FAA CENTER OF EXCELLENCE FOR ALTERNATIVE JET FUELS & ENVIRONMENT

Annual Technical Report

2024

For the period

October 1, 2023 – September 30, 2024

Boston University
Georgia Institute of Technology
Massachusetts Institute of Technology
Missouri University of Science and Technology
Oregon State University
Pennsylvania State University
Purdue University
Stanford University
University of Dayton
University of Hawaii
University of Illinois
University of North Carolina
University of Pennsylvania
University of Tennessee
University of Washington
Washington State University

This work was funded by the US Federal Aviation Administration (FAA) Office of Environment and Energy as a part of ASCENT Project AJFE under FAA Award Number 13-C. Any opinions, findings, and conclusions or recommendations expressed in this material are those of the authors and do not necessarily reflect the views of the FAA or other ASCENT Sponsors.

Table of Contents

Overview Michael P. Wolcott and R. John Hansman, Center Directors	1
Project 001(A) | Alternative Jet Fuel Supply Chain Analysis Lead Investigator: Michael P. Wolcott	7
Project 001(B) | Alternative Jet Fuel Supply Chain Analysis Lead Investigator: Scott Q. Turn	29
Project 001(C) | Alternative Jet Fuel Supply Chain Analysis Lead Investigator: Farzad Taheripour	52
Project 001(D) | Alternative Jet Fuel Supply Chain Analysis Lead Investigator: Lara Fowler	58
Project 001(E) | Alternative Jet Fuel Supply Chain Analysis Lead Investigator: Timothy Rials	74
Project 001(F) | Alternative Jet Fuel Supply Chain Analysis Lead Investigators: Florian Allroggen, Raymond L. Speth	86
Project 002 | Understanding Changes in Aviation Emissions Due to SAF with New Combustor Technology Lead Investigator: Philip D. Whitefield	101
Project 003 | Cardiovascular Disease and Aircraft Noise Exposure Lead Investigator: Junenette L. Peters	105
Project 018 | Community Measurements of Aviation Emission Contributions to Ambient Air Quality Lead Investigator: Kevin J. Lane	117
Project 019 | Development of Aviation Air Quality Tools for Airshed-Specific Impact Assessment: Air Quality Modeling Lead Investigator: Saravanan Arunachalam	133
Project 022 | Evaluation of FAA Climate Tools: Aviation Portfolio Management Tool (APMT) Lead Investigator: Donald Wuebbles	176
Project 023 | Analytical Approach for Quantifying Noise from Advanced Operational Procedures Lead Investigator: R. John Hansman	179
Project 025 | Shock Tube Studies of the Kinetics of Jet Fuels Lead Investigator: Ronald K. Hanson	184
Project 031 | Alternative Jet Fuel Test and Evaluation Lead Investigator: Zachary West	190

Project 033 | Alternative Fuels Test Database Library Lead Investigator: Tonghun Lee	201
Project 037 | CLEEN II System-level Assessment Lead Investigator: Dimitri N. Mavris	213
Project 038 | Rotorcraft Noise Abatement Procedure Development Lead Investigator: Kenneth S. Brentner	227
Project 044 | Aircraft Noise Abatement Procedure Modeling and Validation Lead Investigator: R. John Hansman	241
Project 047 | Clean-Sheet Supersonic Aircraft Engine Design and Performance Lead Investigator: Steven R. H. Barrett	248
Project 049 | Urban Air Mobility Noise Reduction Modeling Lead Investigator: Kenneth S. Brentner	289
Project 051 | Combustion Concepts for Next-Generation Aircraft Engines Lead Investigator: Raymond L. Speth	307
Project 052 | Comparative Assessment of Electrification Strategies for Aviation Lead Investigators: Florian Allroggen, Raymond L. Speth	311
Project 053 | Validation of Low Exposure Noise Modeling by Open-Source Data Management and Visualization Systems Integrated with AEDT Lead Investigator: Juan J. Alonso	319
Project 054 | AEDT Evaluation and Development Support Lead Investigators: Dimitri N. Mavris, Michelle Kirby	333
Project 055 | Noise Generation and Propagation from Advanced Combustors Lead Investigator: Timothy Lieuwen	389
Project 056 | Turbine Cooling Through Additive Manufacturing Lead Investigator: Reid A. Berdanier	432
Project 057 | Support for Supersonic Aircraft En-Route Noise Efforts in ICAO CAEP Lead Investigator: Victor W. Sparrow	449
Project 058 | Improving Policy Analysis Tools to Evaluate Higher-Altitude Aircraft Operations Lead Investigator: Raymond L. Speth	462
Project 059(A) | Jet Noise Modeling to Support Low Noise Supersonic Aircraft Technology Development Lead Investigators: Dimitri N. Mavris, Jimmy Tai	472
Project 059(D) | Physics-Based Analyses and Modeling for Supersonic Aircraft Exhaust Noise Lead Investigator: Sanjiva K. Lele	532

Project 059(E) | Moderate-Fidelity Simulations for Efficient Modeling of Supersonic Aircraft Noise Lead Investigator: Philip Morris	556
Project 060 | Analytical Methods for Expanding the AEDT Aircraft Fleet Database Lead Investigator: Dimitri N. Mavris	576
Project 061 | Noise Certification Streamlining Lead Investigators: Dimitri N. Mavris, Michael Balchanos	590
Project 062 | Noise Model Validation for AEDT Lead Investigators: Dimitri N. Mavris, Victor W. Sparrow	652
Project 064 | Alternative Design Configurations to Meet Future Demand Lead Investigators: Dimitri N. Mavris, Michelle Kirby	689
Project 065(A) | Fuel Testing Approaches for Rapid Jet Fuel Prescreening Lead Investigator: Joshua Heyne	710
Project 065(B) | Fuel Testing Approaches for Rapid Jet Fuel Prescreening Lead Investigator: Tonghun Lee	773
Project 066 | Evaluation of High Thermal Stability Fuels Lead Investigator: Joshua Heyne	788
Project 067 | Impact of Fuel Heating on Combustion and Emissions Lead Investigators: Robert P. Lucht, Carson D. Slabaugh	807
Project 068 | Combustor Wall Cooling with Dirt Mitigation Lead Investigator: Reid A. Berdanier	821
Project 069 | Transitioning a Research nvPM Mass Calibration Procedure to Operations Lead Investigator: Philip D. Whitefield	857
Project 070 | Reduction of nvPM Emissions from Aero-Engine Fuel Injectors Lead Investigator: Wenting Sun	864
Project 071 | Predictive Simulation of nvPM Emissions in Aircraft Combustors Lead Investigator: Suresh Menon	876
Project 072 | Aircraft Noise Exposure and Market Outcomes in the United States Lead Investigators: R. John Hansman, Christopher R. Knittel, Florian Allroggen	898
Project 073 | Fuel Composition Impact on Combustor Durability Lead Investigator: Scott Stouffer	904
Project 074 | Low Emissions Pre-Mixed Combustion Technology for Supersonic Civil Transport Lead Investigator: Adam Steinberg	918
Project 075 | Improved Engine Fan Broadband Noise Prediction Capabilities Lead Investigator: Sheryl Grace	940

Project 077 | Measurements to Support Noise Certification for UAS and UAM Vehicles and Identify Noise Reduction Opportunities Lead Investigator: Eric Greenwood	959
Project 078 | Contrail Avoidance Decision Support and Evaluation Lead Investigator: Ian A. Waitz	1002
Project 079 | Novel Noise Liner Development Enabled by Advanced Manufacturing Lead Investigator: Nicholas Meisel	1011
Project 080(A) | Hydrogen and Power-to-Liquid Concepts for Sustainable Aviation Fuel Production Lead Investigators: Manuel Garcia-Perez, Michael P. Wolcott	1035
Project 080(B) | Hydrogen and Power-to-Liquid Concepts for Sustainable Aviation Fuel Production Lead Investigator: Florian Allroggen	1044
Project 082(A) | Integrated Noise and CO_2 Standard Setting Analysis Lead Investigators: Dimitri N. Mavris, Michelle Kirby	1052
Project 082(B) | Integrated Noise and CO_2 Standard Setting Analysis Lead Investigator: Raymond L. Speth	1066
Project 083 | NO_x Cruise/Climb Metric System Development Lead Investigator: Raymond L. Speth	1069
Project 084 | Noise Modeling of Advanced Air Mobility Flight Vehicles Lead Investigators: R. John Hansman, Jacqueline Huynh	1078
Project 085 | Strategies for Improving En-Route Fuel Efficiency Lead Investigator: Dimitri N. Mavris	1087
Project 086 | Study on the Use of Broadband Sounds to Mitigate Sleep Disruption Due to Aircraft Noise Lead Investigator: Mathias Basner	1102
Project 088 | A Method for Rapidly Assessing Jet Fuel Compatibility with Non-Metallic Materials Lead Investigators: John Graham, Gina Roesch	1107
Project 089 | Characterization of Compositional Effects on Dielectric Constant Lead Investigator: Zachary West	1121
Project 090 | World Fuel Survey Lead Investigator: Zachary West	1129
Project 091(A) | Environmental Impacts of High-Altitude and Space Vehicle Emissions Lead Investigator: Raymond L. Speth	1138
Project 091(B) | Environmental Impacts of High Altitude and Space Vehicle Emissions Lead Investigator: Donald Wuebbles	1144

Project 092 | Advanced Two-Stage Turbine Rig Development Lead Investigator: Reid A. Berdanier	1148
Project 093(A) | Collaborative Research Network for Global SAF Supply Chain Development Lead Investigators: Florian Allroggen, Raymond L. Speth	1163
Project 093(B) | Collaborative Research Network for Global SAF Supply Chain Development Lead Investigator: Scott Q. Turn	1173
Project 093(C) | Collaborative Research Network for Global SAF Supply Chain Development: Latin America Case Lead Investigators: Manuel Garcia-Perez, Michael P. Wolcott	1183
Project 094 | Probabilistic Unmanned Aircraft Systems (UAS) Trajectory and Noise Estimation Tool Lead Investigators: Dimitri N. Mavris, Holger Pfaender	1191
Project 095 | Assessment of Fuel Cells for Powering Modern Business Jets Lead Investigator: Dimitri N. Mavris	1232
Project 096 | Future Transportation System Opportunities and Constraints Lead Investigators: Dimitri N. Mavris, Holger Pfaender	1248
Project 097 | FAST-Tech System Level Assessment Lead Investigators: Dimitri N. Mavris	1261
Project 098 | Low Emissions Lean Pre-Mixed Pre-Vaporized Combustion Technology for Subsonic Civil Transport Lead Investigator: Adam Steinberg	1268
Project 101 | Sustainable Aviation Fuel Repository Lead Investigator: Joshua Heyne	1273
Project 102 | Assessment on Contrail Formation via Combustion of SAF Lead Investigator: Tonghun Lee	1287
Project 103 | Pareto Efficient SAF Yield and Blending Lead Investigator: Joshua Heyne	1295
Publications Index	1312
Funding Tables	1330

Overview

This report covers the period October 1, 2023, through September 30, 2024. The Center was established by the authority of FAA solicitation 13-C-AJFE-Solicitation. The ASCENT website can be viewed at ascent.aero. The next meetings will be held during the months of April and May 2025.

Over the last year, the ASCENT team has made great strides in research, outreach, and education. The team's success includes the following:

- **75 active research projects*.**

The projects are divided into seven main categories: alternative fuels, emissions, noise, operations, tools, aircraft technology innovation, and supersonics. See the project category descriptions for more detail on each category and a summary of the projects. Funding for these projects comes from the FAA in partnership with Transport Canada.

*Note that projects 001, 059, 065, 082 and 093 include several separately funded projects within a single project number. Individual report sections are provided for each of these funded "sub-projects" and are titled Projects 001A-E, 059A-E, 065A-B, 082A-B and 093A-C.

- **200 publications, reports, and presentations by the ASCENT team.**

Each project report includes a list of publications, reports, and presentations. A comprehensive list of the publications, reports, and presentations for all projects is available in the publications index.

- **240 students participated in aviation research with the ASCENT team.**

ASCENT research projects were supported by 199 graduate students and 41 undergraduate students. Each project report includes the names and roles of the graduate and undergraduate students in the investigator's research. Students are selected by the investigators to participate in this research.

- **75 active industry partners involved in ASCENT.**

ASCENT's industry partners play an important role in the Center. Industry partners may contribute matching funds, participate on the Advisory Board, or both. Advisory Board members provide insight into the views of stakeholders, advice on activities and priorities of the Center's co-directors and ensure research will have practical application. The board does not influence FAA policy. Industry partners also play a role in some of the research projects, providing matching funds, resources, and expertise to the project investigators.

Leadership

Dr. Michael P. Wolcott
Center Director and Technical Lead for Alternative Jet Fuels Research
Washington State University
(509) 335-6392, wolcott@wsu.edu

Dr. R. John Hansman
Center Co-Director and Technical Lead for Environmental Research
Massachusetts Institute of Technology
(617) 253-2271, rjhans@mit.edu

Dr. Jonathan Male
Assistant Vice Chancellor for Research and Director of National Laboratory Partnerships
Washington State University
jonathan.male@wsu.edu

Dr. Anna Oldani
Chief Scientific and Technical Advisor for Environment and Energy, Office of Environment and Energy
Federal Aviation Administration
anna.oldani@faa.gov

Research Topics

Research projects within ASCENT are divided into seven categories: alternative fuels, emissions, noise, operations, tools, aircraft technology innovation, and supersonics. The list below includes all ASCENT funded research projects. This report includes research on active projects only. Reports for projects marked as COMPLETE are available on the ASCENT website at: https://ascent.aero/project/.

Alternative Fuels

The development of alternative jet fuels (AJFs) - or sustainable aviation fuels (SAF) - is of great interest to an array of aviation stakeholders, including aircraft and engine manufacturers and airlines. Alternative fuels that are produced from non-fossil feedstocks provide sustainable jet fuel alternatives that not only help alleviate environmental impacts from aviation emissions but can also create jobs in rural areas and lessen our reliance on foreign petroleum supplies.

Effective research and development, co-funded by the federal government and industry, enables SAF development by reducing the costs of producing renewable fuel. ASCENT research provides the scientific expertise and data to evaluate the environmental benefits associated with these sustainable fuels. ASCENT's collaborative R&D activities focuses on evaluating promising sustainable aviation fuel pathways to ensure environmental and social benefits, reduce technical uncertainties, inform aviation emission policies, and promote private sector investment in production.

Projects include:

- 001A-F – Alternative Jet Fuel Supply Chain Analysis
- 025 – National Jet Fuels Combustion Program – Area #1: Chemical Kinetics Combustion Experiments
- 026 – (COMPLETE) National Jet Fuels Combustion Program – Area #2: Chemical Kinetics Model Development and Evaluation
- 027 – (COMPLETE) National Jet Fuels Combustion Program – Area #3: Advanced Combustion Tests
- 028 – (COMPLETE) National Jet Fuels Combustion Program – Area #4: Combustion Model Development and Evaluation
- 029A – (COMPLETE) National Jet Fuels Combustion Program – Area #5: Atomization Tests and Models
- 030 – (COMPLETE) National Jet Fuels Combustion Program – Area #6: Referee Swirl-Stabilized Combustor Evaluation/Support
- 031 – Alternative Jet Fuels Test and Evaluation
- 032 – (COMPLETE) Worldwide LCA of GHG Emissions from Petroleum Jet
- 033 – Alternative Fuels Test Database Library
- 034 – (COMPLETE) National Jet Fuels Combustion Program – Area #7: Overall Program Integration and Analysis
- 052 – Comparative Assessment of Electrification Strategies for Aviation
- 065A-B – Fuel Testing Approaches for Rapid Jet Fuel Prescreening
- 066 – Evaluation of High Thermal Stability Fuels
- 067 – Impact of Fuel Heating on Combustion and Emissions
- 073 – Combustor Durability with Alternative Fuel Use
- 080A-B – Hydrogen and Power-to-Liquid (PtL) Concepts for SAF Production
- 088 – A Method for Rapidly Assessing Jet Fuel Compatibility with non-Metallic Materials
- 089 – Characterization of Compositional Effects on Dielectric Constant
- 090 – World Fuel Survey
- 093A-C – Collaborative Research Network for Global SAF Supply Chain Development
- 099 – Conceptual Analysis of Cryogenic Hydrogen Distribution to Airports
- 100 – U.S.-Canada Cross-Border SAF Supply Chain Analysis
- 101 – Sustainable Aviation Fuel Repository
- 102 – Assessment of Contrail Formation via Combustion of Sustainable Aviation Fuel
- 103 – Pareto Efficient SAF Yield and Blending

Emissions

The demand for passenger and cargo air transportation has grown rapidly over the last several decades. According to the U.S. Bureau of Transportation Statistics (BTS), in 2023 there were 946 million domestic air travelers. The 2024 FAA Aerospace Forecast calls for U.S. carrier domestic passenger growth over the next 20 years to average 2.5 percent per year. This staggering growth is accompanied by airport expansions and increases in emissions from aircraft, ground

services equipment, and vehicle traffic on and near airports. The increases in these activity-based emissions impact the air quality around airports, cumulatively contribute to global climate change, and can negatively affect human health.

ASCENT researchers are analyzing data and improving predictive models to understand the effects of aircraft and ground vehicle emissions, create and refine emission-based analytical techniques at both airport-specific and global scales, and assess how policy changes affect emissions and its impacts.

Projects include:

- 002 – (COMPLETE) Ambient Conditions Corrections for Non-Volatile PM Emissions Measurements
- 013 – (COMPLETE) Micro-Physical Modeling & Analysis of ACCESS 2 Aviation Exhaust Observations
- 014 – (COMPLETE) Analysis to Support the Development of an Aircraft CO2 Standard
- 018 – Community Measurement of Aviation Emission Contribution of Ambient Air Quality
- 019 – Development of Improved Aviation Emissions Dispersion Capabilities for AEDT
- 020 – (COMPLETE) Development of NAS wide and Global Rapid Aviation Air Quality
- 021 – (COMPLETE) Improving Climate Policy Analysis Tools
- 022 – Evaluation of FAA Climate Tools
- 024 – (COMPLETE) Emissions Data Analysis for CLEEN, ACCESS, and Other Recent Tests
- 032 – (COMPLETE) Worldwide LCA of GHG Emissions from Petroleum Jet Fuel
- 039 – (COMPLETE) Naphthalene Removal Assessment
- 047 – (COMPLETE) Clean Sheet Supersonic Aircraft Engine Design and Performance
- 048 – (COMPLETE) Analysis to Support the Development of an Engine nvPM Emissions Standard
- 051 – Combustion Concepts for Next-Generation Aircraft Engines
- 052 – Comparative Assessment of Electrification Strategies for Aviation
- 058 – Improving Policy Analysis Tools to Evaluate Higher-Altitude Aircraft Operations
- 064 – Alternative Design Configurations to Meet Future Demand
- 069 – Transitioning a Research nvPM Mass Calibration Procedure to Operations
- 070 – Reduction of nvPM emissions via innovation in aero-engine fuel injector design
- 071 – Predictive Simulation of nvPM Emissions in Aircraft Combustors
- 074 – (COMPLETE) Low Emissions Pre-Mixed Combustion Technology for Supersonic Civil Transport
- 078 – Contrail Avoidance Decision Support and Evaluation
- 082A-B – Integrated Noise and Emissions CO_2 Standard Setting Analysis
- 083 – NOx Cruise/Climb Metric System Development
- 085 – Strategies for Improving En-Route Fuel Efficiency
- 091A-B – Environmental Impacts of High Altitude and Space Vehicle Emissions

Noise

ASCENT researchers are working to fully understand community noise impacts of aviation including how aircraft noise affects human health and wellbeing and how elements such as motion and atmospheric parameters affect noise. They are also creating tools for analyzing aircraft noise, informing policies related to noise, and conducting outreach and education about aircraft noise reduction efforts.

Projects include:

- 003 – Cardiovascular Disease and Aircraft Noise Exposure
- 004 – (COMPLETE) Estimate of Noise Level Reduction
- 005 – (COMPLETE) Noise Emission and Propagation Modeling
- 007 – (COMPLETE) Civil, Supersonic Over Flight, Sonic Boom (Noise) Standards Development
- 008 – (COMPLETE) Noise Outreach
- 009 – (COMPLETE) Geospatially Driven Noise Estimation Module
- 017 – (COMPLETE) Pilot Study on Aircraft Noise and Sleep Disturbance
- 038 – Rotorcraft Noise Abatement Procedures Development
- 040 – (COMPLETE) Quantifying Uncertainties in Predicting Aircraft Noise in Real-world Situations
- 041 – (COMPLETE) Identification of Noise Acceptance Onset for Noise Certification Standards of Supersonic Airplane
- 042 – (COMPLETE) Acoustical Model of Mach Cut-off
- 043 – (COMPLETE) Noise Power Distance Re-Evaluation
- 044 – Aircraft Noise Abatement Procedure Modeling and Validation

- 049 – Urban Air Mobility Noise Reduction Modeling
- 053 – Validation of Low Exposure Noise Modeling by Open Source Data Management and Visualization Systems Integrated with AEDT
- 055 – Noise Generation and Propagation from Advanced Combustors
- 057 – Support for Supersonic Aircraft En-route Noise Efforts in ICAO CAEP
- 059A-E – Modeling and Measurements of Supersonic Civil Transport Jet Noise
- 061 – Noise Certification Streamlining
- 062 – Noise Model Validation for AEDT
- 063 – Parametric Noise Modeling for Boundary Layer Ingesting Propulsors
- 072 – Aircraft Noise Exposure and Market Outcomes in the US
- 075 – Improved Engine Fan Broadband Noise Prediction Capabilities
- 076 – Improved Open Rotor Noise Prediction Capabilities
- 077 – Measurements to Support Noise Certification for UAS/UAM Vehicles and Identify Noise Reduction Opportunities
- 079 – Novel Noise Liner Development Enabled by Advanced Manufacturing
- 082A-B – Integrated Noise and Emissions CO_2 Standard Setting Analysis
- 084 – Noise Modeling of Advanced Air Mobility Flight Vehicles
- 086 – Study on the Use of Broadband Sounds to Mitigate Sleep Disruption Due to Aircraft Noise
- 094 – Probabilistic Unmanned Aircraft Systems (UAS) Trajectory and Noise Estimation Tool

Operations

Aviation operations result in fuel burn, emissions, and noise impacts. The nature and scale of these effects depends on a number of related factors, including:

- Aircraft flight paths and profiles,
- Schedule and frequency of operations, and
- Aircraft fleet mix.

ASCENT research focuses on identifying and accelerating the implementation of operational concepts that will reduce aviation environmental impacts and/or improve energy efficiency while maintaining the efficiency of the National Airspace System. The research spans multiple phases of flights and targets all environmental impact areas.

Projects include:

- 006 – (COMPLETE) Rotorcraft Noise Abatement Operating Conditions Modeling
- 015 – (COMPLETE) Cruise Altitude and Speed Optimization
- 016 – (COMPLETE) Airport Surface Movement Optimization
- 023 – Analytical Approach for Quantifying Noise from Advanced Operational Procedures
- 038 – Rotorcraft Noise Abatement Procedures Development
- 044 – Aircraft Noise Abatement Procedure Modeling and Validation
- 053 – Validation of Low Exposure Noise Modeling by Open-Source Data Management and Visualization Systems Integrated with AEDT
- 085 – Strategies for Improving En-Route Fuel Efficiency

Tools

The aviation system operation involves complex interactions between many different components when aircraft are on the ground, taking off, in the air, and when landing. Aviation system operations also require the understanding of how to optimize aviation activities, which is best done by implementing advanced modeling tools.

The Federal Aviation Administration's suite of modeling tools have been developed to characterize and quantify the interdependences of aviation-related noise and emissions, impacts on human health and welfare, and the costs and market impacts to industry and consumers under varying policies, technologies, operations, and market scenarios.

The ASCENT researchers are further developing and expanding the capabilities of these modeling tools in a variety of ways, from improving the way basic physical properties are represented and effectively modeled to how new technologies will enter the aircraft fleet and identifying the benefits of such technologies.

Projects include:

- 009 – (COMPLETE) Geospatially Driven Noise Estimation Module
- 011 – (COMPLETE) Rapid Fleet-wide Environmental Assessment Capability
- 012 – (COMPLETE) Aircraft Design and Performance Assessment Tool Enhancement
- 035 – (COMPLETE) Airline Flight Data Examination to Improve flight Performance Modeling
- 036 – (COMPLETE) Parametric Uncertainty Assessment for AEDT2b
- 037 – CLEEN II Technology Modeling and Assessment
- 040 – (COMPLETE) Quantifying Uncertainties in Predicting Aircraft Noise in Real-world Situations
- 043 – (COMPLETE) Noise Power Distance Re-Evaluation (NPD+C) to Include Airframe Noise in AEDT
- 045 – (COMPLETE) Takeoff/Climb Analysis to Support AEDT APM Development
- 046 – (COMPLETE) Surface Analysis to Support AEDT APM Development
- 049 – Urban Air Mobility Noise Reduction Modeling
- 053 – Validation of Low Exposure Noise Modeling by Open-Source Data Management and Visualization Systems Integrated with AEDT
- 054 – AEDT Evaluation and Development Support
- 058 – Improving Policy Analysis Tools to Evaluate Higher-Altitude Aircraft Operations
- 060 – Analytical Methods for Expanding the AEDT Aircraft Fleet Database
- 062 – Noise Model Validation for AEDT

Aircraft Technology Innovation

The evolution of airframes and engines has resulted in modern designs that significantly reduce aviation fuel use, emissions and noise on a per-flight basis. ASCENT researchers conduct the analyses, modeling and testing required to demonstrate the viability of innovative airframe, engine and flight management technologies that reduce noise, emissions, and fuel burn. Future innovations will drive further improvements and the ASCENT research helps accelerate technology development.

Projects include:

- 010 – Aircraft Technology Modeling and Assessment
- 037 – CLEEN II System Level Assessment
- 047 – (COMPLETE) Clean Sheet Supersonic Aircraft Engine Design and Performance
- 050 – (COMPLETE) Over-Wing Engine Placement Evaluation
- 051 – Combustion Concepts for Next-Generation Aircraft Engines
- 052 – Comparative Assessment of Electrification Strategies for Aviation
- 055 – Noise Generation and Propagation from Advanced Combustors
- 056 – Turbine Cooling through Additive Manufacturing
- 059A-E – Modeling and Measurements of Supersonic Civil Transport Jet Noise
- 063 – Parametric Noise Modeling for Boundary Layer Ingesting Propulsors
- 064 – Alternative Design Configurations to Meet Future Demand
- 066 – Evaluation of High Thermal Stability Fuels
- 067 – Impact of Fuel Heating on Combustion and Emissions
- 068 – Combustor Wall Cooling with Dirt Mitigation
- 070 – Reduction of nvPM emissions via innovation in aero-engine fuel injector design
- 074 – (COMPLETE) Low Emissions Pre-Mixed Combustion Technology for Supersonic Civil Transport
- 075 – Improved Engine Fan Broadband Noise Prediction Capabilities
- 076 – Improved Open Rotor Noise Prediction Capabilities
- 077 – Measurements to Support Noise Certification for UAS/UAM Vehicles and Identify Noise Reduction Opportunities
- 092 – Advanced Two-state Turbine Rig Development
- 095 – Assessment of Fuel Cells for Powering Modern Business Jets
- 096 – Future Transportation System Opportunities and Constraints
- 097 – FAST-Tech System Level Assessment
- 098 – Low Emissions Lean Pre-Mixed, Pre-Vaporized Combustion Technology for Subsonic Civil Transport

Supersonics

ASCENT supersonics research supports implementation of new technologies by advancing the understanding of the perception of sonic boom noise over a range of sonic boom levels, assessing Mach cut-off levels that will allow supersonic flight over land and furthering development of supersonic aircraft noise certification standards.

Projects include:

- 007 – (COMPLETE) Civil, Supersonic Over Flight, Sonic Boom (Noise) Standards Development
- 010 – Aircraft Technology Modeling and Assessment
- 022 – Evaluation of FAA Climate Tools
- 041 – (COMPLETE) Identification of Noise Acceptance Onset for Noise Certification Standards of Supersonic Airplanes
- 042 – (COMPLETE) Acoustical Model of Mach Cut-off
- 047 – (COMPLETE) Clean Sheet Supersonic Aircraft Engine Design and Performance
- 057 – Support for Supersonic Aircraft Noise Efforts in ICAO CAEP
- 058 – Improving Policy Analysis Tools to Evaluate Aircraft Operations in the Stratosphere
- 059A-E – Jet Noise Modeling to Support Low Noise Supersonic Aircraft Technology Development
- 074 – (COMPLETE) Low Emissions Pre-Mixed Combustion Technology for Supersonic Civil Transport

Project 001(A) Alternative Jet Fuel Supply Chain Analysis

Washington State University

Project Lead Investigator

Michael P. Wolcott
Regents Professor
Department of Civil & Environmental Engineering
Washington State University
PO Box 642910
Pullman, WA 99164-2910
509-335-6392
wolcott@wsu.edu

University Participants

Washington State University (WSU)

- P.I.s: Michael P. Wolcott, Regents Professor; Christina Sanders, Acting Director, Division of Governmental Studies and Services; Manuel Garcia-Perez, Professor; Xiao Zhang, Professor; and Ji Yun Lee, Assistant Professor
- FAA Award Number: 13-C-AJFE-WaSU-023, 026
- Period of Performance: October 1, 2023, to September 30, 2024
- Tasks:
  1. Prepare and assess design cases
  2. Evaluate the most promising biorefinery concepts for alternative jet fuel (AJF) production
  3. Supplement and maintain the current inventory of biorefinery infrastructures that are useful for AJF production, as identified in the conversion design cases
  4. Update Community Asset and Attribute Model (CAAM) Measures and perform a community social asset assessments
  5. Refine and deploy facility siting tools to determine regional demand and potential conversion sites to be used in regional analyses
  6. Perform a refinery-to-wing stakeholder assessment.
  7. Conduct a supply chain analysis
  8. Provide analytical support for regional Commercial Aviation Alternative Fuels Initiative (CAAFI) and U.S. Department of Agriculture (USDA) jet fuel projects
  9. CAAFI collaboratively supports research, development, demonstration and deployment efforts on sustainable aviation fuel (SAF)/AJF

Project Funding Level

The ASCENT Project 001(A) has received $3,941,805 in Federal Aviation Administration (FAA) funding over its lifetime, $3,666,922 in matching funds, and state-committed graduate school contributions for four doctoral students. Faculty time for Michael Wolcott, Manuel Garcia-Perez, and Xiao Zhang contributed to the cost share.

Investigation Team

Washington State University

Prof. Michael Wolcott (P.I.), Tasks 3, 5, 7, and 8
Christina Sanders (co-P.I.)
Season Hoard (co-P.I.)
Prof. Manuel Garcia-Perez (co-P.I.), Tasks 1, 2, and 7
Xiao Zhang (co-P.I.), Tasks 1 and 2
Assist. Prof. Ji Yun Lee (co-P.I.)
Daniel Mueller (faculty), Tasks 4,6

Michael Gaffney (faculty), Tasks 4, 6
Kristin Brandt (adjoint faculty)
Dane Camenzind (staff engineer)
Lina Pilar Martinez Valencia (postdoctoral research associate)
Santheeb Balaji Velmurugan (graduate student)
Claudia Marcela Valderrama (graduate student)

Commercial Aviation Alternative Fuels Initiative (CAAFI)
Steve Csonka, Office of the Executive Director

Collaborating Researchers

University of Tennessee (UT)
Burton English
Edward Yu

University of Hawaii (UH)
Scott Turn

Massachusetts Institute of Technology (MIT)
Florian Allroggen

Volpe National Transportation Systems Center (Volpe)
Kristin C. Lewis

Project Overview

As part of an effort to realize an "aviation system in which air traffic will move safely, swiftly, efficiently, and seamlessly around the globe," the FAA set a series of goals and supporting outcomes, strategies, and performance metrics (Hileman et al., 2013). The goal entitled "Sustaining our Future" outlines several strategies collectively aimed at reducing the environmental and energy impacts of the aviation system. To achieve this goal, the FAA set an aspirational goal for the aviation industry to utilize one billion gallons of AJF by the year 2018. This goal was created according to economic, emission, and overall feasibility perspectives (Richard, 2010; Staples et al., 2014). Over the past several years, the goals for United States (U.S.) AJF use have been updated with the SAF Grand Challenge that the U.S. will produce and use three billion gallons of SAF by 2030, with an increase to 35 billion gallons in 2050 with a minimum reduction of 50% in lifecycle greenhouse gases (The White House, 2021).

Most approaches to supply chain analyses for AJF optimize feedstock-to-refinery and refinery-to-wing transportation logistics (Bond et al., 2014). One of the greatest barriers to large-scale AJF production is the high capital of greenfield facilities, which translates to risk in the investment community (Huber & Corma, 2007). The cost of cellulosic ethanol plants ranges from $10 to $13 per gallon capacity (Hileman & Stratton, 2014); moreover, the additional processing steps required to convert the intermediate to a drop-in AJF could increase this cost to more than $25 per gallon capacity (Hileman, 2014).

Motivated by the realities of converting these initial commercialization efforts into second-generation AJF, researchers have considered alternative conversion scenarios, including the transitioning of existing facilities (Brown, 2013). The conversion of existing refineries to produce renewable diesel and AJF has been completed on first phase conversions at the following refineries: World Energy®'s Paramount, California, refinery; at Montana Renewables' Great Falls, Montana, refinery; and at Marathon®'s Dickinson, North Dakota, refinery. Conversion is also underway at both the Martinez and Rodeo refineries in California (Marathon, 2022; Phillips 66, 2022). Research on approaches for achieving the SAF Grand Challenge goals for AJF consumption has relied on "switching" scenarios, in which existing and planned capacities are used to produce drop-in fuel (Malina, 2012). These approaches require the identification of existing industrial assets, similar to refinery conversions, which can be targeted for future AJF production. Thus, siting becomes not only an exercise for optimizing feedstock transportation but also a necessary task for aligning this critical factor with the existing infrastructure, markets within regions, and the appropriate social capital for developing this new industry (Henrich, 2007; Seber et al., 2014).

To date, all published AJF supply chain analyses have been limited to stand-alone jet fuel production technologies that do not generate bioproducts. Hence, future studies must consider the potential techno-economic and environmental benefits

® World Energy is a registered trademark of World Management Group, LLC, Boston, Massachusetts.
® Marathon is a registered trademark of Marathon Petroleum Company LP, Findlay, Ohio.

of using the existing industrial infrastructure and the production of co-products with respect to the development of jet fuel production scenarios.

Design cases of stand-alone AJF production facilities will be used in supply chain evaluations. Social asset modeling is not well developed, and efforts are likely to be hampered by difficulties in quantifying social assets when compared with improved environmental performance or reductions in AJF costs. However, the community characteristics of a potential site must be considered when determining preferred locations for a new biorefinery. Community resistance or enthusiasm for the AJF industry can strongly influence the success or failure of a facility (Martinkus et al., 2014; Rijkhoff et al., 2017). Thus, community social asset modeling efforts conducted within this project, such as those based on the CAAM, will inform disciplinary applications and advances. Social factors can have substantial effects, either positive or negative, on project adoption and implementation, particularly in high-technology or energy-related projects (Lewis et al., 2012; Martinkus et al., 2012; Mueller et al., 2020). The consideration of social factors in site selection and implementation decisions can maximize positive social support and minimize opposition and social negatives, thereby substantially promoting the success of a project. In this regard, the CAAM originally piloted in the Northwest Advanced Renewables Alliance project was designed to provide a quantitative rating of select social factors at the county level (Martinkus et al., 2014).

Focusing on regional supply chains, this research aims to identify the key barriers that must be overcome to meet AJF targets. Our team will address this overall goal by developing tools to support the AJF supply chain assessment performed at Volpe. Our efforts will provide facility siting analyses that assess conversion design cases combined with regional supply chain assets and social capacity assessments for communities to act collectively toward development goals. Finally, a refinery-to-wing stakeholder assessment will support modeling and accounting of AJF distribution for downstream fuel logistics.

References

Bond, J. Q., Upadhye, A. A., Olcay, H., Tompsett, G. A., Jae, J., Xing, R., Alonso, D. M., Wang, D., Zhang, T., Kumar, R., Foster, A., Sen, S. M., Maravelias, C. T., Malina, R., Barrett, S. R. H., Lobo, R., Wyman, C. E., Dumesic, J. A., & Huber, G. W. (2014). Production of renewable jet fuel range alkanes and commodity chemicals from integrated catalytic processing of biomass. *Energy & Environmental Science*, *7*(4), 1500–1523. https://doi.org/10.1039/C3EE43846E

Brown, N. (2013, November 20). *FAA alternative jet fuel activities* [Conference presentation]. Continuous Lower Energy, Emissions & Noise (CLEEN) Consortium, Atlanta, Georgia.,

Henrich, E. (2007, August 29-31). *The status of FZK concept of biomass gasification* [Conference presentation]. 2nd European Summer School on Renewable Motor Fuels, Warsaw, Poland.

Hileman, J. I., De la Rosa Blanco, E., Bonnefoy, P. A., & Carter, N. A. (2013). The carbon dioxide challenge facing aviation. *Progress in Aerospace Sciences*, *63*, 84–95. https://doi.org/10.1016/j.paerosci.2013.07.003

Hileman, J. I., & Stratton, R. W. (2014). Alternative jet fuel feasibility. *Transport Policy*, *34*, 52–62. https://doi.org/10.1016/j.tranpol.2014.02.018

Hileman, J. (2013). *Overview of FAA alternative jet fuel activities* [Meeting presentation]. Biomass R&D Technical Advisory Committee, Washington DC.

Huber, G. W., & Corma, A. (2007). Synergies between bio- and oil refineries for the production of fuels from biomass. *Angewandte Chemie International Edition*, *46*(38), 7184–7201. https://doi.org/10.1002/anie.200604504

Lewis, K., Mitra, S., Xu, S., Tripp, L., Lau, M., Epstein, A., Fleming, G., & Roof, C. (2012). *Alternative jet fuel scenario analysis report* (Publication No. DOT/FAA/AEE/2011-05). http://ntl.bts.gov/lib/46000/46500/46597/DOT-VNTSC-FAA-12-01.pdf

Malina, R. (2012, November 27). *HEFA and F-T jet fuel cost analyses* [Presentation]. Massachusetts Institute of Technology, Laboratory for Aviation and the Environment.

Marathon. (2022). *Martinez renewable fuels project*. https://www.marathonmartinezrenewables.com/

Martinkus, N., Kulkarni, A., Lovrich, N., Smith, P., Shi, W., Pierce, J., & Brown, S. (2012, August 27-31). *An innovative approach to identify regional bioenergy infrastructure sites* [Conference presentation]. 55th International Convention of Society of Wood Science and Technology, Beijing, China. https://www.swst.org/wp/meetings/AM12/ppts/smith_paul.pdf

Martinkus, N., Shi, W., Lovrich, N., Pierce, J., Smith, P., & Wolcott, M. (2014). Integrating biogeophysical and social assets into biomass-to-alternative jet fuel supply chain siting decisions. *Biomass and Bioenergy*, *66*, 410-418. https://doi.org/10.1016/j.biombioe.2014.04.014

Mueller, D., Hoard, S., Roemer, K., Sanders, C., & Rijkhoff, S. (2020). *Quantifying the Community Capitals Framework: strategic application of the Community Assets and Attributes Model*. *Community Development*, *51*(5), 535–555. https://doi.org/10.1080/15575330.2020.1801785

Phillips 66. (2022). *San Francisco refinery: the evolution of rodeo renewed*. https://www.phillips66.com/refining/san-francisco-refinery/

Rijkhoff, S. A. M., Hoard, S. A., Gaffney, M. J., & Smith, P. M. (2017). Communities ready for takeoff Integrating social assets for biofuel site-selection modeling. *Politics and the Life Sciences: The Journal of the Association for Politics and the Life Sciences*, *36*(1), 14–26.

Richard, T. L. (2010). Challenges in scaling up alternative jet fuels infrastructure. *Science, 329*(5993):793-796. http://dx.doi.org/10.1126/science.1189139

Seber, G., Malina, R., Pearlson, M. N., Olcay, H., Hileman, J. I., & Barrett, S. R. H. (2014). Environmental and economic assessment of producing hydroprocessed jet and diesel fuel from waste oils and tallow. *Biomass and Bioenergy*, *67*, 108–118. https://doi.org/10.1016/j.biombioe.2014.04.024

Staples, M. D., Malina, R., Olcay, H., Pearlson, M. N., Hileman, J. I., Boies, A., & Barrett, S. R. H. (2014). Lifecycle greenhouse gas footprint and minimum selling price of renewable diesel and jet fuel from fermentation and advanced fermentation production technologies. *Energy & Environmental Science*, *7*(5), 1545–1554. https://doi.org/10.1039/C3EE43655A

The White House. (2021). *FACT SHEET: Biden administration advances the future of sustainable fuels in American aviation*. https://www.whitehouse.gov/briefing-room/statements-releases/2021/09/09/fact-sheet-biden-administration-advances-the-future-of-sustainable-fuels-in-american-aviation/

Task 1 – Prepare and Assess Design Cases

Washington State University

Objectives

In previous years, our team has worked toward completing reviews and final reports of design cases for six stand-alone AJF technologies (Table 1) and four relevant industries (i.e., sugarcane, pulp and paper, corn ethanol, and petroleum refineries). The status of each stand-alone AJF techno-economic analysis (TEA) and report is shown in Table 1. Results on pyrolysis and alcohol-to-jet (ATJ) pathways have been published in the referenced peer-reviewed journals. The work conducted from October 1, 2023, to September 30, 2024, focused on the following objectives:

1. Complete a detailed analysis of a "catalytic hydrothermolysis pathway for jet fuel production," including two publications.
2. Conduct a detailed analysis of a new AJF pathway for hydrothermal liquefaction (HTL) processing.
3. Conduct TEA on the integration of lignin co-product technologies in the ATJ pathway to determine the potential for reducing fuel costs.
4. Develop a new case report focusing on a technology review, an evaluation of lipid conversion processes (hydroprocessed esters and fatty acids [HEFA], catalytic hydrothermolysis [CH], SBI BioEnergy, Forge, Tyton, and decarboxylation), and new technologies for the production of alternative lipids (HTL and sugar-to-lipid).
5. Prepare manuscripts for publication.

Table 1. Evaluated stand-alone alternative jet fuel technologies.

Fuel Type	Literature Review/Design Report Date	Publications	Techno-Economic Analysis (TEA) Model
Pyrolysis	Literature review based on a design report, 138 pages (2017)	*Energy Fuel 33*, 4683, 2019. https://doi.org/10.1021/acs.energyfuels.9b00039; *Fuel Process Technology 195*, 106140, 2019. https://doi.org/10.1016/j.fuproc.2019.106140	A standardized TEA is complete and has been posted on the Washington State University repository.
Alcohol-to-jet (ATJ)	Literature review based on a design report, 28 pages (2015)	*ChemSusChem 11*, 3728, 2018. https://doi.org/10.1002/cssc.201801690	A standardized TEA is complete and has been posted on the Washington State University repository.
Synthetic kerosene and synthetic aromatic kerosene (SK-SKA)	Literature review based on a design report, 36 pages (2015)	Manuscript based on the case design report in preparation	This work was based on a Sasol® process, for which we have not found any significant development since 2016. Because of a lack of adequate process information/data on SK-SKA production from renewable feedstock, we are not able to build a reliable TEA.
Direct sugar-to-hydrocarbon	Literature review based on a design report, 88 pages (2017)	*Biomass and Bioenergy 145:105942,* 2021. https://doi.org/10.1016/j.biombioe.2020.105942	A standardized TEA is complete and available for use by partners.
Virent BioForming process	Literature review based on a design report, 46 pages (2015)	*Biomass and Bioenergy 145:105942,* 202. https://doi.org/10.1016/j.biombioe.2020.1059421	A standardized TEA is complete and available for use by partners.
Catalytic hydrothermolysis (CH)	Literature review based on a design report, 35 pages (2018)	*Renewable and Sustainable Energy Reviews 115:111516,* 2021. https://doi.org/10.1016/j.rser.2021.111516; *Data in Brief 39:107514,* 2021. https://doi.org/10.1016/j.rser.2021.111516	A standardized TEA is complete and has been posted on the Washington State University repository.
Gasification Fischer Tropsch (GFT)	No literature review conducted.	*Biomass and Bioenergy 145:105942,* 2021. https://doi.org/10.1016/j.biombioe.2020.105942	A standardized TEA is complete and has been posted on the Washington State University repository.

® Sasol is a registered trademark of Sasol Limited, Gauteng, South Africa.

Fuel Type	Literature Review/Design Report Date	Publications	Techno-Economic Analysis (TEA) Model
Microchannel GFT (microGFT)	No exhaustive literature review written, capital costs found in the open literature for microchannel FT deemed unreliable.	Capital cost results deemed unreliable	A standardized microGFT TEA was completed; however, the cost information is considered unreliable.
Hydroprocessed esters and fatty acids (HEFA)	No literature review conducted.	*Biomass and Bioenergy 145:105942,* 2021. https://doi.org/10.1016/j.biombioe.2020.105942	A standardized TEA is complete and has been posted on the Washington State University repository.

Research Approach

Background

A detailed literature review was conducted and prepared design case reports on six AJF pathways were prepared, including pyrolysis, ATJ, synthetic kerosene, direct sugar-to-hydrocarbon, Virent® BioForming, and CH. Our team has also collected data from the literature to conduct TEAs for these pathways. The results from these design cases were applied in the development of supply chains and the identification of synergies that may eventually lead to the construction of integrated AJF production systems that take advantage of the infrastructure in a given region. An analysis of the locations of existing infrastructure demonstrated that the U.S. can be divided into regions according to the dominant biomass. Thus, we believe that the generation of advanced biorefinery concepts focused on petroleum refineries, pulp and paper mills, sugarcane mills, and corn ethanol mills is a viable approach for evaluating the synergy among AJF pathways, existing infrastructure, and co-products. Thus, our team can then compare the biorefinery concepts developed for each technology to identify the most promising approach, which can subsequently be used in supply chain analyses.

Stand-alone design case reports were generated by reviewing relevant research in the academic literature and public information provided by commercial entities developing the corresponding technology. The published manuscripts were subjected to an industrial expert review. The reports provide details regarding the processes involved in each conversion pathway and outline the technology readiness and particular barriers to implementation. Publicly available information regarding the commercial processes and research literature will provide a foundation of information to be used in modeling efforts. In cases lacking detailed process engineering information, as possible new models were built to estimate the parameters needed to complete assessments such as techno-economic modeling and supply chain modeling. Aspen Plus primarily generates process models and details, including mass balances, energy balances, energy requirements, and equipment size and cost. These results will also provide the basis for a comparative analysis of design cases, which identify the key advantages and markets for each technology.

Each design case has the following components:

- Feedstock requirements
- Companies developing/commercializing the technology
- Current locations of units in the U.S. and worldwide
- Block and flow diagram of the technology
- Unit operations and process conditions (reactor type, separation unit type, catalysts, product yield, and jet fuel yield)
- Properties of the produced jet fuel
- Identification of potential intermediates
- Current and potential uses of wastes and effluents

® Virent is a registered trademark of Virent, Inc., Madison, Wisconsin.

- Developed co-products
- Potential methods for coprocessing intermediates, wastes, and co-products by using existing infrastructure (e.g., petroleum refineries or pulp and paper mills)
- Preliminary TEA
- Technological challenges and gaps

The ASCENT Project 001(A) team has submitted technical reports and supplementary Microsoft® Excel® files with mass and energy balances and TEAs for the pathways listed. Furthermore, we have conducted a strategic analysis to identify the overall weaknesses of the technologies under study. All files are available for Project 001 team members.

- Pyrolysis-bio-oil hydro-treatment concept (hydro-treated depolymerized cellulosic jet): The TEA is complete.
- ATJ: A manuscript with information on the mass and energy balances and the TEA has been published.
- Fischer Tropsch (FT): Two design cases have been prepared for biomass gasification. The first case focuses on microreactors, and the second design case is applicable to technology based on larger standard reactors (reviews on the TEAs for gasification FT (GFT) and microchannel GFT have been completed). However, the limited reliability of the microreactor capital costs hinders the value of the practical impact of our microreactor TEA study. The TEAs are available for use by partners. In addition to gasification, the harmonized TEA was updated to include power-to-liquids with assistance from collaborators at MIT.
- HEFA: A stochastic TEA was created in MATLAB® and was confirmed to match the completed, deterministic TEA when the assumptions and costs match (the deterministic TEA review is complete). The TEA is now available for use.
- CH: The TEA is complete.
- A stochastic Excel-based spreadsheet version of the HEFA TEA was developed and shared for internal review.
- All TEAs are in the process of being updated to include (1) 2021 cost year, (2) updated operating expense (OPEX) costs, (3) up-to-date feedstock costs, and (4) the addition of a second economic analysis perspective.

Major progress has been made on the analysis of corn ethanol, sugarcane, and petroleum refinery infrastructure that could support jet fuel production. A manuscript on the conversion of corn ethanol mills was published in *Biomass and Bioenergy*. Two additional manuscripts on repurposing either sugarcane mills or petroleum refineries to reduce AJF production costs were also published.

The ASCENT Project 001(A) team has have worked with the Pacific Northwest National Laboratory (PNNL) and completed a case design report on HTL for AJF conversion.

A summary manuscript reviewing several lipid conversion pathways, including SBI, Forge, Tyton, decarboxylation, and coprocessing, entitled “Lipid and bio-processing technologies: an insight into bioconversion potential of process intensification and continuous flow-through reaction (PICFTR), lipid to hydrocarbon (LTH) and TYTON bioenergy” has been prepared.

Milestones

- Produced and prepared corresponding manuscripts for publication a summary report entitled “Lipid and bio-processing technologies: process intensification and continuous flow-through reaction (PICFTR), lipid-to-hydrocarbon (LTH), Tyton, decarboxylation and coprocessing.”
- Updated the five SAF technology TEAs to include policies defined in the 2022 Inflation Reduction Act. Users can now model a variety of policy time horizons, values, and company structure scenarios. Specifically, both a blender tax credit and a production tax credit can be included with starting and ending at user-defined timelines.
- Updated the TEAs to the 2021 cost year. This year was chosen because 2023 cost year is similar to 2021 but does not have complete data yet. The 2022 cost year appears to be a localized maximum that will likely overestimate costs. However, the TEAs can be updated using capital expense (CAPEX) and OPEX factors to whichever cost year a user would like.

® Microsoft and Excel are registered trademarks of Microsoft Corporation in the United States and other countries.
® MATLAB is a registered trademark of The MathWorks Inc., Natick, Massachusetts.

Major Accomplishments

Our team has updated two draft manuscripts, "Hydrothermal liquefaction case design report" and "Lipid and bio-processing technologies: an insight into bioconversion potential of process intensification and continuous flow-through reaction (PICFTR), lipid to hydrocarbon (LTH) and TYTON bioenergy." A manuscript entitled "Comparison of techno-economic and environmental performance of alternative jet fuel production technologies" has been prepared, reviewed, and updated in preparation for FAA review. The ASCENT Project 001(A) team intends to submit these manuscripts to the FAA for review within the next four months. The team is working on the construction of a TEA for lignin extraction and utilization in a biorefinery process.

The ASCENT Project 001(A) team has assisted the International Civil Aviation Organization (ICAO), Committee on Aviation Environmental Protection (CAEP) through participation in the Fuels Task Group (FTG) and the Long-Term Aspirational Goal Task Group. An Excel spreadsheet of publicly announced global AJF producers has been updated, and work with ICAO for integrating the historical portion of these data with their database is ongoing. This year the process and schedule to update and report on this database was established through FTG and approved. Revised fuel projections were requested by and provided to the Modelling and Databases Group (MDG)-and Forecast and Economic Analysis Support Ground (FESG) at the FTG8 meeting in 23-27 September 2024 Montreal, Canada. In addition, a separate U.S. database that does not include ICAO-specific assumptions and data is being maintained to assist in tracking progress toward meeting the SAF Grand Challenge goals.

Six Excel spreadsheet-based TEAs have been published on the WSU repository site to make these tools publicly available for analysis. These TEAs include HEFA, ATJ, FT with both solid and gaseous feedstocks, FT feedstock preparation, pyrolysis, and CH. The TEAs are being used by other ASCENT member universities and interested industry and government parties. These spreadsheet TEAs will be updated and reposted by the first quarter of 2025.

Data generated from the design cases have been made available to ASCENT Project 001(A) partners to assist with supply chain analysis and techno-economic modeling by improving the conversion and cost figure database values. Evaluations of the effects of process variations in the chemical properties of the generated products are being used to provide insight into the challenges that will be faced when AJFs are blended into commercial jet fuel.

Publications

Garcia, A., Sierra-Jimenez, V., Brandt, K., Martinez-Valencia, L. P., Wolcott, M., Male, J., & Garcia-Perez, M. (2024). Holistic methodology to guide the evolution of sustainable aviation fuel production technologies. *Energy & Fuels*, *38*(18), 17706-17716.

Outreach Efforts

During the preparation of design case reports, our team has closely interacted with industrial companies, including Gevo,® LanzaTech,® Sky Energies, and Agrisoma (now NuSeed). These companies have also helped us review reports and draft manuscripts. Our results have been presented to the FAA, Office of the Chief Economist (OCE), U.S. Department of Energy, ICAO, and CAAFI. Six harmonized TEAs have been posted on the WSU Research Repository for public use. The team has also made several presentations for graduate and undergraduate students.

Presentation

Brandt, K., & Malina, R. (2024, February 6). *Process for SAF announcement tracking and short-term projections*. CAEP: CAEP/13 (FTG) Meeting, Geneva, Switzerland.

Awards

None.

Student Involvement

Several graduate students, Sudha Eswaran, Kelly Nguyen, Abid Hossain Tanzil, Anamaria Paiva, and Lina Pilar Martinez Valencia, and one undergraduate student, Kitana Kaiphanliam, participated in the creation, editing, and updating of design cases for stand-alone AJF technologies, relevant existing infrastructure, and lignin co-products.

® Gevo is a registered trademark of Gevo, Inc., Englewood, Colorado.
® LanzaTech is a registered trademark of LanzaTech NZ, Inc., Chicago, Illinois.

Plans for Next Period

- Submit three to five manuscripts on lignin co-product analyses and AJF technology analyses. The following are the proposed manuscripts to be completed this project year:
  - Lipid and bio-processing technologies: process intensification and continuous flow-through reaction (PICFTR), lipid-to-hydrocarbon (LTH), Tyton, decarboxylation, and coprocessing
  - The opportunity for lignin co-products to improve the economics of sustainable aviation fuel production
  - Complete stochastic versions of all the published TEA.
  - Complete and post updated versions of all SAF TEAs.
- Continue to support ICAO work through participation in the CAEP FTG. This includes the regularly scheduled SAF database updates and volume projections and a forthcoming request to update the SAF "Rules of Thumb."

References

National Renewable Energy Laboratory. (2018). *Process design and economics for the conversion of lignocellulosic biomass to hydrocarbon fuels and coproducts: 2018 biochemical design case update* (Publication No. NREL/TP-5100-71949). https://www.nrel.gov/docs/fy19osti/71949.pdf

Task 2 – Evaluate the Most Promising Biorefinery Concepts for AJF Production

Washington State University

Objective

In continuation of work completed from previous years, the ASCENT Project 001(A) team completed our evaluation of biorefinery scenarios for AJF production using corn ethanol, sugarcane, and pulp and paper mills and petroleum refineries. The objective of this task is to conduct detailed TEAs on the integration of lignin co-product technologies and the ATJ pathway to determine the potential for reducing fuel costs.

Research Approach

Background

In this task, the ASCENT Project 001(A) team used design cases for existing infrastructure, AJF production technology, and identified co-products to generate new biorefinery concepts for petroleum refineries, pulp and paper mills, sugarcane mills, and corn ethanol mills. The results from this effort will allow us to identify and select the most commercially feasible biorefinery concepts. Major technical gaps or barriers to the commercialization of each biorefinery concept will also be determined from the results of this study.

The integration of process technologies will be assessed via an approach similar to that for the stand-alone design cases. The integration concepts will be developed by pairing stand-alone cases with these concepts to evaluate the economic and environmental advantages of the integration approaches. Over this period, our team has conducted detailed analyses of ATJ conversion and integration with pulp mill operations. The ASCENT Project 001(A) team has also investigated the potential contribution of lignin co-products to the overall process economy.

A dry-grind corn ethanol mill with a capacity of 80 million gallons of ethanol per year was studied to evaluate potential biorefinery scenarios for AJF production. Similarly, a sugarcane mill with a sugarcane processing capacity of 12,444 tons per day that produces raw sugar, molasses, surplus bagasse, and surplus electricity, was studied. The petroleum refinery used as the base case processes 120,000 barrels of crude oil per day. Five AJF technologies were studied: (1) Virent BioForming, (2) ATJ, (3) direct sugar-to-hydrocarbon, (4) fast pyrolysis, and (5) GFT. A standardized methodology was adopted to compare the biorefinery concepts for a dry-grind corn ethanol mill, sugarcane mill, and petroleum refinery in several integration scenarios with six jet fuel production scenarios. For all cases, our team estimated the fuel minimum selling price (MSP) and greenhouse gas emissions.

A manuscript on the integration of ATJ technologies with pulp mill infrastructure was published. Three additional manuscripts were published with results for corn ethanol mills, sugarcane mills, and petroleum refineries.

The next step in our analysis is to use a p-graph to generate and rank biorefinery concepts utilizing a database of SAF technological pathways built from a database of unitary operations created by our team. A doctoral student has been hired to work on the integration and construction of the database and the use of p-graphs to create new unit operations.

In this year, the ASCENT Project 001(A) team has established an Aspen process model (Figure 1) to analyze methanol to jet fuel (MTJ) production. There are three units in the MTJ process: (1) olefination of methanol (MTO), (2) hydrogenation of oligomers, and (3) fractionation of aviation fuel base stock. The Honeywell® UOP Renewable Jet Fuel Process™/hydro MTO process was referenced to generate C2 and C3 olefins as input feedstocks for oligomerization reaction, and the oligomerized products are hydrotreated to be used as the precursors for SAF. Our team has currently collected literature data to refine the Aspen model. In addition to the Aspen model development, we have completed a draft review paper titled "Methanol to sustainable aviation fuel" in collaboration with PNNL that is under internal review.

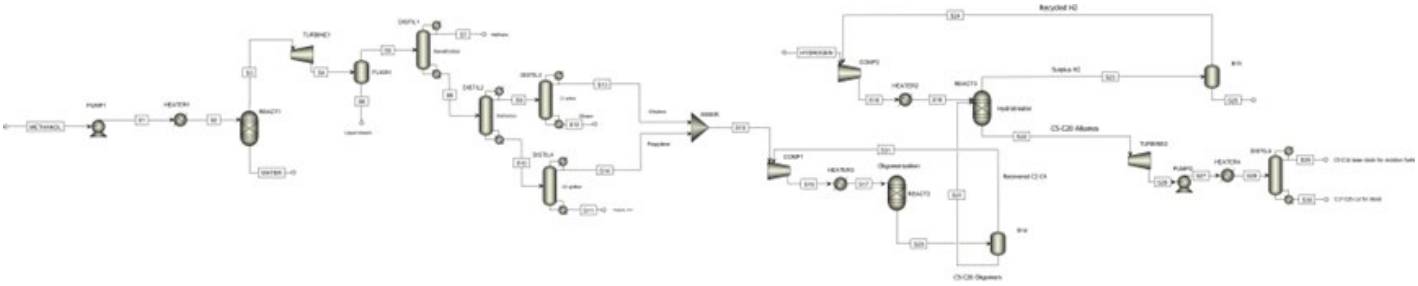

Figure 1. Aspen Plus flow sheet for methanol to aviation fuel base stocks.

Major Accomplishments

None.

Publications

None.

Outreach Efforts

Presentations

Garcia-Perez, M., Garcia, A., & Wolcott, M. (2024, October 2-4). *Methodology to guide the evolution of sustainable aviation fuel production technologies* [Conference presentation]. Sustainable Aviation Futures, North America, Houston, Texas.

Garcia, A., & Garcia-Perez, M. (2024, June 26). *Holistic methodology to guide the evolution of sustainable aviation fuel production technologies* [Conference presentation]. 32nd European Biomass Conference & Exhibition, Marseille, France.

Awards

None.

Student Involvement

Graduate students Claudia Marcela Valderrama, Senthil Subramaniam, Kelly Nguyen, Abid Hossain Tanzil, Lina Martinez Valencia, and Anamaria Paiva, have received training in this project. An undergraduate student, Kitana Kaiphanliam, funded under a National Science Foundation Research Experience for Undergraduates grant, assisted in building techno-economic models for co-product production scenarios.

Senthil Subramaniam, who has been supported by this project, graduated with a PhD degree from WSU in December 2020.

Kelly Nguyen, who has been supported by this grant, graduated with a master's degree from WSU in May 2020.

® Honeywell and the UOP Renewable Jet Fuel Process are trademarks of Honeywell International, Inc., in the United States and other countries.

Abid Hossain Tanzil submitted and defended a doctoral dissertation during the fall 2020 semester.

Plans for Next Period

- Complete a preliminary TEA analysis of MTJ conversion and the internal review of the review paper and submit it to the FAA internal review and then submit it for peer-reviewed journal publication.
- Pending completion of the initial Aspen model, begin work on a TEA to model the economics of MTJ and the impacts of technical and policy options.
- Submit the manuscript "Lipid and bio-processing technologies: an insight into bioconversion potential of process intensification and continuous flow-through reaction (PICFTR), lipid to hydrocarbon (LTH) and TYTON bioenergy."

Task 3 – Supplement and Maintain the Current Inventory of Biorefinery Infrastructures that are Useful for AJF Production, as Identified in the Conversion Design Cases

Washington State University

Objective

The objective of this task is to provide the required periodic evaluation of the databases to add new facilities or update the status of closed facilities in each category to ensure that the geospatially specific assets are current.

Research Approach

The use of existing infrastructure assets is a key component of retrofit approaches for advances in this industry. To differentiate between the relative values of various options, the specific assets must be valued with respect to their potential use within a conversion pathway. Regional databases of industrial assets that might be utilized by a developing AJF industry have been assessed on the national level. These baseline databases have been compiled from a variety of sources, including industry associations, universities, and news outlets. These databases will be expanded, refined, and validated as the conversion design cases indicate additional needs for regional analyses.

Milestones

- Compiled, geolocated, validated, and shared national databases for biodiesel, corn ethanol, energy pellet, pulp and paper, and sugar mill production.
- Evaluated the databases as necessary to add new facilities or to change the status of closed facilities in each category, to ensure that the geospatially specific assets are current.
- Converted the geospatial infrastructure data for use in supply chain resiliency models.
- Updated tools for transportation cost modeling, which should lead to future improvements.

Major Accomplishments

- Compiled, validated, and shared National databases with the ASCENT Project 001(A) teams upon request. All metadata are available for use in regional analyses.
- Updated the count, scale and location of wood pellet mills.
- Geolocated the soybean and canola crushers in the U.S.

Publications

None.

Outreach Efforts

None.

Awards

None.

Student Involvement
None.

Plans for Next Period
This task will be closed out with a final infrastructure write-up and the most recent version of each database posted on the WSU repository next year.

Task 4 – Update CAAM Measures
Washington State University

Objective
The objective of this task is to update the CAAM with the latest available data.

Research Approach
Based on a community capitals framework, the ASCENT Project 001(A) team created the CAAM, which provides quantitative indicators of four social assets: social, cultural, human, and political capital. The CAAM provides quantitative proxy measures of qualitative concepts for initial site-selection assessments. Variations of the model have been applied to the Pacific Northwest, Idaho, Montana, Colorado, and Wyoming. Manuscripts on applications of the CAAM have been published in *Community Development*, *Politics and Life Sciences*, *Biomass & Bioenergy*, and *Frontiers in Energy Research*. The CAAM is currently being updated with the latest available data, with plans to make the CAAM more publicly accessible for use. As the social capital data have not been updated for several years, the research team is updating the data or creating our own measures to be validated in future use.

Milestones
- Conducted an investigation of alternative social capital data sources and measures.
- Met with another research team regarding additional data for potential cultural capital use, the Cultural Vitality Index (CVI) data from Creative West (formerly WESTAF).
- Validated the CAAM by using a private company.

Major Accomplishments
None.

Publications
None.

Outreach Efforts
None.

Awards
None.

Student Involvement
Nathaniel St. Claire, a student from the WSU School of Politics, Philosophy, and Public Affairs, worked on collecting updated data for cultural and human capitals. James Shackelford, also a student from the WSU School of Politics, Philosophy, and Public Affairs, worked on collecting updated data for cultural and human capitals. Both students helped investigate sources for social capital.

Plans for Next Period
- Finalize the alternative for social capital and update of the CAAM.
- Make the CAAM more user friendly.

Task 5 – Refine and Deploy Facility Siting Tools to Determine Regional Demand and Potential Conversion Sites to be Used in Regional Analyses

Washington State University

Objective

This objective of this task is to develop tools to site potential conversion facilities. Two primary tools are needed for this task: (1) a generalized tool to site initial locations that meet the needs of a specific conversion facility type and (2) a tool to select optimal conversion facility sites from the initial set of locations.

Research Approach

The ASCENT Project 001(A) team began developing a geospatial siting pre-selection (GSP) tool in early 2019. This tool is a Python®-based script that automates ArcGIS® to produce points representing locations that suit the needs of a conversion facility. The GSP tool uses a combination of buffer and cost datasets. Buffer datasets ensure that a candidate is sited in proximity to the necessary infrastructure, such as roads, rails, and natural gas pipelines. Because the candidate set generated by using only buffers will be very large, cost datasets have been added to distinguish candidates from each other. Cost datasets represent geospatially variable costs, including electricity, natural gas, and transportation. In early 2020, a graphic user interface was added to the GSP tool to make it more user-friendly. An additional script was developed in 2022 to model the transportation cost inputs for the GSP tool based on the local density of feedstock, the maximum feasible travel distance from the facility for feedstock collection, and regional road characteristics. This script also includes a rudimentary user interface. In 2023, our team performed a retrospective analysis of corn ethanol plants using the GSP, with the objective of performing a pseudo-validation. This study showed that the facility locations of the mature ethanol supply chain were in areas that the GSP would have prioritized for siting, indicating that the tool is likely a good fit for other similar supply chains, such as SAF supply chains. The ASCENT Project 001(A) team also performed an extensive study in 2023 to show how the number of candidates and locations of candidates affect the optimization model solution time. The results of this study showed that a small number of candidates generated by the GSP performed significantly better than the same number of points laid out in a square grid.

The Many-Step Transshipment Solver (MASTRS) is a Python-based script that models large supply chains across multiple levels by building and solving mixed-integer linear programming problems. The model starts with feedstock spread across many locations and then models the distribution and conversion of feedstock into biofuels and other co-products through multiple levels of intermediate facilities that may include temporary storage, pre-treatment, and fuel production, before new products are sent to their destinations. Intermediate facilities may include existing facilities or new candidate facilities that are generated by the GSP tool. The MASTRS output shows the flow of materials throughout the supply chain and the most cost-efficient capacities and locations for new facilities.

The modeling combination of GSP and MASTRS scripts has been implemented for several regional supply chains. MASTRS was first implemented for the Pacific Northwest oilseed-to-jet-fuel supply chain in 2018. Since 2019, the GSP and MASTRS scripts have been used together for two supply chain models for both the production of jet fuel from forest residuals and lumber production byproducts in the Pacific Northwest. The first supply chain model uses single-stage conversion at integrated biorefineries, and the second supply chain model is a multi-stage model with distributed preprocessing facilities.

Milestones

- Continued development of the GSP and MASTRS tools to become more practical.
- Made substantial improvements have been made regarding tool accessibility for new potential users along with the expansion of tool capabilities.

Major Accomplishments

None.

® Python is a registered trademark of Python Software Foundation, Beaverton, Oregon.
® ARCGIS is a registered trademark of Environmental Systems Research Institute, Inc., Redlands, California.

Publications
None.

Outreach Efforts
None.

Awards
None.

Student Involvement
None.

Plans for Next Period
- Begin the process for publishing manuscripts that define the GSP and MASTRS tools.
- Continue implementing the GSP and MASTRS tools in regional supply chain analyses.
- Complete a supply chain analysis for the Bioenergy Alliance Network of the Rockies (BANR).

Task 6 – Perform a Refinery-to-Wing Stakeholder Assessment
Washington State University

Objective
The objective of this task is to extend the stakeholder assessment to a limited sample of informed stakeholders in the remaining sections of the country to provide insight into market and industry dynamics, with the aim of optimizing successful outcomes.

Research Approach
- Conduct online surveys of key stakeholders to inform market and industry dynamics.

Milestones
None.

Major Accomplishments
None.

Publications
None.

Outreach Efforts
None.

Awards
None.

Student Involvement
None.

Plans for Next Period
- Conduct a survey of existing/new renewable diesel producers on what it would take for them to switch a portion of their production to SAF (likely with low, medium, high SAF cut options). Work on this task will restart pending funding approval of current proposal.

Task 7 – Conduct a Supply Chain Analysis

Washington State University
U.S. Department of Transportation Volpe Center

Objective

The objective of this task is to develop a simulation framework for assessing supply chain risk, aimed at providing a quantitative basis for risk-informed decisions on supply chain design and management. To achieve this objective, WSU has developed various models and tools that simulate natural hazards, their interactions with supply chain components, and potential effects on supply chain system performance. WSU and Volpe have each developed modeling tools that apply transshipment optimization to model the geospatial layout of developing supply chains. A comparison of these tools would be useful to identify the strengths and weaknesses of each tool.

Research Approach

Focusing on the use of woody-biomass-to-jet-fuel conversion via fast pyrolysis and the upgrading of a supply chain centered in the northern Rocky Mountains, a series of comparison studies was conducted by using optimization tools from Volpe and WSU. Each modeling approach was required to determine sites for new pyrolysis depots and upgrades to refineries. Forest production data were provided by the land use and resource allocation (LURA) model from the University of Idaho. Pyrolysis depot locations were selected by candidate generation tools included in each approach, and existing petroleum refineries were used as candidates for upgrading refineries. Cities, ports, and airport hubs throughout the U.S. West Coast and Rocky Mountain regions were used as markets for road transportation fuel, bunker fuel, and jet fuel.

Probabilistic Wildfire Risk Assessment

The development of a wildfire risk assessment platform for supply chains requires highly complex tasks that integrate sequential modules, including wildfire simulation, vulnerability assessment, and supply chain analysis, as illustrated in Figure 2. In the wildfire simulation module, our team has developed a set of machine-learning models to identify representative wildfire scenarios, estimate wildfire likelihood, and predict fire growth and suppression. In the vulnerability assessment module, a retrospective approach has been taken to establish a statistical link between potential explanatory variables and supply chain component failures. Finally, the last module has incorporated the impacts of fires on components into supply chain analysis to assess network-wide risks. The outputs from this platform can be used to support risk-informed decisions on cost-effective, wildfire-resilient supply chain layout and operation.

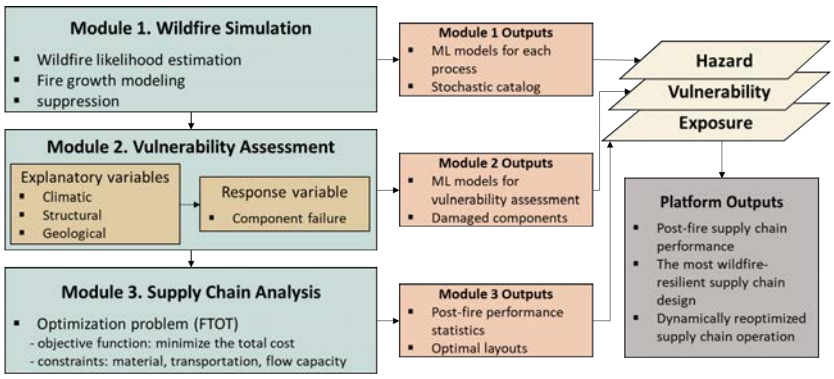

Figure 2. Procedure for the wildfire risk assessment platform for supply chains. FTOT: Freight and Fuel Transportation Optimization Tool; ML: machine learning.

Milestones

None.

Major Accomplishments

- Published a review on the selection and cost estimation of commercially available equipment involved in the collection and adequation of feedstock. The publication includes aggregated information regarding equipment cost, energy consumption, efficiency, feedstock storage, and transportation systems.
- Studied five feedstock types for producing AJF: (1) agricultural residues and grasses, (2) forest residues, (3) urban wood waste, (4) oilseeds, and (5) fats, oils, and greases.
- Submitted a paper titled "Advanced scenario reduction for risk assessment: a hybrid clustering and active learning approach."

Publications
None.

Outreach Efforts
None.

Awards
None.

Student Involvement
Dane Camenzind, a graduate student in Environmental Engineering at WSU, graduated with his Master of Science in September 2019 and is currently employed by WSU as an operations research engineer.

Fangjiao Ma received his doctorate degree in Civil Engineering at WSU in December 2023. In November 2023, he started his new position as a postdoctoral research fellow at the National Oceanic and Atmospheric Administration (NOAA) Cooperative Institute for Severe and High-Impact Weather Research and Operations at the University of Oklahoma.

Plans for Next Period
- Utilize regional supply chain tools to assess forest residuals for SAF using pyrolysis methods, as described in Task 8.
- Submit two journal papers: "Stochastic wildfire set generation: clustering and active learning for enhanced representativeness" and "Predicting wildfire impacts on supply chains: development of a regional risk assessment framework using machine learning models."

Task 8 – Provide Analytical Support for Regional CAAFI and USDA Jet Fuel Projects
Washington State University

Objectives
One of the objectives of this task is to develop a readiness-level tool to assess the status of regional SAF production projects and to use supply chain and stand-alone design cases to support the USDA BANR project in TEA and supply chain analysis. This regional community agricultural project focuses on the use of softwood forest salvage feedstock for fuels via a catalyzed pyrolysis conversion pathway.

A second objective of this task is to assess the regional feedstock, conversion pathways, and MSP for SAF manufactured in the northwest U.S. The aim of this work, requested by the Port of Seattle, is to determine whether the Seattle-Tacoma International Airport can attain a 2028 goal of 10% SAF use by using SAF manufactured in the region from regional feedstock.

Research Approach
The ASCENT Project 001(A) team will assist the regional USDA BANR team in deploying TEA and supply chain analysis for their project. This effort will focus on the use of softwood forest salvage feedstock in a thermochemical conversion process to produce fuels and co-products.

The facility siting tools discussed in Task 5 (i.e., GSP and MASTRS) have been implemented for the BANR supply chain and Port of Seattle project. The most recent model runs included feedstock and markets in an 11-state region including the West Coast and Intermountain West regions in the U.S. Feedstocks include forest residue from logging operations, mill residues from lumber production, and beetle-killed timber. The model results generated by MASTRS will help determine the relationships between facility location, fuel MSP, and conversion facility revenue.

The Port of Seattle project required a detailed feedstock survey for forest residuals, municipal solid waste, and lipids. Forest residuals were quantified with the LURA model for Oregon, Washington, Idaho, and Montana. Regional landfills were identified and located, scales were determined, and the remaining lifetimes were assessed to determine the most viable biorefinery location. The composition of municipal solid waste in the region was determined, as well as a method and related costs for sorting the material to match the SAF conversion pathway. Lipids were separated into two major categories: (1) waste fats, oils, and greases and (2) vegetable oil. Each feedstock was quantified and then paired with a compatible SAF conversion pathway to determine the SAF MSP by using ASCENT-developed TEAs.

Federal (Renewable Fuel Standard, Inflation Reduction Act) and state (CA, OR, WA, IL) policies in the U.S. that incentivize the production of AJF, its co-products, or feedstock (i.e., green dihydrogen [H_2], carbon dioxide [CO_2] capture and utilization) were mapped in a series of flow charts. An initial decision support tool was programmed using Python and converted to an Excel spreadsheet to facilitate its sharing among stakeholders. This tool enables a user to identify applicable policies for specific scenarios and returns generalized values per volume of fuel or mass of feedstock. Values can be selected for different time ranges, confidence interval values, and multiple summary statistics. Graphics were added to the tool in addition to options to export the data. The decision tool underwent ASCENT and external stakeholder review. The output from this tool is a direct input into the harmonized TEAs to more accurately determine the economic viability of an AJF production pathway in the U.S. This will be published in the first quarter of 2025 along with a peer-reviewed paper.

Information about facilities and infrastructure has been supplemented with information about the current consumption of feedstocks. Using information from the U.S. Census Bureau, U.S. Energy Information Administration, California Air Resources Board, and annual company reports, our team has compiled data that show how lipid feedstocks have been consumed for fuels in the U.S. since HEFA fuels were first produced in the U.S. in 2014.

A financial model that uses a system dynamics approach was conceptualized and developed. This model analyzes the effects of federal and state policies on the financial performance of projects to produce SAF. This model can perform both deterministic and stochastic analyses. Three conversion technologies (HEFA, ATJ, FT) and nine feedstocks (including fats, oils, and greases; vegetable oil; municipal solid waste; forest and agricultural residues; first- and second-generation ethanol; direct air capture; and flue gas) have been analyzed. The ASCENT Project 001(A) team will assess the influence of green hydrogen, renewable electricity and gas, and carbon capture utilization and storage on the financial metrics, based on calculations performed by MIT colleagues. A draft manuscript of this work is in progress.

As continuation of the technical support to the CAEP FTG on SAF accounting and reporting systems, a review paper titled “A dual sustainable aviation strategy: voluntary markets and regulatory frameworks” is being drafted. The paper aims to be a critical review on the impacts of regulatory and voluntary frameworks on the industry, examining their correlation to the development of sustainable supply chains, and the scaling up of the renewable energy.

Technical support to the CAEP FTG was provided. This support included (a) maintenance of the global database of SAF fuel production announcements and (b) an update to the SAF “Rules of Thumb” with the addition of two technologies: power-to-liquid and pyrolysis. For power-to-liquid technology, additional information was included to demonstrate the impact of uncertain prices of both green hydrogen and carbon dioxide. CO_2 abatement costs were calculated for new and existing technology and feedstock combinations. This work was presented to Technology Production and Policy subgroup as well as the full the FTG and was published on the ICAO website (https://www.icao.int/environmental-protection/Pages/SAF_RULESOFTHUMB.aspx), replacing the previous version.

An assessment of the practical pathway to meet the SAF Grand Challenge goals was compiled and presented to various industries, academia, and government groups. A more in-depth version of this work, updated with the U.S. production database and related summary statistics is included in a paper that is under internal review. The WSU paper has been started to cover the short-term (2030) goal, and the National Renewable Energy Laboratory will use a Bioenergy Scenario Model to complete the long-term (2050) analysis in a second paper. Both institutions are working to harmonize assumptions and methodologies to provide a cohesive overall analysis. In addition, the SAF Grand Challenge support work

includes participation in a working group that is compiling existing feedstock and supply chain models and identifying gaps that need to be filled. Our team also completed a maximum feedstock price analysis for the USDA OCE for SAF manufactured using HEFA. The maximum price of each analyzed feedstock was determined for a variety of policy scenarios. This work has been extended to be written into a paper with University of Tennessee, Knoxville (UTK) as the lead authors using policy to determine volumes of soybean oil and second crop oils for different price and policy support scenarios.

An inventory of domestic and imported lipid feedstocks was created to support potential SAF production to meet the SAF Grand Challenge. The inventory includes production quantities and prices for various lipids used in fuels including canola oil, soybean oil, corn oil, beef tallow, hog fats, and used cooking oil. Additionally, information about supply elasticity, competition from other markets and recent trends in international trade are also included.

Milestones

- Completed supporting work for BANR, including TEAs and supply chain analyses.
- Made progress in the use of supply chain and stand-alone design cases to support the USDA BANR project in TEA and supply chain analysis.
- Supported the BANR team in creating TEAs for the technologies under consideration.
- Published a review entitled, "Supply chain configuration of sustainable aviation fuel: review, challenges, and pathways for including environmental and social benefits," in *Renewable and Sustainable Energy Reviews* (Martinez-Valencia et al., 2021).
- Published a companion manuscript (Martinez-Valencia et al., 2023) that analyzes the effect of policies that incentivize CO_2e reductions on the financial performance of AJF using municipal solid waste as feedstock and GFT in the *Journal of Cleaner Production*.

Major Accomplishments

- Collaborated with the USDA BANR project team and attended their annual meeting to coordinate analyses. The ASCENT Project 001(A) team currently awaits completion of dead wood estimates to complete the supply chain analysis.
- Modeled analyses with previous forest-residue data.
- Completed the Port of Seattle feedstock and SAF assessment and presented the assessment to the Port of Seattle, which was also released to the public.

Publications

Martinez-Valencia, L., Peterson, S., Brandt, K., King, A. B., Garcia-Perez, M., & Wolcott, M. (2023). Impact of services on the supply chain configuration of sustainable aviation fuel: The case of CO2e emission reductions in the US. *Journal of Cleaner Production, 404*. https://doi.org/10.1016/j.jclepro.2023.136934

Martinez-Valencia, L., Garcia-Perez, M., & Wolcott, M. P. (2021). Supply chain configuration of sustainable aviation fuel: Review, challenges, and pathways for including environmental and social benefits. *Renewable and Sustainable Energy Reviews, 152*. https://doi.org/10.1016/j.rser.2021.111680

Outreach Efforts

- Lina Martinez-Valencia served as the moderator in the discussion panel about Green Hydrogen in Aviation at the Green Hydrogen Summit North America. Seattle, Washington, February 28-29, 2024.
- Lina Martinez-Valencia participated as a panelist in the SAF Policy Landscape at the Workshop "Fueling the Future: Sustainable Aviation Fuel in the Southeast'" in Atlanta, Georgia, October 15, 2024.

Presentations

Brandt, K. (2024, July 3). *ICAO rules of thumb and related TEA tools developed by ASCENT* [Meeting presentation]. ICAO Assistance, Capacity-building and Training for SAF (ACT SAF), 13, virtual.

Brandt, K., & Martinez-Valencia, L. (2023, November 30). *US policy support mechanisms: intro to practical impacts* [Meeting presentation]. ASCENT 93 Lecture Series, virtual.

Brandt, K., & Martinez-Valencia, L. (2024, April 4). *Sustainable aviation fuel TEA examples* [Meeting presentation]. ASCENT 93 Lecture Series. virtual.

Camenzind, D., Brandt, K., Martinez-Valencia, L., Wolcott. M. (2024, September 10*). Drivers of current biofuels development and opportunities for the future* [Conference presentation]. National Sustainability Society Inaugural Conference, Seattle, Washington.
Camenzind, D., & Lewis, K. (2024, September 5). *Fundamentals of supply chain analysis and optimization* [Meeting presentation]. ASCENT 93 Lecture Series, virtual.
Lewis, K., & Camenzind, D. (2024, September 19). *SAF supply chain analyses using the Freight and Fuel Transportation Optimization Tool* [Meeting presentation]. ASCENT 93 Lecture Series, virtual.
Martinez-Valencia, L., Brandt, K., & Wolcott, M. (2024, April 23). *A dual SAF strategy: voluntary market and regulatory frameworks* [Meeting presentation]. ASCENT Spring Meeting. Honolulu, Hawai'i.
Martinez-Valencia, L., & Wolcott, M. (2024, September 16). *Chain of custody methods* [Meeting presentation]. Washington Jet Fuel Group Meeting, Seattle, Washington.
Martinez-Valencia, L., & Wolcott, M. (2024, July 25). *Supply chain steps & types*. ASCENT 93 Lecture Series, Virtual.
Wolcott, M., & Brandt, K. (2024, September 19). *ASCENT SAF research overview & update*. Biomass R&D Operations Committee Meeting, virtual.

Awards
None.

Student Involvement
No students participated in this task during the reporting time frame. Previously supported students include Dane Camenzind, MS in Environmental Engineering at WSU (graduated in September 2019), who is currently employed by WSU as an operations research engineer; and Lina Martinez, PhD in Agricultural and Biological Engineering at WSU (graduated in April 2022), who now works for WSU as a postdoctoral research associate.

Plans for Next Period
- Publish a journal article using the U.S. SAF production database with the updated TEAs and the policy tool.
- Publish the ASCENT policy tool.
- Complete and publish "A dual sustainable aviation strategy: voluntary markets and regulatory frameworks" (review paper) as well as the manuscript based on the system dynamic approach.
- Publish joint paper with UTK that covers the volume of oilseed lipids that match the maximum price biorefineries can pay given different policy scenarios.

Task 9 – CAAFI Collaborative Support of Research, Development, Demonstration and Deployment Efforts on SAF/AJF
CAAFI's Office of the Executive Director
(Partial Year, effective April-September 2024)

Objectives
The objective of this task includes the responsibilities for the CAAFI's Office of the Executive Director to:
- Maintain familiarity with U.S. government, academic and industry SAF activities, and provide expertise in fostering the development and commercialization of SAF as enabled by the various pursuits or interests of these parties.
- Provide technical support to the FAA Office of Audit and Evaluation (AEE) and other agencies associated with the SAF Grand Challenge, as well as to other academic and commercial contributors.
- Lead or assist in facilitating public and private stakeholder engagement with SAF development, ASTM International fuel qualification, and related activities.
- Be responsible for executing an annually-updated set of goals and priorities via a workplan approved by FAA AEE as well as the CAAFI Steering Group.

Research Approach
The CAAFI reinforces the value proposition of synthetic aviation turbine fuels (SATF), including SAF, through use of communications, outreach, and direct stakeholder engagement. CAAFI enhances the SATF Fuel Qualification approach through participation, advisement, and facilitation of producer and original equipment manufacturer (OEM) engagement in the ASTM qualification process, as well as internal coordination discussions with CAAFI research and development (R&D)

and certification teams. CAAFI works to seek alignment of efforts to enable commercial SAF deployment, via leveraging research, partnering across U.S. government agencies, facilitating partnerships among supply chain stakeholders (typical both directly with individual companies and through various trade associations), and supporting innovative fuel acquisition processes. CAAFI implements and shares best practices across the SAF enterprise, including by providing tools and integrating information to support communication and understanding among diverse stakeholders. Finally, CAAFI will support the implementation of the SAF Grand Challenge roadmap by leveraging the above activities to facilitate the execution of the work streams and activities in the roadmap (https://www.energy.gov/sites/default/files/2022-09/beto-saf-gc-roadmap-report-sept-2022.pdf).

All of the above activities are supported through broad exchange of information among SAF stakeholders at our regularly occurring discussions, CAAFI webinars, and via pertinent conferences, workshops, and ad hoc meetings. Pertinent observations from more-formal public activities are published on the CAAFI website: http://www.caafi.org.

CAAFI provides information resources and credible expert technical support to the SAF community through:

- An updated and cohesive communications strategy to leverage a range of outlets for technical information and information exchange.
- A continuously updated CAAFI website with greater functionality, usability across devices, and expanded content.
- Continued and expanded direct interaction with supply chain participants who seek out CAAFI leadership for information, advice, and coordination with other entities.
- Continued and expanded dissemination of information through events, conferences, interviews, written articles, and journal publications.

CAAFI coordinates and aligns with U.S. government agencies' activities in support of the SAF Grand Challenge:

- Regularly coordinating with the Federal SAF Interagency Working Group on needs, goals, and priorities. Providing input on SAF Grand Challenge execution and performance tracking and supporting SAF Grand Challenge work team efforts and tasks.
- Communicating federal funding and program developments to the broader SAF community.
- Communicating the need for long-term, sustained policy support to meet the SAF Grand Challenge goals.
- Collaborating with stakeholders to develop key SAF communications and informational materials (e.g., infographics) that: Reference the best available data; Highlight the potential economic benefits (employment, etc.), environmental, and social benefits of SAF.
- Promote consistency for coherent and clear messaging.

CAAFI facilitates ongoing efforts by ASTM International on:

- Development of a specification for SATF that can be used at higher blend levels up to 100% (complete) synthesized fuels.
- Assessment of options for a more generalized specification for SATF based on composition and other characteristics.
- Evaluation and approval of new SATF pathways.
- Establishment of additional specifications leveraging existing refining infrastructure to produce SAF.
- Support for clearinghouse, prescreening, and other SATF testing for fuel analysis and qualification in collaboration with the FAA-funded ASCENT Center of Excellence.

CAAFI promotes harmonization of sustainability evaluation approaches and tools by:

- Facilitating broader acceptance of methodologies to assess the environmental, social, and economic performance of SAF.
- Facilitating research, demonstration, and commercial scale projects relating to regenerative agriculture/soil organic carbon sequestration.
- Fostering integration with developments in carbon capture and sequestration.
- Identifying concerns about carbon management and permanence with supply chain partners.

CAAFI enables continuing and expanding international engagement through:

- Input to the ICAO through events and direct engagement with working group participants.
- Coordination with other CAAFI-like organizations around the globe to align and complement work efforts.
- Collaboration with global SAF stakeholders on messaging.

Leveraging the above efforts to advance the use and commercial production of SAF by fostering strategic partnerships, identifying opportunities and aligning deployment efforts:

- Facilitating team development to respond to funding opportunities to develop novel feedstocks, SAF commercialization projects, and supply chains.
- Supporting the development of commercial agreements across the SAF supply chain to enable SAF production and use.
- Fostering other supply chain development and deployment partnerships.
- Developing an approach to collaboration with the established biofuel and energy industry and the agricultural sector.

Milestones

- Continued progress on CAAFI via each of the above listed support approaches.
- Hired two program directors – Tim Hughes and Joe Ellsworth.

Major Accomplishments

- Worked collaboratively with BBI International and SAF Magazine, CAAFI co-produced and executed the North American SAF Conference and Expo in St. Paul, Minnesota on September 11-13, 2024.
  - The event showcased many updates for SAF value chain development, as well as providing a forum for major messaging from the principal agencies of the SAF Grand Challenge (USDA, U.S. Department of Energy, and U.S. Department of Transportation/FAA).
  - The event also addressed challenging issues currently facing the SAF industry, as well as highlighting opportunities across the value chain.
  - More than 500 attendees were able to connect with exhibitors showcasing the latest technologies and services in the industry, as well as with their peers in discussing how to move the SAF community forward.
- Conducted interviews for various industry articles, web content, technical papers, and other research activities.
  - Nuseed, James Kendrick, Lisa Gibson (*Ethanol Producer Magazine*), Ben Seal (*Environmental Health News*), Will Guisbond (*The Air Current*), Boeing (ASTM Research Project), WSP (SFO SAFWG Progress Report), University of Manitoba, *Newsweek*, KY Rotary Club

Outreach Efforts

Outreach effort for this task included workshop participation, presentations, general discussions, panel moderation, interviews, and student seminars. The following is a list of outreach efforts participated in during this reporting period:

- Hughes; AURI Bio-Industrial Innovation Center Open House. Waseca, Minnesota, April 08.
- Hughes; AURI New Uses Forum. Mankato, Minnesota, April 09.
- Csonka; ASCENT SAF Spring Meeting. Honolulu, Hawai'i, April 23-25.
- Csonka; CRC Aviation Meeting. Washington, D.C., April 30-May 2.
- Hughes; Low Carbon Fuels Summit, Indianapolis, Indiana, May 1-2.
- Csonka, Hughes, Ellsworth; Strategy & Tactics Discussion with the FAA/Volpe. Cambridge, Massachusetts, May 6-8.
- Hughes; Fast Markets Biofuels & Feedstocks Conference, Chicago, Illinois, May 13-15.
- Csonka; Great Lakes Bioenergy Research Center, Annual Science Meeting and Industry Advisory Board. Lake Geneva, Wisconsin, May 13-16.
- Hughes; Western Illinois University Pennycress Field Day, Macomb, Illinois, May 22-23.
- Csonka; Greater MSP SAF Hub Event. Minneapolis, Minnesota, May 22.
- Hughes; BIO International Conference. San Diego, California, June 3-7.
- Csonka; International Fuel Ethanol Workshop. Minneapolis, Minnesota, June 10-12.
- Csonka; ASTM Committee D02 Summer Meeting. Austin, Texas, June 17-20.
- Hughes; Familiarization visits with Boeing, WSU Tri-Cities, WSU Pullman, and Idaho National Laboratory, July 8-11
- Csonka; Royal Caribbean Cruise Lines Sustainability Meeting. Port Canaveral, Florida, July 12-15.
- Csonka; Center for Bioenergy Innovation, Annual Science Meeting and Industry Advisory Board. Asheville, North Carolina, July 16-18.
- Hughes; International Plant Lipids Meeting. University of Nebraska, Lincoln (UNBL), Lincoln, Nebraska, July 14-18.
- Hughes; Camelina Conference. UNBL, Lincoln, Nebraska, Jul 19

- Csonka; Integrated Pennycress Research Enabling Farm & Energy Resilience (IPREFER) Annual and Advisory Board Meeting. Normal, Illinois, Jul 30-31
- Csonka; CAAFI Strategy & Tactics Discussions with the FAA and A4A. Washington, D.C., August 28-29.
- Csonka, Hughes, Ellsworth; North American SAF Conference & Expo. St. Paul, Minnesota, September 11-13
- Csonka; Argus North America Biofuels Conference, Monterrey, California, September 16-18.
- Csonka; OPIS RFS & RINS Conference, Chicago, Illinois, September 24-25
- Hughes; Hickman and Carlisle Counties visits and Kentucky Climate Summit, Lexington, Kentucky, September 25-26.

Awards

None.

Student Involvement

Student involvement activities occur on a continuing basis via engagement with the universities associated with the Bioenergy Research Centers (i.e., Great Lakes Bioenergy Research Center, Center for Bioenergy Innovation, and their partner institutions), ASCENT Advisory Board Meetings, and USDA National Institute of Food and Agriculture/Agriculture and Food Research Initiative Coordinated Agricultural Projects Sustainable Agricultural Systems efforts (i.e., the Sustainability Programming for Ag Retailers & Certified Crop Consultants [SPARC] and IPREFER). Members of the CAAFI Office of the Executive Director also participate annually with various University forums that promote student engagement in SAF activities (e.g., the UNBL activities highlighted above).

Plans for Next Period

- Release a new CAAFI Website.
- Release a new Commercial Engagement Readiness Level Framework.
- Release a revised Feedstock Readiness Level Framework.
- Execute the next CAAFI General Meeting at the Volpe Center in Boston, Massachusetts, June-03-06, 2025.
- Execute the next North American SAF Conference & Expo in Minneapolis, Minnesota, September 22-24, 2025.
- Target 30-40 outreach activities in the next fiscal year.

Project 001(B) Alternative Jet Fuel Supply Chain Analysis

University of Hawai‘i

Project Lead Investigator

Scott Q. Turn
Researcher
Hawai‘i Natural Energy Institute
University of Hawai‘i
1680 East-West Rd., POST 109
Honolulu, HI 96822
808-956-2346
sturn@hawaii.edu

University Participants

University of Hawai‘i (UH)

- P.I.: Scott Q. Turn, Researcher
- FAA Award Number: 13-C-AJFE-UH, Amendment 005
- Period of Performance: October 1, 2015, to August 4, 2021
- Tasks:
  1.
     1.1 Inform regional supply chains.
     1.2 Identify supply chain barriers in the Hawaiian Islands.

- FAA Award Number: 13-C-AJFE-UH, Amendment 007
- Period of Performance: October 1, 2016, to August 4, 2021
- Tasks:
  2.
     2.1 Inform regional supply chains.
     2.2 Support Indonesian alternative jet fuel (AJF) supply initiatives.

- FAA Award Number: 13-C-AJFE-UH, Amendment 008
- Period of Performance: August 1, 2017, to August 4, 2021
- Tasks:
  3.
     3.1 National lipid supply availability analysis
     3.2 Hawai‘i Regional Project

- FAA Award Number: 13-C-AJFE-UH, Amendment 011
- Period of Performance: May 31, 2019, to August 4, 2021
- Task:
  4. Hawai‘i Regional Project

- FAA Award Number: 13-C-AJFE-UH, Amendment 013
- Period of Performance: June 5, 2020, to August 4, 2021
- Task:
  5. Hawai‘i Regional Project

- FAA Award Number: 13-C-AJFE-UH, Amendment 017
- Period of Performance: October 1, 2021, to September 30, 2022

- Task:
  6. Hawai‘i Regional Project

- FAA Award Number: 13-C-AJFE-UH, Amendment 019
- Period of Performance: December 22, 2022, to December 31, 2023
- Task:
  7. Hawai‘i Regional Project

- FAA Award Number: 13-C-AJFE-UH, Amendment 025
- Period of Performance: August 12, 2024, to August 11, 2025
- Task:
  8. Hawai‘i Regional Project

Project Funding Level

Under **FAA Award Number 13-C-AJFE-UH, Amendment 005**, the Alternative Jet Fuel Supply Chain Analysis–Tropical Region Analysis project received $75,000 in funding from the FAA and cost-share funding of $75,000 from the State of Hawai‘i.

Under **FAA Award Number 13-C-AJFE-UH, Amendment 007**, the Alternative Jet Fuel Supply Chain Analysis–Tropical Region Analysis project received $100,000 in funding from the FAA, cost-share funding of $75,000 from the State of Hawai‘i, and $25,000 of in-kind cost match in the form of salary support for Scott Turn from UH.

Under **FAA Award Number 13-C-AJFE-UH, Amendment 008**, the Alternative Jet Fuel Supply Chain Analysis–Tropical Region Analysis project received $125,000 in funding from the FAA and cost-share funding of $125,000 from the State of Hawai‘i.

Under **FAA Award Number 13-C-AJFE-UH, Amendment 011**, the Alternative Jet Fuel Supply Chain Analysis–Tropical Region Analysis project received $200,000 in funding from the FAA and cost-share funding of $200,000 from the State of Hawai‘i.

Under **FAA Award Number 13-C-AJFE-UH, Amendment 013**, the Alternative Jet Fuel Supply Chain Analysis–Tropical Region Analysis project received $200,000 in funding from the FAA and cost-share funding of $200,000 from the State of Hawai‘i.

Under **FAA Award Number 13-C-AJFE-UH, Amendment 019**, the Alternative Jet Fuel Supply Chain Analysis–Tropical Region Analysis project received $150,000 in funding from the FAA and cost-share funding of $150,000 from the State of Hawai‘i.

Under **FAA Award Number 13-C-AJFE-UH, Amendment 025**, the Alternative Jet Fuel Supply Chain Analysis–Tropical Region Analysis project received $150,000 in funding from the FAA and cost-share funding of $150,000 from the State of Hawai‘i.

Investigation Team

University of Hawai‘i

Dr. Scott Turn (P.I.; Hawa’ii Natural Energy Institute), All Tasks
Dr. Trevor Morgan (assistant researcher; Hawai‘i Natural Energy Institute), Tasks 1–3
Dr. Richard Ogoshi (assistant researcher; Department of Tropical Plant and Soil Sciences), Tasks 1 and 2
Dr. Adel H. Youkhana (junior researcher; Department of Tropical Plant and Soil Sciences), Tasks 1 and 2
Dr. Curtis Daehler (professor; Department of Botany), Task 1
Ms. Sharon Chan (junior researcher; Hawai‘i Natural Energy Institute), Tasks 2, 5, and 7
Mr. Gabriel Allen (undergraduate student; Department of Biochemistry, Task 2
Dr. Jinxia Fu (assistant researcher; Hawai‘i Natural Energy Institute), Task 3
Dr. Quang Vu Bach (assistant researcher; Hawai‘i Natural Energy Institute), Tasks 3,4, 6, and 8
Ms. Sabrina Summers (undergraduate student; Department of Bioengineering), Task 3
Ms. Sarah Weber (undergraduate student; Department of Molecular Biosciences and Biotechnology), Task 3

Mr. Taha Elwir (undergraduate student; Department of Chemistry), Task 3
Dr. Donna Lee (energy crop analyst, Hawai'i Natural Energy Institute), Task 5 and 7
Dr. Elmar Villota (postdoctoral researcher, Hawai'i Natural Energy Institute), Task 5 and 7

Other Lead Personnel

University of Tennessee
Prof. Tim Rials (co-P.I.)
Prof. Edward Yu (co-P.I.)

Washington State University (WSU)
Prof. Michael Wolcott (P.I.)
Prof. Manuel Garcia-Perez (co-P.I.)

Volpe National Transportation Systems Center
Kristin Lewis (principal technical advisor and P.I.)

The Pennsylvania State University
Prof. Lara Fowler (P.I.)

Project Overview

The research effort under **Task 1** has two objectives. The first objective is to develop information on regional supply chains for use in creating scenarios of future alternate jet fuel (AJF) production in tropical regions. Outputs from this project may be used as inputs to regional supply chain analyses being developed by the FAA and Volpe Center. The second objective is to identify key barriers in regional supply chains that must be overcome to produce substantial quantities of sustainable aviation fuel (SAF) in the Hawaiian Islands and similar tropical regions.

The project goals of **Task 1** are as follows:

- Review and summarize the following:
  - The available literature on biomass feedstocks for the tropics
  - The available literature on pretreatment and conversion technologies for tropical biomass feedstocks
  - The available literature on geographic information system (GIS) datasets available for assessing AJF production systems in the tropics
- Identify AJF supply chain barriers in the Hawaiian Islands.

The research effort under **Task 2** has two objectives. The first objective is to develop information on regional supply chains for use in creating scenarios of future SAF production in tropical regions. Outputs from this project may be used as inputs to regional supply chain analyses being developed by the FAA and Volpe Center. This objective includes the development of fundamental property data for tropical biomass resources to support supply chain analysis. The second objective is to support the memorandum of understanding between the FAA and the Indonesian Directorate General of Civil Aviation to promote the development and use of sustainable alternative aviation fuels.

The project goals of **Task 2** are as follows:

- Support the Volpe Center and Commercial Aviation Alternative Fuels Initiative (CAAFI) Farm to Fly 2.0 supply chain analysis.
- Use GIS-based estimates of fiber crop production potential to develop preliminary technical production estimates of jet fuel in Hawai'i.
- Develop fundamental property data for tropical biomass resources.
- Transmit data and analysis results to other ASCENT Project 001 researchers to support the improvement of existing tools and best practices.
- Support Indonesian SAF supply initiatives.

The research effort under **Task 3** has two objectives. The first objective is to support a national lipid supply availability analysis that will inform industry development and guide policy. The second objective is to conduct a targeted supply chain analysis for a SAF production facility based on the Hawai'i regional project.

The project goals of **Task 3** are as follows:

- Support ASCENT partners conducting the national lipid supply availability analysis by contributing information on tropical oilseed availability.
- Evaluate supply chains for targeted waste streams and purpose-grown crops in Hawai‘i to a location in the principal industrial park on the island of O‘ahu.

For the research effort under **Task 4**, the main objective is to conduct bench-scale testing of tropical feedstocks for use in targeted supply chain analysis for a SAF production facility based on the Hawai‘i Regional Project initiated under Amendment 008.

The project goals of **Task 4** are as follows:

- Survey bench-scale systems available for relevant SAF conversion technology options.
- Down-select from the available bench-scale systems to no more than two systems capable of conducting feedstock testing and quantifying product yields and contaminant concentrations.
- Conduct bench-scale feedstock tests and quantify product yields, quality, and contaminant concentrations.

The project goals of **Task 5** are as follows:

- Conduct tropical oil-to-SAF supply chain analyses.
- Develop management strategies for elements present in construction and demolition (C&D) waste that affect use in thermochemical-conversion-based SAF production pathways.

The project goals of **Task 6** are as follows:

- Explore the impacts of HB2386 on waste management in Hawai‘i and potential for waste-based SAF production systems.

The project goals of **Task 7** are as follows:

- Evaluate greenhouse gas (GHG) implications of tropical oil-to-SAF supply chains in Hawai‘i based on life cycle methods.

The project goals of **Task 8** are as follows:

- Evaluate GHG implications of waste management use for SAF production in Hawai‘i based on life cycle methods

Task 1.1 – Inform Regional Supply Chains

University of Hawai‘i

Objectives

This task included two activities: (1) reviewing the archival literature on existing tropical crops and potential new crops that could provide feedstocks for SAF production and (2) reviewing relevant pretreatment and conversion technology options and experiences with the feedstocks identified in (1).

Research Approach

Task 1.1

The archival literature was reviewed to construct an updated database of relevant citations for tropical crops; new potential energy crops were identified and added to the database. Available information on agronomic practices, crop rotation, and harvesting techniques was included. The database was shared to serve as a resource for the ASCENT Project 001 Team and Volpe Center analyses of regional supply chains.

Task 1.2

A database of relevant pretreatment and conversion technology options, and experiences with potential tropical feedstock materials, was assembled from the archival literature and from existing Project 001 Team shared resources. Of particular interest were inventories of material and energy flows associated with the pretreatment and conversion unit operations fundamental to the design of sustainable systems and underlying analyses. Pairings of pretreatment and conversion technology options provided a starting point for the evaluation of tropical biorefineries that can be integrated into the ASCENT Project 001 Team and Volpe Center activities.

Milestones

Task 1.1

- Identified a target list of databases to search for relevant literature.
- Provided an interim report summarizing progress in the literature search.

Task 1.2

- Identified a target list of databases to search for relevant literature.
- Provided an interim report summarizing progress in the literature search.

Major Accomplishments

This work has been completed. A report was produced for each of the two activities, and the two reports were combined into a manuscript published in the journal *Energy & Fuels* (Morgan et al., 2019).

Publications

Peer-reviewed Journal Publication

Morgan, T. J., Youkhana, A., Ogoshi, R., Turn, S. Q., & Garcia-Perez, M. (2019). Review of biomass resources and conversion technologies for alternative jet fuel production in Hawai'i and tropical regions. *Energy & Fuels, 33(4)*, 2699–2762. doi: 10.1021/acs.energyfuels.8b03001

Outreach Efforts

On February 21, 2018, the P.I. participated in a ThinkTech Hawai'i broadcast focused on SAFs, with collaborators from WSU and CAAFI (https://www.youtube.com/watch?v=Ci4oWITPRKQ&feature=youtu.be).

Awards

None.

Student Involvement

None.

Plans for Next Period

None.

Task 1.2 – Identify Supply Chain Barriers in the Hawaiian Islands

University of Hawai'i

Objective

The objective of this task was to identify key barriers in regional supply chains that must be overcome to produce substantial quantities of SAF in the Hawaiian Islands and similar tropical regions.

Research Approach

The UH developed the Hawai'i Bioenergy Master Plan for the State of Hawai'i (http://www.hnei.hawaii.edu/wp-content/uploads/Hawaii-Bioenergy-Master-Plan.pdf), which was completed in 2009. In that plan, UH was tasked with determining whether Hawai'i had the capability to produce 20% of land transportation fuels and 20% of electricity from bio-based resources. To this end, the plan included assessments of (a) land and water resources that can support biomass feedstock production, (b) potential biomass resources and their availability, (c) technology requirements, (d) infrastructure requirements to support logistics, (e) economic impacts, (f) environmental impacts, (g) availability of human capital, (h) permitting requirements, and (i) limitations to developing complete value chains for biomass-based energy systems. In keeping with the stakeholder-driven development of the Hawai'i Bioenergy Master Plan, barriers to the development of regional supply chains for ASCENT were identified through interactions with key stakeholder groups. Green Initiative for Fuels Transition Pacific (GIFTPAC) meetings are held quarterly and attended by biofuel development interests in Hawai'i, including representatives of large landowners, producers of first-generation biofuels, petroleum refineries, electric utilities, the Hawai'i State Energy Office, U.S. Pacific Command, biofuel entrepreneurs, county government officials, and UH. Additional stakeholders are invited as necessary to fill gaps in information and the value chain. These meetings serve as

excellent opportunities to receive stakeholder input, identify barriers to supply chain development, and organize data collection efforts that span supply chain participants.

Milestones

- Introduced activities at the next regularly scheduled GIFTPAC meeting after contract execution
- Prepared an interim report outlining two tropical supply chain scenarios developed in consultation with the Project 001 Team, with input from GIFTPAC participants

Major Accomplishments

This task has been completed. A stakeholder meeting was held and documented in a report submitted to the FAA. The stakeholders identified barriers to SAF production in Hawai‘i and ranked the barriers in order of importance as follows:

1. Economic constraints (e.g., high costs of entry for production factors such as land) throughout the entire production chain;
2. Issues associated with access to capital, including high initial risks and uncertain returns on investment
3. Insufficient government support in the form of incentives and favorable policies to encourage long-term private investment;
4. Cost, availability, and competition for water;
5. SAF production technologies (emerging but not yet demonstrated to have full commercial viability); and
6. Insufficient or inadequate infrastructure (e.g., harbors, roads, fuel distribution infrastructure, irrigation systems) to support the entire production chain.

Several of these barriers also arise at locations in the continental United States; however, those related to water and infrastructure are unique characteristics of an island state.

Publications

None.

Outreach Efforts

This activity engaged stakeholders to identify barriers to SAF production in Hawai‘i. Preparation included reviewing stakeholder lists from previous activities. Facilitators appropriate to the stakeholder group were retained. The stakeholder meeting included a presentation of the scope and goals of the larger ASCENT program and other aspects of the UH ASCENT project.

Awards

None.

Student Involvement

None.

Plans for Next Period

This task is complete, but stakeholder outreach activities will continue under other tasks, as outlined below.

References

Hawai‘i Natural Energy Institute. (n.d.). *Hawai‘i Natural Energy Institute*. hnei.hawaii.edu

Task 2.1 – Inform Regional Supply Chains

University of Hawai'i

Objectives

To build on activities from fiscal year 2016, additional supporting analyses will be conducted for proposed supply chains in Hawai'i, including the following:

- Task 2.1.1 - Support the Volpe Center and CAAFI Farm to Fly 2.0 supply chain analysis
- Task 2.1.2 - Use GIS-based estimates of fiber crop production potential to develop preliminary technical production estimates of jet fuel in Hawai'i
- Task 2.1.3 - Develop fundamental property data for tropical biomass resources
- Task 2.1.4 - Transmit data and analysis results to support the improvement of existing tools (e.g., Policy Analysis System Model [POLYSYS]; https://bioenergykdf.net/content/polysys).

Research Approach

Task 2.1.2 has been conducted by using GIS data to identify areas suitable for purpose-grown crop production of feedstocks for SAF production in Hawai'i. The approach has used GIS layers for land capability class (LCC), slope, and zoning as preliminary screens for suitability. Lands are classified by the Natural Resources Conservation Service with ratings from 1 to 6. LCCs 1–3 are generally suitable for agricultural production, LCC 4 can be productive with proper management, and LCCs 5 or 6 can support less intensive production and may be suitable for forestry. The slopes of terrains affect aspects of production, including mechanization and erodibility. An elevation GIS layer was used to derive a slope layer. Zoning layers were acquired from Hawai'i state and county GIS offices. Only agricultural zoning was deemed suitable for this analysis.

The EcoCrop model was used to develop yield models for the crops selected in Task 1 according to annual rainfall and mean minimum monthly temperature data. EcoCrop includes model parameters on sugarcane, bana grass, five species of eucalyptus, *Gliricidia*, *Leucaena*, *Pongamia*, *Jatropha*, and sorghum. The parameters for sugarcane have been used to provide a base case assessment for comparison with historical sugarcane acreage and yield. Through sensitivity analysis, the model can be tuned to account for differences between parameters developed from global sugar production and a century of production experience in Hawai'i that has been refined through plant breeding to adapt sugarcane varieties to a wide variety of agro-ecosystems. The analysis has purposely avoided land-use conflict with food production by limiting suitability to areas capable of sustaining AJF feedstocks under rain-fed conditions. Areas suitable for SAF production that do not conflict with current agricultural land use (i.e., fallow land) have also been identified.

Pongamia (*Millettia pinnata*) was the initial focus of Task 2.1.3. *Pongamia* is an oilseed-bearing leguminous tree with production potential in Hawai'i and Florida. The tree produces pods containing oil-bearing seeds. Pods, oilseed cake, and oil were evaluated from trees growing on the island of O'ahu. Fundamental measurements of chemical composition were conducted and reported. Torrefaction of pods as a coproduct in oil production has been conducted. An investigation of pretreatment methods to improve pod feedstock properties for thermochemical conversion applications has been completed.

Milestones

- Identified target opportunities to augment POLYSYS, the Alternative Fuel Transportation Optimization Tool (https://trid.trb.org/view/1376122), and conversion modules
- Reviewed previously developed GIS information layers for tropical fiber crops and identified updating requirements
- Conducted preliminary estimates of SAF technical potential in Hawai'i, according to previously developed GIS information layers

Major Accomplishments

The GIS-based analysis of SAF production potential is ongoing. The assessment of potential lands meeting the requirements for LCC, slope, and land-use zoning has been completed. The EcoCrop model was implemented to predict yield as a function of the minimum mean monthly temperature and annual rainfall. This process identified potential SAF feedstock crops for land areas capable of supporting their production under both rain-fed and irrigated conditions. This analysis provided information necessary for determining cropping patterns and assessing costs for transport to processing facility locations. The EcoCrop model's prediction of sugarcane potential was determined, and the results were compared

with historical sugarcane acreage, both rain-fed and irrigated. The EcoCrop's upper and lower values for temperature and rainfall that support optimal sugarcane production were varied to calibrate the prediction against historical acreage. The difference between the EcoCrop values and those representative of conditions in Hawai'i is attributable to improvements due to plant breeding and unique combinations of environmental conditions (e.g., the relatively young volcanic soils present in high-rainfall areas on the island of Hawai'i that enable high drainage rates and accommodate sugar production).

Calibration of the EcoCrop model using historical sugarcane planted acreages was completed in 2018. This effort used a confusion matrix approach for validation (resulting in a kappa value >0.4) and demonstrated that the mean annual temperature was a better indicator of environmental capability than the minimum mean monthly temperature recommended by the EcoCrop developers. This effort highlights the need to adapt models to local conditions. Model predictions for suitable cropping are being compared with current land uses to provide another indicator of agreement.

The GIS analysis of SAF feedstock production potential has been completed. Statewide working maps for each of the species have been summarized in a draft report currently undergoing internal review (Chan et al., draft). This report will serve as the basis for a journal article publication.

Dr. Curtis Daehler (UH, Department of Botany) has completed a report assessing the invasiveness of *Pongamia*. Retrospective analyses have shown that predictive weed risk assessment systems correctly identify many major pest plants, but their predictions are not 100% accurate. The purpose of this study was to collect field observations of *Pongamia* planted around O'ahu to identify direct evidence of *Pongamia* escaping from plantings and becoming an invasive weed. Seven field sites were visited in various environments across O'ahu. Although some *Pongamia* seedlings were found in the vicinity of some *Pongamia* plantings, particularly in wetter, partly shaded environments, almost all observed seedlings were restricted to areas directly beneath the canopies of mother trees. This finding suggests a lack of effective seed dispersal away from *Pongamia* plantings. According to its current behavior in the field, *Pongamia* is not invasive or established outside of cultivation on O'ahu. Because of its limited seed dispersal and low rates of seedling establishment beyond the canopy, the risk of *Pongamia* becoming invasive can be mitigated through monitoring and targeted control of any rare escapes in the vicinity of plantings. Because seeds and seed pods are dispersed by water, future risks of *Pongamia* escape and unwanted spread can be minimized by avoiding planting at sites near flowing water, near areas exposed to tides, or on or near steep slopes. Although vegetative spread by root suckers was not observed around plantings on O'ahu, monitoring for vegetative spread around plantations is recommended; unwanted vegetative spread might become a concern in the future that could be addressed with localized mechanical or chemical control.

Pods, oilseed cake, and oil have been evaluated from a number of trees growing on the island of O'ahu. TerViva, a company pursuing *Pongamia* commercialization, provided material from orchards on O'ahu. Fundamental measurements of chemical composition were made for seeds, pods, extracted oil, and post-extraction seed material. The measured values included carbon, hydrogen, nitrogen, and sulfur elemental composition; energy content; volatile matter, fixed carbon, and ash content; and trace element composition. Oils were characterized for peroxide value, iodine value, fatty acid profile, free fatty acid content, flash point, density, viscosity, and phase transition temperatures. The chemical composition and fuel properties of the oilseed cake and the pod material were characterized. A manuscript summarizing the results of this effort has been published in the journal *ACS Omega* (Fu et al., 2021a).

Coproduct evaluation of *Pongamia* pod feedstock for thermochemical conversion has been conducted. Evaluation included both untreated pods and pods pretreated by a torrefaction process to improve their properties. Torrefaction produces a material with improved grindability, storage stability, diminished oxygen content, and microbial availability. The effects of process conditions on feedstock properties relevant to thermochemical conversion technologies, proximate and ultimate composition, heating value, and Hardgrove grindability index were measured. The chemical structure, reactivity, and changes in elemental composition of the torrefied materials were also investigated. A manuscript summarizing the results of this effort has been published in the journal *Fuel* (Fu et al., 2021b).

Pongamia seedpods are recognized as a potential feedstock for SAF production because of the relatively high oil content of the seeds. *Pongamia* pods are byproduct residues available after seed separation. Pods have high chlorine and potassium content that may be problematic in thermochemical energy conversion systems. Leaching experiments were performed to remove inorganic constituents of the pods and thereby decrease the potential for fouling, slagging, and agglomeration. A manuscript summarizing the results of this effort has been published in the journal *Fuel* (Fu et al., 2021c).

The state tree of Hawai'i, *Aleurites moluccanus* (commonly known as kukui and candlenut), is an oil-nut-bearing tree frequently found in the tropics. Nuts from a number of these trees growing on the island of O'ahu were collected, and the nutshell, oilseed cake, and oil components were fractionated and analyzed for common properties necessary for designing SAF production systems. Results were published in the journal *ACS Omega* (Fu et al., 2023).

Publications

Peer-Reviewed Journal Publications

Fu, J., Summers, S., Morgan, T. J., Turn, S. Q., & Kusch, W. (2021a). Fuel properties of pongamia (*Milletia pinnata*) seeds and pods grown in Hawaii. *ACS Omega*, *6*, 9222–9233. doi:10.1021/acsomega.1c00635

Fu, J., Summers, S., Turn, S. Q., & Kusch, W. (2021b). Upgraded pongamia pod via torrefaction for the production of bioenergy. *Fuel, 291,* 120260. doi: 10.1016/j.fuel.2021.120260

Fu, J., Allen, G., Weber, S., Turn, S. Q., & Kusch, W. (2021c). Water leaching for improving fuel properties of pongamia pod: Informing process design. *Fuel, 305,* 121480. doi: 10.1016/j.fuel.2021.121480

Fu, J., Weber, S., & Turn, S.Q. (2023). Comprehensive characterization of kukui nuts as feedstock for energy production in Hawai'i. *ACS Omega*. 8, 22567-22574.

Written Report

Chan, S., Ogoshi, R. & Turn, S. (2024, draft). Feedstocks for sustainable jet fuel production: An assessment of land suitability in Hawaii. A draft report has been prepared and a draft manuscript is under preparation for publication.

Outreach Efforts

Outreach in this task has focused on interactions with Terviva,® a startup company that has identified *Pongamia* germplasm production and marketing as the central focus of its business plan.

Chan, S., Ogoshi, R. & Turn, S. (2020, July 6-9). *Feedstocks for Sustainable Jet Fuel Production: An Assessment of Land Suitability in Hawaii* [Poster presentation]. 28th European Biomass Conference & Exhibition, Virtual.

Fu, J., Summers, S. & Turn, S. (2020, October 5-7). *Upgraded Millettia Pinnata Pod via Torrefaction for the Production of Bioenergy in Hawai'i* [Oral presentation]. 2020 Thermal & Catalytic Sciences Virtual Symposium, Virtual.

Turn, S. (2019, December 3). *Regional Supply Chain Analysis for Alternative Jet Fuel Production in the Tropics* [Poster presentation]. Hawai'i Aviation and Climate Action Summit, Honolulu, HI.

Fu, J., Allen, G., Weber, S., Turn, S. Q., & Kusch, W. (2021, August 22-26). *Water Leaching for Improving Fuel Properties of Pongamia Pods* [Oral and Virtual presentation]. American Chemical Society Fall 2021 National Meeting, Atlanta, GA, United States.

Fu, J., Summers, S. & Turn, S. (2021, April 5-16). *Upgraded Millettia Pinnata Pod via Torrefaction for the Production of Bioenergy in Hawai'i* [virtual and oral presentation]. American Chemical Society Spring 2021 National Meeting, Virtual.

Fu, J., Weber, S. & Turn, S. (2022, August 21-25). *Comprehensive Characterization of Kukui Nuts for Bioenergy Production in Hawaii* [Oral presentation]. American Chemical Society Fall 2022 National Meeting & Exposition, Chicago, IL, United States.

Awards

A poster entitled "Feedstocks for Sustainable Jet Fuel Production: An Assessment of Land Suitability in Hawai'i" (Chan et al., 2020) was presented at the European Biomass Conference & Exhibition held virtually July 6–9, 2020, and received the Best Visual Presentation Award.

Student Involvement

Three undergraduate students are involved in the project. Their primary responsibility is processing and analyzing samples of biomass materials selected for evaluation as potential SAF feedstocks. The *Pongamia* torrefaction work was the focus of an Undergraduate Research Opportunity Program project for Sabrina Summers, a bioengineering and chemistry double major. The results of her work were presented at the American Chemical Society Fall 2019 National Meeting in San Diego, California. The *Pongamia* pod leaching work was the focus of an Undergraduate Research Opportunity Program project for Gabriel Allen, a biochemistry major.

® Terviva is a registered trademark of Terviva, Inc., Alameda, California.

Plans for Next Period

A report summarizing the GIS analysis of SAF feedstock production potential and a companion manuscript will be completed. Apart from this report and manuscript, this task is complete.

Task 2.2 – Support Indonesian AJF Supply Initiatives

University of Hawai'i

Objective

This task supports the memorandum of understanding between the FAA and the Indonesian Directorate of General Civil Aviation to promote the development and use of sustainable alternative aviation fuels. Under the coordination of the FAA, efforts to establish points of contact and coordinate with Indonesian counterparts are ongoing.

Research Approach

To begin this process, the team will work with the FAA to establish points of contact to coordinate efforts with Indonesian counterparts. Members of the Indonesian Aviation Biofuels and Renewable Energy Task Force include Universitas Indonesia, Institut Teknologi Bandung, and Universitas Padjadjaran. A prioritized list of tasks will be developed in consultation with Indonesian counterparts, and data required to inform sustainability and supply analyses, and potential sources of information will be identified. The information collected may include Indonesian jet fuel use and resources for SAF production, airport locations, and annual and monthly jet fuel consumption patterns. Characterization of sustainable biomass resources with potential for use in producing SAF supplies may include developing preliminary GIS mapping information of their locations and distributions, and preliminary estimates of their technical potential.

Milestones

- Identified points of contact at Indonesian universities participating in the Aviation Biofuels and Renewable Energy Task Force
- Identified research needs and develop a project plan
- Developed data for potential projects

Major Accomplishments

The P.I. traveled to Jakarta, Indonesia, in the first week of August 2017 and met with the following individuals:

- Cesar Velarde Catolfi-Salvoni (International Civil Aviation Organization)
- Dr. Wendy Aritenang (International Civil Aviation Organization)
- Dr. Ridwan Rachmat (Head of Research Collaboration, Indonesian Agency for Agricultural Research and Development)
- Sylvia Ayu Bethari (Head of Aviation Fuel Physical and Chemical Laboratory, Research and Development Centre for Oil and Gas Technology)
- Dr. Ina Winarni (Forest Product Research and Development Center, Ministry of Environment and Forestry)
- Dr. SD Sumbogo Murti (Center of Technology Energy Resources and Chemical Industry, Agency for the Assessment and Application of Technology)

The activities of the tropical supply chain analysis effort were presented to the group, and a general discussion followed. From this introductory meeting, it was concluded that the Indonesian counterparts would seek agreement on how to move forward with future cooperation.

In November 2018, the P.I. traveled to Jakarta, Indonesia, and met with Dr. Wendy Aritenang of the International Civil Aviation Organization's Jakarta office. The same trip included meetings with renewable energy researchers at Universitas Indonesia. After the meeting, Dr. Aritenang suggested several points of contact for future engagement: Frisda Panjaitan from the Palm Oil Research Institute and Tatang Soerawidjaja, Tirto Prakoso Brodjonegoro, and Imam Reksowardojo from the Bandung Institute of Technology.

In October 2022, the P.I. traveled to Jakarta, Indonesia, and met with Dr. Wendy Aritenang. The following day, the P.I. and Dr. Aritenang traveled to Bandung, West Java, Indonesia, to visit the Bandung Institute of Technology and met with faculty members Professor Adiwan Aritenang (Department Head of Regional Planning) and Professors Tatang Soerawidjaja, Tirto

Prakoso Brodjonegoro, and Iman Reksowardojo, from the Faculty of Industrial Technology, Bandung Institute of Technology. Ongoing UH ASCENT activities were presented, and the Bandung Institute of Technology researchers discussed their SAF-related research efforts.

Publications
None.

Outreach Efforts
Outreach efforts by the P.I. are described in the Major Accomplishments section above. In addition, the P.I. participated in the Asia Pacific Economic Cooperation event, "Energy Transition toward Carbon Neutrality, APEC BCG Economy Thailand 2022: Tech to Biz," in Bangkok, Thailand, and gave an oral presentation entitled "US Initiatives on Sustainable Aviation Fuel."

Awards
None.

Student Involvement
None.

Plans for Next Period
This activity is complete.

Task 3.1 – National Lipid Supply Availability Analysis
University of Hawai'i

Objective
In this task, the team will support ASCENT partners working on a national lipid supply availability analysis by sharing data on tropical oilseed availability developed under previous years' activities.

Research Approach
This support will include estimates of *Pongamia* production capability in the state of Hawai'i, in addition to assessments of waste cooking oil and tallow.

Milestones
Milestones will coincide with the schedule of the lead institution (WSU) for the national lipid supply analysis.

Major Accomplishments
Additional seeds and pods were collected from the *Pongamia* trees on the UH campus, Foster Botanical Garden, and Ke'ehi Lagoon Beach Park. Large quantities (tens of kilograms) of material were acquired from TerViva's plantings on the O'ahu North Shore for use in oil evaluation. Two oilseed presses were acquired, and safety documents were developed. Pods, oilseed cake, and oil were evaluated from a number of trees growing on the island of O'ahu. Fundamental measurements of chemical composition were made for seeds, pods, extracted oil, and post-extraction seed material. The measured values included carbon, hydrogen, nitrogen, and sulfur elemental composition; energy content; volatile matter, fixed carbon, and ash content; and trace element composition. Oils were characterized for peroxide value, iodine value, fatty acid profile, free fatty acid content, flash point, density, viscosity, and phase transition temperatures. The development of coproducts from pods and oilseed cake was explored.

Areas in Hawai'i with agricultural zoning suitable for rain-fed production of *Pongamia* have been identified. Conflicts with the current agricultural land use have been identified.

The waste oil resources in Hawai'i are estimated to be on the order of 2–3 million gallons per year, according to the de facto population, and are directed to biodiesel production.

Publications

Peer-Reviewed Journal Publication

Fu, J., Summers, S., Morgan, T. J., Turn, S. Q., & Kusch, W. (2021). Fuel properties of pongamia (*Milletia pinnata*) seeds and pods grown in Hawaii. *ACS Omega, 6*(13), 9222–9233. doi:10.1021/acsomega.1c00635

Outreach Efforts

Data were presented at the April 2019 ASCENT review meeting in Atlanta, Georgia.

Awards

None.

Student Involvement

Three undergraduate students (Sabrina Summers, Sarah Weber, and Taha Elwir) are involved in the project. Their primary responsibility is processing and analyzing samples of biomass materials selected for evaluation as potential SAF feedstocks.

Plans for Next Period

This task is complete. Results will underpin future tasks.

Task 3.2 – Hawai‘i Regional Project

University of Hawai‘i

Objectives

A supply chain based on fiber feedstocks transported to a conversion facility located at the Campbell Industrial Park (CIP) on O‘ahu will be evaluated (Figure 1). The CIP is the current site of two oil refineries. C&D wood waste from the PVT Land Company’s landfill could provide a primary source of feedstock. Other sources will be evaluated from elsewhere on O‘ahu and outer islands, including municipal solid waste streams from outer islands and mining of current waste-in-place stocks. Waste streams and purpose-grown crops form the basis of a hub-and-spoke supply system, with the hub located on O‘ahu. Pipelines for jet fuel transport are in place from CIP to Daniel K. Inouye International Airport and the adjacent Joint Base Pearl Harbor-Hickam. Other coproduct offtakers for alternative diesel fuel include the Hawaiian Electric Company and several military bases, including Schofield Barracks (~50-megawatt alternative fuel-capable power plant under development) and Marine Corps Base Hawai‘i located in Kaneohe Bay. Hawai‘i Gas, a local gas utility, is also seeking alternative sources of methane if methane or feedstock suitable for methane production is available as a coproduct. Hawai‘i Gas currently offtakes feedstock (naphtha) from the refinery.

Figure 1. Possible Locations of Value Chain Participants for a Fiber-Based Alternative Jet Fuel Production Facility at the Campbell Industrial Park, O'ahu.

Research Approach

Task 3.2.G1. Analyze feedstock-conversion-pathway efficiency, product slate (including coproducts), and maturation
To build on activities from previous years, additional supporting analyses will be conducted for proposed supply chains in Hawai'i, as follows:

- Subtask 3.2.G1.1. Assess feedstock suitability for conversion processes (e.g., characterization, conversion efficiencies, and contaminants) (UH and WSU [Manuel Garcia-Perez])
- Subtask 3.2.G1.2. Acquire data on feedstock size reduction, particle size of materials, and bulk densities (UH, WSU [Manuel Garcia-Perez])
- Subtask 3.2.G1.3. Evaluate coproducts at every step of the supply chain (ASCENT Project 001 Team)

Task 3.2.G2. Assess the scope of techno-economic analysis (TEA) issues
This task will determine the current TEA status of targeted SAF production technologies that use fiber feedstocks as production inputs (UH, WSU [Manuel Garcia-Perez], Purdue University [Wally Tyner]).

Task 3.2.G3. Conduct a screening-level GHG life-cycle assessment (LCA)
This task will conduct screening-level GHG LCA on the proposed target supply chains and SAF conversion technologies.
Subtasks:

- Subtask 3.2.G3.1. Assess Massachusetts Institute of Technology (MIT) waste-based GHG LCA tools in the context of application to Hawai'i (MIT [Mark Staples])
- Subtask 3.2.G3.2. Assess requirements to link previously completed eucalyptus energy and GHG analysis to the edge of the plantation with available GHG LCA information for conversion technology options (MIT [Mark Staples], UH)
- Subtask 3.2.G3.3. Identify and fill information/data gaps

Task 3.2.G4. Identify supply chain participants/partners
Subtasks:

- Subtask 3.2.G4.1. Define C&D landfill case
- Subtask 3.2.G4.2. Identify eucalyptus in existing plantations, landowners, leaseholders/feedstock producers, harvesting contractors, truckers, etc. (UH)
- Subtask 3.2.G4.3. Define other feedstock systems as identified (ASCENT Project 001 Team)

Task 3.2.G5. Develop an appropriate stakeholder engagement plan
Subtasks:

- Subtask 3.2.G5.1. Review stakeholder engagement methods and plans from past work to establish baseline methods (UH, WSU [Season Hoard])
- Subtask 3.2.G5.2. Identify and update engagement strategies according to the updated Community Social Asset Modeling/Outreach support tool (UH, WSU [Season Hoard])

Task 3.2.G6. Identify and engage stakeholders
Subtasks:

- Subtask 3.2.G6.1. Identify stakeholders along the value chain and create a database based on value chain location (UH)
- Subtask 3.2.G6.2. Conduct a stakeholder meeting by using the instruments developed in Task 3.2.G5 (UH, WSU [Season Hoard])
- Subtask 3.2.G6.3. Analyze stakeholder response and feedback to the process (UH, WSU [Season Hoard])

Task 3.2.G7. Acquire transportation-network and other regional data needed for the Freight and Fuel Transportation Optimization Tool and other modeling efforts
Subtasks:

- Subtask 3.2.G7.1. Acquire necessary data to evaluate harbor capacities and current usage (UH, Volpe [Kristin Lewis], WSU [Michael Wolcott])
- Subtask 3.2.G7.2. Acquire data on inter-island transport practices (UH, Volpe [Kristin Lewis], WSU [Michael Wolcott])

Task 3.2.G8. Evaluate infrastructure availability
Subtasks:

- Subtask 3.2.G8.1. Evaluate inter-island shipping options and applicable regulation (UH, Volpe [Kristin Lewis], WSU [Michael Wolcott])
- Subtask 3.2.G8.2. Evaluate transport or conveyance options from conversion location to end users and applicable regulation (UH, Volpe [Kristin Lewis], WSU [Michael Wolcott])

Task 3.2.G9. Evaluate feedstock availability
Subtasks:

- Subtask 3.2.G9.1. Refine ground-truth prior evaluations of options for purpose-grown feedstock supply (UH)
- Subtask 3.2.G9.2. Conduct projections of future C&D waste supply and mining of waste-in-place on O'ahu, municipal solid waste, and mining of waste-in-place on other islands (UH)

Task 3.2.G10. Develop a regional proposal
This task will use the information collected in Tasks 3.2.G1–3.2.G9 to develop a regional project proposal.

Milestone
One milestone is associated with each of the subtask activities identified in the Research Approach section above.

Major Accomplishments
The characteristics of the feedstock generated at the landfill have been determined and summarized in a publication (Bach et al., 2021).

The elemental compositions of feedstock materials have been used as the basis for equilibrium analysis of gasification systems using oxygen, steam, and steam–oxygen mixtures to inform process design.

The material flows relevant to the screening-level GHG analysis of C&D waste as SAF feedstock have been assembled. Preliminary discussions of GHG analysis of C&D-based SAF systems with landfill operators have been initiated.

The plans for solid waste management from all counties in Hawai‘i have been used to provide a broader picture of the waste stream composition, diversion, recycling practices, and planned uses.

Publications
Peer-reviewed journal publications

Bach, Q. V., Fu, J., & Turn, S. (2021). Construction and demolition waste-derived feedstock: fuel characterization of a potential resource for sustainable aviation fuels production. *Frontiers in Energy Research, 9,* 711808. doi: 10.3389/fenrg.2021.711808

Bach, Q. V. & Turn, S. (2024, draft). Fate of arsenic and other inorganic elements during gasification of construction and demolition wastes – thermochemical equilibrium calculations. Draft manuscript in process.

Outreach Efforts
Results of the fuel sampling, fuel analyses, and gasification equilibrium analyses were presented at the October ThermoChemical Biomass 2019 Conference in Chicago, Illinois.

Information from this task was included in the talk “Regional Supply Chain Analysis for Alternative Jet Fuel Production in the Tropics” presented at the Hawai‘i Aviation and Climate Action Summit, December 3, 2019, at the Hawai‘i State Capitol, Honolulu, Hawai‘i.

Data acquired under this task were presented to the management of PVT Land Company and their consultants from Simonpietri Enterprises and T. R. Miles Technical Consultants, Inc.

A poster entitled “Construction and Demolition Waste as an Alternative Energy Source: Fuel Characterization and Ash Fusion Properties” was presented at the 2020 Thermal & Catalytic Sciences Virtual Symposium.

Discussion with Dr. Kristin Lewis and Volpe Center staff on the addition of Hawai‘i transportation infrastructure to the Freight and Fuel Transportation Optimization Tool was initiated and deferred until a clearer definition of the system emerges.

As suggested by FAA management, UH worked with the Servicios y Estudios para la Navegación Aérea y la Seguridad Aeronáutica (SENASA) to identify a counterpart university in the Canary Islands, Spain. Universidad de la Laguna (ULL) was selected, and a memorandum of understanding was signed between UH and ULL. A nondisclosure agreement was subsequently signed among SENASA, ULL, UH, and the Spanish company Abengoa Energía, S.A. Regularly scheduled meetings have been held biannually with Professor Dr. Ricardo Guerrero Lemus from ULL to discuss common research themes and were continued in 2023.

Awards
None.

Student Involvement
Three undergraduate students (Sabrina Summers, Sarah Weber, and Taha Elwir) have been involved in sample preparation and in operating the laboratory analytical equipment used for sample analysis.

Plans for Next Period

Manuscripts covering the prediction of gasification product streams including contaminant concentrations will be completed and submitted. Comparative data from bench-scale gasification tests (see Task 4) at ThermoChem Recovery International facilities were received in October 2023. These data will be supplemented with the results of C&D waste sample analyses using a differential thermal analyzer paired with an inductively coupled plasma mass spectrometer (DTA-ICPMS) to provide information on the release of inorganic elements as a function of temperature. Contracting for DTA-ICPMS analytical services at the University of California, Davis, Interdisciplinary Center for Plasma Mass Spectrometry is underway. With these experimental data, the manuscripts will be completed. Note: Although this was anticipated to be completed in 2024, unresolved contracting issues between UH and the University of California, Davis, have delayed the DTA-ICPMS analysis and thus the manuscript preparation and the completion of this task.

References

Bach, Q. V., Fu, J., & Turn, S. (2021). Construction and demolition waste-derived feedstock: fuel characterization of a potential resource for sustainable aviation fuels production. *Frontiers in Energy Research, 9,* 711808. doi: 10.3389/fenrg.2021.711808

Task 4 – Hawai‘i Regional Project

University of Hawai‘i

Objective

This task builds upon results from the previous years' work under the Hawai‘i Regional Project, with a focus on the data and analysis necessary to plan a project that uses C&D waste as feedstock for SAF production. The Task 4 objective is to use C&D feedstock characterization data and thermochemical equilibrium analysis from the previous years to conduct bench-scale gasification tests and to quantify the product gas yield, composition, and contaminant concentrations. These results will be compared with equilibrium prediction used to identify contaminants that must be addressed before end use and will provide the basis for designing contaminant control systems.

Research Approach

Bench-scale gasification tests will be conducted on samples of C&D wastes characterized in the earlier tasks, to measure product yields, identify contaminants, and investigate element partitioning between product phases.

The information gained from the tests will be used to identify opportunities to improve TEA, identify coproducts, inform supply chain participants and stakeholders, and identify necessary infrastructure improvements.

Milestones

- Identified and evaluated capabilities of experimental bench-scale facilities for gasifier tests
- Specified system performance parameters to be measured
- Specified techniques to sample and analyze contaminants
- Selected and engaged an experimental bench-scale facility for testing
- Prepared and shipped feedstock from Hawai‘i to the experimental test facility
- Conducted tests, reduce data, and prepare a summary report of the results

Major Accomplishments

Operational measurements to be conducted as part of the bench-scale tests were summarized, and a test plan was developed; these were used as the basis for entertaining proposals for test services.

Through a competitively structured proposal process, ThermoChem Recovery International, Inc., was engaged to provide bench-scale test services for C&D waste feedstock and other opportunity fuels of relevance to Hawai‘i and the tropics.

A synthetic C&D waste recipe was developed according to the results published in *Frontiers in Energy Research* (Bach et al., 2021). Component fractions in the recipe were determined by a least-squares approach to matching critical fuel characteristics, including volatile matter, fixed carbon, and ash content; higher heating value; and concentrations of the

elements Na, Mg, Al, Si, P, S, Cl, K, Ca, Ti, Cr, Mn, Fe, Cu, Zn, As, Ru, and Pb. This recipe will enable a reproducible C&D waste fuel lot to be assembled and will aid in decreasing test-to-test variability.

In November and December 2021, tests were conducted in the bench-scale facility at the ThermoChem Recovery International facility in Durham, North Carolina. After shakedown testing was completed, two subsequent tests were conducted: (1) a test using *Leucaena leucocephela* stemwood and (2) a test using synthetic C&D waste. Test reports for the two bench-scale gasification tests at ThermoChem Recovery International facilities were finalized in October 2023.

Publications

Peer-reviewed journal publications

Bach, Q. V., Fu, J., & Turn, S. (2021). Construction and demolition waste-derived feedstock: fuel characterization of a potential resource for sustainable aviation fuels production. *Frontiers in Energy Research, 9,* 711808. doi: 10.3389/fenrg.2021.711808

Outreach Efforts

A presentation entitled "Hawai'i Energy Crop and Urban Waste Feedstock Updates" was presented at the ASCENT Spring Meeting in Honolulu, Hawai'i.

Awards

None.

Student Involvement

None.

Plans for Next Period

Planning for additional bench-scale tests at the Gas Technology Institute began in 2023. Moving the mini bench-scale gasifier unit between facilities at the Gas Technology Institute delayed the tests. As of November 2024, the Gas Technology Institute's mini bench-scale unit has not been recommissioned. The principal investigator will re-evaluate the utility of the remaining tests and budgetary issues with the FAA program manager in early 2025.

Test results will be shared with stakeholder communities.

Task 5 – Hawai'i Regional Project

University of Hawai'i

Objective

Task 5.1: Tropical oil-to-SAF supply chain analysis

The goal of Task 5.1 is to develop a model for tropical oil supply chains for SAF and associated coproducts. Hawai'i will be the initial focus, but the modeling tools will be developed for wider use in island settings.

Task 5.2: Contaminants in the gasification of C&D waste

The goal of Task 5.2 is to develop management strategies for elements present in C&D waste that affect its use as a feedstock for thermochemical conversion.

Research Approach

Task 5.1

Prior ASCENT EcoCrop GIS modeling activities identified the growing locations for *Pongamia*, kamani, croton, and *Jatropha*, according to suitable environmental conditions, geography, and zoning. If unavailable, the primary data on the chemical and physical characteristics of these tropical oils and their coproducts (e.g., pods/shell and oilseed cake) were acquired. The project will use these earlier results as the basis for developing supply chain models for AJF production. The model results will identify feedstock production areas as well as locations and scales of primary processing sites for shell and pod separation, oil extraction from seeds, and oil conversion to SAF. Potential sources of hydrogen from oilseed coproducts, other renewable resources, and fossil sources will be analyzed and included in the model. Options for points of

production, SAF production technologies (e.g., Applied Research Associates [ARA], SBI BioEnergies [SBI], or Forge Hydrocarbons [Forge]), transportation strategies, and blend ratios at airports (or for specific end users, e.g., the military) across Hawai'i will affect model outcomes and will be evaluated. Options for coproducts such as animal feeds and high-value materials will be evaluated and incorporated into the model decision-making process. Criteria used to drive the model solution might include minimizing SAF production costs while meeting a minimum total production benchmark or a minimum blending rate for annual state jet fuel consumption. Other criteria, such as system resiliency to extreme weather events and climate change, provision of environmental services, and stakeholder acceptability, will also be of importance and will be used to evaluate model solutions.

Task 5.2
Thermochemical gasification of biorenewable resources is the initial conversion process for two entry points to AJF production: (1) synthesis gas used in the direct production of Fischer–Tropsch liquids and/or (2) green/renewable hydrogen used in biorefineries for hydrotreating lipids or in existing petroleum-refining activities for the production of hybrid jet fuel. Urban wood waste from C&D activities provides a reliable source of biorenewable material and requires a tipping fee for disposal, characteristics that enhance its attractiveness as feedstock. The negative aspects of C&D feedstock are its physical and chemical inhomogeneity. In the latter case, the inorganic elements present in the feedstock can negatively influence the gasification process (e.g., corrosion of, or accumulation on, reactor working surfaces, bed material agglomeration, catalyst deactivation, or pollutant emissions). Using data generated from previous ASCENT Project 001 tasks, this project will assess methods for managing contaminants in C&D feedstocks. This project will be based on gasification systems proposed for the production of synthesis gas/Fischer–Tropsch liquids and green hydrogen. The technology options for contaminant removal or conversion to benign forms will be assessed at each step in the conversion process, including presorting at the waste generation site, sorting/diversion at the C&D waste intake facility, removal by physical/chemical/other methods before gasification, in-situ reactor control methods, and gas cleanup. The technology options based on existing process industries and the scientific literature will be considered. Laboratory-scale testing of removal techniques will be conducted to provide a preliminary assessment of selected promising technology options. The integrated gasification process options and contaminant control options will be evaluated as complete systems to guide system design and to enable system comparisons. The risks associated with technology options will also be assessed to guide implementation and risk mitigation of the system as a whole. The impacts of processing scale (e.g., Mg waste/day) on the selection of technology options will also be assessed.

Milestones

Task 5.1.

- Established a model framework for an oilseed-based SAF supply chain in an island setting, using the scenario of Hawai'i.

Task 5.2.

- Conducted a review of options for managing contaminants along the supply chain and bench-scale tests to confirm the efficacy of options.

Major Accomplishments

On the basis of the *Pongamia* production areas identified by GIS analysis in Task 3 (described above), sites for processing *Pongamia* (pod and seed separation, oil extraction from seed) have been evaluated on each island. Candidate processing sites in the analysis included (a) brownfield sites with industrial zoning and (b) greenfield sites identified as lands with a slope of less than 5%, a contiguous area of 50 hectares, and agricultural zoning. The ArcGIS® "minimized impedance" and "origin-destination" analysis tools were used to determine transportation cost index values for all potential processing facility locations, using the *Pongamia* production estimates and the road network distances from production sites to candidate processing sites. Analyses were performed for each island and included four *Pongamia* production scenarios.

A cost of production analysis for *Pongamia* based on a 25-year orchard lifetime was completed. As *Pongamia* has not been grown commercially in Hawai'i, the analysis included assumptions about the cultural practices and input application rates. The analysis was summarized and shared with stakeholders and subject matter experts for review and comment. Feedback has been incorporated. Analysis has been extended to project a pathway for industry development assuming values for the number of trees planted per year and their cumulative productivity. The production scenarios are being used to explore

® ArcGIS is a registered trademark of ERSI, Redlands, CA.

processing facility scales and technology options that include the unit operations of drying, decortication, oil extraction, and distribution of oil and meal components to the refinery on O'ahu and animal feeding locations across Hawai'i, respectively. Discussions with equipment vendors for drying, decortication, and oil extraction equipment have been productive. Permission to include vendor data as part of techno-economic analyses remains to be resolved.

In an earlier review, camelina (*Camelina sativa*) was not previously identified as a candidate oil seed crop for production in Hawai'i but is nonetheless being pursued as a cover crop in rotation with food crops such as onions, lettuce, etc. In response to interest in producing camelina, UH developed new GIS analysis approaches to evaluate potential production areas. Unlike annual and perennial crops, camelina matures in ~90 days requiring that the growing season be matched to shorter time windows of temperature and rainfall availability. Hawai'i's varied climates, both geographically and seasonally, would require intensive management if grown under rainfed conditions and could require shifting production locations throughout the year. Use of camelina as a cover crop with irrigated food production could alleviate the need to match the plant growth requirements with monthly rainfall. Results of the UH analysis has been used by Pono Pacific to target production areas, engage growers for planting camelina trials, and discuss policy with state executive and legislative branches. The analysis also underpinned a proposal to the U.S. Department of Energy program, Regional Resource Hubs for Purpose-Grown Energy Crops with Pono Pacific and Hawai'i Agriculture Research Center.

Kukui (*Aleurites moluccanus*) is the Hawai'i State tree and bears a nut whose kernel contains 60% extractable oils. Previous work has characterized the fuel properties of the oil, meal, and nut fractions. Kukui is extensively distributed across the Hawai'i landscape zoned for conservation, but little has been done to explore agricultural zoning areas suitable for production. A GIS-based assessment of kukui production using the Eco-Crop model has been initiated.

Elemental analyses of C&D waste from earlier tasks were used as inputs for the thermochemical equilibrium calculation in FACTSage™ 8.0 under different gasification conditions (e.g., bed material, oxidizer, etc.). The results show that the predictions of H_2, CO, and CO_2 in product gas are in good agreement with literature data. In addition, gasification in steam yields the highest H_2 content while that in oxygen yields the lowest. The elements As, Br, Cl, K, Mn, Mo, Na, Pb, S, and Zn were found in the gas phase at different concentrations depending on the feedstock composition and gasification conditions. Some elements (Br, Cl, K, Pb, and Zn) appear to be more volatile than others (As, Na, and S). The elements Ca, Si, P, Ti, Cr, Fe, Ni, Cu, Sr, Ru, and Ba were primarily presented in solid and/or slag phases. Olivine bed material captured a portion of arsenic during the gasification process due to the presence of nickel in its chemical composition. Arsenic species in the product gas stream are predicted to deactivate Fe- and Co-based Fischer-Tropsch catalysts in downstream processes. It is possible to remove arsenic compounds by cooling hot product gas; however, cooling may also result in the condensation of high molecular weight organic compounds (tar). Copper and nickel can be employed as arsenic sorbents with sorptive capacity directly linked to the metals' mass.

Publications

None.

Outreach Efforts

The results of feedstock analyses have been shared with personnel from Par Hawai'i, the refinery located on the island of O'ahu, and with Pono Pacific, a land management company engaged in sustainable agricultural development. Par Hawai'i has announced plans to produce SAF in partnership with Hawaiian Airlines. Pono Pacific is pursuing oilseed production to supply Par Hawai'i with lipids for SAF production via the production pathway for hydroprocessed esters and fatty acids. Mitsubishi Corporation (Americas) personnel interested in SAF-related investment opportunities in Hawai'i have requested briefings on oil seed opportunities. Outreach has also included staff from the Hawai'i State Energy Office's Energy Efficiency and Renewable Energy (EERE) branch and Decarbonization Program.

A presentation entitled "Hawai'i Energy Crop and Urban Waste Feedstock Updates" was presented at the ASCENT Spring Meeting in Honolulu, Hawai'i.

™ FactSage is a trademark of Thermfact/CRCT, Montreal, Canada, and GTT-Technologies, Aachen, Germany. FactSage is a thermochemical software and database package developed jointly between Thermfact/CRCT (Montreal, Canada; www.crct.polymtl.ca) and GTT-Technologies (Aachen, Germany; www.gtt-technologies.de) and is the result of over 30 years of collaborative efforts. The FactSage web site is www.factsage.com.

A poster entitled "Thermochemical Equilibrium Prediction of Ash Behavior during Gasification of Construction and Demolition Waste" was presented at the conference TC Biomass: The International Conference on Thermochemical Conversion Science: Biomass & Municipal Solid Waste to RNG, Biofuels & Chemicals on September 10–12, 2024, Westin Hotel, Itasca, Illinois.

A poster entitled "Alternative Jet Fuel Supply Chain Tropical Region Analysis, Pongamia Supply Chain Optimization" was presented at the ASCENT Fall Meeting in Alexandria, Virginia.

Awards
None.

Student Involvement
None.

Plans for Next Period
Task 5.1
The costs for *Pongamia* delivered to the processing site gate and costs of *Pongamia* processing options will be used with TEA spreadsheets (hydro-processed esters and fatty acids, etc.) developed by WSU collaborators to provide estimates of SAF production costs according to supply chain scenario assumptions. This effort was begun in this reporting period and discussions with equipment vendors are expected to be completed in 2025. In this reporting period, Dr. Kristin Lewis, Dr. Kevin Zhang, and Dr. Alex Oberg from the Volpe Center have engaged on the logistic analysis for this project and Kristin Brandt and Dane Camenzind have engaged on project TEA. These collaborations are expected to continue in 2025.

Task 5.2
A review of additional options for managing contaminants in the gasification process will be conducted. The results of the equilibrium analysis, literature review and contaminant measurements from the bench-scale gasification tests in Task 4 may be used to target bench-scale contaminant control tests. The principal investigator will re-evaluate the utility of the bench scale tests and budgetary issues with the FAA program manager in early 2025.

Task 6 – Hawai'i Regional Project
University of Hawai'i

Objective
The task activities in Year 6 will explore the impacts of Hawai'i State Legislative Bill HB2386 on waste management and the potential for waste-based SAF production systems. HB2386 requires 0.5-mile buffer zones around waste and disposal facilities (including landfills) and restricts facilities from land with conservation-district zoning.

Research Approach
The goal of this task is to assess and evaluate the impacts of HB2386 on waste management strategies in Hawai'i. HB2386 was disruptive to disposal practices for C&D waste on the island of O'ahu, and its impacts are currently not fully understood. The aims of Task 6 are to collect updated waste generation data, elucidate how HB2386 will affect current management strategies, and develop scenarios for waste-based SAF production under the new regulatory environment. The impacts of HB2386 on the capacity to perform landfill mining will also be considered. A preliminary assessment of restricted and unrestricted sites for waste and disposal facilities will be reviewed and refined as necessary.

Milestone
- Evaluated the impacts of removing or diminishing the role of an active C&D landfill as a supply chain participant.

Major Accomplishments
An assessment of available data on urban waste flows across the state has been completed. Sources have included county solid waste management plans, annual reports by county solid waste management offices, and annual legislative reports prepared by the state solid and hazardous waste management branch. Based on these data, estimates of solid waste production across the state have been assembled. Waste composition data available at the county level has been used to

generate production estimates of combustible and noncombustible fractions as well as biogenic and nonbiogenic fractions. The enactment of HB2386 has restricted expansion of the existing C&D landfill on O'ahu and delayed the siting of new landfills on the islands of O'ahu and Kaua'i. Six scenarios for managing waste across the state as an integrated system have been developed. Three of the scenarios split the waste resource between the existing Covanta Honolulu Resource Recovery Venture (H-POWER) waste to an energy plant on O'ahu and a waste-to-SAF production plant using gasification and Fischer-Tropsch technology. The other three scenarios assume that the H-POWER waste-to-energy plant is decommissioned and all of the state's waste is delivered to a larger SAF production facility. Diverting food waste and plastics from the waste streams were also included as scenario options; food waste has alternative use as animal feed or for anaerobic digestion feedstock and plastics are nonbiogenic. Estimates of production potential from the six waste utilization scenarios were completed. Scenarios where H-POWER was decommissioned yielded the highest SAF production values ranging from 38 to 45 million gallons annually. Diverting food waste and plastics from the material fueling the SAF process accounts for the difference of 7 million gallons per year. The scenario with the lowest SAF production potential, 18 million gallons per year, was the result of diverting waste to H-POWER and excluding both food waste and plastics.

Publications
None.

Outreach Efforts
A poster entitled "Municipal Solid Waste (MSW)-based SAF (Alternative Jet Fuel Supply Chain Tropical Region Analysis)" was presented at the ASCENT Fall review meeting in Alexandria, Virginia.

Awards
None.

Student Involvement
None.

Plans for Next Period
In the coming period, possible waste separation locations that meet HB2386 requirements will be identified and used to refine analyses. The preliminary findings will be shared with the waste management community and state and county energy office staffs to garner feedback and refine scenario assumptions.

Task 7 – Hawai'i Regional Project
University of Hawai'i

Objective
Activities proposed for Task 7 will continue to develop the information needed for the Hawai'i Regional Projects begun in previous years. These activities will support efforts by the State of Hawai'i and Hawai'i energy service providers to reduce GHG emissions. Task activities will explore the GHG intensity of *Pongamia* as a feedstock producer in Hawai'i regional pathways.

Research Approach
The goal of this task is to assess and evaluate the GHG implications of a *Pongamia*-based feedstock supply chain for SAF production. Based on analyses from previous years, life cycle inventories (LCIs) for *Pongamia* production, oil extraction, and oil conversion to SAF will be completed. The LCIs will be used to conduct GHG assessments of *Pongamia*-based SAF production systems. Different *Pongamia* land use scenarios, extraction options, and conversion technologies can be considered and compared.

Milestone
- Produced a complete set of LCIs for the *Pongamia* production system.

Major Accomplishments
Production scenarios developed in Task 5 have been used to identify inputs for orchard production of *Pongamia*. This includes material and energy requirements for nursery production of saplings, site preparation, planting and stand establishment, cultural practice (fertilization, weed control, and pruning), harvesting, and orchard removal at the end of productive life. The basis for transport of harvested material between the orchard and processing sites have been established.

Publications
None.

Outreach Efforts
None.

Awards
None.

Student Involvement
None.

Plans for Next Period
Drying, decortication, and oil extraction scenarios currently under development in Task 5 will provide the basis for material and energy flows for *Pongamia* processing. Data for oil and byproduct transport from processing sites to refining assets on O'ahu and animal production facilities will be finalized.

Task 8 – Hawai'i Regional Project
University of Hawai'i

Objective
Activities proposed for Task 8 will continue to develop the information needed for the Hawai'i Regional Projects begun in previous years. These activities will support efforts by the State of Hawai'i and Hawai'i energy service providers to reduce GHG emissions. Task activities in Year 8 will focus on waste-based feedstocks that address MSW and construction and demolition waste currently generated and disposed in landfills across the state.

Research Approach
The goal of this task is to assess and evaluate the GHG implications of waste based SAF production in Hawai'i. Based on analyses from Task 6, waste production across the state will be considered as a single resource to be managed for SAF production. Available data on waste generation by island, waste composition by island, transportation requirements, and conversion technologies will be used as the basis for developing scenarios for SAF production given existing waste management practices. These scenarios will be used to evaluate GHG intensity of SAF production scenarios.

Milestone
- Developed scenarios for waste-to-SAF production options based on available county and state data reporting.

Major Accomplishments
An assessment of available data on urban waste flows across the state has been completed. Six scenarios for managing waste across the state as an integrated system have been developed. Three of the scenarios split the waste resource between the existing H-POWER waste to an energy plant on O'ahu and a waste-to-SAF production plant using gasification and Fischer-Tropsch technology. The other three scenarios assume that the H-POWER waste-to-energy plant is decommissioned and all of the state's waste is delivered to a larger SAF production facility. Based on these six scenarios of waste management for SAF production, preliminary estimates of GHG intensity were developed based on the contributions from feedstock transportation, fuel production, ash disposal, SAF production, and combustion of nonbiogenic components. The scenario that eliminated the use of the existing H-POWER waste-to-energy plant and diverted food waste and mixed plastics from the feedstock stream yielded the lowest GHG intensity, 32 g CO_2e/MJ. The highest value, 53 g

CO_2e/MJ of SAF, corresponded to the scenario where H-POWER was operated, food waste was diverted, and mixed plastics were included in the feedstock steam.

Publications
None.

Outreach Efforts
A poster entitled "MSW-based SAF (Alternative Jet Fuel Supply Chain Tropical Region Analysis)" was presented at the ASCENT Fall review meeting in Alexandria, Virginia.

Awards
None.

Student Involvement
None.

Plans for Next Period
Preliminary findings will be shared with the waste management community and state and county energy offices' staff to garner feedback and refine scenario assumptions.

Project 001(C) Alternative Jet Fuel Supply Chain Analysis

Purdue University

Project Lead Investigator

Farzad Taheripour
Research Professor
Department of Agricultural Economics
Purdue University
403 Mitch Daniels Blvd.
West Lafayette, IN 47906-2056
765-494-4612
tfarzad@purdue.edu

University Participants

Purdue University

- P.I.: Farzad Taheripour, Research Professor
- FAA Award Number: 13-C-AJFE-PU, Amendments 25, 29, 34, 36, 41, 46, 48, 51, 55
- Period of Performance: October 1, 2023, to September 30, 2024
- Tasks:
  1. Provide analyses on induced land use change (ILUC) and direct land use change (DLUC) emissions and other analyses related to land use changes (LUCs) at global, regional, and country levels for national and international biofuel programs that tend to promote supplies of clean fuels. This task provides the required support to calculate a portion of the carbon intensity (CI) of alternative sustainable aviation fuel (SAF) pathways and other biofuels that are related to LUCs.
  2. Collect data, conduct data analyses, and develop economic models to support the United States (U.S.) government agencies and the fuel task group (FTG) of the carbon offsetting and reduction scheme for international aviation (CORSIA)s to develop techno-economic analysis (TEA) in degerming profitability and feasibility of SAF pathways under alternative economic conditions and policy environments.
  3. Improve agro-ecological zone-emission factor (AEZ-EF) model and its emission factors to follow the 2019 International Panel of Climate Change (IPCC) guidelines in assessing land use emission factors and better measure the vegetation and soil organic carbon (SOC) contents of land cover items at a global scale.

Project Funding Level

This project received funding from the Federal Aviation Administration (FAA) as follows:

Amendment 3: $250,000
Amendment 6: $110,000
Amendment 10: $230,000
Amendment 15: $373,750
Amendment 19: $400,000
Amendment 29: $400,000
Amendment 36, 41: $523,000
Amendment 46, $350,000
Amendment 48, $350,000
Amendment 51, $394,844
Amendment 55, $399,865

Current cost sharing for this project year was provided by Neste US, Inc.

Investigation Team

Prof. Farzad Taheripour (P.I.), All Tasks
Prof. Dominique van der Mensbrugghe (co-P.I.), Tasks 3
Prof. Qianlai Zhuang (co-P.I.), Tasks 3
Maksym Chepeliev, (co-P.I.; research economist), Tasks 1
Erwin Corong (co-P.I.; research economist), Task 1
Angel Aguiar (research economist), Tasks, 1
EhsanReza Sajedinia (PhD student), All Tasks
Shuo Chen (PhD student), Tasks 3
Xiangyu Liu (PhD student), Tasks 3
Ye Yuan (PhD student), Tasks 3
Lauren Benavidez (PhD student), All Tasks

Project Overview

The research team of ASCENT Project 001(C) has worked on the three main tasks listed above and made major progress on each task in this performance time period. The first task is focused on providing analyses on ILUC and DLUC assessments for the national and international policies that tend to promote production and consumption of SAF and non-SAF biofuels including corn ethanol, sugarcane ethanol, and biodiesel produced from several types of vegetable oils. This task also considers advancing methodologies for ILUC and DLUC calculations.

The second task aims at supporting the U.S. government agencies and FTG subgroups, including the Core Life Cycle Assessment (LCA), Technology, Production and policy (TPP), Sustainability, and other FTG groups, to accomplish their tasks and achieve their goals. This task considers developing TEA for determining the profitability and feasibility of SAF pathways under alternative economic conditions and policy environments.

The third task focused on various activities including updating the AEZ-EF model to adopt the 2019 IPCC guidelines in assessing lands use emission factors, assessing the existing data and approaches that provide land use emission factors used in the AEZ-EF model; and studying and proposing a methodology to measure, check, and verify changes in the soil carbon content of cropland including SOC at the farm level due to production of SAF or other biofuels.

Task 1 – Provide Required Analyses on ILUC at Global, Regional, and Country Levels

Purdue University

Objectives

The objectives of this task focus on calculating ILUC values and their updates for new SAF pathways, improving ILUC modeling approaches, collecting required data to more accurately estimate ILUC, updating the global trade analysis project for biofuel (GTAP-BIO) database to represent the global economy in recent years, and providing analyses that help to better elucidate LUCs across the world.

Research Approach

Our team collected the required data and developed required analyses for both TEA and LCA to determine the cost structure of each new SAF pathway to be included in the GTAP-BIO model to support ILUC calculations. We then used the modified model to assess the LUCs associated with new SAF pathways.

Milestones

- Calculated new ILUC values upon request by the FTG.
- Developed a new GTAP-BIO database, which represents the global economy in 2014.
- Added several SAF pathways to the new GTAP-BIO database. This new database has been used to develop the required analyses for the 40B provision of the Inflation Reduction Act of 2022.

Major Accomplishments

Accomplishments in Task 1 include providing various assessments for SAF produced in Brazil using corn alcohol-to-jet (ATJ) technology and developing ILUC values for several pathways for the 40B provision of the Inflation Reduction Act of 2022. The pathways included for the 40B provision of the Inflation Reduction Act of 2022 were U.S. corn ethanol-to-jet (ETJ), Brazil sugarcane ETJ, U.S. soy oil hydrotreated esters and fatty acids (HEFA); and U.S. rapeseed (canola) oil HEFA.

Publications

Written Reports

Taheripour, Sajedinia, Chepeliev, and Aguiar have prepared Appendix C of the following report regarding the 40B provision of the Inflation Reduction Act of 2022:

ANL. (2024). Development of R&D GREET 2023 Rev1 to estimate greenhouse gas emissions of sustainable aviation fuels for 40B provision of the Inflation Reduction Act (ANL/ESIA-24/9). Argonne National Laboratory (ANL).

Other Written Reports

- CAEP/13-FTG/06-WP/12 – *Modelling Brazil corn ATJ pathway*, February 5-9, 2024, Geneva, Switzerland.
- CAEP/13-FTG/06-WP/13 – *Updating approved ILUC values according to 2019 IPCC guideline*, February 5-9, 2024, Geneva, Switzerland.
- CAEP/13-FTG/06-WP/16 – *New GTAP-BIO data base and ILUC modelling*, February 5-9, 2024, Geneva, Switzerland.
- CAEP/13-FTG/07-WP/08 – *ILUC values for significant multicropping cases*, May 13-17, 2024, Virtual.
- CAEP/13-FTG/07-WP/09 – *Key discussion points regarding the proposal for significant multicropping cases*, May 13-17, 2024, Virtual.
- CAEP/13-FTG/07-WP/11 – *Proposed revisions in DLUC methodology*, May 13-17, 2024, Virtual.
- CAEP/13-FTG/07-WP/12 – *Removing SOC from ILUC, GLOBIOM ILUC values with 2019 IPCC guidelines, sharing AEZ-EF*, May 13-17, 2024, Virtual.
- CAEP/13-FTG/08-WP/15 – *Proposed revisions in DLUC methodology*, September 20-27, 2024, Montreal, Canada.
- CAEP/13-FTG/08-WP/17 – *Future ILUC tasks and a proposal for ILUC modelling improvements*, September 20-27, 2024, Montreal, Canada.

Outreach Efforts

- Dr. Taheripour participated in ASCENT Advisory Group meetings in Fall 2023 and Spring 2024 and shared the findings of this research with the ASCENT community.
- Dr. Taheripour participated and presented the results of this project at many conferences, seminars, and meetings related to biofuels and their ILUC and DLUC topics. Some examples are:
    - CRC workshop on life cycle analysis of transportation fuels, Argonne National Laboratory, October 3-5, 2023, Lemont, Illinois.
    - Clean Transportation Standard Work Group of Minnesota, Land Use, Water and Ecosystem Services Webinar, Technical Webinar Panel on Land Use, October 16, 2023.
    - Commercial Aviation Alternative Fuels Initiative (CAAFI) Webinar series, October 19, 2023.
    - Opportunities for Climate-Smart Feedstocks in Transportation Fuels, United States Department of Agriculture (USDA) Headquarters, Washington D.C., January 25-26.
    - 2024 Sustainability Workshop, Clean fuel conference, March 11-13, 2024, Kansas City, Missouri.
    - 2024 American and Applied Economic Association (AAEA) Annual Meeting, July 28-30, 2024, New Orleans, Louisiana.
    - Leading the way, Sustainable Aviation Fuels in Illinois, March 21-22, 2024, Chicago, Illinois.
- Dr. Taheripour has reviewed many academic papers for various journals that provide publications in research areas associated with Task 1.

Awards

None.

Student Involvement

- EhsanReza Sajedinia, current PhD student Purdue University, for data collection and running simulations

- Lauren Benavidez, current PhD student, Purdue University, for data collection and working with land use emission data and models

Plans for Next Period

A new International Civil Aviation Organization (ICAO) Committee on Aviation Environmental Protection (CAEP) cycle will begin in 2025. Following the request by FTG, our team plans to use a new version of GTAP-BIO model that represents the world economy in 2017 and update the ILUC values for the CORSIA SAF pathways. In addition, we will develop ILUC assessments for the 45Z provision of the Inflation Reduction Act of 2022.

Task 2 – Collect Data, Conduct Analyses, and Develop Economic Models to Support Policy Decision at National and International Levels for SAF and Other Biofuels

Purdue University

Objectives

The objective of this task is to (1) develop required analyses to support policy decision at national and international levels to promote supplies of cleaner fuels such as SAF and non-SAF pathways for aviation and road transportation, (2) coordinate with the FTG subgroups to avoid conflicts between the ILUC subgroup activities and activities performed by other subgroups, and (3) collaborate with the U.S. government agencies to coordinate policy decision on SAF and non-SAF pathways.

Research Approach

This task considers various assignments and components. Our team uses standard methods to support FTG subgroups, including the Core LCA, TPP, and Sustainability subgroups. We collected data and used economic models including GTAP-BIO and provided appropriate analyses to accomplish this task. Dr. Taheripour is the co-lead of the FTG ILUC group and collaborates with the Core LCA, TPP, and Sustainability FTG subgroups of the ICAO CAEP.

Milestones

- Developed analyses and models to support FTG subgroups,
- Calculated LUCs for SAF pathways.
- Provided required economic analyses.

Major Accomplishments

Supporting International activities

In addition to participating in meetings with FTG subgroups and reviewing their working and information papers, Dr. Taheripour collaborated with the FTG secretary and co-rapporteurs to develop reports for ICAO Steering Group meetings. Examples are presented in the publications (written reports) section. One major accomplishment was developing the required analyses for the 40B provision of the Inflation Recovery Act of 2022. Dr. Taheripour participated in the CAEP13/FTG06, CAEP13/FTG07, CAEP13/FTG08 meetings and many sub-group meetings and was involved in many of the tasks and document preparation activities for these meetings. He also responded to other subgroup requests for help and collaboration. He has led efforts in ILUC modeling and ILUC-related tasks associated with other subgroups. He also joined various meeting with the U.S. government agencies and provided various presentations to discuss and explain ILUC modeling.

Supporting Domestic U.S. Policy Decision

Dr. Taheripour also collaborated with U.S. government agencies such as the Federal Aviation Administration (FAA), USDA, U.S. Environmental Protection Agency (EPA), U.S. Department of Energy (DOE), and Argonne Research Library to develop modeling practices for the use in the U.S. domestic policy analysis regarding the provision of 40B and 45z of the Inflation Reduction Act of 2022.

Publications

Written Reports

- CAEP/13-FTG/06-WP/14 – *Cut-off dates for Low LUC risk practices*, February 5-9, 2024, Geneva, Switzerland.
- CAEP/13-FTG/06-WP/15 – *Definition of marginal land*, February 5-9, 2024, Geneva, Switzerland.
- CAEP/13-FTG/07-WP/10 – *Definition of marginal land for pathway specification*, May 13-17, 2024, Virtual.
- CAEP/13-FTG/07-WP/12 – *Removing SOC from ILUC, GLOBIOM ILUC values with 2019 IPCC guidelines, sharing AEZ-EF*, May 13-17, 2024, Virtual.

Peer-Reviewed Journal Publication

Chen, S., Zhuang, Q., Taheripour, F., Yuan, Y., & Benavidez, L. (2025). Assessment of global land cover changes using satellite data: intermittent and long-term land cover changes from 2001 to 2020. *Environmental Research Letters*, *20*(3). http://dx.doi.org/10.1088/1748-9326/adb5a3

Outreach Efforts

See outreach efforts under Task 1.

- Dr. Taheripour has reviewed many academic papers for various journals that provide publications in research areas associated with Task 2.
- Dr. Taheripour, Dr. Chepeliev, Dr. Aguiar, Sajedinia, Chen, and Yuan attended the ASCENT Advisory Group meetings in Fall 2023 and Spring 2024 and discussed the findings of this task with members of this community.

Awards

None.

Student Involvement

- EhsanReza Sajedinia, current PhD student, Purdue University, for data collection and running simulations
- Shuo Chen, current PhD student, Purdue University, for data collection and running simulations
- Xiangyu Liu, current PhD student, Purdue University, for data collection and running simulations
- Ye Yuan, current PhD student, Purdue University, for data collection and running simulations
- Lauren Benavidez, current PhD student, Purdue University, for data collection and running simulations

Plans for Next Period

- Collaborate with the Core LCA subgroup to refine the mythology of assessing changes in soil carbon content at the farm level.
- Continue to support FTG subgroups, including the Core LCA, and TPP, and sustainability subgroups, in accomplishing the required LCAs for new SAF pathways.
- Continue to develop the required TEAs to include the cost structure of new SAF pathways in the GTAP-BIO database.
- Continue to collaborate with the U.S. government agencies to establish the U.S. domestic policy towards the SAF and non-SAF pathways.

Task 3 – Improvements in AEZ-EF Model

Purdue University

Objectives

The objectives of this task include various research activities to help with better assessment of ILUC values for alternative SAF and non-SAF pathways. These research activities aim at matching the AEZ-EF model's assumption with the latest IPCC guidelines for calculation of land use and land cover changes emissions. In addition, these research activities tend to reassess the soil and vegetation carbon contents of alternative land types using the most recent available data.

Research Approach

To accomplish the objectives of this task, our team revised the AEZ-EF model's assumptions and parameters to follow the 2019 IPCC guidelines. The ASCENT Project 001(C) team detected more recent data on land cover changes, soil carbon content, and above- and belowground vegetation carbon at the global scale at high spatial resolution. After check, verification, and validation of these data items, we aggregated them to match with the AEZ-EF model geographical dimensions, 19 regions and 18 Agroecological Zones.

Milestones

- Updated and used the AEZ-EF to recalculate the ILUC values of SAF pathways. The results of these calculations have been approved and used by the FTG.
- Identified and validated the existing data sources on land use emission factors (soil carbon content). These data items were retargeted to be included in the next version of AEZ-EF model.
- Collected the existing data sources on land cover changes between 2000 and 2020. These data sources are under validation review.
- Collected the existing data sources on land vegetation carbon. These data sources are under validation review.

Major Accomplishments

- FTG has approved the new ILUC values obtained from the revised AEZ-EF model that follows the 2019 IPCC guideline.
- The new AEZ-EF model with IPCC 2019 is now ready to be used in assessing the ILUC values for the 45Z provision of the Inflation Reduction Act of 2022.

Publications

Peer-Reviewed Journal Publication

Taheripour, F., Mueller, S., Emery, I., Karami, O., Sajedinia, E., Zhuang, Q., & Wang, M. (2024). Biofuels induced land use change emissions: The role of implemented land use emission factors. *Sustainability (2071-1050)*, *16*(7).

Conference Papers

Benavidez, L., Baldos, U., Zhuang, Q., Chen, S., and Yuan, Y. (2024, June 5-7). *New induced land use change (ILUC) emissions assessment: Updates from IPCC guidelines and new estimates of soil carbon from the Harmonized World Soil Database (HWSD)* [Conference paper]. 27th Annual Conference on Global Economic Analysis. Colorado State University, Fort Collins, Colorado.

Chen, S., Zhuang, Q., Yuan, Y. and Benavidez, L., (2024, June 5-7). *Global land cover changes under changing climate and socioeconomic conditions from 2001 to 2020* [Conference paper]. 27th Annual Conference on Global Economic Analysis. Colorado State University, Fort Collins, Colorado.

Written Reports

Several working papers and information papers have been produced based on our work for this task. Working and information papers presented at FTG meetings include the following:

- CAEP/13-FTG/06-WP/11 – *Soil organic carbon double counting*, February 5-9, 2024, Geneva, Switzerland.
- CAEP/13-FTG/06-WP/13 – U*pdating approved ILUC values according to 2019 IPCC guideline*, February 5-9, 2024, Geneva, Switzerland.
- CAEP/13-FTG/07-WP/12 – *Removing SOC from ILUC, GLOBIOM ILUC values with 2019 IPCC guidelines, sharing AEZ-EF*, May 13-17, 2024, Virtual.

Outreach Efforts

See outreach efforts under Tasks 1 and 2.

Awards

None.

Student Involvement

- EhsanReza Sajedinia, current PhD student, Purdue University, for data collection and running simulations
- Shuo Chen, current PhD student, Purdue University, for data collection and data processing
- Xiangyu Liu, current PhD student, Purdue University, for data collection and data processing
- Ye Yuan, current PhD student, Purdue University, for data collection and data processing
- Lauren Benavidez, current PhD student, Purdue University, for data collection and data processing

Plans for Next Period

- Continue working to include new emission factors into the AEZ-EF and finalize this task.

Project 001(D) Alternative Jet Fuel Supply Chain Analysis

The Pennsylvania State University

Project Lead Investigator

Lara Fowler
Chief Sustainability Officer, The Pennsylvania State University (Penn State)
Director, Penn State Sustainability
Professor of Teaching, Penn State Law
Affiliate Faculty, Penn State School of International Affairs
The Pennsylvania State University
103 Land & Water Research Building
University Park, PA 16802
814-865-4806
Lbf10@psu.edu

University Participants

The Pennsylvania State University

- P.I.s: Lara Fowler, Chief Sustainability Officer, Penn State Sustainability and Professor of Teaching, Penn State Law; Anne Menefee, Assistant Professor of Energy and Mineral Engineering (starting with funding period beginning June 14, 2022); Armen Kemanian, Professor of Production Systems and Modeling (starting with funding period beginning June 14, 2022); and Seth Blumsack, Professor of Energy Policy and Economics and International Affairs
    - Researchers: Michael Helbing, Executive Director, Penn State Center for Energy Law and Policy; Ekrem Korkut, Legal Research Postdoctoral Associate (position ended June 30, 2024); Yuning Shi, Post Doc, Penn State College of Ag Sciences; Saurabh Bansal, Professor of Supply Chain Management (involvement ended in 2022).
- FAA Award Number: 13-C-AJFE-PSU, RISK-INFORMED ALTERNATIVE JET FUEL (AJF)
- Periods of Performance: **Period A:** August 1, 2017, to January 31, 2022; **Period B:** June 14, 2022, to November 13, 2023; **Period C:** October 1, 2022, to September 30, 2023; and **Period D:** July 1, 2023, to September 30, 2025 (time period extended to 2025 through no-cost extension).
- Tasks:

  Period A (August 1, 2017, to January 31, 2022)

  1.
     1.3.1 Risk–reward profit-sharing modeling for first facilities
     1.3.2 Additional quantification of risk and uncertainties in supply chains (foundational part of Task 1.3.1)
     1.3.3 Supply chain risk analysis tools for farmer adoption
     1.4.1 National survey of current and proposed state and federal programs that monetize ecosystem services
     1.4.3 Support of stakeholder engagement efforts

  Period B (June 14, 2022, to November 13, 2023)

  1.
     1.1 Research on existing federal law and policy drivers
     1.2 Research on existing state and regional law and policy drivers
     1.3 Research on proposed legislation (federal and state)
     1.4 Research on other law/policy issues, as identified by the ASCENT Project 001 team
  2.
     2.1 Work with ASCENT Project 001 team to identify stakeholder engagement opportunities
     2.2 Develop a list of potential stakeholders critical to discussion
     2.3 Develop agenda/materials for critical discussions; meeting facilitation as needed
  3.
     3.1 Work with ASCENT Project 001 team members to identify critical questions, and refine the scope of work related to carbon capture and sequestration (CCS)

3.2 Conduct literature review regarding CCS and its potential use in conjunction with AJFs
3.3 Draft a review manuscript examining opportunities to integrate CCS and AJF

4.

4.1 Work with ASCENT Project 001 team members to identify critical questions, and refine the scope of work related to soil organic carbon (SOC)
4.2 Conduct literature review regarding SOC and its potential relation to AJF
4.3 Draft review manuscript examining opportunities for SOC and AJF

Period C (October 1, 2022, to September 30, 2023)

1.

1.1 Research on existing and proposed federal law and policy drivers
1.2 Research on existing and proposed state and regional law and policy drivers
1.3 Research on other law/policy issues, as identified by the ASCENT Project 001 team

2.

2.1 Work with ASCENT Project 001 to identify stakeholder engagement opportunities

3.

3.1 Research on integration of CCS
3.2 Work with ASCENT Project 001 team to refine the scope of work and current needs
3.3 Research and review paper on geologic carbon storage potential, with emphasis on permanence and risks (both technical and legal)

4.

4.1 Refine global modeling systems using Level 3 Global Administrative Areas (GADM), soils from the International Soil Reference and Information Centre (ISRIC), and weather data from the North American Land Data Assimilation System (NLDAS)
4.2 Use machine learning to generate SOC profiles for business as usual (BAU) conditions, or machine learning and combination of Cycles for automated SOC stock calculations; the initial geographic target is the continental United States (CONUS)
4.3 Apply Cycles-A to the task of fitting sustainable aviation fuel (SAF) crops in the current agricultural matrix of the United States, with focus on oil crops as an example
4.4 Complete a SOC modeling manuscript with the goal of standardizing methods for SOC (and nitrous oxide) calculations in relation to the carbon intensity (CI) of BAU and SAF production scenarios

Period D. (July 1, 2023, to September 30, 2025)

1.

1.1 Research on existing and proposed federal law and policy drivers
1.2 Research on existing and proposed state and regional law and policy drivers
1.3 Research on other law/policy issues, as identified by the ASCENT Project 001 team.

2.

2.1 Work with ASCENT Project 001 team to identify stakeholder engagement opportunities

3.

3.1 Research on integration of CCS
3.2 Work with ASCENT Project 001 team to refine the scope of work and current needs
3.3 Research and review paper on geologic carbon storage potential, with emphasis on permanence and risks (both technical and legal)

4.

4.1 Refine global modeling systems using Level 3 GADM, soils from the ISRIC, and weather data from the NLDAS
4.2 Use machine learning to generate SOC profiles for BAU, or machine learning and combination of Cycles for automated SOC stock calculations; the initial geographic target is CONUS
4.3 Apply Cycles-A to the task of fitting SAF crops in the current agricultural matrix of the United States, with focus on oil crops as an example
4.4 Complete a SOC modeling manuscript with the goal of standardizing methods for SOC (and nitrous oxide) calculations in relation to the CI of BAU and SAF production scenarios

Washington State University (WSU)

- Michael Wolcott, Regents Professor (for funding period from June 14, 2022, to November 13, 2023)
- Kristin Brandt, Staff Engineer (through funding period ending January 31, 2022)

University of Kentucky (UK)
- Burt English, Institute Professor (for work through April 2022); now retired.

Project Funding Level

FAA funding: $150,000 (for Period D, July 1, 2023, to September 30, 2025)
Matching from Penn State: $150,000
Total funding: $300,000

Investigation Team

Period A (August 1, 2017, to January 31, 2022)
- Task 1.3.1 (Bansal; supported by Brandt and English): Risk–reward profit-sharing modeling for first facilities
- Task 1.3.2 (Bansal; supported by Brandt and English): Additional quantification of risk and uncertainties in supply chains (foundational part of Task 1.3.1)
- Task 1.3.3 (Bansal; supported by Brandt and English): Supply chain risk analysis tools for farmer adoption
- Task 1.4.1 (Fowler; supported by Korkut): National survey of current and proposed state and federal programs that monetize ecosystem services
- Task 1.4.3 (Fowler; supported by Korkut): Support of stakeholder engagement efforts

Period B (June 14, 2022, to November 13, 2023)
- Task 1.1 (Fowler, supported by Korkut): Research on existing federal law and policy drivers
- Task 1.2 (Fowler, supported by Korkut): Research on existing state and regional law and policy drivers
- Task 1.3 (Fowler, supported by Korkut): Research on proposed legislation (federal and state)
- Task 1.4 (Fowler, supported by Korkut): Research on other law/policy issues, as identified by the ASCENT Project 001 team
- Task 2.1 (Fowler, supported by Korkut): Work with ASCENT Project 001 to identify stakeholder engagement opportunities
- Task 2.2 (Fowler, supported by Korkut): Development of a list of potential stakeholders critical to discussion
- Task 2.3 (Fowler, supported by Korkut): Development of agenda/materials for critical discussions; meeting facilitation as needed
- Task 3.1 (Menefee): Work with ASCENT Project 001 team members to identify critical questions, and refine the scope of work related to CCS
- Task 3.2 (Menefee): Conduct literature review regarding CCS and its potential use in conjunction with AJFs
- Task 3.3 (Menefee): Draft a review manuscript examining opportunities to integrate CCS and AJF
- Task 4.1 (Kemanian, supported by Wolcott): Work with ASCENT Project 001 team members to identify critical questions, and refine the scope of work related to SOC
- Task 4.2 (Kemanian, supported by Wolcott): Conduct literature review regarding SOC and its potential relation to AJF
- Task 4.3 (Kemanian, supported by Wolcott): Draft review manuscript examining opportunities for SOC and AJF.

Period C (October 1, 2022, to September 30, 2023)
- Task 1.1 (Fowler, supported by Helbing and Korkut): Research on existing and proposed federal law and policy drivers
- Task 1.2 (Fowler, supported by Helbing and Korkut): Research on existing and proposed state and regional law and policy drivers
- Task 1.3 (Fowler, supported by Helbing and Korkut): Research on other law/policy issues, as identified by the ASCENT Project 001 team
- Task 2.1: Work with ASCENT Project 001team to identify stakeholder engagement opportunities
- Task 3.1 (Menefee & Helbing): Research on integration of CCS
- Task 4.1 (Kemanian & Shi): Accounting for SOC and nitrous oxide emissions using agroecosystem models

Period D (July 1, 2023, to September 30, 2025):
- Task 1.1 (Fowler, supported by Helbing and Korkut [through June 30, 2024]): Research on existing and proposed federal law and policy drivers
- Task 1.2 (Fowler, supported by Helbing and Korkut [through June 30, 2024]): Research on existing and proposed state and regional law and policy drivers
- Task 1.3 (Fowler, supported by Helbing and Korkut [through June 30, 2024]): Research on other law/policy issues, as identified by the ASCENT Project 001 team

- Task 2.1: Work with ASCENT Project 001 team to identify stakeholder engagement opportunities
- Task 3.1 (Menefee & Helbing): Research on integration of CCS
- Task 4.1 (Kemanian): Accounting for SOC and nitrous oxide emissions using agroecosystem models

Project Overview

For the first period of performance (Period A), this project focused on developing a qualitative and quantitative understanding of factors to help establish biofuel supply chains for AJFs. Although efforts are being made to establish these supply chains, many face challenges because of a lack of clarity regarding the incentives that stakeholders would require to engage in these supply chains and devote their resources to investing in the facilities required for these supply chains. To this end, this project has two goals:

1. Develop pro forma cash flows that represent the financial status of various participants in biofuel supply chains for AJFs, to inform a transparent risk-sharing tool; and
2. Understand the policy landscape in various parts of the United States to encourage AJF supply chains and identify additional policy initiatives that may be needed.

During the second period of performance (Period B), this project continues to focus on understanding the law and policy drivers associated with AJF, while expanding focus to include two new areas—CCS and SOC—and their potential linkages to AJF.

During the third and fourth periods of performance (Periods C and D), this project continues to stay up to date on the law and policy changes associated with AJF and has also started to focus on important opportunities and knowledge gaps surrounding CCS and SOC. Two new PIs, Dr. Anne Menefee and Dr. Armen Kemanian, were on-boarded to focus on these emerging areas and provide relevant expertise across the ASCENT Project 001 team.

Period A, Task 1.3.1 - Risk-reward Profit-sharing Modeling for First Facilities

The Pennsylvania State University

Objective

Develop a transparent risk-sharing tool to provide all partners with an understanding of the cash flows and risks faced by all supply chain partners.

Research Approach

First, a large number of risk-sharing tools were collected that have been proposed in the supply chain literature. Subsequently, the list was narrowed to 9–12 mechanisms. An Excel[â]-based framework was created in which the cash flows of all supply chain partners are modeled on the basis of data from the techno-economic analyses developed by WSU. This framework incorporates risk-sharing mechanisms.

Milestone

Excel® models were developed for four realistic configurations by using data from techno-economic analysis models developed by WSU.

Major Accomplishments

An Excel®-based framework was developed showing the cash flows of four key stakeholders in AJF supply chains: farmers, preprocessors, refineries, and airlines. The framework shows various risk-sharing contracts that each of the stakeholders could extend to others, as well as the financial burdens or opportunities associated with these mechanisms.
The framework also shows the government's financial burden of supporting these mechanisms. The framework was developed for four levels of refinery capacity. Overall, this framework can be used as a decision support tool by various stakeholders to determine whether to engage in alternative jet biofuel supply chains and negotiate with one another.

[â] Excel is a registered trademark of Microsoft Corporation in the United States and in other countries.

Publications
The risk-sharing tool was provided to the sponsor and training will be provided on its use to the project sponsor upon request.

Outreach Efforts
The risk-sharing tool that was developed has been presented and discussed at three ASCENT advisory committee meetings.

Awards
None.

Student Involvement
None.

Period A, Task 1.3.2 - Additional Quantification of Risk and Uncertainties in Supply Chains (Foundational Part of Task 1.3.1)
The Pennsylvania State University

Objective
Develop methods to rely on expert judgments to quantify uncertainties associated with biofuel supply chains.

Research Approach
A new econometric approach was developed to quantify the probability distributions of uncertain quantities, such as yield or demand, when an expert panel provides judgments regarding the most likely values. This approach exploits the well-known theory of generalized least squares in statistics for the context in which historical data are available to calibrate expert judgments or when these data are not available.

Milestones
This method is described in two manuscripts. In the first manuscript, "Using Subjective Probability Distributions to Support Supply Chain Decisions for Innovative Agribusiness Products," a two-stage procedure was developed to calibrate expert judgments regarding the distribution of biofuel uncertainties, such as the uncertain yields of new varieties of oilseeds, demand, or selling price. In the first step of the procedure, the expert judgments were calibrated by using historical data. Specifically, prior judgments provided by experts were used and compared with actual realizations (such as predicted yield versus actual yield) to determine the frequency with which each expert over- or underestimated the uncertainty (e.g., expert 1 underestimated the yield 60% of the time whereas expert 2 underestimated the yield 90% of the time). In the second manuscript, "Optimal Aggregation of Individual Judgmental Forecasts to Support Decision Making in a R&D Program," this information was used to determine the optimal approach for aggregating the experts' judgments to determine the mean and standard deviation of the probability distributions. In this manuscript, a new optimization protocol was developed for determining the optimal acreage for growing specific crops by considering the estimated mean and standard deviation, as well as incorporating the variability in these estimates. This manuscript won two awards at a professional conference (The Institute of Operations Research and the Management Sciences [INFORMS] conference) in November 2021 and in October 2022.

Major Accomplishments
Theoretical development and a numerical study demonstrated the promise of the econometric approach.

Publications
Peer-reviewed journal publication

Bansal, S., & Gutierrez, G. J. (2020). Estimating uncertainties using judgmental forecasts with expert heterogeneity. *Operations Research*, *68*(2), 363-380. doi: 10.1287/opre.2019.1938

Written reports

Bansal, S., & Wang, T. (2019). Using subjective probability distributions to support supply chain decisions for innovative agribusiness products. Report for the *Federal Aviation Administration*. https://s3.wp.wsu.edu/uploads/sites/2479/2021/05/ASCENT-Project-001D-attachment-1.pdf

Bansal, S., & Gutierrez, G. J. (2021). Optimal aggregation of individual judgmental forecasts to support decision making in a R&D program. Submitted to *Operations Research*. https://s3.wp.wsu.edu/uploads/sites/2479/2021/05/ASCENT-Project-001D-attachment-2.pdf

Outreach Efforts

None.

Awards

- 2021 Decision Analysis Practice Award - INFORMS, November 2021
- 2022 Decision Analysis Best Publication Award – INFORMS, October 2022

Student Involvement

None.

Plans for Next Period

This work has been completed. No plans exist for the next period.

Period A, Task 1.3.3 - Supply Chain Risk Analysis Tools for Farmer Adoption

The Pennsylvania State University

Objectives

Understand farmers' risk preferences over a long duration and how these preferences affect their decisions to grow crops that can support AJF supply chains.

Research Approach

Farmers were surveyed to understand their risk preferences over extended durations. Specifically, farmers were presented with sample yield ranges over extended periods and they were asked to estimate the lowest equivalent guaranteed yield that they would be willing to accept, given the uncertain yields. These responses were used to perform statistical analyses.

Milestones

The survey of farmer's risk preferences was completed and a manuscript was written based on the survey.

Major Accomplishments

Data from 43 farmers were compiled in central Pennsylvania regarding their risk preferences given uncertain yields from their land. The results quantify the loss of value that farmers attribute to an uncertain yield. Results are reported for both 1-year and 10-year horizons. For the 10-year horizon, the results were also reported for an initial yield build-up, which often arises with most biofuel crops. The key takeaways from this study are as follows: (a) farmer valuations of a new crop decrease acutely as the uncertainty in yield increases, and (b) the initial build-up period of low yields can be a large deterrent that inhibits farmers from adopting new crops for the purpose of supporting biofuels.

Publications

A manuscript detailing this work has been written and provided to the sponsor.

Outreach Efforts

None.

Awards
None.

Student Involvement
None.

Plans for Next Period
This work has been completed. No plans exist for the next period.

Period A, Task 1.4.1 - National Survey of Current and Proposed State and Federal Programs that Monetize Ecosystem Services
The Pennsylvania State University

Objective
Conduct a survey and summarize current and proposed state and federal programs to monetize ecosystem services.

Research Approach
This task builds on and continues the work performed under ASCENT Project 001, Task 8.1, which focused on the biomass and water quality benefits to the Chesapeake Bay watershed. In previous years, the biofuel law and policy landscape of the Pacific Northwest and Southeast regions was examined, as well as for the state of Hawai'i. During this most recent time period for reporting (Period C, October 1, 2021, to September 30, 2022), the federal biofuel law and policy was the focus of our approach, as well as how the biofuel law and policy landscape has been affected by international drivers.

Milestones
Our research was previously circulated in three region-specific white papers. In addition, a federal-level white paper was developed in the list of tasks, which was subsequently published (Korkut & Fowler, 2021).

Copies of these documents are available online:
- Western U.S. policy manuscript (with a focus on Washington State, last updated in 2019): Western US Bioenergy Law & Policy - Draft 5.docx
- Southeast policy manuscript (with a focus on Tennessee): Southeast Bioenergy Law & PolicyDraft3.docx
- Hawaii policy manuscript: Hawaiian Biofuel Law & Policy_v5.docx
- Federal-level white paper: 2021_01_08_SAF paper draft_ circulated for review_KCL_NB (1).docx

Major Accomplishments
In addition to developing the white papers described above, the federal-level white paper was adapted for publication (Korkut & Fowler, 2021). A briefing and poster were presented during the ASCENT fall meeting (October 2021). Additionally, P.I. Lara Fowler is involved in another project, funded by the U.S. Department of Agriculture (USDA) National Institute of Food and Agriculture, entitled "Consortium for Cultivating Human and Naturally Regenerative Enterprises" (USDA-NIFA Sustainable Agricultural Systems Award 2020-68012-31824), dubbed the "C-CHANGE" project. She has built upon her work in this ASCENT project to link to the regenerative agriculture work being pursued in C-CHANGE, including providing a briefing on second-generation biofuel law and policy.

Publications
Peer-reviewed journal publications
Korkut, E. & Fowler, L. B. (2021). Regulatory and policy analysis of production, development and use of sustainable aviation fuels in the United States." *Frontiers in Energy Research*, *9,* 750514. doi:10.3389/fenrg.2021.750514.

Outreach Efforts
Presentations
Fowler, L. B., & Lewis, K. (2021, October 6-8). *Sustainable aviation fuel development: Law, policy and the blender's tax credit* [Conference Presentation - Manuscript]. ASCENT 2021 Annual Meeting, Orlando, Florida, United States.

Awards
None.

Student Involvement
Ekrem Korkut graduated from the Penn State School of International Affairs in May 2021 and transitioned to working as a postdoctoral associate on this project (50% of his time; the other 50% is funded by another project).

Plans for Next Period
As noted above, the existing white papers will continue to be adapted for publication. The next step, again, focuses on regional efforts. As needed, support will be provided to working groups under the SAF Grand Challenge. Of note, work on this task was delayed by the lack of a contract in the 4.5 months from February 1, 2022, to June 14, 2022.

References
Korkut, E. & Fowler, L. B. (2021). Regulatory and policy analysis of production, development and use of sustainable aviation fuels in the United States." *Frontiers in Energy Research*, *9,* 750514. doi:10.3389/fenrg.2021.750514.

Period A, Task 1.4.3 - Help Support Stakeholder Engagement Efforts
The Pennsylvania State University

Objective
Facilitate dialogue among producers, industry, government, and other affected stakeholders.

Research Approach
Our work under this objective has focused on stakeholder engagement and facilitation of effective dialogue to help bridge gaps among producers, industry, government, and other affected stakeholders. This role supports the needs of other team members.

Milestone
These efforts have supported stakeholder engagement efforts led by other teams, including but not limited to the regional partners identified in ASCENT Project 001, Tasks 3.1, 3.2, and 3.3.

Major Accomplishments
This set of tasks has been relatively limited, and no major accomplishments have been made to date. Participation in discussions and calls has continued related to potential stakeholder engagement needs.

Publications
None.

Outreach Efforts
None.

Awards
None.

Student Involvement
None.

Plans for Next Period
Future work under this objective will include presenting to the project partners facilitation skills and tactics. Additional support for regional projects will be offered as needed for facilitation and stakeholder engagement sessions as the regional projects move to the deployment stage. As needed, support will be provided to working groups under the SAF Grand Challenge.

Note: Although the proposed contract period was intended to start on February 1, 2022, no contract was in place from February 1, 2022, to June 13, 2022, thus leaving a gap of approximately 4.5 months without funding.

Period B, Task 1- Law and Policy Research

The Pennsylvania State University

Objectives

Understand existing federal law and policy drivers affecting SAF, including participation by the United States in international discussions and agreements (Task 1.1); research existing state law and policy drivers (Task 1.2); research potential law and policy drivers as needed (Task 1.3); and explore other issues identified by the ASCENT Project 001 team as needed (Task 1.4).

Research Approach

Following up on the publication of the *Frontiers in Energy* review of law and policy (Korkut, E. & Fowler, L. B. (2021). Regulatory and policy analysis of production, development and use of sustainable aviation fuels in the United States." *Frontiers in Energy Research*, *9,* 750514. doi:10.3389/fenrg.2021.750514), research began on the recently adopted Blender's Tax Credit and the potential Sustainable Skies Act. In addition, our legal and policy research was updated on different states' activities regarding SAF (including California, Oregon, Washington, and others).

Milestone

Team meetings were conducted, and updates were provided on legal research topics.

Major Accomplishments

Real-time analysis was provided of pending federal legislation (the Inflation Reduction Act) at the request of Project Manager Nate Brown. In addition, information related to the pending Securities and Exchange Commission rulemaking on greenhouse gas emissions accounting was researched and shared.

Publications

Possibilities for another formal publication are being explored.

Outreach Efforts

Presentations

Fowler, L. B., & Korkut, E. (2022, December). ASCENT Project 001 Team Briefing on pending Securities and Exchange Commission Greenhouse Gas Emission rules.

Fowler, L. B. (2022, October). Briefing to Volvo Corporation on Opportunities Related to the Renewable Fuel Standard and SAF.

Fowler, L. B., & Korkut, E. (2022, July). Update on State Legal and Regulatory Opportunities for SAF [Oral presentation]. ASCENT Project 001 Team Meeting.

Fowler, L. B. (2022, June). Legal and Regulatory Drivers of Sustainable Aviation Fuel [Oral presentation]. Global Council for Science and the Environment.

Awards

None.

Student Involvement

None.

Plans for Next Period

Work with the ASCENT Project 001 Team will continue to identify potential law and policy concerns and opportunities. Exploration of how SAF and renewable natural gas might be developed in synergistic ways is planned in the next period.

Period B, Task 2 - Support Stakeholder Engagement Efforts

The Pennsylvania State University

Objective

Facilitate dialogue among producers, industry, government, and other affected stakeholders.

Research Approach

Our work under this objective has focused on stakeholder engagement and facilitation of effective dialogue to help bridge gaps among producers, industry, government, and other affected stakeholders. This role supports the needs of other team members.

Milestone

These efforts have supported stakeholder engagement efforts led by other teams, including but not limited to the regional partners identified in ASCENT Project 001.

Major Accomplishments

This set of tasks has been relatively limited, and no major accomplishments have been made to date. Participation in discussions and calls related to potential stakeholder engagement needs has continued.

Publications

None.

Outreach Efforts

None.

Awards

None.

Student Involvement

None.

Plans for Next Period

Future work under this objective will include presenting to the project partners on facilitation skills and tactics. Additional support for regional projects will be offered as needed for facilitation and stakeholder engagement sessions as the regional projects move to the deployment stage. As needed, support will be provided to working groups under the SAF Grand Challenge.

Period B, Task 3 - Carbon Capture and Sequestration

The Pennsylvania State University

Objective

Understand how CCS could be integrated with sustainable aviation fuel development.

Research Approach

The new area of research involves a technical focus on integration of CCS with liquid fuel production and examination of SOC. For this task, Dr. Anne Menefee focuses on the technical viability and sustainability of integrating liquid fuel production with CCS. Her research is broadly focused on decarbonization of the energy sector; she has extensive experience specifically in carbon sequestration. Across scales, her research ranges from exploring fundamental geochemical–geomechanical feedback in stressed fracture systems that are targeted by subsurface sequestration operations to evaluating the system-level environmental impacts of emerging technologies that can both curb net emissions and be self-sustaining in the market. Most relevantly, she has worked on life-cycle and techno-economic assessments of subsurface technologies for carbon sequestration and waste management in the energy sector.

Milestone
This work started.

Major Accomplishments
None.

Publications
None.

Outreach Efforts
None.

Awards
None.

Student Involvement
None.

Plans for Next Period
Additional consultation with the ASCENT Project 001 Team is needed regarding the proposed and potential next steps. This technical work should support implementation of the SAF Grand Challenge, the International Civil Aviation Organization Committee on Aviation Environmental Protection, and/or both.

Period B, Task 4 - Organic Soil Carbon
The Pennsylvania State University

Objective
Understand how SOC might be integrated with sustainable aviation fuel development.

Research Approach
This is another new area of research identified by the ASCENT Project 001 team. As part of the request on this topic, Dr. Armen R. Kemanian was identified to join the ASCENT Project 001 Team. The research approach for this task involves identifying critical questions and refining the scope of work (Task 4.1); conducting a literature review (Task 4.2); and drafting a review manuscript analyzing the opportunities to link SOC and SAF (Task 4.3).

Milestone
Dr. Kemanian provided an initial presentation of ideas to think about during the August 25, 2022, ASCENT Project 001 team meeting.

Major Accomplishments
None.

Publications
None.

Outreach Efforts
Presentation

Kemanian, A. (2022, August 29). *Agroecosystem Productivity and Carbon Intensity when Producing Aviation Fuel: Amplifying Opportunities and Taming Trade-offs* [Oral presentation]. ASCENT Project 001 Team Meeting, virtual.

Awards
None.

Student Involvement
None.

Plans for Next Period
Additional consultation with the ASCENT Project 001 Team is needed regarding the proposed and potential next steps. As with the technical work associated with CCS, this technical work should support implementation of the SAF Grand Challenge, the International Civil Aviation Organization Committee on Aviation Environmental Protection, and/or both.

Periods C-D, Task 1- Law and Policy Research
The Pennsylvania State University

Objectives
Stay up to date with existing and proposed federal law and policy drivers affecting SAF, including participation by the United States in international discussions and agreements (Task 1.1); research existing and proposed state law and policy drivers (Task 1.2); and explore other issues identified by the ASCENT Project 001 team as needed (Task 1.3).

Research Approach
Following up on our previous law and policy research, the ASCENT Project 001 team stayed abreast of developments related to the Inflation Reduction Act provisions related to SAF, including Producer's Tax Credit (IRC § 45Z), Clean Hydrogen Tax credit (IRC § 45V), and CCSC (IRC § 45Z), as well as broader legal developments that could have an impact on SAF. New corporate disclosure requirements were researched at the state, federal, and international levels. In addition, a 50-state survey of laws and policies impacting SAF development was performed.

Milestone
At biweekly team meetings and semi-annual conferences, updates were provided on legal research topics. Email updates were sent as appropriate regarding significant legal developments.

Major Accomplishments
A presentation on the "Impacts of Law & Policy on SAF Development" was presented in April 2024 at two ASCENT 93 classes. In addition, Information related to the Supreme Court opinion in *Loper Bright v. Raimondo*, in which the Court overturned *Chevron* deference, was researched and shared.

Publications
Peer-reviewed journal publications
Korkut, E. & Fowler, L. B. (2021). Regulatory and policy analysis of production, development and use of sustainable aviation fuels in the United States." *Frontiers in Energy Research*, *9,* 750514. doi:10.3389/fenrg.2021.750514.

Possibilities for another formal publication are being explored.

Outreach Efforts
Presentations
Helbing, M., Fowler, L. B., and Korkut, E. (2023, November). *Sustainable Aviation Fuel Policy in the United States* [Oral presentation]. ASCENT 93 Lecture Series.

Helbing, M, & Korkut, E. (2024, February). *Exploring the Policy Landscape for Livestock Anaerobic Digesters* [Oral presentation]. C-CHANGE Grass2Gas Webinar Series hosted by Penn State Extension. (Renewable natural gas is seen as a potential part of the supply chain for SAF.)

Fowler, L. B. (2024, April), *Legal and Policy Considerations in SAF Financing and Investment* [Oral presentation]. ASCENT 93 Lecture Series.

Helbing, M. & Kemanian, A. (2024, April). *Impacts of Law & Policy, Carbon Capture & Sequestration, and Soil Organic Carbon on SAF Development* [Oral presentation]. Spring 2024 ASCENT Sustainable Aviation Fuel Meeting.

Helbing, M. (2024, June). circulated an email to ASCENT Project01 team with an update about the U.S. Supreme Court's opinion in *Loper Bright Enterprises v. Raimondo.*

Johnson, M. (2024, August). *Preliminary Results of Law and Policy – SAF 50-State Survey* [Oral presentation]. ASCENT Project 001 Team Meeting.
Helbing, M. (2024, October). *Flying into the Future: Sustainable Aviation Fuel and the Policies Impacting its Development* [Oral presentation]. Penn State Earth and Environmental Systems Institute EarthTalks Series.

Awards
None.

Student Involvement
Our third-year law student, Mary Johnson, has researched policies affecting SAF development in all 50 states. She presented preliminary results from her research at the ASCENT Project 001 team meeting on August 12, 2024.

Plans for Next Period
Our team will continue to work with the ASCENT Project 001 Team to identify potential law and policy concerns and opportunities. Our team will also continue to explore how SAF and renewable natural gas might be developed in synergistic ways. Our team will complete compilation of data from our 50-state survey into a distributable format. Finally, our team will engage with other ASCENT Project 001 team members on evaluating the impacts of a potential national low carbon fuel standard policy.

Periods C-D, Task 2 - Support Stakeholder Engagement Efforts
The Pennsylvania State University

Objective
Facilitate dialogue among producers, industry, government, and other affected stakeholders.

Research Approach
Our work under this objective has focused on stakeholder engagement and facilitation of effective dialogue to help bridge gaps among producers, industry, government, and other affected stakeholders. This role supports the needs of other team members.

Milestone
These efforts have supported stakeholder engagement efforts led by other teams, including but not limited to the regional partners identified in ASCENT Project 001.

Major Accomplishments
This set of tasks has been relatively limited. Our team have continued to participate in discussions and calls related to potential stakeholder engagement needs. Those discussions this year included conversations with Steve Csonka from the Commercial Aviation Alternative Fuels Initiative (CAAFI) and Brian Regli from the Pennsylvania Governor's Office of Critical Investments.

Publications
None.

Outreach Efforts
P.I. Lara Fowler held a brainstorming discussion about opportunities related to sustainable aviation fuel and renewable natural gas with the Pennsylvania Department of Agriculture and the Pennsylvania Conservation Commission in December 2023.

Lara Fowler, Michael Helbing, and Ekrem Korkut participated in a discussion with Steve Csonka of the CAAFI and Brian Regli from the Pennsylvania Governor's Office of Critical Investments to respond to questions from the Governor's Office about sustainable aviation fuel and what opportunities might be available within the Commonwealth in February 2024.

Michael Helbing attended the North American SAF Conference and Expo in Saint Paul, Minnesota, in September 2024.

Awards
None.

Student Involvement
None.

Plans for Next Period
Work will continue with other ASCENT partners to facilitate communications with stakeholders. Specifically, the aim is to develop relationships with the Fueling Aviation's Sustainable Transition SAF grant recipients affiliated with the Philadelphia and Pittsburgh airports in Pennsylvania. Future work under this objective will include presenting to the project partners on facilitation skills and tactics. Additional support for regional projects will be offered as needed for facilitation and stakeholder engagement sessions as the regional projects move to the deployment stage. As needed, support will be provided to working groups under the SAF Grand Challenge.

Periods C-D, Task 3 - Carbon Capture and Sequestration
The Pennsylvania State University

Objectives
- Work with ASCENT Project 001 team to identify critical questions and needs surrounding the potential for CCS in SAF/AJF supply chains and support other tasks looking to integrate aspects of CCS (e.g., carbon footprint, techno-economic, and feasibility analyses).
- Conduct literature review to understand the potential opportunities, challenges, research needs, etc.

Research Approach
The initial stages of the CCS task involved in-depth literature review to understand knowledge gaps and existing pathways to integrate CCS into SAF/AJF supply chains. Our approach and objectives were refined through discussions with the ASCENT Project 001 team to focus more on policy and risk related to CCS and to identify hurdles that need to be addressed to (1) enable integration into SAF/AJF supply chains and (2) achieve real and quantifiable emission reductions. As a result of those efforts, Dr. Anne Menefee and Michael Helbing drafted a white paper and circulated it for review among select ASCENT 01 team members. They incorporated that feedback into the white paper and also used it to develop strategies for further research.

Milestone
PI Menefee along with researcher Helbing drafted a white paper discussing technical and policy research about carbon capture and sequestration in SAF development. The white paper was circulated for review in September 2024, updates were presented at the biweekly team meeting in late November, and feedback was received and incorporated.

Major Accomplishments
A white paper was drafted and circulated discussing the technical and policy research about carbon capture and sequestration in SAF development.

Publications
None.

Outreach Efforts
Presentations

Menefee, A. & Helbing M. (2023, November), *Carbon Capture and Sequestration (CCS) with a focus on Geologic Carbon Storage (GCS)* [Oral presentation]. ASCENT Project 001 Team Meeting.

Helbing, M. & Kemanian, A. (2024, April), *Impacts of Law & Policy, Carbon Capture & Sequestration, and Soil Organic Carbon on SAF Development* [Oral presentation]. Spring 2024 ASCENT Sustainable Aviation Fuel Meeting.

Awards
None.

Student Involvement
P.I. Anne Menefee mentored one undergraduate student in the Fall 2023 and Spring 2024 semesters. She mentored an undergraduate student (who was funded through a different program in her department) in Summer 2023 to help conduct initial literature review.

Plans for Next Period
The revised white paper will be disseminated on appropriate platforms (Center for Energy Law and Policy's website at Penn State, submission to CAAFI), and plan to extend our research to address topics raised by ASCENT Project 001 team members in their review of the white paper. For next year, a proposal is in development for a new round of funding, which will include extended research on technical, economic, and policy aspects of CCS. As needed, support and expertise will be provided to other tasks.

Periods C-D, Task 4 - Organic Soil Carbon
The Pennsylvania State University

Objective
Incorporate Penn State expertise on soil carbon and nitrogen cycling in the context of the calculation of the carbon intensity of SAF. This includes incorporating carbon cycling modeling and the inclusion of uncertainty bounds, methods for standardizing calculations that encompass baseline (or reference) scenarios and SAF production scenarios. These methods need to be applicable worldwide, but the initial focus is CONUS. In addition, it is expected that similar work accounting for the nitrogen cycle including the carbon footprint associated to the use of fertilizers and an accounting for the emissions of nitrous oxide, whose equivalent carbon footprint can surpass that of SOC both as a positive or negative climate forcing.

Research Approach
The research approach for this task includes developing a standard method to account for land use and SAF production using Earth State and level three GADM to report calculations on a field basis but also on political units of relevance that are standardized around the world. This task also includes overlaying the NLDAS (reanalysis) climate databases, and ISRIC soils, so that the model Cycles (developed in Dr. Kemanian's lab) can be operated through the cropland domain. Finally, this task includes using machine learning combined with a standard initialization procedure to estimate steady state soil carbon stocks under BAU and alternative SAF production scenarios.

Milestone
The team established a stable database of land use, weather data, and soils, along with automated methods to run simulations with Cycles, and downloaded and curated the USDA-Natural Resources Conservation Service (NRCS) pedon database for machine learning analysis.

Major Accomplishments
Dr. Yuning Shi updated the global weather data from the Global Land Data Assimilation System (GLDAS) reanalysis database, to allow simulation of any crop rotation worldwide.

Dr. Yuning Shi and Dr. Armen Kemanian started developing a 2D version of the model Cycles that will allow simulation of nitrous oxide fluxes in systems with banding of nitrogen fertilizer or manure. Banding is a common practice in crop production. Ignoring nitrogen banding can lead to gross underestimations of nitrogen uptake by crops and alter nitrous oxide emission estimates. The 2D version relies on the use of C-language Variable-coefficients ODE solver (CVODE), a solver for a system of ordinary differential equations maintained by the Lawrence Livermore National Laboratory. So far, water transport in 2D is still being tested, including infiltration that is resolved using a modification of the Green and Ampt method, and water redistribution using Richards equation.

Publications

Dr. Armen Kemanian co-authored a manuscript positing that the return to the soil of high-lignin fermentation byproducts, (i.e., the leftovers of fermenting cellulosic materials for ethanol or other products) can balance or overcome the otherwise expected SOC losses from the removal of corn residues. The manuscript was published in *Environmental Research Letters* on August 2, 2024 (Lynd et al., 2024).

Peer-Reviewed Journal Publication

Lynd, L., Kemanian, A., Smith, J., Richard, T. L., Arifi, A., Bozzetto, S., Fabbri, C., Field, J., Pries, C. H., Kubis, M. (2024). Soil application of high-lignin fermentation byproduct to increase the sustainability of liquid biofuel production from crop residues, *Environmental Research Letters, 19*(8). DOI 10.1088/1748-9326/ad601a

Outreach Efforts

Presentations

Kemanian A., et al. (2023, October 29-November 1). *Understanding how manure and digestate composition affect crop production and nitrogen losses in corn-based systems* [Poster presentation]. Agronomy Society of America meeting, St Louis, MI, United States.

Armen R Kemanian, et al. (2024, March). *Understanding how manure and digestate composition affect crop production and nitrogen losses in corn-based systems* [Poster presentation]. Gamma Sigma Delta society meeting, College of Agriculture - The Pennsylvania State University, University Park, PA, United States.

Helbing, M. & Kemanian, A. (2024, April). *Impacts of Law & Policy, Carbon Capture & Sequestration, and Soil Organic Carbon on SAF Development* [Oral presentation]. Spring 2024 ASCENT Sustainable Aviation Fuel Meeting.

Kemanian, A. (2024, October). *Risk-Informed Alternative Jet Fuel (AJF) Supply Chain Analysis: Top-Down Modeling of Soil Organic Carbon in Cropland* [Oral presentation]. Fall 2024 ASCENT Advisory Committee Meeting.

Awards

None.

Student Involvement

The project has not included students to date. However, P.I. Armen Kemanian intends to recruit a graduate student to work in this project for the Fall 2025 semester once funding commitments are established.

Plans for Next Period

The top-down modeling of the SOC balanced at the county level presented in the ASCENT meeting in Alexandria, VA in October 2024 will be refined and the results summarized in a draft article for publication. Specifically, the analysis to date used SOC from the STATSGO (U.S. General Soil Map) database; it will be replaced with the Soil Grids database from the ISRIC. Carbon input, which were estimated using only grain yield and forage yield, will be updated with a longer statistical time series from the National Agricultural Statistical Service. The target journal is *Global Change Biology – Bioenergy*.

Project 001(E) Alternative Jet Fuel Supply Chain Analysis

University of Tennessee

Project Lead Investigator

Timothy Rials
Professor and Director
Center for Renewable Carbon
University of Tennessee
2506 Jacob Dr., Knoxville, TN 37996
865-946-1130
trials@utk.edu

University Participants

University of Tennessee (UT)

- P.I.: T. Edward Yu, Professor
- FAA Award Number: 13-C-AJFE-UTenn, Amendments 09, 11, 13, 15, 17, 19
- Period of Performance: October 1, 2023, to September 30, 2024
- Tasks:
  1. Conduct regional intermediate oilseed supply analysis for sustainable aviation fuel (SAF)
  2. Assess regional forest biomass feedstock considering feedstock quality variability
  3. Laying the groundwork for developing Regional SAF Economy in Central Appalachia and Tennessee
  4. Conduct soil organic carbon (SOC) analysis in the United States.

Project Funding Level

Total estimated project funding: $2,031,500 (total 10-year funding)
Total federal and non-federal funds: $2,031,500 (total 10-year funding)
The UT Institute of Agriculture, in support of the project, provided faculty salary. Additional nonfederal support was derived from contributions from the stakeholder group.

Investigation Team

Timothy Rials (Project Director – PD), Task 3
T. Edward Yu (P.I.), Tasks 1–4
Joshua Fu (faculty), Task 4
Burton English (faculty), Tasks 1 and 2
Carlos Trejo-Pech (faculty), Task 1
David Hughes (faculty), Task 3
Hannah Rubin (PhD student), Task 4
Kumar Bolakhe (MS student), Tasks 1 and 2

Project Overview

UT leads the project's feedstock production analysis component. This component targets the need to assess and inventory regional forest and agricultural biomass feedstock options and delineate the sustainability impacts associated with various feedstock choices. UT also leads the national lipid supply availability analysis, using the Policy Analysis System Model (POLYSYS) to develop information on the potential effects and feasibility of using lipids to supply aviation fuel. The team at UT facilitates regional deployment/production of SAF by laying the groundwork and developing a regional deployment plan. Additionally, UT collaborates with Purdue University and Pennsylvania State University (PSU) to estimate SOC in the United States in Task 4 to assist the agency in better understanding the related influence of SAF feedstock production.

Task 1 - Conduct Regional Intermediate Oilseed Supply Analysis for SAF

University of Tennessee

Objectives

- Complete the economic viability analysis for intermediate winter oilseeds (winter canola) in the Southeast region.
- Assess the impact of feedstock supply variation on the economics and carbon intensity (CI) of SAF produced from intermediate winter oilseeds in the study area.
- Develop a supply chain related to winter oilseeds and SAF in the study area.

Research Approach

Given their favorable conditions for growing winter canola, Tennessee and Kentucky in the Southeastern United States. constitute the study area in this case. These states have mild winters, sufficient growing season precipitation, and the opportunity to double-crop with traditional annual summer crops. Instead of considering all corn and soybean harvested areas for winter canola, the ASCENT Project 001E team assumed the areas used for winter wheat cultivation for at least one year over the past decade could produce winter canola. Applying the wheat frequency layer from the CropScape portal of the U.S. Department of Agriculture (USDA) National Agricultural Statistics Service (NASS), our team identified around 1.2 million ha of winter wheat harvest area as the potential supply regions. Such an assumption better reflects the regional producers' potential to adopt the relatively new intermediate crop and prevents overestimating winter canola production in this study.

This study modeled the winter canola-based SAF supply chain in four components, as illustrated in Figure 1: (1) farms, (2) oil extraction mills (OEMs), (3) biorefineries, and (4) airport(s). Winter canola will be established and harvested at farms; OEMs purchase and convert canola oilseed into crude oil and canola meal. The crude oil will be transported to biorefineries to produce SAF and other co-products, such as propene, naphtha, and biodiesel, via the hydro-processed esters fatty acid (HEFA) pathway. The SAF will then be transported to associated airports. Our two-stage stochastic mixed integer linear programming (MILP) model selects winter canola cultivation area and facility investment in the first stage. Given the first-stage decisions, operational decisions like crude oil production, SAF production, and procurement of additional feedstocks, subject to uncertainty in feedstock availability, are made in the second stage to maximize the expected profit.

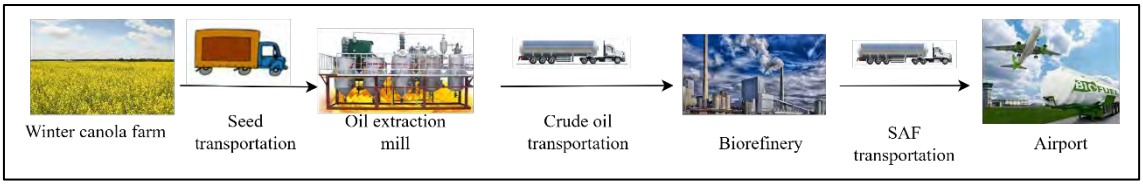

Figure 1. System boundary of winter canola-based SAF production.

The availability of a nearby crushing facility reduces uncertainty for farmers, facilitates the market establishment for winter canola, and lowers shipping costs. Given the OEM's influence, our team evaluated two cases to assess the potential of SAF production subject to the assumption of OEM availability in the system:

- Case I: Assessment of near-term production of SAF utilizing the existing OEM on the border of Tennessee and Kentucky. It is assumed that farmers and SAF producers count on the existing OEM to crush oilseeds for SAF facilities while additional crush facilities are pending.
- Case II: It is assumed that the long-term, large-scale production of SAF will utilize more area for winter canola cultivation, thus requiring the establishment of multiple OEMs alongside the existing OEMs and biorefineries in the region. Industrial parks were considered as a potential location for these additional facilities.

Several assumptions are imposed. The ASCENT Project 001E team followed the techno-economic analysis (TEA) of HEFA conversion pathways provided by the Washington State University ASCENT team. In both cases, the existing road network was used to find the shortest transportation distances between the supply chain components. The feedstock supply regions were decomposed into a grid of 130-km^2 hexagons. Also, the land opportunity cost was adjusted by incorporating the net revenue of winter wheat production and the frequency of wheat harvest within each hexagon. Similarly, our team assigned the different productivity levels to each hexagon based on the winter wheat productivity of each county. The ratio

of the hexagon's productivity to the state's average productivity was then used as the yield factor to incorporate the spatial yield differences.

Winter canola yield varies yearly, which mandates considering several scenarios for winter canola availability when developing a two-stage stochastic supply chain optimization model. The Monte Carlo simulation assuming the Program Evaluation Research Task (PERT) distribution was used to generate scenarios for winter canola supply. In this study, our team considered winter canola yield as a random variable with a mean value (2,800 kg ha^{-1}), representing the most possible outcome within a PERT distribution range of [1,400, 4,200] kg ha^{-1} based on recent field experimental data. The Monte Carlo simulation was run using this distribution for 1,000 iterations across 20 years. Twenty yield intervals were created, each assuming a scenario with a probability distribution obtained from the simulated yield under each scenario, as illustrated in Figure 2.

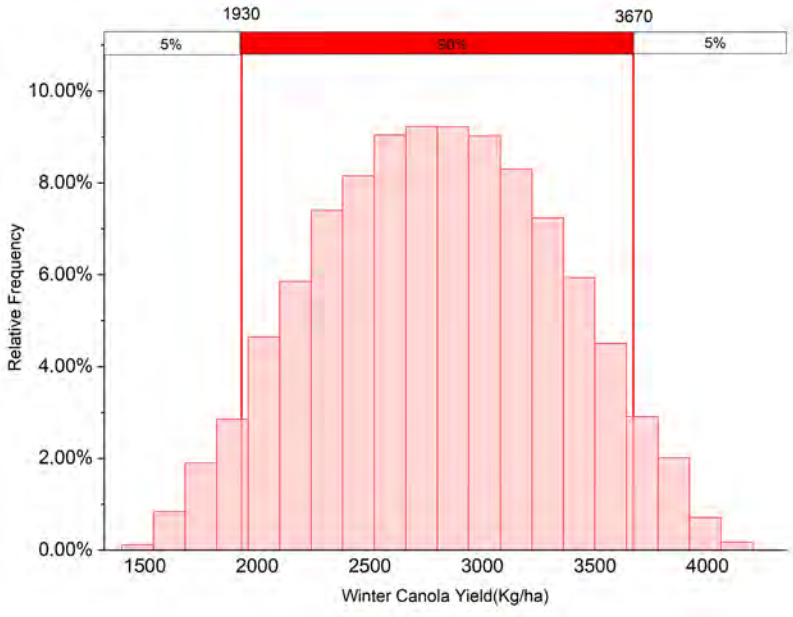

Figure 2. Probability distribution of simulated winter canola yield.

Milestones

- Completed and presented the analysis of SAF production at various national and international professional meetings.
- Developed a Master of Science thesis based on this study, and a derived manuscript is now under review for publication consideration in a prestigious journal in the renewable energy field.

Major Accomplishments

The optimal land allocation for winter canola cultivation and facilities location for Case I and II are determined by the stochastic optimization model. In Case I, 0.2 million ha of land is chosen for winter canola cultivation, with around 85% of the utilized land located in Kentucky. In this case, these locations are selected for their proximity to the only existing OEM, thus lowering oilseed transportation costs. The model selects one biorefinery of 265 million liters yearly (MLY) SAF production capacity (around 373 MLY total production capacity) to adjust the wide range of feedstock yield variations. In Case II, with additional investment in facilities in the longer term, around 0.6 million ha of land in 114 counties are selected annually for winter canola production. Six additional OEMs (in addition to the existing OEM) are placed. Two biorefineries are sited to supply Nashville International Airport (BNA), with one in Tennessee and the other in Kentucky. One biorefinery serving Memphis International Airport (MEM) is situated in southwest Tennessee. The facilities are located near areas with higher oilseed production capacity.

Given the variability in winter canola yield, the estimated volume of SAF supplied to BNA in Case I could fluctuate between 129 MLY and 246 MLY. In Case II, the total SAF supply may vary from 370 MLY to 711 MLY with a 90% likelihood. Specifically, the supply for BNA ranges from 227 MLY to 439 MLY, and ranges from 143 MLY to 272 MLY for MEM.

Figure 3 and Figure 4 show winter canola yield variability introduces substantial risks to the economic viability of SAF production. Our analysis indicates that, after considering co-product revenues, SAF production costs from the HEFA pathway fluctuate between $0.6-$1.7 per liter for Case I and $0.7-$1.7 per liter for Case II, with a 90% likelihood, as shown in Figures 3 and 4. Lower feedstock yields increase the per unit cost of SAF production due to the higher average seed cost, the lower facility utilization rate, and the purchase of additional feedstock at a higher price.

a) Case I: only existing OEM is utilized

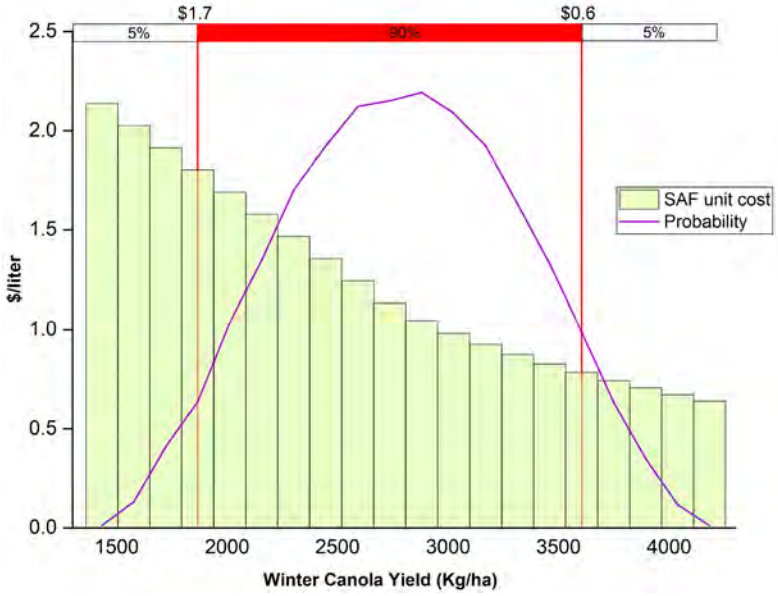

Figure 3. Stochastic per unit cost of SAF production under Case I.

b) Case II: potential OEMs are considered and located

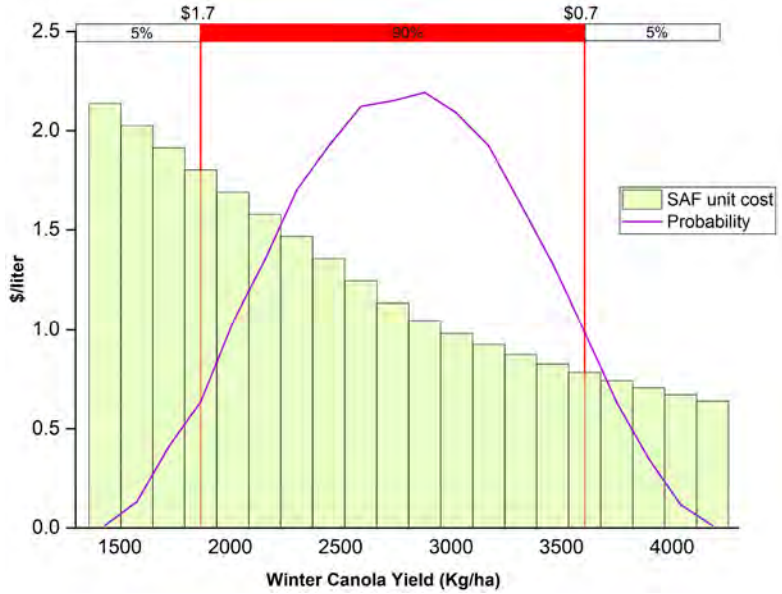

Figure 4. Stochastic per unit cost of SAF production under Case II.

The variability in winter canola yield introduces fluctuations in the CI of the SAF supply chain, highlighting the critical relationship between feedstock yield and the environmental sustainability of SAF. Figure 5 and Figure 6 display the CI over the different yield scenarios in Case I and Case II, respectively. Our estimates show that the CI of SAF in the two cases range from 31 g CO^2e MJ^{-1} to 43 g CO^2e MJ^{-1}, with a 90% likelihood and an expected value of 35 g CO^2e MJ^{-1}.

a) Case I: only existing OEM is utilized

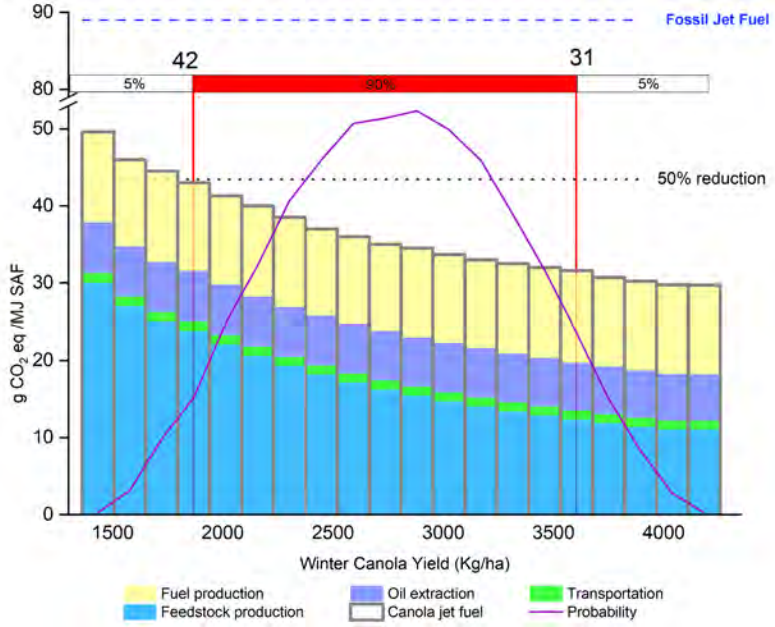

Figure 5. Stochastic Carbon intensity of winter canola-based SAF under Cases I.

b) Case II: potential OEMs are considered and located

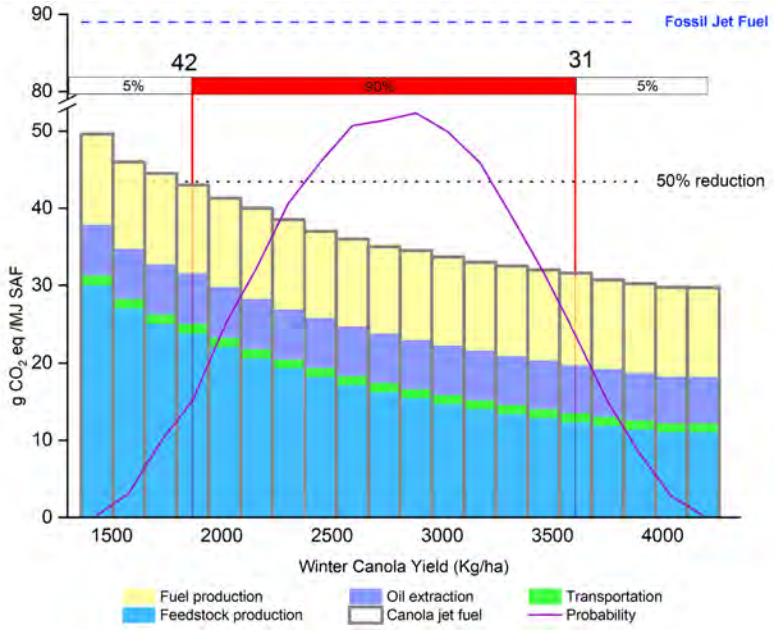

Figure 6. Stochastic Carbon intensity of winter canola-based SAF under Case II.

Publications

Bolakhe, K., Yu, T. E., Sykes, V., Smith, A., & Boyer, C. N. (Manuscript submitted for publication). Assessing a Sustainable Aviation Fuel Supply Chain from Winter Canola and Its Carbon Intensity Considering Feedstock Yield Variations.

Bolakhe, K. (2024). *Stochastic Optimization of Canola-Based Sustainable Aviation Fuel in the Southeastern US* [Master's Thesis, University of Tennessee]. https://trace.tennessee.edu/utk_gradthes/11777/

Outreach Efforts

The study results have been disseminated at various professional meetings. The ASCENT Project 001E team has also presented the findings to producers and state agencies at various Extension field days. Our team also shared the work with the Tennessee Department of Agricultural Commissioners.

Conference Presentations

Bolakhe, K., Yu, T. E., Sykes, V., & Smith, A. (2024, March 18-20). *Developing Sustainable Aviation Fuel System from Winter Oilseeds," Annual International Symposium* [Conference presentation]. Food-Energy-Water Bioeconomies for Net-Zero Transition, Knoxville, Tennessee.

Bolakhe, K., Yu, T. E., Sykes, V., & Smith, A. (2024, May 22-24). *Sustainable Aviation Fuel Supply Chain from Winter Oilseeds and Its Carbon Intensity* [Conference presentation]. 2024 International Transport Forum Summit, Leipzig, Germany.

Bolakhe, K., Yu, T. E., Sykes, V., Smith, A., & Boyer, C. N. (2024, July 28-30). *Evaluating a Stochastic Optimized Sustainable Aviation Fuel Supply Chain from Winter Canola and Its Carbon Intensity* [Poster presentation]. 2024 AAEA Annual Meeting, New Orleans, Louisiana.

Yu, T.E. (2024, September 30 – October 3). *Biomass Feedstock Supply Chain Modeling and Decision Tools for Sustainable Aviation Fuels* [Conference presentation]. 2024 Frontiers in Biorefining 7th International Conference, St. Simons Island, Georgia.

Awards

Southern Agricultural Economics Association's 2025 Outstanding Master's Thesis Award for Kumar Bolakhe's master's thesis, titled "Stochastic Optimization of Canola-Based Sustainable Aviation Fuel in the Southeastern US."

Student Involvement
Graduate student, Kumar Bolakhe, developed the winter canola supply chain optimization model.

Plans for Next Period
- Continue our work on the stochastic analysis focusing on other brassica feasibility in the southeastern area.
- Continue to work on regional SAF analysis using winter canola as feedstock.
- Continue working with stakeholders to further this task.

Task 2 - Assess Regional Forest Biomass Feedstock Considering Feedstock Quality Variability
University of Tennessee

Objectives
The objectives of this study are two-fold: (1) Estimate and compare the potential maximum supply quantity (MSQ) and net revenue (NR) of SAF from forest residues under two scenarios, namely with and without considering ash content variability, and (2) Investigate and differentiate SAF supply chain layout between the two scenarios. The study area is in the southeast United States, as it has gained prominence as a significant supplier of logging residues owing to its abundant and diverse forestry resources, coupled with a thriving wood products industry. This study focuses on a geographical area encompassing Alabama, Arkansas, Georgia, Kentucky, Louisiana, Mississippi, North Carolina, South Carolina, Tennessee, and Virginia, along with a 100-mi buffer surrounding the states' borders.

Research Approach
A two-stage MILP model is developed to incorporate the relationship between feedstock ash content and biofuel yields in optimizing the SAF supply chain. Forest inventory spatial data are gathered from the Forest Inventory and Analysis (FIA) database maintained by the USDA. The sample data are then interpolated to generate the inventory level across the entire study area using the Kriging method. The ASCENT Project 001E team collected 68 different biomass hardwood samples (around 10 kg each) across the southeast. The logging residues' ash content sample data are interpolated using the Kriging method for the entire study area.

Milestones
- Performed analysis of assessment of Regional Forest Biomass Feedstock. Completed (Summer 2024).
- Published a peer-reviewed journal article for this study. A draft manuscript has been developed and will be submitted to a journal after the Program Manger's review.

Major Accomplishments
When assuming constant ash content in the logging residues by using the mean of all collected samples (1.62%) and its corresponding biofuel yield, the annual MSQ of SAF could reach 629 million gal (see Figure 7 (left)). A combination of 18 biorefineries and 85 depots is required under this scenario. The total cost is $5.76 per gal (see Figure 7 (right)). Using a $9.09 per gal price for SAF, its NR reaches $3.33 per gal.

In the scenario of considering spatially heterogenous ash content variation, the MSQ of SAF per year reduces to 540 million gal (see Figure 7 (left)), supplied by 16 biorefineries and 80 depots. In this scenario, the total production cost is $5.92 per gal (up by 2.78% compared to the constant ash content), and the SAF NR is down to $3.17 per gal (a 4.80% reduction). The lower SAF production and higher production cost when considering ash content variations in logging residues are due to lower throughput in conversion (i.e., lower bio-oil yield from the same amount of logging residues) in those areas with high ash content. When the ash variability in feedstock is not considered, feedstock availability and the corresponding SAF production will likely be overestimated.

Figure 8 depicts the estimated quantity of SAF shipped to various airports per year due to the changes in logging residue usage and selection. Seven airports have been identified as destinations of SAF in both scenarios; the heterogeneous spatial distribution of feedstock ash content across the study area creates disparities between the change in SAF shipped to each airport between the two cases. Among them, Charlotte Douglas International Airport (CLT) and Hartsfield-Jackson Atlanta International Airport (ATL) experience the largest decline: The annual SAF consumption decreases from 98 to

72 million gal (a 26.53% reduction) in the CLT and from 148 to 115 million gal in ATL (a 22.30% decrease). The disparity in SAF variation across different airports stems from the spatial heterogeneity of ash distribution. Primarily, the depot near CLT and ATL airports experiences a significant decline in the raw materials harvested due to their higher ash content. Moreover, higher feedstock ash content leads to lower throughput at the biorefinery, resulting in a substantial reduction in the amount of SAF supplied to these two airports.

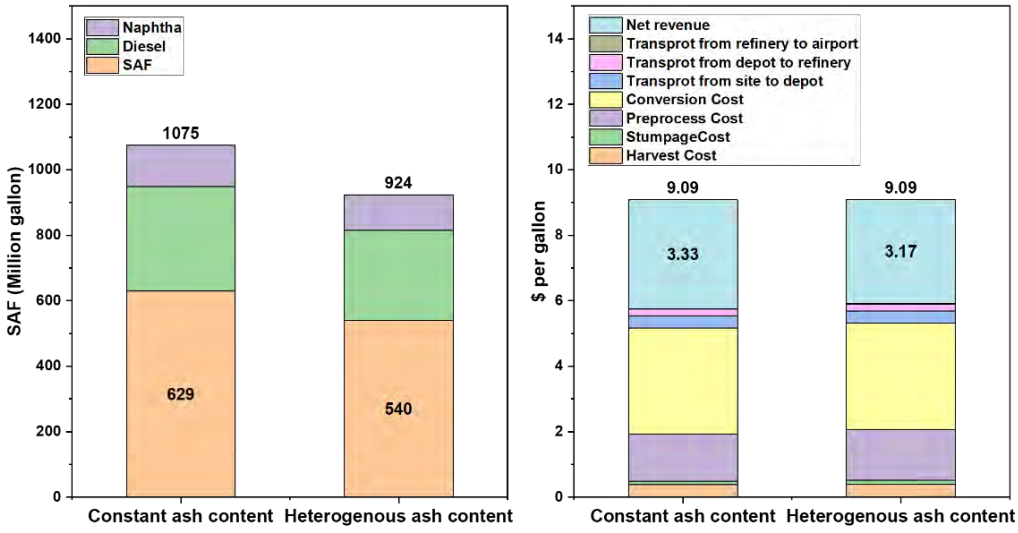

Figure 7. The estimated MSQ and NR under the two scenarios of ash content.

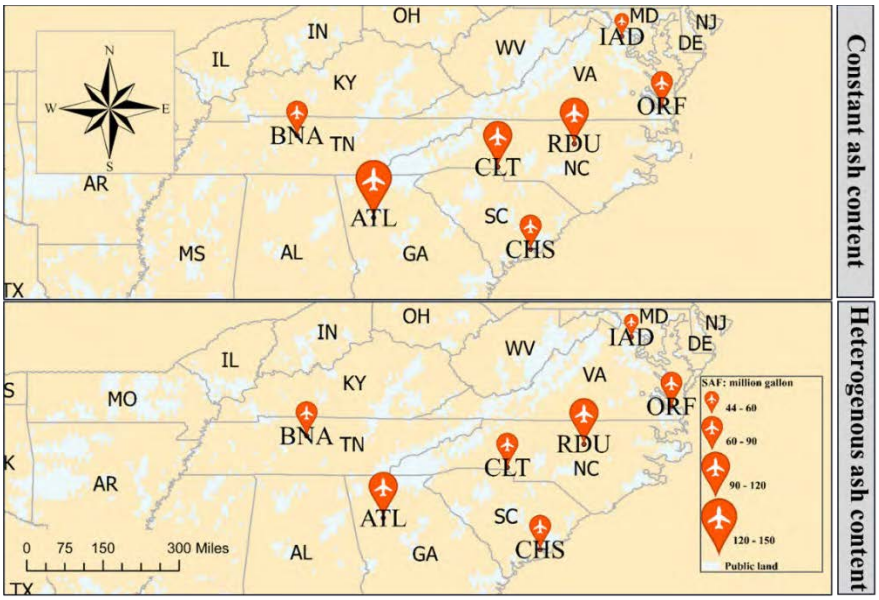

Figure 8. Estimated SAF at airports under the two scenarios of ash content.

Publications

Peer Reviewed Journal Publications

Trejo-Pech, C. O., Yu, T. E., Lanning, D. N., Dooley, J. H., Larson, J. A., & English, B. C. (2024). A Techno-economic Analysis Comparing a Hammermill and a Rotary Shear System to Process Woody Biomass for Biofuel Production. *Energies, 17*, 886. https://doi.org/10.3390/en17040886

Li. P., Yu, T. E., Trejo-Pech, C., Larson, J. A., English, B. C., & Lanning, D. (2024). Assessing the Impact of Preprocessing and Conversion Technologies on the Sustainable Aviation Fuel Supply from Forest Residues in the Southeast U.S. *Transportation Research Record, 2678*(9). https://doi.org/10.1177/03611981241230508

Outreach Efforts

Conference Presentations

Li. P., Yu, T. E., Labbe, C. N., Abdoulmoumine, N., Garcia-Perez, M. Hoyt, K., & English, B. C. (2025, January 5-9). *Optimizing Sustainable Aviation Fuel Supply Chains from Forest Residues Considering the Impact of Feedstock Ash Content Variability* [Conference presentation]. TRB Annual Meeting 2025, Washington, D.C.

Yu, T. E., Li, P., Labbe, C. N., Abdoulmoumine, N., Garcia-Perez, M., & Hoyt, K. (2024, November 20-22). *Sustainable Aviation Fuel Supply Chains Optimization from Forest Residues Considering Feedstock Ash Content Variability* [Conference presentation]. 2024 AFCC Global Biobased Economy Conference and Exhibition, Washington, D.C.

Awards

None.

Student Involvement

Master's graduate students, Pengzhen Li and Kumar Bolakhe, developed the logging residue supply chain model.

Plans for Next Period

- Complete the manuscript with this case study and include the lifecycle analysis in the next period.

Task 3 - Laying the Groundwork for Developing Regional SAF Economy in Central Appalachia and Tennessee

University of Tennessee

Objectives

The team at UT will facilitate regional deployment/production of SAF by completing the groundwork phase of the regional feedstock-to-biofuel pathway and developing a proposal for regional deployment in Central Appalachia.

Research Approach

Conducting a webinar for the potential stakeholders of the SAF supply chain.

Major Accomplishments

The ASCENT Project 001E team invited the leadership of Delta Air Lines, Jeff Davidson, and Minneapolis Airport, Julie Silvis, to share their experience in forming the Minneapolis Saint Paul SAF Hub on January 31, 2024 (see Figure 9). Over 200 registrations were received for this virtual webinar. Both speakers provided insightful information to the audience about the strategies for developing a regional SAF hub. They emphasized the importance of collaboration among stakeholders, including policymakers, airlines, feedstock producers, conversion industries, and financial institutions, to foster the regional SAF ecosystem. The speakers answered many questions from the participants.

Figure 9. Poster of the sustainable aviation fuel stakeholder webinar on January 31, 2024.

Publications
None.

Outreach Efforts
The ASCENT Project 001E team hosted a virtual webinar, *Minnesota's Flight to a Sustainable Future: The Minnesota SAF Hub,* on January 31, 2024, with the leadership of Delta Air Lines, Jeff Davidson, and Minneapolis Airport, Julie Silvis.

Awards
None.

Student Involvement
None.

Plans for Next Period
- Develop a series of webinars for Tennessee SAF regional plans.

Task 4 - Conduct Soil Organic Carbon (SOC) Analysis in the United States
University of Tennessee

Objectives
- To improve SOC baseline estimates in the United States.
- Investigate long-term trends in land use and climate change to enhance our understanding of carbon cycling in complex environments.

Research Approach

The ASCENT Project 001E team proposes to improve SOC estimates and investigate long-term trends in the United States using in situ measurements from soil carbon networks and previous studies and incorporating satellite imagery from the Landsat archive for more complete spatial coverage. In our efforts, the team will compare several machine learning techniques to generate a finer resolution map and better understand SOC dynamics.

Milestones

- Complete the SOC estimation in the top 30 cm of soil with the 30 m spatial resolution for the United States.
- Develop one chapter in a doctoral dissertation and derive a manuscript for peer review and publication.

Major Accomplishments

The ASCENT Project 001E team applied the Random Forest algorithm to the contiguous United States (CONUS) to interpolate SOC between soil observations from 1990 to 2022. The estimated mean SOC map at the spatially and temporally consistent 30 m resolution is shown in Figure 10.

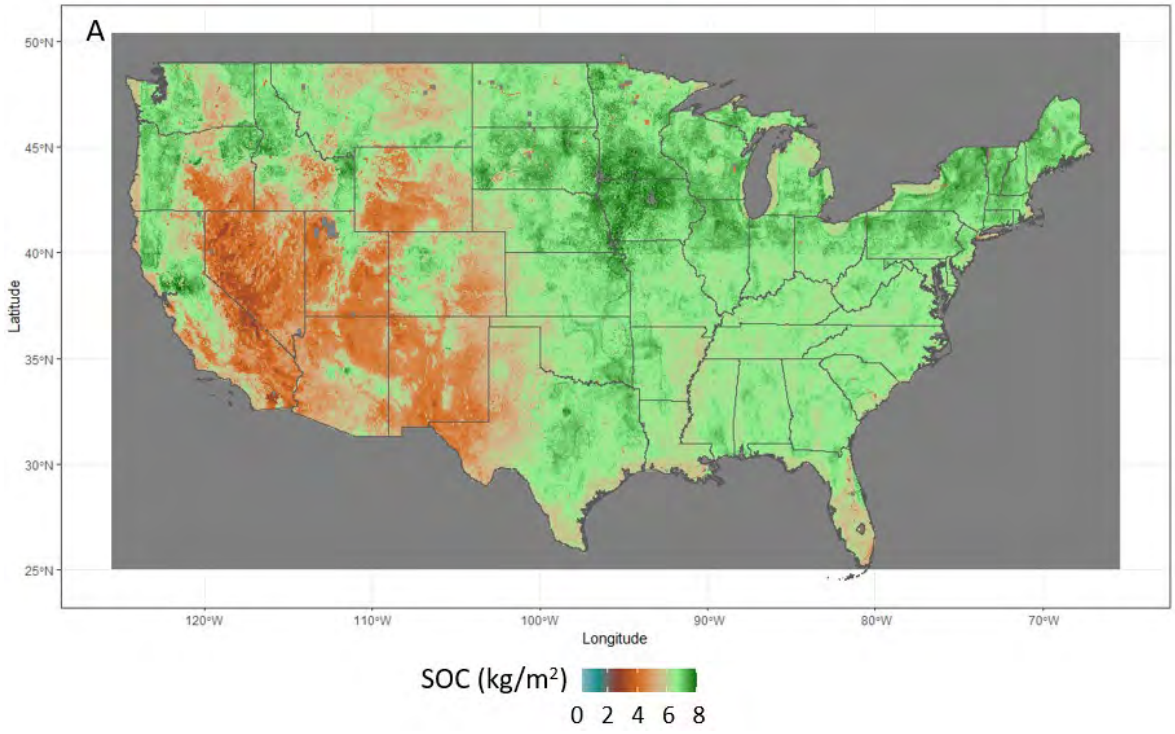

Figure 10. Mean SOC (kg/m2) from 1990-2022 in the top 30 cm of soil.

Using the land cover rasters from the U.S. Geological Survey that were part of the input datasets for the Random Forest algorithm, the land use classes were separated by year and the average total SOC value for each year was calculated in each land use class. Our team found that 60.4 Pg C stored in the top 30 cm of CONUS soils, which falls in the middle of the range of estimates of SOC for the United States (29.3 – 106.2 Pg) over the past decade. Also, about a third of the estimated SOC in the United States is stored in shrubland and grassland soil, and another third is stored in agricultural soil.

Our team grouped the SOC by USDA farm resource region to illustrate the spatial variation in SOC over time. Figure 11 shows that the mean soil carbon values vary among USDA farm resource regions in the United States, given the different sizes of the regions, different land use types, soil types, and climates. The regions with the lowest total SOC estimates were the Mississippi Portal, followed by the Eastern Uplands and the Southern Seaboard. The top three SOC estimates were found in the Basin and Range, Fruitful Rim, and the Northern Crescent.

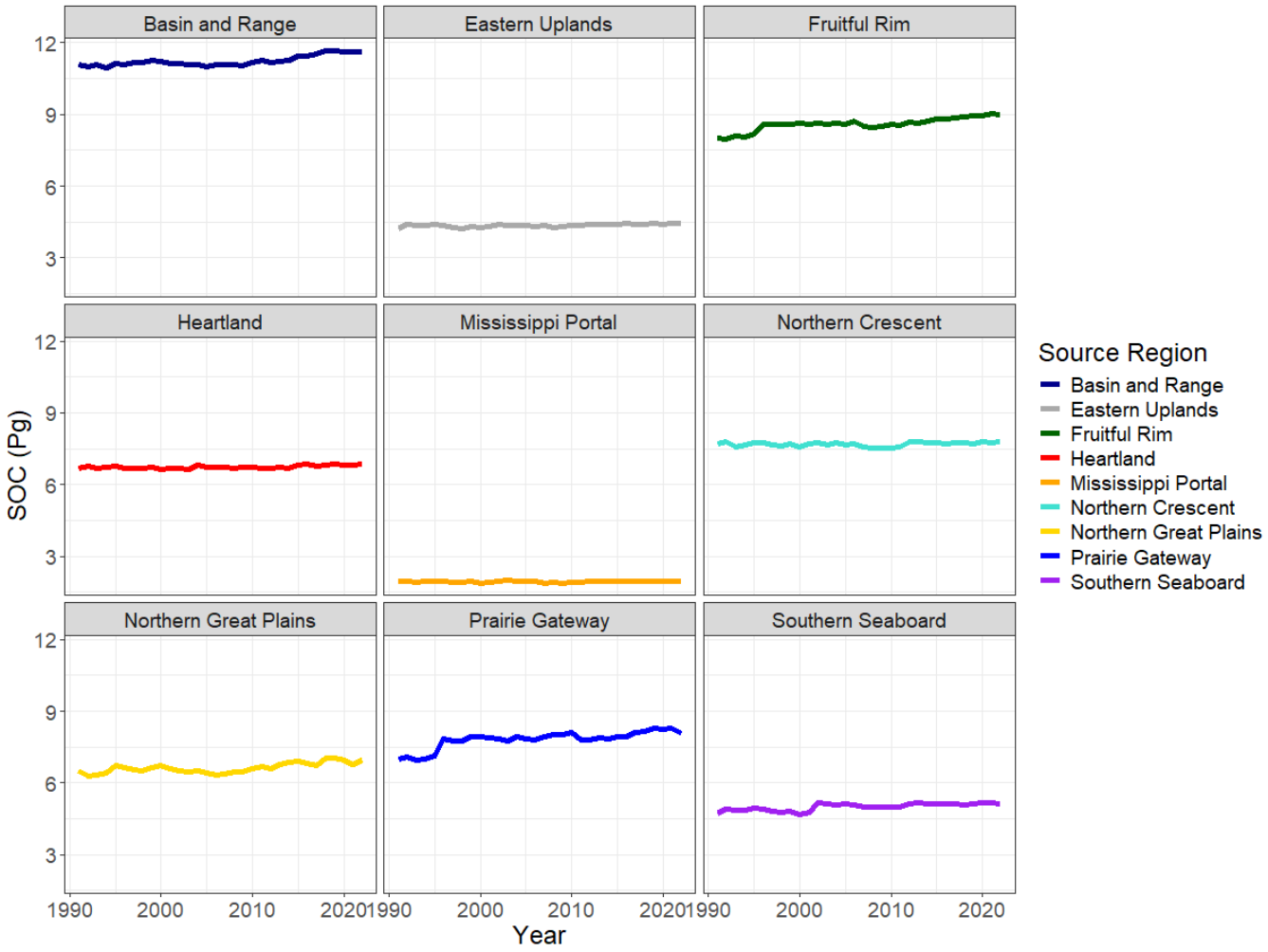

Figure 11. A time series of annual SOC stocks by farm resource region.

Publications

Rubin, H. J., Fu, J. S., & Yu, T. E. (Manuscript submitted for publication). Mapping Historical Soil Carbon in the U.S. with Machine Learning.

Outreach Efforts

None.

Awards

None.

Student Involvement

Hannah Rubin conducted the SOC analysis and included this study as a chapter in her doctoral dissertation.

Plans for Next Period

- Utilize this data layer to evaluate SOC change under some land use management scenarios.

Project 001(F) Alternative Jet Fuel Supply Chain Analysis

Massachusetts Institute of Technology
Hasselt University

Project Lead Investigators

Dr. Florian Allroggen
Executive Director Aerospace Climate & Sustainability; Research Scientist
Laboratory for Aviation and the Environment
Massachusetts Institute of Technology
77 Massachusetts Ave, Building 33-328, Cambridge, MA 02139
617-715-4472
fallrogg@mit.edu

Dr. Raymond L. Speth
Principal Research Scientist
Laboratory for Aviation and the Environment
Massachusetts Institute of Technology
77 Massachusetts Ave, Building 33-322, Cambridge, MA 02139
617-253-1516
speth@mit.edu

University Participants

Massachusetts Institute of Technology (MIT)

- P.I.: Dr. Florian Allroggen
- co-P.I.: Dr. Raymond L. Speth
- FAA Award Number: 13-C-AJFE-MIT, Amendment Nos. 003, 012, 016, 028, 033, 040, 048, 055, 058, 067, 082, 088, 096, 115, 132, and 135
- Period of Performance: August 1, 2014, to December 31, 2024
- Tasks (for reporting period October 1, 2023, to September 30, 2024):
  1. Support and provide leadership for United States (U.S.) participation in the International Civil Aviation Organization (ICAO) Committee on Aviation Environmental Protection (CAEP) to enable appropriate crediting of the use of sustainable aviation fuels (SAF) under the Carbon Offsetting and Reduction Scheme for International Aviation (CORSIA)
  2. Support U.S. participation in the ICAO CAEP by performing core life-cycle analysis (CLCA) to establish default values for use under CORSIA
  3. *(omitted, led by Hasselt University)*
  4. Support knowledge sharing and coordination across all ASCENT Project 001 (A01) universities working on SAF supply chain analyses.

Hasselt University (UHasselt or UH, through subaward from MIT)

- P.I.: Prof. Robert Malina
- Period of Performance: September 1, 2016, to December 31, 2024
- Period of Performance: August 1, 2014, to December 31, 2024
- Tasks (for reporting period October 1, 2023, to September 30, 2024):
  1. Support and provide leadership for U.S. participation in ICAO CAEP to enable appropriate crediting of the use of SAFs under CORSIA
  2. Support U.S. participation in ICAO CAEP by performing CLCA to establish default values for use under CORSIA
  3. Contribute to the development of fuel production assessment for CORSIA-eligible fuels (CEFs)
  4. *(omitted, led by MIT)*

Project Funding Level

The ASCENT Project 001(F) received $4,560,000 Federal Aviation Administration (FAA) funding and $4,560,000 matching funds. Sources of matching funds are approximately $723,200 from MIT, plus 3rd party in-kind contributions of $809,000 from Byogy Renewables, Inc., $1,038,000 from Oliver Wyman Group, $1,155,000 from NuFuels LLC, $401,000 from Savion Aerospace Corp., and $433,800 from Earth Force Technologies.

Investigation Team

Massachusetts Institute of Technology

Dr. Florian Allroggen (P.I.), All MIT tasks
Dr. Raymond L. Speth (co-P.I.), MIT Task 1
Matthew Pearlson (research specialist), MIT Tasks 1
Dr. Niamh Keogh (research scientist), MIT Task 1
Tae Joong Park (graduate research assistant), MIT Tasks 1

Hasselt University

Prof. Robert Malina (P.I.), All UHasselt Tasks
Dr. Alessandro Martulli (postdoctoral associate), All UHasselt Tasks
Teshome Deressa (graduate research assistant), UHasselt Task 2

Project Overview

The overall objectives of A01 are to (a) derive information on regional supply chains to explore scenarios for future SAF production and (b) identify supply-chain-related obstacles to commercial-scale production in the near term and to larger-scale adoption in the longer term. For the reporting period, the MIT/UHasselt team contributed to these goals by (a) providing leadership in the ICAO CAEP CLCA subgroup of the Fuels Task Group (FTG), which has been tasked with calculating life-cycle greenhouse gas (GHG) emissions associated with the use of SAF, (b) performing core life-cycle GHG emission analyses to enable the inclusion of additional SAF pathways under CORSIA or to verify CLCA values calculated by other institutions, (c) contributing to SAF availability assessments, and (d) contributing to knowledge transfer among the A01 team.

Task 1 – Support and Provide Leadership for U.S. Participation in ICAO CAEP to Enable Appropriate Crediting of the Use of SAFs under CORSIA

Massachusetts Institute of Technology
Hasselt University

Objectives

The overall objective of this task is to provide continued leadership and support for the FAA in its engagement with the ICAO CAEP FTG. The specific focus of the work during this reporting period was to (a) develop an actual value method for including fuels produced from atmospheric or waste gas carbon sources in the CORSIA framework, and (b) provide guidance on the inclusion of fuels with significant electricity input in CORSIA.

Research Approach

To achieve the goals outlined above, the team continued to co-lead the CLCA subgroup of the FTG. Prof. Malina acted as a co-lead. This role ensures that Prof. Malina remains a focal point of CLCA research, such that specific research tasks can be guided efficiently and effectively. The following research has been conducted in support of the leadership role:

Actual Value Method for Including Fuels Produced from Atmospheric or Waste Gas Carbon Sources

Currently in CORSIA, only fuels that are produced from biogenic carbon sources and wastes and residues are considered eligible to be considered as SAFs. In consideration of different pathways for SAF production with significant electricity input, the MIT team assessed atmospheric and waste gas carbon sources for inclusion in the actual value document.

As shown in Figure 1, the production and use of SAF made from carbon captured directly from the atmosphere is associated with a closed loop carbon cycle, similar to SAF produced from biogenic feedstock. As such, SAF produced from carbon directly sourced from the atmosphere can be associated with zero combustion emissions.

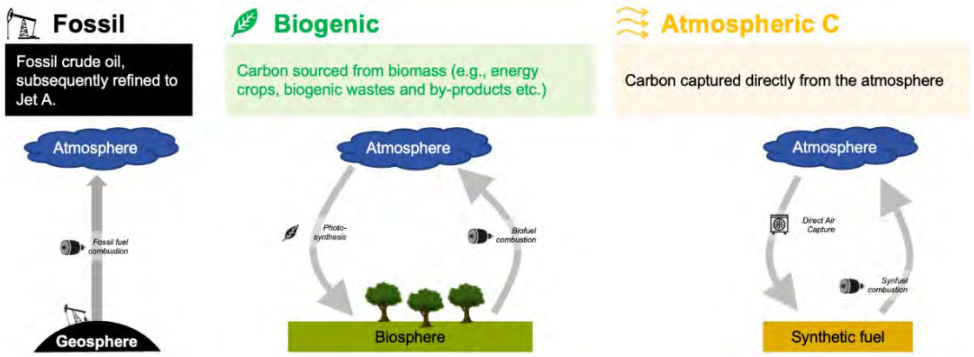

Figure 1. Carbon cycle for CEFs from fossil, biogenic, and atmospheric carbon sources.

In the case of carbon sourced from fossil waste gases (see Figure 2), combustion emissions of a SAF produced could be set to zero if (a) the gas stream is an unintentional and unavoidable results of producing other primary products, (b) the gas stream would be discarded into the atmosphere absent its use for SAF production, and (c) the initial emitter retains the burden of the emission. However, the SAF producer will have to account for (a) any changes in the net realization of climate impacts associated with carbon release (e.g., difference in the global warming potential [GWP] between the waste gas and the carbon dioxide [CO_2] released from SAF combustion), and (b) any impacts of the utilization of the waste gas stream on the initial emitting process (e.g., displacement of heat or electricity production from the waste gas stream).

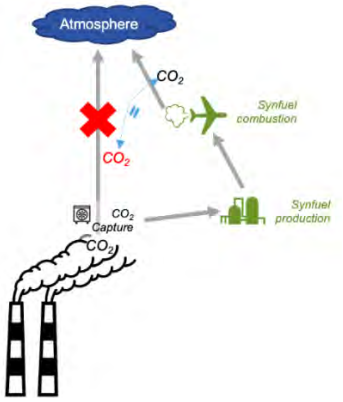

Figure 2. Carbon cycle for CEFs from waste or residue gases.

Guidance on Including Fuels Produced with Significant Electricity Inputs

The team followed the general approach outlined during the previous reporting period and considered two focus areas for developing a framework to calculate the CLCA values of fuels that are produced with significant electricity input.

Embodied Emissions of Electricity and Threshold Development

The MIT team developed a general method to calculate the embodied emissions of power generation and storage facilities:

$$EF_{EMB} = \frac{EMB_{con}+EMB_{RR}+EMB_{decom}}{e_l \times (1-\eta)} \quad \text{(Eq. 1)}$$

where EF_{EMB} is the emissions factor of embodied emissions in g carbon dioxide equivalent (CO_2e)/kWh of electricity, EMB_{con} is the embodied emissions in gCO_2e for the construction of the facility, starting from raw materials (e.g., sand for glass) through production processes (e.g., photovoltaic [PV] cell manufacturing) and installation (e.g., solar panel mounting). EMB_{RR} is the embodied emissions for repair (ex. inverter failure) and replacement (e.g., gearbox fluid change for wind turbine) and EMB_{decom} is the embodied emissions for decommissioning of a plant, including disposal or recycling of

materials. The sum of the embodied emissions from the three stages are normalized by the lifetime power generation (e_l), inclusive of transmission and distribution losses (η).

$$e_l = \sum_{t=1}^{T} RP \times D_t \times l_t \times CF_t \quad \text{(Eq. 2)}$$

where T is the economic life of the power plant, RP is the rated power, D_t is the expected degradation factor in year t, l_t is the expected operating hours in year t, including downtime, and CF is the capacity factor in year t, excluding downtime already captured in lt. Each stage of embodied emissions is calculated using mass and energy balances, and emission factors.

$$EMB_{stage} = \sum_{iM}^{n_M} m_{i_M} EF_{i_M} + \sum_{i\varepsilon}^{n_\varepsilon} \varepsilon_{i_\varepsilon} EF_{i_\varepsilon} \quad \text{(Eq. 3)}$$

where m_{i_M} is the mass (kg) of i_M^{th} material out of n_M materials used in the embodied emissions stage, EF_{i_M} is the emissions factor of i_M^{th} material (gCO_2e/kg), $\varepsilon_{i_\varepsilon}$ is the use of $i_\varepsilon^{\text{th}}$ energy (MJ) type of n_ε energy types used in the embodied emissions stage, and EF_{i_ε} is the emissions factor of $i_\varepsilon^{\text{th}}$ energy type (gCO_2e/MJ). Emission factors can be found in literature or proposed by bottom-up calculations from producers, following CORSIA guidelines (e.g., methane [CH_4], nitrous oxide [N_2O] GWP-100 [global warming potential over a 100-year timeframe] from Intergovernmental Panel on Climate Change [IPCC] Assessment Report [AR]-5). Mass and energy balances should be from the specific supply chain where possible, and reliant on literature and public data where necessary.

The MIT team also developed a sample calculation for embodied emissions factor of electricity by applying this general approach, using data from the literature for solar and wind. Figure 3 below is a partial view of the wind calculator, considering turbine production, electric system, mounting, substation, and end of life treatment for the embodied emission stages. The total emissions footprint is normalized by the lifetime generation, using the rated power, capacity factor, degradation, lifespan, and transmission and distribution losses. Each embodied emission stage uses the emission factors and mass and energy inventory, including metals, plastics, chemicals, wiring, adhesives, electricity, and fuels used for manufacturing and transportation.

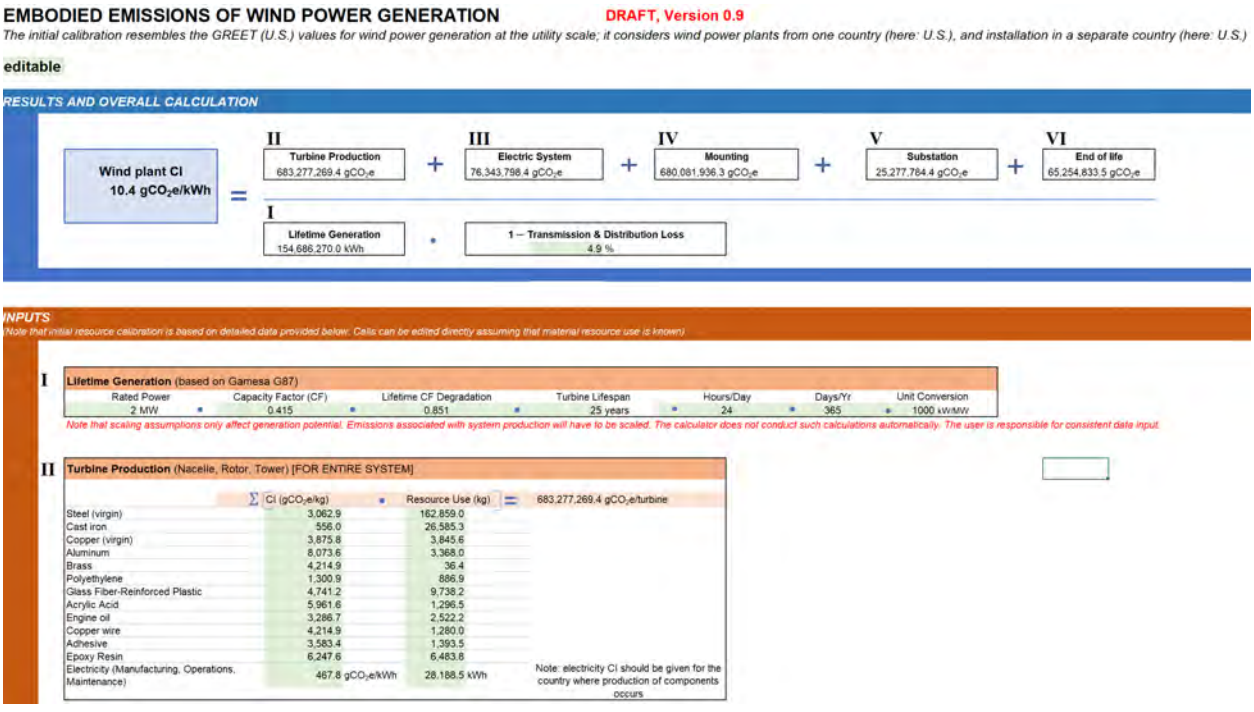

Figure 3. Draft sample calculator for embodied emissions of electricity for a partial view of wind turbine.

Electricity Sourcing
It is not possible to physically trace electricity procured for SAF production processes from a specific electricity generator if transported via the electricity grid. The MIT team investigated a set of electricity sourcing criteria including additionality, temporal matching and deliverability which replicate chain of custody considerations. These criteria are necessary to (a) provide a technology-neutral assessment methodology and (b) avoid concerns at the grid level, especially for emissions and stability.

Additionality defines the degree to which new electricity generation capacity is added in response to demand for CEF production. Additionality ensures balancing of supply and demand considering the large-scale electricity demand that is required for power-to-liquid fuel production and to avoid grid wide emissions impacts. Such a criterion is necessary to prevent double counting of renewable electricity generation deployed for other uses (e.g., grid decarbonization) and to reduce the risk of consequential emissions of displacing renewable electricity from other existing uses (Ricks et al., 2023; Zeyen et al., 2024).

Temporal matching is the timescale over which the generated renewable electricity must match the electricity consumed by the fuel producer. This can be hourly, monthly, or annual. Such criteria can be set to ensure the electricity sourced for SAF production can supply the demand from the SAF production process at any given time, creating a surrogate for a "physical" chain of custody. Hourly time matching is shown to significantly reduce the grid wide emissions impacts, in comparison to annual matching. This is because hourly matching was found to lead to higher capacities for renewable electricity capacity being installed. However, in grids that have an existing high level of low emission power generation sourcing the stringency of hourly matching may not be required (Giovanniello et al., 2024; Ricks et al., 2023; Zeyen et al., 2024).

Deliverability defines the sourcing points from which the procurement of renewable electricity is allowed. Example boundaries of sourcing regions include the same grid, market bidding zones or countries. Deliverability considers the extent to which the electrical path between the renewable electricity supply and fuel producer is physically congested over the lifetime of the supply contract. It has been shown that procurement of electricity over a large geographical area can lead to significant consequential emissions as the introduction of transmission constraints can prevent the physical delivery of the procured electricity (Ricks et al., 2023).

Milestones

- UHasselt and MIT have brought forward analyses to support progress in the areas outlined above. The results have been presented to the FTG during FTG meetings and numerous CLCA subgroup and expert meetings.
- UHasselt and MIT experts participated in and contributed to numerous FTG meetings, including CAEP13_FTG/06 (February 2024), CAEP13_FTG/05 (May 2024) and CAEP13_FTG/08 (September 2024).

Major Accomplishments

1. Drafted (Prof. Malina, co-lead of the FTG CLCA Subgroup) CLCA progress reports for FTG meetings, where CLCA topics were discussed. In addition, Prof. Malina co-led several task group meetings.
2. Prepared detailed proposals enabling the use of additional carbon sources and significant electricity use under the CLCA methodology.

Publications

- CAEP/13-FTG/06-WP/07: Summary of the progress of the CLCA subgroup
- CAEP/13-FTG/06-WP/08: Summary of the progress of consideration for fuels with high electricity input in CORSIA
- CAEP/13-FTG/07-WP/04: Summary of the progress of the CLCA subgroup
- CAEP/13-FTG/07-WP/05: Summary of the progress of consideration for fuels with high electricity input in CORSIA
- CAEP/13-FTG/08-WP/09: Consideration of additional carbon sources for fuels with high electricity input in CORSIA
- CAEP/13-FTG/08-WP/10: Accounting of Electricity for fuels with high electricity input in CORSIA

Outreach Efforts

- Communicated progress on this task during weekly briefing calls with the FAA and other U.S. delegation members to the FTG, as well as during numerous FTG teleconferences between meetings.
- Participated in and contributed to FTG meetings (UHasselt and MIT experts), including CAEP13_FTG/06 (February 2024, Geneva), CAEP13_FTG/05 (May 2024, virtual) and CAEP13_FTG/08 (September 2024, Montréal).

- Led (MIT team) an ad-hoc group to prepare concrete proposals for revision of the actual value document to enable the use of additional carbon sources and significant electricity use.

Student Involvement

Tae Joong Park (graduate student, MIT) was involved in this task.

Plans for Next Period

- Continue its work with the FTG.
- Calculate and propose default CLCA values for additional pathways.
- Continue to lead (Prof. Malina) the CLCA Subgroup.
- Focus on finalization of the actual value method improvement for calculating CLCA values for fuels requiring substantial electricity inputs.

References

Giovanniello, M. A., Cybulsky, A. N., Schittekatte, T., & Mallapragada, D. S. (2024). The influence of additionality and time-matching requirements on the emissions from grid-connected hydrogen production. *Nature Energy, 9*, 197–207. https://doi.org/10.1038/s41560-023-01435-0

Ricks, W., Xu, Q., & Jenkins, J. D. (2023). Minimizing emissions from grid-based hydrogen production in the United States. *Environmental Research Letters, 18*(1), 014025. https://doi.org/10.1088/1748-9326/acacb5

Zeyen, E., Riepin, I., & Brown, T. (2024). Temporal regulation of renewable supply for electrolytic hydrogen. *Environmental Research Letters, 19*(2), 024034. https://doi.org/10.1088/1748-9326/ad2239

Task 2 – Support U.S. Participation in ICAO CAEP by Performing CLCA to Establish Default Values for Use Under CORSIA

Massachusetts Institute of Technology
Hasselt University

Objectives

During the CAEP/11, CAEP/12, and CAEP/13 cycle, the MIT ASCENT Project 001 team took leadership in applying the agreed-upon CLCA method to establish default CLCA values for CEFs. However, the list of pathways is not exhaustive, and further CLCA analysis is required to enable the inclusion of SAF technologies nearing commercialization. During the current reporting period, the team supported (a) a review of mixed animal fat hydroprocessed ester and fatty acid (HEFA) fuels and (b) a sensitivity analysis of CLCA values to investigate the sensitivity of the CLCA default values to changes in input parameters.

Research Approach

CLCA of HEFA fuel from Non-Standard Coconut

During the current reporting period, the team estimated the life cycle GHG emissions of HEFA from non-standard coconut. The system boundaries of calculations as well as the specific data sources used for the calculation are summarized in Table 1.

Table 1. General assumptions for estimating the core life-cycle analysis emissions of hydroprocessed ester and fatty acid fuels from non-standard coconuts. CORSIA: Carbon Offsetting and Reduction Scheme for International Aviation; GREET: greenhouse gases, regulated emissions, and energy use in transportation.

Stage	Assumptions
Feedstock collection and transportation	Non-standard coconut collection is assumed to take place in the Davao region, in The Philippines which has the national largest share of coconut farms (Philippine Statistics Authority, 2022). The feedstock is assumed to be transported for 143 km by medium-truck to the feedstock pretreatment and crude coconut oil facility. Back-hauls are regarded as empty and considered.
Feedstock pre-treatment	Input of electricity (for lighting purposes) and sulfur (for preventing decay) is assumed in feedstock processing (Yani et al., 2022). The electricity mix of The Philippines is considered as electricity grid (Ember, 2023).
Crude coconut oil extraction	Input of steam (to be produced from coal boiler), water, solvent (hexane), and grid electricity is assumed. Output of copra expeller from mechanical process and copra expeller pellet from chemical process are assumed. They are utilized as feed, therefore regarded as co-product. Emissions are allocated to such coproducts on an energy basis. Data source: (Yani et al., 2022) The electricity mix of The Philippines is considered as electricity grid (Ember, 2023).
Crude coconut oil transportation to the fuel production facility	The extracted coconut oil is assumed to be transported first by truck (11 km) to the Port of Davao from where it is transported to the Port of Rotterdam, in Europe. Transportation by ocean tanker (18145 km).
Fuel production	Hydrogen requirements for coconut oil were adjusted compared to those for soybean hydrogen consumption based on the molar stoichiometry of the hydroprocessing reactions. Fatty acid composition of coconut oil based on (Liu et al., 2019) Other energy and utilities inputs are equivalent as in the last calculation from CORSIA.
Fuel transportation and distribution	According to default data from the GREET model, 63%, 8% and 29% of the fuel were assumed to be transported 80 km by truck, 837 km by barge, and 1288 km by rail, respectively. Back-haul is regarded to be empty and considered.

More specifically, the following are noted:

1. The feedstocks involved in this pathway include non-standard coconuts which were recently included in the positive list of wastes, residues and by products of the coconut industry. These feedstocks are assumed to have zero GHG emissions, as they are considered a by-product derived from the coconut industry.
2. The feedstock collection, transportation, and coconut oil extraction are assumed to occur in the Philippines, specifically in the Davao region, which has the largest concentration of coconut farms in the country. The collected coconuts are transported to a facility for feedstock pre-treatment and coconut oil extraction. The crude coconut oil extracted at this facility is then shipped from the Port of Davao in the Philippines to the Port of Rotterdam in Europe, where the production of HEFA fuel is assumed to take place. The assumptions for the fuel production process and transportation are based on the 2023 Greenhouse gases, Regulated Emissions, and Energy use in Transportation (GREET) model (Excel® version). Additionally, the hydrogen requirements for the fuel production stage were adjusted to align with the fatty acid composition of the crude coconut oil. Carbon intensity and GHG emission estimates were derived from the 2023 GREET model.
3. The fuel production stage involves converting the extracted crude coconut oil into SAF by upgrading the feedstock through hydrotreatment and isomerization. Table 2 outlines the inputs and outputs for transforming coconut oil

® Excel is a registered trademark of Microsoft Corporation in the United State and other countries.

into HEFA fuel. It is assumed that the hydrogen consumption during the upgrading of coconut oil may differ from that of soybean oil due to variations in their fatty acid compositions. Coconut oil has a higher content of saturated fatty acids compared to soybean oil, leading to lower hydrogen consumption during the hydrogenation phase of HEFA fuel production. To estimate hydrogen consumption for coconut oil, the molar stoichiometry of hydroprocessing reactions was utilized. This included calculating the reaction stoichiometry for processes such as the conversion of unsaturated triglycerides to saturated ones, propane loss, and decarboxylation. Based on these calculations for coconut oil, the hydrogen input value was adjusted.

Table 2. Inputs and outputs of the feedstock pre-treatment and coconut oil extraction. CCO: crude coconut oil; LHV: lower heating value; UH: Hasselt University.

Parameter	Unit	Non-standard coconuts
		UH
Inputs		
Electricity	MJ/ton copra	23
Sulfur	Ton/ton copra	0.001
Coal	Btu/lb CCO	1600
n-Hexane	Btu/lb CCO	43.5
Electricity, low voltage	Btu/lb CCO	464.6
Outputs		
CCO	lb CCO/ton copra	1459.6
Other		
Coconut oil LHV	MJ/kg	37.8
Copra expeller LHV	MJ/kg	15.7
Allocation factor (energy)	—	85.5%

4. A sensitivity analysis was conducted around key parameters to understand the need for clarification in the pathway specification column of the default value table in the ICAO Document *CORSIA Default Life Cycle Emissions Values for CORSIA Eligible Fuels* (CORSIA, 2024). The results are detailed in Tables 3 through 6.

Table 3. Inputs and outputs of the transformation of coconut oil into hydroprocessed ester and fatty acid fuels. Data is expressed per lb of jet fuel.

Parameter	Unit	Non-standard coconuts
		UH
Inputs		
Coconut oil	lb	1.27
Natural gas	Btu	1548
Electricity, low voltage	Btu	88
Hydrogen	Btu	925
Outputs		
Jet fuel	lb	1.00
Propane fuel mix	lb	0.099
Other		
Total energy input	Btu	2561

Table 4. Estimated greenhouse gas emissions from the production of non-standard coconuts SAF. Data are given in g CO_2e/MJ_{SAF}. HEFA: hydroprocessed esters and fatty acids. UH: Hasselt University.

Stage	Non-standard coconuts
	UH
Feedstock pre-treatment	0.11
Feedstock transportation t. o oil extraction facility	1.29
Coconut oil extraction	13.45
Transport to the SAF facility	2.25
SAF production	9.07
SAF transportation	0.38
Total	***26.55***

Table 5. Sensitivity analysis results for power, coal and natural gas requirements for the production of non-standard coconuts SAF. Data are given in g CO_2e/MJ_{SAF}. NG: Natural gas.

	-20%	-10%	Baseline	+10%	+20%
Power requirements	-1.12	-0.59	26.55	+0.60	+1.12
Coal/NG requirements	-2.69	-1.34	26.55	+1.34	+2.69

Table 6. Sensitivity analysis results for the source of hydrogen production to produce non-standard coconuts SAF. Data are given in g CO_2e/MJ_{SAF}. HTGR: high temperature gas-cooled reactor.

	Natural Gas (Baseline)	Coal	Nuclear (thermo-chemical water cracking)	Nuclear (HTGR)
GHG emissions	26.55	31.75 (+5.20)	23.72 (-2.83)	23.42 (-3.13)

Final Sensitivity Analysis of CLCA Values

A sensitivity analysis was presented at FTG/03 as CAEP/13-FTG/03-IP04 and then updated at FT/04 as CAEP/13-FTG/04-IP03. Pathway specifications for the default value were agreed at the CAEP/13/FTG/04 meeting. The team extended the previously conducted sensitivity analyses by performing the assessment for eight additional SAF pathways. The default CLCA value for a SAF pathway is established as the midpoint of the range of estimates provided by various FTG modeling teams. Consequently, sensitivity analysis cannot be performed on these midpoint values. Instead, the CLCA values were determined using the 2023 GREET model (Rev. 1).

The analysis was conducted for two conversion pathways and a set of different feedstocks: (1) Fischer–Tropsch (FT) jet fuel from agricultural residues and poplar and (2) HEFA from camelina, jatropha and beef tallow (updated coreLCA default value), poultry fat (new coreLCA default value), lard (new coreLCA default value), mix animal fats (new coreLCA default value).

A set of parameter values was varied in the sensitivity analysis:

- Conversion efficiency: Biomass input requirements for the SAF production in its conversion stage were changed by -10% and +10%.
- Heat requirements: Many SAF production pathways require external heat sources during the production process. Those requirements are assumed to be satisfied by natural gas, and we vary these requirements by -10% and +10%.
- Heat source: The default values are modelled with the assumption that external heat requirements are satisfied by natural gas. In the sensitivity analysis, the effect of using a fully decarbonized heat source and the effect of using coal is quantified.

- Electricity requirements: Electricity requirements during SAF production are varied by -10% and +10%.
- Electricity mix: The electricity from the U.S. grid was taken as a base case. The use of the electricity grid of Europe, China, India, and the world average electricity grid was assessed.
- Hydrogen source: Hydrogen is an important input in many SAF pathways. In the default values, it was assumed that hydrogen is produced from natural gas by means of steam methane reformation. In the sensitivity analysis, we quantify the emission effect of hydrogen from a zero-carbon source and hydrogen from coal.

Table 7 provides a summary of the results. Green-shaded cells indicate an emission reduction whereas red-shaded cells indicate an emission increase, with the level of color shading denoting the magnitude of the effect. Darker colors represent stronger effects. A 10% variation in conversion efficiency, electricity requirements, or heat requirements results in an impact of less than 3 g CO2e/MJ SAF across all pathways. Similarly, changes in the assumed electricity grid mix led to an impact of less than 4 g CO2e/MJ. When the heat source is switched to coal, emissions for HEFA pathways—excluding those using camelina and jatropha feedstocks—increase by over 4 g CO2e/MJ, reaching a maximum of 6.38 g CO2e/MJ. For hydrogen production, using coal as the source raises emissions by more than 6 g CO2e/MJ across all HEFA pathways, including those involving camelina and jatropha. These findings align with preliminary sensitivity analyses conducted for other pathways, as presented in FTG03 and FTG04. Figures 4 through 7 show the effect sizes and direction for each of the assessed parameters, broken out by conversion technology and feedstock.

Table 7. Full results of sensitivity analysis. Data is given in g CO_2e/MJ of sustainable aviation fuel. FTJ: fermentation-to-jet; HEFA: hydroprocessed esters and fatty acids.

Pathway	Feedstock	Feedstock conversion		Heat requirements		Heat source		Power requirements		Source of hydrogen		Electricity mix			
		-10%	10%	-10%	10%	Decarbonized source	Coal	-10%	10%	Solar energy	Coal	China	India	Europe	World average
FTJ	Agricultural residues	-0.41	0.50	0.00	0.00	0.00	0.00	0.00	0.00	0.00	0.00	0.00	0.00	0.00	0.00
	Poplar	-0.70	0.86	0.00	0.00	0.00	0.00	0.00	0.00	0.00	0.00	0.00	0.00	0.00	0.00
HEFA	Camelina	-0.88	0.78	-0.26	0.26	-1.23	1.18	-0.13	0.13	-7.78	7.67	0.77	1.12	-0.32	0.26
	Jatropha	-3.09	3.09	-0.37	0.37	-2.32	1.67	-0.11	0.11	-7.78	7.67	0.67	0.97	-0.27	0.23
	Beef tallow	-0.46	0.46	-1.40	1.40	-8.90	6.38	-0.29	0.29	-6.08	5.99	2.49	3.40	-0.37	1.15
	Poultry	-0.63	0.63	-1.31	1.31	-8.05	5.99	-0.29	0.29	-7.48	7.37	1.61	2.12	0.00	0.86
	Lard	-0.41	0.41	-1.10	1.10	-5.94	5.02	-0.25	0.25	-6.77	6.67	2.08	2.86	-0.35	0.95
	Mixed animal fats	-0.46	0.46	-1.15	1.15	-6.49	5.28	-0.26	0.26	-6.66	6.57	2.24	3.07	-0.37	1.02

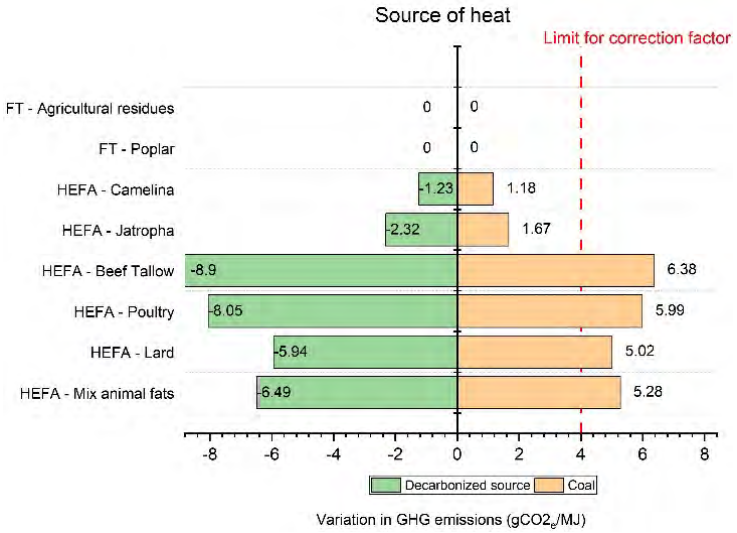

Figure 4. Effect of the source of heat source. FT: Fischer–Tropsch; GHG: greenhouse gas; HEFA: hydroprocessed esters and fatty acids.

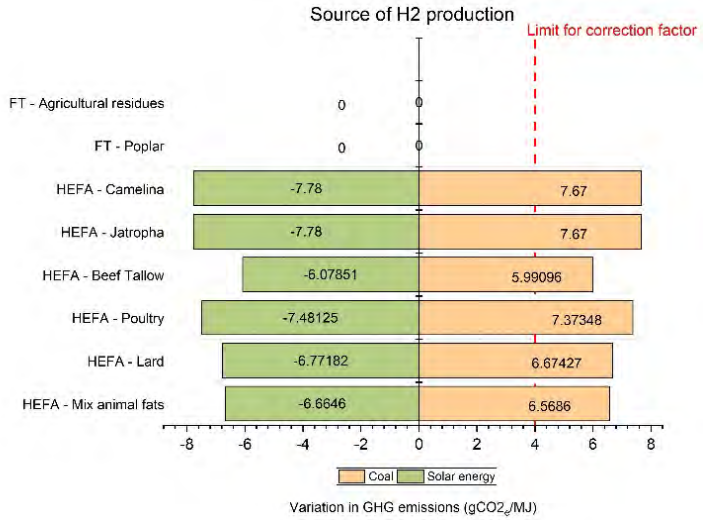

Figure 5. Hydrogen production source. H2: Hydrogen, FT: Fischer–Tropsch; GHG: greenhouse gas; HEFA: hydroprocessed esters and fatty acids.

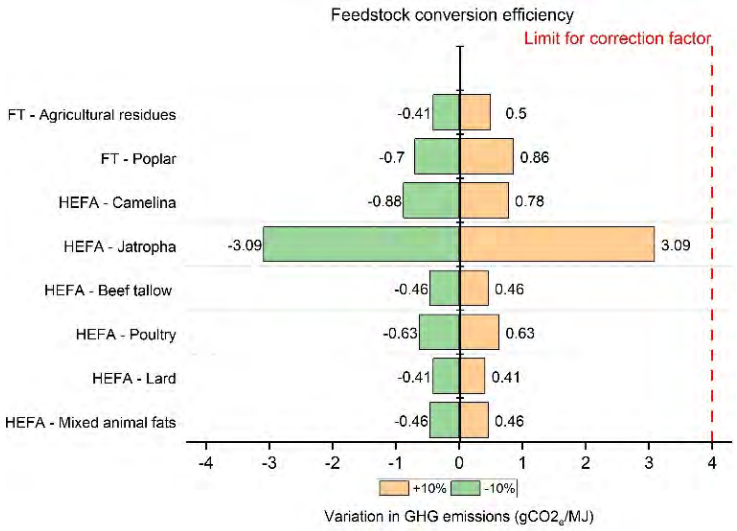

Figure 6. feedstock conversion efficiency (biomass input requirements). FT: Fischer–Tropsch; GHG: greenhouse gas; HEFA: hydroprocessed esters and fatty acids.

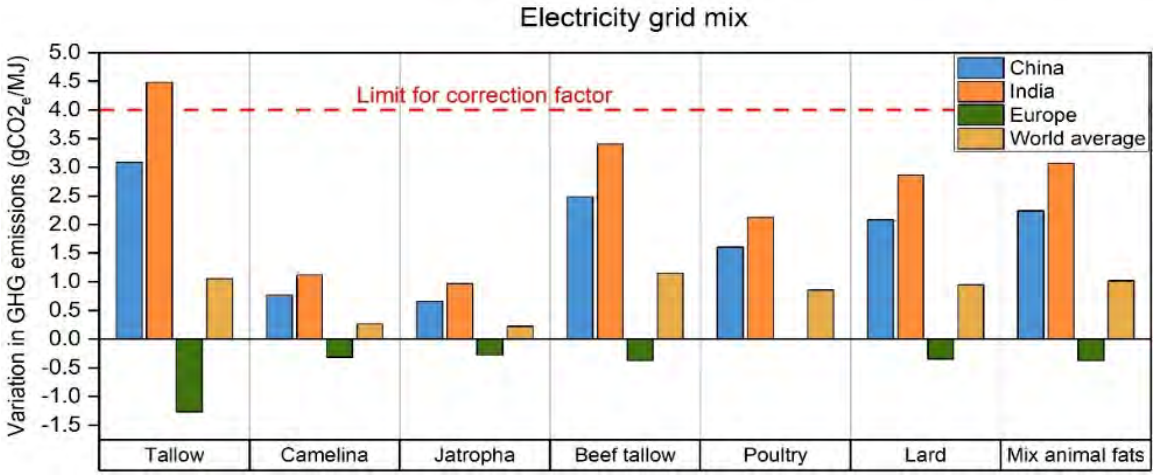

Figure 7. feedstock conversion efficiency (biomass input requirements) and electricity grid mix on the core life-cycle analysis value. GHG: greenhouse gas.

Milestones

- Documented research performed in working papers and information papers submitted to the FTG.
- Discussed the work outlined above with various technical experts.
- Participated in and contributed to the FTG meetings (UHasselt and MIT experts) held during the reporting period, including CAEP13_FTG/06 (February 2024), CAEP13_FTG/05 (May 2024) and CAEP13_FTG/08 (September 2024).

Major Accomplishments

- Finalized sensitivity analysis of the default CLCA values in CORSIA for a broad set of pathways.
- Inclusion of non-standard coconuts HEFA pathway in CORSIA.

Publications

Written Reports

- CAEP13/FTG06/WP07: Progress of the CLCA subgroup, February 2024.
- CAEP13/FTG07/WP04: Progress of the CLCA subgroup, May 2024.
- CAEP13/FTG07/WP16: Proposal for non-standard coconut LCA (FTG Board), May 2024.
- CAEP13/FTG08/WP20: Core-LCA-related items for the FTG Board, September 2024.

Student Involvement

Teshome Deressa (graduate student, UHasselt) was involved in this task.

Outreach Efforts

- Communicated progress on this task during weekly briefing calls with the FAA and other U.S. delegation members to the FTG, as well as during numerous FTG teleconferences between meetings.
- UHasselt and MIT experts participated in and contributed to FTG meetings, specifically CAEP13_FTG/06 (February 2024), CAEP13_FTG/05 (May 2024) and CAEP13_FTG/08 (September 2024).

Plans for Next Period

- Continue to perform attributional CLCA to establish default values for use under CORSIA.
- Participate in the calculation of the pongamia oil to HEFA fuel pathway within CORSIA and additional pathways as needed.

References

CORSIA. (2024). *ICAO document - CORSIA default life cycle emissions values for CORSIA eligible fuels*. Carbon Offsetting and Reduction Scheme for International Aviation (CORSIA). https://www.icao.int/environmental-protection/CORSIA/Documents/CORSIA_Eligible_Fuels/ICAO%20document%2006%20-%20Default%20Life%20Cycle%20Emissions%20-%20October%202024.pdf

Ember. (2023). *The Philippines electricity generation by source*. https://ember-energy.org/countries-and-regions/philippines-the/

Philippine Statistics Authority. (2022). *2022 Selected statistics on agriculture and fisheries* (International Serial Standard No. 1908-2045). https://psa.gov.ph/system/files/main-publication/%2528ons-cleared%2529_SSAF%25202022%2520as%2520of%252030082022_ONS-signed.pdf

Liu, R. J., Guo, X., Cheng, M., Zheng, L., Gong, M., Chang, M., Jin, Q., & Wang, X. (2019). Effects of chemical refinement on the quality of coconut oil. *Journal of Food Science and Technology -Mysore, 56*(6), 3109-3116. http://dx.doi.org/10.1007/s13197-019-03810-w

Yani, M., Toruan, D. P. M. L., Puspaningrum, T., Sarfat, M. S., & Indrawanto, C. (2022). Life cycle assessment of coconut oil product. *IOP Conference Series: Earth and Environmental Science, 1063*(1), 012017. http://dx.doi.org/10.1088/1755-1315/1063/1/012017

Task 3 – Contribute to the Development of the Fuel Production Assessment for CEFs

Hasselt University

Objective

The objective of this task is to contribute to the development of the fuel production assessment for CEFs to the year 2030 and beyond, based on detailed information gathered in a fuel production database. During the reporting period, the team worked jointly with researchers from Washington State University to maintain and update the SAF production analysis database used for the FTG fuel projections. Two work streams were initiated: (1) a database spreadsheet revision, and (2) the development of a new database architecture.

Research Approach

A revision of the existing announcement entries in the database spreadsheet has been carried out. The revision aimed at providing updates to all the announcement entries to reflect the latest information on project locations, statuses, and (planned) production volumes. Moreover, the data have been refined by standardizing company names, identifying duplicates and failed projects, and adding or updating hyperlinks for missing or non-functional links. This work was built upon the recent updates conducted by Washington State University and the FAA for entries based in the U.S.

New Database Architecture Development

The announcement entries were previously stored in a spreadsheet, which lacks structure and consistency. To address this, a new design has been developed to transform the spreadsheet into a relational database using structured query language (SQL). The redesigned database consists of multiple interconnected tables, including the Production Analysis Database and the Announcements Database. Unlike a spreadsheet where data are stored in individual cells, the relational database will organize information into records, with each row representing a unique entry.

Each table includes a column with a unique identifier for its entries (e.g., announcement_ID in the announcements table and production_ID in the production table). The database supports importing and exporting data to and from spreadsheet formats for easy accessibility. The newly developed database architecture will thus be used to generate the scenarios and provide an update on the SAF global production and short-term projections. The update of the scenarios and projections will be provided during the first FTG meeting of the CAEP14 cycle, in May 2025.

Milestone

- Updated and revised the SAF announcements entries and production database.

Major Accomplishments

- Developed the SAF production relational database in SQL.

- Employed the newly developed architecture to provide regular updates on the current global SAF production state and short-term projections.

Publications
- CAEP13/FTG06/WP05: SAF projection process, February 2024
- CAEP13/FTG07/WP15: Update on the SAF database, May 2024

Outreach Efforts
- Communicated progress on this task during weekly briefing calls with the FAA and other U.S. delegation members to the FTG, as well as during numerous FTG and LTAG teleconferences.

Awards
None.

Student Involvement
None.

Plans for Next Period
- Provide an additional update on the scenarios and projections during the first meeting of the new CAEP cycle (CAEP14/FTG01) in May 2025.

Task 4 – Support Knowledge Sharing and Coordination Across All A01 Universities Working on SAF Supply Chain Analyses
Massachusetts Institute of Technology

Objective
The objective of this task is to provide support for coordination of work by all A01 universities on SAF supply chain analysis. The sharing of methods and results decreases the replication of work on similar topics among A01 universities.

Research Approach
The MIT A01 team performed several functions to accomplish this task. Specifically, the team participated in bi-weekly A01 coordination teleconferences, which served as a venue to discuss progress in various grant tasks and learn about the activities of other ASCENT universities.

Milestone
- Presented current research to other ASCENT universities.

Major Accomplishments
- Participated in bi-weekly A01 coordination teleconferences and presentation of current research to other ASCENT universities.

Publications
None.

Outreach Efforts
- Participated in bi-weekly A01 coordination teleconferences and presentation of current research to other ASCENT universities.

Awards
None.

Student Involvement

None.

Plans for Next Period

- Continue to engage in bi-weekly teleconferences and other events to disseminate MIT's A01 work.

Project 002 Understanding Changes in Aviation Emissions Due to SAF with New Combustor Technology

Missouri University of Science and Technology, Aerodyne Research Inc., and The Boeing Company, Pratt and Whitney, and Gulfstream

Project Lead Investigator

Philip D. Whitefield
Professor Emeritus of Chemistry
Department of Chemistry
Missouri University of Science and Technology
400 W 11th Street, Rolla, MO 65409
573-465-7876
pwhite@mst.edu

University Participants

Missouri University of Science and Technology

- P.I.: Prof. Philip D. Whitefield
- FAA Award Number: 13-C-AJFE-MST, Amendments 002, 003, 005, 008, 010, 012, 019, 030 and 033
- Period of Performance: September 18, 2014, to September 30, 2025

Project Funding Level

Project	Funding	Matching	Source
13-C-AJFE-MST-002	$1,288,836.34	$1,288,836.34	EMPA letter
--	$284,613.66	$284,613.66	Transport Canada
13-C-AJFE-MST-003	$500,000.00	$500,000.00	EMPA letter
13-C-AJFE-MST 005	$500,000.00	$500,000.00	EMPA letter
13-C-AJFE-MST-008	$579,234.00	$579,234.00	EMPA letter
13-C-AJFE-MST-010	$725,500.00	$725,500.00	EMPA letter
13-C-AJFE-MST-012	$1,217,221.00	$1,217,221.00	EMPA letter
13-C-AJFE-MST-019	$521,246.00	$521,246.00	GE letter
13-C-AJFE-MST-030	$3,050,812.00	$3,050,812.00	Boeing letter
13-C-AJFE-MST-033	$2,513,003.00	$2,513,003.00	Boeing letter

EMPA = Swiss Federal Laboratories for Materials Science and Technology
GE = General Electric

Investigation Team

Missouri University of Science and Technology Prof. Philip Whitefield, (P.I.)
Prof. Klaus Woelk, (co-P.I.)
Steven Achterberg, (research technician)
Max Trueblood (research technician)

Aerodyne Research, Inc.
Dr. Richard Miake-Lye, (subcontractor)
The Boeing Co.
Dr. Steven Baughum, (subcontractor)
Dr. William Griffin, (subcontractor)
Pratt and Whitney
Dr. Timothy Snyder, (subcontractor)
Gulfstream Aerospace Corporation
Dr. Brian Cook, (subcontractor)

Project Overview

Objectives

In the last quarter of 2022, a decision was made to re-target the ASCENT Project 002 to focus on emissions impacts measurements resulting from the adoption of sustainable aviation fuels (SAF) by current and future anticipated global commercial fleets. Funds were de-obligated and re-obligated to underwrite the cost of these new emissions measurements. The ASCENT Project 002 Missouri University of Science and Technology (MS&T) team, with the guidance of emissions specialists at Boeing, Pratt and Whitney (P&W), and Gulfstream, proposed to make three high-priority ground-based field measurement campaigns of nonvolatile particulate matter (nvPM) and combustion gas emissions from engines on a commercial widebody transport, a business jet aircraft, and a new technology combustor burning both conventional fuels and candidate SAF. These measurements were scheduled to occur in three 21-day test campaigns in the fourth quarter of 2023 (Boeing/ecoDemonstrator; see Link 1 below), and in the fourth quarter of 2024 (Gulfstream; see Link 2 below). Currently the third field campaign with P&W has been delayed due to test cell access and is scheduled to take place at the end of the first quarter (March) of 2025. The analysis and reporting of the data arising from the Boeing and Gulfstream studies is underway. Each campaign has or will be preceded by test design, planning, and preparation, beginning in the second quarter of 2023. The cost to ASCENT Project 002 has been, and will be, to (a) support the MS&T team's participation in and management of the three ground-based emission studies and (b) defray some of the costs incurred for the fuels (i.e., SAFs and conventional jet fuels) that has or will be burned to conduct both ground-based and in-flight emissions testing. During this reporting period, the preparations and execution for the ecoDemonstrator and the Gulfstream subprojects were achieved and both subprojects are currently in the post test analysis stage. Planning and preparation for the P&W combustor test is underway.

Link 1 – Boeing 737-10 EcoDemonstrator Tackles SAF Contrail Study | Aviation Week Network
Link 2 -
https://nam02.safelinks.protection.outlook.com/?url=https%3A%2F%2Fwww.gulfstreamnews.com%2Fen%2Fnews%2F%3Fid%3Dc106d3c5-ffa0-4cf1-adc7-292e3a56dfea%26utm_medium%3Dsocial&data=05%7C02%7Cpwhite%40mst.edu%7Cc677ee6cd01246711ffc08dcfa0e97f6%7Ce3fefdbef7e9401ba51a355e01b05a89%7C0%7C0%7C638660187787269614%7CUnknown%7CTWFpbGZsb3d8eyJFbXB0eU1hcGkiOnRydWUsIlYiOiIwLjAuMDAwMCIsIlAiOiJXaW4zMiIsIkFOIjoiTWFpbCIsIldUIjoyfQ%3D%3D%7C0%7C%7C%7C&sdata=fEol3w3XpAJcXpA%2FrEAOarzcZl90SMKp8TtuWhnYHgg%3D&reserved=0

Work Schedule

- Tasks 1– 3 describes the work required to successfully perform the ground testing associated with an in-flight emissions study on a wide-body airframe (potentially the Boeing-sponsored ecoDemonstrator study), a business jet (the Gulfstream study), and a new technology combustor (the P&W study).
- Task 1 – 3.1: Plan the test matrices for up to a 3-week deployment to a ground testing venue to be provided by the sponsoring original equipment manufacturer (OEM; Boeing, Seattle, WA; Gulfstream, Savannah, GA; and P&W, Hartford, CT). This planning exercise has been undertaken in coordination with the National Aeronautics and Space Administration Mobile Aerosol Laboratory team who are participating in the Boeing and Gulfstream ground tests.
- Task 1 – 3.2: Prepare the MS&T and Aerodyne instrument packages housed in mobile laboratories, including calibration of the individual particulate matter (PM) mass number and compositional systems.
- Task 1 – 3.3: Transport and set up the MS&T and Aerodyne instrument packages (mobile laboratories). This task includes deployment of test personnel to the test site and the interconnection of the instrument packages to the communal sampling probe assembly. During this setup activity, sampling system loss analyses will be performed.
- Task 1 – 3.4: Execute the test matrices defined in Task 1 – 3.1

- Task 1 – 3.5: Tear-down and transport the mobile laboratories and test personnel to their home locations.
- Task 1 – 3.6: Conduct post-test data reduction and analysis including participation in post-test workshops whose locations and times are yet to be defined.
- Task 1 – 3.7: Prepare and deliver interim and final reports.
- Task 1 – 3.8: The OEMs with the assistance of the Federal Aviation Administration (FAA), through this effort, have or will coordinate the procurement, fuel properties analysis, delivery, handling, and loading logistics for various fuels in support of the 2023–2025 emissions testing.

  In the case of the ecoDemonstrator subproject, the fuels burned are as follows:
  - Fuel 1: Low-sulfur Jet A, per ASTM D1655, total percentage by mass maximum objective of 0.0001 (maximum total sulfur target of 1 ppm)
  - Fuel 2: 100% Hydroprocessed Esters and Fatty Acids (HEFA)- straight paraffinic jet fuel (SPK), per ASTM D7566, Tables 1, A2.1, and A2.2
  - Fuel 3: Approved SAF blend (e.g., 30% HEFA-SPK), per ASTM D7566, Table 1

  In the case of the Gulfstream subproject, the fuels burned are as follows:
  - Fuel 1: 100% HEFA- SPK
  - Fuel 2: 30%/70% HEFA-SPK/JET A Blend
  - Fuel 3: 100% Conventional JET A

Milestones

- Task 1 – 3.1: COMPLETED for Boeing, Gulfstream and P&W
- Task 1 – 3.2: COMPLETED for Boeing, Gulfstream and P&W
- Task 1 – 3.3: COMPLETED for Boeing and Gulfstream
- Task 1 – 3.4: COMPLETED for Boeing and Gulfstream
- Task 1 – 3.5: COMPLETED for Boeing and Gulfstream

Major Accomplishments

- Reconfigured ASCENT Project 002 objectives, with new configuration in action.
- Successfully completed planning and preparation phase for SAF studies with Boeing, Gulfstream, and P&W.
- Successfully completed ground tests with Boeing and Gulfstream, with data deposited in Boeing archive.
- Negotiated subcontracts with Aerodyne, Boeing, and P&W.

Publications

Whitefield, P. (2024, October). *Understanding Changes in Aviation Emissions due to SAF with New Combustor Engine Technology* [Oral presentation]. ASCENT Advisory Board Meeting, Alexandria, Virginia.

Outreach Efforts

Currently in negotiation with Gulfstream, P&W, Airbus America, and Honeywell for future follow-on or new SAF focused studies

Awards

None.

Student Involvement

One graduate student (Lauren Kehoe) was employed in this project and five undergraduate research assistants (Dominic Torre, Zachary Alton, Aleck Barchenski, and Zane and Zachary Achterberg) were employed in pre- and post-test activities, including individual component testing and calibration, and data reduction.

Plans for Next Period

- Complete Task 1 – 3.4: For P&W combustor study.
- Complete Task 1 – 3.5: For P&W combustor study.
- Complete Task 1 – 3.6: For Boeing, Gulfstream, and P&W studies.
- Complete Task 1 – 3.7: For Boeing, Gulfstream, and P&W studies.

- Complete Task 1 – 3.8: For P&W combustor study.
- Negotiate, plan, and prepare with Gulfstream, P&W, Airbus America, and Honeywell for future follow-on or new SAF focused studies.
- Communicate results and conclusions from the three field campaigns with publications and presentations.

Project 003 Cardiovascular Disease and Aircraft Noise Exposure

Boston University

Project Lead Investigator

Junenette L. Peters
Associate Professor
Department of Environmental Health
Boston University School of Public Health
715 Albany St., T4W, Boston, MA 02118
617-358-2552
petersj@bu.edu

University Participants

Boston University

- P.I.s: Prof. Jonathan Levy (university P.I.), Prof. Junenette Peters (project P.I.)
- FAA Award Number: 13-C-AJFE-BU-032
- Period of Performance: October 1, 2023, to September 30, 2024

Massachusetts Institute of Technology

- Sub-P.I. and co-P.I.: Prof. R. John Hansman (sub-P.I.), Dr. Florian Allroggen (sub-co-P.I.)
- Tasks:

  Boston University

  1. Present on aircraft noise and health research in the United States (U.S.).
  2. Write up and publish final results on hypertension and nighttime aircraft noise exposure.
  3. Write up and publish final results on the intermediary risk factor of adiposity and aircraft noise exposure.
  4. Perform preliminary analyses of an intermediary risk factor (diabetes) and aircraft noise exposure.
  5. Perform data linking with new cohort and develop data use procedures.
  6. Define request for noise data for additional year and airports.

  Boston University and Massachusetts Institute of Technology

  7. Prepare a third draft of the report on study results related to 2018 FAA Reauthorization, Section 189 for policymakers.

Project Funding Level

Total funding (3-year funding): $2,161,609
Matching funds: $2,161,609
Sources of matching funds: Nonfederal donors to the Nurses' Health Study (NHS) and Women's Health Initiative (WHI) cohorts

Investigation Team

Boston University

Prof. Junenette Peters (P.I.)
Prof. Jonathan Levy (P.I.)

Dr. Levy participates in noise exposure assessment and provides expertise in the areas of predictive modeling and air pollution. Dr. Peters is responsible for directing all aspects of the proposed study, including study coordination, design and analysis plans, and co-investigator meetings.

Harvard University/Brigham and Women's Hospital
Prof. Francine Laden
Prof. Jaime Hart
Dr. Tianyi Huang (*now at the National Institutes of Health*)
Dr. Susan Redline

Dr. Laden and Dr. Hart are our NHS sponsors for this ancillary study. Dr. Hart assigns aircraft noise exposures to the geocoded address history coordinates of each cohort member. Dr. Laden and Dr. Hart also assist in documenting data from the NHS, on the basis of their previous experience in research on air pollution and chronic disease outcomes in these cohorts and in performing appropriate analyses of hypertension and cardiovascular outcomes. Dr. Redline and Dr. Tianyi Huang guide efforts related to noise and sleep disturbance in the NHS and WHI.

University of North Carolina
Dr. Eric Whitsel
James Stewart

Dr. Whitsel is our WHI, National Longitudinal Study of Adolescent to Adult Health (Add Health), and Hispanic Community Health Study/Study of Latinos (HCHS/SOL) sponsor for the ancillary studies. Along with James Stewart, Dr. Whitsel assigns aircraft noise exposure to the geocoded addresses of cohort members. Dr. Whitsel also assists in documenting data from these cohorts based on multiple years of combined leadership and service for the WHI and Add Health morbidity and mortality classification, outcomes adjudication, and ancillary study committees.

Massachusetts Institute of Technology
Prof. R. John Hansman (sub-P.I.)
Dr. Florian Allroggen (sub-co-P.I.)

Dr. Hansman and Dr. Allroggen are responsible for the economic impact analysis and visibility analysis (both analyses reported in previous reports) and participate in drafting the report for policymakers.

Project Overview

Exposure to aircraft noise has been associated with physiological responses and psychological reactions (Bluhm & Eriksson, 2011; Hatfield et al., 2001), including sleep disturbances, sleep-disordered breathing, nervousness, and annoyance (Hatfield et al., 2001; Rosenlund et al., 2001). However, the extent to which aircraft noise exposure increases the risk of adverse health outcomes is still not well understood. The literature, formerly primarily European studies, provided early evidence of a relationship between aircraft noise and self-reported hypertension (Rosenlund et al., 2001), increased blood pressure (Haralabidis et al., 2008; Jarup et al., 2008; Haralabidis et al., 2011; Evrard et al., 2017), antihypertensive medication use (Bluhm & Eriksson, 2011; Greiser et al., 2007; Franssen et al., 2004; Floud et al., 2011), and incidence of hypertension (Eriksson et al., 2010; Dimakopoulou et al., 2017). One study found that aircraft noise exposure was associated with incident diabetes (Eze et al., 2017). Other studies found a stronger but marginal association between aircraft noise and incident diabetes in women and an association with waist circumference (Eriksson et al., 2014; Sakhvidi et al., 2018). Experimental, "everyday," and traffic noise exposures have been related to heart rate variability (El Aarbaoui & Chaix, 2020; El Aarbaoui et al., 2017; Sim et al., 2015; Walker et al., 2016; Kraus et al., 2013), but no study, to date, has reported on heart rate variability relative to aircraft noise. Findings of a cardiovascular relationship were supported by a report by the World Health Organization European Centre for Environmental Health, which evaluated the association between residential exposure to environmental noise and cardiovascular disease and found substantial evidence for biological plausibility and positive associations between environmental noise and hypertension, myocardial infarction, and ischemic heart disease (Babisch & Kim, 2011; WHO, 2018).

The goal of this ongoing project is to continue to examine the potential health impacts attributable to noise exposure resulting from aircraft flights. This project also leverages ongoing work within ASCENT and is responsive to Section 189 of the FAA Reauthorization Act of 2018 (Pub. L. 115-254), which called for a study on the potential health and economic impacts attributable to aircraft overflight noise and an assessment of the relationship between a perceived increase in aircraft noise and increases in aircraft visibility. To date, our work has leveraged existing collaborations with well-recognized and respected studies that have followed over 250,000 participants through the course of their lives to understand factors that affect health. These studies include the NHS and Nurses' Health Study II (NHSII) as well as the

Health Professionals Follow-Up Study. Furthermore, this work has aligned with a concluded effort funded by the National Institutes of Health to examine these associations in the WHI. The research team continues to leverage aircraft noise data for 90 U.S. airports from 1995 to 2015 and has linked these data to demographic, lifestyle, and health data for the participants of long-term health studies. These studies have provided considerable geographic coverage of the U.S., including all of the geographic areas specified in Section 189. Furthermore, our work to date has also included a first-of-its-kind empirical assessment of the economic impacts on businesses located beneath flight paths at selected U.S. airports responsive to the requirements set forth in Section 189 of the FAA Reauthorization Act of 2018.

Our team recently added to the literature by reporting on U.S. studies evaluating the degree to which aircraft noise affects health. A suggestive positive association was found between aircraft noise exposure and the risk of hypertension (Kim et al., 2022). However, there are fewer studies on the potential effect of noise on mental health (Seidler et al., 2017; Wright et al., 2018). Updated guidelines from the World Health Organization reported a lack of high-quality evidence for aircraft noise and mental health and highlighted the need for additional high-quality studies (WHO, 2018; Clark et al., 2020). Potential biological mechanisms of action of noise on health include induced release of stress hormones (Ising & Kruppa, 2004; Spreng, 2000; Selander et al., 2009; Lefevre et al., 2017) and markers of inflammation and oxidative stress, effects on vascular function (Münzel et al., 2017), and indirect effects on sympathetic activity, which is associated with adverse metabolic outcomes (Selander et al., 2009; Grassi, 2006; Mancia et al., 2006; Mancia et al., 2007). To better understand these potential relationships, our team increased the diversity of participants in our studies with a focus on vulnerable populations by adding the HCHS/SOL and Add Health cohorts. Furthermore, the potential impacts of aircraft noise on additional health outcomes beyond those previously explored are being evaluated, including cardiovascular intermediaries and mental health outcomes in NHS, NHSII, WHI, HCHS/SOL, and Add Health.

The overall aims for this multi-year project as it relates to our continuing efforts are as follows:

Tasks under Amendment No. 38:

1. Assign new aircraft noise exposures to geocoded participant addresses for NHS.
   a. Intersect geocoded addresses with day–night average sound level (DNL) aircraft noise exposure levels newly available for 2019 for the currently included 90 airports and for 2015 and 2019 for additional airports.
2. Increase personnel effort (postdoctoral fellow) on noise and health analyses.

Tasks under Amendment No. 32:

1. Assign aircraft noise exposures over time to geocoded participant addresses for HCHS/SOL and Add Health.
   a. Intersect geocoded addresses with DNL and equivalent sound levels for night (L_{night}) and day (L_{day}) aircraft noise exposure levels currently available from 1995 to 2015.
   b. Estimate the percent of participants across noise exposure categories and assess overall trends in participant noise exposure levels over time, including an evaluation of sociodemographic and other predictors of aircraft noise exposure to facilitate the design and interpretation of epidemiological analyses.
2. Estimate the potential association between cardiovascular intermediaries and aircraft noise exposure.
   a. Develop analysis plans and manuscript proposals to gain approval to investigate potential relationships between aircraft noise exposure and health intermediaries or cardiometabolic markers such as adiposity and heart rate variability in the NHS, WHI, HCHS/SOL, and Add Health cohorts.
   b. Perform statistical analyses, undergo manuscript reviews, and present and publish results.
3. Investigate the potential impact of aircraft noise exposure on mental health.
   a. Conduct an in-depth literature search to identify relevant mental health outcomes.
   b. Determine the applicable assessments of these outcomes (i.e., depression and anxiety) within the various cohort studies.
   c. For each cohort, develop an analysis plan and gain approval of manuscript proposals on the potential relationships between aircraft noise exposure and mental health outcomes.
   d. Perform statistical analyses, undergo manuscript reviews, and present and publish results.
4. Explore the addition of noise-related survey questions to Nurses' Health Study 3 (NHS3).

Tasks under Amendment No. 16 as it relates to Section 189 are as follows:

1. Prepare a final draft of the study report related to Section 189 of the FAA Reauthorization Act of 2018 (Pub. L. 115-254) for policymakers.

Task 1 – Present on Aircraft Noise and Health Research in the United States

Boston University

Objective

The aim of this task is to present on U.S.-based research on aircraft noise exposure and health outcomes.

Research Approach

Presentations highlighting published, current, and planned research on aircraft noise exposure and health outcomes in U.S. cohorts were developed and delivered.

Milestone

- Presented on research efforts and results.

Major Accomplishments

- Presented on aircraft noise and health research to the following organizations (example Figure 1):
  - International Society for Environmental Epidemiology (ISEE) Conference
  - Airports Council International (ACI)-North America/American Association of Airport Executives (AAAE) Airport Noise Conference
  - Department of Transportation and FAA Office of Policy, International Affairs, and Environment, and New England regional office

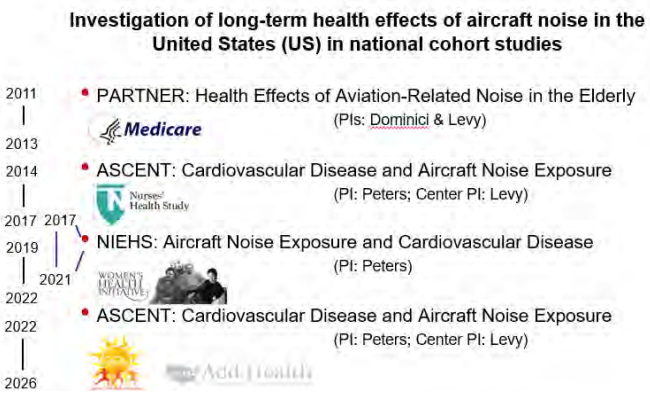

Figure 1. Overview of U.S.-based studies funded through FAA Centers of Excellence (COE) PARTNER and ASCENT and the National Institute of Environmental Health Science (NIEHS) over time, investigating the health effects of aircraft noise in U.S. cohorts.

Task 2 – Write up and Publish Final Results on Hypertension and Night-time Aircraft Noise Exposure

Boston University, Harvard University

Objective

The aim of this task is to write up and publish the final results of our analyses of aircraft noise (L_{night}) and hypertension.

Research Approach

Our team intersected modeled noise exposure surfaces for 1995, 2000, 2005, 2010, and 2015 based on geocoded addresses of the participants over the follow-up period in NHS and NHSII. A large set of a priori variables were selected to

be examined as confounders and/or effect modifiers and used time-varying Cox proportional hazards models to estimate the hypertension risk associated with time-varying night-time aircraft noise exposure, while adjusting for both fixed and time-varying covariates. Sensitivity analyses were also performed to address potential biases.

Milestone

- Published manuscript on aircraft noise (L_{night}) and hypertension.

Major Accomplishments

- Submitted manuscript reporting results on analyses of L_{night} noise and hypertension.
- Responded to journal reviewer comments and revised our manuscript accordingly.
- Published "Long-term nighttime aircraft noise exposure and risk of hypertension in a prospective cohort of female nurses" in the *International Journal of Hygiene and Environmental Health* (Peters et al., 2024).

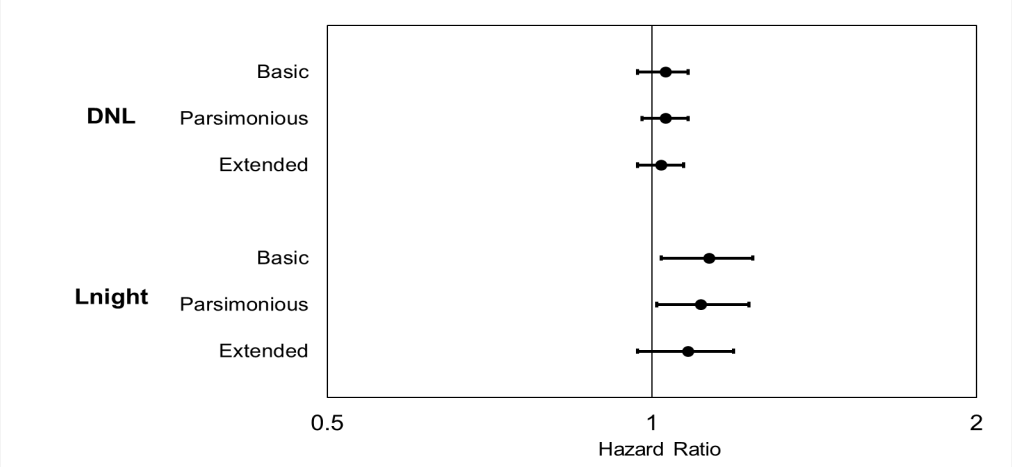

Basic model adjustment: age and calendar year.
Parsimonious model adjustment: basic model + race, physical activity, smoking status, alcohol use, Dietary Approaches to Stop Hypertension, spouse's education attainment, neighborhood socioeconomic status, region of residence, nitrogen dioxide, and fine particulate matter ($PM_{2.5}$).
Extended model adjustment: parsimonious model + body mass index, menopausal status, medications, and family history of hypertension.

Figure 2. Hazard ratios (95% confidence intervals) of the association between aircraft noise at 45 dB and hypertension, comparing previous findings of day-night average sound level (DNL) (Kim et al., 2021) and night-time noise (L_{night}) in the NHS and NHSII (Peters et al., 2024).

Interpretation of night-time noise and hypertension results using the L_{night} 45-dB cut point (Figure 2)
In the combined parsimonious model, the participants in NHS and NHSII exposed to L_{night} levels ≥45 dB had an 11% greater risk of hypertension than the participants exposed to L_{night} levels <45 dB, with a 95% confidence interval (CI) of 1%–23%. In the combined fully adjusted model, the participants exposed to L_{night} ≥45 dB had an 8% greater risk (95% CI: −3%, 19%) than the unexposed individuals. The hazard ratios were relatively stable across the sensitivity analyses, even after controlling for air pollution and shiftwork.

Task 3 – Write Up and Publish Final Results on the Intermediary Risk Factor of Adiposity and Aircraft Noise

Boston University, Harvard University

Objective

The aim of this task is to write up and publish the final results of our analyses on aircraft noise and an intermediary risk marker (adiposity, a measure of cardiometabolic disease).

Research Approach

An analysis plan was developed for studying adiposity and aircraft noise and obtained approval from the NHS oversight committee. Statistical analysis was designed, and a large set of a priori variables were selected to be examined as confounders and/or effect modifiers. The appropriate datasets were compiled and a descriptive statistics analysis was performed. Multivariable multinomial logistic regression was used to estimate the relationship between aircraft noise and longitudinal, repeated measures of adiposity (body mass index [BMI]).

Milestone

- Published analyses on aircraft noise and adiposity.

Major Accomplishments

- Completed and submitted a manuscript reporting the results of analyses on aircraft noise and adiposity.
- Responded to journal reviewer comments and revised our manuscript based on comments.
- Published a paper entitled "Aircraft noise exposure and body mass index among female participants in two Nurses" Health Study prospective cohorts living around 90 airports in the U.S. in *Environment International* (Bozigar et al., 2024).

Table 1. Odds ratio of increasing body mass index (BMI) groups (reference: 18.5–24 kg/m^2) for exposure day–night average sound level ≥55 vs. <55 dB (Bozigar et al., 2024).

Model	BMI Group (kg/m^2)		
	18.5–24.9	25.0–29.9	≥30.0
Model 0: Age	Ref.	1.20 (1.09, 1.31)	1.27 (1.14, 1.42)
Model 1: 0 + demographics & lifestyle	Ref.	1.14 (1.04, 1.24)	1.14 (1.02, 1.28)
Model 2: 1 + environmental	Ref.	1.13 (1.03, 1.24)	1.12 (1.00, 1.25)

Model 0: age, age^2, survey period, cohort; Model 1: 0 + demographics: region, race, individual socioeconomic status, parity, menopausal status, hormone therapy, smoking status, alcohol use, diet quality, physical activity; Model 2: 1 + neighborhood socioeconomic status, greenness, environmental noise, population density.

Interpretation using DNL ≥55 dB as an example (Table 1)
From Model 2, there was 13% higher odds (95% CI: 3%, 24%) of being in the 25.0–29.9 BMI category and 12% higher odds (95% CI: 0%, 25%) of being in the ≥30.0 BMI category versus being in the 18.5–24.9 BMI category among those exposed to aircraft noise (DNL) ≥55 dB compared with those exposed to <55 dB.

Task 4 – Perform Preliminary Analyses of an Intermediary Risk Factor (Diabetes) and Aircraft Noise Exposure

Boston University, Harvard University

Objective

The aim of this task is to generate preliminary results on aircraft noise and diabetes.

Research Approach

An analysis plan was developed for studying diabetes and aircraft noise and obtained approval from the NHS oversight committee. Statistical analysis was designed, and a large set of a priori variables were selected to be examined as confounders and/or effect modifiers. Appropriate datasets were compiled to perform descriptive statistics analysis. We ran preliminary analysis of the form of the relationship between aircraft noise and diabetes risk.

Milestones

- Produced preliminary results to investigate aircraft noise and the risk of diabetes.

Major Accomplishments

- Performed preliminary analyses on the relationship between aircraft noise and risk of diabetes (Table 2 and Figure 3).

Table 2. Number of participants in the Nurses' Health Study (NHS) and Nurses' Health Study 2 (NHSII) at risk for diabetes (did not have diabetes at the time of the first noise measure) and those who developed diabetes during the study period according to day-night average sound level (DNL) categories.

Model	NHS		NHSII	
DNL (dB)	**At Risk**	**Cases**	**At Risk**	**Cases**
<45	90,946	7,076	100,968	6,391
45–49	4,340	313	5,281	276
50–54	2,018	165	2,419	137
55–59	751	60	954	56
60–64	179	17	238	20
≥65	39	3	55	7
Total	98,273	7,634	109,915	6,887

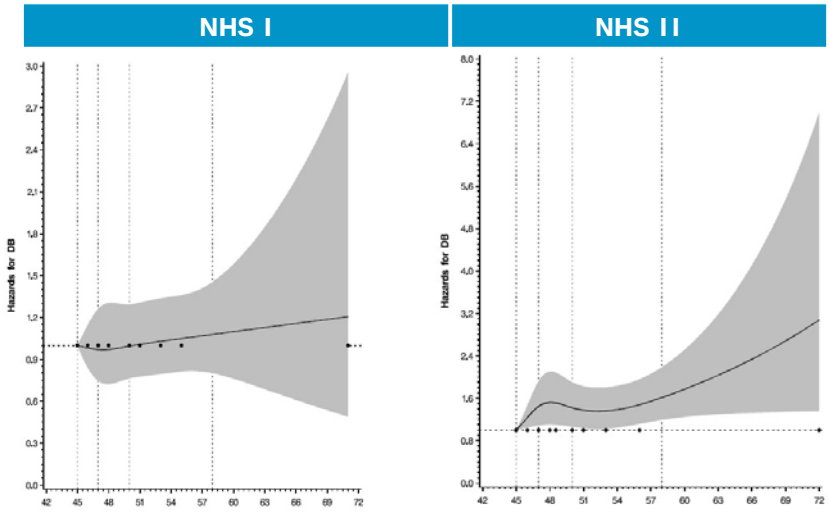

Adjusted for race/ethnicity, individual-level and neighborhood-level socioeconomic status, physical activity, diet, alcohol intake, smoking, family history of Type 2 Diabetes Mellitus, and air pollution

Figure 3. Hazard ratios (line; 95% confidence intervals (gray shade)) of the association between aircraft noise across decibels (dB) and diabetes risk in the Nurses' Health Study (NHS) and Nurses' Health Study 2 (NHSII).

Task 5 – Perform Data Linking with New Cohort and Develop Data Use Procedures

Boston University, University of North Carolina

Objective

The aim of this task is to link airport noise data to participants geocoded addresses.

Research Approach
The geocoded addresses for Add Health participants were intersected with noise contours available from 1995 to 2015. Given the longitudinal nature of this study, noise exposures will be assigned reflecting specific residential addresses over time based on the participant address histories. Our team collaborated in the development and execution of a data use agreement and procedures for use of aircraft noise exposure estimates.

Milestones
- Assigned aircraft noise exposures in Add Health.
- Executed data use agreement.

Major Accomplishments
- Adapted procedures for linking DNL, L_{night}, and L_{day} aircraft noise exposure data to the new cohort.
- Estimated noise exposure for participants of Add Health.
- Developed an Add Health Noise User Guide.
- Executed a memorandum of understanding between the FAA and the University of North Carolina.
- Gained approvals to create a data portal and to access health, sociodemographic, noise exposure, and other relevant cohort data.

Task 6 – Define Request for Noise Data for Additional Year and Airports
Boston University, University of North Carolina, Harvard University

Objective
The aim of this task is to define aircraft noise data request and obtain data for an additional year and additional airports.

Research Approach
More recent data were requested to add to the 5-year incremental data received for 1995 to 2015. The year 2019 was chosen as the additional year to avoid anomalies related to 2020. The locations of participants were reviewed, particularly in new cohorts such as HCHS/SOL, to request 2015 and 2019 data for additional relevant airports not included in the 90 airports previously provided. For the 2019 DNL data, a quality and format review will be performed for the 90 airports before requesting additional metrics and airports.

Milestone
- Requested and obtained data for additional years and airports.

Major Accomplishments
- Investigated study locations and proximate airports to inform the request for additional airports.
- Received the 2019 data and performed the initial review.

Task 7 – Prepare a Third Draft of the Report on Study Results Related to 2018 FAA Reauthorization, Section 189 for Policymakers
Boston University, Massachusetts Institute of Technology

Objective
The aim of this task is to develop a report of overall study results in response to 2018 FAA Reauthorization, Section 189 for policymakers.

Research Approach
Summarized Section FAA Reauthorization Act of 2018 (Pub. L. 115-254), Section 189, *STUDY ON POTENTIAL HEALTH AND ECONOMIC IMPACTS OF OVERFLIGHT NOISE* and provided the background of the study, study methods and data, study findings, and conclusions.

Milestone

- Generated a third draft of the report on overall study results in response to Section 189 for policymakers.

Major Accomplishments

- Provided a revised third draft report summarizing the overall study results in relation to Section 189.

Publications

Peer-Reviewed Journal Publications

Peters, J. L., Grady, S. T., Laden, F., Nelson, E., Bozigar, M., Hart, J. E., Manson, J. E., Huang, T., Redline, S., Kaufman, J. D., Forman, J. P., Rexrode, K. M., & Levy, J. I. (2024). Long-term nighttime aircraft noise exposure and risk of hypertension in a prospective cohort of female nurses. *International Journal of Hygiene and Environmental Health, 12*(263), 114457. doi: 10.1016/j.ijheh.2024.114457. PMID: 39270405

Bozigar, M., Laden, F., Hart, J. E., Redline, S., Huang, T., Whitsel, E. A., Nelson, E. J., Grady, S. T., Levy, J. I., & Peters, J. L. (2024). Aircraft noise exposure and body mass index among female participants in two Nurses' Health Study prospective cohorts living around 90 airports in the United States. *Environment International, 187*, 108660. doi: 10.1016/j.envint.2024.108660. PMID: 38677085

Nguyen, D. D., Levy, J. I., Kim, C., Lane, K. J., Simon, M. C., Hart, J. E., Whitsel, E. A., VoPham, T., Malwitz, A., & Peters, J. L. (2023). Characterizing temporal trends in populations exposed to aircraft noise around U.S. airports: 1995–2015. *Journal of Exposure Science and Environmental Epidemiology.* https://doi.org/10.1038/s41370-023-00575-5

Grady, S. T., Hart, J. E., Laden, F., Roscoe, C., Nguyen, D. D., Nelson, E. J., Bozigar, M., VoPham, T., Manson, J. E., Weuve, J., Adar, S. D., Forman, J. P., Rexrode, K., Levy, J. I., & Peters, J. L. (2023). Associations between long-term aircraft noise exposure, cardiovascular disease, and mortality in US cohorts of female nurses. *Environmental Epidemiology, 7*(4), e259. doi: 10.1097/EE9.0000000000000259

Bozigar, M., Huang, T., Redline, S., Hart, J. E., Grady, S. T., Nguyen, D. D., James, P., Nicholas, B., Levy, J. I., Laden, F., & Peters J. L. (2023). Associations between aircraft noise exposure and self-reported sleep duration and quality in the United States-Based prospective Nurses' Health Study cohort. *Environmental Health Perspectives, 131*(4), 47010. doi: 10.1289/EHP10959

Nguyen, D. D., Whitsel, E. A., Wellenius, G. A., Levy, J. I., Leibler, J. H., Grady, S. T., Stewart, J. D., Fox, M. P., Collins, J. M., Eliot, M. N., Malwitz, A., Manson, J. E., & Peters, J. L. (2023). Long-term aircraft noise exposure and risk of hypertension in postmenopausal women. *Environmental Research, 218*, 115037. doi: 10.1016/j.envres.2022.115037

Kim, C. S., Grady, S. T., Hart, J. E., Laden, F., VoPham, T., Nguyen, D. D., Manson, J. E., James, P., Forman, J. P., Rexrode, K. M., Levy, J. I. & Peters, J. L. (2022). Long-term aircraft noise exposure and risk of hypertension in the Nurses' Health Studies. *Environmental Research*, *207*, 112195.

Outreach Efforts

Presentations

- Presented an oral presentation on current progress during the ASCENT Fall Meeting (October 24–26, 2023) and ASCENT Spring Noise and Operations Meeting (April 9–10, 2024)
- Virtually presented an oral presentation entitled "Aircraft noise research in the U.S. – studies in multiple national cohorts" at the 35th Annual ISEE Conference (September 17–21, 2023).
- Presented an oral presentation entitled "Research on Aircraft Noise and Health in U.S. Cohorts" at the 2023 ACI-North America/AAAE Airport Noise Conference (October 23–25, 2023).

Awards

None.

Student Involvement

The dissertation of Daniel Nguyen (doctoral graduate, Boston University) included a characterization of the temporal trends in aviation noise surrounding U.S. airports. Daniel Nguyen graduated in the spring of 2022 and is currently working for the Centers for Disease Control and Prevention.

The dissertation of Stephanie Grady (doctoral candidate, Boston University) includes developing and performing statistical analyses on noise and hypertension risk, cardiovascular event risk, and biomarkers of neurodegeneration. Stephanie Grady graduated in the spring of 2024 and is currently working as a postdoctoral fellow at Boston University.

Plans for Next Period

(October 1, 2024, to September 30, 2025)

- Submit proposals/analysis plans and generate preliminary results to estimate the relationship between aircraft noise exposure and mental health outcomes (e.g., depression and anxiety).
- Submit proposals/analysis plans and generate preliminary results to estimate the relationship between aircraft noise exposure and sleep outcomes.
- Review analyses, draft the manuscript, and publish on aircraft noise exposure and cardiovascular disease.
- Link aircraft noise data to geocoded addresses of participants in the additional cohort.
- Develop the protocol for accessing aircraft noise exposure data in the additional cohort.
- Document results for policymakers in a final report.

References

Babisch, W., & Kim, R. (2011). Environmental noise and cardiovascular disease. *WHO European Centre for Environmental Health, ed. Burden of disease from environmental noise: Quantification of healthy life years lost in Europe. World Health Organization*, 15-44.

Bluhm, G., & Eriksson, C. (2011). Cardiovascular effects of environmental noise: research in Sweden. *Noise and Health, 13*(52), 212-216.

Bozigar, M., Laden, F., Hart, J. E., Redline, S., Huang, T., Whitsel, E. A., Nelson, E. J., Grady, S. T., Levy, J. I., & Peters, J. L. (2024). Aircraft noise exposure and body mass index among female participants in two Nurses' Health Study prospective cohorts living around 90 airports in the United States. *Environment International, 187*, 108660. doi: 10.1016/j.envint.2024.108660. PMID: 38677085

Clark, C., Crumpler, C., & Notley, H. (2020). Evidence for environmental noise effects on health for the United Kingdom policy context: a systematic review of the effects of environmental noise on mental health, wellbeing, quality of life, cancer, dementia, birth, reproductive outcomes, and cognition. *International Journal of Environmental Research and Public Health*, *17*(2), 393.

Dimakopoulou, K., Koutentakis, K., Papageorgiou, I., Kasdagli, M. I., Haralabidis, A. S., Sourtzi, P., Samoli, E., Houthuijs, D., Swart, W., Hansell, A. L., & Katsouyanni, K. (2017). Is aircraft noise exposure associated with cardiovascular disease and hypertension? Results from a cohort study in Athens, Greece. *Occupational and Environmental Medicine*, *74*(11), 830-837.

El Aarbaoui, T., & Chaix, B. (2020). The short-term association between exposure to noise and heart rate variability in daily locations and mobility contexts. *Journal of Exposure Science & Environmental Epidemiology*, *30*(2), 383-393.

El Aarbaoui, T., Méline, J., Brondeel, R., & Chaix, B. (2017). Short-term association between personal exposure to noise and heart rate variability: The RECORD MultiSensor Study. *Environmental Pollution*, *231*, 703-711.

Evrard, A. S., Lefèvre, M., Champelovier, P., Lambert, J., & Laumon, B. (2017). Does aircraft noise exposure increase the risk of hypertension in the population living near airports in France?. *Occupational and Environmental Medicine*, *74*(2), 123-129.

Eriksson, C., Bluhm, G., Hilding, A., Östenson, C. G., & Pershagen, G. (2010). Aircraft noise and incidence of hypertension—gender specific effects. *Environmental Research*, *110*(8), 764-772.

Eriksson, C., Hilding, A., Pyko, A., Bluhm, G., Pershagen, G., & Östenson, C. G. (2014). Long-term aircraft noise exposure and body mass index, waist circumference, and type 2 diabetes: a prospective study. *Environmental Health Perspectives*, *122*(7), 687-694.

Eze, I. C., Foraster, M., Schaffner, E., Vienneau, D., Héritier, H., Rudzik, F., Thiesse, L., Pieren, R., Imboden, M., von Eckardstein, A., Schindler, C., Brink, M., Cajochen, C., Wunderli, J. M., Röösli, M., & Probst-Hensch, N. (2017). Long-term exposure to transportation noise and air pollution in relation to incident diabetes in the SAPALDIA study. *International Journal of Epidemiology*, *46*(4), 1115-1125.

Floud, S., Vigna-Taglianti, F., Hansell, A., Blangiardo, M., Houthuijs, D., Breugelmans, O., Cadum, E., Babisch, W., Selander, J., Pershagen, G., Antoniotti, M. C., Pisani, S., Dimakopoulou, K., Haralabidis, A. S., Velonakis, V., Jarup, L., & Hyena Study Team. (2011). Medication use in relation to noise from aircraft and road traffic in six European countries: results of the HYENA study. *Occupational and Environmental Medicine*, *68*(7), 518-524.

Franssen, E. A. M., Van Wiechen, C. M. A. G., Nagelkerke, N. J. D., & Lebret, E. (2004). Aircraft noise around a large international airport and its impact on general health and medication use. *Occupational and Environmental Medicine*, *61*(5), 405-413.

Grassi, G. (2006). Sympathetic overdrive and cardiovascular risk in the metabolic syndrome. *Hypertension Research*, *29*(11), 839-847.

Greiser, E., Janhsen, K., & Greiser, C. (2007). Air traffic noise increases prescriptions of cardiovascular drugs in the vicinity of a major airport. *Epidemiology*, *18*(5), S33.

Haralabidis, A. S., Dimakopoulou, K., Velonaki, V., Barbaglia, G., Mussin, M., Giampaolo, M., Selander, J., Pershagen, G., Dudley, M. L., Babisch, W., Swart, W., Katsouyanni, K., Jarup, L. & HYENA Consortium. (2011). Can exposure to noise affect the 24 h blood pressure profile? Results from the HYENA study. *Journal of Epidemiology & Community Health, 65*(6), 535-541.

Haralabidis AS, Dimakopoulou K, Vigna-Taglianti F, Giampaolo M, Borgini A, Dudley ML, Pershagen G, Bluhm G, Houthuijs D, Babisch W, Velonakis M, Katsouyanni K, Jarup L; HYENA Consortium.

Haralabidis, A. S., Dimakopoulou, K., Vigna-Taglianti, F., Giampaolo, M., Borgini, A., Dudley, M. L., Pershagen, G., Bluhm, G., Houthuijs, D., Babisch, W., Velonakis, M., Katsouyanni, K., Jarup, L., & HYENA Consortium. (2008). Acute effects of night-time noise exposure on blood pressure in populations living near airports. *European HeartJournal, 29*(5), 658-664.

Hatfield, J., Job, R. F. S., Carter, N. L., Peploe, P., Taylor, R., & Morrell, S. (2001). The influence of psychological factors on self-reported physiological effects of noise. *Noise and Health, 3*(10), 1-13.

Ising, H., & Kruppa, B. (2004). Health effects caused by noise: evidence in the literature from the past 25 years. *Noise Health, 6*(22), 5–13.

Jarup, L., Babisch, W., Houthuijs, D., Pershagen, G., Katsouyanni, K., Cadum, E., Dudley, M. L., Savigny, P., Seiffert, I., Swart, W., Breugelmans, O., Bluhm, G., Selander, J., Haralabidis, A., Dimakopoulou, K., Sourtzi, P., Velonakis, M., Vigna-Taglianti, F., HYENA Study Team (2008). Hypertension and exposure to noise near airports: the HYENA study. *Environmental Health Perspectives, 116*(3), 329-333.

Kim, C. S., Grady, S. T., Hart, J. E., Laden, F., VoPham, T., Nguyen, D. D., Manson, J. E., James, P., Forman, J. P., Rexrode, K. M., Levy, J. I. & Peters, J. L. (2022). Long-term aircraft noise exposure and risk of hypertension in the Nurses' Health Studies. *Environmental Research*, *207*, 112195.

Kraus, U., Schneider, A., Breitner, S., Hampel, R., Rückerl, R., Pitz, M., Geruschkat, U., Belcredi, P., Radon, K., & Peters, A. (2013). Individual daytime noise exposure during routine activities and heart rate variability in adults: a repeated measures study. *Environmental Health Perspectives*, *121*(5), 607-612.

Lefèvre, M., Carlier, M. C., Champelovier, P., Lambert, J., Laumon, B., & Evrard, A. S. (2017). Effects of aircraft noise exposure on saliva cortisol near airports in France. *Occupational and Environmental Medicine*, *74*(8), 612-618.

Mancia, G., Bousquet, P., Elghozi, J. L., Esler, M., Grassi, G., Julius, S., Reid, J., & Van Zwieten, P. A. (2007). The sympathetic nervous system and the metabolic syndrome. *Journal of Hypertension*, *25*(5), 909-920.

Mancia, G., Dell'Oro, R., Quarti-Trevano, F., Scopelliti, F., & Grassi, G. (2006). Angiotensin–sympathetic system interactions in cardiovascular and metabolic disease. *Journal of Hypertension*, *24*, S51-S56.

Matsui, T. (2004). The Okinawa study: effects of chronic aircraft noise on blood pressure and some other physiological indices. *Journal of Sound and Vibration*, *277*, 469-470.

Münzel, T., Daiber, A., Steven, S., Tran, L. P., Ullmann, E., Kossmann, S., Schmidt, F. P., Oelze, M., Xia, N., Li, H., Pinto, A., Wild, P., Pies, K., Schmidt, E. R., Rapp, S., & Kröller-Schön, S. (2017). Effects of noise on vascular function, oxidative stress, and inflammation: mechanistic insight from studies in mice. *European Heart Journal*, *38*(37), 2838-2849.

Peters, J. L., Grady, S. T., Laden, F., Nelson, E., Bozigar, M., Hart, J. E., Manson, J. E., Huang, T., Redline, S., Kaufman, J. D., Forman, J. P., Rexrode, K. M., & Levy, J. I. (2024). Long-term nighttime aircraft noise exposure and risk of hypertension in a prospective cohort of female nurses. *International Journal of Hygiene and Environmental Health, 12*(263), 114457. doi: 10.1016/j.ijheh.2024.114457. PMID: 39270405

Rosenlund, M., Berglind, N., Pershagen, G., Järup, L., & Bluhm, G. (2001). Increased prevalence of hypertension in a population exposed to aircraft noise. *Occupational and Environmental Medicine, 58*(12), 769-773.

Sakhvidi, M. J. Z., Sakhvidi, F. Z., Mehrparvar, A. H., Foraster, M., & Dadvand, P. (2018). Association between noise exposure and diabetes: a systematic review and meta-analysis. *Environmental Research*, *166*, 647-657.

Seidler, A., Hegewald, J., Seidler, A. L., Schubert, M., Wagner, M., Dröge, P., Haufe, E., Schmitt, J., Swart, E., & Zeeb, H. (2017). Association between aircraft, road and railway traffic noise and depression in a large case-control study based on secondary data. *Environmental Research*, *152*, 263-271.

Selander, J., Bluhm, G., Theorell, T., Pershagen, G., Babisch, W., Seiffert, I., Houthuijs, D., Breugelmans, O., Vigna-Taglianti, F., Antoniotti, M. C., Velonakis, E., Davou, E., Dudley, M. L., Järup, L., & HYENA Consortium. (2009). Saliva cortisol and exposure to aircraft noise in six European countries. *Environmental Health Perspectives*, *117*(11), 1713-1717.

Sim, C. S., Sung, J. H., Cheon, S. H., Lee, J. M., Lee, J. W., & Lee, J. (2015). The effects of different noise types on heart rate variability in men. *Yonsei Medical Journal*, *56*(1), 235-243.

Spreng, M. (2000). Possible health effects of noise induced cortisol increase. *Noise and Health*, *2*(7), 59-63.

Walker, E. D., Brammer, A., Cherniack, M. G., Laden, F., & Cavallari, J. M. (2016). Cardiovascular and stress responses to short-term noise exposures—A panel study in healthy males. *Environmental Research*, *150*, 391-397.

World Health Organization. (2018). *Environmental noise guidelines for the European region*. World Health Organization. Regional Office for Europe.

Wright, D. M., Newell, K., Maguire, A., & O'Reilly, D. (2018). Aircraft noise and self-assessed mental health around a regional urban airport: a population based record linkage study. *Environmental Health*, *17*(1), 1-10.

Project 018 Community Measurements of Aviation Emission Contributions to Ambient Air Quality

Boston University School of Public Health

Project Lead Investigator

Kevin J. Lane
Associate Professor
Department of Environmental Health
Boston University School of Public Health
715 Albany St. T4W
Boston, MA 02118
617-414-8457
klane@bu.edu

University Participants

Boston University School of Public Health (BUSPH)

- P.I.s: Kevin J. Lane, Assistant Professor; Jonathan I. Levy, Professor and Chair
- FAA Award Number: 13-C-AJFE-BU, Amendment 7
- Period of Performance: August 30, 2023, to September 30, 2025
- Tasks:
  1. Continue targeted mobile and stationary monitoring in communities near the Boston Logan International Airport to allow for future analyses of changing aviation source contributions to inform source attribution
  2. Conduct an ambient air pollution monitoring campaign near Dulles International Airport
  3. Provide data to ASCENT Project 019 to conduct calibration and validation of ambient air pollution dispersion models developed by ASCENT Project 019

Project Funding Level

The Federal Aviation Administration (FAA) provided $649,000 in funding. Matching funds were provided by a non-federal donor to the Women's Health Initiative cohort studies as cost-sharing support to Boston University through ASCENT Project 003.

Investigation Team

Boston University School of Public Health

Prof. Jonathan I. Levy, ScD (ASCENT BUSPH Director and ASCENT Project 018 Co-Investigator: Professor of Environmental Health, Chair of the Department of Environmental Health) is the Boston University P.I. for ASCENT. He initiated ASCENT Project 018 and serves as the director of BUSPH ASCENT research.

Prof. Kevin J. Lane, PhD (ASCENT Project 018 P.I.: Associate Professor of Environmental Health, Department of Environmental Health) joined the ASCENT Project 018 team in July 2017. Dr. Lane has expertise in the assessment of ultrafine particle (UFP) exposure, geographic information systems, statistical modeling of large datasets, and cardiovascular health outcomes associated with air pollution exposure. He has contributed to study design and data analysis strategies and, as of October 1, 2017, took over the primary responsibility for project execution. Dr. Lane also contributes to the manuscripts and reports produced.

Dr. Prasad Patil (Assistant Professor) is a machine-learning and regression modeling expert who is assisting Dr. Lane with modeling of the 2017–2019 UFP data.

Sean Mueller (doctoral student) has been analyzing aviation-related particulate number concentration (PNC) results obtained during COVID-19. Daniel Kojis is a doctoral student examining model generalizability and transferability between sites.

Breanna van Loenen and Maria Bermudez (research assistants) are supporting the analysis of mobile monitoring (MM) and stationary monitoring data.

Tufts University

Dr. John Durant, PhD (Associate Professor) oversees the Tufts Air Pollution Monitoring Laboratory (TAPL) team, leads the development of field study design, and contributes to scientific manuscript preparation.

Dr. Neelakshi Hudda, PhD (Research Professor) joined the ASCENT Project 018 team in September 2020 and is managing the TAPL team as well as mobility data analysis, field study design and implementation, and scientific manuscript preparation.

Camille Gimilaro, Olivia Moore, Isabelle Woollacott, and Lily Sandholm (undergraduate students) are working on the MM platform and helping to clean the air pollution data.

Project Overview

The primary goal of ASCENT Project 018 for 2023–2024 was to conduct an air pollution monitoring campaign beneath flight paths to and from the Boston Logan International Airport (BOS), using a protocol specifically designed to determine the magnitude and spatial distribution of UFPs in the vicinity of arrival flight paths. Data were collected to assess whether aircraft emissions, particularly arrival emissions, significantly contribute to UFP concentrations at appreciable distances from BOS. Task 1 aims to further investigate the contributions of variation sources to PNCs at stationary sites using regression and machine-learning models at BOS. Task 2 and 3 leverages the infrastructure previously developed for our field campaign and enable measurements that address a broader set of research questions than those evaluated in the previous monitoring year, with additional data collection for nitrogen dioxide (NO_2) and sulfur dioxide (SO_2) to inform dispersion model validation work being conducted by ASCENT Project 019. Task 4 utilizes the investigation team's insight on monitoring and modeling efforts to provide best-practice recommendations for future monitoring campaigns at other airports and to create a publicly available best-practices report. Finally, Task 5 utilizes the atmospheric dispersion models developed by ASCENT Project 019 for comparison with aviation-attributable pollutant concentrations from our regression models to further investigate the ability of statistical analyses of real-time concentration measurements to capture aircraft source contributions.

Our team has continued our monitoring campaign to collect and analyze community air pollution measurements to determine the contributions of in-flight arrival and departure aircraft to ground-based concentrations. State-of-the-art air pollution monitoring technology that can measure different air pollutants every 1–5 s has been used. Stationary sites have been established at varying distances from flight paths for BOS, with measurements collected across multiple seasons. A MM system (electric vehicle) outfitted with the same monitoring equipment has also been employed to drive throughout these communities to better characterize geographic variations in air pollution. Statistical analyses will compare the stationary and mobile measurements with flight activity data from the United States, FAA, and meteorology to determine aircraft contributions to ground measurements. Our team will compare these source attribution estimates with comparable outputs from atmospheric dispersion models.

A summary of all project methods and data collection is included below to describe the continued application of ASCENT Project 018 data and 2023–2024 study tasks.

Task 1 – Continue Targeted Mobile and Stationary Monitoring in Communities near the Boston International Airport to Allow for Analyses of Changing Aviation Source Contributions to Inform Source Attribution

Boston University School of Public Health

Objectives

The mobile and fixed-site monitoring data collected under ASCENT Project 018 were further analyzed to investigate the spatiotemporal patterns of aviation-related contributions to UFP, as well as the relative influence of flight arrivals and departures in different locations and underneath flights approaching different runways. Broadly, this effort builds on the methodological foundation developed under ASCENT Project 018 and within earlier PARTNER projects, in which our team developed and applied statistical techniques to model short-term pollution measurements with high variability and high autocorrelation. The fact that these data were collected during the pandemic across time periods in which flight activity

changed substantially while traffic followed slightly different patterns provides a “natural experiment” that will enhance our ability to conduct source attribution.

Research Approach

Our team has used two statistical approaches to quantify aviation contributions to community ambient air quality. First, multivariable generalized linear models were used to examine the association between air pollutant concentrations and real-time flight activity, accounting for aircraft locations in space relative to the monitor and including terms for wind speed/direction, temperature, mixing height, and other relevant meteorological covariates. Second, machine-learning regression models, such as random forest modeling and gradient boosts, were applied to improve model performance, while applying Shapley analysis to provide source attribution quantification. Each study site was modeled individually to assess the location-specific impact of aircraft arrivals and departures along with meteorological and other local environmental conditions, and in future work, combined models will be explored. Because of the complexity of interactions among predictors (i.e., flight activity will be influenced by wind speed and direction, which will also affect plume dispersion and resulting concentrations at individual monitors), our team explored advanced statistical techniques for covariate selection and model ensembling, including random forest regression and other machine-learning regression techniques. Preliminary findings from an application of machine-learning techniques to our UFP measurements indicate that machine-learning methods are able to explain more variability than generalized linear models or related techniques. These predictions will subsequently be shared with ASCENT Project 019, where investigators are developing comparable estimates of aviation-attributable concentrations near BOS, and we will conduct analyses to compare predictions from dispersion models and regression models.

Mobile monitoring data were used to (a) generate summary statistics characterizing the spatial and spatiotemporal variability of measured pollutants in the study area, (b) aid in source attribution, and (c) build and evaluate spatially explicit predictive models of pollutant concentrations in the East Boston, Chelsea, Revere, and Winthrop communities. Exploratory spatial data analyses were performed to identify areas of clustering for spatial autocorrelation of PNC within the MM routes, which may warrant further analysis or special treatment in subsequent modeling efforts. Source apportionment of measured pollutants and drivers of variability in the MM data were examined via geographically weighted regression and/or cluster analysis.

With each of the regression models, the amount of measured air pollution attributable to flight is estimated on a short-term and long-term basis. In other words, by zeroing out the flight activity terms and determining the predicted concentrations, the portion of measured concentrations attributable to aircraft arrivals and departures can be ascertained.

Broadly, these analyses make multiple important contributions not available elsewhere. Our team worked with a unique dataset of stationary and mobile measurements collected over the first two years of the COVID-19 pandemic in a variety of locations near a major airport. Advanced statistical techniques were applied to better ascertain source contributions. This work builds upon the aviation air pollution exposure literature and yields novel insights.

Milestones

- Completed significant advancements in mobile monitor spatiotemporal data analysis to elucidate the limitations of stationary monitoring alone in determining accurate UFP exposure across geographic locations in communities around BOS.
- Submitted three manuscripts for publication, two on machine-learning models to predict UFP exposure and one on the particle size distribution of UFPs at the Winthrop monitoring site.
- Presented preliminary machine-learning models at the International Society for Environmental Epidemiology (Sean Mueller).
- Presented results at the International Society for Exposure Science.
- Presented at the Aviation Emissions Characterization (AEC) meeting and ASCENT Fall and Spring 2024 meetings (Kevin Lane).

Major Accomplishments

Our team successfully developed a random forest machine-learning model to predict PNCs based on changing meteorology and flight activity variables. PNC data were collected by TSI® water-based condensation particle counters (CPC) at 1-s

® TSI is a registered trademark of TSI Incorporated, Shoreview, Minnesota.

resolution and then aggregated to 15-min and hourly averages. The model was developed based on 2017 data collected from six stationary air monitoring sites along the 4R/4L runways, which is the most frequently used arrival pathway into BOS. Figure 1 presents corresponding pollution roses, which indicate that the PNC is elevated when the sites are downwind from the airport. PNC data were collected by CPC devices at 1-s resolution and then merged into hourly averages as a proxy for the total UFP.

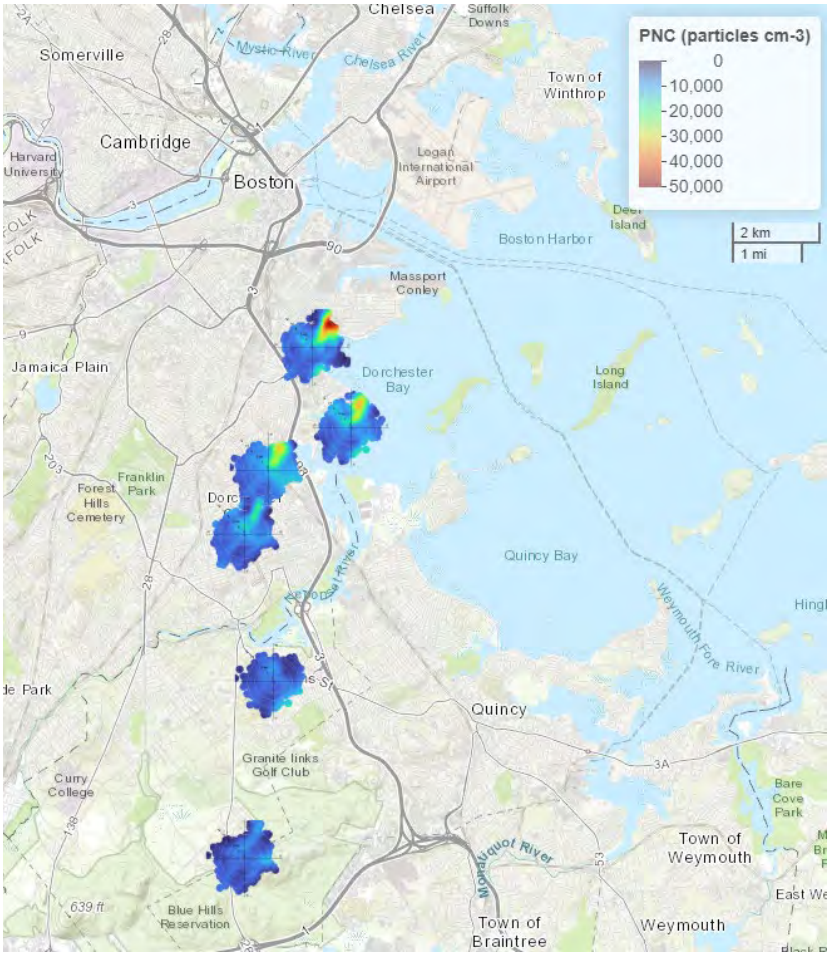

Figure 1. Map of six monitoring sites downwind of the Boston Logan International Airport that were active in 2017. PNC: particle number concentration.

The random forest model predicted UFP concentrations based on changing meteorology and flight activity variables. The model was developed based on 2017 data collected from the six stationary air monitoring sites (i.e., N1, N2, I1, I2, F1, F2) that were active between April and September 2017. The data in Figure 1 were used to develop random forest models for each site. Model performance was evaluated using the coefficient of determination (R^2) and the root mean squared error (RMSE). Prediction variables included in the analysis were meteorological parameters, specifically wind direction, wind speed, temperature, precipitation, humidity, air pressure, and cloud coverage, as well as flight activity variables including total airport arrivals, total departures, and total combined hourly flights. The analysis outlines the associations between these variables and the observed PNC, which were used to train each random forest model to predict the PNC under various conditions. The overall model performance for each individual site measured as R^2 was 0.65–0.73, indicating that our approach has a strong ability to explain the observed variation in PNC at each site.

Our team also assessed variable importance across all of our models. In the overall model (with site indicator included), meteorological variables (including wind direction components) tended to be the most important in predicting the PNC. Figure 2 shows results of variable importance assessment across the site-specific models, with predictors ordered by the importance ranking extracted from the overall model. Blue coloring is indicative of lower ranks (higher importance) while red coloring suggests higher ranks (lower importance). Our team found that, consistent with the overall model results, wind direction components and wind speed tend to be the most important predictors of PNC across all sites, with relatively greater importance of wind direction at sites closer to the airport. Covariates representing flight departures are less important than flight arrivals, consistent with our site selection.

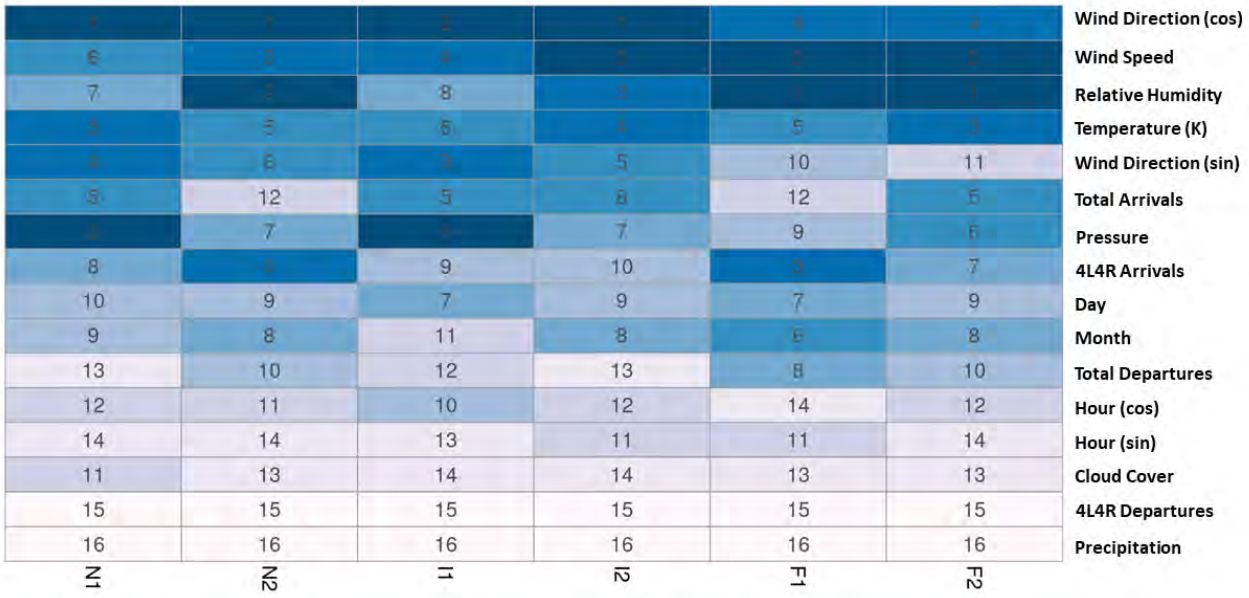

Figure 2. Ranks of relative variable importance for each site-specific model. Variables are ordered by their importance in the overall model as measured by change in MSE when a given variable's values are perturbed. MSE: mean-squared error.

Reinforcing these patterns, Figure 3 shows a variable importance plot for site-specific models at a monitoring location closer to the airport (at monitoring site N1) and further from the airport (at monitoring site F1). The cosine component of wind direction is by far the most important predictor in the model for the N1monitoring site, noting that this covariate captures north and south winds to a greater extent than the sine component and therefore includes the airport impact sector (40-45 degrees). Wind direction covariates are less significant in predicting PNC at monitoring site F1, indicative or a more modest contribution from aviation sources which is consistent with wind roses that illustrate a less pronounced influence of wind direction on concentrations at sites further from the airport (refer to Figure 1).

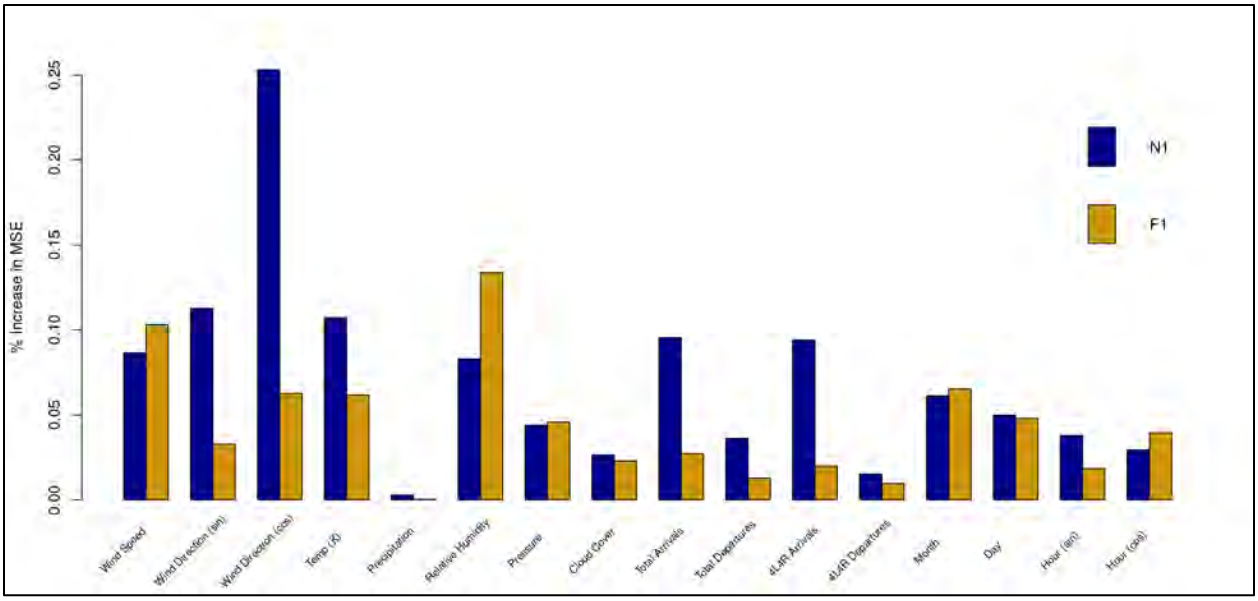

Figure 3. Variable importance plot for a single site-specific models N1 and F1. The percentage increase in MSE refers to the change in MSE when each variable is removed from a given tree. Higher values indicate that the variable is more important in its given model. MSE: mean-squared error.

Meteorological parameters such as wind direction, wind speed, and temperature when flights were arriving on 4R/4L are important, as they show strong contributions in the model to increased PNC. Arriving flights were also observed to make a stronger contribution than departing aircraft at the monitoring sites closest to the airport, which was expected.

Building on the modeling of data collected prior to the COVID-19 pandemic, our team developed additional machine-learning models to assess the contribution of aviation-related activity to the community PNC using SHAP[1] waterfall plots. This approach allows us to quantify the increase or decrease above the hourly average PNC due to all model variables for each hour of the model. Using a gradient boost model, the average PNC prediction of our model was approximately 15,000 #/cm^3 per hour for the study area. SHAP takes each record of data in the model and quantifies each predictor's contribution to increase or decrease the hourly average PNC to explain the difference between the study area mean across all hours and a single observed hourly average. Figure 4 provides an example of one hour of data in the model, for which the PNC was 50,000 #/cm^3. The SHAP plot provides a quantification of each covariate's contribution to the difference between the prediction (50,000 #/cm^3) and mean (15,000 #/cm^3) across all model parameters.

Our results show that surface meteorology had the largest influence on the model – evaluated by mean absolute SHAP value (MASV) ± standard deviation (expressed as a percentage of MASV) across the 10 XGBOOST model runs – with wind direction at 10 m above the surface (2230 ± 2% particles/cm^3), surface temperature (2190 ± 2% particles/cm^3), and wind speed at 10 m above the surface (1910 ± 2% particles/cm^3) demonstrating the highest feature importance (Figure 4). Meteorology has been identified as a significant variable in linear regression models of the near-roadway PNC in Boston and in models developed with data collected under flight-arrival paths. Emissions-related features showed strong positive Spearman's ρ between feature value and SHAP value, indicating the impact of transportation activity on the predicted PNC. Road traffic emerged as the most important emission source of the PNC in our model (1600 ± 4% particles/cm3), exerting a greater global feature importance than any individual runway; the largest aviation impacts on the model predicted PNC were attributed to arrivals at runway 22L (1290 ± 7% particles/cm^3) and departures at runway 22R (840 ± 8% particles/cm^3).

[1] SHAP (Shapley Additive exPlanations) is a game theoretic approach to explain the output of any machine learning model. It connects an optimal credit allocation with local explanations using Shapley values from game theory and related extensions.

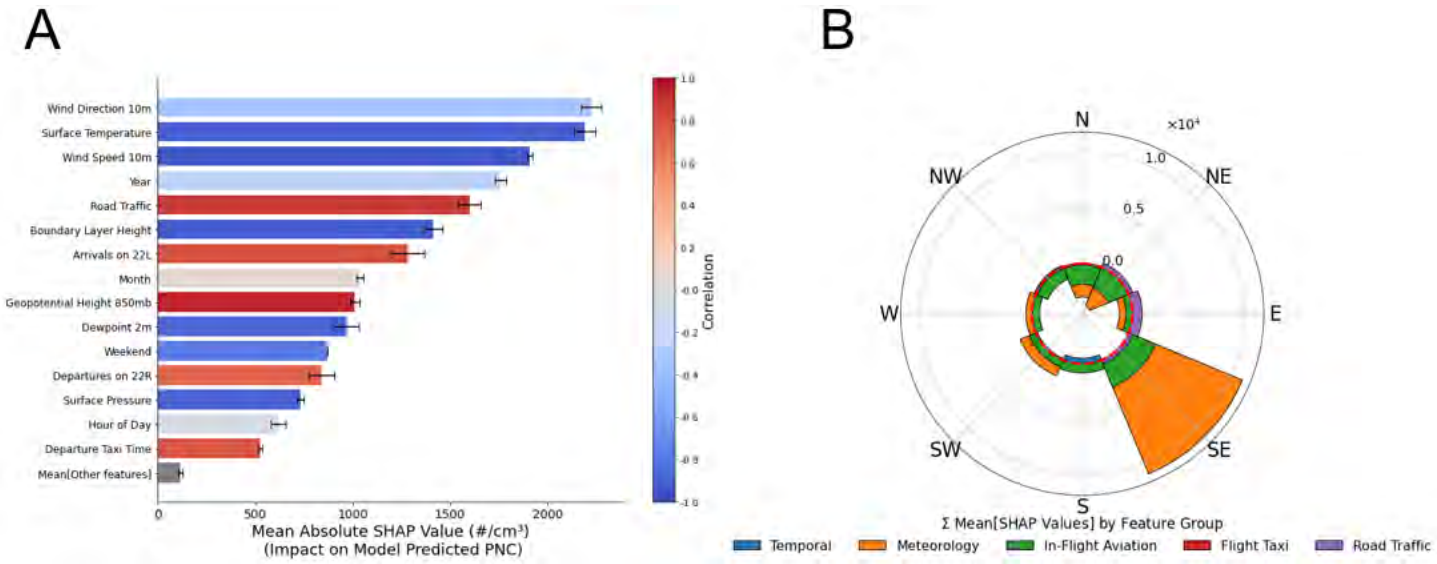

Figure 4. Feature importance via (A) individual features (left) and (B) SHAP Rose (right). (A) The global feature importance of a particular feature is calculated as the Mean Absolute SHAP value (#/cm^3) across all models. Features are ranked by highest mean absolute SHAP value, horizontal lines indicate the variability between model runs, and the color of bars indicates the Spearman correlation between the value of a feature and the corresponding SHAP value (a negative correlation (blue) indicates that a higher feature value is generally associated with a smaller predicted PNC, while a positive correlation (red) indicates that a higher feature is generally associated with an increased predicted PNC). (B) The mean SHAP value (#/cm^3) per aggregate feature category are shown by 45 degree wind sector.

To simplify comparisons among several features and to control unequal representation (e.g., 26 flight operations related variables vs. a single road traffic variable), the features were grouped into broader categories: meteorology, flights, aircraft taxiing, road traffic, and temporal. The overall Markov Shapley value (MSV) for each feature category was computed by first calculating the mean SHAP value of each feature, then averaging these means across all features within the category. While the MSV analysis by feature category aligns with our MASV results (e.g., meteorology shows the highest MSV, and road traffic has higher MSV than flights), segmenting the MSV by 45 degree wind sectors reveals differences in category contributions by wind direction (Figure 4 [left]). During southeast winds (110˚–155˚), when the monitoring site is downwind of the airport, mean predicted PNC increases by 14,300 particles/cm³ compared to the average across all wind directions. This increase is mainly driven by meteorology (11,000 particles/cm³, 77% of the increase above mean) and flights (2,600 particles/cm³, 18%), with minor contributions from road traffic (400 particles/cm³, 3%) and further lower from aircraft taxiing (200 particles/cm³, 1%). In contrast, during easterly winds, road traffic has its highest sector-specific impact (+900 particles/cm³), while flights show a net decrease in predicted PNC (-600 particles/cm³). Notably, road traffic exhibits lower variability across wind sectors (standard deviation [SD] = 370 particles/cm³) compared to flights aviation (SD = 1,450 particles/cm³), indicating that aviation impacts at this site are highly dependent on surface wind direction, with significant contributions occurring only under specific meteorological conditions.

Impact of pandemic-related mobility reductions on UFP levels in a nearby airport community. The natural experiment captured in our study period between 2020-2022 distinguishes aviation-related emissions from ground traffic emissions. Aviation source emissions were differentiated from road traffic emissions by comparing PNC by wind direction and during periods of low flight activity (limited landings and takeoffs) PNC levels to high flight activity (regular landings and takeoffs) PNC levels (Figure 5).

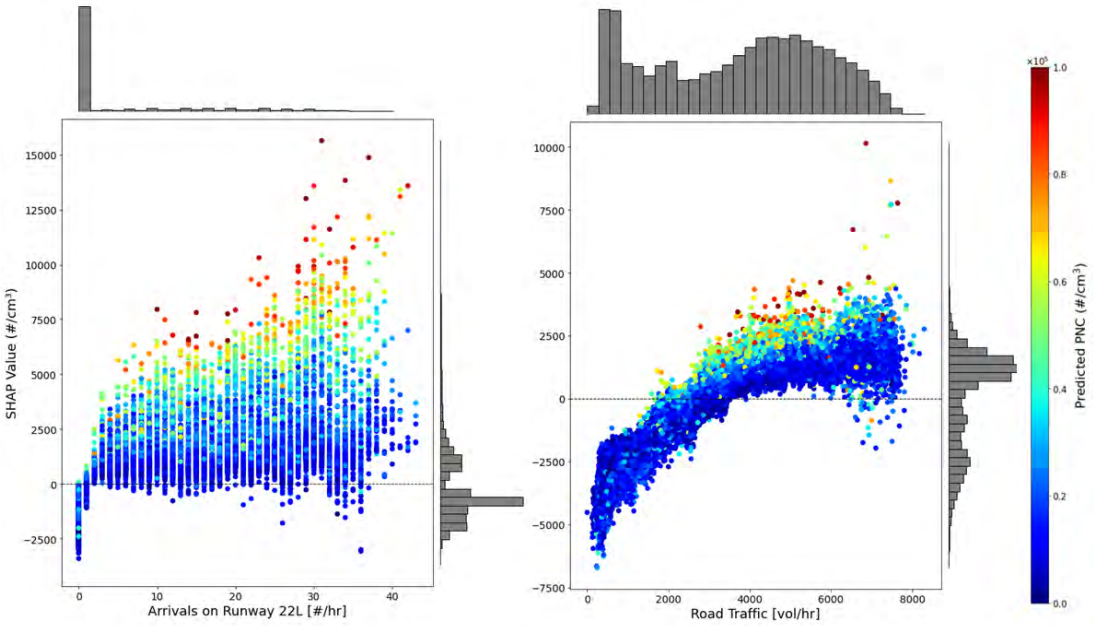

Figure 5. Comparison of PNC concentrations at Chelsea from arrivals on runway 22 and local road traffic.

Our team plans to continue to collect PNC data in communities at BOS and we are in the process of expanding models to all study areas by combining the MM data with stationary models.

Publications

Chung, C. S., Lane, K. J., Black-Ingersoll, F., Kolaczyk, E., Schollaert, C., Li, S., Simon, M. C., & Levy, J. I. (2023). Assessing the impact of aircraft arrival on ambient ultrafine particle number concentrations in near-airport communities in Boston, Massachusetts. *Environmental Research, 225* (15 May 2023). https://doi.org/10.1016/j.envres.2023.115584

Mueller, S. C., Hudda, N., Levy, J. I., Durant, J. L., Patil, P., Lee, N. F., Weiss, I., Tatro, T., Duhl, T., Lane, K. (2022). Changes in ultrafine particle concentrations near a major airport following reduced transportation activity during the COVID-19 pandemic. *Environmental Science & Technology Letters, 9*(9), 706-711. https://doi.org/10.1021/acs.estlett.2c00322

Outreach Efforts

- Presented at the Massport Community Advisory Committee public hearing September 2024.
- Presented at the 2024 International Society for Exposure Science Annual Conference.
- Presented ASCENT Project 018 air pollution monitoring and modeling at the ASCENT Fall 2024 meeting.
- Presented an oral presentation for "Airport Air Quality Monitoring and Source Apportionment" at the FFA AEC Meeting in May 2024.
- Presented an oral presentation at the Aviation Noise and Emissions Meeting, March 2024.

Presentations

Mueller, S., Patil, P., Levy, J. I., Hudda, N., Durant, J. L., Gause, E., Loenen, B. V., & Lane, K. J. (2024, October 20-24). *Examining Impacts of Cross-Validation Approaches on Machine Learning Model Performance for Ultrafine Particle Exposure Assessment* [Oral presentation]. International Society for Exposure Science 2024 Annual Meeting, Montreal, Canada.

Lane, K. J. & Durant, J. (2024, October 29). *ASCENT Project 018 Air Pollution monitoring and Modeling* [Oral presentation]. ASCENT 2024 Fall Meeting, Washington DC.

Lane, K. J. & Durant, J. (2024, May 21-23). *Airport Air Quality Monitoring and Source Apportionment* [Oral presentation]. 2024 Aviation Emission Characterization Roadmap/Emissions Research Meeting, Washington DC.

Awards
None.

Student Involvement
Sean Mueller, PhD student in the Department of Environmental Health, Boston University
Daniel Kojis, PhD student in the Department of Biostatistics, Boston University

Plans for Next Period
- Publish our manuscripts and draft two new manuscripts examining UFP exposures from MM in Boston and Dulles communities.
- Develop a combined stationary and MM machine-learning model using data from 2020–2024.

Task 2 - Conduct an Ambient Air Pollution Monitoring Campaign Near Dulles International Airport
Boston University School of Public Health

Objectives
To expand the generalizability of our work conducted at BOS, our team proposes to conduct mobile and stationary monitoring in 2023-2024 at another airport, Dulles International Airport (IAD), that offers various levels of complexity of urban sources, operations and meteorology. To date, the majority of UFP aviation monitoring and modeling has been conducted at only a few United States airports (i.e., BOS, Seattle-Tacoma International Airport [SEA], and Los Angeles International Airport [LAX]). While our team and other researchers have used these measurements to quantify source contributions, the generalizability and transferability of our findings to other airports need to be systematically analyzed. Specifically, key factors need to be assessed that can impact the ground-level concentrations and thus the relative contribution of airport-related sources. This includes the complexity of urban sources surrounding the airport, airport operations, meteorology, and terrain. By studying these factors systematically, adjustments are made in modeling and resulting estimates. An additional limitation of previous studies is that they have often either been very time-intensive or unable to fully characterize source contributions. Our team, therefore, also wants to help determine a more efficient approach for monitoring and characterizing the air quality impacts at other airports.

Research Approach
Stationary and MM at the new site of IAD. Our team aims to investigate the following questions: (1) Can we distinguish an airport's impact on air quality in near-airport communities? If so, what is the impact? 2) How do we develop a generalized understanding of the impact around airports? To initiate the IAD monitoring campaign, the team has collected analyzed stationary and mobile data in different wind conditions. Preliminary stationary monitoring data were collected at multiple locations near the airport in 2023 with longer term monitoring at three locations from 2023 to 2024 identified in Figure 6. The initial simultaneous stationary data collected from November 1, 2023, to Summer 2024 was used to create pollution roses that inform the scale and magnitude of impact (Figure 6).

Location	Start date	End date	% field data recovery	# days of monitoring	Pollutant
Ashburn	September 2, 2023	February 24, 2024	90%	176	PNC
Barnstead Drive	November 25, 2023	December 13, 2023	100%	19	PNC
Barnstead Drive	November 25, 2023	December 11, 2023	100%	17	NOx
Barnstead Drive	December 22, 2023	December 22, 2023	100%	1	FMPS
Localizer	October 31, 2023	On-going	94%	360	PNC
Localizer	May 23, 2024	September 14, 2024	97%	115	PNC
Brambleton	November 19, 2023	February 24, 2024	100%	98	PNC
Brambleton	June 12, 2024	On-going	100%	135	PNC
Chantilly	November 19, 2023	November 22, 2023	100%	4	PNC, NOx
Spring Knoll	January 1, 2024	January 7, 2024	100%	7	PNC, NOx
Paddock	January 11, 2024	January 14, 2024	100%	4	PNC, NOx
Feltre	December 11, 2023	December 20, 2023	100%	10	PNC
Green Teal	January 15, 2024	January 20, 2024	100%	6	PNC, NOx

Figure 6. Stationary monitoring locations and data collection. Preliminary data collected in 2023 was used to identify primary long-term monitoring site locations for 2024.

Milestones

- Presented our findings at the AEC Roadmap/ASCENT meeting in May 2024 with a showing of the electric vehicle (EV) and instrumentation and monitoring equipment.
- Presented results at the Fall 2024 ASCENT meeting.

Major Accomplishments

Our team has collected over 15 million 1-second measurements of PNC covering three seasons of stationary monitoring in communities near IAD. In Figure 7, each dot represents the hourly average UFP number concentration as a function of wind direction and wind speed. The bearing of each point represents the (hourly average) direction from which the wind is deriving. The distance of each point from the center is proportional to the hourly average wind speed from 0 mph (near the center) to 10 mph (near the outside). The Windrose at left indicates the main directions from which the wind derives at IAD. Northwest winds are common in winter; southwest winds are common in summer. The UFP rose for Localizer shows that (for winter months) the highest concentrations occur during northwest winds. The UFP rose for Brambleton shows that

(for winter months) the highest concentrations occur during southeast winds. These impacts clearly point to the airport as being a major source of PNC at these two sites. Notice that the black dots are as high as 100,000 particle/cm^3.

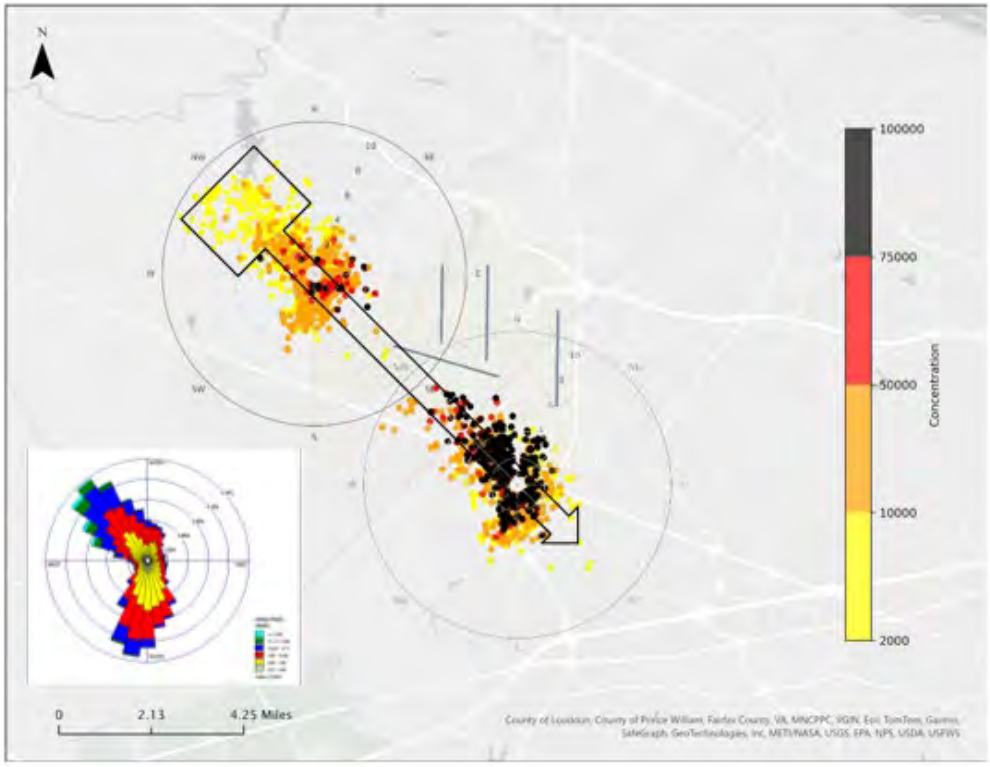

Figure 7. Pollution rose plot for the data at two long-term monitoring sites from fall 2023 through winter 2024.

Our team has collected a robust set of MM data in Dulles communities. Figure 8 shows the adaptive MM routes driven around IAD. In Figure 8, the top panel shows all the roads covered; lower left and right show winter and spring routes, respectively. On each day of monitoring, our team would identify which way the wind was blowing before and during a MM run and then adapt our driving route accordingly to track plumes coming off the airfield. Each run starts with an upwind portion to measure background. Some of these roads have been driven dozens of times, others (e.g., those further from the airport) may have only been driven a few times.

Run No.	Start date/time	End date/time	Duration (hh:mm)	Pollutants
1	11/19/23 8:31	11/19/23 10:15	1:44	PNC, NOx
2	11/22/23 11:39	11/22/2023 19:01	7:22	PNC, NOx, CO2
3	11/23/23 9:48	11/23/23 12:58	3:10	NOx, CO2
4	11/24/23 10:12	11/24/2023 18:56	8:44	PNC, NOx, CO2
5	11/25/23 7:36	11/25/2023 18:11	10:35	PNC, NOx, CO2
6	12/20/23 9:36	12/20/2023 19:14	9:38	PNC, NOx
7	12/21/23 4:15	12/21/2023 15:15	11:00	PNC, NOx
8	12/22/23 9:36	12/22/2023 17:22	7:46	PNC, NOx
9	12/23/23 7:18	12/23/2023 12:24	5:06	PNC, NOx
10	12/25/23 13:43	12/25/2023 20:08	6:25	PNC, NOx
11	12/26/23 9:54	12/26/2023 20:51	10:57	PNC, NOx
12	12/27/23 5:56	12/27/2023 7:41	1:45	PNC, NOx
13	12/28/23 7:25	12/28/2023 23:36	16:11	PNC, NOx
14	12/29/23 11:05	12/29/2023 21:26	10:21	PNC, NOx
15	12/30/23 8:09	12/30/2023 15:38	7:29	PNC, NOx

* Winter runs are grouped by date.

Run No.	Start date/time	End date/time	Duration (hh:mm)	Pollutants
1	5/23/24 15:57	5/23/24 18:25	2:28	PNC, NOx, CO2
2	5/24/24 9:25	5/24/2024 22:16	12:51	PNC, NOx, CO2
3	5/25/24 10:27	5/25/2024 22:13	11:46	PNC, NOx, CO2
4	5/26/24 9:17	5/26/2024 14:32	5:15	PNC, NOx, CO2
5	5/26/24 16:46	5/26/2024 20:26	3:40	PNC, NOx, CO2
6	5/27/24 7:06	5/27/2024 10:17	3:11	PNC, NOx, CO2
7	5/27/24 16:04	5/27/2024 18:43	2:39	PNC, NOx, CO2
8	5/28/24 10:56	5/28/2024 13:00	2:04	PNC, NOx, CO2
9	5/28/24 17:25	5/28/2024 20:24	2:59	PNC, NOx, CO2
10	5/29/24 7:18	5/29/2024 11:20	4:02	PNC, NOx, CO2
11	5/29/24 20:56	5/30/2024 0:20	3:24	PNC, NOx, CO2
12	5/30/24 6:51	5/30/2024 12:58	6:07	PNC, NOx, CO2
13	5/30/24 22:15	5/30/2024 23:55	1:40	PNC, NOx, CO2
14	5/31/24 8:11	5/31/2024 9:58	1:47	PNC, NOx, CO2
15	5/31/24 13:33	5/31/2024 15:17	1:44	PNC, NOx, CO2
16	5/31/24 16:45	5/31/2024 20:11	3:26	PNC, NOx, CO2
16	5/31/24 22:01	5/31/2024 23:57	1:56	PNC, NOx, CO2
17	6/1/24 5:19	6/1/2024 11:22	6:03	PNC, NOx, CO2

* Summer runs are seperated when there is a gap in time > 1 hour.

Figure 8. Mobile monitoring routes and data collection efforts from winter 2023 through spring 2024.

Utilizing the MM data, the PNC and NO_2 data exposures were compared in tandem to identify meteorological and aviation-related conditions that lead to simultaneous peaks in both pollutants. Figure 9 is an example that shows MM results for two pollutants (i.e., PNC and NO_2) for a single day with steady south-southeast winds when downwind from the airport when flights are over the community. Each measurement was made at 1-s resolution (15-20 m). PNC and NO_2 spatial patterns were observed with the downwind spread showing the distance decay gradient, particularly for UFP. Similar and distinct spatial patterns were observed for PNC and NO_2 with far-field NO_2 contributions from departures vs. landings.

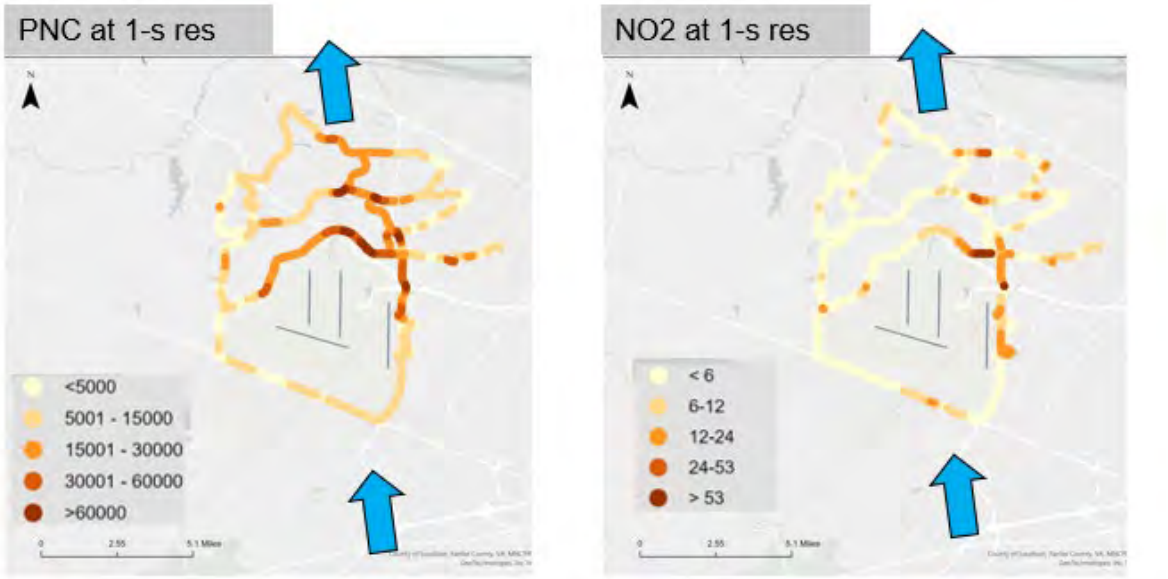

Figure 9. An example of mobile monitoring results for PNC and NO_2 concentrations for a single day with steady south-southeast winds downwind of BOS.

Publications

A manuscript is being developed on the descriptive analyses of the UFP data in Dulles communities.

Outreach Efforts

- Presented our findings at the Spring AEC/ASCENT meeting in May 2024 with a showing of the EV and instrumentation and monitoring equipment.
- Presented results at the Fall 2024 ASCENT meeting.

Awards

None.

Student Involvement

Camille Gimilaro, doctoral student in Civil and Environmental Engineering, Tufts University.

Plans for Next Period

Our team will:

- Continue to collect air pollution data by moving NO_2 and SO_2 equipment to the stationary monitoring sites in Spring 2025.
- Conduct analysis on the transferability of UFP and NO_2 models developed under ASCENT Projects 018 and 019 to IAD in future years of the project. This will inform source attribution statistical models and the AERMOD Modeling System.[2]

[2] AERMOD is a steady-state plume model that incorporates air dispersion based on planetary boundary layer turbulence structure and scaling concepts.

Task 3 – Provide Data to ASCENT Project 019 to Conduct Calibration and Validation of Ambient Air Pollution Dispersion Models Developed by ASCENT Project 019

Boston University School of Public Health

Objectives

Our team is collecting data on $NO/NO_2/NO_x$ at three different sites in Revere, East Boston and South Boston and SO_2 in East Boston to inform calibration and validation of dispersion models created by ASCENT Project 019. Development of descriptive analyses of these datasets continued to inform the ASCENT Project 019 data analysis efforts. Our estimates of aviation-attributable $NO/NO_2/NO_x$ concentrations will be directly shared with ASCENT Project 019 for comparison with dispersion model estimates in future study periods. While our team has constructed numerous regression models for source attribution within ASCENT Project 018, the richness of these datasets (including multiple pollutants, both fixed-site and mobile measurements over a lengthy period, and the potential for synthesizing multiple fixed-site and mobile measurements for the same period) will allow for key refinements that will improve estimation and directly inform dispersion model validation.

Research Approach

Our team has continued working directly with ASCENT Project 019, with the long-term objective of improving dispersion modeling and quantifying arrival and takeoff aircraft contributions to NO_2 concentrations in communities near BOS. In collaboration with ASCENT Project 019, data are shared to provide monitored data and to coordinate the collection of flight activity data to be used in both projects. Team members from ASCENT Project 018 and ASCENT Project 019 are coordinating support of each other's continued progress. ASCENT Project 018 staff have prepared analysis-ready datasets that combine all of our stationary air pollution monitoring data from the 2024 monitoring campaign merged with relevant and timely meteorology data as well as runway-specific flight activity data at BOS and have shared these datasets with ASCENT Project 019 for use in their dispersion models. Figure 10 illustrates the pollution distribution by wind direction and wind speed for each monitoring site during the spring and summer 2024 monitoring campaign.

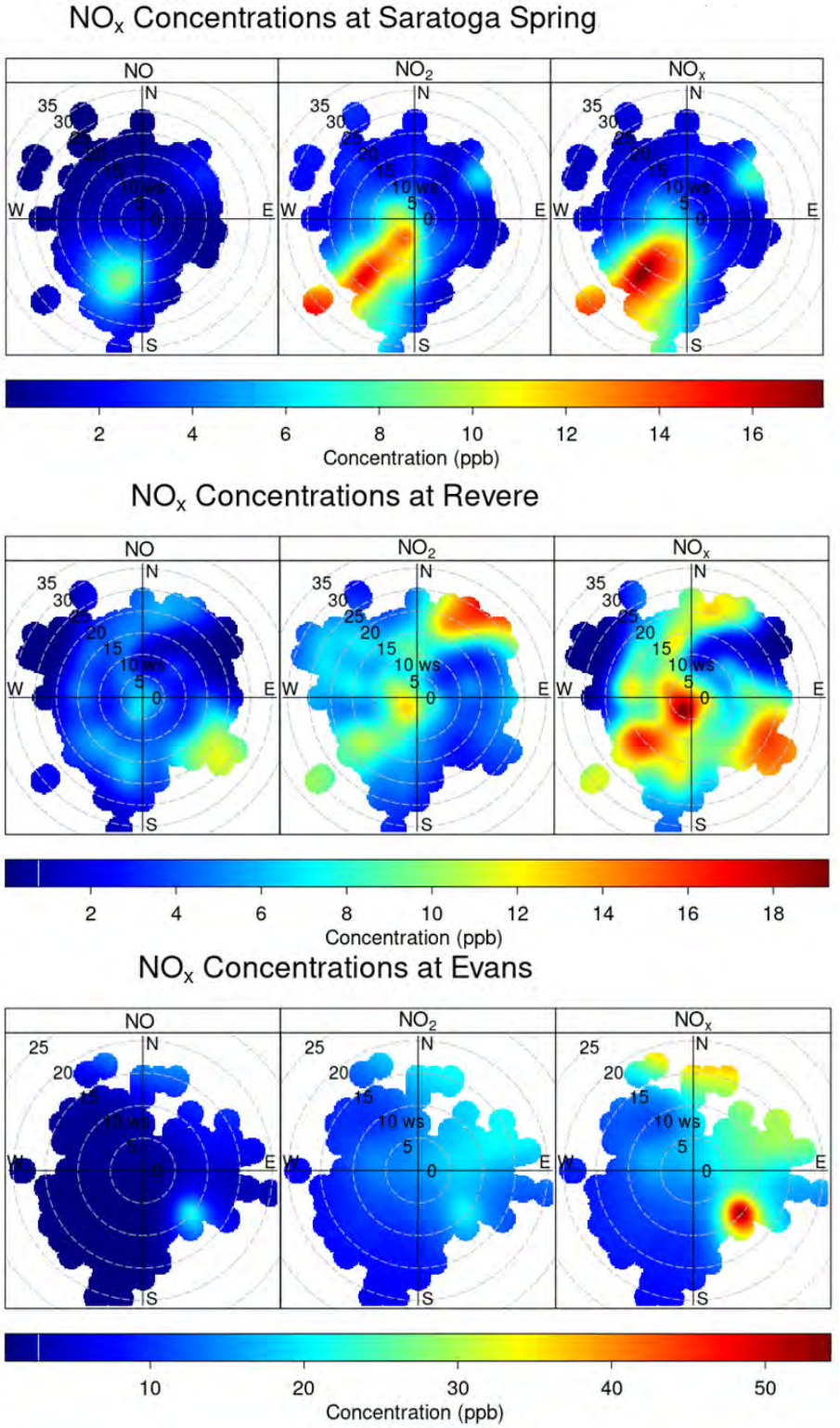

Figure 10. Hourly average $NO/NO_2/NO_x$ pollution rose plots from spring through summer 2024.

ASCENT Project 018 staff have also curated and made available estimates of taxiing time at BOS, geographic information system files of the BOS runway configuration, and a topological analysis of BOS runway and taxiway connectivity to identify potential taxi paths. This sharing of resources across projects allows both teams to avoid duplicating efforts, thus accelerating research progress. Sharing data also ensures that the results of our individual modeling approaches will be comparable, thus providing helpful context in interpreting the varied approaches. To facilitate this data sharing between project groups, ASCENT Project 018 has granted access to their internal data storage and analysis server cluster environment to members of ASCENT Project 019.

Milestones

- Prepared similar analysis-ready data for the current and ongoing stationary and MM campaigns around BOS that are ready to be shared when needed.
- Created a data-processing pipeline to ensure timely updates by periodically cleaning and preparing continuously collected datasets during the current monitoring campaign.

Major Accomplishments

- Shared all analysis-ready data from the Summer 2024 monitoring period with the ASCENT Project 019 team.

Publications

None.

Outreach Efforts

None.

Awards

None.

Student Involvement

None.

Plans for Next Period

- Continue to provide ASCENT Project 019 with additional raw air pollution data as well as modeled PNC and NO_2 and SO_2 contributions.

Project 019 Development of Aviation Air Quality Tools for Airshed-specific Impact Assessment: Air Quality Modeling

University of North Carolina at Chapel Hill

Project Lead Investigator

Saravanan Arunachalam, PhD
Research Professor
Institute for the Environment
University of North Carolina at Chapel Hill
123 W. Franklin St., Suite 330B
Chapel Hill, NC 27516
919-966-2126
sarav@email.unc.edu

University Participants

University of North Carolina at Chapel Hill (UNC Chapel Hill)

- P.I.: Saravanan Arunachalam, Research Professor and Deputy Director
- FAA Award Number: 13-C-AJFE-UNC Amendments 1-21
- Period of Performance: October 1, 2023, to September 30, 2024
- Tasks:
  1. Develop and evaluate a new dispersion model for aircraft sources.
  2. Develop and evaluate a multiscale Weather Research and Forecasting (WRF)-Sparse Matrix Operator Kernel Emissions (SMOKE)-Community Multiscale Air Quality (CMAQ) model application for Boston Logan International Airport (KBOS) focused on ultrafine particles (UFPs).
  3. Implement volatile particulate matter (PM) plume-scale modeling into a CMAQ application

Project Funding Level

The Federal Aviation Administration (FAA) provided $650,000 in funding. The Barr Foundation provided matching cost-share via the Harvard Center for Climate, Health, and the Global Environment.

Investigation Team

Prof. Saravanan Arunachalam, P.I., UNC Chapel Hill Institute for the Environment
Dr. Gavendra Pandey, Air Quality Dispersion Modeler, UNC Chapel Hill Institute for the Environment
Hyeongseok "Darby" Kim, graduate student, UNC Chapel Hill Institute for the Environment
Brian Naess, Geographic Information Systems Specialist, UNC Chapel Hill Institute for the Environment
Dr. Huy Tran, Air Quality Modeler, UNC Chapel Hill Institute for the Environment
Dr. Akula Venkatram, Consultant, University of California at Riverside

Project Overview

Aviation is predicted to grow steadily in upcoming years (Boeing, 2010); thus, a variety of aviation environmental policies will be required to meet emission reduction goals in aviation-related air quality and health impacts. Tools are needed to rapidly assess the implications of alternative policies for an evolving population and atmosphere. In the context of the International Civil Aviation Organization's (ICAO) Committee on Aviation Environmental Protection, additional approaches are required to determine the implications of global aviation emissions.

The overall objective of this project is to develop a new aircraft-specific dispersion model and continue the development and implementation of tools, both domestically and internationally, to allow for an assessment of year-to-year changes in

significant health outcomes. These tools must be acceptable to the FAA (in the context of Destination 2025) and/or other decision makers. More importantly, this new model must have the capability to address the 1-hour form of the nitrogen dioxide (NO_2) National Ambient Air Quality Standard (NAAQS) in the United States (U.S.), as well as to support National Environmental Policy Act (NEPA) and/or NAAQS analyses that may be needed by airports. The developed methods must also rapidly provide output to support a variety of "what if" analyses and other investigations. While the tools for use within and outside the U.S. need not be identical, several goals are desirable for both cases:

- Enable the assessment of premature mortality and morbidity risks due to aviation-attributable PM having a diameter up to 2.5 μm ($PM_{2.5}$), ozone, and other pollutants known to exert significant health impacts.
- Capture airport-specific health impacts at regional and local scales.
- Account for the impact of landing/take-off (LTO) versus non-LTO emissions, including a separation of effects.
- Allow for an assessment of a wide range of aircraft emission scenarios, including differential growth rates and emission indices.
- Account for changes in non-aviation emissions.
- Allow for assessments of sensitivity to meteorology.
- Provide domestic and global results.
- Include quantified uncertainties and differences with respect to U.S. Environmental Protection Agency (EPA) practices, which are to be minimized when scientifically appropriate.
- Be computationally efficient, such that tools can be used in time-sensitive rapid turnaround contexts and for uncertainty quantification.

During this period of performance, the team at the University of North Carolina at Chapel Hill Institute for the Environment (UNC-IE) performed work on Tasks 1 and 2. Task 3 is currently on hold.

Task 1 - Develop and Evaluate a New Dispersion Model for Aircraft Sources

University of North Carolina at Chapel Hill

Objectives

The FAA's Aviation Environmental Design Tool (AEDT) is currently coupled with the American Meteorological Society/EPA Regulatory Model (AERMOD) dispersion model for modeling aircraft sources and is the required regulatory model in the U.S. for modeling airport-level aircraft operations during LTO cycles.

Recent studies have shown several limitations in the use of AERMOD for modeling aircraft sources. The Airport Modeling Advisory Committee developed a series of recommendations in 2011 to improve jet exhaust modeling. Since then, the Airport Cooperative Research Program (ACRP) Project 02-08 developed guidance for airport operators on conducting measurements and modeling of air quality at airports, published in ACRP Report 70 (Kim et al., 2012), with a measurement and modeling study conducted at Dulles International Airport (KIAD). Subsequently, the ACRP Project 02-58 developed the final ACRP Report 171 (Arunachalam, Valencia, et al., 2017) providing dispersion modeling guidance for airport operators for local air quality and health. This study applied four different models—AERMOD, CALPUFF,[1] Second Order Closure Integrated Puff Model with Chemistry (SCICHEM), and the United Kingdom's Atmospheric Dispersion Modeling System for Airports (ADMS-Airport)—for the Los Angeles International Airport (KLAX) and compared model predictions with high-resolution measurements taken during the KLAX Air Quality Source Apportionment Study (AQSAS). Each of these reports identified several limitations with AERMOD and developed a series of recommendations for improving dispersion modeling of aircraft emissions for airport-level air quality.

In 2017, UNC developed the C-AIRPORT dispersion model for application to KLAX (Arunachalam, Isakov, et al., 2017). Initially, C-AIRPORT was designed to be part of the C-TOOLS series of community-scale, web-based modeling systems. The objective of C-TOOLS was to create a web-based interface for modeling multiple source types for short-term or long-term pollutant concentration averages and for analyzing various "what if" scenarios to assess changes in air quality at local scales due to changes in inputs. C-AIRPORT used a line source-based approach to model aircraft sources, based upon the C-LINE modeling system (Barzyk et al., 2015), and a preliminary evaluation of the algorithms against KLAX AQSAS was conducted. Preliminary results at KLAX core sites showed that nitrogen oxide (NO_x) model estimates from all sources were

[1] CALPUFF is an advanced non-steady state air quality dispersion model maintained and distributed by Lake Environmental.

generally comparable to observations except for slight overpredictions, given lack of plume rise. However, overall, aircraft contribution seems low compared to other sources. Further, investigation is needed to continue the evaluation of C-AIRPORT.

Under the previous year's funding, UNC completed development of a modeling framework that addresses known limitations from the above tasks and proposed a viable and suitable approach for modeling pollutants from aircraft sources. The primary objective of this plan was to demonstrate that a robust, improved pollutant dispersion model for aircraft can be developed for U.S. regulatory compliance purposes. The proposed new model will disperse pollutants from aircraft sources in a more technically and scientifically advanced manner (compared with current AERMOD capabilities), with the ultimate goal of becoming a potential U.S. regulatory compliance tool, based on future discussions with the FAA and EPA. This plan will include an itemized list of known limitations along with a corresponding proposed developmental approach and recommendations for addressing the limitations.

As part of the proposed ASCENT research under this task, we will continue to implement the plan with a specific focus on four broad areas. This report provides a very high-level summary here, because the actual specifics of this implementation have been described in previous documents and reports that were independently developed earlier.

Our approach is to ensure that the new model will be "robust" and based on the state of science on physical and chemical processes and associated algorithms.

1. **Source characterization:** Existing approaches in AEDT/AERMOD treat aircraft sources as an area source segment. In the ongoing work, our team is developing two aircraft dispersion models. The first is a simple analytical steady-state plume model, referred to as the aircraft dispersion model (ADM), while the second is a grid-based unsteady-state model, referred to as GADM. In ADM, surface-level aircraft sources are treated as area sources, whereas airborne sources are modeled as pseudo-volume sources. Conversely, in GADM, all aircraft sources are treated as volume sources. To generate input emissions for these models, our team has developed an emission processor called AEDT2ADM. This processor utilizes high-resolution aircraft movement datasets from the AEDT. AEDT2ADM is continuously adapted to enhance its usability for other existing models too, such as AERMOD.

2. **Physical processes:** In previous years, our team already developed an aircraft plume-rise algorithm for the area/volume sources framework (Pandey et al., 2023) by assuming that the different types of aircraft contributing to emissions in any one of the area/volume sources can be represented by a "typical" aircraft whose characteristics computed through a weighted average of the characteristics of aircraft that pass through the area/volume source. Emissions from an aircraft are treated as line thermals that have horizontal momentum and buoyancy. This algorithm is used in ADM and GADM.

   In addition to plume rise, our team will go beyond the initial implementation developed during the previous year, with a new focus on the following:
   a. Treatment of dispersion under low wind conditions and assessment of effects of atmospheric stability
   b. Treatment of dry and wet deposition
      Incorporation of aircraft downwash effects
   c. Treatment of complex terrain and building downwash

3. **Chemical processes:** Our team will go beyond the initial implementation of the previous year, with a new focus on the following:
   a. The 1-hour form of the NO_2 NAAQS
      i) The 1-hour form of the NO_2 NAAQS is a critical issue for air quality around U.S. airports, with several modeling studies showing overestimates compared with observations. It is important that the new model performs adequately to capture this short-term form of the NO_2 NAAQS.
   b. A new detailed chemical mechanism for NO_2 including the generic reaction set (Valencia et al., 2018; Venkatram et al., 1994) or other components
   c. Version of the aerosol treatment as included in the CMAQ and SCICHEM and described by Chowdhury et al. (2015)

4. **Model evaluation**
   a. Ongoing model evaluation has involved evaluating model predictions using only measurements from the KLAX AQSAS for winter 2012. Our team will now consider developing and testing the model for other case studies, including the following:
      i) LAX AQSAS for Summer 2012
      ii) One of three airports (Copenhagen, Madrid, and Zurich) with measurements being undertaken as part of the European Union (EU)-AVIATOR project, a new measurement-modeling study called AVIATOR undertaken in Europe through funding from the EU (see https://aviatorproject.eu/)
         (1) Our team will rely on the AVIATOR team to provide emission inventories for the chosen airport. If emission inventories are not directly available for use, we will obtain airport operations data for the campaign period and develop an inventory using the AEDT.
      iii) New measurements from ASCENT Project 018 investigators at Boston Logan International Airport (KBOS) and KIAD
         (1) This is a new collaboration that will help focus on both designing the monitoring campaign to assist in obtaining valuable data for characterizing the impact of aircraft emissions on air quality and developing the ADM, as well as in source attribution of the measured fields to the aircraft or other source types.
   b. Model evaluation will focus on the model's ability to capture the behavior of the plume related to aircraft sources during LTO cycles at an airport, while comparing with available observations and identifying strengths and weaknesses compared with another existing model.
   c. In collaborating with Boston University (BU), we will rely on BU to perform appropriate cleanup and quality assurance/control of observation data before using these data in our model evaluation routines. Our team will also work closely with BU to ensure appropriate and careful interpretation of the data. UNC and BU have collaborated extensively on similar projects in the past, and we expect to obtain a robust model measurement and modeling assessment from the KBOS study.

Research Approach

1. Source Characterization

1.1 Aircraft Source Characterization in AERMOD

Modeling dispersion of aircraft emissions is challenging because aircraft are mobile sources with varying emissions rates at different elevations depending on the operating mode. The representation of mobile sources, such as motor vehicles and aircraft sources during the LTO cycles, is traditionally represented as AREA or VOLUME sources placed at various heights. AERMOD (v22112) included an option to model on-road mobile sources as LINE segments. However, both source types do not account for plume rise of jet exhaust. Furthermore, the current AREA source treatment does not account for plume meander, which is important in low and variable wind conditions. Currently, AERMOD is the only regulatory tool that can be utilized to demonstrate regulatory compliance in the U.S.; AERMOD allows the user to represent emissions as POINT, AREA, AREAPOLY, LINE, or VOLUME sources. Although the choice of representation is clear in most cases, it is not for atypical sources such as aircraft, which move over the airport and whose exhausts have both horizontal momentum and buoyancy. Here, we compared the results from AERMOD when airport sources are represented as either AREA or VOLUME sources. The data used in the comparison were collected during the summer campaign of the KLAX AQSAS conducted at KLAX in California during the period from July 18 to August 28, 2012. Measured sulfur dioxide (SO_2) concentrations were used in this exercise because most sources close to KLAX emit little SO_2 compared to aircraft. These emissions can be readily quantified because they depend on the sulfur content of aircraft fuel.

1.1.1 Modeling Study Design

In applying AERMOD to KLAX, the FAA's AEDT (version 3e; AEDT3e) was used to model surface as well as airborne aircraft emissions.

1.1.2 AEDT Source Placement and Emissions Comparisons

The number of VOLUME sources to describe TAXI sources is about 14 times the number of AREAs. The reason for this is that each TAXI link is modeled as a single AREA source corresponding to the true length and width of the taxi paths (as a rectangle). In the VOLUME description, each TAXI link is divided into 20 m x 20 m squares housing a VOLUME with a fixed aspect ratio of 1:1. The number of RUNWAY and AIRBORNE sources are 38% and 45% higher in the VOLUME treatment compared to the AREA treatment. Note that in the VOLUME treatment, each aircraft type (e.g., turbojet, turbofan, turboprop, turboshaft, and helicopter) is separated as a separate source for each cuboid. The total SO_2 emissions are distributed among the VOLUMEs and AREAs. However, the total emissions are identical in both source treatments.

1.1.3 Dispersion Comparisons from the Source Treatments of AERMOD (v22112)

Our team compared AERMOD estimates of SO_2 from the two source treatments at the four core sites (AQ, CN, CS, and CE). For this comparison, the same number of sources was used in both treatments by manually converting all the VOLUME sources into AREA sources and fixing the σ_{z_o} as 4.1 m. Figure 1 compares the variation of AERMOD estimated SO_2 concentrations with the friction velocity, u_*, for the two source treatments. It shows that both model estimates do not reflect the behavior of the observed SO_2 concentrations: the concentrations decrease with u_*, with the highest values occurring close to the lowest values of u_*, while the observed maxima occur between $u_* = 0.15$ to $0.3\ m/s$. Furthermore, the maximum concentrations are above 20 ppb, a value that is well above the observed 6.3 ppb. The model estimates are expected to be lower than the observed high values because they do not include background sources.

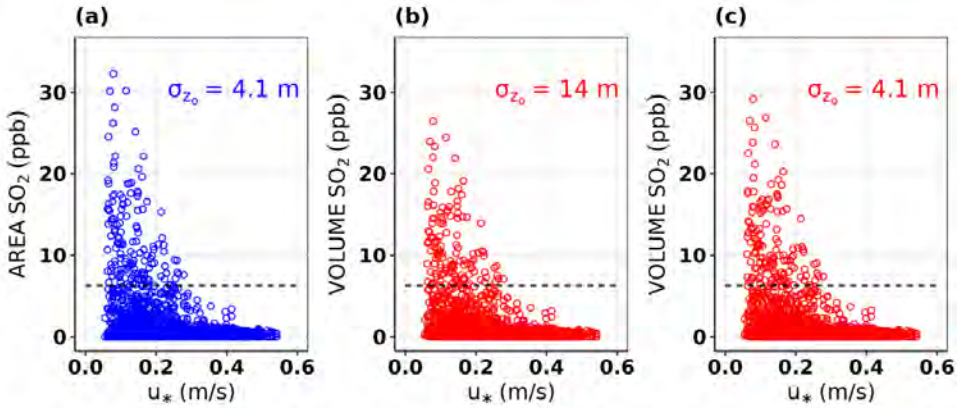

Figure 1. Variation of AERMOD estimates with the friction velocity for (a) AREA, and (b and c) VOLUME source treatments with differing σ_{z_o}. The black dashed line represents the overall maximum observed SO_2 concentration at KLAX.

The VOLUME treatment provides lower estimates at the high end of the concentration distribution as seen in Figure 2. The VOLUME treatment is consistently lower than the AREA description with the discrepancy increasing with the AREA estimate. These differences are most evident at the lowest values of the friction velocity (u_*). The largest difference is about 6 ppb when the AREA model estimate is about 30 ppb.

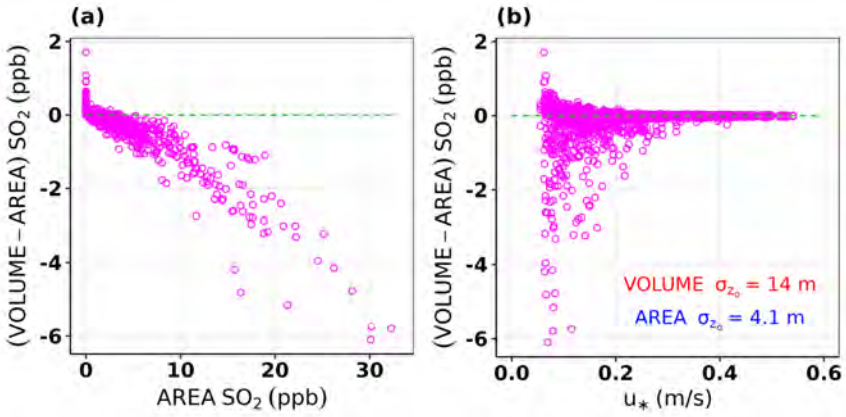

Figure 2. Differences between model estimates from the two source treatments: (a) Comparison against AREA source treatments and (b) comparison against u_*.

The lower values of SO_2 from the VOLUME treatment are associated with higher initial $\sigma_{z_o} = 14\ m$ (AREA $\sigma_{z_o} = 4.1\ m$) and the inclusion of meander. Figure 3 shows that using the same values of $\sigma_{z_o} = 4.1$ m does not remove the trend in the VOLUME estimates: they are still lower, but the values are higher than those in the default VOLUME description. The middle panel of

Figure 3 indicates that the larger $\sigma_{z_o} = 14\,m$ in the VOLUME treatment contributes more than the removal of the meander to the values in the high end of the VOLUME estimates relative to the corresponding AREA estimates. Figure 3(c) shows that results from VOLUME are within 1 ppb of the AREA description when σ_{z_o} values from the two descriptions are set to the same value of 4.1 m, and meander is switched off.

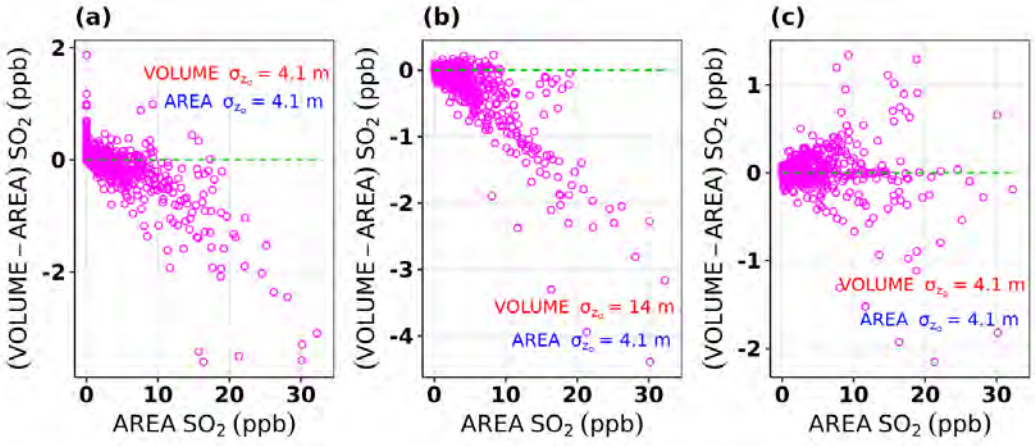

Figure 3. Impact of σ_{z_o} and meander on VOLUME estimates: (a) Left panel uses the same σ_{z_o} for the two source treatments, and the (b) middle and (c) right panels remove meander.

1.1.4 Summary

The analysis presented here shows both treatments of airport sources do not yield AERMOD model estimates that are consistent with the magnitudes and the trends of the observed SO_2 concentrations. The VOLUME description yields lower concentrations than those from the AREA description, but the magnitude of the highest concentrations is about five times larger than the observed values, even when background sources are not included. These results suggest that the inclusion of a plume rise algorithm for aircraft jet exhaust is likely to yield model estimates that are more consistent with observations than those from the current version of AERMOD for both source treatments. Carslaw et al. (2006) show, through an analysis of data collected at Heathrow Airport, that plume rise of jet exhaust gives rise to the observed behavior of concentrations varying with friction velocity. Pandey et al. (2023) provide an approach to modeling plume rise for aircraft sources in AERMOD. The magnitudes of the plume rise estimated by the model are an order of magnitude higher than the 14 m specified in VOLUME. Also, adding plume rise would avoid arbitrary assumptions about the initial vertical spread of the plume in AERMOD. In addition to plume rise, the inclusion of meander in AREA source treatment will enhance the low concentrations and potentially reduce the magnitude of the high concentrations. This work was published in the *Air Quality, Atmosphere, & Health journal* on February 7, 2024 by Pandey et al. (2024a). More details about the study design, emissions, and results, are provided in Pandey et al. (2024a).

2. Physical Processes

2.1 Development and Implementation of an Aircraft Plume Rise Algorithm in AERMOD

The AEDT incorporates AERMOD to estimate concentrations resulting from aircraft emissions, which possess horizontal momentum as well as buoyancy. The current version (v23132) of AERMOD incorporates plume dynamics associated with such emissions as an ALPHA option, which is described in Pandey et al. (2023). AERMET, AERMOD's meteorological processor, does not account for the meteorology of the land-water interface that is likely to be important for airports located on the shorelines of lakes or oceans. An approach to include these effects in AERMOD is described in Pandey et al. (2022). Here, we examined the impact of including plume rise and shoreline effects in AERMOD by evaluating model estimates of NO_x and SO_2 with corresponding measurements made during the AQSAS in the winter and summer seasons of 2012 for 42 days each.

2.1.1 Aircraft Plume Rise Methodology within AERMOD

Aircraft emissions during LTO cycles are transient and buoyant and occur at various altitudes above the ground. AERMOD accounts for emissions at different altitudes and the latest version accounts for plume rise of jet emissions using the approach described in Pandey et al. (2023). Our team incorporated the plume rise algorithm in the AREA source framework

of AERMOD (Pandey et al., 2023) by assuming that the different types of aircraft contributing to emissions in any one of the area sources can be represented by a "typical" aircraft whose characteristics are computed through a weighted average of the characteristics of aircraft that pass through the area source. Emissions from an aircraft are treated as line thermals that have horizontal momentum and buoyancy; the plume is first governed by horizontal momentum, which induces vertical growth of the plume while the velocity in the plume decreases with distance from the aircraft. Buoyancy takes over once the horizontal velocity in the plume is comparable to the mean ambient velocity. Buoyancy results in plume rise and growth of plume dimensions; as in common plume rise treatments, plume rise is terminated either when the plume becomes negatively buoyant in stable conditions or when the rate of plume rise becomes comparable to the standard deviation of turbulent velocity fluctuations outside the plume. The horizontal momentum and the buoyancy of the line thermal associated with jet aircraft emissions are related to aircraft engine characteristics: thrust, fuel burn rate, aircraft velocity, air-fuel ratio, rated power, and engine bypass ratio. Details of the formulation are provided in Pandey et al. (2023).

2.1.2 Modifications in AERMET Meteorology

The meteorological conditions at KLAX can be influenced by processes that are not fully taken into consideration by the AERMET model (Pandey et al., 2022). One of these factors pertains to KLAX's coastal location. When the wind blows from the west, it passes over cold water before reaching the warmer land of the airport. This results in an upward heat flux that creates an internal boundary layer directly above the airport. Consequently, the stable boundary layer predicted by AERMET may not reflect the actual atmospheric conditions that facilitate the dispersion of airport emissions. This possibility is accounted for by using an internal boundary layer model (IBL) (Venkatram, 1977) to simulate the meteorology over KLAX under stable conditions when the winds are westerly. Our team estimated the height of the internal boundary layer using a temperature difference of 2°C between land and water; this value, which is uncertain, is based on data presented by Hsu (1984). The heat flux in the IBL results in positive values of the convective velocity scale w_*. We allow for an alternative treatment of shoreline meteorology based on observations of Rahn & Mitchell (2016), which indicate that onshore flows at KLAX are associated with foggy conditions and a neutral boundary layer whose height is about 400 m. To simulate these conditions, our team has taken the Monin-Obukhov length to be 1000 m, recalculated the friction velocity, and took the convective velocity scale to be zero; these micrometeorological variables govern the vertical and horizontal plume spreads in AERMOD. The default input file produced by AERMET had a maximum roughness length of 0.2 m. This value was increased to 0.3 m when the wind blows from the northeast and southeast quadrants to account for the impact of tall buildings in downtown Los Angeles during these winds. This value of 0.3 m, which is uncertain, allows us to explore the possibility that model performance can improve if the original AERMET file accounted accurately for the effects of downtown buildings.

2.1.3 Emissions

The AEDT3e is used to model aircraft SO_2 and NO_x emissions on the surface as well as airborne. Non-aircraft SO_2 and NO_x emissions estimates are based on the Emissions and Dispersion Modeling System (EDMS) emission inventory of KLAX, which accounts for all the aircraft and non-aircraft sources for winter (02/01/2012 – 03/13/2012) and summer (07/18/2012 – 08/28/2012) seasons of 2012 (Tetra Tech, 2013). The hourly averaged SO_2 and NO_x emissions during winter and summer monitoring seasons include contributions from various sources. The Chevron® refinery contributes 10.92 g/s of SO_2 and 18.66 g/s of NO_x, while other stationary sources contribute 0.05 g/s of SO_2 and 2.20 g/s of NO_x. Marine sources account for 31% of total SO_2 emissions and 40% of total NO_x emissions but have a smaller impact on concentrations due to their distance from the airport (Tetra Tech, 2013). Aircraft emissions are equal to approximately 50% of non-aircraft emissions for SO_2 and NO_x during daytime hours, with larger contributions in the evening. Differences between winter and summer emissions are due to the use of EDMS in the winter study and AEDT in the summer, with the latter providing more accurate data on aircraft operations and taxi emissions.

2.1.4 Model Results

To focus on the impact of aircraft-related emissions on the four core sites (AQ, CN, CS, CE), the concentrations are grouped to reflect the time of day. The hours 1 to 8 describe nighttime, hours 9 to 16 are daytime, and hours 17 to 24 correspond to evening. The impact of the modifications in AERMOD is evaluated at the four core sites during winter and summer using mean concentrations averaged over the hourly bins using line plots. Our team also evaluated model performance using commonly used statistical measures of model performance (Cox & Tikvart, 1990): fractional bias (FB) based on the 26 robust highest concentrations (FB), and fraction of the model estimates with a factor of two of the corresponding observations (FAC2) (Chang & Hanna, 2004). The EPA recommends these metrics to measure the performance of dispersion models that are used in regulatory applications.

® Chevron is a registered trademark of Chevron Intellectual Property, LLC, Houston, Texas.

Model performance statistics are presented for four different cases:

1. *Default*: The meteorological inputs are baseline AERMET outputs, and plume rise of jet emissions is not modeled. This corresponds to the way AERMOD would be normally applied to estimate the air quality impact of airport emissions.
2. *Plume Rise*: This case is the same as case 1, except that plume rise is modeled using the ALPHA option "ARCFTOPT" of AERMOD (v23132); the approach is described in Pandey et al. (2023).
3. *Shoreline*: This case is the same as case 2 except that the meteorological inputs are modified to account for shoreline and urban effects described in Pandey et al. (2022). Shoreline effects are modeled only when AERMET predicts stable conditions during onshore flows.
4. *Neutral*: This case is the same as case 3 except that during both daytime and nighttime, meteorology is treated as neutral rather than unstable to account for the possibility of foggy conditions in LAX during onshore flows.

2.1.4.1 Concentration Averaged over Hourly Bins

The mean concentration variation of the model estimated SO_2 and NO_x concentrations averaged over each hourly bin at the four core sites (AQ, CN, CS, and CE) for the two seasons are compared with corresponding mean observations in Figure 4 and Figure 5.

Figure 4 compares the performance of the four model scenarios through the ratio of the modeled to the measured SO_2 concentrations averaged over the time bins described earlier. The lines above and below unity on the y-axis correspond to modeled limits within a factor of two from the observations. Our team observed that the *Default* version overestimates the concentrations during the early morning and late evening hours at the AQ and CS sites, which are at the far ends of the runways. *Plume Rise* and meteorological modifications reduce this overestimation. However, these modifications reduce the modeled predictions substantially, such that the ratios are now outside the preferred limits indicated by the factor of two lines during the daytime. At the CN site, the modeled concentrations are generally lower than the measured concentrations. The modification to neutral conditions reduces this underestimation during the daytime. At CE, all the modifications to the *Default* version improve model performance to bring the ratios of the modeled to the measured concentrations closer to the one-to-one line. Assuming neutral meteorology appears to make the most noticeable improvements during both daytime as well as nighttime hours. Figure 4, depicting results corresponding to the summer study, shows the *Default* version of the model overestimating SO_2 concentrations during the early morning and late evening hours at all four sites. The overestimation is reduced substantially with the introduction of plume rise, which does not appear to make much difference during the daytime hours, presumably because daytime turbulence overcomes the effects of plume rise. Except for the *Neutral* version, all the scenarios underestimate concentrations during the daytime hours. It is also clear that modifying the AERMET-modeled daytime convective conditions to neutral, and thus reducing turbulent dispersion, leads to improvement in daytime model performance. In addition to this, the change in stable/nighttime onshore flows to neutral further reduces the concentrations at all sites during the early morning hours, whereas in late night hours, it enhances the concentrations.

Figure 5 indicates that during the winter season, all four scenarios of AERMOD underestimate the measured NO_x concentrations at the four sites (AQ, CN, CS, and CE) during the daytime hours. During the early morning and late evening hours, the estimates from the *Default* and the *Plume Rise* scenarios are generally within a factor of two of the model estimates at the CS site primarily because the *Default* version tends to overestimate the impact of emissions as indicated in the modeling of SO_2 concentrations.

All three alternate model scenarios show a substantial improvement in performance compared to *Default* during the summer field study. As in the case of SO_2, the modifications to the model result in reductions in the overestimation of concentrations during the early morning and late evening hours, when plume rise and conversion to unstable conditions reduce ground-level concentrations. It should also be noted that both during the winter and summer field studies, conversion of the daytime unstable conditions and nighttime stable conditions to less dispersive neutral conditions led to an increase in ground-level concentrations, bringing them closer to the one-to-one line.

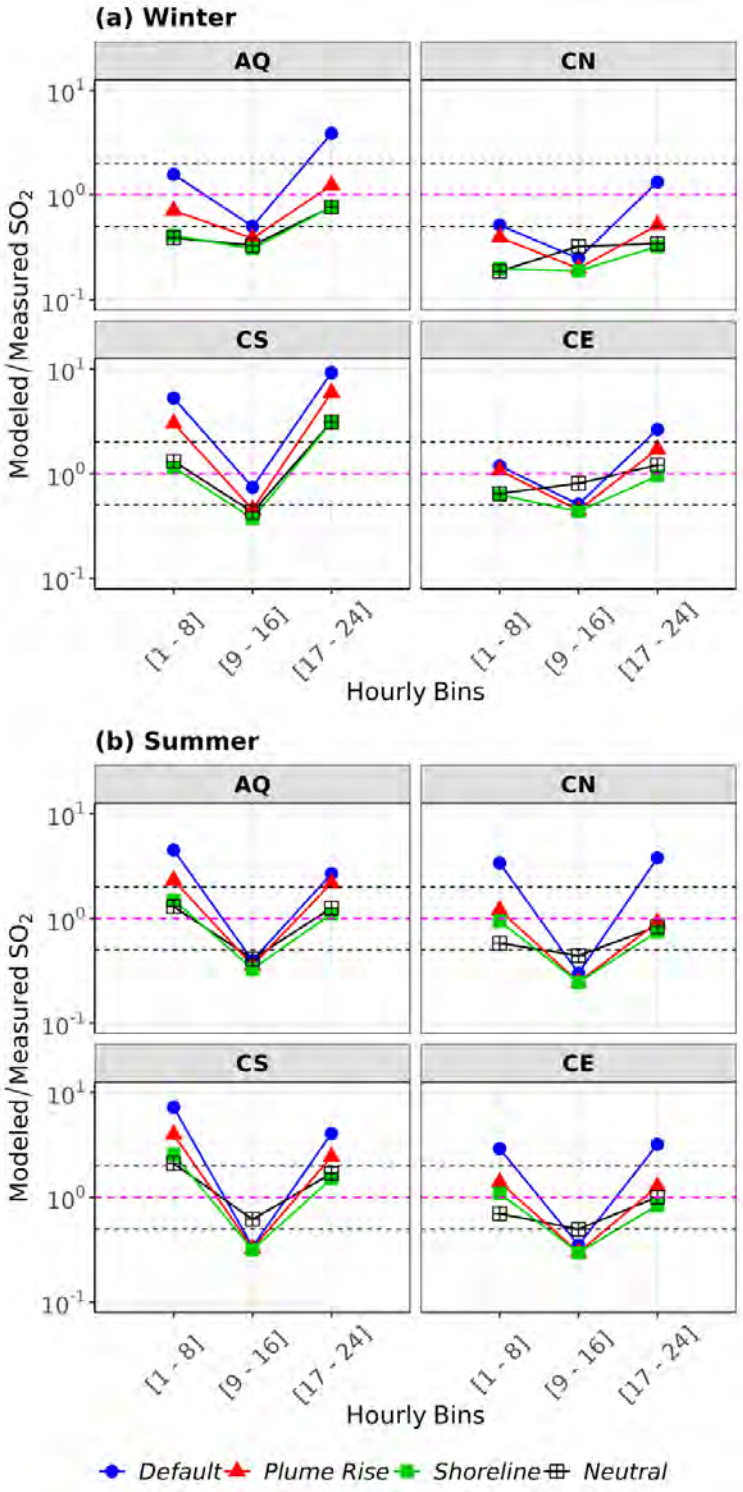

Figure 4. Ratio of modeled to measured SO_2 concentrations averaged over hourly bins at the four sites (AQ, CN, CS, and CE) during the (a) winter and (b) summer studies.

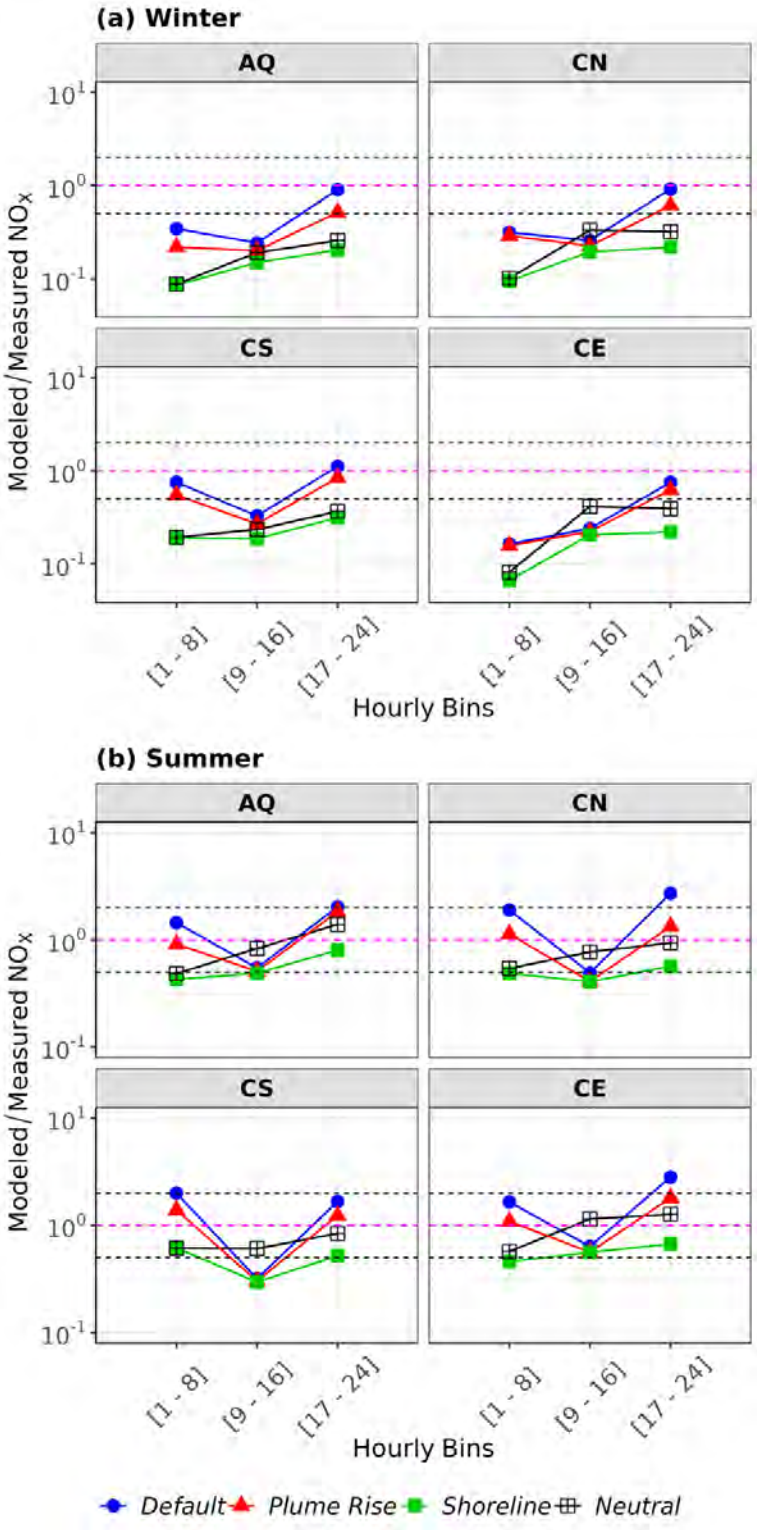

Figure 5. Ratio of modeled to measured NO_x concentrations averaged over hourly bins at the four sites (AQ, CN, CS, and CE) during the (a) winter and (b) summer studies.

2.1.4.2 Regulatory Application of the Model

Because regulatory applications of AERMOD focus on the values at the upper end of the modeled concentration distributions, it is useful to examine the performance of the modified versions of the model statistically, based on the 26 highest values of the modeled and measured concentrations (Cox & Tikvart, 1990) as recommended by the EPA. These statistics are presented in Table 3.

FB is defined by the following equation:

$$FB = 2\frac{(Measured - Modeled)}{(Measured + Modeled)} \quad \text{(Eq. 1)}$$

FAC2 refers to the fraction of modeled values within a factor of two of the corresponding measured values. The ratio of the robust highest concentrations (RHC; Ratio_RHC), is the ratio of the modeled RHC to that of the measured, where the RHC of each set is computed using the 26 highest values.

We have introduced a new metric, "Performance Distance" (PD), based on a three-dimensional coordinate system in which each statistical measure of model performance is measured along each of the three axes. Then a set of three statistics represents a point in this three-dimensional space. Then PD is the Eulerian distance of each of these points from the ideal set, (0,1,0), as follows:

$$PD = \sqrt{FB^2 + \left(1 - \frac{FAC2}{100}\right)^2 + (Ratio_RHC - 1)^2} \quad \text{(Eq.2)}$$

Improvement in the model is indicated by the approach of PD to its ideal value of zero. Note that PD as defined here is only one possible way of combining the three performance indices.

Table 1. Fractional Bias (FB) based on the top 26 highest concentrations, FAC2 (factor of two), and the ratio of robust highest concentrations (Ratio_RHC) for the winter and summer seasons of 2012.

Pollutant	Season	Model	Statistical Measures of Model Performance			
			FB	FAC2 (%)	Ratio_RHC	Performance Distance (PD)
SO_2	Winter	Default	-1.55	89	7.92	7.09
		Plume Rise	-1.53	97	7.51	6.69
		Shoreline	-0.83	52	2.43	1.72
		Neutral	-1.00	63	3.02	2.28
	Summer	Default	-1.36	87	5.27	4.48
		Plume Rise	-1.26	91	4.40	3.63
		Shoreline	-0.63	68	1.92	1.16
		Neutral	-0.75	99	2.20	1.42
NO_x	Winter	Default	-0.37	16	1.46	1.03
		Plume Rise	0	9	1	0.91
		Shoreline	1.01	3	0.33	1.55
		Neutral	1	9	0.33	1.51
	Summer	Default	-1.29	79	4.62	3.85
		Plume Rise	-0.63	89	1.91	1.11
		Shoreline	-0.05	85	1.05	0.17
		Neutral	0.19	86	0.83	0.29

The positive FB and the values of the Ratio_RHC relative to unity suggest the underestimation of the highest concentrations of SO_2 and NO_x during the winter and summer field studies.

For SO_2, the overall FAC2 improves from *Default* to *Plume Rise* model scenarios in both seasons. Additionally, in the summer study, it also improves in the *Neutral* model scenario. On the other hand, for NO_x, all model scenarios in the summer season show improvements in FAC2 relative to *Default*. However, during the winter season, FAC2 is low compared to the summer season due to the differences in the emissions and observations (Table 1).

The PD metrics indicate that the introduction of plume rise and modifications to the input meteorology leads to improvement in the description of SO_2 concentrations in the winter and summer field studies. As Table 1 indicates, the introduction of shoreline meteorology makes the biggest change to model performance expressed in terms of PD. The change to neutral conditions from convective conditions during onshore flows makes a smaller change.

For NO_x concentrations, the introduction of plume rise makes a slight improvement to performance of the *Default* version during the winter study. The modifications to meteorological inputs seem to increase the PD during the winter. On the other hand, during the summer study, the incorporation of plume rise makes the largest improvement to model performance. Modifications to shoreline meteorology and conversion to neutral conditions make smaller contributions to improving the performance of the *Default* version of the model.

2.1.4.3 Sensitivity using Observed Background NO_x Concentrations

During the winter season, more than 45% of the winds originate from the northeast and the southeast directions. This suggests that the core sites CN and CE are impacted by emissions from Los Angeles city core, especially during the late night and early morning hours. This led to a sensitivity analysis in which modeled estimates from non-airport contributions were replaced with observed concentrations of NO_x measured at Air Quality Station (AQS) ID: 06-037-1103 of the California Air Resources Board (CARB) situated in the center part of the Los Angeles city, which is approximately 13 mi from KLAX. This allowed us to avoid the impact of possible limitations in the non-airport emissions inventory on the performance of AERMOD at the core sites. In addition to this, we used summer emissions in winter and limited the mixing height to 200 m. Our team named these new model scenarios as *Default (New_Bg)* and *Plume Rise (New_Bg)*, respectively.

Figure 6 compares the performance of the four model scenarios (*Default*, *Default (New_Bg)*, *Plume Rise*, *Plume Rise (New_Bg)*) through the ratio of the modeled to the measured NO_x concentrations averaged over the time bins described earlier. The lines above and below unity on the y-axis correspond to a factor of two intervals. The *Default (New_Bg)* and *Plume Rise (New_Bg)* versions increase the NO_x concentrations and are close to a one-to-one line, especially at CN and CE sites. The increase in the modeled NO_x concentrations is significant throughout the day because easterly winds that bring non-airport emissions to the receptors are 45% more frequent in winter than in summer.

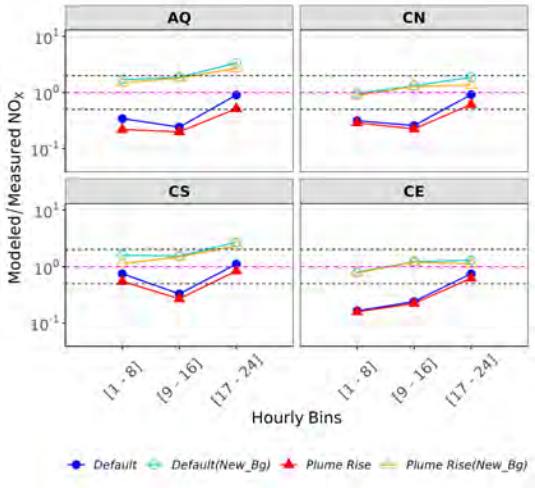

Figure 6. Ratio of modeled to measured NO_x concentrations averaged over hourly bins at the four sites (AQ, CN, CS, and CE) during the winter study.

2.1.4.4 Summary

The model evaluation results from the KLAX AQSAS data show that modifications to AERMOD improve its performance in estimating ground-level concentrations of aircraft emissions, especially compared to the default version. Incorporating plume rise for jet exhaust reduces overestimated concentrations during early morning and late evening hours by up to 50%. Accounting for shoreline meteorology also reduces these overestimations by converting stable to unstable conditions. Underestimations during daytime hours are corrected by adjusting stable conditions to neutral conditions. The summer study showed better model performance, suggesting higher uncertainty in winter emissions and meteorological inputs. Emissions could be more accurate in winter with hourly data from AEDT, as used in the summer study, and by adjusting taxi emissions. The underestimation of NO_x in winter is reduced when observations from the CARB Central Los Angeles monitor replace the modeled non-airport contributions. The analysis indicates that AERMOD provides adequate estimates when aircraft plume rise and shoreline effects are considered. However, gaps in meteorological inputs, such as surface heat flux and boundary layer height, impact model accuracy. The study highlights the need for detailed field light detection and ranging (LIDAR) measurements of aircraft plume behavior, as direct observations of jet exhaust dispersion, especially near runways, are limited. More details are provided in Pandey et al. (2024b).

2.2 Development of AREA Source Meander Algorithm

A variety of sources of pollutant emissions can be represented as area sources. These include manure lagoons, landfills, wastewater treatment ponds, and highways. A group of point sources can also be treated as an area source. The impact of an area source is usually computed by representing the area source as a set of line sources perpendicular to the wind direction. As for point sources, the Gaussian horizontal concentration distribution used to compute the contributions of the line sources is likely to overestimate ground-level concentrations when the wind speed is comparable to the standard deviation of the horizontal velocity fluctuations. Various methods are used to mitigate this overestimation under these conditions, called meander. As an example of one of these approaches, our team examined that of AERMOD. AERMOD includes meander in modeling the impact of point and volume sources but has not yet incorporated it into AERMOD's area source algorithm. This work described an approach to including meander in AERMOD's (v23132) area source algorithm and demonstrates its impact on concentrations associated with area sources.

2.2.1 Treatment of Area Sources

The concentration associated with the plume is given by the commonly used Gaussian formulation, as follows:

$$C_p(x_r, y_r, z_r) = \frac{Q}{2\pi U_s \sigma_z \sigma_y} exp\left(-\frac{(y_r - y_s)^2}{2\sigma_y^2}\right)\left[exp\left(-\frac{(z_r - z_s)^2}{2\sigma_z^2}\right) + exp\left(-\frac{(z_r + z_s)^2}{2\sigma_z^2}\right)\right] \quad \text{(Eq. 3)}$$

where Q is the emission rate, U_s is the mean scalar wind speed evaluated at mean plume height (see Cimorelli et al., 2005, for details), σ_y and σ_z are the horizontal and vertical plume spreads, and the subscripts 's' and 'r' refer to source and receptor. The vertical and horizontal plume spreads depend on the downwind distance $x_r - x_s$, and micrometeorological variables.

The uniform distribution,C_r, is given by the following expression

$$C_r(x_r, y_r, z_r) = \frac{Q}{2\pi r}\frac{V(z_s, z_r, r)}{U_s} \quad \text{(Eq. 4)}$$

$$V(z_s, z_r, r) = \frac{1}{\sqrt{2\pi}\sigma_z(r)}\left(exp\left(\frac{(z_r - z_s)^2}{2\sigma_z^2}\right) + exp\left(\frac{(z_r + z_s)^2}{2\sigma_z^2}\right)\right)$$

$$r = (x^2 + y^2)^{1/2}$$

where r is the distance from the source to the receptor. These two distributions are weighted according to the magnitude of the standard deviation of horizontal velocity fluctuations, σ_v, relative to the mean vector wind speed:

$$C(x_r, y_r, z_r) = f_r C_r(x_r, y_r, z_r) + (1 - f_r) C_r(x_r, y_r, z_r) \quad \text{(Eq. 5)}$$

where

$$f_r = \frac{2\sigma_v^2}{U_s^2} \text{ and } U_s^2 = U_v^2 + 2\sigma_v^2$$

Note that Equation 5 provides the relationship between the vector mean wind speed, U_v, and the mean scalar wind speed, U_s assuming that $\sigma_u = \sigma_v$. It is observed that the maximum value of the weighting factor, f_r, is unity when the wind speed distribution is uniform across 0 to 2π when the vector mean wind speed, U_v, is zero.

AERMOD estimates concentrations associated with an area source by representing it with a convex polygon.
The calculations are performed using a coordinate system in which the x-axis is along the near-surface wind vector.
The contribution of the area source to the concentration at a receptor at (x_r, y_r, z_r) is computed by representing the area by a set of equally spaced line sources that span the along-wind width of the area source.

The concentration caused by a single line can be written as follows:

$$C(x_r, y_r, z_r) = qF_z(x_r - x_l, z_s, z_r)\big(erf(t_2) - erf(t_1)\big)/2 \quad \text{(Eq. 6)}$$

where

$t_1 = \frac{y_r - y_b}{\sqrt{2}\sigma_y(x_r - x_l)}$, and $t_2 = \frac{y_r - y_e}{\sqrt{2}\sigma_y(x_r - x_l)}$

The vertical distribution of the concentration, F_z, which does not vary along y, is commonly described with a Gaussian distribution in AERMOD.

The contribution of a set of *N* line sources on an area source to the concentration at a receptor is written as:

$$C(x_r, y_r, z_r) = q\sum_{i=1}^{i=N} F_z\big(x_r - x_l^i, z_s, z_r\big)F_y\big(x_r - x_l^i\big) \quad \text{(Eq. 7)}$$

where x_l^i is the *x*-coordinate of the i^{th} line source with a length l^i.

Detailed procedure of the numerical solution of Equation 7 is described by Venkatram and Thiruvenkatachari (2023).

2.2.2 Including Meander
Figure 7 shows a line source and the impact of the element *dy* on the concentration at the receptor (x_r, y_r, z_r). It is assumed that the line source is at a height z_s, and the receptor at z_r.

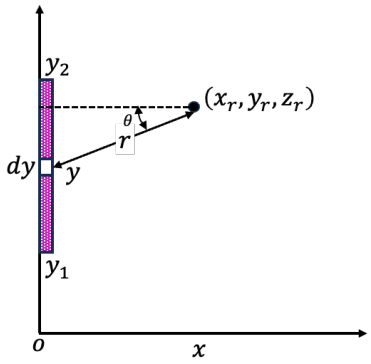

Figure 7. Contribution of an element of the line source to the receptor (x_r, y_r, z_r) using the meander formula.

Then the concentration at the receptor is given by the following equation:

$$C(x_r, y_r, z_r) = \int_{y_1}^{y_2} \frac{q\,dy}{2\pi r}\frac{V(z_s, z_r, r)}{U_s} \quad \text{(Eq. 8)}$$

where *q* is the emission rate per unit length of the line source. Note that the vertical spread, σ_z, is a function of the radial distance from the source to the receptor, $r = (x^2 + y^2)^{\frac{1}{2}}$, as well as micrometeorology. This integral cannot be evaluated analytically for arbitrary σ_z. Evaluating the integral numerically will add computing time to the already resource-demanding

area source algorithm. Thus, it is useful to examine the utility of an analytical approximation derived by first assuming that both and receptor are at ground level, $z_s = z_r = 0$, then the vertical spread grows linearly with *r*, $\sigma_z = \sigma_w r/U_s$, which allows us to write Equation 8 as:

$$C(x_r, y_r, z_r) = \int_{y_1}^{y_2} \frac{q dy}{2\pi r} \sqrt{\frac{2}{\pi}} \frac{1}{\sigma_w} \quad \text{(Eq. 9)}$$

Using the angle ϑ shown in Figure 7, substitute $y = x_r \tan(\theta)$ and $r = x_r/\cos(\theta)$ into Equation 9 and also using $\sigma_z(x_r) = \sigma_w x_r/U_s$, Equation 9 can be written as:

$$C(x_r, y_r, z_r) = \sqrt{\frac{2}{\pi}} \frac{q}{\sigma_z(x_r) U_s} \left(\frac{\theta_2 - \theta_1}{2\pi}\right) \quad \text{(Eq. 10)}$$

where

$$\theta_2 - \theta_1 = tan^{-1}\left(\frac{y_2 - y_r}{x_r}\right) - tan^{-1}\left(\frac{y_1 - y_r}{x_r}\right)$$

Notice that $(\theta_2 - \theta_1)$ is simply the angle subtended by the line at the receptor. For an infinitely long line, the subtended angle is π, and the concentration at the receptor, (x_r, y_r), is one half the value one would obtain if the wind was blowing perpendicular to the line. So, our team proposes the following approximation to the integral in Equation 8, as follows:

$$C(x_r, y_r, z_r) = \frac{qV(x_r, z_r, z_s)}{U_s} \left(\frac{\theta_2 - \theta_1}{2\pi}\right) \quad \text{(Eq. 11)}$$

The vertical distribution function, *V*, is evaluated at x_r, the perpendicular distance of the receptor to the line.

2.2.3 Impact of Meander

In the simulations that follow, our team has taken $z_0 = 0.01\, m, z_s = z_r = 1\, m,$ and $\theta = 225^0$, and the other parameters are allowed to vary. As in AERMET, the minimum $\sigma_v = 0.3\, m/s$. The stability of the surface boundary layer is characterized with the Monin-Obukhov (M-O) length, $L = -\frac{T_0}{g} u_*^3/kQ_0$, where T_0 is the 10 m temperature, *g* is the acceleration due to gravity, *k=0.4* is the von-Karman constant, $u_*$is the surface friction velocity, and Q_0 is the surface kinematic heat flux. A large *L* signifies a deep "neutral" surface layer. A negative *L* corresponds to an "unstable" surface layer in which the height above */L/* is dominated by buoyancy production of turbulence. A "stable" surface layer is described by a positive *L* is one in which shear production is dominant below *L*, while the negative heat flux suppresses turbulence above *L*. In all the figures below, the distances shown are expressed in meters. The emission rate from the source is 1 g/s, and the units of concentration are $\mu g/m^3$.

The reference case is the simulation that does not include meander. The meteorological conditions and relevant statistics for the simulations discussed here are listed in Table 2. The impact of meander is quantified in terms of three statistics: the mean of the concentration without meander, the FB, and the standard deviation of the differences between the cases without and with meander. Figure 8 shows the impact of meandering on plume concentrations under near-neutral conditions when *L*=-1000 m. The scalar wind speed is taken to be $U_s = 0.5\, m/s$ to allow the contribution of meander to the concentrations, 72%, to dominate the plume contribution. Note that the contribution of meander to the concentration at *0.72* does not vary with stability because its value is determined by the minimum value of $\sigma_v = 0.3\, m/s$, which is larger than the value of σ_v computed from M-O similarity.

Panels (a) and (b) of Figure 8 show that, as expected, the major effect of meander is upwind of the source. Panel (c) of Figure 8 shows that concentrations that are small compared to the mean value are enhanced with meandering, while concentrations that are much larger than the mean value are decreased relative to the reference plume case. Table 2 indicates that meandering gives rise to a FB of -8.2%; meander reduces the concentrations. The standard deviation of the differences is 0.82 of the mean. In simulation 2, the M-O length is -10 m, signifying unstable conditions. The FB is -2.6%, and the standard deviation is 0.83 of the mean without meander. In simulation 3, the FB is now -16.8%, and the standard deviation is 0.85. The simulations considered here show that meander has its largest impact during stable conditions, and its least during unstable conditions.

As indicated earlier, the introduction of meandering increases the computing demand of the already resource-hungry area source algorithm. In the simulations considered here, the ratio of computing times with to without meander ranged from a factor of 30 for the stable case, to a factor of 40 for the unstable case. While these statistics will vary with the specifics of the processor, the approximation of Equation 11 will reduce computing time significantly if it is found to yield results that are close to that obtained by the numerical integration of Equation 8.

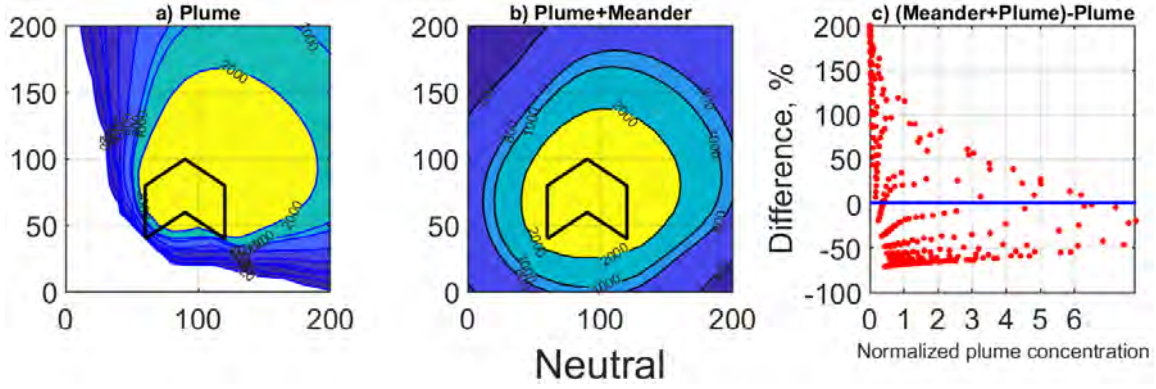

Figure 8. Concentration pattern under neutral conditions. In panel (c), the plume concentration is normalized with the mean of the plume spatial field.

Table 2. Meteorological Inputs and differences associated with including meander in the area source algorithm.

Simulation Number	Scalar Wind Speed(m/s)	M-O Length(m)	f_r (weighting factor)	Plume Mean $\mu g/m^3$	Fractional Bias %	Standard Deviation of difference/Mean
1	0.5	-1000	0.72	1905	-8.2	0.82
2	0.5	-10	0.72	1280	-2.6	0.82
3	0.5	10	0.72	3001	-16.8	0.82

2.2.4 Approximating Meander

Figure 9 compares the results from the approximation, Equation 11, with the exact solution corresponding to the numerical integration of Equation 8 under conditions when the approximation is valid: $z_r = z_s = 0$, and the stability is neutral so that $\sigma_z \sim x$. The small differences between the two results, shown in panel (c) in Figure 9, which occur at concentrations close to zero, are related to the errors in the numerical integration.

Table 3 indicates that the normalized standard deviation of the errors during unstable conditions is 0.4, which is about 25% higher than during stable conditions for this specific set of simulations. Our team has conducted several simulations with a different set of release height, receptor height, wind speed, and M-O length, and example of which is shown in Table 3. The results indicate that the FB does not exceed 25%, which suggests that it might be possible to generalize the result that the maximum FB between the exact and approximate representation of meander is 25%.

Table 3. Meteorological inputs and differences associated with approximating meander in the area source algorithm.

Simulation Number	Scalar Wind Speed(m/s)	M-O Length(m)	f_r (weighting factor)	Exact Mean $\mu g/m^3$	Fractional Bias %	Standard Deviation of difference/Mean
1	0.5	-1000	0.72	1905	24.0	0.35
2	0.5	-10	0.72	1280	23.2	0.41
3	0.5	10	0.72	3001	23.2	0.31
4	1	-10	0.18	645	11.3	0.24

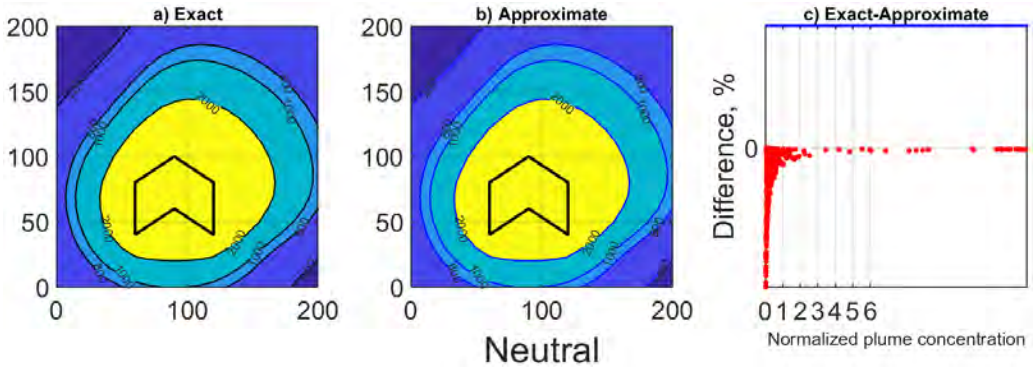

Figure 9. Concentration pattern under neutral conditions and $z_r = z_s = 0$. In panel c, the plume concentration is normalized with the mean of the exact spatial field.

2.2.5 Summary and Conclusions

Note that this formulation for meandering depends on a weighting factor, f_r, in Equation 5, whose functional form is arbitrary. This problem can be avoided by using an alternative approach that expresses the concentration in polar coordinates. As pointed out by Hanna et al. (2003), and formalized by Venkatram et al. (2004), the concentration associated with a point source can also be expressed in polar coordinates

$$C(\theta, z_s, z_r) = Q\frac{P(\theta)}{U_s r}V(z_s, z_r, r) \quad \text{(Eq. 12)}$$

where ϑ is the angle between the line joining the source to the receptor and the mean wind direction, and *P(ϑ)* is the distribution of wind directions about the mean wind direction. In a field study conducted in an urban location, Venkatram et al. (2004) found that this wind direction distribution was close to Gaussian, as follows:

$$P(\theta) = \frac{1}{\sqrt{2\pi}\sigma_\theta} exp\left(-\frac{\theta^2}{2\sigma_\theta^2}\right) \quad \text{(Eq. 13)}$$

where σ_θ is the standard deviation of the wind direction fluctuations about the mean wind direction. Its magnitude determines the impact of the point source at upwind locations. So, this formulation automatically accounts for meandering and thus avoids the arbitrariness of the formulation of the weighting factor, f_r, in Equation 5. The following is a semi-empirical equation (Venkatram et al., 2004) that relates σ_θ to σ_v:

$$\sigma_\theta = \frac{\pi}{\sqrt{3}} tanh\left(\frac{\sigma_v}{U_v}\frac{\sqrt{3}}{\pi}\right) \quad \text{(Eq. 14)}$$

which keeps the value of $\sigma_\theta$between σ_v/U_v and $\pi/\sqrt{3}$ for large σ_v/U_v when P(θ) becomes uniform over 2π.

When applied to a line source perpendicular to the wind direction, the concentration can be expressed as in Equation 8

$$C(x_r, y_r, z_r) = q \int_{y_1}^{y_2} P(\theta) \frac{V(z_s, z_r, r)dy}{U_s r} \quad \textit{(Eq. 15)}$$

and

$$\theta = tan^{-1}(y_r - y, x_r)$$

where $x_r$is the perpendicular distance of the receptor to the line source. Evaluation of Equation 15 requires numerical integration as in the previous case. However, if $z_s = z_r = 0$, and $\sigma_z \sim x$, Equation 15 has the analytical solution:

$$C(x_r, y_r, z_r) = \sqrt{\frac{2}{\pi}} \frac{q}{\sigma_z(x_r) U_s} \frac{(\mathrm{erf}(t_2) - \mathrm{erf}(t_1))}{2} \quad \textit{(Eq. 16)}$$

where

$$t_2 = \frac{\theta_2}{\sqrt{2}\sigma_\theta} \text{ and } t_1 = \frac{\theta_1}{\sqrt{2}\sigma_\theta}$$
$$\theta_2 = tan^{-1}\left(\frac{y_2 - y_r}{x_r}\right) \text{ and } \theta_1 = tan^{-1}\left(\frac{y_1 - y_r}{x_r}\right)$$

where $erf\ (t)$is the error function given by $erf\,(t) = \frac{2}{\sqrt{\pi}} \int_0^t e^{-x^2} dx$. When $x_r < 0$, the receptor is upwind of the line source,

which requires the integral to be expressed as the sum of two integrals, one between θ_2 and π, and the other between θ_1 and -π. The scope of this work does not allow a comparison between these two approaches to treating meander. However, it is useful to show that these approaches yield significantly different concentration patterns as illustrated in Figure 10. The "pancake" approach spreads the concentration pattern further upwind than the "theta" approach but decreases the concentrations downwind of the source relative to the "theta" approach. This results in a FB between these two patterns of -22% indicating the higher downwind concentrations of the "theta" approach.

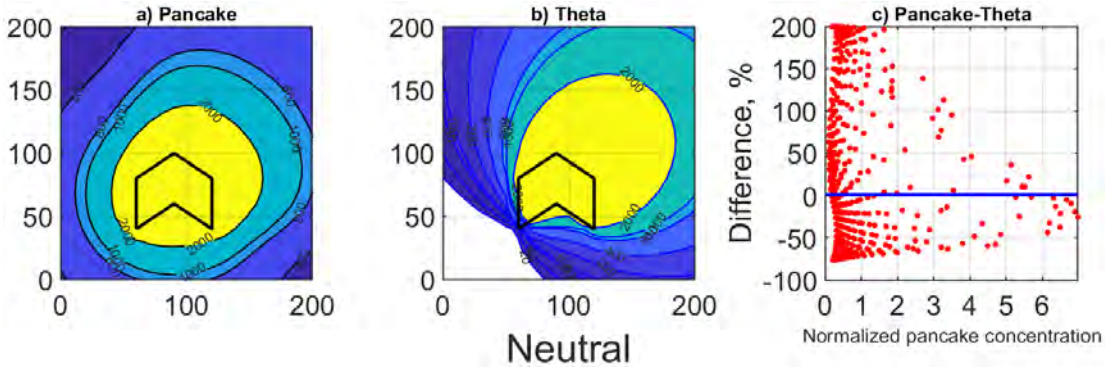

Figure 10. Comparison of concentration patterns produced by two different formulations of meander: Pancake refers to Equations 3 and Theta refers to Equation 12. The simulation corresponds to neutral conditions with M-O length=-1000 m, wind speed= 0.5 m/s and $z_r = z_s = 1$ m. In panel (c), the plume concentration is normalized with the mean of the pancake spatial field.

As expected, the introduction of meandering decreases concentrations downwind of the area source and creates concentrations upwind of the source. The two approaches to meandering yield significantly different results when meandering is a factor. The study conducted by Qian & Venkatram (2011) suggests that the "pancake" approach improves model estimates for point sources during low winds. On the other hand, the analysis of data in Venkatram et al. (2004) suggests that the "theta" approach yields acceptable results for line sources. The inclusion of meander increases the computational demands of the already resource-hungry algorithm for estimating the impact of area sources when the wind speeds are comparable to the standard deviation of the horizontal velocity fluctuations. Our team has proposed an approximation that reduces the computational demand by over a factor of 30. However, it underestimates concentrations relative to those from the numerical integration required to implement meandering. A limited number of simulations indicates that the FB does not exceed 25%. This suggests that it might be possible to adopt the analytical approximation

for meandering by multiplying the results it produces by an appropriate factor, e.g., 1.3. More details are provided in Venkatram et al. (2024).

3. Chemical Processes

3.1 Implementation of a New NO_x Chemistry Option (GRS7) in AERMOD

AERMOD (v23132) allows multiple chemistry options (Table 4) based upon the following NO_x-Ozone (O_3) oxidation and photolysis cycle:

$$NO_2 + h\nu \rightarrow NO + O_3 \quad \text{(R1)}$$
$$NO + O_3 \rightarrow NO_2 + O_2 \quad \text{(R2)}$$

Table 4. Summary of NO_x chemistry options on AERMOD (v23132).

Chemistry Module	Description
Ozone Limiting Method (OLM; Tier 2)	Considers reaction R2; Does not consider reaction R1 Infinite rate constant: NO_2 concentration formed from R2 equal to background O_3 concentration
Plume Volume Molar Ratio Method (PVMRM; Tier 3)	Considers R2; considers entrainment of O_3 background to ensemble plume O_3/NO_x in-plume ratio is used for determining NO_2/NO_x ratio
Ambient Ratio Method (ARM2; Tier 2)	Applied empirical NO_2/NO_x ratio as a function of modeled NO_x concentration to estimate ambient NO_2/NO_x ratio, which is then multiplied with model NO_x to estimate NO_2 (Hendrick et al., 2013; Podrez, 2015) Min and max NO_2/NO_x ratios are specified by modeler. In this study, min = 0.186 and max = 0.717
Travel Time Reaction Method (TTRM; Tier 3) *(Could be employed as additional option TTRM2 for OLM, PVMRM and ARM2*	Implicitly considers both R1 and R2: determines NO_2/NO_x ratio as a function of background O_3, reaction rate constants k1 of R2, and travel time *t* from source to receptor $NO_{frac} = 1 - \exp(-k1[O_3]*t)$.
Generic Reaction Method (GRSM; Beta option)	Explicitly considers both R1 and R2; Requires background O_3, NO_2, and NO_x concentrations (NO_x background = NO_2 background if NO_x data are missing). Considers plume entrainments of background concentration; reaction rate constant R1 is determined as function of solar irradiance

To account for impacts of reactive organic compounds on the NO_x–O_3 cycle, Akula Venkatram et al. (1994) introduced an expansion of NO_x–O_3 to a simplified NO_x–VOC–O_3 cycle, which considers the following seven reactions:

$$NO_2 + h\nu \rightarrow NO + O_3 \quad \text{(R1)}$$
$$NO + O_3 \rightarrow NO_2 + O_2 \quad \text{(R2)}$$
$$ROC + h\nu \rightarrow RP + ROC \quad \text{(R3)}$$
$$RP + NO \rightarrow NO_2 \quad \text{(R4)}$$
$$RP + RP \rightarrow RP \quad \text{(R5)}$$
$$RP + NO_2 \rightarrow SGN \quad \text{(R6)}$$
$$RP + NO_2 \rightarrow SNGN \quad \text{(R7)}$$

where ROC are the reactive organic compounds, RP is the radical pool, SGN is the stable gaseous nitrogen product, and SNGN is the stable non-gaseous nitrogen product. The conversions of volatile organic compounds (VOC) to ROC are as suggested by Venkatram et al. (1994) and presented in Table 5.

Table 5. Reactivity scaling factors.

VOC	VOC species	Reactivity
Propane, benzene	C3H8	0.17
Higher alkanes (≥ C4)	ALKA	0.43
Ethylene	ETHE	10.37
Higher alkenes (> C2), biogenics	ALKE	24.97
Mono-alkyl benzenes	TOLU	8.76
Di- and tri-alkyl benzenes	AROM	24.85
Formaldehyde	HCHO	42.17
Higher aldehydes	ALD2	6.7
Ketones	MEKd	10.49

Our team implemented the above seven reactions (hereafter referred to as GRS7) into AERMOD (v23132) and examined its effect on improving NO_2 simulation over chemistry options listed in Table 4. For this objective, we performed the following actions:

- Introduced new variables and new subroutines to AERMOD for GRS7 implementation. This included modifying AERMOD input/output modules for ROC concentration inputs, error messages, and new variables for debugging purposes.
- Introduced ROC to AERMOD: VOC emissions from aircraft and non-aircraft sources in the KLAX domain (Table 6) were simulated as trace gas to estimate VOC concentrations at the four core sites (CN, CE, CS and AQ). The estimated VOC concentrations at specific receptors were then read in GRS7 when simulating NO_x and NO_2. Details of chemical speciation of aircraft and non-aircraft exhaust are discussed in various studies (Herndon et al., 2006, 2009; Knighton et al., 2009; Wilkerson et al., 2010) based on which our team derived and averaged conversion factor ROC = 14.1 x VOC for all aircraft and non-aircraft source in Table 6.
- In addition to VOC emitted by airport study domain sources listed in Table 6, our team considered VOC emissions from sources that are outside the KLAX modeling domain (i.e., background VOC). This background VOC was derived from an earlier KLAX AQSAS (Tetra Tech, 2013) in which a base case simulation was performed by photochemical model with all airport-related emissions (aircraft, on- and off-airport) removed to provide background concentrations.

Table 6. NO_x and VOC emissions (tons) in the LAX domain.

Source Group Level 1	Source Group Level 2	NO_x		VOC	
		Annual	Summer Episode	Annual	Summer Episode
Aircraft (On-Airport)	Aircraft	3,866	445	368	42
Gate (On-Airport)	On-Airport	649	75	1,541	177
Parking (On-Airport)		311	36	80	9
Roadways (On-Airport)		4,325	498	234	27
Stationary (On-Airport)		1,778	205	1,565	180
Other (On-Airport)		124	14	169	19
Marine (Off-Airport)	Off-Airport	76	9	416	48
Other (Off-Airport)		0.978	0.112	0.329	0.038
Chevron (Off-Airport)		383	44	52	6
Other Stationary (Off-Airport)		119	14	23	3
Roadways (Off-Airport)		1.934	0.223	36	4

3.2 Model configuration

Our team utilized the same AERMOD (v23132) configurations (e.g., plume rise treatment for aircraft emissions and modified meteorological inputs) that were applied in Pandey et al. (2024b). Emission input data (Table 6) was processed by using the FAA's AEDT3e for KLAX-related emissions (i.e., aircraft, taxi, gates) and by EDMS emission inventory for KLAX for non-aircraft sources. Emissions from aircrafts, taxi segments, and gates are all simulated as AREA sources.

Simulations were performed for summer (07/18/2012 – 08/28/2012) episodes with the chemistry options OLM, ARM2, travel time reaction method (TTRM), PVRM, GRSM, and the new chemistry GRS7. Our team utilized modified meteorology inputs as discussed in Pandey et al. (2022), except for surface heat flux (more detail is provided in Section 3.5, "Other Findings"). Note that the modified meteorology inputs only differ from unmodified ones during nighttime (~19:00 – 5:00 local time).

NO_x and NO_2 concentrations simulated at the four core sites (CN, CS, CE, and AQ) are compared with observed values to evaluate AERMOD's NO_2 performance with selected chemistry options. Background NO_x and NO_2 are not included in the simulations given that the off-airport sources (Table 6) are included. Background O_3 plays a vital role in estimating NO_x to NO_2 conversion in all chemistry options except the ARM2. Two scenarios for O_3 background concertation were examined:

- **O3_NW**: Background O_3 hourly concentrations from the South Coast Air Quality Management District (SCAQMD)'s northwest coastal monitor.
- **O3_CMAQ**: Background ozone derived from previous KLAX CMAQ simulation (Tetra Tech, 2013) that exclude emission from KLAX and other non-airport sources within the KLAX AQSAS boundary.

3.3 Model Performance Evaluation

Figure 11 and Figure 12 compare NO_2 performance with all chemistry options. Figure 13 explicitly compares NO_2 performance between GRSM and GRS7 options. In the following discussion, all simulations were performed with O_3_CMAQ background, which is shown to have better NO_2 performance than with the O_3_NW background option.

Findings:

- Observed and simulated NO_2 in all chemistry options peak during the morning hours (07:00 – 09:00) when observed and simulated NO_x are highest during the day (Figure 14).
- As shown in Figure 13, background O_3 is typically less than 30 ppb during the morning hours. During this time, chemistry options that do not consider reaction R1, either implicit or explicit (e.g., ARM2, OLM, PVMRM), have the highest simulated NO_2 among all other options. NO_2 performance is comparable in all chemistry options in the afternoon when O_3 is typically highest (~ 60 ppb) and NO_x is low (<10 ppb).
- The above findings imply that:
  - In the morning hours when background O_3 is low, incorporating NO_2 destruction through photolysis (reaction R1) lowered the simulated NO_2.
  - In the midday and afternoon hours when O_3 is sufficient and NO_x is low, NO_2 formation was mainly driven by oxidation (Reaction R2) and much less by photolysis reactions.
- Simulated NO_2 with the OLM option with consideration of O_3-competition among sources in group (OLMGRPALL) is lower than without consideration of O_3-competition. This finding further illustrates the importance of background O_3 in simulating NO_2 with AERMOD.
- For this KLAX summer case study, the simpler chemistry options (OLM, ARM2, PVMRM, TTRM) have better NO_2 performance than the more complex chemistry options (GRSM, GRS7). However, our team would stress that this finding is not necessarily applicable for all other case studies. This is because NO_2 performance heavily depends on NO_x performance and given the fact the NO_x is underestimated in this LAX case study (Figure 14), NO_2 is expectedly also underestimated.

Although NO_2 performance was marginally improved in GRS7 over GRSM overall (Figure 11 and Figure 12; mean bias was lowered by 0.1 ppb [3%] in GRS7 over GRSM), our team found the difference between the two is significant in the morning hours when background O_3 is low (mean bias was lowered by 1.2 ppb [14%] on average between 07:00 – 09:00 in GRS7). Figure 15 illustrates that incorporating VOC to NO_x chemistry greatly improved simulated NO_2 during these hours when observed NO_2 is typically the highest. Unlike NO_2 photolysis Reaction R1, which has net effect of reducing NO_2 as discussed above, VOC photolysis Reaction R3 and reactions of its by-product RP, in contrast, have the net effect of increasing NO_2 and thus bring the modeled estimate closer to the observed value. GRSM and GRS7 have identical NO_2 performance in the remaining hours of the days when background O_3 was sufficient; NO_x is low during nighttime when there is lack of photolysis.

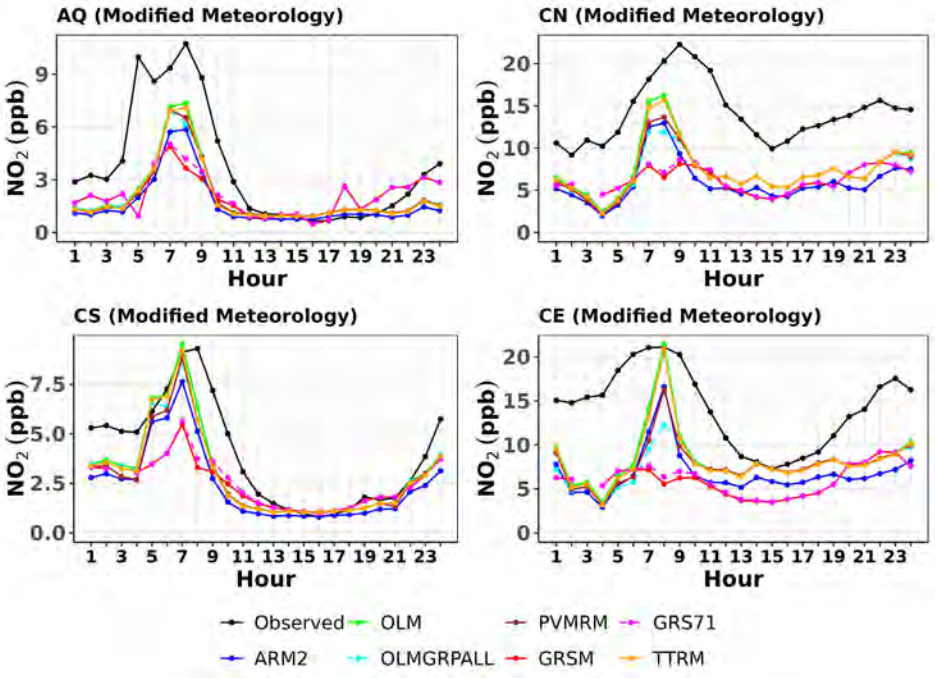

Figure 11. Diurnal plots of observed and predicted (with all the chemistry options) NO_2 concentrations at all four core sites for the summer season of 2012.

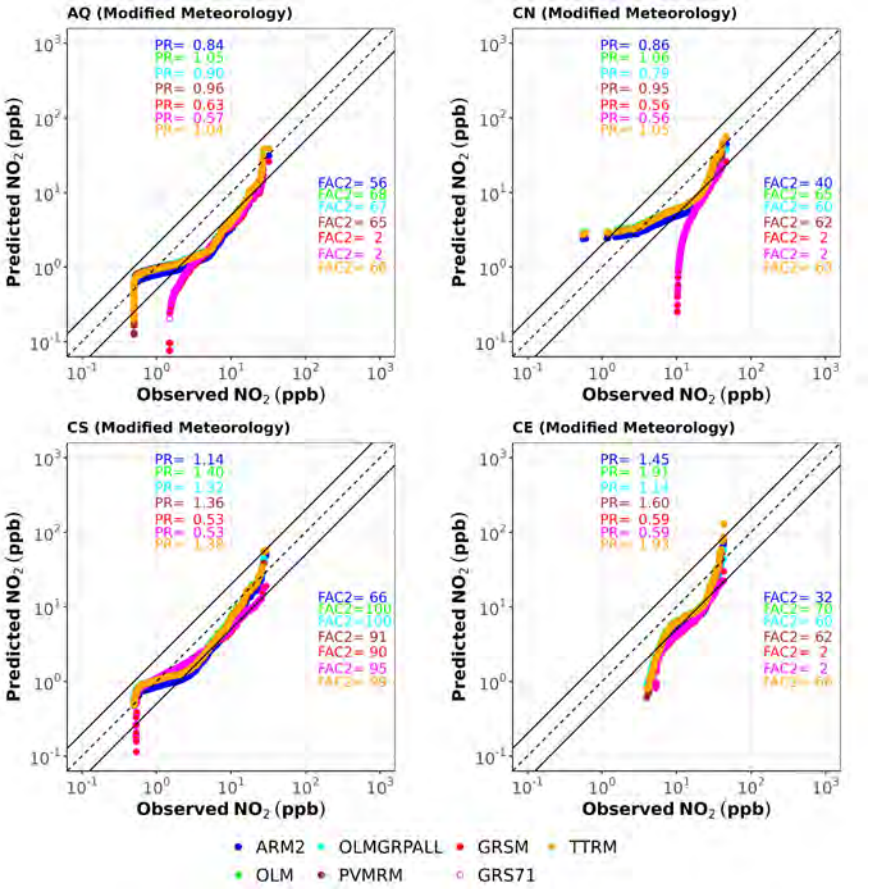

Figure 12. Quantile-Quantile (QQ) concentration distributions of predicted (with all the chemistry options) NO_2 concentrations against observed NO_2 concentrations at all four core sites for the summer season of 2012.

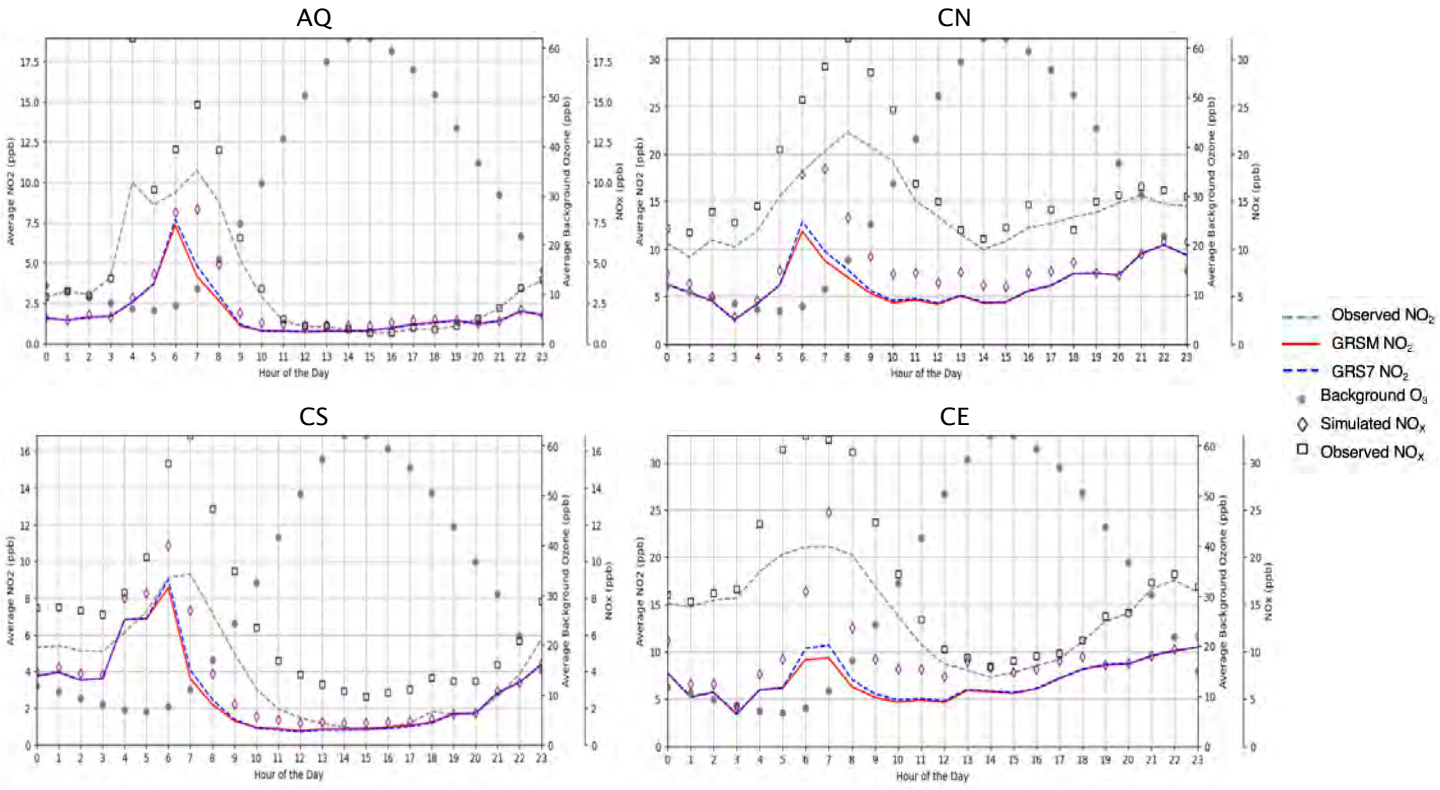

Figure 13. Diurnal plots of observed and predicted (with all the chemistry options) NO_2 concentrations at all four core sites using GRSM and GRS7 chemistry options for the summer season of 2012.

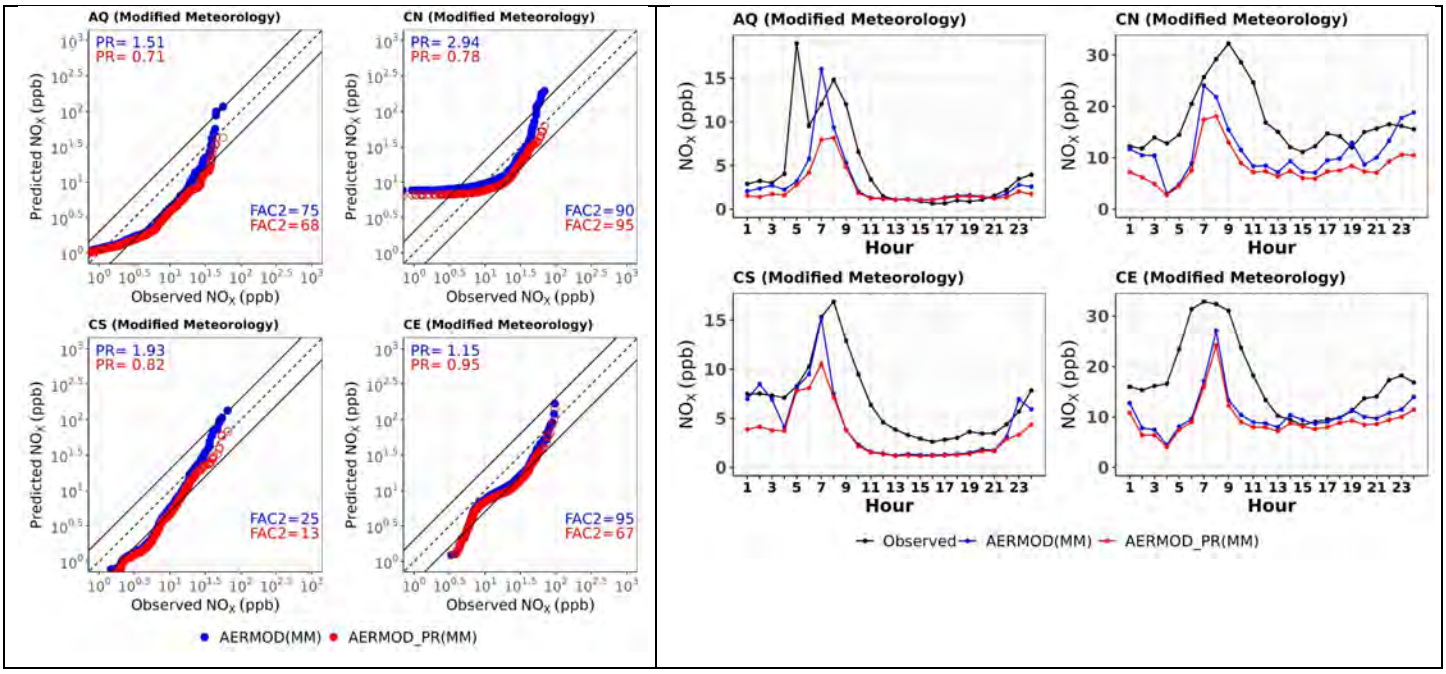

Figure 14. (Left) QQ NO_x concentration and (Right) diurnal plots of observed and predicted NO_x concentrations at four core sites. In this figure, AERMOD_PR indicates simulation with plume rise treatment for aircraft emission.

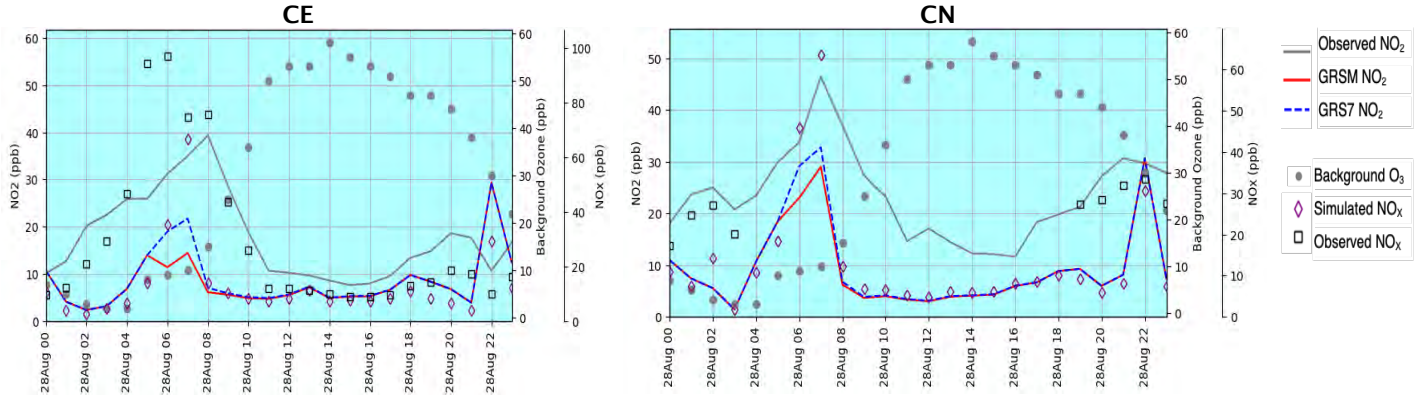

Figure 15. Comparisons of NO_2 performance with GRSM and GRS7 option on August 28, 2012, when observed NO_2 was highest at CE and CN sites.

3.4. Sensitivity Studies

3.4.1 Impact of Background O_3

Overall, background O_3 is higher with O_3_CMAQ than with O_3_NW. Consequently, simulated NO_2 in the morning hours were marginally higher with O_3_CMAQ than with O_3_NW. Figure 16 illustrates the increase of simulated NO_2 on August 28, 2012, using O_3_CMAQ over O_3_NW. No noticeable difference in simulated NO_2 between the two background O_3 options in the remaining hours as background O_3 is sufficient given the low NO_x concentration.

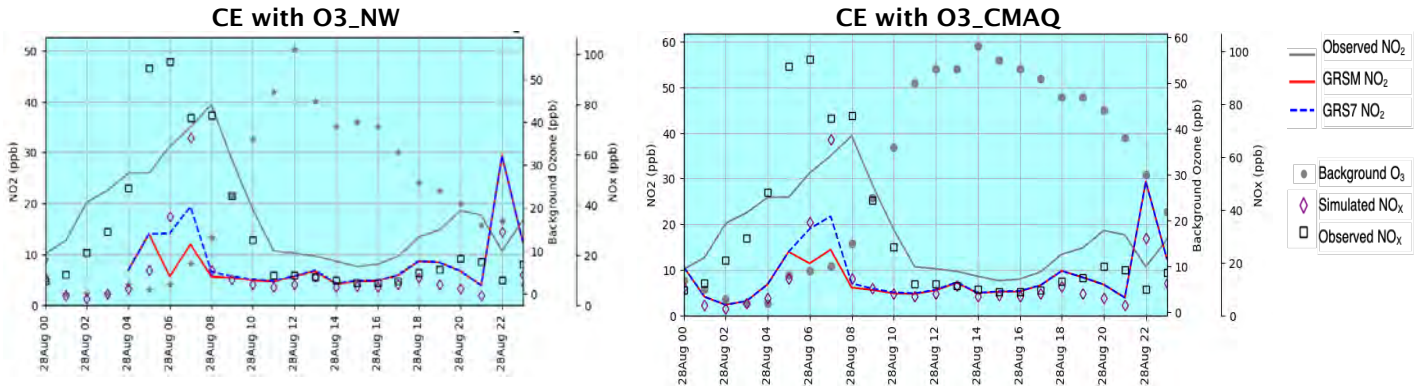

Figure 16. Comparisons of NO_2 performance with GRSM and GRS7 option on August 28, 2012, when observed NO_2 was highest at CE with two background O_3 options.

3.4.2 Impact of Limiting Travel Time

AERMOD limits the concentration-weighted travel time from emitting source to receptor (e.g., chemistry age) to 1 hour in TTRM and GRSM. A similar travel time limit was also implemented in GRS7 for direct comparison with GRSM. However, if non-zero NO_x is simulated at a receptor that is greater than 1 hour in travel time, it is reasonable to assume the chemistry transformation also occurred at the same time scale.

Our team examined the effect of unlimiting the travel time in the GRS7 chemistry option. Figure 17 illustrates the difference in NO_2/NO_x ratio simulated with limited versus unlimited travel time at CE site on August 12, 2012, when travel time at this site was longest (~1.8 hours). A higher NO_2/NO_x ratio (i.e., higher simulated NO_2) was simulated in GRS7 with unlimited travel time than with limited travel time, particularly during morning hours. This finding implies that unlimiting travel time enhances the effect of VOC on VOC–NO_x–O_3 cycle, and in this KLAX case study, enhances NO_2 formation during morning hours. Unlimiting travel time may also enhance the formation of stable nitrogen-product (SGN and SNGN) which are precursors for aerosol formation, although we found formation of SGN and SNGN was very small in this case study.

Overall, our team found that the effect of unlimiting travel time on simulated NO_2 in this KLAX case study is marginal because travel time at all four core sites was less than 1 hour during 90% of simulated hours. However, unlimiting travel time may have a greater effect in other case studies when travel time greater than 1 hour is common.

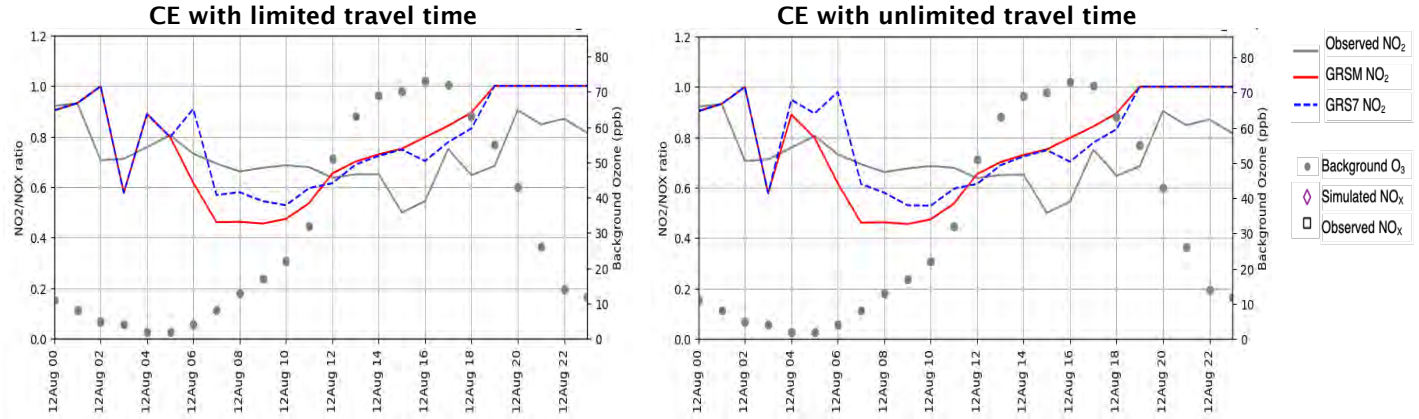

Figure 17. Comparisons of NO_2 performance with GRSM and GRS7 option on August 12, 2012, travel time was longest at CE site with unlimited and limited travel time. Note that unlimited travel time was not applied for simulations with GRSM.

3.5 Other Findings

Our team found a bug in the subroutine PLUMESIZES that came with the distributed AERMOD (v23132) and is called when solving NO_X chemistry in the GRSM option. This bug relates to a dividing by zero issue that occurred during the calculation of plume parameters and resulted in "NaN" values in NO_2 concentrations. Our team discussed this issue with EPA; EPA implemented a bug fix.

Our team performed the AERMOD simulation with modified meteorology inputs as discussed in Pandey et al. (2022), including modified surface heat flux. We found that as AERMOD reverse-calculated solar irradiance from the modified heat flux, it arrived with abnormally high photolysis rate (Reaction R1 in GRSM and in GRS7) which resulted in destruction of NO_2 during evening hours (Figure 18). Because of this artifact, we reverted to using unmodified surface heat flux in all our GRSM and GRS7 simulations.

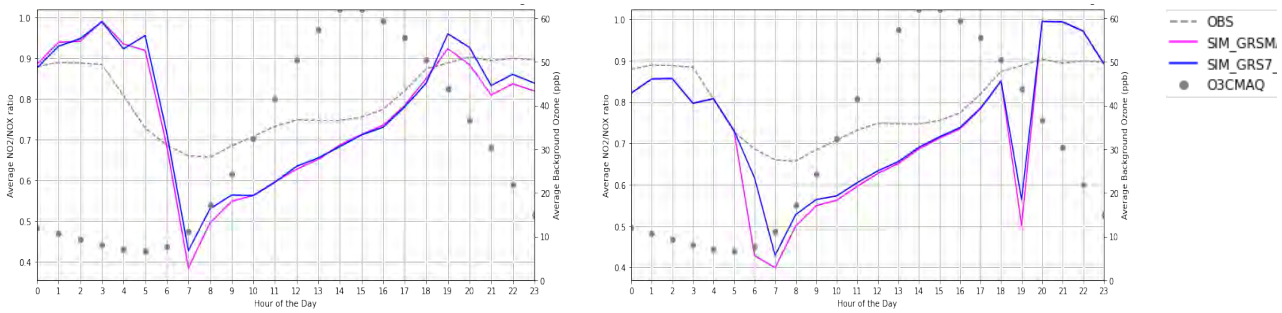

Figure 18. Diurnal average of NO_2/NO_X ratio at CE site simulated with (left) unmodified and (right) modified surface heat flux.

4. Development of Aircraft Dispersion Model

To overcome all the existing issues in aircraft dispersion modeling literature, UNC is developing a new aircraft dispersion model which includes key aspects such as improved source representation of aircraft sources during LTO operations, improved meteorology, new area source treatment with advanced plume rise algorithm for the buoyant exhaust from aircraft as well as with advanced vertical dispersion algorithm, meander during low and variable wind conditions, and additional chemical treatments such as NO/NO_2 and aerosol chemistry. All these characteristics are important to simulate the spatial and temporal distribution of aircraft-emitted pollutants. UNC named this aircraft dispersion model ADM, and an updated gridded version of this model with enhanced physical process is called GADM. Table 7 shows the detailed comparison between ADM and GADM.

Table 7. Comparison of physical and chemical characteristics of ADM and GADM.

	ADM	GADM
Structure of Model	Steady state model in which concentration at each hour is uncoupled from those of previous hours	Unsteady state model in which concentrations preserve memory of previous concentrations
Meteorology	AERMET surface file and vertical wind profile is constructed with Monin-Obukhov similarity theory (MOST)	AERMET surface file and vertical wind profile is constructed with MOST
Source Characterization	• Each area source modeled as a set of line sources, perpendicular to the wind • Number of line sources increased until successive contribution of the area source to a receptor is within specified error	Emissions distributed uniformly into grid volumes with adjustable dimension
Vertical Dispersion	• Modeled with the numerical solution of $u(z)\frac{\partial C}{\partial x} = \frac{\partial}{\partial z}\left(K_z \frac{\partial C}{\partial z}\right)$ • K_z is parameterized based on the Businger approximation • Avoids assumption of Gaussian vertical distribution • Eddy diffusivity modeled with MOST	• Modeled with the numerical solution of $\frac{\partial C}{\partial t} = \frac{\partial}{\partial z}\left(K_z \frac{\partial C}{\partial z}\right)$ • K_z is parameterized based on the Businger approximation • Avoids assumption of Gaussian vertical distribution • Eddy diffusivity modeled with MOST
Horizontal Dispersion	Horizontal contribution of each line source treated analytically with horizontal dispersion as, $\sigma_y = \sigma_v t$	• Following equation solved numerically, $\frac{\partial C}{\partial t} = \frac{\partial}{\partial x}\left(K_x \frac{\partial C}{\partial x}\right)$, $\frac{\partial C}{\partial t} = \frac{\partial}{\partial y}\left(K_y \frac{\partial C}{\partial y}\right)$. • $K_{x,y} = \sigma_v L$, where L = 100 sec • Avoids assumption of Gaussian horizontal distribution
Advection	Plumes from line sources constituting area sources are transported along mean wind	Modeled with numerical solution of $\frac{\partial C}{\partial t} + u\frac{\partial C}{\partial x} + v\frac{\partial C}{\partial y} = 0$ using semi-Lagrangian technique
Plume-Rise	Incorporates aircraft-specific plume rise algorithm (Pandey et al., 2023) with the help of effective distance (based on weighted concentration) from source to receptor	Incorporates aircraft-specific plume rise algorithm (Pandey et al., 2023) by relocating the emission at plume height
Low-wind treatment	Allows plume to disperse upwind of source when wind speeds are low	Advection-diffusion equation accounts for low speeds without numerical problems
Chemistry	Incorporates chemistry schemes using the concept of pollutant age (Venkatram et al., 1994)	Pollutant age, computed with conservation equation, used in chemistry
Concentration Output	Hourly concentrations and ages computed at selected receptors	Hourly averaged concentrations and ages computed at all grid points in model domain

4.1 Preparing ADM/GADM emission inputs

A Python®-based emission processor "AEDT2ADM" has been developed to create the emissions input for ADM and GADM. This emission processor's input data files are the AEDT flight segment and performance data.

During this period of performance, the AEDT2ADM module, which is available on GitHub,® was updated to enhance the output files and fix several bugs discovered during testing. The most important feature added to the module was a code change to allow the user to select standard or gridded output formats for ground-level sources. Standard format, the previous default, allocated emissions to ground polygon shapes like runways, taxiways, and terminals. A new gridded option divides up the ground-level domain into a grid based on the grid size provided by the user. In addition, rated power was added to the engine files for gridded outputs to allow for newer dispersion functionality. Finally, a series of bug fixes and code improvements were added to simplify output files and provide clarity on output file names. The module was pushed into the main branch of the GitHub repository and is now the default branch. The new functionality was thoroughly tested for both summer and winter output files. AEDT2ADM can output data to drive either ADM or GADM.

4.2 Model Evaluation

Both ADM and GADM are validated against the data from the field experiments at KLAX-AQSAS and compared with the existing dispersion model AERMOD using the modified meteorology developed by Pandey et al. (2022). The preliminary results for SO_2 during the summer season from the GADM are encouraging, especially after adding the plume rise associated with buoyant exhaust and horizontal momentum. The high over-predictions are being lowered, and nearly match the diurnal observed concentration magnitudes at all four core sites (Figure 19).

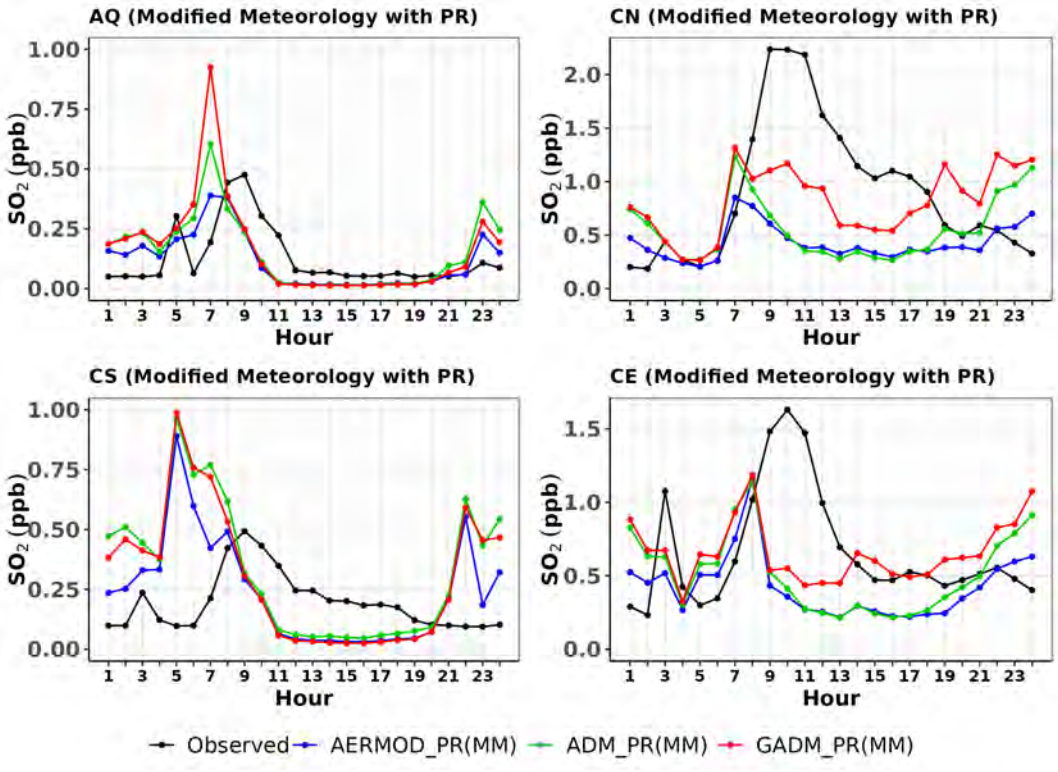

Figure 19. Diurnal modeled and measured SO_2 concentrations during summer season of 2012 at the four sites (AQ, CN, CS, and CE) of KLAX-AQSAS. PR represents the plume rise, and MM represents the modified meteorology.

® Python is a registered trademark of Python Software Foundation, Beaverton, Oregon.
® GitHub is a registered trademark of GitHub, Inc., San Francisco, California.

UNC will finalize all the ADM and GADM development and will evaluate for SO_2 and NO_x both for winter and summer seasons of 2012 for KLAX-AQSAS as well as for other studies.

Milestones

- Evaluated area versus volume source treatment for aircraft sources in AEDT/AERMOD.
- Developed and Implemented new plume rise algorithm in AERMOD for EPA adoption.
- Evaluated plume rise algorithm extensively against KLAX-AQSAS data for two seasons.

Major Accomplishments

- Implementation of UNC's new aircraft-specific plume rise in AERMOD has been adopted by the EPA as an ALPHA option and proposed in the Federal Register Appendix W rulemaking on October 12, 2023.
- Published three papers related to aircraft dispersion.
- Developed a new prototype gridded aircraft dispersion model (GADM) that shows promise for further development and evaluation.

Publications

Venkatram, A., Pandey, G., & Arunachalam, S. (2024). Incorporating meander in area source modeling in AERMOD. *Journal of Air & Waste Management Association*, 1-10.

Pandey, G., Venkatram, A., & Arunachalam, S. (2024). Accounting for plume rise of aircraft emissions and shoreline meteorology enhances AERMOD's description of concentrations measured around Los Angeles airport. *Journal of Air & Waste Management Association*, *74*, 726-742.

Pandey, G. Venkatram, A., & Arunachalam, S. (2024). Modeling the air quality impact of aircraft emissions is area or volume the appropriate source characterization in AERMOD. *Air Quality, Atmosphere & Health, 17*, 1425-1434.

Outreach Efforts

Our team presented our ADM work multiple times, including at the 2024 5th Community Modeling and Analysis System (CMAS) South America conference in Brazil, and the 2024 Aviation Emissions Characterization Roadmap meeting held in Washington, D.C.

Awards

None.

Student Involvement

None.

Plans for Next Period

- Finalize ADM and GADM development with a focus on improved model performance and incorporating other physical processes.
- Finalize a manuscript that shows a detailed comparison of ADM, GADM, and AERMOD using data from KLAX AQSAS.
- Finalize the KBOS AERMOD modeling study.
- Finalize a manuscript that shows a detailed evaluation of plume rise in AERMOD using data from the KBOS study.
- Finalize NO_2 chemistry implementation in ADM and GADM.

References

Arunachalam, S., Isakov, V., Barzyk, T., Venkatram, A., Weil, J., Naess, B., Valencia, A., Seppanen, C., & Brandmeyer, J. (2017, October 9-12). *C-AIRPORT: a new web-based air quality model for community-scale assessments around airports* [Conference presentation]. 18th International Conference on Harmonization within Atmospheric Dispersion Modelling for Regulatory Purposes, Bologna, Italy.

Arunachalam, S., Valencia, A., Woody, M. C., Snyder, M. G., Huang, J., Weil, J., Soucacos, P., Webb, S., Airport Cooperative Research Program, Transportation Research Board, & National Academies of Sciences, Engineering, and Medicine. (2017). Dispersion modeling guidance for airports addressing local air quality health concerns. *Transportation Research Board*. https://doi.org/10.17226/24881

Barzyk, T. M., Isakov, V., Arunachalam, S., Venkatram, A., Cook, R., & Naess, B. (2015). A near-road modeling system for community-scale assessments of traffic-related air pollution in the United States. *Environmental Modelling & Software*, 66, 46–56. https://doi.org/10.1016/j.envsoft.2014.12.00

Boeing. (2010). Boeing Projects $700 Billion Commercial Airplanes Market in North America. Retrieved March 9, 2025, from https://boeing.mediaroom.com/2010-09-02-Boeing-Projects-700-Billion-Commercial-Airplanes-Market-in-North-America

Carslaw, D., Beevers, S., Ropkins, K., & Bell, M. (2006). Detecting and quantifying aircraft and other on-airport contributions to ambient nitrogen oxides in the vicinity of a large international airport. *Atmospheric Environment*, 40(28), 5424–5434. https://doi.org/10.1016/j.atmosenv.2006.04.062

Chang, J. C., & Hanna, S. R. (2004). Air quality model performance evaluation. *Meteorology and Atmospheric Physics*, 87(1–3). https://doi.org/10.1007/s00703-003-0070-7

Chowdhury, B., Karamchandani, P. K., Sykes, R. I., Henn, D. S., & Knipping, E. (2015). Reactive puff model SCICHEM: Model enhancements and performance studies. *Atmospheric environment*, 117, 242–258.

Cimorelli, A. J., Perry, S. G., Venkatram, A., Weil, J. C., Paine, R. J., Wilson, R. B., Lee, R. F., Peters, W. D., & Brode, R. W. (2005). AERMOD: a dispersion model for industrial source applications. Part I: general model formulation and boundary layer characterization. *Journal of Applied Meteorology*, 44(5), 682–693. https://doi.org/10.1175/JAM2227.1

Cox, W. M., & Tikvart, J. A. (1990). A statistical procedure for determining the best performing air quality simulation model. *Atmospheric Environment*. Part A. General Topics, 24(9), 2387–2395. https://doi.org/10.1016/0960-1686(90)90331-G

Hanna, S. R., Britter, R., & Franzese, P. (2003). A baseline urban dispersion model evaluated with Salt Lake City and Los Angeles tracer data. *Atmospheric Environment*, 37(36), 5069–5082. https://doi.org/10.1016/j.atmosenv.2003.08.014

Hendrick, E. M., Tino, V. R., Hanna, S. R., & Egan, B. A. (2013). Evaluation of NO2 predictions by the plume volume molar ratio method (PVMRM) and ozone limiting method (OLM) in AERMOD using new field observations. *Journal of the Air & Waste Management Association* (1995), 63(7), 844–854. https://doi.org/10.1080/10962247.2013.798599

Herndon, S. C., Rogers, T., Dunlea, E. J., Jayne, J. T., Miake-Lye, R., & Knighton, B. (2006). Hydrocarbon emissions from in-use commercial aircraft during airport operations. *Environmental Science & Technology*, 40(14), 4406–4413. https://doi.org/10.1021/es051209l

Herndon, S. C., Wood, E. C., Northway, M. J., Miake-Lye, R., Thornhill, L., Beyersdorf, A., Anderson, B. E., Dowlin, R., Dodds, W., & Knighton, W. B. (2009). Aircraft hydrocarbon emissions at Oakland International Airport. *Environmental Science & Technology*, 43(6), 1730–1736. https://doi.org/10.1021/es801307m

Hsu, S. A. (1984). Effect of cold-air advection on internal boundary-layer development over warm oceanic currents. *Dynamics of Atmospheres and Oceans*, 8(3–4), 307–319. https://doi.org/10.1016/0377-0265(84)90015-0

Kim, B., Rachami, J., Robinson, D., Robinette, B., Wyle, K. N., Arunachalam, S., Davis, N., Baek, B. H., Shankar, U., Talgo, K., Yang, D., Hanna, A. F., Wayson, R. L., Noel, G., Gliff, S. S., Zhao, Y., Hopke, P. K., Kumar, P., Airport Cooperative Research Program, … National Academies of Sciences, Engineering, and Medicine. (2012). Guidance for quantifying the contribution of airport emissions to local air quality. *Transportation Research Board*. https://doi.org/10.17226/22757

Knighton, W. B., Herdon, S. C., & Miake-Lye, R. C. (2009). *Aircraft engine speciated organic gases: speciation of unburned organic gases in aircraft exhaust*. Federal Aviation Administration. https://nepis.epa.gov/Exe/ZyPDF.cgi/P1003YXT.PDF?Dockey=P1003YXT.PDF

Pandey, G., Venkatram, A., & Arunachalam, S. (2022). Evaluating AERMOD with measurements from a major U.S. airport located on a shoreline. *Atmospheric Environment*, 294, 119506. https://doi.org/10.1016/j.atmosenv.2022.119506

Pandey, G., Venkatram, A., & Arunachalam, S. (2023). Accounting for plume rise of aircraft emissions in AERMOD. *Atmospheric Environment*, 314, 120106. https://doi.org/10.1016/j.atmosenv.2023.120106

Pandey, G., Venkatram, A., & Arunachalam, S. (2024a). Modeling the air quality impact of aircraft emissions: is area or volume the appropriate source characterization in AERMOD? *Air Quality, Atmosphere, & Health*. https://doi.org/10.1007/s11869-024-01517-2

Pandey, G., Venkatram, A., & Arunachalam, S. (2024b). Accounting for plume rise of aircraft emissions and shoreline meteorology enhances AERMOD's description of concentrations measured around Los Angeles airport. *Journal of the Air & Waste Management Association* (1995), 74(10), 726–742. https://doi.org/10.1080/10962247.2024.2394104

Podrez, M. (2015). An update to the ambient ratio method for 1-h NO 2 air quality standards dispersion modeling. *Atmospheric Environment*, 103, 163–170. https://doi.org/10.1016/j.atmosenv.2014.12.021

Qian, W., & Venkatram, A. (2011). Performance of steady-state dispersion models under low wind-speed conditions. *Boundary-Layer Meteorology*, 138(3), 475–491. https://doi.org/10.1007/s10546-010-9565-1
Rahn, D. A., & Mitchell, C. J. (2016). Diurnal climatology of the boundary layer in Southern California using AMDAR temperature and wind profiles. *Journal of Applied Meteorology and Climatology*, 55(5), 1123–1137. https://doi.org/10.1175/JAMC-D-15-0234.1
Tetra Tech, Inc. (2013). LAX air quality and source apportionment study. *Los Angeles World Airports*. Available at: http://www.lawa.org/airQualityStudy.aspx?id=7716
Valencia, A., Venkatram, A., Heist, D., Carruthers, D., & Arunachalam, S. (2018). Development and Evaluation of the R-LINE Model Algorithms to Account for Chemical Transformation in the Near-road Environment. *Transportation research. Part D, Transport and environment*, 59, 464–477.
Venkatram, A., Isakov, V., Yuan, J., & Pankratz, D. (2004). Modeling dispersion at distances of meters from urban sources. *Atmospheric Environment*, 38(28), 4633–4641. https://doi.org/10.1016/j.atmosenv.2004.05.018
Venkatram, A., Karamchandani, P., Pai, P., & Goldstein, R. (1994). The development and application of a simplified ozone modeling system (SOMS). *Atmospheric Environment*, 28(22), 3665–3678. https://doi.org/10.1016/1352-2310(94)00190-V
Venkatram, A., Pandey, G., & Arunachalam, S. (2024). Incorporating meander to account for the impact of low winds in area source modeling; AERMOD as a case study. *Journal of the Air & Waste Management Association* (1995), 1–10. https://doi.org/10.1080/10962247.2024.2410450
Venkatram, A., & Thiruvenkatachari, R. R. (2023). Accounting for area sources in air pollution models. *International Journal of Environmental Research and Public Health*, 20(12). https://doi.org/10.3390/ijerph20126110
Venkatram, A., Karamchandani, P., Pai, P., & Goldsteins, R. (1994). The development and application of a simplified ozone modeling system (SOMS). Atmospheric environment, 28(22), 3665–3678.
Venkatram, A. (1977). Internal boundary layer development and fumigation. *Atmospheric Environment* (1967), 11(5), 479–482. https://doi.org/10.1016/0004-6981(77)90011-7
Wilkerson, J. T., Jacobson, M. Z., Malwitz, A., Balasubramanian, S., Wayson, R., Fleming, G., Naiman, A. D., & Lele, S. K. (2010). Analysis of emission data from global commercial aviation: 2004 and 2006. *Atmospheric Chemistry and Physics*, 10(13), 6391–6408. https://doi.org/10.5194/acp-10-6391-2010

Task 2 - Develop and Evaluate a Multiscale Weather Research and Forecasting Sparse Matrix Operator Kernel Emissions Community Multiscale Air Quality (WRF-SMOKE-CMAQ) Model Application for Boston Logan International Airport Focused on Ultrafine Particles

University of North Carolina at Chapel Hill

Objectives

In this project, our team partnered with ASCENT Project 018 investigators from BU to focus on modeling KBOS across various spatial scales. The primary objective was to conduct a thorough intercomparison of measurements and models, with a special emphasis on ultrafine PM, mass, and number concentrations resulting from aircraft emissions.

To achieve this goal, we delved into the utilization of two distinct modeling approaches: the CMAQ and SCICHEM models. The SCICHEM model stands out for its integration of comprehensive gas-, aqueous-, and aerosol-phase chemistry within the advanced Gaussian puff model Second-order Closure Integrated Puff (SCIPUFF) (Chowdhury, 2015). Noteworthy is its capacity to characterize aircraft impacts with high precision in the immediate vicinity of the source as a series of puffs, thereby offering a significant advancement in the estimation of aircraft-attributable PM compared with previous assessments, notwithstanding its potential large computational times.

It is crucial to highlight that while both CMAQ and SCICHEM share a common aerosol treatment, SCICHEM excels in capturing fine-scale details around the airport. A key outcome of this project is the enhancement of predictions related to aircraft-attributable PM compared with previous estimates. It is worth noting that the use of SCICHEM, which focuses solely on PM mass concentrations, necessitated the development of postprocessing routines. These routines were designed to convert PM mass into a UFP number concentration (UFPNC) using a methodology consistent with CMAQ. Additionally, it is important to mention that, until now, SCICHEM has not been employed to predict UFPNC. This effort introduces a novel avenue of research in our project, showcasing our commitment to develop novel model approaches for source treatment.

In 2017, ASCENT Project 018 investigators made multiple measurements of UFPs at seven locations south and west of KBOS. Our team collaborated with BU to obtain these measurements to perform an intercomparison against model outputs.

1. CMAQ-AEDT application for KBOS

To complete this task, our team used a nested application of the WRF-SMOKE-CMAQ modeling system, including the AEDT. CMAQ applied to the northern hemisphere at a resolution of 108 km is downscaled to determine the beginning and boundary conditions for the outermost grid, which is set at a resolution of 12 km. The larger-scale conditions are suitably captured for the outermost grid through the nesting down method. From the immediate outer grid, the next 4-km and 1.33-km grids are nested down in accordance with typical modeling procedures. A transition and improvement of atmospheric conditions are made by this nested technique, which permits a more accurate and thorough depiction of the dynamics as the spatial resolution increases. We used the following to develop this application:

- Meteorology from Modern-Era Retrospective analysis for Research and Applications (MERRA) (Rienecker et al., 2011) downscaled with WRF v3.8 (Skamarock et al., 2008)
- Background emissions from National Emission Inventory (NEI) processed through SMOKE v3.6 (Baek & Seppanen, 2018)
- Aircraft emissions for the 2017 KBOS study from AEDT processed through AEDT Proc (Baek et al., 2012)
- CMAQ v5.33 enhanced with the new aircraft-specific emissions module (Appel et al., 2021)

2. Development of AEDT-UNC (2017) emission inventories for KBOS

An FAA National Airspace System (NAS) called the Performance Data Analysis and Reporting System (PDARS) is an integrated performance measuring tool to help with operational analysis and NAS improvement. The system is made up of a specific network of computers at FAA locations that gather comprehensive data from the air traffic control system using specialist software. PDARS has information about each aircraft operation (e.g., aircraft type, airport, runway, and time of arrival and departure, etc.) and has detailed information about each aircraft operation with real-time tracking, including time, latitude, longitude, and altitude. Our main goal is to enhance our modeling simulation to encompass a whole month, namely July 2017, with PDARS by using AEDT. Our team utilized AEDT3e to create a KBOS specific emission inventory that corresponds with the BU's UFP measurement campaign's duration. Using real-time aircraft operation data to create emissions guarantees more precise calculation of the emissions in the airport vicinity across the designated time frame, compared to other emissions inventories.

3. Comparison of KBOS emissions with different Emission Inventories (EIs)

The EPA provides aircraft emissions estimates in the NEI as a point source for all airports in the U.S. Thus, for KBOS, our team has aircraft emissions during LTO assigned to a single latitude/longitude. While NEI emission inventory provides us with a starting point for use in CMAQ, a few different approaches were explored to refine this and created multiple emissions scenarios.

- The emission scenarios considered in this study are:
  - NoKBOS: NEI 2017 emissions inventory, excluding KBOS (background emission)
  - AEDT2d-2017-N: NEI 2017 emissions inventory with KBOS during LTO cycle
  - AEDT2b-2015-S: 2015 global segment data provided by Volpe, exported for KBOS during LTO cycles
  - AEDT2d-2017-S: 2017 global segment data provided by Volpe, exported for KBOS during LTO cycles
  - AEDT3e-2017-P: 2017 PDARS exported for KBOS during LTO cycles

Besides improvement in spatial allocation in developing emissions estimates, treatment of particle size distribution was also refined in CMAQ as follows:

- Aircraft Specific Aerosol Size Distribution (ASASD) was applied only for KBOS emissions in this study:
  - Geometric Mean Diameter (GMD): 60 nm → 23.2 nm (Moore et al., 2017)
  - Geometric Standard Deviation (GSD): 1.7 nm → 1.56 nm (Moore et al., 2017)
  - Both Geometric Mean Diameter and Standard Deviation (GMDSD) changed as above
  - Emission altitude changes to assign all emissions only at ground (alt 0)

4. Assessment of UFPs through field observations

The ASCENT Project 018 team at BU made field observations of UFPNC in 2017 at seven fixed sites along the aircraft arrival and departure pathways, near KBOS in Figure 20. These monitoring stations were selected because of the varying distances and UFPNC contributions from KBOS. The only one in the northern part of the airport is Chelsea (CHE). Two of the monitoring stations in the southern regions (N1 and N2) are the closest to the airport. I1 and I2 are in the middle and the

last two monitoring stations (F1 and F2) are the furthest distance. UFPNC sample data were collected between April and September 2017, and July 2017 was selected for modeling.

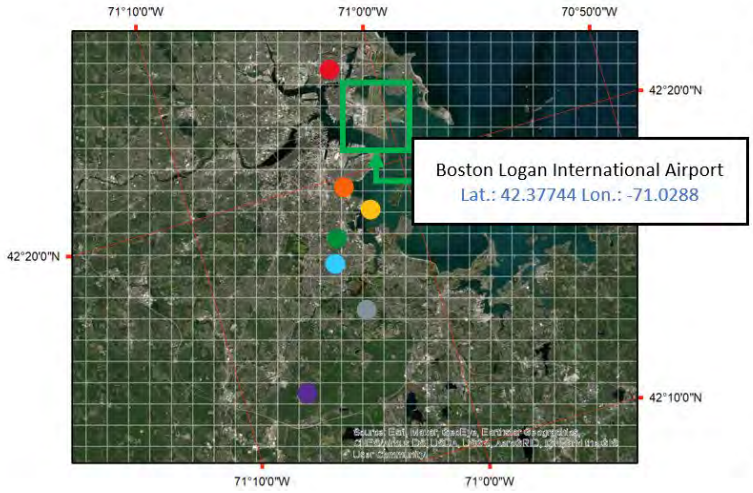

Location	Distance (km)	Color
Airport	-	Green Box
CHE	4	Red
N1	3	Orange
N2	4	Yellow
I1	7	Green
I2	9	Light Blue
F1	12	Gray
F2	17	Purple

Figure 20. CMAQ-based modeling at high resolution 1.33 km x 1.33 km with location of seven monitoring sites near KBOS. CHE: Chelsea.

Research Approach

1. CMAQ-AEDT application for KBOS

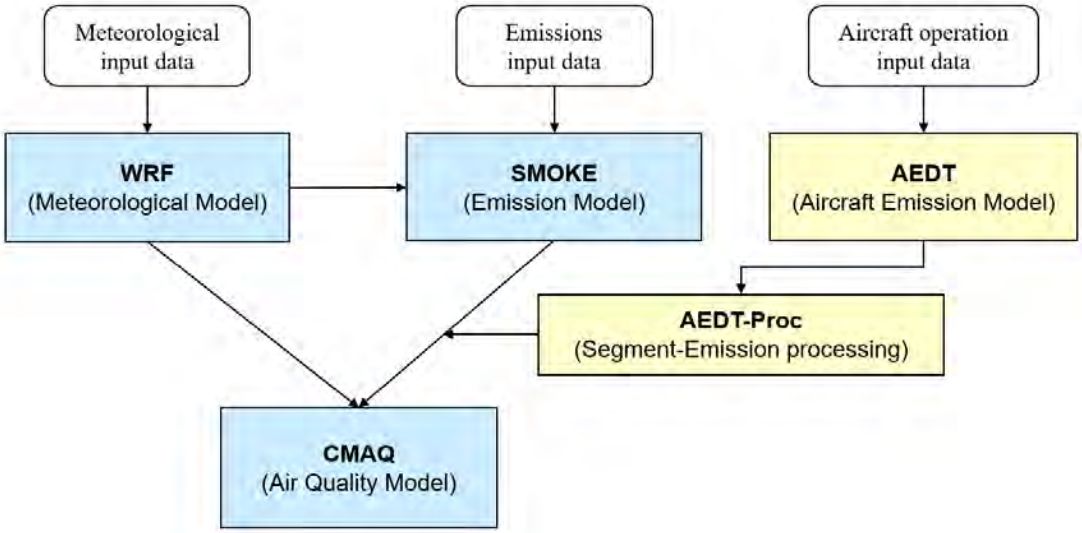

Figure 21. CMAQ application schematic for KBOS with Aviation Environmental Design Tool (AEDT).

UFP concentrations at KBOS were simulated using the WRF-SMOKE-CMAQ modeling framework (Figure 21). The WRF model was used to create meteorological data. The sigma vertical coordinate system, with 35 vertical layers that reach up to 50 hPa (lowest layer approximately 10 to 20 m above ground level) was used in this research.

Background emissions were produced using the SMOKE processing system, except for emissions that came from KBOS by using AEDT2d-2017-N. The particle mass concentration was computed using CMAQ configured with the AERO6 aerosol module and the Carbon Bond 6 V3 mechanism (CB6r3) for the gas-phase chemistry. CMAQ converts particle mass concentration into particle number concentration using particle diameter, particle size distribution, and assumed particle density information (Binkowski & Roselle, 2003). Particle number concentration is estimated by CMAQ for the entire mass and thus one cannot distinguish between non-volatile particulate matter (nvPM) and volatile particulate matter (vPM) components for the number concentrations predicted by CMAQ. In Equation 16, our team used a number of parameters, such as Total Particle Number ($N_{i,j}$), particle geometric diameter ($D_{gi,j}$), particle geometric standard deviation ($\sigma_{gi,j}$), upper diameter cut (UDC), and lower diameter cut (LDC), using the error function (ERF) (Jiang et al., 2006; Meng & Seinfeld, 1994) approach for the concentration of UFPNC. LDC was set at 0.07 µm due to the instrument's low detection limit (LDL) and defined UDC at 0.1 µm, consistent with the UFP definition (Hughes et al., 1998). Our team used a 15-day spin-up period from June 16 to June 30 for the month of July 2017. Initial and boundary conditions were based on the 108-km Northern Hemisphere domain ("108NHEMI").

Our team modeled CMAQ with 35 layers and horizontal resolutions of 12 km, 4 km, and 1.33 km for the study period. Apart from the aircraft emission inventories for KBOS, all simulations used the same default CMAQ parameters, except aircraft specific aerosol size distribution.

$$UFP\ number = \frac{N_i}{2}\left[1+\mathrm{ERF}\left(\frac{\ln(\frac{UDC}{D_{gi}})}{\sqrt{2}\ln\sigma_{gi}}\right)\right]-\frac{N_i}{2}\left[1+\mathrm{ERF}\left(\frac{\ln(\frac{LDC}{D_{gi}})}{\sqrt{2}\ln\sigma_{gi}}\right)\right]+\frac{N_j}{2}\left[1+\mathrm{ERF}\left(\frac{\ln(\frac{UDC}{D_{gj}})}{\sqrt{2}\ln\sigma_{gj}}\right)\right]-\frac{N_j}{2}\left[1+\mathrm{ERF}\left(\frac{\ln(\frac{LDC}{D_{gj}})}{\sqrt{2}\ln\sigma_{gj}}\right)\right] \quad \text{(Eq. 17)}$$

Aitken mode, j = Accumulation mode

where $N_{i,j}$ is the total number particles (particles/cm^3), $D_{gi,j}$ is the geometric diameter (µm), $\sigma_{gi,j}$ is the geometric standard deviation (µm), ERF is the error function, UDC is the upper diameter cut (µm), and LDC is the lower diameter cut (µm).

2. Development of AEDT emission inventory for KBOS by UNC

Besides the three scenarios (AEDT2d-2017N, AEDT2b-2015S, AEDT2d-2017S), which had relatively less fidelity around KBOS, UNC used AEDT3e to build a KBOS emissions inventory to improve aircraft emission data accuracy with high fidelity. Our team modeled three-dimensional segment data for KBOS using data from the PDARS. In Figure 22, our team shows monthly averaged PDARS tracks with arrival and departure for all runways. First, PDARS is used to create representative arrival and departure tracks of aircraft pathway for KBOS by averaging segments. Helicopter and non-aircraft information is filtered out by only choosing 50 segments and then making a segment group for every five segments to smooth segment data with latitude, longitude, and altitude. Then, flight id, aircraft type, operation type, arrival and departure airport, arrival and departure runway, and operation start time are extracted. Using structured query language (SQL) to populate key tables, our team created inputs for KBOS with tracks from PDARS. The LTO segment data obtained from UNC's AEDT run were transformed into gridded emission files using AEDTProc. The CMAQ model-compatible emission input files included multiple pollutants, including NO_x, CO, SO_2, total organic gases (TOG), and PM (primary sulfates, primary organic aerosols, and elemental carbon). LTO cycle emissions were restricted to elevations less than 3,000 ft (about 1,000 m). The new three-dimensional aircraft emission inventory for KBOS created by UNC was then combined with the two-dimensional data from the NoKBOS as background emissions for creating model-ready inputs.

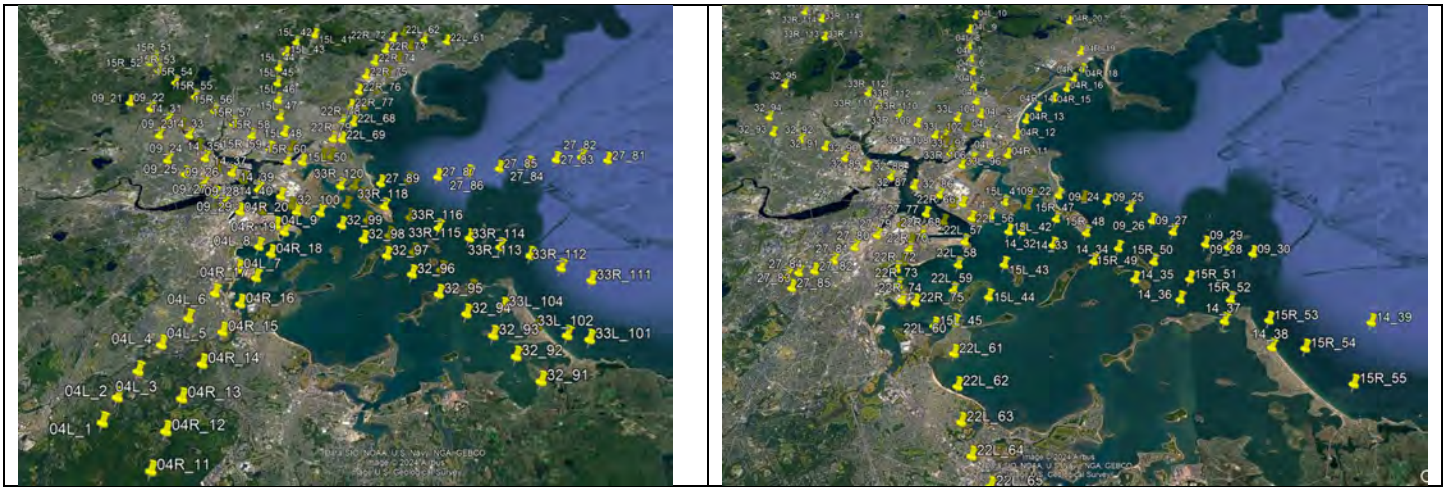

Figure 22. Monthly average of Identification Friend or Foe (July 2017) with arrival (left) and departure (right) by all runways.

3. Comparison of KBOS emissions with different Emission Inventories (EIs)

Using AEDT2b-2015-S, AEDT2d-2017-S, and AEDT3e-2017-P, Figure 23 shows how flight numbers are distributed between the carrier types (i.e., commercial and general aviation). No flight number by carrier type data are provided by EPA in AEDT2d-2017-N.

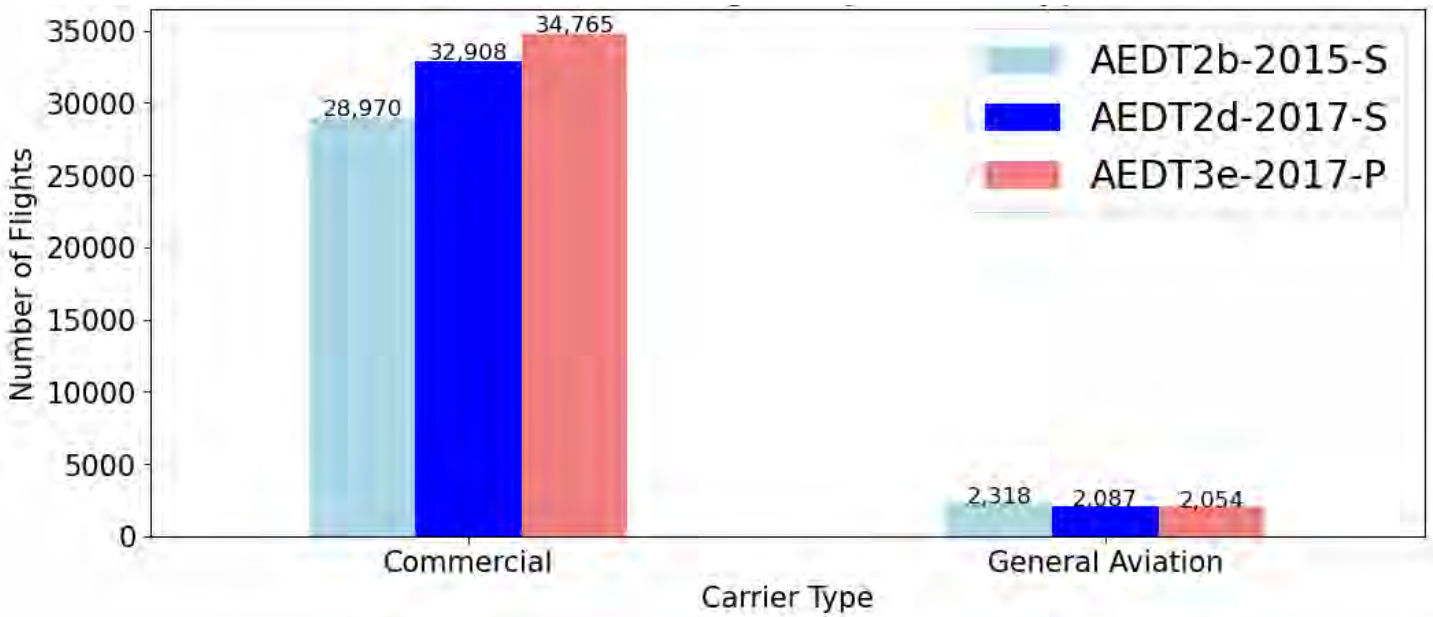

Figure 23. Number of aircraft by carrier type for AEDT2b-2015-S (light blue), AEDT2d-2017-S (blue), and AEDT3e-2017-P (light red).

The commercial aircraft show a consistent increase in the number of flights from 2015 to 2017. The AEDT2b-2015-S dataset reveals 28,970 commercial flights, the AEDT2d-2017-S dataset shows an increase to 32,908 flights, and AEDT3e-2017-P expands to 34,765 commercial flights. The increase in commercial air traffic over a 2-year period can be the reason for this increase. The differences (1,857 flights) between the same year datasets (AEDT2d-2017-S and AEDT3e-2017-P) might be from data collection and reporting method differences.

In contrast, general aviation has far fewer flights across all datasets compared to commercial flights. There were 2,318 flights according to AEDT2b-2015-S. AEDT2d-2017-S and the AEDT3e-2017-P recorded 2,087 flights and 2,054 flights, respectively. This similarity across the 2017 datasets suggests similar data collection methods or flight classifications when comparing flights operated by general aviation to those operated by commercial aircraft. The number of general aviation flights decreased over this 2-year period.

The comparison of datasets also reveals an increase in commercial flights from 2015 to 2017, despite a slight decline in general aviation shown in Figure 23.

Four different emission inventories (AEDT2d-2017-N, AEDT2b-2015-S, AEDT2d-2017-S, and AEDT3e-2017-P) for all key air pollutants are compared in Figure 24. PM is the sum of non-volatile particulate matter (PMNV), Volatile Fuel Organics (PMFO), and Volatile Sulfate PM (PMSO). In the PMNV, AEDT2d-2017-N had over 0.8 tons for July 2017 and AEDT2b-2015-S had less than 0.2 tons for July 2015, but AEDT2d-2017-S and AEDT3e-2017-P were in the middle at roughly 0.5 tons for July 2017. PMFO emissions are significantly lower in both emission inventories (less than 0.1 tons for July) than in the AEDT2d-2017-N and AEDT3e-2017-P (over 0.45 tons for July). The AEDT3e-2017-P, AEDT2d-2017-S, AEDT2b-2015-S, and AEDT2d-2017-N datasets found to be highest to lowest, respectively, for PMSO emissions. The PM difference shows emission inventories have different calculation methods for each PM pollutant, which might come from either the AEDT version or option changes.

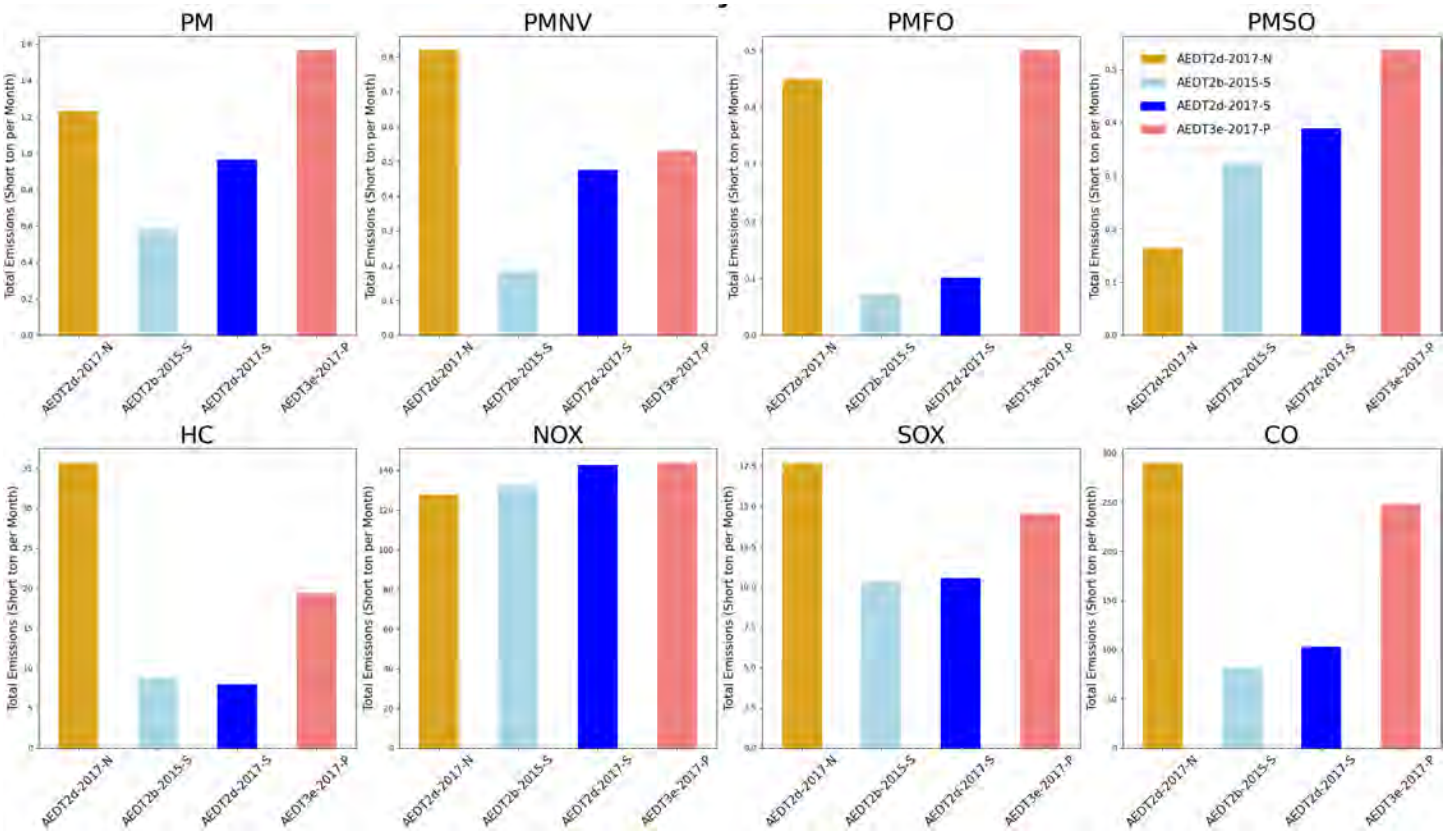

Figure 24. Comparison of four different emission inventories of total emissions for each pollutant.

The AEDT2d-2017-N dataset has the highest hydrocarbon (HC) emissions (35 tons per month) compared to the other datasets. AEDT3e-2017-P records the next-highest emissions for July, at around 20 tons. AEDT2b-2015-S and AEDT2d-2017-S had the lowest HC emissions with July emissions of roughly 5 tons. AEDT2d-2017-S led all datasets in terms of NO_x emissions, which are relatively close with other emission inventories. As seen by the steady emissions in the 120–140 tons per month range reported by AEDT2d-2017-N, AEDT2b-2015-S, and AEDT3e-2017-P, NO_x emissions show less variation

across years and datasets than other pollutants. In AEDT2d-2017-N, SO_x are the highest at almost 17.5 tons per month, followed by AEDT3e-2017-P. AEDT2b-2015-S and AEDT2d-2017-S both show similar July emissions values of roughly 10 tons. While AEDT2d-2017-N shows the highest CO emissions, almost reaching 300 tons for July, AEDT2b-2015-S and AEDT2d-2017-S show far lower emissions, with less than 100 tons for July 2017. Similar to AEDT2d-2017-N, AEDT3e-2017-P showed roughly 250 tons in July 2017.

Even though all datasets showed notable differences in some pollutants within different emission inventories, especially for AEDT2b-2015-S and AEDT2d-2017-S, AEDT3e-2017-P is in comparable emission range. While AEDT2b-2015-S and AEDT2d-2017-S emissions might have similar methods of calculation techniques created by the same provider, Volpe, a later version of AEDT (AEDT3e) used for AEDT3e-2017-P caused differences in emission inventories for each pollutant.

4. Assessment of UFPs through field observations

Figure 25 shows the distribution of UFPNC (# per cm³) across various scenarios at the seven monitoring stations (CHE, N1, N2, I1, I2, F1, and F2) with whiskers representing the 5%–95% interquartile range (IQR). The x-axis represents the observed data (field monitoring station), No KBOS, AEDT2d-2017-N scenarios (Base and GMDSD), the AEDT2b-2015-S scenarios (Base and GMDSD), and AEDT3e-2017-P scenarios (Base, GMDSD, GMDSD_alt0), including variations in altitude zero (alt0). Since AEDT2d-2017-S is still being processed, it was not included in this comparison.

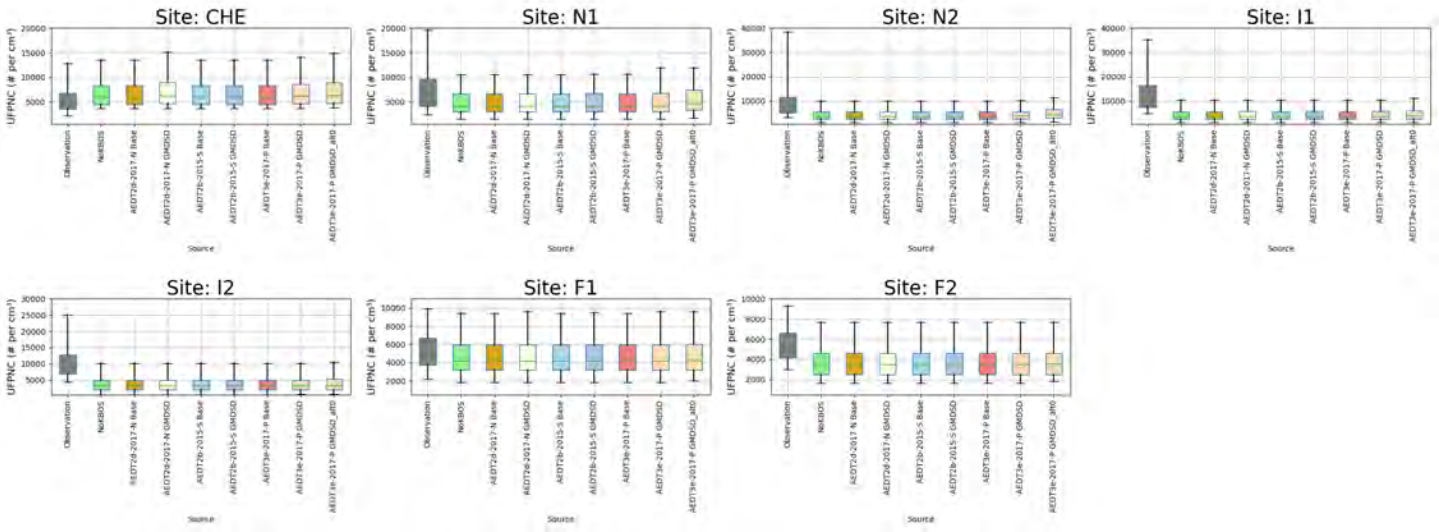

Figure 25. UFPNC comparison observation at seven monitoring stations with eight different scenarios (NoKBOS, AEDT2d-2017-N Base, AEDT2d-2017-N GMDSD, AEDT2b-2015-S Base, AEDT2b-2015-S GMDSD, AEDT3e-2017-P Base, AEDT3e-2017-P GMDSD, and AEDT3e-2017-P GMDSD_alt0).

The observed data in CHE show a median UFPNC value close to 4,800 #/cm³. The median values (about 6,000 #/cm³) in most of base scenarios (AEDT2d-2017-N Base, AEDT2b-2015-S Base, and AEDT3e-2017-P Base) are very similar, demonstrating that the modeled UFPNC agrees with the observed data. All the GMDSD scenarios indicate a higher degree of uncertainty or increased concentrations in the upper ranges by KBOS effect, showing the UFPNC differences compared to the base scenarios.

The N1 site, which is the nearest monitoring station to KBOS, shows a greater range of observed UFPNC than CHE, suggesting that there may be higher impact of KBOS emissions under actual conditions there. The variability and concentration levels vary from CHE and N1 observations because of the local environment or intensity of aircraft effect to each site. Compared to N1 observation, model scenarios from AEDT2d-2017-N and AEDT2b-2015-S were almost 10,000 #/cm³ lower. In AEDT3e-2017-P GMDSD alt0 scenario, the CHE and N1 sites both show higher concentrations, compared to other scenarios, but the UFPNC is still underestimated.

The N2 site is in the path of arriving and departing airplanes using runways 22R, 22L, 4L, and 4R. N2 had the largest concentration of UFPs, with a median UFPNC value near 7,600 #/cm³ and a greater range than the other scenarios. Over 38,000 #/cm³ of maxima in the observed data at N2 suggests there is significant variability because of its location in the flight paths. The significantly lower median values and narrower IQR shown by all other modeled scenarios demonstrate that the modeled scenarios were not able to capture values adequately. The AEDT3e-2017-P GMDSD alt scenario, utilizing real tract data, makes small differences, but UFPNC quantity was underestimated.

The observation shows a median of around 10,500 #/cm³ and maxima that reach about 35,000 #/cm³ at the I1 location. All predicted scenarios had far lower median concentrations and narrower ranges, indicating that the models predicted much lower concentrations of UFPNC than the observed data with the same reason at the N2 site. All modeled scenarios were very similar to each other due to the small influence of KBOS (less than 100 #/cm3), suggesting the particle lifetime might be too short in CMAQ to capture when the monitoring station is more than 5 km distance, as seen with how the KBOS impact dramatically decreased with increasing distance from the airport.

Sites I2, F1, and F2 exhibit similar trends in terms of model underprediction with respect to observations. Particularly when it comes to significant UFPNC brought on by unique characteristics of aircraft emissions and particle number that the model cannot account for, the general underestimation of UFPNC in all sites except CHE highlights the importance of source characterization for models to accurately depict the observed UFP. Although UFPNC at sites F1 and F2 is predicted well by CMAQ when the KBOS effect is minimal, it is hard to capture KBOS impact in modeled scenarios at sites F1 and F2.

In Figure 26, wind direction and UFPNC levels were evaluated for four selected model scenarios and one observation case. NoKBOS modeled scenario adequately represents background conditions when KBOS airport emissions are excluded from AEDT2d-2017-N. The AEDT2d-2017-N Base is modeled by using default emission from the EPA NEI. The baseline for KBOS emissions in the AEDT3e-2017-P GMDSD scenario includes tracks that use the Identification Friend or Foe data with GMDSD applied aircraft specific aerosol size distribution. In the AEDT3e-2017-P GMDSD alt0 scenario, the emission altitude is changed to ground level to maximize aircraft impact on ground from AEDT3e-2017-P GMDSD scenario.

There is a noticeable UFPNC in the southeast, between 125° and 155°, according to the observational data at the CHE monitoring station. Comparing this to the NoKBOS scenario, UFPNC comes mainly from the southwest (235° to 265°) and the southeast (125° to 175°), even though overall UFPNC quantities are lower than in the observation. The UFP directional distribution in AEDT2d-2017-N Base is similar to that in NoKBOS, with no discernible pattern changes. Although the model captures significant UFPNC southeast (between 115° and 155°) at the AEDT3e-2017-P GMDSD scenario, the quantity is still smaller than in observed UFPNC. AEDT3e-2017-P GMDSD alt0 scenario had the best performance of the modeled UFPNC, even if UFPNC levels are still lower than observed levels.

For the N1 site observation, UFPNC peaked at 30° toward the northeast and surpassed 40,000 #/cm³. Although the UFPNC is much lower than the observation, a similar directional impact can be seen in the AEDT2d-2017-N Base scenarios, likely due to meteorological reasons and not from aircraft sources. In contrast to the base scenarios, the AEDT3e-2017-P GMDSD and AEDT3e-2017-P GMDSD alt0 scenario, where UFPNC peaks northward at 0° and climbs to 20,000 #/cm³, the discrepancy is the effect of aircraft emissions. This rise positions AEDT3e-2017-P GMDSD alt0 scenario as having a wind rose pattern that is more in line with the observation, even if the scenario has lower UFPNC compared to observation.

Northeastern UFPNC is significantly concentrated at approximately 10°, with concentrations surpassing 40,000 #/cm³, according to observations made at the N2 site monitoring station. In NoKBOS, AEDT2d-2017-N Base, and AEDT3e-2017-P GMDSD scenarios, there were different UFPNC peaks from the west, particularly at 260° and 300°. The AEDT3e-2017-P GMDSD alt0 scenario repeats this pattern, maintaining higher UFPNC in the west at similar angles. This shows that it was hard to capture UFPNC direction from the N2 site monitoring station with any modeling scenario.

Observation at site I1 shows a prominent UFPNC toward the northeast, with a peak near 350°. The model simulations (NoKBOS, AEDT2d-2017-N Base, and AEDT3e-2017-P GMDSD) show UFPNC westward, with the most pronounced UFPNC occurring between 270° and 310°. The AEDT3e-2017-P GMDSD alt0 scenario presents a slightly higher UFPNC, with the three highest concentrations observed toward the northwest between 310° and 340°. The fact that the UFPNC in this AEDT3e-2017-P GMDSD alt0 scenario outweighs those in AEDT2d-2017-N scenarios and further supports the underestimation of UFPNC impact of ground level in CMAQ.

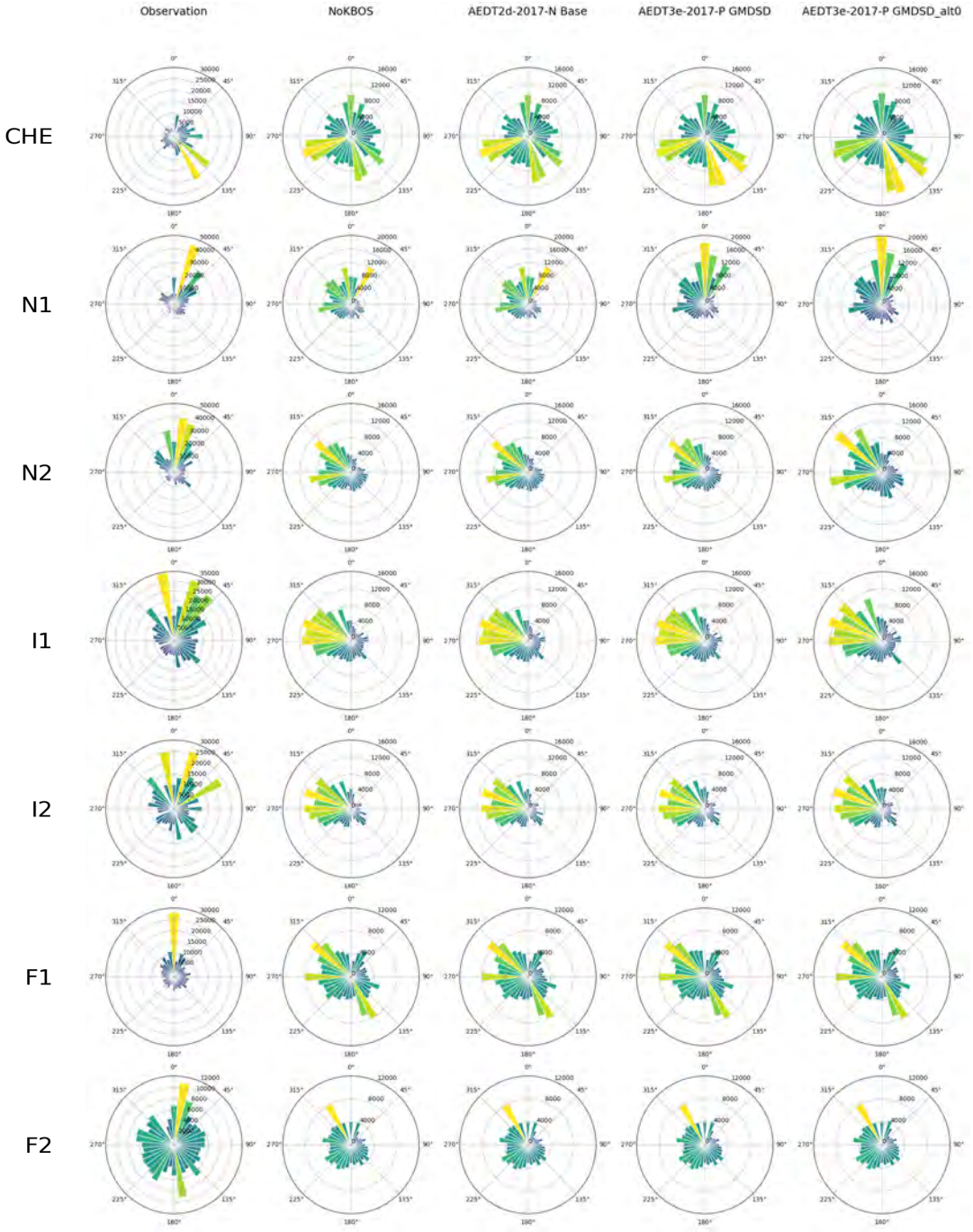

Figure 26. UFP distributions with wind rose analysis at seven monitoring stations across four scenarios: observation, NoKBOS, AEDT2d-2017-N Base, and AEDT3e-2017-P GMDSD alt0.

The UFPNC distribution in site I2 observations showed very similar patterns compared to the site I1 monitoring station, with the highest concentrations occurring toward the northeast, particularly between 20° and 60°. In all modeled scenarios, the UFPNC distribution becomes more concentrated with a noticeable peak in the west (250° to 320°), exhibiting

similar UFPNC distribution patterns at site I2 station. The AEDT3e-2017-P GMDSD alt0 scenario has the highest UFPNC in the modeled concentrations but it hardly recognizes the difference in the monthly mean result.

Observation data at the site F1 monitoring station reveal a large UFP peak toward the north at 0°, with concentrations reaching 20,000 #/cm³. Conversely, the modeled scenarios have decreased UFPNC with directional peaks pointing northwest (305°) and southeast (150°) with no discernible changes in the distribution of UFPNC by KBOS.

The site F2 observation shows UFPNC scattered with clear directional peaks from KBOS, excluding concentration at 10°. The modeled scenarios also show a more noticeable increase in UFP numbers toward the northwest, particularly around 320°, indicating that the direction of UFPNC is pointing towards the location of KBOS, but the differences are found without capturing UFPNC between modeled UFPNC results.

Milestones

- Completed development of KBOS inventories using AEDT for July 2017 and repeated CMAQ simulations.

Major Accomplishments

- UNC was able to use PDARS data for KBOS and created their own airport-level inventory for KBOS, and thus gained AEDT track creation skills and understanding of aircraft operation data in running AEDT.

Publications

None.

Outreach Efforts

None.

Awards

None.

Student Involvement

- Hyeongseok (Darby) Kim, is a PhD student involved in this task, performing CMAQ simulations and AEDT modeling.

Plans for Next Period

- Demonstrate model performance and perform UFP source attribution in CMAQ and emphasize the value of high-fidelity input data and CMAQ modeled grid resolution can adequately characterize UFP contributions from KBOS.

References

Appel, K. W., Bash, J. O., Fahey, K. M., Foley, K. M., Gilliam, R. C., Hogrefe, C., Hutzell, W. T., Kang, D., Mathur, R., Murphy, B. N., Napelenok, S. L., Nolte, C. G., Pleim, J. E., Pouliot, G. A., Pye, H. O. T., Ran, L., Roselle, S. J., Sarwar, G., Schwede, D. B., . . . Wong, D. C. (2021). The Community Multiscale Air Quality (CMAQ) model versions 5.3 and 5.3.1: System updates and evaluation. *Geoscientific. Model Development*, 14(5), 2867–2897.

Baek, B. H., Arunachalam, S., Woody, M., Vennam, P. L., Omary, M., Binkowski, F., & Fleming, G. (2012, October 15-17). *A new interface to model global commercial aircraft emissions from the FAA Aviation Environmental Design Tool (AEDT) in air quality models* [Conference presentation]. 11th Annual CMAS Conference, Chapel Hill, North Carolina.

Baek, B. H., & Seppanen, C. (2018). *Sparse Matrix Operator Kernel Emissions (SMOKE) modeling system*. Zenodo. https://doi.org/10.5281/zenodo.1421403

Binkowski, F. S., & Roselle, S. J. (2003). Models-3 Community Multiscale Air Quality (CMAQ) model aerosol component 1. Model description. Journal of Geophysical Research: Atmospheres, 108(D6). https://doi.org/10.1029/2001JD001409

Chowdhury, B. (2015). Reactive puff model SCICHEM: Model enhancements and performance studies. *Atmospheric Environment*, 117, 242-258. https://doi.org/10.1016/j.atmosenv.2015.07.012

Hughes, L. S., Cass, G. R., Gone, J., Ames, M., & Olmez, I. (1998). Physical and chemical characterization of atmospheric ultrafine particles in the Los Angeles area. *Environmental Science & Technology*, 32(9), 1153–61. https://doi.org/10.1021/es970280r

Jiang, W., Smyth, S., Giroux, E., Roth, H., & Yin, D. (2006). Differences between CMAQ fine mode particle and PM2.5 concentrations and their impact on model performance evaluation in the Lower Fraser Valley. *Atmospheric Environment*, 40(26), 4973–85. https://doi.org/10.1016/j.atmosenv.2005.10.069

Meng, Z., & Seinfeld, J. H. (1994). On the source of the submicrometer droplet mode of urban and regional aerosols. *Aerosol Science and Technology*, 20(3). 253–65. https://doi.org/10.1080/02786829408959681

Moore, R. H., Shook, M. A., Ziemba, L. D., DiGangi, J. P., Winstead, E. L., Rauch, B., Jurkat, T., Thornhill, K. L., Crosbie, E. C., Robinson, C., Shingler, T. J., Anderson, B. E. (2017). Take-off engine particle emission indices for in-service aircraft at Los Angeles International Airport. *Scientific Data*, 4(1), 170198. https://doi.org/10.1038/sdata.2017.198.

Rienecker, M. M., Suarez, M. J., Gelaro, R., Todling, R., Bacmeister, J., Liu, E., Bosilovich, M. G., Schubert, S. D., Takacs, L., Kim, G., Bloom, S., Chen, J., Collins, D., Conaty, A., da Silva, A., Gu, W., Joiner, J., Koster, R. D., Lucchesi, R., . . . Woollen, J. (2011). MERRA: NASA's modern-era retrospective analysis for research and applications. *Journal of Climate*, 24(14), 3624-3648. https://doi.org/10.1175/JCLI-D-11-00015.1

Skamarock, W. C., Klemp, J., Dudhia, J., Gill, D. O., Barker, D., Wang, W., & Powers, J. G. (2008). *A description of the advanced research WRF version 3*. University Corporation for Atmospheric Research. https://doi.org/10.5065/D68S4MVH

Task 3 - Implement Volatile Particulate Matter Plume-Scale Modeling into a Community Multiscale Air Quality Application

University of North Carolina at Chapel Hill

This task is currently on hold.

- Nothing to report.

Project 022 Evaluation of FAA Climate Tools: Aviation Portfolio Management Tool (APMT)

University of Illinois at Urbana-Champaign

Project Lead Investigator

Dr. Donald Wuebbles
Department of Atmospheric Sciences
University of Illinois
105 S. Gregory Street
Urbana, IL 61801
Tel: (217) 244-1568
Fax: (217) 244-4393
Email: wuebbles@illinois.edu

University Participants

University of Illinois at Urbana-Champaign

- P.I.: Dr. Donald Wuebbles
- FAA Award Number: 13-C-AJFE-UI-040
- Period of Performance: October 1, 2023, to September 30, 2024
- Task:
  1. Revisiting High-speed Civil Transports and Their Potential Effects on Ozone and Climate

Project Funding Level

Support from the Federal Aviation administration (FAA) over this time period was about $200,000, with an additional $200,000 in matching in-kind support from the German Aerospace Center (DLR), Germany.

Investigation Team

Dr. Donald Wuebbles (P.I.), All Tasks
Swarnali Sanyal and Dharmendra Singh (postdoctoral students), responsible for conducting studies and performing analyses using the Community Earth System Model (CESM) Whole Atmosphere Community Climate Model (WACCM), a 3-dimensional (3D) atmospheric climate-chemistry model

Task 1 - Revisiting High-speed Civil Transports and Their Potential Effects on Ozone and Climate

University of Illinois at Urbana-Champaign

Major Goals

This project utilizes state-of-the-art modeling and technical knowledge to analyze the potential global environmental effects of aircraft and to perform analyses that underpin the development of analytical tools that can assess the costs and benefits to inform decision making on technology development. The studies rely on state-of-the-art models of the earth system that can provide useful scientific input for considerations by decision makers. The analyses in the project will aid decision making by translating complex models into simpler tools for use in cost-benefit analyses.

Objectives

To quantify the costs and benefits of using advanced aircraft and engine technologies, FAA uses tools that are underpinned by state-of-the-art technical knowledge. These tools are used to inform decision making by providing the

benefits and costs of various options that could enable technology development. The overall objective of this project is to enhance our understanding of the relationships between subsonic and proposed supersonic aircraft and the atmospheric state, and the development and evaluation of the capabilities, limitations, and uncertainties of metrics and simple models (e.g., Aviation Portfolio Management Tool [APMT]) to assist decision makers. This project will use state-of-the-art geophysical models of the earth system that fully represent tropospheric and stratospheric processes to evaluate the costs and benefits of technologies that could advance subsonic aviation and enable supersonic aviation. Specific project goals include the following: (1) science-based evaluation of analytical tools used by the FAA, (2) development of ideas and concepts for the next-generation treatment of aviation's effects on the earth system, (3) updated evaluation and analyses of the science of aviation effects on atmospheric composition, and (4) evaluation of potential environmental effects from assumed fleets of supersonic commercial and business jet aircraft to compare with their benefits in terms of decreased time for air travel.

Research Approach

The study uses the state-of-the-art WACCM that is part of the range of models within the CESM, developed through community-coordinated efforts by the National Center for Atmospheric Research (NCAR). The version of the WACCM used here has 66 layers from the ground to above the mesosphere and provides a comprehensive treatment of tropospheric and stratospheric (and above) chemical processes. The WACCM is one of the most advanced models worldwide for studying atmospheric processes and one of the few with a complete representation of stratospheric and mesospheric processes and higher; for example, it is one of very few models to represent the quasi-biennial oscillation that is important to stratospheric ozone. It has a comprehensive treatment of gas phase, particle based, and heterogeneous chemistry. This makes the WACCM ideal for the study of the environmental impacts from supersonic and subsonic aircraft.

Results and discussion

Various companies and academic institutions have been actively considering the designs of supersonic aircraft. As these new designs are developed, the environmental impact on ozone and climate of these realistic fleets needs to be explored.

In late summer 2023, the ASCENT Project 022 team received emissions for two different supersonic commercial aircraft designs and associated mature fleets from the Massachusetts Institute of Technology (MIT). Model runs for these emissions are complete, and the analysis of findings is almost completed except for finishing the comparison of our WACCM results with those determined by MIT using their model. Our team is currently interacting closely with MIT to compare our analyses. In collaboration with MIT, our team is currently writing a joint journal paper.

A review of current observation and modeling capabilities in treating contrails has been published by the journal *Atmospheric Chemistry and Physics* (Singh et al., 2024).

For the International Civil Aviation Organization (ICAO), Dr. Wuebbles was an invited speaker at a major international workshop on contrails and contrail cirrus. He also coauthored three reports for ICAO Impacts and Science Group (ISG), one based on the contrail workshop, another on nitrogen oxides (NO_x) emissions from aviation, and he co-led one report that updates understanding of potentials environmental impacts of supersonic aircraft.

Milestones

- Completed new studies of supersonic fleets, and our results are being evaluated for comparison with similar modeling studies made by MIT for the potential impacts on ozone and climate of several fleets of supersonic aircraft based on aircraft designs made by MIT. A journal article is being completed.
- Completed and published a review of contrail science.
- Completed and submitted special reports to the ICAO.

Publications

Peer-Reviewed Journal Publications

Singh, D. K., Sanyal, S., & Wuebbles, D. J. (2024). Understanding the role of contrails and contrail cirrus in climate change: A global perspective. *Atmospheric Chemistry and Physics, 24*. https://doi.org/10.5194/acp-24-9219-2024

Written Reports

Eastham, S. D., Wuebbles, D. J., Sparrow, V. W., Rhodes, D., Grewe, V., Baughcum, S. L., Delhaye, D., & Penanhoat, O. (2024). *I.03 Update on Understanding of Potential Impacts of Supersonic Aircraft*. Special report for the International Civil Aviation Organization (ICAO), The United Nations, Montreal.

Lee, D. S., Dickson, N., Altuntas, O., Arunachalam, S., Barrett, S., Baughcum, S., Bonne, N., Block, A., Boehm, A., Brons, R., Burkhardt, U., Carter, W., Catalano, F., Claro, G., Delhaye, D., Eastham, S., Gettelman, A., Goobie, S., Johansson, D., Kagaya, R., . . . Yin, F. (2024). *CAEP Impacts and Science Group (ISG) Contrail Science Workshop Report*. Special report for the International Civil Aviation Organization (ICAO), The United Nations, Montreal.

Prashanth, P., Hauglustaine, D., Arunachalam, S., Eastham, S., Grewe, V., Miake-Lye, R., Skowron, A., Speth, R., Turgut, E. T., Van Velthoven, P., and Wuebbles, D. (2024). *I.01 Air Quality and Climate Impacts Interdependencies and Trade-Offs of Aviation Emissions.* Special report for the International Civil Aviation Organization (ICAO), The United Nations, Montreal.

Outreach Efforts

- Presentations at ASCENT Meetings in Fall 2023, May 2024 and October 2024.
- Presentation made at FAA Air Emissions Characterization Roadmap meeting in May 2024 and October 2024.
- Presentation at U.S. Department of Energy PRE-TRAILS workshop on aviation emissions in October 2024.
- ICAO ISG meetings (monthly) for Dr. Wuebbles.

Awards

None.

Student Involvement

Three postdoctoral students, Swarnali Sanyal, Rachana Pradhan, and Dharmendra Singh, were responsible for the analyses and modeling studies within the project and leading the initial preparation of the project reports.

Plans for Next Period

- Complete and publish studies based on the emission inventories developed by ASCENT Project 010 to consider specific designs of supersonic transports (SSTs) from MIT and compare those results to model analyses done by MIT for the same scenario plus their similar analyses of the Georgia Tech SST fleet.
- Use the results from this study to inform the development of Aviation Portfolio Management Tool – Impacts Climate (APMT-IC) for supersonic impacts (ASCENT Project 058).
- Update analyses of subsonic aircraft fleets for current and projected future time periods.
- Perform additional sensitivity analyses of potential supersonic aircraft fleets to enhance understanding of the envelop of potential impacts on ozone and climate from such aircraft.

Project 023 Analytical Approach for Quantifying Noise from Advanced Operational Procedures

Massachusetts Institute of Technology

Project Lead Investigator

R. John Hansman
T. Wilson Professor of Aeronautics & Astronautics
Department of Aeronautics & Astronautics
Massachusetts Institute of Technology
Room 33-303
77 Massachusetts Avenue, Cambridge, MA 02139
617-253-2271
rjhans@mit.edu

University Participants

Massachusetts Institute of Technology

- P.I.: R. John Hansman
- FAA Award Number: 13-C-AJFE-MIT, Amendment No. 008, 015, 022, 031, 046, and 051
- Period of Performance: October 1, 2023, to September 30, 2024
- Tasks:
  1. Evaluate factors limiting the ability to develop and utilize low-environmental-impact flight procedures.
  2. Review current and proposed air traffic management (ATM) modernization plans for potential environmental impact benefits.
  3. Identify potential opportunities for incorporating operational environmental optimization.
  4. Propose a path forward for high-potential opportunities.

Project Funding Level

The FAA provided $860,000 in funding, and matching funds totaling $860,000 were provided by the Massachusetts Institute of Technology (MIT) (approximately $80,000) and the Massachusetts Port Authority (Massport) (approximately $780,000).

Investigation Team

Prof. R. John Hansman (P.I.), All Tasks
Sandro Salgueiro (graduate student), All Tasks
Clement Li (graduate student), All Tasks
Zhishen Wang (graduate student), All Tasks
Mina Cezairli (graduate student), All Tasks

Project Overview

In this project, the ASCENT Project 023 team is evaluating the noise reduction potential of advanced operational procedures in the terminal (arrival and departure) phases of flight. The noise impact of these procedures is not well understood or modeled in current environmental analysis tools, presenting an opportunity for further research to facilitate ATM system modernization. This project leverages a noise analysis framework previously developed at MIT under ASCENT Project 023 to evaluate a variety of sample procedures. In conjunction, this project contributes to the memorandum of understanding between the FAA and Massport to identify, analyze, and recommend procedure modifications at the Boston Logan International Airport (hereafter, Boston Logan Airport).

Task 1 - Evaluate Factors Limiting the Ability to Develop and Utilize Low-Environmental-Impact Flight Procedures

Massachusetts Institute of Technology

Objectives

This task involves the identification of factors driving operational stakeholder acceptance constraints, which limit when low-environmental-impact procedures may be utilized and, consequently, also impact the feasibility of their implementation. Interviews with stakeholders may be conducted to better understand the operational requirements that different stakeholders have in the context of procedure acceptance.

Research Approach

- Review relevant literature, including prior human-in-the-loop studies, to identify the effects of novel performance-based navigation (PBN) flight procedure concepts on air traffic control (ATC) and pilot tasks.
- Identify the relationship between operational stakeholder concerns and safety, in the context of the implementation of advanced low-noise flight procedure concepts.

Major Accomplishments

- Identified potential mechanisms to mitigate stakeholder concerns, including new merging and spacing tools, and collision mitigation capabilities.
- At the Boston Logan Airport, monitored the use of overlay area navigation (RNAV) global positioning system (GPS) approach procedures throughout the year using flight trajectory data, and identified usage rates for different aircraft and airlines.

Task 2 - Review Current and Proposed ATM Modernization Plans for Potential Environmental Impact Benefits

Massachusetts Institute of Technology

Objectives

This task involves the review of historical, current, and proposed ATM capabilities that influence how operational stakeholders perceive the acceptance of new flight procedure concepts. Examples of capabilities to be analyzed include ATC decision support tools (including merging and spacing tools), trajectory-based operations (TBO), and aircraft navigation capabilities. Both United States and international capabilities are to be reviewed.

Research Approach

- Review relevant literature on both existing and proposed ATM modernization plans, including ATC and pilot decision support tools.
- Analyze noise monitor data from the Boston Logan Airport to evaluate noise benefits achieved with the implementation of new low-noise procedures that were developed as part of prior work.

Major Accomplishments

- Identified a legacy set of ATC decision support tools used for merging and spacing of aircraft on final approach.
- Identified current efforts toward the deployment of new merging and spacing tools, including the Terminal Sequencing and Spacing (TSAS) tool in the United States and Point Merge in Europe.
- Obtained a large set of noise monitor and aircraft trajectory data for a full year of operations at the Boston Logan Airport, enabling new quantitative analyses on the noise effects of procedure changes.
- Analyzed raw noise monitor data for a new overwater required-navigation-performance (RNP AR) approach implemented at the Boston Logan Airport (Runway 33L).
    - Preliminary results show a significant noise reduction associated with the new procedure as measured at a highly impacted area, matching prior modeling results.
- Analyzed raw noise monitor data and flight trajectory data for new departure procedures serving Runways 15R, 22L, and 22R at the Boston Logan Airport.

- Preliminary results showed noise reduction associated with the new procedures as measured at a highly impacted area.

Task 3 - Identify Potential Opportunities for Incorporating Operational Environmental Optimization

Massachusetts Institute of Technology

Objectives

This task will consider the potential of the ATM modernization capabilities identified in Task 2 to address the limitations identified in Task 1 or to enable environmentally desirable trajectories. Potential enhancements or additional capabilities will be identified.

Research Approach

- Review potential effects of ATC and pilot support tools identified in Task 2 towards mitigating the operational stakeholder concerns identified in Task 1.

Major Accomplishments

- Leveraged flight trajectory data to compare track miles between the old procedures and new overwater required-navigation-performance (RNP AR) approach implemented at the Boston Logan Airport (Runway 33L)
  - Preliminary results showed a reduction in track miles flown, leading to fuel burn benefits for the RNP AR procedure.
- Leveraged flight trajectory data to compare track miles between old and new procedures for new departure procedures serving Runways 15R, 22L, and 22R at the Boston Logan Airport.
  - Preliminary results revealed a reduction in track miles flown in all three of the new departure procedures, leading to fuel burn benefits.

Task 4 - Propose a Path Forward for High-Potential Opportunities

Massachusetts Institute of Technology

Objectives

This task will synthesize findings from Tasks 1, 2, and 3 to identify key capability development paths that could enable concepts of low-environmental-impact flight procedures. Areas of investigation will include requirements for each capability, functions served by it, and what changes it may drive in the roles and training of operational stakeholders (controllers and pilots).

Research Approach

- Synthesize findings from Tasks 1, 2, and 3, and identify development paths for future low-noise capabilities.

Major Accomplishments

- Not applicable, pending conclusion of Tasks 1, 2, and 3.

Publications

Peer-Reviewed Journal Publication

Thomas, J, & Hansman, J. (2019). Framework for analyzing aircraft community noise impacts of advanced operational flight procedures. *Journal of Aircraft*, *6*(4). https://doi.org/10.2514/1.C035100

Presentations

Cezairli, M., Salgueiro, S., & Hansman, R. J. (2024) *Analysis of the Implementation of Low-Noise PBN Flight Procedures at Boston Logan Airport* [Conference presentation]. AIAA Aviation Forum, Las Vegas, NV, United States. https://doi.org/10.2514/6.2024-3856

Salgueiro, S., Thomas, J., Li, C., & Hansman, R. J. (2021, January 11-21). *Operational noise abatement through control of climb profile on departure* [Conference presentation.] AIAA Science and Technology Forum and Exposition, virtual.

Salgueiro, S., & Hansman, R. J. (2023). *Identifying, Visualizing, and Communicating Constraints in PBN Flight Procedure Design* [Conference presentation]. AIAA Aviation Forum, San Diego, CA, United States. https://doi.org/10.2514/6.2023-3968

Thomas, J., Yu, A., Li, C., Toscano, P., & Hansman, R. J. (2019, June 17-21). *Advanced operational procedure design concepts for noise abatement* [Seminar presentation]. Thirteenth USA/Europe Air Traffic Management Research and Development Seminar, Vienna, Austria.

Yu, A., & Hansman, R.J. (2019, January 7-11). *Approach for representing the aircraft noise impacts of concentrated flight tracks* [Conference presentation]. AIAA Aviation Forum, Dallas, Texas, United States.

Written Reports

Hansman, R. J., Jensen, L., Huynh, J., O'Neill, G., & Yu, A. (2017). *Block 1 procedure recommendations for Logan Airport community noise reduction*. http://hdl.handle.net/1721.1/114038

Hansman, R. J., Salgueiro, S., Huynh, J., Li, C., Jansson, M., Mahseredjian, A., & Zimmer, K. (2021). *Block 2 procedure recommendations for Logan Airport community noise reduction*. https://hdl.handle.net/1721.1/131242

Outreach Efforts

- September 27, 2017: Poster to the ASCENT Advisory Board
- December 5, 2017: Call with Boeing to discuss procedure for noise impact validity
- March 16, 2018: Discussion with the Minneapolis-St. Paul Airport about metrics
- April 4, 2018: Poster to the ASCENT Advisory Board
- May 7, 2018: Presentation to the FAA 7100.41 PBN Working Group
- June 24, 2018: Discussion with air traffic controllers about dispersion concepts
- July 23, 2018: Briefing at the FAA Joint University Program research update meeting
- October 9, 2018: Poster to the ASCENT Advisory Board
- November 8, 2018: Presentation to the Airline Industry Consortium
- March 3, 2019: Presentation at the Aviation Noise and Emissions Symposium
- October 15, 2019: Presentation to the ASCENT Advisory Board
- November 12, 2019: Presentation to the Airline Industry Consortium
- May 21, 2020: Meeting with operational stakeholders from the FAA 7100.41 process to discuss Block 2 concepts
- September 23, 2021: Public hearing to present Block 2 procedure recommendations for the Boston Logan Airport
- Numerous community meetings
- Numerous briefings to politicians representing eastern Massachusetts (local, state, and federal)
- Briefing to the FAA Management Advisory Council
- In-person outreach and collaboration with Massport, an operator at the Boston Logan Airport, and an ASCENT Advisory Board member
- April 1, 2022: Presentation of a summary of lessons-learned from the Boston project to an audience of FAA, Massport, and HMMH stakeholders
- August 16, 2022: Presentation of work on flight procedure constraints at the FAA Technical Center in Atlantic City, New Jersey, as part of the Joint University Program
- September 20–21, 2022: 7100.41 Working Group meeting at the Boston terminal radar approach control facilities (A90); presentation to air traffic and airline stakeholders on flight procedures proposed for Boston Logan Airport as part of Block 2; approval received for all presented procedures for further implementation work
- April 9–10, 2024: Presentation to the ASCENT Advisory Board
- October 29–31, 2024: Poster to the ASCENT Advisory Board

Awards

- 2018 Department of Transportation/FAA Centers of Excellence Outstanding Student of the Year Award to Jacqueline Thomas
- 2021 Massachusetts Port Authority Logan Stars Award to the MIT International Center for Air Transportation research group
- 2023 American Institute of Aeronautics and Astronautics Orville and Wilbur Wright Graduate Award to Sandro Salgueiro

- 2025 American Institute of Aeronautics and Astronautics Jay Hollingsworth Speas Airport Award for the enhancement of the relationships between airports and their surrounding environment

Student Involvement

Graduate students have been involved in all aspects of this research in terms of analysis, documentation, and presentation.

Plans for Next Period

The next phase of this project will focus on the continuation of all tasks, with a particular focus on the analysis of ATM modernization plans and the identification of potential noise benefits enabled by future capabilities. Current efforts include the analysis of noise monitor data from the Boston Logan Airport, which will be used to quantify the change in noise impacts due to the implementation of Block 1 and Block 2 procedures.

Project 025 Shock Tube Studies of the Kinetics of Jet Fuels

Stanford University

Project Lead Investigator

Ronald K. Hanson
Woodard Professor
Mechanical Engineering Department
Stanford University
452 Escondido Mall
650-723-6850
rkhanson@stanford.edu

University Participants

Stanford University (Stanford)

- P.I.: Prof. Ronald K. Hanson
- FAA Award Number: 13-C-AJFE-SU-027
- Period of Performance: October 1, 2023, to September 30, 2024
- Task:
  1. Chemical kinetics combustion experiments

Project Funding Level

For 2023–2024, the Federal Aviation Administration (FAA) provided $300,000 in funding, and matching funds totaling $300,000 were provided from Stanford University.

Investigation Team

Prof. Ronald K. Hanson, P.I., research direction
Jesse W. Streicher, Research Scientist, research management
Vivek Boddapati, Graduate Student, research assistance
Andrew R. Klingberg, Graduate Student, research assistance

Project Overview

The past year of this program has focused on evaluating and refining strategies for the accurate prediction of jet fuel properties (i.e., chemical and physical) and composition. To achieve this goal, the research focused on two areas: (1) the comparison of previously developed Fourier transform infrared spectroscopy (FTIR)-based linear and nonlinear models against alternative property prediction methods and (2) the analysis of training dataset population distributions to identify areas for improvement in model performance. The results of the infrared (IR) spectral analysis work will be used to establish the strong sensitivity of jet fuels' physical and chemical properties to their molecular structure, with the ultimate goal of developing a rapid pre-screening approach, requiring minimal fuel volume, to streamline the testing and certification process of alternative jet fuels.

Task 1 – Chemical Kinetics Combustion Experiments

Stanford University

Objectives

This work is aimed at developing fuel prescreening tools based on the IR absorption cross-section measurements of jet fuels and their constituent molecules. Specific fuel analysis objectives include developing effective strategies for correlating (a) chemical, physical, and combustion properties, and (b) functional group and molecular species composition of jet fuels with their IR spectra.

Research Approach

An important goal of the current research is to characterize jet fuel composition and properties based on the fuel's mid-IR absorption spectrum, measured using a FTIR spectrometer. Over the past five years, a database of spectroscopic measurements and property data for a variety of jet fuels and jet fuel components has been acquired. Using this database, the ASCENT Project 025 team has developed linear and nonlinear correlations between the spectroscopic properties of jet fuels with fuel composition and with important physical/chemical properties such as density, derived cetane number, net heat of combustion, and flash point. Here, our team will present an overview of the two research areas outlined above, along with the key results obtained over the past year.

Evaluation of FTIR-based models against alternative property prediction methods:
Over the past four years of the ASCENT program, four strategies (Strategies 1-4) were developed for estimating physical and chemical properties, functional group fractions, and molecular species constituents of fuels directly from mid-IR spectra. Strategy 1 utilizes regularized linear models to estimate various physical and chemical properties of hydrocarbon fuels by correlating spectral features with properties. Strategy 2 employs a generalized linear model with grouped-Lasso regularization to characterize the average fuel structure in terms of functional group fractions. Strategy 3 builds upon Strategy 1 by incorporating principal component analysis (PCA) and support vector regression. Strategy 4 leverages the linear additivity of gas-phase spectra and a quadratic programming approach to infer fuel composition through a spectral surrogate.

In the last two years, Strategy 1 elastic-net-regularized linear models and Strategy 3 nonlinear (i.e., principal component analysis and support vector regression) models were trained for different properties by using an expanded training dataset. These models were shown to achieve prediction errors comparable to, if not lower than, standard ASTM property test methods. In the current year, the linear Strategy 1 and nonlinear Strategy 3 models were tested against alternative chemometric methods reported in the literature for different properties. The methodology for comparing different property prediction methods, along with some key results, are discussed below.

A thorough survey of different chemometric methods available in the literature for predicting properties of hydrocarbon fuels was conducted. Specifically, the different types of analytical techniques (e.g., gas/liquid chromatography, infrared spectroscopy, Raman spectroscopy, and nuclear magnetic resonance) and regression methods (e.g., partial least squares regression [PLSR], multiple linear regression [MLR], and artificial neural networks) were identified. Considering the challenges associated with differences in the training datasets and variability in the reported performance metrics, a new methodology was formulated for enabling direct comparison of our FTIR-based property prediction models with alternative prescreening approaches available in the literature. A matrix of available alternative property prediction approaches was first compiled, along with pertinent information about their training datasets, such as the maximum and minimum values for different properties. Following this, the Stanford training dataset was down-selected to only include fuels that lie within the property range used in the alternative method under consideration. This down-selected dataset was then used as the new "testing" dataset to evaluate the relevant error metrics. This enabled a fair comparison between the Stanford strategies and the literature-reported methods on a similar set of fuels. In addition to the prediction error on the down-selected dataset, the error on the overall training dataset, normalized by the range of property values included in the respective dataset, was chosen as an additional performance metric to compare the different prescreening methods. This methodology was applied to compare the performance of our FTIR-based strategies with other prediction methods reported in the literature for the properties: hydrogen-to-carbon (H/C) ratio, density, net heat of combustion (NHC), derived cetane number (DCN), flash point, freezing point, initial boiling point (IBP), and kinematic viscosity (KV). The results for the property NHC are illustrated below in Table 1 and Table 2.

Table 1 shows the comparison of Strategy 1 and Strategy 3 against Johnson et al. (2006), who developed PLSR models based on compositional data obtained using three different techniques: (1) near-infrared (NIR) spectroscopy, (2) Raman spectroscopy, and (3) gas chromatography-mass spectrometry (GC-MS). As seen in Table 1 (top), the Stanford training dataset was observed to span a wider NHC range than the Johnson et al dataset, and the down-selected Stanford dataset had 46 samples (compared to 228 samples in the original dataset). The root-mean-squared error (RMSE) was evaluated on the down-selected dataset using both the original and retrained versions of our Strategy 1 and 3 models. While the NIR-based model of Johnson et al. (2006) was found to have lower error than the original Strategy 1, both the original and retrained Strategy 1 models outperformed the other Johnon et al. (2006) models. The original and retrained Strategy 3 (nonlinear) models have a lower error than the corresponding Strategy 1 (linear) models and also achieve better accuracy than Johnson et al. Similar performance is seen in the range-normalized RMSE metric.

Table 1. Comparison of Strategy 1 and Strategy 3 models for NHC with Johnson et al. (2006) (PLSR models based on NIR, Raman, and GC-MS data): Maximum and minimum NHC values in Johnson et al. (2006) and Stanford datasets (top), and Prediction errors of Johnson et al. (2006) models, and the original and retrained FTIR-based models (bottom).

Johnson et al. dataset		Stanford dataset		Number of Stanford data points within the Johnson et al. range
Min. value	Max. value	Min. value	Max. value	
42.64 MJ/kg	43.24 MJ/kg	40.17 MJ/kg	45.66 MJ/kg	46

Method	Performance metric	Johnson et al.	Strategy 1		Strategy 3	
			Original	Retrained	Original	Retrained
NIR	$RMSE_{reduced}$ (%)	0.146	0.230	0.102	0.117	0.035
	RMSE/(Max – Min)	0.105	0.017		0.012	
Raman	$RMSE_{reduced}$ (%)	0.259	0.230	0.102	0.117	0.035
	RMSE/(Max – Min)	0.186	0.017		0.012	
GC-MS	$RMSE_{reduced}$ (%)	0.218	0.230	0.102	0.117	0.035
	RMSE/(Max – Min)	0.157	0.017		0.012	

Table 2. Comparison of Strategy 1 and Strategy 3 models for NHC with Caswell et al. (1989) (MLR models based on LC/^{1}H NMR data): Maximum and minimum NHC values in Caswell et al. and Stanford datasets (top), and Prediction errors of Caswell et al. (1989) model, and the original and retrained FTIR-based models (bottom).

Caswell et al. dataset		Stanford dataset		Number of Stanford data points within the Caswell et al. range
Min. value	Max. value	Min. value	Max. value	
42.70 MJ/kg	43.20 MJ/kg	40.17 MJ/kg	45.66 MJ/kg	40

Method	Performance metric	Caswell et al.	Strategy 1		Strategy 3	
			Original	Retrained	Original	Retrained
LC/ ^{1}H NMR	$RMSE_{reduced}$	0.060	0.105	0.039	0.051	0.011
	RMSE/(Max – Min)	0.120	0.017		0.012	

Table 2, on the other hand, compares Strategy 1 and Strategy 3 models against Caswell et al. (1989), who developed MLR models based on liquid chromatography (LC) and proton nuclear magnetic resonance (^{1}H NMR) data. Again, the NHC range in the Stanford training dataset was broader than the Caswell et al (1989) dataset, and the down-selected Stanford dataset had 40 samples in this case. The RMSE of the original Strategy 1 model was higher than Caswell et al. (1989). However, the

retrained Strategy 1 and the original and retrained Strategy 3 models outperform Caswell et al. (1989). The range-normalized RMSE of the Stanford models was also significantly lower than the Caswell et al. (1989) model.

In general, the FTIR-based models achieved greater prediction accuracy than most alternative prediction methods for all properties. These strategies thus provide the capability of accurately predicting the physical and chemical properties of alternative jet fuels directly based on their infrared spectra.

Analysis of training dataset population distributions

In machine learning models, there is often a tradeoff between predictive performance and training dataset generalization. Datasets spanning a wider property range ensure that the models are robust and applicable to a broader range of novel fuels. But for some applications, having a specialized dataset (e.g., restricted to a narrow property range or to specific molecular classes) could lead to improved predictive performance on certain kinds of test fuels. To better identify ways to tune the training dataset for different test fuels, the population distribution of the samples in the Stanford training data for each property was analyzed. These population distributions are shown in Figure 1 for six properties: DCN, density, NHC, flash point, KV, and freezing point. In each of the panels, the green faded region represents the ASTM operability range for the corresponding property. In Figure 1, the red dashed line marks the property value of nominal Jet-A (POSF 10325), and the blue dotted lines correspond to the property limits of the sustainable aviation fuel (SAF) samples available in our training dataset.

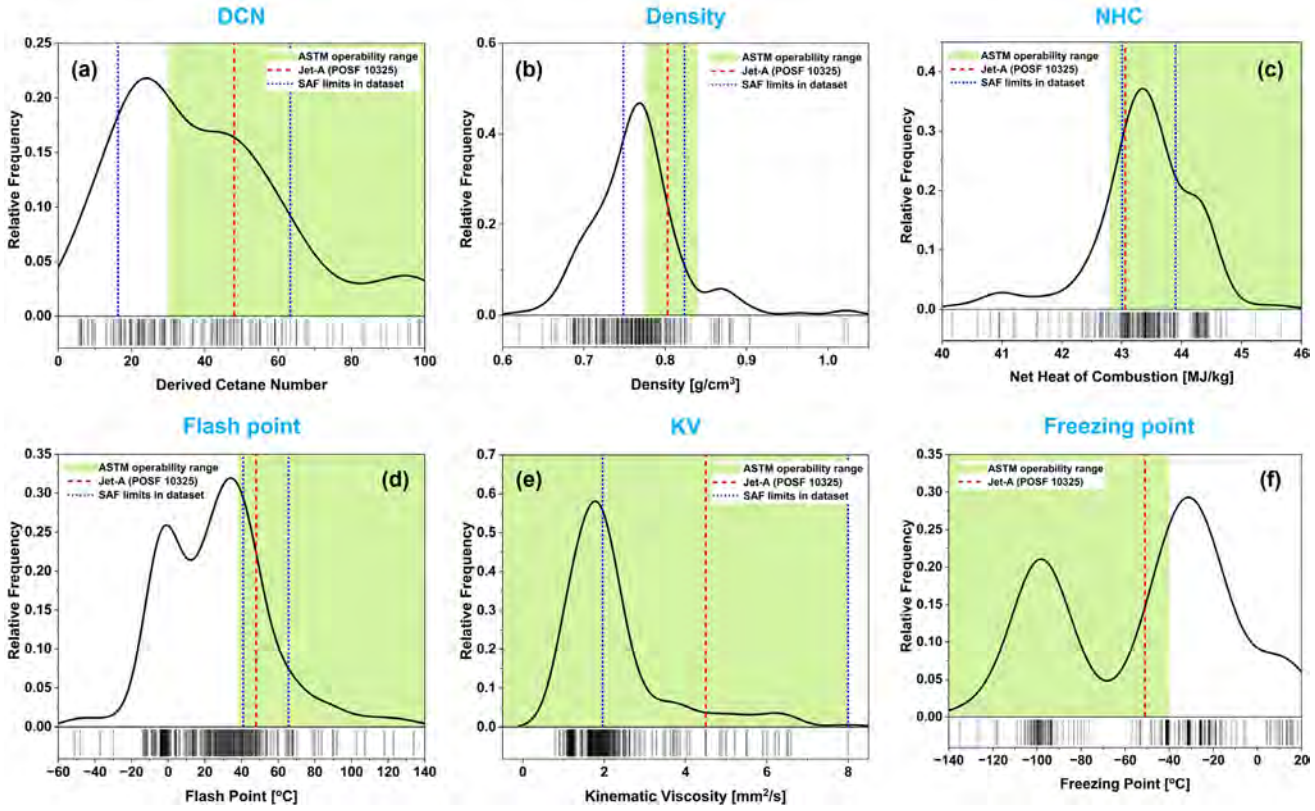

Figure 1. Distribution of samples in the Stanford training dataset for the properties: DCN (a), Density (b), NHC (c), Flash point (d), KV (e), and Freezing point (f). The ASTM operability range, along with the Jet-A and SAF property limits for each property, are marked in the respective plots.

While a majority of the training dataset lies within the ASTM operability range for DCN and NHC, the density training set spans a much wider range than the ASTM limits, as seen in Figure 1 plots a, b, and c. It should be noted that the SAF candidates and blending components typically have properties outside the ASTM range and therefore differ significantly

from nominal Jet-A properties. It is therefore useful to have a wide property range in the training dataset to accurately predict properties of SAF candidates with varied compositions. But it may be desirable to tailor our training data to achieve higher prediction accuracy for specific fuel types/classes. For instance, a training dataset primarily composed of aromatic species could offer higher property prediction accuracy for a synthetic aromatic kerosene (SAK) sample compared to a dataset comprised of multiple molecular classes.

As seen in Figure 1 plot d, most of the flash point data lie outside the ASTM and SAF limits, and it is evident that addition of more fuels with flash points greater than 40°C can improve the sample distribution. The datasets for freezing point and KV are adequately representative of the ASTM operability range but are heavily concentrated around specific property values. This highlights the scope to enhance the dataset uniformity by including more samples within the underrepresented property ranges. Similar insights were obtained through the analysis of the population distributions for the remaining properties. Overall, this analysis highlights potential ways to improve model performance through adjustments to the training dataset, which is a powerful tool to fine-tune the FTIR-based strategies for specific applications or test fuels.

To continually assess the performance of our strategies, 39 new Jet-A samples were recently acquired from the World Jet Fuel Survey (WJFS). The FTIR spectra of these fuels will be analyzed to identify differences in absorption features across various samples. Additionally, a HEFA-SPK (synthetic paraffinic kerosene) SAF sample, along with measured property data, was acquired from ASCENT Project 065A (Professor Josh Heyne), which will be used to test the performance of our models.

Milestones

- Reported experimental results and analysis at the Fall and Spring ASCENT meetings (October 2023 and April 2024)
- Reported and presented results at biannual JANNAF Interagency Propulsion Committee Meetings, December 2023 in Salt Lake City, Utah, and May 2024 in Oklahoma City, Oklahoma.

Major Accomplishments

During this past year of the program, major advances were made in several areas:

- Compared the prediction accuracies of our FTIR-based methodology against alternative prediction methods reported in the literature. Our FTIR-based models demonstrated superior performance over alternative methods in predicting key physical and chemical properties.
- Analyzed the distribution of properties within our training datasets, identifying areas where dataset tuning may improve prediction accuracy.
- Acquired 39 new Jet-A samples obtained from the WJFS and a new HEFA-SPK SAF sample from Project 65A (Professor Josh Heyne).
- Installed a new detector and upgraded the purge setup on our FTIR system. These improvements enhanced the facility's capabilities, allowing us to achieve a better signal-to-noise ratio for future measurements.

Publications

Peer-Reviewed Journal Publication

Boddapati, V., Ferris, A. M., Hanson, R. K. (2024). Predicting the physical and chemical properties of sustainable aviation fuels using elastic-net-regularized linear models based on extended-wavelength FTIR spectra. *Fuel, 356*, 129557.https://doi.org/10.1016/j.fuel.2023.129557

Outreach Efforts

Our IR fuel analysis work was presented at the Fall ASCENT Advisory Committee Meeting (October 24-26, 2023), and at the Spring ASCENT SAF Meeting (April 24-25, 2024). Research was also presented at the biannual JANNAF Interagency Propulsion Committee Meetings (December 4-8, 2023, in Salt Lake City, Utah; and May 6-10, 2024, in Oklahoma City, Oklahoma).

Awards

None.

Student Involvement

Graduate students are actively involved in the acquisition and analysis of all experimental data and model development. Current graduate students, Vivek Boddapati and Andrew Klingberg, performed the IR spectral analysis/fuel prescreening. Jesse Streicher, our current research scientist, has additionally contributed to the project through research management.

Plans for Next Period

- Explore ways of improving the uniformity of training dataset distribution for different properties to eliminate biases (e.g., adding/removing data points within certain property ranges).
- Measure the FTIR spectra of the newly acquired WJFS fuel samples and analyze the data to identify salient spectral differences and subsequently predict the properties of these fuel samples.
- Measure the FTIR spectrum of the newly acquired HEFA-SPK SAF sample and make property predictions using Strategies 1 and 3.
- Begin characterizing the detection limit of NH-containing species in the 2-15 μm wavelength range, with a focus on identifying trace species in complex fuel mixtures.
- Continue expanding the training dataset by measuring the 2-15 μm spectra of relevant neat hydrocarbons, conventional jet fuels, and SAFs. Investigate the value of further extending the wavelength range beyond the 2-15 μm region, particularly to access strong, isolated spectral features corresponding to molecular classes such as cycloparaffins and olefins.
- Explore batch distillation of multi-component fuels as a potential way to isolate molecular classes with weaker spectral features (i.e., cycloparaffins, aromatics, etc.) and possibly identify strategies to make more accurate property predictions based on the FTIR spectra of individual distillate fractions.
- Measure the liquid-phase FTIR spectra of neat hydrocarbons, simple blends, and real fuels. Compare these liquid-phase spectra with vapor-phase FTIR measurements and evaluate the potential merits/demerits of each method.

References

Caswell, H. (1989). Rapid prediction of various physical properties for middle distillate fuels utilizing directly coupled liquid chromatography/proton nuclear magnetic resonance. *Analytical Chemistry, 61*(3), 206-211. https://doi.org/10.1021/ac00178a004

Johnson, K. (2006). Evaluating the Predictive Powers of Spectroscopy and Chromatography for Fuel Quality Assessment. *Fuels, 20*(2), 727-733. https://doi.org/10.1021/ef050347t

Project 031 Alternative Jet Fuel Test and Evaluation

University of Dayton Research Institute

Project Lead Investigator

Zachary West, PhD
Principal Research Engineer
Group Leader, Fuel Science
University of Dayton
300 College Park
Dayton, OH 45458
937-255-4062
zachary.west@udri.udayton.edu

University Participants

University of Dayton Research Institute (UDRI)

- P.I.: Zachary West, Group Leader
- FAA Award Number: 13-C-AJFE-UD
- Overall Period of Performance: April 8, 2015, to September 30, 2025
- Tasks:
  - Period of Performance: April 8, 2015, to March 14, 2016; Amendment No. 006
    1. Evaluate the performance of candidate alternative fuels via the ASTM D4054 approval process
  - Period of Performance: August 13, 2015, to August 31, 2016; Amendment No. 007
    2. Evaluate the performance of candidate alternative fuels via the ASTM D4054 approval process
  - Period of Performance: August 5, 2016, to August 31, 2017; Amendment No. 012
    3. Manage the evaluation and testing of candidate alternative fuels
  - Period of Performance: July 31, 2017, to August 31, 2019; Amendment No. 016
    4. Manage the evaluation and testing of candidate alternative fuels
  - Period of Performance: August 30, 2018, to August 31, 2019; Amendment No. 021
    5. Manage the evaluation and testing of candidate alternative fuels
  - Period of Performance: Extended period of performance end from September 10, 2019, to September 9, 2020; Amendment No. 023
  - Period of Performance: February 5, 2020, to February 4, 2021; Amendment No. 025
    6. Manage the evaluation and testing of candidate alternative fuels
  - Period of Performance: Extended period of performance end from September 9, 2019, to September 9, 2021; Amendment No. 028
  - Period of Performance: February 4, 2021, to February 5, 2022; Amendment No. 032
    7. Manage the evaluation and testing of candidate alternative fuels
  - Period of Performance: August 10, 2021, to February 10, 2022; Amendment No. 033
    - No-cost extension (Amendment No. 033 is not task-specific)
  - Period of Performance: October 1, 2021, to September 30, 2022; Amendment No. 038
  - Period of Performance: October 1, 2022, to September 30, 2023; Amendment No. 043
  - Period of Performance: October 1, 2023, to September 30, 2024; Amendment No. 049
    - No-cost extension
  - Period of Performance: March 19, 2024, to March 18, 2025; Amendment No. 052
  - Period of Performance: August 26, 2024, to September 30, 2024; Amendment No. 056
    - Redirect funds awarded on Amendment No. 024 to ASCENT Project 031
  - Period of Performance: March 19, 2025, to September 30, 2025; Amendment No. 057
    - No-cost extension

Project Funding Level

Amendment	Funding
Amendment No. 006	$309,885
Amendment No. 007	$99,739
Amendment No. 012	$693,928
Amendment No. 016	$999,512
Amendment No. 021	$199,966
Amendment No. 025	$1,926,434
Amendment No. 032	$1,049,700
Amendment No. 038	$499,784
Amendment No. 043	$1,499,940
Amendment No. 052	$1,999,834
Amendment No. 056	$101,888
Total	**$9,380,610**

In-kind cost sharing has been obtained from the following organizations:

Organization	Funding	Year
LanzaTech	$ 55,801	2015
UDRI -- internal funds	$ 43,673	2016
LanzaTech	$ 381,451	2016
Neste	$ 372,000	2017
Boeing	$ 2,365,338	2017
Shell	$ 280,000	2019
IHI	$ 1,150,328	2019
Shell	$ 325,000	2020
Global Bioenergies	$ 6,875,900	2021
Global Bioenergies	$ 290,000	2021
Revo	$ 625,873	2024
University of Sheffield	$ 11,975	2024
Total	**$12,777,339**	

Investigation Team

Dr. Zachary West (P.I.)
Carlie Anderson (staff scientist)
Dr. Amanda Arts (staff scientist)
Shane Kosir (staff scientist)
Susan Mueller (staff scientist)
Linda Shafer (staff scientist)
Dr. Willie Steinecker (staff scientist)
Maria Baker (other professional)
April Landsaw (other professional)
Taylor Nicely (undergraduate student)
CJ Nesbit (undergraduate student)

Project Overview

Alternative jet fuels, also known as synthetic aviation turbine fuel (SATF) or sometimes sustainable aviation fuel (SAF), offer the potential benefits of reduced global environmental impacts, greater national energy security, and stabilized fuel costs for the aviation industry. The Federal Aviation Administration (FAA) is committed to the advancement of "drop-in" SATF. The successful adoption of alternative fuels requires approval for use by the aviation community (i.e., original equipment manufacturers [OEM] and regulators), followed by large-scale production of fuel that is cost-competitive and meets the safety standards for conventional jet fuel. Alternative jet fuels must undergo rigorous testing to become qualified for use and to be incorporated into ASTM International specifications.

Cost-effective, coordinated performance testing capability (in accordance with ASTM D4054) is needed to support the evaluation of promising alternative jet fuels. The objective of this project is to provide the necessary capability to support fuel testing and evaluation of novel alternative jet fuels.

The proposed program should provide the following capabilities:

- Identify alternative jet fuels, including blends with conventional jet fuel, with the potential to be economically viable and to support FAA's NextGen environmental and SAF Grand Challenge goals for testing.
- Perform engine, component, rig, or laboratory tests, or any combination thereof, to evaluate the performance of alternative jet fuels in accordance with ASTM International standard practice D4054.
- Identify and conduct unique testing, beyond that defined in ASTM International standard practice D4054, to support the evaluation of alternative jet fuels for inclusion in ASTM International jet fuel specifications.
- Obtain baseline and alternative jet fuel data to assess the effects of alternative jet fuels on aircraft performance, maintenance requirements, and reliability.
- Coordinate efforts with activities sponsored by the U.S. Department of Defense and/or other governmental parties that may be supporting relevant work.
- Report relevant performance data for the alternative fuels tested, including quantified effects of the alternative fuel on aircraft and/or engine performance and air-quality emissions relative to conventional jet fuel; share reported data with the FAA National Jet Fuel Combustion Program, the ASCENT Center of Excellence membership, and the broader aviation fuels community (e.g., ASTM International, Coordinating Research Council).

Tasks 1 and 2 - Evaluate the Performance of Candidate Alternative Fuels via the ASTM D4054 Approval Process and Manage the Evaluation and Testing of Candidate Alternative Fuels

University of Dayton Research Institute

Objective

Cost-effective, coordinated performance testing capability (in accordance with ASTM D4054) is needed to support the evaluation of promising alternative jet fuels. The objective of this project is to provide the capability necessary to support either (a) the evaluation of to-be-determined alternative fuels selected in coordination with the FAA or (b) a fuel testing and evaluation project with specific alternative fuels in mind.

Research Approach

The intent of this program is to provide the capability needed to perform specification and fit-for-purpose evaluations of candidate alternative fuels, with the aim of providing a path through the ASTM D4054 approval process. The UDRI team can perform many of these evaluations and is prepared to work with other organizations, such as the Southwest Research Institute (SwRI) and OEMs, with unique test capabilities, as needed. These assessments include additional engine, auxiliary power unit, component, and rig evaluations. The UDRI testing capabilities include our campus laboratory facilities and limited efforts at the laboratories of the Fuels Branch of the U.S. Air Force Research Laboratory.

Table 1 and Table 2 list examples of the Tier 1 and Tier 2, respectively, measurements that can be provided by UDRI and its partners.

Table 1. Example Tier 1 Properties.

Test Description	Method
Acidity	ASTM D3242
Aromatics	ASTM D6379
Mercaptan Sulfur	ASTM D3227
Sulfur Content	ASTM D5453
Carbon and Hydrogen Mass	ASTM D5291C
FAME	IP 585
Physical Distillation	ASTM D86
Flash Point	ASTM D93
Freezing Point	ASTM D5972
Net Heat of Combustion	ASTM D4809
Smoke Point	ASTM D1322
Copper Strip Corrosion	ASTM D130
Thermal Stability	ASTM D3241
Existent Gum	ASTM D381 or IP 540
MSEP (Microseparometer Index)	ASTM D3948

Table 2. Example Tier 2 Properties.

Test Description	Method
Bulk Detailed Hydrocarbon Type Composition	UDRI FC-M-101 or FED-STD-791, Method 7508
Hydrocarbon Composition	ASTM D2425
Trace Materials – Polar Organics	UDRI FC-M-102
Total Nitrogen Content	ASTM D4629
Total Halogens (Fluorine, Chlorine)	ASTM D7359
Trace Elements (ICP-MS)	UDRI FC-M-107
Simulated Distillation	ASTM D2887
Thermal Stability, Breakpoint	ASTM D3241
Lubricity (BOCLE)	ASTM D5001
Response to Lubricity Improver	ASTM D5001
Viscosity vs Temperature	ASTM D7042
Specific Heat vs Temperature	ASTM E1269
Density vs Temperature	ASTM D4052
Surface Tension vs Temperature	ASTM D1331A
Isentropic Bulk Modulus vs Temperature	FED-STD-791, Method 7507

Test Description	Method
Thermal Conductivity vs Temperature	ASTM D7896
Water Solubility vs Temperature	ASTM D6304
Air Solubility	FC-M-103
True Vapor Pressure vs Temperature	ASTM D6378 or D2879
Dielectric Constant vs Density	IP 638
Electrical Conductivity and Response to Static Dissipator	ASTM D2624
Storage Stability - Peroxides	ASTM D3703
Storage Stability - Potential Gum	ASTM D5304
Flammability Limits	ASTM E681
Autoignition Temperature	ASTM E659
Hot Surface Ignition Temperature	ISO 20823
Preliminary materials compatibility (Nitrile, Fluorosilicone, Fluorocarbon [Viton] Elastomers)	ASTM D4054 Annex 3 (optical dilatometry)
Derived Cetane Number	ASTM D6890

Extended physical and chemical characterization
In addition to the above physical and chemical fuel evaluation capabilities, UDRI has extensive experience in evaluating microbial growth in petroleum-derived and alternative fuels. These evaluations include standard laboratory culturing and colony counting methods, as well as advanced techniques, such as quantitative polymerase chain reaction and metagenomic sequencing. These methods enable quantitative measurements of microbial growth rates in candidate alternative fuels for comparison with petroleum fuels.

UDRI has extensive experience in the evaluation of elastomer degradation upon exposure to candidate alternative fuels. Various methods are used to evaluate seal swell and O-ring fixture leakage, including optical dilatometry, sealing pressure measurements, fuel partitioning into the elastomer, and the use of a pressurized temperature-controlled O-ring test device.

Moreover, UDRI can perform fuel–material compatibility testing by using ASTM D4054 procedures for fuel soak testing, post-exposure nonmetallic and metallic material testing, and surface and microstructural evaluation. The 68 “short-list” materials and 255 materials on the complete list can be tested.

Milestones

The schedule for this project is dependent on the receipt of alternative fuel candidates for testing. As candidate fuels are received, a testing schedule will be established via coordination with the FAA and collaborators. Our existing relationships with these organizations will help expedite this process.

Major Accomplishments

Virent® Synthesized Aromatic Kerosene
Virent’s synthesized aromatic kerosene (SAK) is an aromatics-only stream produced from a sugar feedstock. The OEM committee has recommended that this candidate be evaluated as a blend with petroleum jet fuel. A few items remain to prior to approval of this fluid through ASTM. However, Virent®’s parent company, Marathon Petroleum Co. (MPC), has decided to close the Virent® research facility; further activities for approval of this SAK will be handled with MPC directly.

Council of Scientific and Industrial Research-Indian Institute of Petroleum
The Council of Scientific and Industrial Research-Indian Institute of Petroleum (CSIR-IIP) has developed a single-step process to convert lipids (i.e., plant-derived oil and animal-derived fats) into hydrocarbons containing aromatic compounds.

® Virent is a registered trademark of Virent, Inc., Madison, Wisconsin.

Multiple fuel samples have been received, and Tier 1 and Tier 2 testing have been completed. The OEM committee has recommended that this fuel proceed along the ASTM full approval pathway (rather than the Fast Track process). OEMs have reviewed the Phase I research report and feedback has been provided to CSIR-IIP.

Methanol to Jet
ExxonMobil (XOM), Honeywell-UOP (UOP), and Topsoe® submitted a combined research report for methanol-to-jet (MTJ) synthetic blending components (SBC). During the entry screening process, it was proposed to separate the report into two separate reports: (1) the primarily isoparaffinic, MTJ-synthetic paraffinic kerosene (SPK) type fluid from XOM and UOP, and (2) the highly cycloparaffinic with aromatics, MTJ-cycloparaffinic kerosene with aromatics (CKA) type fluid from Topsoe.® The MTJ-CKA fluid is considered to be more 'fully formulated' with respect to hydrocarbon classes—'fully formulated' in this sense meaning the blend component contains most/all of the traditional classes of hydrocarbons to include iso-, n-, cyclo-alkanes, along with aromatics—while the MTJ-SPK fluid is more consistent with the existing ASTM D7566 Annex A5 alcohol-to-jet (ATJ)-SPK. The OEM review of both research reports is anticipated in the first quarter of 2025.

Revo
The Revo fuel is a hydroprocessed ester and fatty acid (HEFA)-type fuel containing a higher level of cycloparaffins. Three fuel samples have been received, and Tier 1 and Tier 2 testing have been completed. Revo has decided to perform some additional process optimization and will be submitting additional test data from production plant samples in early 2025.

OMV
The OMV ReOil® candidate is produced from waste plastic pyrolysis oil (WPPO). The OEM committee has approved this fuel for entry to the Fast Track process after reviewing initial fuel property and composition data. Testing is complete on multiple fuel samples. It was recommended to OMV that a WPPO feedstock specification be created through ASTM. OMV is generating additional samples and test data for inclusion in a research report anticipated in early 2025.

CleanJoule®
CleanJoule® entered the ASTM D4054 Clearinghouse this year with a candidate SBC derived from isoprene. The product is exclusively cycloparaffinic and is comprised of a single carbon number. The process involves oligomerization and hydroprocessing. Tier 1 and Tier 2 test data are being generated.

UPM
UPM entered the ASTM D4054 Clearinghouse this year with a candidate SBC derived from crude tall oil (CTO) which is a by-product of the pulp and paper industry. They already have a process, including hydroprocessing and fractionation, to upgrade the CTO into a green diesel product and are looking to expand into jet fuel. The product is a fully formulated SBC that contains a mixed paraffin kerosene along with some aromatics. Tier 1 and Tier 2 test data are being generated.

Shell IH^2 Testing
Shell is still actively seeking a commercialization partner for this technology. As a result, they are putting fuel production and approval activities on hold. The ASCENT Project 031 team is awaiting larger volumes of fuels, as additional Tier 3 testing was recommended by the OEM committee because of the high cycloparaffin level of this fuel.

Publications

Written Reports

Supporting Data for ASTM D7566 revision:

ASTM International. (2018). *Evaluation of LanzaTech-PNNL Ethanol Based Alcohol-to-Jet (LT-PNL ATJ) Synthetic Paraffinic Kerosenes (ATJ-SPKs)* [Research report]. D02-1884.

ASTM International. (2019). R*enewable Jet Fuel Produced by Catalytic Hydrothermolysis (CH)* [Research report]. D02-1914 (Addendum).

ASTM International. (2020). *Evaluation of Synthesized Paraffinic Kerosene from Algal Oil Extracted from Botryococcus braunii (IHI Bb-SPK)* [Fast Track Research Report. D02-1925.

® Topsoe is a registered trademark of Topsoe A/S, Kongens Lyngby, Denmark.
® ReOil is a registered trademark of OMV Downstream GmbH, Vienna, Austria.
® CleanJoule is a registered trademark of CleanJoule, LLC, Salt Lake City, Utah.

ASTM International. (2022). *CHJ Pathway: ReadiJet™ Renewable Jet Fuel Produced by Catalytic Hydrothermolysis (CH)* [Research Report]. D02-2039; ASTM International: West Conshohocken, PA, October 2022.
ASTM International. (2023). *Evaluation of Alcohol-To-Jet Synthetic Kerosene with Aromatics (ATJ-SKA) Fuels and Blends* [Research Report]. D02-2056.
ASTM International. (2023). *Evaluation of Global Bioenergies' Isobutene Derived Synthetic Paraffinic Kerosene (IBN-SPK)* [Research Report]. D02-2054.

Supporting Data for ASTM D1655 revision

ASTM International. (2020). *Modification of ASTM D1655: Co-Processing of Fischer-Tropsch Feedstocks with Petroleum Hydrocarbons for Jet Production using Hydrotreating & Hydrocracking WK69614* [Research Report]. D02-1929.

Outreach Efforts

Presentations on ASCENT Project 031 activities were given at the April 2024 and October 2024 ASCENT meetings. Meetings were held with the OEM technical review panel, FAA, fuel producers, and others at numerous virtual FAA/OEM meetings (generally two meetings per month). Briefings were also given at the United Kingdom Ministry of Defense Aviation Fuels Meeting in Bristol, United Kingdom (March 19-20, 2024), and Coordinating Research Council Aviation Meeting in Alexandria, Virginia (April 29-May 2, 2024).

Awards

None.

Student Involvement

An undergraduate student, Taylor Nicely, assisted with the analysis of FC-M-102 (polars quantification).

Plans for Next Period

- Continue discussions with new fuel producers
- Expect new candidates to enter the ASTM D4504 approval process in the coming months.

Tasks 3 and 4 - Manage the Evaluation and Testing of Candidate Alternative Fuels

University of Dayton Research Institute

Objective

The objective of this work is to manage the evaluation and testing of candidate alternative jet fuels (i.e., SATF, SBC, and SAF) in accordance with ASTM International standard practice D4054 (see Figure 1).

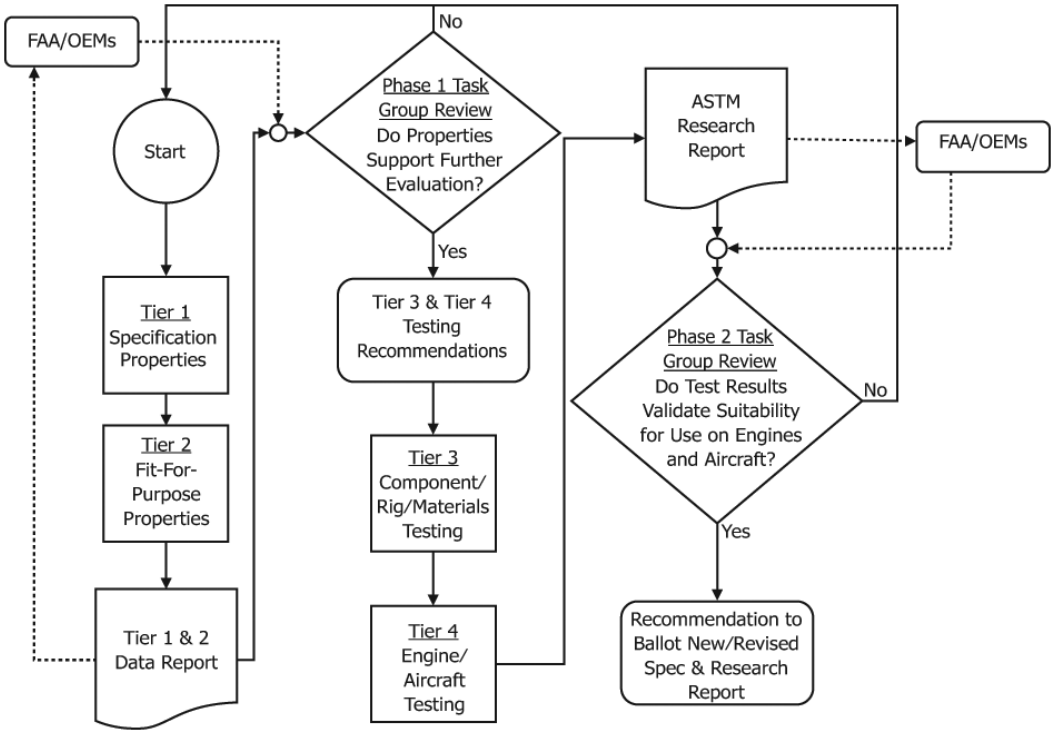

Figure 1. Overview approval process of new aviation fuels from ASTM D4054.

Research Approach

UDRI will subcontract with other research organizations, testing laboratories, and/or OEMs to conduct the following tasks in support of the evaluation and ASTM specification development for alternative jet fuels. The purpose of this project is to manage and coordinate the ASTM D4054 evaluation process to facilitate the transition of alternative fuels to commercial use.

Subtask 1: General support

- Develop and make available an ASTM D4054 process guide describing logistical procedures for the handling of test fuels, documentation requirements, test report issuance and delivery, and contact information, to provide clear instructions for candidate-fuel producers entering the ASTM D4054 process.

Subtask 2: Phase 1 support

- Coordinate the handling of Phase 1 candidate test fuel samples for Tier 1 and Tier 2 testing.
- Review process descriptions provided by the fuel producer to determine the acceptability for incorporation into the Phase 1 research report.
- Review test data from Tier 1 and Tier 2 testing to determine acceptability for incorporation into the Phase 1 research report.
- Issue and deliver a Phase 1 research report to OEMs.
- Review and respond to comments regarding the Phase 1 research report, as submitted by the OEMs, in conjunction with the fuel producer.
- Conduct additional Tier 1 or Tier 2 testing in response to OEM comments, as required.
- Review and consolidate OEM requirements for ASTM D4054 Tier 3 and Tier 4 testing, as submitted by the OEMs.
- Deliver consolidated ASTM D4054 Tier 3 and Tier 4 testing requirements to the fuel producer.

Subtask 3: Phase 2 support

- Coordinate the funding and scheduling of ASTM D4054 Tier 3 and Tier 4 testing with OEMs and other test facilities.

- Coordinate the handling of Phase 2 candidate test fuel samples for Tier 3 and Tier 4 testing.
- Review test data from Tier 3 and 4 testing to determine acceptability for incorporation into the Phase 2 research report.
- Issue and deliver the Phase 2 research report to OEMs.
- Review and respond to comments submitted by OEMs regarding the Phase 2 research report in conjunction with the fuel producer.
- Conduct additional Tier 3 or Tier 4 testing in response to OEM comments, as required.
- Issue and deliver Phase 2 research report addenda reporting the additional Tier 3 or Tier 4 test results, as required.

Subtask 4: OEM review meetings

- Schedule periodic OEM meetings to review the testing status and research report evaluations.
- Identify suitable meeting venues and support equipment.
- Develop agendas and coordinate with attendees for participation in these meetings.
- Record meeting minutes, including agreements, commitments, and other action items.
- Issue and distribute meeting minutes to all attendees.

Subtask 5: Single-laboratory two-dimensional gas chromatography method documentation

- Document UDRI two-dimensional gas chromatography (GCxGC) methods for hydrocarbon type analysis.
- Develop reference materials for the creation of GCxGC hydrocarbon type templates.
- Measure single-laboratory precision of GCxGC methods.

Subtask 6: Multi-laboratory GCxGC method documentation

- Validate the precision of GCxGC methods across multiple laboratories.
- Identify alternative GCxGC methods, including column selection and order and modulation techniques.
- Perform a correlation study to determine the agreement among laboratories, methods, and hardware choices.

Milestones

The schedule for this project is dependent on the receipt of alternative fuel candidates for testing. As candidate fuels are received, a testing schedule will be established via coordination with the FAA and collaborators. Our existing relationships with these organizations will help expedite this process. Figure 2 shows a Gantt chart schedule for the testing and approval of candidate fuels that are currently under evaluation process.

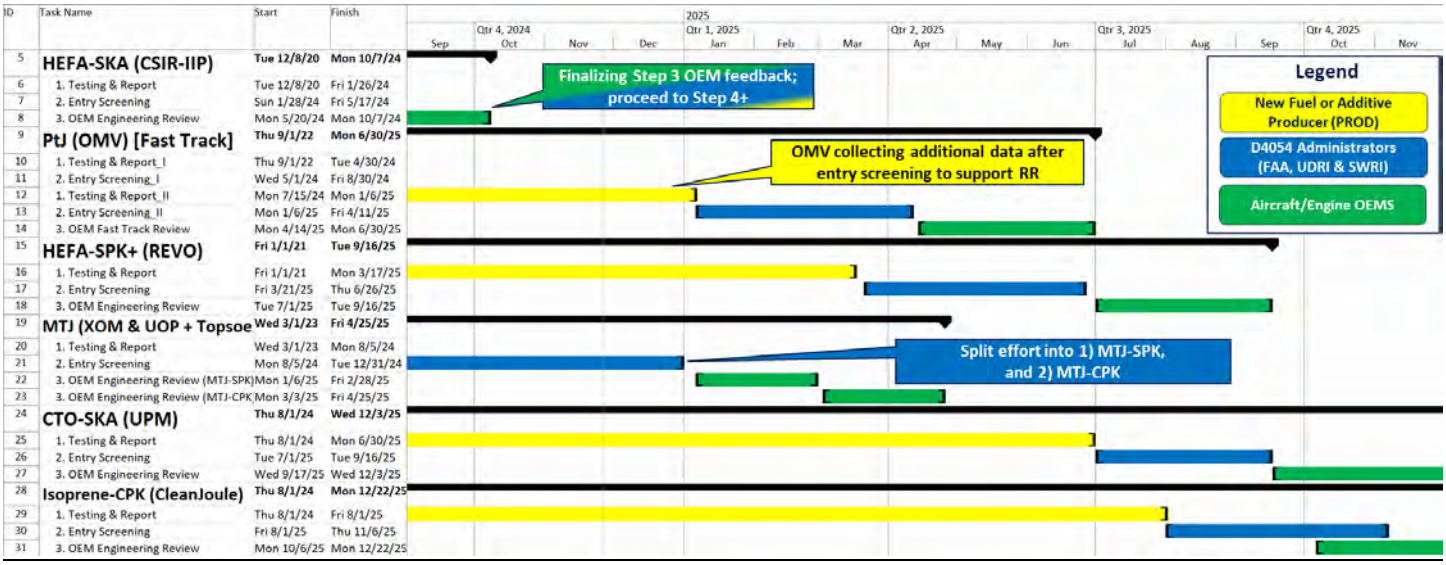

Figure 2. Notional schedule for fuel evaluations.

Major Accomplishments

Detailed Hydrocarbon Type Analysis (via GCxGC)

The ASCENT Project 031 team has further advanced the accessibility and reporting of detailed hydrocarbon type analysis methods using GCxGC technology. In collaboration with the U.S. Navy and U.S. Air Force partners, a Federal Standard Method (FED-STD-791F, Method 7508) was recently published and successfully balloted for inclusion in ASTM D4054. The method is accessible for download from the website https://quicksearch.dla.mil/qssearch.aspx by searching for "FED-STD-791" under the Document ID category.

Inductively coupled plasma mass spectrometry (ICP-MS)

Observations of inconsistent results for dissolved metal/elemental concentrations in fuel evaluated in the ASTM D4054 Clearinghouse have prompted an evaluation of these analyses. In particular, the phosphorus results have presented an issue in ongoing evaluations. UDRI acquired an ICP-MS system and has developed new methods for measuring phosphorous (P) and silicon (Si) via standard addition, as these atoms have interferences that preclude the use of an external calibration curve. In addition to method advancements with P and Si, our team has strived to improve the robustness (i.e., accuracy, precision, and ease of use) of the overall method. The ASCENT Project 031 team have briefed our findings at the Coordinating Research Council Aviation Meeting in Alexandria, Virginia (April 29-May 2, 2024), American Chemical Society (ACS) Fall 2023 national meeting in Denver, Colorado (August 17-21, 2024), and the International Association of Stability, Handling and Use of Liquid Fuels (IASH) 2024 conference in Louisville, Kentucky (September 8-12, 2024).

Civil Aviation Administration of China

The Chinese government has approached the FAA/OEM committee with a request to evaluate two jet fuel additives for approval for use. These additives include a static dissipator additive and a corrosion inhibitor/lubricity improver additive. These additives have been received, and testing has been completed on both additives. Based on an initial review of the results, the OEM committee recommended additional testing, which has also been completed. The OEM committee has commenced communications with representatives of the Civil Aviation Administration of China to find a pathway forward.

OEM committee coordination

Ongoing efforts in ASTM OEM committee coordination continued during this period. These efforts involve coordinating engine and airframer OEM meetings, which have typically occurred in concert with the biannual ASTM Committee D02 sessions and at the annual United Kingdom Ministry of Defense Aviation Fuels Committee meeting in London, United Kingdom. During travel restrictions due to the COVID-19 pandemic, these meetings occurred virtually and more frequently, once or twice per month. SwRI continues to receive funding to aid in coordinating the OEM meetings and in communicating with the OEMs for discussions and research report reviews of new candidate alternative jet fuels. In addition, a Gantt schedule is updated regularly; this schedule shows a queue of candidate fuels and the completed and expected schedules as these fuels move through the ASTM D4054 process of testing, review, balloting, and approval. A recent version of this schedule is shown in Figure 2. In support of the ongoing OEM committee coordination, subcontracts with Boeing, General Electric (GE) Aviation, Honeywell, Rolls Royce, Pratt & Whitney, and SwRI have been extended to our ASCENT grant end date of September 30, 2025.

With the departure of Mark Rumizen from the FAA, and the retirement of the long-time UDRI P.I., Steve Zabarnick, the ASCENT Project 031 team has instituted an OEM review panel scheduling crew to help plan and focus the OEM meeting discussions. This scheduling group currently consists of representatives from UDRI, FAA, SwRI, ASTM J6 Chair, United Kingdom Clearinghouse, European Union Clearinghouse, and European Union Aviation Safety Agency. Our team will be adjusting this group membership as needed. The ASCENT Project 031 team will continue to look for additional ways to optimize and improve the ASTM D4054 process to streamline approval of alternative jet fuels, while maintaining safe operations. Some areas of future improvement our team has identified include the standardization of laboratory testing results (for bespoke Tier 2 testing), creation of a phase I research report template, development of standardized research report feedback, creation and adoption of an OEM review panel terms of reference, and development of an online OEM technical review panel management tool.

Support for Other Related FAA Projects

Due to UDRI's fuel testing capabilities, the ASCENT Project 031 team has supported jet fuel testing for other related FAA projects including fuel samples received from Gulfstream and Pratt & Whitney. Similar to our support for the Boeing EcoDemonstrator program (ca. 2023), our team provided sample analysis to monitor fuel composition and properties during fuel movements in testing campaigns involving synthetic jet fuels or SBCs. Fuel samples have included two HEFA-

SPKs, two Jet A fuels, and blends of HEFA-SPK + Jet A (for a total of 13 fuel samples). Measurements have included, but were not limited to, mono-aromatics, di-aromatics, total aromatics, smoke point, naphthalenes, hydrogen content, gross heat of combustion, net heat of combustion, total sulfur, total nitrogen, flashpoint, density, viscosity, and vapor pressure.

Publications

Written reports

Testing Method of Lubricants, Liquid Fuels, and Related Products: 7508.0—Method for Detailed Hydrocarbon Analysis of Middle Distillate Fuels by Two-Dimensional Gas Chromatography, Fed.-Std.-791F (2024). https://assist.dla.mil

UDRI. (2018). *Flow modulation GCxGC for Hydrocarbon Type Analysis of Conventional and Alternative Aviation Fuels: UDRI Method FC-M-101.* University of Dayton Research Institute (UDRI), Dayton, Ohio, Report No. UDR-TR-2018-40.

UDRI. (2018). *Identification and Quantification of Polar Species in Conventional and Alternative Aviation Fuel Using SPE-GCxGC: UDRI Method FC-M-102*. University of Dayton Research Institute (UDRI), Dayton, Ohio, Report No. UDR-TR-2018-41.

UDRI. (2021). *Reverse Phase Thermal Modulation GCxGC for Hydrocarbon Type Analysis of Conventional and Alternative Aviation Fuels: UDRI Method FC-M-106*. University of Dayton Research Institute (UDRI), Dayton, Ohio,

UDRI. (2023). *UDRI Method FC-M-107: Trace Elemental Determination in Jet Fuel via ICP-MS*. Dayton Research Institute (UDRI), Dayton, Ohio, Report No. UDR-TR-2023-117.

Recent Posters & Presentations

Arts, A. M., Landsaw, A., West, Z. J. (2024, August 20). *Determination of Trace Metals in Aviation Turbine Fuel via ICP-MS* [Poster presentation]. American Chemical Society Fall 2024, Denver, Colorado.

Arts, A. M., Landsaw, A., West, Z. J. (2024, September 8-12). *Determination of Trace Metals in Aviation Turbine Fuel via ICP-MS* [Poster presentation]. 18th International Conference on Stability, Handling and Use of Liquid Fuels, Louisville, Kentucky.

West, Z., Zabarnick, S. (2024, March 19-20). *FAA ASCENT Center of Excellence D4054 Clearinghouse Update* [Conference presentation]. U.K. Ministry of Defense (MoD) Aviation Fuels Conference Meeting, Bristol, United Kingdom.

West, Z. (2024, April 29-May 2). *D4054 Clearinghouse* [Meeting presentation]. 2024 CRC Aviation Committee Meeting, Alexandria, Virginia.

Outreach Efforts

Presentations on ASCENT Project 031 activities were given at the April 2024 and October 2024 ASCENT meetings. Meetings were held with the OEM team, FAA, fuel producers, and other attendees at numerous virtual FAA/OEM meetings (generally two meetings per month). Our team have also met with multiple candidate-fuel producers, including OMV, CSIR-IIP, Revo, ExxonMobil, Chevron, British Petroleum, Vertimass, Virent®/MPC, Captis Aire, Visolis, CleanJoule,® and UPM.

Awards

None.

Student Involvement

An undergraduate student, Taylor Nicely, assisted with the analysis of FC-M-102 (polars quantification). An undergraduate student, CJ Nesbit, assisted with ASTM D2887 (SimDis) analysis.

Plans for Next Period

- Continue coordination of the OEM committee reviews.
- Hold both in-person and virtual OEM committee meetings.

Project 033 Alternative Fuels Test Database Library

University of Illinois at Urbana-Champaign

Project Lead Investigator

Tonghun Lee
Professor
Mechanical Science and Engineering
University of Illinois at Urbana-Champaign (UIUC)
1206 W. Green St.
Urbana, IL 61801
517-290-8005
tonghun@illinois.edu

University Participants

University of Illinois at Urbana-Champaign

- P.I.: Tonghun Lee, Professor
- FAA Award Number: 13-C-AJFE-UI-052
- Period of Performance: October 1, 2023, to September 30, 2024
- Tasks:
  1. Online database development
  2. Chemical kinetic mechanism development

Project Funding Level

FAA funding level: $150,000
Cost-sharing: Software license support from Reaction Design (ANSYS)

Investigation Team

Tonghun Lee (P.I.), All Tasks
Audrey Godsell (Graduate Student), All Tasks

Project Overview

This study continues development of a data library (Alternative Jet Fuels Test Database [AJFTD]) with two main functions, to (1) serve as a comprehensive repository of conventional and sustainable aviation fuel (SAF) test data for the commercial aviation sector and (2) provide fuel analysis techniques applicable to the rapid assessment and prescreening of novel SAFs. Currently, the repository comprises over 24,000 fuel samples and their respective test data, available for download to approved users of the project website. Figure 1 shows the main database web portal, currently housed at the University of Illinois at Urbana-Champaign (https://altjetfuels.illinois.edu). Database data include results from national laboratories, research efforts, airports, and other sources. In 2020, all compiled database data were converted to a new nonstructured query language (NoSQL) format by using a JavaScript® object notation (JSON) schema. This nonrelational structure allows the data to be analyzed using a variety of computational codes.

The catalog of data currently available in the database is primarily assembled from four separate sources. Fuels with POSF (Air Force Research Laboratory fuel database code) number designations were added from the internal database maintained by the Air Force Research Laboratory at Wright Patterson Air Force Base. The second dataset was obtained from Petroleum Quality Information System reports of the Naval Air Systems Command and corresponds to a compilation of fuel data primarily geared for government use. The third set was provided by Metron Aviation, consisting of fuel properties

® JavaScript is a registered trademark of Oracle America, Inc., Redwood Shores, California.

from samples collected at airports through a previous ASCENT project. The dataset resulting from this study has proven valuable by showing the landscape of fuels currently used in commercial aviation and will guide our future efforts focused on capturing this type of data in real time. The final dataset was obtained from the National Jet Fuel Combustion Program within ASCENT.

Though the database already contains a uniquely large collection of publicly available jet fuel data, data collection efforts are ongoing. Data collection is continuing to be pursued both domestically, focusing on airport data, and internationally, focusing on European sustainable aviation programs. The database will document SAF development and usage trends globally to increase our understanding of global fuel infrastructure and variability. Multiple tools for fuel analysis have been implemented on the project website over the years to aid researchers in understanding SAFs. Machine learning techniques for fuel property analysis have been developed in the past. More recently, a graphical interface for assessing fuel two-dimensional gas chromatography (GCxGC) composition information was added to the website. Analysis efforts now encompass the determination of suitable surrogate fuels to model novel SAFs and the development of chemical kinetic models to predict behavior of SAFs in combustion regimes.

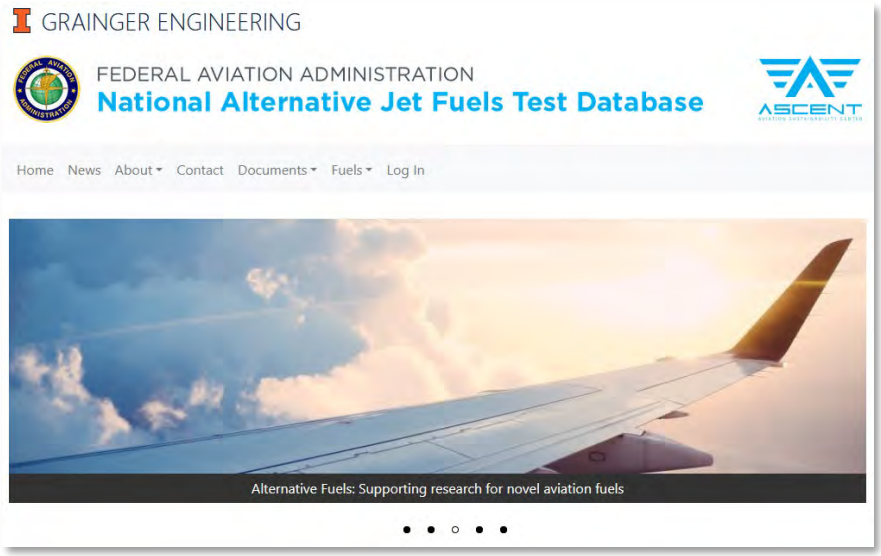

Figure 1. Alternative Jet Fuels Test Database (AJFTD) main webpage (altjetfuels.illinois.edu).

The current goals for the website include:

- Strengthening connections with domestic airports for ongoing real-time data sharing.
- Initiating data sharing with international programs such as ALIGHT and NewJET.
- Developing a common data schema and storage protocols with the World Fuel Survey.
- Developing and refining a methodology for chemical kinetics development based on website data.

Task 1 focuses on data collection and website development efforts, while Task 2 elaborates on the development of analysis techniques for eventual inclusion on the project website.

Task 1 – Online Database Development

University of Illinois at Urbana-Champaign

Objectives

The main objective of this task was to expand and improve the database and its website. The current AJFTD is the second generation of the project website, and new capabilities and improvements are consistently being added. Bugs are fixed as they are discovered, and improvements to the user interface and ease of data access are constant considerations. Data

acquisition efforts continue to seek new data for inclusion on the database. The main Task 1 objectives are summarized as follows:

- Upgrade user interface to aid in the access of fuel data.
- Debug interface where needed.
- Establish fuel data sharing with target domestic airports.
- Forge connections with European programs such as ALIGHT and NewJET.

Research Approach

Website Upkeep

The usability of the database is important to aid users in finding the fuel information they need to conduct impactful research. Likewise, it is important for the website administrators to have the tools they need to improve the experience for website users. To this end, new admin functionalities were added this year.

- **User search feature.** Historically, administrators have been able to search the registered users of the AJFTD. New filters were added, allowing administrators to search by the user's role type (regular or administrator). The quality of the search interface was improved to save time loading the page.
- **Notification settings.** Some administrators receive email notifications when new users request access to the database or when users submit feedback on the website. After improvements this year, administrators can choose whether to receive either of these types of notifications and can remove the permissions of old administrators. In addition, an automated email is sent to users when they request database access. Administrators are now able to edit the content of this email, allowing changes to be easily made as the database evolves.

New administrator functions will continue to be developed, allowing administrators more power to customize website features for the benefit of users.

Website Upgrades

Creating the best user interface for such a large, searchable collection of data is no trivial task, and improvements are constantly being made. This year, upgrades were made to GCxGC data viewing and exporting. For the fuels which contain GCxGC information, expandable tables of the composition data were added and improved on both the fuel viewing and fuel downloading pages. Users can export fuel data into a tab-separated format; this GCxGC data was previously organized in a confusing and difficult-to-parse manner. Improvements this year spread out the GCxGC data in the download file, allowing for the data to more easily be understood and processed.

In addition, a large effort was undertaken to improve the fuels search page. The main fuels search page now displays only the first ten results by default, preventing long load times on the page when many fuels fit the search criteria. Users can click through the pages of results or specify a page number to jump to and can change the number of fuel results per page. Even without entering search criteria, this page architecture appears, allowing users to see the total number of searchable fuel samples available on the database. When search criteria are entered, users can see both the number of results and number of pages of results, as shown in Figure 2.

The old search filters from the previous interface have been moved to the left side of the screen as seen in Figure 2. The way these search boxes function is different from before. Now, when the user clicks inside the box, a dropdown of available search terms appears. Clicking any single term will cause it to appear within the search box next to an "x" which allows the user to easily remove the search term. Multiple search terms can be added to the box, or the user can select the "All" search term, which includes all search terms for the selected search box. Users still have the option to enter their own search string in the "Search by Fuel Name or Description" box at the top of the search boxes (see Figure 2). To initiate any search, the blue "Search" button must be clicked, so the page does not reload in between entering each search criterium. All search features can be cleared at once using the blue "Clear All Filters" button.

Users still have two actions for each individual fuel result. A fuel can be added to a comparison by clicking the blue plus symbol at the right of the fuel entry, or it can be viewed directly by clicking on the blue eye icon. Previously, adding fuels to a comparison popped up a list of the fuels added at the very bottom of the results page. The location of the comparison has been modified to be at the top of the page, under the "Search Fuels" title at the top left (see Figure 2), allowing users to easily see the fuels already in the comparison without scrolling through all the search results. New comparison functionality has also been added; users can now directly view individual fuels from the comparison register, as shown in Figure 3. To view fuels together, users click the "Compare Selected" text at the bottom of the comparison box.

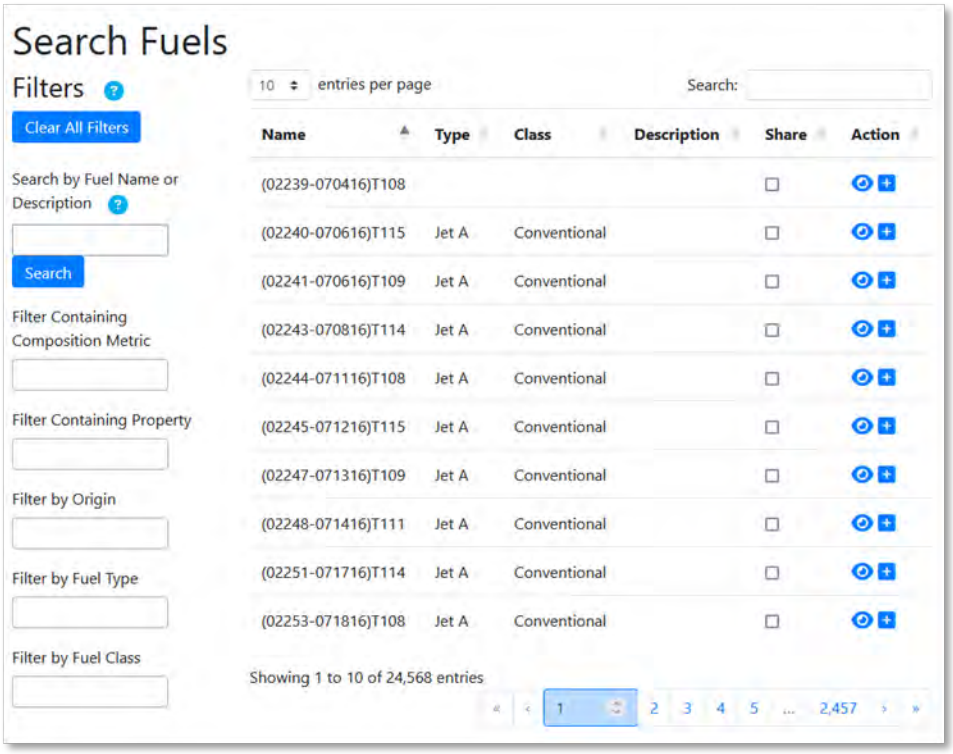

Figure 2. Upgraded fuels search page with added functionality.

The individual and comparison fuel viewing pages were simplified, combining the viewing and exporting functionalities into a single location. Though not shown here, these pages contain brand new search boxes which emulate those on the main fuel search page. Users can select from fuel properties and composition data of interest and view only the data and graphs they are interested in. Likewise, the export functionality now only exports selected data instead of defaulting to all data.

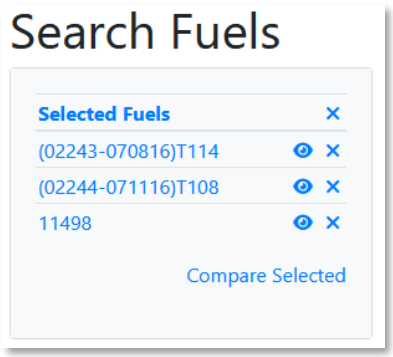

Figure 3. New compare feature to easily add or remove fuels from a comparison.

Despite these improvements to the appearance and usability of the search feature, new methods of improving this and other features on the website are still being developed. Upgrades are key to keeping the website relevant and its data accessible and useful for its broadening range of users.

Airport Data Collection
The AJFTD constantly seeks new data for collection to meet the project's goals of documenting trends in jet fuel usage over time and regionally. In the past, 11 different domestic airports have provided fuel data to the database through a connection with Metron Aviation. These airports are indicated by black squares and their airport code in Figure 4. In the years since, our team has sought to establish robust connections with a few key airports in the United States to set up a foundation for real-time data sharing. The targeted airports are the Chicago O'Hare International Airport (ORD), Seattle-Tacoma International Airport (SEA), San Francisco International Airport (SFO), Daniel K. Inouye International Airport (HNL), and airports in the New York city region, which are governed by a common port authority. This year, data from the years 2021-2023 were received from SFO. Communication has been sent to the other airports, and some progress has been made in obtaining data from HNL. These efforts are ongoing and will continue in the next year.

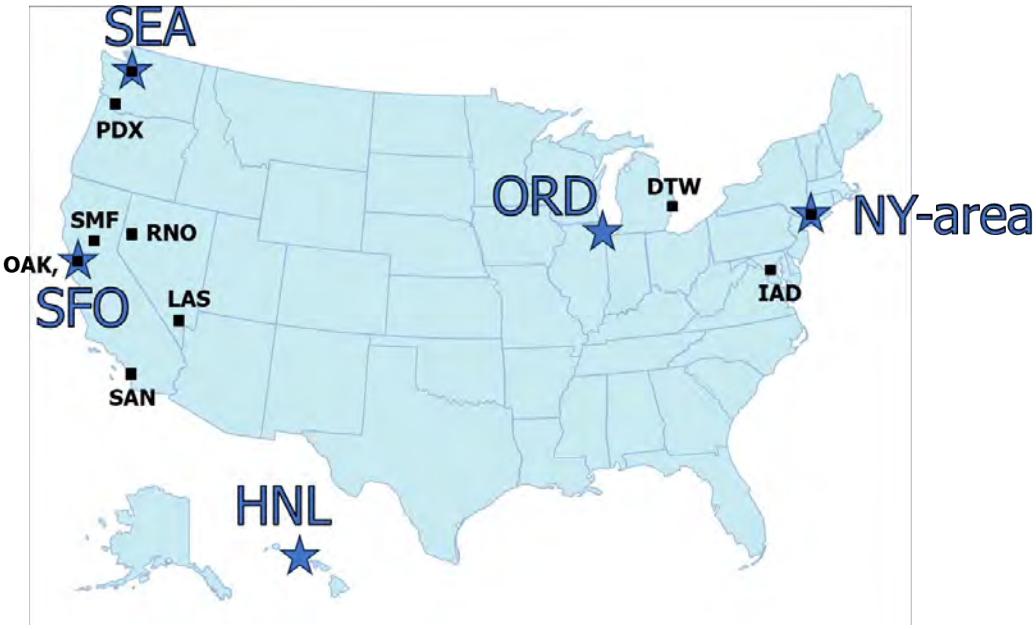

Figure 4. Target airports for data collection (in blue, indicated by stars) and historic database data suppliers (in black or blue, indicated by black boxes).

Research Program Data Collection
The AJFTD serves as a useful location for data storage. We aim to collaborate with other ASCENT projects geared towards data collection, such as the World Fuel Survey project, to establish a common data storage method. One day, these projects may all be integrated into one common database under the FAA, and coordinating data structure among the projects will help with this process.

In addition, connection with more European programs provides valuable breadth to the database. The AJFTD's past connection with JETSCREEN in Europe established a foundation for data sharing with international programs. A common data format, the JSON format, was adopted by both programs and real-time data sharing was set up. European programs ALIGHT and NewJET are our current targets for data collection overseas. This past year marked the first time a representative from the AJFTD attended the ECATS conference in Europe to share information about the database and initiate connections with representatives of ALIGHT and NewJET.

Milestones

3 months

- Followed up with representatives at SEA
- Added new administrator functionality to the AJFTD

6 months

- Presented updates at the Spring SAF ASCENT meeting
- Reached out to SAF developers requesting data
- Begun search interface overhaul
- Completed GCxGC viewing and download updates on the AJFTD
- Identified new target airports for data collection

9 months

- Established contact with HNL representatives
- Completed work on the new fuels search interface

12 months

- Presented updates at the Fall ASCENT meeting

Major Accomplishments

Connections with major airports, SFO and HNL, have been secured and are expected to lead to increased domestic airport data collection in the coming years. In addition, the overhaul of the fuels search interface represents a huge step toward improved usability of the database and continues the evolution of the generation II website into a robust fixture in the fuels research world. Completing large features such as the search interface lays the groundwork for the implementation of more complex analysis techniques in the future, which will help shape the future of SAF in commercial aviation.

Publications

None.

Outreach Efforts

In the last year, the database and data collection efforts have been shared in two different forums:

- **ECATS.** In late Fall of 2023, information about the database was presented at the ECATS conference in the Netherlands. This conference has a strong focus on sustainability in aviation. The title of the talk was “Sustainable Aviation”
- **ASCENT.** In both the Spring and Fall of 2024, project updates were shared at the ASCENT semiannual conferences. These presentations led to productive discussions regarding fuel data acquisition, database usage, and avenues for further outreach.

The database has been made accessible at https://altjetfuels.illinois.edu.

Awards

None.

Student Involvement

This project was primarily conducted by one graduate student (Audrey Godsell).

Plans for Next Period

In the next period, the focus on data collection from target airports will be emphasized. Samples from KHNL will mark the first fuel samples from Hawai‘i in the database. In addition, the team will travel to the New York port authority to meet with stakeholders and share our data collection vision. Meetings with ALIGHT and NewJET leaders are anticipated as well.

The improvement of the database website will continue with efforts such as:

- **User statistics.** The AJFTD historically has only saved data regarding each user’s last date signed in. Updates are planned which will track useful statistics, such as the most downloaded fuel files, the frequency with which the website is accessed, and a report on the most commonly downloaded files per-user.
- **Search interface refinement.** The new fuels search page will continue to be tested to assure the feature is free of bugs. Minor improvements will continue to be made.

Task 2 – Chemical Kinetic Mechanism Development

University of Illinois at Urbana-Champaign

Objectives

The main objective of this task was to investigate the rapid development of chemical kinetic mechanisms for aviation fuels for future integration into the AJFTD. Chemical kinetic mechanisms are critical to practical simulations involving combustion processes and play a fundamental role in certification efforts for new fuels. As new SAFs appear in the aviation industry worldwide, mechanisms will need to be developed to help with numerical simulations in terms of computational fluid dynamics or to support certification. However, creating and reducing detailed chemical kinetic mechanisms requires a substantial amount of computing power and time, often more than is practical for a new SAF that may or may not turn out to be a valuable investment. Thus, methods for rapidly developing reliable and efficient chemical kinetic mechanisms for SAFs are a key ingredient to greater SAF implementation across the world. This effort aims to explore methods for rapidly constraining mechanisms to this end. Specifically, the major goals are as follows:

- Outline and implement a methodology for the rapid development of mechanisms for new SAFs with limited experimental data.
- Perform an example mechanism optimization using the selected approach.
- Quantify uncertainties and effectiveness of the constraining approach.

Research Approach

Methodology

Fuel producers creating new SAFs are likely to produce very small fuel volumes. Scaling up fuel production to the quantities needed for commercial aviation is a costly endeavor, especially if there is no guarantee a new SAF will be approved and certified for use on existing aircraft. Combustion models for new SAFs are necessary as a prescreening tool to determine if a SAF will meet FAA requirements, providing valuable insight to fuel producers looking at whether to invest in production of a certain SAF. These models must be accurate in predicting SAF combustion behavior and should be created with as little dependence on experimental data as possible in accordance with the limited fuel volumes available. Detailed fuel composition information can be determined in a GCxGC apparatus with small fuel volumes; thus, this GCxGC data forms the basis of the mechanism determination approach as discussed.

The methodology for mechanism determination outlined for 2024 is summarized in Figure 5. GCxGC data available on the AJFTD is used to determine an appropriate surrogate to model a SAF of interest. Using established general mechanisms, the breakdown of the surrogate in various combustion environments is simulated. These simulation results are translated into the Hybrid Chemistry (HyChem)[1] mechanism structure, resulting in the stoichiometric coefficients within a set of reactions which govern the initial breakdown of the chosen SAF. The rates of these breakdown reactions are determined from the Hybrid Response-Surface Networks with Stochastic Gradient Descent Ensemble (HRSN-SGDE) approach developed earlier at UIUC. Once reaction stoichiometric coefficients and reaction rates are determined, the new model is constrained towards experimental data to determine which sets of experiments are most critical in rapidly developing mechanisms for new SAFs.

[1] HyChem is an approach to modeling the combustion chemistry of real liquid fuels. The approach takes advantage of the key physics underlying the high-temperature combustion of large hydrocarbon fuels. The approach combines experimentally constrained, lumped reaction steps for fuel pyrolysis and oxidative pyrolysis with detailed reaction model for the pyrolysis and oxidation of the fuel pyrolysis products (Wang et al., 2018).

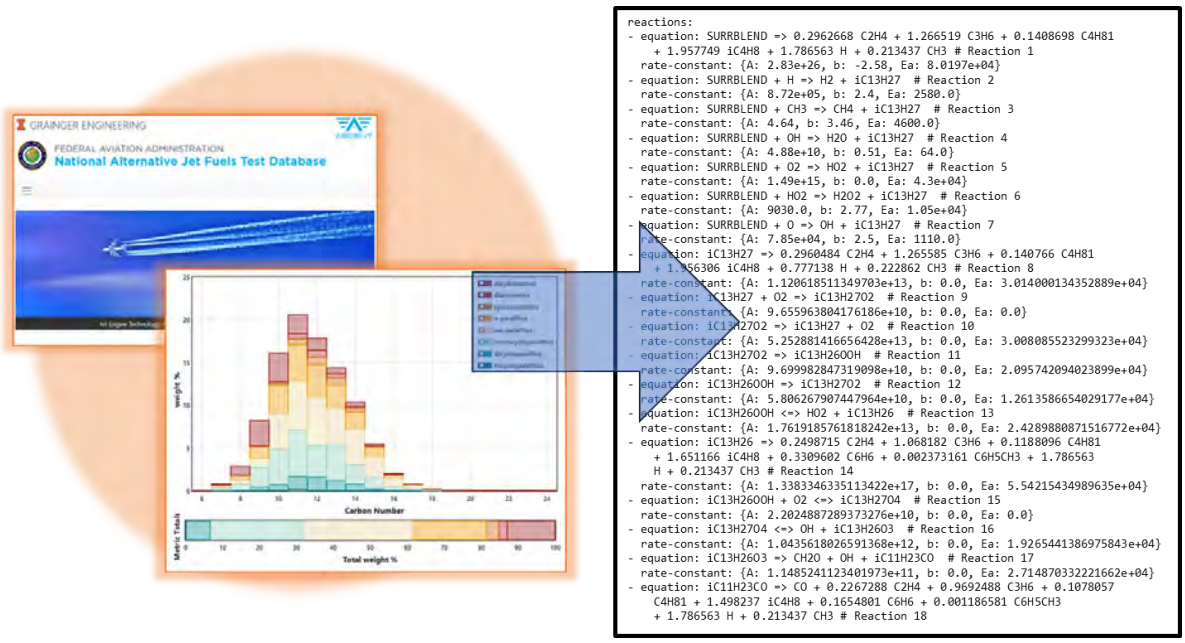

Figure 5. General kinetics approach: transforming AJFTD GCxGC data into a mechanism.

Preliminary Implementation

The feasibility of this method was tested this year by creating a mechanism for a SAF. An alcohol-to-jet (ATJ) fuel manufactured by Gevo® with POSF 11498 was chosen due to the availability of experimental data for this fuel in the literature. In addition, GCxGC data for this fuel was already available on the AJFTD, as seen in Figure 6. The first piece of the mechanism determination methodology involves finding an appropriate surrogate for the fuel of interest. However, the implementation of this surrogate optimization approach was outside the scope of the current methodology; thus, an appropriate surrogate for POSF 11498 was chosen instead based on observation of the fuel's GCxGC diagram. The Gevo® ATJ is a unique fuel comprised mainly of two iso-alkane species: iso-dodecane and iso-cetane. A simple surrogate of a proportional blend of these two components was chosen.

® Gevo is a registered trademark of Gevo, Inc., Englewood, Colorado.

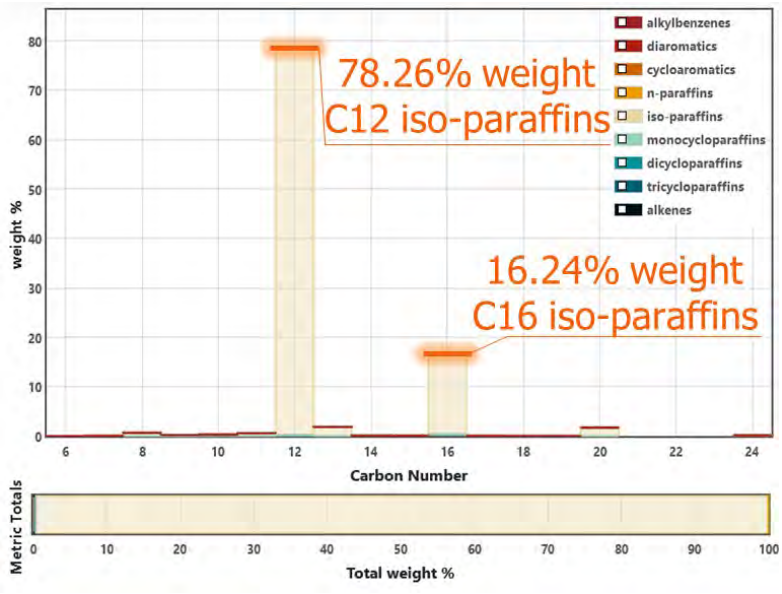

Figure 6. POSF 11498 GCxGC diagram from the AJFTD, with two major constituents labelled.

A HyChem mechanism structure was adopted as a basis for the mechanism determination approach. In this structure, a set of less than 20 reactions describe the breakdown of a "lumped" fuel molecule–representative of the fuel of interest–into smaller hydrocarbon products, or pyrolysis products. From here, a large, descriptive model applicable to any jet fuel takes the reins. For HyChem, this large model is the USC-II[2] mechanism.

The creators of HyChem postulated that most jet fuels have the same key pyrolysis products. Complex jet fuels will break down into many different hydrocarbons, but of these, only about eight smaller hydrocarbon species will be strongly present and will govern the behavior of the post-pyrolysis species mixture. Then, for any new SAF of interest, a researcher need only determine which of these key products are produced from the pyrolysis of the SAF, and what the ratios of the products are to one another. For POSF 11498, the creators of HyChem determined these pyrolysis products by conducting extensive plug flow reactor and shock tube experiments and directly measuring or calculating the concentrations of the products. Here, the goal is to avoid using the high fuel volumes and long experimentation times necessary to conduct these tests. Instead, the plug flow reactor and shock tube experiments were simulated as closely as possible using Cantera[3] simulations. Cantera simulation inputs were the previously-decided-upon surrogate blend for POSF 11498 in addition to an existing general mechanism which included the species iso-dodecane and iso-cetane.

The Cantera simulation results for the POSF 11498 surrogate were used to determine which of the key pyrolysis products were represented and their ratios to one another. This information fed into the mechanism structure in the form of the stoichiometric coefficients of the 18 fuel-specific reactions governing the high- and low-temperature breakdown of the lumped fuel molecule. At this point, the HyChem POSF 11498 mechanism had been modified only in terms of stoichiometric coefficients in the reactions, and not in terms of the reactions' rates. Figure 7 shows in solid blue the original HyChem model against experimental shock tube ignition delay times for POSF 11498. The dashed pink line represents the modified model, with modified stoichiometric coefficients based on the simulation results. The two mechanisms behave similarly, despite the differences in their derivation.

[2] The USC II mechanism was developed at the University of Southern California by Professor Hai Wang. This mechanism aims at representing a wide variety of combustion scenarios.
[3] Cantera is an open-source suite of tools for problems involving chemical kinetics, thermodynamics, and transport processes. Cantera is a sponsored project of NumFOCUS®, a 501(c) nonprofit charity in the United States. NumFOCUS is a registered trademark of NumFOCUS, Inc., Austin, Texas.

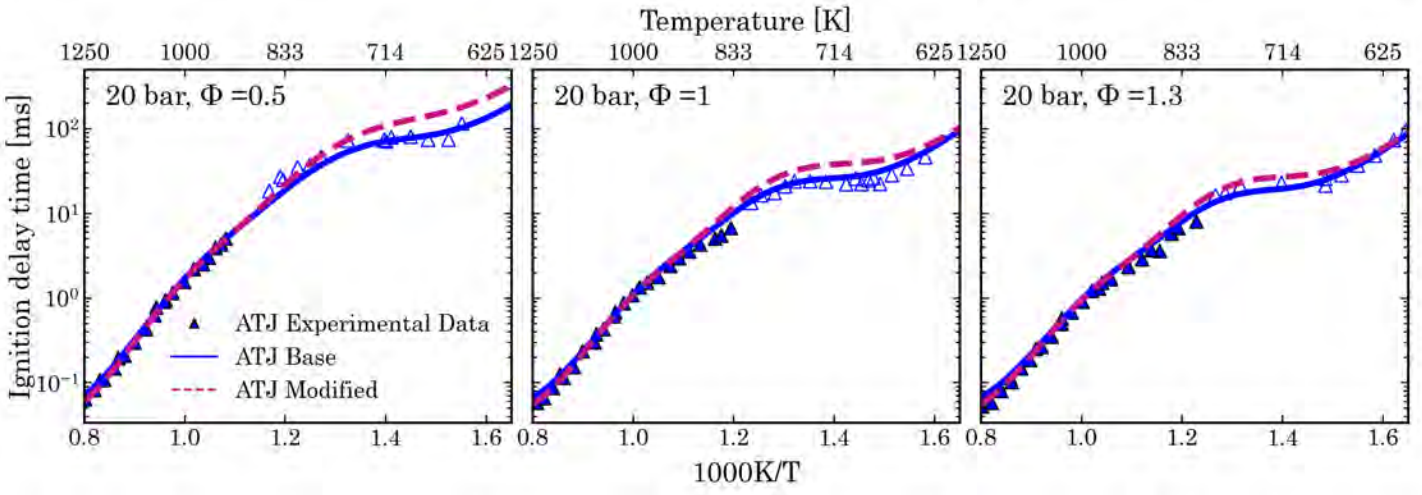

Figure 7. Comparison of the HyChem ATJ model with the modified model.

Next, the reaction rates of the 18 fuel breakdown reactions were determined using the HRSN-SGDE approach. This approach has been described in more detail in past reports and publications by UIUC (Wiersema, Oh, Kim, Godsell, & Lee, 2024; Oh et al., 2023; Wiersema, Kim, Mayhew, Temme, Kweon, & Lee, 2024). Essentially, the HRSN-SGDE approach is a machine learning-based approach which takes in an input of a mechanism to modify and a set of experimental data. In the context of this report, shock tube ignition delay data were used. The machine learning model is trained, creating a response surface which can rapidly estimate ignition delay measurements instead of calculating them each time from a set of input conditions. Once the model is trained, it can very quickly output sets of reaction rate coefficients which would satisfy the input ignition delay data.

Using the HRSN-SGDE approach, the response surface was used to generate 1,000 different models, each with the same stoichiometric coefficients calculated from the Cantera simulations, but with 1,000 unique sets of reaction rate parameters. The distribution of these 1,000 models is plotted in Figure 8 as pink lines alongside experimental ignition delay data. Despite the differences in reaction rate parameters, all the models are able to predict ignition delay reasonably well. This is a very unconstrained problem with many uncertainties. In order to find the best mechanism to help SAF producers, the highest-performing model must be determined, which necessitates narrowing in on the best set of reaction rate parameters. One way to further constrain the problem would be to conduct more experiments with the fuel; however, this would require greater fuel volumes than the SAF creators may be able to produce. Some experiments may be more valuable to perform than others, or perhaps some individual species measurements alongside ignition delay would help constrain the best model with limited fuel volumes. This methodology will be further expanded in the next research period to analyze this problem.

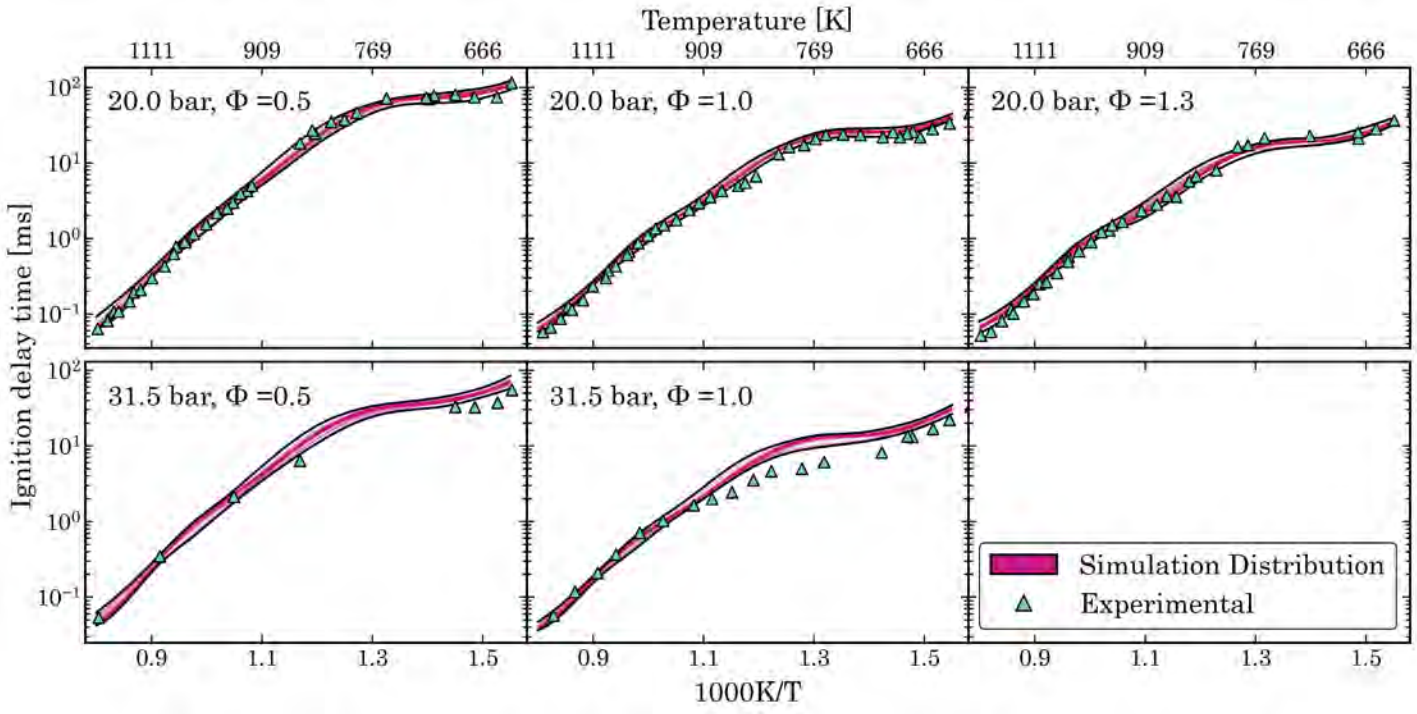

Figure 8. Distribution of models generated for POSF 11498 using the HRSN-SGDE approach.

Milestone

3 months

- Created an outline of methodology

6 months

- Selected a fuel of interest and identify existing experimental data

9 months

- Identified an appropriate existing model for running surrogate simulations
- Conducted surrogate simulations to emulate original HyChem methodology
- Estimated reaction stoichiometric coefficients for fuel breakdown reactions

12 months

- Generated a set of 1,000 models for POSF 11498
- Begun analysis of the initial results

Major Accomplishments

Over the past year, multiple publications have been derived from this work, including peer-reviewed publications.
A repeatable and significant methodology for rapid development of chemical kinetic models based on limited experimental data has been outlined and tested on a SAF. Robust response surface models have been created for POSF 11498 which can be analyzed to quantify the uncertainties in mechanism determination in future work. This methodology is applicable to other SAFs, and much is still to be learned.

Publications

Peer-Reviewed Journal Publications

Oh, J., Wiersema, P., Kim, K., Mayhew, E., Temme, J., Kweon, C., & Lee, T. (2023). Fast uncertainty reduction of chemical kinetic models with complex spaces using hybrid response surface networks. *Combustion and Flame, 254*, 112772.

Wiersema, P., Oh, J., Kim, K., Godsell, A., & Lee, T. (2024). Analysis of constraining a chemical kinetic mechanism using hybrid response surface networks. *Proceedings of the Combustion Institute, 40*, 105522.

Published Conference Proceedings

Wiersema, P., Kim, K., Mayhew, E., Temme, J., Kweon, C., & Lee, T. (2024, Jan 8-12). Development of a gasoline and jet fuel blend kinetic mechanism using hybrid response surface networks. *Proceedings of the 2024 AIAA Science and Technology Forum and Exposition, 0176*.

Outreach Efforts

In the last year, this mechanism development approach and analysis have been shared in two different forums:

- **The Combustion Symposium.** The paper titled "Analysis of constraining a chemical kinetic mechanism using hybrid response surface networks" was presented at the 40th International Symposium on Combustion in Milan, Italy in July 2024. It details the application of a similar constraining methodology, which was adapted to the ATJ study presented here.
- **ASCENT.** In Spring and Fall of 2024, project updates were shared at the ASCENT semiannual conferences. These presentations led to productive discussions regarding fuel data acquisition, database usage, and avenues for further outreach.

Awards

None.

Student Involvement

This project was primarily conducted by one graduate student (Audrey Godsell).

Plans for Next Period

In the next period, work will continue with the mechanism determination approach. Attention will be paid to the following areas:

- **POSF 11498 model analysis.** The HRSN-SGDE results for POSF 11498 will be analyzed and the uncertainties in the mechanisms will be quantified. Analysis here could lead to valuable results which could inform and tailor the methodology for its application to other SAFs.
- **Surrogate optimization.** Overall, the mechanism determination approach has been demonstrated with POSF 11498. However, aspects of the approach have yet to be completely designed or implemented. The surrogate optimization approach is one of these areas that requires attention in the near term. An approach for this surrogate optimization will be outlined and a preliminary implementation is expected to be created in the next period. The surrogate determination piece of the methodology is of special interest because of its potential to be integrated onto the AJFTD as a functionality for users. As this optimization technique is developed, the website architecture which could house such a feature will be considered.

Reference

Wang, H., Xu, R., Wang, K., Bowman, C., Hanson, R., Davidson, D., Brezinsky, K., & Egolfopoulos, F. N. (2018). A physics-based approach to modeling real-fuel combustion chemistry - I. Evidence from experiments, and thermodynamic, chemical kinetic and statistical considerations. Combustion and Flame, 193, 03.019

Project 037 CLEEN II System-level Assessment

Georgia Institute of Technology

Project Lead Investigator

Dimitri N. Mavris
Regents Professor
School of Aerospace Engineering
Georgia Institute of Technology
Mail Stop 0150
Atlanta, GA 30332-0150
(404) 894-1557
dimitri.mavris@ae.gatech.edu

University Participants

Georgia Institute of Technology

- P.I.s: Prof. Dimitri N. Mavris, Dr. Jimmy Tai
- FAA Award Number: 13-C-AJFE-GIT-055
- Period of Performance: October 1, 2023, to September 30, 2024
- Tasks:
  1. Update CLEEN fleet-benefit assessment assumptions
  2. Continuation of CLEEN III modeling of aircraft technologies and advanced configurations
  3. Emissions Assessment Options
  4. Assist FAA with technology modeling process
  5. Update CLEEN fleet-benefit assessment assumptions

Project Funding Level

The Federal Aviation Administration (FAA) provided $472,000 in funding to Georgia Institute of Technology (Georgia Tech). Georgia Tech has agreed to a total of $472,000 in matching funds. This total includes salaries for the project director and research engineers, as well as funding for computing, financial, and administrative support, including meeting arrangements. Georgia Tech has also agreed to provide tuition remission for students, paid from state funds.

Investigation Team

Prof. Dimitri N. Mavris, (P.I.)
Dr. Jimmy Tai, (co-P.I.)
Brennan Stewart, program management/noise modeling
Holger Pfaender, (technical lead), fleet modeling
Supporting Engineers: Carl Johnson and Zhimin Liu
Students: Joao De Azevedo, Krutik Desai, Mitchell Mu, Martina Tehubijuluw, Justin Purser, Todd Goehmann, Tabitha D'Amato, Dante Cyrus, George Blackwell, James Tsangarides, Kayley Lewis, Ballard Huey, Maxwell Home, Nathaniel Green, Flavius Penescu, Aniela Zaremski, Akash Shiri, Anna Conroy, and Vishwa Malaisamy

Project Overview

The objective of this research project is to support the FAA by independently modeling and assessing the technologies that are being developed under the Continuous Lower Energy, Emissions, and Noise (CLEEN) II and CLEEN III programs. This will involve direct coordination and data sharing with CLEEN-funded companies to accurately model the environmental benefits of these technologies at the vehicle and fleet levels.

Georgia Tech was previously selected to perform all system-level assessments for the CLEEN program under Partnership for Air Transportation Noise and Emission Reduction (PARTNER) Project 036 and ASCENT Project 010. As a result, Georgia Tech is in a unique position from both the technical and programmatic standpoints to continue the system-level assessments for CLEEN II. From a technical perspective, Georgia Tech has significantly enhanced the Environmental Design Space (EDS) over the past five years to incorporate advanced, adaptive, and operational technologies targeting fuel burn, noise, and emissions. EDS has been successfully applied to all CLEEN I contractor technologies including the following: General Electric (GE) open rotor, twin annular premixing swirler (TAPS) II combustor, Flight Management System (FMS)-Engine, and FMS-Airframe; Pratt & Whitney geared fan; Boeing adaptive trailing edge and ceramic matrix composite (CMC) nozzle; Honeywell hot section cooling and materials; and Rolls-Royce turbine cooling technologies. As of 2024, Georgia Tech can now state that all CLEEN II Technology modeling has been completed as well. Georgia Tech has also gained extensive experience in communicating system-level modeling requirements to industry engineers and translating the impacts to fleet-level fuel burn, noise, and emissions assessments. This broad technical knowledge base covering detailed aircraft and engine design, as well as high-level benefits assessments, places Georgia Tech in a unique position to assess CLEEN III technologies.

Because the ultimate goal of this work is to conduct fleet-level assessments for aircraft representative of future “in-service” systems, Georgia Tech will need to create system-level EDS models using a combination of both CLEEN II/III and other public domain N+1 and N+2 technologies. The outcomes of the technology and fleet assumptions-setting workshops conducted under ASCENT Project 010 are used for this effort. Non-CLEEN technologies for consideration, along with potential future fleet scenarios, will help to bound the impact of CLEEN II/III on future fleet fuel burn, emissions, and noise.

The FAA was planning to perform a portion of the EDS technology modeling work. Therefore, periodic (i.e., weekly) EDS training sessions were provided to the FAA during a part of the period of performance. This training provided the requisite skill set for using the EDS. In the prior year of this project, Georgia Tech continued modeling activities with the CLEEN III contractors. This modeling process included validation of underlying EDS models, information and data exchange necessary to model the individual technologies, and related EDS modeling activities. In addition, Georgia Tech has assisted the FAA with in-house EDS modeling. This process had increased the number of FAA personnel performing EDS system-level assessment modeling, but due to personnel changes on the FAA side, this effort was discontinued during this performance period.

Work conducted during this period of performance focused on completing vehicle- and fleet-level assessments for CLEEN II. The final technology modeling details for the outstanding CLEEN II technologies have been delivered to Georgia Tech during this performance period. The final vehicle noise assessments have been constructed and delivered to the FAA. Quantifying this impact will provide an understanding of the increased number of operations per day that CLEEN II technologies enable without worsening the surrounding community’s noise exposure. Although airports in the United States are not generally noise constrained, some European airports have limited capacity to meet noise constraints. Understanding the impact of technologies on the future United States fleet will be critical to quantifying the interaction between economic growth (i.e., increased flight operations at a given airport) and community noise impacts. To preserve contractor confidentiality, individual technology impacts on the vehicle airframe and engine will not be reported.

Next year’s work will focus on implementing CLEEN III technologies into EDS as test data becomes available, initializing the CLEEN III fleet-benefit assessment once a sufficient amount of technologies are available, continuing work on furthering emission assessments within EDS with a focus on nonvolatile particulate matter (nvPM) inclusion, and hosting the Spring 2025 CLEEN Consortium.

Milestones

The major milestones which were planned for this performance period and their planned due dates are listed below, (the major accomplishment section will discuss which were achieved):

Task No.	Milestone	Planned Due Date
1	Update CLEEN III Fleet-Benefit Assessment Assumptions	December 30, 2023
2	Continuation of CLEEN III Modeling of Technologies	September 30, 2024
3	Development of Alternative Emissions Assessment Options within EDS	September 30, 2024
5	Finalize CLEEN II Fleet Benefit Assessment	September 30, 2024

Major Accomplishments

- Completed airframe and engine modeling and calibrations for CLEEN III baseline vehicles.
- Updated the public technology set for CLEEN II.
- Included alternative nitrogen oxides (NOx) emission assessment options in EDS.
- Completed the remaining CLEEN II acoustic tech modeling.
- Completed the final CLEEN II fleet noise emission assessment.

Task 1 - Update CLEEN Fleet-benefit Assessment Assumptions

Georgia Institute of Technology

Objectives

During this period of performance, Georgia Tech finalized the project team and FAA agreed on a collection of updated fleet-benefit assessment conditions for incorporation in the preliminary assessments of the CLEEN III program.

Research Approach

The *Project 037 CLEEN II System-level Assessment* (Mavris et al., 2023) for the previous period of performance details the initial updates to the FLEET Assessment Assumption from CLEEN II. This period of performance focused on implementing assumption updates 4 and 7 from Mavris et al. (2023). The implementation process is detailed in the following sections.

Models developed and calibrated for updated 2018 best-in-class baseline vehicles:
Updates to the baseline vehicles were identified in Mavris et al. (2023) along with the classes of included vehicles which would best represent a 2018 best-in-class selection. These vehicles, compared to the CLEEN II baseline vehicles, are shown in Table 1. Airframe and engine modeling for these vehicles has been completed including calibration. Additional work will be performed in the next period to finalize NO_x and Acoustic Emission calibrations.

Table 1. CLEEN III baseline vehicle updates.

Vehicle Class	CLEEN I & II (2010 baseline)	CLEEN III (2018 baseline)
RJ (50-100 pax)	CRJ-900/CF34-8C5	-
SSA (101 – 150pax)	-	E190-E2/PW1922G * + LEAP1B-28 **
LSA (151 - 235 pax)	B737-800/CFM56-7B27	B737-8/LEAP1B-28 * + PW1127 **
STA (236 - 300 pax)	B767-300ER/CF6-80C2B5F	B787-8/GEnX-1B70/P2 *
LTA (301 - 400 pax)	B777-200ER/GE90-94B	B787-10/GEnX-1B76/P2 *
VLA (400+ pax)	B747-400ER/CF6-80C2B5F	B747-8/GEnX-2B67 * (New vehicles updated to B777x in 2025)

* EIS Dates: E190-E2 (2018), B737-8 (2017), B787-8 (2011), B787-10 (2018), B747-8 (2012)
** Notional system with alternative engine architecture

The procedure used to calibrate these vehicles' airframe and engine, was developed under the scope of Georgia Tech work on Project A82A. The procedure used to calibrate is described in detail in the Project A82A annual report. However, for a complete description of the work the ASCENT Project 037 team conducted during this performance period, a write up of the vehicle calibration procedure has been taken from Georgia Tech ASCENT Project 082A annual report *Project 082(A) Integrated Noise and CO2 Standard Setting Analysis* (Mavris et al., 2024).

The process for vehicle model calibration is nominally a two-stage process, starting with engine calibration followed by airframe calibration, matching with publicly available data for engine performance and geometry of the vehicle. The vehicle

calibration was conducted by the ASCENT Project 082A team, and the airframe calibration was conducted by the ASCENT Project 037 team.

The notional engine model is calibrated using publicly available data from the engine Type Certificate Data Sheet (TCDS) and the International Civil Aviation Organization (ICAO) engine emissions databank, *ICAO Aircraft Emissions Databank,* (ICAO 2021). The TCDS provides information on the engine's weight and geometry, while the ICAO databank, (ICAO 2021), supplies key performance values including thrust, fuel flow, emissions indices, overall pressure ratio (OPR), and bypass ratio (BPR) under sea level static (SLS) uninstalled standard day conditions. These data points form the basis for calibrating the model to reflect publicly reported engine performance and physical attributes. EDS integrates various modeling tools to simulate and evaluate engine performance, such as compressor map generation in CMPGEN,[1] flow path and weight modeling through WATE++,[2] and engine cycle analysis via Numerical Propulsion System Simulation (NPSS). These tools work in concert to model the engine's performance at multiple design points, including takeoff, hot day sea level static, top-of-climb, and cruise conditions.

The notional aircraft model is calibrated using publicly available data from the aircraft's Airport Planning Manual (APM). The geometric data, taken from three-dimensional-view published drawings, includes information on the control surfaces of the airplane. Various measurements of the airframe are taken, for example, the height of the tail, the chord length of the leading-edge slats, and many more. The payload-range diagram of the APM is used to determine a design mission for the notional aircraft model. These values are used in various calculations to be implemented in the Flight Optimization System (FLOPS) model. In EDS, FLOPS is executed immediately after the engine design loop has been completed and converged. The engine loop provides an engine deck, basic nacelle dimensions (i.e., length and diameter), and weight. Additionally, FLOPS requires aircraft geometry and mission details (i.e., design range, Mach numbers, altitudes, etc.). It also offers options for more detailed landing and takeoff data, along with performance constraints. FLOPS begins with an initial guess for gross weight (GW) and vehicle geometry, then estimates the weight of internal components like the fuselage, wings, and tail, and results in the estimation of the operating empty weight (OEW). The available fuel capacity is calculated by subtracting OEW and payload weight from the GW. Using this fuel capacity, FLOPS simulates the mission and determines the maximum achievable range.

Public technology set to be updated
The public technology set employed through CLEEN II will be audited for its appropriateness within the near-term to mid-term timelines considered in this study. In addition, the technologies will be reassessed against their expected entry-into-service dates, level of development effort, and evolutionary or aggressive scenario inclusion. Finally, the actual magnitudes of the impacts considered for each technology will be updated to reflect their most realistic values against the updated CLEEN III baseline vehicles.

These updates will be incorporated into a preliminary CLEEN III fleet benefit assessment in the coming period of performance.

Task 2 - Continuation of CLEEN III Modeling of Aircraft Technologies and Advanced Configurations

Georgia Institute of Technology

Objectives

To estimate the impact of CLEEN relevant technologies at the vehicle system-level, each of these technologies must be modeled regarding their impacts to aircraft fuel burn, noise, and emissions using EDS.

Research Approach

Georgia Tech was previously selected to perform all system-level assessments for the CLEEN program under ASCENT Project 010. Because the ultimate goal of this work is to conduct fleet-level assessments for aircraft representative of future "in-service" systems, Georgia Tech will need to create system-level EDS models using a combination of both CLEEN

[1] CMPGEN is a modeling tool used to compute off-design performance of fans, booster, and compressors.
[2] WATE++ is an object-oriented computer code for gas turbine engine weight analysis.

(Phases I, II, and III) and other public domain near-term and midterm Entry into Service (EIS) technologies. Vehicle system-level modeling for all relevant CLEEN technologies will be performed using EDS.

Table 2 presents an update on the vehicle system-level modeling effort regarding each of the CLEEN relevant technologies funded under Phase III of the program. Additionally, it should be noted that, as of the publication of Mavris et al. (2023), there were still outstanding CLEEN II technologies modeling efforts. All CLEEN II technologies models have since been completed and implemented in the CLEEN II final results described in Task 5.

Remaining Modeling Work (Scheduled during the next Performance Period)

- CLEEN III – Collins Large Cell Novel Core Exhaust
  - Georgia Tech has received initial data from Collins and begun implementing it in the system modeling environment.
  - System level modeling effort should be completed in 2025.
- CLEEN III - Delta/MDS/America's Phenix fan blade leading edge coating
  - System level modeling effort was kicked off with the contractor in early 2023.
  - Preliminary modeling has been completed, and Georgia Tech is awaiting data to refine model.
- CLEEN III – Safran Short Inlet
  - System level modeling effort was kicked off with the contractor in mid-2024.
  - Preliminary modeling is underway.
- CLEEN III – Boeing QLG/QHLD/Short Inlet/Intelligent Operations
  - System level modeling effort was kicked off with the contractor in mid-2024.
  - Preliminary modeling is underway.
  - System level modeling effort completion likely targeting completion in 2026.
- CLEEN III - GE MESTANG III, Advanced Brayton Cycle, and Hybrid Electric Integrated Generation
  - System level modeling effort will be kicked off with the contractor in early 2025.
- CLEEN III - Honeywell High Efficient Core technologies
  - System level modeling effort will be kicked off with the contractor in late 2025.
- CLEEN III - Pratt & Whitney Fan Module performance and acoustic technologies
  - System level modeling effort was kicked off with the contractor in mid-2024.
  - Preliminary modeling is underway.

Table 2. CLEEN III Technologies.

Contractor	Technology/Model Impact Area	Fuel Burn	NO_x	Noise	Percentage Complete
Boeing	Quiet Landing Gear			X	20%
	Quiet High Lift System			X	40%
	Advanced Inlet	X		X	20%
	Intelligent Operations	X		X	20%
Collins	Large Cell Novel Core Exhaust			X	50%
Delta/MDS/America's Phenix	Fan Leading Edge Protective Coating	X			20%
GE	MESTANG III	X			5%
	Open Fan	X		X	5%
	Advanced Thermal Management	X			5%
	Hybrid Electric Integrated Generation	X			5%
	Combustor Technology	X	X		5%
	Advanced Acoustics			X	5%
Honeywell	High Pressure Core	X	X	X	10%
	Highly Efficient Fan	X		X	10%
	Compact LPT	X			10%
Pratt and Whitney	Fan Noise Technologies			X	20%
	Fan Performance Technologies	X			40%
	Combustor – Swirlers			X	30%
	Combustor – Cooling Technologies	X			30%
	Combustor- Low Pattern Factor	X			30%
	Combustor – NO_x Reduction		X		20%
Rolls-Royce	Centrifugal Compressor	X			0%
Safran	Short Inlet			X	30%

Task 3 - Emissions Assessment Options

Georgia Institute of Technology

Objective

Georgia Tech has provided the NO_x emissions fleet benefit assessments for both of the first two phases of the CLEEN program. As the CLEEN program continues through Phase III, Georgia Tech will work on reevaluating the assessment approach used in delivering this NO_x emissions benefit to ensure that ASCENT Project 037 has the capability to be ready for any future shifts in NO_x emission metrics modeling.

Research Approach

To date, NO_x emitted in the landing and take-off (LTO) cycle has been exclusively considered as LTO emissions are maintained as an FAA CLEEN Program level metric by which to measure contractor technologies. However, there have been discussions among the community regarding if this will remain the most appropriate metric to express NO_x emissions. To ensure Georgia Tech maintains the capability to model any future standards for NO_x metrics, two additional emissions approaches will be developed for consideration in CLEEN III fleet benefit assessment result articulation: (1) terminal mission NO_x and (2) full mission NO_x. Terminal mission NO_x considers NO_x produced by aircraft below an altitude of 3,000 ft. This assessment approach, though a less common standard than LTO NO_x, considers installation effects, aircraft LTO trajectory, and actual engine operation in this window of the mission. Full mission NO_x considers NO_x produced by aircraft across the complete mission.

Full mission NO_x assessment was fairly straight forward to include in EDS. If NO_x emissions are included as part of the NPSS generated engine deck, then FLOPS includes an option to calculate the NO_x emissions along the full design and off design missions. Thus, inclusion of full mission NO_x simply requires slight modification from the CLEEN II approach, such that NO_x emissions are now included in the engine deck and the option in FLOPS to calculate full mission NO_x is enabled.

Terminal area NO_x assessment is not natively supported by FLOPS and requires new routines to be created in EDS. An additional lookup deck was created in EDS with high granularity relating landing and takeoff altitudes, Mach numbers, throttle settings to $EINO_x$ (the emission index of nitrous oxide) emissions. The detailed takeoff trajectory was extracted from FLOPS, since NO_x emissions are not calculated for each point in the detailed trajectory by FLOPS natively. Each trajectory point is fed into the lookup table to get an emission rate allowing for a segment NO_x emission to be calculated. The segment NO_x emissions are then integrated into a total NO_x emission for the operation.

Although Georgia Tech now has the capability to model alternative NO_x metrics, both Georgia Tech and the FAA agree that LTO NO_x will remain the standard for the CLEEN III program. However, Georgia Tech will continue to development EDS emission analysis capabilities which might become metrics of interest in future phases of the CLEEN program. Adding nvPM emission prediction capabilities will be the focus for the upcoming period of performance.

Task 4 - Assist FAA With Technology Modeling Process

Georgia Institute of Technology

Objective

Georgia Tech will provide the FAA with general EDS training and will offer guidance and feedback regarding the portion of CLEEN III technology portfolio to be modeled in-house at the FAA. This task will allocate Georgia Tech resources to coordinate with FAA on technology simulation tasks and assist the FAA with identifying appropriate programming hooks within EDS, suggesting verification and validation approaches for the technology, and providing any known, available public references on related developments.

Research Approach

During this performance period, Georgia Tech worked with the FAA from October 2023 through January 2024 on training for technology modeling in our EDS environment. However, it was decided in February 2024 that, due to personnel changes with the FAA, this task would be discontinued and Georgia Tech would take over modeling all of the CLEEN III portfolio and FAA will no longer attempt to model some of the CLEEN III technologies in house.

Task 5 - Update CLEEN Fleet-Benefit Assessment Assumptions

Georgia Institute of Technology

Objective

The objective of Task 5 is to evaluate the impact of CLEEN relevant technologies as they are propagated forward into the United States civil fleet of domestic and international departing aircraft, specifically the impact of CLEEN technologies on fleet-level noise, fuel burn, and NO_x emissions.

Research Approach

Vehicle system-level modeling for all relevant CLEEN II technologies will be performed using EDS. Fleet-benefit assessments for aircraft fleet fuel burn, NO_x, and noise through the year 2050 will be performed using the information delivered by the vehicle system-level modeling effort alongside fleet replacement matrices, technology integration scenarios, and projected aviation demand schedules.

CLEEN II Fleet Assumptions

CLEEN II FLEET Assumptions remain unchanged from Mavris et al. (2023).

Final Fuel Burn and NO_x Assessment

The procedure for the CLEEN II Fuel Burn and NO_x assessment remains unchanged from Mavris et al. (2023). The final results are restated in this report so that all CLEEN II Fleet benefits are reported in one complete package.

The final fleet fuel burn result for the estimated annual cost savings attributed to CLEEN I and CLEEN II, relative to the evolutionary scenario, is shown in Figure 1. In Figure 1, it is observed that CLEEN I and CLEEN II contribute a potential annual savings of 1.10 billion dollars and 4.21 billion dollars in 2050, with a combined potential impact of 5.31 billion dollars. This assumes a cost of fuel at $2 per gal and includes all carriers (domestic and foreign flag) flying domestic routes within the United States and international departures from the United States. Results for the estimated cumulative fuel burn savings attributed to CLEEN I and CLEEN II, relative to the evolutionary scenario, are shown in Figure 2. In Figure 2, it is observed that CLEEN I and CLEEN II contribute potential cumulative fuel burn savings of 11.6 and 39.6 billion gal by 2050, with a combined potential impact of 51.2 billion gal. This combined cumulative potential impact of 51.2 billion equates to approximately 500 million metric tonnes (Mt) less carbon dioxide (CO_2) emitted over the same period, which is equivalent to removing about 3.6 million cars from the road. Figure 3 and Figure 4 show these same benefits when only domestic carriers flying domestic routes within the United States and international departures from the United States are considered. Here, it can be seen that CLEEN I and CLEEN II contribute a potential annual savings of 0.90 billion dollars and 3.56 billion dollars, respectively, in 2050, with a combined potential impact of 4.46 billion dollars for domestic carriers. Additionally, it is shown that CLEEN I and CLEEN II contribute potential cumulative fuel burn savings of 9.70 and 33.2 billion gal by 2050, with a combined potential impact of 43.0 billion gal for domestic carriers. This combined cumulative potential impact of 43.0 billion equates to approximately 421 Mt less CO_2 emitted over the same period, which is equivalent to removing about 3.0 million cars from the road.

The amount of LTO NO_x emitted does not vary with the mission distance of the vehicle as the cycle is tied to specific uninstalled engine operation performance. Therefore, LTO NO_x emissions are considered by the Global and Regional Environmental Assessment Tradeoff, (GREAT), tool as a function of the number of operations, not the specific operating distances accomplished by each vehicle. The NO_x fleet assessment maintained the same set of assumptions as the fuel burn analysis, including identical fleet replacement matrices, demand forecast, technology integration scenarios, and scope (United States domestic + international departures) and includes all carriers, (domestic and foreign flag). Again, the impact of CLEEN I and CLEEN II technologies was evaluated by examining the difference between the AG scenario and the AG-C scenario. This result for the estimated annual LTO NO_x savings attributed to CLEEN I and CLEEN II, relative to the evolutionary scenario, is shown in Figure 5. In Figure 5, it can be seen that CLEEN I and CLEEN II potentially contribute an annual impact of 74.13 thousand metric tonnes (kt) and 91.5 kt of LTO NO_x potential savings in the year 2050, respectively, with a combined potential impact of 165.6 kt of LTO NO_x savings. The result for the estimated cumulative LTO NO_x savings attributed to CLEEN I and CLEEN II, relative to the evolutionary scenario, is shown in Figure 6. CLEEN I and CLEEN II potentially contribute cumulative savings of 1.35 and 1.50 Mt of LTO NO_x emissions in the year 2050, respectively. The potential cumulative impact of both phases of the CLEEN program technologies is estimated at 2.85 Mt of LTO NO_x by 2050, compared to the evolutionary scenario.

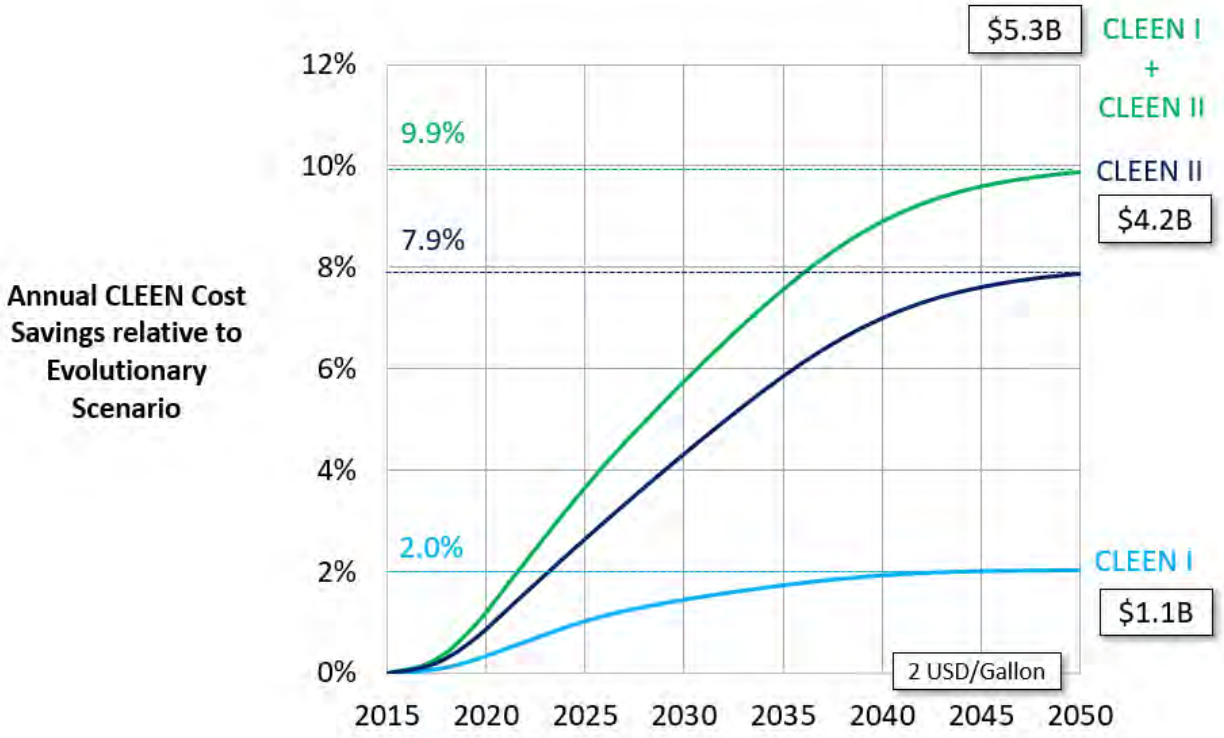

Figure 1. CLEEN technology annual cost savings from United States commercial and foreign flag carriers.

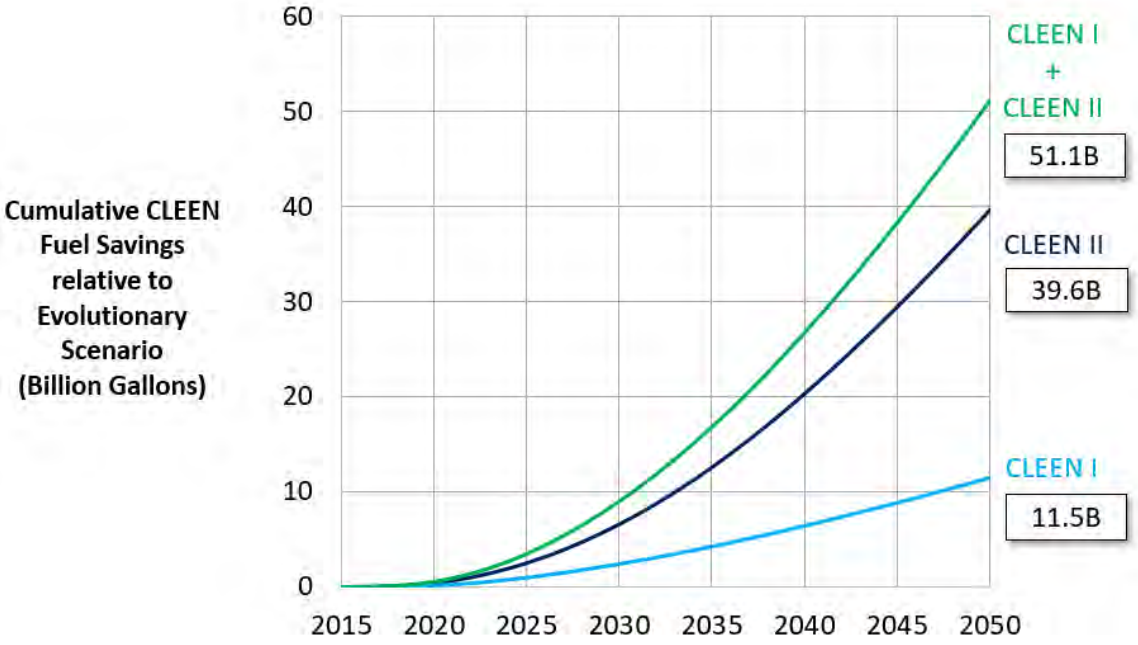

Figure 2. CLEEN technology cumulative fuel savings from United States commercial and foreign flag carriers.

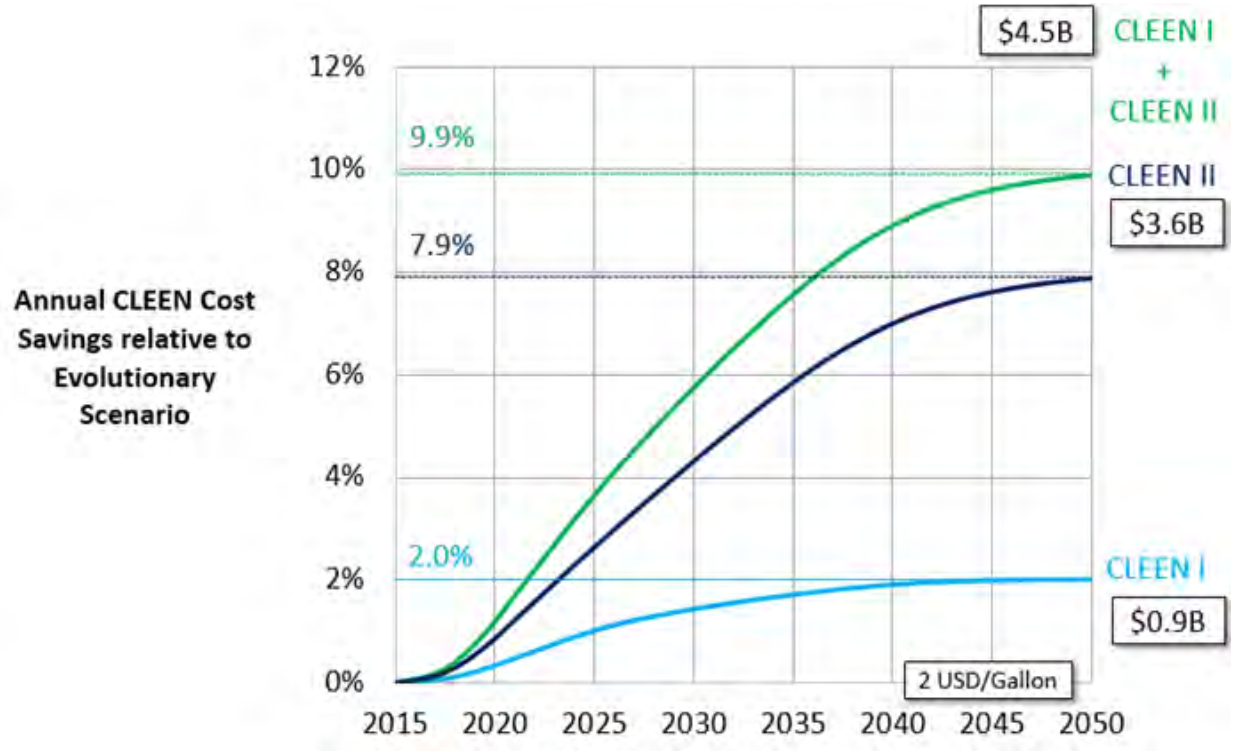

Figure 3. CLEEN technology annual cost savings from United States carriers only.

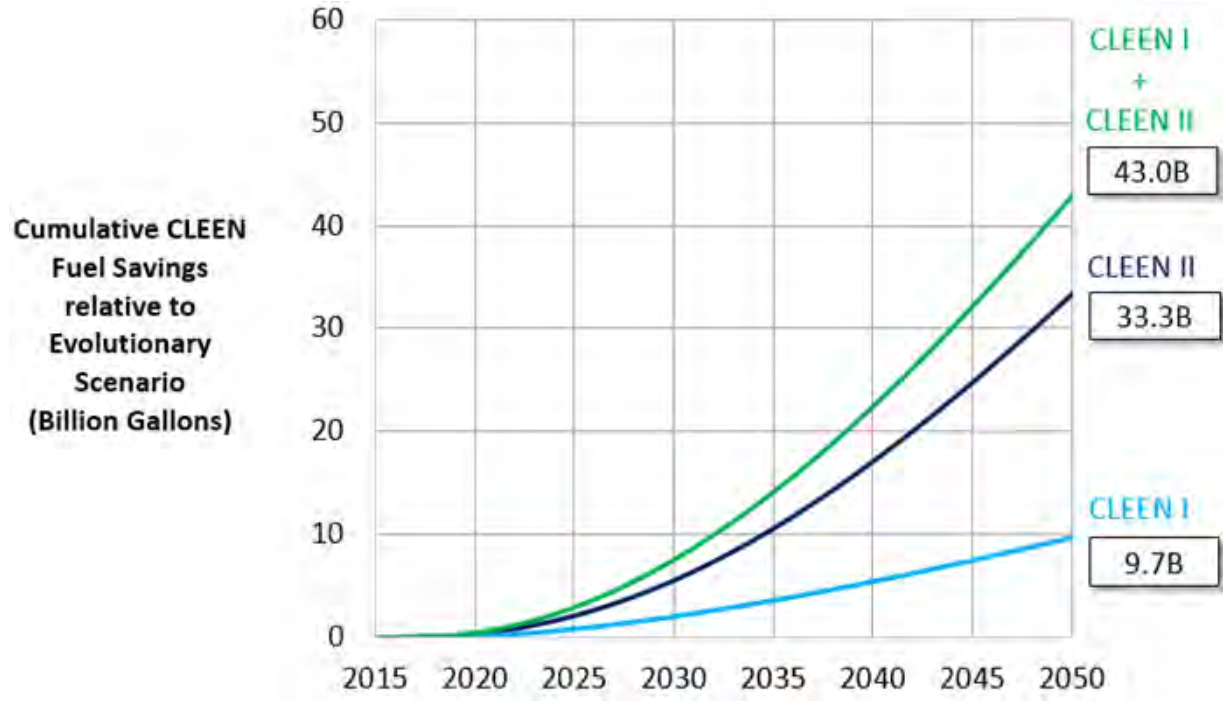

Figure 4. CLEEN technology cumulative fuel savings from United States carriers only.

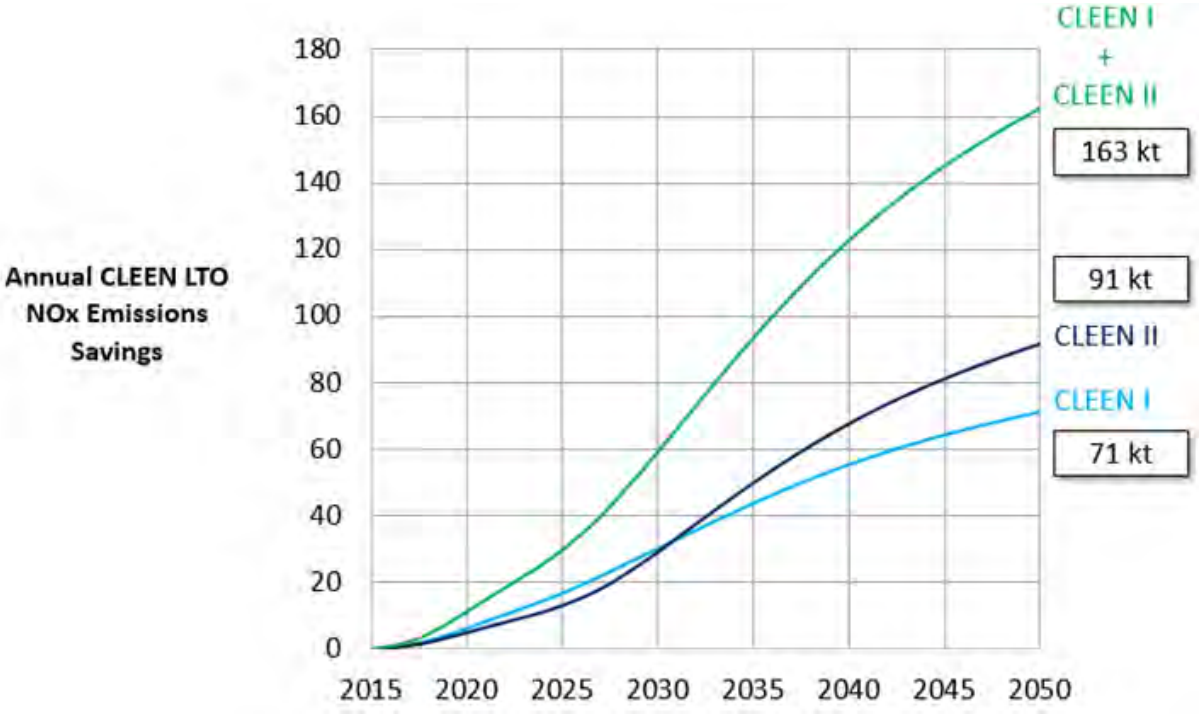

Figure 5. CLEEN technology annual NO_x savings.

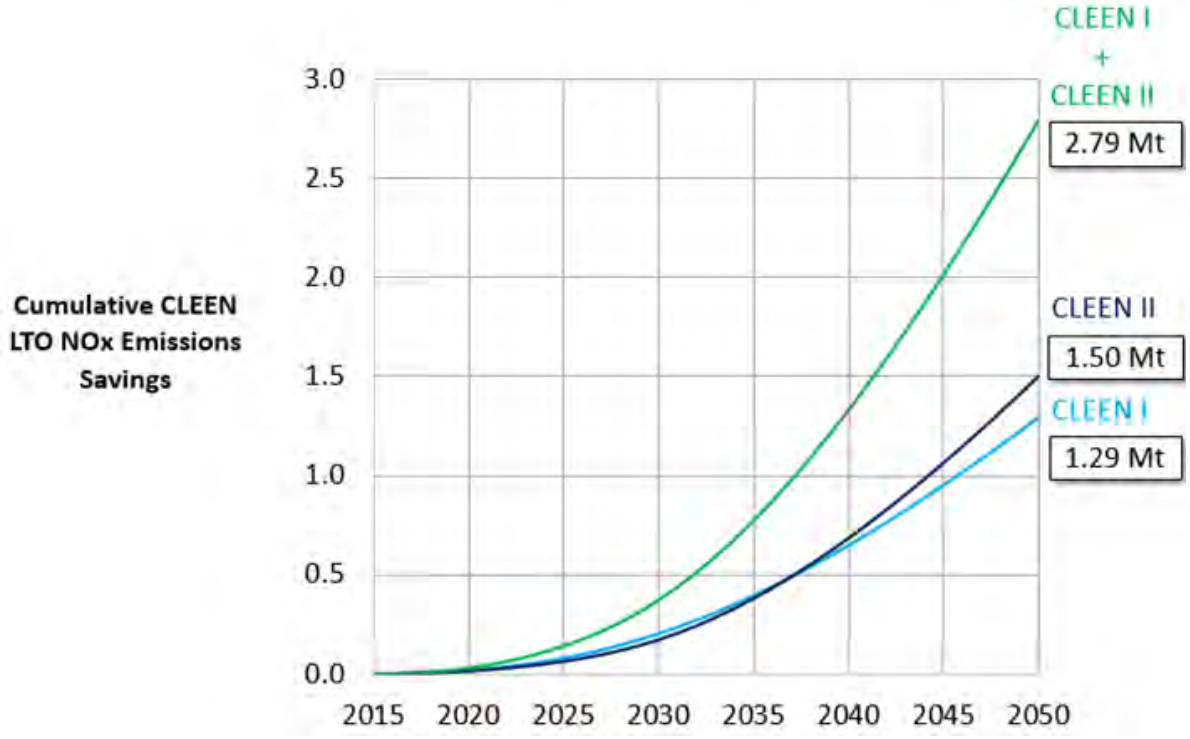

Figure 6. CLEEN technology cumulative LTO NO_x savings.

Final fleet-noise assessment

The following process for assessing the fleet-level noise emissions was described in Mavris et al. (2023) when reporting the preliminary fleet-noise assessment. The fleet-noise assessment has since been finalized; the process is unchanged since Mavris et al. (2023), but now all noise technologies are included along with one correction to a previously implemented technology.

Fleet-level noise emissions results were generated using GREAT in combination with the technology liner assumptions shown in Table 3, the remaining application technology assumptions shown in Table 4 of Mavris et al. (2023), and with the replacement assumptions defined in the fleet fuel burn and emissions studies. The Fan Noise Treatment Module (TREAT) liners serve as baseline technology cases and are evaluated as stock production liners using the Aircraft Noise Prediction Program's (ANOPP's) uncorrected TREAT module.

Table 3. Noise liner technology package definition.

Boeing Compact Nacelle Acoustics
Collins Advanced Acoustics
Honeywell Advanced Acoustics
TREAT - ANOPP Stock Liner

	RJ	SA	STA	LTA	VLA
EV - ADD	TREAT	TREAT	TREAT	TREAT	TREAT
EV - GTF	TREAT	TREAT	TREAT	TREAT	TREAT
EV2 - ADD	TREAT	Boeing	Boeing	Boeing	Boeing
EV2 - GTF	TREAT	Boeing	Boeing	Boeing	Boeing
AG-ADD	HW	Boeing	Boeing	Boeing	Boeing
AG-GTF	Collins	Boeing	Boeing	Boeing	Boeing
AG2-ADD	HW	Boeing	Boeing	Boeing	Boeing
AG2-GTF	Collins	Boeing	Boeing	Boeing	Boeing
AG2-C-ADD	TREAT	TREAT	TREAT	TREAT	TREAT
AG2-C-GTF	TREAT	TREAT	TREAT	TREAT	TREAT
AG-C-ADD	TREAT	TREAT	TREAT	TREAT	TREAT
AG-C-GTF	TREAT	TREAT	TREAT	TREAT	TREAT
CI-AG-ADD	TREAT	TREAT	TREAT	TREAT	TREAT
CI-AG-GTF	TREAT	TREAT	TREAT	TREAT	TREAT
CI-AG2-ADD	TREAT	TREAT	TREAT	TREAT	TREAT
CI-AG2-GTF	TREAT	TREAT	TREAT	TREAT	TREAT

During the vehicle analysis, generic noise contours were generated for each vehicle class and technology integration scenario. In each case, the average 65 day night level (DNL) exposure area was calculated for each analysis year. Output noise results were generated for analysis years set at every five years between 2020 and 2050. The noise fleet assessment maintained the same set of assumptions as the fuel burn analysis, including identical fleet replacement matrices, demand forecast, technology integration scenarios, and scope: United States domestic + international departures and all carriers: domestic and foreign flag. An example resultant noise contour is shown in Figure 7. This notional contour shows how the 65 DNL exposure area changes across each of the technology integration scenarios across vehicles.

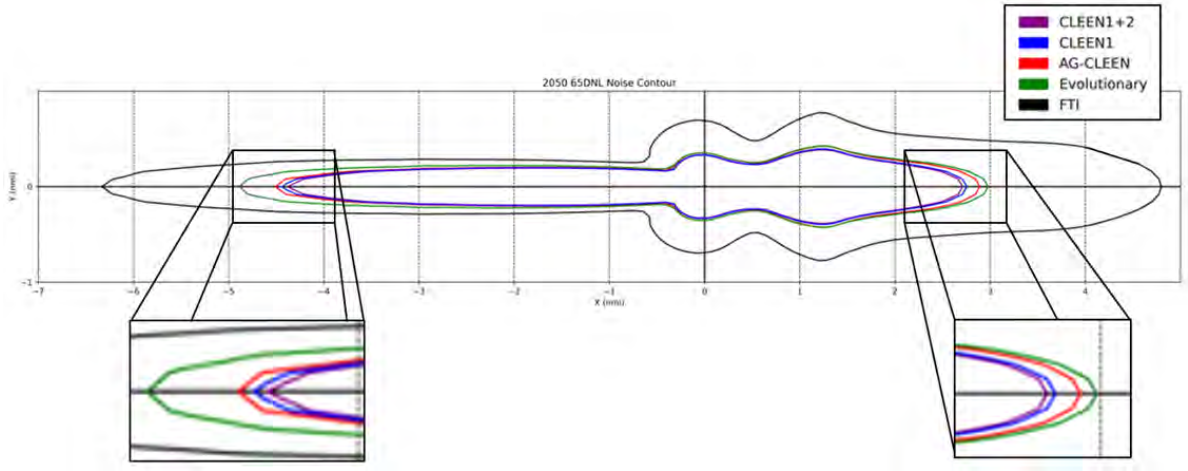

Figure 7. Notional airport 2050 65-DNL noise contour.

In order to isolate the impact of CLEEN I and CLEEN I + II technology sets, the difference between the AG-C (red) line and the CLEEN I (blue) line and CLEEN I + II scenario (purple) line, respectively, as shown in Figure 7 may be calculated. Further, the impact of CLEEN II may be estimated by subtracting the impact of CLEEN I from the impact of CLEEN I + II. The fleet noise assessment computes 65 DNL noise exposure areas across 95 United States airports and averages these to articulate fleet benefits. The result for the estimated average annual 65 DNL exposure area reduction attributed to CLEEN I and CLEEN II, relative to the evolutionary scenario, is shown in Figure 8. In Figure 8, CLEEN I and the cumulative impact of CLEEN I + II potentially contribute an annual noise reduction benefit of 6.3% and 8.6% in 2050, respectively, compared to the evolutionary scenario. This suggests that CLEEN I + II technologies enable increased operations of ~8.6%, with minimal impact to the noise exposure that would be expected in the evolutionary scenario in 2050.

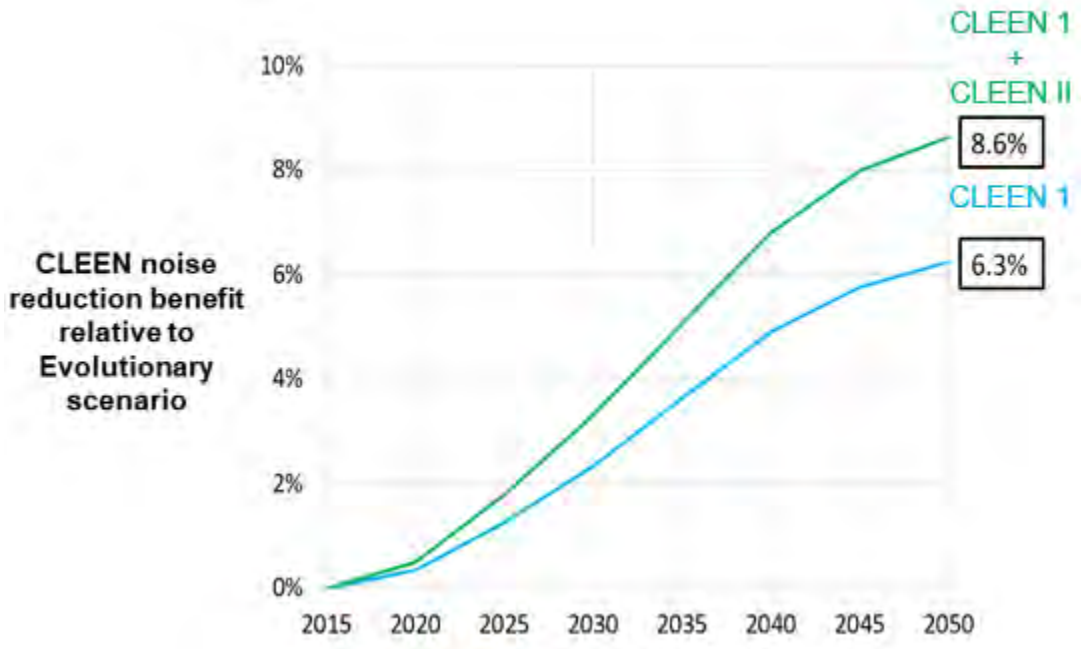

Figure 8. CLEEN technology annual 65-DNL exposure area reduction

Publications
None.

Outreach Efforts
The Georgia Tech attended the spring and fall CLEEN Consortium in 2024. A day of each spring consortium was dedicated to university outreach, which included the opportunity for students to present their contributions to the ASCENT program.

Awards
None.

Student Involvement
In 2024, 18 graduate students received funding from this effort. Two of the graduate students are doctoral track students, Joao De Azevedo and Kayley Lewis, and the other ten, Krutik Desai, Mitchell Mu, Martina Tehubijuluw, Justin Purser, Todd Goehmann, Tabitha D'Amato, George Blackwell, James Tsangarides, Ballard Huey, Maxwell Home, Nathaniel Green, Flavius Penescu, Aniela Zaremski, Akash Shiri, Anna Conroy, Vishwa Malaisamy, are master's degree track students. One additional student, Dante Cyrus, supported this project while receiving funding from the U.S. Air Force.

Plans for Next Period
Future work during the next performance period will focus on completing technology models and integrating models for CLEEN III technologies into EDS as contractor test data becomes available to Georgia Tech. Georgia Tech is planning to host the Spring 2025 CLEEN Consortium in Atlanta, Georgia, and attending the Fall 2025 CLEEN Consortium.

References
ICAO. (2021, June 1). ICAO Aircraft Emissions Databank. https://www.easa.europa.eu/en/domains/environment/icao-aircraft-engine-emissions-databank

Mavris, D., & Kirby, M. (2024). *Project 082(A) Integrated Noise and CO2 Standard Setting Analysis*. https://ascent.aero/project/integrated-noise-and-co2-standard-setting-analysis/

Mavris, D., Tai, J., & Brooks, J. (2023). *Project 037 CLEEN II System-level Assessment*. https://s3.wp.wsu.edu/uploads/sites/2479/2024/08/2023-ASCENT-Annual-Report.pdf

Project 038 Rotorcraft Noise Abatement Procedure Development

The Pennsylvania State University, Continuum Dynamics, Inc.

Project Lead Investigator

Kenneth S. Brentner
Professor of Aerospace Engineering
Department of Aerospace Engineering
The Pennsylvania State University
308 ECoRE Bldg, 556 White Course Drive
University Park, PA
814-865-6433
ksbrentner@psu.edu

University Participants

The Pennsylvania State University (Penn State)

- P.I.: Kenneth S. Brentner, Professor of Aerospace Engineering
- FAA Award Number: 13-C_AJFE-PSU-038, Amendment No. 119
- Period of Performance: October 1, 2023, to September 30, 2024
- Tasks:
  1. Shrouded rotor noise modeling
  2. Broadband noise prediction enhancement
  3. PSU DEPSim aircraft model updates
  4. Application of noise prediction enhancements to abatement procedure analysis
  5. Update PSU Noise Prediction System documentation and sample cases

Project Funding Level

Funding during this period started with Federal Aviation Administration (FAA) funding $150,000; Continuum Dynamics, Inc. (CDI) (Point of contact: Dan Wachspress) provided $150,000 of cost sharing in the form of a 1-year license for the Comprehensive Hierarchical Aeromechanics Rotorcraft Model (CHARM) rotorcraft comprehensive analysis software to Penn State and the FAA or their designee. Penn State provided $20,000 in academic year salary for the principal investigator. This funding ended December 31, 2023, and was not renewed until August 2024, with FAA funding $181,000; Continuum Dynamics, Inc. (Point of contact: Dan Wachspress) will provide $150,000 of cost sharing in the form of a 1-year license for the CHARM rotorcraft comprehensive analysis software to Penn State and the FAA or their designee. Supernal will provide $140,000 in-kind support in the form of costs accrued to collect and extract datasets from a flying test bed Bell 407 and engineering hours.

Investigation Team

Kenneth S. Brentner, P.I., Penn State; acoustic prediction lead on all tasks
Joseph F. Horn, co-P.I., Penn State; flight simulation lead, support for all tasks
Daniel A. Wachspress, co-P.I., CDI; rotor loads, wake integration, and CHARM coupling
Mrunali Botre, co-P.I., CDI; support for rotor loads, wake integration, and CHARM coupling
Sagar Peddanarappagari, Graduate Research Assistant, Penn State; Developing new CHARM models, performing acoustic predictions, distributed electric propulsion simulation (DEPSim) models and documentation for existing noise prediction system

Salma Ibnoukhaiber, Undergraduate Research Assistant, Penn State; broadband noise enhancement, and documentation of Pennsylvania State University (PSU)-Noise Prediction System (NPS) for the Volpe National Transportation System Center (Volpe) and other users.

Project Overview

Rotorcraft noise consists of several components, including rotor noise, engine noise, and gearbox and transmission noise. Rotor noise is typically the dominant component of rotorcraft noise to which the community is exposed upon takeoff and landing, and along the flight path of the helicopter. Rotor noise arises from multiple noise sources, including thickness noise and loading noise (the combination of thickness noise and loading noise is known as rotational noise), blade–vortex interaction (BVI) noise, high-speed impulsive (HSI) noise, and broadband noise. Each noise source has its own unique directivity pattern around the helicopter. Furthermore, aerodynamic interactions among rotors, interactions between the airframe wake and a rotor, and unsteady time-dependent loading generated during maneuvers typically increase loading noise. The combination of all potential rotor noise sources makes the prediction of rotorcraft noise highly complex, although not all noise sources are present at any given time in the flight (e.g., BVI noise usually occurs during descent, and HSI noise occurs only during high-speed forward flight).

In ASCENT Project 006, "Rotorcraft Noise Abatement Operating Conditions Modeling," the project team coupled a MATLAB®-based flight simulation code with CHARM and PSU-WOPWOP to perform rotorcraft noise prediction. The PSU-NPS was used to develop noise abatement procedures through computational and analytical modeling. Although the PSU-NPS cannot predict engine noise or HSI noise, it was thoroughly validated via a comparison between predicted noise levels for a Bell 430 aircraft and flight test data (Snider et al., AHS Forum, 2013) for several observer positions and operating conditions.

In previous work for ASCENT Project 038, representative helicopters were recommended for noise abatement procedure development. These helicopters were selected to enable determination of whether noise abatement procedures could be developed for various categories of helicopters (i.e., two-blade light, four-blade light, two-blade medium, etc.) or whether aircraft-specific design considerations would be required. Aircraft models were established for the following aircraft: Bell 430, Sikorsky S-76C+ and S-76D, Bell 407 and 206L, Airbus EC130 and AS350, and Robinson R66 and R44. Predictions were made before the 2017 FAA/National Aeronautics and Space Administration (NASA) noise abatement flight test to provide guidance for the flight test. After the flight test, a comparison of *A*-weighted sound pressure level time histories and sound exposure level contour plots revealed a problem in the broadband noise prediction, which was subsequently corrected. Initial validation comparisons demonstrated that the simulations were within several A-weighted decibels (dBA) of the flight test data; however, some discrepancies in the simulations (simplifications) remained, thus requiring a detailed examination. Work was also performed on the PSU-NPS, including modifying PSU-WOPWOP to output plots of the maximum dBA, as plotted in the flight test. Further work was conducted to enhance the postprocessing of noise data to enable a direct comparison with flight test data. Detailed analysis of the noise components and noise sources was performed for several helicopters in the 2017 FAA/NASA flight test. Further enhancements were added to compute moving averages and devise strategies for window overlapping in the post proposing of predicted noise data. In the cases studied, de-Dopplerization (used in flight test data processing) and moving observers (used in noise predictions to eliminate Doppler effects) were demonstrated to be effectively equivalent (typically within 0.5 decibels [dB] or less). Next a comparison of the effectiveness of noise abatement procedures by helicopter class was performed by using the 2017 and 2019 flight test data. In particular, the Bell 205, 206, and 407 aircraft were compared for various flight conditions in the flight tests. In the predictions, the Pegg broadband noise prediction did not work as well for some aircraft, and a simple scaling of the broadband noise was considered as a potential correction. Unfortunately, no clear relationship for the scaling among aircraft was observed. In addition, an analysis of the 2019 FAA/NASA flight test was performed by comparison of prediction and experimental data for 3° and 4.5° descents and left and right turns at different bank angles (i.e., 25° and 45°, respectively) for two aircraft, Bell 205 and Sikorsky S-76D. Preliminary coupling between the Penn State noise predictions system and Volpe's Advanced Acoustics Model (AAM) software was implemented.

The objective of this continuing project is to reduce the need for flight testing of each rotorcraft of interest for continued development of low-noise operating procedures. Current guidelines provided to pilots and operators in the Fly Neighborly guide are based on recommendations from manufacturers, but this guidance is not required and is often not provided. Other methods for developing noise abatement procedures at the FAA and NASA are empirical, based on previous flight

® Matlab is a registered trademark of The Mathworks Inc., Natick, Massachusetts.

measurements of specific aircraft. The tasks described below will enable analysis of new flight procedures and noise analysis strategies through computations alone. This year's efforts included further analysis and investigation of the 2017 and 2019 FAA/NASA noise abatement flight tests, development of shrouded rotor noise modeling, updating the flight simulator and enhancing couplings, and prepare documentation and training materials to enable the FAA and their partners to use the PSU-NPS.

References

Snider, R., Samuels, T.O., Goldman, B., & Brentner K. S. (2013). Full-Scale Rotorcraft Broadband Noise Prediction and its Relevance to Civil Noise Certification Criteria, Proceedings of American Helicopter Society 69th Annual Forum, Phoenix, Arizona, May 21–23, 2013.

Task 1 - Shrouded Rotor Noise Modeling

The Pennsylvania State University

Objectives

The primary objective of this task is to utilize shrouded rotor noise prediction capabilities developed as part of task 2 of the 2022-2023 ASCENT Project 038 Annual Report (Wolcott et al., 2023) and test its efficacy against flight test measurements of helicopters equipped with a shrouded tail rotor (also referred to as Fenestron), such as the Airbus EC130. Modeling techniques and their impact are studied and documented.

Research Approach

The 2017 NASA/FAA flight test (Watts et al., 2019) provided acoustic measurements for the EC130 helicopter in hover and various forward flight maneuvers. The shrouded tail rotor geometry was estimated based on publicly available images, including the uneven blade spacing. CHARM is used to derive airloads for the main and tail rotors along with the shroud. The stators and struts in the Fenestron are not currently modeled in CHARM.

Milestones

- Modeled EC130 helicopter Fenestron in CHARM and PSU-WOPWOP.
- Evaluated the acoustic impact of unevenly spaced Fenestron blades.
- Predicted the noise from Airbus EC-130 aircraft flown in the 2017 FAA/NASA flight test.

Major Accomplishments

The EC130 Fenestron features 10 unevenly spaced blades, a design choice aimed at reducing noise by varying the blade passage frequencies and creating destructive interference. Using the tail rotor's diameter (3.28 ft) and chord length (0.2 ft), the blade spacing was estimated (see Figure 1). It is assumed that the aerodynamic effects of uneven blade spacing are minimal and can be neglected for low-speed flight conditions such as hover. Thus, it is currently not directly modeled in CHARM (where the blades are evenly spaced) but is included in PSU-WOPWOP's noise calculations. The tail rotor shroud is modeled as a lifting panel in CHARM, with a tip clearance of approximately 0.01R.

Figure 1. Estimated blade spacing of EC130 tail rotor (Peddanarappagari, 2024).

CHARM's lifting panel method is a potential flow code (Boschnitsch et al., 1999), which does not possess the capability of modeling boundary layer separation commonly observed on tail rotor shrouds in forward flight. Thus, predictions for hovering EC130 are compared with flight test data (Watts et al., 2019). Figure 2 shows a schematic of the flight test during hover, with a semi-circular array of 13 microphones positioned at a radius of 150 m. The EC130 helicopter is hovering around the center of the array, at an altitude of 54 m (~177 ft), ensuring out-of-ground effect conditions. The measured acoustic pressure data was processed through PSU-WOPWOP to obtain various noise metrics.

To assess the impact of uneven blade spacing, the acoustic spectrum of the tail rotor alone (without the shroud) was analyzed. Figure 3(a) compares the predicted acoustic spectra (sound pressure level [dB] vs frequency [Hz]) for evenly spaced and unevenly spaced rotors at microphone 13, which is located directly behind the helicopter where tail rotor noise dominates. It is observed that the evenly spaced rotor exhibits larger peaks at specific frequencies (blade passage frequencies [BPFs]) and lower noise levels in the remaining frequency range. In contrast, the unevenly spaced rotor has slightly lower peaks at more frequencies due to the variation in blade passage frequencies. Similar tail rotor spectral results were found in the 1996 Predictions and Measurements from a Ducted Tail Rotor Project at Bell Helicopter (Andrews et al., 1996). To quantify the effect of blade spacing on overall noise levels, the overall sound pressure level (OASPL) at all microphone locations was also analyzed (Figure 3(b)). The results indicate a reduction in OASPL (~1-5 dB) at certain locations (microphones 1, 2, 3, 11, 12, and 13) and an increase in OASPL (5 dB) at microphone 8. This suggests that the model can capture the effects of uneven blade spacing to some extent.

The predictions can be observed to be within 1-2 dB for all microphones. Good agreement is observed at microphones 1 to 5, where the main rotor noise can be expected to dominate. Similarly, good agreement is found at microphones 10 to 13. However, there is an underprediction of 1-3 dB at microphones 7 to 10, which is likely due to the absence of stators and transmission struts in the model. Incorporating these components into the model is expected to improve accuracy of the prediction.

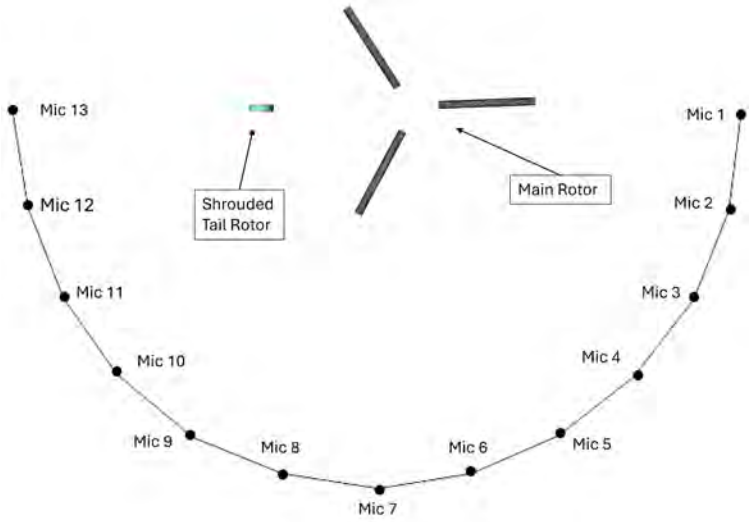

Figure 2. Schematic of helicopter and microphones in hover (Peddanarappagari, 2024) Note: Helicopter rotors enlarged relative to microphone locations for visual representation.

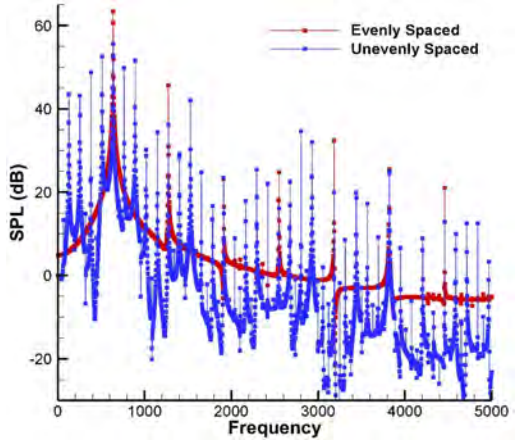

(a) Acoustic spectrum at microphone 13

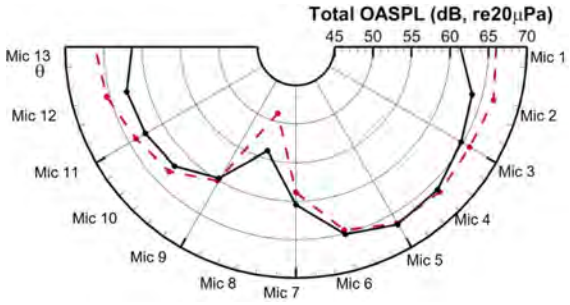

(b) Overall Sound Pressure Level

Figure 3. Comparison of noise from tail rotor: evenly vs unevenly spaced (Peddanarappagari, 2024).

Figure 4 shows a comparison of OASPL between predictions and flight test data for all microphones in the semi-circular array. The flight test OASPL values were averaged over the 33-second duration of flight test case 297473 (Watts et al., 2019) at all 13 microphone locations. Noise predictions were generated for the main rotor, unevenly spaced tail rotor, and shroud using PSU-WOPWOP.

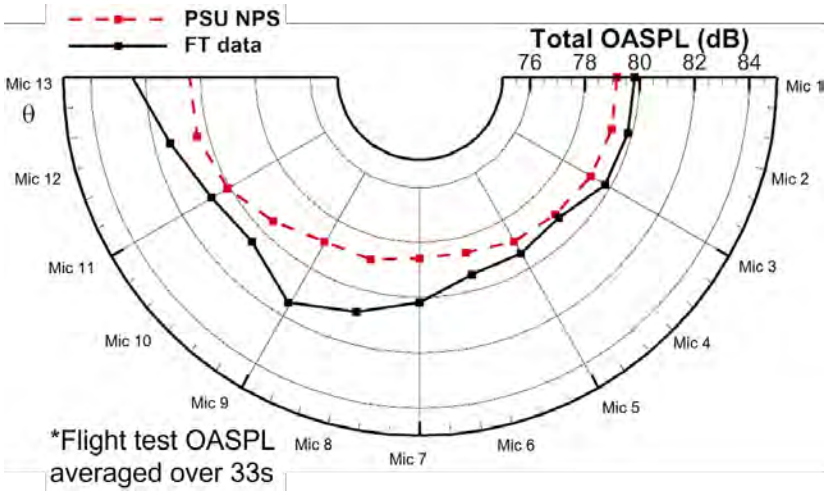

Figure 4. Comparison of noise from tail rotor: evenly vs unevenly spaced (Peddanarappagari, 2024).

Publications

Peddanarappagari, S. (2024). *Updates to Penn State Rotor Noise Prediction System* [Master's thesis]. The Pennsylvania State University.

Outreach Efforts

None.

Awards

None.

Student Involvement

Sagar Peddanarappagari, a graduate assistant working on his Master of Science degree, generated and updated helicopter models and performed the PSU-NPS noise predictions.

Plans for Next Period

Current analysis has helped validate the extracted geometry of the EC130 shrouded tail rotor. The analysis needs to be extended to include modeling of tail rotor-stator interaction noise (likely narrowband). This is expected to improve predictions at hover for some microphones. Empirical methods need to be investigated to model the impact of flow separation at the shroud in forward flight on noise generated. The Brooks, Pope and Marcolini (BPM) self-noise model (Brooks et al., 1989) can offer guidance as it has noise models for isolated airfoils operating in stall.

References

Andrews III, J. R., Riley, Jr, R. G., Rahnke, C. (1996). *Design and Testing of a Ducted Tail Rotor Concept Demonstrator for a Model 222U Helicopter*. Bell Helicopter Textron, Inc., Fort Worth, Texas.

Boschnitsch, A., Usab, Jr., W. J., & Epstein, R. (1999). *Fast Lifting Panel Method*. American Institute of Aeronautics & Astronautics. https://doi.org/10.2514/6.1999-3376

Brooks, T. F., Pope, D. S., and Marcolini, M. A. (1989). *Airfoil Self-Noise and Prediction*. National Aeronautics and Space Administration, NASA RP-1218, 142.

Peddanarappagari, S. (2024). *Updates to Penn State Rotor Noise Prediction System* [Master's thesis]. The Pennsylvania State University.

Watts, M. E., Greenwood, E., Smith, C. D., & Stephenson, J. H. (2019). *Noise Abatement Flight Test Data Report*. National Aeronautics and Space Administration, NASA TM 2019-220264, 734.

Wolcott, M. P., Hansman, R. J., Male, J., & Oldani, A. (2023). *ASCENT Annual Technical Report, 2022-2023*. Washington State University. https://doi.org/10.7273/000006617

Task 2 - Broadband Noise Prediction Enhancement

The Pennsylvania State University

Objective

The objective of this task (Task 8.2 in the 2023-2024 proposal) is to enhance the existing helicopter broadband noise modeling capabilities of the PSU noise prediction system. The task aims to investigate improvements in physics-based and empirical modeling methods.

Research Approach

Previous work in ASCENT Project 038 by Botre (2020) and Zachos (2022) has revealed deficiencies in broadband noise predictions for several helicopters on the order of 6 dB. However, the prediction methodology largely relied on the empirical Pegg (1979) model. The Pegg (1979) model that was calibrated originally from flight test data of medium-weight helicopters offers no path for recalibration using newly measured flight test data (Watts et al., 2019). Zachos (2022) attempted scaling the Pegg (1979) model using an offset determined from flight test data (Watts et al., 2019). While this approach had limited success, it did reveal the potential benefits of recalibrating the Pegg (1979) model. Broadband noise modeling for electric vertical take-off and landing (eVTOL) aircraft in ASCENT Project 049 has largely relied on first-principle methods and can also be applied to helicopters.

Milestones

- Explored new methods for scaling the Pegg model.
- Incorporated broadband noise prediction methods from ASCENT Project 049.

Major Accomplishments

In order to develop new scaling strategies for the Pegg (1979) model, the expression was first rederived. Pegg (1979) did not elaborate on the procedure or the dataset used for calibration. The stated final expression was found to be based on several iterations of expressions originally developed and tuned by Hubbard (1950), with additional corrections by Schlegel et al. (1966) and Munch (1973). Equation 1 below is a generalized version of the original expression for broadband noise stated by Pegg (1979). A constant F, which was calibrated by Pegg and several authors before, was found to be linked to several variables (Equation 2).

$$SPL_{1/3} = 20\log\left(\frac{V_T}{c_0}\right)^3 + 10\log\left[\frac{A_B}{r^2}(cos^2(\theta) + 0.1)\right] + S_{1/3} + f(C_L) + F \quad \text{(Eq. 1)}$$

$$F = 10\log K + 20\log r_K - 10\log[cos^2(\theta_K)] - 10\log I_{ref} + 20\log c_0^3 \quad \text{(Eq. 2)}$$

where $SPL_{1/3}$ is the resultant 1/3rd octave spectrum, and V_T, A_B are the rotor tip-speed and blade area, respectively. The speed of sound is represented by c_0, and the observer/microphone is characterized by its distance from rotor r and angle θ from the axis of rotation. $S_{1/3}$ is a function which provides calibrated weights for different bands of the 1/3rd octave spectrum, while $f(C_L)$ provides empirical corrections based on the operating rotor thrust (which in turn can be linked to helicopter weight and operating condition).

Equation 2 provides an expression for the constant (F) in the Pegg (1979) model which can be calibrated. Here r_K and θ_K represent distance and angle at which the flight test data used for calibration is measured. I_{ref} is the reference sound intensity, while K is a constant that eventually corrects for any differences between predicted 1/3rd octave spectrum using Equation 1 and measured data. Pegg (1979) does not provide the values used for deriving the calibration constant F, but simply states its value as $F = 130$. In its absence, the value of the constants $K\ (3.8e-27), r_K(91.44\ m), \theta_K(105°)$ were adopted from Hubbard (1950) to verify the expression derived in Equation 2. Upon substitution, the value of $F = 142.3$ was derived. This is reasonably close to the original value of 130 from Pegg (1979). Thus, a rederivation of the Pegg (1979) model has revealed the parameters required for calibration with respect to different helicopter models and flight conditions.

Publications
None.

Outreach Efforts
None.

Awards
None.

Student Involvement
Salma Ibnoukhaiber, a senior year undergraduate student in aerospace engineering, has assisted Bhaskar Mukherjee with the derivation of the general Pegg model.

Plans for Next Period
With a greater understanding of the calibrated constant used in the Pegg (1979) model, acoustic data measured during the 2017 FAA/NASA flight tests (Watts et al., 2019) can be used to tune it. However, the data needs to be processed before it can be used for determining the value of the constant F (Equation 2). Tonal and broadband components need to be separated, and main and tail rotor contributions to total noise need to be differentiated. The separated broadband components of main and tail rotors of various helicopters can then be used to tune the constant (F).

References
Botre, M. (2020). *Rotorcraft Noise Prediction System Validation and Analysis for Generating Noise Abatement Procedures* [Doctoral dissertation]. The Pennsylvania State University.

Hubbard, H. H. (1950). *Sound Measurements for Five Shrouded Propellers at Static Conditions*. National Advisory Committee for Aeronautics, NACA-TN-2024.

Munch, C. L. (1973). *Prediction of V/STOL Noise for Application to Community Noise Exposure*. U.S. Department of Transportation, DOT-TSC-OST-73-19.

Pegg, R. J. (1979). *A Summary and Evaluation of Semi-Empirical Methods for the Prediction of Helicopter Rotor Noise.* National Aeronautics and Space Administration, NASA-TM-80200.

Schlegel, R., King, R., & Mull, H. (1966). *Helicopter Rotor Noise Generation and Propagation*. Defense Technical Information Center. https://doi.org/10.21236/AD0645884

Watts, M. E., Greenwood, E., Smith, C. D., & Stephenson, J. H. (2019). *Noise Abatement Flight Test Data Report*. National Aeronautics and Space Administration, NASA TM 2019-220264, 734.

Zachos, D. R. (2022). *Noise Prediction for Helicopter Noise Abatement and eVTOL Design* [Master's thesis]. The Pennsylvania State University.

Task 3 – PSU DEPSim Aircraft Model Updates
The Pennsylvania State University

Objective
Since the transition from the old noise prediction system based on the Helosim flight simulation code (Botre, 2020), helicopter input files need to be adapted for the newly developed PSU DEPSim (Theron et al., 2020). The objective of this task is to transfer input files for helicopters from the old system and validate it with the new noise prediction system (also used in ASCENT Project 049).

Research Approach
Parameters representing the geometry, aerodynamics and dynamics of the helicopter are required for fully coupled flight simulation. Using previously documented values (Botre, 2020), new input files are to be generated based on the format in the DEPSim manual (Theron et al., 2022). Flight test trajectories are simulated using the new system, and noise results are validated.

Milestones
- Generated new helicopter input files for PSU DEPSim.

- Validated noise from maneuvers from various helicopter models against measured flight test data.

Major Accomplishments

Currently four helicopter models have been imported to work with PSU DEPSim: Robinson R44 and R66, Bell 407, and Airbus AS350. Each helicopter has been validated against flight test data recorded for 80 knots level flight (Watts et al., 2019). A trajectory-following controller within PSU DEPSim ensures that the helicopters follow the same flight path as the flight test.

Figure 5 shows a comparison of the simulated and measured (flight test) variation of aircraft Euler angles with time for the R44 helicopter in 80 knots level flight. Reasonable agreement can be observed between the prediction and measurements. Similar agreement for R66 Euler angles were reported in the master's thesis by Peddanarappagari (2024). Figure 6 shows the variation of OASPL with time for a ground microphone. Predicted and measured results are reported for R44 and R66 helicopters. The predicted total noise and flight test match well during approach and flyover (peak).

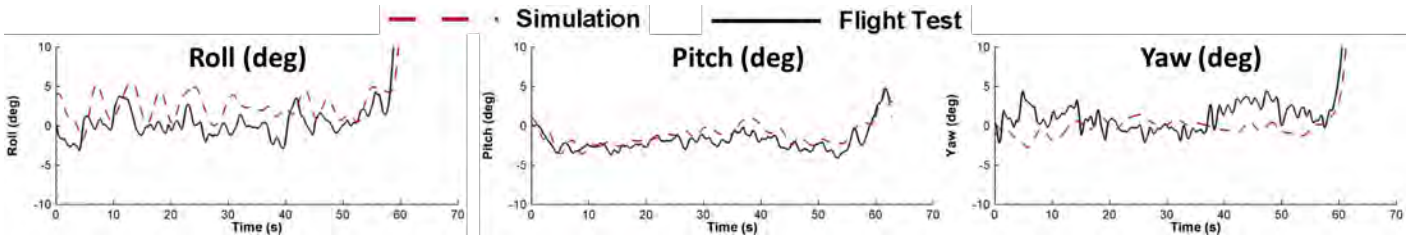

Figure 5. R44 helicopter Euler angles vs time: flight test and simulation (Peddanarappagari, 2024).

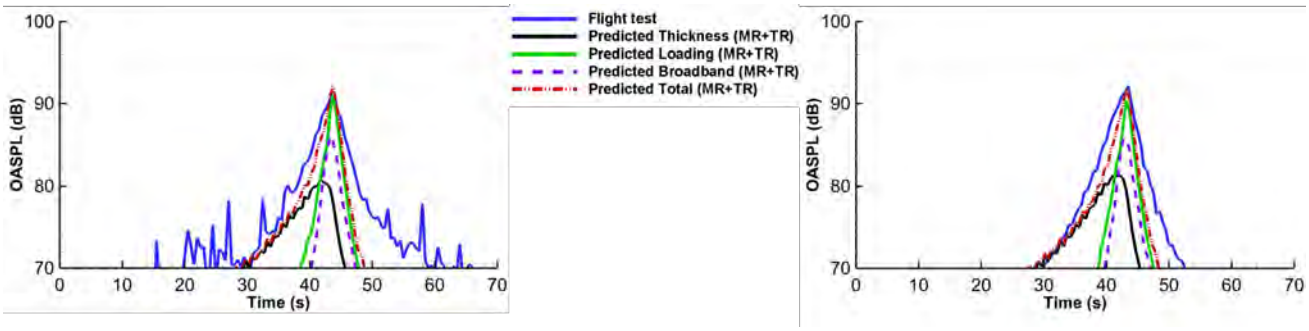

Figure 6. Predicted OASPL vs time compared with flight test data from R44 helicopter (Peddanarappagari, 2024).

However, the Bell 407 and AS350 aircraft were found to have significant deviations in predicted aircraft roll angle (Figure 7). These differences have been attributed to the more complex articulated rotor systems used by these helicopters. The bearingless rotor models in the flight simulation system have not been fully tuned, evidenced also by the retreating side roll for both helicopters. While noise prediction for 80 knots level flight for both seem reasonably accurate (Figure 8), it is expected to introduce errors in BVI noise prediction during maneuvers.

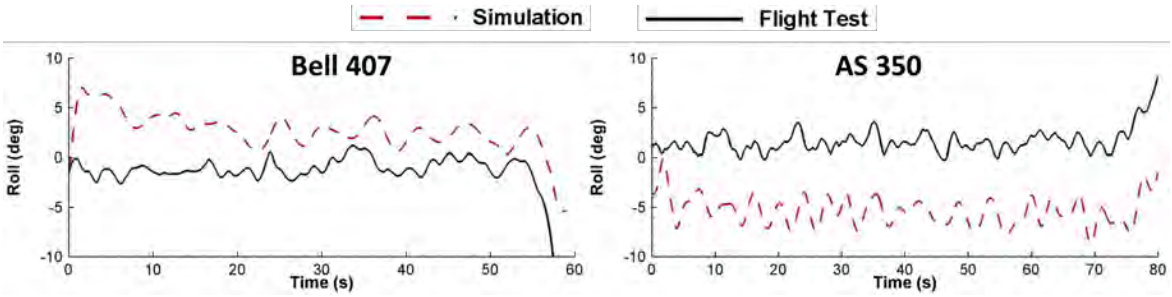

Figure 7. Roll angle vs time for Bell407 and AS350 in 80 knots level flight (Peddanarappagari, 2024).

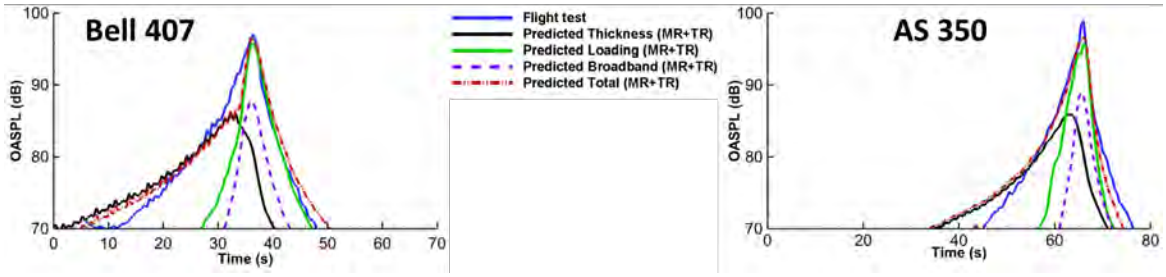

Figure 8. Predicted and measured OASPL vs time: Bell 407, AS 350 (Peddanarappagari, 2024).

Publications

Peddanarappagari, S. (2024). *Updates to Penn State Rotor Noise Prediction System* [Master's thesis]. The Pennsylvania State University.

Outreach Efforts

None.

Awards

None.

Student Involvement

Sagar Peddanarappagari, a graduate assistant working on his Master of Science degree, learned the use of DEPSim simulator and created a new AS350 aircraft model in the new simulator.

Plans for Next Period

The dynamic model parameters of AS350 and Bell 407 aircraft will be refined further to provide a better match between simulation and flight test. Further validation efforts will also include additional medium-weight helicopters from the 2019 NASA/FAA flight test (Pascioni et al., 2021): Bell 205, Sikorsky S-76D, Leonardo AW139, and Airbus MH-65.

References:

Botre, M. (2020). *Rotorcraft Noise Prediction System Validation and Analysis for Generating Noise Abatement Procedures* [Doctoral dissertation]. The Pennsylvania State University.

Pascioni, K. A., Greenwood, E., Watts, M. E., Smith, C. D., & Stephenson, J. H. (2021). *Medium-Sized Helicopter Noise Abatement Flight Test Data Report*. National Aeronautics and Space Administration, NASA TM 20210011459 .

Peddanarappagari, S. (2024). *Updates to Penn State Rotor Noise Prediction System* [Master's thesis]. The Pennsylvania State University.

Theron, J.-P., Horn, J. F., & Wachspress, D. A. (2020, January 21-23). An Integrated Simulation Tool for E-VTOL Aeromechanics and Flight Control Analysis [Meeting presentation]. 2020 VFS Aeromechanics for Advanced Vertical Flight Technical Meeting, San Jose, California.
Theron, J.-P., Jue, A., & Horn, J. F. (2022). *DEPSim Manual* [Version 2.0]. The Pennsylvania State University.
Watts, M. E., Greenwood, E., Smith, C. D., & Stephenson, J. H. (2019). *Noise Abatement Flight Test Data Report*. National Aeronautics and Space Administration, NASA TM 2019-220264, 734.

Task 4 - Application of Noise Prediction Enhancements to Abatement Procedure Analysis

The Pennsylvania State University

Objective

The objective of this task is to design, test, and demonstrate helicopter noise abatement procedures using the new and improved Penn State noise prediction system.

Research Approach

The new noise prediction system has been demonstrated for steady flight conditions, but the system needed to be validated with flight test data for maneuvers. The differences between predicted and measured noise levels during maneuvers are quantified to calibrate the system before using the system to generate new noise abatement procedures.

Milestones

- Validated efficacy of the noise prediction system against maneuvers such as turns, accelerating climbs, etc.
- Demonstrate accuracy of the system in capturing important acoustic events such as BVI, etc.

Major Accomplishments

The efficacy of the noise prediction system was tested by investigating a level retreating-side (left) turn maneuver carried out by an R44 helicopter. The turn is executed at a constant airspeed of 80 knots with a maximum roll angle of 35°. Figure 9 shows that the simulation captures the variation in roll and yaw angles accurately. Figure 10 shows the comparison between measured and predicted noise for the turn. The sound exposure level (SEL) is reasonably captured by prediction (see Figure 10(b)). A region of unusually low noise is apparent on the right-hand side of the predicted contour plot. This can be attributed to the simulation ending before the noise generated by the helicopter reaches the microphone locations in those regions.

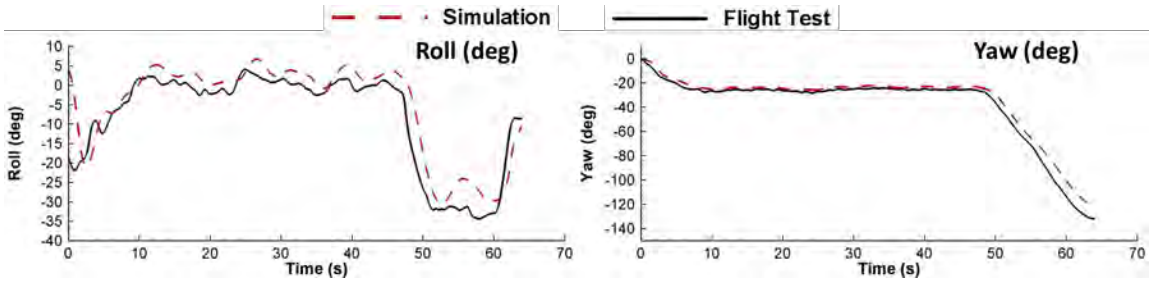

Figure 9. Simulated aircraft roll and yaw compared with flight test data for R44 helicopter flying level left turn (Peddanarappagari, 2024).

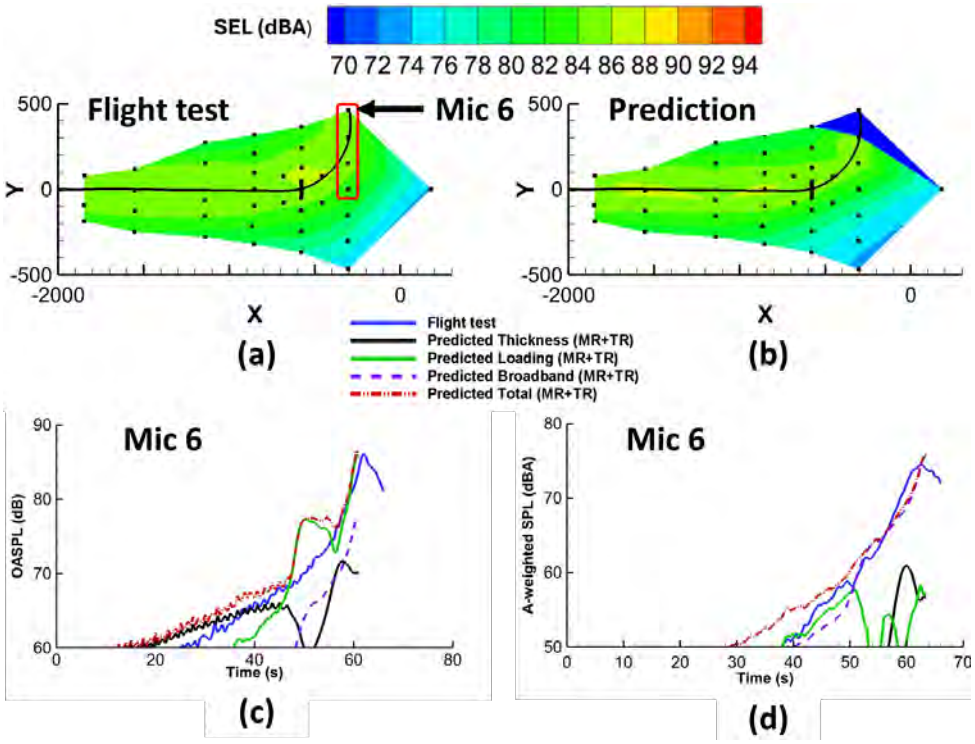

Figure 10. Comparison of predicted noise with flight test data: R44 level left turn 80 knots (Peddanarappagari, 2024).

Figure 10(c) and Figure 10(d) plot the variation of OASPL (dB) and A-weighted (dBA) noise levels with time for microphone 6 (refer Figure 10(a)). The A-weighted sound pressure level (SPL) is overpredicted during the approach phase, while the prediction can be seen to end before the end of the maneuver in the flight test. The A-weighted noise prediction indicates that the broadband noise is the dominant source of noise. On the other hand, Figure 10(c) shows thickness noise to be important when the helicopter is approaching, with loading noise becoming important as it flies over the microphone. An unusual jump is observed in the predictions that is not visible in the measured data. The reason for this jump is being investigated.

Other maneuvers such as descent are yet to be tested using the noise prediction system. The system in the past has used CHARM's wake reconstruction feature (Wachspress & Quackenbush, 2001) to predict impulsive noise events such as BVI. However, the current implementation of PSU-NPS (PSUDEPSim-based) appears to have issues with wake reconstruction, hindering accurate noise prediction of BVI events.

Publications

Peddanarappagari, S. (2024). *Updates to Penn State Rotor Noise Prediction System* [Master's thesis]. The Pennsylvania State University.

Outreach Efforts

None.

Awards

None.

Student Involvement

Sagar Peddanarappagari, a graduate assistant working on his Master of Science degree, set up the cases in preparation for the new computations.

Plans for Next Period

The noise prediction system needs to be updated to include wake reconstruction for calculation of BVI noise. Accurate prediction of other important noise sources such as blade-wake interaction (BWI) and turbulent ingestion noise (TIN) must also be developed before the system can be reliably used to investigate and develop noise abatement procedures.

References:

Peddanarappagari, S. (2024). *Updates to Penn State Rotor Noise Prediction System* [Master's thesis]. The Pennsylvania State University.

Wachspress, D., & Quackenbush, T. (2001). *BVI Noise Prediction Using a Comprehensive Rotorcraft Analysis* [Conference presentation]. Vertical Flight Society Annual Forum & Technology Display - Forum 57, Washington D.C.

Task 5 - Update PSU Noise Prediction System Documentation and Sample Cases

The Pennsylvania State University

Objective

The objective of the current task is to generate updated documentation of the noise prediction system, including user instructions and best practices. A user manual will be distributed to FAA, Volpe, and the FAA Technical Center along with the system for beta testing.

Research Approach

A user manual with instructions on compilation, installation and usage of the system will be documented first. The manual will also contain a brief description of the theoretical background of the components of the noise prediction system. Validation cases will be provided along with a list of best user practices. The manual and the system will be updated based upon the feedback received from beta testers at Penn State and partners at FAA.

Milestones

- Documented installation and setup of DEPSim, CHARM and PSU-WOPWOP including the coupling.
- Described the file structure of the input files including a list of parameters required to simulate new helicopters.
- Identified validation cases and included necessary input files for users to test the system.

Major Accomplishments

Sagar Peddanarappagari gave a seminar on the general composition, input data, file directory structure, and capabilities of the PSU-NPS at the Spring ASCENT Advisory Committee meeting held at Penn State in April 2024. Personnel from FAA, Volpe, and other ASCENT universities attended.

The documentation of the PSU-NPS has continued and significant progress has been made for a software release to Volpe. Figure 11 shows an overview of the current structure of the PSU-NPS user manual. An introduction to the system is provided along with some background on the theory and history of the system. Then a brief description of the constituent codes for PSU DEPSim, CHARM and PSU-WOPWOP is provided. More details on the individual codes can be found in their respective manuals.

The user manual also documents the procedure for installing the system along with the directory structure in which the system operates. A detailed description of the input files required by DEPSim, CHARM, and PSU-WOPWOP is provided along with the files written by the codes as output. Utility codes are also provided with the system to enable the user to process results and visualize them. Best practices are being documented with the examples of operating the system. Work is ongoing to compile validation cases which demonstrate the capabilities of the system to new users.

1 Introduction
- 1.1 Helicopter Noise Background
- 1.2 Introduction to PSU-NPS
- 1.3 Case Example to Operate PSU-NPS: AS350

2 PSU-NPS Description
- 2.1 PSUDEPSim
- 2.2 CHARM
- 2.3 Coupled PSUDEPSim/CHARM
- 2.4 PSU-WOPWOP

3 Installation and Setup
- 3.1 DEPSim
- 3.2 CHARM
- 3.3 PSU-WOPWOP

4 PSU-NPS File Structure

5 PSU-NPS Input Files
- 5.1 DEPSim
  - 5.1.1 *SimFile.inp*
  - 5.1.2 *PSUDEPSimInputData.txt*
  - 5.1.3 *CHARMInputFiles*
  - 5.1.4 *Case File*
  - 5.1.5 *Command File*
- 5.2 CHARM
  - 5.2.1 Run Characteristics Input File (*.inp)
  - 5.2.2 Blade Geometry Input File (*bg.inp)
  - 5.2.3 Blade Dynamics Input File (*bd.inp)
  - 5.2.4 2-D Airfoil Section Data Input File (*af.inp)
  - 5.2.5 Rotor/Wake Input File (*rw.inp)
- 5.3 PSU-WOPWOP
  - 5.3.1 Namelist Input File

6 PSU-NPS Output Files
- 6.1 DEPSim
- 6.2 CHARM
- 6.3 PSU-WOPWOP

7 Utility Programs
- 7.1 Plot_results.m
  - 7.1.1 Description
  - 7.1.2 Results Example
- 7.2 CHARM_LME.m
  - 7.2.1 Description
  - 7.2.2 Results Example
- 7.3 CIFER_freq_proc.m
  - 7.3.1 Description
  - 7.3.2 Results Example

8 Examples to Operate the Noise Prediction System
- 8.1 Predict Noise Using PSU-NPS
  - 8.1.1 Initial Model Creation
  - 8.1.2 DEPSim Simulation: Coupled Example (PSUDEPSim + CHARM Rotor Model)
  - 8.1.3 WOPWOP noise prediction

9 PSU-NPS Validation
- 9.1 Flight Test Data: WOPWOP Processing
- 9.2 Comparison of Predicted Noise to Flight Test Data

Appendix I: Input Reference Tables
- A *PSUDEPSimInput.txt*

Figure 11. Table of contents for the PSU-NPS user manual.

Publications
None.

Outreach Efforts
None.

Awards
None.

Student Involvement
Salma Ibnoukhaiber, a senior year undergraduate student in aerospace engineering, has been working on developing the user manual.

Plans for Next Period
The user manual will eventually be distributed along with the system to users for beta testing. The manual will be continuously updated based on feedback. Additional cases for validation will be included to demonstrate the diverse capabilities of the noise prediction system.

Project 044 Aircraft Noise Abatement Procedure Modeling and Validation

Massachusetts Institute of Technology

Project Lead Investigator

R. John Hansman
T. Wilson Professor of Aeronautics & Astronautics
Department of Aeronautics & Astronautics
Massachusetts Institute of Technology
Room 33-303
77 Massachusetts Avenue
Cambridge, MA 02139
617-253-2271
rjhans@mit.edu

University Participants

Massachusetts Institute of Technology (MIT)

- P.I.: Prof. R. John Hansman
- FAA Award Number: 13-C-AJFE-MIT, Amendment No. 050, 057, 073, 084, 105, 109, 115, 126, and 133
- Period of Performance: September 1, 2018, to September 30, 2025
- Tasks:
  1. Review and identify relevant machine learning and data mining techniques
  2. Apply data mining techniques to relevant noise monitor, aircraft, operator, and flight dynamics data
  3. Expand approach to the analysis of additional airports and aircraft types
  4. Identify operational factors which influence the community noise at specific locations
  5. Assess implications of results to the design of noise abatement procedures

University of California - Irvine (via sub-award from MIT)

- P.I.: Prof. Jacqueline Huynh
- Award Number: MIT Subaward Purchase Order No. 523807
- Period of Performance: September 1, 2020, to September 30, 2025
- Tasks:
  1. Review and identify relevant machine learning and data mining techniques
  2. Apply data mining techniques to relevant noise monitor, aircraft, operator, and flight dynamics data
  3. Expand approach to the analysis of additional airports and aircraft types
  4. Identify operational factors which influence the community noise at specific locations
  5. Assess implications of results to the design of noise abatement procedures

Project Funding Level

The Federal Aviation Administration (FAA) provided $995,000 in funding and $995,000 was provided in matching funds, approximately $201,300 from MIT and $793,700 from the Massachusetts Port Authority.

Investigation Team

Massachusetts Institute of Technology

Prof. R. John Hansman, (P.I.), Tasks 1-5
Sandro Salgueiro, (graduate student, graduated), Tasks 1-5
Merek Homola, (graduate student), Tasks 1-5
Clement Li, (Postdoc), Tasks 1-5

Phillip Hood, (undergraduate student), Tasks 1-5

University of California, Irvine
Prof. Jacqueline Huynh, (co-P.I.), Tasks 1-5
Trinity Lee, (graduate student), Tasks 1-5
Melissa Lepe, (graduate student), Tasks 1-5

Project Overview

This project uses empirical noise data to develop validation methods from noise and flight surveillance datasets and to improve existing noise models. Field measurements of aircraft noise on approach and departure have historically shown significant variation (on the order of 10 dB), which has traditionally been attributed to factors such as varied power settings, aircraft configuration differences, and propagation effects. Recent analyses in this and other ASCENT projects have attempted to account for these factors but have been constrained by limited detailed flight data. This project explores approaches to combine emerging sources of flight data from flight data recorders (FDRs) and other sources such as Automatic Dependent Surveillance-Broadcast (ADS-B) with current and emerging networks of ground noise monitors, to validate or improve aircraft noise models and to validate proposed noise abatement procedures. The rise of data-mining techniques has substantially enabled new insights and modeling capabilities based on the use of large datasets without requiring full a priori knowledge of all relevant physics. The development of advanced data-mining approaches applied to noise modeling is expected to provide insight into aircraft noise prediction for refining or validating noise models and for developing strategies for noise mitigation, through either new aircraft technologies or operational changes. Furthermore, improved noise modeling capabilities are expected to enable more informed decision-making for stakeholders considering the options and consequences of operational or technological changes, thus facilitating the minimization of noise impacts on communities. Because noise is becoming an increasingly important factor in operational decisions regarding airports in the National Airspace System, an accurate understanding of noise impacts is necessary to minimize unnecessary disruptions to, or inefficiencies in, National Airspace System operations.

Task 1 – Review and Identify Relevant Machine Learning and Data Mining Techniques

Massachusetts Institute of Technology
University of California, Irvine

Objectives

Machine learning and data mining techniques appropriate for evaluating relationships between noise monitor, aircraft, operator, and flight dynamics data will be reviewed and identified. These may include, but are not limited to, supervised machine learning on monitor-by-monitor basis, clustering and correlating resulting clusters to noise levels, identification of features/states relevant to observed noise, and intermonitor correlation analysis to investigate trajectory-level effects.

Research Approach

- Identify potential existing data sources for noise validation.
- Develop model of aircraft flight profiles by using existing surveillance (e.g., ADS-B or Airport Surface Detection Equipment, Model-X) data to generate noise estimates (readily available surveillance data are easier and less expensive to acquire than FDR data and data from dedicated flight tests).
- Evaluate flight profiles to understand why some procedures are quieter than others.

Milestones

- Identified Seattle Tacoma International Airport (SEA) noise monitor networks as potential sources of noise data for validation.
- Identified the OpenSky database as a source of flight procedure data for noise validation.
- Identified relevant machine learning techniques beyond simple linear regressions to correlate noise levels to operational factors.

Major Accomplishments

- Identified multilinear regression, clustering, and XGBOOST analysis as data-based modeling approaches to understand changes in noise as a function of operational and weather factors.

Publications

None.

Outreach Efforts

The ASCENT Project 044 team participated in the following outreach efforts:

- Collaboration with Port of Seattle to obtain noise data for arrivals and departures over three years
- Weekly teleconferences and meetings with FAA Technical Monitors
- Outreach and collaboration with Massport, an operator at Boston Logan International Airport (BOS), and ASCENT Advisory Board members
- Presentations at the biannual ASCENT Advisory Board meetings

Awards

None.

Student Involvement

Graduate and undergraduate students have been involved in all aspects of this research in terms of analysis, documentation, and presentation.

Plans for Next Period

Some focuses include using machine learning to understand differences that may exist for different tail numbers and airline differences, as well as multiple partial dependence analysis, to understand interactions amongst different factors as they relate to noise.

Task 2 – Apply Data Mining Techniques to Relevant Noise Monitor, Aircraft, Operator, and Flight Dynamics Data

Massachusetts Institute of Technology
University of California, Irvine

Objectives

Machine learning and data mining techniques identified in Task 1 will be applied to relevant noise monitor, aircraft, operator, and flight dynamics data. The process will begin with SEA noise and OpenSky surveillance data for several aircraft types. Additional data inferred data states, such as flight operation type, will also be considered. From this analysis, the trends or features relevant to the observed noise will be assessed, along with the identification of possible correlations between datasets.

Research Approach

- Identify methods to correct variations in modeled noise due to flap setting, aircraft weight, and ambient atmospheric conditions; apply these methods to departures and approaches at SEA.
- Acquire ADS-B data from the OpenSky Network and atmospheric data from the National Oceanic and Atmospheric Administration's High-Resolution Rapid Refresh; use these data to estimate weight from true airspeed and atmospheric attenuation from relative humidity and temperature.

Milestones

- Developed a method to relate OpenSky surveillance operational data to atmospheric data and noise monitor data at particular time stamps.
- Developed a departure and approach weight estimation method.
- Developed a method to assign flap deployment based on speed for each aircraft.

Major Accomplishments

- Developed a data-driven approach for assessing departure noise as a function of various operational, weather, and carrier factors.
- Validated the arrival and departure weight relations against FDR data from a partner airline.
- Identified contributing noise factors for departure and arrival procedures of various aircraft at SEA from three years of noise monitor recordings for Boeing 737-700, -800, -900, Airbus A319, A320, A321, and Boeing 777 flights.
- Demonstrated the impacts of aircraft configuration and weather on modeled and measured noise over noise monitors of interest at SEA for both approaches and departures.

Publications

Peer-Reviewed Journal Publications

Salguiero, S., Huynh, J. & Hansman. R. J. (2025). Aircraft Takeoff and Landing Weight Estimation from Surveillance Data. *Journal of Air Transportation, 33*(1). https://doi.org/10.2514/1.D0370

Published Conference Proceedings

Huynh, J., Lepe, M., Lee, T., Hood, P., & Hansman, R. J. (2023, November). Comparison of data-based and modeled-based analysis of aircraft departure noise using noise monitor network recordings. In *INTER-NOISE and NOISE-CON Congress and Conference Proceedings* (Vol. 268, No. 5, pp. 3349-3360). Institute of Noise Control Engineering. https://doi.org/10.3397/IN_2023_0484

Outreach Efforts

The ASCENT Project 044 team participated in the following outreach efforts:

- Weekly teleconferences and meetings with FAA Technical Monitors
- Outreach and collaboration with Massport, an operator at BOS, and ASCENT Advisory Board members
- Presentations at the biannual ASCENT Advisory Board meetings

Awards

None.

Student Involvement

Graduate and undergraduate students have been involved in all aspects of this research in terms of analysis, documentation, and presentation.

Plans for Next Period

The additional data mining techniques will be applied on three years of approach and departure radar, weather, and noise monitor data that have been obtained at SEA for multiple aircraft types.

Task 3 – Expand Approach to the Analysis of Additional Airports and Aircraft Types

Massachusetts Institute of Technology
University of California, Irvine

Objectives

The data mining approaches and analysis process from Task 2 will be expanded to additional airports and aircraft types. The modeling approach will be applied to gather data for the additional aircraft and locations. Potential trends or features relevant to the observed noise will be assessed for the larger dataset.

Research Approach

- Examine relevant noise monitor networks at different airports.
- Outreach to different airports to obtain noise monitor data.
- Expand approach to the analysis of additional airports and aircraft types.

Milestone
- Identified and reached out to obtain noise monitor date for analysis from BOS and John Wayne Airport (SNA).

Major Accomplishments
- Collected three years of approach and departure data at BOS for analysis to be done in the next phase.

Publications
None.

Outreach Efforts
The ASCENT Project 044 team participated in the following outreach efforts:
- Weekly teleconferences and meetings with FAA Technical Monitors
- Outreach and collaboration with Massport, an operator at BOS, and ASCENT Advisory Board members
- Presentations at the biannual ASCENT Advisory Board meetings

Awards
None.

Student Involvement
Graduate and undergraduate students have been involved in all aspects of this research in terms of analysis, documentation, and presentation.

Plans for Next Period
The data mining approaches and analysis process from Task 2 will be expanded to additional airports and aircraft types including BOS and SNA which has a unique and aggressive noise abatement procedure in place. This provides an opportunity to significantly expand the range of observed input states and give observably into maneuvers not normally flown at other airports.

Task 4 – Identify Operational Factors Which Influence the Community Noise at Specific Locations
Massachusetts Institute of Technology
University of California, Irvine

Objective
Operational factors from the large dataset and applied data mining techniques in Task 3 will be used to identify any operational factors which influence the community noise. Any observed differences in monitors, airport, and aircraft type will be identified to highlight location- or vehicle-specific trends.

Research Approach
- Use data mining techniques and big data to assess factors with the highest influences on noise levels.

Milestone
- Observed and identified a variety of departure and approach procedures in surveillance data at SEA as sufficient for noise analysis.

Major Accomplishments
- Measured noise levels versus weight, thrust, speed, altitude, weather factors, and airline were examined through a multivariate approach for departures and arrivals.
- For approach procedures, flights for which the speeds were more likely to have been in the clean configuration when the aircraft flew over the monitors were shown to correlate with lower recorded noise levels than flights that were more likely to have been in a dirty configuration when the aircraft flew over the monitors.

- Identified the correlation of aircraft that achieved higher altitudes early in the flight profiles with lower measured noise levels for departure procedures.
- Used different data-mining approaches such as multivariate correlations, clustering, and machine learning applied to the data at SEA to examine trends in variables affecting aircraft noise, including those due to aircraft weight, thrust, distance to the monitor, airspeed, ambient atmospheric conditions, and compounding factors.

Publications
None.

Outreach Efforts
The ASCENT Project 044 team participated in the following outreach efforts:
- Weekly teleconferences and meetings with FAA Technical Monitors
- Outreach and collaboration with Massport, an operator at BOS, and ASCENT Advisory Board members
- Presentations at the biannual ASCENT Advisory Board meetings

Awards
None.

Student Involvement
Graduate and undergraduate students have been involved in all aspects of this research in terms of analysis, documentation, and presentation.

Plans for Next Period
Any observed differences in monitors, airport, and aircraft type will be identified to highlight location- or vehicle-specific trends. In particular, the differences in analysis for procedures at BOS, SEA, and SNA will be examined to evaluate the effectiveness of these noise abatement procedures by a direct comparison.

Task 5 – Assess Implications of Results to the Design of Noise Abatement Procedures
Massachusetts Institute of Technology
University of California, Irvine

Objectives
Implications from Task 4 will be considered in the design of noise abatement arrival and departure procedures. Different flight operations will be explored, and may include cockpit procedures, published procedures, and air traffic control procedures. Results may influence recommended noise abatement techniques and opportunities to improve existing procedures and noise modeling methods.

Research Approach
- Treat noise monitoring data from different airports as experimental data, which could serve as a benchmark for comparing loud versus quiet flights.
- Determine whether learnings can be applied to future departure and approach noise abatement procedure designs.

Milestone
- Performed initial examination of quiet versus loud departure procedures from three years of SEA data.

Major Accomplishments
- Found aircraft altitude and thrust levels to have the strongest correlations with measured noise for the procedures examined.
- Identified weather factors such as relative humidity, temperature, and wind magnitude and direction to have some correlations, albeit weaker, with the measured noise levels on departure.

Publications
None.

Outreach Efforts
The ASCENT Project 044 team participated in the following outreach efforts:

- Weekly teleconferences and meetings with FAA Technical Monitors
- Outreach and collaboration with Massport, an operator at BOS, and ASCENT Advisory Board members
- Presentations at the biannual ASCENT Advisory Board meetings

Awards
None.

Student Involvement
Graduate and undergraduate students have been involved in all aspects of this research in terms of analysis, documentation, and presentation.

Plans for Next Period
The next phase of this project will evaluate how additional variables identified in the previous tasks influence aircraft noise and will inform the design of future advanced flight procedures intended to reduce aircraft noise.

Project 047 Clean-Sheet Supersonic Aircraft Engine Design and Performance

Massachusetts Institute of Technology

Project Lead Investigator

Steven R. H. Barrett
Professor of Aeronautics and Astronautics
Department of Aeronautics and Astronautics
Massachusetts Institute of Technology
77 Massachusetts Avenue
Cambridge, MA 02139
617-452-2550
sbarrett@mit.edu

University Participants

Massachusetts Institute of Technology (MIT)

- P.I.: Prof. Steven R. H. Barrett
- FAA Award Number: 13-C-AJFE-MIT, Amendment Nos. 052, 059, 074, 076, 090, 106, 110, and 115 (NCE to September 30, 2024)
- Period of Performance: March 29, 2019, to September 30, 2024
- Tasks:
  1. Identify mission profiles and operating requirements for propulsion systems
  2. Develop an engine cycle model for a supersonic aircraft propulsion system
  3. Assess environmental footprint of an engine for a supersonic transport aircraft
  4. Evaluate the impact of improved technology on relative performance benefits of clean-sheet and derivative engines
  5. Evaluate the effects of fan diameter and unconventional architectures on the environmental impacts of clean-sheet engines
  6. Assess the effect of variable noise reduction systems on landing and take-off (LTO) emissions for engines for supersonic transport aircraft
  7. Evaluate the impact of advanced take-off trajectories for supersonic transport (SST) using variable noise reduction systems on community noise

Project Funding Level

The ASCENT Project 047 received $1,650,000 in Federal Aviation Administration (FAA) funding and $1,650,000 in matching funds. Sources of matching funds are approximately $340,000 from MIT, plus third-party in-kind contributions of $177,000 from Byogy Renewables, Inc.; $982,000 from NuFuels, LLC; and $151,000 from Savion Aerospace Corporation.

Investigation Team

Prof. Steven Barrett, (P.I.), Tasks 1-7
Dr. Raymond Speth, (co-P.I.), Tasks 1-7
Dr. Choon Tan (co-P.I.), Tasks 1-7
Dr. Jayant Sabnis, (co-investigator), Tasks 1-7
Dr. Prakash Prashanth, (graduate student), Tasks 1, 2, 3, 4, and 5
Dr. Laurens Voet, (graduate student), Tasks 1, 3, 6, and 7
Mr. Wyatt Giroux, (graduate student), Task 5

Project Overview

Engines for supersonic aircraft, compared with those for subsonic aircraft, present unique challenges in terms of fuel consumption, noise, and emissions impacts, because of their unique operating conditions. The propulsion systems currently proposed by the industry are derivative engines (Figure 1) designed around the unmodified core (high-pressure compressor, combustor, and high-pressure turbine) of existing subsonic engines, with modifications to the low-pressure spool (fan and low-pressure turbine).

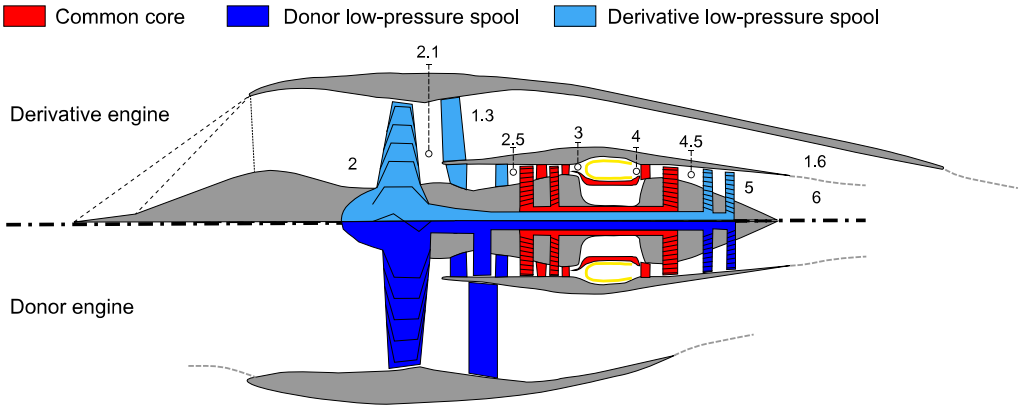

Figure 1. Engine architecture schematic. The lower half shows the subsonic donor engine. The high-pressure spool (red) core is used in the derivative engine (top half) along with modifications to the inlet, fan, and nozzle, as shown in the top half.

This project is aimed at evaluating the design space of "clean-sheet" engines designed specifically for use on civil supersonic aircraft, and to determine the resulting environmental performance of such engines. Unlike previous commercial supersonic engines, which were adapted from military aircraft, or planned propulsion systems derived from current commercial engines, a clean-sheet engine takes advantage of recent advances in propulsion system technology to substantially improve performance and reduce emissions and noise footprints. This project will quantify these benefits for a range of engine designs relevant to currently proposed civil supersonic aircraft. Conventional clean-sheet engines have been examined by the ASCENT Project 047 team. To further characterize the clean-sheet design space, more unconventional engine architectures, namely hybrid-electric systems, are investigated. Specifically, we aim to assess the relative performance of hybrid-electric clean-sheet and conventional clean-sheet engines.

Task 1 - Identify Mission Profiles and Operating Requirements for Propulsion Systems

Massachusetts Institute of Technology

Objectives

The objectives of this task are to (1) identify representative mission profiles of commercial SST aircraft (i.e., characterize stages of the mission by defining parameters such as climb rates and accelerations) and (2) use these mission profiles and representative aircraft parameters (e.g., wing area, drag and lift polars) of civil supersonic aircraft operating in different Mach regimes to derive propulsion system requirements for supersonic aircraft.

Research Approach

Design Space Survey

In Figure 2, the ASCENT Project 047 team presents a set of SST aircraft concepts and existing designs with their respective range and cruise Mach (M) number.

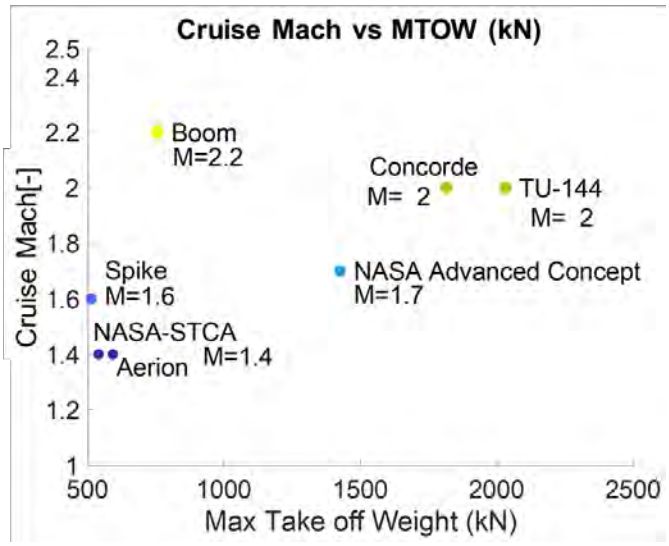

Figure 2. Range versus maximum take-off weight for civil SST aircraft concepts and existing designs.

Figure 2 shows the variability of different concepts and designs for SST. The only existing designs are the Anglo-French Concorde and the Russian Tupolev TU-144 in the Mach 2 regime. However, upcoming companies looking to bring SST back to the market are developing aircraft in different Mach regimes, including low-supersonic (M~1.4), mid-supersonic (M~1.6), and high-supersonic (M~2), and in different weight classes: small business jets and larger airliners.

Mission Profiles

The only existing SST aircraft were the Concorde and Tupolev TU-144. Morisset (1974) compared their performance and shows their mission profiles. A typical mission profile of Concorde is shown in Figure 3. This mission profile is chosen as a case to test the tool to derive propulsion system requirements for an SST aircraft. The mission profile is modeled in SUAVE (Lukaczyk et al., 2015). A comparison of the mission profiles is shown in Figure Figure 3. The descent profile in SUAVE is modeled as a single mission stage because it is assumed that the propulsion requirements during descent will not be critical.

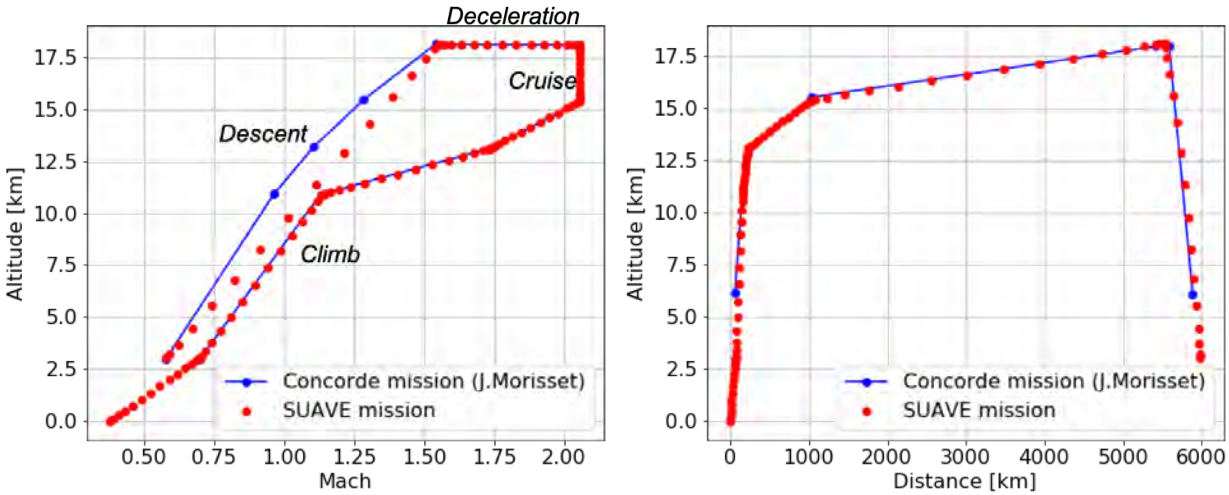

Figure 3. Typical mission profile of Concorde.

Propulsion System Requirements

The SUAVE tool is used to estimate propulsion system requirements for the Concorde aircraft based on the Concorde flight reports (Morisset, 1974). The standard aircraft parameters and aerodynamic coefficients of the Concorde aircraft from the SUAVE tool are used. The propulsion system requirements (i.e., thrust) of the Concorde mission are given in Figure 4 (top). The variation in the drag coefficient of the aircraft during the mission is given in Figure 4 (bottom). The discontinuities in the thrust profile come from jumps in climb rates and in acceleration rates. In Figure 4, the drag coefficient can be seen to sharply increase when crossing the sound barrier. From the thrust profile, the most critical points in the mission can be identified. The engine will need to be able to generate the specified thrust at these points. Therefore, the thrust at these critical points will be a direct input in Task 2 when developing the engine cycle model.

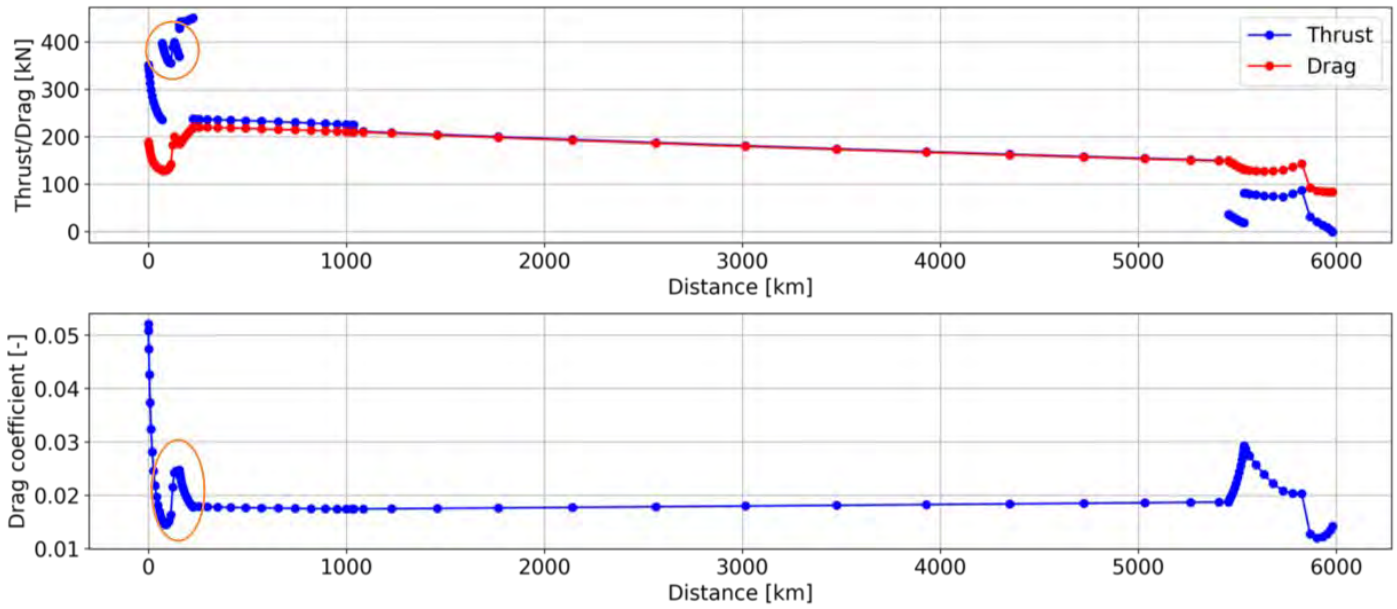

Figure 4. Propulsion system requirements (i.e., thrust and drag) and drag coefficient throughout the mission given in Figure 3. The circled areas indicate the transonic acceleration.

NASA 55-tonne STCA

The National Aeronautics and Space Administration (NASA) has designed a 55-tonne Supersonic Transport Concept Aircraft (STCA) with a cruise Mach number of 1.4 (Berton & Geiselhart, 2019). The aircraft configuration of the STCA is used to derive propulsion system requirements for a small business jet in the low-supersonic Mach regime. The four critical sizing points of the NASA STCA, as illustrated in Table 1, are used in a multiple-design-point (MDP) model in the engine design process.

Table 1. Propulsion system requirements (per engine) for STCA. The top-of-climb conditions are chosen as the aerodynamic design point for any component that is purpose designed for the application.

	Sea Level Static (SLS)	Take-off (TO)	Top-of-climb (TOC)	End-of-cruise (EOC)
Altitude [kft]	0	0	41	51
Mach [-]	0	0.25	1.4	1.4
Thrust [lbf]	16,617	14,140	5,500	3,300

Mission requirements for other aircraft designs will be obtained through collaborations with ASCENT Project 010.

M2.2 Medium SST – 55 passengers, Mach 2.2 Airliner
The mission requirements of a 55-passenger, 4-engine, Mach 2.2 SST – designed by the Georgia Institute of Technology – have been obtained through collaboration with the ASCENT 010 Project.

Milestone(s)

- Conducted a review of the SST concepts and existing designs.
- Identified the appropriate tools to derive propulsion system requirements for an SST aircraft flying a specific mission.

Major Accomplishments

- Conducted a survey of SST concepts and existing designs. Upcoming players in the SST market are developing aircraft in different Mach regimes (i.e., low-, mid-, and high-supersonic regimes) and weight classes (i.e., business jet and airliner).
- Selected SUAVE to derive propulsion system requirements for a supersonic aircraft flying a specific mission profile. For the specific case of a small business jet in the low-supersonic Mach regime, the NASA 55-tonne STCA aircraft (Berton & Geiselhart, 2019).

Publications

None.

Outreach Efforts

- Contacted Boom Supersonic to discuss representative mission profiles and aircraft parameters.
- Prof. Steven Barrett gave a presentation titled "Clean-sheet supersonic engine design and performance" at the ASCENT meeting in Atlanta, GA, on April 19, 2019.
- Dr. Jayant Sabnis gave a presentation titled "Clean-sheet supersonic engine design and performance" at the ASCENT meeting in Alexandria, VA, on October 22, 2019.

Awards

None.

Student Involvement

This task was conducted primarily by Mr. Prakash Prashanth and Mr. Laurens Voet, graduate research assistants working under the supervision of Dr. Jayant Sabnis, Dr. Raymond Speth, and Dr. Choon Tan.

References

Berton, J., & Geiselhart, K. (2019). *NASA 55 tonne Supersonic Transport Concept Aeroplane (STCA) release package*. NASA Glenn Research Center & NASA Langley Research Center.

Lukaczyk, T., Wendorff, A. D., Botero, E., MacDonald, T., Momose, T., Variyar, A., Vegh, M. J., Colonno, M., Economon, T. D., Alonso, J. J., Orra, T. H., and da Silva, C. I. (2015, June 22-26). *SUAVE: An open-source environment for multi-fidelity conceptual vehicle design* [Conference presentation]. 16th AIAA/ISSMO Multidisciplinary Analysis and Optimization Conference, Dallas, Texas. https://doi.org/10.2514/6.2015-3087

Morisset, J. (1974). *Tupolev 144 and Concorde – The official performances are compared for the first time* (NASA-TT-F-15446). NASA. https://ia800507.us.archive.org/11/items/nasa_techdoc_19740011548/19740011548.pdf

Task 2 - Develop an Engine Cycle Model for a Supersonic Aircraft Propulsion System

Massachusetts Institute of Technology

Objective

The objective of this task was to develop an engine cycle deck to analyze clean-sheet and derivative propulsion systems for commercial supersonic aircraft.

Research Approach

The Numerical Propulsion System Simulation (NPSS) tool is chosen to develop the engine cycle decks for clean-sheet and derivative engines, because it is an industry standard tool that facilitates future collaboration with other users of the tool.

Baseline Engine

To develop the derivative engine, a baseline engine is first chosen and modeled. The CFM56-5B engine was chosen for this task because it is the donor engine for the proposed GE Affinity engine. The baseline engine was modeled using published data from Jane's Aero Engines (Gunston, 1996) and data published in the Engine Emissions Databank (EEDB) by the European Union Aviation Safety Agency (EASA) (EASA, 2019). The data published by EASA consist of fuel flow and emission indices of several species at take-off, climb, idle, and approach conditions of various thrust variants of the CFM56-5B engine. The EEDB data can be processed based on the serial number of the tested engines to relate multiple entries in the databank to a common engine, as shown in Figure 5.

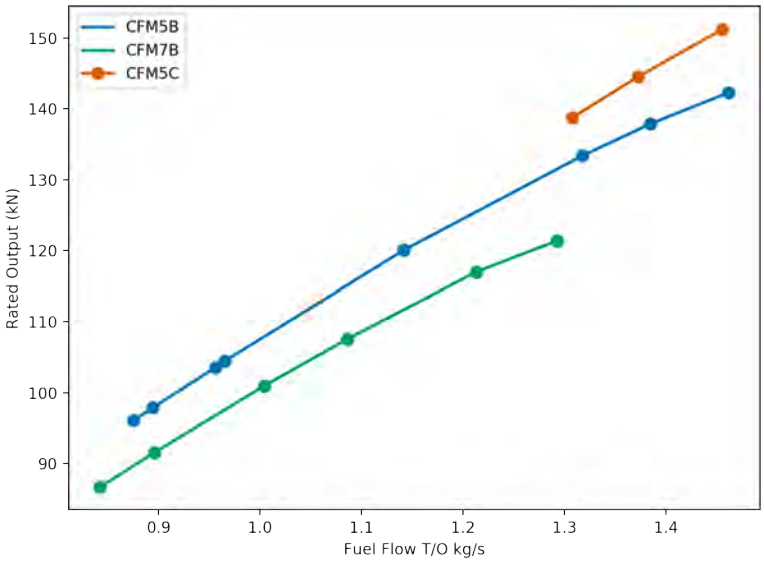

Figure 5. Variants of the CFM56 engine; the CFM56-5B Tech Insertion engine is chosen for the baseline engine.

The engine model (see schematic below) consists of an inlet, fan, low-pressure compressor (LPC), high-pressure compressor (HPC), combustor, high-pressure turbine (HPT), low-pressure turbine (LPT), and nozzles for the bypass and core ducts.

Component parameters such as efficiencies, pressure ratios, and bleed flows for the engine model were varied at a chosen design point. The point chosen for this was the sea-level static thrust of the highest thrust variant of the engine. Subsequent off-design runs were carried out to evaluate whether the model matched the published data on fuel flow at particular thrust levels.

Furthermore, the CFM56-5B and CFM56-7B engines share the same physical core. This information is used to validate the model representing the core specifically by using the core model calibrated to the CFM56-5B data to represent the CFM56-7B engine, by fixing the core components and varying only the low-spool components.

Derivative Engine Model

The thrust requirements of the derivative engine are given in Table 1. As shown in the engine architecture diagram in Figure 1, the derivative engine for supersonic application uses the high-pressure core of the donor subsonic engine. The low-pressure spool consists of a two-stage fan and LPT. An external compression supersonic inlet with two oblique shocks is mounted upstream of the fan, with a pressure recovery modeled using standard oblique shock equations. A fully mixed, variable area nozzle is added downstream of the LPT. The engine is designed such that the nozzle is at the cusp of choke at

take-off conditions to avoid shock-cell noise. Polytropic efficiencies of the turbomachinery components are set to values representative of the CFM56-5B3 technology level. The map scalars of the turbomachinery components in the engine cycle model, the flow areas, and the cooling bleed flow fractions of the CFM56 donor engine core are applied as fixed constants to the derivative engine model.

Clean-Sheet Engine Model
The clean-sheet engine is also designed to meet the propulsion system requirements outlined in Table 1. The engine architecture for the clean-sheet design is the same as the derivative design. However, all the components for the clean-sheet engine, along with the high-pressure core, are purpose-designed. To have a fair comparison between the derivative and clean-sheet engine, the polytropic efficiencies of the turbomachinery are set to the CFM56 values to model the same technology level and turbine cooling flow requirements are met using semi-empirical methods.

Engine Performance Sensitivities
An optimizer coupled with the NPSS models is used to optimize the cycle subject to any constraints (temperature limits and fan diameter limits) for various thrust requirements.

Environmental Footprint Calculations
A first-principles approach is used to evaluate design space constraints imposed by the donor core on the environmental footprint of the derivative engine. The engine cycle deck described above is used to calculate the engine performance in terms of specific fuel consumption (SFC), emissions index and noise of both the derivative and clean-sheet engine. Engine gaseous nitrogen oxides (NO_x) emissions are quantified using the P_3-T_3 method (DuBois & Paynter, 2006). The emission index of NO_x is assumed to be proportional to $P_{t3}^{0.4}$ and a polynomial fit in T_{t3}, constructed based on engine emission data from the International Civil Aviation Organization (ICAO) emission databank, leading to the correlation

$$\frac{\mathrm{EI(NO_x)}}{P_{t3}^{0.4}} = 6.26 \cdot 10^{-8} T_{t3}^3 - 0.00117 T_{t3}^2 + 0.0074 T_{t3} - 15.04 \qquad \text{(Eq. 1)}$$

The aircraft certification cumulative noise levels are computed based on standard methods as summarized in Task 3 (see Table 2).

Milestones

- Developed multiple engine models in NPSS. The donor engine for the supersonic derivative core is chosen to be the CFM56-5B engine.
- Used the derivative engine model to evaluate the impact of design space constraints on the performance of the engine relative to the clean-sheet model.
- Compared the performance of the clean-sheet engine and derivative engines for different thrust requirements.

Major Accomplishments

CFM56-5B3 Model Calibration
Publicly published data were used to build a CFM56-5B3 model in NPSS and calibrate the model at sea-level static conditions as shown in Figure 6.

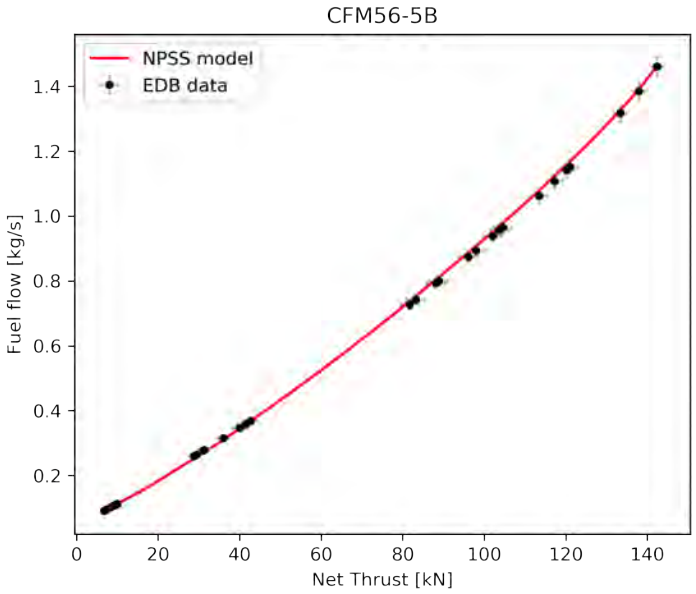

Figure 6. Off-design comparison of the NPSS model and ICAO data from the EEDB for the CFM56-5B engine.

The model is compared with the data available in the EEDB maintained by EASA on behalf of ICAO. The average root mean square (RMS) error for all the landing and take-off (LTO) data points is approximately 2%, suggesting a successful calibration.

The same core is used in a CFM56-7B engine and compared with EEDB data as shown in Figure 7. The average RMS error was approximately 3% in this case (Figure 7).

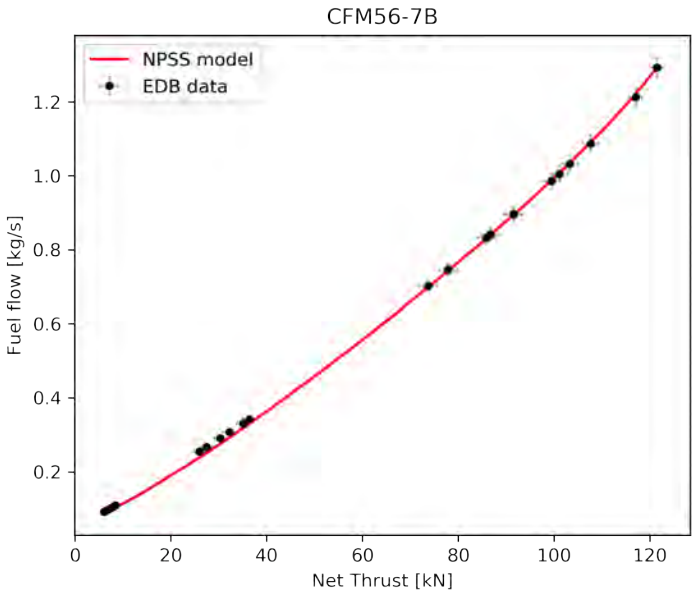

Figure 7. Off-design comparison of the NPSS model and ICAO data from the EEDB for the CFM56-7B engine using the common core.

Derivative Engine Design Space Constraints

Since the core of the derivative engine is sized by the donor-engine (CFM56) cycle, the pressure ratio of the HPC of the derivative engine is not an independent design variable (in contrast to a clean-sheet engine where the HPC pressure ratio is a design variable that can be optimized). The design space of the derivative engine is illustrated in Figure 8. The core of the derivative engine also has cooling flows for the high-pressure turbine sized by the donor engine cycle. Therefore, there are regions of the design space where insufficient cooling flow can result in turbine blade metal temperatures exceeding the set limits. Therefore, the constraints from the donor core limit the feasible design space that can be used for the derivative engine.

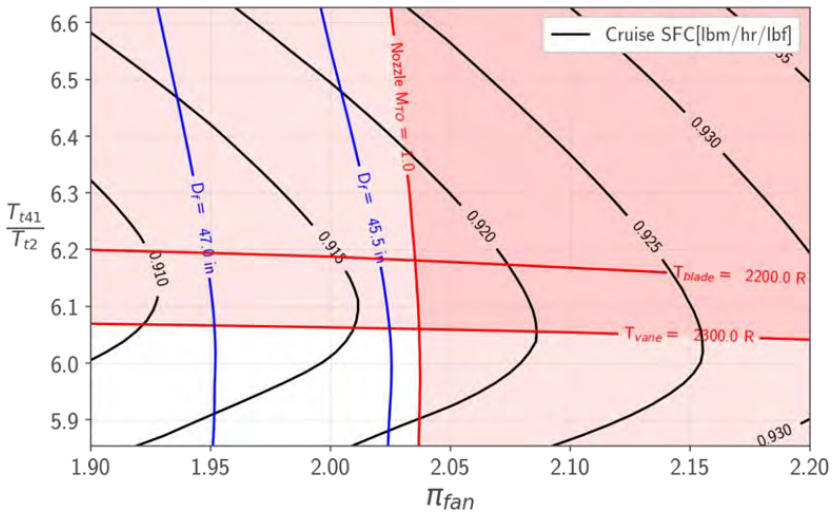

Figure 8. Design space of the derivative engine: turbine inlet temperature over compressor inlet temperature ratio, T_{t41}/T_{t2}, vs. fan pressure ratio, π_{fan}, at the engine aerodynamic design point. The performance contours show the cruise SFC. The resulting fan diameter, D_f, for different designs in the design space is indicated.

Engine Performance Sensitivities

The required thrust of the aircraft impacts the performance of the clean-sheet and derivative engines. At each thrust level, the clean-sheet and derivative engine are optimized to provide minimum SFC. Figure 9 shows the impact that the thrust required has on the fuel consumption and emissions of NO_x. The fan size for both engines is constrained to be 45.5 in. (consistent with the STCA airframe requirement).

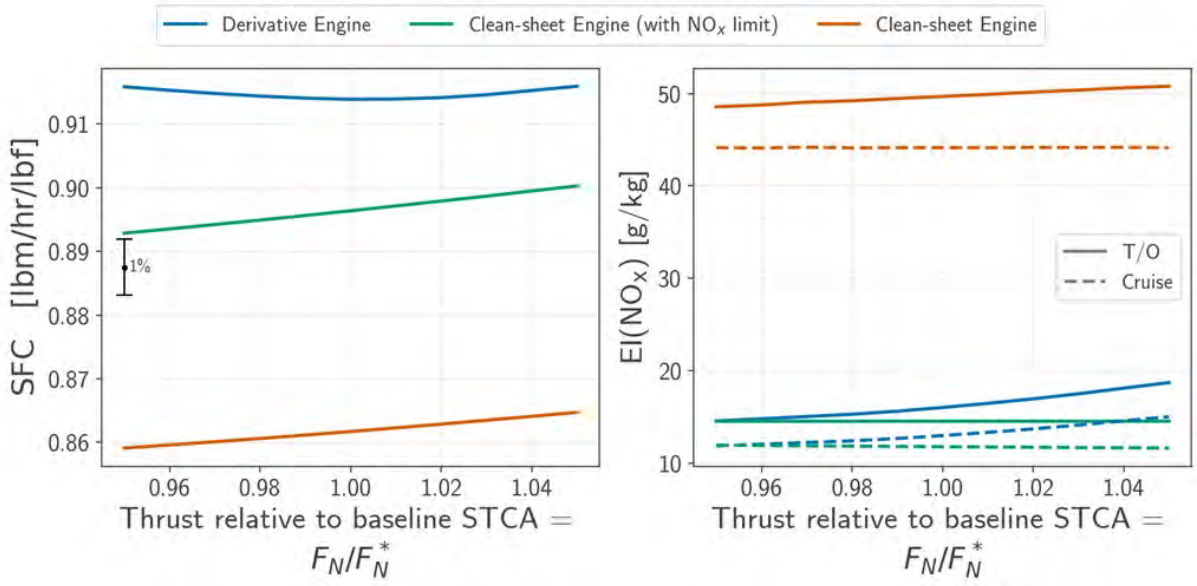

Figure 10. Sensitivities of engine performance parameters (specific fuel consumption at cruise, $\boldsymbol{SFC}$, and NO_x emission index, $\boldsymbol{EINO_x}$, at both design and sea-level static take-off conditions) for a range of thrust requirements. The thrust required is shown as a fraction of the STCA design thrust.

As seen in Figure 11, the clean-sheet engine designed for minimum SFC results in a 5.5 – 6.5% reduction in SFC relative to the derivative. However, assuming the same combustor technology is applied in the clean-sheet engine as the derivative, the emissions of NO_x from the clean-sheet engine that is optimized for minimum SFC is approximately three times greater than the derivative engine. An alternate clean-sheet engine sizing strategy is to impose a NO_x emissions constraint. This results in a 2-3% reduction in SFC relative to the derivative engine. This highlights the need to switch to advanced combustor designs that minimize NO_x emissions if the potential SFC benefits of a clean-sheet engine design are to be realized.

Publications

Voet, L., Prashanth, P., Speth, R., Sabnis, J., Tan, C., & Barrett, S. (2021, January 11–15 & 19–21). *The impact of design space constraints on the noise and emissions from derivative engines for civil supersonic aircraft* [Conference presentation]. AIAA Scitech 2021 Forum, virtual.

Prashanth, P., Voet, L. J. A., Speth, R. L., Sabnis, J. S., Tan, C. S., & Barrett, S. R. H. (2023). Impact of Design Constraints on Noise and Emissions of Derivative Supersonic Engines. *Journal of Propulsion and Power*, *39*(3), 1–10. https://doi.org/10.2514/1.B38918

Outreach Efforts

- Dr. Jayant Sabnis gave a presentation titled “Noise and emission characteristics of commercial supersonic aircraft propulsion systems” at the Aviation Noise and Emissions Symposium on March 5, 2019.
- Mr. Prashanth Prakash and Mr. Laurens Voet gave a presentation titled “Clean-sheet supersonic engine design and performance” at the at the virtual ASCENT meeting on September 30, 2020.
- Mr. Prashanth Prakash and Mr. Laurens Voet gave a presentation titled “Clean-sheet supersonic engine design and performance” at the virtual ASCENT meeting on April 27, 2021.
- Mr. Prashanth Prakash gave a presentation titled “Civil Supersonic Transport Emissions” at the Aviation Emissions Characterization Roadmap 2021 Annual Meeting on May 26, 2021.

Awards

None.

Student Involvement

This task was conducted primarily by Prashanth Prakash, a graduate research assistant working under the supervision of Dr. Jayant Sabnis, Dr. Raymond Speth, and Dr. Choon Tan.

References

DuBois, D., & Paynter, G. C. (2006). Fuel Flow Method 2 for estimating aircraft emissions (SAE Technical Paper 2006-01-1987). SAE International.

EASA (2019). ICAO Aircraft Engine Emissions Databank, version 26A. European Union Aviation Safety Agency (EASA). https://www.easa.europa.eu/easa-and-you/environment/icao-aircraft-engine-emissions-databank

Gunston, B. (1996). *Jane's aero-engines*. Jane's Information Group.

Task 3 - Assess Environmental Footprint of an Engine for a Supersonic Transport Aircraft

Massachusetts Institute of Technology

Objective

The objective of this task is to develop models to assess the environmental footprint of an SST aircraft. Models for both the noise footprint and the emissions footprint will be developed.

Research Approach

The flow chart in Figure 10 illustrates the approach to model the environmental footprint of engines for SST.

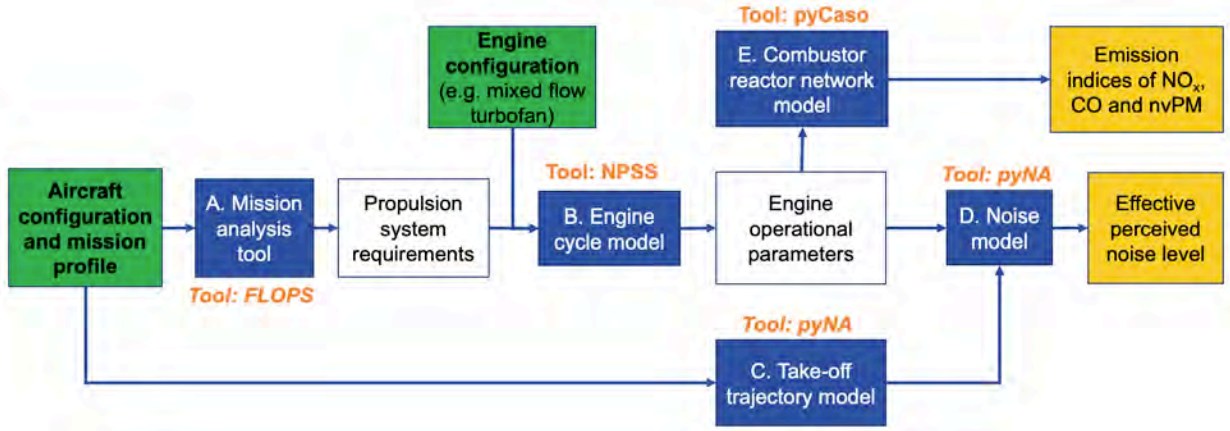

Figure 12. Overview of the framework to model environmental footprint of engines for SST. The mission analysis is performed using the NASA Flight Optimization System (FLOPS) software, the engine cycle model is made in the NPSS tool, the combustor reactor network model (pyCaso) and the aircraft noise and take-off trajectory model (pyNA) are used to calculate emission indices and effective perceived noise levels of the engines.

Emissions Modeling

A chemical reactor network combustor model (pyCaso) was developed to assess the emissions of the engines for SST. The combustor model represents CFM56-TechInsertion rich-quench-lean (RQL) combustor technology. The combustor model is illustrated in Figure 11. A series of perfectly stirred reactors in parallel, representing the primary zone of the combustor, are coupled to a secondary zone plug flow reactor. Similar to the engine model, the emission characteristics of the combustor model are validated against publicly available data from the EEDB.

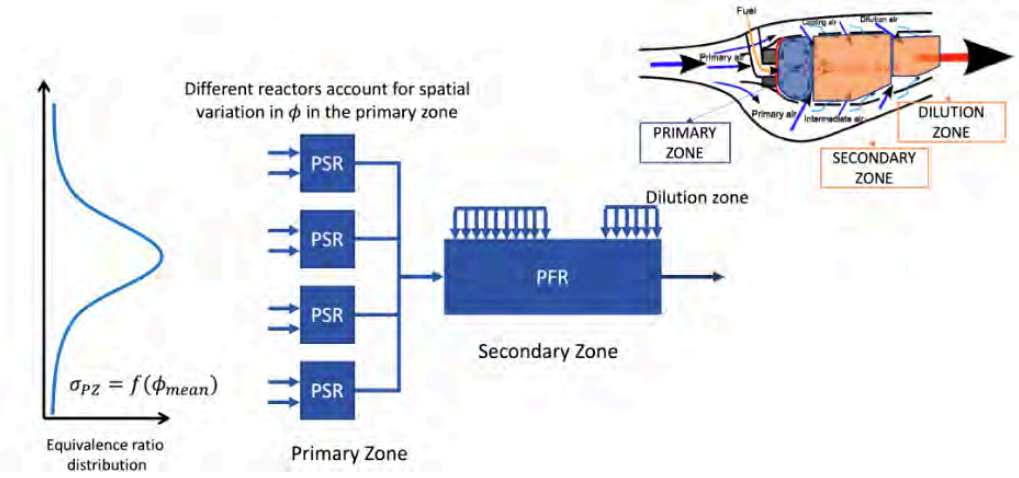

Figure 13. Chemical reactor network combustor model: a series of perfectly stirred reactors (PSR) in parallel, representing the primary zone, combined in parallel with a secondary zone plug flow reactor (PFR). The series of perfectly PRF represents a gaussian distribution, with standard deviation, $\boldsymbol{\sigma_{PZ}}$ being a function of the mean equivalence ratio, $\boldsymbol{\phi_{mean}}$.

Noise Footprint Modeling

A Python Noise Assessment (*pyNA*) model was developed to estimate the engine certification noise levels and assess their sensitivities with respect to engine operating variables. The model is developed in Python within the OpenMDAO framework (Gray et al., 2019); the individual noise modules have been implemented in Julia to be able use its automatic differentiation (AD) libraries for the Jacobian computation. The different noise modules in *pyNA,* as shown in Figure 12, are developed based on the methods from literature listed in Table 2, based on the NASA Technical Memorandum TM-83199 (Zorumski, 1982). The extended design structure matrix (Lambe et al, 2012) of the aircraft noise estimation model is shown in Figure 12.

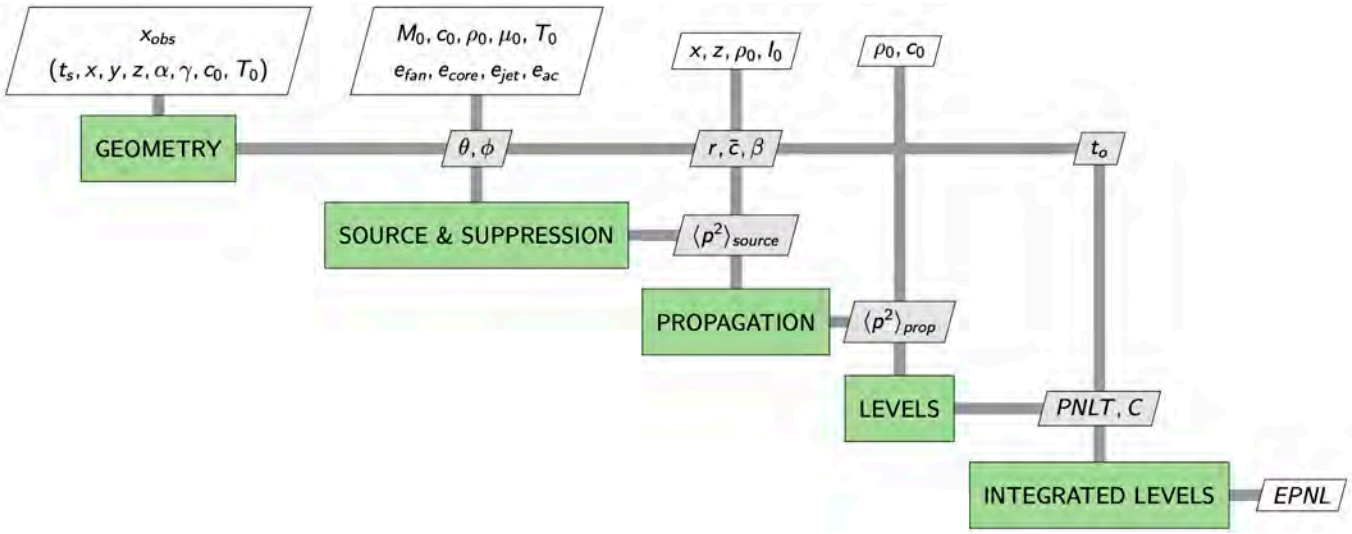

Figure 14. Flow chart of the pyNA model with the different modules required to estimate the effective perceived noise level (EPNL) from engine cycle and fan parameters.

Table 2. Methods for the noise source, propagation, and levels modules.

Module	Method from literature
Noise source modules • Jet mixing noise • Jet shock-cell noise • Combustor noise • Fan broadband and tones (inlet and discharge) • Airframe noise	Single-stream, shock-free jet mixing noise (SAE International, 2021) Circular jet shock cell noise (SAE International, 2021) Emmerling method FAA-RD-74-125 (Emmerling et al., 1976) Heidmann method NASA TM X-71763 (Heidmann, 1979) • with GE Aircraft Engines revision NASA CR-195480 for broadband (Kontos et al., 1996a) • with AlliedSignal revision for fan tones (Hough & Weir, 1996) • with fan treatment NASA CR-202309 (Kontos et al., 1996b) Fink method FAA RD-77-29 (Fink, 1977) • with HSR calibration *NASA CR-2004-213014 (*Golub et al., 2004)
Noise propagation modules • Spherical spreading/characteristic impedance • Atmospheric absorption • Ground reflection and attenuation • Lateral attenuation • Wing shielding module	R^2 law and characteristic impedance ratio Exponential decay using atmospheric absorption coefficient (Montegani, 1979) Chien-Soroka method (Chien & Soroka, 1975) SAE AIR 5662 method (SAE International, 2025), Berton method (Berton, 2021) Maekawa method (copied shielding factors from STCA) (Maekawa, 1968)
Certification Noise Levels modules • Perceived noise level, tone corrected (PNLT) • Effective perceived noise level (EPNL)	ICAO Annex 16 Volume I: Aircraft noise App. 2-13 (ICAO, 2017) ICAO Annex 16 Volume I: Aircraft noise App. 2-13 (ICAO, 2017)

Berton, J. (2021, August 2-6). *Simultaneous use of ground reflection and lateral attenuation noise models* [Conference presentation]. AIAA AVIATION 2021 FORUM, virtual. https://doi.org/10.2514/6.2021-2214

Chien, C., & Soroka, W. (1975). Sound propagation along an impedance plane, *Journal of Sound and Vibration*, 43(1), 9–20.

Emmerling, J., Kazin, S., & Matta, R. (1976). *Core engine noise program Volume III. Prediction methods – Supplement I: Extension of prediction methods, technical report*. Ohio Aircraft Engine Business Group, General Electric Co., Cincinnati, Ohio. https://apps.dtic.mil/sti/pdfs/ADA030376.pdf

Fink, M. R. (1977). *Airframe noise prediction method*. United Technologies Research Center, East Hartford, Connecticut.

Golub, R., Rawls Jr, J. W., & Yeager, J. C. (2004). *High Speed Research Noise Prediction Code (HSRNOISE) user's and theoretical manual*. NASA. https://ntrs.nasa.gov/api/citations/20040200978/downloads/20040200978.pdf

Heidmann, M. F. (1979). *Interim prediction method for fan and compressor source noise* (NASA-TM-x71763). NASA. ntrs.nasa.gov/api/citations/19750017876/downloads/19750017876.pdf

Hough, J. W., & Weir, D. S. (1996). *Aircraft noise prediction program (ANOPP) fan noise prediction for small engines* (NASA-CR-198300). NASA Langley Research Center. ntrs.nasa.gov/api/citations/19960042711/downloads/19960042711.pdf

ICAO. (2017). *Annex 16 to the Convention on International Civil Aviation Environmental Protection Volume 1: aircraft noise* (Ed. 8). International Civil Aviation Organization (ICAO).

Kontos, K. B., Janardan, B., & Gliebe, P. (1996a). *Improved NASA-ANOPP noise prediction computer code for advanced subsonic propulsion systems, Volume 1: ANOPP evaluation and fan noise model improvement* (NASA CR-195480). NASA Lewis Research Center. https://ntrs.nasa.gov/api/citations/19960048499/downloads/19960048499.pdf

Kontos, K. B., Kraft, R. E., & Gliebe, P. R. (1996b). *Improved NASA-ANOPP noise prediction computer code for advanced subsonic propulsion systems, Volume 2: Fan suppression model development* (NASA-CR-202309). NASA Lewis Research Center. https://ntrs.nasa.gov/api/citations/19960048499/downloads/19960048499.pdf

Maekawa, Z. (1968). Noise reduction by screens, *Applied Acoustics*, 1(3), 157–173.

Montegani, F. J. (1979). Computation of atmospheric attenuation of sound for fractional-octave bands (NASA Technical Paper 1412). NASA. ntrs.nasa.gov/api/citations/19790009488/downloads/19790009488.pdf

SAE International. (2025). AIR5662: *Method for predicting lateral attenuation of airplane noise*. https://doi.org/10.4271/AIR5662

SAE International. (2021). *ARP-876F: Gas turbine jet exhaust noise prediction*. https://doi.org/10.4271/ARP876F

The *Geometry* component computes geometrical variables related to the aircraft trajectory relative to the observer position, x_{obs}, i.e., source-observer distance, r; polar and azimuthal directivity angle, (θ, ϕ); elevation angle, β; and observer time, t_O. In the *Source and Suppression* modules, the mean-square acoustic pressure of the different noise sources is computed, and noise suppression is applied to the fan and airframe mean-square acoustic pressure, for the fan liner treatment and the SST airframe calibration, respectively. In the *Propagation* component, the source mean-square acoustic pressure is propagated to the observer through the atmosphere, using the propagation effects listed in Table 2. Finally, the noise levels at the observer, including overall sound pressure level (SPL), tone-corrected perceived noise level (PNLT), and EPNL, are computed in the *Levels* and *Integrated Levels* components.

The Jacobian of the individual noise modules in Table 2 are computed using an AD method. AD provides more accurate derivative computations compared to finite-difference (FD) methods, as well as faster computations compared to FD and complex-step (CS) differentiation methods. The Julia ForwardDiff package (Revels et al., 2016) is used to implement the partial derivatives of the aircraft noise estimation model.

Milestones

- Developed a chemical reactor network–based combustor model, and calibrated NO_x and carbon monoxide (CO) emissions to the EEDB data using combustor inlet values obtained from the NPSS model of the CFM56-5B engine.
- Developed an open-source aircraft noise estimation model estimating the static noise database from relevant engine parameters, the static-to-flight noise projection, and the certification noise levels.
- Provided the sensitivities of the certification noise levels to engine operating parameters by the model to enable multi-disciplinary design optimization and optimal control.

Major Accomplishments

Emissions Model

A framework was developed to estimate the NO_x and CO emissions indices of the donor engine, given the relevant engine parameters using a reactor network model. A comparison of the model developed and the EEDB data is shown in Figure 13. The derivative and clean-sheet engine analyzed in the work described here assumes that the combustor technology used is similar to that of the donor engine and therefore the calibrated parameters are assumed to hold for the clean-sheet engine as well. A soot model to estimate the non-volatile particulate matter (nvPM) concentrations is currently being integrated into the combustor model.

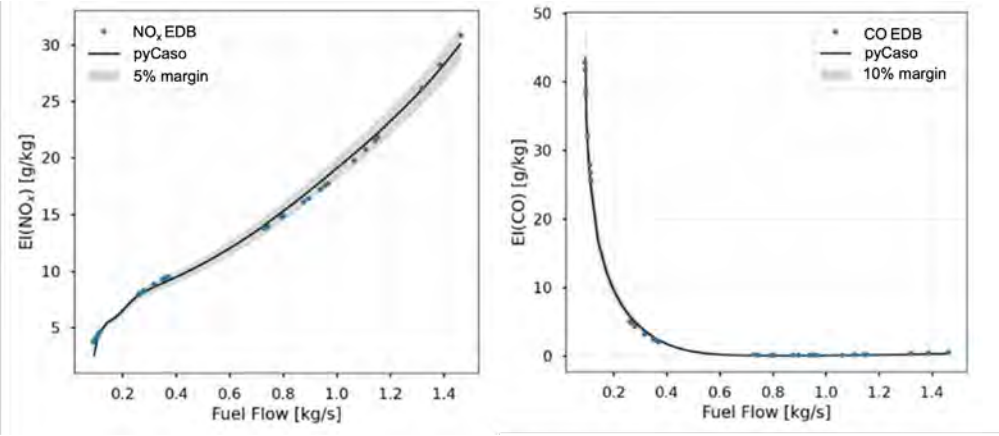

Figure 15. Comparison of NO_x emission indices (left) and CO emission indices (right) of the combustor model and ICAO data from the EEDB.

Aircraft Noise Model (pyNA)

A framework was set up to estimate the noise levels (i.e., SPL, PNLT and EPNL) of the engine given the relevant engine parameters using a semi-empirical model.

Aircraft Noise Estimation Model: Verification

The utility of the aircraft noise model is evaluated based on the noise assessment of the STCA, designed by NASA to evaluate environmental and economic impacts of SST (Berton et al., 2020). The noise modules are evaluated on the standard take-off trajectory, denoted by Berton et al. (2018) as a trajectory that abides by the noise regulation procedures in ICAO Annex 16 for subsonic transport-category airplanes (Berton et al., 2018; ICAO, 2017a). The STCA is a 55-tonne, 8-passenger, Mach 1.4 business tri-jet, cruising at altitudes between 12.5 and 15.5 km (Berton et al., 2020). The STCA noise assessment was performed by Berton et al. (2018) using the NASA Aircraft Noise Prediction Program (ANOPP) (Zorumski, 1982).

The spectral and polar directivity SPL-distribution the fan inlet and discharge, core, jet mixing, and airframe source modules are determined at the zenith point of the flyover observer for a series of one-third octave frequencies, as shown in the polar plots in Figure 14. The engine noise sources are independent of the azimuthal directivity angle, ϕ; the airframe noise source module is plotted for an azimuthal directivity angle, ϕ = 0 deg. The SPL distribution is computed along a circular arc with a 0.3048 m (1 ft) radius from the noise source. The SPL distributions are compared to the NASA STCA ANOPP noise assessment in the polar plots of Figure 14. Excellent agreement is found – a root mean square (RMS) error <0.1dB across polar directivity angles and frequencies – between the current noise model (pyNA) and STCA data for the core, jet mixing and airframe source SPL. Good agreement is found – an RMS error <1.3dB – for the fan inlet and discharge broadband component, although discrepancies can be found in the fan tonal components of the fan inlet and discharge noise.

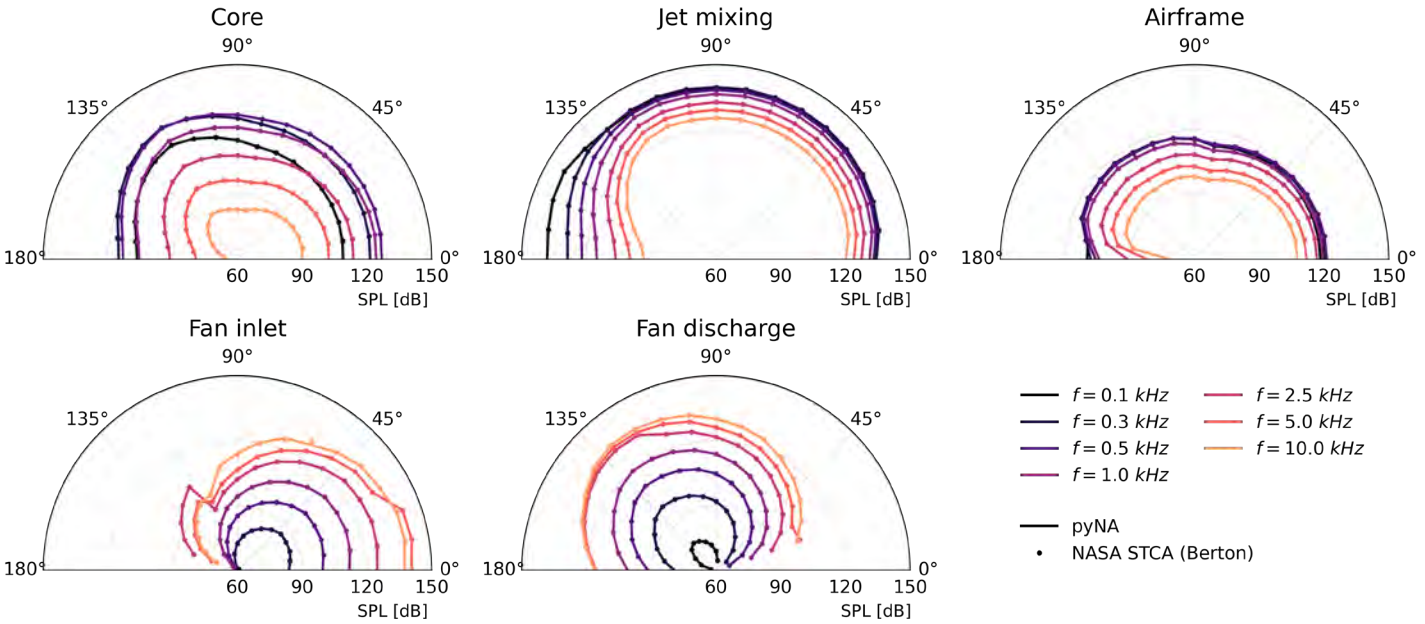

Figure 16. Comparison of the spectral and directional sound pressure level (SPL) distribution at the zenith point of the flyover microphone determined using the current noise model (pyNA) and NASA ANOPP (Berton et al., 2018).

The total PNLT at the lateral and flyover microphones computed by the current noise model (pyNA) is compared to the NASA STCA ANOPP noise assessment in Figure 15. The PNLT curves computed by pyNA have an RMS error of 0.35 PNdB in the domain of dependence of the EPNL, compared to those computed by ANOPP.

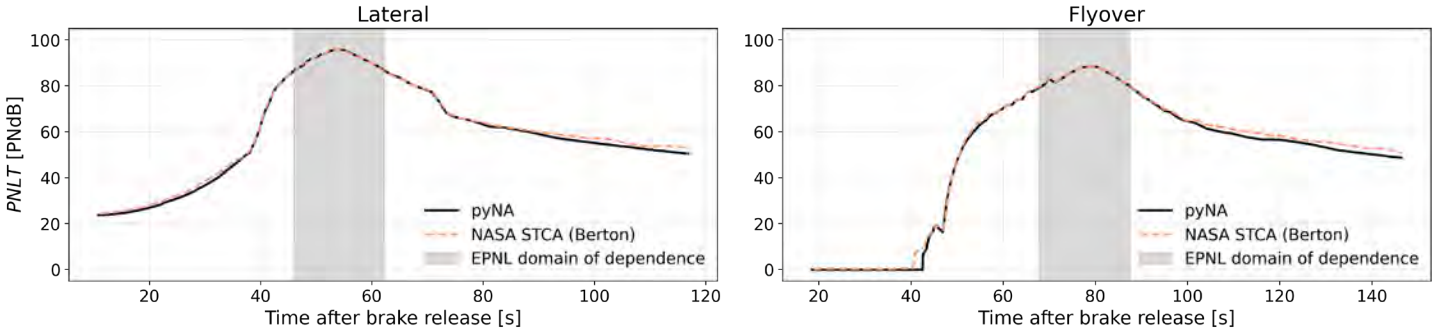

Figure 17. Comparison of the tone-corrected perceived noise level (PNLT) at the lateral (left) and flyover (right) microphone determined using the current noise model (pyNA) and NASA ANOPP (Berton et al., 2018).

The EPNL for individual noise sources and total EPNL are compared to the NASA STCA ANOPP noise assessment in Table 3. A maximum difference across all noise sources of -1.4 EPNdB is found for fan inlet noise source module. This difference is considered acceptable as the fan inlet noise is neither the dominating noise source for the lateral nor the flyover microphone. For the total EPNL, a maximum difference of -0.1 EPNdB is found for the flyover microphone, set mostly by the good agreement for the jet mixing noise source module.

Table 3. Comparison of the individual noise source and total EPNL determined using the current noise model (pyNA) and NASA ANOPP (Berton et al., 2018). The lateral microphone position is assumed to be at the x-location where the aircraft reaches 304.8 m (1000 ft) altitude, i.e., $x_{lateral}$ = 3756 m.

Noise source	Lateral microphone [EPNdB]			Flyover microphone [EPNdB]		
	pyNA	STCA	Δ	pyNA	STCA	Δ
Fan inlet	50.4	49.5	+0.9	35.6	37.0	-1.4
Fan discharge	77.0	76.9	+0.1	71.8	71.8	0.0
Combustor	76.9	77.0	-0.1	73.3	73.6	-0.3
Jet mixing	94.6	94.6	0.0	87.8	87.9	-0.1
Airframe	62.0	-*	-*	64.7	64.8	-0.1
Total	**95.0**	**95.0**	**+0.0**	**88.5**	**88.6**	**-0.1**

*The NASA STCA results for airframe noise source were not available at the lateral microphone.

Sensitivities of noise levels to engine operating variables

The aircraft noise estimation model provides sensitivities of acoustic objective functions with respect to engine operating variables to enable multi-disciplinary design optimization and optimal control. Figure 16 shows the sensitivities of the EPNL at the lateral and flyover microphone with respect to key engine operating variables driving the aircraft noise signature. From Figure 16 it can be seen that noise levels are dominantly sensitive to the jet velocity, as is expected from high specific thrust engines for SST.

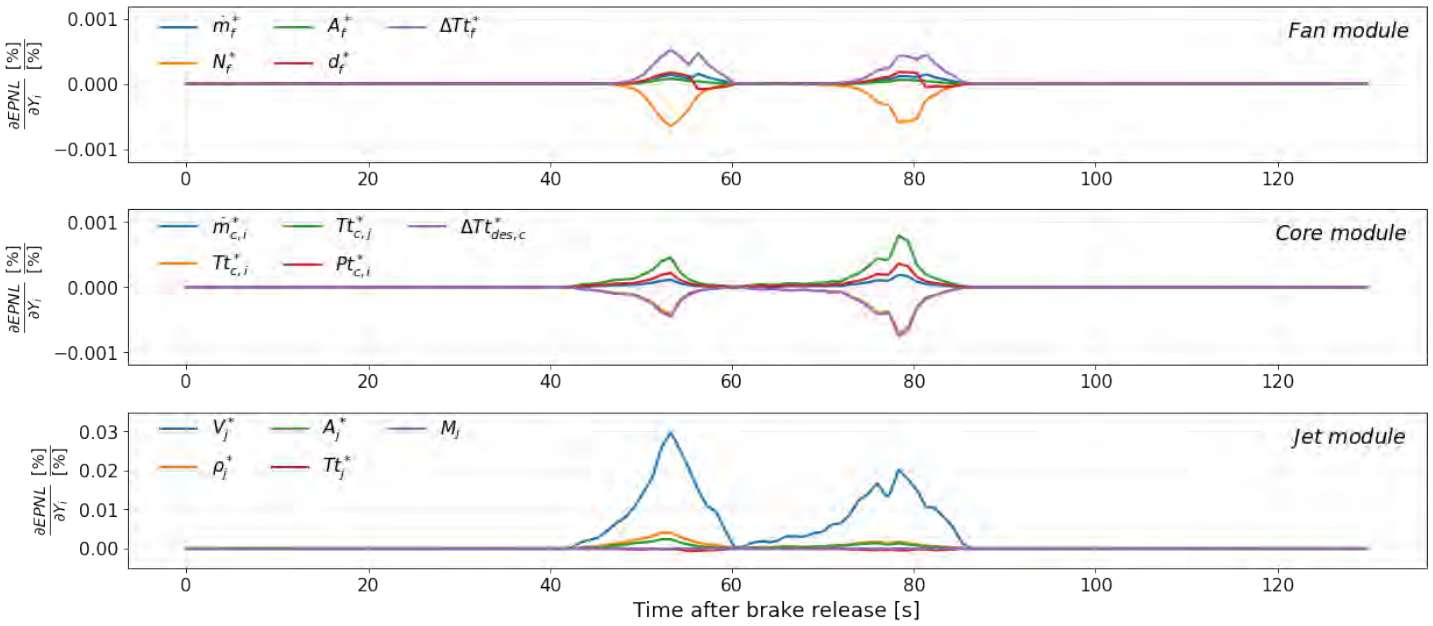

Figure 18. Sensitivities of EPNL along NASA STCA standard take-off trajectory with respect to engine operating variables including the fan (top), core (middle), jet (bottom) for the lateral and flyover microphone.

Sensitivities of Noise Levels to Engine Design Variables

The sensitivities of the environmental performance metrics of a clean-sheet engine with respect to a set of engine design variables are assessed for the NASA STCA business jet. The sensitivities of the environmental performance metrics to engine design variables, $\frac{\partial Y_{env}}{\partial X_{des}}$, are normalized, i.e., $\frac{\partial Y_{env}}{\partial X_{des}}|_{norm} = \frac{\partial Y_{env}}{\partial X_{des}} \cdot \frac{X_{des}}{Y_{env}}$. The normalized sensitivities are given in units of [%]/[%], also known as [pts]. These sensitivities give insight into the design trades of new engine designs configurations during the preliminary design process. The impact of the derivative engine design space constraints imposed by a donor core on the engine environmental performance is briefly considered.

The sensitivities of the environmental performance metrics to engine design variables of the clean-sheet engine without fan size constraint are shown in Table Table 4. The effect of the change in design variables on the fan size is shown in Table 5.

Table 4. Sensitivity of environmental performance metrics with respect to engine design parameters ([%]/[%]). The environmental performance metrics are found to be most sensitive to the fan pressure ratio, π_{fan}.

Environmental Performance Metric	π_{fan}	π_{HPC}	$T_{t,4}/T_{t,2}$	ER_{mix}
Take-off effective perceived noise level, $EPNL_{TO}$	+0.198	-0.019	-0.020	+0.080
Top of climb thrust-specific fuel consumption, $TSFC_{TOC}$	+0.165	-0.114	-0.063	+0.117
Cruise thrust-specific fuel consumption, $TSFC_{cruise}$	-0.040	-0.097	-0.059	+0.013
Take-off NO_x emission index, $EI(NO_x)_{TO}$	+1.978	+1.257	-0.066	+0.259
Cruise NO_x emission index, $EI(NO_x)_{cruise}$	+1.638	+1.786	-0.026	-0.106

Table 5. Sensitivity of fan diameter with respect to engine design parameters ([%]/[%]).

Environmental Performance Metric	π_{fan}	π_{HPC}	$T_{t,4}/T_{t,2}$	ER_{mix}
Fan diameter, d_{fan}	-0.750	+0.063	+0.057	-0.295

From Table 4, it can be seen that the take-off EPNL is most sensitive to the design fan pressure ratio, π_{fan}. The increase in design fan pressure ratio causes an increase in mixed jet velocity and thus, for a given thrust-requirement, reduces the fan size, as shown in Table 5. A similar effect happens for the mixer extraction ratio, ER_{mix}. The increase in jet velocity caused by the increase in fan pressure ratio is the dominant driver of the increased take-off noise levels. Furthermore, from all design variables, the fan diameter is found to have the highest sensitivity to the design fan pressure ratio. This behavior is well-known for subsonic transport engines.

The sensitivity of the take-off noise levels to the engine core design variables, i.e., π_{HPC} and $T_{t,4}/T_{t,2}$, is significantly smaller (factor of 10) compared to that of the design fan pressure ratio. This also shows that, even if the core design variables were constrained by the donor core of a derivative engine design, the impact of such constraints would be relatively small as the take-off noise levels are mainly sensitive to design fan pressure ratio. The low-spool of the derivative engine is purpose-designed to meet the propulsion system requirements. This is unlike the cruise thrust-specific fuel consumption and the take-off NO_x emission index, where the sensitivities to the HPC pressure ratio are of the same order of magnitude as those of the design fan pressure ratio.

At the engine design point, i.e., the top of climb operating point, the sensitivity of thrust-specific fuel consumption (TSFC) with respect to fan pressure ratio is positive, governed by the decrease in propulsive efficiency at higher fan pressure ratios. The sensitivity with respect to HPC pressure ratio and $T_{t,4}/T_{t,2}$ is negative, driven by an increase in thermal efficiency. At the cruise operating point, the sensitivity of TSFC with respect to fan pressure becomes negative due to off-design effects.

At the take-off and cruise operating point, the dominant sensitivities of the NO_x emissions are those with respect to the fan and HPC pressure ratio. Both sensitivities are positive since an increase in the fan and HPC pressure ratios cause an increase in the overall pressure ratio (OPR) resulting in higher $T_t,3$ and $P_t,3$, and thus higher NO_x emissions.

Finally, increasing the HPC pressure ratio for a fixed $T_{t,4}/T_{t,2}$ and ER_{mix} results in a lower total temperature at the HPT exit. Consequently, the mixed jet velocity is lower and therefore, to meet the engine thrust requirement, the engine mass flow will and necessary fan size increases. This results in a positive sensitivity $\partial d_{fan}/\partial \pi_{HPC}$. An increase in $T_{t,4}/T_{t,2}$ at a fixed ER_{mix} similarly results in lower mixed jet velocity, thus increasing the necessary fan size. The sensitivity $\partial d_{fan}/\partial(T_{t,4}/T_{t,2})$ is thus also expected to be positive.

The sensitivities of the environmental performance metrics to engine design variables of the clean-sheet engine with fan size constraint are shown in Table 6.

Table 6. Sensitivity of environmental performance metrics with respect to engine design parameters ([%]/[%]). A constrained fan size results in limited sensitivity of the take-off noise levels with respect to engine design variables.

Environmental performance metric	π_{fan}	π_{HPC}	$T_{t,4}/T_{t,2}$
Take-off effective perceived noise level, $EPNL_{TO}$	-0.007	-0.002	-0.005
Top of climb thrust-specific fuel consumption, $TSFC_{TOC}$	-0.134	-0.088	-0.041
Cruise thrust-specific fuel consumption, $TSFC_{cruise}$	-0.074	-0.094	-0.057
Take-off NO_x emission index, $EI(NO_x)_{TO}$	+1.319	+1.313	-0.016
Cruise NO_x emission index, $EI(NO_x)_{cruise}$	+1.907	+1.763	-0.046

Compared to the results in Table 4, the additional fan size constraint causes the sensitivity of the take-off EPNL with fan pressure ratio, π_{fan}, to become equally insignificant as the sensitivities to the engine core design variables. Since the fan

size and fan face Mach number are fixed, the mass flow through the engine is also fixed. Therefore, the necessary jet velocity to meet the required thrust demand is fixed, resulting in approximately constant take-off noise levels. This effect is specific to high specific thrust engines for SST, having a noise signature dominated by jet noise.

As can be seen from Table 6, the cruise thrust-specific fuel consumption and the take-off NO_x emission index can still be traded by varying the three design variables (π_{fan}, π_{HPC}, and T_{t4}/T_{t2}). The sensitivities of TSFC with respect to all design variables in Table 6 are negative; an increase in both fan and HPC pressure ratios as well as T_{t4}/T_{t2} results in an increase in engine thermal efficiency. The effect of the fan pressure ratio on the propulsive efficiency is now limited because of the constraint fan size. The sign of the sensitivities of engine NO_x emissions with respect to the set of design variables do not change when adding a fan size constraint.

Publications

Voet, L., Speth, R., Sabnis, J., Tan, C., & Barrett, S. (2022). Sensitivities of aircraft acoustic metrics to engine design variables for multi-disciplinary optimization. *AIAA Journal*, *60*(8). https://doi.org/10.2514/1.J061411

Outreach Efforts

- Dr. Jayant Sabnis gave a presentation titled "Noise and emission characteristics of commercial supersonic aircraft propulsion systems" at the Aviation Noise and Emissions Symposium on March 5, 2019.
- Prof. Steven Barrett gave a presentation titled "Clean-sheet supersonic engine design and performance" at the ASCENT meeting in Atlanta, GA, on April 19, 2019.
- Dr. Jayant Sabnis gave a presentation titled "Clean-sheet supersonic engine design and performance" at the ASCENT meeting in Alexandria, VA, on October 22, 2019.
- Mr. Prashanth Prakash and Mr. Laurens Voet gave a presentation titled "Clean-sheet supersonic engine design and performance" at the at the virtual ASCENT meeting on September 30, 2020.

Awards

- Mr. Laurens Voet, 2021, AIAA 2021 Luis de Florez Graduate Award

Student Involvement

This task was conducted primarily by Prashanth Prakash and Laurens Voet, graduate research assistants working under the supervision of Dr. Jayant Sabnis, Dr. Raymond Speth, and Dr. Choon Tan.

References

Berton, J. (2021, August 2-6). *Simultaneous use of ground reflection and lateral attenuation noise models* [Conference presentation]. AIAA AVIATION 2021 FORUM, virtual. https://doi.org/10.2514/6.2021-2214

Berton, J. J., Huff, D. L., Geiselhart, K., & Seidel, J. (2020, January 6–10). *Supersonic technology concept aeroplane for environmental studies* [Conference presentation]. AIAA Scitech 2020 Forum, Orlando, Florida.

Berton, J., Jones, S. M., Seidel, J. A., & Huff, D. L. (2018). Noise predictions for a supersonic business jet using advanced take-off procedures. *Aeronautical Journal, 122*(1250), 556–571. http://dx.doi.org/10.1017/aer.2018.6

Chien, C., & Soroka, W. (1975). Sound propagation along an impedance plane, *Journal of Sound and Vibration*, 43(1), 9–20.

Emmerling, J., Kazin, S., & Matta, R. (1976). *Core engine noise program Volume III. Prediction methods – Supplement I: Extension of prediction methods, technical report*. Ohio Aircraft Engine Business Group, General Electric Co., Cincinnati, Ohio. https://apps.dtic.mil/sti/pdfs/ADA030376.pdf

Fink, M. R. (1977). *Airframe noise prediction method*. United Technologies Research Center, East Hartford, Connecticut.

Golub, R., Rawls Jr, J. W., & Yeager, J. C. (2004). *High Speed Research Noise Prediction Code (HSRNOISE) User's and Theoretical Manual*. NASA. https://ntrs.nasa.gov/api/citations/20040200978/downloads/20040200978.pdf

Gray, J. S., Hwang, J. T., Martins, J. R., Moore, K. T., & Naylor, B. A. (2019). OpenMDAO: An open-source framework for multidisciplinary analysis and optimization. *Structural and Multidisciplinary Optimization, 59*(4), 1075–1104.

Heidmann, M. F. (1979). *Interim prediction method for fan and compressor source noise* (NASA-TM-x71763). NASA. ntrs.nasa.gov/api/citations/19750017876/downloads/19750017876.pdf

Hough, J. W., & Weir, D. S. (1996). *Aircraft noise prediction program (ANOPP) fan noise prediction for small engines* (NASA-CR-198300). NASA Langley Research Center. ntrs.nasa.gov/api/citations/19960042711/downloads/19960042711.pdf

ICAO. (2017a). *Annex 16 to the Convention on International Civil Aviation Environmental Protection Volume 1: aircraft noise* (8th Ed). International Civil Aviation Organization (ICAO).
ICAO. (2017b). *Annex 16 environmental protection. Volume II: Aircraft engine emissions* (4th Ed). International Civil Aviation Organization (ICAO).
Kontos, K. B., Janardan, B., & Gliebe, P. (1996a). *Improved NASA-ANOPP noise prediction computer code for advanced subsonic propulsion systems, Volume 1: ANOPP evaluation and fan noise model improvement* (NASA CR-195480). NASA Lewis Research Center. https://ntrs.nasa.gov/api/citations/19960048499/downloads/19960048499.pdf
Kontos, K. B., Kraft, R. E., & Gliebe, P. R. (1996b). *Improved NASA-ANOPP noise prediction computer code for advanced subsonic propulsion systems, Volume 2: Fan suppression model development* (NASA-CR-202309). NASA Lewis Research Center. https://ntrs.nasa.gov/api/citations/19960048499/downloads/19960048499.pdf
Lambe, A.B., & Martins, J. R. R. A. (2012). Extensions to the design structure matrix for the description of multidisciplinary design, analysis, and optimization processes. *Structural and Multidisciplinary Optimization, 46*(2). 273–284. https://doi.org/10.1007/s00158-012-0763-y
Maekawa, Z. (1968). Noise reduction by screens, *Applied Acoustics*, 1(3), 157–173.
Montegani, F. J. (1979). Computation of atmospheric attenuation of sound for fractional- octave bands (NASA Technical Paper 1412). NASA. ntrs.nasa.gov/api/citations/19790009488/downloads/19790009488.pdf
Revels, J., Lubin, M., & Papamarkou, T. (2016). *Forward-mode automatic differentiation in Julia*. Cornell University, arXiv:1607.07892. https://doi.org/10.48550/arXiv.1607.07892
SAE International. (2021). *ARP-876F: Gas turbine jet exhaust noise prediction*. https://doi.org/10.4271/ARP876F
SAE International. (2025). AIR5662: Method for predicting lateral attenuation of airplane noise. https://doi.org/10.4271/AIR5662
Zorumski, W. E. (1982). *Aircraft noise prediction program theoretical manual part 1-2, technical report*. NASA.

Task 4 - Evaluate the Impact of Improved Technology on Relative Performance Benefits of Clean-Sheet and Derivative Engines

Massachusetts Institute of Technology

Objective

The objective of this first task is to quantify the impact that improvements in technology will have on the relative performance of clean-sheet engine designs over derivative designs. Specifically, we consider the impact of technology improvements in the turbomachinery design, turbine material, cooling technology, and combustor design for low NO_x emissions for the STCA developed by NASA (Berton & Geiselhart, 2019).

Research Approach

We parameterize the technology level of various components as follows:

- **Turbomachinery**
  The technology level of the turbomachinery components (i.e., fan, compressor, and turbines) is quantified by the polytropic efficiency (η_p) of the components.

- **Turbine Material and Cooling Technology**
  The turbine material limits, such as advanced ceramic matrix composites, thermal barrier coatings, and cooling technology, are quantified by the metal temperature that the turbine vanes and blades are allowed to reach (T_{vane} and T_{blade}, respectively).

- **Combustor Technology**
  The design space benefits of a clean-sheet engine design would be more readily accessible if the emissions of NO_x were reduced by using a more advanced combustor model. The combustor technology can be parameterized by using a previously developed reactor network model.

Milestones

- Developed and used a parametrized representation of the technology level of various components to evaluate the impact of improved technology on the performance of clean-sheet and derivative engines.

Major Accomplishments

The sensitivity of the thrust specific fuel consumption to the technology levels of the turbomachinery, turbine material, and cooling were calculated for both clean-sheet and derivative engines. Figure 17 shows that the derivative engine benefits from a 0.33% and 0.46% improvement in SFC per percentage-point improvement in the polytropic efficiency of the LPT and fan, respectively. These sensitivities are calculated for an optimal engine, sized for a fixed propulsion system requirement (on the basis of the thrust requirement of the STCA). Specifically, each point on the graph represents an engine optimized for minimum SFC with the constraints outlined in the previous section. Because the derivative engine uses the donor core, only the fan and LPT can be designed by using the improved technology.

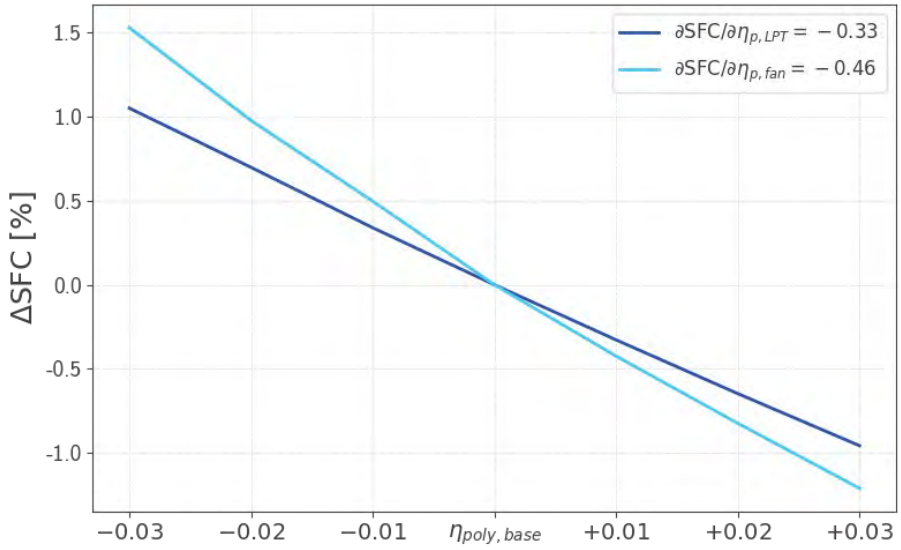

Figure 19. Sensitivity of a derivative engine SFC to the polytropic efficiency of the low-pressure spool components (LPT and fan).

The sensitivities of the clean-sheet engine are different from those of the derivative engine because the core of the engine can be redesigned to obtain an optimal SFC engine at each point. Because the high-pressure spool of the clean-sheet engine is designed, we also calculated the sensitivity of SFC to the polytropic efficiency of the HPC and HPT in addition to the low-pressure spool components, as shown in Figure 18.

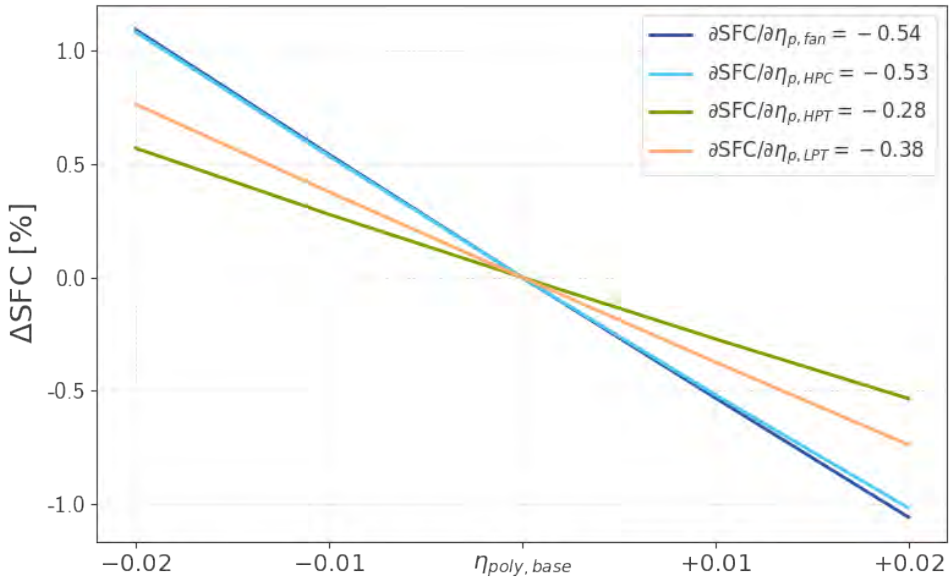

Figure 20. Sensitivity of clean-sheet engine SFC to the polytropic efficiency of the turbomachinery.

For a clean-sheet engine design, the pressure ratio of the engine is limited not by the material limits of the last stage of the HPC but by the imposed constraint on the emission index of NO_x. We found that a 1% increase in the allowable turbine metal temperature results in a 0.25% decrease in the clean-sheet engine SFC.

The cumulative effects of improvements on each of the above engine components are shown for both the derivative and clean-sheet engine in Figure 19. Table 7 shows the assumed magnitude of improvement to the engine components. Improvements in the low-pressure spool and low-NO_x combustor designs have the largest benefit in clean-sheet engine SFC. The clean-sheet engine with advanced technology has a 4.1% lower SFC than the derivative engine with advanced low-pressure spool components.

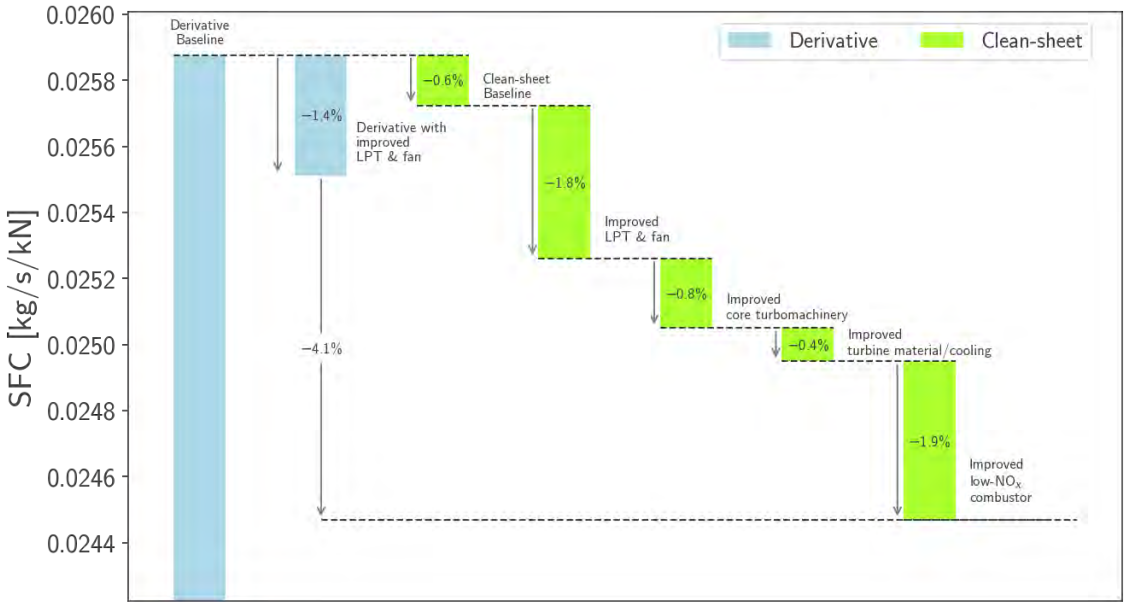

Figure 21. Impact of technology improvements on the SFC of derivative and clean-sheet engines for the STCA.

Table 7. Assumed magnitude of technology improvements for clean-sheet and derivative engines.

Components	Derivative engine	Clean-sheet engine
$\Delta\eta_p$ of low-pressure spool turbomachinery	+0.02	+0.02
$\Delta\eta_p$ of high-pressure spool turbomachinery	-	+0.01
$\Delta T_{metal,HPT}$	-	+100 K
Emission index of NO_x	-	Improved low-NO_x combustor modelled on the PW1133G TALON-X combustor

Publications
None.

Outreach Efforts
- Presented at the ASCENT Advisory Committee Spring Meeting (April 5–7, 2022).
- Presented at the Aviation Emissions Characterization Roadmap Annual Meeting (May 24–26, 2022).

Awards
None.

Student Involvement
This work was performed primarily by graduate research assistant Prashanth Prakash working under the supervision of Dr. Jayant Sabnis, Dr. Raymond Speth, and Dr. Choon Tan.

References

Berton, J., & Geiselhart, K. (2019). *NASA 55 tonne Supersonic Transport Concept Aeroplane (STCA) release package*. NASA Glenn Research Center & NASA Langley Research Center.

Task 5 – Evaluate the Effects of Fan Diameter and Unconventional Architectures on the Environmental Impacts of Clean-Sheet Engines

Massachusetts Institute of Technology

Objective

The objective of this task is to quantify the effects of fan diameter constraints and use of unconventional engine architectures on the emissions of clean-sheet engines. In particular, we examine the combined impact of the following cases:

- Effect of fan diameter on supersonic drag sources, and subsequent impacts on thrust requirements and engine performance.
- Use of hybrid-electric systems powered primarily with conventional fuel alongside a battery-based supplement used during LTO flight.

The work presented is done for the airframe and mission of the STCA developed by NASA (Berton et al., 2020).

Research Approach

The NPSS software (Claus et al., 1991) was chosen for analysis of engine performance and emissions. Because it is an industry-standard tool, it facilitates future collaboration with the broad user base. The clean-sheet engine cycle deck from Prashanth et al. (2023) is used to obtain a baseline design.

Supersonic Drag Sources

Supersonic drag forces on an engine fall primarily into three categories: (1) bypass drag, (2) spillage drag, and (3) wave drag. Bypass and spillage drag represent losses due to off-design operation of a supersonic inlet. In this work, engine inlets are assumed to be operated on-design or to contain variable-geometry components to maintain well-matched operation across the mission. Therefore, we assume that the contributions of spillage and bypass drag are negligible. The effects of such systems (weight, complexity, etc.) are not considered here.

The Fraenkel model for external cowl drag on open-nosed bodies of revolution (as presented by Seddon and Goldsmith [1999]) is used to model the remaining supersonic drag source, wave drag. The aspect ratio of the inlet cross-section (radius/length) is taken to be constant and equal to the value for the existing STCA engine. Fan diameter is used as a proxy for maximum inlet radius and is allowed to vary. A conical profile is conservatively used to minimize drag.

Although the exact value of the wave drag due to the engine inlet cowls on the baseline aircraft is unknown, it can be estimated with the above model. Consequently, the difference in wave drag can be estimated for a clean-sheet engine with a specified fan diameter relative to the baseline design. This difference is then used alongside steady flight assumptions to obtain the difference in thrust requirement relative to the baseline mission presented in Berton et al. (2020).

Previous Hybrid-Electric Assessments

Before implementing a full hybrid-electric NPSS engine model, we first qualitatively assessed the potential benefits of hybrid electrification. We assume an architecture wherein electric systems are used only during the LTO phase of flight, when the greatest demand is placed on the engine. Consequently, the gas turbine component of the engine can be sized more closely to cruise requirements. Similar analyses in subsonic systems (Kang et al., 2022; Lammen & Vankan, 2020; Lents et al., 2016; Seitz et al., 2018) suggest specific fuel consumption benefits on the order of 5%, alongside minor improvements to NO_x emissions. These benefits are hypothesized to manifest through three primary mechanisms:

- Lower peak gas turbine corrected fan speed requirement: This aspect could allow the gas turbine to operate closer to the design condition (100% corrected speed) during cruise, improving component efficiency.
- Lower peak engine turbine-entry-temperature (TET): If the maximum TET point occurs during LTO, electric systems could be used to reduce the TET required by the gas turbine, thereby potentially improving NO_x emissions and propulsive efficiency.

- Lower thrust requirements at pinch points: Electric systems could be used to reduce the thrust requirements of the gas turbine at the pinch points of the mission, thereby allowing the engine to be sized more closely to cruise thrust requirements.

The final mechanism, thrust requirement, was implemented indirectly to maintain the known mission profile. The time in the mission at which a given constraint is placed was varied, and the altitude, Mach number, and thrust requirement could then be calculated at that new time. As an example, the thrust pinch point occurs at 27 kft at a Mach number of 0.85. In a hybrid-electric engine, the gas turbine would not be able to produce sufficient thrust at that point alone and would require assistance by the electric systems. To model this scenario while maintaining the STCA mission profile, the engine is sized for thrust at a slightly later (positive time deviation) or slightly earlier (negative time deviation) mission point. An engine sized for thrust at either of these points will not produce sufficient thrust at the actual thrust pinch point but may be sized more optimally for cruise. This procedure of varying the time at which a thrust constraint is applied is repeated for other key points in the mission.

To test these mechanisms, NPSS is used to examine the sensitivity of emissions metrics to the corrected fan speed, turbine inlet temperature, and thrust requirement (with time as a proxy) at several points in the STCA LTO profile. These points are the thrust pinch point (27 kft., Mach 0.85), the thermal pinch point (42 kft., Mach 1.4), and the aerodynamic design point (ADP); 41 kft., Mach 1.4). Emissions are then evaluated at the beginning of cruise point (44 kft., Mach 1.4) as an estimate of overall cruise emissions.

Major Accomplishments

Supersonic Drag Implementation

The wave drag was first estimated for several supersonic regime Mach numbers for the original STCA engine design. The fan diameter (D_f) was then allowed to vary. The percentage deviation in engine cowl drag area (C_dA) from the baseline STCA design is shown in Figure 20 as a function of Mach number. The drag area of an engine cowl monotonically increases with a local sensitivity of $\partial C_dA/\partial D_f = 3.5$. The drag area relative to the baseline STCA was found to have minimal variation due to the Mach number. At a fixed fan diameter, the change in drag area was between 1.6% at -10% fan diameter and 3.3% at $+10\%$ fan diameter. Notably, the effect of Mach number grows with increasing fan diameter, thus indicating that this effect would need to be accounted for at high fan diameters.

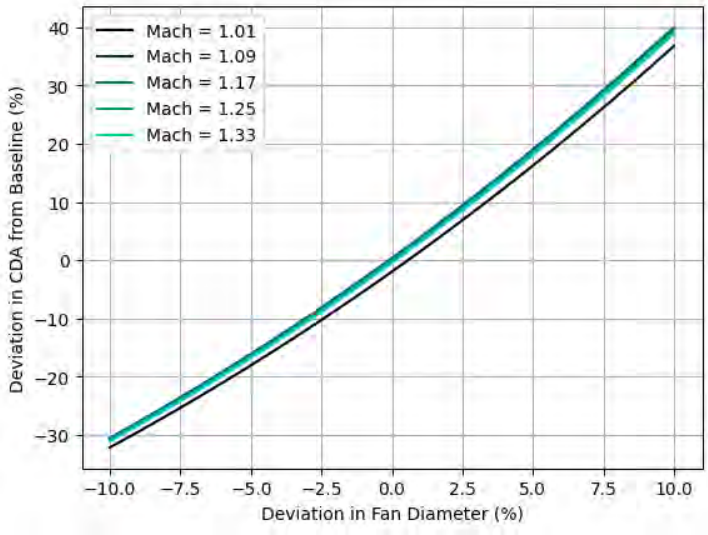

Figure 22. Effect of fan diameter variation on engine external cowl drag area (CDA), as a function of Mach number.

Sensitivities

The supersonic drag model described above was implemented into the NPSS clean-sheet cycle deck, and sensitivities of specific air range (SAR), TSFC, and fan diameter were calculated due to variation in TET, corrected fan speed, and thrust (with time as a proxy). The resulting sensitivities are generally non-linear (Figure 21). Variations in emissions metrics and fan diameter due to turbine inlet temperature have negligible dependence on the point at which the temperature was prescribed, thus suggesting strong correlations between temperature changes at all tested points. We see improved SAR and SFC for increasing turbine inlet temperature, to maxima on the order of 0.5%. SFC was minimized with a corrected fan speed deviation of -5% for all three points of interest. While SAR exhibits a maximum, the value of that maximum is decreased, because of the resultant increase in fan diameter and thus drag.

The emissions and fan diameter sensitivities due to sizing time variation are not smooth, because variations in time equate to variations in altitude, Mach number, and thrust, in accordance with the prescribed LTO mission profile. As such, when an inflection point of the mission (e.g., end of climb) is reached, the behavior of the mission parameters with respect to time changes suddenly. From the time sensitivities, we see SAR and SFC benefits resulting from a positive deviation of time at the thrust pinch point. This finding indicates that sizing the engine thrust to a later point in the mission and producing insufficient thrust at the actual pinch point does improve cruise emissions.

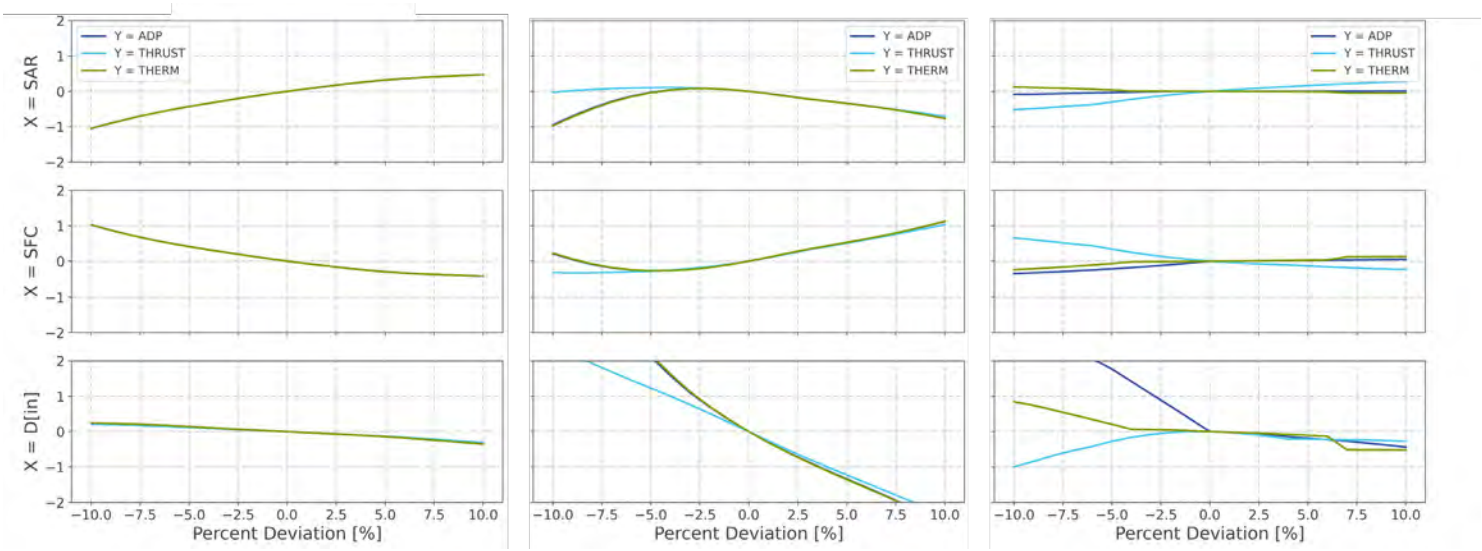

Figure 23. Sensitivity of metric *X* at the beginning of cruise to turbine inlet temperature (left), corrected fan speed (middle), and time (right) at point *Y*.

Mixed Versus Unmixed Performance

An analysis comparing the performance of mixed and unmixed engines performing the STCA mission was also performed, in which mixed engines performed better than unmixed equivalents with respect to fuel mass and efficiency. Specifically, we obtained a 2.2% increase in overall efficiency, broken into a 3.7% gain in thermal, or inner, efficiency and a 1.0% loss in propulsive efficiency. The flow mixer allows some of the hot core stream's thermal energy to be usefully converted to kinetic energy in the cool bypass stream. This energy would otherwise be effectively wasted, as isentropic expansion cannot usefully bring the exhaust to ambient temperature. The effect of this is two-fold. First, the increase in kinetic energy across the mixer increases mass-averaged velocity of the exhaust, decreasing propulsive efficiency by a small amount. Second, the kinetic energy increase effectively reduces requirements on the upstream components. This allows for a decrease in bypass stream size from a fan pressure ratio of 2.17 to 1.80 and from a fan diameter of 1.40 m to 1.26 m. The decreased fan power requirement results in less power dissipating in the turbine and mechanical transfer, boosting the thermal efficiency.

The increase in overall efficiency is balanced by the added mass of a lobed mixer. On a lower fan diameter engine such as an SST aircraft, the mixer mass is relatively low. A similar analysis performed on ultra-high bypass subsonic engines yielded a mixer mass just over twice that for SST, leading to a decrease in useful payload. As such, we conclude that lobed flow mixer should only be considered for low fan diameter applications.

Publications

None.

Outreach Efforts

None.

Awards

None.

Student Involvement

This work was performed primarily by graduate research assistant Wyatt Giroux, working under the supervision of Dr. Prakash Prashanth, Dr. Jayant Sabnis, Dr. Raymond Speth, and Dr. Choon Tan.

References

Berton, J. J., Huff, D. L., Geiselhart, K., & Seidel, J. (2020, January 6-10). *Supersonic technology concept aeroplanes for environmental studies* [Conference presentation. AIAA Scitech 2020 Forum, Orlando, Florida. https://doi.org/10.2514/6.2020-0263

Claus, R. W., Evans, A. L., Lylte, J. K., & Nichols, L. D. (1991). Numerical propulsion system simulation. *Computing Systems in Engineering*, *2*(4), 357–364. https://doi.org/10.1016/0956-0521(91)90003-N

Kang, S., Roumeliotis, I., Zhang, J., Broca, O., & Pachidis, V. (2022). Assessment of engine operability and overall performance for parallel hybrid electric propulsion systems for a single-aisle aircraft. *Journal of Engineering for Gas Turbines and Power*, *144*(041002). https://doi.org/10.1115/1.4052880

Lammen, W., & Vankan, J. (2020, January 6-10). *Energy optimization of single aisle aircraft with hybrid electric propulsion* [Conference presentation]. AIAA Scitech 2020 Forum, Orlando, Florida. https://doi.org/10.2514/6.2020-0505

Lents, C. E., Hardin, L. W., Rheaume, J., & Kohlman, L. (2016, July 25-27). *Parallel hybrid gas-electric geared turbofan engine conceptual design and benefits analysis* [Conference presentation]. 52nd AIAA/SAE/ASEE Joint Propulsion Conference, Salt Lake City, Utah. https://doi.org/10.2514/6.2016-4610

Prashanth, P., Voet, L. J. A., Speth, R. L., Sabnis, J. S., Tan, C. S., & Barrett, S. R. H. (2023). Impact of design constraints on noise and emissions of derivative supersonic engines. *Journal of Propulsion and Power*, *39*(3), 1–10. https://doi.org/10.2514/1.B38918

Seddon, J., & Goldsmith, E. L. (1999). *Intake aerodynamics*. American Institute of Aeronautics and Astronautics Education Series.

Seitz, A., Nickl, M., Stroh, A., & Vratny, P. C. (2018). Conceptual study of a mechanically integrated parallel hybrid electric turbofan. *Proceedings of the Institution of Mechanical Engineers, Part G: Journal of Aerospace Engineering*, *232*(14), 2688–2712. https://doi.org/10.1177/0954410018790141

Task 6 - Assess the Effect of Variable Noise Reduction Systems on LTO Emissions for Engines for Supersonic Transport Aircraft

Massachusetts Institute of Technology

Objective

The engine configurations currently being pursued for the second-generation SST are low or medium bypass turbofans, instead of afterburning turbojets used on Concorde. Such engines, sized for supersonic cruise, are likely to have higher thrust capability at the take-off condition and therefore, may be able to use a programmed thrust cutback (PTCB), allowing the aircraft to perform a take-off at less than 100% of the thermodynamically available thrust. Unlike thrust lapse, PTCB is not a thermodynamic, aerodynamic, nor atmospheric phenomenon but rather, it is a computer-programmed reduction in thrust during the take-off procedure of the aircraft for the purpose of reducing certification noise.

A PTCB designed to reduce certification noise has an impact on the amount of gaseous emissions from the engines during take-off procedures (in this work only NO_x emissions are considered). The objective of this task is to analyze whether a single thrust-setting for the climb-out phase of the engine emissions LTO cycle is representative, or whether the PTCB should be accounted for in the engine emissions LTO cycle.

The objective of this task involves interdependencies between aircraft operations related to PTCB and engine emission certification standards. The noise certification flight profile is chosen as a reference flight profile to analyze these interdependencies. The in-flight emissions during the climb-phase (between 35 ft and 3000 ft) of the noise reference trajectories resulting from different PTCB trajectories are compared to the emissions of the climb mode of the engine emission LTO certification standard. The comparison is done both for the existing subsonic and supersonic engine emission LTO certification standard to assess which is more representative.

Research Approach

The approach employed to address the above-mentioned research objectives is shown in Figure 22. We start from a supersonic aircraft model and an engine model for that aircraft. These are input in a take-off trajectory model that is coupled to a noise model. Minimizing the noise footprint using a variable noise reduction system, gives us a PTCB, characterized by a thrust-setting schedule as a function of time, $\mathrm{TS}(t)$. This thrust-setting schedule is put into a combustor model to estimate take-off emissions (i.e., Method 1 in Figure 22). These emissions are then compared to those in a

baseline trajectory, using a simple power setting schedule, without variable noise reduction systems (VNRS) being applied (i.e., Method 2 in Figure 22). We are interested in comparing the take-off emissions of both these methods.

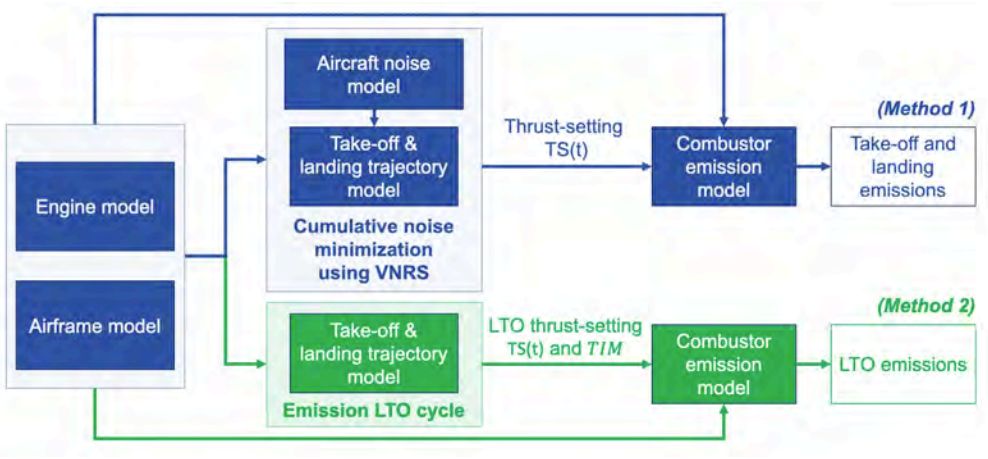

Figure 24. Flow chart of the approach to estimate the effect of VNRS on take-off emissions of engines for SST.

LTO Engine Emissions Certification Cycles

The current subsonic and supersonic LTO emissions cycles indicating thrust setting and time in mode for the different phases are shown in Table 8 and Table 9, respectively (ICAO, 2017b).

Table 8. Subsonic LTO engine emissions certification cycle.

Subsonic Operating Mode	Subsonic Engine Power (percentage of standard day sea-level static thrust, F_{00})	Subsonic Time in Mode
Idle (taxi)	7%	26.0 min
Take-off	100%	0.7 min
Climb out	85%	2.2 min
Approach	30%	4.0 min

Table 9. Supersonic LTO engine emission certification cycle.

Supersonic Operating Mode	Supersonic Engine Power (percentage of standard day sea-level static thrust, F_{00})	Supersonic Time in Mode
Idle (taxi)	5.8%	26.0 min
Take-off	100%	1.2 min
Climb out	65%	2.0 min
Descent	15%	1.2 min
Approach	34%	2.3 min

Modelling Take-off Trajectories

The reference take-off trajectory is composed of five phases, summarized in Table 10. During the ground roll phase, the aircraft accelerates until it reaches rotation speed, $V_{\mathrm{rot}} = k_{\mathrm{rot}} V_{\mathrm{stall}}$ (with k_{rot}=1.3). In the rotation phase, the aircraft pitches up, increasing its angle of attack, α, with a constant rate ($d\alpha/dt$ = 3.5 deg/s) until its net upward force is zero. In the climb phase, the aircraft climbs until it reaches the obstacle height, z_{obstacle}, after which the programmed thrust cutback, $\mathrm{TS}_{\mathrm{PTCB}}$, and pilot-initiated cutback, $\mathrm{TS}_{\mathrm{cb}}$, is applied is applied in the PTCB and cutback phases, respectively. The trajectory stops when the aircraft reaches an altitude $z_{\mathrm{end}} = 1500\,\mathrm{m}$. The first three phases of the take-off trajectory are performed using a

take-off thrust setting $\mathrm{TS_{TO}} = 100\%$. The angle-of-attack, α, serves as control parameter in the climb PTCB and cutback phase and its schedule is determined by optimizing the trajectory for the minimum time to climb to $z_{\mathrm{end}} = 1500\ \mathrm{m}$.

Table 10. Definition of take-off trajectory model.

Phase	Boundary constraint	Path constraint	Control parameters	
			α	TS
Ground roll	$V_{\mathrm{start}} = 0\ \mathrm{m/s} \rightarrow v_{\mathrm{end}} = v_{\mathrm{rot}}$		$\alpha = \alpha_0$	TS=100%
Rotation	$\alpha_{\mathrm{start}} = \alpha_0 \rightarrow \alpha_{\mathrm{end}}\ \mathrm{s.t.}\ F_{\mathrm{up,end}} = 0$		$\frac{d\alpha}{dt} = \mathrm{const}$	TS=100%
Climb	$z_{\mathrm{start}} = 0 \rightarrow z_{\mathrm{end}} = z_{\mathrm{obstacle}}$	$\gamma > 4\%$* $v_{\mathrm{eas}} < 250\ \mathrm{kts}$	$\alpha = \alpha(t)$	TS=100%
PTCB	$z_{\mathrm{start}} = z_{\mathrm{obstacle}} \rightarrow z_{\mathrm{end}} = z_{\mathrm{cb}}$	$\gamma > 4\%$* $v_{\mathrm{eas}} < 250\ \mathrm{kts}$	$\alpha = \alpha(t)$	TS=$\mathrm{TS_{ptcb}}$
Cutback	$z_{\mathrm{start}} = z_{\mathrm{cb}} \rightarrow z_{\mathrm{end}} = 1500\ \mathrm{m}$	$\gamma > 4\%$* $v_{\mathrm{eas}} < 250\ \mathrm{kts}$	$\alpha = \alpha(t)$	TS=$\mathrm{TS_{cb}}$

* This path constraint can be replaced by the one-engine inoperative (OEI) condition.
α = angle of attack
TS = thrust setting

The allowable level of PTCB for the reference trajectory is governed by noise certification regulations and airworthiness standards (ICAO, 2017a): the thrust shall not be reduced below that required to maintain a minimum climb gradient of 4% or steady level flight with one engine inoperative (for multi-engine airplanes), whichever thrust is greater. The aircraft shall not have an indicated air speed of more than 250 kts at altitudes below 10,000 feet MSL. These limits are applied as path constraints of the reference take-off trajectory in Table 10.

Aircraft and Engine Modelling
In this task, two supersonic vehicles are analyzed that span 8–55 passengers and low supersonic (Mach 1.4) to high supersonic (Mach 2.2). The NASA STCA (Berton et al., 2020) is an 8-passenger supersonic business jet with cruise Mach number 1.4 (will be referred to as the NASA STCA). A larger 55-passenger supersonic airliner with cruise Mach number 2.2 designed by Georgia Institute of Technology (subsequently referred to as the M2.2 medium SST) is also analyzed. The engine used in the analysis of the effects of PTCB for the STCA aircraft is a derivative engine, based on the CFM56-5B core, while the engine used for the M2.2 medium SST is a clean-sheet engine (Voet et al., 2021).

Estimating NO_x Emissions
The P_3-T_3 method (DuBois & Paynter, 2006) is used to estimate the engine NO_x emissions. The P_3-T_3 method uses a polynomial regression to model the NO_x emissions from the combustor as a function of the combustor inlet pressure, P_{t3}, and temperature, T_{t3}. We use publicly available data on the NO_x emissions of the CFM56 family of engines from the ICAO EEDB (EASA, 2019) to determine the coefficients needed in our P_3-T_3 method. It is assumed that the emissions index of NO_x scales with $P_{t3}^{0.4}$ as shown in the following equation:

$$\frac{EI(NO_x)}{P_{t3}^{0.4}} = 6.26 \cdot 10^{-8} T_{t3}^3 - 1.17 \cdot 10^{-4} T_{t3}^2 + 0.074 T_{t3} - 15.04 \qquad \text{(Eq. 2)}$$

Since the production of NO_x in a RQL combustor is primarily controlled by the flame temperature and the mixing of the primary zone gas, it is assumed that the above P_3-T_3 correlation is representative of the emissions we expect from a derivative engine that uses the CFM56 core.

The clean-sheet engine designed for the M2.2 medium SST is also assumed to have the same combustor technology as in the STCA engine as well as the CFM56-5B3. This allows us to use the same P_3-T_3 model to estimate emissions of NO_x from the combustor and facilitates a comparison between the two aircraft-engine pairs while holding the combustor technology fixed.

Modeling Take-off Noise

The take-off certification noise levels - in terms of the lateral and flyover effective perceived noise level - are computed using the aircraft noise estimation model, developed as part of Task 3. The side-line (lateral) and flyover noise metrics, defined by ICAO Annex 16 (ICAO, 2017a) are computed for each of the take-off trajectories in the design space. The flyover microphone is located at 6500 m downstream of break release; the location of the lateral microphone is located 450 m away from the runway center line at the position of maximum sideline noise.

Milestone

- Estimated the differences of NO_x pollutant emissions of engines for SST aircraft flying a range of trajectories varying VNRS for two different aircraft configurations.

Major Accomplishments

Estimate of PTCB Range Based on Trajectory Simulations

The possible range of PTCB for the two supersonic vehicles is estimated using take-off trajectory simulations. A single pilot-initiated cutback maneuver is analyzed for the STCA and M2.2 medium SST. The cutback procedure is described by two parameters, namely a cutback altitude, z_{cb}, and a cutback thrust setting, TS_{cb}. The design-space of the single-cutback PTCB is explored by varying both parameters: $z_{cb} \in [25, 750]\text{m}$ and $TS_{cb} \in [50, 100]\%$ for the STCA and $TS_{cb} \in [60, 100]\%$ for the M2.2 medium SST. Thrust settings outside these ranges fail to meet the noise certification and airworthiness requirements for the respective vehicles. A take-off thrust setting $TS_{TO} = 100\%$ is employed. Sample trajectories with and without cutback are shown for the STCA and M2.2 medium SST in Figure 23.

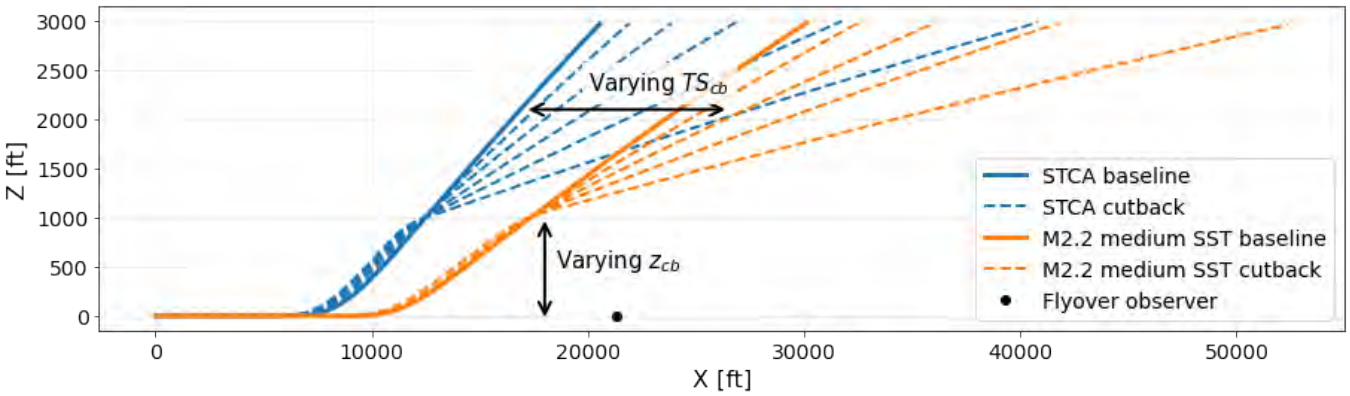

Figure 25. Example of single thrust cutback trajectories for STCA and M2.2 medium SST for $\boldsymbol{z_{cb}}$=1000ft and $\boldsymbol{TS_{cb}} \in [\mathbf{50}, \mathbf{100}]\%$ (for STCA) and $\boldsymbol{TS_{cb}} \in [\mathbf{60}, \mathbf{100}]\%$ (for M2.2 medium SST). The baseline trajectory has a constant thrust setting TS=100%.

The lateral, flyover and cumulative effective perceived noise level as a function of TS_{cb} and z_{cb} is plotted for the single thrust cutback of the STCA and M2.2 medium SST in Figure 24 and Figure 25, respectively.

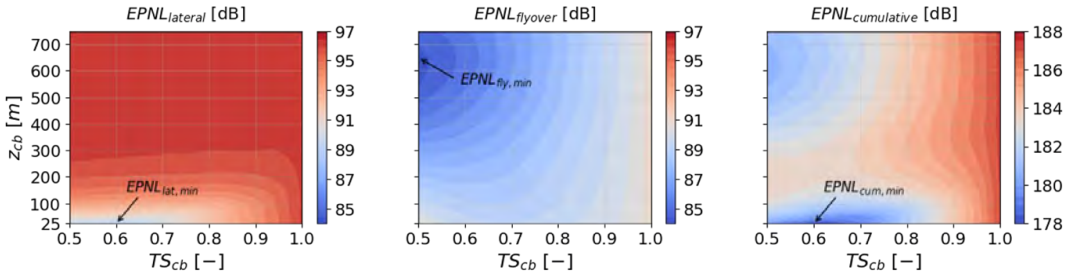

Figure 26. Lateral, flyover and cumulative noise reduction for single cutback trajectories of the STCA.

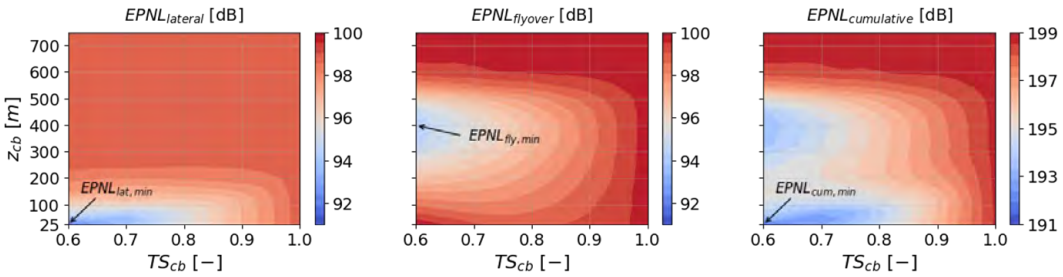

Figure 27. Lateral, flyover and cumulative noise reduction for single cutback trajectories of the M2.2 medium SST.

In Figure 24 and Figure 25, a cutback at low altitudes monotonically decreases the lateral EPNL for both vehicles. A cutback at altitudes z_{cb} > 200 m does not result in improvement in lateral noise anymore, as the aircraft is already past the region of influence of the lateral microphone. For the flyover microphone, a local minimum exists at z_{cb}=650 m for the STCA and at z_{cb}=400 m for the M2.2 medium SST; cutting back later results in more source noise at the flyover microphone and cutting back earlier results in a smaller distance between the aircraft and the flyover microphone increasing noise. For both vehicles, the lateral noise reduction dominates the cumulative noise reduction. Therefore, the point in the feasible design space that results in the minimum cumulative noise occurs at ($TS_{cb} = 60\%, z_{cb} = 25$ m) for both vehicles.

The single cutback minimum noise trajectory is considered a lower bound on the thrust setting during climb-out, whereas a trajectory without any cutback is considered an upper bound. Two additional trajectories, i.e., a standard and advanced trajectory based on the NASA STCA noise assessment (Berton et al., 2020), are also considered with thrust cutbacks in between these bounds. The definitions of these four reference trajectories are shown in Table 11 and their thrust-setting schedules are illustrated in Figure 26.

Table 11. Comparison of reference trajectories.

Name	TS_{TO}	PTCB		Pilot-initiated cutback	
		h_{cb}	TS_{cb}	h_{cb}	TS_{cb}
No cutback	100%	-	-	-	-
Standard	100%	-	-	584.7m	65%
Advanced	100%	15.3m	85%	544.1m	65%
Single CB min. noise	100%	25m (M 1.4, 8 pax) 25m (M2.2, 55pax)	60% (M 1.4, 8 pax) 65% (M 2.2, 55 pax)	-	-

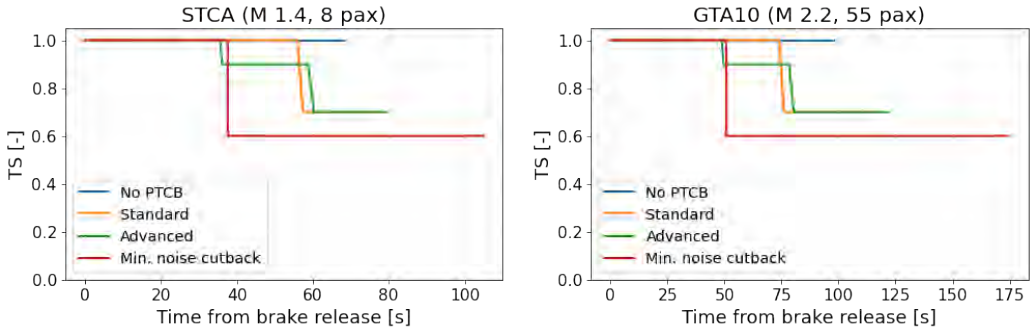

Figure 28. Thrust-setting schedules for trajectories in Table 11 for the STCA and M2.2 medium SST.

Instantaneous Engine Conditions at Various PTCB Levels During Climb Out

The thermodynamic conditions at the inlet to the combustor, T_{t3} and P_{t3}, are shown by the shaded region in Figure 27 at various climb thrust settings for the STCA. The flight Mach number is varied from 0.2 to 0.48 (typical Mach numbers between the aircraft stall speed and $v_{\text{eas}} = 250$ kts) and the flight altitude from 500 to 3000 ft (LTO is considered to consist only of flight phases below 3000 ft altitude). The thermodynamic conditions are normalized by the ICAO LTO conditions for a climb out thrust setting, i.e., 85% of the sea-level static thrust, F_{00}. The thermodynamic conditions for the three cutback trajectories are shown in Figure 27.

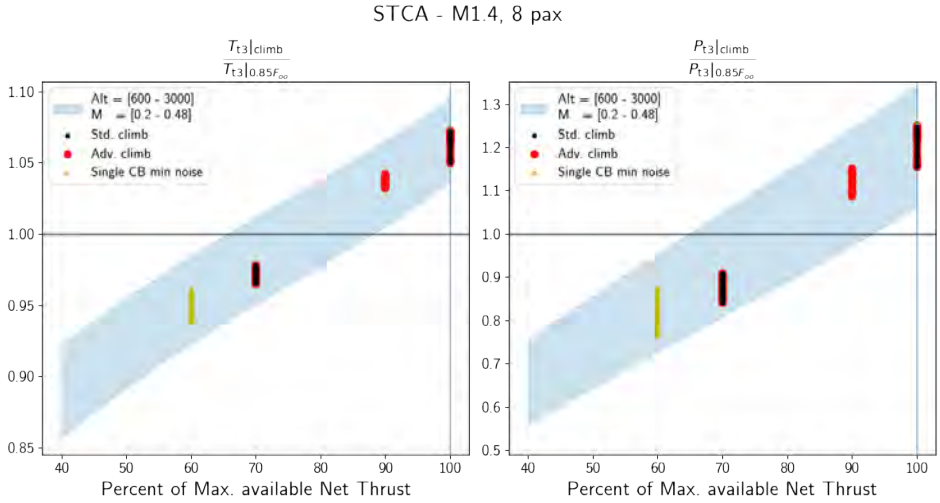

Figure 29. Combustor inlet conditions (P_{t3}, T_{t3}) for flight Mach numbers M ∈ [0.2, 0.48] and altitudes Alt ∈ [500, 3000] ft for the NASA STCA. The black marker and horizontal line indicate the sea-level static conditions at the corresponding thrust setting (TS). The sea level static (SLS) value at 85% F_{oo} corresponds to the ICAO LTO climb out thrust level.

Figure 27 shows that, for the possible range of PTCB identified, the temperature at the inlet to the combustor for the STCA can vary between ~7% below to ~8% above that at the ICAO LTO climb out thrust setting. The pressure at the combustor inlet can vary between ~30% below to 25% above that of ICAO LTO climb out thrust setting.

The instantaneous emission index of nitrogen oxides (EI(NO_x)) for the four trajectories listed in Table 11 are shown in Figure 28. The take-off and climb-out phase of the subsonic certification and supersonic certification LTO cycle are also indicated for reference.

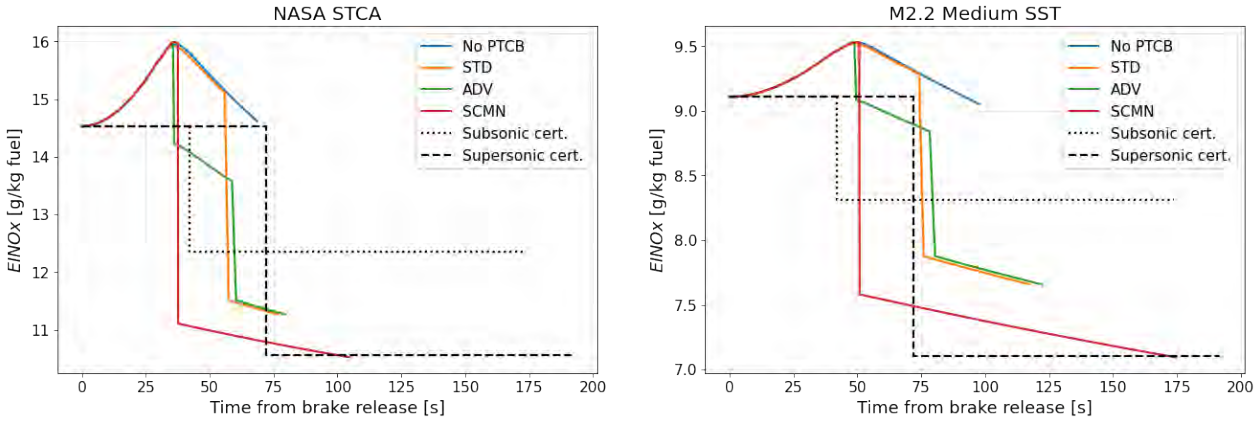

Figure 30. Trajectory instantaneous EI(NO_x) compared to the subsonic and supersonic certification.

The EI(NO_x), during the climb phase relative to the emission index (EI) at the 85% F_{oo} LTO value is shown in Figure 29. We show the trends of the EI(NO_x) values for various PTCB cutback levels for the STCA and M2.2 medium SST.

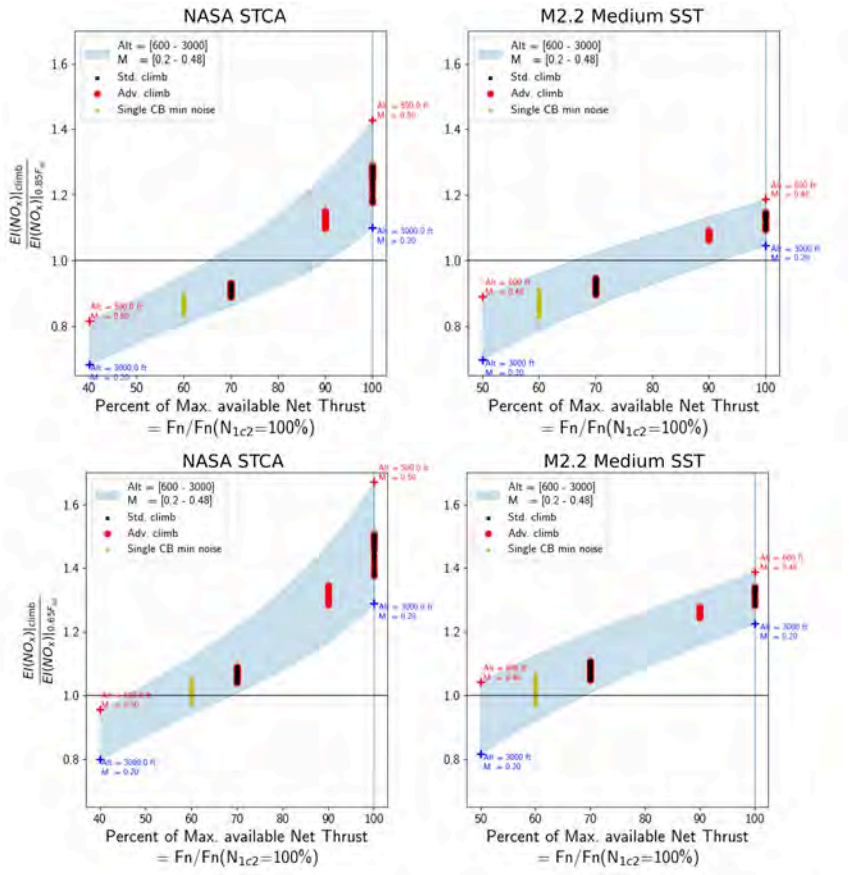

Figure 31. NO_x emissions relative to the 85% (top row) and 65% (bottom row) LTO thrust setting for various flight conditions for two example SST – the 8 passenger M1.4 NASA STCA and M2.2 Medium SST. The black markers indicate the sea-level static conditions at the corresponding thrust setting.

The overall compressor pressure rise (inlet of fan root to combustor inlet) is limited by the maximum allowable T_{t3} based on the materials used in the engine. As the cruise Mach number increases, i.e., from M=1.4 for the STCA to M=2.2 for the M2.2 medium SST) the ram compression increases the inlet temperature and therefore, the allowable compressor pressure ratio reduces. The lower design pressure ratio for the M2.2 medium SST implies a lower T_{t3} in the LTO cycle relative to the STCA. Therefore, the combustor inlet temperatures (and consequently NO_x emissions) are driven by the compressor pressure ratio.

Figure 29 shows that the trend of EI(NO_x) varies for the different aircraft. The STCA climb profile shows that at a 65% thrust setting the EI(NO_x) is approximately 7-12% lower than the LTO value. However, at a thrust setting of 50% (determined by the minimum noise trajectory for a single full-authority digital engine control [FADEC]-controlled cutback event) the EI(NO_x) is 12-20% lower than the LTO value. If the available thrust during climb is higher than the required thrust the PTCB level can be higher (leading to lower TS) and therefore, even lower EI(NO_x) relative to the LTO 85% value. On the other hand, if the required thrust is close to the available thrust then the PTCB level will be lower resulting in EI(NO_x) values greater than the 85% LTO value. For the M2.2 medium SST, at a 65% thrust setting we observer an EI(NO_x) that is ~10% lower than the LTO value. These variations are in part due to the lower required compressor pressure ratios as the cruise Mach number increases. This indicates that the deviation from the LTO 85% value is dependent on the aircraft-engine combination. The

variation in the trends of EI(NO_x) at various flight conditions is observed in the difference between the shaded regions for the two aircraft under consideration.

We observe that the spread of the normalized EI(NO_x) for the STCA is larger at 100% thrust setting relative to the 50% thrust setting. In contrast, the spread at the 100% thrust setting is smaller than the 50% thrust setting for the M2.2 aircraft. This is due to the sensitivity of EI(NO_x) predicted by the P_3-T_3 model to T_{t3}. At lower temperatures ~500-550 K the slope of the EI(NO_x) vs. T_{t3} is higher than the slope at temperatures of 600-650 K. Therefore, for similar variation in T_{t3} the variation in EI(NO_x) is larger for the M2.2 aircraft at lower thrust settings than the STCA.

Estimate of Difference in Integrated Emissions Between Reference Trajectories and LTO Certification Cycles During Climb-Out

The cumulative mass of NO_x emitted from 35 ft up to 3000 ft for the four trajectories is shown in Figure 30 and Figure 31 for the NASA STCA and M2.2 Medium SST, respectively. The comparison of the final cumulative mass of NO_x with the subsonic and supersonic certification LTO cycle, i.e., $m_{NO_x,35<h<3000ft}/m_{NO_x,cert.}$, is shown in Table 12. Note that, for the certification mass of NO_x emitted, $m_{NO_x,cert.}$, only the climb out phase is used.

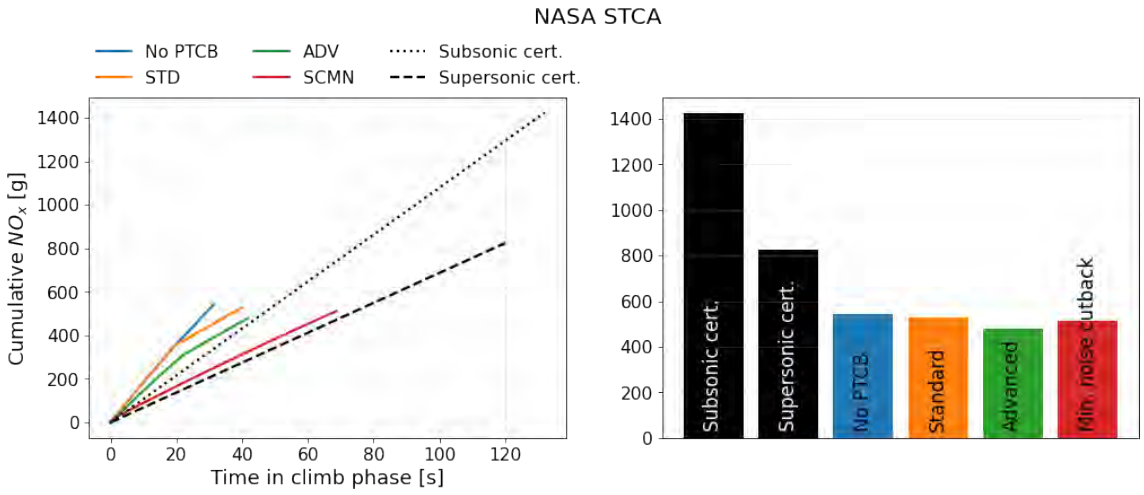

Figure 32. Integrated emissions comparison to subsonic and supersonic certification standards for the M1.4 STCA.

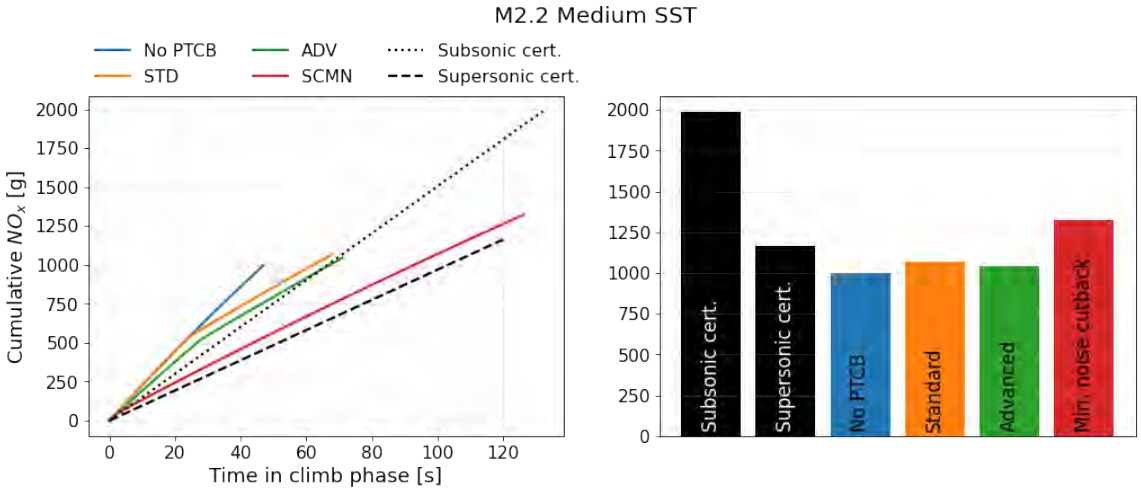

Figure 33. Integrated emissions comparison to subsonic and supersonic certification standards for the M2.2 medium SST.

A comparison of the integrated emissions has been made on a D_p/F_{oo} basis, where only the take-off and climb phases are considered (therefore, further referred to as m_{NO_x}/F_{oo}). The difference in m_{NO_x}/F_{oo} between the four trajectories and the subsonic and supersonic certification LTO cycle are shown in Table 12.

Table 12. Comparison of the climb out $\boldsymbol{m_{NO_x}/F_{oo}}$ ($35 < \boldsymbol{h} < 3000$ ft) for the STCA and M2.2 medium SST with subsonic and supersonic certification LTO cycles (+ means certification cycle is overestimating).

Trajectory name	NASA STCA			M2.2 medium SST		
	$\frac{m_{NO_x}}{F_{oo}}\left[\frac{g}{kN}\right]$	$\Delta_{subsonic}$ [%]	$\Delta_{supersonic}$ [%]	$\frac{m_{NO_x}}{F_{oo}}\left[\frac{g}{kN}\right]$	$\Delta_{subsonic}$ [%]	$\Delta_{supersonic}$ [%]
Subsonic certification	17.8	-	-	14.6	-	-
Supersonic certification	10.3	-	-	8.5	-	-
No cutback	6.8	+61.9	+34.2	7.3	+49.7	+14.1
Standard	6.6	+63.0	+36.1	7.8	+46.3	+8.3
Advanced	6.0	+66.3	+41.8	7.7	+47.4	+10.2
Single CB min. noise	6.4	+64.1	+37.9	9.7	+33.5	-13.6

Table 12 shows that for the STCA aircraft the subsonic certification climb-out time in mode and thrust setting overestimates the mass of NO_x emissions per unit thrust (m_{NO_x}/F_{oo}) of real trajectories by 64% (for the single cutback minimum noise trajectory) to 62% (for no cutback). The supersonic certification time in mode and thrust setting also overestimates m_{NO_x}/F_{oo}, but by smaller margins - 38% to 34% (for the single cutback minimum noise trajectory and no cutback trajectory respectively). For the M2.2 medium SST the subsonic certification climb-out time in mode and thrust setting overestimates m_{NO_x}/F_{oo} by 33.5% to 50%. While the supersonic certification climb-out time in mode and thrust-setting underestimates the m_{NO_x}/F_{oo}, of real single cutback minimum noise trajectory by -13.6% and overestimates m_{NO_x}/F_{oo}, for the no cutback trajectory by 14%, the margin is smaller than the subsonic rules. This suggests that the thrust setting prescribed by the current supersonic certification LTO climb out mode, i.e., 65% F_{oo} is more representative of the real trajectories of the M1.4 STCA and M2.2 Medium SST than the subsonic certification thrust setting of 85% F_{oo}.

Publications
None.

Outreach Efforts
- Mr. Laurens Voet presented an Information Paper titled "Investigation of the effects of VNRS on LTO emissions of engines for supersonic transport aircraft" at the CAEP/12-WG3/5-ESTG meeting on November 3, 2020.
- Mr. Laurens Voet gave a presentation titled "Development of optimal control framework to design VNRS for take-off operations of civil supersonic transport" at NASA Glenn Research Center on July 22, 2021.
- Mr. Laurens Voet gave a presentation titled "Design of variable noise reduction systems for civil supersonic transport certification noise reduction" at the NASA Acoustics Technical Working Group Meeting Fall 2021 on October 19, 2021.

Awards
None.

Student Involvement
This task was conducted primarily by graduate research assistant Laurens Voet, working under the supervision of Dr. Jayant Sabnis, Dr. Raymond Speth, and Dr. Choon Tan.

References
Berton, J. J., Huff, D. L., Geiselhart, K., & Seidel, J. (2020, January 6–10). *Supersonic technology concept aeroplane for environmental studies* [Conference presentation]. AIAA Scitech 2020 Forum, Orlando, Florida.

DuBois, D., & Paynter, G. C. (2006). Fuel Flow Method 2 for estimating aircraft emissions (SAE Technical Paper 2006-01-1987). SAE International.

EASA (2019). ICAO Aircraft Engine Emissions Databank, version 26A. European Union Aviation Safety Agency (EASA). https://www.easa.europa.eu/easa-and-you/environment/icao-aircraft-engine-emissions-databank

ICAO. (2017a). *Annex 16 to the Convention on International Civil Aviation: Environmental Protection - Volume 1: Aircraft Noise* (8th Ed). International Civil Aviation Organization (ICAO).

ICAO. (2017b). *Annex 16 to the Convention on International Civil Aviation: Environmental protection - Volume II: Aircraft engine emissions* (4th Ed). International Civil Aviation Organization (ICAO).

Voet, L., Prashanth, P., Speth, R., Sabnis, J., Tan, C., & Barrett, S. (2021, January 11–15 & 19–21). *The impact of design space constraints on the noise and emissions from derivative engines for civil supersonic aircraft* [Conference presentation]. AIAA Scitech 2021 Forum, virtual.

Task 7 - Evaluate the Impact of Advanced Take-off Trajectories for SST Using VNRS on Community Noise
Massachusetts Institute of Technology

Objectives
The objective of this task is to extend our evaluation of the noise impacts of advanced take-off trajectories to incorporate VNRS. These advanced take-off trajectories are designed and optimized by using the take-off certification noise level as a representative metric for noise around airports. The take-off certification noise level incorporates noise levels measured at two locations, i.e., the lateral and flyover microphones. To assess whether these advanced take-off trajectories are effective in community noise reduction, we calculate community noise contours.

Research Approach
Figure 32 summarizes the noise levels of the advanced take-off trajectories for the NASA STCA using VNRS as measured using the certification noise metric. Reduced cut-back altitudes (from 260 m to 11 m) and increased take-off speeds (from 200 kts to 250 kts) enable as much as 7 EPNdB of cumulative noise reduction. When continuous thrust control (also described as programmed thrust cutback) is used, an additional 3.6 EPNdB of cumulative noise reduction can be achieved. The inherent tradeoff between lateral and flyover noise for the discrete high-altitude and low-altitude thrust cut-back trajectories can be seen in Figure 32. At increased take-off speed, the advanced take-off trajectory with continuous thrust

control avoids this tradeoff by reducing flyover noise without increasing lateral noise, with respect to those with the low-altitude cutback.

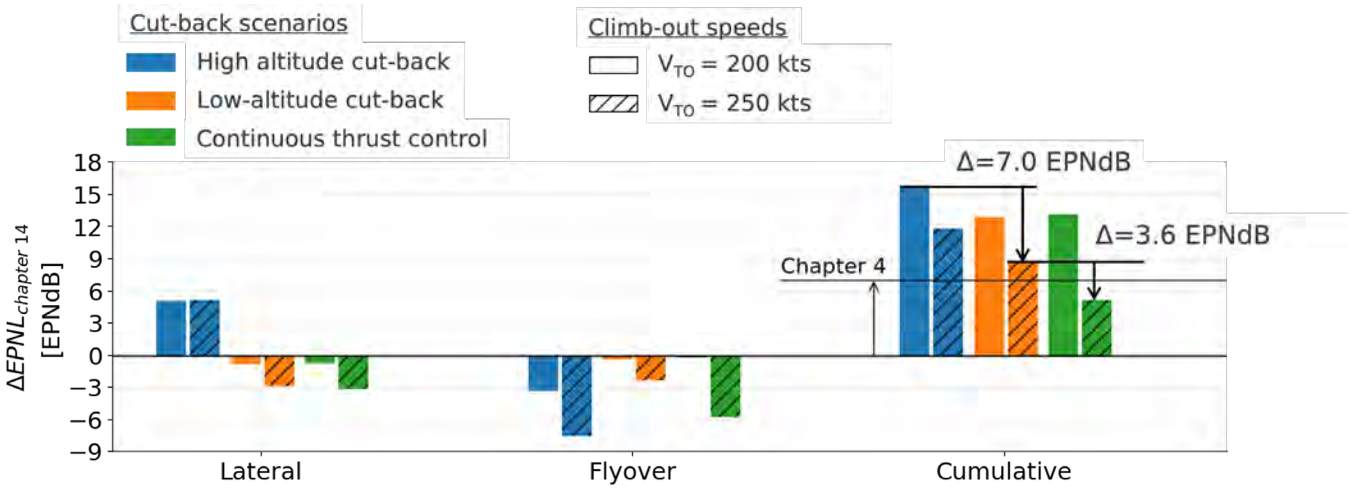

Figure 34. Comparison of the lateral, flyover, and cumulative certification noise levels of standard and advanced trajectories with the ICAO Annex 16 Chapter 14 noise limits (ICAO, 2017). The Annex 16 Chapter 4 noise limits are also indicated for reference.

Programmed high-lift devices have been found to be ineffective in reducing take-off noise for the NASA STCA. Figure 32 shows that, even with the use of advanced take-off trajectories, the NASA STCA is unable to meet current noise limits for subsonic transport set by the ICAO in Annex 16, Volume 1, Chapter 14 (ICAO, 2017). Additional noise reduction might be achieved by incorporating reduced thrust take-off procedures, as explored by Berton et al. (2019) and Olson (1992).

The impact of the advanced take-off trajectories on community noise is shown in the SEL line contours and ΔSEL color contours in Figure 33. In Figure 33, the top left plot shows the community noise contours for the standard take-off trajectory, abiding by the current noise standards for subsonic transport in ICAO Annex 16. The noise is highest underneath the flight path on the centerline and decreases when laterally moving away in the *y*-direction. The center plot on the top row shows the ΔSEL between the high-altitude and low-altitude cut-back.

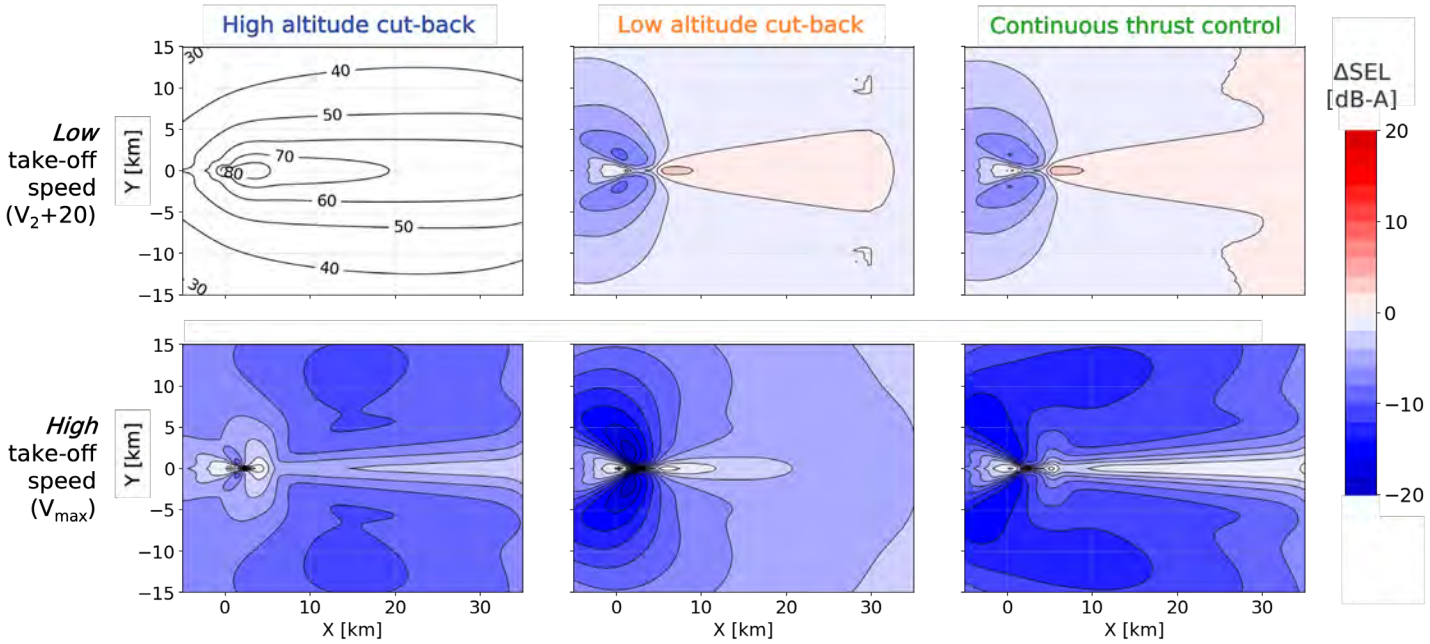

Figure 35. SEL line contours for the NASA STCA standard single thrust cut-back trajectory abiding by the noise standards for subsonic transport defined in ICAO Annex 16 (top left). ΔSEL color contours for the NASA STCA advanced take-off trajectories (top middle and top right, bottom row). The origin is the aircraft brake release point.

With the low-altitude cutback, the community noise contours show the tradeoff between points in the airport vicinity and downstream, indicated by the blue and red regions. This tradeoff is also captured when the certification noise metric is used. At increased take-off speeds, the same tradeoff is observed; however, the average noise is reduced because of the reduced jet shear at higher take-off speeds.

The high-altitude cutback achieves the largest noise reduction in downstream regions, whereas the low-altitude cut-back achieves the largest noise reduction in regions in the vicinity of the airport. With continuous thrust control (at increased take-off speeds), the advanced take-off trajectory achieves noise reduction in the combined region between airport vicinity and downstream. Overall, this trajectory achieves the largest noise reduction relative to all other advanced take-off trajectories.

Figure 34 compares the community noise contours for the high-speed advanced take-off trajectories with continuous thrust control and low-altitude cut-back, i.e., the two trajectories with lowest cumulative noise levels when the certification noise metric is used. With the continuous thrust control trajectory, noise is reduced in the areas where it was already low (away from the flight path, as shown in the line contour of Figure 34), and is not reduced underneath the flight path, where the noise was the highest. These findings illustrate where the certification and community noise metrics are not aligned and thus suggest re-examination of the certification noise metric for SST using advanced take-off trajectories.

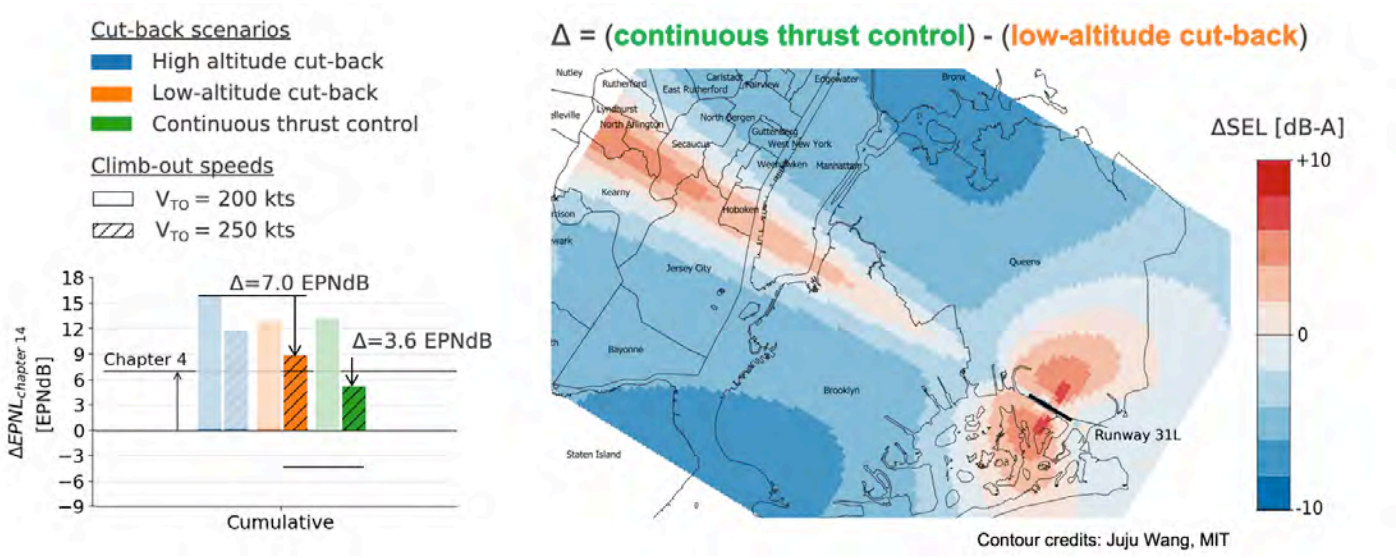

Figure 36. Comparison of certification cumulative noise levels between high-speed continuous thrust control and low-altitude cut-back trajectories (left). ΔSEL color contours for high-speed continuous thrust control and low-altitude cut-back trajectories taking off from runway 31L at New York JFK airport (right).

Milestones

- Used the pyNA aircraft noise estimation tool (Voet et al., 2021) to calculate the community noise contours around airports for the advanced take-off trajectories for SST using VNRS.
- Applied the community noise contours to an existing airport. In this work, the New York John F. Kennedy (JFK) airport is chosen. The departure from JFK is from Runway 31L.

Major Accomplishments

- Applied the use of continuous thrust control (also described as programmed thrust cutback) to achieve an additional 3.6 EPNdB of cumulative noise reduction. At increased take-off speed, the advanced take-off trajectory with continuous thrust control avoids this tradeoff by reducing flyover noise without increasing lateral noise, with respect to those with the low-altitude cutback.
- Found programmed high-lift devices to be ineffective in reducing take-off noise for the NASA STCA.
- Identified that certification and community noise metrics are not aligned, suggesting re-examination of the certification noise metric for SST using advanced take-off trajectories.

Publications

Voet, L., Speth, R. L., Sabnis, J. S., Tan, C. S., & Barrett, S. R. (2022, June 14). *On the design of variable noise reduction systems for supersonic transport take-off certification noise reduction* [Conference presentation]. 28th AIAA/CEAS Aeroacoustics 2022 Conference, Southampton, United Kingdom. https://doi.org/10.2514/6.2022-3052

Voet, L. J. A., Prashanth, P., Speth, R. L., Sabnis, J. S., Tan, C. S., & Barrett, S. R. H. (2024). Automatic Continuous Thrust Control for Supersonic Transport Takeoff Noise Reduction. *Journal of Aircraft*, *61*(1), 291–306. https://doi.org/10.2514/1.C037394

Outreach Efforts

- Presentation at the ASCENT Advisory Committee Spring Meeting (April 5–7, 2022)
- Presentation at the Aviation Emissions Characterization Roadmap Annual Meeting (May 24–26, 2022)

Awards

None.

Student Involvement

This task was conducted primarily by Laurens Voet, a graduate research assistant working under the supervision of Dr. Jayant Sabnis, Dr. Raymond Speth, and Dr. Choon Tan.

References

ICAO. (2017). *Annex 16 to the Convention on International Civil Aviation Environmental Protection Volume 1: aircraft noise* (8th Ed). International Civil Aviation Organization (ICAO).

Olson, E. D. (1992, September 30). *Advanced takeoff procedures for high-speed civil transport community noise reduction*. SAE International. https://doi.org/10.4271/921939

Voet, L., Prashanth, P., Speth, R., Sabnis, J., Tan, C., & Barrett, S. (2021). *The impact of design space constraints on the noise and emissions from derivative engines for civil supersonic aircraft*. [Conference Presentation] AIAA Scitech 2021 Forum. American Institute of Aeronautics and Astronautics. https://doi.org/10.2514/6.2021-1272

Project 049 Urban Air Mobility Noise Reduction Modeling

The Pennsylvania State University
Continuum Dynamics, Inc.

Project Lead Investigator

Kenneth S. Brentner
Professor of Aerospace Engineering
Department of Aerospace Engineering
The Pennsylvania State University
308 ECoRE Bldg, 556 White Course Drive
University Park, PA
814-865-6433
ksbrentner@psu.edu

University Participants

The Pennsylvania State University (Penn State or PSU)

- P.I.: Kenneth S. Brentner, Professor of Aerospace Engineering
- FAA Award Number: 13-C-AJFE-PSU-049, Amendment No. 120
- Period of Performance: October 1, 2023, to September 30, 2024
- Tasks:
  1. Predict and investigate turbulence interaction noise
  2. Compare predictions with flight tests
  3. Investigate time-varying broadband noise of multirotor aircraft
  4. Develop and investigate departure and arrival transition maneuvers
  5. Upgrade and document eVTOL of noise prediction system

Project Funding Level

The funding during this period started with the Federal Aviation Administration (FAA) providing $280,000 in funding. Continuum Dynamics, Inc. (point of contact: Dan Wachspress) provided $75,000 of cost sharing in the form of a 1-year license for the Comprehensive Hierarchical Aeromechanics Rotorcraft Model (CHARM) rotorcraft comprehensive analysis software to the FAA or its designee. Penn State provided $50,000 in equipment cost sharing, and $155,000 in academic year salary for the P.I., corresponding to a total of $280,000 in cost sharing. This funding ended December 31, 2023, and was not renewed until August 2024, with the FAA providing $305,000 in funding. Blue Ridge Research and Consulting LLC (BRRC) will provide $8,975 in-kind support to attend research and biannual meetings, and review software and documentation. Sikorsky, A Lockheed Martin Company, will provide $186,000 in-kind support to attend recuring meetings, provide aircraft configuration data, and acoustic flight measurements for verification and validation of the Penn State noise prediction system (PSU-NPS). Supernal will provide $121,000 in-kind support in the form of costs accrued to collect and extract datasets from a flying test bed Bell 407 as well as engineering hours. Continuum Dynamics, Inc. (Point of contact: Dan Wachspress) will provide $225,000 of cost sharing in the form of a 1-year license for the CHARM rotorcraft comprehensive analysis software to the FAA for its designee and to industrial partners BBRC and Sikorsky. Total cost sharing: $540,975.00.

Investigation Team

The Pennsylvania State University

Kenneth S. Brentner (P.I.; acoustic prediction lead), Tasks 1-5
Eric Greenwood (co-P.I.; acoustics prediction/analysis), Tasks 1-5
Joseph F. Horn (co-P.I.; flight simulation lead), Tasks 2, 4, and 5

Ze Feng (Ted) Gan (graduate research assistant; developing PSU-WOPWOP noise prediction software and performing acoustic predictions), Tasks 2, 3, and 5
Bhaskar Mukherjee (graduate research assistant; software coupling, establishing new aircraft models, developing simulations for new aircraft types, performing acoustic predictions, and developing flight abatement procedures), Tasks 1-5

Continuum Dynamics, Inc.
Daniel A. Wachspress and Mrunali Botre (co-P.I.; rotor loads, wake integration, and CHARM coupling), Tasks 1, 2, 4, and 5

Project Overview

A wide variety of unconventional configurations for urban air mobility (UAM) and electric vertical take-off and landing (eVTOL) aircraft, most with many electrically driven propellers and lifting rotors, have been proposed and are currently under development by companies worldwide. These novel configurations comprise a new category of aircraft that will need to be certified, particularly for acceptable noise levels, given their urban operations. Furthermore, the noise of UAM and eVTOL vehicles is expected to be one of the considerations of passengers and communities. Therefore, first-principles noise predictions of these aircraft will be important for providing the FAA with information independent from that provided by manufacturers and before manufacturer flight test or certification noise data are available. For clarification, unmanned aircraft systems (UAS) (also known as drones), UAM, and eVTOL vehicles all share electric motors as the source of power to drive the rotors; therefore, UAS noise characteristics can also shed light on UAM/eVTOL noise. In most cases, UAM vehicles are likely to use batteries, but the electrical power could come from fuel cells, gas generators, or other sources. Furthermore, although most UAS and UAM vehicles are likely to have VTOL capabilities, such capabilities are not a requirement. In this report, the terms UAM and eVTOL are used synonymously, whereas UASs are eVTOL drones.

In ASCENT Project 038, the helicopter noise prediction system initially developed in ASCENT Project 006 was successful in accurately predicting the noise of helicopters (usually within sound exposure levels of 1 to 3 dBA), when the predictions were compared with results from an FAA/National Aeronautics and Space Administration (NASA) rotorcraft noise abatement flight test performed in August and October 2017. Sound exposure level contours from the flight test were compared with predictions for several flight procedures. The noise prediction system developed in ASCENT Project 038 consisted of the PSU HeloSim flight dynamics simulation code coupled to the CHARM aeromechanics modeling software and the PSU-WOPWOP noise prediction code. This combination with the flight simulation code was demonstrated to be important for noise prediction, which markedly improved when the simulation was modified to track the time-dependent aircraft position, velocity, and attitude flown in an individual run, rather than the nominal flight path.

To build upon the success of ASCENT Project 038, ASCENT Project 049 employs an analogous approach of coupling a flight simulation code with CHARM and PSU-WOPWOP. The PSU HeloSim flight simulation component of the noise prediction system used in ASCENT Project 038 was replaced with DEPSim, a flight simulation code designed for many electrically driven rotors with unique control strategies to fly such vehicles effectively. Coupling of DEPSim with CHARM was performed in work outside ASCENT, whereas DEPSim–CHARM coupling with PSU-WOPWOP was performed in this project.

The goal of this project is to develop a noise prediction system with the initial capability to analyze the noise from UAM and eVTOL vehicles with unique configurations under any flight conditions. This project should enable the FAA, manufacturers, and related entities to investigate how this new class of vehicles—and their noise—might be integrated into the national airspace. Emphasis is placed on modeling the unique features of UAM and eVTOL configurations not commonly seen in conventional rotorcraft, such as rotors with variable rotation speed, and complex unsteady aerodynamic interactions between the many rotors and the airframe. Because UAM vehicles will probably have lower tip speeds to achieve acceptable noise levels, broadband noise is expected to become the dominant rotor noise source; accordingly, rapid physics-based modeling of rotor broadband noise is a goal of this project. Another goal is to use the noise prediction system developed in this project to provide guidance on how to fly these vehicles in a quiet manner through flight operations. Because the analysis and computations are based on fundamental physics, noise abatement procedures for novel vehicles can be developed.

Task 1 – Prediction and Investigation of Turbulent Interaction Noise

The Pennsylvania State University

Objective

The objective of this task is to incorporate PSU-MulTINoise, a new code being developed under ASCENT Project 049, into the noise prediction system. This code computes unsteady airloads generated on blade sections and lifting surfaces due to turbulent interaction. Sources of turbulence include rotor vortex cores, atmospheric boundary layer turbulence, etc.

Research Approach

PSU-MulTINoise currently accepts turbulent intensity and length scale to characterize turbulence via the von Kármán spectrum (von Kármán, 1948) and calculates unsteady airloads generated on an airfoil. This spectrum can be used to characterize small-scale isotropic turbulence commonly observed in the atmosphere. A preliminary investigation on the impact of atmospheric turbulence on eVTOL aircraft noise is conducted. A new reference tiltrotor aircraft is also developed to represent leading eVTOL aircraft designs such as the Joby Aviation® S4.

Milestones

- Developed a utility code that can generate a profile of atmospheric boundary layer and turbulent parameters dependent on local topography and weather conditions.
- Modeled a new tiltrotor reference aircraft (PSU Reference Aircraft 3 [PSU-RA3]) based on Joby S4.
- Investigated the Impact of atmospheric turbulence on a nominal transition maneuver

Major Accomplishments

The atmospheric boundary layer is formed when wind flows over the Earth's surface shown in Figure 1a. Turbulence is generated in this boundary layer due to the presence of terrain features such as vegetation, buildings, etc. Vertical turbulent motion can also be a result of convective thermals due to temperature differences between the ground and surrounding air as shown in Figure 1b. Noise generated due to rotor operating in the turbulence of atmospheric boundary layer has been previously reported to be important (Amiet et al., 1990). Thus, noise due to atmospheric boundary layer turbulence ingestion could be important when the aircraft is flying at low altitude. Little information is available in the literature on its impact on eVTOL noise.

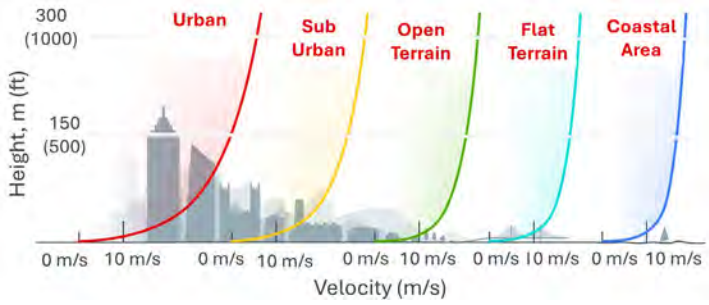

(a) Variation of boundary layer velocity profile with terrain (SimScale, 2024).

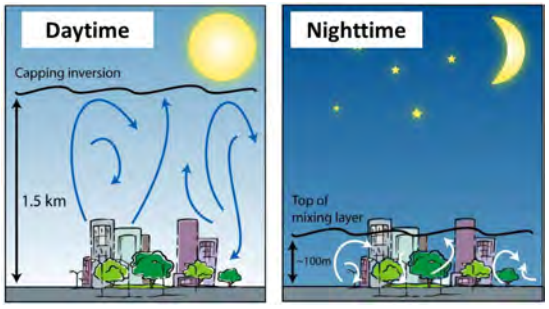

(b) Boundary layer processes (Shaw et al., 2007)

Figure 1. Mechanisms and characteristics of atmospheric boundary layer.

Noise from steady-state boundary layer turbulence interacting with rotors can be predicted using PSU-MulTINoise if a suitable spectral representation of turbulence is identified. Currently, the code has been validated (see ASCENT Project 049 annual Report 2022-2023, Task 4) and takes the turbulent length scale and intensity as inputs to model the homogeneous and isotropic von Kármán power spectrum as:

® Joby Aviation is a registered trademark of Joby Aero, Inc., Santa Cruz, California.

$$S_{ww}(k_{1_n}, k_{2_n}) = \frac{4}{9\pi}\frac{{u'_{RMS}}^2}{k_e^2}\frac{\hat{k}_{1_n}^2 + \hat{k}_{2_n}^2}{\left[1 + \hat{k}_{1_n}^2 + \hat{k}_{2_n}^2\right]^{\frac{7}{3}}} \quad \text{(Eq. 1)}$$

where S_{ww} represents the power spectral density of turbulent upwash velocity w, k_{1_n} and k_{2_n} represent the n^{th} wavenumber of the "frozen" turbulent gust along the chord and span of an airfoil, respectively, u'_{RMS} is the streamwise root mean-square (RMS) of turbulent velocity fluctuations (u'), and k_e is the wavenumber range of energy-containing eddies.

The wavenumbers k_{1_n} and k_{2_n} can be normalized using the integral length scale Λ as:

$$\hat{k}_i = \frac{k_i}{k_e}; \qquad i = 1,2; \qquad k_e = \frac{\sqrt{\pi}}{\Lambda}\frac{\Gamma\left(\frac{5}{6}\right)}{\Gamma\left(\frac{1}{3}\right)} \quad \textit{(Eq. 2)}$$

The magnitude of the spectral density $S_{ww}(k_{1_n}, 0)$ is used to calculate the turbulent gust velocity which is the primary input required for calculating unsteady airloads. Therefore, the key parameters needed to build the energy spectrum of turbulence in the boundary layer are the RMS of turbulent velocity fluctuations u'(m/s) and the characteristic length scale Λ (m). These can be derived using the Monin-Obukhov similarity theory (MOST; Monin & Obukhov, 1954). This theory applies to the atmospheric boundary layer, where surface fluxes are relatively constant. It provides mathematical expressions to model turbulent fluxes and velocity profiles in the boundary layer of the atmosphere.

Inputs to the MOST model include the velocity (u_1, u_2), the temperature (T_1, T_2) of the air at two different altitudes (z_1, z_2), and surface roughness (z_0). The latter is estimated with knowledge of the heights of structures on the terrain. For example, bare land with low grass has an estimated roughness of 0.02 m (Stewart & Oke, 2012). The stability of the boundary layer is determined by the rate at which heat (heat flux Q_H) is transferred from the ground to the air. The atmosphere is considered unstable if $Q_H > 0$, stable when $Q_H < 0$, and neutral otherwise. The result from MOST model is the variation of velocity, turbulent intensity and length scale with altitude based on the local conditions and topography.

Impact of atmospheric boundary layer turbulence was investigated for PSU-RA3. Figure 2a shows an image of the tiltrotor configuration in OpenVSP. It is based on the Joby Aviation S4 aircraft (Figure 2b) but does not use any proprietary information.

(a) PSU-RA3 (b) Joby S4 (evtol.news/joby-s4)

Figure 2. FiTiltrotor eVTOL aircraft.

Acoustic results from a flight test were published in a paper by Pascioni et al. (2022). Two maneuvers from the paper are of interest, departure (T5) and arrival (A4) transition maneuvers. Results from the arrival A4 maneuver are discussed in this report. The arrival maneuver starts at a nominal altitude of 325 ft and 60 knots airspeed and ends with the aircraft in hover (Figure 3).

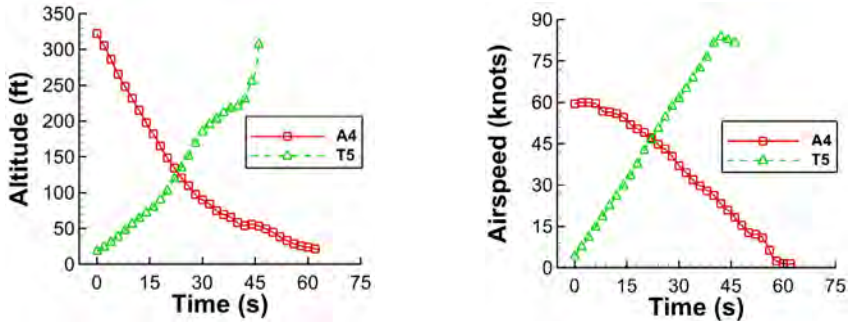

(a) Altitude vs Time (b) Airspeed vs Time

Figure 3. Variation of altitude and airspeed with time for arrival (A4) and departure (T5) maneuvers (based on data published by Pascioni et al. [2022]).

Noise was measured by a set of ground microphones and the $L_{A,max}$ metric was reported. While no measured data on the atmospheric boundary layer turbulence were reported, the nominal atmospheric velocity vs. altitude profile was published in Pascioni et al. (2022) (refer to Figure 4a, black curve with -o- symbol). Assuming the test took place on bare land with low surface roughness, inputs to MOST were adjusted to match the published velocity profile. The velocity-altitude profile shown in red (Δ symbol) can be seen to reasonably match the experimental data.

Based on the velocity profile matched by MOST, the variation of RMS of turbulent fluctuations and length scale with altitude was calculated (Figure 4b). This turbulence-altitude profile was used as input to PSU-MulTINoise for calculating airloads on rotors generated due to turbulence and exported to PSU-WOPWOP for noise prediction.

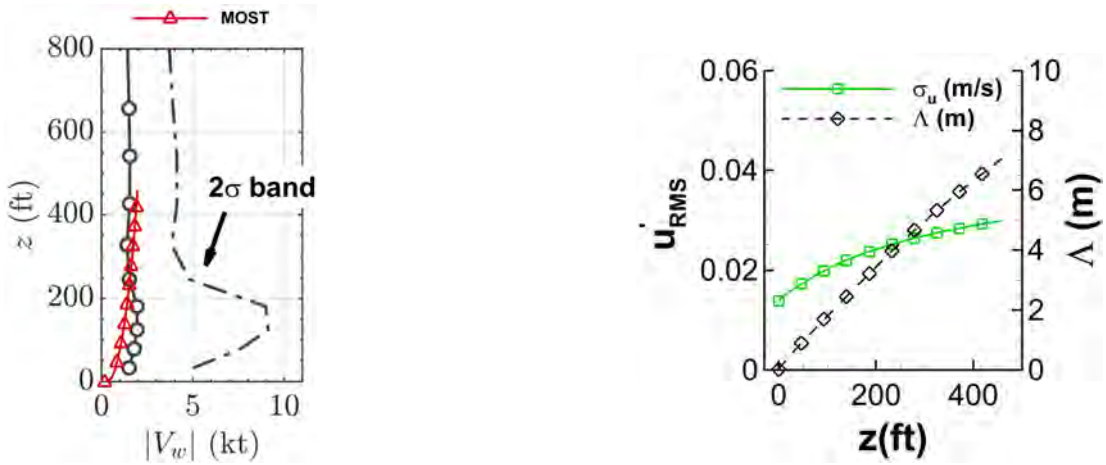

(a) Atmospheric velocity vs altitude profile, measured (Pascioni et al., 2022) vs. MOST theory

(b) RMS of turbulent fluctuations and length scale vs. altitude

Figure 4. Estimated atmospheric boundary layer characteristics for the Joby Aviation S4 flight test.

Figure 5a plots the $L_{A,max}$ noise metric measured during the flight test by a set of ground microphones with Joby Aviation S4 flying the A4 maneuver. Figure 5b and Figure 5c plot predictions for the same maneuver flown by PSU-RA3. Note that PSU-RA3 was not simulated in DEPSim, but the experimentally reported aircraft and rotor states (Pascioni et al., 2022) were used for the simulation.

CHARM was used to calculate the deterministic airloads. While capable of capturing several harmonics of rotor-wake interaction noise, it is not capable of capturing the broadband component. PSU-MulTINoise was used to calculate the airloads generated due to turbulent interaction, and the Brooks, Pope and Marcolini (BPM) model (Brooks et al., 1989) was used to account for the broadband component of self-noise. Two key limitations of the current analysis worth mentioning are: isotropic turbulence modeling and one-dimensional (1-D) calculation of PSU-MulTINoise. In an investigation by Amiet et al. (1990), it was pointed out that turbulence usually undergoes distortion while approaching the rotor disk. This distortion introduces significant anisotropic behavior, not captured by the von Kármán power spectrum (Eq. 1). However, PSU-MulTINoise currently can only model isotropic turbulent interactions. Amiet et al. (1990) also showed that an isotropic assumption can lead to an over-prediction of noise in the order of 20 dBA. For simplicity, Amiet et al. (1990) also discussed using a -20dBA offset to correct for the isotropic assumption. The same offset is used here, thus making this work preliminary.

Figure 5b plots the predicted $L_{A,max}$ from PSU-RA3 aircraft flying the A4 maneuver without the effects of atmospheric boundary layer turbulence. While it captures the trends, it is underpredicting $L_{A,max}$ on the order of 5 to 10 dBA when compared to flight test data (Figure 5a). This underprediction is expected as high frequency broadband noise due to rotor-wake interactions and other sources are not modeled. Figure 5c, which is $L_{A,max}$ prediction with the inclusion of atmospheric boundary layer turbulence ingestion can be observed to underpredict $L_{A,max}$ on the order of 2 to 5 dBA. This demonstrates the potential importance of including this source of noise even for the aircraft flying in seemingly calm conditions.

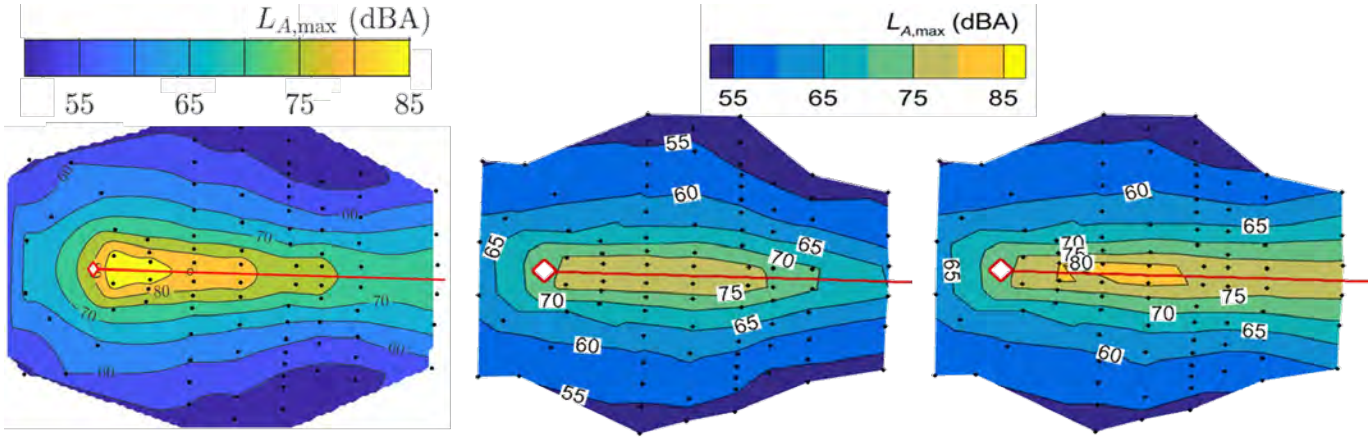

(a) Flight test: Joby S4 (adapted from Pascioni et al., 2022)

(b) Prediction: PSU-RA3

(c) Prediction: PSU-RA3

Figure 5. $L_{A,max}$ contour for A4 arrival maneuver (flight direction: right to left).

Publications

None.

Outreach Efforts

None.

Awards

Bhaskar Mukherjee's work for this task was also partially supported by the Transportation Research Board Airport Cooperative Research Program Graduate Research Awards.

Student Involvement

Bhaskar Mukherjee, a graduate assistant pursuing his PhD at Penn State, is working on physics-based mid-fidelity modeling of broadband noise from various sources of eVTOL aircraft.

Plans for Next Period

- Extend 1-D atmospheric boundary layer turbulence ingestion noise model to two dimensions (2-D).
- Account for turbulence distortion as it approaches the rotor disk in the model to reduce overprediction of turbulence ingestion noise.
- Use the advanced features of CHARM to provide detailed information about the flow field to determine streamline shape and the stress deformation tensor, needed in the turbulence noise model.

References

Amiet, R. K., Simonich, J. C., & Schlinker, R. H. (1990). Rotor noise due to atmospheric turbulence Ingestion. II - aeroacoustic results. *Journal of Aircraft, 27*(1), 15–22. https://doi.org/10.2514/3.45892

Brooks, T. F., Pope, D. S., & Marcolini, M. A. (1989). *Airfoil self-noise and prediction* (p. 142). National Aeronautics and Space Administration (NASA), NASA Langley Research Center, NASA RP-1218. https://ntrs.nasa.gov/api/citations/19890016302/downloads/19890016302.pdf

Monin, A. S., & Obukhov, A. M. (1954). Basic laws of turbulent mixing in the surface layer of the atmosphere. *Tr. Akad. Nauk SSSR Geophiz. Inst., 24*(151), 163-187. https://mcnaughty.com/keith/papers/Monin_and_Obukhov_1954.pdf

Pascioni, K. A., Watts, M. E., Houston, M., Lind, A., Stephenson, J. H., & Bain, J. (2022, June 14-17). *Acoustic flight test of the Joby Aviation advanced air mobility prototype vehicle* [Conference presentation]. 28th AIAA/CEAS Aeroacoustics 2022 Conference, Southampton, United Kingdom. https://doi.org/10.2514/6.2022-3036

Shaw, W. J., Wang, W., Rutz, F. C., Chapman, E. G., Rishel, J. P., Xie, Y., Seiple, T. E., & Allwine, K. J. (2007). *Meteorological integration for the Biological Warning and Incident Characterization (BWIC) system: general guidance for BWIC cities*. Pacific Northwest National Lab (PNNL), Richland, Washington, PNNL-16422. https://doi.org/10.2172/901186

SimScale. (2024, June 30). *Atmospheric boundary layer|pedestrian wind comfort*. https://www.simscale.com/docs/analysis-types/pedestrian-wind-comfort-analysis/wind-conditions/atmospheric-boundary-layer/

Stewart, I. D., & Oke, T. R. (2012). Local climate zones for urban temperature studies. *Bulletin of the American Meteorological Society, 93*(12), 1879–1900. https://doi.org/10.1175/BAMS-D-11-00019.1

von Kármán, T. (1948). Progress in the statistical theory of turbulence. *Proceedings of the National Academy of Sciences of the United States of America, 34*(11), 530–539.

Wachspress, D. A., Quackenbush, T. R., Boschitsch, A. H., Yu, M. K., & Whitehouse, G. R. (2023). C.D.I. Technical note 23 (p. 295). In *Comprehensive Hierarchical Aeromechanics Rotorcraft Model User's Manual*, *Version 7.3.* Continuum Dynamics, Inc., Ewing, New Jersey.

Task 2 – Comparison Between Predictions and Flight Tests

The Pennsylvania State University

Objectives

This task is focused on comparing noise predictions with acoustic data measured in outdoor flight tests and anechoic chamber. The physics of eVTOL and UAS aircraft operations result in high-frequency broadband noise to be the dominant source. Time-averaged broadband noise predictions from the PSU-NPS are compared with experimental data. Differences between both are analyzed to identify methods for improving the prediction. Conversely, experimental data are analyzed to identify characteristics of time-varying broadband noise, with a focus on the impact of blade azimuth phase offsets between rotors during flight.

Research Approach

Noise from a reconfigurable hexacopter in hover was measured on a ground microphone array as part of ASCENT Project 077. Broadband noise predictions using the BPM self-noise model (Brooks et al., 1989) was compared with experimentally measured spectrum. Differences were analyzed, and improvements to the model were made along with its implementation in PSU-WOPWOP.

Simple prediction models for time-varying multirotor broadband noise were developed by supplementing analytical models with flight test and anechoic chamber measurements collected for ASCENT Project 077. These include measurements of the rotor azimuth phase and rotor rotation rates. Summation of the modulation of individual rotors represents the first step towards more formal prediction models. Summation of the broadband noise modulation of multiple rotors makes assumptions not previously validated in the literature, which are discussed and validated below.

Milestones

- Modified the BPM model for smaller unmanned aerial vehicle (UAV)-sized blades that helps improve predictions.
- Developed analysis and prediction frameworks for characterizing multirotor broadband noise modulation, including characterizing the variability of noise with time and between repeated flights.

Major Accomplishments

In ASCENT Project 077, a reconfigurable hexacopter has been built and instrumented for outdoor flight tests. Figure 6a shows the hexacopter flown, while Figure 6b shows the layout of the ground microphone grid used for measuring noise. The hexacopter is hovering over microphone 16 at an altitude of 20 ft. Time-averaged spectrum (0.5 s window) was calculated, and A-weighting was applied. The A-weighted sound pressure level was then derived from the time-averaged spectrum.

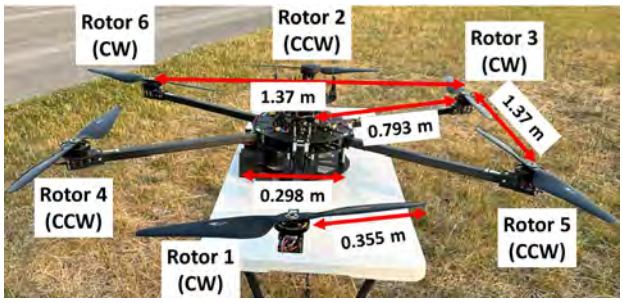

(a) Reconfigurable hexacopter flown for outdoor test

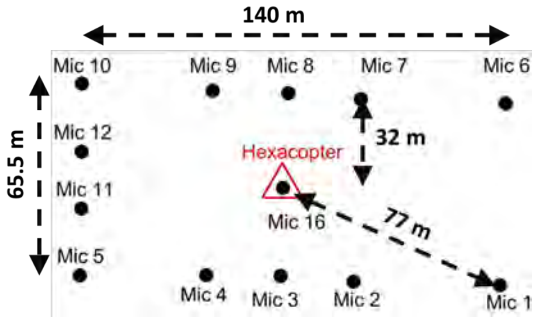

(b) Microphone grid layout

Figure 6. Schematic of hexacopter and microphone grid layout.

Figure 7a shows the variation in A-weighted sound pressure level (SPL) across microphones 1 through 12. Three datasets are plotted: measured, BPM_C (compact formulation) and BPM_{mod} (hybrid compact + noncompact formulation). BPM_C represents the original formulation of the model (Brooks et al., 1989). One of the assumptions in the model was that the blades are acoustically compact (i.e., the chord-to-wavelength ratio (c/λ) is greater than 1). This is a reasonable assumption for modeling self-noise from helicopter blades, which was the original motivation for development of the BPM model. However, small UAS aircraft typically have blades whose chord-to-wavelength ratio (c/λ) are less than 1. Thus, the BPM model was modified (referred here as BPM_{mod}) with a correction for acoustically non-compact blades.

At microphone 16, the measured OASPL is 71.5 dBA and the OASPL predicted using BPM_C and BPM_{mod} are 70.5 dBA and 70.9 dBA. Comparing the A-weighted 1/3rd octave spectrum shows reasonable match (Figure 7b). However, noise predictions by the original BPM_C model at other microphones can be seen to have errors in OASPL on the order of 4 to 8 dBA (Figure 7a). Figure 7c shows the difference in predicted spectrum at microphone 5, with the BPM_{mod} model capturing the shape of the measured spectrum much better than the compact formulation of the BPM_C model. This trend is also observed in predicted OASPL values (Figure 7), where the BPM_{mod} model has a much better prediction than BPM_C with the error in range of 1 to 2 dBA.

To predict multirotor broadband noise modulation, the broadband (BB) SPL time histories generated by individual rotors are summed. The random phase (i.e., incoherence) of noise frequencies characteristic of broadband noise allows summing the mean-squared pressure (MSP) time histories of different rotors. In contrast, the modulation is deterministic, as the modulation frequency is the blade passage frequency (BPF). Therefore, the phase of the modulation must be considered during summation of the broadband noise modulation of different rotors. Results for summing anechoic chamber measurements of individual rotors as shown in Figure 8. Any azimuthal phase offset value can be set using the tachometer measurements. The modulation depths (peak to trough amplitude of SPL time history) of the summed results (+' in Figure 8) match well (within 1 dB) with simultaneous operation of the same rotors with the same phase offset ('x' in Figure 8), for a parametric sweep of phase offset values. This match shows how summation of the broadband noise modulation of individual rotors is a good approach to predicting time-varying multirotor broadband noise. Figure 8 also shows the importance of phase on multirotor broadband noise modulation, including the potential benefits of synchrophasing control to reduce broadband noise modulation. This is because in Figure 8, the modulation depth changes

by more than 5 dB depending on the phase offset value between rotors. The results of Figure 8 were computed by averaging blade passages using cyclostationary analysis, which has been shown in the literature to also be a special case of envelope analysis (Randall et al., 2001). The sum and simultaneous cases did not match as closely when synchronous averaging of the BB SPL time histories of rotors was performed instead of cyclostationary analysis; this shows the benefits of applying cyclostationary and envelope analysis to study rotorcraft broadband noise, despite these methods rarely being applied to rotorcraft noise analysis.

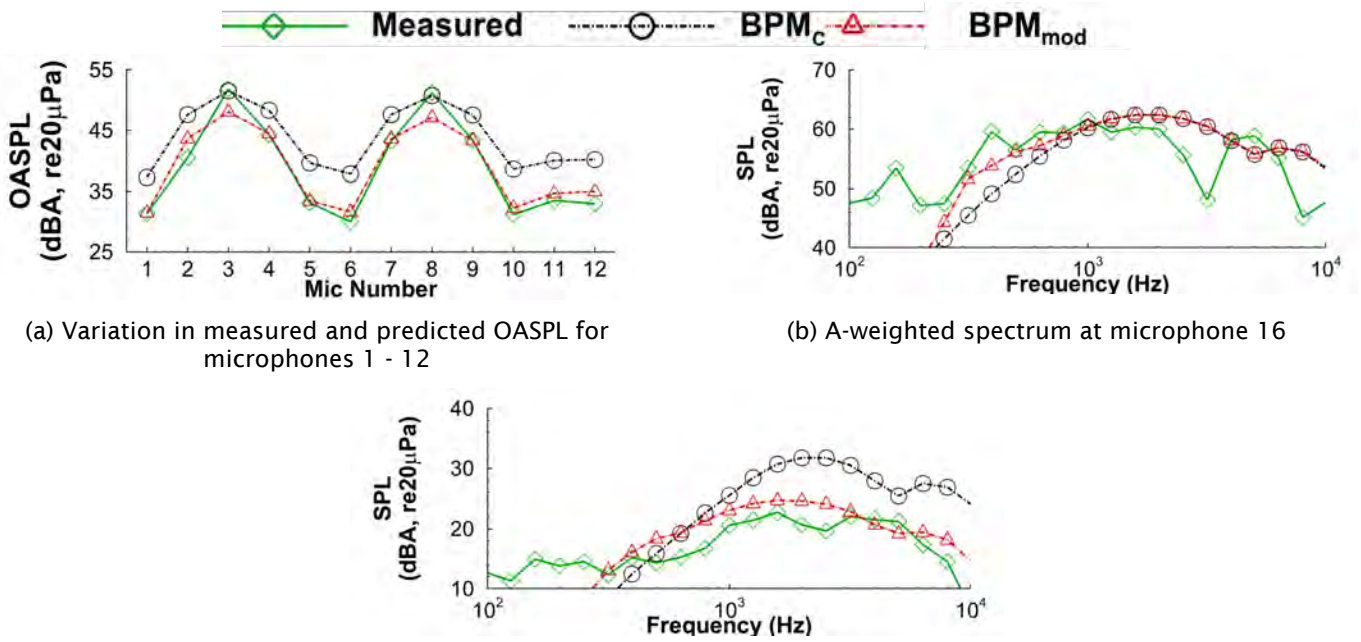

(a) Variation in measured and predicted OASPL for microphones 1 - 12

(b) A-weighted spectrum at microphone 16

(c) A-weighted spectrum at microphone 5

Figure 7. Noise from hovering PSU hexacopter at 20 ft.

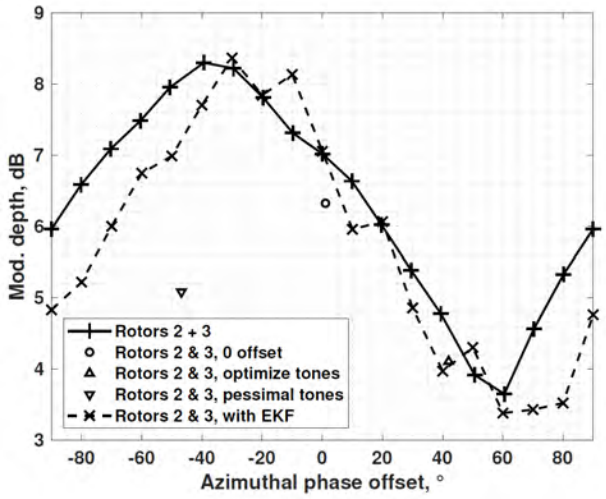

Figure 8. Parametric study of modulation depth of synchrophased anechoic chamber measurements comparing sum (+) vs simultaneous cases (&).

An additional objective previously stated in this work was to predict variations in the noise modulation amplitude. These aperiodic variations between blade passages were observed in flight test measurements in Figure 10 (see Task 3 below). Although Figure 8 studied synchrophased operation of rotors, flight controllers typically vary rotor speeds for flight control. The azimuthal phase offset between rotors was found to follow a uniform random distribution in non-synchrophased anechoic chamber measurements where the rotors were set to the same BPF. Accordingly, the prediction approach described in the previous paragraph was extended by considering an input probability distribution of phase offsets, rather than only considering a single phase offset value for synchrophased operation of rotors. Since the modulation amplitude (or modulation depth) depends strongly on phasing, as seen in Figure 8. This approach predicts a probability distribution for the modulation amplitude. This probability distribution of modulation amplitude is shown in Figure 9a for sinusoidal broadband noise modulation of two rotors summed with uniform random phase. Figure 9a shows that the modulation of the rotors are likely to sum to nearly in-phase (i.e., near fully constructive interference), resulting in high modulation amplitudes being likely to occur, with the median modulation being approximately 71% of the maximum possible value. When the number of rotors N increases, the median modulation amplitude scales with N to the power of -1/2, as shown in Figure 9b. Even for many (e.g., more than 30) rotors, the modulation amplitude plateaus near 20% of the maximum value, which is still likely to be large. Therefore, characterizing the probability distribution of modulation depth might help explain why broadband noise modulation is significant in flight, even for aircraft with many rotors.

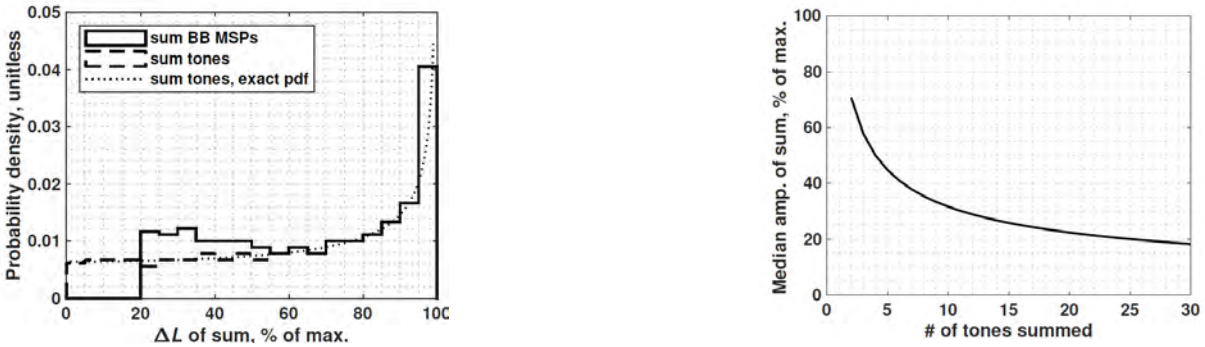

Figure 9. (a) Probability distribution of modulation depth (ΔL) of 2 rotors summed with uniform random azimuthal phasing; (b) Median amplitude of summed sines of equal amplitude.

Publications

Gan, Z. F. T., Tumelero Valente, V., Brentner, K. S., & Greenwood, E. (2024a). Broadband noise modulation of multirotor aircraft, *Journal of the Acoustical Society of America*, *157*, 924–939. https://doi.org/10.1121/10.0035646

Gan, Z. F. T., Tumelero Valente, V., Brentner, K. S., & Greenwood, E. (2024b). Time-varying broadband noise of multirotor aircraft. *Proceedings of Meetings on Acoustics, 54*(1). https://doi.org/10.1121/2.0001946

Outreach Efforts

Presentation

Gan, Z. F. T., Tumelero Valente, V., Brentner, K. S., & Greenwood, E. (2024c, May 13-17). *Multirotor broadband noise modulation* [Conference Presentation]. 186th Meeting of the Acoustical Society of America/Acoustics Week in Canada, Ottawa, Ontario.

Awards

Student Paper Competition - 1 of 5 Winners, *Proceedings of Meetings on Acoustics*, for Gan et al. (2024b).

Student and Early Career Best Presentation Award - 2nd Place, Acoustical Society of America Technical Committee on Noise for Gan et al. (2024c) presented at the *186th Meeting of the Acoustical Society of America/Acoustics Week in Canada*, Ottawa, ON.

Student Involvement

Bhaskar Mukherjee, a graduate research assistant currently working toward his PhD degree at Penn State, analyzed time-averaged broadband noise for this task.

Ze Feng (Ted) Gan, a graduate research assistant currently working toward his PhD degree at Penn State, analyzed time-varying broadband noise for this task.

Plans for Next Period

- Rectify the current implementation of the modified BPM model by using first-principal methods (such as PSU-MulTINoise) to obtain the required parameters of tuning the model. The current implementation of modified BPM model still uses parameters that were obtained from experimental data of compact airfoils.
- Validate predictions of the variation in multirotor broadband noise modulation amplitude using an echoic chamber and flight test measurements.
- Investigate the directivity of multirotor broadband noise modulation in more detail, as it was shown above to differ from the directivity of a single rotor.

References

Brooks, T. F., Pope, D. S., & Marcolini, M. A. (1989). *Airfoil self-noise and prediction*. NASA Reference Publication NASA RP-1218, NASA Langley Research Center, 142. https://ntrs.nasa.gov/api/citations/19890016302/downloads/19890016302.pdf

Randall, R. B., Antoni, J., & Chobsaard, S. (2001). The relationship between spectral correlation and envelope analysis in the diagnostics of bearing faults and other cyclostationary machine signals. *Mechanical Systems and Signal Processing, 15*(5), 945-962. https://doi.org/10.1006/mssp.2001.1415

Task 3 – Investigate Time-Varying Broadband Noise of Multirotor Aircraft

The Pennsylvania State University

Objectives

One objective of this task is to determine the significance of time-varying multirotor broadband noise (a.k.a. multirotor broadband noise modulation) using flight test measurements. This objective is motivated by anechoic chamber measurements taken for ASCENT Project 077 and analyzed in Task 2 of the 2023 annual report for ASCENT Project 049, which found that the importance of time-varying multirotor broadband noise depends significantly on the blade azimuth phase offsets between rotors. This is contrary to predictions in the literature, which predict broadband noise to be fairly constant with time for many rotors, with the modulation depth decreasing as the number of rotors increases (Li & Lee, 2022).

Another objective of this task is to determine the significance and physical sources of broadband noise modulation at modulation frequencies not at the BPF. Broadband noise modulation with the BPF was studied in Task 2 above, but other modulation frequencies were also observed in this work. Psychoacoustics studies of small multirotor UAS report significant noise modulation amplitudes at modulation frequencies much lower than the BPF; and the physical causes responsible for this modulation remain unclear (Gwak et al., 2020; Torija & Nicholls, 2022; Ramos-Romero et al., 2023).

One possible cause of low frequency modulation for multi-rotor aircraft with high BPFs is the presence of beating effects, or simply ‘beats’ for short. Beats arise when tones have closely spaced frequencies, resulting in modulation at a frequency equal to the difference of the tonal frequencies (Feynman et al., 2011). Although beats are typically studied as tones, one could hypothesize that there exists an analogous phenomenon for broadband noise modulation: i.e., for two amplitude-modulated (AM) broadband noise (BBN) signals with closely spaced modulation frequencies. However, this has not been studied in the literature.

Closely spaced BPFs are likely to arise in flight for aircraft with electric rotors with variable rotation speeds: for example, the flight controller may command slightly different rotor rotation speeds to trim the aircraft in hover or axial flight, to counteract the presence of atmospheric disturbances.

Research Approach

Flight test measurements of a hexacopter UAS collected for ASCENT Project 077 are analyzed using advanced signal processing methods such as envelope and cyclostationary analysis. Although these methods have not been widely applied to rotorcraft noise analysis, their fine time resolution enables deeper understanding and more precise and accurate quantification of multirotor broadband noise modulation, including the influence of variations in azimuthal phase.

Prediction models were developed by supplementing simple analytical and numerical models with anechoic chamber measurements collected for ASCENT Project 077. These include not only noise measurements, but also measurements of the time histories of rotor rotation rates.

Milestones

- Determined that time-varying multirotor broadband noise is significant in flight.
- Determined the significance of beats of broadband noise modulation.
- Developed analysis and prediction frameworks for characterizing beats of broadband noise modulation.

Major Accomplishments

BB SPL time histories of flight test measurements are shown for two different microphones in Figure 10. These were computed using the following procedure:

1. Acoustic pressure measurements were bandpass filtered between 5 kHz to 20 kHz to extract broadband noise.
2. Using this filtered acoustic pressure time history, the MSP time history was computed for a window length of 29% of the blade passage period (BPP), with 87.5% overlap between consecutive windows. The window length must be less than a BPP to resolve time variation of broadband noise levels within a blade passage.
3. The time history of the BB MSP is converted to decibels (dB), to obtain the BB SPL time history.

Analyzing the time history of BB SPL rather than time-frequency representations is suitable because the noise frequency content is not significantly detailed but is fairly uniform with frequency.

In Figure 10, for both observers directly below the aircraft and near the rotor disk plane, the modulation depths are significant: approximately 5 to 9 dB. Both observers have similar modulation depths, despite the microphones being at very different far-field distances; this is expected, as for linear acoustics in the far field, the SPL of both modulation peaks and troughs decay at the same rate of 6 dB per doubling of observer distance. Note that the observer along the rotor axis (Figure 10a has similar modulation depths to the observer near the rotor disk plane (Figure 10b). This directivity for six rotors differs from that of a single rotor, where there is greater modulation for observers at small elevation angles relative to the rotor disk plane (Gan et al., 2021). The modulation in Figure 10 predominantly has the BPF (blade passage frequency), although the BPF fluctuates slightly throughout flight; the nominal BPF of 74 Hz is used to normalize the time axis of Figure 10. Other modulation frequencies aside from the BPF are also present, resulting in aperiodic differences between blade passages, which were discussed and predicted in Task 2 above.

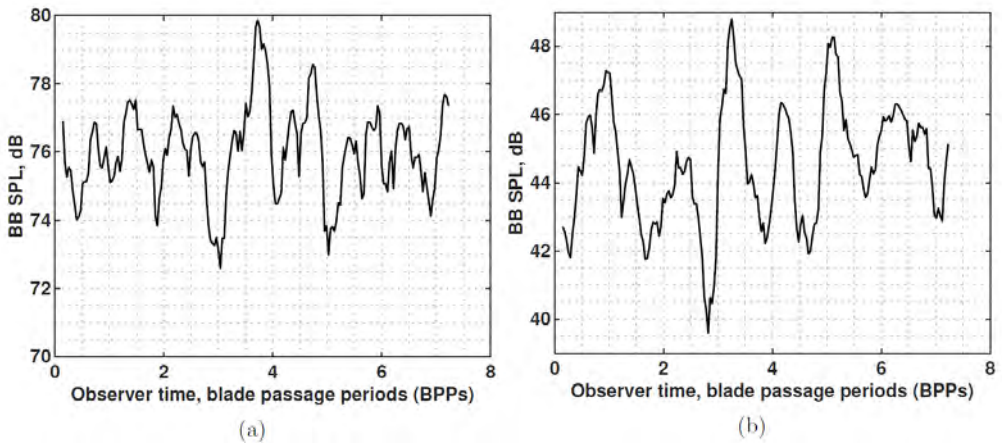

Figure 10. BB SPL time histories for flight test: (a) Microphone 10 ft below aircraft, (b) Microphone: 277 ft away, 17° below rotor disk plane.

Anechoic chamber measurements were also conducted for ASCENT Project 077 for a small hexacopter UAS in a hover condition fixed to a test stand in an anechoic chamber. Only two rotors were operated. The rotors were not synchronized, but set to the same rotor rotation speed setpoint of 2000 rad/s. The resulting BB SPL time history was calculated as described in Task 2 above and shown in Figure 11a. The BB SPL has a clearly visible modulation envelope with a modulation frequency near 2 Hz, which can easily be heard. This modulation frequency corresponds to the 1.8 Hz mean difference between the rotor BPFs. Therefore, the BB SPL envelope seen in Figure 11a is likely caused by beats. The mean BPF difference is small (< 0.3%) compared to the nominal rotor BPF. This demonstrates how even seemingly small offsets in BPF can significantly affect noise. The exact beat frequency differed slightly between repeated trials, ranging from about 0.8 Hz to 1.8 Hz. In each repeated trial, the time variation of the mean BPF difference was found to follow a Gaussian distribution with a standard deviation of 0.8 Hz. Despite this standard deviation being of the same order of magnitude as the mean, these time variations in BPFs did not appear to eliminate beats.

The modulation envelope of the BB SPL time history observed in experiments and as shown in Figure 11a was predicted using a simple analytical model. This model consists of two AM white noise signals with closely spaced AM frequencies. The resulting BB SPL time history of this model is shown in Figure 11b. The beat frequency is easily heard in the acoustic pressure time history auralization of this simple model.

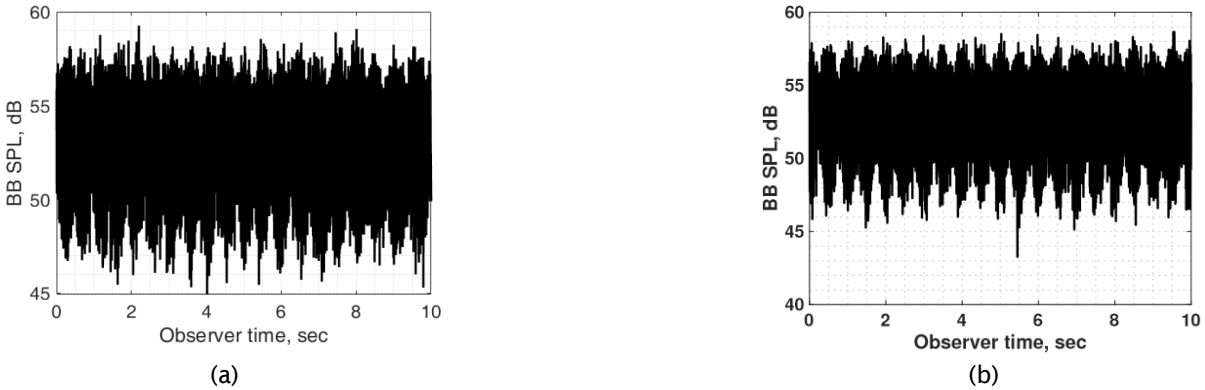

Figure 11. Beats of AM BB noise modulation with closely spaced modulation frequencies: (a) anechoic chamber measurements (b) simple prediction model.

Figure 12a shows the power spectral density (PSD) of the BB SPL time history shown in Figure 11a. This PSD does not show significant content at the beat frequency, but only the BPFs of the individual rotors. In contrast, the PSD of the envelope of

the BB SPL time history clearly shows the beat frequency (see Figure 12b). These conclusions remain unchanged whether the envelope is computed using the magnitude of the Hilbert transform or computing the mean-square time history using a sliding mean-square window, as was used to compute the BB SPL. Furthermore, these conclusions remain unchanged if these PSDs are constructed for the prediction model shown in Figure 11b. The amplitude of the BB SPL envelope was unaffected when sinusoidal time variations in BPFs were introduced into the prediction model. This is consistent with time variations in the BPFs not eliminating beats observed in experiments. However, it is challenging to interpret the physical meaning of the amplitude of the BB SPL envelope, as it does not clearly correspond to any existing physics-based metric.

Finally, the synchrophasing controller developed in ASCENT Project 077 was found to eliminate beats by maintaining a mean BPF difference below 0.01 Hz, an order of magnitude below the lowest modulation frequency humans can easily hear (Fastl & Zwicker, 2006).

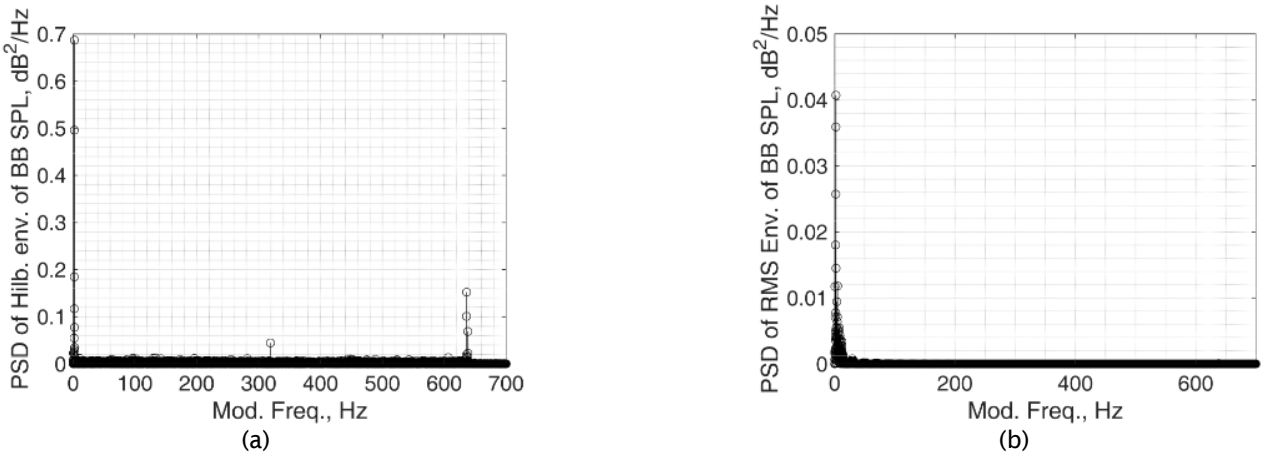

Figure 12. PSD of anechoic chamber measurements: (a) PSD of broadband BB SPL time history, (b) PSD of the envelope of the BB SPL time history.

Publications

Gan, Z. F. T., Tumelero Valente, V., Brentner, K. S., & Greenwood, E. (2024). Broadband noise modulation of multirotor aircraft, *Journal of the Acoustical Society of America*, *157*, 924–939. https://doi.org/10.1121/10.0035646

Outreach Efforts

None.

Awards

None.

Student Involvement

Ze Feng (Ted) Gan, a graduate research assistant currently working toward his PhD degree at Penn State, investigated time-varying broadband noise for this task.

Plans for Next Period

- Study tonal beats and compare their importance to the significance of beats of broadband noise modulation.
- Validate the prediction approach outlined here using flight test measurements taken in ASCENT Project 077, including different maneuvers.

References

Fastl, H., & Zwicker, E. (2006). *Psychoacoustics: facts and models,* (3rd ed.). Springer, Berlin, Heidelberg.

Feynman, R. P., Leighton, R. B., & Sands, M., & California Institute of Technology. (2011). Chap. 48: Beats (Chap. 48). In *The Feynman Lectures on Physics, Volume I: The New Millennium Edition: Mainly Mechanics, Radiation, and Heat*. Basic Books, New York, New York.

Gan, Z. F. T., Brentner, K. S., & Greenwood, E. (2021, January 26-28). *Time variation of rotor broadband noise*. Vertical Flight Society 9th Biennial Autonomous VTOL Technical Meeting, Virtual.

Gwak, D. Y., Han, D., & Lee, S. (2020). Sound quality factors influencing annoyance from hovering UAV. *Journal of Sound and Vibration, 489*(115651). https://doi.org/10.1016/j.jsv.2020.115651

Li, S., & Lee, S. (2022). Acoustic analysis and sound quality assessment of a quiet helicopter for air taxi operations. *Journal of the American Helicopter Society*, *67*(3), 1-15. https://doi.org/10.4050/jahs.67.032001

Ramos-Romero, C., Green, N., Torija, A. J., & Asensio, C. (2023). On-field noise measurements and acoustic characterization of multi-rotor small unmanned aerial systems. *Aerospace Science and Technology, 141*. https://doi.org/10.1016/j.ast.2023.108537

Torija, A. J. & Nicholls, R. K. (2022). Investigation of metrics for assessing human response to drone noise. *International. Journal of Environmental Research and Public Health, 19*(6). https://doi.org/10.3390/ijerph19063152

Task 4 – Develop and Investigate Departure and Arrival Transition Maneuvers

The Pennsylvania State University

Objective

The objective of this task is to design departure and arrival maneuvers aiming to balance the requirements of noise and performance for various eVTOL configurations.

Research Approach

Previous work in ASCENT Project 049 analyzed a notional lift-plus-cruise aircraft departure transition maneuver. However, the version of the noise prediction system used that time was not fully capable of modeling several important sources of broadband noise including rotor-wake interactions, rotor-wing interactions, ingestion of atmospheric turbulence, etc. The noise from the departure transition maneuver needs to be re-calculated by including additional broadband noise sources.

Milestones

- Developed a preliminary computational method for estimating noise sue to ingestion of atmospheric boundary layer turbulence (see Task 1).
- Implemented a convention for categorizing rotor-wake interactions.

Major Accomplishments

As discussed in Task 1 of this report, a new reference aircraft has been developed to represent tiltrotor eVTOL aircraft like the Joby Aviation S4. Noise predictions without inclusion of any airloads generated from turbulent interactions were found to underpredict the $L_{A,max}$ metric by 5 to 10 dBA in comparison to published flight test data. Inclusion of atmospheric boundary layer turbulence ingestion noise using PSU-MulTINoise seemed to reduce the magnitude of under prediction to 2 to 5 dBA. However, additional work still needs to be done in modeling rotor-wake interaction noise. Modeling this source accurately is of greater importance for multi-rotor aircraft. Analysis of free-wake simulations show the significant presence of rotor-wake interactions even for conditions such as hover (Figure 13).

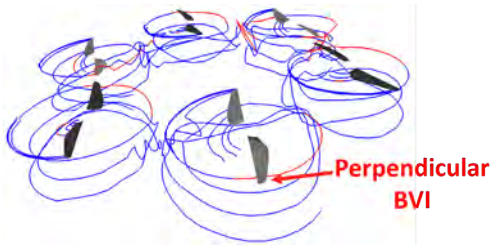

Figure 13. PSU hexacopter: CHARM detecting perpendicular BVI (marked red) during hover at 20 ft altitude.

Publications
None.

Outreach Efforts
None.

Awards
None.

Student Involvement
Bhaskar Mukherjee, a graduate assistant working on his PhD at Penn State, is developing and using the Penn State Noise Prediction System (PSU-NPS) to investigate, design arrival and departure transition maneuvers.

Plans for Next Period
- Develop and test appropriate rotor-vortex interaction models in PSU-MulTINoise. Accurate prediction of noise from transition maneuvers would require modeling rotor-wake interactions. PSU-MulTINoise currently can only model turbulence characterized by the von Kármán spectrum (von Kármán, 1948). However, turbulence in rotor vortex cores is governed by properties such as radius and strength. Its impact is also dependent on the vortex interaction angle and miss distance.

References
von Kármán, T. (1948). Progress in the statistical theory of turbulence. *Proceedings of the National Academy of Sciences of the United States of America, 34*(11), 530–539.

Task 5 – Upgrade and Document eVTOL Noise Prediction System
The Pennsylvania State University

Objective
The objective of this task is to document the eVTOL noise prediction system and its components, including example cases, such that new users can easily learn to use this tool. Work in this task is being coordinated with Task 5 (ASCENT Project 038) as the two projects converge on using the same noise prediction system for helicopters and eVTOL aircraft.

Research Approach
In addition to documentation describing how to use the noise prediction system, example cases are provided to highlight new prediction capabilities and file formats. These example cases also serve as validation cases to ensure that the system is operating as expected. Example cases are automatically validated according to a regression testing procedure (checksuite).

Milestones
- Documented new prediction capabilities for time-varying broadband noise, as summarized in Task 3 above.

- Updated the existing PSU-WOPWOP user manual to include instructions on how to predict time-varying broadband noise.
- Provided example cases and updated the checksuite to automatically validate the file formats of these new time-varying noise results.

Major Accomplishments

A new input file format for self-noise calculations in PSU-WOPWOP using the modified BPM model (refer to BPM_{mod} in Task 2) has been implemented. If chosen by the user, PSU-WOPWOP automatically switches the formulation of BPM model based on local chord-to-wavelength ratio. The new file format also significantly expands the inputs user can provide for the BPM model such as time-varying trailing edge flow angle, sectional eddy convection speed etc. These new inputs will eventually be integrated into the modified BPM model to increase the accuracy of self-noise predictions.

Instructions describing the user input options for predicting time-varying broadband noise were documented in an updated version of the PSU-WOPWOP user manual. The user manual was also updated to describe the new time-varying result file formats, for both single observers (Tecplot® file format) and multiple observers (Plot3D file format). Example cases based on the ideally twisted rotor of NASA (Pettingill et al., 2021) are provided for cases with single and multiple observers. The checksuite was updated to automatically validate time-varying noise result files for multiple observers (Plot3D format). The checksuite was also updated to enable automatic validation of result files located in nested directories.

Publications

None.

Outreach Efforts

None.

Awards

None.

Student Involvement

Ze Feng (Ted) Gan, a graduate research assistant currently working toward his PhD degree at Penn State, documented time-varying broadband noise prediction capabilities for this task.

Plans for Next Period

- Modify the semi-empirical broadband noise models such as the ones originally proposed by Pegg (1979) and Brooks et al. (1989) as calibration techniques are developed and deficiencies identified. PSU-WOPWOP needs to be updated accordingly, including modifying input file formats.
- Updated the checksuite to automatically validate time-varying noise result files for single observers (Tecplot file format). For now, single-observer time-varying noise result files are validated by visual inspection of the results. The checksuite was already updated to automatically validate time-varying noise result files for multiple observers (Plot3D format).
- Update the PSU-WOPWOP user manual to make the tools more accessible to users, including sample cases, which will be described in detail. The user manual revision will also provide more in-depth theory of time-varying broadband noise predictions, including the underlying assumptions. This information has already been outlined in past conference papers published on the work of this project (Gan et al., 2021; Gan et al., 2023).

Example files (e.g., Tecplot layout files) will be provided to illustrate common visualizations, such as spectrograms, contour plots, and hemispheres for a single timestep and contour plot and hemisphere animations between timesteps.

® Tecplot is a registered trademark of Tecplot, Inc., Bellevue, Washington.

References

Brooks, T. F., Pope, D. S., & Marcolini, M. A. (1989). Airfoil self-noise and prediction (p. 142). National Aeronautics and Space Administration (NASA), NASA Langley Research Center, NASA RP-1218. https://ntrs.nasa.gov/api/citations/19890016302/downloads/19890016302.pdf

Gan, Z. F. T, Brentner, K. S., & Greenwood, E. (2022, June 14-17). Time variation of helicopter rotor broadband noise (p. 2914). In *28th AIAA/CEAS Aeroacoustics 2022 Conference*. https://doi.org/10.2514/6.2022-2914 4).

Gan, Z. F. T., Brentner, K. S., & Greenwood, E. (2021, January 27). Time variation of rotor broadband noise (p. 26-28). In *Vertical Flight Society 9th Biennial Autonomous VTOL Technical Meeting, Virtual*.

Pegg, R. J. (1979). *A summary and evaluation of semi-empirical methods for the prediction of helicopter rotor noise.* National Aeronautics and Space Administration (NASA), NASA-TM-80200. https://ntrs.nasa.gov/api/citations/19800007615/downloads/19800007615.pdf

Pettingill, N. A., Zawodny, N. S., Thurman, C., & Lopes, L. V. (2021, January 11–15 & 19–21). Acoustic and performance characteristics of an ideally twisted rotor in hover (p. 1928). In *AIAA Scitech 2021 Forum.* https://doi.org/10.2514/6.2021-1928

Project 051 Combustion Concepts for Next-generation Aircraft Engines

Massachusetts Institute of Technology

Project Lead Investigator

Raymond L. Speth
Principal Research Scientist
Associate Director, Laboratory for Aviation and the Environment
Massachusetts Institute of Technology
77 Massachusetts Ave, Building 33-310, Cambridge, MA 02139
(617) 253-1516
speth@mit.edu

University Participants

Massachusetts Institute of Technology (MIT)

- P.I.: Dr. Raymond L. Speth
- FAA Award Number: 13-C-AJFE-MIT, Amendment Nos. 061, 071, 079, 097, 115, 123, 128, and 133
- Period of Performance: February 5, 2020, to September 30, 2025 (reporting here with the exception of funding level and cost sharing only for the period October 1, 2023, to September 30, 2024)
- Tasks:
  1. Evaluate full-flight effects of alcohol–Jet A dual-fuel Injection on NO_x emissions and fuel consumption
  2. Aerodynamically informed chemical reactor network emissions models for reactive jets-in-crossflow

Project Funding Level

The Federal Aviation Administration (FAA) provided $1,250,000 in funding and $1,250,000 in matching funds were provided from MIT and 3rd party in-kind contributions. Sources of the matching funds are approximately $317,200 from MIT, plus 3rd party in-kind contributions of $674,000 from NuFuels LLC, and $258,800 from Earth Force Technologies.

Investigation Team

Dr. Raymond L. Speth, (P.I.), Tasks 1 and 2
Prof. Steven Barrett, (former P.I.), Tasks 1 and 2
Dr. Jayant Sabnis, (co-investigator), Tasks 1 and 2
Yang Chen, (graduate student), Tasks 1 and 2

Project Overview

The objective of this project is to evaluate the impacts of novel combustion concepts on aircraft engine performance. Specifically, the performance characteristics of interest are engine efficiency and emissions. With advances in material technology in the past 50 years, aircraft engines with higher pressure and temperature ratios have been designed to improve the engine's total efficiency and reduce fuel consumption. However, the increase in combustor temperatures tends to produce higher nitrogen oxide (NO_x) emissions, which account for a substantial portion of aviation's environmental impact. Different combustor techniques have been developed to both reduce emissions and maintain high energy efficiencies. The novel combustion concept currently being investigated in this project is an alcohol–Jet A dual-fuel injection scheme in an axially staged combustor. Research on this topic is a continuation from last year's research. This year, research focused on evaluating the technique when applied to representative flights. Impacts of the technique to mission energy usage and emissions are investigated. Dual-fuel injection's impacts on flights were studied using aircraft design and mission simulation tools (Transport Aircraft System Optimization [TASOPT]), engine modeling tools (Numerical Propulsion System Simulation [NPSS]), and combustor emissions simulation (Pycaso). The second topic under study is the

construction of an aerodynamically informed chemistry model for simulating reactive jets-in-crossflow. This topic is a continuation of Task 2 from the previous year. The modeling techniques utilized for this task make use of chemical solvers including Cantera[1] and Ember[2].

Task 1 - Evaluate Full-flight Effects of Alcohol–Jet A Dual-fuel Injection on NO_x Emissions and Fuel Consumption

Massachusetts Institute of Technology

Objectives

Compared with traditional Jet A dual fuel combustion, combustion of alcohols has been shown to potentially reduce NO_x, unburnt-hydrocarbons (UHC), and soot emissions owing to the hydroxyl group (O–H) within their chemical structures. The oxygen atom from the hydroxyl group acts as a diluent to lower combustion temperature and NO_x emissions. The oxygen, once freed through pyrolysis, also accelerates oxidation of UHCs and reduces their emissions. At the other end of the hydroxyl group, the strong C–O bonding prevents one carbon from forming a C–C structure and reduces soot emissions.

Despite the emissions reduction benefit from alcohol combustion, these fuels have not been widely utilized in aviation due to their reduced specific energy compared with Jet A fuel, which would require airplanes to carry a larger quantity of alcohol fuel compared with Jet A fuel to fly the same distance. To realize the emissions benefits of using alcohol in aircraft engines, it is possible that combining alcohol combustion with a staged combustor design could alleviate the fuel burn penalty from alcohol weight while leveraging the NO_x emissions reduction benefit from alcohol combustion.

An axially staged combustor has fuel injection through two axially arranged locations. The first (pilot) flame zone ensures combustion stability, while the second (main) zone avoids NO_x emissions through lean-burn combustion. As the flow through the pilot zone also passes through the main zone, the effective residence time of pilot zone flow is higher and tends to result in more NO_x emissions. Thus, NO_x reduction techniques applied to the pilot zone are theorized to have larger impacts than those applied to the main zone. Specifically, our team aims to evaluate whether using alcohol in the pilot zone might reduce NO_x emissions more effectively than using alcohol in the main zone. If Jet A fuel is used in the main zone, less alcohol will need to be carried on board and thus the fuel burn penalty will be lower.

Based on the previous year's research, it was noted that during engine ground operations, alcohol-pilot dual-fuel injection can substantially reduce NO_x emissions during the medium power range, which is the power range typically for cruise operations. Also, the additional fuel consumption required for dual-fuel injection is also found to be much lower than for the full alcohol injection case. However, in the previous, mission analysis has not been performed, and different ambient conditions can also affect the emissions analysis. The fuel weight carried for a flight also affects the thrust required and thus the mission fuel burn performance. Therefore, in this task, the chemical reactor network developed in the previous year is incorporated with a conceptual aircraft model to simulate the overall mission performance of dual-fuel injection.

Milestones

- Modified the aircraft design model (TASOPT) to incorporate the change in fuel heating value when switching from jet-fuel to dual-fuel operation mode.
- Added cargo-bay fuel tank model to account for the additional alcohol-fuel storage for dual-fuel injection.
- Optimized a single-aisle aircraft for minimum fuel consumption for different ranges of flight and different fuel schedules.
- Incorporated the additional energy required for alcohol-to-jet (ATJ) fuel conversion into the fuel consumption calculation to have a system level assessment of the energy efficiency of different fuel-injection schedules.

[1] Goodwin, D.G., Moffat, H. K., Schoegl, I., Speth, R. L. & Weber, B. W. (2024). *Cantera: an object-oriented software toolkit for chemical kinetics, thermodynamics, and transport processes* (Version 3.1.0). Zenodo, doi: 10.5281/zenodo.14455267. https://www.cantera.org

[2] Speth, R. L. (2017). *Ember: a quasi-one-dimensional, unsteady flame solver* (Version 1.4.0). Zenodo, doi: 10.5281/zenodo.1004752. https://github.com/speth/ember

- Evaluated the effects of dual-fuel injection on the energy efficiency of flights with different ranges and with and without the additional ATJ energy cost.
- Evaluated the effects of dual-fuel injection on the flight NO_x emissions during different phases of flight.

Major Accomplishments

- Found that a cargo bay fuel tank dramatically increases the mission energy consumption of alcohol-fueled aircraft, as storing alcohol within the cargo bay space allows a more aerodynamically optimal wing size. Additional energy consumption for 1500 nmi full-ethanol flight decreases from 10.5% to 3.8% compared to the baseline jet fuel airplane.
- From in-flight energy consideration only (without ATJ energy cost), found that the ethanol pilot dual-fuel injection schedule reduces the fuel-burn penalty for 3000 nmi missions from 17% in full ethanol injection case to 3.8%, making medium range alcohol flight more practical.
- From system-level energy perspective (with conservative 9.7% ATJ additional energy cost), found that the ethanol pilot dual-fuel injection schedule incurs lower total energy consumption than the full jet-fuel injection case for a flight range below 3000 nmi, making medium range alcohol flight more favorable.
- Observed that because the NO_x emissions reduction effect of ethanol-pilot zone dual-fuel injection is most effective during the cruise power level, ethanol-pilot zone dual-fuel injection reduces total flight NO_x emissions by around 40% compared to the baseline jet fuel airplane.
- Observed that the directional effect on emissions and energy consumption performance of dual-fuel injection are unchanged for different types of alcohol, though the quantitative performance can be affected.

Publications

None.

Outreach Efforts

Results were presented to the FAA ASCENT Project Manager during regular bi-weekly teleconferences.

Awards

None.

Student Involvement

This task was conducted by Yang Chen, working under the supervision of Dr. Jayant Sabnis and Dr. Raymond Speth.

Plans for Next Period

This task is complete.

Task 2 – Aerodynamically Informed Chemical Reactor Network Emissions Models for Reactive Jets-in-Crossflow

Massachusetts Institute of Technology

Objective

To achieve low NO_x emissions and high combustion efficiency, fluid jets in crossflow (JICF) are widely utilized in combustor design, providing quick mixing between reactants. Uses of this technique include the quench flow structure in a rich-quench-lean (RQL) combustor, the main stage fuel injection in a staged combustor, and the hydrogen injection in a micro-mixing injector. Chemical reactor network (CRN) models have been employed previously to assess the performance of and quantify the emissions from combustors using JICF. As showcased by the work performed from Task 1, CRN models can be constructed with parameters, such as fuel-air unmixedness and mixing time scale, to capture the effects of JICF mixing on the NO_x and carbon monoxide (CO) emissions. However, these two parameters are very abstract and for novel combustor concepts with limited experimental data for model calibration, such as multi-stage micro-mixing combustor, determining the parameters can be difficult. This problem can be alleviated if the JICF CRN parameters are linked directly to the physical design parameters for the flow structure, such as momentum ratio and jet diameter, because the physical design can be more easily determined. Also, incorporating this relationship in CRN models enables iterative design and

optimization of a combustor's JICF design to reduce emissions, which can become a more powerful tool in evaluating the performance of more novel combustor in the future.

Previously, constructing CRN directly from flamelet computational fluid dynamics (CFD) simulation has been shown to be a promising way of linking physical design to chemistry model. However, because the CRN model needs to be readjusted through CFD simulation under different physical design conditions, the high computational cost of flamelet models discourages emissions evaluation across a wide range of combustor operating conditions. Therefore, in the current task, further simplification of the flow physics model is performed using analytical models, including potential flow, boundary layer theory, and Lagrange vortex methods. These techniques simplify the flow physics by isolating the important physics from the flow structure, so that computational cost is only spent on simulating the important part. For JICF, the important physics to capture for mixing are the five different vortices structure around the jet include the counter-rotating vortex pair, roll-up vortex, wake vortex, etc. These vortical structures are the primary contributors to the finite rate mixing between the jet and the crossflow. An aerodynamically informed emissions model will be constructed based on these simplified models. The performance of these models in capturing emissions will be compared against the CFD simulation through the technique developed previously.

Milestones

- Evaluated a reduced-order analytical model for jet-in-crossflow in terms of its capability in capturing important JICF parameters, such as penetration depth, jet cross-section size, and entrainment rate.
- Investigate the importance of certain JICF flow features—shear layer vortex and counter-rotating vortex pair—on correctly capturing NO_x emissions.
- Modify the analytical model by adjusting the vortex lifting force and hydrodynamics mass calculation to correctly capture the JICF trajectory prediction
- Construct a correlation-based CRN model for JICF with heat release modeling in-parallel to the analytical model for performance comparison.
- Adjust the correlation model's coefficients to capture JICF trajectory.
- Implement the boundary layer solution for the near field model of the mixing in JICF to provide both the analytical model and correlation model a physical initial condition.
- Utilize the Ember transient flame solver to turn the analytical JICF model into a chemistry model for NO_x emissions capture.

Major Accomplishments

- The modified analytical model is shown to capture experimentally measured JICF trajectory for non-reacting jet.
- The correlation model is shown to capture the experimentally measured JICF trajectory for reacting jet.

Publications

None.

Outreach Efforts

Preliminary results were presented to the FAA Project Manager during regular bi-weekly teleconferences.

Awards

None.

Student Involvement

This task was conducted by Yang Chen, working under the supervision of Dr. Jayant Sabnis and Dr. Raymond Speth.

Plans for Next Period

Further research is on-going to convert the analytical model along with a boundary layer near field model into a chemistry model to capture the NO_x emissions out of a reactive JICF environment. The model performance when applied to a novel combustor technique such as micro-mixing can then be assessed.

Project 052 Comparative Assessment of Electrification Strategies for Aviation

Massachusetts Institute of Technology

Project Lead Investigators

Florian Allroggen
Executive Director, LAE & Research Scientist
Laboratory for Aviation and the Environment
Department of Aeronautics and Astronautics
Massachusetts Institute of Technology
77 Massachusetts Ave, Building 33-328
Cambridge, MA 02139
617-715-4472
fallrogg@mit.edu

Raymond L. Speth
Principal Research Scientist
Laboratory for Aviation and the Environment
Department of Aeronautics and Astronautics
Massachusetts Institute of Technology
77 Massachusetts Ave, Building 33-322
Cambridge, MA 02139
617-253-1516
speth@mit.edu

University Participants

Massachusetts Institute of Technology (MIT)

- P.I.: Dr. Florian Allroggen
- FAA Award Number: 13-C-AJFE-MIT, Amendment Nos. 062, 072, 080, 093, 098, 115, 121, 128, 133, and 138
- Period of Performance: February 5, 2020 to December 31, 2025
- Tasks (reported for the period October 1, 2023, to September 30, 2024):
  1. Develop a suite of roadmaps for aircraft electrification (covered in previous reporting periods; not reported for this period)
  2. Develop a system-level engineering model of power conversion processes and aircraft energy requirements
  3. Develop a model for analyzing the economics and emissions of electrification strategies (covered in previous periods; not reported during the current reporting period)
  4. Analyze the system-level costs and benefits of the electrification strategies
  5. Analyze the benefits of energy storage for PtL fuel production (covered in previous periods; not reported during the current reporting period)

Project Funding Level

The ASCENT Project 052 received $2,185,000 Federal Aviation Administration (FAA) funding and $2,185,000 matching funds. Sources of matching funds are approximately $404,100 from MIT, plus 3rd party in-kind contributions of $460,000 from NuFuels, LLC, and $110,000 from Savion Aerospace Corp., and $214,000 from Google, LLC, and $996,900 from Earth Force Technologies.

Investigation Team

Dr. Florian Allroggen, (P.I.), All tasks

Dr. Raymond L. Speth, (co-P.I.), Tasks 1, 2, and 4
Dr. Niamh Keogh, Tasks 2 and 4
Dr. Prashanth Prakash, Task 1, 2, and 4
Dr. Nicolas Gomez-Vega, (postdoctoral associate), Task 2
Dr. Arthur Brown, (postdoctoral associate), Task 4
Bjarni Kristinsson, (graduate researcher), Task 2

Project Overview

The long-term goal of this project is to quantify the costs, emissions, and environmental impacts (i.e., climate and air-quality impacts) of various electrification approaches for commercial aviation. The electrification pathways include battery-electric ("all-electric") aircraft, as well as aircraft using drop-in sustainable aviation fuels (SAFs) made with substantial electricity input ("PtL") and electricity-intensive non-drop-in fuels, such as liquid hydrogen. The project helps identify the best approach for using one unit of electric energy to power aviation. For this purpose, the ASCENT Project 052 team developed both system-level engineering and system-level economic models, to assess electricity generation, fuel production, fuel transportation and storage, aircraft energy requirements, and aircraft operations. The models analyze different electrification pathways by using what can be described as a "power station to wake" approach. They quantify differences in costs and emissions associated with each electrification approach and compare them to a set of baseline aircraft powered by petroleum-derived fuels or drop-in SAFs made from biomass or waste streams. The outputs are used in a cost–benefit analysis, which provides insights into the net benefits associated with each technology, while also considering each technology's environmental impacts.

Task 2 – Develop a System-Level Engineering Model of Power Conversion Processes and Aircraft Energy Requirements

Massachusetts Institute of Technology

Objective

The objective of this task is to develop and apply system-level models of the entire value-chain power conversion processes, including energy generation, conversion into an energy carrier, transportation, and usage on board the aircraft. The goal of this effort is to understand which fuel provides the most efficient usage of sustainable energy overall. In the reporting period, the ASCENT Project 052 team has made progress on (1) screening of potential non-drop-in fuels and (2) modeling aircraft with non-drop-in cryogenic fuels to calculate their energy demand.

Research Approach

Energy Carrier Screening

The ASCENT Project 052 team evaluates pathways for aviation towards net-zero emissions. This first requires reviewing the four known forces of nature and their associated opportunities for energy storage. After considering projected technical advancements and other constraints (e.g., safety risks), the solution space can be scoped to specific energy carriers and batteries. The goal is to work within the solution space of medium- to long-haul aviation, given that batteries will not have sufficient energy density to propel commercial aircraft between continents. Therefore, molecules that release energy in chemical reactions are the primary solution space to investigate.

Energy carriers are a set of chemical functional groups and compounds that are considered potential aviation fuel candidates. Therefore, high level evaluation and down-selection of the energy carriers is required to reduce the set of attractive aviation candidates, to a manageable size. One of the most important filters identified is that the elemental blocks of the energy carrier must come from sustainable sources, i.e., they must be naturally recycled in the environment, or the emissions can be directly extracted from the atmosphere. This leaves us with the potential elemental building blocks hydrogen (from water, biomass), carbon (from carbon dioxide, biomass), nitrogen (from air), and oxygen (from oxygen, water, carbon dioxide, biomass) which narrows down the solution space to: Alcohols, alkanes, alkenes, alkynes, aromatics, cycloalkanes, ethers, ketones, hydrogen (H) species (i.e., H_2, H_2O_2), nitrogen (N) species (i.e., NH_3, HNO_3, etc.), and, possibly, other chemical compounds composed of H, Carbon (C), N, and Oxygen (O). Other criteria may include gravimetric and volumetric energy density, chemical toxicity, and environmental considerations.

Design of Aircraft for Non-Drop-in Fuels

Non-drop-in fuels require new aircraft designs with an energy efficiency that cannot be determined solely from existing airframes or fuel parameters. For example, liquid hydrogen and methane are two promising non-drop-in fuels that require cryogenic storage inside insulated and pressurized fuel tanks. The team has modeled the energy demand of non-drop-in aircraft via TASOPT.jl, an aircraft design and optimization tool that uses physics-based models. In this reporting period, our team focused on modeling aircraft using cryogenic fuels, such as liquid hydrogen and methane, carried in tanks in the fuselage. For this purpose, models have been implemented and further refined for the tank structural and thermal design and the evolution of the fuel pressure in the tank. Modeling the tank pressure evolution allows us to calculate the amount of fuel venting required.

Cryogenic fuels also introduce new propulsion possibilities that could provide performance improvements. If these fuels are used in a conventional turbofan engine, it is advantageous to vaporize them and heat them up before injecting them in the combustor, instead of using them directly in liquid form. Preheating the fuel results in lower fuel demand to reach the same post-combustion gas temperature. One way to do so is by using heat exchangers integrated into the engine: in addition to heating up the fuel, these could provide engine cycle improvements. To study this possibility, our team has implemented models of tubular heat exchangers coupled to a turbofan engine model in TASOPT.jl. Three different heat exchanger placements were considered in the engine, as shown in Figure 1. Adding the heat exchanger models to an aircraft design code allows us to explore synergies between the engine and the aircraft.

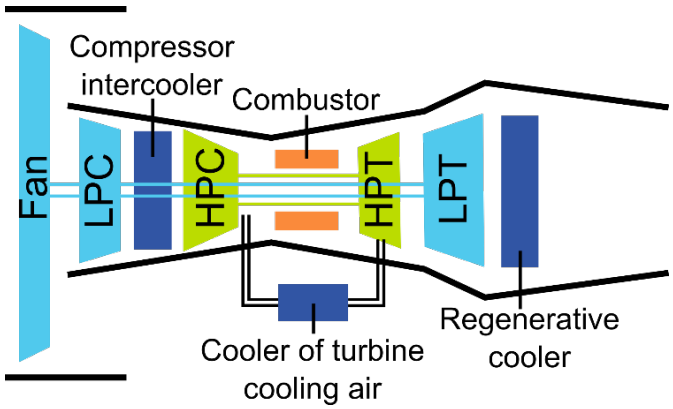

Figure 1. Heat exchanger locations in a turbofan engine.

Milestones

- Completed aircraft design models for cryogenic fuels with turbofan propulsion.
- Prepared two conference papers to disseminate the findings at American Institute of Aeronautics and Astronautics (AIAA) SciTech 2025.
- Presented at the ASCENT 2024 Spring meeting including a presentation on the fuel-down approach.
- Prepared a poster for the 2024 ASCENT Fall meeting.

Major Accomplishments

Energy Carrier Screening

Long-haul operations of commercial aircraft are usually weight-constrained instead of volume-constrained. Therefore, relative to Jet A fuel, the most promising energy carriers are hydrogen and short hydrocarbons (i.e., alkanes, alkenes, and alkynes). Figure 2 visualizes the gravimetric and volumetric energy density tradeoffs of the chemical species relative to fossil distillates. Combustion of alkenes and alkynes will produce a significant amount of soot due to their double and triple carbon-carbon bonds – which makes them less desirable from a pollution perspective. Both hydrogen and methane require cryogenic storage for long-haul aviation deployment. Therefore, the energy intensity of producing them does not represent the actual energy system cost to make energy carriers ready to be filled into aircraft.

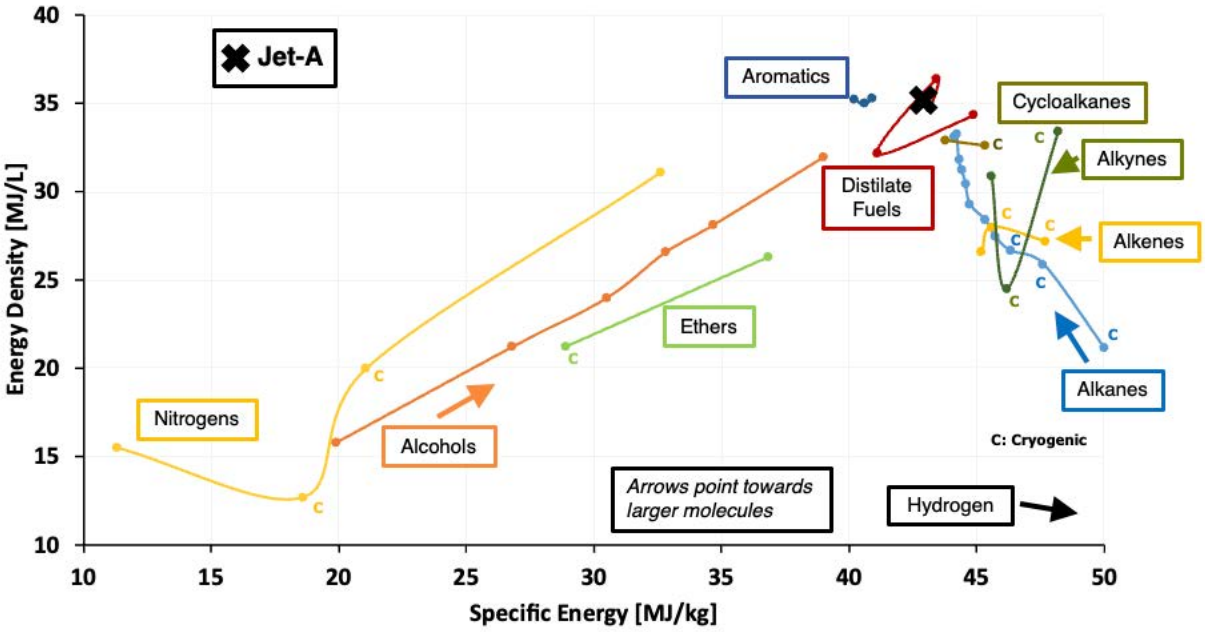

Figure 2. Energy carrier chemical families visualized on a gravimetric vs. volumetric basis. Hydrogen lies outside the boundaries of the figure to show the details of the energy carriers around traditional fossil distillate fuels. Optimum is in the top, right corner.

Design of Aircraft for Non-Drop-in Fuels

A study was completed comparing the energy efficiency of aircraft with jet fuel and hydrogen fuel with either a single-walled or double-walled tank design. Three design missions were considered: short (118 passengers, 2,200 nmi), medium (180 passengers, 3,000 nmi), and long (370 passengers, 7,800 nmi) haul. It was found that the difference between the single-walled hydrogen and jet-fuel aircraft design-mission energy demands is +3.3% in the short-haul mission, -1.6% in medium haul, and -6.3% in the long haul (Gomez-Vega et al., 2025a). A single-walled tank design is found to provide lower energy demand than a double-walled one, mostly due to the difference in weight. Our team also studied the sensitivity of the hydrogen aircraft with single-walled tank to the assumed tank design parameters. The results are shown in Figure 3 in normalized form: the payload-fuel energy intensity (PFEI) is a non-dimensional quantity proportional to the energy consumed per passenger-mile. The normalized PFEI sensitivity represents the percentage change in PFEI for a 1% change in the design variable. Figure 3 shows the sensitivities for the design missions. Our team found that the aircraft design is most sensitive to the design ground temperature, with high sensitivity being shown to the vessel material density, design fuel reserve fraction, and the design heat leakage factor, which models additional heat into the insulated fuel tank.

The effects of introducing heat exchangers in the turbofan powering hydrogen aircraft have been studied further. Our team found that heat exchangers can provide 6.7–9.8% reductions in mission energy demand compared to a case without any heat exchangers, depending on aircraft class (Gomez-Vega, 2025b). Figure 4 shows the change in PFEI, start-of-cruise thrust-specific fuel consumption (TSFC), start-of-cruise lift-to-drag ratio (L/D) and empty mass when heat exchangers are used in a medium-haul mission (180 passengers, 3,000 nmi). All the heat exchanger options considered were found to result in reductions in mission energy demand, with a case with three heat exchangers providing a 9.2% reduction in energy demand. These gains are driven mostly by an improvement in engine TSFC; however, the reductions in PFEI exceed those in TSFC as a result of the coupling between engine performance and aircraft design.

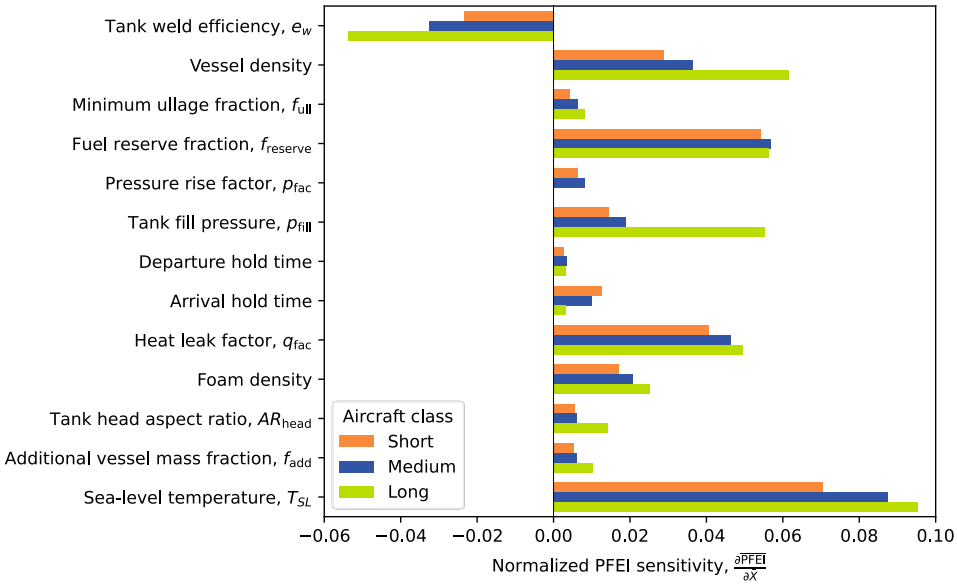

Figure 3. Normalized sensitivity of the PFEI (non-dimensional energy per passenger-mile) to fuel tank design parameters.

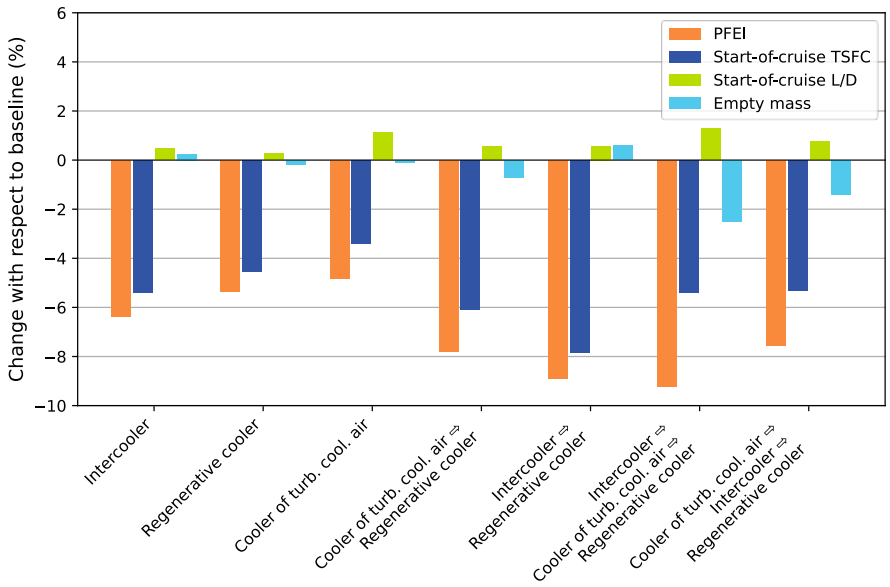

Figure 4. Changes in parameters with respect to a baseline case with no heat exchangers in a medium-haul mission.

Publications

Papers on the impact of heat exchangers on aircraft performance and of cryogenic tank design on aircraft energy efficiency are under preparation. Two conference papers on these topics will be presented at the AIAA SciTech 2025 Forum (Gomez-Vega et al., 2025a; Gomez-Vega et al., 2025b).

Outreach Efforts
Bjarni Örn Kristinsson attended the ASCENT Spring meeting and presented research updates.
Dr. Gomez-Vega attended the 2024 Spring Continuous Lower Energy, Emissions and Noise (CLEEN) meeting and presented the findings. Dr. Gomez-Vega prepared a poster on the accomplishments for the 2024 ASCENT Fall meeting.

Student Involvement
During the reporting period, the MIT graduate student involved in this task was Bjarni Örn Kristinsson.

Plans for Next Period
Over the coming reporting period, the team will continue with modeling efforts to assess various non-drop-in fuels from a system-level perspective, from production to aircraft usage. At the fuel synthesis level, in-depth analysis of methane supply chains will be performed alongside further analysis of other energy carriers. At the aircraft level, models for fuel-cell powered aircraft will be developed.

Task 4 – Analyze the System-level Costs and Benefits of the Electrification Strategies
Massachusetts Institute of Technology

Objective
The objective of this task is to develop system-level analyses for comparing various electrification strategies while integrating the engineering and assessment models developed previously. During the current reporting period, the ASCENT Project 052 team focused on assessing the airport infrastructure required to replace current nine-passenger airliners (mostly: “regional air mobility”) with fully electric aircraft. Specifically, our team produced initial estimates of the number and type of electrical chargers required to recharge every such flight that took place in the United States (U.S.) in 2019.

Research Approach
Regional air mobility (RAM) is a category of airline service flying aircraft with few (≤9) seats to regional airports. About 550,000 such flights took place in the U.S. in 2019. RAM airliners are candidates for replacement with fully electric aircraft. This is because current batteries have low specific energy (energy per unit mass) relative to hydrocarbon fuels and are therefore too heavy to power single-aisle or long-haul airliners. By contrast, the small number of passengers and short ranges (typically ≤450 miles) of RAM flights means that battery-electric RAM airliners may be possible with current battery technology. Hypothesized benefits of electric RAM include lower costs, particularly fuel and maintenance. In addition, tailpipe emissions from burning hydrocarbon fuels are eliminated, potentially reducing both climate and air quality environmental impacts.

The goal of this project is to assess the electrical infrastructure required to support fully electric RAM operations. This is done in three steps. Firstly, a schedule of existing RAM flights is assembled from schedule data for the year 2019. Secondly, all flights are replaced with electric aircraft, and the electricity consumed during each flight is computed with a physics-based aircraft performance model. Finally, the electrical infrastructure required at each airport (i.e., chargers, electricity generation and transmission infrastructure, etc.) is assessed.

Milestones
A flight schedule has been obtained from schedule data, and models for aircraft electricity consumption, and for charging time were developed. Initial estimates for the number of chargers per airport were obtained. A poster was prepared for the ASCENT Fall meeting to disseminate the findings.

Major Accomplishments
An initial study was done to assess the number and type of chargers required to electrify all RAM flights. This number varies as a function of charger power level, because more powerful chargers reduce charging time, leading to fewer overlapping charging-time intervals and hence fewer chargers. The number of chargers increases if the charger is fixed at the gate, as opposed to being mobile or mounted on a vehicle. This is because a fixed charger cannot be used for other

aircraft while an aircraft is blocking a gate or parking position during its turnaround, regardless of whether charging is complete.

Counting the number of overlapping charging intervals at each airport reveals that 500–1,000 chargers are needed to electrify all RAM flights in the U.S. in 2019, depending on charger type(s). These values were computed assuming that all flights will be charged back to the full charge level after each flight. Figure 5 and Figure 6 show the number of chargers required at the top 10 busiest airports in the U.S., ranked in descending order by the average number of daily RAM arrivals. Eight of the 20 busiest RAM airports are in Alaska. This is because over 80% of Alaskan communities lack access to the road system and are only accessible in a timely fashion via air travel. Bethel Municipal Airport in Alaska (the busiest RAM airport) serves as a hub for the roughly 56 villages in the area, none of which are accessible by road. Flights from these villages to Anchorage (the largest city in Alaska) connect through Bethel because its airport is the sole one in the region capable of handling single-aisle jet airliners.

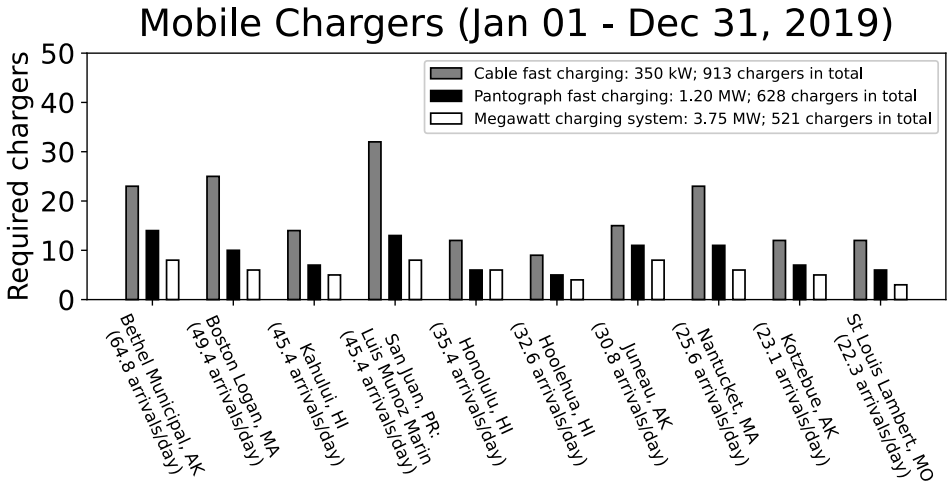

Figure 5. Number of chargers required to electrify all RAM flights in the US, assuming mobile chargers.

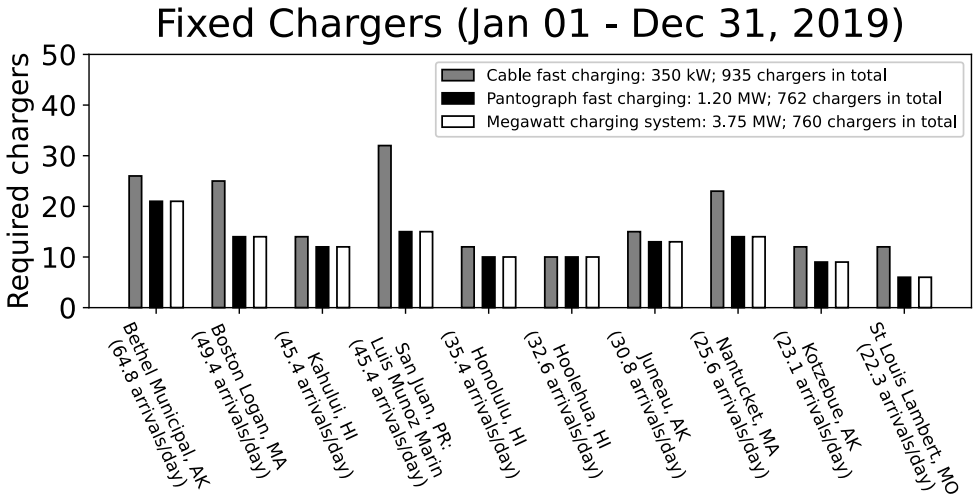

Figure 6. Number of chargers required to electrify all RAM flights in the US, assuming fixed chargers.

Publications
None.

Outreach Efforts
Dr. Brown participated in the National Renewable Energy Laboratory (NREL) Sustainable Aviation Energy Conference in Dallas, Texas, in early April 2024. In addition, Dr. Brown prepared a poster for the 2024 ASCENT Fall meeting to disseminate the findings.

Student Involvement
None.

Plans for Next Period
Over the coming reporting period, the team will conduct a detailed case study on RAM flights in the Bethel, Alaska, area. We will also begin to assess the required electricity generation and transmission infrastructure, possibly including wind turbines, solar panels, and/or battery energy storage systems (BESS).

References
Gomez-Vega, N., Tan, D. Y., Prakash, P., Barrett, S. R. H., Speth, R. L., & Allroggen, F. (2025a, January 6-10). *Influence of Fuel Tank Design on the Energy Demand of Hydrogen Aircraft* [Conference paper]. AIAA SciTech 2025 Forum, Orlando, Florida.

Gomez-Vega, N., Prakash, P., Speth, R. L., & Allroggen, F. (2025b, January 6-10). *Hydrogen Aircraft Design with Heat-Exchanger-Enhanced Turbofan Engines* [Conference paper]. AIAA SciTech 2025 Forum, Orlando, Florida.

Project 053 Validation of Low Exposure Noise Modeling by Open-Source Data Management and Visualization Systems Integrated with AEDT

Stanford University

Project Lead Investigator

Juan J. Alonso
Vance D. and Arlene C. Coffman Professor
James and Anna Marie Spilker Chair of Aeronautics & Astronautics
Department of Aeronautics & Astronautics
Stanford University
Stanford, CA 94305
Phone: (650) 723-9954
E-mail: jjalonso@stanford.edu

University Participants

Stanford University

- P.I.(s): Juan J. Alonso, Professor
- FAA Award Number: 13-C-AJFE-SU-022
- Period of Performance: October 1, 2023, to September 30, 2024
- Task(s):
  1. Complete prototype of Metroplex Overflight Noise Analysis (MONA), including integration of the Aviation Environmental Design Tool (AEDT). Completed.
  2. Validation and verification of AEDT noise predictions in day-night average sound level (DNL) 55-65 dB areas. Completed study (for arrivals into San Francisco International Airport [SFO] Runways 28L/R only) and submitted journal paper, which was published in March 2024.
  3. Data science formats and scientific computing for large-scale airspace analyses. Completed.
  4. Viable alternative approach routes into the San Francisco Bay Area metroplex. Pending/de-scoped.

Project Funding Level

A hiatus in funding meant that no additional funds were received for the work during this reporting period. Although the work of preparing a journal publication continued, no students were funded during the period of performance. The project is expected to restart on January 1, 2025, to complete the study with departure operations from SFO and preparations for conducting similar studies at other airports or different time period at SFO. Even though funding was not received for this period of performance, both Mr. Thomas Rindfleisch and Mr. Donald Jackson contributed a significant portion of their time (approximately 30% full time equivalent [FTE] for Jackson and 50% FTE for Rindfleisch), uncompensated, to the project. In addition, some contractor costs (a small amount this past year) for the continued development of the MONA project visualization website and some minor equipment purchases (and installation costs) were also used to generate cost share for this project. Up until the end of the period of performance for this report, a total of more than $1.85M of cost share has already been generated and accounted for.

Investigation Team

The investigation team is made up of the faculty, graduate and undergraduate students, and collaborators listed below with their respective areas of expertise/areas of contribution:

1. Juan J. Alonso (P.I., Stanford Aeronautics & Astronautics): Overall responsibility for the project and its technical and administrative elements.

2. Brian Munguía (Graduate Student, Stanford Aeronautics & Astronautics): AEDT, cloud-based AEDT study execution, AEDT debugging; departures study development and initial debugging. During the period of performance (October 1, 2023, through September 30, 2024), Mr. Munguía performed a small number of tasks in support of the journal paper submission.
3. Donald Jackson (Collaborator, software developer): Overall MONA project infrastructure (i.e., servers, databases, hardware/software monitoring), geographic information system (GIS), web-based visualization deployment, technical guidance. During the current period of performance, Mr. Jackson continued to maintain our infrastructure database and to ingest and curate the noise data.
4. Thomas Rindfleisch (Co-P.I., Sr. Research Scientist, Emeritus, Stanford University): Noise monitoring and filtering, aircraft trajectory collection/processing, visualization, data analysis. During the period of performance, Mr. Rindfleisch was instrumental in preparing all the data for our journal submission and generating the main manuscript in collaboration with Professor Alonso. October 1, 2023, through September 30, 2024.

Project Overview

The MONA project was started to provide real-time and objective data, analyses, and reports to key stakeholders and policy makers to mitigate the noise impacts of the deployment of new NextGen procedures. This system (a) collects and archives air traffic data using a network of antennae and Automatic Dependent Surveillance-Broadcast (ADS-B) receivers, (b) analyzes noise impacts using a variety of metrics, (c) visualizes resulting large-scale datasets, and (d) uses a network of sound-level monitors (SLMs) to validate and enhance the quality of noise predictions. The focus of this ASCENT project is to improve upon the noise predictions of MONA through tighter integration with AEDT. In particular, our work is focused on the following three tasks: (1) integrate and automate AEDT's noise analysis capabilities, (2) validate and verify (V&V) AEDT's noise predictions in DNL 55-65 dB areas, and (3) propose software engineering/architectural choices for future AEDT development to enhance usability in multiple workflows including application programming interface (API) formulation, visualization interfaces, resilient data acquisition and storage, and cloud computing.

The expected benefits of this project mirror the tasks mentioned above, including (a) ability to automate complex noise analyses in metroplexes so they are available in near-real time after the preceding 24-hr period, (b) a better understanding of the accuracy of AEDT's current noise models in high- (DNL >65 dB) and low-noise (DNL 55-65 dB) areas and the reasons for the discrepancies (if any) in existing predictions, and (c) recommendations to software developers on flexible architectures and APIs for AEDT so that the tool is more versatile and generally applicable. AEDT predictions are built around the policy context of an average annual day. The majority of the V&V results produced and shared by the MONA team had focused on a cumulative daily basis for which flight track data is directly collected. The project thus far has managed to automate the cloud-based analysis (using many parallel instances of AEDT) of *every flight into SFO for a period of an entire year (July 1, 2021, to June 30, 2022)* and therefore some of our results, included in the March 2024 journal publication (Rindfleisch et al., 2024), now contain DNL levels based on the flight operations collected through the MONA system. The focus of the work the MONA team has done so far is on arrivals at SFO with main attention paid to arrivals into Runways 28L/R. Having created the entire framework and having generated data for a full year of arrivals operations, the effort during this past year focused exclusively on creating, submitting, and providing reviews for a journal publication including all of our results to date. The final journal publication in the *Journal of the Acoustical Society of America* (JASA) was made available online and published in Volume 155, Issue 3 in March 2024. The full citation for the 2024 JASA paper, which includes all of our results to date is:

Rindfleisch, T. C., Alonso, J. J., Jackson, D. C., Munguia, B. C., & Bowman, N. W. (2024). A Large-Scale Validation Study of AEDT Noise Modeling for Aircraft Arrivals. *Journal of the Acoustical Society of America*, *155*(3). https://doi.org/10.1121/10.0025276

Background and Previous Accomplishments

The MONA project started approximately six years ago with the main objective of providing real-time and objective data, analyses, and reports to key stakeholders and policy makers to help in mitigating the noise impacts of the deployment of new NextGen procedures. Since then, the MONA team has put together and deployed a system that (a) collects, archives, and makes available air traffic data using a series of networked antennae and ADS-B receivers 24/7, (b) analyzes noise impacts using a variety of metrics (based on both a MONA-developed noise prediction tool and the noise prediction tools within AEDT), (c) visualizes resulting large-scale datasets in a simple, user-friendly fashion using both a bespoke website

and Uber's® kepler.gl and deck.gl large-scale data visualization toolboxes, and (d) has deployed a small network of low-cost, Stanford University-owned, sound-level monitors scattered across the South Bay part of the San Francisco Bay Area and has included the data from the noise monitors deployed by SFO to cross-calibrate measurements by MONA and SFO monitors, collect noise measurements more widely geographically, and enhance noise predictions to describe exactly the actual noise levels experienced.

The longer-term objectives of the MONA project are to (a) ensure the validation and verification of all noise predictions provided (by AEDT or other tools) in both areas near the airport and in other areas further away from the airport, (b) achieve full automation of complex noise analyses in regions around airports in the United States, including AEDT-based noise predictions, (c) make all results web-accessible for in-depth interpretations of historical and proposed changes, (d) eventually study potential alternative traffic patterns in complex airspace to mitigate aviation environmental impacts, and (e) export the proven/validated MONA technology to other airport regions via open-source software/hardware.
The MONA system has matured considerably over the past few years to the point that a full-system prototype has now been operational for some time. In fact, for all arrival operations into SFO, the system is considered to be fully operational. To recall the main elements of the system, the MONA team has deployed a small network of ADS-B/multilateration (MLAT) antennae and has completed the software necessary to merge the data streams from all of these antennae including de-duplication of sightings, identification of aircraft equipment and routes flown, physical interpolation of data missing from the joint observations, and archiving (in appropriate database formats) of the information collected for successive analysis. Moreover, for arrival operations, considerable time and effort has been spent understanding the best ways to utilize AEDT (by understanding the methods to most accurately model aircraft trajectories, aircraft equipment, and aircraft noise) so that any comparisons between experimental data and the results obtained from AEDT may be affected as little as possible by confounding variables. In fact, the MONA team has spent time in using AEDT in multiple ways including the standard version of AEDT that is approved for regulatory use in the United States and an improved version that leverages higher-fidelity aircraft performance models (base of aircraft data [BADA] 4) and detailed descriptions of individual aircraft trajectories (using the so-called altitude and speed controls that result from the ADS-B data and its post-processing).

The MONA system has achieved a level of integration with the Federal Aviation Administration's (FAA) AEDT software that enables fully automatic processing of noise exposure at arbitrary receptor locations for arrival and departure routes into the San Francisco Bay Area airports. The JASA publication and this report include our published and most accurate and comprehensive assessment of the comparison between AEDT predictions and noise-monitoring stations created to date, with an entire year of flights observed at multiple locations. In total, more than 200,000 datapoints give statistical significance to the results that the MONA team has obtained, that are presented here, and were submitted for peer-reviewed publication.

Again, direct research efforts were halted during this past year of performance but work continued, as part of Task 2, to curate the simulation and experimental information for publication in an archival journal. This short yearly report focuses on a summary of the results contained in the2024 JASA paper for arrivals into SFO only. No report on the progress on other tasks is provided in this report, including our departures V&V work, as that work will restart at the beginning of 2025.

Task 2 - AEDT Noise Prediction Assessment in DNL 55-65 and DNL > 65 dB Areas

Stanford University

Our team has previously reported on the development of the MONA system, that data that it acquires, the information processing (both to prepare and post-process AEDT simulations and to filter and curate experimental noise data) that is necessary to V&V the predictions, and the preliminary observations from all the data collected and produced. Last year's report focused on the statistically significant characterization of the discrepancies between the measured noise at two different noise-monitoring stations and the predictions using AEDT in various ways with increasing levels of modeling fidelity. The reader is referred to last year's report for more details. By *statistically significant*, it is meant that the observations and conclusions are based on large amounts of data that are deemed to have converged probability

® Uber is a registered trademark of Uber Technologies, Inc., San Francisco, California.

distributions and statistical moments (e.g., expected value/mean and standard deviations). In other words, we do not attempt to draw conclusions about the predictive qualities of AEDT noise models based on 5 to 10 flights (as has been common in the literature) but that, rather, our focus is on large-enough numbers of observations: at least 10,000 flights/data points for the main aircraft types and over 200,000 flights, over a 12-month period, for our entire study.

Moreover, the actual data from which conclusions are drawn is highly curated to eliminate any noise events that are even slightly unlikely to be the result of aircraft overflights alone, and other situations where multiple aircraft may pass over a noise-monitoring station nearly simultaneously. This is to say that we feel confident that the data presented in this report (directly taken from the JASA paper) is of the highest quality possible. The data presented and associated conclusions/observations, with the limitation to SFO and to arrival operations, has been peer reviewed and approved for publication in JASA.

The remainder of this section is a summary of the key results included in the 2024 JASA paper. For more details, the reader is referred to the full journal article that can be found at https://pubs.aip.org/asa/jasa/article/155/3/1928/3270390/A-large-scale-validation-study-of-aircraft-noise.

Summary of Results from the 2024 JASA Paper

In the United States, the FAA's AEDT is approved to predict the impacts of aircraft noise and emissions. AEDT's critical role in regulatory compliance and evaluating the environmental impacts of aviation requires questioning the accuracy of its noise predictions. Previous studies suggest that AEDT's predictions may lack desired accuracy, especially in regions of relatively low noise (< DNL 55 dB). The journal paper reported on a large-scale study, using 200,000 flight trajectories paired with measured sound levels for arrivals to Runways 28L/28R at SFO, over 12 months. For each flight, two AEDT studies were run: (1) using the approved mode for regulatory filing and (2) using an advanced nonregulatory mode with exact aircraft trajectories. AEDT's per aircraft noise predictions were compared with curated measured sound levels at two locations. On average, AEDT underestimated LAmax[1] by 3.09 dB and sound exposure level (SEL) by 2.04 dB, combining the results from both AEDT noise-modeling modes. Discrepancies appear to result from limitations in the physical modeling of flight trajectories and noise generation, combined with input data uncertainties (i.e., aircraft weight, airspeed, thrust, and lift configuration) and atmospheric conditions. Further V&V investigation is required to ascertain the level of prediction accuracy in departure operations and, possibly, with upcoming improvements to the modeling strategy of terrain and ground effects.

The aims of the study in the 2024 JASA paper were fourfold:

1. To collect a very large, statistically significant set of data, pairing aircraft flight profiles with carefully curated sound level measurements over time and identifying intrinsic limitations in the physical measurements.
2. To select aircraft study cohorts that control, as much as possible, many of the flight variables involved while examining AEDT behaviors for a broad, real-world fleet mix.
3. To tease out statistically significant measures of AEDT metric prediction accuracy and analysis anomalies, aircraft-type by aircraft-type, to reveal internal computational strengths and weaknesses.
4. To provide recommendations for work needed to improve AEDT's noise prediction accuracy.

To model an aircraft flight arrival with AEDT, a detailed study file was created specifying all of the appropriate parameters, including calibrated airspeed, derived from ADS-B ground speed using the National Oceanic and Atmospheric Administration (NOAA) High-Resolution Rapid Refresh (HRRR) atmospheric data (Alexander et al., 2020). In the study, the AEDT's noise predictions were compared using two different modeling approaches:

1. AEDT regulatory mode (AEDT-R): Aircraft Noise and Performance Database (ANP)/BADA 3, with only ground-track positions specified; no altitude or airspeed controls are provided. This is the modeling approach required by the FAA for regulatory purposes.
2. AEDT-AE: BADA 4, with both altitude and airspeed controls specified for each ground-track position.

Our team attempted to use AEDT to the best of its predictive abilities, and for that reason, the FAA and Volpe Center experts were consulted to optimize the preparation of flight-profile data to fit AEDT modeling constraints (e.g., smoothing

[1] LAmax is a tool that uses aircraft performance modeling to estimate aircraft noise levels, and other factors such as fuel consumption, emissions, and air quality. LAmax stands for the highest or maximum sound level of an event.

flight profile parameters and limiting profile altitude or speed changes). User-defined flight modeling profiles were not attempted to be developed, although such efforts might result in a closer match between AEDT predictions and SLM measurements (Meister et al., 2023; NAS, 2018).

To validate the noise predictions of AEDT, we compare and analyze the AEDT-estimated noise metrics (using "trajectory-driven flight performance" modeling [FAA, 2021a]) and ground SLM measurements along each of the three chosen route segments. The AEDT-R results incorporate all aircraft in our fleet mix that have ANP/BADA 3 models, whereas AEDT-AE results are limited to the aircraft types in our fleet mix that have BADA 4 models (FAA, 2021b). The noise predictions for flights on final approach to Runways 28L and 28R are compared with recordings from the SFO monitor NMT-12 in Foster City, 0.4 miles line-of-sight distance from the flight paths. Predictions for approaches along the SERFR-DIRECT route are compared with recordings from one of our project monitors in Palo Alto, 0.9 miles line-of-sight distance from the flight path, at the SIDBY waypoint.

Table 1 summarizes the total number of flights successfully studied for each modeling approach and how various subsets of flights were discarded for failing quality and relevance criteria. The rows in Table 1 describe the results of our data screening. The input AEDT/SLM pairs represent all flight profiles for which a successful AEDT study was run with BADA 3 and/or BADA 4 modeling, and which were detected at the SLM associated with the column heading. These counts exclude flights intended to be modeled as BADA 4, but which AEDT downgraded to BADA 3 modeling. The "Number of pairs skipped as the GA [general aviation]" row is the count of those discarded as general aviation flights. The "pairs skipped for low GoF [goodness-of-fit]" is the count of pairs for which the SLM peak shape was suspect because it was distorted relative to an analytic model peak using our GoF metric (refer to the Appendix in the 2024 JASA paper for more details). The "pairs skipped for multiple PCA [points of closest approach]" is the count of pairs for which the SLM peak was suspect because the arrival time of the sound maximum at the PCA to the SLM could be attributed to more than one aircraft. The "pairs skipped for trajectory criteria" is the count of pairs that do not conform geometrically to the arrival flight path criteria (i.e., distance, elevation, altitude, speed, heading, etc.). Note also that all pairs are collected (flight and corresponding matched SLM peak) by SLM and then partitioned according to route information. Since the ADS-B data does not contain runway information, the first four rows of Table 1 are identical for SFO Runways 28L and 28R. After each aircraft trajectory is followed to the ground, we are able to identify the actual arrival runway and, therefore, rows 5-8 in Table 1 contain information for flights that arrived at either Runways 28L or 28R.

Table 1. Size of AEDT-R and AEDT-AE cohorts for each route segment.

Data volume statistics:	SFO Runway 28L	SFO Runway 28R	SIDBY SERFR-DIRECT
Number of input AEDT/SLM pairs	226 876	226 876	113 113
Number of pairs skipped as GA	4927	4927	2145
Number of pairs skipped for low GoF	55 861	55 861	70 130
Number of pairs skipped for multiple PCAs	9756	9756	525
Number of pairs skipped for trajectory criteria	58 282	105 988	14 020
Number of post-filter pairs	98 050	50 344	26 293
Number BADA 3 pairs	55 793	30 214	14 112
Number BADA 4 pairs	42 257	20 130	12 181

The 2024 JASA paper contains results with both the AEDT-R version (straight out of the box, the version approved for regulatory purposes) and using AEDT-AE (the version that utilizes better aircraft performance models and the possibility of using altitude and airspeed controls that, together with latitude/longitude measurements, can represent the actual trajectory flown by an aircraft exactly). AEDT-AE represents the aircraft performance model and its trajectory with significantly higher fidelity than what is possible in AEDT-R and, therefore, in this summary of the 2024 JASA paper, the results obtained with AEDT-AE are the focus. The reader is referred to the paper for details of the results obtained with AEDT-AE.

AEDT-AE Results

The statistical analysis of the pair-by-pair relations begun between the AEDT-AE LAmax estimates and the corresponding SLM measurements by showing a series of histogram plots, including all of the aircraft and trajectories simulated, and some highlights by aircraft type. Using BADA 4 data from final approaches to SFO Runway 28L (42,257 pairs including 14 ANP performance models), Figure 1 shows histograms of the AEDT-AE LAmax estimates (solid line) and of the SLM LAmax measurements (dotted line). As the histogram labels indicate, the average AEDT-AE LAmax level is 68.59 ± 1.52 dB and that measured by the SLM is 71.32 ± 2.15 dB—on average AEDT underestimates the LAmax value by 2.73 dB. Also, note that the profile of the predicted AEDT values has significant internal structure, indicated by the subpeaks, including one sidelobe at 70.95 dB, and inflection points in the non-Gaussian shape. No discrete subpeaks are present, however, as were prominent in the AEDT BADA 3 predictions (refer to the 2024 JASA paper). This reflects the more sophisticated physics modeled in AEDT BADA 4 and the spread in the trajectories actually flown that are considered in this analysis.

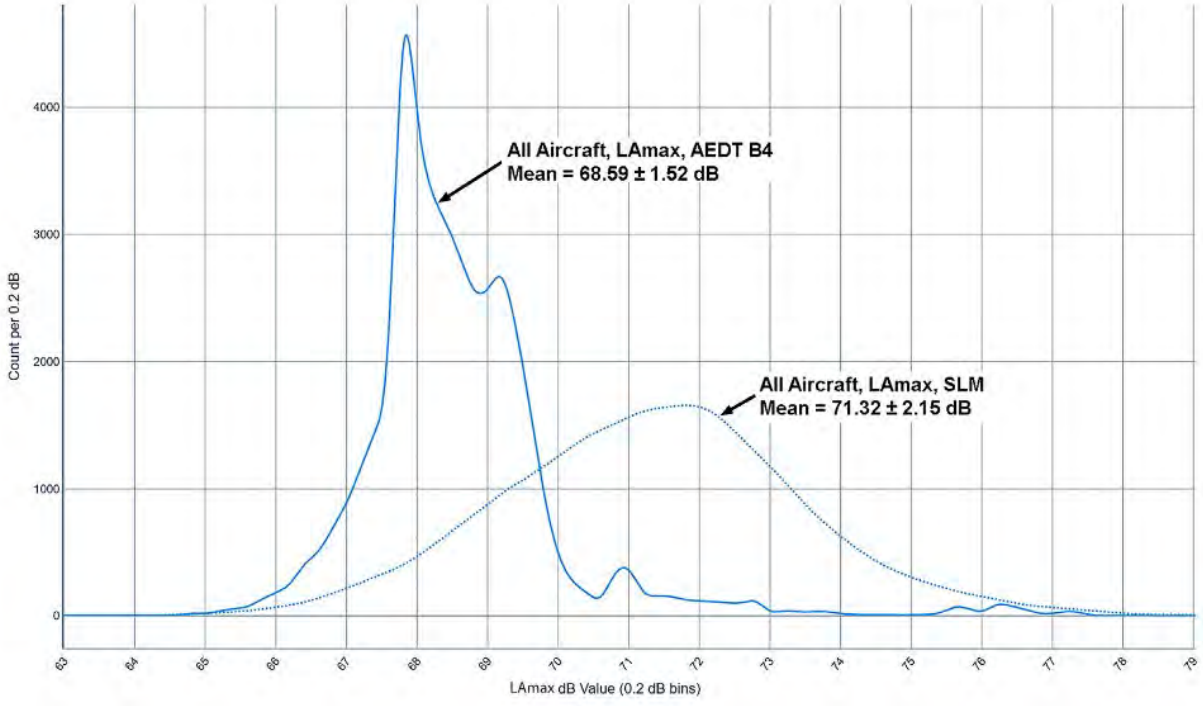

Figure 1. AEDT-AE, SFO NMT-12, Runway 28L. Distributions of predicted LAmax (solid line) and measured LAmax (dashed line) values.

This structure can be elaborated by overplotting histograms for various aircraft sub-cohorts modeled by particular ANP performance models as shown in Figure 2. To simplify the plot, only three major aircraft types are shown. One can see that the AEDT-AE calculations produce histogram profiles with quite varied shapes and that the differences in mean LAmax values between the AEDT-AE predictions and the SLM measurements differ significantly (see the green profile for ANP model 737-800 in particular). It is evident from this plot (and by extension for the entire cohort of aircraft types and ANP performance models) that there are important model-based differences between the estimates AEDT-AE makes and what the SLM measures. These are important in that for the most part the AEDT-AE predictions fall short of the SLM measurements—a result analogous to that seen for the AEDT-R BADA 3 analysis in the 2024 JASA paper.

The AEDT/SLM differences and their distributions can be illustrated by a performance model by computing the metric difference directly for each AEDT/SLM pair and then plotting the histogram of those differences. This comparison is illustrated in the histograms in Figure 3, both for the overall cohort and for a subset of individual ANP performance models for the most frequent types. These differences range from 2.08 dB for the A321-232 performance model to 3.44 dB for the 737-800 model, all with standard deviations ~2 dB (which result from the relatively broad SLM measurement distributions).

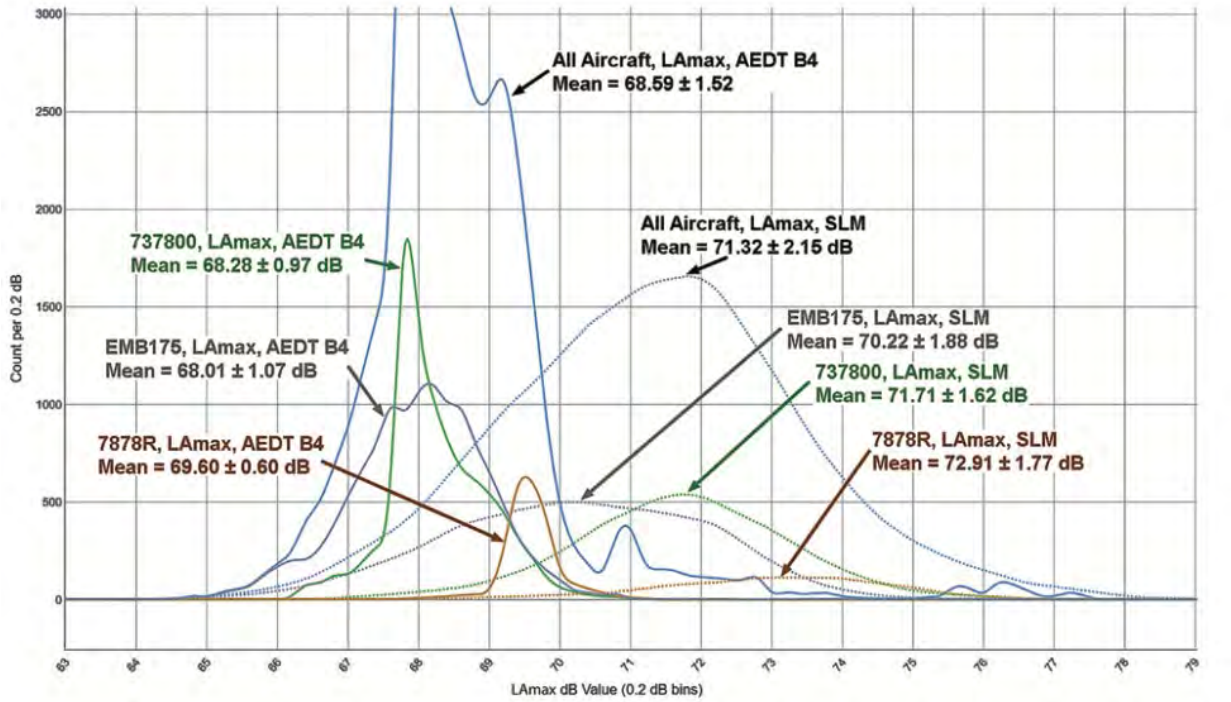

Figure 2. AEDT-AE, SFO NMT-12, Runway 28L. Distributions of predicted LAmax (solid line) and measured LAmax (dashed line) values for selected aircraft.

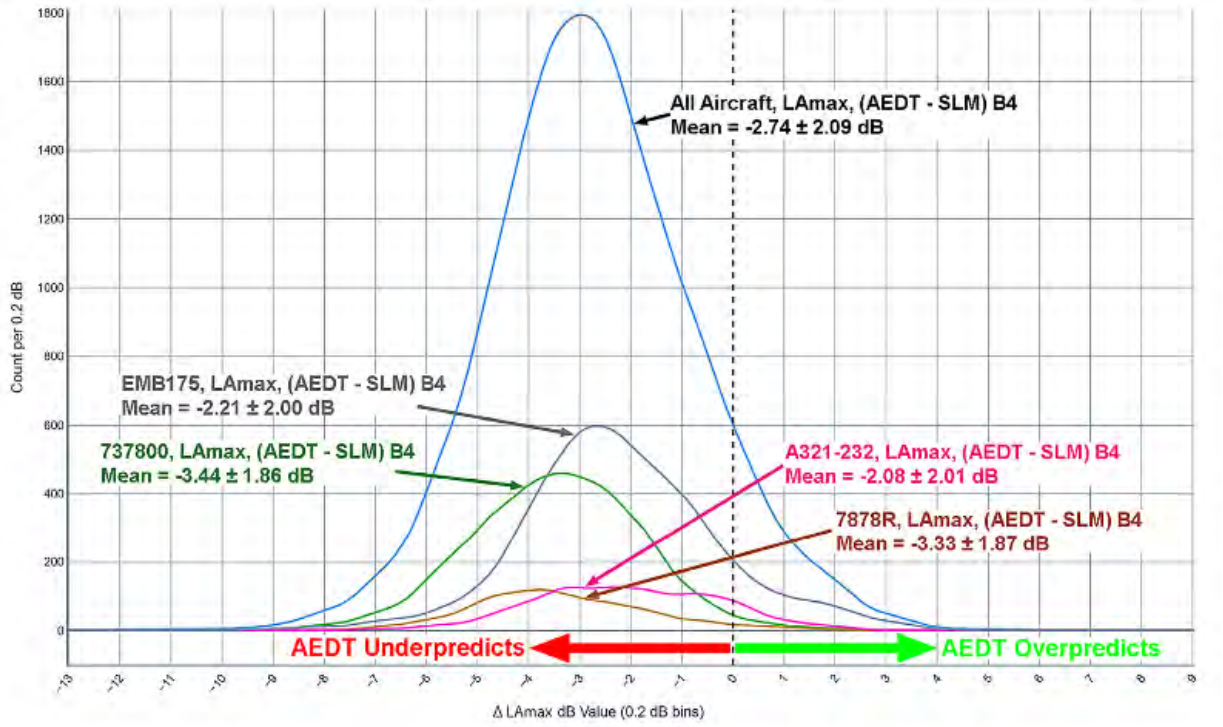

Figure 3. AEDT-AE, SFO NMT-12, Runway 28L. Distributions of LAmax differences (AEDT–SLM) for entire cohort and for selected ANP.

Based on the analyses illustrated in Figures 1, 2, and 3, the difference error statistics is computed for all 14 ANP performance models found in the aircraft cohort. Figure 4 shows an ordered plot of the error values and Table 2 shows the detailed sample flight counts, difference values, and standard deviations. The SEL metric data collected from AEDT-AE study runs and SLM measurements are analyzed with exactly the same approach used for LAmax; the results for the SFO Runway 28L approach are also shown in Figure 4 and Table 2.

As is evident in Figure 4, there are major differences in the accuracy of the AEDT-AE LAmax predictions. For example, the differences for "heavy" aircraft (ANP models 747-400 and 747-8) are relatively small, indicating that the corresponding models seem to be fairly accurate. For the other aircraft though, the accuracy of the AEDT-AE modeling appears to produce systematically low estimates, ranging from 1.6 dB to 3.9 dB. The overall LAmax error weighted by frequency counts is 2.74 dB.

The overall difference between AEDT-AE SEL predictions and SLM measurements for the SFO 28L approach is slightly less, 2.48 dB. On the other hand, the same basic observations about their variable nature and the inability of AEDT-AE to model sound metrics accurately for different ANP performance models apply.

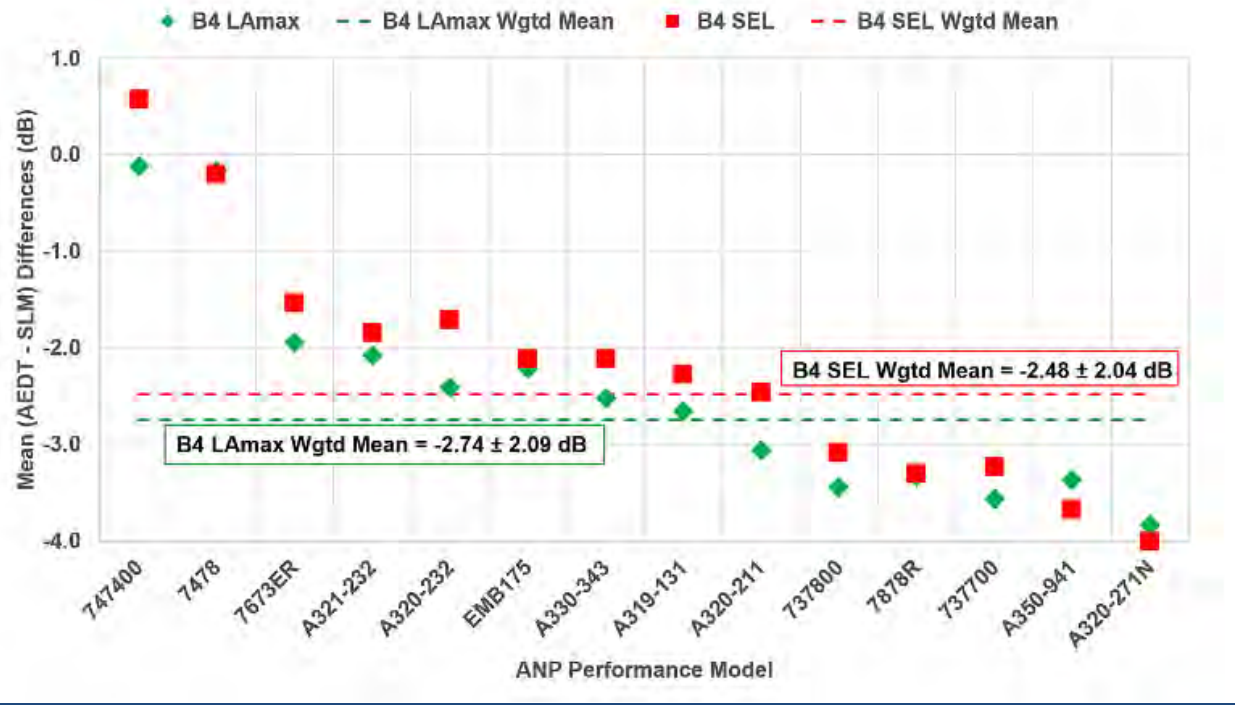

Figure 4. AEDT-AE, SFO NMT-12, Runway 28L. Mean LAmax and SEL differences (AEDT–SLM), by ANP model. The green diamonds for 7478 and 7878 R LAmax are hidden behind the corresponding red SEL squares.

Table 2. AEDT-AE, SFO NMT-12, Runway 28L. Mean and standard deviations of LAmax and SEL differences (AEDT – SLM), by ANP model.

ANP code	BADA code	Subcohort size	AEDT–SLM LAmax difference	AEDT–SLM SEL difference
ALL	All	42 257	−2.74 ± 2.09	−2.48 ± 2.04
737700	B737	2 685	−3.57 ± 1.78	−3.23 ± 1.66
737800	B738, B739	9 793	−3.44 ± 1.86	−3.09 ± 1.72
747400	B744	177	−0.11 ± 1.65	0.57 ± 1.55
7478	B748	304	−0.16 ± 1.35	−0.20 ± 1.30
7673ER	B763	1 212	−1.94 ± 2.06	−1.54 ± 1.96
7878R	B788, B789, B78X	2 408	−3.33 ± 1.87	−3.31 ± 1.77
A319-131	A319	2 251	−2.65 ± 2.22	−2.27 ± 2.12
A320-211	A320	2 072	−3.06 ± 1.83	−2.46 ± 1.76
A320-232	A320	3 196	−2.41 ± 2.19	−1.71 ± 2.05
A320-271N	A20N	661	−3.84 ± 1.96	−4.00 ± 1.85
A321-232	A321	3 167	−2.08 ± 2.01	−1.84 ± 1.83
A330-343	A332, A333, A339	507	−2.52 ± 1.98	−2.12 ± 1.79
A350-941	A359, A35K	970	−3.37 ± 2.43	−3.68 ± 2.36
EMB175	E75L	12 605	−2.21 ± 2.00	−2.12 ± 2.08

SFO Runway 28R AEDT-AE (BADA 4) metric value and difference analysis—Brief summary
The data were analyzed for the final approach to SFO Runway 28R, just as for Runway 28L. Figure 5 and Table 3 summarize the comparisons between AEDT-AE predictions and SLM measurements of LAmax and SEL values.

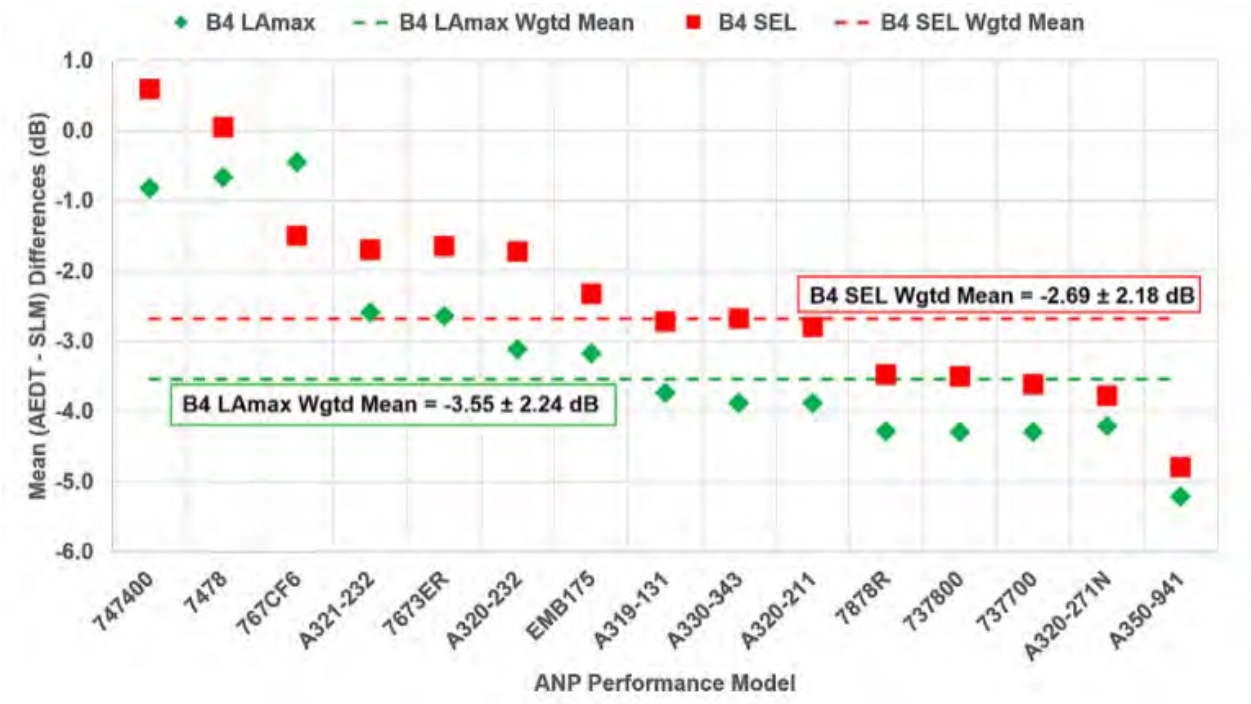

Figure 5. AEDT-AE, SFO NMT-12, Runway 28R. Mean LAmax and SEL differences (AEDT–SLM), by ANP model.

Table 3. AEDT-AE, SFO NMT-12, Runway 28R. Mean and standard deviations of LAmax and SEL differences (AEDT – SLM), by ANP model.

ANP code	BADA code	Subcohort size	AEDT–SLM LAmax difference	AEDT–SLM SEL difference
ALL	All	20 130	−3.55 ± 2.24	−2.69 ± 2.18
737700	B737	870	−4.29 ± 1.68	−3.61 ± 1.62
737800	B738, B739	5 051	−4.29 ± 1.79	−3.50 ± 1.73
747400	B744	269	−0.82 ± 1.96	0.59 ± 1.62
7478	B748	296	−0.66 ± 1.58	0.05 ± 1.52
7673ER	B763	1 500	−2.64 ± 2.33	−1.64 ± 2.13
767CF6	B762	190	−0.45 ± 2.24	−1.50 ± 2.12
7878R	B788, B789, B78X	1 883	−4.28 ± 2.10	−3.47 ± 2.04
A319-131	A319	860	−3.73 ± 2.37	−2.72 ± 2.25
A320-211	A320	1 060	−3.88 ± 1.74	−2.79 ± 1.68
A320-232	A320	1 013	−3.11 ± 2.19	−1.72 ± 2.13
A320-271N	A20N	290	−4.20 ± 2.32	−3.77 ± 2.03
A321-232	A321	2 290	−2.59 ± 1.91	−1.69 ± 1.75
A330-343	A332, A333, A339	247	−3.88 ± 1.76	−2.67 ± 1.70
A350-941	A359, A35K	502	−5.21 ± 2.31	−4.79 ± 2.19
EMB175	E75L	3 528	−3.17 ± 2.17	−2.32 ± 2.10

SIDBY SERFR-DIRECT AEDT-AE (BADA 4) metric value and difference analysis—Brief summary
The data were analyzed for the SERFER-DIRECT approach over the SIDBY waypoint, just as for the final approach to SFO Runway 28L. Figure 6 and Table 4 summarize the comparisons between AEDT-AE predictions and SLM measurements of LAmax and SEL values.

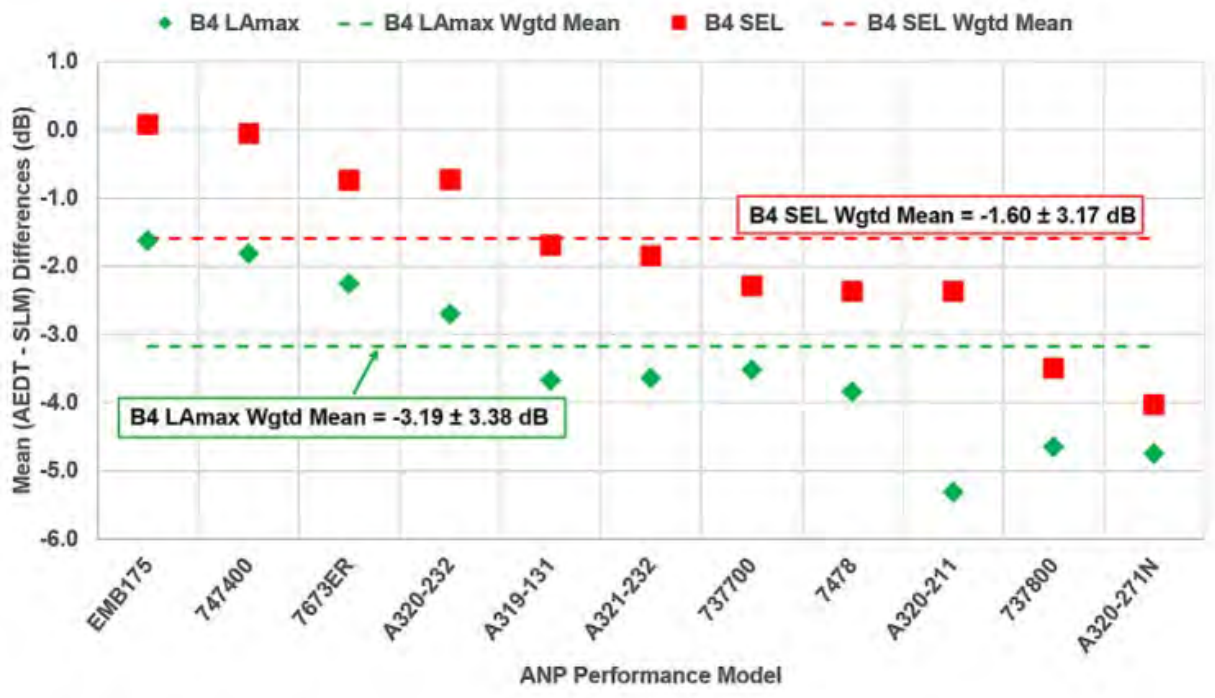

Figure 6. AEDT-AE, SIDBY, SERFER-DIRECT. Mean LAmax and SEL differences (AEDT–SLM), by ANP model.

Table 4. AEDT-AE, SIDBY, SERFER-DIRECT. Mean and standard deviations of LAmax and SEL differences (AEDT–SLM), by ANP model.

ANP code	BADA code	Subcohort size	AEDT–SLM LAmax difference	AEDT–SLM SEL difference
ALL	All	12 181	−3.19 ± 3.38	−1.60 ± 3.17
737700	B737	1 546	−3.52 ± 3.24	−2.29 ± 2.93
737800	B738, B739	2 895	−4.65 ± 2.99	−3.49 ± 2.72
747400	B744	403	−1.81 ± 2.35	−0.05 ± 2.04
7478	B748	366	−3.84 ± 2.32	−2.36 ± 1.99
7673ER	B763	312	−2.25 ± 3.11	−0.74 ± 2.86
A319-131	A319	576	−3.67 ± 3.66	−1.69 ± 3.17
A320-211	A320	546	−5.31 ± 2.61	−2.36 ± 2.36
A320-232	A320	1 323	−2.70 ± 3.28	−0.73 ± 2.90
A320-271N	A20N	243	−4.74 ± 2.58	−4.02 ± 2.47
A321-232	A321	297	−3.64 ± 3.06	−1.84 ± 2.82
EMB175	E75L	3 608	−1.62 ± 3.28	0.08 ± 2.97

Calibrated air speed effects on modeled metric values

An interesting anomaly was noted between AEDT-AE-predicted and SLM-measured LAmax and SEL pairs that can be seen in a pair-wise scatterplot against calibrated air speed (CAS). Figure 7 shows data for two single-aisle aircraft types (ANP performance models 737-700 and 737-800) on final approach to Runway 28L, as observed at SFO NMT-12. AEDT underestimates both LAmax and SEL as noted in the analyses presented above. However, there is another clearly visible effect.

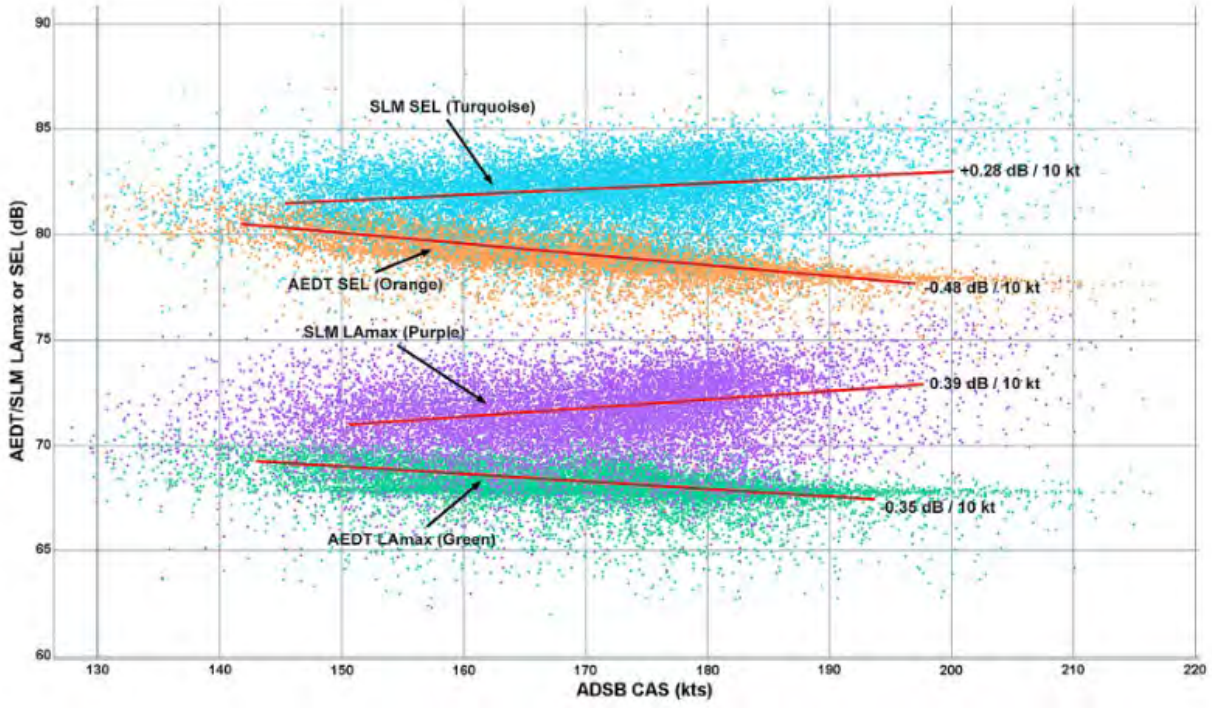

Figure 7. AEDT-AE, SFO NMT-12, Runway 28L. Plots of predicted and measured LAmax and SEL against CAS showing decrease in predicted noise metrics at higher speeds versus increase in measured noise metrics.

With increasing CAS and all other factors remaining constant, physics tells us that sound metrics should increase primarily because of the dependence of airframe noise on airspeed. This effect is indeed observed in the SLM measurements, but AEDT-AE predicts a lessening of noise metrics. The plot shows linear trend lines to illustrate and quantify the rate of metric change, but it is noted that the effect is more complicated than a linear one. This observation is tentatively attributed to the fact that AEDT-AE modeling is based on engine noise estimates, which may in fact decrease as aircraft airspeed changes due to thrust levels, whereas airframe noise sources, especially from auxiliary lift equipment and landing gear deployment, will increase and eventually overpower engine noise, particularly on approach trajectories (Lopes & Burley, 2011). As discussed in the conclusions section, it appears that a more complex and accurate modeling of the physics, particularly of airframe noise, will be needed to make AEDT-AE better conform to ground truth in aircraft arrival situations. Similar results are found for the other route segments (e.g., the final approach to SFO Runway 28R and SERFR-DIRECT over the SIDBY waypoint).

Discussion of AEDT-AE results

For all three route segments, the analyses showed similar AEDT/SLM variation by ANP performance model. AEDT-AE consistently predicts LAmax and SEL values below the levels measured by the SLMs.

Given the complex nature of the AEDT internal calculations, it is difficult to divine exactly the reason for the various underpredictions observed. It is believed that the differences are largely attributable to shortcomings in the SAE-AIR-1845/Doc 9911 model as implemented in AEDT, an underestimation of airframe noise contributions, and a lack of exact knowledge of both the aircraft weight and atmospheric conditions. On the AEDT side, there are many areas of unknown accuracy, such as the validity of noise power distance (NPD) curves derived from certification data and the fact that the modeling is relatively simplistic. For example, without flight operations quality assurance (FOQA) data, the following details are unknown: an aircraft's weight, the thrust employed along the flight profile, when auxiliary lift equipment is deployed, etc. Most often FOQA data are confidential and tightly held by airlines. Weather and atmospheric conditions are similarly hard to control for and would limit the strength of a validation study based on a minimal number of flights.

As with the results from AEDT-R (ANP BADA 3, not described in this summary), the "law of averages" for error cancellation across the fleet mix cannot be relied upon so that AEDT might be able to produce a more accurate average value. In addition, existing AEDT-AE models seem to contradict the expected physics of approach airframe noise generation by not adequately accounting for increased noise levels with increased calibrated airspeed from auxiliary high-lift equipment and landing gear deployment.

Conclusions

In the 2024 JASA paper, as summarized here, a very large dataset of over 200,000 observations was collected and analyzed with pairs of AEDT noise predictions matched with carefully curated SLM noise measurements. The SFO arrivals along three high-density route segments were the focus of our study and the data covered an entire year of observations from July 1, 2021, through June 30, 2022.

Analyses were carried out using the FAA AEDT-R based on ANP/BADA 3 performance modeling with standard profiles and without altitude and speed control data. The resulting statistical data indicate that this type of modeling is overly simplistic and gives far from accurate comparison with ground SLM measurements. For flights passing the SIDBY receptor, it was observed that the estimated altitudes for 9 out of 13 significant aircraft types are significantly below the ADS-B measured altitudes by 2.6 to 4.2 times the standard deviation of the ADS-B altitude distribution. It is noteworthy that, despite these deficiencies, the AEDT-R is the default FAA-approved regulatory mode for AEDT use. Other use of AEDT can go through an approval process on a case-by-case basis.

The analyses also point to a systematic underestimation by AEDT-AE in its predictions for LAmax and SEL metrics by significant but highly varied amounts depending on aircraft type and performance model. AEDT-AE modeling must be improved by adjusting the internal representation of the applicable physics (e.g., the NPD curves and modeling of engine and airframe noise at various stages of flight). In at least some instances, AEDT-AE predicts lower sound metrics (e.g., LAmax and SEL) for aircraft with higher calibrated airspeeds. This contradicts the physics involved and suggests AEDT-AE does not adequately account for airframe noise sources when auxiliary high-lift equipment is in use or landing gear is deployed. It would be ideal to have access to FOQA data, but that is often considered proprietary. It may be possible to estimate factors (i.e., weight, auxiliary lift configuration, etc.) that affect airframe noise generation on average to use more advanced physical models such as the Aircraft Noise Prediction Program (ANOPP2) to better estimate airframe noise (Geissbuhler et al., 2022; Lopes & Burley, 2011; Mahseredjian et al., 2021). Another approach would be to use machine

learning methods to characterize the modeling error in terms of ADS-B data, SLM data, and other flight parameters to improve the accuracy of airframe noise component prediction (Alonso et al., 2023).

Major Accomplishments

- Conducted the largest and most statistically significant study of the discrepancies between measured noise data and predicted noise data (using both AEDT-R and AEDT-AE) at two different locations with vastly different DNL levels. In comparisons with previous studies, which at best use tens of flights to draw conclusions, our study is the first ever to look at hundreds of thousands of flights to draw conclusions. The data observations include a full 12-month period, all relevant aircraft types, and all weather conditions. This study is the first of a kind and our team hopes that additional studies can match the low level of error in our statistics.
- Preparation, submission, revision, and acceptance of the 2024 JASA paper with a detailed evaluation of AEDT noise predictions versus SLM-collected data.

Publications

Peer-Reviewed Journal Publications

Rindfleisch, T. C., Alonso, J. J., Jackson, D. C., Munguia, B. C., & Bowman, N. W. (2024). A Large-Scale Validation Study of AEDT Noise Modeling for Aircraft Arrivals. *Journal of the Acoustical Society of America*, *155*(3). https://doi.org/10.1121/10.0025276

Presentations/Proceedings

Jackson, D.C., Rindfleisch, T.C., & Alonso, J.J. (2021). A System for Measurement and Analysis of Aircraft Noise Impacts. *Engineering Proceedings, 13*(6). https://doi.org/10.3390/engproc2021013006. (Presented at the 9th OpenSky Symposium, Brussels, Belgium, November 18-19, 2021).

Alonso, J. J., Shukla, A., Jackson, D. C., & Rindfleisch, T. C. (2023, Jan 23-27), Improving Noise Predictions of the Aviation Environmental Design Tool (AEDT) Using Deep Neural Networks and Sound-level Monitor Data [Video presentation]. *AIAA SCITECH 2023 Forum*. https://arc.aiaa.org/doi/10.2514/6.2023-0735. (Published online on January 19, 2023).

Outreach Efforts

Over the performance period, a number of outreach activities were made to disseminate the result of our work and to inform the public about the complexities of noise predictions resulting from aircraft overflights. We have participated in the 2023 Aviation Noise and Emissions Symposium and presented at both the San Francisco International Airport Roundtable and the San Francisco International Airport Roundtable Technical Working Group. Finally, we held briefings and visualization demonstrations in our visualization room at Stanford University with various cities and municipalities around the San Francisco Bay Area. Professor Alonso was invited to present the results of the 2024 JASA paper in the University of Michigan Aerospace Engineering Department seminar series.

Awards

None.

Student Involvement

Due to the lack of availability of funding, only PhD Candidate Mr. Brian Munguía has contributed to the work during this performance period. Mr. Nick Bowman (now at the Jet Propulsion Laboratory, but formerly a student in the Computer Science department at Stanford University and a contributor to ASCENT Project 053) also contributed some of his time, as a co-author, to the finalization of the manuscript for the 2024 JASA paper.

Plans for Next Period

The focus of the next year of ASCENT Project 053 (expected to begin January 2025) will be on the completion of the full study. This will include arrivals (presented here) and departures (under investigation) to paint a complete picture of the areas where AEDT-R and AEDT-AE provides the required accuracy in the noise predictions, and to more effectively pinpoint areas of potential noise modeling improvements that may be undertaken by AEDT developers. The full study aims to continuously improve the quality of the predictions and, therefore, the quality of proposed new routes accounting for noise impacts on the ground. Our team will also carry out a number of studies to further improve the accuracy of modeling using AEDT, including terrain and ground effects. Finally, improvement, modularization, and documentation of key elements will be continued for our MONA system software for more effective use in our own studies and for shared use with other

researchers to conduct similar studies at different institutions and airports. A second journal paper is expected to be prepared by the end of this coming year of execution (2025) detailing the entire set of results but focusing on the departure routes. It is expected that the predictions for departure routes, which are dominated by engine noise, to produce better results than those achieved for arrivals.

References

Alexander, C., Dowell, D., Hu, M., Olson, J., Smirnova, T., Ladwig, T., Weygandt, S., Kenyon, J., James, E., & Lin, H. (2020). Rapid refresh (RAP) and high resolution rapid refresh (HRRR) model development. *100th American Meteorological Society Annual Meeting* (AMS, Boston, MA).

Alonso, J., Alonso, Y., Shukla, A., Jackson, D., & Rindfleisch, T. (2023). Improving noise predictions of the aviation environmental design tool (AEDT) using deep neural networks and sound-level monitor data, *AIAA SCITECH 2023 Forum*, p. 735

FAA (2021a). AEDT Version 3d Technical Manual (Federal Aviation Administration, Washington, DC), Sec. 3.9, p. 145.

FAA (2021b). AEDT Version 3d Technical Manual, Section 3.2 (Federal Aviation Administration, Washington, DC), p. 57.

Geissbuhler, M., Behere, A., Rajaram, D., Kirby, M., & Mavris, D. (2022). Improving airport-level noise modeling by accounting for aircraft configuration-related noise at arrival. *AIAA SCITECH 2022 Forum*, p. 1650.

Lopes, L., & Burley, C. (2011). Design of the next generation aircraft noise prediction program: ANOPP2. *17th AIAA/CEAS Aeroacoustics Conference (32nd AIAA Aeroacoustics Conference)*, p. 2854.

Mahseredjian, A., Thomas, J., & Hansman, J. (2021). Advanced procedure noise model validation using airport noise monitor networks. *50th International Congress and Exposition on Noise Control Engineering,* (Institute of Noise Control Engineering Washington, DC).

Meister, J., Schalcher, S., Wunderli, J.M., & Schäffer, B. (2023). Validation of three inherently different aircraft noise calculation programs, *INTER-NOISE and NOISE-CON Congress and Conference Proceedings,* (Institute of Noise Control Engineering, Washington, DC), Vol. 265, pp. 574–581.

NAS (2018). Enhanced AEDT Modeling of Aircraft Arrival and Departure Profiles, Volume 2: Research Report (The National Academies Press, Washington, DC).

Project 054 AEDT Evaluation and Development Support

Georgia Institute of Technology

Project Lead Investigator

Prof. Dimitri N. Mavris
Director, Aerospace Systems Design Laboratory
School of Aerospace Engineering
Georgia Institute of Technology
275 Ferst Drive NW, Atlanta, GA 30332
(404) 894-1557
dimitri.mavris@ae.gatech.edu

Dr. Michelle Kirby
Chief, Civil Aviation Division
Aerospace Systems Design Laboratory
School of Aerospace Engineering
Georgia Institute of Technology
275 Ferst Drive NW, Atlanta, GA 30332
(404) 385-2780
michelle.kirby@ae.gatech.edu

University Participants

Georgia Institute of Technology (Georgia Tech)

- P.I.s: Dr. Dimitri N. Mavris, Dr. Michelle Kirby
- FAA Award Numbers: 13-C-AJFE-GIT-098, 114, and 122
- Period of Performance: September 24, 2021, to September 20, 2023
- Tasks:
  1. Improved departure modeling
  2. Arrival profile modeling
  3. Full flight modeling
  4. System testing and evaluation of the Aviation Environmental Design Tool
  5. Supersonic transport aircraft modeling in the Aviation Environmental Design Tool (formerly ASCENT Project 010)

Project Funding Level

Georgia Tech has received $900,000 in funding for this project. In terms of cost-share details, Georgia Tech has agreed to a total of $900,000 in matching funds. This total includes salaries for the project director, research engineers, and graduate research assistants, as well as computing, financial, and administrative support, including meeting arrangements. Georgia Tech has also agreed to provide tuition remission for the students, paid for by state funds.

Investigation Team

Prof. Dimitri N. Mavris, (P.I.), Tasks 1–5
Dr. Michelle Kirby, (co-Investigator), Tasks 1–5
Dr. Ameya Behere, (co-Investigator), Tasks 1–5
Mr. Jirat Bhanpato, (research faculty), Tasks 1–5
Dr. Raphael Gautier, (research faculty), Tasks 1–5
Dr. Dushhyanth Rajaram, (research faculty), Tasks 1–5
Mr. David Anvid, (research faculty), Tasks 1–5
Tanmay Daga, (graduate student), Task 1

Ranya Almarzooqi, (graduate student), Task 1
Howard Peng, (graduate student), Task 1
Anushka Moharir, (graduate student), Task 2
Hansen Lian, (graduate student), Task 2
Nitya Maruthuvakudi Venkatram, (graduate student), Tasks 2 and 5
Hyungu Choi, (graduate student), Task 3
Yash Vinod, (graduate student), Task 3
Bogdan Dorca, (graduate student), Task 4
Santusht Sairam, (graduate student), Task 4

Project Overview

This project provides data and methods to continue to improve modeling of aircraft weight, takeoff thrust, and departure and arrival procedures within the Federal Aviation Administration's (FAA) Aviation Environmental Design Tool (AEDT), as well as the AEDT's full flight modeling capabilities. Some of the modeling assumptions in the AEDT are considered excessively conservative and could be improved through use of industry and airport flight operation data. Funding for this project will continue to support the implementation of these methods and data in the AEDT. To facilitate these efforts, the Georgia Tech team will use real-world flight data and noise monitoring data to improve departure, full flight, and arrival modeling.

Task 1 – Improved Departure Modeling

Georgia Institute of Technology

Objective

This task aims to improve departure profile modeling in the AEDT. Over the past few years, this task provided recommendations for new noise abatement departure procedures (NADP) to be implemented in the AEDT, improving how flight trajectories are modeled and consequently, giving more accurate fuel consumption and emissions metric results.

In the previous reporting period, it was observed that for the 2021 Threaded Track (TT) dataset, none of the existing departure profiles provided a sufficiently accurate representation of real-world operations. Since then, various parameters, like the aircraft energy share percentage during the climb and the aircraft takeoff weights were analyzed, in a bid to account for the discrepancies existing between the real-world data and the existing departure procedural profiles.

Building on this, further efforts to refine departure profile modeling in the AEDT involved analyzing real-world operations using the flight operations quality assurance (FOQA) calendar year (CY) 2023 data. This analysis focused on aligning the AEDT's modeled departure trajectories with observed operational patterns. Key operational characteristics, or "anchors" such as flap transitions, landing gear retraction, thrust cutbacks, level-offs, and segments of constant calibrated airspeed (CAS), were identified and classified. These anchors were subsequently used to cluster flights exhibiting similar departure patterns. Advanced techniques, such as dynamic time warping (DTW), enabled the identification of distinct departure profiles, which can then be implemented into the AEDT to improve the accuracy of the fuel consumption and emissions reports and noise profiles.

To present these findings, this report is divided into three distinct subsections, each detailing its methodology and development as well as results and discussions:

1. *Aircraft energy share percentage*: This subsection discusses how modifying the division of energy between acceleration and climb, quantified as energy share percentage (ES%), impacts the accuracy of departure profiles in AEDT.
2. *Anchor Classification*: This subsection focuses on identifying and classifying key operational characteristics, such as flap transitions, landing gear retraction, thrust cutbacks, level-offs, and constant CAS segments, to determine patterns in real-world flight behavior.
3. *Clustering*: This subsection details the use of clustering techniques to group flights with similar departure patterns and integrate these distinct profiles into the AEDT for improved trajectory modeling.

Research Approach

The following section gives a detailed explanation of the methodology undertaken for the analysis of aircraft energy share percentage and aircraft takeoff weights. Furthermore, the relevance of the classified anchors and their classification methodologies were also detailed as well as the clustering methodology utilized.

Methodology

1. Energy Share Percentage

Energy Share Percentage refers to the percentage of total available energy being split between acceleration and climb. It is defined as the quotient of change in kinetic energy to sum of change in total energy available (kinetic + potential).

$$ES\% = \frac{\Delta\frac{1}{2}mv^2}{\Delta mgh + \Delta\frac{1}{2}mv^2} \quad \text{(Eq. 1)}$$

If an aircraft has an energy share percentage of *x*, it implies that x% of the total excess energy goes to acceleration and the remaining energy goes to climb. Table 1 shows the energy share percentage of the most popular airframes which are default presets in the AEDT. However, in certain instances, these values were not reflective of actual operational conditions as observed in the real-world data. Based on these observations, new NADP profiles were created for the aircraft with modified ES% and compared against the 2021 TT dataset.

Table 1. Default energy share presets for the Aviation Environmental Design Tool. ES: energy share.

Airframe	AEDT ES%
Airbus A319-131	70
Airbus A320-211	65
Airbus A321-232	70
Airbus A350-941	60
Boeing 737-800	55
Boeing 757PW	55
Boeing 767-300	55
Boeing 787-800	55

Aircraft Takeoff Weight Estimation

The other factor which contributes to differences in real world data and AEDT profiles, could be the variation in takeoff weights. Aircraft Weight (AW) is an important feature, which is required to correctly predict climb rate, emissions, noise, etc. Currently, the AEDT profiles have two distinctions for takeoff weights, namely, Standard and Modified_AW. Modified_AW or Modified Alternate Weight profiles were introduced to AEDT as final recommendations from ASCENT Project 045.

$$Modified\ AW\ (SL_x) = \frac{Standard\ (SL_x) + Standard\ (SL_{x+1})}{2} \quad \text{(Eq. 2)}$$

When CY 2019 FOQA data was analyzed for takeoff weight, it was observed that real world flights were exceeding the weights assigned to Modified_AW for each stage length, being much more evident at lower stage lengths.

1. Anchor Classification

1.1. Flap and Landing Gear Transitions

Flap and landing gear transitions are key events during departure as they significantly affect aircraft performance and environmental metrics. Flap retraction and deployment alter lift and drag, while landing gear retraction reduces aerodynamic drag. Modeling these transitions in the AEDT is necessary because they influence climb gradients and acceleration phases, which impact both noise and fuel consumption profiles. For instance, the NADP1 profile (close-in noise reduction) has steeper climbs and delayed acceleration, which are closely tied with the timing and configuration of

flap and landing gear retractions. On the other hand, NADP2 profiles (distance noise reduction) usually involve earlier flap and landing gear transitions to improve climb performance and reduce fuel burn during later stages of departure.

Proper representation of these transitions allows AEDT profiles to better align with real-world trajectories, as flap retraction speeds and configurations vary by aircraft type and operational procedures. The landing gear classification captures the points where the landing gear moves from a “down” position to an “up” position. This is done by filtering the FOQA data for specific gear positions (0 = up, 2 = down) and identifying the last occurrence of “down” and first occurrence of “up” for each flight. This approach ensures that the key moments of gear retraction are accurately classified.

Similarly, the flap transition classification focuses on capturing meaningful changes in flap positions using a mapping function to find the nearest standardized flap settings for each aircraft type to ensure consistency across varied operational data. Flap transitions are then grouped and filtered to identify significant changes, excluding short-lived or insignificant fluctuations.

By implementing this approach for classifying flap transitions and landing gear retraction, these characteristics were accurately classified across different airframe types, as shown in Figure 1 and Figure 2.

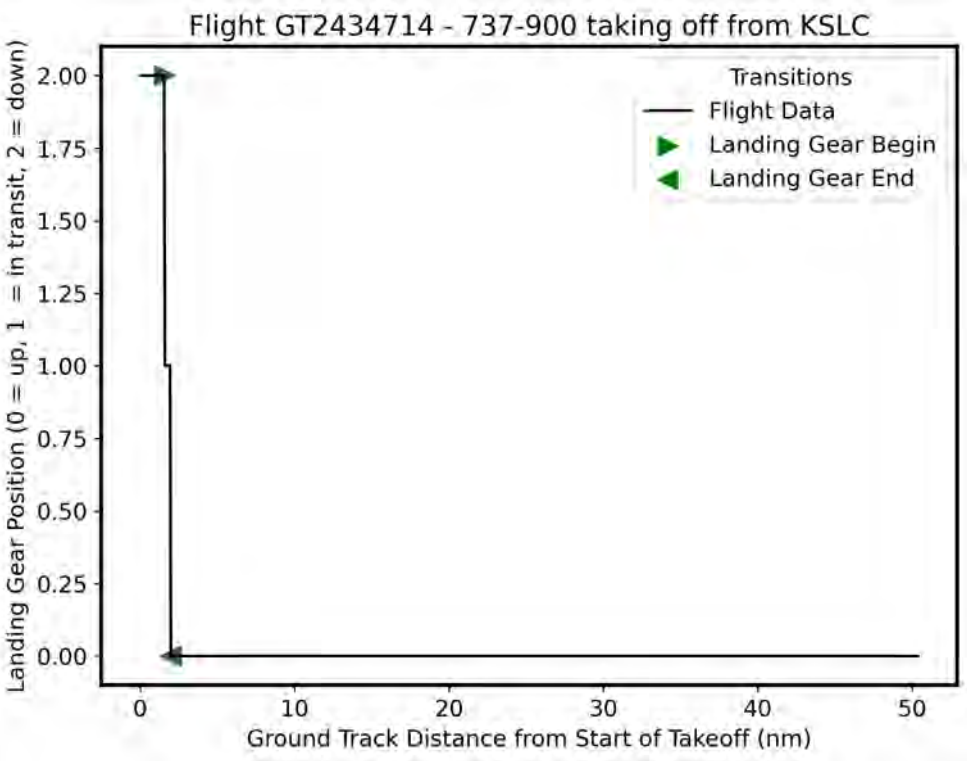

Figure 1. Landing gear retraction anchor classification from Salt Lake City International Airport (KSLC).

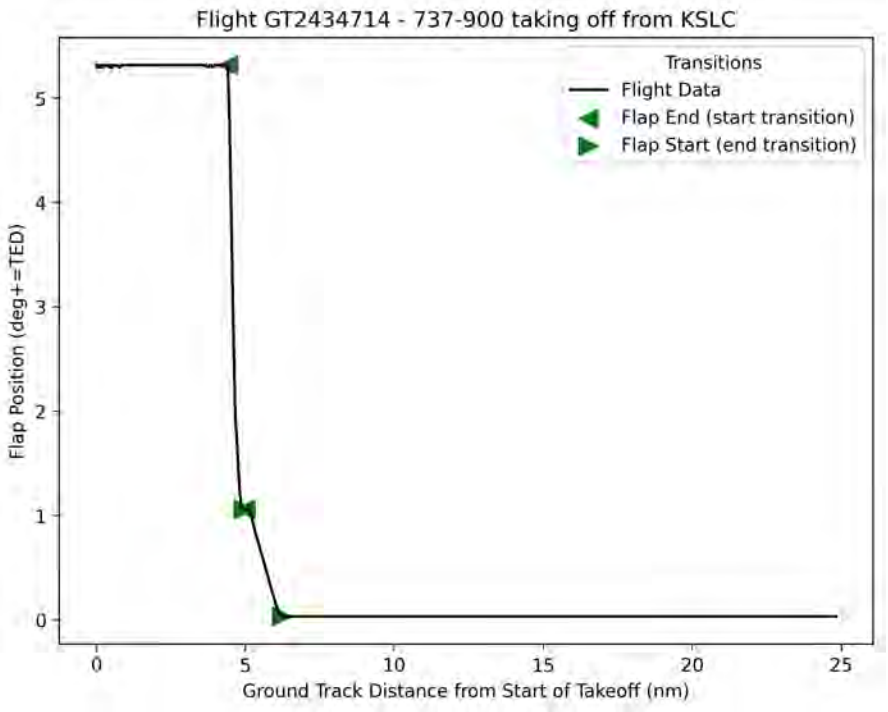

Figure 2. Flap transition anchor classification.

1.2. Thrust Cutback

Thrust cutback occurs when engine thrust is reduced from takeoff to climb thrust at a specific altitude or other trigger condition. This action is crucial for noise abatement and fuel efficiency. Capturing thrust cutback altitudes from FOQA data can potentially enable the AEDT to model more realistic climb profiles. For NADP1 profiles, earlier thrust cutbacks are usually defined to maintain a gradual climb gradient, reducing noise levels in nearby residential areas. In contrast, NADP2 profiles typically have a longer initial climb phase before the thrust is reduced, which enables the aircraft to accelerate and climb more steeply.

The timing, magnitude, and altitude of thrust cutbacks are critical parameters for accurately modeling departure profiles in the AEDT as these parameters dictate the subsequent trajectory of the aircraft as well as fuel consumption and emissions. Thus, proper representation of these thrust cutback parameters across different aircraft types and operational procedures would result in more precise flight profiles.

The thrust cutback classification methodology was tailored to distinguish between Airbus® and non-Airbus airframes due to fundamental differences in how their sensor data reflect thrust transitions. This differentiation was necessary because Airbus airframes often exhibit smoother Normalized Thrust Lever Angle (NTLA) profiles, with fewer detectable fluctuations in the data, as seen in the NTLA plots in Figure 3. The lack of pronounced noise or variability in NTLA for Airbus airframes requires stricter thresholds to reliably identify thrust cutback events.

® Airbus is a registered trademark of Airbus Operations GmbH, Hamburg, Germany.

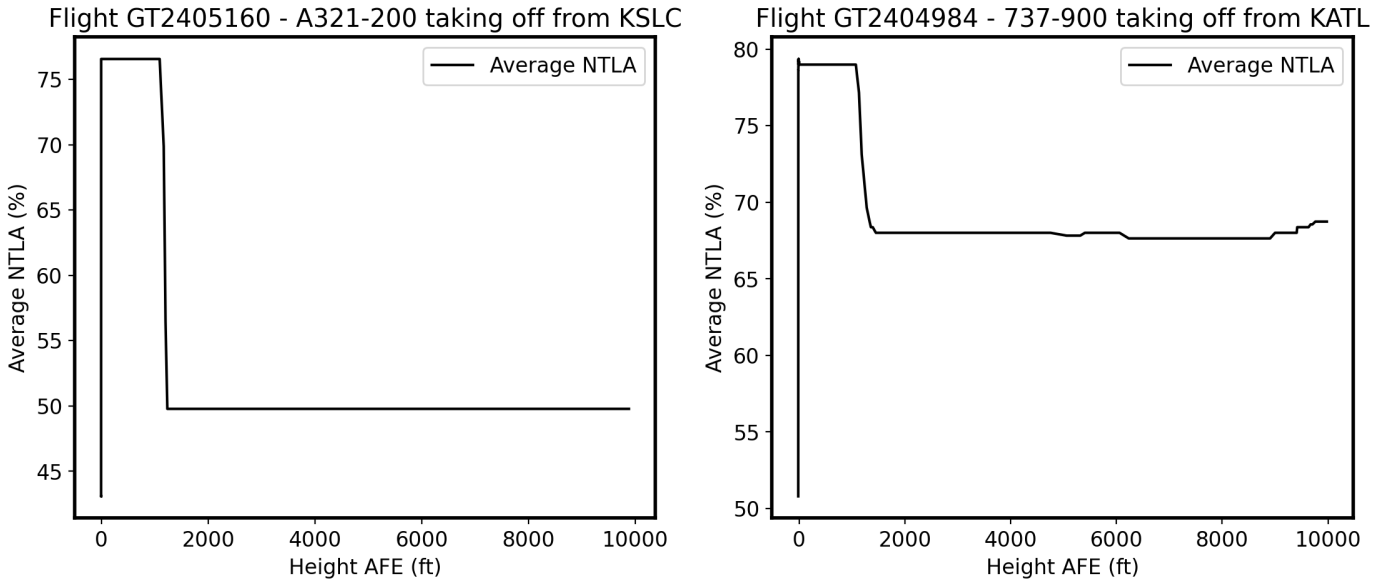

Figure 3. Average NTLA vs. height for the Airbus A321-200 compared to the Boeing 737-900 from KSLC and Hartsfield-Jackson Atlanta International Airport (KATL).

For Airbus airframes, a thrust drop of at least 8% from the baseline NTLA was required to mark the beginning of a cutback. This drop had to persist for a minimum of 5 s to qualify as a sustained event. The end of the cutback was defined as an increase in NTLA of at least 2% from its lowest point during the drop, signaling the recovery phase. In contrast, non-Airbus airframes required a smaller drop threshold of 3% from the baseline NTLA, sustained for at least 10 s to identify a thrust cutback. The recovery was marked by a 1% increase in NTLA from its lowest point.

To further refine the classification, additional criteria were applied uniformly across all airframes. Only thrust cutbacks occurring at altitudes of 2,500 ft above field elevation (AFE) or below were considered, reflecting the operational phases where NADP procedures typically implement thrust reductions. Furthermore, the thrust cutback segment had to begin at least 800 ft above the runway, ensuring that the captured data represented true departure operations and excluding initial takeoff adjustments. Some irregularities in the detected data such as flights with multiple detected cutbacks or NTLA values exceeding 100% are shown in Figure 4. Flights with multiple detected cutbacks were excluded to maintain data integrity and flights exceeding an NTLA of 100% were adjusted to reflect more accurate results.

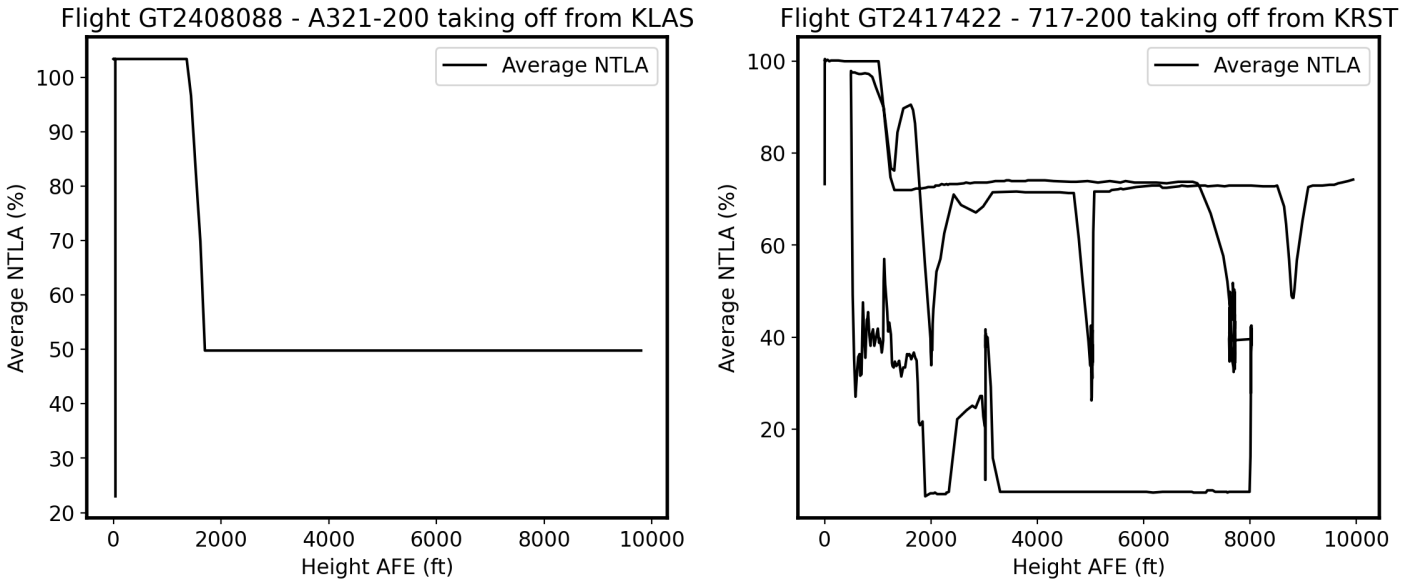

Figure 4. Examples of flights with irregularities from Harry Ried International Airport (KLAS) and Rochester International Airport (KRST).

By defining these precise thresholds, the methodology ensured that thrust cutbacks were accurately classified across different airframe types, as shown in Figure 5.

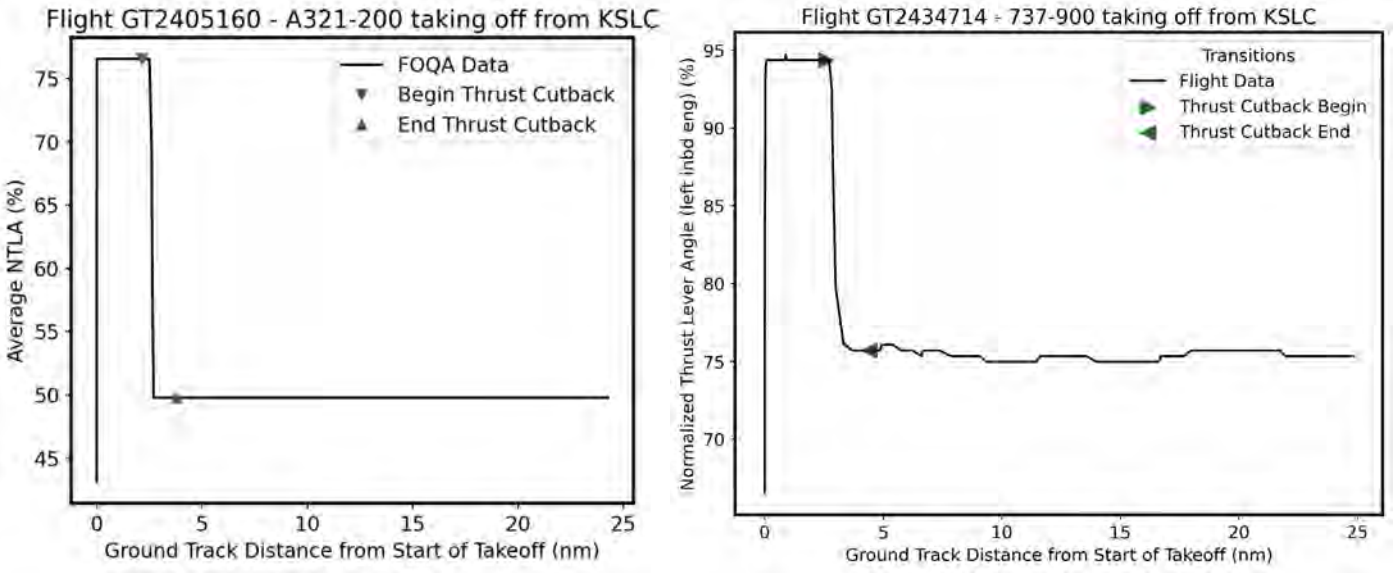

Figure 5. Thrust cutback anchor classification for Airbus and Boeing airframe from KSLC.

1.3. Level-Off Transitions

Level-offs are segments of flight where an aircraft temporarily halts its climb due to air traffic control instructions or operational constraints. These events influence fuel burn and emissions, as engines operate at non-optimal thrust levels. Thus, incorporating level-offs into the AEDT would allow for accounting these operational inefficiencies and provide a clearer picture of their environmental implications.

The methodology for classifying level-offs focused on accurately identifying their start and end points within a defined operational altitude range of 0 to 9,000 ft AFE. A level-off was determined to begin when the aircraft's climb rate dropped below a threshold of 50 ft per nautical mile, indicating a significant reduction in vertical ascent. The end of the level-off was marked when the climb rate exceeded this threshold again, signifying the aircraft's return to its climb phase.

To ensure only meaningful level-offs were classified, additional criteria were applied. Specifically, the horizontal ground track (distance during the level-off had to exceed 1.8 nmi, and the time spent in the level-off had to last at least 10 s. These filters were critical for excluding minor fluctuations in climb rates that do not represent true level-off events. Instead, the classification captured substantial deviations from the climb trajectory.

This refined approach ensured that the level-off anchors were accurately classified across all airframe types and operations, as shown in Figure 6.

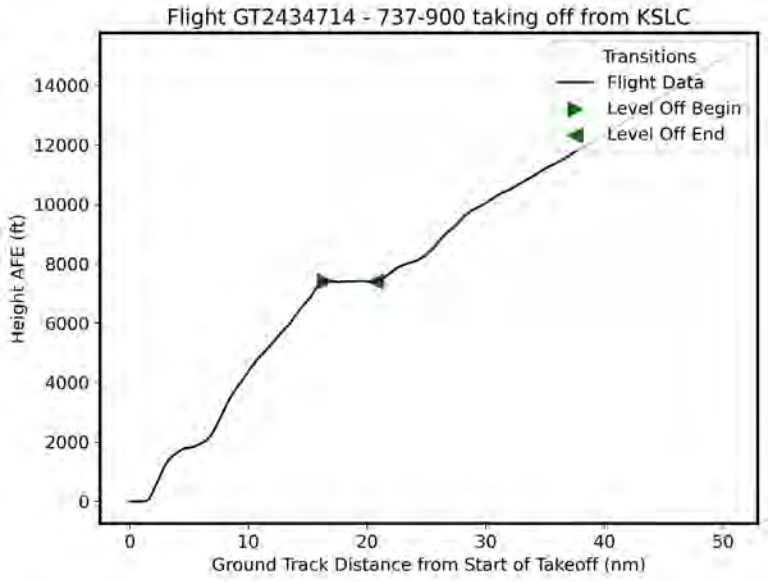

Figure 6. Level-off anchor classification.

1.4. Constant CAS Segment Classification

During specific phases of climb, aircraft maintain a constant CAS while true airspeed (TAS) increases. These segments occur due to standard climb protocols where pilots prioritize maintaining a specific CAS to optimize climb performance and ensure compliance with air traffic control requirements. While this occurs, the aircraft is ascending and experiences decreasing air density, which reduces drag and allows TAS to increase. An example of what a constant CAS segment resembles is shown in Figure 7.

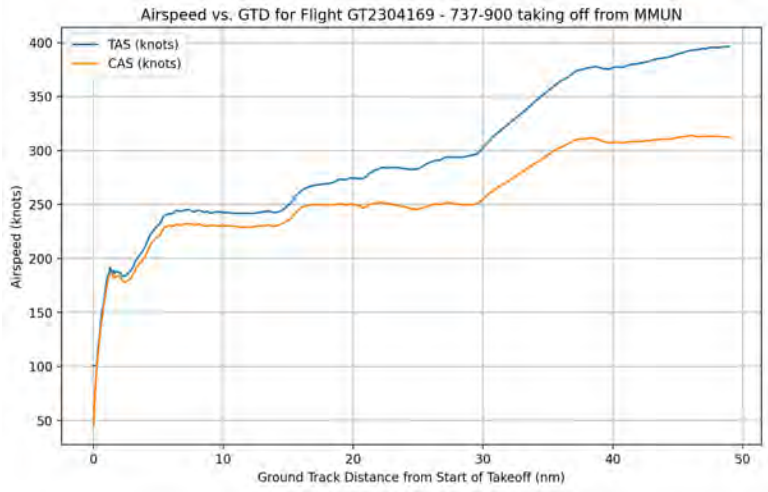

Figure 7. Depiction of constant CAS segment at a ground track distance of 16 to 29 nmi.

Capturing these constant CAS segments is critical for accurately modeling departure trajectories in the AEDT as they represent predictable operational behavior where the aircraft transitions from a focus on climb rate to acceleration efficiency.

The methodology for identifying constant CAS segments relied on analyzing patterns in CAS and TAS to pinpoint sustained periods of constant CAS. A sliding window of five data points was used to evaluate the variability in CAS, where a standard deviation of less than 2 knots indicated a steady CAS. Simultaneously, the TAS gradient within the same window was required to remain below 5 knots to ensure that any increase in TAS was consistent with changes in altitude rather than significant operational adjustments. Consecutive data points that satisfied these criteria were grouped into potential CAS segments.

To ensure only meaningful constant CAS segments were captured, a minimum segment length of 20 data points was applied. This filter excluded short-lived or noisy intervals that might falsely appear as constant CAS behavior.

Thus, this methodology accurately reflects operational practices during climb phases where maintaining a constant CAS is necessary. As shown in Figure 8, this methodology accurately classifies segments of constant CAS in the developed anchor classification algorithm.

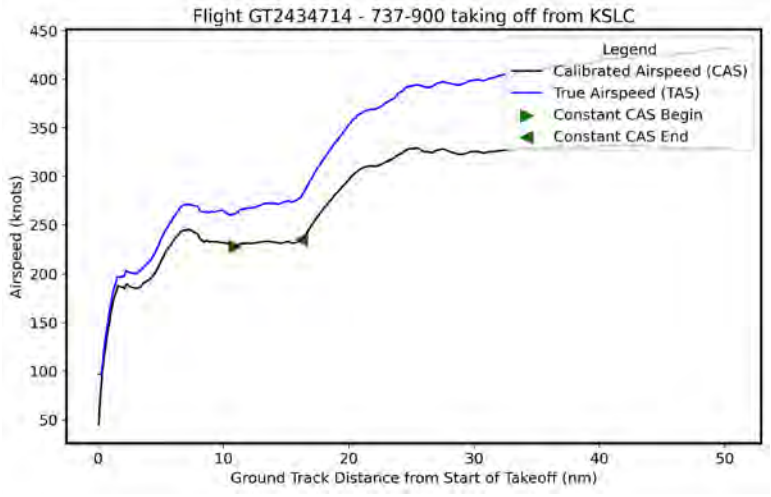

Figure 8. Constant CAS segment anchor classification from KSLC.

2. Clustering Methodology

2.1. Algorithm Selection

The goal of clustering flight trajectories is to identify and group flights with similar operational behaviors during departure. Once the trajectories are grouped or "clustered," features such as height AFE, ground track distance (GTD), thrust cutback, flap transitions, and other operational characteristics need to be analyzed. The analysis can reveal underlying patterns that represent different departure profiles.

To accomplish the task of clustering aircraft trajectories, one needs to identify and group flight records with "similar trajectories." The fundamental assumption here is that similar operational characteristics lead to similar departure profiles. There are different ways to define similarity between flight trajectories. One approach to defining similarity between flight trajectories is on the basis of how "close" they are. This can be identified by calculating the root mean squared error (RMSE) between two time series data, such as altitude and GTD. The closer the RMSE value is between two trajectories, the more similar the trajectories are. The second approach to defining similarity between flight trajectories is based on identifying common trajectory features. That could mean two trajectories having the same number of level-offs and climb profiles, even if they are shifted in time. To get a visual representation of these two approaches, observe Figure 9. According to the first approach, the yellow and blue trajectories are present in the same cluster since they have a lower RMSE. However, according to the latter approach, the green and blue trajectories are present in the same cluster since they have the same number of level-offs and climb performance. In this research effort, the latter approach is of greater relevance to us. The reason is that the blue and green trajectories share similar operational characteristics, but they just differ in their takeoff gross weight. So, the lighter aircraft flies at a higher altitude, which in this case is the green trajectory.

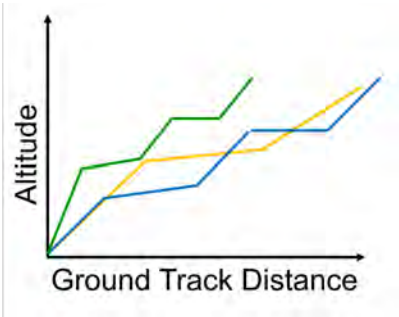

Figure 9. Notional departure trajectories.

To achieve clustering of aircraft trajectories, DTW was used as a primary technique. DTW is a computational technique built using dynamic programming, used to align two time series that may differ in temporal patterns, by finding an optimal match between them. DTW works by stretching and compressing sections of the two-time series that are being compared to minimize the overall distance. It calculates the cumulative distance between points of the two series, creating a warping path that represents the best alignment. A warping distance of zero implies the two time series data are the same. For instance, in the example in Figure 9 above, the blue and green trajectories have the lowest warping distance between them. Multi-dimensional DTW extends this concept to multiple features or dimensions by considering alignment across each dimension simultaneously. This means that if each step has a vector of values instead of a scalar, multi-dimensional DTW aligns the series by treating these vectors as single entities and computing distances for each pair. However, it is computationally expensive because it calculates a matrix of distances between all the possible pairs of inputs, and accounts for dependencies across dimensions and time. Such a pairwise computation has a computational complexity of $O(N^2)$. In simple terms, it means that the computational time increases by a factor of four if the size of the input doubles.

On the other hand, n-dimensional Fast Dynamic Time Warping (FastDTW) is an efficient approximation of multi-dimensional DTW that reduces computational complexity. While standard DTW grows quadratically in time and space, FastDTW approximates the solution using a recursive multilevel approach and grows linearly in time, allowing it to handle larger datasets. However, FastDTW does sacrifice significant accuracy for computational efficiency by approximating the alignment. This could potentially affect cluster quality and precision. The comparison between the two algorithms is summarized in Table 2.

Table 2. Comparing exact DTW algorithm and FastDTW.

	Dynamic Time Warping	**FastDTW**
Time Complexity	Quadratically scales with input size	Linearly scales with input size
Space Complexity	Quadratically scales with input size	Linearly scales with input size
Accuracy	High (optimal alignment)	Moderate or even low
Algorithm Type	Exact	Approximate

Based on the criteria of speed, accuracy, cluster quality, memory efficiency, and ease of implementation, DTW gets a higher score than FastDTW, hence it is used here for clustering. The most important criteria influencing the decision is 'Cluster Quality.' It is a crucial criterion since clustering the aircraft trajectories is challenging when they have smaller differences and are harder to tell apart. The only downside of using a DTW is that it is computationally expensive. Its quadratic time dependence on the input size is a major limiting factor. Dask,® a parallel and distributed computing library, is used to overcome this issue. With Dask, clustering computations were sped up by four times.

2.2. Feature Selection

To perform any clustering algorithm, the features need to be carefully selected. The time series data has a lot of valuable information, and potentially every included parameter can be used as a feature. Some of the potential features that can be used for the clustering the trajectories include:

- Height (AFE)
- GTD
- Flap position
- Thrust cut-back
- Landing gear transition
- Level-off transitions

However, adding many features does not necessarily yield a good result since there is a higher chance that some of them could be highly correlated. Such a selection of features will make the clustering biased towards the correlated features and diminish the influence of the rest of the features. It also increases the computational time. As mentioned earlier, the goal of clustering is to group flights with similar operational behaviors during departure, and it is assumed that flights with

® Dask is a registered trademark of NumFocus, Inc., Austin, Texas.

similar trajectory characteristics could have similar operational behavior. Hence, the features that are selected are as follows:

- Height (AFE)
- GTD
- Flap position
- Thrust Cutback

Level-off transitions are already captured directly by height and GTD. Landing gear transitions only contain 1 or 0 depending on the altitude at which they transition, so they do not contribute much towards the distance calculation by the DTW algorithm. Including thrust cut-back can be helpful, but at the time of writing this report, it has yet to be incorporated into the DTW algorithm. Since the algorithm and features have been selected, the preliminary result of clustering is in the following section.

Results and Discussions

1. Energy Share Percentage

In Figure 10, it is evident that on modifying the energy share percentage (reducing from 70 to 55, in the case of Airbus A321), the NADP profiles show greater resemblance to TT dataset. However, applying this approach to all the airframes in the dataset was a tedious task. It required thorough analysis of airframe/airport/stage-length considerations, which was not feasible given the volume of the dataset.

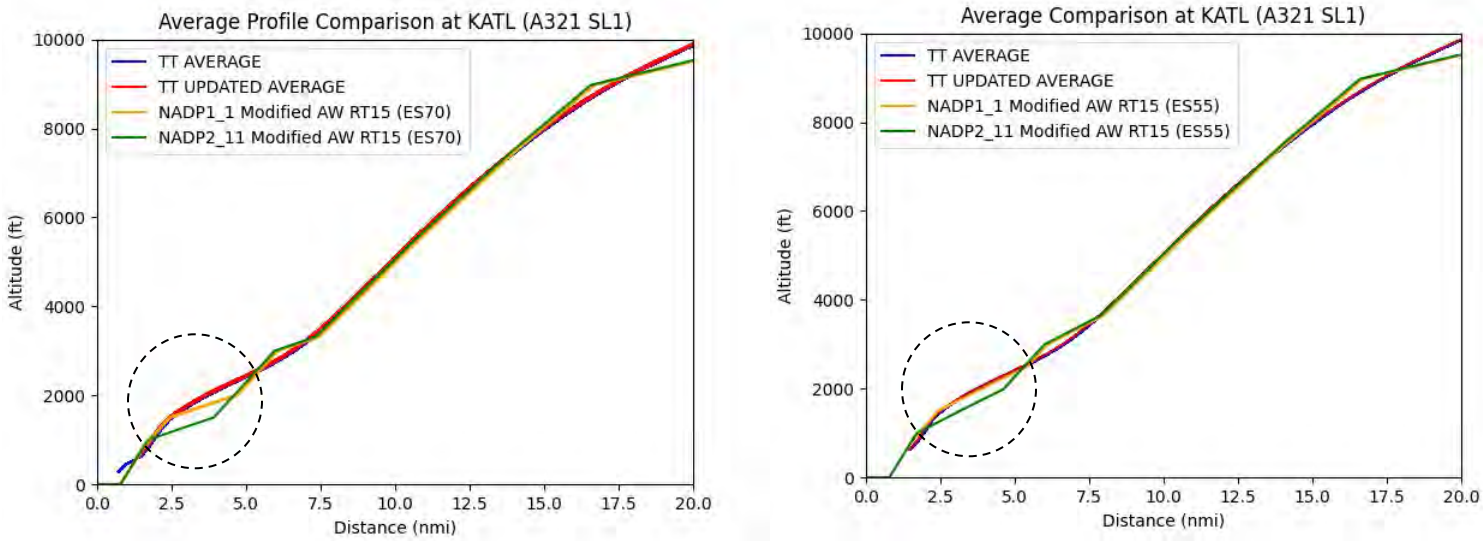

Figure 10. NADP with varying energy share compared with real world data at KATL.

2. Aircraft Takeoff Weight Estimation

To accommodate this, a new approach was implemented, where instead of route lengths, the aircraft weights were to classify the operations at different stage lengths. The approach was implemented on FOQA data initially, due to the presence of aircraft weight in these datasets. This approach led to changes in how flights are distributed across various stage lengths, A significant portion of flights got bumped into a higher stage length as compared to where they would be if the stage length (SL) were classified based on the route length, to comply with the limits of Modified_AW definitions, as shown in Figure 11, Figure 12, and Figure 13.

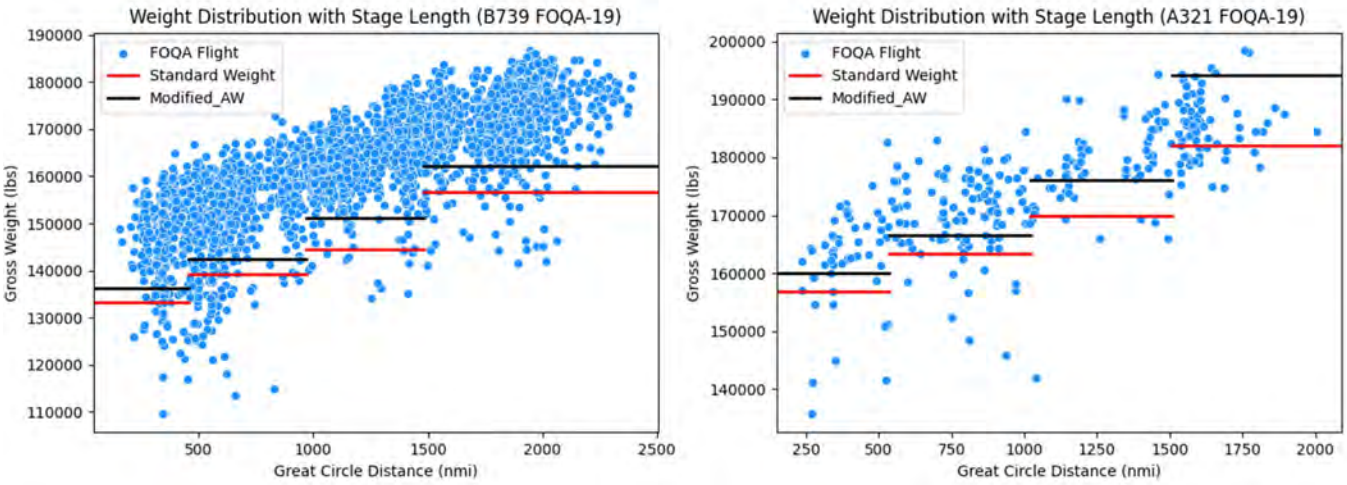

Figure 11. FOQA takeoff weight compared against AEDT definitions for different stage lengths.

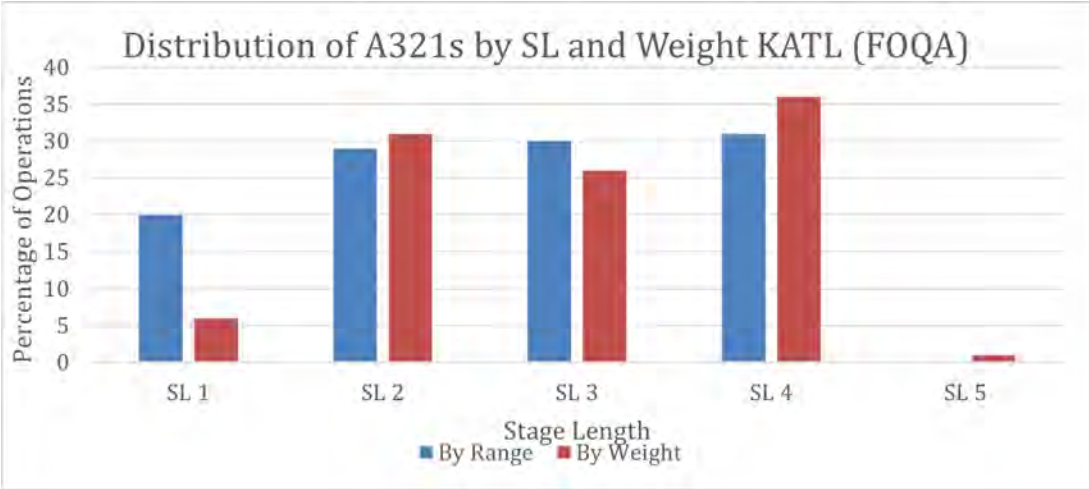

Figure 12. Comparison between SL distribution by range and weight for KATL.

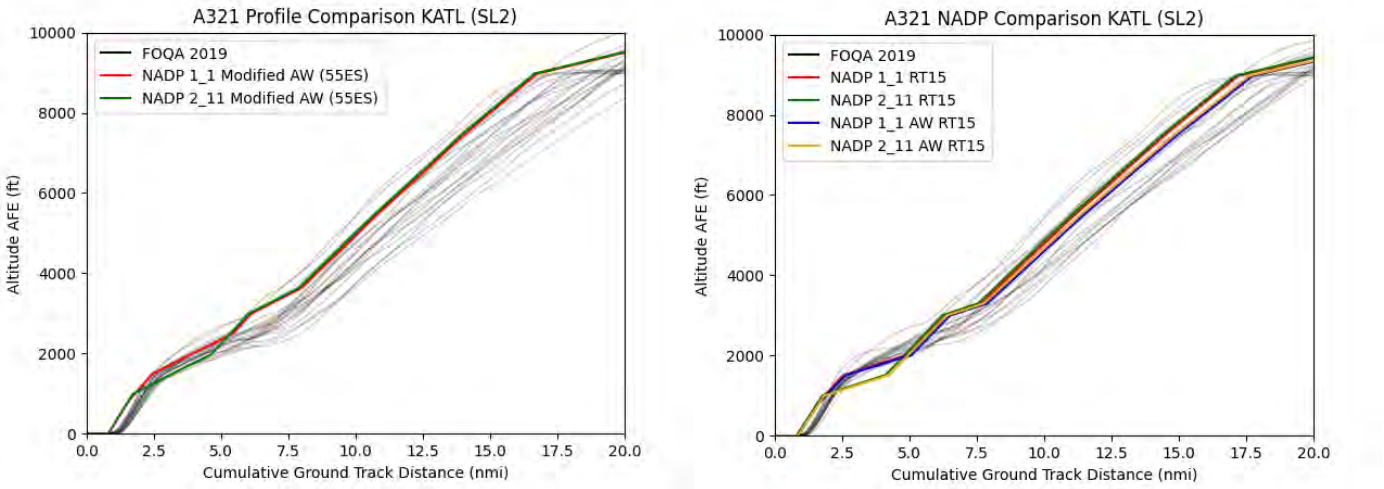

Figure 13. Comparison of profiles with and without modification to energy share for FOQA data for KATL.

The application of this approach showed promising results with FOQA, with the profiles showing similar resemblance to real world data, as one would expect with changing the energy share percentage as well. In fact, at higher altitudes, the weight-based classification methodology showed better resemblance to average real-world operations, as compared to ES calibration methodology.

However, the application of this approach to TT data proposes a challenge, as this weight feature is absent from it. To solve this issue, it was decided to integrate the city-pair based aircraft weights from FOQA for a particular airframe to the TT dataset. The application of this approach at Hartsfield-Jackson Atlanta International Airport (KATL) showed that the profiles were matched for the majority of the segments; however, there were some discrepancies in the thrust cutback region (Figure 14).

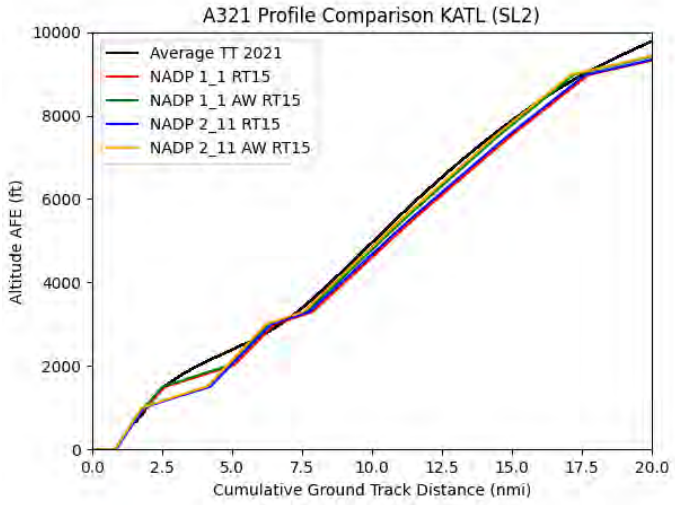

Figure 14. Comparison of Airbus A321 NADP profiles with TT data for KATL.

Apart from Atlanta, this approach was also tried at Salt Lake City International Airport (KSLC) and Los Angeles International Airport (KLAX). The combination of these airports allowed the study to capture the behavior at different elevations, while

maintaining the presence of enough flights to make meaningful observations. Table 3 outlines the airport operations at KSLC and KLAX.

Table 3. Summary of operations at airports in study.

Airport	Elevation	Number of Operations in FOQA Data	Number of Operations in TT Data
Salt Lake City Internation Airport (KSLC)	4226 ft	1821	38028
Los Angeles International Airport (KLAX)	128 ft	1094	253748

Though the flights showed higher resemblance to NADP1_1 RT 15, as evident from Figure 15, the observations showed that similar to KATL, the profiles do not accurately depict the thrust cutback zone. Also, for KSLC, as the distance increased from the airport, the climb rate was not consistent between real world data and AEDT profiles.

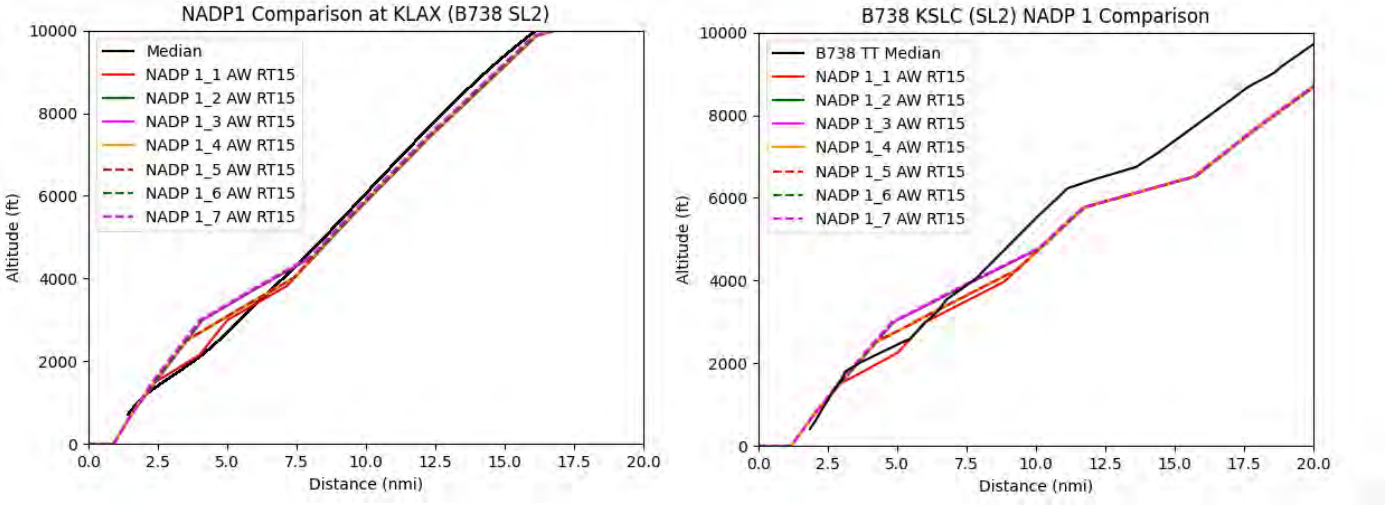

Figure 15. Comparison of B738 NADP profiles with TT data.

2.1. Anchor Classification

The results presented in this section show the classification of key operational characteristics or anchors using the anchor classification methodology. The anchors classified include flap and landing gear transitions, thrust cutback segments, level-offs, and constant CAS segments. The anchors classification algorithm was applied across all airframe types and operational profiles available in the FOQA CY 2023 data. An example of a flight with all anchors is shown in Figures 16 to 19.

Figure 16 demonstrates the classification of flap transitions by depicting flap positions over GTD. The accuracy of the classification of these anchors is shown through the precise identification of start and end points for each event. For instance, the flap transitions correspond to distinct changes in flap settings, starting at approximately 5°, transitions to 1° around 5 nmi into flight and then to 0° shortly after. This reflects expected operational adjustments during the initial climb for a Boeing® 737 aircraft.

® Boeing is a registered trademark of The Boeing Company, Seattle, Washington.

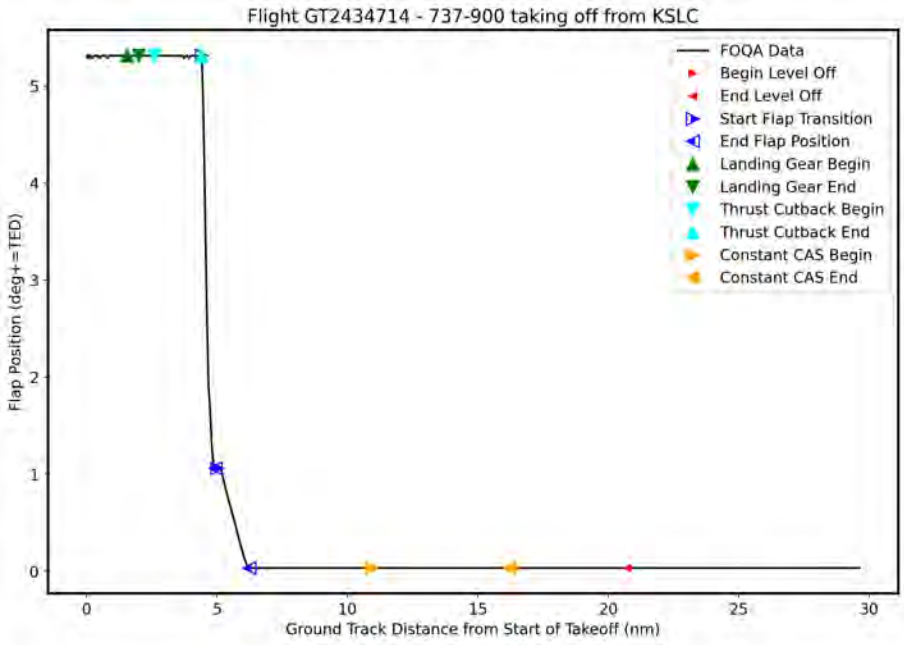

Figure 16. Flap position vs. ground track distance for the Boeing 737-900 flight with all classified anchors from KSLC.

Figure 17 shows NTLA against GTD for the flight, depicting how effectively the anchor classification algorithm captures thrust cutback. The thrust cutback occurs briefly before 5 nmi and decreases from approximately 95% to 75%. These transitions in thrust align with a typical NADP profile where thrust cutback occurs early on in departures before the initial acceleration phase.

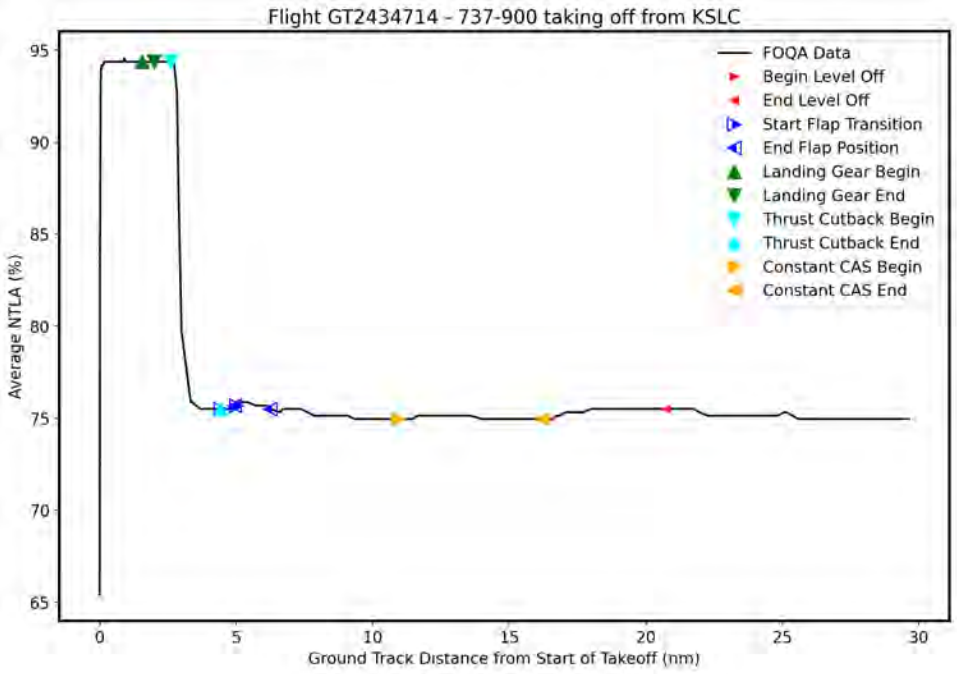

Figure 17. Average NTLA vs. ground track distance for the Boeing 737-900 flight with all classified anchors from KSLC.

Figure 18 depicts the calibrated air speed over GTD for this flight. Comparing Figure 17 to Figure 18, it is clear that the constant CAS segment is correctly classified as when the CAS is constant relative to the TAS (the TAS is increasing over a window where the CAS is more or less constant). Furthermore, this plot also emphasizes that the thrust cutback occurs prior to the initial acceleration phase and the level off in altitude occurs shortly after the constant CAS segment during the final acceleration phase

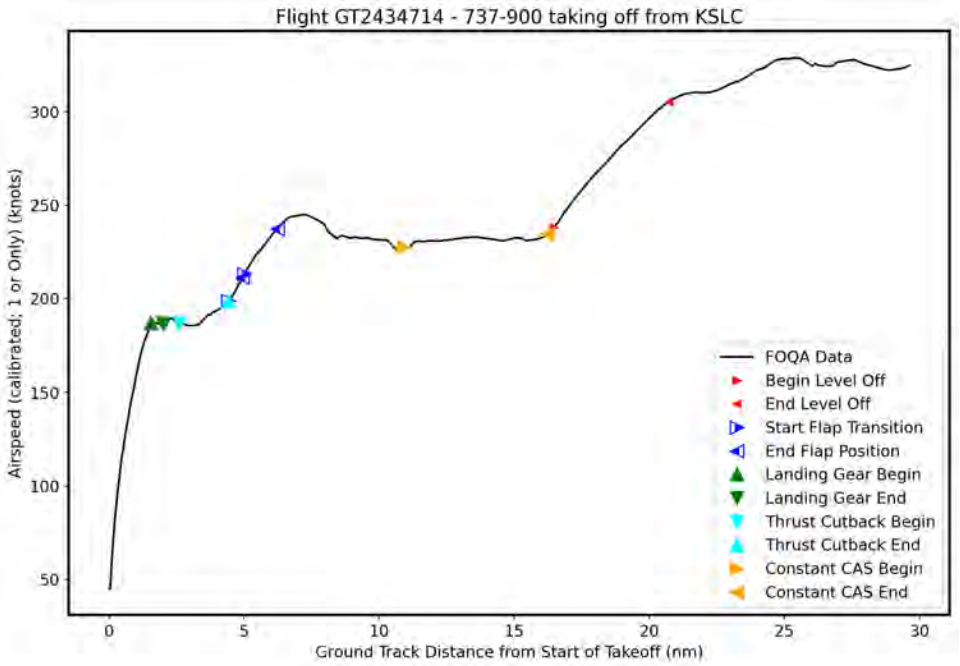

Figure 18. Calibrated airspeed vs. ground track distance for the Boeing 737-900 flight with all classified anchors.

Finally, the height AFE vs. GTD plot is depicted in Figure 19. This plot showcases the interplay between all the anchors. Overall, the results validate the anchor classification methodology and emphasize its importance in capturing the nuances of flight departure operations.

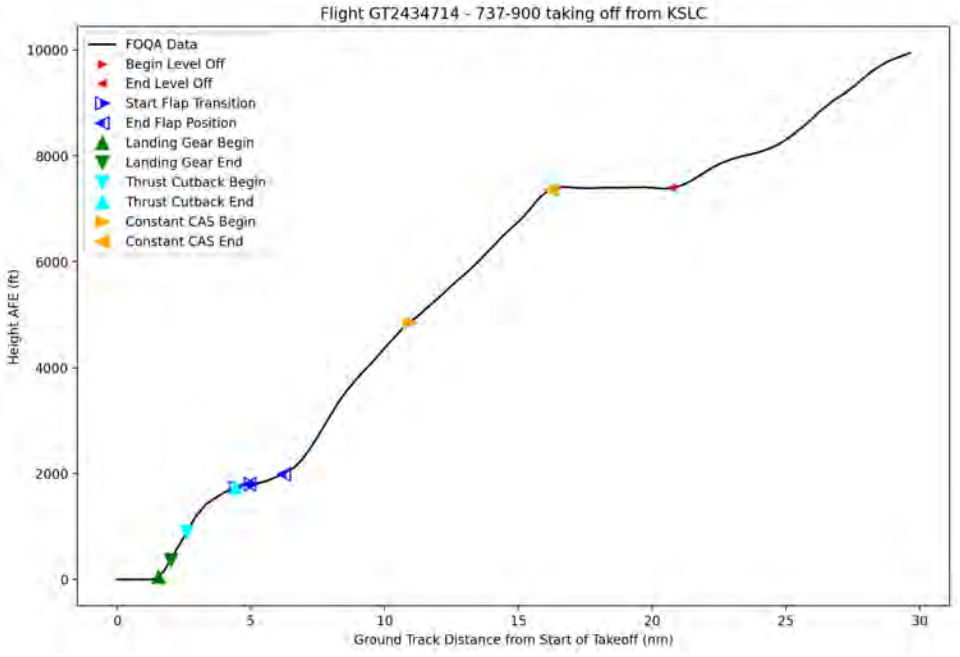

Figure 19. Height AFE vs. ground track distance for the Boeing 737-900 flight with all classified anchors from KSLC.

2.2. Clustering

The DTW algorithm is initially applied on the chosen features of approximately 200 distinct flight records of the Boeing 737-900 prior to its application to all airframes. Ensuring that the algorithm generates high-quality clusters is crucial before it is used on the complete dataset. Usually, the silhouette scores are a good indication of the quality of the clustering algorithm. Though a value above 0.5 is recommended in practice, sometimes a lower value also gives good clustering results, as the exact values of a silhouette score are very dependent on the nature of the problem and the quality of data that is being dealt with. Figure 20 shows the variation of the silhouette score with the number of clusters. Though a value above 0.35 is observed when the number of clusters is 8, all the trajectories can be categorized into four types of clusters:

1. Trajectory Type-1: The first type of trajectories is characterized by no level-offs, and, at most one shallow climb.
2. Trajectory Type-2: The trajectories falling in this cluster often have multiple shallow climbs, but do not contain any level-offs.
3. Trajectory Type-3: These trajectories consist of one level-off, and the rest of the trajectory has a steep or shallow climb.
4. Trajectory Type-4: The last type of trajectories is characterized by multiple level-offs and therefore takes a long time to reach the 15,000 ft mark.

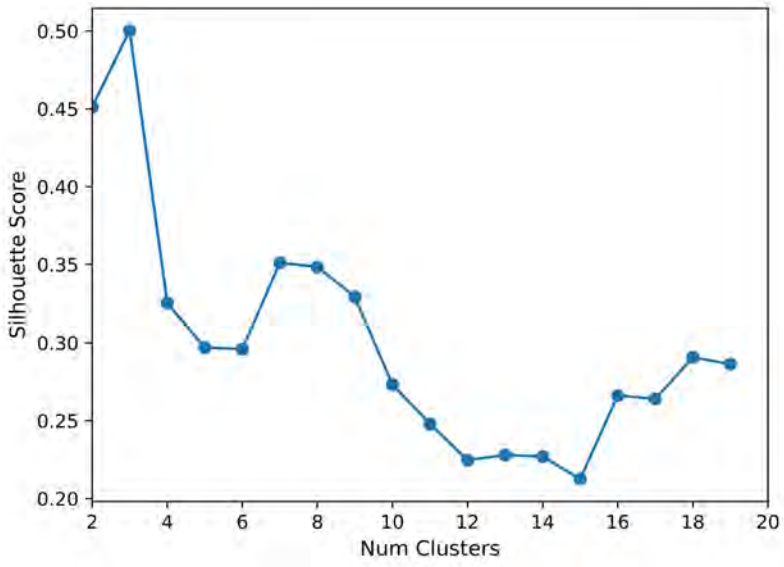

Figure 20. Variation between silhouette score and number of cluster.

It should be noted that there are outliers within each cluster type, as indicated in the plots in Figure 21. These outliers do not belong to that specific type of trajectory. Instead, they might belong to another cluster type. For instance, some of the trajectories in Type-2 belong to Type-1. A very few in Type-1 belong to Type-3 since these outliers in Type-1 have one level-off. This experimentation with a smaller subset of the flight records has, therefore, been useful. Mindlessly applying the algorithm would not only have wasted a lot of computational resources but would have also produced poor quality clusters that would not have yielded any significant insights. Hence, before scaling the algorithm to all the unique flight records, there is a need to fine-tune the algorithm or add another layer of logic that can filter out the outliers that are being miscategorized.

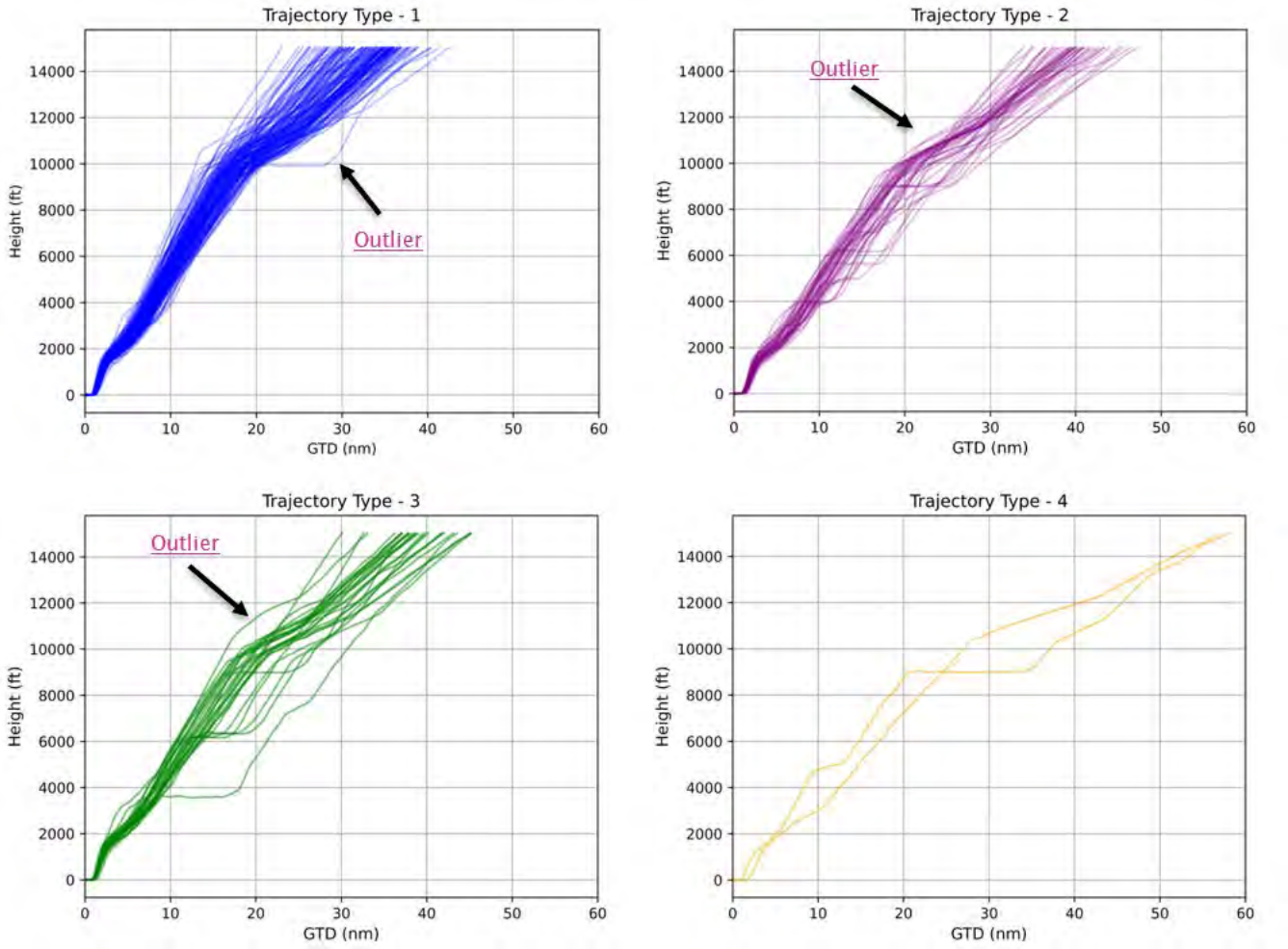

Figure 21. Types of trajectory clusters.

These clusters of trajectories can be visualized conceptually as shown in Figure 22. Imagine two axes forming a plane, with the x-axis being level off and the y-axis being climb. Closer to the origin, there are no level-offs, and the climb is shallow. Far diagonally from the origin, the climb rate is steep, with long level-offs. This plot summarizes the preliminary results of Task 1. Through this research, the ASCENT Project 054 team has qualitatively identified the underlying characteristics that make up different flight trajectories. With this insight, there is a need to refine the algorithm to cluster the trajectories with even higher accuracy to avoid misclassification.

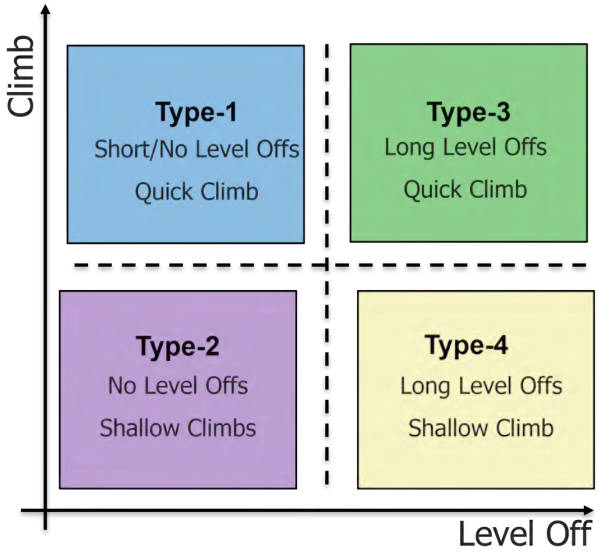

Figure 22. Conceptual visualization of types of trajectory clusters.

Milestones
None.

Major Accomplishments
- Quantified the energy share percentage by modifying the division of energy between acceleration and climb, which impacts the accuracy of departure profiles in the AEDT.
- Identified and classified key operational characteristics for anchor classification, such as flap transitions, landing gear retraction, thrust cutbacks, level-offs, and constant CAS segments, have been identified and classified to determine patterns in real-world flight behavior.
- Selected DTW to perform the trajectory classification after experimenting with a lot of clustering algorithms. Clustering a subset of flight records has revealed distinct characteristics of the four unique types of trajectories.

Publications
None.

Outreach Efforts
- Participated in biweekly calls and biannual ASCENT meetings.

Awards
None.

Student Involvement
Graduate research assistants, Tanmay Daga, Ranya Almarzooqi, and Vishnu Sankar Manivasakan, participated in this task.

Plans for Next Period
The energy share percentage and anchor classification tasks have been completed. Clustering is still a work in progress. The underlying characteristics that make up different flight trajectories have been qualitatively identified during the current clustering efforts. The future tasks are as follows:
- Further refine the DTW algorithm to produce clusters of higher quality and accuracy that can avoid misclassification. Currently, the DTW algorithm occasionally misclassifies certain trajectories, and their number is not negligible, which affects the cluster quality.

- Analyze the clusters for patterns of similarity in the operational behavior of the flight records after accurately clustering the trajectories.
- Propose and carry out improvements to the accuracy of fuel consumption, emissions data, and noise assessments in the AEDT.

Task 2 – Arrival Profile Modeling

Georgia Institute of Technology

Objectives

The current model in AEDT models arrival profiles using specified fixed-point trajectories or manufacturer-provided procedures. The primary objective of Task 2 is to compare data from real-world flights to the AEDT models to make recommendations that will allow the AEDT to better capture aircraft behavior during arrival.

This year, the specific focuses of this task are (1) analyze variations in flap configurations in FOQA data during the arrival phase and evaluate how they deviate from AEDT's standard profile implementation and (2) perform clustering on FOQA data, incorporating variables such as flap schedules and landing gear deployment, to identify patterns and group similar flights for creating improved AEDT arrival profiles. The end goal of this project is to provide recommendations regarding which AEDT arrival profiles should be integrated into the system and what information those profiles should include.

Research Approach

Investigation 1: Flap Variations in FOQA Data vs. AEDT Standard Profile

1. Methodology

In the previous year, an evaluation of arrival trajectories was conducted to identify key level-off characteristics. This analysis laid the foundation for the next phase of the study, which focused on analyzing flap variations along arrival trajectories and assessing their deviations from the AEDT Standard Profile implementation. Recognizing the influence of flap settings on fuel consumption through the aerodynamic drag polar, the study emphasized the relationship between flap configurations and aerodynamic efficiency.

To compare fuel consumption, data was gathered from both the 2021 FOQA dataset and AEDT standard profile. CAS data was extracted from the RSLT_EMISSIONS_SEGMENT table in AEDT using structured query language (SQL) after running emissions inventory metrics. As the flap information was not directly available from AEDT's flight performance reports, calibrated airspeeds were mapped to predefined flap settings from the standard profile. To ensure consistency, airspeed values—initially measured in statute miles per hour—were converted into knots, aligning with AEDT's standard units.

Two approaches were utilized for deriving flap settings. The first approach relied on altitude and GTD from the AEDT Standard Profile, as highlighted in Figure 23, with flap settings aligned to level-off distances at 3,000 ft AFE. The second approach incorporated altitude and calibrated air speed, as shown in Figure 24, correlating specific speed thresholds with flap configurations. Both approaches were applied and validated using step-type checks available within the AEDT, with step-type information also sourced from the standard profile. These checks ensured that flap assignments adhered to expected configurations based on altitude, air speed, and step-type conditions.

Profile ID	Step Number	Step Type	Flap ID	Thrust Level	Altitude AFE (ft)	Calibrated Airspeed (kt)	Distance (ft)	Static Thrust (%)	Angle (°)
STANDARD1	1	Idle Thrust Descend	A_00	Unknown Thrust	6000	248.93			3
STANDARD1	2	Idle Thrust Level	A_00	Idle Approach	3000	249.5	25437		
STANDARD1	3	Idle Thrust Level	A_01	Idle Approach	3000	187.18	3671		
STANDARD1	4	Idle Thrust Level	A_05	Idle Approach	3000	174.66	5209		
STANDARD1	5	Idle Thrust Descend	A_15	Unknown Thrust	3000	151.41			3
STANDARD1	6	Descend	A_30	Unknown Thrust	2817	139.11			3
STANDARD1	7	Land	A_30	Idle Approach			393.8		
STANDARD1	8	Landing Decelerate		Reversed Thrust		139	3837.5	40	
STANDARD1	9	Landing Decelerate		Normal Thrust		30	0	10	

Figure 23. Approach 1 based on altitude and distance to touchdown.

Profile ID	Step Number	Step Type	Flap ID	Thrust Level	Altitude AFE (ft)	Calibrated Airspeed (kt)	Distance (ft)	Static Thrust (%)	Angle (°)
STANDARD1	1	Idle Thrust Descend	A_00	Unknown Thrust	6000	248.93			3
STANDARD1	2	Idle Thrust Level	A_00	Idle Approach	3000	249.5	25437		
STANDARD1	3	Idle Thrust Level	A_01	Idle Approach	3000	187.18	3671		
STANDARD1	4	Idle Thrust Level	A_05	Idle Approach	3000	174.66	5209		
STANDARD1	5	Idle Thrust Descend	A_15	Unknown Thrust	3000	151.41			3
STANDARD1	6	Descend	A_30	Unknown Thrust	2817	139.11			3
STANDARD1	7	Land	A_30	Idle Approach			393.8		
STANDARD1	8	Landing Decelerate		Reversed Thrust		139	3837.5	40	
STANDARD1	9	Landing Decelerate		Normal Thrust		30	0	10	

Figure 24. Approach 2 based on altitude and calibrated air speed.

Flap settings for Boeing 737-900 flights were derived for the top five airports using these two methods. Although the altitude and calibrated speed approach performed reliably, the distance-based approach produced errors for three out of the five airports. Additionally, the methodology was extended to derive flap settings for the Airbus A321-200 aircraft arriving at KSLC, which is at an elevation of 4230.9 ft. Prominent flap positions (0°, 14°, 21°, and 25°) were identified using FOQA data from 327 flight operations at the airport, as shown in Figure 25.

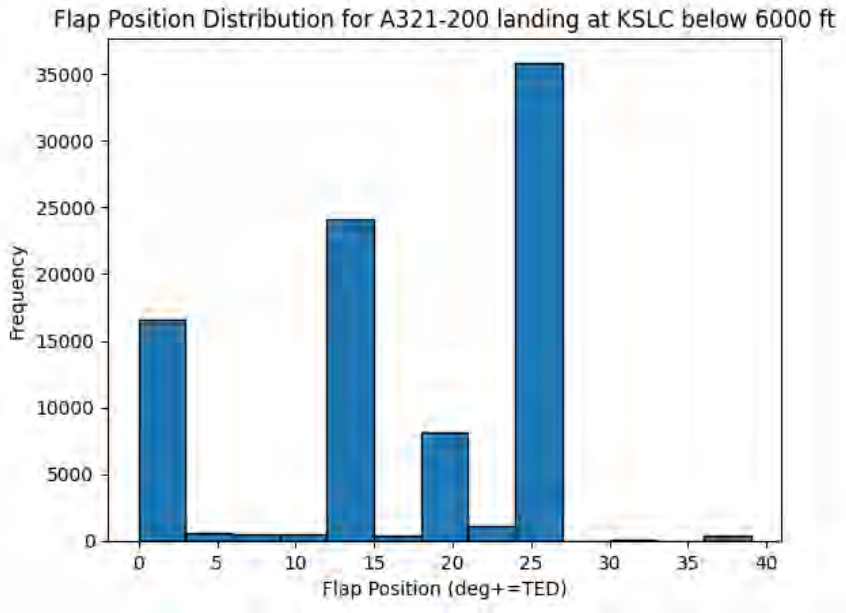

Figure 25. Flap position distribution for Airbus A321-200 arriving at KSLC.

2. Results and Discussion

The comparison of aggregate fuel consumption between FOQA flights and the AEDT Standard Profile revealed that the standard profile provides a good estimate of the median fuel consumption, as depicted in Figure 26. However, when comparing fuel consumption along flight trajectories, significant deviations were observed for flights with median and least fuel consumption when measured against the AEDT Standard Profile. These deviations highlight the sensitivity of fuel consumption to flap configurations, particularly during level-off segments.

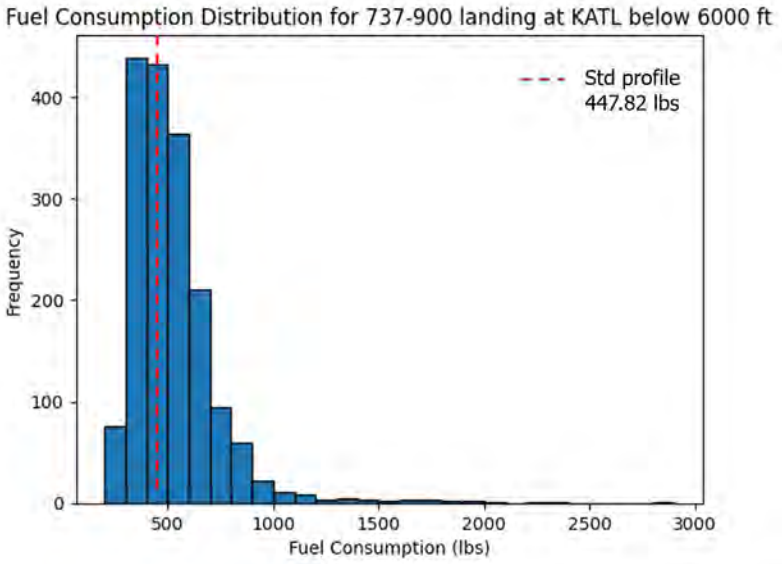

Figure 26. Fuel consumption for Boeing 737-900 FOQA flights and the AEDT standard profile at KATL.

For the Boeing 737-900 standard profile, it was observed that flap settings significantly influence fuel consumption, particularly at lower altitudes. Figure 27 illustrates a notable spike in fuel consumption at 3,000 ft AFE, which corresponds to the transition from 0° to 5° of flap deployment. This spike is evident in both the altitude-based and distance to touchdown plots, where the cumulative fuel consumption for the standard profile deviates from that of the least fuel-consuming flight. These findings emphasize the critical role of flap deployment in shaping fuel consumption patterns and highlight the operational differences between FOQA flights and the AEDT standard profile.

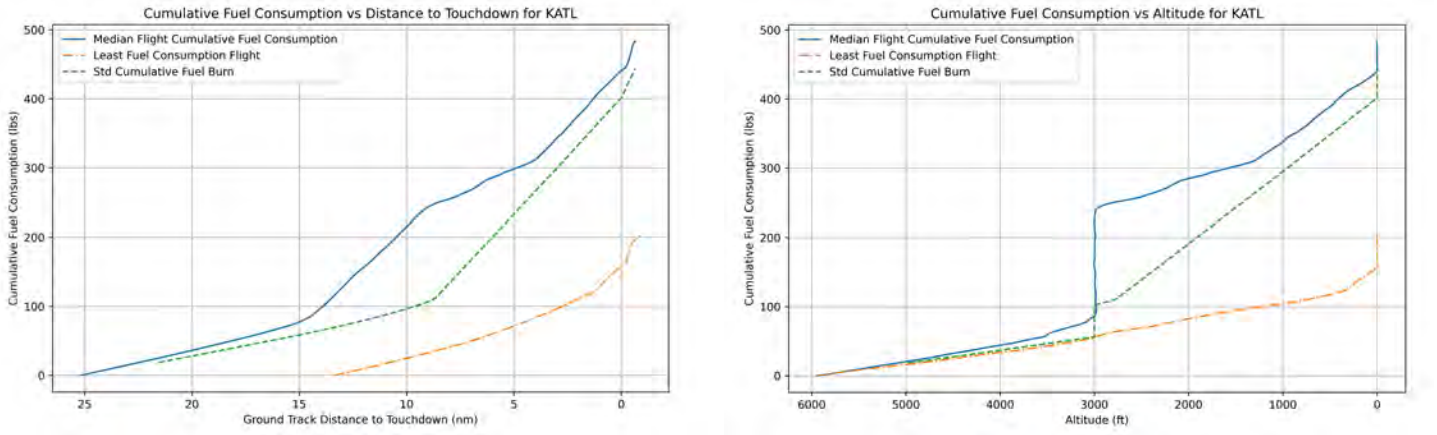

Figure 27. Cumulative fuel consumption vs altitude and distance to touchdown for the Boeing 737-900 arriving at KATL.

While the distance-based flap derivation approach showed inconsistency for certain airports, the altitude and calibrated speed-based approach consistently demonstrated high accuracy and reliability across all analyzed cases. These findings are effectively visualized in Figure 28, which illustrates cumulative fuel consumption and flap positions as functions of altitude and GTD to touchdown. The plots highlight the critical transition points where flap settings change, such as the shift from 0° to 5°, which corresponds to a significant increase in fuel consumption. The color-coded flap positions in the plots clearly delineate the cumulative fuel impact of each setting, providing deeper insights into their aerodynamic and operational significance.

Moreover, the alignment of the calibrated speed-based derivation with actual fuel consumption patterns emphasizes its robustness for accurately capturing real-world operational behaviors. These results underscore the importance of precise flap setting derivations in understanding the variations in fuel consumption across different arrival trajectories.

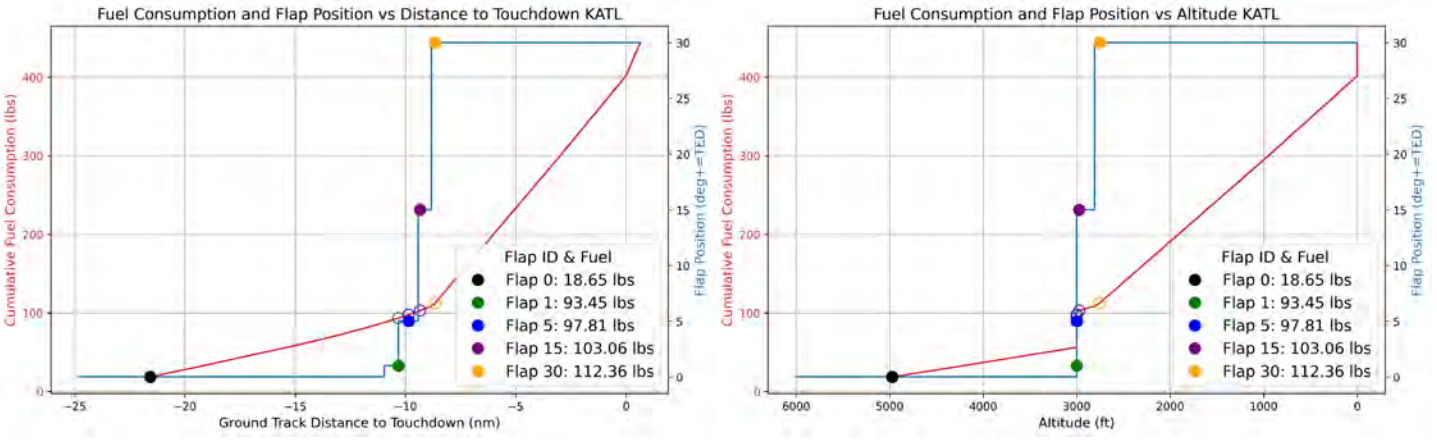

Figure 28. Fuel consumption and flap position as functions of distance to touchdown and altitude for the Boeing 737-900 standard profile at KATL.

For the Airbus A321-200 arriving at KSLC, the analysis of 327 FOQA flight operations identified four prominent flap positions: 0°, 14°, 21°, and 25°. As illustrated in Figure 29, higher flap settings, such as 25°, are predominantly deployed during final approaches, typically below 1,000 ft height above touchdown (HAT), where the increased drag correlates with higher fuel consumption. A flap position of 21° is observed during the approach phase, between 1,000 - 2,000 ft HAT. Lower flap positions, such as 14°, are primarily used during the mid-descent phase, ranging from 2,000 to 4,000 ft HAT. A flap position of 0° is commonly deployed during the initial descent, at altitudes above 4,000 ft HAT. These findings emphasize the dynamic use of flap configurations throughout different phases of descent, contributing to variations in fuel burn and aerodynamic efficiency.

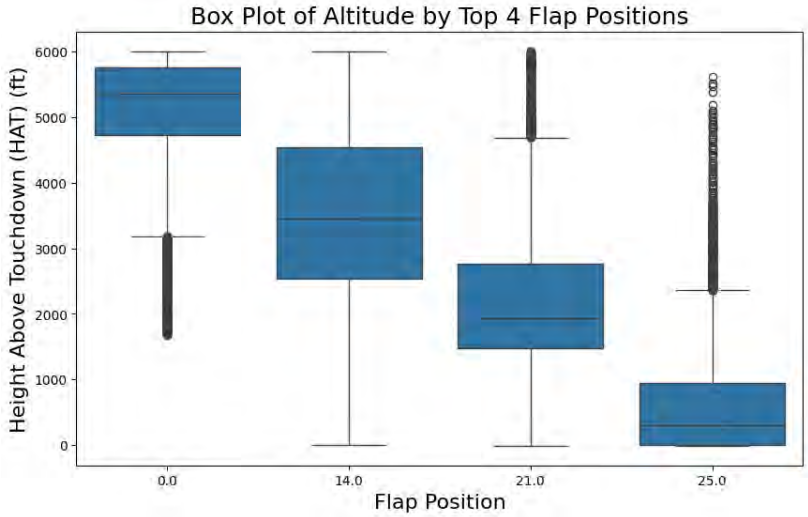

Figure 29. Altitude distribution by prominent flap positions for Airbus A321-200 arriving at KSLC.

Investigation 2: Clustering Efforts

1. Methodology

Mirroring the efforts for modelling more accurate AEDT profiles arrival flight operations in Task 1, a similar attempt to classify flight arrival procedures by clustering around the FOQA CY 2023 flight arrival data was conducted for Task 2. The rational is that by defining and grouping similar flight procedures together, specific patterns and emergent behavior can be found within each group that can ultimately help distinguish different descent patterns from one another that can be modelled in AEDT. To prepare for clustering, features need to be extracted from the FOQA flight operation data which can be defined as meta-parameters for clustering or to define a corresponding AEDT profile. These features correspond to the key operational characteristics of a descent profile and are hereafter referred to as 'anchor points,' much like in Task 1. In essence, they down select a FOQA profile by capturing 'snapshots' of the flight corresponding to flap transitions, landing gear transition, and level-offs that can uniquely define a descent procedure. Much effort was dedicated to not only extracting the 'anchor points' in a time-efficient manner working with the large FOQA CY 2023 dataset but also validating the accuracy of the 'anchor points' and performing outlier analysis to ensure an appropriate level of sensitivity to accurately capture the level-offs and flap transitions. Finally, using these anchor points to define a similarity metric between any two descent procedures, preliminary clustering demonstrations were conducted to demonstrate a capability.

2. Results and Discussion

When determining 'anchor points,' the following criteria were used to define key characteristics of a FOQA descent profile. A level-off was characterized by a descent profile that is 'flat' for at least 1.8 nmi in GTD, with 'flat' being defined as a flight path descent angle of less than arctan (1/50), or 1.15°. In addition, to avoid touchdown from being accidentally recorded as a level-off, level-offs were defined to only occur at heights of 1,000 ft AFE or above. Landing Gear anchor points are defined just as they were in Task 1, at the two points where the landing gear deployment begins and ends. Also, flap transition points were found by detecting when flap positions reached or deviated from a pre-determined flap position. These pre-determined flap positions were calibrated using a mapping function to find the nearest standardized flap settings for each aircraft type after performing data analysis to validate known flap settings for select Boeing and

Airbus airframes.

Validating known flap settings for these airframes was not trivial, because the FOQA data do not exactly match known flap settings, and a degree of rounding needs to be implemented. In addition, while Boeing flap settings are constant across airframe types (for all airframes except the older Boeing 717-200 in the CY 2023 dataset where the flap settings are 0°, 1°, 2°, 5°, 10°, 15°, 25°, 30°, and 40°) as shown in Figure 30, Airbus airframes have different flap configurations as shown in Figure 31.

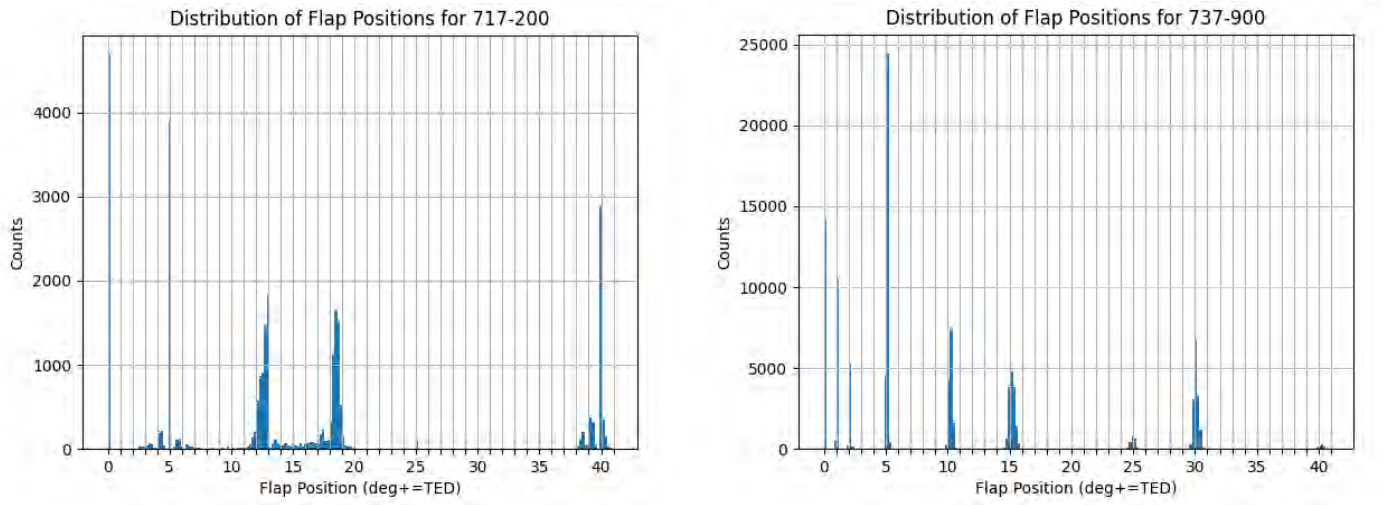

Figure 30. Histograms of found flap positions for select Boeing airframes (FOQA CY 2023 data).

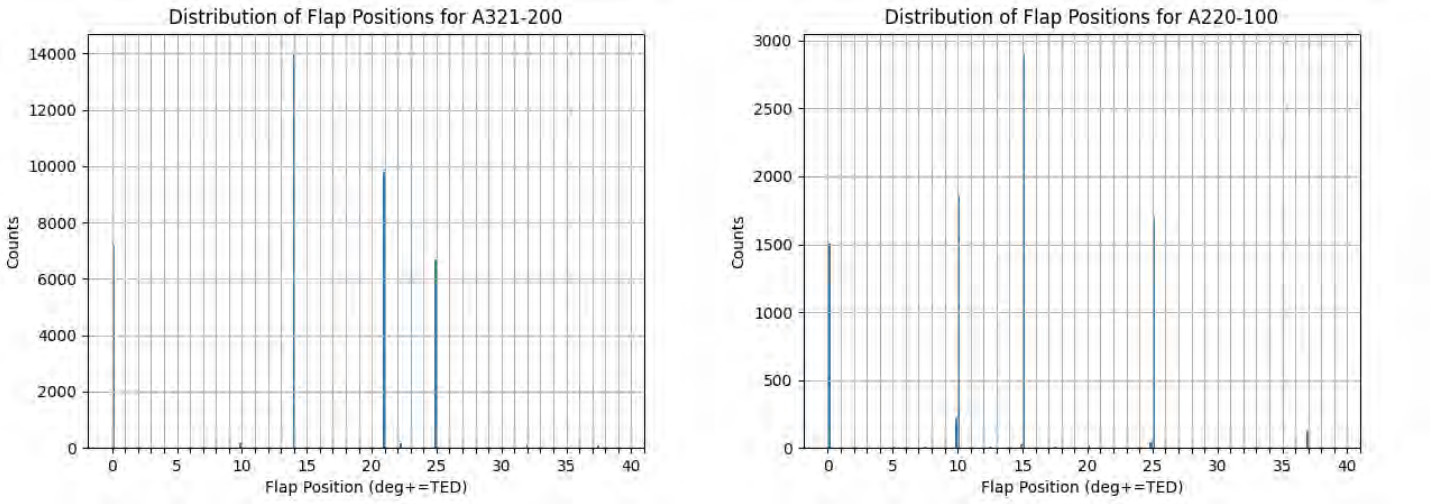

Figure 31. Histograms of found flap positions for select Airbus airframes (FOQA CY 2023 data).

Because of these inconsistencies and slight deviations caused by sensor measurement recorded in the FOQA data, rounding or mapping functions had to be implemented to validate and ensure calculated flap transitions are accurate for each airframe type.

The algorithms for finding anchor points were written to be efficient to work with large datasets (FOQA CY 2023 includes 49,647 flights). Due to a need to prioritize efficiency, outliers were defined as any flight that had to perform a go-around

and discarded, as these descent profiles made it difficult for the algorithm to capture flap transitions and level-offs. Finally, a plotting function to overlay anchor points on a height vs. ground track or flap setting vs ground track trajectory plots was created to visualize the captured anchor points on a per-flight basis as shown in Figure 32.

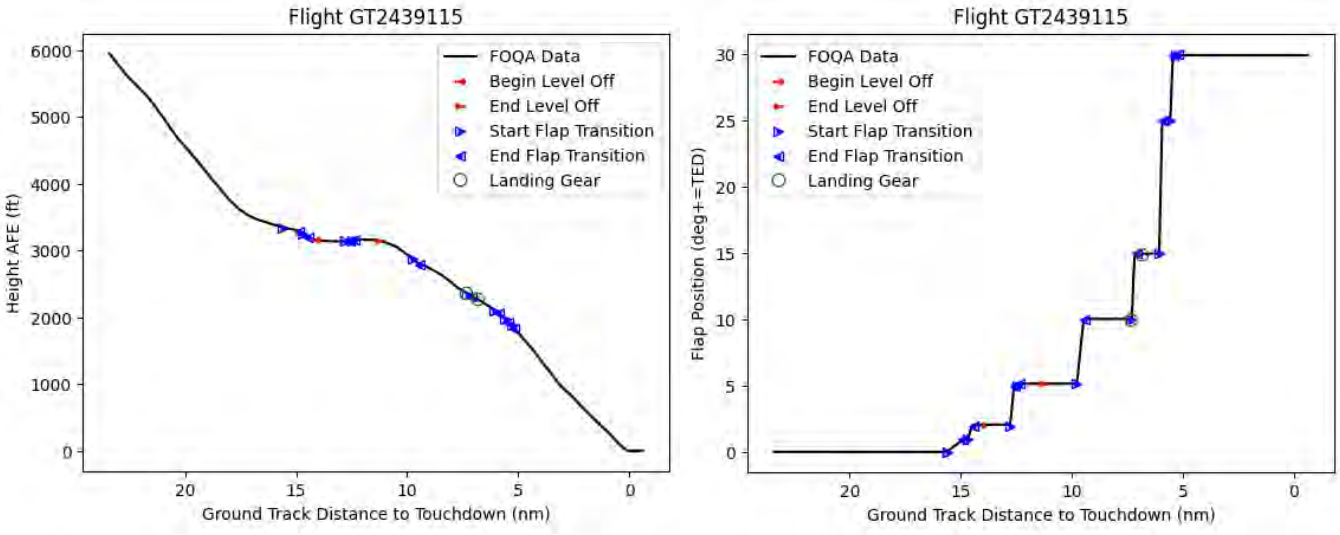

Figure 32. Trajectory plot of height AFE (left) and flap position (right) vs. ground track distance for FOQA CY 2023 data. Trajectory is an arrival of a Boeing 737-900 at Minneapolis-Saint Paul International Airport (KMSP).

Using information from the gathered anchor points, a preliminary clustering effort was conducted. First, the dataset was further restricted to Boeing 737 airframes because the corresponding AEDT profiles can specify an airframe and there was a large sample size to work with in the CY 2023 FOQA data (12,559 trajectories after excluding go-arounds). In addition, an examination of expected emergent behavior was conducted using the anchor points to try and identify trends or features that a clustering algorithm should be able to identify. For example, distinct level-offs occurred at specific peaks of multiples of 1,000 ft AFE as observed in Figure 33.

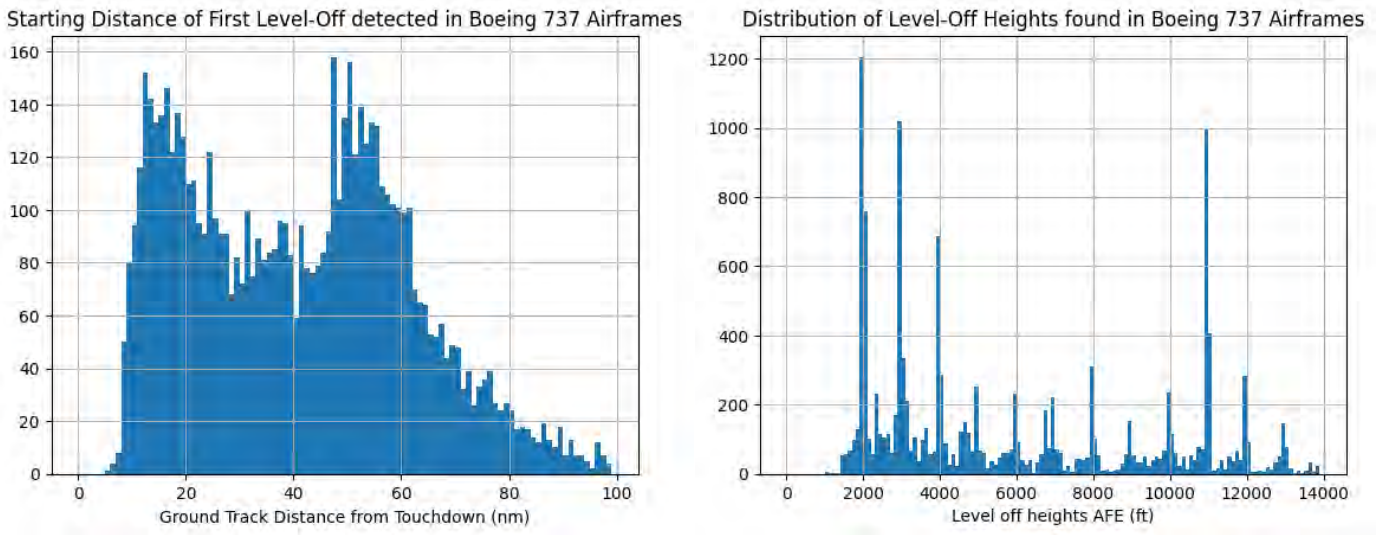

Figure 33. Analysis of level-off occurrences in Boeing 737 airframes.

The relative peaks of level-offs at 2,000, 3,000, and 4,000 ft AFE provides evidence that a clustering algorithm should distinguish this level-off behavior. The high number of level-offs occurring more than 40 nmi from touchdown or above 10,000 ft AFE also suggests that these level-offs should not be classified as belonging to a descent procedure, and should be excluded from the definition of an AEDT descent procedure. Therefore, initial clustering attempts added an additional constraint of limiting FOQA data to under 10,000 ft AFE and under 30 nmi GTD from touchdown.

Similar multi-dimensional analyses were conducted on flap position, to examine where each flap transition occurred (height, GTD, before or after landing gear deployment, level-offs, etc.) and it was determined that all Boeing 737 flights deployed a final flap setting of 25°, 30°, or 40°, which could potentially be loosely correlated with landing airport elevation and/or runway length. However, no real patterns could be distinguished from two-dimensional pair-wise plots.

With the same goal as Task 1 to cluster similar flight trajectories into the same group, a variety of methods and similarity metrics were explored. The hardest question before beginning clustering is defining a similarity metric between any two pair-wise flight trajectories. Because there is so much FOQA data and no real distinct clusters can be viewed from the trajectories (plotting all of them yields a continuous dispersion of trajectories), choosing appropriate features to cluster on is extremely difficult due to trying to balance multi-dimensional effects while trying to avoid the noise and overfitting effects of the curse of dimensionality. Scalar values like number of level-offs, GTD spent at a specific flap value, height of level-offs, can be directly normalized and used as features to cluster on, and some iterations of clustering used this metric. Another predecessor before attempting the DTW clustering method as described in Task 1 that was explored was computing a pair-wise distance metric computing the integral area between any two given trajectories' height vs. ground track plots or flap position vs ground track plots. The same issues that occur with computing similarity across two time-series (vectors) occur, as the computational cost is $O(n^2)$ where n is the number of flights to the order of 10,000 and is infeasible. The time to compute this distance matrix was reduced by just using the subset of precomputed anchor points and linear interpolation rather than the full FOQA data to calculate pairwise similarity values, and this matrix was combined with another similarity matrix of equal weight that included the following (normalized) features: number of level offs, height and distance from touchdown of landing gear deployment, and aggregate (integral GTD) height and flap setting positions.

A variety of clustering algorithms that take as input a distance or similarity matrix were briefly tested to yield preliminary results, including K-medoids, agglomerative, and density-based clustering methods. One such clustering result using K-medoids with 17 clusters (obtained by iterating increasing number of clusters and comparing silhouette scores) was then used for preliminary analysis for Investigation 3 of this task. The distribution of flight trajectories in this clustering result is shown in Figure 34.

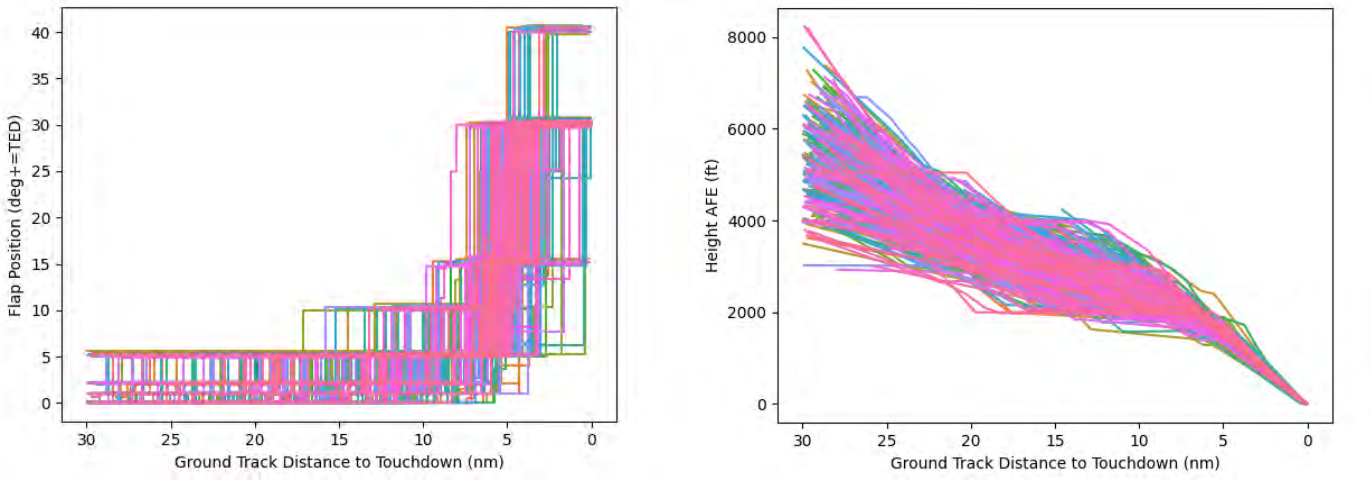

Figure 34. Cluster 1 (out of 17) trajectories plotted using K-medoids, data trained from anchor points.

The preliminary results demonstrate decent results for an initial clustering attempt. A histogram of each cluster's gross weight at touchdown shows no significant deviation between each clusters' operating weight, which is a good indicator

from an AEDT perspective because weight is not an input when defining a descent procedure. However, Figure 35 also shows additional issues with all the methods caused by the continuous distribution nature of all the trajectories. Picking appropriate hyper-parameters like number of clusters, linkage methods, epsilon (for a density-based clustering method), and more causes wildly different results. Oftentimes, the vast majority of number of flights are either classified as outliers, or on the other extreme they are all placed within only one or two clusters. Therefore, there remains additional work on trying to define both proper clustering features, perhaps by switching to DTW, as well as appropriate clustering hyper-parameters to obtain a small, finite number of distinct clusters.

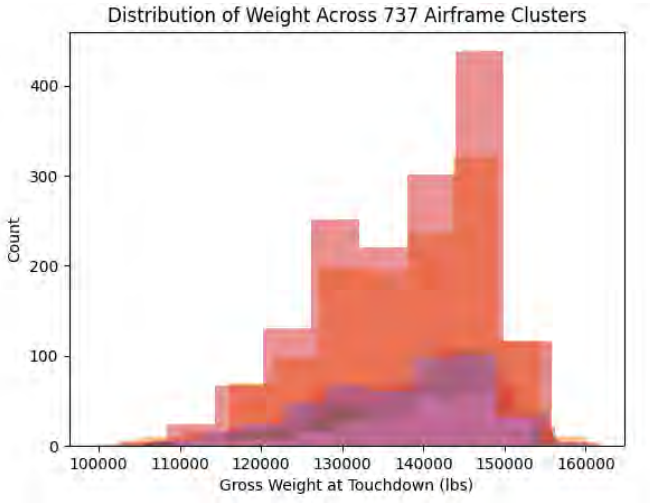

Figure 35. Histogram of final gross weight by luster from preliminary clustering analysis.

Investigation 3: Initial Clustering Analysis

1. Methodology

The analysis focused on examining the two airframes, Boeing 737-900 and Boeing 737-800, represented in the preliminary clustering results. As shown in Table 4, the Boeing 737-900 accounted for most instances, with 1,721 flights, while the Boeing 737-800 had 175 flights. Flights arriving at KATL were analyzed across all clusters simultaneously. Flap transitions were defined as the points where a new flap setting was first detected during each flight. This consistent definition facilitated accurate identification of transitions and enabled a comprehensive comparison of flap behavior across different flights and airframes.

Table 4. Airframe and its instances in initial clustering results.

Airframe	Instances
737-900	1721
737-800	175

The flap transition points for each cluster were collected and averaged to calculate the mean transition values. These mean values were used to visualize cluster-wide trends in flap deployment and transitions. The mean transition points were then marked on the plots to provide a clear representation of typical cluster behavior.

Finally, the resulting plots were overlaid with the AEDT standard trajectory. This step enabled a direct comparison between the behavior of each cluster and the standard reference trajectory provided by the AEDT, highlighting deviations or similarities in flap deployment patterns across clusters.

2. Results and Discussion

The clustering analysis identified distinct behaviors in flap transitions across the clusters, with the mean transition points providing a clear and concise representation of these patterns. The overlay of cluster-specific transition plots with the AEDT standard trajectory revealed notable differences in the timing and configuration of flap settings.

For the Boeing 737-900 airframe, specific clusters exhibited significant variations in flap transition behavior compared to the AEDT standard profile. As shown in Figure 36, certain clusters displayed earlier transitions, with flaps deployed at higher altitudes or greater distances from touchdown than the standard trajectory. In contrast, other clusters demonstrated closer alignment with AEDT expectations. The plot on the left highlight's altitude-based flap transitions, while the plot on the right illustrates transitions with respect to GTD to touchdown. The deviations in the timing of transitions, particularly for flaps 0° and 30°, emphasize operational variability across clusters.

Similarly, deviations were observed for the Boeing 737-800 airframe, particularly in the timing of transitions to higher flap positions such as 30°, underscoring the differences in operational behavior between airframes and clusters.

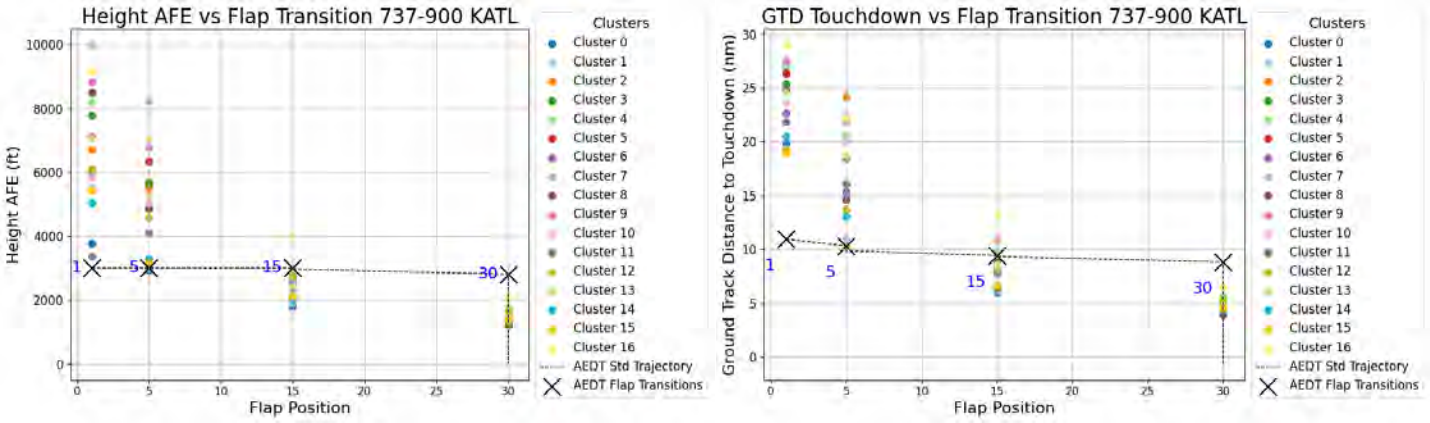

Figure 36. Comparison of altitude and GTD to touchdown vs. flap transitions for Boeing 737-900 arriving at KATL across clusters.

These results underscore the variability in operational behavior captured by the clusters and highlight the need for further investigation to quantify the impact of these deviations on fuel consumption and overall performance. The insights derived from this analysis provide a basis for refining AEDT profiles to better represent real-world operations.

Milestones
None.

Major Accomplishments
None.

Publications
None.

Outreach Efforts
None.

Awards
None.

Student Involvement
Graduate research assistants, Anushka Moharir, Hansen Lian, and Nitya Maruthuvakudi Venkatram, participated in this research.

Plans for Next Period

- Compare AEDT descent profiles starting from 6,000 ft AFE vs. 10,000 ft AFE to assess significant differences in noise contours, considering that FOQA data for arrivals typically begins at 10,000 ft, whereas the AEDT profiles start at 6,000 ft.
- Determine and implement best clustering procedures from defining a similarity metric between flights on FOQA anchor data to differentiate and define distinct descent procedures in the AEDT.

Task 3 – Full-flight Modeling

Georgia Institute of Technology

Objectives

This task aims to improve the usability of the full flight modeling within the AEDT without employing the often complicated and time-consuming process of using the sensor path functionality that is the current standard for AEDT. Over the past years, this task has completed a validation process where its model outputs were compared and validated against the real/historical flight data from the CY 2019 FOQA dataset. Additionally, it examined the characteristics and behavior of thread track data (TTD) and the CY 2023 FOQA dataset, which includes a greater volume of flight data than previous FOQA datasets, to derive insights into flight patterns. The findings from these analyses in prior years have redefined AEDT's potential to support straightforward statistical modeling for analyzing national airspace system flight frequencies, as well as fuel burn and emissions for runway-to-runway operations.

This year's study evaluated the features (parameters) influencing fuel burn using real-world flight data, including TTD and the FOQA dataset, to develop a simplified model for predicting fuel burn in both en-route and runway-to-runway operations. The study provides a foundation for creating efficient and simplified regression or machine learning models by identifying essential variables that considerably impact fuel consumption. This alternative approach offers a practical solution for estimating fuel burn with reasonable accuracy while reducing complexity and eliminating the need for detailed trajectory data.

Another study which is currently ongoing in this task involves using TTD and FOQA CY 2023 data to analyze and compare AEDT's performance models with respect to their calculated fuel burn and emissions metrics. Employing clustering of flights and modeling them using the Sensor Path Import (SPI) tool in the AEDT, this study ultimately aims to use the National Inventory (NAS) database as a basis for recommendations for future improvements in the tool's features.
This report is structured into three distinct sub-sections, each comprising its methodology, findings, and discussion:

1. Correlation analysis utilizing real-world flight data to identify key variables influencing fuel burn.
2. Development of regression and machine learning models to predict fuel consumption for both en-route and runway-to-runway operations.
3. Initial fuel burn analysis of AEDT using clustered core path and real-world flight data.

Research Approach

Investigation 1: Correlation Analysis Utilizing Real-World Flight Data to Identify Key Variables Influencing Fuel Burn

1. Methodology

Developing an accurate and efficient fuel burn prediction model requires identifying the most influential variables. Including all variables is computationally expensive, thus understanding the relationships of key variables is critical for feature selection. Correlation analysis helps measure these relationships, allowing us to select the most relevant variables, which enhances model accuracy while reducing computational complexity.

This study conducted a correlation analysis to determine the key variables affecting fuel burn during the en-route phase of flights. The correlation coefficient, ranging from +1 to -1, measures the strength and direction of the relationship between two variables. A coefficient of +1 indicates a perfect positive correlation, while -1 indicates a perfect negative correlation. A coefficient of 0 signifies no linear relationship between the variables. Our study utilized two data types from the FOQA dataset to analyze fuel burn. The first type is FOQA metadata, which includes essential information related to airports and aircraft, such as departure and arrival airports, runways, aircraft type, engine type, and departure time. From this information, the ASCENT Project 054 team derived each flight's month and season to account for potential seasonal variations in fuel burn. This metadata establishes a foundational framework for each flight, allowing us to analyze fuel burn in relation to specific aircraft characteristics and operational information.

The second type of data is trajectory data, which provides information on aircraft performance and weather conditions throughout the flight. Our analysis focuses specifically on the en-route phase, defined as the period when the aircraft is flying at an altitude of 10,000 ft mean sea level or higher, as it typically represents the longest and most fuel-intensive segment of the flight.

First, the cruise segments were identified for each flight to analyze the trajectory data. Then extracted key metrics were extracted, such as en-route fuel burn, flight time, and flight distance, by combining values across all cruise segments. This allowed our team to focus on the most critical phase of fuel burn. The ASCENT Project 054 team also extracted features related to aircraft performance and weather conditions, such as ground speed, vertical speed, wind speed, wind direction, temperature, pressure, and air density, which are known to influence fuel burn.

To prepare these data points for correlation analysis, we used statistical measures to summarize each performance and weather variable, including median, mean, minimum, maximum, and the 25th and 75th percentiles. This provided a comprehensive profile of each factor, capturing central tendencies and variability. By integrating metadata and trajectory data, our team gained more profound insights into how aircraft characteristics, operational details, and environmental factors collectively influence fuel burn during the cruise phase.

2. Results and Discussion

Using real-world flight data, we identified the most significant variables influencing en-route fuel burn. Figure 37 presents the results of this study based on CY 2023 FOQA dataset, without splitting flight data by city pair. In Figure 37, the analysis highlights key positive correlations between features and en-route fuel burn, showing that variables such as en-route weight, en-route trip distance, and en-route trip time have strong positive correlations. As these values increase, fuel consumption also rises, making them crucial inputs for developing an accurate predictive model.

On the other hand, understanding features with negative correlations is just as important for effective modeling. For example, average air density and average temperature during the cruise phase of flights are strongly negatively correlated with fuel burn. Higher air density or lower temperatures can help reduce fuel burn. These weather-related factors play a significant role in improving fuel efficiency under certain conditions. By analyzing both positively and negatively correlated features of flight performance and weather conditions, valuable insights are gained into how these variables interact, leading to the development of a more effective fuel burn prediction model.

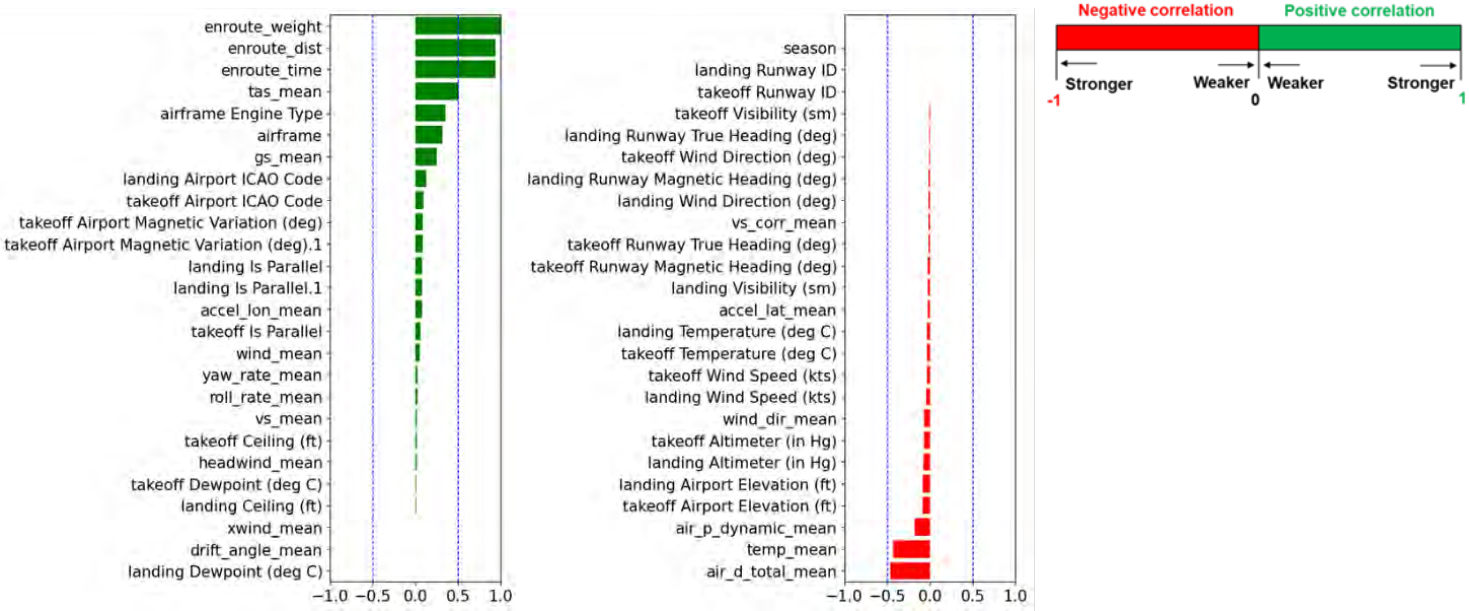

Figure 37. The results of the correlation analysis on en-route fuel burn using CY 2023 FOQA.

Headwinds are commonly assumed to increase fuel consumption during flight, as stronger headwinds add to aerodynamic resistance. However, our correlation study did not confirm this expected relationship. To better understand this discrepancy, our team conducted a detailed analysis of the relationship between headwinds and en-route fuel burn.

Figure 38 shows a scatter plot illustrating the relationship between en-route fuel burn and the average headwind during the cruise phase of flights. The plot, based on the CY 2023 FOQA dataset, reveals a low correlation coefficient of 0.02, indicating no significant relationship between these variables. While it is intuitive to expect stronger headwinds to increase fuel consumption due to higher aerodynamic resistance, the data do not support this assumption.

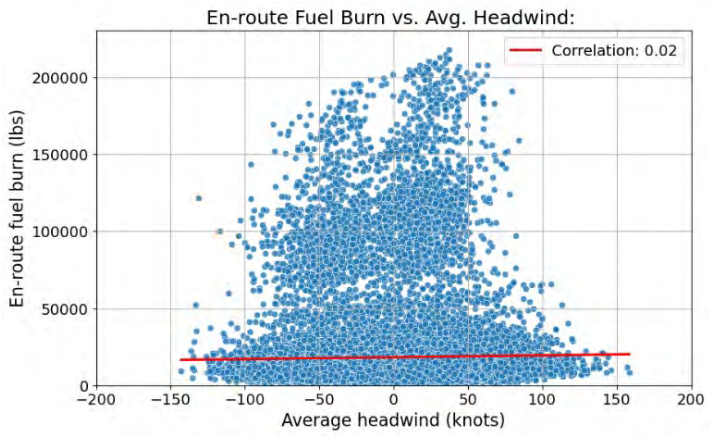

Figure 38. Scatter plot of the relationship between en-route fuel burn and headwind.

This finding suggests that other factors, such as aircraft type, operational procedures, route characteristics, and aircraft weight, play a more significant role in determining fuel consumption. The absence of a clear relationship between headwind and fuel burn underscores the complexity of fuel efficiency, which a single variable cannot fully explain. A more comprehensive analysis that accounts for these additional factors is necessary to better understand the dynamics of fuel consumption during flight.

To enhance the clarity of our analysis, our team first normalized en-route fuel burn by dividing it by flight distance. This step reduces the influence of varying flight distances, allowing us to focus more effectively on the relative impact of headwinds. By standardizing fuel burn in this manner, the specific effect of headwinds can be isolated while minimizing the influence of other variables. With this normalization, our team then examined the relationship between en-route fuel burn per unit distance and headwind to gain deeper insights.

When analyzing specific aircraft types, the relationship between headwind and fuel burn becomes more distinct. For instance, Figure 39 and Figure 40 highlight the Boeing 737-900 and Airbus A321-200, respectively, showing strong positive correlations between fuel burn per nautical mile and average headwind, with correlation coefficients of 0.66 and 0.75. These results indicate that as the headwind increases, fuel consumption per unit distance rises, a finding that aligns well with aerodynamic principles.

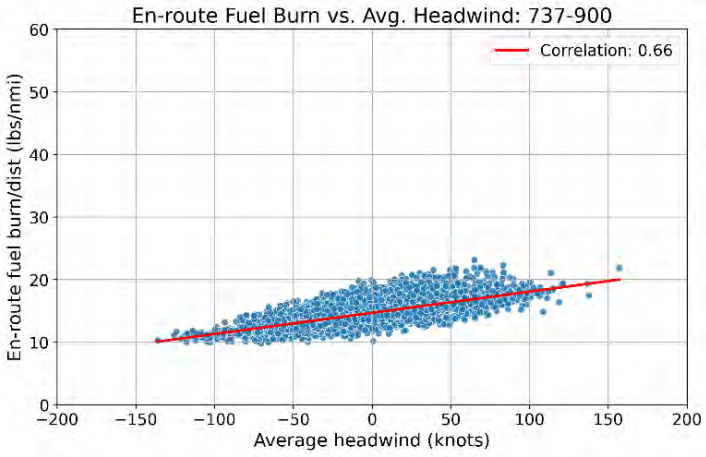

Figure 39. Scatter plot of the relationship between en-route fuel burn per distance and headwind for the Boeing 737-900.

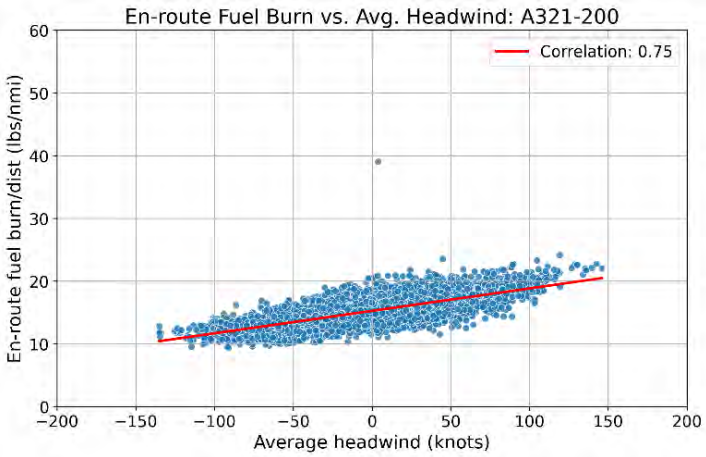

Figure 40. Scatter plot of the relationship between en-route fuel burn per distance and headwind for the Airbus A321-200.

The stronger correlations observed in these individual aircraft analyses suggest that headwind significantly impacts fuel burn when factors such as aircraft type are controlled. In contrast, the aggregated dataset may obscure this relationship due to variability in aircraft type, operational procedures, and other influencing factors. By focusing on specific aircraft types, we can better understand the direct effects of headwinds on fuel consumption, offering more precise and actionable insights for optimizing flight operations.

Investigation 2. Development of Regression/Machine Learning Models to Predict Fuel Burn for Both En-Route and Runway-to-Runway Operations

1. Methodology

The current approach to calculating fuel consumption in the AEDT relies on the SPI tool, which can be both complex and time-consuming. This task aims to develop a simpler, more reliable alternative using regression or machine learning techniques to provide an efficient, accurate fuel estimates alternative to the SPI process. The ASCENT Project 054 team aims to create a predictive model that complements the SPI tool, providing quick and precise predictions with reduced computational demands.

In this study, our team implemented three models— (1) linear regression, (2) decision tree, and (3) random forest—to predict aircraft fuel consumption and identify the most accurate predictor. Each model was evaluated using standard performance metrics, including mean absolute error (MAE), mean squared error (MSE), RMSE, and the coefficient of determination (R^2).

MAE measures the average magnitude of errors between predicted and actual values, with lower values indicating more accurate predictions. MSE calculates the average of squared differences, where a lower value also signifies better performance. RMSE, the square root of MSE, offers an error value in the same unit as the target variable, aiding interpretation. R^2 reflects how well the model explains variability in the target, with values closer to 1 indicating a better fit.

$$MAE = \frac{1}{n}\sum_{i=1}^{n}|Fuel\ Burn_{Actual} - Fuel\ Burn_{Predicted}| \quad \text{(Eq. 3)}$$

$$MSE = \frac{1}{n}\sum_{i=1}^{n}(Fuel\ Burn_{Actual} - Fuel\ Burn_{Predicted})^2 \quad \text{(Eq. 4)}$$

$$RMSE = \sqrt{MSE} \quad \text{(Eq. 5)}$$

As mentioned earlier, this study implemented three types of predictive models. The first is the linear regression model, which assumes a linear relationship between features and fuel consumption. This model is straightforward to interpret and provides clear insights into factors influencing fuel use; however, it may struggle with predictive accuracy in the presence of nonlinear patterns.

The second model is the decision tree, which effectively captures complex nonlinear relationships by iteratively splitting the data and making decisions at each node. This approach allows for insights into the relative importance of each feature, though decision trees are prone to overfitting, making them sensitive to variations in the training data.

The final model, the random forest, addresses this limitation by aggregating multiple decision trees, thereby reducing overfitting and enhancing generalization. By combining the outputs of many trees, random forests capture complex feature interactions, resulting in improved robustness and accuracy of predictions.

The CY 2023 FOQA dataset was utilized to develop predictive models for fuel consumption. To align with the objective of enhancing the AEDT's functionality for fuel burn estimation, the initial approach incorporated the same input parameters used in the SPI tool's calculations. Furthermore, a new feature, was introduced:

- *Route Efficiency:* Defined as the ratio of the great-circle distance to the en-route distance flown.

Key features were identified from the dataset to construct predictive models for both en-route and runway-to-runway fuel consumption. These input features were categorized into two primary groups:

- *Airport and Aircraft Performance Parameters:* Departure airport, arrival airport, takeoff runway, landing runway, airframe, airframe engine type, takeoff direction, landing direction, month, season, flight time, flight distance, and route efficiency.
- *Weather Parameters:* Headwind, wind speed, wind direction, temperature, pressure, and air density.

The initial model focused on predicting en-route fuel consumption to reduce the impact of air traffic control (ATC) procedures at departure and arrival airports. This approach was expanded to include the entire runway-to-runway operation, enabling a more comprehensive estimation of fuel consumption.

The dataset was partitioned into two subsets, with 80% allocated for training and 20% for testing. This systematic division ensured a robust foundation for model validation and performance evaluation.

2. Results and Discussion

This study employed three algorithms (such as linear regression, decision tree, and random forest) to predict fuel burn. The initial model focused on en-route fuel burn to minimize the influence of air traffic control (ATC) procedures at departure and arrival airports. Key airport and aircraft performance features and weather variables from the CY 2023 FOQA dataset were used to train and validate the model.

The performance of the linear regression model is illustrated in Figure 41. In Figure 41(left), the plot shows the relationship between actual and predicted fuel burn, with the red line representing the ideal fit. In Figure 41(right), the plot displays residuals, which measure the differences between actual and predicted values. While the residuals are generally centered around zero, they exhibit broader dispersion and clear patterns, indicating that the model struggles to capture the relationship between input features and fuel burn fully. The residual patterns confirm the model's limitations in addressing the complexities of fuel burn, such as those influenced by varying weather conditions and ATC directives. These challenges are especially evident in longer flights, where external factors like changing winds and ATC rerouting become more pronounced, reducing prediction accuracy.

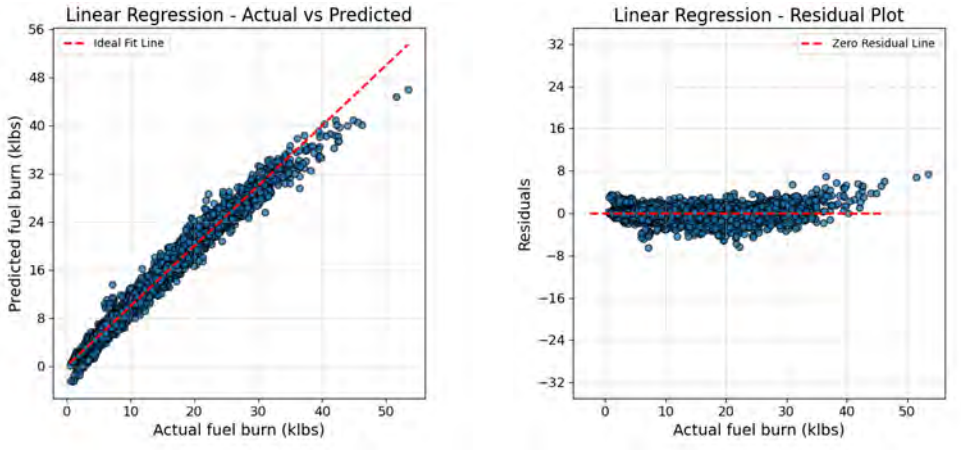

Figure 41. Linear regression analysis for fuel burn prediction.

The linear regression model showed the lowest predictive accuracy among the algorithms tested. Deviations were particularly pronounced at higher fuel burn levels, where predictions consistently underestimated or overestimated actual values. Table 5 summarizes the performance metrics for en-route fuel burn prediction. Among the models tested, random forest performed the best. Random forest achieved the lowest errors, with a MAE of 0.504, MSE of 0.756, and RMSE of 0.870. Additionally, it had the highest R^2 score of 0.992, indicating that it predicts fuel burn with exceptional accuracy and reliability.

Table 5. Comparison of performance metrics for en-route fuel burn predictions.

Metric	Linear Regression	Decision Tree	Random Forest
MAE	0.849	0.690	0.504
MSE	2.566	1.513	0.756
RMSE	1.601	1.230	0.870
R^2	0.972	0.983	0.992

These results demonstrate that the decision tree and random forest models are more effective than linear regression for predicting en-route fuel burn. Their strength lies in their ability to capture complex, nonlinear relationships between variables, resulting in significantly higher accuracy. Based on these findings, our team further developed these two models for fuel burn prediction in runway-to-runway operations.

Figure 42, Figure 43, and Table 6 illustrate the performance of prediction models for both en-route and runway-to-runway operations using the decision tree model. Unlike the previous investigation, this study utilized only airport and aircraft performance features to train and evaluate the models. Table 6 summarizes the predictive performance for fuel consumption during the en-route and runway-to-runway phases. The runway-to-runway model achieved slightly lower values for MAE, MSE, and RMSE compared to the en-route model, indicating marginally higher accuracy. Both models demonstrated strong predictive reliability, achieving a high R^2 value of 0.984.

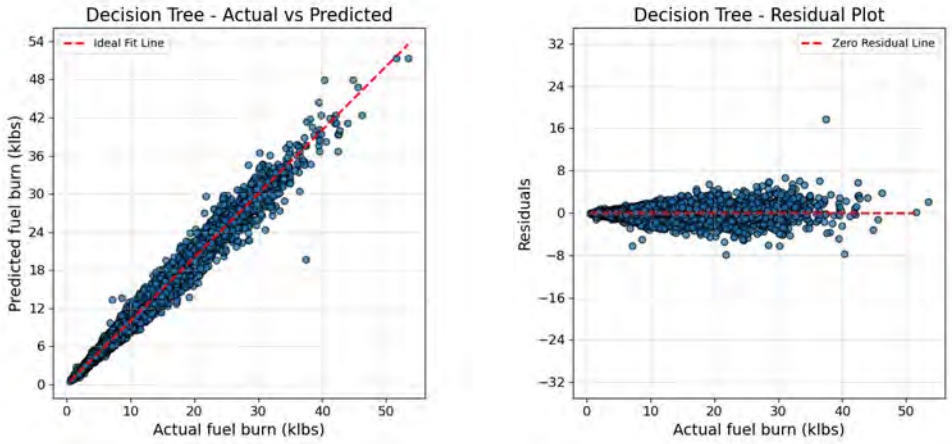

Figure 42. Decision tree for en-route fuel burn prediction.

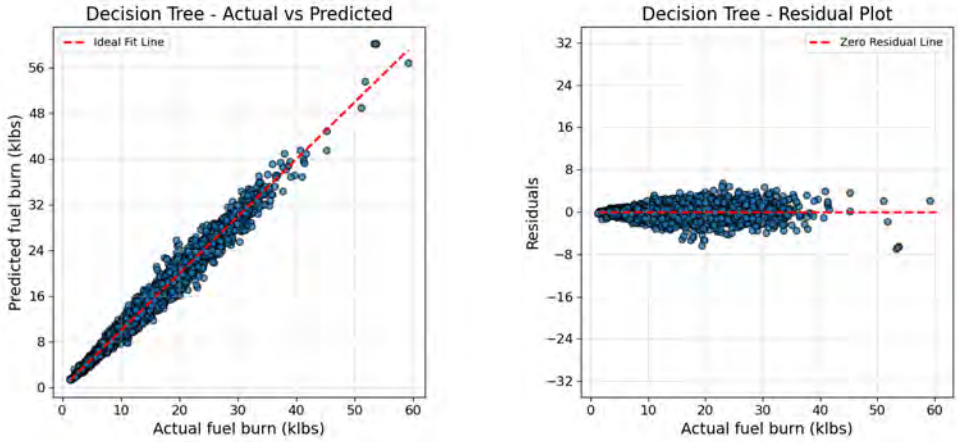

Figure 43. Decision tree for runway-to-runway fuel burn prediction.

Table 6. Comparison of performance metrics for decision tree.

Metric	En-route	Runway-to-Runway
MAE	0.641	0.632
MSE	0.971	0.826
RMSE	0.985	0.909
R^2	0.984	0.984

Overall, the results indicate that the runway-to-runway model provides slightly better performance predicting fuel consumption. This suggests that both approaches are robust and reliable, with the runway-to-runway model offering a slight edge in accuracy.

Similar to the Decision Tree algorithm, the results of the Random Forest's performance metrics are shown in Figure 44, Figure 45, and Table 7. Table 7 summarizes the predictive performance for fuel consumption during the en-route and runway-to-runway phases. The runway-to-runway model achieved slightly lower values for MAE, MSE, and RMSE compared to the en-route model, indicating marginally higher accuracy. Overall, the results indicate that the runway-to-runway model provides slightly better performance predicting fuel consumption. This suggests that both approaches are robust and reliable, with the runway-to-runway model offering a slight edge in accuracy.

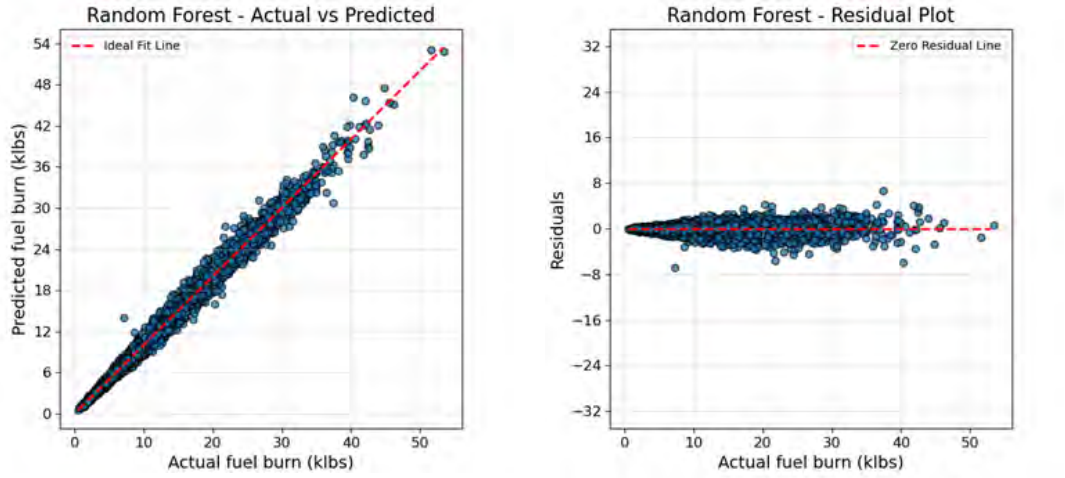

Figure 44. Random forest for en-route fuel burn prediction.

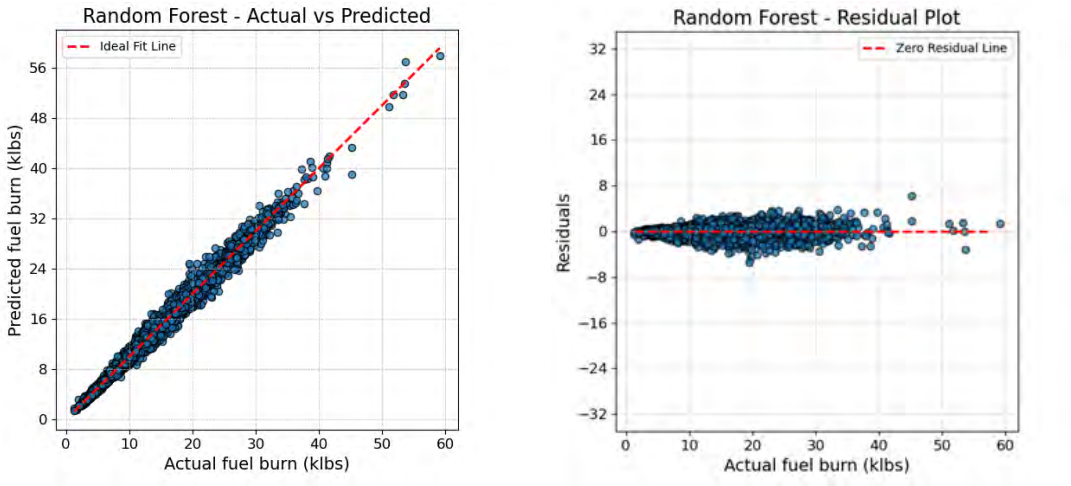

Figure 45. Random forest for runway-to-runway fuel burn prediction,

Table 7. Comparison of performance metrics for the random forest model.

Metric	En-route	Runway-to-Runway
MAE	0.459	0.465
MSE	0.484	0.475
RMSE	0.696	0.689
R^2	0.992	0.991

Investigation 3: Initial Fuel Burn Analysis of the AEDT Using Clustered Core Paths and Real-World Flight Data

1. Methodology

This study aims to build upon the work done by the team in 2021, wherein a fuel burn study was conducted using FOQA CY 2021 data to analyze the AEDT's performance models.

The study began with choosing a set of city pairs to focus upon. For the purposes of the initial study, a total of 12 city pairs were picked. Then, flights belonging to these city pairs were extracted from the FOQA CY2023 dataset. Of these, the city pair of Atlanta International Airport (KATL) and LaGuardia Airport (KLGA) had the most flights, with 263 flights between the outbound and return routes. The city pair with the fewest flights was Kaitaia Airport (KAT) and Minneapolis-Saint Paul international Airport (KMSP), with only 91 flights spread between the outbound and return routes. Table 8 details the composition of the city pairs and number of flights extracted.

Table 8. Total flights selected from FOQA data for selected city pairs.

City Pair	Number of Flights	City Pair	Number of Flights	Great-Circle Distance (nmi)
KATL-KLAS	76	KLAS-KATL	68	1,518
KATL-KLGA	117	KLGA-KATL	146	662
KATL-KMSP	44	KMSP-KATL	47	788
KATL-KSEA	85	KSEA-KATL	98	1,896
KATL-KSLC	105	KSLC-KATL	111	1,382
KLAS-KSLC	56	KSLC-KLAS	66	320

KATL = Hartsfield-Jackson Atlanta International Airport
KLAS = Harry Ried International Airport (Las Vegas, Nevada)
KLGA = LaGuardia Airport (Elmhurst, New York)
KMSP = Minneapolis-Saint Paul International Airport
KSEA = Seattle-Tacoma International Airport

It must be noted that FOQA flights are only a subset of the total flights flown by our partner airline. Additionally, certain city pairs may have a higher number of flights due to factors such as flights generally having higher descent rates to the destination airport.

Once the flights were extracted using an automated Python® script, the 100 trajectory points for each flight were picked based on the great-circle distance of the city pair that flight belonged to. These points are saved, after which a clustering algorithm is performed on them to generate clusters. The previous work done by the team used the Density-Based Spatial Clustering of Applications with Noise (DBSCAN) algorithm. However, as DBSCAN is more susceptible to noise, an alternative algorithm was required. The Hierarchical Density-Based Spatial Clustering of Applications with Noise (HDBSCAN) algorithm is more flexible than DBSCAN and robust against noise, so it was chosen to be implemented into the approach.

® Python is a registered trademark of Python Software Foundation, Beaverton, Oregon.

The HDBSCAN algorithm generates clusters based on grouping of points by comparing the distances between those points. DTW is used to calculate the distance between trajectories in each city pair's flights.

In contrast to DBSCAN, which required two parameters as inputs (thereby two variables affecting clustering results), HDBSCAN just requires a single parameter: the minimum number of points belonging in the vicinity to be considered as a 'core point' (the parameter is called min_samples). To find an optimal value of min_samples, the clustering algorithm was iterated against min_samples values ranging from 2 to 20. Each iteration of the algorithm generates two useful metrics that can be used to compare the goodness between two different results. The first, silhouette score, ideally needs to be as high as possible. The second, the Davies-Bouldin score, needs to be close to 0.8 for that cluster to be called good. The values of these two metrics were compared for each iteration, and an optimal min_samples value was selected for each city pair.

The generated clusters for each city pair are then used to produce a core path, which is the median path of all the flight trajectories present in that cluster. This core path is then converted into operations and trajectory files by the Python script, to be imported into the AEDT using the SPI tool. Finally, a fuel consumption study is performed on the core paths, and results are analyzed.

2. Results and Discussion

The cumulative fuel burn is compared between the generated FOQA core paths and the same core paths modeled in the AEDT. The SPI tool was used to import the core paths, after which a fuel consumption study is run, using the Base of Aircraft Data, version 4 (BADA4) model and Modern-Era Retrospective analysis for Research and Applications, version 2 (MERRA-2) weather data. The cumulative fuel burn is computed for the modeled flights in the AEDT, subtracting the taxi-out and taxi-in phases.

As seen in Figure 46, the clustering algorithm does a satisfactory job in identifying grouped flight trajectories and generates clusters based on them. Proceeding on to inspecting the cumulative fuel burn for each city pair, Table 9 shows a comparison of the cumulative fuel burn computed by the AEDT and the fuel burn from the FOQA core path flight data for each city pair.

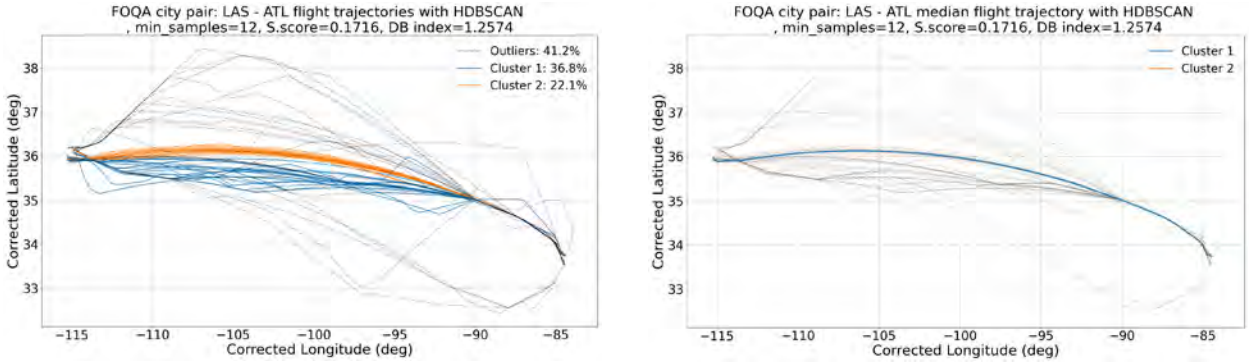

Figure 46. Clusters generated for KLAS-KATL (left); chosen core path for the city pair (right).

Table 9. Comparison of cumulative fuel burn between FOQA data and AEDT output for selected city pairs.

City Pair	Airframe	Cum. Fuel Burn (FOQA) (lb)	Cum. Fuel Burn (AEDT) (lb)	Difference in Fuel Burn (%)
KATL-KLAS	Airbus A321-100	28,103	26,028	-7.4
KLAS-KATL	Boeing 737-900	26,845	27,213	1.3
KATL-KLGA	Airbus A321-100	11,817	11,696	-1.0
KLGA-KATL	Airbus A321-100	13,679	13,817	1.0
KATL-KMSP	Boeing 757-200	14,960	14,078	-5.9
KMSP-KATL	Boeing 737-900	13,804	11,268	-18.44
KATL-KSEA	Boeing 737-900	28,512	26,643	-6.5
KSEA-KATL	Boeing 737-900	23,207	24,242	4.5
KATL-KSLC	Airbus A321-100	25,028	21,424	-14.4
KSLC-KATL	Airbus A350-900	32,210	35,937	11.6
KSLC-KLAS	Boeing 737-900	6,111	5,406	-11.5
KLAS-KSLC	Airbus A321-100	7,743	6,591	-14.8

KATL = Hartsfield-Jackson Atlanta International Airport
KLAS = Harry Ried International Airport (Las Vegas, Nevada)
KLGA = LaGuardia Airport (Elmhurst, New York)
KMSP = Minneapolis-Saint Paul International Airport
KSEA = Seattle-Tacoma International Airport

While a few city pairs have a low difference in cumulative fuel burn between the FOQA data and AEDT output, five city pairs show a relatively higher percentage of difference. The city pair KATL-KLGA is the best-performing city pair with only a 1% difference in fuel burn between the outbound and return routes. However, two city pairs, KATL-KSLC and KSLC-KLAS, show a high difference in fuel burn for both the outbound and return routes. This may arise due to flights between the two city pairs having much higher deviations between the 'optimal' trajectory and the actual flight routes. Figure 47 shows the FOQA flights modeled between the two city pairs.

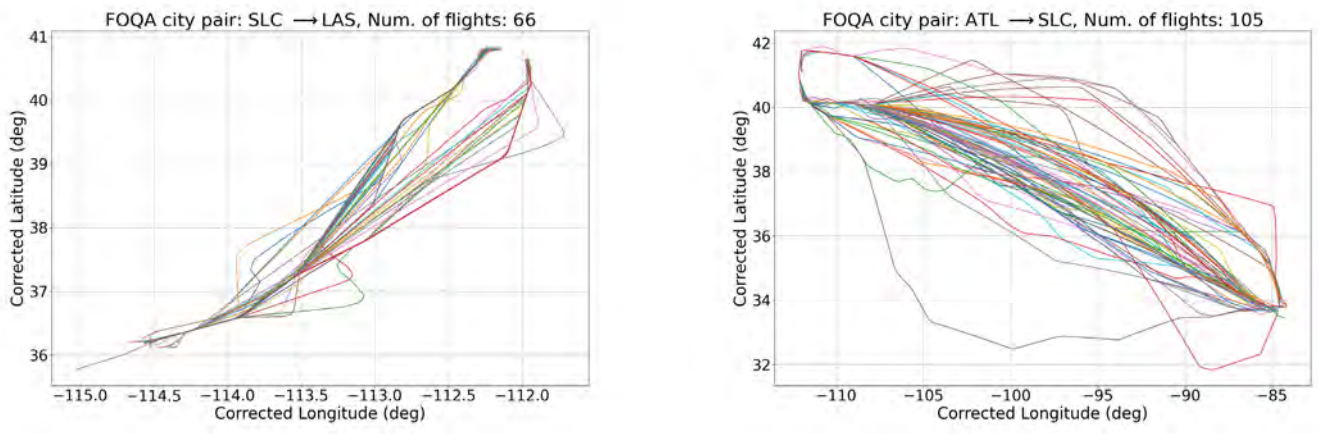

Figure 47. FOQA flights between KSLC to KLAS (left), KATL to KSLC (right).

The findings of this initial study necessitate a revisiting of the data and process to investigate the causes behind discrepancies in fuel burn between the real-world flight data and the computed output generated by the AEDT. As such, that remains to be the primary task before subsequent analysis of TT flights using a similar methodology, which can then be used for further work and recommendations.

Milestones
None.

Major Accomplishments
- Conducted a correlation analysis of en-route fuel burn using real-world flight data, including the TTD and FOQA datasets
- Developed linear regression/machine learning models to predict fuel burn using airport and aircraft performance features

Publications
None.

Outreach Efforts
None.

Awards
None.

Student Involvement
Graduate research assistants, Hyungu Choi and Yash Vinod, participated in this task.

Plans for Next Period
- Enhance the accuracy of fuel burn predictions for runway-to-runway operations by incorporating MERRA-2 weather data. To achieve this, the ASCENT Project 054 team needs to explore and identify effective methods for integrating MERRA-2 data into the modeling process.
- Complete the fuel burn analysis through clustering real-world flight data during the next period.
    - Task 1 will determine the exact cause behind the higher differences in cumulative fuel burn for some FOQA city pairs as opposed to others. Next, the final optimized FOQA core paths will be leveraged to cluster TT flights. The approach planned is to use the median FOQA flight from the cluster(s) for each city pair as a basis to shortlist and extract TT flights for the same city pair. This ensures that the extracted flights belong to the same aircraft type and fly during reasonably similar timelines, for more effective comparison between the two datasets.
    - Once the TT flights are extracted, their trajectories will be collected, and they will be clustered using a similar algorithm to the one used for the FOQA dataset. Iterations will be performed to find the optimal input parameters in this case too.
    - After the clustering is executed, the median of the clustered TT flights is used to produce the TTD core path of that city pair, which will be run as a fuel consumption study in the AEDT after importing it using the SPI tool. The fuel burn and other metrics can then be compared to the actual fuel burn present in the FOQA core path data.

Task 4 – System Testing and Evaluation of AEDT
Georgia Institute of Technology

Objective
To provide the best possible environmental impact modeling capabilities in the AEDT, the FAA Office of Environment and Energy continues to develop the AEDT by improving existing modeling methods and data and adding new functionalities. The FAA Office of Environment and Energy seeks an independent effort in system testing to evaluate the accuracy, functionality, and capabilities of the AEDT, and support future model development. The objective of this task is to provide

the FAA with high-quality systematic testing and evaluation of the capabilities of the AEDT, and to identify gaps in the tools' functionality and areas for further development.

Research Approach

MERRA-2

User reports indicated an incorrect retrieval of weather data during annualizations owing to the utilization of local rather than Coordinated Universal Time (UTC) time during the preparatory phase. The cause was identified as a bug in SQL .NET structure which inadvertently reverted UTC to local time.

These reports were accompanied by further problems arising from the presence of unexpected zero values for altitude during the descent phase of sensor path operations. This issue was traced to the unwitting use of altitude values from the departure phase during arrival.

Examination of the aforementioned user submissions additionally showed a substantial disparity in performance across 11 metrics encompassing both weather-related and conventional performance information. Figure 48 shows a notional example of observed disparity in relative humidity.

A study with 77 sensor path operations for BADA3 and BADA4 respectively spanning primarily Airbus and Boeing aircraft was created with flights from John F. Kennedy International Airport (JFK)-LAX was created and succeeded in recreating the outlined bugs. The worst cases of disparity across BADA3 and BADA4 were isolated for further analysis and determined metrics such as humidity, wind-speed and thrust as further vectors of assessment.

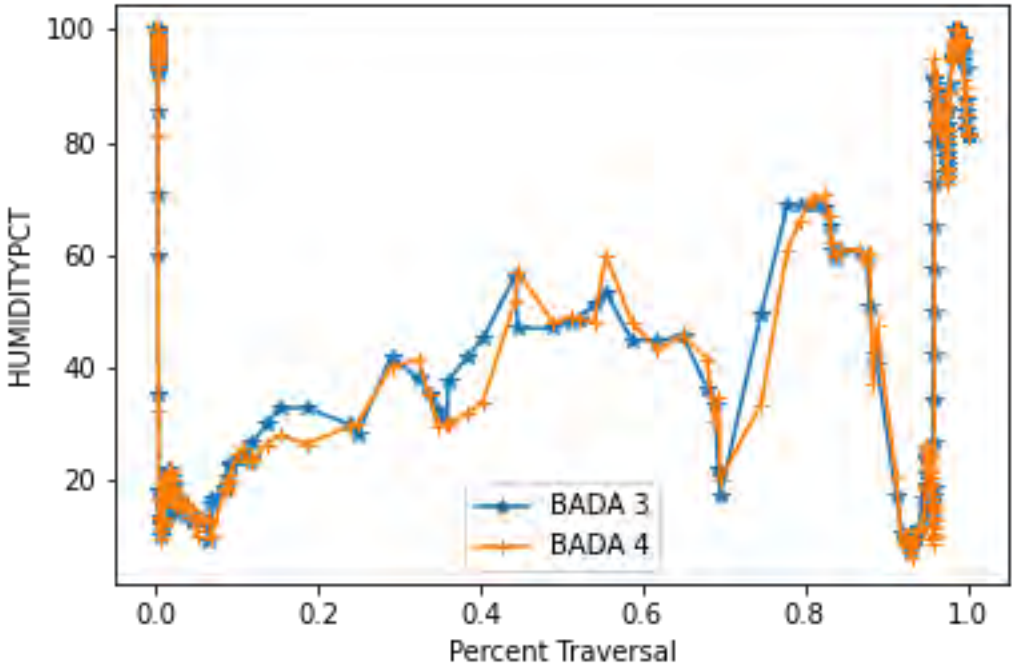

Figure 48. Initially perceived disparity in humidity.

The identified offset in performance metrics were summarily addressed, alongside the reported misuse of local time and incorrect zero altitude values in operations. This has resulted in a current absence of disparity between BADA3 and BADA4 sensor path operations.

Ground Support Equipment/Auxiliary Power Unit Pollutant Metric Testing
AEDT Version 3f (AEDT 3f) expanded the purview of its calculations to encompass greenhouse gases (GHG) based on existing information from major airport emissions sources. These additions were supplemented by alterations to the methods by which the emissions auxiliary power unit (APU) and ground support equipment (GSE) were derived.

The impact of this new methodology was examined via the comparison of emissions inventories across AEDT Version 3e (AEDT 3e) and AEDT 3f in Study Dulles International Airport and Study Rhode Island T.F. Green International Airport (TVD) for all preexisting GSEs and APUs. Initial testing showed GHG values within the expected range and parity across shared metrics for APUs; however, incorrect GHG values and variation beyond an acceptable range for existing inventory metrics in GSE tests.

Further examination revealed two sources of error, namely the improper use of GSEs past their useful life in operations and the improper placement of values in the SQL emissions results table despite correct calculations. Iterations made to address these bugs resulted in an accurate display of emissions value and the exclusion of GSEs operating beyond their prescribed life span.

Tropopause Testing
AEDT 3f heightened the fidelity of its performance calculations by incorporating the meteorological features of the tropopause, providing a more accurate estimate of properties for flights reaching beyond an altitude of 36,000 ft.

The implementation of this feature was tested by the creation of two BADA3 and nine BADA4 operations in both AEDT 3e and AEDT 3f as points of comparison for flights entering the tropopause.

An examination of performance metrics in Figure 49 and Figure 50 alongside temperature values in SQL results tables indicate a proper implementation of the tropopause, owing to the identical ground speeds, deviations in thrust stemming from density differences in the tropopause, and the presence of updated temperature values in AEDT 3f's outputs.

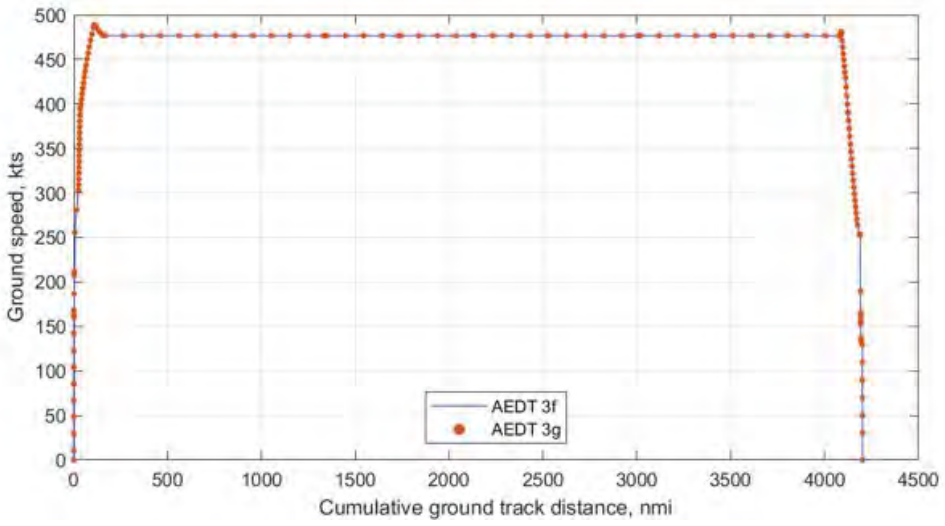

Figure 49. Comparison of ground speed across AEDT versions.

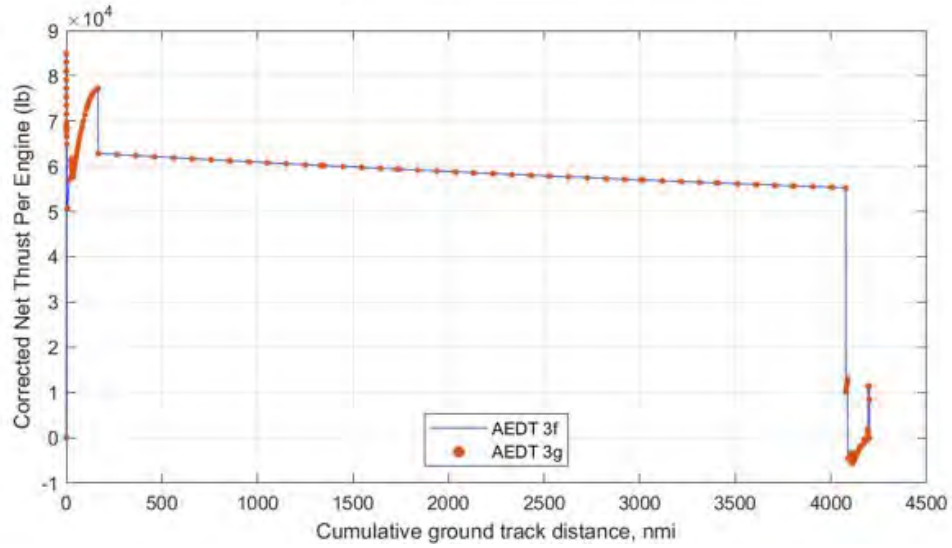

Figure 50. Comparison of thrust across AEDT versions.

TALA/TALC Testing

AEDT 3f modified existing formulas to implement more accurate methods for the calculation of time above A-weighted sound level and time above C-weighted sound level (TALA and TALC) via the incorporation of decibel values from neighboring space and time segments.

The proper functionality of the formula was tested through the creation of single and (ten) aggregated operations of Boeing 737-800 and AIrbusA330-211 arrivals at LAX across a range of receptor density, with the intent to ensure near identical TALA and TALC (on a per-aircraft basis) despite aircraft and receptor additions.

Both Figure 51 and Figure 52 show a proper implementation of the new sound calculation scheme which is invariant in the face of receptor and operation count alterations. Minor graphical user interface (GUI) issues (specifically contour distortion) caused by using the AEDT zoom feature were also resolved during the testing process.

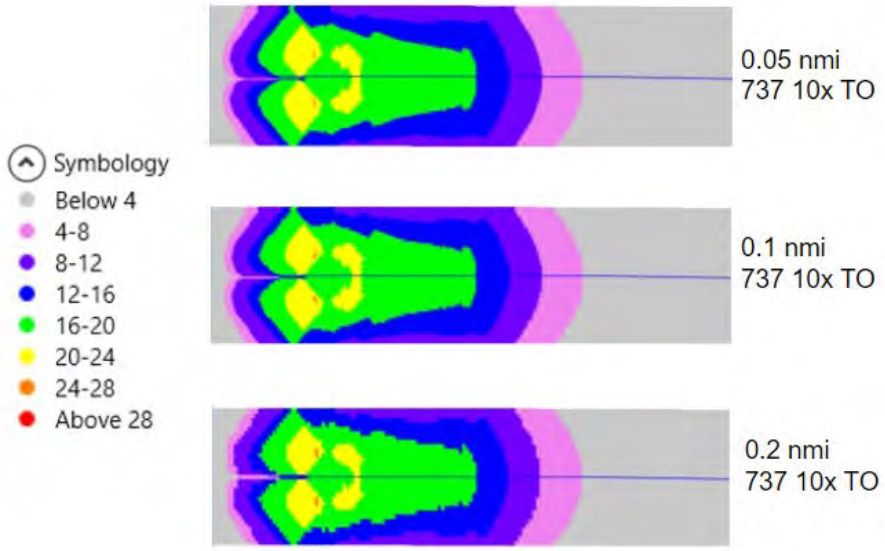

Figure 51. TALA contours for varying Boeing 737 operation count and receptor fidelity.

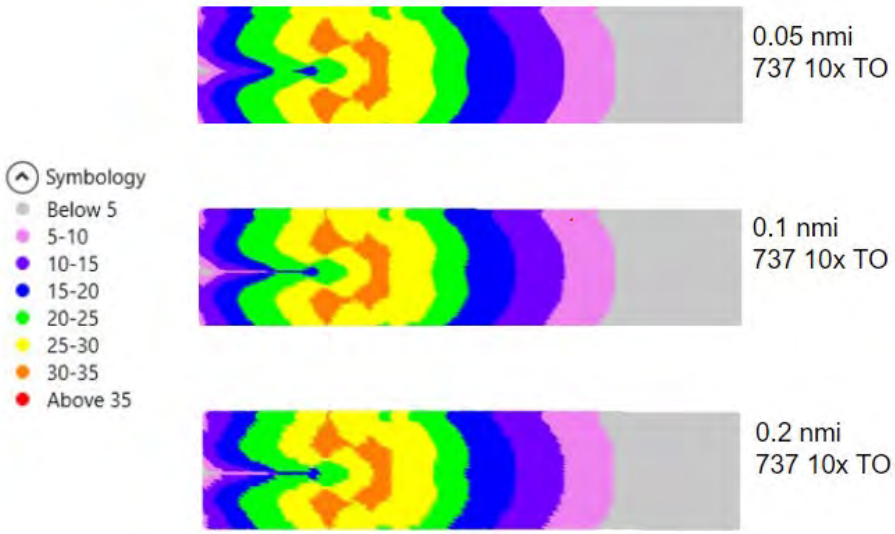

Figure 52. TALC contours for varying Boeing 737 operation count and receptor fidelity.

Milestones
None.

Major Accomplishments
None.

Publications
None.

Outreach Efforts
None.

Awards
None.

Student Involvement
Graduate research assistants, Santusht Sairam and Bogdan Dorca participated in this task.

Plans for Next Period
- Continue system testing efforts to support ongoing AEDT development.

Task 5 – Supersonic Transport Modeling in the Aviation Environmental Design Tool
Georgia Institute of Technology

Objectives
The supersonic transport (SST) modeling task has two primary objectives:
- Develop a predictive model for the propulsion system, encompassing thrust, fuel flow, engine dimensions, weight, and noise generation, and additionally accounting for variations in Mach number, altitude, and throttle setting, to enable comprehensive analysis of performance metrics such as fuel burn, gross weight, takeoff field length, and environmental factors including noise and emission.
- Generate parametric drag polar models for the optimized vehicle that capture aerodynamic performance across the entire flight envelope as a function of Mach number, altitude, and lift coefficient.

Research Approach
Leveraging its suite of sophisticated high-fidelity SST-modeling tools and datasets, Georgia Tech has undertaken the development of a lower-fidelity surrogate model named ASCENT SST. This regression-based specification serves as a comprehensive framework for modeling both propulsion and aerodynamics in SST.

In the past year, the Georgia Tech team has made significant progress in full-flight modeling for the Georgia Tech Mach 1.7, 65-passenger SST model. The primary focus has been on establishing accurate regressions for fuel flow across six selected flight routes. Despite initial validation exercises, which indicated satisfactory performance, further comparisons with the Flight Optimization System (FLOPS) outputs revealed unacceptable error levels in thrust predictions. This report outlines the methodologies employed, challenges encountered, and the steps taken to address these issues.

The six routes chosen for this study are –
- Dubai International Airport (OMDB) – Suvarnabhumi Bangkok International Airport (VTBS)
- Ted Stevens Anchorage International Airport (PANC) – (South Korea) Incheon International Airport (RKSI)
- Los Angeles International Airport (KLAX) – (Hawaii) Daniel K. Inouye International Airport (PHNL)
- Shanghai Pudong International Airport (ZSPD) – Singapore Changi Airport (WSSS)
- RIOgaleão International Airport (SBGL) – (Portugal) Humberto Delgado Airport (LPPT)
- (New York) John F. Kennedy International Airport (KJFK) – Heathrow Airport (EGLL)

The earlier approach involved developing propulsion regressions (thrust and fuel flow rate) and aerodynamic regressions (drag coefficient) (Figure 53). The regressions were developed by dividing the entire working mission domain into different boxes and having a unique regression for each box. For the propulsion regressions, the domain was divided into boxes based on Mach Number (MN), Altitude and Power Code (PC), while for the aerodynamic regressions they were subsonic, transonic and supersonic regions. The power code was calculated from the thrust ratio based on the following relation:

If thrust_ratio ≥ 0.2,

$$PC = \text{thrust_ratio} * 30 + 20 \quad \text{(Eq. 5)}$$

Else if thrust_ratio < 0.2,

$$\text{PC} = \text{thrust_ratio} * \frac{100}{3} + \frac{58}{3} \quad \text{(Eq. 6)}$$

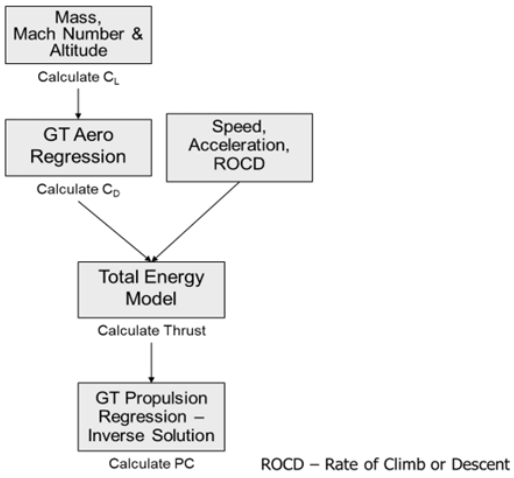

Figure 53. Old methodology implementation by the Volpe National Transportation Systems Center.

However, when these regressions were employed for the selected routes and the obtained results were validated against the FLOPS predictions, unacceptable errors were found for the thrust values (Figure 54). When these errors were studied in detail, the following reasons were identified:

- *Variable Complexity:* Too many variables were used as inputs in our surrogates. The pressure and temperature ratios are functions of MN and altitude. However, in FLOPS, only MN and altitude are used as inputs, potentially leading to discrepancies due to different atmospheric models.
- *Domain Discontinuities:* Dividing the domain into boxes introduced discontinuities at the domain intersections, contributing to error.

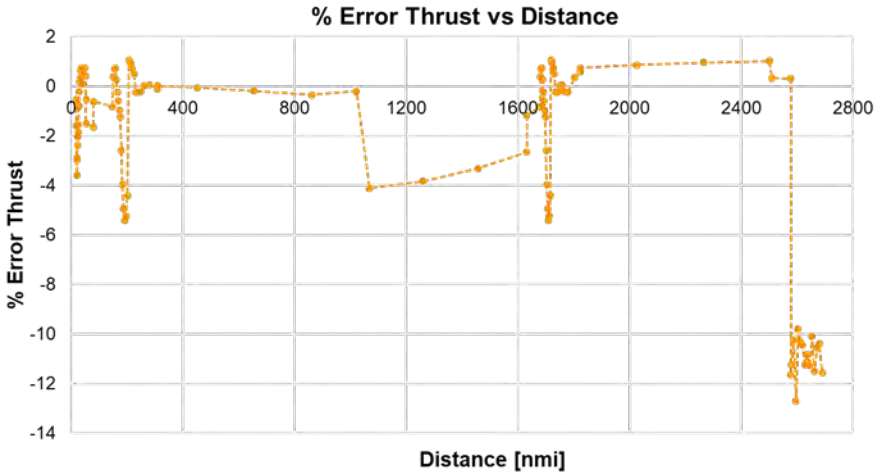

Figure 54. Error in thrust predictions compared to FLOPS for the route from OMDB to VTBS (old methodology).

To address these issues, the following modified approach was implemented:

1. *Fuel Flow Rate (lbm/hr) Regression*: Performed as a function of MN, altitude, and thrust, without dividing the domain into boxes.

2. *Thrust Estimation for Routes*: Implemented using Total Energy Method (TEM) and aerodynamic regressions for drag coefficient (Cd) calculations.
3. *Fuel Flow Prediction:* The estimated thrust was used as input for the fuel flow regression to get the predicted fuel flow.
4. *Validation with FLOPS*: The percentage error for fuel flow was calculated as follows:

$$\%Error = \frac{Actual_{FF} - Predicted_{FF}}{Actual_{FF}} \times 100 \quad (Eq.\ 7)$$

where $Actual_{FF}$ is the fuel flow rate from FLOPS.

Total Energy Model (TEM)

The TEM was implemented based on Equation 8:

$$(T - D)v_{TAS} = m * g_0 * \frac{dh}{dt} + m * v_{TAS} * \frac{dv_{TAS}}{dt} \quad (Eq.\ 8)$$

where

- T is the thrust (lbf)
- D is the drag (lbf)
- v_{TAS} is the TAS
- m is the instantaneous mass
- g_0 is the gravitational acceleration constant = 9.80665 m/s^2
- $\frac{dh}{dt}$ is the rate of climb or descent (ROCD) (ft/min)

Fuel Flow Rate Regressions

For the fuel flow rate regressions, it was observed that a neural network provided the best fit. The specifications of the developed neural network are:

- 2 layers Gaussian Model
- 10 neurons in each layer
- Learning Rate = 0.01
- 75% Training and 25% Validation

The goodness of fit for the developed regression equations are as shown in Figure 55 and the corresponding validation results on two of the six routes are shown in Figure 56.

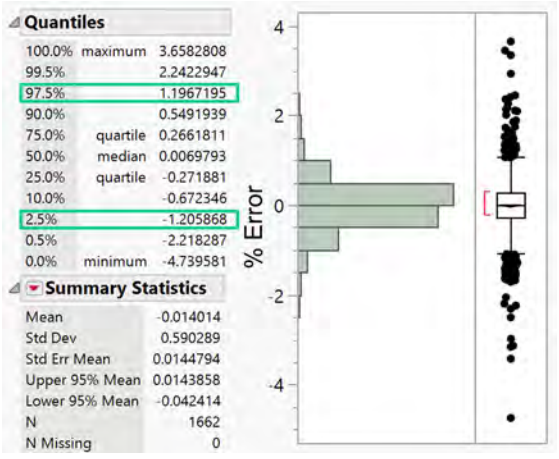

Figure 55. Goodness of fit – fuel flow rate regressions.

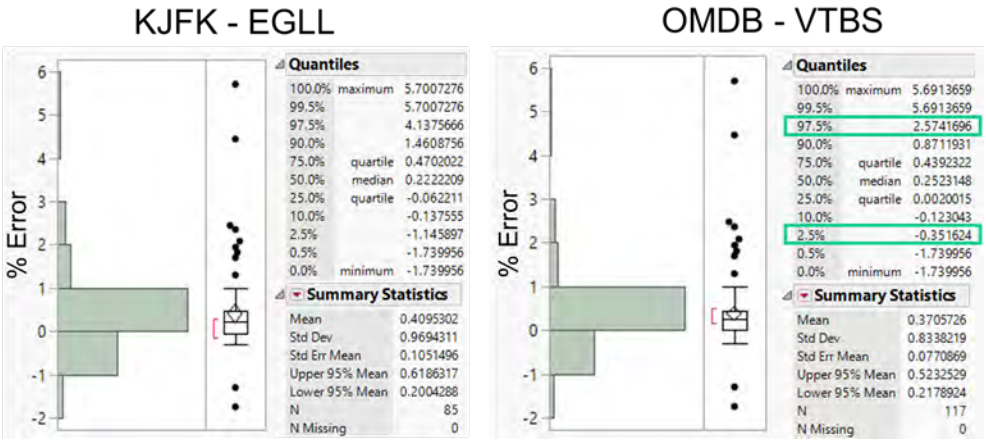

Figure 56. Validation of the fuel flow rate regressions against FLOPS predictions for two routes, KJFK-EGLL (left) and OMDB-VTBS (right).

Aerodynamic Modeling Specifications

For a given aircraft, the aerodynamic modeling component of the specification establishes two sets of key values: (1) a group of four distinct cardinal lift coefficients (C_L) denoted C_{L_i}, and (2) a set of seven distinct cardinal Mach numbers denoted M_i (Figure 57).

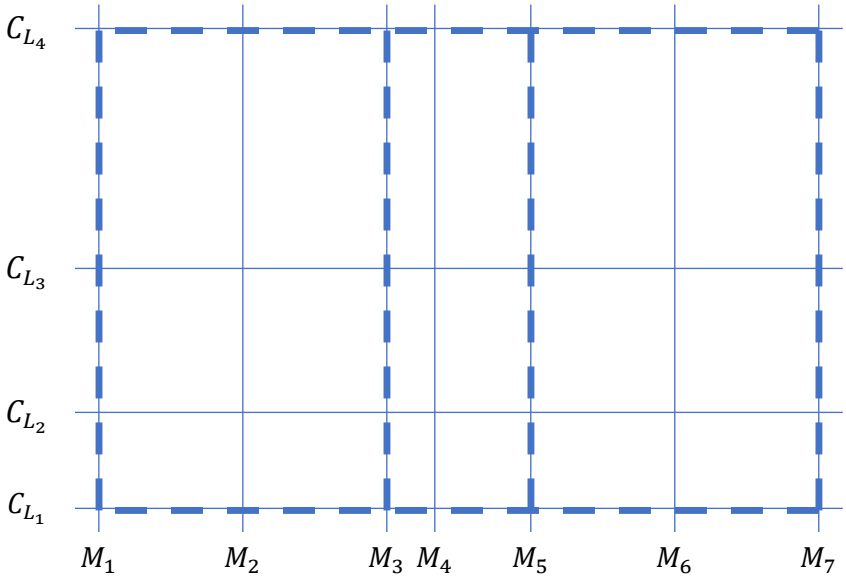

Figure 57. Aerodynamic regressions: boxes definition.

The Mach cardinals M_1 and M_7, along with the lift coefficient cardinals C_{L_1} and C_{L_4}, define the operational state envelope for the aircraft. Specifically, the modeling specification is applicable for {M, C_L} coordinates, where $M_1 \leq M \leq M_7$ and $C_{L_1} \leq C_L \leq C_{L_4}$.

Within the Mach-C_L envelope, Mach cardinals divide the range into three regimes: the "subsonic" regime ($M_1 \leq M \leq M_3$), the "transonic" regime ($M_3 \leq M \leq M_5$), and the "supersonic" regime ($M_5 \leq M \leq M_7$). Each regime corresponds to a structured irregular grid of cardinal values (3 by 4) and has a specific altitude range.

When modeling an aircraft within an aerodynamic sub-domain or along unshared bounds, the drag coefficient C_D at any cardinal grid point $\{M_i, C_{L_j}\}$ is modeled as a function of altitude (h).

$$C_{D_{i,j}} = a_1 + a_2 h + a_3 h^2 + b_{1,i} + b_{2,i} h + c_{1,j} + d_{1,i,j} \quad \text{(Eq. 9)}$$

where

- h is the altitude
- All coefficients are specific to the aircraft and aerodynamic sub-domain
- Coefficients $b_{1,i}$ and $b_{2,i}$ are further specific to the cardinal Mach value M_i
- Coefficient $c_{1,j}$ is further specific to the cardinal value C_{L_j}
- Coefficient $d_{1,i,j}$ is further specific to the combination of cardinal values $\{M_i,\}$

For any supported combination of Mach and lift coefficient {M, C_L}, the drag coefficient is modeled through bi-quadratic interpolation between $C_{D_{i,j}}$ values at cardinal grid points within the relevant Mach regime.

To derive coefficients for the regression of drag coefficients in each SST concept, the design team uses raw aerodynamic data containing the essential Mach number, C_L, altitude values, and their corresponding C_D. The approach involves initially regressing the drag coefficient on these cardinal values through a stepwise fit, followed by quadratic interpolation.

The ASCENT Project 054 team used JMP® for the stepwise regression, considering Mach number, altitude, and C_L. Given the distinct behavior of the drag coefficient in subsonic, transonic, and supersonic phases, three separate boxes are typically created and subjected to regression (Table 10). The chosen set of cardinal values was required to encompass the design mission to prevent extrapolation.

Table 10. Aerodynamic regressions: box definitions.

Box	Mach	Altitude (ft)	CL
Subsonic	0.3, 0.6, 0.8	0–70,000	0, 0.1, 0.25, 0.5
Transonic	0.8, 0.88, 1.05		
Supersonic	1.05, 1.4, 1.7		

Similarly to the process for propulsion regressions, the validation of aerodynamic regressions involves comparing the predicted drag coefficient values from the regression against the actual C_D values derived from the aerodynamic data (Table 11).

Table 11. Assessment of the accuracy of the aerodynamic regressions.

Mode	Points/box	Training Dataset		Validation Dataset	
		Mean (%)	Standard deviation	Mean (%)	Standard Deviation
Subsonic	135/45	-0.01865%	0.97727	0.02687%	0.95778
Transonic	139/41	-0.03778%	1.15181	0.03423%	1.32195
Supersonic	133/47	-0.11692%	1.21366	0.22050%	1.19831

The entire approach was then implemented on the selected mission routes. The results obtained for two of the routes are shown in Figure 58 and Figure 59. The results show that other than certain regions, the overall match of the predicted fuel flow rate with the values from FLOPS is good. The high errors in those specific regions are due to the mismatch in thrust estimated through TEM compared to those predicted by FLOPS. Further analysis of the results showed that the regions of

® JMP is a registered trademark of SAS Institute Inc., Cary, North Carolina.

error are observed at:

- Subsonic to supersonic transition: Occurs in one step in FLOPS.
- Supersonic flight over land: FLOPS decelerates and descends instantaneously, resulting in high ROCD and a sudden drop from supersonic to subsonic speeds.
- Descent phase: Deceleration is not steady and occurs at idle thrust.

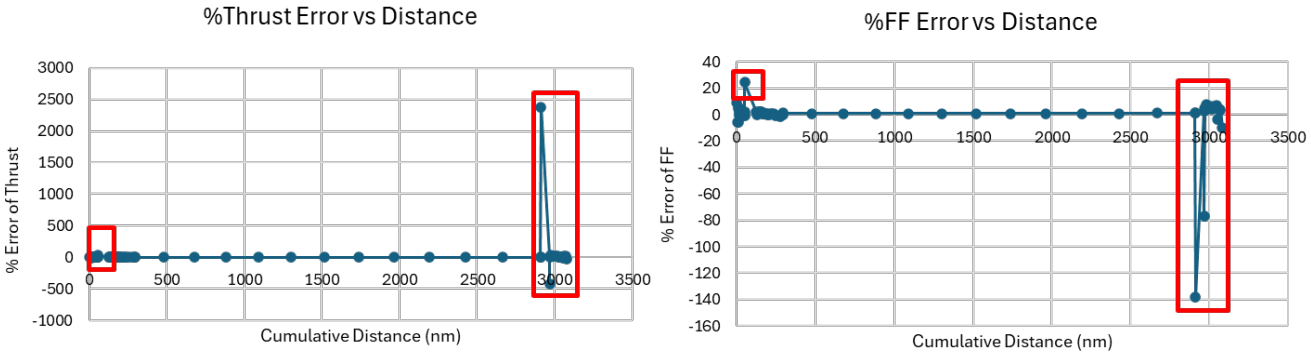

Figure 58. Validation of the modified against FLOPS predictions KJFK-EGLL.

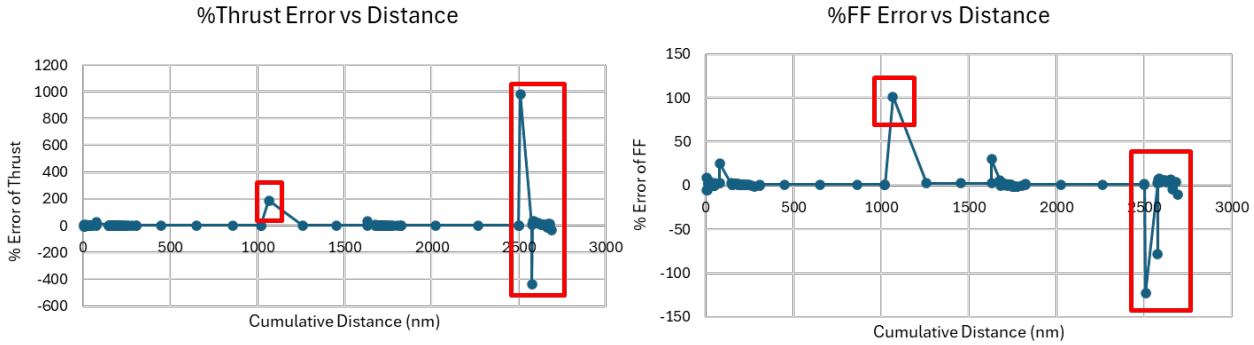

Figure 59. Validation of the modified against FLOPS predictions OMDB-VTBS.

The first two errors are inherent to the FLOPS source code. The first error can be mitigated by modifying the FLOPS climb schedule to model additional subsonic and transonic cruise and climb segments to avoid a single step transition from subsonic to supersonic phases. However, the other error cannot be overcome since the FLOPS code does not allow for multiple descent segments. This updated logic significantly improved the results for three out of the six selected routes: SBGL-LPPT, KLAX-PHNL, ZSPD-WSSS. For the other three routes (KJFK-EGLL, OMDB-VTBS, and PANC-RKSI), there is a subsonic cruise segment before the final descent phase to avoid supersonic flight over land, due to the limitation of FLOPS, which allows only a single descent segment; these decelerations are modeled as instantaneous drops in altitude and speed, resulting in higher errors at these points. For the descent phase, a modified approach was implemented to improve predictions. FLOPS employs idle thrust for all the descent phase, i.e., a thrust ratio of 0.065. Therefore, instead of using the TEM to calculate thrust, a new regression equation was developed for thrust available. This calculated thrust available was then multiplied by 0.065 to get the thrust at different points in the descent phase.

Thrust Available Regressions:
The thrust available surrogates were developed as a function of MN and altitude, and polynomial type regression fit was employed.

$$Thrust\ Available = a_0 + a_1M + a_2M^2 + a_3M^3 + a_4M^4 + a_5M^5 + a_6M^6 + a_7A + a_8A^2 + a_9A^3 + a_{10}A^4 + a_{11}A^5 + a_{12}A^6 + a_{13}MA + a_{14}M^2A + a_{15}M^3A + a_{16}M^4A + a_{17}M^5A + a_{18}A^2M + a_{19}A^3M + a_{20}A^4M + a_{21}A^5M \quad \text{(Eq. 10)}$$

Where M is the MN (dimensionless) and A is the altitude (ft).

The regressions compared to the truth data (engine deck) with less than 5% error (Figure 60).

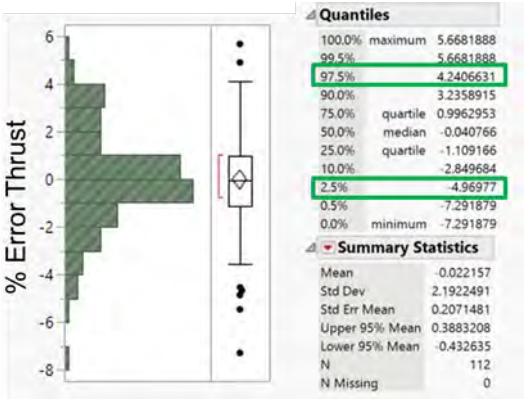

Figure 60. Goodness of fit – thrust available regression.

Overall Validation Results of the Modified Approach for All Six Routes Against FLOPS Data
Figure 61 summarizes the entire approach employed for the ascent and cruise phase and the descent phase.

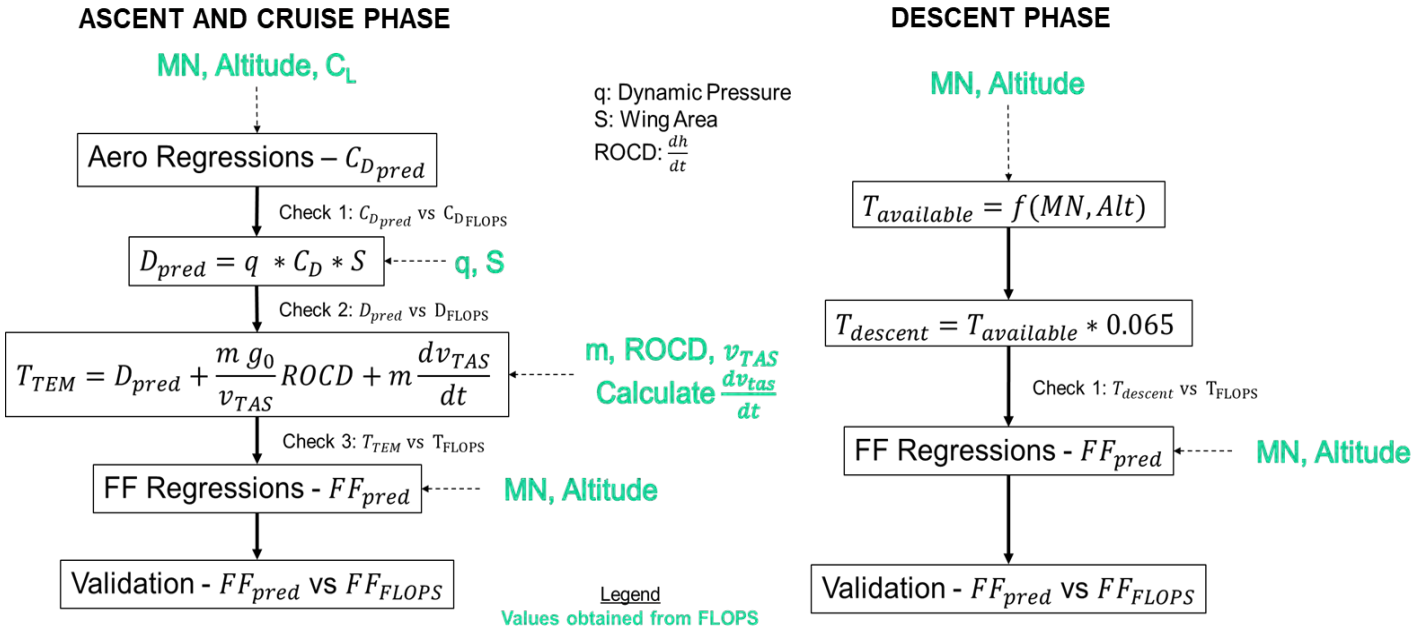

Figure 61. Modeling approach for ascent, cruise, and descent phases.

In order to validate the approach for all the routes, the overall predicted fuel burn and the fuel burn values calculated from the FLOPS fuel burn rate and segment time were calculated and compared against the actual value from FLOPS, the overall error was found to be less than 6% (Table 12).

Table 12. Comparison of fuel burn (lbm) for all six routes against FLOPS.

Route	Actual Fuel Burn (lbm)	FLOPS Fuel Burn (lbm)	% Error	Predicted Fuel Burn (lbm)	% Error
SBGL - LPPT	143,989.00	142,808.86	0.82%	141,421.16	1.78%
KLAX - PHNL	69,023.00	68,706.27	0.46%	68,078.94	1.37%
ZSPD - WSSS	65,715.00	65,415.20	0.46%	64,826.29	1.35%
KJFK - EGLL	102,306.00	101,685.22	0.61%	99,481.06	2.76%
OMDB - VTBS	94,975.00	94,451.85	0.55%	89,687.34	5.57%
PANC - RKSI	122,066.00	121,236.68	0.68%	117,245.10	3.95%

Terminal area: fixed-point profiles
To account for detailed takeoff and landing performance, fixed point profiles are used up to the altitude threshold of 15,000 ft for the departure and 3,000 ft for arrival phase. In this case, smooth connectivity must be ensured between the fixed-point profiles and the rest of the mission.

1. **Detailed Takeoff Segment (one of the off-design missions: OMDB–VTBS)**

Figure 62 depicts the plots of altitude (AFE) and true air speed (knots) against distance (nmi) for the detailed takeoff segment merging into the rest of the mission. The Fixed Point Profile (FPP) for takeoff transitions smoothly to the remaining mission from FLOPS.

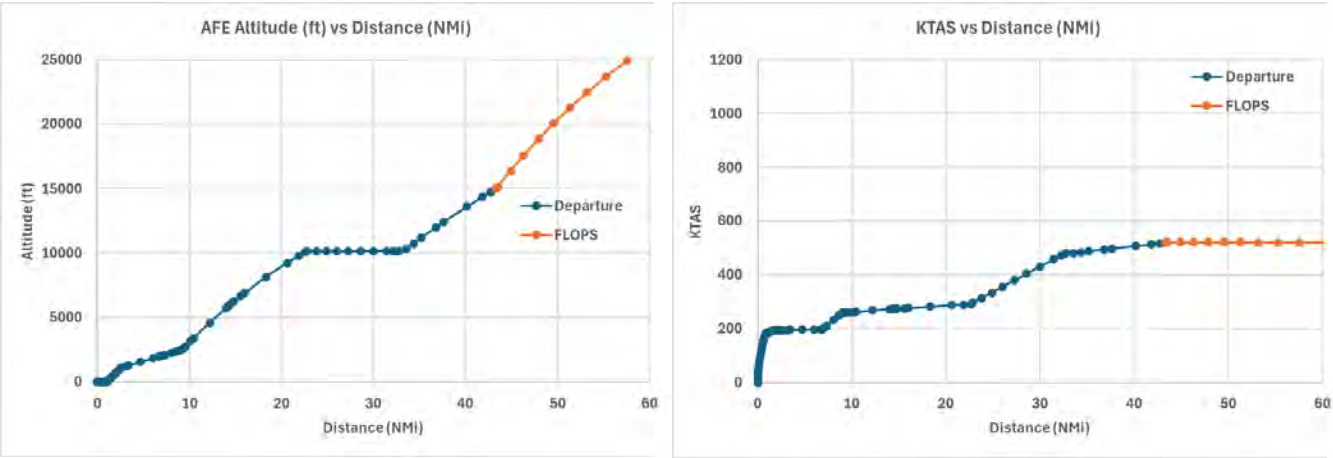

Figure 62. Altitude vs. distance (left) and TAS vs. distance (right), OMDB–VTBS, fixed-point profile takeoff.

2. **Detailed Landing (arrival) Segment (one of the off-design missions: OMDB–VTBS)**

The arrival FPP is modeled as a 3° glide slope from the point of transition into detailed landing (Figure 63[left]). Furthermore, FLOPS also assumes full flops and gear deployment from the specified altitude of descent, in this case, 15,000 ft. However, realistically, full flaps and gear deployment begin at a much lower altitude, thus causing discontinuities in the plots of knots true airspeed (KTAS) vs. distance (Figure 63[right]).

To mitigate these discrepancies and ensure a smooth and consistent transition into arrival, we decided to begin the descent mission from a lower altitude and extend the propulsion and aerodynamic regressions to this altitude to cover the gap.

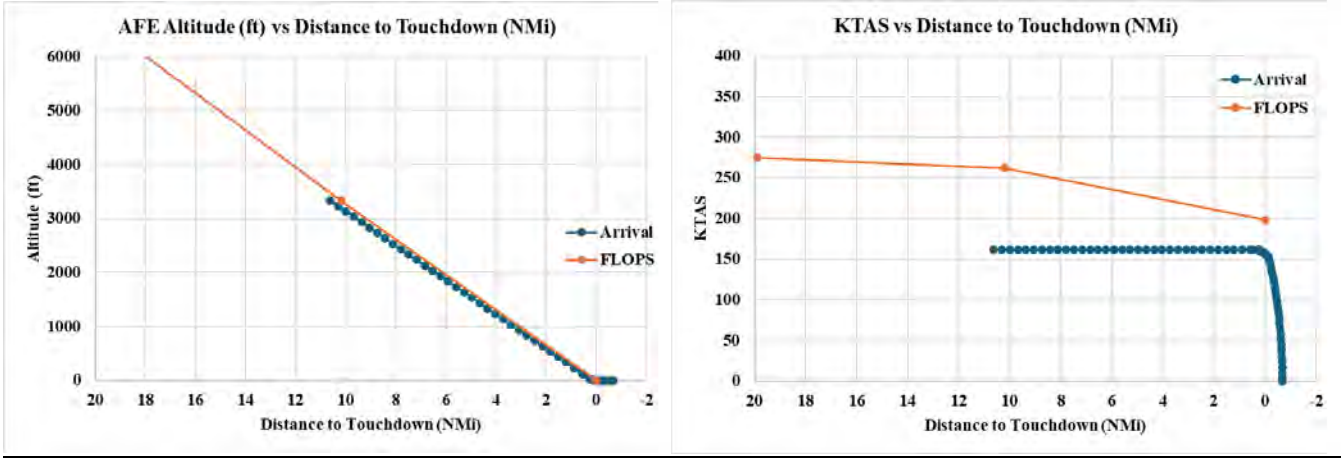

Figure 63. Altitude vs. distance (left) and true airspeed vs. distance (right), OMDB–VTBS, fixed-point profile landing.

Milestones
None.

Major Accomplishments
None.

Publications
None.

Outreach Efforts
- Participated in biweekly calls and attended biannual ASCENT meetings.

Awards
None.

Student Involvement
Graduate research assistant, Nitya Maruthuvakudi Venkatram, participated in this research.

Plans for Next Period
None.

Project 055 Noise Generation and Propagation from Advanced Combustors

Georgia Institute of Technology
RTX Technology Research Center

Project Lead Investigator

Timothy Lieuwen
Professor
Daniel Guggenheim School of Aerospace Engineering
Georgia Institute of Technology
270 Ferst Drive (M/C 0150)
Atlanta, GA 30332-0150
404-894-3041
tim.lieuwen@aerospace.gatech.edu

University Participants

Georgia Institute of Technology (Georgia Tech)

- P.I.s: Prof. Timothy Lieuwen, Prof. Suresh Menon, Prof. Adam Steinberg, Dr. Vishal Acharya, Benjamin Emerson, David Wu
- FAA Award Number: 13-C-AJFE-GIT-058
- Period of Performance: February 5, 2020, to September 30, 2025
- Tasks:
  1. Facility Development: This task addresses the design of experiments that will be performed at Georgia Tech. The task involves coordination between the teams to develop and define the aerodynamic design of a rich-quench-lean (RQL), quick quench, lean burn combustor for this study. This task is led by Tim Lieuwen and Adam Steinberg, with support from Ben Emerson and David Wu.
  2. Simulations of the Experiment: This task includes simulating the Georgia Tech experiment, with a focus on the pre-combustion flow dynamics, flame dynamics, and post-combustion dynamics of pressure and entropy disturbances. This task is led by Suresh Menon.
  3. Reduced-Order Modeling: This task consists of creating a reduced-order model (ROM) framework for the unsteady response of the flame and the generation of entropy disturbances due to unsteady heat release. This task is led by Vishal Acharya.

RTX Technology Research Center (RTRC)

- P.I.s: Dr. Jeffrey Mendoza, Dr. Duane McCormick, Dr. Julian Winkler, Dr. Lance Smith
- FAA Award Number: 13-C-AJFE-GIT-058 (subaward through Georgia Tech)
- Period of Performance: February 5, 2020, to September 30, 2025
- Tasks:
  4. Facility Development: This task addresses the design of experiments that will be performed at RTRC. The task involves coordination between the teams to develop and define the aerodynamic design of an RQL combustor for this study. This task is led by Jeffrey Mendoza, Lance Smith, and Duane McCormick.
  5. Post-Combustion Modeling: This task consists of both post-processing and simulation efforts. First, the post-combustion simulation data from the simulation of the Georgia Tech experiment are mined to investigate the dynamics of entropy fluctuations and their transport. Next, simulations are used to model noise propagation in the post-combustion architecture of the engine. The simulations are split across the different sections: nozzle, turbine, and far-field. This task is led by Jeffrey Mendoza and Julian Winkler.

Project Funding Level

Federal Aviation Administration (FAA) Funding: $4,999,984 (Georgia Tech: $3,000,343; RTRC: $1,999,641)
Cost-Share Funding: $4,772,851 (Georgia Tech: $2,773,210 from Airspace Engineering (AE) school; RTRC: $1,999,641 from company funds)
Total Funding: $9,772,835

Investigation Team

Georgia Institute of Technology

- Prof. Tim Lieuwen, (P.I.), Lead P.I. responsible for overseeing all tasks; specifically, he leads the Georgia Tech experiments and design in Tasks 1 and 2, along with Prof. Steinberg. In addition, he co-leads the modeling tasks in Task 1 for pre-combustion, flame response, and post-combustion modeling, along with Dr. Acharya.
- Prof. Suresh Menon, (co-P.I.), Responsible for simulations of the Georgia Tech experiment.
- Dr. Vishal Acharya, (co-P.I.; Principal Research Engineer), Responsible for all modeling tasks for pre-combustion, combustion, and post-combustion physics, along with Professor Lieuwen. In addition, as an administrative coordinator, he is responsible for general project management, such as project deliverables, group meetings, and interfacing with the FAA project manager.
- Dr. Benjamin Emerson, (co-P.I.; Principal Research Engineer), Responsible for designing and maintaining experimental facilities, as well as experimental operations and management, and graduate students' safety.
- David Wu, (co-P.I.; Research Engineer-II), Responsible for designing and maintaining experimental facilities, as well as experimental operations and management, and graduate students' safety.
- Dr. Achyut Panchal, (Research Engineer), Simulation of the Georgia Tech experiment.
- Sungyoung Ha, (graduate student), Lead experimentalist on the Georgia Tech rig.
- Parth Patki, (graduate student), Working on hydrodynamics modeling subtask (pre-combustion disturbances).
- Guru Charan Ganesh, (graduate student), Working on the entropy dynamics modeling subtask (post-combustion disturbances).
- Leo M. Kastenberg (graduate student), Working on analysis of large eddy simulation (LES) results and responsible for setting new simulations.

RTX Technology Research Center

- Dr. Jeffrey Mendoza, (P.I.; Technical Fellow Acoustics), Leads the RTRC team and oversees its contributions to the project. He leads the subtasks related to modeling, measurements, and simulation for post-combustion disturbances, nozzle interactions, turbine interactions, and far-field sound propagation.
- Dr. Lance Smith, (co-P.I.; Technical Fellow Combustion), Conducting design and measurements of the RTRC experiment. He collaborates closely with the Georgia Tech team to ensure similarities between both experiment setups.
- Dr. Duane McCormick, (co-P.I.; Principal Research Engineer), Conducting design and measurements of the RTRC experiment as well as finite-element calculations in the design process.
- Dr. Julian Winkler, (co-P.I.), Responsible for the simulation tasks at RTRC and focuses on post-combustion disturbances, nozzle interactions, turbine interactions, and far-field sound propagation.
- Dr. Jordan Snyder, conducting design, measurements, and data processing using tunable diode laser absorption spectroscopy and chemiluminescence in the RTRC combustor rig.
- Dr. Kenji Homma, Responsible for far-field sound propagation simulations.
- Dr. Aaron Reimann, Responsible for ROM and high-fidelity (HiFi) modeling of the propagation of direct and indirect noise sources through the turbine nozzle and supports the far-field sound propagation simulations.
- Dr. Sudarshan Koushik, Responsible for post-processing the Georgia Tech LES data to model post-combustion disturbances.

Project Overview

The objective of this project is to develop and validate physics-based design tools that can predict noise production mechanisms and their relative dominance and ultimately reduce the noise output of future engines. The motivation for this project stems from recent and future advances in aircraft engine technology. High-bypass engine technology has significantly reduced the traditionally dominant engine noise sources, namely fan and jet exhaust noise. Noise generated in the combustor has become a dominant source of engine noise for future advanced aircraft designs. In addition, as combustors evolve to increase efficiency and decrease pollutant emissions, methods for predicting and mitigating combustion noise have severely lagged, and legacy methods are insufficient to predict noise from next-generation

combustors. This drawback has motivated the objective of this project, which addresses the critical need for physics-based design tools. The resultant understanding of noise generation and propagation, along with validated noise prediction tools, will enable more rapid and cost-effective designs of low-noise engines for future aircraft.

The project objectives will be achieved through a program of cooperative experiments, high-fidelity simulations, and physics-based ROM. The physical processes involved are tightly coupled and directly determine the project tasks, as shown in Figure 1.

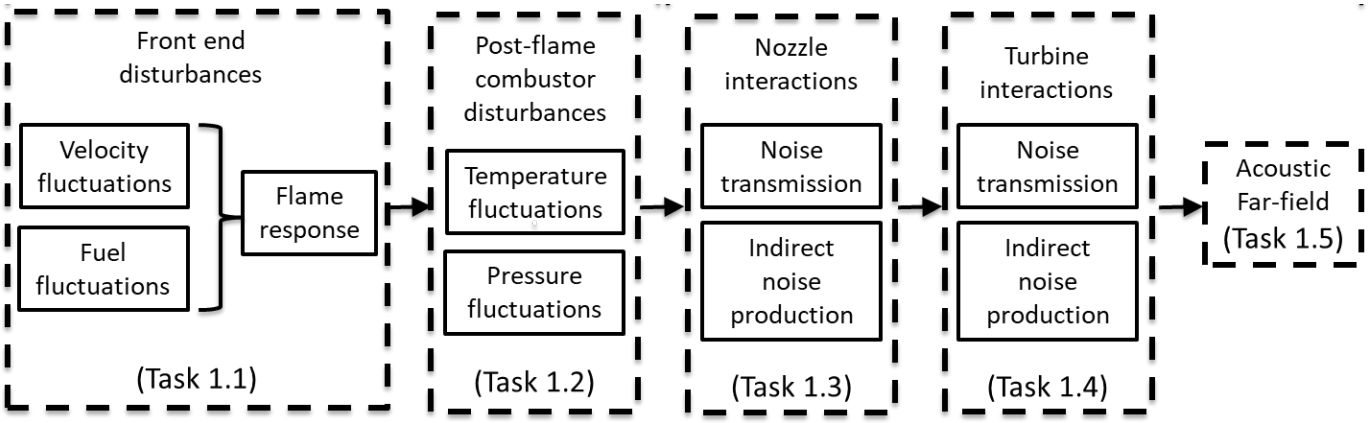

Figure 1. Physical processes and project tasks for noise generation.

The physics of noise generation begins with source disturbances upstream of the combustion zone, which involve unsteady dynamics in the flow and incoming fuel (spray), followed by the response of the combustion zone (flame) to these upstream disturbances. The fluctuations in the unsteady heat release led to the generation of pressure and entropy fluctuations. These fluctuations propagate further downstream in the combustor, interact with the nozzle and turbine, and eventually lead to far-field sound generation. Given the complex interplay of unsteady physics in the various parts of the engine, developing a ROM is challenging.

An important goal of this project is to generate high-quality reference data from both measurements and validated high-fidelity simulations, including measurements of the flow, spray, and flame unsteadiness in the head end of the combustor. Subsequently, the secondary combustion zone is characterized. The generation of entropy and pressure disturbances is then characterized by measurements of temperature and pressure fluctuations, followed by measurements of noise reflection and transmission through the turbine and nozzle section, and sound measurements in the far field. The measurements are accompanied by LES and finite-element simulations that are validated against the measurements. Collectively, these data are generated across a range of operating parameters and provide a source database for the modeling task.

The main goal of this project is to develop a robust design tool that can predict noise at operating points for which prior measurements or data are unavailable. To achieve this goal, two major tasks are necessary. First, ROM and frameworks must be developed for various aspects of the engine architecture: flow/spray models, flame response models, entropy generation models, entropy propagation models, nozzle interaction models, turbine interaction models, and far-field noise generation models. The ROM for each of these aspects involves simplifications and assumptions that are validated against the source database. The validation study and iterative improvement of model predictions serve as the second task to achieve this goal.

In this report, the efforts of both teams, Georgia Tech and RTRC, are summarized from October 2023 to September 2024. The efforts primarily include Georgia Tech rig setups to ascertain the coherence of pressure and heat release fluctuations in both open and ducted flames. The RTRC rig was used to study the relative roles of direct and indirect noise through a combination of measurements and finite element method (FEM) simulations. In addition, progress was made in hydrodynamics modeling, direct noise modeling as well as the entropy source budget from different contributions other than heat release.

Task 1 – Facility Development

Georgia Institute of Technology

Objective

The objective of the task for the Georgia Tech experiment has shifted towards validating the heat release rate (HRR) and pressure modeling efforts and developing new methods for noise source separation. Following the goals of the previous period, an open flame rig was constructed to study the coherence between heat release and combustion noise with plans to utilize it for noise source separation testing as well.

Research Approach

To perform fundamental studies on combustion noise, a turbulent Bunsen burner was constructed as a canonical example. The burner is a piloted premixed methane–air turbulent Bunsen burner, as shown in Figure 2, which was chosen due to its simplicity and broadband frequency characteristics. Furthermore, a good correlation between CH* chemiluminescence intensity and HRR can be expected in atmospheric conditions. Fuel and air are supplied from pressurized bottles which are metered by critical orifices and mixed in a manifold at the base of the setup. The gas then passes through a muffler to minimize upstream noise, which also doubles as a mixing section. Prior to the nozzle, there is a turbulence generator which is followed by a short converging section. The burner nozzle has a diameter of 1 1/8-in. Acoustic data were taken through three PCB® Piezotronics 378B02 free-field microphones placed at various locations from the flame. A Photron® FASTCAM SA-Z1 high speed camera paired with a Lambert™ HiCATT intensifier was used to take high speed images of the flame, and two Thorlabs® PMM01 photomultiplier tubes were used to obtain global chemiluminescence intensity measurements. Both were fitted with 430±10 nm bandpass filters to target CH* chemiluminescence.

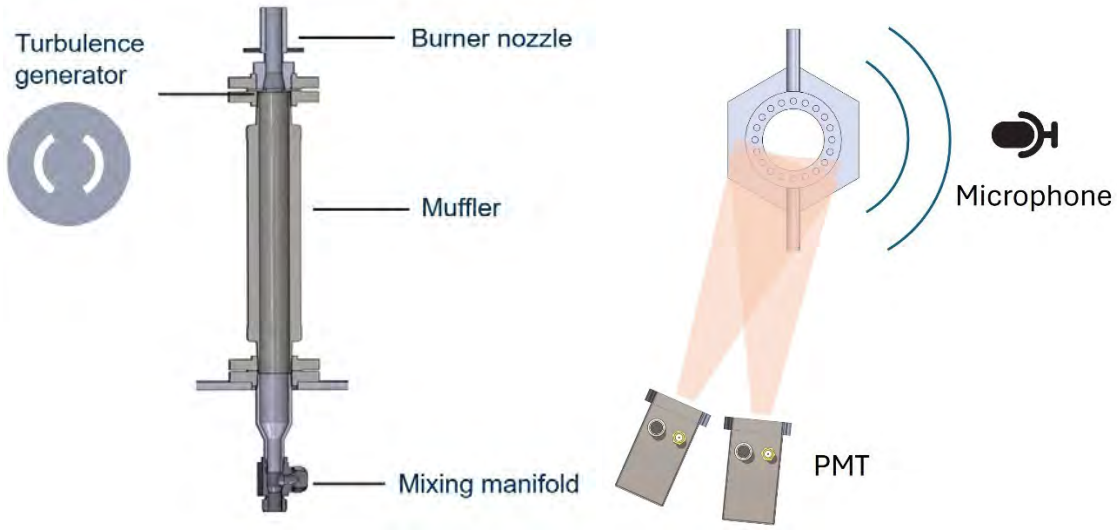

Figure 2. Cross section of experimental apparatus (left) and schematic of diagnostics (right).

Figure 3 shows the acoustic spectra of the burner and background noise of the setup. Combustion noise has a peak near 120 Hz and has a broadband spectrum consistent with literature. After the peak, combustion noise rolls off with a $f^{-\alpha}$ dependence where a power law fit returns a coefficient of $\alpha \approx 2.4$, consistent with previous literature. The spectrum of the global chemiluminescence intensity is also of interest. Figure 4 shows the CH* chemiluminescence intensity spectra from high-speed images and the photomultiplier tube (PMT) which were simultaneously taken at 5000 Hz for 3.5 s normalized

® PCB is a registered trademark of PCB Piezotronics, Inc., Depew, New York.
® Photron is a registered trademark of Photron Limited, Tokyo, Japan.
™ Lambert instruments is a trademark of Tibidabo Scientific Industries, Madison, Connecticut.
® Thorlabs is a registered trademark of Thorlabs, Inc., Newton, New Jersey.

by their mean intensities, respectively. The two spectra were nearly identical, showing that the PMT measurements accurately represent the global fluctuations. It is of particular interest that the peak of the global chemiluminescence intensity occurs at approximately half of the peak frequency of the acoustic spectrum. Figure 4 also shows the transfer function between sound pressure level (SPL) and global chemiluminescence intensity. This follows a f^2 dependence where it rolls off at higher frequencies above 1000 Hz. While this deviation may indicate acoustic noncompactness effects, this is due to the chemiluminescence fluctuation intensity being low at high frequencies where the signal to noise ratio becomes insufficient.

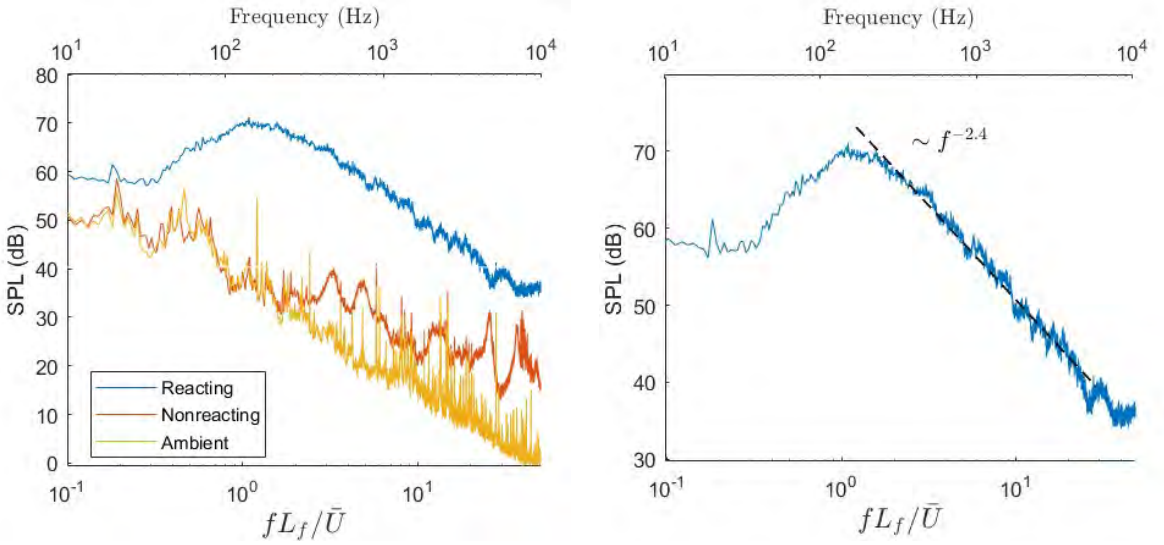

Figure 3. Acoustic characteristics of the burner.

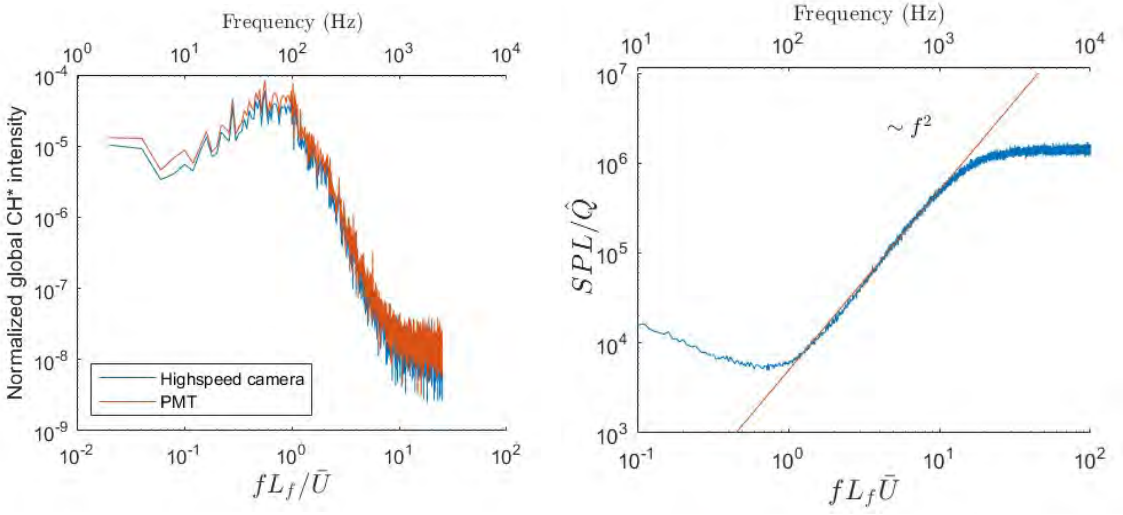

Figure 4. Global chemiluminescence characteristics of the burner.

Figure 5 shows an example of coherence between global chemiluminescence and acoustic pressure fluctuations. Near-unity coherence is observed over a broadband range of frequencies, confirming that coherence between the global heat release and direct combustion noise is indeed unity in the acoustically compact source and far field limit. It should be emphasized that though this result was expected, it is the first data of this nature in the literature. These results also suggest that the low coherence values found in literature may be due to a combination of elevated levels of noise in the system. It is also necessary to determine the cause of coherence drop observed. Figure 5 also shows the coherence between two PMT signals overlaid to the measured coherence along with the predicted coherence from the analytical model. As shown in Figure 2, the two PMTs were identical in hardware and were adjacent to each other with the same viewing window, hence any reduction in coherence between the two signals can be expected to come from random noise in the chemiluminescence measurements. The frequency where coherence drops coincides, suggesting that this coherence drop is due to noise in chemiluminescence measurements, and not a drop in actual pressure heat release coherence. Comparison with the coherence predicted from the model further implies this is the case. At lower frequencies below ~500 Hz, the reduction in coherence is mainly due to noise in the acoustic measurements and generally deviates very little from unity. Above 500 Hz, coherence is reduced according to noise in PMT measurements. This drop in coherence due to noise is gradual, hence it may be potentially possible to apply this to noise source separation even in this region by observing deviations from the trend. Considering that, in general, indirect noise sources manifest at lower frequencies and chemiluminescence intensity is higher at elevated pressures, the application of chemiluminescence to noise source separation in combustors remains a valid consideration.

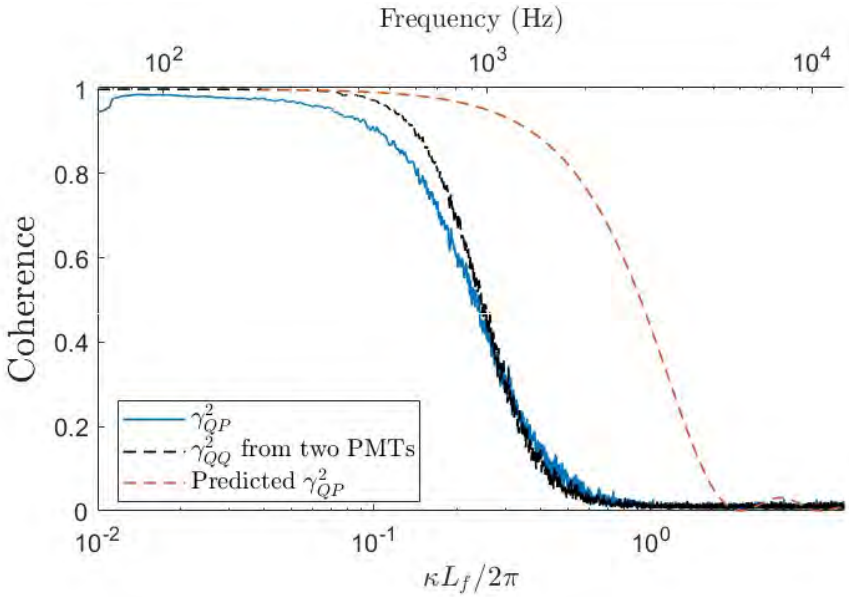

Figure 5. Coherence of global CH* chemiluminescence and acoustic pressure at $x = 10\ cm$ from the burner center, the coherence between two PMT signals, and coherence predicted from the model.

Milestones

- Developed a new canonical open flame rig to study the correlation between HRR and pressure fluctuations.
- Produced measurements of high coherence over a broadband spectrum, which is the first of its kind in literature.

Major Accomplishments

- Constructed a new open flame rig and started collecting data to study the HRR and pressure correlation/coherence.

Publications

Ha, S., & Lieuwen, T. (2024, January 8-12). Coherence between the globally integrated heat release rate and acoustic pressure in an enclosed duct [Conference paper]. AIAA SCITECH 2024 Forum, Orlando, Florida. https://doi.org/10.2514/6.2024-0795

Ha, S., & Lieuwen, T. (2025). Direct combustion noise: Nearfield and non-compactness influences on pressure–heat release coherence. Combustion and Flame, 271. https://doi.org/10.1016/j.combustflame.2024.113811

Outreach Efforts
None.

Awards
None.

Student Involvement
- Graduate student Sungyoung Ha is the lead experimentalist on the Georgia Tech rig.

Plans for Next Period
- Continue the measurement campaign during the next period, with further modifications to the rig to study duct effects and applications to noise source separation.

Task 2 – Simulations of the Experiment
Georgia Institute of Technology

Objectives
The first objective of this task is to validate and justify the compressible reactive LES approach for modeling the Georgia Tech experimental rig. This is considered for two conditions: match point and a higher fuel-air-ratio (FAR) condition, both corresponding to reference conditions in the Georgia Tech experimental campaign. The second objective is to collect time-dependent three-dimensional (3D) snapshots and transfer those to the RTRC and Georgia Tech ROM teams with sample post-processing scripts. As a part of this effort, the 3D dataset is also used for developing a machine-learning (ML) model for unsteady HRR predictions.

Research Approach
Solver Details
A fully compressible Eulerian finite-volume formulation for the gas phase and a Lagrangian formulation for the liquid phase are used in this study. An eddy-viscosity approach with a one-equation subgrid kinetic energy (k_{sgs}) model is used for the closure of gas-phase subgrid-scale fluxes. Because regions in which turbulence is not well established may exist in the plenum or outflow duct, the k_{sgs}-equation coefficients are set to constant values rather than being dynamically computed. Subgrid dispersion for spray particles is modeled with a stochastic separated flow model. Modeling of dense spray, corresponding compressible volume blockage effects, and breakup are also available, as we have previously shown, but these conditions are not considered herein; instead, a dilute injection of spray is considered. A well-established secondary breakup model based on Kelvin–Helmholtz instability is used, and its effect is evaluated in this study.

The combustion is modeled via a finite-rate kinetics approach, by using a two-step, six-species mechanism for kerosene. Subgrid closure for turbulent combustion is provided by a simplified partially stirred reactor model, wherein the mixing time (τ_m) is computed locally by using k_{sgs}, and the chemical time (τ_c) is precomputed for the operating conditions from laminar premixed flame solutions under stoichiometric conditions. Further details about our modeling approach can be found in our recent works and are not repeated herein, for brevity.

The equations are solved at Georgia Tech with the in-house solver LESLIE. LESLIE is a well-established multi-block, structured, fully compressible finite-volume solver. A hybrid second-order central and third-order upwind method is used for the gas-phase evolution. A fourth-order Runge–Kutta solver is used for solving the Lagrangian equations. For computational efficiency, instead of tracking individual Lagrangian particles, the particles are grouped together in "parcels," which are tracked in a Lagrangian manner. A particle-per-parcel value of 8 is used in this work, which has been shown to provide a good balance between accuracy and efficiency for gas-turbine combustor LES.

The current version of the Georgia Tech compressible solver contains three parts: (1) CFDPreProc, (2) LESLIE, and (3) CFDPostProc. CFDPreProc is a pre-processor that can perform functions such as creating a grid and setting boundary

conditions. LESLIE is a core compressible solver that conducts multi-phase reactive LES. The latest LESLIE code (improved during the Year 2 efforts) outputs 3D snapshots of conservative variables that are directly solved for in our compressible framework, including the density, momentum, total energy, and partial densities. Primitive variables remain required for the computation of noise-related quantities; therefore, CFDPostProc computational fluid dynamics (CFD) post-processing software is used to read the conservative variable-based 3D snapshots and compute additional primitive quantities. This code is provided to the RTRC and Georgia Tech ROM teams along with the 3D snapshots. The conservative variables form an exclusive and exhaustive set of variables; therefore, all other quantities can be computed from this set.

Computational Configuration

The computational configuration is shown in Figure 6. The flow from the inlet plenum enters the combustion chamber via two concentric swirlers (one axial and one radial). After the reaction zone, three quench jets on the top, and two on the bottom, are available to reduce the temperature. In addition, multiple small cooling holes are present on the dome plate to decrease the wall temperature. The flow exits the outflow duct through jail bars, which function as a nozzle that chokes the flow.

The boundary conditions are consistent with Georgia Tech experiments. All gas-phase inlet boundary conditions are constant mass flow inlets, based on experimental data inputs. The inflow boundary condition (ahead of the inlet plenum [I] and dilution holes [T1, T2, T3, B1, and B2]) is modeled with a characteristic Navier–Stokes boundary condition. The mass flow rate for the main inflow (I) is set as 93.89 g/s (according to Georgia Tech rig inputs). The total mass flow rates through the top (T1, T2, and T3) or bottom (B1 and B2) dilution holes are 117.03 g/s. The incoming air is at 673.3 K. The flow through the jail bar (J1, J2, and J3) chokes and pressurizes the combustor to the nominal target. With choking, the outflow (O) is supersonic at the domain outlet. The outflow following the choked nozzle is modeled with a sponge boundary condition, but no waves are expected to travel upstream into the combustor chamber from this region, because the nozzle is choked. The quench holes are not resolved; therefore, they are modeled with a porous boundary condition. The mass flow rate specified through the quench holes is 46.72 g/s.

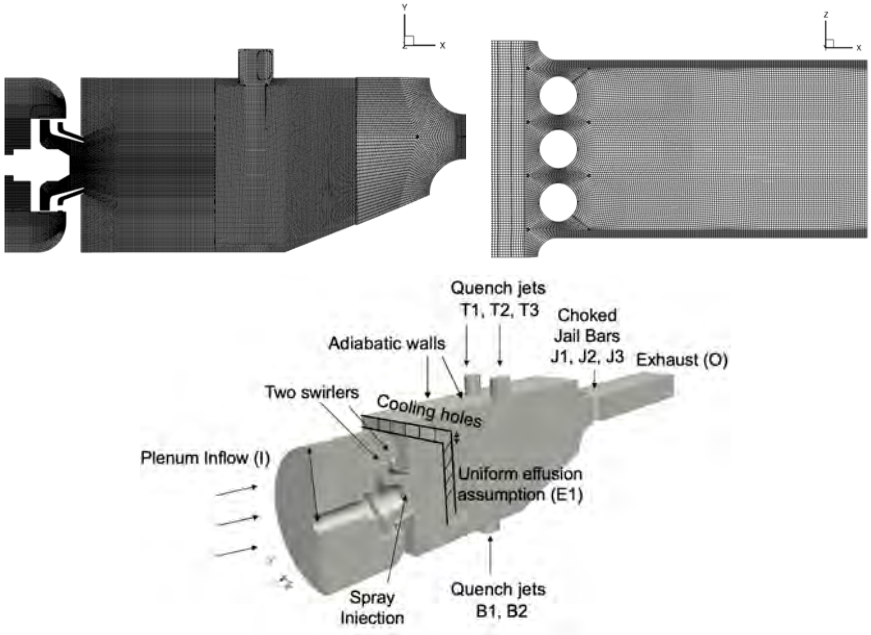

Figure 6. Computational domain for LES. Top: schematics for the multi-block structured grid (main combustor at the center *x*–*y* plane, region behind the jail bars at the center *x*–*z* plane. Bottom: entire computational domain, with key features and corresponding boundary conditions.

The Lagrangian spray droplets are injected in a stochastic manner with two concentric injectors. The mass flow rate is 2.4 g/s through the primary injector and 6.89 g/s through the secondary injector. In the absence of any experimental measurements for this injector, a log-normal size distribution with Sauter mean diameter of 30 μm and 55 μm is injected

in the absence or presence of secondary breakup modeling, respectively. These modeling choices are like the previous gas-turbine LES. The primary injector is modeled as a solid cone injector with a 60° angle; the secondary injector surrounds the primary injector and is modeled as a hollow cone injector with 90° and 120° inner and outer angles, respectively. The injection temperature of the liquid fuel is 330 K, and the velocities are set to 25 m/s. This dilute injection occurs 1 mm downstream of the actual injector plate. This injection procedure is empirical but could be improved in the future, based on experimental insights. The current simulations are with a secondary breakup model based on Kelvin–Helmholtz instability and 55-μm droplets are injected that then break into smaller droplets through a physics-based approach on their own.

The multi-block structured grid has 6.8 million cells and 4,571 blocks, and grid clustering is applied to the near region of the shear flow from the swirler and jail bars. For handling geometrical complexities, six multi-block structure grids are generated with hanging nodes, which are stitched together via an interpolation technique of the same order as the numerical scheme used. Shear layers are resolved with 10–15 points across, and the swirlers have 10 or more points along their span, in agreement with previous LES. Small quench holes on the dome plate are not resolved, but a pre-specified mass flow rate is injected through these holes with a porous boundary condition, as discussed below.

For demonstrating the sufficiency of the LES grid, the turbulent kinetic energy is computed at a representative point in the shear layer, as shown in Figure 7, to capture the inertial subrange. This result has been confirmed at other points within the combustor (e.g., cooling jets, swirling shear layer, etc.), but these data are not shown herein, for brevity. To evaluate the effect and validity of turbulent combustion model, the Partially-Stirred Reactor (PaSR) factor computed as $\tau_c/(\tau_m + \tau_c)$ is saved and its distribution over the entire combustor is shown in Figure 7. The PaSR factor mostly varies between 0.8 and 1 for the current configuration, which indicates that the subgrid mixing is near-ideal.

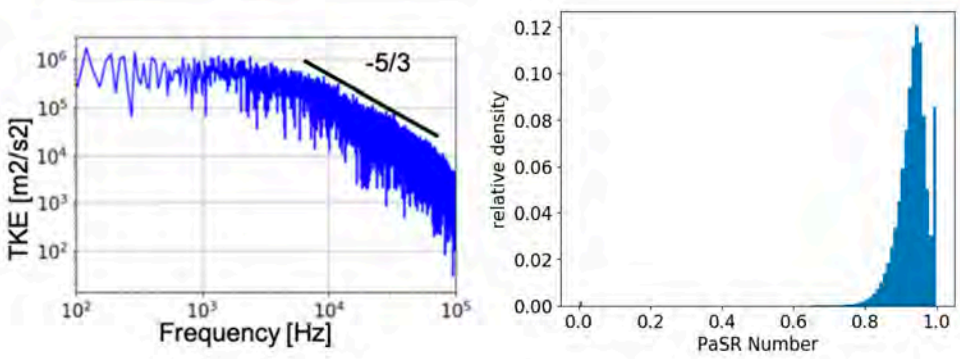

Figure 7. Evaluation of turbulence modeling: Turbulent kinetic energy (TKE) spectrum at a representative point in the shear layer showing at least a decade of inertial range turbulence (left). Histogram of the PaSR factor across the entire combustor for the baseline condition at a representative time-instance (right).

The LES solver is parallelized, and the simulations are run on 1,440 cores. The flow-through time of the combustor is estimated to be 8 ms, according to the entire length of the computational domain and a reference bulk velocity of 30 m/s. Initial transients are neglected for at least the first two flow-through times or until the chamber pressure and volume-integrated HRR stabilize. The statistics are then collected over at least ten additional flow-through times. A simulation for a single flow-through time uses 51,840 central processing unit (CPU) hours on Georgia Tech's supercomputing cluster (Partnership for an Advanced Computing Environment-Phoenix) with Intel® Ivy-bridge i7 processors.

Two operating conditions are of relevance to this rig. The first simulation, "baseline," matches the "Z0" Georgia Tech and RTRC baseline operating conditions and maintains chamber pressure at a target of 0.87 MPa. The next condition uses a higher FAR, in which the fuel mass flow rate is increased by 15%, and the total air mass flow rate is reduced by 8% to maintain the same chamber pressure. This condition coincides with one of the high-FAR conditions in the experimental campaign. These details are summarized in Table 1. All simulations were run with the same solver and model choices.

® Intel is a registered trademark of Intel Corporation, Santa Clara, California.

Table 1. List of simulated operating conditions.

	Fuel Mass Flow Rate	Air Mass Flow Rate	Quench Configuration
Match-point/baseline	9.29 g/s	374.67 g/s	T1, T2, T3, B1, B2
High-FAR	10.68 g/s	344.69 g/s	T1, T2, T3, B1, B2

Validation

For validation and justification of the LES approach, the simulation results at baseline and high-FAR conditions are compared against Georgia Tech experiments, as shown in Figure 8 and . The PJ* chemiluminescence data from the Georgia Tech experiments are compared against the numerical time-averaged line-of-sight HRR predictions (in the absence of CH* or OH* from simulations) at baseline, and this shows a reasonable match in terms of the flame structure in Figure 8.

Next, to evaluate noise predictions, the SPL is computed at several locations within the combustor and is compared against experiments, as shown in Figure 8. The LES results are evaluated in terms of two metrics: (1) the broadband decay rate at higher frequencies, and (2) peak locations and magnitude. The decay rate in SPL matches well between the measurements and LES for 600-2000 Hz at both conditions. However, lower frequencies below 600 Hz show a larger SPL with LES as compared to the experimental measurements, and this is more pronounced for the high FAR case. LES also shows a larger SPL than the measurements for frequencies larger than 2000 Hz. The peaks near 800 Hz, 1100 Hz and 2600 Hz are present in both LES and experiments. As will be shown later, the peak near 2600 Hz corresponds to a longitudinal acoustic mode and its magnitude is predicted to be larger in LES compared to the measurements. The same processing methods are also used for the experimental data, but the total signal length is much longer (several seconds).

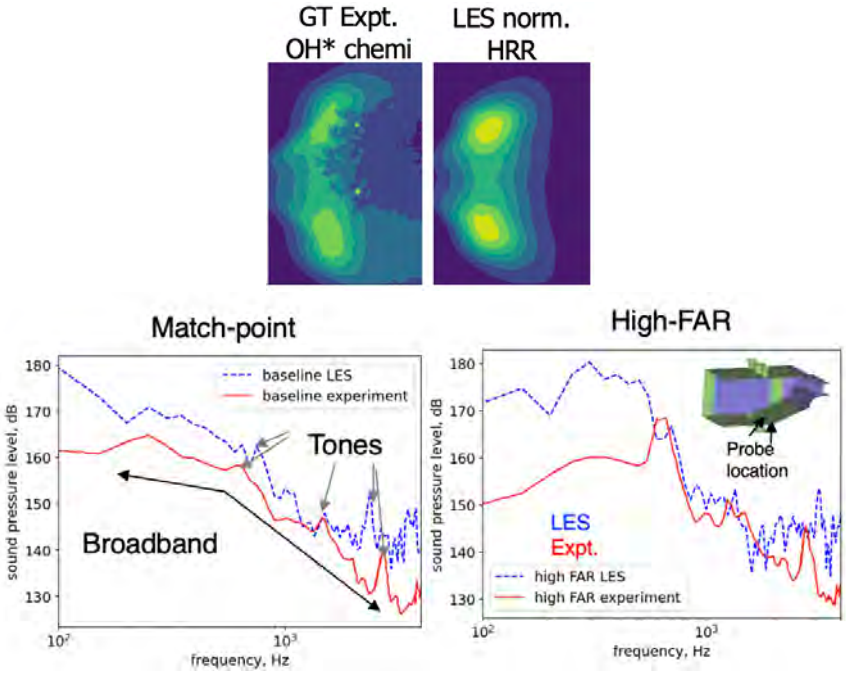

Figure 8. Validation of LES results under baseline and high-FAR conditions against Georgia Tech experiments. Comparison of OH* chemiluminescence data against normalized time-averaged line-of-sight HRR data from LES (top). Schematic showing probe location is included where acoustic data are collected (bottom). Acoustic signature predictions from LES at five probe locations, and comparison against available data from Georgia Tech experiments. LES results are over a 100-ms time window.

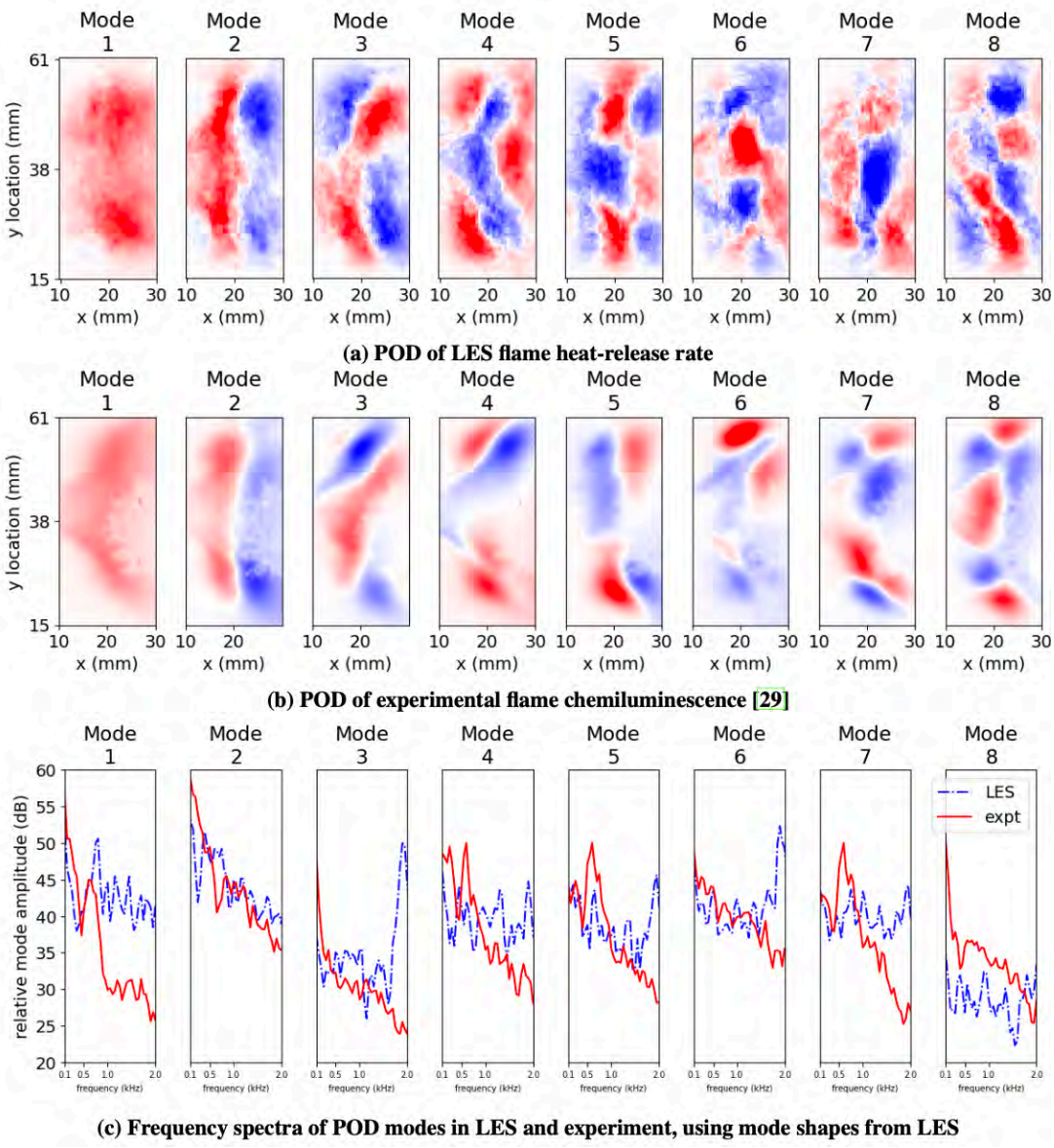

Figure 9. Proper Orthogonal Decompositions of LES HRR and experimental OH* chemiluminescence.

Principal Orthogonal Decomposition Modes

The time-averaged view of the flame does not provide any information about the dynamical features of the flame, which is necessary for noise predictions. The dynamical flame structures of the LES and experiment by looking at a Proper Orthogonal Decomposition (POD) of line-of-sight HRR and chemiluminescence are now compared. The eight primary POD modes are shown in Figure 9. The energy of the fifth mode is less than 20% of the first mode (not shown here) and it is even lower for the higher modes. In terms of comparing the mode shapes between LES and experiments, there is good agreement between experiment and LES for the first four modes, though the latter (with lower energy) mode shapes do not closely align. Next, to understand the spectral significance of these modes, the frequency spectra are compared between the LES and experiment while projecting the LES mode shapes on the unsteady data. This was done to compare spectra one-to-one if the mode shapes are not the same.

The spectral features of the LES and experimental flame match in terms of the peak locations near 800 Hz. However, a difference is noted in terms of the presence of an 1800 Hz peak in the LES data for modes 3 and 5, 6, which is absent in experiments. From the mode shapes, it is noticed that modes 3 and 5, 6 are asymmetrical about the horizontal axis (unlike modes 1, 2, 4). Instead, their top and bottom halves are the negative of each other. Since a conical flame should be symmetric about that axis, it is hypothesized that this mode is associated with the swirl in the flame imposed by the injector, and this is later confirmed using a spectral POD (SPOD) analysis. While the LES is capturing a majority of flame dynamics, the effect of swirl on fluctuating HRR is not matched between LES and experiment and this could be either an artifact of the line-of-sight averaging or modeling deficiencies. In terms of the broadband spectral content, the LES predicted HRR shows a larger high-frequency content for modes 1 and 4. This is unlike the acoustic measurements in the downstream of the combustor that showed a better match within 600-2000 Hz range, although a stronger acoustic longitudinal mode at 2600 Hz, and the reasons for this are unknown and will be explored further in the future.

Based on the frequency spectra for the POD analysis in Figure 9 the frequencies 800 Hz (peaks in both LES and Expt.), 1800 Hz (Peaks in LES but not Expt.), and 2600 Hz (Longitudinal acoustic mode) are selected for further analysis of dynamical features using SPOD. The SPOD shows the mode shapes that are activated at a particular frequency. As an initial verification of the SPOD approach, the longitudinal acoustic mode at 2600 Hz is analyzed using pressure in Figure 10. Pressure antinodes are present near the end and node in the middle near the quench jets. This is also confirmed through computed magnitude and phase along the center axis.

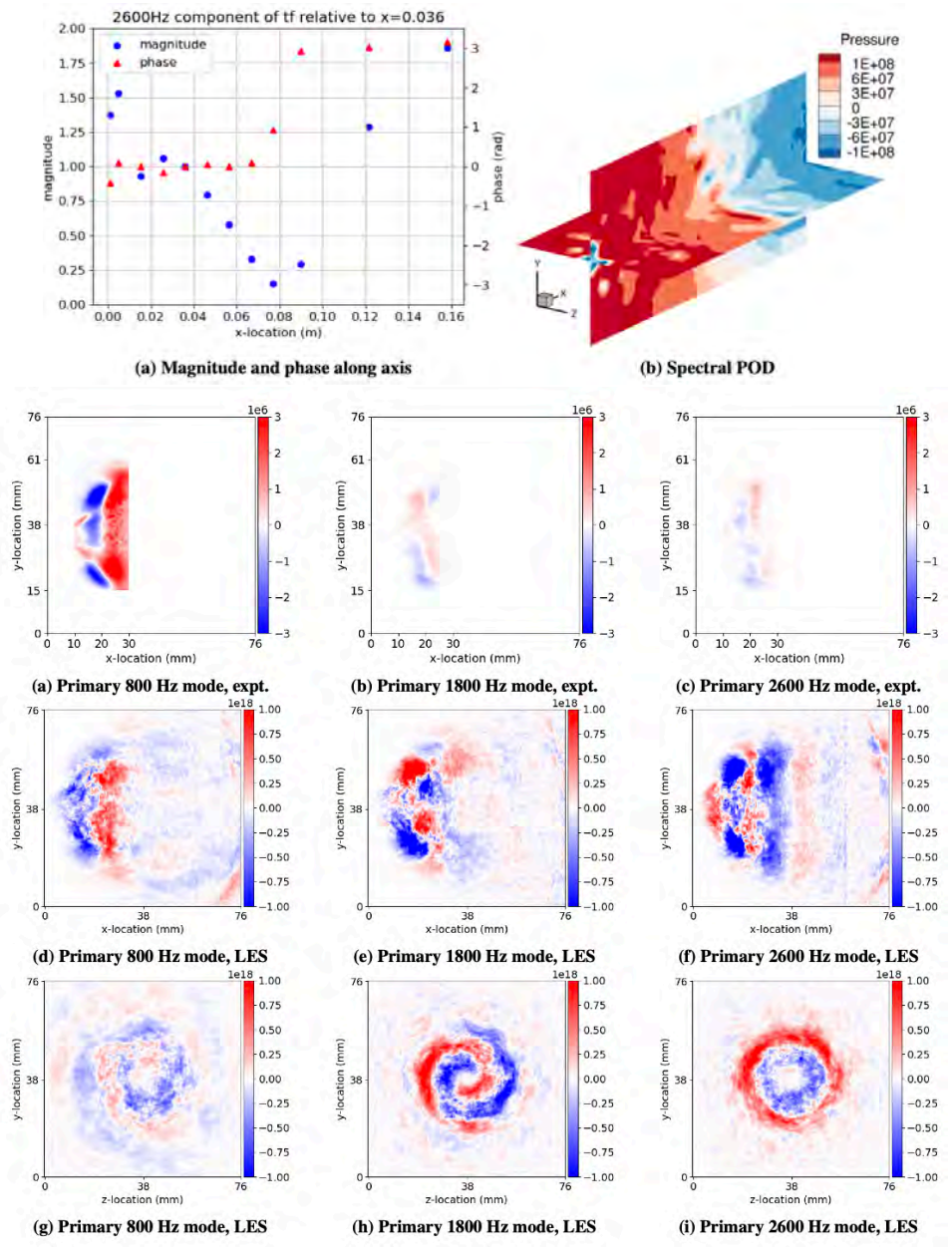

Figure 10. Spectral POD analysis: Longitudinal acoustic mode at 2600 Hz for `baseline' LES visualized using magnitude and phase diagram, and SPOD of pressure (top row). Spectral POD of experimental chemiluminescence data and spanwise and axially averaged HRR from LES (3rd and 4th respectively) in the flame (bottom three rows). The scales from Expt. Chemi and LES HRR are different.

Next, the SPOD of the HRR is analyzed in Figure 10. In the spanwise averaged data (same direction as the LES/experiment comparison in Figure 9), the shape of the 800 Hz and 1800 Hz modes match the modes seen in the 2nd and 3rd POD modes as expected. The 1800 Hz mode also suggests a swirling flame as noted earlier. The 2600 Hz SPOD mode has a similar magnitude to the 1800 Hz mode but is stronger than the 800 Hz mode. This is different from the SPOD analysis of the experimental data which show a much weaker excitation at the acoustic longitudinal mode frequency of 2600 Hz. This comparison is planned to be completed for the high-FAR case in the future.

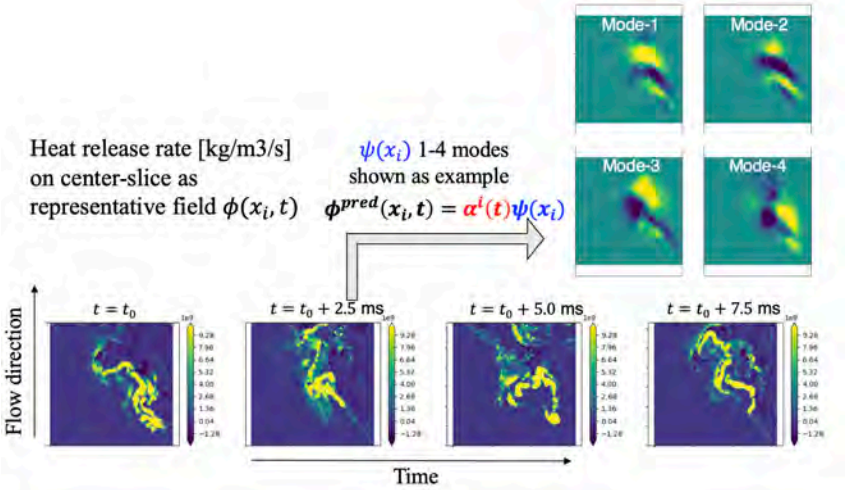

Figure 11. Heat release rate on the center-slice is shown at various times from LES. The 3D HRR field is filtered to a 4X grid for coarse-scale predictions. A POD decomposition is considered on this and the first four POD modes $\psi(x_i)$ and mode coefficients $\alpha^i(t)$ are shown.

Machine Learning for Unsteady Heat Release Rate Predictions

Predicting an unsteady HRR is necessary for ROM of direct and indirect noise. Even though accurate modeling of multiphase turbulent combustion requires LES, it is costly and inappropriate for rapid parametric predictions. Therefore, 3D snapshots from LES dataset are used next to train a ML model. The POD modes were used so far only for validation and post-processing; however, now they are for model development. Figure 11 shows the HRR contours on the center-slice of the combustor at four representative instances. As a first focus, considering the need to predict coarse-scale features of HRR, this 3D flow-field is filtered on a 4X coarse grid and then a POD computation and ML predictions are considered on this data. The resulting POD modes $\psi(x_i)$ and mode coefficients $\alpha^i(t)$ are shown for reference in Figure 12.

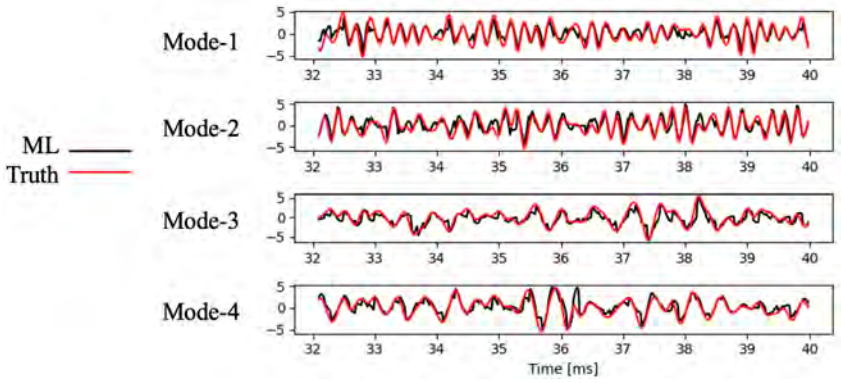

Figure 12. Machine learning predictions are shown for the first four mode-coefficients $\alpha^i(t)$ using long short-term memory (LSTM). The first 40 modes are predicted but only the first four are shown here.

This decomposition results in more than 200 modes; however, considering that the mode energy significantly reduces for higher order modes, it is considered sufficient to model only the first 40 modes to obtain the coarse-scale behavior. If the mode shapes $\psi(x_i)$ remain the same across parametric variations, the problem now reduces to finding the time-evolution of mode coefficients $\alpha^i(t)$ for $i = 1{,}40$. This is done using a ML approach. Long short-term memory (LSTM) model is a supervised learning approach (i.e., needs training data) and it is used for time-series prediction here. The LES data and corresponding POD mode coefficients from 0-30 ms are used for training the model and then the predictions are evaluated for the 30-40 ms time-window.

Representative ML predictions for first four mode coefficients are shown in Figure 12, and the resulting reconstructed (as $\sum_{i=1,40} \alpha^i(t)\psi(x_i)$ and ML predicted HRR on the coarse-grid are shown in Figure 13 at representative time-instances. The coarse-scale behavior is captured reasonably well but ongoing work is considering improvements in this through (a) predicting the mixture fraction, temperature, etc. instead of direct HRR predictions and (b) evaluating the sensitivity to filtering the HRR before predictions.

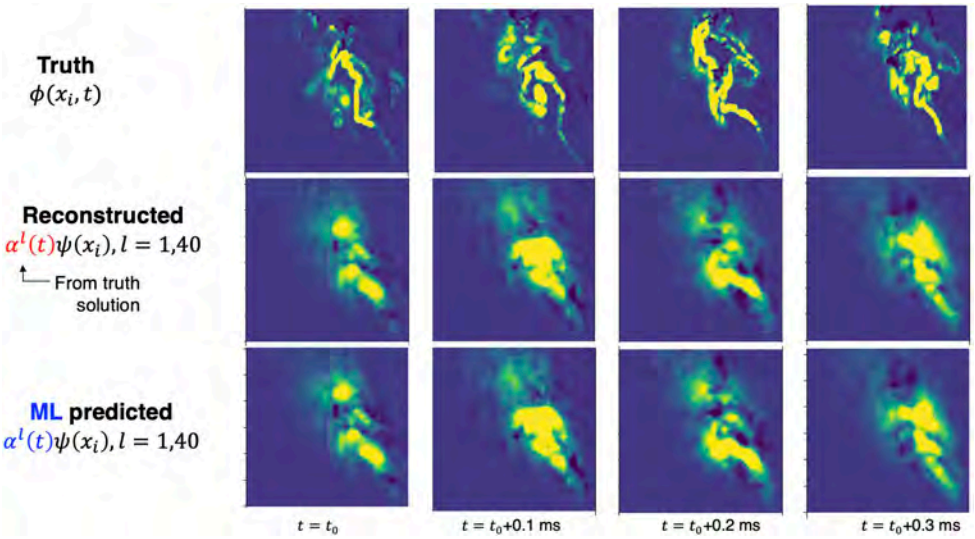

Figure 13. ML predictions are shown for the unsteady HRR. The truth solution is shown for the LES grid, whereas the POD reconstructed solution and ML predictions are on a four times coarser grid for current evaluation using the first 40 modes.

These results do not show the ability of the model to do predictions under conditions that it is not trained on, and this is also a part of an ongoing work with more results expected in the future. As a preliminary evaluation of the ability to extrapolate for the ML model, a LSTM model was trained to predict a sinewave of constant amplitude and frequency, and then an external forcing was added to it in the form of either random noise or in-phase and out-phase sinusoidal disturbances. These results are shown in Figure 14. The in-phase forcing shows a growth in the amplitude whereas the out-phase forcing shows a decay as expected at least for the first four cycles. Furthermore, a random noise of small amplitude (<20%) has no effect, but larger amplitude (50%) causes a growth in the signal. Additional studies are planned in the future, where the unsteady HRR can be forced with external acoustic forcing to study the change in broadband and tonal behavior even though the training data from LES are only at the baseline condition.

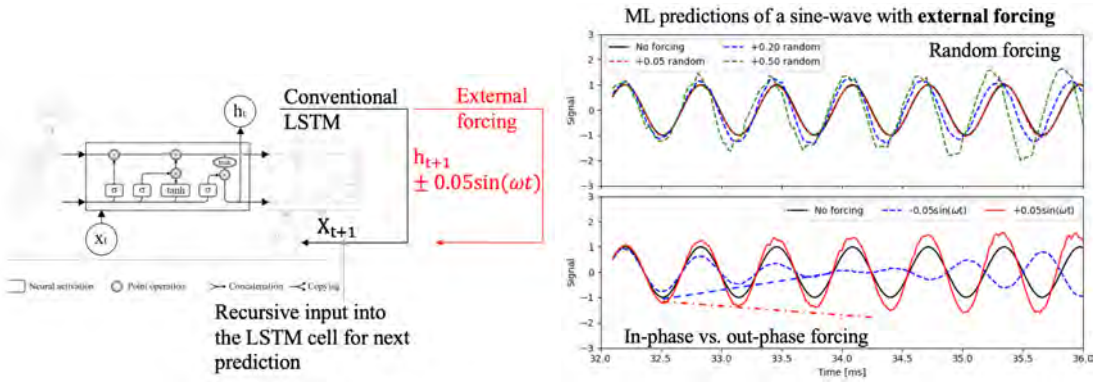

Figure 14. The effect of external forcing is shown on a ML model trained to predict a sinewave of constant amplitude. Both random forcing (with varying amplitude) and in-phase and out-phase sinusoidal forcing are considered.

Data Output and Transfer

The simulations output 3D snapshots of conservative variables. The output frequency of these outputs is 10^4 Hz, and at least 1,000 such snapshots are output for each case over the span of a 100-ms simulation time. The snapshots are collected only after the initial transients for the first two flow-through times have been neglected. A single 3D snapshot is ~1 GB in size. The CFDPostProc software and sample post-processing scripts can (a) compute primitive quantities, such as pressure, temperature, density, and reaction rates; (b) compute derivatives; (c) compute time-averaged quantities; and (d) interpolate data onto another rectangular grid from these files.

In addition to the 3D gas-phase snapshots, the Lagrangian data of the parcel are saved at the same frequency and are available for computing the spray droplet statistics. A post-processing script that translates the Lagrangian quantities onto a Eulerian grid via filtering is also available and provided to other teams. A single droplet snapshot is ~50 MB in size.

Because the 3D gas-phase snapshots are large, they could not be collected at higher frequencies. However, the simulation collects high-frequency data at 10^6 Hz for approximately 200 probe points distributed throughout the computational domain. These points are uniformly placed along the *x*/*y*/*z* directions within the combustor, through the nozzle, and within the exit plenum. These data can be used for accurately computing the frequency characteristics of the system.

Finally, although time-averaged statistics (i.e., mean, root mean square [RMS]) can be computed by using the output 3D snapshots, fine-grained time averaging is also conducted within the code, and the mean and RMS primitive quantities are output for the entire 3D domain. These quantities include the primitive variables, such as velocity, temperature, pressure, density, species mass fractions, and reaction rates. The size of a single time-averaged file is ~4 GB.

Milestones

- Conducted comprehensive validation of LES at baseline and high-FAR conditions against Georgia Tech experiments.
- Collaborated with ROM teams for transfer of at least 1000 3D snapshots for each operating condition and post-processing scripts.
- Performed initial development of a ML model for unsteady heat release predictions.

Major Accomplishments

Efforts during the first three years focused on updating the rig geometry and completing CFD simulations at two conditions. In Year 4, a comprehensive validation of LES against experiments was considered in detail, and 3D snapshots along with post-processing scripts were transferred to Georgia Tech ROM and RTRC teams. A ML-based approach was initiated for ROM of unsteady HRR.

Publications

None.

Outreach Efforts
None.

Awards
None.

Student Involvement
- Graduate student Leo Kastenberg, who is pursuing a master's degree with thesis, worked on developing post-processing scripts for 3D snapshots and worked on detailed validation of the LES results using POD and entropy processing.

Plans for Next Period
- Focus on completion of analysis of the current LES.
- Conduct rig-modifications and simulations for the tonal noise predictions as the details from the experimental campaign become available.
- Continue the development of the ML approach for unsteady heat release prediction by further evaluation of its capability to handle parametric variations and this will be in collaboration with the other reduced-order modeling work in Task 3.

Task 3 – Reduced-Order Modeling
Georgia Institute of Technology

Objective
The overarching objective of this task is to create quick-action ROMs to accurately predict various aspects of noise generation mechanisms that are then collectively fed into a design tool for noise prediction. The specific objective of the Georgia Tech ROM task focuses on the head-end physics in the architecture, namely the flow and spray dynamics, flame dynamics, and generation of entropy disturbances by the flame. The spray/flow dynamics feed into the flame dynamics, thus causing direct combustion noise. The flame dynamics also results in entropy disturbances, which in turn lead to indirect combustion noise at the nozzle. The flame response modeling and the model for the generation of entropy disturbances are provided as inputs to the post-combustion models that will be developed by RTRC. Depending on the prediction results obtained from the RTRC models, these head-end models will be iteratively refined.

Research Approach
In this reporting period, our team focused on tasks pertaining to hydrodynamics, direct noise, and entropy generation budget. Each of these tasks are detailed in their respective subsections below.

Hydrodynamics Modeling
In this reporting period, the hydrodynamics framework was extended to measure the swirling jet global analysis to a 3D Tri-Global problem. Apart from the well-known advantages of swirling jets as canonical flow fields in combustion systems, swirling flows usually result in unsteady hydrodynamic structures that can couple with acoustics. Modeling and predicting the hydrodynamic structures can be important, particularly in the presence of combustion, because these structures can interact with and perturb the flame. Hydrodynamic stability analysis has emerged as a tool for modeling the dynamics of swirling flows in recent decades. This type of analysis is particularly useful for predicting receptivity, or the range of frequencies amplified by the flow. Hydrodynamics provides a transfer function from the background turbulence to large-scale vortical disturbances (which disturb the flame and consequently produce direct noise). Additionally, hydrodynamic stability analysis is particularly valuable for parametric studies determining the sensitivity of the flow response to major design parameters, thus providing a powerful engineering tool. Traditional global hydrodynamic stability analyses have focused on instability generated within the domain (unforced or natural hydrodynamics). The governing equations for this analysis include the linearized continuity and momentum equations in their incompressible form:

$$\nabla \cdot \vec{u}' = 0$$
$$\frac{\partial \vec{u}'}{\partial t} + \left(\bar{\vec{u}} \cdot \nabla\right)\vec{u}' + \left(\vec{u}' \cdot \nabla\right)\bar{\vec{u}} + \frac{\nabla p'}{\bar{\rho}} - \nu \nabla^2 \vec{u}' = 0 \qquad \text{(Eq. 1)}$$

As shown in the previous yearly report, we use a bi-global stability analysis framework, which allows the calculated modes to significantly vary along two coordinates. Using the axisymmetric configuration of the problem, the velocity and pressure disturbances are assumed to take the following harmonic form shown below. The amplitude of the mode is a function of the radial and spatial coordinates, whereas temporal and azimuthal periodicity is maintained by using the frequency ω and azimuthal wave number m. The azimuthal wave number, m, captures the helical modes of swirling jets of interest:

$$g'(r,\theta,z,t) = \hat{g}(r,z)e^{-i(\omega t - m\theta)} \quad \text{(Eq. 2)}$$

Tri-Global stability allows modal features of the flow perturbations to vary in all three spatial directions and the phase of disturbance only captures the temporal terms. In a Cartesian coordinate system, the Tri-Global natural mode is given by:

$$g'(x,y,z,t) = \hat{g}(x,y,z)e^{-i\omega t} \quad \text{(Eq. 3)}$$

Application of the Tri-Global modal expansion to governing Equation 1 and linearization around the 3-D time averaged LES velocity flow shown in Fig. 15 results in the Tri-Global linearized Navier Stokes equations (LNSE). In comparison to their Bi-Global counterpart, the Tri-Global equations are more symmetric in the Cartesian coordinate system. Acknowledging the Tri-Global equations have more computational expense due to the fidelity added by an extra dimension, a centered finite difference scheme is used to obtain the solution to the highly symmetric Tri-Global LNSE. With n nodes in each direction, a centered finite difference 7-point stencil is used to discretize $(n-2)^2$ unknowns. The discretized Tri-Global LNSE for each node can be formulated as a system of linear, coupled equations that represent a generalized eigenvalue problem (GEVP) as:

$$\mathbf{A}\vec{v} = \omega\mathbf{B}\vec{v} \quad \text{(Eq. 4)}$$

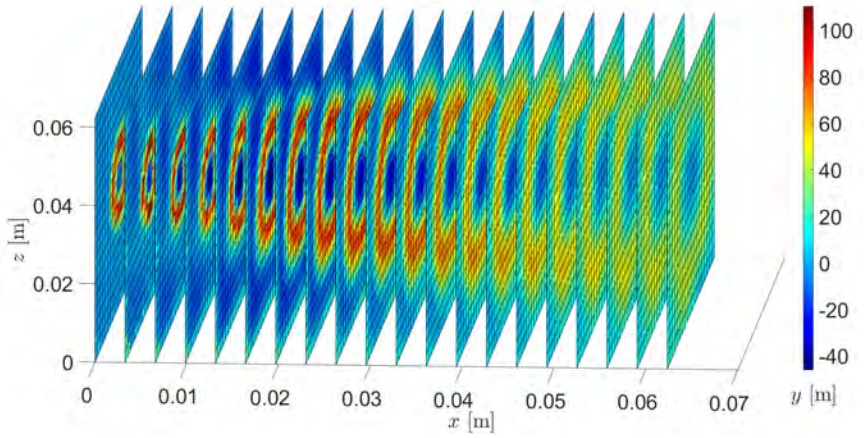

Figure 15. Time averaged LES axial velocity flow field interpolated on cubical mesh.

For a single interior node (i,j,k) of the grid the stiffness ($\mathbf{A} = [\mathbf{A_1}|\mathbf{A_2}|\mathbf{A_3}|\mathbf{A_4}]$) and mass ($\mathbf{B}$) matrices of the GEVP are obtained by the discretized version of the Tri-Global LNSE:

$$\mathbf{A_1} = \begin{bmatrix} -\frac{h}{2}\bar{u} - \nu & -\frac{h}{2}\bar{v} - \nu & -\frac{h}{2}\bar{w} - \nu & h^2\frac{\partial \bar{u}}{\partial x} + 6\nu & \frac{h}{2}\bar{u} - \nu & \frac{h}{2}\bar{v} - \nu & \frac{h}{2}\bar{w} - \nu \\ 0 & 0 & 0 & h^2\frac{\partial \bar{v}}{\partial x} & 0 & 0 & 0 \\ 0 & 0 & 0 & h^2\frac{\partial \bar{w}}{\partial x} & 0 & 0 & 0 \\ -1 & 0 & 0 & 0 & 1 & 0 & 0 \end{bmatrix}$$

$$\mathbf{A_2} = \begin{bmatrix} 0 & 0 & 0 & h^2\frac{\partial \bar{u}}{\partial y} & 0 & 0 & 0 \\ -\frac{h}{2}\bar{u} - \nu & -\frac{h}{2}\bar{v} - \nu & -\frac{h}{2}\bar{w} - \nu & h^2\frac{\partial \bar{v}}{\partial y} + 6\nu & \frac{h}{2}\bar{u} - \nu & \frac{h}{2}\bar{v} - \nu & \frac{h}{2}\bar{w} - \nu \\ 0 & 0 & 0 & h^2\frac{\partial \bar{w}}{\partial y} & 0 & 0 & 0 \\ 0 & -1 & 0 & 0 & 0 & 1 & 0 \end{bmatrix}$$

$$\mathbf{A_3} = \begin{bmatrix} 0 & 0 & 0 & h^2\frac{\partial \bar{u}}{\partial z} & 0 & 0 & 0 \\ 0 & 0 & 0 & h^2\frac{\partial \bar{v}}{\partial z} & 0 & 0 & 0 \\ -\frac{h}{2}\bar{u} - \nu & -\frac{h}{2}\bar{v} - \nu & -\frac{h}{2}\bar{w} - \nu & h^2\frac{\partial \bar{w}}{\partial z} + 6\nu & \frac{h}{2}\bar{u} - \nu & \frac{h}{2}\bar{v} - \nu & \frac{h}{2}\bar{w} - \nu \\ 0 & 0 & -1 & 0 & 0 & 0 & 1 \end{bmatrix}$$

$$\mathbf{A_4} = \begin{bmatrix} -\frac{h}{2\rho} & 0 & 0 & 0 & \frac{h}{2\rho} & 0 & 0 \\ 0 & -\frac{h}{2\rho} & 0 & 0 & 0 & \frac{h}{2\rho} & 0 \\ 0 & 0 & -\frac{h}{2\rho} & 0 & 0 & 0 & \frac{h}{2\rho} \\ 0 & 0 & 0 & 0 & 0 & 0 & 0 \end{bmatrix}$$

$$\mathbf{B} = \begin{bmatrix} 0 & 0 & 0 & i & 0 & 0 & 0 & 0 & 0 & 0 & 0 & 0 & 0 & 0 & 0 & 0 & 0 & 0 & 0 & 0 & 0 & 0 & 0 & 0 & 0 & 0 & 0 \\ 0 & 0 & 0 & 0 & 0 & 0 & 0 & 0 & 0 & 0 & i & 0 & 0 & 0 & 0 & 0 & 0 & 0 & 0 & 0 & 0 & 0 & 0 & 0 & 0 & 0 & 0 \\ 0 & 0 & 0 & 0 & 0 & 0 & 0 & 0 & 0 & 0 & 0 & 0 & 0 & 0 & 0 & 0 & 0 & i & 0 & 0 & 0 & 0 & 0 & 0 & 0 & 0 & 0 \\ 0 & 0 & 0 & 0 & 0 & 0 & 0 & 0 & 0 & 0 & 0 & 0 & 0 & 0 & 0 & 0 & 0 & 0 & 0 & 0 & 0 & 0 & 0 & 0 & 0 & 0 & 0 \end{bmatrix}$$

Due to the presence of a singularity in the mass matrix (as pressure terms are not discretized in the continuity equation), an explicit solution $\mathbf{B^{-1}A}\,\vec{v} = \omega\vec{v}$ to the GEVP is not possible. An iterative technique of shift and invert with a user-defined shift μ is used to transform the GEVP as:

$$\left(\mathbf{A} - \mu\mathbf{B}\right)^{-1}\mathbf{B}\vec{v} = \frac{1}{\omega - \mu}\vec{v} \qquad \text{(Eq. 5)}$$

Natural vortical modes of the 3D flow field were obtained using the Tri-Global finite-difference framework. In the low-frequency region, three unstable modes detected are shown in Table 2 by ascending order of growth rates.

Table 2. Unstable low-frequency Tri-Global modes.

	$\omega_r + i\omega_i$
Mode 1	$0.3234 + 0.0275i$
Mode 2	$0.2989 + 0.0276i$
Mode 3	$0.3198 + 0.0277i$

Contours of axial velocity disturbances for the modes of Table 2 are displayed in Figure 16. Modes 1 and 3 propagate at approximately the same oscillatory frequency and exhibit similar mode shapes along the axial direction. All three modes display a strong presence between the inner and outer shear layers of the jet.

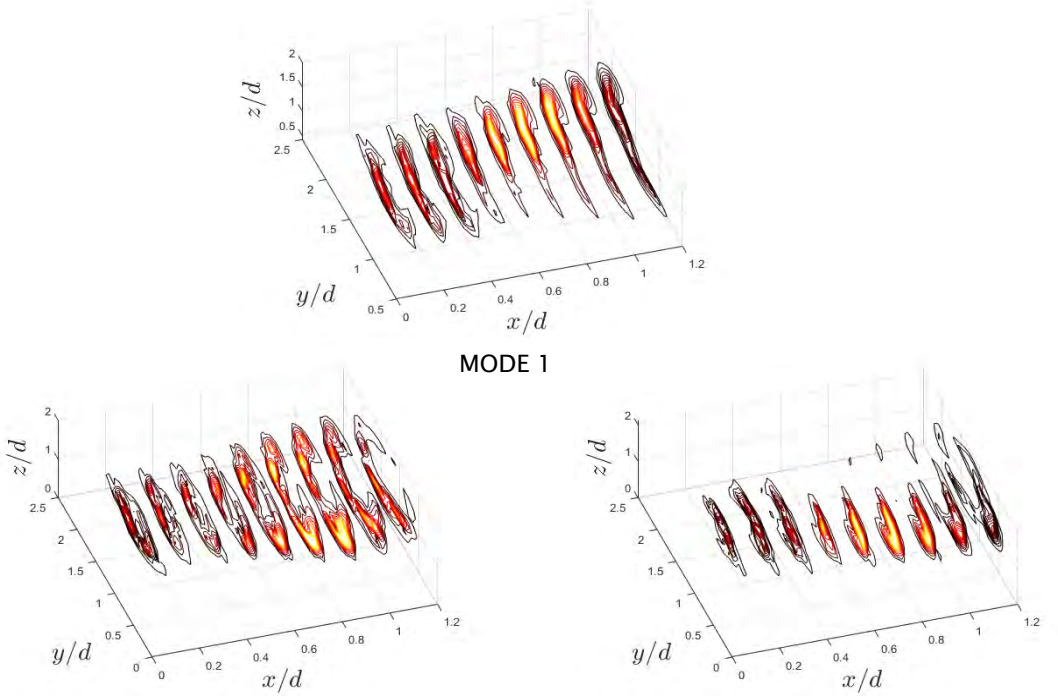

Figure 16. Mode-shapes of axial velocity disturbance corresponding to modes of Table 2.

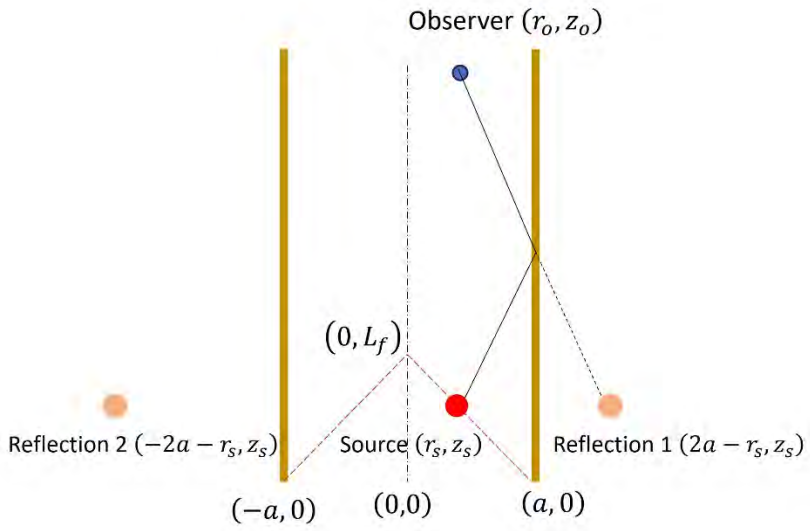

Figure 17. Diagram of the acoustic propagation from a point source on the flame involving a reflection and its equivalent mirror sources. Only one path is shown for simplicity.

Modeling *p'-q'* Correlation/Coherence

The objective of this task is to study the correlation between the HRR measured by chemiluminescence and the generated noise, specifically direct noise. This correlation can be potentially further applied to the separation of direct and indirect noise sources through partial coherence methods. In the literature, experimental attempts to separate indirect and direct noise sources in a combustor have relied on partial coherence methods relating temperature measurements to indirect noise sources. However, high-speed temperature measurements in combustors are difficult to perform, and no high-resolution, high-frequency measurements are currently available in the literature. The coherence between the HRR and direct noise is not fully understood, because little literature has reported coherence, and the few existing studies have shown values well below unity.

Previously as part of this task, an analytical model was developed to study the effects of acoustic noncompactness and nearfield effects on the *p'-q'* coherence of an open flame. It demonstrated how these effects could act to lower the coherence even in the case of a direct noise dominant system. The parameters that govern coherence were identified as (1) the normalized flame correlation length Λ/a, (2) the "compactness factor" a/λ, (3) the distance of the observer R/a, and (4) the flame aspect ratio L_f/a. Furthermore, it was also suggested that coherence is high for a wide range of practical applications. From the perspective of noise source separation, flames are in an enclosed environment, where the acoustic pressure is modified by reflections and duct modes. The analytical model has been extended and applied to a confined scenario to assess the impact of confinement to the results found for the open flame model. Starting from the linear wave equation:

$$\frac{\partial^2 p'(\boldsymbol{x},t)}{\partial t^2} - c_u^2 \nabla \cdot \left(\frac{\rho_u}{\rho_0} \nabla p'(\boldsymbol{x},t) \right) = (\gamma - 1) \frac{\partial q_v(\boldsymbol{x},t)}{\partial t} \qquad \text{(Eq. 6)}$$

The Fourier transformed solution can be written as:

$$p'(\boldsymbol{x}_0,\omega) = \frac{-i\omega(\gamma-1)}{4\pi c_u^2} \oint q' \mathbf{G}(\boldsymbol{x}_s,\boldsymbol{x}_0) dS \qquad \text{Eq. 7)}$$

where $\mathbf{G}(\boldsymbol{x}_s,\boldsymbol{x}_0)$ is the Green's function for a source at $\boldsymbol{x}_s$ and the observer at $\boldsymbol{x}_0$. From here on the Fourier transformed variables are considered. In the free field, it is well known that the Green's function takes the form:

$$\mathbf{G}(\boldsymbol{x_s},\boldsymbol{x_0}) = \begin{cases} \dfrac{e^{ik|\boldsymbol{x_s}-\boldsymbol{x_0}|}}{|\boldsymbol{x_s}-\boldsymbol{x_0}|} & \text{3D freefield} \\ \dfrac{i}{4}H_0^{(1)}\left(\dfrac{2\pi|\boldsymbol{x_s}-\boldsymbol{x_0}|}{\lambda}\right) & \text{2D freefield} \end{cases} \quad \text{(Eq. 8)}$$

where $H_0^{(1)}$ is the Hankel function of the first kind of the zeroth order. Now, it is possible to write the auto spectra of the acoustic pressure G_{pp}, the global HRR G_{QQ}, and the cross spectra G_{Qp} as:

$$G_{QQ} = \iint q'(\boldsymbol{x_{s_1}})q'^{*}(\boldsymbol{x_{s_2}})ds_1 ds_2 \quad \text{(Eq. 9)}$$

$$G_{pp} = \frac{\omega^2(\gamma-1)^2}{16\pi^2 c_u^4}\iint q'(\boldsymbol{x_{s_1}})q'^{*}(\boldsymbol{x_{s_2}})\mathbf{G}(\boldsymbol{x_{s_1}},\boldsymbol{x_0})\mathbf{G}^{*}(\boldsymbol{x_{s_2}},\boldsymbol{x_0})ds_1 ds_2 \quad \text{(Eq. 10)}$$

$$G_{Qp} = \frac{i\omega(\gamma-1)}{4\pi c_u^2}\iint q'(\boldsymbol{x_{s_1}})q'^{*}(\boldsymbol{x_{s_2}})\mathbf{G}^{*}(\boldsymbol{x_{s_2}},\boldsymbol{x_0})ds_1 ds_2 \quad \text{(Eq. 11)}$$

A convenient place to build intuition is a two-dimensional (2D) duct, where reflection effects can be understood in conceptually simple way. Moreover, it is possible to construct a relatively simple Green's function for a 2D duct using the method of images. For each infinitesimal source, it is possible to construct the Green's function by summing the free space Green's function from Equation 8 for all equivalent mirror sources, as described in figure 17. Therefore, assuming no losses at the boundary, the Green's function for an observer inside a 2D duct can be written as:

$$G(\boldsymbol{x_s},\boldsymbol{x_0}) = \sum_{-N}^{N}\frac{i}{4}H_0^{(1)}\left(\frac{2\pi|\boldsymbol{x_n}-\boldsymbol{x_0}|}{\lambda}\right) \quad \text{(Eq. 12)}$$

where $H_0^{(1)}$ is the Hankel function of the first kind of the zeroth order, $\boldsymbol{x_0} = (r_0, z_0)$ is the position of the observer, $\boldsymbol{x_s} = (r_s, z_s)$ is the position of the local point source on the flame, and:

$$\boldsymbol{x_n} = \begin{cases} (2na - r_s, z_s) & n\text{is odd} \\ (2na + r_s, z_s) & n\text{is even} \end{cases} \quad \text{(Eq. 13)}$$

N is infinite but we truncate it such that its value represents the maximum number of reflections considered and n is a reflection index where $|n|$ represents the number of reflections an acoustic path took. $N = 0$ represents an unconfined configuration. It was observed that N=3 is generally sufficient for convergence. It should be noted that for a 2D geometry, the integrals in Equation 9 through Equation 11 are their equivalent line integrals instead of surface integrals. Figure 18 shows iso-contours of coherence for a flat flame at various compactness factors. Comparing an open flame configuration and ducted configuration, the general effect of confinement acts to allow more acoustic pathways to contribute. This may both act to lower or increase coherence depending on the flame geometry and location of the observer. Figure 19 shows a similar plot for varied flame lengths. As with the case of an open flame, coherence is maximum to the side of the flame in the case of a long flame. Such results have implications for sensor placement in combustor diagnostics as well.

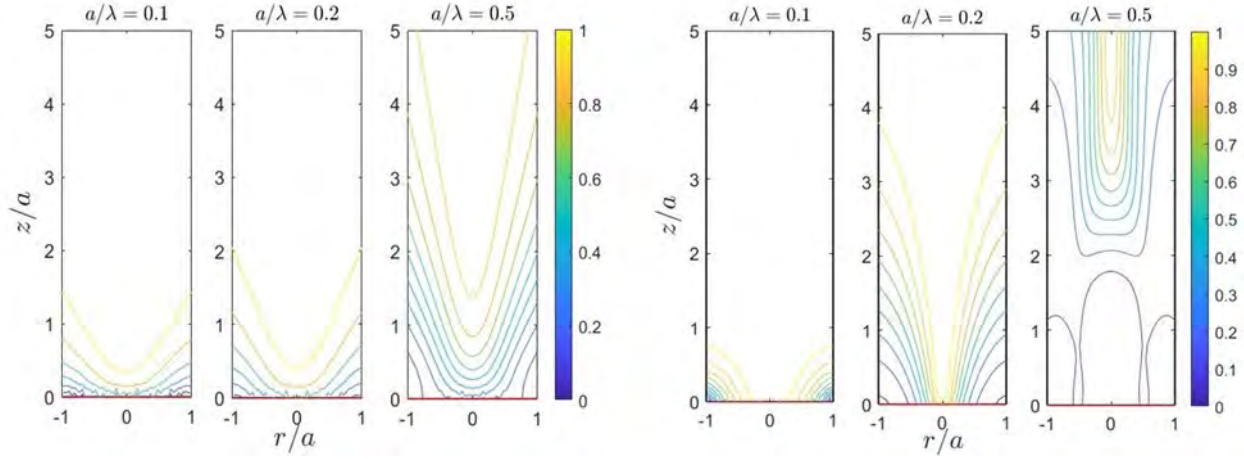

Figure 18. Contour plot of coherence for a flame of $L_f = 0$ of a correlation length $\Lambda/a = 0.1$ for various compactness factors. Unconfined (left) and 2D duct confined with N=3 (right).

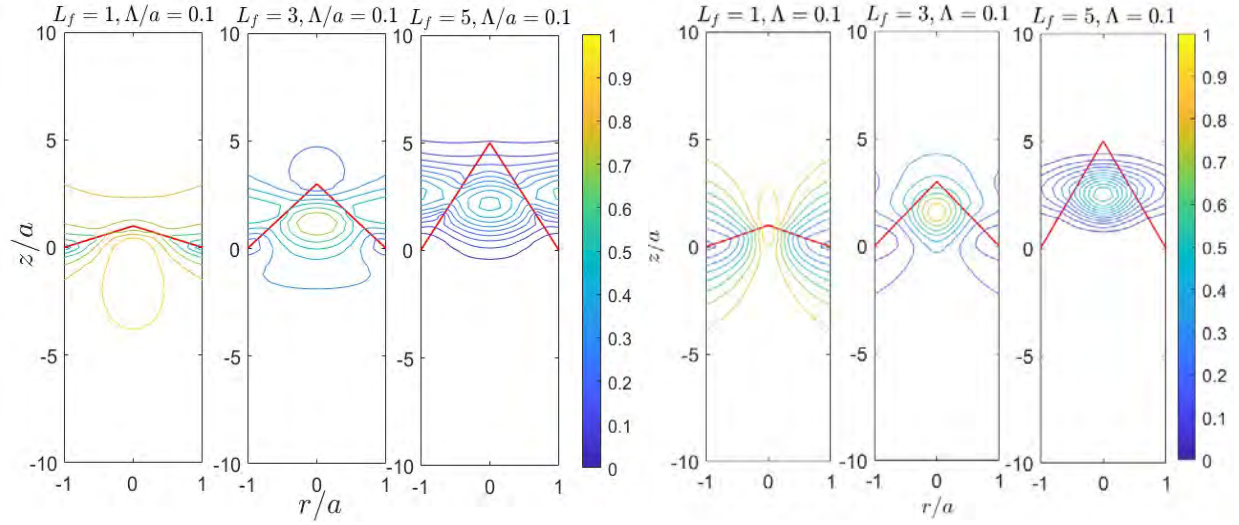

Figure 19. Contour plots of coherence for a flame correlation length of $\Lambda/a = 0.1$ and a compactness factor of $a/\Lambda = 0.2$ for various L_f. Unconfined (left) and 2D duct (right).

Analysis of Entropy Production Mechanisms

In this reporting period, our team has worked on analyzing various mechanisms through which entropy is produced to better understand the dynamics of entropy waves or indirect combustion noise. Prior work has focused on the dynamics of entropy fluctuations by purely considering the heat release term as the dominant source. Although it has been well established in previous studies that for premixed flames, the heat release term produces significant amounts of entropy, in the case of non-premixed flames where diffusion processes need to be considered, estimation of all source terms in the governing equation of entropy needs to be considered. Firstly, simplifications to the governing equation were made to reduce the complexities associated with the diffusion term and then LES simulations were performed in simulating two well-documented flames – Sandia-D and Sydney ethanol spray ETF-2 (Ethanol Flame-2). Using the mean flow field, the time-averaged entropy production rates due to various sources were calculated and budgeted across both flames. Operating conditions were changed around the baseline Sandia-D conditions to understand the sensitivity of production rates. Additionally, far field effects have been analyzed in the integrated production rates as a function of area of integration and the results are presented for all cases of Sandia-D flame. For the spray flame, entropy budget across the flame has been

studied and presented for the baseline conditions. The governing equation for transport and volumetric production rate of entropy in a fluid flow is given as follows:

$$\rho T\frac{Ds}{Dt} = -\nabla\cdot\vec{q} + \overline{\overline{\tau}}:\nabla\vec{u} - \rho\sum_{i=1}^{N_s} D_i\nabla Y_i\cdot\vec{F_i} - \sum_{i=1}^{N_s}\mu_i\left(\dot{\omega}_i + \nabla\cdot\left(\rho D_i\nabla Y_i\right)\right) \quad \text{(Eq. 14)}$$

where ρ is density, T is temperature, $\overline{\overline{\tau}}$ is the shear stress tensor and is modeled using Stokes' hypothesis, $\vec{u}$ is the velocity, D_i and Y_i is the laminar diffusion coefficient and mass fraction of species i, $\vec{F_i}$ is the body force per mass acting on species i, μ_i is the chemical potential of species i, $\dot{\omega}_i$ is the species production rate due to chemical reaction and D/Dt is the substantial derivative. The heat flux vector $\vec{q}$ is given by:

$$\vec{q} = -k\nabla T + \rho\sum_{i=1}^{N_s} h_i Y_i\vec{u}_{D,i} + R_u T\sum_{i=1}^{N_s}\sum_{j=1}^{N_s}\frac{X_j D_{T,i}}{W_i D_{ij}}\left(\vec{u}_{D,i} - \vec{u}_{D,j}\right) + \vec{q}_{rad} \quad \text{(Eq. 15)}$$

where h_i is the specific enthalpy of species i, $\vec{u}_{D,i}$ is the diffusion velocity of species i, $D_{T,i}$ is the thermal diffusion coefficient and D_{ij} is the binary mass diffusion coefficient of species i in otherwise pure j, $\vec{q}_{rad}$ is heat transfer due to radiation. The chemical reaction term $-\sum_{i=1}^{N_s}\mu_i\dot{\omega}_i$ in Equation 14 can be further expanded as:

$$-\sum_{i=1}^{N_s}\mu_i\dot{\omega}_i = -\sum_{i=1}^{N_s}h_{f,i}^0\dot{\omega}_i - \sum_{i=1}^{N_s}\dot{\omega}_i\int_{T_0}^{T}c_{p,i}dT + \sum_{i=1}^{N_s}Ts_i\dot{\omega}_i = \dot{q} - \sum_{i=1}^{N_s}\dot{\omega}_i\int_{T_0}^{T}c_{p,i}dT + \sum_{i=1}^{N_s}Ts_i\dot{\omega}_i \quad \text{(Eq. 16)}$$

where $\dot{q}$ is the HRR, $\sum_{i=1}^{N_s}\dot{\omega}_i\int_{T_0}^{T}c_{p,i}dT$ is the sensible enthalpy change of species i due to chemistry and $\sum_{i=1}^{N_s}Ts_i\dot{\omega}_i$ is the partial entropy term.

The source terms on the right-hand side of Equation 14 represent entropy production due to heat flux, compressibility effects, body force, and chemical reactions respectively. From the expansion of the heat flux vector, entropy production arises due to Fourier's heat conduction, enthalpy transport due to diffusion, full multicomponent diffusion, and radiation, respectively. Moreover, chemical reaction term represents the combined entropy generation due to heat release, sensible enthalpy changes, and partial entropy through species production/consumption. However, in this analysis, a simplified form of transport equation (Equation 14) is considered by making a few assumptions. Assuming that the heat flux is driven purely due to the heat conduction, only the first term on the right-hand side of Equation 15 is considered. For low subsonic flows, i.e., $M \ll 1$, the pressure compression term can be neglected and thus retaining only the viscous dissipation term. Moreover, by assuming that mass diffusion is only driven by Fickian diffusion, second order diffusion effects like *Soret* and *Dufour* as well as full multi-component diffusion effects can be neglected altogether. Additionally, unity Lewis number, Prandtl number, Schmidt number are assumed along with equal mass diffusivities for all the species. The resulting simplified entropy transport equation analyzed in this study is given as follows:

$$\frac{D(\rho s)}{Dt} = \nabla\cdot(\gamma\nabla s) + \frac{1}{T}\overline{\overline{\sigma}}:\nabla\vec{u} + \frac{\gamma c_p}{T^2}\left(\left(\frac{\partial T}{\partial x}\right)^2 + \left(\frac{\partial T}{\partial y}\right)^2 + \left(\frac{\partial T}{\partial z}\right)^2\right) + \sum_{i=1}^{N_s}\gamma\frac{R_i}{X_i}\left(\frac{\partial Y_i}{\partial x}\frac{\partial X_i}{\partial x} + \frac{\partial Y_i}{\partial y}\frac{\partial X_i}{\partial y} + \frac{\partial Y_i}{\partial z}\frac{\partial X_i}{\partial z}\right) - \frac{1}{T}\sum_{i=1}^{N_s}\mu_i M_i\dot{\omega}_i \quad \text{(Eq. 17)}$$

In this simplified form of transport equation (Equation 17), the first term on the right-hand side represents the diffusion of entropy while the rest of the terms represent the volumetric entropy production rate due to viscous dissipation, heat conduction, mass diffusion, and chemical reaction, respectively.

For this study, two well-documented diffusion flames have been identified to simulate – Sandia-D and Sydney ETF-2. The computational domain of dimensions $100d_j \times 100d_j \times 105d_j$, where d_j is the jet-diameter of 7.2 mm, is used for the Sandia-D flame as shown in Figure 20.

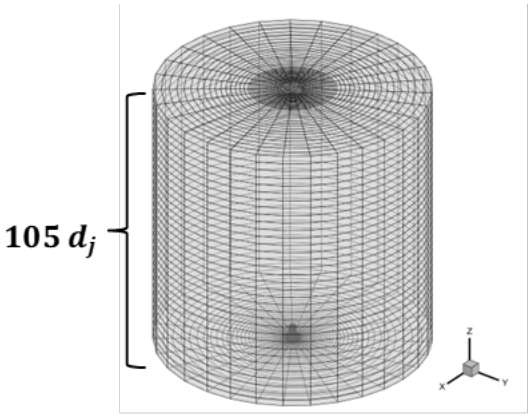

Figure 20. Computational domain of the Sandia-d flame.

As the flame is unconfined, the co-flow inlet of air spans $48\,d_j$ on either side of the jet-inlet. The length of the burner is $5\,d_j$ measured upstream of the jet exit as shown in Figure 20. The flame is stabilized by defining a pilot mixture of hot products of ethyne-air mixture at equivalence ratio of 0.77, spanning $2.5\,\mathrm{d_j}$. The summary of the boundary conditions is provided in Table 3.

Table 3. Boundary conditions of the baseline Sandia-D flame.

	Jet	Pilot	Co-flow
Velocity (m/s)	49.6	11.4	0.9
Temperature (K)	294	1880	291
Pressure (atm)	0.993	0.993	0.993
Y_{CH_4}	0.156	0	0
Y_{O_2}	0.197	0.054	0.233
Y_{CO_2}	0	0.11	0
Y_{H_2O}	0	0.0942	0
Y_{CO}	0	4×10^{-3}	0
φ	2.38	0.77	0

Steady state Reynolds-averaged Navier-Stokes (RANS) simulations were performed to ascertain the dominant integral length scales of the flow and hence obtained the range of turbulent length scales. For LES, since 80% of the TKE is usually resolved, mesh sizing calculations have been performed accordingly. The first cell size is 0.8 mm downstream of the jet exit with the stretch rate of 1.1 in the z-direction. The final cell count stands at 200,000 hexahedral cells with refinements

around the flame region. Furthermore, to assess the validity of the mesh, time series data of velocity were sampled for 15 flow-through times at different probes in the domain, and the TKE spectrum plot was obtained. It was observed that 80-85% of TKE was resolved in the domain.

For the Sydney ETF2 flame, the computation domain of dimensions $97\ \mathrm{d_{js}} \times 38\ \mathrm{d_{js}} \times 38\ \mathrm{d_{js}}$ was considered, as shown in Figure 21, where d_{js} is the spray nozzle jet diameter. The mesh consists of 1.6 million hexahedral cells and like the analysis on the Sandia-D domain, TKE spectrum plot was generated, and Pope's criterion was satisfied. The boundary conditions are provided in Table 4.

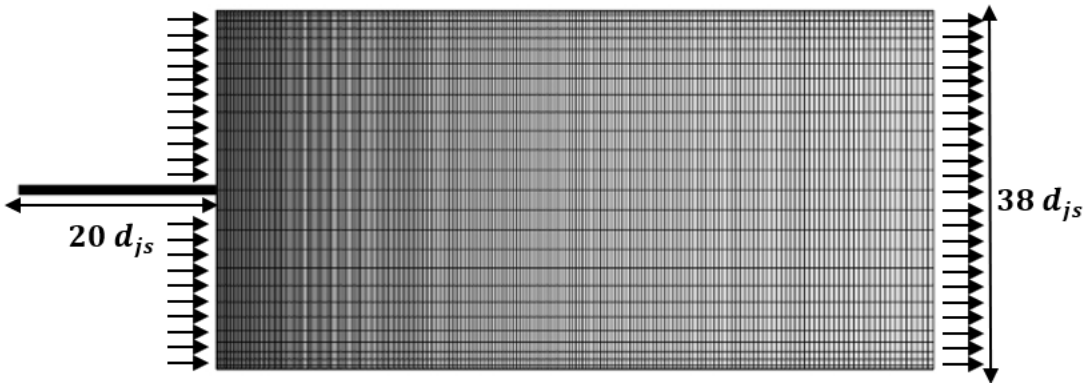

Figure 21. Computational domain of ETF2 spray flame.

Table 4. Boundary conditions of the baseline ETF2 spray flame.

	Jet	Pilot	Co-flow
Velocity (m/s)	36	11.6	4.7
Temperature (K)	273	2400	298
Pressure (atm)	1	1	1
$Y_{C_2H_5OH(g)}$	0.0373	0	0
$Y_{C_2H_5OH(l)}$	1	0	0
Y_{O_2}	0.22	0.07	0.233
Y_{CO_2}	0	0.125	0
Y_{H_2O}	0	0.082	0

The simulations for both the flames were performed using Ansys Fluent 2024 R1 solver. The Wall adapting local eddy-viscosity (WALE) model is used for closure of the sub filter unresolved source terms in the LES equations. Detailed chemistry with pure finite rate effects has been used for modelling the chemical reactions for the Sandia-D flame. The chemical mechanism consists of 16 species and 41 reactions. Species transport model with Stiff Chemistry solver has been used to solve the species' conservation equations. For the spray flame, a single step global chemistry is used for modelling chemical reactions with finite-rate/eddy-dissipation turbulence-chemistry interaction. The equations are discretized using a cell-centered finite volume co-located pressure-based segregated solver. The pressure-velocity coupling is achieved using a SIMPLEC predictor-corrector algorithm. The numerical scheme is second-order accurate in space and a bounded second-order implicit scheme is used for transient formulation. The simulation of the spray flame includes the implementation of a Lagrangian-Eulerian scheme, where the gas phase is treated as a continuum by solving the filtered LES equations, while the

dispersed droplets are tracked individually in the Lagrangian frame of reference. For accurate prediction of the material properties of the species, temperature dependent models like piecewise-polynomial and Sutherland formulations are used for computing specific heat and viscosity, respectively. Mass diffusivity is modeled using the kinetic theory model. Mixing law models are used for calculating the mixture-averaged properties. The entropic source-terms were calculated using a user-defined scalar formulation by treating the production of entropy as a passive scalar in the solution. Additionally, the source terms were volumed averaged locally to filter out the spatial fluctuations. For the transient calculation of both the flames, the Courant-Friedrichs-Lewy (CFL) value of 0.8 was maintained with the time-step size of 25 μs. The LES statistical data are collected over 15 flow-through times for both the Sandia-D and ETF2 flames. The collection of statistics was performed for the Sandia-D flame simulations after 50 flow-through times, while for the ETF2 flame it was performed after 10 flow-through times to wash out the initial transient effects.

First, the qualitative representations of entropy production in the Sandia-D flame due to different sources are discussed, followed by a detailed quantitative analysis of the spatial profiles of the entropy budget, and the influence of operating conditions around the baseline conditions on the same. Similar analysis is presented for the spray flame ETF2 as well. Figure 22 shows the qualitative trends of time-averaged volumetric entropy production rates due to viscous dissipation, heat conduction, mass diffusion, and chemical reaction respectively at the center-plane. It can be observed that the effects of viscous dissipation and heat conduction are highly negligible as seen from the orders of magnitude differences with the effects of mass diffusion and chemical reaction, respectively. Viscous dissipation is dominated by the magnitude of velocity gradients, and as the gradients are stronger at the jet exit, the associated entropy production rates are higher in that region. Furthermore, the effect of viscous dissipation does sustain downstream due to flow acceleration because of gas expansion across the flame, and the resulting velocity gradients drive entropy production. Next, the effect of heat conduction is purely driven by temperature gradients as seen from Equation 17. It can be observed that the effect of heat conduction is the most negligible. Although the temperature gradients are stronger around the flame region, due to turbulent mixing with the cold coflow, the effective gradients become weaker and hence produce the least amount of entropy. The effects of mass diffusion and chemical reaction are the dominant sources of entropy production rates. Species' concentration gradients drive mass diffusion and as the overall effect is summed over all the species, the resulting entropy production is significant. It can also be seen that as the flame grows downstream, forming an over-ventilated flame eventually, the regions of intense species production/consumption increase, thus resulting in wider species radial gradient profiles, and larger entropy production rates. Chemical reaction term is dominated by the species' production rates, and the associated entropy production rates are significant around the flame region. Moreover, as the overall effect is summed over all the species' production/consumption rates, the resulting entropy production is significant.

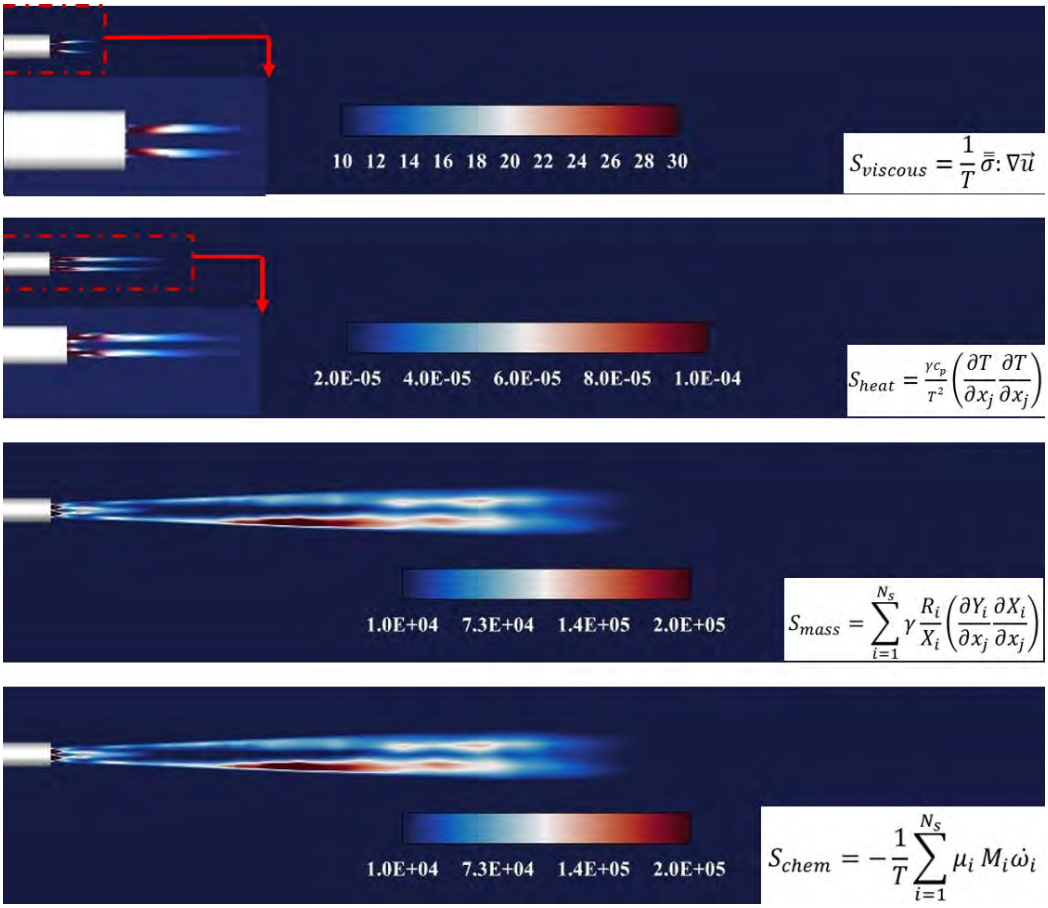

Figure 22. Qualitative representation of entropy production rates (J/K/m^3-s) in the center-plane (x=0) due to a) viscous dissipation, b) heat conduction, c) mass diffusion, and d) chemical reaction.

Next, we look at the spatial variation of the integrated entropy production budget across the flame, by taking slices normal to the flame in the z-direction. Additionally, operating conditions have been varied around the baseline conditions of Sandia-D to understand the sensitivity of the budget to these different conditions. For example, pressure was changed to 2 atm and 5 atm while maintaining the other boundary conditions same as the baseline. Similarly, the jet velocity was modified to $\pm$10 % around the baseline value, and the central jet composition was modified by the same amount. Figure 22 and Figure 23 show the integrated entropy production rate budget of the baseline and the variants across the flame with the x-axis representing the slice position normalized by the jet diameter. The distance between the slices is a jet diameter and it starts from the jet exit and spans all the way up to the outlet.

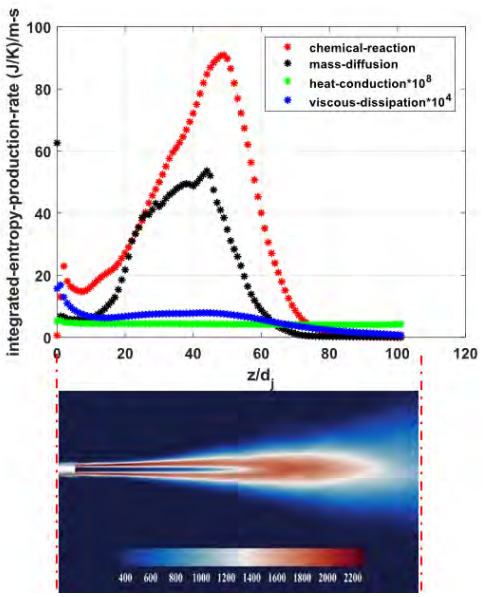

Figure 23. Top: Spatial distribution of integrated entropy production rates (J/K/m-s) across the flame, Bottom: center-plane (x=0) mean temperature field (K)

Figure 23 shows the integrated entropy production rate distribution due to various sources across the flame as represented by mean temperature field (bottom). The effects of heat conduction and viscous dissipation are highly negligible across the flame, confirming the previous observations from the qualitative center-plane distribution. However, at the jet exit, the viscous dissipation effect is slightly significant due to high velocity gradients between the jet and the coflow, resulting in finite values of shear stress and entropy production. The integrated effect of heat conduction is close to zero across the flame and it can be attributed to the bulk mixing with the complete cold coflow resulting in smaller effective temperature gradients, as observed previously.

As the jet flame begins to develop downstream, the entropy production rate associated with chemical reaction increases with distance and reaches a peak around 50-55 jet-diameters, and falls off beyond the flame length, showing the dominating effect of heat release from chemistry. Moreover, the combined effects of sensible enthalpy changes and the partial entropy of the species, along with the heat release, dominates the overall entropy production budget as seen from the plot. The effect of mass diffusion shows a similar trend to the chemical reaction. Interestingly, the contribution from mass diffusion is approximately three times that of the chemical reaction at the jet exit as the radial and axial gradients are significant. Additionally, as the term depends on the gradients of the species, the entropy production associated with mass diffusion increases as the flame grows downstream, producing/destroying species. Furthermore, the radial gradients of the species continue to be significant across the flame, resulting in higher values of integrated entropy production rates.

Figure 24 top row shows the effect of increasing pressures (2-atm and 5-atm) on the integrated entropy budget across the flame. We can see that the production rates of entropy due to mass diffusion and chemical reaction increase significantly with pressure, particularly at 5 atm it can be observed that there is close to two orders of magnitude increase with respect to the baseline conditions. This behavior can be attributed to the increase in mass flow rates of central jet and the coflow at higher pressures, and the associated pressure dependence of the finite rate chemistry. Next, the effect of jet velocity, as shown in Figure 24 middle row, indicates that 10% increment in velocity doesn't show a marked difference with respect to the baseline conditions. However, the case with decrement in jet velocity shows less overall amount of entropy production rates. This is due to the associated decrease in fuel mass flow rate at lower jet velocities and hence lower entropy production rates. Interestingly, the sensitivity of entropy production to lower mass flow rates due to decrease in jet velocity is higher than that of the effect of increment. Next, the effect of equivalence ratio of central jet on entropy production is discussed. Figure 24 bottom row represents the equivalence ratios of 1.91 and 4.45, and the baseline conditions correspond to 2.63. When the jet composition is leaner, the overall entropy production rate decreases with respect to the baseline. This effect is observed due to lesser amounts of rich products available from combustion of methane-air mixture.

Hence the integrated entropy production rates due to chemistry as well as mass diffusion approach zero at approximately 60 jet-diameters. On the other hand, the richer case produces more overall entropy. As the rich products available for combustion downstream is higher, the distribution due to chemical reactions as well as mass diffusion is wider and hence the overall integrated entropy production rates. Interestingly, the effect of mass diffusion in the near field of the leaner case produces significant amounts of entropy due to higher gradients. Moreover, the effect of the scalar dissipation rate due to these gradients seems to affect the local chemistry in the nearby field, resulting in lower entropy production due to chemical reaction.

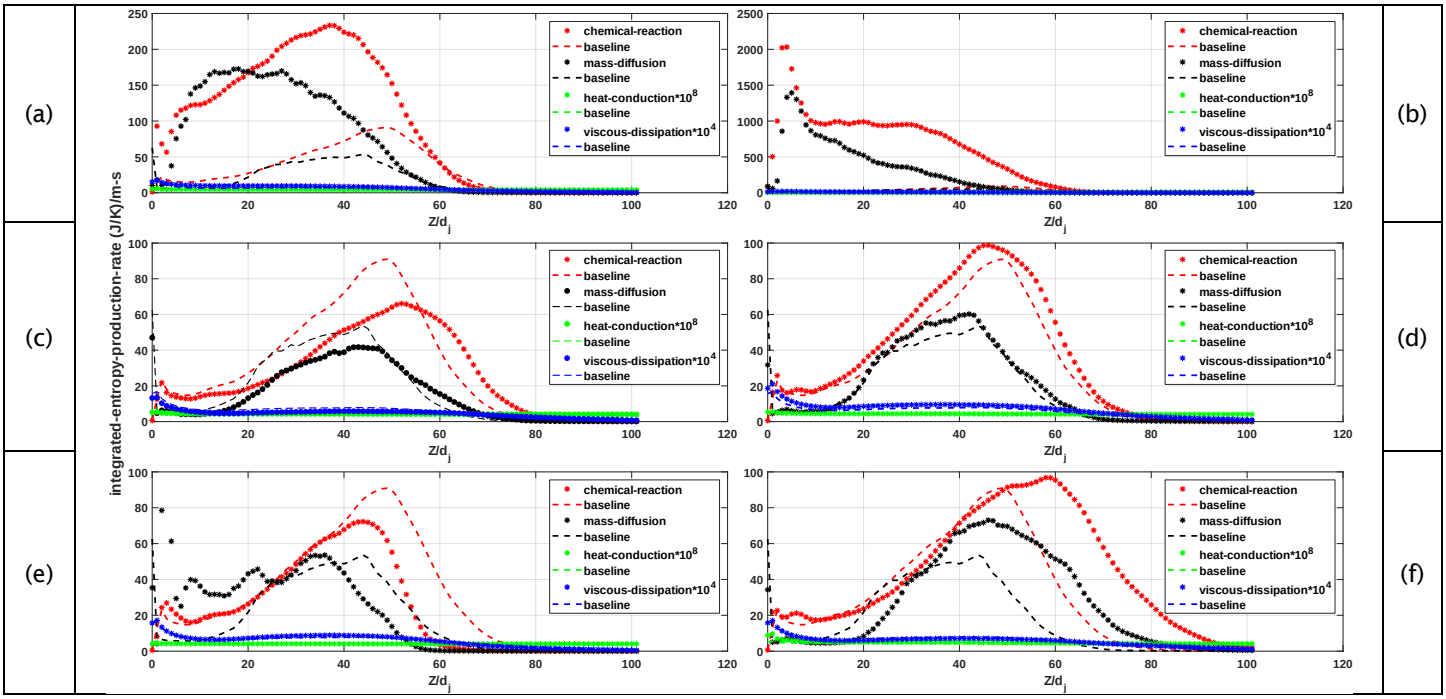

Figure 24. Spatial distribution of integrated entropy production rates (J/K/m-s) across the flame at different operating conditions around the baseline (right to left, up to down): (a) 2-atm, (b) 5-atm, (c) 10% decrement in jet-velocity, (d) 10% increment in jet-velocity, (e) jet equivalence ratio of 1.91, and (f) jet equivalence ratio of 4.45.

Next, the distribution of integrated entropy production rates as a function of area of integration is discussed. Figure 25 represents the above for all cases, with the top row representing the results for the baseline conditions, and the subsequent rows representing the results for 2-atm, 5-atm, 10% decrement/increment in jet-velocity, and jet mixture equivalence ratios (1.91 and 4.45), respectively. The x- axis denotes the radius of the area of integration normalized by the jet-diameter, spanning from 0.1 jet-diameter to the complete slice across the flame. The y-axis represents the slice positions across the flame normalized by the jet-diameter, like previous plots. The columns represent the entropic sources – chemical reaction, mass diffusion, heat conduction and viscous dissipation. It can be observed that across all cases, effects of heat conduction and viscous dissipation are negligible over areas of integration. Additionally, the distribution of integrated entropy production due to heat conduction appears to be quite similar across all the slice locations for each area of integration, reaching its peak value over the complete area of the slice. This represents the contribution of positive temperature gradients existing across increasing areas away from the flame. The distribution of viscous dissipation effects strongly depends on the velocity gradients, which is significant over a particular range of r/d_j – 2.5-3.5 in the near field of the jet exit. This is due to the existence of exceedingly high axial and radial velocity gradients coupled with the effects of hot pilot mixture. The shear, particularly between the pilot mixture, jet and the coflow is stronger due to significant temperature and velocity differences, resulting in higher amounts of entropy production in that region. However, the decrease in the integrated values in larger areas of integration suggests that there is less overall shear due to weaker/negative radial velocity gradients. On the other hand, the effects of mass diffusion and chemical reaction are significant over areas of integration, particularly where the distribution peak occurs, as illustrated by the distribution of

yellow region. This indicates that as the distance increases away from the center of the flame, the radially outward far field effects are stronger, resulting in more entropy production. Specifically, the combined effects of sensible enthalpy changes and the partial entropy of the species for the chemical reaction term as well as the combined effects of species' gradients in mass diffusion, result in more entropy production over increments in areas of integration. This means that although flame is a dominant source of entropy production, the effects in the far field of the flame contribute to the overall integrated entropy production rates. Interestingly, closer to the jet exit, due to the influence of pilot mixture and the exceedingly high axial and radial gradients, the integrated production rates do not show monotonic behavior with the area of integration. This represents the complex nature of the summation over all species as well as magnitude of the species gradients in the nearfield.

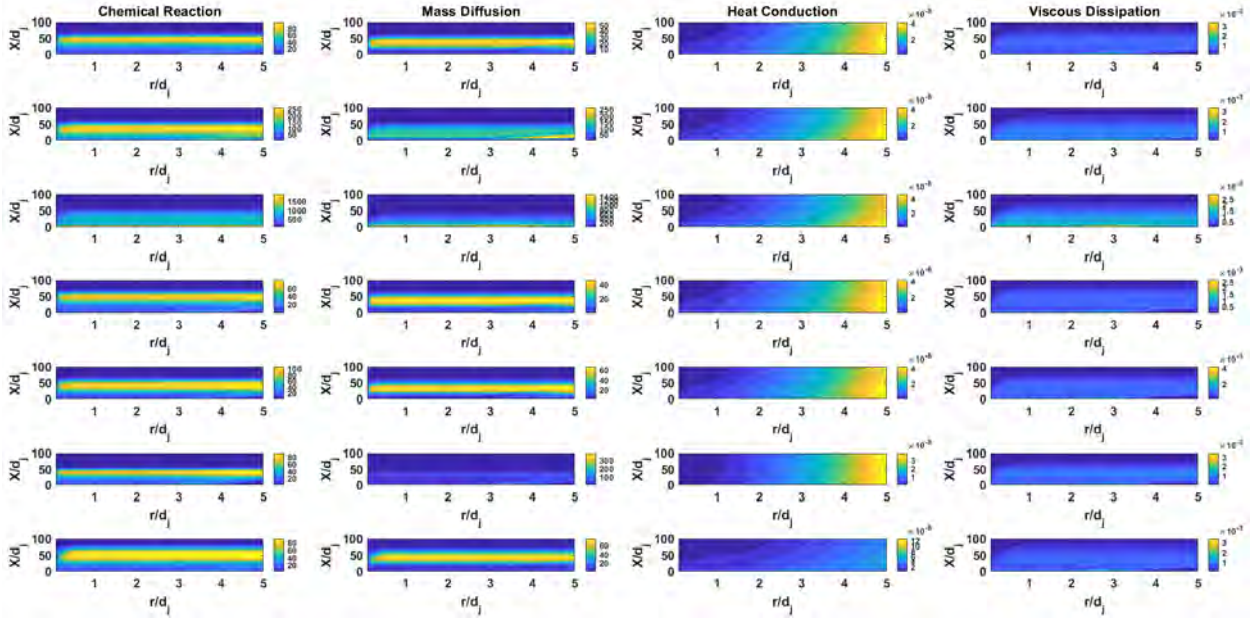

Figure 25. Variation of integrated entropy production rates (J/K/m-s) as a function of area of integration with the columns representing the sources from left to right: chemical reaction, mass diffusion, heat conduction, viscous dissipation. The rows from top to bottom represent the results at different conditions as 2-atm, 5-atm, 10% decrement in jet-velocity, 10% increment in jet-velocity, jet equivalence ratios of 1.91 and 4.45.

Next, the results of the ethanol spray ETF-2 flame are discussed. Figure 26 shows the mean droplet volume fraction in the center-plane (z=0). The origin of the coordinate system is at the center of the jet-exit. The volume fraction field exists only on the upper portion of the nearfield, as indicated by the zoomed-in portion of the field. This behavior arises due to the injection of spray particles only around the positive positions of y, and hence the droplets and the associated phase change effects are captured strongly in that region. Figure 27 (top) show the distribution of integrated entropy production rates across the domain in the streamwise direction, Figure 27 (bottom) represents the mean static temperature field in the center-plane ($z = 0$). Specifically, Figure 27 (top left) represents the production associated with the inlet spray tube up to the jet exit, while Figure 27 (top right) represents the production associated with the flame. Viscous dissipation is the sole contributor to entropy production in the spray tube due to significant velocity gradients in the wall region. Further, the zero-entropy production, because of mass diffusion and chemical reaction arises from the consideration of only pure gaseous species in the calculation. The distribution across the flame highlights that chemical reaction produces significant amounts of entropy, like the observations made previously on the Sandia-D flame. Since combustion occurs only after the phase change, the energy input for evaporation is derived partly from the hot pilot mixture at the jet exit and from the diffusion flame itself. The appearance of two distinct peaks in the production from chemical reaction profile marks the strong influence of the pilot mixture evaporating the liquid fuel and the associated combustion effects in the near field of the jet exit (~ $5d_{js}$), represented by the first peak at the same location. As the hot liquid fuel convects downstream, the gaseous combustion lags, as represented by the drop in the chemical reaction profile as well as from the mean temperature field. Once the flame develops downstream, supported by the phase change of liquid fuel, the entropy

production due to chemistry increases again and reaches the second peak. The decrease in the profile occurs due to lack of combustion further downstream and reaches zero. The most interesting observation in this analysis of the spray combustion case is that mass diffusion produces negligible amounts of entropy, countering the observations made from the Sandia-D flame analysis. This result is attributed to the consideration of only single-step chemistry with five overall species in the domain, whereas detailed kinetics with 16 species were considered for the Sandia-D flame. As the mass diffusion term depends strongly on the summation of the species' gradients of all the species, consideration of detailed kinetics could possibly shed light on the effects of mass diffusion on entropy production. Moreover, the confinement effects would strongly affect the species gradient profiles, both radially and axially, and hence the results would still be quite different from Sandia-D analysis.

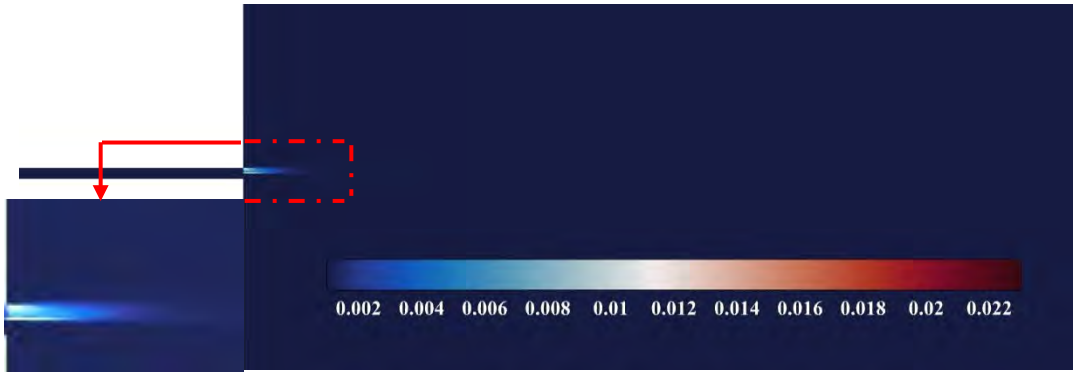

Figure 26. mean droplet volume fraction field in the center-plane (z=0).

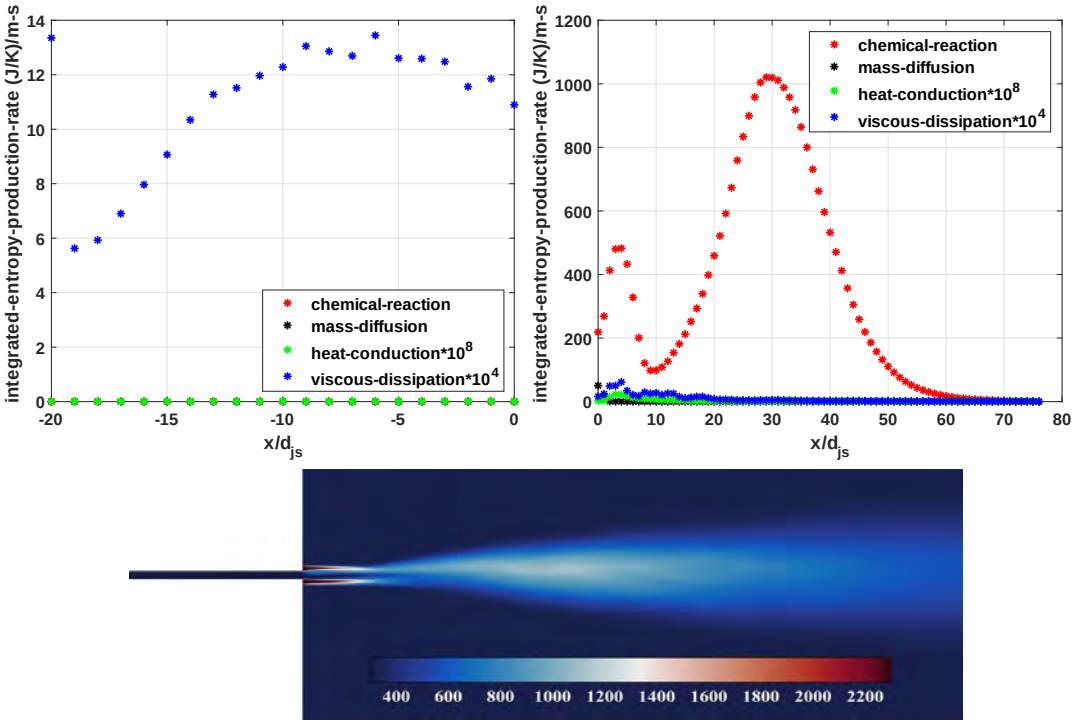

Figure 27. Integrated entropy production rates (J/K/m-s) in the spray inlet tube (top left), downstream of the jet exit and across the flame (top right), and the mean temperature field of the center-plane (z=0) (bottom).

The study in this reporting period has convincingly shown that the mass diffusion term produces significant amounts of entropy in a single-phase gaseous diffusion flame with detailed kinetics, with a comparable magnitude to the dominant chemical reaction term. The sensitivity of operating conditions has shown that at higher pressures, there's orders of magnitude increase in the production rates due to mass diffusion and chemical reactions, because of increasing mass flow rates. Moreover, the decrement in jet velocity has resulted in a significant decrease in the production rates as compared to the increase in the rates with increment in velocity. The composition dependence has shown strong sensitivity to richer equivalence ratios. It was also shown that the radially outward far field effects contribute to more entropy production for all the source terms, indicating that as we move away from the flame, the local flow field still evolves and produces entropy. The analysis on the spray flame showed two distinct peaks in the chemical reaction profile for entropy production. The first peak represents the strong interaction between the pilot gases and the spray near the injection, and the associated entropy production. Interestingly, the mass diffusion effect has been shown to be negligible due to the consideration of single step chemistry with five species only. Hence future studies will focus on the inclusion of detailed kinetics in the simulation of spray flame and investigate its effects on the entropy budget. Furthermore, by accounting for Lewis number effects, particularly for lighter fuels, the future analysis would improve the prediction of mass diffusion effect on entropy production and provide a much stronger support for including the mass diffusion term in the entropy wave generation analysis for indirect combustion noise.

Milestones

- Extended the fidelity of hydrodynamics study to Tri-Global stability by modeling modal characteristics of an extra dimension.
- Studied the differences in p-q coherence when considering duct effects.
- Gained understanding of the true dominance of different entropy source terms for entropy generation and thus indirect noise.

Major Accomplishments

Tri-Global stability analysis works for a 3D base-flow without any assumptions of axi-symmetry used by Bi-Global analysis. A computational effective methodology was developed to obtain Tri-Global natural modes of the time-averaged swirling base-flow obtained by LES flow fields. The coherence modeling analysis extended toward confined configurations to assess applicability to noise source separation. An experiment with a canonical flame was used to verify the analytical results and identify other physical processes affecting coherence. One of the first CFD studies in literature considers canonical diffusion and spray flame configurations to assess the relative dominance of different entropy source terms.

Publications

Peer-Reviewed Journal Publication

Patki, P. A., Emerson, B. L., & Lieuwen, T.C. (2025. Global stability and forced response analysis of swirling flows in aviation combustors. *Journal of Engineering for Gas Turbines and Power, 147*(1).

Published Conference Proceedings

Ha, S., & Lieuwen, T. (2024, January 8-12). *Coherence between the globally integrated heat release rate and acoustic pressure in an enclosed duct* [Conference paper]. AIAA SCITECH 2024 Forum, Orlando, Florida. https://doi.org/10.2514/6.2024-0795

Ha, S., & Lieuwen, T. (2025). Direct combustion noise: Nearfield and non-compactness influences on pressure–heat release coherence. *Combustion and Flame*, *271*, 113811.

Outreach Efforts

None.

Awards

None.

Student Involvement

- Graduate student Parth Patki worked on the hydrodynamic stability task under the mentoring of Ben Emerson.
- Graduate student Sungyoung Ha worked on the coherence modeling task under the mentoring of Vishal Acharya and Tim Lieuwen.

- Graduate student Guru Charan Ganesh worked on the entropy generation task under the mentoring of Vishal Acharya.

Plans for Next Period

- Further consider spray dynamics aspects, such as droplet transport, droplet grouping, and polydisperse sprays, in the flame response framework.
- Validate the ROM with LES data in an ongoing study comparing the ROM equations to the full equations used for the LES.
- Consider a tri-global framework for generic geometry hydrodynamics in hydrodynamics modeling.
- Build and validate the velocity ROM with particle image velocimetry (PIV) measurements from the Georgia Tech experiment task.

Task 4 – Facility Development

Raytheon Technologies Research Center

Objective

The objective of this task is to provide validation data from two RQL combustors that have been tested at RTRC under the program – one that includes "jail-bar" vanes at the combustor exit and closely mirrors the Georgia Tech design, with a specific focus on the higher-pressure operating points that are not possible for the Georgia Tech rig, and another one that corresponds to the Pratt & Whitney® FAA Continuous Lower Energy, Emissions and Noise (CLEEN) single-sector combustor configuration. Collectively, the Georgia Tech and RTRC rig capabilities encompass a broad range of operating conditions, thus resulting in a robust dataset for training the design tools.

Research Approach

During the 2024 reporting period, a fourth test entry was conducted at RTRC in Cell 1 of the Jet Burner Test Stand (JBTS). This test utilized the original ASCENT RQL combustor, first evaluated in 2021 in Year 1 of our program. Figure 28 is a streamwise section of the test rig showing the fuel injector/mixer, window for high-speed chemiluminescence, dilution jets and jail bars that choke the flow (simulating the inlet guide-vane flow field downstream of an aero-combustor).

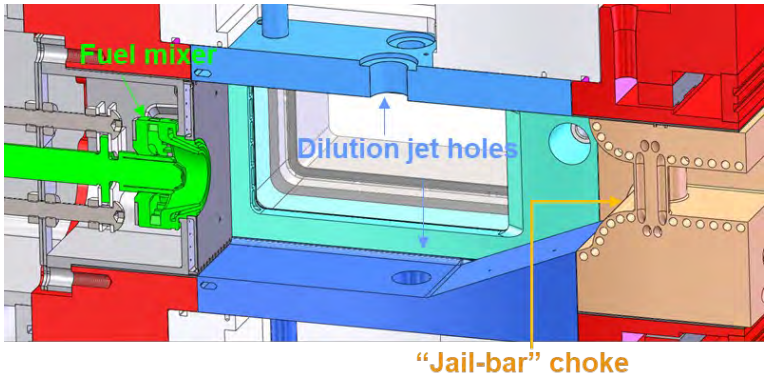

Figure 28. RQL ASCENT combustor.

The purpose of this test entry was to study the combustion noise sensitivity to two geometric changes. First, the fuel mixer was changed by reducing the axial length of the Filmer surface, as shown Figure 29. This surface is where the fuel jet impinges and films before shedding off the trailing edge to be atomized by the counter-rotating shear flows. It is known that this modification can reduce the tone amplitude of a combustion instability. This modification is referred to as the "cutback" configuration. Second, the area of the dilution jets holes was reduced by 10% with "dilution inserts" shown in Figure 30, which were designed such that they could be inserted and removed without a major rig teardown and rebuild.

® Pratt & Whitney is a registered trademark of RTX Corporation, Farmington, Connecticut.

Reducing the dilution jet area increases the jet velocity and hence the penetration into the combustor, thereby altering the mixing in the quench region of the combustor.

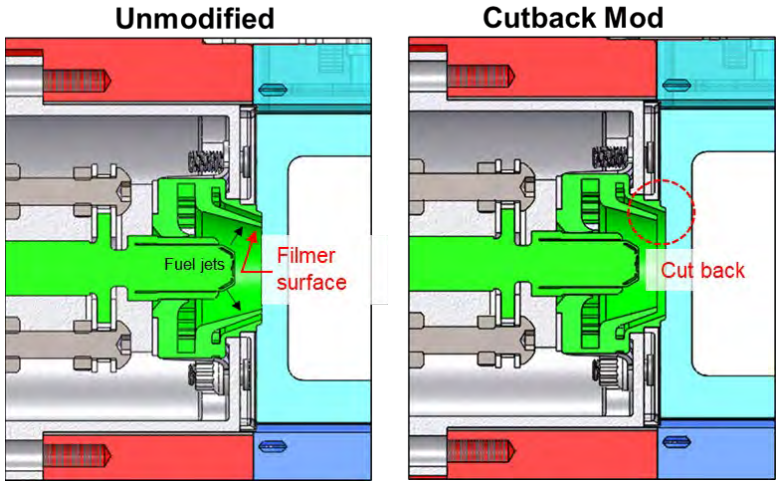

Figure 29. Baseline fuel mixer and "cut back" modification.

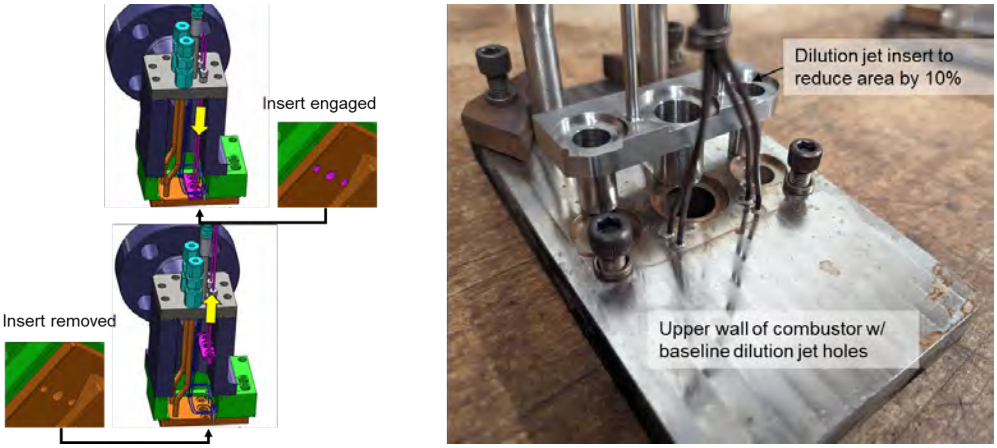

Figure 30. Dilution jet insert for upper combustor wall.

The measurements for this test consisted of dynamic pressures at nine locations (including an array to enable wave decomposition into downstream and upstream propagating components) as shown in Figure 31, chemiluminescence of the heat release field (use to compute an estimated direct noise field), and dual thermocouple (TC) probe for dynamic temperature measurements (used to compute an estimated indirect noise field).

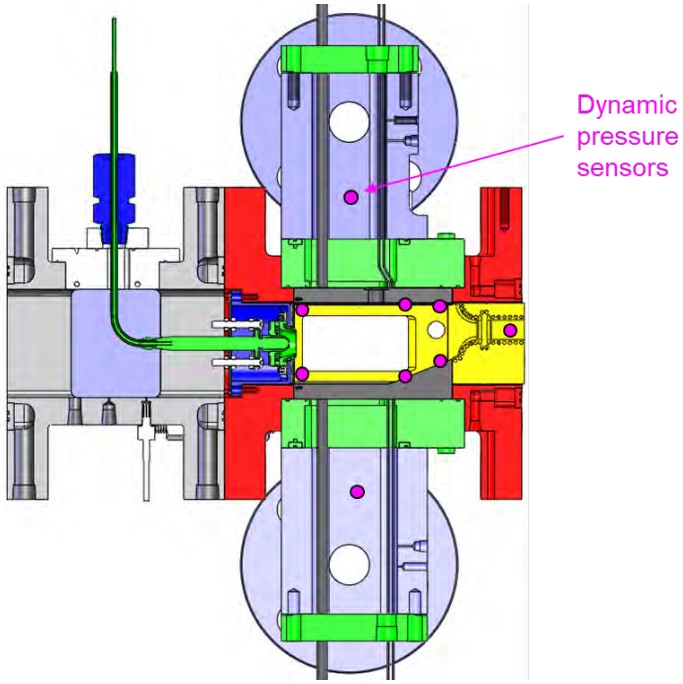

Figure 31. Dynamic pressure sensor locations.

Figure 32 shows the location of the dual TC probe, just upstream of the choke location (jail bars). The intent is to capture the temperature fluctuation that is convected through the choke. The entropy fluctuation due to temperature is then used with compact noise theory to estimate the indirect noise field (discussed later), assuming this entropy fluctuation occurs across the cross section of the combustor. A more accurate approach would be to have multiple probes to provide better spatial fidelity; however, additional probe ports are difficult to accommodate. Also, the probes are expensive and fragile and require particular care. As shown in Figure 32, the probe was mounted on a traverse to allow the probe to be in a retracted position when lighting off to improve the survivability of the wire junctions.

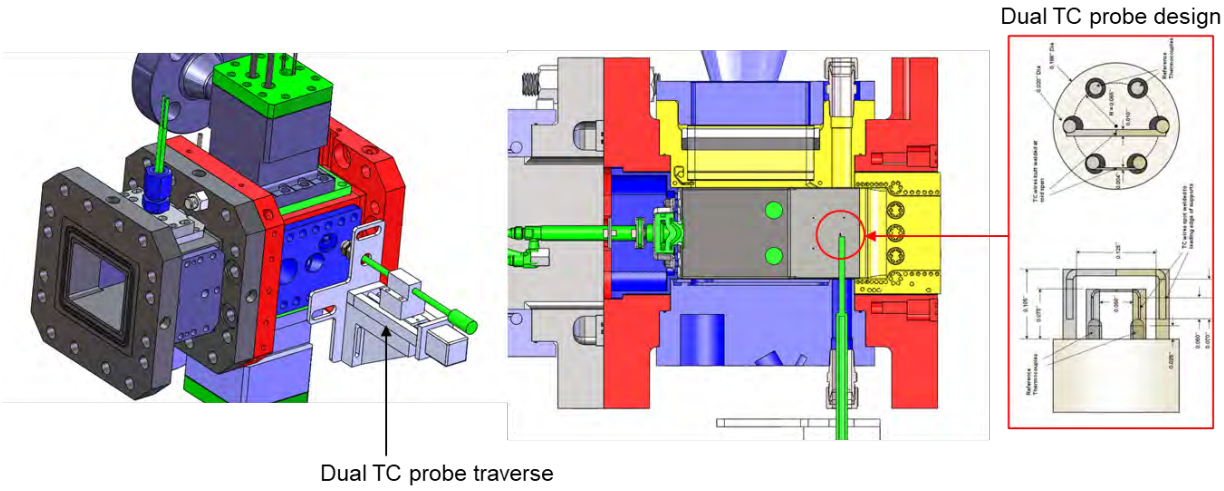

Figure 32. Dual TC probe and rig installation.

The dual TC probe design is shown on the right side of in Figure 32. It consists of two TC butt-welded junctions of different diameters (0.003" and 0.010" or 3-mil and 10-mil) arranged close together in such a manner to avoid wake interaction with the upstream junction. By assuming a linear differential TC response to a fluctuating temperature field based on a time constant, the true fluctuation (in the frequency domain) can be computed. The methodology uses the cross correlation of the two signals to first determine the time constant of the thinner TC wire which is then applied to correct the spectrum. Figure 33 shows an example of the raw and processed data (center plot). The coherence and cross correlation as well as the correction for the true spectrum look consistent with published dual TC probe data with similar time constant. The peaks in the spectra are consistent with tones observed in the corresponding dynamic pressure (see discussion below regarding the relationship between temperature and pressure fluctuation). In summary, the dual TC probe is performing as expected.

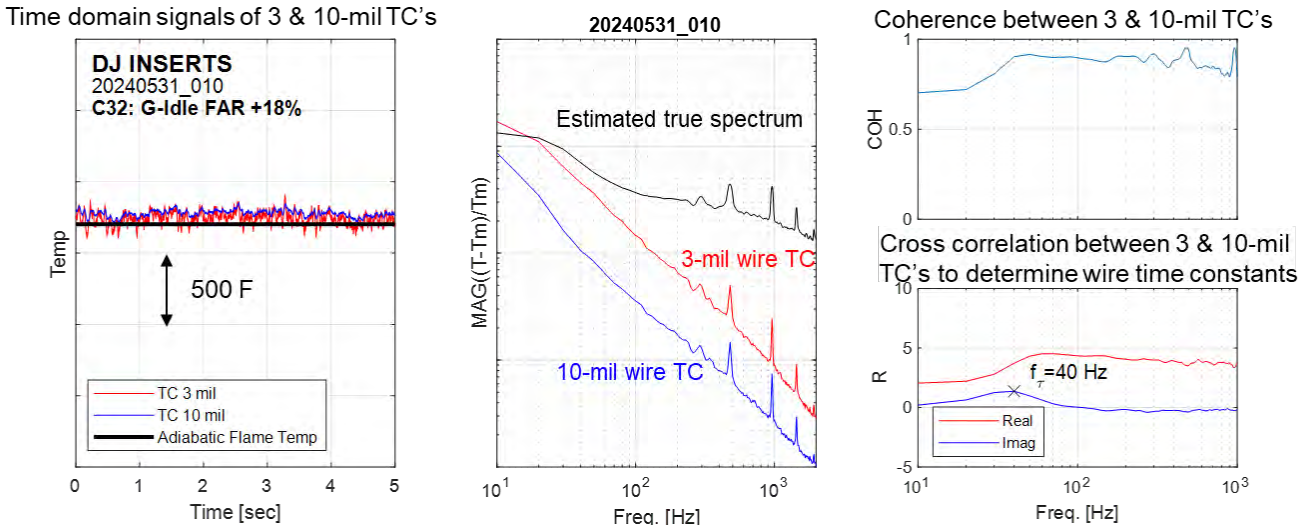

Figure 33. Example dual TC probe raw and processed data.

The representative results from the combustion testing in terms of dynamic pressure at the bulkhead is shown in Figure 34 for a FAR sweep at the cutback cycle point (not to be confused with the swirl cutback modification) for the baseline configuration (lower left), swirler cutback (lower right) and dilution jet inserts (upper right), plus the baseline data obtained for the first test entry in 2021 (upper left). The data demonstrate two conclusions. First, the data are very repeatable (comparing the two baseline configurations taken three years apart). Second, the broadband noise characteristic is surprisingly not overly sensitive to the geometric changes evaluated. The one significant difference notable in the spectra is the tone at about 600 Hz which is significantly diminished or eliminated with swirler cutback, consistent is prior observations for this modification.

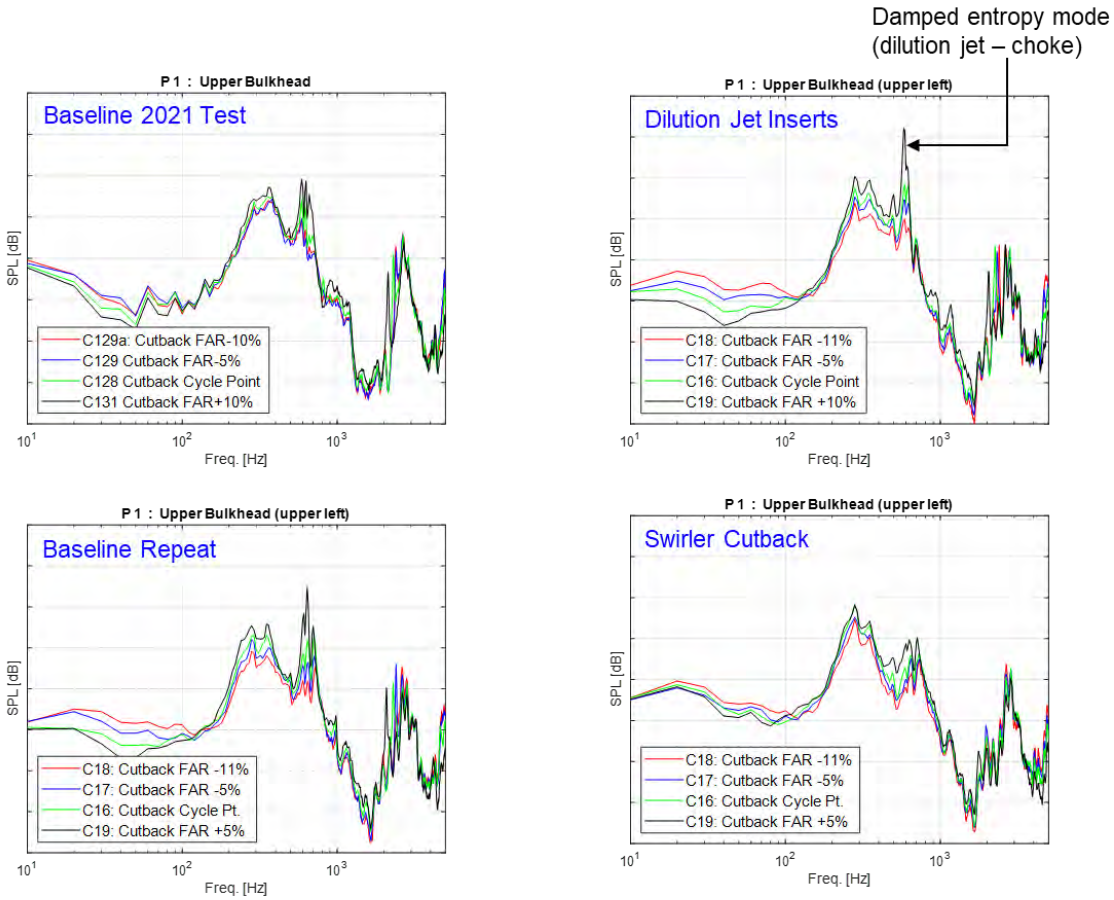

Figure 34. Dynamic pressure spectra at combustor bulkhead.

The specific nature the 600 Hz tone is suspected to be an entropy mode whereby an entropy fluctuation (of the temperature type) associated with a coherent flow structure is accelerated through the choke thereby generating a pressure wave that propagates upstream causing the next flow structure to shed, starting the next cycle of the instability. Computing the convective times from both the front end of the combustor and the dilution jets to the choke found that the latter location had a convective time consistent with the period of the observed tone. Figure 35 provides a visual of the coupling which illustrates cool chunks of the dilution jets as a source of the coherent flow structures (and the unsteady heat release that causes the dynamic pressure response). Figure 35 also illustrates that in addition to the generation of an upstream pressure wave, a downstream propagating wave is also generated.

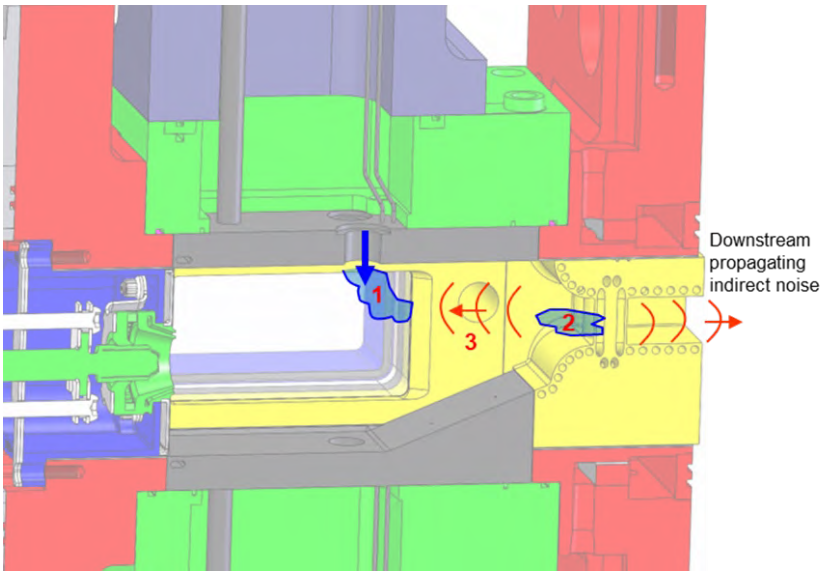

Figure 35. Entropy-combustion feedback loop.

Further corroboration of this entropy mode hypothesis is found by examining the relationship between the dynamic pressures and the unsteady temperature measurements. Figure 36 shows the coherence analysis between the 3-mil TC wire and two dynamic pressure measurements, upstream bulkhead and downstream of the choke, for the ground idle condition where the entropy mode is relatively strong. Figure 36 (top row) is the SPL at the two pressure locations (illustrated at the top of Figure 36) and Figure 36 (bottom row) is the associate coherence of the pressure signal with the 3-mil TC wire signal. Three conditions are plotted that sweep the flow split between front end and dilution jet flow rates (e.g., legend numbers 26:48 indicate 26% front end flow and 48% dilution jet flow). At the bulkhead location, there is a very clear correlation between the SPL tones and the 3-mil TC wire (coherence ~0.5-0.8 around 500-600 Hz). For the 28:46 flow split, the interaction generates a second and third harmonic which also shows up as elevated coherence. The increase frequency at the highest front end flow rate (30:44) is consistent with the higher front-end flow reducing the convection time or cycle period.

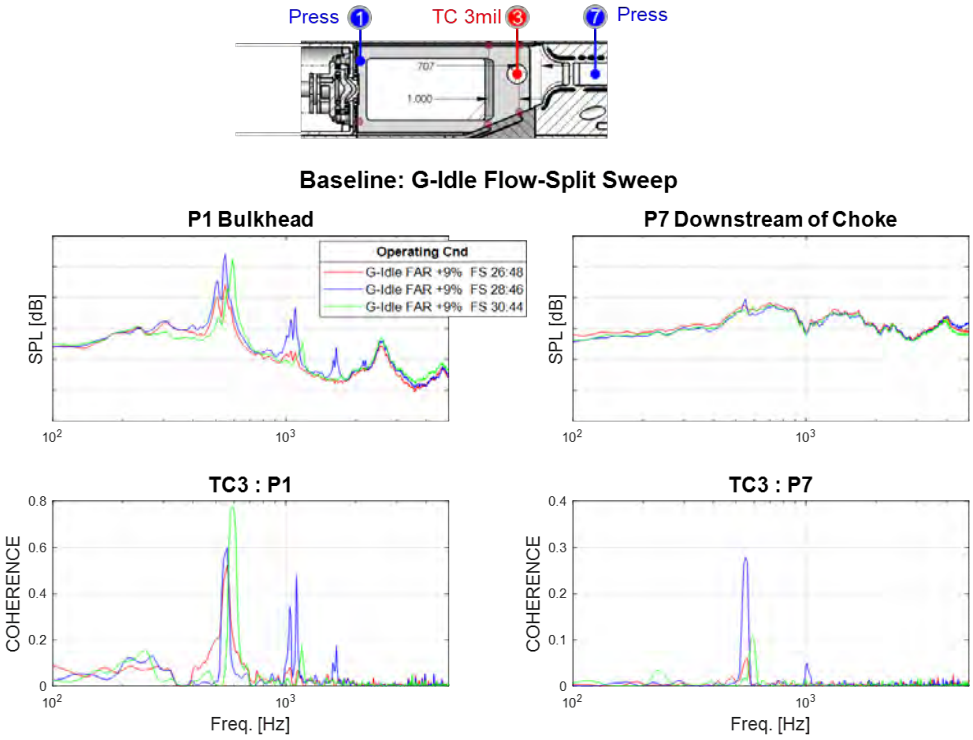

Figure 36. Coherence between unsteady temperature and pressure signals.

For the downstream pressure spectrum, it is notable that frequency content is much different than that at the bulkhead. This is because of the large hydrodynamic pressure oscillations downstream of the choke due to vortex shedding from the jail bars and unsteady shock motion of the under-expanded jets emanating from the throat of the choke. Despite the high level of noise not associated with combustion, there is still a measurable coherence with the 3-mil wire signal. In summary, there is clear evidence that the temperature fluctuation measured by the dual TC probe generates an indirect noise field which in this case, leads to an entropy-mode combustion instability.

The direct and indirect noise fields of the combustion tests were estimated using a finite element acoustics (FEA) model (pressure acoustics solver) shown in Figure 37. A forced response solution was obtained using the chemiluminescence and dynamic temperature data to simulate the direct noise source and indirect noise source, respectively. The pressure acoustics solver does not explicitly include flow which is modeled by impedance conditions where flow is important to the acoustics. Specifically, the pressure drops of the swirler, and the dilution jets are modeled with linearized pressure drop formulation (validated by flowing impedance tube measurements) and the choked exit at the jail bars is modeled using a linearized potential flow solution to derive an impedance boundary condition located upstream of the choke. The direct noise was estimated with a broadband, spherical volume-velocity source based on the spectral analysis of the summed chemiluminescence signal and fuel flow rate. Due to the long wavelengths relative to the combustor, the shape and location of the velocity source is not important. For the indirect noise field estimate, the unsteady temperature signal with compact nozzle theory were used to provide a forced velocity at the choke impedance plane.

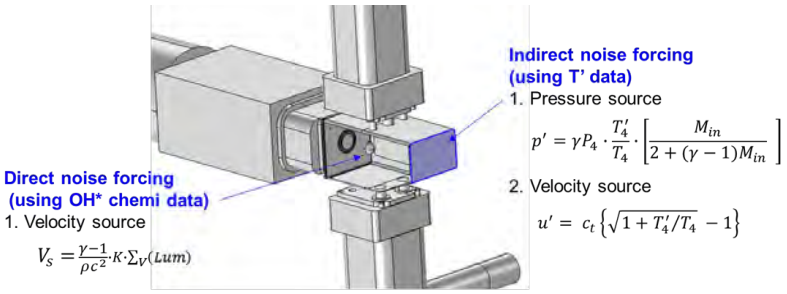

Figure 37. FEA model for estimating direct and indirect noise fields.

The results of estimating the two different noise fields in the combustor are shown in Figure 38. Above 300 Hz, the sum of the direct and indirect fields is consistent with the measured dynamic pressure at the bulkhead; however, below 300 Hz, the results are not consistent with the measurement. There is some additional noise dissipation not accounted for in the FEA model, potentially due to the water-cooled walls. Also, it may be the chemiluminescence signal (OH*) is not the best surrogate for the unsteady heat release. Recent publications indicate the OH* radical has a much longer decay rate than the CH* radical, potentially biasing the results. These potential issues will be investigated by modeling the effect of heat loss on the wall on the acoustic field and using the CH* signal from 2021 data to computer the direct noise estimate.

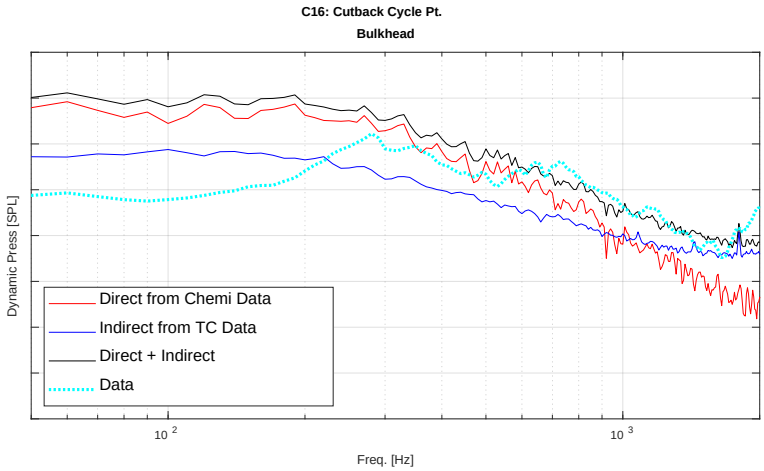

Figure 38. Estimated direct and indirect noise at bulkhead compared with measurement.

As observed in Figure 38, the indirect noise becomes dominant above 1000 Hz. This is consistent with indirect noise estimated from wave decomposition using the dynamic pressure array. This approach and example results are shown in Figure 39. With the array of dynamic pressure taps on the downstream ramp, the acoustic field can be decomposed into a downstream propagating wave (A_{Meas}) and an upstream propagating wave (B_{Meas}) as shown in Figure 39 (top right). Due to the generation of indirect noise, the B component has both a contribution from the reflection due to area change and from the indirect noise. Using a linear potential flow model, the reflection coefficient (R_{Pass}) can be computed for a "passive" choke (only reflects noise, no generation of noise) due to a pure upstream sound source. Using the experimental A component (A_{Meas}) with the modeled passive reflection coefficient, B_{Pass} can be computed. The difference with B_{Meas} can be considered a measurement of indirect noise. The results in the bottom left of Figure 39 show the indirect noise field becomes measurable above 400 Hz and is on the order of 2-4 dB. Compared with the data-driven FEA model discuss above, it shows the indirect noise to dominate the direct noise about 1000 Hz. This is consistent with wave decomposition results that the most observable indirect noise is at the higher frequencies. However, the data-driven FEA model indicates indirect noise over the entire spectrum vs the wave decomposition approach that sees indirect noise above 400 Hz. This inconsistency may be explained by lack of signal-to-noise where the direct noise is highest.

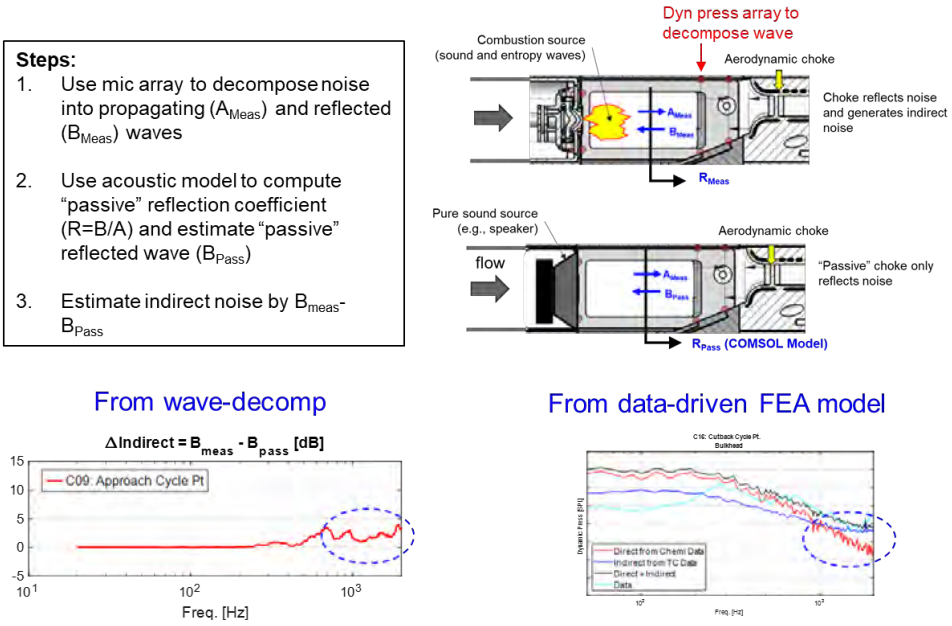

Figure 39. Indirect noise estimate using wave-decomposition.

Milestones

- Successfully completed the fourth RTRC experiment entry.

Major Accomplishments

- Developed methodologies to estimate direct and indirect noise fields.
- Acquired empirical data on combustion noise sensitivity to geometric changes.

Publications

None.

Outreach Efforts

None.

Awards

None.

Student Involvement

None.

Plans for Next Period

- Complete planning and hardware development for the tone campaign test entry program.
- Consider several fuel mixer variations for the tone campaign test. The expected test entry is currently in the first quarter of 2025.

The test rig concept, shown in Figure 40, is the original ASCENT test rig with the jail-bar choke section replaced with a constant area section (note flow is from right-to-left in Figure 40). The choke location is moved downstream and controlled by a variable area elliptic choke. Between the combustor and the choke is a variable length side branch which allows the longitudinal acoustic resonance to be varied. In this way, the combustion instability propensity of a fuel mixer configuration to different resonant frequencies can be studied.

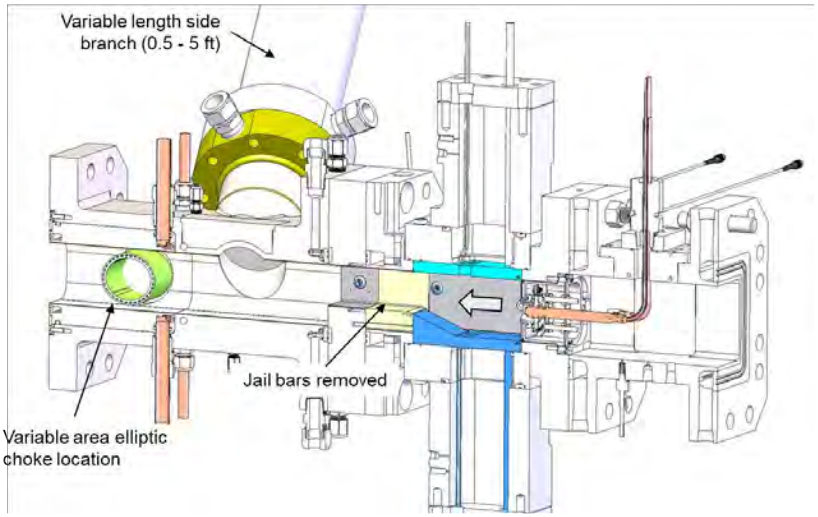

Figure 40. ASCENT rig configured for tone campaign.

A typical dataset consists of taking continuous data over a 3-min period as the plunger in the side branch is swept, changing the length of the side branch from 0.5 to 5 ft. In this manner, the resonant acoustic modes in the combustor vary from high frequency to low frequency. Data collected will be dynamic pressures and dual TC probe signals. The process data consist of a waterfall plot of the combustor response (as observed by dynamic pressure and temperature probes) which identify the frequency where the fuel mixer creates an unsteady heat release field that couples with the acoustic mode. Success will be identifying which fuel mixer geometries have the least coupling with the acoustic modes. High-speed chemiluminescence video (at a fixed side branch length of interest, identify from the sweeps) will be used together with the dynamic pressures and temperature data to understand the physics of the high dynamic and the low dynamic response to develop design methodology that mitigate combustion instability.

Project 056 Turbine Cooling Through Additive Manufacturing

The Pennsylvania State University

Project Lead Investigator

Reid A. Berdanier
Associate Professor
Department of Mechanical Engineering
The Pennsylvania State University
NARCO Building, CATO Park, Room 148
3127 Research Drive
State College, PA 16801
(814) 863-3972
rberdanier@psu.edu

University Participants

The Pennsylvania State University (Penn State)

- P.I.s: Prof. Reid A. Berdanier, Prof. Stephen Lynch, Prof, Karen Thole
- FAA Award Number: 13-C-AJFE-PSU-054
- Period of Performance: February 5, 2020, to September 30, 2025
- Tasks:
  1. Manufacture and test existing FAA Continuous Lower Energy, Emissions, and Noise (CLEEN) II blade designs.
  2. Design new double-wall cooling technologies.
  3. Manufacture and test new double-wall cooling designs for linear cascade.

Project Funding Level

The Federal Aviation Administration (FAA) has provided $1,500,000 of funding to date. In-kind cost-sharing of $1,500,000 has been provided to The Pennsylvania State University by Pratt & Whitney to cover the entire program.

Investigation Team

Prof. Reid A. Berdanier, All Tasks
Prof. Karen A. Thole (co-P.I.), All Tasks
Prof. Stephen Lynch (co-P.I.), Tasks 2 and 3
Assoc. Res. Prof. Michael Barringer, (staff scientist), Task 1
Asst. Res. Prof. Matthew Meier, (staff scientist), Task 1
Scott Fishbone, (project manager), Task 1
Tom Houck (project manager), Task 1
Jeremiah Bunch, (laboratory technician), Task 1
Liam Boyd, (graduate student), Tasks 2 and 3
Nicholas Gailey, (graduate student), Task 1

Project Overview

Gains in the cooling performance of cooled turbine airfoils directly affect the efficiency and durability (lifetime) of turbine engines and therefore are the subject of substantial development. Currently, many cooling designs for turbine airfoils use complex micro-channels placed within the wall of the airfoil to extract heat—a design known as double-wall cooling. However, the geometric complexities (and thus the effectiveness) of the micro-channels are limited by the current design space available through the use of conventional investment casting and core tooling methods to manufacture relatively

small intricate internal cooling features. This project will investigate potential thermal performance and aerodynamic efficiency improvements made possible by exploring the expanded cooling design space opportunities by directly fabricating complex cooling geometries with three-dimensional laser powder bed fusion (L-PBF), a commonly used metal-based additive manufacturing (AM) method. L-PBF AM has begun to find many uses in the gas turbine industry, particularly because of the new design space enabled by this new fabrication method. However, the ability to manufacture high-efficiency, intricate, complex double-wall cooling airfoils design concepts is unknown. This research would generate some of the first thermal performance data at engine-relevant conditions comparing traditional cast airfoils to advanced airfoils manufactured through L-PBF AM. Understanding the potential of new innovative geometric heat transfer cooling design features coupled with unique airfoil cooling configurations will serve as an important guide for future investments in advanced manufacturing and cooling design technologies.

Task 1 – Manufacture and Test Existing FAA CLEEN II Blade Designs

The Pennsylvania State University

Objective

The objective of this task is to measure the as-manufactured shape of FAA CLEEN II turbine blade airfoils with X-ray computed tomography (CT), and to use that information to fabricate additively manufactured copies for direct comparison at the rotating turbine facility at Penn State. The outcomes of this effort will be to (a) provide a direct back-to-back comparison of cast versus additively manufactured airfoils, (b) identify the unknown challenges in creating double-wall designs via AM and translating them into cast parts for commercialization, and (c) learn about and document the design, fabrication, and testing of additive blades that will spin at engine-relevant conditions.

Research Approach

AM blade inspections and testing preparation

Following the delivery of 20 additively manufactured FAA CLEEN II turbine blades in November 2022, a series of tests assessing flow performance and geometric accuracy were conducted in the prior reporting period as preparation for turbine operation. Information about flow characteristics is critical for evaluating thermal characteristics in the turbine rig. Furthermore, verification of geometric accuracy, including surface roughness effects from the AM process, were also important to ensure a full understanding of as-tested geometries.

Steady Thermal Aero Research Turbine (START) rig testing of the FAA CLEEN II blade designs was completed in Quarter (Q)2 and Q3 2024. A rainbow wheel configuration was constructed combining cast and AM versions of the subject blade geometry, and they were evaluated using infrared (IR) thermal imaging. A low, mid, and high blade coolant flow rate was achieved over the test campaign, and IR images were collected for every blade in the wheel while operating at 10,000+ rpm.

Locations of the IR images are shown in Figure 1 across the suction side and pressure side of the blade. Capturing the blade at a fixed radial span height allowed for full surface assessments of blade-to-blade differences. The suction side view closest to the leading edge was not viewable due to the adjacent blade's trailing edge. An additional view taken that is not shown below was the leading edge view, which captured the shower head cooling holes and provides data on the far-forward suction side region.

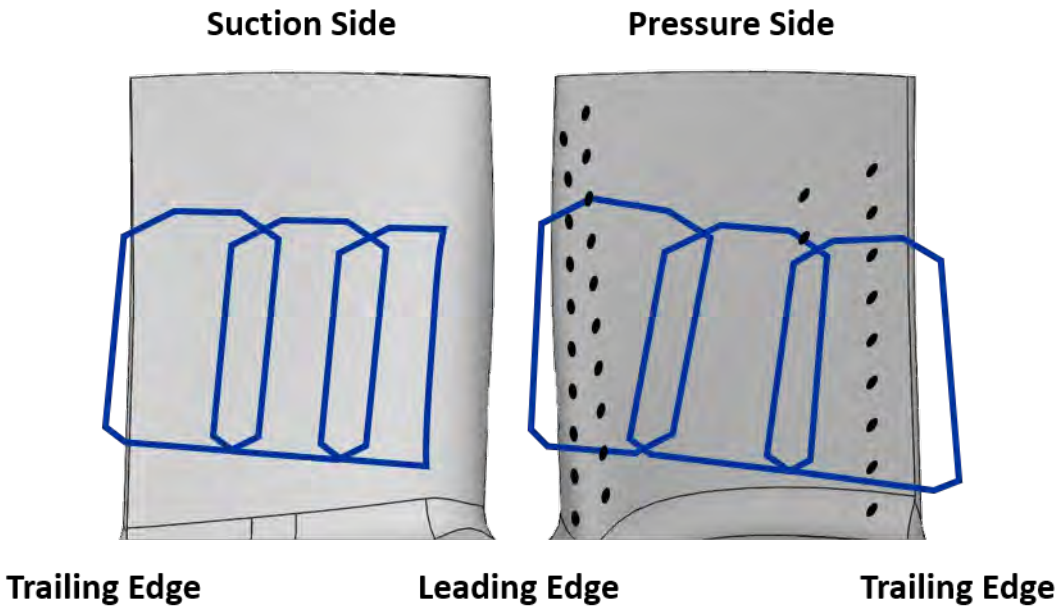

Figure 1. Representation of where IR images were acquired over the surface of the blade.

An area-averaged overall cooling effectiveness ($\overline{\overline{\phi}}$) assessment was made on the pressure side trailing edge view to analyze how well the AM blades performed in comparison to the ideal geometric cast blade. The parameter ϕ is defined as:

$$\phi = \frac{T_\infty - T_s}{T_\infty - T_c}$$

where T_∞ is the main gas path temperature, T_s is the blade surface temperature, and T_c is the blade coolant temperature. The region of interest was located upstream of the cooling holes and is represented as the yellow box shown in Figure 2 for both the high coolant flow and low coolant flow test configurations. Each AM blade $\overline{\overline{\phi}}$ was subtracted from the 'singular' ideal cast blade $\overline{\overline{\phi}}$ where that particular cast blade was used as the basis for the AM design (reference previous reports). The data shown in Figure 2 represent a $\Delta\overline{\overline{\phi}}$ where the greater the $\Delta\overline{\overline{\phi}}$, the hotter the AM blade metal temperature compared to the single cast blade.

For both the high flow and low flow cases in Figure 2, the cast blade had a greater cooling performance when compared to each of the AM blades. On average, $\Delta\overline{\overline{\phi}} = 0.07$ for the high flow test and $\Delta\overline{\overline{\phi}} = 0.05$ for the low flow test. The decreased $\Delta\overline{\overline{\phi}}$ at lower cooling flows suggests that manufacturing variations have less impact on blade cooling when less internal flow is present. When assessing blade-to-blade differences, the range of $\Delta\overline{\overline{\phi}}$ varies from $\Delta\overline{\overline{\phi}} = 0.041$ up to $\Delta\overline{\overline{\phi}} = 0.106$ for the high flow test condition. The large range of $\Delta\overline{\overline{\phi}}$ is due to the individual blade characteristics that occur from the AM process.

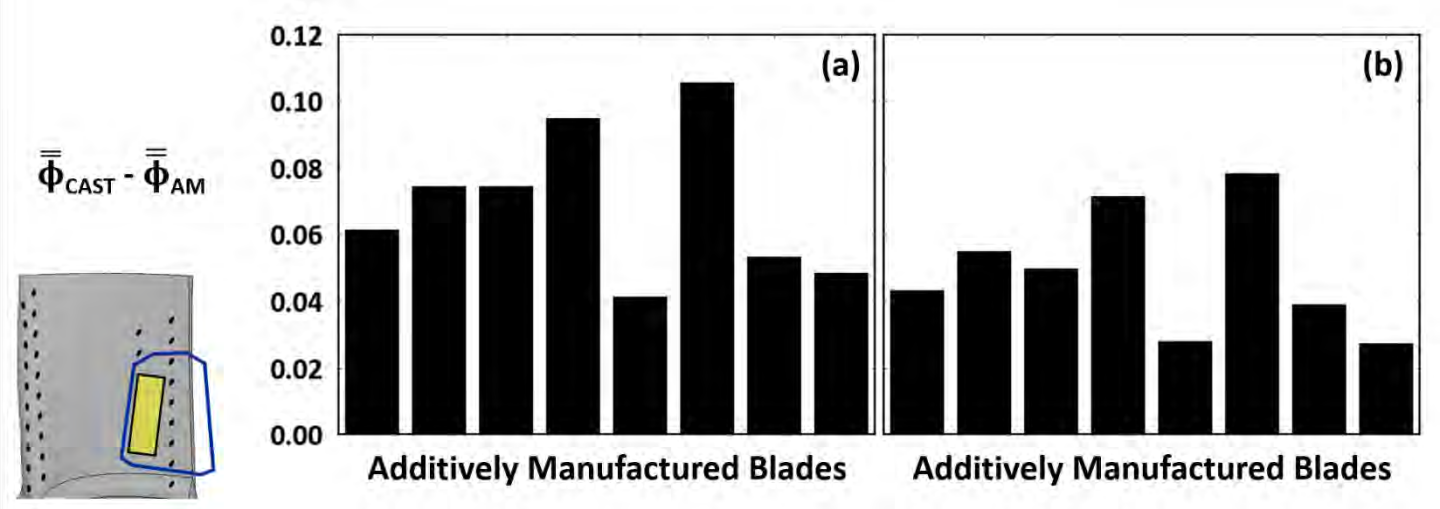

Figure 2. Area-averaged cooling effectiveness comparison between a singular cast blade and multiple AM blades for (a) high flow and (b) low flow cooling conditions.

One consideration for the increased blade temperatures was the difference in the thermal conductivity of the AM blades versus the cast blades. A one-dimensional (1D) heat transfer analysis approximates a $\Delta\bar{\bar{\phi}} = 0.0013$ for the high flow condition, which does not account for the differences in cooling performance. Additional post-test coolant flow studies are planned to understand how much coolant is being supplied to specific sections of the blade. It is expected that the AM blades will have a reduction in flow rate passing through the trailing edge feed plenum, which therefore would lead to the increase in temperature seen within the trailing edge area of interest. Additional analysis is underway following completion of the test program, which will continue to combine information from internal CT inspections, external geometry analyses, bench flow characteristics, and thermal performance in the turbine rig.

For the next phase of this research program, preparations are underway to manufacture an additional round of AM turbine blades with double-wall geometries. A primary focus of this next campaign is dependent on an understanding of roughness influences from existing fielded turbine blades across a range of operating environments and run times. With this information, select discrete roughness values will be targeted for future AM builds to better read across fielded engine operation and connectivity with the AM test programs.

The roughness inherent to AM parts manufactured using L-PBF is a key contributor to the heat transfer performance. Based on this, it is important to understand the driving factors associated with rough surfaces from AM components. To this end, new turbine blades are set to be manufactured with controlled external surface roughness. However, prior to determining the magnitude of average external surface roughness to select as target values for AM airfoils, there was a need to first correlate AM roughness scales with known roughness scales already existing in the turbine design space. More specifically, a series of airfoils with varying pedigree were evaluated to determine how roughness can vary in operational engine components. For purposes of this initial assessment, data were extracted from three unique airfoils matching the descriptions outlined in Table 1.

Table 1. Description of Airfoils Analyzed in this Study.

Airfoil	Description
a	Vane, low run time
b	Vane, high run time
c	Blade, high run time

The surface roughness study of airfoils outlined in Table 1 was completed using a Keyence® VK-3100 optical profilometer located in Penn State's Materials Characterization Laboratory. The profilometer used the focus variation scanning method to measure airfoil surface profiles with horizontal resolution of 2.7 μm and vertical resolution 0.1 nm. Scan locations were chosen based on visual appearance and size limitations of the profilometer. Various measurement locations on both pressure and suction sides were chosen, and an example scan result is shown in Figure 3.

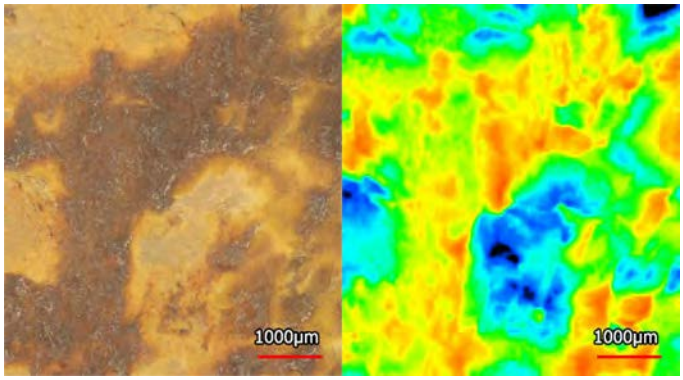

Figure 3. Typical optical image obtained from profilometer (left) and resulting surface height heatmap (right).

Raw data were postprocessed using the Keyence® VK-X3000 Multifile Analyzer software. Mathematical corrections were applied to the raw data to account for surface curvature. Figure 4 shows a subset of the measured surfaces with height plots corresponding to marked locations.

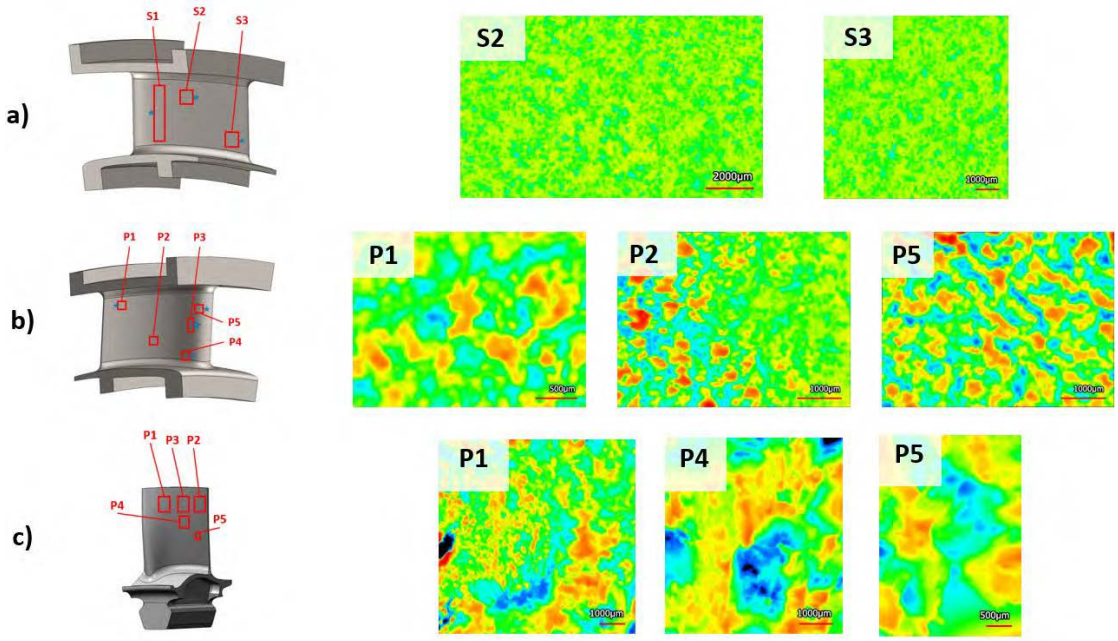

Figure 4. Three sample airfoils scanned with callouts to locations where surface scans were obtained. Heatmaps of representative surface scans for each airfoil surface are shown with normalized color bar. Airfoil (a) was a low run time vane, (b) a deteriorated (high run time) vane, and (c) a deteriorated (high run time) blade.

® Keyence is a registered trademark of Keyence Corporation, Osaka, Japan.

Surface roughness measurements were calculated for each image. Arithmetical mean height (Sa) and root mean square height (Sq) were chosen for comparison across samples. Values for these metrics corresponding to the images in Figure 4 are shown below in Table 2.

Table 2. Area Average Surface Roughness Values of Surface Scans in Figure 4.

Airfoil	Location	Sa [µm]	Sq [µm]
a	S2	4.6	6.0
	S3	4.0	5.3
b	P1	12.3	15.5
	P2	13.1	18.3
	P5	17.5	21.8
c	P1	15.9	21.2
	P4	18.4	23.5
	P5	14.6	17.8

In Table 2, the surface roughness values indicate that the high run time vane (b) and blade (c) saw significant surface deterioration compared to the low run time vane (a). In some cases, surface roughness was seen to increase as much as four to five times comparing the low versus high run time airfoils. Another observation was the difference in surface geometry patterns that arise on deteriorated surfaces. Airfoil (a) was observed to have uniform surface geometry as expected for a newly manufactured part. However, when comparing (a) to deteriorated (b) and (c), surface features become larger in size and patterns turned nonuniform. The quantitative and qualitative surface deterioration from this work provides insight into how surfaces degrade and how performance might change as run time increases, and it will inform the next phase of manufacturing for AM turbine blades supporting this project.

Task 2 – Design New Double-wall Cooling Technologies

The Pennsylvania State University

Objective

The objective of this task is to develop novel double-wall cooling designs that feature the microchannel concepts being explored in the literature and which can be achieved via AM. The designs will be generated with advice from Pratt & Whitney, so that the concepts can be leveraged for commercialization. The designs will be packaged into cascade test articles that will be measured in the high-speed linear cascade at Penn State with IR thermography.

Research Approach

Design of linear cascade test articles

This task was completed in 2022, but several important highlights are discussed in this section because they continue to support the efforts in Task 3. In this task, several novel microchannel cooling geometries were developed according to concepts in the literature, some of which have previously been demonstrated with AM. Figure 5 shows several of the designs, which were grouped by type. Pin fin designs include a standard circular pin (manufactured through AM by Kirsch and Thole (2017a), and a triangular pin design tested by Ferster et al. (2018). These designs are expected to have high pressure loss but also high cooling effectiveness. The second grouping is for ribs (turbulators), which do not span the entire channel but act to locally trip the flow. The discrete W shape designed by Wright et al. (2004) is a conventional design, but the wavy S-shaped ribs designed by King and Pietraszkiewicz (2018) is based on a patent and may have similar effects to the wavy channels studied by Kirsch and Thole (2017b). The channel-only configurations include the baseline empty microchannel that replicates the existing FAA CLEEN II design, and a wavy microchannel that is based on the findings of Kirsch and Thole (2017b).

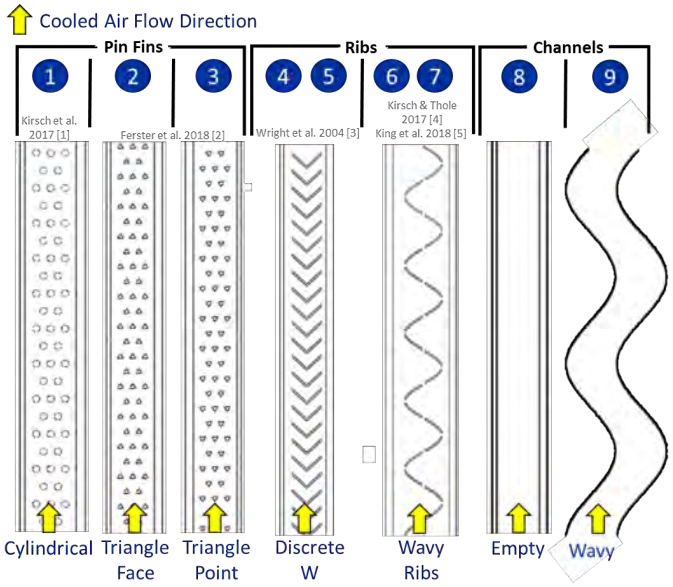

Figure 5. Novel cooling concepts packaged into the microchannels in this study.

These geometries were packaged into a linear cascade (two-dimensional profile) airfoil for testing in the high-speed linear cascade at Penn State. An example of the airfoil with surface microchannels, and the full test article including a mounting base and embedded pressure and temperature instrumentation ports, is shown in Figure 6. The designs of Figure 5 were packaged into the microchannels to create eight unique test articles.

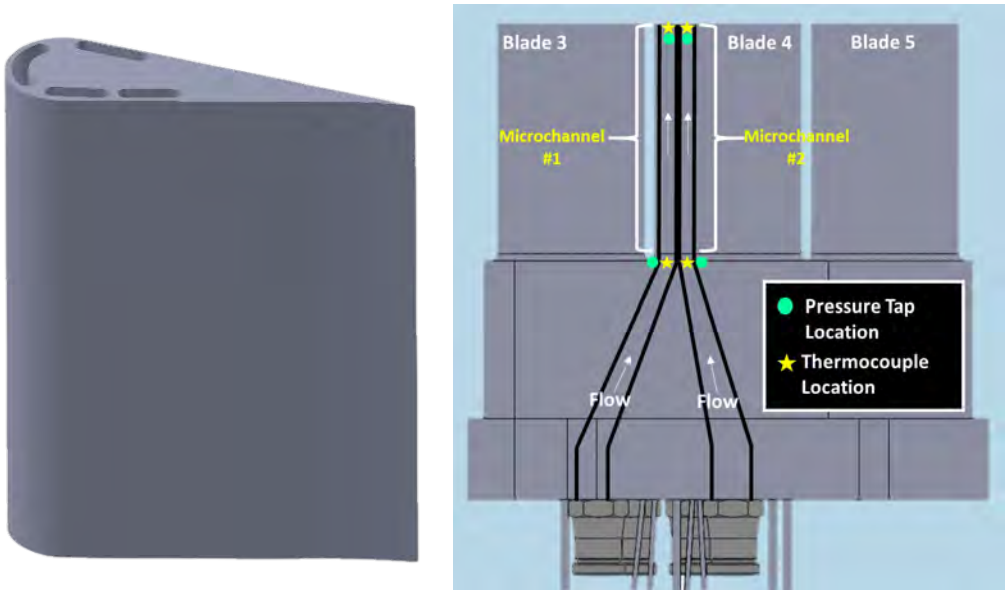

Figure 6. Example airfoil with microchannels (left), and airfoils packaged into an additively manufactured test article with embedded instrumentation ports.

Task 3 – Manufacture and Test Novel Double-wall Cooling Designs for Linear Cascade

The Pennsylvania State University

Objective

The objective of this task is to measure the performance of the AM microchannels in the linear cascade airfoil and rank the performance of the novel geometries. This process includes measuring the pressure decrease and the surface temperature of the airfoils with the novel microchannel geometries. Our team has also developed a novel measurement technique to obtain the overall convection coefficient in the microchannels by using coolant and surface temperature measurements.

Research Approach

Fabrication of linear cascade hardware

In the previous reporting period, the novel microchannel test airfoils with internal geometries indicated in Figure 6 were manufactured by Vertex Manufacturing and were received in 2022.

Current experimental data

Experimental data for microchannel cooling designs were collected in late Q4 calendar year (CY) 2023 in the high-speed linear cascade at Penn State with instrumented thermocouples, pressure taps, and an IR camera used to measure surface temperature. The cooling effectiveness Φ is used for comparison and is calculated using the following formula:

$$\frac{T_{aw}^{*} - T_s}{T_{aw}^{*} - T_{m,i}}$$

where T_{aw}^{*} is the adiabatic wall (recovery) temperature, T_s is the surface temperature, and $T_{m,i}$ is the coolant inlet temperature. The adiabatic wall temperature has been calculated using isentropic relations in tandem with computational fluid dynamics (CFD) pressure loading profiles at each external condition tested. The experimental hardware setup can be seen below in Figure 7.

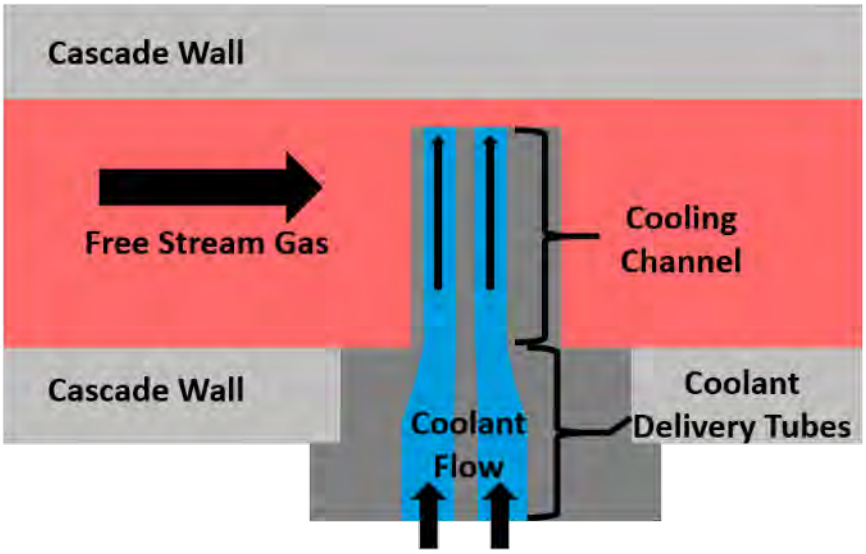

Figure 7. Pressure-side and suction-side views of the airfoil, and view locations on the following plots.

A diagram of how the different plotting regions relate to the physical blade is shown in Figure 8. The vertical arrow indicates the direction of increasing height on the blade surface. The horizontal arrow points from the leading edge of the airfoil to the trailing edge. The space between the pressure side and suction side is representative of the area not captured by the IR camera, which includes the stagnation zone.

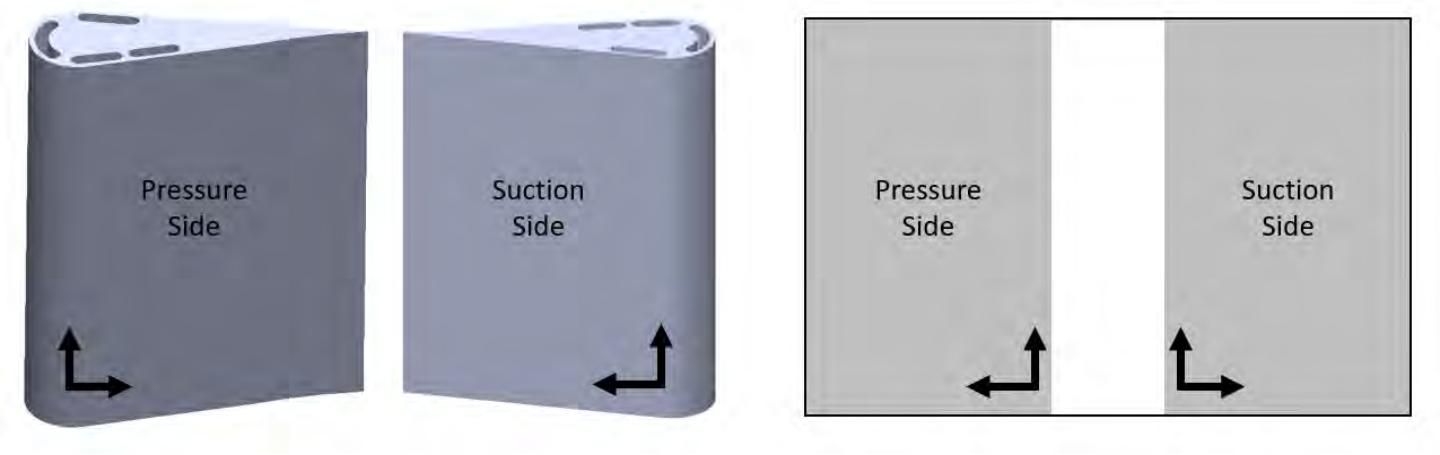

Figure 8. Pressure-side and suction-side views of the airfoil, and view locations on the following plots.

Below in Figures 9,10, and 11 experimental data are shown in contour plots in which all four internal cooling channels are flowing at an internal Reynolds number of 20,000. Each figure shows both the pressure side and the suction side of the airfoil on the left and right side of the plot, respectively. The surface temperature has been recorded using an IR thermal imaging camera and has been calibrated and dewarped onto two dimensional planes before being normalized and plotted.

In Figure 9, the cascade is set to a condition of no back pressure at Ma = 0.81, which leads to an external Reynolds number of about 245,000. In Figures 10, 11, and 12, the cascade is provided with a pressure higher than ambient through the use of a downstream valve to hold the external Reynolds number constant at 340,000 while the exit Mach number is varied. It can be observed that the contours of cooling effectiveness in Figure 9 are different than in Figures 10, 11, and 12. The contours of cooling effectiveness in Figures 10, 11, and 12 are all very similar. This supports the fact that the external heat transfer coefficient (which is an important component of the overall cooling effectiveness) is a function of Reynolds number and is not affected by Mach number, when the Reynolds number is held constant. This is only tested for subsonic Mach numbers, but this is typical of the range of commercial aircraft engines.

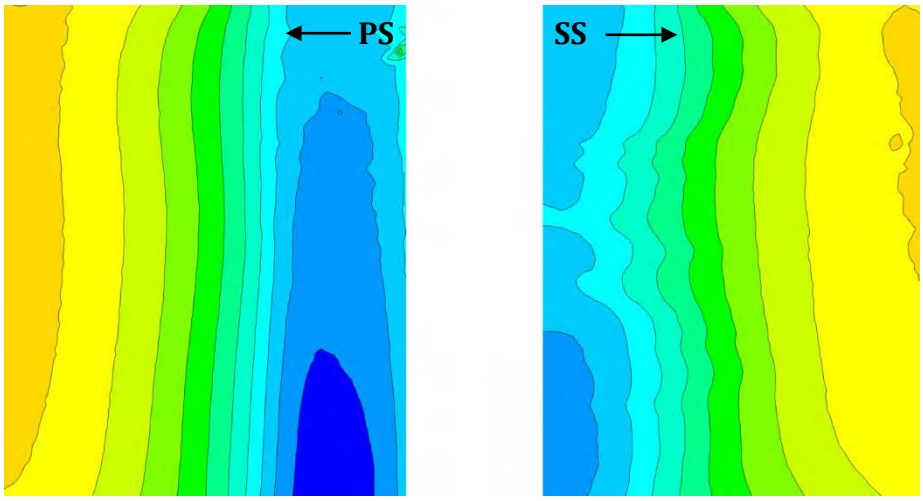

Figure 9. Ma = 0.81, external Reynolds number = 245,000, all channels flowing at an internal Reynolds number of 20,000.

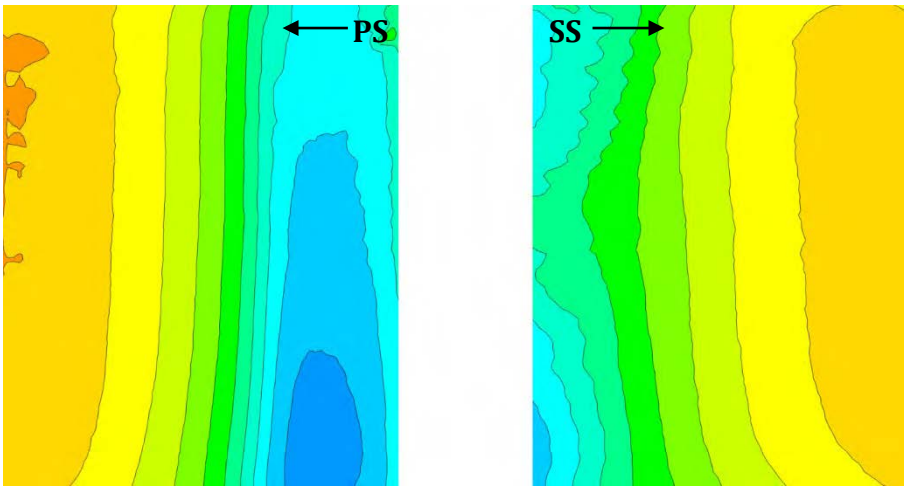

Figure 10. Ma = 0.81, external Reynolds number = 340,000, all channels flowing at an internal Reynolds number of 20,000.

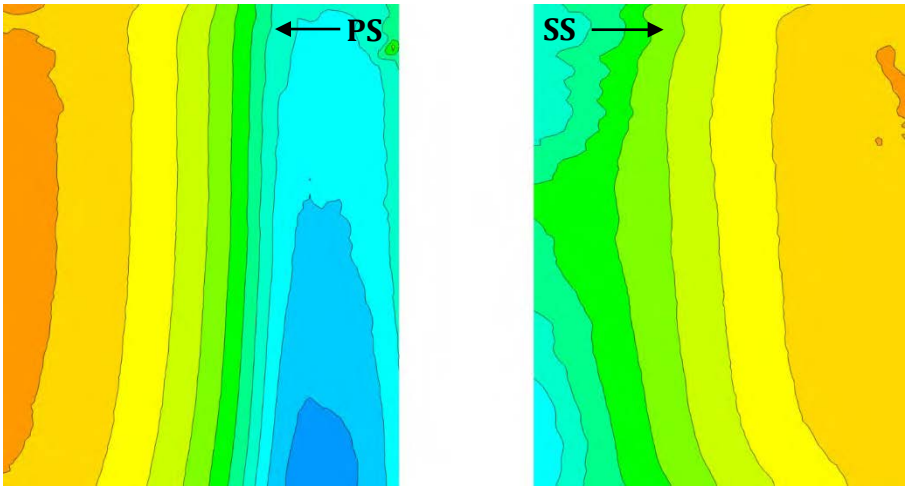

Figure 11. Ma = 0.70, external Reynolds number = 340,000, all channels flowing at an internal Reynolds number of 20,000.

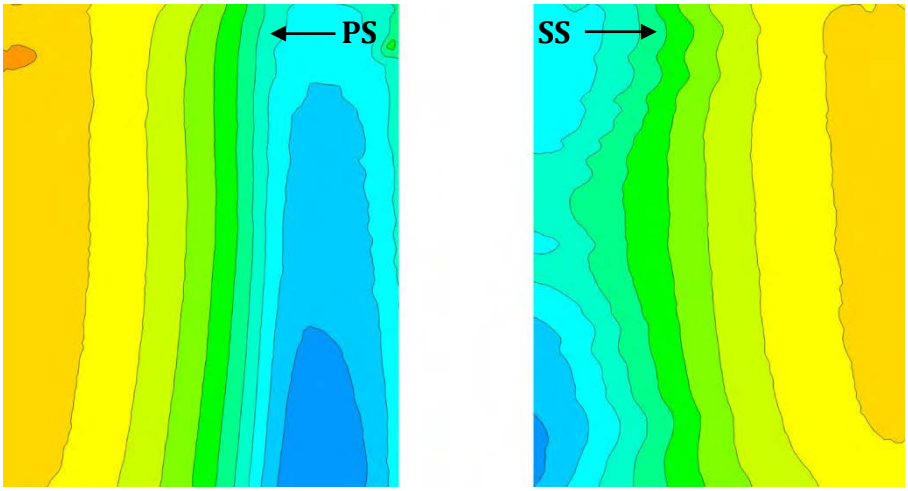

Figure 12. Ma = 0.90, external Reynolds number = 340,000, all channels flowing at an internal Reynolds number of 20,000.

In Figure 13, three different internal channel geometries are shown. These three geometries were tested in the cascade, and the cooling effectiveness contours for each are shown in Figures 14, 15, and 16. Each data point shown was recorded with an exit Mach of 0.81, external Reynolds number of 340,000, and an internal Reynolds number of 20,000 with all four channels flowing. Figure 14 is the same as Figure 10 above, repeated for ease of comparison. In comparison to the empty channel, both rib designs show significant differences in effectiveness contours. The W-Rib channels have much higher cooling effectiveness near the base of the channel, but that cooling effectiveness decreases at a faster rate than either of the other designs. This is likely due to the added turbulence that the tightly packed ribs add to the flow. The coolant entering the channel is immediately tripped into turbulence leading to an increase in the internal heat transfer coefficient. The increased rate of decline in this effectiveness is likely due to the coolant heating up to a higher temperature early into the channel. The S-Rib channel design behaves differently. This design shows a similar cooling effectiveness near the base of the channel as the empty channel but exhibits the ability to continue this cooling level further down the channel, leading to a more uniform cooling effectiveness. The lack of a major increase at the base of the channel could be due to the ribs being much less densely packed than in the W-Rib channel design.

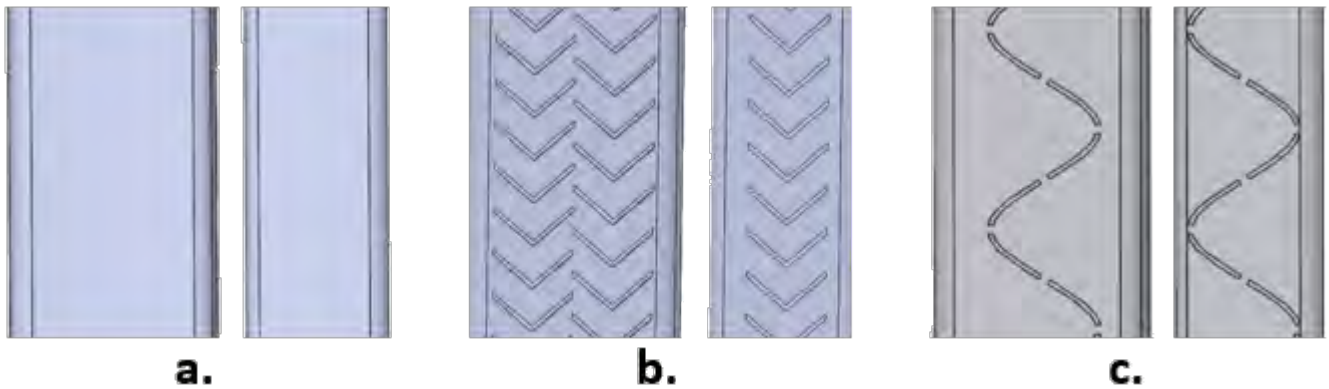

Figure 13. Internal channel geometries; a) Empty channel design. b) W-Rib channel design. c) S-Rib channel design.

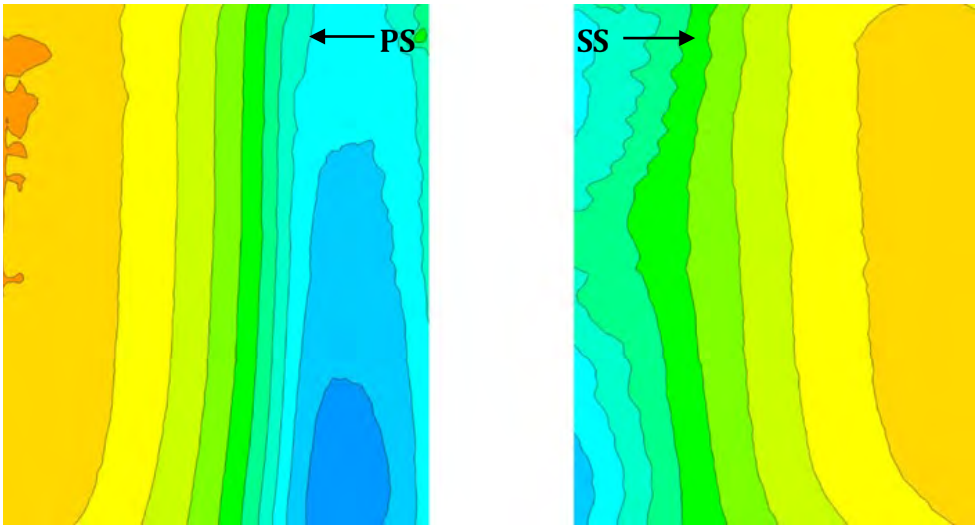

Figure 14. Empty Channels flowing at $\mathrm{Re}_{\mathrm{int}} = 20{,}000, \mathrm{Re}_{\mathrm{ext}} = 340{,}000, \mathrm{Ma} = 0.81$.

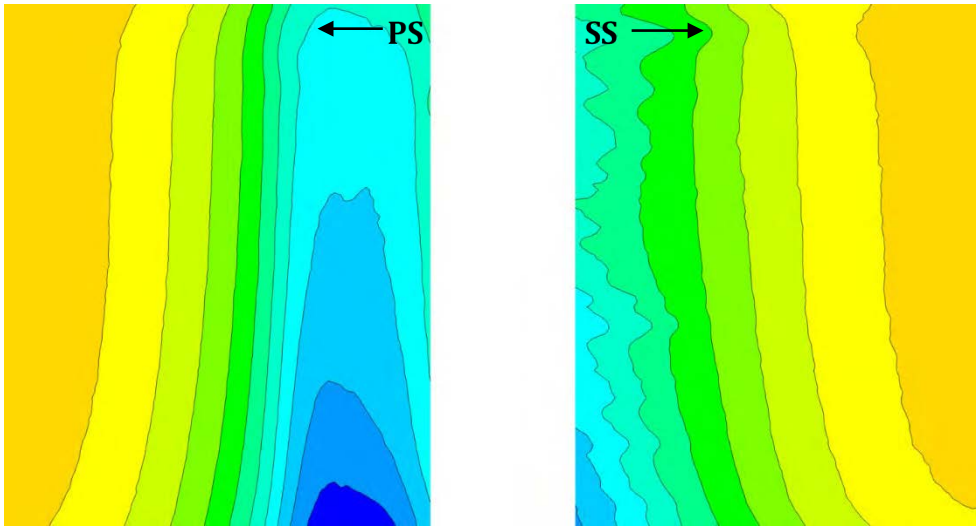

Figure 15. W-Rib Channels flowing at $\mathrm{Re}_{\mathrm{int}} = 20{,}000, \mathrm{Re}_{\mathrm{ext}} = 340{,}000, \mathrm{Ma} = 0.81$.

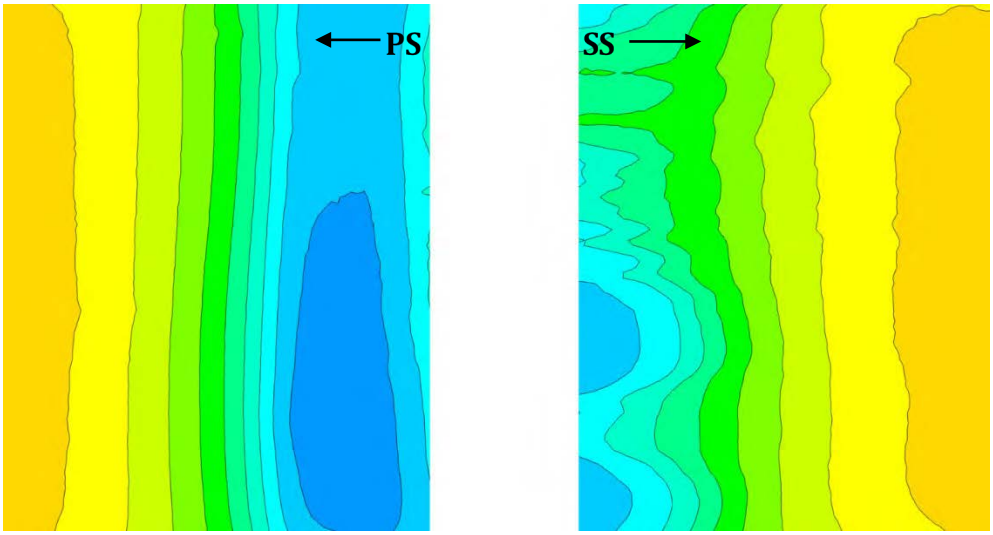

Figure 16. S-Rib Channels flowing at $\mathrm{Re}_{\mathrm{int}} = 20{,}000, \mathrm{Re}_{\mathrm{ext}} = 340{,}000, \mathrm{Ma} = 0.81$.

To better understand the cooling effectiveness of these different geometries, CT data were analyzed. An example of a typical cross section after processing is shown in Figure 17. In Figure 17, the black area is the channel being analyzed. CT scan data were processed in a similar manner for all three tested geometries. This analysis provided hydraulic diameters at ten distinct slices or cross sections. These hydraulic diameters were normalized by the design intent hydraulic diameter and the results of this analysis can be seen in Figure 18. The empty channel design and the W-Rib design printed well compared to design intent. Both designs showed that on average the hydraulic diameter was less than 1% underbuilt. The S-Rib design, however, was more significantly underbuilt with an average hydraulic diameter nearly 8% smaller than design intent.

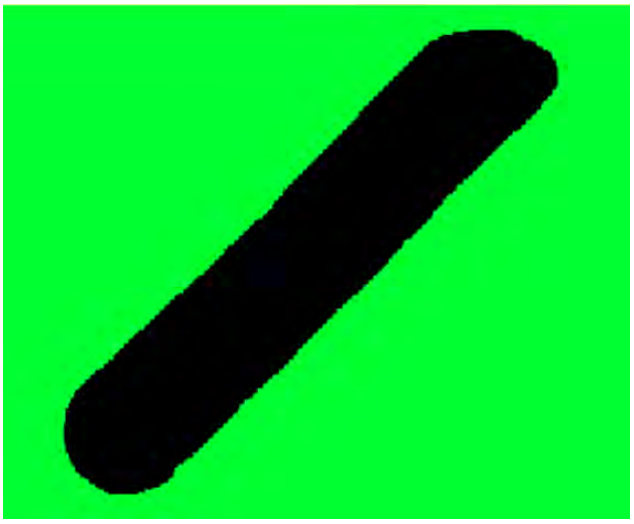

Figure 17. Cross section of microchannel CT scan after processing.

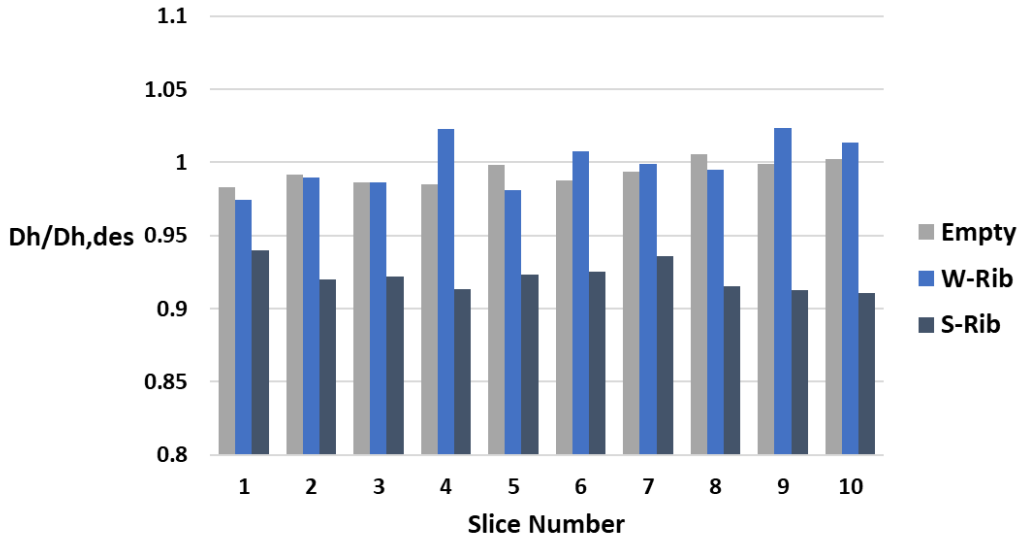

Figure 18. Hydraulic diameter analysis of the three tested channel geometries.

In addition to the cooling effectiveness testing which took place in the high-speed linear cascade, benchtop testing was done to determine the friction factor. This nondimensional parameter can help provide insight to losses associated with each channel design. In this analysis, the CT data were used to provide real cross-sectional areas and perimeters.
The friction factor data can be seen in Figure 19. Both the Reynolds number and the friction factor were normalized by a selected design point. As expected, the empty channel design produced the lowest friction factor. The W-Rib design showed very similar but slightly increased friction factor, while the S-Rib design showed more significant increases. One possible reason for the significant difference is the resolution of the ribs. Qualitative analysis of the CT scan data revealed that the shape of the ribs had much better resolution in the S-Rib channels, while the ribs in the W-Rib channels printed poorly. With poor rib resolution in the W-Rib channels, the losses become much more similar to the empty channel that does not have any ribs.

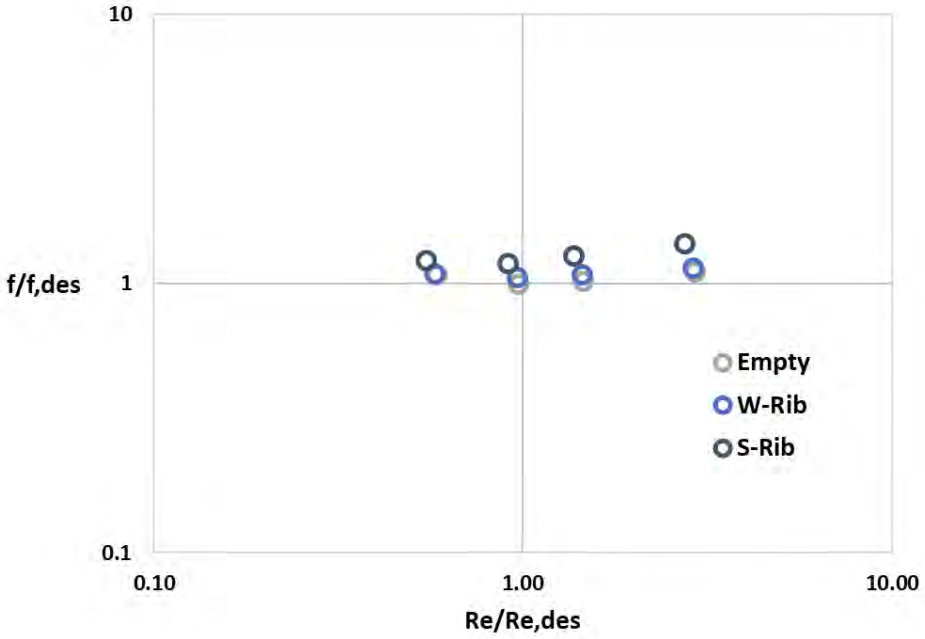

Figure 19. Normalized friction factor data for the three tested geometries.

Milestones

Milestone	Due date	Estimated date of completion	Actual date of completion	Status
Workplan	3/4/20	3/4/20	3/5/20	Completed
COE meeting 1	4/1/20	4/1/20		Cancelled
COE meeting 2	10/1/21	10/1/21	10/28–10/29/21	Completed
COE meeting 3	10/26/22	10/26/22	10/26–10/28/22	Completed
COE meeting 4	10/24/23	10/24/23	10/24/23	Completed
COE meeting 5	10/31/24	10/31/24	10/29-10/31/24	Completed
Annual report	12/20/24	12/13/24	12/13/24	Completed
Project closeout	9/30/25	9/30/25		

Major Accomplishments

After several years of preparation, this year included the successful test of AM turbine blades created based on a CT-scanned cast turbine airfoil. This test program represented one of the first to operate AM blades at operational speeds representative of engine-scaled conditions in a turbine test environment. Furthermore, it represented the first test of its kind to operate a rainbow wheel, concurrently testing cast and AM blades together. Although the data from this test are still under analysis, there is still a lot to learn about the comparisons between cast and AM airfoils, and this ongoing research program is continuing to help close that gap.

Publications

None.

Outreach Efforts

Research findings were presented throughout this year, as shown below.

Event	Date	Attendees
Bi-weekly calls	Every 2 weeks	Pratt & Whitney (PW) aerodynamics/durability engineers
Quarterly calls with turbine OEMs	Once per quarter	Industry partners: Solar, Siemens, Honeywell
Center of Excellence bi-annual meetings	5/20/2024 and 12/9/2024	PW aerodynamics/durability engineers and management
Center of Excellence bi-annual meetings	1/18/2024	Solar Turbine engineers
Dept. of Energy (DOE) National Experimental Turbine (NExT) annual review meeting	11/18/2024	DOE, NASA, PW, Solar, Siemens, Honeywell
NASA university leadership initiative meeting	10/2/2024	NASA, FAA, PW, Collins, RTRC, Howard University, Georgia Institute of Technology
Turbine Engine Technology Symposium	9/11/2024	ONR, AFOSR, AFRL, PW, GE, Honeywell, Williams International, Kulite

Our findings on learning from AM to Solar Turbines were presented at the November Center of Excellence on January 18, 2024, and to Pratt & Whitney at the May (5/20/2024) and December (12/9/2024) program reviews. We also reported on additive manufacturing learning at the Turbine Engine Technology Symposium (TETS). The TETS meeting, which took place on September 11, 2024, is a Department of Defense-focused meeting attended by a range of gas turbine manufacturers, defense contractors, and small business researchers.

Awards

Graduate student Nicholas Gailey won a second-place award for his poster presentation at the National Aeronautics and Space Administration (NASA) ImaginAviation Symposium in February 2024.

Student Involvement

Liam Boyd, a master's degree student, started on the project in Summer 2022. Liam conducted computational simulations of microchannels and experimentally testing microchannel geometries to study the effectiveness of certain designs and the predictive capabilities of modern CFD. After finishing his research at Penn State, Liam is now a staff engineer at General Electric Aerospace.

Nicholas Gailey is a PhD student who led the experimental analysis of AM turbine blades in the START rig. Nicholas has led the development of advanced IR thermal imaging capabilities in the START Lab at Penn State, including the mapping of two-dimensional images to three-dimensional geometries. Nicholas is expected to complete his PhD in Summer 2025.

Plans for Next Period

New sets of AM turbine blades will be manufactured and prepared for testing in the START Lab at Penn State. These blades will be specifically targeting different roughness levels to better understand the relative influence of internal and external roughness effects associated with the additive manufacturing process.

Experimental testing of microchannel designs for friction factor (benchtop) and surface temperature (linear cascade) will be conducted in 2025 and compared to CFD predictions to determine whether design level CFD can predict experimentally observed behavior. CT information will inform modifications for the CFD to assess the importance of as-manufactured dimensions on prediction accuracy.

References

Ferster, K. K., Kirsch, K. L., & Thole, K. A. (2018). Effects of geometry, spacing, and number of pin fins in additively manufactured microchannel pin fin arrays. *Journal of Turbomachinery*, *140*(1), 011007. https://doi.org/10.1115/1.4038179

King, C., & Pietraszkiewicz, E. F. (2018). *U.S. Patent No. 10,156,157*. Washington, DC: U.S. Patent and Trademark Office.

Kirsch, K. L., & Thole, K. A. (2017a). Pressure loss and heat transfer performance for additively and conventionally manufactured pin fin arrays. *International Journal of Heat and Mass Transfer*, *108*, 2502-2513. https://doi.org/10.1016/j.ijheatmasstransfer.2017.01.095

Kirsch, K. L., & Thole, K. A. (2017b). Heat transfer and pressure loss measurements in additively manufactured wavy microchannels. *Journal of Turbomachinery*, *139*(1), 011007. https://doi.org/10.1115/1.4034342

Wright, L. M., Fu, W. L., & Han, J. C. (2004). Thermal performance of angled, V-shaped, and W-shaped rib turbulators in rotating rectangular cooling channels (AR= 4: 1). *Journal of Turbomachinery, 126*(4), 604-614. https://doi.org/10.1115/1.1791286

Disclaimer

This research was funded by the U.S. Federal Aviation Administration Office of Environment and Energy through ASCENT, the FAA Center of Excellence for Alternative Jet Fuels and the Environment, Project 056 through FAA Award Number 13-C-AJFE-PSU-109 under the supervision of Joshua Glottmann. Any opinions, findings, conclusions or recommendations expressed in this material are those of the authors and do not necessarily reflect the views of the FAA.

Project 057 Support for Supersonic Aircraft En-Route Noise Efforts in ICAO CAEP

The Pennsylvania State University

Project Lead Investigator

Victor W. Sparrow
United Technologies Corporation Professor of Acoustics
Graduate Program in Acoustics
The Pennsylvania State University
411 Engineering Collaborative Research and Education Building (ECoRE)
566 White Course Drive
University Park, PA 16802
814-865-6364
vws1@psu.edu

University Participants

The Pennsylvania State University (Penn State)

- P.I.: Professor Victor W. Sparrow
- FAA Award Number: 13-C-AJFE-PSU Amendments 55, 77, 86, 100, 115, 117, and 122
- Period of Performance: February 5, 2020, to September 30, 2025
- Tasks:
    1. Procedures for sonic boom certification
    2. Assessing secondary sonic boom propagation
    3. Investigating seismic networks for measuring sonic booms
    4. Host ASCENT noise meeting in Spring 2024

Project Funding Level

This project focuses on multiple tasks at Penn State and its subcontractors Farmingdale State University and RACC Consulting, LLC. The Federal Aviation Administration (FAA) funding to Penn State in 2024 was $400,000. Matching funds are expected to meet cost sharing on all tasks. In 2024, FAA granted Penn State's request for reduced cost sharing to 25% of the total project costs. In-kind contributions have been pledged by Boom Supersonic ($120,000), Exosonic ($220,000 in 2024; however, Exosonic is ceasing operations, so this cost share is uncertain at the time of this writing), Gulfstream ($250,000), and Pivotal Supersonics (previously known as Global SST; $75,000).

Task 3, investigating seismic networks, was initiated by the Project P.I. using funds from the United Technologies Corporation Professorship within the Penn State College of Engineering. This 2023 and 2024 financial support from the Penn State College of Engineering is gratefully acknowledged.

Investigation Team

Penn State
Prof. Victor W. Sparrow, (P.I.), Tasks 1, 2, 3, and 4
Joshua Kapcsos, (Acoustics graduate research assistant), Task 1
Dr. Sampath Rathnayaka (Geosciences postdoctoral scholar), Task 3
Prof. Andrew Nyblade, (Geosciences professor), Task 3
Farmingdale State College, **State University of New York** (subrecipient of Penn State)
Kimberly A. Riegel, (Physics co-investigator), Tasks 2 and 3
RAC Consulting, LLC
Robbie Cowart (Research scientist), Task 1

Boom Supersonic (industrial partner)
Michael Rybalko, Gus Silva, et al.
Exosonic (industrial partner)
John Morgenstern
Gulfstream (industrial partner)
Brian Cook, Matthew Nickerson, Joe Gavin, Nick Ward, and Charles Etter
Pivotal Supersonic (previously known as Global SST; industrial partner)
Steve Ogg

Project Overview

Passenger aircraft development is on the verge of a true revolution. Companies such as Boom Supersonic, Gulfstream Aerospace Corporation, Lockheed Martin, Exosonic, Pivotal Supersonics, and others are reaching the point at which they can build and deliver to users aircraft capable of flying supersonically in an environmentally responsible way. This development will allow for decreased air transportation travel times, to the great benefit of society.

New supersonic aircraft must be certified as being sufficiently quiet to not excessively disturb the public. Preparation for such a certification process has been ongoing for several years in the FAA Office of Environment and Energy (AEE). Working with its international partners in the International Civil Aviation Organizations (ICAO)'s Committee for Aviation Environmental Protection (CAEP), the FAA has been laying the groundwork for certification standards. The FAA's efforts have been supported by both universities and other governmental agencies. Specifically, Penn State has supported the FAA/AEE through Projects 8 and 24 in the PARTNER Center of Excellence (COE) and more recently in Projects 7, 41, and 42 of the ASCENT COE. Summaries of these research efforts can be found on the website ascent.aero. To date, a group of six candidate metrics for en route supersonic certification have been agreed upon in the CAEP's Working Group 1 (WG1) (Noise Technical) Supersonic Task Group (SSTG). Multiple schemes for certification have been generated. Several schemes have been eliminated from further consideration, and others are currently being evaluated for possible implementation. Procedures have been proposed for acquiring and processing ground measurement of the en route supersonic noise, but all possibilities remain under discussion. The extent to which atmospheric conditions will affect the measurements, and the requirements and roles of numerical simulations of the noise propagating from the aircraft to the ground are being considered. One particularly challenging aspect is the influence of the atmosphere in distorting the acoustic pressure signatures, owing to atmospheric turbulence, and the subsequent effects on the metric values. These gaps are only several of those that must be filled.

All these topics are being worked on, in a stepwise manner, in FAA and in WG1's SSTG. Efforts in the completed ASCENT Project 41 have been aimed at supporting the FAA with technical expertise in the development of the certification procedures and gaining an initial understanding of secondary sonic booms. Secondary sonic booms, also known as over-the-top sonic booms, are the sound energy that travels upward at heights above the aircraft cruise altitude and lands at distant locations. Secondary sonic booms are the reason why the Concorde[1] was requested to transition from supersonic to subsonic speeds at substantial distances before entering the continental United States airspace. ASCENT Project 41 ended in early 2021, and ASCENT Project 57 is now in its fifth year. However, much work remains to be done, and efforts lasting several more years will be required to advance certification standards for supersonic aircraft.

In 2025 and beyond, continued support for supersonic aircraft noise efforts will be necessary for the FAA and its international partners to fill technical solution gaps and continue progressing toward certification procedures. Although other universities and industries will continue their focus on aircraft design and landing and takeoff studies, continued work on en route supersonic noise issues will be essential, because these issues remain the greatest barrier to the use of environmentally responsible supersonic aircraft. ASCENT Project 57 will support the ongoing activities in ICAO CAEP and their WG1 (Technical Noise), with a focus on establishing supersonic aircraft en route procedures and metrics for noise certification standards, and to support the interface with the ICAO Air Navigation Commission to address related noise issues.

In the 2020 through 2025 project period, the emphasis will be on continuing the research support for supersonic aircraft en route procedures, including the utilization of an agreed-upon reference-day atmosphere, the establishment of techniques for incorporating measurement data and simulations into a draft certification procedure, and the consideration

[1] The Concorde was a specifically designed aircraft for supersonic flight.

of off-design flight speed sonic booms, such as focus booms and acceleration booms. Support will also be provided for a more comprehensive analysis of the National Aeronautics and Space Administration's (NASA's) SonicBAT dataset and efforts in developing methods to remove the effects of atmospheric turbulence on measured acoustic pressure waveforms to support certification. The research in 2020 through 2025 will also need to consolidate and process the results of research from 2019 to 2020 on the topic of secondary sonic booms as a potential noise issue for the initial supersonic airplanes. This material will be of particular interest to ICAO's Air Navigation Commission because it could affect the operation of supersonic aircraft in the near term.

Task 1 – Procedures for Sonic Boom Certification

The Pennsylvania State University
RAC Consulting, LLC

Objectives

ASCENT Project 57 is a transition from ASCENT Project 41, Identification of Noise Acceptance Onset for Noise Certification Standards of Supersonic Airplanes. As national aviation authorities move toward developing noise certification standards for low-boom supersonic airplanes, several research gaps exist in areas including signature fidelity, metrics, metrics sensitivity to real-world atmospheric effects, and adjustments for reference conditions. The objective of Task 1 is to support the FAA in the development of technical standards for civil supersonic aircraft under the ICAO CAEP. This effort provides the FAA with technical noise expertise regarding the development of noise certification standards for future civil supersonic passenger aircraft, primarily in the area of en route noise (sonic boom) minimization and/or abatement.

Task 1 in ASCENT Project 57 focuses on research initiatives necessary to develop an overland supersonic en route noise certification standard. An objective is to improve the turbulence model in nonlinear propagation code KZKFourier by introducing atmospheric profiling and ground blocking methodologies. Additional work focuses on providing direct research support for ICAO/CAEP/WG1's SSTG and Procedures subgroup (PrSG) meetings and discussions.

Research Approach

Background

The KZKFourier propagation code is an augmentation of the Burgers equation into a KZK propagation equation to include nonlinearity, diffraction, and absorption in directional sound beams, to simulate wind and temperature fluctuation effects of the atmospheric boundary layer (ABL), according to the Ostashev and Wilson (2015) model. During the 2019–2020 academic year, PCBoom 6.7.1.1 and KZKFourier were used above and within the atmospheric boundary layer, respectively, to simulate turbulence effects of atmospheric boundary layer heights of 268.2, 411.4, and 1026.7 m, corresponding to SonicBAT Flight 5 conditions. Information regarding this endeavor appears in the 2020 report for ASCENT Project 057. After propagating shaped boom signatures through ten randomly generated atmospheres, the data were shared with the WG1/SSTG/PrSG, in which zero-padding and spiking artifacts were discovered near the beginnings and ends of certain ground signatures; the plots shown in the 2020 report did not span the entire retarded time domain of the ground waveform data. These artifacts were corrected in the 2020–2021 academic year, as described in the 2021 report for ASCENT Project 57. In the 2021–2022 academic year, Penn State expanded the shaped boom database to 20 realizations at NASA's request, conducted a parameter check on KZKFourier for boundary layer thicknesses, freezing temperatures, and turbulence parameters, conducted a grid refinement study on KZKFourier, and initiated a reference-day crosscheck with international members of the CAEP's WG1 (Noise Technical); these milestones are described in the 2022 report for ASCENT Project 57. The 2023 report for ASCENT Project 57 reviews an extension of the reference-day crosscheck to evaluate participant noise metrics, an investigation of the numerical interpolation methods of the KZKFourier solution, and the introduction of atmospheric profiling in KZKFourier, in which humidity was profiled in the molecular relaxation module for the first time.

Progress Toward Implementation of Ground Blocking in KZKFourier

It is important to include the effects of a realistic atmospheric profile during sonic boom simulation. Atmospheric variables such as humidity, pressure, density, and temperature realistically vary by altitude. NASA requested Penn State investigate improving the atmospheric turbulence model in KZKFourier, which models the primary sonic boom carpet with atmospheric turbulence included. This is now in progress; the introduction of humidity profiling in KZKFourier can be found in the 2023 report for ASCENT Project 57. The current year has been focused on the progress toward implementation of a height-dependent ground blocking methodology to further improve the turbulence model.

The original released version of KZKFourier does not consider the effect of the ground on the turbulent eddies in the atmospheric boundary layer; in reality, the proximity of the eddies to the ground affects their shape, as an eddy cannot penetrate the ground. While KZKFourier considers scalar (temperature) and both shear- and buoyancy-induced vector (wind) turbulence, height-dependent ground blocking affects only the buoyancy-induced vector turbulence. At the 186th meeting of the Acoustical Society of America in May 2024, Dr. D. Keith Wilson presented an equation (Wilson et al., 2024) to implement ground blocking by applying natural exponential factors to a two-dimensional cross spectrum (ϕ_{33}) between propagation heights, z_1 and z_2, and wavenumbers, κ_1 and κ_2 as follows:

$$\hat{\phi}_{33} = (\kappa_1, \kappa_2; z_1, z_2) = \phi_{33}(\kappa_1, \kappa_2; z_2 - z_1) - \phi_{33}^*(\kappa_1, \kappa_2; z_1)e^{-\kappa_\perp z_2} - \phi_{33}(\kappa_1, \kappa_2; z_2)e^{-\kappa_\perp z_1} + \phi_{33}(\kappa_1, \kappa_2; 0)e^{-\kappa_\perp (z_1 + z_2)}.$$

Because KZKFourier uses a three dimensional (3D) turbulence spectrum (E) as prescribed in *Acoustics in Moving Inhomogeneous Media* (Ostashev & Wilson, 2015) and not a two-dimensional (2D) cross spectrum as Wilson's ground blocking method requires, KZKFourier is being modified to conciliate with the above exponential factors. Cotté and Blanc-Benon (2007) refer to a doctoral dissertation by Chevret (1994) that suggests the conversion factor from a 3D to 2D spectrum is $2\pi\kappa$. As shown in Figure 1, this conversion factor results in a spectrum that is similar to Wilson's 2D cross spectrum and factor of $4\pi\kappa^4/(\kappa_1^2 + \kappa_2^2)$ that returns E from a cross spectrum. Penn State is currently working on using these conversion factors to modify the KZKFourier spectrum such that the ground-blocking methodology can then be implemented within the C++ code.

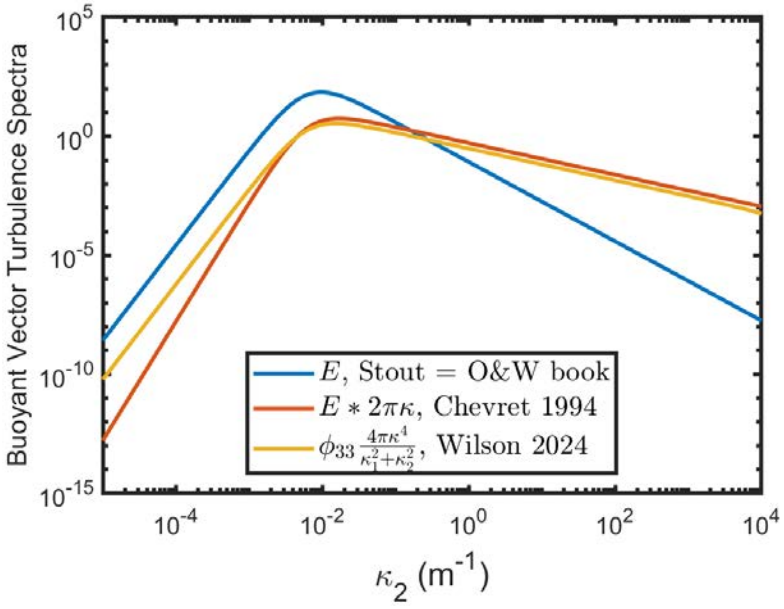

Figure 1. Buoyant vector turbulence spectra as it appears in three-dimensional E in KZKFourier, as multiplied by Chevret conversion factor to 2D, and as compared to a 2D cross spectrum ϕ_{33}.

Direct Support for CAEP/WG1 meetings

Research conducted in ASCENT Project 57 supports many aspects of sonic boom science, including the simulation of conventional N-wave sonic booms and low noise acoustic pressure signatures of future shaped supersonic aircraft in realistic atmospheric environments. Current work includes development and implementation of algorithms to model the effects of atmospheric turbulence, ultra-long-distance propagation of secondary booms, signal processing and metric evaluation of low signal-to-noise target acoustic pressure signatures in the presence of various levels of background noise, all of which supports the FAA with technical expertise and research science to continue development of noise certification standards for future civil supersonic passenger aircraft.

Within the ICAO-CAEP, the WG1 on aircraft noise is responsible for noise standards and recommended practices. At the FAA's request, ASCENT Project 57 began supporting the SSTG within WG1, which is tasked with supersonic en route/sonic boom noise standards, in April 2024 through RAC Consulting, LLC. Figure 2 provides a summary of subgroups organized under the SSTG. The PrSG is a subset of the SSTG which concentrates efforts on understanding all aspects of candidate noise certification schemes under consideration by the WG1. The Test Procedures ad hoc group (TPahg) is a subset of the PrSG which has been tasked to derive and document en route noise test procedures for consideration by the WG1 to include in a future noise certification procedure. The Scheme Drafting Subgroup is another recently established subset of PrSG tasked with outlining and drafting detailed process steps of the candidate schemes.

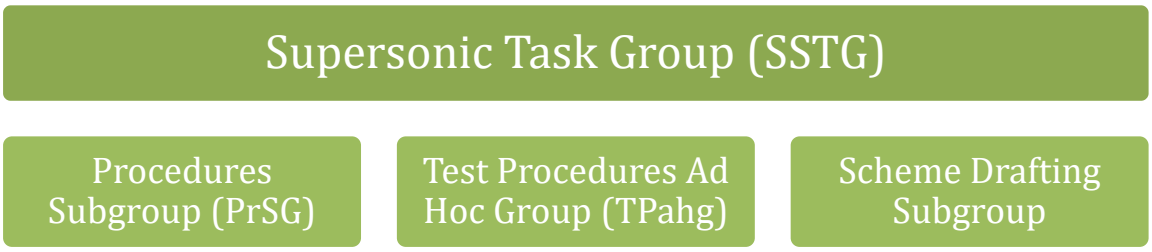

Figure 2. Groups organized around developing supersonic en route noise certification procedures.

During the second quarter of 2024, 12 virtual meetings were held via telecon across the SSTG, PrSG, and TPahg, leading up to and following the seventh WG1 meeting (WG1-7) held in May. During this time, TPahg was paused but anticipated to restart in the second half of 2024. As noted above, the telecons led to several technical papers for WG1-7 and inputs for the WG1 report to the third, and final, CAEP Steering Group meeting in the CAEP/13 cycle.

In the third quarter, activities included 21 virtual meetings, largely in preparation for the eighth, and final, WG1 meeting (WG1-8) of the CAEP/13 cycle. Key points of discussion centered mostly on technical and research activities that carry well beyond CAEP/13. During this period, much attention was given to the scheme drafting group, formed in the final weeks of the second quarter of 2024, and tasked to create a more detailed set of process steps for the candidate certification schemes. As one of the research scientists for ASCENT Project 57, planning was initiated for a virtual SSTG workshop to be held in December 2024 along with discussion of workshop priorities, objectives, and possible agenda topics. TPahg telecons were restarted in July 2024 and focused on developing portions of text for en route noise test procedures. In preparation for WG1-8, a technical report summarizing CAEP/13 supersonic en route noise activities was prepared for the upcoming CAEP/13 meeting in February 2025.

In addition to the above-mentioned activities, six other virtual meetings were supported with either partial or the full ASCENT Project 57 research team. These sessions were to review and discuss ongoing research in support of en route/sonic boom procedures, active work on secondary sonic boom, and research cost-sharing activities across multiple ASCENT Project 57 industry partners. The ASCENT Project 57 research team discussed ongoing work into multi-path signature evolution and unique measurement techniques for secondary boom, when appropriate, within the CAEP/WG1 subgroups.

In total, 42 virtual sessions have been held across task and subgroups, including one 2-day virtual workshop in December 2024 and four technical papers that were prepared for WG1 meetings, along with a final summary report and technical report of supersonic en route noise activities in the CAEP/13 cycle.

Milestones

Significant progress has been made in improving the turbulence model in KZKFourier, beginning with the inclusion of uniform humidity profiling in its molecular relaxation module and currently toward a ground blocking methodology. With the similar buoyancy-induced vector turbulence spectra shown in Figure 1, groundwork has been laid to implement height-dependent ground blocking in KZKFourier.

Major Accomplishments

The 3D buoyancy-induced vector turbulence spectrum in KZKFourier has been converted to a spectrum that is similar to a 2D cross spectrum needed to implement a ground-blocking methodology, and the consideration of these ground effects

will lead to more accurate simulated sound metrics and annoyance evaluation for NASA and its upcoming X-59 Quesst[2] quiet supersonic technology demonstrator.

Publications

Published Conference Proceedings

Kapcsos, J. L., & Sparrow, V. W. (2023). Progress update on inclusion of atmospheric profiling for sonic boom propagation through turbulence. *The Journal of the Acoustical Society of America*, *154*(4_supplement), A148. https://doi.org/10.1121/10.0023078

Outreach Efforts

None.

Awards

Joshua Kapcsos received the 2nd place award from the Acoustical Society of America Technical Committee on Noise for the Student and Early Career Best Paper Award; for the presentation "Progress update on inclusion of atmospheric profiling for sonic boom propagation through turbulence" given on December 5, 2023, at the Acoustics 2023 meeting in Sydney, Australia.

Student Involvement

Joshua Kapcsos was the Penn State graduate research assistant who worked on ASCENT Project 57 during the 2023–2024 academic year.

Plans for Next Period

Penn State will continue developing atmospheric profiling schemes in KZKFourier for other atmospheric quantities (e.g., temperature). The modified buoyancy-induced vector turbulence spectrum will be used to implement a ground-blocking methodology such that height-dependent ground effects are considered during propagation.

References

Chevret, P. (1994). *Simulation numérique des effets de la turbulence sur la propagation du son dans l'atmosphère* (Publication No. 94-18) [Doctoral dissertation, L'école Centrale de Lyon]. Centre Acoustique. https://acoustique.ec-lyon.fr/publi/chevret_thesis.pdf

Cotté, B., & Blanc-Benon, P. (2007). Estimates of the relevant turbulent scales for acoustic propagation in an upward refracting atmosphere. *Acta Acustica United with Acustica, 93*, 944-958.

Kapcsos, J. L., & Sparrow, V. W. (2023). Progress update on inclusion of atmospheric profiling for sonic boom propagation through turbulence. *The Journal of the Acoustical Society of America*, *154*(4_supplement), A148.

Ostashev, V. E., & Wilson, D. K. (2015). *Acoustics in moving inhomogeneous media* (2nd ed.). CRC Press, Boca Raton, FL.

Wilson, D. K., Ostashev, V. E., Hart, C. R., & Kamrath, M. J. (2024). Verifying turbulence models in the atmospheric boundary layer by acoustical means. *The Journal of the Acoustical Society of America, 155*(3_supplement), A200.

Task 2 – Assessing Secondary Sonic Boom Propagation

The Pennsylvania State University
Farmingdale State College, State University of New York

Research Approach

Overland secondary sonic booms

In previous work, secondary sonic booms were modeled from flights approaching the United States coastlines and around Edwards Air force Base (EAFB) in Edwards, CA. Using NASA's PCBoom program seems to work effectively for this modeling purpose, although the research team does not yet have any experimental evidence validating the PCBoom secondary boom predictions.

[2] Quesst is NASA's mission to demonstrate the X-59, an experimental supersonic aircraft built by Lockheed Martin Skunk Works® (registered trademark of Lockheed Martin Corporation, Bethesda, Maryland) and NASA Aeronautics.

Last year, the research team initiated a new set of studies regarding secondary sonic booms and the effects of topography. The Concorde is well known to have produced secondary booms in New England in the late 1970s, as described in Rickley and Pierce (1980). These secondary booms were no longer heard when sufficient coastal buffer distances were introduced to keep the secondary booms off the coastlines. Simultaneously, the U.S. Air Force regularly flies supersonically around EAFB in California, and the sounds of secondary booms do not appear to be reported regularly. What is the difference? Last year's work indicated that one possibility is that the secondary boom signal might be affected by surface topography of the land, given that topography is one difference between overwater and overland flight. Over water, the water surface is fairly flat except during exceptional weather conditions. Secondary sonic booms have two types: type I (also called direct) secondary booms and type II (also called indirect) secondary booms. The difference is that type I secondary booms initially head upward and do not interact with the ground surface until they are heard on the ground, whereas type II secondary booms initially head downward, form the primary boom carpet, reflect back into the atmosphere, and eventually head back to the ground, where they are heard as secondary booms. Both type I and type II secondary booms require favorable upper-atmospheric winds to be heard at all. However, only type II booms require surface reflection. Our work last year indicated that type II secondary sonic booms could be affected by the topography of the ground reflections. This work was reported in the proceedings of the European Acoustics Association's Forum Acusticum 2023 in Torino, Italy, in September 2023, which are available by open access (Sparrow & Riegel, 2023). These results need to be verified under less stringent conditions, perhaps by a full-wave model instead of a ray-trace model. This is an area of future work.

The other significant question which has come up again and again regards the duration of the secondary sonic boom signatures. As clearly seen in the report of Rickley and Pierce (1980), the secondary sonic boom signatures can have a duration on the order of 30 s, sometimes shorter, sometimes longer. The prediction code PCBoom produces signatures on the order of 1 s in duration. Why is there such a large difference?

Rickley and Pierce (1980) suggested the received signatures in their secondary boom measurement campaign had energy coming from different directions (azimuths). This spurred a new research direction for the ASCENT Project 57 research team to ascertain why the secondary sonic boom energy came from multiple azimuths. The key seems to be that as the sonic boom is being created, there is sound energy emanating from multiple positions along the supersonic flight path, and this is called multipath. (The aircraft is moving, and it is continuously making the sound.) This is quite different from the long distance sound from a fixed-location loud source like an explosion. For an explosion there is a definite beginning and ending of the sound. However, for a supersonic aircraft, the sound is being shed from multiple locations, and because a real atmosphere will move the sound rays around, a distant listener to this sound will hear contributions from the sonic boom from different aircraft positions. Figure 3 depicts the overall multipath concept.
To provide some technical underpinning to this view, the ASCENT Project 57 research team ran a case where a Concorde aircraft was approaching the United States East Coast. As the aircraft approached, different meteorological conditions were utilized in PCBoom, corresponding to the state of the atmosphere at those different positions along the aircraft trajectory. The current PCBoom version does not allow for the input of a true 3D atmosphere, just a vertical profile. However, by using different vertical profiles along the flight track, Penn State and Farmingdale State College were able to show that the secondary boom rays do move substantially due to the meteorology, confirming the notion that this allows rays to arrive at different times at the secondary boom ground locations, extending the duration of the noise event. The details of these calculations were written up in AIAA-3187 (Sparrow & Riegel, 2024), presented at the 30th American Institute of Aeronautics and Astronautics (AIAA)/Council of European Aerospace Societies (CEAS) Aeroacoustics Conference held June 4-7, 2024, in Rome, Italy.

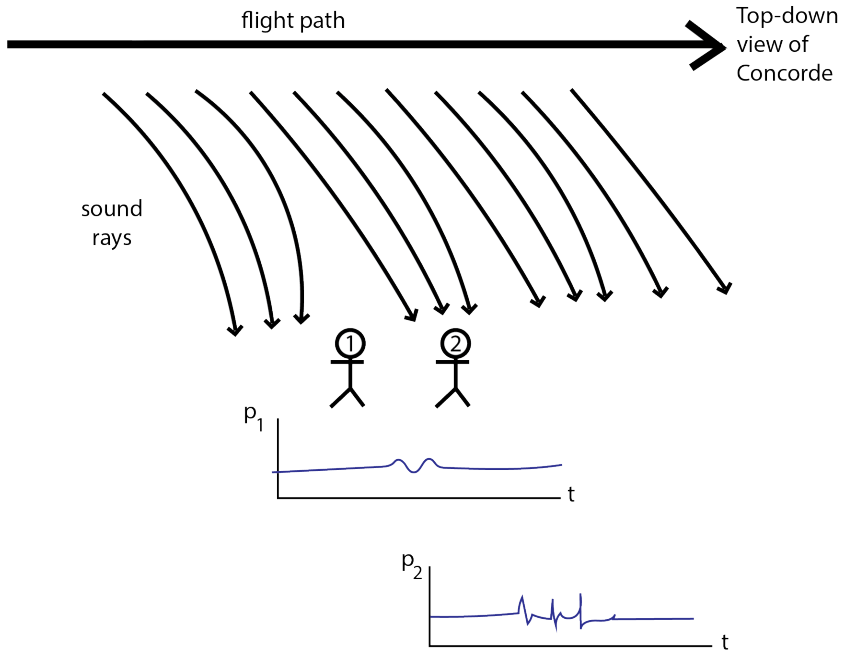

Figure 3. Multipath geometry to explain the long duration of secondary boom signatures. Due to atmospheric inhomogeneities bending the sound rays, person 1 hears sound p_1 at a low-level sound while person 2 hears sound p_2 including arrivals from multiple azimuths, creating a sound many seconds in duration. Note: These are not actual sonic boom signatures, and the diagram is for illustrative purposes. (From AIAA-3187, copyright American Institute of Aeronautics and Astronautics, Inc., 2024.)

Milestone

The project has put forward a concept in line with Rickley and Pierce (1980) that gives a basis for explaining the long duration of secondary sonic boom signatures.

Major Accomplishments

New simulations were performed changing the meteorology along the supersonic flight path in PCBoom, perhaps for the first time.

Publications

Conference Presentation

Sparrow, V. & Riegel, K. (2024, June 4-7). *Multipath interpretation of secondary sonic boom signatures* [Conference Presentation]. AIAA/CEAS Aeroacoustics Conference, Rome, Italy, AIAA-3187). https://doi.org/10.2514/6.2024-3187

Outreach Efforts

None.

Awards

None.

Student Involvement

None.

Plans for Next Period

In Task 2, work will continue toward obtaining accurate acoustic signatures for secondary sonic booms; this work will be essential to assess community impact. The project team will also determine the feasibility of prediction of the impact location of secondary sonic boom rays from upcoming test flights of the X-59 Quesst aircraft.

References

Rickley, E. & Pierce, A. (1980). *Detection and assessment of secondary sonic booms in New England* (Report No. FAA-AEE-80-22). Defense Technical Aviation Center, Fort Belvoir, Virginia.

Sparrow, V., & Riegel, K. (2023, September 11-15). The role of topography for secondary sonic boom reflection. *Proceedings of the Forum Acusticum 2023 - 10th Convention of the European Acoustics Association, EAA 2023, Torino, Italy,* 2221-3767. https://appfa2023.silsystem.solutions/atti/000361.pdf

Sparrow, V., & Riegel, K. (2024, June 4-7). *Multipath interpretation of secondary sonic boom signatures* [Conference presentation]. 30th AIAA/CEAS Aeroacoustics Conference, Rome, Italy, AIAA-3187. https://doi.org/10.2514/6.2024-3187

Task 3 – Investigating Seismic Networks for Measuring Sonic Booms

The Pennsylvania State University
Farmingdale State College, State University of New York

Objective

The pressure signals from a sonic boom, triggered by supersonic flights, can generate detectable ground motions along and across the land surface of flight paths (Cates & Sturtevant, 2002). Cates and Sturtevant (2002) and Rathnayaka et al. (2023) have shown that existing seismic networks in Southern California can detect seismic signatures from primary sonic booms. In 2024, this work has focused on investigating seismic data processing procedures needed to isolate ground motions from sonic booms recorded on seismic stations, a procedure which can be used in future studies assessing primary and secondary sonic booms from various supersonic flights.

Research Approach

The sonic boom event used in our analysis was triggered at approximately 19:34:00 UTC on October 14, 2022, near EAFB, in California during an air show commemorating the 75th anniversary of the first supersonic flight. The supersonic pass was created by an F-22 aircraft flying in a westward (260˚) direction at an altitude of 30,000 ft (~9.1 km). The precise location of the initiation of the boom signal is not well known. Here we focus only on the primary sonic boom event recorded at seismic station CI.EDW2 located near EAFB, which belongs to the Southern California Seismic Network (https://scedc.caltech.edu). The data processing approach developed in this study can be applied to other supersonic passes at various locations for identifying primary and secondary sonic booms.

Data and methods

The seismic station (CI.EDW2) used in this study consists of a three-component broadband seismometer recording ground motions at 100 samples/s. Only the vertical component of ground motion was requested and used. The seismic data and the instrument response were downloaded from the Southern California Earthquake Data Center (SCEDC; https://scedc.caltech.edu/data/waveform.html). The sonic boom information was provided by NASA.

The schematic representation of the data processing procedure is illustrated in Figure 4 and Figure 5. After raw data (velocity seismograms) retrieval, a bandpass filter from 0.1 to 0.5 Hz and 45 to 50 Hz was applied to the raw data to prevent amplifying noise during the frequency-domain deconvolution used to remove the instrument response.
The instrument response was then deconvolved from the vertical component velocity seismogram, and the velocity waveform was converted to displacement. The displacement seismogram was subsequently cut to begin 0 s prior to the event recorded time and 120 s after the event origin time, ensuring that the primary boom arrival was contained within the waveform and then demeaned, detrended, and tapered, and finally filtered from 1-20 Hz with a four-pole two-pass Butterworth bandpass filter.

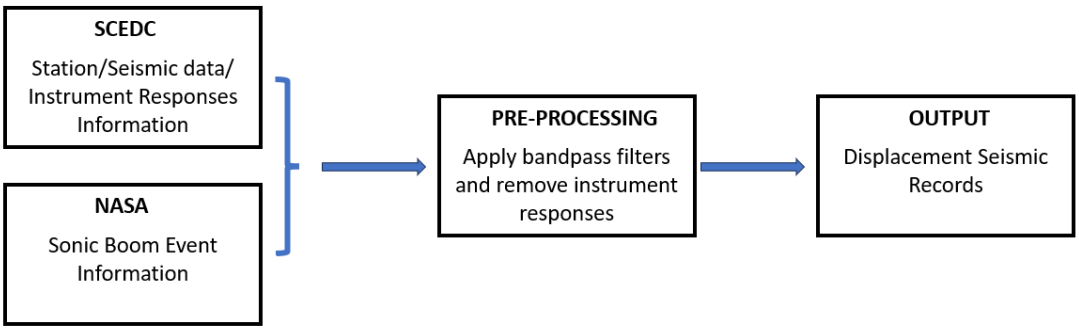

Figure 4. Schematic representation of the seismic data processing procedure. SCEDC: Southern California Earthquake Data Center. NASA: National Aeronautics and Space Administration.

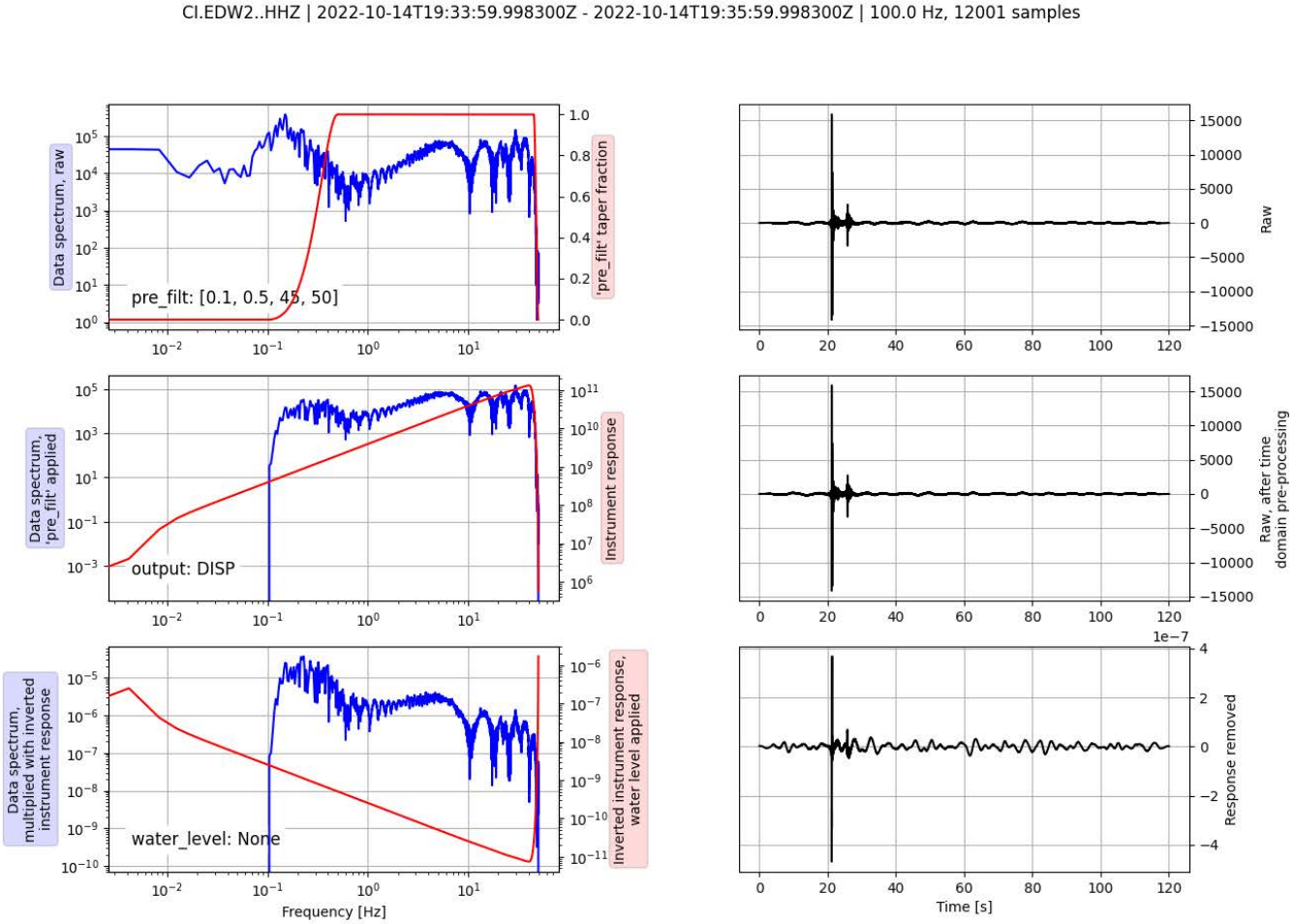

Figure 5. Illustrations of frequency (left panel) and time domain (right panel) waveforms and instrument response during processing steps.

Figure 5 provides a graphical representation of the main processing steps that are followed to remove instrument responses from raw seismic data records and to convert data into displacements. In the upper left of Figure 5, two spectra are seen. The blue spectrum with the legend on the left represents raw seismic data (counts) plotted in the frequency domain, and the red spectrum with the legend on the right represents the prefilter taper fractions (0.1 to 0.5 Hz and 45 to 50 Hz) that will be applied to the data prior to multiplying with the inverse spectrum. The upper right of Figure 5 shows the raw seismic data plotted in the time domain. The middle left of Figure 5 shows two spectra, and here the blue represents the prefiltered raw data spectrum and the red represents instrument responses plotted versus frequency. The middle right figure shows the raw seismic waveform after time domain preprocessing (i.e., after applying the prefilters). The lower left of Figure 5 now shows the data spectrum (blue color) after multiplying the inverted instrument response (red color) with the raw data spectrum shown in blue on the middle left of Figure 5. Finally, the lower right of Figure 5 shows the instrument response removed displacement seismic records plotted in the time domain. It should be noted that there are two ways to prevent amplifying noises during the instrument response removal procedure. One method is to specify a water level which represents a clipping of an inverse spectrum and limits amplification to certain maximum-cutoff values (water level in dB). The other method (i.e., used in this study) is to taper the waveform data in the frequency domain prior to multiplying with the inverse instrument response. The water level approach may strongly suppress the valid or wanted part of the spectrum if the output unit is not the native quantity of the instrument; therefore, the other approach is utilized.

Results

Figure 6 illustrates a displacement seismic record section of a supersonic boom event recorded on the CI.EDW2 station. For detecting the primary boom detection, the processed data were manually inspected for an N-type wave signature, as illustrated on Figure 6c (PARTNER project 8 annual report, 2005). The effective sound speed in the upper atmosphere may vary from 0.2 km/s to 0.4 km/s, which can be used as a guide for detecting sonic boom signals at various distance ranges (Rathnayaka et al., 2023). The infrasound microphone recording of a primary boom is shown on Figure 6c (PARTNER project 8 annual report, 2005). The U-wave type waves shown in Figures 6b and 6c result from the aircraft accelerating up to its supersonic cruise speed. The U-waves are triggered earlier in the flight while the aircraft is accelerating, but the sound reaches the ground after the N-wave arrivals due to the aircraft traveling faster than the speed of sound.

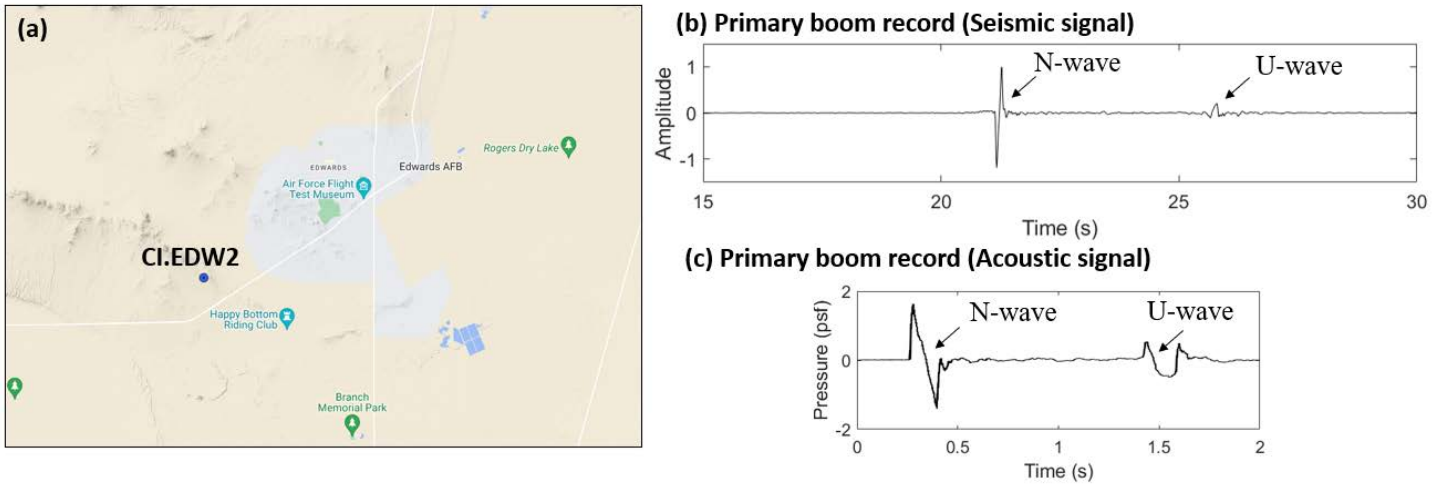

Figure 6. (a) Map of the location of seismic station CI.EDW2 near the west gate of EAFB. (b) N- and U-type (primary sonic boom) seismic signals recorded at station CI.EDW2. (c) Pressure trace for primary boom event modified from the PARTNER project 8 annual report (2005).

Summary

The goal of this work was to develop a seismic data processing procedure for detecting primary sonic boom signals (N- and U- type waves) recorded on seismic stations. The data processing approach used in this study can be applied to other supersonic flights at various locations for different distance ranges for identifying primary and/or secondary sonic boom records on different seismic networks.

Special Acknowledgments
The project team thanks NASA overall, particularly Edward Haering of the NASA Armstrong Flight Research Center, for making us aware of the existence of the October 2022 air show and for providing tremendous support throughout this investigation. The financial support in 2023 to enable Task 3 was provided by the Penn State College of Engineering through the United Technologies Corporation Professorship. This support is gratefully acknowledged.

Milestone
The seismic data processing approach illustrated in this study can be applied to detect primary and/or secondary boom events for any supersonic flight.

Major Accomplishments
ASCENT Project 057 Task 3 extended knowledge of the recording capability of primary booms by existing seismic stations. The project can now continue identifying secondary booms to understand primary and secondary boom carpets.

Publications
Peer-Reviewed Journal Publications
Rathnayaka, S., Nyblade, A. A., Sparrow, V. W., & Riegel, K. A. (2023). Air show primary sonic boom across a Seismic network. *Journal of the Acoustical Society of America, 154*(4-supplement), A147-A147. https://doi.org/10.1121/10.0023074

Published Conference Proceedings
Rathnayaka, S., Nyblade, A. A., Sparrow, V. W., & Riegel, K. A. (2023, December 4-8). *Air show primary sonic boom across a Seismic network* [Abstract presentation]. Proceedings of the 185th Meeting of the Acoustical Society of America, Sydney, Australia.

Outreach Efforts
None.

Awards
None.

Student Involvement
None.

Plans for Next Period
In Task 3, the team will continue to work on identifying signatures for primary and secondary sonic booms from various supersonic passes, an essential step toward assessing community impact.

References
Cates, J. E., & Sturtevant, B. (2002). Seismic detection of sonic booms. *The Journal of the Acoustical Society of America*, *111*(1), 614-628.
Rathnayaka, S., Nyblade, A. A., Sparrow, V. W., & Riegel, K. (2023). Air show primary sonic booms across a seismic network. *The Journal of the Acoustical Society of America*, *154*(4_supplement), A147-A147. https://doi.org/10.1121/10.0023074

Task 4 – Host ASCENT Noise Meeting in Spring 2024
The Pennsylvania State University

Research Approach and Results
In 2023 Penn State was identified by FAA/AEE as the ASCENT participating school to host the Spring 2024 ASCENT Noise and Operations Meeting. Hence, this Task 4 was created for the purpose of hosting the meeting in April 2024. The task is not expected to continue beyond 2024.

Dr. Sparrow and the research team worked with Penn State's Office of Conferences and Institutes to ensure that adequate space, remote access (such as Zoom®), hotel rooms, morning coffee, etc., were available to host a meeting that works well for FAA employees, industrial partners, interested stakeholders, and ASCENT principal investigators across the spectrum of noise and operations projects supported by FAA.

The Spring 2024 ASCENT Noise and Operations Meeting was held April 9-10, 2024, at the Penn Stater Hotel and Conference Center located at 215 Innovation Blvd., State College, PA, 16803. The uniquely horseshoe-shaped and terraced Forum Room in the Penn Stater Hotel and Conference Center was utilized to provide a conducive environment for this type of technical review and discussion by all participants. Because of the location, distant from alternative options, breaks and lunches were provided to all who attended. Virtual participants were hosted with no problems.

On April 9, 2024, there were nine technical presentations and a bus tour out to The Pennsylvania State University Unmanned Aircraft Systems Research Laboratory (PURL) partially supported by FAA ASCENT projects. This laboratory is in the Penn State Department of Aerospace Engineering, and it is located adjacent to the State College (PA) Regional Airport. On April 10, 2024, there were nine additional technical presentations.

It was an honor to host this meeting. Penn State is in a good position if FAA ever wanted host a similar type of meeting in the future. But for now, Task 4 has been completed successfully.

® Zoom is a registered trademark of Zoom Communications, Inc., San Jose, California.

Project 058 Improving Policy Analysis Tools to Evaluate Higher-Altitude Aircraft Operations

Massachusetts Institute of Technology

Project Lead Investigator

Dr. Raymond L. Speth
Principal Research Scientist
Associate Director, Laboratory for Aviation and the Environment
Massachusetts Institute of Technology
77 Massachusetts Ave, Building 33-322, Cambridge, MA 02139
speth@mit.edu

University Participants

Massachusetts Institute of Technology (MIT)

- P.I.: Dr. Raymond L. Speth
- FAA Award Number: 13-C-AJFE-MIT, Amendment Nos. 064, 089, 099, 115, 120, 128, and 133
- Period of Performance: September 1, 2023, to September 30, 2024
- Reporting Period: October 1, 2023, to September 30, 2024
- Tasks (tasks completed before this reporting period are listed as completed):
  1. Develop a set of emissions scenarios for high-altitude aviation (completed)
  2. Extend and validate MIT's existing atmospheric simulation capabilities (completed)
  3. Extend the current GEOS-Chem[1] sensitivities for enhanced input resolution
  4. Develop a reduced order model and parametrization of contrails for simplified climate models
  5. Develop and Update Operational Tools Capable of Quantifying Environmental Impacts of Aviation
  6. Investigate dependence on aviation emissions impacts on non-aviation factors

Project Funding Level

The ASCENT Project 058 has received $1,720,000 Federal Aviation Administration (FAA) funding and $1,720,000 matching funds. Sources of matching funds are approximately $309,200 from MIT, plus 3rd party in-kind contributions of $391,000 from NuFuels, LLC, and $127,000 from Savion Aerospace Corp., and $414,000 from Google, LLC, and $478,800 from Earth Force Technologies.

Investigation Team

Prof. Raymond L. Speth, (P.I.), All Tasks
Dr. Prakash Prashanth, All Tasks
Shreya Sharma, (graduate research assistant), Task 1
China Hagström, (graduate research assistant), Task 2
Carla Grobler, (graduate research assistant), Task 3, 4

Project Overview

Companies are proposing, developing, and testing aircraft operating at higher altitudes such as commercial supersonic aircraft and high-altitude, long-endurance (HALE) unmanned aerial vehicles, which offer the potential to become enablers for new use cases and business models in the aviation sector. However, the combustion emissions of these vehicles will

[1] GEOS-Chem is a global three-dimensional model of atmospheric chemistry drive by meteorological input from Goddard Earth Observing System (GEOS) of the National Aeronautics and Space Administration (NASA) Global Modeling and Assimilation Office.

have atmospheric impacts which differ from conventional subsonic aviation due to the higher altitudes of emission. Emissions at higher altitudes are associated with a different chemical environment, longer emission lifetimes, and greater distances over which the emissions will be transported. Furthermore, new developments in emissions impact estimation have enabled a more nuanced view of the environmental consequences of conventional aircraft activity. This includes the recognition that both their climate and air quality impacts vary depending on the prevailing conditions of the emission and the time horizon of the assessment.

In ASCENT Project 058, our team is working to quantify the environmental consequences of aviation emissions, incorporating information about altitude, location, and timing. In pursuit of this object, our team intends to (1) extend the current GEOS-Chem sensitivities for enhanced input resolution, (2) develop a parametrization of contrails, (3) develop and update operational tools capable of quantifying environmental impacts of aviation, and (4) investigate the dependence of aviation emissions impacts on non-aviation factors.

Task 3 – Extend the Current GEOS-Chem Sensitivities for Enhanced Input Resolution

Objective

The objective of this task is to extend the GEOS-Chem sensitivities derived during the previous period of performance by focusing on specific areas as well as aircraft class and missions. The output would be a many-to-many mapping of emissions at different altitudes and latitudes to spatially and temporally resolve environmental outcomes. In addition to regional differences here we hope to develop sensitivities to key routes, and aircraft types.

Research Approach

Previous work on ASCENT Project 058, has shown that most of the fuel burn occurs in cruise, in altitudes between 8-13 km and during landing and take-off below 1 km (Grobler et al., 2019). Work during this period sought to define the geopolitical regions which currently have the largest share of impacts, and where this share is expected to increase in the future. The International Civil Aviation Organization (ICAO) air passenger forecasts predict the Asia Pacific region to account for almost half the total share of fuel burn in 2043 (this region in 2023 only accounted for about one third of the total aviation fuel burn).

For our analysis, this region is defined to be a combination of two groups of countries as defined by the world bank: (1) South Asia and (2) East Asia and Pacific. The highlighted countries are shown in Figure 1.

Figure 1. Countries in the Asia subset: (1) South Asia (red) and (2) East Asia and Pacific (pink).

In consideration of the pre-COVID year 2019, since air traffic is still recovering to pre-pandemic levels, flights in this 'Asia' dataset are chosen which either land or take-off from the highlighted countries. Furthermore, this Asia subset is split into long-, medium-, and short-haul flights. Long haul flights are defined here as those which are longer than 2,000 nm and short haul flights are those which are shorter than 500 nm. The remaining flights are classified as medium- or mid-haul flights. A summary of the fuel burn for these cases is tabulated in Table 1.

Table 1. Summary of the fuel burn for Asia-long, -mid, -short, and non-Asia flights.

Quantity/Subset	Global	Asia - Long	Asia - Mid	Asia - Short	Non-Asia
Fuel burn (Tg)	258	61	21	35	141
NO_x (Tg)	4.11	1.11	0.31	0.55	2.13

The geographical distribution of the emissions was obtained using the Aircraft Emissions Inventory Code (AEIC). The spatial distribution of these flights and the associated fuel burn is seen in Figure 2 and Figure 3:

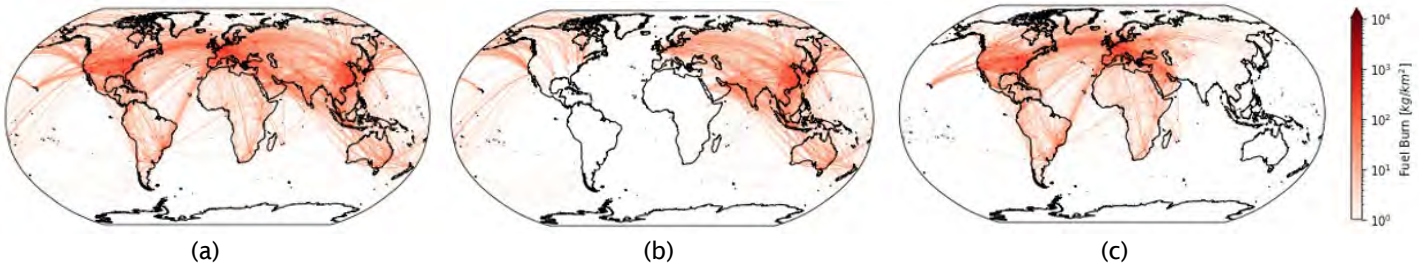

(a) (b) (c)

Figure 2. Distribution of fuel burn for (a) global aviation, (b) Asia aviation, and (c) non-Asia aviation in 2019.

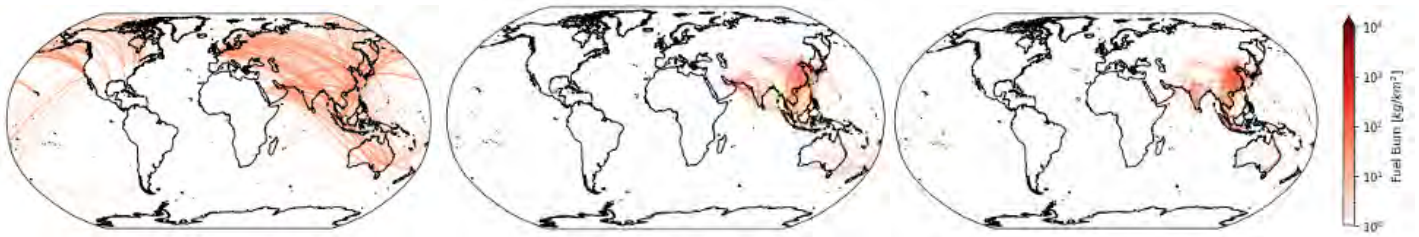

(a) (b) (c)

Figure 3. Distribution of fuel burn for (a) long-haul, (b) mid-haul, and (c) short-haul flights originating or ending in Asia in 2019.

Additionally, the AEIC is used to obtain the fuel burn as a function of altitude for the different cases as shown in Figure 4. Most of the fuel burn for both the cases is concentrated in the 9-12 km range in cruise (consistent with prior findings in this project). In Figure 4(a), it is observed that on average, flights in Asia tend to cruise higher than the non-Asia flights. Additionally, the long-haul flights fly at higher altitudes compared to the mid and short haul flights (with the mid haul flights flying slightly higher than the short haul flights). Most of the fuel burn in this set occurs in cruise in the long-haul flights.

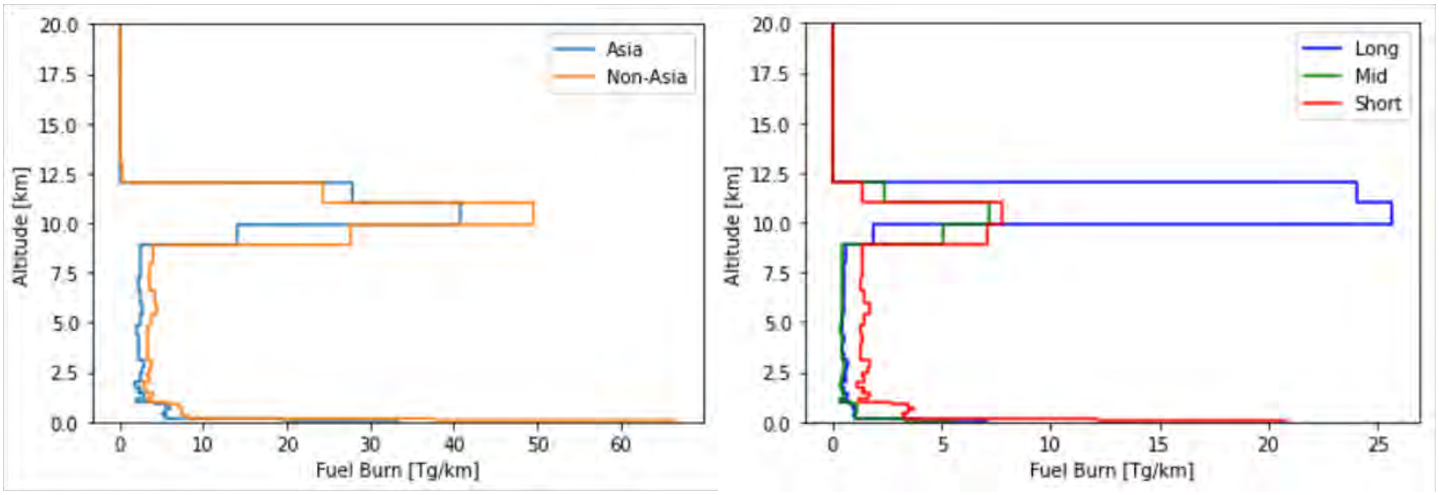

(a) (b)

Figure 4. Plot showing the distribution of fuel burn with altitude for (a) Asia and non-Asia flights and (b) long-, medium-, and short-haul flights.

Milestone

Emissions and fuel burn inventories for specific regions (Asia) were calculated using the AEIC and flight schedules for 2019.

Major Accomplishments

Fleet-wise fuel burn analysis was conducted for flights in the highest emission intensity region of South Asia, East Asia, and the Pacific.

Publications

None.

Outreach Efforts

None.

Awards

None.

Student Involvement

During the reporting period of academic year (AY) 2023-2024, the MIT graduate student, Shreya Sharma, was involved in this task.

Plans for Next Period

Short-term:

- Use the generated emissions inventory as an input to the GEOS-Chem High Performance (GCHP) chemical transport model to obtain changes in concentration of species of interest that impact air quality (ozone [O_3] and particulate matter 2.5 [$PM_{2.5}$]).
- Extend a similar analysis to other global regions and different aircraft types and missions.

Long-term:

- Use the increased resolution data from the GCHP simulations identify technology options by flight class and route to minimize aviation's climate and air quality impacts.
  - It will also facilitate the evaluation of landing and take-off policies in specific regions or airports.

- Additionally, it will assist in assessing the impact of novel aircraft technologies and alternative energy sources, such as sustainable aviation fuels (SAF).

References

Grobler, C., Wolfe, P. J., Dasadhikari, K., Dedoussi, I. C., Allroggen, F., Speth, R. L., Eastham, S. D., Agarwal, A., Staples, M. D., & Sabnis, J. (2019). Marginal climate and air quality costs of aviation emissions. *Environmental Research Letters, 14, 114031*, doi: 10.1088/1748-9326/ab4942.

Task 4 – Develop a Reduced Order Model and Parametrization of Contrails for Simplified Climate Models

Objectives

The objective of this task is to understand the dependence of uncertainty and variability in cruise altitude and environmental parameters (such as relative humidity) on contrail impacts. As described in Figure 5, the agreement between reanalysis and experimental data sources differs, but the drivers and effects of this disagreement remain unknown. We aim to develop reduced order models of high-resolution plume-based contrail models (APCEMM) and radiative transfer codes (LibRadTran) which can then be used to understand the relative contribution of various uncertainty sources. Furthermore, this approach may provide the ability to map contrail radiative impacts from flights to respective uncertain and variable conditions, such as emissions location, time, and composition. These radiative impacts, determined at least in part by these reduced order models, when incorporated into an economic impact assessment tool (APMT), facilitates policy analysis of various aviation emissions scenarios including subsonic and supersonic aviation. In future work under this task, our team will also coordinate with ASCENT Project 022 as needed to compare respective modelling of contrail impacts.

Research Approach

During this period efforts were made to define the methods of production for a reduced-order contrail impact model. The production and integration of this reduced order (parametrized) model will be a substantial improvement in fidelity compared to the current treatment of contrails using a global average impact per flight distance or fuel burn. Now, contrail properties are treated as spatio-temporally dependent and account for variations in emissions composition. This will further enhance contrail impact estimation including the ability to estimate uncertainties associated with contrail climate impacts.

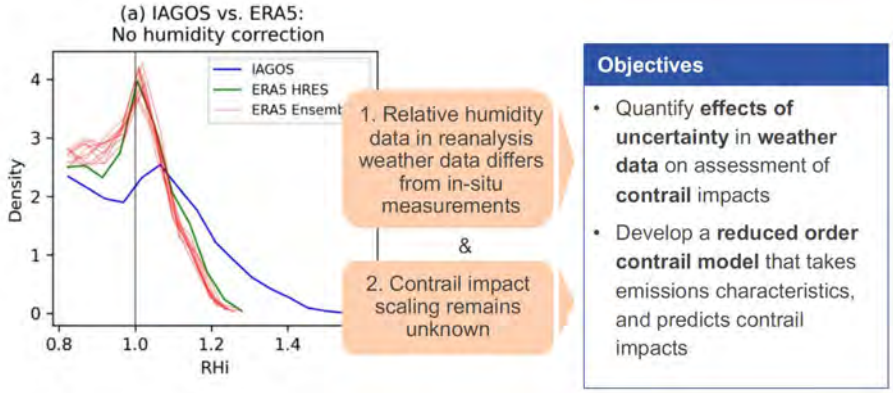

Figure 5. Improving contrail impact assessment through recognition of shortcomings in data agreement and quantifying impacts of uncertainty and variability. (IAGOS vs ERA5: Teoh et al., 2022).

Initial work this period included investigating methods of production for a parametrized paired contrail and radiative forcing (RF) model. Tools required to estimate contrail properties and impacts were investigated and compared. To create a contrail RF modelling pipeline the models chosen were the Aircraft Plume Chemistry and Microphysics Model (APCEMM) to model the contrail formation and properties and LibRadTran to calculate the radiative impact of the contrails.

To construct the parametrized model, the polynomial chaos expansion (PCE) approach was identified as a computationally efficient means for reduced-order modelling and subsequent uncertainty quantification. ERA5[2] reanalysis data and GRUAN in-situ data sources were defined as current and baseline data sources for meteorological data, respectively to be used in the training of the PCE model.

Looking forward, efforts were made to identify where future parametrized updates will likely fit into the code structure of operational tools (see Task 3). This modularity will allow rapid policy analysis tools like Aviation Climate and Air quality Impact (ACAI) tool to model the underlying drivers of contrail climate impacts. Further, producing a contrail parametrization model will allow greater flexibility and improved speed in cost evaluation of impacts.

Milestones

- Identified suitable tools to model contrails and calculate the radiative impact.
- Identified PCE as a suitable approach for reduced order modeling.

Major Accomplishments

- Identified appropriate meteorological reduced order model training datasets.
- Performed initial work on producing a reduced order contrail model.

Publications

Hagström, C., Waitz, I., Eastham, S., & Barret, S. (2024, April 14-19). *Uncertainty quantification of contrail climate impacts using non-intrusive polynomial chaos* [Poster presentation]. The 2024 General Assembly of the European Geosciences Union, Vienna, Austria.

Outreach Efforts

- Initial approach was presented at the ASCENT meeting in Washington, D.C., held in October 2024 by Dr. Prakash Prashanth.
- Progress in all tasks was communicated during biweekly briefing calls with the FAA and reported in quarterly progress reports.

Awards

None.

Student Involvement

During the reporting period of AY 2023-2024, the MIT graduate student, China Hagström, was involved in this work.

Plans for Next Period

Short-Term:

- Develop reduced order contrail models.
- Develop reduced order contrail pipeline and model suitable for ACAI.
- Apply tools to support decision making and policy analysis.

Long-Term:

- Quantify uncertainty in contrail impacts due to uncertainty in weather data.
- Quantify underlying drivers of contrail impact variability.

References

Teoh, R., Schumann, U., Gryspeerdt, E., Shapiro, M., Molloy, J., Koudis, G., Voigt, C., & Stettler, M. E. J. (2022). Aviation contrail climate effects in the North Atlantic from 2016 to 2021, *Atmospheric Chemistry and Physics, 22*(16), 10919–10935. https://doi.org/10.5194/acp-22-10919-2022

[2] ERA5 is the fifth generation European Centre for Medium-Range Weather Forecasts (ECMWF) atmospheric reanalysis of the global climate covered the period from January 1940 to present. ERA5 is produced by the Copernicus Climate Change Service at ECMWF.

Task 5 – Develop and Update Operational Tools Capable of Quantifying Environmental Impacts of Aviation

Massachusetts Institute of Technology

Objective

The objective of this task is to operationalize the results of Tasks 1 and 2. This includes aligning APMT with the latest scientific consensus by updating underlying climate submodules. The outcome is a re-engineered version of the APMT using Julia[3] for climate and air quality impacts. The ASCENT Project 058 team aimed to maintain the original APMT structure while implementing an updated software infrastructure using the Julia programming language resulting in the ACAI model. The migration to Julia provides new opportunities for increased computational performance.

The new version of the APMT is calibrated using updated sensitivity data and upgraded to provide monetized impacts that consider gridded variabilities such as cruise altitude. The monetized outputs are based on recently published U.S. Environmental Protection Agency (EPA) methods for deriving social cost of greenhouse gasses, including an updated surface temperature model containing updated Equilibrium Climate Sensitivity and Transient Climate Response values (EPA, 2023). These cost metrics support rapid evaluation of strategies to reduce aviation's climate and air quality impacts. Additionally, ozone layer impacts are integrated into the updated model. The spatio-temporal sensitivities and cost metric improvements provide further insights into cost sensitivity to regional emissions and emissions at various altitudes. These efforts will facilitate a rational comparison of the impacts of emissions from supersonic and subsonic aviation.

Research Approach

During this period, the primary focus was on obtaining, validating, and verifying the aircraft fleet data, and incorporating them into our emissions code within the APMT. Additionally, the new structure, now referred to as ACAI, was written in Julia to accept gridded emissions inputs and addressed areas for improved computational efficiency. Finally, our team investigated the feasibility of increasing the ACAI model's capabilities to incorporate non-volatile particulate matter (nvPM) emissions as part of a contrail impact assessment.

During this reporting cycle, high resolution aircraft fleet data were incorporated into our emissions inventory code. This involved refining aircraft engine matching using data obtained from the Cirium® Fleets Analyzer and splitting the flights in OAG® schedule data from broader aircraft categories, to represent individual aircraft subtypes. The ACAI model now includes a module quantifying the air quality health impacts developed during this reporting period. Additionally, preliminary radiative forcing (RF) and air quality sensitivity data for nitrogen oxides (NO_x) were assimilated from previous ASCENT Project 058 work. Monetization of both climate and air quality impacts is integrated within this single model. Finally, to address uncertainty quantification a Monte Carlo approach is implemented currently. A summary of these changes can be found in Figure 6.

[3] Julia is a high-performance, open-source, general purpose programming language designed for scientific computing, machine learning, and data mining.

® Cirium is a registered trademark of LexisNexis Risk Solutions Data Services Limited, London, United Kingdom.

® OAG is a registered trademark of OAG Aviation Worldwide Limited, Bedfordshire, United Kingdom.

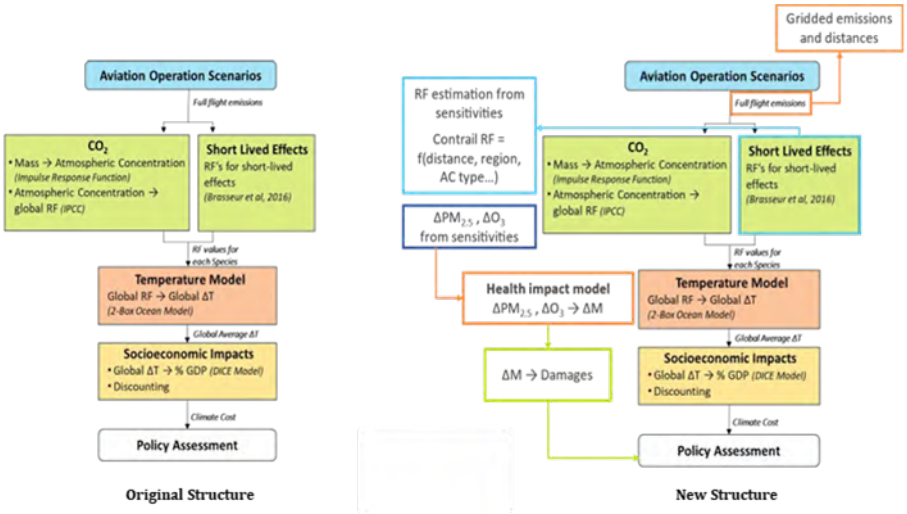

Figure 6. Schematic attributing methodological changes from the original APMT to ACAI.

Milestones

- Created a new framework for the APMT which includes air quality and climate impact quantification in a consistent manner.

Major Accomplishments

- Completed the conversion of APMT to use Julia.
- Integrated gridded emission species from fleet emissions.
- Quantified monetary impacts on climate and air quality from supersonic transport and subsonic emissions.
- Quantified air quality impacts in the ACAI model.
- Performed preliminary RF and air quality sensitivities integration.

Publications

None.

Outreach Efforts

- Progress in all tasks was communicated during biweekly briefing calls with the FAA and reported in quarterly progress reports.

Awards

None.

Student Involvement

During the reporting period of AY 2023-2024, the MIT graduate student, Carla Grobler, was involved in this task.

Plans for Next Period

Short-Term:

- Incorporate emissions sensitivities for additional emission types ($PM_{2.5}$, surface O_3, and columnal O_3).

Long-Term:

- Improve the resolution of contrail impact assessment within the ACAI model. This may include updates to the ACAI temperature model and implementation of higher resolution "stretched grid" emissions sensitivity simulations.
- Efforts also include updating existing impulse response functions (IRFs) based on shared socioeconomic pathway (SSP) scenarios.
- This work along with Task 3 will develop a reduced order contrail model for ACAI integration.

References

EPA. (2023). *Report on the social cost of greenhouse gases: estimates incorporating recent scientific advances*. U.S. Environmental Protection Agency (EPA). https://www.epa.gov/system/files/documents/2023-12/epa_scghg_2023_report_final.pdf

Task 6 – Investigate Dependence of Aviation Emissions Impacts on Non-Aviation Factors

Massachusetts Institute of Technology

Objective

The objective of this task is to produce a historical assessment of the impacts of aviation emissions. This historical assessment addresses quantification of factors such as variable emissions indices and how an evolving chemical background has affected – and will affect – the total impacts of aviation. The ASCENT Project 058 team investigated aviation's historical emissions, present-day climate impacts, current damages due to marginal emission changes, and potential pathways to reach net-zero climate impacts by 2050.

Research Approach

The ASCENT Project 058 team extended and finalized the emissions inventory, utilizing high-quality matching method based on data acquired from Cirium. From 1980 to 2019 total contrail impacts have increased but the impact per unit of contrail distance has decreased. The trends in these impacts are observed to be highly sensitive to the criteria determining if a contrail likely evaporated. Finally, our team used these data to perform an evaluation of how changes in both aviation and non-aviation emissions over time have affected the estimated climate and air quality impacts of aviation (Grobler, 2024).

Trends in Historical Emissions

First, the research develops a consistent bottom-up emissions inventory for commercial civil passenger aviation from 1980 to 2019, quantifying how emissions patterns such as spatial, temporal, and compositional characteristics have varied over time. Results show that, while fuel consumption increased by 330%, capacity, measured as available seat miles, grew by 560%. This growth has been regionally heterogeneous, with the emissions share over Asia growing from 7% to 23%, while emissions share over North America decreased from 55% to 25%. Over this time, the share of nighttime fuel consumption increased from 30% to 38%, due to an increase in aircraft utilization. Additionally, there has been a shift in the emissions composition, with the NO_x emissions index increasing by 20%, while the non-volatile particulate emissions index decreased by 70%.

Contrail Impacts' Trends in Conjunction with Non-Aviation Factors

Our team quantified aviation's present-day climate effects using the bottom-up emissions inventory. Using APCEMM and ERA5 reanalysis weather data, results indicate that contrail impacts increased by 460% from 1980 to 2019, outpacing growth in annual fuel consumption. The underlying drivers did not remain constant. The fraction of flight segments that cause contrails increased by 32%, while the radiative forcing per distance of contrail decreased by 24%. Our team quantified for the first time how different assumptions regarding the treatment of contrails mixing with ambient air could change their lifetime by a factor of three.

Climate Dependence on Aviation Impacts

Our team then calculated the impacts of marginal changes in aviation emissions on climate and air quality. Climate and air quality impacts are monetized on a per unit emissions basis, using a simplified climate model and sensitivities from the GEOS-Chem global chemistry-transport model. Cruise emissions account for 90% of impacts per fuel unit, with 49-81% arising from air quality effects depending on the discount rate. Collectively NO_x, carbon dioxide (CO_2), and contrails cause 97% of the total impact. Our team found that the equilibrium climate sensitivity, climate damage function, and value of statistical life contribute to the greatest uncertainty in outputs.

Alternative Energy Pathways to Net-Zero

Our team also evaluated pathways through which alternative energy carriers and avoidance of non-CO_2 impacts could lead aviation towards net-zero climate impacts by the year 2050. The follows alternative energy carriers were considered:

synthetic fuels from biomass, synthetic fuels from green hydrogen and atmospheric CO_2, and the direct use of green liquid hydrogen. We find that 50% of fleet-wide contrail length can be avoided for a 0.88% fleet-wide fuel burn penalty. Avoiding subsequent contrails has an additional 20% fuel avoidance penalty, requiring double the additional fuel. Assuming continued efficiency gains and 50% avoidance of contrails, such an energy transition could reduce annual lifecycle aviation CO_2 emissions by 89-94% compared to year-2019 levels. This is despite a 2-3-fold growth in demand by 2050.

Major Accomplishments

- Continued work from the previous year, finalizing aspects of the emissions inventory.
- Submitted abstract (Grobler, 2023) for the 2023 American Geophysical Union (AGU) Fall Meeting.
- Received acceptance of and published the doctoral dissertation, *Past, present, and future climate impacts of aviation* (Grobler, 2024).

Publications

Dissertation

Grobler, C. (2024). *Past, present, and future climate impacts of aviation* [Doctoral dissertation, Massachusetts Institute of Technology]. Massachusetts Institute of Technology. https://dspace.mit.edu/handle/1721.1/154000

Presentation

Grobler, C., Agarwal, A., Fritz, T., Elmourad, J., Prashanth, P., Xu, X., Meijer, V., Florian, A., Eastham, S. D., & Barrett, S. R. (2023, December 11-15). *Assessing the evolution of contrail impacts from 1980 to 2019* [Conference presentation]. The American Geophysical Union (AGU) Fall Meeting 2023, San Francisco, California.

Outreach Efforts

- Fleet data results were presented by Dr. Prakash Prashanth at the Aviation Emission Characterization (AEC) Roadmap meeting in Washington, D.C., held in May 2024.
- Progress in all tasks was communicated during biweekly briefing calls with the FAA and reported in quarterly progress reports.

Awards

None.

Student Involvement

During the reporting period of AY 2023-2024, the MIT graduate student, Carla Grobler, was involved in this task.

Plans for Next Period

None.

References

Grobler, C. (2024). *Past, present, and future climate impacts of aviation* [Doctoral dissertation, Massachusetts Institute of Technology]. Massachusetts Institute of Technology. https://dspace.mit.edu/handle/1721.1/154000

Grobler, C., Agarwal, A., Fritz, T., Elmourad, J., Prashanth, P., Xu, X., Meijer, V., Florian, A., Eastham, S. D., & Barrett, S. R. (2023, December 11-15). *Assessing the evolution of contrail impacts from 1980 to 2019* [Conference presentation]. The American Geophysical Union (AGU) Fall Meeting 2023, San Francisco, California.

Project 059(A) Jet Noise Modeling to Support Low Noise Supersonic Aircraft Technology Development

Georgia Institute of Technology

Project Lead Investigators

Dimitri N. Mavris
Regents Professor
School of Aerospace Engineering
Georgia Institute of Technology
Mail Stop 0150
Atlanta, GA 30332-0150
404-894-1557
Dimitri.mavris@ae.gatech.edu

Jimmy Tai
Senior Research Engineer
School of Aerospace Engineering
Georgia Institute of Technology
Mail Stop 0150
Atlanta, GA 30332-0150
404-894-0197
jimmy.tai@ae.gatech.edu

University Participants

Georgia Institute of Technology (Georgia Tech or GT)

- P.I.s: Dr. Dimitri N. Mavris (P.I.), Dr. Jimmy Tai (co-P.I.)
- FAA Award Number: 13-C-AJFE-GIT-070
- Period of Performance: October 1, 2022, to December 31, 2023

Project Funding Level

The ASCENT Project 059(A) is funded at the following levels: Georgia Tech, $100,000.

Georgia Tech has agreed to a total of $100,000 in matching funds. This total includes salaries for the project director, research engineers, and graduate research assistants, as well as computing, financial, and administrative support, including meeting arrangements. Georgia Tech has also agreed to provide tuition remission for the students, paid for by state funds. During the period of performance, in-kind cost sharing is also obtained for cost share.

Investigation Team

Georgia Institute of Technology

Dimitri N. Mavris, P.I.
Jimmy Tai, Co-Investigator
James Kenny, Project Manager/Technical Lead, Primary technical developer, project manager, and student advisor
Jai Ahuja, Supporting Engineer, Supporting technical developer, aerodynamics subject matter expert (SME)
Students: Student technical support role involved completing various tasks to support completion of supersonic inlet code, actual tasks varied depending on timeframe support provided.
Noah Chartier, Graduate Research Assistant, Provided technical support from 2021 to 2022, co-developed majority of the inlet code with James Kenny
Andrew Tai, Undergraduate Research Assistant, Supported between late 2021 to early 2022

Sijian Tan, Graduate Research Assistant, Supported inlet code development from mid-2022 to end of period of performance.

Project Overview

The original purpose of this project was to develop and assess computational tools to simulate the flow and noise of civil supersonic aircraft engines and to identify novel methods for noise reduction. In addition to noise predictions, the impact of the noise reduction methods on overall engine performance would be assessed. The predictions would include consideration of the engine inlet, engine cycle, mixers and ejectors, and unsteady jet exhaust. Accurate prediction of the engine exhaust flow would enable the noise generated by the theoretical system to be computed. Predictions were to be assessed through comparison with available experimental measurements provided by ASCENT Project 059 research partners focusing on experimental methods.

In discussion with the Federal Aviation Administration (FAA), the overall direction of the project was changed in fiscal year (FY) 2022 of the project. Instead of developing and simulating jet noise reduction technologies, ASCENT Project 059(A) will provide an assessment of the benefits addressing the supersonic jet noise problem through a different approach—considering the supersonic inlet's effects on maintaining thrust while jet noise devices are employed on the engine nozzle, and ensuring a retention of jet noise reduction, precluding the necessitation of a higher throttle setting, which could potentially negate any benefits seen to thrust. To support this, models for inlet performance, a coupled engine and aircraft model, and jet noise technology models were required to be developed and integrated. Although the primary objectives anticipated for ASCENT Project 059(A) being supported by experimental data provided by other ASCENT Project 059 technical partners, including the work of jet noise experimentation teams, experimental data to be used in this simulation was not able to be generated by the technical partners due to technical difficulties. As such, the Georgia Tech team was required to perform extensive literature review and develop modeling capabilities to simulate jet noise reduction technology designs and their effects and integrate into their broader models.

As a result of this change, the research goal for the Georgia Tech team in Year 2 shifted to pursue means to identify a thrust–noise break-even relationships for arbitrary and real nozzle-based jet noise reduction technologies. In the final year of the project (Year 3), this objective was superseded by a more focused approach in modeling the effects of a parameterized family of supersonic chevrons applied to a fixed 65-passenger aircraft model with a design Mach number of 1.7, using a supersonic mixed-flow turbofan engine model with axisymmetric plug nozzle. The study seeks to understand if a custom-designed supersonic inlet, which functions acceptably well while installed on a vehicle for an entire supersonic transport (SST) mission profile would be able to recover the thrust lost due to chevrons applied to that fixed engine and aircraft configuration. If it were not, researchers sought to determine how much better variable geometry features applied to the same inlet could perform, again, attempting to minimize thrust loss and retain noise reduction properties provided by the chevrons. This study seeks to identify whether an improved and variable geometry inlet can recover thrust lost by the nozzle technology installed on an engine, while precluding the need to resize the engine, which would likely increase the likelihood of greater noise production due to increased thrust, and also precluding the need for the landing and take-off (LTO) throttle setting to be increased, having the same effect as an upsized engine. This slight modification to the scope of the previously defined primary research objective removes the ambiguity associated with coupling arbitrary sets of thrust loss values with noise reduction values in reasonable proportions to one another, which would be performed for a thrust-noise breakeven analysis, instead, pursuing designs which could actually be encountered by actual jet noise reduction devices applied to nozzles.

Also in Year 2, the goal of implementing low-fidelity, low-speed aerodynamics models to be implemented for the supersonic inlet and new variable-geometry models to determine whether any thrust lost by the addition of the jet noise technology can be recovered by sole use of inlet variable geometry (including the external compression inlet ramps or cone, a variable-geometry cowl lip, and potentially blow-in doors), without further manipulation of the throttle were to be developed. These tasks were retained and completed in the work presented below. In future work, higher-fidelity modeling capabilities may be incorporated into the zeroth-order inlet performance tool, if this area of study appears promising because of work completed here. Essentially, our team sought to identify and explore ways to facilitate rapid exploration of installed engine configurations, ensure that the selected nozzle-based jet noise technology does not degrade aircraft thrust to an extent that the technology is no longer beneficial, and to determine the effectiveness of off-design variable-geometry configurations for conditions of low speed/high inlet air demand conditions.

Project Introduction

As previously discussed, the main objectives of this research project in the first two years (Year 1 and Year 2) were twofold. First, to facilitate the capability to perform thrust-noise break-even studies for arbitrary nozzle-based jet noise technologies. Second, to develop capabilities to identify the impacts of supersonic inlet configurations and designs on thrust recovery—thus ultimately determining whether off-design supersonic inlet configurations can recover the thrust detriment from noise technologies used for jet noise regulation compliance. Because of the Georgia Tech team's departure from being coupled with Pennsylvania State University (PSU) researchers, and the modification of the overall project direction, the major project milestones for Years 2 and 3 were modified. Furthermore, as the Year 3 objective was redefined to explore the impacts of a specific jet noise reduction technology, chevrons, the project milestones listed below were modified even further and extended to capture the discrete sections of work completed to answer the research questions proposed.

Regarding earlier project milestones, such as Task 2.2 which was previously described as "Determination of boundary conditions from 'Vision SST Engine Cycle'," the replacement task for this period was to continue improvement of Task 2.1, "Assembly of zeroth-order methods to predict inlet performance." At the initially projected due date for Task 2.1, the supersonic inlet analysis tool developed during Year 1, although functional, was found to lack many capabilities necessary to analyze the installed inlet performance across the SST mission profile. While the project only sought to understand LTO performance, the design and installation of an advanced inlet configuration which would operate in a realistic SST mission profile, resulting in a realistic SST engine and aircraft design was sought out to serve as the baseline for this work. Some, but not all, of these lacking capabilities included the abilities to predict required inlet capture area, accurately calculate internal shock quantity and positioning and the associated losses for mixed compression conditions for a supersonic two-dimensional (2D) inlet to (1) predict and determine additive (pre-entry) drags and cowl lip suction forces, (2) predict the location and corresponding strength of the normal shock when swallowed, and (3) accurately predict the low-speed aerothermodynamic losses associated with conditions of low-speed and high-air-demand conditions (i.e., take-off). Furthermore, our team used all of Year 2 to improve the supersonic inlet analysis tool's user interface and perform debugging to achieve highly robust performance across a variety of supersonic inlet geometries and mission profiles—from external compression to mixed compression inlets, as well as from transonic design Mach numbers to low hypersonic values (1.2 to 5) and off-design cases. As a result of this work, the tool was found to be able to perform well in all explored and conditions compared to published inlet data. Additionally, the tool was integrated with the team's internal supersonic aircraft and engine sizing and synthesis tool (Flight Analysis for Supersonic Transports [FASST], also used for ASCENT Project 010), by converting the inlet code into a rapid-running executable. However, despite the development of an executable, it was determined that the creation of conventional inlet maps for use with the engine cycle and vehicle sizing tool was the best option due to runtime and flexibility—inlet map generation capability was developed late in Year 3.

From the outset of this project, a highly functional supersonic inlet analysis tool was found to be required to perform thrust recovery analyses, in accordance with the initial goal of the project. Therefore, the focus for the Year 1 and Year 2 was on the robust development of this capability. Although it was intended for continued development of the supersonic inlet tool to take a secondary role during the third and final year (Year 3) of this project, some improvements were required prior to the execution and facilitation of the jet noise reduction-break-even study. Specifically, the low-speed aerodynamic model and its validation were required, and this took several months of effort. As a result, the final project deadline and subsequent milestones were extended via a No-Cost Extension, which was requested for the project grant completion, and approved by the FAA. As a result, the final project deadline was shifted to February 29, 2024. Further work was required to perform code integration and ensure robust and reliable results, with the inlet performance data implemented in the engine cycle and noise analysis, and as such, the work proceeded well past the approved No-Cost Extension date, mentioned previously. Rationale and technical complications which necessitated this are outlined in the section titled "Comments on Schedule Modifications."

The integration of the supersonic inlet analysis and design code developed under this project, as well as the engine cycle code and noise prediction codes all needed to be integrated for the results in question to be determined. Additionally, a supersonic engine and aircraft needed to be selected and adapted to employ an inlet designed for the SST design mission, and the identification and selection of a reasonable jet noise reduction method with thrust and noise performance relationships needed to be performed. Lastly the installation of these models into the overall engine cycle needed to be performed and the study utilizing the fixed engine and aircraft with modifications to the nozzle and variable geometry inlet needed to be performed, for thrust degradation, and then noise impacts, using the cycle results to capture the jet stream thermodynamic properties. All these tasks comprise the overall objective of accomplishing an investigation into the

main research goals. These tasks are all captured, along with modified planned due dates and actual and projected completion dates in the Milestones table, below.

Project Milestones
The major milestones and planned due dates are as follows:

Task No.	Milestone	University	Planned Due Date	Planned/Actual Completion Date
1	Selection of initial geometry in coordination with other Project 059 Investigators	PSU and Georgia Tech	12/15/2020	12/15/2020
2.1	Final assembly of zero-order methods to predict inlet performance: Complete supersonic inlet analysis code	Georgia Tech	1/30/2023	9/15/2023
2.2	Determination of boundary conditions from "Vision SST Engine Cycle"—collaboration efforts: Identify engine and operating conditions for inlet studies to be performed	Georgia Tech	5/31/2023	10/30/2023
~~3~~	~~Internal and external modeling of jet exhaust flow for noise modeling~~	~~PSU and Georgia Tech~~	~~8/1/2022~~	~~Cancelled~~
~~4~~	~~Script construction for generation of ANOPP custom jet noise source~~	~~PSU and Georgia Tech~~	~~9/1/2022~~	~~Cancelled~~
5	Submission of 2022 Annual Report	Georgia Tech	12/1/2022	3/1/2023
6	Extension of zeroth-order methods for inlet performance to include low-speed aerodynamics	Georgia Tech	4/15/2023	10/30/2023
7	Establish overall modeling and simulation framework	Georgia Tech	6/1/2023	4/30/2024
8	Development of inlet variable geometry methods and models for improving LTO thrust	Georgia Tech	7/1/2023	2/15/2024
9	Development and design of SST inlet to be used as baseline model and off-design inlet maps	Georgia Tech	7/30/2023	3/30/2024
10	Development and implementation of nozzle-based jet noise reduction methods for engine cycle effects	Georgia Tech	8/30/2023	4/15/2024
11	Completion of the full thrust recovery and noise effects study	Georgia Tech	2/1/2024	11/15/2024
12.1	Submission of FY2023 Annual Report	Georgia Tech	2/1/2024	6/3/2024
12.2	Submission of interim final project report (intermediate results)	Georgia Tech	2/29/2024	6/3/2024
12.3	Submission of the final project report (completion of project)	Georgia Tech	2/29/2024*	11/22/2024

**Indicates planned date based on no-cost-extension, pushing official project end date to 2/29/2024*

Comments on Schedule Modifications

Based on the Project Milestone table and previously submitted annual reports, the project timeline has significantly deviated from the initially planned one. There are several factors which contributed to this large deviation in task completion, which are predominantly technical in nature. First, while the project was overall focused on the integration of inlet performance predictions into an installed engine cycle model, the development of zeroth-order inlet models which could capture any appreciable benefit to the engine cycle and noise model needed to be carefully developed and tested to ensure realistic performance and the ability to design a bespoke supersonic inlet for application to a selected engine cycle and aircraft. One reason for the prioritization of this task was due to the predicted sensitivity of the inlet performance predictions using the inlet design and analysis tool developed in this project, translating to thrust.

Since deviations from a baseline inlet at the LTO conditions would be studied primarily, the ability to discern even seemingly negligible performance benefits relating to the inlet pressure recovery was crucial to answering the primary research question of, "can the inlet recover sufficient thrust without compromising noise benefits to ensure that supersonic jet nozzle noise technologies are feasible?" As such, despite the low fidelity of the modeling efforts—which were pursued due to the desire for enabling rapid assessments without the use of complex computational fluid dynamics (CFD) analyses and high-fidelity inlet computer aided design (CAD) models and meshes to be developed for single analyses—accuracy was determined to be critical. To ensure accuracy, the inlet tool performance was validated against various inlet performance studies in the public domain, and gradually extended and improved, with component models being verified and validated using Inlet Performance Analysis Code (IPAC) case runs, where those component models are also used, and in the case of the addition of the low-speed aerodynamics model, validating with CFD runs performed by competent inlet designers and CFD experts. A detailed discussion regarding the process for this development will be discussed in Tasks 2.1 and 6; however, it can be summarized that this improvement took much longer than initially intended to ensure accuracy when compared to experimentally tested inlets and the execution of CFD runs to validate the low-speed aerodynamics models.

Due to the aforementioned factors, the time required to complete the inlet analysis tool, which was employed for the purposes of generating the baseline inlet in this study, and the variations of it utilizing variable inlet geometry, along with the addition of the capability of modeling the variable geometry, the tool development process took a disproportionate amount of time to complete, rendering the majority of the remaining study to be compressed into a much tighter schedule. As a result, the final study could not be completed by the initial deadline, despite the best effort of the researchers.

A second factor contributing to the delay in schedule was the requirement to effectively perform integration among the three tools required for the study. The study required the use of an engine cycle and aircraft modeling tool, FASST, developed in-house by Georgia Tech's Aerospace Systems Design Laboratory (GT-ASDL), which employs several National Aeronautics and Space Administration (NASA) tools, including CMPGEN[1] for compressor map generation, Numerical Propulsion System Simulation (NPSS) for cycle design and modeling, and FLight Optimization System (FLOPS), for aircraft optimization and mission profile analysis. The study also required use of the Aircraft Noise Prediction Program (ANOPP), NASA noise prediction module, which is coupled to Environmental Design Space (EDS) to allow for analysis of a designed engine and aircraft system. Lastly, the inlet design tool, Supersonic Inlet Performance Code (SIPC) was developed for this project and based in Python.® While it was clear that the tools could all be used together, the action of performing software integration and ensuring consistent cycle performance, and ultimately, noise predictions through the ANOPP, required the ability to create inlet performance inputs in a means compatible with FASST. Doing so required a significant amount of trial and error and presented a non-trivial learning curve for the researchers. In Year 2, an approach was pursued to package SIPC as an executable to be called upon each iteration of the execution of the engine model. This approach proved to be too complicated to ensure consistent results and could not be effectively integrated to ensure accurate inlet performance predictions for each run. As such, this process was abandoned for a simplified approach to generate supersonic inlet maps and install them into the engine cycle for rapid and seamless use when called by the cycle model. The understanding of how to generate inlet performance maps analytically required a notable amount of research, culminating in a discussion with a senior technologist at the Inlets and Nozzles Branch at the NASA Glenn Research Center (Dr. John Slater). As a result, this effort contributed to a push in the overall project completion timeline.

[1] CMPGEN is a modeling tool used to compute off-design performance of fans, booster, and compressors.
® Python is a registered trademark of Python Software Foundation, Beaverton, Oregon.

A third major factor contributing to research complexity and timeline shift was the need to accurately model nozzle noise technologies, along with their thrust and noise effects. In the first two years (Year 1 and Year 2) of the project, it was anticipated that other ASCENT Project A059 research partners would provide experimental data to correlate nozzle geometries and factors which could be replicated and modeled analytically by the engine cycle modeling code. However, at the end of Year 2, it was understood that it would not be possible to obtain these data from the partner researchers, and alternative means to achieve this task were sought out, due to its critical function in accomplishing the ASCENT Project 059(A) research goals. As a result, a deep literature review was performed to support this task, ultimately yielding the finding that a dearth of experimental data existed in the public domain explicitly coupling jet noise technologies to thrust loss and noise reduction. Some significant publications were identified which answered this question, but these were isolated to the exploration of these trends in chevrons on supersonic engines and nozzles. A set of experimental papers published by NASA nozzle experts were used, primarily by the late Dr. John Seiner, which explored the use of parametric families of chevrons on the F404 engine and axisymmetric converging-diverging nozzle (Seiner, 1995 and others). The studies found the noise and thrust impacts associated with take-off conditions and were thereby applicable for use in the research presented here, while some assumptions were made for compatibility and consistency of the use in the study, which are detailed in the sections below.

Lastly, the explicit procedures for using these tools, in concert with one another to answer the correct research questions, were not clear at the outset of the project, and took time well into the software integration phase to understand. The FASST operates by running several iterations of engine cycle model and vehicle model, finally converging to meet initial cycle and aircraft requirement inputs provided by the user. As such, it generates an inlet design for each iteration and performs an off-design analysis to identify whether the engine can meet the requirements provided by the user. The ANOPP is integrated into the FASST run scheme, to generate input files from FASST vehicle outputs, and then an ANOPP analysis is performed. Non-trivial modifications of the FASST code were necessary to ensure that the variable geometry inlet study could be performed as desired. This involved ensuring that the engine models could use the variable geometry inlet maps in the off-design conditions without modifying the engine design at all—as the engine and nozzle configuration were to remain fixed in order to answer the primary research question. Additionally, modifications of execution procedure and codes, and deeper research into capabilities of the ANOPP for use in the noise reduction study were performed, specifically, the addition of supersonic chevrons and their parametrized impacts on noise at LTO conditions.

In summary, it is with the deepest sincerity and humility that the researchers who are performing this work apologize for the late nature of the submission of this work and the final results and findings, which we believe will be of interest to the SST research community. While technical challenges were encountered and overcome, compliance with agreed-upon timelines is a priority and not taken lightly. It is hoped that the work presented here is notable enough to justify the tardiness of terminal reporting of it. The team is grateful for the understanding, patience, and support of the FAA.

Major Accomplishments

Year 1 and Year 2 of work largely comprised creating and developing the supersonic inlet analysis code and refining its capabilities. Year 1 of effort was focused primarily on the assembly of various zeroth-order methods to conduct this inlet analysis, whereas Year 2 efforts were focused primarily on making the tool useful and suitable for the ASCENT Project 059(A) research goals. Year 1 accomplishments included the following:

1. **Task 2.1 - Final assembly of zero-order methods to predict inlet performance**
    - Completed a simple parametric 2D analysis tool able to predict the following:
        - Pressure recovery between freestream and engine face
        - Oblique and normal shock predictions
        - Inlet geometry schematic for verification
        - Bleed, bypass, and spillage drags
    - Validated tool performance against several published 2D inlets.
        - Good agreement with mixed compression M_d = 5.0 inlet provided in an IPAC manuscript (Barnhart, 1998).
        - Good agreement with external compression M_d = 2.3 inlet in *Fundamentals of Aircraft and Airship Design* (Nicolai & Carichner, 2013).
        - Analysis and validation of Performance of Installed Propulsion System Interactive (PIPSI) "R2DSST" M_d = 2.3 mixed compression inlet; currently underway (Kowalski & Atkins, 1979).

During Year 2 of ASCENT Project 059(A) efforts, capability gaps were closed, and several capabilities were improved:

1. **Task 2.1 - Final assembly of zero-order methods to predict inlet performance**

- Identified and improved many capability gaps between the Year 1 supersonic inlet analysis tool and needs including:
  - Inlet–engine airflow matching → bypass mass flow determination
  - Inlet capture area sizing
  - Cowl lip suction and additive drag predictions
  - Nacelle wave drag predictions
- Improved mixed compression inlet performance prediction.
- Improved accuracy of location and strength of internal oblique shock train.
- Improved accuracy of location and strength of internal terminal normal shock.
- Completed the initial integration of supersonic inlet tool and supersonic engine and aircraft analysis and design tools (FASST).

Finally, many significant Year 3 tasks were completed, requiring the modification of the initial milestones and task list to facilitate answering the primary research questions proposed. Year 3 accomplishments include the following:

1. **Task 2.1 - Final assembly of zero-order methods to predict inlet performance**
   - Enabled critical spillage and spillage drag calculations at high supersonic Mach numbers into the SIPC.
   - Improved cowl lip suction calculations based on Crosthwaite et al. (1967).
   - Developed and inlet choking condition prediction and limitations into the SIPC.
   - Extended additive drag predictions to include detached normal shock conditions into the SIPC.
   - Improved subsonic diffuser duct loss prediction models into the SIPC.
   - Developed and added an automated mass flow sizing approach for user-defined normal shock position into the SIPC.
   - Developed and added capability to photographically scale inlet into the SIPC.
   - Developed and added angle of attack effects to inlet model into the SIPC.
   - Developed and added increased fidelity in the inlet model to capture external normal shock-oblique shock interactions into the SIPC.
   - Developed and added the ability to visualize oblique shock-normal shock interactions and a three-dimensional (3D) view of inlet configuration into the SIPC.
   - Developed and added the ability to run batches of inlet cases into the SIPC for design space exploration.
   - Added ram drag calculation into the SIPC.
   - Completed the inlet modeling tool for the project.
2. **Task 6 - Extension of zeroth-order methods for inlet performance to include low-speed aerodynamics**
   - Developed and added a low-speed viscous aerodynamic model into the SIPC and validated with CFD.
3. **Task 7 - Establish overall modeling and simulation framework**
   - Performed initial integration work using an example inlet, and the selected engine and aircraft design to be used in project studies.
   - Determined and evaluated an approach for coupling inlet, aircraft, and noise codes.
   - Identified the ANOPP noise modeling approach for use with chevrons.
4. **Task 8 - Development of inlet variable geometry methods and models for improving LTO thrust**
   - Developed and added ramp bleed ports and throat bypass models into the SIPC.
   - Developed and added blow-in door models into the SIPC.
   - Developed and added variable geometry cowl lip models into the SIPC.
5. **Task 9 - Development and design of SST inlet to be used as baseline model and off-design inlet maps**
   - Designed the baseline inlet model for selected M=1.7 65-passenger SST vehicle with the mixed-flow turbofan (MFTF) engine.
   - Adapted the baseline inlet model to use previously developed blow-in doors, variable geometry cowl lips, and ramp bleed and throat bypass models for off-design and verified functionality across the flight profile.
   - Developed process for analytically generating inlet maps for all off-design conditions using the standardized inlet map format presented in Kowalski (1979).
   - Developed inlet maps for baseline inlet, variable geometry cowl lip, blow-in doors, and hybrid (both).
6. **Task 10 - Development and implementation of nozzle-based jet noise reduction methods for engine cycle effects**
   - Performed a literature review to identify potential nozzle-based jet noise technologies to be modeled, which provided a thrust and noise relationship.

- Identified research papers with experimental and analytically derived data which correlated jet noise reduction to thrust loss using chevrons.
- Determined an approach for implementing chevrons into the cycle model to capture thrust losses and the impact to engine cycle, as well as the effects on jet noise in ANOPP.

7. **Task 11 - Completion of the full thrust recovery and noise effects study**
   - Integrated inlet maps, and fixed engine and aircraft models to ensure functionality and confirm study procedure.
   - Added chevrons for three parametrized designs defined in aforementioned reference into the NPSS nozzle element and ensured functionality.
   - Integrated inlet maps, fixed engine and aircraft models, and chevron models to ensure functionality and confirm study procedure.
   - Ran a baseline engine case and established the ANOPP performance values for baseline inlet, fixed engine and aircraft, and clean nozzle (no chevrons) for a comparison datum.
   - Determined the necessary chevron geometry and inlet variable geometry cases to be studied.
   - ***In-process:***
     - ***Completing studies and compiling data.***
     - ***Performing analysis of data and necessary model reruns.***

Task 1 - Select Jet Nozzle Geometry

Georgia Institute of Technology
Pennsylvania State University

Objective

The objective of this task was initially to unify and maximize the impact of work across relevant ASCENT projects; Georgia Tech and PSU will coordinate efforts to select an initial jet nozzle geometry. In work with Dr. Krishnan Ahuja, the experimental data from this standard geometry (gathered in ASCENT Project 059) will be used to inform the work of ASCENT Project 059(A).

Research Approach

The combined PSU and Georgia Tech research team will work together to identify promising geometries for use across the ASCENT projects. The selected geometry must be relevant to the project goals, and also achievable regarding experimental measurement, computational analysis, and other supporting tasks. Specific evaluation criteria may include jet velocity reduction and thrust loss.

This task was completed during Year 1 of work. Although the results of this effort were not used to complete the inlet analysis code, it was helpful in identifying and converging upon the ultimate objective of the project and establishing cooperative working relationships with other ASCENT Project 059(A) partners.

Milestone

- Selected a notional jet nozzle geometry. This project task was completed early in the project (Year 1). The nozzle geometry was superseded in Year 3 in favor of one which was employed on an engine and aircraft model which were designed initially for ASCENT Project 010.

Major Accomplishments

- Selected an initial nozzle configuration.
- Established a collaboration with Georgia Tech experimental lab and PSU.

Publications

None.

Outreach Efforts

None.

Awards
None.

Student Involvement
None.

Plans for Next Period
None.

Task 2 - Translate Installed Cycle Performance Requirements into Boundary Conditions
Georgia Institute of Technology

Objective
The objective of this task is to leverage engine cycle modeling capabilities to determine the installed thrust for an engine of interest that is appropriate for commercial SST. The thermodynamic properties across this mixed flow turbofan engine, alongside the install thrust value, are used to characterize the mixer exit, nozzle entrance, and nozzle exit operating conditions during take-off. Because the initial testing and high-fidelity simulations are not (yet) representative of a mixed flow turbofan, these operating conditions (i.e., total pressure, total temperature, mass flow, geometry, etc.) will inform the testing team regarding relevant testing conditions.

Research Approach
Task 2.0 - Determine Installed Thrust
To ensure that minimum thrust is lost during implementation of potential jet noise reduction technology, the installed thrust requirement must be determined, because it is directly proportional to jet velocity. A major contributor to installed thrust is inlet performance, which is highly dependent on how the engine is integrated with the vehicle. Therefore, the primary element of Task 2 is to investigate zeroth-order methods to predict inlet performance for different inlet designs and off-design configurations.

Task 2.2 - Generate Boundary Conditions
Initially, the objective of this task for Georgia Tech was to analyze the engine cycle developed by ASCENT Project 010 to estimate the best operating conditions for LTO to minimize certification noise levels. This task was updated to reflect the required boundary condition/experimental data generated by project partners, to be used in Tasks 7 and 8. Additionally, the timeline was updated to reflect when these data were required by the ASCENT Project 059(A) team. Some beneficial data for modeling will include mixer and nozzle conditions, i.e., total temperature, total pressure, and mass flow rate, as well as measured thrust vs. noise for each tested jet noise reduction technology or mixer type. This task was completed in Year 3.

Task 2.1 - Zero-order Methods to Predict Inlet Performance
A major contributor to installed thrust is inlet performance, which is highly dependent on how the engine is integrated with the vehicle. To capture thrust recovery due to improved inlet performance, the Georgia Tech team must develop a means to predict inlet performance across the SST flight envelope, particularly at low-speed conditions during which jet noise is most prominent (i.e., LTO).

During Year 1, the Georgia Tech team completed an initial the model development for the 2D inlet case, by developing a modular 2D supersonic inlet anlaysis tool (see Figure 1). In addition, the team has completed an initial validation of the 2D inlet case with satisfactory preliminary results (refer to Figure 2).

Table 1 compares the developed tool's predicted total pressure recovery to that produced by IPAC across the mission-relevant range of freestream Mach numbers (Barnhart, 1998). Here, the supersonic inlet is designed for a freesteam Mach number of 5, and evaluated across a range of lower "off-design" operating freestream Mach settings. The maximum and average error values were found to be 3.69% and 0.82%, respectively, across this range.

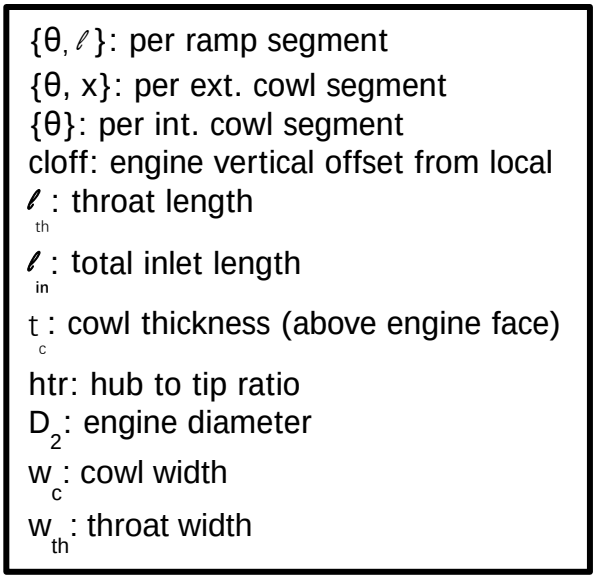

Figure 1. Geometry inputs to define inlet in Year 1 supersonic inlet analysis code.

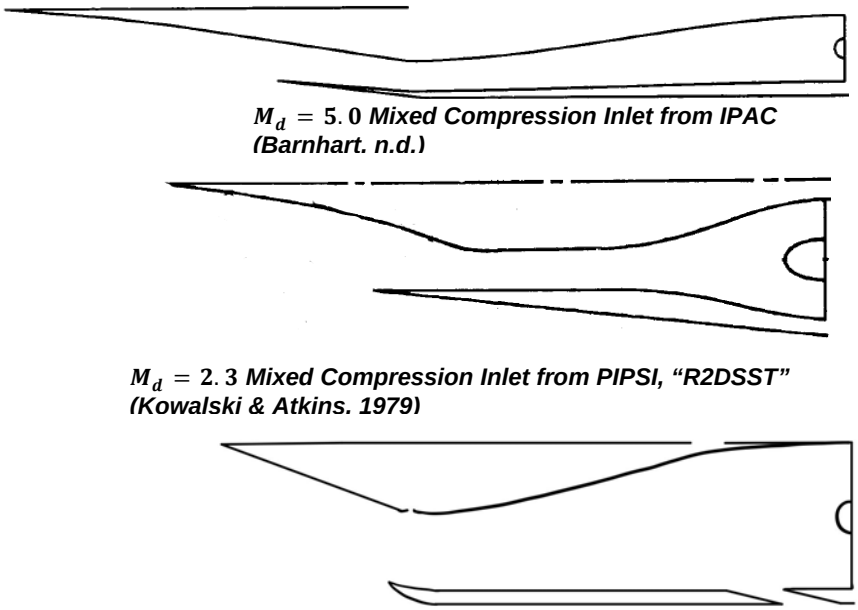

$M_d = 5.0$ ***Mixed Compression Inlet from IPAC (Barnhart. n.d.)***

$M_d = 2.3$ ***Mixed Compression Inlet from PIPSI, "R2DSST" (Kowalski & Atkins. 1979)***

$M_d = 2.3$ ***External Compression Inlet from Nicolai & Carichner (2013)***

Figure 2. Three 2D supersonic inlets used to validate the Year 1 inlet analysis tool; top inlet performance results are displayed in Table 1.

Table 1. Validation case: total pressure recovery.

Freestream Mach number	Modeled	Reference	Error (%)
0.01	0.9586	0.9608	−0.23
0.2	0.9586	0.9608	−0.23
0.4	0.9586	0.9608	−0.23
0.6	0.9586	0.9608	−0.23
0.8	0.9586	0.9608	−0.23
1.0	0.9586	0.9608	−0.23
1.2	0.9517	0.9539	−0.23
1.4	0.9404	0.9456	−0.55
1.6	0.9233	0.9285	−0.56
1.8	0.8767	0.8816	−0.55
2.0	0.8107	0.8153	−0.57
2.5	0.8591	0.8760	−1.97
3.0	0.7873	0.7875	−0.03
4.0	0.6618	0.6427	2.88
5.0	0.5349	0.5152	3.67

Table 2 compares the developed tool's predicted total drag coefficient and that produced by IPAC across the mission-relevant range of freestream Mach numbers (Barnhart, 1998). This drag term includes the contributions of spillage, bleed, and bypass drag on the engine inlet. Again, the supersonic inlet is designed for a freesteam Mach number of 5 and is evaluated across a range of lower "off-design" operating freestream Mach settings. The maximum and average error values were found to be 9.88% and 1.19%, respectively, across this range.

Table 2. Validation case: total drag coefficient.

Freestream Mach number	Modeled	Reference	Error (%)
0.01	0.0000	0.0000	0.00
0.2	0.0000	0.0000	0.00
0.4	0.1976	0.1799	9.88
0.6	0.3086	0.3024	2.05
0.8	0.3831	0.3811	0.53
1.0	0.4809	0.4797	0.25
1.2	0.6537	0.6617	−1.21
1.4	0.3953	0.3855	2.53
1.6	0.3264	0.3265	−0.01
1.8	0.3245	0.3250	−0.15
2.0	0.3426	0.3411	0.45
2.5	0.3007	0.3000	0.23
3.0	0.2994	0.2987	0.23
4.0	0.2315	0.2307	0.35
5.0	0.0175	0.0175	0.00

The developed inlet performance analysis tool is intended to help identify competitive supersonic inlet designs for overcoming negative performance impacts accompanying noise reduction nozzle technologies across the flight envelope and as identifying the resulting behaviors associated with low-speed performance and off-design ramp (and other variable geometry) configurations of the inlet. To this end, a sensitivity study was performed to evaluate inlet variable-geometry settings that may be capable of recovering thrust across off-design flight segments (i.e., LTO).

For Year 2, the inlet performance tool was extended to include several capabilities for performance modeling, as listed in the Major Accomplishments section. One simple capability added for Year 2 was a schematic showing the user where the external oblique shocks are located with respect to the external portion of the supersonic inlet (Figure 3). This schematic allows users of the supersonic inlet analysis script as a standalone tool (i.e., not coupled to an engine/airframe sizing and synthesis tool) to quickly identify whether an external shock system is attached to the inlet, or a detached shock system has been formed. In work for Year 3, the normal shock system, whether external or internal, will be included in the schematic. Additionally, the subsonic diffuser portion (the internal inlet section closest to the engine face) will reflect the actual curvature reflected in the model (here, it is straight, without curvature).

Figure 3. Inlet and shock schematic enabled in supersonic inlet tool during Year 2 work.

In addition to the modeling fidelity improvements listed in the Major Accomplishments section, many more stations and the physical properties of airflow at those stations can be modeled as a consequence of the Year 2 work. Instead of simply considering the total pressure recovery and drags, as displayed for the Year 1 work in Table 1 and Table 2, the work of Year 2 enabled a much closer examination of the supersonic inlet performance at each station. The performance of the inlet at each of these additional stations was compared with those from the published results of the M = 5.0 mixed compression inlet from IPAC (shown at top in Figure 2). Detailed results for the M = 3.0 off-design case of this inlet are shown in Table 3; the design case and other off-design cases down to M = 0.01 had similar performance results with respect to the validation error. As described previously, a greater level of fidelity regarding flow station performance and improvements in the accuracy of the model were achieved. Using the Year 2 inlet analysis tools, the team had found an improvement in accuracy regarding total pressure recovery (total pressure ratio across the entire inlet) as a consequence of the improvement in shock location predictions and internal reflected shock quantities.

Table 3. Validation results for IPAC M = 5.0 inlet and M = 3.0 off-design case.

Outputs	Local calculated	Local reference	Error (%)	Cowl lip calculated	Cowl lip reference	Error (%)	Throat calculated	Throat reference	Error (%)
Flow area (ft^2)	0.6905	0.6905	0.0000	0.3953	0.3955	0.0594	0.1600	0.1598	−0.1126
Mach number	3.0000	3.0000	0.0000	2.3982	2.3990	0.0335	1.3149	1.3140	−0.0700
Static pressure (lbf/ft^2)	156.7630	156.3000	−0.2962	390.6043	389.5000	−0.2835	1,960.9823	1,959.0000	−0.1012
Static temperature (R)	389.9700	390.0000	0.0077	508.6205	507.7000	−0.1813	812.6533	811.5000	−0.1421
Density (slg/ft^3)	0.0002	0.0002	−0.2490	0.0004	0.0004	−0.2472	0.0016	0.0014	−13.3433
Velocity (ft/s)	2,905.4154	2,904.0000	−0.0487	2,650.0449	2,649.0000	−0.0394	1,838.3284	1,835.0000	−0.1814
Total pressure (lbf/ft^2)	5,753.6784	5,743.0000	−0.1859	5,694.5814	5,684.0000	−0.1862	5,545.0869	5,534.0000	−0.2003
Total temperature (R)	1,093.6709	1,092.0000	−0.1530	1,093.6709	1,092.0000	−0.1530	1,093.6709	1,092.0000	−0.1530
Mass flow (lbm/s)	21.8556	21.8200	−0.1630	15.0913	15.0700	−0.1411	13.2882	13.2700	−0.1370
$\frac{P_{T_1}}{P_{T_L}}$	$\frac{P_{T_1}}{P_{T_{L\,REF}}}$	$\frac{P_{T_{TH}}}{P_{T_1}}$	$\frac{P_{T_{TH}}}{P_{T_{1\,REF}}}$	$\frac{P_{T_2}}{P_{T_{TH}}}$	$\frac{P_{T_2}}{P_{T_{TH\,REF}}}$	$\frac{P_{T_X}}{P_{T_Y}}$ (across normal shock)	$\frac{P_{T_X}}{P_{T_{Y\,REF}}}$ (across normal shock)	Number of internal shocks	Number of internal shocks (reference)
0.9897	0.9900	0.9737	0.9740	0.8164	0.8174	0.897	.8952	3	3

During Year 3 work, many significant progresses were made, and the overall completion of the inlet modeling tool was completed. First, critical spillage determinations and the ability to calculate drag forces for them was developed. While in Year 2, the ability to determine subcritical spillage was developed and added into the inlet model, critical spillage at higher

Mach numbers was not present. Critical spillage is experienced when the normal shock in a shock system is swallowed by a mixed compression inlet, but the oblique shocks are not converged upon the cowl lip. An example of this can be seen in Figure 4, from Barnhart (1998). It can be seen that since the oblique shocks do not converge on the cowl lip (i.e., the lower protruding surface), and streamtube area entering the inlet is less than the total capture area, denoted as A_c. This creates a spillage effect, since the overall mass flow which could be captured by the inlet is not able to be due to the oblique shock system, and a momentum drag is incurred. While this is only relevant to supersonic conditions, an inlet with realistic performance predictions for the entire SST mission profile needed to be designed, and this condition and capability needed to be added to the inlet model.

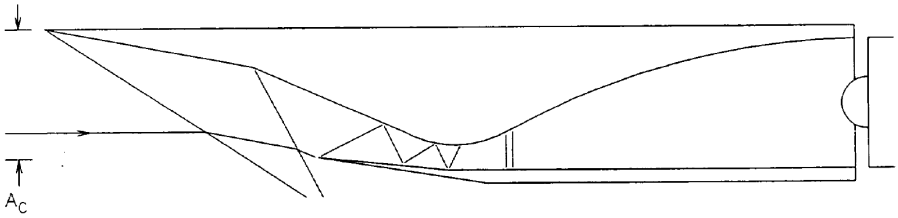

Figure 4. Critical spillage due to oblique shocks (Barnhart, 1998).

Another improvement to the inlet performance tool was the improvement of cowl lip suction calculations based on Crosthwaite et al. (1967), "Preliminary Design Methodology for Air-Induction Systems." Although the IPAC technical report (Barnhart, 1998) outlines a basis for cowl lip suction calculation based on this reference, the researchers could not achieve consistent performance for the cowl lip suction calculation using the equations provided by the IPAC report. In several cases, when running the IPAC example 2D inlet with a design Mach number of 5.0, cowl lip suction values varied from the reference calculations up to 5%. As a result, a simplified approach found in the original work from which the IPAC equations were derived was used, enabling agreement and improvement with highest error of 2% for the worst case in the validation dataset. Another improvement predicated on improving the physics modeling of the inlet code was to add a choking condition prediction for the different points of convergence inside the inlet duct and provide an error which would yield an invalid case run to the user. As a consequence of the conservation of mass and compressibility effects, the mass air flow through an inlet is limited by its smallest area. The inlet code requires a user (or engine deck) input for engine demand, bleed, and bypass—the components or sum of which can choke the inlet either at the cowl lip entrance, or later, at the throat (most likely). If this is the case, it is important for the user model the condition in which no more mass flow can be demanded by the engine, bleed ports (for boundary layer control), or bypass (for shock system stability control). As such, adding this functionality ensured a more accurate physical representation of the operation of an inlet across the mission profile of the vehicle, especially LTO conditions, at which extreme amounts of air are required to operate. This furthermore enabled the user to know when the inlet needed to be upsized for a condition, or variable geometry compression ramps needed to have their deflection angles changed.

In the case in which the inlet experiences a detached normal shock—one that is located in front of any compressed surface—also known as a bow shock, additive drag is still experienced. Additive drag is the sum of cowl lip suction forces, the low-pressure suction phenomenon due to air flowing in the reverse direction of the streamtube, over the inlet cowl lip, and drag due to spillage. While the drag due to spillage was developed, implemented, and validated for other operating conditions, it was added for the supersonic condition during which there is extremely low mass air flow demand into the inlet. This improvement, again, was to ensure the overall prediction of the inlet maps was physically accurate for overall mission modeling. For reference, the inlet generally used for component model validation is shown in Figure 5. In Year 3, as previously discussed, there were further modifications and improvements to the inlet modeling code which were performed, including the improvement of subsonic diffuser duct loss predictions. This task was identified as necessary, as the partial total pressure recovery which was calculated as the loss in total pressure between the inlet throat and the engine fan face was providing worse (lower) total pressure recovery values than those predicted by the IPAC code. As such, the source data employed by IPAC, found in Crosthwaite et al. (1967), were digitized, added to the code as a lookup table, and revalidated in order to ensure better agreement with IPAC output values.

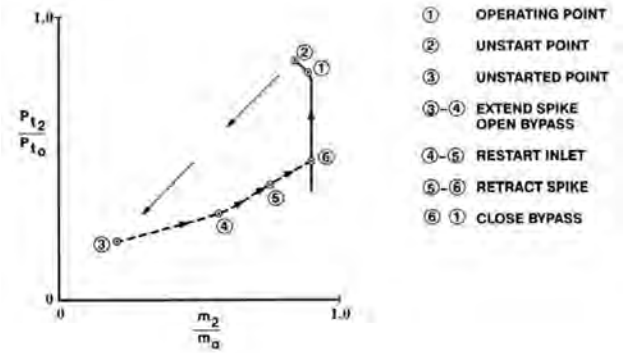

Figure 5. SR-71 inlet operation and operability chart on "Cane Curve" shows the effects of inlet unstart (Anderson, 2014).

In previous versions of the supersonic inlet design code, the prediction of the internal normal shock was limited to being defined by the user using a throat Mach number definition, assuming that the internal oblique shock train would eventually become detached after enough internal shock reflections in the converging inlet duct wall, terminating at the throat. However, this assumption did not reflect the physics of the problem particularly well, upon deeper examination of the problem, nor did it truly enable a full analytical physics-based approach to understanding the performance of the inlet. Specifically, the inlet normal shock position is a consequence of the backpressure provided by the engine and bypass demands. An example of a started mixed compression inlet shown in Figure 4, where the normal shock is swallowed into the inlet duct. As the converging duct is an unstable location for a normal shock to reside (position of high shock instability), the normal shock, if swallowed, will lie at the throat, or past it inside the subsonic diffuser duct (which is a diverging duct, and geometry much more amenable to keeping a shock in place) (Seddon & Goldsmith, 1999). In practical operation, if the inlet is in the started condition, this necessitates that the inlet is moving fast enough to form all external oblique shocks, and also that the engine and bypass demand are sufficiently high to retain the normal shock. If the demand (backpressure) is too low (high), the normal shock will pop out of the inlet duct and the system will be in what is known as an "unstarted" condition. Two examples of this can be found in Figure 5. Since the normal shock position is exclusively dependent upon the inlet-engine-aircraft system operating conditions, it was crucial to ensure that the position was a response due to these factors, and not an independent modeling input provided by the user. This model was defined based on compressible flow relationships defined in Seddon and Goldsmith's "Intake Aerodynamics" (Seddon & Goldsmith, 1999), and positions were defined not by axial coordinates, but rather inlet cross-sectional areas segmented between inlet stations defined commonly defined across various inlet literature sources and shown in Figure 6. This method was validated successfully and ensured accurate determination of the position of the normal shock when swallowed. Previous work to define the normal shock on the external ramps when the unstarted condition was completed and validated against IPAC outputs in Year 2 of work, so effects of normal shock positioning across the entire range of inlet operation were fully captured upon the completion of this task.

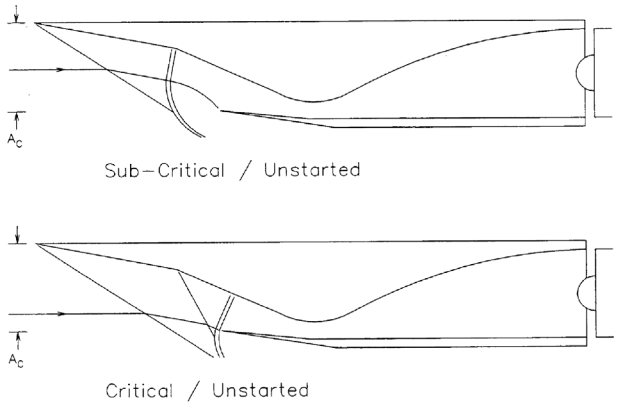

Figure 6. Examples of unstarted inlet conditions for mixed compression 2D inlet (Barnhart, 1998).

Additionally, a design analysis condition was defined to ensure that the inlet would remain in the started condition while performing analyses such as the generation of inlet performance maps. As will be described in later sections pertaining to the generation inlet performance maps for the selected inlet and engine models, inlet performance maps are generated for supersonic conditions assuming that the shock remains swallowed, since an unstarted inlet in a supersonic condition causes a highly unstable engine transient conditions, such as compressor stall or surge. This was a significant factor in the operability of the SR-71 axisymmetric inlet, which proved to be the most challenging feature of the entire aircraft design (Anderson, 2014).

As such, it was useful to automate two features to facilitate the retention of this condition in use of the analytical tool. First, a required mass flow rate for the inlet to retain the normal shock in the swallowed condition, and second, the ability to perform analysis keeping the normal shock fixed in a position defined by the user. For the first feature, Equation 1 defines the required mass flow for keeping the engine started condition, also assuming that the operating condition of the aircraft is sufficiently fast to create oblique shocks on all external ramps and a terminal normal shock after them. The maximum amount of mass flow ingested by the inlet at a given condition while the normal shock is swallowed is referred to as the critical mass flow ratio:

$$\frac{A_{0I}}{A_C}_{Critical} \quad \text{(Eq. 1).}$$

This value changes as the vehicle speed drops below the design Mach number for the inlet, as the geometry of the inlet is created to ensure a shock-on-lip condition, which prevents critical spillage from occurring. When the oblique shocks are no longer focused on the cowl lip, the oblique shocks are formed, starting on the compression ramps at a more shallow angle than in the design condition, and the streamtube of air which is able to be swallowed by the inlet is constrained by the compression of the streamtube as a result of the off-design compression of the external oblique shocks. An example of this can be seen in Figure 4, where the captured streamtube area is less than the forward-projected capture area defined by rectangle formed from the cowl lip to the bottom of the first compression ramp (and along the inlet sidewalls, not pictured in the axial cross section), and denoted as A_C. When the inlet (as shown) is operating at the design condition, the streamtube captured by the inlet (corresponding to the mass flow ingested by it) is in full flow and is equal to the capture area, since the external oblique shocks are concentrated on the cowl lip. So, to accomplish this task, it was necessary to identify a means to find the maximum ingested mass flow when the $\frac{A_{0I}}{A_C}_{Critical} \neq 1$ (where 1 represents the on-design condition and full flow). The total ingested mass flow is at the maximum when the following condition is met: $\frac{A_{0I}}{A_C} = \frac{A_{0_{eng}}}{A_C} + \frac{A_{0_{bld}}}{A_C} + \frac{A_{0_{byp}}}{A_C} = \frac{A_{0I}}{A_C}_{Critical}$. This was performed by calculating the streamtube area compression due to the oblique shocks moving backwards from the cowl lip, at each oblique shock intersection with the streamtube, to the inlet "local" position, which can be seen in the inlet position schematic in Figure 7. This approach needed to be parametric and conditional such that the $\frac{A_{0I}}{A_C}_{Critical}$ value could be determined across the entire flight regime. Again, it should be mentioned that while this particular task was not necessary for the determination of thrust benefit at LTO conditions, a new inlet, which worked for an installed engine on a vehicle performing an actual SST mission profile, needed to be defined for this task. To do this, performance at all mission points needed to be able to be ascertained. The second task listed above was to enable the fixing of the normal shock and understanding the resulting aerothermodynamic properties of the flow which result from these properties. This was notionally achieved in Year 2 of work with the model; however, the initial attempt at fixing the normal shock internally provided incongruous flow patterns between the first half (from freestream to throat) and the second half (from throat the engine fan face) of the inlet. The approach determined here allowed users to study the effects of the flow and perform the inlet design at off design configurations by modifying the ramp angles, and ensuring the normal shock was able to remain in a stable location for the off-design supersonic conditions.

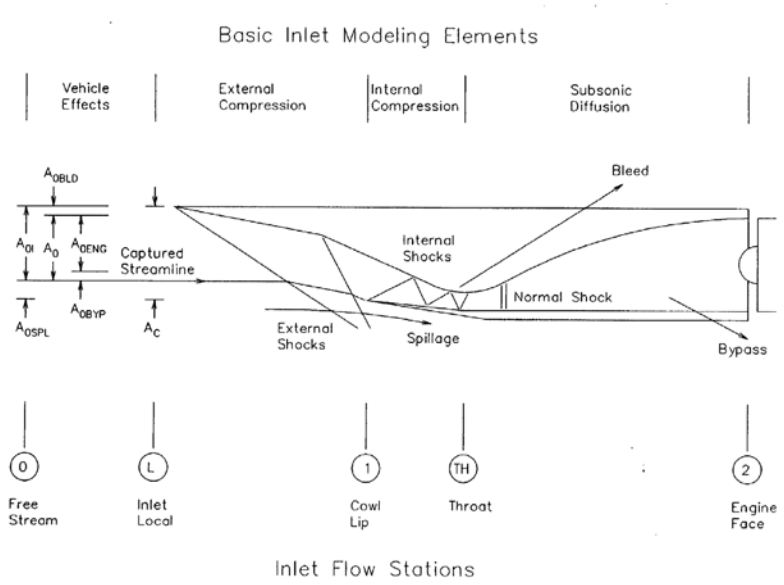

Figure 7. Commonly-defined inlet flow stations (Barnhart, 1998).

Another feature which was useful for the initial definition and design of the inlet to be used in the SST configuration for the study was the ability to size the inlet photographically. Previously, individual sizing parameters, such as ramp lengths, cowl lip width, engine fan diameter, and the like, were defined and would need to be redefined for each successive permutation of inlet design, even if a simply scaled-down or scaled-up version of the inlet was desired. This enabled the researchers to initially employ already-designed inlet models to various engines and have a baseline from which to begin inlet studies. An example of the scaling enabled by this step can be seen in Figure 8.

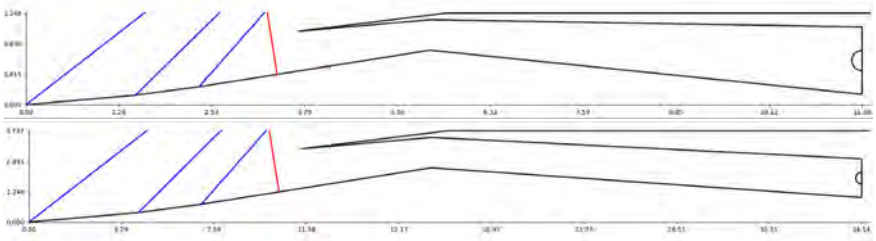

Figure 8. Identical inlets in off-design condition sized for different capture areas with same engine ($\mathrm{Ac} = 1$ (top), $\mathrm{Ac} = 3$ (bottom)).

Yet another useful feature for understanding performance of the inlet across the SST mission profile was the addition of angle of attack effects in SIPC. While most inlet maps, and the IPAC inlet analysis code, do not account for inlet performance effects with modified angles of attack, it was important to account for this in the predicted inlet performance here, as a high angles of attack for SSTs are nearly inevitable for LTO conditions. While the plot generated by SIPC does not show the effects of modifications of angle of attack (see Figure 9). The external shock train prediction, due to the change in incident flow and position of the normal shock due to the ingested flow to the inlet, can be seen clearly in Figure 10. The normal shock in the top image shows the operation of the IPAC-defined $M_D = 5.0$ inlet at $\alpha = 0°$, while in the bottom image in Figure 9, where for the same inlet configurations and operating conditions, $\alpha = 8°$. It can be seen that the normal shock is positioned farther from the cowl lip due to less ingested airflow entering the inlet due to the oblique shock train, and the oblique shocks have a lower shock angle, despite maintaining the same ramp angle. These effects are further propagated to all following aerothermodynamic predictions at all stations and were able to be reflected in the inlet performance maps.

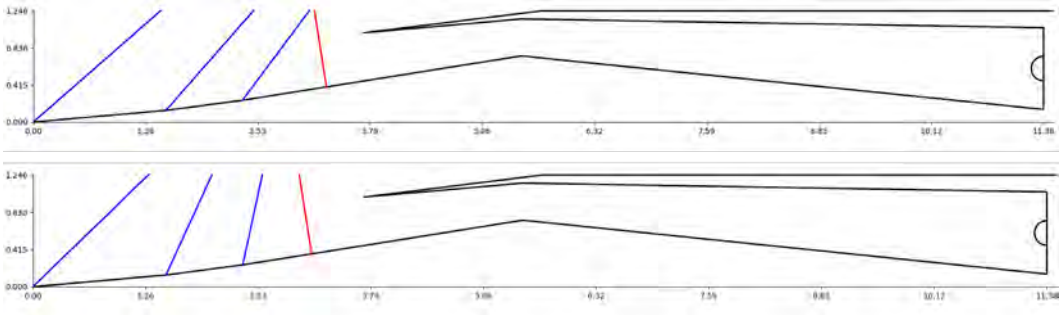

Figure 9. Effects of change in angle of attack: top α = 0°, bottom α = 8°.

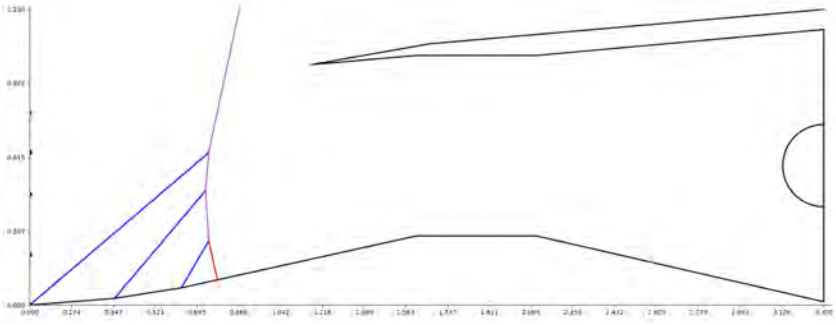

Figure 10. Example M=1.7 SST inlet experiencing external oblique-normal shock interactions (purple lines).

While in the previous year of work, it was assumed in off-design supersonic conditions, where the normal shock is not swallowed, that the normal shock and oblique shocks had no significant physical interaction. As such, any interaction between the two shock systems was not modeled. This was addressed by the team after some cursory CFD modeling was performed to better understand this phenomenon and if it was significant, and it was determined to be so. As such, an understanding of the compressible flow effects was sought, using in part, Seddon and Goldsmith (1999). Additionally, the explanation of the interactions of shocks was explained in Chapter 7.4 of Seddon and Goldsmith (1999). Seddon and Goldsmith (1999) indicates that instead of the weak oblique shocks which are seen in standard compression regimes at the ramp surface turning angles for supersonic flow, any interaction between normal shocks and oblique shocks would yield a strong oblique shock, rendering a stronger oblique shock instead of being replaced by the normal shock. As such, this effect was added to be modeled. In the weak oblique shock condition, the resulting flow after the shock remains supersonic, and only becomes subsonic after a terminal normal shock (which necessarily occurs). In a strong oblique shock condition, the flow which follows the shock becomes subsonic and no normal shock is experienced. Since the oblique shock equation has two solutions (supersonic and subsonic), the conditional to select which one in the root finder scheme was appropriately selected to model this phenomenon. Additionally, a visualization approach was developed and added to the code to show when this oblique-normal shock interaction occurs to the user (shown in Figure 11). The resulting strong shock can be seen as the purple line—and it can be seen that the oblique shocks modify the typically orthogonal shape of the normal shock (when measured from the compression ramp surface).

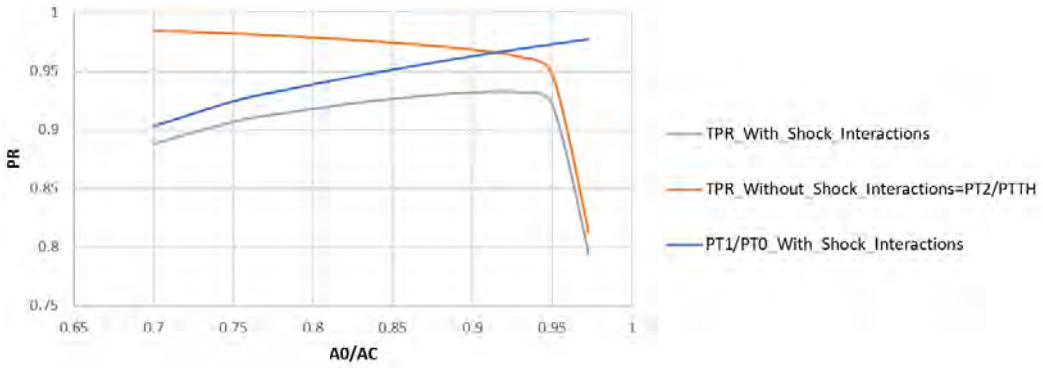

Figure 11. Total pressure recoveries for M=1.7 SST inlet comparing the modeling with and without shock interactions.

It can be seen in Figure 11, that the total pressure recoveries for an inlet at a fixed supersonic Mach number and in an off-design condition (since the normal shock is external to the inlet, and thus unstarted), the inlet performance "cane curve" shows nontrivial losses when only allowing the calculation of these normal-oblique shock interactions to take place. Here, for lower mass flow ratios ingested by the inlet, the difference in total pressure recovery from the non-interaction case is approximately 1%, while at higher mass flow ratios, it is closer to 0.25%. This affects the off-design performance of the inlet and likely, the overall design selected in the design phase.

To allow a better understanding of the inlet design, a 3D schematic generation was developed, which provides a movable 3D plot in the Python Matplotlib plot screen upon completion of the SIPC's execution. An example of this 3D print is shown in Figure 12.

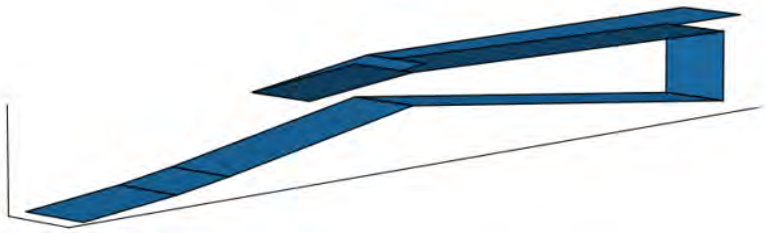

Figure 12. 3D schematic of M_D = 5.0 inlet.

To further illustrate the design variables and parametrization of the inlet, which is employed by the SIPC code, a schematic is provided in Figure 13. As can be seen, although the code is currently only capable of modeling 2D (rectangular cross-section) inlets, all possible geometric variables are considered and used in modeling. Another capability added to the inlet design and analysis code for this task was to enable the running of batches of inlet design cases, using a spreadsheet as the input file, for a user-defined quantity of inlet analysis cases. In the batch run capability, the code is able to vary any geometry variable, flight condition variable, or engine operating condition variable, and the results are collected and summarized in final comma separated value (CSV) file. A summary of the inlet user inputs is defined in Table 4 including units and variable descriptions. All of these variables are able to be varied in the input CSV file using the batch running capability, allowing for the running of many cases to generate inlet performance maps, or perform a design space exploration (DSE) for different geometries and configurations. The geometry variables which define the inlet are listed in Table 4, and are also shown in the schematic of the inlet in Figure 14. In addition to explaining the SIPC-defined lengths and angles mapped to a generic 2D supersonic inlet, the image captures the parameterization approach utilized in SIPC (see Table 4).

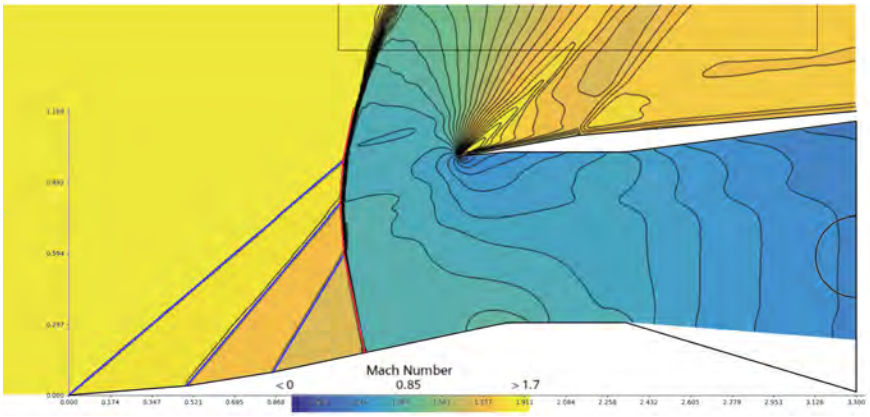

Figure 13. Reynolds-averaged Navier-Stokes (RANS) CFD model for SST inlet to validate external oblique-normal shock interactions.

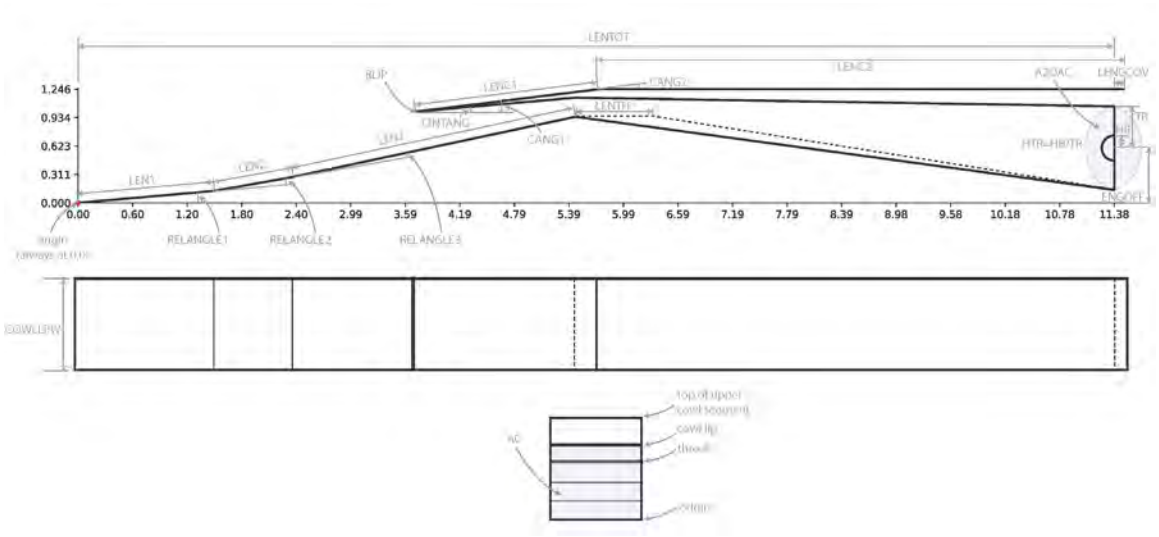

Figure 14. M_D =5.0 Inlet from IPAC report (Barnhart, 1998) defined using SI. PC variables Illustrating parameterization approach.

Table 4. SIPC input variables and units.

Variable Category	Variable Name	Description (Units)
AMBIENT	ALT	Altitude (ft)
	MACH	Freestream Mach number
	ALPHA	Angle of attack (degrees)
CAPTURE GEOMETRY	AC	Capture area (sqft)
	COWLLPW	Cowl lip width (ft)
FLOW CALCULATION	SET_AS	Flag to set normal shock position and keep there, if started
	AS_RATIO	Area ratio of normal shock position to throat area
	SIZED_FLOW	Flag to size the flow to keep mass flow equal to critical ingested mass flow rate
COWL GEOMETRY	NUMSEG	Number of cowl segments (ft)
	CANG1	Respective angles of the cowl lengths WRT horizontal (first one), then each other (relative) (ft)
	CANG2	Respective angles of the cowl lengths WRT horizontal (first one), then each other (relative) (ft)
	CINTANG	Internal cowl lip angles, relative after first angle (fron horizontal) (ft)
	LENC1	Length of each external cowl segment along the hypotenuse (ft)
	LENC2	Length of each external cowl segment along the hypotenuse (ft)
	RLIP	Lip Radius (ft) ;Sharp lip radius = 0
	LENTH	Length of throat section (constant area duct) (ft)
	LENTOT	Total inlet length, user-provided value by-design (ft)
EXTERNAL RAMP GEOMETRY	NRAMPS	Number of external ramps
	RELANGLE1	Angle of first ramp relative to previous (degrees)
	RELANGLE2	Angle of second ramp relative to previous (degrees)
	RELANGLE3	Angle of third ramp relative to previous (degrees)
	LEN1	Length of first ramp along the hypotenuse (ft)
	LEN2	Length of second ramp along the hypotenuse (ft)
	LEN3	Length of third ramp along the hypotenuse (ft)
ENGINE FACE GEOMETRY	A2OAC	Fan area ratio (Fan area/Capture area)
	HTR	Engine hub-to-tip ratio
	ENGOFF	Offset of the middle of the spinner (and engine) from the beginning of the ramps (i.e. y=0) (ft)
	LENGCOV	Length of the external cowl which is past the engine face (ft)
FLOW RATES	A0ENGOAC	Engine flow rate required as a fraction of catured flow
	ABLDOAC	Bleed flow rate as a fraction of captured flow
	ABYPOAC	Bypass flow rate as fraction of captured flow
SETUP	SDFRIC	Subsonic diffuser skin friction factor (real number)
	DEBUG	Debug print output off = 0, on = 1
	LIPLOSS	Lip loss calculations on = 1, off = 0
	PLOT	Plot inlet and resulting shock system on = 1, off=0
	SOL	Adjust ramp/cowl lengths for shock on lip/focus point (off = 0, on = 1)
	SOLOFF	Focal point above cowl lip for external shocks

Although a significant and disproportionate amount of time compared to other tasks was expended on Task 2, a great deal of improvements in modeling capabilities for the inlet were achieved because of it. At this point, it should be noted, that although NASA's IPAC was available to use for reference, it was not able to be used due to its restricted nature (only available to persons of the United States), while several graduate students which worked on the project over its course were international students. Additionally, the IPAC lacked several features which were desired to be used by the researchers, such as the shock visualization capability, shock interaction/strong oblique shock predictions, and low speed aerodynamic viscous models, among other things. Extensions of the IPAC would have been exceedingly difficult, if possible, even if not restricted, as the source code was not easily available to the researchers, and is a Fortran code, a language not regularly used by the researchers. As such, in order to design a bespoke inlet for this research effort, and to ensure that the inlet maps for use in later parts of this project to be accurate, work on the inlet design code was critical. Once completed, the inlet code, SIPC, allowed the researchers to complete the aforementioned tasks.

Milestones

- Completed the final assembly of zero-order methods to predict inlet performance.

Major Accomplishments

- Enabled critical spillage and spillage drag calculations at high supersonic Mach numbers into SIPC.
- Improved cowl lip suction calculations based on Crosthwaite et al. (1967).
- Developed and inlet choking condition prediction and limitations into SIPC.
- Extended additive drag predictions to include detached normal shock conditions into SIPC.
- Improved subsonic diffuser duct loss prediction models in the SIPC.
- Developed and added an automated mass flow sizing approach for user-defined normal shock position into
- Developed and added the capability to photographically scale the inlet into SIPC.
- Developed and added angle of attack effects to the inlet model in SIPC.
- Developed and added increased fidelity in the inlet model to capture external normal shock-oblique shock interactions in the SIPC.
- Developed and added the ability to visualize oblique shock-normal shock interactions and a 3D view of inlet configuration into SIPC.
- Developed and added the ability to run batches of inlet cases into SIPC for design space exploration.
- Added ram drag calculation into SIPC.

Publications

None.

Outreach Efforts

None.

Awards

None.

Student Involvement

Over the course of the work, several graduate students worked on the task of developing the inlet modeling capability. In total, this project funded the studies of four graduate students, for different proportions in the past three years, and all of them worked on this task.

Plans for Next Period

Task 2 is complete.

Task 6 - Extension of Zeroth-Order Methods for Inlet Performance to Include Low-Speed Aerodynamics

Georgia Institute of Technology

Objectives

The objectives of this task are for the completion the project, to capture the effects of the inlet operating at LTO conditions, and to facilitate low-speed aerodynamics modeling for the supersonic inlet, including the viscous effects encountered by supersonic inlets during LTO conditions. The initial inlet analysis model, used in Year 1 and Year 2 of the project, uses a simple viscous loss relationship, which is scaled depending on the freestream air Mach number and the sharpness and radius of the inlet cowl lip, taken from the IPAC publication's equations (Barnhart, 1998). This loss model does not account for the potential improvements achieved by modulating the variable geometry of the inlet to maximize airflow, and minimize the viscous effects incurred by incoming air when pulling around the cowl lip and sidewalls.

Research Approach

Several approaches were followed to identify computationally low-cost methods for determining low-speed aerodynamics over the supersonic inlet ramps, cowl lip, or compression center cone:

- Perform a literature review to identify analytical methods for modeling low-speed viscous flow over a flat ramp with varying angles of attack or incidence.
- Implement these methods within the script and compare results for validation against published sources and published experimental data.
- Perform flat-plate loss approximations and compare them with experimental data and the results achieved.
- Select the method yielding the best results with reasonable computation execution time.

As was mentioned in previous sections, it was important to ascertain any potential benefit or loss contributed by the inlet on the installed engine regarding thrust and impacts to noise. As such, the extension of the Task 2.1 effort, in adding a low-speed aerodynamic module to the supersonic inlet design and analysis code was anticipated to be important to achieving the overall research study. Several approaches were attempted to develop a low-cost low-speed aerodynamics module of the zero-order fidelity to integrate with the developed inlet code. These attempts employed flat-plate approximations, as well as more sophisticated approaches accounting for boundary layer skin friction losses and were validated by Reynolds-averaged Navier-Stokes (RANS) CFD runs performed by the researchers.

Viscous loss models associated with low-speed aerodynamics (below M=0.8) were developed and implemented in a viscous aerodynamics module and integrated into the inlet code. Several functions were developed from different references to model losses on the different sections and account for different phenomena and then integrated together. First, a model to capture the effects of skin friction driven total pressure losses on the external ramps was developed. The function computes the flat plate average turbulent skin friction coefficient on the external ramps using the Prandtl-Schlichting relationship for turbulent flow. This model also uses a relationship to add compressibility corrections to the skin friction equation, as most of the inlet code's compressibility effects were previously captured either through the prediction of shock effects, or compressible effects inside the inlet duct—prior to this effort, there were no viscous losses associated with the external compression ramps. The curves relating the Reynolds number of the flow to the incompressible turbulent flow before the compressible correction (Equation 4.3.7 from McLean [2012], shown in Figure 15) and is defined in McLean (2012) with the compressibility correction for skin friction.

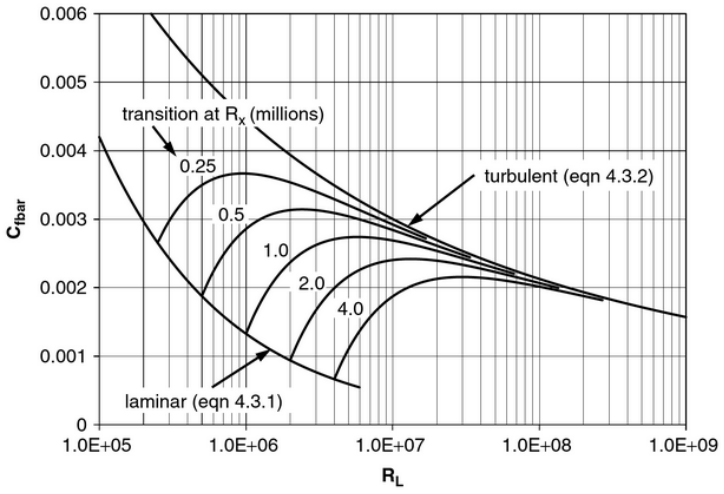

Figure 15. Prandtl-Schlicting relationship for incompressible turbulent flow (McLean, 2012).

The second relationship in the viscous flow module for external compression is similar to the previous one, except it is for the flow inside of the converging duct of the 2D inlet, and not the external compression ramps. This set of equations computes the turbulent skin friction coefficient in a 2D channel model of the internal converging duct utilizing the correlations identified in Dean (1978). As the rectangular duct loss model identified in Dean (1978) was for incompressible flow, the compressibility correction from McLean (2012) was employed here as well.

The third relationship identified for use in the low-speed viscous flow model is the calculation of total pressure losses on external ramps due to boundary layer skin friction. The model was derived from Seddon and Goldsmith's *Intake Aerodynamics* text, Equation 3.4 and employed using logic obtained from Chapters 2 and 3 (Seddon & Goldsmith, 1999). Here, an empirical factor defined by Seddon and Goldsmith (1999), the external wetted surface area, the ambient freestream dynamic pressure seen by the external ramps, and external skin friction values were calculated and used to find the change in total pressure due to boundary layer skin friction on the ramps, using Equation 3.4. Here, I is the duct integral, $q_\infty$is the freestream dynamic pressure, $\frac{A_\infty}{A_C}$ represents the ingested mass flow ratio, J is the position ratio defined by the surface area of the wetted flow divided by the inlet cross sectional area at the investigated location, and C_{fd} , C_{fa} are friction coefficients for the duct and the cross sectional area, respectively.

$$\frac{\Delta P}{q_\infty} = IC_{Fd}\frac{\rho_\infty}{\rho_c}\left(\frac{A_\infty}{A_c}\right)^2 + JC_{Fa}\left(\frac{A_c}{A_\infty}\right) \quad \text{(Eq. 2)}$$

The next relationship computes the incompressible flow and the critical flow ratio below which pre-entry losses due to boundary layer skin friction occur. it was derived from data taken from Seddon and Goldsmith (1999) (shown in Figure 16). This was adapted to application for compressible flow using Figure 16.

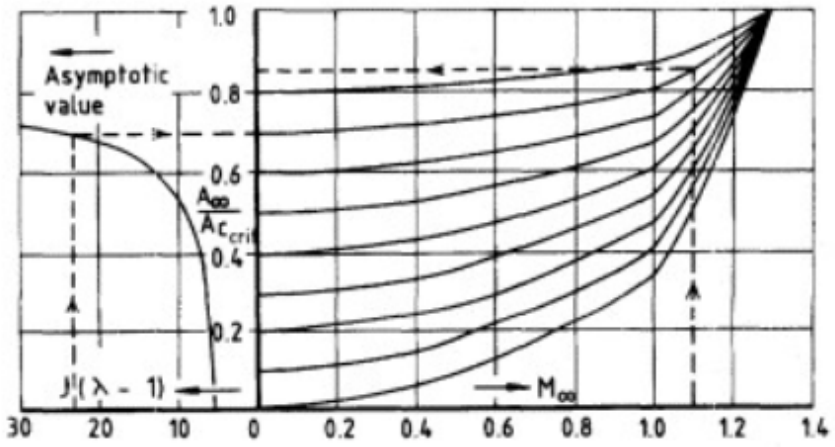

Figure 16. Critical flow ratio for pre-entry separation from intake aerodynamics (Seddon & Goldsmith, 1999).

The fifth relationship used in the viscous flow module computes the total pressure losses in the converging duct due to boundary layer skin friction—similar to the third viscous model described above, except adapted for the 2D duct. Lastly, a parametric model was developed to determine the separation losses for pre-entry flow due to boundary layer effects at low speed if the demanded flow ratio was less than the critical flow ratio. This model employed equations and approaches found in Seddon and Goldsmith (1999), Chapters 3 and 7.

The model was assembled and validated after several months of effort in attempting different approaches, and then it was validated using CFD runs, as previously discussed. The effects of pressure due to low speed aerodynamics validation can be seen using the final inlet design ($M_D = 1.7$), in Figure 17. The validation achieved across several runs for Mach 0.3 can be seen in Figure 18. It can be seen that the effects of the losses from the local position (ramp start location) to the throat (through converging duct) agree well for the baseline inlet model for pressure losses as the mass flow rate at the throat (WTH) is varied and normalized by the inlet height (depth in ft).

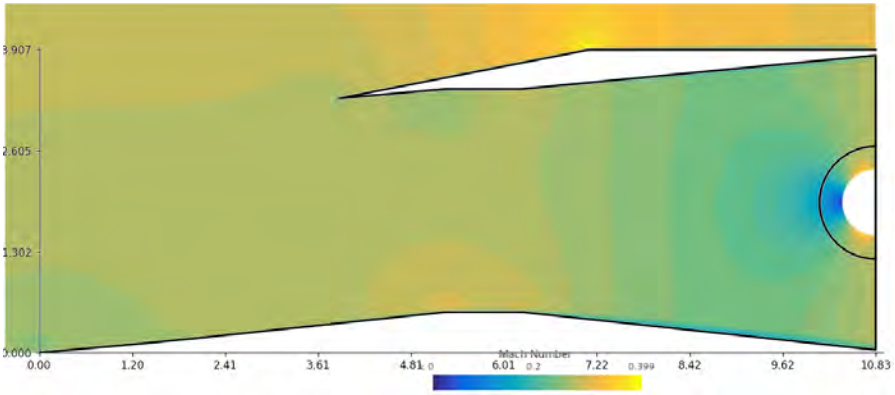

Figure 17. CFD run with the selected inlet design at M=0.2.

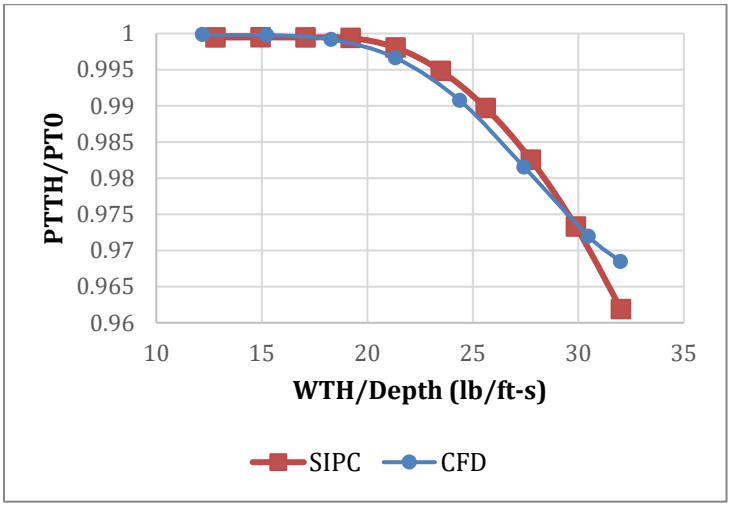

Figure 18. Validation of low-speed losses model in the SIPC vs. CFD run.

A similar study was performed for the larger capture area modification to the baseline inlet achieved using the variable geometry cowl lip (VGCL), which will be described in Task 8. This comparison proved the loss model performed with much worse agreement but nonetheless provided aggressive losses due to low-speed aerodynamics effects compared to the CFD run and thereby was retained as it provided a more conservative prediction of the overall inlet performance by underpredicting. The error between the SIPC and CFD models at the highest normalized throat mass flow rate was 2.2%, and the capture area was assumed to be 20% larger than the baseline inlet shown in Figure 18, which is shown in Figure 19.

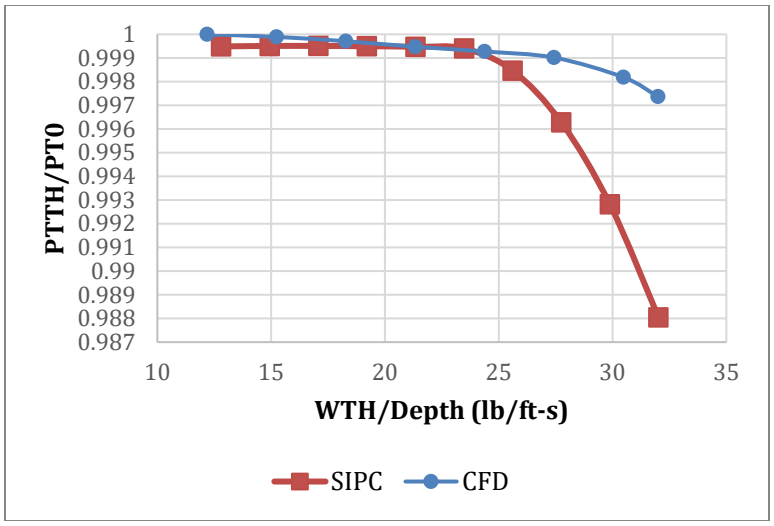

Figure 19. CFD validation results for the baseline inlet with variable geometry cowl lip (20% larger capture area).

The loss model was shown to have acceptable error when compared to CFD runs, which were used as a baseline truth model, and they were retained and used for the remainder of the study, specifically in the generation of the inlet maps.

Milestone

- Extended zeroth-order methods for inlet performance to include low-speed aerodynamics.

Major Accomplishments

- Developed and added a low-speed viscous aerodynamic model into the SIPC and validated with CFD.

Publications

None.

Outreach Efforts

None.

Awards

None.

Student Involvement

None.

Plans for Next Period

None.

Task 7 – Establish Modeling and Simulation Tool Integration

Georgia Institute of Technology

Objective

Since the research being pursued for the work described in this report was performed using analytical modeling and simulation approaches, it was necessary to identify suitable tools, however disparate, to accomplish the required tasks. The tasks to be accomplished by modeling and simulation tools were the following:

1. Inlet modeling: Needed to capture the effects of the inlet and generate performance data to be implemented into an engine cycle modeling tool.
2. Engine cycle model: Needed to capture the installed effects of the engine, including inlet and nozzle, along with jet noise reduction devices (chevrons).
3. Vehicle and mission model: Needed to capture system-level effects of installed engine during SST mission profile, specifically at LTO conditions.
4. Noise modeling: Needed to understand the potential benefits or degradations of an advanced inlet on an engine with adding variable geometry to an inlet and jet noise reduction technologies to the nozzle.

Research Approach

Several different tools were assessed to accomplish each of these tasks for the research effort, but the following were selected: (1) SIPC for inlet modeling, due to the flexibility of design, extensibility for future tasks, capability beyond IPAC in compressible flow modeling and low speed aerodynamics module, and the ability to be used by non-United States students, (2) FASST, an engine-vehicle sizing and synthesis code developed by GT-ASDL, which employs NASA's tools NPSS for engine cycle modeling, (3) CMPGEN for engine compressor map generation, (4) FLOPS for mission profile optimization and vehicle sizing and synthesis, and lastly (5) ANOPP, which is integrated into FASST, for noise prediction as a result of the engine and vehicle modeling results. A basic flowchart outlining the modeling framework utilized for this research is presented in Figure 20.

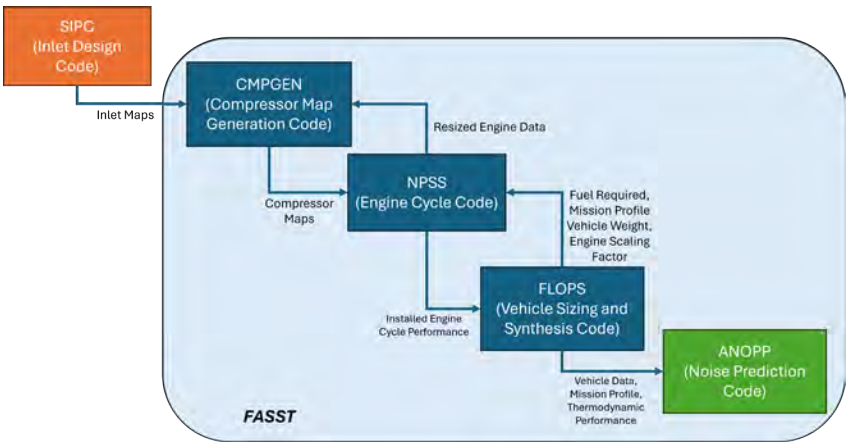

Figure 20. Flowchart of the modeling framework used in ASCENT Project 059(A).

Once the notional framework was determined, it was necessary to identify specific inputs and outputs provided by each section and connect them appropriately, in the correct format. For a first iteration testing of the framework and its component tools' integration, the tools in FASST were kept constant, which is to say, that they were not further modified for the purposes of the study at hand. This was in part due to the fact that necessary modifications to the iterative sizing process and software run order were not known or understood at the time of the initial framework integration. Modifications to the framework were identified after the specific inlet designed for the study was installed onto the selected engine and aircraft models, and the jet noise reduction methods were determined. These subtasks were performed in Task 11.

As shown in Figure 20, FASST is a supersonic vehicle sizing and synthesis tool which performs engine modeling, aircraft modeling, and mission profile optimization for the designed aircraft system. The tool utilizes user inputs to define criteria for engine and aircraft sizing, and initial guess points, such as maximum T4, turbomachinery calibration factors and map operating points, thrust targets for different segments (i.e., take-off, cruise, supersonic pinch point, top of climb and sea level static), mission profile altitudes, design mission range, and many others. Inputs used are passed initially to CMPGEN, which determines an initial set of turbomachinery compressor maps which are used in the first iteration of the engine code. After this first iteration is completed, the engine is resized to meet the demands of the required thrust in the NPSS model. After the engine is designed, the aircraft variables from the user input are utilized and the vehicle is modeled in FLOPS, with the installed engine for the design and off-design missions. After the vehicle has converged to an appropriate

size to fly with the designed cycle, meeting the requirements input by the user, it enters the "environmental off-design" analysis phase. In this phase, emissions and noise are determined, as well as detailed mission profile segments, such as take-off, approach, and landing. For the purposes of this project, only the noise module which utilizes ANOPP was run, as the other modules produced results which did not pertain to noise or thrust at LTO conditions.

Coupling the codes in the FASST was not necessary, as it was already performed as part of the code development, and used in several research projects, including ASCENT Project 010, where several SST vehicles and engines were developed and presented. It will be seen in the section describing Task 11, however, that FASST required modifications to achieve the objective of the research task sought here. Since the assembly of codes which defined FASST was already completed, the chief objective of this task was to determine a means to integrate inlet performance into the engine cycle and have those results propagated to final off-design performance and noise analysis. In Year 2 of work, researchers attempted to modify SIPC into rapidly running executable which could be called for each FASST iteration, changing the inlet design for each iteration. This task was notionally completed, but the variation in inlet design performed for each iteration could not be achieved with reliability.

It was found that the inlet code was not developed enough to allow for the prediction of normal shock position and redesign of the inlet variable geometry ramps with suitable accuracy to be utilized for the work at hand. Due to the desire to complete the project on time, the effort was abandoned, in favor of working on the development of SIPC to enable more robust predictions for off-design performance. Additionally, it should be noted that the executable-based approach for inlet performance prediction was initially sought due to the difficulty in understanding how to generate inlet performance maps, as there was a lack of any clear guidance in the literature. The pursuit of, and the accomplishment of, determining an inlet map generation process was completed by a deep literature review, independent research between several research engineers at the GT-ASDL (who were researchers on the project), and discussion with subject matter experts. This will be described in greater detail in Task 9.

As part of the inlet performance prediction integration into the overall modeling and simulation framework, it was determined that the use of conventional inlet maps was desired. In order to do this, the implementation of inlet maps into FASST had to be explored and developed, and the ability to generate maps using SIPC was also necessary. While a previously-defined set of inlet maps could have been used to perform a basic version of the study, the researchers determined that there was no reliable way to modify the models of experimental inlet data to attempt to add variable geometry, which is a key feature of the study presented in this document. As such, the inlet map integration exercise for this step was performed with an inlet from the PIPSI software, described in reference (Kowalski, 1979). An example of an inlet map, one of eight, shown in Figure 21. The eight-map format defined by PIPSI utilizes maps to describe all of the off-design operating conditions of the inlet, with several factors being implicit in them, and opaque to the user—specifically inlet geometry and ramp angles at off-design conditions.

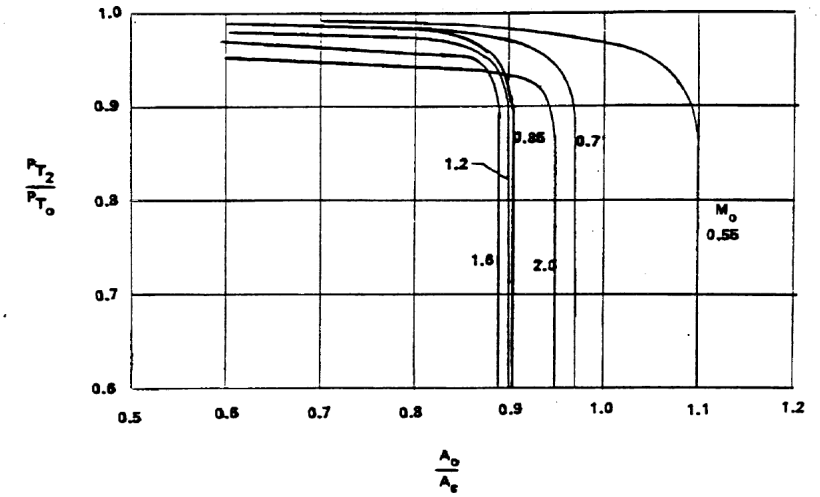

Figure 21. Inlet total pressure recovery map for ATS2 inlet from PIPSI (Kowalski, 1979).

A list of the maps defined for each inlet modeled in FASST, and used together to achieve a full picture of the inlet performance across engine cycle design and off-design points, is summarized as the following:

1. Inlet Recovery vs. A0/AC & Local Mach (TABLE 2A) → Cane curves to find Total Pressure Recovery of inlet
2. Buzz A0/AC vs. Local Mach (TABLE 2D) → Operability check of required inlet mass flow vs. buzz limit (lower bound)
3. Distortion A0/AC VS. Local Mach (TABLE 2E) →Operability check of required inlet mass flow vs. distortion limit (upper bound)
4. CD Spill vs. A0I/AC & Local Mach (TABLE 3) →Determination of spillage drag
5. CD Bleed vs. A0Bleed/AC & Local Mach (TABLE 4) →Determination of bleed drag
6. CD Bypass vs. A0Bypass/AC & Local Mach (TABLE 5) → Determination of bypass drag
7. A0Bleed/AC vs. A0/AC & Local Mach (TABLE 6A) →Determination of required bleed mass flow
8. A0Bypass/AC vs. A0Engine/AC & Local Mach (TABLE 7) →Determination of required bypass mass flow

The order of table lookups associated with the inlet installation using the PIPSI maps will be explained here. The engine mass flow demand is determined by the engine cycle model and then the required bypass mass flow, which was experimentally determined to be necessary for retaining a normal shock to stay "started" (if any), is determined from Table 7 (as defined in list above). Once the engine and bypass mass flow demands are known, these values sum to determine the value of $\frac{A_0}{A_C}$, which is a primary feature used for determining other flows. Then, the value of $\frac{A_0}{A_C}$ is then checked against Tables 2D and 2E (as defined in list above) for possible buzz and distortion effects due to mass flow through the inlet, which is too high, or too low. Buzz occurs in the inlet subsonic diffuser when the mass flow passing through it is too low, and an oscillatory behavior creates a harmonic oscillation which can potentially cause a compressor surge or stall (Seddon & Goldsmith, 1999). On the other end of the spectrum of inlet operability allowance, distortion is the effect seen when too much mass flow is passed through the inlet and creates uneven pressure distributions at the compressor (fan, in this case) face. This can have similar effects to buzz and could be detrimental to engine performance in off-design conditions (Seddon & Goldsmith, 1999). These values, like the others included in the inlet maps from PIPSI, were derived experimentally. If the $\frac{A_0}{A_C}$ values for the operating point under consideration are between the buzz and distortion limits, then Table 6A (as defined in PIPSI workflow list, above) is used to find the required boundary layer bleed mass flow ratio. The sum of $\frac{A_0}{A_C}$ and bleed mass flow rate yields the total ingested mass flow rate, $\frac{A_{0I}}{A_C}$, which determines the amount of spillage experienced by the inlet at any condition. As such, then Tables 3, 4, and 5 (as defined in PIPSI workflow list, above) enable the drag coefficients of spillage, bleed, and bypass to be determined. This is performed by the engine code each time the engine model is run. The means of installing the inlet performance determined SIPC was found to be best performed using inlet maps, and an example inlet map from PIPSI (Kowalski, 1979) was used to check this integration prior to the execution of the actual study.

As the final part of this task, it was sought to establish the functionality of ANOPP and its integration with FASST in a way that was usable in the study at hand. ANOPP is a NASA noise prediction code with many nuanced modules, requiring an expert to fully understand and utilize all of its capabilities. Furthermore, the tool's capabilities continue to grow regularly, being continually developed by NASA researchers. A GT-ASDL researcher who serves as a noise analyst and ANOPP expert was able to assist in ensuring that ANOPP was set up to study jet noise at LTO conditions. This involved a modification in the user inputs to switch on the jet noise so as to not be confounded by other noise sources. Additionally, the employment of chevrons was selected due to the ability to model their noise effects in ANOPP, and their effects on the engine cycle in NPSS. ANOPP has a chevron-specific noise prediction function which is based on empirical regressions using the "Stone 2" jet noise prediction module, which enables the study of jet noise effects based on the parametric scaling of the ratio of the wetted perimeter of the nozzle exhaust to the wetted perimeter of the chevron exit. With some geometric studies and comparison, these values were easy to ascertain from the selected chevron geometries selected for study in Task 10 but were performed for an arbitrary nozzle perimeter ratio for the completion of this initial task. Once this was completed, the task was considered complete.

Milestone

- Established modeling and simulation tool integration—engine cycle, inlet design, and noise analysis tools.

Major Accomplishments

- Performed initial integration work using example inlet, and selected engine and aircraft design to be used in studies.
- Determined and evaluated an approach for coupling inlet, aircraft, and noise codes.
- Identified ANOPP noise modeling approach for use with chevrons.

Publications

None.

Outreach Efforts

None.

Awards

None.

Student Involvement

None.

Plans for Next Period

Task 7 is complete.

Task 8 – Development of Inlet Variable Geometry Methods and Models for Improving LTO Thrust

Georgia Institute of Technology

Objective

The objective of this task was to find new ways to potentially enable the recovery of thrust when jet noise devices were added to the nozzle of the SST engine, by adding new ways for the inlet to function in the off-design condition. While it is possible that the baseline advanced inlet made for the selected 65-passenger SST with MFTF engine could provide sufficient thrust recovery, it was sought to determine how much more thrust from the baseline inlet model, variable geometry permutations of it could.

Research Approach

The capability to add several variable geometry configurations to a baseline inlet was sought in order to determine if these new configurations would allow for greater performance at high mass flow demand conditions, such as those seen at LTO. The variable geometry capabilities investigated by the researchers included a VGCL and blow-in doors; a third configuration in which both the VGCL and blow-in doors were manipulated was sought to be modeled. Variable geometry is typically employed in 2D supersonic inlets, but it is primarily used for the control of oblique shocks and the variation of the throat area to prevent mass flow restrictions and choking, thereby improving engine operability at supersonic speeds. After several iterations of design, the inlet designed here only used variable geometry for LTO conditions as described in this task, and no variable geometry. The purpose of this was to reduce weight and complexity when compared to highly complex inlet designs for SSTs such as the Concorde inlet. As such, the two variable geometry modeling additions described here were the only means utilized for the final study to modulate mass flow apart from the engine demand, bypass doors, and boundary layer bleed.

First, in order to facilitate a study into how to appropriately use bleeds, bypass and blow-in doors for a SST inlet without using variable geometry external compression ramps, the ability to draw bleed from ramps was added to the model, as well as bypass from the throat. As seen in Figure 7, boundary layer bleed is typically considered to be taken from the throat, while the bypass is taken from just forward of the engine face at station 2. Due to the decision to use a fixed inlet (no variable geometry external compression ramps), these options were needed in addition to the conventional positions of the bleed and bypass doors to prevent choking and improve operability. This was completed by replicating the bleed and bypass stations in SIPC in their new positions, ensuring that the mass flow ejected from them experienced the

appropriate friction losses, and ensuring that the downstream flow resulting from the mass flow extraction was appropriately modeled.

Second, a model to simulate blow-in doors was added to the inlet code. Blow-in doors are spring-loaded devices which have been employed on subsonic commercial transports for many years but were ultimately rejected despite their improvement in performance due to the increase in mass flow provided when the differential pressure between inlet and ambient static pressures were significant enough, due to noise problems (Marsh et al., 1983; McPike, 1972; Little & Russell, 1976; Aviation Stack Exchange, 2021). While this could clearly provide a potential problem for supersonic engines, which operate with much greater thrust than the subsonic engines referenced in Marsh et al. (1983), McPike (1972), Little & Russell (1976), and Aviation Stack Exchange (2021), this modeling option was desired to be explored in the case that technological improvements in noise shielding could potentially counteract this for future SST vehicles. Additionally, it can be seen in a schematic of the Concorde inlet in Figure 22, that blow-in doors were used for their ability to improve take-off mass flow rates (Slater, 2020). In combination with the first inlet modeling improvement subtask listed under this task, the blow-in doors were able to be modeled at the throat, as well, which could potentially provide a practical improvement in noise reduction over the aft-mounted blow-in doors on the Concorde inlet, which are much closer to the engine face. No SIPC schematic was developed to illustrate the blow-in doors, so it is not shown, here.

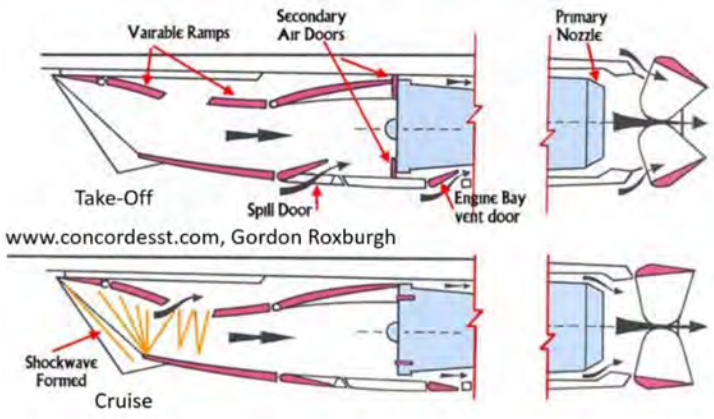

Figure 22. Schematic of Concorde inlet operation at take-off and cruise; spill/blow-in door used for take-off (Slater, 2020).

The last subtask for this task was to develop a model for the increase of capture area by allowing for a VGCL. Although initially conceived by the researchers as a novel concept, this design was found to have been implemented in several cases in actual vehicles for the purpose of increasing air quantity at take-off conditions. An example can be seen in the Eurofighter Typhoon EF2000, where the rectangular pitot inlet utilizes VGCLs for its bifurcated inlet design, seen in Figure 23 (Aircraft Recognition Guide, 2018). This concept was mirrored and implemented into the SIPC, enabling a pivot of the cowl lip just forward of the throat, and increasing the capture area 20%. This concept was evaluated and proved to show a large increase in capture area, with a decrease in friction losses compared to the baseline inlet. The SIPC-generated schematic of the VGCL superimposed upon the baseline inlet used for this study is shown in Figure 24. The improvements here assisted in the overall completion of the project by adding the ability to consider new ways to increase mass flow provided to the engine for thrust compensation. The results of this implementation will be shown in later sections.

Figure 23. Eurofighter Typhoon VGCL inlet (Aircraft Recognition Guide, 2018).

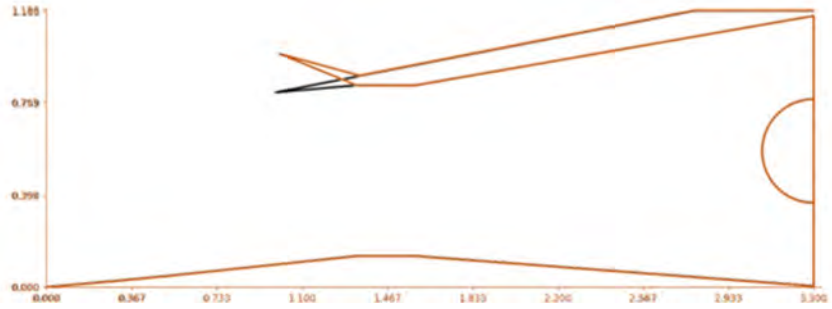

Figure 24. M=1.7 SST inlet used in study: Baseline inlet (black) vs. VGCL geometry activated (orange).

Milestone

- Completed the development of inlet variable geometry methods and models for improving LTO thrust.

Major Accomplishments

- Developed and added ramp bleed ports and throat bypass models into SIPC.
- Developed and added blow-in door models into SIPC.
- Developed and added VGCL models into SIPC.

Publications

None.

Outreach Efforts

None.

Awards

None.

Student Involvement
None.

Plans for Next Period
None.

Task 9 – Development and Implementation of SST Inlet to be used as Baseline Model and Off-design Inlet Maps
Georgia Institute of Technology

Objective
The objective of this task was to (1) identify and select the engine and vehicle to be used as the baseline for the thrust-noise study executed in Task 13, (2) design an inlet specifically for the vehicle selected from subtask 1, (3) understand how to analytically develop inlet maps, and (4) generate inlet maps for the inlet designed in subtask 2. These objectives were accomplished as part of three subtasks.

Accomplishing these specific tasks would enable a baseline installed engine to be developed from which the chevron and variable geometry inlet models could be compared with regards to thrust recovery and noise impacts.

Research Approach
The first task required to proceed with the analysis of jet noise reduction using inlet geometries was to select an engine and airframe to be used in the FASST as the basis for the nozzle and inlet study. A supersonic vehicle which could utilize a supersonic inlet and converging-diverging supersonic nozzle was required. As those components would be required for any SST design to which the study may apply. Beyond this, the details of the vehicle class and engine size were inconsequential, as the study here seeks to determine benefits of the inlet from an established baseline. As such, several engine and aircraft models developed by the GT-ASDL were considered, but the 65-passenger SST with a design Mach number of 1.7 was selected due to its extensive testing, model robustness across many operating conditions tested, and the fact that it had already been presented and investigated by ASCENT Project 010. A schematic of the vehicle is shown in Figure 25.

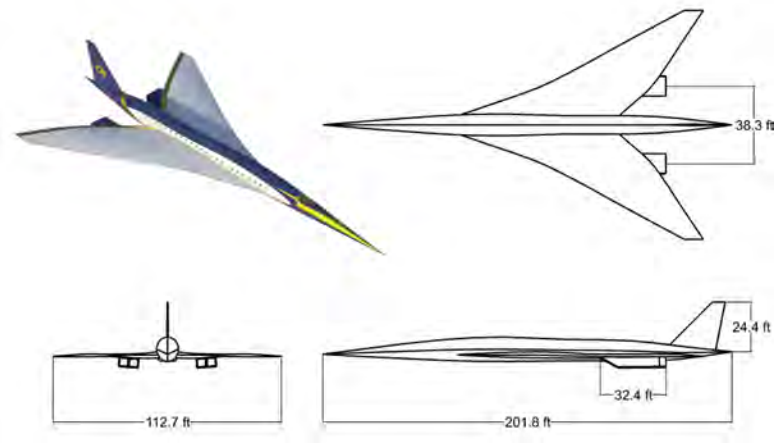

Figure 25. GT-ASDL SST (initially presented in ASCENT Project 010).

The GT-ASDL vehicle was developed using the FASST and several aerodynamics tools; the researchers used RANS CFD for aerodynamic shaping of the fuselage and outer mold line, along with multi-fidelity and parametric polar drags generated with tools developed in-house and used RANS CFD for LTO drag estimation. The propulsion cycle was modeled in NPSS using parametric loss models and multi-design point sizing, sizing for the supersonic pinch point, and satisfying operating

criteria for cruise, take-off, top of climb and sea-level static conditions. A summary of the vehicle performance data is in Table 5.

Table 5. Summary of GT-ASDL 65-passenger SST.

Passengers	65
Design Range	4,250 nmi
Cruise Mach	1.7
Max Take-off Field Length	11,000 ft
Approach Speed	165 kts

The engine developed for the ASCENT Project 010 and used here was a mixed-flow turbofan architecture which was designed in NPSS. The engine design parameters considered were the fan pressure ratio, overall pressure ratio, design turbine rotor inlet temperature, bypass ratio, and max turbine rotor inlet temperature. These parameters were varied to meet the design point and simultaneously meet the criteria of the aforementioned satisfaction points in a simultaneous multi-design point sizing approach. The engine utilizes two controls in order to affect thrust and noise conditions, fuel flow to affect the speed and thermodynamic states of the turbomachinery, and the nozzle throat, to affect the jet stream thermodynamic properties. A schematic of the engine layout as defined in NPSS is shown in Figure 26.

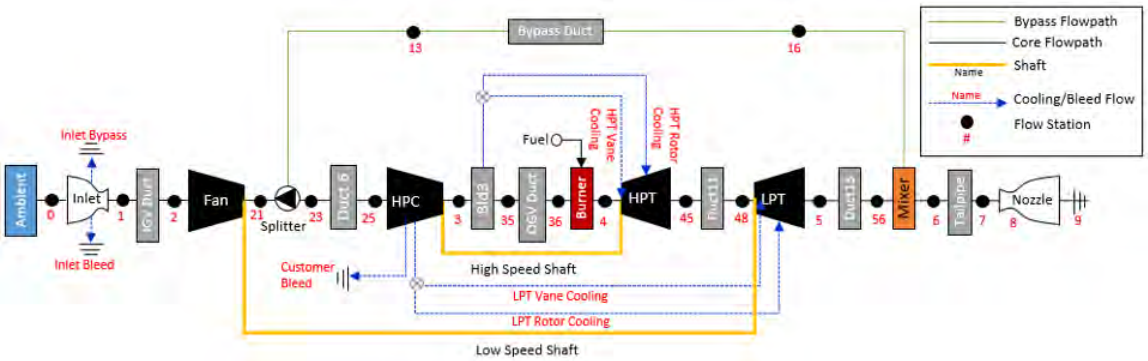

Figure 26. Schematic of NPSS Model of non-afterburning MFTF used on 65-passenger vehicle.

Ultimately, the vehicle designed could perform a 4,250 nmi mission with 13,650 lb of payload, using 156,611 lb of block fuel, and requiring 10,832 ft to take-off and 10,442 ft to land, with a cruise thrust-specific fuel consumption (TSFC) of 1.023. The vehicle employed a predefined inlet utilized from the PIPSI installation volume (Kowalski, 1979), ATS2 inlet, for each engine. This approach enabled a quick modeling of the inlet performance of the vehicle, but when it was developed, an inlet design capability to generate maps and utilize them in the FASST did not exist. As such, it was a suitable experiment to develop a new inlet for the 65-passenger GT-ASDL SST for the performance of this study.

The inlet was designed to be a 2D supersonic inlet with non-variable geometry and only utilizing external compression for the shock train management. This design selection was based on guidance from Seddon and Goldsmith's "Practical Intake Aerodynamic Design" (Seddon & Goldsmith, 1993) and Kowalski's guidance from the PIPSI documentation in Kowalski (1979). A chart of this guidance is shown in Figure 27. Investigating this chart in Figure 27, from early research and implementation on vehicles, up until the development of PIPSI (circa 1979), many different inlets were developed for use across a spectrum of design Mach numbers. The trend of increased numbers of oblique shocks corresponding to an increase in operating Mach number can be seen—this is used to mitigate the strength of the normal shock when it occurs in the inlet. It can also be seen here that it is recommended for the design of a supersonic inlet to be used at M=1.7 to use between two shocks and three shocks, and external compression. It can also be seen that this flight regime corresponds to a recommendation of variable geometry, but as this is at the initial stages of the supersonic regime, that recommendation can be seen as flexible. The driving factor in inlet design, as guided by Figure 27, is to minimize complexity and length of the inlet insofar as one can gain benefit from the simplest design. As such, variable geometry should be avoided for the low supersonic operating conditions since it adds a significant amount of weight and can add potential for failure in flight.

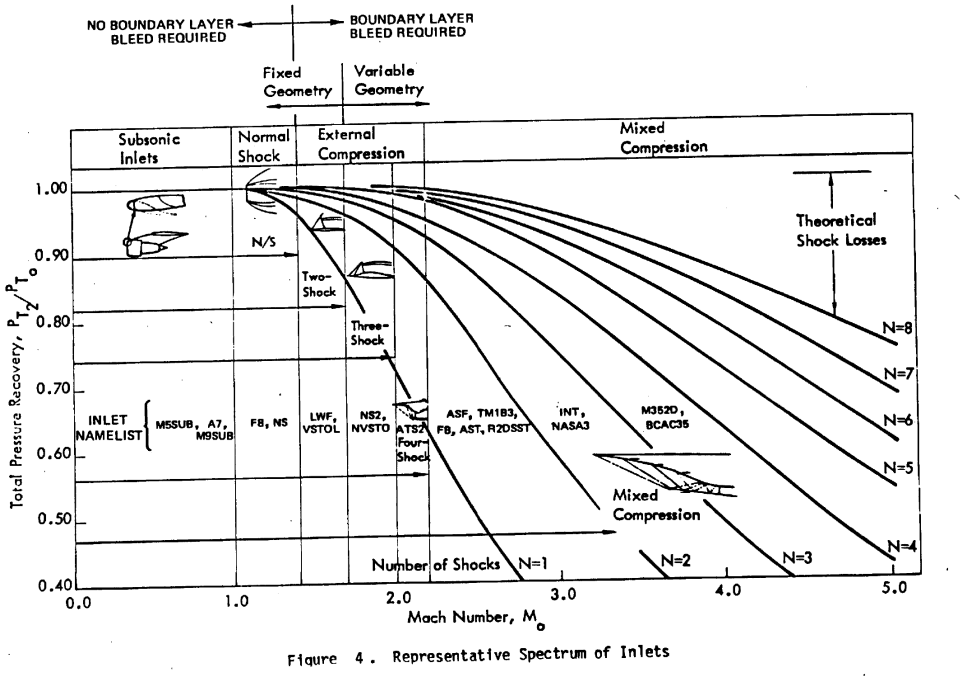

Figure 4. Representative Spectrum of Inlets

Figure 27. Recommended inlet designs for Mach numbers 0 to 5 (Kowalski, 1979).

Using this as guidance, the inlet design pursued for this study to be implemented on the GT-ASDL vehicle utilized three short fixed external compression ramps and was developed to be as short as possible to minimize weight, while still trying to take advantage of the benefits of the length of a subsonic diffuser, which slows down the flow of the ingested air just prior to the compressor face, and uses an isentropic diffusion surface to try to reduce the amount of pressure lost across it. In order to determine the appropriate size of the inlet, the uninstalled engine was run in NPSS. An engine deck was developed to identify the maximum mass flow required at all points of the previously defined SST mission. Once this was determined, the capture area was sized and the external ramp angle was determined based on maximizing total pressure recovery, and the condition that the external oblique shock had to meet the cowl lip at the cruise condition, to minimize the critical drag experienced there. A non-scaled model of the resulting inlet operating at the cruise condition, as generated by the SIPC shown in Figure 28. It can be seen that three oblique shocks form on the turning surfaces of the external compression ramps, converging at the cowl lip above them. A normal shock is formed and is positioned at the cowl lip, which serves as the critical operating condition for external compression ramps. Lastly, a strong oblique shock results at the cowl lip as a result of the normal shock-oblique shock interactions there. It can also be seen that a small, straight channel exits past the cowl lip, which serves as a safety region in the case of transients during which the normal shock may be swallowed.

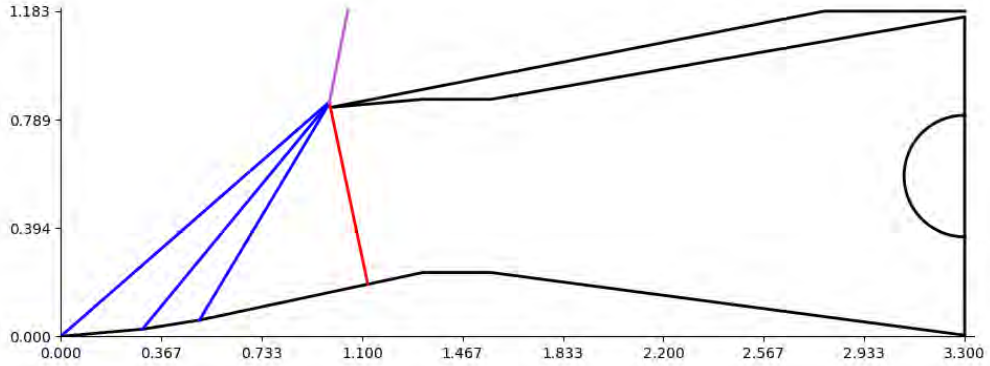

Figure 28. M=1.7 SST Baseline inlet at cruise condition (M=1.7).

After the inlet was designed, the variable geometry options developed in the prior task were evaluated and implemented at take-off conditions between M=0.01 and 0.3, based on the SST mission profile. The VGCL modification can be seen in Figure 24, and the aerothermodynamic effects of increasing mass flow and the associated were seen in the SIPC output files for the LTO conditions, as well. The bypass doors and VGCL each enabled a maximum mass flow to increase at LTO conditions of 20% of the capture area. As such, the baseline inlet capture area was assumed to be 1.2, and with both VGCL and blow-in doors activated, the inlet could use an effective capture area of 1.6 in the LTO regime. The inlet was modeled with functions actuated closed after rotation to minimize drag effects.

The process for generating inlet maps using the analytical inlet analysis tool then had to be determined and applied to get maps for the baseline inlet (no variable geometry), the VGCL case (only VGCL actuated), the blow-in doors case (only blow-in doors actuated), and then the hybrid case (both VGCL and blow-in doors actuated). The four different inlet maps used at the different conditions all employed the same inlet performance data in the operating regions outside of M=0.01 to M=0.3, as they were modeled to represent exploratory variations of the same inlet. The basis for inlet map generation took a significant amount of time (three months) and required input from subject matter experts and several papers and textbooks. Of note, Seddon and Goldsmith's texts (Seddon & Goldsmith, 1999; Seddon & Goldsmith, 1993) were of tremendous help, as was the paper describing the operation of the SR-71 inlet by Anderson (2014). Additionally, credit should be given to Dr. John Slater, the head of inlet design and analysis at NASA Glenn Research Center, who assisted in the researchers' understanding of map generation and provided validation of the approach.

Inlet maps are used to form a functional picture of the operational performance of an inlet for any point in the sky for which it was designed. In this way, inlet maps seek to inform the engine or aircraft designer about the predicted effects of installing a specific inlet design in all potential points which the inlet could see in flight. The primary inlet maps generated using the PIPSI format (Kowalski, 1979) describe the inlet's total pressure recovery, required mass flows for bypass and bleed, and drags associated with spillage, bypass, and bleed, along with reference maps which show the ideal performance case for each Mach number. The generation of the inlet maps, therefore, is akin to also performing the off-design control logic of the inlet and in the case of variable geometry ramps. However, in the case of fixed geometry, the maps are generated using variation of the engine mass flow at each Mach number from the lowest required mass flow to the highest required mass flow in the uninstalled engine deck as a guide for what would be required by the inlet. Additionally, bleed schedules need to be determined, using similar PIPSI maps as a guide, since these are typically generated experimentally. In this case, no bypass was used for internal shock positioning control, since the normal shock is not intended to be swallowed but was used to ensure external normal shock positioning to retain it at the cowl lip position and ensure minimized critical drag. Summaries of some of the inlet performance maps are shown in Figures 29 through 32, where they are compared side-by-side with a similar external compression inlet (ATS2 from PIPSI [Kowalski, 1979]) to illustrate the similarity in shape and numerical value.

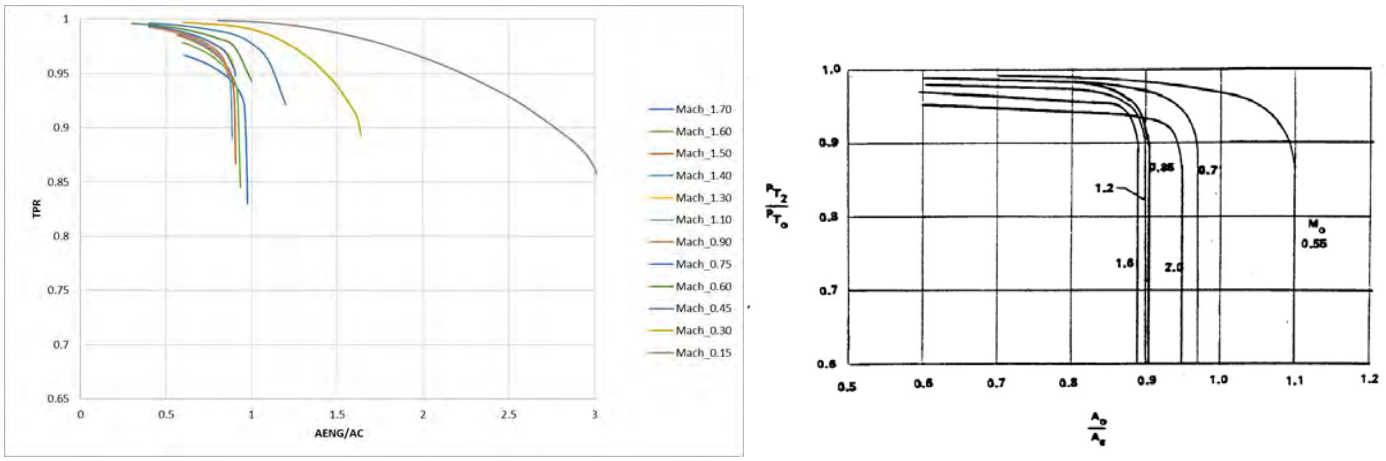

Figure 29. Total pressure recovery vs. mass flow ratio vs. Mach number (Kowalski, 1979).

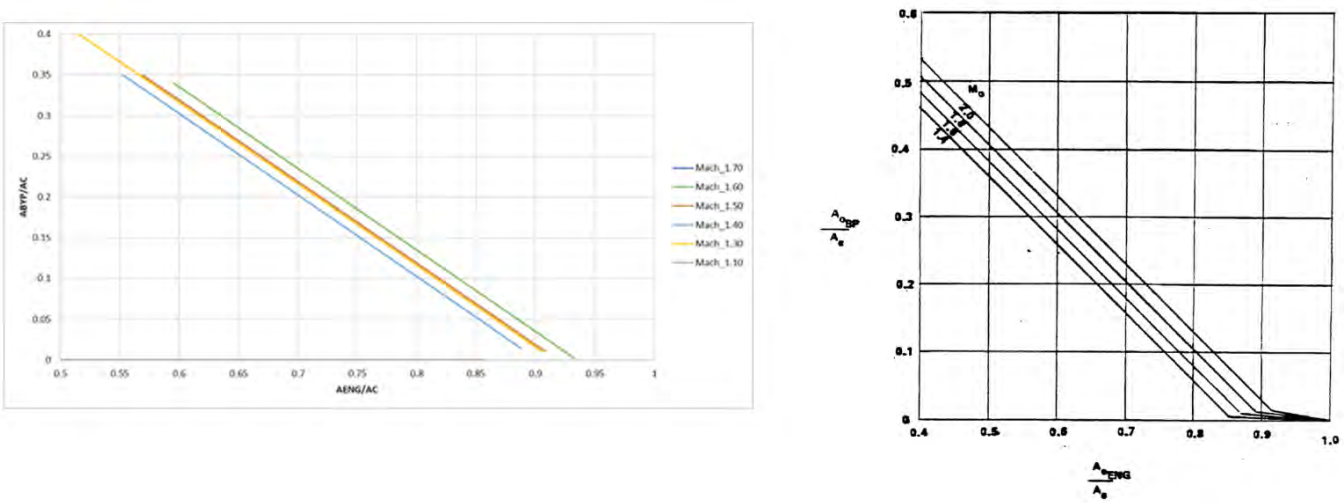

Figure 30. Engine mass flow ratio vs. required bypass mass flow ratio (Kowalski, 1979).

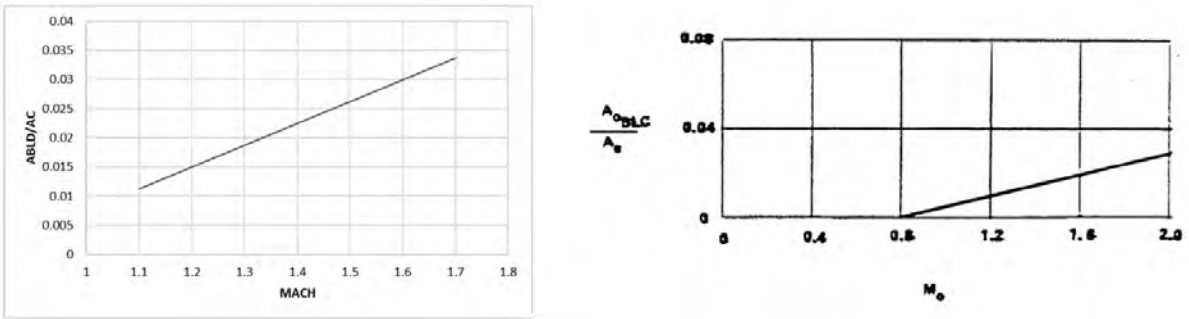

Figure 31. Required bleed mass flow ratio vs. Mach number (Kowalski, 1979).

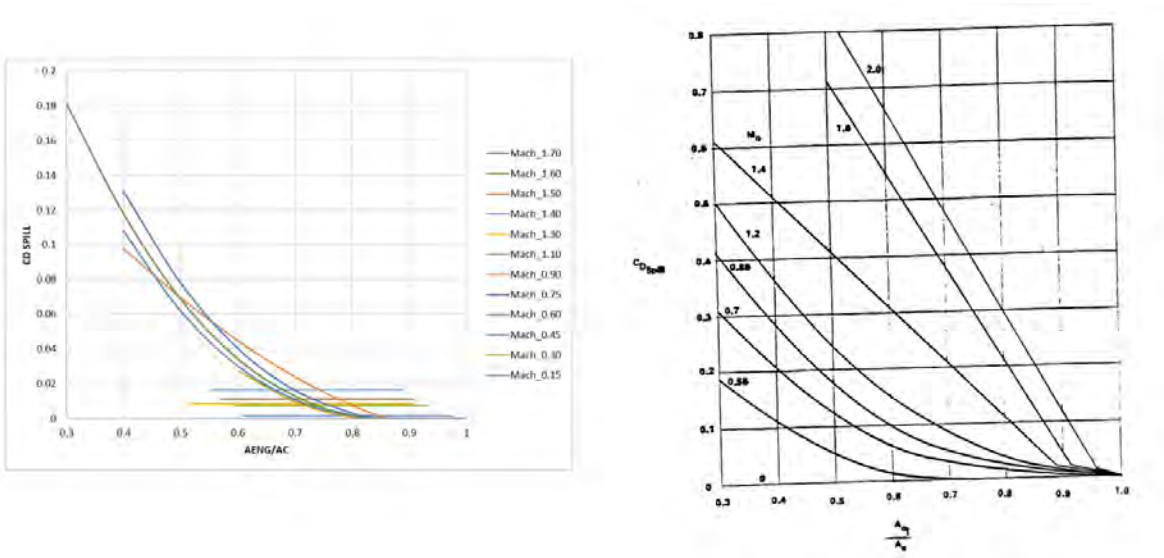

Figure 32. Spillage drag vs. mass flow ratio (Kowalski, 1979).

Finally, the inlet maps were generated for the variable geometry cases (i.e., baseline, VGCL, blow-in doors, and hybrid) defined previously and added to separate map files to be used in the FASST with integration with the GT-ASDL SST vehicle. Results for the cane curve (characteristic curve) map for the M=0.3 condition comparing the four cases can be seen in Figure 33. It can be seen that any means to increase capture area benefits the performance of the inlet for high mass flow ratios (engine demands), which are typically seen in the take-off condition. These maps account for viscous losses seen at low-speed conditions and the additional losses experienced by the air as a consequence of needing to move around the cowl lip due to the mass flow ratio being larger than 1 (implying that the streamtube area is larger than the capture area). Additionally, it can be seen that even if noise due to the implementation of blow-in doors is potentially an issue, significant benefit can still be achieved by only using the VGCL to increase airflow. Furthermore, an alternative to increase the area change due to the VGCL exists, as only one VGCL geometry was considered for this study.

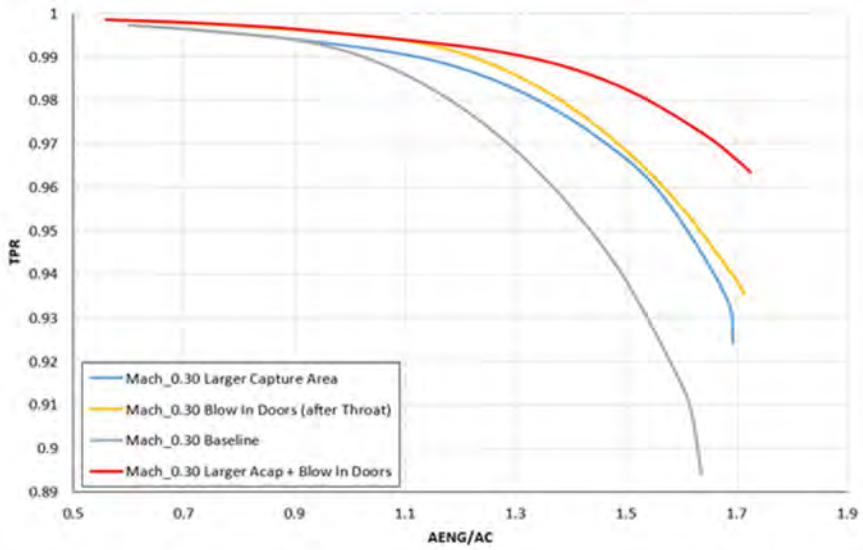

Figure 33. Cane curves for variable geometry inlet cases at M=0.3 take-off condition.

Milestone

- Completed the development and design of the SST inlet to be used as the baseline model and off-design inlet.

Major Accomplishments

- Designed the baseline inlet model for the selected M=1.7 65-passenger SST vehicle with MFTF engine.
- Adapted the baseline inlet model to use previously developed blow-in doors, VGCL, and ramp bleed and throat bypass models for off-design and verified functionality across the flight profile.
- Developed a process for analytically generating inlet maps for all off-design conditions using the standardized inlet map format presented in Kowalski (1979).
- Developed inlet maps for baseline inlet, VGCL, blow-in doors, and hybrid (both).

Publications

There are currently no publications for this effort; however, the researchers are pursuing a conference paper at 2025 AIAA Propulsion and Energy Forum to explain the development of the SIPC and analytical process for generating inlet maps.

Outreach Efforts

None.

Awards

None.

Student Involvement

None.

Plans for Next Period

None.

Task 10 – Development and Implementation of Nozzle-based Jet Noise Reduction Methods for Engine Cycle Effects

Georgia Institute of Technology

Objective

The objectives of this task are to determine a means to analytically model these features for several jet noise technologies and determine the metrics of interest (thrust loss and jet noise level) for them. This task was critical to model the effects of jet noise technologies on a supersonic engine to determine if the inlet can recover the thrust degraded by the nozzle technologies applied. As such, the jet noise technology modeling needed to account for thrust losses, effects on the exhaust stream, and the levels of noise resulting from the nozzle exhaust.

Research Approach

A key enabler for the completion of this research is a relationship between a jet noise technology's functional approach and effectiveness for noise reduction (mixing, noise insulation, etc.) and its effects on thrust losses. While many novel concepts have been investigated in the annals of aerospace research regarding reducing jet noise, and descriptions of the physical phenomena which contribute to noise reduction, it was found by the researchers that it is uncommon for those investigations into noise effects to be similarly investigated with corresponding effects on net thrust. As many technologies could be conceived which perform this function effectively, and have been implemented, many of them would generate losses in thrust which would render the device without net benefit to the installed engine. As such, for the purposes of this study, a means to couple these factors needed to be identified.

For the first two years (Year 1 and Year 2) of the project, it was anticipated that other ASCENT Project 059 partners would be able to experimentally or computationally derive relationships of thrust loss and noise benefit for unique nozzle-based jet noise technologies. After these relationships were determined experimentally, they would be provided to the ASCENT Project 059(A) team for use in the modeling and simulation described here. However, in Year 3, it was found that this

would not be possible, and an approach for modeling these behaviors would need to be found and implemented independently. To do this, a large literature review was performed, looking at a wide variety of jet noise technologies including chevrons (Bridges & Brown, 2004), contour shaping of the nozzle (Karon & Ahuja, 2017) , corrugations (Tinney et al., 2020), microfluidic injection (Morris et al., 2013), microvortex generators (Lui, 2021), and others.

More than 20 papers on the subject were carefully examined for potential use in this application, but their references are omitted for brevity. Ultimately, while some of the papers showed some relationships between thrust and noise benefits (very few, however), none also provided a scalable geometric or other factor which could be parameterized and implemented into the modified FASST framework used for this project except one paper, "An Aerodynamic and Acoustic Assessment of Convergent-Divergent Nozzles with Chevrons," by Frate and Khavaran (2011). This paper provides a means to parametrically define the chevron geometry using penetration depth, length and effective width as a percentage of base width and uses a RANS CFD code to find comprehensive results of thrust loss and noise benefit for installation on a modeled F400 series C-D nozzle. A parametric design of experiments based on these different chevron design parameters was developed and CAD models of the chevrons were generated for use in the CFD modeling. An illustration of the chevron parameters is shown in Figure 34, as well as the full matrix of their design of experiments (DOE) for the parameterization of the chevron geometries (Table 6), and the resulting performance values (Figure 35).

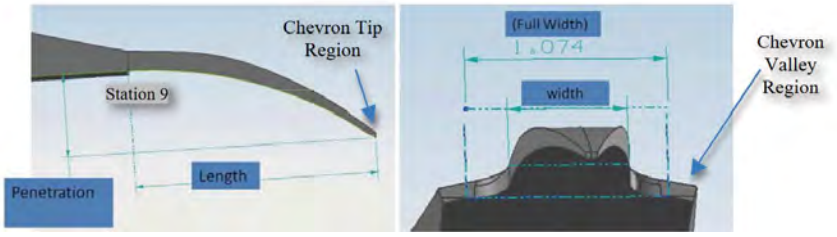

Figure 34. Parameterization of chevron geometries from Frate and Khavaran (2011).

Table 6. Chevron geometry DOE matrix from Frate and Khavaran (2011).

Serial	Configuration	Penetration (inches)	Length (inches)	Width (% of max)
1	P05L13W08	0.45	1.25	80
2	P03L08W06	0.3	0.75	60
3	P03L08W10	0.3	0.75	100
4	P03L18W06	0.3	1.75	60
5	P03L18W10	0.3	1.75	100
6	P06L08W06	0.6	0.75	60
7	P06L08W10	0.6	0.75	100
8	P06L18W06	0.6	1.75	60
9	P06L18W10	0.6	1.75	100
10	P02L13W08	0.2	1.25	80

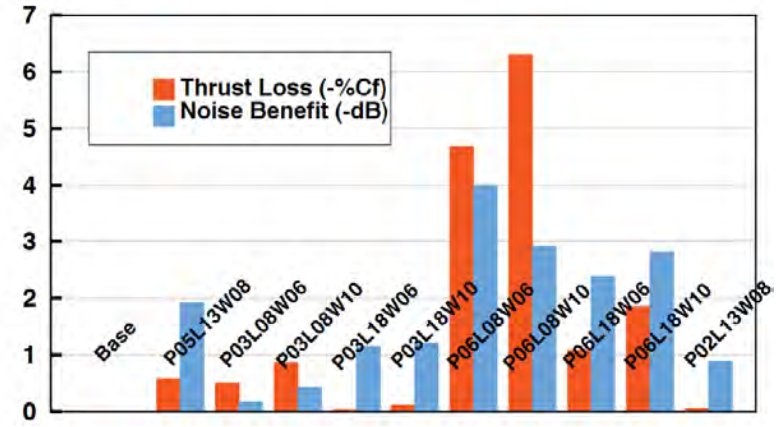

Figure 35. %Cfg loss and noise benefit for each tested chevron geometry in Frate and Khavaran (2011).

After this information was found, a sufficient set of data was determined to be in possession for the sake of performing the thrust-noise study. The means for modeling this experimental data and implementing them into the modified FASST framework was outlined in Task 7. The thrust losses for each nozzle technology were adapted to be modeled in the cycle modeling as a scalar on the gross thrust of the nozzle, using the gross thrust coefficient. Then, the effects on the jet noise and jet exhaust were modeled using the Stone 2 Jet Noise module within the ANOPP, which provides experimentally determined relationships for chevron noise benefits using a geometric relationship between the chevron nozzle wetted perimeter and the clean nozzle wetted perimeter, in a variable named "PER1." The geometries of the chevrons were scaled to the GT-ASDL SST MFTF engine nozzle size as they were normalized by the diameter of the F404 nozzle and rescaled to fit the GT-ASDL nozzle, assuming the performance remains similar when changing size, calculated on a spreadsheet. Once the effectiveness of this approach was determined by experimentation, the task was considered complete. The specific details regarding the chevron geometries selected and a comparison against the performance of similar chevron configurations are described in the task and section following this one.

Milestone

- Completed the development and implementation of nozzle-based jet noise reduction methods for engine cycle effects.

Major Accomplishments

- Performed a literature review to identify potential nozzle-based jet noise technologies to be modeled, which provided a thrust and noise relationship.
- Identified research papers with experimental and analytically derived data which correlated jet noise reduction to thrust loss using chevrons.
- Determined an approach for implementing chevrons into the cycle model to capture thrust losses and impact to engine cycle, as well as effects on jet noise in ANOPP.

Publications

None.

Outreach Efforts

None.

Awards

None.

Student Involvement

None.

Plans for Next Period
Task 10 is complete.

Task 11 – Completion of the Full Thrust Recovery and Noise Effects Study
Georgia Institute of Technology

Objective
The objective of this task is to integrate the products of all the previously completed tasks into the modified FASST modeling framework and ensure that the analysis methodology was sound. This involved modifying the FASST code even further to achieve the desired outcome for the study, which had been briefly mentioned previously. Additionally, it required manipulation and further adjustment of input data, such as the inlet maps and chevron nozzle parameters to ensure accurate modeling. A run matrix of experiments was compiled to understand the effects of the chevrons and inlets on noise and thrust, and analysis will be performed to identify the net effects of these devices on a baseline system. Upon completion of this task, the overall project was completed.

Research Approach
Introduction
Developing a suitable study to explore the topic at hand was difficult, due to the exclusively analytical approach and novelty of the effort. As such, several permutations of the study were investigated over time, and contributed to the tardiness of the submission of the final project results and findings. The approach in previous years to accomplish the primary research objectives was to investigate the necessary throttle push amount required to meet the take-off thrust requirements in spite of the installation of jet noise technologies added to the nozzle, and then proceed to see if the inlet could make up the difference in thrust push, precluding its necessity. Furthermore, this study was to be completed for a set of arbitrary nozzle technologies without any mapping to geometry or physical characteristics, since experimental data could not be ascertained. However, after attempting to model this, it was found that a simpler approach could be used to address the same research objectives in a more direct way. This modified approach was to:

1. Develop a baseline installed engine model with an unmodified inlet and clean nozzle (no chevrons).
2. Run the baseline installed engine model and aircraft in the FASST (and ANOPP) to obtain the baseline datum for comparison.
3. Add parameterized chevron geometries and thrust effects, as well as the record effects and run in the FASST/ANOPP to obtain losses due to chevrons.
4. Perform step 3 with variable geometry inlet settings.
5. Record and analyze data to understand the net effects of the inlet on jet noise.

Performing these steps would enable the same understanding as what was previously proposed, but in a much more straightforward manner. As such, it was important to develop a matrix of runs to execute, which can be seen in Table 7.

Table 7. Off-design Installed Engine FASST Run Matrix.

Run	Nozzle Model	Inlet Map
1	Round	Baseline
2	Chevron 1	Baseline
3	Chevron 2	Baseline
3	Chevron 3	Baseline
4	Round	VGCL
5	Chevron 1	VGCL
6	Chevron 2	VGCL
7	Chevron 3	VGCL
8	Round	Blow-In
9	Chevron 1	Blow-In
10	Chevron 2	Blow-In
11	Chevron 3	Blow-In
12	Round	Hybrid
13	Chevron 1	Hybrid
14	Chevron 2	Hybrid
15	Chevron 3	Hybrid

Modeling and Simulation Environment

The standard version of FASST utilizes many iterations of runs to ensure that the vehicle is sized to meet the requirements set by the user in the input file; this process was described in detail in Task 7. However, for FASST to run a selected off-design inlet and nozzle configuration and provide that data to ANOPP for a congruous noise output, it was necessary to identify a means for modeling a fixed engine, converging in a single iteration, and enabling the modification of the nozzle and inlet performance in the off-design study, only. Performing this task required that baseline vehicle did not resize itself to minimize block fuel burn after the installation of new inlet maps, but rather that the final 65-passenger vehicle model was achieved on the first run of the code.

By modifying the FASST code slightly, this was achieved, and the baseline engine and vehicle system results could be consistently obtained through a single run. Then,FASST needed to be prevented from resizing when an improved inlet was installed, as the sizing algorithm consistently wanted to downsize the engine and vehicle due to improved thrust.
The addition of the ability to prevent downsizing was beneficial in that improved inlet maps (from the baseline) could be added the model and run in the off-design condition to achieve the desired result, while maintaining the same initial baseline engine. To the knowledge of the researchers, this effort had not been considered with the FASST framework prior to this work, and it required substantial trial and error to ensure consistent results and the final off-design cycle data passed through to ANOPP for the noise performance prediction.

The primary tool utilized to model jet noise in the context of this research is the Stone Jet Noise module (hereafter referred to as ST2JET), developed by the NASA Glenn Research Center as an adjunct module to predict jet noise and suppression device effects outlined in a technical manual, found in reference (Stone et al., 2009). The Stone Jet Noise module was developed over several years, using a combination of experimental and analytical techniques, serving effectively as a hybrid predictive noise model to provide detailed suppressed jet noise predictions for subsonic and supersonic applications. Additionally, the module has provision for plug nozzles, which is what was selected for use in the SST vehicle which was employed in this study.

Since the model was able to model supersonic nozzle flow, plug nozzles, and had a parametric chevron suppression model, and integrated directly with NASA's ANOPP tool, it served as the ideal jet noise prediction environment to perform the studies presented here. Earlier versions of the Stone Jet Noise model, which were carried over into the most recent

version, ST2JET, included the initial development of jet noise prediction models which would serve to predict noise suppression based on the previously described wetted perimeter ratio and specific noise components. These components include mixing noise components (i.e., intermediate scale, large scale and small scales), and shock noise components (i.e., inner and outer streams), merged mixing noise, and plug separation noise. It should be noted that not all of these effects are seen by all aircraft. For example, inner stream plug separation noise only appears for high bypass ratio and low mixed jet velocity nozzles and operating conditions, so likely not applicable for most small SSTs (Stone et al., 2004). Additionally, certain elements, including plug and downstream shock noise are mitigated entirely by the presence of suppression modification to nozzle exit planes (Stone et al., 2004). Many different nozzle configurations for single and dual-flow nozzles with chevrons were compared against supersonic and subsonic experimental data produced for NASA (Janardan et al., 2000), with good agreement across the ranges of operation which were considered.

Chevron Modeling Approach

It should be noted that the primary objective of the work presented here was to determine if supersonic 2D inlet configurations with variable geometry provisions would be able to provide sufficient increased mass flowrates with minimal separation losses during the LTO conditions, when chevrons or other noise suppression devices are added, such that they can overcome the loss of thrust introduced by the suppression devices, while maintaining the noise benefit gained by them at the proposed conditions. In this work, other types of noise are neglected, and only jet noise is analyzed for impact with regards to chevron and inlet installation on the previously described engine and vehicle system. Since this was the chief objective, it was determined that the precise modeling and matching of specific chevrons and their performances was not necessary. However, it was necessary to select and model jet noise suppression devices in a way that affected both jet noise and thrust proportionally. For example, if an arbitrary jet noise reduction device was selected to be implemented which created jet noise benefit but introduced no thrust degradation. It is likely that the laws of physics were somehow violated. Similarly, if too large a thrust degradation was introduced for a jet noise reduction model, with too little of a jet noise benefit, it is unlikely that such a device would ever be selected as a candidate to be installed on an SST to begin with. As a result, it was crucial to identify some nozzle-based jet noise reduction models which captured behavior between these two extremes. To do this, the public literature regarding jet noise reduction devices was extensively reviewed to ensure that thrust loss and noise benefits obtained by the chevron types selected and described in the previous section were (a) reasonable with regards to the thrust degradation and noise benefit ratio and (b) could be modeled reasonably with the tools available. The development of the ST2JET noise model regressions is well developed and explained in references (Stone et al., 2009; Stone et al., 2004; Stone et al., 2003; Stone, 2001), but are extensive and are thus beyond the scope of the study presented here.

The chevron geometries selected to modify the round plug nozzle employed by the GT-ASDL SST engine to achieve a realistic noise-thrust relationship were based primarily on the Frate and Khavaran geometries also described in the previous section. Although those chevrons were adapted to a fighter jet converging-diverging nozzle, the NASA and Office of Naval Research/Naval Research Laboratory efforts to identify jet noise reduction methods for F404 engines were the only chevron-based experiments found in public literature with clear geometry schematics and definitions, thrust degradation and noise reduction performance results, and experimental operating conditions. Several extensions of initial studies by Henderson and Bridges (2010), using the F404 style supersonic tactical nozzle can be seen in Lui (2021), Frate & Khavaran (2011), Liu et al. (2022), and Rodriguez et al. (2022). The general chevron parametrization scheme incorporates penetration depth and length as fractions of round nozzle diameter, and width scaled by the width of the nozzle facet. An example of an experimental chevron nozzle used in this series of studies is shown in Figure 36. While these chevrons were created for use on an F404 converging-diverging nozzle of a smaller scale, their performance values and geometries were selected to be used and adapted for use on the GT-ASDL SST nozzle, which uses a different configuration—a converging-diverging plug nozzle. Although these nozzles utilize different architectures, the nozzle area ratios seen by converging-diverging nozzles and the plug nozzle used in this study are very similar in the take-off condition in which the nozzle jet is overexpanded.

Figure 36. Chevron nozzle with removable chevrons from experimental study (Henderson & Bridges, 2010).

Some modeling limitations when adapting the Frate and Khavaran chevrons were experienced. First, the chevrons employed in the F404 studies impinged on the jet stream, which is commonly seen across the F404-style chevron studies, which can be seen in the studies listed previously. This creates a smaller effective exit area, which influences jet velocity, and likely, thrust. Although a parametric modification to the effective A_9 to simulate the impingement of the chevrons was attempted to be modeled, it was not able to be achieved within the time required for the completion of the work presented here. However, the nozzle area ratio (A_9/A_8) was found to be similar for the overexpanded cases during take-off, which likely would result in little effect from the impingement effects with regards to effects on expanded jet velocity and thrust.

Additionally, the plug nozzle employed in the GT-ASDL SST model utilizes a translating plug which attempts to achieve perfect exhaust expansion across most operating conditions. As such, when the area was reduced during the work to modify the throat area due to chevron addition, the plug would consistently translate to maintain an area that would yield a similar overexpansion condition of the jet during take-off. To determine the effects of chevron impingement fully, future work would need to be completed to affect the throat area, A_8, and the nozzle effective exit area, A_9, and determine the second-order effects which propagate from it.

However, some slight impingement can be observed in the installation of chevrons within the Stone Jet modeling documentation (this can be seen in one of the schematics of a validation case nozzle configuration used in Janardan et al. [2000], shown in Figure 37), and thus to some extent it can be assumed that a reduction in area introduced by chevrons is already incorporated into the semi-empirical relationships developed in Stone et al. (2003) and Stone (2001). Here, it is stated that the model assumes the chevron contour "is a smooth continuation upstream of the original exit plane" (Stone, 2001), and in the same paragraph, the authors briefly discuss how penetration (impingement) of the chevrons are proprietary in their model, but "acknowledged to be in the order of boundary layer thickness" (Stone, 2001). Due to this linguistic ambiguity, it is somewhat unclear whether the penetration effects are fully captured in the ST2JET chevron models. While the penetration utilized in the model presented here is much more significant, it is only notional in the sense that it is only reflected in the model by the PER ratio (an overall perimeter ratio), and as such can simply represent a longer, and not deeper penetrating chevron. As a result, this limitation is assumed to have a negligible effect, unless trying to precisely match the performance of the F404 chevrons presented by Frate and Khavaran. The definition of the PER ratio utilized by the researchers and applied in the ST2JET module using Equation 3, assuming the nozzles described in both the numerator and denominator have the same round (baseline) geometry, and chevrons serve as an addition or augment. While generalized equations to determine the PER value are found in Stone et al. (2009), the relationship can be simply defined as such:

$$PER = \frac{Perimeter\ of\ chevron\ nozzle\ including\ plug\ perimeter}{Perimeter\ of\ round\ nozzle\ including\ plug\ perimeter} \quad \text{(Eq. 3)}$$

Another modeling limitation can be seen in the fact that the chevrons in the nozzle configuration employed in the study here were attached to the throat (see Figure 37). Chevrons in the F404-style converging-diverging nozzle types are attached at the nozzle exit, which likely produces a different effect in both noise benefit and thrust degradation; however,

since the models implemented by the experiments which informed and validated the ST2JET module utilized throat-attached chevrons in their installation, it was assumed that such a configuration for the supersonic plug nozzle is both acceptable and standard. The primary concern regarding this limitation is that the chevrons from Frate and Khavaran utilized for the study cannot be explicitly matched, which is a similar problem to the first limitation.

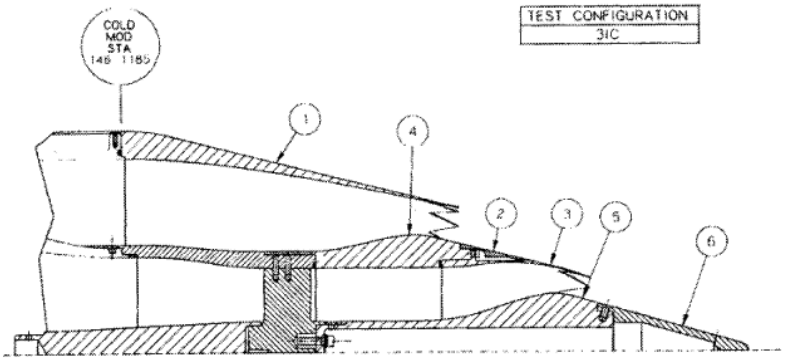

Figure 37. Chevron nozzle test configuration 3IC from Janardan et al. (2000), used in validation for Stone et al. (2004).

Since these modeling limitations exist, and the chevron geometry which was employed in this study cannot match a published model precisely, it was necessary to perform a comparison against other chevrons. This was primarily to understand the chevrons' performance and installation-level impacts on thrust and noise, and to understand whether the chevron models employed in the study here were reasonable and would yield sufficient insight when installed in a broader system level analysis. These comparison results are presented in Figure 38, after the results of the study are shown, for a clear comparison of reasonability. Further discussion regarding the limitations and their effects is provided in the next section.

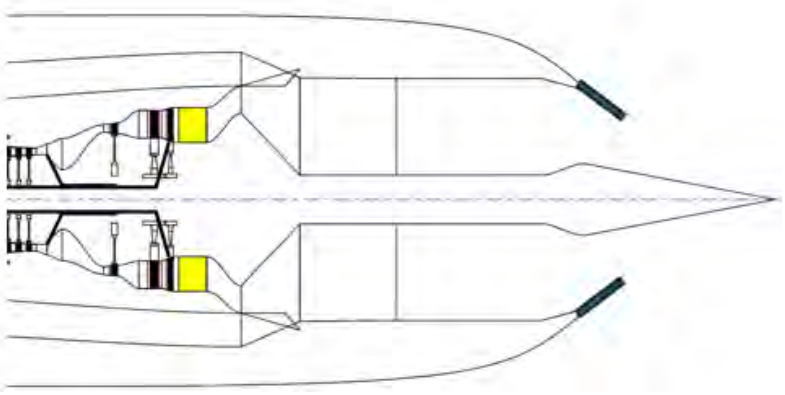

Figure 38. WATE++[2] Schematic of GT-ASDL plug nozzle with notional chevrons for visualization.

Chevron Model Development

As previously discussed, the selection of chevrons to be implemented into the study presented here required the satisfaction of several factors. First, the chevron model needed to be adaptable to the round (clean) plug nozzle under consideration and shown, in the manner presented in Figure 37. While the placement of the chevrons at the plug nozzle throat did not affect the flow area or downstream thermodynamics, as mentioned as a modeling limitation, the throat is the functionally correct position for the chevrons on this nozzle design, and as such, this needed to be utilized for the determination of the PER variable. Second, the chevron PER ratio could not exceed 1.5 as discussed in Stone et al. (2009).

[2] WATE++ is an object-oriented computer code for gas turbine engine weight analysis.

The documentation for the ST2JET module claims that while the model can provide nominal accuracy in prediction up to PER=2.0, the values between 1.5 and 2.0 are extrapolated from experimental data. As a result, chevron sizes needed to provide a wetted chevron to round nozzle (inclusive of plug circumference) perimeter ratio of less than 1.5. Additionally, the chevron models to be adapted for the purposes of this study needed to have results for thrust loss (to be employed in the study as a C_{fg}factor) and noise reduction values (for comparison and verification with the study results which used the ST2JET module). Lastly, the geometry in the literature accompanying the chevron performance data needed to provide a facet width to properly parameterize and scale the chevron width based on the nondimensional values provided.

Of all of the literature surveyed and described in the previous section, the chevron models from Frate and Khavaran were selected to be adapted to the full-scale model used on the GT-ASDL SST engine. The chevron geometries from Frate and Khavaran (2011) were normalized by round nozzle exit diameter and scaled to the GT-ASDL SST nozzle size. In the study, 12 chevrons were used, each placed on a standard facet of the F404 nozzle, with a small gap introduced by the variable geometry nozzle, referred to as a facet gap. This gap needed to be included in the overall calculation of the PER value in order to arrive at an accurate noise reduction value. As a note, ST2JET does not model chevron gaps, and assumes the chevrons are placed flush against one another—supersonic chevrons in this configuration could not be ascertained, so the chevron gaps were included in the PER calculation, despite the inevitable introduction of some deviation from noise reduction performance seen by the Frate and Khavaran chevrons. This was deemed acceptable in the adaptation of these chevron models for two reasons. First, since the only geometry variable seen by the NPSS and ANOPP model is the PER value, it can be understood that the chevrons modeled by the ST2JET module are of a similar shape, but individually smaller, to cover the overall gaps which are seen in the Frate and Khavaran nozzle configurations. As a result, this will lead to a lower noise benefit calculation, which was deemed acceptable, since the concern in adapting an experimental model to the model at hand was potentially having a disproportionately large noise benefit. Second, the chevrons adapted for the models presented here for the thrust recovery study only need to be similar in performance to the experimental ones, and an exact match between the two models was not possible to begin with.

After the geometries of the Frate and Khavaran chevrons were scaled to the size of the GT-ASDL SST nozzle, the PER values inclusive of plug perimeter were calculated, and a gross thrust coefficient, C_{fg}, were calculated for all the scaled chevron models. A summary of the baseline chevron geometries and the related geometry and performance values are seen in Figure 4, along with the scaled versions of the same chevron designs, denoted as “scaled.” Inclusive of the plug circumference (which is specified in the ST2JET documentation, as well as in Stone et al. [2009]), the PER values for all these chevrons are nearly all above 1.5, except for two, P03L08W06 and P03L08W10, which are highlighted in Table 8; these were selected to serve as the basis for the chevrons utilized for the inlet thrust recovery study. As can be seen here, gross thrust coefficients are assumed to be constant with an increase in size (which will be discussed in a later section), and the PER values are constant, since the chevron geometries were normalized by the nozzle exit diameter and a plug was included using the same hub-to-tip ratio as the GT-ASDL SST nozzle.

Table 8. Frate and Khavaran adapted chevron geometry values and scaled to GT-ASDL SST nozzle size (Frate & Khavaran, 2011).

Chevron Name	Penetration [inches]	Length [inches]	Width [%D_9]	Width [inches]	Chev. Leg Length [inches]	Chevron Perimeter Each [inches]	Total Perimeter of Chevrons [inches]	Total Perimeter with Plug [inches]	PER1 no plug	PER1 with Plug	C_{fg}
P05L13W08	0.45	1.25	80	0.8592	1.3218	2.7925	33.5104	41.7694	2.2952	1.9752	0.9842
P03L08W06	0.3	0.75	60	0.6444	0.8163	1.7393	20.8719	29.1310	1.5015	1.3775	0.9850
P03L08W10	0.3	0.75	100	1.0740	0.9224	1.9400	23.2796	31.5387	1.6527	1.4914	0.9814
P03L18W06	0.3	1.75	60	0.6444	1.7794	3.6091	43.3086	51.5677	2.9107	2.4385	0.9897
P03L18W10	0.3	1.75	100	1.0740	1.8305	3.7099	44.5190	52.7780	2.9867	2.4958	0.9889
P06L08W06	0.6	0.75	60	0.6444	0.8163	2.0261	24.3137	32.5728	1.7176	1.5403	0.9434
P06L08W10	0.6	0.75	100	1.0740	0.9224	2.2008	26.4095	34.6685	1.8493	1.6394	0.9274
P06L18W06	0.6	1.75	60	0.6444	1.7794	3.7557	45.0684	53.3274	3.0212	2.5217	0.9793
P06L18W10	0.6	1.75	100	1.0740	1.8305	3.8527	46.2327	54.4917	3.0943	2.5768	0.9716

Chevron Name	Penetration [inches]	Length [inches]	Width [%D_9]	Width [inches]	Chev. Leg Length [inches]	Chevron Perimeter Each [inches]	Total Perimeter of Chevrons [inches]	Total Perimeter with Plug [inches]	PER1 no plug	PER1 with Plug	C_{fg}
P02L13W08	0.2	1.25	80	0.8592	1.3218	2.6736	32.0834	40.3425	2.2056	1.9077	0.9896
P05L13W08 Scaled	3.77	10.48	80	7.2018	11.0790	23.4070	280.8840	350.1115	2.2952	1.9752	0.9842
P03L08W06 Scaled	2.51	6.29	60	5.4014	6.8421	14.5790	174.9484	244.1758	1.5015	1.3775	0.9850
P03L08W10 Scaled	2.51	6.29	100	9.0023	7.7318	16.2608	195.1299	264.3573	1.6527	1.4914	0.9814
P03L18W06 Scaled	2.51	14.67	60	5.4014	14.9151	30.2511	363.0130	432.2405	2.9107	2.4385	0.9897
P03L18W10 Scaled	2.51	14.67	100	9.0023	15.3436	31.0965	373.1584	442.3859	2.9867	2.4958	0.9889
P06L08W06 Scaled	5.03	6.29	60	5.4014	6.8421	16.9831	203.7976	273.0250	1.7176	1.5403	0.9434
P06L08W10 Scaled	5.03	6.29	100	9.0023	7.7318	18.4470	221.3644	290.5918	1.8493	1.6394	0.9274
P06L18W06 Scaled	5.03	14.67	60	5.4014	14.9151	31.4803	377.7631	446.9906	3.0212	2.5217	0.9793
P06L18W10 Scaled	5.03	14.67	100	9.0023	15.3436	32.2935	387.5225	456.7500	3.0943	2.5768	0.9716
P02L13W08 Scaled	1.68	10.48	80	7.2018	11.0790	22.4103	268.9232	338.1506	2.2056	1.9077	0.9896

An examination of the contents of Figure 39, which shows the relationship between PER ratio and thrust degradation in comparison to the round nozzle, while relationships exist that correlate the two metrics, the relationship between PER and thrust is not linear. Rather, linear relationships exist within subsets of families of chevron types when grouped by penetration and length. Intuition would dictate that a higher perimeter ratio would yield a higher thrust loss, but this is not the case. Despite this, because of the observed relationship within similar penetration and length families, this PER- C_{fg} relationship was used to develop the extrapolated family of chevrons for the study presented here.

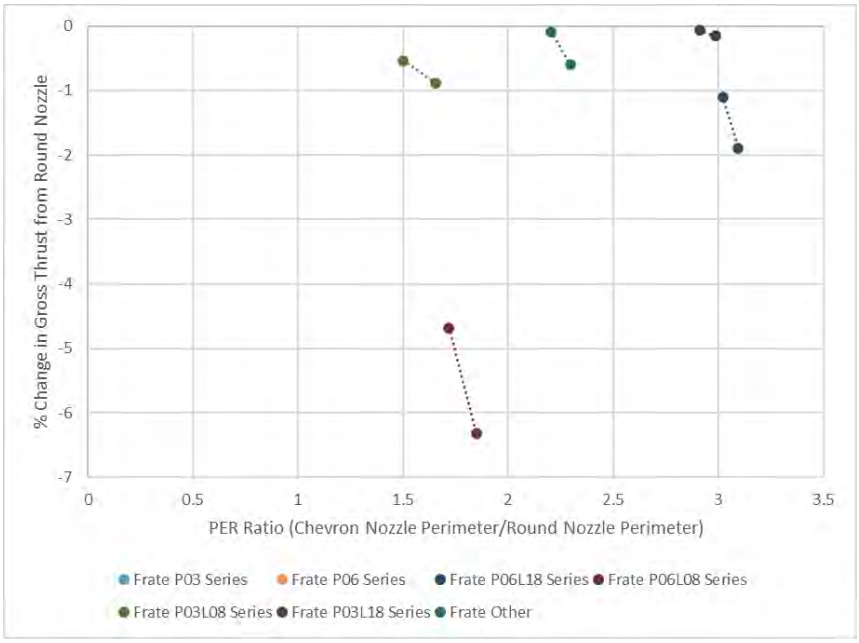

Figure 39. PER vs. change in gross thrust from baseline nozzle for unscaled Frate and Khavaran chevrons.

Using the geometry and performance data generated in the previously described step, two notional chevrons models with lower PER values were generated by linear extrapolation. The only objective with this step was to ensure that chevrons with lower PER values were obtained and evaluated with the GT-ASDL SST engine and nozzle configuration, due to the limitation

of the ST2JET module requirements for PER and the limited experimental data found in published literature pertaining to supersonic chevrons. A summary of the chevron inputs developed from the previously described steps can be seen in Table 9 and Figure 40, along with the baseline chevron. Note that the baseline nozzle is assumed to have a gross thrust coefficient, and as such, a scalar was employed to achieve the desired overall gross thrust degradation seen in the experimental data. The values in Table 9 match the selected geometry and performance values shown in Table 8.

Table 9. Summary of chevron inputs.

	PER1With Plug	CFG Scalar	CFG
Baseline	1.0000	1.0000	0.9900
Chevron 1	1.3775	0.9949	0.9850
Chevron 2	1.4914	0.9914	0.9814
Chevron 3	1.2500	0.9991	0.9890
Chevron 4	1.3000	0.9975	0.9875

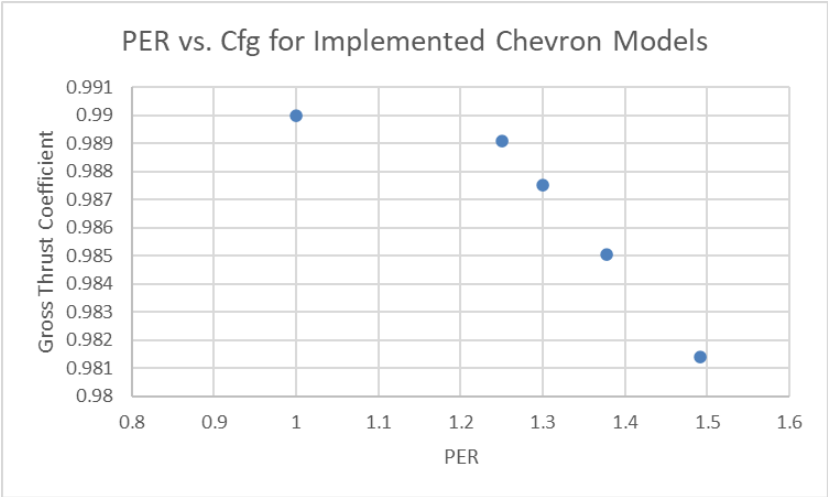

Figure 40. PER vs. C_{fg} for chevron models used in Installation study.

Baseline Chevron Installation Results, NPSS Modeling Setup, and Comparison

Upon completion of the development of the chevron models to be used in the broader study, these results needed to be evaluated against those seen in published data. As such, the chevrons were each installed on the previously described GT-ASDL SST engine with the baseline M=1.7 2D inlet with no variable geometry implemented. These individual cases serve as the baselines from which the variable geometry inlet cases were performed and compared against. After a significant amount of pre-processing to determine reasonable baseline chevron values, they were added to the NPSS and ANOPP models in the forms shown in Figure 40. The PER value is added in the FASST environment by the user, and it propagated through the runs to be used in ANOPP after the engine and vehicle performance is determined by the preceding parts of FASST (CMPGEN for compressor map generation, NPSS for engine cycle modeling and engine deck creation, and WATE++ for engine flow path calculation). The C_{fg}value is used in an off-design script, after the baseline, fixed engine and vehicle are run in the primary FASST run, in order to ensure each run uses the same engine and vehicle, with only inlet and chevron parameters changing, for a clear “apples-to-apples” comparisons between the configurations outlined in Table 7.

The ANOPP configuration selected for this study was to only consider jet noise resulting from the ST2JET module, with the ability to model shock noise turned on. The take-off model was taken from the Cutback-Approach (CBAP) output file

generated from the ANOPP after running, since it provided the most detailed take-off noise performance results with take-off conditions matching those generated by ANOPP. A custom take-off script which runs NPSS in off-design was created to model the take-off conditions defined in the FLOPS file for the baseline GT-ASDL SST vehicle. From this, the inlet and chevron nozzle inputs are added and modify the baseline engine solved earlier in the FASST run, affecting the take-off model with the desired inputs defined in the experiment run matrix in Table 7. These performance data are used in the calculation of the state tables for the ANOPP noise prediction, and as such, the take-off script performance output and the ANOPP jet noise prediction of the modified engine configuration are coupled. Due to the modeling setup as described, only $C_{fg}$and PER were required to define in the framework used for the study. While it is likely that higher fidelity models could improve jet noise prediction, the level of fidelity provided by this integration was deemed acceptable due to the validation of ST2JET with similar nozzle configurations, the proven reliability of NPSS and the FASST environment in previous studies, and their physics-based coupling.

After the baseline chevron data (seen in Table 9) were generated, they were input into the FASST modeling environment as described previously. Then, the systems-level metrics sought for this study, namely change in decibel noise reduction from the baseline round nozzle using overall sound pressure level (OASPL) at a selected 110° of directivity (a common angle presented in literature used for validation), and percent change in installed thrust from the baseline round nozzle. A summary of these values can be found in Table 10, highlighted in dark gold; the corresponding Frate and Khavaran (2011) chevron performance results are provided in light gold above them. These values are placed in the same table as a similar family of chevrons from the selected F404-style chevron nozzle studies, seen in Frate & Khavaran (2011), Liu et al. (2022), and Rodriguez et al. (2022). In the cases of the chevrons from Liu et al. (2022) and Rodriguez et al. (2022), detailed geometry was not provided regarding facet width and facet gap width.

Table 10. GT-ASDL and example F-404 style chevron geometry and performance results.

Run	Penetration [$\%D_9$]	Length [$\%D_9$]	Width [$\%L_F$]	PER	NPR	D_9 [in]	L_f [in]	$\%\ \Delta F_g$	ΔdB OASPL @110°	Reference
P06L20W100	6	20	100%	2.57	2.7	1.450	0.3072	-0.7600	-0.1764	Rodriguez [29]
P06L20W100	6	20	100%	2.57	3.0	1.450	0.3072	-0.61%	-1.6294	Rodriguez [29]
P08L20W100	8	20	100%	2.60	2.7	1.450	0.3072	-1.3900	-1.1764	Rodriguez [29]
P12L20W100	12	20	100%	2.70	2.7	1.450	0.3072	-3.2000	-0.7794	Rodriguez [29]
P08L20W80	8.9	25	80%	2.60	2.7	1.450	0.3072	-1.0400	-1.2277	Rodriguez [29]
P10L20W100	10	20	100%	2.08	2.7	3.167	0.6711	-2.2000	-0.67702	Liu [28]
P06L20W100	6	20	100%	1.98	2.7	3.167	0.6711	-0.76	-0.8575	Liu [28]
P06L20W100	6	20	100%	1.98	3.0	3.167	0.6711	-0.61%	-0.4436	Liu [28]
P08L20W100	8	20	100%	2.02	2.7	3.167	0.6711	-1.39	N/A	Liu [28]
P05L13W08	8.87	24.66	80%	2.29	3.0	5.068	1.074	-0.6047	-1.9330	Frate [22]
P03L08W06	5.91	14.79	60%	1.50	3.0	5.068	1.074	-0.5345	-0.1835	Frate [22]
P03L08W10	5.91	14.79	100%	1.65	3.0	5.068	1.074	-0.8855	-0.4427	Frate [22]
P03L18W06	5.91	34.53	60%	2.91	3.0	5.068	1.074	-0.0647	-1.1663	Frate [22]
P03L18W10	5.91	34.53	100%	2.98	3.0	5.068	1.074	-0.1511	-1.2203	Frate [22]
P06L08W06	11.83	14.79	60%	1.71	3.0	5.068	1.074	-4.6814	-3.9956	Frate [22]
P06L08W10	11.83	14.79	100%	1.84	3.0	5.068	1.074	-6.3120	-2.9157	Frate [22]
P06L18W06	11.83	34.53	60%	3.02	3.0	5.068	1.074	-1.1015	-2.4028	Frate [22]
P06L18W10	11.83	34.53	100%	3.09	3.0	5.068	1.074	-1.8952	-2.8185	Frate [22]

Run	Penetration [$\%D_9$]	Length [$\%D_9$]	Width [$\%L_F$]	PER	NPR	D_9 [in]	L_f [in]	$\% \Delta F_g$	ΔdB OASPL @110°	Reference
P02L13W08	3.94	24.66	80%	2.21	3.0	5.068	1.074	-0.0918	-0.8963	Frate [22]
Chevron 1	0.05	0.1479	60%	1.37	2.0	42.48	9.002	-0.5100	-5.1	GT-ASDL
Chevron 2	0.05	0.1479	100%	1.49	2.0	42.48	9.002	-0.8684	-6.1	GT-ASDL
Chevron 3	Notional	Notional	Notional	1.25	2.0	42.48	9.002	-0.0910	-3.7	GT-ASDL
Chevron 4	Notional	Notional	Notional	1.30	2.0	42.48	9.002	-0.2520	-4.3	GT-ASDL

Frate, F., & Khavaran, A. (2011, January 4-7). *An aerodynamic and acoustic assessment of convergent-divergent nozzles with Chevrons* [Conference paper]. 49th AIAA Aerospace Sciences Meeting including the New Horizons Forum and Aerospace Exposition, Orlando, Florida. https://doi.org/10.2514/6.2011-976

Liu, J., Khine, Y. Y., Saleem, M., Rodriguez, O. L., & Gutmark, E. (2022, June 14-17). *Comparison of the Thrust-Based Noise Reduction Performance between Micro-vortex Generators and Chevrons* [Conference presentation]. 28th AIAA/CEAS Aeroacoustics Conference, Southampton, United Kingdom. https://doi.org/10.2514/6.2022-2970

Rodriguez, O. L., Saleem, M., Gutmark, E., & Liu, J. (2022, January 3-7). *Implementation of chevrons as a noise reduction system for a supersonic tactical nozzle* [Conference presentation]. AIAA SciTech 2022 Forum, San Diego, California, & virtual. https://doi.org/10.2514/6.2022-0682

As a result, the detailed geometry from Frate and Khavaran (2011) was utilized to obtain a related PER value for comparison. As the same nozzle configuration (i.e., axisymmetric, 12-facet, variable geometry, converging-diverging F404 style nozzle) with a similar schematic, is shared across the aforementioned studies, it was assumed this was an acceptable approach. In comparing the GT-ASDL chevron geometries to the published ones, a significant increase in noise reduction is achieved, despite the PER value being notably smaller than most of the other chevrons listed, while the thrust loss is more or less in family with the other chevrons shown. This result can be seen in Table 10 and Figure 41. There are several potential explanations for this phenomenon. First, the difference in size from the nearest nozzle, used by Frate and Khavaran (2011), is nearly 8.5 times smaller than the full-size nozzle used in the study presented here. By investigation into the studies which presented the results in Table 10 and Figure 41 it can be found that operating conditions, nozzle size, and experimentation setup likely all have an effect on predicted sound level.

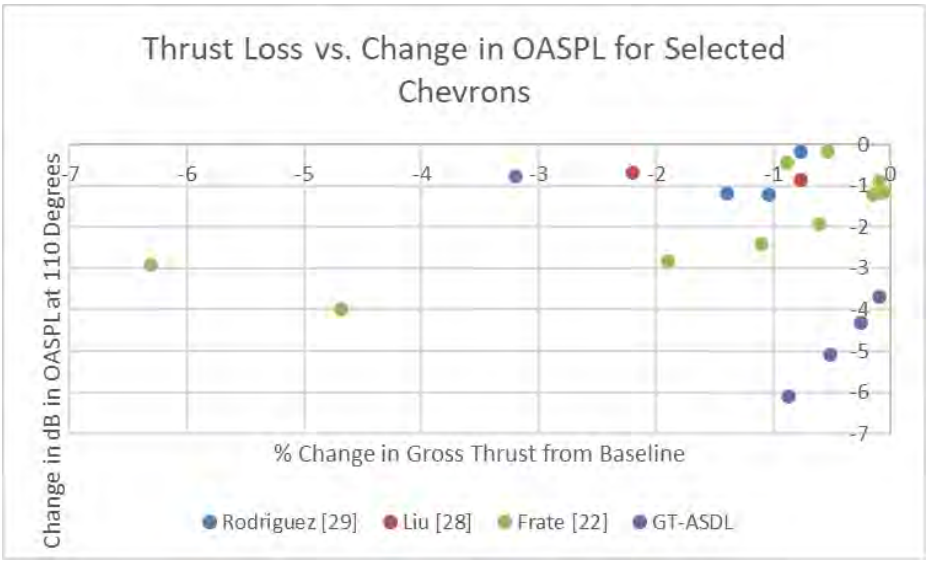

Figure 41. Thrust loss vs. change in OASPL at 110° for selected chevrons.

For identical chevron configurations defined in Rodriguez et al. (2022) and Liu et al. (2022) for the P06L20W100 chevron nozzle, it can be seen that variations occur in OASPL measured at 110° of directivity, when the nozzle pressure ratio (NPR) and nozzle diameter are measured. These experiments are an excellent comparison point to try to understand the basic effects of geometry and operating conditions on chevrons, since both experiments (1) use the same chevron parametrization for length, width, and penetration, (2) use the same NPR, NTR, freestream Mach number operating conditions, (3) use identical nozzle area ratios between the throat and nozzle exit areas, and (4) they are attached to an identical format, but different sized nozzle. It should also be noted that these studies both utilized large eddy simulations (LES) for determination of thrust loss, but Rodriguez et al. (2022) employed an acoustic test rig for physical experimental data. As such, those data are trusted more when considering the effect of change of NPR on the OASPL reduction values. Regardless of accuracy, it can be seen that for identical models, significant differences in OASPL reduction can be seen both as a function of nozzle size, and operating conditions, namely NPR. Conversely, when comparing these papers, the difference in gross thrust for the different sized nozzles in these studies remains the same. The observations discussed here can be gleaned in Figure 42.

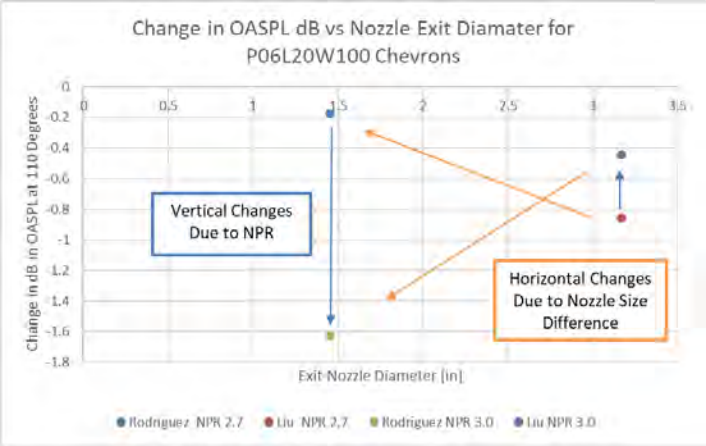

Figure 42. Noise reduction vs. nozzle exit diameter for P06L20W100 chevrons of the two studies performed, comparing Liu and Rodriguez based chevron designs.

Upon further inspection of the results presented in Table 10, it can be postulated that nozzle size is a key driver in jet noise reduction. As mentioned previously, the GT-ASDL chevron nozzles achieve substantially better jet noise reduction performance than smaller nozzles; it is not immediately clear if noise reduction is heavily dependent on nozzle exit area and overall scale effects. For this reason, a normalized metric was sought to determine if the noise reduction levels from literature and those found from the study at hand related to primarily to nozzle size, and secondarily to chevron geometry and size (both of which are related parameters). It is shown in Figure 43 that each group of chevrons (including the previously analyzed families of Frate chevrons, shown in Figure 39) generally yields a trend of increasing normalized jet noise reduction with increasing values of PER. The trend has outliers, and this is typically because (a) in the case of the best-performing Frate chevrons, the PER values are very low and it can be seen that higher values of penetration with shorter length affects the flow at the exit plane more significantly than other chevron geometries in the group, and (b) potential experimental deviations seen in the directivity trend seen in Liu et al. (2022), seen in red in Figure 43. Another observation is that the GT-ASDL chevrons selected, while lower in PER values compared to the other chevrons, yield a similar normalized jet noise reduction level to several other chevrons. In this way, our team has effectively confirmed that the chevrons which were modeled here are both acceptable in thrust degradation and jet noise reduction performance, when size effects are considered. Lastly, to confirm the validity of the noise reduction model, we will consider two other performance trends of the chevron nozzles utilized for the study at hand, noise composition breakdown, and an OASPL directivity comparison against other many other chevrons to identify some trends and close the book on verification and comparison of the GT-ASDL chevron models.

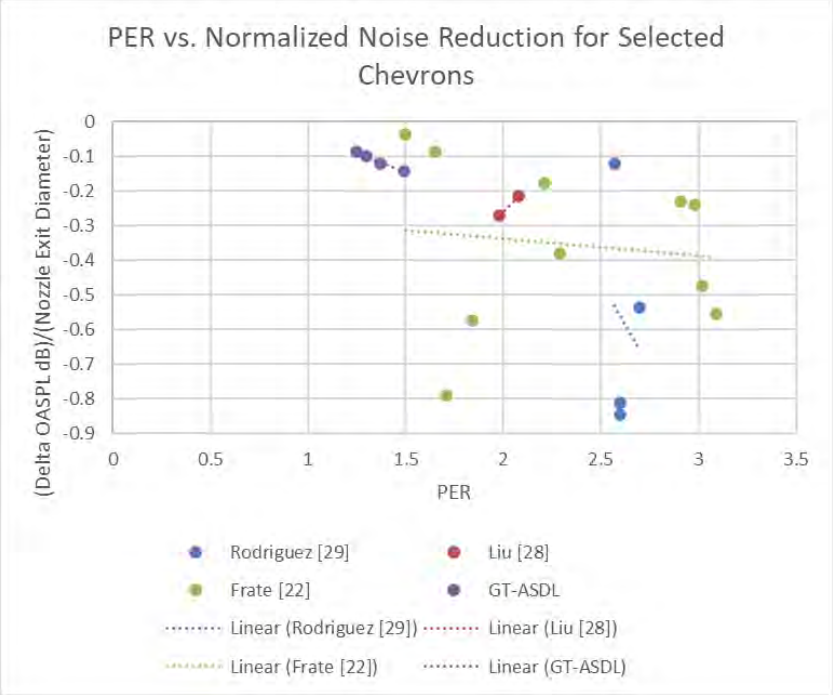

Figure 43. Normalized Jet Noise Reduction vs. PER.

An examination of a standard directivity angle vs. OASPL noise reduction plot is shown in Figure 44. While not initially obvious, the chevron trends for the GT-ASDL chevrons (labeled chevrons 1-4) are roughly similar to those of Liu et al. (2022), with a delayed dip in performance. The trends in Liu et al. (2022) were recorded at a smaller set of directivity angles, which prevents more comprehensive understanding of the trends. Additionally, the curves from Liu et al. (2022) dip lowest towards the standard observation angle of 110°, where the experimental ones are lowest closer to 0°. A final observation is from the supersonic jet from Chen et al. (2024). Despite employing an unrelated chevron geometry (on a supersonic cold conical nozzle), the magnitudes of noise reduction are fairly similar to a median of what was obtained through chevrons 1-4 (see Figure 44). Additionally, with Chen et al. (2024) and Liu et al. (2022), their Mach numbers at the nozzle exhaust plane are 1.2 and ~1.5, respectively. They also both experience shocks—as will be discussed here, the Mach number in the nozzle exhaust plane for the experimental chevrons with plug nozzle is, on average, very close to 1.01 and has no shock noise component for take-off from the ANOPP predictions. As such, the difference in chevron and nozzle geometry and operating conditions can also likely be attributed to the lack of shock in the experimental nozzle results.

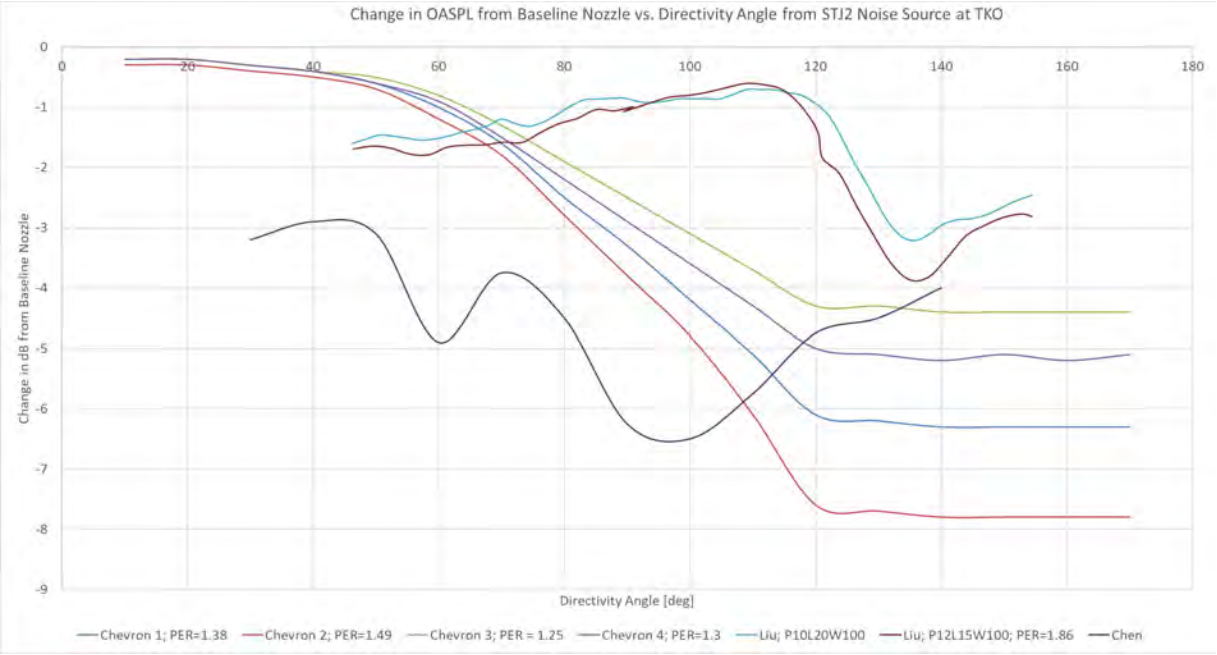

Figure 44. Directivity angle vs. OASPL noise reduction for a selection of chevrons.

After sufficient investigation and comparison, it was determined that the chevron models utilized for the GT-ASDL SST engine and vehicle models were reasonable and deviation from nearest points of comparison were justifiable. It was found that the normalized baseline chevron jet noise reduction values were similar in magnitude to experimental values, thrust loss magnitudes correspond well to other chevron nozzles even of different scales and operating conditions, variations in operating condition and size contributed most to deviation. Most importantly, it was determined that the differences from (deltas) across chevron performance data need to be reasonably accurate, which it seems to be.

Inlet Thrust Loss Mitigation Study

Recall from the initial discussion in earlier sections of this report that the primary objective of the research was to identify whether a variable geometry supersonic inlet which performs well at cruise could potentially mitigate the drawbacks associated with jet noise reduction devices at LTO (effects on other segments not considered here). To do this, an inlet was designed with three modes of variable geometry which could allow for higher mass flow into the engine with lower duct and separation losses at low speeds—a VGCL, blow-in doors, and a hybrid mode which enabled both. Separate inlet maps were created using a process defined by SIPC, an inlet design and analysis tool developed for the completion of this task. Nozzles were modeled and added to the NPSS and ANOPP models to model the effects of chevrons on noise and thrust, and the installed combinations of these inlets and nozzles were implemented and modeled in the FASST integrated modeling environment to obtain results comparing noise and thrust degradation compared to a round nozzle with the baseline inlet using no variable geometry (the baseline case). Some important results of the study are shown in Figure 45.

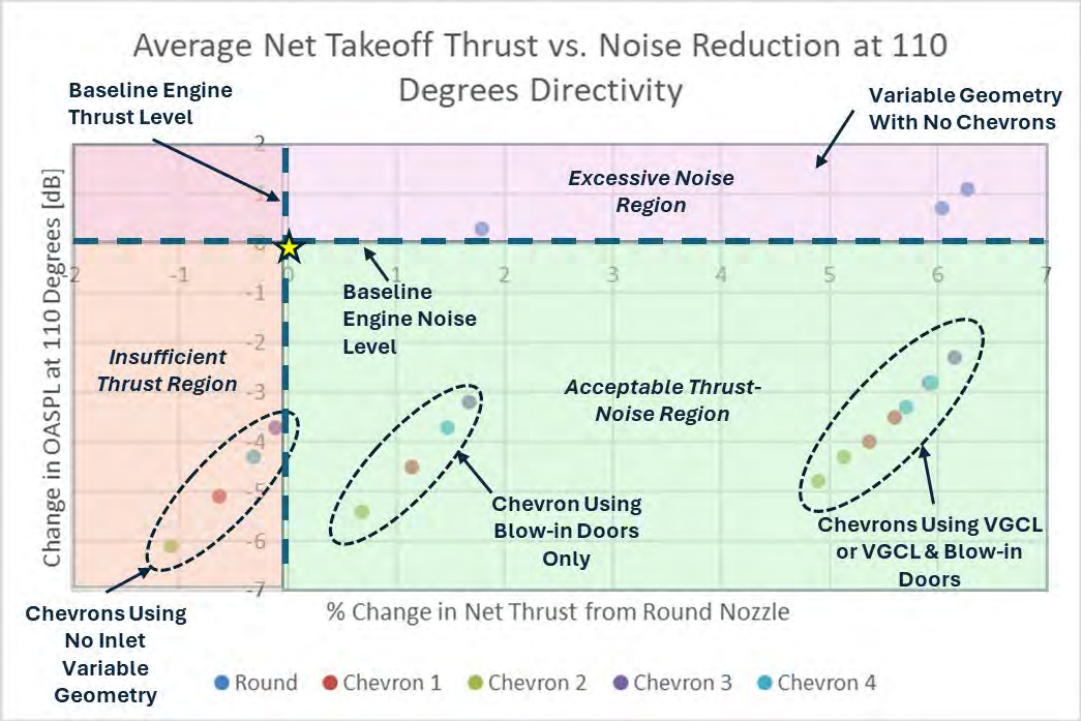

Figure 45. Average net take-off thrust vs. noise reduction at 110° directivity.

In Figure 45, the percent change in average installed (gross thrust – inlet ram drag – inlet drags) net thrust compared to change in OASPL at 110° directivity in decibels is presented. Several visual overlays have been added to the basic chart to aid in explaining the results. The results of thrust-noise relationship points were color-coded by the chevron type and their respective inlet types are grouped and identified using arrows. It can be seen here that the pink-shaded area above 0 dB change in OASPL is labeled the excessive noise region; this is because, if chevrons are being implemented on SST, achieving worse noise performance is unacceptable. Similarly, the orange-shaded area to the left is the insufficient thrust region, which is to the left of the 0% change in net thrust from round nozzle line (vertical axis). If an installation performs worse than the baseline case, it is an unacceptable configuration for the aircraft. A star marks the origin simply for quick reference since the axes are not bright due to the region overlays. We can see that, as predicted, for the cases in which engine has chevrons installed, but the inlet is not using any variable geometry, the noise reduction is excellent, but the thrust introduced by the chevrons cannot be overcome. Similarly, some points appear in the excessive noise region, and upon investigation, these are the variable geometry cases which employ no chevrons to mitigate increased jet noise as a result of increased mass flow into the engine. The remaining points exist within the acceptable thrust-noise region in which thrust degradation and noise benefit is equal to or greater than the baseline configuration. On the lower left side of the acceptable thrust region, the four cases which use blow-in doors only have good noise befit compared to the baseline, but only slight improvement in thrust over it. This follows logically, since the blow-in doors were limited in the inlet model to take in a small amount of air to prevent excessive noise which can be introduced by inlet blow-in doors positioned near the fan face. Lastly, a mix of chevron cases which use either the VGCL alone, or VGCL and blow-in doors together are observed. They provide significant improvements in thrust and maintain nearly the same noise level as the blow-in door cases.

Similar graphics were developed for the net take-off thrust vs. noise reduction at 60° and 90° of directivity as shown in Figure 46 and Figure 47. However, in these charts, the results are more complicated. While the regions previously defined remain intact, and the relative improvement in net take-off thrust has remained the same, the level of noise reduction has reduced dramatically, and as a result, most of the VGCL and hybrid VGCL/blow-in door cases are in the excessive noise region at this angle of directivity. At this angle of observation, only the chevron cases with blow-in doors are operating in the acceptable noise region.

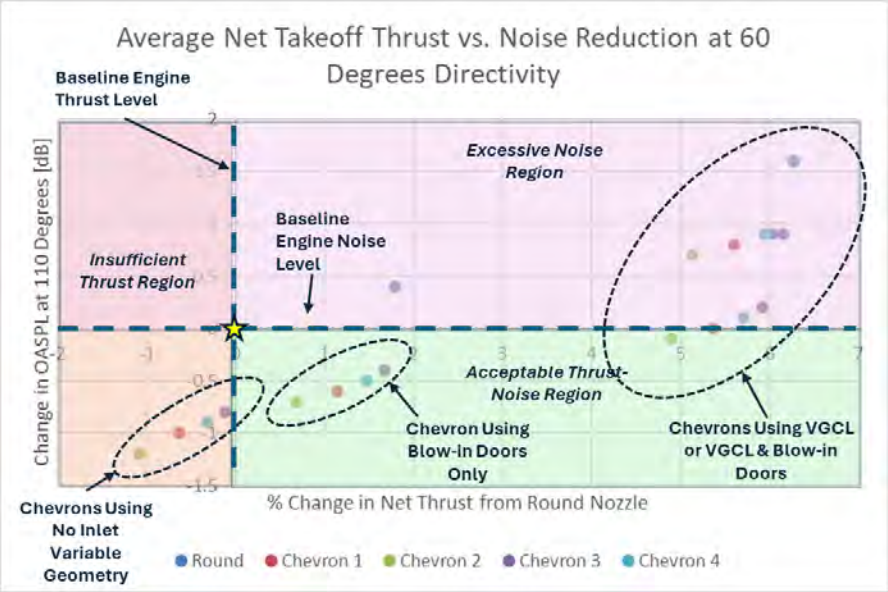

Figure 46. Average net take-off thrust vs. change in jet noise at 60° directivity.

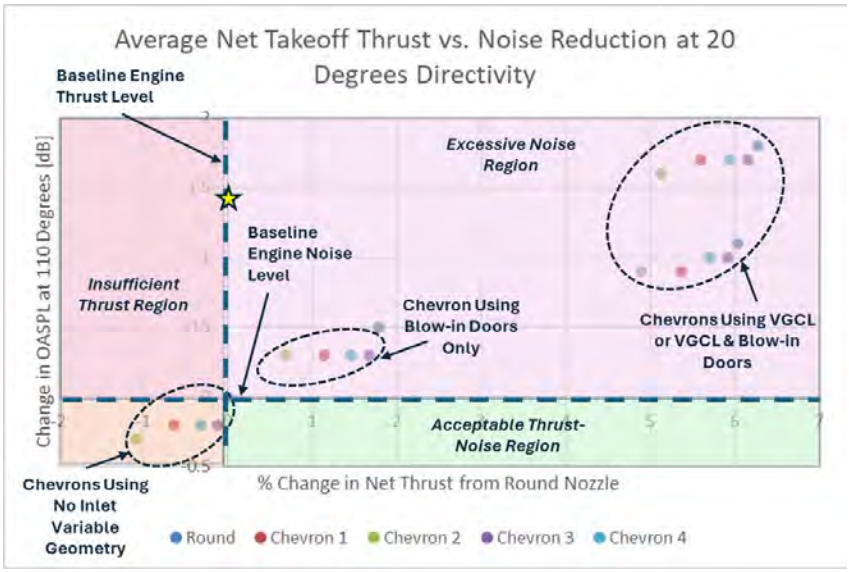

Figure 47. Average net take-off thrust vs. change in jet noise at 20° directivity.

Similarly, we see an even more interesting result in Figure 47 for the same study for 20° directivity. Here, the noise reductions, even with the chevrons, are not sufficient to break even with the baseline case if they use inlet variable geometry. And the cases which use chevrons, but no inlet variable geometry produce acceptable noise benefit, cannot produce sufficient thrust to enable the vehicle to take-off (break even with the baseline case). This trend of seeing worse noise benefit as the directivity angle decreases towards zero is shown in Figure 48, which shows the change in OASPL at various directivity angles for the different cases examined in this study. As Figure 44 shows, the general trend for the nozzle with jet stream noise benefit increases as directivity angle increases. Most inlet and nozzle combinations have worse noise performance than the baseline case for directivity angles between 10° and 60°. The linear-shaped results

above the noise breakeven line are attributed to the cases which utilize variable geometry inlet configurations with no chevrons and should be ignored when determining thrust-noise behavior of the proposed engine installations.

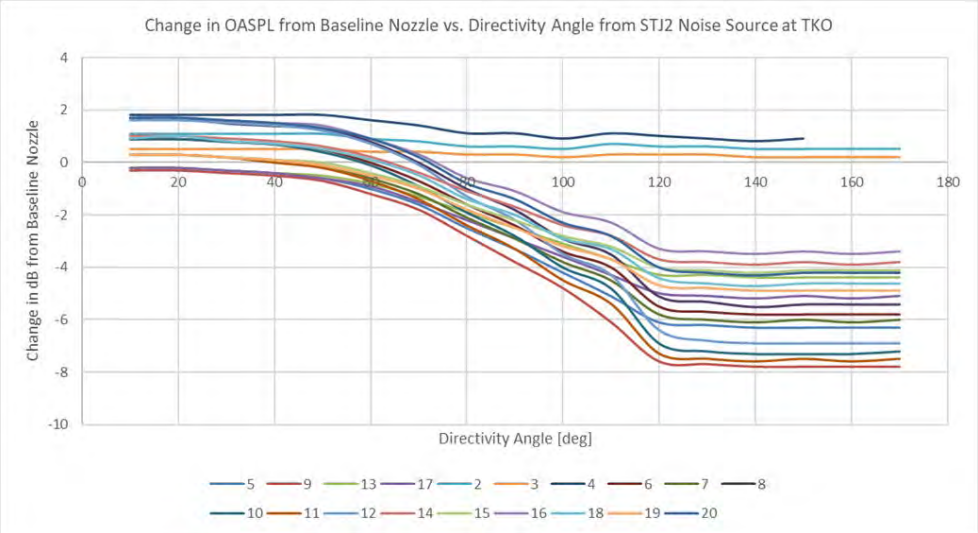

1	Baseline	Round
2	VGCL	Round
3	BlowIn	Round
4	BlowInVGCL	Round
5	Baseline	Chevron1
6	VGCL	Chevron1
7	BlowIn	Chevron1
8	BlowInVGCL	Chevron1
9	Baseline	Chevron2
10	VGCL	Chevron2
11	BlowIn	Chevron2
12	BlowInVGCL	Chevron2
13	Baseline	Chevron3
14	VGCL	Chevron3
15	BlowIn	Chevron3
16	BlowInVGCL	Chevron3
17	Baseline	Chevron4
18	VGCL	Chevron4
19	BlowIn	Chevron4
20	BlowInVGCL	Chevron4

Figure 48. Change in OASPL from baseline nozzle [dB] vs. directivity angle θ for all tested installation configurations.

Discussion and Conclusions

Based on the results shown in Figures 45 to 48, several takeaways can be identified:

- Variable geometry inlet configurations are capable of overcoming the losses introduced by a notional set of chevrons added to a supersonic engine nozzle at take-off conditions.
- The blow-in door model maintains a strong noise reduction performance and still ensures sufficient thrust benefit to break even with the losses introduced by the chevrons (in most cases, perform slightly better).
- The VGCL and VGCL/blow-in door hybrid configurations of inlet variable geometry produce high levels of thrust improvement, but at the expense of noise increase.
  - The rate of increase in noise (decrease in noise benefit) seen with these configurations was better than anticipated (low decrease in noise benefit for much higher thrust).
- As observed in Figures 46 to 48, nearly all inlet/chevron configurations experienced noise degradation from the baseline for directivity angles between 10° and 60°.
  - It is unclear whether this quality would render the inlet variable geometry incapable of performing the task of overcoming the thrust and enabling a breakeven with the baseline noise performance (i.e., the louder nozzle across 50° of directivity is acceptable and the other directivity angles are more important (or the inverse could be true, as well).
  - Investigation into this could be accomplished with future work.
- Since the chevron models and variable geometry models implemented are notional and based on studies into published literature and engineering assessments, it is possible other better performing chevrons or better performing installation combinations exist which could fully mitigate the effects seen in the lower directivity angles.
- Chevron models were only adapted from literature because of the inability to obtain relevant jet noise and thrust relationships from other ASCENT Project 059 partners, as initially anticipated—future work should incorporate the addition of experimental data with new jet noise reduction techniques.
  - Literature has been published regarding microvortex generators and tab devices which could also be modeled at low effort to perform a similar but lower fidelity function.
- The noise analysis was performed at a single point ~9 ft in altitude from the lift-off point of the aircraft—further analysis could be completed to identify a more comprehensive set of data.
- The development of the inlet design and analysis code proved to be the most demanding component of the project, taking nearly two and a half years to complete; the proper adaptation of chevron models and their

justification and comparison to those in published literature, as well as the development of the overall study framework was a close second in complexity

Parting Thoughts
The Georgia Tech team would like to thank the FAA ASCENT community and leadership for their support, guidance and understanding in the completion of this project over the last four years. This project has supported several students through their graduate careers and ultimately turned one into a full-time research engineer at Georgia Tech. We are grateful for the opportunity to work on this project and attempt to contribute to the field of civil aviation and supersonics.

Milestone

- Completed the full thrust recovery and noise effects study.
- Completed the presentation and analysis of the final results.

Major Accomplishments

- Integrated inlet maps, and fixed engine and aircraft models to ensure functionality and confirm study procedure.
- Added chevrons for four parametrized designs defined in aforementioned reference into the NPSS nozzle element and ensured functionality.
- Integrated inlet maps, fixed engine and aircraft models, and chevron models to ensure functionality and confirm the study procedure.
- Ran a baseline engine case and established ANOPP performance values for the baseline inlet, fixed engine and aircraft, and clean nozzle (no chevrons) for a comparison datum.
- Determined necessary chevron geometry and inlet variable geometry cases to be studied.
- Performed thrust-noise degradation studies.
- Performed a comparison and analysis of selected/designed chevron nozzle models with those found in published literature.
- Identified a relevant jet noise model and parameters for inclusion in the study and performed analysis of the results.

Publications

The ASCENT Project 059(A) will seek to publish these findings at AIAA SciTech 2026 with the acknowledgement of the FAA ASCENT team's support.

Outreach Efforts

None.

Awards

None.

Student Involvement

None.

Plans for Next Period

None.

References

Aircraft Recognition Guide. (2018). *Eurofighter Typhoon*. https://www.aircraftrecognitionguide.com/eurofighter-typhoon

Anderson, J. T. (2014, May 1). *How supersonic inlets work: Details of the SR-71 mixed compression inlet geometry and operation* [Conference presentation]. 11th Aircraft Engine Historical Society (AEHS) Convention, San Diego, California. https://www.enginehistory.org/Convention/2014/SR-71Inlts/SR-71Inlts.shtml

Aviation Stack Exchange. (2021). Why do the 737-100's JT8Ds, and no others, have suck-in doors. https://aviation.stackexchange.com/questions/70316/why-do-the-737-100s-jt8ds-and-no-others-have-suck-in-doors

Barnhart, P. J. (1998). *Inlet performance analysis code developed*. NASA Research and Technology. https://ntrs.nasa.gov/search.jsp?R=20050177169

Bridges, J., & Brown, C. (2004, May 10-12). *Parametric testing of chevrons on single flow hot jets* [Conference paper]. 10th AIAA/CEAS Aeroacoustics Conference, Manchester, Great Britain.

Chen, B., Li, W., Fei, W., & Zhengwu, C. (2024). Experimental study of the noise suppression of supersonic impinging jets with chevrons. *Applied Acoustics, 221*.

Crosthwait, E. L., Kennon, I. G., & Roland, H. L. (1967). Preliminary design methodology for air-induction systems (SEG-TR-67-1). Systems Engineering Group, Research and Technology Division, Air Force Systems Command, Wright-Patterson Air Force Base, Ohio.

Dean, R. B. (1978). Reynolds number dependence of skin friction and other bulk flow variables in two-dimensional rectangular duct flow. *Journal of Fluids Engineering, 100*, 215–223.

Frate, F., & Khavaran, A. (2011, January 4-7). *An aerodynamic and acoustic assessment of convergent-divergent nozzles with Chevrons* [Conference paper]. 49th AIAA Aerospace Sciences Meeting including the New Horizons Forum and Aerospace Exposition, Orlando, Florida. https://doi.org/10.2514/6.2011-976

Henderson, B., & Bridges, J. (2010, June 7-9). *An MDOE investigation of chevrons for supersonic jet noise reduction* [Conference paper]. 16th AIAA/CEAS Aeroacoustics Conference, Stockholm, Sweden. https://doi.org/10.2514/6.2010-3926

Janardan, B.A., Hoff, G. E., Barter, J. W., Martens, S., Gliebe, P. R., Mengle, V., & Dalton, W. N. (2000). *AST critical propulsion and noise reduction technologies for future commercial subsonic engines: Separate flow exhaust system noise reduction concept evaluation* (NASA/CR-2000-2100039). General Electric Aircraft Engines and Allison Engine Company. https://ntrs.nasa.gov/api/citations/20010061345/downloads/20010061345.pdf

Karon, A. Z., & Ahuja, K. K. (2017, June 5-9). *Reduction of jet noise by the nozzle-exit boundary layer* [Conference paper]. 23rd AIAA/CEAS Aeroacoustics Conference, Denver, Colorado. https://doi.org/10.2514/6.2017-3859

Kowalski, E. J. (1979). *Computer code for estimating installed performance of aircraft gas turbine engines, Vol 1: Final report.* NASA Lewis Research Center. https://ntrs.nasa.gov/citations/19800004788

Little, J. W., & Russell, R. E. (1976, March 21-15). *Status report: Subsonic aircraft noise reduction* [Conference paper]. ASME 1976 International Gas Turbine and Fluids Engineering Conference, New Orleans, Louisiana. https://doi.org/10.1115/76-GT-116

Lui, J. (2021, August 2-6). *Supersonic jet noise reduction using micro vortex generators* [Conference presentation]. AIAA Aviation 2021 Forum, virtual. https://doi.org/10.2514/6.2021-2183

Liu, J., Khine, Y. Y., Saleem, M., Rodriguez, O. L., & Gutmark, E. (2022, June 14-17). *Comparison of the thrust-based noise reduction performance between micro-vortex generators and chevrons* [Conference presentation]. 28th AIAA/CEAS Aeroacoustics Conference, Southampton, United Kingdom. https://doi.org/10.2514/6.2022-2970

Marsh, A. H., Chapkis, R. L., & Blankenship, G. L. (1983). *Study of noise-certification standards for aircraft engines, volume 3: Selection and evaluation of engine-noise-certification concept*. Dytec Engineering Inc., Long Beach, California. https://apps.dtic.mil/sti/citations/ADA137805

McLean, J. D. (2012). *Understanding aerodynamics: Arguing from the real physics*. Wiley.

McPike, A. L. (1972). Community noise levels of the DC-10 aircraft. *Journal of Aircraft, 9*(8), 542-547. https://doi.org/10.2514/3.59033

Morris, P., McLaughlin, D., & Kuo, C-W. (2013). Noise reduction in supersonic jets by nozzle fluidic inserts. *Journal of Sound and Vibration, 332*(17), 3992-4003.

Nicolai, L. M., & Carichner, G. E. (2013). Turbine engine inlet design (Ch. 15). In *Fundamentals of Aircraft and Airship Design: Volume 1*. American Institute of Aeronautics and Astronautics (AIAA).

Rodriguez, O. L., Saleem, M., Gutmark, E., & Liu, J. (2022, January 3-7*). Implementation of chevrons as a noise reduction system for a supersonic tactical nozzle* [Conference presentation]. AIAA SciTech 2022 Forum, San Diego, California, & virtual. https://doi.org/10.2514/6.2022-0682

Seddon, J., & Goldsmith, E. L. (1999). *Intake aerodynamics*. Blackwell Science.

Seddon, J., & Goldsmith, E. L. (1993). *Practical intake aerodynamic design*. AIAA Education Series.

Seiner, J., & Gilinsky, M. (1995, June 19-22). *Nozzle thrust optimization while reducing jet noise* [Conference paper]. Fluid Dynamics Conference, San Diego, California. https://doi.org/10.2514/6.1995-2191

Slater, J. W. (2020, August 24-28). *A study of the internal aerodynamics of the Concorde inlet* [Conference presentation]. AIAA Propulsion and Energy 2020 Forum, virtual.

Stone, J. R. (2001). *Separate flow nozzle jet noise source separation and correlation extension to enhanced mixing configurations*. MTC Report to GE Aircraft Engines.

Stone, J. R., Krejsa, E. A. and Clark, B. J. (2003, January 6-9). *Semi-empirical model for coannular nozzle component noise extraction and correlation including the effects of noise reduction devices* [Conference paper]. 41st Aerospace Sciences Meeting and Exhibit, Reno, Nevada. https://doi.org/10.2514/6.2003-1060

Stone, J. R., Krejsa, E. A., & Clark, B. J. (2004). *Jet noise modeling for supersonic business jet application* (NASA/CR-2004-212984). Modern Technologies Corporation, Middleburg Heights, Ohio. https://ntrs.nasa.gov/api/citations/20040050631/downloads/20040050631.pdf

Stone, J. R., Krejsa, E. A., & Clark, B. J. (2009). *Jet noise modeling for suppressed and unsuppressed aircraft in simulated flight* (NASA/TM-2009-215524). NASA Glenn Research Center. https://ntrs.nasa.gov/api/citations/20090015381/downloads/20090015381.pdf

Tinney, C. E., Valdez, J., & Murray, N. (2020). Aerodynamic performance of augmented supersonic nozzles. Experiments in Fluids, 61(2). https://link.springer.com/article/10.1007/s00348-019-2866-3

Project 059(D) Physics-based Analyses and Modeling for Supersonic Aircraft Exhaust Noise

Stanford University

Project Lead Investigator

Sanjiva K. Lele
Professor
Department of Aeronautics & Astronautics
Stanford University
Stanford, CA 94305
Phone: (650) 723-7721
E-mail: lele@stanford.edu

University Participants

Stanford University (Stanford)

- P.I.s: Dr. Sanjiva K. Lele, Dr. Juan J. Alonso
- FAA Award Number: 13-C-AJFE-SU-024
- Period of Performance: September 30, 2023, to October 1, 2024
- Tasks:
  1. Develop and refine research plans in coordination with ASCENT Project 059 partners
  2. Perform large eddy simulation (LES)-based simulation, modeling, and validation of jet noise predictions
  3. Conduct Reynolds-averaged Navier–Stokes (RANS)-based simulation, modeling, and validation of jet noise predictions

Project Funding Level

This project receives $200,000 per year from the Federal Aviation Administration (FAA), in-kind matching from Stanford, and cost-share matching from Gulfstream Aerospace Corporation.

Investigation Team

Dr. Sanjiva K. Lele (P.I.; Department of Aeronautics and Astronautics)
Dr. Juan J. Alonso (P.I.; Department of Aeronautics and Astronautics)
Gao Jun Wu (PhD student; Department of Aeronautics and Astronautics)
Tejal Shanbhag (PhD student; Department of Aeronautics and Astronautics)
Kristen Matsuno (PhD student; Department of Mechanical Engineering)
Olivia Martin (PhD student; Department of Mechanical Engineering)

Project Overview

Improved methods for predicting and reducing noise for civil supersonic aircraft would be highly valued by the research and technology development community engaged in civil supersonic aircraft development. In addition to aircraft and engine companies, organizations such as the National Aeronautics and Space Administration (NASA), FAA, and the U.S. Department of Defense (DoD), and the research and technology community would also benefit from improved methods and tools. Supersonic jet noise tools with predictive capabilities can be used to design improved noise mitigation systems and to provide estimates of noise for certification studies.

This project involves the coordinated development of both low- and high-fidelity approaches for jet noise predictions for civil supersonic aircraft being considered in ASCENT and involves the tasks listed above. High-fidelity simulations of the jet exhaust flow and noise will be developed for a carefully selected subset of configurations and operating points being

evaluated by the Georgia Institute of Technology (Georgia Tech) team. In parallel, Reynolds-averaged Navier–Stokes (RANS) computations of a broader range of configurations and operating conditions relevant for civil supersonic aircraft will be performed and used to develop improved jet noise source models and more accurate far-field noise propagation kernels. The noise source and noise propagation modeling will leverage high-fidelity simulation data and ongoing Georgia Tech experiments, as well as other noise and flow measurements available in the archival literature. Our goal is to understand the predictive quality of RANS-based noise prediction approaches with improved source and/or propagation models so that designers can better capture tradeoffs typical in the development of full civil supersonic aircraft configurations.

Task 1 – Develop and Refine Research Plans in Coordination with ASCENT Project 059 Partners

Stanford University

Objectives

The objective of this task is to design a simulation study that covers the range of operating conditions and nozzle configurations relevant for civil supersonic jet exhaust. The research plan must be inclusive of the current test plan from our experimental partner at Georgia Tech.

Research Approach

Planning involved discussions with ASCENT Project 059 partners and reaching out to external advisors at NASA and elsewhere in academia and industry. Based on these efforts, it was determined that the project should focus on axisymmetric dual-stream nozzles with an internal mixer and with the possibility of an internal and/or external nozzle plug. Our team has also searched for nozzle configurations and flow and noise measurement data in the archival literature that would be deemed relevant for civil supersonic aircraft and that could be used in the development of noise prediction methods. A comprehensive exploration indicated that the bulk of jet noise data including studies of noise reduction concepts were in the regime of moderate to high bypass ratios and were thus not particularly relevant for civil supersonic aircraft. While this affirmed the need for the planned laboratory measurement campaign by ASCENT Project 059 partner Georgia Tech, it also highlighted the need to use the most relevant data from the published literature to kickstart the modeling and simulation effort. Two specific datasets associated with jet noise tests at NASA Glenn Research Center were thus identified.

Georgia Tech Dual-Stream Nozzle

A coannular nozzle geometry with a variable-length mixing duct has been designed and is being evaluated extensively by the team at Georgia Tech. Following discussions among project collaborators and key stakeholders, a test matrix has been determined for the Year 1–2 experimental efforts. The jet Mach numbers for the two streams each vary between $M_j = 0.4$ and $M_j = 1.0$, and the length of the nozzle mixing duct can be adjusted to be 0.7, 1.0, 2.0, and 3.0 times the length of the nozzle diameter, $D_e = 1.7''$.

Bridges and Wernet Internal Mixer

Bridges and Wernet (2004) (at the NASA Glenn Research Center) reported flow and noise measurements for internally mixed two-stream nozzles with variations in the mixer duct length and mixer geometry. The operating conditions involve transonic and low supersonic jet exhaust velocity with a moderate bypass ratio. This configuration has also been used in previous RANS-based noise prediction studies by Rolls Royce® and Purdue University, along with a more recent large eddy simulation (LES) study. Our team has been in touch with Rolls Royce and NASA regarding the nozzle geometry and measurement data. It is hoped that the geometry and data will become available in the future. This configuration is of interest to us because it is unique in providing both jet flow measurements and far-field noise for conditions relevant to civil supersonic flights.

Recent Jet Noise Measurements at NASA Glenn Research Center

As part of NASA's Commercial Supersonic Technology Project, under the Advanced Aero Vehicle Program, Dr. Bridges at NASA Glenn Research Center (personal communication, 2020) completed jet noise measurements on specially designed modular nozzle configurations at operating points selected to be relevant for commercial supersonic aircraft. Far-field acoustic measurements have been made available (Bridges et al., 2021), and PIV measurements of the jet have also been

® Rolls Royce is a registered trademark of Rolls-Royce PLC, London, Great Britain.

made available for select operating conditions (Bridges & Wernet, 2023). Our team is interested in exploring a selected subset of NASA's test matrix in our ASCENT Project 059 studies. Our team has obtained the computer-aided design (CAD) geometry for the nozzle and began early efforts in geometry cleaning and mesh generation.

Milestones

- Determined and followed the simulation plan (Years 1–2, complete).
- Studied the effects of mixing enhancement devices under heated jet conditions (Year 3, complete).
- Finalized and focused on trying to understand and improve noise discrepancies between the LES predictions and experimental measurements (Year 4).

Major Accomplishments

- Developed a research plan regarding the nozzle geometry and flow conditions to be studied. The plan includes both the experimental study by our partner at Georgia Tech and other relevant works from NASA Glenn Research Center.

Publications

None.

Outreach Efforts

Communication with researchers at NASA Glenn Research Center has been established, and ideas for collaboration have been exchanged.

Awards

None.

Student Involvement

Four graduate students have been involved in this part of ASCENT Project 059. G. Wu and K. Matsuno have conducted literature research on relevant jet experiments and simulations that involve similar flow conditions and nozzle mixing devices. T. Shanbhag has performed literature reviews on acoustic modeling of jet noise. K. Matsuno recently completed her Ph.D. O. Martin has joined the project and is helping with the simulations of the mixer nozzle.

Plans for Next Period

- Continue to refine our research plan according to ongoing discussions among teams of ASCENT Project 059.
- Select nozzle geometries with noise mitigation concepts that are of interest to industrial partners for the development of next-generation supersonic civil transport aircraft.

References

Bridges, & Wernet. (2004). Cross-Stream PIV Measurements of Jets with Internal Lobed Mixers (NASA/TM-2004-213206). NASA Glenn Research Center. https://ntrs.nasa.gov/citations/20040152075

Bridges. (2020). Personal Communication.

Bridges, J. E., Podboy, M. P., Gary, G., & Wernet, M. (2021). Plug20 test report (NASA/TM-20210010291). NASA Glenn Research Center. http://ntrs.nasa.gov/api/citations/20210010291/downloads/TM-20210010291.pdf

Bridges, J., & Wernet, M. P. (2023). Plug20 test report: Particle image velocimetry (PIV) measurements (NASA TM-20230006779). NASA Glenn Research Center. https://ntrs.nasa.gov/api/citations/20230006779/downloads/TM-20230006779.pdf

Task 2 – Perform LES-based Simulation, Modeling, and Validation of Jet Noise Predictions

Stanford University

Objectives

In collaboration with ASCENT partners in ASCENT Project 059, the objective of this task is to develop physics-based analyses for supersonic aircraft exhaust noise. The main goal of these analyses is to develop improved jet noise prediction methods using a multi-fidelity approach. As part of the high-fidelity approach, LES will be conducted for a carefully selected set of configurations and operating points corresponding to tests conducted by the experimental team at Georgia Tech. The LES data will provide turbulence flow statistics and will be leveraged for acoustic source modeling.

Research Approach

NASA Plug20 Internal Lobed Mixer and Axisymmetric Splitter

In the past project year, efforts have been dedicated to high-fidelity modeling of the NASA Plug20 dual-stream nozzle with an internal plug and lobed mixer (configuration 122Am5pInt) and an internal plug and axisymmetric splitter (configuration 122Am0pInt), shown in Figure 1. LES and far-field acoustics modeling by the permeable Ffowcs Williams–Hawkings (FWH) formulation were performed using a compressible solver, CharLES, developed by Cascade Technologies (now part of Cadence Design Systems). LES-FW-H acoustic predictions for the 122Am5pInt nozzle have been obtained at Setpoint 1183 (summarized in Table 1) because of its relevance to industry collaborators and because experimental far-field acoustic measurements were available at this setpoint (Bridges & Wernet, 2004). Acoustic predictions for the 122Am0pInt nozzle have been obtained at Setpoint 7 (subsonic, unheated) and Setpoint 1183.

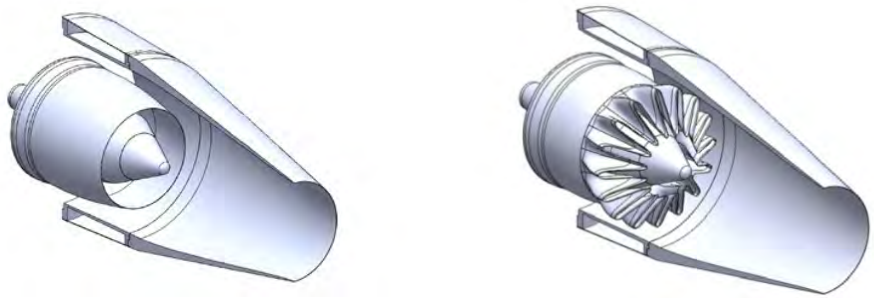

Figure 1. Detailed nozzle geometries. 122Am0pInt, confluent nozzle with an internal plug (left), 122Am5Int, confluent nozzle with an internal plug plus lobed mixer (right). Images obtained from Bridges et al. (2021).

Table 1. Operating conditions for NASA geometries.

Setpoint	NPR (nozzle pressure ratio)	NTRc (nozzle temperature ratio – core)	NTRb (nozzle temperature ratio – bypass)	Mfj (coflow Mach number)
1183	1.8	2.90	1.20	0.3
7	1.857	1.0	1.0	0

In Figure 2, far-field acoustic predictions for the 122Am0pInt nozzle are compared to the experimental measurements. At the unheated setpoint, the LES-FWH acoustic predictions agree very well with the experimental measurements across all angles. There is slight under-prediction of the high frequency noise at upstream angles and overprediction of high frequency noise at far downstream angles, but agreement is particularly good in the mid-to-low frequency range. At the

heated setpoint (Setpoint 1183), the LES-FWH results agree well with the experimental measurements at far downstream angles, though the LES-FWH is missing the spectral hump around St = 1. At sideline and upstream angles, however, large discrepancies are observed across all frequencies. The overall sound pressure level (OASPL) is under-predicted by 4-5 dB in upstream and sideline angles. Similar underpredictions have been reported by researchers at NASA Ames Research Center (Stich et al., 2024). In the next project year, we plan to run simulations at Setpoint 4200 for nozzle configuration 122Am0pInt. This setpoint has equation heating of both core and bypass streams (NTR = 1.31, NPR = 2.0, Mfj = 0). These results will help us to better understand whether the noise underprediction at Setpoint 1183 is related to heating of the jet or the temperature and velocity differentials between streams.

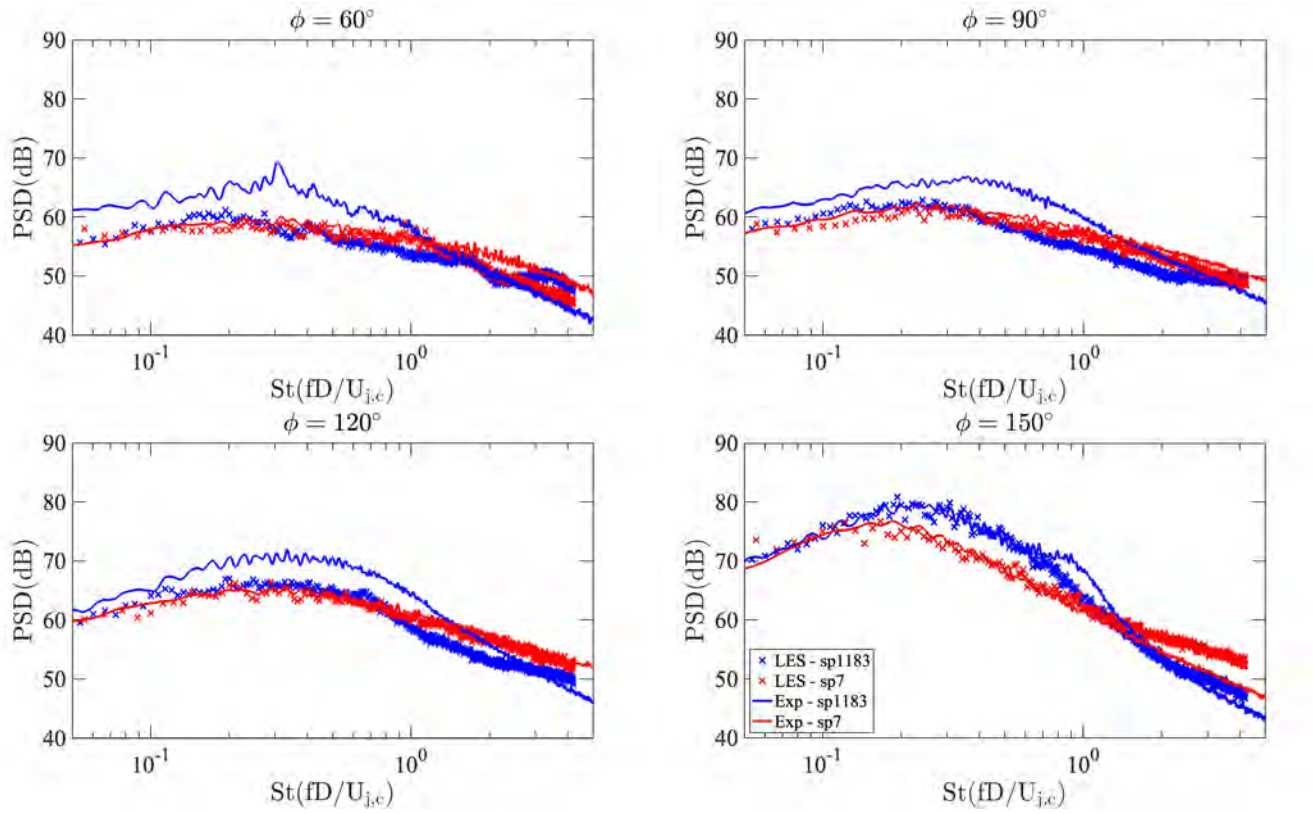

Figure 2. Far-field acoustic predictions using the LES-FWH method (marked with x's) compared to experimental measurements (lines) at Setpoint 1183 and Setpoint 7 for the 122Am0pInt nozzle.

For the 122Am5pInt nozzle, acoustic predictions have been obtained at Setpoint 1183. One goal of this study was to understand the sensitivity of the far-field acoustics to our modeling choices. Three of the most important modeling choices we chose to investigate were:

1. Mesh resolution inside the nozzle
2. FWH surface placement
3. External boundary layer modeling

In order to test the mesh resolution inside the nozzle, two different meshes were generated, referred to as Mesh A and Mesh B, shown in Figure 3. The finest level of refinement ($\Delta x/D = 0.005$) is colored in dark gray. For Mesh A, the finest level of refinement ended at x/D = -1.1. For Mesh B, the finest refinement region is extended outside the nozzle to x/D = 0.5.

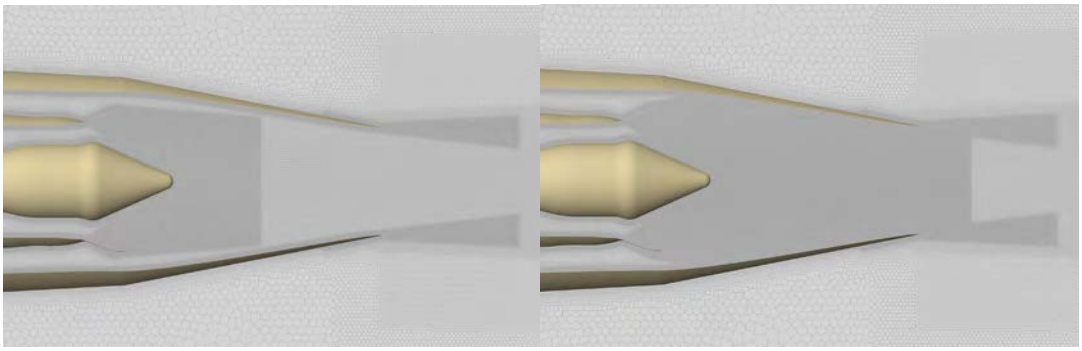

Figure 3. Mesh refinement inside the 122Am5Int nozzle with internal plug and lobed mixer. Mesh A (left), Mesh B (right). The region of finest refinement ($\Delta x = 0.005$) is shown in dark gray.

To evaluate the FWH surface placement, four different FWH surfaces were generated. Surface 'S1' is closest to the jet, followed by surfaces 'S2' and 'S3.' Surfaces S1, S2, and S3 all have 12 equally spaced end caps in the region x/D = [40, 45]. Surface '$S2_{ext}$' is the same as surface S2 except the end caps are extended to x/D = [45, 50]. These four FWH surfaces are shown in Figure 4.

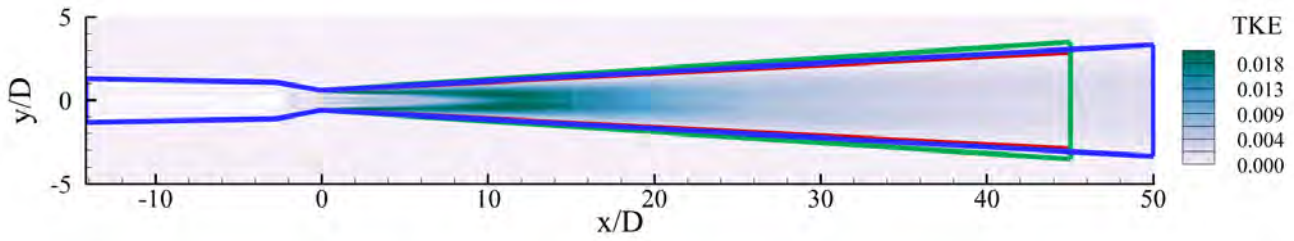

Figure 4. FWH sampling surfaces plotted on top of the turbulence kinetic energy profile at Setpoint 1183. Surface S1 is plotted in red, surface S2 is plotted in orange, surface S3 is plotted in green, and surface $S2_{ext}$ is plotted in blue. Surface S2 falls directly underneath surface $S2_{ext}$.

At Setpoint 1183, a boundary layer is expected to develop on the nozzle exterior due to the non-negligible flight stream ($M_f = 0.3$). How this boundary layer is modeled will impact the shear layer extending from the nozzle lip and refraction of sound by the shear layer. Mesh A and Mesh B have refinement on the nozzle exterior and a wall-model is applied in the region x/D > -6.0. In order to quantify the sensitivity of the results to these choices, a third mesh was generated, referred to as Mesh C, with minimal refinement on the nozzle exterior and an adiabatic no-slip boundary condition (no wall model). Profiles of the mean streamwise velocity and turbulence kinetic energy (TKE) just upstream of the nozzle exit are shown in Figure 5 for Mesh B and Mesh C. Mesh B has a thicker, more-turbulent boundary layer than Mesh C.

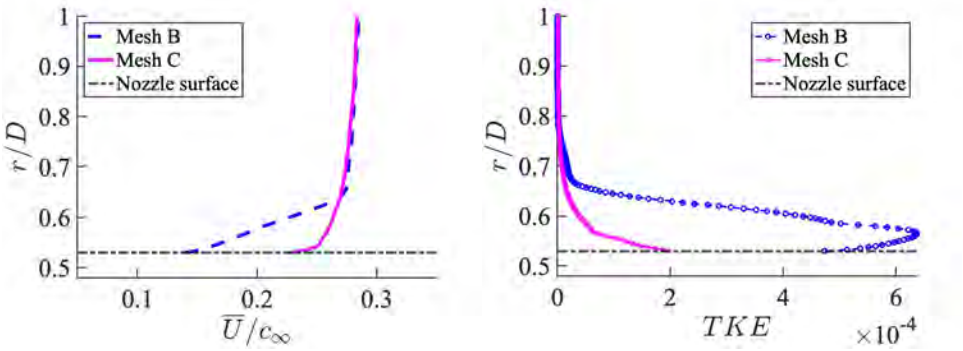

Figure 5. Profiles of mean streamwise velocity and TKE on the nozzle exterior just upstream of the nozzle exit (x/D = -0.1) for Mesh B and Mesh C.

Far-field acoustic predictions for nozzle 122Am5pInt are shown in Figure 6 at Setpoint 1183. Results computed on Mesh A, Mesh B, and Mesh C are compared to the experimental measurements. LES-FWH results for Mesh B are shown for all four different FWH sampling surfaces. These results show that the LES-FWH predictions are insensitive to the FWH sampling surfaces evaluated and differences in the external boundary layer model. Results computed on Mesh A and Mesh B are also nearly identical, which suggests that the mesh in the mixing region inside the nozzle is sufficiently fine and could potentially be coarsened even further. The LES-FWH results agree very well with the experimental measurements at far downstream angles. At sideline directions, high frequency noise is underpredicted by the LES and the spectral hump around St = 1.5 is not captured. This spectral hump is believed to be due to internal mixing from the lobed mixer and is often referred to as 'excess' noise. At far upstream directions, the noise discrepancy ranges from about 3-10 dB across the frequency spectrum. The OASPL is underpredicted by 5-6 dB at sideline and upstream angles. Researchers at the NASA Ames Research Center similarly are not predicting the high-frequency noise and the spectral hump around St = 1.5, though they observe better agreement at low frequencies in the upstream direction (Stich et al., 2024).

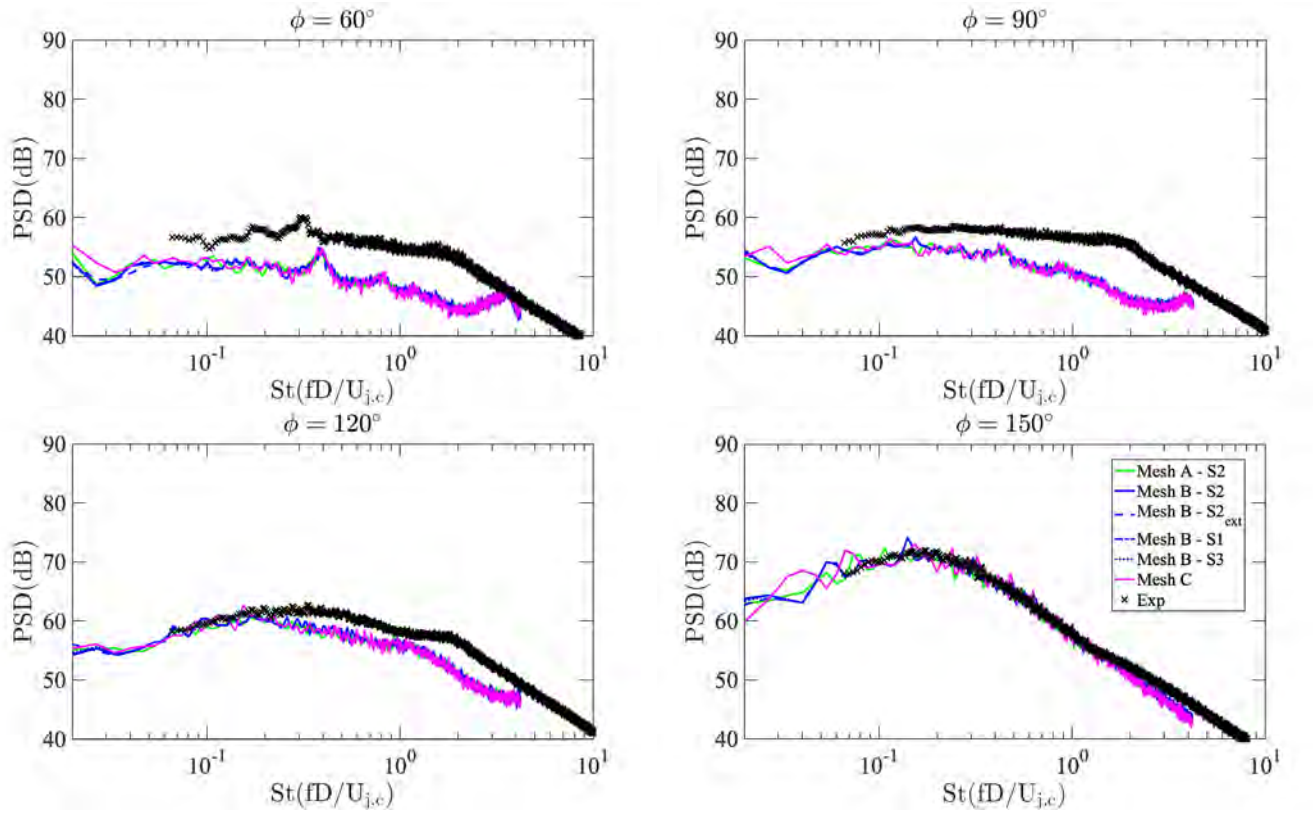

Figure 6. Far-field acoustic predictions using the LES-FWH method compared to experimental measurements at Setpoint 1183 for the 122Am5pInt nozzle.

To better characterize the internal mixing and identify the source of the 'excess' noise around St = 1.5, time-resolved volumetric data were sampled inside the nozzle. To save on compute costs, data were sampled surrounding two mixer lobes. Table 2 contains details regarding the volumetric sampling grid. Spectral proper orthogonal decomposition (SPOD) was used to analyze the volumetric data. The SPOD modes were computed based on Chu's compressible energy norm. Parameters of the SPOD, such as the number of flow snapshots used, number of blocks, and % overlap between blocks, are given in Table 3.

Table 2. Volumetric sampling grid parameters.

x	r	θ	N_x	N_r	N_θ	Δx	Δr_{max}	$(\Delta\theta)r_{max}$
[-2.5, 0]	[0, boundary]	$[\pi/16,\ 5\pi/16)$	126	80	68	0.02D	0.011D	0.01D

Table 3. Parameters of spectral proper orthogonal decomposition.

$\frac{\Delta t c_\infty}{D}$	N_{snaps}	N_{blocks}	$N_{snaps/block}$	$N_{overlap}$	St_{max}
0.05	4500	11	750	375 (50%)	6.6

The resulting SPOD spectrum is shown in Figure 7. A spectral hump is observed in the SPOD spectrum around St = 1, which is similar to the spectral hump in the far-field experimental acoustic measurements. In Figure 8, the pressure fluctuations associated with the SPOD modes at select frequencies on the spectral hump are shown. Pressure fluctuations shed from the lobed mixer propagate downstream and couple with the near-wall pressure. These pressure fluctuations will be scattered by the sharp nozzle lip, producing far-field acoustics that scale with U^5. Bridges (2023) found that the 'excess' noise generated by the lobed mixer that had minimal flight stream dependence scaled with $(U_c+U_b)^5$, where U_c is the core stream velocity and U_b is the bypass stream velocity. Bridges suggested that this noise was generated by the shear layer extending from the lobed mixer interacting with the nozzle lip and/or the plug. This hypothesis by Bridges (2023) appears to agree with the findings presented here. Our team believes it is highly likely that the 'excess' noise is generated by coherent structures shed from the lobed mixer interacting with the nozzle lip. It remains unclear, however, why this noise is not accurately captured in the LES.

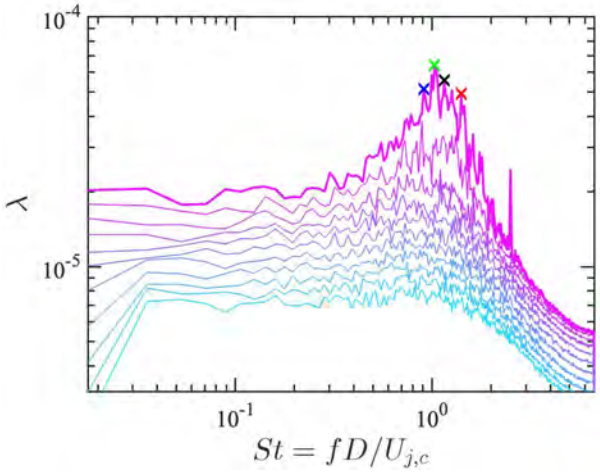

Figure 7. SPOD spectrum computed using Chu's compressible energy norm. Frequencies St = 0.91, St = 1.03, St = 1.16, and St = 1.41 are marked with x's.

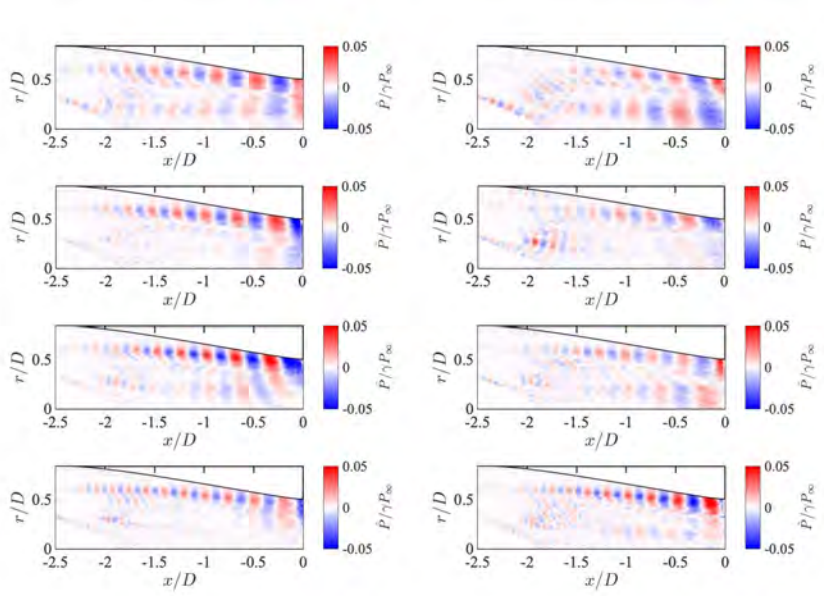

Figure 8. Pressure component of SPOD modes. Frequencies St = 0.91, St = 1.03, St = 1.16, and St = 1.41 are shown in rows 1-4, respectively. The leading SPOD mode at each frequency (left column), and the second SPOD mode at each frequency (right column).

One hypothesis is that there is a form of aeroacoustic resonance inside the nozzle that amplifies the structures shed from the mixer. Our team assessed this theory by searching for an upstream-traveling wave that could serve as a feedback mechanism. We separate the SPOD modes into +/- phase speed components by performing a streamwise Fourier transform on each SPOD mode. Since the nozzle is converging, and the SPOD modes are sampled onto a curvilinear mesh defined by coordinates (r, θ, η), we performed a non-uniform Fourier transform along the η direction, rather than x. The coordinate η represents the distance along the mesh at a constant (r, θ) position. This decomposition is performed over the region $x \in (-1.75,0)$, which is just downstream of the plug and lobed mixer. In Figure 9, the magnitudes of the Fourier components are plotted for the leading SPOD modes across a range of frequencies. The x-axis is the wavenumber, and the y-axis corresponds to different (r, θ) positions. For frequencies in the range of approximately St ≤ 1.85, we observe energy in the negative wavenumber region of the spectrum. This suggests that there may be upstream-propagating modes inside the nozzle. Interestingly, this range of frequencies contains the frequencies where the hump is observed in the SPOD spectrum. Our team is currently working on performing linear stability analysis (LSA) using the mean flow data inside the nozzle to assess whether (1) an upstream-traveling duct mode is supported inside the nozzle at these frequencies, (2) whether the shapes of the eigenfunctions from LSA agree with filtered SPOD data, and (3) whether the band-of-existence of this duct mode aligns with the spectral hump in the experimental measurements.

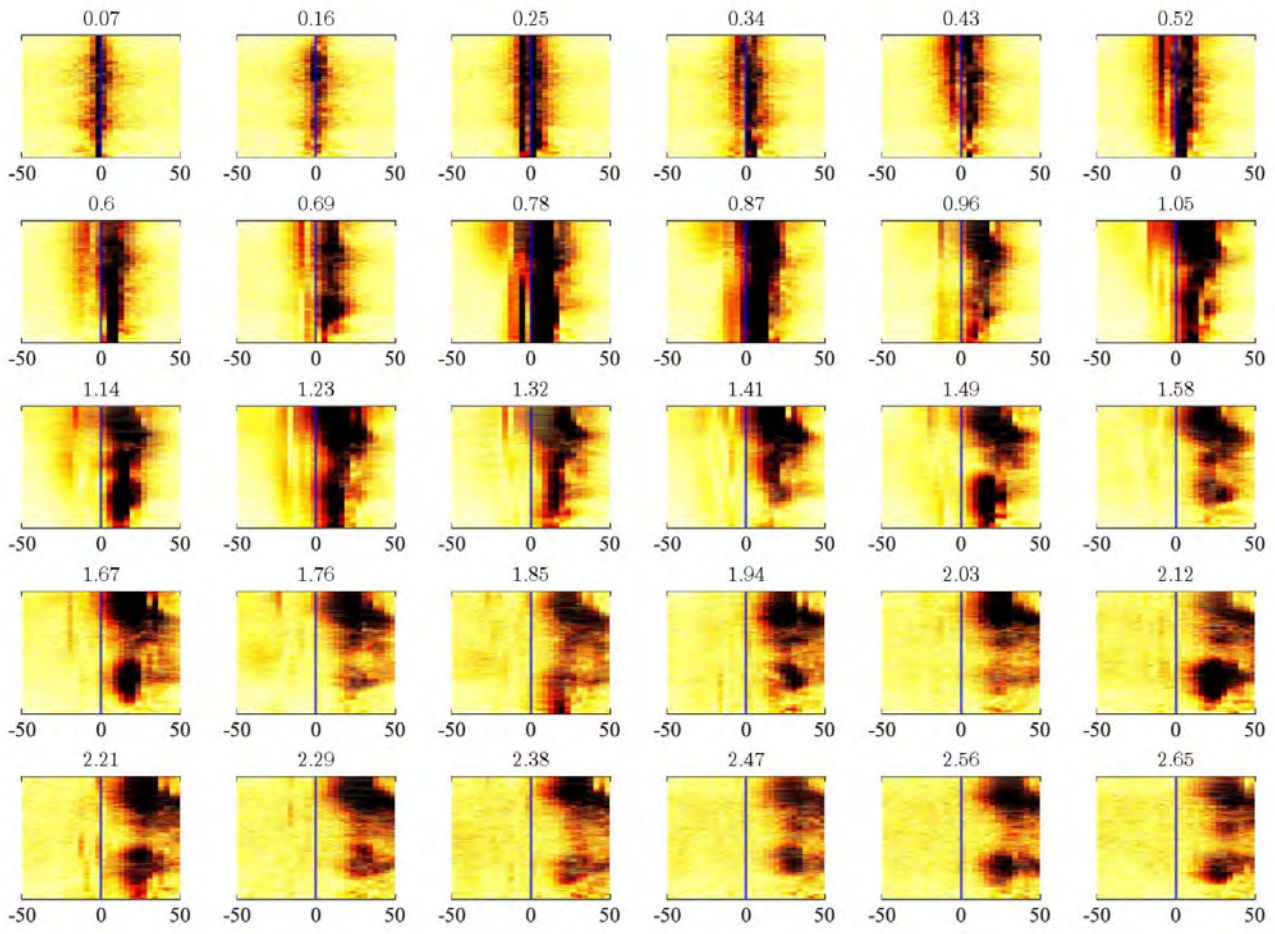

Figure 9. Magnitudes of the Fourier components for the leading SPOD modes at frequencies in the range St = [0.07, 2.65]. The x-axis is the wavenumber k (non-dimensionalized by the nozzle diameter), and the y-axis corresponds to different (r, θ) positions. The blue line at k = 0 is used to highlight the zero wavenumber.

Comparison of Different Coaxial Geometries

This subsection gives a detailed analysis of the flow features inside the nozzle by comparing results from different nozzles, including the Georgia Tech primary nozzle, the Georgia Tech coannular nozzle, and the NASA 122Am0pInt nozzle, for conditions in which the core and bypass streams have the same nozzle pressure ratio and nozzle temperature ratio. Under ideal isentropic expansion, the dual streams would have a (velocity ratio) VR = 1 and a (temperature ratio) TR = 1, therefore behaving as a single jet. However, because of the presence of viscous boundary layers and shear layers in the mixing duct, the flow is not fully mixed at the nozzle exit, which results in a reduction in thrust. Figure 10 shows the nozzle geometries being evaluated, and Figure 11 presents the velocity field inside the nozzles. The values of the mass flow rate and thrust from these configurations are given in Table 4 and are found to be lower than their ideal isentropic conditions. A more detailed analysis has been reported by Wu et al. (2024).

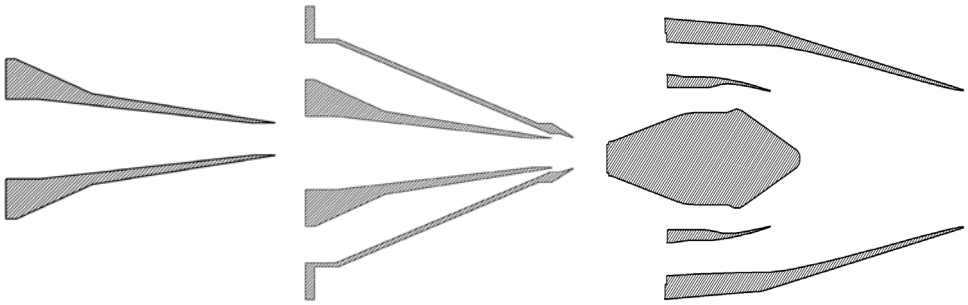

Figure 10. (a) Georgia Tech primary nozzle; (b) Georgia Tech coaxial nozzle; (c) NASA 122Am0pInt nozzle.

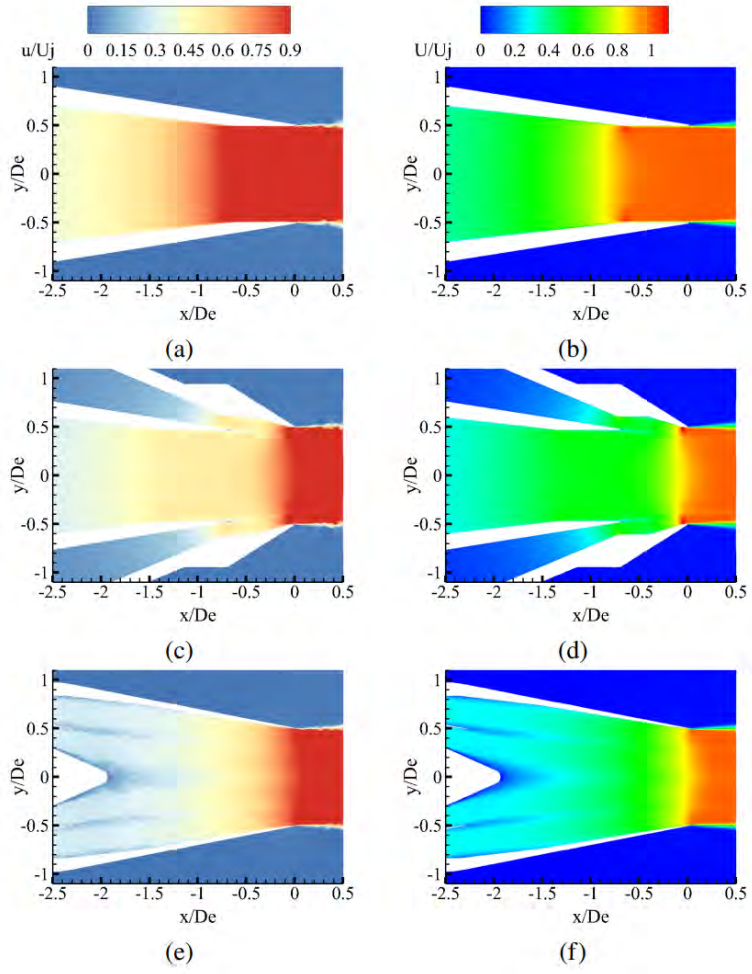

Figure 11. Instantaneous ([a], [c], [e]) and time-averaged streamwise velocity ([b], [d], [f]) inside the nozzles. From the top to the bottom row: Georgia Tech primary nozzle, Georgia Tech coaxial nozzle, NASA 122Am0pInt nozzle.

Table 4. Mass flow rate, ideal thrust, and actual thrust values for the three different nozzles. Values in brackets are the percentage differences of the actual thrust from the ideal thrust.

Nozzle	M_j	D_e	$\dot{m}/(\rho_0 c_0 A_e)$	$T/(\dot{m}c_0)$, ideal	$T/(\dot{m}c_0)$
Georgia Tech primary	0.80	1.6''	0.828	0.756	0.750 (-0.833%)
Georgia Tech coaxial	0.80	1.7''	0.821	0.756	0.740 (-2.09%)
NASA 122Am0pInt	0.98	6.0''	1.037	0.900	0.871 (-3.22%)

Comparison of a Dual-Stream Jet with the Fully Mixed Equivalent Single-Jet Condition

To study the aeroacoustic effects of temperature and velocity differences between the dual streams, LES results of Setpoint 1183 for the two NASA nozzles, 122Am0pInt and 122Am5pInt, are compared. In addition, the fully mixed equivalent single-jet (FMESJ) condition for Setpoint 1183 is determined based on Tanna's criteria (Tanna, 1980). The FMESJ flow parameters are summarized in Table 5. Under the ideal expansion assumption for each stream, the FMESJ has the same mass flow rate, exit area, and thrust as Setpoint 1183. The FMESJ simulation has been conducted using the NASA 122Am0pInt nozzle.

Table 5. Summary of the fully mixed equivalent single-jet (FMESJ) flow parameters.

Setpoint	NPR (nozzle pressure ratio)	NTR (nozzle temperature ratio)	Mfj (coflow Mach number)
1183-FMESJ	1.849	1.606	0.354

Figure 12 shows far-field acoustics for the three test points for two polar angles, $\phi = 60^{\circ}$ and $\phi = 150^{\circ}$. For the downstream direction, where $\phi = 150^{\circ}$, the FMESJ, labeled as SP1183-FMESJ, is approximately 10–15 dB quieter than Setpoint 1183, labeled as SP1183, for the same nozzle for St <1. This result agrees with the previous finding by Tanna and Morris (1985). The addition of the lobed mixer in the 122Am5pInt nozzle reduces the noise by 5–10 dB. As St increases above 1, the noise difference between SP1183-FMESJ and SP1183-Mixer diminishes. In contrast, for the upstream polar angle, SP1183-FMESJ has additional noise peaks at St = 0.2, 0.3, 0.6, 1.2, and 2.4. A more detailed discussion of these results has been provided by Wu et al. (2024).

Thrust comparisons between the 122Am0pInt nozzle, 122Am5pInt nozzle, and the SP1183-FMESJ are given in Table 6. Both NASA nozzles show a reduction of about 7% from the ideal thrust value of a FMESJ that is perfectly expanded at the nozzle exit, and 3-4% from a non-ideally expanded FMESJ. It should be noted that the FMESJ conditions for the two NASA nozzles are assumed to be the same, despite the slight differences in measured effective exit area ratios as reported by Bridges et al. (2021). Additional details can be found in Wu et al. (2024).

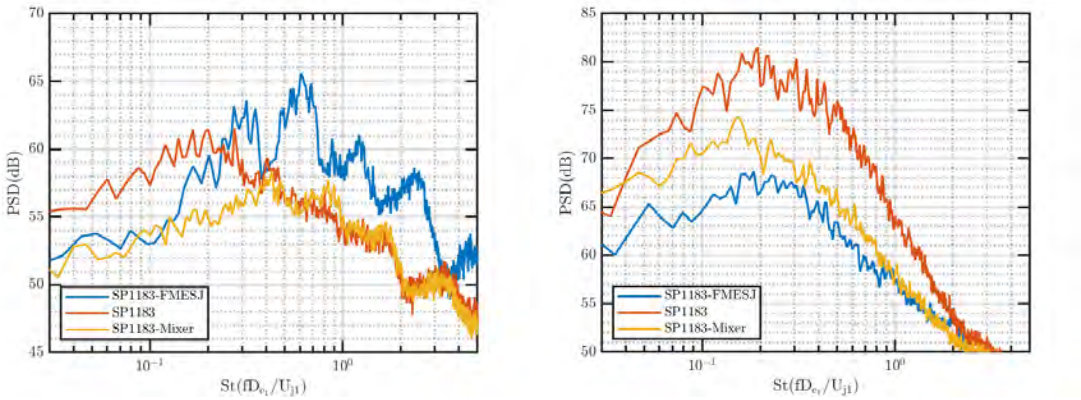

(a) $\phi = 60°, r/D_e = 100$ (b) $\phi = 150°, r/D_e = 100$

Figure 12. Comparison of far-field noise emitted from Setpoint 1183 for the NASA 122Am0pInt nozzle (labeled as SP1183), the NASA 122Am5pInt nozzle (labeled as SP1183-mixer), and the fully mixed equivalent single jet for the NASA 122Am0pInt nozzle (labeled as SP1183-FMESJ). PSD: power spectral density.

Table 6. Mass flow rate, ideal thrust, and actual thrust values for the NASA nozzles at Setpoint 1183, compared to the FMESJ condition. Values in brackets are the percentage differences of the actual thrust from the ideal thrust.

Nozzle	D_e	$\dot{m}/(\rho_0 c_0 A_e)$	$T/(\dot{m}c_0)$, ideal	$T/(\dot{m}c_0)$
NASA 122Am0pInt	6.0''	0.804	1.14	1.05 (-7.31%)
NASA 122Am5pInt	6.0''	0.815	1.14	1.06 (-6.56%)
1183 - FMESJ	6.0''	0.812	1.14	1.10 (-3.31%)

Milestones

- Conducted LESs for test cases corresponding to the NASA Plug20 experiment for two different coaxial nozzles with an internal plug.
- Identified and characterized numerical errors associated with the mesh inside the nozzle, the FWH sampling surface, and the external boundary layer model.
- Performed acoustics and thrust comparisons between the Georgia Tech and NASA nozzles and fully mixed equivalent single-jet conditions.

Major Accomplishments

- Made steady progress in the high-fidelity simulations of jet noise in accordance with the test plan established by our ASCENT Project 059 partners.
- Conducted LESs have been conducted for the Georgia Tech coannular nozzle and two NASA nozzles from the Plug20 campaign using the compressible solver CharLES developed by Cascade Technologies. For the NASA nozzles, agreement between the LES and experimental measurements is particularly good at downstream angles, though discrepancies are observed at upstream and sidelines angles. Further investigation of these discrepancies is planned for Year 4.
- Quantified the thrust loss due to mixing inside the nozzle as well as viscous effects in the boundary layer for the NASA nozzles and the Georgia Tech primary and coaxial nozzles using the LES data.

Publications

Wu, G. J. (2024). *Towards quieter supersonic flight: a computational aeroacoustic study of high-speed jets* (Ch.4) [Doctoral dissertation, Stanford University]. Stanford University.

Shanbhag, T. K., Zhou, B. Y., Ilario, C. R. S., & Alonso, J. J. (2024, January 8-12). *An AD framework for jet noise minimization using geometrical acoustics* [Conference paper]. AIAA SCITECH 2024 Forum, Orlando, Florida.

Wu, G. J., Martin, O. G., & Lele, S. K. (2024, June 4-7). *Computational aeroacoustic study of coannular nozzles with internal mixing geometries at high transonic Mach numbers* [Conference paper]. 30th AIAA/CEAS Aeroacoustics Conference, Rome, Italy.

Shanbhag, T. K., Zhou, B. Y., Ilario, C. R. S., & Alonso, J. J. (2024, June 4-7). *Adjoint-based jet noise minimization using geometrical aeroacoustics* [Conference paper]. 30th AIAA/CEAS Aeroacoustics Conference, Rome Italy.

Martin, O. G., Wu, G. J., & Lele, S. K. (2024, July 29-August 2). *Noise predictions of a dual-stream jet with forced internal mixing* [Conference paper]. AIAA Aviation Forum and ASCEND 2024, Las Vegas, Nevada.

Shanbhang, T. K. (2024). *RANS-based methods for the prediction and reduction of jet noise* [Doctoral dissertation, Stanford University]. Stanford University.

Outreach Efforts

Communication with ASCENT Project 059 partners and NASA scientists has been established. Deeper collaboration with the Georgia Tech experiments and with NASA scientists is expected as the project progresses further.

Awards

None.

Student Involvement

Two graduate students, G. Wu and O. Martin, participated in this task for Year 3. G. Wu has since graduated from Stanford.

Plans for Next Period

- Perform LES at two additional supersonic set points for the 122Am5pInt NASA Plug20 nozzle configuration (1203 and 1233). This will enable us to assess the ability of the LES-FWH method to capture broadband shock-associated noise.
- Compare the near-field velocity statistics at set point 1203 to PIV measurements, which have been made available (Bridges and Wernet, 2023).
- Perform LES at Setpoint 4200 for the 122Am0pInt NASA Plug20 nozzle configuration. These results will help us to understand whether the noise underprediction at Setpoint 1183 is related to heating of the jet or the temperature differential between streams.
- Use the LES data to perform linear stability analysis (LSA) inside the 122Am5pInt nozzle and assess the potential of resonance developing between the downstream-traveling coherent structures shed from the lobed mixer and upstream-traveling duct modes.

References

Bridges, J., & Wernet, M. P. (2023). Plug20 test report: particle image velocimetry (PIV) measurements (NASA TM-20230006779). NASA Glenn Research Center. https://ntrs.nasa.gov/api/citations/20230006779/downloads/TM-20230006779.pdf

Bridges, J. (2023, June 12-16). Diagnosing Noise Features of Internally Mixed, External Plug Exhaust Systems [Conference paper]. *AIAA AVIATION 2023 Forum*. https://doi.org/10.2514/6.2023-3210

Bridges, J. E., Podboy, M. P., Gary, G., & Wernet, M. (2021). Plug20 test report (NASA/TM-20210010291). NASA Glenn Research Center. http://ntrs.nasa.gov/api/citations/20210010291/downloads/TM-20210010291.pdf

Bridges, & Wernet. (2004). Cross-Stream PIV Measurements of Jets with Internal Lobed Mixers (NASA/TM-2004-213206). NASA Glenn Research Center. https://ntrs.nasa.gov/citations/20040152075

Stich et al. (2024). Noise Prediction of Multi-Stream Internally Mixed Jets with External and Internal Plugs Using Large-Eddy Simulation [Conference Paper]. *AIAA/CEAS Aeroacoustics Conference*, Rome Italy. https://arc.aiaa.org/doi/10.2514/6.2024-3377

Tanna, H. K., & Morris, P. J. (1985). The noise from normal-velocity-profile coannular jets. *Journal of Sound and Vibration, 98*(2), 213-234. https://doi.org/10.1016/0022-460X(85)90386-4

Tanna, H. K. (1980). Coannular jets—Are they really quiet and why? *Journal of Sound and Vibration, 72*(1), 97-118. https://doi.org/10.1016/0022-460X(80)90710-5

Wu, G. J., Martin, O. G., & Lele, S. K. (2024, June 4-7). Computational aeroacoustic study of coannular nozzles with internal mixing geometries at high transonic Mach numbers [Conference paper]. *30th AIAA/CEAS Aeroacoustics Conference*, Rome, Italy. https://arc.aiaa.org/doi/10.2514/6.2024-3198

Task 3 – Conduct RANS-Based Simulation, Modeling, and Validation of Jet Noise Predictions

Stanford University

Objectives

The objective of this task is a coordinated development of both low- and high-fidelity approaches for jet noise predictions. For the low-fidelity approach, RANS computations of a broader range of configurations and operating conditions relevant for civil supersonic aircraft will be performed and used to develop improved jet noise source models and more accurate far-field noise propagation kernels.

Research Approach

Turbulent Scales Modeling

The ASCENT Project 059D team is continuing work to model the turbulent length and time scales used in standard RANS-based acoustic source models. In previous work, our team studied the two-point fourth order velocity fluctuation correlation data extracted from LES databases of round jet simulations at Mach numbers of 0.5 and 0.9. In this research period, the same framework has been applied to extract the turbulent length and time scales at different points in the hydrodynamic source-containing region from this unsteady flow data on the basis of two common frameworks used in high frequency modeling, assuming that the spatial and temporal components of these correlation functions are separable. The validity of the widely applied assumption that these turbulent scales may be assumed universally proportional to the dimensionally derived dissipation scales arising from RANS-based turbulent quantities is investigated. Our team has found that this assumption breaks down over the potential core, where in the context of both the source models studied, the length and time scales appear to be relatively constant (see Figure 13). In the case of the time scale, we find that the constant of proportionality is not in fact constant over space but may be well approximated by a simple radial weight function. Our proposed 'weighted scales' model offers improved predictive capability as compared with the baseline Ribner source model for an unseen jet case (see Figure 14). The similarity of both the length and time scale distributions between the two Mach numbers studied, supported by the experimental and numerical observations of previous authors, suggest that this type of prediction framework could be widely applicable across jet operating conditions (see Figure 15 and Figure 16). However, this assumption will require further verification. This could take the form of either repeating the type of 'scale extraction' analysis performed in the present work on a more extensive set of unsteady simulations or experimental measurements or testing the far field predictions of similar weighted scales models against other jet noise experiments.

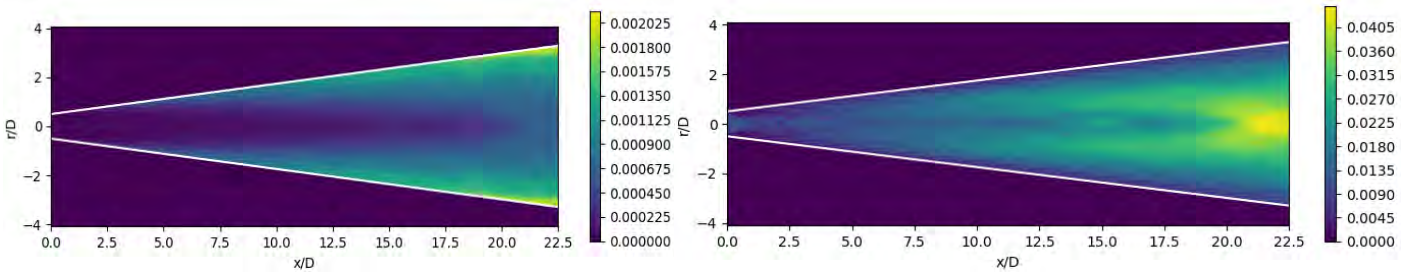

Figure 13. LES consistent scales for RANS modeling, time scale (left) and length scale (right).

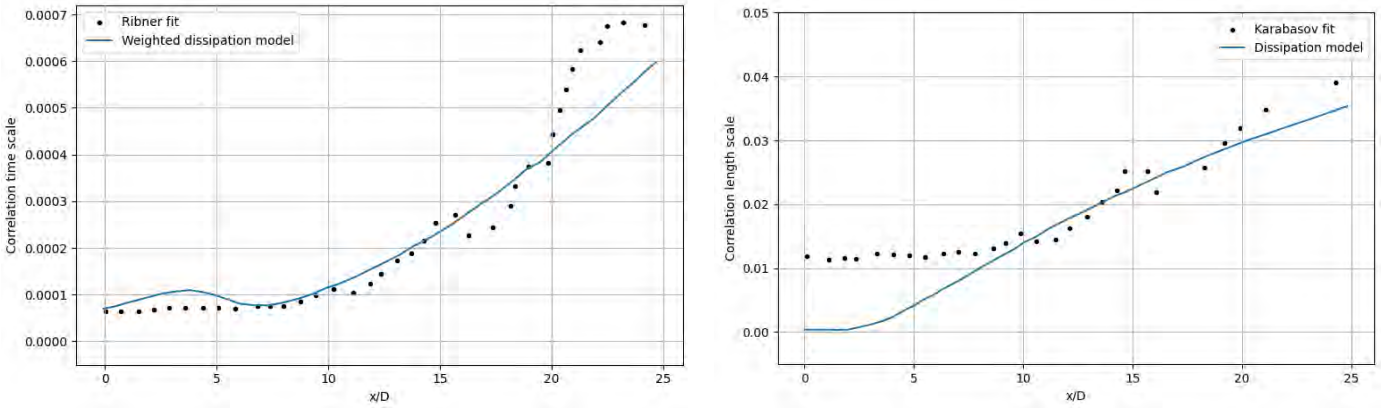

Figure 14. Comparison of fitted LES scales (symbols) and weighted dissipation model scales (line) along jet centerline.

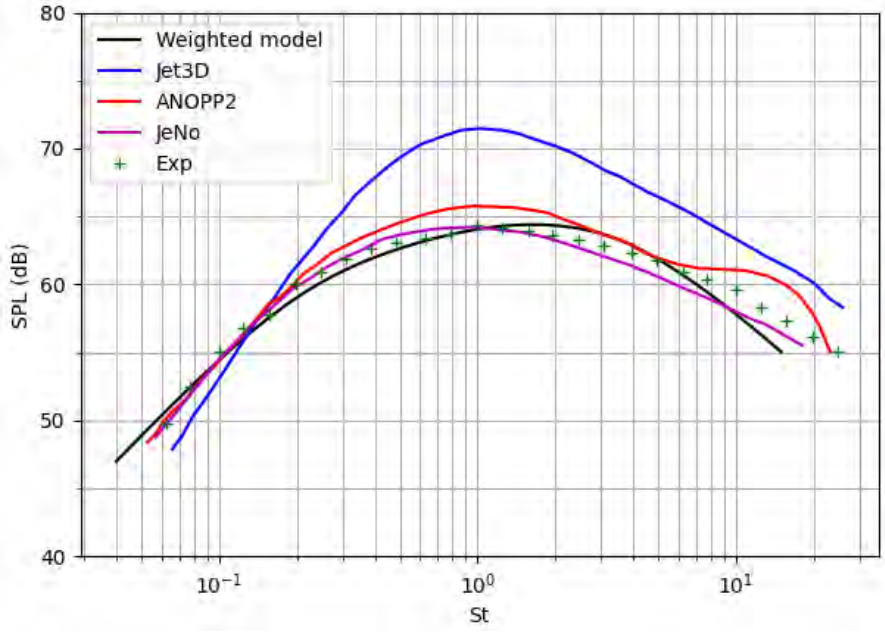

Figure 15. Convergent straight nozzle, M = 0.5: far field spectrum at r = 50.8D, θ = 90 deg

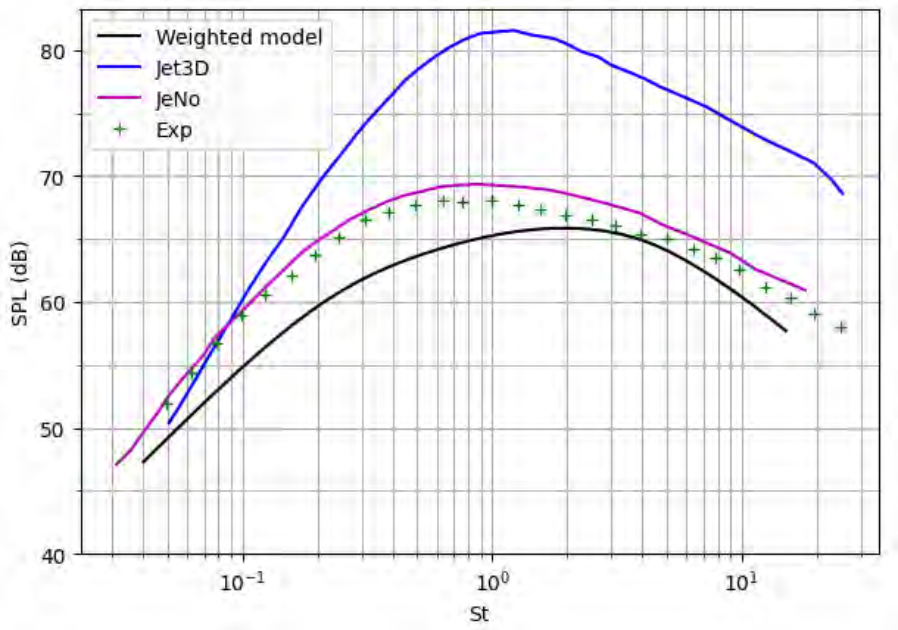

Figure 16. Convergent straight nozzle, M = 0.5: far field spectrum at r = 50.8D, θ = 50 deg

Wavepacket Jitter Modeling

The ASCENT Project 059(D) team continued our effort towards modeling far field noise associated with the large-scale coherent structures in the jet flow. Our team proposed a predictive model form of the near field turbulent velocity fluctuation cross spectral density, based on a line source representation building upon the previous works of Crow, Mollo-Christensen (1967), Cavalieri and Agarwal (2014). Resolvent analysis was used, augmented by a RANS-based eddy viscosity model, to deduce properties of the wavepacket spatial structure. This information was then used to reconstruct the cross-spectral density matrix (CSD), which is augmented with an explicit model of axial coherence decay along the wavepacket structure, observed experimentally as jitter. The coherence function used to represent the stochastic effects of jitter in the frequency domain is chosen to require minimal model parameter tuning, while offering an improved representation of the true CSD. The values of these parameters are selected, both based on LES conical nozzle round jet data at Mach number 0.5 and 0.9, and experimental measurements of far field acoustic directivity for round jets at subsonic Mach numbers between 0.4 and 0.9. In both cases, there is an observed linear scaling of the coherence length scale with wavelength (see Figure 17), supporting the hypothesis of this and previous works, that the wavepacket sources considered exhibit self-similar properties, not only in their spatial growth and decay but also in their streamwise coherence. However, while the LES-consistent parameters show this linearity between the coherence length and the acoustic wavelength, the experiment-consistent parameters suggest that the hydrodynamic wavelength is more relevant. The resulting global source model is demonstrated to be capable of low frequency noise prediction on a round jet test case at M = 0.9, and a promising degree of agreement with experimentally measured far field directivity profiles is obtained (see Figures 18 and 19). With an unchanged parameter set, the model also has some preliminary applicability to supersonic jet cases, with minor modifications to the CSD construction methodology. Additional details on this work can be found in Shanbhag (2024).

Given the relatively small amount of data used to select model parameters in this study, it will be important to repeat the model calibration in further work, using a greater variety of axisymmetric jet data across different Mach numbers and temperature ratios, to verify the trends that we observe. The recent experimental works of Hasparyk et al. (2024) have suggested that properly calibrated global source models proceeding along the lines in this work may be capable of shallow angle acoustic predictions accurate to within 1.5 dB of measured values, underlining the potential value of developing these methods further.

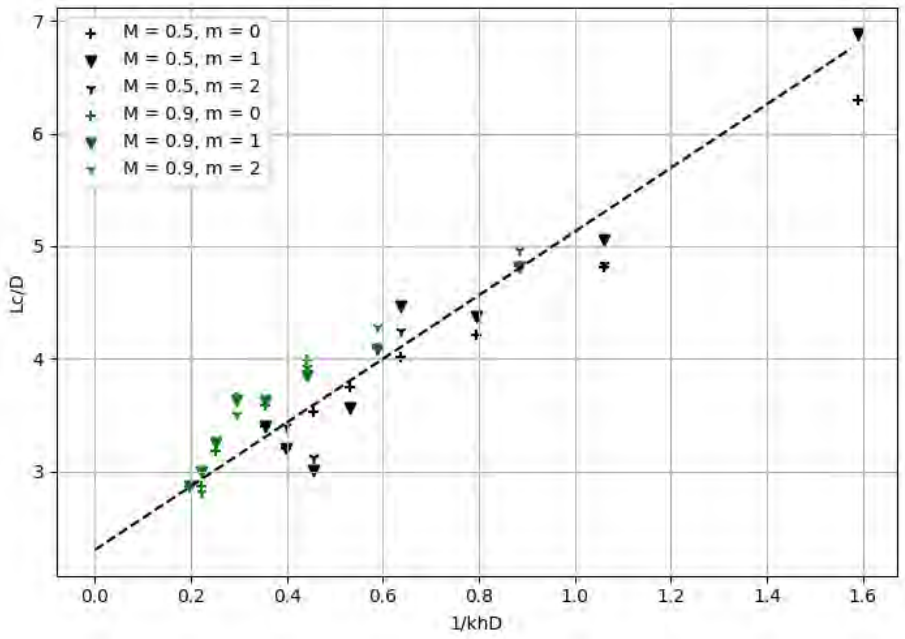

Figure 17. Optimal value of coherence length scale parameter vs. acoustic wavelength.

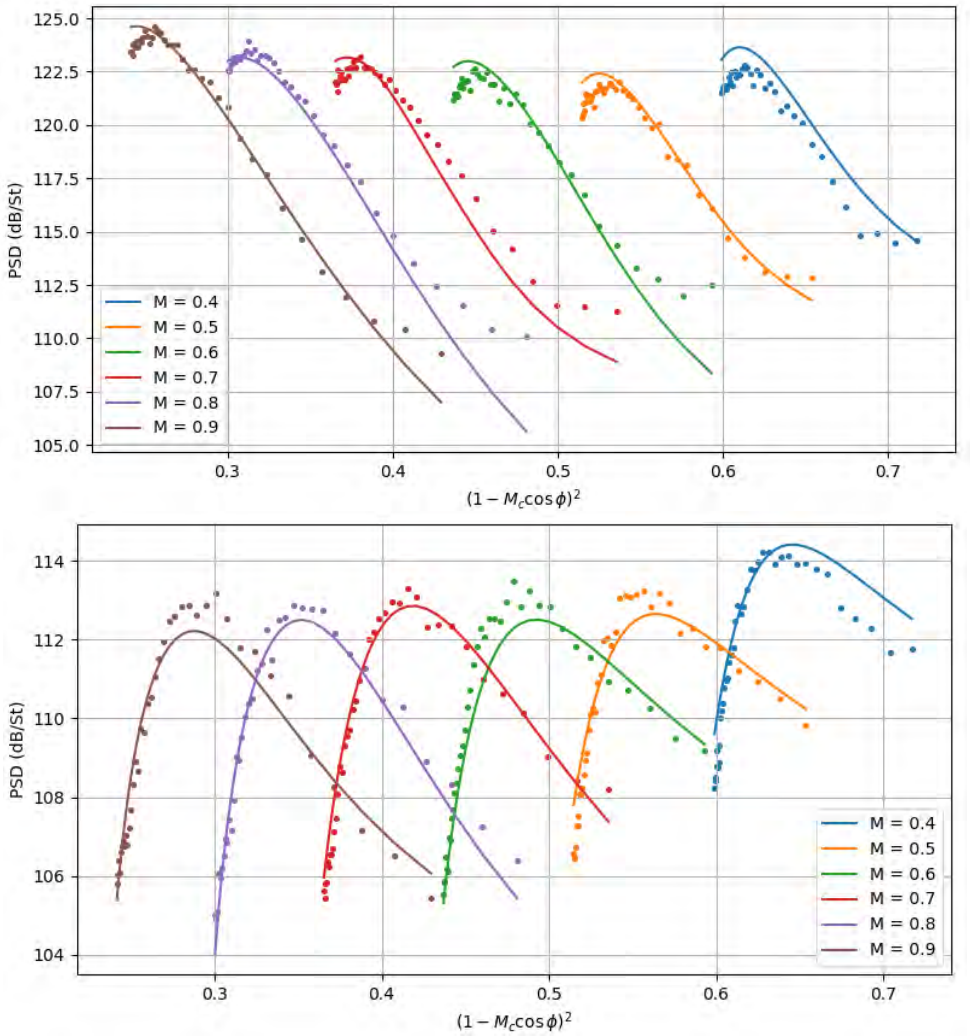

Figure 18. Predicted acoustic directivity for Poitiers jet compared against experimental measurements (Hasparyk et al., 2024) St = 0.2 (upper) and St = 0.6 (lower).

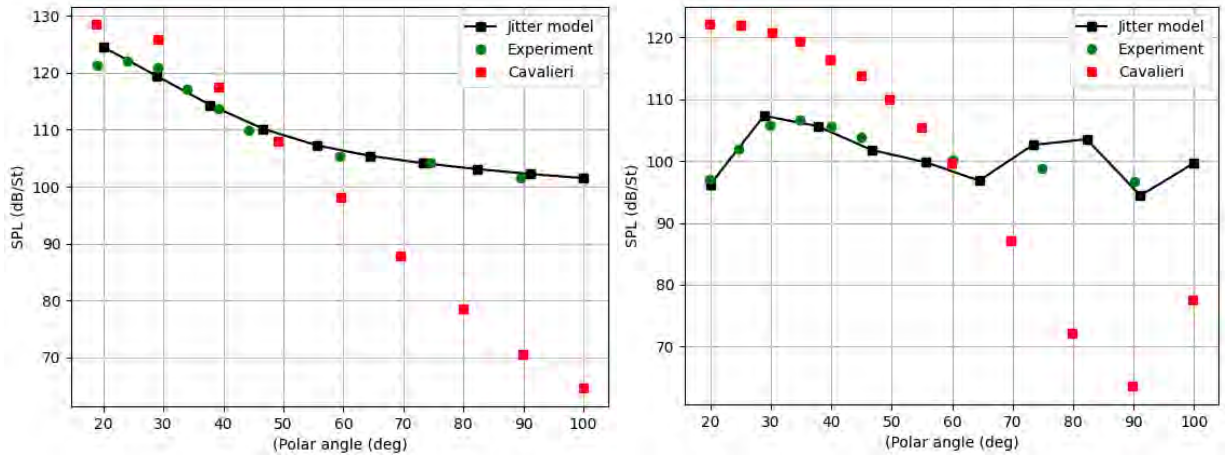

Figure 18. Comparison of M = 0.9 round jet directivity at St = 0.2 (left) and St = 0.75 (right).

Adjoint (AD) Framework for Chevron Design Optimization

The ASCENT Project 059(D) team applied our previously developed framework for efficient adjoint-based design to the optimization of two baseline nozzle geometries. Our design framework allows the incorporation of realistic constraints on quantities such as thrust. The optimal designs produced show the capability of such a design framework to make significant noise reductions through minor geometric alterations. The alterations in geometry and flow field observed appear to be logically consistent with the conclusions drawn by the parametric design studies of previous authors looking to minimize jet noise through shear layer interference.

Figure 20 and Figure 21 show the results of a series of gradient-driven design iterations, beginning from the Poitiers round nozzle geometry. The results of two optimization problems are shown here: (1) the unconstrained problem, in which the computed nozzle thrust is allowed to vary freely, and (2) the constrained problem, in which thrust is maintained within 10% of the baseline value via incorporation of a penalty function. While this implementation does not guarantee satisfaction of the thrust constraint at every design iteration, the converged result of the optimization problem should satisfy the constraint exactly. The chosen design objective in both problems was the averaged sound pressure level (SPL) at St = 0.1, St = 0.3 and St = 1.0, computed over four equally azimuthally spaced sideline observers placed at r = 50D from the nozzle exit. It should also be noted that both problems were run under one additional constraint: that the nozzle exit area was not permitted to increase beyond a certain point. This was found to be necessary during early design iterations, when the direction of the parameter gradient tended to open the nozzle exit - beyond a certain point this would result in the development of a choked throat and weak normal shock system. As an internal shock would be unacceptable to nozzle performance, this constraint was added to all design iterations and enforced via a backtracking line search along the computed gradient direction.

Comparing the two optimized geometries, both develop along similar lines. When prevented from simply expanding at the exit to reduce axial flow velocity, the nozzle instead develops an azimuthal radius asymmetry or 'waviness', similar to what is seen in a lobed mixer design. The amplitude of this waviness is significantly greater in the unconstrained case, whose geometry grows into something closer resembling lobes. The constrained case develops a squarer exit profile, whose final area is slightly contracted compared to the initial design point. Looking then at the relative performance of the two optimized geometries, the overall noise improvement in the constrained case is not much worse than that in the unconstrained case, with reductions of 12dB and 15dB respectively. This suggests that while traversing this region of the design space, disruption of the shear layer, and the shape and amplitude of the associated turbulent kinetic energy field, via relatively small azimuthal variations has more impact on the far field noise than changes in the bulk axial velocity via exit area variations. It can also be seen that the single frequency noise objective monotonically reduces over both optimization problems, albeit to a lesser extent than the overall noise objective. This suggests that although the changes made during the design process have not resulted in crossover explicitly, they have resulted in an overall 'flattening' of the spectrum, with the higher frequency part of the spectrum being raised in comparison to the low frequency part. This is illustrated clearly by the optimized geometry spectra plotted in Figure 22. In both cases, however, the nozzle 'squaring' that results in noise reduction also results in significant thrust deviation, corresponding to a loss of approximately 7% even

in the constrained case. In a realistic optimization scenario, this would represent a design trade-off skewed too far in favor of noise reduction at the expense of propulsive performance. Repeating these optimizations with significantly tighter aerodynamic constraints will be important to demonstrate the real-world applicability of the method.

Considering the observed geometry changes in the context of existing design studies, there have been a number of investigations into the performance of similarly 'squared' or rectangular exit nozzles as compared to the round jet baseline. The conclusions of these studies have varied. The work of Tam and Zaman (2000) pointed out that beyond an initial region of evolution, both the flow field and radiated sound field associated with a square or rectangular jet is, “quite axisymmetric and practically the same as that of a circular jet.” In contrast, the experimental studies of Massey, Ahuja and Gaeta (2004), which examined unheated subsonic jets issuing from rectangular nozzles of varying aspect ratio, found that sideline OASPL was lowered for the rectangular geometries compared with the round baseline. Furthermore, this noise reduction effect was found to be more pronounced in lower AR rectangular exits, suggesting that an optimal geometry closer to a square is not unreasonable. The subsequent experiments of Bridges (2012) corroborated these observations and further noted that the non-square rectangular geometries result in an azimuthally varying effect on OASPL, whereby a reduction in noise was observed on the narrow side of the nozzle, but noise on the wide side was increased. It is possible that repeating this optimization problem without azimuthal averaging of the noise objective may therefore result in larger aspect ratio, narrowing in the direction of the chosen observer. Further work on this topic would include application of the framework to a greater range of baseline geometries, and investigation in detail the effects of different parameterizations of the geometry, and the outcomes of optimizing for multiple objectives.

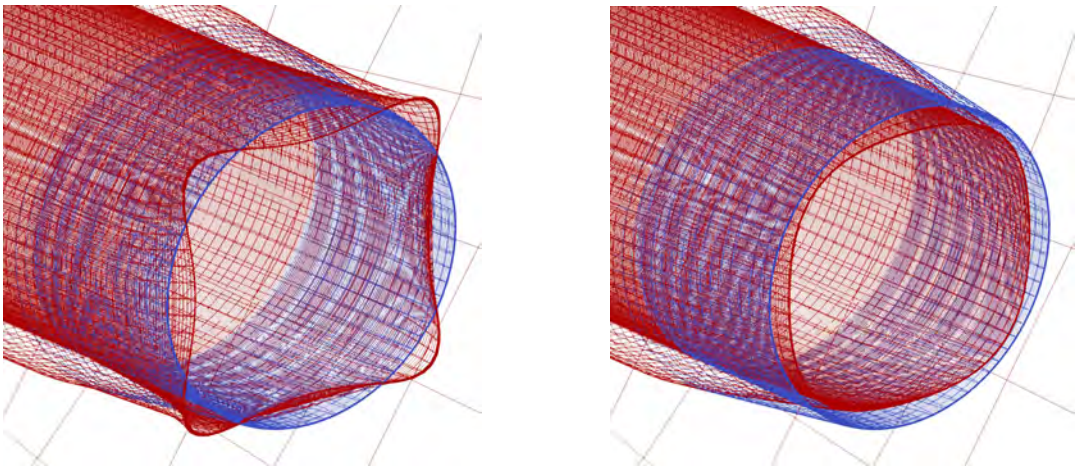

Figure 19. Poitiers jet optimization results: unconstrained (left) and constrained (right) cases.

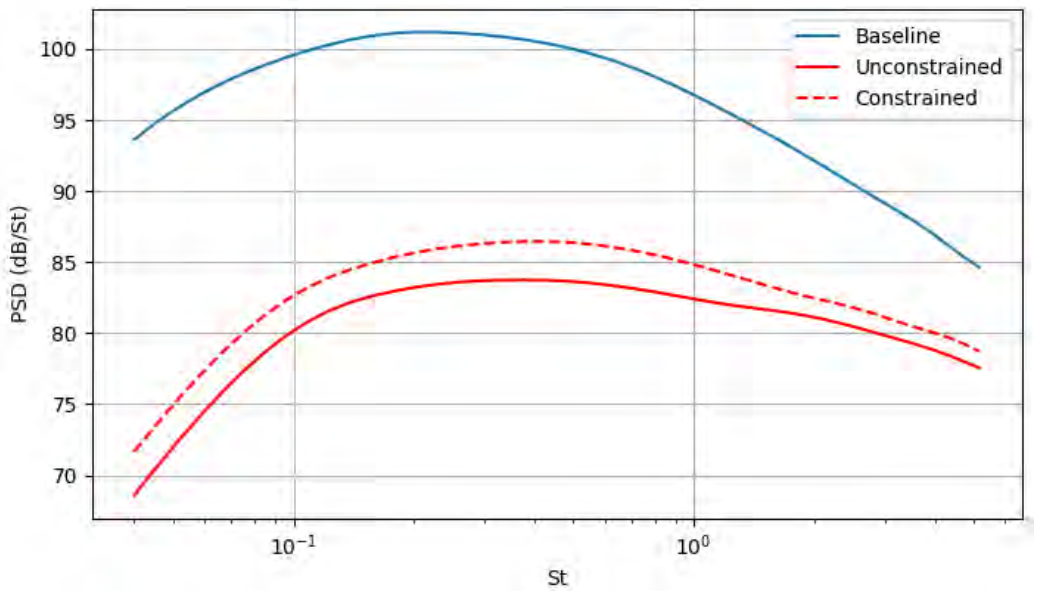

Figure 21. Baseline and optimized far field spectra for Poitiers optimization cases.

Milestones

- Applied our modular implementation of the low-fidelity (RANS-based) acoustic prediction tool and AD-enabled adjoint design framework to two simple nozzle optimization problems.
- Extended our predictive model for the shallow-angle low-frequency component of jet noise based on resolvent analysis.

Major Accomplishments

- Demonstrated a simple predictive model of the acoustic line source CSD, using an eddy viscosity-augmented resolvent analysis to deduce coherent wavepacket structures in the hydrodynamic region of a jet, coupled with an explicit modified exponential function to account for the effects of axial coherence decay and the corresponding jitter. Preliminary predictions of far field noise using this model have shown reasonable agreement with experimental measurements.
- Demonstrated our AD-enabled framework for RANS-based jet noise minimization via a set of gradient-driven optimization steps on round and chevron baseline nozzle geometries. The resulting geometry changes are physically consistent with the conclusions of previous parametric study into the variation of nozzle geometries and jet flow fields for the purpose of noise reduction.

Publications

Shanbhag, T. K. (2024). *RANS-based methods for the prediction and reduction of jet noise* [Doctoral dissertation, Stanford University], Stanford University.

Outreach Efforts

None.

Awards

None.

Student Involvement

T. Shanbhag has led the efforts with geometrical acoustics, AD-enabled nozzle optimization, and wavepacket jitter modeling described for Task 3.

References

Bridges, J. (2012). Acoustic Measurements of Rectangular Nozzles with Bevel. *18th AIAA/CEAS Aeroacoustics Conference (33rd AIAA Aeroacoustics Conference)*.

Cavalieri, A.V.G., & Agarwal, A. (2014). Coherence decay and its impact on sound radiation by wavepackets. *Journal of Fluid Mechanics*, 748:399–415. https://doi.org/10.1017/jfm.2014.186

Crow, S.C. (1972). Acoustic gain of a turbulent jet. *Annual Meeting of the APS Division of Fluid Dynamics*.

Crow, S.C., & Champagne, F.H. (1971). Orderly structure in jet turbulence. *Journal of Fluid Mechanics*, 48(3):547–591.

Hasparyk, B., Jordan, P., Lesshafft, L., Pickering, E., & Colonius, T. (2024). Resolvent Modeling of Subsonic Jet Noise [Conference Paper]. *30th AIAA/CEAS Aeroacoustics Conference*. https://arc.aiaa.org/doi/10.2514/6.2024-3199

Hasparyk, B., Jordan, P., Martini, E., & Lesshafft, L. (2024). The Shape of Subsonic Jet Noise. *30th AIAA/CEAS Aeroacoustics Conference*. https://arc.aiaa.org/doi/10.2514/6.2024-3199

Massey, K., Ahuja, K., & Gaeta, R. (2004). Noise scaling for unheated low aspect ratio rectangular Jets [Conference Paper]. *10th AIAA/CEAS Aeroacoustics Conference*. https://arc.aiaa.org/doi/10.2514/6.2004-2946

Mollo-Christensen, E. (1967). Jet Noise and Shear Flow Instability Seen From an Experimenter's Viewpoint. *Journal of Applied Mechanics*, 34(1):1–7. https://doi.org/10.1115/1.3607624

Tam, C.K.W., &. Zaman, K.B.M.Q. (2000). Subsonic jet noise from nonaxisymmetric and tabbed nozzles. *AIAA Journal*, 38(4):592–599. https://arc.aiaa.org/doi/10.2514/2.1029

Project 059(E) Moderate-fidelity Simulations for Efficient Modeling of Supersonic Aircraft Noise

The Pennsylvania State University

Project Lead Investigator

Philip Morris
Boeing/A.D. Welliver Professor Emeritus
Department of Aerospace Engineering
Pennsylvania State University
233C Hammond Building
University Park, PA 16802
814-863-0157
pjm@psu.edu

University Participants

Pennsylvania State University (Penn State)

- P.I.s: Dr. Philip Morris (P.I.), Dr. Daning Huang (co-P.I.)
- FAA Award Number: 13-C-AJFE-GIT-070
- Period of Performance: January 1, 2024, to December 31, 2024
- Tasks:
  1. Grid generation and large eddy simulations (LESs)
  2. Hybrid Reynolds-averaged Navier–Stokes (RANS) and LES approach for noise efficient predictions

Project Funding Level

The ASCENT Project 059€ is funded at the following level: $100,000 from Federal Aviation Administration (FAA) and $100,000 in cost-sharing funding provided by Gulfstream Aerospace Corporation, a General Dynamics Company.

Investigation Team

Dr. Philip Morris (P.I.), All Tasks
Dr. Daning Huang (co-P.I.), All Tasks
Ms. Dana Mikkelsen (graduate student), All Tasks
Mr. Aravinth Sadagopan (graduate student), Computational fluid dynamics (CFD) tasks

Project Overview

The purpose of this project is to develop and assess efficient computational tools to simulate the flow and noise of civil supersonic aircraft engines.

The prediction of noise from supersonic jets, particularly when noise reduction devices are present, is a challenging computational task. Methods based on RANS solutions are relatively inexpensive to perform and provide satisfactory predictions of the average flow field, even for quite complicated geometries. The subsequent prediction of noise according to acoustic analogies is highly efficient but faces difficulties when the nozzle does not have simple axisymmetric geometry. Methods based on LESs provide considerably more information than those based on RANS methods about the unsteady flow and the noise generated. However, LESs are computationally expensive, particularly when the engine geometry is complex. This complexity is encountered in the case of nozzles with noise reduction devices, such as internal mixers. Noise predictions based on LES can be made quite efficiently by using the Ffowcs Williams and Hawkings (FW-H) acoustic analogy (Farassat and Succi, 1982; Ffowcs Williams and Hawkings, 1969), but long-time records are required to predict the noise radiated to far-field observers, thus adding additional expense to LES.

The approach in ASCENT Project 059(E) strikes a compromise between the accuracy and high computational cost of LES and the noise prediction limitations of RANS-based simulations. The simulations being conducted in the initial stage of the project use RANS, and these calculations serve as a starting point for the LES. In anticipation of the addition of internal mixers to the nozzle geometries, only RANS simulations are planned to be conducted for the internal flow; then LES, coupled with the FW-H acoustic analogy, will be used to predict the external flow and the noise generated. The RANS solution at the jet exit will be used as an initial condition for the external LES. This process will require the addition of some unsteady information, as guided by a very limited number of LESs. This approach will reduce the total computational cost because it removes much of the geometric complexity and the associated grid requirements for LES of the internal flow.

The utility of this approach is that it will make LES for nozzles with noise reduction devices more accessible to more users, particularly industry engineers with limited computational resources and time available to perform multiple simulations in the design process.

In addition, the LES-based predictions will be supplemented by more traditional acoustic analogy approaches based on RANS. As described below, the future research direction will combine a RANS-based acoustic analogy approach for noise radiation to large angles to the jet downstream axis and a very coarse LES approach for noise radiation in the peak noise radiation direction.

If successful, ASCENT Project 059(E) will develop methods to predict the noise generated and radiated by civil supersonic aircraft engines. The developed tools should enable airframe and engine manufacturers to assess the noise impacts of engine design changes, and to determine whether the designs will meet current or anticipated noise certification requirements.

Project Direction Change

During the first project year (Year 1), because of a change in direction from the originally proposed research, the original project was split into two parts. A new ASCENT Project 059(A), being conducted at the Georgia Institute of Technology (Georgia Tech), examines the effects of different inlets and the introduction of noise reduction devices on the performance of selected engine cycles and geometries. A new ASCENT Project 059(E), which is the topic of this report, focuses on the prediction of the flow and noise from different nozzle configurations.

Major Accomplishments

The tasks for this project year included continued RANS simulations and LESs. The focus was on the Georgia Tech dual-stream nozzle. LES simulations were performed at Gulfstream Aerospace, by using different grid resolutions to determine the flow resolution relative to different turbulent length scales. An acoustic analogy code was based on Tam and Auriault's model (Tam & Auriault, 1999) and integrated with output from the RANS simulations. Noise predictions with this method have been made for the Georgia Tech dual-stream nozzle and compared with measurements.

Task 1 - Grid Generation and LESs

Pennsylvania State University
Gulfstream Aerospace

Objectives

The objectives of this task are to (1) develop a grid based on the natural scales of the turbulence and (2) use this grid to make flow and noise predictions for the dual-stream nozzle designed by Georgia Tech. This converging nozzle has a core nozzle exit diameter of 0.04064 m, a bypass duct exit diameter of 5.334 cm, and an exhaust nozzle with an exit diameter of 4.32 cm. The nozzle has a length of 3.02 cm.

Research Approach

One of the major questions that arises when developing an LES simulation is the selection of the appropriate size for both the grid resolution and the time step. If the discretization is too coarse, the solvers will not converge to give accurate data. However, there is a point at which further refinement of the grid and time steps results in increased computation times that do not reflect an adequate improvement in the solution. The challenge is finding that point without participating in

costly trial and error exercises. This report investigates grounding the grid discretization, and thus also the time discretization, within the concept of the turbulent energy cascade.

In the present approach, three length scales were used, listed from largest to smallest: (1) the energy-containing length scale characterized by a mixing length, (2) the Taylor microscale, which is an intermediate length scale between the dissipation range and the inertial subrange at which fluid viscosity affects the turbulence in the flow, but the kinetic energy is not dissipated into heat, and (3) the Kolmogorov microscale, which characterizes the smallest length scale where viscous dissipation effects dominate. These scales can be estimated based on a RANS simulation.

To begin with, a polyhedral grid of arbitrary grid size was generated in SimCenter®-STAR CCM+[1]. This grid contained twelve levels of grid refinement that fanned out from the nozzle exit, with the finest refinement near the nozzle exit and growing coarser with each subsequent level. The refinement regions chosen were arbitrary, with the denser regions kept smaller to conserve grid and file size. Figure 1 shows the grid near the nozzle exit, and the refinement cones are shown in Figure 2.

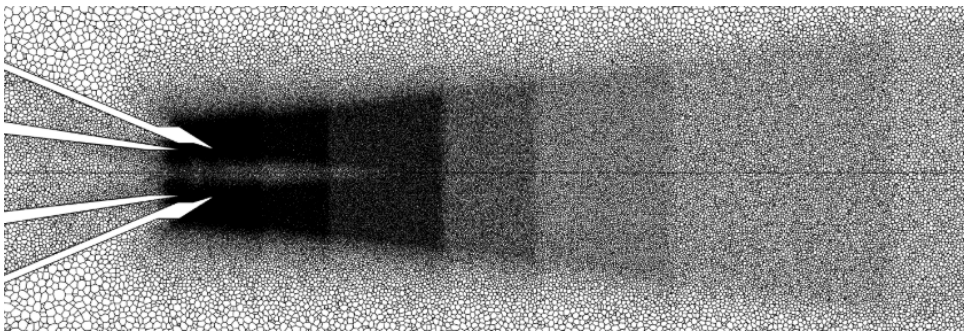

Figure 1. Grid refinement to 15 jet diameters downstream.

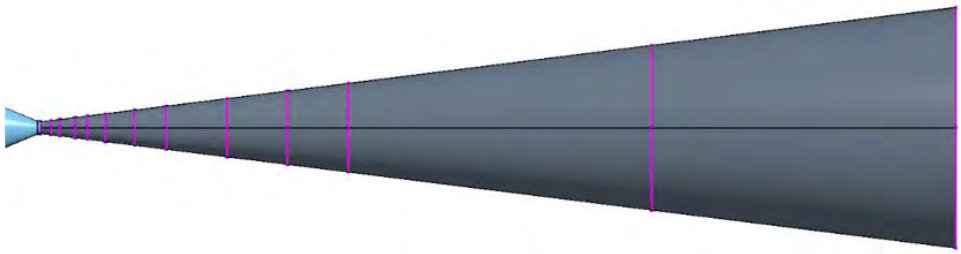

Figure 2. Grid refinement cones extending to 2.5, 5, 7,5, 10, 20, 30, 40, 50, 100, and 150 diameters downstream.

The smallest grid size used at the nozzle exit was 0.01 inches, or 0.625% of D_j. The largest grid size at 150 D_j downstream was 1.5 inches, or 93.75% of D_j.

Figure 3 shows the Taylor microscale, turbulent mixing length, and grid length extracted from a RANS calculation at each x / D_j location. The initial grid created for this simulation ("original grid") was biased close to the Taylor microscale, so the grid length was increased to fall more evenly between the two length scales ("adjusted grid").

® SimCenter is a registered trademark of Siemens Industry Software N.V., Leuven. Belgium.
[1] SimCenter STAR CCM+ is a multiphysics CFD software that models complex fluid dynamics applications for real-world conditions including single-phase, multiphase, reacting, heat transfer, aeroacoustics, and fluid-structure interaction simulations.

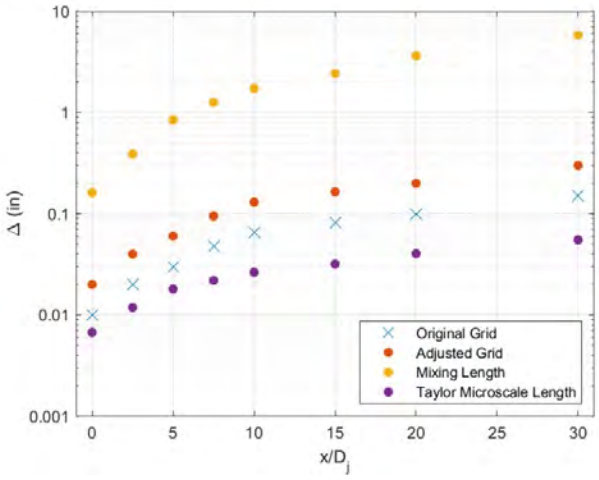

Figure 3. Grid length Δ in relation to Taylor microscale and mixing length up to 30 diameters downstream.

To estimate what fraction of the turbulent energy was captured by the grid, the Pao energy spectrum (Pao, 1965) was used as a guide. Figure 4 shows an example in which the wavenumbers associated with the extracted mixing length, Taylor microscale, and Kolmogorov length scales fall on the calculated energy spectrum. Also shown is the location of the wavenumber associated with a targeted 80% resolution of turbulent kinetic energy and the wavenumber associated with the grid length at an x / D_j of 9.89. For both the centerline and the lipline at each location, the grid length fell between the 80% mark and the Taylor microscale length. Therefore, the grid was technically over-resolved and had a smaller cell size at that location than necessary to resolve 80% of the turbulent kinetic energy. However, to better capture the turbulence intensity in the initial mixing layers, further grid refinement was added to the free shear layer. To further refine the grid around the free shear layer without making the grid prohibitively large, the grid refinement cones shown in Figure 1 and Figure 2 were adjusted. The cones were given a smaller radius, shown in Figure 5, and hollowed out in the middle of the potential core where the refinement wasn't necessary, shown in Figure 6. This refined grid contained 62.7 million cells.

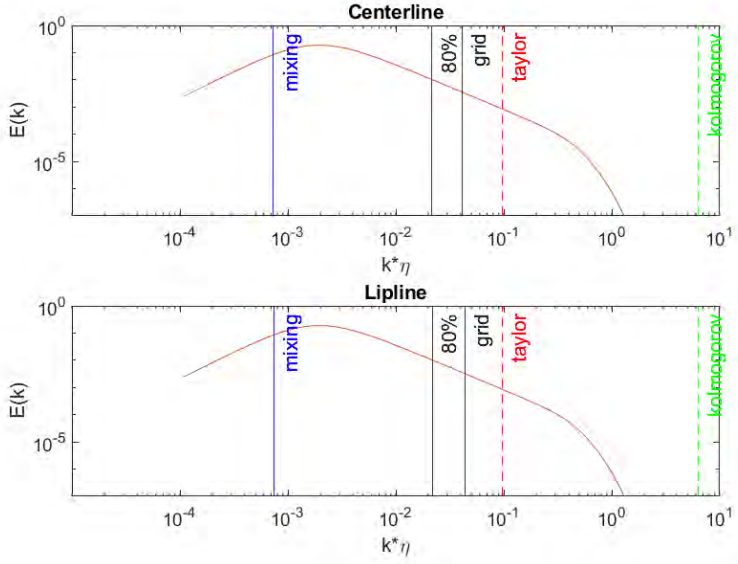

Figure 4. Pao energy spectrum at *x/Dj* = 9.89 for the centerline (top) and lipline (bottom).

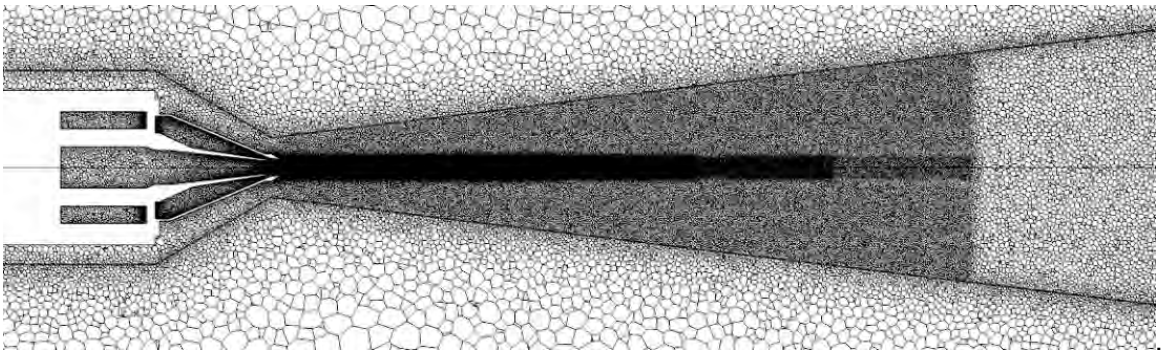

Figure 5. New grid refinement to 65 diameters downstream.

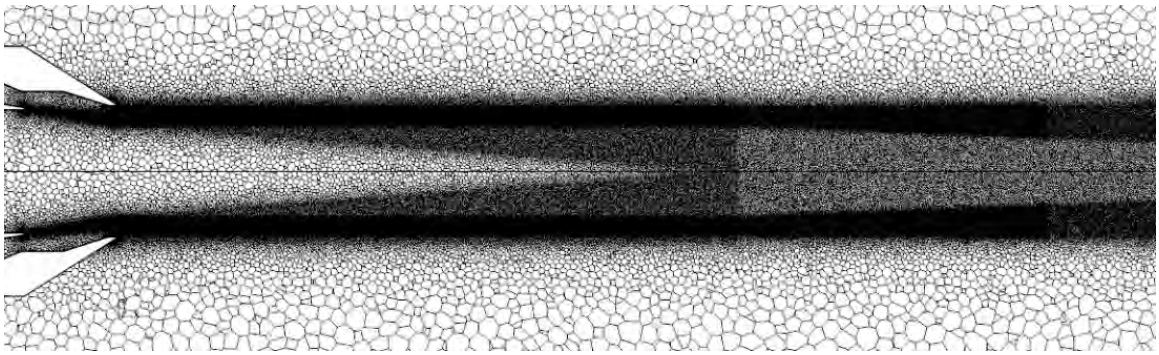

Figure 6. New grid refinement to 8 diameters downstream.

A LES for the two-stream jet was run with the nozzle pressure ratio (NPR), NPR = 1.39, and total temperature ratio (TTR)= 1.0 for both the core and bypass flow. The simulation ran for 12 days, with a total central processing unit (CPU) time of 546,288 hours. 40,000-time steps were collected, with a time step length of 1 μs.

The simulated flow field was validated against experimental values obtained by Georgia Tech. The experiments were conducted at the same conditions as those used in the simulation. Figure 7 and Figure 8 show the centerline and lipline mean axial velocity profiles, respectively, shown as U/U_j where U_j is the jet exit velocity. Figure 7 shows that the potential core of the LES flow was slightly shorter than that for the experimental flow. These results are like the velocity profiles obtained by Brès et al. (2018) with the LES solver CharLES. For the current study, the LES slightly underpredicts the axial velocity for both the centerline and the lipline but shows good overall agreement.

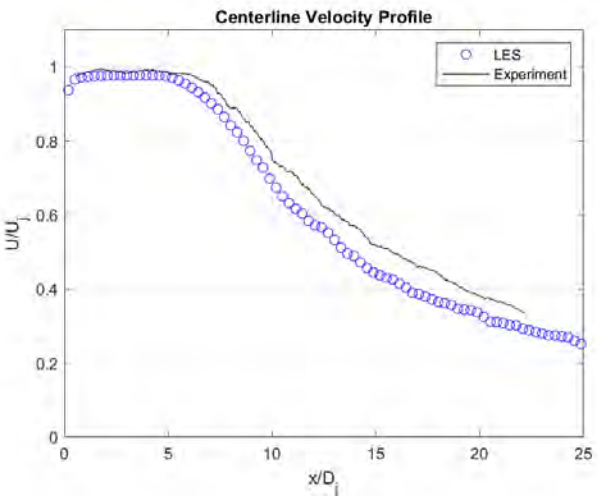

Figure 7. Centerline velocity profiles, U / U_j.

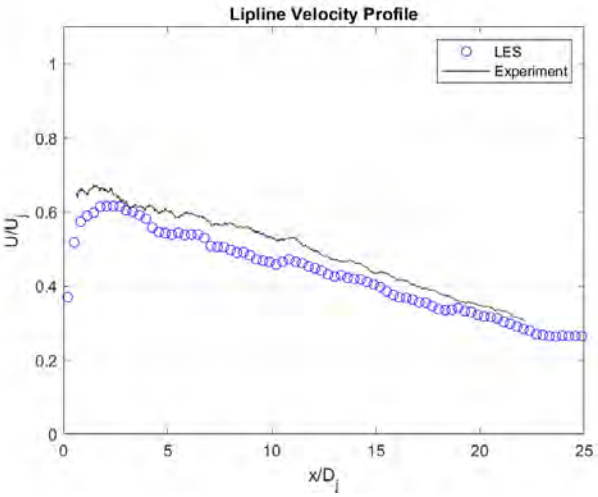

Figure 8. Lipline velocity profiles,

The corresponding turbulence intensities are shown in Figure 9 and Figure 10 for the centerline and lipline, respectively. Figure 9 shows that the LES misses the peak value and slightly underpredicts the turbulence intensity but shows good overall agreement with experiments. Figure 10 indicates that on the lipline the turbulence intensity was overpredicted near the nozzle exit in the LES. The boundary layer at the jet exit in this simulation was not fully turbulent. This results in a rapid increase in levels as the quasi-laminar flow transitions as if the initial boundary layer were laminar.

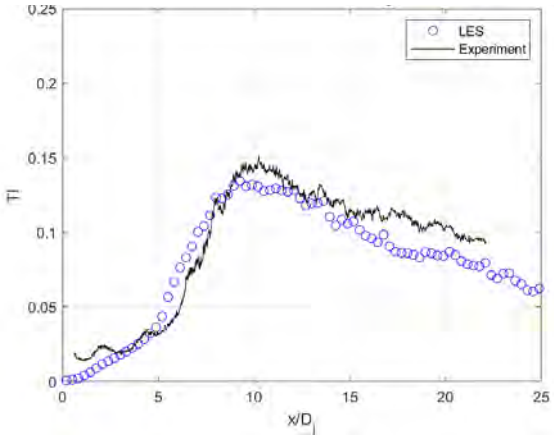

Figure 9. Centerline turbulence intensity profiles.

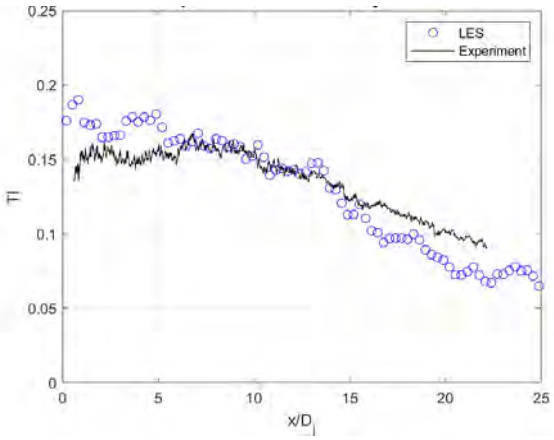

Figure 10. Lipline turbulence intensity profiles.

Acoustic data were extracted from STAR CCM+ using the built-in FW-H solver at radial distances of 50, 75, 100, 125, 150, 175, 180, and 200 jet radii. The distance of 180 radii corresponds to the radial distance at which experimental data were taken at Georgia Tech. Data were recorded at azimuthal angles of 20°, 30°, 40°, 50°, 60°, 70°, 80°, 90°, 100°, and 110° from the downstream, with 100° and 110° being sideline angles. Welch's power spectral density (PSD) estimate was used to calculate the PSD for the data points taken at 180 radii, the distance at which experimental data were taken. The azimuthal angles available at this distance were only 30° and 40°; therefore, the data used in the comparison at 90° were extrapolated from the data taken at 100 radii by using the equation,

$$PSD = 10\log\left(\frac{P_{xx}}{p_0^2}\right) - 20\log\left(\frac{r}{r_0}\right) \quad \text{(Eq. 1)}$$

where P_{xx} is the power spectral density estimate given by Welch's method, p_0 is 2×10^{-5} Pa, and r/r_0 is the ratio of the desired radius to the radius being extrapolated from, in this case 180 radii and 100 radii, respectively. Figure 11 and Figure 12 show these comparisons to experiments.

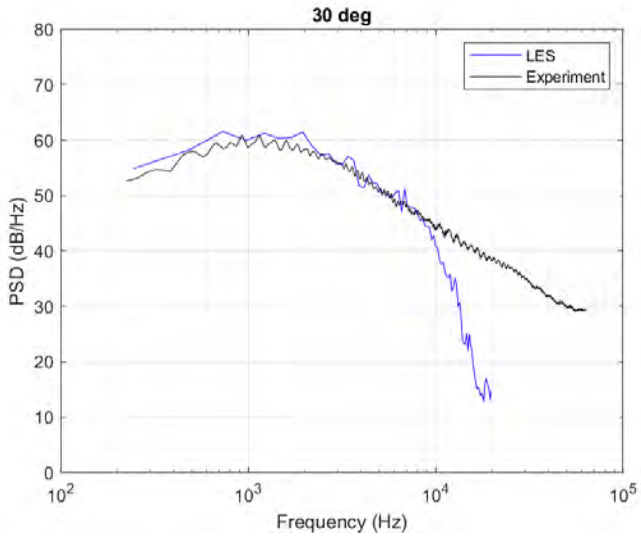

Figure 11. PSD comparison with experiments for 180r_j at 30°.

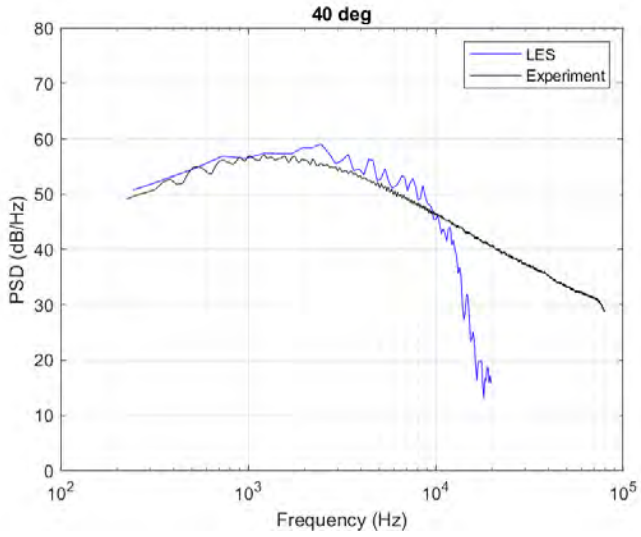

Figure 12. PSD comparison with experiments for 180 RJ at 40°.

The results obtained from the LES show good agreement with the experimental data at all angles, but show better agreement at small angles, with the data taken at 30° being the closest match. The LES captured lower frequencies better than higher frequencies, as expected. At each azimuthal angle, the PSD for the LES drops off sharply after 10,000 Hz due to limitations in the grid resolution, a behavior common to all LES simulations. A longer period of data collection would probably minimize the large fluctuations in the PSD most visible in Figure 13.

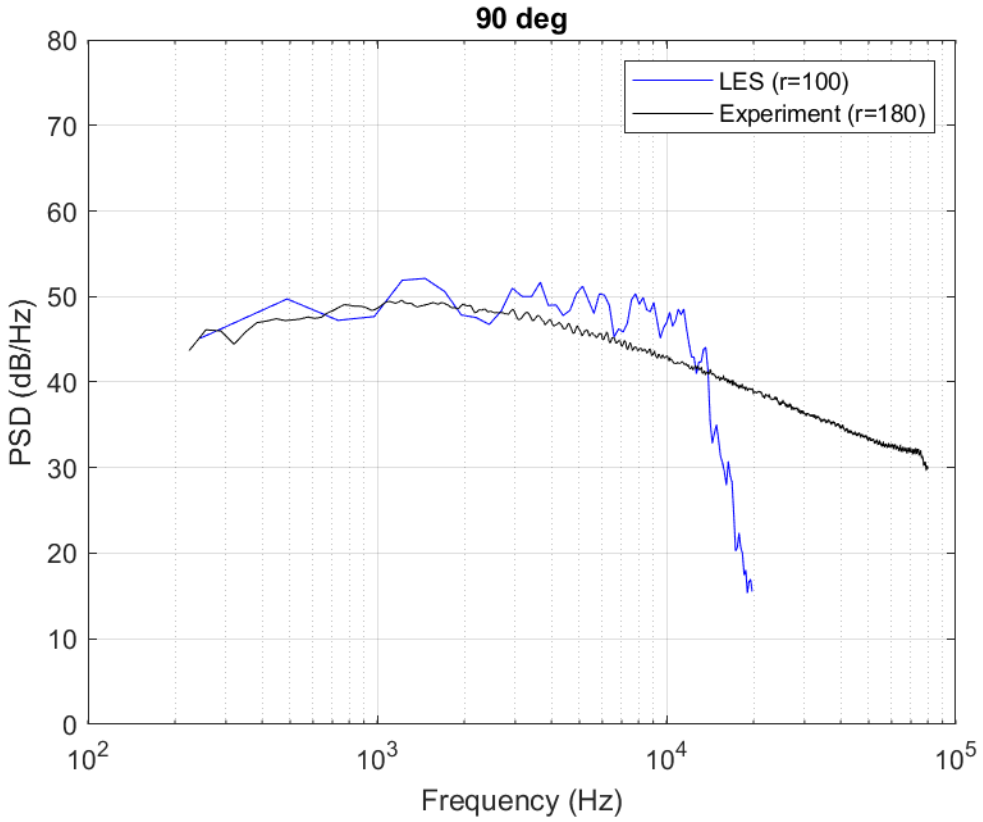

Figure 13. PSD Comparison with experiments for 180 RJ at 90°.

Task 2 - Hybrid RANS and LES Approach for Noise Efficient Predictions

Pennsylvania State University

Objectives

The basic objective of this task is to develop a less computationally expensive approach. The basic concept and initial results were described in last year's annual ASCENT report. A summary and task progress are described below.

Research Approach

The idea arose from experimental results providing convincing evidence that jet noise consists of two characteristic source mechanisms. This was first proposed by Tam et al. (1996), who identified a small-scale similarity spectrum and a large-scale similarity spectrum. With these two spectral shapes, the radiated noise spectra of jets from a wide range of operating conditions could be matched very successfully. The original comparisons by Tam et al. (1996) were made for supersonic jets, but Viswanathan (2002) has shown that the same similarity spectra can be used to represent both subsonic and supersonic jet noise. A more recent overview of the "two-source model" has been given by Tam (2019). The two similarity spectra are shown in Figure 14.

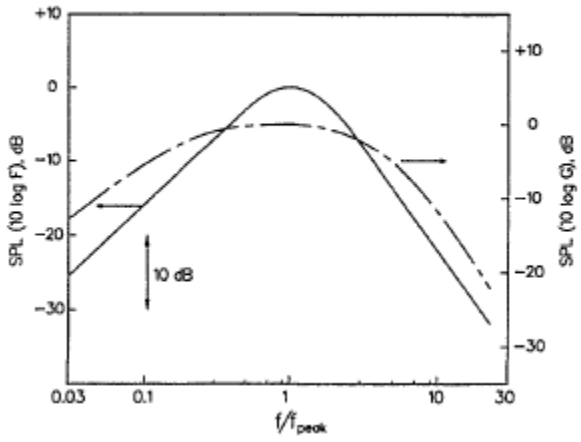

Figure 14. Similarity spectra for the two components of turbulent mixing noise. -------, large turbulent structures/instability wave noise; --- -- ---, fine scale turbulence noise.

Figure 15 shows how jet noise spectra at three polar angles can be decomposed into the two similarity spectra. At 90°, the full spectrum is described by the small-scale similarity spectrum. At 145°, both similarity spectra are required to match the full spectrum. Finally, at 165°, the large-scale similarity spectrum contributes almost completely to the full spectrum except for a possible contribution from the small-scale similarity spectrum at high Strouhal numbers. These examples are for an unheated $M_j = 0.51$ jet. For a higher Mach number, the large-scale similarity spectrum dominates over a wider-angle range. In addition, Tam and Zaman (2000) have shown that the same similarity spectrum can be used to represent the noise radiation to sideline directions for nozzles with tabs or rectangular nozzles, thus indicating that nozzle geometry has little influence on the noise radiation in these directions.

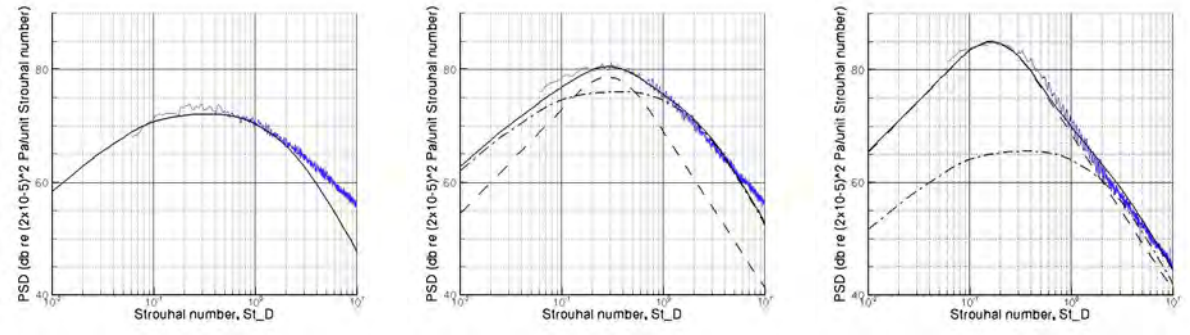

Figure 15. Demonstration of how the two similarity spectra can represent the full radiated noise spectrum at different polar angles: 90° (left), 145° (center), and 165° right).

This behavior, particularly for the small-scale similarity spectrum, is similar to that displayed by the noise predictions using the Tam and Auriault (1999) prediction method for the noise from small-scale turbulence. Figure 16 shows predictions of jet noise from a convergent nozzle at the same acoustic Mach number of 0.875. One is unheated and has a static temperature ratio of 2.5.[2] The upper set of data are for the heated jet, and the lower set is for the unheated case. Predictions for three acoustic analogy models were performed by Gryazev et al. (2023). The models were those developed

[2] These data were obtained as part of the Strategic Investment in Low-carbon Engine Tech program and were performed at QinetiQ.

by Tam and Auriault (1999) and Khavaran and Bridges (2004), as well as the generalized acoustic analogy (GAA) by Goldstein and Leib (2008). The predictions for the Tam and Auriault model follow the trend seen in Figure 15, whereas the other models follow the experimental data more closely, because these models, particularly the GAA, attempt to model a non-isotropic source to represent noise radiation to large angles. The GAA model relies on LES to obtain the properties of the non-isotropic source, and whether the same properties would be retained if the geometry or complexity of the jet nozzle were different is unclear.

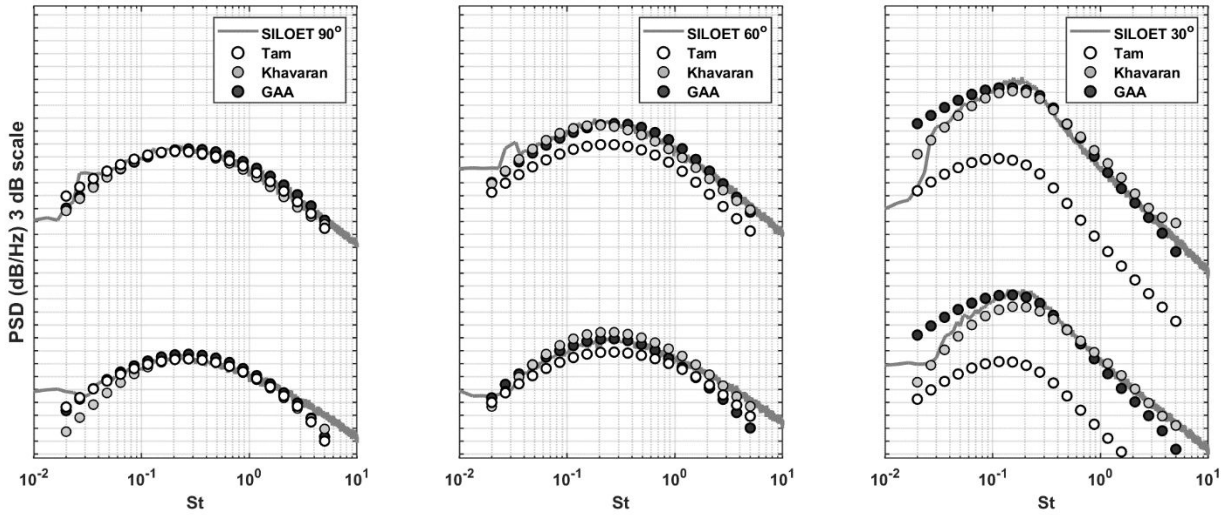

Figure 16. Noise spectra predictions of the cold (bottom) and hot (top) Strategic Investment in Low carbon Engine Technology (SILOET) jet, using the correlation scales based on the turbulent kinetic energy and dissipation rate reconstructed from RANS: comparison.

These findings suggest that Tam and Auriault's model (Tam and Auriault, 1999) can represent the noise radiated by small-scale turbulence. The difference between the small-scale noise prediction and the full spectrum can be attributed to the contribution from the large-scale turbulence.

During this year, the focus has been on predicting the contribution from the large-scale turbulence. This work is described in under the next two tasks. In the meantime, a code has been written to implement the acoustic analogy model of Morris and Boluriaan (2004). This model allows the scales needed in the acoustic analogy model to be a function of frequency.

Task 3 - Coarse LES Flow Simulations

Pennsylvania State University

Objective

The objective of this task is to use a coarse grid LES and the FW-H acoustic analogy to predict the radiated noise in the peak noise direction.

Research Approach

The STAR CCM+ simulation was initialized using steady state RANS, and then LES was implemented. A second-order central difference scheme was used with the turbulence modeled using the Dynamic Smagorinsky model with a filter width ratio of 2, and model coefficient $c_t = 3.5$. A second-order finite difference scheme discretizes the temporal derivatives with a time step of 15 μs.

The coarse LES uses polyhedral finite volume cells to form the mesh, and a cross section of the mesh grid is shown in Figure 17. A very fine mesh of 0.4-mm discretizes the region downstream of the round nozzle exit to resolve the small

amplitude instability that is generated in the shear layer. The diameter of the round nozzle exit is $D_j = 0.0432$m. The mesh resolution of the nozzle jet core flow ranges from 1-mm at the inlet to 2-cm downstream at $x / D_j = 15$. Additional mesh resolution of 1-mm was provided throughout the volumetric region outside and inside the FW-H surface to capture the unsteady vortical structures. The far field surfaces at $y / D_j = 293$ and $x / D_j = 280$ were prescribed with surface cell size of 0.15 m. An instantaneous contour plot of vortical structures downstream of the round jet is also shown in Figure 18.

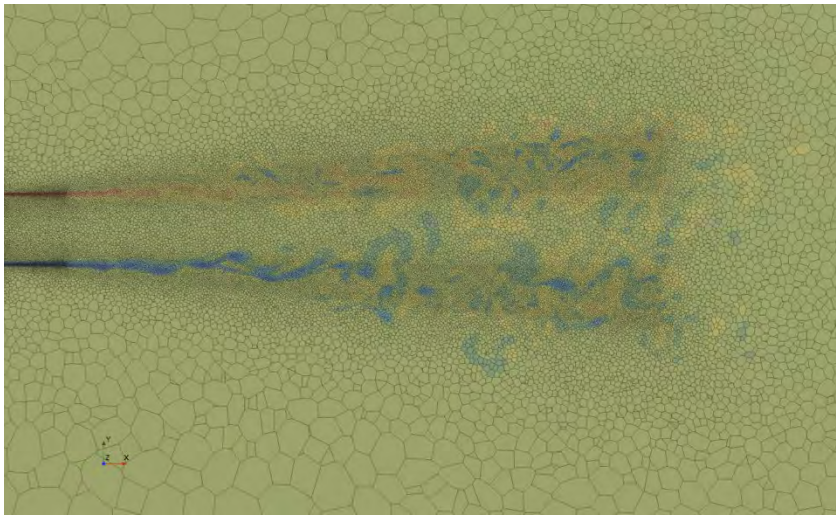

Figure 17. Coarse LES mesh grid with vorticity contours.

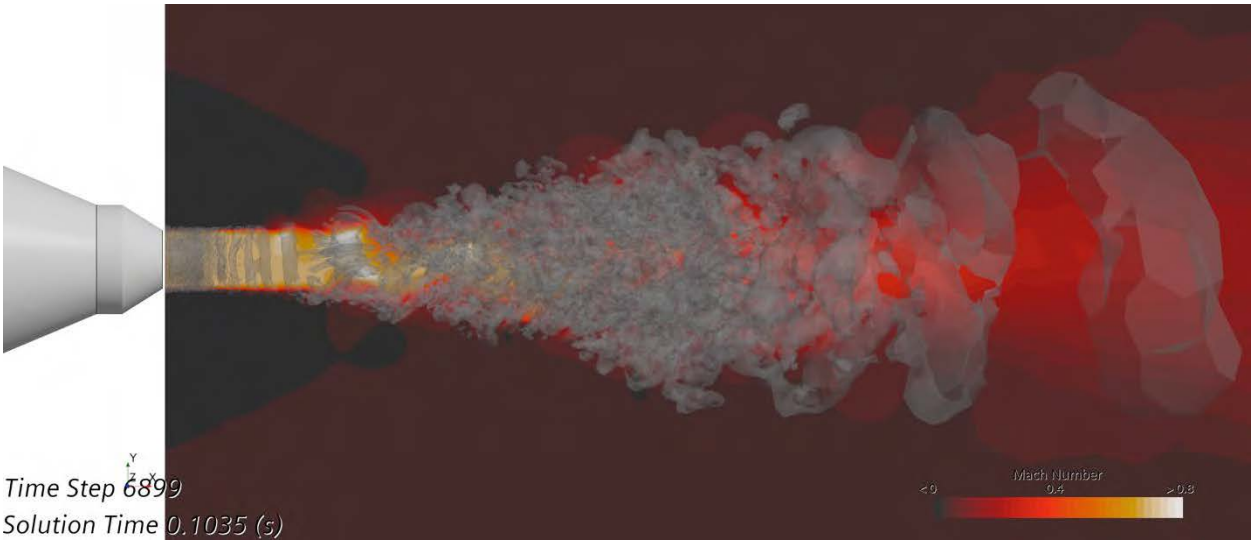

Figure 18. Q-criterion visualization of the vortex structures and Mach number contours in the jet cross-section.

To help to understand the flow field, the unsteady streamwise velocity was used to extract energy optimal modes in space-time using the spectral proper orthogonal decomposition (SPOD) method. The spectral densities are shown in Figure 19. The corresponding mode shapes at distinct frequencies of interest are shown in Figure 20.

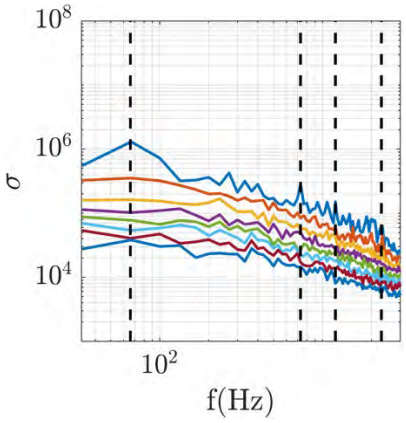

Figure 19. Spectral density of the unsteady streamwise velocity data using the SPOD method; black lines highlight the frequencies at 67, 733, 1200, and 2333 Hz.

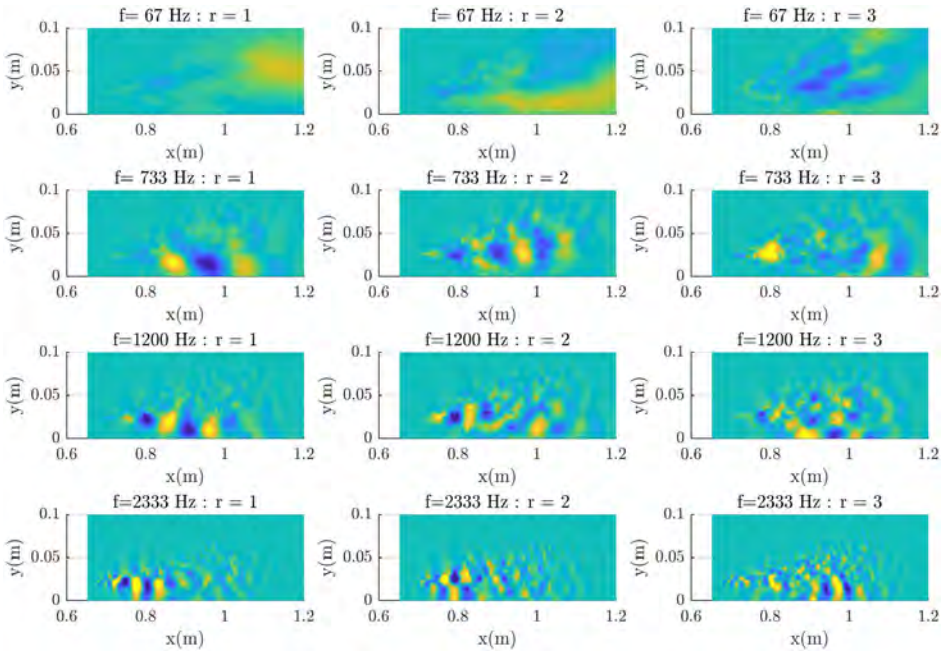

Figure 20. Dominant SPOD modes of streamwise velocity perturbation up to rank (r) 3 at four distinct frequencies (f), 67, 733, 1200, and 2333 Hz.

The turbulence intensity (TI) from the coarse LES and experimental values from particle image velocimetry (PIV) are compared in Figure 21. The perturbations in the coarse LES start downstream of the nozzle exit whereas there was a finite amplitude perturbation at the nozzle exit from the nozzle boundary layer in the experiment. This difference changes the distribution of TI downstream of the nozzle in the coarse LES. The mesh resolution was improved in the downstream region in the computation with the outflow disks; however, any mismatch in the flow field dynamics could be improved by adding instabilities in the shear layer due to upstream flow conditions. The perturbations from the upstream nozzle boundary layer play an important role in the downstream flow field.

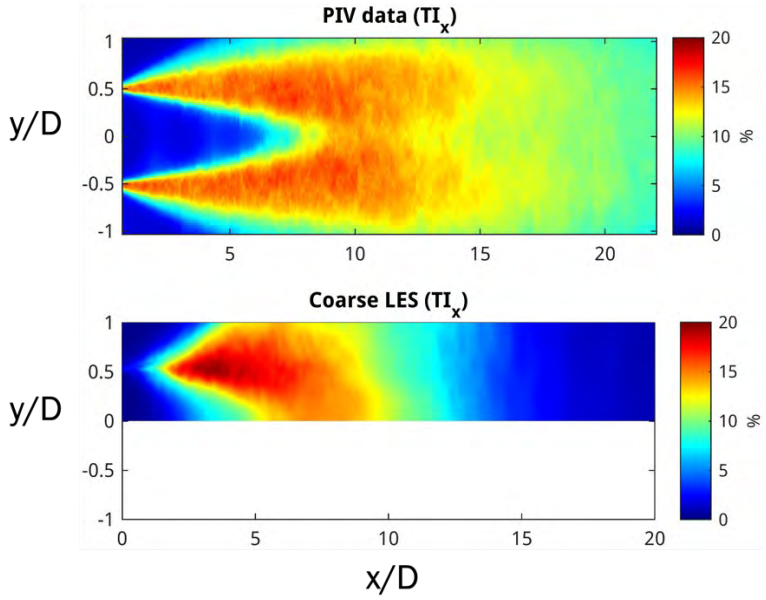

Figure 21. Distribution of the turbulence intensity (Ti) contours using streamwise velocity perturbations.

The time-averaged streamwise velocity is compared with the PIV measurements in Figure 22.

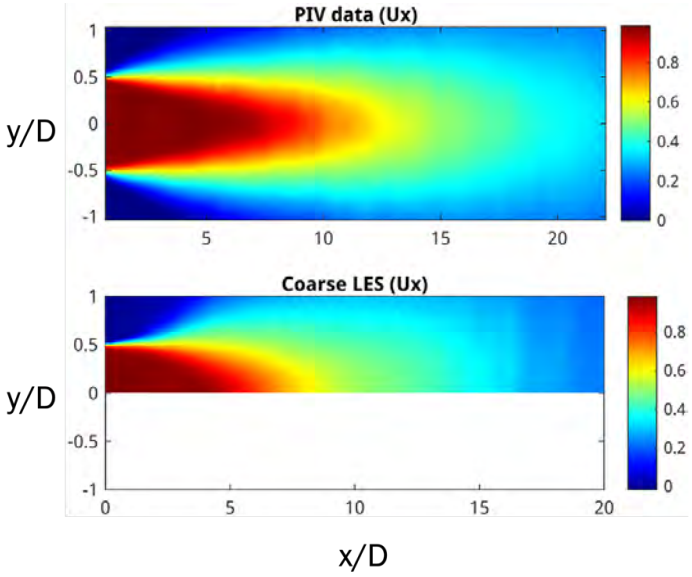

Figure 22. Time-averaged streamwise velocity contours (U / U_j) compared with PIV measurements.

The effect of downstream mesh resolution was studied by comparing the turbulence intensities of streamwise velocity perturbations at several streamwise locations in Figure 23. The absence of upstream perturbations from the nozzle boundary layer was evident at x/D = 0.69. A reasonable match was observed in the TI values up to x/D = 8.04. Further

downstream, the coarse mesh diffuses the velocity perturbations, and the amplitude of TI decreases significantly compared to the experiment.

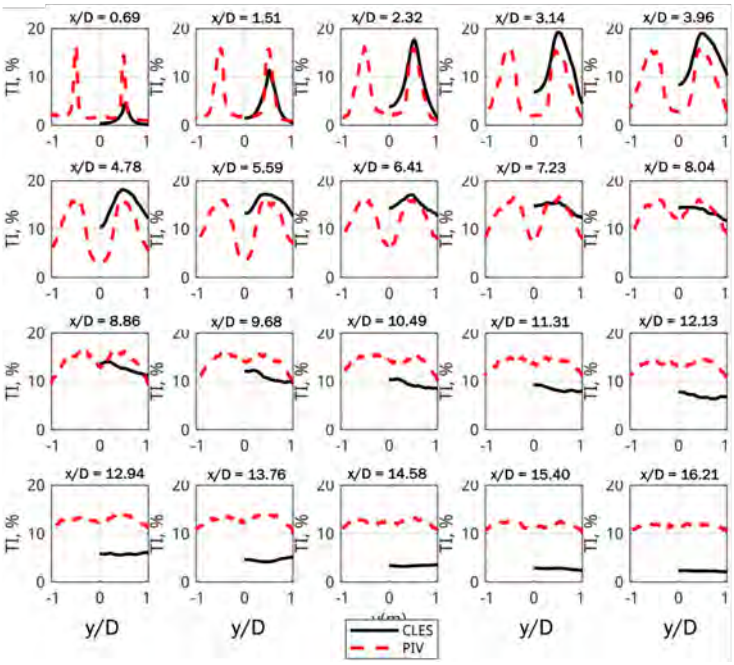

Figure 23. Comparison of turbulence intensity from coarse LES and experimental PIV at different axial locations.

Task 4: Coarse LES Noise Predictions

Pennsylvania State University

Objective

The objective of this task is to build upon the less computationally expensive approach described in the previous section. The ASCENT Project 059(E) team spent time this year developing a FW-H solver for the noise radiation prediction given data obtained from the coarse LES data. The basic formulation and initial results are described below.

Research Approach

The coarse LES solver produces the time history of transient pressure, velocity, and density on the FW-H surface. The FW-H data were subsequently supplied to a FW-H solver, based on the well-known F1A formulation, for noise radiation prediction.

A Python® code was written for the FW-H calculations, and it performs two tasks. First, given the scattered spatiotemporal data extracted from the FW-H surface in STAR CCM+, the code interpolates the data onto a multi-block structured grid, which consists of a conic surface surrounding the jet flow and a circular plane closing the cone in the downstream direction. To accurately interpolate the data on a curved surface, the three-dimensional (3D) conic unstructured surface was first mapped to a 2D structured surface. The data were interpolated by cubic splines on the two-dimensional (2D) surface and then mapped back to a 3D structure conic surface, as shown in Figure 24. Furthermore, the grid can be refined in regions where spatial variation is strong, e.g., near the nozzle, as shown in Figure 25.

® Python is a registered trademark of Python Software Foundation, Beaverton, Oregon.

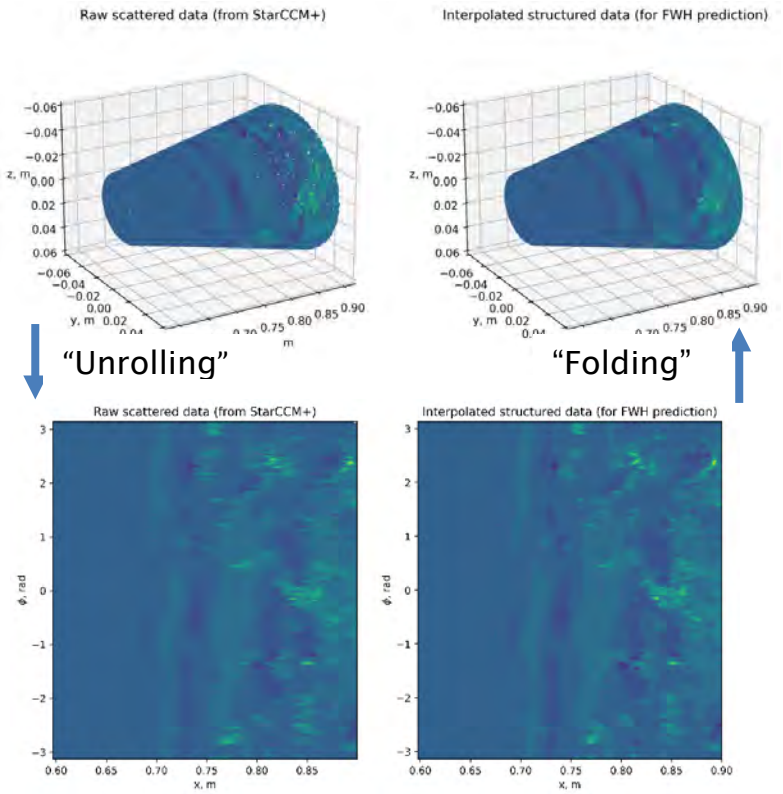

Figure 24. Algorithmic development for FW-H data interpolation.

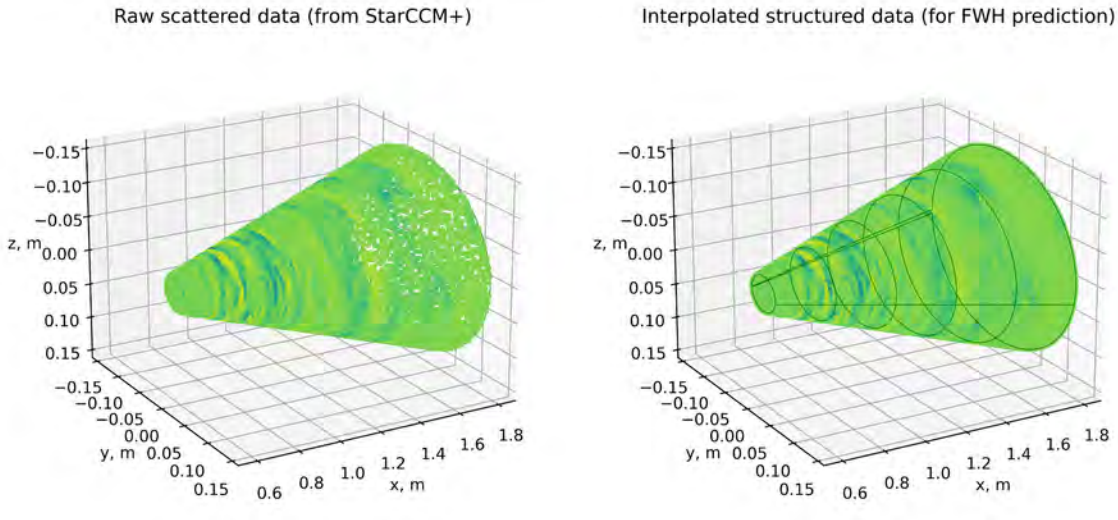

Figure 25. Raw scattered data from STAR CCM+ and interpolated structured data for FW-H prediction.

Given the locations of observers, the FW-H code calculates the far-field acoustic pressure, where the FW-H formulation was simplified due to the stationarity of the FW-H surface and the observers. Two formulations were attempted for the FW-H

calculation. The first method was the time-domain F1A formulation (Farassat and Succi, 1982), in which the time-domain pressure fluctuations at the observers were computed first and then converted to sound pressure level. The second formulation was based on the Fourier transform of the F1A formulation (Mendez et al., 2013), in which the spectra of the pressure fluctuations at observers were computed directly from the time-domain FW-H data. The two formulations were tested using data synthesized from a monopole source placed at the origin with multiple observer locations, shown in Figure 26 (left). For the time-domain version, the FW-H prediction matched well with the analytical solutions at all observer locations with errors less than 1.5%, and the error decreased as the grid was further refined. For the frequency-domain version, the FW-H prediction also captured accurately the dominant frequency and achieved agreement in the amplitude, when compared to the analytical solutions, shown in Figure 26 (right).

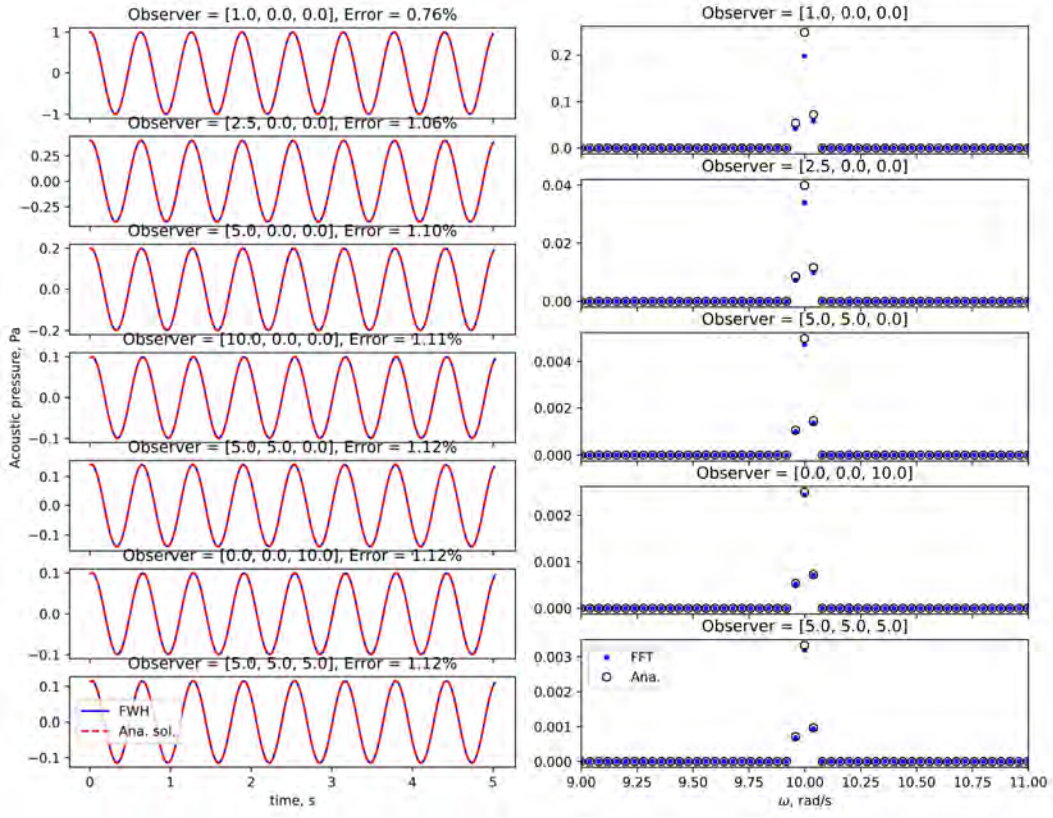

Figure 26. Comparison of predicted far field pressure for a monopole source at the origin. Time-domain prediction (left); frequency-domain prediction (right).

A special treatment for the acoustic prediction of jet noise uses a nested set of FW-H surfaces, as shown in Figure 27. The nested FW-H surfaces included a series of equally spaced closing disks; these disks were leveraged to eliminate the pseudo-sound generated by the convection of slow vortices in the vicinity of the downstream end of the FW-H surface (Shur et al., 2005). A description of the FW-H surface is given in Figure 27. 'L1' is the location of the first disk. The spacing between two consecutive disks is $0.5D_j$, and the distance between the first and the last disks is $5D_j$. The outflow disks were averaged to cancel out the effects of turbulent eddies (vortical motions) passing through the outflow disks. The open surfaces provide inaccurate results at lower frequencies, in addition to loss of information at shallow angles. The acoustic predictions are expected to improve at upstream angles with such modifications. The effect of closure was limited to lower frequencies.

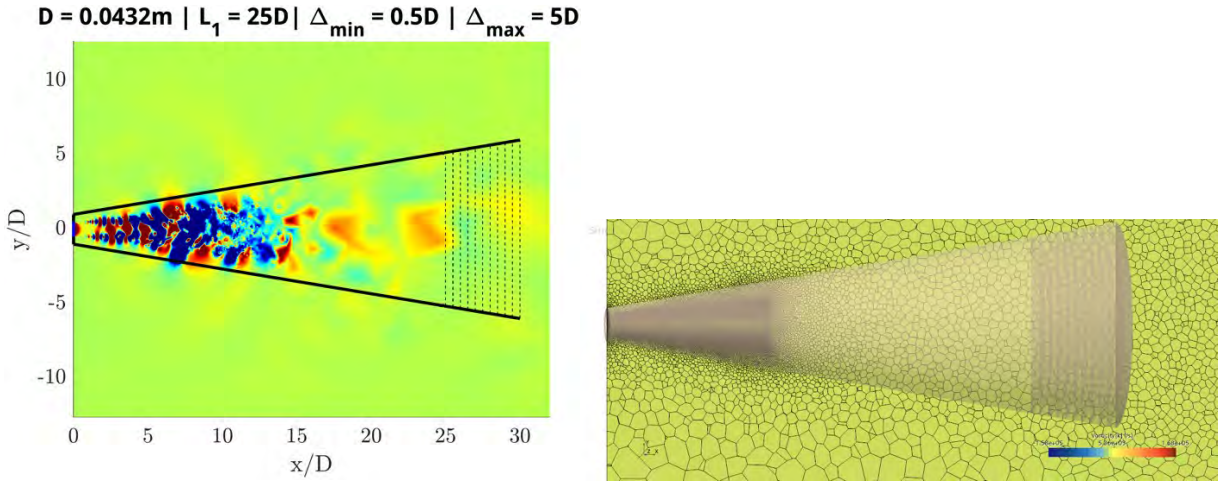

Figure 27. FW-H surface. Surface relative to jet flow (left); FW-H surface grid (right).

In the time-domain approach, the sound pressure level (SPL) was computed from predicted time-domain pressure fluctuation via the Welch algorithm with Hann window. In Figure 28, the SPL prediction shows a peak near 1 kHz for each observer, which qualitatively matches with the experimental data. However, on average, there was an over-prediction of 10 dB. Furthermore, for each observer, there was a low-frequency peak, whose SPL was nearly the same as that of the main peak near 1 kHz. Lastly, due to the time resolution of the FW-H data, the SPL up to approximately 3 kHz was available.

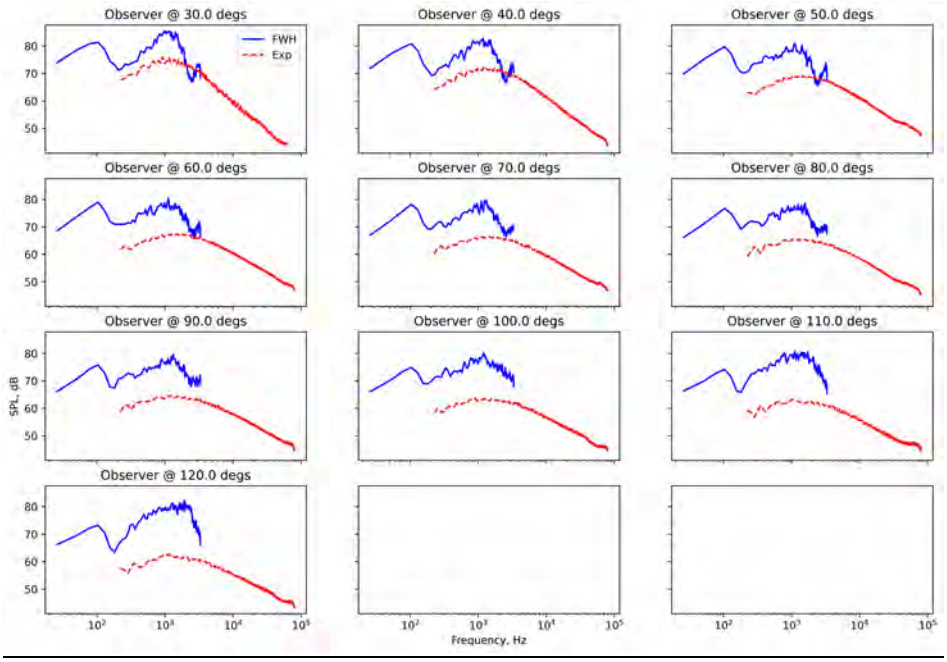

Figure 28. Acoustic prediction at each observer based on time-domain formulation.

The initial noise predictions based on data generated from the coarse LES have been disappointing and the reasons for this are still under investigation. It is planned to address this issue as a task in the next period's work.

Milestones

Table 1 shows the anticipated list of milestones for the next research period.

Table 1. Anticipated tasks and milestones for the next research period.

Task No.	Milestone	Planned due date
Task 1	Continue debugging FW-H code using coarse LES data	March 31, 2025
Task 2	Extend acoustic analogy approach to apply to non-circular jets	March 31, 2025
Task 3	Submit final ASCENT report	April 30, 2025

Publications

Mikkelsen, D. (2024). *Large-eddy simulation of jet noise using the energy cascade* {Master's thesis, Pennsylvania State University]. Pennsylvania State University.

Outreach Efforts

- Presentation at the ASCENT Spring 2024 Advisory Board meeting.

Awards

None.

Student Involvement

The Penn State team included one graduate research assistant, Dana Mikkelsen, who has been the lead on computational fluid dynamics simulations. During the year, Dana Mikkelsen left Penn State to become a full-time employee of Gulfstream Aerospace. She graduated with n Master of Science in Aerospace Engineering in December 2024. A senior graduate student, Mr. Aravinth Sadagopan, has been providing computational support.

Plans for Next Period

- Complete outstanding project tasks.
- Validate the FW-H code in both the frequency and time-domain.
- Apply the acoustic analogy approach to additional nozzle geometries and operating conditions.

References

Brès, G. A., Jordan, P., Jaunet, V., Le Rallic, M., Cavalieri, A. V. G., Towne, A., Lele, S. K., Colonius, T., & Schmidt, O. T. (2018). Importance of the nozzle-exit boundary-layer state in subsonic turbulent jets. *Journal of Fluid Mechanics, 851*, 83–124. https://doi.org/10.1017/jfm.2018.476

Farassat, F., & Succi, G. P. (1982). The prediction of helicopter rotor discrete frequency noise. *American Helicopter Society*, 497-507. https://api.semanticscholar.org/CorpusID:107210864

Ffowcs Williams, J., & Hawkings, D. L. (1969). Sound generation by turbulence and surfaces in arbitrary motion. *Philosophical Transactions for the Royal Society of London. Series A, Mathematical and Physical Sciences*,

Goldstein, M. E., & Leib, S. J. (2008). The aeroacoustics of slowly diverging supersonic jets. *Journal of Fluid Mechanics, 600*, 291-337.

Gryazev, V., Markesteijn, A. P., & Karabasov, S. A. (2023). Robustness of reduced-order jet noise models. *AIAA Journal, 61*(1), 315-328.

Khavaran, A., & Bridges, J. (2004, May 10-12). *Modelling of turbulence generated noise in jets* [Conference paper]. 10th AIAA/CEAS Aeroacoustics Conference, Manchester, Great Britain. https://doi.org/10.2514/6.2004-2983

Mendez, S., Shoeybi, M., Lele, S. K. & Moin, P. (2013). On the use of the Ffowcs Williams-Hawkings equation to predict far-field jet noise from Large-Eddy Simulations. *International Journal of Aeroacoustics, 12*(1-2), 1-20.

Morris, P. J. & Boluriaan, S. (2004, May 10-12). *The prediction of noise from CFD data* [Conference paper]. 10th AIAA/CEAS Aeroacoustics Conference, Manchester, Great Britain. https://doi.org/10.2514/6.2004-2977

Pao, Y.-P. (1965). Structure of turbulent velocity and scalar fields at large wavenumbers. *Physics of Fluids, 8(6), 1063-1075.*

Shur, M.L., Spalart, P.R. & Strelets, M.Kh. (2005). Noise prediction for increasingly complex jets. Part I: methods and tests, *International Journal of Aeroacoustics, 4*(3-4), 213–246.

Sinha, A., Rodríguez, D., Brès, G. A., & Colonius, T. (2014). Wavepacket models for supersonic jet noise. *Journal of Fluid Mechanics, 742*, 71-95.

Tam, C. K. (2019). A phenomenological approach to jet noise: the two-source model. *Philosophical Transactions of the Royal Society A, 377*(2159), 20190078.

Tam, C. K., & Auriault, L. (1999). Jet mixing noise from fine-scale turbulence. *AIAA journal, 37*(2), 145-153.

Tam, C., Golebiowski, M., & Seiner, J. (1996, May 6-8). *On the two components of turbulent mixing noise from supersonic jets* [Conference paper]. *Aeroacoustics conference*, State College, Pennsylvania. https://doi.org/10.2514/6.1996-1716

Tam, C. K., & Zaman, K. B. M. Q. (2000). Subsonic jet noise from nonaxisymmetric and tabbed nozzles. *AIAA journal, 38*(4), 592-599.

Viswanathan, K. (2002). Analysis of the two similarity components of turbulent mixing noise. *AIAA journal, 40*(9), 1735-1744.

Project 060 Analytical Methods for Expanding the AEDT Aircraft FLEET Database

Georgia Institute of Technology

Project Lead Investigator

Dimitri N. Mavris
Director, Aerospace Systems Design Laboratory
School of Aerospace Engineering
Georgia Institute of Technology
270 Ferst Drive, Mail Stop 0150
Atlanta, GA 30332-0150
404-894-1557
dimitri.mavris@ae.gatech.edu

University Participants

Georgia Institute of Technology (Georgia Tech)

- P.I.: Prof. Dimitri N. Mavris
- FAA Award Number: 13-C-AJFE-GIT-104
- Period of Performance: October 1, 2022, to September 30, 2024
- Tasks:
  1. Enhancement of the Aviation Environmental Design Tool (AEDT) Fleet database (Fleet dB)
  2. Analytical method development

Project Funding Level

The current Federal Aviation Administration (FAA) funding for this project is $150,000 from September 21, 2022, to September 30, 2024. Georgia Tech has agreed to a total of $150,000 in matching funds.

Investigation Team

Dr. Dimitri N. Mavris (P.I.), All Tasks
Dr. Michelle R. Kirby, All Tasks
Dr. Mayank Bendarkar, All Tasks
Dr. Ameya Behere, All Tasks
Dr. Styliani I. Kampezidou, All Tasks
Bilal Mufti (graduate student), Task 2

Project Overview

The AEDT relies on aircraft noise and performance (ANP) data provided by aircraft manufacturers to support the calculation of aircraft trajectories and noise at receptors by using aircraft performance information and noise-power-distance relationships for specific aircraft/engine combinations. In the ANP/Base of Aircraft Data (BADA) workflow, ANP performance data are also used in the calculation of emissions inventories and air quality dispersion. However, not all aircraft in the fleet are represented in the ANP database. When ANP data are not available for a specific target engine/airframe combination, AEDT uses a substitute aircraft from the ANP database to model the target aircraft by closely matching the certification noise characteristics and other performance parameters. However, a problematic issue is that the best substitute according to noise criteria does not always match the best substitute for emissions criteria. In addition, substitute aircraft do not capture the environmental benefits of newer aircraft with noise- and emissions-reduction technologies, thus resulting in overly conservative noise and emissions estimates.

The goal of this research is to increase the accuracy of AEDT noise and emissions modeling of aircraft not currently in the ANP database. Georgia Tech will identify, and review aircraft not currently modeled in the AEDT, and will collect information and necessary data to better understand the characteristics of these aircraft. Various statistical analysis methods will be used to classify the aircraft into different types in terms of size, age, technologies, and other engine/airframe parameters. Quantitative and qualitative analytical methods will be identified and evaluated for each aircraft type, to develop ANP noise data for the aircraft. Validation data from certification data or airport planning documents will be gathered to validate the methods. After validation, the models will be applied to develop ANP and noise data for the aircraft. Finally, recommendations and guidelines will be developed for implementing the developed data in the AEDT, to expand the AEDT Fleet dB to include noise and performance data for aircraft currently not in the ANP database.

The flowchart in Figure 1 presents an overview of the project approach. The first step is to identify the necessary aircraft parameters that will be used to better estimate the substitution aircraft. These parameters are already included in the internal data (Fleet dB) or will be collected from external resources.

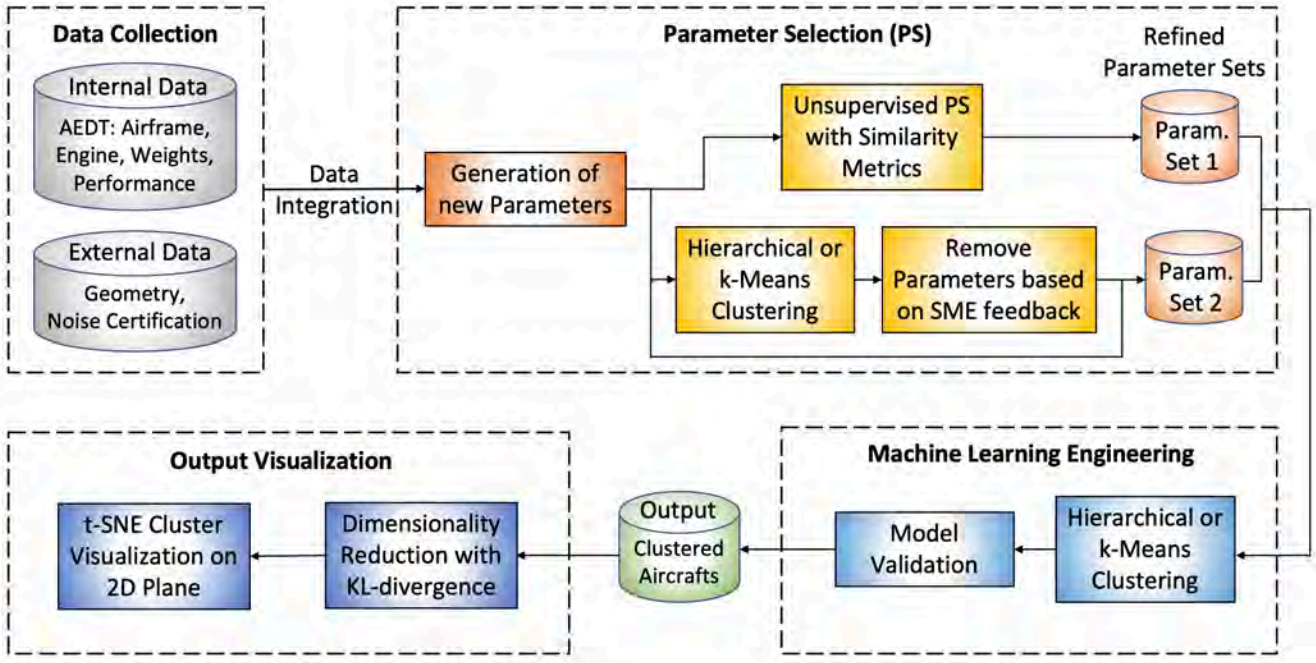

Figure 1. Overview of ASCENT Project 060 tasks and workflow.

Task 1 – Enhancement of the AEDT Fleet Database

Georgia Institute of Technology

Objective

The objective of Task 1 is to identify aircraft that are not currently modeled with ANP data in the AEDT for noise and emissions modeling. In the AEDT Fleet dB, specific aircraft engine/airframe combinations are defined by a series of ANP and noise coefficients that are used with the BADA and SAE-AIR-1845 algorithms to conduct performance, emissions, and noise modeling. The AEDT Fleet dB contains representative aircraft for the entire fleet; some aircraft are modeled according to ANP data, whereas others are represented by substitution aircraft. This task involves the identification of aircraft that do not have ANP data and determining whether those substitutions can be improved or enhanced by creating an ANP extension database. In addition, this task reviews the quality of the AEDT Fleet dB entries.

Research Approach

Creating the ANP extension database - Aircraft without ANP data in AEDT

The aircraft not currently modeled with ANP data are identified by reviewing the AEDT Fleet database and conducting a literature survey. The identified aircraft of interest are further investigated to identify gaps between them and the substitution aircraft in terms of performance, noise, and emissions. This step involves reviewing the existing literature on these aircraft and acquiring the information and data necessary to better determine their engine/airframe characteristics. In addition, the ANP data in the AEDT Fleet dB are studied to summarize key parameters for which the analytical methods can be used.

The AEDT Fleet dB consists of 3,626 airframe/engine combinations; only 269 have available ANP data (native), whereas the remaining 3,357 do not (proxy). The proxy aircraft have a unique equipment identification (ID) (the primary key in the Structured Query Language [SQL] database) and a default equipment ID, which is assigned as the equipment ID of the closest native aircraft, in terms of ANP similarity. The native aircraft have a matching equipment ID and default equipment ID. This substitution enables proxy aircraft to borrow ANP data from the native aircraft for the purposes of conducting environmental analyses and studies. The AEDT Fleet dB uses proxy aircraft because of the intensity of effort required to generate the required ANP definition by a manufacturer; this use of proxies was assumed to be reasonable for modeling purposes on an average basis decades ago.

In last year's research efforts, a down-selection process was developed to focus on most of the United States commercial fleet of aircraft which contribute the majority of noise, emissions, and fuel burn. Through this process, approximately 990 unique equipment IDs were chosen as the basis for the ANP extension database. External data sources to the AEDT Fleet dB were identified and gathered, which included European Union Aviation Safety Agency (EASA) noise certification data, type certification data sheet (TCDS) parameters from EASA and FAA, and manufacturers' airport planning documents and websites. The main parameters of interest were to include the noise certification data for the proxy aircraft.

Creating the ANP extension database - Noise certification data population for the ANP extension database

To populate the ANP extension database with noise data, two sources of the EASA certification noise level databases were used until the questionable unique entries could be rectified (1) for jets and (2) for propellers for the three certification noise levels. The questionable unique entries are specifically the combination of the airframe, the engine and its emissions ID number, and noise certification if data exists for that combination. The limit, margin, and cumulative noise values in effective perceived noise in decibels (EPNdB) units were extracted. The methods used for matching comprised the following steps. In the ANP database, a total of 990 airframe/engine candidate combinations for noise data population were selected. The population procedure was started by selection of a specific airframe of interest (e.g., the Airbus A321-200 Series AIRFRAME_MODEL and "common aircraft name"). For that airframe, a specific engine, ENGINE_MODEL, among the different options available, was selected (e.g., the CFM56-5B3/2P). After the specific airframe/engine combination was defined, the same combination was searched and selected in EASA certification noise level database. For matching to be performed, the selected airframe/engine combination in EASA was required to be unique. To ensure this unique matching, a set of successive selection criteria was used involving the following sequence of steps:

1. Use the EASA TCDS to verify that the variants are actually on the airframe; use the EASA certification noise level database (e.g., Model Aircraft Database Jets) to cross-reference that the engine is certified for noise.
2. Use the EASA TCDS to verify that the engine emissions and thrust parameters in the ANP database are correct.
3. Identify and register identified differences by matching the ANP Equipment ID and EASA Record number.
4. For the certified airframe/engine combination in the EASA certification noise level database, select the maximum take-off weight (MTOW).
5. If no unique combination is obtained, proceed to select the maximum landing mass.
6. If the combination still has more than one option, the maximum cumulative noise level can be selected.
7. In cases in which multiple airframe/engine combinations have the same noise values, the first entry is selected.
8. Finally, if more than one combination remains after application of the preceding criteria, the most recent modification date for the data of the remaining combinations is selected. This modification date corresponds to the most recent date when the existing values for the selected combination were entered in the database.

The rationale underlying these selection criteria was to choose the most representative noise value of the combination selected. After a unique combination was found, the corresponding noise value was transferred from the EASA database to ANP extension database. To increase the number of combinations available for which noise values were obtained, engines with similar designation codes for some airframes were utilized. In this case, the criterion for selection was a direct comparison of the main parameters (bypass ratio, overall pressure ratio, and rated thrust) of the similar engines were

selected. If the parameters were within 5% of each other, the combination was considered valid and was added to the ANP database. This process yielded data for less than 60% of the 990 unique equipment IDs of interest, which would be used in Task 2 for the analytical methods. It should be noted that the noise certification data gathering was an extremely labor-intensive process.

Creating the ANP extension database - Quality assessment of the unique equipment IDs
Upon further investigation of a unique equipment ID entry for which noise data could not be established, erroneous and questionable entries were identified when the ENGINE_MODEL was cross-referenced to FAA or EASA airframe TCDS. Four variables in the AEDT Fleet dB represent the proper entry in the flying fleet: AIRFRAME_MODEL, ACFT_DESCR, MANUF_DESC, and ENGINE_MODEL. In last year's research efforts, only a portion of these erroneous entries were documented, which was finalized in the current research.

Milestone
- Developed a framework for new external data to be used in Task 2.

Major Accomplishments
- Populated new extension database and created additional certification database.

Publications
None.

Outreach Efforts
- Participated in bi-annual ASCENT meetings.

Awards
None.

Student Involvement
None

Plans for Next Period
- Finalize and document the issues uncovered with the existing Fleet dB for the AEDT development team.

References
NoisedB. (2023). *Noise Certification Database Version 2.34.* Noise Certification Database, Ministère Chargé Des Transports. https://noisedb.stac.aviation-civile.gouv.fr/bdd

Task 2 – Analytical Method Development
Georgia Institute of Technology

Objective
The objective of Task 2 is to develop analytical methods and solutions that can improve the modeling of aircraft types (airframe/engine combinations) that are not included in the ANP database. In this process, machine learning (ML) and data mining (DM) approaches are used to analyze aircraft features (both internally and externally collected), ANP data, and environmental output data, as well as to gain insights and evidence of better model substitution and approximation.
The following research questions can be answered while developing these more advanced analytical methods:
- How can substitutions be better assigned for aircraft types not included in the ANP database?
- How can representative aircraft models be better chosen to develop more ANP data, with the aim of more sufficiently covering the entire population?
- Which aircraft features should be used in the identification of aircraft substitution?
- How can the current ANP data be better used to approximate the remaining aircraft with greater flexibility?

Research Approach

The data-driven analytical methods used in this task are based primarily on ML and DM techniques. The solutions to the outlined research questions consist of multiple ML/DM algorithms. In general, the analytical techniques relevant to this project can be classified into five categories: (1) clustering, (2) dimensionality reduction, (3) regression, (4) feature selection, and (5) data visualization.

The research method is illustrated in Figure 1. It begins with a data fusion step, wherein various data sources are queried and merged with the AEDT Fleet dB to create the ANP extension database, as detailed in Task 1. The ANP extension database contains 3,626 airframe/engine combinations with 112 columns. The total number of airplanes with nitrogen oxide (NO_x) emissions data is 2,361, which decreases to 575 when noise data are also included. Of these, only 269 aircraft have data from the ANP database. Most of the efforts in the past year have focused on finalizing this dataset and conducting preliminary analytical method development. This report provides a cumulative summary of the progress made over several years and includes results and analyses from applying ML and DM methods to the complete datasets.

Past efforts concentrated on unsupervised clustering techniques to group similar aircraft using the dataset from Task 1. Within each cluster, native aircraft (with ANP data) were identified as potential substitutes for other aircraft lacking ANP data. These efforts, however, were limited by the size of the available dataset and focused on finding a single native aircraft as a combined substitute for both noise and emissions metrics. This approach posed challenges because the features influencing clustering for noise metrics did not always align with those for emissions metrics.

In the current work, separate clustering algorithms were developed and applied to noise and emissions data, independently. The goal was to identify distinct feature sets and native aircraft for both noise and emissions metrics, thereby addressing the limitations of the previous approach. Two clustering algorithms, k-means (KM) and agglomerative hierarchical clustering (AHC), were tested extensively.

After thorough evaluation, AHC was selected as the preferred method due to its ability to:

1. Identify hierarchical relationships among aircraft by constructing a dendrogram, which provides interpretable insights into the proximity of aircraft features.
2. Accommodate clusters of varying sizes and shapes, making it more robust for complex datasets.
3. Incorporate domain-specific constraints or feedback directly into the clustering process, aligning well with expert-driven analysis for both noise and emissions metrics.

Clustering for Noise-Based Metrics

The AHC clustering algorithm was implemented to identify representative native aircraft for clusters of airframe/engine combinations based on noise metrics. A dataset of 575 unique aircraft/engine combinations was used for this analysis, ensuring sufficient diversity and representation across various aircraft types.

Feature Selection

The feature set for noise-based clustering was developed iteratively with guidance from subject matter experts (SMEs) and empirical testing. Initially, the clustering was conducted using only the three primary noise metrics: (1) flyover noise, (2) approach noise, and (3) lateral noise. Based on the clustering results, additional parameters were incrementally introduced, starting with the MTOW and followed by selected engine and airframe parameters.

After multiple iterations of clustering and analysis, a finalized feature set was determined, as shown in Table 1. This feature set captures critical aspects from aircraft geometry, performance, engine characteristics, and noise metrics, ensuring a comprehensive representation of parameters relevant to noise modeling.

Table 1. Selected SME parameters for noise-based clustering.

Group	Parameter	Units
Geometry	Wing aspect ratio	-
Performance	Maximum Takeoff Weight (MTOW)	Kg
Engine	Pressure ratio	-
	Total thrust	kN
Noise	Flyover noise	EPNdB
	Approach noise	EPNdB
	Lateral noise	EPNdB

Selection of Number of Clusters

The silhouette score is a widely used metric for evaluating the quality of clustering. It measures how similar an object is to its own cluster (cohesion) compared to other clusters (separation). The silhouette score for a single data point (i) is defined as:

$$s(i) = \frac{b(i) - a(i)}{\max\left(a(i), b(i)\right)}$$

where $a(i)$ is the mean intra-cluster distance for point (i) (average distance to other points in the same cluster) and $b(i)$ is the mean nearest-cluster distance for point (i) (average distance to points in the nearest cluster not containing (i)).

The silhouette score ranges from -1 to 1. A score close to 1 indicates that the point is well-clustered. A silhouette score close to 0 suggests that the point lies on the boundary between two clusters. A negative value silhouette score indicates incorrect clustering. Unlike the elbow method used with KM clustering (which relies on inertia), the silhouette score is particularly well-suited for hierarchical clustering algorithms like AHC, as it evaluates both intra-cluster cohesion and inter-cluster separation, making it ideal for datasets with varying cluster shapes and densities.

The plot of the silhouette score against the number of clusters is shown in Figure. 2. The silhouette score defined earlier is for a single data point, but in this case, the scores represent the mean silhouette score across all data points in the dataset. This cumulative score is calculated as the average of individual silhouette scores for all data points as follows:

$$Mean\ Silhouette\ Score\ = \frac{1}{n}\sum_{i=1}^{n} s(i)$$

The mean silhouette score provides a comprehensive metric to evaluate the overall quality of clustering, reflecting the balance between intra-cluster cohesion and inter-cluster separation. In Figure 2, the score generally increases as the number of clusters (n) increases, peaking at n = 10. Beyond n = 10, the silhouette score begins to decline, indicating that adding more clusters reduces the overall cluster quality by fragmenting well-defined clusters. The peak at n = 10 suggests an optimal balance between intra-cluster cohesion and inter-cluster separation. This observation aligns with the dataset's complexity and dimensionality, where 10 clusters sufficiently capture the diversity of noise-based features without overfitting or creating unnecessary splits.

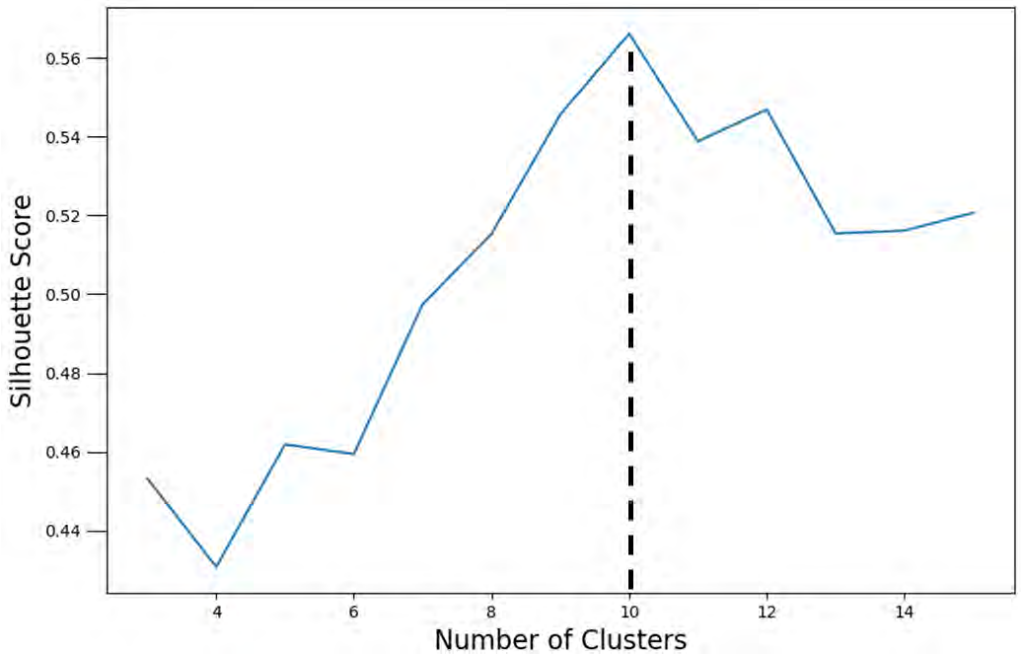

Figure 2. Variation of mean silhouette score with number of clusters.

To visualize the clustering results in two dimensions, t-distributed Stochastic Neighbor Embedding (t-SNE) was employed. Figure 3 illustrates the t-SNE projection of the dataset with 10 clusters derived from AHC clustering. It can be observed that most of the clusters show clear separation, suggesting unique feature distribution. However, some mixing is observed between clusters 2 and 4, potentially due to similarities in noise-related features for certain aircraft. This overlap will be analyzed further in subsequent sections.

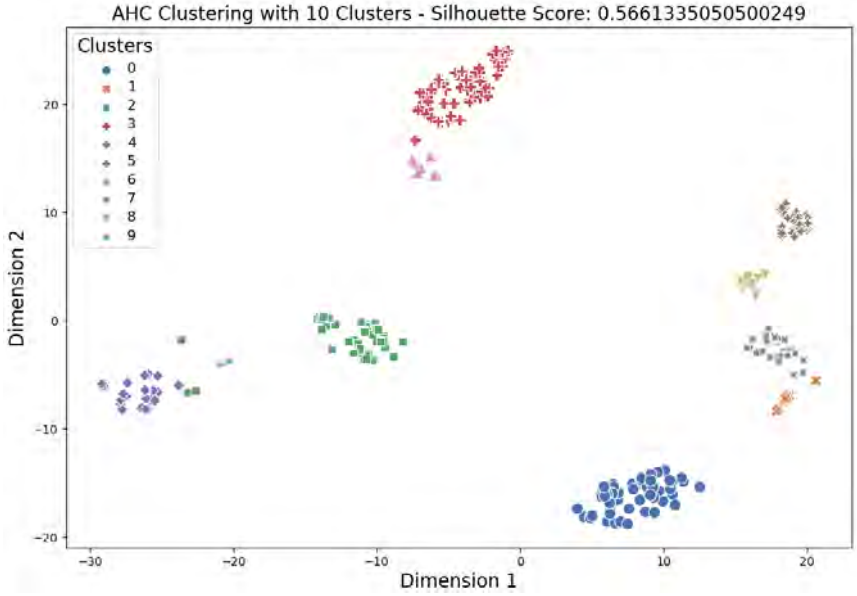

Figure 3. t-SNE projection of noise-based AHC clustering.

Grouping of Aircraft by Clusters

The analysis of feature importance, as shown in Figure 4, highlights the predictors that significantly influenced the noise-based clustering results. Among these, the pressure ratio emerged as the most critical parameter, contributing 45.21% to the clustering process. This result aligns with expectations since the pressure ratio directly impacts engine performance and noise generation. The wing aspect ratio ranked second with a contribution of 23.40%, reflecting its influence on aerodynamic efficiency and noise characteristics during flight operations. The lateral noise level, which ranks third, provides a direct measure of noise emissions and plays a pivotal role in differentiating aircraft noise profiles. Lower-ranked features, such as the MTOW and flyover noise level, contributed less to the clustering process due to their relatively lower variability across the dataset and similarity with another parameter in the feature set. Nonetheless, these features remain valuable in refining the boundaries between clusters and enhancing the overall robustness of the grouping.

	Clusters		
Predictor	**Contribution**	**Portion**	**Rank**
Pressure Ratio	903.979	0.4521	1
Wing Aspect Ratio	467.844	0.2340	2
Lateral Noise Level (EPNdB)	264.923	0.1325	3
total_thrust (kN)	181.353	0.0907	4
MTOM (kg)	112.080	0.0561	5
Approach Noise Level (EPNdB)	51.022	0.0255	6
Flyover Noise Level (EPNdB)	18.115	0.0091	7

Figure 4. Parameter importance for noise-based clustering.

Figure 5 provides a comprehensive view of the aircraft groupings across the 10 clusters derived from the noise-based clustering process. In Figure 5, the blue bars represent proxy aircraft without ANP data, while the red bars indicate native aircraft available in the ANP database. These groupings reveal meaningful patterns where aircraft with similar noise characteristics are effectively clustered together. For instance, cluster 6 predominantly consists of newer-generation aircraft, including the A320Neo and B737-Max series. These newer generation, small, single-aisle aircraft demonstrate reduced noise levels, attributed to their advanced engine designs and aerodynamic enhancements. Similarly, cluster 4 comprises regional jets such as the CRJ900 and ERJ145, which share comparable operational profiles and engine configurations. Larger aircraft, such as the B747 and A380, are grouped in cluster 1, characterized by higher noise levels due to their size and thrust requirements. Similarly, traditional single-aisle aircraft are mostly grouped in cluster 3 and wide-body aircraft are grouped in cluster 7. These coherent groupings validate the effectiveness of the clustering methodology in identifying native aircraft for proxy substitution.

The scatter plots in Figure 6 illustrate the relationships between the three primary noise metrics—flyover noise, approach noise, and lateral noise—and further validate the clustering results. The plot of flyover noise versus approach noise reveals that aircraft with higher approach noise levels, such as those in clusters 0 and 1, also exhibit higher flyover noise levels, a trend consistent with larger aircraft and high-thrust engines. A similar positive correlation is observed between flyover noise and lateral noise, with cluster 0 displaying the highest values due to the inclusion of larger aircraft. The plot of approach noise versus lateral noise provides additional insights into the distinctiveness of clusters, with smaller regional aircraft, such as those in clusters 4 and 5, occupying the lower end of the noise spectrum. Despite the overall distinctiveness of the clusters, some overlap is observed between clusters. This overlap could indicate shared design or operational characteristics among the aircraft in these clusters, as the clustering is carried out not just with noise-metrics but using aircraft engine, performance, and geometric characteristics as well.

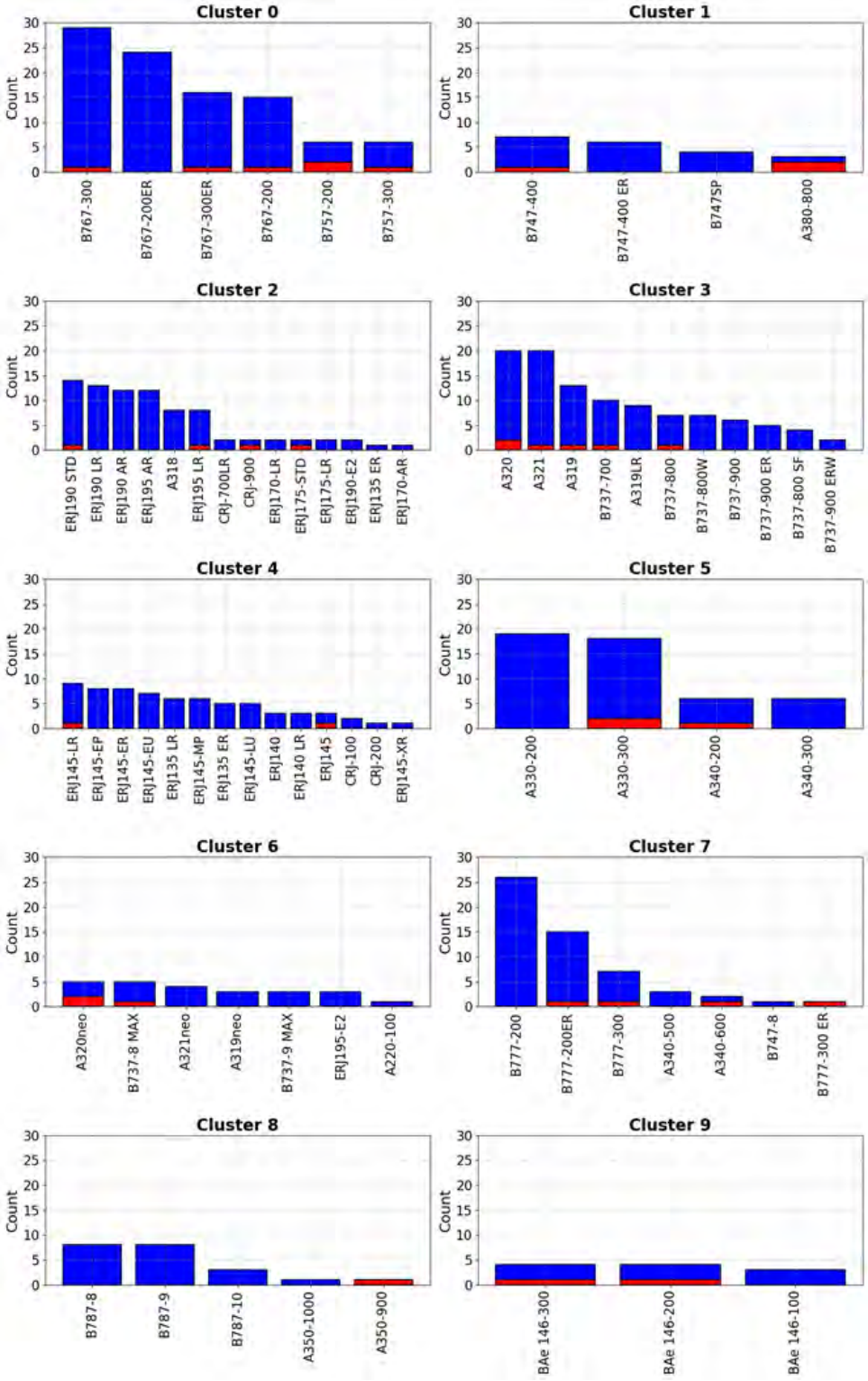

Figure 5. Aircraft grouping in noise-based clusters.

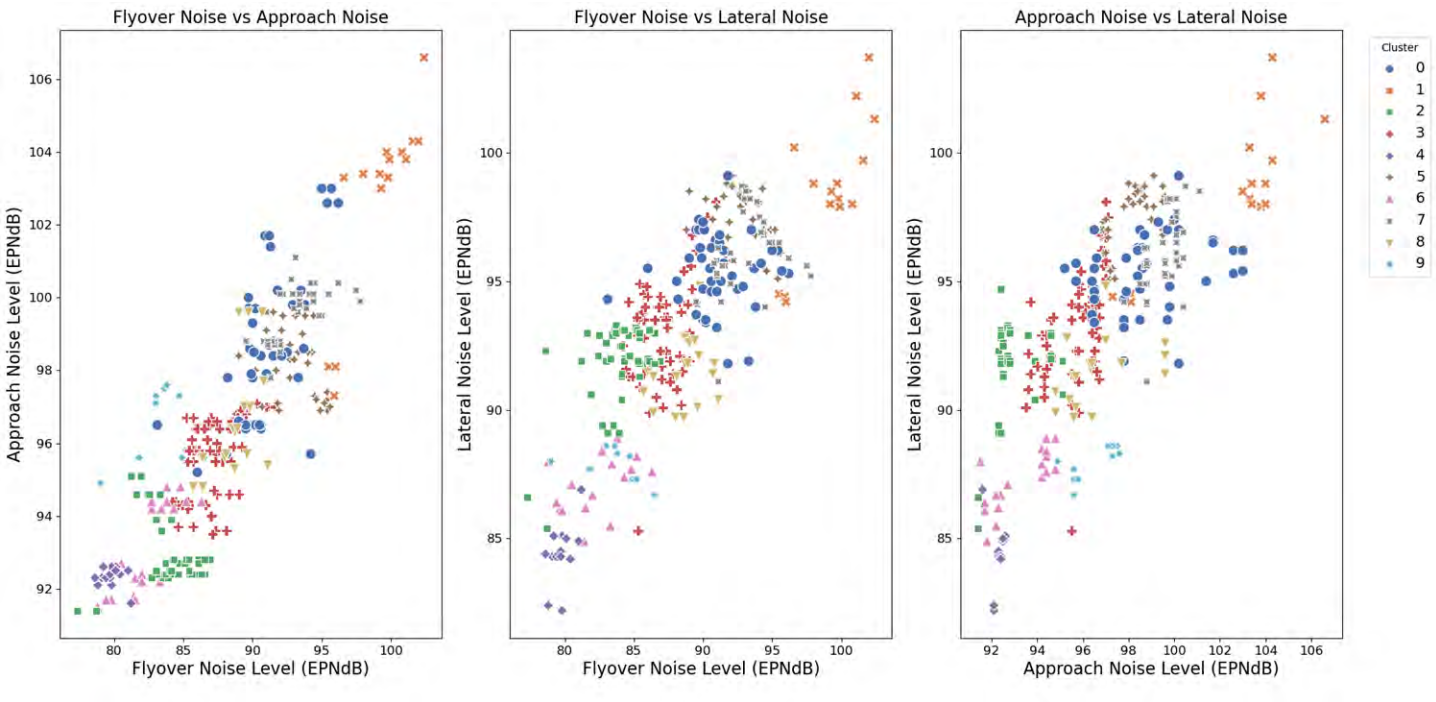

Figure 6. Scatter plots for noise metrics colored with clusters.

Overall, the noise-based clustering effectively groups aircraft with similar noise profiles and ensures that each cluster includes at least one native aircraft for substitution in the ANP database. The feature importance analysis, cluster groupings, and scatter plot visualizations collectively validate the clustering methodology and highlight the potential for improved modeling and substitution of proxy aircraft in the ANP database.

Clustering for Emissions-Based Metrics

The clustering analysis for emissions-based metrics was conducted on a dataset of 2,369 unique aircraft/engine combinations. After applying filters to address missing or incorrect values for various features, 869 combinations were selected for clustering.

Feature Selection

The feature set for emissions-based clustering was developed iteratively with input from SMEs. The initial clustering was conducted using only the emission metric NO_x DP/Foo[1] Average (Avg) (g/kN) and rated thrust, as these were identified as critical factors influencing emissions. Subsequent iterations involved the gradual inclusion of additional parameters such as engine pressure ratio, bypass ratio, and geometric configuration metrics. The final feature set, presented in Table 2, captures key parameters from geometry, performance, engine characteristics, and emissions.

This iterative approach validated the initial hypothesis that a consistent feature set might not be suitable for both noise-based and emissions-based clustering. While there is some overlap in the selected features, the emission-focused analysis required distinct features that better capture the determinants of engine emissions. As a result, independent sampling and feature selection were necessary to identify native aircraft replacements for noise and emissions data in the ANP database.

[1] The mass, in grams (Dp), of any pollutant emitted during the reference landing and take-off (LTO) cycle, divided by the rated output (Foo) of the engine.

Table 2. Selected SME parameters for emissions-based clustering.

Group	Parameter	Units
Geometry	Wing aspect ratio	
Performance	Maximum Takeoff Weight (MTOM)	Kg
Engine	Pressure ratio	
	Rated Thrust	kN
	Bypass ratio	
Emissions	NO_x Dp/Foo Avg	g/kN

Selection of Number of Clusters

To maintain consistency with the noise-based clustering analysis, the number of clusters was set to 10 (n=10) for emissions-based clustering. The t-SNE projection for the clustering results, shown in Figure 7, provides a visual representation of the cluster separations. The projection demonstrates that most clusters are well-separated, with minimal overlap between them. Although clusters 3, 4, and 8 exhibit proximity to one another, there is no significant overlap or erroneous assignment of data points. This indicates that the feature set and the selected number of clusters are appropriate for accurately grouping aircraft based on emissions metrics.

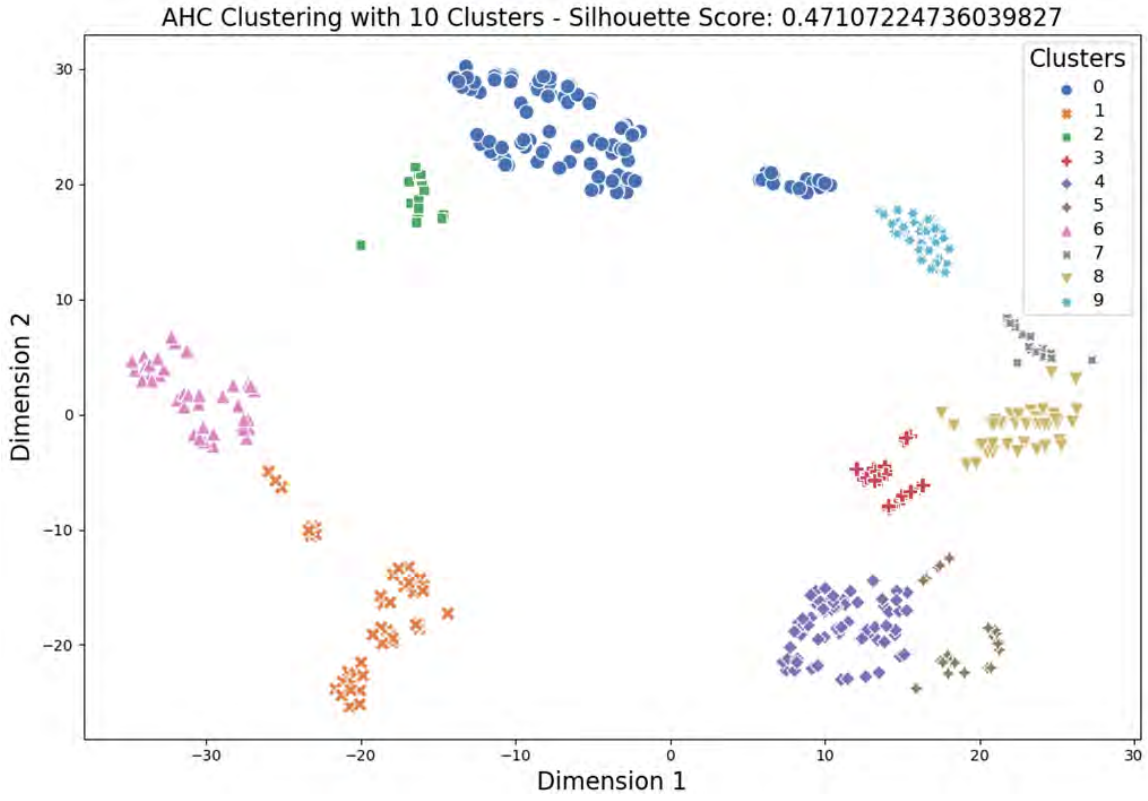

Figure 7. t-SNE projection of emissions-based AHC clustering.

Grouping of Aircrafts by Clusters

The importance of selected features on the clustering results is summarized in Figure 8. Among the features, rated thrust emerges as the most significant, contributing approximately 53% to the overall clustering outcomes. This result is consistent with expectations, as thrust is a key driver of engine emissions and serves as an effective proxy for characterizing aircraft emissions performance. The second most important feature is the wing aspect ratio, which

contributes 28.6%. This parameter indirectly influences emissions by impacting the aerodynamic efficiency of the aircraft, which in turn affects fuel burn and emissions per flight. Other features, such as the pressure ratio and bypass ratio, ranked third and fifth respectively, reflect the technological advancements in engine design that reduce emissions. Interestingly, NO_x DP/Foo Avg, the direct emissions metric, is ranked last. This can be attributed to the lower variability of this parameter across aircraft in comparison to the engine and geometric features, which serve as stronger differentiators for clustering. Moreover, it is also possible that the variation in noise metrics is similar to another feature which is already being captured by the clustering algorithm making it seem less influential on overall clustering results.

	Clusters		
Predictor	Contribution	Portion	Rank
Rated Thrust (kN)	2613.98	0.5306	1
Wing Aspect Ratio	1409.24	0.2860	2
Pressure Ratio	419.10	0.0851	3
MTOM (kg)	248.17	0.0504	4
B/P Ratio	174.11	0.0353	5
NOx Dp/Foo Avg (g/kN)	62.04	0.0126	6

Figure 8. Parameter importance for emissions-based clustering.

The clustering results for emissions-based metrics and the selected feature set are presented in Figure 9. Similar to the noise-based clustering results, the algorithm demonstrates a meaningful grouping of aircraft based on their emissions characteristics. Advanced, next-generation aircraft equipped with modern engine technologies and improved aerodynamic designs are grouped into distinct clusters (clusters 2 and 7). For example, aircraft such as the B777-8X, B777-9X, B787, and A350 are clustered together due to their lower emissions profiles enabled by advanced engine designs and optimized aerodynamic configurations. The inclusion of these wide-body aircraft in a single cluster underscores the clustering algorithm's capability to capture and group aircraft with shared performance and emissions characteristics effectively. Regional jets are also distinctly grouped into separate clusters, reflecting their unique operational profiles and emissions characteristics. This pattern is observed due to the lower rated thrust and bypass ratios typically associated with regional jets, which differentiate them from larger commercial aircraft.

Each cluster includes at least one native aircraft that can serve as a representative to complete the emissions data for the proxy aircraft in that cluster. In fact, most clusters contain more than one native aircraft, providing flexibility and redundancy in the substitution process. For example, clusters containing both wide-body and regional aircraft provide multiple options for emissions modeling, ensuring greater accuracy and robustness in completing the ANP database. Overall, the clustering outcomes for emissions-based metrics highlight the robustness of the selected features and the clustering methodology. By ensuring distinct groupings of aircraft types and the availability of native aircraft in each cluster, the results establish a strong foundation for improving emissions modeling in the ANP database.

Conclusion for Task 2

Task 2 successfully developed and applied ML and DM techniques to improve the modeling of aircraft types not represented in the ANP database. By conducting independent clustering analyses for noise and emissions metrics, tailored feature sets were identified, ensuring that the unique characteristics of each metric were effectively captured.
The clustering results demonstrated the robustness of the selected methodologies, as distinct aircraft groupings emerged, reflecting shared performance and environmental characteristics. Importantly, each cluster contained at least one native aircraft, enabling the accurate substitution of proxy aircraft in the ANP database.

The comparison of clustering results for noise (Figure 5) and emissions (Figure 9) clearly indicates that separate proxies are necessary for noise and emissions. The distinct feature sets and clustering outcomes for each metric underscore the challenges of using a single proxy to satisfy both noise and emissions modeling requirements. Independent proxies allow for more accurate representation of environmental impacts, aligning with the specialized characteristics of each metric.

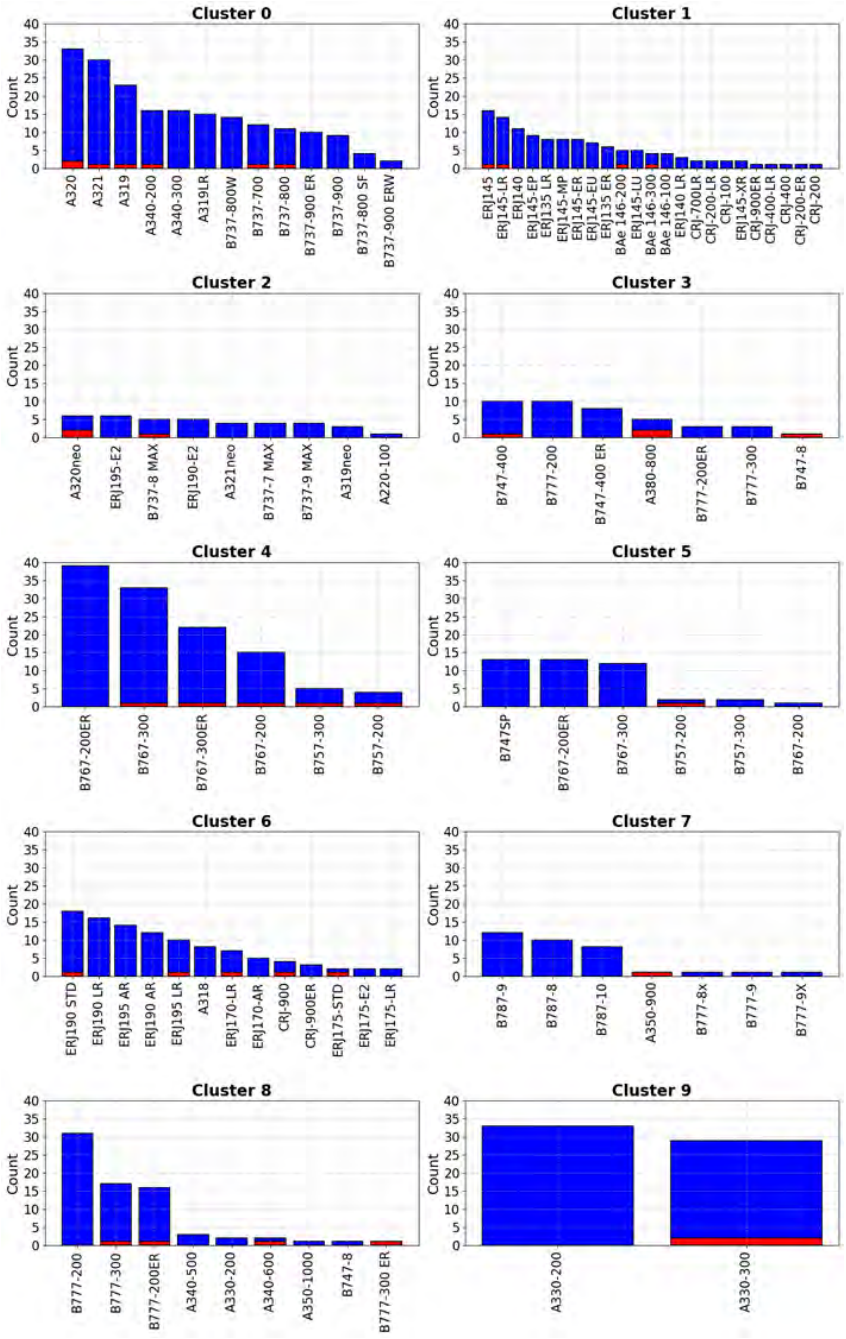

Figure 9. Aircraft grouping in emissions-based clusters.

The use of t-SNE projections and feature importance analyses further validated the clustering process, providing insights into the parameters driving aircraft grouping. Together, these advancements significantly enhance the accuracy and flexibility of the ANP database, enabling better noise and emissions modeling for unrepresented aircraft and laying the groundwork for future improvements in aviation environmental modeling.

Major Accomplishments

- Conducted a literature study on databases to collect performance, emissions, and noise data for target aircraft.
- Created a new template for the Fleet extension database, and external data were gathered.
- Gathered external databases to augment the extension database.
- Conducted a literature survey on analytical methods in clustering, dimensionality reduction, feature selection, and data visualization.
- Conducted unsupervised clustering analyses on the available Fleet extension database to better group similar aircraft and provide insights into the parameters driving the groupings.
- Developed independent clustering for noise- and emissions-based metrics using advanced analytical methods including AHC. Tailored feature sets were identified for both metrics, ensuring distinct aircraft groupings aligned with environmental modeling goals.
- Validated the clustering results through t-SNE projections, parameter importance analyses, and postprocessing visualizations, such as bar charts and scatterplot matrices, highlighting the effectiveness of the feature sets and clustering methodology in identifying native aircraft for proxy substitution.

Publications

None.

Outreach Efforts

- Participated in bi-annual ASCENT meetings.

Awards

None.

Student Involvement

Styliani I. Kampezidou and Cristian Puebla-Menne (graduate students, Georgia Tech) conducted research on potential analytical techniques to use for the clustering.

Plans for Next Period

- **Refinement of Clustering Approaches:** Further refine noise- and emissions-based clustering by analyzing overlapping clusters and incorporating additional features to improve the distinction between clusters.
- **Collection of Missing Feature Data:** Attempt to collect data for missing feature values in the airframe/engine combinations that were excluded due to incomplete data, thereby extending the database and improving the coverage of aircraft in the clustering process.
- **Development of Hybrid Substitution Models:** Investigate hybrid substitution models using multiple native aircraft within clusters to improve the flexibility and accuracy of ANP data synthesis for proxy aircraft.
- **Combined Clustering for Noise and Emissions**: Conduct clustering using both noise and emissions metrics and feature sets, along with the extended ANP database, to explore the possibility of identifying a combined proxy aircraft that satisfies both noise and emissions modeling requirements.

References

Maaten, L. V., & Hinton, G. E. (2008). Visualizing Data using t-SNE. *Journal of Machine Learning Research, 9*, 2579-2605. https://www.jmlr.org/papers/volume9/vandermaaten08a/vandermaaten08a.pdf

Melit Devassy, B., & George, S. (2020). Dimensionality reduction and visualisation of hyperspectral ink data using t-SNE. *Forensic Science International*, *311*, 110194. https://doi.org/10.1016/j.forsciint.2020.110194

Project 061 Noise Certification Streamlining

Georgia Institute of Technology

Project Lead Investigator

Prof. Dimitri N. Mavris
Director, Aerospace Systems Design Laboratory
School of Aerospace Engineering
Georgia Institute of Technology
Aerospace Systems Design Laboratory
Weber Space Science & Technology Building, Room 301A
275 Ferst Drive, NW, Atlanta, GA 30332
404-894-1557
dimitri.mavris@ae.gatech.edu

Dr. Michael Balchanos (co-P.I.)
Senior Research Engineer, Aerospace Systems Design Laboratory
School of Aerospace Engineering
Georgia Institute of Technology
Aerospace Systems Design Laboratory
Weber Space Science & Technology Building, Room 313B
275 Ferst Drive, NW, Atlanta, GA 30332
404-894-9799
michael.balchanos@asdl.gatech.edu

University Participants

Georgia Institute of Technology (Georgia Tech)

- P.I.s: Dr. Dimitri N. Mavris and Co-P.I. : Dr. Michael Balchanos
- FAA Award Number: 13-C-AJFE-GIT-066
- Period of Performance: October 1, 2023, to September 30, 2024
- Tasks:
  1. Define Model-Based Standard Framework.
  2. Develop a library of UAS and testing procedures
  3. Document and model noise testing and certification procedures based on existing practices
  4. Develop alternative procedures and assess their performance with existing tools (proof-of-concept)

Project Funding Level

The total amount of current funding from the Federal Aviation Administration (FAA) for ASCENT Project 061 is $250,000 for a 12-month period of performance. The Georgia Institute of Technology has agreed to a total of $83,333 in matching funds.

Investigation Team

Georgia Institute of Technology

Prof. Dimitri N. Mavris, (P.I.), Tasks 1-4
Dr. Michael Balchanos, (co-P.I.), Tasks 1-4
Dr. Jimmy Tai, (senior research engineer), Tasks 1-4
Dr. Evan Harrison, (research engineer II), Tasks 1-4
Balaji Ravikanti (graduate student), Tasks 1-4
Hussein Ali (graduate student), Tasks 1-4
Hajar Mali (graduate student), Tasks 1-4

Mika Xu (graduate student), Tasks 1-4
Nathnael Geneti (graduate student), Tasks 1-4
Martin Poretti (graduate student), Tasks 1-4

All team members are affiliated with the Aerospace Systems Design laboratory (ASDL), under the School of Aerospace Engineering at Georgia Tech. Please refer to Figure 1 for a breakdown of the Georgia Tech ASDL Team.

Figure 1. ASCENT Project 061 Georgia Tech Aerospace Systems Design Laboratory (ASDL) team.

Past technical advisors who contributed to the tasks:

- **Mr. David Anvid**, Senior Research Engineer, provided guidance on best practices for noise certification testing, observed and articulated from an industry point of view.
- **Dr. Sehwan Oh**, postdoctoral researcher, focused on exploring current certification regulations, understanding their structure (i.e., hierarchy, associations, etc.) linked to Task 1, and providing input on the application of discrete event and agent-based methods as part of the efforts planned for Task 4.
- **Dr. Etienne Demers Bouchard,** postdoctoral researcher, focused on exploring process modeling methods from literature and formulating a canonical problem to assess the feasibility and applicability of various methods.

Former students who have contributed to the tasks:

- **Ms. Mika Xu,** a second-year Master of Science (MSc) student, contributed to the model-based systems engineering (MBSE) efforts for representing the UAS certification process in systems modeling language (SysML).
- **Mr. Rahul Rameshbabu,** a third year Doctor of Philosophy (PhD) student, supported activities in developing a parametric and interactive decision support tool.
- **Mr. Paul Wang,** a second-year PhD student, was involved in the formulation of a MBSE verification model for UAS.
- **Mr. Daewoon Kim,** a second-year MSc student, was leading the team's MBSE efforts for representing the baseline certification process in SysML.
- **Mr. Nathaniel Omoarebun,** a fifth-year PhD student, was supporting the team's MBSE efforts and SysML modeling activities.
- **Mr. Tyler Wills,** a second-year MSc student, was supporting the team's efforts in process improvement modeling (PIM) methods and process simulation.

- **Mr. Merc Taneri,** a second-year MSc student, was leading the team's efforts in PIM methods, stochastic process simulation (Markov chain Monte Carlo [MCMC]), and interactive visualization.
- **Ms. Shireen Datta,** an MSc student, supported efforts in documenting current procedures and exploring regulation-driven requirements, which are now included in the verification model.
- **Ms. Fatma Karsten,** a PhD student, worked on flight testing plan implementation and an effective perceived noise level (EPNL) calculation module within the MBSE verification model.
- **Mr. Arnaud Ballande**, an MSc student, worked on a process simulation capability for evaluating equivalent procedures under the PIM task.
- **Ms. Hayden Dean,** a PhD student, was instrumental in capturing and understanding current regulations and certification procedures, as dictated by the Certification Procedures for Products and Articles, 14 C.F.R. § 21 (2025), and Noise Standards: Aircraft Type and Airworthiness Certification, 14 C.F.R. § 36 (2025), as well as Advisory Circulars (AC) for Noise Standards: Aircraft Type and Airworthiness Certification, with a particular focus on AC 36-4D (FAA, 2017) and an emphasis on guidance instructions regarding flight testing for noise certification.
- **Ms. Domitille Commun,** a PhD student, worked on implementing a discrete event simulation (DES) model-based process simulation capability for the certification baseline.

Project Overview

Noise certification procedures (with their inclusion of equivalent procedures) have served aviation stakeholders (i.e., original equipment manufacturers [OEM], regulators, operators, airports, etc.) well since the 1960s (Metzger, 1970; Ollerhead, 1968; Senzig et al., 2018). With new vehicle types and new technologies (including new entrants, digital technologies for airframes, propulsion, and measurements, etc.), it is necessary to critically examine the existing certification processes. Key features of current certification practices include equivalent procedures and supporting technology, which many OEMs utilize 14 C.F.R. § 36 (2025). Equivalent procedures are anticipated for both existing and new standards to further accommodate innovation in the future.

The project objective is to examine current noise certification procedures and identify opportunities to streamline the noise certification process while recommending process updates for building the flexibility needed to accommodate all air vehicle types. ASCENT Project 061 seeks to propose quantifiable process improvements and facilitate the application of traditional systems engineering for complex systems and MBSE, while leveraging these methods for the management of regulatory requirements. To perform the proposed research under this 4-year effort, Georgia Tech has teamed with several industrial partners with extensive experience in noise certification. Each industrial partner brings expertise for different types of vehicles, such as large subsonic transports, propeller-driven small aircraft, and rotorcraft.

The ASCENT Project 061 team is seeking to accomplish the following high-level goals:

- Identify opportunities for increased efficiency (by expediting steps and simplifying processes) and flexibility in current noise certification processes to accommodate multiple vehicle categories.
- Formulate and evaluate revised noise certification processes for current vehicle types and offer recommendations to the FAA (i.e., ACs for Part 36, AC 36-4D [FAA, 2017], etc.).
- Develop process modeling methods to enable quantitative assessments of noise certification.
- Facilitate the application of traditional systems engineering processes for complex systems and MBSE, leveraging these methods for the management of regulatory requirements.
- Leverage the technical expertise acquired in investigating and modeling noise regulatory frameworks and recommend procedures for certification testing and analysis to the FAA for small propeller-driven vehicles and UASs.

Overall ASCENT Project 061 roadmap and statement of work

An overview of the ASCENT Project 061 roadmap toward goals and milestones is shown in Figure 2.

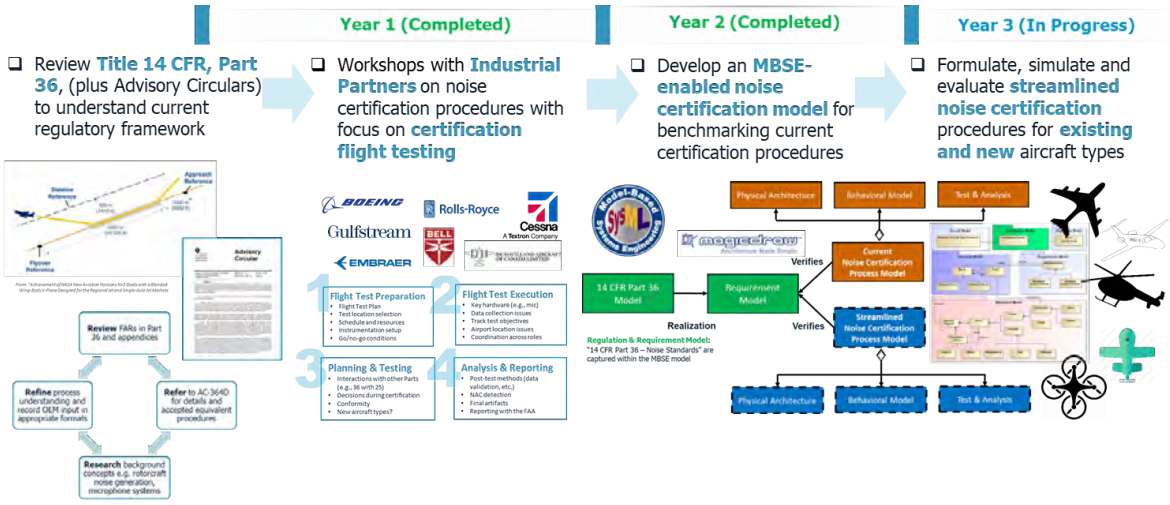

Figure 2. Roadmap toward a model-based framework for exploring current and streamlined noise certification. AC: advisory circular; CFR: Code of Federal Regulations; FAR: Federal Acquisition Regulation; MBSE: model-based systems engineering; NAC: nonacoustical change; OEM: original equipment manufacturer.

The main goal is to provide recommendations to the FAA in the form of feasible equivalent procedures, supported by the latest technologies/hardware, as well as analysis techniques to support the certification of future air vehicle types. These recommendations should be accompanied by evidence that the suggested equivalent procedures are fully in compliance with ACs for Part 36 (FAA, 2017) and use case examples for future air vehicles (e.g., small propeller-driven aircraft and UASs). To implement this roadmap and achieve the targeted outcomes, the team will engage in four main tasks, along with the subtasks that have been prioritized for year 4 of ASCENT Project 061. These tasks are summarized as follows:

- Task 1: Define Model-Based Standard Framework.
- Task 2: Develop a library of UAS and testing procedures.
- Task 3: Document and model noise testing and certification procedures based on existing practices.
- Task 4: Develop alternative procedures and assess their performance with existing tools (proof-of-concept).

General direction for Year 4 (2023-2024)

The FAA's Office of Environment and Energy (AEE) has suggested a timeframe for pivoting to UAS category certification as part of the year 4 effort (2023-2024). The main task for the Georgia Tech team is to investigate the feasibility and applicability of current ASCENT Project 061 models and analysis tools for exploring procedures and flight test planning to support noise certification of small propeller-driven UAS. To further align with the goals of the Committee on Aviation Environmental Protection Working Group 1, the use of the ASCENT Project 061 model-based framework will be demonstrated for standard-setting problems, where decisions on noise standard formulation will be driven by criteria related to the effectiveness of certification rules, as well as the certification testing burden. The above need is motivated by the primary issue with UAS certification, in that the spectrum of possible and available configurations covers a large class of aerial systems with completely different characteristics, as shown in Figure 3.

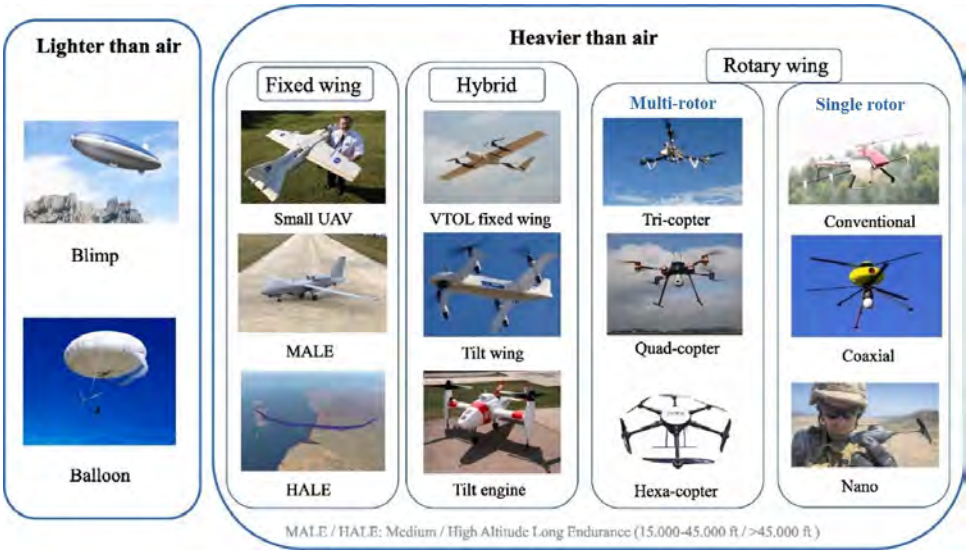

Figure 3. Overview of unmanned aerial system concepts. UAV: unmanned aerial vehicle; VTOL: vertical takeoff and landing.

It is assumed to be unlikely that UAS noise certification will be addressed as a "clean sheet of paper" process. Multiple efforts are underway to establish guidance for noise certification, similar to that for the transport category.
The International Civil Aviation Organization (ICAO) is the recognized authority for developing and establishing a global baseline for noise standards and stringencies. The harmonization of certification requirements among national airworthiness authorities is desirable.

Goals and technical challenges
The high-level goals for this direction are to (1) recommend testing procedures for UAS noise certification and, through the proposed methodology, (2) ensure traceability between regulations, testing requirements, and certification procedures. As part of the planned capability demonstration for the model-based framework, the request for the Georgia Tech research team is to demonstrate the effectiveness of a standard-setting framework for UAS/urban air mobility (UAM) vehicles enabling the formulation and evaluation of standards that meet criteria of being environmentally beneficial, technically feasible, and economically viable.

The key challenges that have been identified and will be addressed by the Georgia Tech research team are as follows:

- There is currently a large spectrum of UAS designs and configurations under testing for production. As the FAA is preparing to release guidance for UAS noise certification, it is important to determine whether the MBSE-enabled method developed under ASCENT Project 061 is sufficiently flexible to accommodate UAS testing actions and to help establish a workflow that meets current and upcoming regulations.
- As there are currently no general regulations and the application of current certification procedures is on a case-by-case basis (e.g., recently completed certification framework for the Matternet® UAS), it is important to assess whether current testing procedures are effective for UASs.

Hence, the FAA is requesting that the ASCENT Project 061 team use the established framework to demonstrate its effectiveness in assisting the FAA through the assessment of Notice of Proposed Rulemaking (NPRM) plans, as these are being iterated before they become approved as part of the UAS noise certification standards.

As a starting point for the literature search, 14 CFR § 36 Appendices G and J are considered the only aircraft noise certification standards that might be applicable for noise certification of small, unmanned aircraft systems (sUAS) in the

® Matternet is a registered trademark of Matternet, Inc., Menlo Park, California.

United States, but a number of additional standards will be reviewed and included in formulating certification practices, including the following:

- ICAO Annex 16, Volume 1, Chapters 8, 10, 11, and 13
  - These are applicable to all fixed wing aircraft, rotorcraft, and tiltrotors below a maximum takeoff weight (MTOW) of 3,175 kg.
- NASA Ref. Publication 1258, *Aeroacoustics of Flight Vehicles: Theory and Practice* Volume 1 & 2, August 1991.

Statement of work/task definitions for UAS noise certification research

Following the emphasized focus on UAS certification, the ASCENT Project 061 team further adjusted the statement of work (SOW) towards the development of use cases that address the FAA's needs for UAS noise certification. This SOW is based on the idea of integrating UAS certification goals into the model-based framework, which relies on an MBSE-based capture of the regulatory framework and PIM components. This development will entail the generation of multiple libraries that enable flexibility of use across a broader range of UAS configurations and support traceability between regulations, requirements, and elements of the library.

The tasks that have been implemented under the 2023-24 SOW are the following:

Task 1: Define Model-Based Standard Framework

1.1 Create a comprehensive noise standards database.
1.2 Breakdown the noise standards into logical elements.
1.3 Define a validation process for noise standards.

Task 2: Develop a library of UASs and testing procedures

2.1 Complete technical documentation of UAS configurations.
2.2 Complete technical documentation of UAS noise testing equipment.
2.3 Define UAS noise test plans.
2.4 Define possible simulation techniques.

Task 3: Develop a noise certification procedure based on existing practices

3.1 Transfer noise testing plans to the MBSE model.
3.2 Transfer noise testing data to the MBSE model.
3.3 Develop a full noise test plan.
3.4 Implement a validation process.

Task 4: Develop alternative procedures and assess their performance with existing tools

4.1 Develop alternative testing procedures using the elements library.
4.2 Transfer alternative procedures to the PIM.
4.3 Report on the performance of the alternative procedures.
4.4 Develop a proof-of-concept demonstration of the PIM capabilities.

Framework Demonstration Use Case for Standard Setting

As part of the framework capability demonstration, the ASCENT Project 061 team has scoped a problem that is specific to decision making for standard setting. In contrast to Tasks 1 to 4 listed above that mostly cover the development steps of the framework, the following tasks are specific to the demonstration exercise:

Task D.1: Define Model-Based Standard Framework

- Create a comprehensive database that synthesizes noise standards information from various sources including the FAA, European Union Aviation Safety Agency (EASA), and International Organization for Standardization (ISO).
- Analyze the existing standards to supplement a text-based definition of a standard by (1) identifying the categories of information necessary to sufficiently define a standard and then (2) use them to compare the existing standards.

Task D.2: Evaluate the Applicability of Existing Standards to UAS and UAM Vehicles

- Create a database of noise measurements (from publicly available test campaign data) for a variety of UAS/UAM configurations.
- Conduct a comparative analysis between UAS and UAM vehicles in terms of configuration, weight, operational altitudes, etc.
- Evaluate existing standards pertaining to prescribed test procedure altitude, speed, etc.
- Re-adjust and validate the standard framework once data for UAM vehicles is available.

Task D.3: Incorporate Process Complexity and Test Process Sensitivity Assessment to the Standard-Setting Framework

- Model and simulate the noise certification testing as a stochastic process.
- Quantify and assess the complexity level of the process using a set of complexity metrics.
- Identify trends related to the test conditions (i.e., altitude, speed, and weight).
- Conduct sensitivity analyses (e.g., histogram overlays and prediction profilers) to assess and compare different alternative processes.

Task D.4: Incorporate Economic Viability Assessment to the Standard-Setting Framework

- Conduct a time and cost analysis of the certification processes associated with the proposed standards to evaluate the overall economic impact on applicants to ensure the standards do not impose unnecessary economic burden.

Matrixing of parallel ASCENT project efforts

Within the topic of UAS testing and certification for noise, there are currently three related, but unique, ASCENT research efforts (Figure 4):

- ASCENT Project 077: Measurements to Support Noise Certification for UAS/UAM Vehicles and Identify Noise Reduction (The Pennsylvania State University)
- ASCENT Project 009/094: Geospatially Driven Noise Estimation Module (Georgia Tech ASDL)
- ASCENT Project 061: Noise Certification Streamlining (Georgia Tech ASDL)

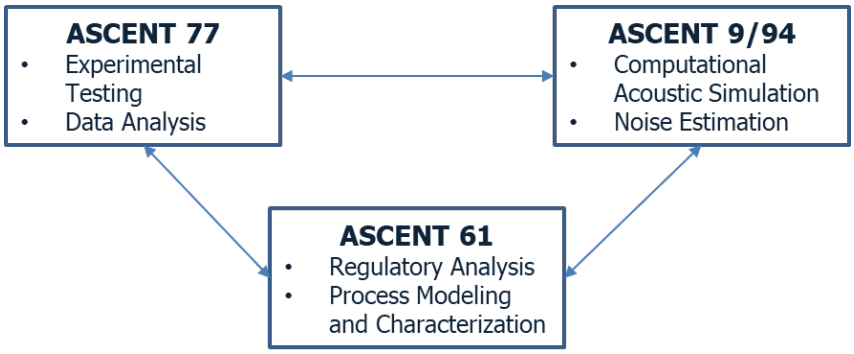

Figure 4. Coordination with parallel ASCENT work related to unmanned aerial system certification.

To preclude "mission creep" into other projects' remit and to leverage the work of the other ASCENT project teams, the ASCENT Project 061 team has been coordinating on a regular basis with ASCENT Project 077 and ASCENT Project 009/094 team members (as highlighted in Figure 4). The main collaboration areas are the following:

- ASCENT Project 077: Data sharing. Experimental test data provides real-world input for noise certification modeling. The results of the ASCENT Project 077 testing efforts provide a better understanding of the most significant parameters affecting UAS noise characteristics. The weighting of these parameters may influence modifications to the existing MBSE model.
  - Comparison of field geometry, test equipment, and basic flight profiles in addition to UAS configuration, weight, and vehicle performance
- ASCENT Project 009/094: Evaluation of possible vehicle operational environments and the practical impacts of noise profiles on the public. While the ASCENT Project 009/094 efforts do not provide direct technical data for MBSE modeling, these efforts do provide context for how noise level outputs from the certification process are applied to an operational environment.

Summary of major accomplishments to date

- Performed a literature search and documented regulations and current testing standards for small UAS (14 CFR § 36 Appendix G, J, and H, and recent NPRMs)
- Completed the **architecting and implementation of a noise certification modeling and assessment framework** for transport and UAS category aircraft.
  - The traceable structure for UAS noise certification requirements uses the MBSE verification model developed for the transport category.

  - The MBSE framework can accommodate multiple UAS types and allows for process effectiveness and flexibility evaluation.
  - Finalized the model-based architecture and delineated key requirements across UAS standards for representation in the knowledge graph.
- Completed **development of the PIM**, which is a key enabling analysis module under the ASCENT Project 061 framework:
  - Developed and implemented metrics with the analysis.
  - Used stochastic Monte Carlo methods for capturing and simulating process uncertainties in the PIM.
  - Applied the PIM as a demonstration example for a typical plan for UAS noise testing to better capture the process and properly estimate the cost, staff, and time implications.
  - Calibrated the model using noise data provided by the 2021 Causey campaign (James et al., 2021).
- Formulated use cases aligned with the needs and recommendations provided by the OEM partners, with a focus on **exploring implications of alternative testing procedures on regulatory compliance.**
  - Focused on **process simplification** (e.g., lateral microphone placement or removal, if trusted analysis is used) for a set of scenarios and experiments.
  - Focused on exploring alternatives **for standard setting** for the overall framework demonstration.
- Reviewed and provided comparison of the UAM noise standards with the UAS standards for demarcation of categories.
- Developed a **visualization environment** in the JMP® software to aid as a use case demonstrator and decision support environment.
- Published articles with the American Institute of Aeronautics and Astronautics (AIAA) for the SciTech 2024 and participated in the Quiet Drones Symposium 2024.

In the following sections, key contributions are highlighted, along with detailed descriptions of technical progress, research approaches, key milestones, and accomplishments for each task.

References

Certification Procedures for Products and Ports, 14 C.F.R. § 21 (2025). https://www.ecfr.gov/current/title-14/chapter-I/subchapter-C/part-21

Federal Aviation Administration. (2017). *Advisory Circular 36-4D – Noise Standards: Aircraft Type and Airworthiness Certification*. https://www.faa.gov/documentLibrary/media/Advisory_Circular/AC_36-4D.pdf

International Civil Aviation Organization. (2018). Annex 16 to the Convention on International Civil Aviation: Environmental protection, Volume I – Aircraft noise (9th ed.). ICAO.

Metzger, F. B., & Foley, W. M. (1970). *Stol aircraft noise certification-a rational approach*. SAE Transactions. 700325. https://doi.org/10.4271/700325

Noise Standards: Aircraft Type Certification, 14 C.F.R. § 36 (2025). https://www.ecfr.gov/current/title-14/chapter-I/subchapter-C/part-36

Ollerhead, J. (1968). *Subjective Evaluation of General Aviation Aircraft Noise* (Technical Report NO-68-35).

Senzig, D.A. & Marsan, M. (2018). *UAS Noise Certification*.

Senzig, D. A., Marsan, M., Cutler, C. J., and Read, D. R., Sound Exposure Level Duration Adjustments in UAS Rotorcraft NoiseCertification Tests, 2018.
URL https://rosap.ntl.bts.gov/view/dot/37057.

® JMP is a registered trademark of SAS Institute Inc., Cary, North Carolina.

Task 1 - Define Model-Based Standard Framework

Georgia Institute of Technology

Objectives

In support of the main research objective of ASCENT Project 061 Task 1 focuses on examining current noise standards (Task 1.1) and benchmarking against current industry practices in how these standards are adopted and implemented (Tasks 1.2 and 1.3).

Task 1: Define Model-Based Standard Framework

1.1 Create a comprehensive noise standards database
1.2 Breakdown the noise standards into logical elements
1.3 Define a validation process for noise standards

Research Approach

Task 1.1 Create a comprehensive noise standards database

For Task 1.1, the main goal was to create a comprehensive database that synthesizes noise standards information from various sources including the FAA, EASA, and ISO. The task objective was to gain an understanding of current UAS and UAM noise standard frameworks in terms of their intent and structure. In particular, our team conducted a thorough literature review of noise standards for UAS and UAM vehicles that were issued by the FAA, EASA, and ISO. Figure 5 illustrates some of the existing standard references that were explored during this process. A traceable and manageable model-based environment is necessary to keep track of relationships and dependencies between all standards.

Along with the extensive review of existing noise standards, the research team aimed to obtain a fundamental understanding of the noise standard framework starting from the general regulatory intent which is to limit the annoyance to communities where UAS/UAM operate. The generation of standards that can successfully achieve this intent requires an understanding of how UAS/UAM vehicles produce noise and what are the key sound features that represent the human auditory system response. This fundamental understanding will provide the basis for understanding the noise measurement procedures and the choice of noise metrics in the existing noise standards as demonstrated in Figure 6.

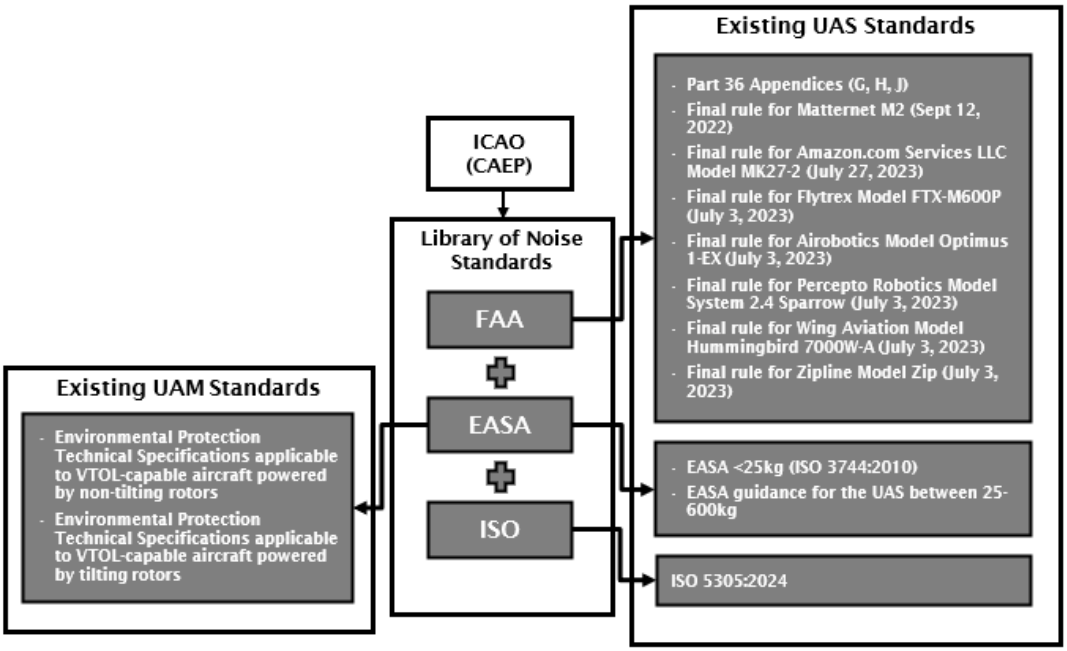

Figure 5. Existing noise standards frameworks.

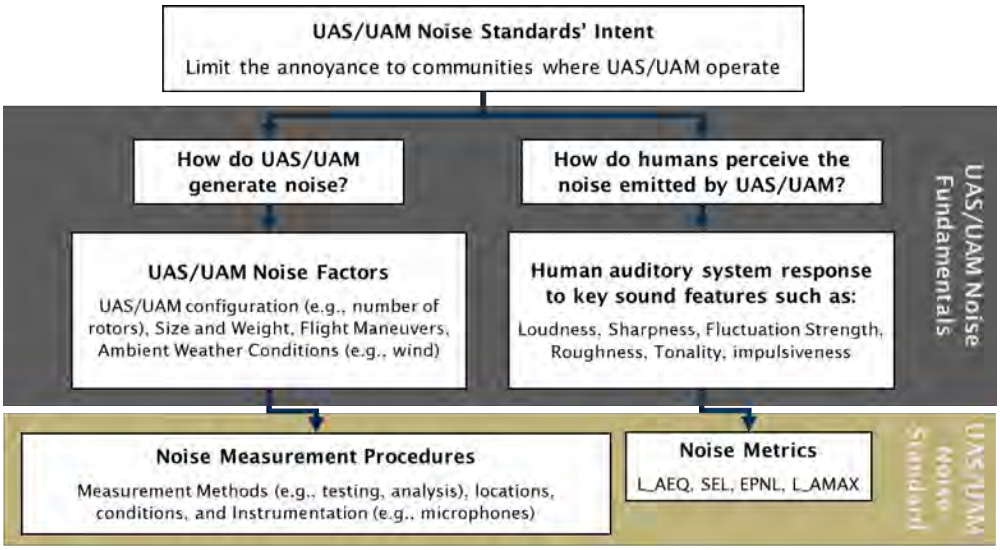

Figure 6. Noise standards intent, noise factors, key sound features and how they relate to the standards.

Moreover, another motivating factor for creating the noise standards database is to examine the existing body of standards and identify the differences and similarities between them. Figure *7* illustrates a relationship diagram used to visually determine the different associations between the existing standards from different entities. This examination aims to produce two outcomes: (1) establishing a demarcation between UAS and UAM noise standards (as illustrated in Figure 8) and (2) enabling the identification of gaps within current UAS/UAM noise standards.

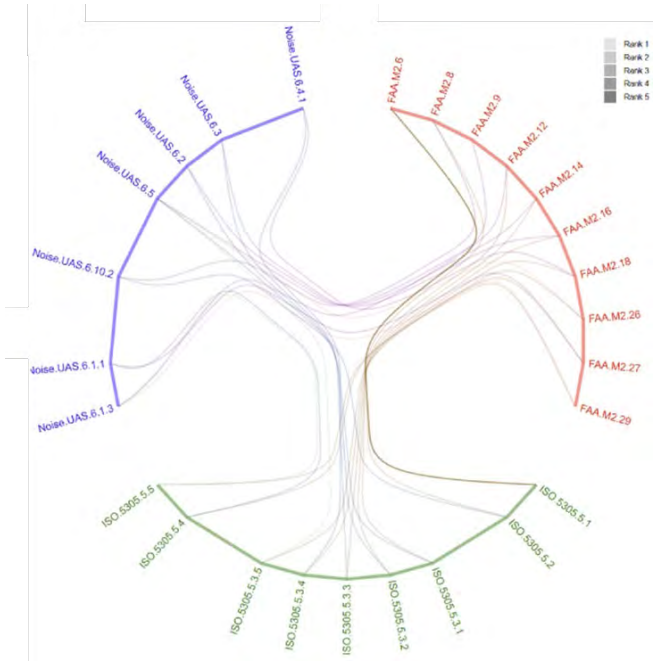

Figure 7. Relationship diagram showing the associations between the existing standards from different entities.

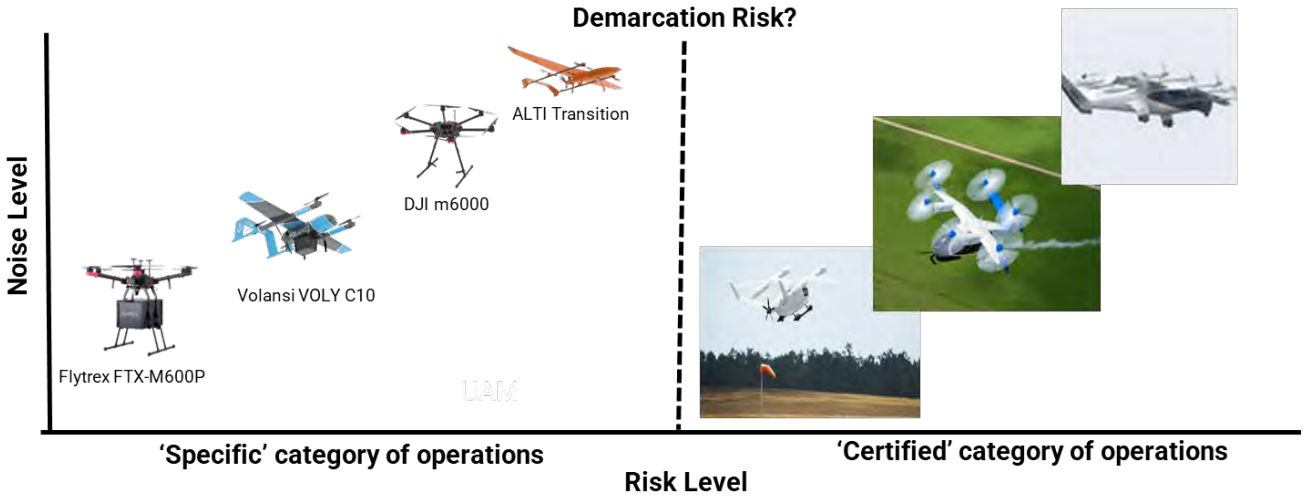

Figure 8. Demarcation between UAS and UAM noise standards.

To investigate the demarcation between the UAS and UAM noise standards, a case study considering the EASA's UAS and UAM noise standards was formulated by our team. By comparing the EASA's UAS Noise Measurement Guidelines and Environmental Protection Technical Specifications (EPTS) for vertical takeoff and landing (VTOL) capable aircraft as shown in Table 1. It is evident that weight cannot be considered as the demarcation parameter since the weight range of both frameworks overlap. Instead, the EASA uses "Risk" as a demarcation parameter between the UAS and UAM noise standards. In general, the EASA defines risk as the potential harm based on the environment, vehicle type, and nature of the operation (EASA, 2023). Higher risk operations require stricter regulations and certifications to ensure safety. Based on this definition, the EASA also provides three categories of risk:

1. Open (Low Risk): Drones are operated in visual line-of-sight under specific limits (e.g., weight, height), typically over nonpopulated areas, with no need for prior authorization (EASA, 2024a)
2. Specific (Low to Medium Risk): Requires an authorization due to higher risks (e.g., flying near people or complex environments) and needs an operational risk assessment (EASA, 2019)
3. Certified (High Risk): For the most dangerous operations (e.g., over urban areas or transporting people) where certification of both the drone and operator is mandatory (EASA, 2024b)

This delineation leads to trying to determine the influence of risk classification on the applicable noise standards. To this end, understanding the risk of annoyance to communities where UAS/UAM vehicles operate in terms of factors such as weight, configuration and concept of operations (CONOPS) is crucial to quantify risk, and thus produces a risk classification that can be mapped to applicable noise standards (i.e., noise metrics, test types, the number of microphones, etc.). The goal of this procedure is to propose proportional applicable noise standards corresponding to certain risk levels. Determining the proportionality of noise standards to the vehicle risk classification requires the evaluation of the Economic Viability (Economic Burden) of alternative noise standards in terms of time, cost, and process complexity.

One of the benefits of the outcome of Task 1.1 is that team members quickly became more knowledgeable of basics on noise standards in preparation for Task 1.2 (breakdown of standards) and were able to build a comprehensive MBSE representation (in SysML) of the current framework (see Task 3.1).

Task 1.2 Breakdown the noise standards into logical elements

Once a comprehensive database of existing noise standards has been established, the second step is to analyze existing standards to supplement a text-based definition of a standard. This is done by identifying the categories of information necessary to sufficiently define a standard and then use it to compare the existing standards. Our team aimed to demonstrate the flow of procedures, associations, and dependencies across the standard framework items. This was achieved by establishing a clear breakdown of noise standards in a proper structural arrangement as shown in Figure 9. This breakdown was inspired by the works of Bendarkar et al. (2023) and Fazal et al. (2022). Bendarkar et al. (2023) provided a structural hierarchy of FAA regulations comprising four layers, (1) part, (2) subpart, (3) grouping, and

(4) paragraph. Whereas Fazal et al. (2022) constructed a regulatory framework identifying three main categories of regulatory statements, (1) regulation requirement, (2) regulation context, and (3) regulation test.

Table 1. Comparison between EASA's UAS Noise Measurement Guidelines and EPTS for VTOL capable aircraft.

	EASA EPTS applicable to VCA	EASA guidance for the UAS between 25-600kg
Weight Range	< 80,000 kg	25 kg – 600 kg
Prescribed Tests	Takeoff (TF), Approach (AP), Level Flyover (LF), Hover (H)	Level Flyover (LF), Hover (H)
Noise Metrics	EPNL (TF, AP, LF), L_AEQ (H)	SEL (LF), L_AEQ (H)
# of Microphones	3 (TF, AP, LF, H*), 9 (H) Inverted Ground Microphones	1 (LF, H) Inverted Ground Microphone
Noise Limits	87.0314 + 9.9673 log10 M (TF) 85.0314 + 9.9673 log10 M (LF) 90.0314 + 9.9673 log10 M (AP) in EPNdB	Not Applicable
# of runs	6 runs (TF, AP, LF, H)	6 runs (LF, H)

Breaking down standards into logical elements facilitates systematic comparison and helps to identify essential information needed to establish standards and ensure traceability. The breakdown in Figure 9 organizes standards into sections, paragraphs, and equations, ensuring clear and systematic representation. It also ensures uniformity, enabling diverse standards to seamlessly fit into a consistent framework. A breakdown was created for each of the noise standards gathered in the database.

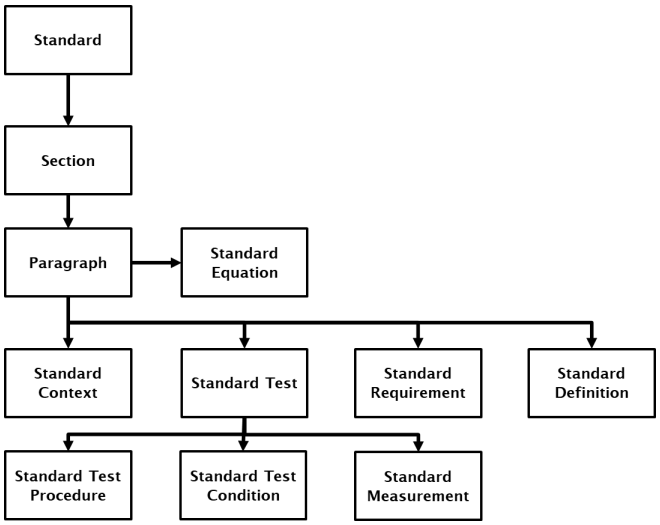

Figure 9. Standards breakdown and elements.

Establishing a breakdown of noise standards is a crucial first step in creating a model-based standards setting framework. As mentioned previously, one of the aims of the model is to provide a traceable and manageable model-based environment to keep track of relationships and dependencies between all the standards. In addition, the complexity of this process becomes apparent by examining the intricate networks created between standard framework items. The MBSE model can aid in nullifying this complexity by capturing the process of creating the certification plan in addition to other

supplementary domain knowledge within one model that is the singular source of truth. More information about the MBSE model's representation of the framework that was created in MagicDraw® is provided in Task 3.1.

A critical element of the standard breakdown is the standard requirement. Defining and maintaining a good set of requirements is vital for the successful design, development, and operation of systems, products, and processes. A requirement is defined as "a statement that identifies a system, product or process' characteristic or constraint, which is unambiguous, can be verified, and is deemed necessary for stakeholder acceptability" (International Council on Systems Engineering, 2006). "Good" requirements are those having attributes such as necessary, unique, unambiguous, clear, concise, complete, consistent, technically feasible/achievable/obtainable, traceable, measurable/quantifiable, verifiable (e.g., testable), able to be validated, operationally effective, and survivable and singular as outlined by the U.S. Department of Defense (DoD) *Systems Engineering Guidebook* (2022). In addition, requirements can vary in their type, which encompasses functional, nonfunctional, design, performance, certification, etc. (Firesmith, 2005).

The FAA Writing Standards provide a useful guide for defining the requirements to satisfy the desirable requirement attributes outlined by the DoD *Systems Engineering Guidebook* (2022) that are nonfunctional in nature (detailed in the Task 1.3). These standards include word choice such as using "must" instead of "shall," using short sentences and short paragraphs, limiting the use of abbreviations and acronyms, etc. (FAA, 2003). While converting the standards into requirements, the following considerations were taken (Kim et al., 2023):

- Not all standards needed to be converted into requirements.
- A single standard often needed to be broken down into multiple requirements. Conversely, multiple standards were sometimes merged into a single requirement.
- The standards do not always provide all the necessary information, so additional metrics and clarifying information were gathered from literature reviews and other noise standards related documents.

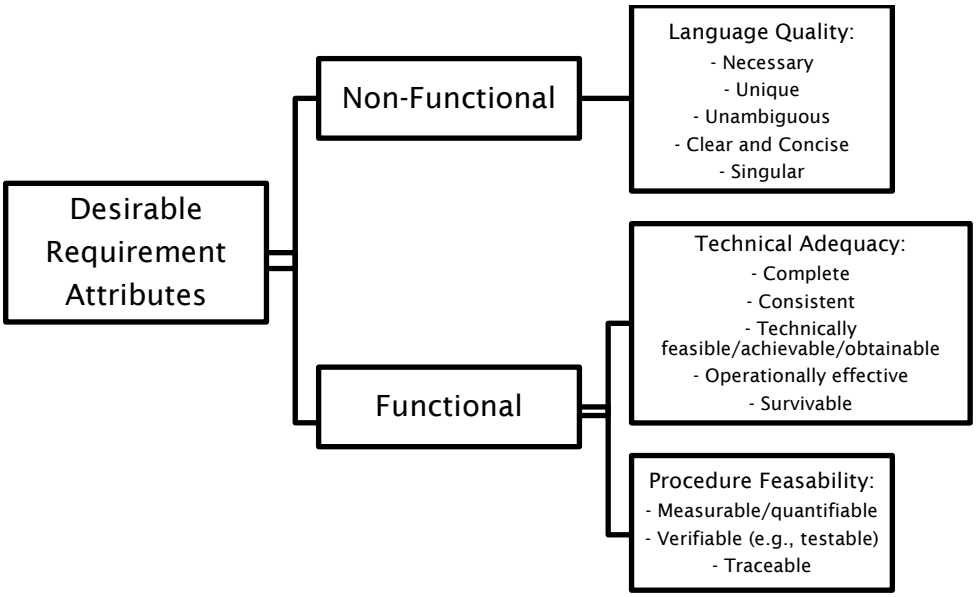

Figure 10. Attributes of desirable requirements.

Task 1.3 Define a validation process for noise standards.
Following the creation of a standards database and the breakdown of standards into their elements, it is imperative to verify noise standard requirements satisfy the desirable requirement attributes. The attributes can be classified into functional and nonfunctional categories, as illustrated in Figure 10. Functional attributes are concerned with the feasibility and technical adequacy of the requirements, whereas nonfunctional attributes are those concerned with language quality. Functional attributes require data for verification, unlike nonfunctional attributes. To this end, the standards requirements

® MagicDraw is a registered trademark of No Magic, Inc., Allen, Texas.

analysis process (outlined in Figure 11) provides a framework that allows for the verification of regulatory requirements' adherence to the desired requirement attributes. The outline indicates that once the requirements are defined, data needs to be collected using flight testing data. Raw data are then processed by applying procedures such as correlating noise measurement data with position, calculating the required noise metrics (e.g., sound exposure level [SEL]), and applying the necessary data corrections (duration adjustments). The processed data are then used to verify the requirements. Additionally, the requirements can also be checked for functional attributes in the presence of available test data and experience. This is an iterative process, so there is a feedback element that allows for the refinement of the requirements such that it will satisfy the desired requirement features.

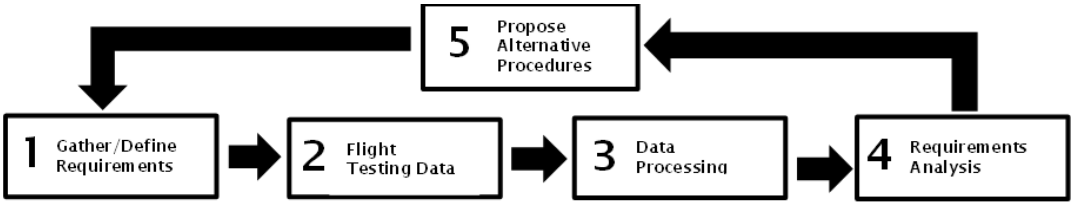

Figure 11. Noise standards requirements analysis process.

The iterative nature of the requirements analysis process dictates whether a standard requirement is deemed unsatisfactory or can be improved in terms of functional attributes; alternative standard requirements need to be proposed (as shown in Figure 11). These alternative requirements are meant to bridge the current gap that exists between current noise standards and UAS/UAM certification needs. Proposing alternative requirements will contribute to capturing the uniqueness of UAS/UAM vehicles while also addressing the challenges associated with their certification (i.e., operational and noise metric limitations). The proposed standards may include the use of different noise metrics, microphone setups, or additional flight tests that better capture the specific mission profile of UASs. Such suggestions could convert to opportunities for potential process streamlining if recommended practices are uncoordinated with current procedures.

The alternative standard requirements can be generated by identifying combinations in the morphological matrix shown in Table 2. The options provided by the matrix are surveyed from literature including FAA, EASA, and ISO noise standards.

Table 2. Noise standards morphological matrix.

Morphological Matrix					
Flight Test Profile	**Flyover**	**Hover**	**Vertical Takeoff/Landing**	**Infrastructure Inspection**	**Maneuver**
Microphone Type	Ground microphone	Inverted ground microphone	Elevated microphone on a tripod	Elevated microphone on a crane (higher altitude)	-
Microphone Array Design	Linear (horizontal)	Circular	Vertical, elevated microphone array	-	-
Noise Measurement Metric	Sound exposure level (SEL)	A-Weighted maximum sound level (LAMAX)	Equivalent sound level (LAEQ)	Effective perceived noise level (EPNL)	-
...	...	...	...	...	...

The objective for generating alternative noise standards is to explore options for formulating a streamlined noise certification process. The following target objectives for streamlining the certification process are currently under consideration:

- Reduce the number of steps in the process, with anticipated savings in time and cost.
- Replace steps in analysis, data preparation, and post-processing with digital tools.
- Enhance automation on procedural tasks (e.g., data retrieval, queries, processing, and report generation).
- Simplify setup requirements to facilitate more test locations/weather windows.

In general, the process of assessing the alternative noise standards can be approached by conducting a series of tradeoff studies between alternative noise standards' technical feasibility and economic viability to find the best alternative in the design space illustrated in Figure 12. Technical feasibility or standard effectiveness can be interpreted as the standard's ability to capture UAS/UAM noise sources and their impact on communities. On the other hand, economic viability, also referred to as economic burden, evaluates the alternative standard time, cost, and complexity.

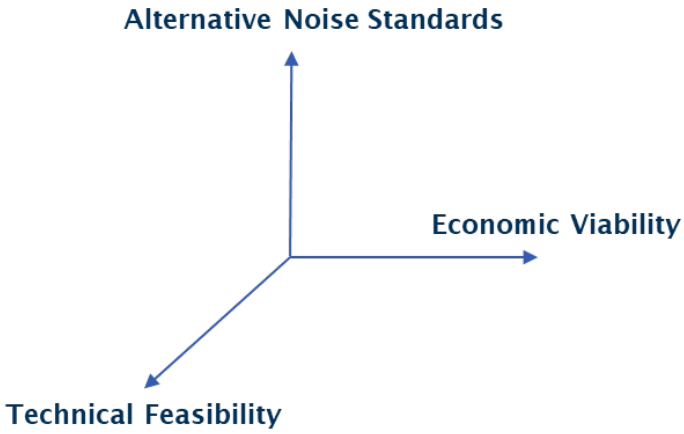

Figure 12. Alternative noise standards tradeoff space.

Along with the selection of the alternative noise standards of interest, the outcome of this exercise is to present certain use cases for which a feasibility demonstration of an equivalent procedure would be possible. This effort would require data for calibrating the standard-setting model against various UAS and UAM vehicle configurations. Additionally, this effort would require data to showcase quantifiable improvements against the process criteria listed above, while meeting the same noise standards constraints and requirements as the benchmarked certification procedure. The quantitative assessment, which will be supported under the PIM module developed under Task 4, is the main enabler for allowing an iterative process until process alternatives can meet the expectations for process streamlining and simplification.

As mentioned above, the existing connections and synergies with other ASCENT projects are expected to provide the resources needed to support the demonstration of this framework as a platform for evaluating equivalent procedures.

Milestones

Between October 2023 and September 2024, the following milestones were achieved:

- Completed the exploration and assessment of NPRM (86 FR 48281) (FAA, 2022), which presents only the noise certification basis for one new model of UAS seeking type certification, the Matternet® M2.
- Reviewed the recently approved remotely piloted aircraft (RPA) for noise certification of small UAS category vehicles.

Major Accomplishments

- Performed a literature search and documented regulations and current testing standards for small UAS.
- Defined a traceable structure for UAS noise certification requirements, using the MBSE verification model developed for the transport category.
- Published articles with AIAA SciTech 2024.

Publications

Published Conference Proceedings

Ravikanti, B., Ali, H., Balchanos, M., Harrison, E. D., & Mavris, D. N. (2024, January 8-12). *MBSE-Enabled System Verification of Unmanned Aerial System Noise Certification* [Conference presentation]. 2024 AIAA SciTech Forum, Orlando, Florida.

Balchanos, M., Ravikanti, B., Ali, H., Mali, H., D Harrison, E., & N Mavris, D. (2024, September 9-11). *A Regulatory Analysis and Process Improvement Decision Support Framework for Unmanned Aerial System (UAS) Noise Certification* [Conference presentation]. Quiet Drones 2024 Symposium, Manchester, United Kingdom.

Written Reports

Balchanos, M., Mavris, D. (2024). December 2023 ASCENT Quarterly Report, ASCENT Project 061 - Noise Certification Streamlining. Award number 13-C-AJFE-GIT-066.
Balchanos, M., Mavris, D. (2024). March 2024 ASCENT Quarterly Report, ASCENT Project 061 - Noise Certification Streamlining. Award number 13-C-AJFE-GIT-066.
Balchanos, M., Mavris, D. (2024). June 2024 ASCENT Quarterly Report, ASCENT Project 061 - Noise Certification Streamlining. Award number 13-C-AJFE-GIT-066.
Balchanos, M., Mavris, D. (2024). September 2024 ASCENT Quarterly Report, ASCENT Project 061 - Noise Certification Streamlining. Award number 13-C-AJFE-GIT-066.
Balchanos, M., Mavris, D. (2023). Annual Report (period ending September 2023), ASCENT Project 061 - Noise Certification Streamlining. Award number 13-C-AJFE-GIT-066.

Outreach Efforts

- Completed follow-up meetings with OEM partners for feedback on the certification model.
- Presented the model-based framework in two webinars.
- Completed a project overview and capability demonstration to the Volpe National Transportation Systems Center (Volpe) and requested information for model finetuning.
- Participated in conferences (2024 AIAA SciTech Forum and Quiet Drones 2024 Symposium).

Awards

None.

Student Involvement

All participating graduate students have supported Task 1 activities by contributing to the literature, conducting ground searches, and reviewing current regulations and FAA-instructed certification procedures. Recent efforts to document current regulations for UAS noise certification are currently led by Balaji Ravikanti.

Plans for Next Period

- Demonstrate an equivalent procedure (EP) assessment through certification modeling across different UAS configurations.
- Explore alternatives for the standard setting.
- Publish peer-reviewed journal articles with *AIAA Journal* and AIAA SciTech.

References

Bendarkar, M. V., Harrison, E., Fields, T. M., Glinski, S., García, E., & Mavris, D. N. (2023). An Extended MBSE Framework for Regulatory Analysis of Aircraft Architectures. 2023 AIAA AVIATION. https://doi.org/10.2514/6.2023-3611
European Union Aviation Safety Agency. (2019, June 11). *Specific Category - Civil Drones | EASA*. https://www.easa.europa.eu/en/domains/drones-air-mobility/operating-drone/specific-category-civil-drones
European Union Aviation Safety Agency. (2023). *Environmental Protection Technical Specifications (Noise) Applicable to VTOL-Capable Aircraft Powered by Non-Tilting Rotors*. https://www.easa.europa.eu/en/downloads/139022/en
European Union Aviation Safety Agency. (2024a, July 10). *Open Category - Low Risk - Civil Drones | EASA*. https://www.easa.europa.eu/en/domains/drones-air-mobility/operating-drone/open-category-low-risk-civil-drones
European Union Aviation Safety Agency. (2024b). *Certified Category - Civil Drones | EASA*. https://www.easa.europa.eu/en/domains/drones-air-mobility/operating-drone/certified-category-civil-drones
Fazal, B., Glinski, S., Harrison, E., Fields, T. M., Bendarkar, M. V., García, E., & Mavris, D. N. (2022, June 29-July 1). *An MBSE Framework for Regulatory Modeling of Transport Category Airplanes*. AIAA AVIATION 2022 Forum, Chicago, Illinois, AIAA 2022-3256. https://doi.org/10.2514/6.2022-3256
Federal Aviation Administration. (2003). *FAA Writing Standards*. https://www.faa.gov/documentlibrary/media/order/branding_writing/order1000_36.pdf.
Firesmith, D. (2005). Are your requirements complete. *The Journal of Object Technology, 4*(1), 27. https://doi.org/10.5381/jot.2005.4.1.c3

International Council on Systems Engineering. (2006). *Systems Engineering Handbook: A Guide for System Life Cycle Processes and Activities*, version 4.0, INCOSE-TP-2003-002-03. http://www.las.inpe.br/~perondi/21.06.2010/SEHandbookv3.pdf

Kim, D., Taneri, M., Omoarebun, E.N, Wills, T., Balchanos, M., & Mavris, D. (2023, January 23-27). *MBSE-Enabled System Verification and Process Improvement of Transport Aircraft Certification*. AIAA SciTech 2023 Forum, National Harbor, MD, AIAA 2023-1897. https://doi.org/10.2514/6.2023-1897

U.S. Department of Defense. (2022). *Systems Engineering Guidebook*. Office of the Under Secretary of Defense for Research and Engineering, Washington, D.C. https://ac.cto.mil/wpcontent/uploads/2022/02/Systems-Eng-Guidebook_Feb2022-Cleared-slp.pdf.

Task 2 - Develop a Library of UAS and Testing Procedures

Georgia Institute of Technology

Objectives

Task 2: Develop a library of UAS and testing procedures

2.1 Complete technical documentation of UAS configurations
2.2 Complete technical documentation of UAS noise testing equipment
2.3 Define UAS noise test plans
2.4 Define possible simulation techniques

Research Approach

Task 2.1 Complete technical documentation of UAS configurations

Research tasks on investigating and archiving technical documentation of UAS configurations, as well as recommended procedures for noise testing, started in July 2022. Due to the lack of historical data about the noise generated by most UAS models, the FAA is unable to provide generally applicable noise standards for UAS (FAA, 2021). This insufficiency in data is caused primarily by the novelty and variety of UAS, such that no clear categorization of the systems is currently established. Figure 13 illustrates this problem by listing some of the different UAS configurations currently available.

The aforementioned problem is exacerbated by the various mission profiles of UAS systems and their different operating environments (Kim, 2022). As an alternative measure, the FAA issues Rules of Particular Applicability (RPA) for applicants who wish to certify their product for noise (FAA, 2023). To achieve this, the FAA assumes that the fundamental physics of UAS operation and noise are scalable if UAS share comparable characteristics with crewed aircraft. As a result, the current noise standards for crewed aircraft outlined in 14 CFR § 36 (2025) can be applied to UAS or extrapolated for testing lower-weight UAS at lower altitudes. An example of this is the “Noise Certification Standards: Matternet Model M2 Aircraft” (FAA, 2021), which is the first RPA establishing a noise certification basis for a single model of aircraft described only for the Matternet® Model M2 (FAA, 2021). These RPAs alongside the Volpe UAS Testing Campaign’s noise measurement reports have been valuable for documenting testing procedures and in identifying the most important technical challenges for UAS noise testing.

So far, depending on the availability of data, only multirotor UAS were encompassed within the scope of the provided analysis. This includes vehicles such as the Matternet® Model M2, Tarot X8, and Flytrex® FTX M600P. The three UASs are depicted in Figure 13. The Matternet® Model M2 was issued the first RPA by the FAA in 2022; therefore, it was used for benchmarking efforts early in the pivot toward UAS from the transport category. Tarot X8 is employed by the ASCENT Project 077 team for their noise measurement testing campaigns. Thus, in collaboration with ASCENT Project 077, a dataset was obtained from the testing campaign and was used to investigate the noise generated by Tarot X8 within the scope of the benchmarked regulations. Finally, the Flytrex® FTX M600P is the system under test (SUT) for the most recent case study under this project. Its noise certification standards were issued on July 3, 2023, and upon collaboration with the ASCENT Project 094 team, a dataset was obtained from the Causey Noise Measurement Testing Campaign that facilitated this case study. More details about the case study are provided in Task 4.

® Flytrex is a registered trademark of Flytrex Aviation LTD, Tel Aviv, Israel.

(a) Matternet® M2 (b) Tarot X8 (c) Flytrex® FTX M600P

Figure 13. Unmanned aerial systems (UASs) analyzed within this project.

Task 2.2 Complete technical documentation of UAS noise testing equipment
Part of the motivation behind looking at RPAs and Volpe UAS noise measurement campaigns' reports, as well as collaborating with the ASCENT Project 077 team, is to generate technical documentation on UAS noise testing equipment. The equipment employed within a testing procedure includes everything from pressure sensors (i.e., microphones), to data recorders, weather data microstations, aircraft tracking systems, etc. This equipment will be supported by data measurement and collection software.

Microphones are the most critical element in noise testing. Figure 14 showcases three types of microphones that can be utilized during noise testing: (1) ground microphones, (2) inverted ground microphones, and (3) elevated microphones. Ground microphones, including the inverted ones, tend to minimize interference with directed or reflected sound, and reduce measurement uncertainty related to the microphone elevation; however, ground microphones tend to be more complex to set up and more costly than the elevated microphones. In contrast, elevated microphones are simpler to set up and less expensive, but elevated microphones suffer from interference with directed and reflected sound. All microphones utilized for noise measurement are outfitted with windscreens to ensure reliable acoustic measurements while minimizing noise due to weather variations (e.g., rain and wind) and birds.

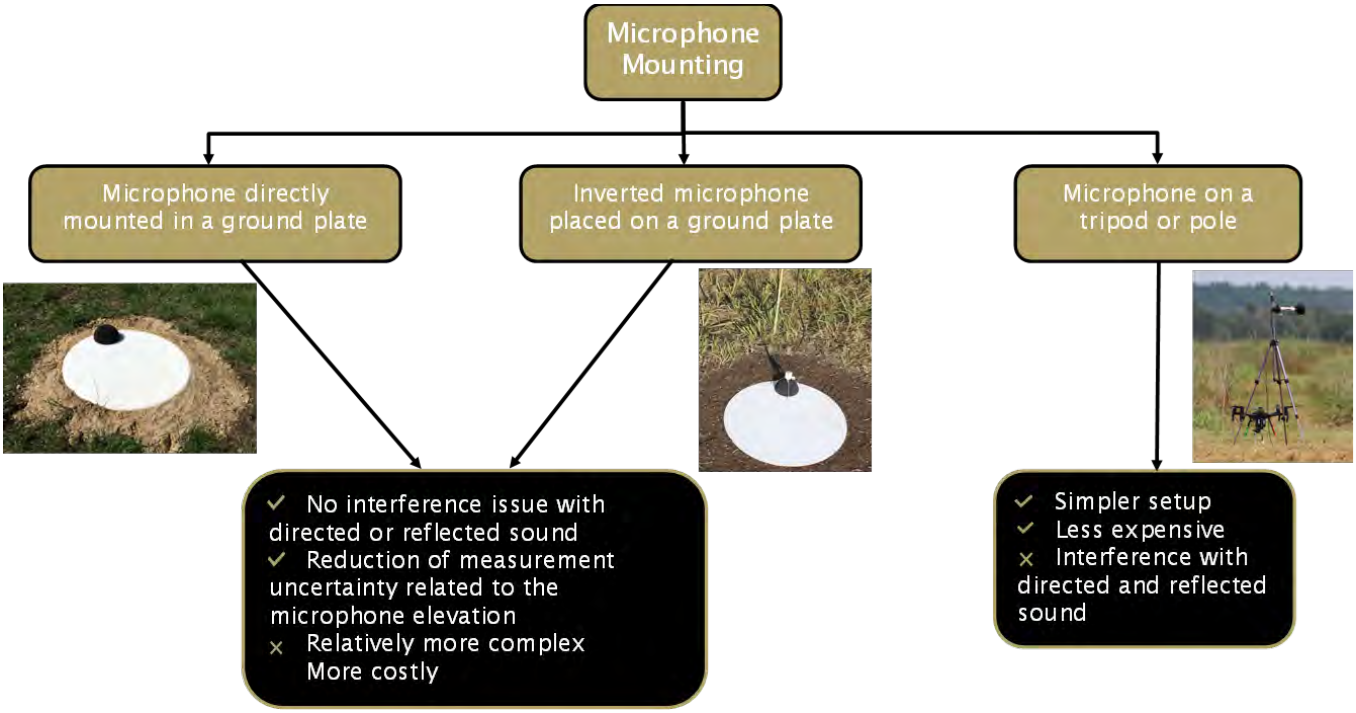

Figure 14. Microphone types and corresponding advantages and disadvantages.

The pressure fluctuations captured by the microphones are digitized via a data recorder. Data recorders are also used to power microphones and control the timing, synchronization, and data transfer between the input module and external host such as a computer. Moreover, meteorological conditions are continuously monitored during acoustic measurements. Weather data logging can be collected via weather microstations connected to anemometers and temperature/humidity sensors, as shown in Figure 15.

Figure 15. Anemometers for Weather data acquisition equipment.

Time-space-position information for UASs within a noise testing procedure is captured by aircraft tracking systems such as the Survey and Tracking Apparatus for Research in Transportation (START) depicted in Figure 16. START is a tracking system developed by Volpe "for the purpose of deriving precise positioning and timing information from UAS and other automated platforms" (James et al., 2021).

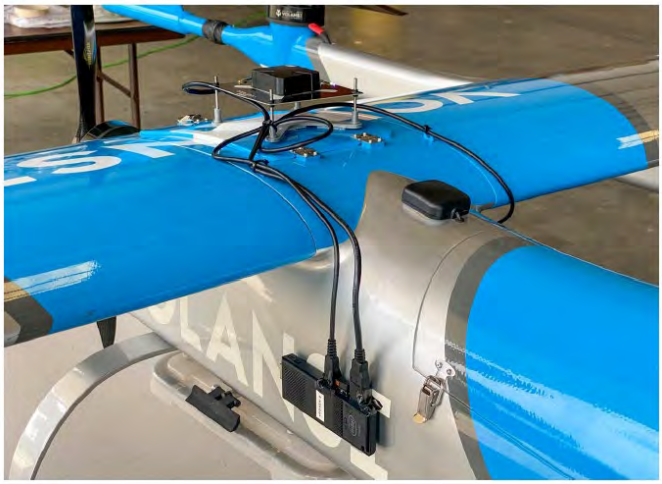

Figure 16. Survey and Tracking Apparatus for Research in Transportation (START) aircraft tracking system.

Task 2.3 Define UAS noise test plans

Research tasks on investigating and archiving technical documentation of UASs, as well as recommended procedures for noise testing, started in July 2022. One of the key studies that the ASCENT Project 061 team has started to document, which has been valuable in identifying the most important technical challenges for UAS noise testing, is the document titled "Noise Measurement Report: Unconventional Aircraft" by the Choctaw Nation of Oklahoma (July 2019). The practice

described for UAS noise testing took place on a grassland, which, taking the flight envelope into consideration, is not suitable due to the following reasons:

- Dense areas can have a different "perceived" noise
- High altitudes and dense areas over buildings and hard surfaces can have different reflective behaviors
- Within buildings, noise can be reflected, amplified, or attenuated

Part of this grassroots effort in discovering the state of the art is the technical documentation on UAS noise testing equipment. By assessing testing procedures from a regulatory perspective, we can build some simple alternatives under the system verification model (Figure 17 shows examples). Finally, the UAS noise test plans must be defined and executed. Physical testing will not cease to exist, but simulation techniques are needed for testing process alternatives.

A major part of the study for this cycle involved gathering available experimental test data to aid in understanding both the sensitivity of noise metrics to flight test parameters or test setup parameters and the times and costs associated with various sub-steps of a noise testing procedure. Note that the experimental noise testing campaign is more rigorous in many ways compared with the certification noise testing procedures. This enabled us to compare various microphone locations, flight conditions, and metrics, which is not possible when limited to the data typically available from certification-type noise testing procedures.

The experimental test campaign whose data were extensively utilized in this cycle of the study was the Causey test campaign. The objective of the testing campaign was "to gather data on UAS noise emissions in compliance with the UAS noise regulations specified in 14 CFR § 135." Unlike other test campaigns, which may not be compliant with certification norms, the Causey campaign is explicitly meant to gather certification quality data. The report provides the acoustic measurements and resultant dataset. FAA, Volpe, and Blue Ridge Research and Consulting (BRRC) were the parties involved. Chris Hobbs (FAA) headed UAS flight operations, Robert Samiljan (Volpe) coordinated the vehicle tracking data collection, and Michael James (BRRC) managed the acoustic data collection.

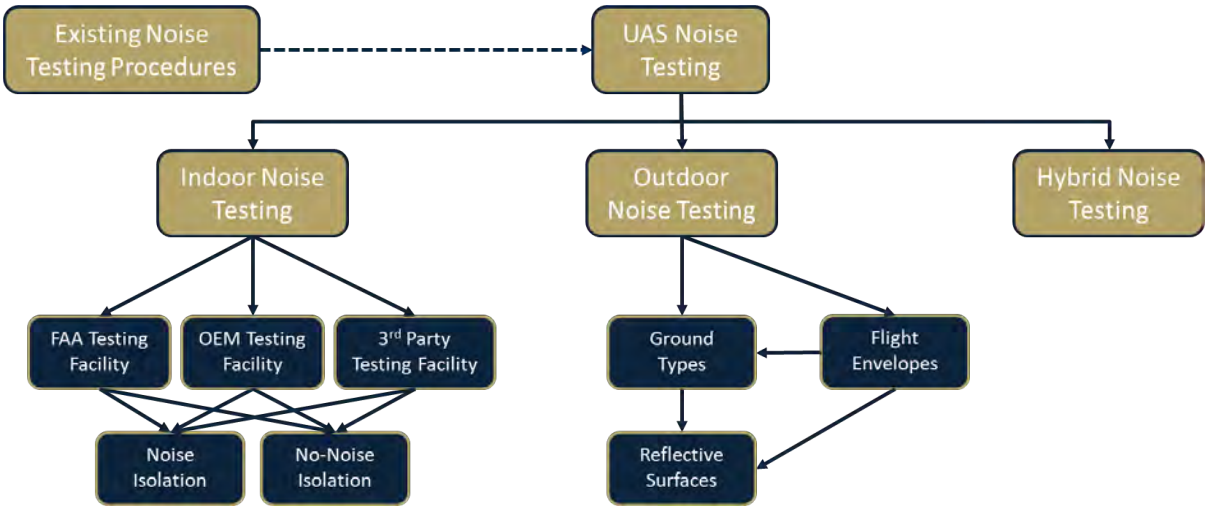

Figure 17. Alternative noise testing procedures for an unmanned aerial system (UAS). OEM: original equipment manufacturer.

Table 3 lists the empty and maximum weights of the test vehicles shown in Figure 18. Vehicles performed flyover and hover operations for multiple flight conditions. The weight of the Flytrex® FTX-M600P is comparable to the Matternet® M2 (for which there is an existing recent noise regulation linked in references), which has a MTOW of 29 lb, including a 4-lb payload. However, it is worth noting that the Flytrex® FTX M600P is a hexacopter, whereas the Matternet® M2 is a quadcopter. An RPA for the noise certification of Flytrex FTX-M600P was approved recently, alongside six other vehicles of the same class. Flight conditions are derived based on various combinations of weight, speed, and altitude. Three groups of "test points" were conducted (namely, level flyover operations; hover operations; and idle, takeoff, landing, or

operational level flyover operations). The campaign took place from July 26 to July 29, 2021. Each day, a different vehicle underwent testing.

Table 3. Causey test campaign vehicle weights.

Weight	Flytrex® FTX-M600P	Volansi® VOLY C10	DJI® m210
Empty (lb)	26.8	51.4	11.8
Max (lb)	33.4	55.0	-

Figure 18. Test vehicles of Causey testing campaign.
From left to right, Flytrex® FTX-M600P, Volansi® VOLY C10 and DJI® m210.

An additional day of Flytrex® FTX-M600P measurements was conducted to capture new test points and repeat two flyover test points to account for day-to-day variations. The goal was to complete six repeated test flights of each condition; however, some test points were repeated more than six times, as will be discussed in later sections.

Figure 19 illustrates the Causey testing campaign layout. This view is later used in the visualization environment that is to host all the key details of a test procedure to enable effective decision-making.

® Volansi is a registered trademark of Volansi, Inc., Concord, California.
® DJI is a registered trademark of SZ DJI Technology Company, LTD, Shenzhen, China.

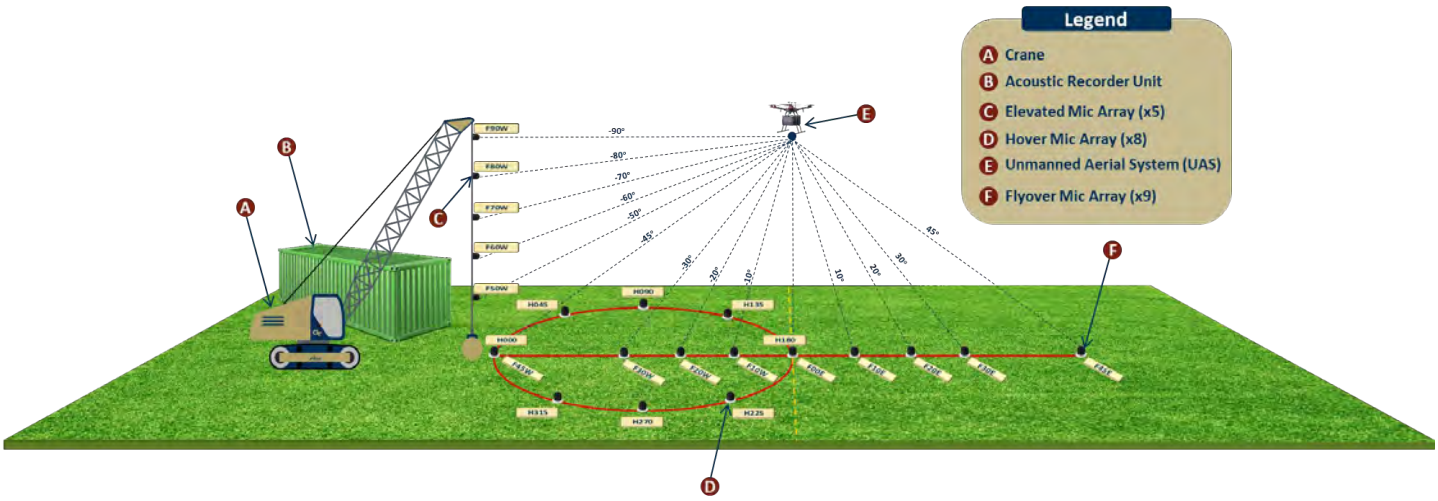

Figure 19. Causey test campaign concept of operations.

Task 2.4 Define possible simulation techniques

Within the scope of this project, the MBSE model was used to assess current noise certification procedures. Typically, MBSE methods are used to represent a vehicle's lifecycle and enable the use of data and information as an integrated systems engineering approach. In the case of ASCENT Project 061, the product is a process architecture, within which current procedures will be assessed and equivalent procedures will be proposed, defined, implemented, and tested within this environment. The full MBSE model formulation for certification and implementation is shown in Figure 20.

The validation process contains the steps needed to demonstrate that vehicle noise levels calculated from flight testing results are meeting requirements. Part of meeting the requirements is the instrumentation setup, which is implemented as a logical architecture within the model. A library of instrument model representations is also constructed, from which alternative instrumentation lineups can be modeled. The latter feature is key, as this framework should allow for the evaluation of equivalent procedures (e.g., ground microphone placement). Other components of the verification model are the test procedures and the test report checklist, which are prototyped as activity diagrams in SysML, as well as the vehicle configurations represented as a state machine.

Completing the verification model is any applicable regulation text in the form of a SysML verification thread. With the verification model in place, the user can import any UAS model, perform the certification equivalent process by executing the verification model, and then generate a final report which would contain the instrument validation document and flight test plan. It is crucial that the overall framework be implemented in a highly modular fashion to obtain the needed flexibility for testing equivalent procedure alternatives and to accommodate a broader range of air vehicle designs and configurations. The SysML implementation currently comprises the following modules:

1. Requirement translation and constraints
2. Noise testing instrument architecture
3. Procedures, protocols, and behavior
4. SUT
5. System verification model overview
6. Auto-report generation and output to process evaluation model

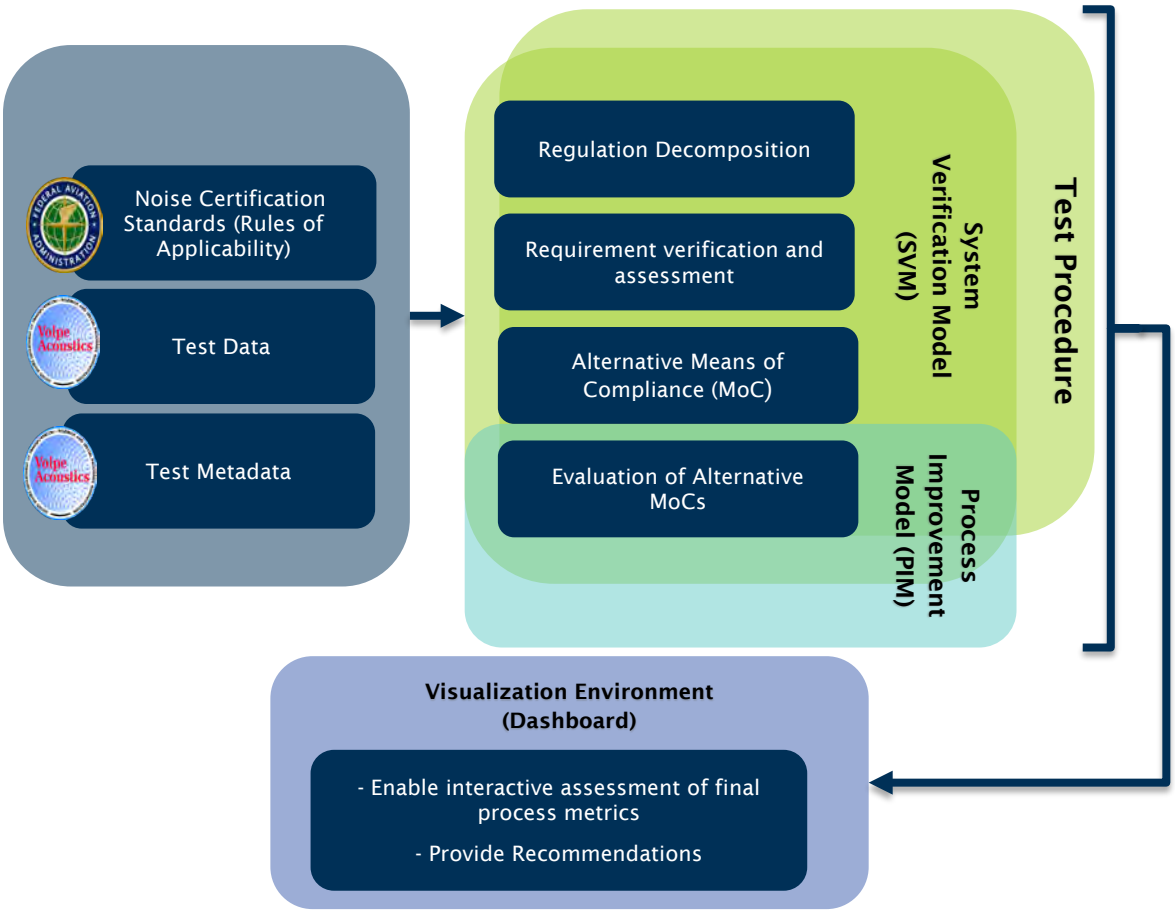

Figure 20. Model-based systems engineering (MBSE) verification model structure.

Event process modeling
With detailed guidance from the documents listed above, event-driven processes were defined and created within the certification model. Additions include modeling of the test-day acoustic collection process and test scenario event processes (i.e., flyover, hover).

Library creation
A new task was identified to command the creation of libraries within the certification model, to allow for added flexibility and modularity. Current libraries include the aircraft library, microphone library, and data amplifier library. The SUT representation has been modified to allow for adaptability to various UAS types and configurations.

Aircraft testing environment
Another finalized improvement on the certification model is the modeling of the UAS test environment, including the flight test setup configuration. With input from documents such as RPAs and Volpe UAS noise measurement campaign reports, the model was updated and refined to include various instrumentation system architectures.

Noise calculation
UAS noise certification only requires a flyover test, but noise certification also specifies a supplemental hover test to augment the process of collecting noise data that will inform the generation of generally applicable noise standards for UAS. The hover test, as described by the FAA in the noise certification standards for the Matternet® M2, is a voluntary test that "will not be used to inform the applicant's airworthiness or type certification basis or be evaluated against any noise limits or regulatory criteria for noise certification purposes" (FAA, 2021). So far, UAS RPAs have described two noise

metrics for noise measurements: (1) SEL for the flyover test and (2) equivalent sound level (L_{eq}) for the hover test (FAA, 2021).

1. **Sound Exposure Level:**
   SEL is an energy-averaged A-weighted sound level over a specified period of time or single event, with a reference duration of 1 s. SEL can be calculated using two methods, defined as follows (Bennett & Pearsons, 1981):

   1.1- Continuous time integration:

$$L_{AE} = 10\log_{10}[\frac{\int_{t_1}^{t_2} 10^{\frac{L_A(t)}{10}} dt}{1\ sec}]$$

   where t_1 and t_2 define the time interval, and $L_A(t)$ is the time function of A-weighted sound level during the time for $t_1 - t_2$.

   1.2- Temporal sampling:

$$L_{AE} = 10\log_{10}[\sum_{i=1}^{n} 10^{\frac{L_A(i)}{10}} \Delta t]$$

   where $L_A(t)$ is the instantaneous A-weighted sound level for the n^{th} sample, n is the number of samples taken during the observational period, and Δt is the time interval between samples.

   As mentioned previously, UAS RPAs prescribe the use of SEL for the flyover test, in which they specify that the integration time $t_2 - t_1$ in practice must not be less than the time interval during which $L_A(t)$ first rises to within 10 dB(A) of its maximum value (L_{Amax}) and last falls below 10 dB(A) of its maximum value. In addition, the regulations allow for the use of an integrating sound level meter to obtain L_{AE} directly rather than manually calculating L_{AE} (FAA, 2021).

2. **Equivalent Sound Level:**
   L_{eq} is the level of the A-weighted sound energy averaged over a specified period of time. Similar to L_{AE}, it can be calculated by two methods, defined as follows (Bennett & Pearsons, 1981):

   2.1- Continuous time integration:

$$L_{eq} = 10\log_{10}[\frac{\int_{t_1}^{t_2} 10^{\frac{L_A(t)}{10}} dt}{t_2 - t_1}]$$

   where t_1 and t_2 define the time interval, and $L_A(t)$ is the instantaneous A-weighted sound level.

   2.2-Temporal sampling:

$$L_{eq} = 10\log_{10}[\frac{1}{n}\sum_{i=1}^{n} 10^{\frac{L_A(i)}{10}}]$$

   where $L_A(t)$ is the instantaneous A-weighted sound level for the n^{th} sample and n is the number of samples taken.

   UAS RPAs prescribe the use of L_{eq} for hover tests only. Similar to L_{AE}, the regulations allow for the use of an integrating sound level meter to obtain L_{eq} directly rather than calculating it manually (FAA, 2021).

Before L_{AE} and L_{eq} are calculated, corrections must be applied to the measured data to account for uncertainties related to the measurement system, microphone and recording system used, background noise, actual flight path, and meteorological conditions present when the measurements were taken.

The use case described in Task 4 utilizes a Python® code to parse through the sound pressure time-history (audio) signals obtained from the Flytrex® FTX M600P flyover and hover tests during the Causey UAS Acoustic Measurements campaign and calculate both L_{AE} and L_{eq} based on the equations above. Regarding the implementation of noise metric calculations, there is no option for directly performing such analyses within the SysML-based certification model. A possible solution is to create a function in Matlab® and then incorporate the analysis in the verification thread.

Milestones

- Reviewed UAS testing procedures from the literature.
- Obtained useful test data from collaborators.
- Established connections with OEMs and other research teams for further investigations.

Major Accomplishments

- Created scripts required to generate multiple noise metrics from raw frequency domain data.
- Documented UAS noise testing practices and processes.

Publications

None.

Outreach Efforts

- Provided full year 4 performance review to the FAA AEE.
- Facilitated technical discussions and feedback provided by Volpe.
- Collaborated with the ASCENT Project 077, Dr. Eric Greenwood's research group, and Flytrex Aviation LTD.

Awards

None.

Student Involvement

All students participated in the collection and review of UAS noise testing practices and processes. Hussein Ali led the review of available noise testing data and the creation of scripts of noise metrics evaluation.

Plans for Next Period

Identify use case examples to plan for demonstration, based on selected areas of improvement for alternative procedures and their evaluation.

References

Bennett, R., & Pearsons, K. (1981). *Handbook Of Aircraft Noise Metrics (CR-3406).* National Aeronautics and Space Administration (NASA), N81-21871. https://ntrs.nasa.gov/api/citations/19810013341/downloads/19810013341.pdf

Federal Aviation Administration. (2021). *Noise Certification Standards: Matternet Model M2 Aircraft.* https://www.federalregister.gov/documents/2021/08/27/2021-17769/noise-certification-standards-matternet-model-m2-aircraft

Federal Aviation Administration. (2023). *Noise Certification of UAS/AAM using Rules of Particular Applicability.* https://www.faa.gov/about/office_org/headquarters_offices/apl/aee/noise/uas_noise_certification

James, M., Salton, A., Downing, M., & Calton, M. (2021). *Causey UAS Acoustic Measurements.* Blue Ridge Research and Consulting, Asheville, North Carolina.

Kim, D., Karagoz, F., Datta, S., Balchanos, M., Anvid, D., Harrison, E., & D.N. Mavris (2022). *A Model Based Systems Engineering Approach to Streamlined Noise Certification of Transport-type Aircraft.* In 33rd Congress of International Council of the Aeronautical Sciences ICAS, Stockholm, Sweden, 2022.

Noise Standards: Aircraft Type Certification, 14 C.F.R. § 36 (2025). https://www.ecfr.gov/current/title-14/chapter-I/subchapter-C/part-36

® Python is a registered trademark of Python Software Foundation, Beaverton, Oregon.
® Matlab is a registered trademark of The Mathworks Inc., Natick, Massachusetts.

Read, D. R., Senzig, D. A., Cutler, C. J., Elmore, E., & He, H. (2020). *Noise Measurement Report: Unconventional aircraft - Choctaw Nation of Oklahoma: July 2019*. Retrieved February 21, 2025, from https://rosap.ntl.bts.gov/view/dot/49647/dot_49647_DS1.pdf

Task 3 - Develop a Noise Certification Procedure Based on Existing Practices

Georgia Institute of Technology

Objectives

The focus of Task 3 is to develop an overall definition of a more flexible certification process and the evaluation criteria for determining that the procedure is more streamlined than the baseline. The pivot to a UAS focus is well aligned with the objectives of this task, where flexibility will be driven by the requirement for the MBSE model to accommodate a range of UAS configurations and payloads. Task 3 will build upon the capabilities of the integrated MBSE platform and leverage contributions from all other tasks. The following tasks will be conducted under Task 3:

Task 3: Develop a noise certification procedure based on existing practices

3.1. Transfer noise testing plans to the MBSE model
3.2. Transfer noise testing data to the MBSE model
3.3. Develop a full noise test plan
3.4. Implement a validation process

Research Approach

Tasks 3.1 and 3.2 Transfer noise testing plans and data to the MBSE model.

Task 3.1 seeks to define what is meant by a “flexible” process. One way to define the “flexible” process is to determine whether the introduction of a different vehicle configuration leads to many incompatibilities with the streamlined process under evaluation. For instance, it is important to assess how the UAS configuration affects the microphone technology and quantity needed and microphone placement in the testing facility. Task 3.1 will involve testing procedures and producing mapping compatibilities between vehicle configurations and testing procedures. A set of criteria and evaluation metrics is needed to assess the combinations of vehicle configuration, testing procedures, and uncertainty factors against regulatory-derived requirements, which will be implemented within the MBSE certification framework. Hence, a proposed set of flexibility criteria for the certification process could include the following considerations:

- Compatibility and applicability of equivalent procedures
  - Alternatives in the testing procedure should be accounted for in the model for verification (i.e., more microphones vs. more flight test points)
- Complexity (e.g., if a switch to another configuration requires more steps to setup) and additional instrumentation if a vehicle is more sensitive to variations in certain factors during testing
- Sensitivity to weather and other aleatory uncertainties

The defined criteria will be tested and applied in other tasks; hence, this task is considered complete.

Table 4. National instance table.

#	Name	lateral_distance	hover_height_0	lateral_distance	AGL_45	hover_height_9	radial_90
1	new_req_datapoint	3	4	1	2	7	2
2	new_req_datapoint1	3	3	1	1	2	1
3	new_req_datapoint2	2	3	3	4	4	4

A regulation paragraph can contain both quantitative requirements and inspectional requirements. Quantitative requirements refer to those that contain numbers or a range of numbers to be met. Inspectional requirements usually do not contain numbers but ask the test procedure to follow the instructions or guideline given in the paragraph. In the verification model, such paragraphs cannot be directly adopted but need functional breakdown. For quantifiable requirements, the subjects for which the quantified constraints are designed are identified and separated from each other

for the convenience of validation. For an inspectional requirement, a straightforward number is not available to make constraint out of, but a simple 'yes' or 'no' test can be implemented to address the requirement. With the above modification logic, our team used the function of the requirement diagram in the MBSE model to delineate each requirement within each regulation paragraph. The requirements are constructed with several blocks in addition to the two archetypes mentioned above. Figure 21 shows the formal requirement breakdown process with the help of a requirement from the noise regulations of the Matternet® M2. Table 4 above shows the mapping of the broken down requirements to the test data which enables verification of the requirements.

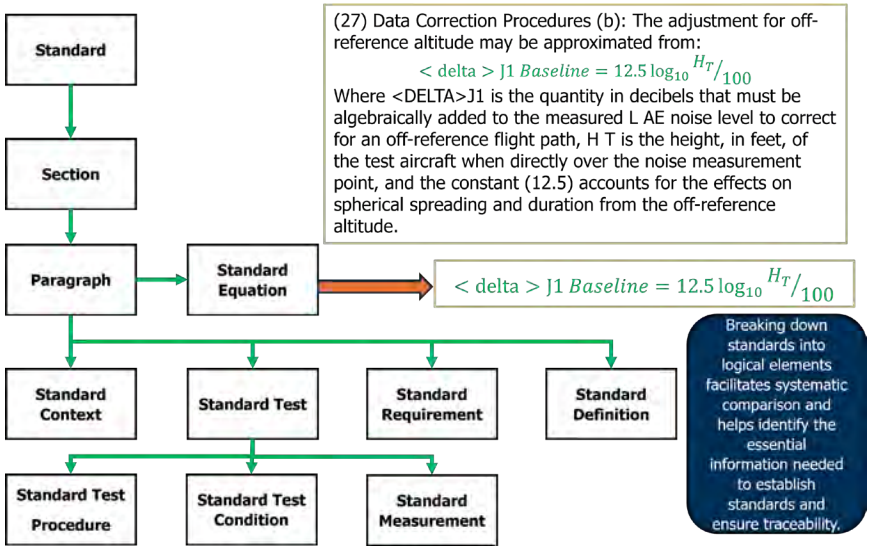

Figure 21. Requirements breakdown highlighting standard equation element.

Figures 22 and 23 show the various standard elements that make up a requirement paragraph with the help of noise certification requirements of the Matternet® M2. A standard equation element of requirement paragraphs enforces the usage of such equations for data correction/adjustment for consistency among all applicants and/or test runs. Similarly, a standard requirement is naturally a part of a requirement paragraph that spells out a metric and the corresponding threshold that needs to be met. In parallel with the requirement breakdown process, the compatibility of existing standards with the rapidly evolving UAS category vehicles is analyzed. This analysis helps assess alternative approaches that could enhance the effectiveness of these standards. One such study targets the confidence interval requirement shown in Figure 22. Another study assessed the suitability of the duration adjustment equation highlighted in Figure 23.

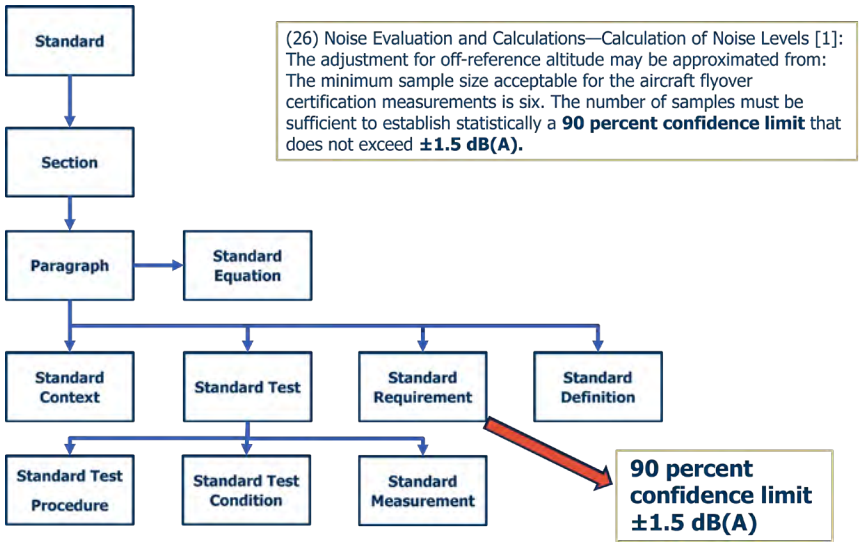

Figure 22. Requirements breakdown highlighting standard requirement element.

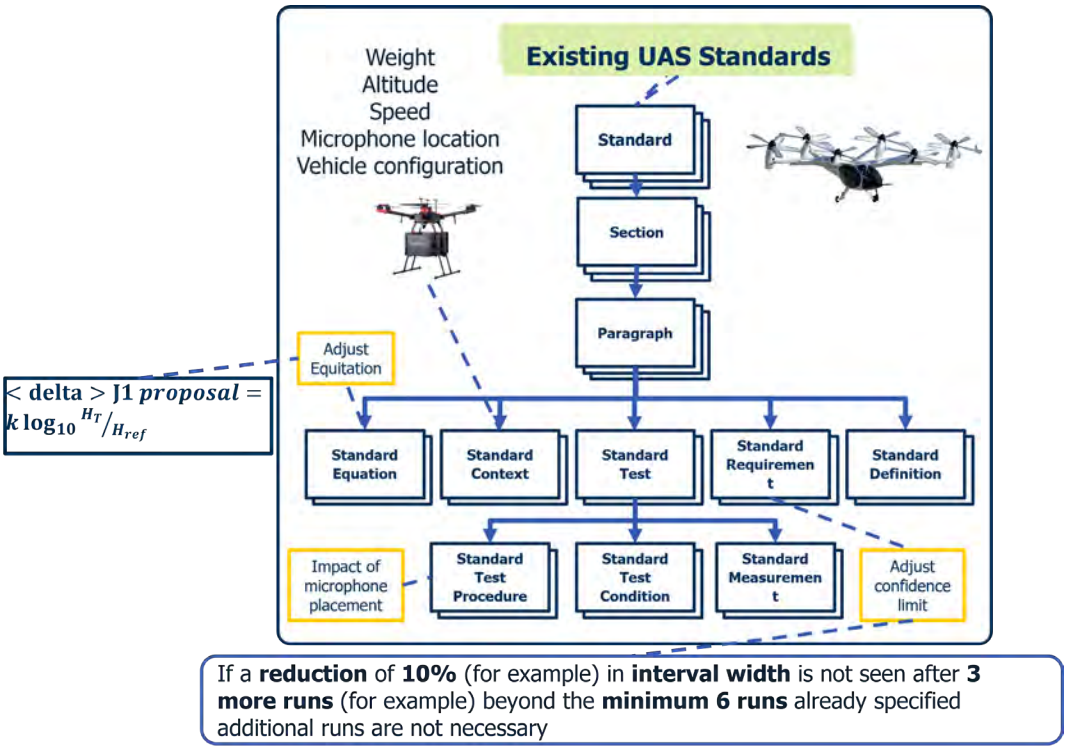

Figure 23. Model-based systems engineering certification framework version for unmanned aerial systems (UASs) to test category flexibility in equivalent certification procedures.

With the MBSE model, testing data can be validated against the requirements instantly after processing. For the convenience of the users, data should be populated in the form of an instance table shown in Figure 21, aligning data to each corresponding constraint. The MBSE model validates data provided to each constraint instantly.

The workflow proposed is extended to an integrated framework for flexible assessment of the certification process and is expected to be reusable for a broader set of UAS configurations, as highlighted in Figure 23.

Task 3.3 Develop a full noise test plan

The certification framework for UASs developed under Task 3, and the use of the PIM completed under Task 4, allow our team to measure process flexibility, efficiency, complexity, and other figures of merit as part of comparing alternatives to the baseline. Framing this problem as a decision-making problem in this context, an "alternative" would be a version of the baseline certification process with a specific combination of a testing plan, instrumentation selection, and a setup for measurements and processing methods, as dictated by a possible equivalent procedure.

A typical flight test procedure can be divided into five major sections corresponding to four days of carrying out different activities or tasks, as shown in Figure 24. These sections are not necessarily carried out over consecutive days as any two sequential sections can be separated by days, if not months, depending on the testing campaign and the scheduling and planning of the parties involved.

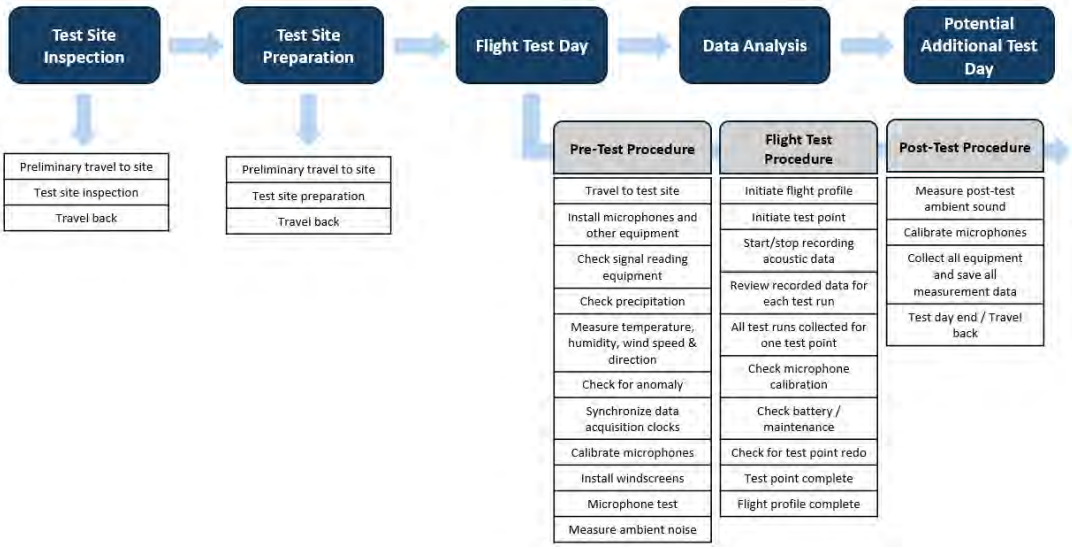

Figure 24. Outdoor noise testing procedure layout for unmanned aerial systems (UAS) noise measurements.

The flight test procedure can be described in the following steps (refer to Figure 24 for the detailed steps for each day of the testing process):

(1) Test Site Inspection. The team visits the potential test site to evaluate its suitability for conducting noise testing. This consists of assessment of the site location and surroundings in terms of proximity to noise-sensitive areas, weather conditions, and levels of background noise (e.g., traffic, birds, construction noise, or sound reflections off nearby buildings). The type of ground surface is also important as it could influence the noise measurement results. Common ground surfaces considered can include grass, concrete, asphalt, and open terrain. Grass tends to be the most preferred ground surface due to its ability to absorb sound and reduce sound reflections compared to hard surfaces; however, this requires the grass to be well maintained and free from tall vegetation. The elevation and uniformity of the ground surface are also crucial to avoid measurement inconsistencies. The overall site area is also evaluated by checking whether it can properly accommodate equipment installation, and distances and altitudes required for flight tests. Following this inspection, the test site is either approved, if deemed appropriate for the testing requirements, or denied, if it does not

meet certain criteria or would lead to test measurement complications or inconsistencies. The necessary permits for conducting UAS flights at the selected location and ensuring regulatory compliance are obtained.

(2) Test Site Preparation. Once the test site is approved and permits are obtained, a second visit to the test site is necessary to prepare the site prior to the actual flight test day. This consists of clearing the site of any obstacles or potential hazards, mowing grass, if needed, and marking the positions of microphones and other equipment installation. This requires having a clear flight plan for the specific flight paths, altitudes, and maneuvers to be performed by the UAS on the flight test day. The UAS to be flown is also inspected to ensure it is functioning properly prior to the flight test day.

(3) Flight Test Day. The flight test day can be delineated into three main action lists:

- Pre-test Procedure: All microphones, recording equipment, and other equipment are installed and deployed. Weather measurements are initiated, and microphones are calibrated and tested prior to the installation of windshields and measurement of ambient noise. Throughout this procedure, multiple checks are conducted to ensure proper functioning of all devices and adequate meteorological conditions for testing.
- Flight-test Procedure: Flight test profiles (i.e., flyover, hover, takeoff, and landing, etc.) are initiated. Within each flight profile, multiple test points can be conducted under different conditions including altitude, weight, and speed. To ensure the accuracy and reliability of measurements, each test point is repeated for a minimum of six test runs. After the completion of each test point, multiple checks are carried out to assess the need for microphone recalibration, maintenance, or battery changes for UASs, or a complete redo of the test point upon the detection of any anomalies or inconsistencies in the measurements.
- Post-test Procedure: Once all flight profiles are completed, the ambient sound is measured, the microphones are calibrated, all microphones and equipment are collected, and measurement data are saved.

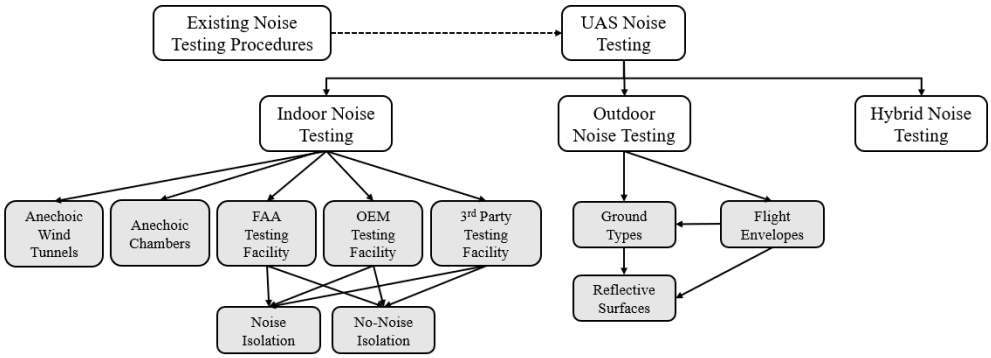

Figure 25. Noise testing types for unmanned aerial systems.

(4) Data Analysis. The data collected during the flight test day are postprocessed and analyzed. Raw measurements are translated in terms of noise metrics of interest, and any sources of inconsistency or interference with the measurements can be revealed. Consequently, the need for replacement or additional measurements is decided at this step.

(5) Potential Additional Test Day: Based on the results of the data analysis from the flight test, an additional flight test day might be necessary. This would either consist of a partial repeat of some test measurement points or a full flight retest if significant interference appears to have been present throughout the entire flight test day or throughout a major of the flight test.

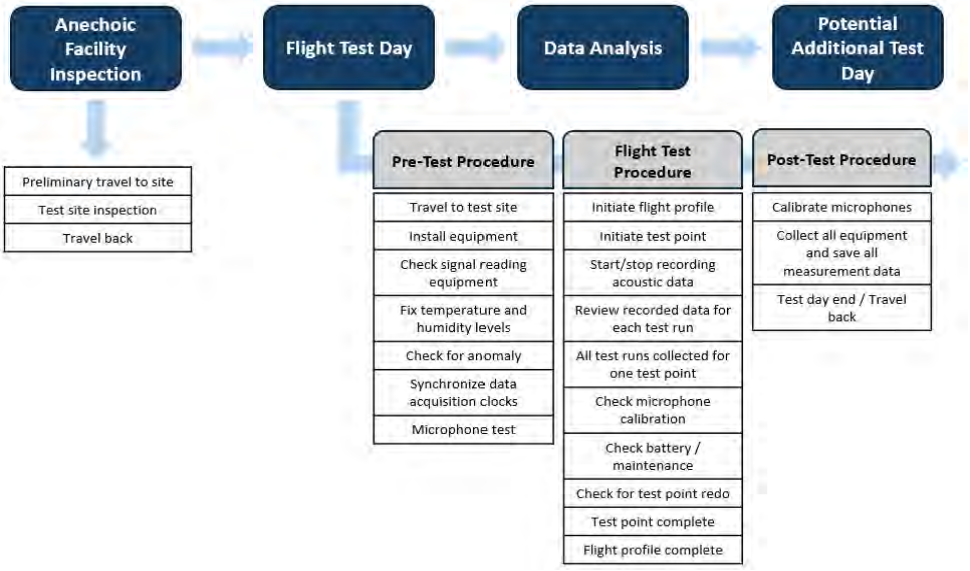

Figure 26. Indoor noise testing procedure layout for UAS noise measurements.

Similarly to the outdoor noise testing procedure for UASs described above, an indoor testing procedure can be formulated for UASs that can be tested in an enclosed space such as anechoic chambers or anechoic wind tunnels (Figure 25). The indoor testing consists of a smaller number of phases and steps considering the controlled nature of the testing environment which reduces the complexity of tasks to be carried out and increases the likelihood of measurements success due to the lack of weather or background noise interferences. Consequently, the corresponding procedure (Figure 26) does not require any travel for test site preparation nor any continuous tracking of weather changes. Moreover, microphone installation and pre-calibration tasks are also eliminated as these are usually installed and calibrated beforehand by the facility. Additionally, the use of windscreens, previously needed for outdoor testing due to wind interference, is no longer essential.

After the model has been calibrated with inputs and parameter definitions that will be obtained from noise testing data resulting from ASCENT Projects 077 and 094, the model will rely on statistical analysis and an identification of process bottlenecks and showstoppers. Another set of metrics of interest will target the impact quantification of process complexities and will be used to indicate gaps and further drive certification process simplification using technologies and estimation methods (e.g., virtual sensing and instrumentation), where process steps could be reduced or eliminated.

As a means of facilitating a scenario-based parametric decision-making capability, the ASCENT Project 061 team has been developing an interactive visualization environment. Through the use of visual representations of the process and key analysis outputs, this environment serves as a user-friendly interface for requirement validation, exploration of process alternatives and their impacts, detection of process shortcomings and gaps, and ranking for the selection of test plans, instrumentation, and noise measurement data analysis against user-set criteria. The ranked alternatives are validated through an assessment of the equivalency for a procedure to standard regulatory practices. A notional representation of the final version of this environment is shown in Figure 27.

Figure 27. Graphical user interface for process specification.

As interactive dashboard development is often approached as a spiral development; the capabilities and features included in the current version are as follows:

- Histograms to visualize each metric of a given procedure. To compare procedures, it may be helpful to overlay the histograms for the respective procedures to visually compare time, cost, etc.
- Sensitivity plots to help select from alternative procedures to improve upon the current baseline. These sensitivities can indicate how robust an alternative is to unforeseen variability in the procedure steps in terms of time or cost it takes to complete the step. For example, how sensitive the overall cost improvement (with respect to the baseline) of an alternative is to the cost it takes to complete the alternatives' first step. This information can be presented to the decision maker in the form of a matrix of plots like the prediction profiler plot in the JMP® statistical software.
- For multivariate and multicriteria problems, a spider chart (radar plot) is used to compare process alternatives against multiple criteria. This chart can help to drive the evaluation of all tested process alternatives and map the strengths and weaknesses of each alternative against the prioritized evaluation criteria.
- The highest ranked process as a chain of events to rank order key steps identified by the PIM in the order of importance for a given procedure.
- A requirements satisfaction section to present an assessment review of whether requirements are being met, which includes providing guidance toward the exploration of procedures and technologies that would help close any gaps and meet all requirements. In this part, the focus is on data analytics supported by the Monte Carlo process simulations using probabilistic inputs. Hence, the results are typically in the form of distributions for the metrics of interest, and allow for exporting means, median values, and cumulative distribution functions to assess whether constraints and requirements are being met.
- A high-level concept graphic (OV-1) charts for physical representation of the test setup and easier communication with OEMs and decision makers as needed.

Using this visualization environment, decision makers can determine the feasibility of alternative procedures, compare alternatives relative to the baseline, and down-select between alternative procedures based on sensitivity to input values. On the actual model demonstrator, alternative procedures will be compared based on sensitivities. The sensitivity plots, along with the histograms and the complementary plots, will be used to select an alternative to the current baseline procedure that has the desired balance between mean performance, variability, and robustness in terms of relevant metrics such as overall time and cost of the procedures.

To enable the multicriteria, parametric, and interactive capability for rapid exploration of certification alternatives, the PIM, which executes a process simulation through Markov chains[1] and graph analysis, can allow probabilistic Monte Carlo simulations for investigating the limitations of each process alternative. This capability is primarily the focus of Task 4 and is presented in the following section (Figure 36 of the Task 4.1 Develop alternative testing procedures using the elements library) of this report.

[1] A Marcov chain, named after Andrey Markov, is a mathematical stochastic process (framework) for describing the sequence and/or states where transitions occur in a given state that are dependent on the probability of the state attained in the previous event and time elapsed (e.g., the probability that n+1th steps will be x depends only on the nth step, not the complete sequence of steps that came before n).

Task 3.4 Implement a Validation Process

A particular instance to illustrate the analysis of alternatives proposed is regulatory paragraph J36.205(b) of 14 CFR § 36, Appendix J, which prescribes the method of adjustment for test flight altitudes during flyover noise measurements that deviate from the reference altitude prescribed in the regulatory paragraph 14 CFR § 36 J36.3(c). Figure 28 (Figure 5 from Volpe test campaigns SEL Duration Adjustment Studies Senzig et. al. 2018) shows that the higher the test flight altitude deviation is from the reference altitude on which the correction curve is based, the higher the error is that results from the adjustment. The test campaigns by Volpe (Senzig et. al. 2018) evaluated these errors by means of the difference in adjusted noise measurement values and actual noise measurement values at various altitudes. Referring to the morphological matrix discussed earlier (refer to Table 3; Task 1.3), an alternative procedure can emerge from any one of the procedural steps such as data processing methods, as in this particular use case. This again bolsters the need for a traceable platform that has the capability to conduct a holistic assessment of all potential certification bases.

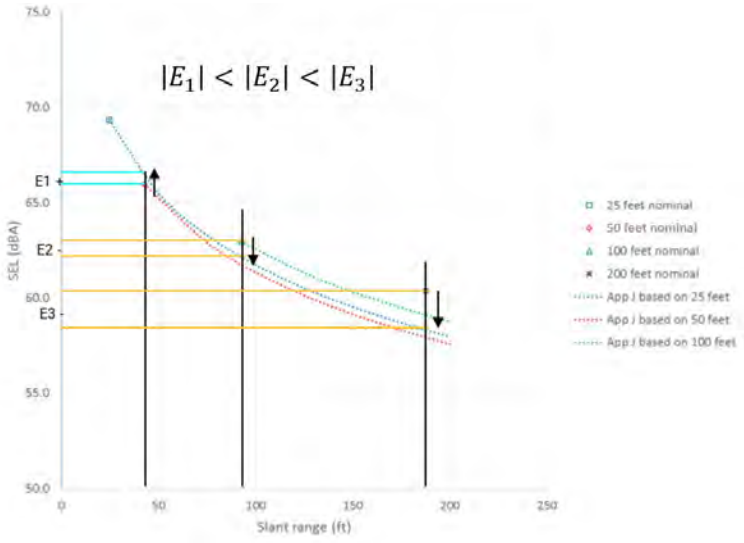

Figure 28. 14 CFR § 36 Appendix J duration adjustments applied to various altitudes (Figure 5 of SEL Duration Adjustment Studies).

Figure 29 below shows the microphone array configuration employed by the Causey testing campaign (James et al., 2021) that generated data analyzed by the Cutler-Wood et al., (2022). The same experimental data was used to conduct the duration adjustment study discussed in this section in the context of analysis of alternatives.

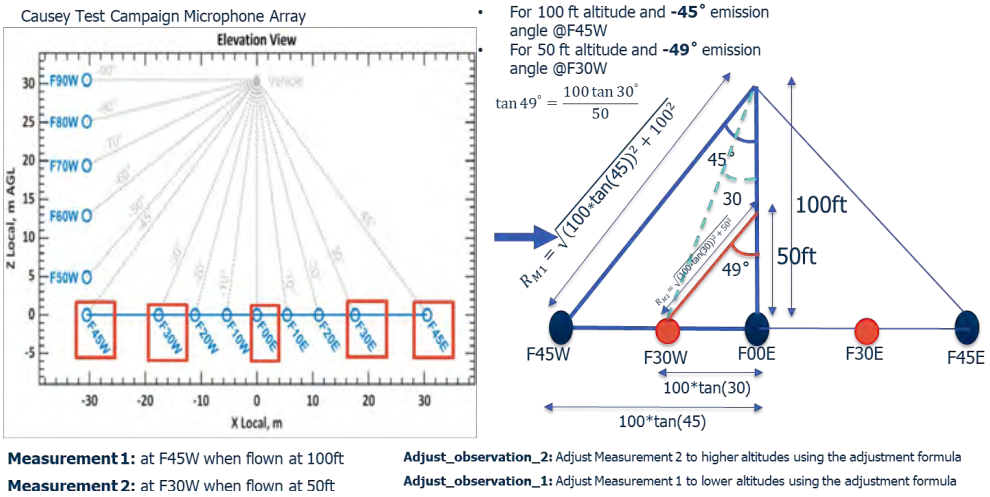

Figure 29. Causey microphone configuration and measurement nomenclature.

Each alternative procedure can have different ramifications on different paragraphs of a regulatory noise standard. Consider, for instance, the alternatives illustrated in Figure 30 for the duration adjustment equation. The variation of noise with respect to emission angles is represented using noise spheres in Cutler-Wood et al., (2022). To determine the utility of the proposed alternative in the context of the duration adjustment requirement alone, it is necessary to know the effects of emission angle and flight profile parameters such as hover flight altitude and weight of the vehicle on the variability in the measurement. It can be seen from Figure 30 that various fixed factor adjustments proposed do not necessarily guarantee a conservative adjustment of the true measurements to different altitudes. The fixed factor adjustments are specified in the RPA corresponding to the Matternet M2 (FAA 2022), the other RPAs (FAA 2023) issued by the FAA. Hence, as highlighted in Figure 23, it is worth considering vehicle specific k-factor adjustment regimen given the wide variety of configurations with varied noise generation and propagation characteristics emblematic of the UAS category.

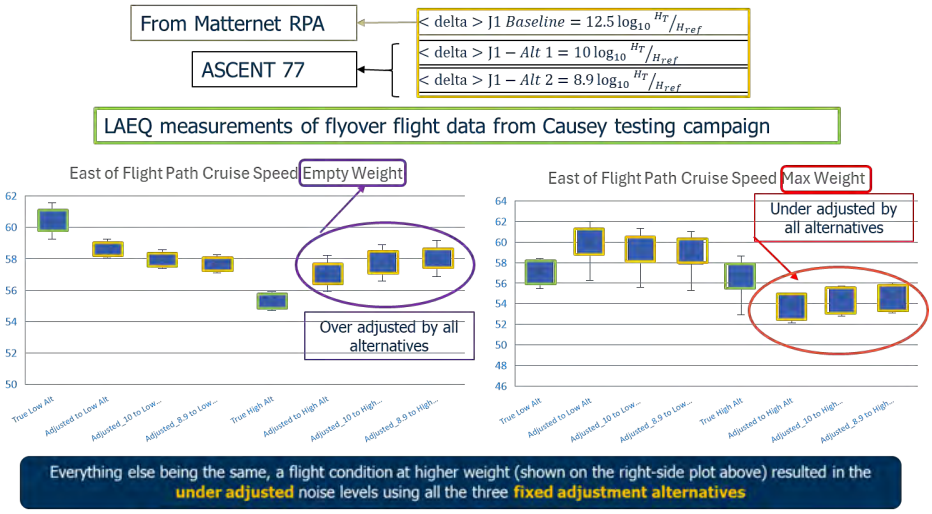

Figure 30. Application of the fixed factor duration adjustments to the noise measurements

Figure 31 shows the microphone array configuration employed by the FAA and collaborating researchers (James et al.,2021) to acquire noise data necessary to understand the effects (Cutler-Wood et al., 2022)). The vehicle deployed for the experimental campaign belongs to the small UAS category.

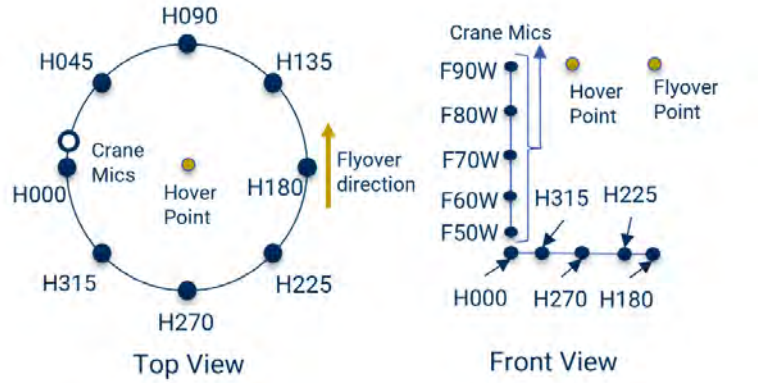

Figure 31. Experimental microphone array configuration (not to scale).

Experimental results consisted of higher-weight and lower-weight flights that were flown at an altitude of 100 ft and repeated five and six times, respectively. Our team evaluated the average confidence interval of SEL measurements of various subsets of a given number of repeats and plotted the results as shown in Figure 32. Figure 32 highlights the effect that vehicle weight has on variability in noise measurement. It can be observed that a higher weight configuration results in higher variability. Figure 32**,** however, does not illustrate a strict relationship in emission angle and weight, and further investigation may highlight the same. The ASCENT Project 061 team also observed that a greater number of runs is required to achieve a confidence interval limit of ± 1.5 dBA (SEL) at higher weight configuration. In view of this, it is proposed if a reduction of 10% (for example) in interval width is not seen after three additional runs (for example) beyond the minimum of six runs already specified, additional runs are not necessary, noting that further reduction variability may not be possible for the given combination vehicle configuration and test flight profile.

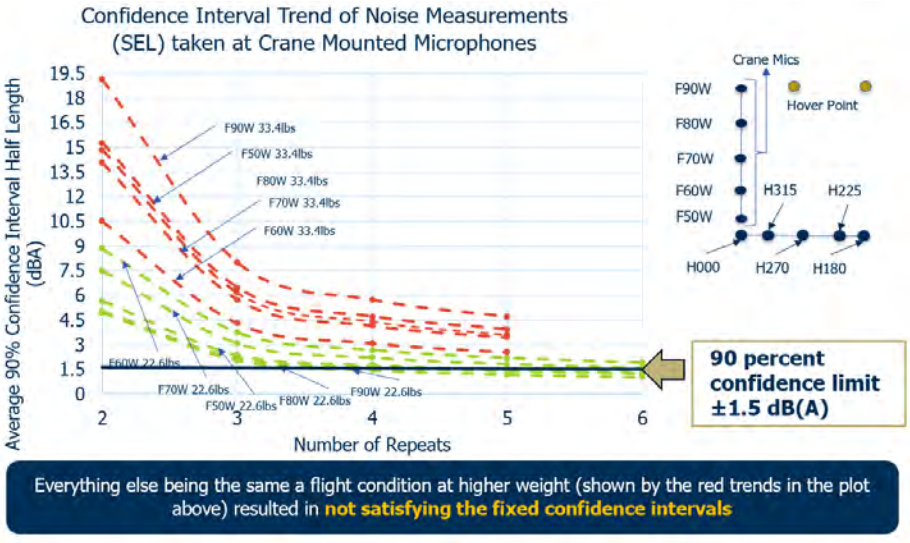

Figure 32. Effects of vehicle weight and emission angle on noise variability in hover flight.

Figure 33 shows the average confidence interval trends for a flyover flight condition that was repeated the highest number of times. Although this flight condition is different from the hover flight condition, it highlights the trend of the average confidence interval of SEL over a higher number of runs. Hence, our team noted that although fewer microphones are required for the alternative method as shown in in the left panel plot of Figure 30, the number of repeats required to achieve the confidence interval limit make the alternative method, as shown in the right panel plot of Figure 30, preferable.

Ultimately, to arrive at a decision, the costs and times of additional microphones and their setup need to be compared with those of additional flights.

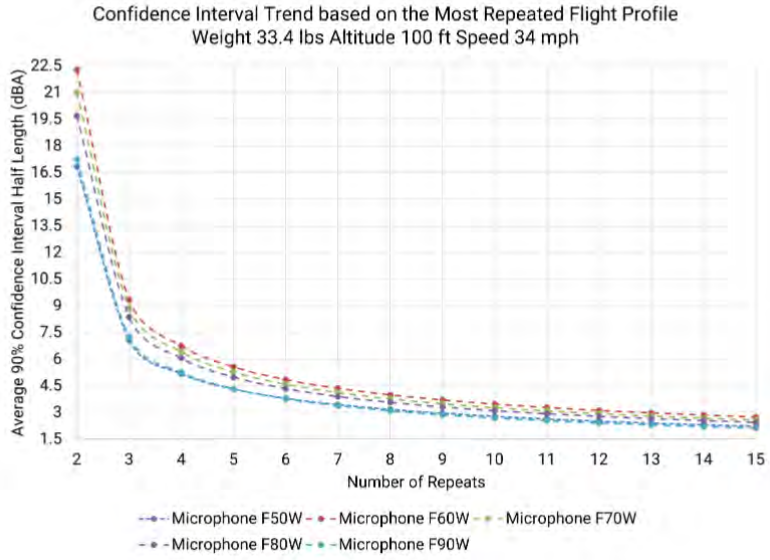

Figure 33. Effects of emission angle on noise variability in flyover flight.

Milestones
See the milestones under Task 1.

Major Accomplishments
- Developed metrics and integrated the PIM under a parametric interactive decision support environment. The concept has been demonstrated through a minimum viable project exercise.
- Formulated and applied the PIM to a typical plan for UAS noise testing.
- Conducted a preliminary analysis of noise measurement data and utilized resulting insights for requirement analysis.

Publications
None.

Awards
None.

Student Involvement
The full student team (Hussein Ali, Nathaniel Geneti, Hajar Mali, Martin Poretti and Balaji Ravikanti) has participated in brainstorming sessions toward formulating the integrated certification process assessment framework for UASs.

Plans for Next Period
- Demonstrate a simple use case, where a number of feasible alternatives lead to comparisons with the process baseline. The use case and the improvement propositions within the alternative options will be formulated with input from subject matter experts and current gaps to meet certification targets.
- Conduct extensive analysis of the noise data available to inform regulatory rulemaking.

References

Cutler-Wood, C., Barzach, M., Hobbs, C. M., & Shirayama, S. (2022, June 27-30). *Estimating Unmanned Aircraft Takeoff Noise Using Hover* [Conference paper]. QUIET DRONES Second International e-Symposium on UAV/UAS Noise, virtual. https://rosap.ntl.bts.gov/view/dot/64152

Federal Aviation Administration. (2022). *Noise Certification Standards: Matternet Model M2 Aircraft*. https://www.federalregister.gov/documents/2022/09/12/2022-19639/noise-certification-standards-matternet-model-m2-aircraft

Federal Aviation Administration. (2023). *Noise Certification of UAS/AAM using Rules of Particular Applicability*. https://www.faa.gov/about/office_org/headquarters_offices/apl/aee/noise/uas_noise_certification

James, M., Salton, A., Downing, M., & Calton, M. (2021). *Causey UAS Acoustic Measurements*. Blue Ridge Research and Consulting, Asheville, North Carolina.

Noise Standards: Aircraft Type and Airworthiness Certification, 14 C.F.R. § 36 (2023). https://www.ecfr.gov/current/title-14/chapter-I/subchapter-C/part-36

Senzig, D. A., Marsan, M., Cutler, C. J., & Read, D. R. (2018). *Sound Exposure Level Duration Adjustments in UAS Rotorcraft Noise Certification Tests*. Volpe National Transportation Systems Center, Cambridge, Massachusetts. https://rosap.ntl.bts.gov/view/dot/37057

Task 4 - Develop Alternative Procedures and Assess Their Performance with Existing Tools (Case Study)

Georgia Institute of Technology

Objectives

Task 4 seeks to explore options for evaluating noise certification within the MBSE certification framework. The purpose of this task is to allow a performance baseline to be established for current procedures and to allow for the evaluation and comparison of more flexible process alternatives as they are formulated within Tasks 2 and 3. The breakdown of tasks under Task 4 is as follows:

Task 4: Develop alternative procedures and assess their performance with existing tools

- 4.1 Develop alternative testing procedures using the elements library
- 4.2 Transfer alternative procedures to the PIM
- 4.3 Report on the performance of the alternative procedures
- 4.4 Develop a proof-of-concept demonstration of the PIM capabilities

Research Approach

The goal of Task 4 is to identify process modeling approaches for the purpose of simulating and evaluating the performance of a noise certification procedure. Task 4 delivers a solution that, in a broader sense, is referred to as the PIM. Tasks 4.1 to 4.3 focus on PIM implementation, whereas Task 4.4 integrates the PIM into the current MBSE framework. The PIM must analyze the process performance and interface with the verification model for completing steps regarding requirements and compliance. The PIM must also be flexible and reusable within the verification thread and must accommodate UAS configurations. An overview of the integrated verification thread and the PIMs is shown in Figure 34.

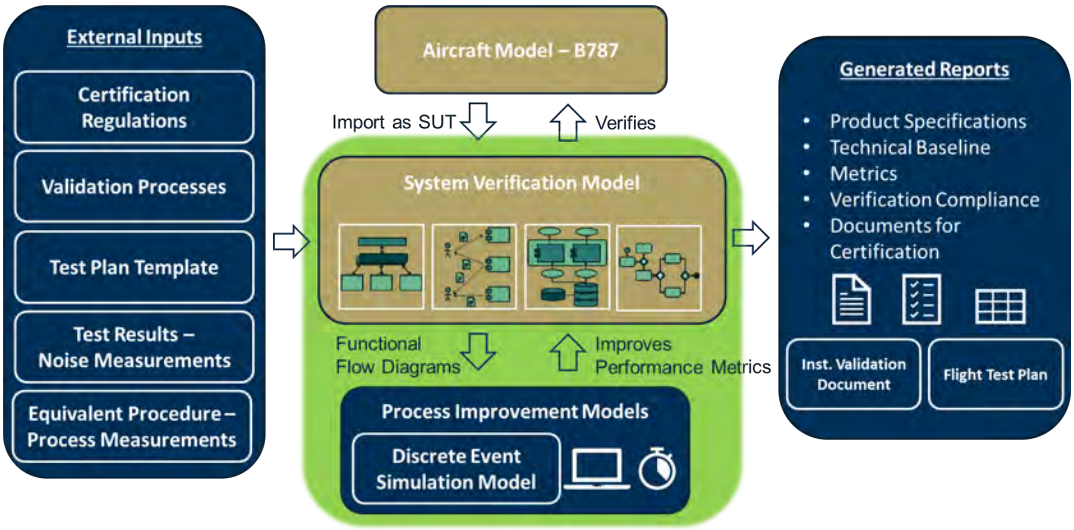

Figure 34. Integration of the process improvement model within the model-based systems engineering certification framework. SUT: system under test.

Task 4.1 Develop alternative testing procedures using the elements library.
The team has completed a literature review on process modeling methods to enable process simulation. These methods are listed below:

- DES, where a clock tracks the duration of the transition between model states
- Agent-based simulation methods
- System dynamics
- MCMC simulation methods

These techniques are evaluated on the basis of their ability to capture and simulate actual industry-applied procedures, and to interface with the verification thread. For simulating a simple process that is representative of transport category certification, the DES modeling approach appears to be the most effective. To demonstrate feasibility, a proof-of-concept version was developed using the DES method in a Python®-based environment. The chosen example covered the testing process for a flyover approach, as shown in Figure 35. The objective was to demonstrate that a process model, as defined in the MBSE framework, can be simulated using DES. With the MBSE model states imported, DES can track the clock and return time points at each event conclusion. The DES results are then fed back as input in turn updating the process diagram in the verification model, which then checks the process model against requirements and compliance.

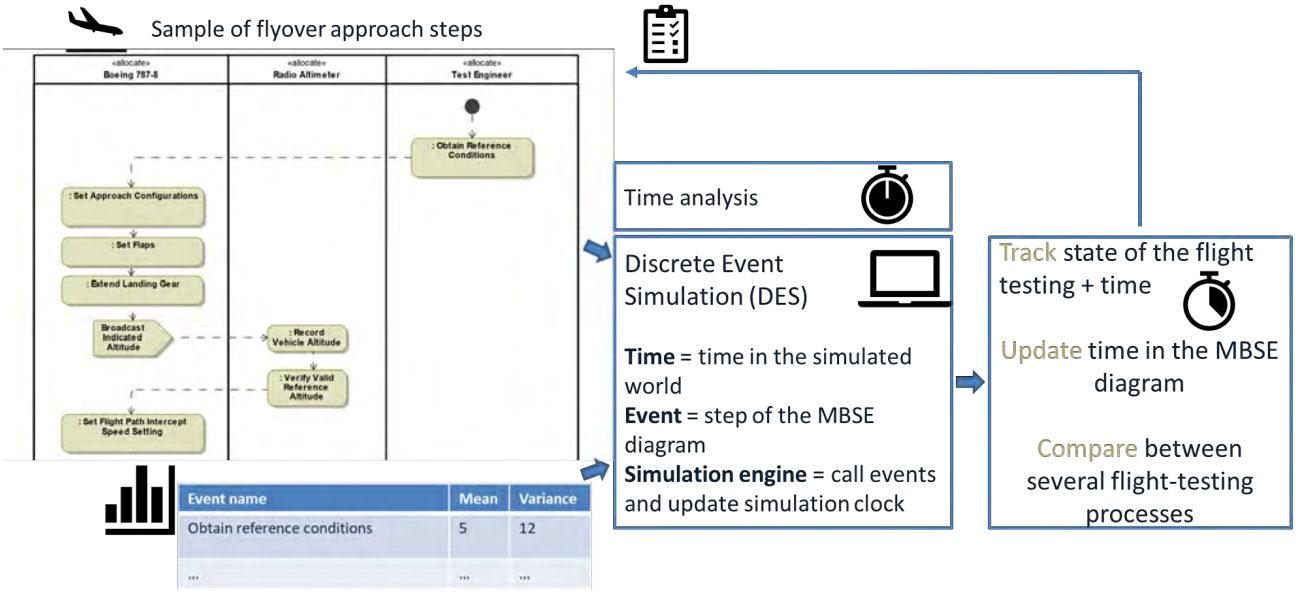

Figure 35. Discrete event simulation for a flyover approach. MBSE: model-based systems engineering.

However, because flight testing procedures are impacted by uncertainties, a different modeling approach is needed. To account for uncertainties, a probabilistic model using Markov chains has been developed to improve the accuracy of how interactions and emerging effects are captured. This approach is better suited to support use cases, with the objective of further process simplification, especially for flight testing portions, instrumentation setup, and measurement systems. This simplification could involve eliminating or replacing steps and potentially using advanced data-driven or physics-based modeling approaches as a substitute.

Because of the extension of DES to Markov chain approaches and the need for large samples, the ASCENT Project 061 team adopted the MCMC approach, where a Markov chain model is used to run a Monte Carlo study to collect sample runs, given an input probability matrix and stakeholder value function. Each run is associated with an incurred time, cost, and accuracy penalty. The output is provided in the form of activity diagrams and responses that are fed back to the verification model within the MBSE framework. Through the requirement model within the MBSE framework, the MCMC simulation data are imported to perform acceptance–rejection sampling, where each run (with its associated metric) is accepted or rejected by requirements/constraints within the verification model. The format of the MCMC simulation data follows the form of a step-by-step sequence (similar to a DES).

Summarizing the development of the PIM, the implementation path is shown in Figure 36, which illustrates the interface with the verification model. Using a similar flyover approach plan example as in Figure 35, the process model informs the PIM, which converts the flyover approach test into an executable simulation model. Based on the type of requirement test selected by the user, the appropriate response values, parametric settings for baseline values (i.e., time, cost, resources, disruption risks, accuracy penalty, etc.), and distributions for Monte Carlo simulations are chosen. The Monte Carlo simulation then generates the PIM metrics and prepares the dataset for verification.

For this task, the literature search, exploration of modeling options and selection, and proof-of-concept implementation are now completed.

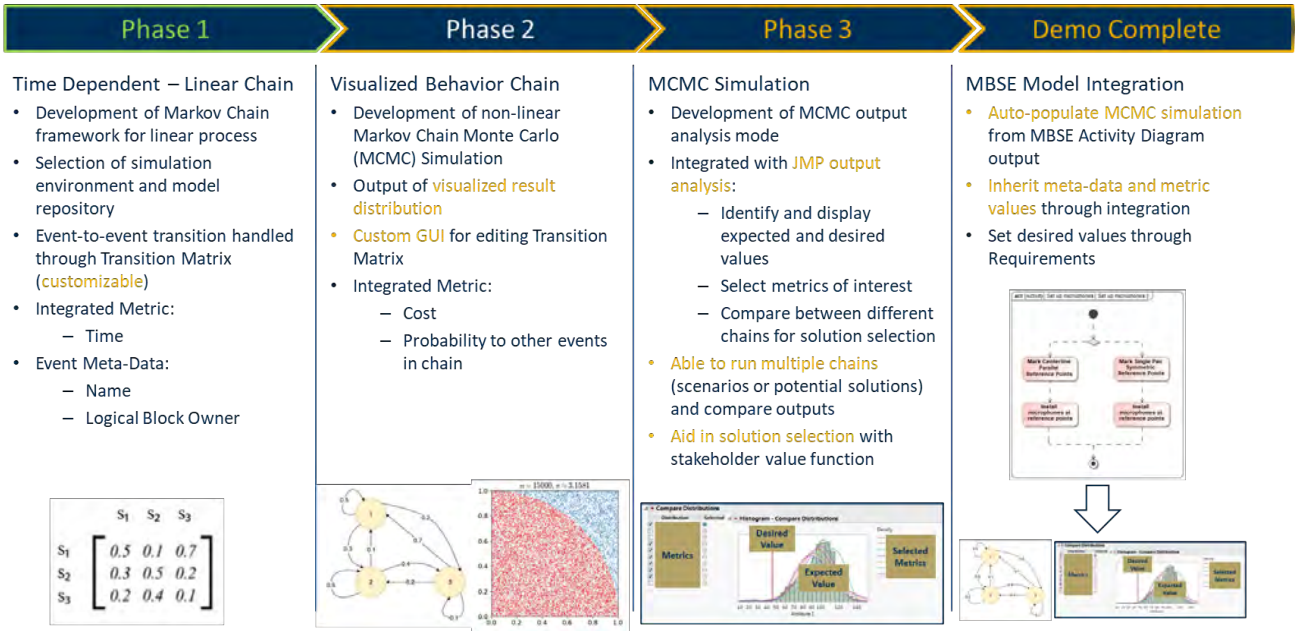

Figure 36. Functional development plan based on a process improvement model. GUI: graphical user interface; MBSE: model-based systems engineering.

Task 4.2 Transfer alternative procedures to the PIM.
With the PIM model now available in a flexible and customizable format, in Task 4.2 our team sought to expand the process simulation and analysis toward metrics that will link to use case objectives and process selection of improved alternatives.

The selected metrics should allow for a quantitative comparison of current and proposed streamlined noise certification process options. The updated list of identified metrics is as follows:

- Time: The schedule cost incurred to complete event.
- Cost: The budget cost incurred to complete event.
- P(Failure): The probability of repeating an event or reverting to a previous event (does incur time and cost [full or partial] in each occurrence).
- P(Success): The probability of moving out of the current event.
- Accuracy penalty: The impact on overall accuracy value for executing the event (does not incur an additional cost in each occurrence).
- Process complexity metrics: These metrics are one of the latest additions to the model and allow the model to capture the level of uncertainty and risks corresponding to a specific testing procedure. More complex procedures are highly susceptible to causing significant schedule and budget overruns.

The proposed integrated model uses a system verification model with external inputs, such as current certification regulations, validation processes, and test plan templates. This results in an interconnected model for the UAS, referred to as the SUT, which evaluates the validity of a certain certification procedure and generates alternative procedures suggesting one or a combination of modifications related to the utilized noise measurement metric, microphone type or array design, or flight profile (i.e., flyover, hover, vertical takeoff/landing, etc.). Figure 37 provides a general overview of the integrated structure of the system verification model, the PIM, and the visualization environment.

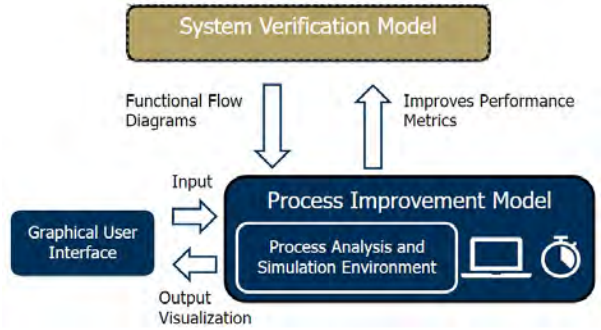

Figure 37. Integration of system verification model, process improvement modeling, and graphical interface.

In addition to the flight test procedure diagrams describing the sequence of events constituting the flight tests, different detailed reports can be generated as outputs of the system verification model. The PIM assesses the performance of the baseline flight test procedure and other alternative procedures in terms of overall time and cost. The PIM captures a typical noise testing process. Certain events within that process have feedback loops indicating that one event or a set of events is to be repeated due to the detection of anomalies or calibration issues. Hence, some events can have different outcomes and, depending on the likelihood of each outcome, the overall flight test sequence would differ and lead to a different overall time and cost of the entire process. This steers the focus toward a probabilistic modeling approach, in which it is desirable that each event exclusively depends on the previous event. Moreover, to properly account for uncertainty and risks in predictions and decision-making, it is crucial for these flight tests to be simulated multiple times. With all these elements taken into consideration, a suitable approach for modeling a flight test procedure is using a Markov chain. To maintain a simplified terminology for the PIM, the flight test procedures extracted from the system verification model are to be considered flight test processes and the events are to be referred to as steps.

The PIM implements a Matlab® script incorporating the mathematical representation of the flight test process to be analyzed using Monte Carlo simulations. Two Microsoft Excel® files are used as inputs to the script; the first file includes all the steps of the flight test process and the probabilities of occurrence of each outcome, and the second file contains the assigned time and cost values for each step.

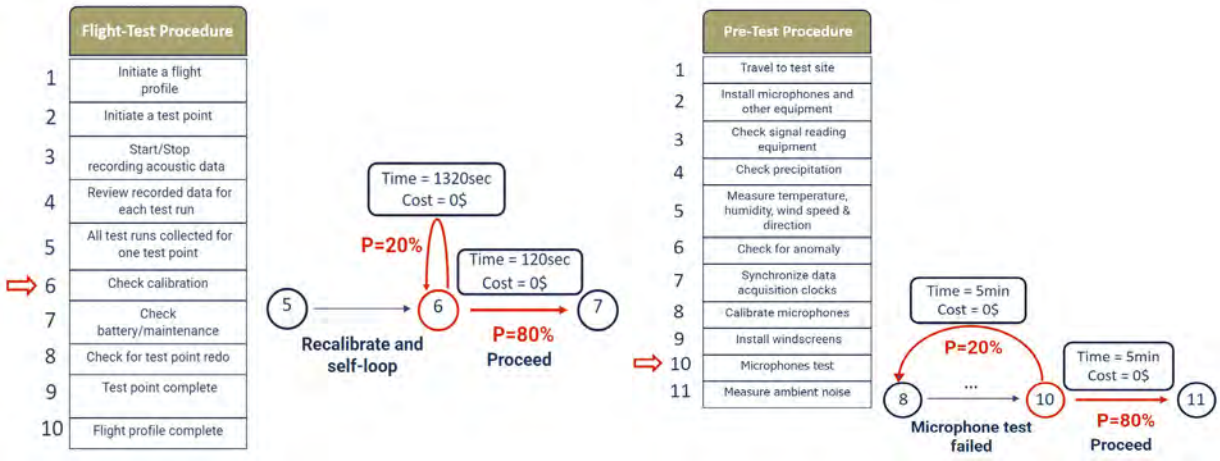

Figure 38. Example of self-loop (left figure) and feedback loop (right figure) within the noise testing process.

® Microsoft and Excel are registered trademarks of Microsoft Corporation in the United States and other countries.

As noise testing is captured as a stochastic process, most of the steps can lead to different outcomes depending on many factors, including human error, unstable weather conditions, equipment malfunction, unsatisfactory measurements, etc. These variations are modeled using feedback loops and self-loops in the Markov chain, in which the former represents the need to go back to a previous task in case an anomaly is detected, whereas the latter refers to the need to repeat the current task. Each potential outcome has a specific probability of occurrence assigned to it. Figure 38 portrays examples of a self-loop and a feedback loop within the process. In Figure 38, step 6 of the flight-test procedure consists of checking the calibration of the microphones after the completion of each test point. This step is crucial to avoid potential complications such as reducing confidence in the validity of noise test results, lacking a traceable chain of measurement standards, and impacting data comparability across multiple instruments. In this example, a probability of 20% is set for the need to recalibrate, which entails a longer time compared to the alternative outcome of not needing recalibration with 80% probability. Similarly, step 10 of the pre-test procedure consists of two potential outcomes for the microphone test; either the test fails, and the staff need to take the windscreens off, recalibrate the microphones, reinstall the windscreens and test again (probability of 20%), or the microphone test is successful (probability of 80%) and the following step is initiated.

In addition to evaluating the effectiveness and efficiency of different testing alternatives in terms of their resulting time and cost, capturing and understanding the complexity of the testing layout is also crucial as it helps identify improvement points within the process to better streamline it and reduce the uncertainty and error proneness related to it.

Two categories of metrics have been implemented to quantify the complexity level of a testing procedure; four metrics that are dependent only on the structure of the noise testing process, and one metric that is dependent on the outcome of the Monte Carlo simulations. This simulation-dependent metric is the Redundancy and Rework Index (RRI), and it indicates the percentage of steps in the process that are redundant or have been reworked, such as measurement repetitions or microphones' re-calibration. This metric highlights areas in the process where efficiency improvements might be necessary to reduce the uncertainty level related to those steps and minimize repetitions and corrections, as follows:

$$RRI = \frac{R}{T}$$

where R is the number of repeated or reworked steps and T is the total number of steps.

RRI is computed for each Monte Carlo simulation. Since each of the 10,000 design of experiment (DoE) cases contains 10,000 Monte Carlo runs, the mean and standard deviation of RRI is calculated for each DoE case then calculated again over all cases to get a final mean RRI and standard deviation for the overall noise testing process. As for the process-dependent complexity metrics, these include:

- Cyclomatic Complexity, which calculates the number of unique and independent paths (different sequence of nodes and edges) to go through the process such that full testing coverage is ensured, as follows:

  $$CC = E - N + 2P$$

  where E is the number of edges, N is the number of process steps, and P is the number of connected components.

- Control Flow Complexity, which indicates how much decision-making and iteration is present within the process based on the control flow structure, as follows:

  $$CFC = D + L$$

  where D is the number of steps with multiple potential paths and L is the number of feedback loops and self-loops.

- Decision Density, which measures the concentration of decision points in the process (as shown in the following equation). A lower decision density value indicates fewer decision points leading to less uncertainty relative to the total number of steps. In contrast, a higher value would indicate the opposite.

  $$DD = \frac{D}{T}$$

- Process Entropy, which measures the unpredictability in the process flow. A high level of entropy indicates that there are many possible task outcomes(paths), making the process more complex and more difficult to predict. Lower entropy, however, means fewer paths, and a more structured and predictable process.

  For a step i with j potential paths:

$$\sum_{j=1}^{n} p_{ij} = 1$$

  where p_{ij} is the probability of occurrence of path j at step i.

  Process entropy for step i:

$$PE_I = -\sum_{j=1}^{n} p_{ij} \log\left(p_{ij}\right)$$

  Overall process entropy:

$$PE = \sum_{i=1}^{m} PE_i = -\sum_{i=1}^{m}\sum_{j=1}^{n} p_{ij} \log\left(p_{ij}\right)$$

Task 4.3 Report on the performance of the alternative procedures.
The objective of Task 4.3 is to produce a baseline of a noise certification procedure simulation and to propose a calibration step, as process data become available from ASCENT Project 061 partners. The analysis workflow for the PIM module is shown in Figure 39. The goal of the workflow within the PIM is to analyze the complexity of the process and to identify potential bottlenecks by assessing time, cost, and node/step criticalities. The workflow is completed in three basic steps:

1. **Definition of test data:** This step includes a test plan, setup, instrumentation and recording information, and sound pressure level measurement data.
2. **Process representation as an event chain through graph modeling:** In this step, the process is converted and represented as a weighted directed graph. Each node represents a step in the process, and the edges represent transitions between steps. The progression through the steps is represented by probabilities and parameters at each step.
3. **Execution of the MCMC algorithm:** The simulation starts from a node, and a "roll the dice" (i.e., generate a random number) function is performed. Depending on the outcome and the probability of each path, the algorithm selects the next node. A learning factor is utilized to update the probabilities of progressing through the steps (increased probability the second time).

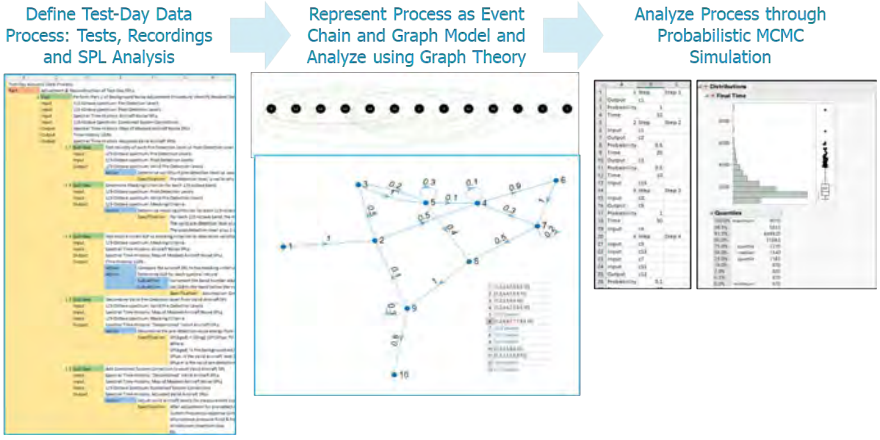

Figure 39. Analysis workflow based on the process improvement model. MCMC: Markov chain Monte Carlo; SPL: sound pressure level.

The analysis of different alternative procedures in noise flight testing relies on the evaluation of different performance criteria or metrics of interest to which the user may allocate different levels of importance. The outputs of this analysis heavily contribute to the decision-making alongside the regulatory adherence in which the requirements' satisfaction of each alternative procedure is evaluated. In the context of the suggested PIM, progression through the steps is associated with probabilities and parameters. Hence, tracking the propagation of these metrics of interest is enabled within the Monte Carlo simulations. Induced costs and time throughout the process are the focus of the current efforts. When combined with the sequencing of events of each process simulation, these outputs can provide insight into process complexity and induced risks and allow the anticipation of potential bottlenecks in the process.

Noise certification testing processes are represented using Markov chains within a probabilistic simulation environment. This approach relies on random variables, which are functions assigning real numbers to each potential outcome within the sample space of a random experiment. This approach also entails that every event solely depends on the previous event, thus preventing the propagation of uncertainties throughout the process. The entire process can be visualized using weighted directed graphs, in which every node represents a step within the noise testing process and the edges indicate the transitions between nodes. A valid representation of the certification testing process requires every node on the graph to be able to eventually reach the final step, thus ensuring process continuity by calculating the "connected components" in the graph. Figure 40 depicts the need to ensure continuity within the demonstrative process. The illustration on the left of Figure 40 depicts the demonstrative process in which step 7 cannot reach the final step; whereas the corrected Markov chain representation on the right of Figure 40 implements process continuity for each step.

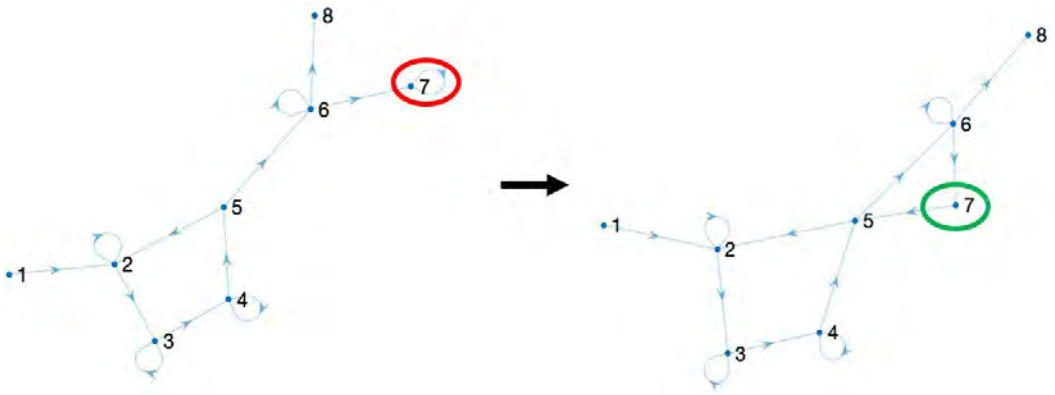

Figure 40. Illustration of process continuity in a sample flight test process.

Every edge of the Markov chain representation is assigned to a probability characterizing the likelihood of moving from one node to another, thus mapping different potential paths to be taken. The Monte Carlo method is implemented to achieve repeated random sampling during the simulation. This method generates a random number that is compared to the cumulative sum of the row corresponding to the current step of the transition matrix, which contains all potential probabilities connecting any two nodes. The next step is chosen once the random number is less than or equal to the smallest cumulative sum. Each Monte Carlo simulation follows a specific path that is dictated by the method. To achieve accurate estimates, the Monte Carlo simulation must be repeated multiple times by increasing the number of runs set within the Matlab script. This underlines an important trade-off between the accuracy of the results and the script execution time. In this work, the analysis was first exclusively targeting the most influential steps of the noise testing process as they will be the main sources of variation within the results. This approach allows for the reduction of computational time for PIM execution while ensuring the accuracy and reliability of the results. This can be accomplished by implementing PageRank centrality, which is a metric providing the average time spent at each node during a random process simulation. The average for each node is weighted according to the probabilities of reaching a node and the value of the associated parameter. These key (i.e., most influential) steps were varied in each simulation using DoEs. In addition to the identification of key steps, the code introduces the capability of detecting bottlenecks within the process giving enough insight about steps susceptible to causing delays or complications within the process workflow.

Table 5. Identification of noise testing equipment and other expenses.

	Fixed Costs	Variable Costs
Equipment	Microphones	Batteries
	Windscreens	Personnel payment
	Weather sensors	
	Time-position tracker	
	Crane or poles (for elevated microphones)	
	Calibrators	
	Travel expenses	
	Test site rental	

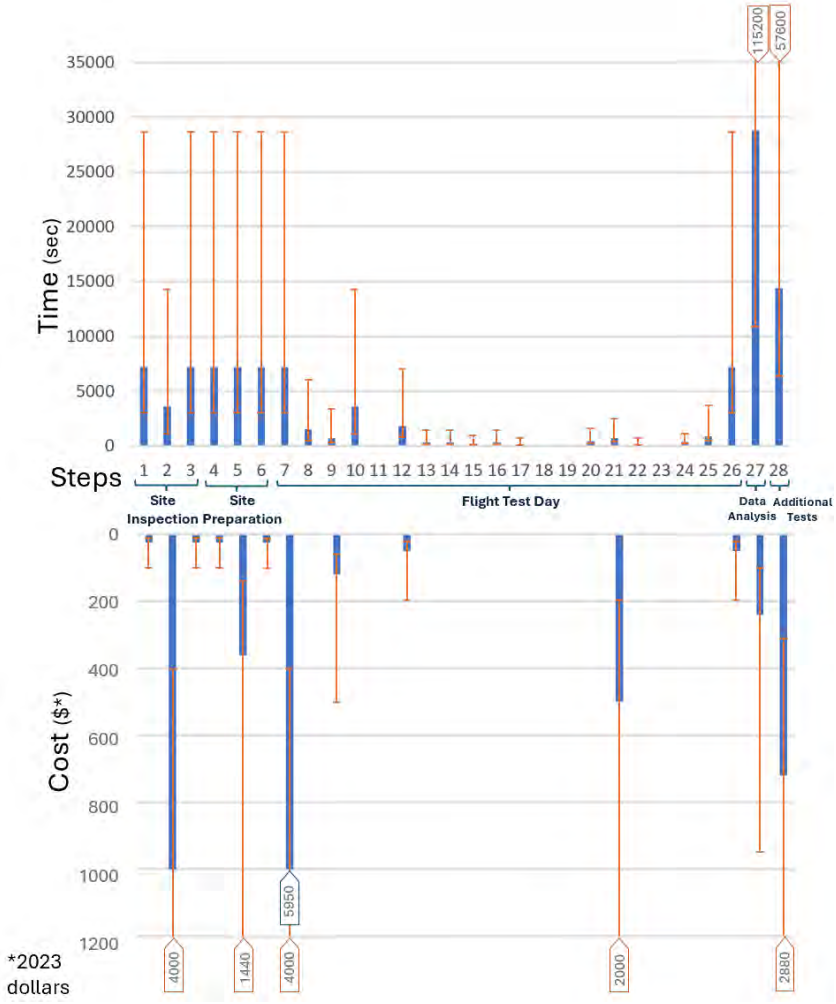

Figure 41. Time and cost estimates related to each noise testing phase and step.

As the model has been significantly expanded, the DoE is now conducted on all the steps of the process to enable a full analysis of the results and a comprehensive evaluation of testing alternatives. Furthermore, this approach allows us to explore a wide range of variables and assess their impact on the total time and cost of the noise testing process.
The inputs (i.e., individual times and costs) are now varied by multiplying the values by factors between [0.4, 4]. Figure 41 depicts the allocated time and cost to each step of the process with the hairline indicating the range of variation.
The baseline cost values have been estimated based on the list of equipment that has been used during the Causey Airport noise testing campaign. This served as a crucial starting point to formulate a more comprehensive list of equipment (Table 5) for which the prices have been either estimated or looked up online. The costs have been divided into two categories: (1) fixed costs consisting of all pieces of equipment, travel expenses, and rentals and (2) variable costs such as the battery replacements for UAS or the personnel payment that depend on the duration of testing and/or the number of personnel. To generate this DoE, the Latin Hypercube Sampling (LHS) has been selected as the space-filling method of choice. Each process simulation has been conducted for the 10,000 DoE cases such that each case is repeated for 10,000 Monte Carlo runs.

The number of personnel available during each phase of testing can highly impact the time required to conduct certain tasks and eventually the total time of testing. Figure 42 showcases an example of the impact of the number of microphones and the number of personnel on the time needed to install the microphones. It has been assumed that one individual can install a single microphone in 5 minutes, and that one individual is always on standby as they could be carrying out a different task in parallel or supervising the installation process. In Figure 43, to help with the visualization of this plot, it has been broken down into two different plots such that the left plot displays the change in time with respect to the number of personnel for the installation of 10 microphones and the right plot shows the change in time with respect to the number of microphones for a total of six personnel members. For example, considering a total of 10 microphones and six personnel members are on site, only five members can participate in the installation process. The installation team would simultaneously install one microphone each then install the remaining five microphones, which requires a total duration of 10 minutes.

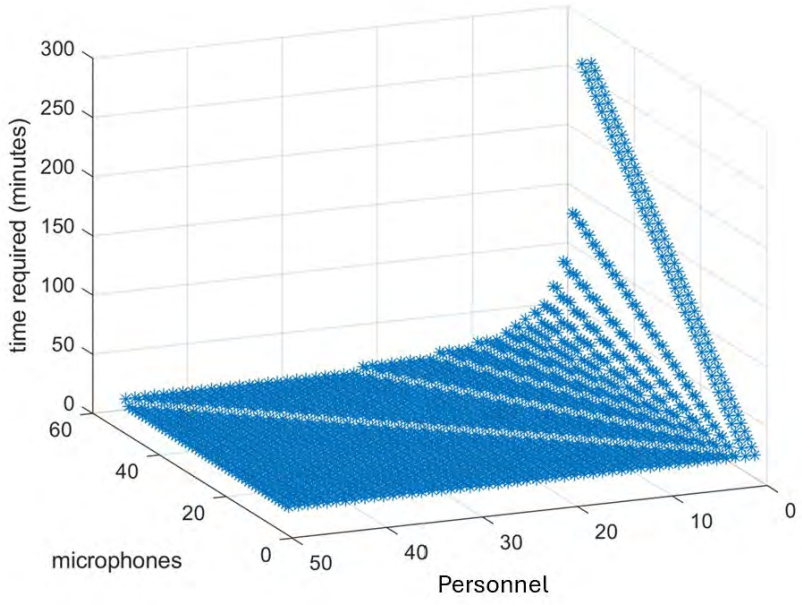

Figure 42. Three-dimensional plot of the impact of number of microphones and personnel variations on microphone installation time.

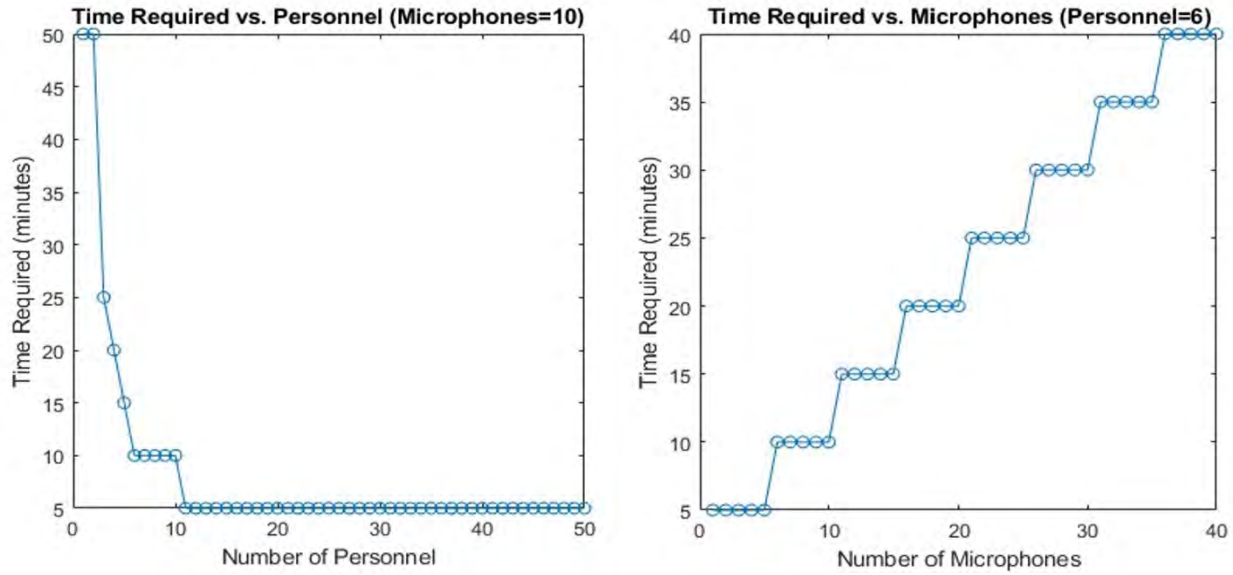

Figure 43. Two-dimensional projects of the impact of number of personnel on installation time of 10 microphones (left) and the impact of the number of microphones on equipment installation time for a team of six personnel (right).

The baseline process for the PIM exclusively considers a hover flight profile with three test points with a minimum of six runs per test point. Each test point refers to a test condition with a specific combination of weight, speed, and altitude. With the use of only one microphone, UASs will fly at three different locations relative to that microphone (Figure 44). The analysis is turned into a parametric analysis capable of automatically changing the types of flight profiles and number of test points based on a set of user-defined inputs without having to manually modify the values in the input files. This enables the modeling of any combination of flight procedures, thus capturing noise testing campaigns of any desired size. Other user-defined inputs apply to parameters that would simultaneously affect multiple steps of the process in different ways, such as the number of staff members, number of microphones, travel duration to the test site, etc. Manually assessing and incorporating the changes due to variation in these parameters can be very tedious, as many steps can be directly or indirectly affected. Thus, all the impacted steps are identified beforehand, and the effects are quantified and mathematically modeled in terms of time and cost consequences. Once the user identifies any combination of parameters, the code will automatically implement the corresponding changes to the time and cost values in the input file of the baseline process.

Figure 44. Baseline noise testing process (hover flight profile).

Calibration is an essential step for ensuring model accuracy and the validity of results and findings. This task requires a completed process simulation capability, which will be calibrated against a baseline that captures current certification testing plans and processing steps. The pivot to the UAS category has included plans to interface with ASCENT partners who can provide testing plans and noise datasets to be used as calibration data and overall process information. This task will be one of the key focus topics for the ASCENT Project 061 year 3 activities. Scalability issues are bound to arise as this model is expanded to reflect the full verification thread; thus, the next step is to discuss options for data that ASCENT Project 061 partners could provide for further calibrating the model, according to the use cases of preference.

Task 4.4 Develop a proof-of-concept demonstration of the PIM capabilities

In a proof-of-concept demonstration of the complete certification process simulation capability within the PIM, the ASCENT Project 061 team has been formulating use case examples based on scenarios provided by OEM partners. For these examples, simulation runs are being executed to test modifications and proposed improvements over the baseline process. Under this task, a first demonstration of the PIM has been completed. For this example, the goal is to assess the impact of a simplified noise collection/analysis process for the Waco Aircraft® YMF-5 propeller aircraft.

The baseline (original) process was formulated within the PIM and executed using the best estimates for time and cost. The term "best" implies that our team had to rely on rationalized assumptions that were initially formulated by input from OEM partners. As this information could be of a sensitive nature for most OEMs, guidance was provided at a higher level, without any limitations on how the information would be distributed. Hence, for this example, a simplified process for flight segment testing is proposed, where a certain calculation is removed from the standard process. As shown in Figure 45, the simplified process removes step 18, the calculation of the second flight segment, while other steps were updated with new values to capture the updated process.

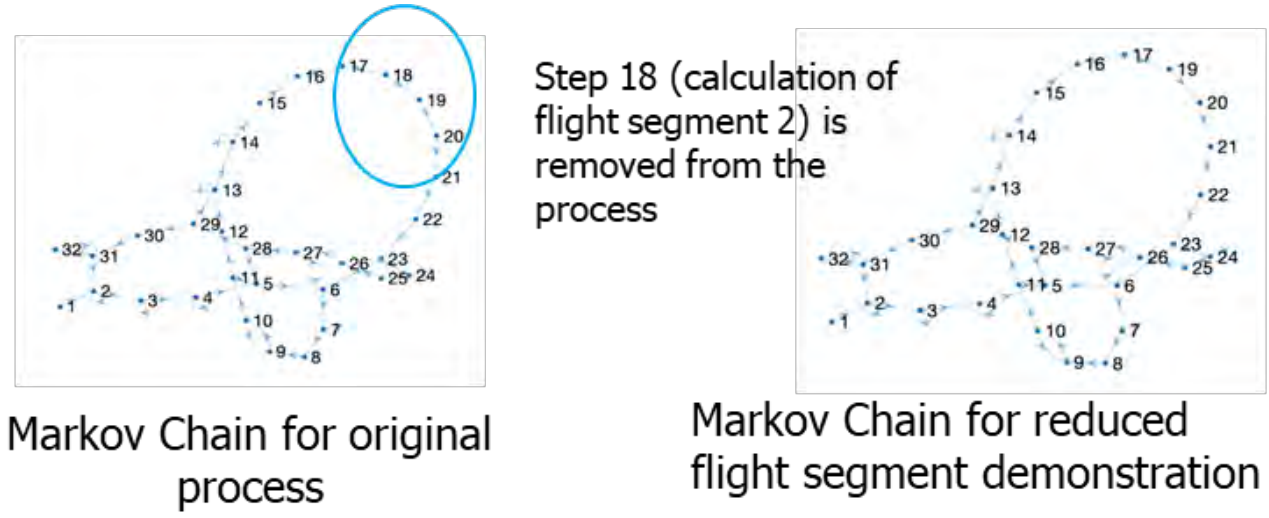

Figure 45. Process modification with step 18, the calculation of the second flight segment, is removed from the Markov chain flight-testing process.

A comparison of the two process alternatives is presented in Table 6. The results were obtained from an MCMC analysis and comparison between the baseline and simplified process. The PIM was able to quantify measurable savings in time and cost. In particular, the average process cost shows a reduction of 16%, and the average process time shows a decrease of 2%. The results are highlighted in Figure 46, where the Monte Carlo simulation data are plotted as distributions for the cost and time required for the process.

® Waco Aircraft is a registered trademark of Dimor Group Inc., Battlecreek, Michigan.

Table 6. Summary of cost ($) and time (hr) improvements.

		Mean
Original	**Cost($)**	166,770
	Time(hr)	155
Reduced Segments	**Cost($)**	140,430
	Time(hr)	151

With this fundamental example showcased under this task, the groundwork is set for scaling up the PIM to more comprehensive modifications, which would also include technology impact forecasting functions. As this practice will now be exclusive to the UAS category, the ASCENT Project 061 team's priorities are to investigate current noise testing plans and procedures and to be able to propose promising equivalent procedures.

Case Study 1

The FAA's Notice of Proposed Rulemaking (NPRM) for the Matternet® Model M2 Aircraft (FAA, 2022a) outlines the use of a single microphone mounted on a tripod or pole, positioned 4 feet above the ground, for unmanned aircraft (UA) noise certification measurements. This proposed rule aims to streamline the process and reduce costs and workload by utilizing a single microphone. However, the possibility of using multiple microphones for hover noise testing was also explored to shorten testing time and enhance efficiency. Notably, the FAA is open to reviewing and approving multiple microphone configurations if deemed beneficial by the applicant. Consequently, a model-based approach is necessary to comprehensively evaluate and select between the proposed single-microphone setup and the alternative multiple-microphone configuration.

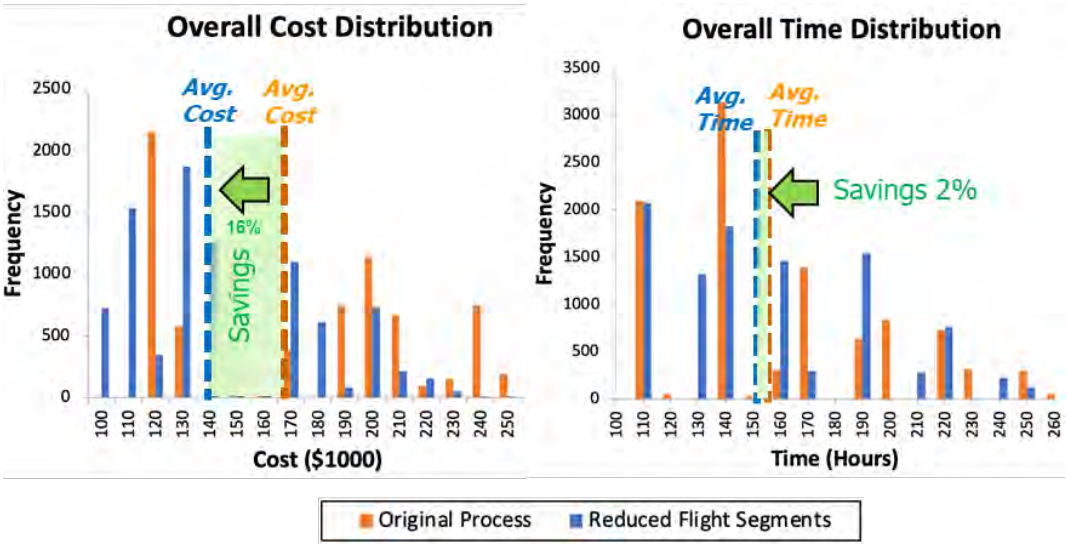

Figure 46. Execution of Markov-chain-based Monte Carlo analysis and comparison between the baseline and simplified process.

Following the adoption of rule for applicability for the Matternet® M2 aircraft, the FAA introduced subsequent noise certification standards for other models, including the Flytrex® FTX-M600P. In this section, the PIM capabilities are utilized to compare the single-microphone configuration (baseline process) with the multiple-microphone configuration (alternative

process) for a UA hover test, using the Flytrex® FTX-M600P aircraft as a case study. According to the hover test conditions specified in paragraph 16, subparagraphs (b) through (e) of the Flytrex® noise certification standards (FAA, 2023), the baseline configuration involves the aircraft hovering at three distinct spatial locations relative to the single microphone, as depicted in Figure 47. Conversely, the alternative configuration uses three microphones, requiring the aircraft to hover at a single spatial location relative to these microphones, as shown in Figure 48. A representation of the Markov Chain for both the baseline and alternative processes is provided in Figure 49.

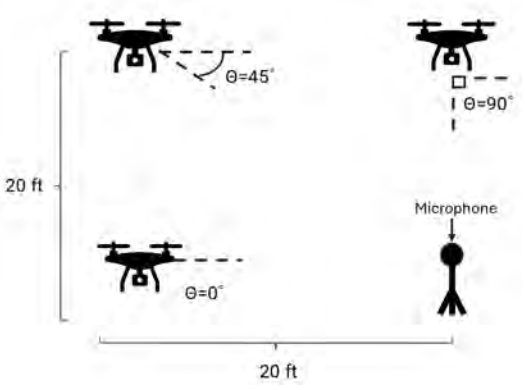

Figure 47. Microphone layout for the baseline process during the hover measurements.

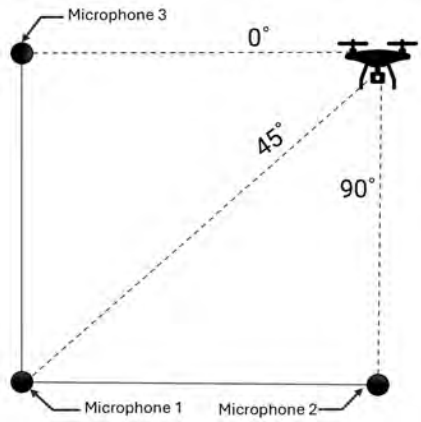

Figure 48. Microphone layout for the alternative process during the hover measurements.

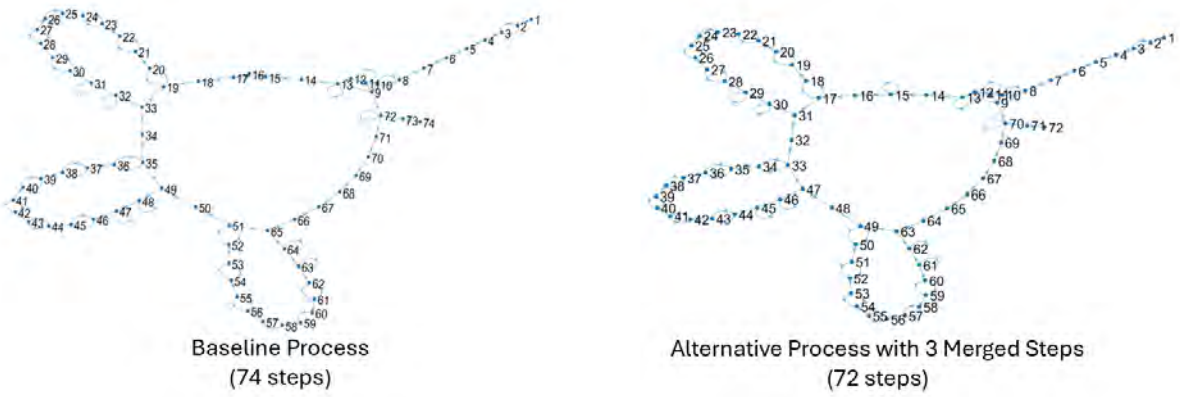

Figure 49. Markov Chain representation for the baseline process (left) and alternative process (right).

As outlined in the case study setup, a DoE consisting of 2,000 cases, each with 10,000 Monte Carlo simulations, was conducted. Process simulations for both the baseline and alternative configurations were performed to create a parametric, interactive decision-making environment. This environment enables the comprehensive comparison of test processes using various visualization techniques, including operational viewpoints, histogram overlays, and sensitivity analysis plots. This section provides an analysis of the process simulations for the baseline and alternative configurations for the Flytrex® FTX-M600P case study, accompanied by visualizations to support interpretation of the results.

The operational viewpoint of the case study test setup, shown in Figure 50, combines the schematic diagrams, providing a more realistic and comprehensive visual representation of the test setup. Following this, process simulations for both the baseline and alternative configurations were performed, producing key output metrics, specifically mean time and mean cost, for each case in the DoE. Histogram overlays were used to visually compare the two processes in terms of time and cost, as seen in Figure 51 and Figure 52. These figures demonstrate that the baseline process results in both lower mean

time and mean cost compared to the alternative process. The higher cost of the alternative process is expected due to the additional microphones, which incur extra costs for equipment, installation, and calibration.

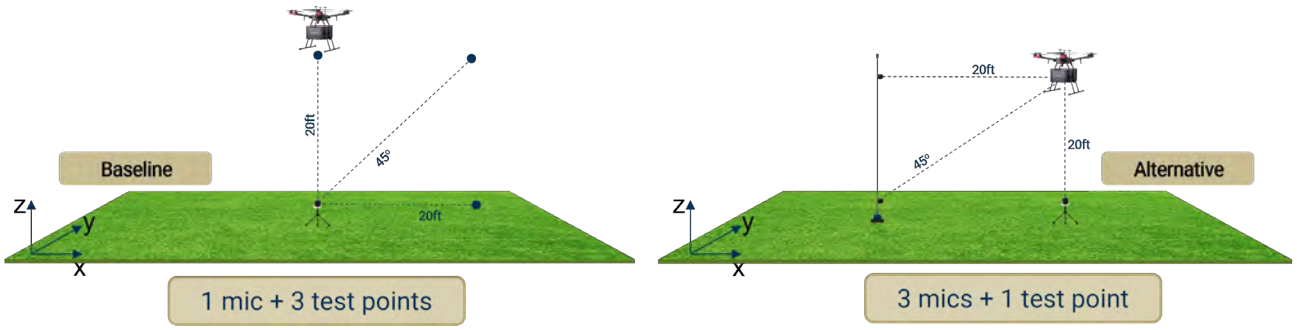

Figure 50. Operational viewpoint of baseline vs. alternative test set up for Flytrex® FTX-M600P.

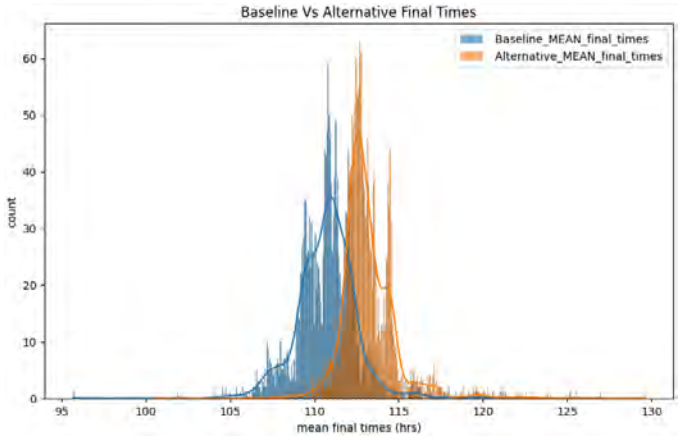

Figure 51. Baseline vs. alternative mean final times overlay.

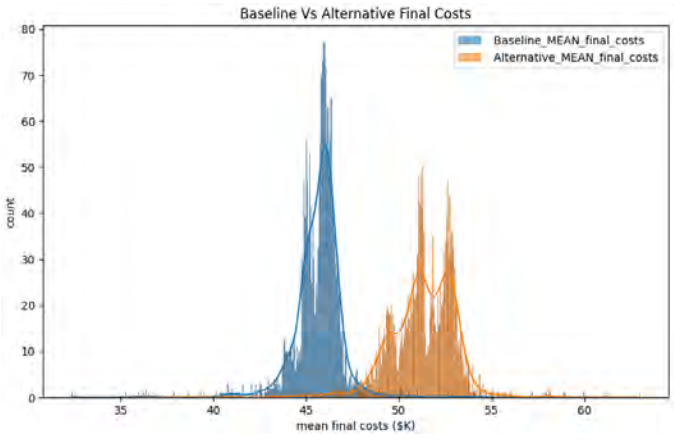

Figure 52. Baseline vs. alternative mean final costs overlay.

The time metric, however, exhibits more variability and is influenced by factors such as calibration time and the likelihood of test failures. Under the specific parameter values used in the model, the baseline process results in a shorter mean time. This indicates that the additional time required for microphone installation and calibration in the alternative process outweighs the time lost due to potential test failures. However, if the probability of test failure and the calibration time for a single microphone were increased, there could be cases where the alternative process proves more time efficient. In such cases, the single microphone in the baseline process would require repeated setup and calibration at various test points, extending the total test duration.

Histogram overlays provide a useful means of comparing baseline and alternative processes by visualizing the mean distributions of PIM outputs, such as time and cost. However, histogram overlays do not capture the variability of these metrics in relation to input parameters across different steps in the noise testing process. Understanding this variability is crucial for assessing a testing process's robustness to uncertainties. Tools like the JMP® Prediction Profiler offer dynamic visualization capabilities, displaying relationships between input predictors (e.g., time or cost for specific testing steps) and output metrics. To enable interactive decision making, meta or surrogate models are needed to map input parameters to PIM outputs. However, the non-normal distribution observed in the Monte Carlo simulations necessitated the evaluation of various probability density functions (PDFs) to replicate the data accurately. Among these, the log-normal distribution proved most suitable, demonstrating the closest match with minimal error, as shown in Figure 53, and further validated by reconstructing the Monte Carlo distribution using random samples within the parameters of the log-normal PDF (i.e., μ, σ, and scale), as depicted in Figure 54.

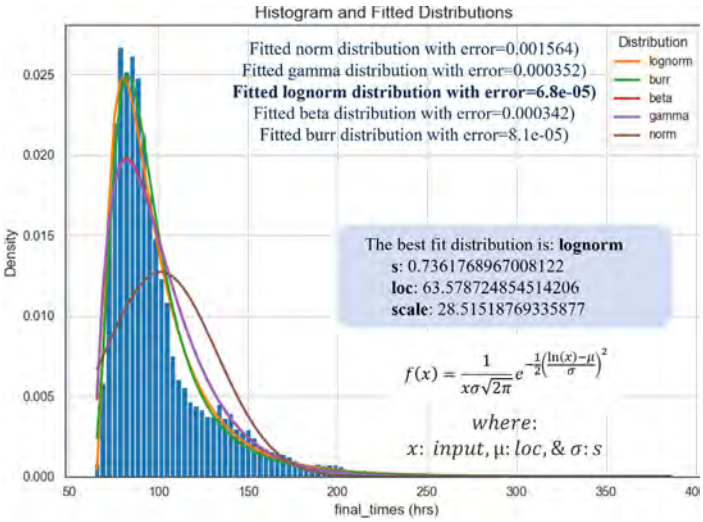

Figure 53. Sample Monte Carlo distribution of a single DoE case.

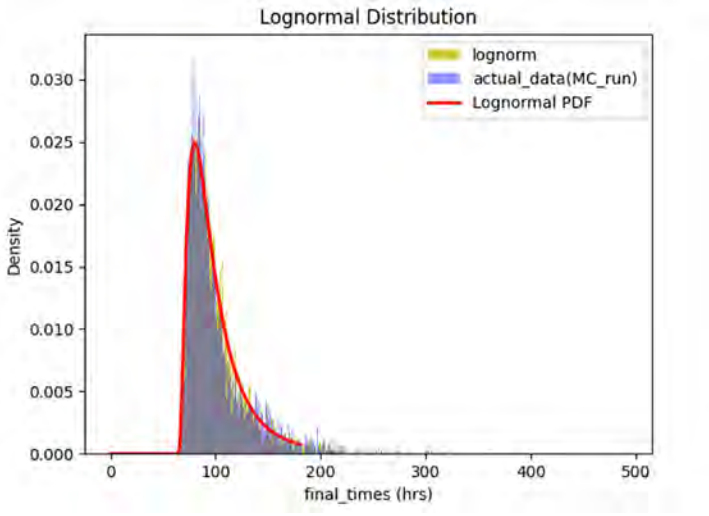

Figure 54. Actual vs predicted Monte Carlo distribution fit using log-normal PDF.

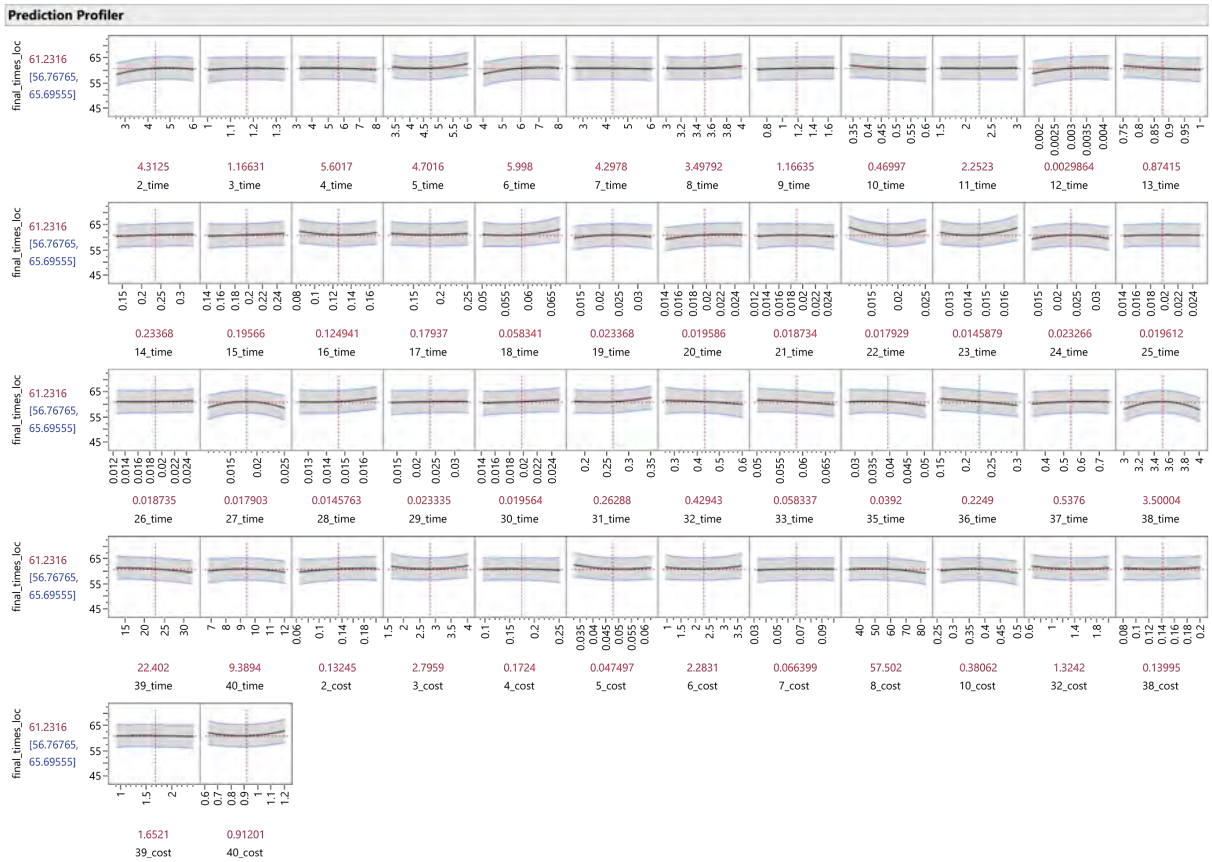

Figure 55. Prediction profiler plot of alternative process time generated using JMP.®

Using the log-normal PDF, calculations were performed for each case in the DoEs. The resulting parameters of the log-normal PDF served as output metrics and were instrumental in developing surrogate models. For instance, focusing on the μ (location) parameter for the time associated with the alternative process, Prediction Profiler plots were generated (Figure 55) to evaluate the sensitivity of this output metric to the time allocated for each step in the testing process. Analysis of the predictor variables within the model revealed that steps 36 and 12 were statistically significant in predicting the location parameter, prompting a deeper investigation into their influence. This analysis, illustrated in Figure 56, shows the impact of holding step 12 constant while varying the time for step 36. The results reveal a significant correlation, including a directional change, emphasizing the importance of these steps in influencing variability. While this study primarily examines the location parameter for time in the alternative process, similar insights can be extended to other parameters and metrics for both baseline and alternative processes.

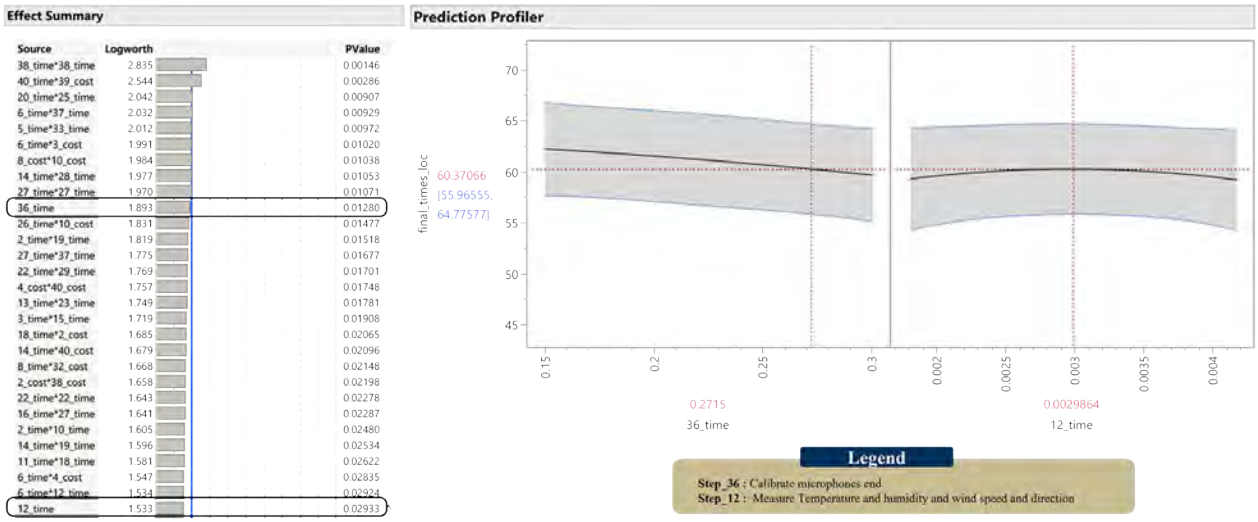

Figure 56. Key steps sensitivity plot generated using JMP.®

Case Study 2

The International Organization for Standardization (ISO) provides detailed methodologies for measuring sound pressure levels in its ISO 3744 standard (International Organization for Standardization, 2010), which outlines microphone positioning, test point selection, and the number of test runs required for various flight profiles. Additionally, ISO 5305 (International Organization for Standardization, 2024) specifies configurations and microphone layouts for testing UASs in anechoic chambers or wind tunnels. EASA adopts a proportional, risk-based framework for UAS operations, classifying them into three categories: (1) open, (2) specific, and (3) certified. The EASA category, applicable to UAS with a maximum takeoff mass (MTOM) up to 600 kg (1323 lb), includes guidelines for noise emission assessments. EASA has also proposed noise assessment standards for air taxis under the Environmental Protection Technical Specifications (EPTS), covering vertical take-off and landing (VTOL) aircraft with tilting and nontilting rotors.

This section presents and analyzes results from the PIM for the second case study, which evaluates various testing procedures defined by existing standards and guidelines for UA and VTOL aircraft. To align with these regulatory standards, three models were developed for noise testing across different vehicle categories: (1) low risk indoor testing (UAS with MTOM ≤ 25 kg), (2) medium risk outdoor testing (25 kg < MTOM ≤ 600 kg), and (3) high risk outdoor testing (VTOL with 600 kg < MTOM ≤ 80,000 kg). The high-risk model for outdoor testing specifically addresses VTOL aircraft with tilting rotors. Table 7 summarizes the testing procedures from these guidelines, forming the basis for creating simulations to replicate certification noise testing and outlining the corresponding test runs for each category. To enable sensitivity analysis and account for cost and time uncertainties, the DoE excludes travel-related process steps, as their extended durations could disproportionately influence results. Only unique process steps are included as variables, with repetitive tasks represented by a single instance.

Table 7. Testing procedures set by existing standards and guidelines for UA and VTOL aircraft.

	ISO 3744 (UAS ≤ 25kg)	EASA (UAS ≤ 600kg)	EASA (VTOL ≤ 80000kg)
Risk Level	Low Risk	Medium Risk	High Risk
Testing Type	Indoor Testing	Outdoor Testing	Outdoor Testing
Flight Profiles	Hover	Flyover - Hover	Takeoff - Approach - Hover - Flyover
Test Points	1 MTOW (hover)	1 MTOW + 1 ETOW (hover)	1 MTOW (takeoff) 1 MLW (approach) 1 MTOW (hover) 3 MTOW (flyover)
Test Runs	3 runs/test point	6 runs/test point	6 runs/test point
# of Microphones	10	1	9 total: 3 (takeoff- approach - flyover) 9 (hover)

The low-risk category indoor testing involves fewer tasks (27 steps yielding 32 variables, with 16 time and 16 cost variables) compared to outdoor procedures for medium-risk (146 steps yielding 44 variables) and high-risk (116 steps yielding 44 variables) categories. Notably, the medium risk outdoor testing procedure has slightly more steps due to the requirement to conduct tests at both maximum and empty takeoff mass, as outlined in Table 7.

A DoE with 10,000 cases was constructed, each case undergoing 10,000 Monte Carlo runs to account for the inherent variability in the simulation. The PIM was used to calculate the mean final time and cost for the testing procedures across all cases. Histograms of these outputs for the three categories are shown in Figure 57 and Figure 58. From the overlay of mean final times, it is evident that low-risk indoor testing requires the least time due to its controlled environment and reduced uncertainties. Interestingly, while medium-risk outdoor testing includes more steps and variables than high-risk outdoor testing, the latter exhibits slightly longer mean final times across the DoE cases.

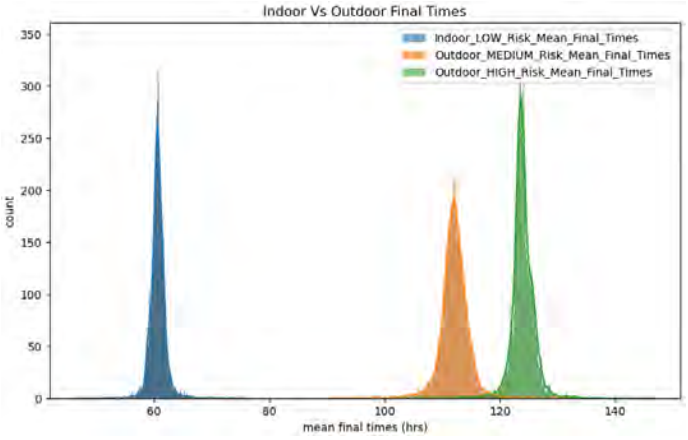

Figure 57. Indoor vs outdoor testing final times overlay.

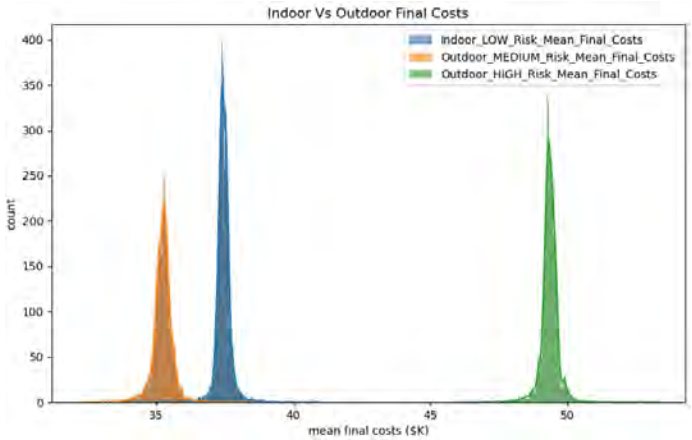

Figure 58. Indoor vs outdoor testing final costs overlay.

In terms of costs, high-risk outdoor testing is the most expensive, driven by the need for nine microphones and multiple flight test profiles and test points. Surprisingly, medium-risk outdoor testing incurs slightly lower costs than low-risk indoor testing. This unexpected result is primarily due to the number of microphones utilized during each testing procedure.

Analyzing the complexity metrics of the three testing alternatives discussed earlier and applying the metrics outlined in Task 4.2 reveals that the low-risk indoor testing procedure consistently achieves the lowest scores across all metrics. This indicates it is the most efficient and least uncertain approach. The high-risk outdoor testing procedure ranks second, while the medium-risk outdoor testing procedure has the highest scores, making it the least efficient and most uncertain. Table 8 below summarizes the calculated complexity scores for each testing category.

Table 8. Process complexity scores of testing procedures.

	Low Risk (ISO 3744)	Medium Risk (EASA)	High Risk (EASA)
# of Steps (N)	27	146	116
Cyclomatic Complexity	0.2321	0.2823	0.2735
Control Flow Complexity	0.2839	0.363	0.3534
Process Entropy	0.1441	0.2837	0.2732
Decision Density	0.4074	0.5342	0.5172
Overall Complexity	**0.1489**	**0.3336**	**0.3068**

Table 9 presents the overall time, cost, and complexity scores for the three testing procedures discussed, highlighting the relative difficulty of certification for each category. The low-risk indoor testing procedure stands out with the lowest overall time and complexity, making it the easiest option for certification. In contrast, the high-risk outdoor testing procedure has the highest time and cost, making certification more challenging.

Table 9. Overall Time, Cost and Complexity of testing Procedures.

	Low Risk (ISO3744)	Medium Risk (EASA)	High Risk (EASA)
Overall Time	60h 38min	112h 05min	123h 56min
Overall Cost	$37,459.83	$35,236.86	$49,353.97
Overall Complexity	0.1489	0.3336	0.3068

Further Model Implementations

The earlier case studies demonstrated the ability of the Process Evaluation Model to evaluate and quantify the certification burden of various noise testing procedures, as defined by different regulatory standards, in terms of time, cost, complexity, and risks of schedule or budget overruns. In contrast, the next section explores the time and cost impacts of performing the same noise testing procedure under varying conditions. This analysis supports improved planning and resource management, including decisions regarding equipment, personnel, and test location selection. To illustrate the advantages of this capability, three use cases were developed, simulated, and analyzed.

(1) Alternative Testing Location and Weather Effects

Noise testing may be conducted at various locations, with the optimal test site depending on factors such as proximity, site area, ground type, background noise, and weather conditions. These factors significantly impact testing duration, overall expenses, measurement quality, and the likelihood of requiring an additional day to repeat measurements. This use case compares two noise testing processes under different travel distances and weather conditions:

- **Baseline Process**: The test site is 2 hours away, with stable weather expected.
- **Alternative Process**: The test site is 40 minutes away, but weather conditions are less stable, with a higher likelihood of rain and strong winds.

While the alternative process reduces travel time and expenses, it increases the probability of adverse weather, leading to higher chances of test run rejections and additional test days for measurement repetitions. This presents a trade-off between travel-related time and costs and those associated with weather-impacted noise measurements.

To model these scenarios, travel time and costs, along with weather-related probabilities, were adjusted, and each process was simulated using 10,000 Monte Carlo runs to account for the inherent uncertainty. Table 10 summarizes the mean time and cost results, while Figure 59 and Figure 60 visualize the total time and cost distributions for each process, displaying a sample of 50 Monte Carlo runs for clarity. The results show that the alternative process incurs higher costs and nearly doubles the testing duration, indicating that shifting to a closer location with unstable weather is not advisable for this scenario.

Table 10. Mean time and mean cost (across 10,000 Monte Carlo runs) of the baseline process vs. the alternative process.

	Baseline process	Alternative Process
Average Time (h)	45.655	90.781
Average Cost ($)	18602.542	34600.877

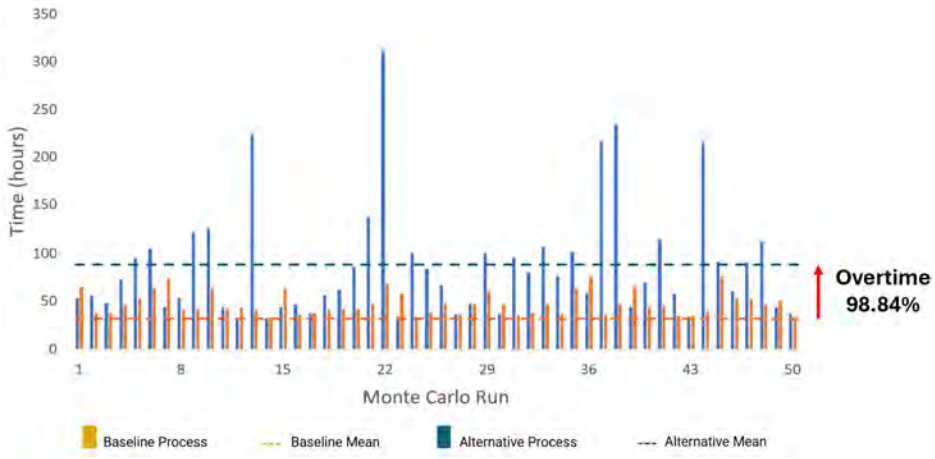

Figure 59. Total time (sample of 50 Monte Carlo runs) and mean time (10,000 Monte Carlo runs) between the baseline and alternative processes.

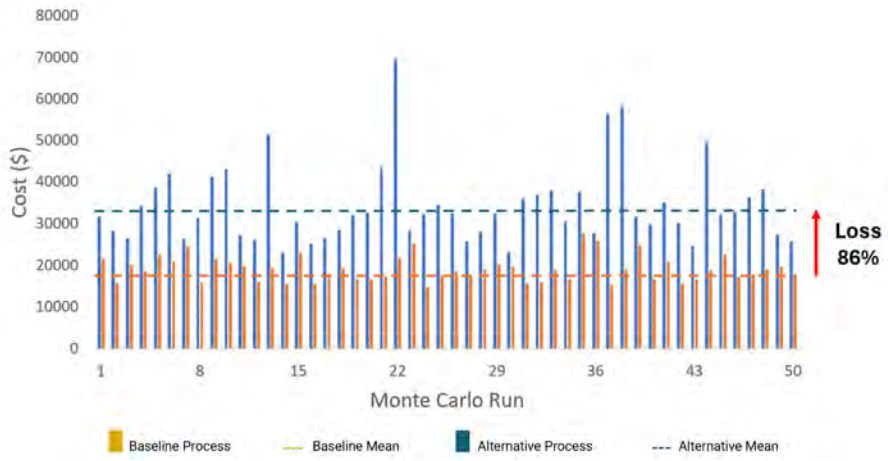

Figure 60. Total costs (sample of 50 Monte Carlo runs) and mean cost (10,000 Monte Carlo runs) of the baseline and alternative processes.

(2) Alternative Dispatching and Sequencing of Tasks

Parallel processing enables multiple tasks to be executed simultaneously, leading to a significant reduction in the overall noise testing time. This use case evaluates the impact of parallel processing by comparing two testing approaches:

- **Baseline Process**: All tasks are performed sequentially.
- **Alternative Process**: While some tasks depend on others and cannot be performed in parallel, and others involve uncertainty requiring separate handling to maintain accuracy, three specific tasks— (1) synchronizing data acquisition clocks, (2) calibrating microphones, and (3) installing windscreens—are executed simultaneously.

Figure 61 illustrates the Markov Chain representations of the baseline process, which includes 74 steps, and the alternative process, which reduces the total steps to 72 by merging three tasks for parallel execution. Table 11 outlines the mean time for each process, showing that the alternative process saves 2.25 hours, a 4.02% reduction in total testing time (as depicted in Figure 62).

This example demonstrates the potential for significant time savings through parallel task execution in noise testing, provided sufficient on-site personnel are available to optimize task allocation.

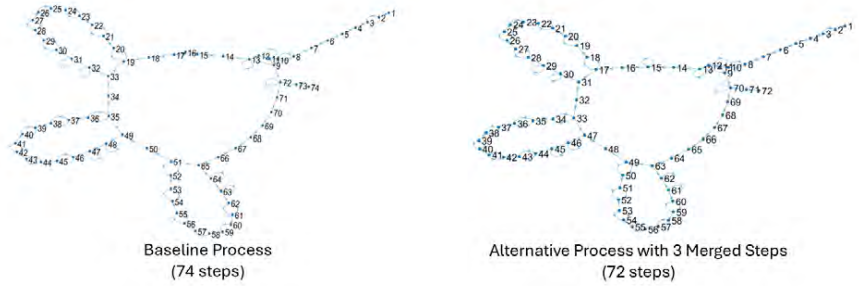

Figure 61. Markov Chain representation for the baseline process (left) and alternative process (right).

Table 11. Mean time (across 10000 Monte Carlo runs) of the baseline process vs. the alternative process.

	Baseline process	Alternative Process
Average Time (h)	55.798	53.554

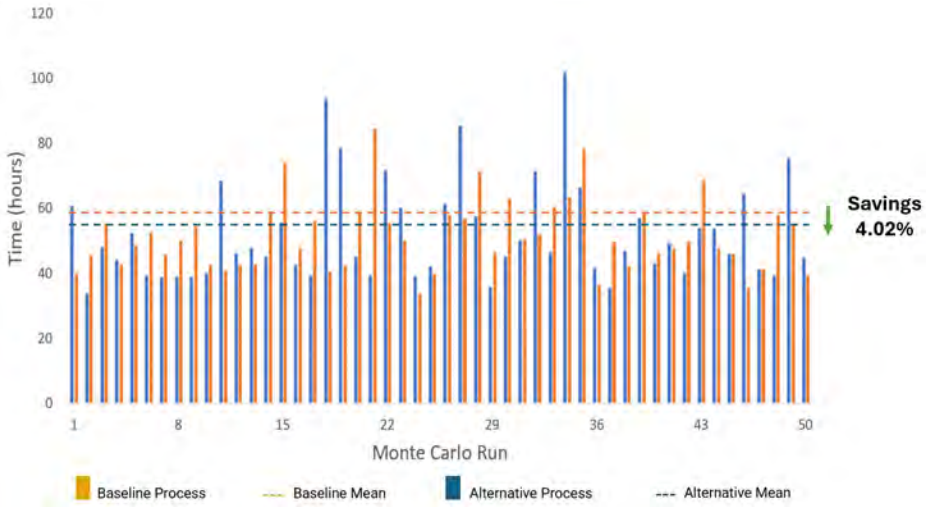

Figure 62. Total time (sample of 50 Monte Carlo runs) and mean time (10,000 Monte Carlo runs) of the baseline and alternative processes.

(3) Effects of Personnel Structure on Small Certification Testing vs. Large Testing Campaigns
Increasing the number of personnel may raise immediate payroll costs, but it can potentially shorten testing durations or enhance test quality, potentially reducing long-term expenses. This use case explores the effects of doubling the personnel assigned to each of the five phases of the noise testing process (Table 12). Two scenarios are modeled and analyzed: a standard noise certification process and a larger experimental noise testing campaign. The baseline personnel numbers are estimated for demonstration purposes, with user-defined inputs that the model adjusts automatically.

Table 12. Mean time (across 10,000 Monte Carlo runs) of the baseline process vs. the alternative.

Noise Testing Phase	Baseline process: Number of Personnel	Alternative Process: Number of Personnel
Site Inspection	2	4
Site Preparation	1	2
Flight Test Day	3	6
Data Analysis	1	2
Additional Test Day	2	4

Increasing the number of personnel reduces the time needed for site inspection, preparation, and the installation and calibration of equipment. However, it also raises travel and payroll expenses. With a larger team, parallel task execution is enhanced, leading to more efficient resource utilization, though this also adds complexity to the process. In the baseline certification scenario, a single microphone is used, whereas the larger campaign involves 21 microphones. Expanding the team reduces time for site setup and equipment calibration but increases costs for travel, wages, and equipment, particularly if elevated setups (e.g., poles or cranes) are required.

The results show that doubling personnel reduces total testing time by 12.19%, saving 5.67 hours. However, total costs increase by 45.15% (see Table 13, Figure 63, and Figure 64). While the alternative process achieves time savings, the higher personnel costs outweigh the benefits of reduced work time.

Table 13. Mean time and mean cost (across 10000 Monte Carlo runs) of the baseline process vs. the alternative process.

	Baseline process: Certification Testing	Alternative Process: Certification Testing	Baseline process: Large Experimental Campaign	Alternative process: Large Experimental Campaign
Average Time (h)	45.655	40.092	55.798	44.591
Average Cost ($)	18,602.54	27,001.99	47,955.98	56,273.50

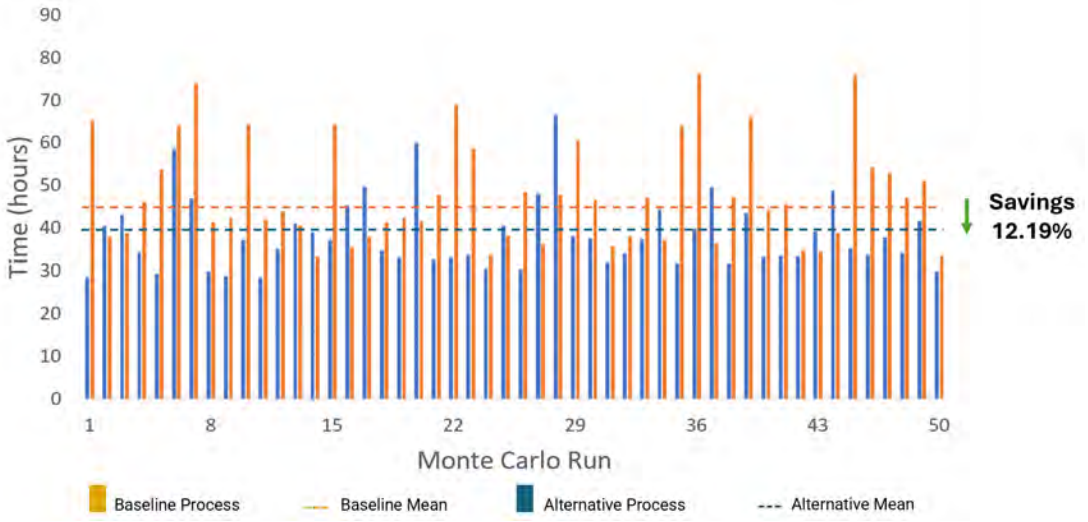

Figure 63. Total time (sample of 50 Monte Carlo runs) and mean time (10,000 Monte Carlo runs) between the baseline and alternative processes for certification testing.

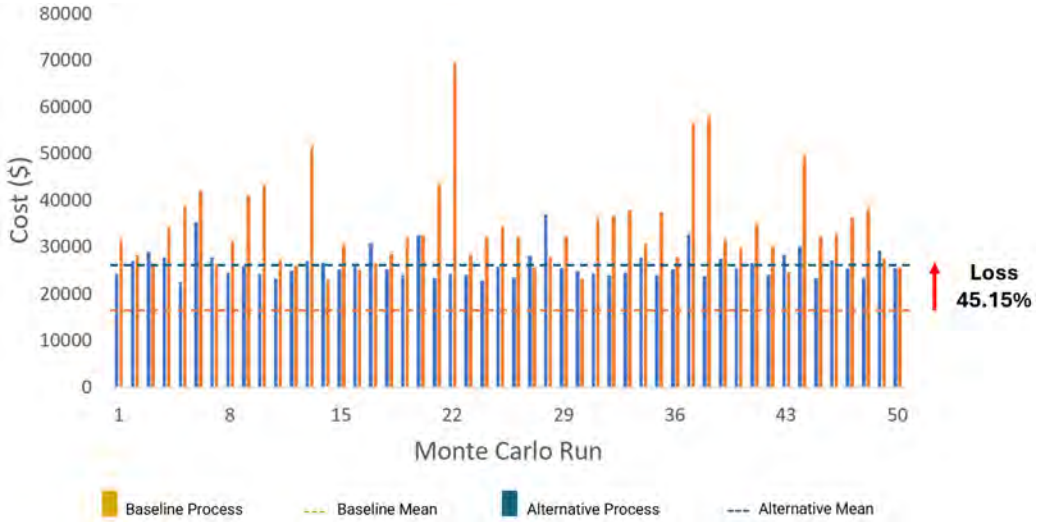

Figure 64. Total costs (sample of 50 Monte Carlo runs) and mean cost (10,000 Monte Carlo runs) of the baseline and alternative processes for certification testing.

Doubling the personnel team for a larger testing campaign results in a 20.09% reduction in time, significantly higher than the 4.02% savings observed for smaller certification testing (see Table 13 and Figure 65). Additionally, the financial loss is reduced to 17.34%, compared to 45.15% for certification testing (see Table 13 and Figure 66). The increased efficiency of additional personnel becomes more pronounced with the expansion of equipment, such as microphones, enabling more parallel task execution.

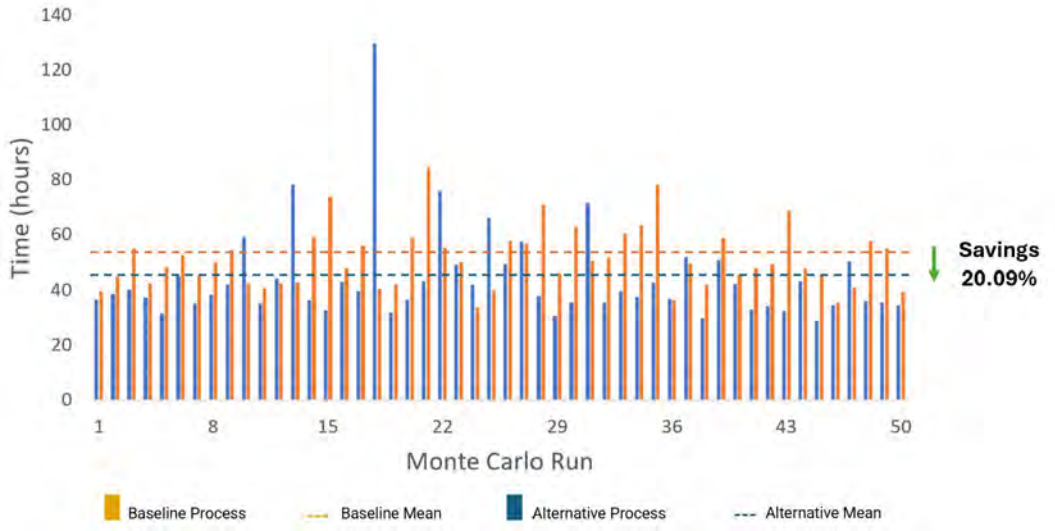

Figure 65. Total time (sample of 50 Monte Carlo runs) and mean time (10,000 Monte Carlo runs) between the baseline and alternative processes for experimental testing campaign.

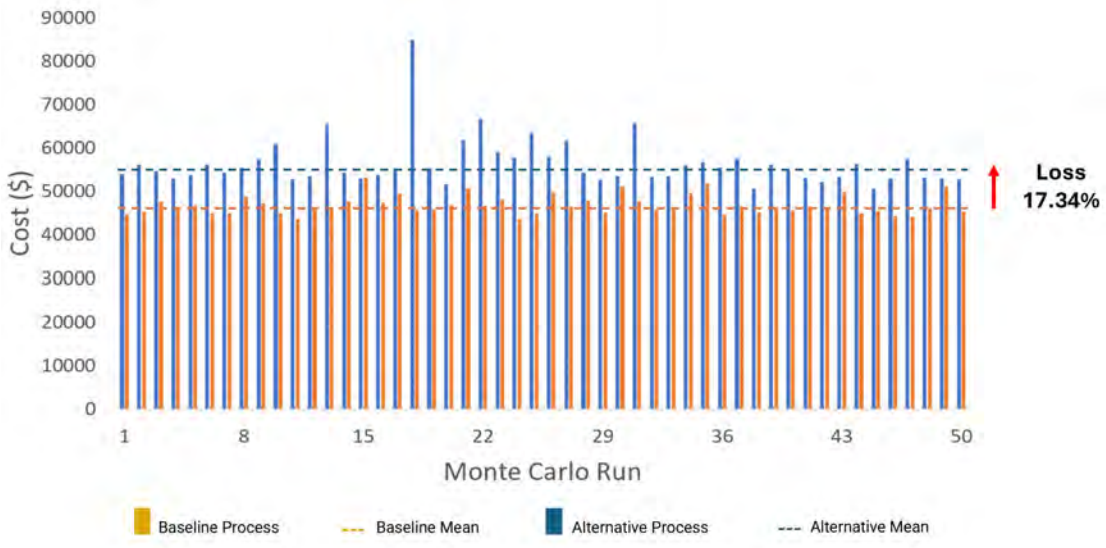

Figure 66. Total costs (sample of 50 Monte Carlo runs) and mean cost (10,000 Monte Carlo runs) of the baseline and alternative processes experimental testing campaign.

Milestones

Please refer to the milestones listed under Task 1.

Major Accomplishments

- Developed a small-scale PIM using DES as a deterministic modeling exercise.
- Developed a more comprehensive stochastic model using stochastic MCMC methods, formulated in a way that enables seamless integration into the verification thread within the MBSE framework.
- Defined a starting set of metrics as a working solution with a focus on process efficiency improvements.
- Designed approach for integrating the PIM with the verification model within the MBSE framework.

- Finalized PIM analysis workflow with the use of Monte Carlo simulation for Markov chain models of the certification testing process.
- Integrated workflow with the MBSE verification model.
- Obtained proof-of-concept use case for assessing the impact of process simplification through quantifiable outcomes, which has been supported by the current working version of the MCMC-enabled PIM module.
- Further improved and tuned the existing PIM with automation and parametrization of user-defined input data to make the model representative of any desired process.
- Applied the PIM to a typical plan for UAS noise testing to better capture the process and properly estimate the cost, staff, and time implications.

Publications
None.

Outreach Efforts
- Presented concepts to FAA and Volpe partners, who provided feedback on the tools and analysis methods.
- Participated in discussions with experts in the field with similar applications (i.e., process simulations for industrial systems, manufacturing, supply chains, etc.).

Awards
None.

Student Involvement
Although a small portion of the team has been leading the technical approach of PIM development, this task has involved the full team. Recent efforts to extend the PIM capabilities have been led by Hajar Mali, and the dashboard and visualization of results have been led by Nathnael Geneti.

Plans for Next Period
- Continuation with the PIM development steps toward a full verification model scale capability for the UAS category.
  - Iterate on noise measurement data to be used for PIM improvements.
  - Calibrate the model with input from UAS OEM data.
- Formulate a simple certification problem for each vehicle type and use it as a pilot for comparing and selecting the appropriate method.
- Improve assessment of certification burden for various standards.
- Further integrate results and PIM analysis in the interactive decision support tool.

References
Federal Aviation Administration. (2022a). *Noise Certification Standards: Matternet Model M2 Aircraft.* https://www.federalregister.gov/documents/2022/09/12/2022-19639/noise-certification-standards-matternet-model-m2-aircraft

Federal Aviation Administration. (2023). *Noise Certification Standards: Flytrex, Inc. Model FTX-M600P aircraft.* https://www.faa.gov/media/31186

International Organization for Standardization. (2010). Acoustics – Determination of sound power levels and sound energy levels of noise sources using sound pressure – Engineering methos for an essentially free field over a reflecting plane (ISO Standard No. 3744:2010). https://www.iso.org/standard/52055.html

International Organization for Standardization. (2024). Noise Measurements for UAS (unmanned aircraft systems) (ISO Standard 5305:2024. https://www.iso.org/standard/81111.html

ASCENT Project 061 Year 4 Recap

The following key tasks and activities have been completed within the ASCENT Project 061 Year 4 performance period:

- Developed **a certification framework** to explore options for **standard setting** to support **noise certification of Emerging Technology Aircraft (ETA),**
- Demonstrated applicability of the current ASCENT Project 061 framework for noise certification of rotor or small propeller-driven UASs.
  - Formulated use cases that are aligned with needs and recommendations provided by OEM partners, with a focus on exploring implications of alternative testing procedures on regulatory compliance and highlighting the benefits of process simplification (e.g., lateral microphone placement or removal, if trusted analysis is used).
  - Provided a demonstration by assessing a simplified noise collection/analysis process.
- Developed **traceable and consistent methodology** to analyze Means of Compliance (MoC) alternatives for supporting rulemaking recommendations.
  - Model-based methods (e.g., MBSE) to **map regulatory-driven requirements to testing procedures.**
- Performed UAM noise **standards review** and **comparison with the UAS standards for demarcation** of categories.
- Engaged in a broader outreach of ASCENT Project 061 to the aviation community on noise certification, including:
  - Participation in ASCENT fall/spring meetings
  - Discussions with UAS OEMs
  - Publication of articles with AIAA and for the SciTech 2024/2025 meetings
- Provided annual and quarterly reports, which are available on the ASCENT Knowledge Services Network database.
- Prepared peer reviewed publications for conferences, such as Scitech 2024 and Quiet Drones Symposium 2024.

Project 062 Noise Model Validation for AEDT

Georgia Institute of Technology
The Pennsylvania State University

Project Lead Investigators

Prof. Dimitri N. Mavris
Director, Aerospace Systems Design Laboratory
School of Aerospace Engineering
Georgia Institute of Technology
Mail Stop 0150
Atlanta, GA 30332-0150
404-894-1557
dimitri.mavris@ae.gatech.edu

Victor W. Sparrow
United Technologies Corporation Professor of Acoustics
Graduate Program in Acoustics
The Pennsylvania State University
411 Engineering Collaborative Research and Education Building (ECoRE)
566 White Course Drive
University Park, PA 16802
814-865-6364
vws1@psu.edu

University Participants

Georgia Institute of Technology (Georgia Tech)

- P.I.s: Prof. Dimitri N. Mavris, Dr. Michelle R. Kirby, and Dr. Mayank V. Bendarkar
- FAA Award Number: 13-C-AJFE-GIT Amendments 61, 82, 106, 125, 144, 160, and 164
- Period of Performance: September 27, 2021, to March 14, 2025
- Task:
  1. Noise modeling in the Aviation Environmental Design Tool (AEDT) with automation (Georgia Tech)

The Pennsylvania State University (PSU)

- P.I.: Prof. Victor Sparrow
- FAA Award Number: 13-C-AJFE-PSU, Amendments 59, 83, 89, 106, 114, and 122
- Period of Performance: October 1, 2021, to March 14, 2025
- Task:
  2. Assessing the use of high-fidelity meteorological data in AEDT noise calculations (PSU)

Project Funding Level

The project is funded by the Federal Aviation Administration (FAA) at the following levels: Georgia Tech: $235,000; PSU: $140,000. Cost-sharing funding is described below.

Georgia Tech has agreed to a total of $235,000 in matching funds. This total includes salaries for the project director, research engineers, and graduate research assistants, as well as computing, financial, and administrative support, including meeting arrangements. Georgia Tech has also agreed to provide tuition remission for the students, paid for by state funds.

For PSU, Spire Global is providing cost-sharing funds in the form of meteorological data and research support. The point of contact for this cost-sharing is Ms. Ashley O'Neil (703-853-8468; ashley.oneill@spire.com). Metropolitan Washington Airports Authority is providing sound level meter data from Dulles International Airport (IAD) as in-kind cost-sharing; the point of contact is Mr. Mike Jeck (703-417-1204; michael.jeck@mwaa.com). Raleigh-Durham International Airport is providing sound level meter data from Raleigh-Durham International Airport (RDU) airport as in-kind cost-sharing; the point of contact is Mr. John Wiatrak (919-840-7748; john.wiatrak@rdu.com). Additional in-kind cost-sharing is being provided by the PSU College of Engineering to meet the required matching of $140,000.

Investigation Team

Georgia Institute of Technology

Prof. Dimitri N. Mavris, (P.I.)
Dr. Michelle R. Kirby, (co-investigator)
Dr. Mayank Bendarkar, (co-investigator)
Mr. Jirat Bhanpato, (research faculty)
Humfrey Kimanya, (graduate student)
Cristina Llongueras, (graduate student)
Sonal Mehta, (graduate student)

The Pennsylvania State University

Prof. Victor Sparrow, (P.I.)
Harshal Patankar, (graduate student)
Pierce Hart, (postdoctoral scholar)

Project Overview

The focus of this project is to assess the accuracy of the AEDT in estimating noise in the vicinity of airports as well as further afield. The foundation of AEDT noise modeling is based on the Integrated Noise Modeling (INM) tool, which has undergone several validation and verification efforts in the past, specifically at the Denver International Airport (DEN), and has shown continual improvements in the agreement between modeling predictions and measurement data. During the development of the AEDT, multiple algorithm updates have occurred. This project seeks to quantify the new noise modeling capabilities through comparison with field measurement data from DEN and other airport monitoring systems. The research team will develop a detailed model validation plan, review the plan with the FAA for concurrence, execute the plan, and make recommendations for future AEDT development. The research, once completed, is expected to provide a noise model validation benchmark that can be used not only to respond to questions regarding AEDT noise prediction accuracy, but also to allow the tool development team to prioritize further development of modeling features and enhancements. The research team will also collaborate with PSU on the assessment of the noise propagation assumptions and the use of higher-fidelity weather data.

Task 1 - Noise Modeling in AEDT With Automation

Georgia Institute of Technology

Background and Objective

In the past decade, demand for air passenger services growth has increased, with a long-term average exceeding 5% in terms of revenue passenger miles (Juniac, 2019). To mitigate the environmental impacts of this growth in aviation, and to maximize the economic benefits that can be achieved through higher efficiency and performance, the National Aeronautics and Space Administration (NASA) Environmentally Responsible Aviation project has suggested aggressive goals (Suder, 2012). This set of goals includes a target to reduce the noise emissions created by aviation over the 2015, 2020, and 2025 timeframes. The first step in mitigating noise emissions is having the capability to model them with a high level of accuracy. The FAA's AEDT (Federal Aviation Administration, n.d.) has among the most advanced capabilities for both modeling aircraft operations and computing-associated environmental metrics. The AEDT is a software system that models aircraft performance in space and time to estimate fuel consumption, emissions, noise, and air quality consequences. AEDT's primary objective is to facilitate the environmental review of federal actions associated with changes in airports, airspace, and other applicable aviation activities.

Several past efforts have studied the improvement of modeled procedures in the AEDT or the comparison between AEDT capabilities and real-world operational data. Noise abatement departure procedures (NADP) are commonly used to mitigate community noise, close to the airport or further afield. Lim et al. (2020) have provided a set of 20 NADP profiles suitable for modeling a large variety of operations that are typically observed in the real world. Behere et al. (2020) and Lim et al. (2020) have focused on quantifying the impacts of such NADP profiles on noise modeling and have identified the most representative NADP profiles. The AEDT has also been used in the creation of alternative rapid noise modeling tools (Levine et al., 2019; Monteiro et al., 2018), in comparing aviation environmental impact mitigation strategies (Yu & Hansman, 2019), and in various other community noise quantification studies (Yu & Hansman, 2019; Salgueiro et al., 2021; Thomas & Hansman, 2019). Other efforts have focused on using large amounts of real-world data to produce reduced-order models for rapid computation of noise impacts (Behere, Rajaram, et al., 2021) or for estimating the impacts of average types of operations at different airports (Behere, Bhanpato, et al., 2021).

Prior studies related to noise model validation date back to the AEDT's predecessor, INM. Several prior efforts have focused on validating the AEDT or INM to quantify the agreement between the model predictions and the data recorded from actual operations. Page et al. (2000) investigated a 1997 dataset from DEN to determine how INM's prediction accuracy changed with different thrust prediction methods. They found that the manufacturers' look-up values of normalized thrust were the most accurate. They then used this information to improve the noise-power-distance (NPD) curves in INM from historical manufacturer data. Forsyth & Follet (2006) used the same 1997 DEN data to update the INM's database, with an emphasis on higher altitudes. Spectral classes were created to correct the NPD information with respect to Society of Automotive Engineers (SAE) AIR-1845 atmospheric absorption. In another study performed with the 1997 DEN data, Plotkin et al. (2013) studied options to further enhance the modeling capability by accounting for the effects of weather and terrain.

Since the introduction of the AEDT by the FAA in 2015, numerous studies have been performed on it. Hobbs et al. (2017) proposed an easily implementable method for including ground cover effects on noise propagation calculations by using algorithms originally implemented in the Advanced Acoustic Model (Page et al., 2000). These algorithms use optical straight-ray theory, as adapted for acoustics, to model noise propagation, in addition to the Fresnel ellipse method. This process has been found to improve noise propagation calculations with respect to empirical data, on data from Portland International Airport, San Francisco International Airport (SFO), and Oakland International Airport. Downing et al. (2019) investigated a method for including terrain and manufactured structural effects in AEDT's noise propagation calculations in 2019. Three separate models were evaluated with respect to their ability to accurately predict how buildings and barriers affect aircraft noise: the Traffic Noise Model (TNM) (Hastings, 2019), SoundPLAN® 7.4 (which uses ISO 9613-2), and the National Cooperative Highway Research Program's Reflection Screening Tool. After validation using data from Los Angeles International Airport (LAX) and Long Beach Airport, the TNM method was recommended as the best option because its noise calculations have variability and consistency similar to those of AEDT's baseline calculations.

Giladi & Menachi (2020) developed a methodology to validate the AEDT noise model using published flight paths and Automatic Dependent Surveillance-Broadcast (ADS-B) data at three different locations. They found the AEDT to underestimate actual noise levels based on a handful of operations. Following a similar methodology, Jackson et al. (2021) developed an automated framework for modeling large datasets of real-world flight trajectories in the AEDT using ADS-B data. Alonso (2022) reports preliminary findings of that framework applied to over 86,000 arrival operations at SFO for a couple of noise monitor locations. In a study using flight operations quality assurance (FOQA) data for AEDT noise model validation, Gabrielian et al. (2021a) presented an automated framework to model FOQA data as fixed-point profiles (FPP) within the AEDT. This was followed by an evaluation of AEDT's noise prediction capability while using high-fidelity weather data (Gabrielian et al., 2021b). Shaw & Sparrow (2022) investigated acoustic impedance and atmospheric absorption using high-fidelity meteorological data to improve the AEDT noise model. Further work on using appropriate averages based on inhomogeneous meteorological profiles, instead of relying on homogeneous annual average weather, to improve noise predictions is presently underway (Mavris & Sparrow, 2022). Preliminary results of a comparative assessment of AEDT noise modeling assumptions at SFO were presented last year (Willitt et al., 2024). ASCENT Project 062 annual report from 2023 provided updates on modeling FOQA flights in the AEDT Ver. 3c for SFO for the calendar year 2019 (Mavris & Sparrow, 2023). This year's report focuses on updates to the FOQA processing pipeline to process additional years' data at different airports and reports the preliminary results obtained at the Minneapolis-Saint Paul International Airport (MSP) and Seattle-Tacoma International Airport (SEA) for the calendar year 2021.

® SoundPLAN s a registered trademark of SoundPLAN GmbH, Backnang, Germany.

The remainder of this report provides information on noise modeling data sources, AEDT assumptions, and automation capabilities developed for the current work. It also discusses the results generated for the bulk flight operations modeled, along with particular or aggregate insights.

Research Approach

The research approach used for the present year mimics last year's approach applied to newer datasets to increase the size of the validation study (Mavris & Sparrow, 2023). Some important aspects of it are repeated here for completeness. Readers interested in the details are directed at prior annual reports (Mavris & Sparrow, 2023). The present work focuses on updates made to the framework and results from the 2021 datasets at MSP and SEA airports.

The two essential elements in this modeling are (1) the data sources used during modeling and (2) the modeling assumptions and alternatives available for each assumption.

Data Sources Used

The two main datasets relevant to this work include the flight operations data and noise monitoring data and are described below:

1. ***FOQA*** data are recorded by the airline operating the flight. FOQA systems record large amounts of data at one recording per second (i.e., 1 Hz). These data have been used for several safety-related applications in prior work (Puranik & Mavris, 2018; Lee et al., 2020). The important elements of FOQA data in this report relate to the detailed time history of parameters such as altitude, speed, thrust, weight, configuration (i.e., flaps and gear), and so on, for each flight modeled in the AEDT. These flights consist of the Boeing® 717-200, 737-800, 737-900, 757-200, 757-300, and 777-200ER/LR, Airbus® A319-100 and A320-200, and Airbus 220 airframes.

2. ***Noise monitoring data*** contain the following key parameters: a noise monitor identification (ID), noise monitor locations, sound exposure level (SEL), and the maximum, A-weighted sound level (L_{max}) metrics of associated noise events, the time of the noise event, and the flight operation correlated to the noise event. The flight ID and the time of closest approach in the noise monitor data allow flights to be matched to the appropriate flight from FOQA data, thereby matching the aircraft configuration and the time of the noise event with the noise metric value. The locations of the noise monitors are used in flight modeling within the AEDT. The noise monitor data are used as a benchmark comparison for noise results calculated by the AEDT.

The framework for modeling and automation developed in this report is independent of the data source used and will need to be modified only to account for the availability of parameters if other data sources are used. In this report, data used are obtained from flight operations at two airports, MSP and SEA for calendar years 2019 (SEA only) and 2021 (both MSP and SEA).

Modeling Assumptions and AEDT Capabilities

Modeling in the AEDT offers users multiple settings for critical assumptions related to the modeling of performance and noise. A matrix of alternatives for these options is shown in Table **1** and Table **2**. Although the possible options and their combinations may be large, not all listed options are compatible or included in the present work. These limitations are noted while discussing the modeling assumptions individually.

® Boeing is a registered trademark of The Boeing Company, Seattle, Washington.
® Airbus is a registered trademark of Airbus Operations GmbH, Hamburg, Germany.

Table 1. Modeling options for departure operations.

Assumption	AEDT default	Option 2	Option 3	Option 4	Option 5
Thrust	Full	FOQA	RT05	RT10	RT15
Weight	AEDT **	FOQA	Alternative weight		
Ground track	Standard	FOQA			
Procedure	Standard	FOQA	NADP1_1	NADP2_11	
Weather	Standard	FOQA	ASOS	High fidelity	
Surface	Soft	Hard			
Terrain	None	Actual			
Flaps	AEDT	FOQA			
Gear	AEDT	FOQA			
NPDs	AEDT	NPD+C			

** Based on stage length.
ASOS = Automated Surface Observing System
RT = Reduced Thrust (5 or 10 or 15 percent).
NADP = Noise Abatement Departure Profile (1 or 2)
NPD+C = Noise Power Distance + Correction

Table 2. Modeling options for arrival operations.

Assumption	AEDT default	Option 2	Option 3	Option 4	Option 5
Thrust	Full**	FOQA			
Weight	AEDT	FOQA			
Ground track	Standard	FOQA			
Procedure	Standard	FOQA			
Weather	Standard	FOQA	ASOS	High fidelity	
Surface	Soft	Hard			
Terrain	None	Actual			
Flaps	AEDT	FOQA			
Gear	AEDT	FOQA			
NPDs	AEDT	NPD + C			

** Arrival thrust is calculated using force-balance.
ASOS = Automated Surface Observing System
NPD+C = Noise Power Distance + Correction

Several settings are available under every assumption (row) in Table **1** and Table **2**, which can affect the performance and noise for each flight operation. This section provides a summary of each option and how it might potentially affect the calculations. For further details, readers are referred to the AEDT Technical Manual (Ahearn et al., 2016).

1. ***Thrust settings***: The options for thrust in the AEDT can be seen through some of the procedures in the FLEET database. Apart from a full thrust assumption, the true thrust value at different points along the departure or arrival is available from FOQA data and can be used. RT15 corresponds to a 15% reduced thrust during the takeoff procedure. Investigation of thrust settings upon takeoff and cutback in ASCENT Project 045 identified that 15% reduced thrust is regularly used by operators in real-world scenarios. This decrease in takeoff and cutback thrust results in a 30% decrease in the area of the 80-dB SEL contour for a single-aisle aircraft (Mavris et al., 2018). Other options available within the AEDT include 5% and 10% reduced thrust; however, these options are not studied in the present work. The final thrust option available is the actual thrust from the flight given in FOQA data.

2. ***Procedure:*** The FLEET database has two types of profiles that can be used: procedural profiles and FPPs. Procedural profiles define an aircraft's thrust, speed, and trajectory in a series of steps. Examples of procedural profiles include the standard profile, NADP1, and NADP2. FPPs fully define the location and state of the aircraft in the sky, as well as its state: thrust and speed. FPPs are used to model FOQA data within the AEDT because they include the speed and thrust from flight data and can prescribe the trajectory and performance as flown in the actual flight.

3. ***Weight:*** Standard departure weight is defined by trip distance (stage length) within the AEDT. Modified alternative weight procedures are available within the AEDT that can be combined with the standard or reduced thrust procedures. Alternatively, FOQA weight can be used for AEDT procedures. FOQA weight can also be used within the AEDT while employing FPPs. However, weight does not affect noise computation for FPPs because all performance parameters, such as thrust, are already prescribed. Information regarding weight, thrust, and speed can be used in one FPP for each flight modeled.

4. ***Ground track:*** The ground track comprises the latitude and longitude points on the ground of the aircraft during its flight. The default AEDT modeling for ground tracks is straight into the airport along with the extended runway centerline that the aircraft is using upon arrival, or straight out of the airport upon departure. These default settings are likely to result in incorrect predictions compared with real-world noise observations and are therefore not included in the current analysis. The FOQA ground track data, reflecting the true flight paths into or leaving airports, are used in the present work.

5. ***Weather:*** The default weather settings used in AEDT studies are in the AIRPORT database. These settings include temperature, relative humidity, wind speed, sea-level pressure, and dew point, which affect performance for the procedural profiles and acoustic calculations for all profiles. The wind direction is always assumed to be a headwind direction. Although the AEDT can use high-fidelity weather data in multiple formats, the present work is limited to the default setting.

6. ***Surface and terrain***: The surface options within the AEDT are available for propeller aircraft, including hard and soft surface options that affect the ground reflection and other properties in noise calculations. For the present work, AEDT default values of soft ground surface and flat terrain are used. The correct real-world elevations of the noise monitors are used to calculate the slant distance to the aircraft.

7. ***Flaps and landing gear:*** The flap and gear schedule for modeling in the AEDT are provided with each of the procedures. For FOQA FPPs, the AEDT infers a flap and gear schedule from the corresponding standard profile. However, unless the analysis is using NPD data with correction for configurations, the flap and gear configuration does not affect the calculated noise when using an FPP. The present work visualizes the errors in AEDT SEL predictions against FOQA flap and gear settings because these affect the real-world noise measured at monitoring stations.

8. ***NPD curves:*** Noise calculations in the AEDT rely on NPD curves derived in a process similar to that used in aircraft noise certification. Noise levels are obtained as a function of observer distance via spherical spreading through a standard atmosphere. In noise analysis, the AEDT applies other correction factors to obtain the desired sound field metrics at the location of the receiver. NPD + configuration (NPD + C) curves that may enable more accurate noise

prediction due to aircraft configuration and speed changes are under study (Mavris, 2019) and are not included in the present work.

Compatibility of Settings

Of the settings discussed previously, those varied in this study include the procedures and profiles, thrust, and weight. Importantly, not all these variations are compatible with one another. For example, the FOQA FPPs are incompatible with reduced thrust or alternative weight settings because FOQA FPPs specify the thrust at every step and the weight at the start of the takeoff or landing segments, whereas the reduced thrust or alternative weight settings calculate these parameters with respect to the standard profile. Likewise, FOQA thrust values cannot be used in a procedural profile because they are numerical (in pounds); whereas the procedural profiles require thrust type and step type definitions that subsequently produce their own thrust values. Consequently, a compatibility matrix is created, yielding the actual number of combinations for flights to be modeled. Arrival profiles have fewer combinations of modeling settings than departure profiles. The only profiles available for arrivals are the standard and FPP from FOQA data, and one thrust setting is available.

In the present study, the combination of settings yields seven different jobs per noise metric for departures. For arrival modeling, it yields two different jobs for each noise metric. Running these cases on the hundreds of flights modeled at MSP and SEA for 2021 requires an automation capability that is described below.

Automation Capability

An automation capability was developed to manage these combinations in a time-efficient manner. Automation is required not only for setting up the many combinations of settings within the AEDT (also called pre-AEDT automation) but also for post-processing of the results generated (post-AEDT automation). The pre-AEDT automation consists of nine structure query language (SQL) automation scripts (Figure 1). The user specifies the profiles to be modeled (either procedural or FPP), the ground tracks, and a combination matrix. This matrix maps profile IDs and ground track IDs together with runway specifications to model the correct combinations from the matrix options in Table 1 and Table 2. These scripts work on multiple AEDT and user-created databases to set up the studies. After scripts 0a through 4b have been executed, script 5 can be executed, which gathers all the information from the previous scripts and sets up the metric results within a new AEDT study. After the user runs all studies within the AEDT graphical user interface, the results, including performance, emissions, and noise, are exported into comma separate value (CSV) files with a batch report run tool. Each case in the combination test matrix results in two reports – the SEL and L_{max} noise metrics, which are then processed with MATLAB® and Python® post-processing scripts (post-AEDT automation).

® Matlab is a registered trademark of The Mathworks Inc., Natick, Massachusetts.
® Python is a registered trademark of Python Software Foundation, Beaverton, Oregon.

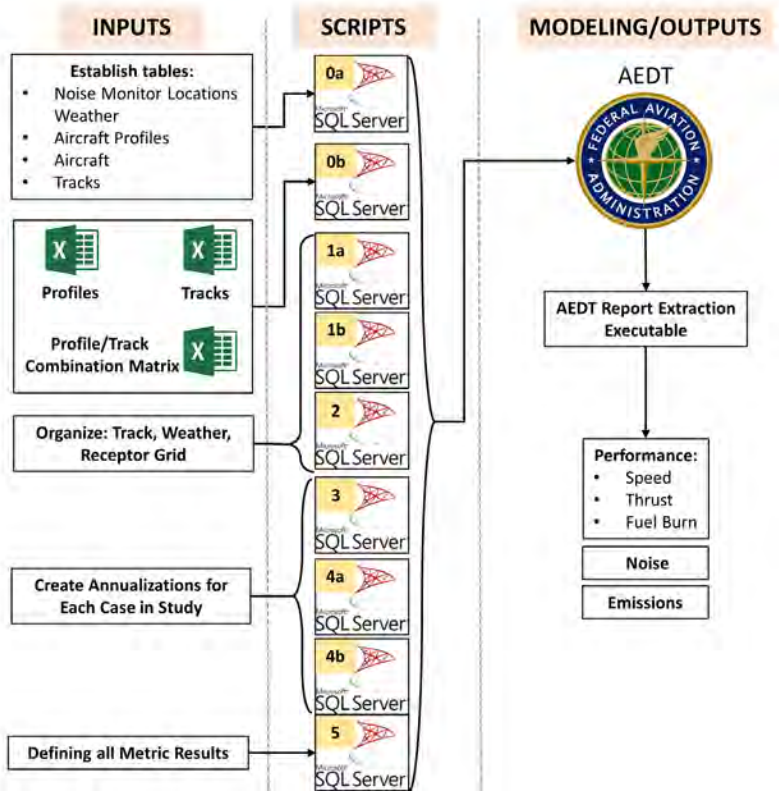

Figure 1. Noise modeling process automation steps.

FOQA Data Pre-processing

Figure 2 shows the data pre-processing pipeline to get the FOQA data ready for insertion into the AEDT. The full FOQA data are sampled at 1 Hz and includes thousands of data points per flight which makes it difficult to insert directly into the AEDT. For that reason, the data are first split to keep only the terminal area operations (removing the en-route data) and further split into arrival and departure operations at different airports. The next step involves down-sampling FOQA data to reduce the number of data points from thousands to roughly 200-400 per departure or arrival operation. For this, L2-normalization is applied to a selected subset of FOQA columns necessary for AEDT modeling so each N-dimensional data point becomes a unit vector. Ramer–Douglas–Peucker (RDP) algorithm, an iterative end-point fit algorithm, is then applied twice — once for the aircraft configurations (i.e., flap, gear), and once for the remaining continuous performance and trajectory parameters. Error between the downsampled points and the full FOQA time series is computed using Euclidean distance to keep points that would reproduce the time series up to a tolerance. This results in each flight being downsampled to an unequal number of points. This process is only applied after lift-off and before touchdown and the FOQA points over the runway portion are not downsampled. The raw FOQA points over the runway as well as the downsampled points away from the runway are kept for the vertical profile used to define FOQA_FPPs. An example illustration of the points kept is shown in Figure 3. A verification study was conducted to see the noise impact from this process as shown in Figure 4, and the tolerance value was selected accordingly to minimize the noise modeling error. The tolerance selected retains approximately 50% of the data points, resulting in the 200-400 points being kept as described earlier.

Further filtering is applied to the ground track after downsampling. Ground track points over the runway and up to at least 500 ft away from the runway threshold are excluded. Additionally, airborne points are filtered such that the spacing between them is at least 500 ft. This ensures sufficient spacing for AEDT modeling during low-speed segments and during turns, as shown in Figure 5. The ground tracks were then used with both the FOQA_FPPs and AEDT procedural profiles in modeling the different flights discussed in the rest of this work.

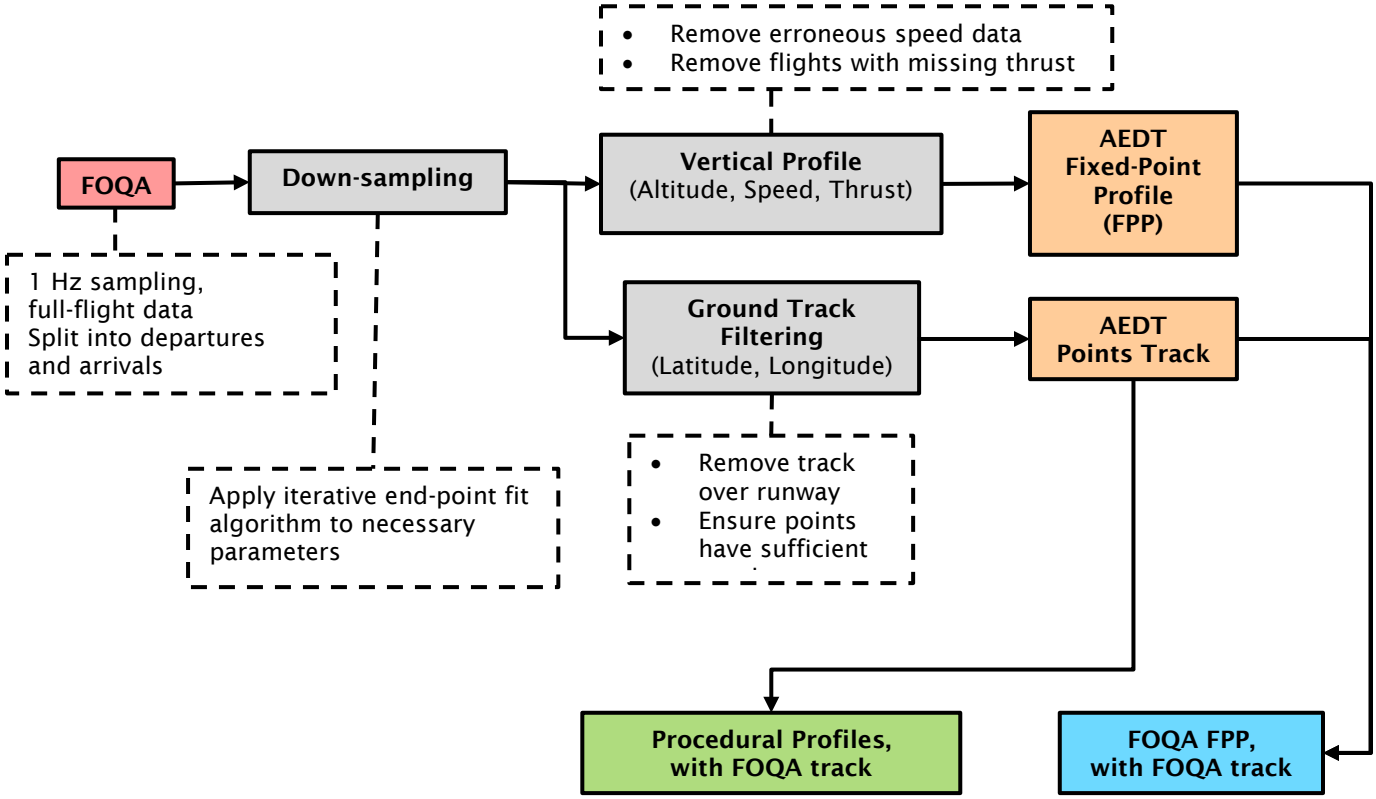

Figure 2. Pipeline for pre-processing FOQA data.

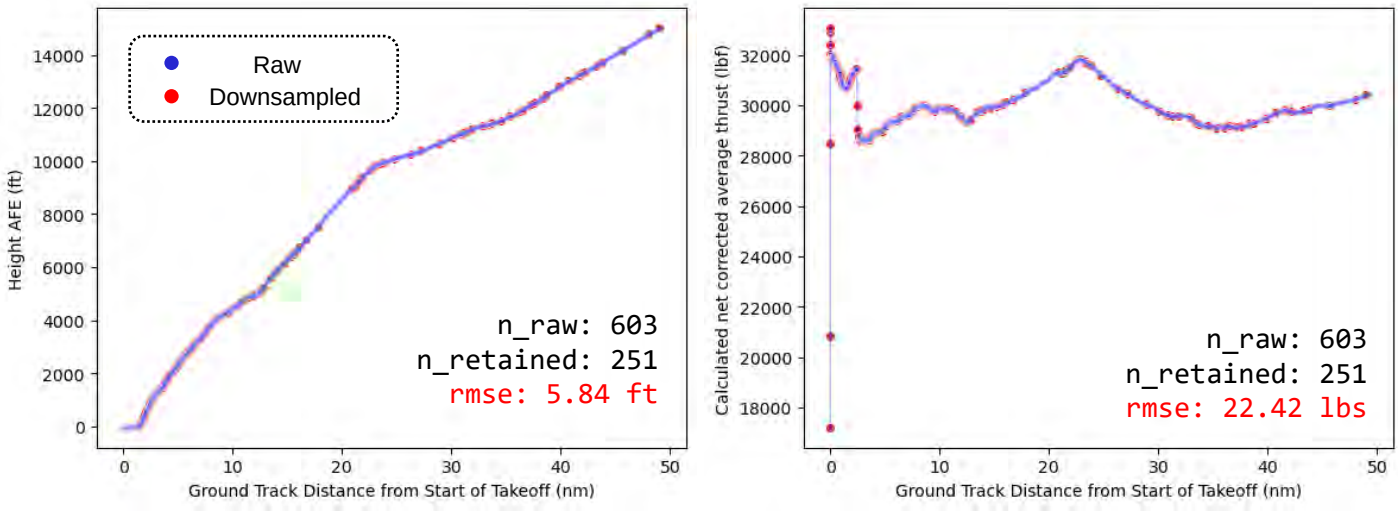

Figure 3. Example downsampled altitude and thrust profiles for a single departure flight.

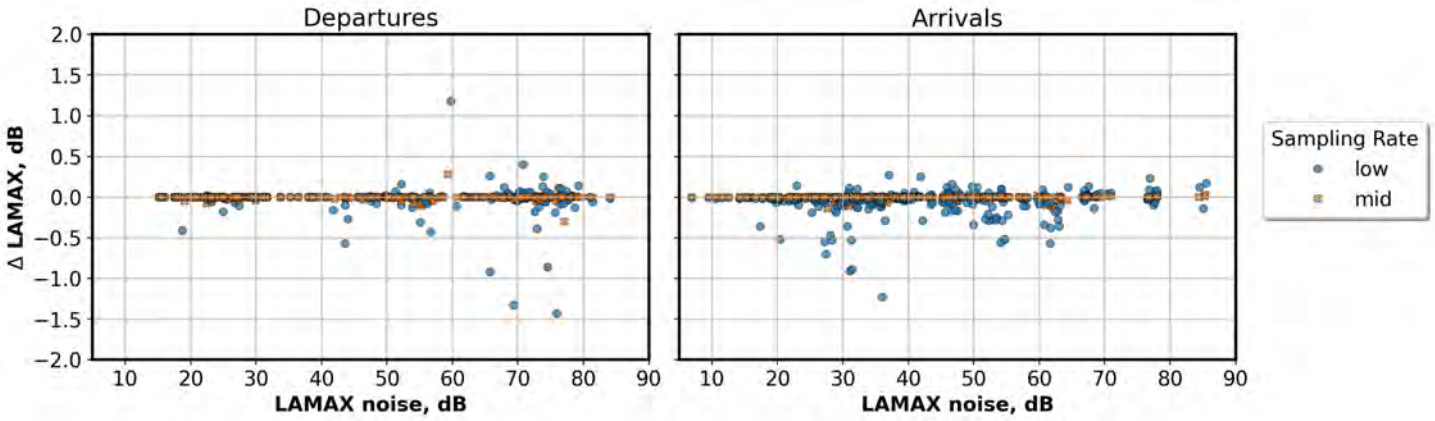

Figure 4. Downsampling impacts on LA_{max} noise at mid and low sampling rates (~50% and ~20% of points retained, respectively).

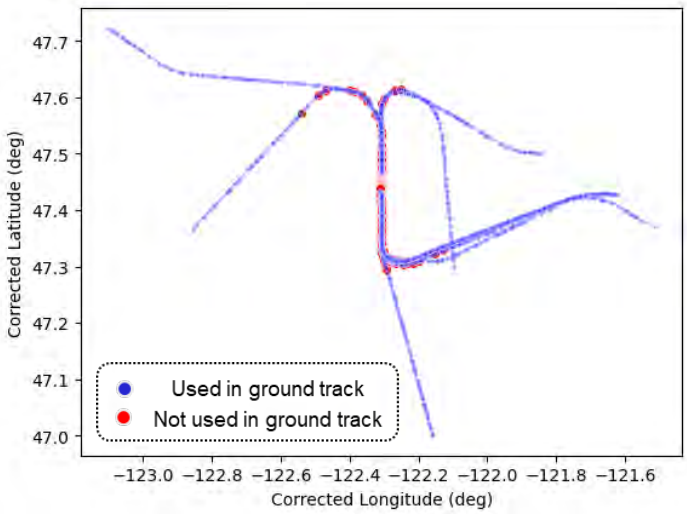

Figure 5. Example ground track filtering results for departure flights.

The processed dataset is then used to generate input files for the AEDT automation pipeline as shown in Figure 1. During this process, each FOQA aircraft type is mapped to the available Aircraft Noise and Performance (ANP) database aircraft IDs.

Table 3 details the mapping used in the present work. Note that some airframes do not have native ANP ID available for modeling, specifically the Boeing 737-900 and Airbus A220-100, A220-300, A330-200, and A330-900.

Table 3. FOQA airframe and their respective ANP aircraft mapping.

FOQA		AEDT		Matching Airframe
Aircraft Type	**FOQA Airframe**	**ANP Aircraft ID**	**Default Equipment Airframe**	
B737	B737-800	737800	Boeing 737-800 Series	Yes
	B737-900	737800	Boeing 737-800 Series	No
B757	B757-200	757PW	Boeing 757-200 Series	Yes
	B757-300	757300	Boeing 757-300 Series	Yes
B767	B767-300/ER	7673ER	Boeing 767-300 ER	Yes
	B767-400ER	767400	Boeing 767-400 ER	Yes
A220	A220-100	737700	Boeing 737-700 Series	No
	A220-300	737700	Boeing 737-700 Series	No
A320	A319-100	A319-131	Airbus A319-100 Series	Yes
	A320-200	A320-232	Airbus A320-200 Series	Yes
	A321-200	A321-232	Airbus A321-200 Series	Yes
A330	A330-200	A330-343	Airbus A330-300 Series	No
	A330-300	A330-343	Airbus A330-300 Series	Yes
	A330-900	A330-343	Airbus A330-300 Series	No
A350	A350-900	A350-941	Airbus A350-900 series	Yes

Preliminary Results

Prior year's report (Mavris and Sparrow, 2023) presented findings of the AEDT validation framework described earlier on FOQA and noise monitoring data for SFO for calendar year 2019. For the present report, the results discussed here include findings from SEA for 2019 followed by findings for MSP and SEA airports for calendar year 2021. In total, 891 departure and 913 arrival operations were correlated with the noise data to identify 3807 departure and 2553 arrival noise events. The detailed breakdown of these is provided in the respective sections for the airports. The number of noise events is greater than the number of flights because some flights triggered multiple monitors. The flights have been given arbitrary flight IDs (GT-xxx) to anonymize the real-world flight details. A few considerations for what noise events can be considered relevant events for validation were discussed in last year's report (Mavris & Sparrow, 2023) and are discussed here again for completeness. The AEDT does not apply wind when modeling noise propagation, while noise measurement under precipitation or high winds is likely to be inaccurate. Therefore, all the noise events were correlated with Automated Surface Observing System (ASOS) weather data to exclude events that show winds greater than 10 knots or non-zero precipitation. Similarly, noise events with elevation angles (see Figure 6) less than 20° typically show anomalous behavior. This behavior was confirmed in the 2021 datasets presented here and therefore such events have been removed from processing as well. Slant distances (see Figure 6) over 7,000 ft were found to cause disproportionately higher prediction errors. Due to absence of time-history noise data, it was difficult to associate these noise events with aircraft operations

with high precision. As a result, all noise events above 7,000 ft slant distances have been removed from the results discussed below. The totals listed above are the noise events processed after these exclusions were made.

The metric used to measure the accuracy of AEDT predictions in this study is the ΔSEL metric defined below.

$$\Delta SEL = SEL_{AEDT} - SEL_{Measured} \quad \text{(Eq. 1)}$$

Since ΔSEL subtracts the measured SEL value from the AEDT predicted value, negative values indicate underprediction while positive values indicate overprediction from the AEDT. ΔSEL is also referred to as SEL error in the discussion below.

Since the FOQA ground tracks are used with all modeled profiles, every noise event can be categorized based on the slant distance and elevation angle of the aircraft with respect to the noise monitor, as shown in Figure 6. For the analysis that follows, a noise event is considered overhead if the elevation angle is ≥50˚ and is sideline otherwise.

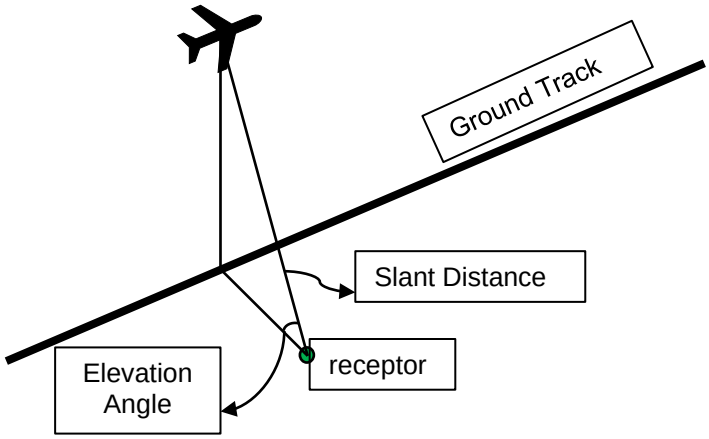

Figure 6. Notional representation of elevation angle and slant distance.

SEA 2019 - Aggregate Flight Modeling Results

Noise monitoring data for SEA were available as time history data consisting of 1-s L_{eq} values for July to December 2019, as well as SEL measurements of noise events for the entire year. The locations of noise monitors around the SEA airport are shown in Figure 7, and the FOQA flight tracks for operations at SEA for 2019 are shown in Figure 8.

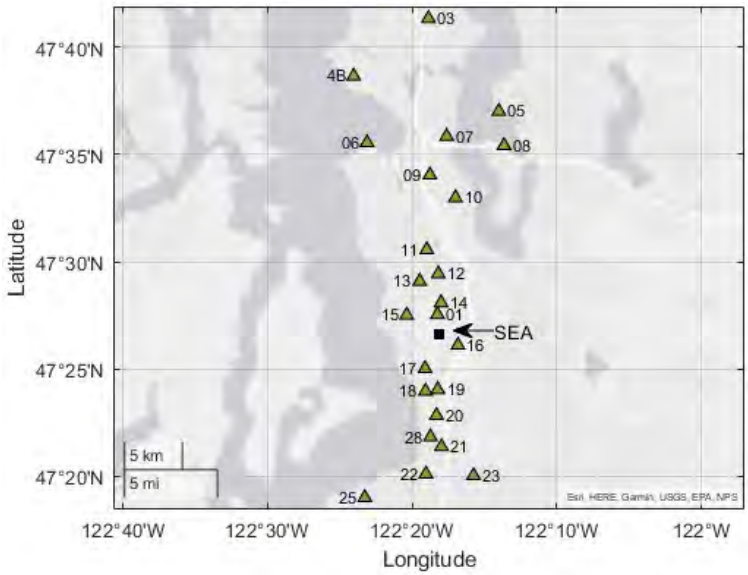

Figure 7. Locations of noise monitors around SEA.

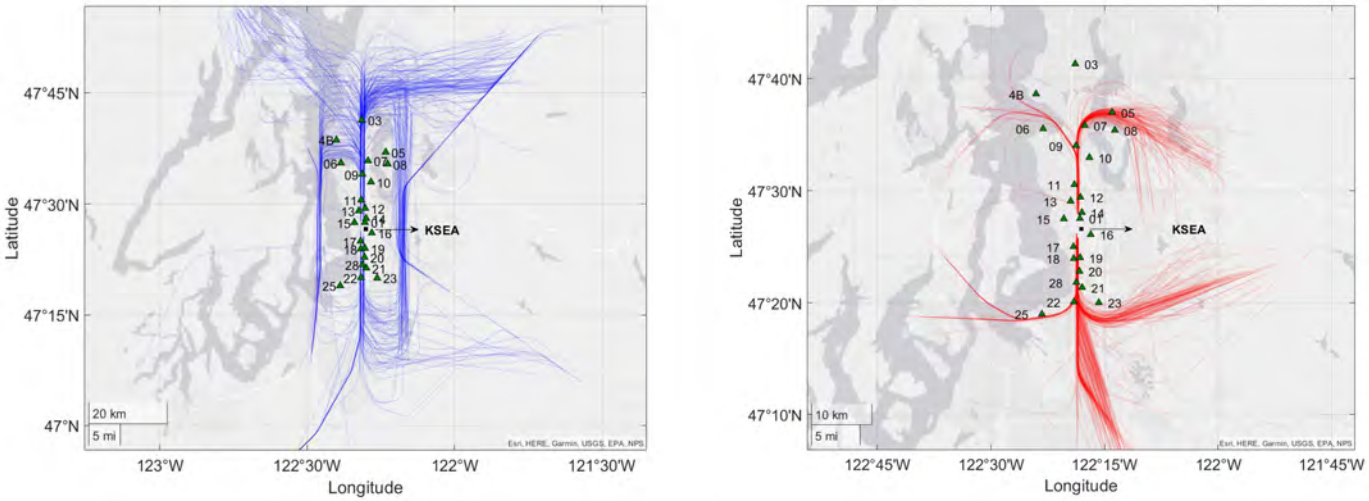

Figure 8. Modeled FOQA arrival (left) and departure (right) tracks for SEA for 2019.

To process the noise time history data for SEA, a dashboard was created that merged the FOQA and noise monitoring data. The developed dashboard enables the user to line up the FOQA flights with noise monitoring data to capture noise events by calculating the SEL, L_{max}, and background sound levels (L_{90}). The dashboard allows the user to visualize the 1-s L_{eq} values captured by noise monitors closest to the flight of interest. A user can manually identify a noise event and capture and export the SEL, L_{max}, and L_{90} values at the closest point between the flight and noise monitor. A snapshot of the dashboard is shown in Figure 9. In it, an arrival flight's noise event at SEA Monitor 12 (topmost in red) is captured. Presently, a total of 76 departure and 87 arrival FOQA operations have been correlated with noise data, resulting in 113 arrival and 198 departure noise events, respectively. After matching SEA-provided SEL noise events with FOQA data for the first 6 months

of 2019, an additional 33 departure and 6 arrival noise events were identified. For SEA, flights with ambient wind speeds greater than 10 knots and nonzero precipitation were excluded prior to modeling in the AEDT.

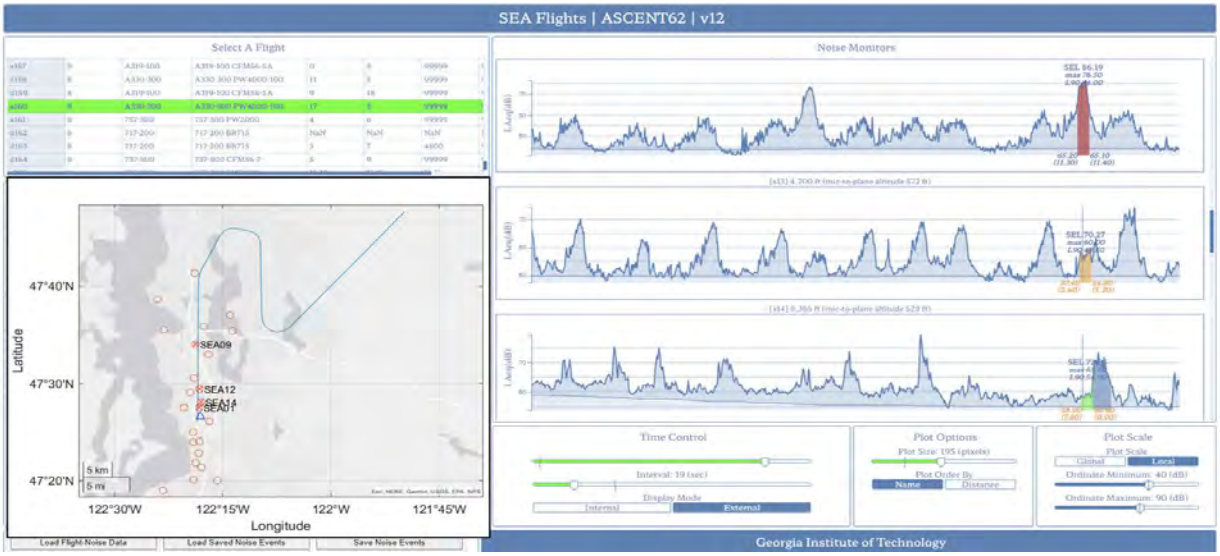

Figure 9. Developed dashboard to capture event sound exposure level (SEL) and maximum, A-weighted sound level (L_{max}) from Seattle-Tacoma International Airport (SEA) noise time history data.

Further processing of correlated noise events based on noise time history (1-s Leq) and closest point of approach of FOQA tracks resulted in just 108 departure and 8 arrival noise events (25 departure flights, 8 arrival flights) where the L_{max} peak coincides exactly with the closest point of approach of the FOQA flight for all monitors triggered by the same flight. The resulting ΔSEL error metric (SEL predicted – measured) for the different profiles is shown in Figure 10. Since the SEA 2019 data were requested in 2022 and more than three years had passed, a little over five months of noise history data was available to be matched to FOQA data. This partially explains the low number of noise events matched to FOQA data from that year. Due to the limited number of noise events identified, no significant statistical inference may be drawn from the SEA 2019 results and there was little use in attempting to identify further trends in this dataset. However, the dashboard capability that matches FOQA data with noise time histories will be invaluable in processing the 2021 and 2023 datasets from SEA in the future.

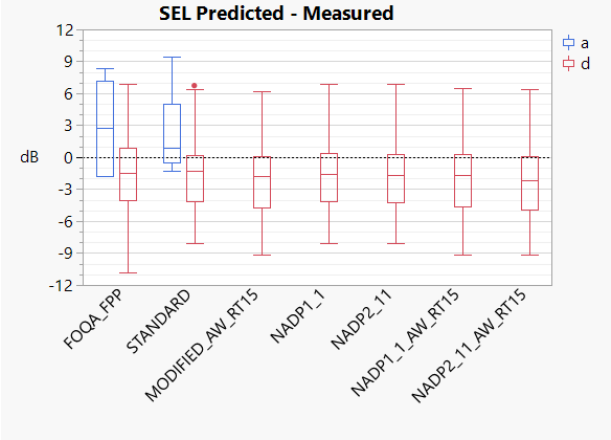

Figure 10. SEA 2019 - Predicted − measured sound exposure level (SEL) (dB) noise box plot for matched 108 departure and 8 arrival noise events at all monitors split by arrivals (A) and departures (D). _AW_RT15: Alternate Weight Reduced Thrust 15%, NADP: Noise Abatement Departure Procedure (1 or 2), FOQA_FPP: Flight Operations Quality Assurance Fixed Point Profile.

MSP 2021 - Aggregate Flight Modeling Results

For MSP, the noise monitoring data for calendar year 2021 obtained included noise events (SEL and L_{max} metrics) correlated with flight registration numbers. To match FOQA data to the noise events identified by the MSP airport noise office, a two-step procedure was followed. First, FOQA flights that were at the closest point of approach to every triggered noise monitor were identified by matching the timestamps between the noise events and the flight tracks. Second, the aircraft registration numbers were matched to ensure that any errors due to the FOQA matching algorithm or the airport noise-flight mapping algorithm are filtered out. MSP 2021 dataset included 683 departure (red) and 618 arrival (blue) flight tracks as shown in Figure 11. All noise events with wind speeds greater than 10 knots and non-zero precipitation were discarded, since the AEDT is not designed to predict noise well in those scenarios. Many outliers in the ΔSEL values were found when elevation angles were less than 20°. These noise events were also likely to have high slant distances (greater than 7000 ft). Lessons learned from the analysis of SEA 2019 noise time history data pointed towards a higher chance of incorrect noise measurements due to terrain or other effects in these cases. Discarding them resulted in a total of 337 arrival flights and 399 departure flights being mapped to a total of 1023 arrival and 1263 departure noise events at MSP for 2021.

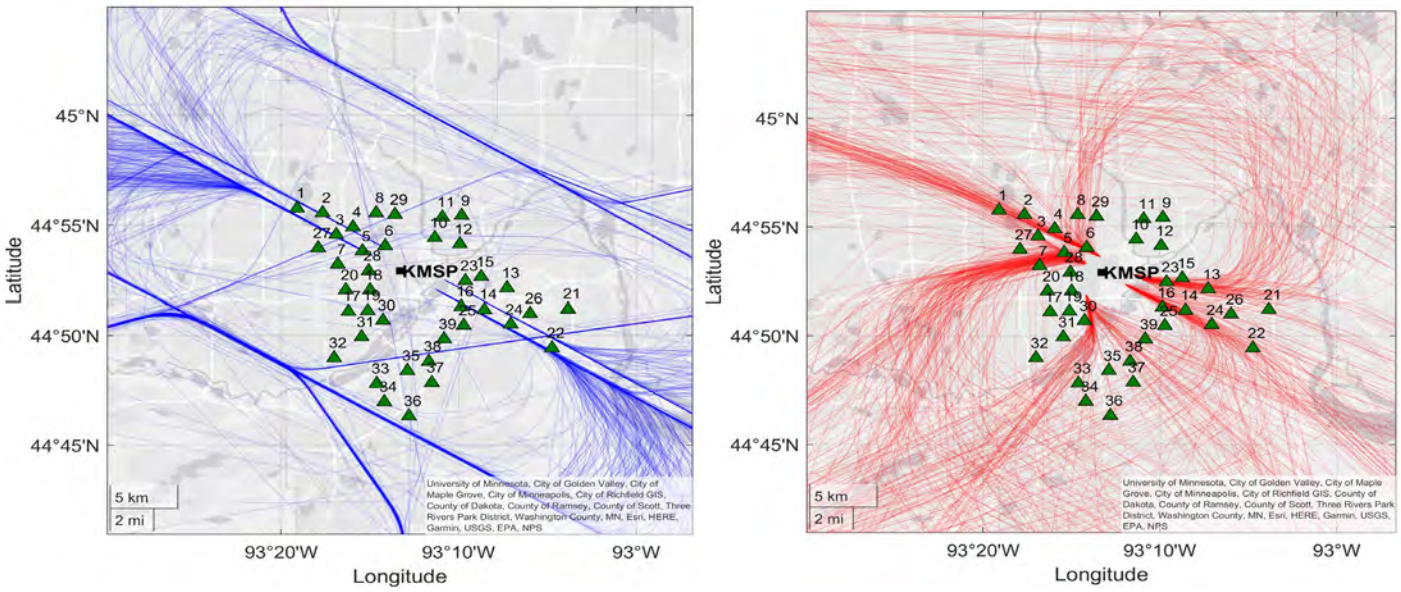

Figure 11. MSP 2021 - Modeled flight operational quality assurance (FOQA) data: 618 arrival (left) and 683 departure (right) tracks overlaid with noise monitors around the airport.

Figure 12 shows the ΔSEL (predicted – measured SEL) for the 337 arrival and 399 departure flights modeled in the AEDT using six different departure and two different arrival profiles from the MSP 2021 database that resulted in a total of 1023 arrival and 1263 departure noise events mapped to the noise monitoring data. For the arrivals, both FOQA fixed point profiles as well as the standard profile shows a median SEL prediction error less than 1 dB on either side and the 25th and 75th percentiles for ΔSEL at roughly [-1, 2] dB. The FOQA departure profile shows the best SEL prediction error among the six modeled profiles, with median SEL underprediction of around 1 dB and the 25th and 75th percentiles for ΔSEL at roughly [-3, 0] dB.

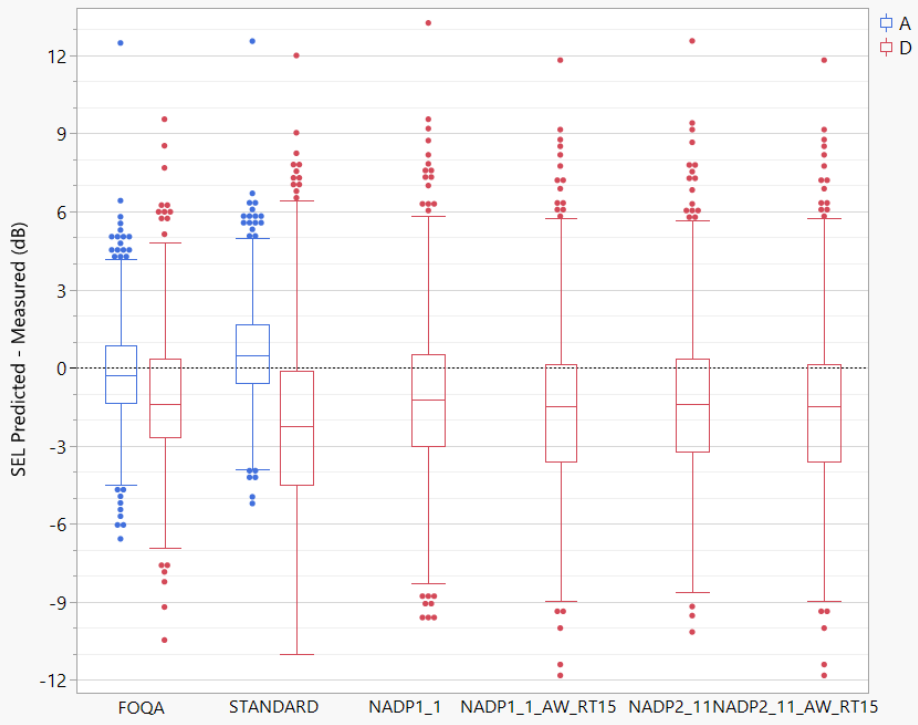

Figure 12. MSP 2021 Predicted − measured sound exposure level (SEL) (dB) noise box plot for matched 1263 departure and 1023 arrival noise events at all monitors split by arrivals (A) and departures (D). _AW_RT15: Alternate Weight Reduced Thrust 15%, NADP: Noise Abatement Departure Procedure (1 or 2), FOQA: Flight Operations Quality Assurance Fixed Point Profile.

Figure 13 shows the trend of ΔSEL against the maximum sound level (L_{max}) metric split by arrivals (blue) and departures (red). The departures show a weak trend towards underprediction of the SEL metric with increasing L_{max} levels. There could be numerous factors (i.e., airframe, stage lengths, weight assumptions, etc.) confounding this result that need to be investigated to better understand this result.

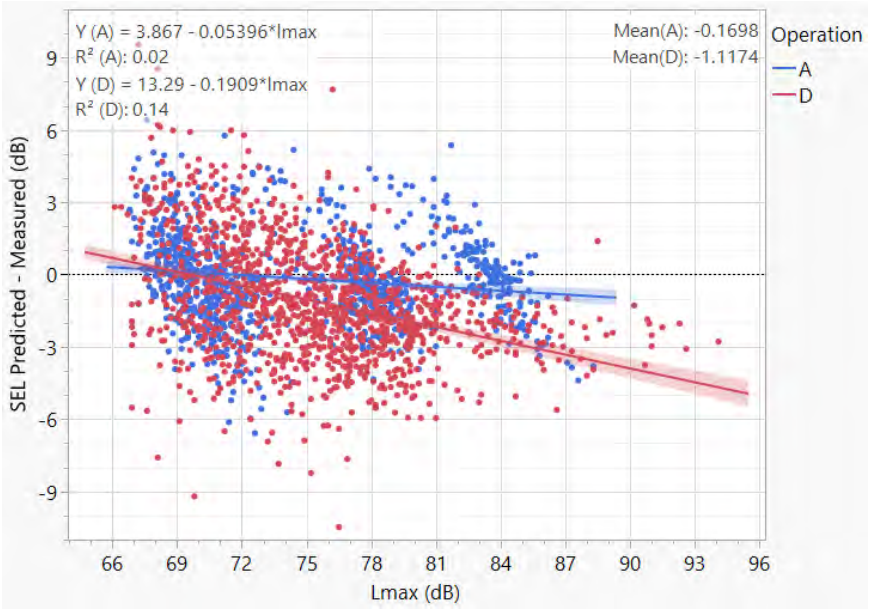

Figure 13. MSP 2021 Predicted − measured sound exposure level (SEL) (dB) vs. maximum sound level (L_{max}) for matched 1263 departure and 1023 arrival noise events at all monitors split by arrivals (A) and departures (D) for the FOQA profile.

Figure 14 shows the ΔSEL metric box plots by aircraft types for all noise monitors from the MSP 2021 dataset. A detailed breakdown of FOQA aircraft type and the ANP aircraft used in the modeling is provided in Table **3**. The Airbus 320 and the Boeing 737 families consist of a large majority of the noise events (over 400 arrival/departure noise events each) mapped between the FOQA data and noise monitoring data from MSP for 2021. The Airbus A350, Boeing 757, Airbus A330, and Airbus 220 families have roughly 20 to 75 noise events each for arrivals or departures. The Boeing 737 family was modeled using the Boeing 737-800 native ANP aircraft, and results show median SEL prediction errors within ±1 dB. The Airbus A320 family (which for the present dataset includes the Airbus A319/320/321 airframes) was modeled using Airbus A319-131, A320-232, and A321-232 native ANP aircraft. The results for the Airbus A320 family show median SEL prediction errors within ±1 dB for arrivals and underprediction of 2-4 dB for departures. The Airbus A350 family was modeled using the Airbus A350-941 native ANP aircraft, and the results show median SEL overprediction of 2-3 dB for arrivals and ΔSEL between [-1,2] dB for departures. Since the Airbus A220 family does not have a native ANP aircraft in the AEDT, it was modeled using Boeing 737-700 ANP ID and the results show median SEL overprediction errors of 3-6 dB. The Airbus A330 family was modeled using the A330-343 native ANP aircraft and the results show median SEL overprediction errors between 1-3 dB for arrivals and underprediction errors between 1-3 dB for departures. The Boeing 757 family was modeled using the Boeing 757-300/757PW native ANP aircraft, and the results show median SEL overprediction errors between 0-3 dB for arrivals and ΔSEL between [-6,2] dB for departures. For the Boeing 767s (modeled using 7673ER/767400 native ANP aircraft), too few noise events have been identified to draw meaningful conclusions. It is important to note that the prediction errors mentioned here are confounded by other parameters like the stage length (modeled weight), airframe-engine combination, flaps and landing gear settings, etc. that need to be studied before drawing any conclusions on the impact of different airframes on AEDT SEL prediction capability.

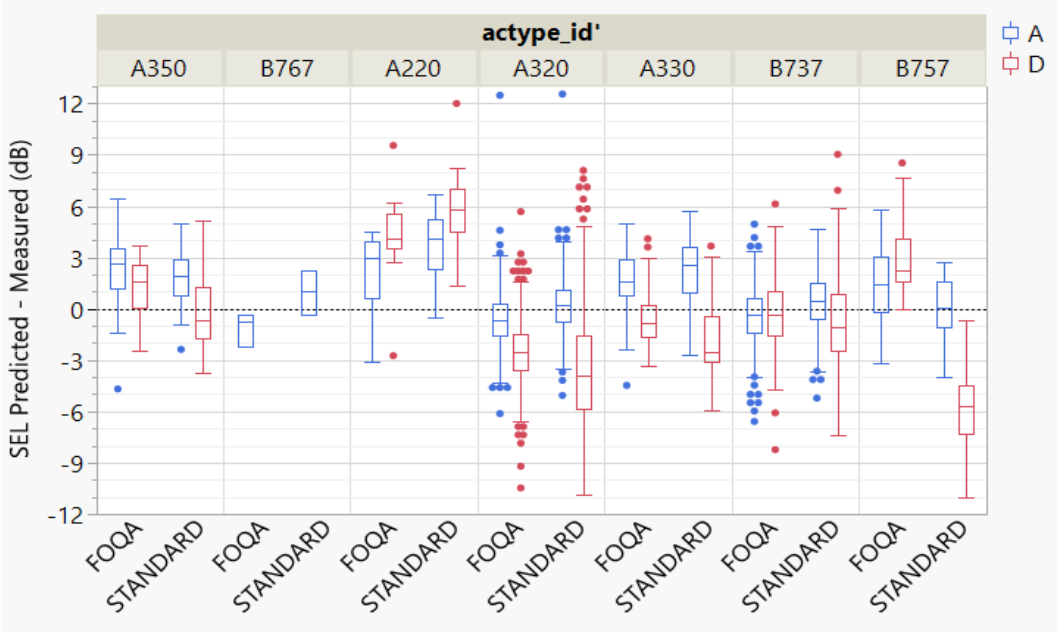

Figure 14. MSP 2021 Predicted − measured sound exposure level (SEL) (dB) noise box plot by aircraft type for all monitors split by arrivals (A) and departures (D). A350 (#A = 41, #D = 46), B767 (#A = 3, #D = 0), A220 (#A = 39, #D = 17), A320 (#A = 421, #D = 598), A330 (#A = 32, #D = 37), B737 (#A = 436, #D = 490), B757 (#A = 61, #D = 75). FOQA: Flight Operations Quality Assurance Fixed Point Profile, #A: number of arrivals, #D: number of departures.

Figure 15 shows the ΔSEL box plots for the MSP 2021 dataset split by the stage lengths of the operations. For arrivals into MSP, stage length was defaulted to 1, while departures out of MSP were assigned stage length according to the origin-destination pairs. A more accurate method to define stage-lengths might be to use the FOQA weight for each operation and will be explored in future work. Figure 16 shows the difference in prediction accuracy when accounting for the elevation angle. Elevation angles less than 20° were omitted in data processing. Elevation angles $\in [20°, 50°)$ represent sideline noise events, while those $\in [50°, 90°]$ represent overhead noise events. The results of Figure 15 and Figure 16 follow the general results shown in Figure 12, showing no particular trend with the stage lengths or elevation angles.

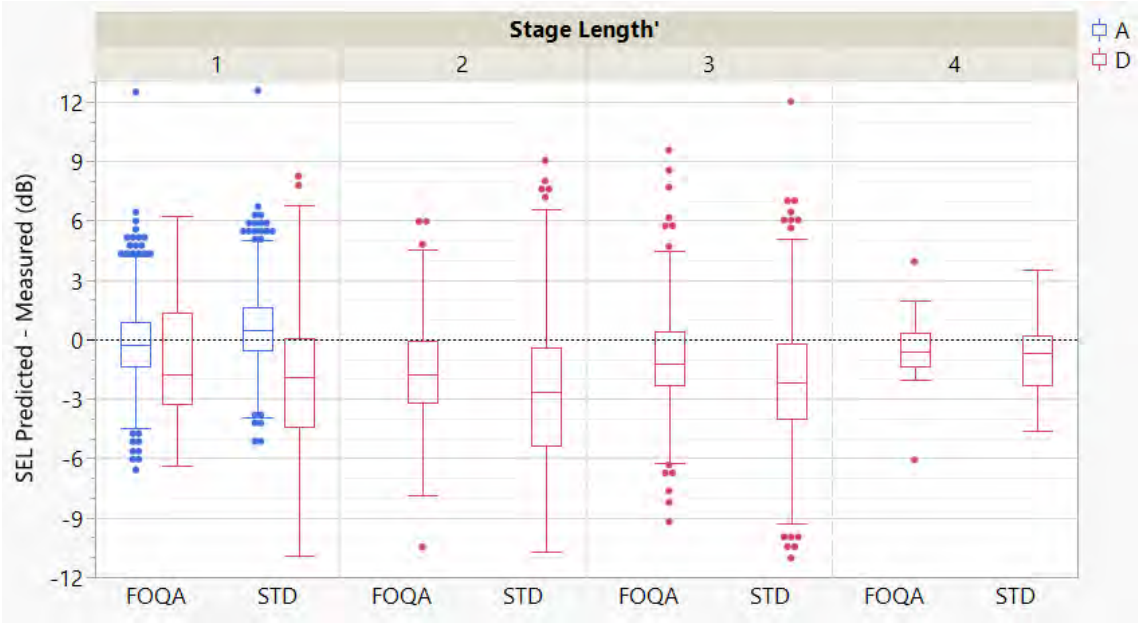

Figure 15. MSP 2021 Predicted − measured sound exposure level (SEL) (dB) noise box plot by stage length (SL) (based on origin-destination pairs) for all monitors split by arrivals (A) and departures (D). SL1 (#A = 1023, #D = 125), SL2 (#D = 418), SL3 (#D = 689), SL4 (#D = 28). FOQA: Flight Operations Quality Assurance Fixed Point Profile.

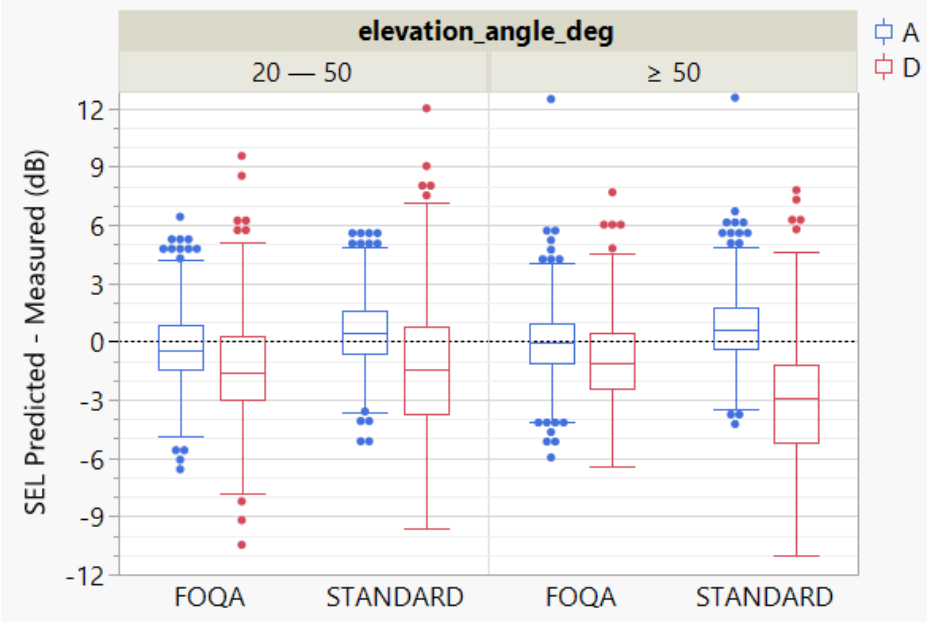

Figure 16. MSP 2021 Predicted − measured sound exposure level (SEL) (dB) noise box plot by elevation angles for all monitors split by arrivals (A) and departures (D). Elevation angles less than 20° were omitted. FOQA: Flight Operations Quality Assurance Fixed Point Profile.

SEA 2021 - Aggregate Flight Modeling Results

For SEA, the noise monitoring data for calendar year 2021 obtained included noise events (SEL and L_{max} metrics) correlated with flight registration numbers. To match FOQA data to the noise events identified by the SEA airport noise office, a two-step procedure was followed. First, FOQA flights that were at the closest point of approach to every triggered noise monitor were identified by matching the timestamps between the noise events and the flight tracks. Second, the aircraft registration numbers were matched to ensure that any errors due to the FOQA matching algorithm or the airport noise-flight mapping algorithm are filtered out. SEA 2021 dataset included 869 departure (red) and 826 arrival (blue) flight tracks as shown in Figure 17. All noise events with wind speeds greater than 10 knots, non-zero precipitation, elevation angles less than 20°, as well as slant distances over 7000 ft were discarded for the same reason stated under MSP 2021 results. This resulted in a total of 568 arrival flights and 467 departure flights being mapped to a total of 1522 arrival and 2436 departure noise events at SEA for 2021.

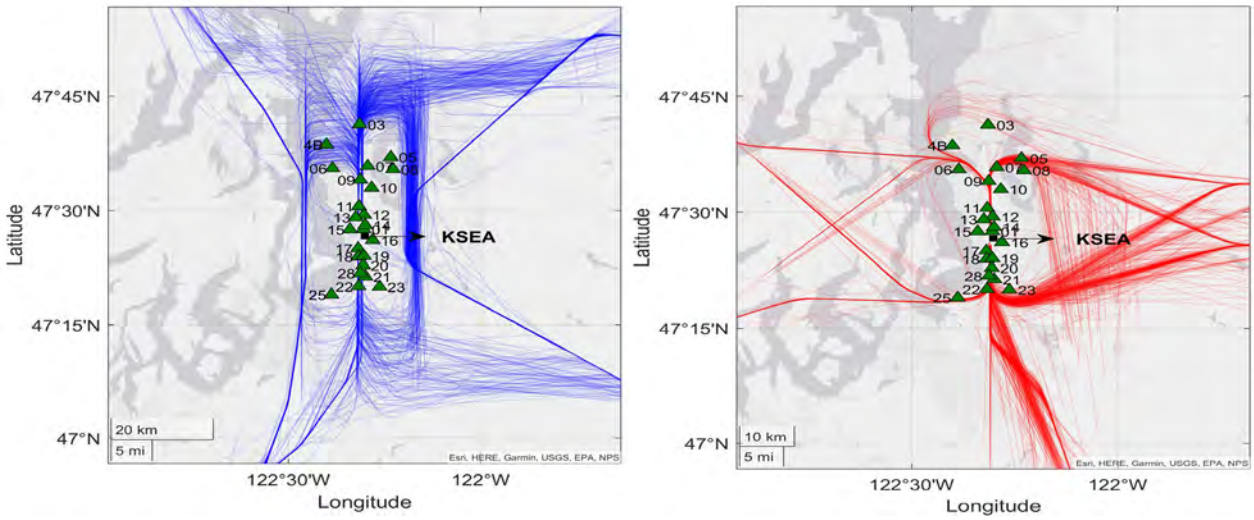

Figure 17. SEA 2021 - Modeled flight operational quality assurance (FOQA) data: 826 arrival (left) and 869 departure (right) tracks overlaid with noise monitors around the airport.

Figure 18 shows the ΔSEL (predicted – measured SEL) for the SEA 2021 flights modeled in AEDT using six different departure and two different arrival profiles that resulted in a total of 1522 arrival and 2436 departure noise events mapped to the noise monitoring data. For the arrivals, both FOQA fixed point profiles as well as the standard profile show a median SEL prediction error of less than 1 dB, with the 25th and 75th percentiles for ΔSEL at roughly [-1, 2] dB. All six of the departure profiles also show a median SEL prediction error less than 1 dB, with the 25th and 75th percentiles for ΔSEL at roughly [-2, 2] dB. The minimum values of the box and are set as 1.5*IQR below the 25th percentile, while the maximum values are set as 1.5*IQR above the 75th percentile, where interquartile range (IQR) is 75th percentile – 25th percentile. Any values beyond these are denoted as outlier data points by the statistical software being used for this analysis.

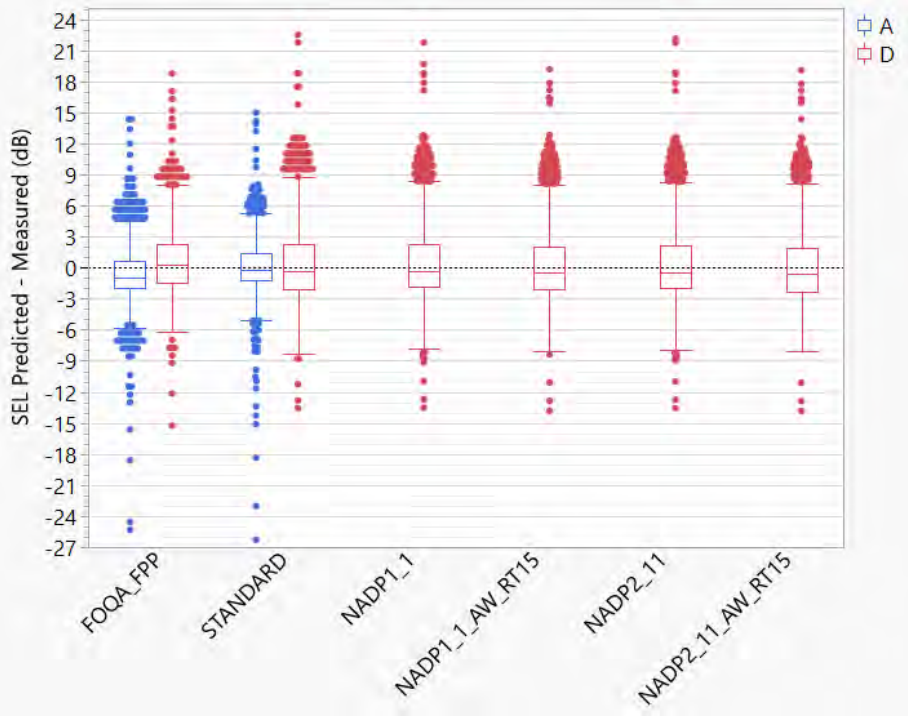

Figure 18. SEA 2021 - Predicted − measured sound exposure level (SEL) (dB) noise box plot for all noise events at all monitors split by arrivals (A) and departures (D). _APTW: profile with airport weather, _ASOS: Profile with automated surface observing system weather _AW_RT15: Alternate Weight Reduced Thrust 15%, NADP: Noise Abatement Departure Procedure (1 or 2), FOQA_FPP: Flight Operations Quality Assurance Fixed Point Profile.

Figure 19 shows the trend of ΔSEL against the maximum sound level (L_{max}) metric split by arrivals (blue) and departures (red) for the FOQA fixed point profile using SEA 2021 data. The departures as well as arrivals show a weak trend towards the underprediction of the SEL metric with increasing L_{max} levels. There could be numerous factors (i.e., airframe, stage lengths, weight assumptions, etc.) confounding this result that need to be investigated to better understand this result.

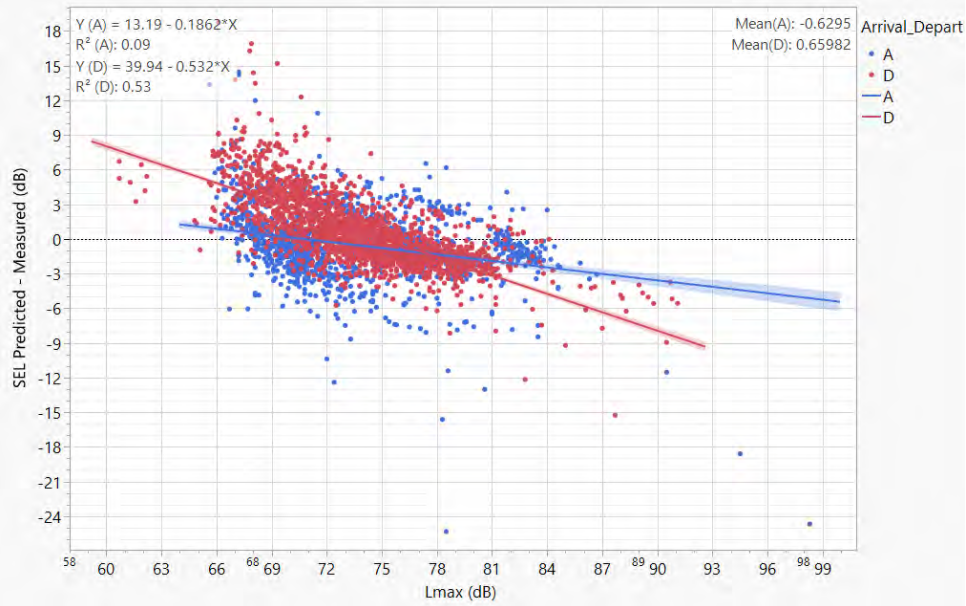

Figure 19. SEA 2021 Predicted − measured sound exposure level (SEL) (dB) vs. maximum sound level (L_{max}) for matched 2436 departure and 1522 arrival noise events at all monitors split by arrivals (A) and departures (D) for the FOQA profile.

Figure 20 shows the ΔSEL metric box plots by aircraft types for all noise monitors from the SEA 2021 dataset. A detailed breakdown of aircraft type and the ANP aircraft used in the modeling is provided in Table 3. The Airbus 220, Boeing 737 and 757 families consist of a large majority of the noise events mapped between the FOQA data and the noise monitoring data from SEA for 2021. The Boeing 767, Airbus A320, and Airbus A330 families have double-digit noise events each for arrivals or departures. The Airbus A350 family just had a handful of noise events in this dataset. The Boeing 737 family was modeled using the Boeing 737-800 native ANP aircraft, and the results show median SEL prediction errors within $[-2, 0]$ dB. The Boeing 757 family was modeled using the Boeing 757-300/757PW native ANP aircraft, and the results show median SEL prediction errors between [0,1] dB for the FOQA profile as well as the standard arrival profile, while standard profile departures show unusual median prediction error around -5 dB. The Airbus A220 family was modeled using the Boeing 737-700 native ANP aircraft, and the results show median SEL overprediction errors of around 2 dB for arrivals and 4 dB for departures using FOQA profile, while using Standard profile, the median overprediction error is around 3 dB for arrivals and 7 dB for departures. The Airbus A320 family (which for the present dataset includes the Airbus A319/320/321 airframes) was modeled using Airbus A319-131, A320-232, and A321-232 native ANP aircraft, and the results show median SEL prediction errors within [-2, -1] dB for arrivals and between [-5, -3] dB for departures. The Airbus A330 family was modeled using the Airbus A330-343 native ANP aircraft, and the results show median SEL prediction errors of 0 dB for arrivals and between [-2, -1] dB for departures. For the Boeing 767s (modeled using Boeing 7673ER/767400 native ANP aircraft), results show median SEL prediction errors [-2, -1] dB for arrivals and [-4, -3] dB for departures. For the Airbus A350 family (modeled using the Airbus A350-941 native ANP aircraft), too few noise events have been identified to draw meaningful conclusions. Just as in the case of the results from the MSP 2021 dataset, for these results based on SEA 2021 data, it is important to note that the prediction errors mentioned here are confounded by other parameters like the stage length (modeled weight), airframe-engine combination, flaps and landing gear settings, etc. that need to be studied before drawing any conclusions on the impact of different airframes on AEDT SEL prediction capability.

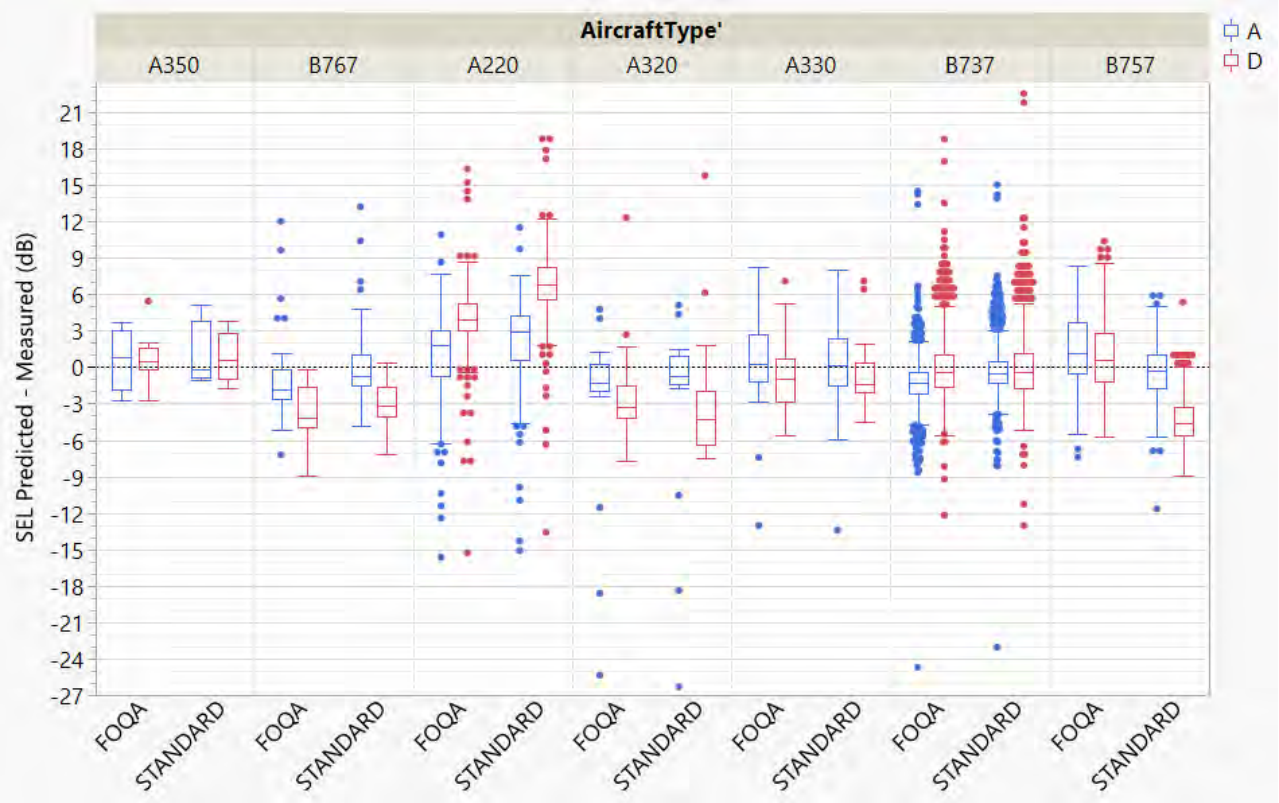

Figure 20. SEA 2021 Predicted − measured sound exposure level (SEL) (dB) noise box plot by aircraft type for all monitors split by arrivals (A) and departures (D). A350 (#A = 4, #D = 12), B767 (#A = 33, #D = 13), A220 (#A = 242, #D = 354), A320 (#A = 20, #D = 32), A330 (#A = 50, #D = 58), B737 (#A = 919, #D = 1443), B757 (#A = 254, #D = 524). FOQA_FPP: Flight Operations Quality Assurance Fixed Point Profile, #A: number of arrivals, #D: number of departures

Figure 21 shows the ΔSEL box plots for the SEA 2021 dataset split by the stage lengths of the operations. For arrivals into SEA, stage length was defaulted to 1, while departures out of SEA were assigned stage length according to the origin-destination pairs. A more accurate method to define stage-lengths might be to use the FOQA weight for each operation and will be explored in future work. Figure 22 shows the different in prediction accuracy when accounting for the elevation angle. Elevation angles less than 20° were omitted in data processing. Elevation angles $\in [20°, 50°)$ represent sideline noise events, while those $\in [50°, 90°]$ represent overhead noise events. The results of Figure 21and Figure 22 follow the general results shown in Figure 18, showing no particular trend with the stage lengths or elevation angles.

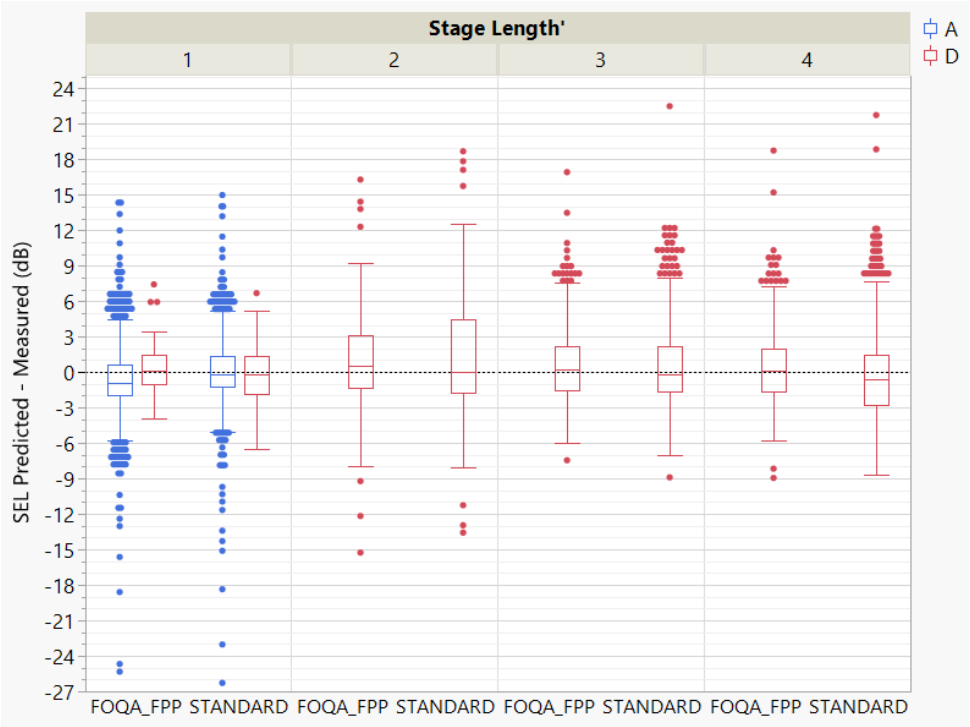

Figure 21. SEA 2021 Predicted − measured sound exposure level (SEL) (dB) noise box plot by stage length (SL) (based on origin-destination pairs) for all monitors split by arrivals (A) and departures (D). SL1 (#A = 1522, #D = 38), SL2 (#D = 714), SL3 (#D = 592), SL4 (#D = 1092). FOQA_FPP: Flight Operations Quality Assurance Fixed Point Profile.

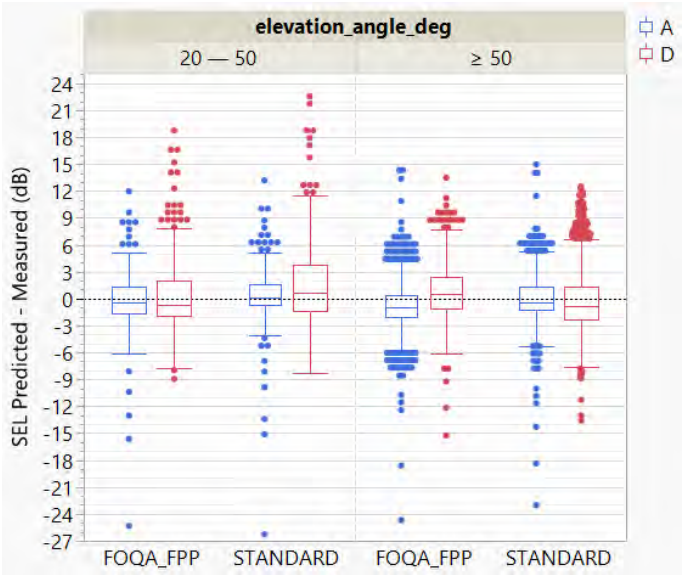

Figure 22. SEA 2021 Predicted − measured sound exposure level (SEL) (dB) noise box plot by elevation angles for all monitors split by arrivals (A) and departures (D). Elevation angles less than 20° were omitted. FOQA_FPP: Flight Operations Quality Assurance Fixed Point Profile.

The AEDT is designed to be accurate on average while modeling the sound exposure of operations over a long duration at a place of interest. The present preliminary results confirm that fact and show that the AEDT has a median SEL prediction error of between [-2, 1] dB from the MSP 2021 dataset and between [-1,0] dB from the SEA 2021 dataset over thousands of noise events across different monitoring locations. Although these results are important in validating the AEDT, it is important to recognize the limitations of the results presented here. This study reports results from two airports, MSP and SEA, with their varied geography and climate, for the year 2021, while matching FOQA flight data to airport noise monitoring SEL measurements. While the authors have taken sufficient care in selecting noise events that meet stringent quality criteria to compare AEDT predictions with real-world operations, detailed noise time-histories were not processed for the year under consideration at the time of writing this report. For the next year of the project, data from additional airports and the years 2021 and 2023 will be processed. This should provide sufficient results to generate confidence in AEDT's noise model for different weather and geographic conditions and for varied operations.

Milestones

None.

Major Accomplishments

Georgia Tech accomplishments

- Completed successful implementation of the AEDT automation pipeline for (a) modeling real-world flights in various settings and (b) extracting and visualizing results from noise modeling efforts.
- Successfully ran 1804 flights at all identified settings from the test matrix and analyzed over 6360 noise events (3807 departure and 2553 arrival) to generate preliminary validation results.
- Excluded noise events with wind speeds >10 knots, non-zero precipitation, elevation angles less than 20° and slant distances > 7000 ft to ensure high quality of results.
- Presented SFO 2019 and MSP 2021 results at 2024 ASCENT spring and fall meetings.
- Analysis for 2023 noise validation data at the following airports: SEA, MSP, SFO, IAD, and RDU, is under progress.
- Coordinated with the PSU team to provide AEDT performance data required for tasks relevant to high-fidelity weather modeling.

Publications

Willitt, A., Bendarkar, M. V., Bhanpato, J., Kirby, M., Abelezele, S., & Mavris, D. N. (2024, Jan). Preliminary AEDT noise model validation using real-world data. AIAA SCITECH 2024 Forum. Orlando, FL, January 2024.

Outreach Efforts

Held biweekly calls with the FAA, the Volpe Center, and Airborne Tactical Advantage Company (ATAC) and participated in biennial ASCENT meetings.

Awards

None.

Student Involvement

Georgia Tech

Sonal Mehta and Humfrey Kimanya worked on noise modeling and data processing for SEA 2019 dataset. Humfrey Kimanya and Cristina Llongueras worked on noise modeling and data processing for SEA 2021 and MSP 2021 datasets.

Plans for Next Period

Georgia Tech

- Complete noise data analysis for SEA, MSP, SFO, IAD, RDU airports for the years 2021 and 2023.
- Provide insights into the statistical significance of results at various noise monitoring stations.
- Develop the interactive dashboard containing the modeling results with all different settings combined for performing trade-off studies.
- Collaborate with PSU to complete analysis of the impact of high-fidelity weather on noise predictions and measurement.

References

Ahearn, M., Boeker, E., Gorshkov, S., Hansen, A., Hwang, S., Koopmann, J., Malwitz, A., Noel, G., Reherman, C. N., Senzig, D. A., et al. (2016). *Aviation Environmental Design Tool (AEDT) technical manual version 2c*. FAA.

Alonso, J. J. (2022). Project 053 validation of low-exposure noise modeling by open-source data management and visualization systems integrated with AEDT. In *ASCENT 2022 Annual Report*. ASCENT. https://s3.wp.wsu.edu/uploads/sites/2479/2023/05/ASCENT-Project-053-2022-Annual-Report.pdf, last accessed 28 Dec 2025.

Behere, A., Bhanpato, J., Puranik, T. G., Kirby, M., & Mavris, D. N. (2021, January 11). *Data-driven approach to environmental impact assessment of real-world operations* [Conference presentation]. AIAA SciTech 2021 Forum, virtual. https://doi.org/10.2514/6.2021-0008

Behere, A., Isakson, L., Puranik, T. G., Li, Y., Kirby, M., & Mavris, D. (2020, June 15). *Aircraft landing and takeoff operations clustering for efficient environmental impact assessment* [Conference presentation]. AIAA Aviation 2020 Forum, virtual. https://doi.org/10.2514/6.2020-2583

Behere, A., Lim, D., Li, Y., Jin, Y.-C. D., Gao, Z., Kirby, M., & Mavris, D. N. (2020, January 6). *Sensitivity analysis of airport level environmental impacts to aircraft thrust, weight, and departure procedures* [Conference presentation]. AIAA SciTech 2020 Forum, Orlando, Florida. https://doi.org/10.2514/6.2020-1731

Behere, A., Rajaram, D., Puranik, T. G., Kirby, M., & Mavris, D. N. (2021). Reduced order modeling methods for aviation noise estimation. *Sustainability*, *13*(3), 1120. https://doi.org/10.3390/su13031120

Downing, J. M., Calton, M. F., Page, J. A., & Rochat, J. L. (2019). *Improving AEDT modeling for aircraft noise reflection and diffraction from terrain and manmade structures* (Tech. Rep. ACRP 02-79). Airport Cooperative Research Program.

Federal Aviation Administration. (n.d.) *Aviation Environmental Design Tool (AEDT)*. https://aedt.faa.gov/

Forsyth, D. W. & Follet, J. I. (2006). *Improved airport noise modeling for high altitudes and flexible flight operations* (NASA/CR-2006-21451). NASA.

Gabrielian, A. B., Puranik, T. G., Bendarkar, M. V., Kirby, M., Mavris, D., & Monteiro, D. (2021a, August 2). *Noise model validation using real world operations data* [Conference presentation]. AIAA Aviation 2021 Forum, virtual. https://doi.org/10.2514/6.2021-2136

Gabrielian, A., Puranik, T., Bendarkar, M., Kirby, M., & Mavris, D. (2021b). Validation of the aviation environmental design tool's noise model using high fidelity weather. *INTER-NOISE and NOISE-CON Congress and Conference Proceedings*, *263*(2), 4810–4822. https://doi.org/10.3397/IN-2021-2846

Giladi, R., & Menachi, E. (2020). Validating aircraft noise models. *Proceedings, 59*(1). doi:10.3390/proceedings2020059012, URL https://www.mdpi.com/2504-3900/59/1/12.

Hastings, A. L. (2019). *Traffic Noise Model 3.0 - technical manual* (Tech. Rep. FHWA-HEP-20-012). U.S. Department of Transportation, Volpe National Transportation Systems Center.

Hobbs, C. M., Gurovich, Y. A., Boeker, E., Hasting, A., Rapoza, A., Page, J., Volpe, J. A., Airport Cooperative Research Program, Transportation Research Board, & National Academies of Sciences, Engineering, and Medicine. (2017). *Improving AEDT noise modeling of mixed ground surfaces*. Transportation Research Board. https://doi.org/10.17226/24822

Jackson, D. C., Rindfleisch, T. C., and Alonso, J. J. (2021). A system for measurement and analysis of aircraft noise impacts. *Engineering Proceedings, 13*(1), doi:10.3390/engproc2021013006. https://www.mdpi.com/2673- 4591/13/1/6

Juniac, A. (2019). *IATA annual review 2018*. International Air Transport Association (IATA). https://www.iata.org/publications/Documents/iata-annual-review-2018.pdf

Lee, H., Madar, S., Sairam, S., Puranik, T. G., Payan, A. P., Kirby, M., Pinon, O. J., & Mavris, D. N. (2020). Critical parameter identification for safety events in commercial aviation using machine learning. *Aerospace*, *7*(6), 73. https://doi.org/10.3390/aerospace7060073

LeVine, M. J., Bernardo, J. E., Pfaender, H., Kirby, M., & Mavris, D. N. (2019). Demonstration of a framework for comparing aviation environmental impact mitigation strategies. *Journal of Aircraft*, *56*(3), 1116–1125. https://doi.org/10.2514/1.C035170

Lim, D., Behere, A., Jin, Y.-C. D., Li, Y., Kirby, M., Gao, Z., & Mavris, D. N. (2020, January 6*). Improved noise abatement departure procedure modeling for aviation environmental impact assessment* [Conference presentation]. AIAA SciTech 2020 Forum, Orlando, Florida. https://doi.org/10.2514/6.2020-1730

Mavris, D., Kirby, M., Lim, D., Li, Y., Pfaender, H., Levine, M., Brooks, J., Behere, A., Gao, Z., Chan Jin, Y., & Kim, J. (2018). *Project 045 takeoff/climb analysis to support AEDT APM development* (Tech. Rep.). ASCENT.

Mavris, D. (2019). *Project 043 noise power distance re-evaluation.* ASCENT. https://s3.wp.wsu.edu/uploads/sites/2479/2020/05/ASCENT-Project-043-2019-Annual-Report.pdf, last accessed 14 Dec 2025.

Mavris, D. N., & Sparrow, V. W. (2022). Project 062 noise model validation for AEDT. In *ASCENT 2022 Annual Report*. ASCENT. https://s3.wp.wsu.edu/uploads/sites/2479/2023/06/ASCENT-Project-062-2022-Annual-Report.pdf, last accessed 13th Nov 2023.

Mavris, D. N., & Sparrow, V. W. (2023). Project 062 noise model validation for AEDT. In *ASCENT 2023 Annual Report*. https://s3.wp.wsu.edu/uploads/sites/2479/2024/04/ASCENT-Project-062-2023Annual-Report.pdf

Monteiro, D. J., Prem, S., Kirby, M., & Mavris, D. N. (2018, January 8). *React: A rapid environmental impact on airport community tradeoff environment* [Conference paper]. 2018 AIAA Aerospace Sciences Meeting, Kissimmee, Florida. https://doi.org/10.2514/6.2018-0263

Page, J. A., Hobbs, C. M., Plotkin, K. J., & Stusnick, E. (2000). *Validation of aircraft noise prediction models at low levels of exposure* (NASA/CR-2000-210112). NASA. https://ntrs.nasa.gov/api/citations/20000068518/downloads/20000068518.pdf

Plotkin, K. J., Page, J. A., Gurovich, Y., Hobbs, C. M., et al. (2013). *Detailed weather and terrain analysis for aircraft noise modeling*. U.S. Department of Transportation, Volpe National Transportation Systems Center.

Puranik, T. G., & Mavris, D. N. (2018). Anomaly detection in general-aviation operations using energy metrics and flight-data records. *Journal of Aerospace Information Systems*, *15*(1), 22–36. https://doi.org/10.2514/1.I010582

Salgueiro, S., Thomas, J., Li, C., & Hansman, R. J. (2021, January 11). *Operational noise abatement through control of climb profile on departure* [Conference presentation]. AIAA SciTech 2021 Forum, virtual. https://doi.org/10.2514/6.2021-0007

Shaw, E., & Sparrow, V. (2022). Modeling acoustic impedance and atmospheric absorption around airports using high-fidelity weather data. *INTER-NOISE and NOISE-CON Congress and Conference Proceedings, 264*, 104–110, doi:10.3397/NC-2022-698.

Suder, K. (2012, July 30). *Overview of the NASA environmentally responsible aviation project's propulsion technology portfolio* [Conference paper]. 48th AIAA/ASME/SAE/ASEE Joint Propulsion Conference & Exhibit, Atlanta, Georgia. https://doi.org/10.2514/6.2012-4038

Thomas, J. L., & Hansman, R. J. (2019). Framework for analyzing aircraft community noise impacts of advanced operational flight procedures. *Journal of Aircraft*, *56*(4), 1407–1417. https://doi.org/10.2514/1.C035100

Willitt, A., Bendarkar, M. V., Bhanpato, J., Kirby, M., Abelezele, S., & Mavris, D. N. (2024, January 8-12). *Preliminary AEDT noise model validation using real-world data* [Conference presentation]. AIAA SciTech 2024 Forum. Orlando, Florida. https://doi.org/10.2514/6.2024-2107

Yu, A., & Hansman, R. J. (2019, June 17). *Approach for representing the aircraft noise impacts of concentrated flight tracks* [Conference paper]. AIAA Aviation 2019 Forum, Dallas, Texas. https://doi.org/10.2514/6.2019-3186

Task 2 - Assessing the Use of High-fidelity Meteorological Data in AEDT Noise Calculations

The Pennsylvania State University

Objective

One challenge in validating aircraft noise models is knowing the state of the atmosphere during field tests. As a part of ASCENT Project 062, in collaboration with our industrial partner Spire Global, the PSU team has previously provided relevant high-fidelity meteorological data to support the AEDT noise model validation work being conducted by Georgia Tech. At present, the AEDT noise model uses high-fidelity meteorological data only for performance calculations. For noise calculations, the AEDT does not use high-fidelity meteorological data directly (e.g., when calculating the acoustic impedance adjustment or the atmospheric absorption adjustment). As an exploratory step, PSU is investigating the possibility of incorporating high-fidelity meteorological data in AEDT noise calculations without modifying the noise model in the AEDT. The ultimate goal is to suggest enhancements to the AEDT that will enhance the predictive capability of AEDT's noise calculations with respect to real-world measurement data.

Research Approach

AEDT's noise model currently assumes homogeneous weather conditions for noise calculations. The weather conditions used in noise calculations are typically ground-based measurements, such as the airport weather (typically an annual average). Although real-world weather is known to rarely be homogeneous, the impact of meteorological inhomogeneity on AEDT's noise calculations must be investigated to determine whether it substantially affects AEDT noise prediction capabilities. One possibility of incorporating high-fidelity weather data in AEDT noise calculations is to explore the use of averages of meteorological variables (e.g., temperature and humidity) based on high-fidelity meteorological data. If this

approach leads to a noticeable improvement in AEDT noise calculations, it could enable AEDT noise calculations to be improved without changing the existing integrated noise model in the AEDT. To explore this possibility, the PSU team is working with real-world flight and noise measurement data provided by Georgia Tech for flights departing from SFO. The aircraft tracking data and performance results from the AEDT (provided by Georgia Tech) are used by PSU in its in-house ray-tracing code to predict noise levels near the ground. Previous work (Sparrow et al., 2022; Sparrow et al., 2023) demonstrated confidence in the in-house ray-tracing code by comparing in-house predictions with AEDT noise results. For this year's work, the in-house ray-tracing code is used to incorporate meteorological inhomogeneity in noise predictions. The goal is to assess if using appropriate average based on the layered (inhomogeneous) meteorological profiles improves predictions when predicting noise levels on the ground. Another area explored in this year's work is seasonal variations in SEL predictions based on daily average weather (averaged over 0 to 2 km altitude) instead of using annual average airport weather.

Data Overview from SFO

The Georgia Tech team shared AEDT noise and performance results with PSU for arrivals and departures from SFO. For the noise monitors located around SFO (shown in Figure 23), the measured SEL and L_{max} (maximum, A-weighted sound level) data were also shared by Georgia Tech. Excluding the cases with precipitation, strong winds, or unusable noise monitor data, there were 149 flights including both arrivals and departures. The PSU team decided to focus only on the 63 departure flights since departures tend to be louder. The departure events were analyzed using the previously validated physics-based in-house code.

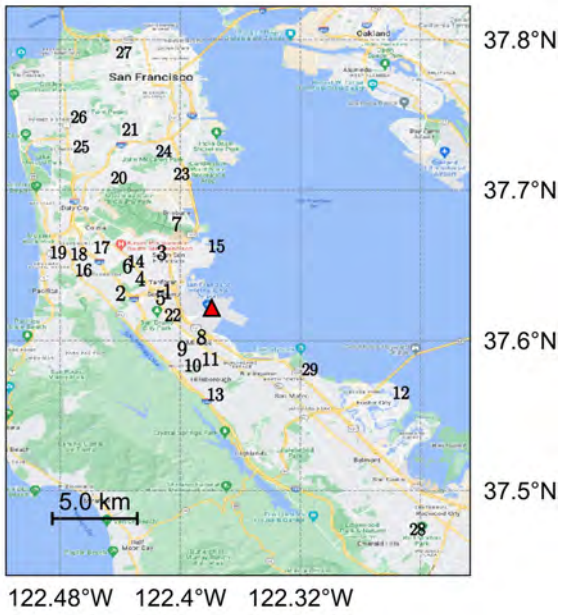

Figure 23. Locations of the noise monitors around SFO.

Figure 24 shows the spread of the available departure events across seasons. It can be seen from Figure 24 that the events are not evenly distributed in time from March 2018 to August 2019. In fact, in some months there are no events for which the flight data and noise data are available.

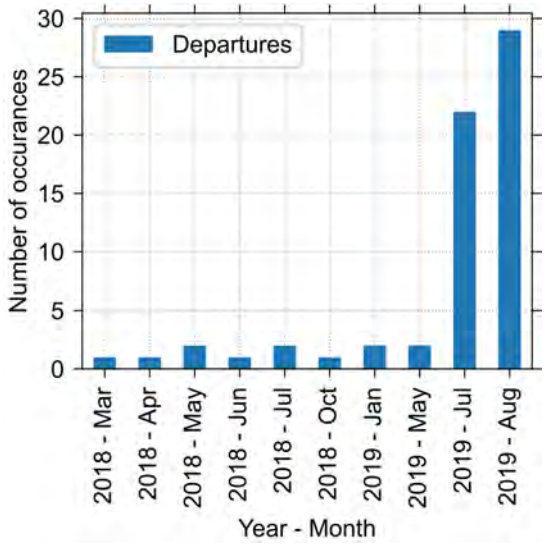

Figure 24. Monthly distribution of the departure events from SFO from March 2018 to August 2019.

Noise Predictions Using Daily Weather (averaged over 0 to 2 km)
Using the hourly ERA5 reanalysis data (a high-resolution global climate reanalysis dataset produced by the European Centre for Medium-Range Weather Forecasts (ECMWF) as part of the Copernicus Climate Change Service (C3S), 2017), inhomogeneous meteorological conditions were averaged over the day of each departure flight. Further, the meteorological conditions were averaged over the nine standardized heights in the ERA5 reanalysis data from 0 to 2 km to arrive at the homogenous conditions to be used in noise predictions instead of the annual airport weather at the surface.

Figure 25 shows the comparison of the AEDT annual average airport weather (temperature and specific humidity shown with a green star) with the daily average weather for the days of the departure flights from SFO. It is important to note that the daily average weather shown in Figure 25 is obtained by taking the average of the meteorological variables over the heights between 0 to 2 km. The median temperature (dashed black line) and the median specific humidity (dashed orange line) is not far off from the annual average airport weather values used in AEDT (green star). The daily average weather shown in Figure 25 is dominated by the weather data between July 2019 and August 2019.

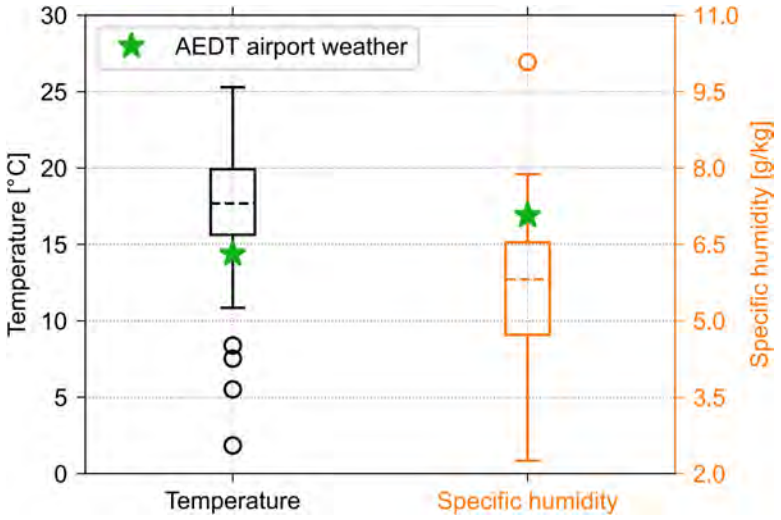

Figure 25. Comparison of the AEDT airport weather with the ERA5 daily average weather (averaged over 0 to 2 km) for the days of the departure flights from SFO (dominated by July/August data). The temperatures are shown in black (left), and the specific humidity is shown in orange (right).

Using the annual average airport weather (like in the AEDT) and the daily average weather obtained from ERA5 data, numerical experiments were conducted using the in-house code for 142 noise events spread across 20 noise monitors (shown in Figure 23). Figure 26 shows the difference between SEL prediction (in-house) and measured data from the noise monitors. It is clear from Figure 26 that the median error (red line) in SEL predictions is about 1 dB when assuming annual average weather conditions (like in the AEDT). There is a small improvement (about 0.5 dB) in median SEL predictions when utilizing daily average weather for the flights/days being looked at. As observed previously, since the data are dominated by events in July/August, these results do not paint a good statistical picture.

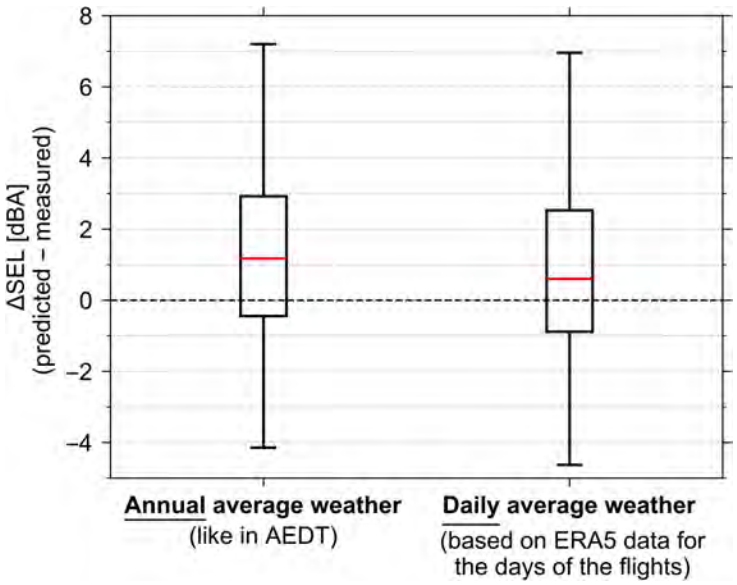

Figure 26. Comparison of the error in SEL predictions using the annual average airport weather and the daily average weather (averaged over 0 to 2 km) based on the ERA5 data for the days of the departure flights.

Seasonal Variation in SEL Predictions Based on Daily Average Weather

Ideally, a dataset with a uniform distribution of departures throughout the year would allow us to comment on the seasonal variation in error when predicting SEL. As an alternative, we picked one aircraft departure trajectory shown in Figure 27 and analyzed the event using 365 meteorological profiles (one for each day of 2019) for the noise received at monitor number 25 shown in Figure 23.

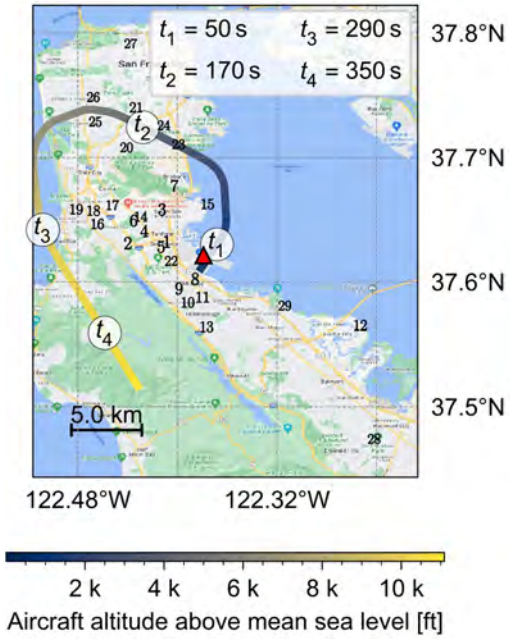

Figure 27. Aircraft departure trajectory and locations of noise monitors around SFO (shown with a red triangle).

Hourly ERA5 data were downloaded for a whole year (2019) and daily average meteorological profiles were calculated for temperature and humidity (shown in Figure 28). This allowed us to calculate SEL predictions throughout the year and look at a statistically representative spread in predictions. One important caveat in these calculations is that we reused the thrust data from the AEDT output (provided by Georgia Tech) for SEL calculations for all the days of 2019. Thrust data provided by Georgia Tech team correspond to the annual average airport weather (and thereby is unchanged for each day of 2019).

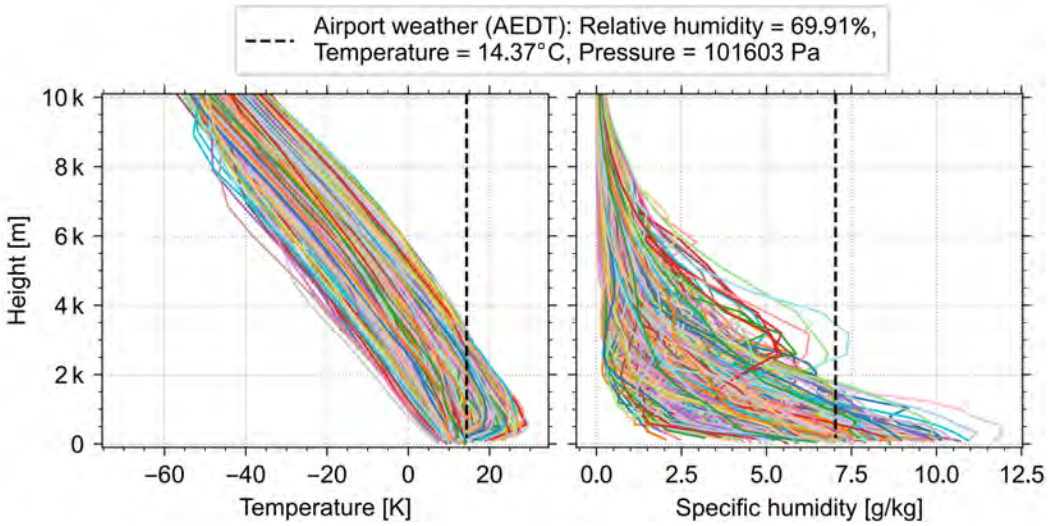

Figure 28. Daily average of the hourly temperature and the specific meteorological profiles (colored lines) for each day of 2019. AEDT annual average airport weather for SFO (dashed vertical line).

Two Methods of Handling Absorption and Comparison Results

Using the temperature and humidity profiles shown in Figure 28, SEL predictions were made using PSU in-house code with two methods of handling absorption. The first method used to calculate SEL uses daily average weather (ERA5 data averaged over 0 to 2 km) for calculating atmospheric absorption (results shown with blue color in Figure 29). The second method of calculating SEL assumed layered profiles for calculating the atmospheric absorption (results shown with red color in Figure 29). Both methods assumed straight rays for propagation to be consistent with the AEDT. All the results shown in Figure 29 use SEL prediction based on the annual average airport weather as a reference to show the seasonal variation in SEL predictions. From Figure 29, it is evident that for the chosen flight-monitor combination at SFO, assuming annual average airport weather results in underpredicted SEL for winter and spring (likely due to colder and dryer weather). For summer and autumn seasons, assuming annual average airport weather results in overprediction of SEL (likely due to warmer and more humid weather). Across all the seasons, the median difference in SEL prediction is less than a decibel when using daily weather instead of the annual average airport weather. Hence, in this particular instance, the AEDT appears to be doing fine predicting the median annual SEL based on the annual-average airport weather. Looking at the results across all seasons, using the annual average airport weather instead of the daily average weather, the SEL is underpredicted by 1.4 dB or overpredicted by 3.7 dB (barring the outliers). Using layered atmosphere for absorption calculations can have an influence of anywhere from 0.5 to 4.0 dB when predicting SEL as compared to using average meteorological data (from 0 to 2 km) for absorption calculations. It is important to highlight that the slant distance involved for the flight-monitor combination is less than 5 km. Depending on the exact weather conditions, longer slant distances can potentially worsen underprediction/overprediction due to the difference in daily weather versus annual average weather.

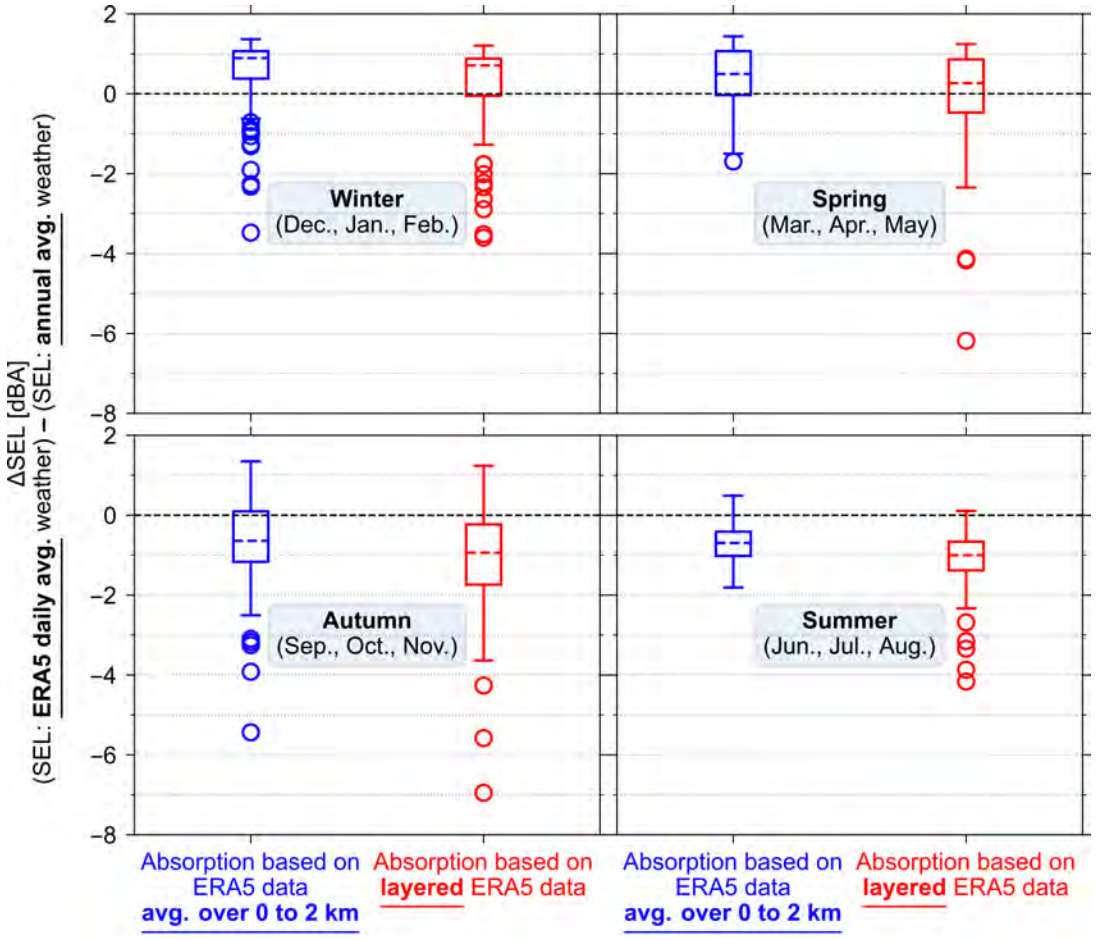

Figure 29. Seasonal variation in SEL predictions (monitor# 25) for entire year (2019) using two ways of including atmospheric absorption.

This study needs to be extended to additional airports and a more even distribution of flights throughout the year to see if the differences with AEDT noise calculations extend to those situations.

New Relationship with Raleigh-Durham International Airport

In the past year, RDU was established as an additional cost share partner. The airport possesses several traits which are of interest for noise-model validation in the AEDT. RDU is a mid-sized airport, carrying over 14.5 million passengers in fiscal year 2023, as compared with SFO, a previously studied airport, which carried more than 3 times the number of passengers at 47.1 million in the same fiscal year. While operating on a smaller scale, the airport has shown a significant interest in sustainability practices. As a result, they possess noise monitors, positioned either side of the singular main runway (see Figure 30).

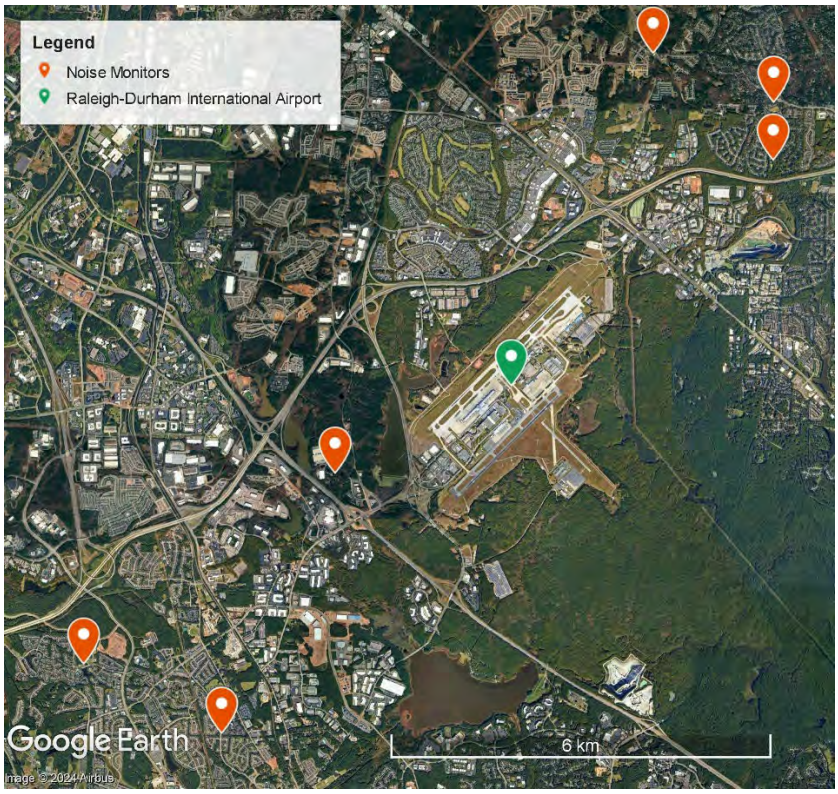

Figure 30. Locations of noise monitors around RDU.

Some of the other features of interest that make RDU an appealing choice for AEDT noise model validation is its climate. Per National Oceanic and Atmospheric Administration (NOAA) reports the mean daily average temperature between 1991-2020 fluctuated from a low of 41.9°F in January while peaking at 80.5°F in July (NOAA, 2024). By comparison a map of the mainland United States average temperature, shown in Figure 31, the North Carolina region appears within the more moderate temperature bounds. Additionally, unlike SFO, the airport is not positioned near a body of water, which can have a significant impact on the noise received from arriving or departing aircraft. The research team looks forward to working with noise monitor data from RDU in the near future.

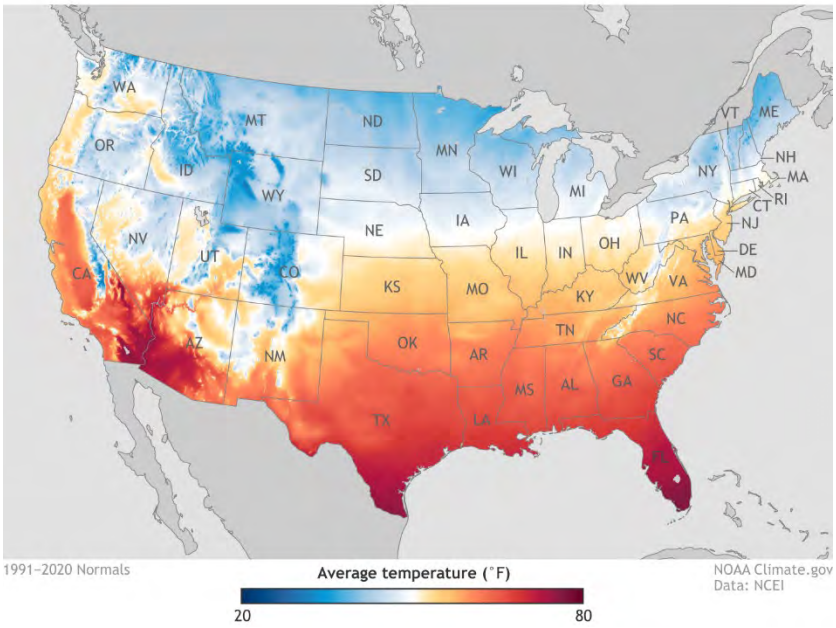

Figure 31. NOAA report of United States annual average temperature between 1991-2020 (NOAA, 2024).

Milestones

None.

Major Accomplishments

- Analyzed a departure flight-monitor combination based on daily weather (averaged over 0 to 2 km altitudes) for an entire year (2019) using PSU's validated in-house ray-tracing code. For the conditions near SFO airport and the flight-monitor geometry analyzed, the median difference in predicted SELs when using the daily average weather instead of the annual average weather is less than 1 dB. At the same time, a considerable spread in SELs was observed for specific days predicted across seasons (from 1.4 dB underprediction to 3.7 dB overprediction depending on the season).
- Examined two methods of including absorption based on inhomogeneous ERA5 reanalysis data in noise calculations using PSU's validated in-house ray-tracing code. Depending on the exact weather conditions, the noise predictions using atmospheric absorption based on a layered meteorological profile did seem sometimes to differ significantly from predictions obtained using an average based on the inhomogeneous meteorological profile.
- Identified conclusions based on PSU's preliminary results which are consistent with the previous work by Plotkin et al. (2013) who had similar findings, i.e., using an appropriate average based on inhomogeneous meteorological profiles can improve noise predictions instead of relying on homogeneous annual average weather.

Publications

None.

Outreach Efforts

- Attended biweekly calls with the FAA and Georgia Tech.
- Participated in semiannual ASCENT meetings.

Awards

None.

Student Involvement

PSU graduate research assistant, Harshal Patankar, contributed to this task. Harshal Patankar worked on PSU's physics-based in-house noise calculations and analyzing real-world aircraft noise events near SFO using ERA5 reanalysis weather for a whole year (2019). PSU post-doctoral scholar, Pierce Hart, also contributed to this task.

Plans for Next Period

- Continue to support the Georgia Tech team, consider the differences in AEDT noise predictions with and without high-fidelity weather, and assess whether updating the atmospheric absorption and acoustic impedance adjustments with high-fidelity weather will have a noticeable effect on AEDT noise predictions.
- Examine more flights, other weather conditions, and other airports, in collaboration with Georgia Tech to generalize the results shown in this report.
- Continue working with the Washington Metropolitan Airports Authority, RDU, and other airports, as needed, to support ongoing and future AEDT noise validation efforts in conjunction with Georgia Tech, as advised by the FAA.
- Provide the relevant high-fidelity meteorological data to support AEDT noise model validation work being conducted by Georgia Tech using high-fidelity meteorological data (obtained by PSU either through collaboration with Spire Global from alternative sources if needed), as demonstrated in the ASCENT Project 062 annual report in 2021 (Sparrow et al., 2021).

Special Acknowledgments

The contributions to ASCENT Project 62 by industrial partners Spire Global, Metropolitan Washington Airports Authority, and RDU were incredibly important for this project. Our research team gratefully acknowledges their essential and exemplary support to the PSU research efforts described here.

References

Copernicus Climate Change Service. (2017). *ERA5: Fifth generation of ECMWF atmospheric reanalyses of the global climate. Copernicus Climate Change Service Climate Data Store (CDS)*. https://cds.climate.copernicus.eu/

NOAA. (2024). *NOWdata – NOAA online weather data*. https://www.weather.gov/wrh/climate?wfo=rah

NOAA. (2021). *New maps of annual average temperature and precipitation from the U.S. Climate Normals*. https://www.climate.gov/news-features/featured-images/new-maps-annual-average-temperature-and-precipitation-us-climate

Plotkin, K. J., Page, J. A., Gurovich, Y., & Hobbs, C. M. (2013). *Detailed weather and terrain analysis for aircraft noise modeling* (No. Wyle Report 13-01). U.S. Department of Transportation, National Transportation Systems Center.

Mavris, D. & Sparrow, V. (2021). Project 062 noise model validation for AEDT. In *ASCENT 2021 Annual Report*. ASCENT. https://s3.wp.wsu.edu/uploads/sites/2479/2022/10/ASCENT-Project-062-2021-Annual-Report.pdf

Mavris, D. & Sparrow, V. (2022). Project 062 noise model validation for AEDT. *In ASCENT 2022 Annual Report*. ASCENT. https://s3.wp.wsu.edu/uploads/sites/2479/2023/06/ASCENT-Project-062-2022-Annual-Report.pdf

Mavris, D. & Sparrow, V. (2023). Project 062 noise model validation for AEDT. *In ASCENT Project 2023 Annual Report*. ASCENT. https://s3.wp.wsu.edu/uploads/sites/2479/2024/04/ASCENT-Project-062-2023Annual-Report.pdf

Project 064 Alternative Design Configurations to Meet Future Demand

Georgia Institute of Technology

Project Lead Investigator

Prof. Dimitri N. Mavris
Director, Aerospace Systems Design Laboratory
School of Aerospace Engineering
Georgia Institute of Technology
Atlanta, GA 30332-0150
404-894-1557
dimitri.mavris@ae.gatech.edu

Dr. Michelle Kirby
Chief, Civil Aviation Division
Aerospace Systems Design Laboratory
School of Aerospace Engineering
Georgia Institute of Technology
Atlanta, GA 30332-0150
404-385-2780
michelle.kirby@ae.gatech.edu

University Participants

Georgia Institute of Technology (Georgia Tech)

- P.I.s: Dr. Dimitri N. Mavris and Dr. Michelle Kirby
- FAA Award Number: 13-C-AJFE-GIT-062
- Period of Performance: September 30, 2023, to September 30, 2024
- Tasks:
  1. Improvement of Advanced Concept Aircraft (ACA) representation in Modeling and Databases Group (MDG)/Forecasting and Economic Analysis Support Group (FESG) models
  2. Alternative design approaches to meet demand.
  3. Exploring physics-based boundaries of the possible

Project Funding Level

The Federal Aviation Administration (FAA) provided $500,000 in funding, and Georgia Tech has agreed to a total of $500,000 in matching funds. This total includes salaries for the project director, research engineers, and graduate research assistants, as well as funds for computing, financial, and administrative support, including meeting arrangements. The Georgia Tech has also agreed to provide tuition remission for the students, paid from state funds.

Investigation Team

Prof. Dimitri N. Mavris, (P.I.), All Tasks
Dr. Michelle Kirby, (co-P.I.), All Tasks
Dr. Jon Gladin, (technical lead), All Tasks
Dr. Yu Cai, (technical lead), All Tasks
Dr. Jiacheng Xie, (technical lead), All Tasks
Mr. Dev Patel, (graduate student researcher), Tasks 1 and 2
Mr. Tuna Ergan, (graduate student researcher), Tasks 2 and 3

Ms. Emmanuella Okonkwo, (graduate student researcher), Task 1
Ms. Akshiti Parashar, (graduate student researcher), Task 2
Mr. Cem Kocer, (graduate student researcher), Task 3

Project Overview

The purpose of ASCENT Project 064 is to improve upon the modeling approach used in the first two years of research and to provide insights or recommendations to the MDG regarding a more realistic approach to modeling ACA at the fleet level. In addition, the project will address alternative means of designing aircraft beyond the usual adoption of technologies with the payload and range capability of the existing fleet.

Task 1 - Improvement of ACA Representation in MDG/FESG Models

Georgia Institute of Technology

Objective

The objective of this task is to investigate potential opportunities for improving how ACAs are modeled within the fleet to benefit current analyses and probable future analyses. The traditional approach to modeling future aircraft types in the fleet has been to define a proxy aircraft that the new aircraft entering the fleet will replace and then establish a change in benefit. Although this process worked for evolutionary aircraft of the past, it does not work for ACAs, which may have markedly different performance behavior from that of conventional aircraft, such as different cruise altitudes and speeds or different range capabilities for the same seat class. To model an ACA within the MDG modeling tools, manufacturers would need to provide the necessary performance, emissions, and noise coefficients defined by SAE (Society of Automotive Engineers) AIR (Aerospace Information Report) 1845 and the Base Aircraft Data (BADAv3). Prior research in this area, specifically for a blended wing body, has shown limitations in the accuracy of these tools in capturing the expected performance.

Within the Environmental Design Space (EDS), algorithms exist to create the necessary performance, emissions, and noise coefficients needed by MDG's modeling tools. Although the coefficients can be determined, how the ACA actually flies within MDG tools may not be correct, and modifications to the framework may be required. This task will investigate the shortcomings of the MDG tools for ACAs and provide recommendations to the model developers regarding means of improvement or new methods that must be developed.

Research Approach

Step 1 – Validate the Modeling and Simulation Environment and Inconsistency Elimination

The first step is to validate the modeling and simulation environment on which the ACA model is established and eliminate the inconsistencies between the EDS and MDG's modeling tool (i.e., Aviation Environmental Design Tool [AEDT]).
The validation process was conducted using a notional tube-and-wing aircraft model calibrated based on the Airbus® A320neo aircraft and Pratt & Whitney® PW-1127G engine. The model was created in the EDS, and performance, emissions, and noise coefficients were generated based on the EDS analysis results. These coefficients were used to create an AEDT Standard Input File (ASIF) by identifying the corresponding coefficients necessary to define a new user-defined aircraft within the AEDT. A pipeline that converts EDS outputs into the AEDT aircraft definition and noise spectral data was established, enabling modeling refinements between the two analysis tools.

After obtaining the coefficients for the notional Airbus A320neo model, terminal area operations were modeled in the AEDT to determine the performance, noise, and emissions during the standardized departure and arrival procedures. Specifically, departure operations from stage lengths 1 to 6, corresponding to expected takeoff weight for various trip lengths, and arrival operations at stage length 1, corresponding to expected landing weight, are modeled. These operations were modeled in the AEDT at the South Lafourche Leonard Miller Jr. Airport (KGAO) Runway 18 and for straight in-and-out trajectories. The same terminal area operational procedures were also analyzed in the EDS, using the National Aeronautics and Space Administration (NASA) Flight Optimization System (FLOPS). The inputs provided to the FLOPS were obtained using the same EDS model that was used to generate AEDT coefficients, and the departure and arrival procedures were defined as the same as those used in the AEDT. If the performance analysis results from the FLOPS match closely to

® Airbus is a registered trademark of Airbus Operations GmbH, Hamburg, Germany.
® Pratt & Whitney is a registered trademark of RTX Corporation, Farmington, Connecticut.

those from the AEDT with a small error margin, the modeling and simulation environment would be validated and could be used for ACA model development.

Step 2 – ACA Identification for the Future Fleet
The second step is to identify the most likely ACA to enter the fleet in the future. This task includes identification of the potential airframe, propulsion, energy sources, and operational improvements possible for the different seat-class aircraft over time. This step will heavily leverage work performed in the previous two years in identifying relevant technologies for future vehicles but will now focus on ACAs. These technologies and concepts may include, but are not limited to, blended wing bodies, truss-braced wings (TBWs), boundary layer ingestion, hybrid-electric propulsion, drop-in and non-drop-in fuels, supersonic aircraft, and cruise speed reductions. A transonic TBW (TTBW) was selected because substantial research funds have been spent by the U.S. government to develop the theoretical and practical model of the TBW and TTBW aircraft. For the purposes of this task, the TTBW is relevant, because it is a highly efficient "new" airframe, and it has several differences in terms of mission profile concerning a traditional tube and wing design (typically higher altitude). Although it does not use nontraditional fuel sources by definition (even though it could), its configuration is substantially different from that of the conventional tube and wing aircraft.

Step 3 – Establishment of a Quantitative Model for the ACA
The third step is to establish a quantitative model for the ACA using the EDS once it is validated in Step 1. A stable notional TTBW aircraft was modeled and calibrated to closely match the geometry, weight, and performance of the configuration presented in the Subsonic Ultra Green Aircraft Research (SUGAR) phase 3 study by Boeing.® This aircraft was selected because this TTBW is expected to be deployed by the year 2035. In the process of calibrating the TTBW aircraft in EDS, geometric parameters, engine parameters, weight distribution, mission profile, aerodynamic parameters, and performance parameters from the SUGAR report were used as references.

Table 1 compares the output obtained from the EDS and Boeing SUGAR report.

® Boeing is a registered trademark of The Boeing Company, Seattle, Washington.

Table 1. Comparison between the Environmental Design Space (EDS) model and Boeing Subsonic Ultra Green Aircraft Research (SUGAR) report data.

Component	Parameter	Unit	SUGAR Report	EDS Model
Wing	Area	ft^2	1,477.1	1,566.4
	Aspect ratio		19.55	19.56
	Span	in	2,039.3	2,100.5
	Taper ratio		0.35	0.35
	Sweep 25%	°	12.52	20.46
	Dihedral	°	-1.5	-1.5
Vertical tail	Area	ft^2	292.99	292.99
	Aspect ratio		0.82	0.82
	Span	in	186.6	186.0
	Taper ratio		0.8	0.8
	Sweep 25%	°	43.5	43.5
Horizontal tail	Area	ft^2	276.94	276.94
	Aspect ratio		4.93	4.93
	Span	in	443.3	443.4
	Taper ratio		0.35	0.35
	Sweep 25%	°	31.6	31.6
Fuselage	Width	ft	12.39	12.39
	Depth	ft	13.88	13.88
	Compartment length	ft	93.92	93.92

Step 4 – Creation of Performance, Emissions, and Noise Coefficients for the AEDT
The fourth step is to create the performance, emissions, and noise coefficients needed by the AEDT using the EDS by using the calibrated ACA model from Step 2 to generate AEDT coefficients and obtain noise contours. Input files were generated to be used in the AEDT environment using the calibrated TTBW aircraft from the EDS.

Following the same procedure in Step 1, this step involves modeling the TTBW terminal area operations in the AEDT to obtain performance, noise, fuel burn, and emissions results of the TTBW departure and arrival profiles as defined by the EDS. These operations are modeled at Hartsfield–Jackson Atlanta International Airport (KATL) Runway 09L, assuming the AEDT 10-year average weather conditions to facilitate comparisons. Full flight operations are modeled using real-world aircraft trajectories to obtain performance, fuel burn, and emissions results of the TTBW. This is accomplished by using the AEDT sensor path modeling, which utilizes BADAv3 to compute aircraft performance during en route operations, given real-world position (latitude, longitude), altitude, and ground speed data. Real-world trajectories are sampled from 2021 Threaded Track data using top routes departing KATL flown by Airbus A320neo at various stage lengths. Figure 1 illustrates the sampled trajectories to be used in sensor path modeling. Additionally, the notional Airbus A320neo model developed in Step 1 is used as a reference aircraft to enable comparisons of the TTBW terminal area and full flight results against a similar baseline aircraft already defined in the AEDT to identify unexpected behaviors.

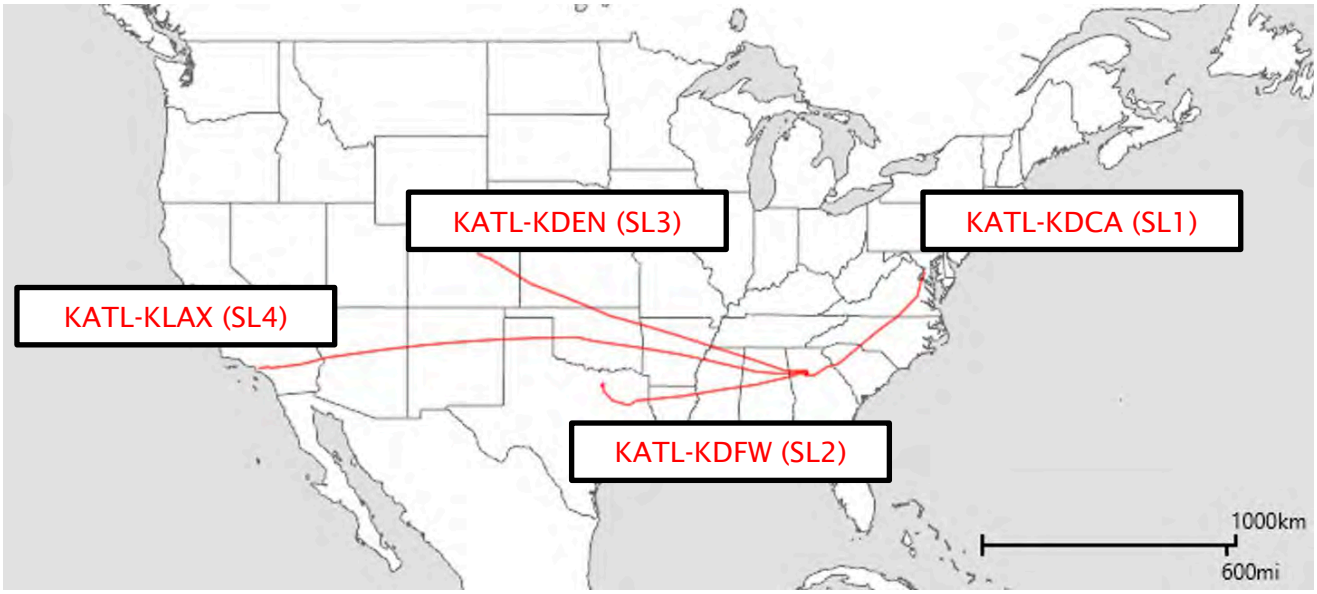

Figure 1. Sampled real-world trajectories for full flight modeling in *the* AEDT.

Step 5 – Results Analysis for the EDS
The fifth step is to analyze the results from EDS outputs and compare the results against baseline aircraft to validate whether EDS parameters behave as expected in the AEDT. This is followed by determining whether gaps exist for modeling ACA within the fleet modeling tools of MDG; and suggesting potential opportunities to improve how ACA is modeled within the fleet to benefit current analyses, as well as probable future analyses. The TTBW results are compared against the baseline Airbus A320neo aircraft model in the AEDT to validate whether EDS parameters behaved as expected in the AEDT.

Milestones

- Completed Step 1 – Identified and addressed inconsistencies in flight profile definitions between the EDS and AEDT.
- Completed Step 2 – Selected a TTBW aircraft.
- Completed Step 3 – Modeled and calibrated a notional TTBW aircraft to closely match the configuration presented in the Boeing SUGAR phase 3 report. Improvements to the TTBW aircraft model are still ongoing.
- Partially completed Step 4 – Established a pipeline to convert definitions of calibrated TTBW aircraft from the EDS to the AEDT environment. The generation of performance, emission, and noise coefficients of TTBW for the AEDT will be finished soon.
- Step 5 is in progress. The TTBW results will be compared against the baseline aircraft (Airbus A320neo) to validate whether EDS parameters behaved as expected in the AEDT.

Major Accomplishments

- Gained an improved understanding of the impact of the TTBW aircraft as a potential alternative design by the aircraft manufacturers.
- Calibrated an EDS model of the TTBW aircraft (Boeing SUGAR phase 3) and established a modeling pipeline between the EDS and AEDT. Multiple iterations of the TTBW have been modeled in the AEDT.

Publications

None.

Outreach Efforts

- Attended ASCENT biannual meetings.

Awards
None.

Student Involvement
This task involves two graduate students: Dev Patel and Emmanuella Okonkwo.

- Dev Patel contributed to the following project tasks:
  - Developed the notional Airbus A320neo model in EDS and generated performance, emissions, and noise coefficients for the AEDT based on the EDS analysis results.
  - Established a TTBW model in EDS, calibrated based on Boeing's SUGAR concept.
  - Obtained performance, emissions, and noise coefficients and created a TTBW model in the AEDT.
- Emmanuella Okonkwo contributed to the following project tasks:
  - Ran the AEDT for both the notional Airbus A320neo and TTBW models.
  - Compared the notional Airbus A320neo departure and arrival trajectories between EDS and the AEDT to address the inconsistencies in the flight profile definition between the two environments.

Plans for Next Period
- Refine and improve the calibrated model to generate more stable AEDT coefficients for AEDT modeling.
- Perform analysis to determine whether gaps exist for modeling ACAs within fleet modeling tools.

Task 2 - Alternative Design Approaches to Meet Demand
Georgia Institute of Technology

Objective
The objective of this task is to determine the efficiency opportunity if the fleet operates with single-aisle aircraft with a design range closer to that actually flown on a day-to-day basis. That is, how would the aircraft design change if a single-aisle aircraft were sized to be optimal to fly within a continent (1,000–2,000 nm range) and at a slower Mach number (e.g., 0.7)? To meet the longer-range requirements, a separate single-aisle design could be used for any longer ranges (closer to current single-aisle designs). Shorter ranges and lower aircraft speed requirements open the technology space to the consideration of alternative means of propulsion systems beyond the traditional turbofan engines running on conventional jet fuel. This task will use the EDS to redesign a single-aisle aircraft to meet market demand and establish a notional entry-into-service schedule for the fleet and will determine the market-share split within the seat class for how the market share would grow with time. The outcomes will serve as the basis for the MDG fleet modeling tools to quantify the benefit at the fleet level. This task will exercise the connection with MDG tools and improve current modeling practices for goal setting or stringency analysis.

The outcomes of this task are anticipated to include quantification, at the vehicle level, of the benefits and interdependencies of designing an aircraft to a new paradigm, and the implications of that approach in the fleet-level environmental footprint of aviation. Applications for this task include establishing realistic production rates for future designs, modifications to the assumed manufacturing production rates based on historical trends, changes in the market-share assumptions within a seat class or competition bin, and the nonrecurring costs of developing a new aircraft (in lieu of modifying an existing product).

Research Approach
The approach applied for this research task follows that applied in the original long-term aspirational goals (LTAG) International Civil Aviation Organization (ICAO) Committee on Aviation Environmental Protection (CAEP) study, for which Georgia Tech performed the vehicle modeling and assessment tasks in support of the FAA. The vehicle modeling and technology assessment parts are improved to better reflect the impacts of future technologies on engine and aircraft performance. Additional variables are incorporated into the design space to enable evaluation of the effects of reducing cruise speed and design range. The major steps applied in this task are shown in Figure 2.

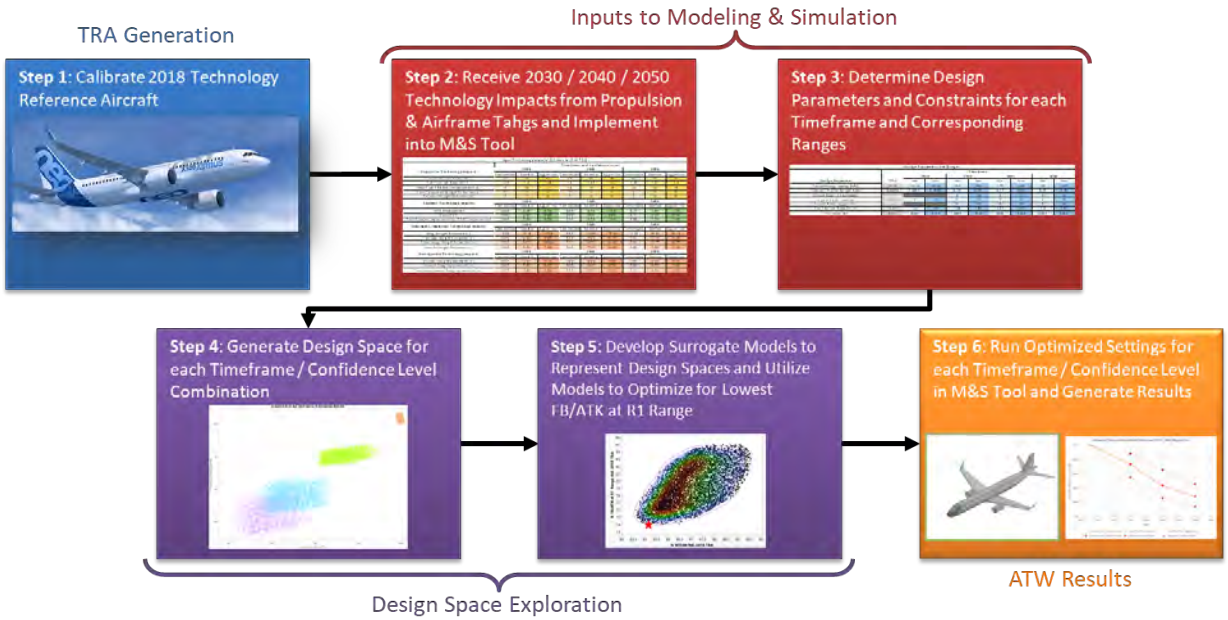

Figure 2. Long-term aspirational goal (LTAG) advanced tube and wing aircraft assessment method.

Step 1 - Technology Reference Aircraft Generation
The test case used in this research task is the narrow-body aircraft, while the same alternative design approaches can be used for aircraft in different classes. The Airbus A320neo aircraft equipped with the Pratt & Whitney PW-1127G geared turbofan engine was selected as the technology reference aircraft (TRA). A notional Airbus A320neo aircraft model was developed in the EDS built upon the 2018 narrow-body TRA model created for the LTAG study. The key updates made to the LTAG aircraft model include the calibrations of the aircraft noise and the takeoff and landing performance. Table 2 outlines key design specifications of the TRA model.

Table 2. Key design specifications of the technology reference aircraft (TRA) model.

Parameter	Unit	Value
Number of passengers	-	153
Design range	nm	3,420
Cruise Mach number	-	0.78
Maximum cruise altitude	ft	41,000
Maximum ramp weight	lb	175,047
Maximum sea-level static thrust	lb	2 × 27,080
Reference wing area	ft^2	1,341
Wingspan	ft	112.8
Takeoff field length	ft	6,619
Landing field length	ft	6,512

Step 2 - 2035 Technology Modeling
The alternative design approaches proposed in this research task are considered to be applied to the design of a new aircraft expected to enter into service around 2035. To evaluate the effectiveness of alternative design approaches,

technologies to be matured by 2035 need to be infused into the new design. The 2035 technology impacts applied in this task are identified from the LTAG study and summarized in Table 3. These impacts represent the improvements in key design and performance parameters due to the expected evolution of technology through research and development. The propulsion system of the 2035 design is still the geared turbofan engine but, along with the advanced cycle design, new engine components built on new materials and improved manufacturing process are expected to improve overall engine efficiency and reduce engine weight. The structural technologies mainly include innovative composite materials and their associated manufacturing process to decrease the weights of aircraft structural components. The drag reductions introduced by aerodynamic technologies are mainly due to the advanced aerodynamic shape optimization. The values of the technology impact factors shown in Table 3 are determined based on the 2030- and 2040-level technology improvements summarized in the LTAG report. For a conservative estimation, only the moderate confidence of the LTAG technology forecast is utilized.

Table 3. Impacts of 2035 technologies on the TRA model.

Technology Impact	Improvement
Small core efficiency	+13.5%
Core component weight	-3.0%
Propulsor weight	-3.0%
Thrust-specific fuel consumption due to power extraction	-0.525%
Wing weight	-11.85%
Fuselage weight	-8.35%
Empennage weight	-9.52%
Nacelle weight	-6.25%
Viscous drag	-2.38%
Induced drag	-0.175%
Total aerodynamic drag	-2.53%

Aside from the technologies listed above, the reduced cruise speed also opens an opportunity for natural laminar flow (NLF) technology. NLF reduces aircraft skin friction drag by shaping the airfoil to delay the boundary layer transition from laminar to turbulence. When the cruise speed reduces from the transonic to subsonic regime, the wave drag decreases and skin friction drag becomes the dominating factor, so there is a need to decrease skin friction drag for better aerodynamic efficiency. Meanwhile, a lower sweep angle may become feasible as the wave drag decreases, which discourages crossflow instability and benefits the implementation of NLF.

Instead of modeling the skin friction drag reduction due to the NLF as a constant, this research improves the NLF modeling approach of the LTAG study by incorporating additional influencing factors, including the Mach number, Reynolds number, and sweep angle. Specifically, in this task, the NLF is modeled using the flat plate approximation and analyzed using NASA's aircraft design tool FLOPS. The percentage of the laminar region on the wing surface is computed as the ratio between the transition Reynolds number and the local Reynolds numbers at different spanwise locations. The local Reynolds numbers are computed based on the altitude, Mach number, and local chord lengths, whereas the transition Reynolds number is determined by the leading-edge sweep angle using the crossflow instability and the Tollmien-Schlichting instability theories. The regions enclosed by control surfaces, behind the nacelles, and near the fuselage are assumed turbulent because of large disturbances.

The proposed NLF modeling method was applied to NASA's CRM (Common Research Model)-NLF model for validation. The calculated percentage of the laminar region on the wing was compared to the experimental result documented in the literature. Figure 3 shows the laminar area computed for the CRM-NLF model using the proposed method. The Mach number and Reynolds number of the validation case are at 0.86 and 1.5×10^7, respectively. The upper surface laminar portion calculated by the proposed model is 55.6%, which matches closely the experimental result of 56.0%. The cruise lift-

to-drag ratio improvement was also compared between two sides, with the proposed model being 6.87% and the experimental result being 6.81%.

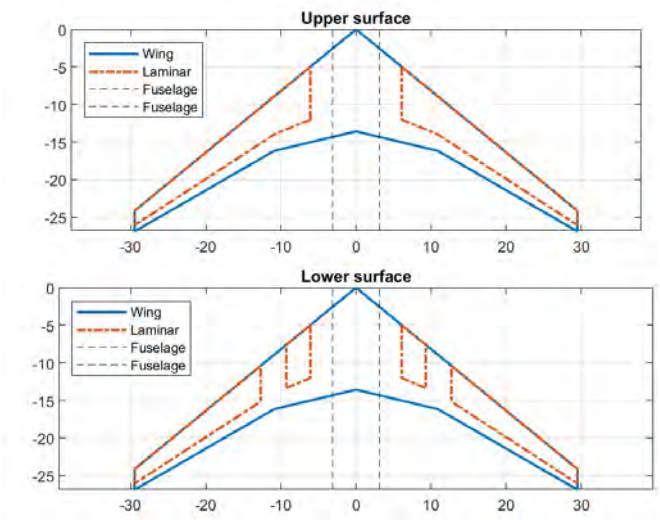

Figure 3. Laminar region on wing surfaces of CRM-NLF model.

Step 3 - Design Space Exploration

The design space of interest is constructed by the design variables and their associated ranges shown in Table 4. Aside from the variables used in the LTAG study, additional wing geometric parameters are added to the design space to maximum the benefits of reducing cruise speed and design range. The design objective is to minimize the block fuel at the design mission. The constraints considered in the optimization are summarized below:

- Takeoff field length at maximum takeoff weight (MTOW) and sea-level International Standard Atmosphere (ISA) condition no longer than 6,619 ft
- Landing field length at maximum landing weight and sea-level ISA condition no longer than 6,512 ft
- Wingspan no longer than 118 ft (Aircraft Design Group III)
- Excess fuel capability at the design mission must be non-negative
- Fan diameter no longer than 86.04 ft
- Core size parameter no smaller than 2.8
- Maximum high-pressure compressor temperature no higher than 1800 R

The first three constraints ensure the new aircraft has the same capability with existing airport facilities as the Airbus A320neo. The fan diameter constraint ensures ground clearance of the nacelle. The last two constraints ensure the high-pressure compressor is manufacturable and its operating temperature does not exceed the temperature limit of the material.

To sample the design space, 10,000 design-of-experiment (DoE) cases are generated by applying the Latin hypercube design to the design variables listed in Table 4. These DoE are run through the EDS design environment twice with two settings: (1) the NLF model turned off and (2) the NLF model activated. Based on the responses of the sampling cases, surrogate models are established between metrics of interest (i.e., design objective and constraints) and design variables using two-layer neural networks. To ensure that the established surrogate models are sufficiently accurate to replace true functions, multiple validation metrics are evaluated, including R-squared, the root mean squared error, the actual vs. predicted plot, and the residual vs. predicted plot. Using these surrogate models, a set of constrained optimizations are performed to obtain optimal designs at different scenarios, and these designs are then re-evaluated in the EDS to determine the fuel burn improvements.

Table 4. Design variables and ranges.

Design Variable	Timeframe		
		2035	
	TRA	Minimum	Maximum
Design range (nm)	3,420	1,500	3,420
Cruise Mach number	0.78	0.70	0.80
Thrust-to-weight ratio	0.31	0.28	0.33
Wing loading (lb/ft^2)	131	128	134
Fan pressure ratio	1.52	1.375	1.55
Overall pressure ratio	45.8	41	51
Maximum turbine entry temperature (R)	3,360	3,334	3,519
Wing aspect ratio	9.5	9.0	11.5
Wing taper ratio	0.19	0.15	0.25
Wing average thickness to chord	0.138	0.1	0.14
Wing quarter-chord sweep angle (°)	25.3	15	27

Step 4 - Fleet-Level Impact Evaluation
Although an aircraft's fuel consumption decreases with a reduced design range due to a smaller vehicle size and thrust requirement, the reduced range could limit the number of flight operations that the aircraft can fly. To assess the impacts of reducing design range on the fleet operation, this task also performs a fleet analysis build upon the design space exploration results obtained from Step 3. Assume the optimal designs with reduced design range and cruise speed replacing the single-aisle aircraft in the current fleet starting from 2035, multiple fleet evolution scenarios are analyzed.

The fleet analysis is performed using the in-house tool Global and Regional Environmental Aviation Trade-Off (GREAT). In GREAT, all aircraft are categorized into seat classes based on their passenger capacities. These seat classes include short thin haul (SHT), small regional jet (RJ-S), large regional jet (RJ-L), turboprop (TP), small single aisle (SSA), large single aisle (LSA), small twin aisle (STA), large twin aisle (LTA), and very large aircraft (VLA). The evaluation of the fleet composition depends on the retirements of old aircraft and the replacements of new aircraft. Each seat class in GREAT is model with a retirement curve derived based on historical data. The replacement is modeled using a structure matrix considering three aspects: (1) chronological, (2) mission capabilities, and (3) environmental feasibility. This implies that the newer generation of aircraft will replace the older aircraft starting the year it is brought into service. Meanwhile, the new aircraft's capabilities with respect to the design range, payload, and seat class must be equal to or more than that of the previous aircraft that it is replacing. Finally, the fuel burn or emissions produced by this aircraft need to be improved compared to the older aircraft.

Figure 4 depicts the retirement and replacement algorithm used in GREAT.

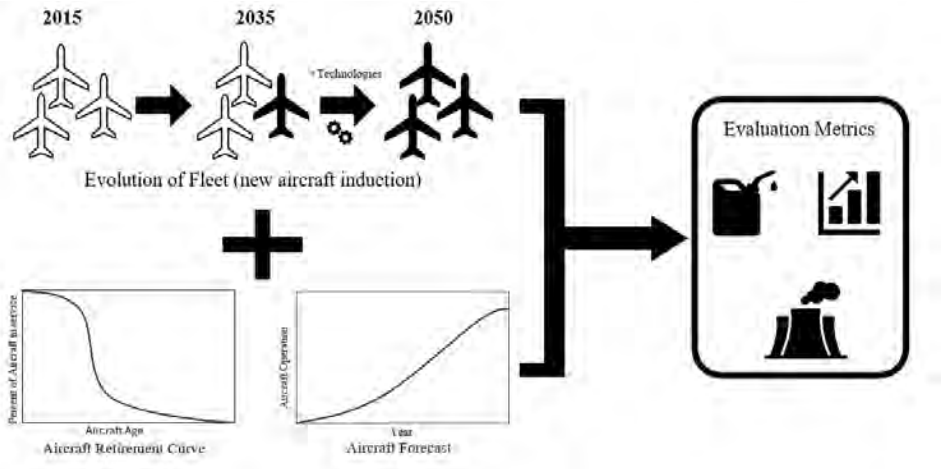

Figure 4. Retirement and replacement algorithm in GREAT.

The forecast model of the future flight demands integrated in GREAT is established based on the Boeing Commercial Market Outlook (CMO). As shown in Figure 5, this forecast model includes the COVID years and provides information on the forecasted recovery of air travel demand in post-COVID years. The black curve in the plot represents the growth in total operations from 2015 to 2050. Note that since the Boeing CMO only predicts the operations until 2041, the growth rates between 2041 and 2050 are based on extrapolation. The color bars in Figure 5 denote the percentage of total operations covered by different classes of aircraft. For each class, the shaded bar represents the aircraft that are out of production, while the bright bar represents the aircraft that are still in production.

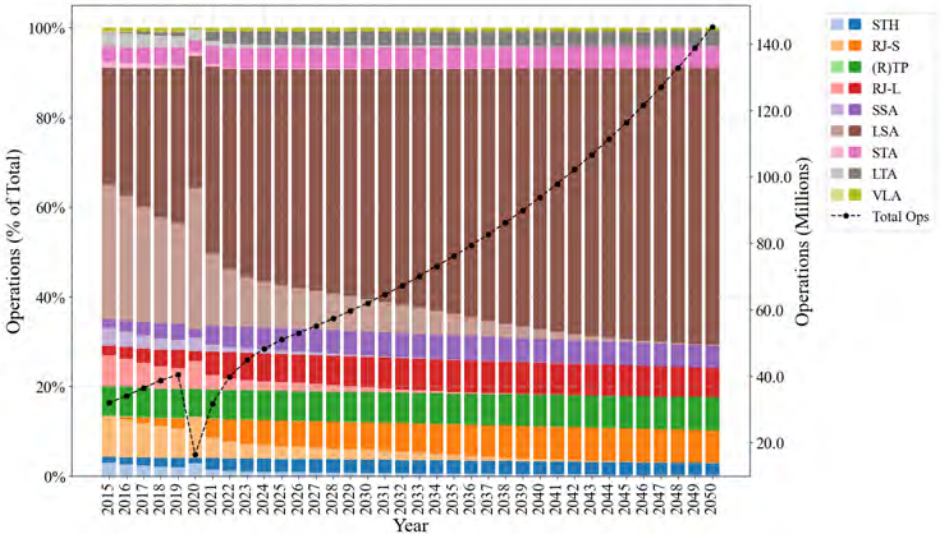

Figure 5. Commercial aviation growth forecast and business as usual scenario used in GREAT.

In this task, a baseline "business-as-usual" scenario is first established, followed by 12 scenarios using the optimized vehicles replacing the existing fleet, as summarized in Table 5. In the baseline scenario, no newly designed aircraft is introduced, and the industry maintains production of existing vehicles with anticipated annual market and operations growth. This represents the current situation in the real world. The scenario includes cases such as waiting until novel concept programs come to fruition or new vehicles arriving later than 2035 to have a meaningful impact on 2050. It could

also represent new models being introduced in the fleet being less impactful. Twelve other scenarios were sketched to utilize the findings of the vehicle design study and the resultant optimized vehicle.

Table 5. Vehicle production and replacement scenarios of consideration. ATA: Air Transport Association.

Scenario	Optimized Aircraft	Design Range (nm)	Replaced Aircraft Class
1	Business as usual		
2	ATA 1	3,420	LSA only
3	ATA 1	3,420	LSA and SSA
4	ATA 2	3,000	LSA only
5	ATA 2	3,000	LSA and SSA
6	ATA 3	2,500	LSA only
7	ATA 3	2,500	LSA and SSA
8	ATA 4	2,000	LSA only
9	ATA 4	2,000	LSA and SSA
10	ATA 5	1,700	LSA only
11	ATA 5	1,700	LSA and SSA
12	ATA 6	1,500	LSA only
13	ATA 6	1,500	LSA and SSA

The outputs from the tool include total operations conducted by that aircraft, annual distance covered, fuel burn, and carbon and nitrogen oxides (NO_x) emissions. To evaluate the global impact induced by the introduction of newly designed vehicles compared to the non-replacement scenario, these metrics are added up for the particular seat class and plotted against the time period in consideration.

Milestones

- Calibrated and established a TRA mode based on the Airbus A320neo aircraft and Pratt & Whitney PW-1127G engine.
- Determined 2035 technologies and their impacts on aircraft and engine characteristics from the LTAG study.
- Developed and integrated a NLF modeling approach considering aircraft geometry and flight condition into the EDS.
- Formulated design variables, objectives, and constraints.
- Generated and ran DoE cases through the EDS to sample the design space.
- Established surrogate models based on DoE cases, on which a set of constrained optimizations were performed to evaluate the benefits of the proposed alternative design approaches.
- Identified optimal designs sized for different design ranges from the constrained single-objective optimization.
- Defined and established fleet analysis scenarios in GREAT.
- Performed a global-level fuel burn evaluation assuming the optimal designs replacing the aircraft in the single-aisle fleet starting from 2035.

Major Accomplishments

The major accomplishes of this task include two parts: one is the optimized 2035 single-aisle aircraft design with reduced cruise speeds at multiple design ranges; the other is fleet-level fuel burn impacts of introducing these optimized design into fleet operations.

Part 1 - Vehicle-Level Assessment

Figure 6 illustrates the fuel burn reduction obtained from different sets of constrained optimizations. The blue bars in the waterfall charts (in represent the design created by resizing the TRA with the 2035 technologies listed in Table 3 infused.

This design is assessed at both the design mission (3,420-nm range) and off-design missions (ranges <3,420 nm). The result shows that 2035 technologies (excluding NLF) can reduce the fuel burn by 12% compared to the TRA. The orange bars denote the design generated by not only applying 2035 technologies but also optimizing the engine and airframe design variables listed in Table 4. Note that for these orange bars, the cruise speed and design range remain the same as for the Airbus A320neo. The result shows that optimizing engine and airframe can introduce around 7% fuel reduction, in addition to the 2035 technologies at both design and off-design missions. The purple bars represent the design established by reducing cruise speed simultaneously with optimizing engine and airframe. The cruise Mach number is optimized for the block fuel at the design mission and remains constant for all off-design missions. With the cruise speed reduced, the NLF is also assumed to be equipped on the aircraft. It is seen from the purple bars that using NLF at the reduced cruise speed can introduce around 8% fuel burn reduction compared to operating the aircraft at a higher cruise Mach number, and the benefit is more significant as the mission range increases. The five yellow bars at the bottom of the chart denote five designs resized with respect to reduced design ranges. For each design range, the airframe, engine cycle, and cruise speed are also reoptimized. Compared with the aircraft sized for the 3,420-nm design range but operating at shorter ranges, the aircraft directly sized for a shorter range can save the fuel burn up to 4.1% when the design range is reduced to 1,500 nm due to its smaller thrust, weight, and geometric scales.

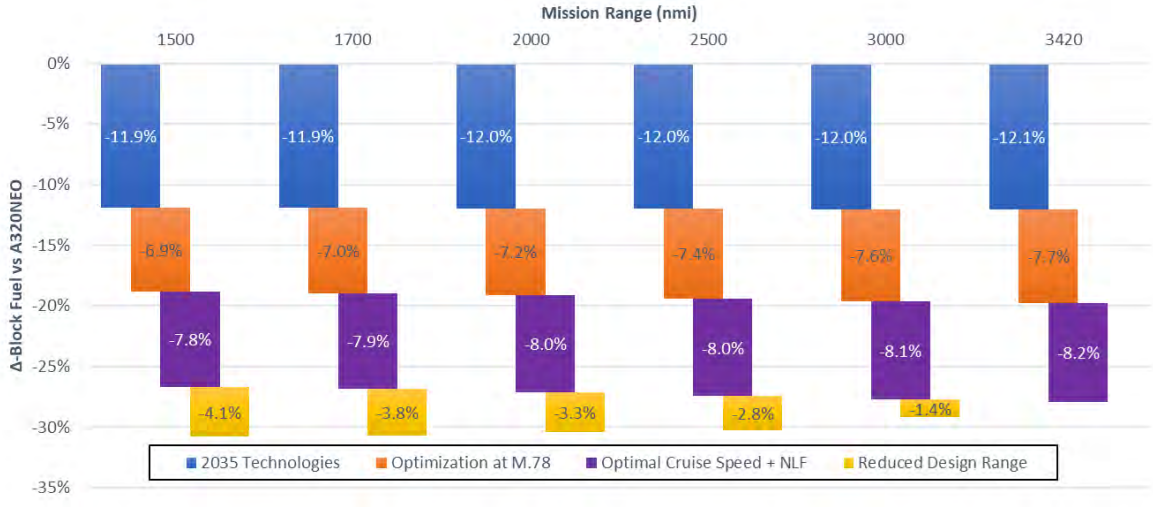

Figure 6. Block fuel reduction compared to the TRA model. NLF: natural laminar flow.

Part 2 - Fleet-Level Assessment

Execution of the scenarios in GREAT provides several outputs, including but not limited to operations, distance flown, fuel consumption, and carbon and NO_x emissions. In this study, the output metrics are fleet fuel burn and the number of operations, which are used to evaluate the environmental impact of the various designs and the percentage of flights each reduced-range vehicle can cover. With the staggered introduction of the vehicle into the existing fleet, starting with production ramp-up from 2035 onward and reaching full-scale production by 2040, the impact until the year 2050 is analyzed.

Figure 7 illustrates the projected percentage reduction in fleet-level fuel consumption across various design ranges over the years 2030 to 2050. Each line represents a specific scenario, with the optimized aircraft replacing the LSA class or replacing both the LSA and SSA classes when the flight distances are at or below the design ranges of those vehicles. The trend shows a consistent decrease in fuel consumption over time. Depending on the aircraft design and the replacement setting, the cumulative global fuel burn reduction in 2050 spans between 5.4% and 6.5% compared to the business-as-usual scenario.

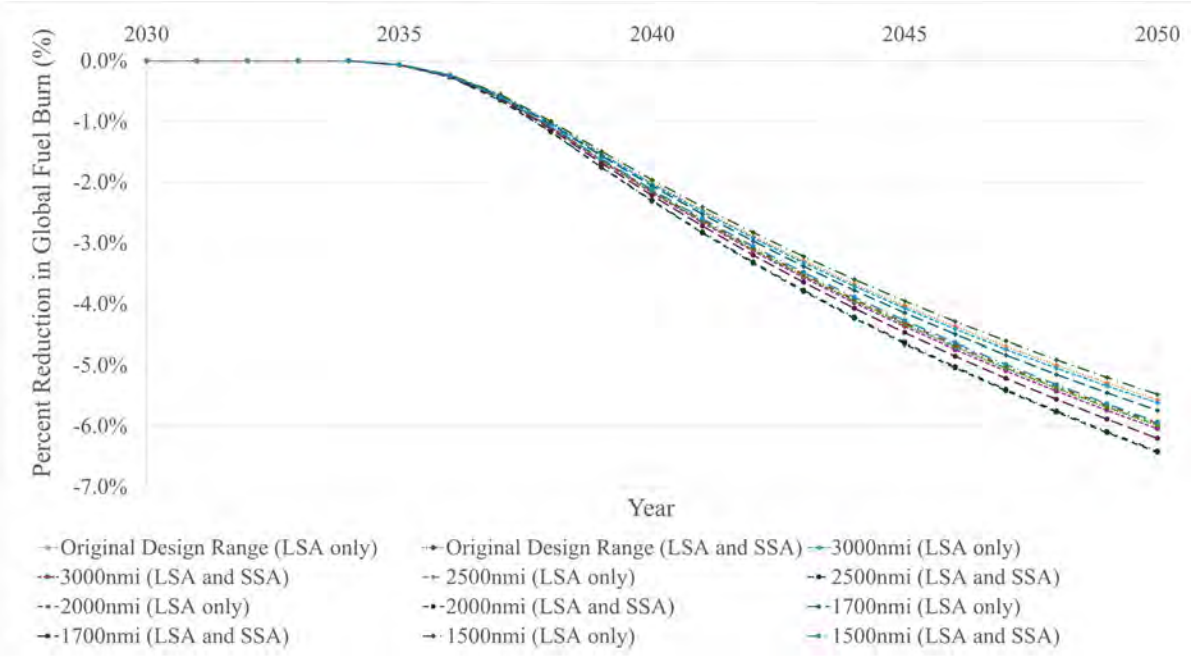

Figure 7. Percentage change in total fuel burn for all scenarios compared to business as usual.

Figure 8 displays the cumulative fuel burn reduction in 2050 in scenarios where the optimal designs only replace the LSA class vehicles. The green bars represent the fuel burn reduction in the LSA fleet. The blue bars represent the fuel burn reduction in the entire fleet with all aircraft classes considered. Note that in these scenarios, other than LSA, all other aircraft classes are kept at the same settings as used in the baseline scenario. It is seen that as the aircraft's design range decreases, the benefit in fleet fuel burn first increases but then shrinks. This non-monotonic trend reflects the trade-off between the vehicle size and its mission capability: a smaller aircraft sized for a shorter design range may exhibit a higher fuel efficiency compared to a larger aircraft operating at short-distance flights, but it cannot be used to replace the aircraft operating at long-distance missions due to the limited range capability. As shown in Table 6, when the design range reduces to 1,500 nm, only 94% of the LSA flights can be operated by the new design, indicating that about 6% of the operations still rely on old aircraft. Among all new designs, Air Transport Association (ATA) 3, sized and optimized for a 2,500 nm range, results in the largest reduction of fuel burn, with the values being 14.3% in the LSA fleet and 6.0% in the entire fleet.

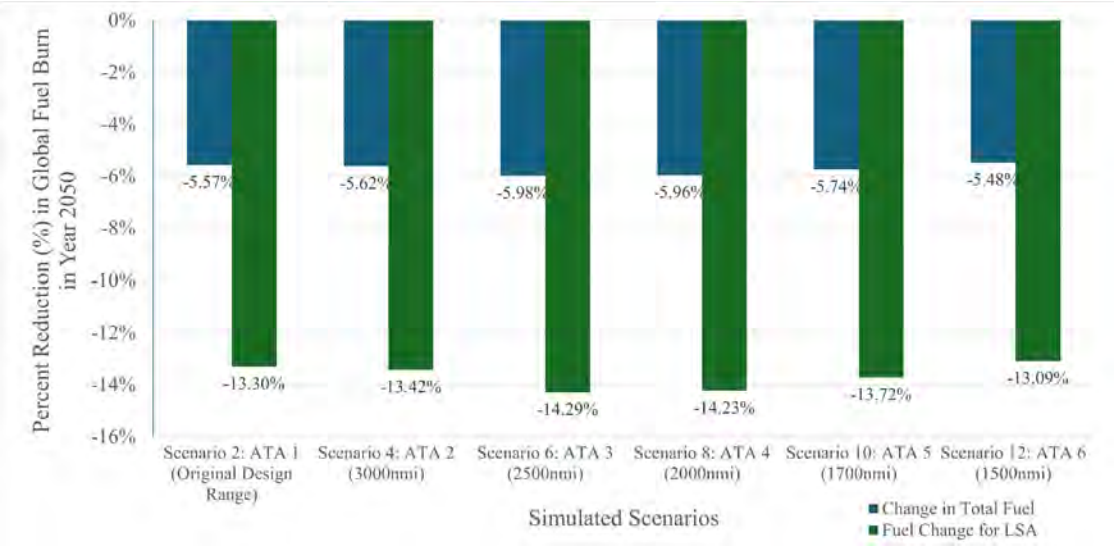

Figure 8. Fleet fuel burn reduction in 2050 of scenarios ATAs replacing only LSA.

Table 6. Percentage of SSA and LSA operations replaced by reduced-range optimal designs.

Aircraft	Design Range (nm)	SSA Operations	LSA Operations
ATA 2	3000	99.996%	99.959%
ATA 3	2500	99.992%	99.722%
ATA 4	2000	99.858%	98.509%
ATA 5	1700	99.469%	96.353%
ATA 6	1500	98.947%	94.059%

Figure 9 presents the cumulative fuel burn reduction in 2050 in scenarios where the optimal designs replace both SSA and LSA classes. The orange bars in the chart indicate that the optimal designs have more benefits for the SSA fleet fuel reduction than for the LSA fleet, especially when the design range is below 2,500 nm. This is mainly because short-range vehicles can be used in more SSA operations compared to LSA operations, as shown in Table 6. In addition, since short-range ATAs are sized and optimized to design ranges closer to typical SSA operational flight distances than conventional SSA or LSA, their improvements in fuel efficiencies at these short-range off-design missions are more significant. If only considering the SSA fleet, the design that introduces the most significant cumulative fuel burn reduction is ATA 5 sized for 1,700 nm. However, in terms of the entire fleet, the one that brings the largest fleet fuel burn reduction is still ATA 3. Comparing Figure 8 and Figure 9 replacing the SSA fleet with ATA 3 on top of LSA replacement only brings an extra 0.45% benefit (from 5.98% to 6.43%) in the entire fleet fuel consumption, even though ATA 3 reduces SSA fleet fuel burn by 14.9%. This small change reveals the minimal impact of the SSA class on the entire fleet.

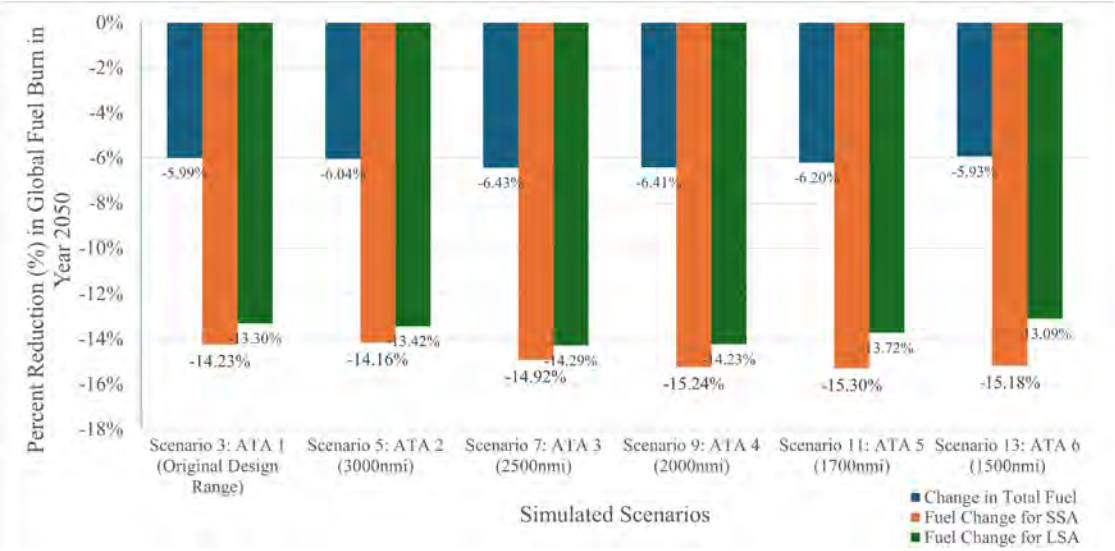

Figure 9. Fleet fuel burn reduction in 2050 of scenarios ATAs replacing SSA and LSA.

Publications

Conference Proceedings

Patel, D., Ergan, T., Cai, Y., Gladin, J., & Mavris, D. (2025, January 6-10). *Performance assessment and mission-based optimization for next-generation single-aisle aircraft conceptual design* {Conference presentation]. AIAA SciTech 2025 Forum, Orlando, Florida. https://doi.org/10.2514/6.2025-0001

Ergan, T., Parashar, A., Xie, J., Kirby, M., & Mavris, D. (2025, January 6-10). *Fleet-level and global emissions impact analysis of mission-optimized next-generation single-aisle aircraft* [Conference presentation]. AIAA SciTech 2025 Forum, Orlando, Florida. https://doi.org/10.2514/6.2025-2168

Outreach Efforts

- Attended ASCENT biannual meetings.
- Presented *Performance assessment and mission-based optimization for next-generation single-aisle aircraft conceptual design* and *Fleet-level and global emissions impact analysis of mission-optimized next-generation single-aisle aircraft* at the AIAA SciTech 2025 Forum, Orlando, Florida (January 6-10, 2025).

Presentations

Patel, D., Ergan, T., Cai, Y., Gladin, J., & Mavris, D. (2025, January 6-10). *Performance assessment and mission-based optimization for next-generation single-aisle aircraft conceptual design* {Conference presentation]. AIAA SciTech 2025 Forum, Orlando, Florida. https://doi.org/10.2514/6.2025-0001

Ergan, T., Parashar, A., Xie, J., Kirby, M., & Mavris, D. (2025, January 6-10). *Fleet-level and global emissions impact analysis of mission-optimized next-generation single-aisle aircraft* [Conference presentation]. AIAA SciTech 2025 Forum, Orlando, Florida. https://doi.org/10.2514/6.2025-2168

Awards

None.

Student Involvement

This task involved three graduate students: Dev Patel, Tuna Ergan, and Akshiti Parashar.

- Dev Patel contributed to the following project tasks:
  - Created the TRA model in the EDS based on the Airbus A320neo aircraft and Pratt & Whitney PW-1127G engine.
  - Identified 2035 technologies and their impacts on aircraft and engine characteristics from the LTAG study and infused them into the TRA to establish the 2035 baseline model.

    - Generated sampling cases using DoE and ran the cases through the EDS.
    - Performed two sets of constrained single-objective optimizations: (1) fuel burn and (2) cumulative noise.
    - Determined optimal designs for the fleet analysis.
- Tuna Ergan contributed to the following project tasks:
    - Formulated and validated the NLF modeling approach and implemented the approach into the EDS.
    - Determined design variables, objectives, and constraints for the design space exploration.
    - Created surrogate models for objectives and constraints using artificial neural networks based on the results of DoE cases.
    - Performed constrained multi-objective optimization using the Monte-Carlo approach and identified Pareto Frontiers between fuel burn and noise metrics at different ranges.
    - Established representative models for the identified optimal designs in GREAT.
    - Defined fleet analysis scenarios in GREAT.
- Akshiti Parashar contributed to the following project tasks:
    - Configured GREAT for the evaluation of fleet impact induced by reducing design range and cruise speed.
    - Performed the fleet analysis in GREAT based on the defined scenarios to obtain fleet-level fuel burn from 2015 to 2050.
    - Evaluated global-level fuel burn reduction assuming the optimal designs replacing the aircraft in the single-aisle fleet starting from 2035.

Plans for Next Period

- Improve low-speed aerodynamic analysis for takeoff and landing performance assessment.
- Include noise analysis to evaluate the potential noise reduction induced by 2035 technologies, airframe and engine optimizations, and reduced cruise speed.
- Evaluate the opportunity to increase payload when sizing aircraft with respect to lower design ranges.

Task 3 - Exploring Physics-Based Boundaries of the Possible

Georgia Institute of Technology

Objective

The objective of this task is to examine the physics-based limitations of efficiency for various propulsion architectures considered for future ACA. This type of study is beneficial in that it aids the FAA in understanding the boundaries of the possible, rather than building from a baseline by applying specific individual technologies that benefit efficiency. Depending on any follow-on actions from the LTAG task group analyses, this task may also include the identification of barriers for ACA and their propulsion systems, or additional supporting analysis.

Research Approach

Step 1 - Reference Engine and Aircraft Model

The first step is to establish a state-of-the-aircraft aircraft and corresponding engine model to use as a baseline to evaluate the potential of future turbofan engines. In this task, the notional Airbus A320neo model developed in Task 2 is selected as the baseline. This model was developed in the EDS and calibrated based on the public domain data of the Airbus A320neo aircraft and Pratt & Whitney PW-1127G engine.

Step 2 - Engine Efficiency Improvement

With the advancement in engine design methods, engine materials, and engine manufacturing process, it is expected the thermal and propulsive efficiencies of gas turbine engines will be improved over the next few decades. To determine the possible performance boundary of the turbofan architecture, it is necessary to quantify the potential improvements in engine component efficiencies. The ICAO LTAG Report Appendix M3 Technology Subgroup Report (ICAO, 2022) provided a projection of efficiencies of engine core components at the years of 2030, 2040, and 2050. The projection was made for different classes of aircraft, and for each class each year, there are three levels of confidences: (1) conservative, (2) medium, and (3) aggressive. This task takes the 2050 aggressive prediction as the reference to maximize the improvements in core efficiencies in order to explore the boundary. Table 7 compares the efficiencies of engine components between the 2050 aggressive projection and the baseline Airbus A320neo model.

Table 7. Engine components' efficiencies. LPC: low-pressure compressor; HPC: high-pressure compressor; HPT: high-pressure turbine; LPT: low-pressure turbine.

Component	Baseline Airbus A320neo Engine Model	LTAG 2050 Aggressive Prediction	Improvement
Fan (adiabatic)	92.5%	93.4%	+0.9%
LPC (polytropic)	91.5%	93.3%	+1.8%
HPC (polytropic)	91.4%	93.3%	+1.9%
HPT (adiabatic)	89.0%	90.7%	+1.7%
LPT (adiabatic)	91.1%	93.1%	+2.0%

Step 3 - Small Core Size Effect

One contributing factor to the engine component efficiency is the core size effect. As the turbofan engine continues to strive for higher bypass ratios to promote propulsive efficiency, the core size is becoming smaller and smaller. Meanwhile, future airframe technologies will reduce the aircraft drag and the thrust required, encouraging smaller size engines for future aircraft. However, as the engine core becomes smaller, rotor tip clearance, knife-edge seal clearances, and edge thicknesses cannot be scaled down with the engine core size. All these non-scalable features introduce penalties to high-pressure compressor (HPC) efficiency. Figure 10, adopted from Evan et al. (2022), illustrates how HPC polytropic efficiency is affected by the engine core flow rate. The orange curve represents the current technology level, which is applied on the baseline Airbus A320neo model. The orange dash curve is shifted from the solid curve by 25% improvement in HPC efficiency, as predicted by the LTAG study. This curve is utilized in the 2050 narrow-body aircraft engine model. The blue curve represents an ideal scenario where clearances can be scaled with the core size, which is used in a practical ideal engine model created in this task. All these curves are digitalized in EDS.

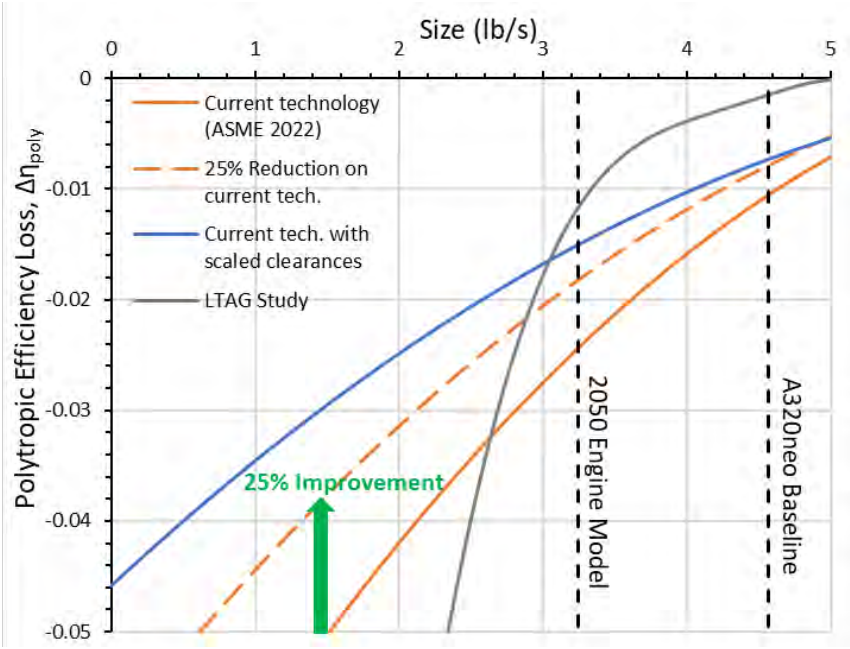

Figure 10. Engine core size effect.

Step 4 - Aircraft Systems Impacts

Engine efficiency is also affected by the aircraft systems that consume pneumatic, hydraulic, electric, and mechanical power. These systems include but are not limited to environmental control system (ECS), ice protection system (IPS), aircraft control system, and avionic system. The pneumatic power is mainly provided by the bleed air extracted from the

engine compressor. The hydraulic and electric power are mainly converted from the mechanical power extracted from the engine shaft. With the technological improvements in aircraft equipment systems and secondary power distribution systems, it is expected that less bleed air and power extractions will demand from the engine, improving the engine propulsive efficiency. The LTAG study predicted that the thrust-specific fuel consumption (TSFC) of the narrow-body aircraft engine at the aerodynamic design point would be reduced by 1.67% due to the improvements in bleed and power extraction, as listed in Table 8. Furthermore, enabled by the electrification of aircraft systems, bleed air from the engine compressor may not be needed. In the bleedless architecture, aircraft systems are mainly driven by the electric power converted from the mechanical power extracted from the engine shaft. Table 8 presents the engine TSFC improvement at different power extraction settings when the bleedless architecture is applied.

Table 8. Aircraft systems impact on engine TSFC.

Architecture	Bleed	Power extraction	TSFC change
Baseline A320neo	2	75	--
2050 engine model	1.25	50	-1.67%
Bleedless architecture	0	250	-2.57%
	0	225	-2.76%
	0	200	-2.96%

Step 5 - Engine Materials
Advanced composite materials and improved manufacturing processes are expected to not only enable the engine components to sustain higher pressure ratios and temperatures but also reduce the overall engine weight. Based on historical trends and literature reviews, the LTAG study predicted that the core component weight can reduce by 8% in 2050 compared to the current technology level. This weight reduction will bring a secondary benefit to the fuel burn reduction. Aside from the LTAG study, this task also investigates the ceramic matrix composite (CMC) technology. Preceding literature suggests that CMC can increase the maximum temperature limit by 300 R and provide a weight saving of 66% when it is applied to the turbine.

Step 6 - Engine Cycle Optimization
To maximize the benefits of engine technologies, the engine needs to be resized with optimal cycle parameters. In this task, the engine cycle parameters include bypass ratio (BPR), overall pressure ratio (OPR), fan pressure ratio (FPR), high-pressure compressor pressure ratio (HPCPR), and turbine entry temperature (T4max). The optimization process follows the steps described in Task 2, where surrogate models are developed based on the responses of the DoE sample cases run through the EDS. The objective function is to minimize the fuel burn of the notional Airbus A320neo model at an economic mission. Table 9 presents the optimized cycle of the 2050 engine and compares it to the baseline model.

Table 9. Optimized engine cycle parameters.

Design Variable	Baseline Airbus A320neo Engine Model	Optimized 2050 Engine Cycle
BPR	11.6	14.5
OPR	45.8	61.0
FPR	1.52	1.45
HPCPR	17.0	17.5
T4max (R)	3091	3144

Step 7 - Fuel Burn Evaluation
The possible boundary of the turbofan engine is evaluated based on the aircraft-level fuel consumption at an economical mission that is most frequently flown by the narrow-body aircraft. With Steps 2 to 6 implemented sequentially, several engine models are established and integrated with the notional A320neo aircraft model. The fuel burn is evaluated at the

900-nm mission with the design payload. The fuel reductions due to efficiency improvement, size effect reduction, aircraft system architecture, engine weight, and engine cycle optimization are evaluated in a stepwise manner.

Milestones

- Finished literature review on turbofan engine efficiency, engine materials, core size effects, and bleedless aircraft system architecture.
- Established 2050 narrow-body aircraft model based on the aggressive prediction made in the LTAG study.
- Created a practical ideal engine model by assuming scalable tip clearances, large-core efficiencies, and bleedless architecture on the 2050 engine model.

Major Accomplishments

The major accomplishments of this task include the evaluations of contributions of different engine technologies to the fuel burn efficiency when retrofitting the state-of-the-art aircraft with a new turbofan engine, as well as the development of a practical ideal engine model to explore the boundary of the turbofan architecture.

Figure 11 displays the reductions of the 900-nm mission block fuel when engine technologies are progressively applied to the notional Pratt & Whitney PW-1127G engine. Note that the airframe is fixed as the notional Airbus A320neo model during the evaluation, but only the engine model is updated. The practical ideal engine shown in the last bar is established by assuming bleedless architecture with 200 hp power extraction and scalable tip clearances on top of the aggressive core efficiency improvement prediction, engine weight reduction, and the application of CMC. Overall, with all potential engine technologies applied and the idealized core size effect, the turbofan engine can reduce the fuel burn at the economical mission by 20% for the Airbus A320neo aircraft compared to the current technology level. It is seen that the core efficiency improvement has made the most significant contribution to the engine fuel efficiency, reducing the economical mission block fuel by 7.4%. Meanwhile, engine cycle optimization also has a considerable impact on the fuel burn reduction due to the increased OPR and T4max and decreased FPR.

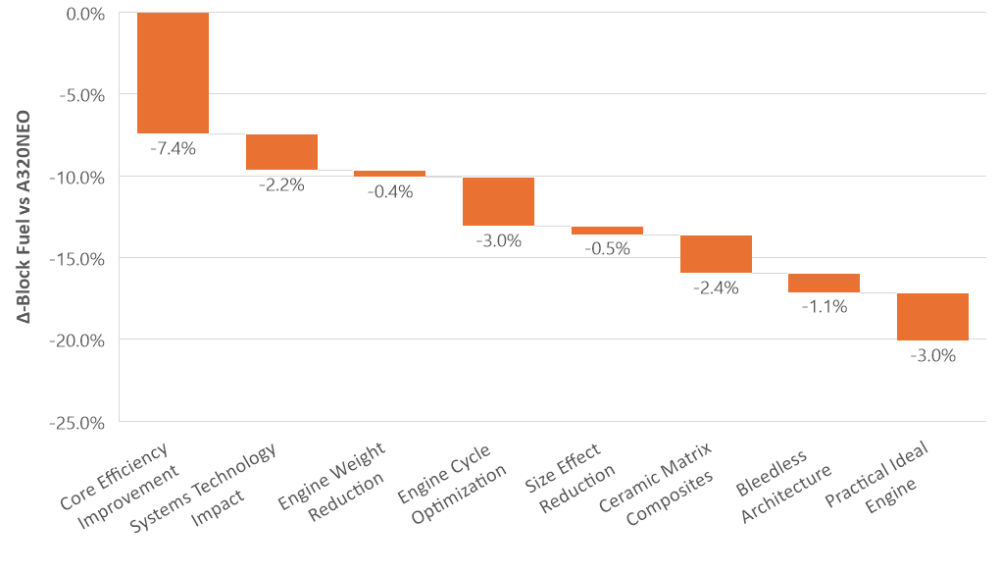

Figure 11. Potential block fuel reductions due to engine technologies.

Publications

None.

Outreach Efforts

- Attended ASCENT biannual meetings.

Awards
None.

Student Involvement
This task involves two graduate students: Cem Kocer and Tuna Ergan.

- Cem Kocer contributed to the following project tasks:
  - Literature review on turbofan engine efficiency improvement, small core size effects, and bleedless architecture.
  - Created a parametric model to represent the small core size effects based on the literature and implemented the model in the EDS.
  - Modeled the impacts of CMC on engine cycle and weight in the EDS.
  - Evaluated fuel burn reduction due to size effect reduction, CMC, and bleedless architecture.
  - Created a practical ideal engine model by assuming scalable tip clearances, large-core efficiencies, and bleedless architecture on the 2050 engine model.
- Tuna Ergan contributed to the following project tasks:
  - Literature review on turbofan engine efficiency and engine materials improvements.
  - Integrated 2050 engine models into the TRA model to assess the aircraft-level fuel consumption.
  - Evaluated fuel burn reduction due to improvements in engine efficiency, engine materials, bleed, and secondary power extractions.

Plans for Next Period
- Add inlet, fan, and nozzle technologies from the FAA's Continuous Lower Energy, Emissions and Noise (CLEEN) Program and other literatures to the 2050 "practical" ideal turbofan engine model.
- Investigate the impact of engine core size on HPT efficiency.
- Establish parametric model for the secondary power extraction and subsystems weights of the bleedless architecture.

References
1. Evans, S., Nolan, S., Botros, B., Port, B., Chin, P., Kulkarni, S., & Stephens, J. (2022, June). Clearance Sensitivity Mitigation in Small Core Compressors. In *Turbo Expo: Power for Land, Sea, and Air* (Vol. 86090, p. V10AT29A014). American Society of Mechanical Engineers.
2. International Civil Aviation Organization. (2022). Report on the Feasibility of a Long-Term Aspirational Goal Appendix M3, Technology Subgroup Report, ICAO.

Project 065(A) Fuel Testing Approaches for Rapid Jet Fuel Prescreening

Washington State University

Project Lead Investigator

Joshua Heyne
Bioproducts, Sciences, and Engineering Laboratory Director, Associate Professor
School of Engineering and Applied Science
Washington State University
2710 Crimson Way, Richland, WA 99354
509-372-7461
joshua.heyne@wsu.edu

University Participants

Washington State University (WSU)

- P.I.: Joshua Heyne
- FAA Award Number: 13-C-AJFE-UD, Amendments 26, 31, 34, and 42
- Period of Performance: October 1, 2023, through September 30, 2024. Cost share is from the German Aerospace Center (DLR).
- Task:
  1. Prescreening of sustainable aviation fuels (SAF)

Investigation Team

Washington State University

Joshua Heyne (P.I.) coordinating all team members (both ASCENT and non-ASCENT efforts) and communicating prescreening results with SAF producers.
David Bell (PhD student) developing comprehensive two-dimensional gas chromatography (GCxGC) vacuum ultraviolet (VUV) detection methods and software.
Zhibin (Harrison) Yang (PhD student) conducting Tier Alpha prediction and Tier Beta measurements.
Conor Faulhaber (PhD student) conducting seal swell, sulfur, and nitrogen measurements
Josh Ledezma (undergraduate student) conducting seal swell measurement.
Gabriela Nicacio (undergraduate student) conducting various lab tests.

Project Overview

The ASCENT Project 065(A) focuses on further developing the Tier Alpha and Tier Beta test methods, which can help minimize the fuel volume needed for testing and improve a fuel's potential for meeting ASTM approval criteria. Tier Alpha refers to low-volume analytical testing approaches (i.e., GCxGC, nuclear magnetic resonance, and infrared analytical testing). Tier Beta tests focus on directly assessing the physical and chemical properties of a fuel rather than predicting properties from GCxGC methods.

Task 1 - Prescreening of Sustainable Aviation Fuels

Washington State University

Objective

The objective of this task is to develop a tiered prescreening process for new alternative jet fuels that uses low fuel volumes and will improve a fuel's potential to meet ASTM approval criteria. This work facilitates the flow of meaningful

information to fuel producers when their production processes are at a low technology readiness level while simultaneously strengthening a producer's readiness for the approval process.

Research Approach

Previous annual reports summarized significant progress toward prescreening SAF candidates. The motivation, conceptual application, detailed description, and examples of this effort were described in publications in peer-reviewed journals in the first 18 months of this project. Prior to this report, the ASCENT Project 065(A) team has reported 13 publications. This report documents five additional peer-reviewed journal articles, published between October 1, 2023, and September 30, 2024. Citations for the articles are listed in the *Publications* section below and are provided as Appendices A-D:

- Paper 14 - "Quantitation of olefins in sustainable aviation fuel intermediates using principal component analysis coupled with vacuum ultraviolet spectroscopy" (Kosir et al., 2023) in *Frontiers in Fuels*. (Presented in Appendix A.)
- Paper 15 - "Volatility measurements of sustainable aviation fuels: A comparative study of D86 and D2887 methods" (Yang et al., 2024) in *ACS Sustainable Chemistry and Engineering*.
- Paper 16 - "Perspective on fuel property blending rules for design and qualification of aviation fuels: A review" (Boehm et al., 2024) in *Energy & Fuels*. (Presented in Appendix C.)
- Paper 17 - "Dielectric constant predictions for jet-range hydrocarbons: Evaluating the Clausius–Mossotti relation and correcting for molecular dipole moments" (Faulhaber et al., 2024) in *Energies*. (Presented in Appendix D.)
- Paper 18 - "Assessing the effect of composition on dielectric constant of sustainable aviation fuel" (Yang et al., 2025) in *Fuel*. (Presented in Appendix B.)

Milestones

- Performed Tier Alpha testing a total of 358 times.
- Performed Tier Beta testing a total of 203 times.
- Determined the maximum blending ratio for 41 SAF candidates.
- Developed a refinement strategy/distillation optimization for 24 fully synthetic SAF candidates.

Major Accomplishments.

- Developed method to identify olefins in jet fuel using GCxGC-VUV.
- Made many strides on improving aviation fuel blending rules, including a novel blending rule for distillation curves.
- Participated in numerous prescreening collaborations with groups at National Renewable Energy Laboratory (NREL), Massachusetts Institute of Technology (MIT), Pacific Northwest National Laboratory (PNNL), and other groups withing WSU.
- Measured the dielectric constant in numerous fuels and mixtures resulting in two publications.

Publications

Peer-reviewed Journal Publications

Boehm, R. C., Yang, Z., Bell, D. C., Faulhaber, C., Mayhew, E., Bauder, U., Eckel, G., & Heyne, J. S. (2024). Perspective on fuel property blending rules for design and qualification of aviation fuels: A review. *Energy and Fuels, 38*(18), 17128–17145. https://doi.org/10.1021/acs.energyfuels.4c02457

Faulhaber, C., Bell, D. C., Boehm, R., & Heyne, J. S. (2024). Dielectric constant predictions for jet-range hydrocarbons: Evaluating the Clausius–Mossotti relation and correcting for molecular dipole moments. *Energies, 17*(18), 4700. https://doi.org/10.3390/en17184700

Kosir, S., Feldhausen, J., Bell, D. C., Cronin, D., Boehm, R., & Heyne, J. (2023). Quantitation of olefins in sustainable aviation fuel intermediates using principal component analysis coupled with vacuum ultraviolet spectroscopy. *Frontiers in Fuels, 1*. https://doi.org/10.3389/ffuel.2023.1246950

Kumar, A., Bell, D. C., Yang, Z., Heyne, J., Santos, D. M., Wang, H., Zuo, P., Wang, C., Mittal, A., Klein, D. P., Manto, M. J., Chen, X., & Yang, B. (2024). A simultaneous depolymerization and hydrodeoxygenation process to produce lignin-based jet fuel in continuous flow reactor. *Fuel Processing Technology, 263*. https://doi.org/10.1016/j.fuproc.2024.108129

Yang, Z., Bell, D. C., Boehm, R. C., Marques, P. F., Boze, J. A., Kosilkin, I. V., & Heyne, J. S. (2024). Assessing the effect of composition on dielectric constant of sustainable aviation fuel. *Fuel, 380*. https://doi.org/10.1016/j.fuel.2024.133230

Yang, Z., Bell, D. C., Cronin, D. J., Boehm, R. C., Heyne, J., Ramasamy, K. K. (2024). Volatility measurements of sustainable aviation fuels: A comparative study of D86 and D2887 methods. *ACS Sustainable Chemistry and Engineering, 12*(19), 7414–7420. https://doi.org/10.1021/acssuschemeng.4c00678

Outreach Efforts

Presentations

Heyne, J. S. (2024, September). *SAF center at Paine Field* [Panel]. Aerospace Futures Alliance, 19th Annual Aerospace Summit, Tacoma, Washington.

Heyne, J. S. (2024, September)*Towards decarbonizing aviation with sustainable aviation fuel: Some technical challenges and opportunities* [Seminar]. University of Georgia – Athens, School of Engineering and Chemistry Department, Athens, Georgia.

Heyne, J. S. (2024, July 26). *Towards biobased sustainable aviation fuel: Some technical challenges and opportunities in sustainable aviation fuels* [Keynote presentation]. NSF Innovative Nexus for Food, Energy and Water Systems, University of Illinois Urbana-Champaign, Urbana, Illinois.

Heyne, J. S. (2014, April 16). *Driving change: Alternative fuel strategies and athlete branding in the modern era* [Lecture]. Washington State University, Entrepreneurial Faculty Ambassadors, Science Pub Talk, Pullman, Washington.

Heyne, J. S. (2024, March 4). *Fuel analysis, qualification, and standardization* [Seminar]. University of Washington, William E. Boeing Department of Aeronautics and Astronautics, Seattle, Washington.

Heyne, J. S. (2024, February). *Fuel analysis, qualification, and standardization* [Lecture]. ASCENT 93: Global Supply Chain Development Series, virtual.

Heyne, J. S. (2024, January). *ASCENT 101: SAF repository* [Keynote presentation]. Commercial Aviation Alternative Fuels (CAAFI) Research & Development Committee Lecture Series, virtual.

Fuller, C & Heyne, J. S. (2024, January). Some local SAF efforts and overviews [Keynote presentation]. CleanTech Alliance, Perkins Coie, Seattle, Washington.

Heyne, J. S. (2024, January). *Navigating the shift: understanding fuel property variations in the move to 100% SAF* [Panel]. 2024 AIAA SciTech Forum, Sustainable aviation fuels: Moving towards 100% SAF, Orlando, Florida.

Heyne, J. S. (2023, December). *Future horizons: present insights and emerging trends in sustainable aviation fuel* [Lecture]. Campus seminar, WSU Everett, Everett, Washington.

Heyne, J. S. (2023, October). *Clear skies ahead: Sustainable aviation fuel work at WSU Tri-Cities* [Panel]. WSU Tri-Cities: Research Week, Clean Energy & the Environment Panel, Richland, Washington.

Heyne, J. S. (2023, October). *Clear skies ahead: The evolution and expansion of sustainable aviation fuel* [Keynote presentation]. Discovery Series: A Technology Alliance Program, Perkins Coie, Seattle, Washington.

Heyne, J. S. (2023, October). *WSU Tri-Cities bioenergy: research, programs, & priorities* [Keynote presentation]. Northwest Environmental Business Council, Northwest Bioenergy Summit, Three Rivers Convention Center, Kennewick, Washington.

Heyne, J. S. (2023, October). *Sustainable aviation fuel: existing pathways, contemporary developments, and a potential future fuels* [Panel]. Northwest Environmental Business Council, Northwest Bioenergy Summit: Biofuels section, Kennewick, Washington.

Heyne, J. S. (2024, September 16). *Drop-in solutions to minimize aviation fuel sooting* [Panel]. International Civil Aviation Organization (ICAO), Symposium on non-CO_2 Aviation Emissions, Montréal, Canada.

Heyne, J. S. (2024, May). *SAF property predictions from gas chromatography predictions* [Panel]. United Kingdom Department for Transport's Advanced Fuel Fund: Sustainable Aviation Fuel Innovation Programme, QEII Centre, London, United Kingdom.

Awards

- Joshua Heyne, 2024, *Energy and Fuels* Rising Star

Student Involvement

- David Bell (PhD student) leads this effort.
- Zhibin (Harrison) Yang (PhD student) participates in this effort.
- Conor Faulhaber (PhD student) participated in this effort.
- Joshua Ledezma (undergraduate student) participated in this effort
- Gabriela Nicacio (undergraduate student) participated in this effort.

Plans for Next Period

- Expand testing to include numerous new testing equipment. These include an ignition quality tester (IQT), inductively coupled plasma–optical emission spectroscopy (ICP-OES), graphite furnace, ball-on-cylinder lubricity evaluator (BOCLE), titration, and more.
- Publish developments towards an improved freezing point blending rule.
- Continue to develop our O-ring swell measurements to test the effects of fuel cycling on O-ring swell. This is in addition to the work we perform for fuel producers through tier alpha and tier beta.

APPENDIX A

Quantitation of Olefins in Sustainable Aviation Fuel Intermediates Using Principal Component Analysis Coupled with Vacuum Ultraviolet Spectroscopy

Kosir, S., Feldhausen, J., Bell, D. C., Cronin, D., Boehm, R., & Heyne, J. (2023). Quantitation of olefins in sustainable aviation fuel intermediates using principal component analysis coupled with vacuum ultraviolet spectroscopy. *Frontiers in Fuels, 1*. https://doi.org/10.3389/ffuel.2023.1246950

1. Introduction

Sustainable aviation fuel (SAF) represents the only near-term solution to reducing emissions associated with commercial air travel (Staples et al., 2018). SAF represents a subset of alternative jet fuel that, in addition to being from a non-petroleum source, produces fewer CO_2 and particulate matter (PM) emissions compared to conventional jet fuel (Kosir et al., 2019). Olefins are a common product of processes relevant to SAF, including gasification, deoxygenation, and fermentation (Zacharopoulou and Lemonidou, 2018). Olefins are generally limited to less than 1% in jet fuel (ASTM D7566, 2022) because of their poor thermal stability, which can result in the formation of coke and gum. Methylindene blended at 3% in synthetic paraffinic kerosene (SPK) exhibited nitrile rubber O-ring swelling less than conventional jet fuel, which raises O-ring swell concerns (Graham et al., 2011). Additional internal O-ring testing indicates that olefins have low O-ring swell, similar to their saturated counterparts. It follows that the accurate detection of olefins in SAF is necessary for safe aircraft operation.

The olefin detection method specified in ASTM D7566 is the bromine index (ASTM D2710, 2020), which requires up to ~12 mL of fuel and provides no information about the nature of the olefins. Vacuum ultraviolet spectroscopy (VUV) can potentially provide more information about the olefins by providing unique spectra for hydrocarbon classes (Schug et al., 2014) while using as low as ~1 mL of fuel when coupled with gas chromatography (GC). Such low-volume olefin quantitation constitutes Tier α prescreening, which can save fuel producers significant production costs by detecting promising SAF candidates at early stages and helping to make process refinements (Yang et al., 2021). For reference, Tier 1 and 2 testing following ASTM D4054 requires approximately 20-100 gal of fuel. Currently, ASTM D8071 is the only approved method for olefin quantitation using vacuum ultraviolet spectroscopy (ASTM D8071, 2021). It uses a 1D GC-VUV configuration and is geared toward gasoline samples. The identity of the measured VUV spectra is compared against a reference VUV library, with up to three coeluting species considered simultaneously. Extension to 2D GCxGC-VUV offers the advantage of improved separation resolution. The literature for GCxGC-VUV olefin quantitation, hereafter referred to as the deconvolution method, uses a single reference spectrum to represent each hydrocarbon class (Lelevic et al., 2021). Deconvolution is then carried out by assuming that the resulting spectrum is a linear combination of two reference spectra. Olefin quantitation is performed by taking the olefin/non-olefin proportion in each template region and multiplying it by the VUV relative response factors.

Principal component analysis (PCA), a technique for reducing the dimensionality of data, is applied to VUV spectra in this paper. PCA produces vectors that result in maximum variance in an N-dimensional feature space. These vectors are called principal components (PCs), which can be constructed to align with important features and neglect unimportant features. The original data can then be transformed and manipulated in the PC space. In the case of VUV spectra, the features being reduced are the number of wavelengths required to describe spectral features. As shown in the Results section, two PCs can describe 82% of the variance for absorbances across 3240 wavelengths spanning from 125 nm to 240 nm. A PC template, which can be used in place of a GCxGC template, was created using PCs. Several recent papers have applied PCA to VUV spectra (Santos et al., 2018; Roberson and Goodpaster, 2019; Roberson et al., 2020; Tanen et al., 2020; Cruse and Goodpaster, 2021); however, this paper represents the first application of PCA to fuel templating to the best of the authors' knowledge.

The method developed in this paper uses PCA to identify and quantify olefins and other hydrocarbons without the use of a GCxGC template. The objective of this work is to apply PC quantitation to a highly olefinic fuel intermediate. Deciphering olefins from cyclic molecules is a challenge for mass spectrometry, which is a common detector for GC systems. The PC results will be compared to the deconvolution method (Lelevic et al., 2021)which relies on a GCxGC template and spectral deconvolution as described above. The PC results generated will also be validated against ^{13}C and ^{1}H NMR, which is a common method for hydrocarbon quantitation.

2. Materials and Methods

2.1 Principal Component Quantitation

FID and VUV data were collected using previously published methods (Feldhausen et al., 2022; Heyne et al., 2022). A highly olefinic fuel intermediate from an anonymous source was screened in this paper. The PCA model was generated using 298 VUV spectra from 12 different hydrocarbon groups that did not contain heteroatoms. The spectra were first interpolated so that the absorbances were all at the same wavelengths. The spectra were smoothed using the SciPy Savitzky-Golay filter with a polynomial order of three and a window length of 324. Each spectrum was then normalized by its sum. The PCA model was trained using the Scikit-learn PCA package with four PCs in total.

The screening VUV spectra had to be aligned with the FID peaks, which tend to drift behind their respective VUV spectra, as depicted in Supplementary Figure 1. Alignment was accomplished by finding the local maxima of VUV absorbance, and then aligning them with their respective FID peaks as identified by the FID software. The VUV data, which has retention times associated with two columns, RT_1 and RT_2, was converted into a 2D matrix using the NumPy histogram2d package. VUV maxima were then detected using the SciPy maximum filter package with a footprint of 100. VUV spectra were integrated from 130-135 nm to compare the peak sizes on an equal basis. This range was selected because hydrocarbon groups have VUV features of similar absorbances (Lelevic et al., 2021).

The VUV-FID phase shift was calculated as follows:

$$Phase\ shift\ = \sum(VUV_i - FID_i)/N \qquad \textit{(Eq. 1)}$$

Here, N is the number of VUV maxima used, VUV_i is the elution time of the VUV maxima, and FID_i is the elution time of the trailing FID peaks. Once a VUV-FID phase shift was determined, it was subtracted from RT_1 for all of the FID data. The fuel intermediate VUV spectra went through the same preprocessing as the training data before being run through the PCA model. The signal-to-noise ratio of the absorbances was calculated over the range of 130-135 nm, and noisy VUV peaks with signal-to-noise ratios less than 10 were dropped. Once the fuel intermediate VUV spectra were processed, they were categorized using the PC template on a timestep basis. The coupled FID peaks were used to determine the mass contribution of the identified VUV spectra, as reported in Figure 4.

2.2 Reference GCxGC-VUV Quantitation

The PC method presented in this work will be compared against the existing approach that is based on the deconvolution procedure presented in the literature [3,4,8]. The method requires importing the GCxGC hydrocarbon group-type template from ChromSpace into Python and overlaying the template onto the VUV dataset so that each of the VUV timesteps can be classified into a corresponding hydrocarbon group. Because olefins most commonly elute within the *iso*-alkane and cycloalkane regions, these regions undergo further olefinic analysis while the other regions rely solely on GC-FID data for quantification. The olefinic content is determined by resolving the linear combination of a representative olefin spectrum and a representative saturate spectrum. With a ratio of olefins to saturates, a weighting can then be applied to the GC-FID group result for a final mass-based olefinic quantitation.

2.3 NMR Quantitation

^{13}C and ^{1}H NMR spectra were acquired at 125.65 and 499.67 MHz, respectively, on an Agilent 600 MHz instrument at room temperature in 5 mm NMR tubes. Quantitative ^{13}C NMR spectra were acquired over a spectral width of 250 ppm, applying acquisition and relaxation delay times of 3 and 5 s, respectively. 1024 scans were collected and combined. Quantitative ^{1}H spectra were obtained using acquisition and relaxation delays of 3 and 8 s, respectively. 128 spectra were collected and combined. All chemical shifts were referenced to the $CDCl_3$ solvent (77.16 ppm for ^{13}C, and 7.26 ppm for ^{1}H). The ^{13}C test mixture was prepared by mixing 0.40 mL of the sample with 0.15 mL of $CDCl_3$ (containing 0.05 M chromium(III) acetylacetonate, added to reduce T1 relaxation time), and the ^{1}H test mixture was prepared by mixing 0.05 mL of the sample with 0.75 mL of $CDCl_3$. The $CDCl_3$ and chromium(III) acetylacetonate were obtained from Sigma-Aldrich. The NMR spectra were processed using the MestReNova 10.0.2 software package. An automatic baseline correction and phase correction were performed before further data analysis.

3. Results

3.1 Principal Component Template

A PC template was created by plotting PC_1 versus PC_2, as shown in Figure 1. PC_1 and PC_2 comprise 66% and 16% of the explained variance in the VUV spectra, respectively. PC_3 and PC_4 have been omitted because they offer only a marginal improvement, capturing 7% and 4%, respectively, of the explained variance in the VUV spectra. Six distinct regions can be identified, including aromatics, diaromatics, conjugated dienes, cyclodienes, olefins, and alkanes. The olefin region comprises linear alkenes, branched alkenes, cycloalkenes, and unconjugated dienes. The alkane region comprises *n*-alkanes, *iso*-alkanes, monocycloalkanes, and dicycloalkanes. In general, species are more saturated at higher values of PC_1. Linear alkenes progress from *cis*-2-pentene to 1-tetradecene as PC_1 increases, indicating that longer linear alkene spectra behave similarly to alkanes. This can be explained by a dilution of the double bond as the length of the aliphatic chain increases. The meaning of the positive and negative PC values are discussed in the paragraph following Figure 2.

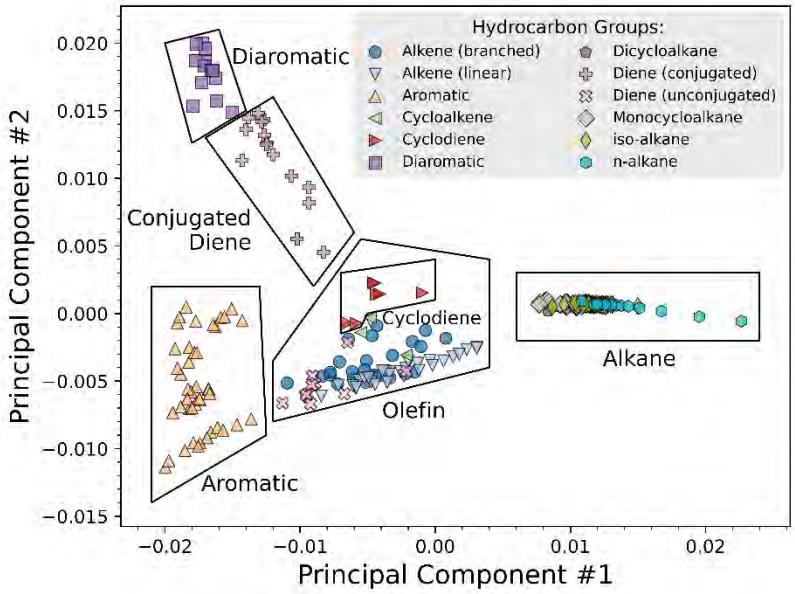

Figure 1. Principal component template generated using PC_1 and PC_2, with template regions in boxes. Specific hydrocarbon groups are listed in the legend.

The loadings of each principal component were plotted against their respective wavelengths to determine which spectral features the principal components align with, as shown in Figure 2. Each PC has a unique set of loadings associated with each feature. Once the loadings are determined, the PC is calculated as a linear combination of the original variables:

$$PC_i = w_{i1}X_1 + w_{i2}X_2 + \cdots + w_{ip}X_p \qquad (Eq.\ 2)$$

Here, w_{ip} is a loading, X_p is an absorbance, i is the principal component index, and p is the wavelength index. Loadings range from -1 to 1, with higher absolute values representing features that align more closely with a PC. A feature and PC are positively correlated when the loading is positive, and negatively correlated when the loading is negative. The loadings in Figure 2 are low because a large number of features were used in this study.

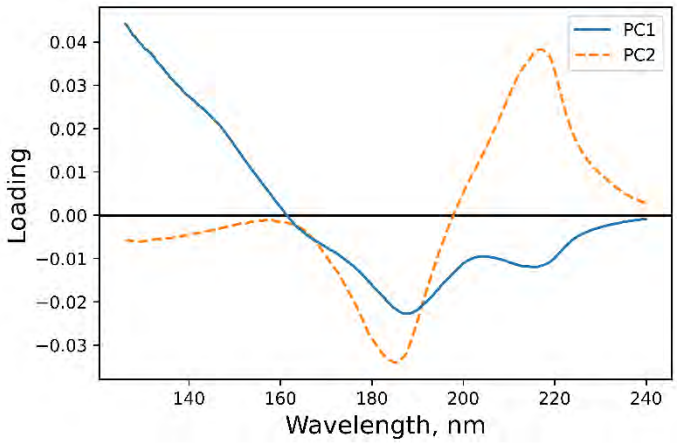

Figure 2. Loadings for PC_1 and PC_2 across the VUV wavelengths. Large positive loadings indicate a strong positive correlation between a principal component and a wavelength, and vice versa for large negative loadings.

PC_1 has positive loadings below 160 nm and negative loadings above 160 nm. This explains why alkanes, which have spectral features at low wavelengths, have positive PC_1 values. The opposite is true for aromatics, which have spectral features at 180 nm. PC_2 crosses the x-axis at 200 nm, with negative loadings at 160-200 nm and positive loadings at 200-240 nm. Aromatics have spectral features at 180 nm, while diaromatics have spectral features at 220 nm. It follows that aromatics and diaromatics diverge over PC_2 in Figure 1, with aromatics exhibiting negative PC_2 values and diaromatics exhibiting positive PC_2 values. It should be noted that while spectra can readily be converted to PCs, the opposite is not typically true. Unless the nonzero loadings of a PC are confined to a narrow wavelength range, a given PC has multiple possible spectra. This is evidenced by the aromatic/diaromatic divergence over PC2 in Figure 1.Olefin Quantitation –

3.2 Deconvolution Method

The GCxGC template used in this study is shown in Figure 3, with the hydrocarbon groups called out in the legend. In general, the volatility of species increases from left to right and polarity increases from bottom to top. GCxGC-VUV analysis using the deconvolution method for the fuel intermediate determined that it consists of 93.4 wt% olefins on an FID area basis, which is 0.95 times that of the PC method. This is likely due to olefins eluting in stencil regions other than those that were assigned to olefins, such as the *n*-alkane regions. The remaining species are as follows: 2.8 wt% *iso*-alkanes, 0.9 wt% monocycloalkanes, and 0.1 wt% dicycloalkanes. 2.8 wt% of the species were not identified because they fell outside of the GCxGC template regions.

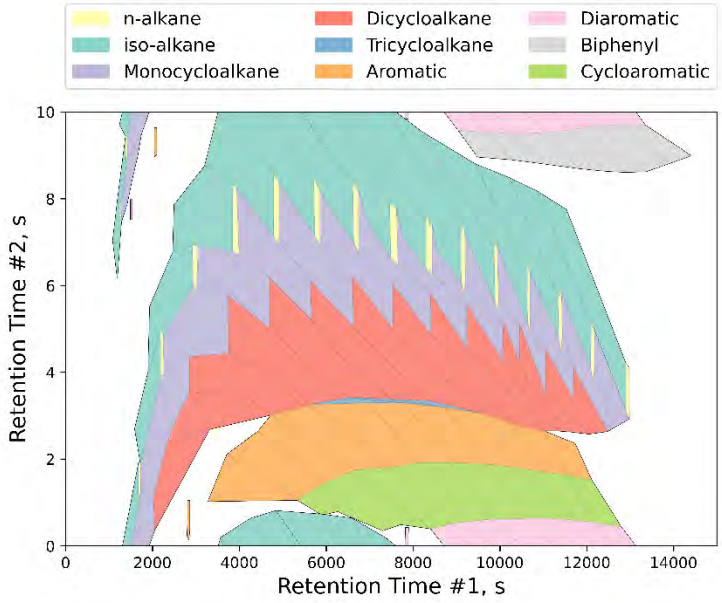

Figure 3. GCxGC template used for the deconvolution method, with hydrocarbon regions indicated by color.

3.3 Olefin Quantitation – Principal Component Method

PC olefin analysis for the fuel intermediate is depicted in Figure a, and Figure 4b isolates the trace species to give a better sense of their location. After the signal-to-noise filter was applied, 75.0 wt% of the spectra remained. The identified spectra are 98.3 wt% olefins with a small alkane region at $RT_1 \approx 1000$ s and trace amounts of cyclodienes. A significant fraction of the alkane peaks falls outside of the GCxGC template at $RT_1 \approx 1000$ s. 99.5 wt% of the spectra were matched, indicating that the signal-to-noise processing was effective at removing noisy spectra.

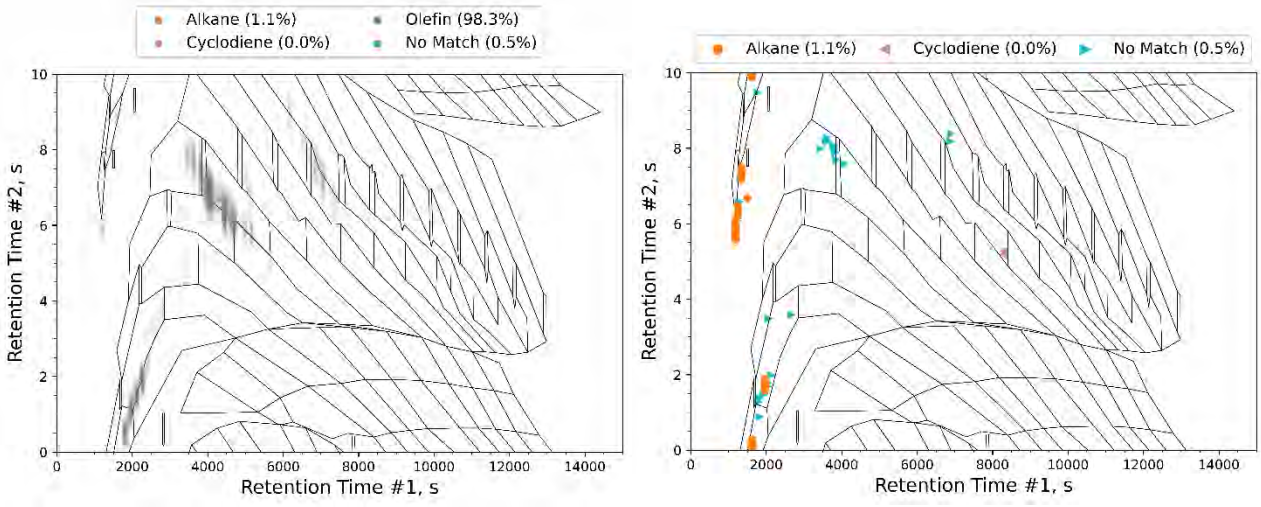

Figure 4. a (left): Quantitation for the fuel intermediate, with larger FID peak areas represented by darker circles. The GCxGC template is overlayed for reference. b (right): Quantitation for the fuel intermediate with uniform shading for only the trace species. The GCxGC template is overlayed for reference.

Representative *n*-alkane, olefin, and cyclodiene spectra from this analysis are shown in Figure 5. As expected, the alkane spectrum has a large feature below 160 nm, and the olefin spectrum has a characteristic hump at ~190 nm. The cyclodiene spectrum is right-shifted to ~200 nm compared to the olefin spectrum, as expected from its higher PC_2 value. The cyclodiene spectrum represented only 0.01 wt% of the sample, illustrating the ability of the PC method to resolve trace olefin peaks. The unmatched spectra are plotted over the PC template in Supplementary Figure 2. Most of the spectra fall below or between the olefin and alkane regions.

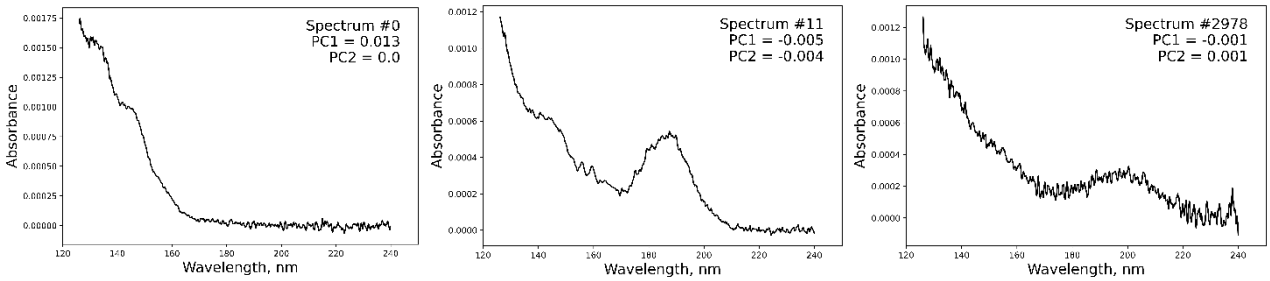

Figure 5. Representative alkane (left), olefin (middle), and cyclodiene (right) spectra from Figure 4a.

3.4 Olefin Quantitation – NMR

As a means of validating the quantitative GCxGC-VUV analysis of the fuel intermediate investigated in this study, the mixture was analyzed via quantitative ^{13}C and ^{1}H NMR (see Supplementary Figure 3). By integrating key regions of each spectrum and presenting these values as a proportion of the whole, the mol% of hydrogen and carbon accounted for by key functional group types was determined. The values obtained are summarized in Table 1. This data suggests that the fuel intermediate mixture is a pure hydrocarbon (i.e., containing negligible quantities of common heteroatoms), contains little aromatic content, and has a high proportion of aliphatic C-C double bonds.

Table 1. Quantitative ^{13}C and ^{1}H NMR data for key functional group types of the fuel intermediate analyzed in this study.

Nuclei	Type	Quantity (mol%)	Integration region (ppm)
H	Aromatic H	0.7	6.2-10.7
	Olefinic H	3.7	4.3-6.2
	Paraffinic H (*n*-, *iso*-, & cyclo)	95.7	0.5-4.3
C	Olefinic + Aromatic C (mol%)	9.9	100-155
	Paraffinic C (*n*-, *iso*-, & cyclo) (mol%)	90.1	5-55

4. Discussion

The PC quantitation approach presented in this paper represents an alternative approach to olefin quantitation that relies on a PC template rather than a GCxGC template. One outcome is that quantitation with the GCxGC template resulted in an olefin concentration of 0.95 times that of the principal component method due to olefins falling outside of the expected GCxGC regions. The ability of the PC method to detect and quantify species that fell outside of the GCxGC template regions can help with template adjustment. In Supplementary Figure 2, unmatched VUV spectra were readily identified for further analysis. Other merits of the PC approach are: (1) it allows for visualization of VUV spectra on a timestep basis, (2) it has more nuanced hydrocarbon identification, and (3) it doesn't rely on a single seed spectrum for quantitation. The trace cyclodiene detection depicted in Figure 4b illustrates merit #2. These cyclodienes, which were present at 0.01 wt%, were not detected by the deconvolution method.

One shortcoming of the PC approach is that it is currently unable to perform spectral deconvolution. One possible approach for PC deconvolution is to take the distance of a spectrum from the centroids of PC regions. It remains to be seen whether this would result in linear behavior in the PC space as the relative proportion of spectra is varied. Another possibility is that VUV spectra could be identified using the PC approach then deconvolution could be performed using the literature methods (ASTM D8071, 2021; Lelevic et al., 2021) to handle coelution. The PC approach could also benefit from coupling with the GCxGC template to enable more nuanced identification of hydrocarbon groups that are not present in the PC template (e.g., *iso*-alkanes, monocycloalkanes, and dicycloalkanes). Finally, the limits of detection of the VUV detector affect the comprehensiveness of this analysis. As mentioned in Section 3.3, 25 wt% of the spectra were not included in the quantitation because they did not meet the signal-to-noise criteria. Whether this is due to detector limits or coelution, coupling with the GCxGC template can potentially overcome this shortcoming.

Both ^{13}C and ^{1}H NMR agree with the GCxGC-VUV data qualitatively because they indicate that there is a significant amount of olefins and alkanes present in the sample. Direct comparison of the GCxGC-VUV with the NMR data is not possible because they are reported on a molecular and atomic basis, respectively. The ^{1}H NMR picked up 0.7 mol% of aromatics, while the GCxGC-VUV did not detect any aromatics. It is unlikely that the unmatched spectra in Supplementary Figure 2 are aromatics, given that they are closer to the olefin and alkane regions. Additionally, species from the sample did not elute in the GCxGC template regions associated with aromatics, as is evident from a comparison of Figures 3 and 4. The aromatics shown in Table 1 merit further study. A comparison study should be carried out in the future between the olefin quantitation method presented here and the bromine index (ASTM D2710) for validation purposes. Additional SAF intermediates should also be tested to ensure that the PC approach is valid over a wide compositional range.

5. References

ASTM D2710: Standard Test Method for Bromine Index of Petroleum Hydrocarbons by Electrometric Titration (2020). West Conshohocken doi: 10.1520/D2710-20.

ASTM D7566: Standard Specification for Aviation Turbine Fuel Containing Synthesized Hydrocarbons (2022). West Conshohocken doi: 10.1520/D1655-10.2.

ASTM D8071: Standard Test Method for Determination of Hydrocarbon Group Types and Select Hydrocarbon and Oxygenate Compounds in Automotive Spark-Ignition Engine Fuel Using Gas Chromatography with Vacuum Ultraviolet Absorption Spectroscopy Detection (GC-VUV) (2021). West Conshohocken doi: 10.1520/D8071-21.

Cruse, C. A., and Goodpaster, J. V. (2021). A systematic study of the absorbance of the nitro functional group in the vacuum UV region. *Anal. Chim. Acta* 1185. doi: 10.1016/j.aca.2021.339042.

Feldhausen, J., Bell, D. C., Yang, Z., Faulhaber, C., Boehm, R., and Heyne, J. (2022). Synthetic aromatic kerosene property prediction improvements with isomer specific characterization via GCxGC and vacuum ultraviolet spectroscopy. *Fuel* 326, 125002. doi: 10.1016/j.fuel.2022.125002.

Graham, J. L., Rahmes, T. F., Kay, M. C., Belières, J.-P., Kinder, J. D., Millett, S. A., et al. (2011). Impact of Alternative Jet Fuel and Fuel Blends on Non-Metallic Materials Used in Commercial Aircraft Fuel Systems. Federal Aviation Administration report.

Heyne, J., Bell, D., Feldhausen, J., Yang, Z., and Boehm, R. (2022). Towards fuel composition and properties from Two-dimensional gas chromatography with flame ionization and vacuum ultraviolet spectroscopy. *Fuel* 312, 122709. doi: 10.1016/j.fuel.2021.122709.

Kosir, S., Behnke, L., Heyne, J., Stachler, R., Flora, G., Zabarnick, S., et al. (2019). Improvement in Jet Aircraft Operation with the Use of High-Performance Drop-in Fuels. *AIAA SciTech Forum*. doi: 10.2514/6.2019-0993.

Lelevic, A., Geantet, C., Moreaud, M., Lorentz, C., and Souchon, V. (2021). Quantitative Analysis of Hydrocarbons in Gas Oils by Two-Dimensional Comprehensive Gas Chromatography with Vacuum Ultraviolet Detection. *Energy and Fuels* 35, 13766–13775. doi: 10.1021/acs.energyfuels.1c01910.

Roberson, Z. R., and Goodpaster, J. V. (2019). Differentiation of structurally similar phenethylamines via gas chromatography–vacuum ultraviolet spectroscopy (GC–VUV). *Forensic Chem.* 15. doi: 10.1016/j.forc.2019.100172.

Roberson, Z. R., Gordon, H. C., and Goodpaster, J. V. (2020). Instrumental and chemometric analysis of opiates via gas chromatography–vacuum ultraviolet spectrophotometry (GC-VUV). *Anal. Bioanal. Chem.* 412, 1123–1128. doi: 10.1007/s00216-019-02337-5.

Santos, I. C., Smuts, J., Choi, W.-S., Kim, Y., Kim, S. B., and Schug, K. A. (2018). Analysis of bacterial FAMEs using gas chromatography – vacuum ultraviolet spectroscopy for the identification and discrimination of bacteria. *Talanta* 182, 536–543. doi: 10.1016/j.talanta.2018.01.074.

Schug, K. A., Sawicki, I., Carlton, D. D., Fan, H., McNair, H. M., Nimmo, J. P., et al. (2014). Vacuum ultraviolet detector for gas chromatography. *Anal. Chem.* 86, 8329–8335. doi: 10.1021/ac5018343.

Staples, M. D., Malina, R., Suresh, P., Hileman, J. I., and Barrett, S. R. H. (2018). Aviation CO2 emissions reductions from the use of alternative jet fuels. *Energy Policy* 114, 342–354. doi: 10.1016/j.enpol.2017.12.007.

Tanen, J. L., Lurie, I. S., and Marginean, I. (2020). Gas chromatography with dual cold electron ionization mass spectrometry and vacuum ultraviolet detection for the analysis of phenylethylamine analogues. *Forensic Chem.* 21. doi: 10.1016/j.forc.2020.100281.

Yang, Z., Kosir, S., Stachler, R., Shafer, L., Anderson, C., and Heyne, J. S. (2021). A GC×GC Tier α combustor operability prescreening method for sustainable aviation fuel candidates. *Fuel* 292. doi: 10.1016/j.fuel.2021.120345.

Zacharopoulou, V., and Lemonidou, A. A. (2018). Olefins from Biomass Intermediates: A Review. *Catalysts* 8. doi: 10.3390/catal8010002.

APPENDIX B

Assessing the Effect of Composition on Dielectric Constant of Sustainable Aviation Fuel

Yang, Z., Bell, D. C., Boehm, R. C., Marques, P. F., Boze, J. A., Kosilkin, I. V., & Heyne, J. S. (2024). Assessing the effect of composition on dielectric constant of sustainable aviation fuel. *Fuel, 380*. https://doi.org/10.1016/j.fuel.2024.133230

1. Introduction

Commercial aviation is one of the safest means of travel. This is due to a combination of industry regulations, rigorous pilot training, and redundancy of aircraft components. Safety is and always will be paramount on commercial airlines and at the forefront of development efforts toward commercial airlines' net-zero 2050 carbon emission goals [1]. Sustainable aviation fuel (SAF) is the key contributor to this goal. Other technologies have been envisioned, including hydrogen and electrification. However, the technology readiness level of these technologies are low, rendering them unlikely to contribute as much as SAF toward the carbon emissions goal by 2050 [2–4].

Several currently approved synthetic blending component pathways in ASTM D7566-22 are allowed to be blended up to 50 %v (A3 and A7 are limited to 10%v) with conventional jet fuel for commercial usage. The blend limits of these various annexes are due to differences in fuel properties outside of the petroleum experience, such as density and material compatibility (i.e., O-ring seal swell). Another concern raised by aircraft manufacturers is possible inaccuracy in fuel gauging due to the difference in the dielectric constant between conventional jet fuels and 100% paraffinic SAF. With the diversification of SAF feedstocks, conversion processes, and product compositions, there remains significant uncertainty in regard to the impact all this has on the dielectric constant and other properties. As per ASTM D4054, dielectric constant and many other properties are considered "fit-for-purpose" properties, which are not controlled explicitly by the fuel specifications (ASTM D1655, UK MoD Def Stan 91-091, ASTM D7566, MIL-DTL-83133, MIL-DTL-5624, etc.). Despite not being explicitly regulated, these properties are vital for engine and airframe fuel system design and undergo assessment during the ASTM D4054 approval process.

Precise fuel quantification aboard aircraft is essential for ensuring operational safety and efficiency. Fuel quantity indicating systems (FQIS) on contemporary aircraft, typically employ capacitance or speed of sound methods to gauge fuel levels, with the former being more widespread. These systems are influenced by fuel characteristics, with capacitance-based FQIS leveraging the Clausius-Mossotti relation to correlate the measured dielectric constant with fuel density. Consequently, fuel mass, rather than volume — which can fluctuate with temperature changes experienced during flight — is utilized to ascertain the aircraft's operational range. The system computes the on-board fuel mass by combining volume measurements with density calculations, derived from capacitance readings. While some aircraft enhance FQIS accuracy with onboard densitometers for direct density measurement, this feature is not universal.

Capacitance based FQIS gauging relies on the following major parameters: dielectric constant, voltage, frequency, and geometry. The latter three are fixed in the aircraft design, so the only variable parameter is the dielectric constant. The dielectric constant (i.e., relative permittivity) is a function of the fuel composition and temperature. The major aircraft manufacturers use some combination of historical data to design their FQIS. In practice, deviation from the hard-coded Clausius-Mossotti line will cause either an over or under-estimation of fuel on board. A fuel gauging error of ±6% is typical [5], supposing that the dielectric constant is treated as a constant independent of temperature and fuel type. By introducing dielectric compensation, this error is reduced to ±2.5% [5], where the compensator is typically located at the bottom of the fuel tank. Most aircraft have a densitometer installed, but the industry is now increasingly using the densitometer only on the ground due to air bubbles (outgassing), vibrations in-flight, etc. Where the dielectric constant, density, and temperature of the uplifted fuel during refueling are measured and then mapped to dielectric and temperature sensors in all tanks, density can also be inferred using the Clausius-Mossotti relationship, which contributes about ±1.2% [5] to overall accuracy error.

Two latest world fuel surveys of performance and fit-for-purpose properties for aviation jet fuels include ARINC 611 [6] and CRC 647 [7]. A total of 172 jet fuel samples from around the world were collected and characterized, generating a total of 1200 data points on density and dielectric constant. This data was used to correlate density and dielectric constant using the Clausius-Mossotti relationship. Relatively similar slopes and intercepts are observed for both data sets. While both of these surveys are excellent, it should be recognized that 172 samples are a small fraction of the total population. This data is suitable for highlighting trends and average values; however, the relatively modest data set does not accurately define the distribution's shape and should not be used to deduce the range's extreme property values.

Unlike other properties that are mentioned in ASTM D4054, the dielectric constant of aviation fuel is largely unstudied. Sen et al. [8] were able to observe that dielectric constants of mixtures of liquid hydrocarbons exhibited linear relationships with volume fraction by investigating light alkanes (C2-C7) and some hydrocarbon mixtures using a slotted line technique at 1.2 GHz and at atmospheric pressure over a temperature range of 115-295 K. Pan et al. [9] explored the dielectric constant and Clausius-Mossotti functions for liquid mixtures containing nitrogen, argon, and light hydrocarbons. The liquefied natural gas densities were determined from accurately measured dielectric constants and compositions. Sharma

et al. [10] studied the measurement of dielectric parameters of aviation fuel at various frequencies using the cavity perturbation technique, which showed that the dielectric constant of jet fuel is a function of frequency at X-band frequencies. Brazier et al. [11] studied the effect of pressure on the density, viscosity, and dielectric constant of some light hydrocarbons. While there is some published research on the dielectric constant of hydrocarbons, there are no published studies on the effect of synthetic blend components or sustainable aviation fuel or jet fuel composition on the dielectric constant and the Clausius-Mossotti relationship.

Here, we report the dielectric constant and density measurement for four conventional fuels, thirty-four neat jet fuel range hydrocarbons, thirty-two mixtures, and six synthetic blending components (SAF) over a range of 10 to 30 °C. One hundred and seventy-two different jet fuel dielectric constant and density measurements over the range of -35 to 70 °C were gathered from two reports to establish a conventional jet fuel experience range. These new data are used to investigate the effect of SAF on the dielectric constant and evaluate two different blending rules for dielectric constant estimation of jet-range hydrocarbon mixtures, while the mined data is used to characterize the conventional fuels experience range.

2. Materials and Methods

2.1. Reference Materials

Forty-five hydrocarbon materials were sourced from five vendors and six fuel producers. The details of these materials are included in Table 1.

Table 1. The hydrocarbons used in this study, including the source and purity.

Name	Type	Supplier	Purity
hexane	*n*-alkane	Sigma-Aldrich	>99%
heptane	*n*-alkane	ACROS	99%
octane	*n*-alkane	ACROS	99%
nonane	*n*-alkane	ACROS	99%
decane	*n*-alkane	Thermo Scientific	99%
undecane	*n*-alkane	Thermo Scientific	99%
dodecane	*n*-alkane	Thermo Scientific	99%
tridecane	*n*-alkane	TCI	>99%
tetradecane	*n*-alkane	Thermo Scientific	>99%
2,3-dimethylbutane	*iso*-alkane	Thermo Scientific	>98%
2,2,4-trimethylpentane	*iso*-alkane	Thermo Scientific	99%
2,6,10-trimethyldodecane	SPK	Amyris	N/A
2,2,4,4,6,8,8-heptamethylnonane	*iso*-alkane	Thermo Scientific	98%
cyclohexane	cycloalkane	Thermo Scientific	99%
methylcyclohexane	cycloalkane	Thermo Scientific	99%
cycloheptane	cycloalkane	TCI	99%
cyclooctane	cycloalkane	Thermo Scientific	>99%
ethylcyclohexane	cycloalkane	ACROS	>99%
1,2-diethylcyclohexane	cycloalkane	TCI	98%
1,2,4-trimethylcyclohexane	cycloalkane	TCI	>96%
tert-butylcyclohexane	cycloalkane	Thermo Scientific	>99%
1,4-dimethylcycloctane (DMCO)	SPK	Mukund Karanjikar, CleanJoule	N/A
trans-decalin	cycloalkane	TCI	>98%
cis-decalin	cycloalkane	TCI	98%
bicyclohexyl	cycloalkane	TCI	>99%
toluene	aromatic	Thermo Scientific	99%
ethylbenzene	aromatic	Thermo Scientific	99%
n-propylbenzene	aromatic	Thermo Scientific	98%
m-xylene	aromatic	TCI	>99%
o-xylene	aromatic	TCI	98%

Name	Type	Supplier	Purity
p-xylene	aromatic	Thermo Scientific	99%
n-hexylbenzene	aromatic	Alfa Aesar	98%
1,2,3-trimethylbenzene	aromatic	Sigma-Aldrich	>89%
1,2,4-trimethylbenzene	aromatic	TCI	>98%
1,3,5-trimethylbenzene	aromatic	TCI	>97%
1-methylnaphthalene	aromatic	Thermo Scientific	96%
tetralin	aromatic	Thermo Scientific	97%
n-butylbenzene	aromatic	Thermo Scientific	>99%
A-1 (POSF 10264)	Jet A	AFRL, Tim Edwards	N/A
A-2 (POSF 10325)	Jet A	AFRL, Tim Edwards	N/A
A-3 (POSF 10289)	Jet A	AFRL, Tim Edwards	N/A
Hydroprocessed Esters And Fatty Acids (HEFA)	SPK	World Energy	N/A
Fischer-Tropsch Synthesized Paraffinic Kerosine (FT-SPK)	SPK	AFRL, Tim Edwards	N/A
Synthetic Aromatic Kerosene (SAK)	SAK	Virent	N/A
Alcohol-To-Jet Synthetic Paraffinic Kerosene (ATJ)	SPK	AFRL, Tim Edwards	N/A
JP-10	Jet Fuel	AFRL, Tim Edwards	N/A

2.2. Density and Dielectric Constant Measurement

The Stanhope-Seta equipment, JetDC, was used to measure both density and dielectric constant according to IP PM FC/21. The JetDC has a density range from 0 to 900 kg/m3, a dielectric constant range from 1 to 2.5, and a temperature range from 0 to 40 ˚C with a temperature resolution of 0.01 ˚C. An existing standard test method (ASTM D924) for relative permittivity for electrical insulating liquids provides a procedure for measurements at frequencies between 45 and 65 Hz. This is a different frequency than is used for the equipment installed on airplanes, and these lower frequencies have significant interference from water. Thus, the new JetDC (5000 Hz) was designed for conventional jet fuel and SAF.

A brief description of the standard test method follows. Forty ml of liquid sample is injected into the instrument at 20 ˚C test cell temperature. The sample chamber is then cooled to 10 ˚C before steadily increasing to a final temperature of 40 ˚C. The liquid sample is then discharged, and the instrument is cleaned with 150 mL of petroleum ether and allowed to air-dry.

The permittivity measurement consisted of an inner, outer, and guard electrode with a known cell constant. The capacitance is measured at each temperature at an excitation frequency of 5000 Hz. The density measurement utilized a resonance-type measurement with an accuracy of 0.5 kg/m3. The relative permittivity (ε_r) is calculated using Equation 1.

$$\varepsilon_r = C_s/C_0 \qquad \textit{(Eq. 1)}$$

In Equation 1, C_s is the dielectric to the capacitance of a given configuration of electrodes with the materials present and C_0 is the dielectric to the capacitance of the same configuration of electrodes in a vacuum. In the case of this equipment, C_s is defined as the capacitance in pF of the cell containing the test portion at the test temperature. C_0 is defined as the cell constant in pF at the test temperature; its calculation is shown in Equation 2.

$$C_0 = C_{cyclohexane}/\varepsilon_{r\ cyclohexane} \qquad \textit{(Eq. 2)}$$

Where $C_{cyclohexane}$ is the capacitance of the cell containing certified reference cyclohexane, and $\varepsilon_{r\ cyclohexane}$ is the certified value for relative permittivity of the certified reference cyclohexane.

2.3. Clausius-Mossotti Relationship

Two forms of the Clausius-Mossotti relationship are represented in Equations 3 [12] and 4 [5], respectively. In these equations, the dielectric constant at a given temperature (dimensionless) is denoted by ε_r, the molecular weight of the fuel (g/mol) is denoted by MW, the molar polarizability (cm3/mol) is denoted by R, and the fuel density at a given temperature

(g/cm3) is denoted by $\boldsymbol{\rho}$. For jet fuel, the published values [5] for the constants A and B are 1.0 $\pm$ 10% and 0.3658, respectively.

$$\frac{\varepsilon_r-1}{\varepsilon_r+2}=\frac{\rho R}{MW} \quad (Eq.\ 3)$$

$$\frac{\varepsilon_r-1}{\rho}=A+B(\varepsilon_r-1) \quad (Eq.\ 4)$$

While Equation 3 is true only for materials with no permanent dipole moment, it may be particularly useful for the prediction of dielectric constant for conceptualized fuels or even neat hydrocarbons because polarizability, density, and molecular weight are each readily predictable or well documented. Equation 4 is generally true, but the constants are dependent on the material and heretofore have been determined empirically, via linear regression, by collecting density and dielectric constant data over a series of temperatures. By ignoring the material dependence of A and B and rearranging Equation 4 to Equation 5, the density of fuel is estimated from its measured dielectric constant. A prominent goal of this research is to inform the aviation research community of the implication of ignoring the material dependence of A and B as the composition of (potential) future jet fuels deviates from the composition of fuels used to generate the reference database that was used to establish the constants, A and B for jet fuel.

$$\rho=\frac{(\varepsilon_r-1)}{\{A+B(\varepsilon_r-1)\}} \quad (Eq.\ 5)$$

2.4. Reference Database for Conventional Jet Fuels

Per ASTM D4054, the dielectric constant is considered a fit-for-purpose property. It is not controlled explicitly by the fuel specifications but is important for capacitance-based FQIS gauging. As such, it is important to establish the experience range of Clausius-Mossotti plot data for conventional jet fuel. Combined, the datasets from ARINC 611 and CRC 647 account for 1200 data points from 172 different Jet A fuel samples. The ARINC data was taken at -35 to 25 ˚C at 10 ˚C increments and the CRC data was taken at various temperature increments from -35 to 70 ˚C. The Clausius-Mossotti plot is generated for each of the 172 fuel samples to derive a conventional jet fuel experience range for both the slope and intercept. It should be noted that the ARINC data was published in 1999 and the CRC was published in 2006. It is certainly possible that modern Jet A fuel has lower aromatic content and lower cycloalkane content due to industry-wide changes in petroleum refining practices [13]. However, any year-over-year trend in the average composition of jet fuel is believed to be small relative to the worldwide variation in jet fuel composition observed over any 12-month period since records of jet fuel composition have been kept.

2.5. Blending Rule for Mixture

Predicting the dielectric constant of fuel blends is particularly valuable, given the impracticality of conducting dielectric constant measurements for every individual blend ratio. Two blending rules were evaluated against measurement. One predicts the mixture's dielectric constant directly from the component volume fraction and dielectric constant, and the other predicts the mixture's dielectric constant from the mixture polarizability and molar volume. The volume fraction blending rule, expressed here as Equation 6, was first introduced by Sen et al. [8] for light alkanes (C2-C7). We apply it here to liquids because the dielectric constant is linear with density, and density has a volume fraction blending rule. In this equation, $\boldsymbol{\varepsilon_{r\,mix}}$ denotes the dielectric constant of the mixture and v_i and $\varepsilon_{r\,i}$ are the volume fraction and neat dielectric constant, respectively of the ith component. The advantage of this blending rule is that no additional information regarding the mixture is required to do the calculation.

$$\boldsymbol{\varepsilon_{r\,mix}} = \sum \boldsymbol{v_i} * \boldsymbol{\varepsilon_{r\,i}} \quad (Eq.\ 6)$$

For nonmagnetic materials with no permanent dipole, the dielectric constant, ε_r is related to the polarizability (R) by a simple algebraic expression written here as equation 7. The blending rule for polarizability, expressed here as Equation 8, has been widely disseminated [14] and is extraordinarily accurate. Moreover, the polarizability of saturated hydrocarbons can be predicted with excellent accuracy via a group additivity approach [15]. The accuracy of such models applied to aromatic hydrocarbons is not well understood, and thus the 'effective polarizability' (defined as the result of Equation 7) of aromatic species in fuel may require substantially more intricate models or determination from measured density and dielectric constant. Once the polarizability of the mixture is determined from Equation 8, it is straightforward to rearrange Equation 7 to calculate the dielectric constant or the molar volume of the mixture provided the other is known. It cannot be used to simultaneously predict both density and dielectric constant. In other words, this analysis is ideal for mixtures with well-known composition, from which molar volume can be readily determined. However, for commercial fuel, which is

a complex mixture with incomplete composition illumination, a more direct approach for estimating the dielectric constant of a mixture of fuels, such as Equation 6, is preferred.

$$R = V_m * \frac{\varepsilon_r - 1}{\varepsilon_r + 2} \quad (Eq.\ 7)$$

$$R_{mix} = \sum v_i * R_i \quad (Eq.\ 8)$$

3. Results and Discussion

A Clausius-Mossotti plot is provided in Figure 1, showing all 1200 data points (open circles) from the database described in the abovementioned section and the best-fit line (dash lines) through these points. The slope and intercept of the combined data are 0.35944 and 1.0005, respectively, which is consistent with the published value [5] for constant A is 1.0 ± 10%, and constant B is 0.3658. Since the dielectric constant varies inversely with temperature, the lower-left of this plot is populated by the higher-temperature portion of the CRC dataset and is not a reflection of any fuel composition differences between the two datasets. The cluster of 18 blue points below the trend line originates from three fuel samples drawn from different places around the world. All three samples have a lower aromatic content (14.1 v%) compared to the CRC average (20.0 v%) and elevated total cycloalkanes content (42.5 v%), especially in dicycloalkanes content (23. 5v%) compared to CRC average of 21.1 v% and 9.0 v%, respectively. It is worth noting that the lowest aromatic sample is a 100% synthetic fuel from South Africa with 5.6 v% aromatic content and a 2.6 v% total cycloalkanes content. However, this fuel has a dielectric constant that is well within the conventional fuel range. The technical reason behind this observation will be discussed in a later section. The linearity of dielectric constant with respect to temperature for jet fuel in the liquid range is also investigated, where the temperature range is restricted (-35 to 25 ˚C for ARINC data and -35 to 70 ˚C CRC data) to avoid highly non-linear features that present in many properties as the temperature approaches a phase transition (freezing or boiling). The average R-square value for the 172 dielectric constant versus temperature correlations is exceptional, 0.99989.

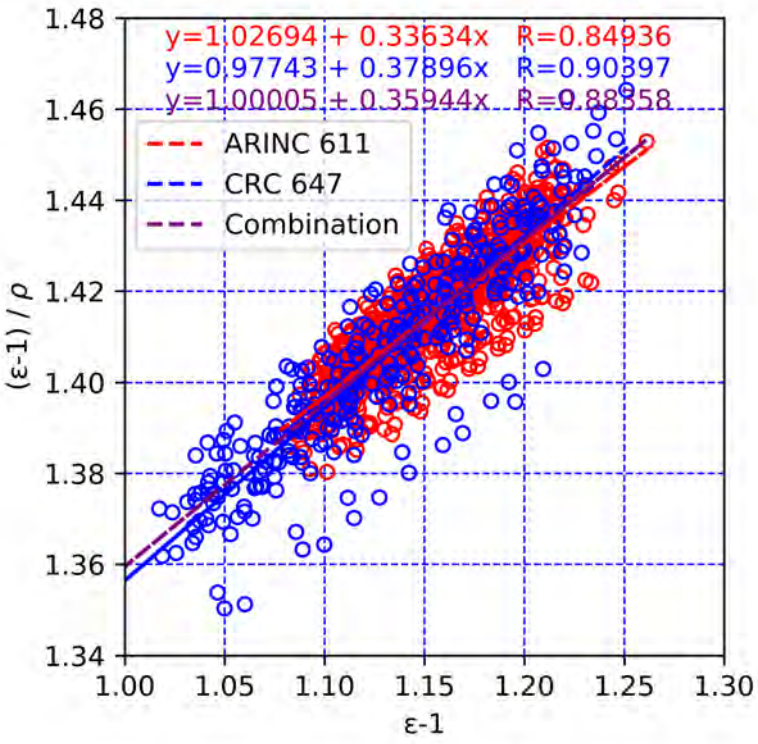

Figure 1. Clausius-Mossotti relationship for 172 different jet fuel samples. The dielectric constant and density of 114 Jet A sample at -35 to 25˚C are from ARINC report (red open circles), and dielectric constant and density of 57 Jet A sample at -35 to 70˚C are from CRC report (blue open circles). In addition, the best fit line of ARINC data (red dash line), CRC data (blue dash line), and the combination of both report (purple dash line) are also reported.

It is understood that different hydrocarbon types (normal, iso, cycloparaffins, aromatics, diaromatics) have different dielectric properties (absolute values at a given temperature and slopes of dielectrics vs. density relationship) [16]. The typical distribution of hydrocarbons that were historically present in turbine fuels (e.g., aromatic content around 16-18 v%), resulted in a combination of dielectric values that aviation industry and fuel probe manufacturers accepted as typical for design and calibration of fuel quantity indication systems. Most modern aircraft rely on these properties for the accurate gauging of fuel on board.

Fuels with unique distribution of hydrocarbons such as those that lack of an entire hydrocarbon type, aromatics or cycloparaffins will have dielectric properties that are outside of the typical experience (e.g., absolute value or slope). Use of such fuels in fuel systems that rely on an average hardcoded relationship of dielectric permittivity vs. density will result in inaccurate estimation of fuel quantity. While historically there were cases of petroleum refineries releasing fuels with very low aromatic content, no issues operating aircraft relying on dielectric properties for fuel quantity indication have been reported.

Due to the nature of the production process fuels from unconventional sources often lack one or more type of hydrocarbons. For example, HEFA SPK predominantly consists of iso-paraffins, virtually no aromatics, and has a relatively low proportion of cycloparaffins. As a result, dielectric properties of emerging fuels (SAF) are likely going to be outside of the current typical experience. Better understanding of how chemistry of emerging fuels impacts dielectric properties is needed.

Since it is virtually impossible to find fuels with properties near the outer corners of the experience range, selected single molecules and simple mixtures are used to represent the corners of the real fuel experience range. Single molecule hydrocarbons that represent major hydrocarbon types found in turbine fuels were chosen for this study. These included n-paraffins, iso-paraffins, cycloparaffins, and aromatics. Each type is represented by different substitution patterns, providing insight into the structure – dielectric property relationship.

To better understand the different hydrocarbon type effects on the Clasusius-Mossotti relationship, data from the thirty-four individual hydrocarbon molecules and nine fuels (10 to 30˚C) are plotted in Figure 2, where the 172 reference jet fuels were also extrapolated/interpolated to 10 to 30˚C to create a back-to-back comparison. In general, the saturated hydrocarbons were clustered at the bottom left of Figure 2, where n- and iso-alkanes were mostly on the same line as the reference fuels but at a lower density. This is no surprise since n- and iso-alkanes makes up most of the jet fuel composition. The cycloalkanes fall below the reference fuel line, while the polycycloalkanes are positioned farther away from it. The dielectric constant of cycloalkanes, n-alkanes and iso-alkanes are similar. The reason that cycloalkanes deviate from the trendline is because of the difference in density at a given temperature. The unsaturated hydrocarbons, or aromatics, are on the top right corner of the Clasusius-Mossotti plot. It is observed that all three 100% paraffinic SAFs (HEFA, FT-SPK, and ATJ) exhibit similar dielectric constants and Clausius-Mossotti relationship. This finding is consistent with expectations, given that these SAFs consist entirely of normal and branched alkanes. Contrastingly, SAK is primarily composed of mono-aromatic compounds [16]. This chemical composition accounts for its proximity to other mono-aromatic fuels on the Clausius-Mossotti plot. Note the large difference between the dielectric properties of o-xylene and p-xylene. This interesting observation is discussed in a later section.

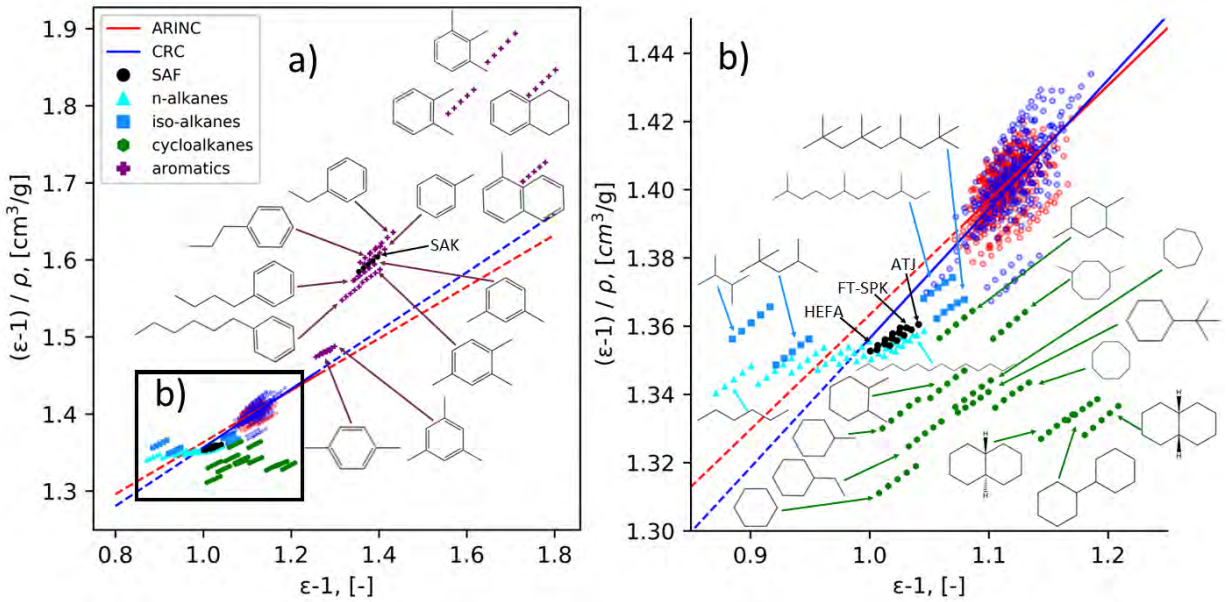

Figure 2. Clausius-Mossotti relationship of neat hydrocarbons that are in the jet fuel range. All 172 reference Jet A were interpolated/extrapolated to 10 to 30 °C to compare with the measurement done on JetDC. The neat molecule's structure was also presented next to the data point for better illustration.

To further assess the variation in fuel samples and hydrocarbon type, the constants of the Clausius-Mossotti relationship were computed for each temperature series of each fuel sample, and these values are shown in Figure 3. The locus of points corresponding to petroleum fuels resides along a straight line. Linear extrapolation of this line to a lower slope (higher intercept) brings it into the data corresponding to all neat iso and normal alkanes (nC6 to nC14) provided in Table 1. Most of the data corresponding to cycloalkanes resides to the left (or below) this line, while most of the data corresponding to unsaturated hydrocarbons resides to the right (or above) this line. Such a feature-level difference between different hydrocarbon types raises concern that future fuels, with markedly different compositional characteristics relative to conventional fuels, may require software (or gauging) changes to aircraft systems used to determine fuel quantity. The purpose of Figure 3 is not to compare pure aromatics with conventional jet fuel but to see the effect of the hydrocarbon group type on the Clausius-Mossotti relationship.

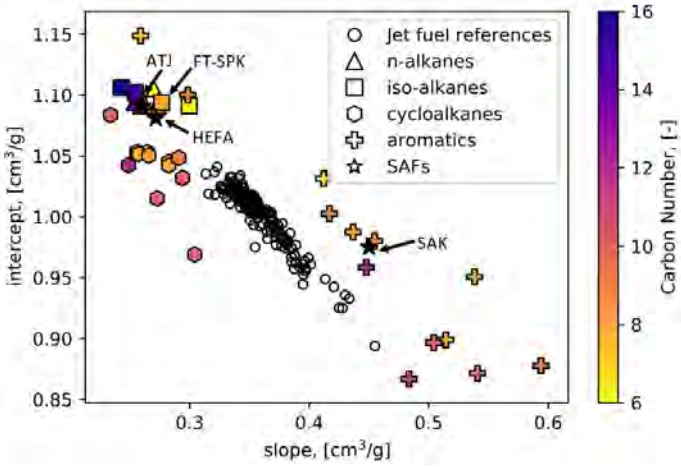

Figure 3. The slope and intercept of all 172 Jet A (black open circles) and neat molecules (solid-colored circles). A color gradient also presents the carbon number associated with individual molecules.

Since the Clausius-Mossotti relationship is an algebraic manipulation of density, and dielectric constant, there is merit in investigating each property independently. Figure 4 illustrates the density (a) and dielectric constant (b) slope and intercept as a function of temperature. While the three different isometric variances of xylene have similar densities, their dielectric constants vary considerably. One interesting observation that could be made is that the conventional fuel density range could be met with just n- and iso-alkanes and cycloalkanes; no aromatic would be needed. In the SAF community, it is of great interest to use cycloalkanes to replace aromatic to satisfy the density and material compatibility (e.g., seal swell) requirement while reducing the sooting propensity of the blended fuel.

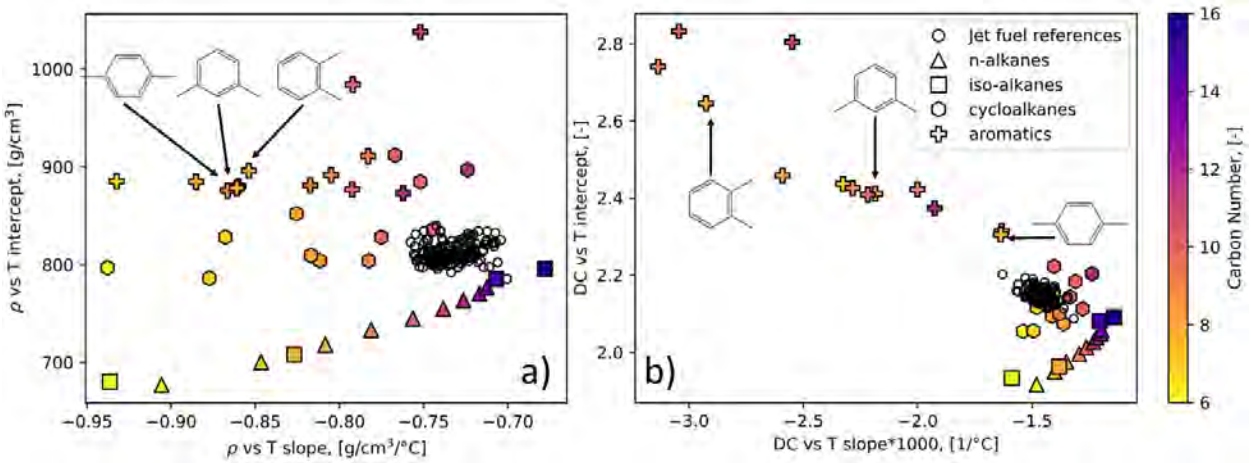

Figure 4. Density (a) and dielectric constant (b) slope and intercept as a function of temperature, the open black circles are the reference jet fuels. Some of the aromatics molecule's structure was presented next to the data point for better illustration. A color gradient also presents the carbon number associated with individual molecules.

The slope from the Clausius-Mossotti plot strongly correlates with the molecule's permanent dipole moment, as shown in Table 2. The correlation coefficient of the slope of the dielectric constant and permanent dipole moment on selected aromatics is 0.89. This explains why the saturated compounds were all clustered in the bottle right of the figure. This also explains the large difference between o-xylene and p-xylene in the Clausius-Mossotti plot. Upon examination of Figure 4 it becomes clear that some amount of aromatics is required in a mixture in order to match the dielectric properties range of conventional jet fuel. Since both n- and iso-alkanes and cycloalkanes are on the bottom right of the conventional fuel, some of the top left aromatic points will be needed to bring the blended fuel into the conventional fuel range.

Table 2. The slope of dielectric constant with respect to temperature and permanent dipole moment of selected aromatics. The permanent dipole moment of aromatic compounds are taken from the work of Zhao et al. [17].

Molecules	DC slope*1000, [˚C]	Permanent dipole moment, [D]
1,2,3-trimethylbenzene	-3.1346	0.660
o-xylene	-2.9254	0.582
toluene	-2.3262	0.343
1-methylnaphalene	-2.5492	0.318
ethylbenzene	-2.5912	0.297
1,2,4-trimethylbenzene	-2.0012	0.291
m-xylene	-2.1864	0.271
p-xylene	-1.6376	0.081
1,3,5-trimethylbenzene	-1.6336	0.047

Being able to accurately predict the dielectric constant of blends of two fuels is also of significant interest since dielectric constant measurement on every single blend ratio is not feasible. The Clausius-Mossotti relationship can be predicted before any blending occurs. In light of this, the accuracy of the two abovementioned blending rules were investigated against 24 neat molecules and fuels at various blend ratios, which include 40 mixtures and 200 data points. The mixtures

consist of neat molecule to neat molecules, neat molecules to fuel, and fuel to fuel blending. For detailed information regarding neat molecules, mixture blend ratio, etc., please refer to the supplemental information.

Both the volume fraction and polarizability blending rules achieved excellent results. Figure 6 shows the dielectric constant measurement versus prediction for both volume fraction (green open circles) and polarizability (red x markers) blending rules. The predicted points corresponding to the volume fraction blending rule employed only the neat molecules/fuels' dielectric constant; no other information is required by this model. The volume fraction blending rule achieved a mean absolute error (MAE) of 0.0038, mean standard error (MSE) of 0.000039, mean error (ME) of 0.0037, and R-squared of 0.9942. For the predictions corresponding to the polarizability blending rule, neat component data, including dielectric constant, density, and MW, were employed to determine the fuel polarizability and molar volume, respectively. The polarizability blend rule achieved a MAE of 0.002, MSE of 0.000011, ME of 0.0004, and R-squared of 0.9983. As seen visually and numerically in Figure 6, MAE and ME values are nearly equal to one another. The volume fraction blending rule appears to result in a small bias higher than the measured data.

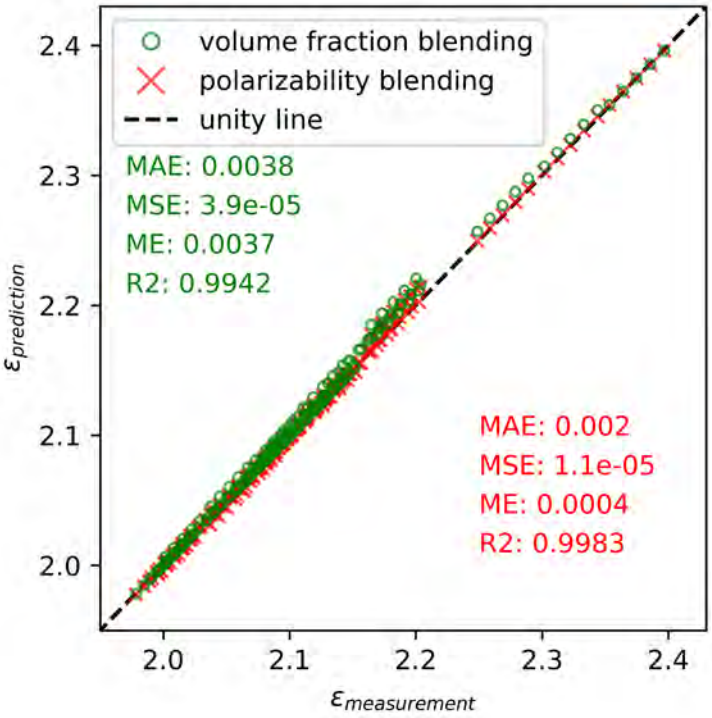

Figure 6. Prediction versus measurement of the dielectric constant of volume fraction (green open circles) and polarizability (red x) blending rules. The black dashed line represents the unity line.

Aromatics are needed for 100% drop-in capacitance based FQIS compatibility. The fuel community has demonstrated a strong interest in the development of 100% drop-in SAF options while simultaneously aiming to reduce or eliminate aromatics in these fuels to address particulate matter emissions. In recent years, many publications have illustrated the ability of cycloalkanes to complement SPKs [18], e.g., density, material compatibility [19], while lowering the sooting potential of the fuel [20,21]. In contrast to those previous studies, cycloalkanes do not complement n- and iso-alkanes. Instead, here they adversely affect the Clasusius-Mossotti relationship. Meaning, replacing aromatics with cycloalkanes is not an option for this property. The precise quantity and type of aromatics required remains unclear at this stage for 100% drop-in capacitance based FQIS compatibility. Furthermore, mono-aromatic compounds, such as those found in SAK, can offer enhanced dielectric constant to most 100% paraffinic SAF pathways, while simultaneously reducing overall particulate matter emissions when compared to traditional jet fuels [16].

4. Conclusion

In this study, we presented the Clausius-Mossotti relationship experience based dielectric permittivity measurements of 172 worldwide conventional jet fuels. Additionally, the effect of hydrocarbon types (studied as pure single molecule compounds) and substitution pattern on the dielectric constant and subsequent Clausius-Mossotti relationship was investigated. We showed that the permanent dipole moment of jet fuel range hydrocarbons has a strong correlation with the orthogonal distance away from the Clausius-Mossotti relationship commonly accepted in modern capacitance-based FQIS. We conclude that to reach the current jet fuel experience range for both the dielectric constant and the Clausius-Mossotti relationship, SAF made from 100% paraffins will most likely require a minimal concentration of aromatics in order to avoid gauging accuracy issues.

Two blending rules for predicting dielectric properties of simple mixtures were investigated and achieved excellent results when compared to direct measurements. These blending rules can help provide understanding into how particular jet fuel compositions will impact the FQIS performance. This can also provide insight into if additional empirical testing is needed to understand the dielectric vs. density relationship for a particular fuel composition.

This study clearly showed that different hydrocarbon classes have different dielectric permittivity and most importantly different slopes of dielectric vs. density relationship. This has further reinforced the need to move to a model in which the dielectric vs. density relationship is determined for each flight cycle to allow use of a wider range of fuel compositions and greater accuracy.

5. References

[1] Air Transport Action Group. WAYPOINT 2050. 2021.
[2] Collins JM, McLarty D. All-electric commercial aviation with solid oxide fuel cell-gas turbine-battery hybrids. Appl Energy 2020;265:114787. doi:10.1016/J.APENERGY.2020.114787.
[3] Nicolay S, Karpuk S, Liu Y, Elham A. Conceptual design and optimization of a general aviation aircraft with fuel cells and hydrogen. Int J Hydrogen Energy 2021;46:32676–94. doi:10.1016/J.IJHYDENE.2021.07.127.
[4] Ng KS, Farooq D, Yang A. Global biorenewable development strategies for sustainable aviation fuel production. Renew Sustain Energy Rev 2021;150:111502. doi:10.1016/J.RSER.2021.111502.
[5] Langton R, Clark C, Hewitt M, Richards L. Aircraft Fuel Systens. Wiltshire, UK: WILEY; 2009.
[6] ARINC. Guidance for the design and installation of fuel quantity systems, ARINC REPORT 611-1. ANNAPOLIS, MARYLAND: 1999.
[7] Hadaller OJ, Johnson JM. WORLD FUEL SAMPLING PROGRAM, CRC Report No . 647. ALPHARETTA, GA: 2006.
[8] Sen AD, Anicich VG, Arakelian T. Dielectric constant of liquid alkanes and hydrocarbon mixtures. J Phys D Appl Phys 1992;25:516–21. doi:10.1088/0022-3727/25/3/027.
[9] Pan WP, Mady MH, Miller RC. Dielectric constants and Clausius-Mossotti functions for simple liquid mixtures: Systems containing nitrogen, argon and light hydrocarbons. AIChE J 1975;21:283–9. doi:10.1002/aic.690210209.
[10] Sharma S, Kaur D. Measurements of Dielectric Parameters of Aviation Fuel at X-Band Frequencies Using Cavity Perturbation Technique. Int J Wirel Microw Technol 2016;6:48–55. doi:10.5815/ijwmt.2016.06.05.
[11] Brazier DW, Freeman GR. The effects of pressure on the density, dielectric constant, and viscosity of several hydrocarbons and other organic liquids. Can J Chem 1969;47:893–9. doi:10.1139/v69-147.
[12] Rysselberghe P Van. REMARKS CONCERNING THE CLAUSIUS-MOSSOTTI LAW n.d.
[13] Speight JG. The Refinery of the Future. Second. Laramie, Wyoming: Elsevier; 2020. doi:https://doi.org/10.1016/C2017-0-04272-6
[14] Corson D, Lorrain P. Introduction To Electromagnetic Fields And Waves. San Francisco and London: W. H. FREEMAN AND COMPANY; 1962.
[15] C. Teixeira-Dias JJ, Murrell JN. The calculation of electric polarizabilities of hydrocarbons with particular attention to the bond-additive property. Mol Phys 1970;19:329–35. doi:10.1080/00268977000101341.
[16] Moses C. Review of Bulk Physical Properties of Synthesized Hydrocarbon: Kerosenes and Blends. WRIGHT-PATTERSON AIR FORCE BASE, OH 45433-7542: 2017.
[17] Zhao J, Zhang R. Proton transfer reaction rate constants between hydronium ion (H 3O+) and volatile organic compounds. Atmos Environ 2004;38:2177–85. doi:10.1016/j.atmosenv.2004.01.019.
[18] Kosir S, Heyne J, Graham J. A Machine Learning Framework for Drop-in Volume Swell Characteristics of Sustainable Aviation Fuel. Fuel 2020;274:1–7. doi:10.1016/j.fuel.2020.117832.
[19] Faulhaber C, Kosir ST, Gawelek K, Boehm R, Heyne JS. Optical Dilatometry Measurements for the Quantification of Sustainable Aviation Fuel Materials Compatibility 2022. doi:10.2514/6.2022-1240.

[20] Yang Z, Xu Z, Feng M, Cort JR, Gieleciak R, Heyne J, et al. Lignin-based jet fuel and its blending effect with conventional jet fuel. Fuel 2022;321:124040. doi:10.1016/j.fuel.2022.124040.
[21] Boehm RC, Yang Z, Heyne JS. Threshold Sooting Index of Sustainable Aviation Fuel Candidates from Composition Input Alone: Progress toward Uncertainty Quantification. Energy & Fuels 2022. doi:10.1021/acs.energyfuels.1c03794.

APPENDIX C

Perspective on Fuel Property Blending Rules for Design and Qualification of Aviation Fuels: A Review

Boehm, R. C., Yang, Z., Bell, D. C., Faulhaber, C., Mayhew, E., Bauder, U., Eckel, G., & Heyne, J. S. (2024). Perspective on fuel property blending rules for design and qualification of aviation fuels: A review. *Energy and Fuels, 38*(18), 17128–17145. https://doi.org/10.1021/acs.energyfuels.4c02457

1. Introduction

The aviation industry is aggressively pursuing alternative low-carbon propulsion technologies and sustainable aviation fuel (SAF) as a means to decarbonize the sector. This shift is driven by initiatives from multiple national governments and the International Civil Aviation Organization (ICAO), which have implemented policies and challenges to accelerate the adoption of cleaner aviation solutions. As a result, there is a growing focus on developing chemical conversion technologies that can transform renewable feedstocks into jet fuel. In the United States, the SAF Grand Challenge has set an ambitious target of producing 35 billion gallons of sustainable aviation fuel annually by 2050, underscoring the urgency and scale of the decarbonization effort in the aviation industry.1 In addition to this 2050 goal, the SAF Grand Challenge aims to facilitate the annual production of 3 billion gallons domestically by 2030, or approximately 10% of domestic jet fuel consumption.

The Environmental Protection Agency (EPA) reports that D4 and D6 renewable jet fuel production has seen a significant increase in recent years.2 In 2023, 26 million gallons of SAF were generated, and in the first half of 2024 alone, production has already reached 27 million gallons.2 Looking ahead, domestic SAF production capacity projections are expected to surpass 2 billion gallons annually by the end of 2028.3 This projected capacity is a substantial increase from current levels, representing nearly 80 times the production achieved in 2023. To further contextualize this growth, consider that in 2020, the combined production of biodiesel and renewable diesel, which have less stringent technical requirements compared to jet fuel, was 13.6 billion gallons.4 The fact that SAF production is projected to reach 2 billion gallons annually by 2028, despite the more rigorous technical standards, highlights industry expectations and collective urgency of the aviation enterprise to decarbonizing.

Bridging the gap between decarbonization targets and actual production values is a substantial challenge, particularly in the case of novel SAF routes. The process of developing a new SAF pathway is both time-consuming and expensive, with an estimated cost of $100 million to produce sufficient volumes (approximately 100 gallons) of material to enter the ASTM D4054 qualification process. This qualification process alone can take multiple years, and companies may face bankruptcy along the way. Even after successful qualification and approval (resulting in an update or addition to ASTM D7566), the technology must undergo significant scale-up, initially requiring a demonstration facility before a commercial facility can be developed. These additional steps further contribute to delays and costs in the process. To align new technologies, manage expectations, and communicate likely approved blend ratios or illustrate hard limits on a given pathway's ability to produce an acceptable aviation fuel or blend stock, predictive models are employed from the inception of a novel SAF route.5

Currently, in the United States and Europe, aviation turbine fuels must adhere to the stringent specifications detailed in ASTM D1655 for Jet A and Jet A-1 to be considered fungible and suitable for use in the existing fuel infrastructure, aircraft, and engines. Renewable carbon can be incorporated into an ASTM D1655-compliant fuel through two primary methods: co-processing with fossil carbon or blending an ASTM D7566-approved renewable blend component (SAF) with fossil-based fuel. (It should be noted that there will likely be 100% drop-in [ASTM D1655 compliant] and non-drop-in [or Jet-X] SAF pathways in the coming years and decades.) These processes and specifications must be strictly followed to ensure that the resulting fuel containing renewable carbon meets the required standards before it can be introduced into the fungible supply network.

However, the specifications for renewable or synthetic blend components (ASTM 7566) are significantly more restrictive and rigorous compared to those for conventional fossil-based fuels. This is because fuel properties that fall outside the range defined by historical experience with Jet A or Jet A16 fuel may be incompatible with existing infrastructure, including combustors, flow control logic or hardware, storage tanks, seals, handling procedures, fuel additives, and software. These heightened requirements are in place to guarantee that the introduction of renewable or synthetic components does not compromise the safety, performance, or compatibility of the aviation fuel supply.

The evaluation process (ASTM D4054) identifies and establishes appropriate property limits to control fuels made from any process/feedstock other than petroleum refining. To date, eleven conversion processes have fully passed through the evaluation process and blends of up to 10 %v or 50 %v of the products of these processes with conventional jet fuel or crude oil is allowed and controlled by ASTM D7566 or annex A1 of ASTM D1655.7 While eight processes have a corresponding annex to ASTM D7566 that ensures its production pathway is in control, there are also four “extended requirements” that apply to the finished (blended) product in addition to those called out by ASTM D1655. Further amendments to the controlling documents are expected as the blend fraction of SAF in conventional fuel increases and the diversity of commercialized SAF products potentially warrants blending multiple SAF pathways to meet the aforementioned

2030 and 2050 goals. To inform new specifications, it is important to characterize the impacts of fuel-fuel blending on the safety and performance properties of the finished product using blending rules derived from fundamental physics.

To address these challenges, it is crucial for developers of SAF to employ probabilistic fuel property prediction methods based on modest production volumes8,9 or the anticipated composition of the considered production stream. These predictions can significantly de-risk pathway development of SAF and illuminate high risk blend components early, potentially saving thousands of gallons of fuel and tens to hundreds of millions of dollars throughout the product development lifecycle, from the earliest phases to full-scale commercialization. By utilizing these prediction methods, SAF developers can ensure that their fuels meet the stringent specifications required for compatibility with existing infrastructure and engines, while also minimizing the costs and risks associated with developing new SAF pathways. Of course, for a prediction method to be useful, it is important to quantify its accuracy uncertainty. Here, information is collected from numerous, independent sources in order to document the model accuracy of simple blending rules for seventeen properties, as applied to arbitrary mixtures of aromatic and saturated hydrocarbons within the jet fuel volatility range. Heretofore, no such compilation of blending rule accuracy has been published.

2. Fuel Property Targets

Fuel property targets based on the specifications (direct or inferred) in the controlling documents help fuel developers select target composition, feedstock, conversion approach, parameters such as pressure, temperature or catalysts used in various stages of the conversion process, biocrude refinement strategy, and blending strategy with other bioproducts or petroleum products. The financial impacts of these decisions emphasize the importance of modeling final fuel properties based on compositional data. The availability of component composition and property values of theoretical fuels can vary widely and generalized strategies for estimating model parameters that account for 2nd order mixing effects are unknown to the authors. It is therefore difficult for researchers or developers to assemble the information required to leverage models that require input beyond composition and component property values, further motivating the use of the simplest model that affords acceptable prediction accuracy. Conversely, gaps in compositional or component property data, as required to leverage simple blending rules, can be filled by methods such as Monte Carlo sampling 10–13 or machine learning, 14 which facilitate a probabilistic interpretation of fuel property predictions.

Multi-dimensional optimizations employed for distillation cuts, 15 conversion process parameters, 16 specification alteration trade studies,17 etc. may invoke blending rules millions of times, magnifying the impact of computational time. In this context the functional requirements on the chosen blending rules may be skewed more toward ease of use and less toward accuracy than the functional requirements on the chosen blending rules applied to a less generalized outcome. For example, fuel surrogate development 12,18,19 is all about matching a suite of properties of very complex, natural fuels to those of engineered surrogates, comprised of few (<25) components that are readily procurable in high-grade purity. Throughout their development cycle, surrogate fuels (real or imagined) have no gaps in component property or composition data, and it may be possible to assemble the information necessary to incorporate second order mixing effects into the property predictions. Since surrogate defining routines iterate across a relatively small number (<25) of plausible constituents, blending rules may be invoked thousands of times instead of millions, as required for optimizations iterating across many (~1150) plausible constituents, and thus the impact of model computational time is minor. Presumably, the more complex fundamental models improve the probability of attaining a match to all of the chosen target property target on the first attempt. In contrast, simple blending rules facilitate complex optimizations and expedite the flow of important information between aviation fuel stakeholders.

Within the context of modeling, composition-property relationships can be distinguished by three distinct categories. The first category treats the fuel as a singular entity, predominantly employing machine learning or regression techniques. 14,20–24 These models stand out for their exemption from requiring blending rules, although their applicability is confined to fuels similar to those in their training datasets. The second category, in contrast, perceives fuel as a mixture of various components. It necessitates not only precise blending rules but also comprehensive data on all constituents present in the fuel. The third category represents a hybrid approach. 14,23,25 26,27 It conceptualizes fuel as a 'mean component'. This category is distinguished by its training on both fuels and individual components, enabling it to autonomously learn the blending rules required for accurate analysis. The second category has an advantage in terms of accountability and also on extrapolation to unknown fuels. In this paper, we examine the blending rules, since they are, besides accurate data of all constituents of the fuel, crucial for models of the second category.
Within the first category, fuel properties can be estimated from regression models that relate a set of measured properties, e.g., Nuclear magnetic resonance (NMR), Fourier transform infrared (FTIR), Raman, etc. to the properties of interest. An excellent review of these methods has been reported by Vozka and Kilas in 2020 28 and the points made there will not be

repeated here, except as needed. These models suffer from, not only an undetermined isomeric population distribution but also an undetermined distribution of carbon number within each family. Moreover, certain properties, the distillation curve for example, are strongly impacted by characteristics that are not significantly informed by the optical or magnetic properties of the mixture, and thus cannot be predicted by any model that exclusively uses such data to inform the model. The other fundamental issue with regression models is that input to the model would be very difficult to determine without making a physical measurement, and thus composition optimizations, involving property estimates for millions of composition variants, would be extremely difficult or problematic to execute.

Regarding simple blending rules of the second category, sixteen scalar products between a concentration vector (mass, mole, or volume fraction) and a properties vector can be used to estimate thirty-one properties, including a nominal predicted value and confidence intervals. The goal of this article is to document the uncertainty of these models when applied to mixtures of hydrocarbons that are potentially significant components in jet fuel; C7-C18 alkanes and aromatics. These scalar product models apply to mixtures of complex fuels as well as mixtures of pure components and everything in-between, which is particularly valuable for anticipating fuel properties in advance of blending fuels from different sources. Additionally, one model that is somewhat more complex than a scalar product will be discussed. Each of the property models to be discussed in this article is listed in column A of Table 1 while column B provides a listing of other relevant properties that can be determined from those listed in column A. Most of these property-property relationships are exact; the uncommon exceptions are discussed in Section 3.

Table 1. Fuel Characteristic Listings.

A. Properties Derived from Blending Rules	B. Properties Derived from Column A	C. Composition Limit Specified in ASTM D4054	D. Properties Impacted by Trace Levels of Impurities or Additives	E. Controlled Bulk Properties Not Covered Here
Carbon number, C#	Molecular weight, Mw	C8-C16 Population distribution of aromatics (report)	Conductivity vs concentration of additive	Autoignition temperature
Hydrogen number, H#	Hydrogen to carbon ratio, H/C	C8-C16 Population distribution of paraffins (report)	Corrosion of copper	Hot surface ignition temperature
Density, □	Percent hydrogen, %H	Copper	Distillation loss	Upper flammability limit
Lower heating value, LHV	Molar volume, Vm	Cycloalkanes	Distillation residue	Bulk modulus vs temperature and pressure
Heat capacity, Cp	Higher heating value, HHV	Existent gum	Effect on clay filtration	
Thermal conductivity, k	Energy density, ED	Fatty acid methyl esters	Effect on coalescer filters and monitors	
Kinematic viscosity, □	Isentropic expansion factor, □	Halogens	Electrical conductivity	
Surface tension, □	Thermal diffusivity, □H	Mercaptan sulfur	Lubricity	
Freeze point, Tfp	Dynamic viscosity, □	Naphthalenes	Microseparometer rating	
Vapor pressure, Pvap	Prandtl number, Pr	Nitrogen (fuel bound)	Potential gums	
Distillation curve (ASTM D2887, infinite-plate limit), Tn	Ohnesorge number (fuel dependent terms), Oh'	Peroxides	Response to CI/LI additive	
Lower flammability limit, LFL	Distillation curve (ASTM	Polar organic molecules (report 13 classes)	Thermal stability	

A. Properties Derived from Blending Rules	B. Properties Derived from Column A	C. Composition Limit Specified in ASTM D4054	D. Properties Impacted by Trace Levels of Impurities or Additives	E. Controlled Bulk Properties Not Covered Here
	D86, one-plate limit), Tn			
Flash point, Tflash	Refractive index, n	Tetralins and Indanes	Water solubility vs temperature	
Dielectric constant, □	Smoke point, Sp	Total acidity	Compatibility with additives	
Threshold sooting index, TSI		Total aromatics	Toxicity	
Derived cetane number, DCN		Total sulfur	Air solubility	
Elastomer swell, Sw		Trace elements (22 listed at <100 ppb)		
		Water		
		Antioxidant (approved additive)		
		Metal deactivator (approved additive)		
		Fuel system icing inhibitor (approved additive)		
		Electrical conductivity improver (approved additive)		
		Leak detection tracer (approved additive)		
		Biocide (approved additive)		
		Corrosion inhibitor / Lubricity improver (approved additive)		
		Water scavenger (approved additive)		

In addition to physiochemical properties, ASTM D4054 also addresses the concentration of certain elements, molecules or types of molecules, and these are listed in column C of Table 1. Of course, measurements are required to acquire this data for real fuel samples, but for conceptual fuels or blends of component fuels that have fully characterized composition, the obvious blending rules are exact.

Column D of Table 1 lists fuel properties that are controlled by ASTM D4054 and influenced significantly by certain types of impurities that may be present in some aviation fuel samples at less than 1 %m. While it may not be possible to estimate these properties from detailed composition, it may be possible, in some cases, to predict the outcome of blending two or more fuels for which the property-of-interest was measured. No attempt is made here to document or assess any such model.

Column E of Table 1 lists four properties which are theoretically predictable from detailed bulk composition characterization, but which are not predicted well by simple blending rules. The models required to make predictions of autoignition temperature or a hot surface ignition temperature should involve detailed chemical kinetics and fully described temperature, pressure and gas phase species concentrations as a function of time. The upper flammability limit (UFL) can be estimated by using a model similar to that used for the lower flammability limit, but some of the approximations used in that model do not hold at relatively high fuel concentration. Intuition suggests that better estimates of UFL could be attained from more comprehensive, yet un-parameterized physical models. The bulk modulus of fuels at standard temperature and pressure could be predicted well by a simple blending rule that employs component

concentration and property data inputs, such a model is not expected to hold at conditions (temperature and pressure) approaching a phase boundary or at supercritical conditions. While the prediction of each of these four properties is certainly interesting and important, a characterization of the generality and accuracy of available (or developing) models is beyond the scope of this article.

While columns C-E of Table 1 contribute to its convenient compilation of important jet fuel properties, the focus of this article is on documenting the accuracy of and generality of the blending rules that can be used to predict the fuel properties listed in column A and the property-to-property relationships (or definitions) that can be used to predict the fuel properties listed in column B. In most applications the uncertainties of these blending models are small compared with the uncertainties introduced by the values of their inputs. For example, Hall et al. 29 have recently published an excellent presentation of properties of C8-C16 hydrocarbons from which the undetermined isomer uncertainty term can be inferred, and an approach (a.k.a. category 3) taken to reduce this uncertainty has been described elsewhere. 30,31 The uncertainty introduced through incomplete property vectors boils down to the accuracy of a quantitative structure property relationship (QSPR) model or the accuracy of the model used to describe the temperature dependence of the property. Citations to important works describing these models will be provided in the discussion section. Promising recent advances in the approach for developing QSPR models have been proposed by Pan et al. 32 and a thorough discussion of prior work on this topic has been provided by Landera et al. 33 Here the focus is on blending rule uncertainty, so discussion of models used to get component property data is limited.

A partial assessment (2 data points) of models available for the prediction of four important fuel properties has recently been given elsewhere. 34 Here, the focus is on documenting model uncertainty for every property of interest to the stakeholder community, and to juxtapose that uncertainty term with other sources of uncertainty in predictions. As such, each of the blending rules foreshadowed by Table 1 is documented in the discussion section, along with a characterization of its accuracy. Uncertainties are communicated with a unity plot when available, and by a standard deviation (σ), a mean absolute error, or a mean error. Unless there is reason to believe otherwise, quadrature addition of random error originating with each term in the scalar product is assumed for multicomponent mixtures, and in the absence of any evidence to the contrary we assume the variance of each term depends linearly on its concentration alone as described by equation 1. Evidence supporting the validity of this assumption is included or cited in the discussion section relating to some of the blending rules.

Property/property relationships (formulae) are also documented within the same subsection as the blending rule(s) that serve as source terms them, and the accuracy of the approximate (or empirically motivated) property/property relationships are qualified but not quantified. Generally, the uncertainty terms applicable to these relationships are also estimated by quadrature addition as represented by equation 2, where property Z is a function of properties, x_1 and x_2.

$$\sigma_{mix}^2 = \sigma^2 * \sum_i \tilde{c}_i^2 \;\; | \;\; \tilde{c}_i = \min(c_i, (1 - c_i)) \qquad (Eq.\ 1)$$

$$\sigma_Z^2 = \left(\frac{dZ}{dx_1}\right)^2 * \sigma_{x1}^2 + \left(\frac{dZ}{dx_2}\right)^2 * \sigma_{x2}^2 \qquad (Eq.\ 2)$$

6. Blending Rules Selection, Generality and Accuracy Documentation

3.1 Conservation of Mass

The average number of carbon or hydrogen atoms per molecule in a mixture is determined exactly by the scalar products expressed as equation 3. In these identities, $\vec{X}$ is the mole fraction vector, $\overrightarrow{C_n}$ is a vector of integer values corresponding to the number of carbon atoms characterizing the concentration bin (from the stenciled region of a chromatogram) and $\overrightarrow{H_m}$ is a vector of integer values corresponding to the number of hydrogen atoms characterizing the concentration bin. While these models introduce no error whatsoever, there is some uncertainty attributed to their inputs.

$$C\# = \langle \vec{X} \,|\, \overrightarrow{C_n} \rangle \text{ and } H\# = \langle \vec{X} \,|\, \overrightarrow{H_m} \rangle \qquad (Eq.\ 3)$$

The undetermined isomer uncertainty as well as the component property value uncertainty are zero in these models, whenever the input data applies to discrete molecules or bins of molecules (isomers) having the same empirical formula. In these cases, the only uncertainty entering into predictions of carbon number (C#) and hydrogen number (H#) is that associated with the concentration vector, which typically comes from a GCxGC experiment. While the GCxGC analytical approach has already garnered widespread use and value, the effort to standardize it to group types quantification of hydrocarbons35 is in its infancy. This complicates uncertainty determination, but lab to lab reproducibility tests have been

performed 36 and are expressed here as Equation 4, which fits their published reproducibility data. The true uncertainty could be larger due to bias consistent across experiments, such as FID response factor inconsistencies, 37 stencil errors, volatility overlap between isomers in different hydrocarbon families, column health, numerical peak integration bias, unnoticed retention time wrap-around, etc. That being said, there are also factors that could render the error smaller such as the fact that that concentration vector must sum to one and the high likelihood that miss-appropriated peaks on a chromatogram, the main source of error, would be off by a single carbon number. For chromatogram stencil bins that encompass thousands of isomers, such as C15 iso-alkanes for example, it is possible to miss a large fraction of the mass in the bin if many of the isomers are present at a concentration that is below the detection limit of the experimental method. 38

$$\sigma_y = 0.26 * \bar{y}^{\,0.28} \qquad \textit{(Eq. 4)}$$

Armed now with C# and H#, the hydrogen to carbon ratio (H/C) can be determined without any uncertainty contribution from the model itself, which is, as its name implies, a straightforward ratio, documented as Equation 5. This property is used in correlation-based models for lower heating value and sooting propensity as well as physical models of combustion products. The average molecular weight of the molecules comprising a fuel sample is given by equation 6, where 1.008 g/mol is the atomic weight of hydrogen and 12.011 g/mol is the atomic weight of carbon, and the fuel's mass fraction of hydrogen is documented by Equation 7. A fuel's molecular weight is used to convert between mass and mole concentration units and to convert between density and molar volume, which is discussed in the next subsection, while the mass percent hydrogen is used in the conversion of higher heating value, HHV (i.e., gross heat of combustion) into lower heating value, LHV (i.e., net heat of combustion).

$$\mathrm{H/C} = \mathrm{H\#/C\#} \qquad \textit{(Eq. 5)}$$

$$\mathrm{Mw_{fuel}} = 12.011 * \mathrm{C\#} + 1.008 * \mathrm{H\#} \; = \langle \vec{X} \,|\, \overrightarrow{\mathrm{Mw}} \rangle \qquad \textit{(Eq. 6)}$$

$$\%\mathrm{H} = 1.008 * \mathrm{H\#/Mw_{fuel}} \qquad \textit{(Eq. 7)}$$

3.2 The Ideal Solution

It is well-known that solutions do not always blend linearly, and the resulting density of a combination of two fluids is not the simple weighted average of the two. Nevertheless, the approximation represented by equation 8 is documented here because of its simplicity and because the uncertainty it introduces into jet fuel property predictions is small compared to uncertainty originating from the model inputs. In this equation, V_m is molar volume, ρ is density, and $\vec{v}$ is the concentration vector in terms of volume fractions. The denominator used for volume fractions is the sum of component volumes, not the mixture volume, and thus $\vec{v}$ is a unit vector.

$$V_{m,fuel} = \langle \vec{X} \,|\, \overrightarrow{V_m} \rangle \quad \text{or} \quad \rho_{fuel} = \langle \vec{v} \,|\, \vec{\rho} \rangle \qquad \textit{(Eq. 8)}$$

$$\sigma = 0.007 * \rho_{fuel} * \mathrm{sqrt}\left(\sum_i \tilde{v}_i^2\right) \;|\; \tilde{v}_i = \min\left(v_i, (1 - v_i)\right) \qquad \textit{(Eq. 8.1)}$$

A unity plot showing 146 recently published 39 measurements and predictions of density at 15 ˚C of two-constituent mixtures of species likely to be found in jet fuel is shown in Figure 1. In this dataset each constituent may be a single component, a 50/50 by volume blend of single components or a complex mixture such as jet fuel. The largest modelling errors are observed when the final mixture contains two or three species which is consistent with the presumption expressed by equation 1. The standard deviation of the model error is given by equation 8.1 and is consistent with previous determinations made from more limited datasets. 40 In comparison, a recently published regression model imbued with composition data from GCxGC-FID experiments attained 0.1% mean absolute percentage error. 41 In contrast, the standard deviation of the distribution of molar volumes applicable to a given hydrocarbon class is approximately 10% of the mean for that class. 29 Moreover, the uncertainty in the density prediction is very small relative to the acceptable range for jet fuel which is 0.775-0.840 g/ml. Even for compositions identified with full isomeric detail, where the model error is not dwarfed by its input uncertainty, having a prediction uncertainty that is less than 1% of the nominal prediction is hardly motivation to seek out a more accurate model in the applications of note here. Nonetheless, readers who are interested in more accurate mixing rules to predict the density (or molar volume) of fuels may consult Nabipour et al. 42 as a starting point.

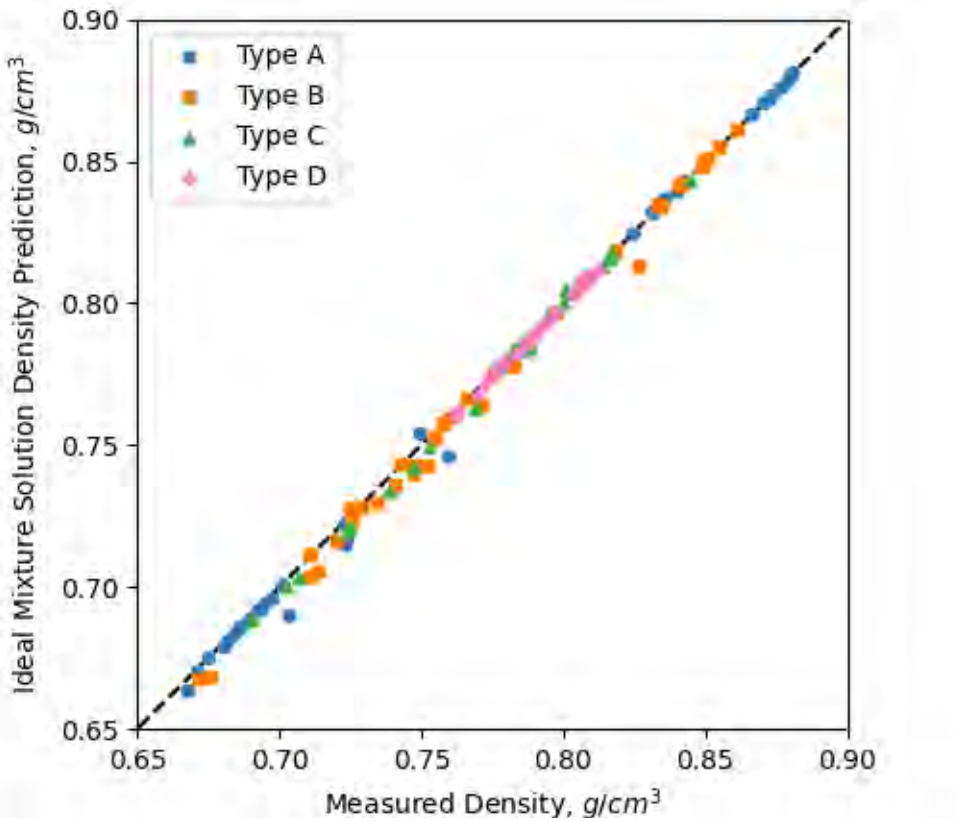

Figure 1. Unity Plot for Ideal Solution Approximation. Binary mixtures of aliphatic and aromatic hydrocarbons within the jet fuel volatility range. Type A: Both mixture constituents are comprised of a single component. Type B: One mixture constituent is a single component; the other is a 50/50 (by volume) mixture of two components. Type C: One mixture constituent is a single component; the other is a complex mixture. Type D: Both mixture constituents are complex mixtures.

The fuel density is a fundamental property to which many other properties are correlated, notably for aviation including speed of sound and dielectric constant, which are measurements taken in flight, along with fuel volume to gage fuel mass and latent heat available to power the aircraft. The density of the fuel that is in an aircraft should be known as accurately as possible, through direct measurement, primarily for this reason. Pre-application, however, equipment manufacturers design their hardware to accommodate any fuel that conforms to the specification range; 0.775-0.840 g/ml at 15 °C. From the perspective of SAF developers, that is the target, period. The density estimates noted here are used to guide blending formulations and as input to several other property estimates as discussed below, which are also driven by a target range. It is presumed here that a <1% prediction error is small compared to the margin producers develop between the fuel specification limits and the property goals they set internally for their product.

3.3 Conservation of Energy

Enthalpy (per unit mole, or mass) is a state function and therefore the change in enthalpy between any two states of the system is not dependent on the path taken to connect them. This, of course, applies to heats of formation, heat of combustion, and the general form of the exact blending rule is given by equation 9. In this expression ΔH refers to a change in enthalpy, c refers to the units of the concentration vector (mass or mole) and ΔH_{mixing} refers to the heat of mixing. For the liquid phase, the heat of mixing is not quite zero in real mixtures, and by neglecting this contribution in the application of equation 5 a negligibly small error, expressed by equation 9.1, is introduced. The values reported here are based on the measurements of Lundberg. 43 Boehm et al. 44 discussed in detail the other sources of uncertainty in the so-called 'tier alpha' method as applied to seventeen different complex mixtures. While the modeling error received a

mention in that article, it contributes ~100 times less than the measurement uncertainties of the component concentrations and enthalpies and ~1000 times less than the uncertainty attributed to undetermined isomers.

$$\Delta H_{c,fuel} = \langle \vec{c} \mid \overrightarrow{\Delta H_c} \rangle + \Delta H_{mixing,c} \qquad (Eq.\ 9)$$

$$\Delta H_{mixing,kg,liq} = 0.0 \text{ to } 0.3 \text{ kJ/kg} \qquad (Eq.\ 9.1)$$

Equation 9 applies to the higher and lower heating values, HHV and LHV of the fuel (a. k. a. gross and net heat of combustion) as well as the gas or liquid phase heat of formation, any of which may be used in engineering models applied to combustion, engine performance and aircraft drag. The product of LHV with (mass) density yields the energy density (ED, equation 10) which may be used in engineering models to determine volumetric flow rates, fuel system pressure losses, and heat transfer, for example. For specialty SAF (not conforming to ASTM D1655) the energy density of the fuel would also be used for fuel passage and orifice sizing as well as airplane fuel tank sizing. 17

$$ED_{fuel} = LHV * \rho_{fuel} \qquad (Eq.\ 10)$$

The temperature derivative of equation 5 results in the heat capacity, C_p and this is expressed as equation 11, where the derivative of the heat of mixing term has been dropped as an approximation. The uncertainty introduced by this approach is negligible in the gas phase because intermolecular forces do not significantly perturb the saturated degrees of freedom of motion associated with molecular translation and rotation or the largely unsaturated degrees of freedom of motion associated with intramolecular vibrations. In the liquid phase however, none of these assertions are true. The degrees of freedom associated with 'hindered' rotation of molecules or intermolecular (or lattice) vibrations (sourced back to translation and rotation of gasses) contribute significantly to its temperature-dependent heat capacity and these lattice vibrations are wholly determined by intermolecular forces which are certainly different for heterogeneous terms (the left side of equation 11) than they are for homogeneous terms (the right side of equation 11). The impact of these intermolecular forces is referred to here, and in the cited literature, as excess heat capacity.

Eighty-one measurements of binary aromatic hydrocarbon blends have indicated that the contribution of excess heat capacity is within +/-0.9% of the bulk fluid heat capacity.45 Beyond this example, the vast majority of work related to the evaluation and prediction of multi-component liquid heat capacity is focused on polar molecules, which are present only in trace amounts in aviation turbine fuel. Sharma et al. 46 observed a maximum 12.8% deviation from Equation 11 for 803 total heat capacity measurements of binary and ternary polar compound mixtures. This is consistent with 1083 measurements by Malik et al., 47 who reported a maximum 12.5% contribution of mixing towards the bulk fluid heat capacity, as well as earlier studies. 48,49 In both the polar and non-polar studies cited here, blend ratios containing large mole fractions of multiple components (e.g., 0.5/0.5 binary or 0.45/0.45/0.1 ternary ratios) exhibited the highest excess heat capacity supporting the application of equation 1 to the heat capacity blending rule. Since this has not been proven and it is unclear whether trace polar molecules may have a disproportional impact on heat capacity, the evaluation of heat capacity for complex mixtures, such as aviation turbine fuels, represents an area of fuels research in need of attention. Nevertheless, the discussion in the following paragraph applies under the assumption that equation 1 is applicable to the heat capacity blending rule when applied to aviation fuels.

$$C_{p,c,fuel} = \langle \vec{c} \mid \overrightarrow{C_{p,c}} \rangle \qquad (Eq.\ 11)$$

$$\sigma \approx 0.06 * C_{p,c,fuel} * \text{sqrt}\left(\sum_i \tilde{c}_i^2\right) \;\; || \;\; \tilde{c}_i = \min\left(c_i, (1 - c_i)\right) \qquad (Eq.\ 11.1)$$

At first blush, an error of 12.5% is concerning because accurate heat capacity is necessary (but not sufficient) to execute accurate heat transfer analyses of fuel systems to get accurate fuel temperature and enthalpy at inlet to the fuel nozzle and the combustor, where fuel temperature also impacts, exponentially, viscosity and thermal stability of fuel. However, upon closer inspection, the estimated uncertainty of equation 11 for many component mixtures is less concerning. Assuming the 12.5% max observed error of 1083 data points (215 mixtures) is three standard deviations off and the mean error is zero, then the random error in the heat capacity prediction is given by equation 11.1. The leading scalar, 6% is still concerning, but the sum of the square of the mole fractions is a small number for many component fuels. Even for SAF with very few components, which are typically limited to a maximum blend ratio of 10 %v with a conventional jet fuel, the sum of the mole fractions squared is unlikely to exceed 0.028, below which the standard deviation of the model error is less than 1%.

Returning now to the gas phase, for which the error in equation 11 is negligible, there is little interest in knowing the heat capacity of vaporized jet fuel, as it along with the fuel latent heat of vaporization is baked into the LHV application of equation 9. A rare demand for the vaporized fuel heat capacity occurs during detailed redesign of premixing chambers within combustors, where fluid dynamics is very complex, but temperature gradient estimates which employ fuel vapor heat capacity are necessary to illuminate potential root cause of observed coking or autoignition issues that show during a design validation test.

The heat capacity of the combustion products is more interesting than the heat capacity of vaporized fuel under normal circumstances, as it is used to calculate adiabatic flame temperature. The combustor exhaust gas heat capacity, more precisely the ratio of the temperature derivatives of enthalpy and internal energy at constant pressure (C_p) and volume (C_v) respectively, should be used in turbine performance models to calculate the work achievable through adiabatic or isentropic expansion. 50 The isentropic expansion factor (γ) is defined by equation 12. It varies with temperature, air humidity, and the combustion products of the fuel (which stem from the fuel to air ratio in the combustor and the hydrogen to carbon ratio of the fuel). Nonetheless for engineering purposes, γ is frequently treated as a constant based on the properties of dry air at some reference temperature.

$$\gamma = C_{p,exhaust}/C_{v,exhaust} \quad (Eq.\ 12)$$

NASA polynomials 51 covering the full temperature range of interest are available for all components of air as well as the combustion products, so $C_p(T)$ can be treated as a known quantity. The other heat capacity term C_v is just a little more complicated. A blending rule analogous to equation 11 could be used but is not necessary. To first order the difference between C_p and $C_v$is equal to the universal gas constant (R), so C_v follows from C_p. Optionally, R may be scaled by the gas' compressibility factor (Z) or replaced by the value of $(C_p - C_v)_{air}$at a reference temperature and pressure for which both values are known and applicable to the operating environment of the turbine (up to 40 atm). Engineers may even go so far as to represent this difference for each exhaust gas component by its exact value, 52 which is given by equation 13, where T is temperature, α_T is the coefficient of thermal expansion and β is the isothermal compressibility. This, of course, is only possible because (PV_mT) equation of state models exist for each of the components. Fuel effects enter here through H/C as it influences the proportion of H2O and CO2 in the exhaust gas and through LHV as it influences the fuel to air ratio necessary to achieve a mission-point-demanded level of thrust, both of which are easily determined from composition.

$$(C_p - C_v)_T = T * V_m * \frac{\alpha_T^2}{\beta} \approx (C_p - C_v)_{ref} \approx Z * R \approx R$$
(*Eq. 13*)

3.4 Other Thermal Properties

The Prandtl number (Pr), defined as the ratio of kinematic viscosity (ν) to thermal diffusivity (α_H), is a significant factor in heat transfer correlations and is represented here by equation 14. 53 The thermal diffusivity is the ratio of thermal conductivity (k) to heat capacity per unit volume ($\rho * C_p$), as indicated by equation 15. The kinematic viscosity term is discussed in section 2.5, Fluidity Properties, while the thermal conductivity term is discussed in this section.

$$Pr_{fuel} = \nu_{fuel}/\alpha_{H,fuel} \quad (Eq.\ 14)$$

$$\alpha_H = k_{fuel}/C_{p,fuel} * \rho_{fuel} \quad (Eq.\ 15)$$

$$\alpha_H = \langle \vec{Y} \,|\, \overrightarrow{\alpha_H} \rangle \quad (Eq.\ 16)$$

A direct blending rule for Prandtl number might avoid compounding of uncertainties, but to the best of the authors knowledge, no such blending rule exists. Similarly, the authors are not aware of any published evaluation of a blending rule for thermal diffusivity. Equation 16, where $\vec{Y}$ is the mass fraction vector, is proposed here. However, it is unclear whether directly-measured, component thermal diffusivity data is significantly more precise than component thermal diffusivity data that is derived from conductivity, density and heat capacity measurements. Applying equation 16 to binary mixtures of isooctane and heptane, we found mean error of 7.43% relative to the archival literature on thermal diffusivity data of hydrocarbon mixtures. 54,55

Thermal conductivity prediction of liquid mixtures has been the subject of several archival studies, including most recently Rokni et al. 56 and Malatesta and Yang. 57 A prevalent theme in thermal conductivity models for mixtures is to employ a generalized form of a thermal conductivity model for pure materials, where a blending rule is used to generate the inputs. These two studies employed an entropy scaling approach, for which several inputs are required that may not be generally available, including the reduced residual entropy, an equation of state, and a collision integral. Most of the more sophisticated models require the critical temperature, volume and pressure as input to a sub-model buried in layers of detail. While there is no questioning the superior accuracy with model evolution beyond the mass fraction weighted average model proposed in 1956, 58 it remains to be seen whether such accuracy is truly worth the cost in terms of computational resources, human labor or outright loss of applicability to complex mixtures that have never been produced. This simple blending rule is expressed here as equation 17.

$$\mathrm{k_{fuel}} = \langle \vec{\mathrm{Y}} \,|\, \vec{\mathrm{k}} \rangle \qquad (Eq.\ 17)$$

Using temperature (only) dependent models published by NIST, 59 Yang et al. [90] generated five sets of data with temperature equal to 288, 323, 358, 393 or 428 K, spanning the range of fuel temperature that would potentially be encountered during the normal operation of an aircraft. The standard relative deviation of these datapoints ranges from a low of 17.3% at 288 K to a high of 19.4% at 428 K with no apparent correlation with carbon number or family. The jet fuel conductivity values reported by Malatesta and Yang 57 are all within the scatter of the neat material conductivity values in this database, hinting that a simple scalar product model may in fact be good enough for engineering purposes despite the decades of development of more elaborate models. Evidence to the contrary, perhaps motivating some of the early work toward the development of elaborate models, includes a fact pointed out by Baroncini et al. 60 that the conductivity of some binary mixtures of polar (and presumably associated) organic molecules does not follow interpolation rationale. We consider such mixtures to be well outside the range of potential aviation fuels, which are comprised of many non-associated species. Considering two articles 61,62 documenting the thermal conductivities of binary mixtures of normal alkanes with other normal alkanes or aromatics, the maximum observed error of the scalar-product blending rule is 2.6%.

3.5 Fluidity Properties

The fuel dependent factor (Oh') of the Ohnesorge number ($Oh = Oh' * L_{char}^{-0.5}$), defined by equation 18, combines three fuel properties that are known to influence atomization of fluids into a single property that is significantly more correlated with important spray characteristics and outcomes such as ignition 63,64 than viscosity, surface tension (σ) or density. To the best of the authors knowledge no one yet has proposed a blending rule for Oh'. Such a rule, to directly calculate Oh' from composition and component Oh' could be convenient, but is unlikely to reduce prediction uncertainty because there is no direct measurement of Oh' to apply to the components separately. In this section the errors associated with the blending rules for viscosity and surface tension are discussed, where emphasis is placed on viscosity because it varies with composition and temperature much more so than density or surface tension and because it also contributes strongly to the Prandtl and Reynolds numbers.

$$Oh' = \nu * \sqrt{\rho/\sigma} \qquad (Eq.\ 18)$$

Hernandez et al. 65 recently compared thirty different blending rules for the viscosity of petroleum-based fuels using 303 measured data points of biodiesel and petroleum/biodiesel binary blends. Nine of the thirty blending rules showed a relative standard error below 5%. The Arrhenius blending rule, 66 represented here by equation 19, was among the most accurate and the most straightforward. Separately, Boehm et al. 39 determined the accuracy of this model by comparing 675 measured and predicted viscosities of simple to complex mixtures of aliphatic and aromatic hydrocarbons in the jet fuel volatility range. Equation 19.1 summarizes their accuracy assessment where $\xi(T)$ equals 0.132 at -40 ˚C and 0.096 at -20 ˚C. The unity plot they published is reproduced here as Figure 2. It very clearly shows less error with increasing mixture complexity, thereby supporting the presumption expressed by equation 1 (8.1, 11.1, 19.1, etc.).

$$\nu_{fuel} = \langle \vec{X} \,|\, \vec{\nu} \rangle \qquad (Eq.\ 19)$$

$$\sigma = \xi(T) * \nu_{fuel} * sqrt\left(\textstyle\sum_i x_i^2\right) \;\; | \, x_i \leq 0.5 \qquad (Eq.\ 19.1)$$

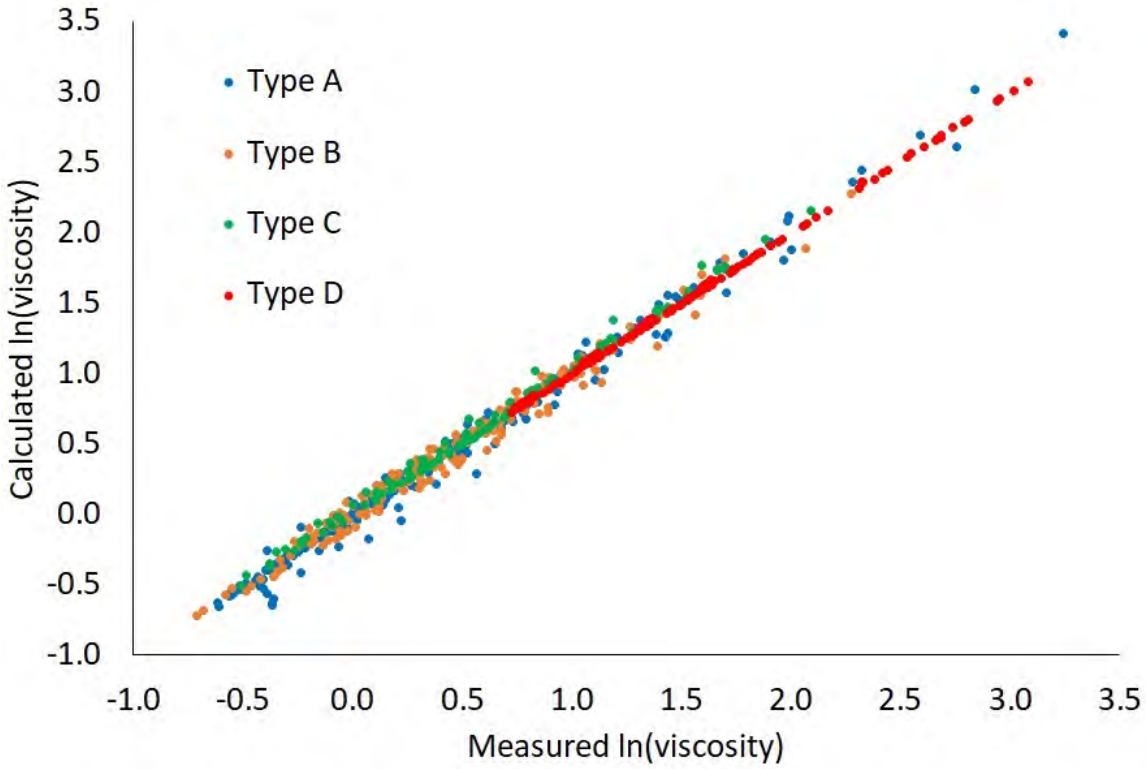

Figure 2. Unity Plot for Arrhenius Blending Rule. Binary mixtures of aliphatic and aromatic hydrocarbons within the jet fuel volatility range. Type A: Both mixture constituents are comprised of a single component. Type B: One mixture constituent is a single component; the other is a 50/50 (by volume) mixture of two components. Type C: One mixture constituent is a single component; the other is a complex mixture. Type D: Both mixture constituents are complex mixtures. The reference viscosity is 1 cSt. This figure has been previously published 39 and is reproduced here with permission from *Frontiers in Energy Research.*

The surface tension at 22 ˚C of 29 jet-fuel-range molecules extracted from DIPPR database 67 is 18 to 40 mN/m, with a strong dependency on hydrocarbon family that mirrors that of density and hydrocarbon family. The blending rule for mixtures of aliphatic and aromatic hydrocarbons in the jet fuel range, equation 20, is simplified from the general form published in 1986 by Hugill and Van Welsene. 68 The interaction terms are all set to 1 since aviation fuels are non-associated mixtures and the density of the vapor phase is set to 0 since it is much less than the liquid phase density at -10 to 40 ˚C, corresponding to the reference temperature range for which (lab-ambient-pressure) surface temperature measurements are required by ASTM D4054. This formulation is consistent with earlier expressions of the blending rule dating back to 1929 69 but a detailed, statistical analysis of its error, when applied strictly to mixtures of aliphatic and aromatic hydrocarbons has not been published to the best of our knowledge. There is, however significant, even if anecdotal, evidence 68 that a linear interpolative blending rule for surface tension is reasonable, particularly for these types of mixtures. Using data from Schmidt 70 and Bezerra 71 with a total of 55 sets of data points, this blending rule has a mean absolute error of 1.07 dyne/cm and a mean relative error of -2.85%.

$$\sigma_{fuel}^{0.25} = \left\langle \vec{X} \middle| \overrightarrow{\sigma^{0.25}} \right\rangle \qquad (Eq.\ 20)$$

The phase transition from liquid to solid has obvious and severe implications with regard to fluidity, so the freeze point (T_{fp}) is classified here as a fluidity property. Boehm et al. 72 showed that the freeze point of 41 simple to complex mixtures containing n-tridecane and/or bicyclohexyl is determined by the concentration of that component along with its phase transition thermal properties; heat of fusion (ΔH_{fus}), entropy of fusion (ΔS_{fus}), freeze point (T_{fp}), and heat capacity ($C_{p,solid}$ and $C_{p,liq}$). It was therefore proposed that the freeze point of fuel is the maximum freeze point of its components,

restated here as equation 21, where the subscript, 'mix' refers to any mixture of aliphatic and aromatic hydrocarbons having the same mole fraction of component, i as the fuel of study. This idea goes back to first principles and illuminates the physics supporting earlier work 73–75 that technically was directed toward understanding the relationship between the freeze point of fuel and normal paraffins concentration and size distribution. In this theory, every fuel component would have a corresponding freeze point predicted by equation 22.

$$T_{fp,fuel} = \max\{T_{fp,mix,i}\} \quad (Eq.\ 21)$$

$$T_{fp,mix,i} = \frac{\Delta H_{fus,i} + x_i * (C_{p,solid,i} - C_{p,liq,i}) * (T_{fp,i} - T_{fp,mix,i})}{\Delta S_{fus,i} + x_i * (C_{p,solid,i} - C_{p,liq,i}) * \ln\left(\frac{T_{fp,i}}{T_{fp,mix,i}}\right) + \zeta * \Delta S_{mixing}} \quad (Eq.\ 22)$$

The inputs to equation 22 pertain to the pure material unless otherwise specified and ζ is a parameter between 0 and 1 that can be tuned for each component, accounting for the difference between the entropy of mixing of an ideal solution and the actual entropy of mixing of the fuel. By default, $\zeta = 0.25$, resulting in a conservative freeze point prediction that could be too high (never too low) by upwards 20 ˚C at low mole fractions where the change in freeze point with concentration is steep. The implication of this conservatism from the perspective of fuel formulation is that a lower-than-truly-necessary cap on the concentration of that component would be set. With tuning, the model error reduces to less than 5 ˚C, where tuning can be accomplished by varying ζ to attain the best fit to freeze point data of prepared binary mixtures containing the subject molecule and some low-freeze solvent such as iso-octane. Mixtures containing two or more components that freeze out of solution at nearly the same temperature are the least likely to be well-approximated by equation 22, however the main issue with this model is the sparsity of input data to supply it. The DIPPR database 67 contains the freeze point temperature of approximately 200 molecules in the jet fuel range and just a few of those also have heat or entropy of fusion. Also, the heat capacity terms in equation 15 should be evaluated at the midpoint temperature between the freeze point of the pure component and the freeze point of that component in the solvated state, meaning the liquid state is supercooled. Boehm et al. 72 suggested using the pure-component heat capacity models proposed by Naef 76 with extrapolation to the temperature of interest. For materials with a known freeze point temperature but unknown heat (or entropy) of fusion, Boehm suggested using Walden's rule of thumb estimate for entropy of fusion, which is 56.5 J/mol/K. 77 It is not known how much (data input uncertainty) error is introduced into the component freeze point prediction by this approximation. Another issue with equation 22 is that it is difficult to solve for materials with a low entropy of fusion as the denominator flips between positive and negative values during the iteration. Some revision may be necessary to ensure that the first two terms in the denominator never sum to a value less than zero.

The good news is that common sense can be applied to equation 21. There is no need to include any component whose neat freeze point is below -40 ˚C and there is no need to include any component whose mole fraction is below a threshold value, approximately 5%. A mixture containing mostly high freeze point components (higher than -40 ˚C), all at very low concentration, may not technically freeze at -40 ˚C or higher, but its viscosity may be higher than the 12 cSt limit. The freeze point model is a good tool to catch formulations with too much of any one high freeze point component, or to identify a need for freeze point measurements of surrogate mixtures containing the proposed fraction of the at-risk component(s). The viscosity blending rule is a more convenient tool for evaluating fluidity.

Using the data published by Affens et al.74 as additional evidence supporting the premise behind equations 21 and 22, the data they provide for the normal alkanes from C12 to C17 can be used to tune equation 22 or serve directly as a prediction curve for any fuel mixture that contains those normal alkanes. As noted by Solash et al.73, these are the molecules that are most commonly responsible for the freeze point of fossil, aviation fuels. Similar datasets for all high-freeze-point components of SAF that are not normal alkanes do not yet exist.

3.6 Volatility Properties

Volatility properties consist of vapor pressure as a function of temperature, the distillation curve corresponding to the mass recovered vs. temperature resulting from a specified procedure and apparatus at ambient pressure, and the composition of the vapor phase throughout the non-equilibrium transformation between the liquid phase and the vapor phase. From the perspective of fuel formulation design, fuel volatility is all about its vapor pressure. The gas phase composition follows from the vapor pressure and so does the distillation curve, given an accurate model of the still and its operating conditions.

According to Dalton's Law, the total pressure is the sum of the partial pressures (p_i) of each component in the gas phase, reproduced here as equation 23. There is no modeling error associated with this blending rule. The estimation of partial pressures of components in real gas mixtures is a topic covered in chemistry education 78,79 and differences between real gasses and ideal gasses (for which the partial pressure is equal to the component mole fraction times the total pressure of the system, $RT/V_{m,gas}$) can be significant, particularly for dense gasses and molecules with unusually strong intermolecular interactions. While the aviation industry stakeholders do indeed care about gas properties at pressures up to approximately 50 atm and temperature up to 750 ˚C, they also care about understanding potential issues such as cavitation which can be caused by incipient boiling with the fuel delivery system, fuel leakage through valves after stopcock caused by vapor pressure exceeding the valve's cracking pressure, droplet evaporation rate before/during ignition and the accel to idle, and droplet evaporation rate at flight idle and throughout throttle chop transients where the combustor inlet air temperature and pressure are relatively low. At these conditions, the deviation of real gas properties from ideal gas properties is negligible relative to other sources of error in equation 24, which is Raoult's Law. In this equation, $P_{vap,i}$ is the vapor pressure of pure component i.

$$P_{tot} = \sum_i p_i \quad \textit{(Eq. 23)}$$

$$p_i = \mathrm{x}_{\mathrm{liq,i}} * P_{vap,i} = \mathrm{x}_{\mathrm{gas,i}} * P_{tot} \quad \textit{(Eq. 24)}$$

In a provocative article published 28 years ago, Hawkes 80 proclaimed that Raoult's Law is deceptive. While the tone of that article may be harsh, at least as it applies to mixtures of aliphatic and aromatic hydrocarbons in the jet fuel range, additional experimental data are needed to develop any correction to Raoult's Law. Pending this result, equation 24 should be used only when necessary. For example, the gas phase composition of partially evaporated droplets may be required to evaluate the chemical properties of the front end of the distillation.

The distillation curve represents the distribution of boiling points present in a fuel. Typically, distillation curve properties are reported as, T_n where n refers to a volume percent distilled, and T is the temperature at which that amount of fuel has vaporized. There are two common ways to measure distillation curve: standard distillation (ASTM D86) and simulated distillation (ASTM D2887). ASTM D86 is the referee method called out in ASTM D7566 even though it carries more experimental error. ASTM D2887 is a gas chromatography method relating chromatographic elution time with boiling point. Physically the differences in the results are dramatic; D86 is effectively a one theoretical plate separation whereas D2887 can be estimated as infinite theoretical plates. Both methods are required by ASTM D4054.

Distillation curve blending has not been explored in depth. Two distillation curves are controlled by ASTM D4054. The relevant experiments are described in ASTM D2887 and ASTM D86. The ASTM D2887 distillation curves are interpreted from gas chromatographic data. As such, the response from common peaks in each chromatogram can be combined in proportion to their mass fraction, consistent with the mass response of the flame ionization detector. There is no uncertainty introduced by the blending rule, as conservation of mass applies rigorously. However, if the raw data is obscured by reporting, the reported datasets can be partitioned into bins of discrete temperature range(s) and the mass in each bin proportionately summed over all mixture constituents. 81 While conservation of mass is invoked as the rationale for this blending rule, some uncertainty is introduced by the transformation between reported distillation curve points and the assignment of mass into bins. Its efficacy is shared in Figure 3, which is pulled from work in progress involving 46 mixtures, 21 points each. 81

For D86 distillation curve prediction, the difficulties in calculating vapor pressure manifest in uncertainty of distillation curve prediction. While an approach like the D2887 method described above may be acceptable, no analysis of its efficacy has been performed. More commonly, the vapor pressure is predicted from equations 23 and 24 along with some model of the distillation experiment wherein the composition of the liquid phase is updated with each increment of vapor removed from the system. Typically, the total pressure in the experiment is one atmosphere so the vapor phase component mole fractions equal their partial pressures.

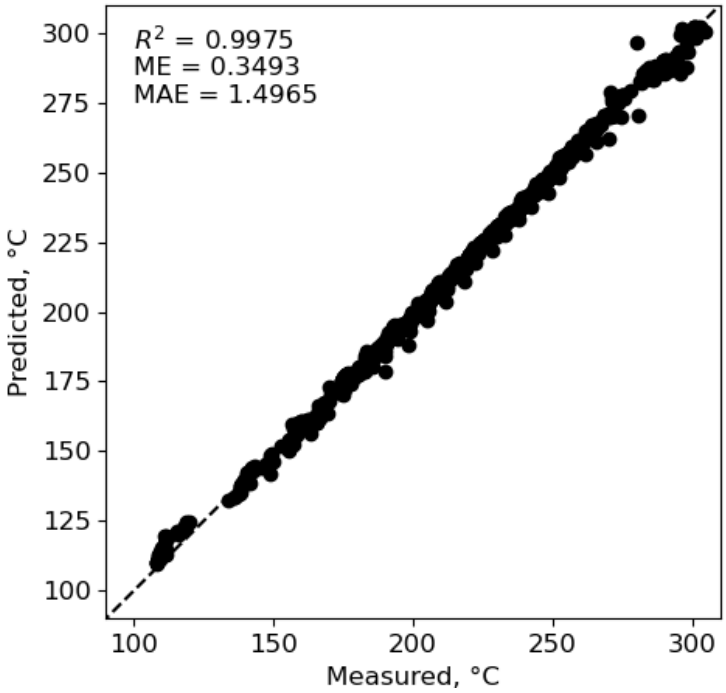

Figure 3. Unity Plot for Distillation Curve (via ASTM D2887) Predictions Based on Components' Distillation Curves.

3.7 Fire Safety Properties

The upper (UFL) and lower (LFL) flammability limits measure, respectively, the maximum and minimum fuel/air ratio required for ignition. In 1891, Le Chatelier 82 used a small set of data to propose a blending rule, represented here by equation 25, for determining the flammability limits of combustible gases commonly used in practical applications. Le Chatelier's rule has since been derived under somewhat differing sets of assumptions; 83–85 the most significant being that adiabatic temperature rise or the heat rise at the flammability limit (FL) is the same for all species. The mole fraction vector in equation 25 includes only the combustible components and the flammability limit refers to either the upper or lower limit. This form of the blending rule is particularly practical because a large amount of single-species fuel component flammability limit data exists within the archival literature, 86–89 data compilations 90 and most Material Safety Data Sheets, to name a few sources. However, the compiled data sources may preferentially report the most conservative measurements. 91

$$1/FL_{fuel} = \langle \vec{X} \mid \overrightarrow{1/FL} \rangle \qquad (Eq.\ 25)$$

The accuracy of equation 25 is satisfactory when applied to the LFL and offers a respectable guess when applied to the UFL. Coward and Jones 86 reviewed flammability limits for a wide range of flammable gas mixtures and qualitatively described good adherence to Le Chatelier's rule for light hydrocarbons with air. More recently, Liekhus et al. 88 found a mean relative error (MRE) of 8.5% for the LFL of 27 mixtures containing volatile organic compounds and Kondo et al. 87 showed 1.21% and 7.19% MRE for the LFL and UFL, respectively, of 86 mixtures. Beneficial in the context of this work, hydrocarbons are found to be particularly consistent with Le Chatelier's rule, and the predicted flammability limits tend to bracket the experimentally observed limits. Modifications to reduce blending rule error do exist, 85,87,88 but their added complexities render the equations impractical for most applications related to aviation fuel. Lastly, the recent work of Qi et al. 92 contains a comprehensive review of flammability limits, including prediction methods for flammability limit data not found in the other cited works.

Although not represented by equation 25, the limits of flammability also depend on the relative oxygen (or oxidizer) to inert concentration in the mixture as well as the starting temperature of the experiment. Rowley 91 suggests modifications to the models to account for these variations, and also suggests an extension of these concepts to predict the flash point temperature (T_{flash}). While this is an intriguing idea, the incentive to develop a new flashpoint point model is rather low

because a number of empirical correlations already exist that appear to be satisfactorily predictive for petroleum distillate fuels and SAF alike. Thorough reviews of these models have been recently published. 93,94 The Wickey model, 95 which is reproduced here as equation 26 was found to be the most consistent, with a global mean absolute error of 1.72 ˚C. 94 In this empirical model, each flash point is converted to a unitless, flash point index (FPI), the blending rule is applied to the index, and the that result is then converted back into a temperature.

$FPI_{fuel} = \langle \vec{v} \mid \overrightarrow{FPI} \rangle$ where each component in $\overrightarrow{FPI}$ is determined as follows:

$$\log_{10}(FPI) = -6.1188 + 4345.2/(383 - T_{flash}) \quad (^{\circ}\text{F units}) \qquad (Eq.\ 26)$$

Extension of flammability models to non-standard inlet temperatures, pressures, and 'air' compositions is more intriguing because combustors within turbine engines operate over a wide range of inlet temperatures and pressures (and potentially water content – such as some ground-based power plants that are subject to stringent NOx emissions regulations), while afterburners operate with inlet air that is approximately 1000 ˚C, which is well above the standard reference temperature of 20 ˚C and they receive vitiated air instead of clean air to oxidize the fuel that is supplied to them. Nonetheless, flammability models extended to non-standard inlet conditions are regarded as out-of-scope for this review.

3.8 Electromagnetic Properties

For nonmagnetic materials with no permanent dipole, the dielectric constant, ε_r (a.k.a. relative permittivity), refractive index, n and polarizability (α), are all relatable through simple algebraic expressions written below as equations 27 and 28, in which $N_A$is Avogadro's number and ε_0 is the permittivity of free space.79 A blending rule, can be applied to either polarizability 96,97 or dielectric constant. 97,98 These blending rules are reproduced here as equations 29 and 30, respectively. Since the 'effective' polarizability of a mixture (α_{fuel}) is not directly observable, the accuracy assessment of equation 29 is tied to equation 27. In other words, the dielectric constant of a mixture can be estimated from equation 30 directly or it can be estimated from equation 27 by using the effective polarizability from equation 29 along with a known molar volume as independent variables to determine the dielectric constant. In recent benchmarking against 160 dielectric constant measurements99 of samples consisting of both simple and complex mixtures of aliphatic and aromatic hydrocarbons within the jet fuel range, Yang et al. 97 found 0.0013 MAE and 0.0003 ME between measured and predicted values of dielectric constants when the fuel dielectric constant was calculated from equations 27 and 29, and 0.0038 MAE and 0.0037 ME when the dielectric constant was calculated directly from equation 30. While these metrics indicate superior accuracy by using the equations 27 and 29, Yang et al. emphasize that the accuracy of this approach depends on the concentration of species with non-zero dipole moments and the magnitude of those dipole moments. Equation 30, however, is more generally applicable, easier to use and its accuracy is believed to be well represented by the assessment they executed. In contrast, a particularly useful utility of equation 27 is to calculate dielectric constant data for non-polar fuel constituents based on modeled polarizabilities. 100

$$\alpha = \left(\frac{3\varepsilon_o}{N_A}\right) * V_m * \frac{\varepsilon_r - 1}{\varepsilon_r + 2} \qquad (Eq.\ 27)$$

$$n = \sqrt{\varepsilon_r} \qquad (Eq.\ 28)$$

$$\alpha_{fuel} = \langle \vec{X} \mid \vec{\alpha} \rangle \qquad (Eq.\ 29)$$

$$\varepsilon_{r,fuel} = \langle \vec{v} \mid \overrightarrow{\varepsilon_r} \rangle \qquad (Eq.\ 30)$$

3.9 Chemical Properties

With rare exceptions to be discussed here, the chemical properties of complex mixtures such as fuel do not lend themselves to prediction by simple algebraic models. Rather, chemical kinetic models are needed and excellent work has been published showing that kinetic models of surrogate fuels that match the H/C, Mw, derived cetane number (DCN) and threshold sooting index (TSI) of a corresponding real fuel are able to predict its combustion properties. 18,19 The execution of such a model to predict combustion properties is too computationally intensive to be done within the innermost loop of a fuel composition optimization. That said, algebraically simple blending rules for H/C and Mw, two of the four target properties used for fuel surrogate development, are exactly accurate as discussed in section 2.1 Conservation of Mass Models. The other two property targets (TSI and DCN) are discussed in this section, before discussion of elastomer/fuel compatibility.

The threshold sooting index, defined by equation 31, was introduced in 1983 101 as a tool to normalize smoke point data from different experiments. A year later it was leveraged to establish a method to predict the sooting tendency of mixtures based on the sooting tendencies of its constituents 102 which was later validated by several research teams. 103–106 This blending rule is reproduced here as equation 32. A similar blending rule can also be applied to a unified sooting index 107 or a yield sooting index 108 which invoke different raw data to represent sooting tendency. Motivated by a dearth of experimental data to supply the blending rule, Boehm et al. 106 integrated the (linear) TSI blending rule with a linear QSPR (quantitative structure property relationship) model to estimate TSI_{fuel} based on the integrated carbon fragment counts of the fuel, where the blending rule for each carbon fragment is exact, obeying the conservation of mass principle. The standard deviation of that QSPR model was estimated to be 4.5 TSI, slightly less than a more general QSPR model for sooting tendencies of oxygenated fuels that was published a few months earlier. 107 In contrast, the standard deviation of the uncertainty ascribed to the blending rule, equation 32 was estimated to be less than one index point. On the other side, the real variation between isomers within the same concentration bin, as defined by a stenciled region with a chromatograph from a GCxGC/FID experiment is much, much larger than one index point because branching has a large impact on TSI but no impact at all on molecular weight.

$$Sp_{fuel} = b * Mw_{fuel}/(TSI_{fuel} - a) \quad (Eq.\ 31)$$

† a & b are calibration coefficients for a specific operator and experimental arrangement and are calibrated by the smoke points of methylcyclohexane & 1-methyl naphthalene.

$$TSI_{fuel} = \langle \vec{X} \mid \overrightarrow{TSI} \rangle \quad (Eq.\ 32)$$

Historically, the cetane number, or the propensity of a fuel to auto-ignite under reference conditions, was measured in a CFR engine per ASTM D613. Over the last several decades the derived cetane number or DCN has gained favor in the combustion field for its ease of use, repeatability, modest footprint in the lab, and reproducibility across labs. Subsequent to its widespread use, the DCN has been found to correlate to aviation relevant metrics. The derived cetane number is calculated from the ignition delay according to the procedures and equipment described in ASTM. 109 DCN and the initial metric, cetane number, have long been used as metrics to characterize ignition quality of fuels used in compression-ignition engines. It has also been shown 110 to be strongly correlated with lean blow out of continuous flow combustors. Moreover, its correlation with gas-phase autoignition delay time is strong over a range of temperature, pressure and equivalence ratio conditions. 111,112 Regression models leveraging input from FTIR analysis of drop-size fuel samples have been shown to predict DCN of validation set samples with an RMS error of 1-2 index points. 113–115 Similar efforts have also used liquid phase IR absorption to predict DCN using linear and non-linear models with similar accuracy. 24 Aside from the drawback of needing at least a drop of sample fuel to get the FTIR spectral feature inputs, the regression models cannot predict the DCN of partially vaporized fuel because the FTIR spectrum may vary significantly from one distillation fraction to another and to the best of the authors knowledge there is not yet a standardized experimental method to attain FTIR data of the vapor fraction of 2-phase samples, nor is there a processing methodology to relate such data to distillation fractions.

The extent of vaporization and the mixedness of the vapor phase of the fuel inside a jet-engine combustor, leading up to forced ignition, lean blow out, autoignition forward of the intended flame front and even normal operating conditions for that matter are difficult to model accurately with computational fluid dynamics, or any other approach. To assess fuel effects on combustion metrics such as these, complex chemical kinetic models are required, but the human and machine labor involved to do this is extensive, requiring days or weeks to complete each fuel assessment on each combustion metric. At low fuel readiness level, such a drain on resources is impractical. A more tractable approach, relating the vapor fraction of the fuel throughout the vaporization transient to its DCN, in combination with other 1D models of the combusting system, affords stakeholders an early indication of whether the compositional differences between a SAF concept product and a conventional jet fuel will have a deleterious effect on the combustion metric of study. Equation 33 is one model for making this connection.

$$DCN_{fuel(gas)} = \langle \vec{c} \mid \overrightarrow{DCN} \rangle \quad (Eq.\ 33)$$

The maximum uncertainty associated with equation 33 is large, see Figure 4. The model itself has a mean absolute relative error of 2.9%. Moreover, when the blending rule is applied to partially vaporized fuel, the gas phase composition uncertainty can also be significant, as discussed in section 2.6 Volatility Properties. Additionally, the uncertainty regarding

the property vector input is particularly substantial for a DCN blending rule. The database of measured pure component DCN values is so sparse that other models 18,24,114,11618,114 must be used to populate $\overrightarrow{DCN}$ which leads to significant database uncertainty. Moreover, the undetermined isomer uncertainty is particularly large for DCN because this property is known 29 to be strongly impacted by branching, while the GCxGC stencil regions encompass all molecules having the same number of carbons that belong to the same hydrocarbon family.

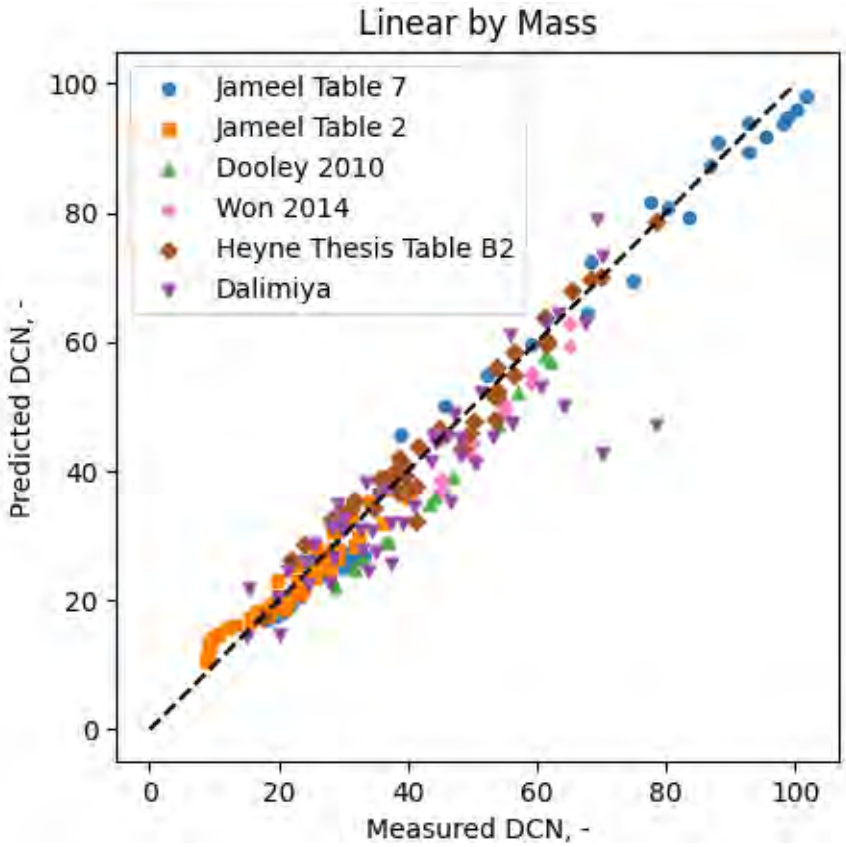

Figure 4. Unity plot showing DCN blending rule error. Data sources: 117,117,118,118,119,119–121.

The material compatibility of fuel is primarily concerned with the intercalation of certain fuel constituents into elastomeric materials. Effects of the fuel/elastomer interaction are commonly quantified with volume swell measurements during an O-ring soak test. These tests require days or even weeks of soak time to complete and the results vary between manufacturing batches of O-rings. 122–126 The testing complications present a challenge to the establishment of material compatibility requirements in the fuel approval process, as a comprehensive database of standard component swell values is sparse and therefore limiting for both proposed fuel evaluations and scientific studies aimed at predictive blending rules. Informed by the available literature, Kosir et al. 127 proposed the linear volumetric blending rule found in Equation 34.

$$Sw_{fuel} = \langle \vec{v} \mid \overrightarrow{Sw} \rangle \qquad (Eq.\ 34)$$

This rule was validated by Faulhaber et al. 122 for binary blends of 4 single dopant molecules from different hydrocarbon classes at 3%v to 40%v in a SAF comprised entirely of aliphatic hydrocarbons. These 24 results, along with 28 additional swell measurements of binary and ternary mixtures, are found in Figure 5. For this demonstration, single-species swell was quantified using measurements of each molecule doped at 8%v in synthetic paraffinic kerosene (SPK) and extrapolated to 100%v. This was done to avoid O-ring test sample degradation that can occur during soak tests using single species aromatic solvents. Volume swell of fuels, on the other hand, were simply measured at 100%v.

The MAE for these 52 total measurements is 1.23%v/v. Comparing this to the O-ring swell experience range for conventional jet fuel found with this experimental method (8.3-17.1%v/v), the total uncertainty ranges between 7-15% of the swell expected for elastomer compatibility. However, it is expected that experimental error comprises a large portion of this uncertainty. Further O-ring swell measurement campaigns will afford more comprehensive validation of this rule and associated experimental error, including investigation of potential interaction effects in complex mixtures and the impact of trace amounts of heteroatoms.123,125,128,129 A key part of these continuing efforts will be the collection of single component swell data to construct a model based on observed relationships between elastomer swell and other molecular properties or structural identifiers to predict the swell of compounds that are not readily available for measurement, building on the works of Graham et al. 125 and Landera et al. 33 whose respective models relate elastomer swell with Hansen solubility parameters. 11131

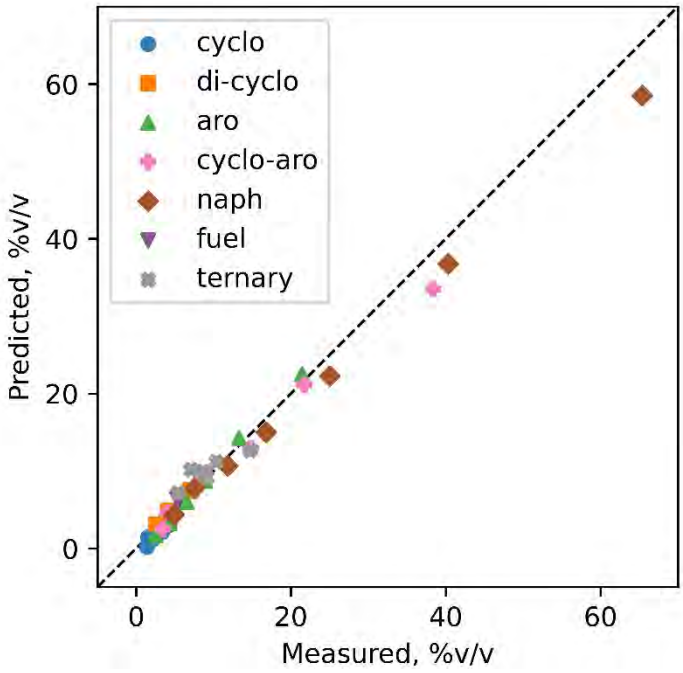

Figure 5. Unity plot showing O-ring volume swell blending error for 42 mixtures measured using optical dilatometry method of Faulhaber et al. 122 The legend indicates hydrocarbon type of species doped in SPK, except for 'fuel' and 'ternary', which indicate fuel-fuel blends and single-species/single-species/SPK blends, respectively.

7. Challenges to Property Predictions for Jet Fuel Design and Qualification

Looking forward, there are five themes poised for advancements. These include; 1) quantification of prediction uncertainty category one (regression) and three (hybrid) models, 2) dissemination of probabilistic property prediction software, 3) integrating category one (regression) with category two (blending rules) models to refine the composition characterization, addition hybridization opportunities to reduce model uncertainty, and 5) prediction impurity-sensitive properties such as those listed in column D of Table 1. A brief paragraph is devoted to each of these themes.

Throughout the sciences, there has been widespread application of machine learning to develop interpolative relationships between different characteristics of the population. Few of the articles that showcase these models address potential overfitting errors or uncertainties arising from epistemic errors (population is not representative of the sample for which a property estimate is desired) or heteroscedastic errors arising from non-uniformity of variances over the range of independent variables. Two notable exceptions include the work of Oh22 work of 14Tools that are excellent at finding and leveraging strong correlations between features that are distributed throughout a large population 132 are not necessarily applicable to problems where the variation in the uncharacterized population (desired prediction) may be substantially different from the variation observed in the characterized population (training, validation and test sets). To the point, more education is needed around the application limits of regression-based models.

Frequently, the results of machine-learning models are published, absent disclosure of the model itself. While it may be reasonable to presume that independent researchers could acquire the same data used in the original research and follow the same prescription to derive a similar, interpolation scheme, this presumption is unprovable without definition of the original model. De-motivating the creation of such models or models for which uncertainty quantification is incomplete could be accomplished by making the models that do include comprehensive uncertainty quantification more readily available. This article assists to that end. Additionally, the revision-controlled software that utilizes the blending rules discussed in this article and makes the uncertainty determinations could be made available on-line along with the NIST database upon which it relies.

One potential application of machine-learning models which has not been explored in detail is an integration with blending rules; tier-alpha models,10 where both models use species concentration data from a GCxGC experiment as input. Perhaps the coefficients of the regressed model could serve as probabilistic constraints to be imposed on the selection of isomers used to represent a particular hydrocarbon bin in the tier-alpha model framework. The isomeric population distributions that bring the tier-alpha-like 10 prediction into alignment with the regressed model interpolation for one property (or set of properties) may be used to narrow the undetermined isomer contribution to the tier-alpha-like predictions of other properties.

There are, in fact, many opportunities to integrate different modelling approaches and to maximize their utilization of disparate data streams to reduce overall prediction uncertainty. Simple examples of this notion include utilization of C#, H# and total aromatics content to bound the total concentration of cycloalkanes. It is more complicated to simultaneously leverage GCxGC data, spectroscopic data, and physiochemical properties. One tactic would be to let any piece of data serve as a constraint within the tier-alpha framework. For example, NMR data could provide information on chain branching, which could, in principle, be imposed on the isomeric selections with the tier-alpha framework. Another possibility would be to create a model integration method whereby the probabilistic predictions of different modelling approaches are encouraged to inform one another; resulting in an integrated property prediction with a narrower uncertainty band.

While each of the four potential advances which have been noted so far are interesting in their own right, the biggest gap in SAF property predictions has to do with the properties listed in column D of Table 1. These properties are believed to be strongly influenced by impurities and other components that may be present in fuel at very low concentration; perhaps even below the detection limit of analytical methods that focus on qualification and quantification of individual components within a mixture. A review of existing models to estimate these properties is needed, and we believe such a review will reveal significant gaps to be filled by future research and development.

8. Conclusion

A summary of each blending rule assessment is provided in Table 2. Raoult's Law, for vapor pressure is left off the list because its accuracy, when applied to mixtures of many components, is not known. This is the most impactful gap within our collective knowledge of model accuracy because it has a direct bearing on the ASTM D86 distillation curve (e.g. T_{10}, T_{50}, T_{90}) and the gas phase concentration. Overall, thirty-two different fuel properties can be estimated

Table 2. Summary of Blending Rules Accuracy Assessments.

Property	Blending Rule Uncertainty	Number of Data Points Used	Source
Carbon number	0	CoM †	
Hydrogen number	0	CoM	
Density	MARE 0.24, [%]	675	39
Lower heating value	ME 0.15, [kJ/kg]	27	43
Liquid heat capacity	MRE 0.9, [%]	81	133
Thermal conductivity	Max 2.6, [%]	22	61,62
Kinematic viscosity	MARE 3.9, [%]	675	39
Surface tension	MRE -2.85, [%]	55	70,71
Freeze point	Max 20, [˚C]	41	72
Distillation curve (ASTM D2887)	MAE 1.5, [˚C]	966	134
Lower flammability limit	MRE 1.3 [%]	86	87
Flash point	MAE 1.72, [˚C]	153	94
Dielectric constant	MAE 0.0038, [-]	200	135
Threshold sooting index	MAE < 2, [-]	confounded	106
Derived cetane number	MARE 2.9, [%]	278~100	117–121
Elastomer swell	MAE 1.23 [%v/v]	52	122

† Conservation of mass (CoM)

from simple algebraic models involving sixteen scalar products, one simple equation of state model, and well-known property-property relationships. Six of the base properties including carbon number, hydrogen number, lower heating value, heat capacity of the gas phase, dielectric constant and the distillation curve as defined by ASTM D2887 are predicted essentially exactly by the scalar product blending rule since intermolecular forces have no substantive effect on these properties. Another six base properties can be predicted from composition and component data with model uncertainty that is small relative to other sources of uncertainty. These properties include density, liquid-phase heat capacity, threshold sooting index, elastomer seal swell, flash point, and the lower flammability limit. Three properties that depend significantly on intermolecular forces include kinematic viscosity, surface tension and thermal conductivity. Even these properties are reasonably well approximated by a scalar-product blending rule, having prediction uncertainties less than 4% when applied exclusively to mixtures of aliphatic and/or aromatic hydrocarbons. The freeze point can also be predicted well (<5 ˚C) from composition provided there is also a collection of reference data for each high-freeze-point component as a function of concentration in a reference, hydrocarbon solvent. Absent the reference data, however, freeze point predictions can be too high by as much as 20 ˚C. The derived cetane number, which intuitively should be modeled through detailed kinetics is well approximated by a simple blending rule for many mixtures. However, the scalar-product blending rule applied to some mixtures does result in a DCN prediction error greater than 20%.

9. References

(1) Goldner, W.; Bredlau, J.; Brown, N.; Haq, Z.; Brown, C.; Galperin, D.; Craig, K.; Csonka, S.; Fitzgerald, J.; Hileman, J.; Hoffman, B.; Lewis, K.; Oldani, A.; Reed, V.; Rowe, I.; Rumizen, M.; Shmorhun, M.; Spaeth, J.; Steinbach, R.; Wiselogel, A.; Wolcott, M. SAF Grand Challenge Roadmap Flight Plan for Sustainable Aviation Fuel; 2022. https://www.energy.gov/sites/default/files/2022-09/beto-saf-gc-roadmap-report-sept-2022.pdf (accessed 2024-05-22).
(2) US Environmental Protection Agency. RINs Generated Transactions. https://www.epa.gov/fuels-registration-reporting-and-compliance-help/rins-generated-transactions (accessed 2024-05-22).
(3) Commercial Aviation Alternative Fuels Initiative. US SAF Production Potential. https://www.caafi.org/focus_areas/docs/US_SAF_Production_Potential_March2024.pdf (accessed 2024-05-22).
(4) International Energy Agency: IEA. Renewables 2021; 2021.

(5) Heyne, J.; Rauch, B.; Le Clercq, P.; Colket, M. Sustainable Aviation Fuel Prescreening Tools and Procedures. Fuel 2021, 290, 120004. https://doi.org/https://doi.org/10.1016/j.fuel.2020.120004.
(6) Martin, D.; Wilkins, P. Petroleum Quality Information System (PQIS) 2011 Annual Report; Defense Technical Information Center: Fort Belvoir, VA, 2011.
(7) The International Civil Aviation Organization (ICAO). ICAO Global Framework for Aviation Alternative Fuels: Conversion Processes. https://www.icao.int/environmental-protection/GFAAF/Pages/Conversion-processes.aspx.
(8) Heyne, J.; Bell, D.; Feldhausen, J.; Yang, Z.; Boehm, R. Towards Fuel Composition and Properties from Two-Dimensional Gas Chromatography with Flame Ionization and Vacuum Ultraviolet Spectroscopy. Fuel 2022, 312, 122709. https://doi.org/https://doi.org/10.1016/j.fuel.2021.122709.
(9) Feldhausen, J.; Bell, D. C.; Yang, Z.; Faulhaber, C.; Boehm, R.; Heyne, J. Synthetic Aromatic Kerosene Property Prediction Improvements with Isomer Specific Characterization via GCxGC and Vacuum Ultraviolet Spectroscopy. Fuel 2022, 326, 125002. https://doi.org/https://doi.org/10.1016/j.fuel.2022.125002.
(10) Yang, Z.; Kosir, S.; Stachler, R.; Shafer, L.; Anderson, C.; Heyne, J. S. A GC × GC Tier α Combustor Operability Prescreening Method for Sustainable Aviation Fuel Candidates . Fuel 2021, 292 (September 2020), 120345. https://doi.org/10.1016/j.fuel.2021.120345.
(11) Heyne, J.; Rauch, B.; Le Clercq, P.; Colket, M. Sustainable Aviation Fuel Prescreening Tools and Procedures. Fuel 2021, 290, 120004. https://doi.org/https://doi.org/10.1016/j.fuel.2020.120004.
(12) Bell, D.; Heyne, J. S.; August, E.; Won, S. H.; Dryer, F. L.; Haas, F. M.; Dooley, S. On the Development of General Surrogate Composition Calculations for Chemical and Physical Properties. AIAA SciTech Forum - 55th AIAA Aerospace Sciences Meeting 2017. https://doi.org/10.2514/6.2017-0609.
(13) Flora, G.; Kosir, S.; Behnke, L.; Stachler, R.; Heyne, J.; Zabarnick, S.; Gupta, M. Properties Calculator and Optimization for Drop-in Alternative Jet Fuel Blends. In AIAA Scitech 2019 Forum; American Institute of Aeronautics and Astronautics Inc, AIAA, 2019. https://doi.org/10.2514/6.2019-2368.
(14) Hall, C.; Rauch, B.; Bauder, U.; Le Clercq, P.; Aigner, M. Predictive Capability Assessment of Probabilistic Machine Learning Models for Density Prediction of Conventional and Synthetic Jet Fuels. Energy & Fuels 2021, 35 (3), 2520–2530. https://doi.org/doi.org/10.1021/acs.energyfuels.0c03779.
(15) Yang, Z.; Boehm, R. C.; Bell, D. C.; Heyne, J. S. Towards Sustainable Aviation Fuel Distillation Optimization. Fuel 2023, 353, 129136. https://doi.org/doi.org/10.1016/j.fuel.2023.129136.
(16) Miller, J. H.; Tifft, S. M.; Wiatrowski, M. R.; Thathiana Benavides, P.; Huq, N. A.; Christensen, E. D.; Alleman, T.; Hays, C.; Luecke, J.; Kneucker, C. M.; Haugen, S. J.; Sànchez Nogué, V.; Karp, E. M.; Hawkins, T. R.; Singh, A.; Vardon, D. R.; Nogué, S. Journal Pre-Proof Screening and Evaluation of Biomass Upgrading Strategies for Sustainable Transportation Fuel Production with Biomass-Derived Volatile Fatty Acids. iScience 2022, 105384. https://doi.org/10.1016/j.isci.2022.105384.
(17) Boehm, R. C.; Faulhaber, C.; Behnke, L.; Heyne, J. On Selecting Optimum Composition of Sustainable Aviation Fuels for Engine and Aircraft Efficiency. submitted.
(18) Won, S. H.; Haas, F. M.; Dooley, S.; Edwards, T.; Dryer, F. L. Reconstruction of Chemical Structure of Real Fuel by Surrogate Formulation Based upon Combustion Property Targets. Combust Flame 2017, 183, 39–49. https://doi.org/10.1016/J.COMBUSTFLAME.2017.04.032.
(19) Kang, D.; Kim, D.; Kalaskar, V.; Boehman, A.; Violi, A. Experimental Characterization of Jet Fuels under Engine Relevant Conditions – Part 2: Insights on Optimization Approach for Surrogate Formulation. Fuel 2019, 239, 1405–1416. https://doi.org/10.1016/J.FUEL.2018.10.006.
(20) Caceres-Martinez, L. E.; Kilaz, G. Kinematic Viscosity Prediction of Jet Fuels and Alternative Blending Components via Comprehensive Two-dimensional Gas Chromatography, Partial Least Squares, and Yeo-Johnson Transformation. J Sep Sci 2024, 47 (5), 2300816. https://doi.org/doi.org/10.1002/jssc.202300816.
(21) Vozka, P.; Kilaz, G. Determination of Jet Fuel System Icing Inhibitor by GC×GC-FID. Talanta 2020, 218, 121146. https://doi.org/https://doi.org/10.1016/j.talanta.2020.121146.
(22) Oh, J.-H.; Oldani, A.; Solecki, A.; Lee, T. Learning to Predict Sustainable Aviation Fuel Properties: A Deep Uncertainty Quantification Viewpoint. Fuel 2024, 356, 129508. https://doi.org/https://doi.org/10.1016/j.fuel.2023.129508.
(23) Berrier, K. L.; Freye, C. E.; Billingsley, M. C.; Synovec, R. E. Predictive Modeling of Aerospace Fuel Properties Using Comprehensive Two-Dimensional Gas Chromatography with Time-Of-Flight Mass Spectrometry and Partial Least Squares Analysis. Energy & Fuels 2020, 34 (4), 4084–4094. https://doi.org/10.1021/acs.energyfuels.9b04108.
(24) Dalmiya, A.; Sheyyab, M.; Mehta, J. M.; Brezinsky, K.; Lynch, P. T. Derived Cetane Number Prediction of Jet Fuels and Their Functional Group Surrogates Using Liquid Phase Infrared Absorption. Proceedings of the Combustion Institute 2023, 39 (1), 1495–1504. https://doi.org/https://doi.org/10.1016/j.proci.2022.08.104.
(25) Kehimkar, B.; Hoggard, J. C.; Marney, L. C.; Billingsley, M. C.; Fraga, C. G.; Bruno, T. J.; Synovec, R. E. Correlation of Rocket Propulsion Fuel Properties with Chemical Composition Using Comprehensive Two-Dimensional Gas

Chromatography with Time-of-Flight Mass Spectrometry Followed by Partial Least Squares Regression Analysis. J Chromatogr A 2014, 1327, 132–140. https://doi.org/10.1016/j.chroma.2013.12.060.
(26) Mehta, J. M.; Lynch, P. T.; Mayhew, E. K.; Brezinsky, K. Evaluation of Chemical Functional Group Composition of Jet Fuels Using Two-Dimensional Gas Chromatography. Energy & Fuels 2023, 37 (3), 2294–2306. https://doi.org/10.1021/acs.energyfuels.2c03514.
(27) Hall, C.; Creton, B.; Rauch, B.; Bauder, U.; Aigner, M. Probabilistic Mean Quantitative Structure–Property Relationship Modeling of Jet Fuel Properties. Energy & Fuels 2021, 36 (1), 463–479. https://doi.org/10.1021/acs.energyfuels.1c03334.
(28) Vozka, P.; Kilaz, G. A Review of Aviation Turbine Fuel Chemical Composition-Property Relations. Fuel 2020, 268, 117391. https://doi.org/10.1016/j.fuel.2020.117391.
(29) Hall, C.; Bell, D. C.; Feldhausen, J.; Rauch, B.; Heyne, J. Quantifying Isomeric Effects: A Key Factor in Aviation Fuel Assessment and Design. Fuel 2024, 357, 129912.
(30) Heyne, J.; Bell, D.; Feldhausen, J.; Yang, Z.; Boehm, R. Towards Fuel Composition and Properties from Two-Dimensional Gas Chromatography with Flame Ionization and Vacuum Ultraviolet Spectroscopy. Fuel 2022, 312, 122709. https://doi.org/10.1016/J.FUEL.2021.122709.
(31) Feldhausen, J.; Bell, D. C.; Yang, Z.; Faulhaber, C.; Boehm, R.; Heyne, J. Synthetic Aromatic Kerosene Property Prediction Improvements with Isomer Specific Characterization via GCxGC and Vacuum Ultraviolet Spectroscopy. Fuel 2022, 326, 125002. https://doi.org/10.1016/J.FUEL.2022.125002.
(32) Pan, Q.; Fan, X.; Li, J. Automatic Creation of Molecular Substructures for Accurate Estimation of Pure Component Properties Using Connectivity Matrices. Chem Eng Sci 2023, 265, 118214. https://doi.org/10.1016/J.CES.2022.118214.
(33) Landera, A.; Bambha, R. P.; Hao, N.; Desai, S. P.; Moore, C. M.; Sutton, A. D.; George, A. Building Structure-Property Relationships of Cycloalkanes in Support of Their Use in Sustainable Aviation Fuels. Front Energy Res 2022, 9. https://doi.org/10.3389/FENRG.2021.771697.
(34) Watanasiri, S.; Paulechka, E.; Iisa, K.; Christensen, E.; Muzny, C.; Dutta, A. Prediction of Sustainable Aviation Fuel Properties for Liquid Hydrocarbons from Hydrotreating Biomass Catalytic Fast Pyrolysis Derived Organic Intermediates. Sustainable Energy Fuels 2023, 7, 2413–2427. https://doi.org/10.1039/d3se00058c.
(35) Committee D02.04.0L. ASTM D8396 Standard Test Method for Group Types Quantification of Hydrocarbons in Hydrocarbon Liquids with a Boiling Point between 36 °C and 343 °C by Flow Modulated GCxGC – FID. Astm International: West Conshohocken, PA 2022, pp 1–25. https://doi.org/10.1520/D8396-22.
(36) Johnson, K.; Loegel, T.; Metz, A.; Wrzesinski, P.; Shafer, L.; Striebich, R.; West, Z. Method for Detailed Hydrocarbon Analysis of Middle Distillate Fuels by Two-Dimensional Gas Chromatography; NAVAIR public release 2020-361, 2020.
(37) Schofield, K. The Enigmatic Mechanism of the Flame Ionization Detector: Its Overlooked Implications for Fossil Fuel Combustion Modeling. Prog Energy Combust Sci 2008, 34 (3), 330–350. https://doi.org/10.1016/J.PECS.2007.08.001.
(38) Bell, D. C.; Feldhausen, J.; Spieles, A. J.; Boehm, R. C.; Heyne, J. S. Limits of Identification Using VUV Spectroscopy Applied to C8H18 Isomers Isolated by GC×GC. Talanta 2023, 258, 124451. https://doi.org/10.1016/J.TALANTA.2023.124451.
(39) Boehm, R. C.; Hauck, F.; Yang, Z.; Wanstall, C. T.; Heyne, J. S. Error Quantification of the Arrhenius Blending Rule for Viscosity of Hydrocarbon Mixtures. Front Energy Res 2022, 10 (Sec. Bioenergy and Biofuels). https://doi.org/doi.org/10.3389/fenrg.2022.1074699.
(40) Sanghvi, M. K. D.; Kay, W. B. Volume Changes on Mixing in the Cyclohexane-n-Heptane-Benzene System. Chem Eng Sci 1956, 6 (1), 10–25. https://doi.org/10.1016/0009-2509(56)80006-7.
(41) Vozka, P.; Modereger, B. A.; Park, A. C.; Zhang, W. T. J.; Trice, R. W.; Kenttämaa, H. I.; Kilaz, G. Jet Fuel Density via GC × GC-FID. Fuel 2019, 235, 1052–1060. https://doi.org/https://doi.org/10.1016/j.fuel.2018.08.110.
(42) Nabipour, N.; Daneshfar, R.; Rezvanjou, O.; Mohammadi-Khanaposhtani, M.; Baghban, A.; Xiong, Q.; Li, L. K. B.; Habibzadeh, S.; Doranehgard, M. H. Estimating Biofuel Density via a Soft Computing Approach Based on Intermolecular Interactions. Renew Energy 2020, 152, 1086–1098. https://doi.org/10.1016/J.RENENE.2020.01.140.
(43) Lundberg, G. W. Thermodynamics of Solutions XI. Heats of Mixing of Hydrocarbons. J Chem Eng Data 1964, 9 (2), 193–198.
(44) Boehm, R. C.; Yang, Z.; Bell, D. C.; Feldhausen, J.; Heyne, J. S. Lower Heating Value of Jet Fuel from Hydrocarbon Class Concentration Data and Thermo-Chemical Reference Data: An Uncertainty Quantification. Fuel 2022, 311. https://doi.org/10.1016/j.fuel.2021.122542.
(45) Fortier, J. L.; Benson, G. C. Heat Capacities of Some Binary Aromatic Hydrocarbon Mixtures Containing Benzene or Toluene. J Chem Eng Data 1979, 24 (1), 34–37. https://doi.org/10.1021/je60080a015.
(46) Kumar Sharma, V.; Malik, S.; Solanki, S. Thermodynamic Studies of Molecular Interactions in Mixtures Containing Tetrahydropyran, 1,4-Dioxane, and Cyclic Ketones. J Chem Eng Data 2017, 62 (2), 623–632. https://doi.org/10.1021/acs.jced.6b00606.

(47) Malik, S.; Gupta, H.; Sharma, V. K. Topological Investigation of Ternary Mixtures: Excess Heat Capacities. J Mol Liq 2017, 233, 319–325. https://doi.org/10.1016/J.MOLLIQ.2017.03.024.
(48) Jamieson, D. T.; Cartwright, G. NEL Report No. 648: Properties of Binary Liquid Mixtures: Heat Capacity; East Kiibride, U.K., 1978.
(49) Teja, A. S. Simple Method for the Calculation of Heat Capacities of Liquid Mixtures. J Chem Eng Data 1983, 28 (1), 83–85. https://doi.org/10.1021/JE00031A025/ASSET/JE00031A025.FP.PNG_V03.
(50) Hall, N.; Glenn-Research-Center; NASA. Isentropic Compression. https://www.grc.nasa.gov/www/k-12/airplane/compexp.html (accessed 2023-10-08).
(51) McBride, B. J.; Zehe, M. J.; Gordon, S. NASA Glenn Coefficients for Calculating Thermodynamic Properties of Individual Species; Cleveland, OH, 2002.
(52) BYJU. CP – CV for Non-Ideal Gases. https://byjus.com/chemistry/cp-cv-for-non-ideal-gases/ (accessed 2023-10-08).
(53) Bergman, T. L.; Lavine, A. S.; Incropera, F. P.; Dewitt, D. P. Fundamental of Heat and Mass Transfer, 7th ed.; John Wiley & Sons, 2011.
(54) Isidro-Ojeda, M. A.; Calderón, A.; Marín, E. Thermal Diffusivity of Heptane-Isooctane Mixtures. Thermochim Acta 2020, 689, 178616. https://doi.org/10.1016/J.TCA.2020.178616.
(55) Bedoya, A.; Alvarado, S.; Calderón, A.; Marín, E. Thermal Transport Properties of Heptane-Isooctane Mixtures. Thermochim Acta 2018, 666, 190–196. https://doi.org/10.1016/J.TCA.2018.07.003.
(56) Rokni, H. B.; Moore, J. D.; Gupta, A.; McHugh, M. A.; Mallepally, R. R.; Gavaises, M. General Method for Prediction of Thermal Conductivity for Well-Characterized Hydrocarbon Mixtures and Fuels up to Extreme Conditions Using Entropy Scaling. Fuel 2019, 245, 594–604. https://doi.org/10.1016/J.FUEL.2019.02.044.
(57) Malatesta, W. A.; Yang, B. Aviation Turbine Fuel Thermal Conductivity: A Predictive Approach Using Entropy Scaling-Guided Machine Learning with Experimental Validation. 2021. https://doi.org/10.1021/acsomega.1c02934.
(58) Tsederberg, N. V. Thermal Conductivity of Binary Liquid Solutions.". Teploenergeti Ka 1956, 3 (9), 42–48.
(59) Lemmon, E.W., Bell, I.H., Huber, M.L., McLinden, M. O. NIST Standard Reference Database 23: Reference Fluid Thermodynamic and Transport Properties-REFPROP. National Institute of Standards and Technology, Standard Reference Data Program: Gaithersburg 2018.
(60) Baroncini, C.; Latini, G.; Pierpaoli, P. Thermal Conductivity of Organic Liquid Binary Mixtures: Measurements and Prediction Method. Int J Thermophys 1984, 5, 387–401.
(61) Ogiwara, K.; Arai, Y.; Saito, S. Thermal Conductivities of Liquid Hydrocarbons and Their Binary Mixtures. Industrial & Engineering Chemistry Fundamentals 2002, 19 (3), 295–300. https://doi.org/10.1021/i160075a011.
(62) Wada, Y.; Nagasaka, Y.; Nagashima, A. Measurements and Correlation of the Thermal Conductivity of Liquid N-Paraffin Hydrocarbons and Their Binary and Ternary Mixtures. Int J Thermophys 1985, 6 (3), 251–265. https://doi.org/10.1007/BF00522147/METRICS.
(63) Boehm, R. C.; Colborn, J. G.; Heyne, J. S. Comparing Alternative Jet Fuel Dependencies Between Combustors of Different Size and Mixing Approaches. Front Energy Res 2021, 9. https://doi.org/10.3389/fenrg.2021.701901.
(64) McKinley, G. H.; Renardy, M. Wolfgang von Ohnesorge. Physics of Fluids 2011, 23 (12). https://doi.org/10.1063/1.3663616/257457.
(65) Hernández, E. A.; Sánchez-Reyna, G.; Ancheyta, J. Evaluation of Mixing Rules to Predict Viscosity of Petrodiesel and Biodiesel Blends. Fuel 2021, 283, 118941. https://doi.org/10.1016/J.FUEL.2020.118941.
(66) Arrhenius, S. A. On the Internal Friction of Dilute Aqueous Solutions. Z. Physik. Chem. 1887, 1, 285.
(67) Wilding, W. V.; Rowley, R. L.; Oscarson, J. L. DIPPR® Project 801 Evaluated Process Design Data. Fluid Phase Equilib 1998, 150–151 (151), 413–420. https://doi.org/10.1016/S0378-3812(98)00341-0.
(68) Hugill, J. A.; Van Welsenes, A. J. Surface Tension: A Simple Correlation for Natural Gas + Conensate Systems. Fluid Phase Equilib 1986, 29 (C), 383–390. https://doi.org/10.1016/0378-3812(86)85038-5.
(69) Hammick, D. L.; Andrew, L. W. The Determination of the Parachors of Substances in Solution. J. Chem. Soc. 1929, 0 (0), 754–759. https://doi.org/10.1039/jr9290000754.
(70) L. Schmidt, R.; C. Randall, J.; Lawrence Clever, H. The Surface Tension and Density of Binary Hydrocarbon Mixtures: Benzene-n-Hexane and Benzene-n-Dodecane. J Phys Chem 2002, 70 (12), 3912–3916. https://doi.org/10.1021/j100884a027.
(71) Bezerra, E. S.; Santos, J. M. T.; Paredes, M. L. L. A New Predictive Model for Liquid/Air Surface Tension of Mixtures: Hydrocarbon Mixtures. Fluid Phase Equilib 2010, 288 (1–2), 55–62. https://doi.org/10.1016/J.FLUID.2009.10.011.
(72) Boehm, R. C.; Coburn, A. A.; Yang, Z.; Wanstall, C. T.; Heyne, J. S. Blend Prediction Model for the Freeze Point of Jet Fuel Range Hydrocarbons. Energy & Fuels 2022, 36 (19), 12046–12053. https://doi.org/10.1021/acs.energyfuels.2c02063.

(73) Solash, J.; Hazlett, R.; Hall, J.; Nowack, C. Relation between Fuel Properties and Chemical Composition. 1. Jet Fuels from Coal, Oil Shale and Tar Sands. Fuel 1978, 57 (9), 521–528. https://doi.org/https://doi.org/10.1016/0016-2361(78)90036-4.
(74) Affens, W.; Hall, J.; Holt, S.; Hazlett, R. Effect of Composition on Freezing Points of Model Hydrocarbon Fuels. Fuel 1984, 63 (4), 543–547. https://doi.org/https://doi.org/10.1016/0016-2361(84)90294-1.
(75) Cookson, D. J.; Lloyd, C. P.; Smith, B. E. Investigation of the Chemical Basis of Kerosene (Jet Fuel) Specification Properties. Energy & Fuels 1987, 1 (5), 438–447. https://doi.org/10.1021/EF00005A011.
(76) Naef, R. Calculation of the Isobaric Heat Capacities of the Liquid and Solid Phase of Organic Compounds at and around 298.15 K Based on Their "True" Molecular Volume. Molecules 2019, 24 (8), 1626. https://doi.org/10.3390/MOLECULES24081626.
(77) Walden, P. Heat of Fusion, Specific Cohesion, and Molecular Complexity at the Melting Point. Elektrochem 1908, 14, 713.
(78) Hayez, B. Approximate Equation To Calculate Partial Pressures in a Mixture of Real Gases. J Chem Educ 2018, 95 (11), 1982–1988. https://doi.org/10.1021/acs.jchemed.8b00185.
(79) Atkins, P. W. Physical Chemistry, Third.; Freeman and Company: New York, 1986.
(80) Hawkes, S. J. Raoult's Law Is a Deception. J Chem Educ 1995, 72 (3), 204.
(81) Yang, Z.; Bell, D. C.; Cronin, D. J.; Boehm, R.; Heyne, J.; Ramasamy, K. K. Volatility Measurements of Sustainable Aviation Fuels: A Comparative Study of D86 and D2887 Methods. ACS Sustain Chem Eng 2024, 12 (19), 7414–7420. https://doi.org/10.1021/acssuschemeng.4c00678.
(82) Le Chatelier, H. Estimation of Firedamp by Flammability Limits. Annals of Mines 1891, 19 (8), 388–395.
(83) Burgess, M. J.; Wheeler, R. V. The Lower Limit of Inflammation of Mixtures of the Paraffin Hydrocarbons with Air. Journal of the Chemical Society, Transactions 1911, 99, 2013-2030.
(84) Mashuga, C. V; Crowl, D. A. Derivation of Le Chatelier's Mixing Rule for Flammable Limits. Process Safety Progress 2000, 19 (2), 112--117.
(85) Chen, C.-C.; Liu, S.-H.; Kang, X. Evaluating Lower Flammability Limit of Flammable Mixtures Using Threshold Temperature Approach. Chem Eng Sci 2018, 185, 84–91. https://doi.org/https://doi.org/10.1016/j.ces.2018.04.011.
(86) Coward, H. F.; Jones, G. W. Limits of Flammability of Gases and Vapors, 503rd ed.; US Government Printing Office: Washington DC, 1952.
(87) Kondo, S.; Takizawa, K.; Takahashi, A.; Tokuhashi, K.; Sekiya, A. A Study on Flammability Limits of Fuel Mixtures. J Hazard Mater 2008, 155 (3), 440–448. https://doi.org/https://doi.org/10.1016/j.jhazmat.2007.11.085.
(88) Liekhus, K. J.; Zlochower, I. A.; Cashdollar, K. L.; Djordjevic, S. M.; Loehr, C. A. Flammability of Gas Mixtures Containing Volatile Organic Compounds and Hydrogen. J Loss Prev Process Ind 2000, 13 (3–5), 377–384. https://doi.org/10.1016/S0950-4230(99)00034-0.
(89) Zabeta, M. G. Flammability Characteristics of Combustible Gases and Vapors; Pittsburg, PA, 1964. https://doi.org/https://doi.org/10.2172/7328370.
(90) NFPA. Fire Protection Guide to Hazardous Materials; Spencer, A. B., Colonna, G. R., Eds.; National Fire Protection Agency: Quincy, MA, 2002.
(91) Rowley, J. R. Flammability Limits, Flash Points, and Their Consanguinity: Critical Analysis, Experimental Exploration, and Prediction, Brigham Young University, 2010.
(92) Qi, C.; Yan, X.; Wang, Y.; Ning, Y.; Yu, X.; Hou, Y.; Lv, X.; Ding, J.; Shi, E.; Yu, J. Flammability Limits of Combustible Gases at Elevated Temperatures and Pressures: Recent Advances and Future Perspectives. Energy & Fuels 2022, 36 (21), 12896–12916. https://doi.org/10.1021/acs.energyfuels.2c02567.
(93) Phoon, L. Y.; Mustaffa, A. A.; Hashim, H.; Mat, R. A Review of Flash Point Prediction Models for Flammable Liquid Mixtures. Ind Eng Chem Res 2014, 53 (32), 12553–12565. https://doi.org/10.1021/IE501233G/SUPPL_FILE/IE501233G_SI_001.PDF.
(94) Santos, S. M.; Nascimento, D. C.; Costa, M. C.; Neto, Antonio MB Fregolente, L. V. Flash Point Prediction: Reviewing Empirical Models for Hydrocarbons, Petroleum Fraction, Biodiesel, and Blends. Fuel 2020, 263, 116375. https://doi.org/10.1016/j.fuel.2019.116375.
(95) Wickey, R. O.; Chittenden, D. H. Flash Points of Blends Correlated. Hydrocarbon processing 1963, 42 (6), 157–158.
(96) Corson, D. R. Introduction to Electromagnetic Fields and Waves; WH Freeman: San Francisco, 1962; p 116.
(97) Yang, Z.; Bell, D.; Boehm, R.; Fischer Marques, P.; Bose, J.; Kosilkin, I.; Heyne, J. Assessing the Effect of Composition on Dielectric Constant of Sustainable Aviation Fuel; 2024.
(98) Sen, A. D.; Anicich, V. G.; Arakelian, T. Dielectric Constant of Liquid Alkanes and Hydrocarbon Mixtures. J Phys D Appl Phys 1992, 25 (3), 516. https://doi.org/doi:10.1088/0022-3727/25/3/027.
(99) Sen, A. D.; Anicich, V. G.; Arakelian, T. Dielectric Constant of Liquid Alkanes and Hydrocarbon Mixtures. J Phys D Appl Phys 1992, 25 (3), 516–521. https://doi.org/DOI 10.1088/0022-3727/25/3/027.

(100) Teixeira-Dias, J. J. C.; Murrell, J. N. The Calculation of Electric Polarizabilities of Hydrocarbons with Particular Attention to the Bond-Additive Property. Mol Phys 1970, 19 (3), 329–335. https://doi.org/10.1080/00268977000101341.
(101) Calcote, H. F.; Manos, D. M. Effect of Molecular Structure on Incipient Soot Formation. Combust Flame 1983, 49 (1–3), 289–304. https://doi.org/10.1016/0010-2180(83)90172-4.
(102) Gill, R. J.; Olson, D. B. Estimation of Soot Thresholds for Fuel Mixtures. Combustion Science and Technology 1984, 40 (5–6), 307–315. https://doi.org/10.1080/00102208408923814.
(103) Yan, S.; Eddings, E. G.; Palotas, A. B.; Pugmire, R. J.; Sarofim, A. F. Prediction of Sooting Tendency for Hydrocarbon Liquids in Diffusion Flames. Energy & Fuels 2005, 19 (6), 2408–2415. https://doi.org/10.1021/EF050107D.
(104) Mensch, A.; Santoro, R. J.; Litzinger, T. A.; Lee, S.-Y. Sooting Characteristics of Surrogates for Jet Fuels. Combust Flame 2010, 157, 1097–1105. https://doi.org/10.1016/j.combustflame.2010.02.008.
(105) Yang, Y.; Boehman, A. L.; Santoro, R. J. A Study of Jet Fuel Sooting Tendency Using the Threshold Sooting Index (TSI) Model. Combust Flame 2007, 149 (1–2), 191–205. https://doi.org/10.1016/j.combustflame.2006.11.007.
(106) Boehm, R. C.; Yang, Z.; Heyne, J. S. Threshold Sooting Index of Sustainable Aviation Fuel Candidates from Composition Input Alone: Progress toward Uncertainty Quantification. Energy & Fuels 2021. https://doi.org/10.1021/acs.energyfuels.1c03794.
(107) Lemaire, R.; Le Corre, G.; Nakouri, M. Predicting the Propensity to Soot of Hydrocarbons and Oxygenated Molecules by Means of Structural Group Contribution Factors Derived from the Processing of Unified Sooting Indexes. Fuel 2021, 302, 121104. https://doi.org/10.1016/J.FUEL.2021.121104.
(108) McEnally, C. S.; Pfefferle, L. D. Improved Sooting Tendency Measurements for Aromatic Hydrocarbons and Their Implications for Naphthalene Formation Pathways. Combust Flame 2007, 148 (4), 210–222. https://doi.org/10.1016/j.combustflame.2006.11.003.
(109) ASTM Research Report D02-1531, Diesel Fuel Ignition Quality Tester (IQTTM) - Development of the IQTTM Model to Calculate the Derived Cetane Number (DCN).
(110) Colket, M.; Heyne, J. Fuel Effects on Operability of Aircraft Gas Turbine Combustors, August.; AIAA, Progress in Astronautics and Aeronautics, 2021. https://doi.org/10.2514/4.106040.
(111) Min, K.; Valco, D. J.; Oldani, A.; Kim, K.; Temme, J.; Kweon, C. B. M.; Lee, T. Autoignition of Varied Cetane Number Fuels at Low Temperatures. Proceedings of the Combustion Institute 2019, 37 (4), 5003–5011. https://doi.org/10.1016/J.PROCI.2018.05.078.
(112) Kim, K.; Lee, W.; Wiersema, P.; Mayhew, E.; Temme, J.; Kweon, C.-B. M.; Lee, T. Effects of the Cetane Number on Chemical Ignition Delay. Energy 2023, 264, 126263. https://doi.org/https://doi.org/10.1016/j.energy.2022.126263.
(113) Wang, Y.; Ding, Y.; Wei, W.; Cao, Y.; Davidson, D. F.; Hanson, R. K. On Estimating Physical and Chemical Properties of Hydrocarbon Fuels Using Mid-Infrared FTIR Spectra and Regularized Linear Models. Fuel 2019, 255, 115715. https://doi.org/10.1016/j.fuel.2019.115715.
(114) Al Ibrahim, E.; Farooq, A. Prediction of the Derived Cetane Number and Carbon/Hydrogen Ratio from Infrared Spectroscopic Data. Energy & Fuels 2021, 35 (9), 8141–8152. https://doi.org/10.1021/ACS.ENERGYFUELS.0C03899/ASSET/IMAGES/LARGE/EF0C03899_0007.JPEG.
(115) Boddapati, V.; Ferris, A. M.; Hanson, R. K. On the Use of Extended-Wavelength FTIR Spectra for the Prediction of Combustion Properties of Jet Fuels and Their Constituent Species. Proceedings of the Combustion Institute 2023, 39 (1), 1347–1355. https://doi.org/https://doi.org/10.1016/j.proci.2022.08.041.
(116) Abdul Jameel, A. G.; Naser, N.; Issayev, G.; Touitou, J.; Ghosh, M. K.; Emwas, A.-H.; Farooq, A.; Dooley, S.; Sarathy, S. M. A Minimalist Functional Group (MFG) Approach for Surrogate Fuel Formulation. Combust Flame 2018, 192, 250–271. https://doi.org/https://doi.org/10.1016/j.combustflame.2018.01.036.
(117) Dooley, S.; Won, S. H.; Chaos, M.; Heyne, J.; Ju, Y.; Dryer, F. L.; Kumar, K.; Sung, C. J.; Wang, H.; Oehlschlaeger, M. A.; Santoro, R. J.; Litzinger, T. A. A Jet Fuel Surrogate Formulated by Real Fuel Properties. Combust Flame 2010, 157 (12), 2333–2339. https://doi.org/10.1016/J.COMBUSTFLAME.2010.07.001.
(118) Heyne, J. S. Direct and Indirect Determinations of Elementary Rate Constants H+ O 2: Chain Branching; the Dehydration of Tertiary-Butanol; the Retro Diels-Alder Reaction of Cyclohexene; the Dehydration of Isopropanol, Princeton University, 2014.
(119) Sheyyab, M.; Lynch, P. T.; Mayhew, E. K.; Brezinsky, K. Optimized Synthetic Data and Semi-Supervised Learning for Derived Cetane Number Prediction. Combust Flame 2024, 259, 113184. https://doi.org/10.1016/J.COMBUSTFLAME.2023.113184.
(120) Won, S. H.; Dooley, S.; Veloo, P. S.; Wang, H.; Oehlschlaeger, M. A.; Dryer, F. L.; Ju, Y. The Combustion Properties of 2,6,10-Trimethyl Dodecane and a Chemical Functional Group Analysis. Combust Flame 2014, 161 (3), 826–834. https://doi.org/https://doi.org/10.1016/j.combustflame.2013.08.010.

(121) Abdul Jameel, A. G.; Naser, N.; Emwas, A.-H.; Dooley, S.; Sarathy, S. M. Predicting Fuel Ignition Quality Using 1H NMR Spectroscopy and Multiple Linear Regression. Energy & Fuels 2016, 30 (11), 9819–9835. https://doi.org/10.1021/acs.energyfuels.6b01690.
(122) Faulhaber, C.; Borland, C.; Boehm, R.; Heyne, J. Measurements of Nitrile Rubber Absorption of Hydrocarbons: Trends for Sustainable Aviation Fuel Compatibility. Energy & Fuels 2023, 37 (13), 9207–9219. https://doi.org/10.1021/acs.energyfuels.3c00781.
(123) Romanczyk, M.; Ramirez Velasco, J. H.; Xu, L.; Vozka, P.; Dissanayake, P.; Wehde, K. E.; Roe, N.; Keating, E.; Kilaz, G.; Trice, R. W.; Luning Prak, D. J.; Kenttämaa, H. The Capability of Organic Compounds to Swell Acrylonitrile Butadiene O-Rings and Their Effects on O-Ring Mechanical Properties. Fuel 2019, 238, 483–492. https://doi.org/10.1016/j.fuel.2018.10.103.
(124) Liu, Y.; Wilson, C. W. Investigation into the Impact of N-Decane, Decalin, and Isoparaffinic Solvent on Elastomeric Sealing Materials. Advances in Mechanical Engineering 2012, 2012. https://doi.org/10.1155/2012/127430.
(125) Graham, J. L.; Striebich, R. C.; Myers, K. J.; Minus, D. K.; Harrison, W. E. Swelling of Nitrile Rubber by Selected Aromatics Blended in a Synthetic Jet Fuel. Energy & Fuels 2006, 20 (2), 759–765. https://doi.org/10.1021/ef050191x.
(126) Anuar, A.; Undavalli, V. K.; Khandelwal, B.; Blakey, S. Effect of Fuels, Aromatics and Preparation Methods on Seal Swell. Aeronautical Journal 2021, 125 (1291), 1542–1565. https://doi.org/10.1017/aer.2021.25.
(127) Kosir, S.; Heyne, J.; Graham, J. A Machine Learning Framework for Drop-in Volume Swell Characteristics of Sustainable Aviation Fuel. Fuel 2020, 274 (April), 117832. https://doi.org/10.1016/j.fuel.2020.117832.
(128) J. Gormley, R.; D. Link, D.; P. Baltrus, J.; H. Zandhuis, P. Interactions of Jet Fuels with Nitrile O-Rings: Petroleum-Derived versus Synthetic Fuels. Energy & Fuels 2009, 23 (2), 857–861. https://doi.org/10.1021/ef8008037.
(129) Corporan, E.; Edwards, T.; Shafer, L.; Dewitt, M. J.; Klingshirn, C.; Zabarnick, S.; West, Z.; Striebich, R.; Graham, J.; Klein, J. Chemical, Thermal Stability, Seal Swell, and Emissions Studies of Alternative Jet Fuels. Energy & Fuels 2011, 25 (3), 955–966. https://doi.org/10.1021/ef101520v.
(130) Hansen, C. M. Three Dimensional Solubility Parameter and Solvent Diffusion Coefficient. Importance in Surface Coating Formulation, 1967.
(131) Hansen, C. M. Three Dimensional Solubility Parameter and Solvent Diffusion Coefficient. Importance in Surface Coating Formulation, Panish Technical Press, 1967.
(132) Ho Manh, L.; Chen, V. C. P.; Rosenberger, J.; Wang, S.; Yang, Y.; Schug, K. A. Prediction of Vacuum Ultraviolet/Ultraviolet Gas-Phase Absorption Spectra Using Molecular Feature Representations and Machine Learning. Journal of Chemical Information and Modeling 2024, 64 (14), 5547–5556. https://doi.org/10.1021/acs.jcim.4c00676.
(133) Luc Fortier, J.; C. Benson, G. Heat Capacities of Some Binary Aromatic Hydrocarbon Mixtures Containing Benzene or Toluene. J Chem Eng Data 2002, 24 (1), 34–37. https://doi.org/10.1021/je60080a015.
(134) Yang, Z.; Cronin, D. J.; Bell, D.; Boehm, R. C.; Heyne, J. S.; Ramasamy, K. K. Effect of Sustainable Aviation Fuel Blending on Distillation Curve; 2024.
(135) Yang, Z.; Bell, D. C.; Boehm, R. C.; Marques, P. F.; Boze, J. A.; Kosilkin, I. V.; Heyne, J. S. Assessing the Effect of Composition on Dielectric Constant of Sustainable Aviation Fuel. submitted 2024.

APPENDIX D

Dielectric Constant Predictions for Jet-Range Hydrocarbons: Evaluating the Clausius–Mossotti Relation and Correcting for Molecular Dipole Moments

Faulhaber, C., Bell, D. C., Boehm, R., & Heyne, J. S. (2024). Dielectric constant predictions for jet-range hydrocarbons: Evaluating the Clausius–Mossotti relation and correcting for molecular dipole moments. *Energies, 17*(18), 4700. https://doi.org/10.3390/en17184700

1. Introduction

Sustainable aviation fuel (SAF) has been identified as a leading prospect for meeting the decarbonization goals of commercial aviation [1]. To advance this technology, a joint effort by the United States' Department of Energy, Department of Agriculture, Department of Transportation, and Federal Aviation Administration has put forth a number of domestic SAF production targets, including 3 billion gallons of SAF by 2030 and 35 billion by 2050 (10% and 100% of the United States' projected fuel demand, respectively) [2]. Standing in the way of these goals are a number of obstacles, not the least of which is the compatibility of the current operational aircraft fleet with novel SAFs. Currently, in-flight fuel safety and performance characteristics are maintained by a maximum 50%v blending limit for SAF in conventional petroleum-based fuels [3]. Ensuring full fleet compatibility past this limit is a critical step towards meeting the stated industry targets.

Many SAF compositions significantly vary from those of conventional petroleum jet fuel (Jet-A), and ongoing regulatory efforts are in place to ensure safe operation for aircraft utilizing SAFs. Due to the high cost of developing novel fuels, the community benefits from reliable predictive methods for fuel properties critical to engine and fuel system function. One of these properties, the dielectric constant, is central to an empirical version of the Clausius–Mossotti relation (C-M) with density used in capacitance-based fuel quantity indicator systems (FQISs) [4]. If this relationship for a prospective SAF is far outside of the expected fuel values used by the system, then a significant error in density can occur as a result, potentially leading to an incorrect indicated fuel mass on board the aircraft [5,6]. All of the currently approved (up to 50%v) low-aromatic SAFs would fall into this category if they were to be allowed up to 100%v [7,8].

The conventional fuel dielectric constant is highly dependent upon aromatic content. Existing SAF technologies that contain little-to-no aromatics, such as synthetic paraffinic kerosene (SPK) or cycloparaffinic kerosene (CPK), do not match the conventional fuel experience range for density as a function of the dielectric constant [9]. Both density and the relationship between density and the dielectric constant restrict, to varying degrees, the blend fraction of low-aromatic synthetic fuels, which are otherwise viewed favorably in terms of LHV, sooting propensity, and thermal stability [10]. An O-ring seal swell is an additional fuel property of concern to engine and aircraft manufacturers that is driven largely by aromatics in conventional fuels [11]. The inclusion of cycloalkanes at larger fractions is currently seen as a low-sooting alternative to induce adequate seal swell and density [12,13], but cannot be used to improve fuel gauging relative to the Jet-A range [7]. Understanding how to improve the viability of low- or zero-aromatic SAFs in the entirety of current aircraft systems requires accurate prediction methods for the properties of aromatic species and potential substitutes, namely certain cycloalkanes.

Here, the dielectric constant is predicted using a two-part model. First, QSPR polarizability predictions from Wang et al. [14] and density measurements are applied to the theoretical version of the Clausius–Mossotti relation, which assumes no permanent molecular dipole moments [15,16], to demonstrate its efficacy in jet fuel applications. Second, the permanent dipole moments of 240 molecules are calculated from first principles and are used as an independent variable in a second-degree binomial regression to predict the difference between the empirical dielectric constant data of Yang et al. [7] and the Clausius–Mossotti dielectric calculation. Adding the terms of this regression to the theoretical Clausius–Mossotti relation results in a new, computationally inexpensive dielectric constant prediction method that, when used in tandem with the blending rules verified by Yang et al. [7], can be easily implemented into fuel-composition optimizations to effectively forecast fuels that will maintain compatibility with current aircraft fuel systems, including FQISs, while exhibiting advantageous performance properties [10,17,18].

2. Materials and Methods

The 230 dielectric constant and density measurements (46 molecules at 10, 15, 20, 25, and 30 °C) found in Yang et al. [7] are utilized here along with 10 additional data points, 1,3,5-trimethylcyclohexane (TCI America, Portland, OR, USA, Purity >98.0%) and cis-1,3-dimethylcyclohexane (TCI America, Portland, OR, USA, Purity >99.0%), each at the same 5 temperatures as the previous study, for model development. The 10 added measurements can be found in Tables S1 and S2 of the Supplementary Information (SI). The temperatures considered here cover a moderate fraction of the expected range for an in-service jet fuel. However, historical jet fuel dielectric constant data [19,20] indicate a linear relationship on the Clausius-Mossotti plot for each fuel over a more comprehensive temperature range, −35 to 70 °C. Although currently unavailable, single-species dielectric constant data over a wider temperature range, which will improve modeling efforts, will be a focus of future experimental work. To provide further context towards the dipole moments of jet-range hydrocarbons (C7 to C18), the permanent dipoles of 1827 molecules found in the NIST Web Thermo Tables Version 2-2012 [21] are computed and discussed.

Polarizability is a relatively easily predicted property, and multiple QSPR/QSAR models exist for this purpose [14,22]. Here, polarizability is predicted using Wang et al.'s Model 2E [14]. This is a simple QSPR model built with 420 experimental polarizability data points and has a coefficient of determination (R2) equal to 0.9978. While the present study employs quantum mechanical calculations for the dipole moment, this empirical model was favored for predicting polarizability values. In addition to added simplicity, this choice is based on Wang et al.'s comparison of Model 2E to quantum mechanical molecular polarizabilities, which showed superior performance of Model 2E relative to the experimental values.

The dipole moment represents the solution to the dipole operator with respect to the electronic wave function of the molecule at its ground electronic energy state [23]. These two steps, optimizing a molecule's atomic coordinates to its ground state and evaluating the wave function, are somewhat computationally expensive even for hydrocarbons. Additionally, molecules often have multiple electronic energy local minima, representing different electronic states for the same molecule. Accounting for all of these conformations requires additional iterations of an already time-consuming calculation.

Fortunately, easily accessible computational quantum chemistry software packages [24,25] exist for running calculations for the molecular dipole moment. With the species' isomeric SMILES string [26] and a random number generator 'seed' as inputs, RDKit Version 2023.09.05 [27] was used for obtaining initial atomic coordinates. Then, the Psi4 software package Version 1.9.1 [24] was employed to handle the quantum mechanical calculations using the Hartree–Fock method [23] and 6-31G** basis set [28,29]. To account for the presence of multiple local electronic energy minima, this computation was repeated with 100 different atomic coordinate seeds for each species in the database. The average of the 100 dipole moment calculations for each molecule was then stored for use in property predictions. Additionally, it is important to note that the basis set and level of theory used here are simplistic and computationally inexpensive relative to what can be found in work dedicated to determining optimal dipole calculation methods [23,30,31]. Improved dipole calculations would, in all likelihood, lead to improved dielectric predictions, at the cost of computational time not afforded to the work shown here.

As mentioned, the prediction method for the dielectric constant described here consists of two parts. The first part stems from the Clausius–Mossotti relation (Equation (1)) for the dielectric constant (ε_{CM}) with Avogadro's number (N_a), molar volume (V_m), and molecular polarizability (α) [15].

$$\frac{\varepsilon_{CM}-1}{\varepsilon_{CM}+2} = \frac{4\pi}{3} N_a \alpha V_m \qquad (Eq.\ 1)$$

Solving Equation 1 for the dielectric constant results in Equation 2.

$$\varepsilon_{CM} = \frac{\frac{8\pi N_a \alpha}{3V_m}+1}{1-\frac{4\pi N_a \alpha}{3V_m}} \qquad (Eq.\ 2)$$

The original development of the Clausius–Mossotti relation was for applications to substances without a significant permanent dipole moment, such as noble gases or simple aliphatic hydrocarbons [15,16]. Hydrocarbons are generally considered non-polar due to the similar electronegativities of hydrogen and carbon (2.1 and 2.5, respectively). However, the hydrogen/carbon (H/C) ratio and structural differences between hydrocarbon classes (n-/iso-alkanes, cycloalkanes, aromatics, etc.) does introduce a small and varied dipole moment. This implies that Equation (2) may underrepresent the impact of dipole moments on the dielectric constant, or that, in other words, some hydrocarbons can have non-negligible permanent dipole moments. A more comprehensive overview of the Clausius–Mossotti relation in aviation applications can be found in the works of Yang et al. [7] and Kosir et al. [9].

Part two of the model presented here aims to address the potential impacts of the dipole moments of molecules. Using data for 48 neat molecules, the difference between the measured dielectric constant and the result of Equation (2) was calculated. A second-degree binomial regression was performed on this dataset with the dipole moment acting as the independent variable. Multiple forms of regression, with and without forcing the y-intercept term to zero, were considered. Ultimately, the second-degree binomial form with an intercept equal to zero was chosen for its high accuracy compared to the other forms considered and its semblance to the theoretical applications of dipole moments in dielectric constant calculations [32]. The results of the regression, including 5 k-fold cross-validation scores indicating no overfitting, can be found in Figure S1 and Table S3 of the SI. The dielectric constant prediction for a given species (ε) was computed according

to Equation (3) as the sum of the Equation (2) result (ε_{CM}) and the output of this regression with the dipole moment (μ) as calculated by the method described above.

$$\varepsilon_{CM,\mu} = \varepsilon_{CM} + 0.9263\mu^2 + 0.2655\mu \qquad (Eq.3)$$

3. Results and Discussion

3.1 Dipole Moment Calculation

Figure 1 shows the results of the dipole moment calculations for the NIST database of 1827 jet-range hydrocarbons. While confirmation of these values remains difficult due to the lack of available dipole moment data in the archival literature, this self-consistent dataset is convenient for understanding molecular dipole moments relative to hydrocarbon class and carbon number, as well as the variance of dipoles within these descriptors. It is suitable for relating Equation (2) model error to the calculated dipole moment; however, the coefficients of the regression are specific to the dipole calculation method presented in this article.

The most polar hydrocarbons common to aviation turbine fuels, di-aromatics, have dipole moments well below 1 Debye (D), which is often considered non-polar within the context of heteroatom-containing hydrocarbons, as well as most inorganic compounds. For clarity, dipole moments are discussed here in terms that are relative to the ranges shown in Figure 1. For example, a high dipole moment for a constituent fuel molecule would be 0.6 D.

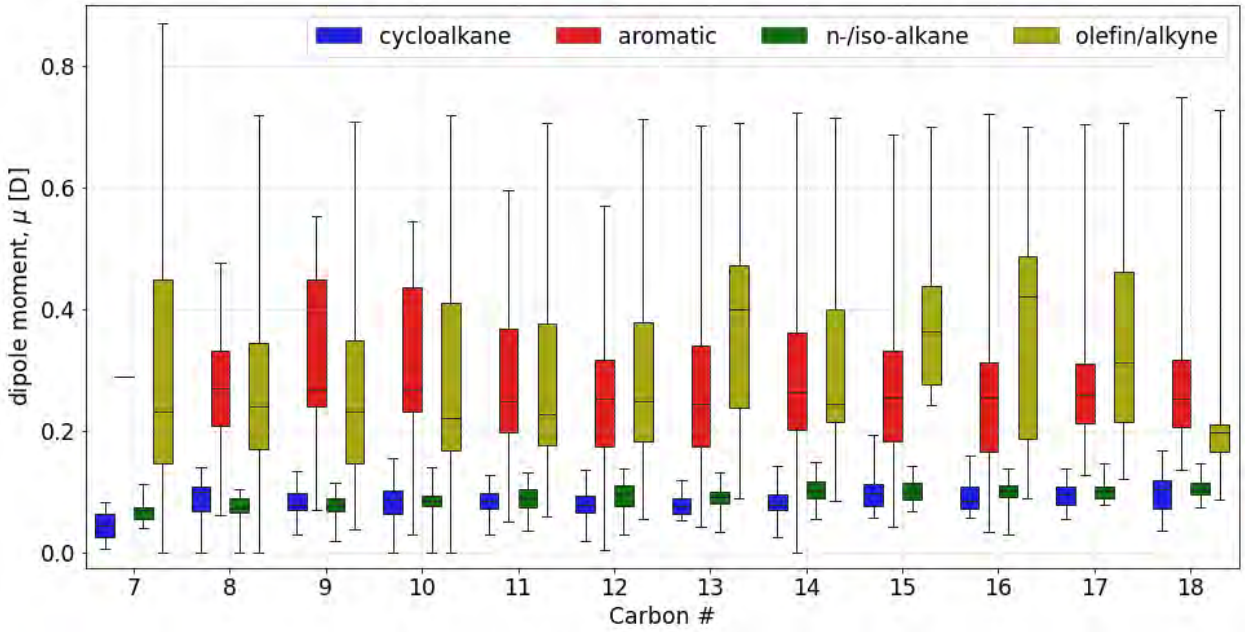

Figure 1. Calculated dipole moments sorted by carbon number and general hydrocarbon class. Cycloalkanes include mono, di, and tricycloalkanes. Aromatics include alkylbenzenes, di-aromatics, and cyclo-aromatics. Olefins include linear and branched alkenes, alkynes, and dienes.

As expected, n-, iso-, and cyclic alkanes all have a much lower mean dipole moment across all carbon numbers compared to unsaturates (aromatics, olefins, and alkynes). Unsaturated compounds also show a much higher variance within carbon number groups, with some species exhibiting lower dipole moments than many alkanes. This makes the identification of carbon-number trends among unsaturated compounds difficult. Alkanes show a slight increase in the dipole moment with higher carbon number, likely due to an increased opportunity for branching.

3.2 Model Performance

The dielectric constant measurements of 48 neat molecules at five temperatures were compared with values predicted from the Clausius–Mossotti relation (Equation (2)) using the measured density and QSPR-calculated polarizability [14] as inputs. As shown in Figure 2 and Table 1, the majority of n-, iso-, and cycloalkanes in the dataset show good agreement

with this equation due to the relatively low dipole moments of most aliphatic hydrocarbons. However, the two additional cycloalkanes measured for this study, 1,3,5-trimethylcyclohexane and cis-1,3-dimethylcyclohexane, show a MARE nearly five times higher than the rest of the alkanes in the dataset and have the two largest dipole moments within the alkanes in the dataset. Since these molecules appear much nearer to the conventional fuel range compared to other alkanes, it is important to ensure that the dielectric constant can be correctly predicted for similar molecules. This is discussed further in Section 3.3. Additionally, for unsaturated molecules exhibiting higher dipole moments, Equation (2) consistently underestimated the dielectric constant leading to a poor overall R2 of 0.54 for the Clausius–Mossotti relation. Given the importance of aromatics for meeting the conventional jet fuel range for the dielectric constant, and the potential impact of certain cycloalkanes as higher-performing substitutes for aromatics in synthetic fuels, Equation (2) alone is not sufficient for accurate predictions.

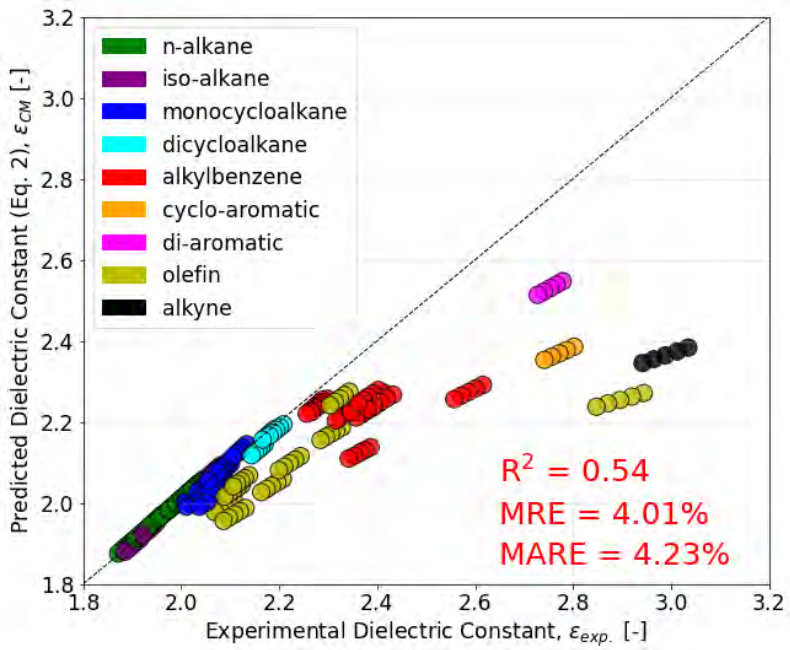

Figure 2. Unity plot for dielectric predictions via the Clausius–Mossotti relation (Equation (2)) with accuracy metrics for the entire dataset. R2 = coefficient of determination, MRE = mean relative error, MARE = mean absolute relative error.

The results for the dipole-corrected C-M model described by Equation (3) are shown in Figure 3 below. The Equation (3) predictions for alkanes remain mostly consistent with those from the standalone C-M relation, while the predictions for aromatics and olefins are most affected by the inclusion of a weighted dipole moment term. This is supported by Table 1, where the accuracy increases significantly for alkylbenzenes, cyclo-aromatics, and di-aromatics. The correction of these groups is the main contributor to the much-improved R2 of 0.92 for the overall model.

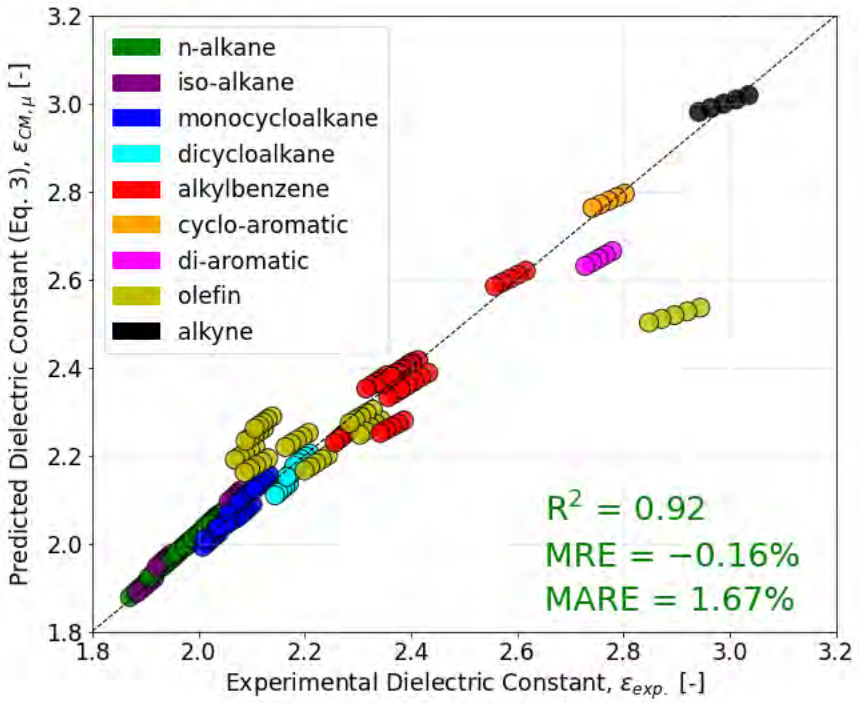

Figure 3. Unity plot for dielectric predictions via the dipole-corrected Clausius–Mossotti model (Equation (3)) with accuracy metrics for the entire dataset.

Olefins did not show an obvious improvement with the dipole correction compared to the other hydrocarbon classes. While the MARE for these molecules slightly improved from 6.76% to 4.80% with the dipole moment correction, over half of the molecules see an overcorrection in the dielectric constant from the additional model term. This indicates that partial saturates, whether cyclic or linear, may have electronic or magnetic [9] properties that are beyond what is described by a singular dipole moment term. While this represents one limitation of the current work, it is of relatively low concern because jet fuel typically contains less than 2.5%v of olefins measured by ASTM D1319 [19,33].

Table 1. Error metrics for the two dielectric constant models presented here.

	Clausius–Mossotti (Figure 2)		Dipole-Corrected Model (Figure 3)	
HC Class	**MRE [%]**	**MARE [%]**	**MRE [%]**	**MARE [%]**
N-alkane	−0.45	0.45	−0.97	0.98
Iso-alkane	−0.08	0.27	−1.16	1.16
Monocycloalkane	0.73	0.85	−0.02	0.43
Dicyclocycloalkane	0.78	0.78	0.82	0.82
Alkene	6.76	6.76	−0.77	4.80
Cyclo-aromatic	14.53	14.53	−0.24	0.35
Alkyne	20.89	20.89	−0.36	0.63
Di-aromatic	8.11	8.11	3.86	3.86
Alkylbenzene	5.98	5.98	0.61	1.27

Another impact of the dipole moment correction is the slight decrease in accuracy for n-alkanes, iso-alkanes, and dicycloalkanes. The change in accuracy between the two models in Table 1 correlates with the dipole moment calculations found in Figure 1. Specifically, these molecules all have small, but nonzero, dipole moments. When applied to Equation (3), this confounds what is otherwise a highly accurate prediction from the C-M relation (Equation (2)) where no dipole moments are assumed. The error for these molecules in the dipole-corrected model still appears reasonably close to the unity line, although its impact on the relationship with density is more pronounced and will be discussed in Section 3.3.

Most of the monocycloalkanes behave similarly with regard to the dipole correction; however, the group at large sees a slight improvement in accuracy due to the much-improved predictions for 1,3,5-trimethylcyclohexane and cis-1,3-dimethylcyclohexane. These molecules exhibit higher polarity than the rest of the cycloalkanes, and thus are not well characterized by the Clausius–Mossotti model alone (Equation (2)). Because cycloalkanes are seen as desirable for improving the density and seal swell characteristics of SPK SAFs, which are almost entirely composed of n- and iso-alkanes, it is important to accurately capture the dielectric behavior of the entire spectrum of cycloalkanes. Additionally, the disproportionate influence of aromatic molecules on fuels meeting the Jet-A experience range for the dielectric constant implies that cycloalkanes exhibiting higher dipole moments could actually contribute positively towards SAFs meeting this property constraint.

3.3 Impacts on Model Application

This work provides a method for predicting the dielectric constant of aviation turbine fuel. However, as mentioned before, aircraft FQISs function under the assumption that the onboard fuel resembles the conventional fuel range on the Clausius–Mossotti plot. Using historical dielectric constant data for 172 fuels at 10°, 15°, 20°, 25°, and 30 °C from ARINC 611-1 and CRC 647 [19,20], the Jet-A experience range is shown in Figures 4 and 5 as a reference point to evaluate how the models presented here (Equations (2) and (3)) performed for each hydrocarbon class in a fuel-gauging application. The impact of hydrocarbon class in relation to the Clausius–Mossotti Jet-A range is discussed at length in previous work [7], so it will not be repeated. However, an important detail to point out in these plots is the close proximity in Figures 4b and 5b of the two additional cycloalkane molecules measured, 1,3,5-trimethylcyclohexane (thin diamonds) and cis-1,3-dimethylcyclohexane (stars), to the conventional fuel range.

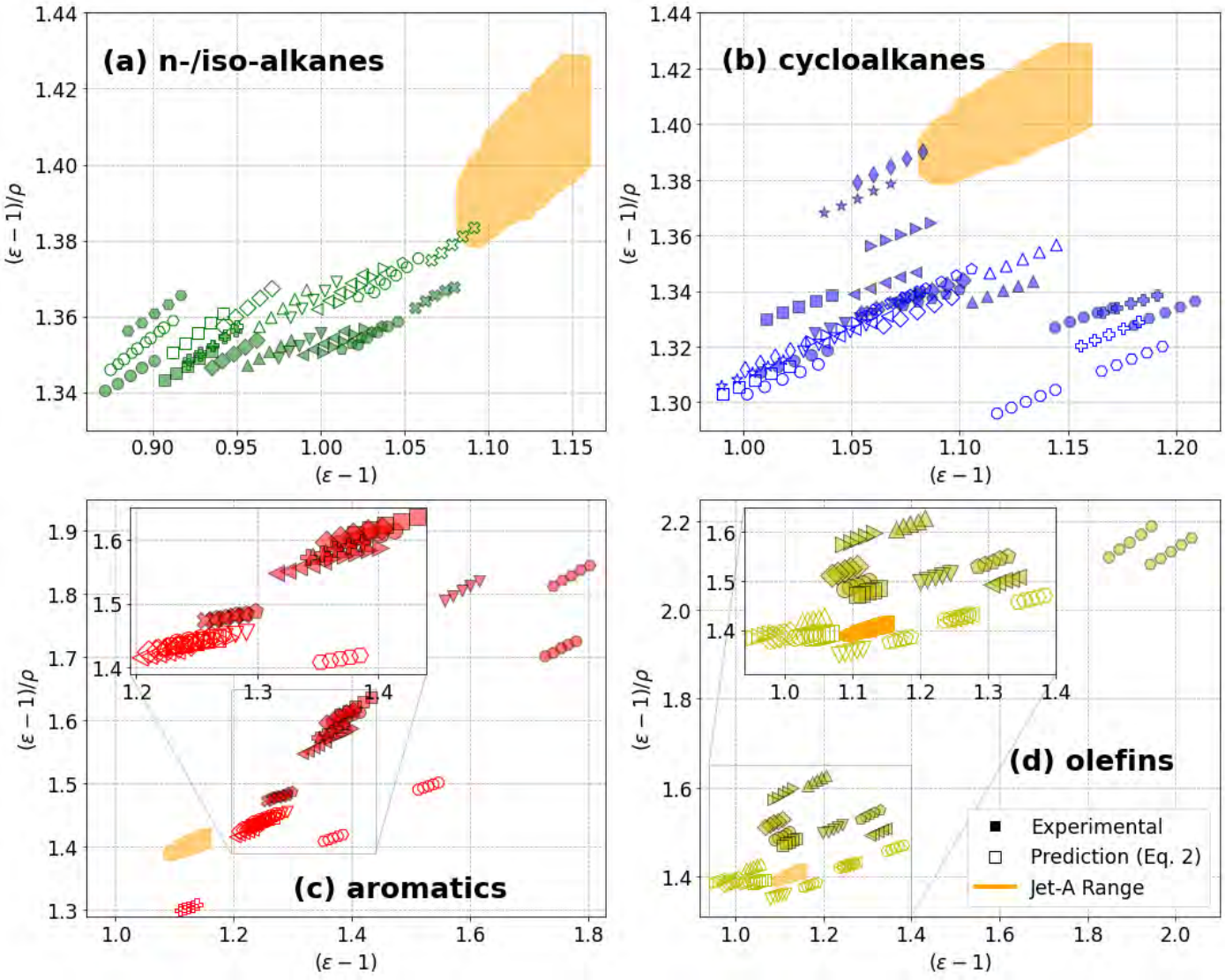

Figure 4. Clausius–Mossotti plots containing experimental results (closed symbols) and predictions from the Clausius–Mossotti relation shown in Equation (2) (open symbols). Each subplot (and color) focuses on one general hydrocarbon class: n-/iso-alkanes (a), cycloalkanes (b), aromatics (c), olefins, and alkynes (d). Each molecule is identified by a unique shape. The Jet-A experience range, based on ARINC and CRC historical data, is shown in orange.

Given the results shown in Figure 2, the results shown in Figure 4 are largely unsurprising. The placements of more polar hydrocarbons, aromatics (Figure 4c) and olefins (Figure 4d), are poorly predicted by the theoretical Clausius–Mossotti relation (Equation (2)). Barring the two additional cycloalkanes measured for this study, the cycloalkanes predictions from Equation (2) are found well below the Jet-A range, in general alignment with the experimental values. Figure 4a, on the other hand, demonstrates a consistent overprediction of the n-/iso-alkanes on the Clausius–Mossotti plot despite displaying low errors for Equation (2) predictions in Figure 1 and Table 1. Because these molecules have much lower density than the other hydrocarbon classes, errors in the dielectric constant are exacerbated on the Clausius–Mossotti plot. The small increase in dielectric error for n-/iso-alkanes in the dipole-corrected (Equation (3)) model further demonstrates this effect on the Clausius–Mossotti plot in Figure 5a. However, because these molecules display relatively little variance across species for FQIS implications (or O-ring seal swell, for that matter), they can be adequately represented in fuel-composition optimizations with the properties of a commercially available SPK or iso-paraffinic solvent.

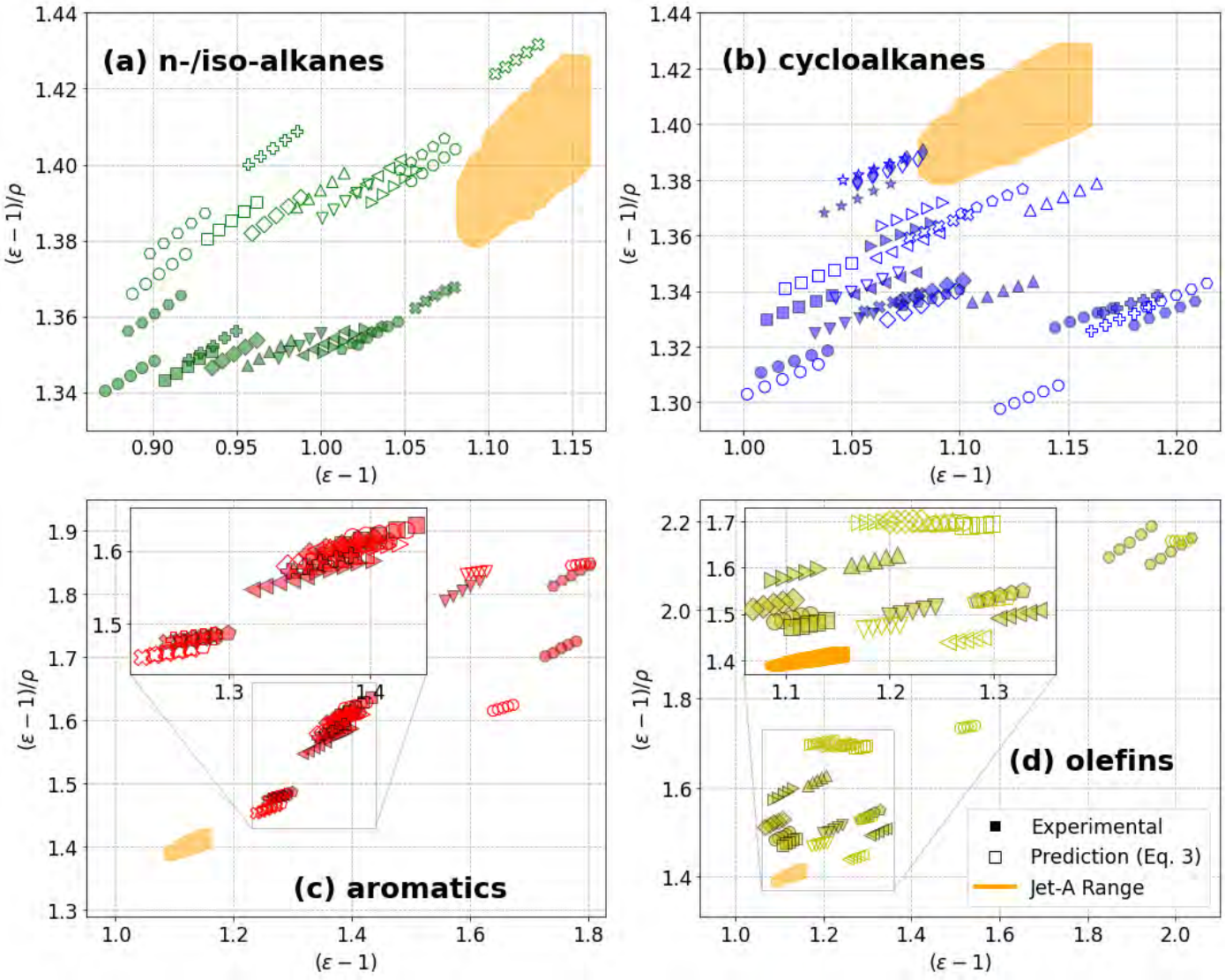

Figure 5. Clausius–Mossotti plots containing experimental results (closed symbols) and predictions from the dipole-corrected Clausius–Mossotti relation shown in Equation (33) (open symbols). Each subplot (and color) focuses on one general hydrocarbon class: n- and iso-alkanes (a), cycloalkanes (b), aromatics (c), olefins, and alkynes (d). Each molecule is identified by a unique shape. The Jet-A experience range, based on ARINC and CRC historical data, is shown in orange.

Figure 5b,c,d show predictions more consistent with the experimental values for cycloalkanes and aromatics. The improved prediction capabilities for aromatics offer the opportunity for identifying the most desirable species for improving FQISs' compatibility while taking the sooting impacts of the molecule into consideration. Additionally, the improvement in accuracy for 1,3,5-trimethylcyclohexane (thin diamonds) and cis-1,3-dimethylcyclohexane (stars) indicate this method's potential to forecast the dielectric constant values for more polar cycloalkane species that may offer some benefit in reducing the need for aromatics in aviation fuel. The improvement in prediction accuracy for molecules near the Jet-A range comes at the cost of some cycloalkanes showing overpredictions on the y-axis of the Clausius–Mossotti plot. This underlines that there are other electromagnetic properties impacting the dielectric constant that are uncharacterized by this model. However, the range of species near the Jet-A range on the Clausius–Mossotti plot is fairly narrow, making experimental validation of these molecules for model applications much simpler than evaluating the entirety of jet-range hydrocarbons.

With this in mind, Figure 6b illustrates that certain cycloalkanes from the NIST database may positively contribute towards fulfilling the constraints of the Clausius–Mossotti Jet-A range when using the dipole-corrected model (Equation (3)) for dielectric constant prediction. Alternatively, Figure 6a shows that predictions made on the same database using only the Clausius–Mossotti relation (Equation (2)) significantly impact the solution space for modeling FQIS-compatible fuel compositions from this database.

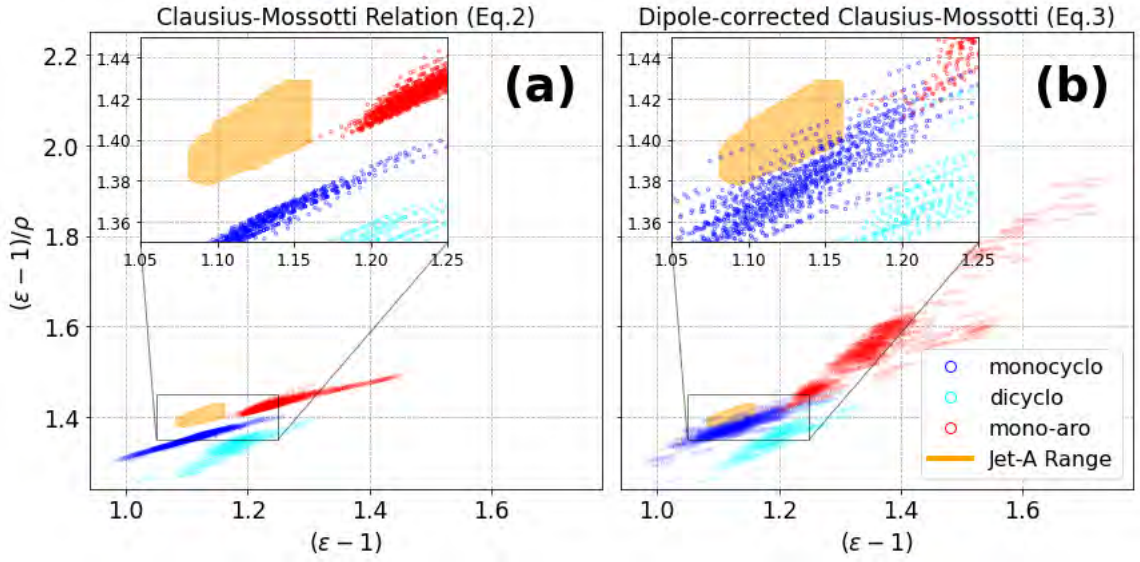

Figure 6. Clausius–Mossotti plot displaying predictions from (a) the Clausius–Mossotti relation (Equation (2)) and (b) the dipole-corrected model (Equation (3)) for the NIST database molecules of interest for blending with current SPK products (monocycloalkanes, dicycloalkanes, and mono-aromatics). The Jet-A range is shown in orange as a reference point.

While not insignificant, the applications of the dipole-corrected model presented here are limited to research or production efforts at low fuel readiness levels [34] seeking to evaluate fuel compositions in relation to the Jet-A range on the Clausius–Mossotti plot. This model does not sufficiently capture the temperature dependence of the dielectric constant, which is leveraged in aircraft FQISs in the form of the gauging slope and intercept [9]. A closer look at Figure 3 shows that the slope of the temperature series for many molecules is not consistent with the unity line. This is likely the result of some temperature dependency that has not been assessed for some of the model inputs, namely polarizability and the dipole moment. Although some work has been performed to show the impact of temperature on the electronic properties of molecules [35,36], accurately calculating this dependency is beyond the scope of this work.

4. Conclusions

This work evaluated the Clausius–Mossotti relation (Equation (2)), which assumes negligible molecular dipole moments, for predicting the dielectric constant of aviation jet-range hydrocarbons and proposes Equation (3) as a more accurate prediction method using a simple correction for dipole moments calculated using open-source computational chemistry software. Both models (Equations (2) and (3)) were evaluated over a training dataset of density and dielectric constant measurements for 48 neat molecules at five temperatures each. The relatively high dipole moments of aromatic molecules led to poor prediction accuracy over the entirety of the dataset (R2 = 0.54, MRE = 4.01%, MARE = 4.23%) when Equation (2) was used. With the addition of model terms accounting for the dipole moment, Equation (3) showed significantly improved error metrics (R2 = 0.92, MRE = −0.16%, MARE = 1.67%) by more accurately capturing the behavior of aromatics and polar cycloalkane species. Both models showed low accuracy for olefins, which is of little concern due to their relatively low concentration in jet fuels. Predictions from both models had small error metrics for the dielectric constant values of n-/iso-alkanes, but presented exacerbated inaccuracies on the Clausius–Mossotti plot used in fuel-gauging applications, due to the low density of these molecules. More computationally intensive dipole moment calculations would likely improve these predictions and may be the subject of future work. Despite this, the authors suggest the current dipole-corrected model (Equation (3)) as appropriate for use in exploratory fuel-composition optimizations where the n-/iso-alkane fraction of the solutions can be represented with existing SPK products to highlight the influence of aromatics and cycloalkanes on fuel

performance and operability properties, e.g., sooting propensity, energy density, volumetric density, elastomer O-ring seal swell, and dielectric constant-based FQISs, that are currently of high interest to the community.

Nomenclature

α	Molecular polarizability.
ASTM	ASTM International.
C-M (or CM)	Clausius–Mossotti relation.
CPK	Cycloparaffinic kerosene.
D	Debye.
ε	Dielectric constant.
FQIS	Fuel quantity indicator system.
μ	Permanent dipole moment.
Na	Avogadro's number.
NIST	National Institute of Standards and Technology.
QSPR/QSAR	Quantitative structure property/activity relationship.
R2	Coefficient of determination.
SAF	Sustainable aviation fuel.
SPK	Synthetic paraffinic kerosene
Vm	Molar volume.

5. References

Air Transport Action Group. Waypoint 2050: Balancing Growth in Connectivity with a Comprehensive Global Air Transport Response to the Climate Emergency: A Vision of Net-Zero Aviation by Mid-Century; Air Transport Action Group: Geneva, Switzerland, 2021. Available online: https://aviationbenefits.org/environmental-efficiency/climate-action/waypoint-2050/ (accessed on 16 June 2024).

SAF Grand Challenge Roadmap Flight Plan for Sustainable Aviation Fuel; US Department of Energy: Washington, DC, USA, 2022. https://www.energy.gov/sites/default/files/2022-09/beto-saf-gc-roadmap-report-sept-2022.pdf (accessed on 25 January 2023).

ASTM D7566-22a; Standard Specification for Aviation Turbine Fuel Containing Synthesized Hydrocarbons 1; ASTM: West Conshohocken, PA, USA, 2023. https://doi.org/10.1520/D7566-22A.

Connors, M. A Systems Design Approach to Fuel Measurement in Hybrid-Electric Aircraft; Vertical Flight Society: Fairfax, VA, USA, 2020.

Brasfield, R.G. Patent: Fuel Gaging System. WO1984001428A1, 12 April 1984.

ASTM D924; JetDC 88500-0 Measurement of Dielectric Constant of Aviation Turbine Fuel IP PM-FC/21. Available online: https://www.stanhope-seta.co.uk/ (accessed on).

Yang, Z.; Bell, D.C.; Boehm, R.C.; Fischer Marques, P.; Boze, J.A.; Kosilkin, I.V.; Heyne, J.S. Assessing the Effect of Composition on Dielectric Constant of Sustainable Aviation Fuel. Available online: https://ssrn.com/abstract=4700499 (accessed on 22 May 2024).

ASTM D7566-23b; Standard Specification for Aviation Turbine Fuel Containing Synthesized Hydrocarbons 1; ASTM: West Conshohocken, PA, USA, 2024. https://doi.org/10.1520/D7566-23B.

Kosir, S.; Landsaw, A.; Steinecker, W.H.; West, Z.J.; Zabarnick, S. Synthetic Blend Component Study: The Effects of Hydrocarbon Composition on Aviation Fuel Dielectric Constant. Energy Fuels 2024, 38, 16451–16457. https://doi.org/10.1021/acs.energyfuels.4c02342.

Boehm, R.C.; Faulhaber, C.; Behnke, L.; Heyne, J. The Effect of Theoretical SAF Composition on Calculated Engine and Aircraft Efficiency. Fuel 2024, 371, 132049. https://doi.org/10.1016/j.fuel.2024.132049.

Faulhaber, C.; Borland, C.; Boehm, R.; Heyne, J. Measurements of Nitrile Rubber Absorption of Hydrocarbons: Trends for Sustainable Aviation Fuel Compatibility. Energy Fuels 2023, 37, 9207–9219. https://doi.org/10.1021/acs.energyfuels.3c00781.

Yang, Z.; Xu, Z.; Feng, M.; Cort, J.R.; Gieleciak, R.; Heyne, J.; Yang, B. Lignin-Based Jet Fuel and Its Blending Effect with Conventional Jet Fuel. Fuel 2022, 321, 124040. https://doi.org/10.1016/j.fuel.2022.124040.

Muldoon, J.A.; Harvey, B.G. Bio-Based Cycloalkanes: The Missing Link to High-Performance Sustainable Jet Fuels. ChemSusChem 2020, 13, 5777–5807. https://doi.org/10.1002/cssc.202001641.

Wang, J.; Xie, X.Q.; Hou, T.; Xu, X. Fast Approaches for Molecular Polarizability Calculations. J. Phys. Chem. A 2007, 111, 4443–4448. https://doi.org/10.1021/jp068423w.

Van Rysselberghe, P. Remarks Concerning the Clausius-Mossotti Law. J. Phys. Chem. 1932, 36, 1152–1155.

Talebian, E.; Talebian, M. A General Review on the Derivation of Clausius-Mossotti Relation. Optik 2013, 124, 2324–2326. https://doi.org/10.1016/j.ijleo.2012.06.090.
Kosir, S.; Stachler, R.; Heyne, J.; Hauck, F. High-Performance Jet Fuel Optimization and Uncertainty Analysis. Fuel 2020, 281, 118718. https://doi.org/10.1016/j.fuel.2020.118718.
Kroyan, Y.; Wojcieszyk, M.; Kaario, O.; Larmi, M. Modeling the Impact of Sustainable Aviation Fuel Properties on End-Use Performance and Emissions in Aircraft Jet Engines. Energy 2022, 255, 124470. https://doi.org/10.1016/j.energy.2022.124470.
Hadaller, O.; Johnson, J. World Fuel Sampling Program; Coordinating Research Council: Alpharetta, Georgia, 2006.
ARINC611-1; ARINC Report 611-1 Guidance for the Design and Installation of Fuel Quantity Systems. ARINC: Annapolis, MD, USA, 1999.
Kroenlein, K.; Muzny, C.; Kazakov, A.; Diky, V.; Chirico, R.; Magee, J.; Abdulagatov, I.; Frenkel, M. NIST Standard Reference 203: TRC Web Thermo Tables (WTT) Version 2-2012-1 Professional; National Institute of Standards and Technology: Gaithersburg, MD, USA, 2012.
Bosque, R.; Sales, J. Polarizabilities of Solvents from the Chemical Composition. J. Chem. Inf. Comput. Sci. 2002, 42, 1154–1163. https://doi.org/10.1021/ci025528x.
Szabo, A.; Ostlund, N. Modern Quantum Chemistry: Introduction to Advanced Electronic Structure Theory; Dover Publications: Mineola, NY, USA, 1996.
Smith, D.G.A.; Burns, L.A.; Simmonett, A.C.; Parrish, R.M.; Schieber, M.C.; Galvelis, R.; Kraus, P.; Kruse, H.; Di Remigio, R.; Alenaizan, A.; et al. 1.4: Open-Source Software for High-Throughput Quantum Chemistry. J. Chem. Phys. 2020, 152, 184108. https://doi.org/10.1063/5.0006002.
O'Boyle, N.M.; Banck, M.; James, C.A.; Morley, C.; Vandermeersch, T.; Hutchison, G.R. Open Babel: An Open Chemical Toolbox. J. Cheminform. 2011, 3, 33. https://doi.org/10.1186/1758-2946-3-33.
Weininger, D. SMILES, a Chemical Language and Information System. 1. Introduction to Methodology and Encoding Rules. J. Chem. Inf. Comput. Sci. 1988, 28, 31–36. https://doi.org/10.1021/ci00057a005.
Landrum, G. RDKit: Open-Source Cheminformatics. Q2 2010. Version 2023.09.05. Online Documentation: https://www.rdkit.org (accessed on 23 January 2024).
Hariharan, P.C.; Pople, J.A. The Influence of Polarization Functions on Molecular Orbital Hydrogenation Energies. Theor. Chim. Acta 1973, 28, 213–222. https://doi.org/10.1007/BF00533485.
Francl, M.M.; Pietro, W.J.; Hehre, W.J.; Binkley, J.S.; Gordon, M.S.; DeFrees, D.J.; Pople, J.A. Self-Consistent Molecular Orbital Methods. XXIII. A Polarization-Type Basis Set for Second-Row Elements. J. Chem. Phys. 1982, 77, 3654–3665. https://doi.org/10.1063/1.444267.
Hait, D.; Head-Gordon, M. How Accurate Is Density Functional Theory at Predicting Dipole Moments? An Assessment Using a New Database of 200 Benchmark Values. J. Chem. Theory Comput. 2018, 14, 1969–1981. https://doi.org/10.1021/acs.jctc.7b01252.
Zapata, J.C.; McKemmish, L.K. On the Computation of Dipole Moments: A Recommendation on the Choice of the Basis Set and the Level of Theory. J. Phys. Chem. 2020, 124, 7538–7548. https://doi.org/10.1021/acs.jpca.0c06736.
Caleman, C.; Van Maaren, P.J.; Hong, M.; Hub, J.S.; Costa, L.T.; Van Der Spoel, D. Force Field Benchmark of Organic Liquids: Density, Enthalpy of Vaporization, Heat Capacities, Surface Tension, Isothermal Compressibility, Volumetric Expansion Coefficient, and Dielectric Constant. J. Chem. Theory Comput. 2012, 8, 61–74. https://doi.org/10.1021/ct200731v.
ASTM D1319-20a; Standard Test Method for Hydrocarbon Types in Liquid Petroleum Products by Fluorescent Indicator Adsorption 1. ASTM: West Conshohocken, PA, USA, 2020. https://doi.org/10.1520/D1319-20A.
CAAFI. Fuel Readiness Level (FRL); CAAFI: Bristol, UK, 2010. Available online: https://www.caafi.org/information/pdf/FRL_CAAFI_Jan_2010_V16.pdf (accessed on 13 June 2024).
Sharipov, A.S.; Loukhovitski, B.I.; Starik, A.M. The Influence of Vibrations of Polyatomic Molecules on Dipole Moment and Static Dipole Polarizability: Theoretical Study. J. Phys. B At. Mol. Opt. Phys. 2017, 50, 165101. https://doi.org/10.1088/1361-6455/aa7f80.
Miller, T.M.; Bederson, B. Atomic and Molecular Polarizabilities—A Review of Recent Advances. Adv. At. Mol. Phys. 1978, 13, 1–55. https://doi.org/10.1016/S0065-2199(08)60054-8.

Project 065(B) Fuel Testing Approaches for Rapid Jet Fuel Prescreening

University of Illinois at Urbana-Champaign

Project Lead Investigator

Tonghun Lee
Professor of Mechanical Science & Engineering
University of Illinois at Urbana-Champaign
1206 W. Green St., Urbana, IL 61801
517-290-8005
tonghun@illinois.edu

University Participants

University of Illinois at Urbana-Champaign (UIUC)

- P.I.: Professor Tonghun Lee
- FAA Award Number: 13-C-AJFE-UI-051
- Period of Performance: October 1, 2023, to September 30, 2024
- Tasks:
  1. Characterization of pressure effects on lean blowout (LBO) behavior as a part of M1 combustor development
  2. Spray Breakup Characterization for Multi-Fuel Analysis

Project Funding Level

Federal Aviation Administration (FAA) funding level: $150,000
Cost Sharing: 100% matching funds provided by software license support from Converge, Inc.

Investigation Team

Prof. Tonghun Lee, (P.I.), All Tasks
Casey O'Brien, (graduate student), experimental efforts in characterizing the M1 combustor, including laser and optical diagnostics

Project Overview

This study is aimed at introducing a new compact test rig (Army research combustor [ARC] M1), developed with original equipment manufacturer (OEM) support within the National Jet Fuel Combustion Program (NJFCP), that can screen fundamental combustor behavior with much lower fuel volumes (approximately gallons) before tier 3 and 4 tests in the ASTM D4054 evaluation. In the NJFCP, the referee rig at the Air Force Research Laboratory (AFRL) was used as a foundational test rig for this goal. The M1 may have the potential to perform screening tasks at reduced fuel volumes (approximately gallons rather than hundreds of gallons) in a simplified and open architecture that can be readily shared and operated at different locations at a fraction of the cost. Both the Army Research Laboratory (ARL) and Argonne National Laboratory (ANL) have been and will be partners in the effort to fully characterize the M1 facility. If successful, these efforts will allow fuel providers and OEMs to conduct basic combustor tests by using an identical testing architecture and identical test conditions at multiple test locations, in contrast to the referee rig, which is housed in a secure government facility (AFRL). Tests in smaller test rigs can provide a platform for individual suppliers or researchers to independently evaluate their new fuels and to make predictions without requiring the use of one single facility. Over time, as test data are accumulated, the potential for test rigs, such as the M1 to predict actual tier 3 and 4 performances will increase, potentially reducing the burden of relying on capital-intensive ASTM rig and engine tests.

Background of the M1 Combustor

Under the FAA-funded NJFCP, the referee rig combustor at AFRL was used to determine the sensitivity of combustor performance parameters, such as LBO and ignition parameters, to the chemical composition of novel fuels. The results from this investigation were instrumental in establishing a relationship between fuel chemistry and its effects on combustor performance. Prof. Tonghun Lee's research group conducted a substantial portion of the laser and optical diagnostic work for the referee rig as part of the NJFCP, including quantitative-phase Doppler particle analysis, which provided key quantitative data for the simulation efforts.

Although the referee combustor used in the NJFCP program provides valuable information, a few key issues were identified. One issue is that the combustor requires hundreds of gallons of fuel to operate, which likely would be not available for many of the new sustainable aviation fuels (SAF) that would become available in the near future in the initial phase of production. The second issue is that the referee combustor lacks adequate optical access for diagnostics as a research combustor. Most significantly, it does not have windows on the top where laser beams can be inserted. Finally, the combustor itself is in a secure military facility (AFRL) and is not readily accessible to the general community. For these reasons, a smaller, compact, and less expensive option was needed; thus, the M1 combustor was developed with both the FAA and ARL (FAA NJFCP member). The M1 was designed as a joint effort between the University of Illinois and select OEMs who were involved with the referee combustor. The M1 combustor would run with moderately high-pressure air and would require a few gallons of fuel instead of hundreds of gallons. If this type of low-cost combustor can be well characterized, it can help prescreen SAFs as new fuels become available.

The dimensions and a magnified view of the M1 combustor are included in Figure 1. This combustor was built to be modular so that components can be easily switched out to suit the needs of different optical and laser diagnostics. The combustor includes four-sided optical access to allow for maximum flexibility in the diagnostics. The modular aspect was designed to allow us to transport the combustor easily to other locations for measurements, primarily because our team envisioned using x-ray imaging for fuel spray characterization at ANL as well as combustion characterization with velocity field and radical species measurements at UIUC. With this approach, the ASCENT Project 065(B) team can ensure that we are able to characterize the M1 combustor in an unprecedented way to enable wide adoption in the academic/industrial community as a test platform for new fuel blends. After this characterization is complete, the basic physics, dimensions, and operational envelope of the combustor will be openly shared with the academic and commercial sectors. This work is expected to provide a common platform not only for prescreening SAFs but also for performing other sustainability-related experiments involving novel fuels in a laboratory setting. It can also be noted that the combustor and surrounding hardware were designed specifically to be inexpensive (low flowrate requirements, lower pressure requirements, low fuel requirements on hardware) so that other labs could replicate this setup with reasonable resources.

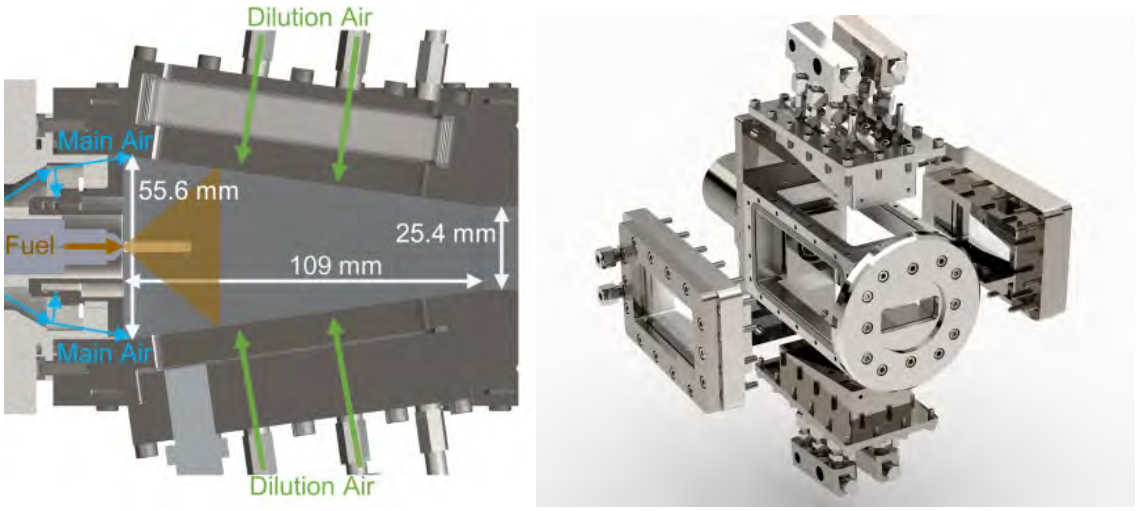

Figure 1. M1 combustor.

Task 1 – Characterization of Pressure Effects on LBO Behavior as a Part of M1 Combustor Development

University of Illinois at Urbana-Champaign

Objectives

In this task, LBO measurements are conducted for four different fuels and two combustor pressures. The fuels are selected to have a wide range of properties to isolate fuel effects on LBO behavior. Previously, a strong correlation was observed between physical fuel properties and LBO behavior, demonstrating that atomization and vaporization are rate-limiting steps for the M1 combustor because of the significantly smaller length scales compared with previous tests on the referee combustor. Two pressures are evaluated to determine whether higher pressure can produce favorable combusting conditions to create a transition from physically dominated LBO performance to a more chemical regime. By collecting LBO measurements at well-controlled, relevant operating conditions across different pressures, a comprehensive characterization matrix can be obtained to demonstrate how the operating regime of the M1 can be matched to previous large-scale testing for comparing fuel effects. This work should aid in the integration of alternative jet fuels into our current infrastructure by providing insight into how a model combustor can be utilized to observe real-scale effects while using much lower fuel volumes than other large-scale test rigs.

Research Approach

Throughout the NJFCP, the referee combustor and several other combustors were carefully characterized under a variety of relevant operating regimes, including blowout and ignition. These studies were conducted under a range of standard operating conditions that are relevant to gas turbine operational regimes and are likely to expose differences between fuels with varying properties. Although experiments in the referee combustor have provided valuable data regarding fuel effects near LBO, operating the referee rig has several disadvantages. The scale of the referee combustor results in large air and fuel flow rate requirements, thus making setup and operation expensive, particularly for studies of new alternatively derived fuels, which may be difficult to manufacture. Therefore, the ability to obtain similar results from a smaller combustor with decreased fuel and air requirements would be beneficial. The M1 combustor uses substantially less air and fuel, thereby reducing the overall instrumentation expense and complexity, as well as the volume of fuel needed to conduct tests over a range of conditions. With these advantages, the M1 combustor could be used to evaluate the performance of new fuels with much less fuel, thereby decreasing the supply requirements for a potential new fuel supplier. To achieve this goal, we must ensure that the trends observed in a smaller combustor convey the physics observed in other test combustors, such as the referee combustor.

Overview of LBO Testing

Performing LBO measurements on a combustor in a reliable and repeatable manner involves careful control of all combustor operating parameters, including fuel flow rate, air flow rate, air temperature, and combustor pressure. To ensure that combustor conditions are stable before LBO testing is conducted, the combustor is ignited at a fuel flow rate above the LBO point, and combustion is sustained at that flow rate until the air outlet temperature reaches a steady-state condition. After steady-state temperatures are reached, the fuel flow rate is slowly reduced until a blowout occurs. For these experiments, the fuel flow rate is reduced by approximately 0.05 g/min per second. This slow ramp rate helps ensure that the combustor wall temperature does not bias the LBO point toward a lower value, owing to heat transfer from the hot combustor itself back into the flame. While the fuel flow rate is being stepped down, all other combustor properties are closely monitored to ensure that they remain within the specified parameter ranges. The specific LBO point is monitored by simultaneously recording a photodiode signal at 100 kHz and all other combustor parameters at 50 Hz. The LBO point is determined for each test by finding the equivalence ratio for the point at which the photodiode signal indicates that blowout occurred. The testing matrix (Table 1) for this experiment is applied under conditions that can provide a consistent comparison to previous experiments conducted at UIUC as well as in the referee combustor. An example of broadband imaging near the LBO point is captured in Figure 2. Observable variations in flame distribution for one imaged frame within the combustor reveal a high flame concentration at the top with a sparse concentration at the bottom. This demonstrates the stochastic nature of LBO testing, which is an oscillatory process where the flame can be locally extinguished and reignited with the recirculation of hot products. Because of this stochasticity, a total of 15 tests are conducted for each condition to account for variation in the results and provide high-confidence data. Currently, the combustor pressure is monitored using a pressure transducer with a recording frequency capable of capturing vibrations up to 2000 Hz.

Table 1. Targeted combustor operating conditions.

Fuels	F-24, C-1, C-3, C-5
Combustor Absolute Pressure (kPa)	202.65, 303.98
Main Air Flow Rate (g/s)	43.38, 65.07
Air Preheat Temperature (K)	394
Pressure Drop (%)	3

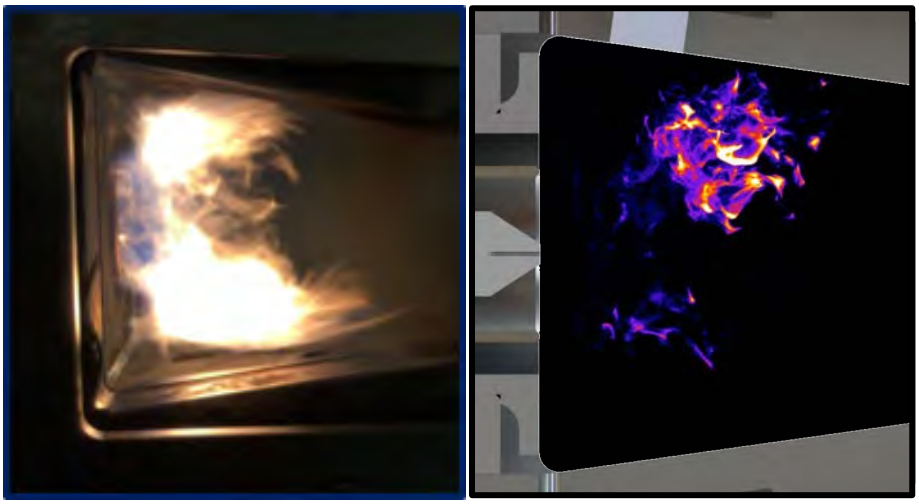

Figure 2. Imaging of a near-lean-blowout event in the M1 combustor at 20,000 frames per second.

Nozzles Utilized in LBO Testing

In the comprehensive evaluation of the ARC-M1, prior investigations included a meticulous comparison of three distinct hollow-cone pressure swirl nozzles—designated as A, B, and C as outlined in Table 2. The fuel atomization among these nozzles was characterized by utilizing advanced X-ray phase-contrast imaging techniques at the ANL. Intriguingly, the comparative analysis revealed that Nozzle B exhibited superior performance in terms of atomization and remarkable stability at low equivalence ratios. In contrast, both Nozzle A and Nozzle C, while sharing similarities in performance, lagged significantly behind Nozzle B in terms of atomization efficiency and operational stability. Despite the similar dimensions and characteristics for Nozzle B and Nozzle C, their distinct internal geometries resulted in disparate flow characteristics. Notably, the large difference in injection pressure exhibits a relationship to atomization performance, with higher injection pressures generally corresponding to enhanced atomization. Previously, all three nozzles exhibited strong dependence of the equivalence ratio at LBO to physical properties such as distillation temperature and viscosity of the fuels. Leveraging these insights, our team strategically selected Nozzle B for subsequent higher-pressure testing, with the specific aim of mitigating the reliance of LBO behavior on atomization and vaporization dynamics.

Table 2. Properties of fuel nozzles tested in experiments.

Nozzle	Approximate minimum diameter (μm)	Approximate cone angle	Flow rate at 100 p sid (L/hr)	Injection pressure at F-24 l ean blowout (psid)
Nozzle A	344	90°	6.2	29.2
Nozzle B	150	80°	2.25	45.9
Nozzle C	150	80°	4.60	32.5

Fuels for LBO Testing

In these experiments, four different fuels are tested in the M1 combustor to probe the effects of fuel properties on combustion behavior at these critical conditions. In addition to a reference fuel, the tested fuels consist of F-24 (comprising Jet A fuel and military-specific additives) and three fuels from the NJFCP with specific properties designed to probe the edges of the jet fuel operational envelope. Fuel C-1 has been developed with a low derived cetane number (DCN) and a relatively flat boiling curve. Fuel C-3 has been formulated to have a high viscosity, and fuel C-5 has been developed with an extremely flat boiling curve with respect to those of other fuels. Table 3 shows selected important parameters of each fuel for comparison, demonstrating some of the key features of the fuels chosen for testing.

Table 3. Comparison of key properties of the four tested fuels.

Fuel	Key features	Derived cetane number	Heat of combustion (MJ/kg)	H/C ratio	Stoichio-metric air/fuel ratio	Kinematic viscosity at 40 °C (cSt)	Surface tension (dynes/cm)
F-24	Jet A with additives	48.6	43.2	1.94	14.70	1.36	23.6
C-1	Low cetane	17.1	43.8	2.18	15.03	1.53	21.0
C-3	High viscosity	47.0	43.3	1.97	14.65	1.78	24.2
C-5	Flat boiling	39.6	43.0	1.94	14.68	0.83	22.2

LBO Performance Results

Figure 3 illustrates the results of a principal component analysis (PCA) applied to the fuel property dataset. The PCA was conducted to address the issue of multicollinearity among fuel properties, as many of these variables are interrelated (e.g., viscosity, surface tension, distillation temperatures). By reducing the dimensionality of the dataset, PCA identifies underlying trends and simplifies the analysis by decomposing the fuel properties into three key components: physical dependence (PD), chemical dependence (CD), and droplet dependence (DD). These components capture nearly 95% of the total variance in the dataset, providing a compact yet comprehensive representation of the variables that govern LBO behavior. Figure 4 complements this by summarizing the experimental LBO conditions and providing a detailed correlation analysis between the global equivalence ratio at LBO (ϕ_{LBO}) and these variables, highlighting key trends across different pressure regimes. The use of PCA, combined with rigorous experimental controls, ensures that observed trends are not confounded by multicollinearity or external factors like airflow dynamics. By carefully matching volumetric flow rates and pressure drops between conditions, the study isolates the effects of pressure on LBO behavior. These findings provide valuable insights into the distinct physical and chemical regimes governing LBO and the guidelines to adapt small scale combustor physics to larger gas turbine physics essential for prescreening fuel at low volumes.

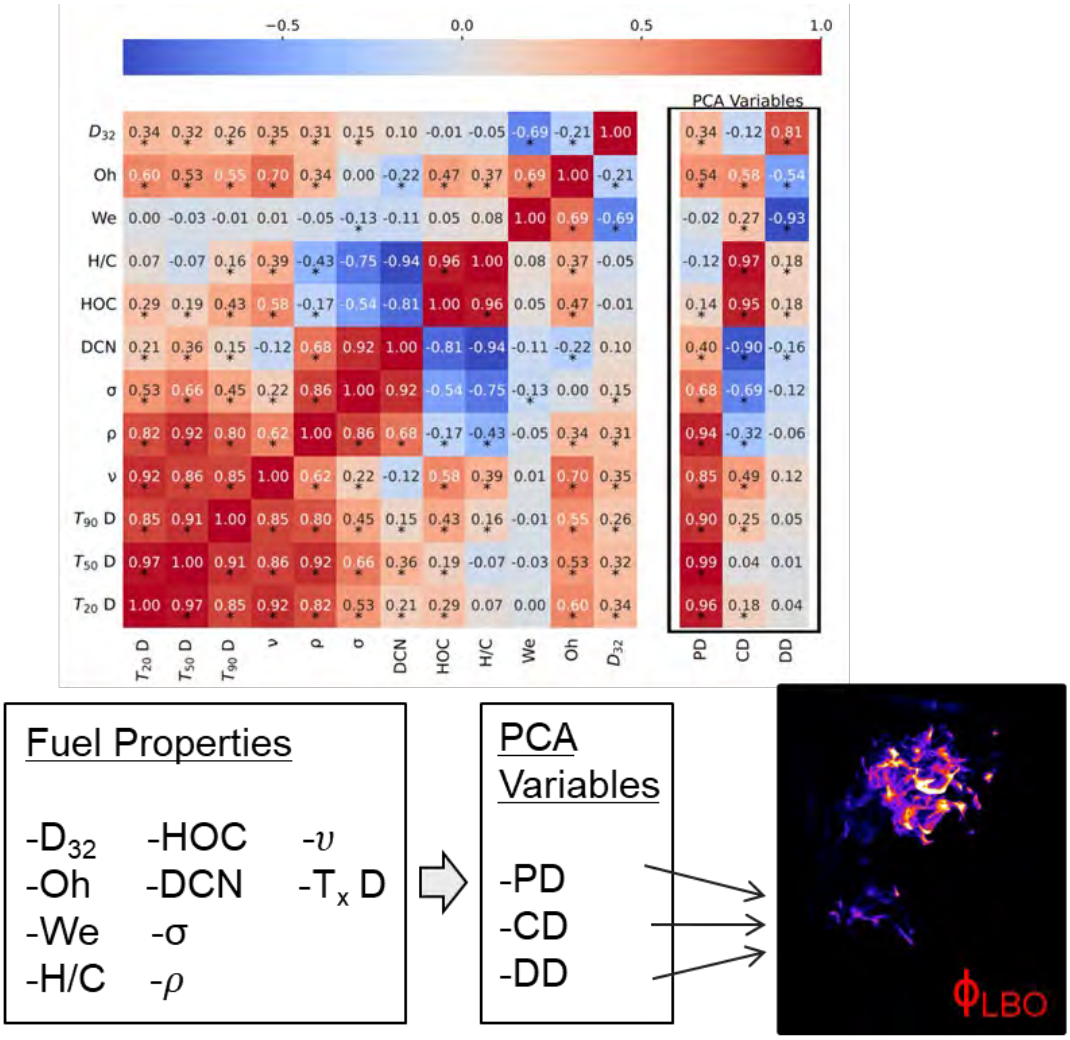

Figure 3. Principal component analysis of key fuel properties. The coefficients for the PCA are shown in the table (top).

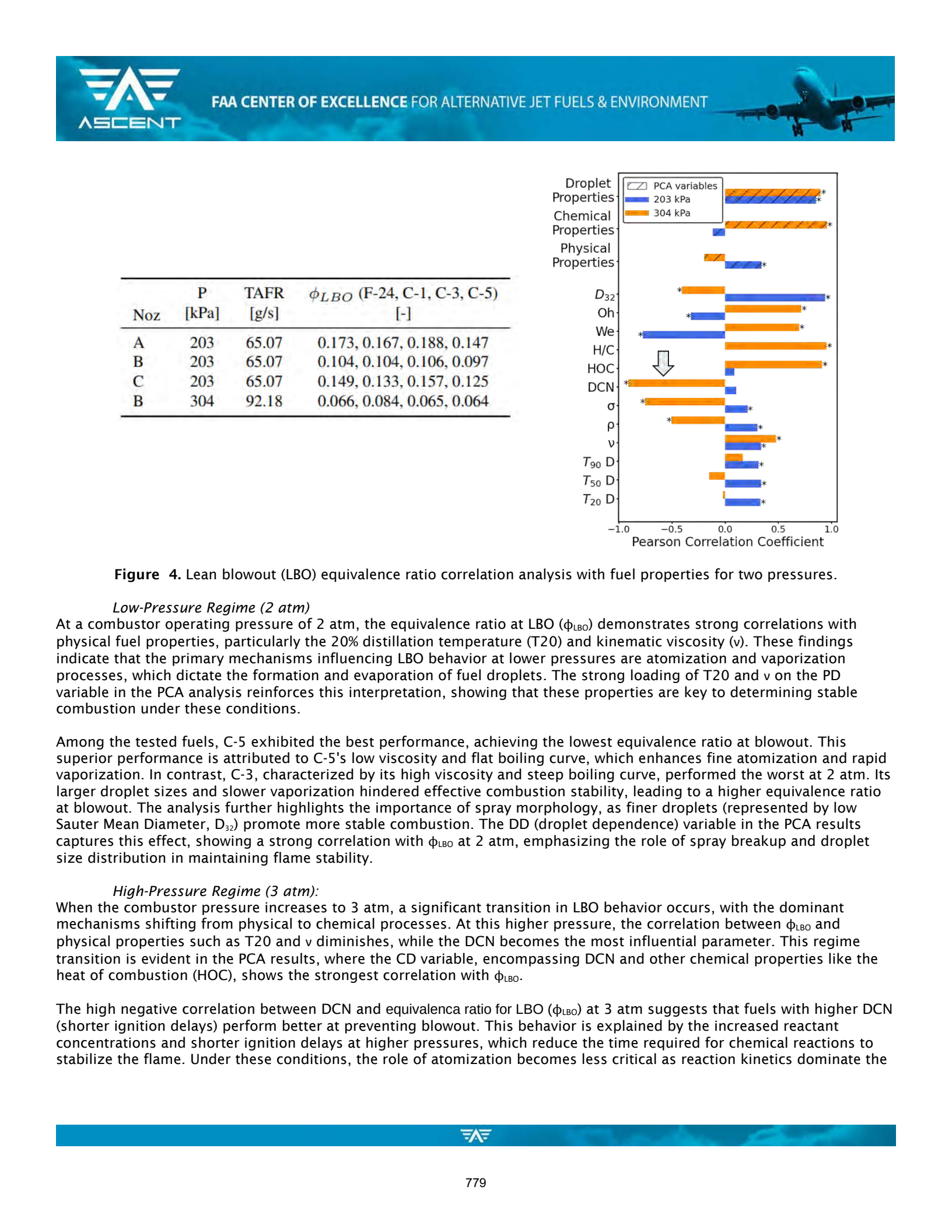

Noz	P [kPa]	TAFR [g/s]	ϕ_{LBO} (F-24, C-1, C-3, C-5) [-]
A	203	65.07	0.173, 0.167, 0.188, 0.147
B	203	65.07	0.104, 0.104, 0.106, 0.097
C	203	65.07	0.149, 0.133, 0.157, 0.125
B	304	92.18	0.066, 0.084, 0.065, 0.064

Figure 4. Lean blowout (LBO) equivalence ratio correlation analysis with fuel properties for two pressures.

Low-Pressure Regime (2 atm)

At a combustor operating pressure of 2 atm, the equivalence ratio at LBO (ϕ_{LBO}) demonstrates strong correlations with physical fuel properties, particularly the 20% distillation temperature (T20) and kinematic viscosity (ν). These findings indicate that the primary mechanisms influencing LBO behavior at lower pressures are atomization and vaporization processes, which dictate the formation and evaporation of fuel droplets. The strong loading of T20 and ν on the PD variable in the PCA analysis reinforces this interpretation, showing that these properties are key to determining stable combustion under these conditions.

Among the tested fuels, C-5 exhibited the best performance, achieving the lowest equivalence ratio at blowout. This superior performance is attributed to C-5's low viscosity and flat boiling curve, which enhances fine atomization and rapid vaporization. In contrast, C-3, characterized by its high viscosity and steep boiling curve, performed the worst at 2 atm. Its larger droplet sizes and slower vaporization hindered effective combustion stability, leading to a higher equivalence ratio at blowout. The analysis further highlights the importance of spray morphology, as finer droplets (represented by low Sauter Mean Diameter, D_{32}) promote more stable combustion. The DD (droplet dependence) variable in the PCA results captures this effect, showing a strong correlation with ϕ_{LBO} at 2 atm, emphasizing the role of spray breakup and droplet size distribution in maintaining flame stability.

High-Pressure Regime (3 atm):

When the combustor pressure increases to 3 atm, a significant transition in LBO behavior occurs, with the dominant mechanisms shifting from physical to chemical processes. At this higher pressure, the correlation between ϕ_{LBO} and physical properties such as T20 and ν diminishes, while the DCN becomes the most influential parameter. This regime transition is evident in the PCA results, where the CD variable, encompassing DCN and other chemical properties like the heat of combustion (HOC), shows the strongest correlation with ϕ_{LBO}.

The high negative correlation between DCN and equivalenca ratio for LBO (ϕ_{LBO}) at 3 atm suggests that fuels with higher DCN (shorter ignition delays) perform better at preventing blowout. This behavior is explained by the increased reactant concentrations and shorter ignition delays at higher pressures, which reduce the time required for chemical reactions to stabilize the flame. Under these conditions, the role of atomization becomes less critical as reaction kinetics dominate the

process. Despite this shift, C-5 remains the best-performing fuel, maintaining its effectiveness due to its favorable physical properties.

Transition Between Regimes

The transition from the low-pressure to high-pressure regime highlights a shift in the dominant mechanisms governing LBO behavior. At 2 atm, LBO is primarily driven by atomization and vaporization processes, with physical properties like T20 and ν playing critical roles. As pressure increases to 3 atm, the regime transitions to one dominated by chemical properties, with DCN emerging as the primary driver of LBO behavior. This regime transition reflects the changing importance of physical and chemical factors: at lower pressures, finer atomization and faster vaporization are essential for maintaining stable combustion, while at higher pressures, enhanced mixing and ignition kinetics reduce the reliance on physical properties and shift the focus to chemical reactivity. This shift is further validated by the PCA results, where the contributions of PD and DD decline at higher pressures, while CD becomes the dominant factor influencing ϕ_{LBO}. As pressure increases, reactant concentrations rise, mixing improves, and ignition delay decreases, resulting in a reduced reliance on atomization and an increased dependence on chemical properties.

Milestones

- Completed the experimental phase (3 months), wrapping up both low-pressure and higher-pressure LBO testing across the test matrix.
- Conducted an initial analysis to identify and characterize the dominant LBO regimes (6 months), focusing on the transitions between physical and chemical property dependencies.
- Refined the analytical framework, incorporating insights from scaling parameters, PCA results, and advanced diagnostic data to enhance the interpretation of experimental findings (9 months).
- Finalized the analysis and prepare a detailed manuscript for submission to a peer-reviewed journal (12 Months).

Major Accomplishments

Our comprehensive investigation into the LBO behavior of the M1 combustor has provided a robust framework for simplifying the comparison between small-scale and real-scale combustors. By examining a wide range of operating conditions—spanning different pressures and the interplay of chemical and physical fuel properties—we have established a foundational approach for analyzing combustion performance across scales. Future efforts will focus on developing specific scaling parameters to bridge the differences in length and time scales between small and real-scale combustors. This next step is crucial for ensuring that insights gained from compact systems can be reliably translated into real-world applications, ultimately guiding the optimization of combustion system designs.

Publications

Dasgupta, D., & Som, S. (2024, June). Fuel property impact on lean blow out for sustainable aviation fuels in gas turbine combustors. In *Turbo Expo: Power for Land, Sea, and Air* (Vol. 87943, p. V03AT04A073). American Society of Mechanical Engineers.

Wood, E. J., Mayhew, E., Motily, A., Temme, J., Kweon, C. B., & Lee, T. (2021). Lean blowout dependence on fuel properties and combustion conditions in the ARC-M1 single-cup swirl combustor. In *AIAA SciTech 2021 Forum* (p. 0652).

Outreach Efforts

All test data will be made accessible through https://altjetfuels.illinois.edu/.

Awards

None.

Student Involvement

This task was primarily conducted by Casey O'Brien (PhD Student).

Plans for Next Period

The focus will shift towards expanding LBO testing to include a wider range of new alternative fuels. This effort aims to balance the contributions of the physical property regime—driven by fuel atomization and evaporation—and the chemical property regime, dominated by fuel reactivity. Testing at two pressures, 2 bar and 3 bar, will provide a systematic framework to explore the transitions between these regimes, where the dependence of LBO on fuel properties follows

distinct dynamics. The expanded test matrix will include various fuel types, such as blends of hydrotreated esters and fatty acids (HEFA), Jet A, synthetic paraffinic kerosene (SPK), fuels high in cycloparaffin content, and alcohol-to-jet (ATJ).

In addition to expanding the fuel range, emphasis will be placed on scaling parameters to bridge the differences in length and time scales between small-scale and real-scale combustors. These scaling efforts are essential for translating insights from compact systems into actionable knowledge for real-world applications, enabling more accurate predictions of combustion performance across systems of varied sizes.

To gain a deeper understanding of the mixing and chemistry timescales in the combustor, the analysis will also focus on simultaneous planar laser-induced fluorescence (PLIF) and particle image velocimetry (PIV). By combining these advanced diagnostic techniques with computer vision and sophisticated data analysis methods, we aim to extract detailed information on the interaction of mixing and combustion processes. This approach will provide critical insights into the coupling of chemical reactions and fuel-air mixing, further refining our understanding of the dynamics governing LBO and enhancing the predictive capability of combustion models.

Task 2 – Spray Breakup Characterization for Multi-Fuel Analysis

University of Illinois at Urbana–Champaign

Objectives

In this task, the ASCENT Project 065(B) team aims to develop and implement a robust framework for analyzing spray breakup dynamics across a range of alternative fuels. While the framework has been validated using the fuel F-24, it is designed for easy adaptation to fuels with diverse physical properties, including viscosity and surface tension, which play a critical role in atomization and vaporization processes. Fuels such as C-1, C-3, and C-5, for which extensive experimental droplet data have been collected in previous campaigns, will serve as the initial test cases for expanding the framework's capabilities.

The ultimate goal is to isolate fuel-specific effects on primary breakup dynamics, enabling a deeper understanding of how these properties impact downstream processes like droplet formation and, ultimately, LBO behavior. By combining computational approaches, including optical flow and computational fluid dynamics (CFD), with experimental validation, this task aims to significantly reduce the reliance on physical testing for characterizing new fuels. The framework provides a predictive pathway to evaluate alternative fuels, focusing on the fuel breakup process in the primary spray region, which is critical for determining atomization and vaporization rates in combustion systems.

Research Approach

Spray breakup characterization has historically relied on extensive experimental testing under a wide range of operating conditions. However, such physical testing can be both resource- and time-intensive, particularly for alternative fuels that are limited in availability or require significant effort to produce. This task leverages a novel computational approach, utilizing an unsupervised optical flow machine learning model, to predict flow vectors and model the primary breakup process. This optical flow model is trained on experimental measurements, ensuring its predictions align with observed physics. By comparing optical flow predictions to CFD results, we aim to establish a mutual validation framework, enabling the refinement of CFD models and enhancing the reliability of simulations for new fuels. By focusing on the primary spray breakup, this framework bypasses the need for exhaustive downstream droplet analysis, instead providing direct insights into atomization mechanisms. This work contributes to the integration of sustainable jet fuels by bridging the gap between experimental and computational methodologies, ensuring real-world applicability with reduced fuel and air requirements.

Droplet Visualization through Experimental Approaches

Building upon prior investigations that primarily focused on understanding the impact of fuel spray nozzles on LBO behavior, research endeavors have extended to the detailed analysis of droplet data associated with various nozzles and pressures. Leveraging the capabilities of the Advanced Photon Source (APS) at the ANL, comprehensive droplet data have been collected, aiming to uncover insights into the intricacies of fuel atomization and its correlation with combustion dynamics. An image of the APS facility with the setup utilized for droplet measurements is shown in Figure 5.

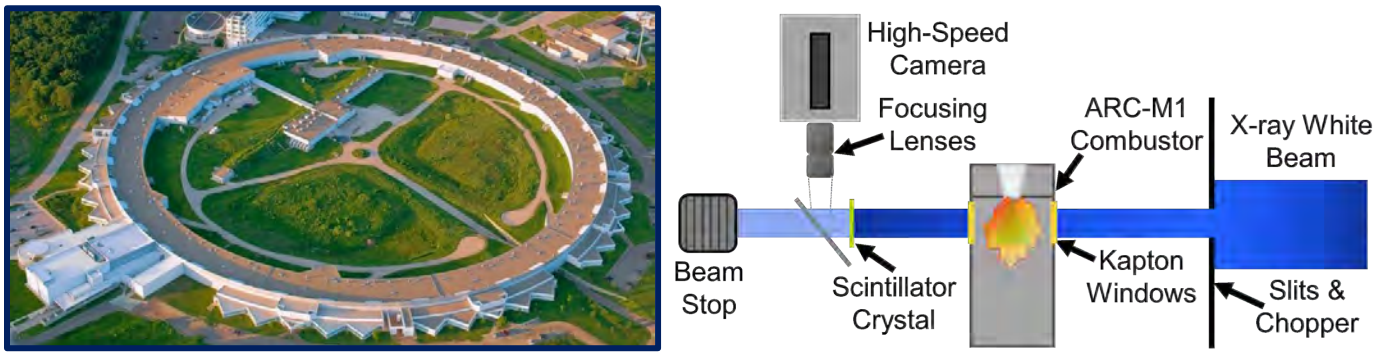

Figure 5. Advanced Photon Source facility at the ANL (left) and the ARC M1 setup (right).

In this study, high-speed X-ray phase-contrast imaging was employed to characterize the ARC-M1. This imaging method was utilized to visualize and analyze the liquid fuel spray exiting the pressure-swirl atomizing nozzle of the operating combustor. The experimental setup includes an unfocused polychromatic X-ray white beam from the APS bending magnet source, controlled by slits and a mechanical chopper to manage beam size and exposure time. Kapton windows on the combustor facilitate high levels of X-ray transmission. The transmitted X-rays pass through the combustor and reach a Yttrium Aluminum Garnet: Cerium (YAG:Ce) scintillator crystal, which emits visible light directed to a high-speed camera for imaging. The imaging setup includes a Photron SA-Z high-speed camera with specific lenses and settings, synchronized with the synchrotron's electron circulation frequency. A water-cooled beam stop absorbs unused X-rays downstream of the setup. Phase contrast imaging leverages the difference in the index of refraction between the liquid fuel and hot gases, creating enhanced contrast at the liquid edges due to Fresnel diffraction patterns. This technique effectively captures the liquid fuel spray within the combustor, unaffected by varying gas temperatures.

Optical Flow Modeling

In this study, the ASCENT Project 065(B) team introduced an unsupervised machine learning (ML) approach for analyzing fuel spray dynamics, which leverages the unique capability of training directly on experimental data without the need for labeled datasets. This methodology is particularly advantageous in experimental fluid dynamics, where acquiring labeled data is often infeasible due to the complexity of phenomena like primary breakup in fuel sprays. Our model incorporates a multifaceted architecture with several computational heads, each designed to perform specific tasks that contribute to the overall analysis. These tasks include extracting essential features of the spray, predicting motion between consecutive frames (denoted I_t to I_{t+1}), and generating pixel-wise velocity fields across the entire image.

At the core of the model lies a robust convolutional architecture, which enables it to capture and represent intricate features of the spray dynamics effectively. The prediction of motion is carried out hierarchically, progressing from coarse to fine spatial scales. This multi-scale approach ensures that both global motion trends and fine-grained details are accurately captured, resulting in detailed and precise velocity field predictions. Additionally, the model incorporates several innovations that enhance its predictive capabilities. Notably, a self-attention mechanism is integrated into the architecture, allowing the model to differentiate effectively between background motion and the motion of the fuel spray. This feature is particularly important in regions with low contrast or complex flow structures, where traditional methods might struggle. Furthermore, the model employs a structural similarity loss function (SSIM), which focuses on preserving spatial structures and textures during motion prediction. SSIM is particularly effective at maintaining the integrity of fine details, ensuring that the predicted motion remains physically realistic compared to utilizing a basic photometric loss (the difference between pixel values of a predicted image that is translated with the vectors and a reference image).

The architecture of the model, as illustrated in Figure 6, highlights the interplay between its various components, from convolutional layers to attention mechanisms and flow refinement. These elements work in tandem to generate robust predictions that accurately reflect the spray dynamics. The performance of the model was evaluated against UPFlow, a state-of-the-art optical flow model widely used in realistic optical flow applications. The evaluation used several key metrics, including mean absolute error (MAE) of pixel values, multi-scale structural similarity (MS-SSIM), and learned perceptual image patch similarity (LPIPS). Each metric provides unique insights into the quality of the predictions:

1. Multi-Scale Structural Similarity (MS-SSIM): MS-SSIM measures the perceptual similarity between predicted and reference images by assessing structural information across multiple spatial scales. Unlike pixel-wise metrics such as MAE, MS-SSIM captures how well the structural integrity of the image is preserved, making it highly relevant for analyzing flow fields where spatial consistency is critical. MS-SSIM values range between 0 and 1, with higher values indicating better preservation of structural features. This metric is particularly sensitive to edge regions and fine-scale details, ensuring that predictions align with the physical characteristics of the spray.
2. Learned Perceptual Image Patch Similarity (LPIPS): LPIPS measures the perceptual distance between predicted and reference images by comparing deep features extracted from neural networks trained on large datasets. This metric evaluates how closely the predicted image matches human perception, focusing on the overall similarity in texture, structure, and appearance. LPIPS values range from 0 to 1, with lower values indicating more accurate predictions. By accounting for high-level perceptual similarities, LPIPS provides a complementary perspective to MS-SSIM, ensuring that the predictions not only preserve structural details but also align with the overall appearance of the reference image.

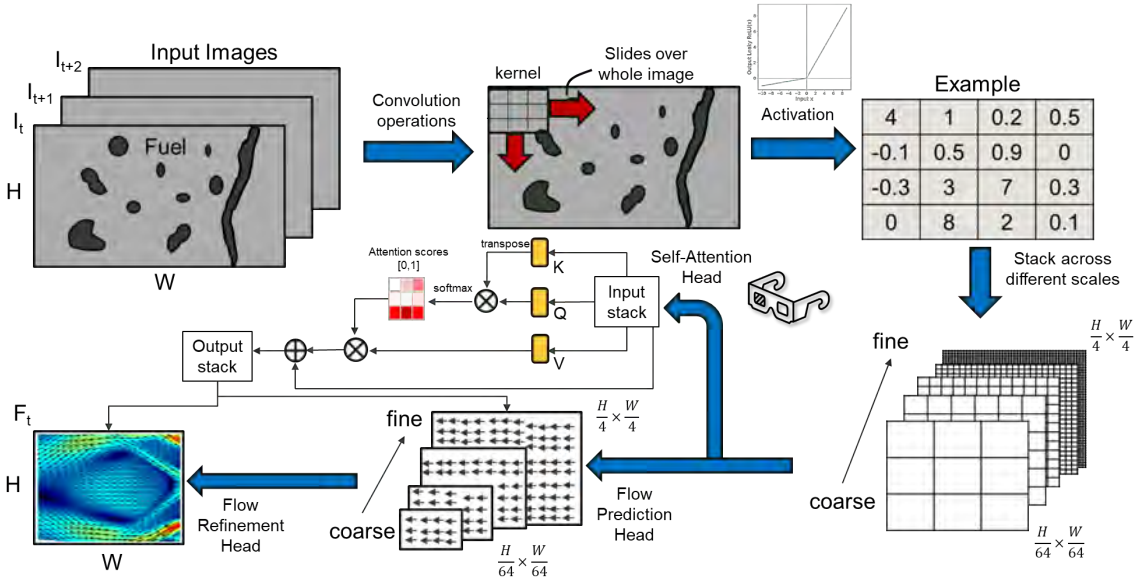

Figure 6. Optical flow model architecture diagram.

The comparison study was conducted under controlled experimental conditions using F24 fuel. The experimental setup included a combustor air temperature of 50°C, a combustor pressure of 1 atm, and a pressure drop (ΔP/P) of 1.75% from the plenum to the combustor. The fuel flow rates varied between 35, 30, and 26 g/min, with measurements taken at various positions (i.e., lower, center, upper) and distances (upstream near the nozzle and downstream). This report focuses on the upstream droplet spray region, where the primary breakup occurs, as this region presents the most complex spray dynamics, and the results are summarized in Table 4.

Table 4. Comparison of optical flow model to state-of-the-art model.

Model	Condition	MAE (pixels)	Standard Deviation	RMSE		MS-SSIM	LPIPS
Desired ouput:		↓	↓	↓		↑	↓
Ours	C _35.0	**3.27 (1.28%)**	**5.72**	**6.2**	**0.963**	**0.020**
	C_30.0	**2.75 (1.08%)**	**4.76**	**5.18**	**0.974**	**0.015**
	C _26.0	**2.48 (0.97%)**	**4.23**	**4.61**	**0.979**	**0.012**
	L _35.0	**2.37 (0.93%)**	**4.28**	**4.93**	0.965	0.014
	L_ 30.0	**2.11 (0.83%)**	**3.76**	**4.34**	**0.974**	0.011
	U _35.0	**2.35 (0.92%)**	**4.07**	**4.62**	**0.969**	0.013
	U_ 30.0	**2.02 (0.79%)**	**3.45**	**3.92**	**0.978**	**0.01**
	U _26.0	**1.8 (0.71%)**	**3.04**	**3.44**	**0.983**	**0.008**
UPFlow: state-of-the-art optical flow	C _35.0	4.62 (1.81%)	7.81	8.48	0.939	0.028
	C_30.0	4.25 (1.67%)	7.17	7.82	0.947	0.025
	C _26.0	4.04 (1.58%)	6.79	7.39	0.951	0.023
	L _35.0	2.9 (1.14%)	4.7	5.39	0.965	**0.012**
	L_ 30.0	2.77 (1.09%)	4.45	5.11	0.968	0.011
	U _35.0	3.11 (1.22%)	4.97	5.62	0.961	0.013
	U_ 30.0	2.83 (1.11%)	4.54	5.15	0.967	0.012
	U _26.0	2.68 (1.05%)	4.3	4.86	0.97	0.011

Our results demonstrate that the proposed model consistently outperforms UPFlow across nearly all spray conditions and metrics. While UPFlow shows a marginal advantage in LPIPS for the 35 g/min lower section, our model excels in other metrics, highlighting its robustness and versatility. Figure 7 provides an example of the predicted flow vectors (x and y components) for an instantaneous velocity field in the primary breakup region. The vectors illustrate the conical divergence of the spray from the centerline, confirming the physical realism of the predictions. the model captures detailed velocity fields across the liquid sheet breakup and droplet formation regions. This capability enables a direct analysis of how aerodynamic and inertial forces interact to shape the spray. Figure 8 presents a quantitative summary of the x- and y-component velocities using cumulative distribution function (CDF) plots derived from five distinct slices taken along the x- and y-directions of the spray region. These CDFs consolidate the velocity distribution at each slice, highlighting variations in breakup behavior and offering a clear depiction of spatial and directional asymmetries. Such detailed and accurate predictions are crucial for understanding the dynamics of spray breakup and dispersion.

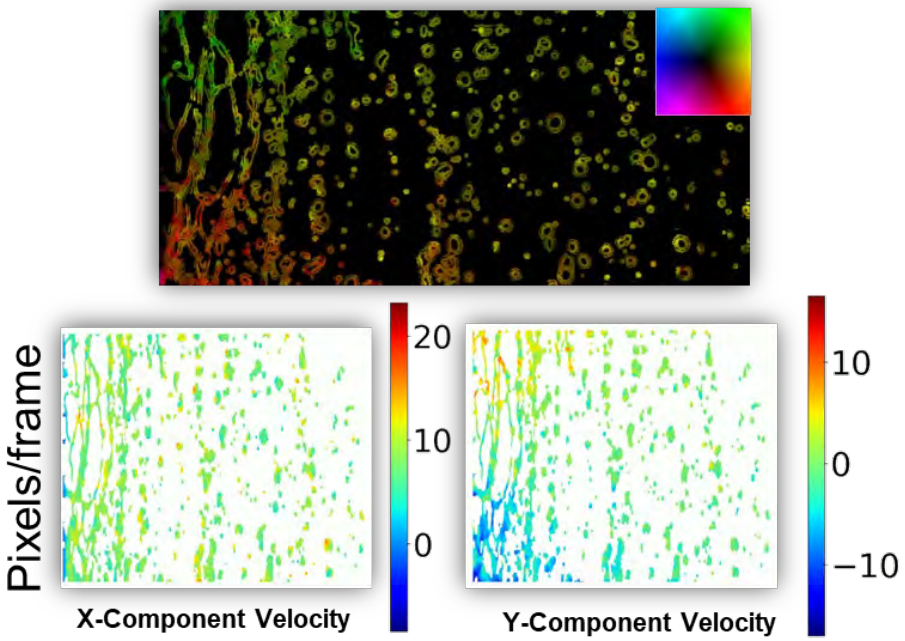

Figure 7. Instantaneous Velocity predictions for both X and Y components in upstream fuel spray of F-24 fuel.

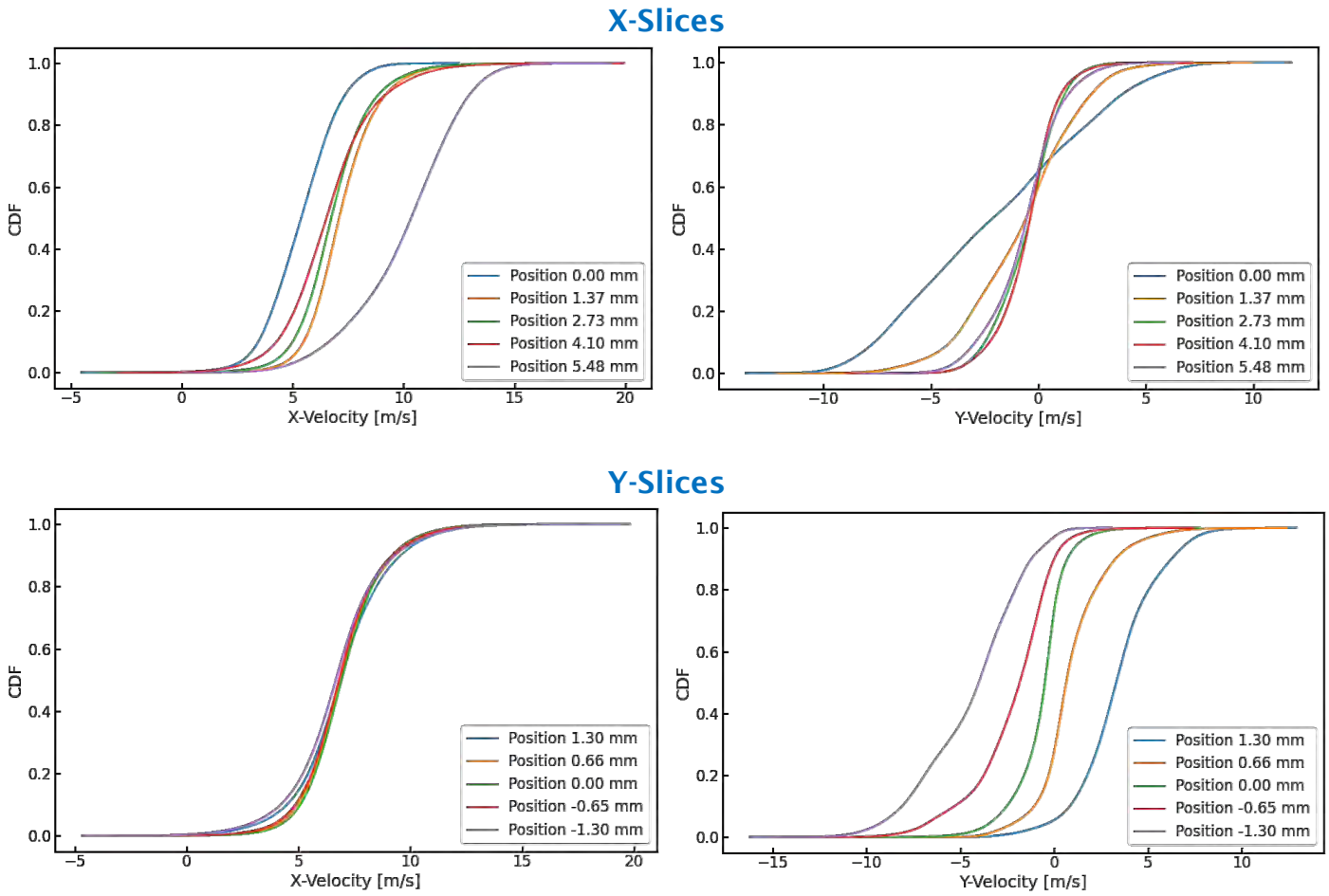

Figure 8. X and Y component velocity profiles of the fuel spray visualized as cumulative distribution function (CDF) plots at five selected slices in the x- and y-directions.

The model offers significant advantages over traditional methods such as Phase Doppler Particle Analysis (PDPA). PDPA is inherently limited to pointwise measurements, requiring extensive sampling to reconstruct the global spray morphology. Moreover, it relies on strong assumptions, such as treating particles as perfectly spherical, which can lead to inaccuracies in characterizing irregularly shaped droplets and ligaments in the spray. In contrast, our model overcomes these limitations by providing a spatially resolved analysis of the entire spray field, offering simultaneous insight into both primary and secondary breakup dynamics without the need for extensive spatial interpolation.

Connection to SAF

The convective velocity of fuel spray plays a pivotal role in understanding and predicting fuel spray breakup, particularly in small-scale combustors. In these systems, where length scales are reduced, atomization and vaporization processes dominate the spray dynamics. Accurate characterization of these processes is critical to potentially decouple the chemical effects of different fuels from their physical behavior, aiding in the development of alternative fuels.

Our findings suggest that primary breakup dynamics are especially critical, as they determine the initial spray morphology, which subsequently affects atomization and vaporization. In previous studies, we observed clear trends between downstream droplet sizes and fuel properties like surface tension and viscosity. In the primary breakup region, these properties are expected to exert an even greater influence, creating distinct spray morphologies that highlight differences between fuels.

Understanding these dynamics is particularly important for advancing the use of SAF in small-scale combustors. By accurately modeling the atomization and vaporization processes, we can better predict fuel behavior and performance, paving the way for more effective integration of SAFs into aviation systems. This study provides a foundation for further exploration of how fuel properties influence spray behavior under combusting conditions.

Milestones

- Performed initial testing of optical flow on spray images (3 months).
- Tuned the hyperparameters and loss functions on previous model (6 months).
- Developed innovative approaches to optical flow architecture (9 months).
- Conducted training and evaluation of spray metrics over a large dataset (~57600 images) (12 months).

Major Accomplishments

We have successfully developed and validated an advanced machine learning-based framework to characterize spray breakup dynamics for multi-fuel analysis. This process involved the following key achievements:

1. Machine Learning Model Development: Designed a robust, unsupervised optical flow model capable of accurately predicting instantaneous velocity fields in the spray breakup region. The model incorporates novel parameters to accurately differentiate background and spray motion, ensuring realistic predictions of droplet and ligament dynamics.
2. Integration of Experimental Data: Applied the model to high-fidelity imaging data of fuel sprays from a pressure-swirl nozzle. The dataset focused on a baseline fuel (F-24, essentially Jet A) and multiple flowrates, capturing diverse spray conditions at different spray locations. These datasets enabled a detailed analysis of primary and secondary breakup phenomena.

Publications

Oh, J. H., Wood, E., Mayhew, E., Kastengren, A., & Lee, T. (2023). Sequence2Self: Self-supervised image sequence denoising of pixel-level spray breakup morphology. *Engineering Applications of Artificial Intelligence, 126*, doi: 106957.

Outreach Efforts

All experimental spray breakup data, including high-speed videos, processed velocity fields, and droplet size distribution measurements, will be made publicly accessible via altjetfuels.illinois.edu.

Awards

None.

Student Involvement

This task has been primarily conducted by Casey O'Brien (PhD student).

Plans for Next Period

Global LBO performance will be explored in greater depth by integrating insights from LBO testing with optical flow analysis. Additionally, optical flow techniques will be applied to experimental datasets for fuels C-1, C-3, and C-5, aiming to develop scientific relationships that improve predictions of spray morphology based on fuel properties. Efforts will also focus on bridging simulation work with the quantitative results derived from the spray and combustion behavior. This will involve performing detailed spray simulations and enhancing existing combustor simulations to better capture the interplay between spray dynamics and combustion processes.

Project 066 Evaluation of High-Thermal-Stability Fuels

Washington State University

Project Lead Investigator

Joshua Heyne
Bioproducts, Sciences, and Engineering Laboratory Director, Associate Professor
School of Engineering and Applied Science
Washington State University
2710 Crimson Way, Richland, WA 99354
(937) 229-5319
joshua.heyne@wsu.edu

University Participants

Washington State University (WSU)

- P.I.s: Assoc. Prof. Joshua Heyne and Assoc. Res. Prof. Randall Boehm
- FAA Award Number: 13-C-AJFE-WaSU-036
- Period of Performance: October 1, 2023, to September 30, 2024
- Tasks: (Leveraging tools developed under this project, award number 13-C-AJFE-UD)
  1. Publish work relating to energy efficiency (Complete)
  2. Evaluate the cost and availability of critical SAF components, necessary to achieve optimal benefits.
  3. Evaluate the Thermal Stability of Potential SAF
  4. Fuel Property Estimates of Optimized SAF Compositions (Complete)
  5. Suggest optimal fuel properties for non-drop-in SAF (Complete)

Project Funding Level

The Federal Aviation Administration (FAA) provided $200,000 in funding. Cost-sharing funding is provided by Boom Technology, Inc. ($100,000) and WSU ($100,000).

Investigation Team

Washington State University

Assoc. Prof. Joshua Heyne, (P.I.), All Tasks
Assoc. Res. Prof. Randall Boehm, (co-P.I.), All Tasks
Conor Faulhaber, (graduate research student), All Tasks

Boom Technology, Inc. (Boom Technology)

Akshay Ashok, (team leader), Task 1 (Boom Technology)

Project Overview

It has long been understood that increasing the reliance on jet fuel as a primary coolant for both the engine and the aircraft has significant performance and efficiency benefits relative to the use of air as a coolant (Bruenig & Chang, 1999), but fuel degradation and coking at high temperatures restrict how much heat can be put into the fuel. In some military applications, the performance benefits are sufficiently large to justify the creation of specialty fuels such as JP7 and Jet Propellant Thermally Stable (JPTS), which can tolerate much higher temperatures than petroleum-derived Jet A or Jet A1 (JP8) fuels (Edwards, 2007). In land-based applications of gas turbines, weight is of little consequence; thus, the operations of waste heat recovery (WHR) for plant efficiency or the cooling of combustor inlet temperature for emission reductions can be accomplished in a wide variety of ways, all of which are impractical for flight because of their impact on the mass of the power plant. Nonetheless, these applications provide some common examples of how controlling the air temperature along its flow path through the engine can have a large impact on performance, durability, and energy efficiency (Wilfert

et al., 2007). The flurry of works relating to fuel deoxygenation (Zabarnick et al., 2020) and other ways to decrease coking propensity and its impacts (Mancini et al., 2004) is largely motived at the sponsorship level by these benefits.

More recently, sustainable aviation fuels (SAF) have received much attention because they can contribute to high-priority geopolitical goals to diversify energy supply chains and reduce greenhouse gas emissions. Most of these efforts have focused on streamlining the evaluation and approval processes to use synthetic fuels at some blend ratio with petroleum-derived jet fuel to create a so-called drop-in fuel that can be used within existing infrastructure without objection from any stakeholders (Colket & Heyne, 2021). Additionally, there have been discussions regarding characteristics of synthetic blend components (e.g., low aromatics, high specific energy, and high thermal stability) that would make these components attractive to consider as potential specialty fuels (i.e., JPTS) or high-performance fuels. Kosir et al. (2020) recently published work highlighting the efficiency gain that could be realized by using fuels with high specific energy, via lower aircraft weight at take-off, with less mass to lift and hold against the force of gravity.

The weight of fuel uplifted to an aircraft, as necessary to complete its mission, is certainly an important component to consider in assessing the integrated engine/aircraft energy demand and efficiency. The energy efficiency of the engine is also expected to be influenced by other fuel properties, including the following:

- **Hydrogen/carbon (H/C) ratio:** Through its impact on combustor exhaust gas composition, this ratio has a small impact on the ratio of heat capacities (gamma), combustor exit temperature, and work extracted during expansion through the turbine, even when the total enthalpy created at the combustor is unchanged.
- **Viscosity:** Viscosity impacts the heat transfer coefficients, which determine how much waste heat is recovered by the fuel (coolant) and delivered back to the engine via the combustor.
- **Energy density:** Energy density, measured in joules per liter (J/L), impacts volumetric flow rates, which also impacts heat transfer coefficients.
- **Specific heat:** Specific heat also has some effect on heat transfer coefficients, but perhaps more importantly has a direct impact on the temperature rise in the fuel per unit of heat energy absorbed, which in turn may impact the coking rate.
- **Coking rate:** Also known as fuel thermal stability, the coking rate drives several high-level design decisions relating to the thermal management of an engine.

References

Bruening, G. B., & Chang, W. S. (1999). Cooled cooling air systems for turbine thermal management. *Proceedings of the ASME 1999 International Gas Turbine and Aeroengine Congress and Exhibition. Volume 3: Heat Transfer; Electric Power; Industrial and Cogeneration*, Indianapolis, Indiana. https://doi.org/10.1115/99-GT-014

Colket, M., & Heyne, J. (2021). *Fuel effects on operability of aircraft gas turbine combustors*. The American Institute of Aeronautics and Astronautics, Inc. https://doi.org/10.2514/4.106040

Edwards, T. (2007). Advancements in gas turbine fuels from 1943 to 2005. *Journal of Engineering for Gas Turbines and Power, 129*(1), 13–20. https://doi.org/10.1115/1.2364007

Kosir, S., Stachler, R., Heyne, J., & Hauck, F. (2020). High-performance jet fuel optimization and uncertainty analysis. *Fuel, 281*. https://doi.org/10.1016/j.fuel.2020.118718

Mancini, A. A., Ackerman, J. F., Richard, L. K., & Stowell, W. R. (2004). *Method and coating system for reducing carbonaceous deposits on surfaces exposed to hydrocarbon fuels at elevated temperatures* (6808816 B2). General Electric Company.

Wilfert, G., Sieber, J., Rolt, A., Baker, N., Touyeras, A., & Colantuoni, S. (2007). *New environmental friendly aero engine core concepts*. https://api.semanticscholar.org/CorpusID:73527508

Zabarnick, S., West, Z. J., Arts, A., Griesenbrock, M., & Wrzesinski, P. (2020). Studies of the impact of fuel deoxygenation on the formation of autoxidative deposits. *Energy Fuels, 34*, 13814–13821. https://doi.org/10.1021/acs.energyfuels.0c02603

Task 1 – Publish Work Relating to Energy Efficiency

Washington State University and Boom Technology, Inc.

Objectives

The objective of this task is to estimate the impact of fuel property variation on engine-level specific fuel consumption (SFC), considering conceptual design trades involving the outer mold line and the aircraft thermal management systems, as well as direct fuel effects on gross weight at takeoff.

Research Approach

To accomplish this task the tools developed previously under ASCENT Project 066 (award number 13-C-AJFE-UD) were used in conjunction with dual-objective optimizations of SAF composition over a database containing 1,121 molecules. To ensure meaningful results, a filter on compositions was applied to eliminate those with properties outside of fuel specifications, as predicted via algebraic blending rules. Additionally, Boom Technology contributed to this goal by mission analyses for baseline and alternative aircraft architectures, where the alternative aircraft architectures exploited higher fuel specific energy and/or energy density. Boom Technology also evaluated a variety of thermal management architectures of their own conceptualization.

Evaluation of Aircraft Configuration Concepts That Leverage Theoretical SAF (100% non-drop-in, Jet-X) Properties

Proprietary models developed by Boom Technology were used to derive linear relationships that relate changes in aircraft weight and drag components to changes in mission fuel consumption, to assess sensitivities. The weight derivative is used to evaluate changes in mission fuel weight to aircraft component sizing differences, namely, heat exchangers, fuel tanks, the fuselage, wings, and engine based on revised fuel burn requirements. In total, seven cases have been considered. Configuration B/L is the baseline design, which is compatible with conventional fuel or drop-in SAF. Configuration A incorporates efficiencies of reduced fuel weight made possible by an exclusive diet of SAF with 2% (or more) higher enthalpy per unit mass (lower heating value [LHV]) than the reference petroleum-derived jet fuel, A-2 as defined by the National Jet Fuel Combustion program, allowing the airline to reduce fuel weight while maintaining overall range. Configuration B incorporates resizing of the central fuel tank, fuselage, wings, and engine to exploit an exclusive diet of SAF with 8% (or more) higher energy density (ED) than the reference fuel without consideration of alternative aircraft volume requirements such as passengers, cargo, and systems. Configuration C combines aircraft resizing of configurations A and B, consistent with SAF having 1% higher LHV and 4% higher ED. Configuration D evaluates the technical feasibility of using fuel as the coolant for the (cabin) environmental control system (ECS). Configuration E evaluates the technical feasibility of using fuel as the coolant in the ECS precooler. Configuration F evaluates the merit of using fuel (instead of air) as the coolant in the hydraulic system. The results of these studies are summarized in Table 1.

Table 1. Aircraft architecture trade study summary.

Case	Δ Weight†	ARES	Δ Range (nm)	Fuel Temperature
A	-0.75%	1.8%	105	No change
B	-1.3%	3.2%	190	No change
C	-1.0%	2.3%	130	No change
D	Not feasible		Fuel temperature ≈ cabin temperature	
E	Not feasible		Fuel temperature exceeds safety limits	
F	-400 to -500 lbs	0.30%	15	120°C

† Aircraft maximum gross weight. ARES: aircraft relative enthalpy savings.

Additionally, Boom Technology employed proprietary mission analysis tools, considering trans-ocean flights represented by Vancouver–Tokyo and New York–London, to estimate the SFC benefit of increasing LHV. They found 0.43% (enthalpy basis) improved SFC per 1 MJ/kg increase in specific energy. This benefit can be realized on any aircraft provided the fuel's specific energy is known to (and leveraged by) the airline prior to fueling the aircraft.

Milestones

- Verified transfer function (0.43% per 1 MJ/kg specific energy) relating mission fuel enthalpy demand requirement to fuel enthalpy per unit mass.
- Recognized that aircraft would be designed differently if the fuel specifications called out a higher (minimum threshold) limit on specific energy. Estimated impact of aircraft design changes.
- Recognized that aircraft redesign to leverage higher ED of worst-case fuel may be technically beneficial but pragmatically more difficult than leveraging higher specific energy of worst-case fuel. Estimated impact of aircraft design changes.
- Evaluated alternative aircraft thermal management architectures intended to leverage the higher thermal stability (and higher flash point, min-to-min basis) of 100% SAF relative to conventional fuels.

Major Accomplishments

- By designing to a minimum ED requirement that is 4% higher than the current design point reference fuel and increasing the threshold specific energy of the reference fuel by 1% (both of which are attainable for optimized, 100% SAF without aromatics), supersonic aircraft can be made, at most, 2.3% more energy efficient.

Publications

Boehm, R. C., Faulhaber, C., Behnke, L., & Heyne, J. S. (2024). The effect of theoretical SAF composition on calculated engine and aircraft efficiency. *Fuel, 371*(B). https://doi.org/10.1016/j.fuel.2024.132049

Outreach Efforts

None.

Awards

None.

Student Involvement

Conor Faulhaber, a PhD student at WSU, contributed significantly to the latest manuscript, specifically in data curation, visualization, and editing.

Plans for Next Period

None. This task is complete.

Task 2 – Evaluate the Cost and Availability Drivers of Critical SAF Components, Necessary to Achieve Optimal Benefits

Washington State University

Objective

The objective of this task is to begin construction of a pathway to bridge the gap between optimal fuel composition and producible fuel composition.

Research Approach

Accomplishing this task is matter of shopping for identified components or mixtures that contain a sizeable proportion of the identified components and mixtures and also understanding how close available mixtures are the ideal fuel, and how the differences between the ideal and available fuels impact fuel properties.

Evaluation of Cost and Availability of Optimal SAF Drivers

Major segments of the publication cited in Task 1 are reproduced under the Results heading, and these form the basis for the discussion provided here.

One molecule, 3-ethyldecane was found at elevated concentration in almost all of the converged sets of solutions (Pareto fronts) regardless of which pair of objective functions were optimized: aircraft-level relative enthalpy savings (ARES),

engine-level relative enthalpy savings (ERES), LHV, or ED. A thorough search of suppliers of this chemical was conducted, none were found. At this time, our approach for acquiring this chemical is to purchase mixed and refined iso-paraffinic solvent, selected over a narrow distillation range inclusive of the expected normal boiling point of 3-ethyldecane. That commercially available mixture would then have additional separation methods (e.g., column chromatography and/or additional distillation), applied in our lab to further elevate the purity of 3-ethyldecane such that we can confirm its properties, most notably it LHV, density, viscosity, and freeze point. Its freeze point, in particular, represents a notable risk because National Institute of Standards and Technology (NIST) reports this property to be 72°C based on a study conducted in 1941 (Petrov et al., 1941) of which we are skeptical. As synthetic pathways that yield a concentration of 3-ethyldecane are not known, those that theoretically do have such a characteristic should be highlighted by potential fuel producers as particularly desirable. Meanwhile, the optimizations further highlighted the following composition characteristics.

When LHV and ERES were simultaneously optimized by varying the composition of the theoretical fuels, the corresponding composition was comprised mostly of iso-alkanes with one or two branches and having an average molecular weight of 151 g/mol. Very few cyclo-alkanes were represented in these solutions, but among those nearly all contained at least one 5-membered ring. To meet the fuel (mass) density constraint, these solutions contained alkyl benzenes, where such species having 10 or 12 total carbon atoms were preferred over other carbon numbers. From a producibility perspective it would be exceedingly difficult to match the precise mole fractions of individual isomers that were selected by this optimization, and such an approach is not recommended. Rather, producers should select pathways to match the broad targets identified here: lightly branched iso-alkanes having an average molecular weight of 151 g/mol, and separately a synthetic aromatic pathway that yields alkyl benzenes exclusively, with a target carbon number in the 10-12 range. While cyclo-alkanes with five membered rings can be added to this mixture, for example to meet density specification while reducing sooting propensity, such molecules are difficult to make and would not be part of a cost effective, near-term, future SAF.

When energy density and ARES were simultaneously optimized by varying the composition of the theoretical fuels, the corresponding composition was even more strongly comprised of iso-alkanes. These solutions had essentially no aromatics content, which was surprising because they were also constrained to meet (mass) density specifications. To accommodate higher density, the average molecular weight of the iso-alkanes in this set was 175 g/mol, much higher than the solutions noted in the prior paragraph. Also, the iso-alkanes, on average had significantly more branching. Cyclo-alkanes made up nearly 9% of these compositions, and like above, none of the identified cyclo-alkanes contained a ring with six carbons; rather, most of these had 8 to 10 carbons in the ring. Such species may be easier to synthesize than cyclo-alkanes with 5-carbon rings. Before going down that path, however, it is advised here that the industry decides whether to favor energy density or LHV. The ASCENT Project 066 team believes that LHV will be prioritized.

Results

The converged pareto fronts for each of the three dual-objective fuel composition optimizations are shown in Figure 1. The ARES is communicated by the horizontal axis, and particularly relevant property variations are communicated by two separated vertical axes and two separate color bars that are tied to symbol fill color or border color, respectively. Energy density and vapor pressure were deemed particularly relevant because they were among the objective functions considered for this study. Kinematic viscosity was deemed particularly relevant because it has a strong influence on atomization characteristics and is highly sensitive to fuel composition. The threshold sooting index (TSI) was deemed particularly relevant because it has a strong influence on contrail formation and represents a significant value-opportunity for SAF relative to petroleum-derived fuels.

ARES, for the representative aircraft and mission, can be improved by up to 0.40% relative to nominal petroleum-derived Jet A fuel by using fuel that has been optimized for efficiency. However, the virtual SAF composition affording that level of improvement does not meet all the requirements of ASTM D7566 (ASTM International, 2022). Notably, the aromatics concentration is too low. Upon filtering the solutions shown graphically in Figure 1 to a minimum aromatics concentration of 8.0 %v, the remaining best-case fuel composition results in ARES is 0.33%. This composition, as is the case for most of the solutions shown in Figure 1, is limited by vapor pressure at 160°C. The energy density of this solution is 34.3 GJ/m^3, which is within the experience range of petroleum-derived Jet A fuel (34.0-35.6 GJ/m^3, 95% confidence interval) (Martin & Wilkins, 2011). Indeed, all the calculated properties of this solution fall within the experience range of petroleum jet fuel and, therefore, it can be considered as a potential drop-in, 100% SAF candidate (SAF100).

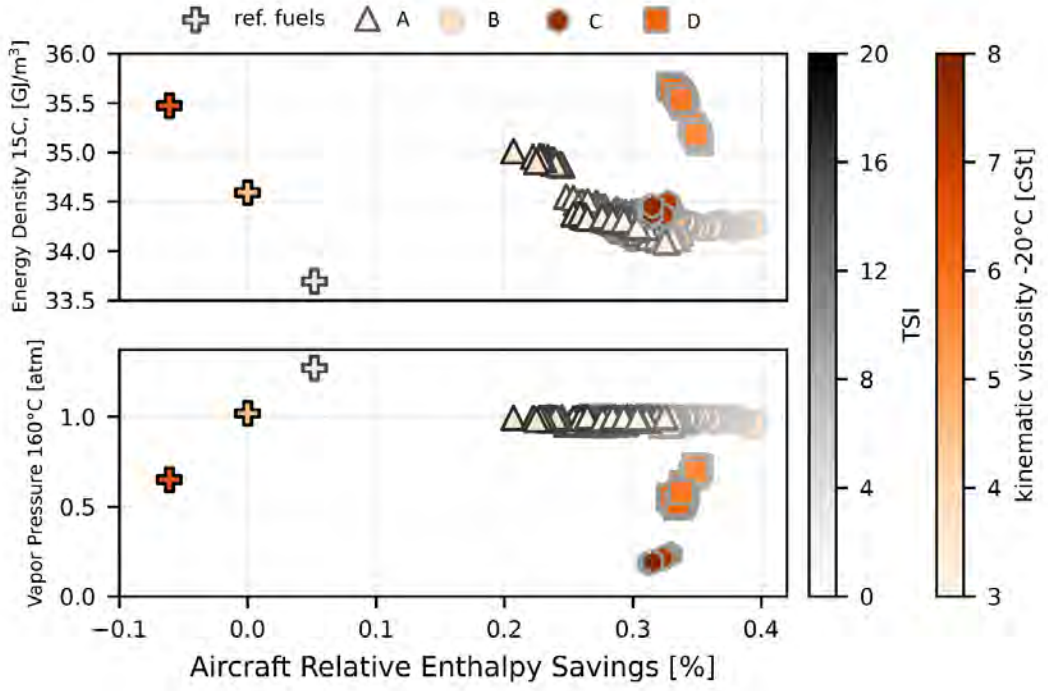

Figure 1. Jet-X optimization summary. (A) Results from a LHV/ERES optimization using the full database; (B) results from a LHV/ERES optimization using database consisting of ethylbenzene and 79 iso-alkanes with a single branch; (C) results from a vapor-pressure/ARES optimization using the full database; and (D) results from an ED/ARES optimization using the full database.

Note that viscosity and TSI tend to decrease as ARES increases along each of the pareto fronts. The implication of this is that SAF affords an opportunity to simultaneously improve fuel efficiency and atomization characteristics while decreasing a principal driver (soot) to contrail formation. Also note that increasing fuel energy density tends to drive viscosity higher, whereas decreasing vapor pressure (to mitigate phase transitioning within the fuel system) drives viscosity all the way up to its specification limit, adding considerable technical challenge to meeting cold-day ignition requirements. Vapor pressure at 160°C is the limiting property for the LHV/ERES optimizations, where LHV stands for lower heating value, also known as specific energy or net heat of combustion, and fuel (mass) density is also near its specification limit in these two optimizations. The difference between the full (1,121 molecules) and engineered (ethyl benzene and 79 iso-alkanes) database in the LHV/ERES optimizations is subtle, suggesting that significant composition variation is possible with limited impact on performance.

Figure 2 represents a summary of six different dual-objective optimizations (LHV and ERES), each completed over a different database of molecules to choose from. As with the results summarized by Figure 1, it is clear from Figure 2 that both viscosity and TSI tend to decrease as ARES increases, although the two databases that contain aromatic molecules produce results with higher TSI and lower viscosity than the three databases that do not contain aromatic molecules. Vapor pressure is limiting for each database except the one that contains only iso-alkanes. In that case, density is limiting. The two databases that contain only cycloalkanes result in solutions with higher energy density than the two databases that include aromatics as well as non-cyclic-alkanes, and the one database that contains only iso-alkanes with a single branch. However, the ARES of the cyclo-alkane solutions are lower than the ARES of the other databases. Moreover, the solutions represented by (D) in Figure 1 reveal that higher energy density can also be achieved by increasing the molecular weight of iso-alkanes in the SAF, where the composition detail of that Pareto front is discussed below.

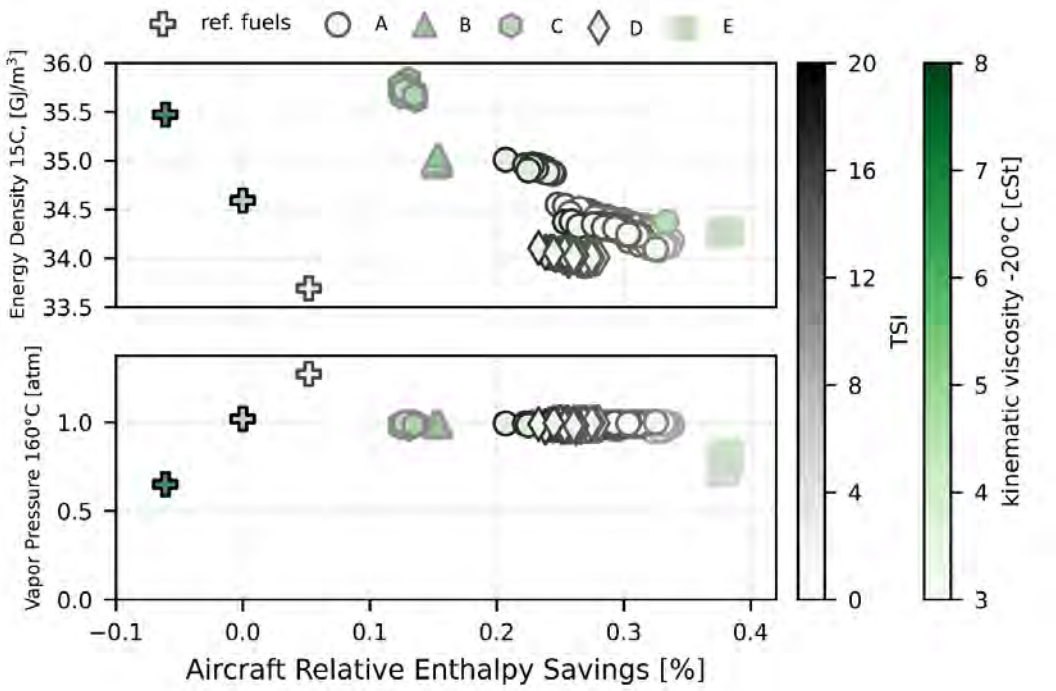

Figure 2. Results from specific-energy/engine-relative-enthalpy-savings (LHV/ERES) optimizations. (A) Full database; (B) database containing only mono-cycloalkanes; (C) database containing only mono-, bi-, and tri-cycloalkanes; (D) database containing no cycloalkanes; and (E) database containing 79 iso-alkanes with a single branch.

Composition characteristics of optimized Jet-X and SAF100 candidates

The prominent composition characteristics of the average of each pareto front shown in Figure 1 are discussed below.

The LHV/ERES optimization over the full database gave precedence (77.8%) to iso-alkanes over other hydrocarbon types. In particular, 3-ethyldecane accounted for 17.0 molar percentage ($\%_{mol}$) of the average composition and was the only compound present at greater than $10\%_{mol}$. As is evident from Figure 3, the optimization favored iso-alkanes with one or two branches, together accounting for $65.3\%_{mol}$ of the Pareto front solutions. The average molecular weight of the alkanes in the Pareto front was found to be 151.0 g/mol, with notably higher weighting of species with 10 or 12 carbon atoms. The relative paucity of iso-alkanes with 11 carbon atoms within the pareto is not yet fully explained and should not be taken too literally.

Cycloalkanes, including mono-, bi-, and tri-cycloalkanes, comprised just 9.7 %mol of the pareto front solutions. Among the cycloalkanes, nearly all contained a 5-membered ring and nearly half comprised species without any alkyl group branching. The average molecular weight of the identified cycloalkanes was quite low, with carbon number (C#) ranging from 7 to 10. The most prominent cycloalkane was bicyclo[2.2.1]heptane, which accounted for $2.5\%_{mol}$ of the pareto front average. Aromatics, including alkylbenzenes, naphthalenes, indanes, and tetralins constituted $12.5\%_{mol}$ of the pareto front solutions. Nearly all of these were alkylbenzenes. Although no single aromatic molecule exceeded $3\%_{mol}$, those with a total of 12 carbon atoms accounted for nearly half of all aromatic content.

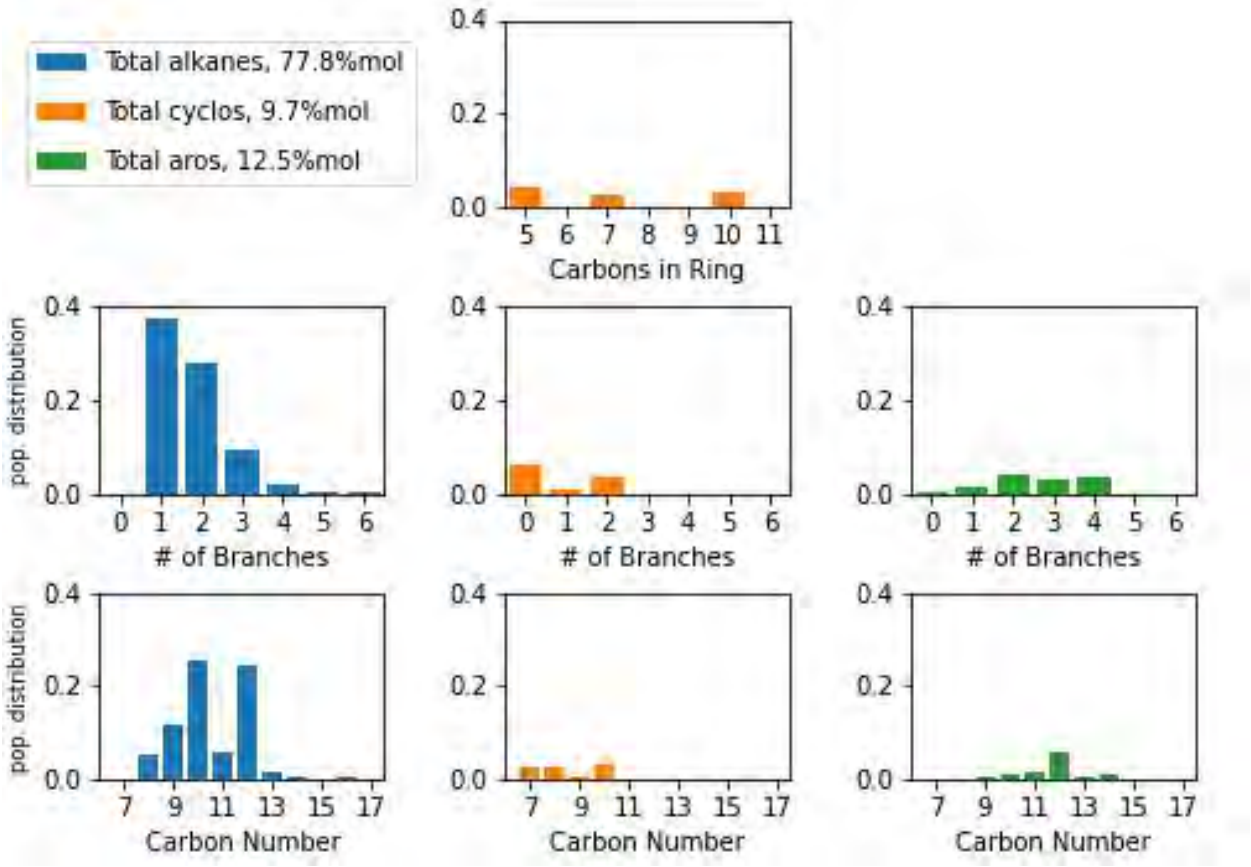

Figure 3. Composition characterization, the result of a LHV/ERES optimization using the full database. Carbons-in-ring is defined as the total number of carbon atoms that are linked into a ring, including mono-, bi-, and tri-cycloalkanes. The total mole percentage of species with a degree of unsaturation (DoU) equal to 2, 3, 5, or 7 is 3.6%$_{mol}$, where DoU is defined as (1 + C# – H#/2).

The LHV/ERES optimization initiated from a database containing ethylbenzene and 79 iso-alkanes with one branch resulted in an average (of 250 points) pareto front that contained 11.3%$_{mol}$ ethylbenzene and 88.7%$_{mol}$ iso-alkanes. The carbon number distribution, shown in Figure 4, of the iso-alkanes in these solutions was found to have much in common with the result from the LHV/ERES optimization over the full database. Like the former optimization, two molecules, 3-ethyldecane (19.1%$_{mol}$) and 3-ethyloctane (15.3%$_{mol}$) had significantly elevated concentrations relative to other species. However, one molecule, 6-pentyldodecane (9.3%$_{mol}$), was favored by this optimization but not by the similar optimization over the full database. This observation illustrates that solutions are not unique and that potential shortcomings of one solution can be overcome with little or no loss of performance benefit. For example, if one solution has a freeze point that is too high because of a too-high concentration of a high-freeze-point component, the concentration of the offending component(s), such as 3-ethyldecane or 6-pentyldodecane, can be restricted to an acceptable level, and the optimization will find an alternative composition that is nearly as good.

The ED/ARES optimization that began with the full database containing 1,121 molecules also favored iso-alkanes (91.4%$_{mol}$) over all other hydrocarbon types. The two most favored molecules by this optimization were 3-ethyldecane (14.9%$_{mol}$) and 5,10-dimethyltetradecane (7.1%$_{mol}$), and a total of 28 molecules were present at concentrations higher than 1%. A notable advantage of a fuel with many constituents is that its freeze point should be quite low. However, the producibility of such fuel, precisely as defined by the optimized compositions, is challenging. The path forward here is to produce mixtures that reproduce the higher-level composition characteristics shown in Figure 5 as closely as is pragmatic while also targeting specific representation of the most prevalent species in these definitions.

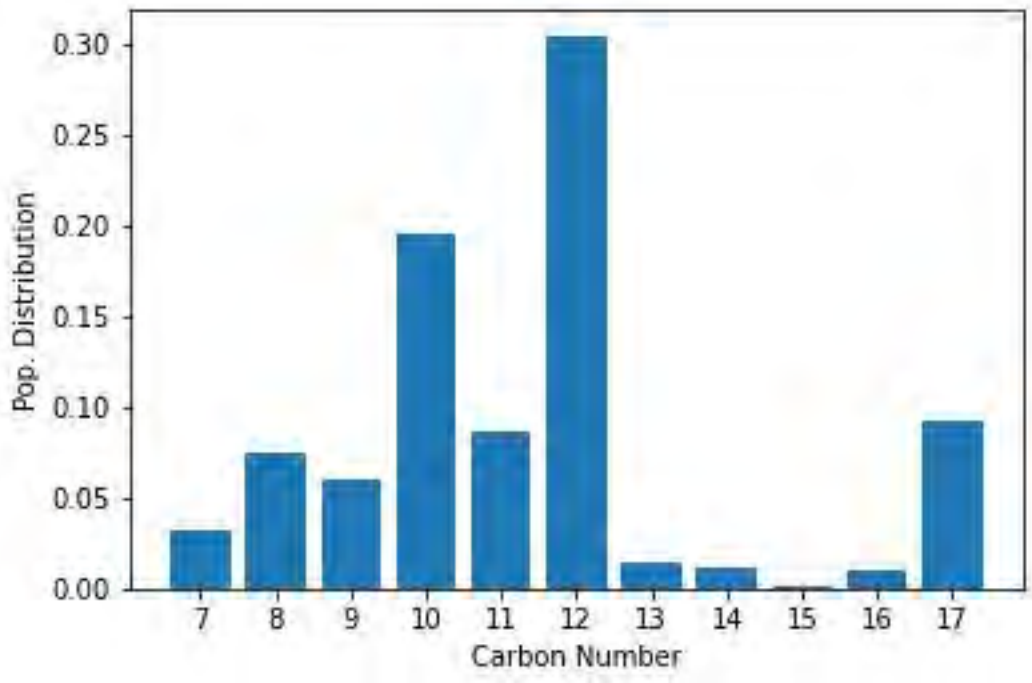

Figure 4. Composition characterization: result of an LHV/ERES optimization using a database containing ethylbenzene and 79 iso-alkanes with a single branch. The four most abundant species, on average, in this set of 250 compositions are 3-ethyldecane (19.1 $\%_{mol}$), 3-ethyloctane (15.3 $\%_{mol}$), ethylbenzene (11.3 $\%_{mol}$), and 6-pentyldodecane (9.3 $\%_{mol}$). LHV: lower heating value; ERES: engine-level relative enthalpy savings.

Although 3-ethyldecane was highlighted by all the optimizations, clear compositional differences exist between those solutions optimized for LHV and ERES and those optimized for ED and ARES. The ED/ARES optimized candidates contained essentially no aromatic materials, instead containing iso-alkanes with higher molecular weight (174.6 g/ml vs. 152.3 g/ml) and more branching than their LHV/ERES optimized counterparts. The characteristics of the selected cycloalkanes also differed significantly. The ED/ARES optimization identified significant content of compounds with 8-, 9-, and 10-membered rings in addition to one bridged ring compound, bicyclo[3.3.3]undecane. Conversely, the LHV/ERES optimization identified primarily cyclopentanes and di-cyclopentanes. The often-discussed molecule decalin (Liu & Wilson, 2012; Muldoon & Harvey, 2020; Undavalli et al., 2023) was present in the full database but was not selected by any of the optimizations.

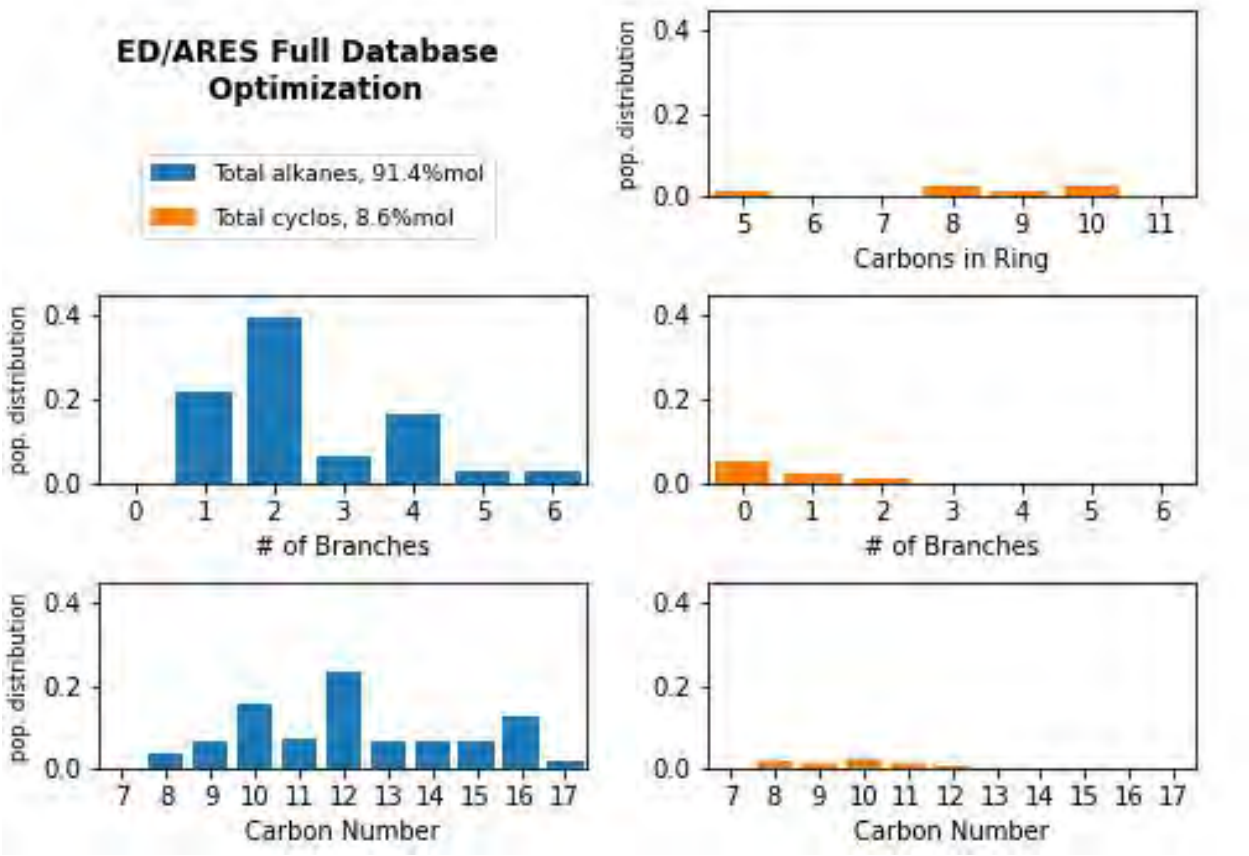

Figure 5. Composition characterization: result of an ED/ARES optimization using the full database. Carbons-in-ring is defined as the total number of carbon atoms that are linked into a ring, including mono- and bi- (or di-) cycloalkanes. ED: energy density; ARES: aircraft relative enthalpy savings.

The composition resulting from the ARES/Vapor-Pressure optimization will not be discussed here because these solutions present too much risk to cold ignition requirements while affording a potential benefit that no original equipment manufacturer has requested.

Milestones

- Created new internal code for fuel composition optimization, more amenable to large databases and Boolean-type constraints than our previously used solver, Mixed Integer Distributed Ant Colony Optimization (MIDACO).
- Finalized validation of properties database containing 1,121 molecules.
- Recognized and documented effects of hydrocarbon class on aircraft fuel economy.
- Established entitlement for direct fuel effect on aircraft fuel economy for both drop-in and non-drop-in, 100% synthetic fuels.
- Documented composition characteristics of optimized 100% SAF fuels (both drop-in and non-drop-in).

Major Accomplishments

- Established entitlement for direct fuel effect on aircraft fuel economy for both drop-in and non-drop-in, 100% synthetic fuels.
- Documented composition characteristics of optimized 100% SAF fuels (both drop-in and non-drop-in).

Publications

Boehm, R. C., Faulhaber, C., Behnke, L., & Heyne, J. S. (2024). The effect of theoretical SAF composition on calculated engine and aircraft efficiency. *Fuel, 371*(B). https://doi.org/10.1016/j.fuel.2024.132049

Outreach Efforts

None.

Awards

None.

Plans for Next Period

None. This task is complete. Note that every time a change in fuel composition is proposed that will drive existing fuels closer toward an ideal composition, it will come with consideration of its producibility and cost.

References

ASTM International. (2022). *ASTM D7566-22: standard specification for aviation turbine fuel containing synthesized hydrocarbons*.

Liu. Y., & Wilson, C. W. (2012). Investigation into the impact of n-decane, decalin, and isoparaffinic solvent on elastomeric sealing materials. *Advances in Mechanical Engineering, 2012*. https://doi.org/10.1155/2012/127430

Martin, D., & Wilkins, P. (2011*). Petroleum Quality Information System (PQIS) 2011 annual report*. Defense Technical Information Center.

Muldoon, J. A., & Harvey, B. G. (2020). Bio-based cycloalkanes: the missing link to high-performance sustainable jet fuels. *ChemSusChem, 13*, 5777–5807. https://doi.org/10.1002/CSSC.202001641

Petrov, A. D., Pavlov, A. M., & Makarov, Y. A. (1941). Synthesis of 3-ethyldecane and of 2, 5-dimethylhendecane. *Zhurnal Obschei Khimii* (Russian Journal of General Chemistry), *2*, 1104–1106.

Undavalli, V., Gbadamosi Olatunde, O. B., Boylu, R., Wei, C., Haeker, J., Hamilton, J., & Khandelwal, B. (2023). Recent advancements in sustainable aviation fuels. *Progress in Aerospace Sciences, 136*. https://doi.org/https://doi.org/10.1016/j.paerosci.2022.100876

Task 3 – Evaluate the Thermal Stability of Potential SAF

Washington State University

Objective

The goal of this task is to investigate synergies between typical impurities in conventional jet fuel and various organic nitrogen molecules with an emphasis on typical impurities in bioproducts made from waste streams via hydrothermal liquification (HTL).

Research Approach

- Create worst-case petroleum fuel by spiking one aliquot of the sample with the polar extract of a different aliquot of the same sample.
- Create worst-case bioproduct by spiking one aliquot of the sample with the polar extract of a different aliquot of the same sample.
- Execute ASTM D3241 on various blends of the two spiked sample streams (replication required).

Document comparison in terms of two metrics pulled from characterization of the test articles via ellipsometry: the peak and area of the curve showing the angular (360°) average deposit thickness at different axial planes along the length of the test specimen.

Preliminary Results

1. **Jet Fuel Thermal Oxidation Tester (JFTOT) and Impurity Measurements to Date**

To date, 41 PAC's Alcor JFTOT® tests have been run on 17 different fuels or fuel blends. Two of these sample-stock are conventional Jet A fuel while eight of these are synthetic, hydrocarbon mixtures at various stages of fuel readiness level. One is a binary blend of two different synthetic products and the other six are doped versions of one of the conventional fuels. The majority of these tests were measurements of a conventional Jet A fuel (referred to here as "R1") sourced from a local airport. Procuring this fuel was the most convenient and cost-effective way to acquire the large volumes of fuel needed for JFTOT testing, and it has provided an initial platform for understanding and developing our thermal stability measurement capabilities. This includes performing the liquid-liquid extraction method found in Link et al. (2005) and Link et al. (2007) with an additional step of methanol removal via distillation, as a proof of concept for accelerating the JFTOT coking process by doping fuel with extracted polar molecules. This strategy has an advantage over previous doping studies in that the amount of the fuel's naturally occurring polars are controlled rather than just a small number of commercially available, hydrocarbons that contain a heteroatom. Table 2 summarizes this information.

Table 2. Breakdown of JFTOT tests run to date.

Fuel Source	# of Samples	# of JFTOT Tests
Conventional Jet A (R1, R1+dopant)	7	30
Externally supplied synthetic hydrocarbon mixtures	10	11
Total	17	41

At the time, the best available analytical capabilities to evaluate this extraction was Pacific Northwest National Laboratory (PNNL) elemental analysis for total sulfur and nitrogen content. Table 3 displays the increased sulfur and nitrogen content in the extracted sample relative to the original R1 conventional fuel, indicating that this "first-pass" effort was ten times more effective at separating nitrogen-containing species from R1 than sulfur-containing species although both were dramatically enriched in the extract relative to the fresh R1 sample. Additionally, two-dimensional gas chromatography (GCxGC) results indicated that the methanol solvent had been removed entirely from the extracted polars, making this sample suitable to dope fuel for JFTOT testing.

Table 3. Results of elemental analysis run on the neat conventional Jet A sample, the polars removed from the Jet A fuel using liquid-liquid extraction, and the concentration of sulfur and nitrogen in the polar extract relative to the neat fuel.

Fuel	Total Sulfur [ppm]	Total Nitrogen [ppm]
Jet A	458.17	9.08
Jet A polars	659.49	39.76
Relative Increase	43.9%	438.9%

The results of six JFTOT tests at 260°C, including four runs of the neat R1 fuel and two runs of the R1 fuel doped with the extracted polar sample at 1.5%m, are shown in Figure 6. While these results are not comprehensive, they show that the deposit thickness can be significantly increased by a small amount of polar dopant extracted from just 75mL of the original fuel. The ability to control the amount of natural polars in a fuel is important to diversify the experimental campaign due to the difficulty of acquiring fuels with a variety of polars in the volumes needed for JFTOT tests. By refining the method shown here to improve the extraction, reduce the time needed for methanol removal, and expand the analytical techniques used to characterize the polar extract, this will become a valuable method for achieving the objectives of this research.

® JFTOT is a registered trademark of Petroleum Analyzer Company, L.P., Housten, Texas. JFTOT is a globally recognized standard for jet fuel thermal oxidation testing.

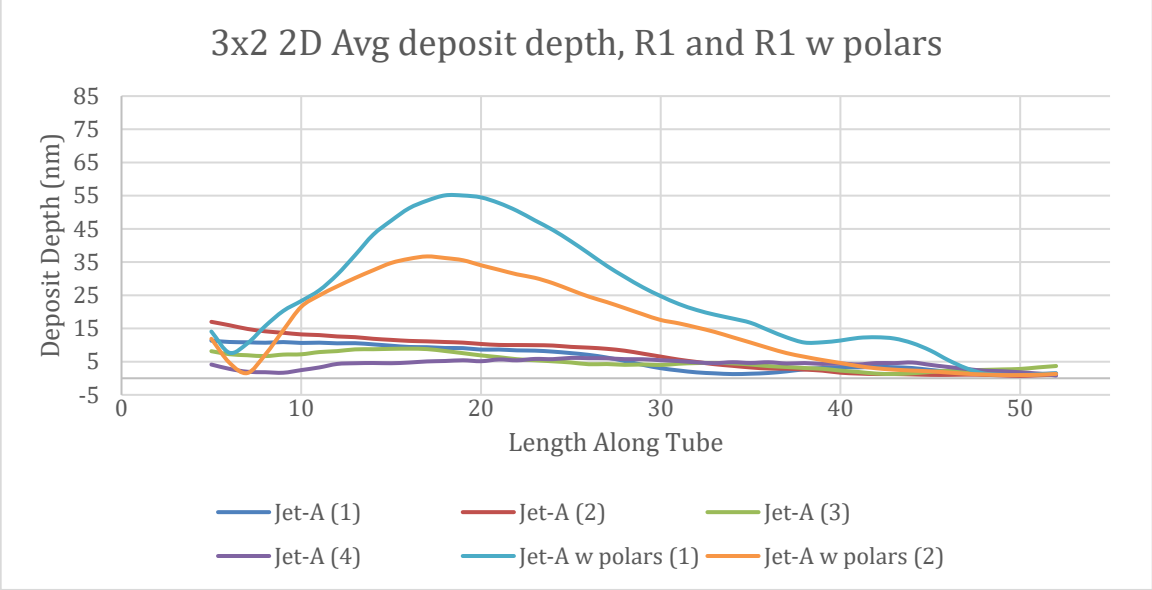

Figure 6. Results of JFTOT testing for four replicates of a neat Jet A fuel, and two separate polar-doped Jet A fuel samples.

Milestones

- Commissioned JFTOT.
- Commissioned process for doping fuel with naturally occurring polar species.

Major Accomplishments

None.

Publications

None.

Outreach Efforts

None.

Awards

- Conor Faulhaber, Distinguished Graduate Research Program (DGRP) appointment, PNNL.

Student Involvement

Conor Faulhaber, a graduate student at WSU, is leading this effort.

Plans for Next Period

- Standardize methodology for amplifying both SAF and petroleum fuel impurities for the purpose of accessing the impact of typical SAF impurities on thermal stability of SAF/petroleum fuel blends.
- Publish at least one paper on the topic of the effect of organic nitrogen materials on fuel properties such as thermal stability and elastomer seal swell.

References

Link, D. D., Baltrus, J. P., & Zandhuis, P. (2007). Isolation and identification of nitrogen species in jet fuel and diesel fuel. *Energy & Fuels, 21*(3), 1575–1581. https://doi.org/10.1021/ef060451q

Link, D. D., Baltrus, J. P., & Zandhuis, P., Hreha, D. C. (2005). Extraction, separation, and identification of polar oxygen species in jet fuel. *Energy and Fuels, 19*(4), 1693–1698. https://doi.org/10.1021/ef040095q

Task 4 – Fuel Property Estimates of Optimized SAF Compositions

Washington State University

Objective

The objective of this task is to highlight which fuel property specifications restrict the fuel composition such as to limit how much energy efficiency can be improved through fuel effects.

Research Approach

Define the detailed composition of theoretical fuels with favorable (optimized) energy efficiency characteristics and then predict as many properties as possible for these fuels based on their respective compositions using the blending rules discussed in Boehm et al. (2024).

Discussion

More than 50 properties of more than 2,250 optimized, theoretical fuels that were defined by the composition optimizations described in Task 1 are listed here as Table 4, which is an embedded Excel® file. The average compositions of each of four important dual-objective optimizations are listed in Table 5, which is also an embedded Excel file. Due to the bulkiness of the data, average compositions are used to communicate main effects. The individual, theoretical fuel composition corresponding to each row in Table 4 is available upon request. These two tables, Table S1 (Table 4) and Table S2 (Table 5), were included in Boehm et al. (2024) as supplemental material, respectively.

Table 4. Fuel properties of optimized, theoretical fuels.

Database	fill	solutions	Mission_	ERES	ARES	LPwhr
DBconv	gray	43.239	-0.00026	-0.02578	0.052047	10288.81
DBconv	gray	43.058	0.00E+00	0	0	9991.46
DBconv	gray	42.878	0.000164	0.016444	-0.06096	9518.506
DBeng1	tab:blue	44.2044	-0.00098	-0.09776	0.395189	10012.1
DBeng1	tab:blue	44.20245	-0.00098	-0.09783	0.394284	10005.57
DBeng1	tab:blue	44.2024	-0.00098	-0.09785	0.394238	10006.62
DBeng1	tab:blue	44.20195	-0.00098	-0.09771	0.394194	9997.831
DBeng1	tab:blue	44.20115	-0.00098	-0.09785	0.393704	10001.49

Table 5. Averaged compositions (mole fraction) of optimized, theoretical fuels.

Molecule	Pvap/ARES	ED/ARES	HV/ERES en	HV/ERES fu	Global Avg
3-ethylde	6.77E-02	1.49E-01	1.91E-01	1.70E-01	1.32E-01
3-ethyloct	6.06E-04	0.00E+00	1.53E-01	2.34E-02	2.97E-02
5,10-dime	1.86E-05	7.10E-02	0.00E+00	0.00E+00	2.37E-02
ethylbenz	0.00E+00	0.00E+00	1.13E-01	1.73E-04	1.89E-02
6-pentyld	0.00E+00	6.54E-05	9.25E-02	0.00E+00	1.54E-02
undecane	3.85E-03	2.29E-04	8.31E-02	0.00E+00	1.52E-02
2,2-dimet	3.53E-03	3.72E-02	0.00E+00	0.00E+00	1.36E-02
cyclodeca	2.09E-05	2.34E-02	0.00E+00	2.96E-02	1.27E-02

® Excel is a registered trademark of Microsoft Corporation in the United States and other countries.

Milestones
None.

Major Accomplishments
None.

Publications
Boehm, R. C., Faulhaber, C., Behnke, L., & Heyne, J. S. (2024). The effect of theoretical SAF composition on calculated engine and aircraft efficiency. *Fuel, 371*(B). https://doi.org/10.1016/j.fuel.2024.132049

Outreach Efforts
None.

Awards
- Conor Faulhaber, DGRP appointment, PNNL

Student Involvement
Conor Faulhaber, a graduate student at WSU, led the effort for this task.

Plans for Next Period
None. This task in complete.

References
Boehm, R, C., Yang, Z., Bell, D. C., Faulhaber, C., Mayhew, E., Bauder, U., Eckel, G., & Heyne, J. S. (2024). Perspective on Fuel Property Blending Rules for Design and Qualification of Aviation Fuels: A Review. *Energy & Fuels, 38*, 17128–17145. https://doi.org/10.1021/acs.energyfuels.4c02457

Task 5 – Suggest Optimal Fuel Properties for Non-Drop-In SAF
Washington State University

Objective
The objective of this task is to inform the decision-making process around specifications for non-drop-in, 100% SAF (Jet-X).

Research Approach
This is an organic off-shoot of the theoretical fuel composition optimization work discussed in Task 1. While some discussion of this work was made in the publication noted in Task 1, the highlights of this effort are discussed below.

Discussion
First, it is worthwhile to distinguish limiting properties from optimal properties. For example, many potential SAF products have physically a maximum allowable blend fraction with conventional fuel based on unfavorable freeze point or flash point of the hypothetical finished fuel. Since the specified limits on these properties are motivated by safety concerns, they cannot be altered. This logic applies to most of the properties specified in ASTM D1655, D7566 and/or D4054. Notable exceptions include (mass) density, dielectric constant and minimum aromatics content (for seal swell). Regardless of how Jet-X is eventually defined, it is very likely to have significantly different or no requirements pertaining to these three properties than conventional (ASTM D1655) jet fuel. Optimal properties include a subset of those restricted on just one side of the distribution. These include most notably, LHV, viscosity, energy density, and thermal stability. Moreover, depending on priorities stemming from issues that are outside the scope of this project, they may include sooting propensity (which is sometimes represented by aromatics content) or total sulfur.

To achieve optimal (maximum) LHV, the fuel composition will be constrained by the flash point requirement as its composition is driven toward the highest possible hydrogen carbon ratio, manifested by low molecular weight iso-alkanes. Such species also, typically, have lower viscosity than average conventional jet fuel (Martin & Wilkins, 2011) which is favorable with respect to combustion figures of merit as well as heat transfer characteristics. The maximum LHV is also

constrained by thermal stability, as cyclo-alkanes with a lot of ring strain (e.g., three or four carbons in the ring) as well as alkenes and alkynes tend to be relatively easy to oxidize, which is a critical step in the overall coking mechanism. Finally, the LHV can be constrained by energy density requirements because it is possible for the product of (mass) density with LHV (which is energy density) to decrease as LHV increases and there is an implicit lower limit on energy density which is based on available space to use for fuel tanks.

The tradeoffs between the benefits of higher LHV verses higher energy density favor higher LHV for two reasons. The viscosity tends to increase with the increasing (mass) density that is necessary to achieve higher energy density. While either fuel would presumably meet all combustor operability requirements, the fuel with lower viscosity (the high LHV fuel) would likely pass with more margin. From an aircraft design perspective, the higher-LHV fuel is also generally preferred because it is harder to take advantage of higher energy density than LHV. Many aircraft design concepts are significantly more influenced by gross weight at take-off than available space for fuel tanks. Enabling a smaller fuel tank, in these cases does not help significantly. Moreover, LHV increases can be exploited by any aircraft that is certified to operate on the defined fuel, whether it was designed specifically for a steady diet of such fuel.

In short, the optimal properties of theoretical SAF are those reported in row 6 of Table 2, which are extracted here for convenience and summarized in Table 6. This theoretical fuel has the highest LHV of any we found and met all specifications of drop-in SAF except those related to aromatics content which include the specified minimum aromatics content (8% by volume), dielectric constant experience range, and compatibility with elastomers with prior in-service exposure to fuel with aromatics. While the exclusion of these properties would automatically render it non-drop-in, it is also possible that such a fuel would require some dosing with the approved lubricity improver/corrosion inhibitor in order to meet lubricity requirements as it would be free of any naturally occurring impurities that would promote lubricity.

Table 6. Fuel properties of representative, best-case theoretical fuel. (2 pages)

Property	Units	Value	Comments
ERES	%	-0.098	Slight negative impact stems from H_2O/CO_2 impact on heat capacity
ARES	%	0.395	Drop-In Benefit
LPwhr	W	10012.1	Waste Heat Recovery at Low Power (LP), A2 fuel has 9,991.5 W
LPsav %	%	-0.091	ERES at Low Power reference condition
HPwhr	W	62142.4	Waste Heat Recovery at High Power (HP), A2 fuel has 61,195.5 W
HPsav %	%	-0.104	ERES at High Power reference condition
MW	kg/mol	0.1602	Average Molecular Weight (MW)
LHV	MJ/Kg	44.204	Lower Heating Value (LHV), A2 fuel has 43.058 MJ/Kg
ED 15C	MJ/L	34.27	Energy Density (ED) at 15°C, A2 fuel has 34.59 MJ/L
ED 85C	MJ/L	31.92	Energy Density at 85°C, linear
kvisc -40C	cSt	7.59	
kvisc -20C	cSt	3.80	A2 fuel has 4.6 cSt
kvisc 15C	cSt	1.66	
kvisc 85C	cSt	0.67	
TSI	unitless	5.0	A2 fuel has 22.2 Threshold Sooting Index (TSI)
Smoke Point	mm	71.2	A2 fuel has 25.3 mm
density 15C	Kg/L	0.775	Minimum allowed by fuel quality control specifications, at 15°C
density 85C	Kg/L	0.722	density is linear with temperature, at 85°C
MV 15C	L/mol	0.207	Molar Volume (MV) at 15°C
MV 85C	L/mol	0.222	Molar Volume at 85°C, linear
Cp 15C	J/mol/K	346.1	A2 has 310.2
Cp 85C	J/mol/K	388.5	heat capacity is linear with temperature
K 15C	W/m/K	0.130	Thermal conductivity at 15°C, low sensitivity to fuel composition
K 85C	W/m/K	0.119	thermal conductivity is linear with temperature
alpha 15C	unitless	0.486	Cp/Cv A2 has 0.519
alpha 85C	unitless	0.423	
Prandtl 15C	unitless	3.419	A2 fuel has 3.756
Prandtl 85C	unitless	1.572	
H-C ratio	unitless	2.168	A2 fuel has 1.904, H-C: Hydrogen to Carbon
Pvap -40C	atm	0.000263	
Pvap 25C	atm	0.0120	
Pvap 85C	atm	0.125	
Pvap 160C	atm	0.974	Restricted to a maximum of 1.0 by user constraint. A2 fuel has 1.019.
nalkanes mfrac		0	A2 fuel has 20.0%
isoalkanes mfrac	fraction	0.992	A2 fuel has 29.7%
cycloalkanes mfrac		0	A2 fuel has 25.1%
dicycloalkanes mfrac		0	

Property	Units	Value	Comments
tricycloalkanes mfrac		0	
total cyclos mfrac		0	A2 fuel has 31.8%
alkylbenzenes mfrac	fraction	0.008	A2 fuel has 12.9%
cycloaromatics mfrac		0	
naphthalenes mfrac		0	
other mfrac		0	
total aromatics mfrac	fraction	0.008	A2 fuel has 18.5%; Note: 0.8% is 10 times lower than spec minimum
polarizability		21.62	A2 fuel has 21.28
dielectric constant 288K		2.07	A2 fuel has 2.12
refractive index 293K		1.439	A2 fuel has 1.446
surface tension 295K	mN/m	23.43	Low sensitivity to fuel composition
Oh 295	m^0.5	0.00030	A2 fuel has 0.00035 Ohnesorge Number (Oh) (lower is better for atomization)
DCN 288	unitless	49.4	A2 fuel has 48.3 Derived Cetane Number (DCN)
iBP	°C	162	iBP: initial boiling point
T10	°C	170	
T20	°C	178.5	
T30	°C	186.5	
T40	°C	194.5	
T50	°C	202.5	
T60	°C	211	
T70	°C	222	
T80	°C	240.5	
T90	°C	278.5	
fBP	°C	295	
T50-T10	°C	32.5	A2 fuel has 28.6°C
T90-T10	°C	108.5	A2 fuel has 67.8°C

Milestones
None.

Major Accomplishments
None.

Publications
Boehm, R. C., Faulhaber, C., Behnke, L., & Heyne, J. S. (2024). The effect of theoretical SAF composition on calculated engine and aircraft efficiency. *Fuel, 371*(B). https://doi.org/10.1016/j.fuel.2024.132049

Outreach Efforts
None.

Awards

- Conor Faulhaber, DGRP appointment, PNNL.

Student Involvement

Conor Faulhaber, a graduate student at WSU, led the effort for this task.

Plans for Next Period

None. This task in complete.

References

Martin, D, & Wilkins, P. (2011). *Petroleum quality information system (PQIS) 2011 annual report*. Defense Technical Information Center.

Project 067 Impact of Fuel Heating on Combustion and Emissions

Purdue University

Project Lead Investigators

Robert P. Lucht
Ralph and Bettye Bailey Distinguished Professor of Combustion
School of Mechanical Engineering
500 Allison Road
Purdue University
West Lafayette, IN 47907-2014
765-714-6020
Lucht@purdue.edu

Carson D. Slabaugh
Associate Professor
School of Aeronautics and Astronautics
500 Allison Road
Purdue University
West Lafayette, IN 47907-2014
765-494-3256
cslabau@purdue.edu

University Participants

Purdue University

- P.I.s: Dr. Robert P. Lucht and Dr. Carson D. Slabaugh
- FAA Award Number: 13-C-AJFE-PU-038
- Period of Performance: October 1, 2020, to September 30, 2024
- Task:
  1. Investigate the effects of fuel heating on combustion and emissions for aviation gas turbines

Project Funding Level

The ASCENT Project 067 was funded by the Federal Aviation Administration (FAA) at the level of $250,000 for the project period from June 5, 2020, to June 4, 2021; an additional $250,000 for the time period from June 5, 2021, to September 30, 2022; an additional $250,000 for the time period from October 1, 2022, to September 30, 2023; and an additional $200,000 has been approved for the project period of October 1, 2023, to September 30, 2024. A no-cost extension of this funding period is now in place. The required cost-sharing 1:1 match of $950,000 was provided by Purdue University.

Investigation Team

Prof. Robert P. Lucht (P.I.)
Prof. Carson D. Slabaugh, (co-P.I.)
Thomas McLean, Tristan Shahin, Ben Murdock, Zander Hodge, and Keaton Koenig (graduate students), Responsible for the design of system components, such as the fuel heating system, and will be responsible for executing test operations.
Dr. Rohan Gejji, Research Engineer, Help graduate students with their design projects and supervising test operations.
Dr. Bahman Habibzadeh, Current FAA Program Manager
Dr. Prem Lobo, Program Manager from October 1, 2022, to September 30, 2023

Project Overview

The goal of this project is to evaluate the effects of heating jet fuel before injection in an aviation gas turbine combustor on combustion efficiency, pollutant emissions, and dynamics. In an aircraft engine, heat that would otherwise be wasted can be directed into the fuel to increase its sensible enthalpy before injection. Thermochemistry dictates that this increase in sensible enthalpy must lead to lower fuel consumption for a given combustor exit temperature. However, the effects of elevated fuel temperature on combustion performance characteristics (e.g., the fuel spray pattern, spatial distribution of reaction zones, pollutant emissions, and combustion dynamics) are not yet well understood. The ASCENT Project 067 team will perform experiments with heated fuels by using a piloted, partially premixed fuel injector located in an optically accessible combustor. This process will allow us to apply advanced laser diagnostic techniques to compare the behavior of the combustor at different fuel temperatures over a wide range of operating conditions.

The platform for the planned experiments is the Combustion Rig for Advanced Diagnostics (COMRAD). The test rig (Figure 1) is designed to operate at steady-state conditions with thermal power as high as 8 MW, inlet air pressure (P_3) as high as 4.0 MPa, and inlet air temperature (T_3) as high as 1,000 K. To facilitate operation at these conditions, the test article is made of aviation-grade alloys, and is thoroughly water cooled, and the inner windows are film cooled with heated nitrogen. Before this project, extensive testing with ambient-temperature fuels was performed in this test rig, with a focus on 5- and 10-kHz particle image velocimetry (PIV) measurements in the downstream boundary condition window section, and 50- and 100-kHz PIV measurements in the flame zone.

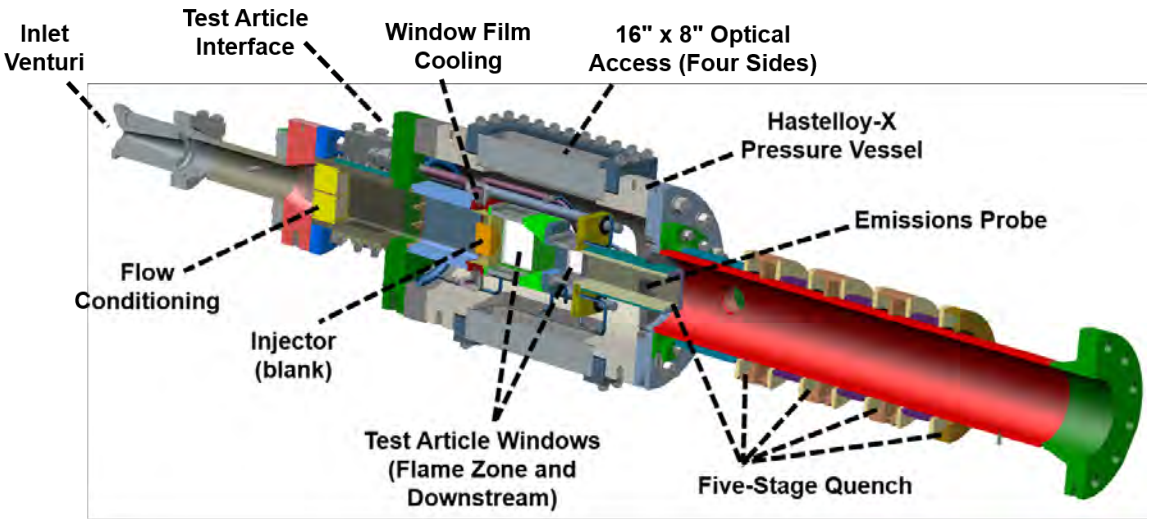

Figure 1. Schematic diagram of the Combustion Rig for Advanced Diagnostics (COMRAD).

Task 1 - Investigate the Effects of Fuel Heating on Combustion and Emissions for Aviation Gas Turbines

Purdue University

Objective

The goal of this project is to determine the effects of fuel heating on the performance of aviation gas turbines. Fuel heating can potentially lead to higher efficiency but can also lead to changes in the fuel distribution pattern and in the locations of reaction zones in the combustor. These changes may also affect pollutant emissions and combustion dynamics during engine operation. The ASCENT Project 067 team will perform experiments using heated fuels and measure the fuel distributions, reaction zone distributions, pollutant emissions, and combustion dynamics at a range of fuel temperatures from near room temperature to above the supercritical temperatures for hydrocarbon fuels.

Research Approach

Our team will perform experiments with heated fuels by using a piloted, partially premixed fuel injector located in an optically accessible combustor. This experimental system will allow us to apply advanced laser diagnostic techniques to compare the behavior of the combustor at different fuel temperatures over a wide range of operating conditions. These advanced diagnostic techniques include fuel planar laser-induced fluorescence (PLIF) imaging to monitor fuel distribution patterns, hydroxyl (OH) radical PLIF (OH PLIF) imaging to monitor reaction zones, and PIV to measure the flow fields. We will also measure emissions with probe sampling and will use pressure transducers to measure combustion dynamics.

Facility Overview

COMRAD is supplied by facility fluid systems including heated air, heated nitrogen, high-pressure water, and liquid jet fuel. Two types of liquid jet fuel were used separately for this work: (a) Jet A fuel and (b) Shell® gas-to-liquids (GTL) GS190, a Fischer-Tropsch synthetic paraffinic kerosene (FT-SPK). The rig features a piloted swirl injector (shown schematically in Figure 2), housed inside a duct within a large-windowed pressure vessel enabling optical access to the entire flame from four sides. Figure 3 shows a diagram of the test rig. Combustion air is supplied to the test article at 755 K and up to 20 bar. After it is metered, the air passes through a flow conditioner and into the air plenum, which supplies both the pilot and main sections of the injector.

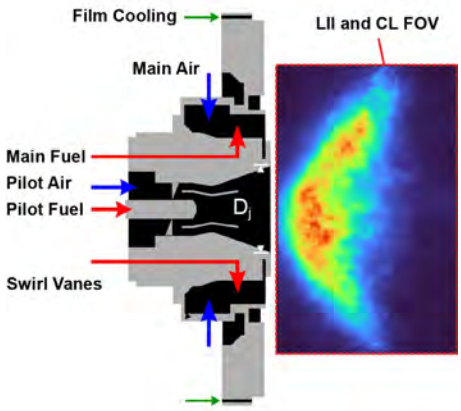

Figure 2. Schematic of injector indicating reactant flow routing as well as the laser-induced incandescence (LII) and OH* chemiluminescence (CL) fields of view (FOV) relative to an averaged LII image.

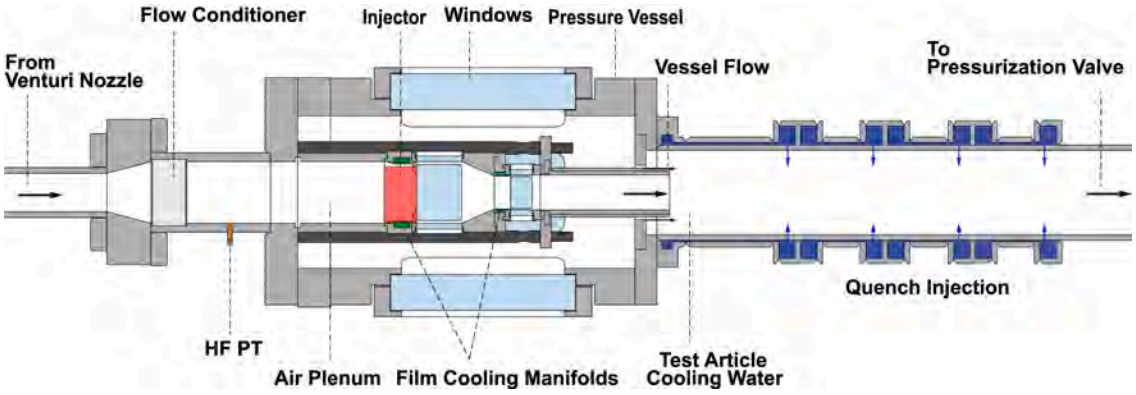

Figure 3. Schematic representation of the combustor, highlighting primary features. HF PT: high-frequency pressure transducer.

® Shell is a registered trademark of Shell Trademark Management B.V., The Hague, The Netherlands.

Liquid jet fuel is supplied to the injector at temperatures as high as 590 K by an 81-kW fuel heater. The fuel heater (Figure 4) comprises a stack of copper blocks with 20 cartridge heaters inserted into each block. Fuel flows in stainless steel tubes through three independent circuits, two pilot circuits, and one main circuit. The mass flow rates in each circuit are measured with Coriolis flow meters. In the fuel heater, the stainless-steel tubes are clamped between each pair of copper blocks before being delivered to the test rig. The temperature of the fuel is monitored both in the fuel heater (to ensure that no phase change is encountered) and immediately upstream of the injector. Fuel passes through approximately 50 cm of trace-heated tubing from the heater to the test rig. The tubing is air-jacketed within the test rig to inhibit heat transfer from the heated air before the injector is reached. To prevent coking in the fuel lines at high fuel temperatures, the fuel tank is sparged with nitrogen for 30 minutes before use to remove dissolved oxygen, and the tank ullage is purged with nitrogen during the experiment. A dissolved oxygen sensor (Mettler Toledo® Inpro 6850i) is used to ensure that the levels of dissolved oxygen remain below 0.2% of the fully saturated level during the experiment. An inert gas purge circuit is used to prevent the collection of stagnant fuel in the heater and the tubing to the experiment when fuel is not flowing to the experiment. This purge displaces the fuel to a collection tank through a bypass circuit and counter-flow heat exchanger that cools the fuel temperature to ambient temperature with water as the heat transfer medium.

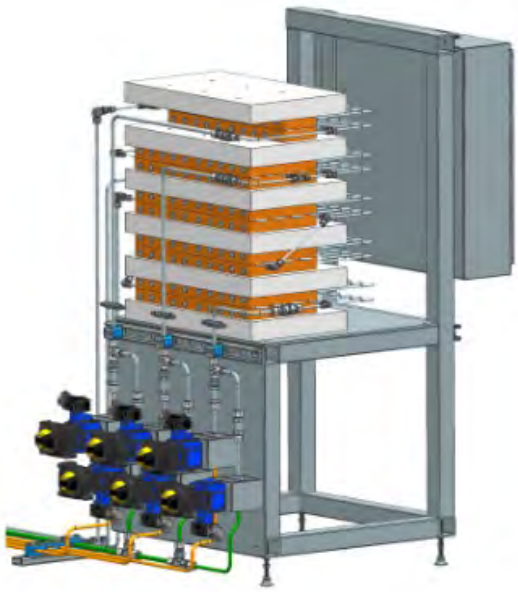

Figure 4. Computer-aided design rendering of the fuel heater.

At the injector, fuel is injected into two co-swirling flows of air separated by a bluff body. The inner flow forms the pilot flame, and the outer flow forms the main flame, where most of the fuel is burned. The fuel flow rates to the pilot and main circuits are separate to enable independent control of the fuel/air ratio in each part of the flame. The pilot flame is operated at a higher fuel/air ratio than the main flame, allowing the main flame to stabilize as the pilot products mix with the main reactants. The main reactant stream is assumed to be partially premixed when it reaches the flame, but the pilot flame is mostly non-premixed.

The flame zone is contained by a rectangular duct with a height/width ratio of approximately 1.4. Fused quartz windows are installed on each side of the duct to enable imaging of the flame, which is not presented in this work. These windows are film cooled with heated nitrogen at approximately 590 K to lessen the thermal load created by the flame. The film cooling flow rate is independently controlled but is set to a constant fraction of the combustion air flow rate. The duct then

® Mettler Toledo is a registered trademark of Mettler-Toledo GmbH, Greifensee, Switzerland.

contracts vertically to a height/width ratio of approximately 0.75. Downstream of this contraction, another windowed section is present. A separate supply of heated air flows through the pressure vessel at the same pressure as the combustor, and this flow merges with the test article flow in a pipe, where water is radially injected into the flow to cool it. An electrically actuated butterfly valve is installed at the exit of the flow path to back-pressurize the combustor. The inner duct is coated with a thermal barrier coating and cooled by internal water channels. This cooling water is directed into the flow at the exit of the inner duct.

Heated air and nitrogen sources are metered with sonic Venturi nozzles, high-pressure water is metered with cavitating Venturi nozzles, and jet fuel is metered with Coriolis flow meters. The test rig is equipped with pressure transducers (GE® PMP50E6) and K-type thermocouples (Omega® GKMQSS-062G) for flow metering and in several different locations throughout the flow path. These instruments are sampled at 100 Hz to monitor the operating conditions, and a National Instruments® LabVIEW virtual instrument is used to display measured values and send commands to pneumatically and electrically actuated valves in the test cell. The relative uncertainties of calculated mass flow rates have been determined to be below 0.83% for gases and below 0.10% for liquid fuel according to the Kline–McClintock[1] method, with a 95% confidence interval. A high-frequency pressure transducer (Kulite® WCT312M-70BARA) is installed in the air plenum to monitor acoustic oscillations.

During testing operations in Spring 2024, a facility water softener failure resulted in damage to the water-cooled portions of the test article. The damage to the exhaust duct of the combustor was severe and the cost of the repair was more than $50,000. Because the this was a facility issue, Purdue University insurance rather than the FAA project paid for the repair, but the exhaust duct had to be refabricated, and it has taken over six months to complete that fabrication. We are now in the process of reassembling the test rig and should be operational before early January 2025.

Laser-Induced Incandescence

LII is an in-situ method for determining soot levels in a combustion flow field. The diagnostic was first applied to a lab scale laminar diffusion flame (Yale burner) to validate the accuracy of the experimental setup and then used to investigate soot formation for both rich and lean dome operation in COMRAD. Comparison of soot levels between several different fuels has begun with noticeable decrease in signal for synthetic fuels lacking aromatics such as World Energy® hydro-processed esters and fatty acids (HEFA) across all operating conditions. LII measurements provide valuable information of the spatial locations for particulate formation in the combustor flow field. GE Aerospace is very interested in the types and number of particulates that are in the combustor exhaust.

Two-dimensional LII measurements can be obtained in a flame by using a laser sheet that passes through a plane of interest and measuring the incandescence signal with a camera. Comparative soot volume fraction measurements can be determined by gating the detection device around the entire incandescence signal.

A Quanta-Ray® Pro-290 Nd:YAG laser is used to generate a 1064 nm beam at a frequency of 10 Hz. Using an excitation wavelength of 1064 nm reduces poly-aromatic hydrocarbon (PAH) laser-induced fluorescence (LIF) and excitation of diatomic carbon (C_2) molecules. The beam is attenuated to the desired power with a half-wave plate and a thin-film polarizer allowing for a max of 240mJ down to as low as 8.5mJ. A set of cylindrical lenses (f = -50, +300) is used to expand the beam in a vertical direction and collimate it. Two horizontal cylindrical focusing lenses (f = +150) are then used to focus the beam into a sheet with a variable focal length. The focal point of the laser sheet is aligned with the center line of the injector. For the Yale burner experiments, the sheet is 44 mm wide and 0.40 thick at the focal point. For the experiments in COMRAD, the sheet is 48.49 mm wide and 0.53 mm thick at the focal point. The sheet is introduced to the experiment from above, perpendicular to the injector's face. The sheet is aligned with the center of the injector while ensuring vertical alignment using a reflected beam. A diagram of the setup used for the COMRAD testing is shown in Figure 5.

® GE is a registered trademark of General Electric Company, Schenectady, New York.
® Omega is a register trademark of Omega Engineering, Inc., Stamford, Connecticut.
® National Instruments is a registered trademark of National Instruments Corporation, Austin, Texas.
[1] The Kline-McClintock Method is used to determine the uncertainty of a calculation given certain measurements and the tolerances on those measurements. The method defines the uncertainty as a range where the true value lies in.
® Kulite is a registered trademark of Kulite Semiconductor Products, Inc., Leonia, New Jersey.
® World Energy is a registered trademark of World Management Group LLC, Boston, Massachusetts.
® Quanta-Ray is a registered trademark of Newport Corporation, Irvine, California.

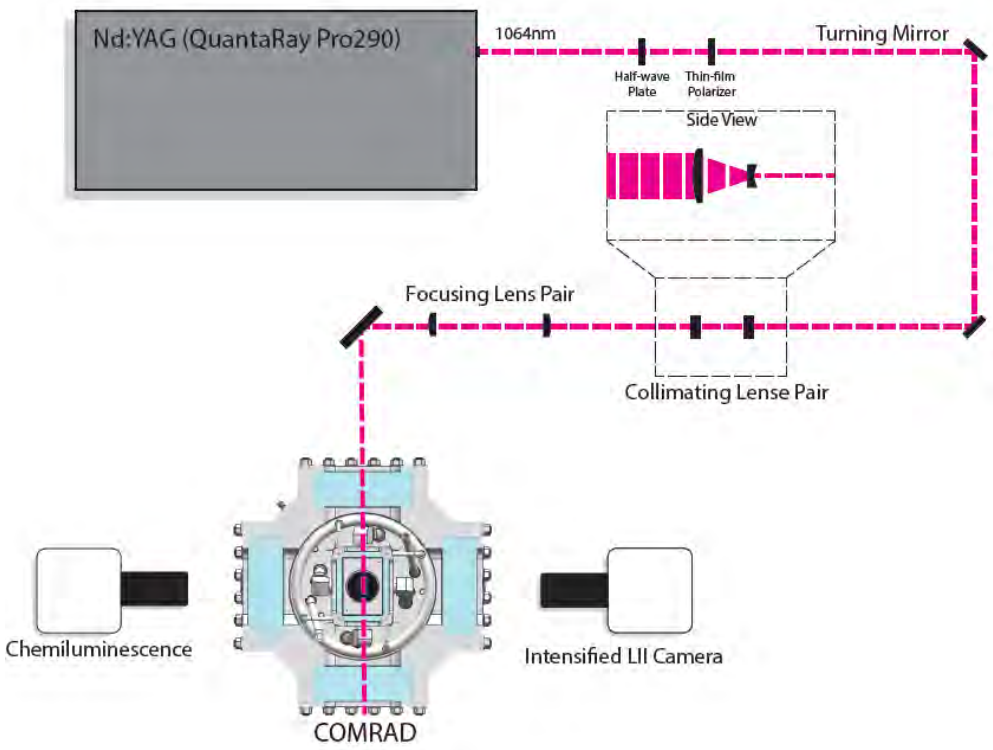

Figure 5. LII diagnostic setup in COMRAD.

An intensified ultrahigh-speed complementary metal-oxide-semiconductor (CMOS) camera (Phantom® TMX and Lambert™ High-speed Intensified Camera Attachment [HiCatt]) measures the LII signal emitted from soot within the flame. A gate time of 5 μs is used to capture the incandescence with the arrival of the laser occurring approximately 500 ns after the beginning of the gate. The camera is operated in burst mode to take an image of the background 20 μs before the laser pulse and an image of the LII signal gated around the arrival of the laser pulse. This is used for background subtraction in post-processing. The camera was equipped with a 105 mm lens to achieve the desired spatial resolution. A bandpass filter centered at 450 nm with a 20 nm bandwidth isolates the LII signal at a wavelength with negligible interference from C_2 emissions. A shortpass filter with a cut-off wavelength of 900 nm is used to block any scattered 1064 nm laser light from reaching the camera.

LII Measurements in a Laminar Diffusion Flame

Prior to attempting LII measurements in the COMRAD test rig, our team performed LII experiments in a well-characterized sooting laminar flame. This allowed us to optimize experimental parameters such as the details of the time gate for the detection of the LII signal and also allowed us to develop data analysis methods. The Yale burner is a steady axisymmetric laminar diffusion flame that has been studied extensively in the combustion community including our own coherent anti-Stokes Raman spectroscopy (CARS) measurements of the temperature field (Satija et al., 2019). Another consideration for performing these measurements in the Yale burner is that we were using the infrared 1064-nm out of the Q-switched Nd:YAG laser, a beam that presents significant eye hazards. Our team wanted to gain experience with working this beam prior to attempting alignment in the test cell for the COMRAD experiments.

A schematic diagram of the Yale burner is shown in Figure 6. Air enters co-axially into a plenum and diffuses through a manifold of glass beads for flow conditioning. Gaseous fuel enters a manifold through the bottom of the burner and exits

® Phantom is a registered trademark of Vision Research, Inc., Wayne, New Jersey.
™ Lambert is a trademark of Lambert Instruments, Netherlands.

through an uncooled fuel tube. The inner diameter of the fuel tube is 4 mm with a wall thickness of 0.38 mm. It is surrounded by a concentric air annulus that is 74 mm in diameter.

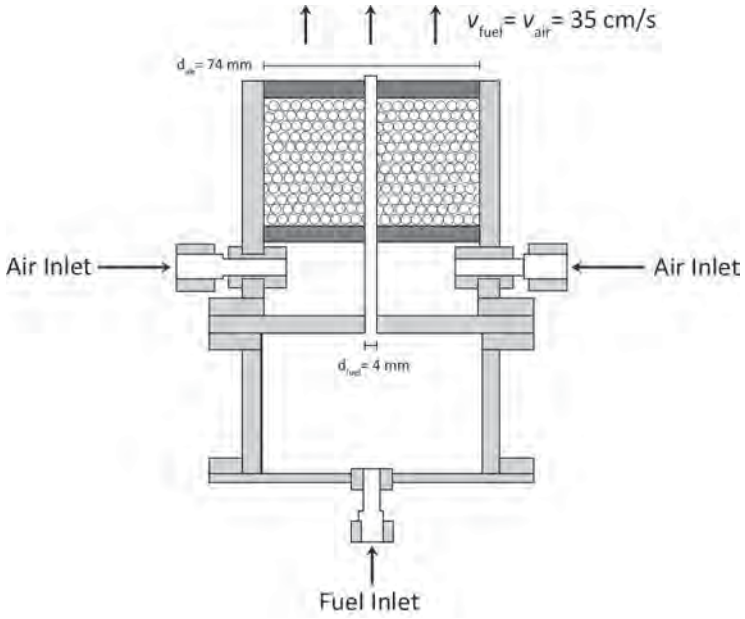

Figure 6. Schematic diagram of Yale burner.

The test conditions used in this study match an International Sooting Flame (ISF) workshop target dataset for the Yale burner. Ethylene diluted with nitrogen in various percentages is used as the fuel. Synthetic air with 79% N_2 and 21% O_2 is the oxidizer. The flow rates for fuel and air in the conditions evaluated are set so that both cold flow exit velocities are equal to 35 cm/s. Fuel and air velocities were validated in the experimental setup using an air velocity transducer (TSI® Model 8645-12). The fuel fraction varies for each condition while the total mass flow rate for fuel and diluent is constant at 0.264 standard liter per minute (SLPM). Fuel fractions of 32%, 40%, 60%, and 80% are evaluated to create a spectrum of flames ranging from lightly sooting to heavily sooting. Details for each flame condition are shown in Table 1.

Table 1. Yale Burner co-flow diffusion flame ISF target conditions

Condition	f_{fuel} [%]	$\dot{m}_{air}$ [SLPM]	$\dot{m}_{C2H4}$ [SLPM]	$\dot{m}_{N2}$ [SLPM]	Flame height [mm]
A	32	90	0.0845	0.1795	29
B	40		0.1056	0.1584	35
C	60		0.1584	0.1056	56
D	80		0.2112	0.0528	80

The LII signal intensity was measured at various laser pulse energies to generate a curve showing the relationship between laser sheet fluence and peak LII signal (shown in Figure 7). Prior to flame on, a power meter is used to measure the average energy per pulse at the location of the flame. These measurements are taken after all losses occurred through the beam path and thus represent the true energy reaching the soot. Operation of the laser at the plateau region (shown in Figure 7) is optimal for soot volume fraction measurements because it ensures that non-uniformity in the laser sheet has a minimal effect on the LII signal. This plateau region is caused by the soot reaching the sublimation threshold leading to increased cooling rates.

® TSI is a registered trademark of TSI Incorporated, Shoreview, Minnesota.

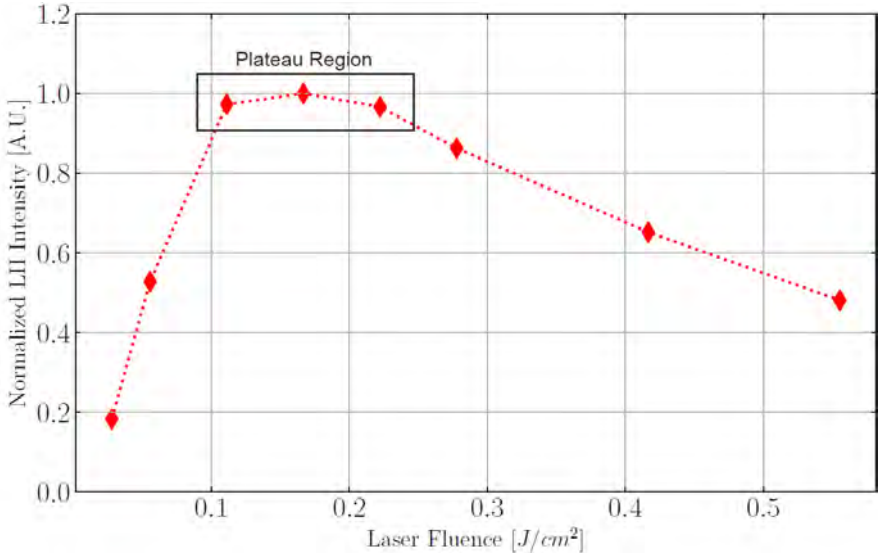

Figure 7. Normalized peak LII intensity as a function of laser fluence.

Based on the fluence curve seen in Figure 7, a target average laser sheet fluence of 0.17 J/cm^2 was used for all experimentation within the Yale burner. This fluency was associated with a laser power at the burner of 30 mJ. There is general agreement that with the selection of appropriate parameters and conditions, LII signal intensity can be assumed to vary linearly with soot volume fraction. The measured LII signal only provides a qualitative value proportional to the soot volume fraction in a flame. A calibration coefficient is therefore required to obtain soot volume fraction measurements from LII. Calibration was performed in this study using results from Smooke et al. (2005) for a nearly identical burner and the same test conditions. A constant average Ke = 10 was assumed throughout the flame with a constant $E\ (m)$ value of 0.40 from Snelling et al. (2005).

The experimental soot volume fraction is plotted in Figure 8 as the fuel fraction is increased from 32% to 80%. It should be noted that the color scale of each image is set by the maximum value in individual sub-images. The results show an expected increase in peak soot volume fraction with increases in fuel fraction. A higher percentage of ethylene in the fuel results in greater amounts of fuel pyrolysis within the flame that drives soot production. Another clear trend is the shift in the location of the peak soot volume fraction from the center to the outer edges of the flame as the fuel fraction is increased. This increase in soot volume fraction and transition to the wings of the flame has been observed in previous experiments in the Yale burner for the given conditions. This phenomenon has been connected to an increased residence time for soot growth by Smooke et al.

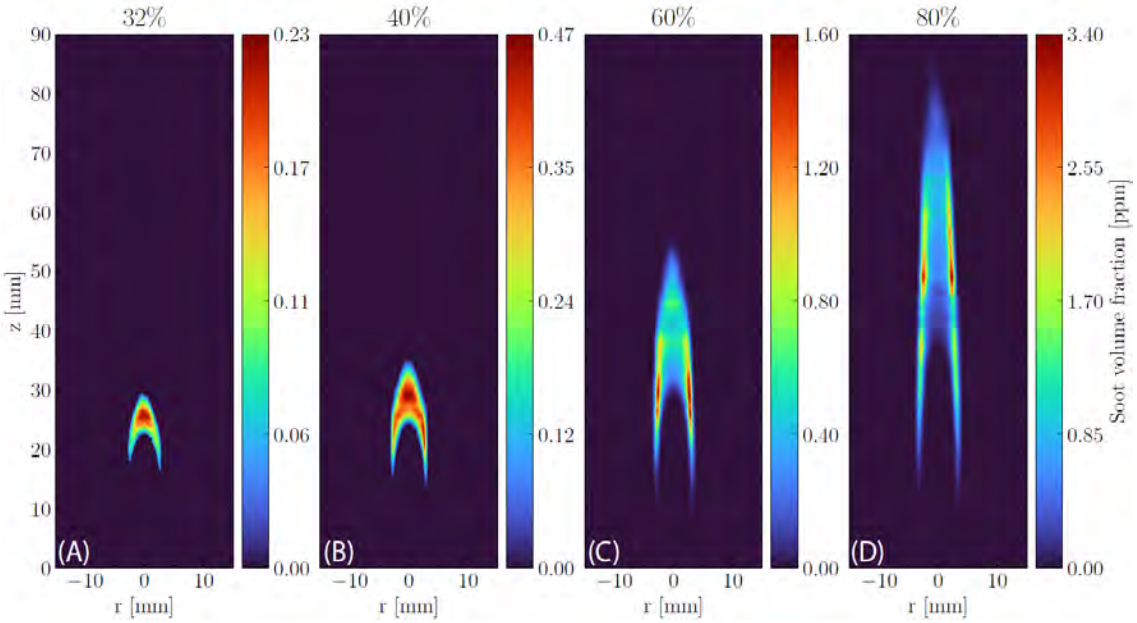

Figure 8. Soot volume fraction comparison with changes in fuel fraction.

LII Measurements in COMRAD

Simultaneous time-integrated LII and broad-band chemiluminescence measurements were taken in the COMRAD experimental facility. A list of the experimental conditions is provided in Table 2. All experiments were operated at a nominal air inlet pressure of 1 MPa, temperature of 755 K, and mass flow rate of 0.585 kg/s. In addition to the inlet conditions, the pressure loss across the injector, pilot to main fuel mass flow split, and pressurization/cooling fluid conditions were constant throughout the experiments. The primary variables explored in the experimentation demonstrated here are the global equivalence ratio (ϕ_{total}) and the type of fuel used (Jet A fuel or HEFA). These conditions were chosen from true engine operating conditions.

Table 2. Test conditions for LII in COMRAD. The parameters listed in the table are inlet pressure, inlet air temperature, total equivalence ratio, pilot to total fuel mass flow fraction, and air mass flow rate. Maximum deviation from target condition is indicated using ±.

Condition	P_3 [MPa]	T_3 [K]	Φ_{total}	Pilot/Total [%]	$\dot{m}_{air}$ [kg/s]
1	1.00 ± 0.04	755 ± 20	0.40 ±0.009	30.0 ± 0.9	0.585 ± 0.006
2			0.45 ± 0.021		
3			0.50 ± 0.005		
4			0.55 ± 0.006		
5			0.60 ± 0.013		

A fluence curve was developed for the high-pressure flame using the same method described above or the Yale burner. These measurements were intended to inform the correct laser power operation to reach the sublimation threshold. The results of these measurements are included in Figure 9. All measurements were taken at Condition 5 using Jet A as the fuel.

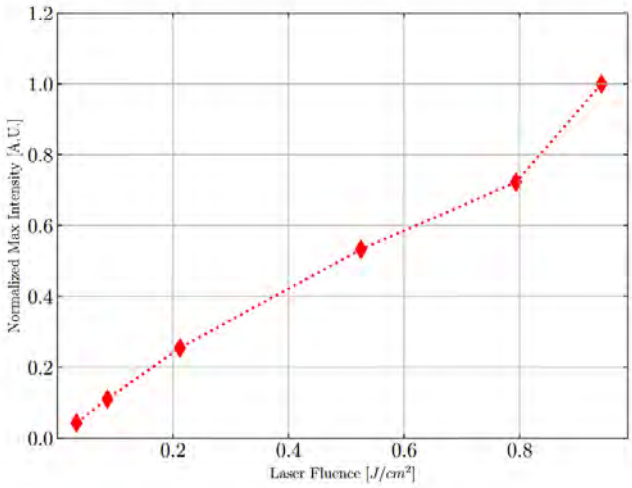

Figure 9. High-pressure normalized fluence curve at condition 5.

The fluence curve is assumed to be the same for liquid fuels because the optical characteristics of liquid fuels are similar. In the current configuration, ∽0.95 J/cm^2 was the greatest achieved laser fluence. Data from McGrath et al. (2024) conducted in a swirl-stabilized Jet A fueled combustor at 0.41 MPa had a peak of LII intensity at 0.24 J/cm^2. The lack of a peak or plateau at this fluence indicates a dependence on chamber pressure affecting the required laser fluence to vaporize soot. This agrees with the Clausius-Clapeyron relation where an increase in pressure should increase vaporization temperature. This increased temperature also results in a higher LII signal output at the detection wavelength due to Planck's law. This additional LII signal output is beneficial for the distinction of soot from background irradiance. While the sublimation threshold was not reached for this set of experimental data, all conditions were run at a constant fluence of 0.545 J/cm^2 to compare qualitative soot quantities in the flames.

An example of single-shot background subtracted LII signals in the Jet A fuel flame with an equivalence ratio of 0.6 can be seen in Figure 10. The t = 0 ms is associated with the first laser shot that entered the test article after the camera was triggered. The time between these images is much greater than the residence times of the combustor. Therefore, these images are not representative of the evolution of the soot within the combustor and instead demonstrate "instantaneous" soot pockets. This behavior of pocket development is congruent with expected soot development in a turbulent liquid-fueled flame. The soot develops in locally rich regions and then processes down the combustor until turbulence introduces lean mixtures to the pocket where the soot can then be consumed.

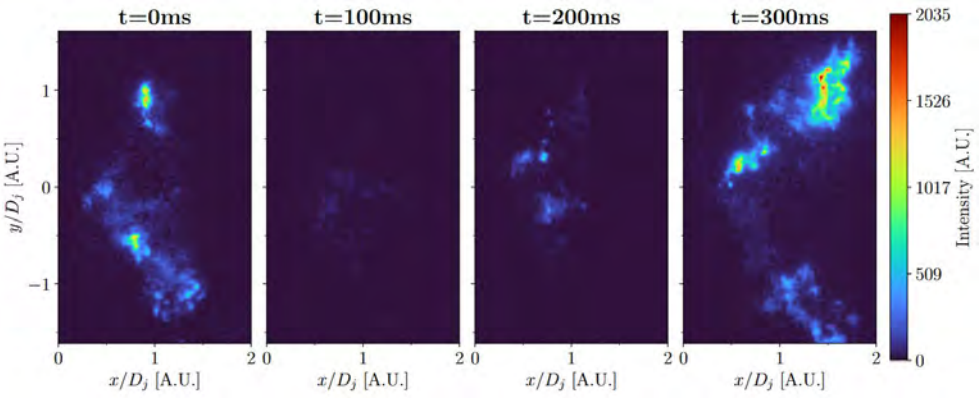

Figure 10. Background subtracted LII images in a Jet A fueled flame at Condition 5

To determine the locations of the highest soot population in the flame, instantaneous soot images are averaged over a set of greater than 500 images. These averaged images are provided in Figure 11 for both Jet A fuel and HEFA-fueled conditions. The HEFA-fueled flame had a much lower soot content than the same condition using Jet A fuel. Specifically, the peak averaged LII signals of the Jet A fuel cases are greater than nine times that of the peaks in the corresponding HEFA cases. One of the major differences between the chemical composition of these two fuels is the presence of single-ring aromatics. The Jet A fuel used during testing was measured to be 17.2% aromatic hydrocarbons by volume. The drastic difference in soot production between these two cases emphasizes just how critical these aromatics are in the production of soot at aircraft-relevant conditions.

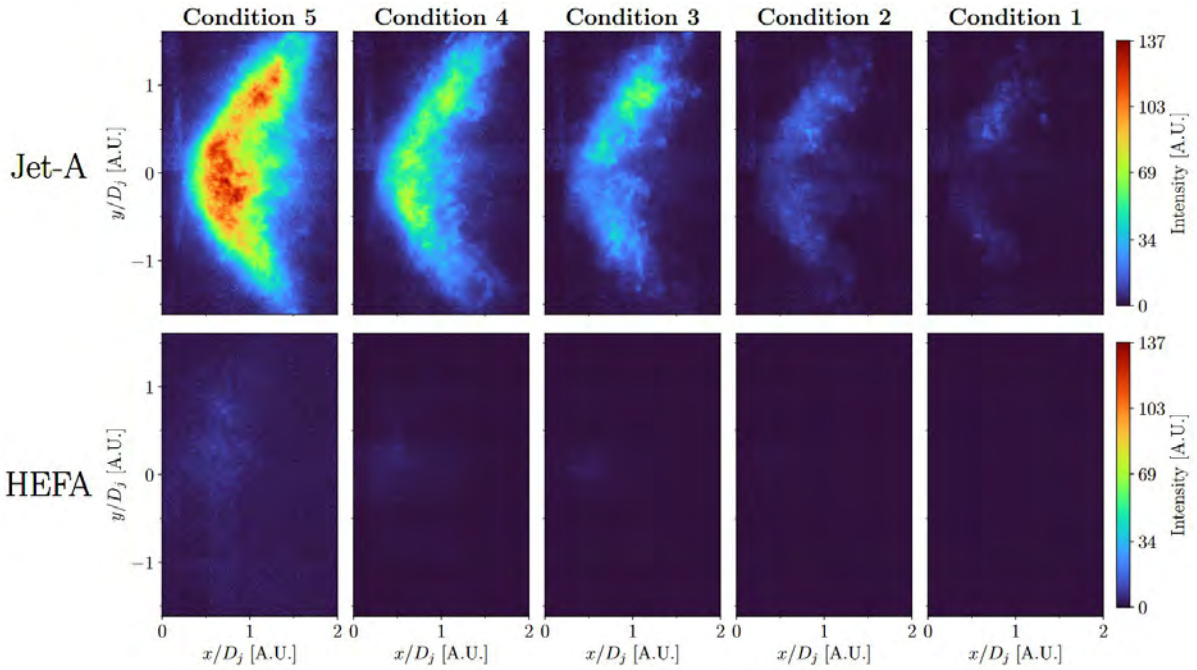

Figure 11. Averaged LII signal for all condtions. Top images are Jet A fueled where the bottom are HEFA. Φ is decreasing from left to right.

As the equivalence ratio decreases the location of peak soot does not change. Both the Jet A fuel and HEFA flames have the most soot in the central recirculation zone (CRZ). There are two locations within this CRZ where hot products may be introduced to reactants (thus inducing pyrolysis) and then are caught in a vortex increasing the resonance time and lifetime of soot in the flame before consumption due to oxidation. These locations are approximately: x/D*j* = 0.5; y/D*j* = -.25 and x/D*j* = 0.75; y/D*j* = 0.75. Further experimentation at conditions with PIV data is required to gain a true understanding of correlations between the flame structure and soot development.

By summing the signal along the columns, an axial distribution of the LII signal can be developed across conditions. Figure 12 shows both these values: (A) normalized to the highest signal count across all averaged Jet A fuel conditions and (B) normalized to the peak value in each one of the conditions. This same plot was produced for the HEFA conditions, but the general shape is similar and thus conclusions that could be drawn from it are identical. Figure 12A shows a clear decrease in the total amount of soot for flames with lower equivalence ratios. This agrees with the principles of soot inception and experimental results from pre-mixed Jet A fuel flames. Additionally, Figure 12B shows that along with this decrease in the amount of soot, the soot is also consumed further upstream in flames of lower equivalence ratio. The consumption of soot closer to the injector benefits the aircraft's operation and longevity because it reduces the chance of soot deposition on the turbine blades.

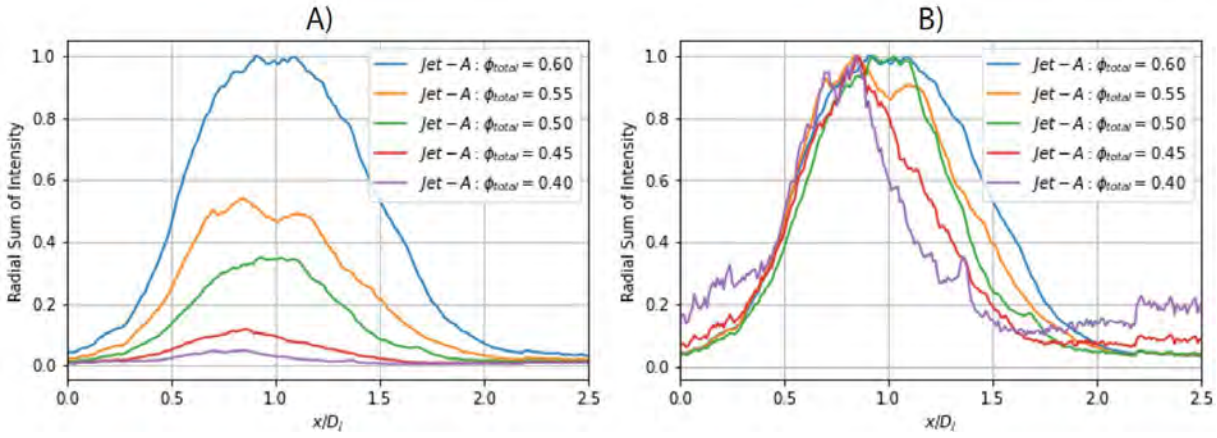

Figure 12. Axial distribution of soot in Jet A fuel flame.

Based on our previous work measuring emissions during this project, one of the counter-intuitive findings from this study was an increase in unburnt hydrocarbons with a decrease in equivalence ratio. The results of this experiment make it clear that unburnt hydrocarbons cannot be broadly correlated with soot volume fraction within the flame region.

Milestones

- Completed the full-scale facility reconfiguration in the test cell housing this experiment allowing for the continued operation of the COMRAD test rig.
- Applied the previously developed LII system for the measurement of soot formation and oxidation processes in the combustion zone to COMRAD. Measurements were taken in the combustor utilizing Jet A fuel and synthetic aviation fuel (SAF) (World Energy HEFA) at a variety of equivalence ratios.
- Procured synthetic aromatic kerosene (SAK) for testing in COMRAD. This SAK will be mixed into synthetic paraffinic kerosenes (SPK) to match the aromatic content.

Major Accomplishments

- Continued our development of laser-induced incandescence for determining soot levels in our combustion flow field.
- Applied the diagnostic to a lab-scale co-flow diffusion flame before being applied to the gas turbine combustor.
- Testing in COMRAD was performed with Jet A fuel and SAF (World Energy HEFA) for a range of equivalence ratios at a pressure of 1.0 MPa with LII measurements.

Publications

Peer-Reviewed Journal Publications

Philo, J. J., Shahin, T. T., McDonald, C. T., Gejji, R. M., Lucht, R. P., & Slabaugh, C. D. (2023). Effect of fuel temperature on the structure of a high-pressure liquid-fueled swirl flame, *Fuel, 354*. 129142. https://doi.org/10.1016/j.fuel.2023.129142

McDonald, C. T., Shahin, T. T., Philo, J. J., Gejji, R. M., Fish, D. D., Slabaugh, C. D., & Lucht, R. P. (2025). Emissions measurements in a liquid-fueled aviation gas turbine combustor with heated fuels. *ASME Journal of Engineering for Gas Turbines and Power, to be submitted.*

Hodge, A. J., Shahin, T. T., Gejji, R. M., Philo, J. J., Lucht, R. P., & Slabaugh, C. D. (2025). Fuel temperature effects on combustion stability of a high-pressure liquid-fueled swirl flame. *Journal of Propulsion and Power, 41*(1), 53-63. https://doi.org/10.2514/1.B39592

Published Conference Proceedings

McDonald, C. T., Philo, J. J., Shahin, T. T., Gejji, R., Slabaugh, C. D., & Lucht, R. P. (2021, August 9). *Effect of fuel temperature on emissions and structure of a swirl-stabilized flame* [Conference presentation]. AIAA Propulsion and Energy 2021 Forum, virtual. https://doi.org/10.2514/6.2021-3480

Hodge, A., Shahin, T., McLean, T., Gejji, R., Lucht, R., & Slabaugh, C. (2024, January 8-12). *Fuel temperature effects on combustion stability of a high-pressure liquid-fueled swirl flame* [Conference presentation]. AIAA SciTech 2024 Forum, Orlando, Florida. https://doi.org/10.2514/6.2024-1241

McLean, T. N., Koenig, K. C., Murdock, B. K., Shahin, T. T., Hodge, A. J., Gejji, R. M., Slabaugh, C. D., & Lucht, R. P. (2025, January 6-10). *Laser-induced incandescence measurements in a high-pressure swirl-stabilized flame* [Conference presentation]. AIAA SciTech 2025 Forum, Orlando, Florida. https://doi.org/10.2514/6.2025-1580

Outreach Efforts

None.

Awards

None.

Student Involvement

Three PhD students (Tristan Shahin, Ben Murdock, and Zander Hodge) and one master of science (MS) student (Keaton Koenig) are currently working on the project. John Philo graduated in March 2022 with his PhD after working on the project and is currently employed at Blue Origin. Colin McDonald graduated in September 2022 with his MS degree and accepted a position with Astra (Merced, California), where he is responsible for setting up a new rocket engine test facility. Thomas McLean graduated in May 2024 with his MS degree after working on the project and is currently attending U.S. Air Force Flight School.

The project provides outstanding research experiences for the graduate students, including the design of system components for, and the operation of, a sophisticated aviation gas turbine combustion test rig, as well as application of advanced laser diagnostic methods for measurements in this test rig. As noted above, the graduate students have been responsible for designing system components, such as the fuel heating system, and for executing test operations.

Plans for Next Period

The focus for the next period of this project will be a detailed comparison of a selected SAF with a well-characterized petroleum-based fuel, Jet A or fuel A2 from the National Jet Fuel Combustion Program. The SAF will be a mixture of SPK and SAK, and the composition will be selected in consultation with other FAA ASCENT researchers and our collaborators at GE Aerospace. The nominal SAF composition is expected to be 92% SPK (World Energy HEFA) and 8% SAK (single-ring aromatic compounds from Virent®). SAFs with SAK contents as low as 4% and as high as 30% will also be investigated, depending on the availability of supplies from Virent. We may also explore petroleum-based single-ring aromatic compounds if we cannot obtain enough SAK from Virent.

We plan to expand our operational test matrix to include conditions of significant interest to GE Aerospace. Thus far in our test program, the relative equivalence ratios for the pilot and main have been fixed. GE Aerospace is interested in expanding the test matrix to investigate the effect of varying equivalence ratios in the main and pilot on hot fuel effects, especially as it relates to nitrogen oxides (NO_x) formation. Along these same lines, pilot-only operation is of significant interest. We will also explore the effects of fuel heating for rich dome operation, implemented by supplying sufficient fuel in the streams to create a globally rich mixture.

Additionally, LII will be used to further investigate soot formation for rich dome operation and expand on the measurements taken in lean dome operation. Additional funding will allow us to expand the operational test matrix to include conditions with higher pilot to main fuel, globally rich conditions, and further fuel composition blends. The LII measurements will provide valuable information of the spatial locations for particulate formation in the combustor flow field for engines using both conventional Jet A fuel and a variety of SAFs. We are also interested in both nonvolatile and volatile particulate formation. GE Aerospace has shown considerable interest in the types and number of particulates that are in the combustor exhaust. Further experimentation with differing laser sheet location and increased laser repetition rate are both of considerable interest to gain further special and temporal resolution. The effects of passing through the turbine on particulate emissions are not well understood. In addition to LII, our previous diagnostic methods of PIV and OH PLIF will be applied to probe the flow field for selected operating conditions.

® Virent is a registered trademark of Virent, Inc., Madison, Wisconsin.

References

McGrath, R., Juergensmeyer, J., Bond, R., Bugay, E., Wehe, S., Wu, D., Steinberg, A., Sun, W., & Mazumdar, Y. C. (2024). Planar laser-induced incandescence for the study of soot production in a multi-sector RQL Jet A combustor. *Applications in Energy and Combustion Science*, *18*, 100269. doi:10.1016/j.jaecs.2024.100269

Satija, A., Chang, Z., Lowe, A., Thomas, L. M., Masri, A., & Lucht, R. P. (2019). CARS thermometry in laminar sooting ethylene-air co-flow diffusion flames with nitrogen dilution. *Combustion and Flame, 208*, 37-44. doi: 10.1016/j.combustflame.2019.06.025

Smooke, M. D., Long, M. D., Connelly, B. C., Colket, M. B., & Hall, R. J. (2005). Soot formation in laminar diffusion flames, *Combustion and Flame, 143*, 613–628. doi: 10.1016/j.combustflame.2005.08.028

Snelling, D. R., Smallwood, G. J., Liu, F., Gülder, O. L., & Bachalo, W. D. (2005). A calibration independent laser-induced incandescence technique for soot measurement by detecting absolute light intensity, *Applied Optics, 44*, 6773–6785. doi:10.1364/AO.44.006773

Project 068 Combustor Wall Cooling with Dirt Mitigation

The Pennsylvania State University

Project Lead Investigator

Reid A. Berdanier
Associate Professor
Department of Mechanical Engineering
The Pennsylvania State University
NARCO Building, CATO Park, Room 148
3127 Research Drive
State College, PA. 16801
(814) 863-3972
rberdanier@psu.edu

University Participants

The Pennsylvania State University (PSU)

- P.I.s: Prof. Karen Thole, Prof. Reid A. Berdanier, Dr. Michael Barringer, Prof. Stephen Lynch
- FAA Award Number: 13-C-AJFE-PSU-057
- Period of Performance: June 5, 2020, to September 30, 2025
- Tasks:
  1. Manufacturing and testing of combustor liner cooling concepts with small coupons
  2. Testing of scaled models of optimal cooling concepts
  3. Profile simulator for the Steady Thermal Aero Research Turbine (START)

Project Funding Level

For the entire 4-year effort ASCENT Project 068 received $1,250,000 Federal Aviation Administration (FAA) funding, and matching funds of $1,250,000 were provided by Pratt & Whitney.®

Investigation Team

Prof. Reid A. Berdanier (P.I.), Management, reporting, and oversight of all technical tasks
Prof. Karen A. Thole (co-P.I.), Management, reporting, and oversight of all technical tasks
Assoc. Prof. Stephen Lynch (co-P.I.), Management, reporting, and oversight of Tasks 1–3
Assoc. Res. Prof. Michael Barringer (research advisor), Task 3
Scott Fishbone (project manager), Tasks 1–3
Tom Houck (project manager), Tasks 1–3
Kyle McFerran (graduate student), Tasks 1 and 2
Chad Schaeffer (graduate student), Task 3

Project Overview

A critical issue related to the current operation of gas turbines is the ingestion of dirt and other fine particles that lead to dirt buildup and reduced cooling of hot section components, such as the liner walls of the combustion chamber. With increasing need to fly in dirty environments, the criticality of operations in dirty environments is increasing. Modern gas turbine engines typically use a double-walled combustor liner with impingement and effusion cooling technologies, whereby impingement cooling enhances the backside internal cooling, and effusion cooling creates a protective film of coolant along the external liner walls. Dirt accumulation on the internal and external surfaces severely diminishes the heat transfer capability of these cooling designs. This study also investigates the development of a combustor profile simulator

® Pratt & Whitney is a registered trademark of RTX Corporation, Farmington, Connecticut.

upstream of the Steady Thermal Aero Research Turbine (START) test turbine. Combustor profiles affect turbine performance and durability. As combustor designs evolve, particularly the liner cooling technologies, understanding the impacts on the turbine is important. This study investigates practical designs applied to combustor walls to decrease dirt accumulation and also explores the development of a profile simulator that can replicate relevant temperature and pressure profiles upstream of a test turbine.

Task 2 – Testing of Scaled Models of Optimal Cooling Concepts

The Pennsylvania State University

Objective

The objective of this task is to produce an effective cooling design for combustor walls that is insensitive to dirt accumulation at existing or lower coolant flow rates. Various parameters such as dirt deposition, flow behavior, and heat transfer effectiveness will be investigated and quantified to compare the efficiency of candidate designs. Improved understanding of the underlying reasons for dirt sensitivity and deposition behavior is also being sought. During this past year, the ASCENT Project 068 team took two primary approaches to the problem: (1) identify the impact of dirt deposition on the cooling performance of a typical double-wall combustor liner and (2) identify a novel geometry to replace the double-wall liner design with a triple-wall combustor liner.

Research Approach

Background

The project focuses on the impacts of ingestion of dirt and other fine particulate matter in gas turbine engines. These particles are known to block the cooling holes and passages needed to effectively cool combustion chamber walls. Gas turbine engines often use double-walled combustor liners comprising impingement and effusion cooling plates (Figure 1). The impingement plate enhances backside internal cooling, and the effusion plate creates a protective film of coolant along the external liner walls. As particulate matter accumulates on these plates, the heat transfer performance severely decreases, thus ultimately leading to component failure.

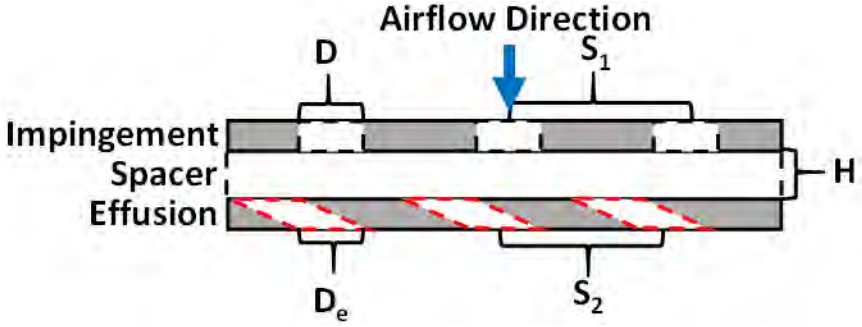

Figure 1. Schematic of double-walled combustor liner geometry.

A coupon design of a double-wall combustor liner consisting of an impingement, spacer, and effusion plate is shown in Figure 2, along with the testing facility in which the coupons are installed. The impingement plate has straight holes resulting in high-velocity jets that impinge on the backside of the effusion plate, which is exposed to the hot main gas path. The spacer plate creates a small controllable gap between the impingement and effusion plates. The effusion plate uses cooling holes angled at 30° to create a film effect along the external wall exposed to the hot combustion gases.

The goal of this research is to determine the impact of dirt deposition on the ability to cool the double wall containing the hot combustion gases in the gas turbine engine. To understand the effects of dirt deposition on the combustor cooling, heat transfer coefficients on all four surfaces (top and bottom of both the impingement and effusion plates) need to be calculated. A three-case proposal utilizing thermal resistive networks can be used to measure these respective heat transfer coefficients. Case 2, shown in Figure 3, demonstrates the resistive network for calculating the heat transfer coefficient on the bottom (cold) side of the effusion plate. This past year, work has been based on this specific case. A more in-depth description of the heat transfer experimental methodology is provided in last year's annual report.

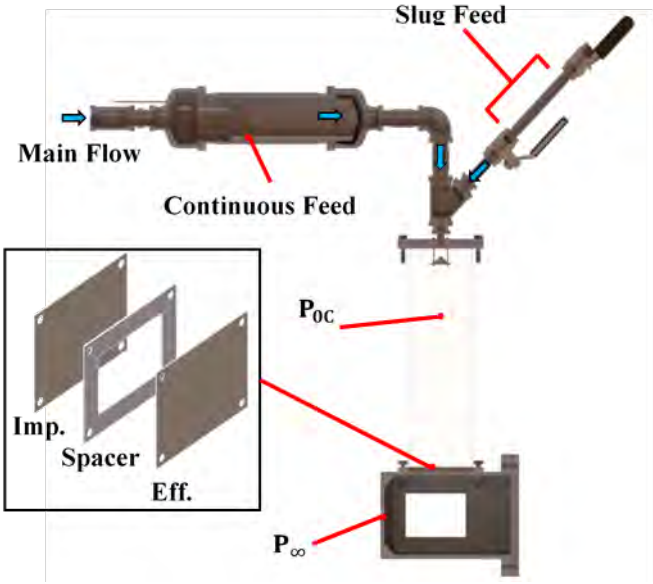

Figure 2. Schematic of the double-walled combustor liner configuration.

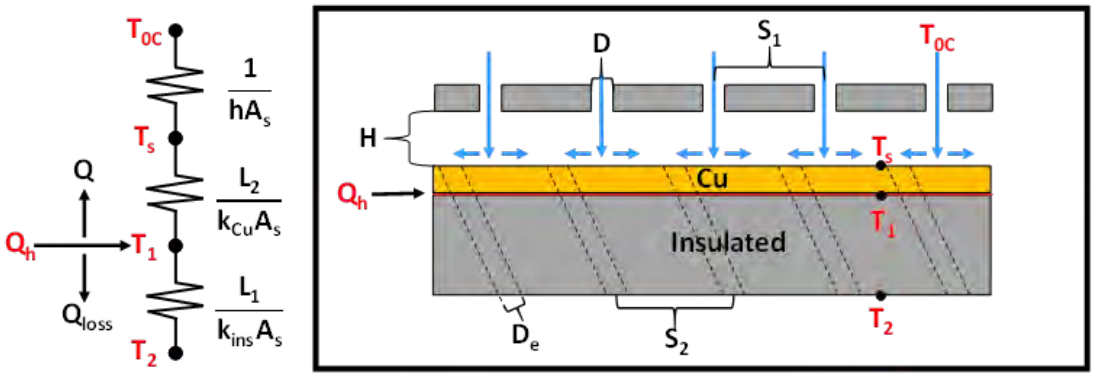

Figure 3. Thermal resistive network (left) used to calculate the convective heat transfer coefficient on the impinging side of an effusion plate. Next to the resistive network is the heater coupon (right) with dimensions used for heat transfer testing. Experimentally measured values are shown in red.

The three cases allow for calculation of the four heat transfer coefficients for dirt and no-dirt tests. In each case, one of the cooling plates is made of insulation, whereas the other plate is made of copper, an electric heater, and insulation. For the resistive network in Figure 3, the composite coupon made up the effusion plate. Of note, testing last year was performed with an effusion plate without effusion holes. Effusion holes were not evaluated because literature data were available for only plates without effusion holes. Five thermocouples were implemented throughout the composite coupon to measure the appropriate temperatures in the thermal resistive network. Ultimately, these thermocouple measurements were used to solve the heat transfer coefficient (h_1) in Equation 1.

$$h_1 = \frac{Q}{A_s(T_s - T_{0C})} \qquad \text{(Eq. 1)}$$

Impacts of Dirt Deposition on a Double-Wall Liner Design

Heat transfer tests are performed using the dirt test rig shown in Figure 2. Last year, convective heat transfer results were shown for a no-effusion heater coupon for several height to diameter (H/D) ratios, where this ratio was adjusted by changing the spacing between the impingement and effusion plates. This year, heat transfer tests were performed on an effusion plate with effusion holes, shown in Figure 4, over a range of H/D values between 3 < H/D < 10. An array of 5 x 11 cooling holes was used for both the impingement and effusion plates, with effusion holes being angled at 30° with respect to the horizontal surface.

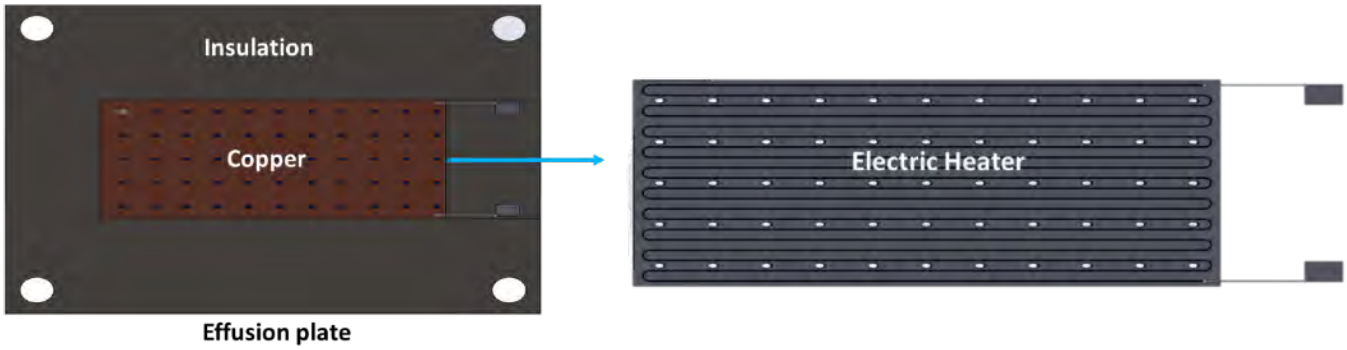

Figure 4. Heater composite consisting of insulation, an electric heater, and copper used for heat transfer testing of the effusion hole test plate.

Two different injection amounts were evaluated in this study, which led to two different testing conditions: (1) matched deposition and (2) matched supply. For the matched deposition condition, a mass of dirt was injected that resulted in 0.175 ± 0.015 g of dirt accumulation on the test plate surface. A target deposition mass of 0.175 g was chosen because prior dirt tests in the lab had similar deposition masses. The mass of injected dirt needed to achieve this matched deposition varied between 2 to 4.8 g for different mass flow rates and plate-to-plate spacings. In contrast, a constant 2 g of dirt was injected for the matched supply tests, which resulted in deposition masses between 0.05 to 0.175 g on the test plate surface. Overall, the two test conditions were conducted to isolate the effects of deposition mass and injection mass on the heat transfer coefficients (HTC).

For the heat transfer testing of the effusion plate without cooling holes, a constant Reynolds number (Re_d) was maintained throughout the dirt injection process. In contrast, a constant pressure ratio (PR) was maintained during dirt injection for the heat transfer testing on the effusion-cooled plate. Pressure taps located upstream of the impingement plate and downstream of the effusion plate were used to monitor the PR across the double-walled liner with Equation 1. A PR range of 1.01 < PR < 1.1 was evaluated for the effusion-cooled plate.

$$PR = \frac{P_{0C}}{P_{\infty}} \quad \text{(Eq. 2)}$$

As dirt was injected into the system, the upstream mass flow rate (and hence pressure) decreased, because dirt blocked the impingement and effusion cooling holes, thus reducing the overall flow area. The flow parameter (FP), shown in Equation 3, was monitored during testing to quantify these blockage levels caused by the deposition.

$$FP = \frac{4\dot{m}\sqrt{RT_{0C}}}{\pi P_{0C} N D_i^2} \quad \text{(Eq. 3)}$$

With the FP being directly related to the mass flow rate, a decrease in the mass flow rate resulting from the blockage of cooling holes leads to a reduction in FP (RFP). An increase in flow blockage is quantified by an increase in the RFP, which is defined in Equation 4.

$$RFP = \frac{FP_{clean} - FP_{dirty}}{FP_{clean}} \times 100 \quad \text{(Eq. 4)}$$

Heat transfer coefficients for the dirty plate were less than those for the clean plate for all tests conducted in this study. The addition of dirt on the test plate surface had a twofold effect on the heat transfer. First, the deposition functioned as an extra layer of insulation which shielded the test plate from the cooling air. Second, the deposition structures that formed impacted the flow field of the impinging jets, which also led to reductions in cooling. Augmentations that compared Nusselt numbers (Nu) for the dirty (Nu_d) and clean (Nu_0) test plates, as defined in Equation 5, gave insight into the negative effects the deposition had on cooling within the double-walled liners. The augmentation is a positive number because the addition of dirt always led to reductions in the HTC (and hence Nusselt number). This reduction in the HTC is representative of a cooling reduction on the target plate surface. As the reductions in cooling from dirt accumulation increased, the augmentation increased.

$$\text{Augmentation} = \frac{Nu_0 - Nu_d}{Nu_0} * 100 = \left.\frac{\Delta Nu}{Nu_0}\right|_{Re_d,PR} \quad \text{(Eq. 5)}$$

The augmentations compare reductions in Nusselt numbers at a constant Red or at a constant PR. The results of this current study are the basis of a new literature paper that was written and submitted to the 2024 Turbo Expo Conference (McFerran et al., 2025). For the effusion hole plate, this means that the dirty HTC was compared to the clean HTC at the dirty Re_d for the Re_d-based augmentation and at the clean Re_d for the PR-based augmentation. In Figure 5, an example Re_d- and PR-based augmentation for the effusion hole plate is shown for a PR = 1.045. There is a reduction in the flow for the same pressure ratio due to blockage where Re_d decreased from Re_d = 1800 (clean) to 1200 (dirty). The augmentation then compares the dirty Nu at Re_d = 1200 to the clean Nu predicted by the clean trendline at Re_d = 1200 and 1800 for the Re_d- and PR-based augmentation, respectively. Testing performed on the no-effusion plate maintained a constant Re_d so only Re_d-based augmentations could be made between the dirty and clean HTCs which is also shown in Figure 5.

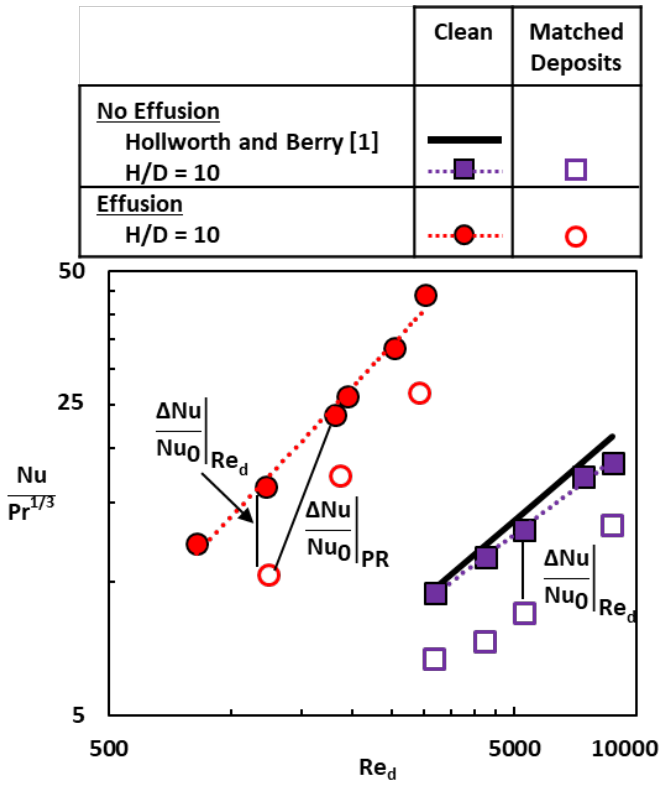

Figure 5. Heat transfer coefficient in terms of a Nusselt number as a function of Red for both test plates at a H/D = 10. Dirty heat transfer measurements have 0.175 g of deposition on the cold-side effusion plate surface. Example augmentations are shown for each test plate.

Heat transfer results in terms of a Nusselt number are plotted in Figure 6 as a function of Reynolds number (Re_d) for the effusion hole plate over a range of H/D from 3 < H/D < 10 and Re_d from 800 < Re_d < 3500. This Re_d range corresponds to the range of pressure ratios evaluated which were between 1.01 < PR < 1.1. Heat transfer coefficients for the clean and dirty plates are shown in Figure 6, where dirty tests had 0.175 g of dirt deposition on the effusion plate surface. The heat transfer results for the no effusion plate are also shown for 10 < H/D < 15 for a Re_d range of 3200 < H/D < 8400. The range of Re_d for the no-effusion plate was chosen to match the literature, and it differed from the Re_d range for the effusion hole plate because the effusion hole plate was designed to match typical combustor liner pressure ratios. Heat transfer coefficients for the effusion hole plate are 300% higher than those for the no-effusion plate. A higher heat transfer coefficient indicates better cooling, which would be expected for the effusion hole plate because of the cooling that occurs through the coupon from the effusion holes. These results verified that having effusion holes led to enhanced cooling on the cold-side effusion plate surface. The addition of effusion holes led to improved internal cooling of the effusion plate. Additionally, less crossflow resulted on the cold-side surface of the effusion hole plate compared to the no-effusion plate because air exited through the effusion holes and not out of the sides. Increasing the crossflow reduced the strength of the impinging jets which diminished the cooling for the no-effusion plate.

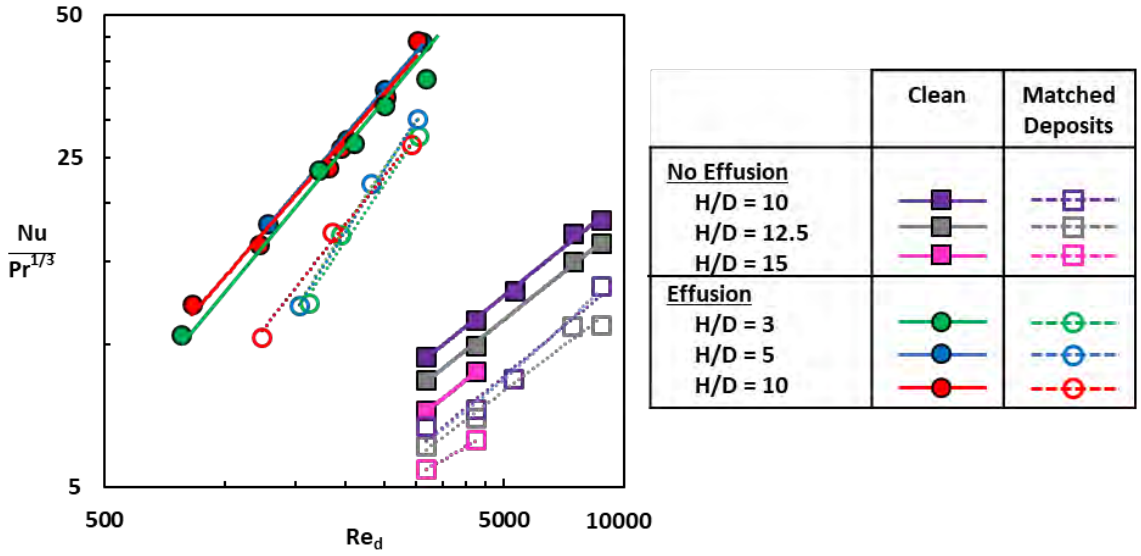

Figure 6. Heat transfer results in terms of a Nusselt number as a function of Reynolds number for both the effusion plate without cooling holes and the effusion-cooled plate.

For all tests performed on the no-effusion plate, an increase in the plate-to-plate spacing resulted in lower HTCs, which means less cooling. In contrast, the effusion hole plate showed no differences in HTCs for an increase in plate to plate spacing. These results can be explained by the localized flowfield effects of heat transfer that resulted from the jet flow (Gardon & Arkfirit, 1966; Gardon & Arkfirit, 1965; Choi & Kim, 2022). As the impinging jet traveled towards the target surface, a momentum exchange with the surrounding fluid leads to development of a shear layer that expands as the plate-to-plate spacing increases. This shear layer leads to a decrease in the centerline jet velocity. As the plate-to-plate spacing increases, the diminishing centerline velocity combined with a widening of the jet leads to a decreasing HTC at the stagnation point (Gardon & Arkfirit, 1966; Choi & Kim, 2022). As shown in the literature for up to H/D of 8, there is an increase in the mixing of the jet with the surrounding fluid from increased turbulence, which leads to increased heat transfer in the jet stagnation region (Gardon & Arkfirit, 1966; Choi & Kim, 2022). This increase in heat transfer from turbulence dominates the decrease in heat transfer from diminishing centerline velocities and widening of the impinging jets as H/D increases to 8. Gardon and Akfirat (1965) showed that beyond H/D of 8, the turbulence intensity (TI) did not continue to increase and that the decreasing jet velocity and increasing jet width began to dominate, decreasing the stagnation HTC. The data shown in Figure 6 support their finding on why HTCs for the no-effusion plate decreased as H/D increased beyond 10.

Another important finding by previous studies (Gardon & Arkfirit, 1966; Choi & Kim, 2022) is that heat transfer performance at H/D less than 10 was affected by the formation of a secondary peak in heat transfer radially out from the stagnation region due to the boundary layer transitioning from laminar to turbulence. As H/D decreased from 10, which encompasses the 3 < H/D < 10 range evaluated for the effusion hole plate, these secondary spikes in heat transfer resulted in increased HTCs radially out from the stagnation region. These physics explain the average HTC trends for an increasing H/D from 3 to 10, where the increase in stagnation zone heat transfer and decrease in lateral downstream heat transfer led to equivalent average heat transfer coefficients for the changing H/D on the effusion hole plate.
A computational study performed by Choi and Kim (2022) also showed that average HTCs were constant over a H/D range of 1-10 for an effusion hole plate.

The accumulation of dirt on both test plates led to a reduction in the HTC for all plate-to-plate spacings as shown in Figure 6. Re_d- and PR-based augmentation results for both test plates are shown in Figure 7 over several Re_d and PRs. It is important to note the magnitude of these augmentations range between 20-55%, which signifies the highly negative impact dirt has on cooling performance in a double-walled liner. As a reminder, a higher augmentation represents a higher reduction in the HTC and hence a higher cooling reduction due to dirt. In Figure 7, the effusion hole plate with a matched supply had an increase in Re_d-based augmentations as the plate-to-plate spacing increased, which shows that the reductions in the HTC from dirt increased as H/D increased.

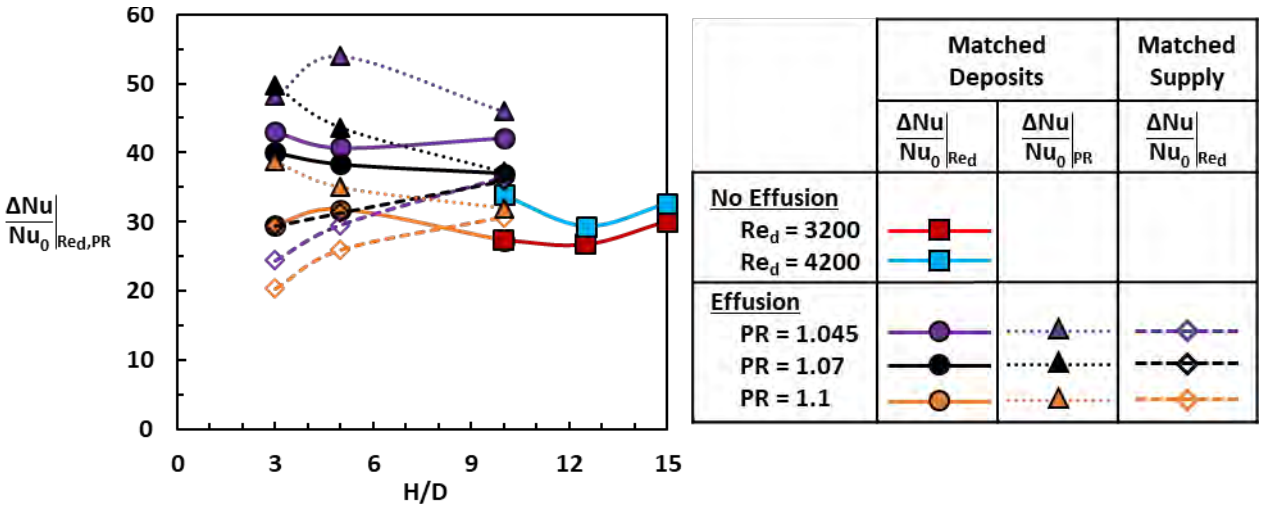

Figure 7. Re_d- and PR-based augmentations comparing the heat transfer coefficient for the clean and dirty plates across a range of H/D for both test plates. For matched deposits, 0.175 g of dirt was on the test plate surface; for matched supply, a total of 2 g of dirt was injected.

For matched deposit cases, both test plates demonstrated a constant Re_d-based augmentation as a function of the H/D ratio. In contrast, PR-based augmentations for matched deposits on the effusion hole plate show that an increase in H/D led to a decrease in cooling reductions. Overall, the PR augmentations, which are more representative of true engine conditions, are higher than all of the Re_d augmentations for a constant H/D. As H/D increased, the difference between the PR- and Re_d-based augmentations decreased. This result has to do with the RFP, which is shown to decrease as H/D increased for the effusion hole plate in Figure 8. As the RFP decreased, the difference between the clean and dirty Re_d also decreased, which would lead to decreased differences between the PR and Re_d-based augmentations.

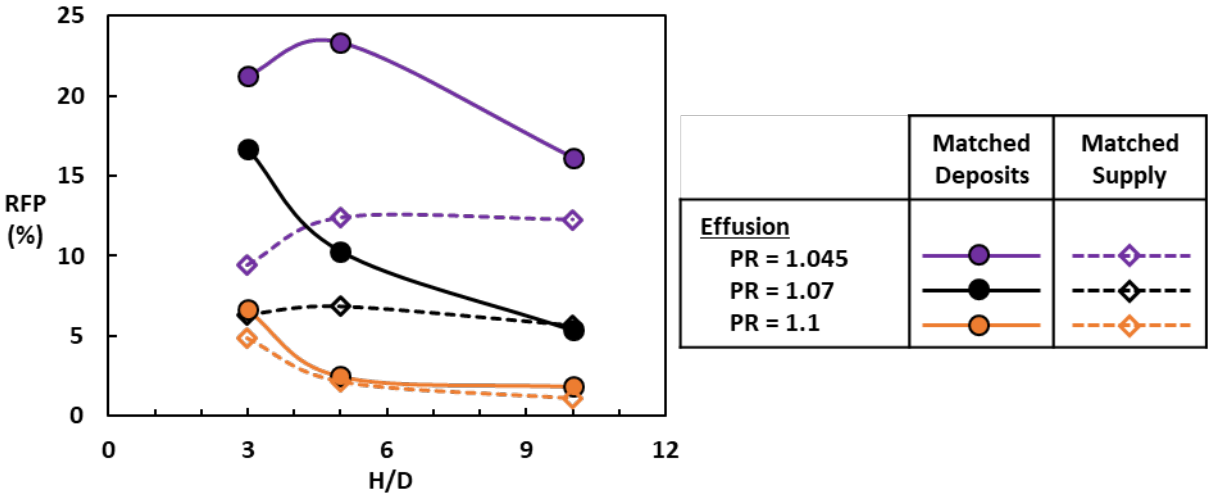

Figure 8. RFP as a function of H/D for the effusion hole plate. For matched deposits, 0.175 g of dirt was on the test plate surface; for matched supply, a total of 2 g of dirt was injected.

For a matched deposition, there was at least a 3% reduction in the RFP as the plate-to-plate spacing increased from 3D to 10D, as shown in Figure 8. The PR-based augmentations in Figure 7 for the effusion hole plate followed similar trends to the RFP trends in Figure 8 for a matched deposit. For a matched supply, the RFP was constant as a function of H/D as shown in Figure 8. Although not plotted, the PR-based augmentation followed a similar trend to this RFP, which demonstrates that RFP is an important predictor of the PR-based augmentations.

Different dirt injection amounts explain the RFP trends observed as a function of H/D. Throughout the testing, the amount of dirt needed to achieve matched deposition amounts decreased as H/D increased, which suggests that dirt was more readily captured on the effusion hole plate surface as the plate-to-plate spacing increased. For example, at a PR of 1.045, the injected mass of dirt needed to reach matched deposits on the effusion hole plate for a H/D of 10 was 2.8 g, but for a H/D of 3, an injection mass of 4.4 g was needed. An explanation for this trend resides in experimental observations made on the back-side impingement plate surface, which showed a decrease in dirt buildup as H/D increased. These observations suggest that as H/D increased, the dirt was less likely to rebound off of the effusion plate surface and stick to the impingement plate, leading to more deposition on the test plate surface.

With the injection mass decreasing for matched deposits as H/D increased, it is no surprise that the RFP also decreased in Figure 8. From the standpoint of flow blockage, it would be expected that a decrease in RFP would correlate with a decrease in the Re_d-based augmentation. However, Figure 7 showed that the Re_d-based augmentation was constant as a function of H/D for a matched deposit, which contradicts the RFP trends.

Likewise, for the matched supply case, the RFP was constant as a function of H/D as shown in Figure 8, which suggests that plate-to-plate spacing had minimal impact on the RFP. However, the Re_d-based augmentation shown in Figure 7 increased as H/D increased. These results suggest that the deposition structures must be considered to fully understand the cooling reductions.

The deposition patterns for different H/Ds are shown in Figure 9 for both test plates with a matched deposit. For the no-effusion plate, as the plate-to-plate distance increased from 10D to 15D, the conical mound region became flatter with decreasing peak heights. These results align with the flow field physics of the jet widening as the H/D increased which led to wider, flatter deposition structures (Fallon et al., 2023).

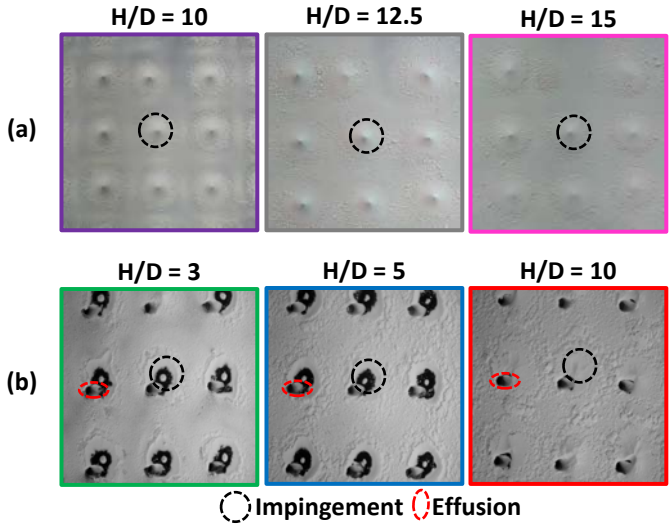

Figure 9. Observed deposition patterns across a H/D range of 3 < H/D < 15 for (a) the no-effusion plate at a Red = 3200 and (b) the effusion hole plate at a PR = 1.045. A black dotted circle is the impingement location, and a red dotted circle is the effusion hole.

For the effusion hole plate, an increase in the plate-to-plate spacing showed an increase in stagnation region deposition. The centerline velocity decreased as H/D increased and, as a result, the decreased velocity led to more deposition in the stagnation region which is clearly shown in Figure 9b. Additionally, a H/D of 3 and 5 for the effusion hole plate showed development of a conical mound in the center of a black ring, which was the exposed test plate. Surrounding this region are dirt thicknesses that have a crater-like topology, which align with the boundary layer regions that transition from laminar to turbulent flow.

Three-dimensional scanning of the test plates provided a quantitative analysis of deposition thicknesses for both test plates over a range of plate-to-plate spacings. In Figure 10, laterally averaged dirt thicknesses for the effusion hole plate at a PR = 1.045 with matched deposition show the trends discussed previously for the observed deposition, specifically those regarding the stagnation region peak heights. It is important to note that the lateral average plots are not the actual deposition heights but rather a line average. For example, the stagnation region peak averaged with an area of no dirt buildup will result in a peak that is half of the stagnation peak height.

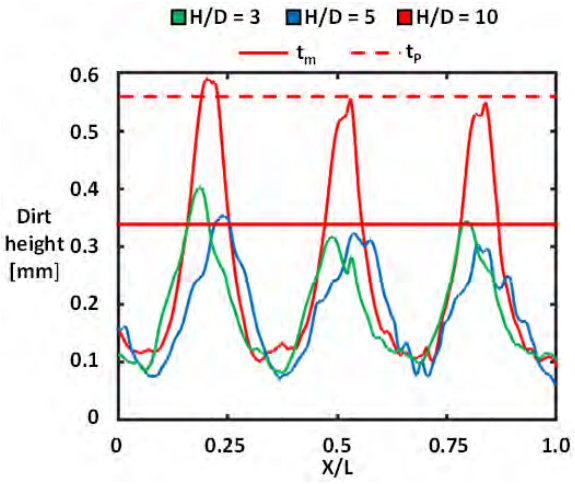

Figure 10. Laterally averaged dirt heights for the effusion hole plate at a PR of 1.045 for 3 < H/D < 15. The mean dirt thickness (tm) and the peak dirt thickness (tb) are shown for the effusion hole plate at H/D = 10.

For the no-effusion plate, it was observed that as H/D increased, the peak height decreased, which was a result of the jet width increasing. In contrast, the peak height increased as H/D was increased from 3 to 10 for the effusion hole plate, which is shown in Figure 10. This difference was a result of the decreasing centerline velocity that occurred over this H/D range. Cooling reductions, shown in Figure 7, were more severe for the effusion hole plate with a matched supply as H/D increased, which correlated well with the peak height increasing. The stagnation zone where the conical mounds formed is the region of dominant heat transfer, so if more dirt accumulated in this region, increased augmentations (and hence increased cooling reductions from dirt) would be expected. This result explains why the Re_d-based augmentation (Figure 7) is constant for the matched deposition test as a function of H/D. For an increase in H/D, the beneficial results of a decreasing RFP are countered by the increased deposition in the jet stagnation region. These results demonstrate that in addition to the level of flow blockage, the deposition structures play an important role in the reductions of heat transfer.

Mean (t_m) and peak (t_p) thicknesses were calculated from the lateral averages, as shown for the effusion hole plate at a H/D of 10 in Figure 10. These values were used to calculate an effective heat transfer coefficient that incorporated a uniform layer of dirt having these heights onto the cold-side effusion plate surface, where usage of t_p resulted in the most extreme approximation. This extra layer of dirt adds an insulating effect in the thermal resistive network from Figure 3. Even with this extra conductive layer of thickness, the convection accounted for at least 76%-92% of the total thermal resistance between the heater surface and the impinging free stream across all tests using the peak height thickness, t_p. This quantitative analysis supports the conjecture that the influence of the deposition topology on the impingement flow field is an important factor in the observed reductions on cooling.

Next, the effects of jet Reynolds number on heat transfer rates were analyzed. The convective heat transfer is highly dependent on the impinging Re_d. Referring back to Figure 6, the HTC increased as the Re_d increased for both test plates. Dirt deposition led to cooling reductions, which are shown in terms of a Re_d-based augmentation as a function of Re_d in Figure 11 for both test plates. Augmentation results are presented as a function of Re_d so that comparisons could be made for both test plates. For the no-effusion plate, Re_d-based augmentation results in Figure 11 show that the cooling reductions from dirt have a local maximum as a function of Re_d for a H/D of 10. At this H/D of 10, there is a local maximum of 35% in the augmentation at a Re_d = 5300.

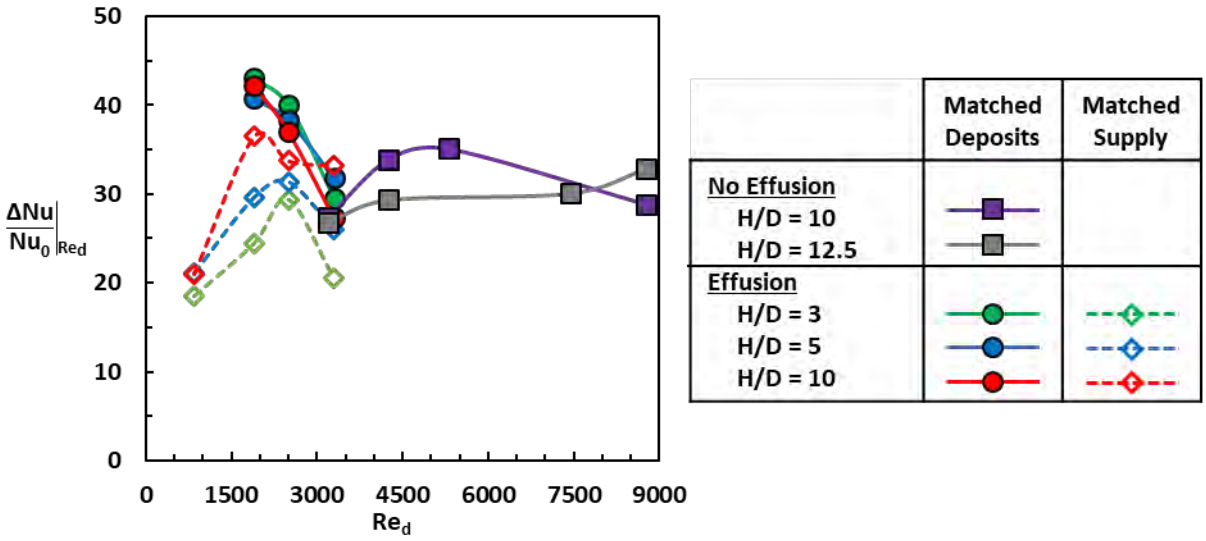

Figure 11. Re_d-based augmentation comparing the heat transfer coefficient for the clean and dirty plates across a range of Re_d for both test plates. For matched deposits, 0.175 g of dirt was on the test plate surface; for matched supply, a total of 2 g of dirt was injected.

Similarly, the effusion hole plate appeared to follow a similar trend, at least for a matched dirt supply condition. Over a Re_d range of 850 < Re_d < 3300, which corresponded with the range of PR from 1.02 < PR < 1.1, the effusion hole plate had a maximum in augmentation at a Re_d between 1800-2500 for all H/D. These augmentation results show that for a given H/D, there was a Re_d that had the most negative effects on cooling.

For a matched deposit condition, data were only obtained for a PR between 1.045-1.1 because the amount of dirt needed to achieve 0.175 g of dirt deposition was unfeasible due to the high RFP. However, for the range of PR evaluated, there was a strong trend showing that as the Re_d increased (and PR increased), the reductions in cooling decreased. PR-based augmentation results are not shown in Figure 11, but followed similar trends as the RFP which are shown in Figure 12.

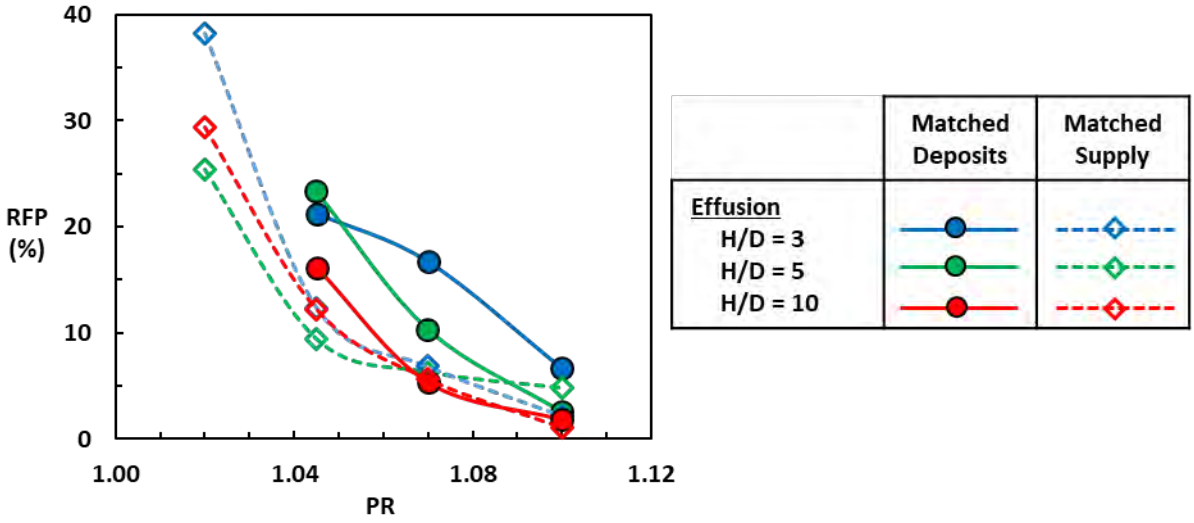

Figure 12. RFP as a function of PR for the effusion hole plate for 3 < H/D < 10. For matched deposits, 0.175 g of dirt was on the test plate surface; for matched supply, a total of 2 g of dirt was injected.

The RFP in Figure 12 shows a strong correlation between increasing PR and decreasing RFP for the effusion hole plate, which shows that as the jet velocity increased, the blockage of the cooling holes also decreased. This result occurred because an increasing flow velocity pushed more dirt through the impingement and effusion holes. Overall, with less blockage occurring as the pressure ratio increased, it is reasonable that the reductions in cooling also decreased because more of the impinging flow could impact the effusion plate surface and properly exit through the cooling holes.

The only exception to this trend occurred as the PR decreased from 1.045 to 1.02 for a matched supply, where an increase in the RFP did not correlate with an increase in the cooling reductions shown in Figure 12. This trend is observed because as the PR was decreased, the amount of dirt buildup on the effusion plate surface decreased, which overcame the effects of an increasing RFP. For example, a PR of 1.02 at a H/D of 3 yielded 0.058 g of deposition on the effusion plate, while a PR of 1.1 yielded a mass of 0.130 g. As the deposition mass decreased, the heat transfer augmentations also decreased because the effects the deposition had on the flow field were less severe. For a given H/D, it is believed that there is a Red value at which these effects of decreasing plate deposition mass begin to dominate the effects of RFP. This is another example demonstrating that flow blockage and the deposition structures both play equally important roles in cooling reductions.

Matched deposit dirt structures are shown for both test plates over several mass flow rates in Figure 13. For both test plates, there was a decrease in the peak height and greater overall spread of dirt as the mass flow increased. For the matched deposit case on the effusion hole plate, the decreasing RFP and decreasing peak heights aligned with a decreasing cooling reduction as the Red increased. As was stated previously, a decreasing deposition thickness in the jet stagnation region led to less severe effects on the HTC because this was the dominant area of heat transfer.

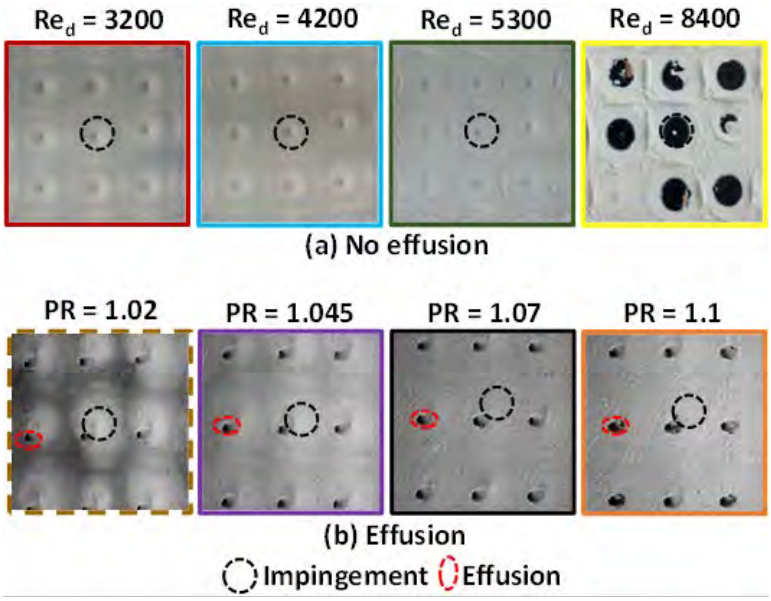

Figure 13. Observed deposition patterns for (a) the no-effusion plate and (b) the effusion hole plate for several mass flow rates at a H/D = 10. All deposition patterns are for a matched deposit, except for the effusion hole plate at a PR = 1.02 which is shown for a matched supply. A black dotted circle denotes the impingement jets, and a red dotted circle denotes the effusion holes.

Also shown in Figure 13 are deposition patterns for a PR of 1.02 with a matched supply. Outside of deposition in the stagnation region, there was little spread of dirt across the test plate surface as indicated by the black regions on the surface. This observation supports the decreased augmentation from PR of 1.045 to 1.02 because an increased area on the effusion plate surface was directly exposed to the cooling flow, which led to decreased cooling reductions. A similar observation for the no-effusion plate explains why the augmentation in Figure 11 is less for a Re_d of 3200 than that for Re_d of 5300, which had a greater spread of dirt.

Scans of each of the deposition patterns in Figure 14 were used to show side-view lateral averages of the deposition thicknesses for the effusion hole plate at a H/D of 10. Laterally averaged results are only shown for the effusion hole plate because both plates showed similar trends for a changing mass flow rate. The laterally averaged results show the decreased peak heights as the flow rate was increased. It is also interesting to see how the ridge region thickness at an X/L of 0.35 and 0.65 increased as the PR increased, which shows the dirt was pushed away from the jet stagnation zone.

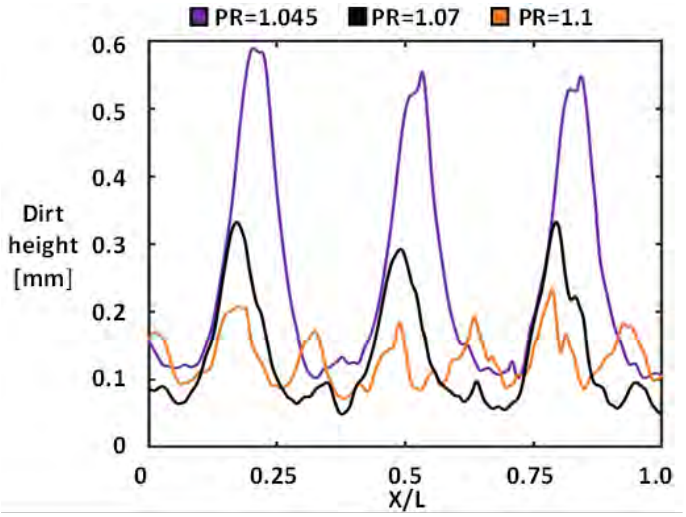

Figure 14. Laterally averaged dirt heights for the effusion hole plate for 1.045 < PR < 1.1 at a H/D of 10.

In summary, heat transfer testing was performed on an effusion hole plate holes for several pressure ratios and H/Ds. Overall, heat transfer coefficients are higher for the effusion hole plate compared to the coefficients obtained in prior quarters on a no-effusion plate. The effects of plate-to-plate spacing on cooling differed for the two test plates. For the clean, no-effusion plate, increasing the H/D from 10 to 15 resulted in a decrease in heat transfer. In contrast, for the clean, effusion hole plate, an increase in H/D from 3 to 10 resulted in similar heat transfer coefficients. The impingement flow physics explains why these heat transfer results occurred. An analysis of the flow blockage, deposition thickness, and deposition mass showed that decreasing all three were important factors in less severe cooling reductions.

Changing the jet Reynolds number and pressure ratio also impacted how deposition influenced target plate heat transfer. As the PR increased, the level of flow blockage in the impingement and effusion holes decreased, which suggested that greater flow rates resulted in more dirt being pushed through the cooling holes. Likewise, increased Red led to decreased dirt deposition heights and hence to decreased cooling reductions. It was observed that a decrease in the deposition mass, deposition height, and RFP all affected the heat transfer coefficients.

Novel Triple-Wall Combustor Liner

In developing methods for a dirt-insensitive combustor liner, a triple-walled liner was designed to include an additional impingement plate upstream of a double-walled liner, as seen in Figure 15b. The middle impingement plate, Imp-025, and the effusion plate, Eff-033, were designed in a similar fashion to prior double walled liners from our lab, which consisted of 5 x 11 arrays of cooling holes (Fallon et al., 2023). The three-digit number following each of the plate names represents the diameter of the cooling holes, where 025, for example, means 0.025 inches. Impingement holes were perpendicular to the effusion plate surface and offset from the effusion hole entrances, which were angled at 30° with respect to the horizontal surface. The Imp-025 and Eff-033 plates were used for all baseline 2-layer testing performed during this quarter, as seen in Figure 15a. An impingement plate, Imp-06, with cooling holes in a 4 x 10 array was added upstream of this double-walled liner for the purpose of encouraging more dirt capture on Imp-025 than Eff-033.

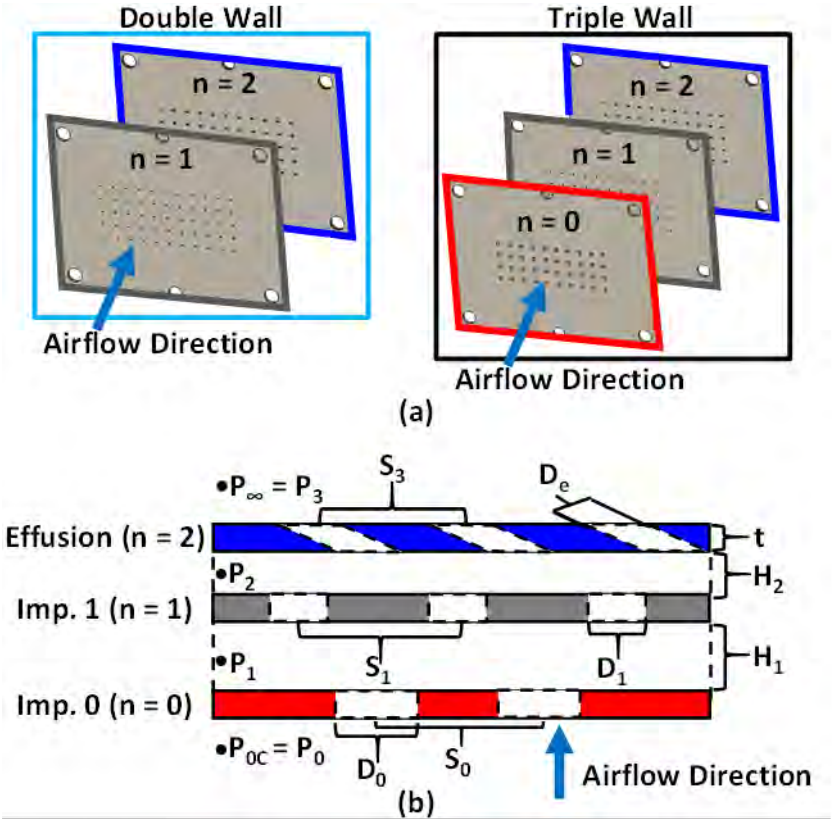

Figure 15. (a) Side view of a double-walled and triple-walled liner used for dirt mitigation studies. (b) Side view of a triple-walled liner including pressure ratio definitions.

Table 1. Triple-walled Liner Parameters.

	H/d	t/d	α	Pressure Split (%)
Imp-125	10	1	0.08	0.1
Imp-09	10	1	0.042	0.4
Imp-06	10	1	0.019	2.0
Imp-025 Pins Diamond Fence	3	2	0.018	17
Eff-033	N/A	2	0.005	82

$$\alpha = \frac{\text{Impingement Flow Area}}{\text{Total Flow Area}}$$

$$\frac{t}{d} = \frac{\text{Plate thickness}}{\text{impingement diameter}}$$

Pressure correlations were utilized to develop flow areas for each of the plates as well as the plate thicknesses to match previous testing done within the lab. The parameters developed for each of these are shown in Table 1. Imp-125, Imp-09, and Imp-06 refer to the three different diameters tested for the first impingement plate, which were used to analyze the effects of first plate pressure split on deposition, where increased diameters resulted in decreased pressure splits which is

shown in Table 1. Pressure split is defined in Equation 6, where it represents each individual plate pressure contribution to the total pressure drop across all 3 plates.

$$\text{Pressure split} = \frac{\Delta P_{individual}}{\Delta P_{Total}} * 100 \quad \text{(Eq. 6)}$$

The H/D spacing between Imp-06 and Imp-025 was set at 10, while the H/D ratio between the Imp-025 and Eff-033 was set at 3. This decision was made based on previous testing (McFerran et al., 2025) which showed that as H/D increased, dirt was more likely to be captured on the plate. Because the goal is to increase capture on imp-025 and decrease capture on eff-033, a larger H/D was chosen for Imp-06 than Imp-025.

The 4 x 10 array dimensions for Imp-06 differed from the 5 x 11 array dimensions of the other two plates because the impingement jets from Imp-06 were designed to impact in the center of the Imp-025 cooling holes, which can be seen in Figure 16. Designing the impinging jets in the center was done to keep the dirt as far from each of the Imp-025 cooling holes as possible. Ultimately, deposition on Imp-025 is not as big a detriment to the combustor wall as deposition on Eff-033 because Eff-033 is the plate that needs maximum cooling due to high temperature exposure.

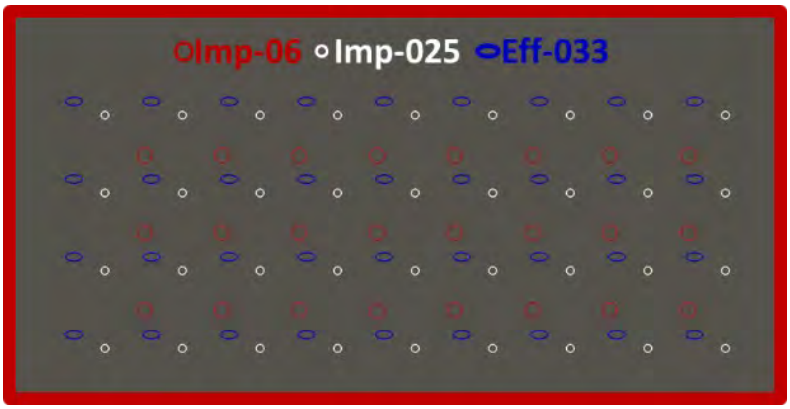

Figure 16. Top-down view of the impingement and effusion holes locations for each layer.

Geometric surface structures were also designed on the Imp-025 surface with the goal of capturing more dirt on this layer than Eff-033. The four designs of surface structures tested (i.e., pins, diamonds, fence, and tall fence) are shown in Figure 17b. For each of these designs, the Imp-06 plate was used as the first layer impingement plate. The goal of the pin design was to block a direct flow of the impinging jets from Imp-06 to the cooling holes of Imp-025. Without a direct path to the hole, the dirt would be more likely to deviate from the flow field path and not funnel into the holes. The diamond and fence designs were designed to cause a sharp velocity gradient at the base of a wall in which the flow would need to go up and over because past studies (Fallon et al., 2023; Singh et al., 2013; Lundgreen, 2017) have shown that particulate has a difficult time following flows with sharp velocity gradients. The pin and diamond designs had heights equal to a quarter of the plate-to-plate spacing between Imp-06 and Imp-025, while the fence and tall fence designs were 1/6th and 1/3rd of the plate-to-plate spacing, respectively. A side view in Figure 17a shows the height of the pins compared to the plate-to-plate spacing.

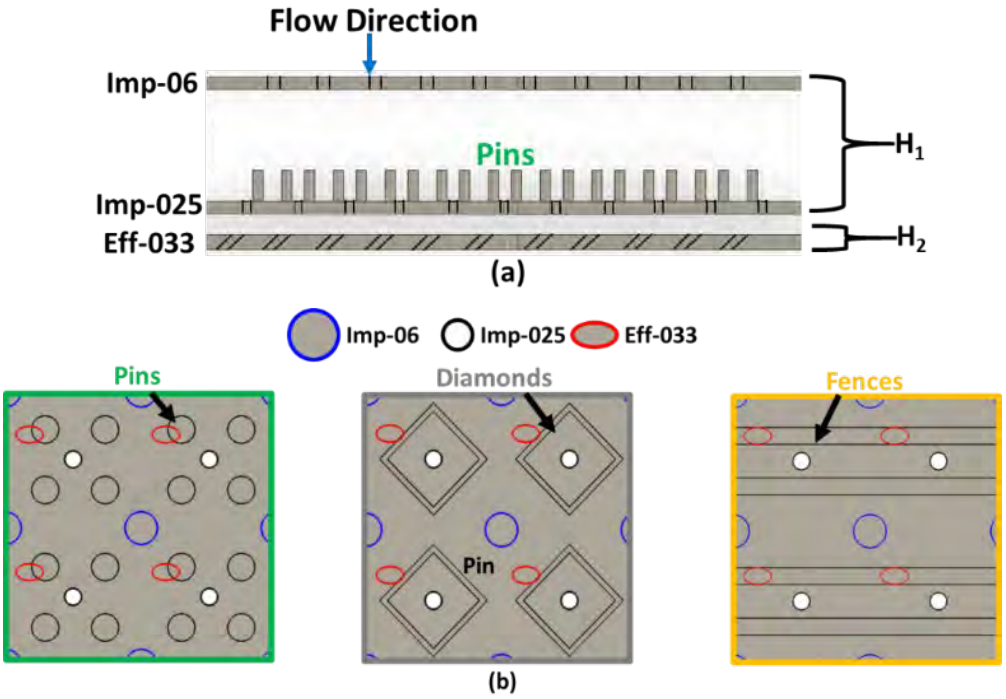

Figure 17. (a) Sideview of the pin design on Imp-025 where H_1/D equals 10 and H_2/D equals 3. (b) Top view of the four different designs tested on Imp-025. Note that two different fence heights were tested for the fence design.

Prior to each test, the mass of each layer of the triple-walled liner was recorded and assembled at the base of the plenum. Clean pressure and FP measurements were made on each clean layer to obtain the clean test conditions. Dirt was then injected via a slug feed method discussed in previous quarters, causing dirt to deposit on all three layers of the combustor liner. After injection, pressure and FP measurements are once again taken and the entire rig was disassembled. Upon disassembly, each of the layer's masses were measured and the differences in mass between the dirty (mf) and clean (m0) plates gave the mass of dirt on each layer.

First, the effects of first plate pressure split were analyzed for the 3-layer composites by adjusting the diameters of the first plate impingement holes (Imp-06, Imp-09, or Imp-125). A pressure split of 2% PR, 0.4% PR, and 0.1% PR were tested for Imp-06, Imp-09, and Imp-125, respectively, where PR was equal to 1.045 across the entire assembly for both double-walled and triple-walled testing. Results for the percentage of dirt captured per layer are shown in Figure 18 for both the 2-layer and 3-layer walls. For each of these tests, 2.0 g of dirt was injected. As the pressure split across the first plate increased, the percentage of dirt found on the Imp-025 plate compared to that on Eff-033 also increased. For the Imp-06 plate which had a 2% PR pressure split, only 17% of the total dirt distribution ended up on the effusion plate, which is an 83% reduction in deposition compared to the 2-layer design. Even Imp-125 performed very well, resulting in more than a 50% reduction in the Eff-033 deposition while only contributing 0.1% to the total pressure ratio.

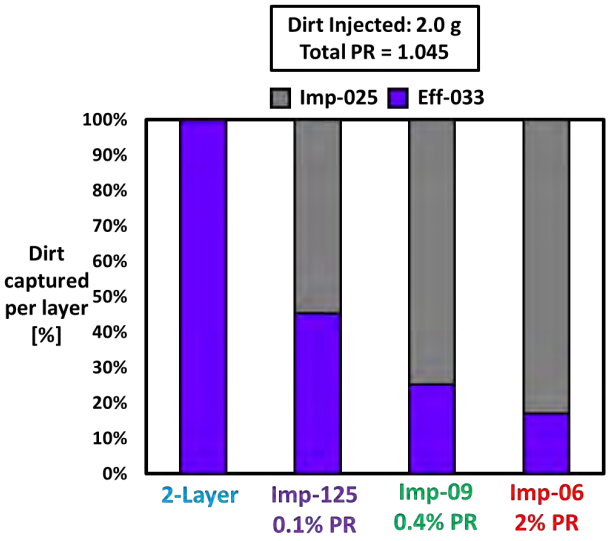

Figure 18. Percentage of dirt captured on Imp-025 and Eff-033 for Imp-125, Imp-09, and Imp-06 as the first (cold-side) liner.

The RFP was also analyzed as a function of % PR for each of these three designs, as shown in Figure 19. As the % PR increased across the first impingement plate, the RFP decreased, which means that there was less overall flow blockage as the first plate pressure split increased. Therefore, as the % PR increased, the RFP and deposition mass on Eff-033 decreased. This trend suggests that the effusion plate is the layer that has the greatest impact on flow blockage because the flow blockage decreased as deposition on the effusion plate decreased. Experimental observations of the deposition patterns also support this trend, as dirt buildup in the holes was visualized during testing.

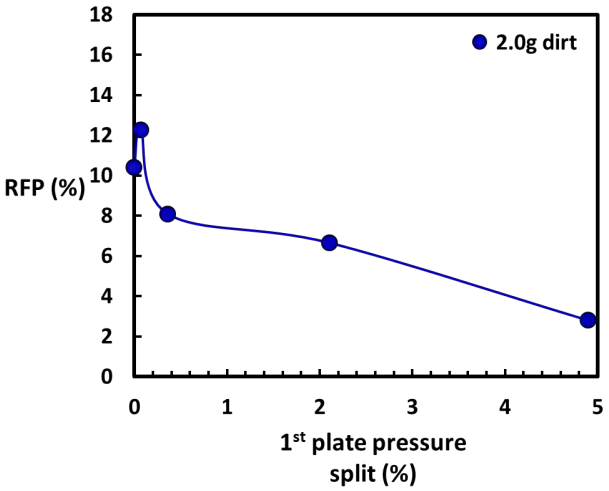

Figure 19. The reduction in flow parameter as a function of first plate pressure split for an injection of 2.0 g of dirt at a total pressure ratio of 1.045.

An analysis of the individual pressure splits before and after dirt injection, as seen in Figure 20, show that the pressure split across Eff-033 increased as dirt was injected into the system. This result supports the idea that the effusion plate contributes the most to the total flow blockage because despite a decrease in the mass flow rate, the pressure split across this plate increased. The only way for this to happen is if the flow area on this plate decreased which would indicate flow

blockage. Also, in Figure 20, the clean PR across each of the plates shows the increase in PR across the first impingement plate as the diameter of the holes were decreased.

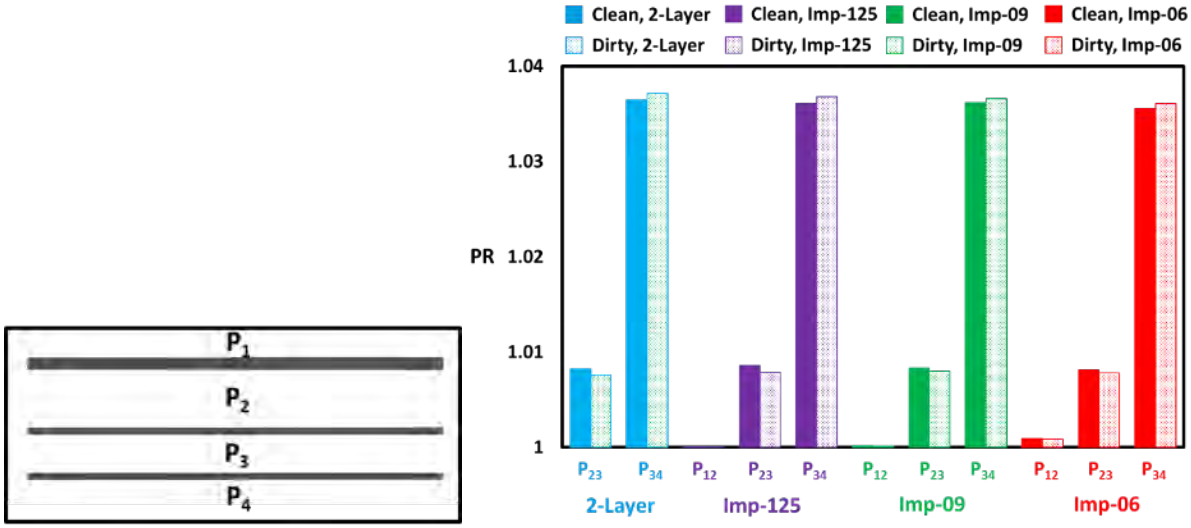

Figure 20. Pressure splits across each of the liner walls for the 2-layer and 3-layer designs used to analyze the effects of first plate pressure splits.

Any pressure split across the first impingement plate is a pressure loss, which reduces efficiency because more cooling air would be needed to effectively cool the effusion wall. However, as this pressure split increased, the deposition mass on Eff-033 and the RFP decreased. As a result, it is important to consider how the benefits of increased dirt reductions can outweigh the negative impacts of increased pressure losses, especially considering the significant impact dirt deposition has on cooling as seen in previous quarters (McFerran et al., 2025).

The Imp-06 plate was chosen as the first impingement plate for the rest of testing because it resulted in the greatest reductions in deposition on the effusion plate compared to Imp-09 and Imp-125. The next set of tests studied the effects of dirt injection on deposition distributions, where injection masses of 0.5 g, 1.0 g, 1.5 g, and 2.0 g were evaluated. Studying different injection masses was also useful in quantifying the benefits of a triple-walled liner over time because deposition increases over time in an engine. It was found that capture percentages for the Imp-025 and Eff-033 layers were insensitive to injection mass, as seen in Figure 21. At each of the tested injection masses, the percent of dirt captured on Eff-033 compared to Imp-025 ranged between 17-20%.

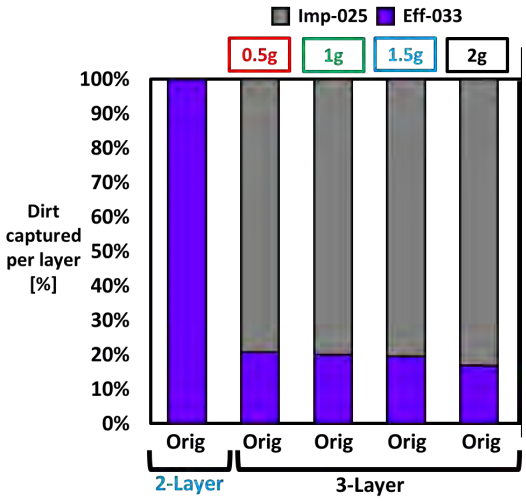

Figure 21. The percentage of dirt captured on the baseline 2-layer and 3-layer designs with injection masses between 0.5 and 2.0g.

Although not shown in a plot, the individual pressure splits once again demonstrated that the effusion plate pressure split increased as dirt was injected into the system, despite a reduction in the flow parameter. This change in pressure split for the effusion plate increased as the dirt injection mass increased, and this is a result of the increase in RFP that occurred as the injection mass increased, as shown in Figure 22. These results are shown for both the 2-layer and 3-layer designs. As the injection mass increased, the RFP increased for double and triple-walled liners because with more dirt, there is inherently a greater likelihood of flow blockage. However, the RFP for the 3-layer design was 40% less than that for the 2-layer design at the same injection mass. These results further support the idea that the effusion plate is the main driver of RFP because the deposition mass on Eff-033 was less for the 3-layer design than the 2-layer design, so a decrease in the RFP would also be expected.

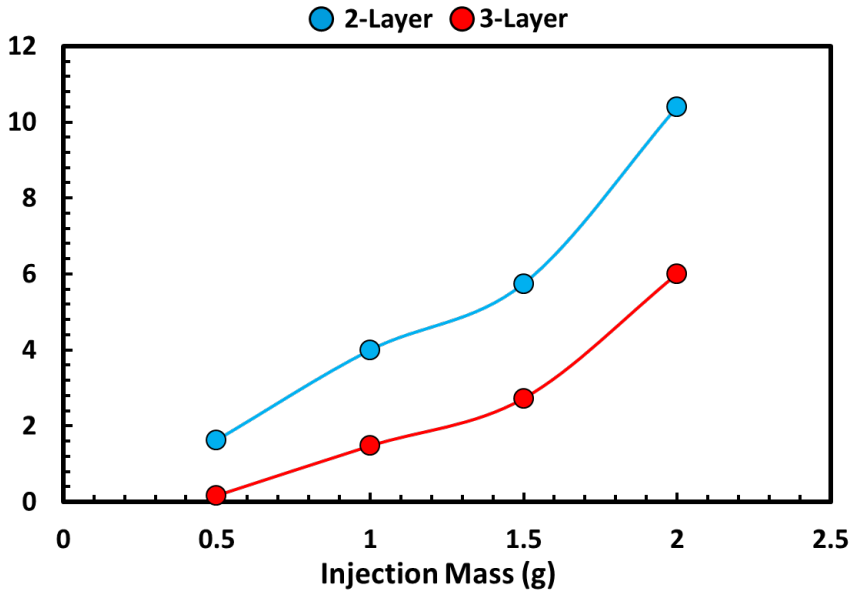

Figure 22. Reduction in Flow Parameter for the baseline 2-layer and 3-layer designs as a function of dirt injection mass.

Finally, the feature designs introduced in Figure 16 were added to the Imp-025 plate with the goal of further enhancing dirt capture on this layer as opposed to Eff-033. The dirt capture per layer is plotted in Figure 23, which compares the four designs (i.e., pin, diamond, fence, and high fence) to the 2-layer baseline and 3-layer baseline. Each of these tests were performed with 2.0 g of dirt injection at a PR of 1.045. Results in Figure 23 show that the pin and diamond designs reduced deposition on the effusion plate by 5% compared to the 3-layer design with the regular Imp-025 plate. In contrast, the fence and high fence designs performed 1-2% worse than the 3-layer with regular Imp-025 in terms of deposition distribution on the effusion plate.

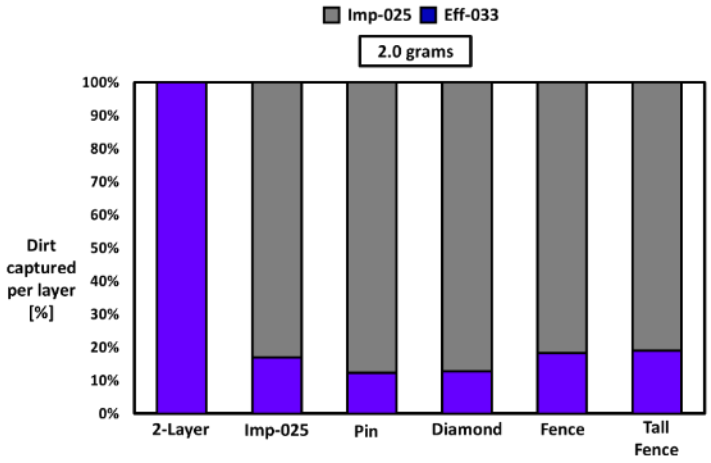

Figure 23. The percentage of dirt captured on Eff-033 and Imp-025 with the pin, diamond, fence, and tall fence designs for an injection mass of 2.0g and PR of 1.045.

Despite having slight differences in dirt distribution among the different layers, the RFPs for the pins, diamond, fence, and tall fence designs were slightly less than that for a 3-layer with the regular Imp-025 plate as shown in Figure 24. However, the high fence had an RFP about 25% higher than any of the other structural designs. The effusion plate was once again the main driver of this RFP. Experimental observations of the deposition patterns in Figure 25 show some of the dirt buildup occurring in the effusion holes which contributes to flow blockage. Additionally, these microscopic images show the deposition patterns on the imp-025 plate for each of the designs. The deposition patterns have similar characteristics to patterns seen previously, where conical mounds form in the regions of direct impingement.

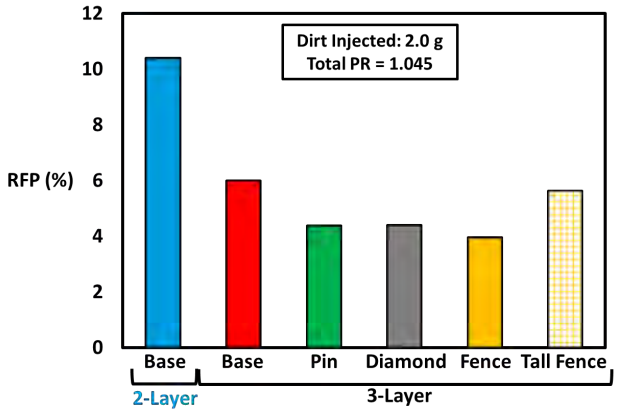

Figure 24. RFP for the 2-layer and 3-layer baseline and structural designs.

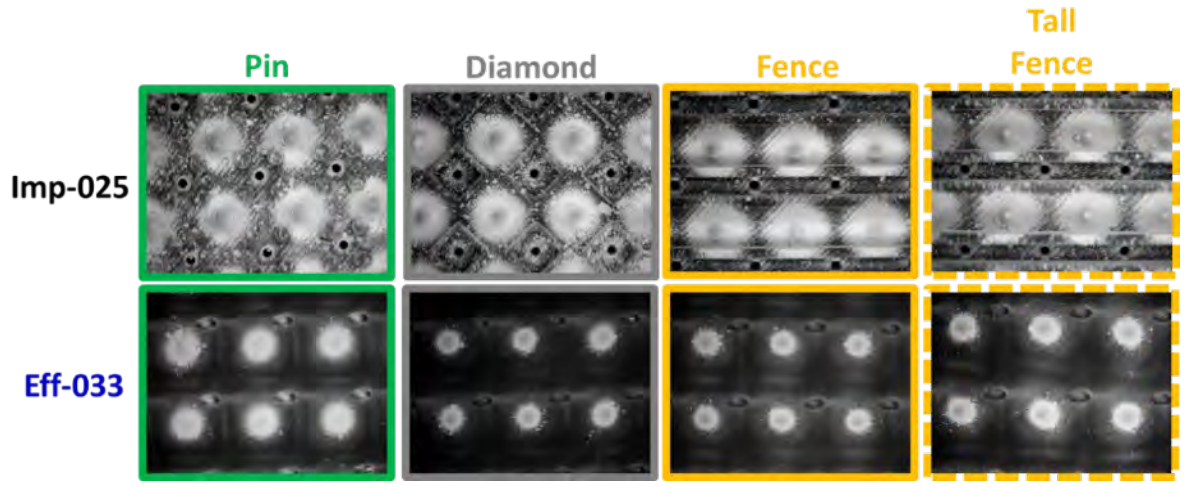

Figure 25. Deposition patterns on the Imp-025 and Eff-033 plates for each of the structural designs evaluated.

Also, during this past year, there was a focus on the effects of different particle sizes and different dirt compositions to see whether the triple wall remains effective for these conditions. Figure 26 show the effect of particle size using the US Air Force Research Laboratory (AFRL)-05 (original) test dirt by expanding the largest particle diameter from 1 μm to 10 μm. As already discussed, for the double wall, it is expected that 100% of the dirt is deposited on the effusion plate. The results in Figure 26 show that, similar to those of the 1 μm particle that the triple wall is still effective.

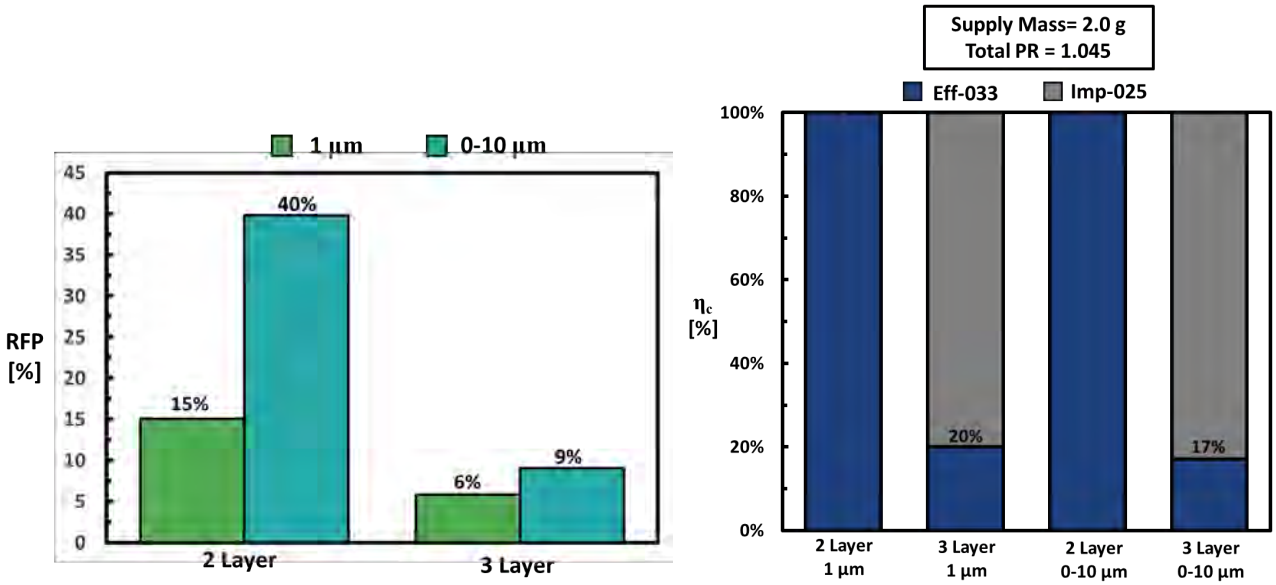

Figure 26. Comparison of capture efficiency and reduction in flow parameter for two different particle sizes using the AFRL-05 test dust.

Also shown in Figure 26 is that the reduction in flow parameter also was reduced, meaning that more flow resulted when using the triple-wall due to less flow blockage even when the particle size increased. However, it is important to note that for both the double- and triple-wall designs the overall RFP increased, indicating that the larger particles had a tendency to block the cooling holes more readily as expected. Figure 27 shows images on the effusion plate of these blockages comparing the smaller and larger particle size tests.

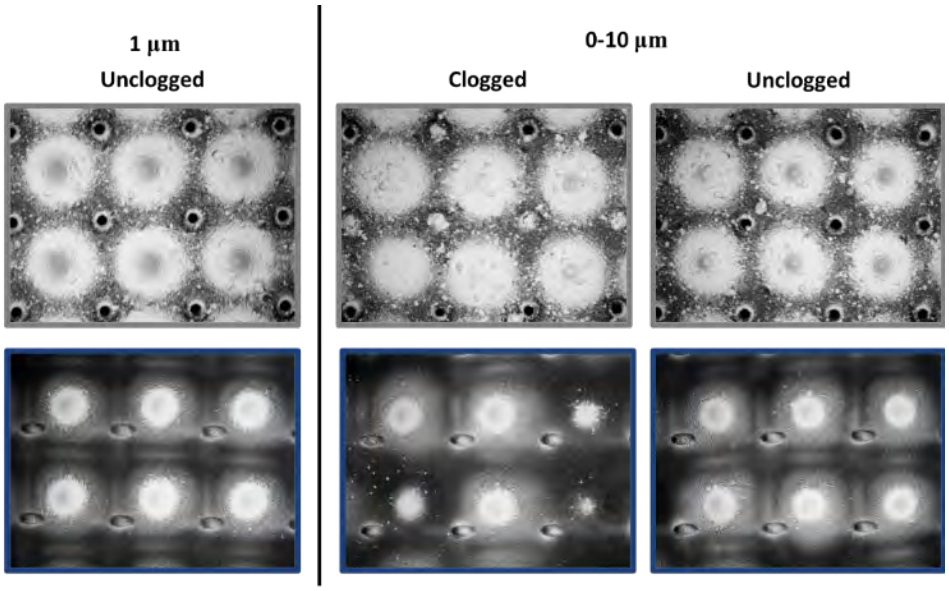

Figure 27. Comparison of deposition patterns for two different particle sizes using the AFRL-05 test dust.

One of the simplified tests that was conducted during this reporting period was also to heat the dirt to temperatures relevant to turbine conditions. Based on the data shown in Figure 28, there is a dramatic effect of temperature especially when nearing turbine operating temperatures. These results indicate the importance of testing at relevant temperatures.

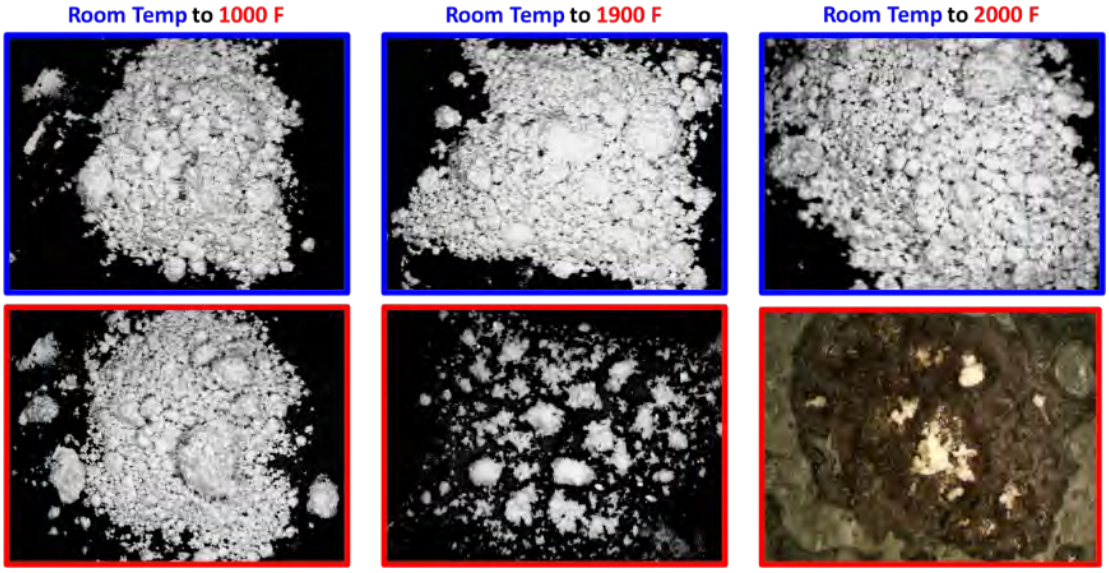

Figure 28. AFRL-05 test dust as a function of exposure temperatures.

In summary, a triple-walled liner was developed in which an impingement plate was added upstream to a typical double-walled liner. It was shown that the inclusion of this plate can lead to reductions in dirt deposition on the effusion plate because more of the dirt deposits on the middle impingement plate, which acts as a sacrificial filter. With there not being a strong need to cool this middle plate, deposition on this surface is not that significant compared to deposition on the effusion plate. Testing was performed for several % PRs across the first impingement plate, dirt injection masses, and

structural designs. Overall, the reduction in deposition on the effusion plate also led to decreased reductions on the cooling flow due to dirt blockage, which is another benefit of the 3-layer design. It was also shown that the no matter the particle size, there was an improved performance of reduced impacts on the external effusion hole wall.

Task 3 – Profile Simulator for START

The Pennsylvania State University

Objectives

The objective of this task is to (1) develop and integrate a non-reacting profile simulator to be placed upstream of the START test turbine, and (2) understand the impacts of a range of temperature and pressure profiles, representative of current and future combustors, on turbine efficiency and durability.

Background

The ability to replicate combustor-relevant temperature and pressure profiles is important in learning how to improve engine performance with typical aviation fuels, sustainable aviation fuel, and other fuels. These profiles, which exit the combustor that then enter the turbine, impact turbine efficiency and durability. This task involves developing a non-reacting profile simulator that can simulate relevant combustor non-dimensional flow and thermal fields. Figure 29 illustrates the need for placing a combustor simulator upstream of the START test turbine. The data in Figure 29 show the range of nonuniformities of non-dimensional temperatures ($\overline{T}/T_m$) that occur at the exit of the combustor, which affects turbine performance. The profiles labeled "Engine Profile 1" through "Engine Profile 4" are from Barringer et al. (2004) and show a variety of combustor exit profile shapes influenced by liner wall dilution and effusion flows. Five additional profiles are shown for comparison including "Engine Profile 5" and "Engine Profile 6" obtained from gas turbine OEMs (OEM Engineer Manufacturers, 2022), an OEM engine profile ("Engine Profile 7") from Karalus et al. (2019), a typical engine profile ("Engine Profile 8") from Povey et al. (2007), and a final profile showing the current START facility inlet temperature profile for the National Experimental Turbine (NExT) that is nearly uniform. Because various fuels will be used for combustion in the future, simulating these profiles will become even more essential.

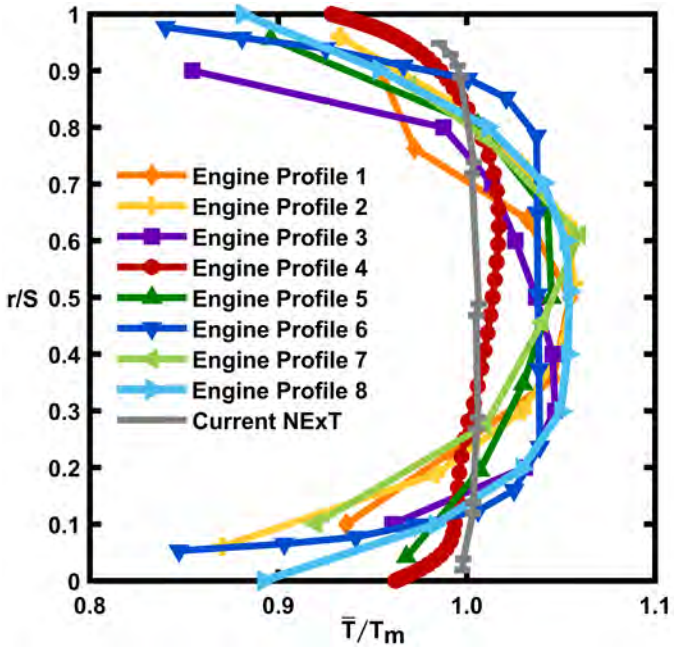

Figure 29. Combustor exit profiles from the literature, indicating non-uniform temperatures ($\overline{T}/T_m$).

A combustor profile simulator is being designed and implemented into the START rig upstream of the turbine test section. The purpose of the simulator is to replicate the temperature and pressure profiles at elevated turbulence levels that are

characteristic of the flow exiting a modern gas turbine combustor. A number of generalized temperature profile shapes are being targeted for the design including a radial mid-span peaked, outer diameter (OD) peaked, inner diameter (ID) peaked, and a flat uniform profile. The simulator device consists of a series of solid and perforated walls that form a central chamber, similar in concept to a gas turbine engine combustion chamber.

To achieve the range of temperature and pressure profiles, our team conducted predictive computational fluid dynamics (CFD) simulations using steady Reynolds-averaged Navier–Stokes to understand the impacts of different flow features on the resulting profiles. Simultaneously, the START team engaged a design firm to develop the hardware necessary to achieve the profiles developed through the CFD studies.

Recall, the central chamber of the simulator design includes three axial rows of dilution holes and several rows of effusion holes in both the inner and outer diameter liner walls. The first dilution row is used for turbulence generation, whereas the second and third dilution rows are used for temperature profile generation. The effusion flow is used to tailor the temperature in the near-wall regions. The dilution holes will be drilled into the annular walls, which are removable to allow different dilution hole diameters and corresponding momentum flux ratios to be studied.

The domain of the CFD simulation began at the axial inlet of the central chamber and ended at the turbine vane leading edge. The flow inlets for the simulation domain included the main gas path central chamber inlet, approach flow plenums for the dilution holes, and effusion zone liner walls. All of the flow inlets were designated as mass flow inlets, including the approach flow paths leading to the dilution holes, which provided more realistic flow interactions between the dilution jets and mainstream crossflow. The temperature of the first-row dilution jets was set to match the temperature of the flow at the main gas path inlet in order to maintain the majority of the total flow at an elevated temperature level above the second/third row dilution flow and effusion flow. This elevated flow temperature, illustrated in Figure 30 by the red colored flow vectors, helps to produce a mass-averaged flow temperature at the turbine vane inlet plane that matches the design target for conducting the turbine experiments. The temperature of the second/third row dilution flow is illustrated at a lower temperature level in orange, and finally the effusion flow is illustrated at an even lower level in blue. Overall, the three levels of flow temperatures are used to establish the target mass-averaged flow temperature entering the turbine vanes. The turbine vane inlet was set as a pressure outlet boundary condition, defined using the static pressure at the turbine vane leading edge. All of the boundary conditions are summarized in Figure 30.

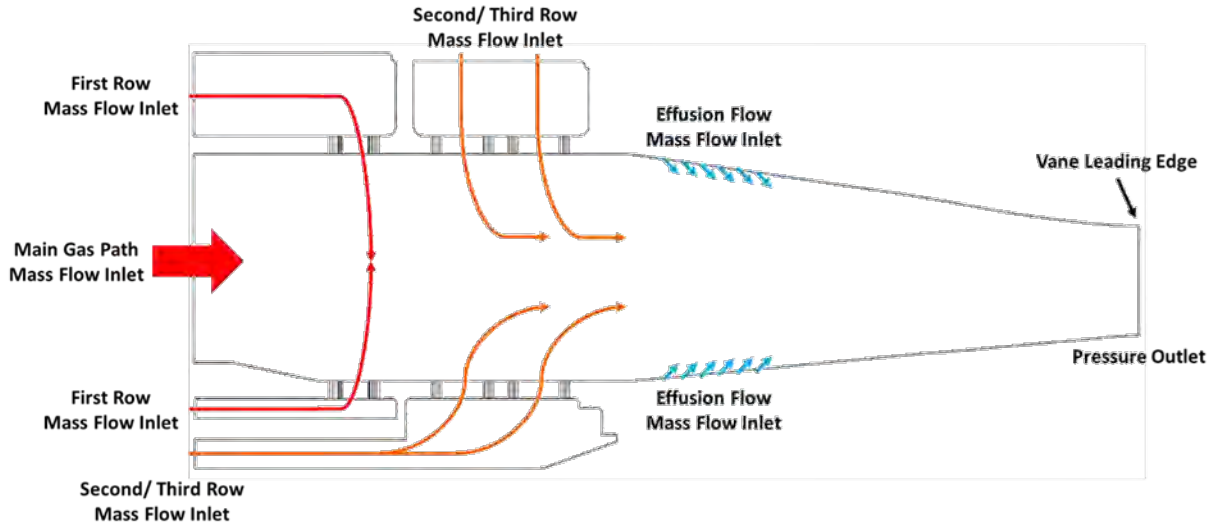

Figure 30. Diagram of boundary conditions used for the SimCenter®-STAR CCM+[1] CFD simulations.

® SimCenter is a registered trademark of Siemens Industry Software N.V., Leuven. Belgium.
[1] SimCenter STAR CCM+ is a multiphysics CFD software that models complex fluid dynamics applications for real-world conditions including single-phase, multiphase, reacting, heat transfer, aeroacoustics, and fluid-structure interaction simulations.

Profile Simulator Results

The setup work for CFD simulations, including mesh generation and a grid independence study, and the execution of the CFD simulations were completed during Q3 and Q4 of 2023. Two different 2-level fractional factorial Design of Experiments (DoE) were completed. The second DoE included four more additional factors than what was included in the first DoE. The 12 factors as part of the second DoE are shown in Table 2 and included (1) dilution row 1 mass flow rate, (2) dilution row 1 hole diameter, (3) dilution row 3 OD mass flow rate, (4) dilution row 3 ID mass flow rate, (5) effusion flow OD mass flow rate, (6) effusion flow ID mass flow rate, (7) dilution row 3 OD hole diameter, (8) dilution row 3 ID hole diameter, (9) dilution row 3 OD total temperature, (10) dilution row 3 ID total temperature, (11) effusion flow OD total temperature, and (12) effusion flow ID total temperature. The second CFD design of experiments allowed more variables to be studied in order to generate a wider range of profile shapes. Since both DoEs were a 2-level design, the maximum and minimum of the respective ranges were used for the hole diameters and mass flow rates. The changes made to the first-row dilution flow and holes described by the first two factors were to understand the effects of turbulence on the profile shape. The remaining ten factors were changed to study their effects on the exit temperature and pressure profile shapes.

Table 2. Factors for the 2-level, 12-factor fractional factorial DoEs.

Factor Number	Input factors	Lower Level	Upper Level
1	$\dot{m}_1/\dot{m}_t$ [%]	0.18	0.22
2	D_1/S [-]	0.23	0.45
3	$\dot{m}_{3,\,OD}/\dot{m}_t$ [%]	8.8	11
4	$\dot{m}_{3,\,ID}/\dot{m}_t$ [%]	8.8	11
5	$\dot{m}_{e,\,OD}/\dot{m}_t$ [%]	3.8	6.3
6	$\dot{m}_{e,\,ID}/\dot{m}_t$ [%]	3.8	6.3
7	$D_{3,\,ID}/S$ [-]	0.39	0.55
8	$D_{3,\,OD}/S$ [-]	0.39	0.55
9	$T_{3,\,OD}/T_m$ [-]	0.55	0.75
10	$T_{3,\,ID}/T_m$ [-]	0.55	0.75
11	$T_{e,\,OD}/T_m$ [-]	0.55	0.75
12	$T_{e,\,ID}/T_m$ [-]	0.55	0.75

The non-dimensional temperature profiles predicted by the simulations at the exit plane of the combustor profile simulator for the second CFD design of experiments are shown in Figure 31 for the grid-independent 20 million cell mesh.
The shapes of the engine profiles are mostly in the profile range capability predicted by CFD simulations. The shaded gray region of Figure 31 represents the range of profiles that correspond to the DoE case configurations. The short-dashed black lines represent individual CFD DoE case profiles. The steepest wall gradients characteristic of Engine Profile 3 and 6 were not captured by the second DoE test matrix. However, this does not mean that the simulator is not able to produce temperature profiles with steeper gradients along the walls. Steeper gradients might be possible since the CFD DoE only varied 12 factors that had settings of the minimum or maximum within their selected ranges and did not encompass all the factors as part of the simulator's flexibility.

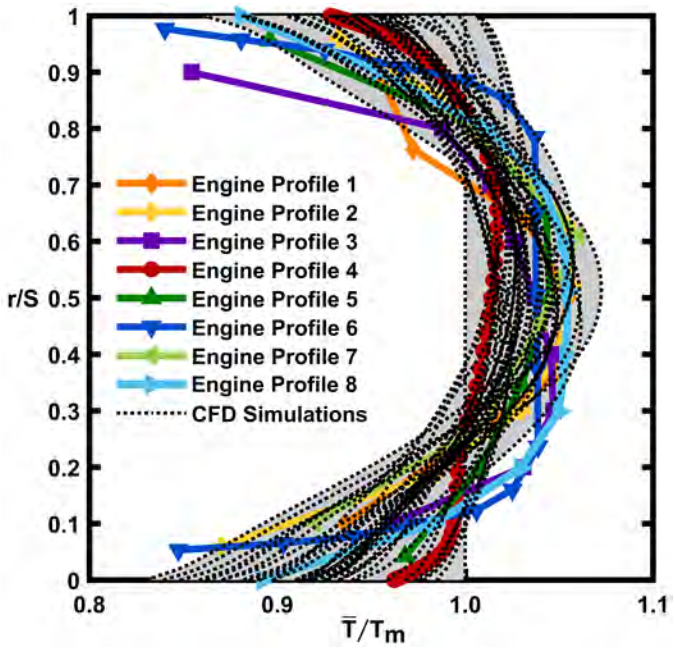

Figure 31. Several non-dimensional total temperature profiles at the simulator exit from the second CFD design of experiments, plotted in the radial span direction (r/S) and circumferentially averaged, with comparisons to typical engine profiles.

Recall, the design targets for the new profile simulator include a radial mid-span peaked, OD peaked, ID peaked, and a flat uniform profile. The profile results from the second CFD design of experiments that best matched the design targets were selected and plotted in Figure 32 for easier visibility. The four simulation-predicted profiles shown in Figure 32, designated as 'Center Peaked', 'ID Peaked', 'OD Peaked', and 'Uniform', are more representative of the engine profiles than what was previously found in the first CFD design of experiments using a 2-level 8-factor approach. The shaded gray region in Figure 32 is the same as that shown in Figure 31, which represents the full-range of profiles produced by the second CFD DoE.

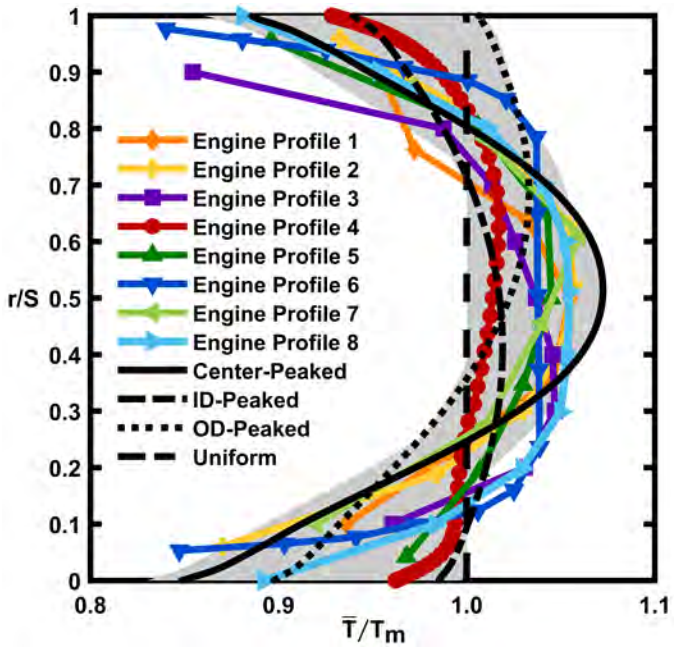

Figure 32. Range of non-dimensional total temperature profiles from the second CFD design of experiments, plotted vs. radial span location and compared to the example engine combustors.

A sensitivity analysis was completed during the current reporting period on the profile results from the second CFD DoE to understand how each of the 12 input factors affect the exit temperature shape. The sensitivity analysis determines which factors significantly affect the profile shape so that targeted profiles can be produced. An analysis of variance (ANOVA) was conducted on the predicted exit profile shapes at eleven discrete radial locations that correspond to the measurement locations of the traverse system probes in the START rig. However, only three radial locations—10%, 50%, and 90% radial span—are presented to illustrate the importance of the sensitivity analysis. The ANOVAs conducted allowed the percent contribution of each input factor to be calculated for each of the 11 radial span locations. The percent contributions of each factor to the temperature profile shape were determined by calculating the ratio of the individual factor's sum of squares to the total sum of squares. The individual factor's sum of squares refers to the variation in the non-dimensional temperature at a specific radial span location that can be contributed to that factor, while controlling the other factors. The total sum of squares is the sum of the individual factors sum of squares within a particular ANOVA. The percent contributions for each of the 12 factors at 10%, 50%, and 90% span can be seen in Figure 33. The largest, secondary, and tertiary contributors to the profile shape at 10% span was the injection temperature the ID effusion flow, the injection temperature of the ID third-row dilution flow, and the mass flow rate of the ID effusion flow, respectively. At 50% span the first-row dilution hole diameter was the largest contributor and was significantly higher than the rest of the contributors. The largest, secondary, and tertiary contributors to the profile shape at 90% span were the injection temperature of the OD effusion flow, first-row dilution hole diameter, and injection temperature of the OD third-row dilution flow, respectively. The percent contributions of the injection temperature of the OD third-row dilution flow and mass flow rate of the OD effusion were very close in being the tertiary contributor at 90% span. However, based on the 36 simulations that were part of the ANOVA, the injection temperature of the OD third-row dilution flow had a slightly higher percent contribution when compared to the mass flow rate of the OD effusion flow. This is similar to the percent contributions at 10% where the injection temperature of the ID third-row dilution flow had a higher contribution than the mass flow rate of the ID effusion flow. The largest contributors for 10% and 90% radial span intuitively make sense since the effusion flow is designed to blanket the chamber walls. The first- and third-row dilution flow do not mix effectively with the effusion flow at low and high radial spans leading to a large contribution of the effusion temperatures. At 50% span, the first-row dilution hole diameter has a large effect on the turbulence generated. For a case when the turbulence in the simulator is high, the hot flow of the main gas path and first-row dilution mix well with the colder third-row dilution flow. As the flows mix, the bulk average exit flow is lower when compared to a case with low turbulence levels. For a low turbulence case, the flows do not

mix comparatively as well, allowing hot main gas path and first-row dilution flow to continue downstream creating a hot mid-span peak in the temperature profile.

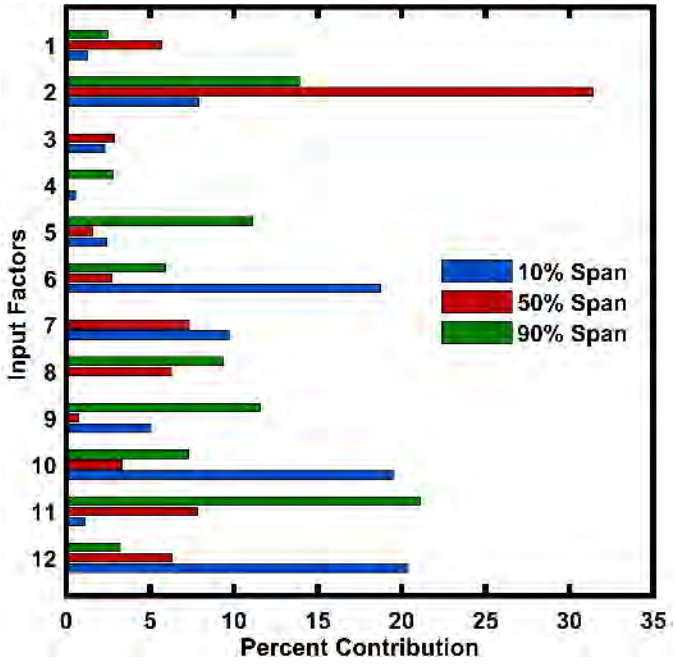

Figure 33. Results from the second DoE sensitivity analysis for (a) 10% span, (b) 50% span, and (c) 90% span, illustrating the impact of individual factor effects on the exit temperature profile metric $\overline{T}/T_m$.

One reason for the selection of the four target profiles was to allow the target profiles to be studied in depth using a higher fidelity computational model and experiments. It was previously determined that the Reynolds-averaged Navier Stokes (RANS) model provides a good prediction of the flow physics, such as jet penetration depth and bulk averaged velocities, but large eddy simulation (LES) modeling is needed to accurately capture the turbulence created by the mixing process of the dilution jets. Understanding how well the RANS simulations predict the temperature profiles is important in determining the viability of using RANS as a predictor for the various flow and geometry configurations in which the profile simulator can be installed and operated. The center-peaked target profile was selected as the preliminary case to transition to LES modeling.

Prior to a transition from RANS to LES, a more in-depth RANS simulation (REV-7), was completed that included the domain regions defined by the upstream strut, profile plate, and downstream turbine vane. The turbine vane used is from the PSU NExT geometry. This updated CFD domain can be seen in Figure 34, with the axial location of the turbine inlet traverse rakes marked in green and axial location of the vane leading edge (LE) marked in blue. The perforated profile plate acts to reduce the air pressure to enable proper injection of the dilution and effusion flows into the central chamber. The profile plate is interchangeable and contains an engineered perforated pattern that facilitates the desired air mass flow distribution throughout the simulator. In addition to creating a pressure loss, the profile plate is used to reduce the aerodynamic wake effect of the strut's presence in the main flow and to create a uniform flow field entering the central chamber. The struts function as a passageway to distribute cooling air to the inner diameter annulus flow paths and to structurally support the inner hardware components.

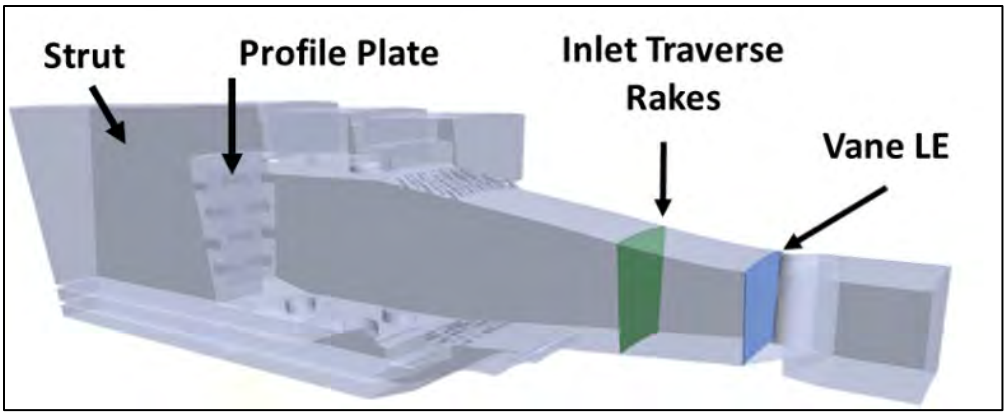

Figure 34. Combustor simulator CFD domain including the upstream strut region, profile plate, and downstream turbine vane (NExT).

The results of the RANS simulation were very encouraging. Figure 35 compares the non-dimensional radial temperature profiles for the 'center-peaked' target profile using the REV-7 simulation domain to the REV-6 domain. Comparisons are shown for axial locations aligned with the vane LE and with the turbine inlet rakes. The REV-7 profile that is axially aligned with the vane LE is not quite as peaked near mid-span (r/S = 0.5) as the REV-6 profile that is also aligned with the vane LE. This slight difference in peak shape is likely attributed to including the NExT vane in the simulation for the REV-7 case, in that the vane's presence had an effect on the flow and thermal fields. The CFD results were extracted at the inlet rake location because this is where physical rakes will be located when the simulator is installed in the rig. Four rakes will measure the air pressure and temperature in the annulus across the full 360° circumferential direction. The experiments will allow the comparison of the predicted radial profiles with what is actually measured in the rig. This comparison is important for validation purposes. The REV-7 profile that is axially aligned with the inlet rakes is further peaked than both the REV-7 profile aligned with the vane LE and the REV-6 profile aligned with the vane LE. This increase in peak shape for REV-7 at the inlet rakes is due to the axial location being further upstream. At locations further upstream, not as much mixing from the turbulence has taken place enabling the hotter flow near the mid-span region to remain intact.

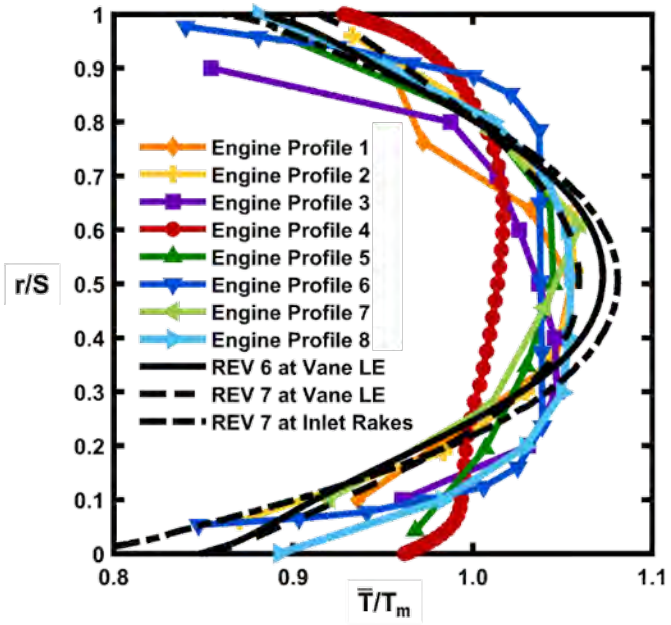

Figure 35. Radial temperature profiles located at the vane leading edge and turbine inlet rakes using the simplified DoE geometry (REV-6) and a more complete geometry (REV-7).

The RANS modeling method used in the CFD DoE study and planned LES modeling method for the higher-fidelity simulations have not yet been validated with experimental results. To validate the modeling methods, both a RANS and LES simulation will be run that uses the same combustor liner geometry as reported by Shrager et al. (2018, 2019). Shrager et al. (2018, 2019) reported flow field measurements and heat transfer performance of the liner wall in the form of overall effectiveness, but overall effectiveness measurements will not be part of the new simulator studies. Therefore, only validation of the computational modeling methods to the flow field measurements will be made. The study performed by Shrager et al. (2018, 2019) presented turbulence levels surrounding the dilution jet, as well as sensitivities to jet momentum flux ratio and freestream turbulence intensity. The outward facing effusion hole geometry as seen in Figure 36 was the selected test case for validation, which includes the highest dilution jet momentum flux ratio of I = 30 and highest freestream turbulence intensity of TI = 13%. This particular case had the most interesting flow phenomena producing a flow field that was significantly different than the other cases. The outward facing effusion hole case formed coherent vortices both upstream and downstream of the dilution jet which can be seen in Figure 37a and Figure 37b.

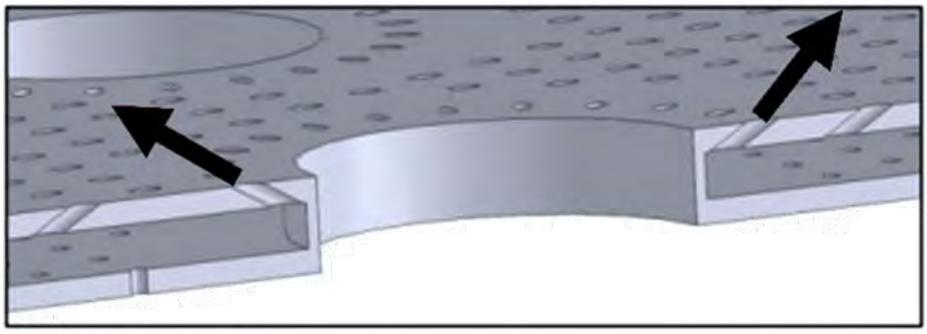

Figure 36. The combustor liner geometry used in the experimental study by Shrager et al. (2018, 2019) showing the large dilution hole with surrounding effusion holes pointing radially outward, that was also used in the current computational simulations to validate modeling methodology.

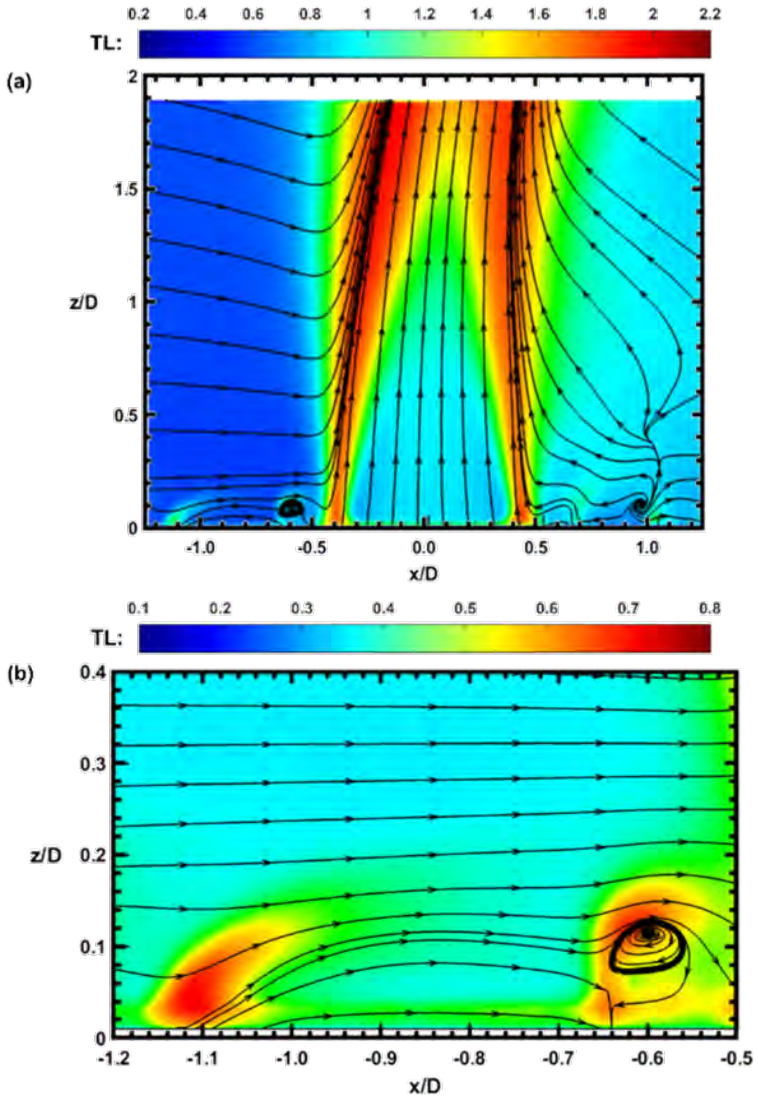

Figure 37. Turbulence intensity contours from experiments by Shrager et al. (2018) for the outward facing effusion hole configuration with a dilution jet momentum flux ratio of I = 30 and a freestream turbulence intensity of TI= 13% showing the flow field (a) near the dilution jet and (b) near the effusion holes.

Five different turbulence models were evaluated to determine the agreement with the experimental results. The five turbulence models that were used included (1) the realizable k-ε model, (2) the k-ω Shear-Stress Transport (SST) model, (3) an incompressible model, (4) a linear pressure strain Reynolds Stress model, and (5) the elliptic blending Reynolds Stress model. The realizable k-ε model is the same RANS turbulence model that was used in the simulator profile simulations. Newly generated turbulence contours with overlaid streamlines are shown in Figure 38a-e from the various turbulence models and compared to the experimental results in Figure 38f. The computational predictions show that the incompressible turbulence model matches well with the realizable k-ε turbulence model. This finding was a good validation check since the flow is well below Mach number 0.1 and can be treated as incompressible. The streamlines in the realizable k-ε simulation and incompressible simulation compare the best to the experimental streamlines. The results from the k-ω SST model, Reynolds Stress with linear blending model, and Reynolds Stress with elliptic blending model all show that the streamlines downstream of the dilution jet do not match well with the experimental streamlines. For all five turbulence models, the turbulence levels are severely underpredicted when compared to the experimental results. This

finding is consistent with literature and was not all too surprising. In addition, the jet penetration is underpredicted for all five turbulence models when compared to the experimental results.

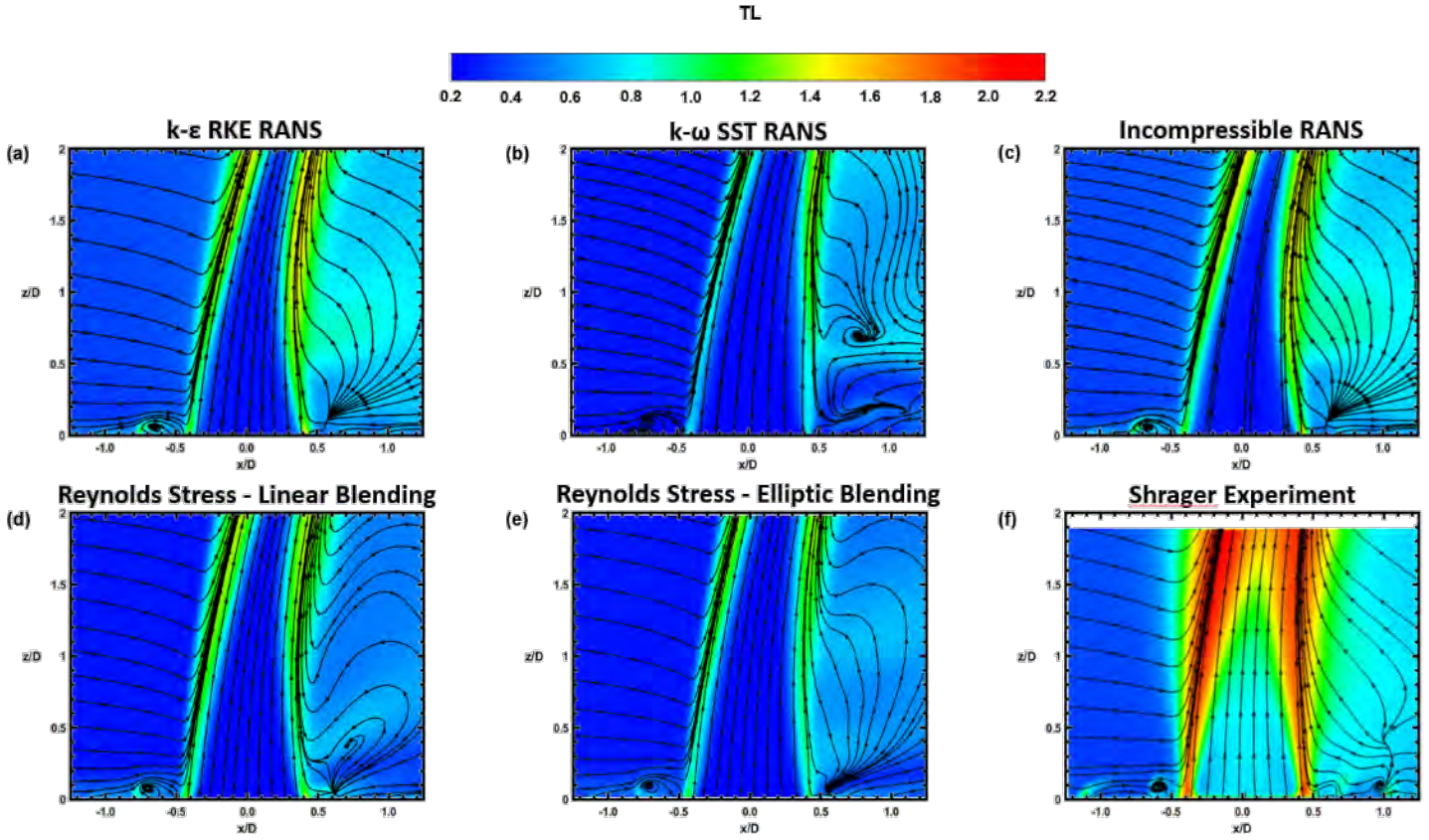

Figure 38. Predicted turbulence intensity contours for the outward facing effusion hole configuration with a dilution jet momentum flux ratio of I = 30 and a turbulence intensity of TI= 13% using the (a) realizable k-ε turbulence model, (b) k-ω SST turbulence model, (c) incompressible turbulence model, (d) Reynolds Stress turbulence model with linear blending, (e) Reynolds Stress turbulence model with elliptic blending, all compared to (f) experimental results from Shrager et al. (2018).

The realizable k-ε predictions compared to the Shrager et al. (2018) experimental results are shown in Figure 39. Figure 39 compares experimentally measured contours of normalized axial velocity, normalized spanwise velocity, and turbulence intensity to the realizable k-ε predictions. When comparing the experimental axial velocity contour shown in Figure 39a to the predicted axial velocity contour shown in Figure 39d, the flowfield upstream of the dilution jet is predicted accurately. The prediction does not compare well with the experimental results inside the dilution jet and downstream of the dilution jet. Within the dilution jet, the axial velocity is overpredicted. This can be explained by the fact that the jet trajectory does not penetrate as far into the mainstream in the computational predictions compared to the experimental results. Resulting from this jet turning, the flow velocity becomes stronger in the axial direction. The spanwise velocity of the experimental results shown in Figure 39b compares adequately with the spanwise velocity of the predicted results shown in Figure 39e. The predicted spanwise velocity is a little overpredicted in the dilution jet core when compared to the experimentally measured results but overall, the results agree well with each other. When comparing the turbulence intensity contour of the experimental results shown in Figure 39c to the predicted results shown in Figure 39f, the turbulence intensity is severely underpredicted within the dilution jet and downstream of the dilution jet. In all three contours it can be seen that the jet penetration is underpredicted for the realizable k-ε simulation when compared to the experimental results. When looking at the predicted streamlines, the streamlines are well predicted upstream of the dilution jet. Within the dilution jet the streamlines follow the jet as expected and show the underpredictions of the jet penetration clearly. Downstream of the dilution jet, the predicted streamlines do not match well with the experimental streamlines.

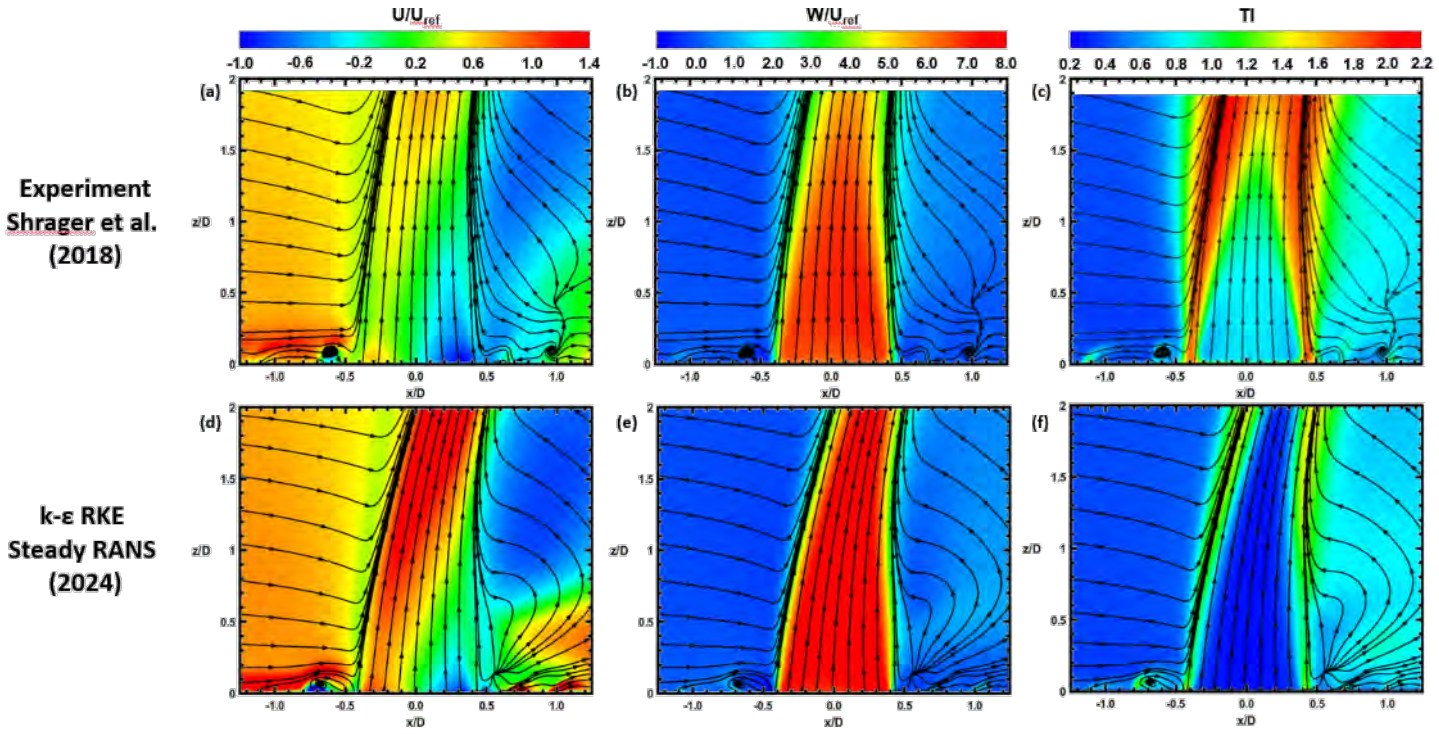

Figure 39. Experimentally measured (a) normalized axial velocity, (b) normalized spanwise velocity, and (c) turbulence intensity contours with streamlines overlaid from Shrager et al. (2018) compared to realizable k-ε turbulence model predicted (d) normalized axial velocity, (e) normalized spanwise velocity, and (f) turbulence intensity contours with streamlines overlaid for the outward facing effusion hole configuration with a dilution jet momentum flux ratio of I = 30 and a turbulence intensity of TI = 13.

The severe underprediction of the turbulence intensities and jet penetration led to further investigation into the current simulation's inlet boundary conditions. To produce the correct inlet turbulence boundary conditions, a RANS and LES simulation was completed this reporting quarter that included the turbulence bar grid used in the experiment. Both the RANS and LES bar grid simulations were run using the geometry domain shown in Figure 40 that extends the full wind tunnel height of 0.55 m and the full wind tunnel width of 1.11 m of the experimental setup. The boundary conditions include an inlet velocity set to a uniform 3.4 m/s with the bar grid located 15 bar diameters upstream of the computational domain inlet corresponding to the Shrager experiments. The domain exit boundary condition was set as a static pressure outlet with the pressure being equal to the experiment atmospheric pressure and was located at the same axial position as the exit for the computational domain. The simulation using the LES bar grid was run for four flow field times before any results were extracted to ensure the results were statistically stationary. A flow field time was defined and calculated by dividing the total domain length by the volume average axial velocity, as calculated from the RANS simulation. Once the bar grid simulation was considered statistically stationary, results were collected for an additional 9.5 flow field times. An appropriate timestep was determined after the bar grid LES solution had been initialized so that the convective Courant number was never greater than unity. After each statistically stationary timestep a table was exported containing values for the three components of velocity and static temperatures for each cell located on the blue plane, as designated in Figure 40. Once the simulation was completed, a master table that varied with time was imported into the domain and upon running RANS and LES, the turbulence decay from the grid bars to the experimental measurement plane agreed very well. This process provided the correct inlet boundary conditions to help further evaluate the poor prediction of the jet penetration and turbulence levels.

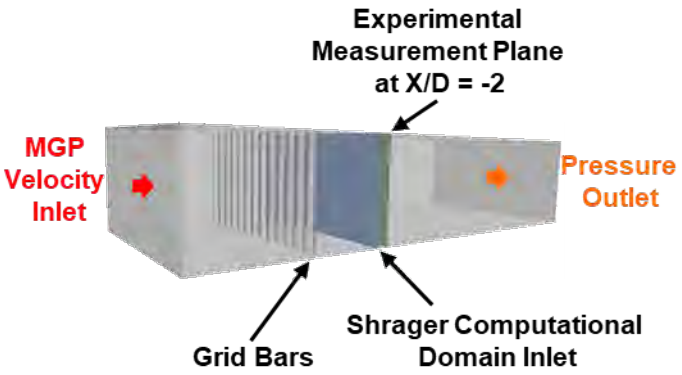

Figure 40. Bar grid domain used to extract inlet boundary conditions for the computational simulations corresponding to the Shrager experiments.

Rerunning the computational simulations of the Shrager experiments using the realizable k-ε RANS and LES models with the new inlet boundary conditions did improve the solution stability; however the jet penetration and turbulence levels were still severely underpredicted. A thorough analysis was then completed by examining the original particle image velocimetry (PIV) data from Shrager et al. (2018) to ensure the reported turbulence levels were not artificially elevated due to PIV processing settings, and that the reported momentum flux ratio was correct. The results of this recent in-depth analysis indicated the turbulence levels were not artificially elevated due to the chosen PIV processing settings. It was found that the PIV settings originally chosen were appropriate for the data, and high turbulence levels reported at the core of the jet can be attributed to the selected turbulence intensity nondimensionalization parameter. The turbulence intensity definition in the denominator used the average main gas path (freestream) velocity located at the domain inlet. The average freestream velocity was only 3.4 m/s while the velocity fluctuations within the dilution jet flow were around the same order of magnitude. This similarity between the jet flow velocity fluctuations and freestream velocity leads to higher dilution jet turbulence intensities than if the fluctuations were nondimensionalized by the dilution jet's local mean velocity. The dilution jet's mean velocity is an order of magnitude higher than the jet velocity fluctuations. When the dilution jet turbulence levels are defined using local jet velocities, the turbulence levels compare better to what is expected. In addition, the recent in-depth analysis showed that the momentum flux ratio reported by Shrager et al. (2018) was correct. A 2.8% and 2.9% error were seen when comparing the RANS dilution and effusion jet momentum flux ratios to the experimental data, respectively.

Beginning in January of 2024, manufacturing was started on the various profile simulator hardware components. Currently, the hardware components are 90% complete through the manufacturing process, and the estimated completion of all simulator components is mid-November 2024. Before the simulator is shipped to PSU, a trial fit of all main hardware components will be performed. This trial fit will ensure the components mate with each other as intended and none of the parts have to go back out for machining rework. This trial fit process will save PSU valuable time when the simulator arrives.

Over the past year, work was performed to begin procuring other miscellaneous parts that are needed for experimentally testing the simulator, such as the 360˚ traverse components, flow valves, flow meters, and general instrumentation. An instrumentation plan is being developed to establish (1) a bill of materials for the instruments and sensors that need to be ordered, (2) the details related to instrumentation installation and placement, and (3) the details related to the egress of sensor tubes and wires. The instrumentation will include temperature, pressure, and flow measurement devices placed throughout the simulator device to dial in experimental operation settings that enable the simulator to produce the target profiles. In addition, these measurement instruments can help aid in CFD validation by providing accurate experimental data that can be compared back to the computational predictions.

Milestones

Milestone	Completion Date	Status
Workplan	3/5/20	Completed
COE Meeting 1	10/29 - 10/29/21	Completed
COE Meeting 2	10/26 - 10/28/22	Completed
COE Meeting 3	10/24/23	Completed
COE Meeting 4	10/29 - 10/31/24	Completed
Annual Report	12/13/24	Completed

Major Accomplishments

- Successfully demonstrated improved dirt management for combustor liners through the implementation of a triple-wall cooling design. (Task 2)
- Completed manufacturing of the combustor profile simulator. In addition, more detailed computational predictions of the flowfield to meet the needs of the START facility have been completed with higher fidelity simulations being ramped up. (Task 3)

Publications

McFerran, K., Thole, K. A., & Lynch, S. P. (2025). Dirt ingestion impacts on cooling within a double-walled combustor liner. *ASME Journal of Turbomachinery, 147*(8), 081019. https://doi.org/10.1115/1.4067464

Schaeffer, C. B., Barringer, M. D., Lynch, S. P., & Thole, K. A. (2025). Influence of dilution and effusion flows in generating variable inlet profiles for a high-pressure turbine. *ASME Journal of Turbomachinery*, 147(3), 031003. https://doi.org/10.1115/1.4066560

Schaeffer, C. B., Barringer, M. D., Lynch, S. P., & Thole, K. A. (2025). *Comparison of predicted and measured combustor-relevant flow fields* (GT2025-15782). (in progress).

Outreach Efforts

- Presented periodically to Pratt & Whitney through this joint collaboration.
- Presented the combustor simulator concept to the U.S. Department of Energy, Siemens Energy, Honeywell, and Pratt & Whitney. Industry partners are very supportive of this direction and provide guidance.

Awards

Chad Schaeffer won a third-place poster award for a poster focused on the profile simulator design and corresponding computations that he presented at the National Aeronautics and Space Administration (NASA) ImaginAviation University Poster Session.

Student Involvement

Kyle McFerran earned his Master of Science in Mechanical Engineering in August 2024. Kyle started working for Pratt & Whitney starting in September 2024. Chad Schaeffer is performing CFD simulations and assisting in the design of the combustor profile simulator. Chad successfully passed the PhD comprehensive examination in April 2024. All students participate in weekly meetings with their advisors (Berdanier/Thole/Lynch) and in regular meetings with Pratt & Whitney. They regularly present their findings to Pratt & Whitney, including to a larger Pratt & Whitney audience at the biannual Center of Excellence meetings (June and November).

Plans for Next Period

- Optimize the multi-wall combustor liner design and evaluate associated heat transfer performance benefits (Task 2).
- Begin integration for the profile simulator into the START rig and continue with higher fidelity computational simulations (Task 3).

References

Barringer, M. D., Thole, K. A., & Polanka, M. D. (2004, June 14-17). Developing a combustor simulator for investigating high pressure turbine aerodynamics and heat transfer. *Proceedings of the ASME Turbo Expo 2004: Power for Land, Sea, and Air. Volume 3: Turbo Expo 2004,* Vienna, Austria. https://doi.org/10.1115/GT2004-53613

Choi, W., & Kim, S. (2022). Effect of effusion hole arrangement on jet array impingement heat transfer. *International Journal of Heat Mass Transfer, 192*, 122900.

Fallon, B., McFerran, K., Fox, S., Thole, K.A., & Lynch, S.P. (2023, June 26-30). Comparison of dirt deposition on double-walled combustor liner geometries. *Proceedings of the ASME Turbo Expo 2023: Turbomachinery Technical Conference and Exposition. Volume 13C: Turbomachinery — Deposition, Erosion, Fouling, and Icing; Design Methods and CFD Modeling for Turbomachinery; Ducts, Noise, and Component Interactions*, Boston, Massachusetts

Gardon, R., & Akfirat, J.C. (1965). The role of turbulence in determining the heat-transfer characteristics of impinging jets. *Journal of Heat Mass Transfer, 8*(10), 1261-1272.

Gardon, R., & Akfirat, J.C. (1966). Heat transfer characteristics of impinging two-dimensional air jets. *Journal of Heat Mass Transfer, 88*(1), 101-107.

Karalus, M., Krishnamoorthy, N., Reynolds, B., & Mallouppas, G. (2019, June 17-21). An assessment of the implicit non-iterative PISO solution procedure for the prediction of combustor performance. *Proceedings of the ASME Turbo Expo 2019: Turbomachinery Technical Conference and Exposition. Volume 4B: Combustion, Fuels, and Emissions*, Phoenix, Arizona. https://doi.org/10.1115/GT2019-90950

Lundgreen, R. K. (2017, June 26-30). *Pressure and temperature effects on particle deposition in an impinging flow proceedings of the ASME Turbo Expo 2017: Turbomachinery Technical Conference and Exposition. Volume 2D: Turbomachinery*, Charlotte, North Carolina. https://doi.org/10.1115/GT2017-64649

McFerran, K., Thole, K. A., & Lynch, S. P. (2025). Dirt ingestion impacts on cooling within a double-walled combustor liner. *ASME Journal of Turbomachinery, 147*(8), 081019. https://doi.org/10.1115/1.4067464

OEM Engine Manufacturers. (2022). *Private communication with OEM engine manufacturers requesting combustor exit profiles at the vane inlet.*

Povey, T., Chana, K. S., Jones, T. V., & Hurrion, J. (2007). The effect of hot-streaks on HP vane surface and endwall heat transfer: An experimental and numerical study. *ASME Journal of Turbomachinery, 129*(1), 32–43. https://doi.org/10.1115/1.2370748

Shrager, A. C., Thole, K. A., & Mongillo, D. (2018). Effects of effusion cooling pattern near the dilution hole for a double-walled combustor liner—Part II: Flowfield measurements. *ASME Journal of Engineering for Gas Turbines and Power, 141*(1), 011023. https://doi.org/10.1115/1.4041153

Shrager, A. C., Thole, K. A., & Mongillo, D. (2019). Effects of effusion cooling pattern near the dilution hole for a double-walled combustor liner—Part 1: overall effectiveness measurements. *ASME Journal of Engineering for Gas Turbines and Power, 141*(1), 011022.

Singh, S., Reagle, C., Delimont, J., Tafti, D., Ng, W., & Ekkad, S. (2013). Sand transport in a two pass internal cooling duct with rib turbulators. *International Journal of Heat and Fluid Flow*, 46, 158-167. https://doi.org/10.1016/j.ijheatfluidflow.2014.01.006

Disclaimer

This research was funded by the U.S. Federal Aviation Administration Office of Environment and Energy through ASCENT, the FAA Center of Excellence for Alternative Jet Fuels and the Environment, Project 68 through FAA Award Number 13-C-AJFE-PSU-109 under the supervision of Joshua Glottmann. Any opinions, findings, conclusions or recommendations expressed in this material are those of the authors and do not necessarily reflect the views of the FAA.

Project 069 Transitioning a Research nvPM Mass Calibration Procedure to Operations

Missouri University of Science and Technology, Aerodyne Research Inc., & U.S. Air Force Arnold Engineering Development Center

Project Lead Investigator

Philip D. Whitefield
Professor Emeritus of Chemistry
Department of Chemistry
Missouri University of Science and Technology
400 W 11th Street, Rolla, MO 65409
573-465-7876
pwhite@mst.edu

University Participants

Missouri University of Science and Technology (MS&T)

- P.I.: Prof. Philip D. Whitefield
- FAA Award Number: 13-C-AJFE-MST, Amendments 014, 020, and 023
- Period of Performance: June 5, 2020, to January 31, 2024
- Task:
  1. Investigate the validity of the centrifugal particle mass analyzer mass calibration research approach for non-volatile particulate matter certification measurement systems

Project Funding Level

Project	Funding	Matching	Source
13-C-AJFE-MST; Amendment 014	$846,707.00	$846,707.00	EMPA letter
13-C-AJFE-MST; Amendment 020	$100,853.00	$100,853.00	FOCA letter
13-C-AJFE-MST; Amendment 023	$99,999.00	$99,999.00	GE letter

Investigation Team

Missouri University of Science and Technology Prof. Philip Whitefield, (P.I.)
Steven Achterberg, (research technician)
Max Trueblood, research technician
William Satterfield, research technician
Aerodyne Research, Inc. (ARI)
Dr. Richard Miake-Lye, (subcontractor)
Arnold Engineering Development Center (AEDC)
Dr. Robert Howard, (subcontractor)

Project Overview

This project is designed to investigate the validity of the centrifugal particle mass analyzer (CPMA) mass calibration research approach. The assessment will extend across all non-volatile particulate matter (nvPM) mass ranges encountered during certification tests. The primary goal will be the successful transitioning of the research methods to operations. The project will begin with a laboratory assessment leading to dedicated turbine engines as the test sources at the U.S. Air Force (USAF) AEDC. The challenge mass devices for calibration (micro-soot sensor [MSS], laser-induced incandescence

monitor, and cavity attenuated phase shift monitor) will be provided by the North American Reference nvPM Measurement System, together with the CPMA and other necessary instruments, such as a DMS500 particulate analyzer, and aerosol mass spectrometer.

Task 1 – Investigate the Validity of the Centrifugal Particle Mass Analyzer Mass Calibration Research Approach for Non-volatile Particulate Matter Certification Measurement Systems

Missouri University of Science and Technology

Objectives

The objectives of this task are to acquire the components of a CPMA-based mass calibration system similar to that described in Society of Automotive Engineers SAE E31 discussion paper DP-32 (presented by Dr. G. Smallwood) from the annual SAE E31 committee meeting on June 17–21, 2019, in Saclay, France; assemble the system; and evaluate its performance.

Research Approach

Subtask 1.1 (Completed)

Acquire the components of a CPMA-based mass calibration system similar to that described in SAE E31 discussion paper DP-32 (presented by Dr. G. Smallwood) from the annual committee meeting on June 17–21, 2019, in Saclay, France. The CPMA-based system has also been referred to as the CPMA-Electrometer Reference Mass Standard (CERMS).

Subtask 1.2 (Completed)

Assemble and test the CPMA-based mass calibration system's performance at MS&T's laboratories, by using a miniature combustion aerosol standard (Minicast) as the nvPM generation source (Figure 1). Compare the laboratory performance of the MS&T CPMA-based mass calibration system with that of two highly similar systems owned and operated by the University of Alberta and the Canadian National Research Council (NRC).

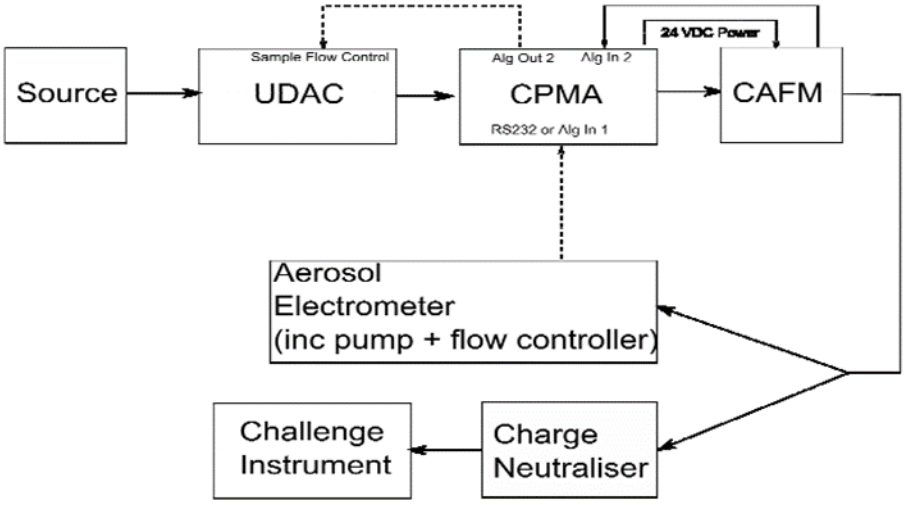

Figure 1. Schematic diagram of the CPMA-based mass calibration system.

Subtask 1.3 (Completed)

Investigate the validity of the CPMA mass calibration research approach across all nvPM mass ranges encountered during certification tests, to successfully transition the methods to operations.

Subtask 1.3a (Completed)
Deploy (transport and install) the North American Reference System, including the CPMA-based mass calibration system and ancillary diagnostic suite, with the USAF's AVL® nvPM measurement system and the two Canadian CPMA systems, at engine testing facilities at Arnold Air Force Base in Tennessee, which will include the J85 turbojet and a gas-turbine-based "start cart" as nvPM sources.

Subtask 1.3b (Completed)
Evaluate the performance of the three CPMA-based mass calibration systems, surveying across all mass ranges by using the start cart as the nvPM source; compare these results with concomitant mass calibration data acquired with SAE E-31 OCEC-based mass calibration methods.

Subtask 1.3c (Completed)
Demonstrate the performance with an nvPM emissions test on the J85 engine, with calibration including standard elemental carbon/organic carbon (EC/OC) analysis, as well as the CPMA-based calibration system described in DP-32.

Subtask 1.3d (Completed)
Decouple the diagnostic suites from the Arnold Air Force Base engine facilities and transport them back to Missouri and Massachusetts.

Subtask 1.4 (Completed)
Analyze and interpret the data gathered in Subtasks 1.2 and 1.3.

Subtask 1.5 (In Preparation)
Prepare and deliver a final report.

Milestones

- Developed and reviewed a laboratory-based assessment strategy.
- Acquired and tested essential components for the assessment study, including a Minicast nvPM source, a sample mixing and distribution plenum, and a semi-continuous EC/OC analyzer (Sunset). Substantial effort has been invested in assuring the performance of the analyzer, with modest success. The MS&T team has worked closely with Sunset and will send a representative to the forthcoming engine demonstration. Backup manual EC/OC sampling will be performed at the engine demonstration.
- Operated the CPMA mass standard source in conjunction with the and MSS mass monitors.
- Performed a laboratory-based performance comparison of the MS&T CPMA-based calibration system has undergone against two Canadian CPMA-based calibration systems.
- Conducted engine emissions testing performance at AEDC.
- Completed performance evaluation of multiple CPMA systems.
- Implemented and executed manual EC/OC.
- Completed assessment tests using start cart.
- Completed assessment tests using J85.
- Completed data reduction and analysis.

Major Accomplishments

Essential diagnostic equipment has been acquired, and work on Subtasks 1.2 and 1.3 is complete. The laboratory-based measurements and engine-specific measurements have been completed. Figure 2 and Figure 3 are schematic diagrams of the two instrument configurations used in the engine-specific assessment tests conducted at Arnold Engineering Development Center (AEDC). The configuration in Figure 2 is designed for intercomparison of the performance of the three Centripetal Particle Mass Analyzer (CPMA) systems made available for the project. The configuration in Figure 3 was used to demonstrate a CPMA-based calibration of optical mass measurement instruments, specifically the Micro Soot Sensor (MSS), laser induced incandescence (LII), and Cavity Attenuated Phase Shift (CAPS) system. The configuration in Figure 3 also included a filter-based system (Teflon® and quartz) to perform thermo-gravimetric total OC/EC measurements with the

® AVL is a registered trademark of AVL List GMBH, Graz, Austria.
® Teflon is a registered trademark of The Chemours Company FC, LLC, Wilmington, Delaware.

NIOSH 5040 method (NIOSH, 2003). During a 3-week period in April 2023, the instrumentation was assembled as described, and the measurements were made.

The project has undergone its data analysis and interpretation phase, and the final report has been prepared by the ASCENT Project 069 team. The members of the ASCENT Project 069 team and their results, conclusions and recommendations are summarized below.

The ASCENT Project 069 team is comprised of the following team members:

- The ASCENT Project 069-funded research was led by P.I. Phil Whitefield MS&T, and Co P.I.s Rick Miake Lye (ARI) and Robert Howard (AEDC). They were supported by Klaus Woelk, Steven Achterberg, Max Trueblood, Dave Satterfield (MS&T), and Ben Naught (ARI)
- The NRC Canada team was led by P.I. Greg Smallwood supported by Rym Mehri and Brett Smith
- The University of Alberta team was led by P.I. Jason Olfert supported by Robert Nishida
- The U.S. Environmental Protection Agency (EPA) team was led by Robert Giannelli supported by John Kinsey, Jeff Stevens, Samuel Johnson, and David Kittelson.

An anticipated outcome of this study, "Transitioning A Research nvPM Mass Calibration Procedure to Operations," was to demonstrate that the CERMS system was a field-deployable, user-friendly, low cost mass calibration system for nvPM measurements during engine emissions certifications. Based on the CERMS in its current state of development and in consideration of the results of this study, the ASCENT Project 069 team believes the CERMS has demonstrated potential to reduce the uncertainty associated with the current reference for mass concentration instruments, EC, but does not fully satisfy the desired operational criteria due to some issues that were observed. Additionally, calibration with a CERMS should be done by a competent laboratory. As a result, the team recommends that a follow-on evaluation study is justified addressing the unresolved issues described in this report.

It is important to note that using the CERMS is fundamentally different from the traditional calibration method. In the CERMS, the principle is to provide a stream of particles of known mass concentration. Whereas the traditional calibration requires a concurrent measurement of EC to establish the concentration of particles from the calibration source.

In terms of assessing the reproducibility of CERMS, the uncertainties in this study indicate that it may be capable of lowering the uncertainty associated with the calibration of the mass concentration instruments. This uncertainty could be significantly reduced if the recommendations to minimize the bias between CPMAs is investigated.

Future experiments should include using different particulate matter measurement techniques in similar configurations (including the aerosol mass spectrometer [AMS]), to investigate if the CERMS system, dilution, and/or other aspects not considered here, lead to the losses of the volatile particulate matter.

Although some of the issues encountered by the ASCENT Project 069 team are a result of instrument limitations (penetration through the instruments and hence low concentration), further studies are recommended to address the issues encountered during this study. These recommended future studies would have the following objectives.

- Objective 1: Reduce the reproducibility uncertainty. The reproducibility for CERMS was largely attributed to the CPMA reproducibility, such that reducing the CPMA uncertainty will have a direct impact on reducing the CERMS uncertainty. The CPMA response could be potentially traceably calibrated using certified reference material (CRM) particles of a known narrow mass distribution.
- Objective 2: Understand the impact of particle conditioning on CERMS. Simultaneous characterization of the particles (using different laboratory and engine sources) upstream and downstream of the CPMA would be informative to understand the effect of the CPMA classification (in time) on the particle composition, with and without the use of a catalytic stripper.
- Objective 3: Increase the CERMS output mass concentration. Determine the influence of the CPMA model (Mk I or Mk II) on the classified particles and penetration through the instrument. Investigate the use of high transmission efficiency chargers in place of the Unipolar Diffusion Aerosol Charger (UDAC).
- Objective 4: Optimize CERMS set point determination. Address the shift in the UDAC charging efficiency in time or changes in the experimental setup.
- Objective 5: Determine performance of CERMS under realistic calibration conditions. Compare CERMS and TOA in the context of a calibration as intended with a gas turbine source across a representative concentration range. This

will require a direct comparison of the EC to the electrometer, without any other instruments, and may result in low concentrations on the filter used for EC analysis due to shorter acquisition periods.

- It is recommended that future experiments should use low sulfur jet fuel to avoid poisoning of the catalytic stripper.

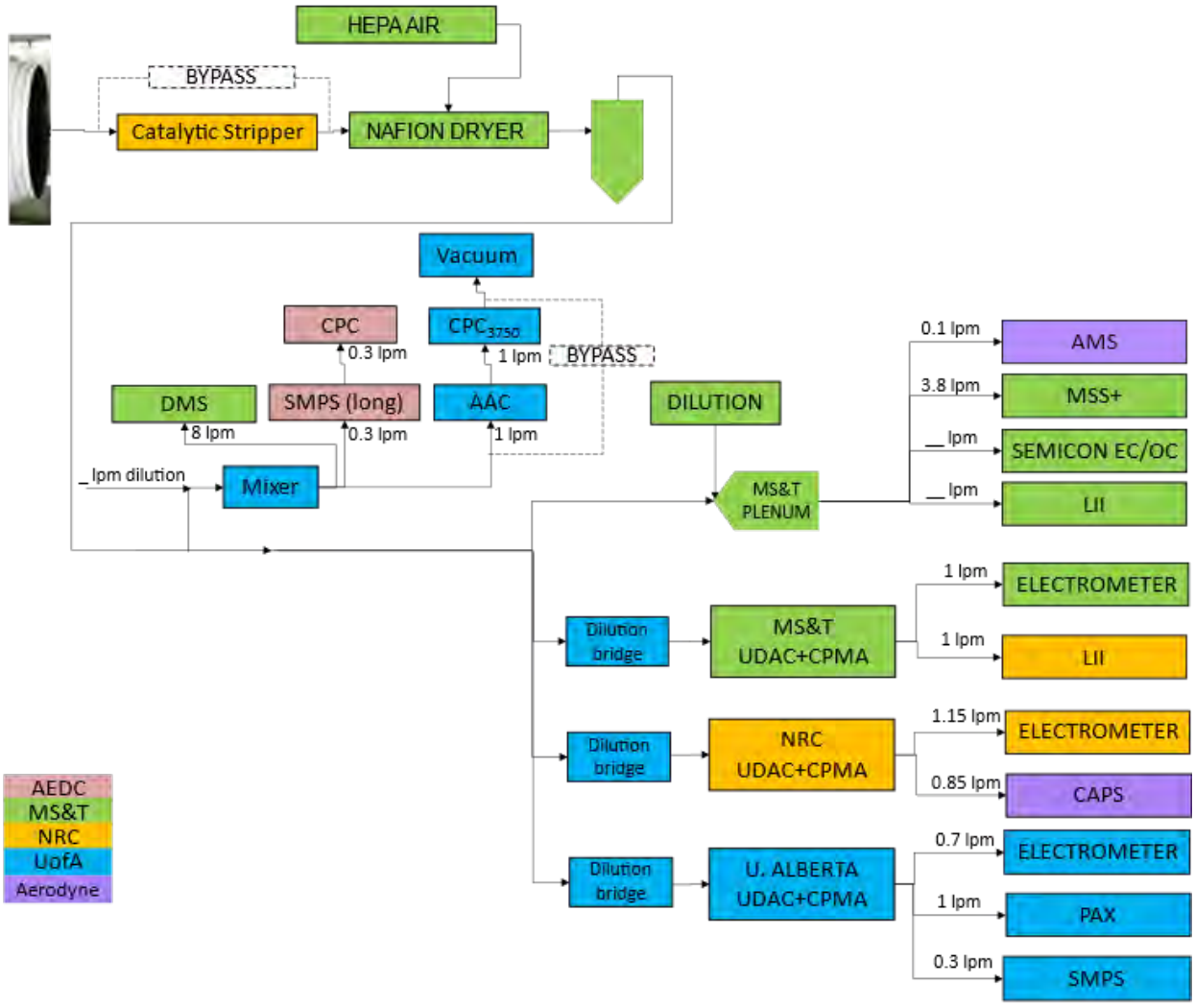

Figure 2. Instrument configuration 1.

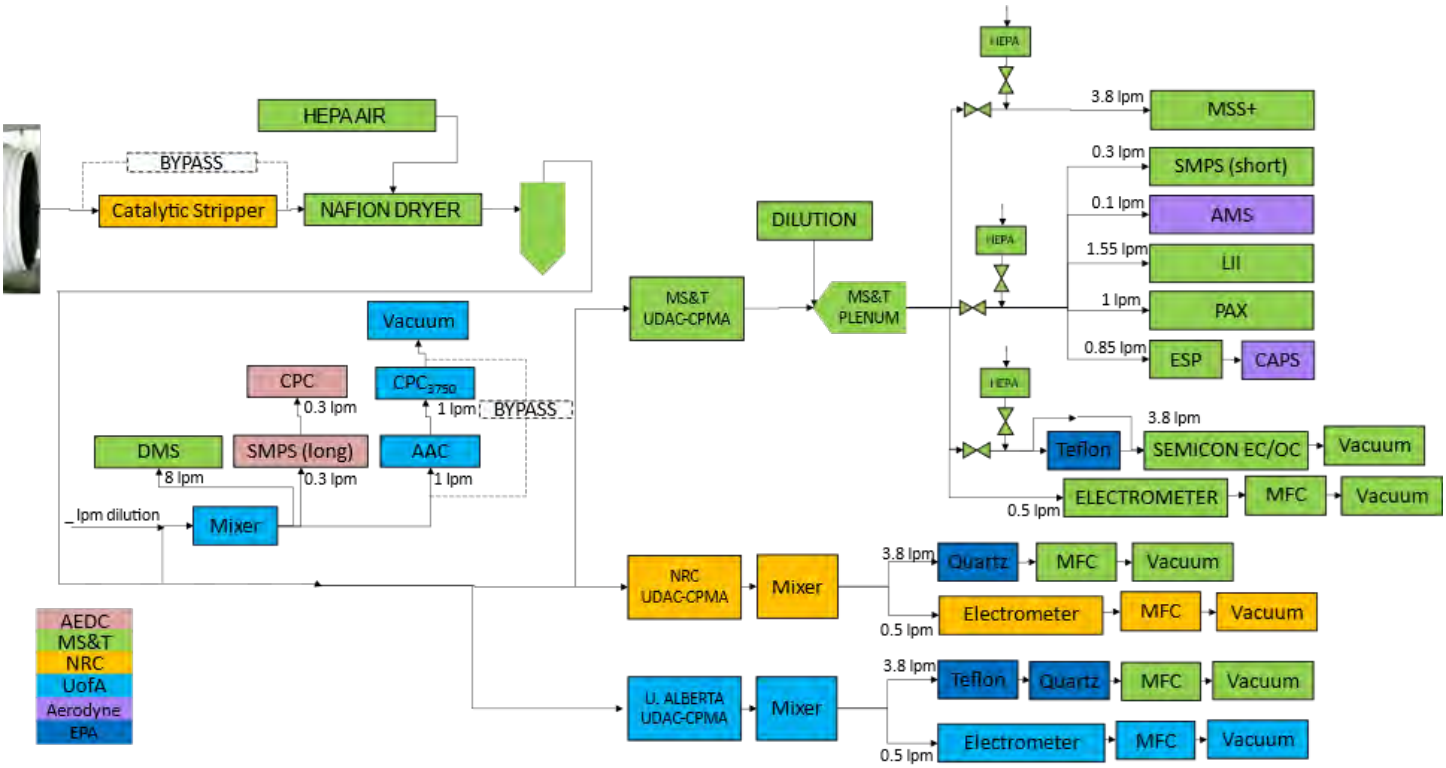

Figure 3. Instrument configuration 2.

Publications

Published Conference Proceedings

Whitefield, P. (2023, May). *Transitioning a research nvPM mass calibration procedure to operations* [Oral presentation]. ASCENT Advisory Board Meeting, Alexandria, Virginia.

Whitefield, P and Offert, J. (2023, October). *Transitioning a research nvPM mass calibration procedure to operations* [Oral presentation]. ASCENT Advisory Board Meeting, National Academy of Science, Washington D.C.

Whitefield, P and Offert, J. (2024, January). *Transitioning a research nvPM mass calibration procedure to operations* [Oral presentation]. SAE E31 Meeting, Albuquerque, New Mexico.

Whitefield, P. (2024, October). *Transitioning a research nvPM mass calibration procedure to operations* [Oral presentation]. ASCENT Advisory Board Meeting, Alexandria, Virginia.

Outreach Efforts

The CPMA-based mass calibration system has been transported to Canada for a laboratory-based intercomparison study.

Awards

None.

Student Involvement

One graduate student, Godwin Ogbuehi, and two undergraduate students have been assigned to this project.

Plans for Next Period

The advisory/research team plans to brief the SAE E31committee, Committee on Aviation Environmental Protection Working Group 3, Federal Aviation Administration, EPA, and NRC on the results, conclusions and recommendations of the study to date and seek support for a follow-on program targeting the future research objectives described above.

Reference

DP-32

National Institute for Occupational Safety and Health. (2003). *NIOSH Manual of Analytical Methods (NMAM)* (4th Ed.): Diesel Particulate Matter (as Elemental Carbon) (Method 5040, Issue 3). https://www.cdc.gov/niosh/docs/2003-154/pdfs/5040.pdf

Project 070 Reduction of nvPM Emissions from Aero-Engine Fuel Injectors

Georgia Institute of Technology

Project Lead Investigator

Wenting Sun
Associate Professor
School of Aerospace Engineering
Georgia Institute of Technology
270 Ferst Drive, Atlanta, GA 30332
404-894-0524
wenting.sun@aerospace.gatech.edu

University Participants

Georgia Institute of Technology (Georgia Tech)

- P.I.: Dr. Wenting Sun
- FAA Award Number: 13-C-AJFE-GIT-080
- Period of Performance: September 01, 2023, to September 30, 2024
- Task:
  1. Spray characterization and measurement of non-volatile particulate matter formation

Project Funding Level

The total amount of funding from the Federal Aviation Administration (FAA) is $1,500,000. The funding match includes $1,350,000 from the Georgia Institute of Technology and $150,000 from Honeywell.®

Investigation Team

Georgia Institute of Technology

Wenting Sun, (P.I.), Task 1,3
Adam Steinberg, (co-P.I.), Task 1
Ellen Yi Chen, (co-P.I.), Task 1
Shawn Wehe, (research engineer), Task 1,3
Rahul Vishwanath, (postdoctoral fellow), Task 1,3
Dominic Olimid, (graduate student), Task 1
Eric Douglas, (graduate student), Task 1
Adhav Arulanandan, (graduate student), Task 1
Andrew Fan, (graduate student), Task 1

Honeywell. Inc

Rudy Dudebout, (co-P.I.), Task 2
Fang Xu, (co-P.I.), Task 2

Project Overview

Reducing non-volatile particulate matter (nvPM) from gas turbine engines is essential for improving air quality and decreasing the environmental impact of aviation. However, predicting and controlling nvPM remains a challenge because of the complicated physical and chemical processes at play. The proposed research will characterize the fuel spray and nvPM

® Honeywell is a registered trademark of Honeywell International, Inc., Charlotte, North Carolina.

formation for optimizing the design of an aeronautical gas turbine fuel injector to reduce nvPM at flight-relevant conditions. In this project, the ASCENT Project 070 team developed a sector combustor containing three fuel injectors. The sector combustor is a generic rich-quench-lean (RQL) jet engine combustor equipped with the actual fuel injectors used in Honeywell's auxiliary power unit (APU). The combustor was fabricated through three-dimensional (3-D) printing, and the fuel injectors are directly provided by Honeywell. The combustor and high-pressure system were detailed in a previous report and are presented briefly in the next section. The research focus of this year is on conducting an experimental campaign to characterize droplet size and measure nvPM volume fraction distribution in the primary zone of the combustor, a region between the fuel injector and downstream quenching holes. The performance of combustion in this rich region dictates the overall performance of the combustor therefore it is the research focus of this project.

Task 1 – Spray Characterization and Measurement of Non-volatile Particulate Matter Formation

Georgia Institute of Technology

Objective

The objective of Task 1 is to obtain drop-size distribution for spray injectors using phase doppler particle anemometry (PDPA) and to quantify the nvPM volume fraction by laser-induced incandescence (LII) under a broad range of conditions for Jet A fuel and sustainable aviation fuel (SAF), respectively.

Research Approach

In this year, droplet-size distributions are obtained to characterize liquid fuel spray using PDPA at different pressure, inlet temperature, and equivalence ratio conditions in both reacting and non-reacting conditions. **This is the first such measurement performed in a three-sector combustor housed in a pressure vessel due to its unconventional configuration.** Additionally, quantitative measurements of soot volume fraction have been obtained using two-color LII at different operating conditions. Both these measurements are performed using Jet A fuel and SAF to compare the combustion characteristics of both the fuels and their blends. The SAF employed in this study is the hydroprocessed esters and fatty acids (HEFA) from World Energy. Results are presented below in corresponding sections.

Subtask 1.1: Droplet-size measurement using PDPA

PDPA utilizes the light scattering interferometry technique wherein interference signals are created by two intersecting laser beams in a small measurement volume of interest. As individual particles/droplets move through this volume, a shift in the frequency of scattered light is detected which is proportional to the particle velocity. Additionally, there is a phase shift in the detected interference signal which is proportional to the size of the particle. Hence, simultaneous information on particle velocity and size can be obtained with high spatial and temporal accuracy using this technique. One of the major advantages of PDPA is that the fringe patterns produced by the particles are obtained only from the scattered light signals produced within the probe volume, which eliminates signal interference from other sources. For environments with high spatial and temporal variations in density, the technique suffers from beam steering, which gives rise to low signal to noise ratios.

For measuring droplet sizes, PDPA requires off-axis scattering angles in the range of 30-70 degrees. This presents a challenge for confined combustors housed in pressure vessels wherein such scattering angles are not available. To overcome this difficulty, a creative mirror system has been proposed and mounted inside the pressure vessel to obtain scattering angles up to 40 degrees in the plane of measurement.

The PDPA system (from Dantec Dynamics®) consists of a diode-pumped solid state (DPSS) laser transmitter capable of emitting a pair of 1000 mW, 561 nm laser beams, with each beam frequency shifted by 40 MHz using a Bragg cell. Although the system can operate with two pairs of laser beams at 532 nm and 561 nm, only one pair is utilized for droplet-size measurements. The laser beam pair is then sent into a transmitter probe (TSI, Inc.) through fiber optic cables, where a lens having a focal length of 61 cm is used to focus the two beams into the sample measurement volume. The phase-shifted light scattered from the droplet in the small measurement volume is then collected by a receiver module through two mirrors placed and aligned such that the collection angle of the scattered light is approximately 40 degrees. The collected light passes through a three slit mask mounted onto the receiver, where the light through each of the slits is

® Dantec Dynamics is a registered trademark of Dantec Dynamic, Inc., Mahwah, New Jersey.

focused separately and transmitted through fiber optical cables into the basic spectrum analyzer (BSA). The analyzer is capable of measuring signal bursts at frequencies up to 400 kHz and subsequently produce instantaneous drop-size distributions.

The combustor wall (liner) includes three Honeywell aircraft swirl injectors on the dome face, representing typical multiple sectors of an aeroengine combustor, as illustrated in Figure 1b. The combustion liner has four fused quartz windows for optical access. Two windows on opposing sides enable laser access across all three injectors, and two windows on top provide visual access to the rich-burn and lean-burn regions. The mirror system is mounted onto the inner face of the quartz vessel window flange as shown in Figure 1a. It consists of two mirrors, with the first mirror having a 7.5 cm diameter clear aperture and the second mirror having a 15 x 10 cm rectangular area. They are aligned together to collect the scattered light from the droplets and focus onto the PDPA receiver module. The entire mirror system mount is made of stainless steel to minimize material deformation from high temperature air flowing through the vessel. The measurement region was restricted to a 5 cm x 5 cm area on left-hand side of the central nozzle as shown in Figure 1a, due to the constraints on the current PDPA and mirror system.

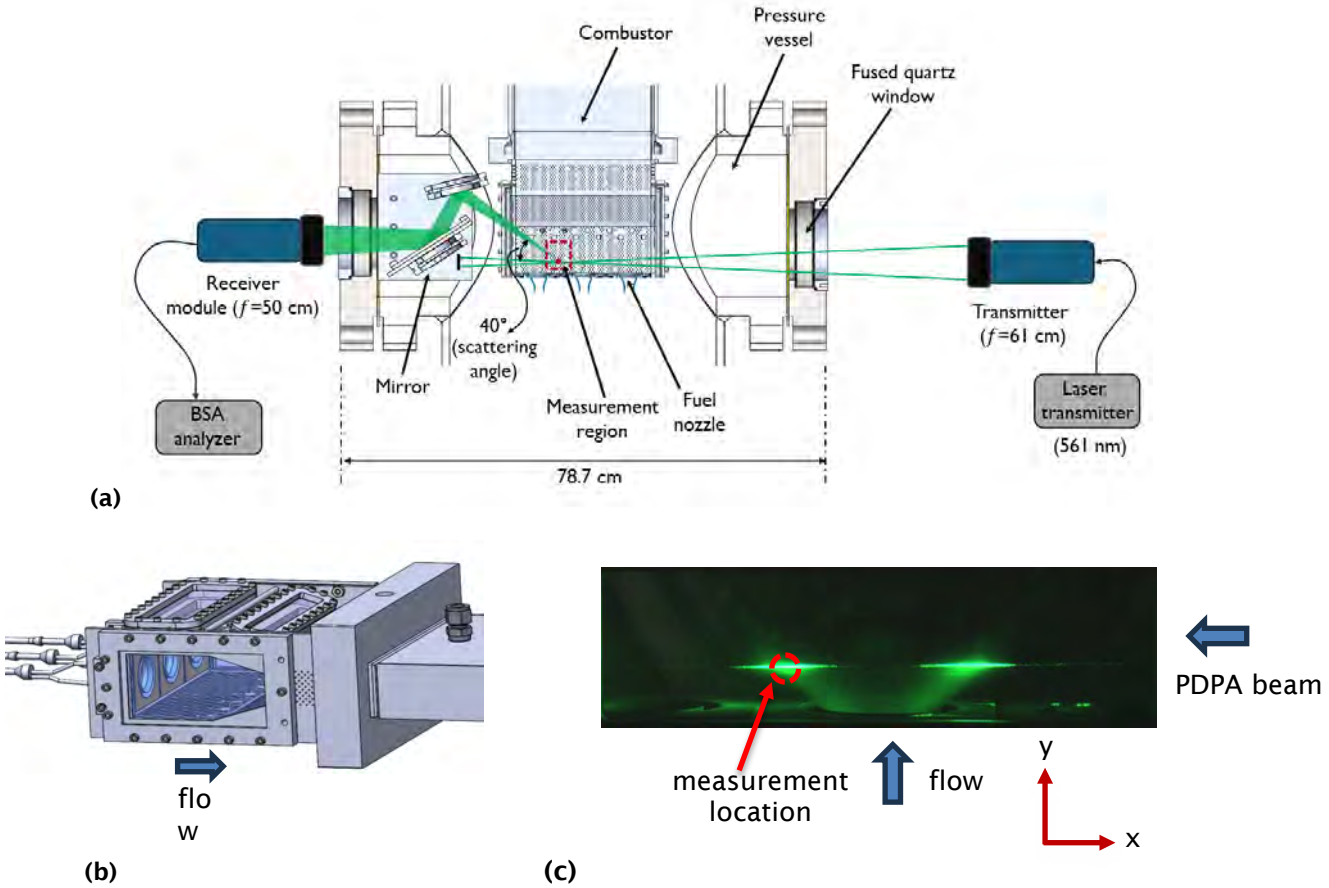

Figure 1. (a) Schematic of the PDPA setup showing the two-mirror configuration to obtain required scattering angles in a confined vessel for the depicted measurement region. (b) View of the combustor depicting the three fuel nozzles and quartz windows for optical access. (c) Raw image of Mie scattering from the central injector spray along with the PDPA laser beam oriented in the vertical plane (perpendicular to the flow direction) passing through the spray. PDPA: phase doppler particle anemometry, BSA: basic spectrum analyzer.

Experiments are performed at both cold flow and reacting flow conditions to study the effect of combustion environment on droplet vaporization and subsequent drop-size. In all cases, only the central injector is operated so that the droplets do

not cover the combustor windows which will affect PDPA measurements, especially in cold-flow conditions. A total of four operating conditions were chosen with varying pressure (0 psig, 35.3 psig, 85.3 psig), preheat temperature (450 K, 600 K), and global equivalence ratio (0.264, 0.315) for both Jet A fuel and SAF. It is to be noted that since the combustor is run on a RQL concept, the local equivalence ratios in the rich-burn region immediately downstream of the nozzles may vary from 1.22 to 1.45, depending on the global equivalence ratio. Although only the central injector is utilized while operating the combustor for PDPA measurements, the local equivalence ratio for that injector should remain the same. For cold flow conditions, ten measurement locations were chosen, whereas for reacting conditions only four locations were chosen where minimal soot was present just downstream of the nozzle dump plane along the spray cone.

At every spatial location, a total of 10,000 instantaneous measurements were made for all cases. But in certain conditions where the signal to noise ratio was slightly poor, the total measurement counts reduced. Nonetheless, the frequency distributions were repeatable for all conditions. The current fuel injectors utilized in this study are pre-filming air blast-type assisted with surrounding swirl air for jet breakup. Figure 2 shows the number frequency and Sauter mean diameter (SMD) distribution at various spatial locations for a non-reacting Jet A fuel spray at 35.3 psig pressure and 450 K preheat temperature. Zero on the x-axis represents the center axis of the center fuel injector. The Y axis represents the distance from the combustor dome face. The droplet diameters are typically in a broad range of 1-100 μm at most locations, although the maximum frequencies are within the small range of 10-40 μm suggesting good atomization at these operating conditions. Due to the right skewed nature of the number frequency distributions, the SMD values tend to shift towards larger diameters, but the peak diameters are always lower.

It can be seen from the results shown in Figure 2, the SMD values of the droplets reduced with increasing axial distance downstream of the injector along the spray cone as the swirling air assists in secondary atomization of the spray. Another reason for the decrease of SMD along the flow direction is vaporization of the droplets while flowing downstream. It is to be noted that the present PDPA system can detect droplets only in the range of 0.1-170 μm based on the slit size and mask used on the receiver module. As seen from the frequency distributions, this range was sufficient to cover the entire spray as the probability of detecting droplets larger than 150 μm was almost negligible.

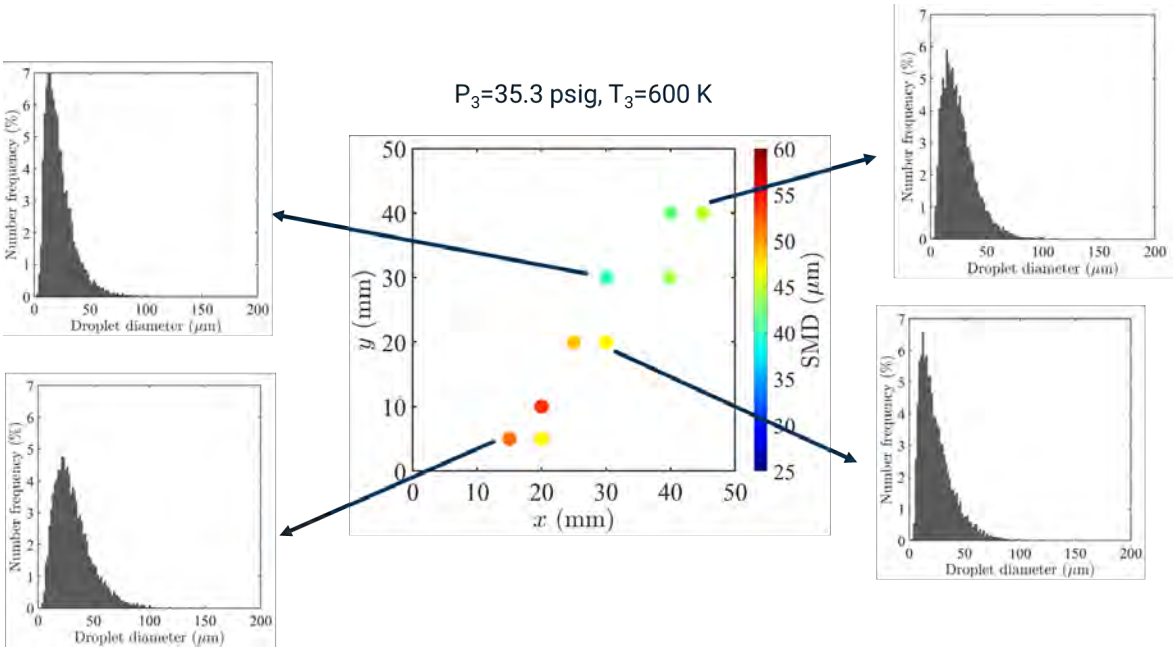

Figure 2. Sauter mean diameters (SMDs) and number frequency distributions from PDPA measurements for non-reacting Jet A fuel spray at 35.3 psig pressure and 450 K preheat temperature.

Figure 3 shows the SMD values measured at different operating conditions for Jet A in non-reacting spray. Apart from the general trend of decreasing diameters with increasing downstream distance, there are trends observed with different

pressures and preheat temperatures. With increasing operating pressure, the SMD decreases for a given location and preheat temperature. This is due to the increase in Reynolds number of the surrounding air causing larger relative velocities between the liquid and gas phase, thereby inducing faster primary breakup of liquid jet and subsequent smaller droplets. The amount of reduction is highly dependent on the Reynolds number range or the operating pressure. The reduction in SMD due to increasing preheat for surrounding air is due to droplets being able to evaporate faster as they travel downstream of the fuel nozzle. Compared to the atmospheric conditions, the mean SMD values have decreased by more than two times when the combustor is operated at 85.3 psig pressure at a preheat of 600 K. Our results suggest that measurements and characterization need to be conducted in practical engine operating conditions.

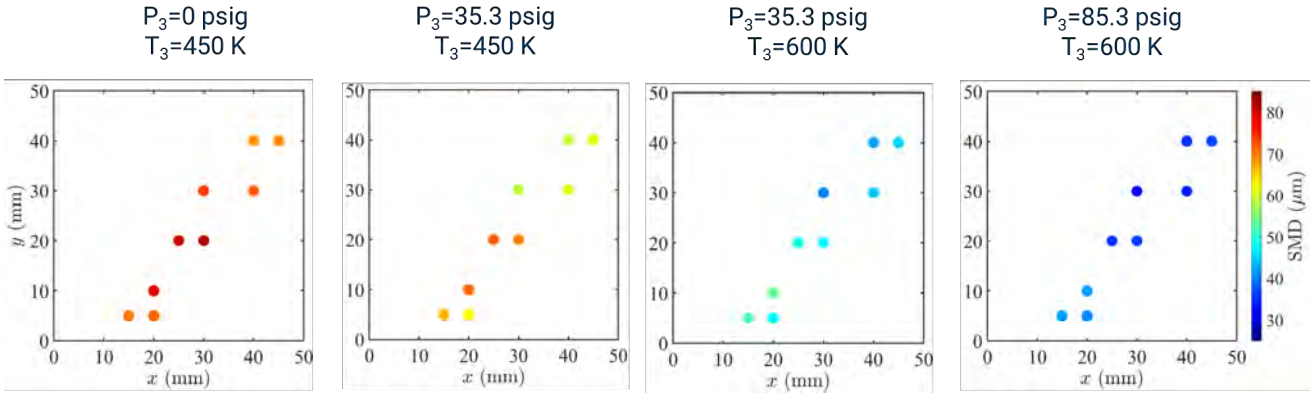

Figure 3. Spatial variation of Sauter mean diameter (SMD) values for non-reacting Jet A fuel spray at different operating conditions.

To study the effect of reacting conditions on the spray, measurements were performed with the same PDPA configuration at the same operating conditions. It is to be noted that the current combustor operates liquid spray flames that produce large amounts of soot, especially in the primary zone of the combustor. Since the soot particles are mostly in solid phase at the measurement region, they can be detected as particles by the device which corrupts the actual droplet signals. To avoid this, the measurement region is confined to a small region 10-20 mm downstream of the dump plane within the spray cone. This region is largely devoid of soot, apart from small fluctuations in the flame where soot/flame can be entrained into these regions. Four measurements points (matching the non-reacting conditions) were possible for all the reacting conditions. The number frequency distributions for non-reacting and reacting conditions are compared in Figure 4 for Jet A fuel at 35.3 psig pressure and 600 K preheat at two different locations. For the reacting case, the distributions seem to shift towards larger diameters for all locations. This is counter-intuitive in the sense that reaction/flame should help the droplets evaporate faster adding to the preheat leading to smaller droplets. The plots in Figure 4 suggests that the smaller droplets not only evaporate faster but are almost non-existent, leaving only the larger droplets being detected. Hence, it is very possible that the SMD values are considerably higher in the reacting cases as compared to the non-reacting cases owing to the disappearance of small droplets which are vaporized promptly. An increase in almost 15-20 μm is observed for SMD in reacting cases compared to their non-reacting counterparts. This change was consistently observed for all cases at the same spatial location and operating conditions. Additionally, these distribution changes also provide information on the number of smaller diameter droplets available in reacting cases at any downstream location. If it were a non-sooting flame, reliable measurements (uncorrupted from the presence of soot) would be possible in the entire flame region providing a good insight on droplet evaporation and breakup for comparison between non-reacting and reacting conditions. It is worth mentioning that the signal to noise ratio was much lower in reacting cases at the same measurement location due to laser extinction as the laser beam passes through the flame/spray regions from the side nozzles before reaching the measurement zone. Additionally, the large density differences within the flow leads to beam steering causing the PDPA focal region to keep shifting, in turn reducing the signal rate.

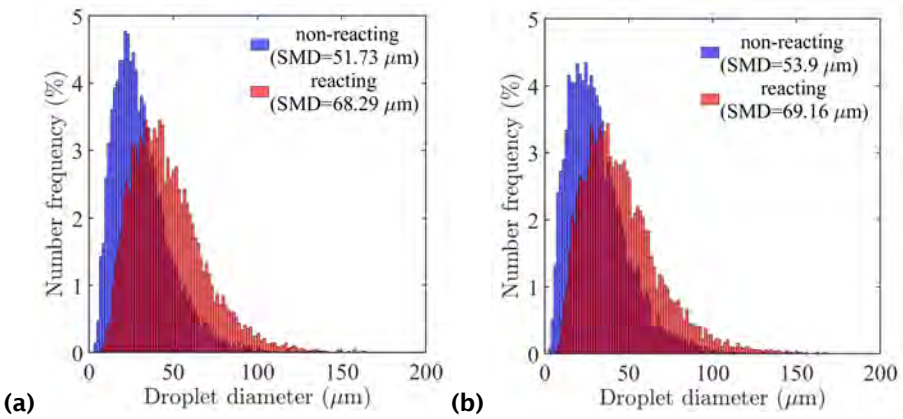

Figure 4. Comparison of number frequency distributions for Jet A fuel at reacting and non-reacting conditions with 35.3 psig pressure and 600 K preheat temperature for locations (a) *x*=15 mm, *y*=5 mm (b) *x*=20 mm, *y*=10 mm.

The second part of the measurements involved utilizing SAF for the measurements at the same conditions as Jet A fuel. The SAF used here is a HEFA-based fuel with almost negligible amount of aromatic content in it. Figure 5 shows the comparison in number frequency distributions between Jet A fuel and SAF in the non-reacting case for the same operating conditions. It is seen that the SAF spray produces slightly smaller droplets compared to Jet A fuel spray, giving a smaller SMD value. This is mostly due to the changes in physical properties of the two different fuels. The SAF utilized in this study has ~10% lower surface tension as compared to Jet A fuel. Reduction in surface tension helps in formation of new surface areas promoting droplet/jet breakup, thereby creating smaller droplets. This can also be looked at in terms of Weber number which is inversely proportional to the surface tension force. The higher the Weber number, better is the atomization quality of the liquid spray. Also, at temperatures above 100° C, the vapor pressure of SAF is ~5% higher than Jet A fuel which can contribute to better vaporization and smaller droplets. The variation in SMD values at different operating conditions followed similar trends as Jet A fuel at all the measurement locations. Similar trends were observed for reacting cases between Jet A fuel and SAF as shown in Figure 6. The frequency distributions for SAF case shifted towards smaller diameters, suggesting an overall reduction in SMD for a given condition and location.

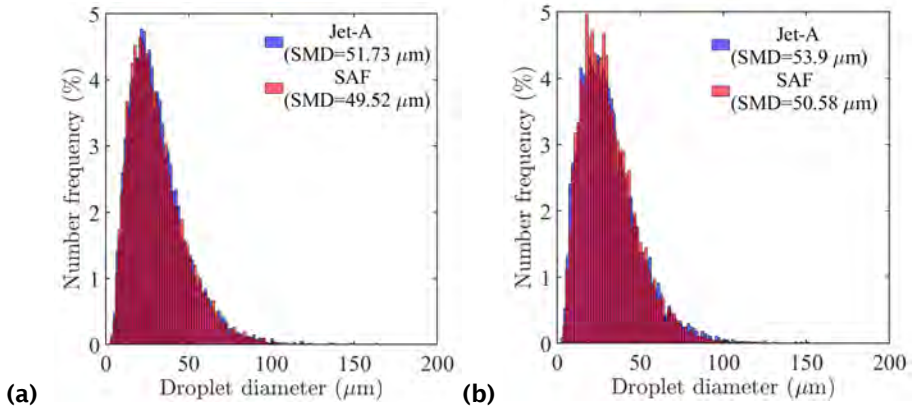

Figure 5. Comparison of number frequency distributions for Jet A fuel and SAF at non-reacting conditions with 35.3 psig pressure and 600 K preheat temperature for locations (a) *x*=15 mm, *y*=5 mm (b) *x*=20 mm, *y*=10 mm.

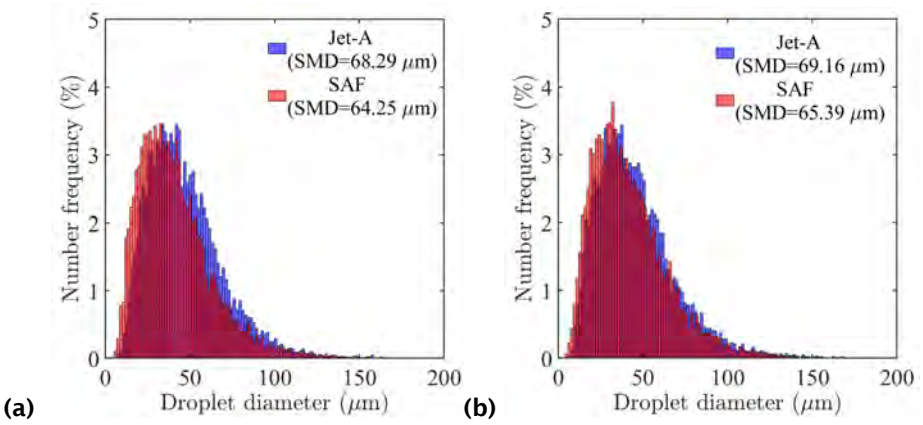

Figure 6. Comparison of number frequency distributions for Jet A fuel and SAF at reacting conditions with 35.3 psig pressure and 600 K preheat temperature for locations (a) x=15 mm, y=5 mm (b) x=20 mm, y=10 mm.

Since the availability of SAF is limited at the current scenario due to production/supply issues, blending sustainable fuels with neat Jet A fuel is considered a viable option. Due to small changes in physical and chemical properties of these blended fuels as compared to their neat counterparts, their spray and combustion characteristics are still not well known. Hence, measurements were also performed at the same locations by blending the neat fuels in a 50-50% by volume (further referred to as 50-50 blend). Figure 7 shows the SMD comparison between the neat fuels and their blend for 35.3 psig pressure and 600 K preheat. From the previous discussions, it was seen that SAF generally produced slightly smaller droplets. Interestingly, the 50-50 blend does not show a very clear trend for a given operating condition. As seen from the SMD comparison, the 50-50 blend produced slightly larger SMDs compared to their neat fuels closer to the nozzle. But for locations more downstream (y > 20 mm), the SMD values were comparable to neat Jet A fuel. In the present study, physical properties such as surface tension, viscosity and density for the 50-50 blend generally lie in between their neat fuel properties. Hence, their behavior in spray breakup and atomization is expected to occur in the same trend. But the results show that the atomization behavior can change significantly with location (which can be a proxy for time) and/or operating conditions. While PDPA can measure the SMD, it cannot measure the absolute number of droplets. However, the SMD is controlled by the existing droplets regardless of their absolute number. Therefore, there exists a possibility that at more downstream locations, SAF component in the blend might evaporate faster and hence, most droplets in the measurement region are from Jet A fuel, thus the droplet size (SMD) is dominated by Jet A fuel. Therefore, it is closer to the results of Jet A fuel even the 50-50 blend. In fact, the vapor pressure of the blend in the current study is slightly lower compared to their neat fuels. So, this might affect the droplet size based on the location within the spray. Further investigations are necessary to draw firm conclusions on understanding the atomization behavior of blended fuels, which will be conducted in future testing.

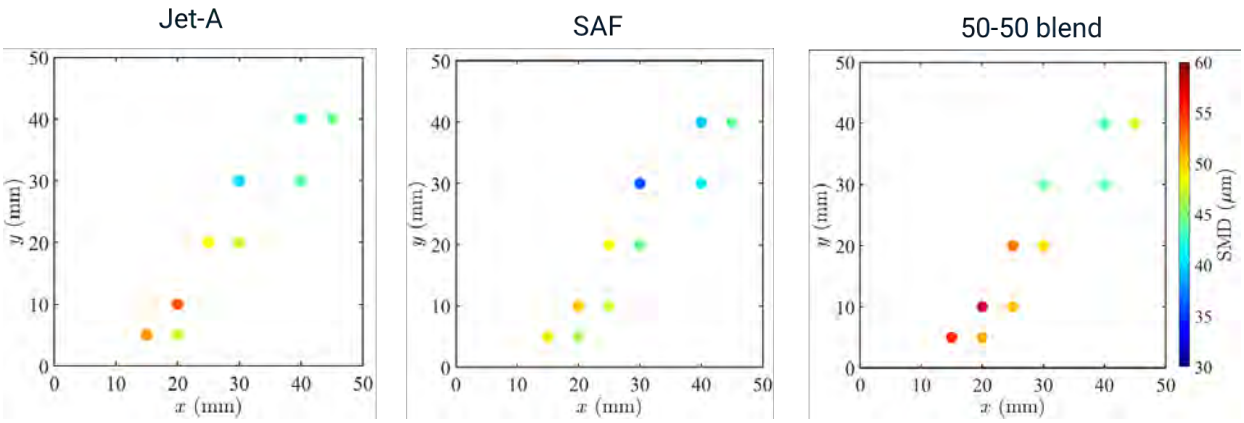

Figure 7. Spatial variation of Sauter mean diameter (SMD) values for non-reacting spray with neat Jet A, neat SAF and 50-50 blend at operating conditions of 35.3 psig pressure and 600 K preheat temperature.

Subtask 1.2: Two-color LII for nvPM/soot measurements

LII involves heating soot particles using a short pulsed high-energy laser instantaneously. When the particles absorb this energy, they re-emit through radiation in a broadband wavelength spectrum governed by Planck's law. This resulting magnitude of the incandescence signal just after the laser pulse absorption can be correlated with the particle volume fraction, whereas the signal decay rate profile is dependent on the primary particle size in the detection region. To quantify the volume fraction, the incandescence signal must be calibrated with a known value of soot concentration in a standard burner using a different detection technique. This can also be done using an in-situ extinction technique in the same flame simultaneously with LII. But these methods incur high uncertainties in the calibration, mainly due to unknown soot optical properties. In this study, a calibration lamp of known radiance-wavelength relationship is utilized where the camera intensity can be calibrated. The main advantage of this method relies upon the fact that the quantification is completely independent of the flame conditions, type of fuel and the optical setup. In fact, any errors that might occur due to the parameters within the optical setup is auto compensated even though the errors due to unknown soot optical properties still exist.

The schematic of the LII setup used in the current study is shown in Figure 8a. The soot particles are heated using a ~2 J/pulse Nd:YAG laser (Quanta-ray® Pro-250) emitting a 1064 nm beam having a pulse width of 8-12 ns. The infrared wavelength of 1064 nm helps in avoiding interference due to laser induced fluorescence occurring from polycyclic aromatic hydrocarbons either present inherently in the fuel or formed after combustion. The gaussian laser beam is then shaped into a collimated sheet of nearly top hat profile using a three-lens combination, consisting of a cylindrical concave lens (f=-25.4 mm) and two cylindrical convex lenses (f=400 mm and f=1000 mm). After the first lens, the diverging sheet was passed through an iris to obtain only the central part of the gaussian profile before hitting the second lens. Another iris restricted the final collimated sheet height to about 27 mm with a beam waist of <1 mm at the combustor centerline. The laser energy was controlled to obtain a fluence of around 0.3-0.4 J/cm^2 throughout the sheet height, to operate within the low-fluence LII regime where the incandescence signal is nearly independent of the fluctuations in laser energy. The broadband incandescence signal emitted by the soot particles after laser absorption is captured using an intensified charge coupled device (CCD) camera (PI-MAX® 4) after passing through an image splitter. The image splitter (LaVision®) consists of a splitting prism which separates the same imaging area to be viewed at two different wavelengths filtered at 447±60 nm and 680±42 nm. This helps in obtaining soot temperature through two color incandescence detection instantaneously throughout the imaging region. The camera intensities at both the wavelengths are calibrated using the known radiance from a calibration lamp mounted inside an integrating sphere (Sphere Optics®), see Figure 8b. The light source is kept at the same location as the laser sheet with the exact detection setup and settings as the LII images. The LII signal was captured with an exposure time of 80 ns after the peak laser absorption with the camera and the laser being

® Quanta-ray is a registered trademark of Newport Corporation, Santa Clara, California.
® Pi-Max is a registered trademark of Teledyne Digital Imaging US, Inc., Thousand Oaks, California.
® LaVision is a registered trademark of LaVision GmbH, Gottingen, Germany.
® Sphere Optics is a registered trademark of SphereOptics GmbH, Herrsching, Germany.

timed using a delay generator. The images were flat-field corrected for spatial intensity variation through the imaging path and camera response. A total of 500 images were captured for each experimental condition to obtain mean soot volume fraction distributions.

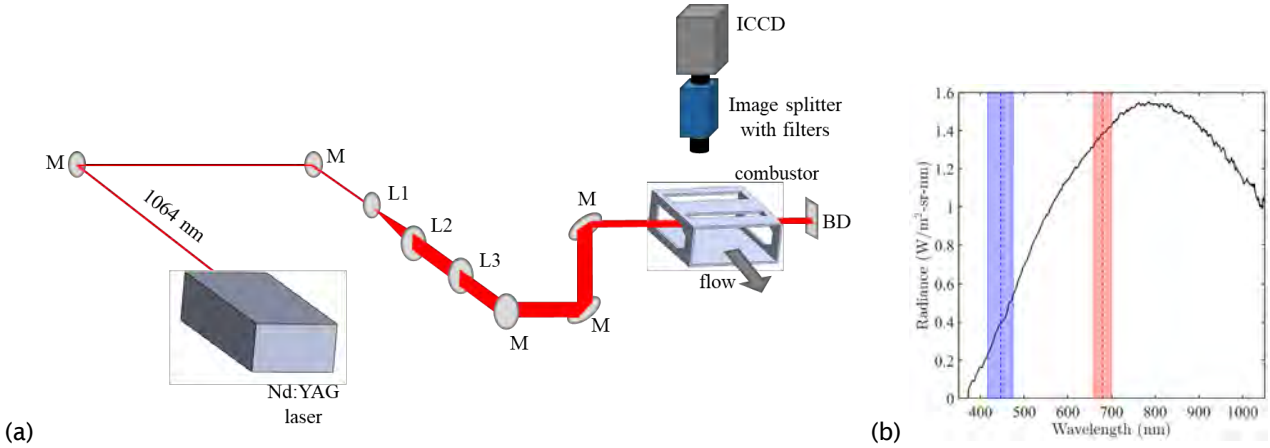

Figure 8. (a) Schematic of the two-color LII setup. The image splitter splits the image and passes through two filters centered at 447 nm and 680 nm onto the ICCD. L1: cylindrical concave lens (f=-25.4 mm), L2: cylindrical convex lens (f=400 mm), L3: cylindrical convex lens (f=1000 mm), M: mirror, BD: beam dump. (b) Radiance curve for the calibration lamp as a function of wavelength. The blue and red regions depict the detection wavelength for the current study using the filters on the splitter.

The image pairs acquired for a given test condition is first split to obtain intensities from the two different wavelengths separately to match the exact regions of interest on both the images. Since the pixelated intensities tend to give erroneous values when dividing the pixel values from the two image pairs, the images are smoothened using a 3 x 3 convolution filter. After applying the flat-field correction and removing any background noise, the soot temperature values are obtained using the Planck's law for blackbody radiation. The ratio of soot absorption function ($E(m)$) values at two different wavelengths is taken as 1.0. For the low-fluence LII regime, soot temperature values should not exceed the sublimation temperature, which is usually considered to be around 4000 K. The averaged soot temperature distribution for the case of Jet A fuel at the global equivalence ration (ϕ_g) of 0.2 with 35.3 psig pressure and 450 K preheat is shown in Figure 9a. The temperature values lie below 4000K in the entire region, satisfying the low-fluence LII criterion. Although a laser sheet with uniform fluence should heat up the soot particles uniformly to the same temperature instantaneously, the differences in soot temperatures spatially can be due to several factors. The soot maturity will not be uniform throughout the flame and hence nascent soot and mature soot will heat up differently. Additionally, the laser fluence along the sheet is not completely top-hat; the fluence drops slightly towards the upstream direction. Nonetheless, the soot volume fraction is not affected by the differences in temperature as the current study uses the two-color ratiometric method in the low-fluence regime.

Once the soot temperature is obtained at all locations, the raw LII signals can be quantified using the radiance values from the calibration lamp at the same camera settings. The mean soot volume fractions (f_v) for the Jet A fuel case at ϕ_g=0.2 is shown in Figure 9b. The masked regions in images are due to the quench holes of the combustor inadvertently appearing in one of the image pairs which could not be avoided in the present measurements. The mean f_v values are below 5 ppm at most of the locations throughout the flame regions. The maximum values occur near the shear region of the conical spray where the main reactions occur as expected. The high values near the borders of the flame are due to insufficient signals over time leading to a higher mean. So, the actual time-averaged values should be lower than the values depicted in Figure 9b. Due to the highly turbulent nature of the flame along with the swirling nature of the flow, the soot detection probabilities are much lower than a laminar flame case at a given location. Hence, 500 images may not be sufficient for obtaining a converged soot volume fraction distribution for a given condition. Another important feature to notice in the contours is that the laser extinction along the beam path from right to left in Figure 9b can also make the f_v values to appear to be decreasing for the same regions downstream of the different fuel injectors. This absorption will be hard to correct as the soot concentration and their extinction coefficients must be known instantaneously throughout the flame

region. Improvements to most of these measurement features will be made in future campaigns to obtain more accurate soot distributions.

To study the effect of the type of fuel, the same LII measurements were made with SAF as the fuel at similar conditions to Jet A fuel. Since SAF has different fuel physical and chemical properties, the soot formation tendencies are expected to differ.

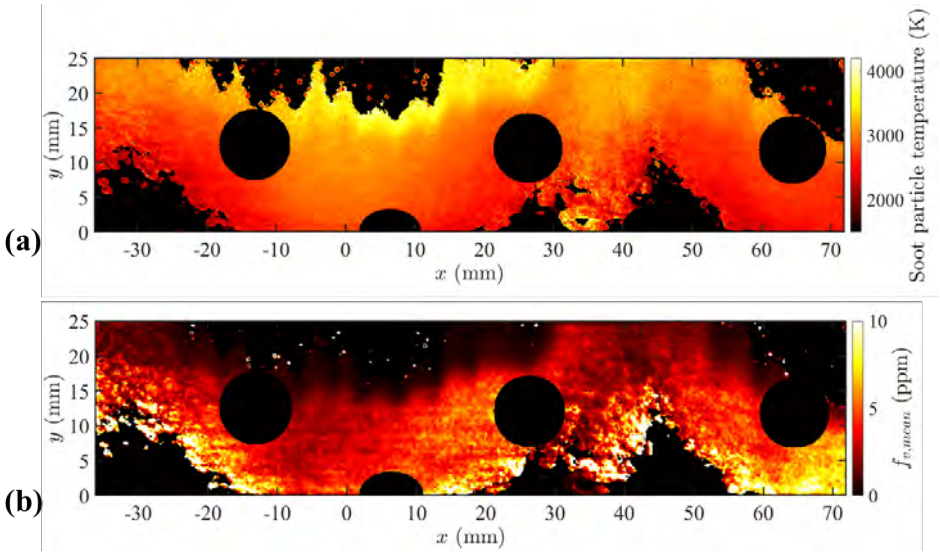

Figure 9. Spatial mean contours of (a) soot particle temperature and (b) soot volume fraction for Jet A combustion at 35.3 psig pressure, 450 K preheat and global equivalence ratio of 0.2. The black masked regions are from the quench holes appearing in the images.

The f_v contours for both Jet A fuel and SAF are shown in Figure 10 for the same operating conditions and global equivalence ratio. There is a considerable difference seen in the soot volume fraction values for the case of SAF as compared to Jet A fuel. The f_v values are almost 2-3 times lower for SAF at the same spatial locations as the Jet A fuel case. This is mainly due to the chemical composition of SAF utilized in the current study. As there is a negligible number of aromatics present in SAF, the tendencies for soot precursor formation is reduced leading to reduced overall soot production. Comparing the spray properties in the previous section, SAF also produced slightly smaller droplets as compared to Jet A fuel which will contribute to better fuel-air mixing and more complete combustion. Although the contribution from differences in spray is much lower as compared to the contribution from the chemical effects, the combined effects help in reducing soot formation considerably in the case of SAF combustion. Further processing of LII results is underway at more operating conditions for both Jet A fuel and SAF which will provide a comprehensive understanding of soot formation properties of these fuels at different conditions. These results will be reported in the next year's annual report.

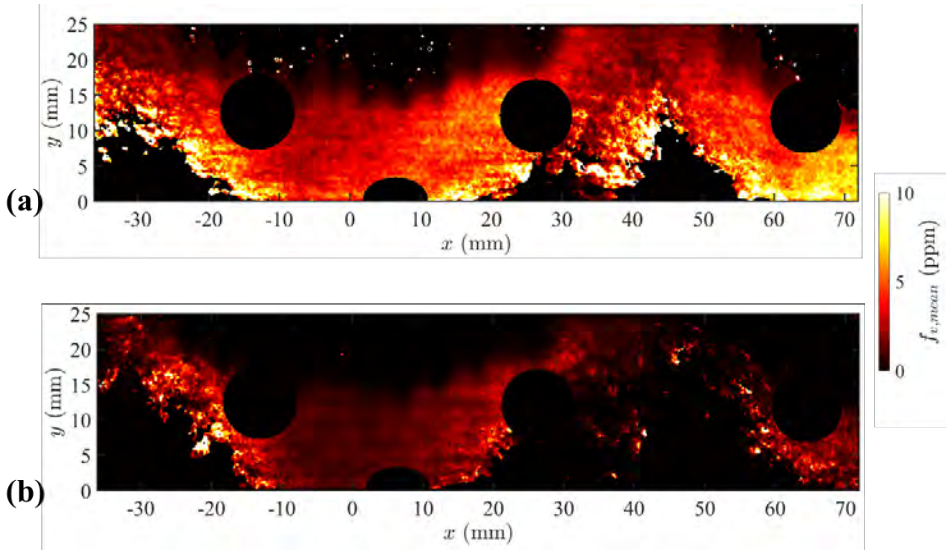

Figure 10. Spatial mean contours of soot volume fraction for (a) Jet A fuel and (b) SAF reacting flow at 35.3 psig pressure, 450 K preheat and global equivalence ratio of 0.2. The black masked regions are from the quench holes appearing in the images.

Milestone

- Conducted systematic PDPA and two-color LII measurements at different combustor operating conditions with Jet A fuel, SAF, and a 50-50 blend of Jet A fuel and SAF, respectively.

Major Accomplishments

- Conducted spatially resolved droplet size measurements in a confined sector combustor using PDPA for Jet A fuel, SAF, and a 50-50 blend of Jet A fuel and SAF.
- Conducted two-color LII measurements to obtain nvPM volume fraction distributions at different combustor operating conditions for Jet A and SAF.
- Compared the differences between Jet A and SAF in terms of spray properties and nvPM formation.

Publications

McGrath, R., Juergensmeyer, J., Bond, R., Bugay, E., Wehe, S., Wu, D., Steinberg, A., Sun, W., & Mazumdar, Y. C. (2024). Planar laser-induced incandescence for the study of soot production in a multi-sector RQL Jet A combustor. *Applications in Energy and Combustion Science, 18*, 100269. https://doi.org/10.1016/j.jaecs.2024.100269

Vishwanath, R., Bibik, O., Olimid, D., Douglas, E., Wehe, S., Mazumdar, Y. C., Steinberg, A., & Sun, W. (2025, January 12-16). *Drop-size measurements using phase doppler particle anemometry in a confined high-pressure sector combustor* [Conference presentation]. AIAA SciTech 2025 Forum, Orlando, Florida.

Juergensmeyer, J., Miller, J., Bond, R., Mcgrath, R., Wehe, S., Sun, W., Mazumdar, Y. C., & Steinberg, A. (2025, June 16-20). Measurement of particulate matter and its oxidation in a multi-sector rich-quench-lean combustor. ASME Turbomachinery Technical Conference & Exposition 2025, Memphis, Tennessee.

Outreach Efforts

None.

Awards

Dr. Wenting Sun received the Hiroshi Tsuji Early Career Researcher Award (2023). This award is awarded by the Combustion Institute, which recognizes early career researchers who have demonstrated excellence in fundamental or applied combustion science and have achieved a significant advancement in their field within four to ten years of

completing a doctoral degree or equivalents. Dr. Wenting Sun was made an American Institute of Aeronautics and Astronautics (AIAA) Associated Fellow in 2023.

Dr. Adam Steinberg was made a fellow of The Combustion Institute in 2023.

Student Involvement

Four graduate students, Adhav Arulanandan, Dominic Olimid, Eric Douglas, and Andrew Fan, from Georgia Tech worked on Task 1.

Plans for Next Period

- Conduct PDPA, two-color LII, and OH radical planar laser induced fluorescence (OH PLIF) measurements in a new combustor configuration for Jet A fuel, SAF, and their blends at a large range of operating conditions.
- Continue detailed combustor design and comprehensive thermal stress analysis.

Project 071 Predictive Simulation of nvPM Emissions in Aircraft Combustors

Georgia Institute of Technology

Project Lead Investigator

Suresh Menon
Professor at the School of Aerospace Engineering
Georgia Institute of Technology
270 Ferst Drive, Atlanta, GA 30332-0150
404-894-9126
suresh.menon@aerospace.gatech.edu

University Participants

Georgia Institute of Technology (Georgia Tech)

- P.I.: Prof. Suresh Menon
- FAA Award Number: 13-C-AJFE-GIT-067
- Period of Performance: October 1, 2023, to September 30, 2024
- Tasks:
  1. Kinetic Modeling: Improvement in soot kinetic models and chemistry of jet fuels under rich-quench-lean combustor operating conditions
  2. Nucleation Modeling: Predicting incipient particle nucleation rates according to polycyclic aromatic hydrocarbon dimerization rates from molecular dynamics simulations
  3. Surface Growth and Aggregation Modeling: Reaction-transport-limited growth of soot particle models for cluster-cluster aggregation
  4. Large eddy simulation of soot formation inside a rich-quench-lean combustor

Project Funding Level

The current Federal Aviation Administration (FAA) funding is for a 3-year effort (July 2020 to September 2023), with a request of $500,000 per year from ASCENT (per year). An additional request for a no-cost extension has been approved. cost-sharing is provided as follows:

- Georgia Tech provides cost-sharing for its share of $150,000 per year. The Georgia Tech point of contact is Kevin Ellis (kevin.ellis@aerospace.gatech.edu).
- Raytheon Technologies Research Center (RTRC) provides cost-sharing of $250,000 per year. Dr. Colket is a consultant on this project with many years of experience in soot modeling. The RTRC contact is John LaSpada (LaSpadJW@RTRC.utc.com).
- The University of Michigan (UM) provides cost-sharing in the amount of $100,000 per year. The UM point of contact is Alexandra Thebaud (thealexi@umich.edu).

A no-cost extension (NCE) until September 2025 has been granted.

Investigation Team

Georgia Institute of Technology

Prof. Suresh Menon: (P.I.), Task 4
Mr. Shubham Karpe: (Student), Task 4

Raytheon Technologies Research Center

Dr. Miad Yazdani, (co-P.I.), Task 3
Dr. Steve Zeppieri, (co-P.I.), Task 1
Dr. Meredith Colket, (co-investigator), Task 1

University of Michigan
Prof. Angela Violi, (co-P.I.), Task 2
Mr. Jacob Saldinger, (Post doc), Task2

Project Overview

This project is being used to establish a new multiscale approach to predict soot formation in aircraft combustors. A hierarchy of first-principles simulation methods is being used to account for the multiscale physics of the formation and transport of non-volatile particulate matter (nvPM, also called soot in literature). The final objective is to use this multiscale approach to model the physics in large eddy simulation (LES) of realistic gas turbine combustors. The layers of empiricism that currently exist are targeted and isolated, for example, in particle inception models, the roles of precursor species in nucleation, the particle shape assumptions and their impact on surface growth, the sensitivity of predictions to particle size distribution, and the ad hoc coagulation/coalescence mechanisms. The ASCENT Project 071 team already has all modeling tools, but a systematic coupling of these tools in a multiscale, multiphysics strategy has yet to be accomplished by any research group. Hence, this study provides insights into establishing new predictive abilities by integrating these capabilities.

The multiscale and multiphysics layers of collaborations among the cost-sharing groups are summarized in Figure 1 and Figure 2 and briefly described herein. As the main goal of the current work was to establish this hierarchy of physics-based approach in a realistic reacting environment, Georgia Tech conducted LES simulations of a single-sector rich-quench-lean (RQL) model combustor at conditions based on ASCENT Project 070. This information was translated into useful parametric space for the establishment and evaluations of different modeling approaches under representative conditions mimicking real combustion environments. The kinetics group at RTRC conducted a study to understand the role of gas-phase kinetics in predicting important species potentially labeled as soot precursors. The information on detailed kinetics from RTRC was used in a UM study and the process of nucleation by Georgia Tech to evaluate its effects on posterior soot predictions at RQL combustion conditions. In the UM study, research is conducted on the propensity of gas-phase species to form dimers (considered the building blocks of soot inception) under flame conditions. The molecular dynamics-based studies identified key soot precursors and the rates of formation of soot nuclei under RQL combustion-relevant conditions. This nucleation rate was provided to Georgia Tech to update the source terms associated with nucleation processes through a method of moment soot model, and the information on the structures of these soot nuclei was also provided to RTRC for modeling surface growth and aggregation processes. Outputs from the aggregation studies in RTRC in the form of global surface growth and aggregation models will then be used by Georgia Tech to update the source term of surface growth and aggregation models in the moment models. At Georgia Tech, LES studies of soot formation from RQL combustor were conducted to identify a feasible range of conditions where the individual soot physics is predicted using global soot models, and the inputs obtained from the collaborators were assembled in a standalone solver as a final deliverable for the project.

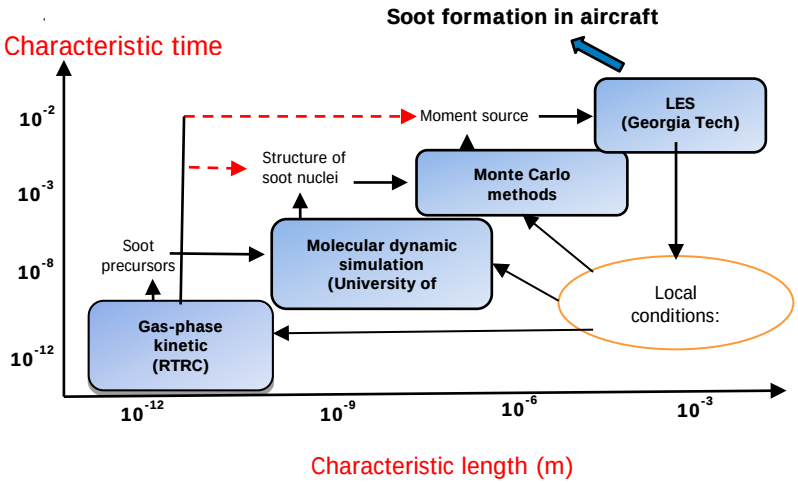

Figure 1. Multiscale collaborative efforts to improve nvPM (soot) predictions. LES: large eddy simulation.

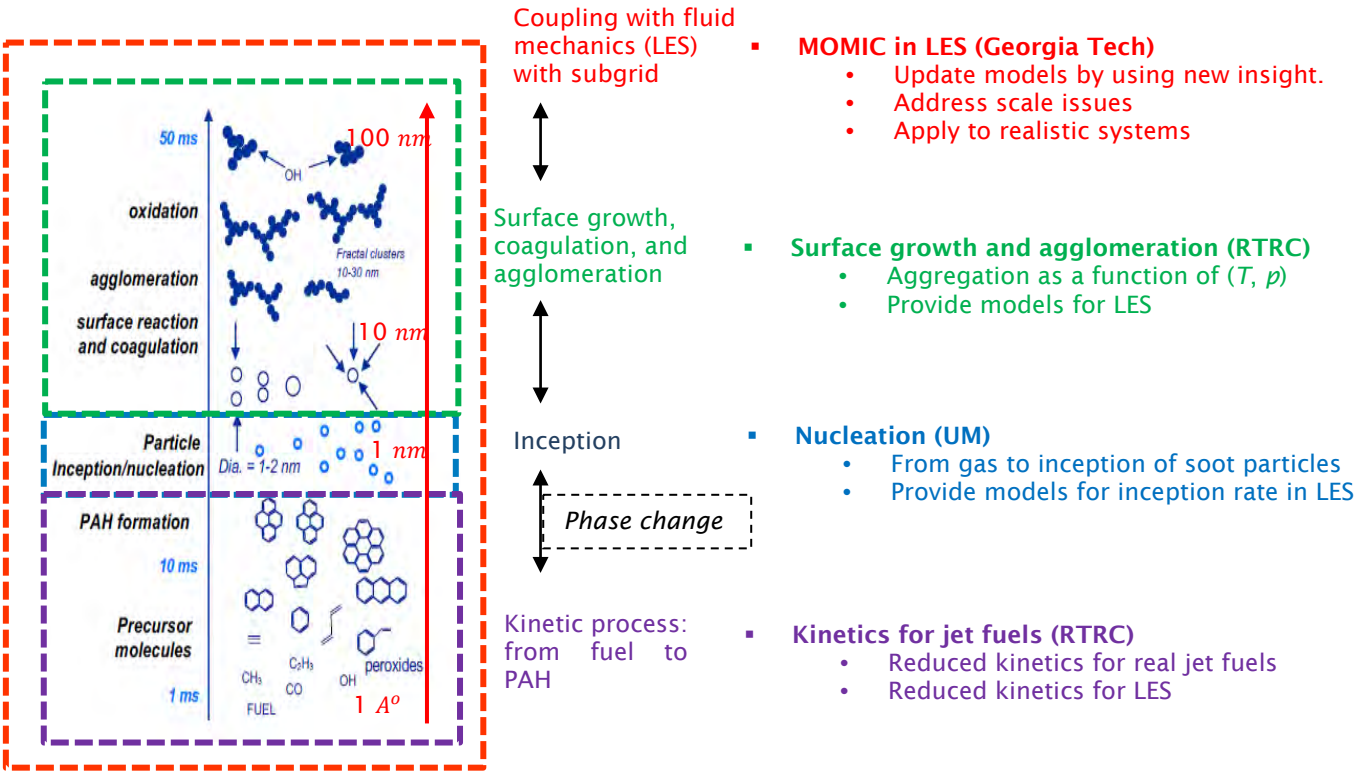

Figure 2. Multiscale collaborative efforts to improve nvPM (soot) predictions.
PAH: polycyclic aromatic hydrocarbon, LES: large eddy simulation.

Task 1 – Kinetic Modeling: Improvement in Soot Kinetic Models and Chemistry of Jet Fuels under Rich-Quench-Lean Combustor Operating Conditions

Raytheon Technologies Research Center

Objective

The objective of this task was to develop a validated, detailed chemical kinetics model of parent fuel decomposition and oxidation reactions, with a special focus on fuel-rich chemistry, to enable the accurate evolution of polycyclic aromatic hydrocarbon (PAH)/soot precursor formation and incipient soot particle formation, and the evaluation and improvement of reduced-order soot formation models. Year 1 fuel activities focused on ethene, whereas Year 2 efforts shifted the focus to Jet A fuels. In Year 3, efforts continued toward optimizing fuel chemistry and soot kinetics at RQL-relevant conditions. Finally, a detailed chemical kinetics model and a reduced soot kinetic model were developed as final deliverables through these studies.

Research Approach

Development of detailed gas-phase kinetics and reduced order soot kinetics

The schematic in Figure 3 shows the coupling among the LES, nucleation, and kinetic activities focused on during this project, where T, P, and ϕ represent the temperature, pressure, and equivalence ratio of the surrounding gas phase, respectively. Georgia Tech conducted LES simulations (described in detail in Task 4) of combustion physics inside the RQL combustor using a globally reduced two-step mechanism. These conditions, shown in Figure 4, were provided for the optimization of jet fuel chemistry and the soot kinetics model. Moreover, PAH represents the polycyclic aromatic

hydrocarbon species considered as the soot precursors. The objective of the current kinetic efforts was focused on down selecting the detailed kinetic model of jet fuels. This kinetic model was provided back to Georgia Tech for assessment and coupling to their moment-based soot model. The information regarding the involved precursor species characteristics (n_{PAH}, d_{PAH}) and concentrations were provided as inputs into the nucleation studies at UM to assess their ability to form dimers.

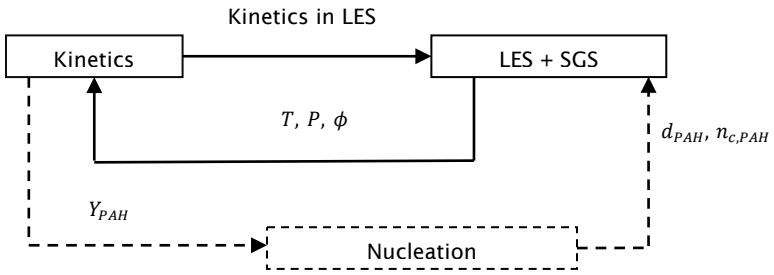

Figure 3. Coupling of LES–kinetic activities. LES: large eddy simulation

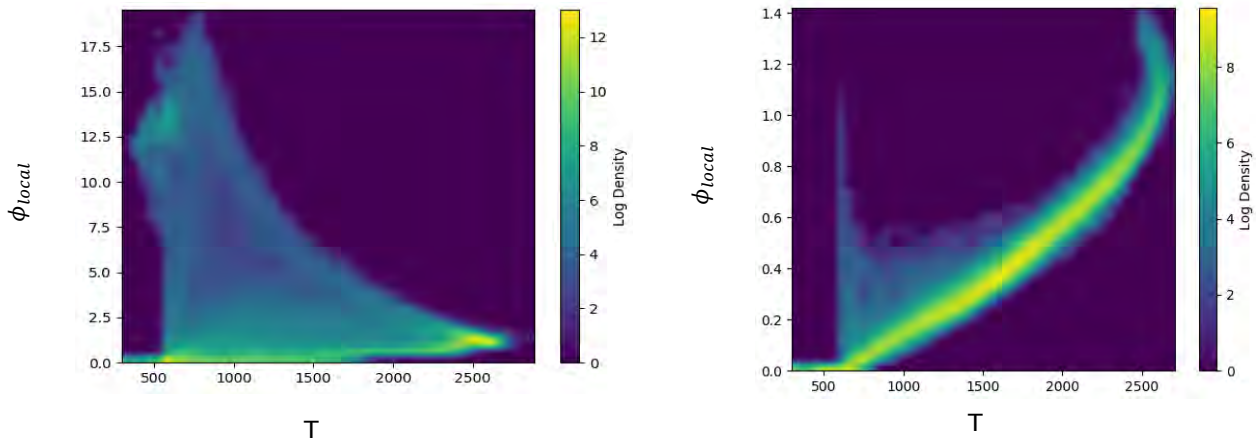

(a) Rich primary zone

(b) Lean secondary zone

Figure 4. Local conditions obtained from the LES simulations of RQL combustor at Georgia Tech. The heat maps correlate with the density of the number of points with such conditions. Representative conditions from this sample data were chosen for RTRC kinetic activities.

In Year 3, the efforts were focused on the completion and assessment of chemical kinetics models coupled to PAH formation for logistic (Jet A) fuels. In our prior annual efforts, four different chemical mechanisms were assessed.

To summarize, the HyChem (Wang et al., 2018) method was used, in which semi-empirical reactions treat the parent fuel decomposition process to the relevant intermediate hydrocarbon species, and the Strategic Environmental Research and Development Program (SERDP) technique, in which compositions of several surrogate hydrocarbon species are formulated that capture the bulk properties of the fuel of interest. (For example, Jet A fuel would be considered a binary blend of *n*-dodecane and *m*-xylene.) The HyChem model was coupled with both the SERDP and King Abdullah University of Science and Technology (KAUST) PAH-chemistry (Selvaraj et al., 2016) models for analysis, and the SERDP model was coupled with the SERDP PAH-chemistry model. Finally, the Caltech-mech (Blanquart et al., 2009) model was appended with the HyChem model to incorporate additional reactions related to the decomposition of Jet A fuels. The overall layout of the workflow adopted in this effort is highlighted in Figure 5. This assessment is carried out using a perfectly stirred reactor

configuration where a mixture of Jet A fuel (assumed as 77% nC12, 23% *m*-xylene) and air is subjected to the following conditions *P*: 1-5.8 atm, τ_{res}: 1-25 msec, ϕ : 0.5–5.5, T: 1400–2300 K.

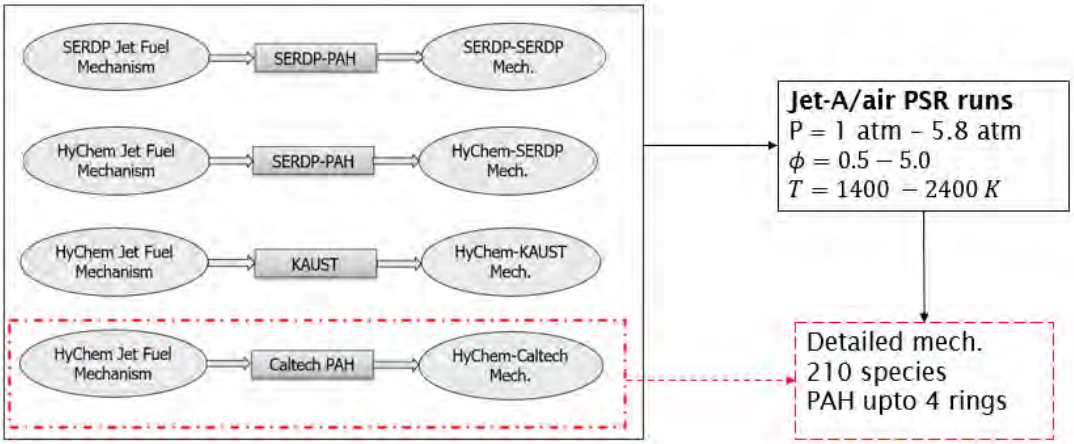

Figure 5. Assessment of detailed gas-phase chemical mechanisms. The red dashes depict the final delivered gas phase kinetics through RTRC kinetic activities.

The key outcomes of kinetic activities are discussed briefly here. The results obtained from the assessment of all detailed gas phase mechanisms are provided in Figure 6. As seen in Figure 6a, overall predictions of temperature are similar for all mechanisms. Some visible differences arise in the range of higher equivalence ratios. The benzene (C_6H_6) profiles and acetylene (C_2H_2) profiles are in qualitative agreement among mechanisms except the Pitsch mechanism (Langer et al., 2023), which must be investigated further. Encouragingly, both the HyChem models and the Caltech-mech model have an overall satisfactory agreement.

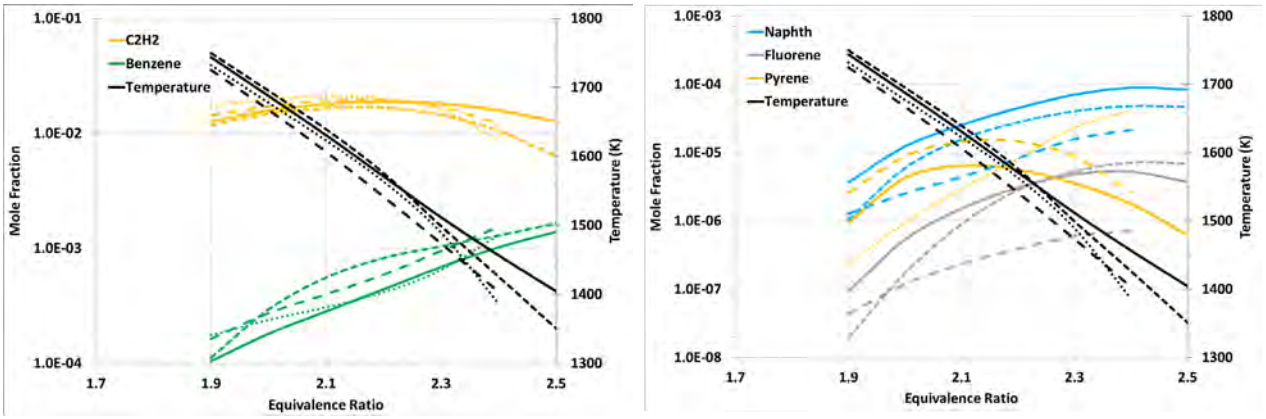

(a) Comparison of major precursor species.

(b) Comparison of heavier PAH species.

Solid:	**Caltech Mech**
Dash:	**Pitsch et al.**
Dot:	**Hychem/Kaust Mech.**
Long Dash:	**Hychem/SERDP Mech.**

Figure 6. Assessments of key soot relevant characteristics among different detailed mechanisms.

The nucleation studies at UM required addressing the formation of heavier PAH species which play a critical role in the inception of soot particles. In this regard, a comparison of major PAH species used in the state-of-the-art nucleation models was conducted across a range of conditions. Such an assessment for key species such as naphthalene ($C_{10}H_8$), fluorene ($C_{13}H_{10}$), and pyrene ($C_{16}H_{10}$) is provided in Figure 6b. The results suggest a wider spread of PAH species among all four mechanisms that may be crucial in predicting the early nucleation stages of soot formation in large-scale simulations. The Pitsch mechanism was relatively new and required further assessment and hence was not preferred in the subsequent analysis.

Finally, to conclude upon the final piece of kinetic activities at RTRC, analysis is presented herein to compare predictions of soot formation using a new particulate matter reduced order model (PM-ROM). The PM-ROM model was developed as an optimization of rates for the Lindstedt soot model (Leung et al., 1991). Sufficient details about such reduction/optimization processes are available in our previous annual efforts. The PM-ROM is based on the well-known Lindstedt two-equation soot model. The two equations are used to determine the soot mass and soot number concentrations generated in the system. The necessary rates for model closure are particulate inception/nucleation, particulate surface growth, surface oxidation, and particle coagulation. In the original Lindstedt model (Leung et al., 1991), the key particulate matter (PM)-forming species is acetylene, molecular oxygen is the key soot oxidation species, and a single Arrhenius rate expression is used for each step. The RTRC formulation extends the original premise by adding benzene as a key PM-forming species and the hydroxyl radical as another oxidation species, and by using a double Arrhenius rate expression for both the inception and surface growth processes, thus enabling the model to capture the well-known and experimentally observed "soot bell" concentration profile with respect to temperature. As the objective was to generate a higher fidelity PM-ROM model for use in RQL computational fluid dynamics (CFD) studies, a numerical shooting fitting procedure was used to establish rate coefficients that enabled the PM-ROM model to identically match the soot concentration levels generated via detailed kinetic analysis coupled with moment-based soot calculations. In the most recently developed PM-ROM, the reduced model was calibrated against perfectly stirred reactor (PSR) calculations at the elevated pressure (5.8 atm) and air temperature (600 K) conditions of RQL combustor operation. The nominal reactor residence time for these calculations was 5 ms, and the fuel-air equivalence ratio spanned from 1.8 to 2.5. The detailed mechanism used was the previously discussed HyChem-Caltech mechanism. The agreement between the soot concentrations generated via detailed kinetics and method of moments (MOM) and the PM-ROM are shown in Figure 7, indicating good agreement.

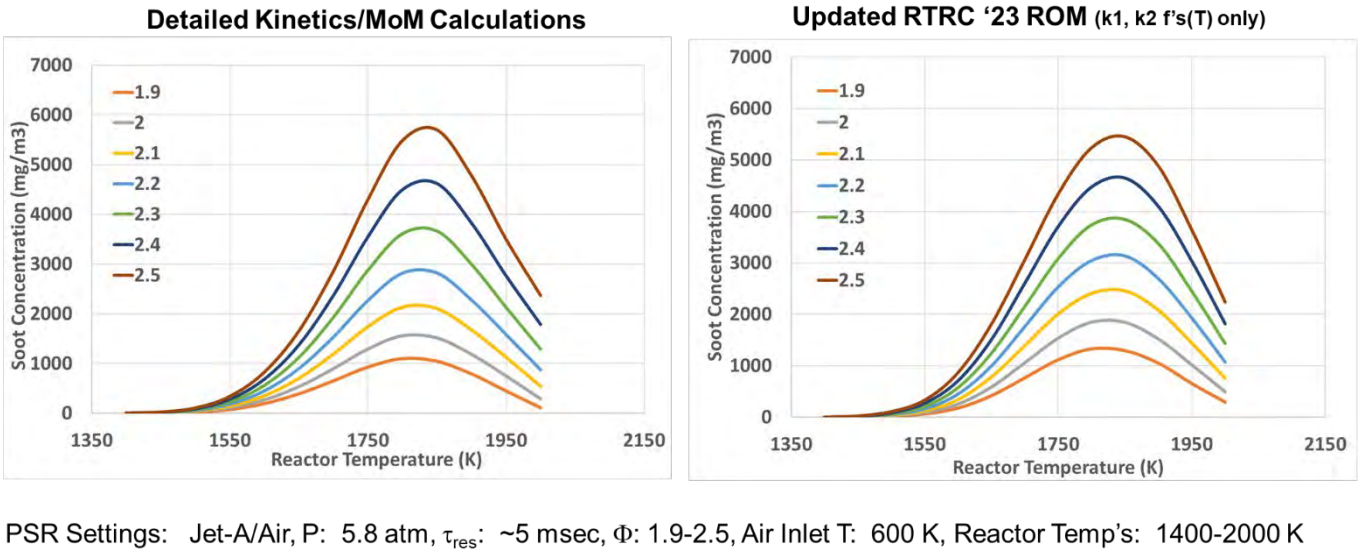

Figure 7. Comparison of soot concentrations generated from the two modeling approaches listed at nominal RQL combustor conditions. MOM: Method of Moments.

The goal of this year's activities was to determine whether a suitably compact mechanism that incorporates both Jet A fuel and PAH/PM kinetic information could be developed. From the analysis conducted to date, the detailed mechanism has

been constructed, and the PM-ROM has also been optimized to match its predictions with a detailed MOM model. The PM-ROM model will be used by Georgia Tech for CFD analysis of an RQL combustor.

Milestone

- Delivered detailed Jet A fuel chemistry and optimization of the PM-ROM for soot kinetics to other team members for further assessment. The work at RTRC is complete for this project.

Major Accomplishments

- Detailed Jet A fuel chemistry and optimized PM-ROM at RQL-relevant conditions.

Publications

None.

Outreach Efforts

None.

Awards

None.

Student Involvement

None.

Plans for Next Period

- Submit the final report by the end of September 2025.

Task 2 – Nucleation Modeling: Predicting Incipient Particle Nucleation Rates According to Polycyclic Aromatic Hydrocarbon Dimerization Rates from Molecular Dynamics Simulations

University of Michigan

Objective

The objective of this task is to develop models for nanoparticle inception, a critical step in predicting emissions. This effort bridges the work on gas-phase chemistry (RTRC) with the model for particle growth (RTRC) and provides inputs for the moment model (Georgia Tech) and growth models (RTRC) using atomistic simulations.

Research Approach

The current models for nanoparticle inception in the literature are insufficient in replicating an array of experimental observations, most notably the molecular structures observed in flames. The main focus of the current research was to design a predictive model that can accurately present chemical and physical growth trajectories for PAHs, considering their varied compositions, mass, and form. The information regarding concentration levels of such PAHs was used from the detailed gas-phase kinetics developed at RTRC. Additionally, the background temperature conditions to explore the stability of such PAHs were used from the local temperature conditions established using the high-fidelity reacting flow simulations of a practically relevant RQL combustor at Georgia Tech (see Figure 4). Once such an approach is established, it is critical to reduce this information in an expression that can reflect these physics-based rates. These reduced rates are now provided to conduct further Monte Carlo-based growth studies of incipient soot particles at RTRC. Furthermore, these reduced rates are also provided to Georgia Tech to add as an alternative robust nucleation model to their moment models.

To summarize, such work is conducted at the scales relevant to particle inception using high-fidelity molecular dynamics (MD) simulations. In our earlier annual efforts, the MD approach and its capability to identify key molecular structural properties of PAHs that can impact their dimerization capabilities were established. Furthermore, the approach of using innovative machine learning (ML) framework was also introduced. ML enabled us to perform a wide range of parametric investigations that were inaccessible due to the expensive nature of MD simulations. The success of such ML-based

predictions in predicting free-energy barriers (ΔA) is shown in Figure 8. Moreover, the Lasso regularization in the ML model helped us to extract critical features of importance by providing valuable insights regarding their influence on the dimerization ability of PAHs. Detailed discussions regarding these results were already provided in our previous annual efforts and hence are not repeated here for brevity.

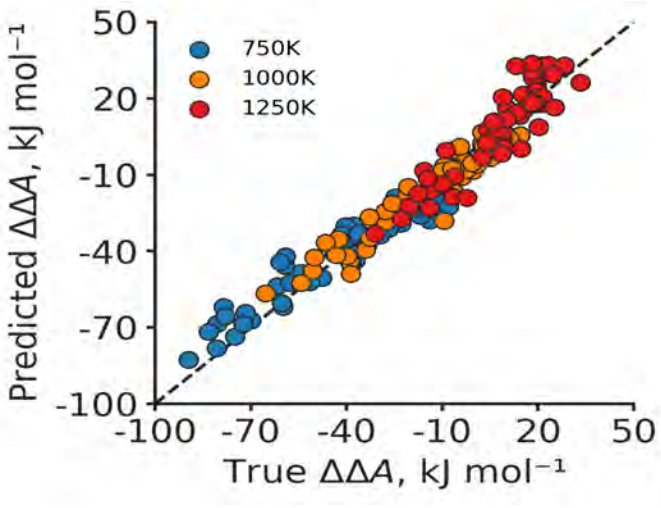

Figure 8. ML-assisted free-energy barrier analysis across a range of conditions.

To conclude upon the MD activities at UM, a brief discussion of the final deliverable from our current annual efforts is provided. In these efforts, a reduced nanoparticle inception model was developed. The model used information on the PAH species benzopyrene (A_4R_5).

The optimized rate constant can be approximated as shown in Equation 1.

$$k_f \left(\frac{L}{mol.s}\right) = \text{A T exp -} \left(\frac{G_f}{RT}\right) \quad \text{(Eq. 1)}$$

In this equation, the preexponential factor (A) is obtained as 2.0837×10^{10} 1/K/s, whereas the activation free energy is computed as:

$$G_f \text{ (kJ/mol)} = g_o + g_1 T + g_2 T^2 \quad \text{(Eq. 2)}$$

g_o, g_1, and g_2 are the constants with respective uncertainty as noted below.

$$\begin{aligned} g_o &= -4.12147 \quad +/- 0.4233 \quad (10.27\%) \\ g_1 &= 0.101723 \quad +/- 0.001069 \quad (1.051\%) \\ g_2 &= 5.55181e\text{-}06 \quad +/- 5.515e\text{-}07 \quad (9.935\%) \end{aligned} \quad \text{(Eq. 3)}$$

Finally, this information is provided to the models described in Task 3 for Monte Carlo simulations of post-inception growth as well as the nucleation rate expression in the moment-based soot model at Georgia Tech.

Milestone

- Develop a reduced nanoparticle inception model based on benzopyrene (A_4R_5).

Major Accomplishments

- Established machine learning-based MD predictions for nucleation rates due to A_4R_5 dimerization. This information is provided to both RTRC and Georgia Tech. The work is considered complete for this project.

Publications
None.

Outreach Efforts
None.

Awards
None.

Student Involvement
PhD student (Mr. Jacob Saldinger) at UM participated in this work.

Plans for Next Period
- Submit the final report by the end of September 2025.

Task 3 – Surface Growth and Aggregation Modeling: Reaction-Transport-Limited Growth of Soot Particle Models for Cluster–Cluster Aggregation
Raytheon Technologies Research Center

Objective
The objective of this task is to develop a physics-based framework for the prediction of soot particle growth after the inception process. The growth consists of agglomeration due to collisions between the primary particles and surface growth because of direct deposition of the precursors on the aggregate. The final aggregate fractal structure and its temporal evolution as a function of local conditions are of interest. This model will provide the morphology characteristics and the growth rate of the particles, which will serve as inputs into the moment-based soot models at Georgia Tech.

Research Approach
Soot particles from nucleation stages undergo various surface growth processes and form primary particles. These primary particles are spherical and typically have diameters of 1–10 nm. The focus of this effort is to understand the evolution of the fractal dimension of aggregates from the formation of primary particles to final fractal aggregates, through processes of surface growth and aggregation. Experimentally, the structures of these soot particles have been demonstrated to be dependent on the local conditions (e.g., the local equivalence ratio). These surface growth processes can occur because of heterogeneous reactions of gas-phase precursors on solid soot particle surfaces (reaction-limited growth) or through the transport of soot precursors in high-speed flames (transport-limited growth). Most of the current growth models account for only reaction-limited growth and ignore transport-limited growth as well as cluster–cluster interactions, which may be important in aggregate formation. In this work, information on background gas-phase species contributing to soot particles, the structure of the initial soot nuclei, and the local conditions are merged to understand the fundamental processes contributing to the formation of large soot aggregates.

The coupling of the growth framework that was developed at RTRC with inputs from MD simulations at UM, described in Task 2, and the LES study at Georgia Tech, to be described in Task 4, is briefly highlighted in Figure 9. The growth module takes the number density and size distribution of incipient soot particles from nucleation as an input, then tracks the growth of such particles along the statistically averaged path lines, which have varying background LES conditions in the form of temperature (T), pressure (P), and local equivalence ratio (ϕ), as detailed in Figure 10. The output from such studies in the form of the parametrized fractal dimension (D_f) will be used in the method of moment soot model.

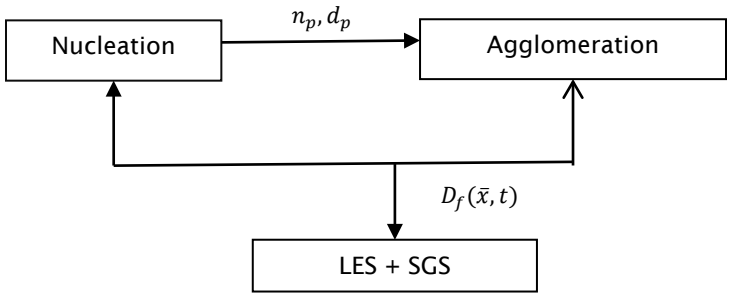

Figure 9. Post-inception growth of soot particles (LES–RTRC–UM coupling). LES: large eddy simulation.

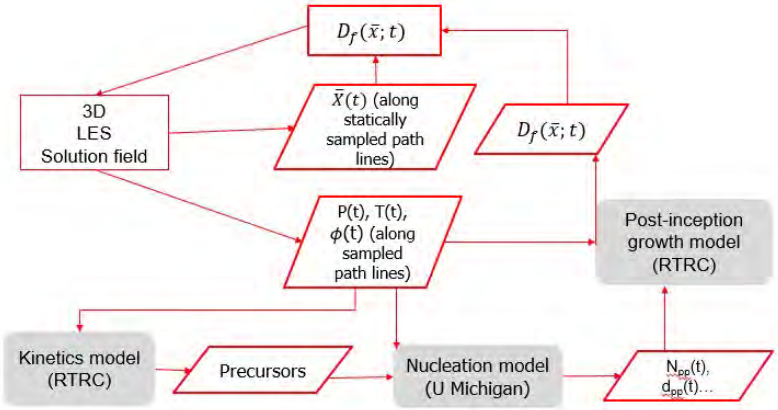

Figure 10. One-way coupled strategy for growth of soot particles. LES: large eddy simulation.

In the current annual efforts, the nucleation model provided by MD simulations (Equation 1) at UM was coupled with the MC simulation framework at RTRC. With this updated framework and the conditions highlighted from LES simulations of RQL combustor at Georgia Tech (to be discussed in Task 4), a parametric investigation was conducted across a range of conditions. The fractal dimension was estimated from such simulations and some results are highlighted in Figure 11.

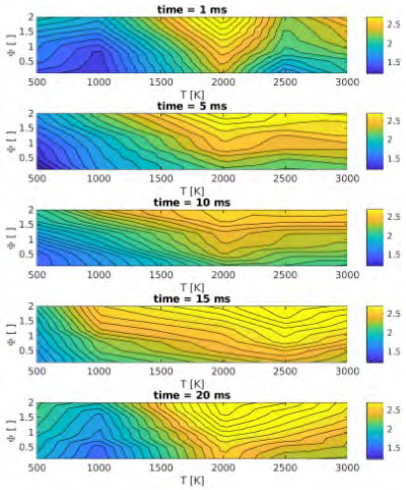

Figure 11. Fractal dimension as a function of parametric background conditions in RQL.

Milestone

- Tabulated the fractal dimension as a function of local residence time and equivalence ratio as feedback to moment soot model at Georgia Tech.

Major Accomplishments

- Performed one-way coupled demonstration of RQL-LES to parametrize the fractal growth of soot. This work may continue during the NCE for a two-way coupling demonstration.

Publications

None.

Outreach Efforts

None.

Awards

None.

Student Involvement

None.

Plans for Next Period

- Submit the final report by the end of September 2025.

Task 4 – Large Eddy Simulation of Soot Formation inside a Rich-Quench-Lean Combustor

Georgia Institute of Technology

Objective

The objective of this task is to develop a physics-informed LES framework to model soot formation in turbulent reacting configurations, focusing on both canonical settings, and a spray combustor of practical relevance. In the most recent annual efforts, the moment-based soot model was coupled with the LES framework to investigate soot evolution in canonical premixed and non-premixed flames. In the current annual effort, simulations, and analysis of soot formation from the RQL spray combustor are presented. Finally, a comparative assessment after coupling different modeling inputs obtained from sections discussed earlier is presented.

Research Approach

LES studies of turbulent sooting problems are challenging because of the multiscale nature of soot inception, coagulation, and surface growth that must be modeled in a highly turbulent and reactive environment, typically in a complex combustor. Most prior studies have focused on global models that approximate small-scale physics. Consequently, many available models account for the underlying physics. In contrast, simulations require some approximations, because the computational resources will never meet the simulation requirements. In the current effort, our team is balancing contributing to the prediction of soot formation physics in a realistic gas turbine combustor with the need to obtain high-fidelity, reliable predictions by using advanced models. To achieve this goal, our past LES capability is leveraged with baseline soot models and then compare their predictions against the models obtained from the current research efforts. Qualitative comparisons are provided wherever applicable. In earlier work, soot evolution was tracked with MOMIC, wherein the first six moments of the particle size distribution function were used. However, in complex configurations such as RQL, the six-moment approach was reduced to a 3-equation monodisperse model to reduce the numerical challenges; however, the description of nucleation, growth, oxidation, condensation, and aggregation processes was kept the same.

The full set of compressible reacting multispecies Navier–Stokes equations cannot be solved directly, because a direct numerical simulation is not feasible for practical applications. For LES, the large-scale flow features are resolved, and subgrid modeling is used for the smaller scales. The LES governing equations are obtained by filtering the compressible

form of Navier-Stokes equations using a low-pass filter with a cut-off length equal to the grid size (Δ). The gas-phase governing equations contain source terms due to the Lagrangian dispersed phase. Under the assumptions of point particle modeling, the equations of motion for the dispersed phase are solved using a Lagrangian framework. The LES formulations of all models for transport, thermodynamics, shear stress, heat flux vectors, and Lagrangian dispersed phase have been verified in the past on lab-scale swirl spray combustors (Menon & Ranjan, 2016) and as complex RQL spray configuration (Panchal & Menon, 2022) similar to the one of current interest. As the main focus of the current work is soot modeling, the relevant formulation of baseline soot models is discussed next.

To account for soot formation and growth, three additional transport equations are solved for three soot scalars (Nmira et al., 2023). These scalars represent the soot concentration (Y_{cs}), the soot aggregate number concentration (N_D), and the soot primary particle number concentration (N_{ps}). The global soot properties of engineering interests are then obtained as volume fractions ($f_v = Y_{cs}/\rho_s$), mean particle diameter $\left(d_p = \left(\frac{6Y_{cs}}{\pi\rho_s N_D}\right)^{\frac{1}{3}}\right)$, and mean number of primary particles per aggregate $\left(n_p = \frac{N_{ps}}{N_D}\right)$. In all these relations, the density of soot is assumed to be constant (= 1800 kg/m^3). The kinetics model describing the source terms for all these processes is highlighted here briefly. In the current work, two types of kinetics are primarily available: (1) Lindstedt model and (2) PAH-based model.

In the Lindstedt model (Leung et al., 1991), nucleation is assumed to occur via acetylene gas phase species. An empirical relation is used to correlate nucleation rate with acetylene concentration. A similar empirical relation is used to account for surface growth due to acetylene concentration. The oxidation rate is accounted for by the expression involving O_2 oxidation. A PMROM (delivered through Task1 by RTRC) is also coupled in our framework as an alternative to the Lindstedt model.

In the PAH-based soot model, nucleation is associated with the dimerization of naphthalene (A_2). However, the higher PAH species such as pyrene (A_4), or benzopyrene (A_4R_5) can also be used in the same framework if they are part of gas-phase chemistry. The models accounting for the condensation of PAH on soot surfaces are also considered. The hydrogen-abstraction-C_2H_2-addition (HACA) growth kinetics (Appel et al., 2000) is used to represent surface growth and oxidation reactions. Furthermore, soot particles are assumed to grow spherically until the primary particles reach a critical diameter (d_{cr}) and start forming aggregates with a fractal dimension of 1.8 afterward. In the current work, d_{cr} value is taken as 10 nm. The coagulation of particles is assumed to occur via free molecular, transitional, and continuum coagulation.

Within LES, small-scale fluctuations are not directly resolved and hence closure modeling is necessary to represent their effects. In this work, an eddy viscosity type subgrid model with dynamic coefficients (LDKM) is used to obtain the closure of subgrid momentum stresses and subgrid enthalpy flux. For the subgrid turbulence chemistry soot interactions, the code is equipped with a multiscale linear eddy model (LEM)-based closure model, partially stirred reactor model, laminar chemistry approximations, etc. The use of a standalone LEM to address multiscale soot physics was demonstrated in our past annual efforts as well as presented at the 75th American Physical Society's Division of Fluid Dynamics Meeting in November 2022. However, this model is computationally quite intense for LES applications of the RQL combustor. Therefore, in this work, a partially stirred reactor model was used to account for soot-turbulence interactions. Finally, an optically thin radiation model suggested at the International Sooting Flame (ISF) workshop was used to account for radiative heat losses due to soot.

LES of Soot Formation in RQL Combustor

A. Computational Setup and Numerical Methodology

The computer-aided design (CAD) model of the realistic LES rig in the Year 3 effort is shown in Figure 12a. The RQL burner simulated at Georgia Tech is a subsection (only one swirler) and is represented in Figure 12b. Few approximations were made at the inlet sections due to proprietary constraints leading to uncertainty near the injector location.

In summary, the computational domain from the inlet plenum to the outlet duct is considered. The overall components of the combustor consist of the swirler, fuel injector, quench jets, effusion surfaces, and the outlet duct. The main combustor has the primary rich zone from the dump plane to the quench jets and the secondary lean burn zone post-quench jets.

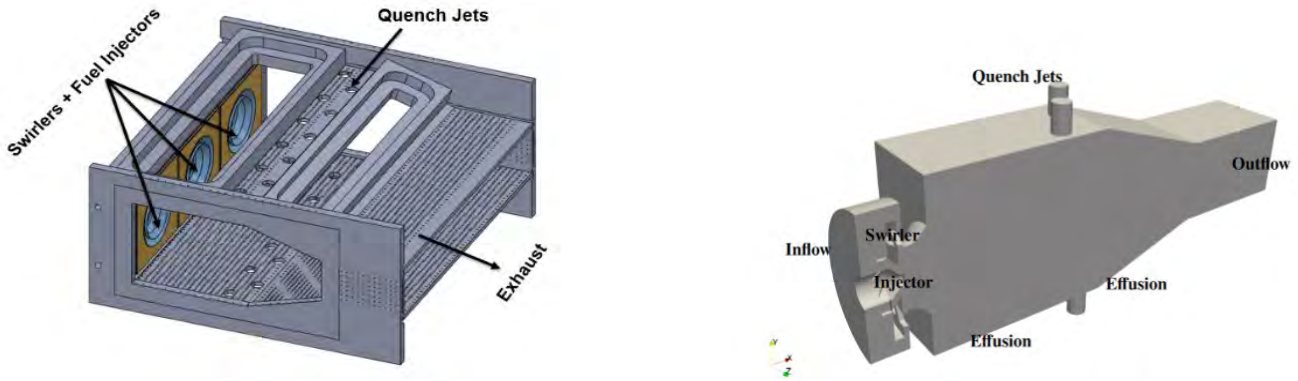

(a) Three-swirler RQL experimental rig (b) Model single-injector combustor with periodic BC

Figure 12. Computational aspects of the sector RQL rig investigated in the current work.

The computational domain is discretized using 6.3 million finite-volume cells. A multi-block structured grid with hanging nodes is generated to manage the geometric complexities of the combustor. Shear layers are resolved with minimum grid points of 0.25 to 0.7 mm consistent with previous LES simulations (Panchal & Menon, 2022). Swirlers have 10 points along their span. The grid quality is on average above 0.9 with a minimum value of 0.7 near dilution jets and geometrically complex swirled regions. The stretching ratio of 1.01 is applied on average with a maximum value of 1.2 near the outlet channel and the inlet plenum where no complex physics occurs.

The parts that are stitched together with hanging nodes use an interpolation scheme of the same order of accuracy as the numerical scheme. The geometry is further split into 5,141 blocks. Characteristic-based constant mass inflow boundary conditions are used at the primary inflow and inflow for quench jets. Periodic boundary conditions are used in the z-direction (spanwise-direction) as the current work focuses only on the single section of the multi-sector grid. At the outflow, the domain is extended by 30% of the combustor length, and a relaxing sponge boundary condition is applied. Small effusion holes are present throughout the walls in the primary and secondary zones of the combustor for wall cooling. Such holes are difficult to resolve in LES and hence are modeled using an effusion boundary condition. The air split for the combustor is 18% from the dome face (resulting in the equivalence ratios of 0.66 and 1.14 in the primary zone of the combustor), 44% from the two rows of quench holes, 7% from effusion cooling holes in the rich-burn region, and 19% for the effusion cooling holes in the lean-burn, taper, and exhaust regions.

For numerical simulations, a well-established Eulerian-Lagrangian (EL) finite volume solver (LESLIE) is used. In the current work, the numerical scheme for the gas phase is of second-order accuracy in time while a hybrid scheme for spatial discretization is employed, which dynamically switches between a second order accurate MacCormack central scheme and a third order-accurate Monotone Upstream-centered Schemes for Conservation Laws (MUSCL) scheme. A fourth order-accurate Runge-Kutta method for time integration is used for the Lagrangian phase.

B. Soot Formation Using the Lindstedt Model

Initially, to study soot formation in this configuration, our team employed the Lindstedt soot model. Three-dimensional (3-D) iso-surfaces of soot volume fractions along with their corresponding source terms of nucleation, growth, and oxidation are shown in Figure 13.

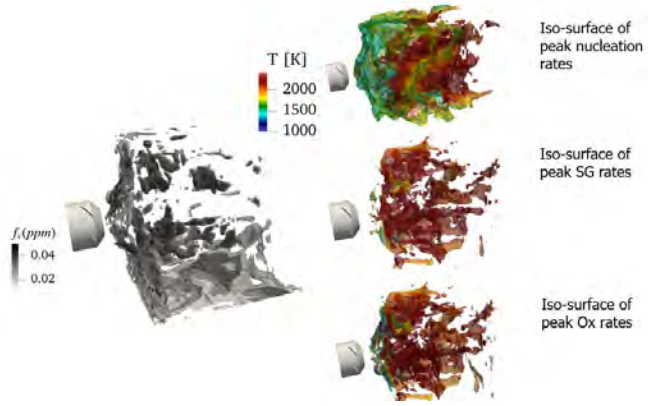

Figure 13. Contours of soot volume fraction and subprocesses near the fuel injector.

Our team further looked at the relevance of all subprocesses in the mixture fraction (Z) space. Here, the mixture fraction is computed using Bilger's formula as shown in Equation 4. Z_c, Z_H & Z_{ox} are the local elemental mass fractions of carbon (C), hydrogen (H), and oxygen (O) whereas W_c, W_H, and W_o represent their respective atomic weights. Additionally, the subscript ox & f represent their contributions from the fuel and oxidizer stream, respectively.

$$Z = \frac{\left(\frac{2(Z_C - Z_{C,ox})}{W_C} + \frac{(Z_H - Z_{H,ox})}{2W_H} - \frac{(Z_O - Z_{O,ox})}{W_O}\right)}{\frac{2(Z_{C,f} - Z_{C,ox})}{W_C} + \frac{(Z_{H,f} - Z_{H,ox})}{2W_H} - \frac{(Z_{O,f} - Z_{O,ox})}{W_O}} \quad \text{(Eq. 4)}$$

In mixture fraction space, a value of Z greater than Z_{st} (=0.0635) indicates a rich regime, characterized by a higher proportion of fuel relative to oxidizer, whereas ($Z < Z_{st}$) denotes the fuel-lean regime and Z_{st} represents the stoichiometric mixture fraction. Typically, the critical subprocesses related to soot formation, such as nucleation, surface growth, and oxidation, predominantly occur in the rich regime due to the reduced presence of oxidizer, which limits the complete combustion of the fuel. This observation is validated through a conversion of the entire LES dataset into mixture fraction space as shown in Figure 14. As depicted in the scatter plot in Figure 14, which shows 3-D unsteady LES data at a time, the majority of nucleation, surface growth, and oxidation rates are found to the right of the red line, indicating their occurrence in the rich regime ($Z > Z_{st}$).

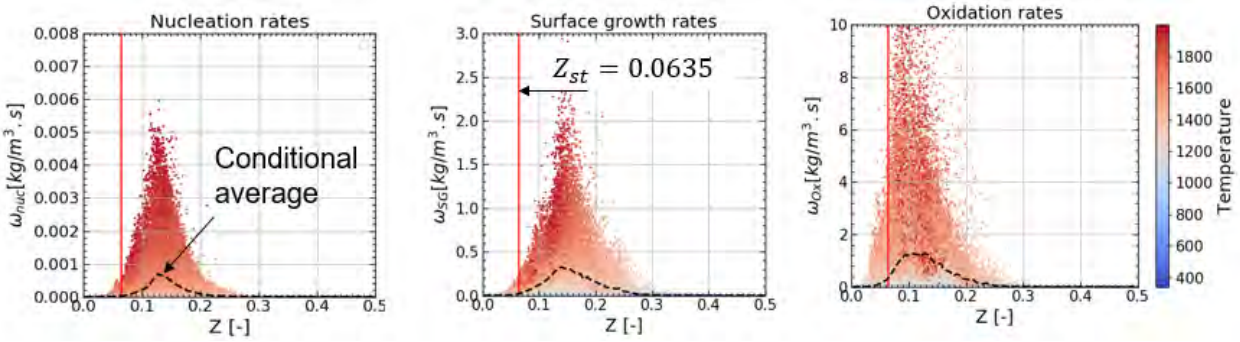

Figure 14. Scatter plot of soot source terms in the mixture fraction space.

RQL simulation data were post-processed to identify conditions favorable for soot formation. Figure 15 provides an overview of our LES simulations. In Figure 15a, the overall geometry of the combustor used for these simulations is shown.

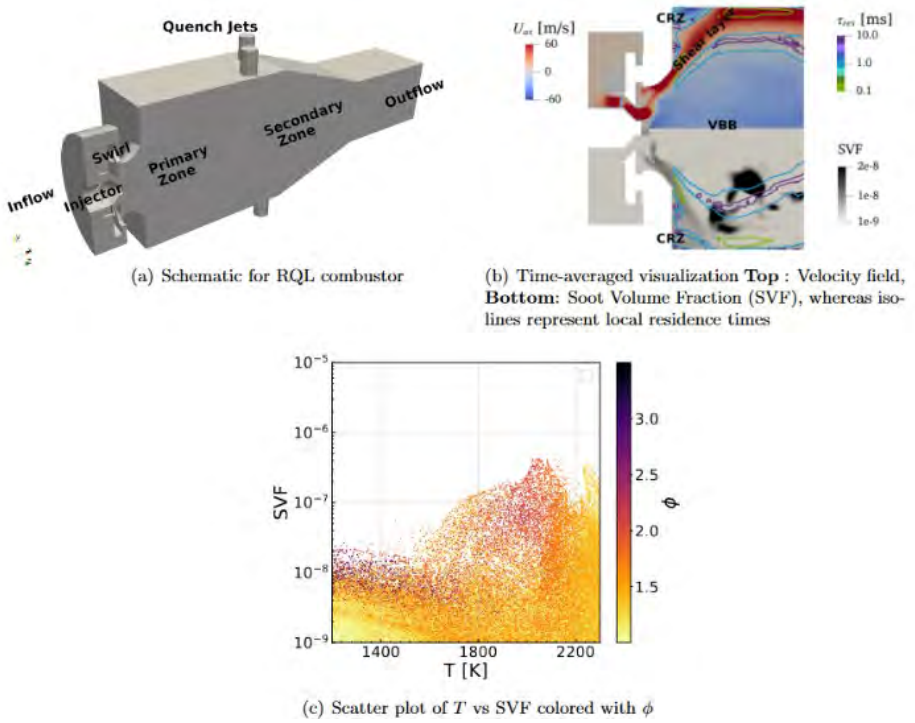

(a) Schematic for RQL combustor

(b) Time-averaged visualization **Top** : Velocity field, **Bottom**: Soot Volume Fraction (SVF), whereas isolines represent local residence times

(c) Scatter plot of T vs SVF colored with ϕ

Figure 15. Parametric conditions from CFD simulation for model assessment and optimization. RQL: rich-quench-lean.

Figure 15b presents a qualitative velocity field and soot formation visualization in the primary zone of the RQL combustor. The simulations effectively capture key characteristics of swirl-stabilized flames, including the vortex breakdown bubble (VBB) and corner recirculation zone (CRZ), which are separated by a shear layer. The lower half of Figure 15b shows that soot formation begins near the injector and predominantly follows the shear layer. Soot accumulates in recirculation zones such as the CRZ and VBB, where significant soot growth occurs. Additionally, isolines in Figure 15b depict the time scales within these zones, indicating that typical time scales for the recirculation zones (i.e., VBB and CRZ) are around 10 ms, while shear layers exhibit much shorter time scales, around 0.1 ms. Finally, Figure 15c displays the averaged local conditions (ϕ, T) within zones showing prominent soot formation. This detailed view of the RQL simulation data highlights areas prone to soot production, providing valuable insights for further analysis. The post-processed analysis suggests that the major envelope of local conditions where soot exists is observed to be $\phi \in [1.6 - 3.2]$, $T \in [1400 - 2200]\ K$, $\tau_{res} \in [0.1 - 10]\ ms$.

With the establishment of sooting LES RQL simulations, our team has shared the resulting data with our collaborative partners as outlined below. Initially, the entire dataset is transformed into a representation of equivalence ratio (ϕ) vs. temperature (T), as depicted in Figure 4 in the description of Task 1. This transformation is crucial for kinetic model optimization and for assessing the model using zero-dimension (0-D) configurations. Additionally, our team has statistically averaged the RQL LES data over two to three flow-through times to capture information along the streamlines. These averaged data have been provided to the RTRC team to support their modeling efforts as shown in Figure 4. The overall framework for data transmission is shown in Figure 16.

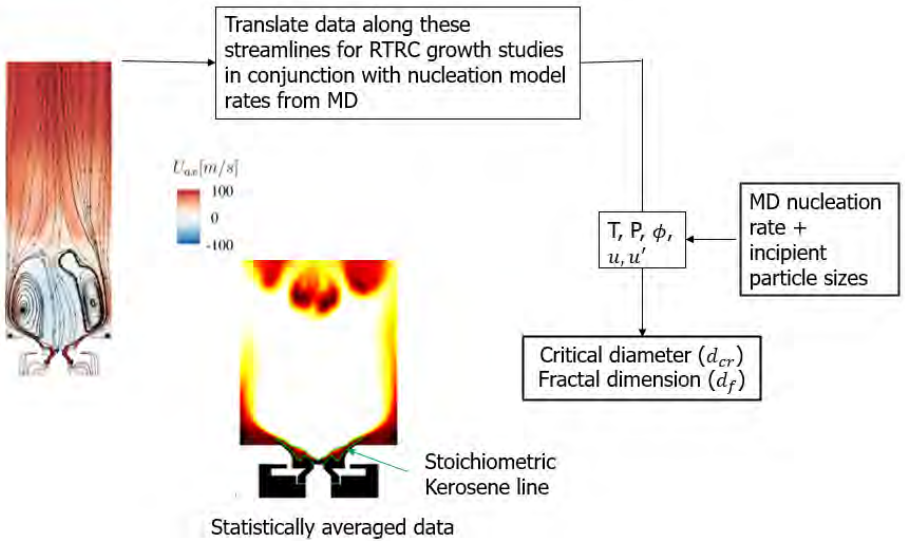

Figure 16. One-way coupled data along the RQL CFD streamlines.

Coupling of Inputs in the Modeling Framework at Georgia Tech

In this section, Georgia Tech activities about the coupling of different inputs obtained through Task 1 to Task 3 are highlighted. A 0-D model was used where the inputs of detailed kinetics and PM-ROM from RTRC, the nucleation model at Michigan, and surface fractal characteristics from RTRC are coupled and their effects are demonstrated sequentially in our modeling capabilities. The gas-phase kinetic mechanism is quite detailed in terms of the number of species (210 species) and is notably stiff and generally less suitable for large-scale CFD applications. Therefore, our team did not pursue RQL simulations with this approach. Instead, this detailed mechanism was utilized in our 0-D model, which provides valuable insights into soot formation trends within the primary zone of RQL combustors. The 0-D model requires equivalence ratio (fuel/air ratio), temperature (T), pressure (P), and residence times (τ_{res}) as inputs that were established from our RQL simulations as described earlier. This allowed us to analyze the effects of various kinetic models involved in soot formation in a controlled manner.

Effects of PM-ROM by RTRC

First, our team compared the performance of these models across a range of equivalence ratios and temperatures prevalent within the RQL combustor. The comparative predictive trends are shown in Figure 17, showing that while the Lindsted model predicts the peak of soot volume fraction at higher temperatures (~2100 K), the PAH-based model locates this peak at approximately 1800 K. The PM-ROM also predicts the same peak and qualitatively similar trend to temperature when compared with the PAH-based soot model.

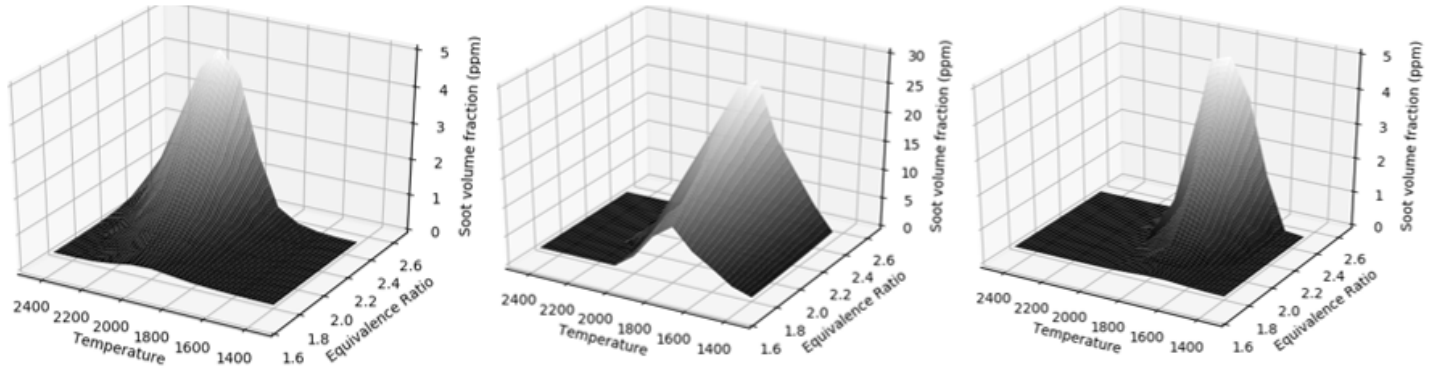

(a) Lindstedt model (b) PAH-based soot model (c) PMROM

Figure 17. Effects of gas-phase chemistry on soot volume fraction at representative conditions of RQL combustor.

Incorporating the Nucleation Effects (UM to Georgia Tech)

Based on the preliminary assessment of the nucleation model established in the previous quarterly effort, our analysis of such comparison was extended this quarter. Our team also included feedback on the model that is implemented in this approach. This model was implemented and the observed soot volume fraction for a range of conditions with increasing ϕ (1.8 – 2.5) is shown in Figure 18. The physics-based nucleation studies using molecular dynamics at Michigan suggested the rate expression as shown in Section 2 of the current work. Changing to a physics-based nucleation model, the trend of soot bell curve with temperature persists. However, the overall soot volume fraction seems to drop by an order of magnitude as compared to the baseline pyrene model. Such deviations may be less prominent in the lower temperature ranges where soot growth is dominated by surface growth. These are still preliminary results as the nucleation model is under investigation from added MD simulations at Michigan.

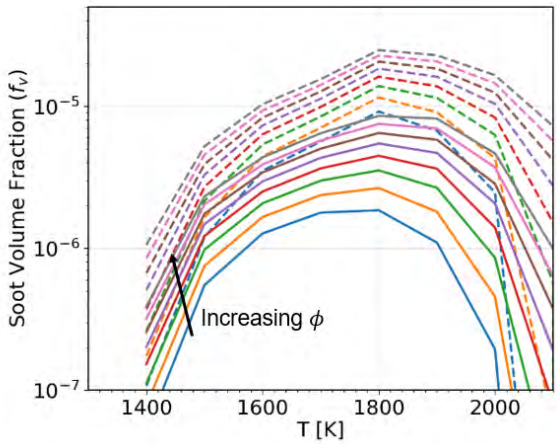

Figure 18. Effects of nucleation on soot volume fraction at RQL conditions. Solid lines: New nucleation model incorporated in Soot Modeling at Georgia Tech, Dashed lines: Baseline nucleation model based on pyrene dimerization.

Incorporating fractal characteristics (RTRC to Georgia Tech)

The typical structure of soot (morphology) determines its average surface area which influences various background processes such as rates of surface reactions and collisions of soot particles. Therefore, including such morphological details in the soot models can be quite important. Most of the models available in the literature or commercial solvers disregard the fractal structure of soot and assume these particles as spherical particles which can impact the sizes of such particles. A typical aggregate formation of such soot particles is shown in Figure 19. In our modeling, based on the physics of soot formation, initial formation is assumed to occur via spherical coalescence till the primary particle size (d_p) reaches

a critical transition criterion (d_{tr}) and after this point, particles are assumed to aggregate with constant fractal dimension (d_f) of 1.8.

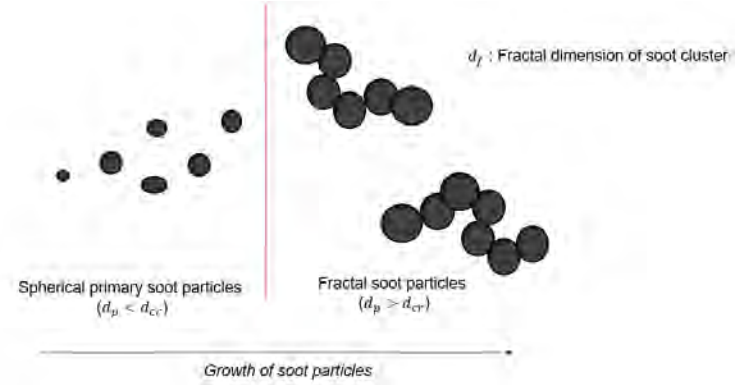

Figure 19. Fractal modeling of soot particles in the current work.

In our current work, the knowledge gained from Monte Carlo RQL simulations was used to improve the existing models to account for physics-based predictions of soot fractal growth. Task 3 discussed the preliminary results on predicted fractal characteristics of soot from Monte Carlo simulations. Here, the effects of these two key quantities (d_{cr} & d_f) were assessed for the overall soot volume fraction predictions. The results are presented here for a few representative conditions at a temperature of 1400-1800 K and an equivalence ratio of 2.4 (see Figure 20 for reference). Currently, our team looked at residence time of 8.5 ms (relevant to recirculation zones of the combustor). The spherical model assumes no fractal formation of soot, whereas different aggregate models are defined based on representative values of key quantities. These results suggest that including such aggregates may not have a significant impact on the volume fraction (hence mass) predicted from these models. Especially, the transition criterion (d_{cr}) has an impact on soot volume fraction till the point where the aggregation model kicks off, after which the impact diminishes. Even though the current results suggest a marginal impact on soot volume fractions, these models will most certainly have a critical impact on the size and number of particles estimated and will be explored in our future efforts.

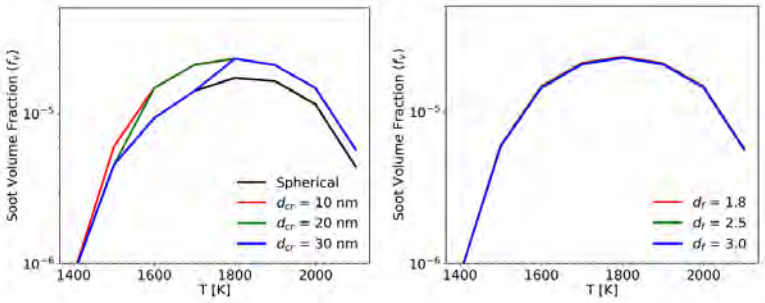

(a) Effect of critical diameter (d_{cr}) (b) Effect of fractal dimension (d_f)

Figure 20. Effects of aggregate inputs on soot volume fraction predictions.

PM-ROM in 1-D Gas Phase Laminar Flame Propagation

As the next phase of investigation, our team specifically focused on the propagation of a laminar flame through a rich premixed gas phase mixture under RQL-relevant conditions. The physics of soot formation in this scenario is depicted in the schematic shown in Figure 21. This setup allows for an examination of the role of aggregation models in the post-flame environment. In this configuration, a premixed reactant mixture enters the one-dimensional (1-D) domain from the left side and burns at the flame front. Due to an insufficient amount of oxidizer, the fuel-rich mixture cannot completely combust, leading to the decomposition of leftover fuel into soot. Various stages of soot formation occur behind the flame.

Immediately after the flame front, influenced by the kinetic model, nucleation, surface growth, and oxidation processes initiate the formation of soot, which continues to aggregate as it progresses downstream.

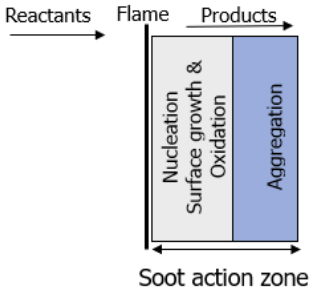

Figure 21. Schematic of laminar flame propagation.

Initially, the impact of various soot kinetic models was assessed by comparing the PM-ROM model against the Lindstedt model. Due to the current gas phase mechanism's lack of aromatic species, our team was unable to utilize the PAH-based soot model. As shown in Figure 22, the PMROM model predicts slightly less soot accumulation than the Lindstedt model. Also, the sensitivity of incorporating an aggregation model was explored, which helps characterize the structure of soot aggregates forming behind the flame, as depicted in Figure 23. The baseline model posits that aggregation effects commence once the primary particle reaches a critical diameter of 27 nm, with a fractal dimension of 1.8. Incorporating the aggregation model enhances the rate of particle coagulation, leading to a decrease in soot aggregate density. However, as aggregation increases the overall surface area available for soot reactions, it consequently raises the soot volume fraction. The aggregation model specifically influences the sizes of the particles formed behind the flame; without it, the model predicts large, spherical particles, whereas with aggregation, a cluster of soot aggregates composed of primary spherical particles is predicted.

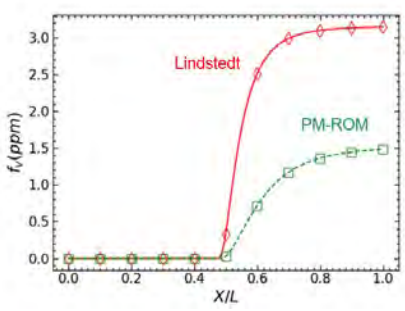

Figure 22. Soot volume fraction behind the laminar flame propagation.

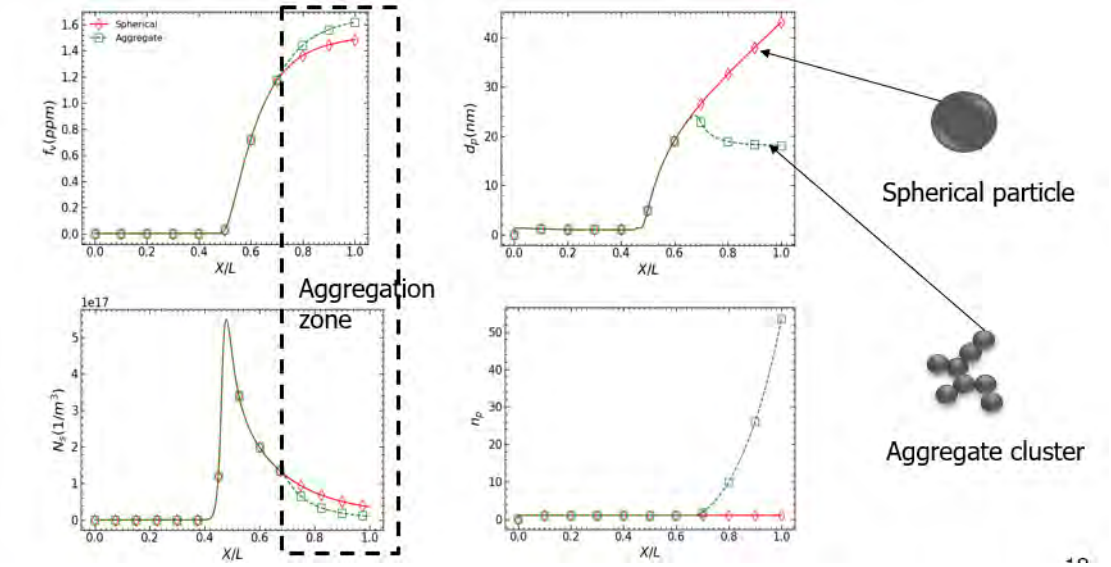

Figure 23. Aggregate characteristics of nvPM formed behind the laminar flame propagation.

PMROM in 3-D Gas-Phase Turbulent Premixed Flame Propagation

Our team performed 3-D calculations of turbulent premixed flames of gasified Jet-A2 fuel as a final investigation case. The schematic for the configuration is shown in Figure 24. Specifically, the laminar premixed flames investigated in the earlier section are superimposed on top of the isotropic turbulence field such that the flame turbulence interactions fall in a thin reaction zone $\left(\frac{u'}{S_l} = 10 \,\&\, \frac{l}{\delta_f} = 6.2\right)$ where, u' represents the turbulence intensity, S_l represents the laminar flame speed, l represents the turbulent length scale and δ_f is the flame thickness. The grid resolution is 96 x 96 x 96 for a physical domain of 15 x 15 x 15 mm. Characteristic inflow-outflow conditions are applied in the streamwise direction whereas periodicity is applied in the cross-streamwise and spanwise direction. The initial turbulence field is generated using a well-developed direct numerical simulation of isotopic turbulence in the same periodic domain and then filtered back to the LES grid. The fuel kinetics is based on the same 41-species skeletal mechanism derived from detailed mechanism (Wang et al., 2018) reduced by T. Lu and coworkers at the University of Connecticut using direct relation graph approach (Lu & Law, 20005). To model the unresolved sub grid stresses, our team employed a well-established Localized Dynamic k_{sgs} model (LDKM). Additionally, the partially stirred reactor (PaSR) model was used to incorporate the effects of turbulence-chemistry interactions due to unresolved subgrid interactions between chemistry and turbulence. All the simulations were conducted using Georgia Tech's super-computing cluster (PACE-phoenix) with Intel Ivy-bridge i7 processors.

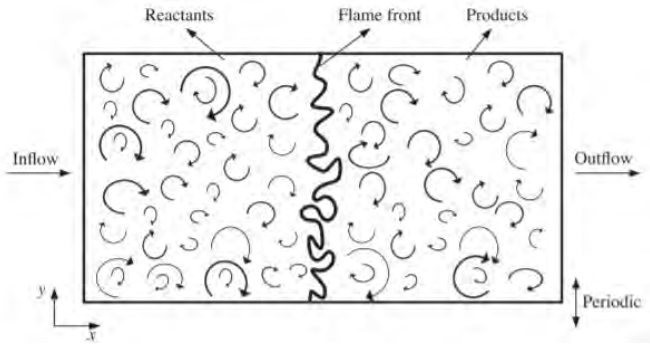

Figure 24. Schematic of the Turbulent Premixed Flame.

Figure 25 shows the inflow and outflow vorticity contours and the wrinkling of the initially planar surface due to background turbulence. The overall qualitative zones of soot nucleation, growth, and oxidation behind the flame are shown in Figure 26. In a premixed flame, soot formation heavily depends on the type of fuel, C/O ratio as well as the residence time, the soot aging, and the residual soot may leave the system. Moreover, as highlighted from the maximum contour lines of the nucleation, surface growth, and oxidation processes, the processes occur simultaneously; however, their relative magnitudes may differ significantly.

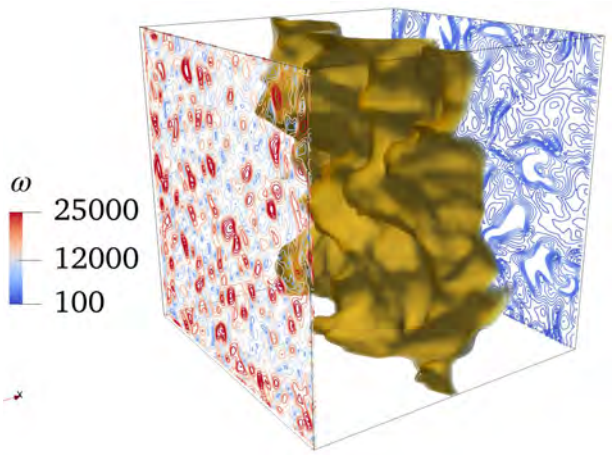

Figure 25. Vorticity at the Inflow and Outflow planes along with wrinkled flame surface.

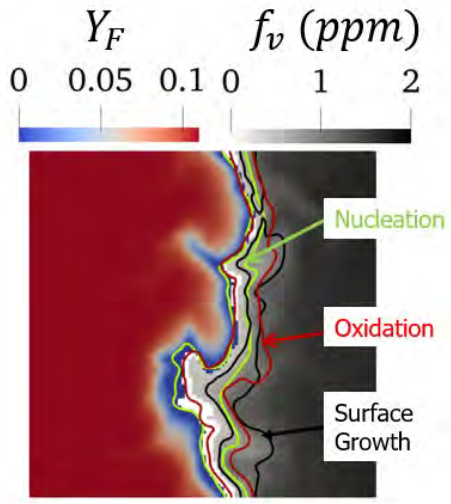

Figure 26. Consumption of gas phase fuel (left) formed soot levels (right) superimposed with contour lines of soot sub-processes in a turbulent premixed flame.

Milestones

- Studied (LES) soot formation within RQL complex rig the Lindstedt soot model.
- Performed standalone assessments of PM-ROM, nucleation model from UM, and aggregation characteristics from RTRC on soot volume fraction predictions.
- Calculated RTRC PM-ROM in 1-D laminar flame and LES of 3-D turbulent premixed flame.

Major Accomplishments

- Developed assembly of inputs from all cost-share partners in a standalone soot module.

Publications

None.

Outreach Efforts

None.

Awards

None.

Student Involvement

PhD student Shubham Karpe was involved in the development of the soot modeling framework at Georgia Tech.

Plans for Next Period

- Demonstrate the ability of LES to capture the trend of soot volume fractions in the primary zone of the RQL combustor as a function of global fuel/air ratios.
- Provide all the modeling tools in a standalone soot package to FAA. A final report will be submitted by the end of September 2025.

References

Appel, J., Bockhorn, H., & Frenklach, M. (2000). Kinetic modeling of soot formation with detailed chemistry and physics: Laminar premixed flames of C2 hydrocarbons. *Combustion and Flame*, *121*(1-2), 122-136. https://doi.org/10.1016/S0010-2180(99)00135-2

Blanquart, G., Pepiot-Desjardins, P., & Pitsch, H. (2009). Chemical mechanism for high temperature combustion of engine relevant fuels with emphasis on soot precursors. *Combustion and Flame*, *156*(3), 588-607. https://doi.org/10.1016/j.combustflame.2008.12.007

Frenklach, M. (2002). Method of moments with interpolative closure. *Chemical Engineering Science, 57*(12), 2229–2239. https://doi.org/10.1016/s0009-2509(02)00113-6.

Langer, R., Mao, Q., & Pitsch, H. (2023). A detailed kinetic model for aromatics formation from small hydrocarbon and gasoline surrogate fuel combustion. *Combustion and Flame, 258*, 112574. https://doi.org/10.1016/j.combustflame.2022.112574

Leung, K. M., Lindstedt, R. P., & Jones, W. P. (1991). A simplified reaction mechanism for soot formation in non-premixed flames. *Combustion and Flame, 87*(3-4), 289–305. https://doi.org/10.1016/0010-2180(91)90114-Q

Lu, T., & Law, C. K. (2005). *A directed relation graph method for mechanism reduction.* Proceedings of the Combustion Institute, *30*(1), 1333–1341. https://doi.org/10.1016/j.proci.2004.08.145

Menon, S., & Ranjan, R. (2016). Spray combustion in swirling flow. *Coarse-Grained Simulation and Turbulent Mixing*, *351*.

Nmira, F., Bouffard, A., & Consalvi, J. L. (2023). Flamelet/transported PDF simulations of ethylene/air jet turbulent non-premixed flame using a three-equation PAH-based soot production model. *Combustion Theory and Modelling*, *27*(6), 820-851. https://doi.org/10.1080/13647830.2023.2224755

Panchal, A., & Menon, S. (2022). Large eddy simulation of fuel sensitivity in a realistic spray combustor II. Lean blowout analysis. *Combustion and Flame*, *240*, 112161. https://doi.org/10.1016/j.combustflame.2022.112162

Selvaraj, P., Arias, P. G., Lee, B. J., Im, H. G., Wang, Y., Gao, Y., Park, S., Sarathy, S. M., Lu, T., & Chung, S. H. (2016). A computational study of ethylene–air sooting flames: Effects of large polycyclic aromatic hydrocarbons. *Combustion and Flame*, *163*, 427-436. https://doi.org/10.1016/j.combustflame.2015.10.017

Wang, H., Xu, R., Wang, K., Bowman, C. T., Hanson, R. K., Davidson, D. F., Brezinsky, K. and Egolfopoulos, F. N. (2018). A physics-based approach to modeling real-fuel combustion chemistry-I. Evidence from experiments, and thermodynamic, chemical kinetic and statistical considerations *Combustion and Flame, 193,* 502-519. https://doi.org/10.1016/j.combustflame.2018.03.019

Xu, Z., & Meakin, P. (2008). Phase-field modeling of solute precipitation and dissolution. *The Journal of Chemical Physics, 129*(1), 014705. https://doi.org/10.1063/1.2948949

Project 072 Aircraft Noise Exposure and Market Outcomes in the United States

Massachusetts Institute of Technology

Project Lead Investigators

R. John Hansman
T. Wilson Professor of Aeronautics & Astronautics
Department of Aeronautics & Astronautics
Massachusetts Institute of Technology
77 Massachusetts Avenue, 33-303
Cambridge, MA 02139
617-253-2271
rjhans@mit.edu

Christopher R. Knittel
George P. Shultz Professor of Applied Economics
Sloan School of Management
Massachusetts Institute of Technology
77 Massachusetts Avenue, E62-527
Cambridge, MA 02139
617-324-0015
knittel@mit.edu

Florian Allroggen
Executive Director Aerospace Climate & Sustainability & Research Scientist
Department of Aeronautics and Astronautics
Massachusetts Institute of Technology
77 Massachusetts Avenue, 33-328
Cambridge, MA 02139
617-715-4472
fallrogg@mit.edu

University Participants

Massachusetts Institute of Technology (MIT)

- P.I.: Prof. R. John Hansman
- Co-P.I. s: Professor Christopher R. Knittel and Dr. Florian Allroggen
- FAA Award Number: 13-C-AJFE-MIT, Amendment Nos. 075, 081, 094, 111, 115, and 130
- Period of Performance: August 11, 2020, to August 11, 2025
- Tasks (tasks listed below are general project tasks; reporting includes the period from October 1, 2023, to September 30, 2024):
  1. Literature review (not reported; completed during past reporting periods)
  2. Empirical identification strategy and scope of dataset (not reported; completed during past reporting periods)
  3. Calculation of noise impact metrics
  4. Cleaning and aggregation of housing transaction dataset (not reported; completed during past reporting periods)
  5. Descriptive analysis of dataset (not reported; completed during past reporting periods)
  6. Empirical analysis
  7. Social economic analysis of noise exposure and noise exposure impacts

Project Funding Level

The ASCENT Project 072 received $1,080,000 Federal Aviation Administration (FAA) funding and $1,080,000 matching funds. Sources of matching funding include approximately $236,300 from MIT, plus 3rd party in-kind contributions of $519,000 from NuFuels, LLC, and $79,000 from Savion Aerospace Corp., and $245,700 from Earth Force Technologies.

Investigation Team

Prof. R. John Hansman, (P.I.), all tasks
Prof. Christopher R. Knittel, (co-P.I.), Tasks 1, 2, 4, 5, and 6
Dr. Florian Allroggen, (co-P.I.), all Tasks
Dr. Xibo Wan, (postdoctoral associate), Tasks 1, 2, 4, 5, and 6
Dr. Jasdeep Mandia, (postdoctoral associate), Tasks 4 and 6
Zhishen Wang, (graduate student), Tasks 3, 5, 6, and 7

Project Overview

As enplanements at United States (U.S.) airports have increased by almost 50% over the past two decades, the number of Americans exposed to substantial levels of aircraft noise has decreased. However, considerable concerns regarding aircraft noise remain in some airport communities. This project leverages revealed preference approaches to infer the "implicit price" of aircraft noise exposure from market outcomes in U.S. airport communities. More specifically, the research team quantifies the capitalized disutility associated with aircraft noise exposure through analyzing the empirical relationship between aircraft noise exposure and transaction values for residential properties in communities surrounding U.S. airports. The project leverages potential changes in noise exposure associated with quasi-experimental settings (e.g., the opening of new runways or changes in arrival and departure paths) to empirically identify potential effects on house prices. The results provide insight into the average impacts of noise exposure on residential property values, while also assessing dynamic adjustment processes and potential heterogeneities in revealed preferences, by targeting factors such as time, location, or noise exposure patterns.

Task 3 – Calculation of Noise Impact Metrics

Massachusetts Institute of Technology

Objective

The goal of this task is to calculate aircraft noise exposure in communities surrounding selected U.S. airports. These analyses will be used to derive noise exposure changes associated with changes in flight trajectories (e.g., owing to new runways or new procedures).

Research Approach

The MIT team uses the Aviation Environmental Design Tool (AEDT) to model noise exposure according to historical flight track data at high temporal and spatial resolution. A high-resolution approach is required because the noise changes in performance-based navigation procedures are expected to be highly localized. One limitation of AEDT is in processing speed. Because it calculates noise for each flight track individually, a single day of flights can require hours to process. To circumvent this limitation, a fast model was developed at MIT under this project (Jansson, 2021). This model uses AEDT outputs for various aircraft types to set up a noise lookup table. Next, it uses flight track data, either from the Airport Surface Detection Equipment Model X (ASDE-X) or Threaded Track data provided by the FAA and applies the noise-power-distance curves from AEDT to obtain accurate noise data on an annual scale.

The tool is currently set up to calculate the day night average sound level (DNL). It also computes the number of instances an overflight event is above a certain peak sound level (L_{max}) threshold over a day – which we refer to as N_{above}. For example, an N_{60} of 25 indicates that 25 overflight events had an L_{max} of 60 dB or greater that day. We use N_{above} in addition to DNL in our assessments.

Milestone

- Ran the AEDT to model noise exposure for three U.S. airports, for Boston Logan International Airport (BOS), Seattle-Tacoma International Airport (SEA), and Charlotte Douglas International Airport (CLT).

- Analysis was conducted for N_{60} in addition to DNL metrics.

Major Accomplishments
- Performed detailed noise analyses for the year 2019 for BOS, SEA, and CLT.
- Conducted additional analysis to support economic impact analyses as described in Task 7.

Publications
None.

Outreach Efforts
The team presented during the ASCENT fall meeting in 2024.

Awards
None.

Student Involvement
Graduate student Zhishen Wang worked on Task 3.

Plans for Next Period
- Continue refinement of the modeling approach and simulation of noise exposure at additional airports.

Task 6 – Empirical Analysis
Massachusetts Institute of Technology

Objective
The goal of this task is to empirically analyze the impacts of aircraft noise exposure on residential property values. For this purpose, the team uses the identification strategies developed previously under Task 2 (see reports for previous periods) and empirically estimates the parameters in the model using the datasets developed previously under Tasks 3 and 4. Through this process, the research team can obtain estimates of the price effects of aircraft noise exposure for residential properties, while controlling for other impacts such as the characteristics of a house or neighborhood, or general price trends.

Research Approach
The model developed previously is estimated by using empirical methods for regression analysis. Initial analyses are available for BOS, Chicago O'Hare Airport (ORD), and SEA.

During the current period of performance, the ASCENT Project 072 team analyzed whether the response to noise exposure is homogeneous across the regions surrounding an airport. Most importantly, the team studied differences in noise exposure responses with (1) the value of houses and (2) noise exposure levels. Variation with house values could stem from differences in sensitivity to aircraft noise exposure with wealth. Variation with prior aircraft noise exposure levels could be driven by how a fixed change in noise levels may be perceived differently in a quiet versus a noisy environment.

Milestone
- Used preliminary model specifications (see reports for previous periods) to gain initial insights into the variation in house price responses to noise exposure.
- Performed preliminary analyses for three airports, BOS, ORD, and SEA, to compare results and understand their robustness.

Major Accomplishments
- Obtained average estimates of the impact of noise exposure on house prices during previous periods of performance (see reports for previous periods). During this period of performance, the ASCENT Project 072 team

gained further insights into whether the responses to noise exposure are homogeneous across the regions around an airport.

- Analyzed whether changes in house prices differ with (1) the value of houses and (2) noise exposure levels. Preliminary results are shown in Tables 1 and 2, which show the regression coefficients and their standard deviations for different house price quintiles and different noise exposure groups.

The results indicate that (1) house price response to changes in aircraft noise exposure tends to be stronger with higher property values and (2) noise response to changes in aircraft noise exposure tends to be statistically significant at lower noise levels. These findings require further analysis and are not fully consistent across the airports considered so far. It remains to be seen whether these findings could be artifacts of the datasets (e.g., distribution of neighborhoods around the airports) or sample size (e.g., high noise values can only be found for a relatively small number of properties).

Table 1. Results of regression analysis by quintiles of house prices. Regression coefficients represent the percentage house price in response to a 1% change in DNL for the group. Note that the regression model is run individually with data for each house price quintile so that the average coefficient does not reflect the results for the pooled data. Statistical significance level is indicated by asterisks where *p<0.10,**p<0.05,***p<0.01. The analysis is preliminary.

dB Range	Boston		Chicago		Seattle	
	Coef.	S.D	Coef.	S.D	Coef.	S.D
<= 40 dB	0.108	0.216	-0.127***	0.062	-0.155***	0.075
40-50 dB	-0.391***	0.092	-0.349***	0.104	-0.818***	0.199
50-60 dB	-0.078	0.157	0.762	0.747	0.945	0.839
> 60 dB	-0.205	0.546	.	.	.	.

Table 2. Results of regression analysis by prior aircraft noise exposure levels. Regression coefficients represent the percentage house price in response to a 1% change in DNL for the group. Note that the regression model is run individually with data for each noise exposure group so that the average coefficient does not reflect the results for the pooled data. Statistical significance level is indicated by asterisks where *p<0.10,**p<0.05,***p<0.01.. The analysis is preliminary.

Quintile	Boston		Chicago		Seattle	
	Coef.	S.D	Coef.	S.D	Coef.	S.D
First (Lowest)	-0.122	0.087	-0.128	0.092	-0.195**	0.107
Second	-0.022	0.024	0.005	0.027	-0.04	0.032
Third	0.002	0.023	-0.023	0.021	-0.063***	0.025
Fourth	0.032	0.031	-0.045**	0.027	-0.078***	0.035
Fifth (Highest)	-0.135*	0.087	-0.408***	0.071	-0.194***	0.088

Additional analyses in future periods and under Task 7 could shed further light on the underlying trends and the validity of these findings.

Publications

A manuscript which summarizes the methods and results for BOS, SEA, and ORD is under preparation.

Outreach Efforts
The research team presented during the ASCENT spring and fall meetings in 2024.

Awards
None.

Student involvement
Graduate student, Zhishen Wang, worked on Task 6.

Plans for Next Period
- Continue to refine the analysis by leveraging data for additional airports and by assessing potential variation in noise exposure response across different airports and regions surrounding airports.

Task 7 – Economic Analysis of Noise Exposure and Noise Exposure Impacts
Massachusetts Institute of Technology

Objective
This task aims to assess potential household economic implications in aircraft noise exposure and its impacts. Initially, the research team will analyze noise exposure with respect to the distribution of the population. Based on the results, variation in impacts with economic variables will be assessed in a data-driven approach.

Research Approach
To assess the distribution of noise exposure around airports, the ASCENT Project 072 assessed noise exposure normalized by distance to the airport. The normalization by distance is pursued because flights generate higher ground-level noise exposure while at low altitude, upon takeoff and landing in close proximity to the airport. As such, proximity to the airport can be expected to be correlated with increased noise exposure. Grid-level noise exposure data for BOS (using data derived under Task 2) can be used to show the correlation between distance to the airport and noise exposure (see Figure 1 for BOS).

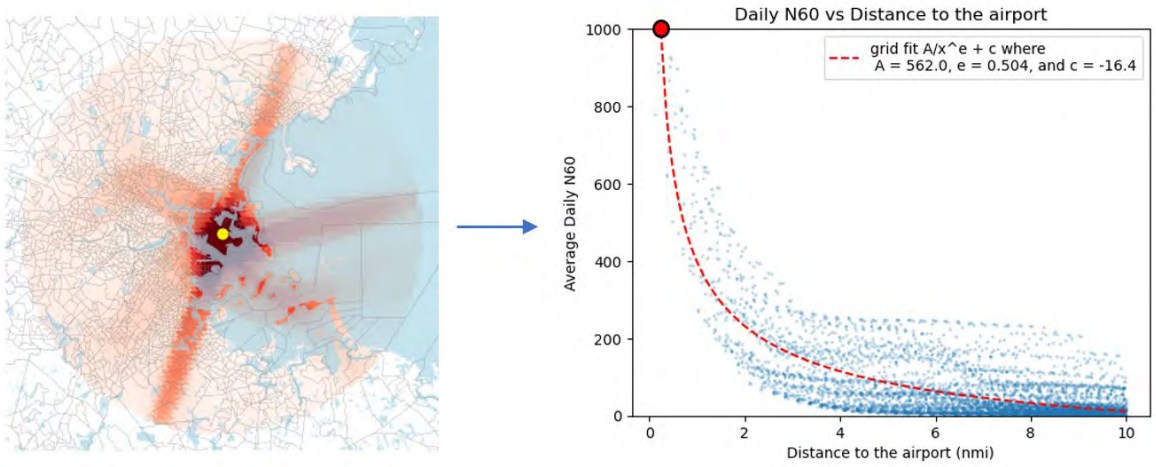

Figure 1. Modeled aircraft noise exposure for BOS and correlation with distance to airport; year 2019 data. Data are preliminary.

Based on the data shown in Figure 1, the "expected" noise exposure level can be derived, which is based on distance to the airport. It is evident that noise level at a given distance is subject to variation, especially at higher distances from the

airport (e.g., due to runway orientations and dominant operational patterns). Yet, the fit allows us to prescribe an expected "equal" noise level given distance to the airport. Locations where the noise may be more or less than the expected exposure based on distance to the airport can now be identified (see Figure 2).

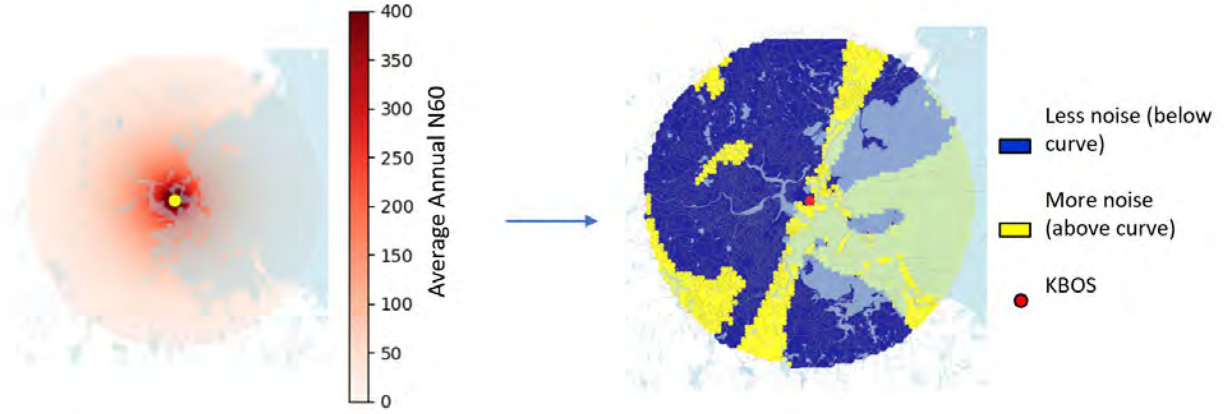

Figure 2. Modeled aircraft noise exposure for BOS and correlation with distance to airport; year 2019 data. Analysis is preliminary.

Milestone

- Developed an initial approach for analyzing inequality in noise exposure around airports.

Major Accomplishments

- Developed an initial approach for analyzing inequality in noise exposure.
- Gathered data (e.g., from the U.S. Census) to analyze the household economic correlations with noise exposure.

Publications

None.

Outreach Efforts

The team presented the approach in a presentation during the ASCENT spring and fall meetings in 2024.

Awards

None.

Student involvement

Graduate student, Zhishen Wang, worked on Task 7.

Plans for Next Period

- Perform analysis for additional airports to assess potential social economic implications in aircraft noise exposure.
- Analyze the correlations between noise exposure and household economic characteristics.

Project 073 Fuel Composition Impact on Combustor Durability

University of Dayton Research Institute

Project Lead Investigator

Scott Stouffer
Group Leader, Combustion Group, Fuels and Combustion Division
University of Dayton Research Institute
300 College Park, Dayton, OH 45469-0043
937-255-7277
Scott.Stouffer@udri.udayton.edu

University Participants

University of Dayton Research Institute

- P.I.: Scott Stouffer, PhD, PE
- FAA Award Number: 13-C-AJFE-UD, Amendment 029
- Period of Performance: August 11, 2020, to September 30, 2021
- Period of Performance: August 10, 2021, to February 10, 2022: Amendment 036
- Period of Performance: October 1, 2021, to September 30, 2022: Amendment 040
- Period of Performance: October 1, 2022, to September 30, 2023: Amendment 044
- Period of Performance October 1, 2023, to September 2025: Amendment 54
- Task:
  1. Perform radiation measurements of various fuel types in the referee combustor to evaluate the effect of fuel composition on combustor liner lifetime

Project Funding Level

Amendment No. 029	$299,148
Amendment No. 040	$199,865
Amendment No. 044	$200,000
Amendment No. 054	$130,000
Total	**$829,013**

Investigation Team

Dr. Scott Stouffer, (P.I.), project direction
Mr. Tyler Hendershott, (research engineer), combustor operations
Dr. Jeff Monfort, (research engineer), radiation measurements
Mr. Harry Grieselhuber, (technician), combustor testing
Mr. Jeff Gross, (technician), combustor testing

Project Overview

In this study, the effects of fuel chemical composition on radiative heat transfer and the resulting combustor liner lifetime will be evaluated. Alternative fuels contain ratios of hydrocarbon types that may substantially differ from those in familiar petroleum-based fuels. In petroleum-based fuels, higher aromatic levels are known to contribute to greater particulate matter loading radiative heat transfer and reduced combustor liner lifetimes. Consequently, aromatic compounds are limited to 25 vol% in the ASTM D1655 (ASTM International, 2023) jet fuel specification. Some candidate alternative fuels contain synthetically produced aromatic compounds and cycloparaffins, which must be evaluated for their radiative heat

transfer characteristics. The measurements collected in this project will provide insights into the effects of fuel type on liner lifetime. Several fuel types will be investigated, including a synthetic aromatic kerosene, a baseline Jet A fuel, and a fuel high in cycloparaffins (e.g., Shell® IH²® fuel). Diagnostic methods to be used in the investigation include the measurement of wall and gas temperatures, and the use of infrared (IR) cameras and radiometers.

Task 1 – Perform Radiation Measurements of Various Fuel Types in the Referee Combustor to Evaluate the Effect of Fuel Composition on Combustor Liner Lifetime

University of Dayton Research Institute

Objective

The objective of this program is to provide insights into the effect of fuel type on engine combustor liner lifetime. This study will ensure that candidate drop-in fuels will perform satisfactorily in jet engines and will not increase the need for engine maintenance or decrease flight safety. The findings of this study may also indicate which fuel composition changes may reduce radiative heat transfer and therefore increase combustor liner lifetime.

Research Approach

Fuel chemical composition is well known to strongly affect soot formation, smoke production, and radiative heat flux in gas turbine combustors (Chin & Lefebvre, 1990). Studies of petroleum-based fuels with varying levels of aromatic levels have indicated that these properties increase with the overall content of aromatic species. Other parameters such as hydrogen content, hydrogen/carbon ratio, and smoke point have also been correlated with liner temperatures, but the effects of individual types of aromatic species have not been well studied. Candidate alternative fuels may meet the overall limits for aromatic species but may contain individual species or mixtures of species that are markedly different from those in petroleum-derived fuels. Radiation heat transfer to combustor liners is a major issue affecting the durability and operational envelope of gas turbine engines. Radiation can cause high heat fluxes, thus resulting in localized heating, hotspots, and high thermal gradients along and across the liner. Increases in liner temperature can decrease liner durability (Gleason & Bahr, 1980). Intense heating can cause problems with low cycle fatigue, cracking, and buckling of the liner and, in extreme cases, localized melting of the liner. The combustor walls can be convectively cooled by effusion or film cooling; however, film cooling typically imposes a cycle performance penalty, along with elevated levels of carbon monoxide (CO) and unburnt hydrocarbons, particularly at low power settings. Because of concerns regarding the effects of fuel type on radiation, the radiant heat flux is considered a figure of merit by aircraft engine original equipment manufacturers in the evaluation of alternative fuels for aircraft use (Colket et al., 2017).

The radiation from a gas turbine flame has two main components: (a) "non-luminous" radiation from product gases, such as carbon dioxide (CO_2), H_2O, and CO, and (b) luminous radiation from non-volatile particulate matter (principally soot).

Non-luminous radiation corresponds to the IR region and has a spectral distribution, whereas the luminous radiation is broadband, and a fraction of the radiation appears at visible wavelengths. Typically, as the pressure is increased, the luminous radiation from soot particles becomes the dominant source of heat flux to the liner walls. Whereas the convective component of the wall heat transfer depends on the fluid dynamics and gas temperature distribution near the walls, the peak radiant fluxes are related to the combinations of high-temperature gas and non-volatile particulate matter.

The emissivity of the combustion gases is typically related in an expression such as:

$$\epsilon_g = 1 - exp\left[-aPL(ql)^{0.5}T_g^{-1.5}\right] \quad \text{(Eq. 1)}$$

where ϵ_g= emissivity of the combustion gases (non-dimensional)
P = gas pressure in kPa
l = characteristic length factor, which is a function of combustor geometry
T_g = gas temperature in K

® Shell is a registered trademark of Shell Trademark Management BV, The Hague, The Netherlands.
® IH² is a registered trademark of Gas Technology Institute, Des Plaines, Illinois.

q = fuel-to-air ratio
L = luminosity factor

The luminosity factor is set to 1 for gaseous emissivity. For sooting flames associated with liquid aviation fuels, the luminosity is greater than 1 and can be correlated with the fuel composition. Several relations between luminosity and fuel type have been reported in the literature (Lefebvre, 1999; Naegeli & Moses, 1980; Clark, 1982). In general, the luminosity factor has been found to decrease with increasing hydrogen/carbon ratio and decreasing aromatic content of the fuel. Other correlations in the literature have addressed the correlations with smoke point and naphthalene content. Although IR has been used as a diagnostic tool in basic flame experiments (Rankin et al., 2012), very little work using multiple radiometers and/or planar measurements of IR emissions in practical combustors has been reported in the literature. The referee rig combustor is ideal for assessing radiation heat transfer because the walls are heavily cooled—a condition that tends to suppress the convective component and thus the background radiant heating from opposing walls, so that the wall heat transfer is primarily from the flame radiation.

The referee rig combustor was developed to conduct experimental combustion research. Highlights of previous contributions to the evaluation of alternative fuels include the following:

1. Experimental measurements of lean blowout (LBO) for fuels at conditions of interest to original equipment manufacturers and the National Jet Fuels Combustion Program, which have resulted in the unexpected finding of a high correlation between the derived cetane number and the LBO limit.
2. Experimental measurements of boundary conditions for the combustor, including air flow splits to support numerical combustion modeling efforts.
3. Development of cold air and cold fuel capabilities for the facility, to enable atmospheric cold start ignition experiments to be conducted over a range of conditions.
4. Further extension of the facility's ability to allow altitude relight experiments to be conducted with a range of fuels at simulated altitudes of 25,000 ft.
5. Examination of the effects of heated fuels on combustion characteristics and emissions.

The work with the referee rig combustor has yielded publications that detail cold start ignition (Hendershott et al., 2018), ignition at elevated temperatures (Stouffer et al., 2017), LBO characteristics (Corporan et al., 2017; Esclapez et al., 2017; Colborn et al., 2020), particulate and gaseous emissions (Corporan et al., 2017), acoustic response (Monfort et al., 2017), flow through the liner effusion passages (Erdmann et al., 2017; Briones et al., 2017), spray characteristics (Mayhew et al., 2017), and altitude relight (Stouffer et al., 2020; Stouffer et al., 2021).

Milestones

The anticipated major milestones and planned due dates are as follows:

Milestone	Planned due date
Provided test plan	December 1, 2020
Conducted initial instrumentation experiments	September 2022
Perform detailed testing for a range of fuels	April 1, 2025
Complete final report	September 30, 2025

Major Accomplishments

Improvements in Instrumentation

In the past year, our team made improvements to the instrumentation for the purpose of better characterizing the radiation and conditions of the flow. The improvements included:

1. The installation of emissions probes into the exhaust.
2. Adding exhaust thermocouples to capture the exhaust temperature.
3. The installation of three radiometers to characterize the axial distribution of emitted radiation.
4. The use of round sapphire windows to image radiation over wide wavelength ranges (0.3 to 4 μm)
5. Addition of a visible/near IR camera

Figure 1 shows the installation of the thermocouples and the three emissions probes at the combustor exit. The probes were used to sample both particulate emissions and gaseous emissions of the gases. The gaseous emissions were

measured with a Fourier transform infrared analyzer (FTIR) and a flame ionization detector (FID), and the particulate emissions were characterized by using condensation particle counters to measure the particle number density. The three emissions probes are at the same spacing as used in previous work with this combustor and were aligned with the vertical combustor centerline. The probes were cooled with a closed-circuit process fluid that maintained the temperature at 150°C, for the purpose of thermally quenching combustion reactions of the gases entering the probe.

The purpose of the thermocouple rake is to measure the gas temperature at the exit to determine if the actual heat release during combustion is the same between two fuels at the same test conditions. Theoretically the heat release at a fixed fuel air equivalence ratio may be calculated by $\Delta H = \dot{m}_f(LHV)$, However, this calculation does not consider the combustion efficiency. The thermocouples were chromel-constantan (type K) and were located between the cooled emissions probes in small uncooled rakes additively manufactured from inconel 718. The rakes had Kiel-head radiation shields.

One concern that the ASCENT Project 073 team had with using cooled emissions probes and thermocouple probes close to each other was that when the probes were placed in back purge mode, the nitrogen emitted from the probe tip would interfere with the thermocouple measurements. Fortunately, our team found that there was no effect of the emissions purge gases on the measured gas temperatures.

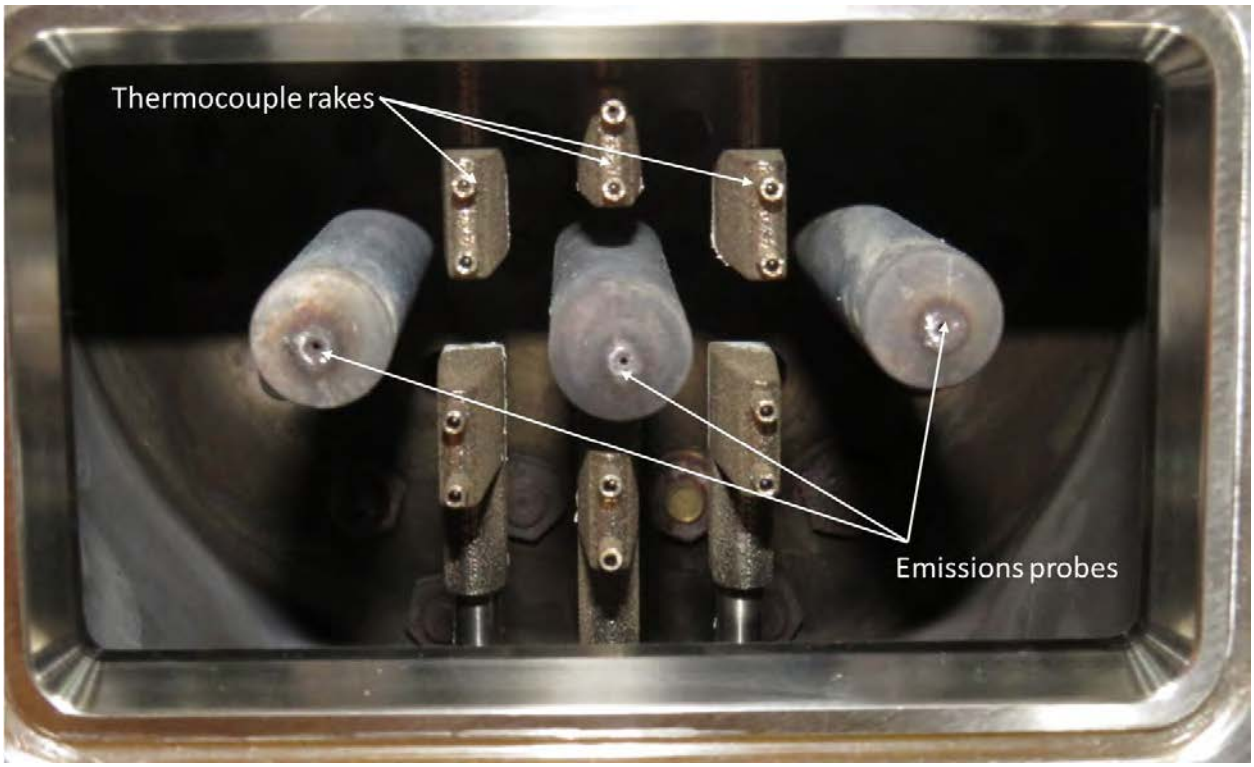

Figure 1. Thermocouples and emissions probes installed at the exit of the combustor.

A side wall radiometer panel was developed that allowed the installation of three radiometers to study the longitudinal variation in the radiative loading. Figure 2 shows the internal view of the panel the radiometers are mounted along the centerline of the combustor side wall and are numbered from 1 (upstream) to 3 (downstream location). Figure 3 shows the external view of the instrumented panel with the associated plumbing of water cooling and nitrogen film cooling for the three gauges. The radiometers were manufactured by Vatell Corporation and have a 120° collection angle for the radiation. During tests, after steady temperatures are reached in the combustor, the radiometer signal is expected to be steady. However, the first tests showed that soot collected on the gauge surface caused a drop in the output of the gauges at steady combustion conditions.

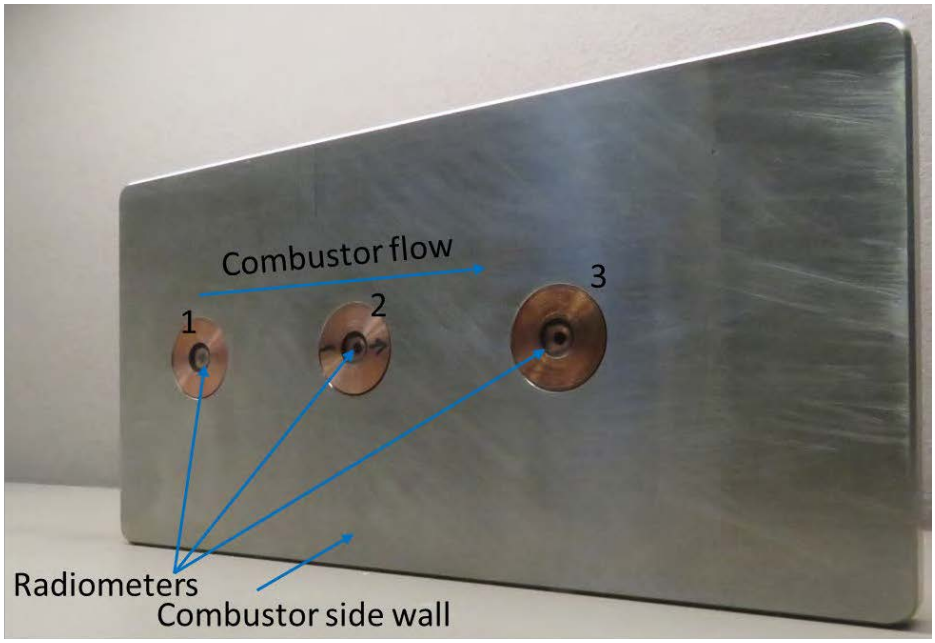

Figure 2. Combustor radiometer section (inside view).

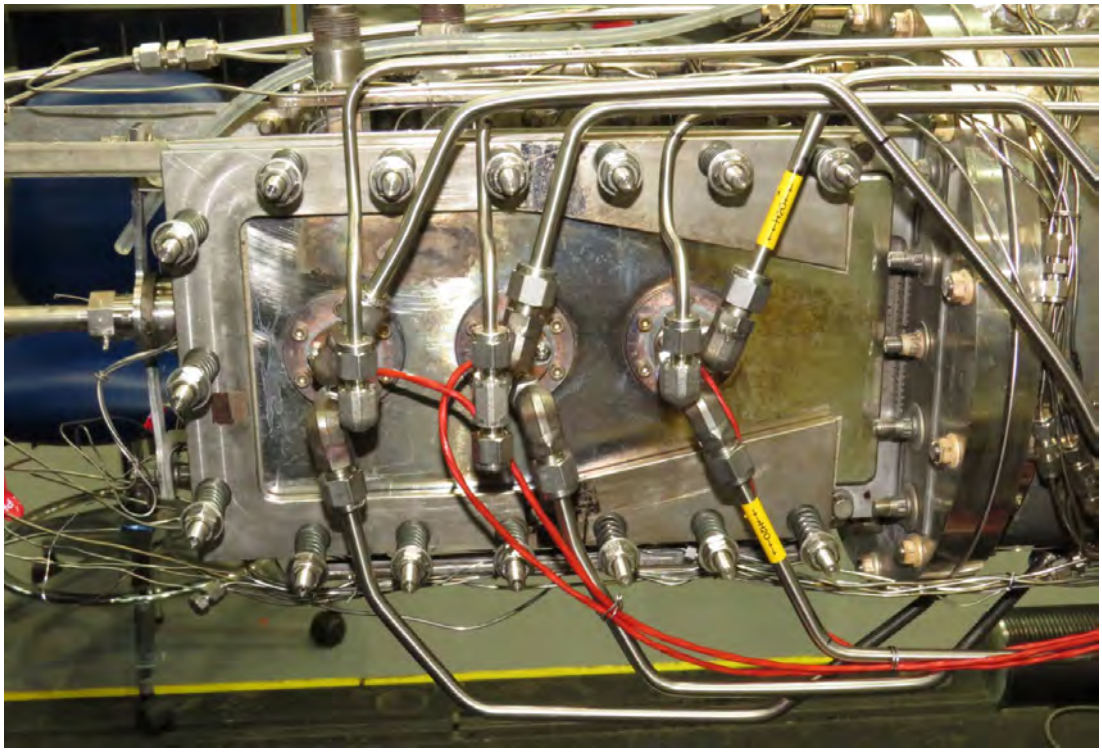

Figure 3. Combustor side wall with radiometers installed (outside wall view).

Because of this, our team developed an additional air purge using film cooling cover shields for the gauges in addition to the nitrogen purge for the gauge. The additional air flow to protect the radiometers was only 3% of the total combustor flow. The shield design is shown in Figure 4 and creates a film through a narrow slot that passes over the gauge surface. A small amount of air is passed through two holes through the side panel and are directed by the film cooling cover to create a thin film of air over the gauge surface. This film in combination with the gauge cooling was sufficient to mitigate the soot deposits on the gauge surface. Figure 5 shows a photo of the film cooling shields installed on the internal wall of the radiometer panel.

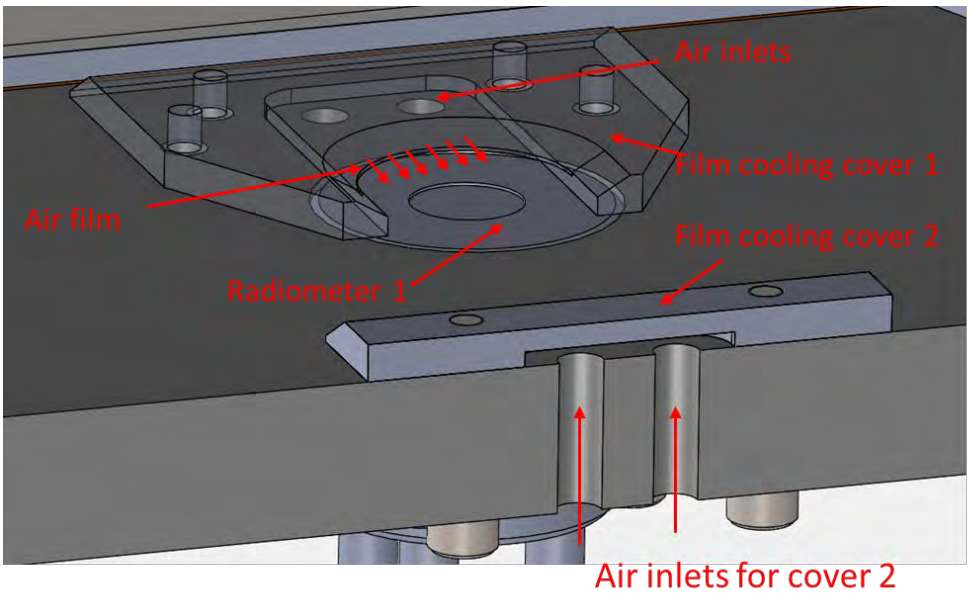

Figure 4. Film cooling approach for radiometers using plenum air.

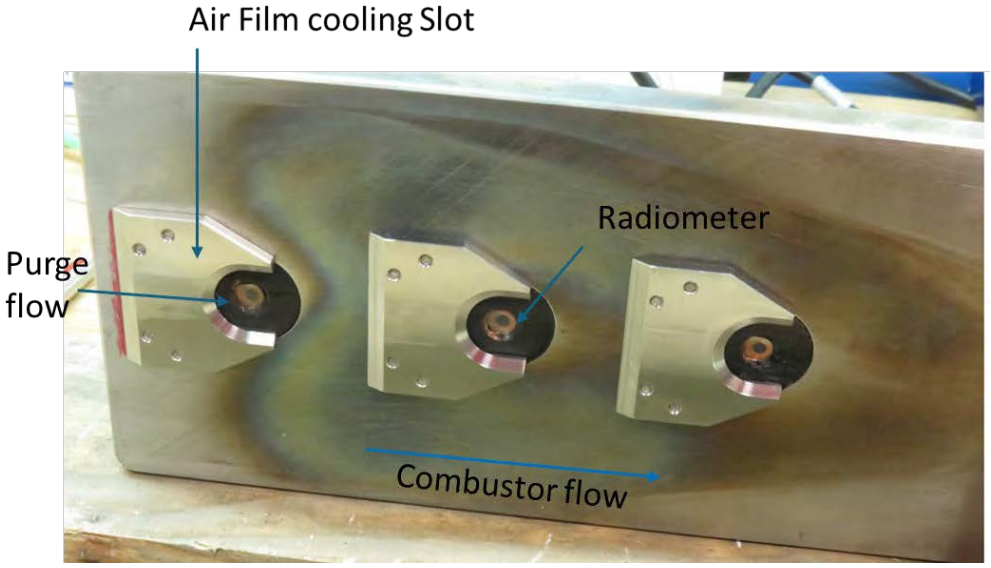

Figure 5. Additional air purge for mitigation of soot deposits on radiometers.

At the beginning of the program, large-scale sapphire windows were purchased to allow for visualization of the IR radiation with IR cameras in the spectral range of 1.5 to 5 μm. The intent was to obtain large-scale IR images in the combustor and to use filters to sample spectral regions that are dominated by either blackbody radiation from the soot or by radiation from major radiating gaseous species (H_2O, CO_2, and CO). The referee rig uses two sets of windows for visualization: (1) an inner set installed on the combustor walls that is exposed to the combustion gases and (2) an outer set that is installed in the surrounding pressure vessel. The inner windows which were exposed to large thermal gradients, caused by contact with the hot combustion gases, failed because of thermal cracking.

Building on the lessons learned from the previous experiments, the ASCENT Project 073 team developed an alternative configuration for the inner combustor window using round port windows installed in a metal side panel. Initial experiments used a round window. With this configuration, our team was able to measure IR radiation through the window in proof-of-concept experiments. This window design was extended to more ports as shown in Figure 6. Unfortunately, the sapphire windows in this configuration also broke, which required us to shift our emphasis to working with more robust quartz windows.

Figure 6. Window design for IR visualization: (a) proof-of concept-IR window, (b) multiple IR port design window.

Quartz windows were used for visualization of radiation from the combustor. The quartz windows have a useful transmissivity of 0.3 to 2.5 μm which is less than that available from sapphire (0.3 to 4.5 μm). Our team employed two different IR cameras to visualize the radiation that passed through the quartz windows. The first was an IR camera (FLIR® SC6800) which was used to measure IR radiation over the range of 1.05 to 4.5 μm. The IR radiation at wavelengths 2.5 um was attenuated by the quartz windows. The radiation in this range is from a combination of gaseous radiation (principally from H_2O, CO_2, and CO) and the radiation from emission from soot particles.

The second camera is a FLIR Blackfly 16S2M, which has strong sensitivity throughout the entire visible spectrum, and extends slightly into the near-infrared range, with a cutoff wavelength of approximately 1100 nm. The wavelength range was selected specifically to target emission primarily from soot particles, and to avoid many of the longer-wavelength bands commonly associated with emission from combustion species such as H_2O, and CO_2. The camera is coupled with a lens with a focal length variable between 4 and 12 mm. The combination of the sensor size, camera position, focal length, and aperture diameter result in an image that captures the visible extents of the combustor, with a depth of field approximately equal to the width of the combustor. These settings allow for any point within the volume of the combustor to be visualized in an approximately equivalent manner, thus preserving the possibility of drawing spatial comparisons between different regions within the combustor.

A series of narrow band-pass filters were used in conjunction with the camera to spectrally resolve the emission. Five filters were chosen, with central wavelengths of 500, 600, 700, 800, 950 nm, and full-width half-maximum bandwidth of 25 nm, ensuring no overlap between the filtered ranges. At each operating condition, a series of images were collected at a frame rate of approximately 100 frames per second, for a duration of approximately 5 s. The long capture duration, when viewed

® FLIR is a registered trademark of Teledyne Flir, LLC, Thousand Oaks, California.

in conjunction with the fact that the combustor naturally exhibits fluctuations on the order of 300-600 Hz, allows for sufficient data needed for statistically significant average images. The process is repeated at each condition for each of the five filters, with special attention being devoted to ensuring that the rig is maintained at a constant operating condition throughout.

Following capture, each image is corrected to account for variations in camera efficiency as a function of wavelength and to account for non-ideal transmission through each filter. As needed, each image can also be corrected for exposure time differences between conditions, allowing for more direct comparison.

Fuels Studied

The fuels for the experiments are listed in Table 1 which shows a top-level breakdown of the chemical constituents. The fuels are listed in order of increasing total aromatic fraction. The Fischer Tropsch (FT) fuel is a low aromatic fuel consisting mainly of iso-paraffins. The A2 fuel is a "middle of the road" Jet A fuel studied extensively in the National Jet Fuels Combustion Program. A 50% blend of the A2/FT fuel was also considered to examine the effect of lowering the aromatic content of Jet A fuel. A mixture of synthetic aromatic kerosene (SAK) and JP8 fuels, was also studied, this fuel contained more than twice the number of single ring aromatic compounds (alkybenzenes) but lower levels of diaromatics, and cycloaromatics. A final blend of aromatic compounds (30% volume) mixed with FT (70%) fuel was created to examine the effect of high levels of both total aromatics and diaromatic compounds on soot and radiation.

Table 1. Properties of the fuels studied.

	volume %								Empirical Fomula		
	Aromatics				Paraffins						
Fuel	Total Alkylbenzenes	Total diaromatics	Total Cycloaromatics	Total Aromatics	Total Iso paraffins	Total n-paraffins	Total Cycloparaffins	Total Paraffins	C	H	MW
Fischer Tropsch (FT)	0.37	0.02	0.13	0.51	94.31	0.32	4.87	99.49	10.80	23.50	153.2
50% FT/50% Jet A	6.10	0.93	1.47	8.50	62.88	10.77	17.85	91.51	11.10	22.74	156.1
Jet A (A2)	11.84	1.84	2.81	16.49	31.46	21.23	30.83	83.52	11.40	22.10	159.0
JP8/SAK Blend	23.36	0.62	1.35	25.33	33.62	23.18	17.87	74.67	10.50	19.90	146.0
70% FT/ 30% Aromatic Blend	24.50	3.73	1.92	30.15	66.21	0.23	3.41	69.85	10.48	19.56	145.5

Experimental Results

Experiments were conducted at inlet conditions of combustor air (T_{air}) = 394K, fuel temperature (T_{fuel})= 322K, combustor pressure (P_{cmb})= 207kPa. The air pressure drop (ΔP_{dome}) was either 2.5% or 3% of plenum pressure and the global fuel air equivalence ratio (ϕ) was either 0.16 or 0.2. Note that the global equivalence ratios are fuel lean because of the excessive dilution provided by the transpiration film cooling on the liners, but the local equivalence ratio in the recirculation region downstream of the swirler is rich for $\phi_{global} > 0.16$.

The average exhaust temperature at the combustor exit is shown in Figure 7 for the $\phi = 0.16$, $\Delta P = 2.5\%$ condition. The average absolute temperature varied by less than 1.4% at the exit of the combustor. Similar results were shown at other equivalence ratios. Therefore, the overall heat release for all the cases was close, which is required for meaningful comparison of fuel effects on the radiation because of the strong relationship between temperature and radiation.

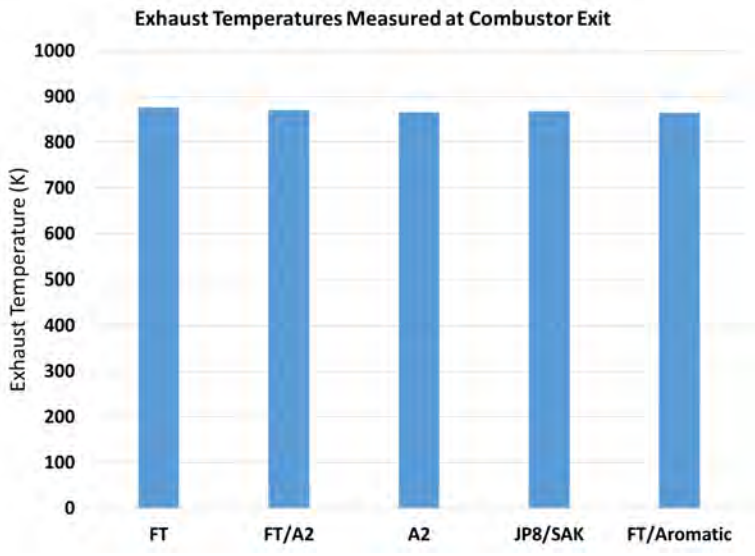

Figure 7. Exhaust temperatures at combustor exit P_{cmb} = 207kPa, ϕ = 0.16, ΔP = 2.5%, T_{air} = 394K.

The particle number densities, primarily from soot particulates, were measured using condensation nuclei counters (CNC) from probes located at the combustor exhaust. The results, shown in Figure 8, show that the lowest number of particulates occurred for the FT fuel and the greatest for the FT/aromatic fuel blend. In general, the total particulates tracked with increases in the total aromatic and diaromatic levels. Note that the particle number density dropped for the SAK/A2 fuel mixture even though the overall aromatic level increased. It is thought that this result is because the higher level of diaromatics present in the neat A2 fuel compared to the blend causes a higher level of soot.

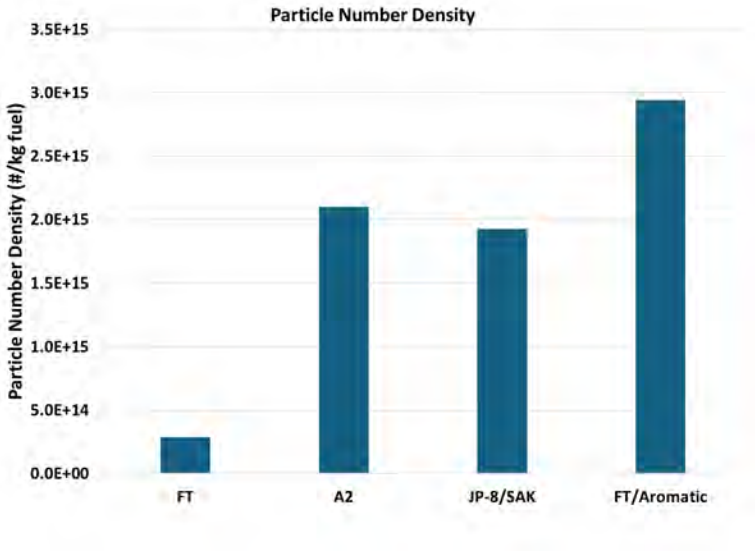

Figure 8. Particle number density measured at combustor conditions at P_{cmb} = 207kPa, ϕ = 0.16, ΔP = 2.5%, T_{air} = 394K.

The radiometer results are shown in Figure 9. The radiometer signal measures the total integrated radiation within the 120 degree collection angle that is transmitted to the individual gauge location. For all fuels, the radiometer signal drops from the two upstream gauges to the downstream gauge. The highest gauge output is seen for gauge 2 (the middle gauge) for

all cases except the aromatic blend case, which had the highest particulate levels. The highest overall radiation levels measured by radiometer 1 in the upstream position for the high aromatic fuel blend case.

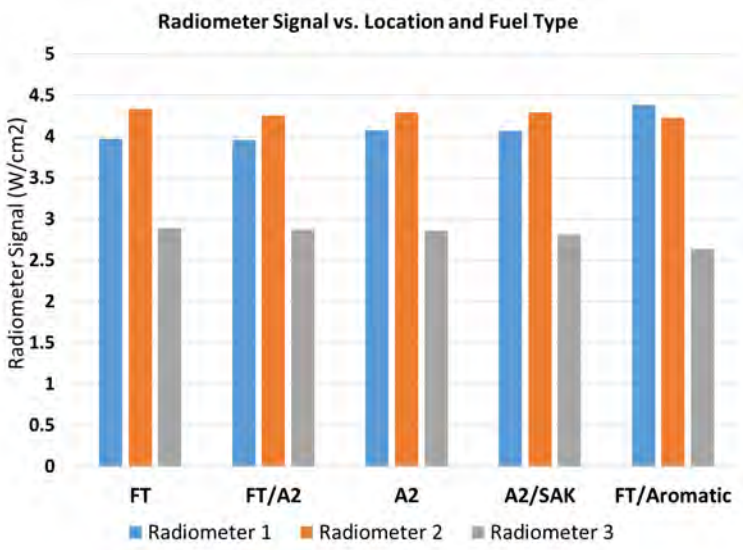

Figure 9. Radiometer measurements at combustor conditions at P_{cmb} = 207kPa, ϕ = 0.16, ΔP = 2.5%, T_{air} = 394K.

Figure 10 shows the time-averaged IR images for the fuels at 2.5% ΔP_{dome}, ϕ_{global} =0.16. At this wavelength, the radiation is expected to be mainly from the soot particles. Note that the intensity level increases dramatically from the FT fuel to the aromatic fuel. The images were further characterized by examining the radiation in the image contained in a 1-in. diameter circle in line with each of the three images. The results are shown in Figure 11. The highest levels were observed for the upstream location and decreased dramatically with axial location. Also note that the fuel trends for magnitude for each of the gauges resemble the trends for the particulate emissions.

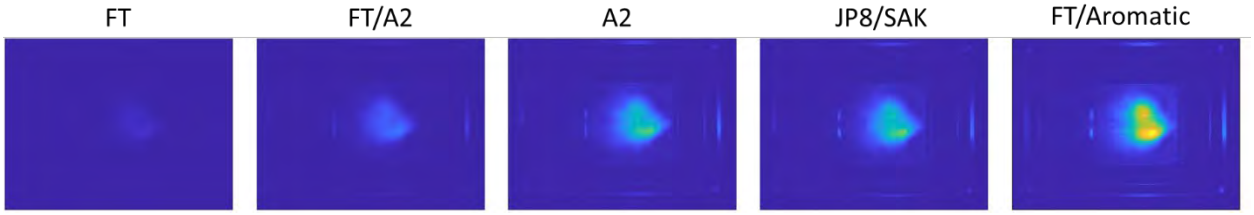

Figure 10. Radiation at 0.95 μm for P_{cmb} = 207kPa, ϕ = 0.16, ΔP = 2.5%, T_{air} = 394K.

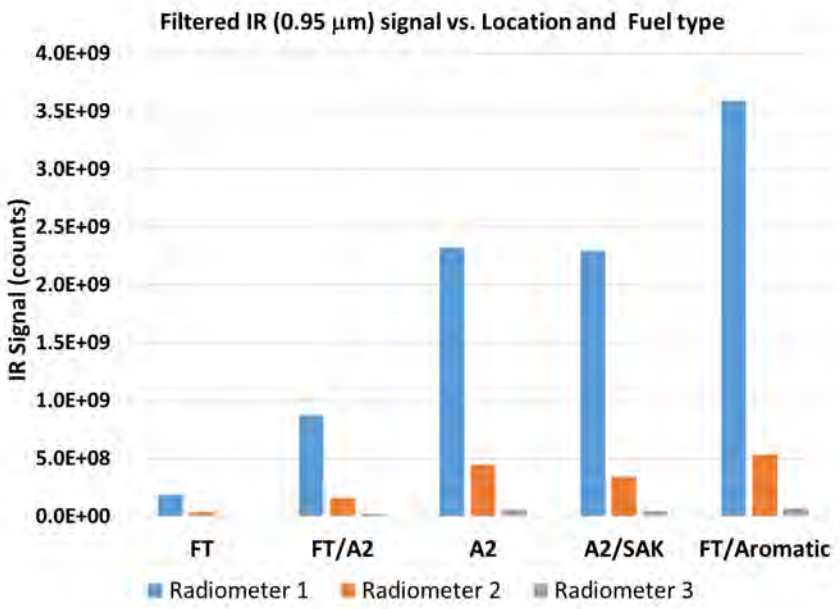

Figure 11. Radiation at 0.95 mm in line with the radiometer locations. P_{cmb} = 207kPa, ϕ = 0.16, ΔP = 2.5%, T_{air} = 394K.

The broadband radiation (1.05-2.5 um) was measured for three of the fuels and the time averaged images are shown in Figure 12. The ranking of the images shows a similar trend to that shown at the shorter wavelength, although the differences between the fuels are not as pronounced as that shown at the shorter wavelength. Note that over this range of wavelengths both radiating gases and particulate matter are expected to contribute to the overall radiation measured by the camera. A similar spatial analysis of the images was conducted to extract the signal from 1-in. circles in line with each of the three radiometers. The results, shown in Figure 13, are similar to those in Figure 11, but the magnitude of the differences was less. It is thought that the difference between these two trends is caused by the presence of the radiation from the gases which is only measured at the longer wavelengths (above 1 um).

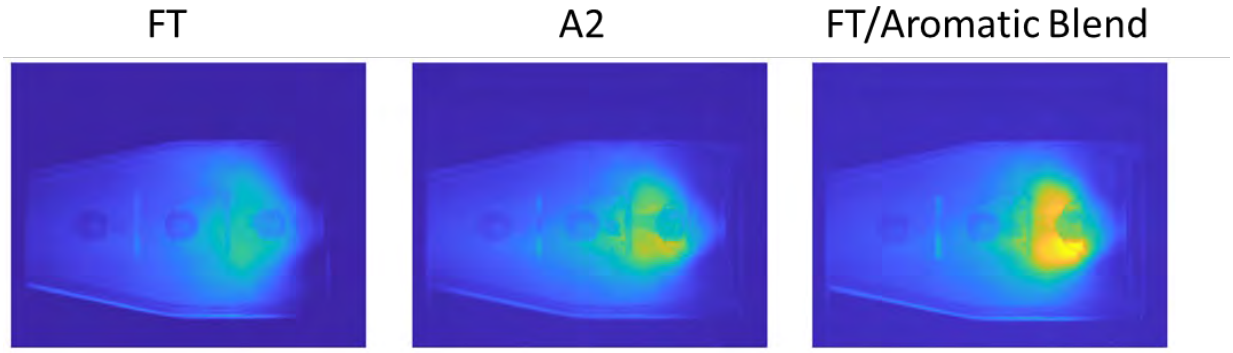

Figure 12. The broadband IR (1.05 -2.5 um) signal measured at P_{cmb} = 207kPa, ϕ = 0.16, ΔP = 2.5%, T_{air} = 394K.

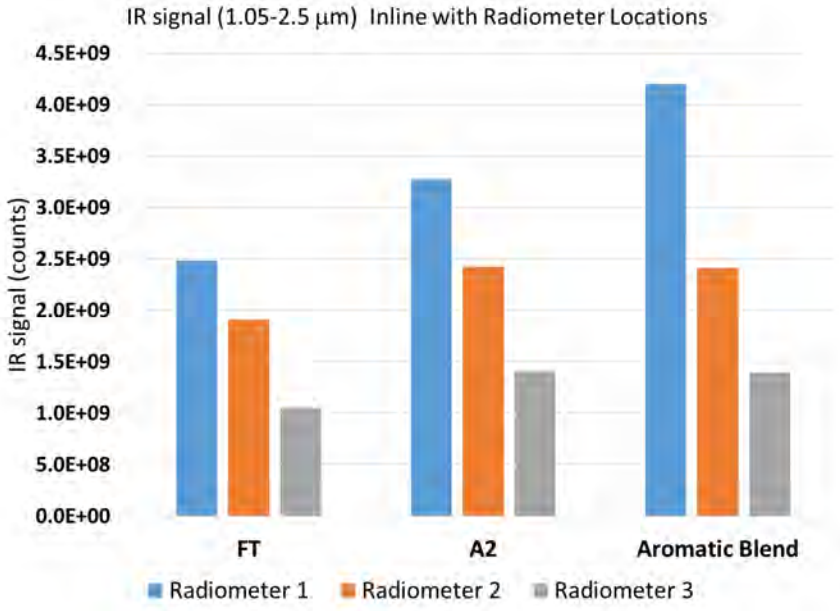

Figure 13. Broadband IR signal in line with the gauge locations P_{cmb} = 207kPa, ϕ = 0.16, ΔP = 2.5%, T_{air} = 394K.

The images for the near-IR images (0.95 μm) showed a large effect of fuel type on image intensity. The radiation in this spectral range is principally due to radiation emitted from the soot particles. The results in this range are consistent with the results of the particulate emissions measurements, which show pronounced increases in particulate levels (principally soot) as the aromatic content increases. The images of the IR radiation in the range of 1-2.5 μm also show similar trends (radiation increasing with aromatic content), but the results show a less pronounced effect of fuel type on radiation than that observed in the 0.95 mm range. It is thought that the observed effect is because of the combined effect of radiation from gases and particulates in this wavelength range. Note that concentration levels of the two major radiating gas species (CO_2 and H_2O) will be expected to be close, with small variations due to fuel composition, so that at the same temperature and pressures, the contributions of the gas radiation will be expected to be similar for all of the fuels studied. The results from the radiometer, which measures the sum of all radiation in the broad spectral region between 0.3 and 5 μm showed very small changes in between the gauges. Based on the conditions of our experiment thus far, our team hypothesizes that that the emission from the gases is obscuring the effect of the pronounced differences in the radiation from the soot when considering radiation over the entire wavelength range. As pressure increases, the contribution of the radiation from particulate emissions is expected to increase in importance relative to the importance of the emission from the gases.

The plan for the next series of experiments is to conduct the experiment at different pressures to allow further insight into the relative contributions of gaseous and particulate radiation. Planned instrumentation will include near infrared and infrared imaging along with radiometer measurements of emissions measurements of gas and particulates. For the infrared images, further spectral filtering of the IR images will be explored to allow separation of the effects of radiation from gases and particulates.

Publications

None.

Outreach Efforts

As part of this work, there have been discussions with the National Aeronautics and Space Administration Glenn Research Center on modeling, specifically using the data from this effort to validate combustion models of the Referee Combustor that incorporate radiation calculations within the CFD framework.

Awards
None.

Student Involvement
None.

Plans for Next Period
- Process the visible and near IR images to gain further insights into the effects of temperature and particle concentration on the radiation from the particulate matter.
- Conduct future tests are at higher pressures and consider high cycloparaffin fuels. It is thought that at the test conditions, the radiation from soot, while showing a strong relation to fuel type, does not overwhelm the gaseous component of the radiation, resulting lower fuel differences in the broad-spectrum radiation detected by the radiometer. The radiating gases (CO_2, H_2O, and CO) are expected to be similar for a given temperature and pressure condition for all the fuels. The ratio between particulate (soot) and gaseous radiation is expected to change as pressure increases.

References

ASTM International. 2023. *Standard specification for aviation turbine fuels*. ASTM International.

Briones, A. M., Stouffer, S., Vogiatzis, K., & Rankin, B. A. (2017, January 9). *Effects of liner cooling momentum on combustor performance* [Conference publication]. 55th AIAA Aerospace Sciences Meeting, Grapevine, Texas. https://doi.org/10.2514/6.2017-0781

Clark, J. A. (1982). Fuel property effects on radiation intensities in a gas turbine combustor. *AIAA Journal*, *20*(2), 274–281. https://doi.org/10.2514/3.7908

Chin, J. S., & Lefebvre, A. H. (1990). Influence of fuel composition on flame radiation in gas turbine combustors. *Journal of Propulsion and Power*, *6*(4), 497–503. https://doi.org/10.2514/3.25462

Colborn, J., Heyne, J. S., Hendershott, T. H., Stouffer, S. D., Peiffer, E., & Corporan, E. (2020, January 6). *Fuel and operating condition effects on lean blowout in a swirl-stabilized single-cup combustor* [Conference publication]. *AIAA Scitech 2020 Forum*, Orlando, Florida. https://doi.org/10.2514/6.2020-1883

Colket, M., Heyne, J., Rumizen,M., Gupta, M., Edwards, T., Roquemore, W., Andac, G., Boehm, R., Lovett, J., Williams, R., Condevaux, J., Turner, D., Rizk, N., Tishkoff, J., Li, C., Moder, J., Friend, D., & Sankaran, V. (2017). Overview of the National Jet Fuels Combustion Program. *AIAA Journal*, 55(4), 1087-1104. https://doi-org /10.2514/1.J055361

Corporan, E., Edwards, J. T., Stouffer, S., DeWitt, M., West, Z., Klingshirn, C., & Bruening, C. (2017, January 9*). Impacts of fuel properties on combustor performance, operability and emissions characteristics* [Conference publication]. 55thAIAA Aerospace Sciences Meeting, Grapevine, Texas. https://doi.org/10.2514/6.2017-0380

Erdmann, T. J., Burrus, D. L., Briones, A. M., Stouffer, S. D., Rankin, B. A., & Caswell, A. W. (2017, June 26-30). Experimental and computational characterization of flow rates in a multiple-passage gas turbine combustor swirler. *Proceedings of the ASME Turbo Expo 2017: Turbomachinery Technical Conference and Exposition. Volume 4B: Combustion, Fuels and Emissions,* Charlotte, North Carolina. V04BT04A076. https://doi.org/10.1115/GT2017-65252

Esclapez, L., Ma, P. C., Mayhew, E., Xu, R., Stouffer, S., Lee, T., Wang, H., & Ihme, M. (2017). Fuel effects on lean blow-out in a realistic gas turbine combustor. *Combustion and Flame*, *181*, 82–99.

Gleason, G. C. & Bahr, D. W. (1980, March 10-13). Fuel property effects on life characteristics of aircraft turbine engine combustors. *Proceedings of the ASME 1980 International Gas Turbine Conference and Products Show. Volume 1A: General*, New Orleans, Louisiana. 80-GT-55. https://doi.org/10.1115/80-GT-55

Hendershott, T. H., Stouffer, S., Monfort, J. R., Diemer, J., Busby, K., Corporan, E., Wrzesinski, P., & Caswell, A. W. (2018, January 8). *Ignition of conventional and alternative fuel at low temperatures in a single-cup swirl-stabilized combustor* [Conference publication]. 2018 AIAA Aerospace Sciences Meeting, Kissimmee, Florida. https://doi.org/10.2514/6.2018-1422

Lefebvre, A. H. (1999). *Gas turbine combustion* (2nd Ed.), Taylor and Francis, Philadelphia.

Mayhew, E., Mitsingas, C. M., McGann, B., Hendershott, T., Stouffer, S., Wrzesinski, P., Caswell, A. W., & Lee, T. (2017, January 9). *Spray characteristics and flame structure of jet and alternative jet fuels* [Conference publication]. 55th AIAA Aerospace Sciences Meeting, Grapevine, Texas. https://doi.org/10.2514/6.2017-0148

Monfort, J. R., Stouffer, S., Hendershott, T., Wrzesinski, P., Foley, W., & Rein, K. D. (2017, January 9). *Evaluating combustion instability in a swirl-stabilized combustor using simultaneous pressure, temperature, and chemiluminescense measurements at high repetition rates* [Conference publication[. 55th AIAA Aerospace Sciences Meeting, Grapevine, Texas. https://doi.org/10.2514/6.2017-1101

Naegeli, D. W. & Moses, C. A. (1980, Mar 10-13). Effects of fuel properties on soot formation in gas turbine engines. *Proceedings of the ASME 1980 International Gas Turbine Conference and Products Show. Volume 1A: General*, New Orleans, Louisiana. https://doi.org/10.1115/80-GT-62

Rankin, B. A., Blunck, D. L., Katta, V. R., Stouffer, S. D., & Gore, J. P. (2012). Experimental and computational infrared imaging of bluff body stabilized laminar diffusion flames. *Combustion and Flame*, *159*(9), 2841–2843. https://doi.org/10.1016/j.combustflame.2012.03.022

Stouffer, S. D., Hendershott, T. H., Colborn, J., Monfort, J. R., Corporan, E., Wrzesinski, P., & Caswell, A. (2020, January 6). *Fuel effects on altitude relight performance of a swirl cup combustor* [Conference publication]. AIAA Scitech 2020 Forum, Orlando, Florida. https://doi.org/10.2514/6.2020-1882

Stouffer, S., Hendershott, T., Monfort, J. R., Diemer, J., Corporan, E., Wrzesinski, P., & Caswell, A. W. (2017, January 9). *Lean blowout and ignition characteristics of conventional and surrogate fuels measured in a swirl stabilized combustor* [Conference publication]. 55th AIAA Aerospace Sciences Meeting, Grapevine, Texas. https://doi.org/10.2514/6.2017-1954

Stouffer, S. D., Hendershott, T. H., Boehm, R., Lovett, J. (2021). Chapter 4: The referee rig combustor. In *Fuel effects on operability of gas turbine combustors*. The American Institute of Aeronautics and Astronautics, Inc. https://doi.org/10.2514/4.106040

Project 074 Low Emissions Premixed Combustion Technology for Supersonic Civil Transport

Georgia Institute of Technology

Project Lead Investigator

Adam Steinberg
Professor
School of Aerospace Engineering
Georgia Institute of Technology
Phone: (404) 897-1130
E-mail: adam.steinberg@gatech.edu

University Participants

Georgia Institute of Technology (Georgia Tech)

- P.I.: Prof. Adam Steinberg, School of Aerospace Engineering
- FAA Award Number: 13-C-AJFE-GIT-142
- Period of Performance: August 11, 2020, to September 30, 2024
  Period of Performance Covered in Report: October 1, 2023, to September 30, 2024
- Tasks:
  1. Execution of Experimental Campaign 3, performing hydroxyl (OH) Planar Laser Induced Fluorescence (PLIF), Mie scattering, and Phase Doppler Particle Analyzer (PDPA) measurements with conventional and alternative fuels
  2. Data analysis to determine fuel properties, droplet sizes, evaporation lengths, flame surface densities, and lean blow-out (LBO) limits

Project Funding Level

The Federal Aviation Administration (FAA) provided $3,102,994 in funding. Cost-sharing is provided by Georgia Institute of Technology ($1,544,950) and GE® Research ($1,558,044).

Investigation Team

Georgia Institute of Technology

Prof. Adam Steinber (P.I.), Management, reporting, technical oversight of all tasks, oversight of optical diagnostics in Task 1.
Ellen Mazumdar (Co-P.I.), Assistant Professor, Oversight of OH PLIF measurements in Task 1.
Prof. Joseph Ofelein (Co-P.I.), Oversight of first-principles LES in Task 2 and overall coordination of Task 2.
Prof. Jerry Seitzman (Co-P.I.), Oversight of gas phase fuel/air mixing diagnostics in Task 1.
Oleksandr Bibik, Senior Research Scientist, Task 1
Mitchell Passarelli, Graduate Research Assistant, Task 1
Sundar Ram Manikandan, Graduate Research Assistant, Task 1
Samuel Wonfor, Graduate Research Assistant, Task 1
Andrew Zheng, Graduate Research Assistant, Task 1
Arihant Jain, Graduate student, Task 1
Ijeoma Obi, Graduate student, Task 1
Sriram Kalathoor, Graduate Research Assistant, Task 2
Coleman Pethel, Research Assistant (Undergraduate student), Task 1
Mihir Rao, Research Assistant (Undergraduate student), Task 1

® GE is a registered trademark of General Electric Company, Schenectady, New York.

Andrew Semelka, Research Assistant (Undergraduate student), Task 1
Neilay Amin, Research Assistant (Undergraduate student), Task 2
Preethi Mysore, Research Assistant (Undergraduate student), Task 2
Katrina Potak, Research Assistant (Undergraduate student), Task 2
Rachel Wilder, Research Assistant (Undergraduate student), Task 2

GE Research

Krishna Venkatesan (Co-P.I.), Principal Engineer, Oversight of combustor operation in Task 1 and data collection for Task 3.
Hannah Bower, Research Engineer, Task 1
Fei Han, Engineering Manager, Task 3
John Hong, Lead Engineer, Task 1
Nick Magina, Task 3
Victor Salazar, Lead Engineer, Task

GE Aviation

Michael Benjamin (Co-P.I.), Consulting Engineer, Oversight of combustor design in Task 1, coordination of GT/GE LES collaboration in Task 2.
R. Narasimha Chiranthan, Task 2
Manampathy Giridharan, Task 2
Hiranya Nath, Task 2

Project Overview

Market demand for high-speed transport is expected to drive a rapid re-emergence of commercial supersonic transport (CST) aircraft over the coming decades. This impending CST revival and the increasingly harmful impacts of anthropogenic climate change mandate advancements in CST-focused environmentally compatible technologies and policies. Compared with subsonic aircraft, engines for CST aircraft will (a) operate at significantly lower overall pressure ratio (OPR) and bypass ratio (BR), (b) experience higher combustor inflow temperatures (T_3), lower pressures (p_3), and higher fuel/air ratios (FAR) at cruise, and (c) cruise at higher altitudes. The reduced OPR and BR result in increased thrust-specific fuel consumption, thus increasing fuel burn and making it fundamentally more challenging to reduce emissions. Furthermore, the combination of low OPR and high cruise T_3 and FAR result in complicated trade-offs between nitrogen oxides (NO_x) at cruise and other emissions (carbon monoxide [CO], nonvolatile particulate matter [nvPM] and unburnt hydrocarbons [UHC]) at lower power.

Several recent studies have assessed potential CST fleet emissions and environmental impact based on currently deployed rich burn-quench-lean burn combustors (typically Tech Insertion combustors) designed for subsonic transports (Kharina et al., 2018; Berton et al., 2020; Hassan et al., 2020; Speth et al., 2021). These studies demonstrate that innovations in combustor architecture will be required to meet emissions and efficiency targets, helping enable an environmentally compatible CST market. Despite the high T_3 and FAR, peak flame temperatures must be moderated to meet NO_x targets, while also maintaining efficiency and achieving low CO, UHC, and nvPM. This will require increased fuel-lean premixing before combustion.

Lean premixed prevaporized (LPP) combustors are a promising path to lowering emissions from future CST engines. In LPP, fuel is injected, partially prevaporized and partially premixed with air before the reactants enter the combustor. While the concept of LPP is not new (e.g., Niedzwiecki, 1992), achieving good vaporization and mixing in a flight-appropriate package previously has been challenging. However, these issues can potentially be alleviated by the high T_3 in CST combustors (which results in faster vaporization) and advanced manufacturing to enable compact rapid-mixing flow elements.

However, the ability of current design methodologies to predict the operability and emissions of LPP combustors under relevant conditions is unproven. Hence, there is a critical need to generate high-quality experimental data at CST combustor conditions, coupled with the development/validation of computational fluid dynamics (CFD) simulations and reduced-order thermoacoustic models. This project addresses this need through a combination of experiments, large eddy simulations (LES), and thermoacoustic modeling, all applied in a novel LPP combustor of interest to future CST applications. This report focuses on analysis of LBO and thermoacoustic dynamics, the majority of which was performed by PhD candidate Mitchell Passarelli.

Task 1- Analysis of Combustor Performance with Conventional and Alternative Fuels

Georgia Institute of Technology

Objectives

The overarching objectives of Task 1 were to (1) demonstrate the operability of the LPP combustor at the conditions of interest, including demonstrating the potential to hit National Aeronautics and Space Administration (NASA) long-term NO_x goals for supersonic cruise, (2) measure and understand any thermoacoustic dynamics in this combustor, (3) measure and understand the process of LBO in this combustor, (4) measure and understand the impact of using sustainable aviation fuel (SAF) in this combustor, and (5) provide quantitative data with which to develop and validate predictive models, particularly LES and thermoacoustic solvers. Objectives (1) and (2) were fully achieved during the previous reporting periods. Objectives (3) and (5) were largely completed during previous reporting periods. The focus of the last reporting period was on the impact of SAFs, including collection of additional LBO boundaries and extensive data for validation of LES with both conventional fuels and SAF.

Research Approach

1. Experiment

1.1 Configuration and Operating Conditions

Experiments were conducted at GE Research in Niskayuna, New York, in a lean premixed prevaporized combustor that has been detailed in previous studies (Passarelli et al., 2024; Passarelli et al., 2023; Passarelli et al., 2022; Salazar et al., 2023). Figure 1a shows a conceptual schematic of the combustor dome face, which contains four bluff-body stabilized LPP main flames surrounding a non-premixed swirling pilot. Figure 1b shows the side view, with a simplified flow field adapted from (Lovett et al., 2011). For the optical diagnostics measurements, quartz windows were used for the side and top walls of the combustor. The combustor bottom wall is optically inaccessible, as it houses the ignitor.

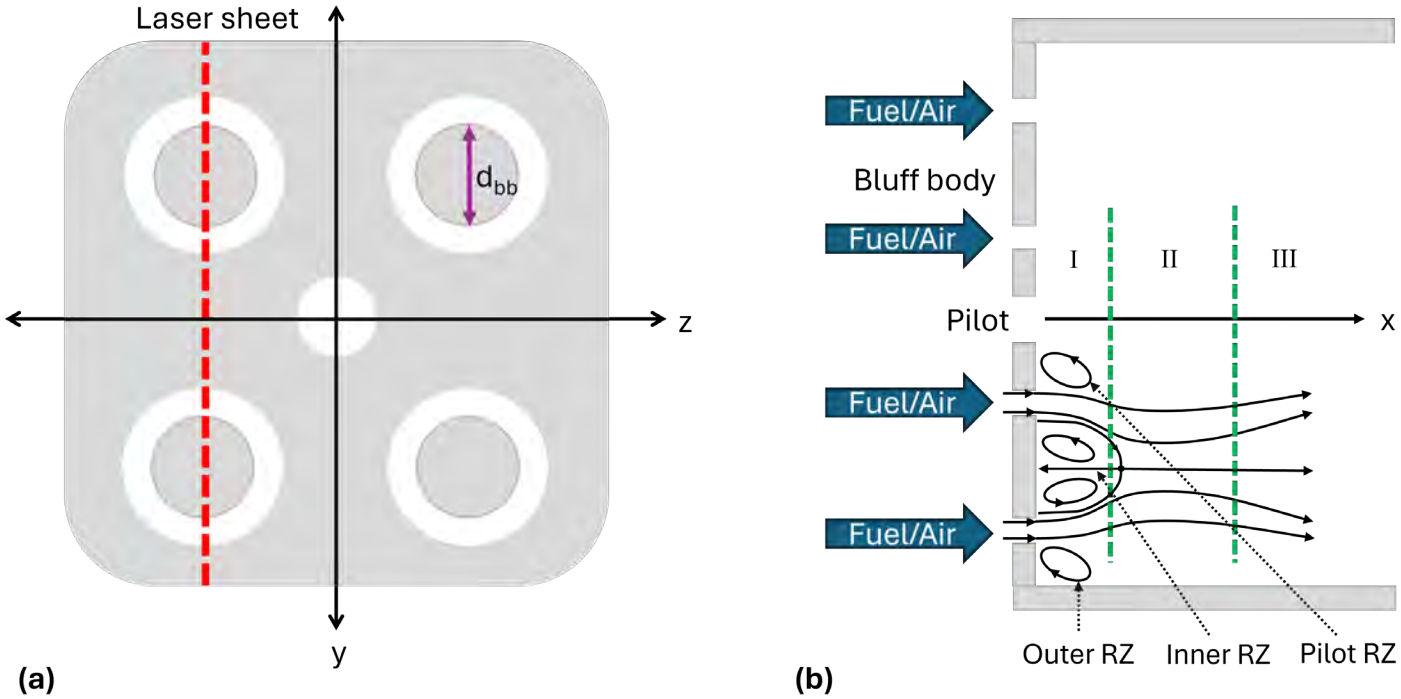

Figure 1. Schematic of combustor dome face (a) and side view of notional flow field (b).

Three liquid fuel lines supply the combustor, one to the pilot and the other two to the top and bottom mains flames. A torch ignitor is located inside the combustor to ignite the fuel-air mixture. All the air, fuel, and water flows to the test rig are individually metered and controlled. Within the mixer are discrete fuel injectors arranged azimuthally, and the angular

positions of these injectors vary slightly from main-to-main. The operating conditions of the combustor for the majority of experiments are detailed in Table 1. The FAR sweep targets four nominal conditions tested at all air preheat temperatures T_3. A finer FAR sweep also is performed to precisely identify the LBO conditions, with the specific FAR values depending on T_3. The exact values of T_3 are not provided here but instead normalized by a reference temperature $T_{3,\mathrm{ref}}$. $T_{3,\mathrm{ref}}$ is in a range that results in significant, but not complete, fuel pre-vaporization. FAR varies by keeping air mass flow rate constant while changing fuel mass flow rate. The pilot is kept at an equivalence ratio of $\phi = 1$.

Table 1. Test condition summary.

Parameter	Values		
Fuel	100% SAF, 100% Jet A, 50/50 volumetric blend		
Reactant pressure p_3 (bar)	7.9		
Nominal FAR of mains	0.055, 0.050, 0.045, 0.040		
Reactant temperature T_3	$0.93T_{3,\mathrm{ref}}$	$T_{3,\mathrm{ref}}$	$1.10T_{3,\mathrm{ref}}$
LBO Sweep Main FAR	0.046, 0.044, 0.043, 0.042	0.044, 0.043, 0.042, 0.041	0.042, 0.041, 0.039

The SAF used in this work is a hydrotreated esters and fatty acids (HEFA) fuel manufactured by World Energy®. HEFA fuel distillation profiles mimic those of the petroleum-derived jet fuels (C8 to C16 hydrocarbons), but their distribution may differ. In terms of chemical composition, HEFA fuels are primarily composed of saturated n-paraffins and isoparaffins with negligible aromatics or cycloparaffins (Vozka et al., 2018). In comparison, Jet A fuel aromatic and cycloparaffinic content is typically around 18% and 30%, respectively.

Samples of fuels used in this study were analyzed by the National Renewable Energy Laboratory (NREL) to determine physical and chemical properties, which are presented in Table 2. The values marked with an asterisk are not yet measured, and thus are calculated from literature correlations (EPA, 2007). All fuel properties comply with ASTM D1655 standards (ASTM International, 2023), except for the 100% SAF density. Lack of aromatics contributes to a higher hydrogen/carbon (H/C) ratio and lower heating value (LHV) for the HEFA, which is expected to yield less soot formation and lower fuel mass consumption rates, respectively. Other measured properties included freeze and flash point, and distillation curves, which are omitted for succinctness but also complied with standards.

Table 2. Fuel chemical and physical properties. ICN: Indicated cetane number.

Property	HEFA	Blend	Jet A
Density (g/cm3) at 288 K	0.747	0.775	0.793
ICN	59.5	54.3	48.6
LHV (MJ/kg)	44.0*	43.6*	43.3
Viscosity (mm2/s) at 258 K	4.140	4.827	3.613
H/C ratio	2.15	2.03	1.92
Vapor pressure (kPa) at 311 K	3.04	2.84	2.62
Surface tension (mN/m) at 295 K	23.72	24.77	25.85
ASTM D86 distillation temperature at 10% recovered (K)	437	445	458

® World Energy is a registered trademark of World Management Group, LLC, Boston, Massachusetts.

ASTM D86 distillation temperature at 90% recovered (K)	524	523	521

1.2 Optical Diagnostics

1.2.1 OH Planar Laser Induced Fluorescence (PLIF)

In OH PLIF, a laser is used to excite OH radicals, and their subsequent fluorescence is captured using an intensified camera. OH exists at detectable quantities in product gases at temperatures above about 1550 K; in premixed flames, the OH PLIF signal is a good demarcation of the flame surface topology (Sweeney & Hochgreb, 2009; Carter & Lee, 2022).

OH PLIF was stimulated by using a neodymium-doped yttrium aluminum garnet (Nd:YAG) laser (EdgeWave™ InnoSlab IS300-2-L, 532 nm, 10 kHz, 10 mJ/pulse) to pump a tunable dye laser (Sirah™ Rhodamine 6G). The dye laser output at approximately 566 nm was frequency-doubled to yield an ultraviolet (UV) pulse with energy of approximately 340 µJ. The dye laser output was tuned to excite the Q1(9) transition of OH in the $A^2\Sigma^+ - X^2\Pi(1,0)$ band near 283.9~nm (Saini et al., 2020; Fugger et al., 2020).

The optics used to form the laser sheet and transmit it into the combustor are shown in Figure 2. The laser sheet is positioned along the centerline of one set of mains, as shown in Figure 1a. The sheet is 50 mm long with a beam waist of approximately 1 mm. As shown in Figure 2, the residual sheet that does not get reflected into the test section is impinged on a phosphor-coated plate placed after the final mirror. The resultant phosphorescence is imaged by a camera (FLIR Blackfly®) with a colored glass filter. This camera captured 100 PLIF laser pulses per test point, enabling a mean laser sheet intensity profile correction.

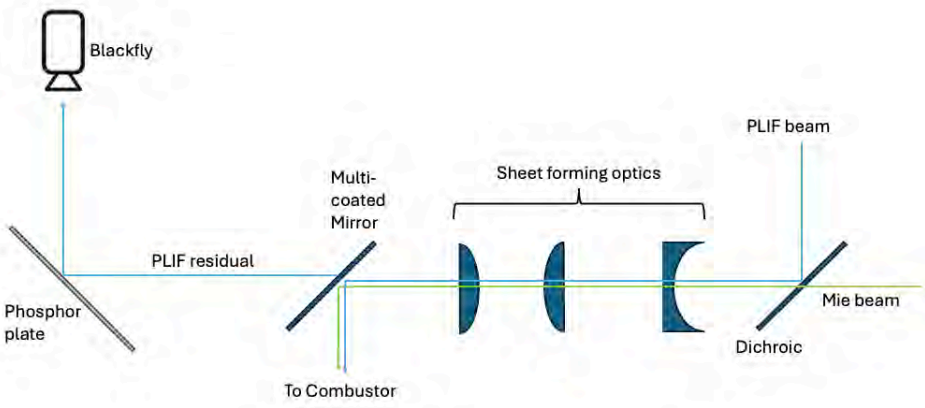

Figure 2. Simplified schematic of optical layout.

Images were recorded using a 308±10 nm filter, UV objective lens (Cerco™ 100 mm, f/# = 2.8) and a high-speed camera (Photron® SA-5) coupled to an image intensifier (Invisible Vision™ UVi 2550B-10, gate time of 100 ns, 896 x 848 pixels). The camera recorded 15,068 frames (1.5068 s) per test point with a projected pixel size of 119.2 micron/pixel. The limiting spatial resolution of the PLIF system is expected to be set by signal integration across the depth of the ca. 1 mm laser sheet thickness, particularly in the highly turbulent wrinkled flames studied here.

™ Edgewave is a trademark of EdgeWave GmbH, Germany.
™ Sirah is a trademark of Sirah Lasertechnik GmbH, Germany.
® Blackfly is a registered trademark of Teledyne FLIR, Wilsonville, Oregon.
™ Cerco is a trademark of Cercolens, France.
® Photron is a registered trademark of Photron Limited, Tokyo, Japan.
™ Invisible Vision is a trademark of Invisible Vision Limited, United Kingdom.

1.2.2 Fuel Droplet Mie Scattering

Mie scattering was used to qualitatively describe the fuel sprays and their downstream penetration. Mie scattering from the fuel droplets was generated from the output of an Nd:YAG laser (Quantel® Evergreen EVG00200, 532 nm, 10 Hz, 160 mJ/pulse). The Mie laser sheet optics also are shown in Figure 2. Data were acquired using a high-speed camera (Phantom® v7.3) due to its low minimum exposure time, though not all frames contained Mie scattering data from the 10 Hz laser. For each test point, 1184 frames with Mie scattering were collected at an exposure of 1μs.

1.2.3 Phase Doppler Particle Analysis

A TSI® Flow and Size Analyzer (FSA) 3500 two-component Phase Doppler Interferometer system was utilized to measure local droplet size and velocity parallel and radial to the mixer axis during operation. For these tests, measurements were performed only at $T_{3,\mathrm{ref}}$ (FAR = 0.040 and 0.050) and $1.10T_{3,\mathrm{ref}}$ (FAR = 0.050). All the measurements were performed at the main tubes plane as depicted in Figure 1a. Since the PDPA is a single point measurement, mapping the entire spray region is quite time consuming. Therefore, in this campaign, vertical scans at two select axial locations: $x = 1$ mm and $x = 10$ mm from the mixer face, were only performed.

2. Data Analysis Techniques

2.1 Flame Surface Density

Flame surface density (FSD) is of fundamental interest in premixed turbulent combustion and defined as the reaction layer surface layer per unit volume:

$$\Sigma_{3\mathrm{D}} = \lim_{\Delta x \to 0} \frac{A_{\mathrm{T}}}{\Delta x^3} \qquad \text{(Eq. 1)}$$

where $\Delta x$and A_{T}re interrogation box side length and wrinkled flame surface area, respectively (Candel & Poinsot, 1990). In planar measurements, it is common to approximate the FSD as the flame perimeter per unit area in the laser sheet:

$$\Sigma_{2\mathrm{D}} = \frac{L_{\mathrm{T}}}{\Delta x^2} \qquad \text{(Eq. 2)}$$

for small Δx. The accuracy of the two-dimensional (2D) approximation has been experimentally shown to be in reasonable agreement with three-dimensional (3D) measurements, though a multiplicative factor is needed to quantitatively align 2D and 3D FSD data (Filatyev et al., 2005; Han et al., 2018; Bell et al., 2007). Here, we are concerned with FSD spatial distributions and trends with operating conditions/fuels, which do not require consideration of such factors.

While there are multiple definitions of the flame front, location of peak heat release is generally accepted as a common standard (Sweeney & Hochgreb, 2009). This location tends to approximate coincident with the point of maximum gradient in both temperature and OH concentration. In ideal unstretched laminar flame calculations, OH concentration rises from zero in the unburned reactants to a peak within the flame front, before relaxing to the equilibrium product concentration (Sweeney & Hochgreb, 2009). However, experimental data are confounded by multiple factors, such as temperature dependence, signal quenching, noise, and spatial resolution. In instantaneous images, there can be significant noise from the intensifier and laser profile variability. The location of the maximum gradient along a flame surface may also vary due to local stoichiometry in flames will local composition variations (Chaib et al., 2023). High pressure gas turbine environments cause signal quenching and highly convoluted turbulent flames that are difficult to identify in image processing. This study defines the flame front as the location of peak OH signal gradient, as it is clear that regions with no signal mark no reaction or products.

Several steps are required to reliably determine a flame surface topology from OH PLIF images in the high-pressure, partially premixed flames studied here. Initial image processing steps include spatial calibration, cropping, background subtraction, flat-field intensifier response correction, and a beam profile correction. To calculate FSD, the OH PLIF images undergo a preprocessing algorithm followed by edge detection in MATLAB.® In general, one desires an algorithm to maximize tradeoffs between computational expense and supervision, without sacrificing accuracy. The preprocessing algorithm requires tuning of two main thresholding parameters, which is comparable to other algorithms in the literature

® Quantel is a registered trademark of Lumibird, France.
® Phantom is a registered trademark of Vision Research, Inc., Wayne, New Jersey.
® TSI is a registered trademark of TSI Incorporated, Shoreview, Minnesota.
® Matlab is a registered trademark of The Mathworks Inc., Natick, Massachusetts.

(Chaib et al., 2023). Here, edge detection utilizes the Canny method (Canny, 1986), which is broadly used across the combustion field, but introduces another thresholding tuning parameter.

Due to absorption of laser energy as the laser sheet traversed the combustor from top to bottom, the OH PLIF signal-to-noise ratio was higher in the upper portion of the combustor, as shown in Figure 3. Therefore, flame surfaces and FSD are only analyzed in the upper half of the combustor. While the combustor exhibits some asymmetry in operation, the general flame behavior is assumed to be similar in each main. FSD fields are calculated using a 5 x 5-pixel (0.59 x 0.59 mm) window. This window is swept over all pixels in an image to calculate FSDs centered at each pixel, followed by a temporal average of all images for a test point. Tuning parameters and window size were selected via a sensitivity study and kept consistent across test points.

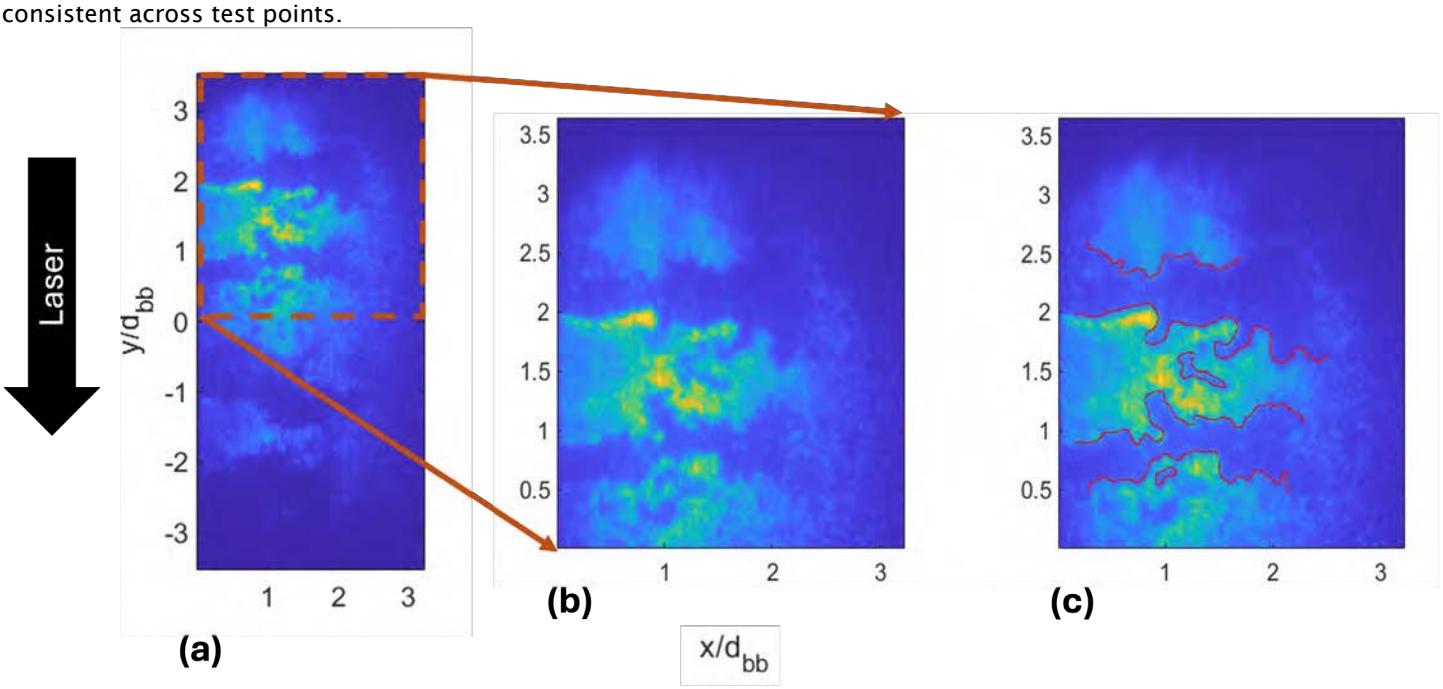

Figure 3. Example implementation of edge finding algorithm. (a) Raw image, (b) isolated region of interest from pilot midplane to top of the combustor, and (c) application of edge detection algorithm. Coordinates are normalized by bluff body diameter. Flow progresses from left to right.

2.2 Fuel Penetration Depth

To determine fuel depth penetration, x_{dp}, Mie scattering images first undergo dark-field and background subtraction. Additionally, due to soot deposition on the windows over the testing day, thresholding is applied to the areas impacted by the residues. To remain consistent with PLIF analysis, only the top main is analyzed. After preprocessing, pixel values are averaged along the y-axis. The axial coordinate at 30% of the maximum mean intensity is defined as x_{dp}.

2.3 Blow-off Characterization

LBO limits in bluff-body flames previously have been reviewed in Shanbhogue et al. (2009) and Tuttle (2010). Blow-off occurs due to competition between flow and chemical time scales, which is captured by Damköhler vs. Reynolds number correlations. The blow-off process is multifaceted, and complications can arise from chemical and aerodynamic interactions in multi-element combustors. Nonetheless, Damköhler number correlations have been shown to do a good job of collapsing LBO data across different combustors (Shanbhogue et al., 2009; Cavaliere et al., 2013).

The blow-off process described by Shanbhogue et al. (2009) is divided into two stages. In the first stage, as the Damköhler number in a stable flame is decreased, the local strain rate intermittently exceeds the extinction strain rate, creating holes in the flame from local extinction events. In the second stage, decreasing Damköhler number further causes more frequent extinction events, and the holes in the flame sheet lead to larger scale disruptions like flame flapping. Finally, further decrease of Damköhler number leads to blow-off.

Calculation of blow-off Damköhler and Reynolds numbers in this work follows the methodology from Passarelli et al. (2024). Reynolds number is computed as:

$$\mathrm{Re} = \frac{\rho_3 u_{\mathrm{main}} d_{\mathrm{bb}}}{\mu_3} \quad \text{(Eq. 3)}$$

where ρ_3 and μ_3 are the reactant mixture density and viscosity, respectively, assuming perfectly mixed, completely vaporized fuel and air. The characteristic flow speed, u_{main}, is computed from the one-dimensional (1D) continuity equation using the total mass flow rate through a single main. Damköhler number is defined as $\mathrm{Da} = \tau_{\mathrm{f}}/\tau_{\mathrm{c}}$, where the flow timescale τ_f is calculated using the empirical correlation for laminar boundary layer momentum thickness (Shanbhogue et al., 2009):

$$\tau_{\mathrm{f}} = \frac{35 d_{\mathrm{bb}}}{u_{\mathrm{main}} \mathrm{Re}^{1/2}} \quad \text{(Eq. 4)}$$

and the chemical timescale τ_c is calculated as the ratio of the unstretched laminar flame thermal thickness δ_{f}^0 and speed S_{L}^0.

Numerical simulations in Cantera[1] using the 1D freely propagating premixed laminar flame model were used to determine the flame and thermodynamic properties. Surrogate blends were used to model the tested fuels. The HEFA was modeled using pure n-dodecane (Liang et al., 2024); the Jet A fuel used n-dodecane/iso-octane/toluene 42.7/33.0/24.3 mol% (Dooley et al., 2010); and the blend used a 50/50 mix of its constituent surrogate components. The Chemical Reaction Engineering and Chemical Kinetics (CRECK) surrogate kerosene mechanism for low and high temperature kinetics, which has been extensively validated and implemented across the literature, is used for all fuels (Ranzi, 2014). Blow-off conditions are defined from the OH PLIF images, when no significant signal is observed in the inner recirculation zone (RZ) (see Figure 1b) for the entire duration of the recording.

3. Results and Discussion

3.1 Fuel Penetration Depth

Figure 4 presents temporal mean Mie scattering images for $T_3 = T_{3,\mathrm{ref}}$. The analogous figures for other T_3 are omitted for brevity, but the trends are similar. The slight curving of the signal towards the centerline for $x/d_{\mathrm{bb}} > 1$, particularly at the lower FARs, is associated with the flow around the inner recirculation zone and contraction of this zone as LBO is approached. In bluff body combustors, the general flow pattern is as shown in Figure 1b (Lovett et al., 2011); previous particle image velocimetry measurements in this combustor are consistent with this image (Passarelli et al., 2023). Adopting terminology from Lovett et al. (2011), downstream of the inner RZ ($x/d_{\mathrm{bb}} > 1$ from Passarelli [2023] in this combustor) the flow enters a transition region, referred to as the close out region (COR). The streamlines in the COR initially converge towards the centerline of the bluff body, similar to the Mie signal behavior from $1 \lesssim x/d_{\mathrm{bb}} \lesssim 1.5$.

[1] Cantera is an open-source suite of tools for problems involving chemical kinetics, thermodynamics, and transport processes. Cantera is a sponsored project of NumFOCUS,® a 501(c) nonprofit charity in the United States. NumFOCUS is a registered trademark of NumFOCUS, Inc., Austin, Texas.

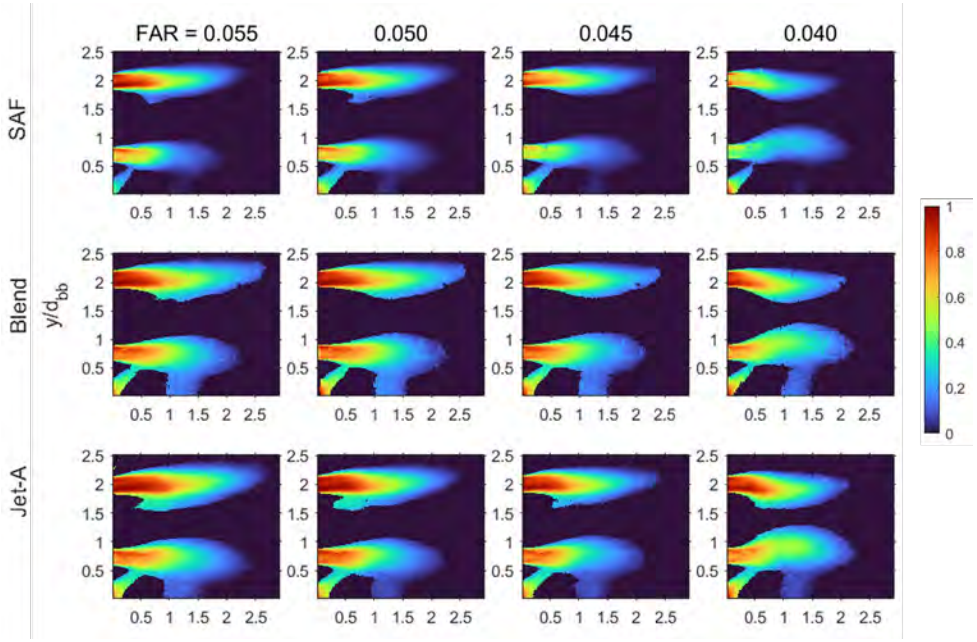

Figure 4. Temporal mean spray fields for $\boldsymbol{T_3 = T_{3,ref}}$ at nominal FARs. Colorbar represents a spray field normalized by the max intensity for presented test points. Flow progresses from left to right.

Figure 5 plots x_{dp} vs. FAR for all test conditions. As expected, higher T_3 lead to faster vaporization and lower penetration depths. Penetration depth also decreases with decreasing FAR due to the lower fuel flow rate that needs to be vaporized by the fixed air flow rate. Most notably, the SAF consistently has a lower penetration depth than the blend and fossil Jet A fuel. This is due to a combination of (i) lower surface tension promoting droplet breakup, (ii) higher vapor pressure indicating more volatility, and (iii) the distillation curve behavior, where the SAF showed the lowest boiling points of the fuels (see Table 2). Furthermore, the blend and fossil Jet A fuel have significant overlap, indicating that the less volatile components of the fossil fuel persist. The preferential vaporization of less volatile components of SAF/fossil blends has been observed previously but understanding its impact on combustion chemistry remains an open question (Xing et al., 2024).

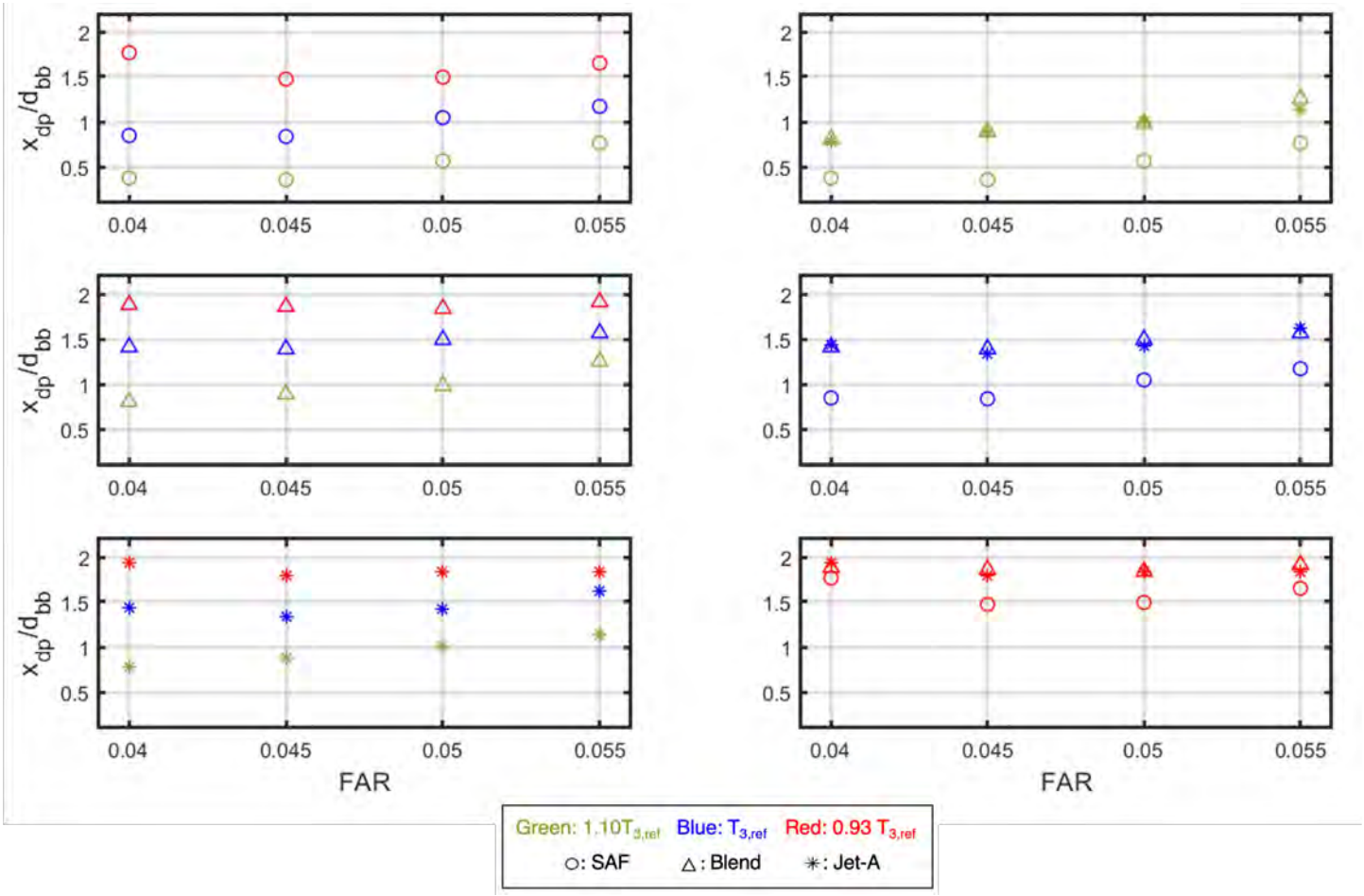

Figure 5. Penetration depth versus FAR for temperature sweeps by fuel (left) and fuel sweeps by temperature (right). Quantitative Droplet Characteristics.

A key objective of the PDPA campaign was to investigate the droplet size changes with reduction in FAR from the nominal value (i.e., 0.05) down to the blow off limit. In a previous campaign employing Jet A fuel, flame videos and OH* imaging showed that the flame transitions from attached at the mixer face to lifted once the FAR is reduced below FAR ~0.045. Therefore, in this study, we compare FAR of 0.040 and FAR of 0.050 cases to understand the droplet behavior at these extreme conditions. It should be mentioned that both the velocity and droplet size data are normalized for comparisons and absolute magnitudes can be made available upon request.

Velocity and droplet size results for the FAR variation at two axial locations, $x = 1$ mm and $x = 10$, are shown in Figure 6 and Figure 7. At $x = 1$ mm, the droplets concentrate mainly around the annular regions of the mains tubes. It should be noted that a significant number of droplets were found at the exit of the bluff body for the FAR = 0.040 case for the Jet A fuel because, at high FAR (>=0.045), the flame is attached to the mixer exit face and, therefore, most of the droplets are consumed by the flame. At low FARs, on the other hand, the flame is lifted and the droplets exiting the mixer are far from the reaction zone.

Figure 6 shows that the velocity profiles follow similar trends for all FARs and that their maximum magnitudes take place at the inner and outer shear layers of each tube, passing through a minimum somewhere between these two shear layers. Except for the FAR = 0.040 case, where the velocities are higher, the velocities look very similar for all the three cases. As the droplets move downstream, at $x = 10$ mm, the velocity profile changes and droplets are found for FAR = 0.050 along almost the entire vertical scan. Velocity magnitude, in all cases, was observed to be much higher than those at $x = 1$ mm. It should be noted that at $x = 10$ mm, the droplets coming from the pilot nozzle may confound the results. Overall, the

velocities of both fuels SAF and Jet A fuel behave in a similar way suggesting that the flow effect on the droplets is relatively similar for both fuels.

A key outcome of this work was to obtain droplet size for SAF and compare it to Jet A fuel. This is done in terms of profiles of the Sauter mean diameter D_{32}. The droplet size trends are shown in Figure 6e and Figure 6f. To help visualize the subtle differences, the top and bottom tube have been divided for $x = 1$ mm and are presented in a magnified view in Figure 7. Here we can see that the droplets show a minimum at the center of the annular regions and then quickly grow as they move to the edges and outside the annulus. There are some variations between the four annular regions, which could be due to variation in atomization caused by the difference in fueling between them. However, there is consistency between annular regions with respect to FAR dependency (i.e., the droplets decrease in size as the FAR decreases for a given fuel). This droplet size dependency with FAR has been observed before for other fuel nozzles tested in the same combustor. This is mainly due to a degradation in atomization as the fuel flow is increased while all other parameters are kept constant. Figure 7 shows that, at FAR = 0.040, the droplets near the bluff body region (Jet A fuel only) are much smaller is size than those in the annular regions. Typical droplet sizes are of the order of half the size of the droplets found in the annular main regions. At $x = 10$ mm (Figure 6), the droplets have decreased in size, which can be attributed to vaporization as they are convected downstream the flame. The higher FAR case had bigger droplets.

Comparing the SAF and Jet A fuel droplet sizes (Figure 6 and Figure 7) suggests that the SAF droplet size is smaller than that of Jet A fuel. Also, there are variations that seem to be jet dependent with the higher differences for the bottom jet, where Jet A fuel shows much bigger droplets. The droplet size trend with SAF is consistent with the Mie scattering measurements for the same operating conditions taken during the same campaign. The smaller droplet size for SAF can be explained in part by the physical properties of the fuel. That is, the fuel analysis performed by NREL, for the two fuels reported here, indicate that SAF has lower viscosity, surface tension, and boiling point. Therefore, for the same operating conditions, this could enable smaller droplets and faster vaporization as the fuel droplets convect towards the flame.

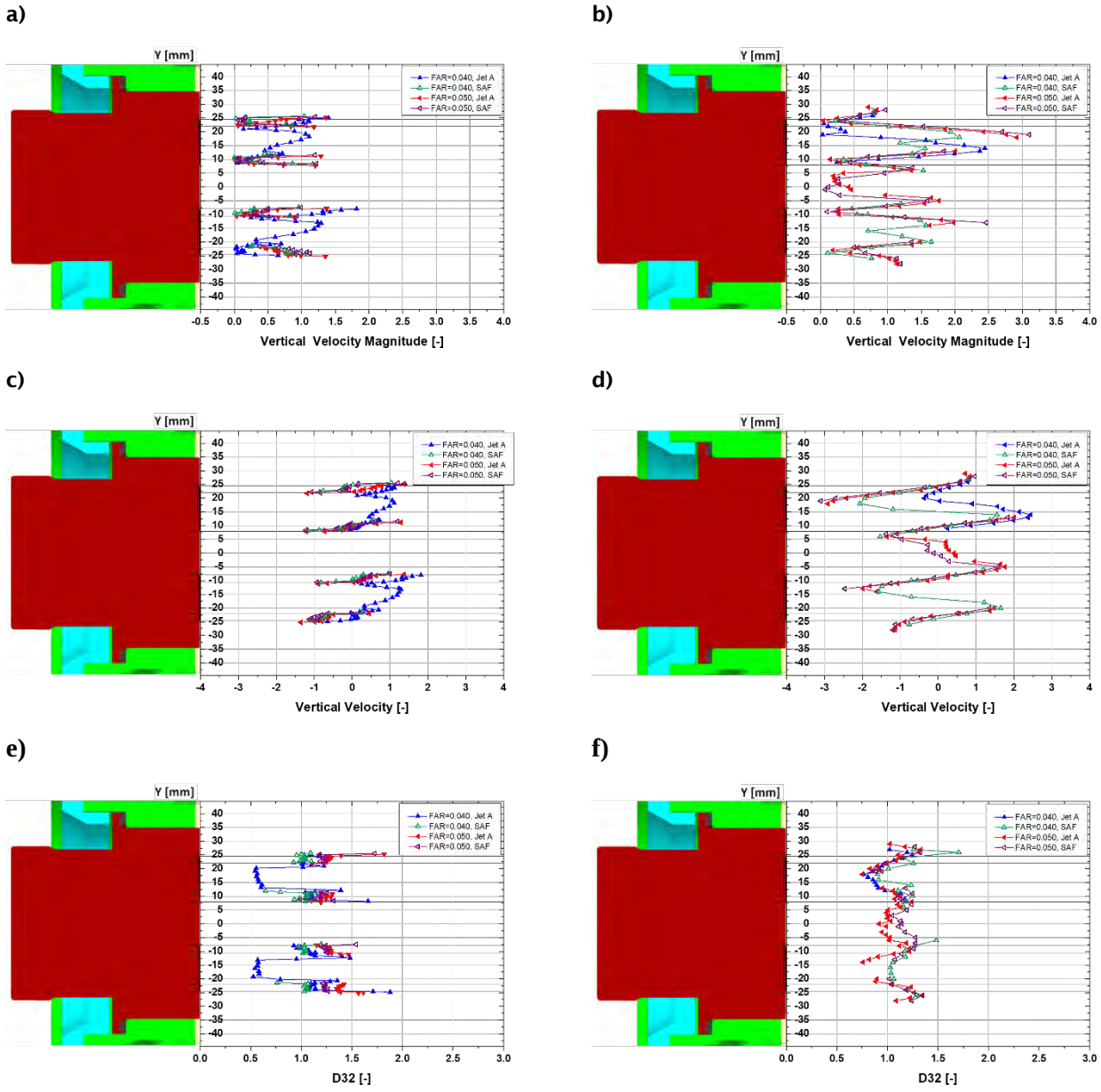

Figure 6. Impact of FAR on droplet speed, velocity, and size at two axial locations $x = 1$ mm (left column) and $x = 10$ mm (right column).

a)

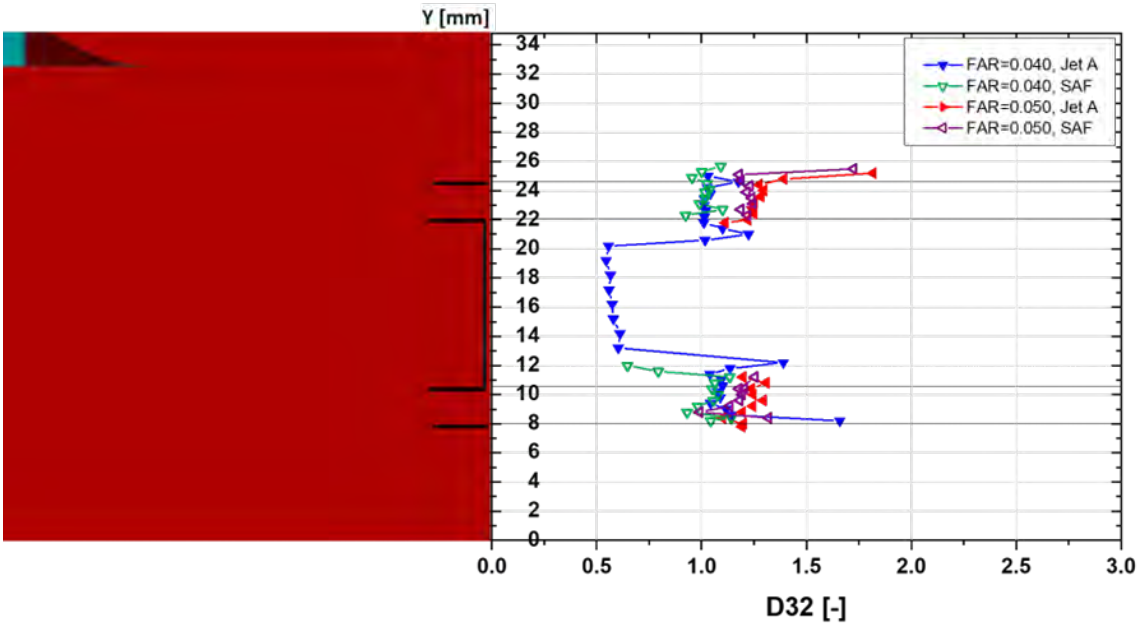

b)

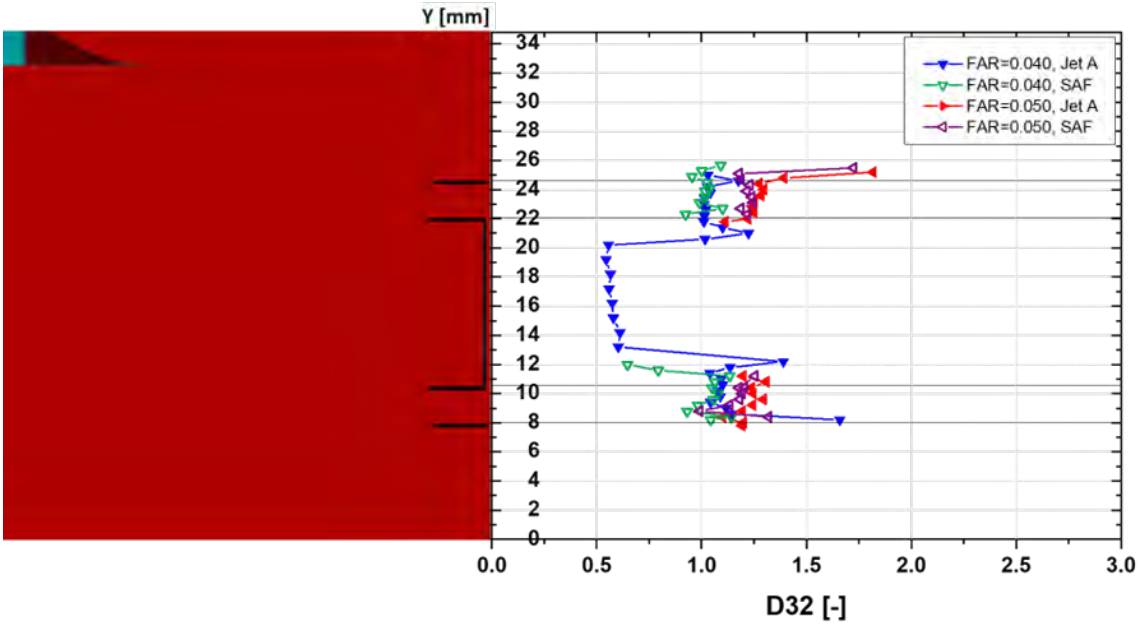

Figure 7. Impact of FAR on droplet size at axial location $x = 1$ mm showing a magnified view of the (a) top main tube and (b) bottom main tube.

The droplet size behavior as a function of T_3 is presented in Figure 8 and Figure 9. Figure 8 shows that, in general, the velocity follows similar trends, with the vertical coordinate, for both T_3 and fuels. At $x = 10$ mm, the velocities increase, and the velocity profiles seem to be more consistent for all cases. Magnified views of velocity are presented in Figure 9, showing smaller droplets at higher T_3s. This is expected because higher T_3 will increase the temperature difference that drives droplet vaporization. Regarding SAF and Jet A droplet differences, the SAF also shows consistently smaller droplets. The differences are also jet dependent with the highest differences observed for the bottom jet.

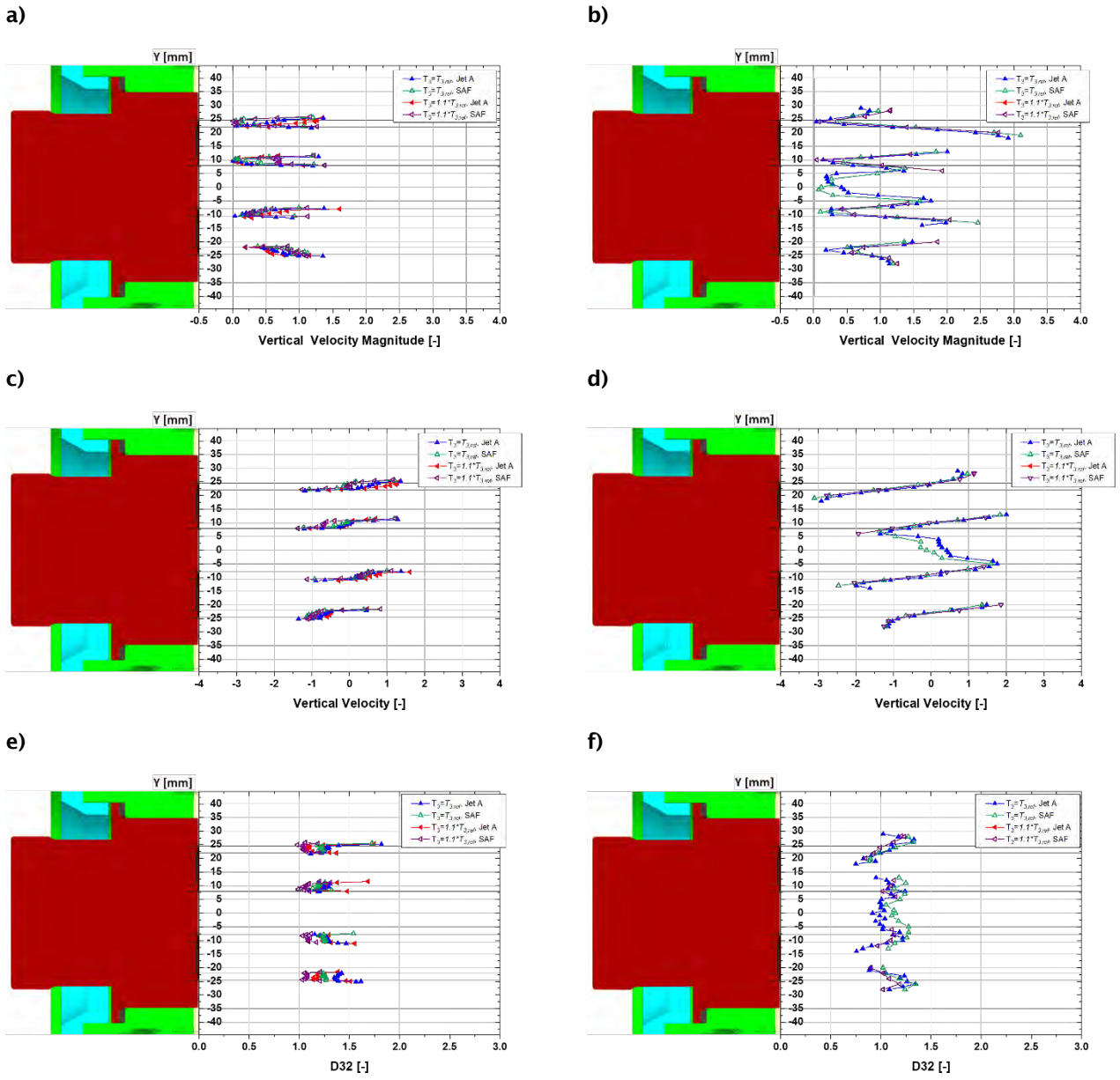

Figure 8. Impact of T_3 on droplet speed, velocity, and size at two axial locations $x = 1$ mm (left column) and $x = 10$ mm (right column).

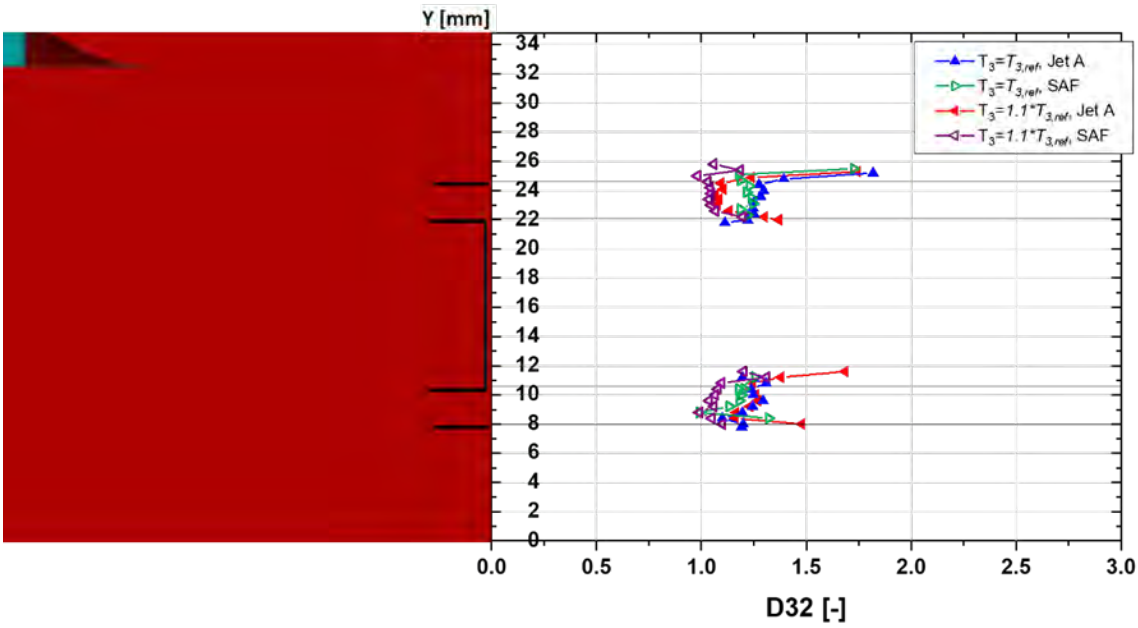

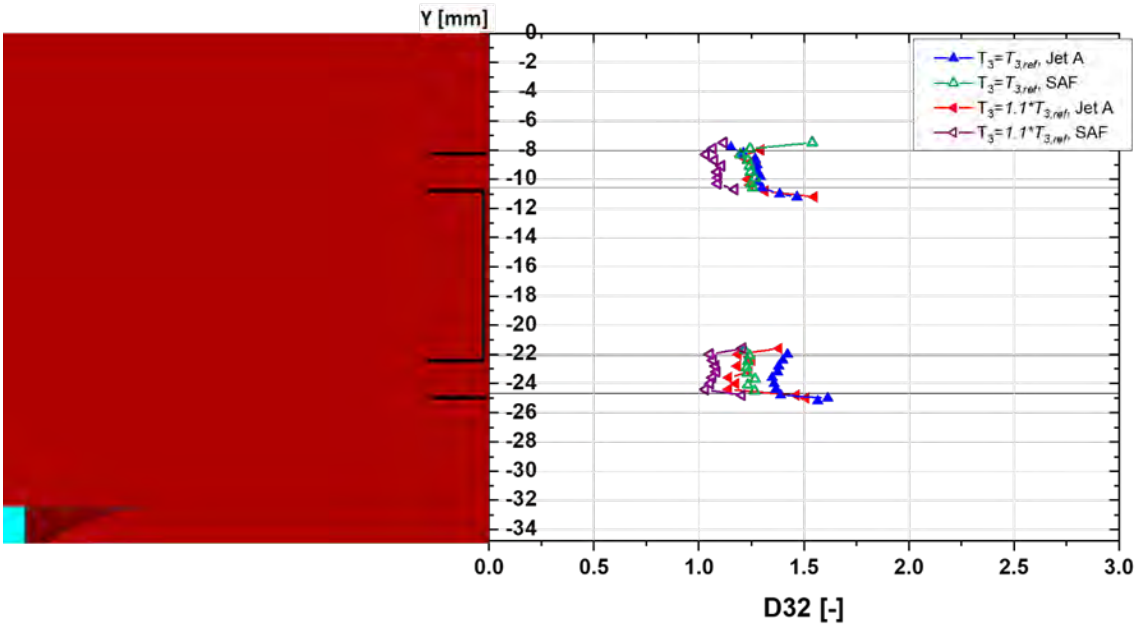

Figure 9. Impact of T_3 on droplet size at axial location $x = 1$ mm showing a magnified view of the (a) top main tube and (b) bottom main tube.

3.2 Flame Topology

The highly turbulent nature of the flow and flame is evident in the sample instantaneous OH PLIF image sequence in Figure 10. The image sequence also shows evidence of local extinction holes in the flame surface, consistent with approaching LBO (Shanbhogue et al., 2009). These holes allow for transport of mass and energy between reactants and products, and enhanced preheating and radical generation that have a favorable influence on the flame particularly in the inner RZ. As shown, the flame is able to "heal'" itself and remain attached.

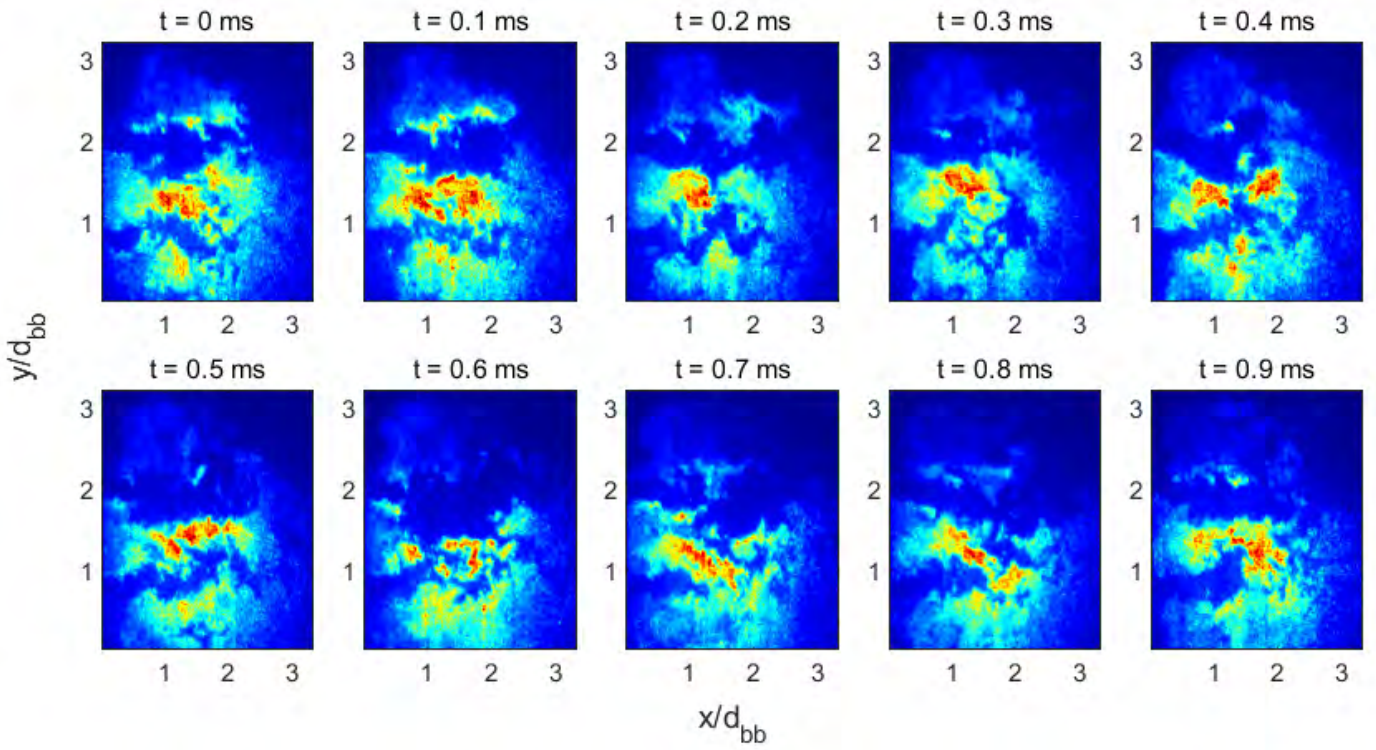

Figure 10. Instantaneous sequence of OH PLIF images for SAF, $\boldsymbol{T_3 = T_{3,\mathrm{ref}}}$ at FAR = 0.043. Flow from left to right.

Figure 11 presents 2D temporal mean FSD fields at $T_3 = T_{3,\mathrm{ref}}$ for varying FAR across all three fuels. Analogous figures for the other T_3 are omitted for brevity, but the fields and trends are similar. The FSD fields with the SAF consistently have higher values near the dome face for $x/d_{bb} < 0.5$. There is also a clear near-field reactant stream visible in the SAF that is less prevalent in the blend and Jet A fuel datasets. The Laser Induced Fluorescence (LIF) signal in this region is likely due to the aromatic content in the latter fuels, which is not present in the HEFA. Due to the varying fuel composition of kerosene fuels, the excitation of mono- and di-aromatics results in broadband fluorescence emission from 260-420 nm, which is resulting in crosstalk between fluorescence signals.

Referring to Figure 1b, the flame is anchored at the lip of the bluff body, and one observes the characteristic inner RZ directly downstream of the dome face. The flames are found in the shear layers surrounding the reactant streams where the boundary layers have separated from the edge of the bluff-body (Shanbhogue et al., 2009). As mentioned, downstream of the recirculation zone, the flow transitions from a recirculating flow to a wake flow. The transitional COR region features a convergence and then divergence of the flame surface from the centerline. Downstream of the COR, the flame surface diverges from the centerline due to entrainment.

As blow-off is approached (moving left to right in Figure 11), the recirculation zone becomes shorter in the x-direction, and the COR becomes thinner in the y-direction. The reduction of the recirculation zone is attributed to the reduced dilation rates (Tuttle, 2010). It has also been shown that as equivalence ratio drops and flame speed decreases, the flame moves closer to the unstable shear layer. The high strain rates in the shear layer can cause local extinction, as evidenced by the

holes in the flame. Eventually, excessive strain rates caused by shear layer vortices cause the flame sheet to become non-reactive, and the flame can no longer be sustained leading to blow-off (Chaudhuri et al., 2010).

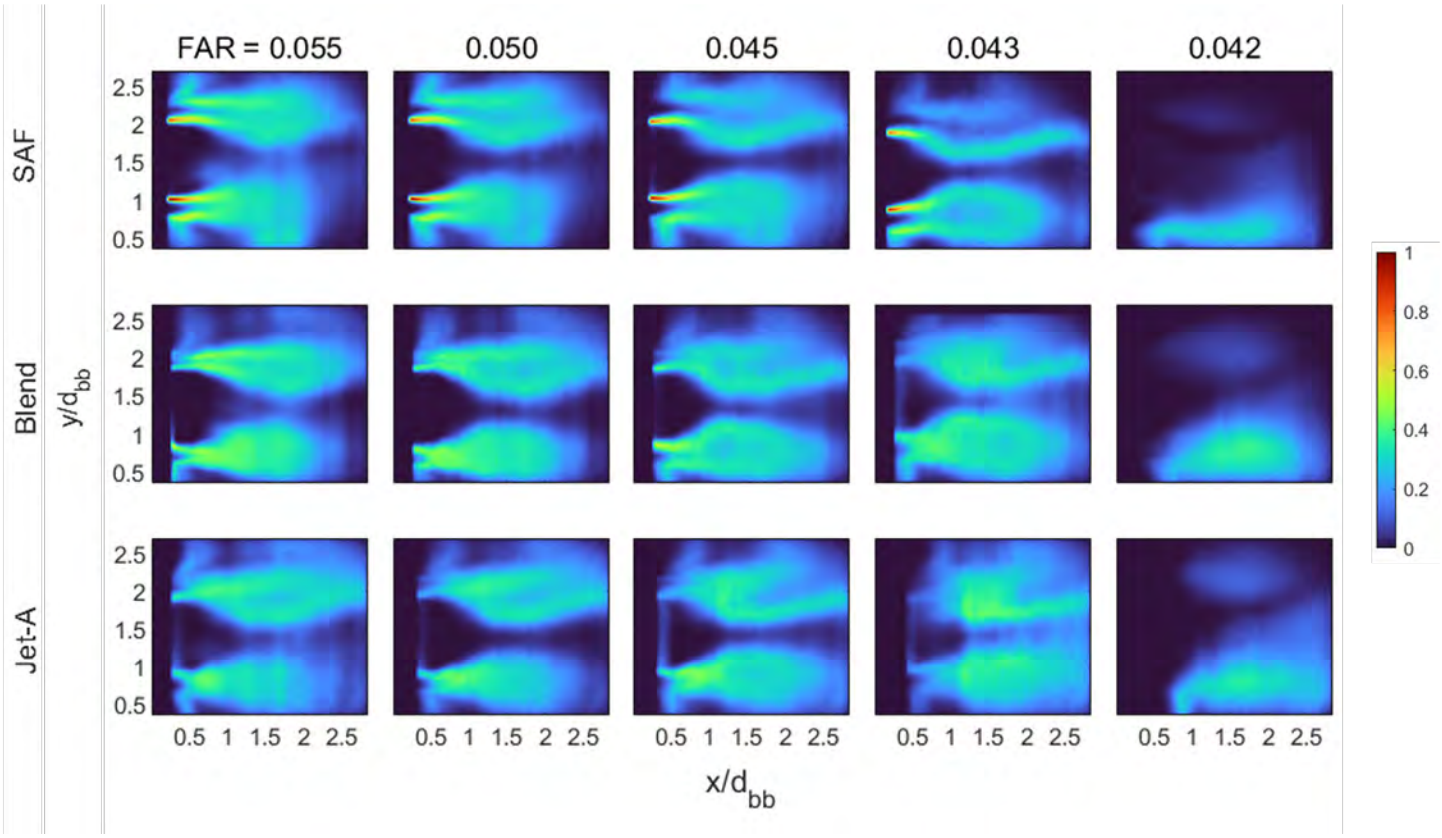

Figure 11. Temporal mean FSD fields for $T_3 = T_{3,\mathrm{ref}}$. Colorbar represents FSD normalized by the max FSD for presented test points. Flow progresses from left to right.

3.3 Blow-off Behavior

It previously was shown that differing physical fuel properties caused systematic differences in fuel penetration depth. As mentioned, the physics limiting processes for LBO due to fuel property affects are said to be governed by a competition between mixing/evaporation rate and chemical kinetic rate (Colket & Heyne, 2021). When fuel/air mixing occurs rapidly relative to the combustion chemistry or has already occurred prior to combustion as in LPP systems, LBO is kinetically limited and vaporization/mixing disparities we observed may be insignificant. The HEFA has a higher H/C ratio, LHV, and indicated cetane number (ICN), which suggests that it may be more resistant to blow-off (Rock et al., 2019). However, Table 3 show no significant trends at a given T_3.

Table 3. LBO FAR for different T_3 and fuel.

	HEFA	Blend	Jet A
$0.93T_{3,\mathrm{ref}}$	0.044±0.0003	0.045±0.0003	0.043±0.0003
$T_{3,\mathrm{ref}}$	0.042±0.0004	0.042±0.0004	0.042±0.0004
$1.10T_{3,\mathrm{ref}}$	0.039±0.0004	0.040±0.0004	0.039±0.0004

These similarities can be explained by blow-off Damköhler vs. Reynolds number correlations detailed earlier. First examining Re for a given T_3, primary disparities between fuels would be due to varying ρ_3 and μ_3, as $\dot{m}_{\mathrm{main}}$ is kept constant

for each fuel. However, due to the very lean nature of the mixture, these differences are minimal and therefore Re_{LBO} is approximately the same across fuels. For Da_{LBO}, it then follows that τ_f would also be approximately constant.

Additionally, δ_f^0 and S_L^0 in τ_c did not significantly vary across fuels. Experiments in previous studies have also shown that S_L^0 between HEFA blends and Jet A fuel are similar (Munzar et al., 2014; Hui et al., 2012). S_L^0 has a strong dependence on adiabatic flame temperature, which is directly controlled by LHV (Hui et al., 2012). While the LHV of the HEFA is slightly higher than the Jet A fuel, the difference is not significant enough to have meaningful impacts on S_L^0.

Figure 12 presents the LBO limits in the current experiments against data from the literature (Shanbhogue et al., 2009) for axisymmetric bluff bodies. The data from this study (blue dots), and previous campaigns (orange dots) are grouped towards the lower limit, indicating more robustness to LBO. The blow-off results across fuels are therefore encouraging for further applications of this combustor and LPP.

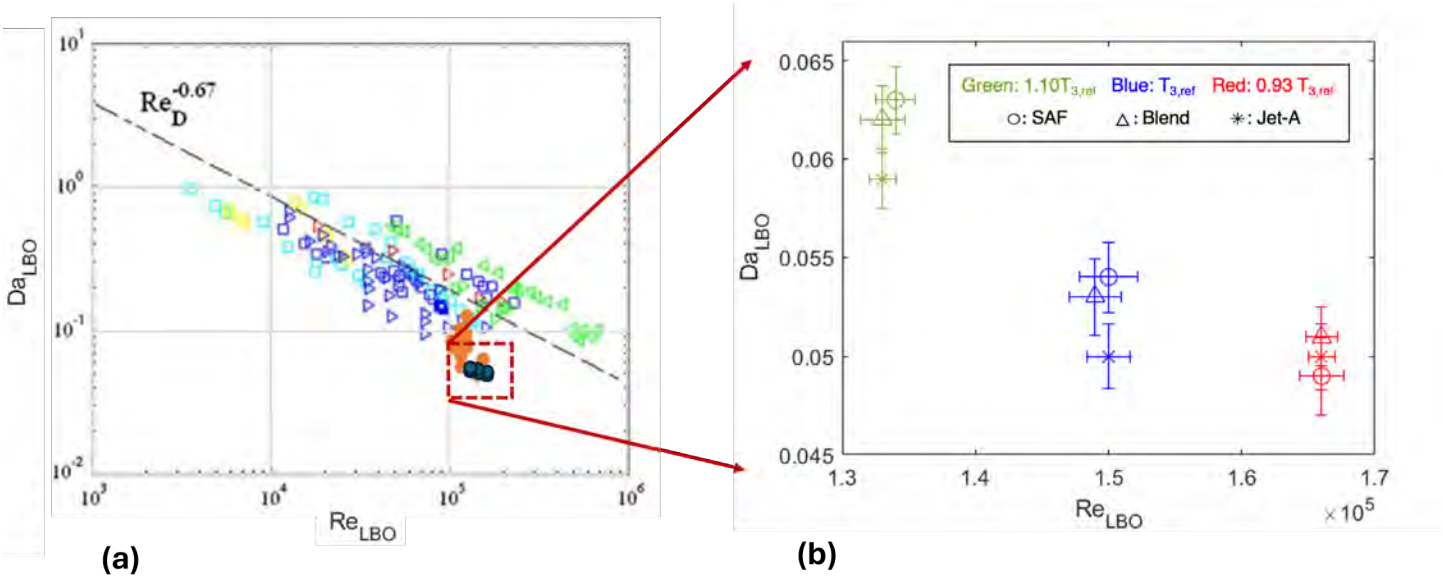

Figure 12. Blow-off Damköhler number (Da) vs. Reynolds number (Re). (a) Data from this study (solid blue) overlayed on axisymmetric bluff bodies from Shanbhogue et al. (2009). (b) Detailed view of blow-off Damköhler number vs. Reynolds number for the current study.

Milestones

- Completed campaign 3.
- Completed data analysis from campaign 3.

Major Accomplishments

- Measured the impact of fuel properties on spray characteristics.
- Measured the flame structure and FSD fields in LPP combustor.
- Demonstrated robust operation with SAF, despite atomization/vaporization differences.
- Established LBO correlation based on Damköhler and Reynolds numbers for LPP combustor, including SAF.

Publications

Jain, A., Obi, I., Mazumdar, Y. C., Salazar, V., Kodali, M., Venkatesan, K., & Steinberg, A. M. (In preparation). Flame structure, spray, and blowout of a lean premixed prevaporized combustor with conventional and sustainable jet fuels. *AIAA Journal*.

Jain, A., Obi, I., Mazumdar, Y. C., Salazar, V., Kodali, M., Venkatesan, K., & Steinberg, A. M. (2025, January 6-10). *Flame structure, spray, and blowout of a lean premixed prevaporized combustor with conventional and sustainable jet fuels* [Conference paper]. AIAA SCITECH 2025 Forum, Orlando, Florida.

Passarelli, M. L., Wonfor, S. E., Zheng, A. X., Mazumdar, Y., Steinberg, A. M., Bower, H., Hong, J., & Venkatesan, K. (2024, June 24-28). *Blowoff characteristics of a bluff-body stabilized, multi-element, lean premixed pre-vaporized combustor for supersonic transport applications* [Conference paper]. ASME Turbo Expo 2024: Turbomachinery Technical Conference and Exposition, London, United Kingdom. https://doi.org/10.1115/GT2024-129322

Zheng, A. X., Manikandan, S. R., Wonfor, S. E., Steinberg, A. M., & Mazumdar, Y. C. (2023). Planar time-resolved laser-induced incandescence for pressurized premixed Jet A combustion. *Applied Physics B: Lasers and Optics, 129*(71).

Salazar, V., Venkatesan, K., Han, F., Wonfor, S., Passarelli, M., Zheng, A., & Steinberg, A. M. (2023, January 26-30). *Acoustic and optical flame transfer function measurements in a high-pressure lean-burn aero-engine combustor fueled with Jet A* [Conference paper]. ASME Turbo Expo 2023: Turbomachinery Technical Conference and Exposition, Orlando, Florida. https://doi.org/10.1115/GT2023-103222

Passarelli, M. L., Wonfor, S. E., Zheng, A. X., Mazumdar, Y. C., Seitzman, J. M., Steinberg, A. M., Salazar, V., Venkatesan, K., & Benjamin, M. (2023). *Forced and unforced dynamics of a lean premixed prevaporized combustor for civil supersonic transport* [Conference paper]. AIAA SCITECH 2023 Forum, National Harbor, Maryland. https://doi.org/10.2514/6.2023-0920

Passarelli, M. L., Wonfor, S., Zheng, A. X., Manikandan, S. R., Mazumdar, Y. C., Seitzman, J. M., Steinberg, A. M., Bower, H., Hong, J., Venkatesan, K., & Benjamin, M. (2022, January 3-7). *Experimental characterization of a lean prevaporized premixed combustor for supersonic transport applications* [Conference presentation]. AIAA SCITECH 2022 Forum, San Diego, California. https://doi.org/10.2514/6.2022-2347

Student Involvement
Arihant Jain (PhD Student), Ijeoma Obi (MS Student), Mitchell Passarelli (PhD Student, graduated) contributed to this task.

Awards
None.

Plans for Next Period
Task 1 is complete. The effort to further advance LPP combustion will continue under ASCENT Project 098, focused on advancing the technology readiness level (TRL) for subsonic aircraft engines.

Task 2 - Computational Simulations of Combustor
Georgia Institute of Technology

Objective
The objective of this task is to develop and validate best practices for industry-scale simulations of LPP combustion. This involves a combination of industry- and research-scale CFD simulations, predominantly using LES.

Research Approach
To benchmark current CFD approach against experimental data, unsteady CFD simulations were performed for experimental conditions explored during Year 2 (2022-2023). Predictions from the industrial scale LES simulations were compared against the experimental measurements of 2D fuel-air mixing, 2D combustor heat release imaging and droplet sizing from phase Doppler Interferometry. Based on comparison of CFD to experimental data at two different FARs, it was concluded that the initially assumed droplet distribution, as well as accurate modelling of evaporation and fuel-air mixing, are key to better matching with observed experimental trends. The computational fuel injection model likely needs further improvement, requiring a better definition of fuel evolution at the injection boundary for better prediction of the amount of liquid versus vapor fuel at combustor inlet. Also, boundary conditions from the CFD simulations were provided to the NREL for reduced domain modelling and code-code comparison, as part of benchmarking the industrial scale simulations against state-of-the-art high-fidelity simulations.

The activity in 2023 helped identify deficiencies in the liquid fuel injection method employed in the CFD simulations. To address the inadequacy, the computational team is investigating a high-fidelity fuel injection process based on a hybrid volume of fluid (VoF)/discreet particle method (DPM) approach. The idea is to generate the fuel-injection by employing a sub-model and, additionally, to run the full-model unsteady CFD simulation using VoF based fuel-injection. Unsteady CFD simulations at Year 2 experimental conditions with the high-fidelity injection process are in progress and will be compared and contrasted against the previous CFD and experimental measurements.

The industrial-scale LES of the burner has been completed. The high-fidelity LES being conducted by NREL is ongoing under U.S. Department of Energy funding. The project team will continue to collaborate with NREL regarding boundary conditions and validation data.

Milestones
- Completed the LES of Year 2 conditions using industry-scale simulations.
- Transmitted the boundary conditions for high-fidelity simulations
- Established a hybrid fuel injection model.
- Obtained and processed spray, flame, and velocity data for simulation validation.

Major Accomplishments
- Identified changes in boundary conditions required for more accurately simulating LPP fuel injection.
- Progressed a partnership with NREL.

Publications
None.

Student Involvement
Arihant Jain (PhD Student), Ijeoma Obi (MS Student), Mitchell Passarelli (PhD Student, graduated) contributed to this task.

Awards
None.

Plans for Next Period
Task 2 is complete. The effort to further advance LPP combustion will continue under ASCENT Project 098, focused on advancing the TRL for subsonic aircraft engines. The NREL team will continue the high-fidelity LES that is being conducted under DoE funding. The ASCENT Project 074 team will continue to work with NREL to assess the simulations against the experimental data.

Task 3 - Analysis of Thermoacoustic Dynamics
Georgia Institute of Technology

Objectives
The objectives of this activity were to (1) measure the forced response of the LPP combustor to acoustic perturbations, (2) model the response using GE's thermoacoustic solver tools, (3) improve and validate these tools, as appropriate, and (4) physically explain the processes leading to thermoacoustic dynamics in this experiment.

Research Approach
Due to timing of the reports, proposal approvals, and no-cost extensions, the thermoacoustic measurement and modeling tasks were completed prior to the previous ASCENT Project 074 report. No further activities were required during this past performance period to complete the task objectives.

Milestones
- Completed the measurement of flame transfer functions.
- Completed the analysis of forced experimental results.
- Completed the preliminary analysis of flame transfer functions using network modeling.

Major Accomplishments
- Performed the first measurements of flame transfer functions and forced response of this type of LPP combustor.

Publications

None.

Student Involvement

Mitchell Passarelli (PhD Student, graduated) contributed to this task.

Awards

None.

Plans for Next Period

Task 3 is complete. The effort to further advance LPP combustion will continue under ASCENT Project 098, focused on advancing the TRL for subsonic aircraft engines.

References

ASTM International. (2023). ASTM D1655-22a: Standard specification for aviation turbine fuels. https://doi.org/10.1520/D1655-22A

Bell, J. B., Day, M. S., Grcar, J. F., Lijewski, M. J., Driscoll, J. F., & Filatyev, S. A. (2007). Numerical simulation of a laboratory-scale turbulent slot flame. *Proceedings of the Combustion Institute, 31*(1), 1299–1307. https://doi.org/10.1016/j.proci.2006.07.186

Berton, J. J., Huff, D. L., Geiselhart, K., & Seidel, J. (2020). Supersonic technology concept aeroplanes for environmental studies. In *AIAA Scitech 2020 Forum* (p. 0263).

Candel, S. M., & Poinsot, T. J. (1990). Flame stretch and the balance equation for the flame area. *Combustion Science and Technology, 70*(1-3), 1–15. https://doi.org/10.1080/00102209008951608

Canny, J. (1986). A computational approach to edge detection. *IEEE Transactions on Pattern Analysis and Machine Intelligence, PAMI-8*(6), 679–698. https://doi.org/10.1109/TPAMI.1986.4767851

Carter, C. D., & Lee, T. (2022). LIF theory and practice (Ch. 5, pp. 181–254). In A. Steinberg & S. Roy (Eds.), *Optical Diagnostics for Reacting and Non-reacting Flows: Theory and Practic*e. American Institute of Aeronautics and Astronautics, Reston, Virginia.

Cavaliere, D. E., Kariuki, J., & Mastorakos, E. (2013). A comparison of the blow-off behaviour of swirl-stabilized premixed, non-premixed and spray flames. *Flow, Turbulence and Combustion, 91*(2), 347–372. https://doi.org/10.1007/s10494-013-9470-z

Chaib, O., Zheng, Y., Hochgreb, S., & Boxx, I. (2023). Hybrid algorithm for the detection of turbulent flame fronts. *Experiments in Fluids, 64*(5), 104. https://doi.org/10.1007/s00348-023-03651-6

Chaudhuri, S., Kostka, S., Renfro, M. W., & Cetegen, B. M. (2010). Blowoff dynamics of bluff body stabilized turbulent premixed flames. *Combustion and Flame, 157*(4), 790–802. https://doi.org/10.1016/j.combustflame.2009.10.020

Colket, M., & Heyne, J. (2021). *Fuel effects on operability of aircraft gas turbine combustors*. Progress in Astronautics and Aeronautics, American Institute of Aeronautics and Astronautics, Reston, Virginia.

Dooley, S., Won, S. H., Chaos, M., Heyne, J., Ju, Y., Dryer, F. L., Kumar, K., Sung, C.-J., Wang, H., Oehlschlaeger, M. A., Santoro, R. J., & Litzinger, T. A. (2010). A jet fuel surrogate formulated by real fuel properties. *Combustion and Flame, 157*(12), 2333–2339. https://doi.org/10.1016/j.combustflame.2010.07.001

EPA. (2007). *Methodology for thermal efficiency and energy input calculations and analysis of biomass cogeneration unit characteristics* (EPA-HQ-OAR-2007-0012). U.S. Environmental Protection Agency (EPA). https://www3.epa.gov/ttn/atw/utility/fnl_biomass_cogen_TSD_04_19_07.pdf

Filatyev, S. A., Driscoll, J. F., Carter, C. D., & Donbar, J. M. (2005). Measured properties of turbulent premixed flames for model assessment, including burning velocities, stretch rates, and surface densities. *Combustion and Flame, 141*(1), 1–21. https://doi.org/10.1016/j.combustflame.2004.07.010

Fugger, C. A., Hsu, P. S., Jiang, N., Yi, T., Slipchenko, M. N., Felver, J. J., Smith, T. E., Emerson, B. L., Lieuwen, T. C., & Roy, S. (2020). 10-kHz simultaneous dual-plane stereo-PIV and OH-PLIF imaging. *Applied Physics B, 126*(10), 167. https://doi.org/10.1007/s00340-020-07522-4

Han, D., Satija, A., Gore, J. P., & Lucht, R. P. (2018). Experimental study of CO_2 diluted, piloted, turbulent CH_4/air premixed flames using high-repetition-rate OH PLIF. *Combustion and Flame, 193*, 145–156. https://doi.org/10.1016/j.combustflame.2018.03.012

Hassan, M., Pfaender, H., & Mavris, D. (2020). Design tools for conceptual analysis of future commercial supersonic aircraft. In *AIAA Aviation 2020 Forum* (p. 2620).

Hui, X., Kumar, K., Sung, C.-J., Edwards, T., & Gardner, D. (2012). Experimental studies on the combustion characteristics of alternative jet fuels. *Fuel, 98*, 176–182. https://doi.org/10.1016/j.fuel.2012.03.040.13

Kharina, A., MacDonald, T., & Rutherford, D. (2018, July). Environmental performance of emerging supersonic transport aircraft. ICCT.

Liang, Y., Liu, X., Yang, M., Hui, X., & Wang, J. (2024). Investigating the oxidation characteristic of a hydro-processed bio-jet fuel: Experimental and modeling study. *Combustion and Flame, 270*, 113778. https://doi.org/10.1016/j.combustflame.2024.113778

Lovett, J. A., Cross, C., Lubarsky, E., & Zinn, B. T. (2011, June 6-10). *A review of mechanisms controlling bluff-body stabilized flames with closely-coupled fuel injection* [Conference paper]. ASME 2011 Turbo Expo: Turbine Technical Conference and Exposition, Vancouver, British Columbia. https://doi.org/10.1115/GT2011-46676

Munzar, J. D., Zia, A., Versailles, P., Jiménez, R., Bergthorson, J. M., & Akih-Kumgeh, B. (2014, June 16-20). C*omparison of laminar flame speeds, extinction stretch rates and vapor pressures of Jet A-1/HRJ biojet fuel blends* [Conference paper]. ASME Turbo Expo 2014: Turbine Technical Conference and Exposition, Düsseldorf, Germany. https://doi.org/10.1115/GT2014-25951

Niedzwiecki, R. W. (1992, April). Low emissions combustor technology for high-speed civil transport engines. In *NASA. Langley Research Center, First Annual High-Speed Research Workshop, Part 2*.

Passarelli, M. (2023). *An experimental characterization of a multi-element lean premixed pre-vaporized combustor for supersonic transport applications* [Doctoral dissertation, Georgia Institute of Technology]. Georgia Institute of Technology

Passarelli, M. L., Wonfor, S. E., Zheng, A. X., Mazumdar, Y., Steinberg, A. M., Bower, H., Hong, J., & Venkatesan, K. (2024, June 24-28). *Blowoff characteristics of a bluff-body stabilized, multi-element, lean premixed pre-vaporized combustor for supersonic transport applications* [Conference paper]. ASME Turbo Expo 2024: Turbomachinery Technical Conference and Exposition, London, United Kingdom. https://doi.org/10.1115/GT2024-129322

Passarelli, M. L., Wonfor, S. E., Zheng, A. X., Mazumdar, Y. C., Seitzman, J. M., Steinberg, A. M., Salazar, V., Venkatesan, K., & Benjamin, M. (2023). *Forced and unforced dynamics of a lean premixed prevaporized combustor for civil supersonic transport* [Conference paper]. AIAA SCITECH 2023 Forum, National Harbor, Maryland. https://doi.org/10.2514/6.2023-0920

Passarelli, M. L., Wonfor, S., Zheng, A. X., Manikandan, S. R., Mazumdar, Y. C., Seitzman, J. M., Steinberg, A. M., Bower, H., Hong, J., Venkatesan, K., & Benjamin, M. (2022, January 3-7). *Experimental characterization of a lean prevaporized premixed combustor for supersonic transport applications* [Conference paper]. AIAA SCITECH 2022 Forum, San Diego, California. https://doi.org/10.2514/6.2022-2347

Ranzi, E., Frassoldati, A., Stagni, A., Pelucchi, M., Cuoci, A., & Faravelli, T. (2014). Reduced kinetic schemes of complex reaction systems: Fossil and biomass-derived transportation fuels. *International Journal of Chemical Kinetics, 46*(9), 512–542. https://doi.org/10.1002/kin.20867

Rock, N., Chterev, I., Emerson, B., Won, S. H., Seitzman, J., & Lieuwen, T. (2019). Liquid fuel property effects on lean blowout in an aircraft relevant combustor. *Journal of Engineering for Gas Turbines and Power, 141*, 071005. https://doi.org/10.1115/1.4042010

Saini, P., Chterev, I., Pareja, J., Aigner, M., & Boxx, I. (2020). Effect of pressure on hydrogen enriched natural gas jet flames in crossflow. *Flow, Turbulence and Combustion, 105*(3), 787–806. https://doi.org/10.1007/s10494-02000148-8

Salazar, V., Venkatesan, K., Han, F., Wonfor, S., Passarelli, M., Zheng, A., & Steinberg, A. M. (2023, January 26-30). *Acoustic and optical flame transfer function measurements in a high-pressure lean-burn aero-engine combustor fueled with Jet A* [Conference paper]. ASME Turbo Expo 2023: Turbomachinery Technical Conference and Exposition, Orlando, Florida. https://doi.org/10.1115/GT2023-103222

Shanbhogue, S. J., Husain, S., and Lieuwen, T. (2009). Lean blowoff of bluff body stabilized flames: Scaling and dynamics. *Progress in Energy and Combustion Science, 35*(1), 98–120. https://doi.org/10.1016/j.pecs.2008.07.003

Speth, R. L., Eastham, S. D., Fritz, T. M., Sanz-Morere, I., Agarwal, A., Prashanth, P., ... & Barrett, S. R. (2021). *Global environmental impact of supersonic cruise aircraft in the stratosphere* (No. E-19920).

Sweeney, M., & Hochgreb, S. (2009). Autonomous extraction of optimal flame fronts in OH planar laser-induced fluorescence images. *Applied Optics, 48*(19), 3866–3877. https://doi.org/10.1364/AO.48.003866

Tuttle, S. G. (2010). *Blowoff behavior of bluff body stabilized flames in vitiated and partially premixed flows* [Doctoral dissertation, University of Connecticut]. University of Connecticut ProQuest Dissertations & Theses, 3428890. https://doi.org/https://www.proquest.com/dissertations-theses/blowoff-behavior-bluff-bodystabilized-flames/docview/757375950/se-2

Vozka, P., Šimáček, P., & Kilaz, G. (2018). Impact of HEFA feedstocks on fuel composition and properties in blends with Jet A. *Energy & Fuels, 32*(11), 11595–11606. https://doi.org/10.1021/acs.energyfuels.8b02787

Xing, J., An, Z., & Kurose, R. (2024). Analysis and flamelet modeling of preferential evaporation in SAF/Jet A spray flames. *Proceedings of the Combustion Institute, 40*(1–4), 105707. https://doi.org/10.1016/j.proci.2024.105707

Project 075 Improved Engine Fan Broadband Noise Prediction Capabilities

Boston University & Raytheon Technologies Research Center

Project Lead Investigator

Sheryl Grace
Associate Professor
Mechanical Engineering
Boston University
110 Cummington Mall, Boston, MA 02215
617-353-7364
sgrace@bu.edu

University Participants

Boston University (BU)

- P.I.s: Sheryl Grace – Associate Professor, Mechanical Engineering
- FAA Award Number: 13-C-AJFE-BU Amendment 022
- Period of Performance: November 1, 2023, to October 30, 2024
- Tasks:
  1. Fan-wake surrogate model creation
  2. Improved low-order model
  3. Rig test planning

Project Funding Level

Year 3 Funding (January 1, 2023, to June 1, 2024):
Federal Aviation Administration (FAA): $400,000 total ($150,000 to BU, $250,000 to Raytheon Technologies Research Center [RTRC])
Matching Funds: $400,000 total ($200,000 from BU [datasets, faculty time, graduate student stipend], $200,000 from RTRC [personnel time, Pratt & Whitney® (P&W)])

Year 4 Funding (March 18, 2024, to May 31, 2025):
FAA: $201,044 total ($105,286 to BU, $95,758 to RTRC)
Matching Funds: $201,044 from BU (datasets, AeroAcoustics Research Consortium [AARC] previous funding, faculty time)

Investigation Team

Boston University
Sheryl Grace (PD/P.I.), Tasks 1, 2 & 3
Nuo Li, graduate researcher (PhD), Tasks 1 & 2
Theo Favier, graduate researcher (Master of Science [MS]). Tasks 1& 2
Amarylis Wiltz, undergraduate researcher, Task 1
Raytheon Technologies Research Center
Jeff Mendoza (Co-PD/P.I.), Tasks 1, 2 & 3
Craig Aaron Reimann, Tasks 2 & 3
Julian Winkler, Tasks 1, 2 & 3
Dmytro Voytovych, Task 1

® Pratt & Whitney is a registered trademark of RTX Corporation, Farmington, Connecticut.

Dustin Frohnapfel, Task 3
Matt Kennedy, Task 3

Project Overview

The noise signature of contemporary turbofan engines is dominated by fan noise, both tonal and broadband. Accepted methods for predicting the tonal noise have existed for many years. Furthermore, engine designers have methods for controlling or treating tonal noise. This is much more challenging for broadband noise. Thus, it is clear that further reductions in engine noise will require accurate prediction methods for the broadband noise to enable design decisions. Interaction noise from the fan-stage is a dominant broadband mechanism in a modern high bypass engine and is created by the interaction of the turbulence in the fan-wakes with the fan exit guide vanes (FEGVs). This project leverages prior development of low-order models for the prediction of fan broadband interaction noise. Gaps in the low-order approach are addressed based on knowledge gained from computation and experimentation. In particular, a method for determining the inflow into the stator via a machine learning (ML) algorithm is being developed. The low-order method will also be validated against full- and rig-scale data and appropriate development undertaken based on the findings.

Task 1 - Fan-wake Surrogate Model Creation

Boston University
Raytheon Technologies Research Center

Objective

The objective of this task is to build a surrogate model using machine learning that will work with performance level unsteady Reynolds-Averaged Navier-Stokes (URANS) to specify the mean flow, turbulent kinetic energy, and turbulent length scale at locations along the helical fan-wake path.

Research Approach

Subtask 1.1&2: Development of Autoencoder & Development of Decoder

The ML was applied to this problem in Year 4 of the ASCENT Project 075 and our team continued to use the decoder part of a neural network. Four wake flow parameters are learned in the region downstream of the fan. The mean flow axial and circumferential velocities and the turbulent kinetic energy and turbulence length scale are learned using a two-dimensional (2D) Convolution Neural Network (CNN). In the 2D method, the data are made of axial slices of the wake flow.

TensorFlow® is used for the ML and is integrated into a Python® wrapper. In Year 4, the CNN was improved and evaluated against alternatives. One improvement was in the number of interpolated points on the 2D axial slice of wake data. By selecting 64 points in the circumferential direction and 64 in the radial, the image being constructed with the ML breaks down much more easily and the sizes of the different ML layers are more easily fit.

Subtask 1.3: Identification & Creation of Training Data

The focus of Year 4 was *Subtask 1.3b: Creation of additional training data.* A collaborator from the Institut Supérieur de l'Aéronautique et de l'Espace (ISAE-Supaero) in Toulouse, France, was also identified during the Year 3. Professor Bauerheim's team has been developing canonical fan geometries with some basis in existing rig-scale fans that have been tested in the past. His group has also performed rotor-alone type RANS simulations for the fan geometries they have developed. A data usage agreement was sought but it continued to stall. Finally, Professor Bauerheim made much of his data open-source. The ISAE team found a way to share their RANS results for 59 different fans with the ASCENT Project 075 team. The results of our initial ML applied to this new database are included as an appendix in the form of the American Institute of Aeronautics and Astronautics (AIAA) aviation abstract that describes the work. In short, the ML works exceptionally well with this database.

® TensorFlow is a registered trademark of Google LLC, Mountain View, California. TensorFlow is a software library for ML and artificial intelligence that is used across a range of tasks, but mainly for training and inference of neural networks.
® Python is a registered trademark of Python Software Foundation, Beaverton, Oregon.

Additionally, to increase the database for the ML, BU PhD student Nuo Li learned how to implement the SU2[1] computational software. However, it was shown that the turbulence model did not give adequate results for use in building the needed turbulence length scale. Subsequently, the Cadence® Fidelity® Flow[2] was acquired. The team at BU can now run fan-alone simulations using Cadence Fidelity Flow. The results are still being analyzed to determine if the turbulence parameters are well behaved. It is assumed this software will work because of its similarity to the previously used FINETurbo[3] software that ISAE applied for their RANS analysis of their 59 fans.

Subtask 1.4: Application of Surrogate Model to Relevant Fan Geometries
The CNN ML predictions were applied to the previous database that contains the swept, leaned, and low blade count fans. And now it has been applied to the new database of 59 fans. It is of interest to know how the ML learned parameters work together with the low-order acoustic method to predict the final expected power level in the bypass duct for the cases. Last year's report showed how this played out for the original database. The use of ML learned parameters for analysis on three of the new fans is shown in Appendix A. Based on the results of the analysis in Appendix A, either direct RANS inputs or ML inputs can be used together with the low-order model with similar outcomes. The cases for which ML does not achieve the desired modeling outcome include fan geometries or operating points that require extrapolation from the database, which is expected.

The ability to consider the noise from so many different fan stages has led to further insights into fundamentals of fan stage broadband interaction noise. From the original database, the overall sound levels were viewed as they related to the fan efficiency plots as shown in Figure 1. The lowest noise point along any speed line does not line up with the highest efficiency point. It can also be seen by the black dots that the three main operating points that are the focus of testing and simulation—approach, cutback, and takeoff—are not at high efficiency points nor at low noise points.

[1] SU2 is an open-source collection of software tools written in C++ and Python for the analysis of partial differential equations (PDEs) and PDE-constrained optimization problems on unstructured meshes with state-of-the-art numerical methods.
® Cadence and Fidelity are registered trademarks of Cadence Design Systems, Inc., San Jose, California.
[2] Cadence Fidelity Flow is a computational fluid dynamics (CFD) platform allows for the simulation of a wide range of complex fluid dynamics problems, such as multiphase flows, reactive flows, and turbulent flows, from industrial to academic applications.
[3]Stand alone FINETurbo used by ISAE. Originally developed by NUMECA before being purchased and modified by Cadence (https://www.numeca.de/en/news/fine-turbo-version-17-1/).

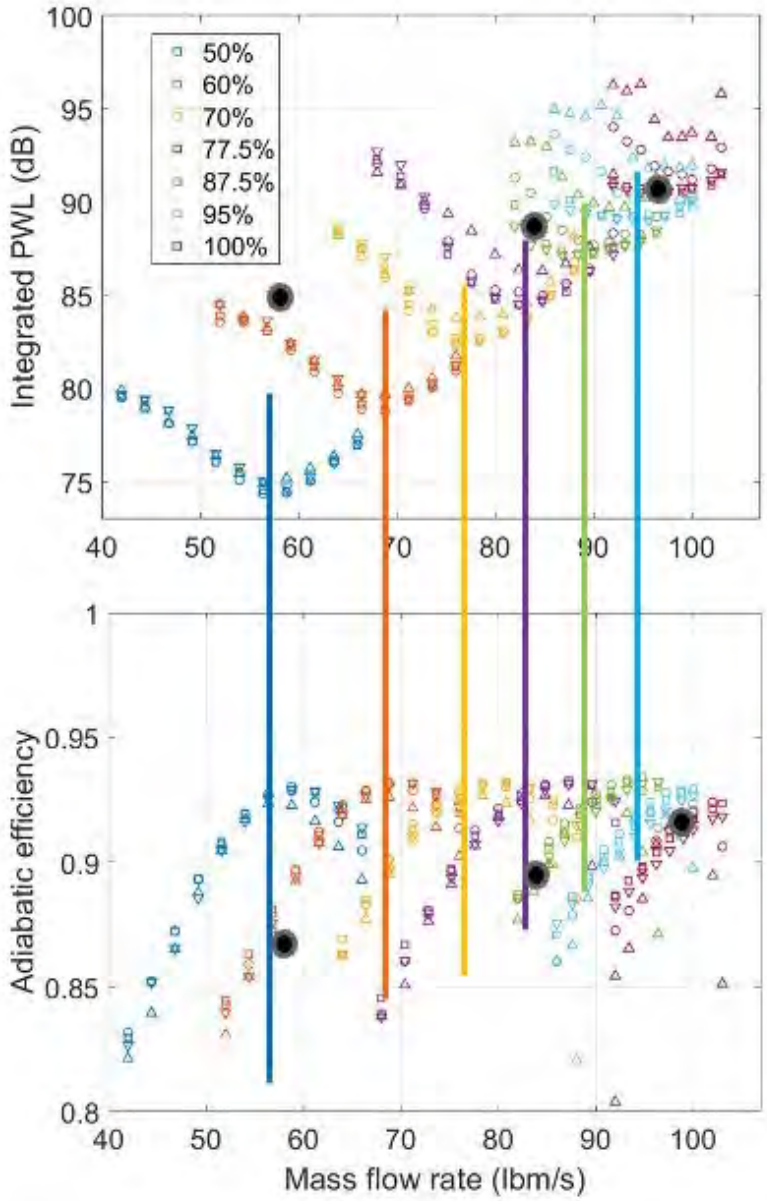

Figure 1. Top: Downstream noise. Bottom: Fan efficiency. Different leaned fans with same FEGV: Downward triangles: -10◦. Squares: 0◦ (BL). Circles: 15◦. Upward triangles: 30◦

The new dataset does not have complete operating lines. Four-Five operating points are available for any given fan as shown in Appendix A. Thus, for the new database, the same type of comparison between the low noise point and max efficiency cannot be completed. However, the investigation led to an effort to identify the relationship between noise and efficiency. To this end, different Mach number scalings (M^n with different n values) were evaluated and a collapse in the data was found when n=5. The broadband noise was analyzed in 1/3 octave bands and over the entire spectrum. The scaled values are shown vs. efficiency for the 59 fans in the new database. Single trend lines seem to be appearing. This means that a very simple algebraic method for estimating the overall broadband noise of a fan-stage based on the fan efficiency may be available in the future. This would be a very useful design tool.

Milestones

- Validated and refined the ML surrogate model.
- Improved the ML model and applied the model to a new database with success.

Major Accomplishments

- Improved the 2D CNN models for fan wake parameter prediction.
- Applied ML to a new dataset.
- Completed acoustic analysis using the low-order method of all of the fans in the new database.
- Evaluated SU2 and Cadence flow software to provide a method for creating and analyzing additional fans in the future.

Publications

Li, N., Zhange, Y., Winkler, J., Reinmann, C. A., Voytovych, D., Joly, M., Lore, K. G., Mendoza, J., & Grace, S. M. (2024). Development of fully low-order prediction of fan broadband interaction noise via integration of machine learning. *AIAA Journal, 62*(6). https://doi.org/10.2514/1.J063148

Li, N., Winikler, C., Reinmann, A., Voytovych, D., Joly, M., Lore, K. G., Mendoza, J., & Grace, S. M. (2023, June 12-16). *Machine learning aided fan broadband interaction noise prediction for leaned and swept fans* [Conference paper]. AIAA AVIATION 2023 Forum, San Diego, California, Virtual.

Outreach Efforts

- Presented at several university seminars and highlighted this work, including Embry Riddle University (November 2023), Virginia Tech (September 2024), and University of California (UC) Irvine (November 2024).

Awards

None.

Student Involvement

Nuo Li, graduate researcher (PhD) develops the ML and adopted and tested the two possible CFD codes, Theo Favier, graduate researcher (MS) worked on defining the thickness geometry for the fans in the new dataset, and Amarylis Wiltz, undergraduate researcher, ran parametric studies to help tune the ML method.

Plans for Next Period

- Continue refinement and validation of the ML surrogate model.
- Develop and add additional fans to analysis.
- Consider scenarios for when the database includes fans with different flow paths (fans with differing radial extents) and how ML is implemented and performs under these conditions.
- Consider combining the two databases.

Task 2 - Improvement of Low-order Model

Boston University
Raytheon Technologies Research Center

Objective

The objective of this task is to validate the low-order method against full-scale test data. The existing low-order methods are regularly applied to the Source Diagnostics Test (SDT) cases and as such have been well validated against this test, which represents one scaled fan and multiple FEGV configurations. The low-order method might also require reformulation to account for other real-flow effects.

Research Approach

Subtask 2.1: Ability to Predict Full-Scale Results

The low-order method will be applied to a full-scale geometry with available validation data. Due to the difference in frequency range of interest for the full-scale case, as compared to the scaled fans, it is surmised that the low-order method will require grid adjustments and integral extent adjustments. Such improvements to the low-order method will be completed as part of this task.

The test of the low-order method related to the FAA Continuous Lower Energy, Emission and Noise (CLEEN) Program I rig, and full-scale engine demonstration cases are still in progress. While this effort did not get attention this year, it remains in the background as something that must still be addressed. The results did not indicate that the low-order method performed well for the full-scale setting.

Acquisition of a computational fluid dynamics (CFD) tool at BU during this past year will aide in moving this investigation forward. Our team will perform analysis on the SDT fan stage for both the rig and full-scale setting. The acquisition of this CFD tool will allow for investigation of the questions that arose when analyzing the CLEEN fan.

A focus in Year 4 was improving the capability for the low-order method to handle FEGV sweep. The core cascade solver and its integration into the broadband noise calculation was studied carefully. The method by which sweep is characterized internally in the calculation was updated and the results improved. This improvement also allowed the low-order method to be used to study the impact of FEGV placement downstream of the fan on the fan-stage noise. In this study, the BU-Rotor-Stator Internation (RSI) code was verified against an alternative low-order method (referred to here as the Hanson method). It was through an agreement with Optis that their software OptiSound® was purchased and used to obtain the Hanson method predictions. The outcomes of this study were presented at the Aeroacoustics conference in 2024 (Li et al., 2024, listed under publications below).

The most important outcomes from the study are:

1) The BU-RSI and Hanson method do not react to changes in the mean flow in the same way. The BU-RSI has a stronger reaction to mean flow acceleration.
2) The BU-RSI and Hanson method do not react to changes in the length scale exactly the same. The Hanson method tilts the spectrum more as length scale changes.
3) Both methods, the BU-RSI and Hanson method, predict that as the SDT FEGV is moved very close to the fan, the overall broadband interaction noise only changes by about 1dB.

In Year 2, *Subtask 2.2: Inclusion of Tip Flow Impact on the Low-Order Model* and *Subtask 2.3: Inclusion of Inflow Distortion Impact on the Low-Order Model* were discussed.

Milestones

- Validated the low-order model on new geometry, specific the test rig-scale vs. full-scale applicability. The low-order method has been improved to more accurately model swept vane cases (which is the case for both the AneCom AeroTest 1 (ACAT1) and the FAA CLEEN I geometries). The low-order method was verified against the Hanson method (some differences were seen). It was applied to study the effect of moving an FEGV closer to the fan and the results indicate that there is little broadband noise penalty to shortening the interstage gap.
- Completed final improvements to low-order model. The low-order model has been applied to several cases that have accompanying experimental data for validation: (a) the ACAT1 geometry and now to the FAA CLEEN I rig- and full-scale geometries, and (b) the rig-scale cases, ACAT1 and FAA CLEEN I, show good agreement between the predicted and measured acoustics. In all cases, the approach prediction is slightly high. The source of this discrepancy is not understood yet. The FAA CLEEN I full-scale case has not been accurately predicted.

Major Accomplishments

- Obtained the RANS solver that works for fan alone simulation to provide the opportunity for studying the rig scale vs. full-scale setting noise scenario in the future.
- Acquired and used OptiSound software to verify BU-RSI method.
- Improved the method for accounting for FEGV sweep in the low-order acoustic method.
- Completed a computational study of FEGV placement.

® OptiSound is a registered trademark of Optis Consultants, Inc., Sherbrooke, Quebec.

Publications

Li, N., Winkler, J., Reinmann, C. A., Voytovych, D., Mendoza, J., & Grace, S. M. (2024). Effect of straight and swept FEGV placement on fan broadband interaction noise. In *30th AIAA/CEAS Aeroacoustics Conference (2024)* (p. 3161). https://doi.org/10.2514/6.2024-3161

Outreach Efforts

- Discussed this topic in presentations at Virginia Tech and UC Irvine in Fall of 2024.

Awards

None.

Student Involvement

Nuo Li, graduate researcher (PhD), worked on the low-order model.

Plans for Next Period

- Update the low-order model dependent on the results of the full-scale studies and perform further comparisons to the OptiSound results.
- Complete final improvements to low-order model.

Task 3 - Rig Test preparation

Boston University
Raytheon Technologies Research Center

Objectives

The objective of this task is to perform experiments in the RTRC Acoustic Research Tunnel (ART) to (a) acquire key aerodynamic and acoustic data to support the validation of low-order and mid- (RANS) to high- (VLES, LBM Very Large Eddy Simulation, Lattice Boltzman Method) fidelity CFD models, and (b) assess the noise trends and scaling laws of different fan stage.

Research Approach

RTRC began designing the rig for the planned experiments. After careful study, it was concluded that additional funds were necessary in order to fully design the desired rig and complete the experiments. A stop work was ordered related to the fan rig development while a new proposal was developed that outlined the funding needs. The proposal was submitted and approved. Once it was approved, funding was issued and work recommenced.

The rig being designed is a scaled version of the P&W Fan Rig 2 from the FAA CLEEN I program. The flow path will focus solely on the bypass, thus eliminating the need for a core. The configurations that are planned include the P&W baseline design, as evaluated at the National Aeronautics and Space Administration (NASA) previously, and either a rotor-alone (no FEGV) configuration or a shifted FEGV configuration.

As Year 4 concludes, the fan and hub design will be completed, and fabrication will be sourced. The FEGV and bifurcations have preliminary layouts. The nacelle aerodynamic design is complete, and the mechanical design is in progress allowing for additive manufacturing considerations. The electric motor drive from previous programs is being adopted.

The Gantt chart for the project (Figure 2) shows the best estimate for completion of the tests.

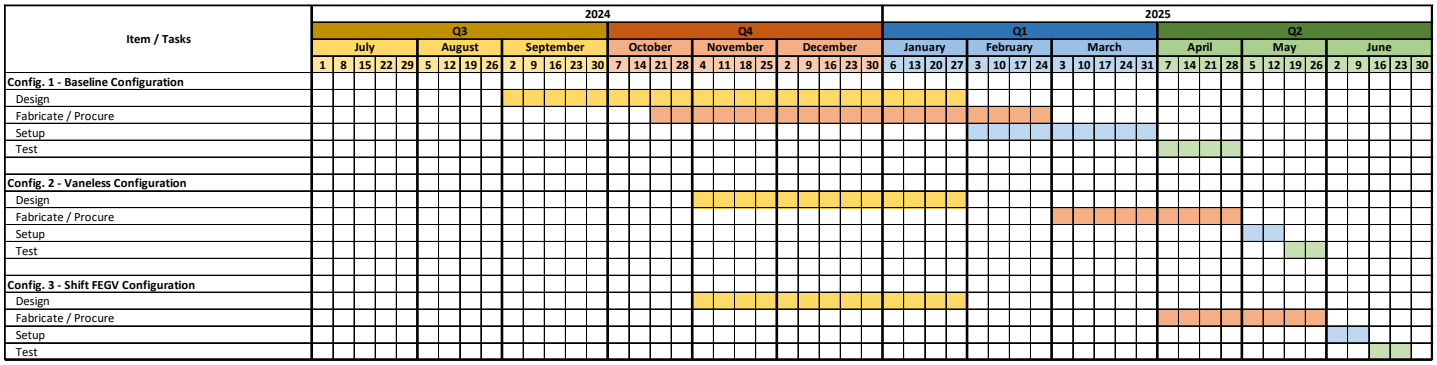

Figure 2. RTRC rig development and test schedule.

Meetings have commenced to discuss in detail the flow and acoustic data acquisition. The final test matrix will be developed as the rig comes together.

Milestones

- Continued ongoing final rig design.
- Test rig shakedown and complete rig testing. The rig will be built in early 2025 and the tests will commence around May 2025.

Major Accomplishments

- Participated in multiple meetings between RTRC/BU and P&W to determine the exact test capabilities.
- Determined the specification of additional funds needed to fully design and complete the rig test.

Publications

None.

Outreach Efforts

None.

Awards

None.

Student Involvement

None.

Plans for Next Period

- Test rig shakedown.
- Complete rig testing.

APPENDIX A

Low-Order Methods for Analysis of Impact of Fan Design on Fan Stage Broadband Interaction Noise

Nuo Li*,Sheryl M. Grace†
Boston University, Boston, MA, 02215, U.S.A.

The fan stage is a dominant source of noise in modern high-bypass ratio engines. Fan blade design plays a crucial role in both fan stage aerodynamic performance and noise. This work explores the impact of fan blade design on the fan stage downstream propagated broadband rotor-stator interaction (RSI) noise using low-order methods. A dataset with 59 fan blade geometries at multiple operating points is used as a basis of this study. A RANS-informed cascade model is used to predict the broadband interaction noise. A generative machine learning model is employed to explore operating points not available in the original dataset. Fan isentropic efficiency is shown to be inversely proportional to the fan stage broadband interaction noise when the integrated sound power is scaled by M^6.

I. Introduction

Increase in bypass ratio (BPR) and decrease in fan pressure ratio has became a major design trend in modern and future turbofan engines for better efficiency. The design trend has led to a shift of the dominant broadband noise source from jet noise to fan noise.

Resolving the broadband acoustic signal numerically requires computationally expansive simulations such as Large Eddy Simulation (LES) [1, 2] or Lattice Bolzmann Method using Very large Eddy Simulation (LBM/VLES) [3, 4]. The early design phase of an engine can benefit from more efficient low-order models [5–8]. In this work, the focus is on a low-order model for the rotor-stator interaction (RSI) broadband noise, which is a major source of fan-stage noise. The low-order model relies on the mean fan wake velocity and turbulence quantities upstream of the Fan Exit Guide Vane (FEGV). These can be obtained from lower fidelity simulations such as steady Reynolds averaged Navier-Stokes simulations(RANS).

RANS is widely utilized in engine design due to its lower cost and ease of automation when coupled with modern gridding softwares. Still there is a push to further speed up the low-order predictions. A method that has been considered is surrogate fan wake models using machine learning (ML). Such a ML method was demonstrated in a previous study [9]. In Ref. [9], a generative convolutional neural network (CNN) model was introduced to predict the mean flow and turbulence quantities in the fan wake. Ref. [10] utilized a U-net based CNN model with upsampling to determine the flow in a multistage compressor.Ref. [11] demonstrated an application of a U-net based model to predict fan wake entropy and fan efficiency.

This study extends the research presented in Ref. [9] by applying the ML to the fan database described in Ref. [11] and provided by Fesquet et al. from ISAE-SUPAERO. The fan database is also used to study the broadband noise produced by the multitude of fan geometries in the database. The broadband noise is computed using the BU-RSI cascade model [12] with RANS based fan wake flow input. The acoustic trend and its associated correlation with rotor alone efficiency will be discussed. The generative ML model is then used to obtain the fan wake input needed for the acoustic calculation at operating points not available in the database.

II. Method

The current dataset consists of RANS fan-alone simulations for 59 fan geometries at several operating points on 4 speed lines totaling 298 cases. Examples of 9 fan geometries are depicted in Fig. 1. The dataset was provided by Fesquet et al. [11] and is derived from 6 main rotor geometries: the Akira DGEN-380, NASA R37 and R67, the Safran LP4 fan, EC Lyon ECL5, and ISAE-SUPAERO PropHyDis. The final geometries are all 14-blade fans generated by interchanging the design parameters of the original geometries and fitted into the 352mm-diameter duct associated with

*Graduate Student, Mechanical Engineering Department, AIAA Student Member
†Associate Professor, Mechanical Engineering Department, AIAA Associate Fellow.

the DGEN-380 fan stage. The steady-RANS simulations were set up using fan alone, periodic domains and employ the Mentor's $SSTk-\omega$ turbulence model [13]. The Cadence Fine/Turbo Euranus solver was used for the simulation and Cadence Autogrid5 was used to create the mesh.

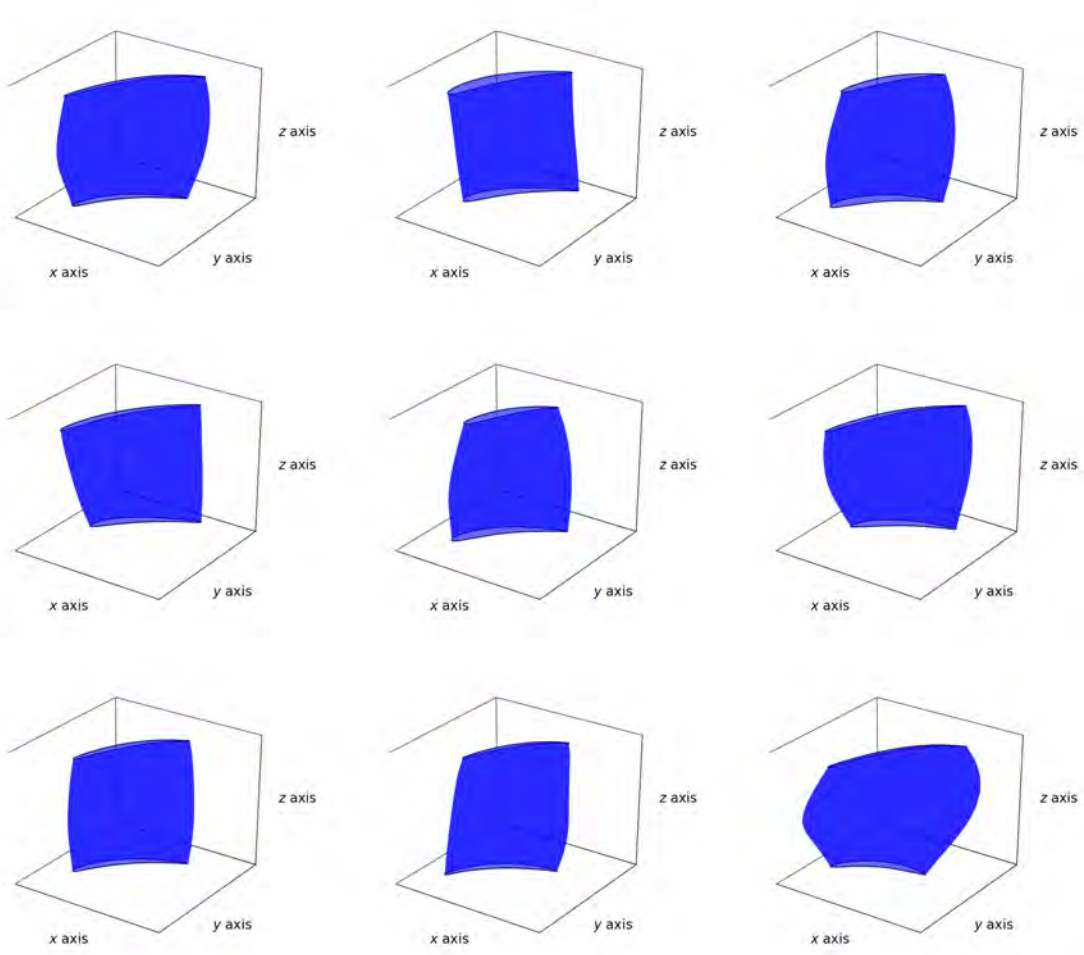

Fig. 1 Example blade geometries

An FEGV must be defined to complete the fan stage in order to consider interaction noise. The FEGV geometry has been created by modifying the NASA SDT baseline vane based on basic information available for the DGEN-380[14]. In particular, the FEGV has 40 vanes and a chordlength of 1.28in (0.0033m). In the low-order method, FEGV radial strips from hub to tip are transformed into flat-plate cascades and analyzed. As such, the flat plate geometry at each radial location is defined with the same global stagger profile as the SDT.

The acoustic result is computed by the cascade model based on Ventres et al. [8] and later expanded and improved by Envia & Nallasamy[15], and Grace [12]. The simulation is carried out in the frequency-wavenumber domain. The model considers a linear, 2-D flat plate cascade interacting with a turbulent wake carried by the mean flow U as depicted in Fig. 2. The unsteady blade loading depends only on the disturbance normal to the vane, which has the form $\tilde{u}_2(r, \mathbf{k}, \omega)e^{i\mathbf{k}(z\cos\chi x_1 - sh\sin\chi x_2)}$ where $\mathbf{k} = (k_1, k_2, 0)$ and s is

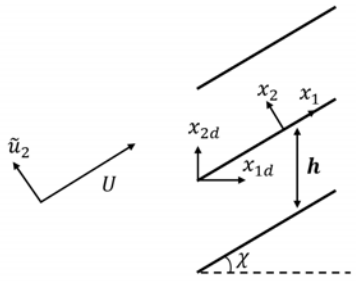

Fig. 2 Linear cascade definition

the vane index. The vane loading distribution $\tilde{f}(r, z, \mathbf{k}, \omega)$ can be obtained by solving the integral function

$$e^{i\mathbf{k}z} = \int_b^{-b} K_c(z - z')\tilde{f}(z, \mathbf{k}, M)\frac{dz'}{b} \tag{1}$$

where K_c is a kernel function derived in [8], and z is the coordinate along the chord. This vane response to a unit amplitude disturbance is convolved with the turbulence statistics to obtain the expected value of the vane response [8]. The Liepmann turbulence spectrum [16] is used to model the fan wake turbulence in the frequency-wave number domain. The duct acoustic power is then computed via Green's method for every cut-on circumferential and radial mode.

Previous study using this model [12, 17] showed that the computed sound power level is highly dependent on the definition of the vane stagger angle χ: a larger stagger angle will lead to a higher sound power. However, it was also shown that the acoustic trends with fan RPM and fan wake turbulence levels etc. are consistent given any stagger definition.

The low-order broadband interaction noise calculation is dependent on the cicumferentially-averaged values of mean axial velocity (v_x), mean tangential velocity (v_t), turbulence intensity (u'), and turbulence length scale (Λ) upstream of the FEGV. Isotropic turbulence is assumed so that when these input parameters are derived from RANS data, $u' = \sqrt{2/3TKE}$ and turbulence length scale is determined by $\Lambda = 0.43\frac{TKE^{1/2}}{0.09\omega}$.

While the acoustic model is often informed by input extracted from RANS. Earlier study [9, 18] showed reasonable accuracy in acoustic predictions made by coupling the low-order acoustic calculation with a ML surrogate for the input. In that study, a fan dataset was created with 8 fans of varying lean and sweep. Now, the generative CNN model is being applied to a new dataset with more fan design variations.

The ML developed for the fan wakes utilizes only the decoder part of a CNN. The model takes the following blade design parameters and operating point information as inputs:

- Rotor RPM (0D)
- Mass flow rate (0D).
- Leading edge radial location (1D)
- Trailing edge radial location (1D)
- Relative leading edge axial location (1D)
- Relative trailing edge axial location (1D)
- Relative trailing edge circumferential location (1D)
- Chord (1D)
- Stagger (1D)
- Inlet metal angle (1D)
- Outlet metal angle (1D)
- Blade thickness at five chordwise control points (1D)

The 0D inputs are scalars and the 1D inputs are specified at several spanwise equally-spaced locations along the fan. Currently, 5 spanwise sections are used. This provides the latent space that would be produced by an encoder.

The training data are the fan wake flow parameters at 30 equally-spaced axial slices downstream of the fan between 0.06m to 0.22m as measured from the fan stacking axis. At each axial location, the RANS solution is interpolated onto 64×64 points in the circumferential and radial directions.

The inputs are concatenated into a 1D array for each axial slice in the training data. The concatenated input is followed by fully-connected layers to transform the input into a single 1/8 scale feature map (8×8 for the current output resolution). It is then passed to eight transposed CNN layers with three strided layers to expand the feature maps into 1/4 scale, 1/2 scale and finally the full scale output.

III. Results

The results for the ML model's performance on the new multi-fan dataset are discussed first. Three geometries were extracted from the dataset and reserved for testing. They are shown in Fig. 3. The training data then consists of the remaining 56 geometries. The model is trained in four channels for each wake flow parameter (v_x, v_t, TKE, Λ). Two mean error metrics are defined, both are averaged over an axial slice: (1) The relative error, e, is calculated by point-to-point difference on the full axial slice between the ML prediction and the CFD solution normalized by the averaged CFD value. (2) The circumferential averaged relative error, e_{circ}, is determined by first taking the

circumferential averaged values for the ML prediction and the CFD, then, their differences are normalized by the slice averaged CFD value. In most cases, e_{circ}, is lower than e as it ignores any phase misalignment.

An example prediction for an axial slice near the FEGV leading edge is shown in Fig. 4 using test geometry 1 at 9000 RPM, 9.4 kg/s. The ML predictions exhibit good agreement with the target CFD solution exhibiting a 1% error for the velocity fields. The TKE relative error is notably larger than the velocity error mainly due to the scale of its variation between the wake center and background. The prediction errors for test geometry 2 are similar to test geometry 1 and examples are omitted for brevity. Test geometry 3 is a more challenging case due to its thicker profile which leads to large flow separation. It is considered a less preferable design. An example prediction for this geometry is shown in Fig. 5 at 12000 RPM, 9,84 kg/s, a slightly larger error is observed, but the model is still able to capture the wake profile. However, for an off-design, heavily stalled case, the results as seen in Fig. 6 are not good. This is considered the most challenging extrapolation case. The model completely fail to predict the wake under this condition. Previous studies [9, 18] have shown a very limited extrapolation capability using a generative CNN model. This is still true even with a more diverse dataset. Fesquet et al. [11] also noted that their transformative U-net failed to extrapolate the flow field for this stalled condition.

It is of interest to understand how an acoustic prediction using the low-order method is affected by using input either from RANS or from the ML surrogate model. As mentioned above, a single FEGV was created to complete the fan-stage for any fan in the dataset. In Fig. 7, the predicted broadband interaction sound power spectrum downstream of the fan stage with inputs from cases in figs. 4 to 6 are compared. The solid line shows the prediction when RANS data are used as input to the acoustic calculation and the dotted lines show the prediction when the ML surrogate model provides the input. The black and red lines show errors are less than 1 dB. This is typical for any fan geometry at an on-design operating point. For the heavily stalled case depicted by the blue lines, a very large error of more than 10 dB difference at 1 kHz arises. This is expected given that the ML prediction is very different than the CFD results for this case.

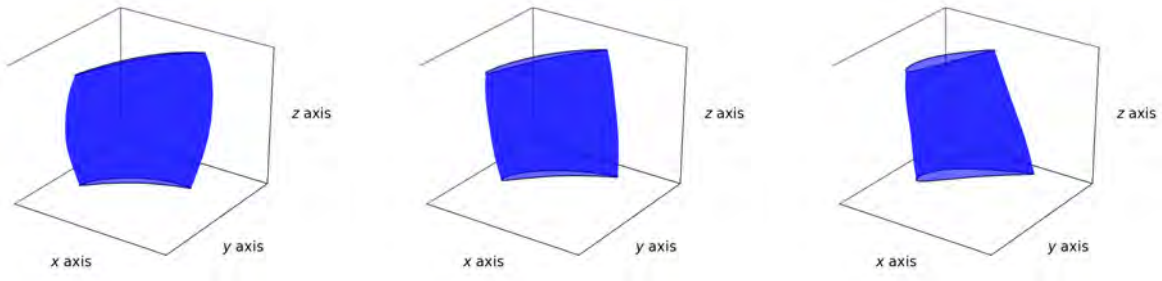

(a) Test Geometry 1 (b) Test Geometry 2 (c) Test Geometry 3

Fig. 3 Diagrams of test geometries

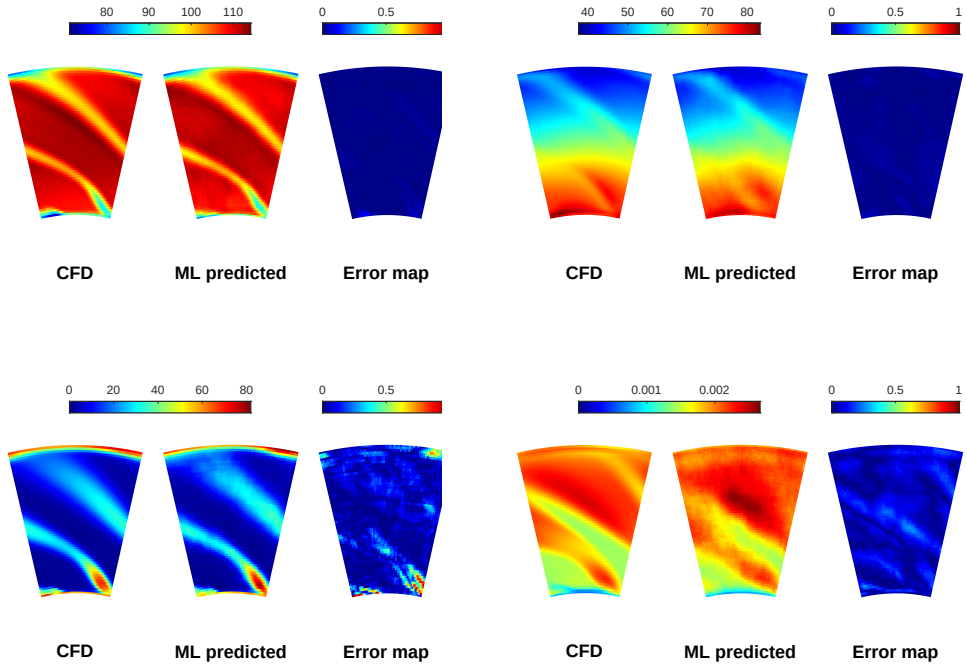

(c) $TKE(m^2/s^2), e = 0.102, e_{circ} = 0.04$ (d) $\Lambda(m), e = 0.072, e_{circ} = 0.051$

Fig. 4 Flow fields at axial slices upstream of FEGV. Test geometry 1 at 9000RPM, 9.4kg/s

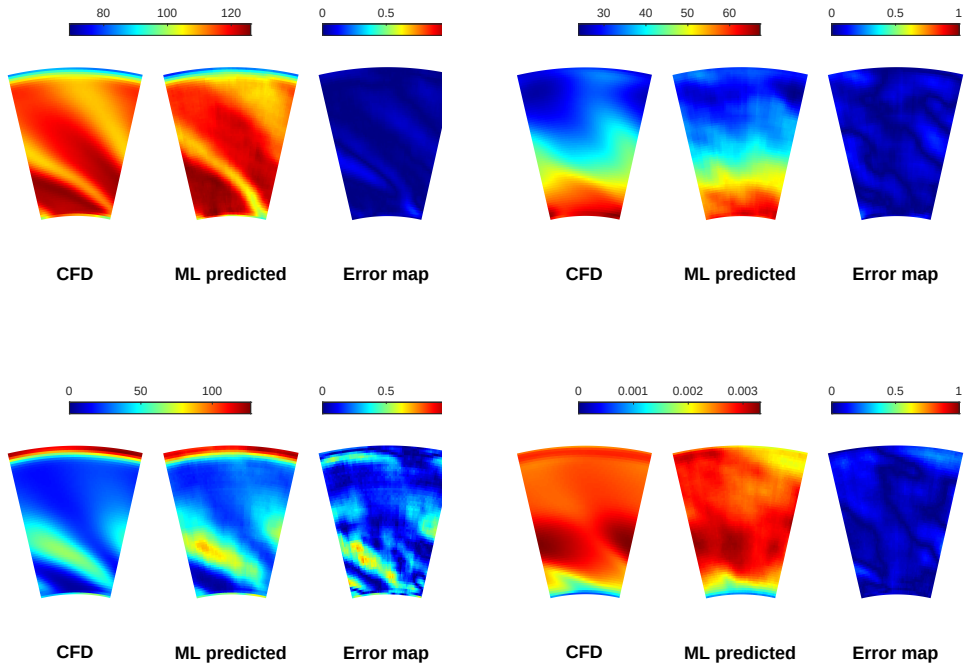

(c) $TKE(m^2/s^2), e = 0.217, e_{circ} = 0.18$ (d) $\Lambda(m), e = 0.065, e_{circ} = 0.026$

Fig. 5 Flow fields at axial slices upstream of FEGV. Test geometry 3 at 12000RPM, 9.84kg/s

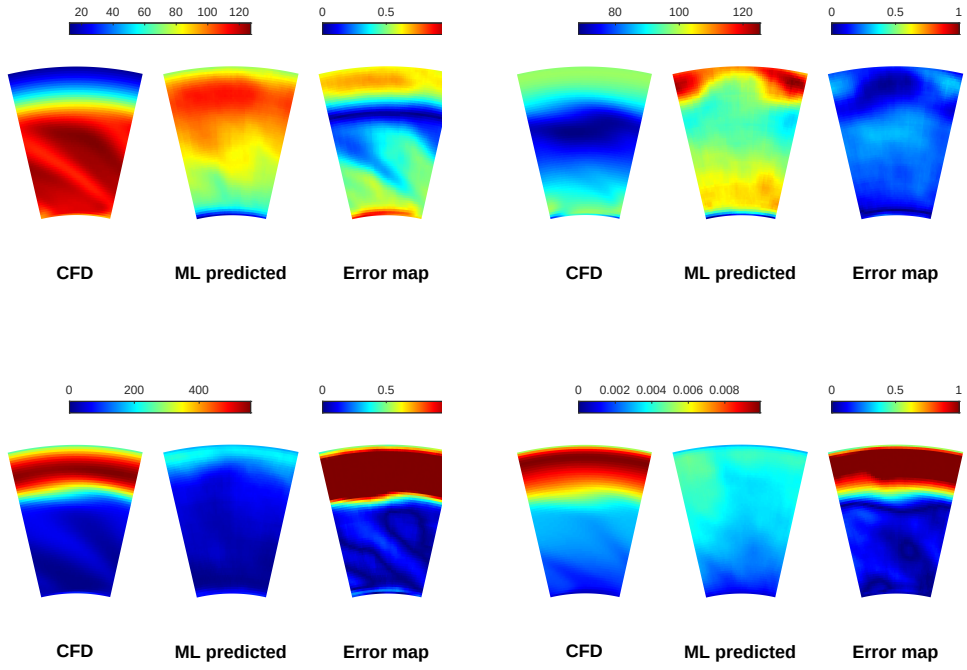

(c) $TKE(m^2/s^2), e = 0.666, e_{circ} = 0.64$ (d) $\Lambda(m), e = 0.374, e_{circ} = 0.369$

Fig. 6 Flow fields at axial slices upstream of FEGV. Test geometry 3 at 15000RPM, 8.19kg/s

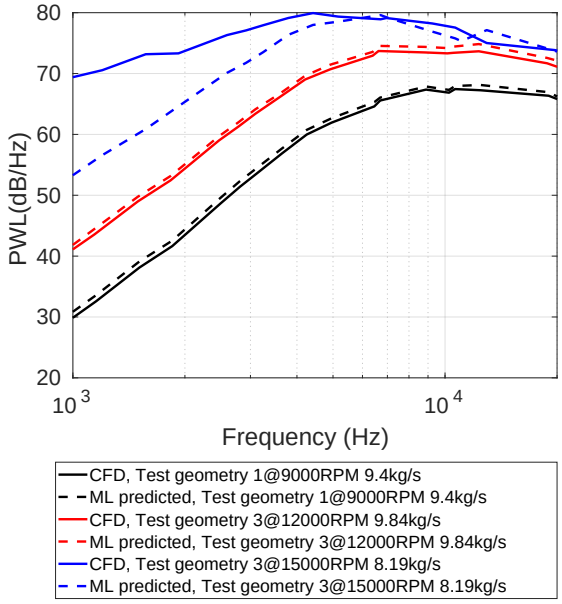

Fig. 7 Sound power spectra predicted using CFD and ML predicted inputs.

Access to the new fan dataset enabled a study of fan-stage acoustics that is discussed here. The results in this section were all obtained using the low-order acoustic method with input taken directly from the RANS simulations. The study was motivated by the expectation that there may be a correlations between fan performance and noise when considering multiple fan blade designs at different operating points. Indeed, in [17] it was found that the overall sound power level (OAPWL) does not perfectly mirror the isentropic efficiency curve for a single rotor. However, it was found in [18] that at any given operating point (mass flow rate and rotor speed), the OAPWL is inversely proportional to the fan efficiency for fans with different lean and sweep. In this work, the correlation is analyzed across the larger set of fan geometries. The original goal of the creation of this dataset was to sample geometries with largest physical distance possible among each other within a reasonable sample size as described in [11] by blending the design parameters from 6 main existing main geometries, which annihilated the original design point, and the operating points were determined by the flow coefficient $\hat{\phi}_p$. For most fans, at least two operating points with $\hat{\phi}_p = 0.3$ and 0.45 were simulated, in which their mass flow rates as well as thrust are different for each rotor.

In an effort to eliminate the effect of operating point in the correlation, a scaled sound power was considered. Previous studies suggested that gust-airfoil or gust-flat plate interaction noise is highly dependent on Mach number [19]. Some studies [20, 21] suggested a scaling exponent of 4-5.2 between the acoustic pressure and Mach number. Here, the scaled sound power level is defined as

$$PWL_{scaled} = PWL + 10\log_{10}(\frac{M}{M_{ref}})^6 \tag{2}$$

where M is the absolute Mach number upstream of the stator, and $M_{ref} = 0.3$ is the reference Mach number.

Figs. 8 show the scaled sound power level as functions of isentropic efficiency, η_{is} at four $1/3$ octave bands. The $1{,}250Hz$ nominal band is integrated from the range of $1{,}122Hz-1{,}413Hz$, the $4{,}000Hz$ nominal band is integrated from $3{,}548Hz-4467Hz$, the $8{,}000\ Hz$ nominal band is integrated from $7{,}079Hz$ $8913Hz$ and the $12{,}500Hz$ nominal band is integrated from $12{,}220Hz-14{,}130Hz$. Fig. 9 shows the overall sound power level integrated from $1{,}000Hz$ to $20{,}000Hz$. Consistent trends can be observed showing a inversely proportional relation between sound power and fan isentropic efficiency for all geometries and operating points. The trends are nearly independent of fan speed represented by the marker color. Still, the slight shift in trend with respect to fan speed at low frequency, i.e. Fig. 9(a) indicates that the sound power scaling may be frequency-dependent. This will be further investigated in the final paper. Two distinct curves are observed representing two operating points with different $\hat{\phi}$ (which also implies different inlet flow angles at the leading edge of the FEGV). At higher frequency, i.e. Fig. 8(c) and Fig. 8(d), the scaled PWL becomes less dependent on both flow coefficient and isentropic efficiency. Trend lines fitted to these correlations can provide instantaneous design feedback pertaining to the expected broadband noise from a new fan design based on its operating curve.

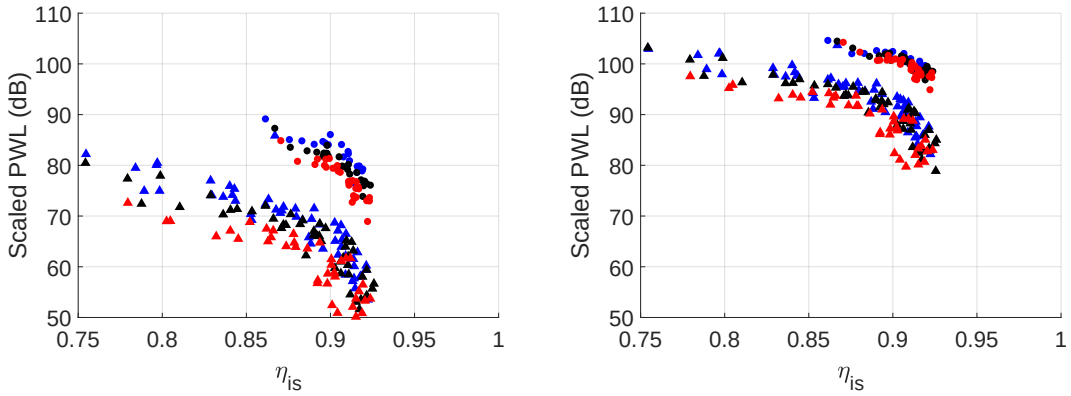

(a) 1,250 Hz (b) 4,000 Hz

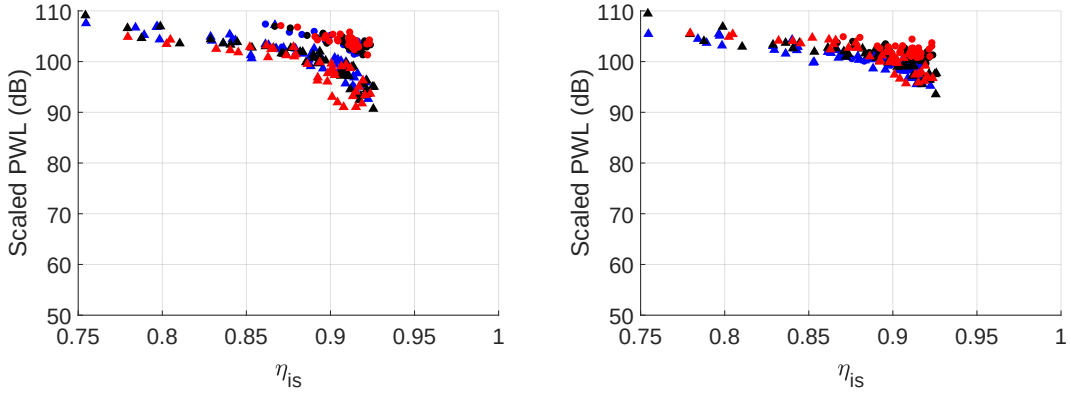

(c) 8,000 Hz (d) 12,500 Hz

Fig. 8 Scaled sound power level as functions of isentropic efficiency at $1/3$ Octave bands. Blue:7000 RPM, black: 9000 RPM, red: 12000 RPM. Circles: low flow coefficient, triangles: high flow coefficient.

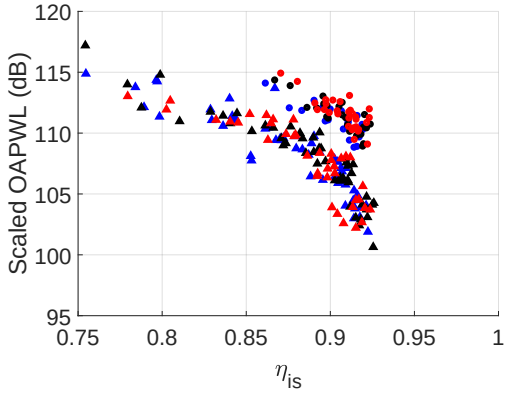

Fig. 9 Scaled OAPWL as functions of isentropic efficiency. Blue:7000 RPM, black: 9000 RPM, red: 12000 RPM. Circles: low flow coefficient, triangles: high flow coefficient.

IV. Conclusions and final paper

A study is performed to investigate the impact of fan blade design on fan-stage broadband interaction noise using low-order methods. The time-averaged flow field is supplied by steady RANS simulations of a dataset consisting of 59 fan geometries. It is shown that the Mach number-scaled aft-propagated interaction noise level is inversely proportional to the fan-alone isentropic efficiency. Additionally, a generative ML fan wake surrogate is assessed using the RANS fan solutions and the parameterized blade geometry as input. Promising results are obtained from the ML fan wake surrogate showing the capability to predicting the fan wake of a fan blade geometry at an on-design operating point.

The final paper will include a more detailed study of the sound power relation to the fan efficiency with fitted trendlines. Results from another fan stage configuration with larger diameter, NASA SDT, and other blade geometries designed based on the SDT may be considered for comparisons. Additional RANS simulations may be performed using Cadence Fidelity Turbo for more fan geometries and operating points.

Acknowledgments

This research was funded by the U.S. Federal Aviation Administration Office of Environment and Energy through ASCENT, the FAA Center of Excellence for Alternative Jet Fuels and the Environment, project 75 through FAA Award Number 13-C-AJFE-BU under the supervision of Christopher Dorbian. Any opinions, findings, conclusions or recommendations expressed in this material are those of the authors and do not necessarily reflect the views of the FAA. Additional funding has come from RTRC and the BU Mechanical Engineering Department. The development of the low-order acoustic method was funded through the Ohio Aerospace Institute on a grant from the AeroAcoustics Research Consortium. Authors would like to acknowledge Jean Fesquet and Michaël Bauerheim from ISAE-SUPAERO for providing the dataset.

References

[1] Leonard, T., Sanjose, M., and Moreau, S., "Large Eddy Simulation of a scale-model turbofan for fan noise source diagnostic," *AIAA Paper No. 2016-3000*, 2016, pp. 1–24.

[2] Bres, G. A., Wang, K., Ivey, C. B., Bose, S. T., Okubo, G., Kamatsuchi, T., and Tanaka, H., "Predictions of Fan Noise and Performance at Transonic Operating Conditions Using GPU-Accelerated Large-Eddy Simulationss," *AIAA Paper 2024-3162*, 2024.

[3] Casalino, D., Ribeiro, A., Fares, E., Nolting, S., Mann, A., Perot, F., Li, Y., Lew, P.-T., Sun, C., Gopalakrishnan, P., Zhang, R., Chen, H., and Habibi, K., "Towards Lattice-Boltzmann Prediction of Turbofan Engine Noise," *AIAA Paper No. 2014-3101*, 2014, pp. 1–30.

[4] Casalino, D., Hazir, A., and Mann, A., "Turbofan Broadband Noise Prediction using the Lattice Boltzmann Method," *AIAA Journal*, Vol. 56, No. 2, 2018. doi:10.2514/1.J055674.

[5] Hanson, D. B., and Horan, K. P., "Turbulence/Cascade Interaction – Spectra of Inflow, Cascade Response, and Noise," *AIAA Paper No. 98-2319*, 1998, pp. 688–698. doi: 10.2514/6.1998-2319.

[6] Posson, H., Moreau, S., and Roger, M., "Broadband noise prediction of fan outlet guide vane using a cascade response function," *Journal of Sound and Vibration*, Vol. 330, 2011, pp. 6153–6183.

[7] Masson, V., Posson, H., Sanjose, M., Moreau, S., and Roger, M., "Fan-OGV interaction broadband noise prediction in a rigid annular duct with swirling and sheared mean flow," *AIAA Paper No. 2016-2944*, 2016.

[8] Ventres, C., Theobald, M. A., and Mark, W. D., "Turbofan Noise Generation Volume 1: Analysis," Tech. Rep. CR-167952, NASA, July 1982.

[9] Li, N., Zhang, Y., Winkler, J., Reimann, C., Voytovych, D., Joly, M., Lore, K., Mendoza, J., and Grace, S., "Machine Learning Aided Low-Order Predictions of Fan Stage Broadband Interaction Noise," *AIAA Journal*, Vol. 62, 2024. doi:10.2514/1.J063148.

[10] Bruni, G., Maleki, S., and Krishnababu, S. K., "Deep learning modelling of tip clearance variations on multi-stage axial compressors aerodynamics," *arXiv*, 2023. doi:10.48550/arXiv.2310.04264.

[11] Fesquet, J., Bauerheim, M., Rojda, L., Bousquet, Y., and Binder, N., "Application of Deep Learning for Fan Rotor Blade Performance Prediction in Turbomachinery," *Proceedings of ASME Turbo Expo 2024: Turbomachinery Technical Conference and Exposition*, 2024. doi:10.1115/GT2024-127348.

[12] Grace, S., "Fan Broadband Interaction Noise Modeling Using a Low-Order Method," *Journal of Sound and Vibration*, Vol. 346, 2015, pp. 402–423.

[13] Menter, F., "Improved Two-Equation $k - \omega$ Turbulence Modesl for Aerodynamic Flows," Tech. Rep. 103975, NASA, October 1992.

[14] Thacker, A., and Rosa, N., "Measurements of fan efficiency at low pressure ratio," *Proceedings of 15th European Conference on Turbomachinery Fluid dynamics and Thermodynamics*, 2023. doi:10.29008/ETC2023-232.

[15] Nallasamy, M., and Envia, E., "Computation of rotor wake turbulence noise," *Journal of Sound and Vibration*, Vol. 282, 2005, pp. 649–678.

[16] Hinze, J. O., *Turbulence*, McGraw-Hill International Book Co., New York, etc., 1975.

[17] Li, N., Wachtmann, B., Ramsarran, T., Winkler, J., Reimann, A., Voytovych, D., Mendoza, J., and Grace, S. M., "Fan-stage broadband interaction noise trends," *AIAA Paper No. 2022-2884*, 2022. doi:10.2514/6.2022-2884.

[18] Li, N., Winkler, J., Reimann, A., Voytovych, D., Mendoza, J., and Grace, S. M., "Machine Learning Aided Fan Broadband Interaction Noise Prediction for Leaned and Swept Fans," *AIAA Paper No. 2023-4297*, 2024. doi:10.2514/6.2023-4297.

[19] H. M. Atassi, M. D., and Davis, C. M., "Acoustic Radiation from a Thin Airfoil in Nonuniform Subsonic Flows," *AIAA Paper No. 90-3910*, 1993.

[20] SINGER, B., BRENTNER, K., LOCKARD, D., and LILLEY, G., "SIMULATION OF ACOUSTIC SCATTERING FROM A TRAILING EDGE," *Journal of Sound and Vibration*, Vol. 230, No. 3, 2000, pp. 541–560. doi:https://doi.org/10.1006/jsvi.1999.2628.

[21] Jiang, S., Wang, Y., Yan, Z., Zhang, R., and Hu, Z., "Variations with Mach number for gust–airfoil interaction noise," *Physics of Fluids*, Vol. 35, No. 2, 2023, p. 026111. doi:10.1063/5.0139656, URL `https://doi.org/10.1063/5.0139656`.

Project 077 Measurements to Support Noise Certification for UAS and UAM Vehicles and Identify Noise Reduction Opportunities

The Pennsylvania State University

Project Lead Investigator

Eric Greenwood
Assistant Professor of Aerospace Engineering
Department of Aerospace Engineering
The Pennsylvania State University
422 ECoRE Building
556 White Course Drive
University Park, PA 16802
814-863-9712
eric.greenwood@psu.edu

University Participants

The Pennsylvania State University (Penn State or PSU)

- P.I.: Eric Greenwood, Assistant Professor of Aerospace Engineering
- FAA Award Number: 13-C-AJFE-PSU-112
- Period of Performance: March 15, 2024, to March 14, 2025
- Tasks:
  1. Experimental and computational investigations of uncrewed aircraft system (UAS) noise generation during takeoff and landing
  2. Computational investigation of rotor-airframe interaction noise
  3. Development and testing of a reconfigurable multirotor UAS
  4. UAS noise measurement and analysis of variability
  5. Development of a source separation process for distributed propulsion vehicles
  6. Noise reduction through synchrophasing
  7. Air data system integration and calibration

Project Funding Level

The ASCENT Project 077 received $500,000 awarded by the Federal Aviation Administration (FAA). The ASCENT Project 077 received $495,933 cost-sharing funding from Beta Technologies for labor, flight test support, and technical data.

Investigation Team

Eric Greenwood (P.I.), All Tasks
Kenneth S. Brentner (co-P.I.), Tasks 1 and 2
Eric N. Johnson (co-P.I.), Tasks 2 and 5
Vítor T. Valente (senior personnel), Tasks 2, 3, 5, and 6
Joel Rachaprolu (graduate research assistant), Tasks 3 and 4
Rupak Chaudhary (graduate research assistant), Tasks 1 and 2
EzzEldin ElSharkawy (graduate research assistant), Tasks 4 and 7

Project Overview

Measurement techniques for conventional propeller-driven aircraft and rotorcraft are well established. These techniques typically assume that the acoustic state of the vehicle does not change over the duration of a steady-state pass over a microphone or microphone array. UAS and Urban Air Mobility (UAM) platforms violate the steadiness assumption used in the measurement and modeling of conventional aircraft noise. Rotor or propeller states, such as the rotational speed or blade pitch angle, vary continuously and independently as the vehicle control system responds to atmospheric perturbations. Many of these vehicles use distributed propulsion systems, in which the rotors or propellers are not locked in phase. When multiple rotors or propellers operate at similar blade passing frequencies, coherent addition of the tonal noise results in lobes of acoustic radiation that are tightly focused on certain directions. As the phase relationships between the rotors change over time, the directionality of these lobes varies. Consequently, the noise cannot be modeled as a single stationary source, and no two flight passes will result in the same noise radiation pattern on the ground. Moreover, because numerous possible combinations of control inputs can result in the same flight condition, unique mapping of the overall flight condition of the vehicle to a corresponding acoustic state is no longer present. This project is aimed at developing noise measurement techniques and data analysis methods that can reduce this variability, thereby allowing for repeatable characterization of UAS and UAM noise.

Task 1 – Experimental and Computational Investigations of UAS Noise Generation during Takeoff and Landing

The Pennsylvania State University

Objective

The goal of this task is to understand the noise of small multirotor vehicles during the approach to landing and climb from takeoff. These maneuvers are relevant to a variety of proposed commercial applications for these aircraft, including package delivery.

Research Approach

The reconfigurable hexacopter developed in previous years of the project was flown at Mid-State Regional Airport (KPSB) along approach and climb trajectories over an array of microphones to understand takeoff and landing noise. The same aircraft and flight conditions were also simulated using the Penn State Noise Prediction System (NPS), which can provide additional insight into the physical mechanisms of noise generation. This system includes models of the vehicle's flight dynamics, aerodynamics, and noise generation.

Milestones

- Conducted various takeoff and landing maneuvers to understand the noise of small multirotor UAS under these conditions.
- Applied the Penn State NPS to understand how the major noise sources of the vehicle vary as the flight condition changes.

Major Accomplishments

Outdoor acoustic measurements were conducted at KPSB in Philipsburg, Pennsylvania, near the end of Runway 16.
The microphone array employed for data collection is depicted in Figure 1. The relative locations of the three microphones (used in this study) to the hover point (microphone 16 [M16]) are detailed in Table 1 along with information on their installation.

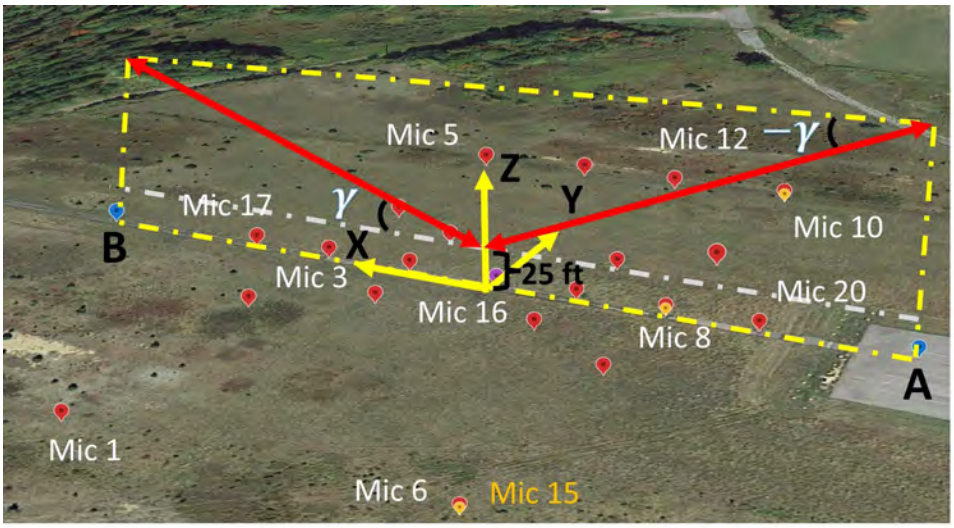

Figure 1. Overview of microphone (mic) locations and trajectory.

Table 1. KPSB microphone locations relative to microphone 16.

Microphone No.	X (ft)	Y (ft)	Installation
M3	100	0	Inverted
M8	-100	0	Inverted
M16	0	0	Inverted

Twenty-one microphones are inverted (indicated in red in Figure 1) and positioned at ground level, while the remaining three are mounted on tripods at a height of 4 ft above the ground (indicated in yellow in Figure 1, M13, M14, and M15 which are collocated with ground-plane microphones M6, M8, and M10, respectively). To study takeoff and landing maneuvers, the hexacopter takes off and ascends to a specified height above point A (as shown in Figure 1). Then it starts a descending maneuver towards the simulated landing zone (LZ), where the vehicle comes to a stop at an altitude of 25 ft above ground level. The vehicle hovers for 4 s at that position and then proceeds to start the climb maneuver, aiming for the same altitude as it started the descent, directly above point B. This complete maneuver cycle is then repeated in the reverse direction, and the entire process is repeated twice on each flight to assess variability.

Points A and B are each 250 ft away from the LZ. The altitude at points A and B varied from 50 ft to 200 ft in steps of 25 ft, thereby varying the flight path angle of the ascent and descent portions of the trajectory. The altitude at the landing point was kept at 25 ft in all cases. Additional repeats were performed for each different initial altitude. The hexacopter flies over the microphones along the direction of the flight path in the following order: M20, M8, M19, M16, M18, and M17. Negative flight path angles (γ) indicate descents, positive represents climbs, and zero represents level flight. Wind speeds during the tests ranged from 0 to 8 knots, as measured using a ground-based wind station on a 4 ft tripod. Aircraft state data and ground-based acoustic measurements are synchronized using global positioning system (GPS) time. Acoustic pressures from ground-plane inverted microphones are adjusted to a free-field equivalent by removing the pressure doubling.

A model of the large reconfigurable UAS, described in Task 2, has been developed by using the Penn State NPS. The NPS, described by Figure 2, is a simulation architecture consisting of three subsystems: (a) PSU Distributed Electric Propulsion Simulator (PSUDEPSim), (b) Comprehensive Hierarchical Aeromechanics Rotorcraft Model (CHARM), and (c) PSU-WOPWOP. PSUDEPSim is a flight simulation model for multirotor aircraft developed at Penn State. PSUDEPSim is used to compute the aircraft's flight state as it undergoes steady or maneuvering flight. PSUDEPSim can be coupled to a higher-fidelity aerodynamics model to capture the effects of interactions among components of the aircraft, such as the rotors. In the

Penn State NPS, PSUDEPSim is coupled with CHARM to form DEPSim. CHARM, developed by Continuum Dynamics, Inc., is a rotorcraft comprehensive analysis platform including a higher-order free vortex rotor wake method and a panel method for aerodynamic bodies and surfaces, such as the fuselage and wings of UAM aircraft. In addition to providing aerodynamic data in DEPSim for flight dynamic simulation, CHARM produces high-resolution rotor airloads for input into aeroacoustic propagation tools, such as PSU-WOPWOP. PSU-WOPWOP is a general-purpose Ffowcs Williams–Hawkings equation solver that uses Farassat's formulation 1A for tonal noise prediction. Broadband noise, specifically airfoil self-noise, is predicted using the semiempirical Brooks, Pope, and Marcolini (BPM) model. PSU-WOPWOP uses the time-dependent data (i.e., geometry, motion, sectional airloads, and angle of attack) generated from CHARM as inputs to compute the noise at any number of observers on the ground or moving with the aircraft.

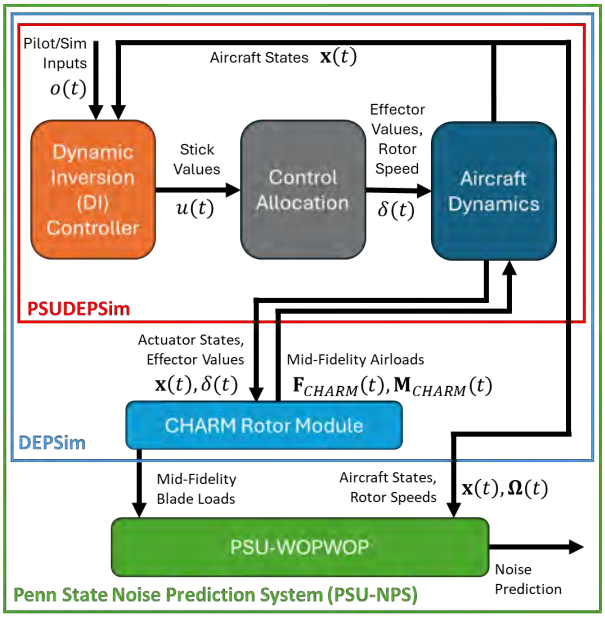

Figure 2. Overview of the different components of the PSU-NPS.

Figure 3 represents the layout of the large reconfigurable UAS developed by Penn State in a hexacopter configuration. The rotor diameter is 0.71 m, and the vehicle weight is 151 N (15.4kg [34 lb]). The front of the vehicle is aligned with the X-axis. For the current study, the hexacopter flies in an "X" configuration, with two rotors toward the front of the vehicle.

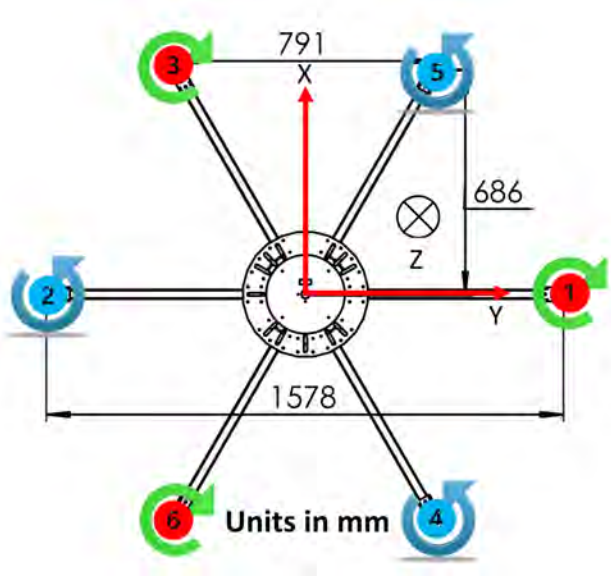

Figure 3. Schematic of the hexacopter layout.

To validate the capabilities of the current Penn State NPS, a comparison is made between the predicted and measured motor angular speed, vehicle attitude, and overall sound pressure level (OASPL) of the PSU-Reconfigurable hexacopter during both hover and forward flight at 10 mph (8.7 kts [4.5 m/s]). Motor angular speed and OASPL comparisons were presented in last year's report.

Flight Simulation Validation

Figure 4 plots the measured and predicted vehicle attitude during level flight at 10 mph. As observed, both roll and yaw angles remain close to zero (see Figure 4b) during computation with some fluctuations from zero over time in the experimental case (see Figure 4a). The experimental vehicle pitch data exhibit variations between -6.5° and -5°, while the computational model predicts a constant vehicle pitch of -5.5°.

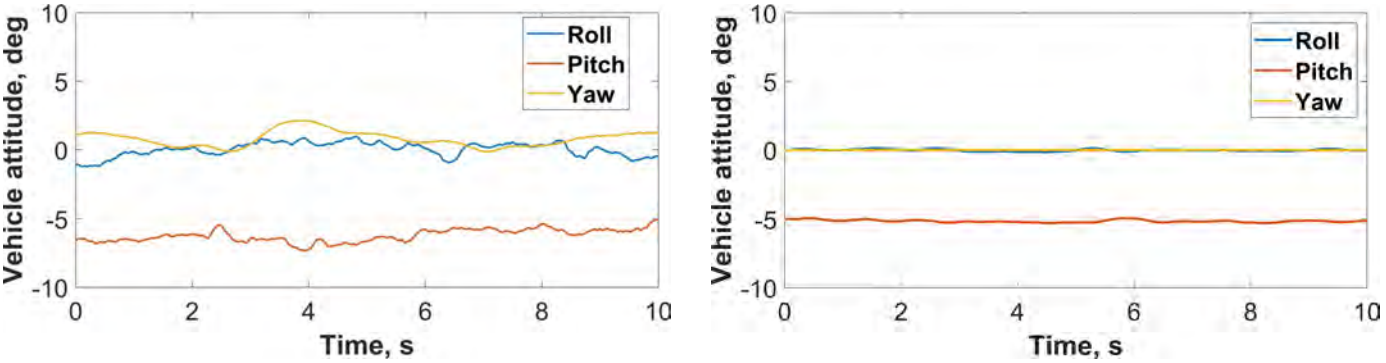

(a) Experimental.

(b) Computational.

Figure 4. Comparison of vehicle attitude between experiment and computation during level flight at 10 mph.

Experimental Results from Takeoff and Landing Maneuvers

Climb and descent maneuvers were performed at various flight path angles (γ) and forward speed (V_x). The aircraft noise directivity is defined in this paper using the emission angle (ϕ) shown in Figure 5. The emission angle is 90° when the vehicle is directly above the microphone, less than 90° when the vehicle is approaching the microphone, and greater than

90° when the vehicle departs from the microphone (see Figure 5) Sound pressure level (SPL) time history calculations are performed using 0.5-s non-overlapping segments of pressure time series data with a Hann window. Power spectral density spectrograms use 0.5-s segments of data with a 50% overlap and a Hann window. All SPLs are computed using a reference pressure of 20 μPa.

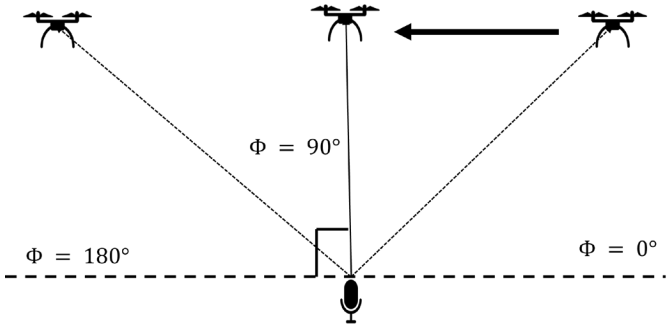

Figure 5. Emission angle nomenclature.

Figure 6 plots the variation of normalized SPL vs. emission angle for both climb and descent maneuvers. The SPL is normalized to a fixed distance of r_{ref} = 1 m (3.28 ft) using spherical spreading using Equation 1.

$$SPL_{norm} = SPL_{meas} + 20\log_{10}\left(\frac{r}{r_{ref}}\right) \quad \text{(Eq. 1)}$$

For climb maneuvers, the shallower flight path angles have higher peak noise levels than the steeper flight path angles (see Figure 6a). For climb conditions, at the lower flight path angles, the change in noise levels due to changes in the flight path angle primarily occurs at emission angles less than 90°, i.e., toward the front of the aircraft. A different variation in noise with flight path angle is seen for the descent conditions, as shown in Figure 6b. For the steepest descent conditions, a lower noise level is observed at emission angles less than 90° (i.e., when the vehicle is approaching the observer) and is higher behind the aircraft (i.e., for emission angles greater than 90°). Conversely, for the shallower flight path angles, higher noise levels are observed behind the aircraft and lower noise levels toward the front. Note that for the steepest descent angles (>20°), the speed of the aircraft was limited to avoid an excessive sink rate, as described previously, which may also contribute to the observed variations in noise for these conditions.

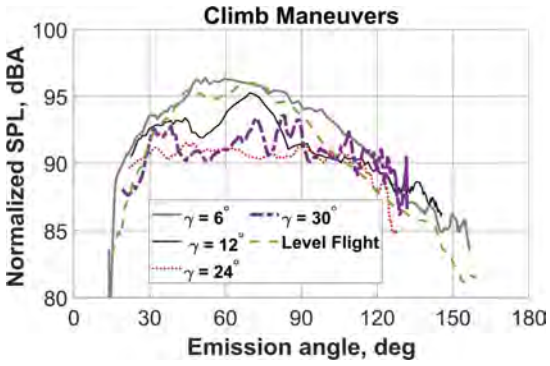

(a) Climb

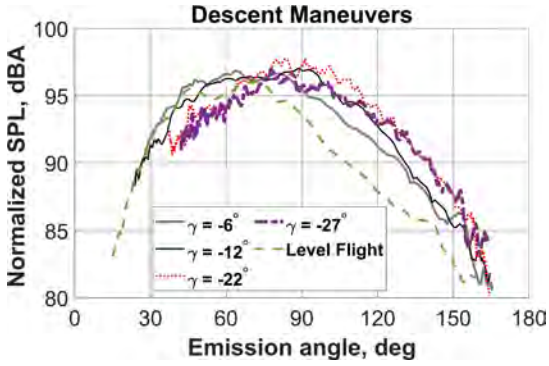

(b) Descent

Figure 6. Comparison of normalized A-weighted SPL vs. emission angle at different flight path angles for Microphone 8 during climb and descent, at a forward speed of 10 mph.

Figure 7 depicts the normalized spectrogram for climb and descent maneuvers at a flight path angle of 6°. The black dashed line represents the variation in emission angle over time, to aid in the interpretation of the results. The vehicle is above the microphone when the emission angle is 90° correlating with time t = 6 s during a climb with a flight path angle

of 6°. The tones are prominent across the entire range of emission angles and remain fairly consistent in level. Broadband noise levels are minimal for the climbing flight condition, except directly underneath the vehicle. Broadband noise occurs across a wider range of emission angles for the descending flight condition, especially ahead of the aircraft.

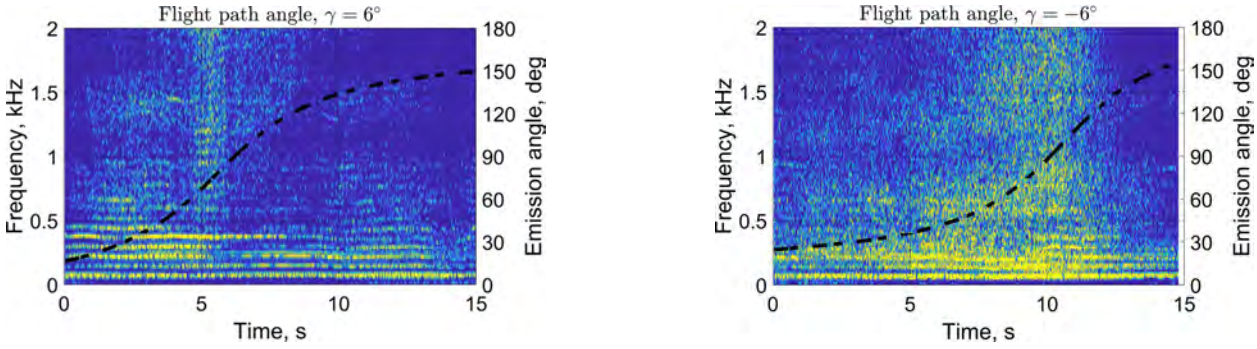

(a) Climb. (b) Descent.

Figure 7. Distance normalized spectrogram at a flight path angle of $\gamma = 6°$ for M8 during climb and descent, with a forward speed of 10 mph. Black dashed line shows emission angle.

Computational Results from Takeoff and Landing Maneuvers

Figure 8a depicts the variation of vertical force with respect to the change in azimuth within the rotor disk. Figure 8a serves as an indicator of the extent of rotor-rotor interactions during the climb maneuver. Notably, the near-zero values with small positive and negative patches suggest minimal interaction between the rotors. Figure 8b depicts the variation of vertical force with respect to the change in azimuth within the rotor disk during descent. Figure 8b reveals significantly larger regions with greater changes in vertical airloads compared to the climb maneuver. This phenomenon is attributed to the increased rotor wake interactions with the blades during descent. The red regions in Figure 8b represent areas where the vertical airloads increase with respect to the previous azimuthal positions. The wake passes close above the blade element, leading to an increase in the sectional angle of attack and thus an increase in vertical sectional airloads. Conversely, when the wake passes below the blade element, the reduction in the sectional angle of attack leads to a decrease in the vertical sectional airloads.

(a) Climb (b) Descent

Figure 8. Variations in vertical force with respect to azimuth $\left(\frac{dF_z}{d\psi}\right)$ in rotor disk during climb and descent at a flight path angle of γ = 15°, with a vehicle speed of 10 mph.

Figure 9 illustrates the variations of A-weighted SPL with the flight path angle for different noise sources at the same vehicle speed of 10 mph. The observer is positioned in front of the vehicle at a distance of 20R, and at an angle 20°below the vehicle plane. Loading noise increases during steeper descent maneuvers, while it decreases during steeper climb maneuvers. Steeper descent maneuvers result in more rotor-rotor interactions, whereas during climb, there is lesser rotor wake rolling up into the rotor with an increase in the climb flight path angle, and the wake gets convected downward,

leading to fewer interactions. Higher rotor-rotor interactions result in higher noise levels. Broadband noise (BPM self-noise) exhibits minimal variations with the flight path angle. Total noise increases during steeper descent maneuvers, and decreases during steeper climbs, primarily due to the higher loading noise during steeper descents.

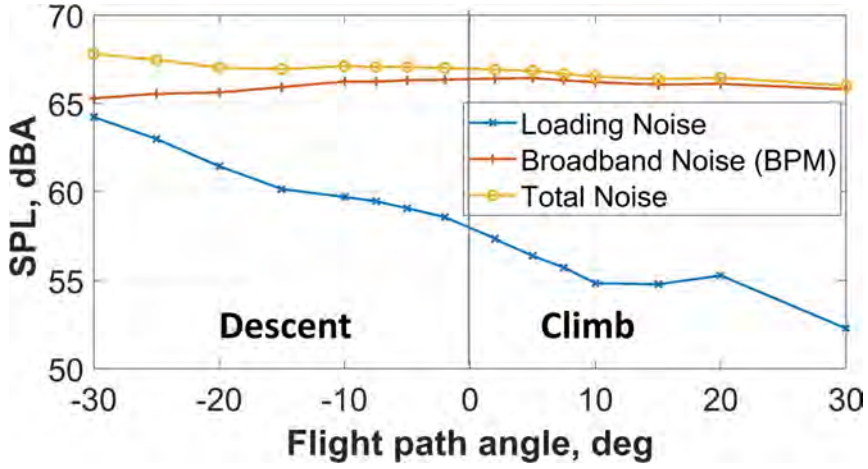

Figure 9. A-weighted SPL variation with flight path angle.

A total of 35 maneuvers with various combinations of forward speed and sink rate were conducted with the Penn State NPS. Figure 10a specifically focuses on the variations in A-weighted SPL for loading noise. The analysis reveals that loading noise decreases as forward speed increases. Conversely, a higher sink rate is associated with increased loading noise. The total noise is the sum of loading noise and broadband noise (self-noise), with broadband noise typically being the dominant contributor to the predictions. This analysis reveals a trend of decreasing total noise as forward speed increases (see Figure 10b). Conversely, lower forward speeds combined with high sink rates lead to increased total noise, while higher forward speeds with lower sink rates result in a decrease. An initial comparison of the measured and predicted results indicates that the predicted trends are consistent with the behavior observed in the measured data. Tonal noise levels are generally in good agreement; however, the predicted broadband noise levels are significantly higher than what is observed in measurements.

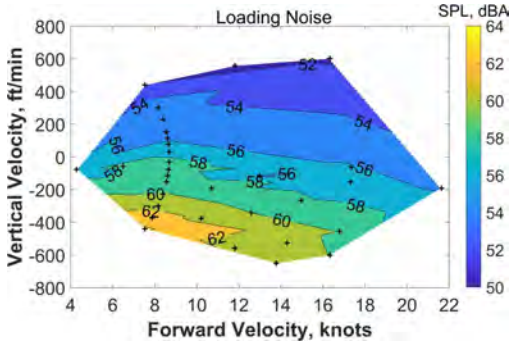

(a) Loading noise.

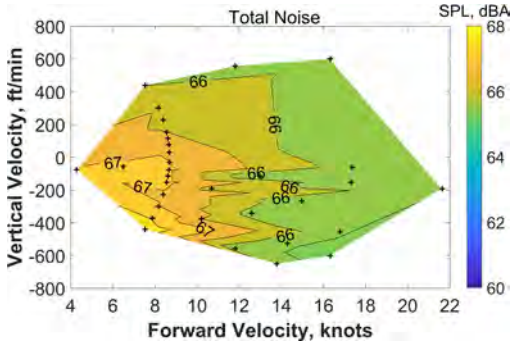

(b) Total noise.

Figure 10. A-weighted SPL variation with forward velocity and sink rate.

Publications

Chaudhary, R., Valente, V., Mukherjee, B., Jue, A., Brentner, K. S., & Greenwood, E. (2024, May 7-9). *Understanding takeoff and landing noise for small multirotor vehicles* [Conference presentation]. Vertical Flight Society's 80th Annual Forum & Technology Display, Montreal, Canada.

Outreach Efforts

- Participated in monthly meetings with the FAA and an external advisory board consisting of a dozen interested parties from government and industry.

Awards

None.

Student Involvement

Rupak Chaudhary, a Penn State Doctoral student, is the primary person responsible for conducting UAS noise predictions by using the Penn State NPS (including DEPSim, CHARM, and PSU-WOPWOP). These predictions include the flight dynamics of the vehicle based on the DEPSim multirotor flight simulation code, including the variation in rotor revolutions per minute (RPM) required to perform the maneuver. The resulting acoustic predictions are compared with experimental data from both outdoor acoustic flight test measurements and laboratory experiments conducted under controlled conditions.

Plans for Next Period

- Refine the Penn State NPS to better match in the experimental result in frequency domain.
- Conduct simulations for different maneuvers that are representative of multirotor aircraft operations to comprehensively study the generated noise and inform the development of UAS noise measurement techniques.
- Study varied vehicle configurations to understand how vehicle configuration changes influence radiated noise.

Task 2 – Computational Investigation of Rotor-Airframe Interaction Noise

The Pennsylvania State University

Objective

The objective of this task is to investigate rotor-airframe interaction noise in UAS and UAM vehicles, focusing on configurations ranging from single rotor-airframe setups to full multirotor vehicles, and to explore methods for reducing rotor-airframe interaction noise.

Research Approach

The Penn State NPS was employed to study rotor-airframe interaction noise. Initially, the noise from a single rotor-airframe structure was analyzed, focusing on factors influencing the noise and the noise directivity of individual sources. Subsequently, some design changes that could reduce this noise are explored. Finally, rotor-airframe interaction noise was examined for a full multirotor vehicle.

Milestones

- Studied single rotor-airframe interaction noise.
- Analyzed rotor-airframe interaction noise reduction methods.
- Examined rotor-airframe interaction noise for a full vehicle.

Major Accomplishments

The rotor (R = 0.355 m) and airframe (a strut with a 25.4 mm square cross-section) used in this study are the same as those employed by Task 1. The two-bladed rotor and strut were modeled in OpenVSP[1] and imported into CHARM, with a rotor-strut separation of Δ/R = 0.2 and the rotor positioned 0.793 m from the center. The CHARM/PSU-WOPWOP interface was employed to calculate airloads and noise during hover at 1875 RPM (clockwise direction). Figure 11a shows the wake geometry during hover, with the majority of the rotor wake convected downwards. The default settings were adjusted to allow wake filaments to pass through the strut, despite the model being inviscid. Figure 11b illustrates the variation of vertical forces (F_z) with respect to azimuth (ψ) within the rotor disc during hover. The greater variation in vertical airload within the rotor disc is at the azimuthal location above the strut and is attributed to the influence of the strut.

[1] OpenVSP is an open-source aircraft design tool which allows aircraft and rotor geometries to be quickly developed in terms of common engineering parameters.

(a) Rotor-strut wake structure.

(b) Variations in vertical force with respect to azimuth.

Figure 11. Single rotor-strut during hover.

The airloads and blade geometry data were used to compute the noise using PSU-WOPWOP for a single rotor-strut in hover. Figure 12a illustrates the tonal acoustic pressure time history of different noise sources for an observer positioned 20 m below the rotor. The term "isolated rotor" refers to the case where the airloads were computed without the airframe, while "rotor only" refers to the case where the airloads were computed with the strut present, but the acoustic prediction only propagates the noise from the rotor blade surfaces. Likewise, "strut only" uses the aerodynamic simulation of both the rotor and strut but only propagates noise from the strut surfaces. "Rotor + strut" includes noise radiated from both the rotor and strut.

The acoustic pressure for the isolated rotor is predicted to be a nearly sinusoidal waveform. Adding the aerodynamic influence of the strut on the rotor, in the "rotor only" case, results in a small fluctuation in the pressure near the negative peaks of the sinusoidal waveform, showing a limited influence of the strut on the rotor noise for this condition. On the other hand, the noise radiated from the strut is impulsive. Note that the predicted strut acoustics are based entirely on the fluctuating hydrodynamic pressure on the panel surface and do not fully model acoustic scattering effects. The acoustic pressure peaks when the rotor wake vortices pass over the strut, causing the peaks to occur at different times compared to the rotor alone.

Figure 12b shows the acoustic pressure contribution from the strut noise source with varying rotor-strut separation distances and orientations for an observer positioned 20 m below the rotor-strut during hover. "Square" refers to the cross-section where the flat surface faces the rotor wake, while "diamond" refers to the cross-section where the surface is angled at 45°. No significant changes between the two strut orientations are observed. However, the acoustic contribution from the strut decreases as the rotor-strut separation distance increases.

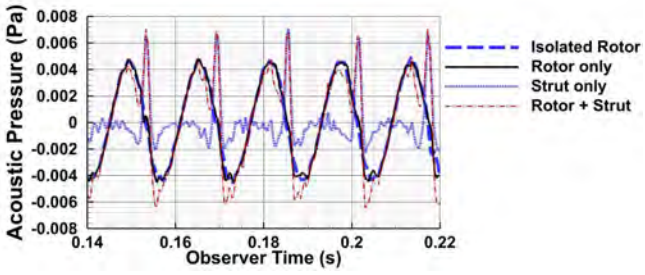

(a) Different noise source components.

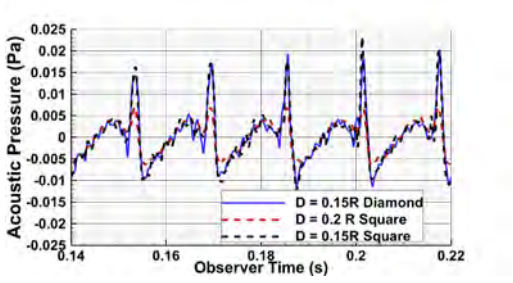

(b) Different rotor-strut distances and orientations.

Figure 12. Acoustic pressure time history for observer 20 m below rotor-strut during hover.

The acoustic noise hemisphere is used to analyze noise directivity. Figure 13a shows the lower noise hemisphere for the isolated rotor case, where the rotor is positioned 0.793 m from the center. The directivity resembles a typical loading noise

dipole pattern during hover. The rotor noise increases due to the influence of the strut (see Figure 13c). A significant directivity pattern is observed due to the presence of the strut (see Figure 13d). Figure 13b illustrates the lower noise hemisphere for the rotor and strut, with higher noise levels observed on both sides and beneath the strut.

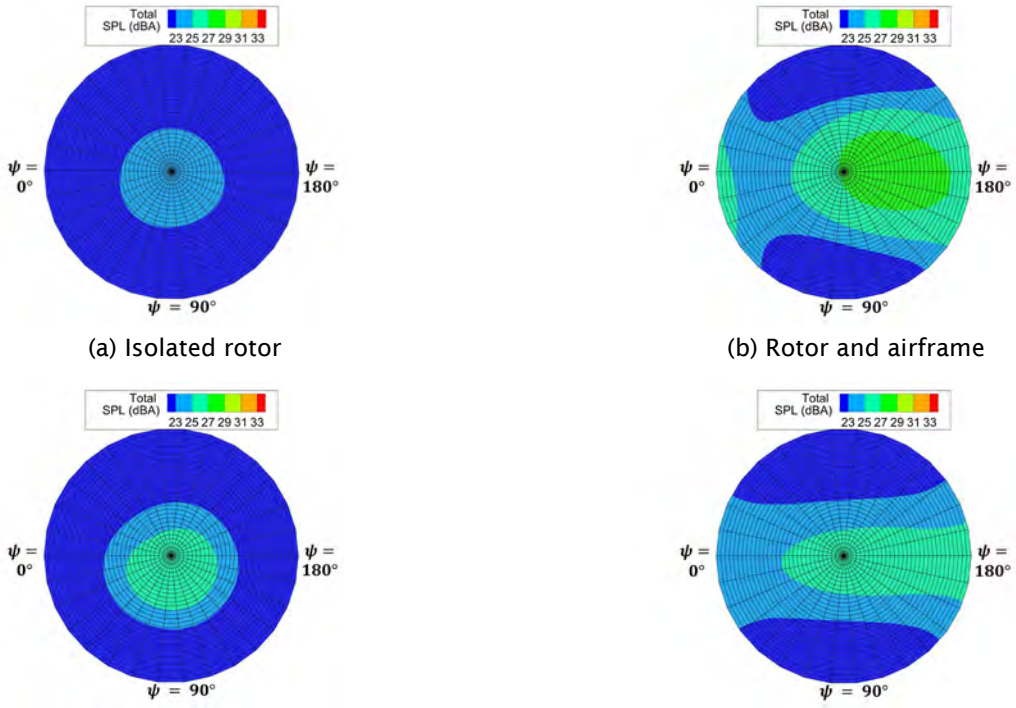

(a) Isolated rotor

(b) Rotor and airframe

(c) Rotor only

(d) Airframe

Figure 13. Stereographic projection of lower noise hemisphere of radius 50R during hover.

Noise Reduction Methods

Two strategies for mitigating rotor-strut interaction noise by changing the geometry were investigated. In the first, the strut is offset horizontally from the rotor axis, such that the blade and the strut are no longer parallel to one another during the interaction. In the second, the strut is inclined vertically, so that the distance between the rotor blade tips and the strut is higher than that between the rotor blade root and the strut. Figure 14b illustrates the noise hemisphere with the strut positioned 0.3R from the rotor's center (see Figure 14a), showing a significant reduction in noise compared to the strut aligned with the rotor's centerline. When the strut is aligned with the rotor's center, the rotor blades interact with the strut at a single azimuthal position, resulting in higher impulsive loading. In contrast, offsetting the strut causes the rotor blades to pass over the strut across a range of azimuthal angles, with the blade tip and root passing at different moments. This reduces impulsive loading and, consequently, lowers overall noise levels. Inclining the strut (see Figure 15a) increases the distance between the rotor tip and the strut, thereby reducing aerodynamic interaction and lowering pressure fluctuations in the strut. Figure 15b shows a significant reduction in noise for the strut inclined at 30° compared to the horizontal strut (see Figure 13d).

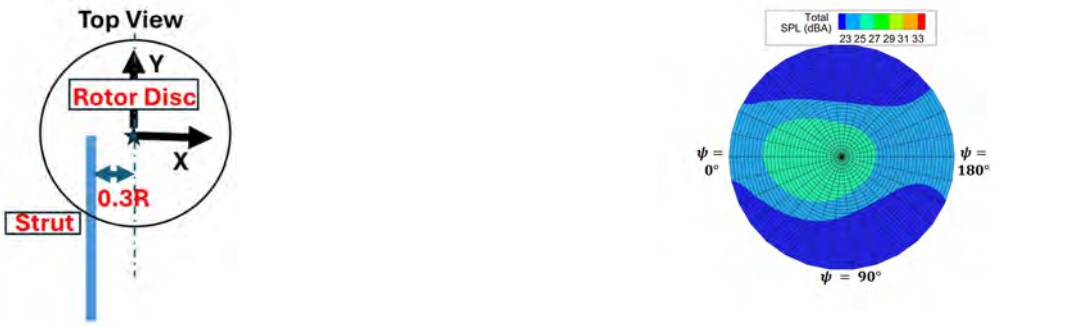

(a) Strut offset schematic.

(b) Strut 0.3R offset from center.

Figure 14. Strut offset schematic and stereographic projection of lower noise hemisphere of radius 50R during hover.

(a) Inclined strut schematic.

(b) Strut inclined at 30° from horizontal.

Figure 15. Inclined strut schematic and stereographic projection of lower noise hemisphere of radius 50R during hover.

Full Vehicle Rotor-Strut Interaction Noise

Figure 16 illustrates the wake structure of the hexacopter in hover with all rotors operating at 1900 RPM and synchronized to the same phase. The wakes generated by adjacent rotors are in close proximity, increasing the likelihood of rotor-rotor interactions.

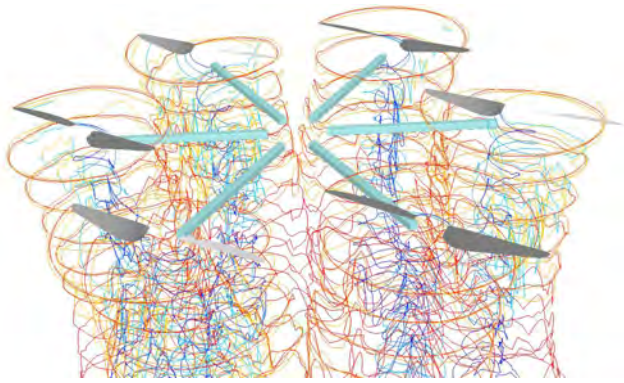

Figure 16. Hexacopter wake structure during hover.

Figure 17 illustrates the significant variation in airloads observed at azimuth angles below the airframe and in regions where the wakes of two rotors are in close vicinity.

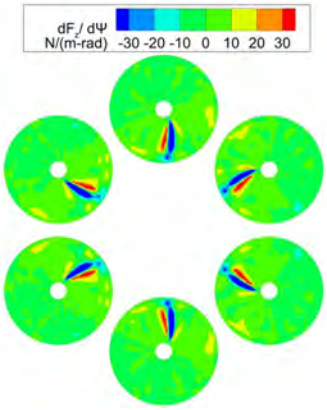

Figure 17. Variations in vertical force with respect to azimuth $\left(\frac{dF_z}{d\psi}\right)$ in rotor disk during hover.

Figure 18 presents the predicted acoustic pressure time history radiated from the different components for an observer located 20 m in front of the vehicle. As seen previously for the single rotor-strut case, the airframe generates impulsive noise with higher harmonic components, which significantly impacts the total acoustic pressure (from both the rotor and the airframe). Notably, there are two pressure peaks from the rotor and airframe during each rotor revolution.

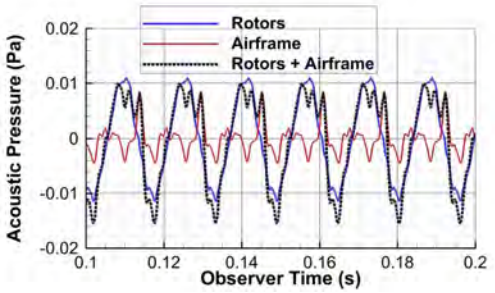

Figure 18. Acoustic pressure time history for observer 20 m infront of vehicle during hover.

Publications

None.

Outreach Efforts

- Participated in monthly meetings with the FAA and an external advisory board consisting of a dozen interested parties from government and industry.

Awards

None.

Student Involvement

Rupak Chaudhary, a Penn State Doctoral student, is the primary person responsible for conducting UAS noise predictions by using the Penn State NPS (DEPSim/CHARM/PSU-WOPWOP).

Plans for Next Period

- Continue studying noise directivity for the complete vehicle at various rotor RPMs and phase offsets,
- Further develop and implement noise reduction methods for the full vehicle.

Task 3 – Development and Testing of a Reconfigurable Multirotor UAS

The Pennsylvania State University

Objective

The objective of this task is to design and develop a multirotor UAS vehicle that can be easily reconfigured, to explore the acoustic effects of different UAS vehicle configurations and their influence on the noise measurement and data processing approaches developed in this project.

Research Approach

Small and large reconfigurable multirotor UAS aircraft architectures were developed in previous years of the project, with the smaller vehicle serving as a testbed for design concepts that were later integrated into the larger, more capable aircraft. Developmental ground and flight testing was performed before flights for acoustic data collection. These initial tests focused on the hexacopter configuration, to ensure a higher level of redundancy during initial testing. Onboard instrumentation includes a real-time kinematic Differential Global Positioning System (DGPS), an inertial measurement unit, individual rotor RPM and phase measurements, and an air data system. During the current reporting period, an additional UAS configuration was developed using the same large reconfigurable UAS architecture as the previously developed hexacopter configuration.

Milestones

- Identified acoustically significant configuration changes to be made on the vehicle.
- Performed the initial design of the vehicle and selection of sensors.
- Designed the control system.
- Conducted ground and flight testing.

Major Accomplishments

A second large vehicle using a different configuration was added to the portfolio of UAS used in this project. This new version has an X8 configuration, i.e., four arms with coaxial motors set up shown alongside with the hexacopter version in Figure 19. The X8 includes two additional motors, and two fewer arms, compared to the hexacopter. The main body of the vehicle was kept identical to the hexacopter. The landing gear height was increased in this new model to increase ground clearance for the bottom rotors on each arm. A modification to the landing gear was also included to prevent the vehicle from tilting on the ground, reducing the risk of damaging the rotors during landing.

Figure 19. Photograph of the large reconfigurable UAS currently being used in experimental acoustic measurements. On the left, the X8 coaxial configuration. On the right, the hexacopter configuration.

Improvements were also made to both vehicles over the last year, including a new radio control system, capable of transmitting in both 2.4GHz and 900MHz, was installed. Switching between the two frequencies happens automatically. This significantly improved the reliability and range for each mission. The onboard data recording system used to record RPM and phase for each rotor was improved to account for the additional motors of the X8 coaxial configuration. Data from each motor are independently acquired and correlated with the GPS time for synchronization with acoustic data collected at ground level. The standalone air data system, described in Task 7, can be exchanged between both vehicles. This system includes another onboard computer and a commercially available sonic-anemometer-based weather station to measure wind speed, wind direction, air temperature, static pressure, and relative humidity, among other parameters. The equipment is installed 44 cm above the upper rotor plane for the X8 coaxial configuration.

In addition to the new UAS described previously, the following additional upgrades have been made to the aircraft over the reporting period:

- Upgraded firmware for all motors.
- New signal distribution board, connecting each motor to the main board that reads RPM.
- New onboard data recording board supporting up to 8 motors.
- General maintenance of other systems and mechanical parts.

The gross weight of each aircraft is approximately 36 lb. The weights are similar, because while the X8 coaxial configuration has additional motors and a larger landing gear, the airframe has two fewer arms than the hexacopter configuration.

Publications

Rachaprolu, J., Valente, V. T., ElSharkawy, E., & Greenwood, E. (2024, May 7-9). *Multirotor noise source separation and characterization from ground-based acoustic measurements* [Conference presentation]. Vertical Flight Society's 80th Annual Forum & Technology Display, Montreal, Canada.

Chaudhary, R., Valente, V., Mukherjee, B., Jue, A., Brentner, K. S., & Greenwood, E. (2024, May 7-9). *Understanding takeoff and landing noise for small multirotor vehicles* [Conference presentation]. Vertical Flight Society's 80th Annual Forum & Technology Display, Montreal, Canada.

ElSharkawy, E., Valente, V.T., Rachaprolu, J.S., Greenwood, E. (2024, July 29-August 2). *Calibration of an air data system for small multirotor aircraft* [Conference presentation]. AIAA AVIATION Forum and ASCEND 2024, Las Vegas, Nevada.

ElSharkaway, E., Valente V.T., Rachaprolu, J., Greenwood, E. (2024, September 7-9). *Effect of wind on multirotor UAS noise measurements* [Conference presentation]. Quiet Drones 2024 Symposium, Manchester, United Kingdom.

Outreach Efforts

- Participated in monthly meetings with the FAA and an external advisory board consisting of a dozen interested parties from government and industry.
- Shared technical data regarding the reconfigurable multirotor UAS with investigators from the National Research Council Canada, Georgia Institute of Technology, University of Salford, Texas A&M University, and National Aeronautics and Space Administration (NASA) Langley Research Center. Discussions are ongoing regarding potential opportunities for collaboration.

Awards

None.

Student Involvement

Dr. Vítor T. Valente is primarily responsible for the design, assembly, and configuration of the UAS. Joel Rachaprolu (Penn State Doctoral student) and EzzEldin ElSharkawy (Penn State Master's student) participated in the planning and executing the flight tests and acquiring measurements. Dr. Valente served as the remote pilot in command and the safety pilot for the UAS during flight testing. Dr. Valente graduated over the Summer of 2024, but remains working on the project as senior personnel.

Plans for Next Period

- Continue use of both aircraft for acoustic data collection.
- Explore different and new maneuvers and test conditions.
- Develop and add new features and systems to the aircraft as needed to support other research tasks.

Task 4 – UAS Noise Measurement and Analysis

The Pennsylvania State University

Objective

The objective of this task is to conduct an acoustic flight test campaign to collect noise measurements for a variety of UAS vehicles under a variety of operating conditions and configurations.

Research Approach

Acoustic measurements of a flying UAS were conducted at KPSB, surrounded by the Moshannon State Forest and Black Moshannon State Park near Philipsburg, Pennsylvania. Research noise measurements were made for the large reconfigurable research UAS described in the previous tasks. The vehicle was flown through a range of operating conditions, including hover, forward flight at several speeds, climb and descent, yaw and maneuvers for calibration of the weather system onboard. For all maneuvers, the aircraft was flown at different altitudes, from near ground level to 400 ft above ground level, to evaluate the ability to scale UAS noise measurements made at one flight altitude to another, given the relatively low noise levels of small UAS. Acoustic measurements were made with Penn State's networked, battery-powered, and field-deployable acoustic data acquisition system capable of sampling at a frequency as high as 125 kHz at 24-bit resolution with subsample accurate GPS time synchronization across all nodes. A microphone array was designed to capture both spatial and temporal variations in the radiated noise. Weather instrumentation was also deployed, including measurements of wind speed, direction, temperature, pressure, and humidity, both on the vehicle and at ground level near the ground control station. The weather station used at ground level is the same make and model of the one mounted on the vehicle.

Milestones

- Collected a baseline acoustic, performance, and meteorological dataset of UAS noise measurements.
- Analyzed the data to quantify and understand the variability in UAS noise.

Major Accomplishments

Additional ground-plane microphone installations were fabricated, thereby allowing the acoustic array to be expanded to as many as 36 individual microphone locations. With these additional microphones, an expanded acoustic array configuration was developed for UAS testing at KPSB. This configuration strategically places microphones in both linear

and grid patterns to capture the acoustic field generated by an aircraft in flight, using ground noise footprint predictions made under Task 1. Linear arrays, aligned parallel and perpendicular to the expected flight path, are intended to measure the variation in noise levels along and across the flight trajectory. Additionally, the square arrangement of four microphones near the center of the array (M21–M24) is included to enhance the spatial resolution of acoustic data during maneuvers over the center of the array.

Figure 20 shows two recently used versions of the microphone array configuration. The second configuration includes two concentric circles: the inner circle has a radius of 30 ft while the outer circle has a radius of 100 ft from the center microphone; this array was deployed to measure noise during some of the airspeed calibration tests described in Task 7.

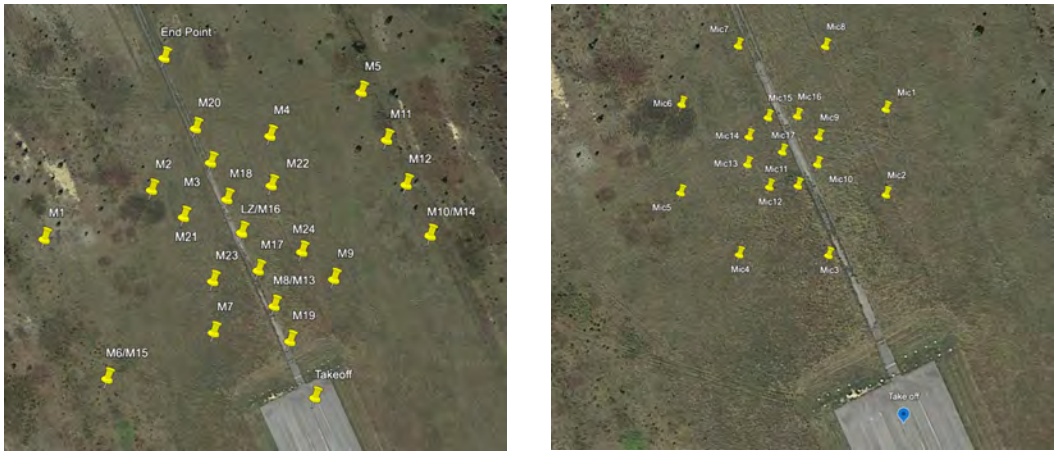

Figure 20. Two versions of the microphone array configuration flown by the UAS team.

Prior to acoustic measurements and between flight test measurements of the aircraft, measurement of the ambient noise is recorded to understand the signal-to-noise ratio (SNR) of the measurements. Figure 21 shows the ambient noise spectra overlayed with aircraft noise spectra for a hover flight condition measured at two distinct microphones. Note that the ambient and aircraft measurements were taken approximately within 30 min of one another. The aircraft hovered at an altitude of 100 ft above ground level during the measurement. The top plot is for a microphone located directly under the aircraft, and the bottom plot is for the microphone located about 200 ft horizontally from the hover point. The A-weighted SPL of the ambient is approximately 25 dBA at both locations, with the aircraft noise measuring 65 dBA at the microphone below the hover point and 54 dBA at the microphone 200 ft away from hover point.

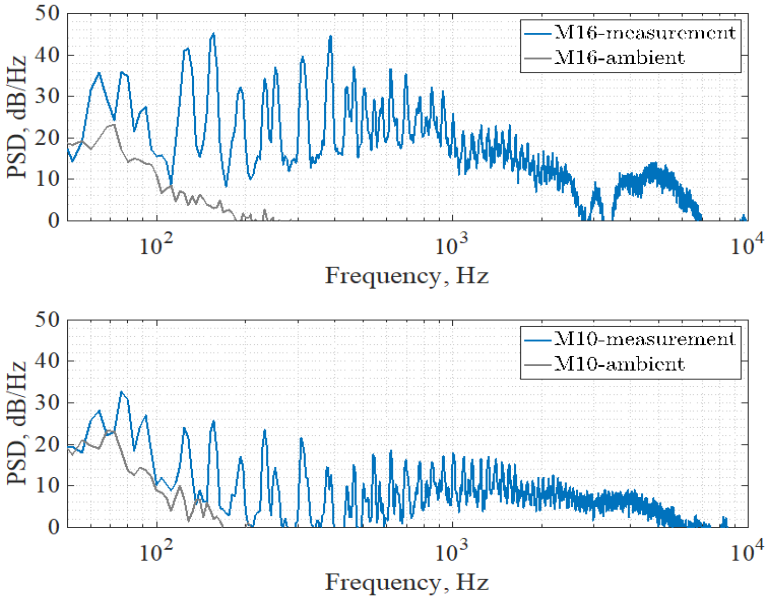

Figure 21. Acoustic spectra for ambient noise versus hovering flight at 100 ft altitude at two microphone locations, microphone below the aircraft (top) and microphone 200 ft from the hover point (bottom).

A summary of conditions flown date (including data from previous years of the project) for acoustic measurements of the large reconfigurable UAS is provided in Table 2. The range of altitude and ground speed set points flown is listed, as applicable. Multiple repeated runs were conducted for nearly every condition, often across multiple test days to collect data under varied conditions.

Table 2. Summary of conditions flown to date.

Maneuver	Description	Altitude range (ft)	Speed range (mph)
Hover	Takeoff and move toward the center of the array. Hover for approximately 30 s above center microphone at the center of the array at each altitude set point.	10–360	N/A
Flyover	Takeoff, climb to the desired altitude. Flyover in a straight line passing the last line of the microphone. Yaw and return on the same path, at the same altitude.	10–200	10–20
Ascent/descent	Takeoff and climb to the desired initial altitude. Apply a constant flight path angle toward the 25-ft altitude at the center of the array. Climb again toward the end of the array. Yaw and return, performing the same maneuver.	50–200 as initial set point	10
Yaw	Takeoff and climb to the desired altitude. Flyover condition until directly above center microphone. Yaw and return.	25–125	10–20
Air data: flyover	Takeoff and climb to the desired altitude. Successive upwind/downwind flyover pairs across a range of speeds.	100	5–20

Air data: octagon	Takeoff and climb to the first way point. Follow an octagonal circuit at constant speed.	50–100	5–10
Air data calibration	Takeoff and climb to the desired altitude. Perform upwind/downwind flyover above center line of microphones. Move to hover at the far most microphone on the right. Perform a flyover in both directions perpendicular to the first flyover. Flights at a range of speeds.	50	4-27
Flyover with added weight	6.8 lb were added to the vehicle in hexacopter configuration and a flyover condition was evaluated.	50	20
Hover with added weight	6.8 lb were added to the vehicle in hexacopter configuration and a series of hover measurements were performed.	20-100	N/A
N/A = not applicable			

The team also conducted measurements in different wind conditions (up to 12 knots) measured at the ground level. These flights aimed to provide data for the calibration of the air data system onboard of the vehicle. Conditions where the gross weight of the vehicle was increased were also evaluated. Measurements of flyover and hover conditions at different altitudes were taken with additional 6.8 lb on the vehicle in the hexacopter configuration, with the variation in OASPL shown in Figure 22.

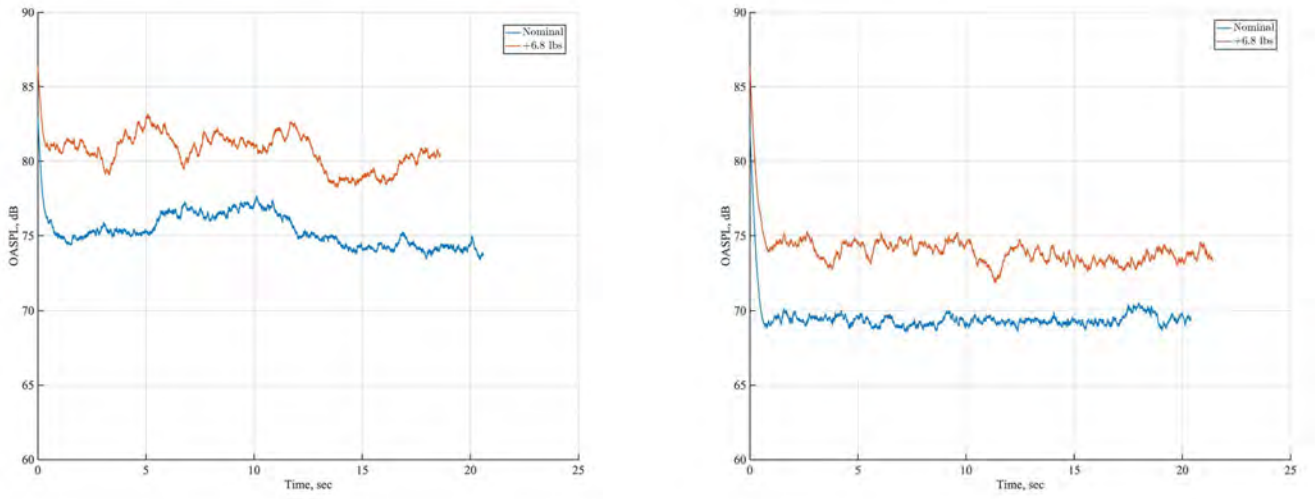

Figure 22. OASPL time histories for conditions with and without added weight at two different altitudes, a hover altitude at 40 ft (left) and a hover altitude at 80 ft (right).

An investigation was conducted to compare the performance of inverted ground plane microphones and elevated microphones in acoustic measurements, as shown in Figure 23. The goal was to analyze the SNR of each setup and identify any filtering effects that could influence the quality of acoustic data. For this study, Welch's method was applied to data collected during a controlled hover test at 50 ft above the center of a microphone array. Microphones were placed at the center and the outer ring of the array, 100 ft from the center. Both setups were evaluated under ambient conditions and during the hover test, using 20 s of data to calculate the power spectral density (PSD). The PSD for all four microphones during the hover measurement are compared in Figure 24. No corrections are applied for pressure doubling or ground effects. As expected, the elevated microphones (8 and 19, plotted in red) show a "comb filter" like interference pattern due to ground reflections, which is not present for the ground plane microphones (M1 and M17).

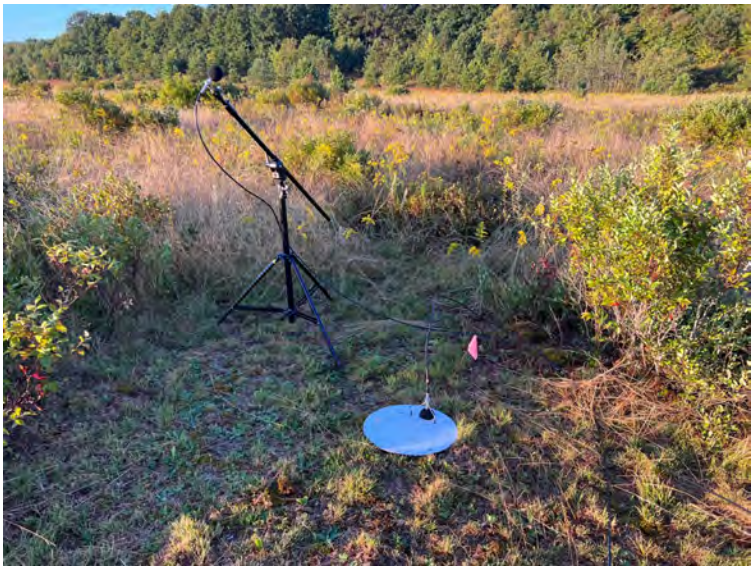

Figure 23. Photograph of collocated elevated and ground plane microphone configurations.

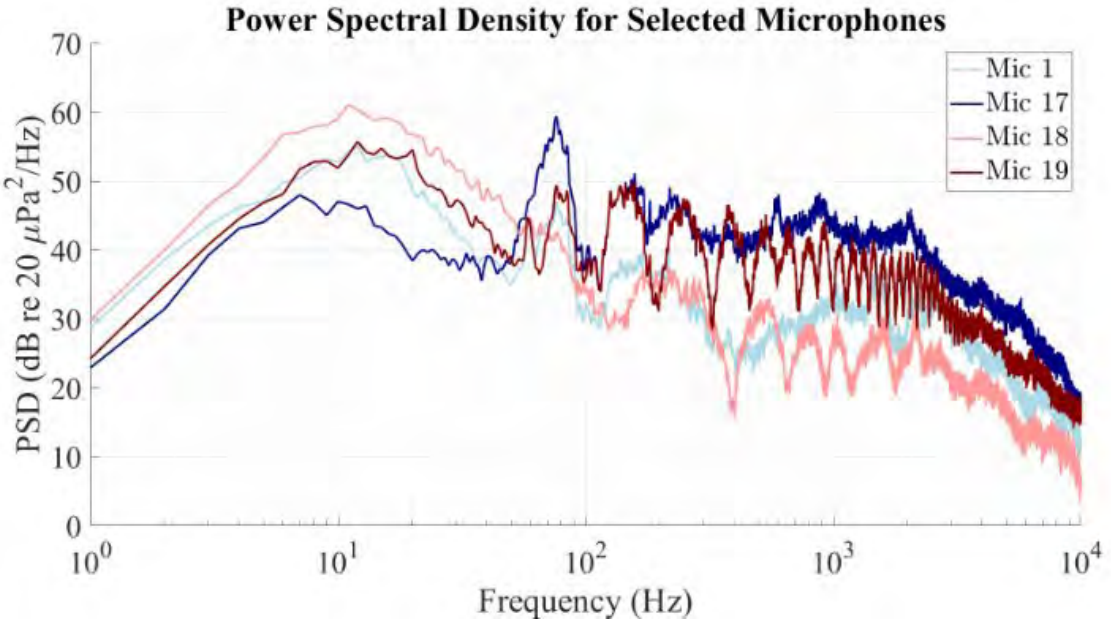

Figure 24. Acoustic spectra during hover for elevated and ground plane microphones at two locations. M17 and M1 are both ground plane microphones, with M17 located at the center of the array and M1 offset laterally by 100 ft. Likewise, M19 and M18 are both elevated microphones, located at the center of the array (M19) and offset by 100 ft (M18).

By comparing the hover spectra to the ambient spectra at each location, the SNR could be computed at each frequency. Figure 25 plots the spectra for the two microphones located at the center of the array, under the hovering aircraft. Note that the aircraft does not generate significant noise below the blade passing frequencies, clustered around 70 Hz. As such,

the SNR is poor (5-10 dB) below this frequency but increases to 20-30 dB for the first blade passing frequency, with the higher SNR observed for the inverted ground plane installation. Up to 500 Hz, the elevated microphone approaches the SNR of the ground plane microphone at the frequencies where ground reflections add constructively to the directly measured signal. Above 500 Hz, the SNR of the ground plane microphone is better (about 10 dB) at all frequencies. Similar results are seen for the offset microphone, Figure 26, except that ground reflections add constructively to the elevated microphone signal at difference frequencies, due to the different reflection geometry at this elevation angle.

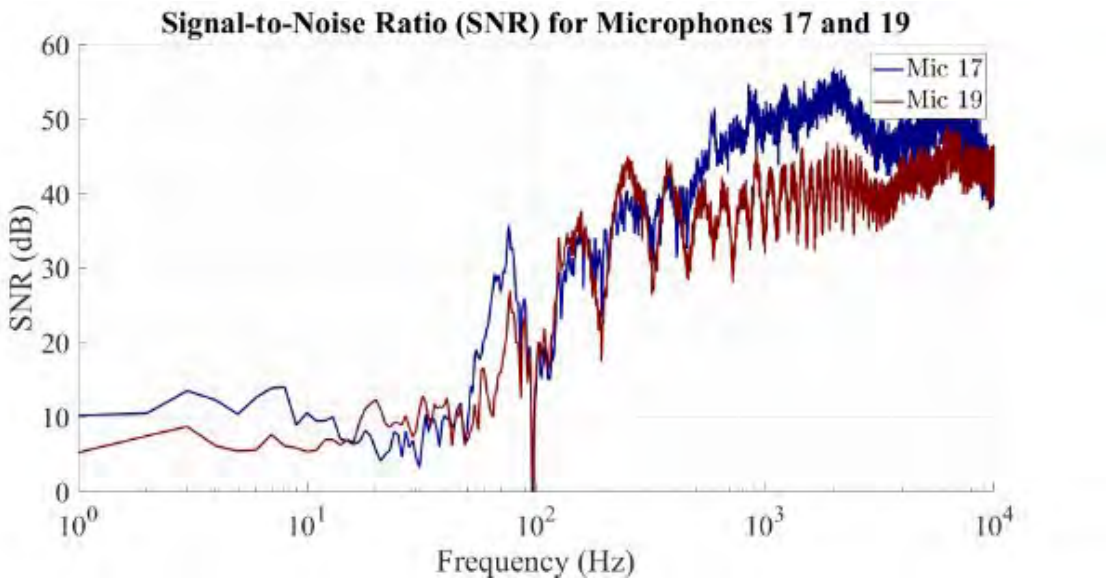

Figure 25. Signal-to-noise ratio spectra for elevated (M19) and ground plane (M17) microphones directly underneath the hovering aircraft.

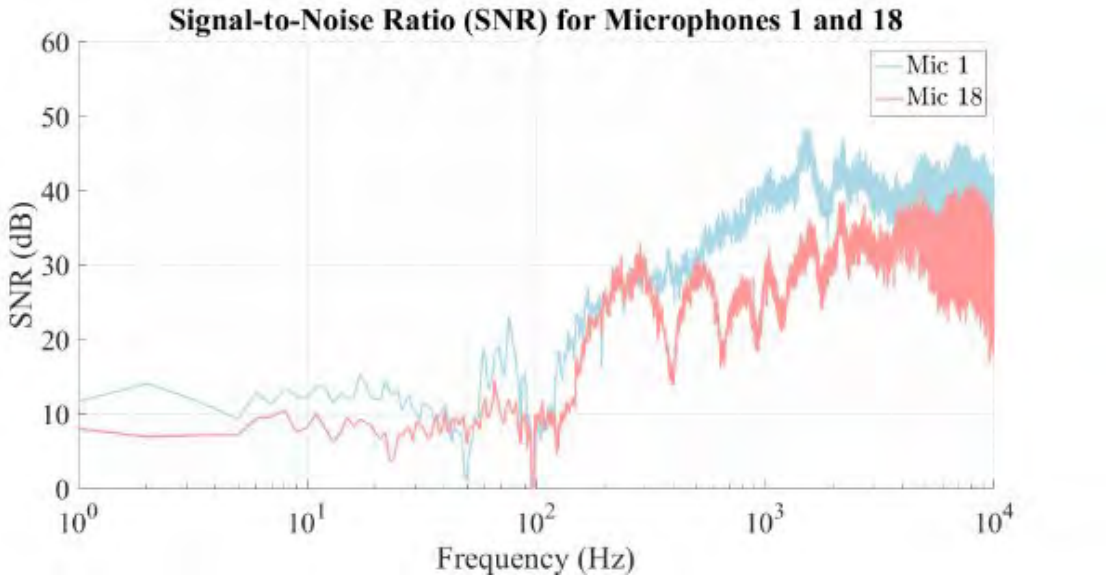

Figure 26. Signal-to-noise ratio spectra for elevated (M18) and ground plane (M1) microphones 100 ft to the side of the hovering aircraft.

Publications

Chaudhary, R., Valente, V., Mukherjee, B., Jue, A., Brentner, K., S., & Greenwood, E. (2024, May 7-9). *Understanding takeoff and landing noise for small multirotor vehicles* [Conference presentation]. Vertical Flight Society's 80th Annual Forum & Technology Display, Montreal, Canada.

Rachaprolu, J., Valente, V.T, ElSharkawy, E., & Greenwood, E. (2024, May 7-9). *Multirotor noise source separation and characterization from ground-based acoustic measurements* [Conference presentation]. Vertical Flight Society's 80th Annual Forum & Technology Display, Montreal, Canada.

ElSharkawy, E., Valente, V.T., Rachaprolu, J.S., Greenwood, E. (2024, July 29-August 2). *Calibration of an air data system for small multirotor aircraft* [Conference presentation]. AIAA AVIATION Forum and ASCEND 2024, Las Vegas, Nevada.

ElSharkaway, E., Valente V.T., Rachaprolu, J., Greenwood, E. (2024, September 7-9). *Effect of wind on multirotor UAS noise measurements*. Quiet Drones 2024 Symposium, Manchester, United Kingdom.

Outreach Efforts

- Participated in monthly meetings with the FAA and an external advisory board consisting of a dozen interested parties from government and industry.
- Provided data collected for UAS under this task to collaborators at the University of Salford and NASA Langley Research Center to enable psychoacoustic evaluations of UAS noise by using their auralization and human participant testing capabilities.

Awards

None.

Student Involvement

Dr. Vítor T. Valente, Joel Rachaprolu and Rupak Chaudhary (Penn State Doctoral students), and EzzEldin ElSharkawy (Penn State Master's student) conducted acoustic flight testing of large reconfigurable UAS and participated in analysis of the measured data.

Plans for Next Period

- Continue analysis of data collected during the current reporting period in the next period. These efforts will include the processing of all UAS flyover data into acoustic hemispheres, with an emphasis on characterizing the statistical variability of noise levels emitted over all frequencies and directions.
- Investigate of the variation in acoustic characteristics with changes in nominal flight conditions will continue, including changes in flight speed and flight path angle (i.e., climb and descent).
- Conduct a more detailed comparison of differences between data measured by using inverted ground-plane and elevated microphones, including the changes in spectral quantities and the effect on integrated noise metrics, such as the sound exposure level and effective perceived noise level.
- Collect data for a wide range of UAS configurations and operating conditions.
- Investigate a new array designs to help decouple the variations in noise over time from the variations with emission angle.
- Evaluate additional conditions with added weight for both vehicle configurations. Different variations in terms of weight added will also be evaluated.
- Repeat the evaluation of the previous conditions with the hexacopter configuration for the X8 coaxial configuration and conduct a study of the differences.

Task 5 – Development of a Source Separation Process for Distributed Propulsion Vehicles

The Pennsylvania State University

Objective

The objective of this task is to develop a process for separating the noise generated by rotors or propellers at non-constant, but potentially similar RPM values from flyover measurements of UAS and UAM vehicles. By separating noise

generated from each rotor, it may be possible to develop a more repeatable characterization of the noise of the entire aircraft.

Research Approach

The source separation process (SSP) developed in this task is mainly a two-step process that combines a time-domain de-Dopplerization procedure and Vold-Kalman order tracking filter. The flowchart in Figure 28 outlines the steps of the SSP. This approach will de-Dopplerize ground-based acoustic measurements and separate the individual rotor noise components, with the capability to extract time-varying impulsive noise. Performing this source separation in the specified time domain will enable the application of a wide range of post-processing techniques in both the time and frequency domains. Moreover, the need to characterize the acoustic directivity of these aircraft requires that the processed data be projected onto an acoustic hemisphere to illustrate the noise radiation patterns.

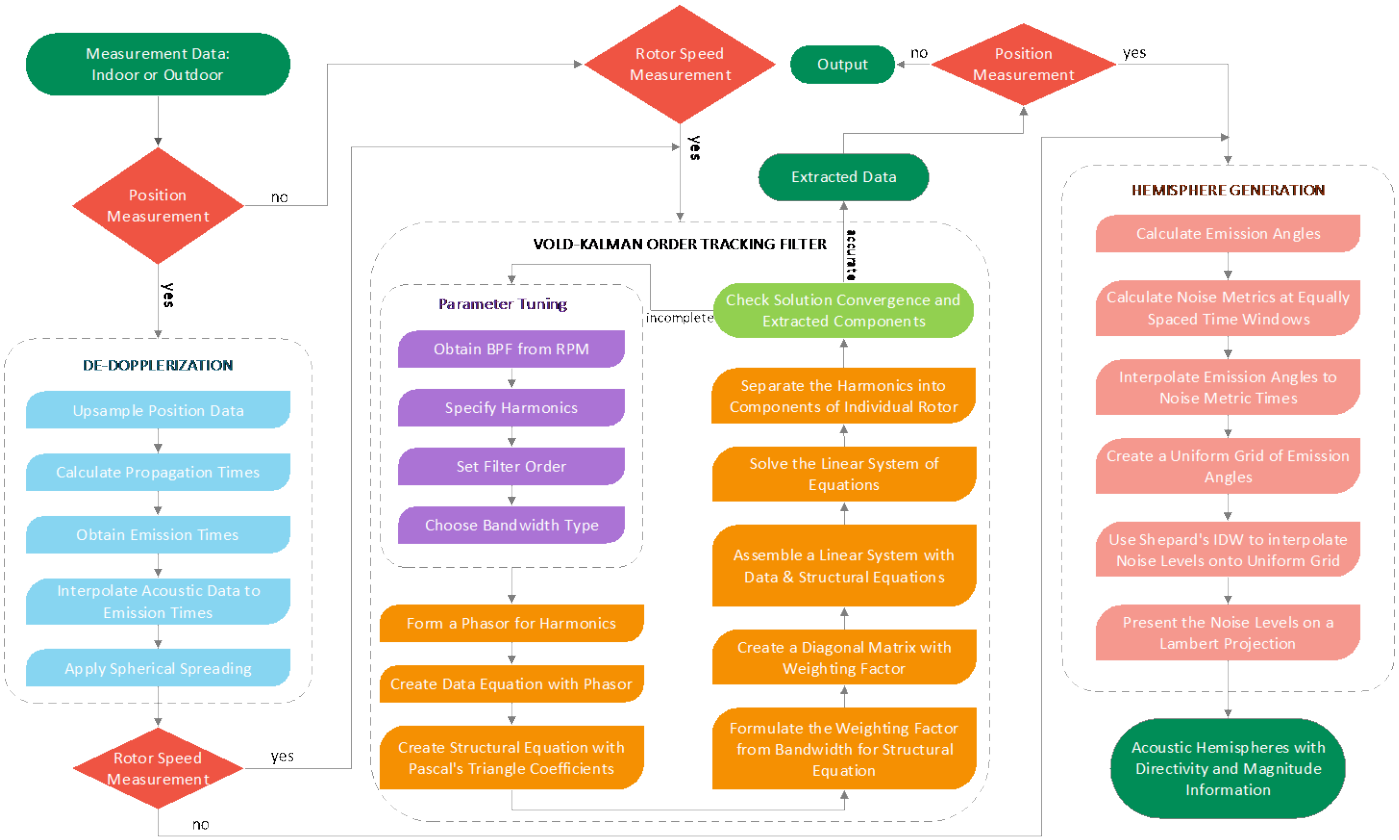

Figure 27. Flowchart of the system architecture of the SSP.
BPF: blade passing frequency. IDW: inverse distance weighting.

Each step of the SSP was verified on computational and experimental/flight test data to assess the performance. Acoustic analysis with the SSP components was also performed, in which individual steps of the SSP were isolated and applied to different datasets. The Vold-Kalman filtering technique[2] was applied to anechoic wind tunnel acoustic measurements from a coaxial rotor. A combination of de-Dopplerization and order tracking is used to analyze acoustic flight test data. This process was applied to the Bell 430 helicopter in the previous reporting period. During the current period, the process was

extended to separate the tonal noise generated by individual rotors of the large reconfigurable UAS described in previous tasks.

Milestones

- Developed a SSP for stationary acoustic measurements.
- Implemented a de-Dopplerization approach to covert non-stationary measurements to a stationary frame.
- Applied the process to simulated and measured data to evaluate the effectiveness of the separation.
- Applied the process to multirotor aircraft acoustic measurements to extract acoustic components for each rotor.

Major Accomplishments

The developed SSP was applied to acoustic measurements of large reconfigurable UAS in a hexacopter configuration. The process relies on the newly developed individual motor RPM measurement capability described and implemented on aircraft in Task 2. Prior research has identified that longitudinally grouped rotor pairings (i.e., for hexacopter the forward-, mid-, and aft-rotor pairs) operate at distinctly different rotor speeds and blade passing frequencies in forward flight conditions. The rotor numbering for the separated hexcopter data is identical to the schematic previously presented in Figure 3.

The measured time history of the rotor RPM for each of the rotors is shown in Figure 28 for a forward flight condition. The forward flight condition is performed at an altitude of 100 ft and at a speed of 20 mph. The accuracy in altitude tracking was within 6 in. and the aircraft was quite steady during the flyover. Although the condition is nominally steady, RPM variations occur over time as the vehicle responds to atmospheric disturbances.

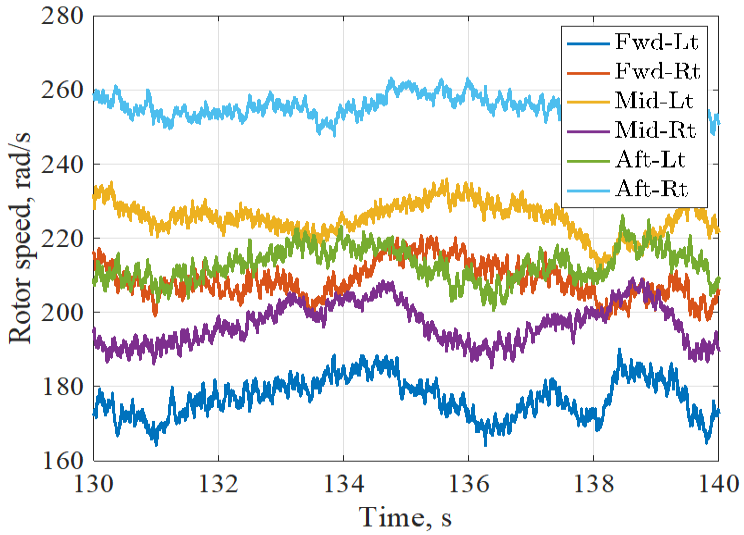

Figure 28. Rotor RPM time history in forward flight.

During the time period shown, the aircraft fly directly over the microphone. A clear difference is observed in the acoustic energy of all the individual rotors. From theory and previous research, a correlation can be expected in the trends of the rotor speed of the rotors and the tonal SPL. From Figure 28 and Figure 29, this trend is evident in the case SPL of the forward flight measurements. In addition to this, the SPL trend in the microphone measured at a different location but for the same test case shows is consistent.

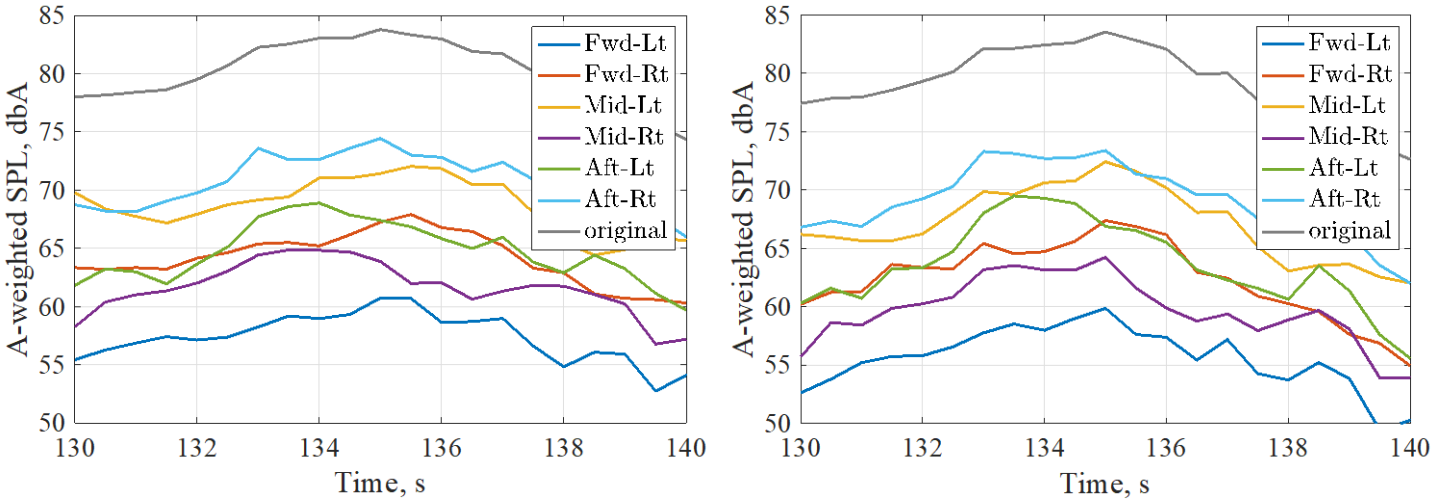

Figure 29. Separated tonal SPL of each rotor plotted with the measured SPL of the aircraft for microphone on the aircraft flight path (left) and microphone at 80 ft (~51 deg elevation) starboard side of the aircraft (right).

The acoustic data for multiple microphones were separated for a forward flight case. The separated data were processed to understand the variation of individual rotor tonal noise levels and the variation of this SPL with time. The separation was performed for the first 15 harmonics of the rotor blade passing frequencies.

Taking a look at the acoustic pressure-time histories of the separated data of each rotor shown in Figure 30, the acoustic characteristics of the different rotors are clearly distinct. The trend seen previously that higher rotor speed has higher levels is seen in the acoustic pressures (i.e., the higher RPM rotors have distinctly different waveforms with higher peak-to-peak values than the rotors with lower rotor speeds).

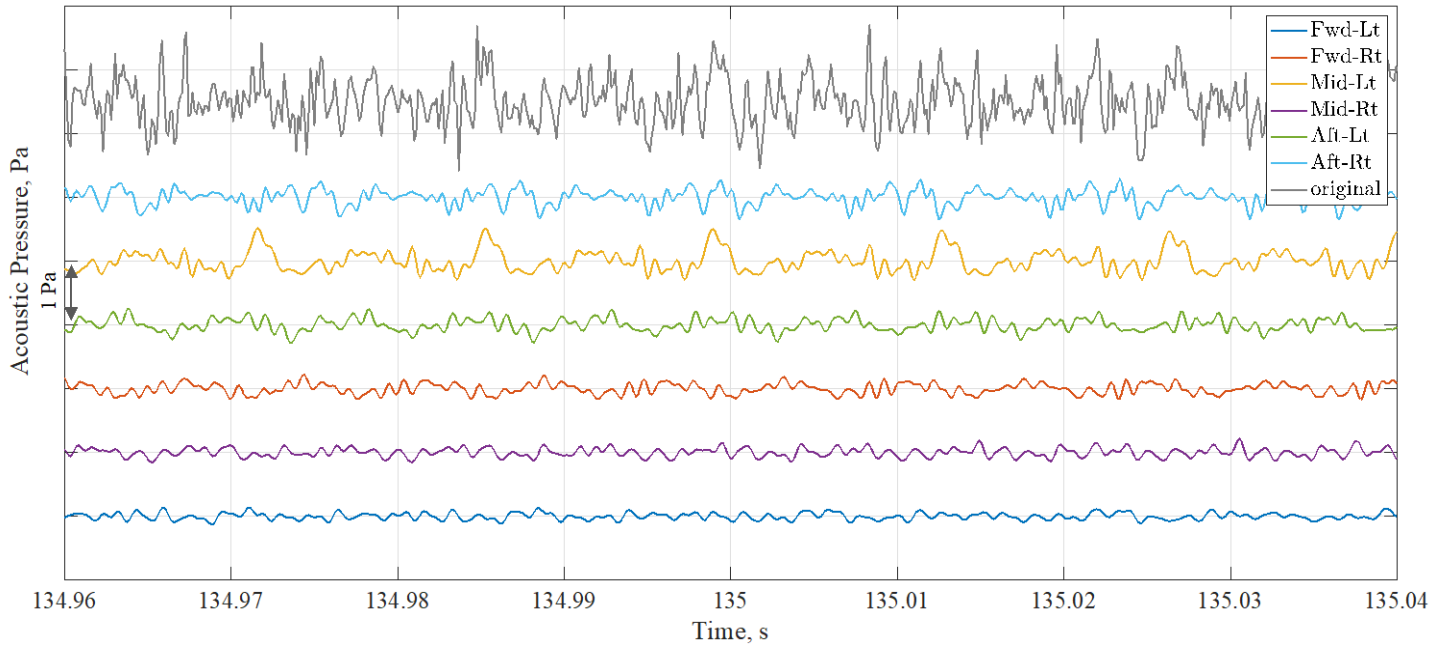

Figure 30. Separated acoustic pressure time series signals for each rotor on the aircraft over a short time window.

Publications

Rachaprolu, J., & Greenwood, E. (2024). Helicopter noise source separation using an order tracking filter. *Journal of the American Helicopter Society, 69*, 012006. https://doi.org/10.4050/JAHS.69.012006

Rachaprolu, J., Valente, V.T, ElSharkawy, E., & Greenwood, E. (2024, May 7-9). *Multirotor noise source separation and characterization from ground-based acoustic measurements* [Conference presentation]. Vertical Flight Society 80th Annual Forum & Technology Display, Montreal, Canada.

Outreach Efforts

- Participated in monthly meetings with the FAA and an external advisory board consisting of a dozen interested parties from government and industry.
- Provide the SSP developed under this task to Blue Ridge Research and Consulting, which has applied the method to isolate noise generated by an UAM vehicle.

Awards

None.

Student Involvement

Joel Rachaprolu, a Penn State Doctoral student, developed and evaluated the SSP on computational data and extended the application of the process to helicopter flight test data and UAS flight test data.

Plans for Next Period

All major milestones for the task have been completed. However, in the next period, the SSP will be applied to a wider range of conditions to validate its accuracy. Improvements will be made, as necessary, to increase the robustness of the process for future use on multirotor vehicles.

Task 6 – Noise Reduction through Synchrophasing

The Pennsylvania State University

Objective

The objective of this task is to develop and experimentally validate an active noise reduction approach for multirotor aircraft based on phase synchronization of the rotors.

Research Approach

A fully electronic rotor phase control scheme was developed for a hexacopter small UAS (sUAS) designed and built at Penn State. The process begins by characterizing the acoustics of each rotor of the vehicle by using an acoustic array installed in Penn State's flow-through anechoic chamber. These acoustic signals were processed to allow the results to be generalized to any other far-field observer location. An optimization approach was then applied to identify the rotor phase combinations that reduce the noise of the vehicle at one or more observer locations. An electronic phase controller was then used to maintain the target phase relationships between the rotors, and the radiated noise of the entire vehicle was measured and assessed.

Milestones

- Developed a phase control method based on a semi-empirical approach.
- Performed implementation and evaluation of the phase control method in real flight conditions.

Major Accomplishments

A phase control scheme was developed, implemented on a small multirotor vehicle, and validated in Penn State's flow-through anechoic chamber.

Experimental approach

The vehicle was mounted on a stand inside the Penn State flow-through anechoic chamber, as shown in Figure 31. The plate supporting the vehicle was mounted on a six-axis load cell, which was itself mounted on a gimbal allowing the orientation of the vehicle to be changed. Initially, the gimbal was locked, such that the vehicle was level with the horizon.

The microphone array inside the anechoic chamber was installed vertically and fixed on a rotating arm at approximately 60 in. from the center of the vehicle. A schematic of the microphone array is shown in Figure 32. The arm with the microphone array can rotate in azimuth over a range from 104°. The array includes eleven 0.5-in. microphones (M1–M11) and one 0.25-inch microphone (M12). The 0.25-in. microphone, physically located in between microphones M9 and M10, was installed to monitor noise at frequencies above 20 kHz.

Figure 31. Photograph of the experimental setup.

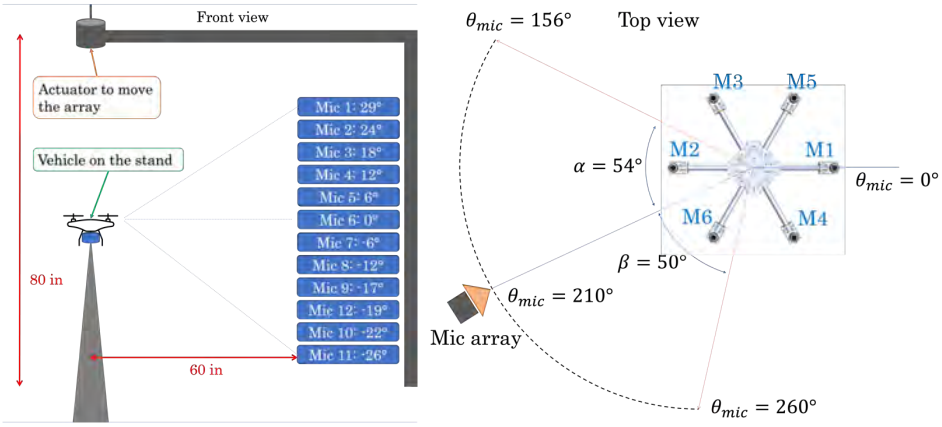

Figure 32. Microphone array configuration. Side view (left) and top view (right).

Rotor characterization and phase optimization

The rotor characterization and phase optimization processes are intended to find the lowest noise combination of relative phases between all rotors. The phases are optimized to produce the lowest overall SPL at one or more microphone locations by using a semiempirical modeling process. Each motor is characterized individually, i.e., acoustic signal is acquired for each rotor at a range of microphone array angles. The goal is to generate a single average acoustic pressure waveform for each elevation angle that is characteristic of the noise generated by the rotor over one revolution.

Figure 33 shows the result of this characterization for motor number 2. Because the acoustic signal will be offset in phase at different microphone array positions, a phase compensation offset is applied to allow the data to be generalized to other locations, according to the assumption that the microphones are in the far field of a single rotor. The phase compensation process considers two main effects: the relative distance between the rotor and the microphone, accounting for the propagation time delay; and the azimuth angle of the array relative to the rotor, accounting for the rotating sound

field generated by the rotor. By transforming these two terms into phase offsets, all measured waveforms for a single rotor can now be averaged into a single waveform representing the noise observed at an arbitrary reference location (chosen as the location of microphone six at array azimuth 180°). Similarly, these phase offsets can later be subtracted from the average single to predict the relative phase of the waveform at any other location. This characterization process was repeated for all six rotors on the vehicle.

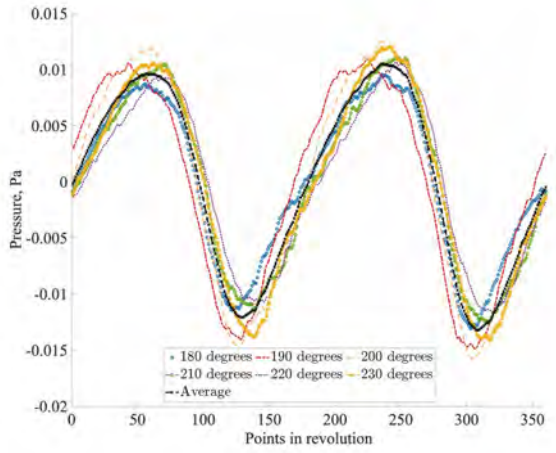

Figure 33. Result of the characterization step for motor 2.

The optimization problem aims to minimize the average mean square pressure across a subset of observers by adjusting the set of relative phases. The objective of the optimizer is to select the phase offsets that minimize the sum of the mean squared pressures at each observer location in the target region, thus reducing the average SPL in that region. Alternatively, the sum of the mean squared pressures can be maximized to determine the phase combinations that will increase the SPL in the target region. Using the previously described phase compensation process, the noise generated by each rotor can also be predicted across a range of azimuth angles. The noise of multiple rotors is then predicted for each azimuthal location assuming linear superposition of the acoustic signals associated with each individual rotor. This assumption implies that the aerodynamic, and therefore acoustic, states of the individual rotors are not significantly altered by the presence of the other rotors on the vehicle. This procedure results in a simple semiempirical prediction model for the harmonic noise of the entire aircraft in hovering flight that includes the acoustic interference effects between the rotors, as shown as an example in Figure 34. Given appropriate acoustic characterization data, the process can be repeated for other observer elevation angles and rotor speed set points.

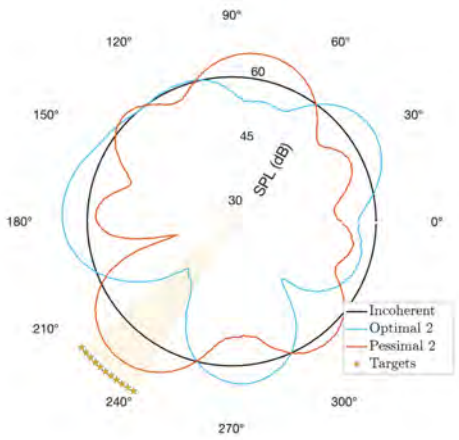

Figure 34. Result of a prediction condition for a region with ten observers from 220° to 240° for both the most attenuation (optimal) and most amplification (pessimal) cases.

Three main experimental conditions were analyzed: stationary, nonstationary and generating torques. For each one of them, different target locations, number of observers and RPM setpoints were used.

Experimental Evaluation of Stationary Conditions

Figure 35 shows the results for 1850 rad/s rotational speed setpoint with a target noise control region between 180° to 200° azimuth. The measured and predicted in-plane noise levels are plotted against the azimuth angle as a polar plot. Black lines represent the incoherent case without phase control, red lines the “pessimal” solution intended to amplify noise levels in the target region, and blue lines the “optimal” solution intended to attenuate noise in the target region. The solid lines are always representative of predictions based on the waveform characterization. Multiple lines are plotted for the measured data, showing the measured OASPL, the SPL of the first four harmonics, including the blade passage frequency (BPF) tone, and the SPL of the BPF alone.

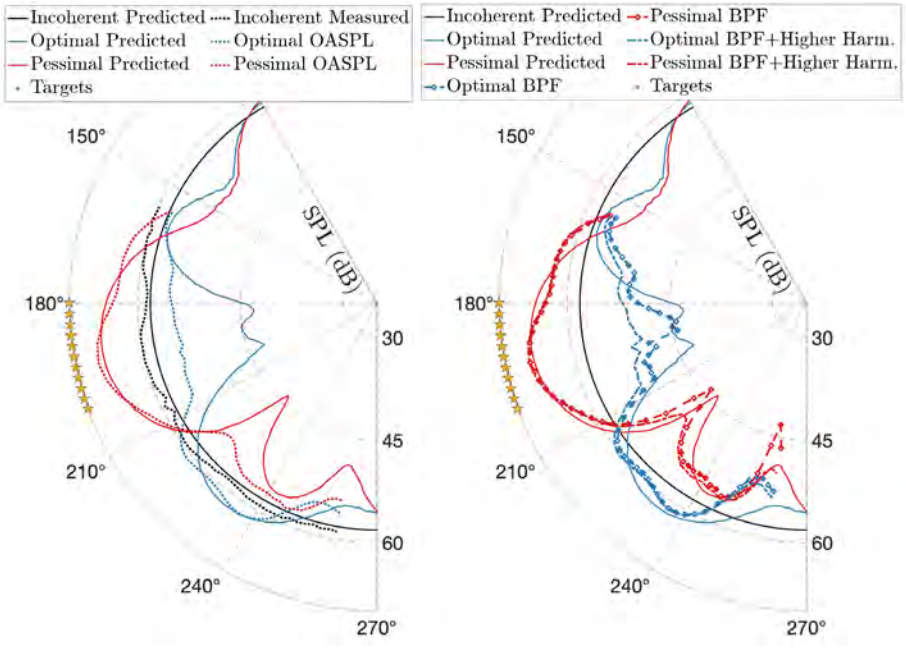

Figure 35. Comparison between measurements and predictions for an observer region between 180° to 200°.

The ability of phase control to affect the noise at elevation angles above and below the plane of the rotors was also investigated for the same condition, using measurements collected from different microphones. Figure 36 displays the measured SPL contours versus both the azimuth and elevation angles for both the optimal (left) and pessimal (right) set of rotor phases. Separate plots are provided for the OASPL, SPL over the tonal noise dominated frequency range, and BPF SPL. The red vertical lines delimit the target noise control region azimuth. The red horizontal line shows the targeted in-plane elevation angle used for the optimization.

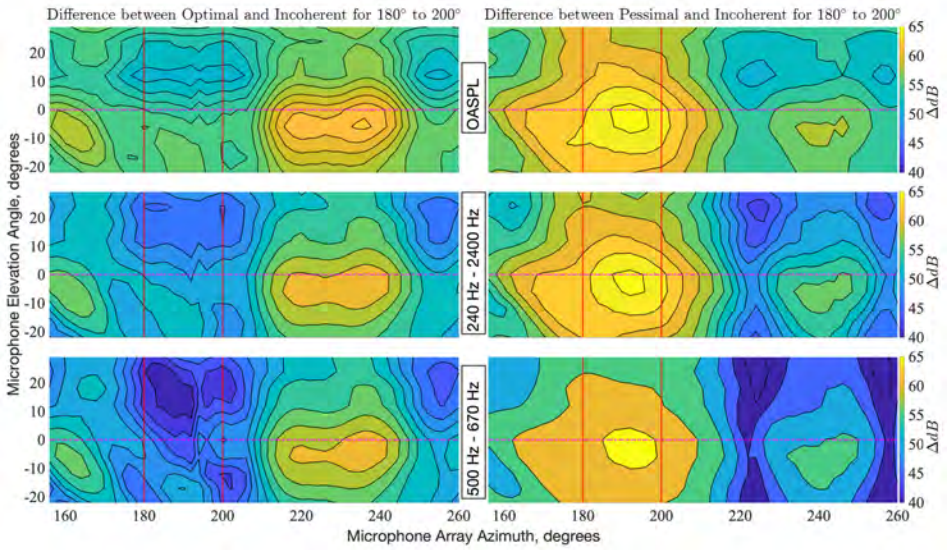

Figure 36. Measured SPL over different frequency ranges for optimal (left) and pessimal (right) phase control with a target region of 180° to 200° azimuth at 1850 rad/s.

Figure 37 plots data from the same measurement, but this time as a difference from the measured incoherent, or random phase, case at 1850 rad/s. Negative values, shown in blue, represent the amount of attenuation achieved by applying phase control, whereas positive values, shown in red, represent the amplification.

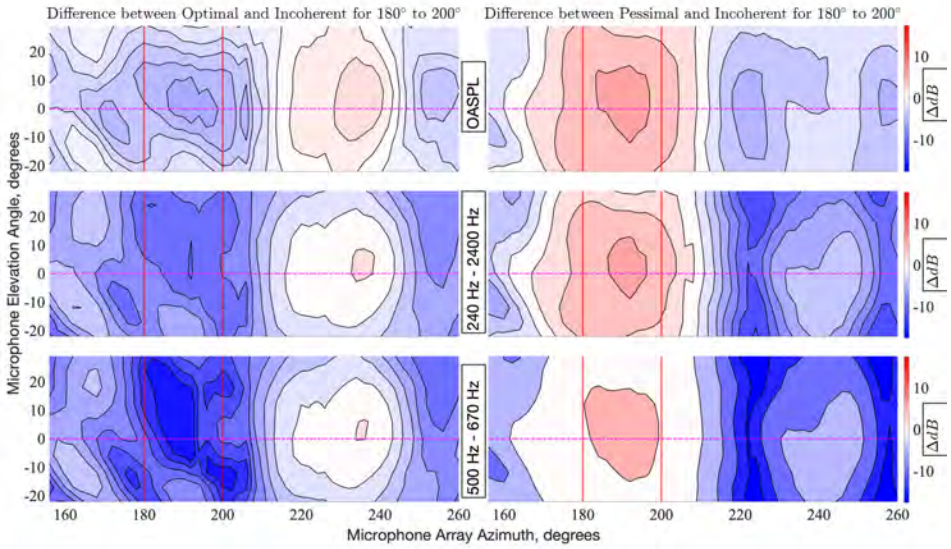

Figure 37. Measured SPL over different frequency ranges for optimal (left) and pessimal (right) phase control with a target region of 180° to 200° azimuth at 1850 rad/s.

The use of phase control to effect global, rather than directional, noise control was also investigated. In this case, the target noise control region was extended to a circle around the aircraft, with individual observers placed at 5° intervals from 1° to 356°. The rotational speed setpoint was 2000 rad/s. Noise levels are reduced below the incoherent level in nearly all directions, only slightly exceeding the incoherent level in the largest lobe. There is a good agreement between predictions and measurements across the entire measured region. This result is presented in Figure 38.

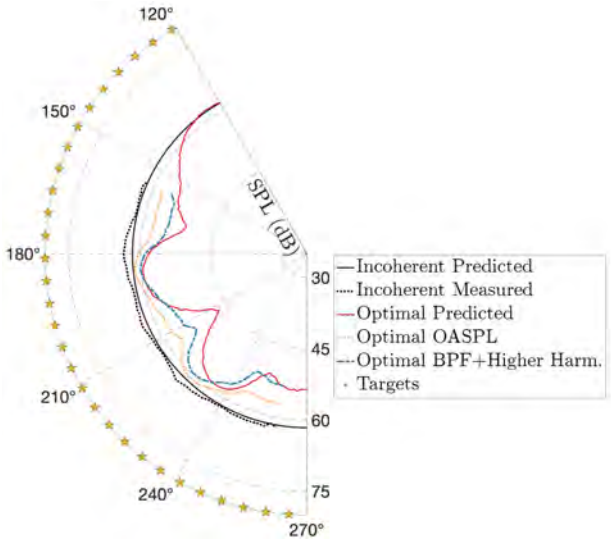

Figure 38. Tonal SPL for global noise attenuation at 2000 rad/s.

Experimental Evaluation of Nonstationary Conditions

Experimental measurements were taken to verify the method under varying observer location. Consider a case where the observer region varies from 180° to 240° azimuth under 25 s. The comparison between the predicted values for the optimal and pessimal conditions is illustrated separately in Figure 39 and Figure 40. Each figure not only shows the overall SPL but also includes two additional curves. These curves highlight the processed pressure data, which underwent time-domain analysis using a band-pass filter. The filtering was applied to isolate frequencies corresponding to either the region including the first four harmonics or only a region that comprehends the first harmonic. The plots demonstrate that the prediction for the optimal case aligns closely with the data filtered within the [500,670] Hz range. However, the data including the first four harmonics, spanning [240,2400] Hz, show some attenuation but does not fully achieve the predicted level of reduction. The unfiltered measured data deviate by approximately 9 dB from the predicted value at its minimum point.

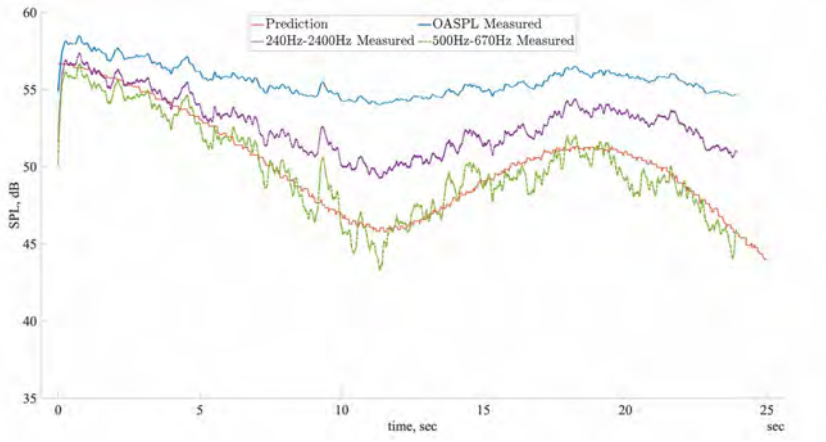

Figure 39. Comparison between predicted and measured optimal condition, with limited frequency analysis for the measured data.

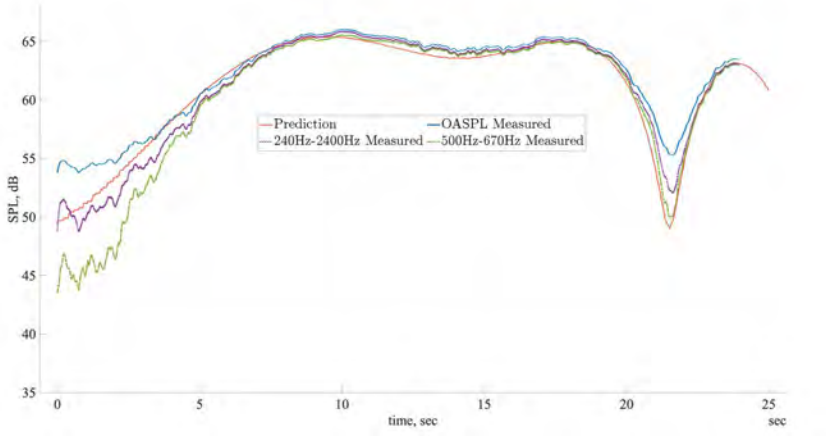

Figure 40. Comparison between predicted and measured pessimal condition, with limited frequency analysis for the measured data.

Figure 41 displays the difference between measured SPL and measured incoherent contours versus both the time and elevation angles for the optimal set of rotor phases. The vertical line shows where the microphone array was positioned. The horizontal line shows the targeted in-plane elevation angle used for the optimization. Negative values, shown in blue,

represent the amount of attenuation achieved by applying phase control, whereas positive values, shown in red, represent the amplification.

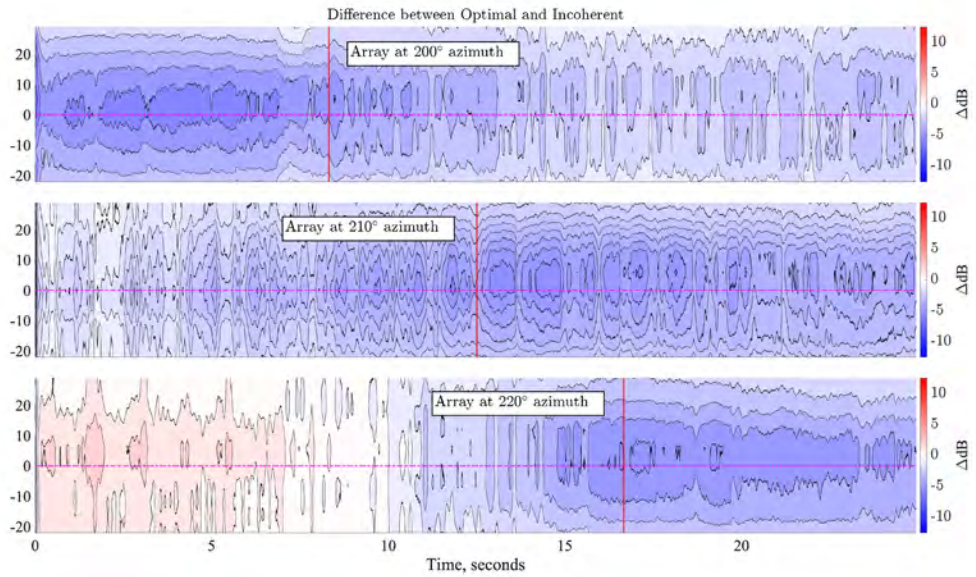

Figure 41. Change in SPL relative to incoherent over different frequency ranges for optimal at different time instants for independent runs.

Generating Torques

Another study aimed to assess the efficacy of the phase control method under conditions characterized by more dynamic variations in the RPM set point. To achieve this, the control over a single degree of freedom is examined. In addition to identifying the optimal and the pessimal condition, the incoherent case is also studied. The main difference between this condition and previous studies resides in the fact that now motors will be divided into groups, and not varying their RPM set point altogether. This grouping strategy is predicated on the similarity of RPM among rotors, ensuring that phase control remains a viable and effective method despite the differentiated angular velocity settings. The optimization algorithm was adjusted to incorporate varying RPM set points tailored to each rotor, segmenting the test duration into five distinct zones: three where all motors maintain same RPM and two where motors within a specific group have similar angular velocity. At first, all motors have the same commanded RPM; then, the initial transition is applied according to the degree of freedom of interest; shortly after, all motors return to the initial condition; then, the transition is applied in the other direction; finally, all motors return to the initial set point and remain until the end of the test.

Acoustic measurements for three runs for each of the optimal, pessimal and incoherent cases were taken when examining generating moments in the roll axis. Figure 42 presents the average sound pressure level for each distinct case. A clear distinction is observed between the optimal and pessimal phase sets, even when the roll command remains constant. Regions 1, 3, and 5 exhibit similar SPL magnitudes, indicating that the algorithm effectively manages varying RPM set points between rotors.

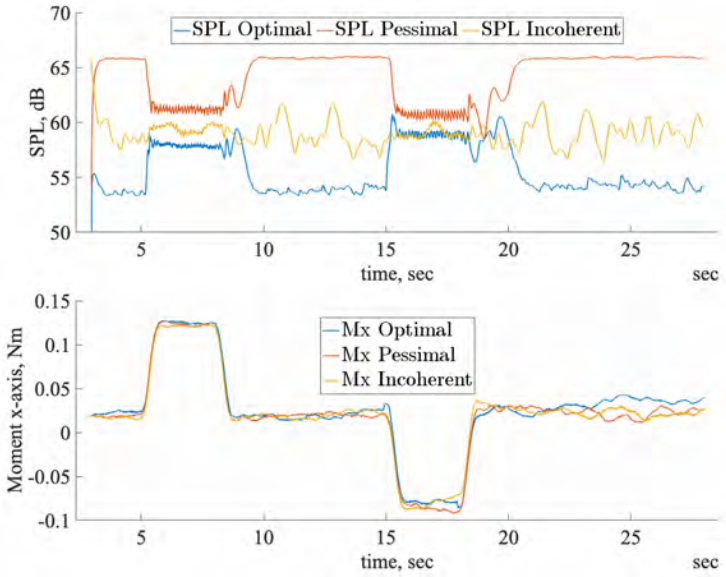

Figure 42. Average acoustic measurements for roll doublet and the averaged moment generated in the x-axis.

Combining Attitude and Phase Control for Noise Attenuation

The strategy presented in this task was taken one step further and integrated with an attitude controller, with the objective of enabling noise reductions during unsteady maneuvering flight conditions. Preliminary results shown in Figure 43 demonstrate that it is possible to achieve a certain level of acoustic attenuation and amplification while generating moments. Although the behavior is not homogeneous throughout the experiment, these initial findings still demonstrate the potential of phase synchronization in controlling acoustic emissions in rotor systems while simultaneously varying rotor RPM to control the vehicle attitude. Further investigation of the desired attitude in different conditions, in terms of amplitude and frequency of oscillation, should be conducted to refine the strategy before introducing this strategy into a real flight condition.

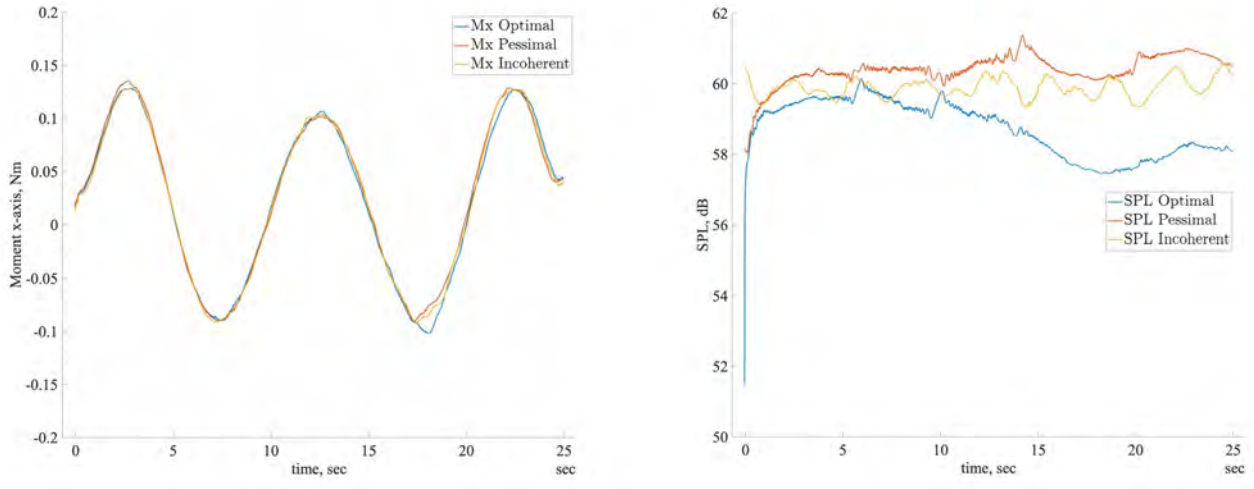

Figure 43. Preliminary results of combining an attitude controller with phase control. On the left, the moments generated in the x-axis. On the right, the correspondent SPL for the same run.

Publications

Valente, V., Johnson, E., & Greenwood, E. (2024, May 7-9). *An experimental evaluation of electronic propeller phase synchronization.* Vertical Flight Society 80th Annual Forum & Technology Display, Montreal, Canada. https://doi.org/10.4050/F-0080-2024-1194

Valente, V., Johnson, E., & Greenwood, E. (In revision). An experimental evaluation of electronic propeller phase synchronization. *Journal of American Helicopter Society*.

Valente, V. (2024). *Multiple rotor acoustic control* [Doctoral dissertation, The Pennsylvania State University]. The Pennsylvania State University.

Valente, V., Khamvilai, T., Greenwood, E., Johnson, E. (2025, May 20-22). *Combining attitude and phase control for noise attenuation on multiple rotor vehicles* [Abstract submitted]. Vertical Flight Society Forum 81, Virgina Beach, Virginia.

Outreach Efforts

- Participated in monthly meetings with the FAA and an external advisory board consisting of a dozen interested parties from government and industry.
- Shared technical data regarding the reconfigurable multirotor UAS with investigators from the National Research Council of Canada, the Georgia Institute of Technology, the University of Salford, Texas A&M University, and the NASA Langley Research Center. Discussions are ongoing regarding potential opportunities for collaboration.

Awards

None.

Student Involvement

Dr. Vítor T. Valente was responsible for preparing the vehicle setup, including developing the method, defining test points, collecting and analyzing the data.

Plans for Next Period

- Adapting the method to a modified fixed-wing vehicle UAS, followed by an outdoor flight evaluation of the effectiveness of the synchrophasing approach in reducing noise under realistic atmospheric conditions. The use of a fixed wing aircraft simplifies the control problem, as all propellers can be operated at the same RPM to generate the required net thrust, while aerodynamic control surfaces are used to balance moments. Additionally, this configuration is highly relevant to numerous electric short-takeoff and landing (eSTOL) UAM aircraft under development, as well as several eVTOL (electric vertical takeoff and landing) UAM aircraft when configured for cruise.
- Conduct an analysis inside the anechoic chamber to verify the possibility of merging an attitude controller and the phase control. This will allow for an eVTOL vehicle configuration to have some control of the noise generated while maintaining desired attitude. The results should ultimately provide recommendations for implementing the phase control method on a flying multirotor aircraft.

Task 7 – Air Data System Integration and Calibration

The Pennsylvania State University

Objective

The objective of this task is to integrate an air data system into the large reconfigurable UAS platform. This includes calibrating the air data system for inflow and installation effects, verifying the accuracy of the calibration results, and exploring how the air data can be used to better understand the effects of wind on multirotor UAS noise measurements.

Research Approach

An air data system, based on a commercially available sonic anemometer-equipped weather station, was developed and integrated into the reconfigurable UAS platform. This system measures airspeed, wind speed, temperature, pressure, and humidity, synchronized with vehicle state data using an independent GPS. Multiple flight and wind tunnel test procedures were designed to characterize aerodynamic installation effects on airspeed measurements, including calibration of the system across a range of operating conditions. Calibration methods leveraged GPS-assisted upwind–downwind flyover runs

to account for wind effects and produce corrected airspeed estimates. Additionally, the impact of angle of attack on airspeed accuracy was quantified in a controlled wind tunnel environment. The calibrated system was further validated in level, ascent, and descent flight conditions. Finally, the integrated air data system enabled an investigation of the relationship between wind, airspeed, and noise metrics during flyover tests, contributing to a deeper understanding of UAS noise behavior under varying wind conditions.

Milestones

- Integrated a sonic anemometer-based air data system into the reconfigurable UAS platform.
- Developed and validated airspeed calibration procedures to correct for aerodynamic installation effects.
- Used the air data system to characterize the aerodynamic state of the UAS during various flight conditions, including level flight, ascent, and descent.
- Investigated the effects of wind speed, airspeed, and flight dynamics on noise metrics, including the sound exposure level (SEL) and equivalent level (L_{eq}), during flyovers.

Major Accomplishments

First, a review of prior research was conducted to evaluate different options for measuring air data onboard the aircraft during flight. The multirotor UAS's small size, low flight speeds, and ability to fly in different directions makes using a conventional Pitot probe air data system on these aircraft impractical. However, atmospheric researchers have had success in recent years in using weather stations equipped with sonic anemometers on multirotor UAS to characterize meteorological data, including wind speed and direction, in the atmospheric boundary layer. During these measurements, the vehicle enters a hover over a fixed point on the ground. Prior research has shown a good correlation between measurements made on UAS and those made using fixed ground stations or light detection and ranging (LIDAR). In contrast, when the vehicle is in motion, the aerodynamic flow field around the aircraft and the weather station itself is expected to affect the local velocity measured by the probe. These aerodynamic “installation effects” are known to significantly affect airspeed measurements made on conventional aircraft with Pitot probes; however, the magnitude of installation effects on multirotor UAS is not well understood. To answer this question, and to provide high-quality air data both during and between acoustic data collection runs, a sonic anemometer-based air data system was developed and integrated into Penn State’s large reconfigurable UAS platform.

The air data system incorporates an Airmar® 150 WX weather station, including a sonic anemometer, as well as measurements of air temperature, static pressure, and relative humidity. The weather station also includes an independent GPS sensor, which is used to synchronize the measured air data in time with the vehicle’s state data. A separate onboard computer is used to record data from the weather station, as described in Task 3. The weather station and its accompanying data acquisition system were designed, fabricated, and secured to the UAS. The mounting of the weather station includes some 3D-printed parts, an 0.5-in polyvinyl chloride pipe to elevate the sensor above the rotors on the vehicle, and a case for the data acquisition system. Indoor tests have been conducted to ensure that the system is safe to fly outdoors, as well as ensuring that the height above the rotor plane is sufficient to avoid rotor inflow effects in hover. Figure 44 plots the time history of the measured wind speed during indoor hover tests. The measured wind speed is close to 0 (within 0.2 m/s), as expected, because the aircraft is in hover and isolated from outside winds.

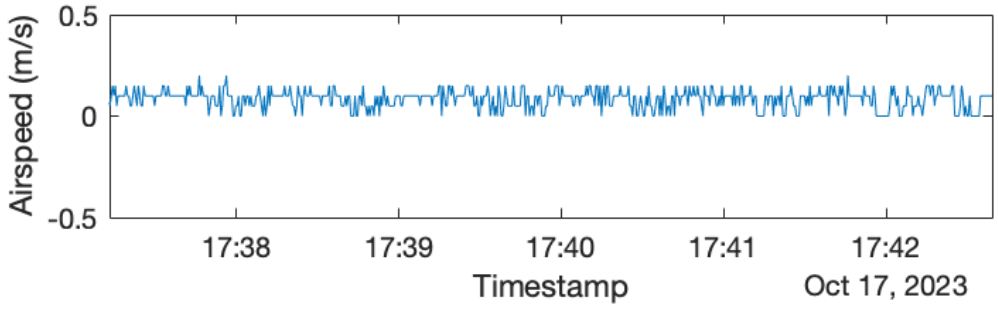

Figure 44. Wind speed time history during indoor hover testing.

® Airmar is a registered trademark of the Airmar Technology Corporation, Milferd, New Hampshire.

After indoor testing, procedures were developed to quantify the aerodynamic installation effects of the air data system, with the goal of establishing a calibration curve to correct the measured data to true airspeeds. These procedures are based on the GPS-assisted airspeed calibration methods used on conventional aircraft. The primary approach used consists of upwind and downwind flyover runs, wherein the UAS flies over the microphone array at a constant ground speed along one heading, then immediately flies back to the starting point at the same ground speed along the opposing heading. If the wind speed and direction are assumed to be constant during both upwind and downwind runs, the average airspeed measured along the flight direction should equal the constant ground speed.

Figure 45 plots the measured airspeed components during one upwind–downwind flyover pair with a constant ground speed of 7.82 m/s. The difference in airspeed between the upwind and downwind legs is caused by the mean wind over the ground; averaging the upwind and downwind airspeed measurements produce an estimate of the true airspeed accounting for wind effects. Differences between the average measured airspeed and the ground speed can be attributed to aerodynamic installation effects. This process is repeated across a range of airspeeds, to characterize how these effects change as the airspeed increases.

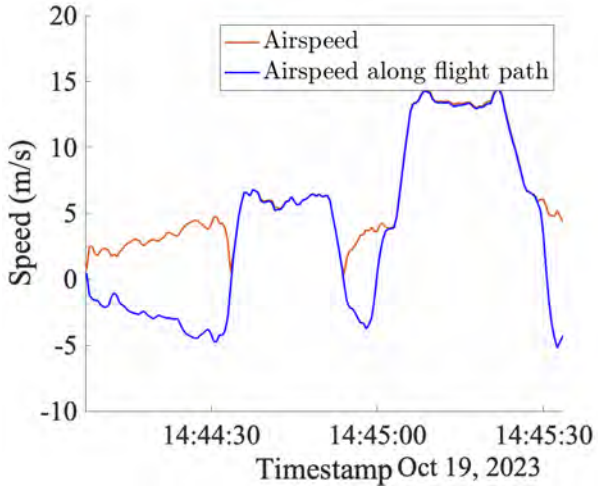

Figure 45. Measured airspeed during a flyover run at 7.82 m/s.

Figure 46 plots the measured airspeed versus the estimated true airspeed for upwind–downwind pairs from 2.24 to 8.94 m/s. This plot indicates an increasing difference between the measured and true airspeed as the speed of the aircraft increases. This error appears to grow linearly as the airspeed increases. A calibration curve characterizing this offset can be developed by fitting a linear trend line to the measured airspeed, which has a correlation coefficient, R^2, of 0.988, indicating close agreement with a linear model. The error bars shown on the measured airspeed data represent the statistical variation in airspeed measured during each run and are far smaller than the offset between the true and measured airspeeds, thereby indicating that the installation effects for airspeed measurements are significant.

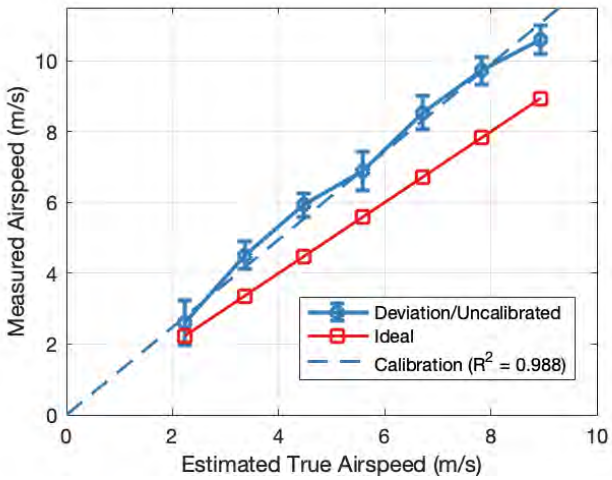

Figure 46. Measured airspeed vs. ground speed.

The calibration was validated using data from separate flight tests conducted over a shorter 61 m distance. Airspeeds from back-to-back upwind and downwind runs were corrected using the calibration curve. Comparing calibrated and uncalibrated airspeeds at a commanded ground speed of 8.94 m/s showed that uncalibrated airspeeds had a 20.2% error, which was reduced to 1.8% after calibration. This is shown in Figure 48.

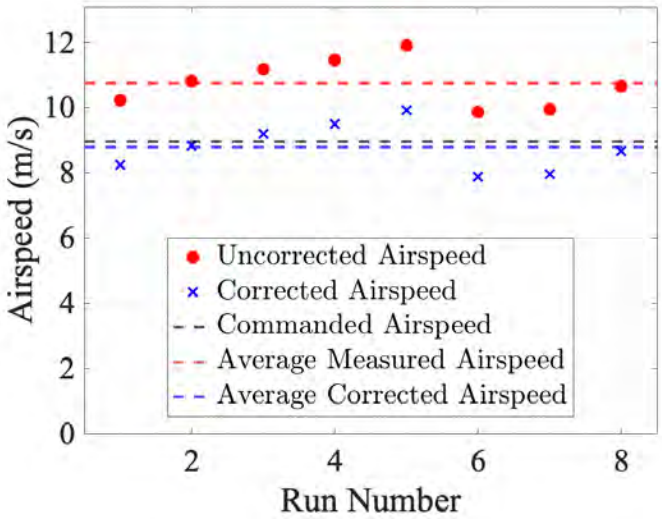

Figure 47. Comparison of calibrated and uncalibrated airspeeds across multiple level flight runs at 8.94 m/s ground speed.

Wind tunnel experiments were conducted in Penn State's Flow-through Anechoic Chamber to evaluate the effect of angle of attack on sonic anemometer airspeed measurements. The chamber, featuring a closed-circuit wind tunnel with an adjustable contraction nozzle and acoustically treated collector, was configured to provide a controlled test environment. The weather station was mounted on a custom fixture that allowed pitch and yaw adjustments, simulating a range of flight attitudes. The angle of attack varied between -25° and 25° in 5° increments, while flow speeds ranged from 1.64 m/s to 11.95 m/s, representing typical UAS operating conditions. The setup ensured accurate alignment with the open jet flow, enabling a detailed analysis of how angle of attack influences airspeed measurements. A sketch of the wind tunnel and image of the wind tunnel test set up are shown in Figure 48 and Figure 49, respectively.

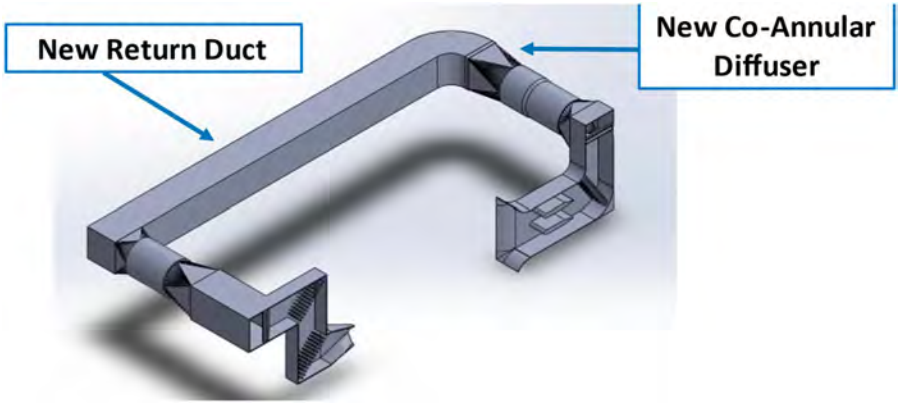

Figure 48. Drawing of the Penn State Flow-through Anechoic Chamber open jet wind tunnel circuit.

Figure 49. Weather station test setup in the Penn State Flow-through Anechoic Chamber open jet wind tunnel.

Figure 51 plots the normalized wind speed measured by the anemometer against the angle of attack. The wind speed is normalized versus the measured wind speed at zero angle of attack for all five flow speeds evaluated, to facilitate a comparison of the angle of attack effects across all flow speeds. In general, the effect of angle of attack changes is similar for each of the flow speeds, with an increase in measured wind speed for increasing angles of attack. However, the effect of angle of attack changes on the measurement is relatively small, with less than a ±10% variation in the measured wind speed across a large angle of attack range.

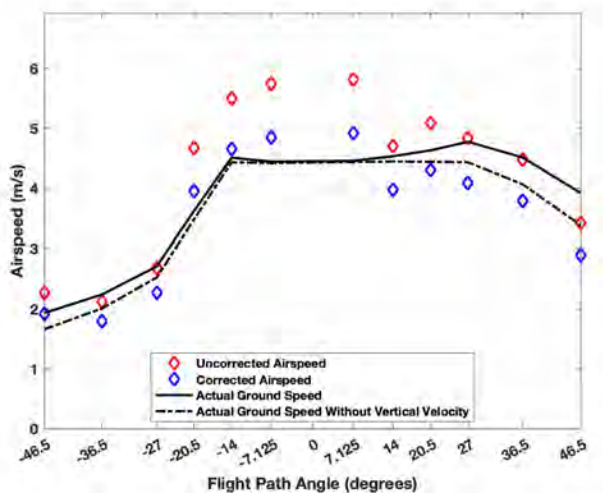

Figure 50. Comparison of calibrated and uncalibrated airspeeds across multiple ascent-descent flight runs.

In addition to level flight, the UAS was flown in ascent and descent maneuvers with flight path angles ranging from -46.5° to 46.5°, and a commanded ground speed of 4.47 m/s. At moderate angles (~14°), the actual ground speed closely matched the commanded speed, while at steeper angles, it decreased due to climb/sink rate limits. The calibration developed for level flight was applied to these data, with the results shown in . The calibrated airspeeds aligned well with the average ground speed, supporting the suitability of using the level flight calibration for these conditions. However, the two-dimensional (2D) ground speed (i.e., neglecting the vertical velocity) has slightly better agreement with the calibrated airspeed than the full 3D inertial speed at the steepest climb angles, suggesting that accuracy may be improved for these conditions by using a fully 3D sonic anemometer.

Utilizing the new integrated air data system, the effects of wind on acoustic measurements of multirotor UAS were explored. Figure 51 shows data for a sample flight run at 2 m/s, highlighting variations in ground speed, airspeed, and A-weighted SPL during the flyover. Figure 52 presents three plots showing the relationships between SEL and ground speed, airspeed, and wind speed, while Figure 53 shows similar plots for L_{eq} computed over the same “10 dB down” duration as the SEL. Together, these results demonstrate the complex interactions between wind conditions, flight dynamics, and noise emissions for multirotor UAS. They provide a foundation for optimizing noise measurement techniques and understanding the environmental impact of UAS operations.

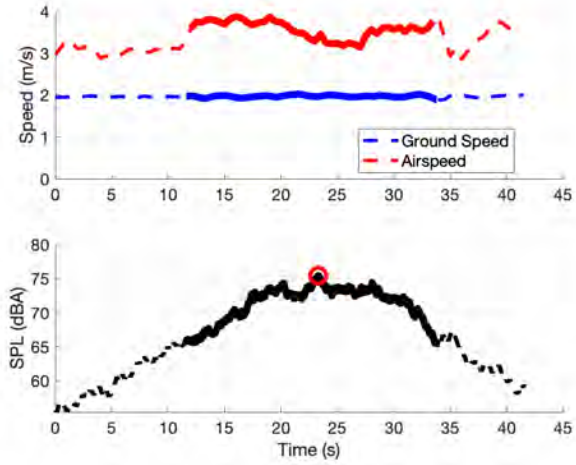

Figure 51. Flight test at 2 m/s ground speed showing ground speed, airspeed, and A-Weighted SPL time history.

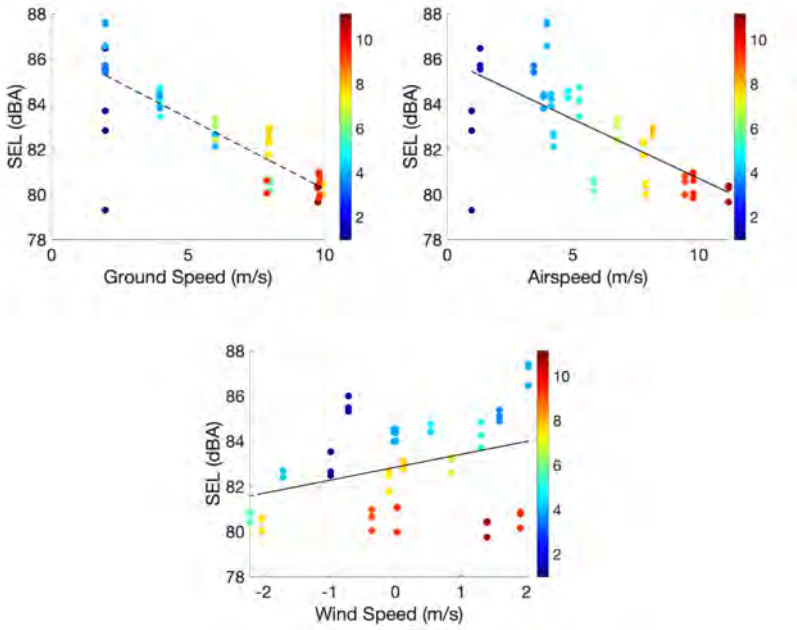

Figure 52. Relationship between SEL and ground speed, airspeed, and wind speed.

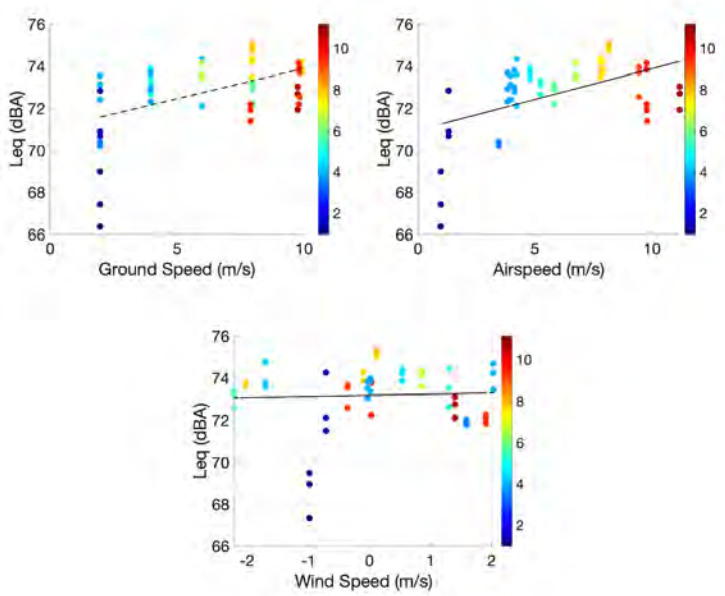

Figure 53. Relationship between Leq and ground speed, airspeed, and wind speed.

The SEL is found to decrease with increasing flight speed, whereas the equivalent level increases with increasing flight speed. This suggests that although the noise generation of the aircraft does increase as the speed of the aircraft increases. This has a smaller effect on the SEL than the reduction in duration with increasing flight speed. The correlation between SEL and ground speed is somewhat stronger than the correlation between SEL and airspeed, which can be expected since the variation in SEL is primarily due to the change in duration. However, the variation in noise metrics is generally consistent regardless of whether airspeed or ground speed is used to define the flight condition. Likewise, the wind speed was not strongly correlated with either noise metric. A weak correlation suggests that tailwinds may result in lower SEL, and headwinds increased SEL. No significant correlation was found with L_{eq}. It should be noted that the wind speeds captured in the present study varied between 0 and 2.2 m/s. Higher wind speeds are likely to have a more significant impact on the measured noise. In future flights, data will be collected under higher wind conditions, with the aim of establishing wind speed limits for repeatable acoustic data collection.

Publications

ElSharkawy, E., Valente, V.T., Rachaprolu, J.S., Greenwood, E. (2024, July 29-August 2). *Calibration of an air data system for small multirotor aircraft*. AIAA Aviation Forum and ASCEND 2024, Las Vegas, Nevada. https://doi.org/10.2514/6.2024-4393

ElSharkaway, E., Valente V.T., Rachaprolu, J., Greenwood, E. (2024, September 8-11). *Effect of wind on multirotor UAS noise measurements*. Quite Drones 2024, Manchester, United Kingdom. https://rosap.ntl.bts.gov/view/dot/79378

Outreach Efforts

- Participated in monthly meetings with the FAA and an external advisory board consisting of a dozen interested parties from government and industry.

Awards

None.

Student Involvement

EzzEldin ElSharkawy, Penn State Master's student, has been primarily responsible for the development, programing, and analysis of data produced by the onboard air data system. Dr. Vitor Valente has assisted in developing the air data system and conducted all test flights.

Plans for Next Period

- Run additional tests to improve and validate the air data system calibration methods.
- Use the calibrated sensor to conduct wind profile measurements at different heights and spatial locations throughout the test site.
- Correlate data to ground-based meteorological measurements. Measured air and meteorological data will be correlated to the aircraft flight state and acoustic data to better understand the effects of environmental conditions on noise generation and propagation.

Project 078 Contrail Avoidance Decision Support and Evaluation

Massachusetts Institute of Technology

Project Lead Investigator

Ian A. Waitz
Professor of Aeronautics and Astronautics
Vice President for Research
Massachusetts Institute of Technology
77 Massachusetts Ave, Building 3-240, Cambridge, MA 02139
(617) 253-0218
iaw@mit.edu

University Participants

Massachusetts Institute of Technology (MIT)

- P.I.: Prof. Ian Waitz
- FAA Award Number: 13-C-AJFE-MIT, Amendment Nos. 086, 100, 115, 125, 128, 133, and 139
- Period of Performance: October 1, 2021, to September 30, 2024
- Reporting Period: September 20, 2023, to September 30, 2024
- Tasks:
  1. Contrail forecast module
  2. Contrail identification module
  3. Contrail observability module

Project Funding Level

The ASCENT Project 078 received $2,250,000 Federal Aviation Administration (FAA) funding and $2,250,000 matching funds. Sources of matching funds are approximately $333,100 from MIT, plus 3rd party in-kind contributions of $469,000 from Savion Aerospace Corp., and $463,000 from Google, LLC, and $984,900 from Earth Force Technologies.

Investigation Team

Prof. Ian Waitz (P.I.), All Tasks
Dr. Prakash Prashanth, All Tasks
Dr. Florian Allroggen (co-investigator), All Tasks
Dr. Raymond Speth (co-investigator), All Tasks
Maria Paula Barbosa (graduate student), Tasks 1
Marlene V Euchenhofer (graduate student), Tasks 1, 3
Olivier Ng'weno Kigotho (graduate student), Tasks 1, 2
Louis Robion (graduate student), Tasks 1

Project Overview

Condensation trails (contrails) are the line-shaped ice clouds that form behind aircraft. These contrails and subsequent contrail cirrus are thought to account for around half of the climate warming attributable to aviation. Contrail avoidance through vertical and horizontal flight path changes is estimated to cause fuel burn penalties at the few percent level. As such, it is a potentially cost-effective way to mitigate aviation's climate impacts. However, contrail avoidance has not been demonstrated at scale, and a comprehensive toolset to support the approach has not been developed. The goal of this project is to create a contrail avoidance decision support and evaluation tool that can be trialed to optimize and evaluate

the benefits, costs, and practicality of contrail avoidance. In addition, subject to agreement with industry partners, our team will seek to test contrail avoidance in a way that has no negative implications for air traffic control or safety.

This project aims to satisfy four specific objectives: (1) to develop the capabilities necessary to predict the formation and impacts of contrails from a given flight, (2) to evaluate the financial costs and environmental benefits of deviating from that path to avoid a contrail, including uncertainty, (3) to integrate these capabilities into an operational tool that can provide near-real-time estimate of the costs and benefits of a contrail avoidance action, informed by automated, coordinated observational analysis and modeling, and (4) to evaluate the effectiveness of these tools in a safe, scientifically sound real-world experiment.

The objectives outlined above will be met through a work program that comprises the following tasks:

1. Contrail forecast module
2. Contrail identification module
3. Contrail observability module

The following tasks will be included under future periods of performance (i.e., not funded through current submission) but provide an outlook for follow-on work in future project years.

4. Airline and air traffic control integration
5. Contrail radiative impacts analysis
6. Experiment evaluation module

What follows in this document is a description of the tasks, including research progress and next steps.

Task 1 - Contrail Forecast Module

Massachusetts Institute of Technology

Objective

The goal is to develop a contrail forecast module that predicts the likelihood of persistent contrail-forming conditions in the hours before the flight, and in real time during a flight. This is intended to allow airlines to decide ahead of time to consider whether flights should use contrail avoidance, to file flight plans accounting for the best estimated cruise altitude, and to adjust in real time (subject to pilot workload and air traffic control constraints).

Research Approach

Development of the MIT Contrail Avoidance Support Tool and MIT Contrail Avoidance Support Tool-Board

MIT Contrail Avoidance Support Tool (MCAST) and its web interface MCAST-board integrate contrail detection and forecasting capabilities developed in this project to provide a nowcast of persistent contrail forming regions in near-real time. They have been improved and restructured to enable making the project open source, and MCAST-board's functionalities have been expanded to support student research. First, the integration of images from low-Earth orbit satellites equipped with higher resolution sensors (VIIRS) allows for comparison of contrail observability as a function of instrument resolution and background conditions. This has sparked new research directions which are now being explored in Task 2. Second, new tools in the web interface enable manually matching contrails to the flights that formed them. This supports human labelers in a contrail-flight matching task and led to the creation of the manual attribution dataset used to test automated contrail-flight matching algorithms in Barbosa (2024).

MCAST-board was also used during the 2023 Boeing® ecoDemonstrator campaign for nowcasting contrail forming regions and live verification of contrail formation.

Development of Contrail-Flight Matching Algorithms

Matching contrails to the flights which formed them is a necessary component for verifying a contrail avoidance strategy's effectiveness. It provides a quantitative measure, on a per flight basis, of the change in contrail length due to an avoidance action based on a given contrail-forming region forecast. It can also be used to complement these forecasts by providing additional altitude information about the detected contrails; for a contrail matched to a given flight, Automatic Dependent

® Boeing is a registered trademark of The Boeing Company, Seattle, Washington.

Surveillance-Broadcast (ADS-B) data provide the altitude of the contrail at the time it was created, an approach we investigate further in Task 2. The focus of this section is on quantifying the matching accuracy of different flight attribution approaches. This is presented in detail in Barbosa (2024), and the methodology and highlights of this study are briefly presented in this report.

Contrails are identified on a Geostationary Operational Environmental Satellites (GOES)-16 image at time (T) using the same detection algorithm as in Task 2 (Meijer et al., 2022), and FlightAware® ADS-B data from the past four hours are used to find previous aircraft trajectories. These trajectories are advected to the time (T) using ERA5[1] wind data, placing flight tracks near the contrails they would have formed had they created one. Matching between discretized flight trajectories (flight segments) and detected contrails is decided by geometrical comparisons of distance and orientation and can include altitude information as well. The weighting of these terms is determined by parameters representing the associated uncertainties with advection of the flight tracks, the computation of orientation differences, and in the contrail altitude retrievals. Different weights, some of which time-varying, were tested in a parameter sweep to find optimal values.

Accuracy is evaluated on a dataset of 180 manual labels of unique contrail-flight attributions pairs. Each contrail is tracked through portions of its lifetime leading to 1980 manual contrail-flight attributions. Though instrument limitations and labeler errors can sometimes lead to misattributions, this dataset is used as the basis of algorithm performance comparisons (see Figure 1).

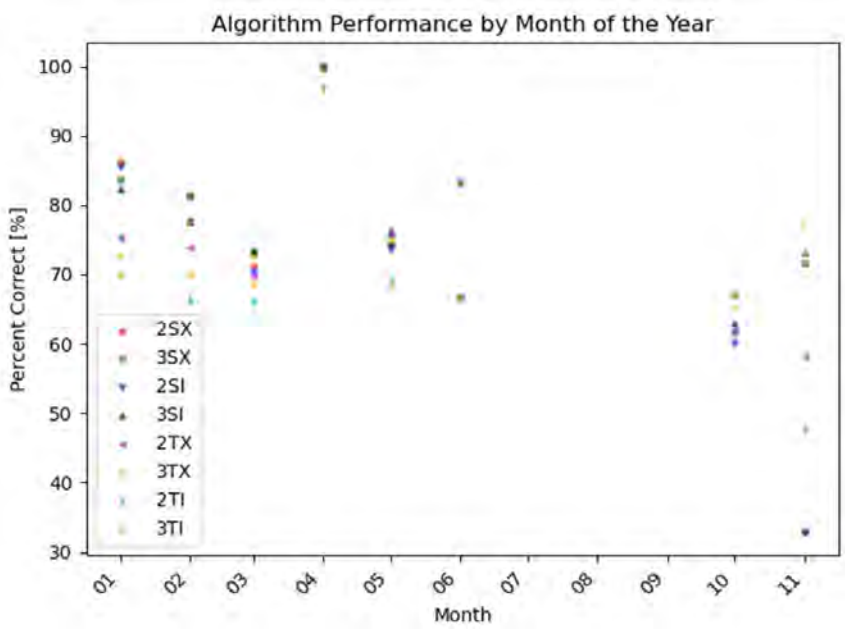

Figure 1. Comparison of different flight-matching algorithms accuracy as a function of time of year. Percent of correct is the percentage of correct contrail-flight matches by the automated algorithm compared to the manually labelled dataset. No clear trend is apparent, though November appears to be an outlier, likely due to the limited size of the labeled dataset. Different algorithms may have similar accuracies but do not necessarily match the same contrails correctly, highlighting a sensitivity that requires further studies.

On average, the highest performing algorithm is 3SX with 76.2% of contrails being matched to the correct flight. The 3SX algorithm includes information about contrail altitudes, has time invariant parameters and only includes flight segments as candidate matches for contrails. The same algorithm without the inclusion of altitude information has an accuracy of 73.3%

® FlightAware is a registered trademark of FlightAware, LLC, Houston, Texas.
[1] ERA5 is the fifth generation European Centre for Medium-Range Weather Forecasts (ECMWF) atmospheric reanalysis of the global climate covering the period from January 1940 to present. ERA5 is produced by the Copernicus Climate Change Service (C3S) at ECMWF.

meaning that at the cost of small reduction in accuracy, contrail-flight matches could be used as an independent estimation of contrail altitudes.

Updates to the Aircraft Plume Chemistry, Emissions, and Microphysics Model
Aircraft Plume Chemistry, Emissions, and Microphysics Model (APCEMM) (Fritz et al., 2020) is the primary contrail model used in this project. It is open source and undergoing active development through a collaboration between MIT, Cambridge University, and Imperial College London. New model versions have focused on improving its fidelity, particularly on the tracking of water vapor field and ice crystals during the plume's evolution. Under ASCENT Project 078 funding, work is underway to decouple APCEMM's Early Plume Model (EPM) from its mature plume evolution model. Bypassing the EPM would allow the testing of the plume evolution using different initializations, namely using in-situ data collected during the ecoDemonstrator campaign. These data comprise both direct measurements of chemical and aerosol concentrations, as well as light detector and ranging (LIDAR) cross-sections of very young contrails. It would enable testing and validation of APCEMM components for different atmospheric and fuel compositions by separating uncertainties tied to modeling of the aircraft and early plume from the later stages of the contrail's evolution.

Milestone

- Developed and evaluated the performance of automated flight matching algorithms.

Major Accomplishments

- Created a dataset of manual contrail-flight matches.

Publications

Barbosa, M. P. (2024). *Relationship between synoptic scale meteorology, aircraft parameters, and observable contrails* [Master's thesis, Massachusetts Institute of Technology]. Massachusetts Institute of Technology. https://hdl.handle.net/1721.1/157807

Kigotho, O. N. (2024). *Design of experiments for contrail avoidance* [Master's thesis, Massachusetts Institute of Technology]. Massachusetts Institute of Technology. https://hdl.handle.net/1721.1/155413

Meijer, V. R. (2024). *Satellite-based analysis and forecast evaluation of aviation contrails* [Doctoral dissertation, Massachusetts Institute of Technology]. Massachusetts Institute of Technology). Massachusetts Institute of Technology. https://hdl.handle.net/1721.1/155350

Outreach Efforts

- Poster presenting a machine learning regressor trained to estimate the altitude of contrail using geostationary imagery was presented at the American Geophysical Union (AGU) Fall 2023 Meeting (December 11-15) in San Franscisco, California. FAA support was acknowledged.
- Poster presenting an ensemble Kalman filter developed to improve the temporal consistency of contrail detection on satellite imagery was presented at the 2023 AGU Fall 2023 meeting. FAA support was acknowledged.
- Poster evaluating the performance of probabilistic algorithms which match detected contrails on GOES-Advanced Baseline Imager (ABI) imagery to the flights that formed them was presented at the European Geosciences Union General Assembly 2024 (EGU24) (April 14-19) in Vienna, Austria. FAA support was acknowledged.
- Presentation showcasing the groundwork to infer persistent contrail forming regions directly from satellite observations for use in contrail forecasting was presented at EGU24. FAA support was acknowledged.
- Presentation describing the ongoing work to couple APCEMM with the in situ measurements obtained during the 2023 ecoDemonstrator campaign was presented during the Pycontrails Workshop at the General Electric 2024 LEAD Symposium (October 1-2) in Niskayuna, New York. FAA support was acknowledged.
- Presented at the ASCENT Fall Meeting October 2024, in Alexandria VA.

Presentations

Meijer, V., Eastham, S. D., Barrett S. R. H. (2023, December 11-15). *Contrail height estimation using geostationary satellite imagery* [Poster presentation]. AGU Fall 2023 Meeting, San Franscisco, California.

Robion, L., Meijer, V., Speth, R., Eastham, S. D., Barrett S. R. H., (2023). *Enabling contrail avoidance through robust contrail detections* [Poster presentation]. AGU Fall 2023 Meeting, San Franscisco, California.

Barbosa, M. P., Barrett, S. R. H., Eastham, S. D., Meijer, V., Robion, L. (2024, April 14-19). *Evaluation of robust flight attribution algorithm for contrail avoidance* [Poster presentation]. EGU24, Vienna, Austria.

Robion, L., Meijer, V., Speth, R., Eastham, S. D., Barrett S. R. H., (2024, April 14-19). *Robust satellite-based tracking of contrail forming regions* [Conference presentation]. EGU24, Vienna, Austria.
Robion, L., Prashanth, P., (2024, October 1-2). *Contrail modelling informed by flight campaign measurements* [Conference presentation]. 2024 LEAD Symposium, Niskayuna, New York.

Awards
None.

Student Involvement
The research and communication for this task was conducted primarily by MIT graduate research assistants, Maria Paula Barbosa, Marlene V Euchenhofer, Olivier Ng'weno Kigotho, and Louis Robion.

Plans for Next Period
- Further test updated forecasts with the new contrail height estimates to evaluate the effectiveness of proposed flight deviations around contrail forming regions.
- Finish decoupling APCEMM early plume model to analyze ecoDemonstrator measurements as initialization data for the mature plume.

References
Barbosa, M. P. (2024). *Relationship between synoptic scale meteorology, aircraft parameters, and observable contrails* (Master's Thesis. Massachusetts Institute of Technology.
Fritz, T. M., Eastham, S. D., Speth, R. L., & Barrett, S. R. (2020). The role of plume-scale processes in long-term impacts of aircraft emissions. *Atmospheric Chemistry and Physics*, *20*(9), 5697-5727.
Meijer, V. R., Kulik, L., Eastham, S. D., Allroggen, F., Speth, R. L., Karaman, S., & Barrett, S. R. (2022). Contrail coverage over the United States before and during the COVID-19 pandemic. *Environmental Research Letters*, *17*(3), 034039.

Task 2 - Contrail Identification Module
Massachusetts Institute of Technology

Objective
The objective of this task is to develop a real-time contrail identification module that locates contrails both horizontally and vertically.

This module will be necessary to evaluate whether avoidance has been successful. Furthermore, this module will enable contrail forecasting approaches that are based on contrail detections, and that might prove to be more reliable for shorter lead times than approaches based on numerical weather forecasts. The initial version will use GOES satellite observations combined with an MIT-developed (under National Aeronautics and Space Administration [NASA] sponsorship) deep learning approach to identify contrails from space. Future developments could add other satellite products and ground and other observations.

Research Approach
New Contrail Height Estimation Approach
The ASCENT Project 078 team's previous height estimate approach was purely based on remote sensing and relied on the radiances of pixels that our model identifies as part of a contrail. Using the radiances of all available wavelengths, an altitude probability distribution is calculated for each pixel (Meijer, 2024). Currently, the mean of this distribution is used to retrieve the altitude of the contrail pixel. During the assessment of our computing pipeline, our team identified that this approach was not sufficiently accurate for our operational purposes – potentially due to temperature variations in the upper troposphere being too small to provide sufficient information to distinguish nearby altitudes.

Therefore, the ASCENT Project 078 team decided that a new approach to estimate the altitude of detected contrails is required. Our team attributes contrails to flights and takes advantage of the flights' known altitude to estimate the altitude of the contrails. This approach led to a more precise estimate of the persistent contrail forming regions altitude.
The altitude estimation accuracy was defined by the likelihood of each of the following outcomes: (1) the contrail is

avoided successfully, (2) the contrail is avoided successfully, but the flight also makes a contrail at the deviated altitude, (3) no contrail is avoided, but no new contrail is formed at the deviated altitude, and (4) a no contrails is avoided, but a new contrail is formed at the deviated altitude, as shown in Figure 2.

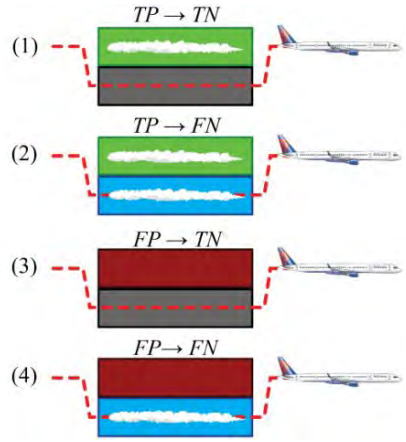

Figure 2. Four possible outcomes for performing a contrail avoidance deviation. A deviating from a true positive (TP) to true negative (TN) avoids a contrail. Deviating from a TP to a false negative (FN) has no effect on the number of contrails formed. Deviating from a false positive (FP) to a TN also has no effect. Finally, deviating from a FP to a FN creates a new contrail that otherwise would not have been formed.

Our team compared estimates using both radiative temperature and a new automated attribution method to altitudes determined by manually attributing flight and LiDAR scans—from the Cloud-Aerosol Lidar with Orthogonal Polarization (CALIOP)—of the top-heights of contrails. While this could be done only in regions where the flight density was sufficiently low to manually attribute contrails, the results were promising, as shown in Figure 3. A significant increase in the likelihood of outcome 1 was observed where a contrail is avoided, and a significant decrease was observed in outcome 3 where we deviate to no effect.

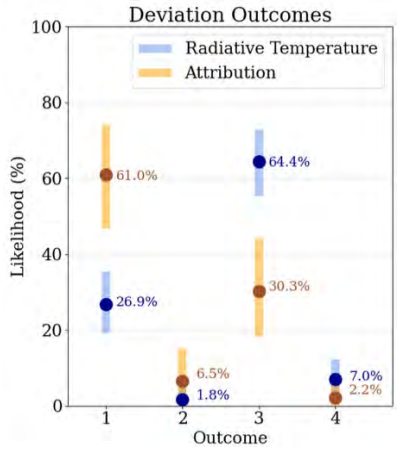

Figure 3. Likelihood and 95% credible intervals of each of the outcomes shown in Figure 2.

The ASCENT Project 078 team is confident that using attribution to estimate the altitude of contrails increases the likelihood of outcome 1 and decreases the likelihood of outcome 3.

Milestone

- Developed an attribution-based contrail height estimation method.

Major Accomplishments

- Demonstrated the flight attributions lead to higher precision in the altitude estimates, such that successful contrail avoidance is more likely.

Publications

None.

Outreach Efforts

None.

Awards

None.

Student Involvement

The research and communication for this task was conducted primarily by MIT graduate research assistant, Olivier Ng'weno Kigotho.

Plans for Next Period

- Adapt the height estimation code to take inputs and produce outputs that can be integrated into MCAST.
- Quantify how well the height estimation code works for secondary purposes: contrail tracking and contrail attribution.

References

Meijer, V. R. (2024). *Satellite-based analysis and forecast evaluation of aviation contrails* [Doctoral dissertation, Massachusetts Institute of Technology]. Massachusetts Institute of Technology. https://hdl.handle.net/1721.1/155350

Task 3 - Contrail Observability Module

Massachusetts Institute of Technology

Objective

The goal of this task is to assess the limitations of the sensing platform used and to develop an understanding for how this quantitatively affects our capabilities in performing and measuring successful operational contrail avoidance. Furthermore, this module aims to provide insights into the practical observability implications of contrails on satellite imagery. While recent work (Driver et al., 2024) investigated the resolution-based observability limitations of remote sensing for satellite detection using synthetic contrail data, there is a need for a systematic analysis using real satellite imagery. The ASCENT Project 078 team is therefore generating a comparison dataset of contrails identified on infrared imagery from two different satellite platforms and eventually open source the data to support the research efforts of the broader scientific community.

Research Approach

Contrail Observability Limitations

Our nowcasting pipeline currently fully relies on imagery from the ABI onboard the geostationary satellite GOES-16. The platform's continental United States (CONUS) product covers the full contiguous United States (U.S.) and has a temporal resolution of one image every five minutes, making it operationally feasible for our approach. However, the limited spatial resolution of the images, which range between two and three kilometers per pixel is a limitation of the geostationary satellite imager. This leads to an observability gap, i.e., contrails do not appear on the imagery right after formation but only once they have grown wide enough relative to the remote sensing instruments spatial resolution. Further, some contrails might not be observable at any point throughout their life due to not reaching a critical width or optically deep enough, or by not being distinct enough from the background. In either of these cases, this implies that our method could miss clusters or regions of contrails due to limited spatial resolution and thus not initiate deviations where they might be necessary.

Quantification Approach
Infrared imagery from VIIRS, an instrument that is currently onboard three satellites in the low Earth orbit (NOAA-20, NOAA-21, SUOMI NPP), is used. This instrument generates images at a spatial resolution at a factor 3.5 times higher (pixel width 750 m or below). The polar orbits of these satellites, however, limit use to two overpasses over the U.S. per satellite per day, as well as coverage of maximum half the contiguous U.S. Therefore, our team cannot use the imagery from VIIRS for our nowcasting pipeline, but it allows us to assess resolution-based contrail observability limitations by comparing images between GOES-ABI and VIIRS when data from the latter are available.

For this, human-labeling contrails were started on respective images from both instruments on seasonably distributed scenes. With these human-observable contrail labels, comparisons are run regarding total number of observed contrails, total contrail length, and area coverage of contrail labels, among others. Then, trends are investigated with meteorological conditions.

Intermediate findings
The ASCENT Project 078 team found that on average, about four times as many contrails are observed on VIIRS, compared to GOES-ABI imagery (see Figure 4 below). This results in additional avoidance regions being derived from VIIIRS labels that do not appear from running the same approach based on GOES-ABI labels. Our team needs to consider – and investigate next – whether these 'missed' contrails appear on GOES-ABI imagery at a later point to address the question of whether VIIRS, in many cases, picks up contrails that are short-lived and therefore assumed to be of lower impact on the climate than potentially the more likely persistent ones that are resolved on GOES-ABI imagery.

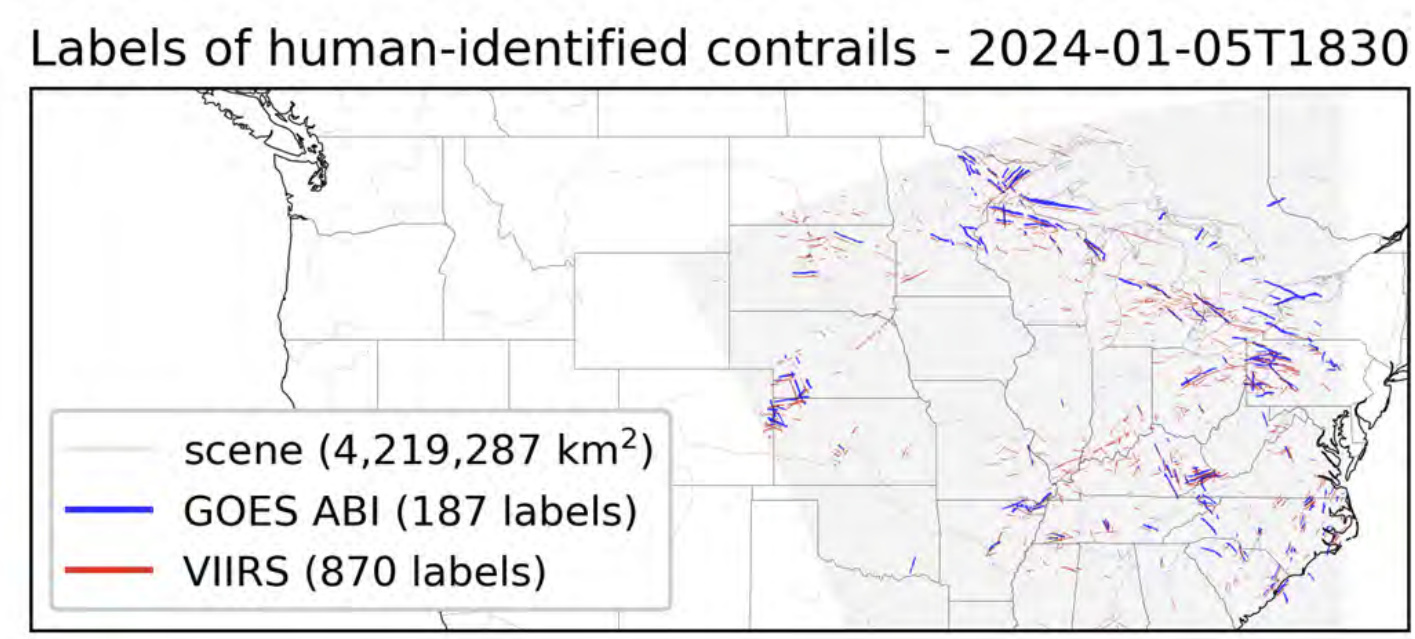

Figure 4. Comparison of labels of identified contrails on GOES-ABI imagery vs VIIRS imagery at the same point in time. The extent of the scene is limited to the extent of the VIIRS swath which covers about 50% of the contiguous U.S. here. The same contrail appears slightly shifted in location on the two input images due to the parallax effect (different viewing geometry on the same object, elevated from the ground).

Milestone

- Set up a pipeline for generating and analyzing labels of contrails observed on GOES-ABI and VIIRS infrared imagery, respectively.

Major Accomplishments

- Created a dataset of 11 human-labeled GOES-ABI scenes, and for 5 of them, labeled their corresponding VIIRS scene.
- Adapted flight attribution algorithm to run on human contrail labels to generate three-dimensional avoidance polygons from these labels.

Outreach Efforts

- Presented poster comparing the visibility and area coverage of contrails captured for one specific scene comparing GOES-ABI and VIIRS (instrument on LEO—Low Earth Orbit—satellites) imagery at EGU24. FAA support was acknowledged.

Presentation

Euchenhofer, M. V., Ross, I., Eastham, S. D., Meijer, V., & Waitz, I. A. (2024, April 14-19). *A comparison of contrail detectability from LEO and GEO satellite images* [Poster presentation]. EGU24, Vienna, Austria.

Publications

None.

Awards

None.

Student Involvement

The research and communication for this task was conducted primarily by MIT graduate research assistant, Marlene V. Euchenhofer.

Plans for Next Period

- Investigate trends in observability of contrails with meteorological factors.

References

Driver, O. G. A., Stettler, M. E. J., & Gryspeerdt, E. (2024). *Factors limiting contrail detection in satellite imagery* (p. 1-28). EGUsphere. https://egusphere.copernicus.org/preprints/2024/egusphere-2024-2198/

Project 079 Novel Noise Liner Development Enabled by Advanced Manufacturing

The Pennsylvania State University
RTX Technology Research Center
Altair Engineering
Cornerstone Research Group

Project Lead Investigator

Nicholas Meisel
Associate Professor
School of Engineering Design and Innovation
The Pennsylvania State University
University Park, PA 16802
nam20@psu.edu

University Participants

The Pennsylvania State University (PSU)

- P.I.: Nicholas Meisel, Associate Professor of Engineering Design
- FAA Award Number: 13-C-AJFE-PSU-079
- Reporting Period: October 1, 2023, to September 3, 2024
- Tasks:
  1. Refine Rapid Design-Build-Test Methodology for Acoustic Liners
  2. Investigate Manufacturability Variations in Polymer Additively Manufactured (AM) Liners
  3. Evaluate Multi-Objective Performance of Polymer AM Liners
  4. Expanding Acoustic Understanding of Liners Under Grazing Flow

Project Funding Level

The ASCENT Project 079 received $1,200,000 from the Federal Aviation Administration (FAA) with match from The Pennsylvania State University ($110,000), RTX Technology Research Center ($450,000), Altair Engineering ($400,000), and Cornerstone Research Group ($240,000).

Investigation Team

The Pennsylvania State University

Nicholas Meisel (P.I.), Project management, task coordination, and student advising
Allison Beese (co-P.I.), Student advising, Tasks 1, 2, and 3, and
Eric Greenwood (co-P.I.), Student advising, Task 1
Alden Packer (graduate student; PhD), Task 1
Eric Goldberg (graduate student; Master of Science [MS]), Tasks 2 and 3
Joeseph Windows (graduate student, MS), Task 2

RTX Technology Research Center (RTRC)

Jeff Mendoza (P.I.), Project coordination and management at RTRC
Julian Winkler (co-P.I.), Acoustic analysis and evaluation as part of Tasks 1 and 4
Aaron Reimann (co-P.I.), acoustic analysis and evaluation as part of Tasks 1 and 4
Kenji Homma (investigator), Acoustic analysis and evaluation as part of Tasks 1 and 4
Paul Braunwart (investigator), Acoustic analysis and evaluation as part of Tasks 1 and 4

Altair Engineering (Altair)
Eric Nelson (P.I.), Multi-objective design optimization as part of Tasks 1 and 3
Cornerstone Research Group (CRG)
Akiva Wernick (P.I.), Direct mesh generation as a part of Task 1

Project Overview

PSU in collaboration with industrial partners, RTRC, Altair, and CRG, along with government collaborator, the National Aeronautics and Space Administration (NASA) Langley Research Center (LaRC), will help the FAA develop and advance innovative engine acoustic liner technology to meet the demands of low noise for future aircraft. Specifically, the team will develop and demonstrate a method to rapidly design, manufacture, and evaluate novel structures that enhance noise attenuation in aircraft engines. Analysis and experimental testing will be used to characterize the effect of lattice topology, geometry, and features size to attenuate noise while ensuring the manufacturability of these complex structures in different materials. Advanced manufacturing technologies will be used to enable rapid design-build-test cycles for liner development, including assessment of structural integrity and acoustic performance. Promising engine liner designs and their performance will be documented to aid future advancements in aircraft engine noise reduction.

The overall project approach includes the following steps:

1. Establish a set of acoustic requirements for future aircraft engine designs.
2. Design and analyze lattice-based acoustic liners using advanced software tools.
3. Perform rapid, iterative prototyping and testing to identify promising designs and materials.
4. Conduct detailed assessments of manufacturability.
5. Perform acoustic and structural evaluations of novel liners in collaboration with NASA LaRC.
6. Document results and archive data for the FAA.

Task 1 - Refine Rapid Design-Build-Test Methodology for Acoustic Liners

The Pennsylvania State University
RTX Technology Research Center
Altair Engineering
Cornerstone Research Group

Objective

The objective of this task is to further refine the rapid design-build-test methodology for low-noise acoustic liners that can enhance noise attenuation in aircraft engines.

Research Approach

Previously, in Year 2, Altair joined the research team to contribute to the selection of optimum lattice structures through the use of their HyperStudy® software – a multidisciplinary design study software that enables engineers to explore and optimize product performance and robustness. HyperStudy guides users to explore data trends, perform trade-off studies, and optimize performance and reliability of a design solution, while considering multiphysics constraints. HyperStudy was combined with nTopology[1] and COMSOL[2] Multiphysics to generate and analyze three-dimensional (3D) models of lattice-based acoustic liners (see Figure 1).

® HyperStudy is a registered trademark of Altai Engineering, Inc., Troy, Michigan.
[1] nTopology is a software that enables users to create complex geometries, optimize designs, and automate workflows for 3D printing. It utilizes implicit modeling and field-driven design to enhance design iteration and engineering capabilities. nTopology is a software developed by nTOP, which is a registered trademark of nTopology Inc., New York, New York.
[2] COMSOL Multiphysics is a general-purpose simulation that includes a finite element analyzer, solver, and simulation software for various physics and engineering applications, especially coupled phenomena and multiphysics. COMSOL is a registered trademark of Comsol AB, Stockholm, Sweden.

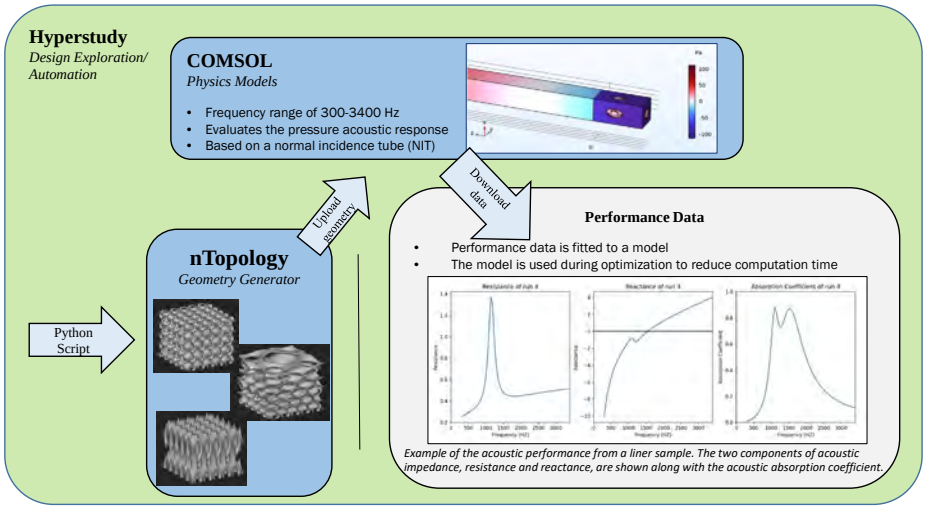

Figure 1. Design-analysis portion of methodology enabled by combining nTopology (for 3D model generation), COMSOL Multiphysics (for acoustic analysis) in Altair HyperStudy (for automation and visualization of results).

Once combined, HyperStudy was used to generate acoustic liner design alternatives through design of experiments using either space filling or other sampling strategies. To facilitate this, the team previously created a four-panel dashboard within HyperStudy (see Figure 2) that contained information about the input parameters, acoustic responses, and sampled parameter space. Using this dashboard, a designer can quickly sort through the data for a given response, select a design sample, review its acoustic response, and visualize the corresponding lattice geometry.

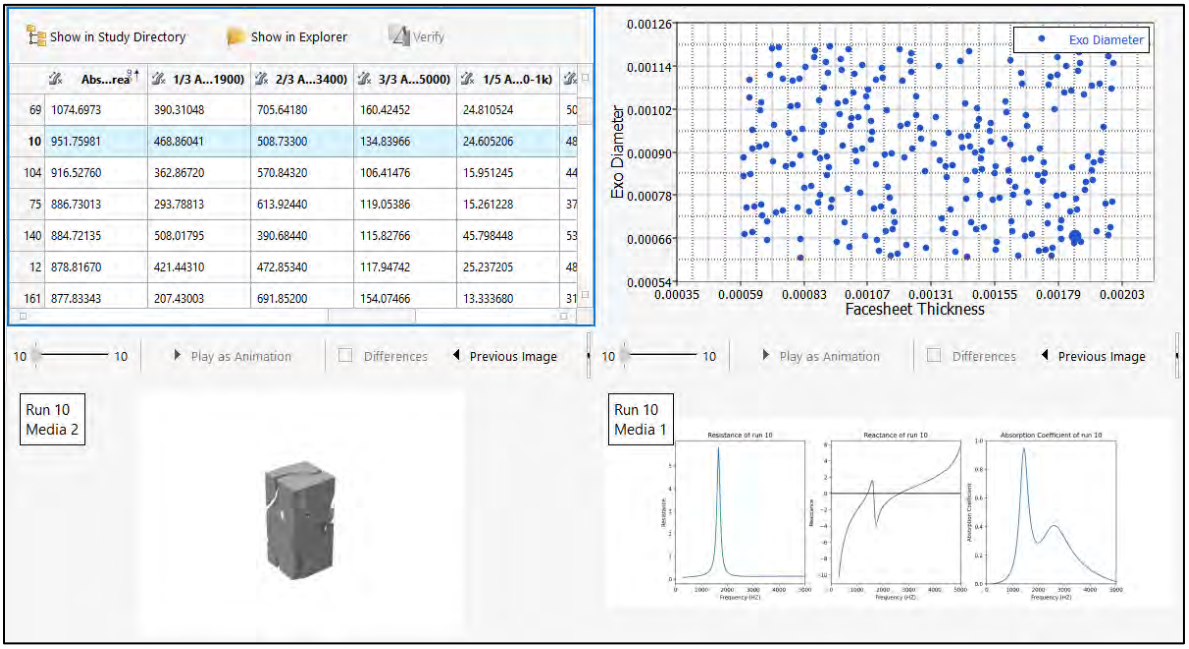

Figure 2. Design exploration dashboard in HyperStudy allows a designer to (a) sort through the sample data for a given response, (b) observe where the input parameters sit in the design space, (c) view the lattice structure geometry, and (d) view plots of the acoustic simulation data.

Two response objectives were selected as examples to validate the framework's operation and the accuracy of the models used within the workflow: (1) low-frequency absorption and (2) mid-frequency absorption. Lattices of interest centered on triply periodic minimal surfaces (TPMS), which are a subset of lattice structures that are periodic in three dimensions with mathematically defined parameters that govern the unit cell periodicity in each direction. Previous work identified both the Schwarz-P and Gyroid TPMS structures as possible candidates for acoustic liners. Across all of the samples generated within the HyperStudy software, modeling predicted that Schwarz-P-based liners performed better than Gyroid-based liners in the low frequency range (300-1900Hz), while Gyroid-based liners performed better in the mid-frequency range (1900-3400Hz). It was with this understanding that a representative Schwarz-P acoustic liner and a representative Gyroid-based liner were selected in direct response to the low absorption curve area objective and the mid-frequency absorption objective, respectively. These samples were then fabricated using AM for experimental validation. Two-inch square specimens (see Figure 3 and Figure 4) were created according to the required specifications of the testing equipment through the vat photopolymerization process. The samples were washed and fully cured prior to any experimental measurement. X-ray computed tomography (XCT) was used to verify the build integrity of the fabricated samples.

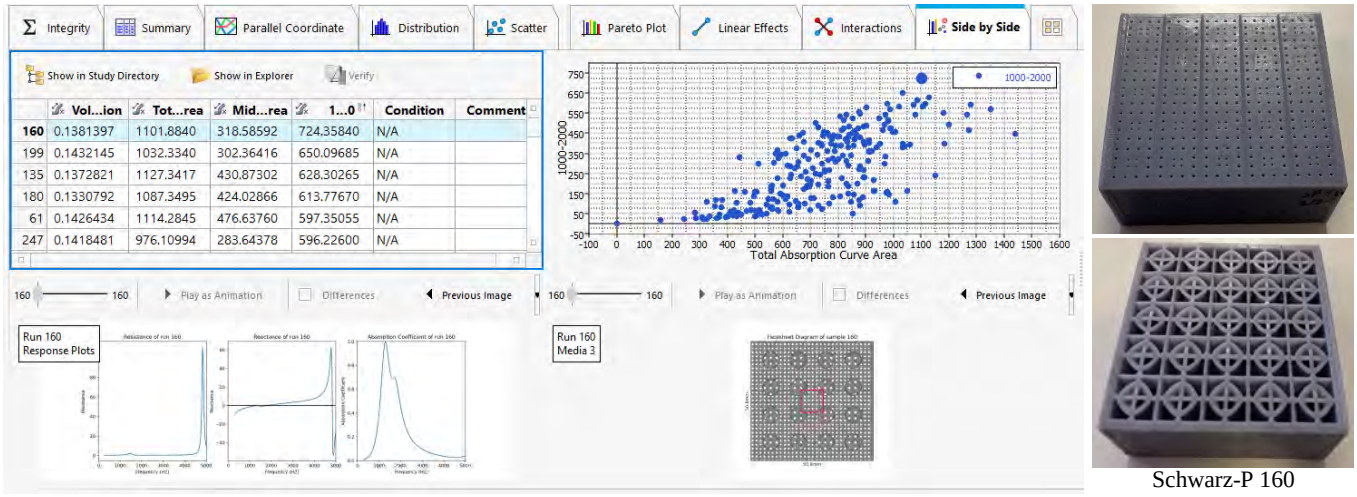

Figure 3. Schwarz-P lattice selection (from space filling design of experiments approach). Selected run 160 based on absorption over 1K-2K Hz band and comparison of volume fraction for top three candidates in that frequency range.

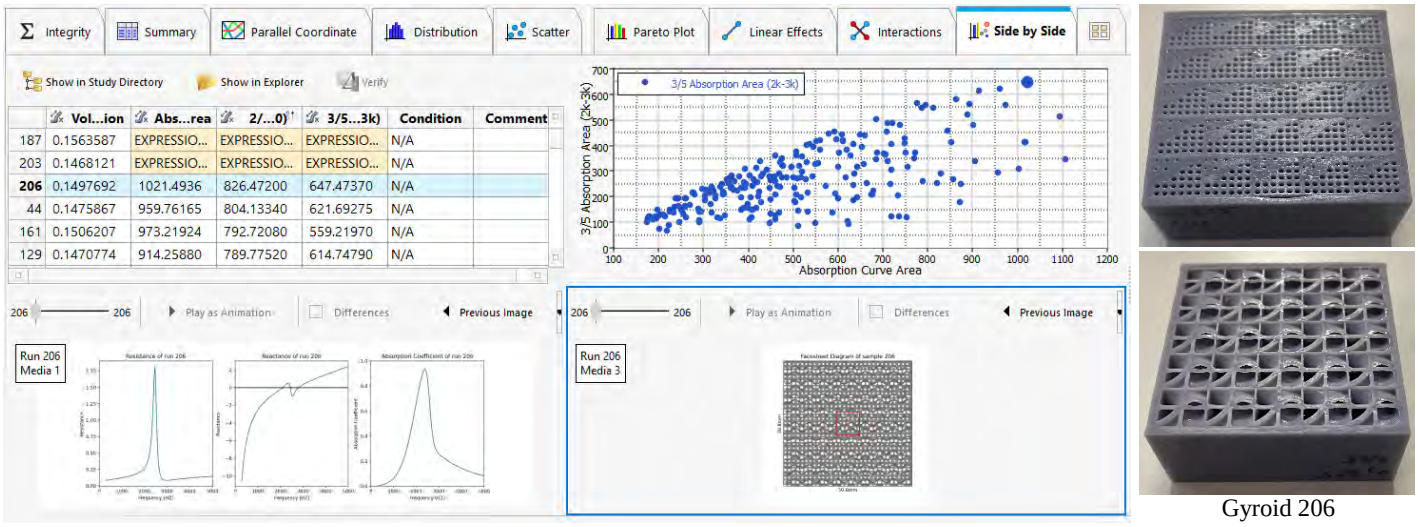

Figure 4. Gyroid lattice selection. Selected run 206 based on absorption over 2K-3K Hz band and comparison of volume fraction for top three candidates in that frequency range.

A normal incidence tube (NIT) located at PSU (Figure 5) was used to measure the acoustic performance of fabricated samples. The acoustic liner samples were loaded into the tube such that the face sheet was flush with the PSU NIT end wall at the mid-tube flange (sample side). An aluminum plunger was positioned and tightened against the back side of the samples to increase immobility. After the tube sections were assembled, the amplifier for the acoustic driver was turned on to generate a broadband noise source. A Bruel and Kjaer data acquisition system read pressure measurements from the two microphones mounted in the tube and a Python® script converted the time domain pressure data to frequency domain data, effectively separating the broadband noise source into individual frequencies. A transfer function method was used to calculate the resistive and reactive components of impedance as well as the absorption coefficient from the pressure data. To mitigate uncertainty related to the operation of the tube, each sample was completely removed from the NIT and retested three times. Even though the samples were symmetric, the orientation of the samples was also changed in each test.

Figure 5. PSU NIT is used to evaluate a 2-in. square sample for its acoustic impedance and absorption.

The performance plots from the manufactured Schwarz-P sample are shown in Figure 6, with data from the experimental results, the COMSOL Multiphysics predictions, and a high-fidelity computational verification using the Lattice Boltzmann Method (LBM). In the absorption coefficient plots, the low frequency region of interest was shaded; in this region, we can see that absorption for sample SP160 was high, as predicted by the design framework. The COMSOL Multiphysics results match well with the high-fidelity LBM. The experimental results exhibit different behavior, which is attributed to air leakage in the experimental setup and/or defects from the manufacturing process. Nonetheless, the experimental results showed high performance for SP160 in the shaded area.

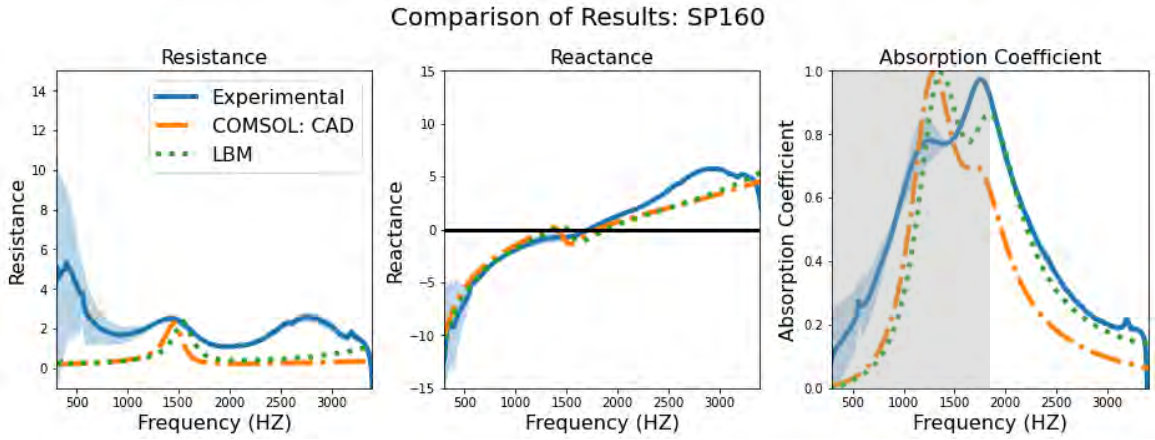

Figure 6. The plots show the experimental validation results of the selected Schwarz-P acoustic liner. The shaded region in the Absorption Coefficient plots show the lower frequency response objective range that was used to select this sample. The shaded outline of the experimental results curve represents the uncertainty found through replicated experiments.

® Python is a registered trademark of Python Software Foundation, Beaverton, Oregon.

As mentioned, a Gyroid acoustic liner design was also selected from the mid-frequency range optimization (1860 – 3420Hz). Again, the sample was selected from the extreme of the performance ranges, with sample G206 having a high absorption in the specified frequency range. The experimental results were compared with the COMSOL predictions and LBM verification; the G206 sample showed the desired response of having a high absorption in the mid-frequency range (shaded region of Figure 7) for COMSOL Multiphysics, LBM, and the experimental. This sample showed moderately good alignment between the COMSOL Multiphysics predictions and the experimental results, with LBM results also in alignment.

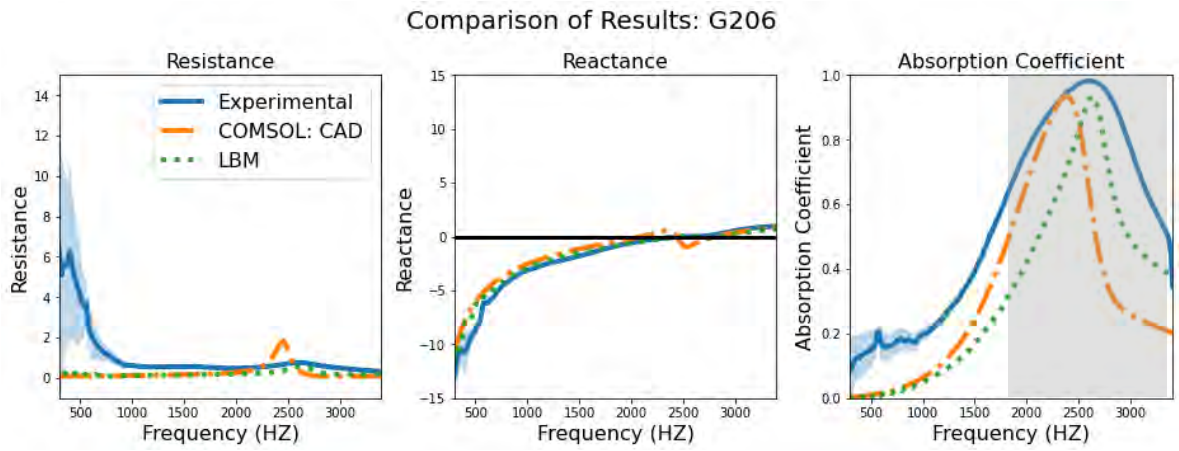

Figure 7. Plots comparing the results of Gyroid-based acoustic liners are shown. Similar to the Schwarz-P results, the shaded regions in the Absorption Coefficient plots indicate the middle frequency objective response that was used to select these samples. The shaded outline of the experimental results curve represents the uncertainty found through replicated experiments.

Milestones

- Demonstrated the use of the HyperStudy dashboard to identify high-performing candidates.
- Implemented NIT testing for additively manufactured liner specimens.
- Validated experimental findings against simulated predictions of acoustic performance.

Major Accomplishments

- Refined the overall functionality of the Design-Test-Build Framework through HyperStudy wrapping.
- Quantified performance differences in acoustic performance between Gyroid and Schwarz-P TPMS structures.
- Identified experimental error occurring between physical testing and COMSOL Multiphysics/LBM models.

Publications

Packer, A., Nelson, E., Mavrudieva, D., Liedtke, P., Winkler, J., Reimann, C., Homma, K., Goldberg, E., Mendoza, J., Simpson, T., & Manahan, M. (2024). A design optimization framework applied to additively manufactured acoustic liners. *Additive Manufacturing*. In Review.

Outreach Efforts

None.

Awards

None.

Student Involvement

One graduate student was involved in this task. Alden Packer, a PhD student in mechanical engineering who worked closely with RTRC, Altair, and CRG to refine the design-analysis portion of the framework.

Plans for Next Period

With CRG joining the team late in the current period of performance, the next period will focus on leveraging their existing meshing algorithms to help better automate the existing design framework for different lattice topologies and design variations. CRG will work closely with Penn State, Altair, and RTRC on this integration, which will help to better generalize the acoustic analysis portion of the existing framework.

Task 2 – Investigate Manufacturability Variations in Polymer AM Liners

The Pennsylvania State University

Objective

The objective of this task is to identify, measure, and account for the presence of manufacturing variations and defects in TPMS liners created via vat photopolymerization AM.

Research Approach

Because wall thickness is difficult to define and may vary along a unit cell, a tool was needed to find the true thickness range of a TPMS lattice design to understand the physical tolerances involved when printing specimens like those described in Task 1. To investigate this, a verification tool created in nTop was used to directly assess lattices that would be meshed and exported for printing. The geometry used for reference was a TPMS 8 mm3 Schwarz-P unit cell with thicknesses ranging from 0.2 mm to 0.8 mm. An analysis workflow was adapted from the existing nTop Knowledge Base resource used to (1) identify the true average thickness of a Schwarz-P lattice and (2) observe regions with lowest and highest average thickness in a unit cell. To achieve this, a custom block was used to generate a field of equally spaced points throughout a mesh. The point map used 0.1 mm spacing across a meshed unit cell, with 500 relaxation iterations to evenly distribute points on the mesh. Examples of two candidate geometries with 0.4 mm and 0.8 mm approximate thickness setpoints are shown in Figure 8. After employing the thickness point map, it is evident that Schwarz-P walls are consistently thicker than designed, with average thicknesses being 44-48% greater than targeted.

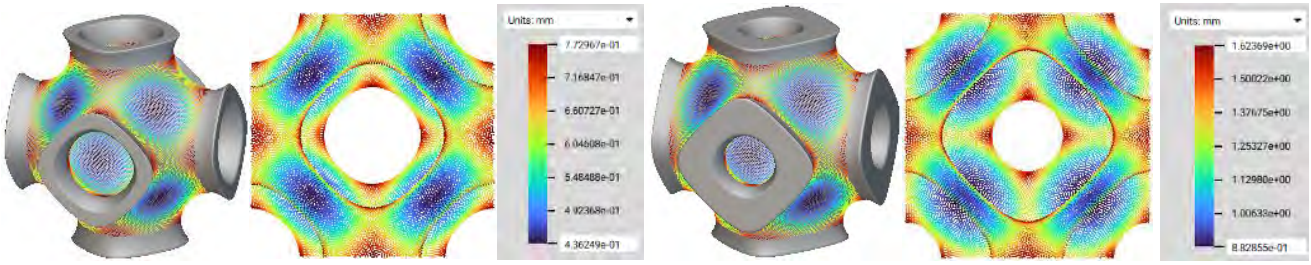

Figure 8. Thickness variations in a 0.4 mm (Left) and 0.8 mm (Right) Schwarz-P unit cell.

Understanding these variations in implicit modeling thickness allows for a better understanding of the weakest regions to expect for structural performance, as well as thin features expected when printing. With the computational variation identified, physical samples were fabricated on an AnyCubic® Photon Mono X 6K LCD Masking printer using a layer height of 0.05 mm and Elegoo® ABS-Like ultraviolet (UV) resin. An Elegoo Mercury X resin wash and cure station was used for post-processing. The wash station consists of a circulating bath which was filled with 95% isopropyl alcohol (IPA), and the cure station uses lights paired with Fresnel lenses to emit UV light at a 405 nm wavelength. The AnyCubic printer uses a top-down printing approach to cure layers at the bottom of the resin vat, where the Z-axis moves a build plate to the bottom of the vat, offset by the layer height (before each subsequent layer) above a fluorinated ethylene propylene (FEP) film that sits over an LED screen. The build plate is 245 mm by 197 mm with a working Z-height of 122 mm.

Development of samples began with design considerations based on design for AM rules to produce defect-free, high-quality prints. These considerations required an understanding of the print limitations and tolerances for the printer. For example, geometries used a minimum wall thickness of 0.3 mm to avoid layer adhesion to the FEP film. An initial set of

® AnyCubic is a registered trademark of Shenzhen AnyCubic Technology Co., Ltd., Shenzhen, China.
® Elegoo is a registered trademark of Shenzhen Elegoo Technology Co., Ltd., Shenzhen, China.

eight samples, each with varied unit cell designs and feature sizes, served as a testbed for systematically identifying failure and defect forms in candidate liners. Common feature parameters between these test artifacts were four 3 mm perimeter walls and a 3 mm thick face sheet. Sample dimensions measured 48 x 48 x 24 mm, with the face sheet spanning 48 x 48 mm on the top face and zero backing on the bottom face to allow for ease of resin removal. Differences between samples evaluated included changes to the lattice infill. Both Gyroid and Schwarz-P lattices were evaluated, with variations in unit cell packing, and aspect ratios. Backing braces were added to aid in the printability of structures by anchoring tapered lattice faces with larger contact points. Lastly, face sheet perforations were adjusted in size, spacing, and shape to accommodate the open areas of each lattice. A series of defects are shown in Table 1, with descriptions of failure areas, failure modes, and lessons learned.

Table 1. Overview of defects for printed lattices with walls and face sheets.

A)		Constraining thin lattice infills with thick border walls led to cracking at interfaces from post-cure warpage. Thick-to-thin regions for both the lattice infill and support braces are sensitive to cracking and delamination.	**D)**	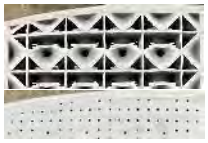	Partial delamination from the build surface resulted in distorted features, both for lattice overhangs and face sheet perforation locations. Bottom layer exposure time should be increased for parts with vulnerable geometries.
B)		Thick lattices and backing braces were prone to post-cure cracking due to uneven curing. Large feature sizes internal to the liner lead to uneven exposure leading to residual stresses and part distortions.	**E)**		Insufficient IPA washing and drying led to residue and ragging on surfaces throughout the sample. After a post-cure, excess resin mixed with IPA leads to surface degradation, and bonded debris is impossible to remove.
C)	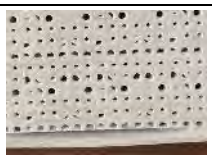	Thick walls were prone to partial delamination from the face sheet side of liners. Perforations near border regions can minimize contact surfaces between subsequent layers which then yield to FEP adhesive forces.	**F)**		Interlayer delamination due to FEP adhesion led to downstream defects on bridged surfaces and tapered contact points of lattices. Flat, thin surfaces, especially when bridging, can bulge and impact the cure surface of future layers.

Due to residual stresses from thick liner walls, lattice infills were found to warp like in Table 1(A-B). Dividing walls varying from 0.4-mm to 0.6-mm were evaluated to support individual unit cells and maintain local resonation for acoustic testing efforts. For samples undergoing post-print warpage, thin dividing walls were observed to undergo distortions in place of other lattice features. These defects were not found to be consequential to the overall quality and performance of the structure. Unlike in Table 1(B), where thick support braces exacerbated shrinkage-based warpage, thin walls like in Table 1(F) were deformed but preserved the unit cells (outside of the four cells which failed during printing). While defects like distortion cracking and post-processing flaws were deemed important to avoid, thin barrier walls were not considered detrimental and were incorporated in subsequent designs to alleviate unit cell warpage.

With general defect modes identified, imaging was performed on lattice samples with warped aspect ratios and scaled liner geometries with perforate sheets. This study was used to confirm dimensionality of parts and to ensure nominal process parameters yielded accurate geometries. Image analysis was established as a verification tool for printed infills and liner face sheets to supplement other cost-prohibitive analysis methods like XCT and microscopy used in prior ASCENT development efforts. Lattice samples measuring 48 x 48 x 24 mm with 12 x 12 x 8 mm unit cells were printed flat with the 48 x 48 mm face on the build plate. Unit cell warpage was analyzed by comparing a profile of the implicit geometry to lens-corrected and thresholded lattice profiles. Because TPMS lattices contain two different surfaces, surfaces at the center of each unit cell were defined as endo and were isolated after applying the edge detection feature in the software ImageJ. The particle analysis feature was used to select centroids. A custom macro was used to; (1) identify the centroid of each boundary and (2) create an orthogonal major and minor axis from the centroid to the boundary edges. The major and minor axes were then divided to determine an aspect ratio (AR). Aspect ratios for the 16 endo openings were calculated and plotted as four segments of four points for each row, denoted by the reference images in Figure 9. AR values increase when unit cells are longer in the X (horizontal) direction and decrease when unit cells are longer in the Y (vertical) direction. Fluctuations about AR = 1 indicate stretching of the geometry.

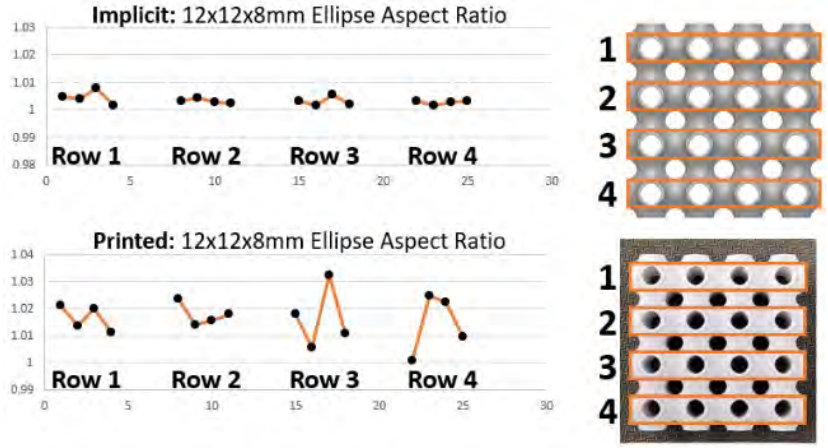

Figure 9. Variations in aspect ratio for implicit profile (Top) and printed profile (Bottom).

The first plot in Figure 9 describes aspect ratio variations for the implicit geometry to verify the accuracy of boundary and centroid detection. All unit cells contain an aspect ratio between 1 and 1.01, indicating symmetry for all unit cells, as expected. The second plot describes results for a printed geometry, with greater variation shown on the same ±0.025 scale. Aspect ratios fluctuated about 1.015 with a standard deviation of 0.0016. The AR>1 average may suggest mild warpage in the X direction, but these minor variations likely fall within error tolerances from the image correction and boundary detection strategies. Overall, no significant warpage was identified for this geometry and print orientation.

One successfully printed full-scale liner section was also used to identify the accuracy of holes designed to be 0.6-mm in diameter. A vertically printed liner (built with the 125 x 25 mm face contacting the build plate) was imaged and carefully thresholded to isolate holes throughout the top face. Capturing all holes at once led to some measurement inconsistencies due to poor resolution at boundaries; so, five images were taken and analyzed to generate the full series of data. Because holes showed varying degrees of circularity, initial runs led to inconsistent distributions of diameter measurements. Instead, each particle (representing a hole) was measured for area and assumed to be a circle, through which an estimated diameter was calculated. Pillar holes on the center and sides, as well as small tears around them, were manually removed from particle analysis results. Overall, there were 2,146 holes captured in the particle analysis as summarized in the thresholded image and histogram in Figure 10.

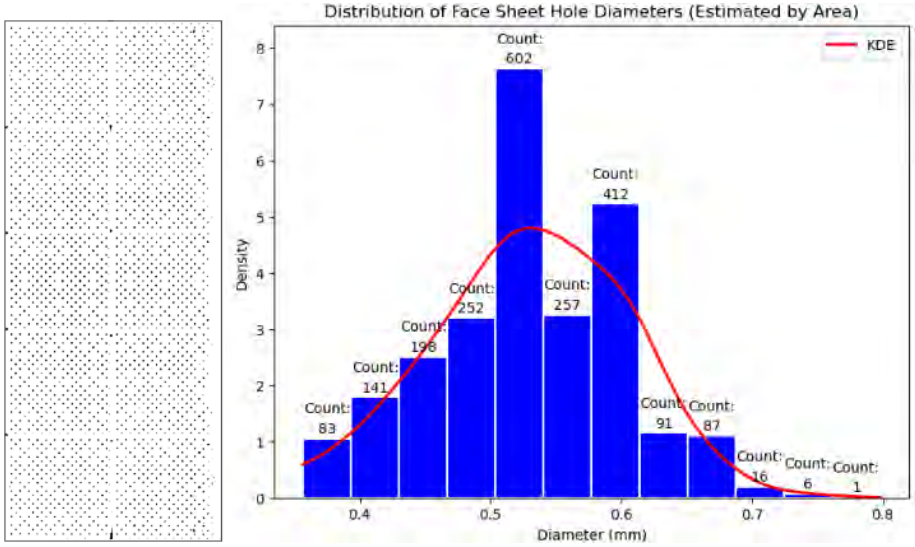

Figure 10. Full face sheet for visualization purposes (left); Histogram of estimated face sheet hole diameters with a kernel density estimator (KDE) fit (right).

Estimated diameters were binned and plotted in a histogram to identify the distribution of hole diameters, and a KDE fit was added to find the point of highest probability density. Results indicated a large range of hole sizes, primarily in the 0.35-0.7 mm range. The average diameter determined from the total range was 0.516 mm with a standard deviation of 0.10 mm, indicating a 14% reduction in average hole size from the targeted 0.6 mm. The gaussian KDE function was used to find the highest frequency hole diameter within a ±0.025 mm range, found to be 0.53 mm or 11.7% reduction in mode hole size. Both results fall in line with an approximate 10% decrease for 0.7-mm hole sizes and smaller. Based on the frequency and mode diameter results, these percentages can be used as a correction factor to estimate design diameters at 0.67-0.68 mm to achieve a 0.6-mm target. This correction assumes the shrinkage rate is proportional at a 0.1 mm design increase and is specific to the geometry and print parameters.

Milestones

- Established a method for understanding implicit TPMS lattice model thickness variations.
- Addressed manufacturing failures that may occur during the production of polymer TPMS lattice structures.
- Specified an experimental approach to identify error distributions which can later be integrated with HyperStudy.

Major Accomplishments

- Identified common defects in the vat photopolymerization process for TPMS liners and how to avoid these defects.
- Quantified inconsistencies in circularity within the endo surfaces of TPMS lattices.
- Measured the distribution of hole accuracy in manufactured face sheet pores.

Publications

Goldberg, E. (2024). *Polymer prototyping of acoustic liner designs to support transition to metal additive fabrication.* [Master's thesis, The Pennsylvania State University]. The Pennsylvania State University, University Park, Pennsylvania.

Outreach Efforts

None.

Awards

None.

Student Involvement

Two graduate students were involved in this task. Eric Goldberg, an MS student in additive manufacturing and design, and Joseph Windows, an MS student in mechanical engineering. Both worked to identify key manufacturability challenges and determine how they might be later accounted for in the Design-Build-Test framework.

Plans for Next Period

- Focus on further expanding this exploration of manufacturability.
- Correlate identified variations and defects with manufacturing process parameters (e.g., layer thickness, build rate, post-processing steps, etc.) to develop mitigation and compensation strategies. These strategies will be used alongside Altair's existing machine learning and artificial intelligence software tools to help ensure error compensation in design and manufacturing.

Task 3 – Evaluate Multi-Objective Performance of Polymer AM Liners

The Pennsylvania State University
Altair Engineering

Objective

The objective of this task is to expand and evaluate the range of component-level and system-level metrics relevant to multi-objective design optimization crucial to expansion of the design-build-test framework beyond only acoustic properties.

Research Approach

While the focus of this ASCENT research is on the acoustic performance of AM liners, other factors will become relevant as the team moves closer to full-scale deployment of the AM liner concept. This includes the liners' structural characteristics, which can be better understood and predicted using mechanical testing. Because resin printing is not guaranteed to be the end-application direction, determining performance of full liner systems was not an initial goal and a simpler scenario was planned for comparative assessment of Schwarz-P lattice behavior. Following geometry relationships for lattice features aligned in the compressive load direction, effective modulus is expected to change when varying unit cell aspect ratios. Thus, samples were produced to characterize the deformation and proportional response to uniaxial compression.

Lattice samples were produced without face sheets, backings, or sidewalls, and the first round of testing focused on Schwarz-P structures that were 48 x 48 x 24 (X, Y, Z) mm in size. Each sample was loaded with the 24 mm side as the gage thickness, as this dimension closely resembles the thickness of a single degree of freedom (SDOF) liner infill. The primary lattice design used a lattice with a targeted 0.4-mm wall thickness with unit cell dimensions of 8 mm^3. Three samples were fabricated in a vertical (XZ) orientation with a 24 x 48 mm face parallel to the build plate, and three samples were fabricated in a horizontal (XY) orientation with a 48 x 48 mm face parallel to the build plate. For the two batches of otherwise identical samples, the consequence of layer-wise effects was of interest for process planning to optimize print orientations. Optimization of lattices for a given frequency band commonly leads to unit cells being warped either horizontally or vertically; so, a test case for each was fabricated for Schwarz-P lattices. First, a horizontally stretched condition using 12 x 12 x 8 mm (U, V, W) unit cells, and second, a vertically stretched condition using 8 x 8 x 12 mm (U, V, W) unit cells, were fabricated with the same bounding lattice dimensions of 48 mm x 48 mm x 24 mm (X, Y, Z). Both cases were fabricated in the vertical orientation to reduce variability. Lastly, a test case using a doubled wall thickness with the first geometry (8 mm^3) was included in the test array. An overview of the unit cell dimensions, print orientations, and volume fractions of the samples selected for testing are listed in Table 2.

Table 2. Lattice samples printed for compression testing.

Approx Thickness	Unit CellU	Unit Cell V	Unit Cell W	Samples Printed	Number of Cells	Volume Fraction	Reference Model
0.4 mm	8	8	8	3 *XY* 3 *XZ*	108	17.12%	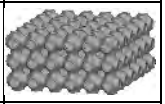
0.4 mm	12	12	8	1 *XZ*	48	13.08%	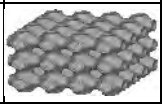
0.4 mm	8	8	12	1 *XZ*	72	14.96%	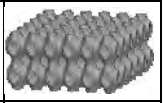
0.8 mm	8	8	8	1 *XZ*	108	34.29%	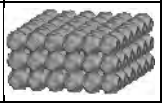

Samples were compression tested on an MTS® servomechanical test frame with a 10 kN load cell. The crosshead speed was selected as a modification on ASTM D1621 (ASTM International, 2023), where the rate of displacement for cellular rigid polymer materials is specified at 10% of the sample gage height per minute ± 0.25 mm/min which yields 0.04 mm/s based on a 24-mm gage. To accurately capture anomalies like cracking for a sample with half the suggested specimen thickness, the crosshead rate was slowed to 0.1 mm/s for each test. MTS software was used to acquire voltages (representing force at the crosshead) at a rate of 1 Hz. Due to slack in the MTS system and the low loads expected, measuring displacement directly from the crosshead was expected to be too insensitive to provide accurate results for thin polymer lattices. Digital image correlation (DIC) was employed for accurate measurements of displacement which could be mapped back to load measurements. DIC allows for tracking of a series of points during testing, typically using speckled paint added to a flat surface, across either the substrate of the test article or the fixtures used to perform the test, shown in Figure 11.
A two-camera setup was used, with one focused on the rectangular fixtures and one on the lattice face for reference photos. Images were captured at 1 frame per second to match the MTS readouts for voltage. Each test was programmed to run until 4 mm of crosshead displacement and then return to 0 mm at the same 0.01 mm/s rate.

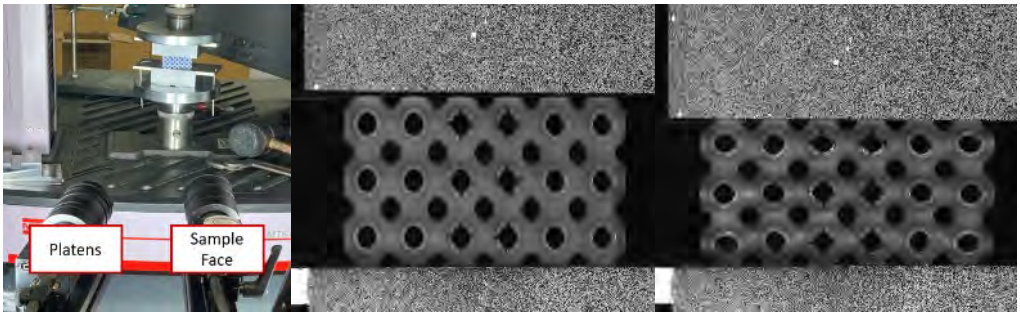

Figure 11. Setup of cameras for digital image correlation (left); Camera 2 images of a lattice face before and after deformation with speckled platens (right).

Results for both vertical prints and flat prints are shown in Figure 12. Representative DIC images are included for each sample to indicate the amount of deformation experienced throughout each test. Maximum forces exhibited on the horizontally printed samples were averaged at 1.32 kN with a standard deviation of 0.12 kN as well as an average force/displacement (F/D) slope of 1.41 kN/mm in the linear region. These geometries were loaded with layers in line with

® MTS is a registered trademark of Illinois Tool Works Inc., Glenview, Illinois.

the load direction, meaning that samples were mounted in the same orientation in which they were printed. Vertically printed samples with the same geometry and test configuration were found to consistently exceed the performance of samples printed horizontally, indicating that orientation of samples does play a role, even for structures with symmetrical features. This is consistent with previous work which showed that, in Schwarz-P lattices with loading transverse to the layers (flat prints), loading leads to stress risers at the thinnest regions of the deformed structure where layer-wise bonds are weak.

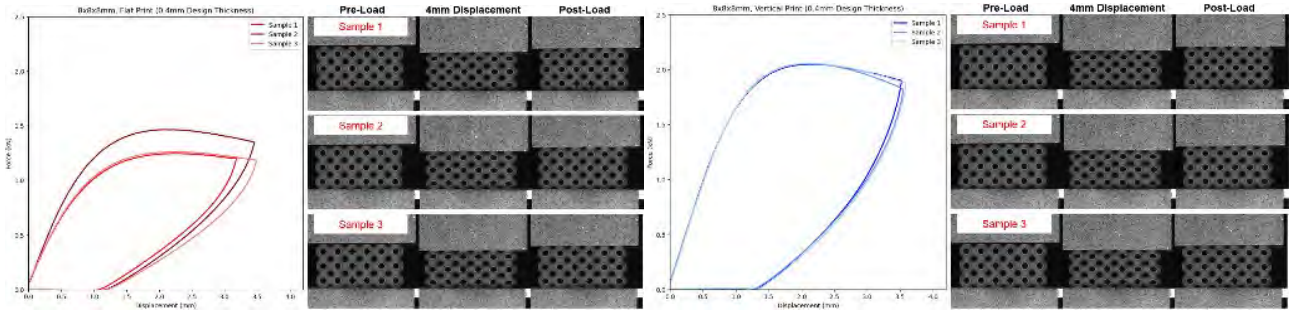

Figure 12. F/D curves for 8 mm³ 0.4 mm samples printed horizontally (left) and vertically (right).

Tests for changes in geometry beyond the base 8 mm³ 0.4 mm design extended to three samples with permutations in design variables. One candidate sample for each of the three geometry variations (increased wall thickness, vertically stretched, and horizontally stretched) was evaluated and compared to study effects of increased material on stiffness and effects of anisotropy. Results for these tests are shown in Figure 13. As with the baseline lattice tests, DIC images are included for each sample for reference. For the 8 mm³ 0.8 mm wall thickness sample, F_{max} was 3.8 times greater than the average 0.4-mm geometry F_{max}. The F/D for the 0.8-mm wall thickness sample was 2.5 times greater than the linear slope of the average 0.4-mm geometry. The 12 x 12 x 8 mm warped unit cell sample underperformed as compared to baseline geometries printed in the same vertical orientation. This can be explained by the lower volume fractions of this design and by the lack of alignment of geometric features with the load direction. The 8 x 8 x 12 mm sample had a higher F_{max} and F/D than the baseline geometries but also dropped off more quickly after its peak. This illustrates the greater stiffness of the geometry due to better alignment for compression, but greater susceptibility to deformation due to the lower volume fraction.

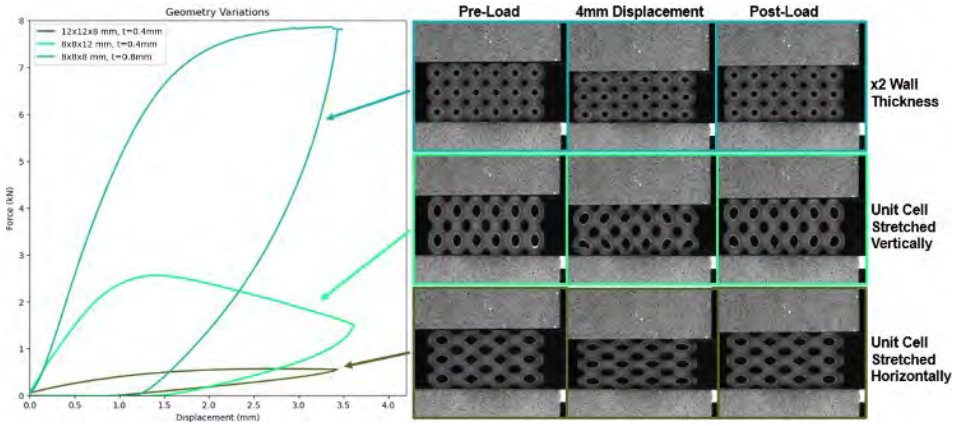

Figure 13. F/D curves for lattice geometry variation samples.

Altair SimSolid® 2024 was used to validate the results of the geometries printed and mechanically tested so that relationships could be made between real-world testing and modeled performance. Altair SimSolid is a structural solver that does not rely on meshing like traditional finite element analysis (FEA) software, and instead uses nodes applied to computer-aided design (CAD) geometry for its functions. This allows for flexible boundary conditions that do not require tetrahedrons or other mesh element shapes to be used to approximate a model. The fully curvature-based lattices that were imported were instead described by point clouds mapped to a CAD representation of each sample type. For these lattices, describing the boundaries with a tetrahedral mesh requires high element counts and intensive central processing unit (CPU) resource consumption, making a meshless solver favorable. Further, unlike traditional meshing, CAD representations do not over- or under-approximate curved surfaces. A tolerance value of 0.2 mm was found to appropriately rebuild samples without compromising accuracy. CAD models are shown with segmented faces in Figure 14.

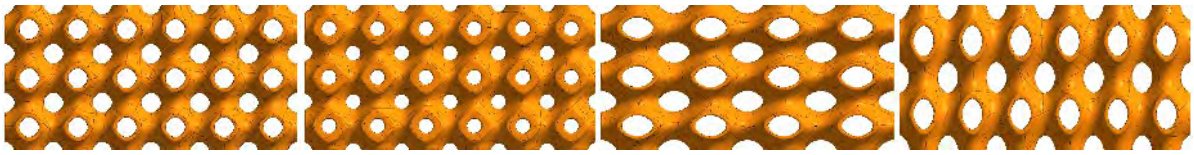

Figure 14. Examples of Schwarz-P geometries represented as a series of CAD faces.

For each imported geometry, thick plates were placed at top and bottom boundaries and were given a modulus value of 2.1E5 MPa. The software allows multiple imported parts to have connections automatically applied at contact points. For the chosen lattice geometries, bottom and top faces each have 36 semi-circular edges that do not have flat CAD faces to assign mates to, making manual boundary condition setup difficult in other FEA programs. Automatic connections were placed, with 72 connectors established between the lattice and plates. With the help of the Altair team, solver input settings were established for simulation passes. Orientation-varied samples were shown to have well-defined differences in behavior under identical loading conditions; thus, Altair SimSolid results were compared to a test in each configuration.

Simulations provided reaction forces (R) at the maximum 0.5 mm displacement. R values were compared to compression F/D plots for the four unique geometries trialed. A slope value was estimated from 0 mm to 0.5 mm to assess relative stiffness values that can be compared to earlier stress-strain results. These proportionalities can allow for better comparison between F/D curves that have differing magnitudes. In addition to the variations in geometry, simulation results for the 0.8 mm^3 0.4 mm condition were mapped to both a flat and vertical Sample 1 test to identify how closely they match to a homogenous material with no degradation in performance due to layer-wise weaknesses. Two plots are shown in Figure 15 with reaction forces overlaid with an experimental compression curve with a linear regression used to calculate the slope. Red arrows and lines indicate the build orientation of each scenario. F/D slopes in the linear region describe stiffness and were used for comparison as the geometry is too complex to be described by a maximum or principal stress in the solver. The same R value is used for both plots as simulations only account for input geometry and properties which did not change. Simulation results fit much more closely for the vertical print test than the flat print test; this was expected, as the modulus value was applied to an isotropic structure. Results can be interpreted in two ways. The first is that vertically printed Schwarz-P geometries are inherently stronger than horizontal counterparts due to fabrication inconsistencies from poor adhesion, under-curing, or warpage. A second interpretation is that layer orientation plays a large role in deformation mechanisms.

® Altair SimSolid is a registered trademark of Altai Engineering, Inc., Troy, Michigan.

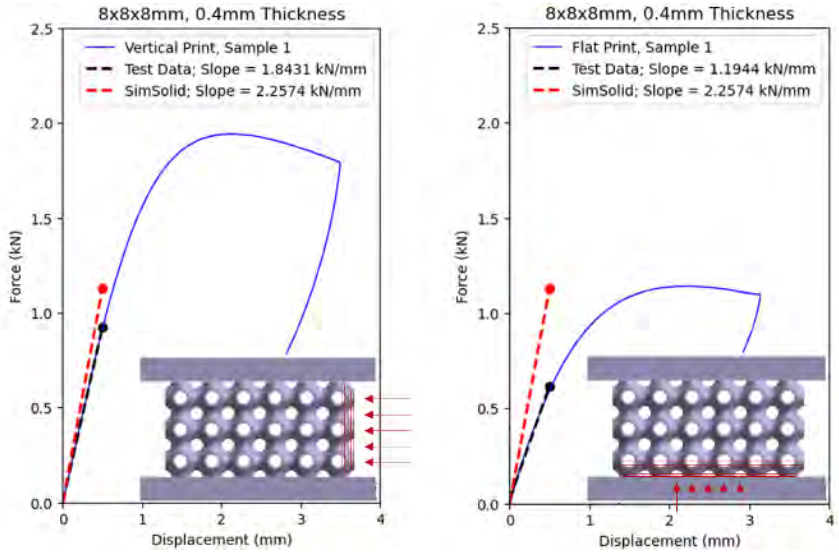

Figure 15. F/D at 0.5 mm of (Left) vertical and (Right) flat print orientations compared to the reaction force slope at 0.5 mm. Arrows indicate the build direction.

Slopes from reaction force at 0.5 mm were next applied to the three other Schwarz-P geometries, shown in Figure 16. Reaction forces for each simulation fit closely with each compression curve. As shown in Table 3, simulation results were roughly 20% greater than experimental results for vertically printed 0.4 mm thick lattices, with similar relationships for the isotropic unit cell as well as unit cell warped variations. For the 0.8 mm thick lattice, simulation results were only ~13% greater than experimental. Simulations assume an isotropic material with 100% density; so, the overapproximated performance is expected. However, it can be inferred that TPMS lattices with thin walls are more greatly impacted by the printing process.

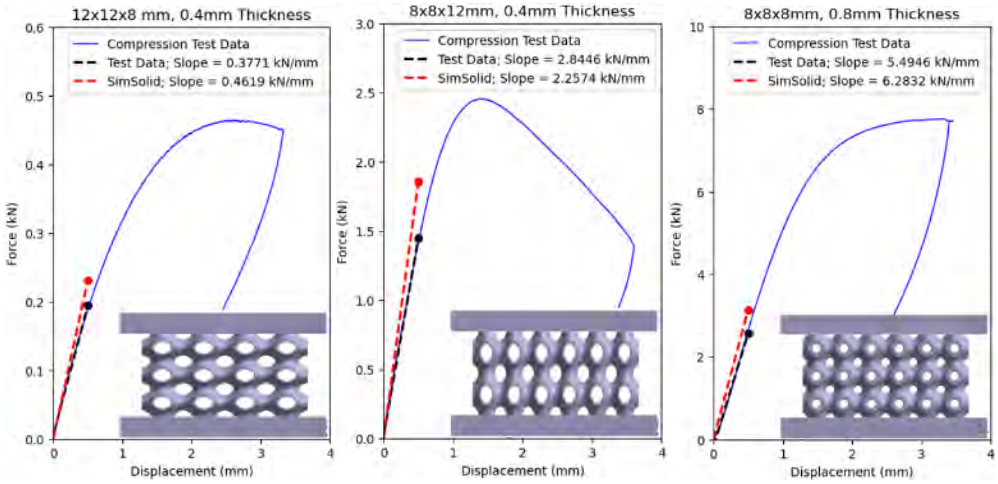

Figure 16. F/D at 0.5 mm of 12 x 12 x 8 mm (left), 8 x 8 x 12 mm (center), and 8 mm^3 0.8 mm (right) samples compared to the reaction force slope at 0.5 mm.

Table 3. Simulation values compared to experimental compression test data.

Sample	Reaction Force (kN)	R Slope (kN/mm)	F/D Slope (kN/mm)	Slope Ratio, $\left(\frac{F}{R}\right)$
8 mm³ 0.4 mm, Vertical	1.1287	2.2574	1.8431	0.8165
8 mm³ 0.4 mm, Flat			1.1944	0.5291
12x12x8 mm	0.23097	0.4619	0.3771	0.8164
8x8x12 mm	1.8565	2.2574	2.8446	0.7936
8 mm³ 0.8 mm	3.1416	6.2832	5.4946	0.8745

Altair SimSolid also provides a visualization of deformation which can be magnified by a scale factor. DIC images at 4 mm displacement were compared to simulations with a scale factor of 8 to predict deformation at the same displacement. As shown in Figure 17, plastic deformation visualized using the 8X scale factor matches well with compression samples. The 8 x 8 x 12 mm geometry showed much greater plastic deformation in the DIC profile as compared to the visualization; while this does not truly predict deformation, it supports the result that relative performance for the vertically stretched geometry compared to the simulated reaction force was lower than other vertically printed structures. As shown in the top right corner of the 8 mm³ 0.8 mm lattice, cracking occurred in the thick geometry. This sample was printed vertically (XZ), so the crack formation seen is likely to be along a layer line. The scaled prediction shows the maximum deformation that the outer unit cells of the structure that the experimental sample may have experienced, indicating that this high-stiffness sample may fail more readily due to lower relative energy absorption capacity.

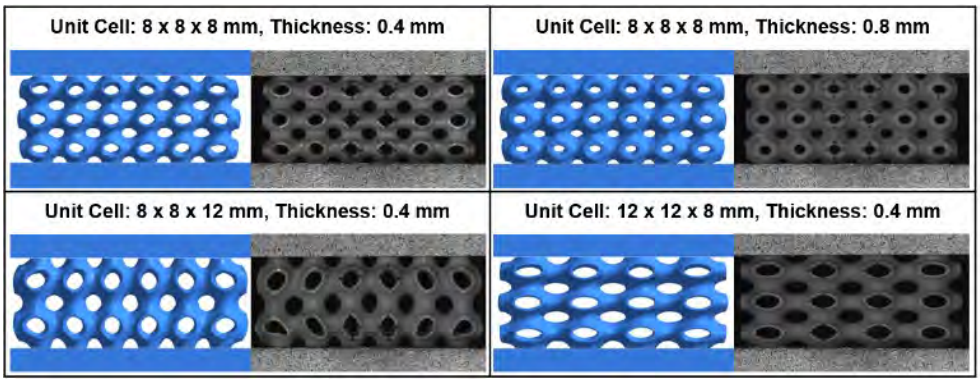

Figure 17. DIC images of lattices compressed at 4 mm displacement compared to 8X scaled simulation results.

Milestones

- Demonstrated the validity of using DIC to analyze compressive properties of lattice-based liners.
- Integrated nTop models with Altair SimSolid for computational predictions of strength.
- Categorized key variations in lattice design that may affect compressive strength.

Major Accomplishments

- Established pilot design of experiments testing regimen to support multi-objective optimization efforts.
- Quantified the effects of build orientation and unit cell aspect ratio on lattice strength.
- Validated experimental compression tests with Altair SimSolid computational simulations.

Publications

Goldberg, E. (2024). Polymer prototyping of acoustic liner designs to support transition to metal additive fabrication [Master's thesis, The Pennsylvania State University]. The Pennsylvania State University, University Park, Pennsylvania.

Outreach Efforts

None.

Awards
None.

Student Involvement
One graduate student was involved in this task. Eric Goldberg, an MS student in additive manufacturing and design, worked closely with Altair to analyze the proposed liner structures using Altair SimSolid.

Plans for Next Period
- Leverage the structural findings from this period and incorporate them into a multi-objective decision framework alongside the existing acoustic properties.
- Conduct further exploration of additional relevant metrics for integration into the framework, including, but not limited to weight, volume, drag, and economic analysis. Understanding such metrics will enable us to move our liner approach closer to full-scale implementation.

Task 4 – Expanding Acoustic Understanding of Liners Under Grazing Flow
RTX Technology Research Center

Objective
The objective in this task is to evaluate the acoustic performance of liners under grazing flow measured using an education method.

Research Approach
The current period was focused on testing a liner sample at the NASA Grazing Flow Impedance Test (GFIT) facility (see Figure 18) and utilizing the results to verify and improve our design tools. In Year 2, RTRC fabricated an AM liner sample, suitable for this initial testing at NASA, 20 × 2.5 × 1 in. (length [i.e., total assembled length], width, depth). The sample is fabricated using a Carbon® M2 printer with EPX82 epoxy resin. Due to the size limitations of the printer, four individual sections of 5-in. in length each were printed and joined afterwards (see Figure 19). The tested design is the first of two designs to be evaluated at NASA. The second design is being fabricated by PSU and was tested at the end of 2024. In the GFIT facility, acoustic impedance is educed from an array of microphones on the wall opposite the acoustic liner material (test sample). The transmission loss (TL) is determined from the sound pressure level (SPL) difference between last and first mic, yellow dots in Figure 18 indicate locations upstream and downstream of the liner sample. The impedance and TL are key results compared between the test and predictions and in the summary to follow.

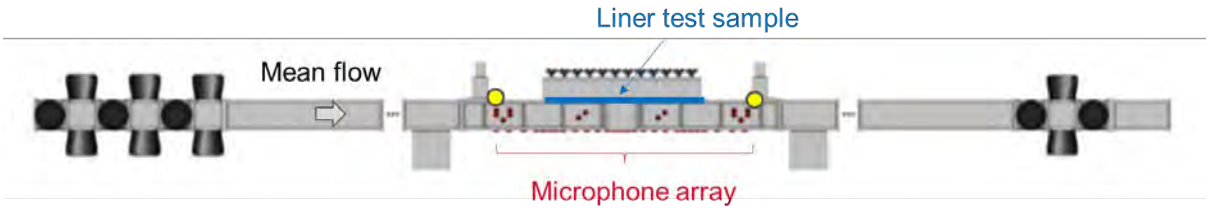

Figure 18. NASA GFIT facility flow and sound sources, microphone locations, and the liner test sample. Yellow dots indicate the positions in the duct used to estimate the TL of the material.

® Carbon is a registered trademark of Carbon, Inc., Redwood City, California.

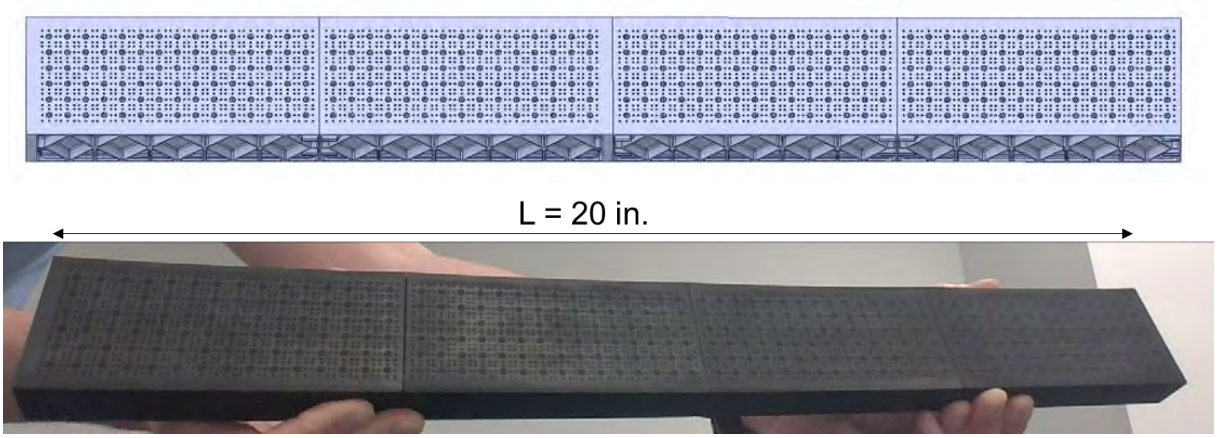

Figure 19. Illustrations of the joined (4 sections, 5-in. in length) initial design tested at the NASA GFIT.

As previously described, RTRC utilized a two-step process for the design of the two TPMS liner configurations. In summary, the first step is the prediction of the acoustic impedance using a virtual normal incidence impedance tube based on finite element (FE) modeling. Then the predicted acoustic impedance is applied as an acoustic boundary condition representing the liner in a virtual grazing flow test model (which emulates NASA's grazing flow test setup) to predict the insertion loss and down-select leading concepts for acoustic testing. At this step, the liner is not explicitly modeled; the normalized impedance boundary condition (with flow) is specified via a table. TL is determined from modal basis acoustic power at inlet and outlet or from difference in SPL between first and last virtual mic (similar to what is done in the NASA test). The intent of this initial round of testing and corresponding designs was for an assessment of our design tool and improving performance and not necessarily to test the best performing TPMS design. In addition, the designs target performance in the measured frequency range of the GFIT facility, ~500Hz to 3,000Hz.

The RTRC team made both pre-test and post-test predictions of liner performance. The comparison with NASA results below will focus only on the post-test predictions. In addition, data were acquired for Mach numbers M=0.0, 0.3, and 0.5, only M=0.3 results are presented as salient trends are similar for all conditions. A summary of the differences between pre- and post-prediction is provided in Figure 20. Figure 20 shows the difference in impedance and TL for pre- and post-test predictions, post-test results indicated by the solid lines and pretest are indicated by the dashed lines. The pre-test predictions were essentially as designed estimates from the process described. There are two main differences accounted for with the post-test predictions: (1) differences between the assumed grazing flow Mach number and actual test Mach numbers utilized and (2) differences in the manufactured liner geometry versus the initial design intent.

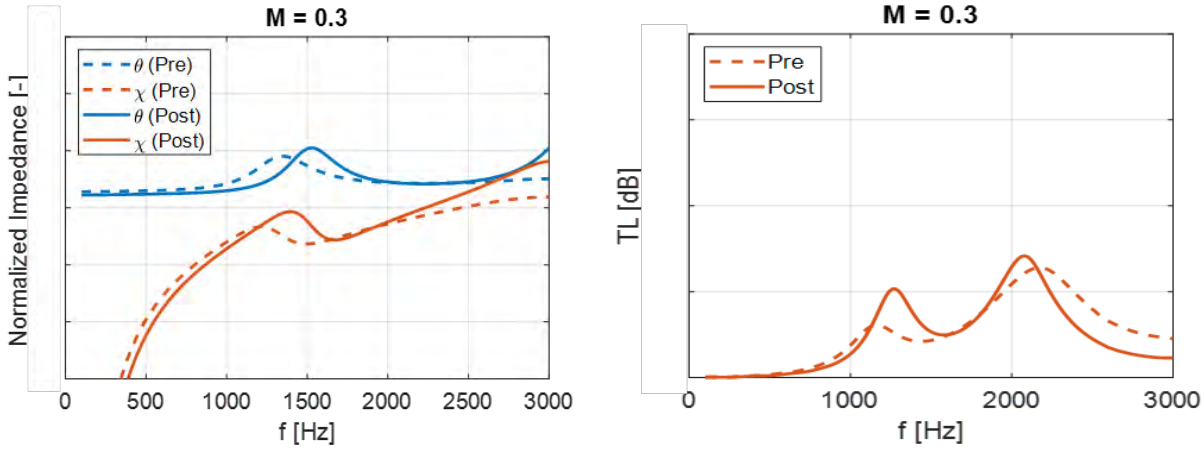

Figure 20. Comparison pre- vs. post-test predictions, for a single SPL in the duct. [θ - Resistance, χ - Reactance].

Mean flow Mach numbers were assumed to be the average Mach values in pre-test estimates but were changed to the nominal Mach numbers from the test for post-test estimates. The geometry model was updated (from pre-test predictions) to account for finite wall thickness and actual bulb shape that was used for printing (adjusted through several iterations), the volume split and neck size changed slightly, see the illustration in Figure 21. These geometry changes transformed the actual design closer to an iso-surface (from the simple mathematical geometry expressions for TPMS structures) of zero compared to the design value of 0.3 in pre-test predictions. As indicated in Figure 20, the biggest difference resulting from these changes are in the zero crossings of the reactance slightly shifting the peaks and correspondingly slightly moving the resistance peaks. This is an expected outcome due to the volume differences described in the bulb region and larger surrounding cavity.

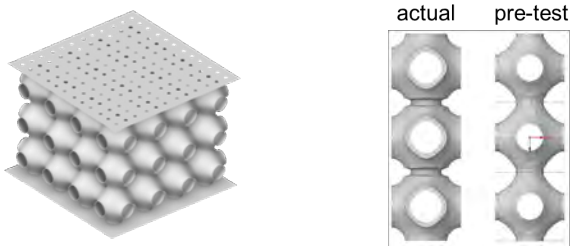

Figure 21. Comparison of TPMS bulb layer through the thickness illustrating the actual AM part and design (pre-test).

The normal impedance, resistance and reactance, and TL are shown in Figure 22 and Figure 23, respectively. Each figure shows the normalized impedance or TL as a function of frequency for M=0.3 and for increasing sound pressure level in the duct for L1 = 110dB, L2 = 120dB, L3 = 130dB, L4 = 140dB, and L5 = 150dB, respectively, as measured just upstream of the liner. As observed in Figure 22, excellent agreement is achieved up to 130 dB (L3) for all but the low-end frequency values. Of greatest importance is the region near the first resonance (~1300Hz-1600Hz depending on SPL) and over the range of ~750Hz to 2500Hz. It is likely that the response below 750Hz in the data is, at least partially, due to the poor performance of the eduction method in regions of low sound attenuation. Deviations between predicted and test occur near first resonance (~1300Hz) at the higher SPL where L5 shows the biggest differences between test and prediction in both resistance and reactance. We believe these effects are attributed to non-linear effects currently not captured in the prediction tool. It is noted that for the M=0.5 case, differences at resonance are slightly reduced for L4 and L5 compared to M=0.3. Overall, there is good agreement in the normalized impedance across all Mach numbers and duct SPLs.

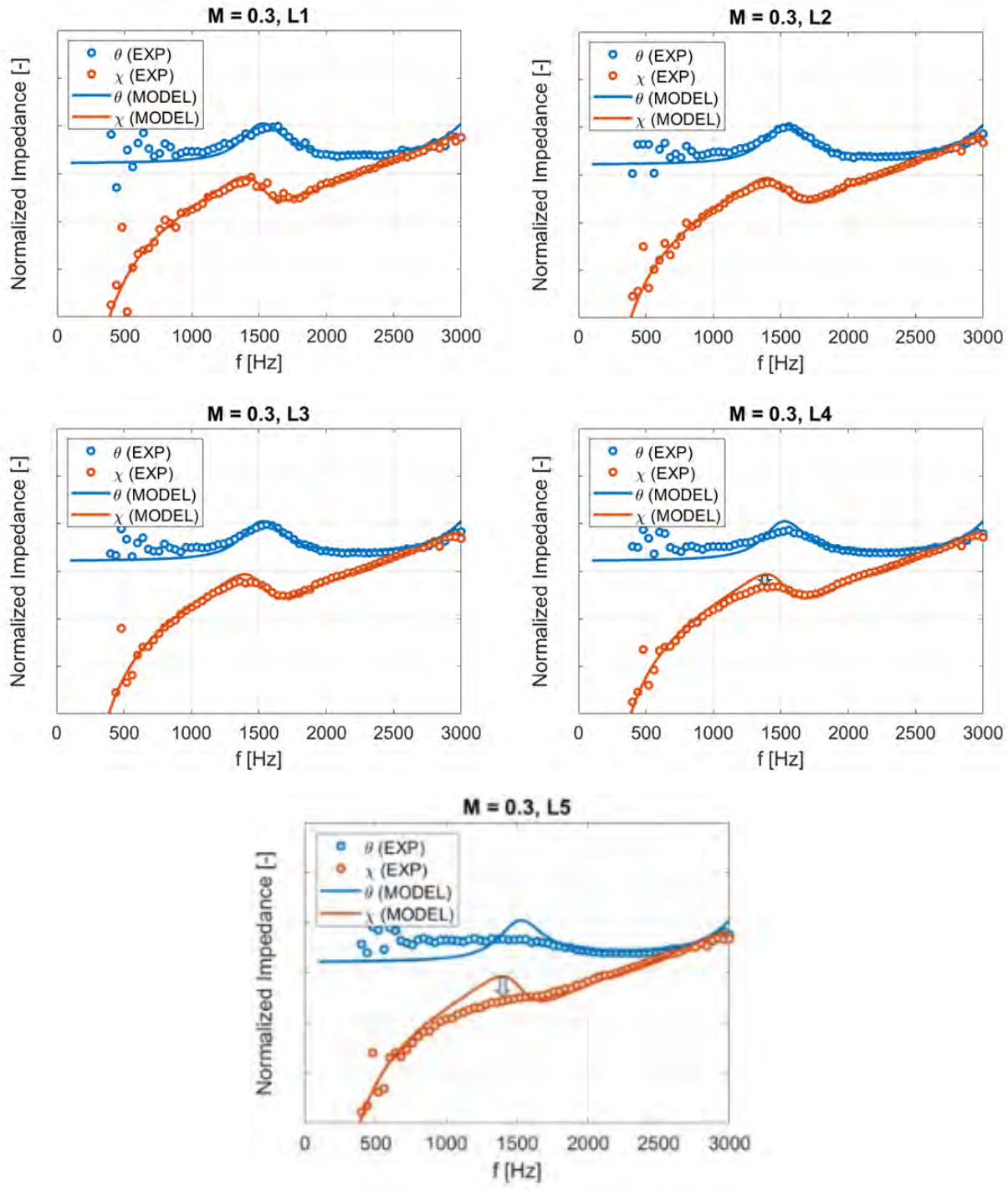

Figure 22. Comparisons of normalized impedance (resistance and reactance) for M = 0.3.
[θ - Resistance, χ - Reactance, L1 = 110dB, L2 = 120dB, L3 = 130dB, L4 = 140dB, and L5 = 150dB]]

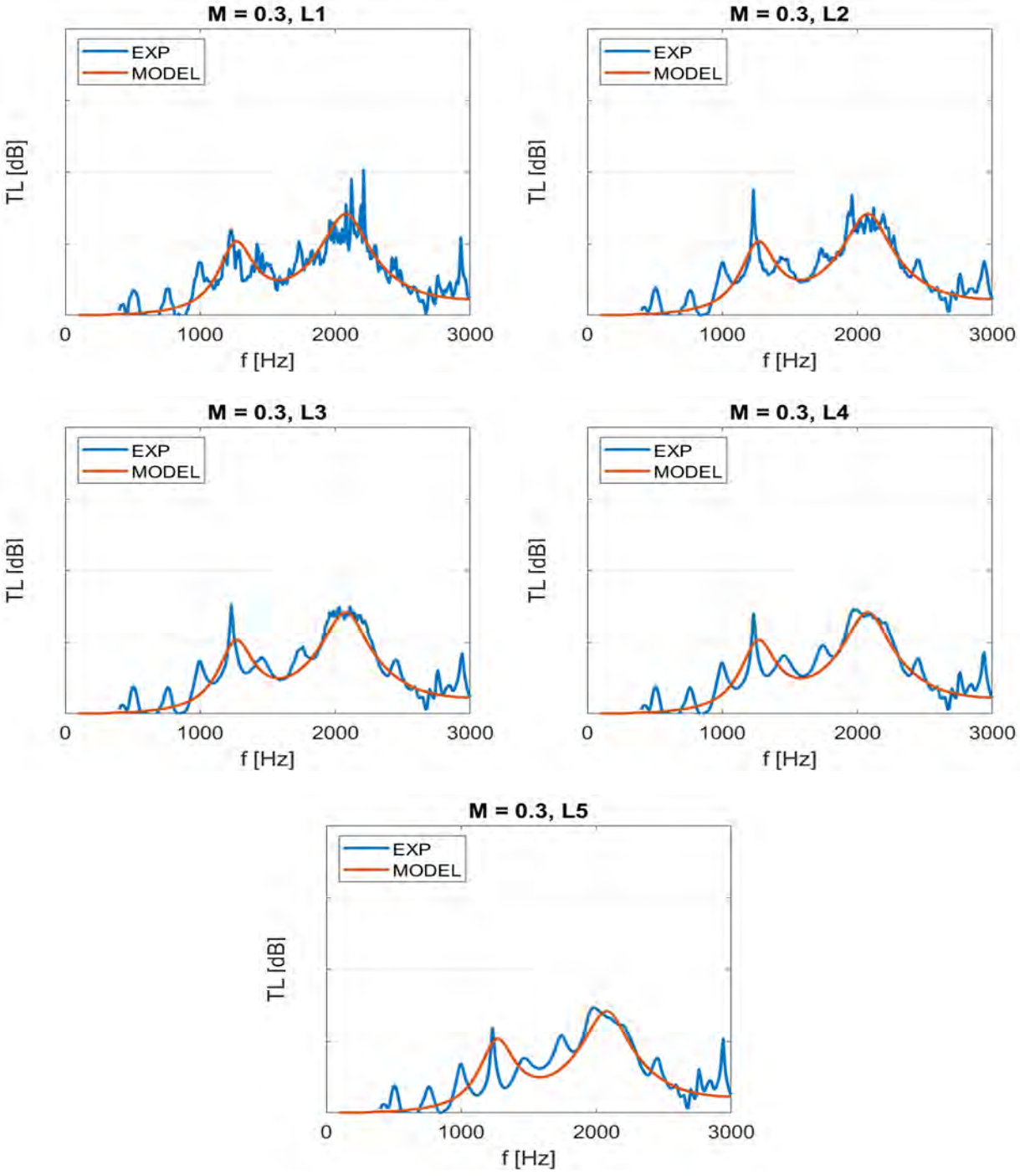

Figure 23. Comparison of Transmission Loss for M = 0.3.
[L1 = 110dB, L2 = 120dB, L3 = 130dB, L4 = 140dB, and L5 = 150dB]]

Figure 23 shows the TL loss comparison between the NASA test data (blue) and the post-prediction (orange) for M=0.3 and for all five in-duct SPLs (L1-L5) as previously defined. Overall, good agreement between the measured test results and the post-predictions except for the slight waviness in the test results. This waviness can partially be explained by reflections in the flow duct facility, as a two-microphone technique at the inlet was used to extract the incident pressure on the microphones and reduced the waviness significantly above 1000Hz in the test results. More microphones could provide additional filtering; although, the team is satisfied with the results of this first teat entry.

The TL performance at the two peaks is captured very well in all conditions shown. The two peaks in the TL data are related to the bulb volume and the volume outside the bulbs. More peaks are expected due to the number of bulbs in the design; however, other peaks fall outside the measured test range. Note, at the M=0.0 case the first peak is significantly reduced for the higher SPLs, L3 to L5 where it is expected that the SPL effects will dominate the liner performance compared to when grazing flow is added.

A successful first test of a liner in the presence of grazing flow was achieved. Steps taken to improve predictions included (1) modeling the actual (manufactured) bulb thickness and geometry and (2) matching the nominal Mach number from the test instead of using the average Mach number. Excellent agreement between educed impedance from test data and modeled impedance and between predicted and measured TL, indicating that flow effects are accurately accounted for and substantiating the GFIT model for TL.

Based on the learnings of this first test entry, additional updates to the model will consider non-linear effects, currently not incorporated. Non-linear SPL effects are noticeable in the test data and impacting the first resonance. This effect is currently not accounted for in model and hence performance is overpredicted. A summary is provided below of where this is most noticeable in the impedance data:

- M = 0 effect is pronounced for SPL >= 130 dB
- M = 0.3 effect is pronounced for SPL >= 140 dB
- M = 0.5 effect is pronounced for SPL >= 150 dB

An additional sample is being prepared by PSU for another grazing flow test at NASA's GFIT facility, this is the second design (design 2). The plan is to get pressure loss measured across the sample in addition to acoustic impedance and the insertion loss of the liner. This testing is targeting late 2024, depending on NASA facility availability. In addition, RTRC has invested capital funding into upgrades to its Grazing Flow Facility (GFF) for future testing. Sound absorption of acoustic liners is measured using a normal impedance tube; however, liner impedance measured in normal impedance tubes does not accurately represent acoustic liners installed in aircraft nacelles due to dependency of impedance on high-speed flow grazing over the liner. Therefore, liner impedances in the presence of grazing flow must be measured in specialized test facilities such as NASA's GFIT or RTRC's GFF.

In the grazing flow impedance test setup shown in Figure 24(a), a liner sample is installed into a duct where sound propagates along the duct in the presence of forced air flow. In this setup, an axial microphone array over the liner is used to measure the sound field distribution across the liner, then the eduction method is performed to inversely determine the liner impedance. This contrasts with an in-situ method, where the impedance of the liner is determined by two or more probe microphones directly installed into the internal structure of the liner, enabling very localized measurements. The in-situ impedance method is only practical for conventional acoustic liners with relatively simple internal geometries. The impedance of advanced liners with more complex internal structures has to be determined by an eduction method.

To enable the impedance measurement of advanced liners in this program, RTRC developed our in-house liner eduction code based on NASA's Prony method. The Prony method is a data-driven approach where liner impedance is determined by measuring the axial (complex) wavenumber of the propagating waves using the axial microphone array. The code has been rigorously validated by multiple approaches. For this work, we used NASA's publicly available data from their GFIT facility to validate the results from RTRC's eduction code.

In parallel to the impedance eduction code development, internal capital funds were used to upgrade the RTRC GFF, as shown in Figure 24(b). One of the upgrades included a new test section. The cross-sectional height of the duct was reduced, which was found (based on simulation) to be beneficial for improving the accuracy of liner impedance eduction results (by ensuring the plane-wave propagation in the duct to higher frequencies). This was accomplished by introducing tapered duct inserts that effectively reduced the duct cross-sectional area by half. Other design features like liner section length, microphone array position and count, acoustic drivers, and data acquisition system were also updated to enable

accurate liner education measurements. In addition to the acoustic measurements, accommodations were incorporated into the duct section to allow for flow characterization of the new test section. Thus, this allows for both flow and sound pressure level measurements to be made at the sample location to verify the operating condition and expected noise levels at the sample.

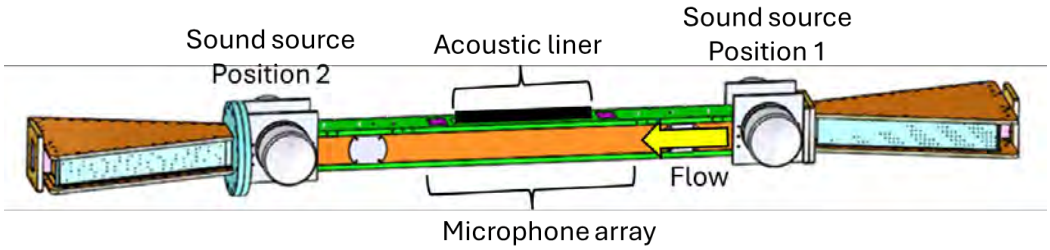

(a)

(b)

Figure 24. RTRC's GFF liner test facility (sound source, acoustic liner, and microphone array); (a) GFF liner facility schematic; (b) GFF liner facility photo.

Milestones

- Detailed acoustic evaluation of acoustic liner design based on Schwarz-P TPMS.
- Refined predictions using the manufactured part and true test conditions.
- Developed eduction code estimate impedance of more complex acoustic liner designs.
- Utilize simulation and eduction code to finalize upgrade design of RTRC's GFF.

Major Accomplishments

- Matured TPMS liner technology to TRL4/TRL5 with relevant grazing flow and upstream sound source.
- Validated process for impedance eduction of liner samples in a grazing flow environment using Prony's method.
- Completed the capital upgrade project for the RTRC GFF to enable liner eduction measurements and initiated shakedown testing.

Publications

None. Our team is working on publication of the grazing flow results with NASA. We also plan to prepare one or two conference publications once the experimental evaluation is complete.

Outreach Efforts

None.

Awards

None.

Student Involvement

None.

Plans for Next Period

- Leverage the RTRC facility for evaluating the performance of advanced liner concepts under development.
- Fabricate additional acoustic liner samples for grazing flow impedance testing and compare experimental results to predicted values.
- Begin to assess the aerodynamic losses on our designs.
- Refine and update analysis and simulation models as needed.
- Conduct additional testing of acoustic performance and material evaluation for successful manufacturing of the proposed liner concepts.
- Shift focus to acoustic liner designs for a specific section of the engine, moving from component-level tradeoffs (e.g., weight, acoustic performance, structural integrity) to subsystem-level tradeoff studies (e.g., weight, cost, drag).

References

ASTM International. (2023). *ASTM D1621: Standard test method for compressive properties of rigid cellular plastics*. doi:10.1520/D1621-16.

Project 080(A) Hydrogen and Power-to-Liquid Concepts for Sustainable Aviation Fuel Production

Washington State University

Project Lead Investigators

Manuel Garcia-Perez
Professor and Chair
Biological Systems Engineering Department
Washington State University
LJ Smith, Room 205, PO Box 646120, Pullman, WA 99164-6120
509-335-7758
mgarcia-perez@wsu.edu

Michael P. Wolcott
Regents Professor
Department of Civil & Environmental Engineering
Washington State University
PO Box 642910, Pullman, WA 99164-2910
509-335-6392
wolcott@wsu.edu

University Participants

Washington State University (WSU)

- P.I.s: Prof. Manuel Garcia-Perez, Prof. Michael P. Wolcott
- FAA Award Number: 13-C-AJFE-WaSU-031
- Period of Performance: October 1, 2023, to September 30, 2024
- Tasks:
  1. Evaluate the strengths and weaknesses of hydrogen production and power-to-liquid (PtL) concepts in the United States
  2. Co-location and incorporation of hydrogen technologies into existing sustainable aviation fuel (SAF) production and infrastructure
  3. Evolution of SAF production pathways to integrate alternative hydrogen and carbon sources

Project Funding Level

The ASCENT Project 080 received $450,000 in Federal Aviation Administration (FAA) funding and $450,000 in matching funds. State-committed graduate school contributions for PhD students and faculty time for Michael Wolcott, Manuel Garcia-Perez, Xiao Zhang, and Su Ha contribute to the cost share. WSU funding is reported for this reporting period.

Investigation Team

Washington State University

Prof. Manuel Garcia-Perez (P.I.), Tasks 1, 2, and 3
Prof. Michael Wolcott (P.I.), Tasks 1, 2, and 3
Prof. Xiao Zhang (Co-PI), Tasks 1, 2 and 3
Prof. Su Ha (Co-PI), Tasks 1, 2 and 3
Dr. Jonathan Male (Co-P.I.), Tasks 1, 2, and 3
Aidan Garcia (research associate), Tasks 2 and 3
Kristin Brandt (staff engineer), Tasks 1, 2, 3, and 6
Valentina Sierra (graduate research assistant), Tasks 1 and 2

Collaborating Researchers

Corinne Drennan, Pacific Northwest National Laboratory (PNNL)

Project Overview

The aviation industry is under pressure to reduce its greenhouse gas (GHG) emissions. SAFs are considered the most promising approach for achieving the sector's GHG emissions reduction targets. To date, no comprehensive assessment exists for analyzing how different carbon, hydrogen, and energy sources can be combined with different conversion processes to produce SAF with high GHG emission reductions and low costs. The goals of this project are to (a) evaluate the strengths and weaknesses of hydrogen production and PtL concepts, (b) assess the state of the art for the integration of hydrogen production, different carbon sources (including atmospheric carbon dioxide [CO_2] capture), and PtL production with existing infrastructure (SAF production and industries), (c) analyze the cost and environmental impacts of these production pathways, and (d) synthesize this information and obtain rules on how to best combine carbon, hydrogen, and energy sources with different conversion technologies to improve environmental impacts and costs. This research will enable the identification of new pathways to optimize SAF production for maximum GHG reductions with minimal fuel costs.

Approved SAF pathways commonly use photosynthesis-derived carbon from sugars, lignocellulosic materials, or lipids. Some SAF technologies that are currently being investigated include those based on hydro-processed ester and fatty acid synthetic paraffinic kerosene (HEFA-SPK), Fischer–Tropsch (FT) synthetic paraffinic kerosene (FT-SPK), Fischer–Tropsch synthetic kerosene with aromatics (FT-SKA), synthesized iso-paraffins (SIP), Virent® BioForming synthesized aromatic kerosene, hydrodeoxygenation synthesized kerosene, catalytic hydro-thermolysis, alcohol-to-jet (ATJ) fuel, hydropyrolysis (Shell® IH²®), fast pyrolysis, and hydro-processed depolymerized cellulosic jet fuel. The jet fuels produced from eight paths (FT-SPK, HEFA-SPK, SIP, FT-SKA, ATJ, catalytic hydro-thermolysis, and HEFA) (ASTM, 2024a) and by co-processing lipids and FT biocrude in refineries (ASTM, 2024b) are now approved by ASTM International (formerly known as the American Society for Testing Materials) for use in commercial aircraft. Although these processes can result in substantial GHG reductions, their production costs are still substantially higher than those of conventional jet fuels derived from petroleum distillation ($0.88–$3.86/L) (Tanzil et al., 2021).

Previous studies (Tanzil et al., 2021) have shown that the quality of the carbon source determines the SAF yield. For example, although lignocellulosic materials are ten times cheaper than lipids (on a mass basis), the latter's quality as a carbon source makes triglyceride-derived fuels much cheaper (two to five times) than those derived from cellulose, hemicellulose, or lignin. Carbon in organic matrices containing a higher level of oxygen, nitrogen, and sulfur is more challenging to convert to jet fuel because of the penalties associated with the removal of oxygen, nitrogen, and sulfur, a process that typically consumes hydrogen. Carbon in polymeric molecules is also more challenging to convert to jet fuel because it requires costly molecular weight reduction technologies and often lacks selectivity to the targeted jet fuel cut. Carbon in the form of aliphatic molecules can be more easily converted to jet fuel than carbon as aromatics which has a higher tendency to form coke. Carbon sources such as CO_2, biomass, coal, petroleum, and municipal solid waste (MSW) must be thoroughly investigated as feedstocks for SAF production. Because carbon is the highest-weight element in jet fuel production, high fuel yields can only be achieved in processes with high carbon conversion efficiencies.

Most technologies that produce SAF consumed large amounts of hydrogen, ranging from 2 mass % of the produced fuel for ATJ (Snowden-Swan et al., 2017) to 11-12 mass % for pyrolysis (Brandt et al., 2022). Although hydrogen can currently be produced by many pathways using low-carbon-intensity electrons produced by wind and solar farms, current hydrogen production is mainly based on steam methane reforming (SMR), which is associated with significant CO_2 emissions. Commonly considered paths for hydrogen production include (a) steam and dry reforming of hydrocarbons, (b) water electrolysis, (c) plasma arc decomposition, (d) water thermolysis, (e) thermochemical water splitting, (f) thermochemical conversion of biomass (biomass gasification and biofuel reforming), (g) photovoltaic electrolysis, photocatalysis, and photochemical methods, (h) dark fermentation, (i) high-temperature electrolysis, (j) hybrid thermochemical cycles, (k) coal and petroleum gasification, (l) MSW gasification, (m) fossil fuel reforming, (n) biophotolysis and photo-fermentation, (o) artificial photosynthesis, and (p) photo-electrolysis (Dincer & Acar, 2015). One goal of this project is to evaluate the

® Virent is a registered trademarks of Virent, Inc., Madison, Wisconsin.
® Shell is a registered trademark of Shell Trademark Management B.V., The Hague, The Netherlands.
® IH² is a registered trademark of Gas Technology Institute, Des Plaines, Illinois.

strengths and weaknesses of hydrogen production concepts, determine how they can be integrated with existing infrastructure to produce cheap green hydrogen, and identify the potential impact of these technologies in producing SAF.

In some biomass and waste conversion processes, CO_2 and methane (CH_4) are produced as a side product or as the starting material. To meet the specifications for SAF, hydrogen will be needed to hydrogenate alkenes and hydrotreat oxygenates. Utilizing waste CO_2 and CH_4 can increase the amount of carbon obtained from resources in the SAF while reducing emissions. This can be done in conjunction with hydrogen production with a lower carbon intensity. Our analysis will examine the trade-offs between enhanced carbon utilization, the effects of increased renewable energy use, the need for stability in the grid and energy storage, access to lower-carbon-intensity hydrogen against positive impacts on environmental indicators, the cost impact of such changes, and technology uncertainty in emerging science and engineering.

References

ASTM. (2024a). *Standard Specification for Aviation Turbine Fuel Containing Synthesized Hydrocarbons* (D7566; Version 24D). https://doi.org/10.1520/D7566-24D

ASTM. (2024b). *Standard Specification for Aviation Turbine Fuels* (D1655; Version 24a). https://doi.org/10.1520/D1655-24A

Brandt, K., Tanzil, A. H., Martinez-Valencia, L., Garcia-Perez, M., & Wolcott, M. P. (2022). *Pyrolysis techno-economic analysis* (v. 2.2). Washington State University. https://doi.org/10.7273/000002563

Dincer, I., & Acar, C. (2015). Review and evaluation of hydrogen production methods for better sustainability. *International Journal of Hydrogen Energy*, *40*(34), 11094–11111. https://doi.org/10.1016/j.ijhydene.2014.12.035

Snowden-Swan, L. J., Zhu, Y., Bearden, M. D., Seiple, T. E., Jones, S. B., Schmidt, A. J., Billing, J. M., Hallen, R. T., Hart, T. R., Liu, J., Albrecht, K. O., Fox, S. P., Maupin, G. D., & Elliott, D. C. (2017). *Conceptual biorefinery design and research targeted for 2022: Hydrothermal liquefaction processing of wet waste to fuels* (p. 1-40). Pacific Northwest National Laboratory, 27186. https://www.osti.gov/servlets/purl/1415710

Tanzil, A. H., Brandt, K., Wolcott, M., Zhang, X., & Garcia-Perez, M. (2021). Strategic assessment of sustainable aviation fuel production technologies: Yield improvement and cost reduction opportunities. *Biomass and Bioenergy*, *145*, 105942. https://doi.org/10.1016/j.biombioe.2020.105942

Task 1 - Evaluate the Strengths and Weaknesses of Hydrogen and PtL Concepts in the United States

Washington State University

Objectives

The objective of this task is to perform a literature review and develop design cases for hydrogen and PtL concepts.

Research Approach

In this task, the ASCENT Project 080 team will identify areas that require more research and development to reduce technology uncertainty. Specifically, our team analyzed six technologies for hydrogen production: (a) steam reforming, (b) dry reforming, (c) water electrolysis, (d) gasification of carbonaceous materials (biomass, coal, bitumen, and MSW) (with steam and CO_2), (e) thermal decomposition of hydrocarbons (methane pyrolysis with capture and use of solid carbon), and (f) fossil fuel reforming. This task is being conducted by WSU and PNNL and started during 2022. The main goal of this task is to build design cases for each of these hydrogen production technologies (i.e., mass, energy balances, and techno-economic analysis [TEA]) and identify the strengths and weaknesses of each technology studied. A team of hydrogen production experts from WSU and PNNL meets weekly with a PhD student and post-doctoral associate from WSU to guide them in the literature review and in the creation of a road map for constructing design cases and identifying the opportunities and challenges for each of the technologies studied.

Milestones

- Worked on two main deliverables: (a) a literature review of hydrogen production technologies within the context of SAF production, and (b) mass, energy balances, and TEAs of standalone hydrogen production technologies.
- Completed the first draft of a literature review for hydrogen production within the context of SAF technologies, and it is currently under internal review.

- Developed TEAs of hydrogen production technologies to estimate the minimum selling price and GHG footprint for each. These results are now available for internal use and are being finalized for publication.

Major Accomplishments

- Completed the first draft of a literature review on the TEAs of hydrogen production technologies (low and high-pressure gasification, steam reforming, methane partial oxidation, autothermal oxidation, methane pyrolysis, and low- and high-temperature water electrolysis) and have identified several promising pathways in which hydrogen production technologies are integrated with gasification.
- Developed standardized design cases to estimate hydrogen production costs for each of the technologies studied. These cases will provide a harmonized set of process models, TEA and Lifecycle analysis results for future studies utilizing hydrogen from various sources, and they have already proved useful as reference values for Task 2.
- Developed a method to account for policy support from Inflation Reduction Act section 45.
- Updated the methodology for our TEA to a cost of equity (COE) model during this project. This methodology represents a more realistic assessment of the risk and profits assumed by investors in a plant project.
- Worked on the development of detailed equipment costing assumptions. The manuscript containing these results will be submitted shortly.

Publications

Sierra, V., Wolcott, M., Zhang, X., Ha, S., Male, J., Garcia, A., Brand, K., Garcia-Perez, M., Drennan, C., & Holladay, J. (Under review). *Emerging and commercial hydrogen production technologies for SAF manufacturing: A comparative literature review*. Washington State University.

Outreach Efforts

- Presented the preliminary results at the ASCENT Spring 2022 and Fall 2022 meetings on April 5–6, 2022, and November 25–26, 2022, respectively.
- Presented the preliminary results at the Civil Aviation Alternative Fuels Initiative meeting on June 1–3, 2022, in Washington, D.C.

Presentation

Sierra-Jimenez, V., Brandt, K., Wolcott, M., Male, J., Garcia-Perez, M. (2024, November 20-21). *Hydrogen Production Techno-economic and Carbon Intensity Insights for a Sustainable Energy Transition in the U.S.* [Poster presentation]. Re+CHARGE H_2 Conference (PNWH2 Hub), Seattle, Washington.

Student Involvement

Valentina Sierra, a graduate student majoring in biological systems engineering at WSU, performed the literature review of hydrogen production technologies and the role that hydrogen has in SAF production. She also worked with Kristin Brandt on the TEA of these technologies.

Plans for Next Period

- Publish the revised literature review and the standardized improved TEAs.

Task 2 - Co-location and Incorporation of Hydrogen Technologies into Existing SAF Production and Infrastructure

Washington State University

Objective

The goal of this task is to estimate the cost reduction potential of the inclusion and co-location of hydrogen production with existing SAF production technologies and infrastructure.

Research Approach

This task involves both a theoretical and applied approach. The first is the updating of current SAF production and TEA models to account for the inclusion of green hydrogen (using data from Task 1). The second is the investigation of specific

mechanisms by which that inclusion can be improved.

In the first subtask, the ASCENT Project 080 team evaluated the impact of each of the emerging hydrogen production technologies on existing SAF technologies, including those based on (a) HEFA, (b) Virent BioForming synthesized aromatic kerosene, (c) ATJ fuel, (d) natural sugar to hydrocarbon (SIP), (e) fast pyrolysis and the gas-to-fuel process, and (f) selective carbonization/CO_2 gasification/steam reforming/FT processes. These technologies are all hydrogen limited to some degree, meaning that emerging hydrogen production technologies may improve their yields and carbon intensity. Detailed analysis would furnish us with a hydrogen cost and carbon intensity (CI) threshold to justify its inclusion in SAF production and what SAF technologies stand to benefit most from supplemental hydrogen. Our team conducted weekly meetings with WSU, PNNL experts, and our PhD students to identify hydrogen production opportunities in existing industries (i.e., petroleum refineries, dams, metallurgical industry, etc.). Our main goal is to estimate cost reduction opportunities that would arise if the emerging hydrogen production technologies were co-located with some of these industries.

In the second subtask, our team studied how hydrogen is used in hydrotreatment steps. Hydrogen utilization for SAF production typically occurs in a hydrotreatment step that varies depending on the technology (Tanzil et al., 2021; Han et al., 2019). This step can proceed from a simple hydrogenation, hydrodeoxygenation, hydrocracking, or all of them together, depending on the technology (Han et al., 2019). Especially troublesome is the hydrotreatment of oligomers and materials with a high tendency to form coke (Han et al., 2019). In this subtask, we will develop a detailed phenomenological mathematical model for the hydrotreatment step of the HEFA and fast pyrolysis pathways, which the team will then use to study potential strategies to reduce hydrogen consumption during SAF production (Chen et al., 2019; Plazas-González et al., 2018). This type of model requires a detailed description of the chemical composition of the feedstock, the reaction mechanism, and associated kinetics (Gutiérrez-Antonio et al., 2018; Talib Jarullah, 2011; Boesen et al., 2011 Jenišťová et al., 2017; Tieuli et al., 2019; Hachemi & Murzin, 2018). The modeling work will complement studies in batch and continuous hydrotreatment reactors with different catalysts to validate the mathematical model.

Milestones

- Used our cost heuristic to evaluate the effect of many hydrogen production technologies on a simplified gasification model as an offshoot of our holistic assessment of SAF (Task 3). The introduction of technical constraints for a simplified oxygen gasification model yielded a tipping point of about 2.75 $/kg hydrogen. An assessment of this simplified gasification model with different oxidizers (dioxygen [O_2], steam, and CO_2) indicated that current gasification technologies (O_2, steam) do not justify its inclusion in these simplified cases.
- Created a design case for our standard gasification TEA that accepts external hydrogen to verify these results in more detail.
- Conducted an investigation of hydrogen efficiency in hydrotreatment which began January 2023 with a literature review of catalytic hydrotreatment reactions.
- Began development of atomistic models of hydrotreatment processes and a description of pyrolysis oils in terms of representative compounds.
- Developed a gasification process using supplemental hydrogen and continued work on the development of TEA for gasification/methanol/FT and pyrolysis-hydrotreatment technologies.

Major Accomplishments

Our work shows potential for synergy between co-located syngas processes and high-temperature electrolysis. In addition to gasification's elevated temperatures providing plentiful high-quality heat, fuel synthesis ejects 22% to 28% of the fuel's heating value as waste heat under ideal conditions (Lange, 2007). Results for simplified models of current gasification technologies do not indicate performance improvements from supplemental hydrogen, and we are verifying these results in more detail. We have made progress on a literature review on pyrolysis oils hydrotreatment reactions and a preliminary atomistic model of pyrolysis oil molecules catalytic hydrogeneration.

Publications

Denson, M. (2023). *Contributions to understanding oligomeric sugars derived from biomass pyrolysis* [Doctoral dissertation, Washington State University]. Washington State University.

Outreach Efforts

None.

Awards
None.

Student Involvement
Aidan Garcia, a research associate at WSU, is working on the TEA and process models. Melba Denson, a PhD student at WSU, has contributed applied and theoretical hydrotreatment work to this task as part of her thesis.

Plans for Next Period
- Complete our detailed investigation of hydrogen's effect on gasification's cost and CI.
- Update our pyrolysis TEA to include external hydrogen and perform the same analysis. The remaining TEA cases (HEFA, ATJ) already account for supplemental hydrogen and should be relatively easy to modify.
- Continue our review of different hydrotreatment technologies associated with producing SAFs and the mathematical models used to describe the operation of these reactors.

References
Boesen, R. R. (2011). *Investigation and modelling of diesel hydrotreating reactions* [Doctoral dissertation, Technical University of Denmark]. Technical University of Denmark. https://backend.orbit.dtu.dk/ws/portalfiles/portal/6470295/Thesis+Rasmus+R.+Boesen+2010+final.pdf

Chen, Z., Feng, S., Zhang, L., Shi, Q., Xu, Z., Zhao, S., & Xu, C. (2019). Molecular-level kinetic modelling of fluid catalytic cracking slurry oil hydrotreating. *Chemical Engineering Science*, *195*, 619–630. https://doi.org/10.1016/j.ces.2018.10.007

Gutiérrez-Antonio, C., Soria Ornelas, M. L., Gómez-Castro, F. I., & Hernández, S. (2018). Intensification of the hydrotreating process to produce renewable aviation fuel through reactive distillation. *Chemical Engineering and Processing - Process Intensification*, *124*, 122–130. https://doi.org/10.1016/j.cep.2017.12.009

Han, Y., Gholizadeh, M., Tran, C.-C., Kaliaguine, S., Li, C.-Z., Olarte, M., & Garcia-Perez, M. (2019). Hydrotreatment of pyrolysis bio-oil: A review. *Fuel Processing Technology*, *195*. https://doi.org/10.1016/j.fuproc.2019.106140

Hachemi, I., & Murzin, D. Yu. (2018). Kinetic modeling of fatty acid methyl esters and triglycerides hydrodeoxygenation over nickel and palladium catalysts. *Chemical Engineering Journal*, *334*, 2201–2207. https://doi.org/10.1016/j.cej.2017.11.153

Jeništová, K., Hachemi, I., Mäki-Arvela, P., Kumar, N., Peurla, M., Čapek, L., Wärnå, J., & Murzin, D. Y. (2017). Hydrodeoxygenation of stearic acid and tall oil fatty acids over Ni-alumina catalysts: Influence of reaction parameters and kinetic modelling. *Chemical Engineering Journal*, *316*, 401–409. https://doi.org/10.1016/j.cej.2017.01.117

Lange, J. (2007). Lignocellulose conversion: an introduction to chemistry, process and economics. *Biofuels, Bioproducts and Biorefining: Innovation for a Sustainable Economy, 1*(1), 39–48.

Plazas-González, M., Guerrero-Fajardo, C. A., & Sodré, J. R. (2018). Modelling and simulation of hydrotreating of palm oil components to obtain green diesel. *Journal of Cleaner Production*, *184*, 301–308. https://doi.org/10.1016/j.jclepro.2018.02.275

Talib Jarullah, A. (2011). *Kinetic parameters estimating hydrotreating reactions in trickle bed reactor (TBR) via pilot plant experiments; Optimal design and operation of an industrial TBR with heat integration and economic evaluation* [Doctoral. dissertation, University of Bradford]. University of Bradford. https://bradscholars.brad.ac.uk/bitstreams/01cfae05-bc0d-4a5e-9611-a465899e3e13/download

Tanzil, A. H., Brandt, K., Wolcott, M., Zhang, X., & Garcia-Perez, M. (2021). Strategic assessment of sustainable aviation fuel production technologies: Yield improvement and cost reduction opportunities. *Biomass and Bioenergy*, *145*. https://doi.org/10.1016/j.biombioe.2020.105942

Tieuli, S., Mäki-Arvela, P., Peurla, M., Eränen, K., Wärnå, J., Cruciani, G., Menegazzo, F., Murzin, D. Y., & Signoretto, M. (2019). Hydrodeoxygenation of isoeugenol over Ni-SBA-15: Kinetics and modelling. *Applied Catalysis A: General*, *580*, 1–10. https://doi.org/10.1016/j.apcata.2019.04.028

Task 3 – Evolution of SAF Production Pathways to Integrate Alternative Hydrogen and Carbon Sources

Washington State University

Objective

The objective of this task is to identify new pathways to optimize SAF production for maximum GHG reductions with minimal fuel costs.

Research Approach

This task is being conducted in two steps. In the first step, the WSU–PNNL panel of experts met weekly with the PhD student to discuss the potential for combining the SAF pathways studied under Task 2 with alternative carbon sources (i.e., MSW, sludges from wastewater treatment plants, CO_2). In the second step, our team evaluated the potential integration of these technologies with the new hydrogen production technologies discussed in Task 1. We used the information collected to propose design and synthesis rules (diagrams) to help visualize how the source of carbon, hydrogen, and available energy and the type of conversion technology impact on the main environmental and economic sustainability indicators. Our team aimed to use this exercise to identify better paths for SAF production.

Milestones

Our team followed a holistic path to identify desired production pathways. The following milestones were achieved as part of this effort:

- Correlated the minimum fuel selling price from 32 SAF TEAs with a model proposed by Lange (2016). The model estimates the production SAF cost of product yield, feedstock, and other supplied costs. Our analysis estimated an average conversion cost of $330 per tonne of feedstock processed, which is consistent for the chemical industry.
- Developed three purely stoichiometric mass balances to estimate the effect of deoxygenation method (e.g., oxygen removal as O_2, H_2O, or CO_2) on production cost. Although water deoxygenation proved to be most advantageous, all idealized models proved viable, ruling out stoichiometry alone as a limiting factor in fuel production. These simple models were also used to study the effect of hydrogen, plastics, and carbon sequestration on the overall performance of these ideal technologies.
- Analyzed biomass gasification technologies for more detailed optimization. We concluded that existing technologies for the conversion of biomass into syngas are limited by very low carbon conversion efficiencies. To achieve carbon conversion efficiencies close to 100%, the introduction of outside hydrogen and energy is necessary. While low-temperature gasification technologies have higher cold-gas efficiencies, the use of existing high-temperature gasification technologies may allow for better yields and heat integration with hydrogen technologies through reactive quenching by reverse water gas shift (Hillestad et al., 2018). Additionally, close to one-third of the syngas energy is lost when syngas is converted to SAF, presenting a limitation that must be addressed. Our team worked on the development of modern technologies to address these issues.
- Developed preliminary models for standard gasification and gasification with integrated electrolysis. Our base-case is modelled on the results of Swanson (Swanson et al., 2010).
- Identified relevant case studies for methanol synthesis (Tan et al., 2015) and heat integration during syngas cleaning (de Oliveira et al., 2023).

Major Accomplishments

The ASCENT Project 080 team has learned that the most critical factor governing production cost is fuel yield, which is directly related to carbon conversion efficiency. However, to maximize carbon conversion efficiency, it is critical to remove oxygen in the form of water by reacting it with hydrogen, which requires the introduction of hydrogen from outside the system. Currently, gasification is the leading technology for producing syngas as an intermediate. Current gasification systems must be optimized for maximum carbon conversion efficiency. An overall mass and energy balance shows that typical gasification systems are oxygen-, energy-, and hydrogen-deficient and that current designs sacrifice carbon efficiency to address the lack of energy and hydrogen. This issue can be addressed by augmenting hydrogen and energy from outside the system. Furthermore, the carbon dioxide (CO) in syngas affords a carbon/oxygen (C/O) ratio that is much higher than the C/O ratio of biomass, requiring oxygen addition to the system. Syngas also has an energy content higher than that of the fuel produced; therefore, nearly one-third of the system's energy is released as heat. Heat integration is critical to maximizing the economic viability of technologies producing syngas as an intermediate. Because hydrogen must

be produced externally to maximize fuel production yields, hydrogen production technologies and their potential synergisms with SAF production must be carefully studied to develop optimized systems.

For this purpose, our team has produced a holistic analysis of the hydrogen market's effect on the potential of oxygen, steam, and CO_2 gasification technologies. This overall analysis was then integrated with the hydrogen production technologies examined in Task 1 to forecast which pathways will become favorable as the hydrogen market evolves. We have also produced a Microsoft Excel®-based model that accounts for both stoichiometric and thermodynamic constraints in fuel production from biomass. This tool has not been utilized but could theoretically be updated and deployed for the testing of basic process optimization. Our extended Lange model has been placed into a Python® module that allows the calculation of economics for simple stoichiometric processes. We can easily extend this model to accept generalized user inputs, if needed for public outreach. Through this analysis our team was able to determine a tipping point of 2.50 $/kg for the inclusion of hydrogen in stoichiometric SAF production processes. Without the availability of hydrogen below this price, removal of biogenic oxygen in the form of CO_2 is more cost effective than removal in the form of water for the stoichiometric models evaluated. The results of this holistic analysis have been published in *ACS Energy and Fuels* (Garcia et al., 2024). These results are currently being evaluated in more detail using standard techno-economic methods.

Publications

Peer-Reviewed Journal Publication

Garcia, A., Sierra-Jimenez, V., Brandt, K., Martinez-Valencia, L. P., Wolcott, M., Male, J., & Garcia-Perez, M. (2024). Holistic methodology to guide the evolution of sustainable aviation fuel production technologies. *Energy & Fuels, 38*(18), 17706–17716. https://doi.org/10.1021/acs.energyfuels.4c02795

Presentations

Garcia, A., & Garcia-Perez, M. (2024, June 24-27). *Holistic methodology to guide the evolution of sustainable aviation fuel production technologies* [Conference Presentation]. European Biomass Conference, Marseille, France.

Garcia-Perez, M., Garcia, A., & Wolcott, M. (2024, October 2-4). *Holistic methodology to guide the evolution of sustainable aviation fuel production technologies* [Conference presentation]. Sustainable Aviation Futures, North America, Houston, Texas.

Garcia-Perez, M., Garcia, A., & Wolcott, M. (2024, July 28-31). *Holistic methodology to guide the evolution of sustainable aviation fuel production technologies* [Conference presentation]. American Society of Agricultural and Biological Engineers (ASABE) 2024, Anaheim, California.

Garcia-Perez, M., Garcia, A., & Wolcott, M. (2022, October 24-27). *Production of cheap sustainable aviation fuels (SAFs): Balancing economic and environmental imperatives* [Conference presentation]. Sustainable Energy for a Sustainable Future, San Pedro, San Jose.

Outreach Efforts

- Participated in biweekly meetings with our panel of experts and have been progressing toward the goals of this task.
- Completed a literature review of hydrogen production technologies, their TEAs, and the synthesis of new SAF production pathways.
- Presented at the Spring 2022 ASCENT meeting (April 5–7, 2022) and at the Civil Aviation Alternative Fuels Initiative meeting in Washington, DC (June 1–3, 2022).
- Presented our work at the October 2022 Fuel Task Group meeting in Alexandria, Virginia.
- Presented our results in poster format at the 2023 and 2024 Northwest Bioenergy Summit (Tri-Cities and Spokane, Washington).
- Presented our results at the Spring 2024 and Fall 2024 ASCENT meetings in Hawai'i and Alexandria, Virginia, respectively.

Student Involvement

Valentina Sierra (PhD student), Anika Afrin (master's student), Aidan Garcia (research associate), and Robert Macias (research associate) contributed to this task. Claudia Valderrama-Ríos, a biological systems engineering PhD candidate at WSU, is developing the integrated case for gasification for this task.

® Microsoft and Excel are registered trademarks of Microsoft Corporation in the United States and other countries.
® Python is a registered trademark of Python Software Foundation, Beaverton, Oregon.

Plans for Next Period

- Evaluate these results in more detail as part of our previously mentioned study of integrated gasification technologies.
- Evaluate each model with an refuse-derived fuel feedstock to further evaluate the effect of fossil carbon on abatement costs. In addition to providing results about the viability of supplemental hydrogen and carbon sources on SAF production, these case studies will better inform our heuristic correlation.

References

de Oliveira, Diego C., Lora, E. E. S., Venturini, O. J., Maya, D. M. Y., & Garcia-Perez, M. (2023). Gas cleaning systems for integrating biomass gasification with Fischer-Tropsch synthesis-A review of impurity removal processes and their sequences. *Renewable and Sustainable Energy Reviews, 172*. https://doi.org/10.1016/j.rser.2022.113047

Hillestad, M., Ostadi, M., Serrano, G. D. A., Rytter, E., Austbø, B., Pharoah, J. G., & Burheim, O. S. (2018). Improving carbon efficiency and profitability of the biomass to liquid process with hydrogen from renewable power. *Fuel, 234*, 1431–1451. https://doi.org/10.1016/j.fuel.2018.08.004.

Lange, J. P. (2016). Catalysis for biorefineries-performance criteria for industrial operation. *Catalysis Science and Technology, 6*(13), 4759–4767. https://doi.org/10.1039/c6cy00431h

Swanson, R. M., Satrio, J. A., & Brown, R. C. (2010). *Techno-economic analysis of biofuels production based on gasification* (No. NREL/TP-6A20-46587). National Renewable Energy Lab.(NREL), Golden, Colorado. https://www.nrel.gov/docs/fy11osti/46587.pdf

Tan, E. C. D., Talmadge, M., Dutta, A., Hensley, J., Schaidle, J., & Biddy, M. (2015). *Process design and economics for the conversion of lignocellulosic biomass to hydrocarbons via indirect liquefaction. Thermochemical research pathway to high-octane gasoline blendstock through methanol/dimethyl ether intermediates* (No. NREL/TP-5100-62402). NREL, Golden, Colorado. https://www.nrel.gov/docs/fy15osti/62402.pdf

Project 080(B) Hydrogen and Power-to-Liquid Concepts for Sustainable Aviation Fuel Production

Massachusetts Institute of Technology

Project Lead Investigators

Florian Allroggen
Executive Director Aerospace Climate and Sustainability
Laboratory for Aviation and the Environment
Massachusetts Institute of Technology
77 Massachusetts Ave, Building 33-328
Cambridge, MA 02139
617-715-4472
fallrogg@mit.edu

University Participants

Massachusetts Institute of Technology (MIT)

- P.I.: Dr. Florian Allroggen
- FAA Award Number: 13-C-AJFE-MIT, Amendment Nos. 091, 101, 115, 124, 128, 133, and 136
- Period of Performance: October 1, 2021, to December 31, 2025
- Tasks during current reporting period (October 1, 2023, to September 30, 2024): (additional tasks to be reported separately by Washington State University)
  1. Develop methods for assessing the economic and environmental impacts of promising sustainable aviation fuel (SAF) production pathways
  2. Apply models to analyze the economic and environmental footprint of SAF production pathways
  3. Analyze the prospects of direct air capture (DAC) of atmospheric carbon dioxide (CO_2) to provide a carbon source for SAF production

Project Funding Level

The ASCENT Project 080(B) received $950,000 Federal Aviation Administration (FAA) funding and $950,000 matching funds. Sources of matching funds are approximately $264,100 from MIT, plus 3rd party in-kind contributions of $101,000 from Savion Aerospace Corp., and $213,000 from NuFuels LLC, and $371,900 from Earth Force Technologies.

Investigation Team

Florian Allroggen (P.I.), Tasks 4, 5, and 6
Niamh Keogh (Research Scientist), Tasks 4, 5 and 6
Tae Joong Park (graduate research assistant), Tasks 4 and 5
Tara Housen (graduate research assistant), Task 6

Project Overview

The aviation industry is under pressure to reduce its greenhouse gas (GHG) emissions. The use of SAF is considered the most promising approach to meet the industry's emission targets. To date, no comprehensive assessment exists which analyzes how different carbon sources, hydrogen sources, and conversion processes can be combined to achieve the highest reductions in GHG emissions at low costs. The goals of this research project are to (1) evaluate the strengths and weaknesses of hydrogen production and power-to-liquid (PtL) concepts in comparison to current SAF production pathways; (2) assess how hydrogen production and PtL production can be integrated with existing production and distribution infrastructure; and (3) analyze the impacts these technologies could have on the current production of SAF (e.g., environmental footprint, cost). The focus of the MIT team will be on analyzing the environmental and economic

impacts of novel fuel production pathways. Furthermore, the MIT team is conducting an analysis of DAC technologies, as well as assessments on how existing SAF pathways can be optimized from a lifecycle GHG emissions perspective.

Task 4 - Develop Methods for Assessing the Economic and Environmental Impacts of Promising SAF Production Pathways

Massachusetts Institute of Technology

Objective

The objective of this task is to define a method for assessing the economic and environmental impacts of promising fuel production pathways. For this purpose, the ASCENT Project 080(B) team developed techno-economic assessment (TEA) and life-cycle assessment (LCA) models. The TEA model calculates the minimum selling price of a specific fuel. The LCA model computes its lifecycle GHG emissions. Because the exact process layout and process characteristics (e.g., mass and energy balances, capital expenditures, operating expenditures) of novel fuel production pathways are subject to uncertainty, the results will include sensitivity studies. This approach obtains insights into the range of economic and environmental impacts associated with fuels from novel fuel production pathways.

Research Approach

The modeling chain used to explore the emissions reduction potential and associated cost impacts of electrifying the SAF production process is outlined using the ethanol-to-jet (ETJ) process with corn grain feedstock. The team reconstructed the United States (U.S.). LCA value from Carbon Offsetting and Reduction Scheme for International Aviation (CORSIA) (ICAO, 2022), which was based on Greenhouse gases, Regulated Emissions, and Energy use in Technologies (GREET®) 2011, using GREET 2022 (Rev. 1) (Argonne National Laboratory, 2022a), GREET 2022 Aviation module (Argonne National Laboratory, 2022b), and International Civil Aviation Organization (ICAO)-GREET 2019 (Argonne National Laboratory, 2022c). This baseline is 8 g carbon dioxide equivalent (CO_2e)/MJ lower and accounts for efficiency improvements since the original analysis; the remaining differences are attributable to the use of older GREET versions.

Figure 1 shows the carbon intensity reduction strategies used for this study. All direct combustion of carbonaceous fuels in the primary supply chain is replaced with onshore wind electricity with battery storage, inclusive of embodied emissions (15.7 g CO_2e/kWh) (Argonne National Laboratory, 2022a). This includes all heating energy used in natural gas (NG), liquefied petroleum gas, diesel, residual oil, coal, biomass, and landfill gas boilers (Argonne National Laboratory, 2022a) being substituted with resistance heating electric boilers (Engineer Live, 2021). All existing electricity use from the U.S. grid is replaced with onshore wind electricity with battery storage. In farming, off-road equipment (tractors) (Lagnelöv et al., 2021), irrigation units (Husker Power Products, 2023), pumps (Honda, 2023), and generators powered by diesel, gasoline, and NG are replaced with equivalent electric units (U.S. Department of Energy, n.d.). For material inputs such as fertilizer, herbicide, and insecticide use, where there is no direct combustion in the primary jet fuel supply chain, the secondary supply chain (i.e., inputs into fertilizer production) is electrified. This includes ammonia (NH_3) produced from electrolytic hydrogen (H_2), electrified transportation of inputs (battery trucks [Tesla Semi, 2023], rail [Popovich et al., 2021], and NH_3 fuel cell–powered ocean tankers and barges [Korberg et al., 2021]), and electrified off-road mining equipment (battery trucks [Henrio et al., 2023] for phosphoric rock hauling for monoammonium phosphate [$NH_4H_2PO_4$]). H_2 from proton exchange membrane (PEM) electrolysis powered by wind replaces H_2 from steam methane reforming in the hydro-processed ester and fatty acid (HEFA) process. Carbon capture and sequestration (CCS) is deployed for the biogenic CO_2 released during the fermentation process. Corn and jet fuel transport and distribution are electrified.

Compared to previous work, the work reported here is based on detailed modeling of the electrification steps.

® GREET is a registered trademark of UChicago Argonne, LLC, Chicago, Illinois.

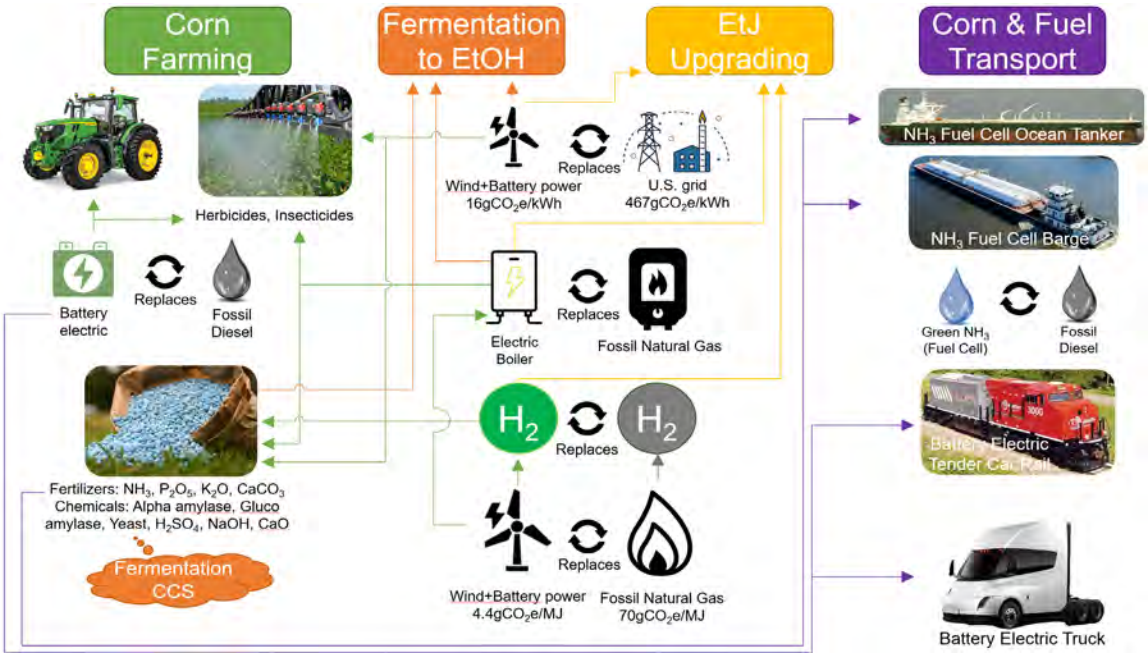

Figure 1. Strategies for reducing the carbon intensity of the corn ETJ pathway, using electrification. Electrolytic hydrogen is produced via proton exchange membrane (PEM) (low temperature) electrolyzer from onshore wind electricity with battery storage, replacing "gray" H_2 from steam methane reforming (SMR) using fossil NG. Note that this is a simplified schematic and not an exhaustive analysis of every element of the lifecycle assessment. HEFA: hydro-processed ester and fatty acid, LPG: liquefied petroleum gas, LFG: landfill gas.

Milestone

- Presented the initial modeling approach to the FAA and other stakeholders.

Major Accomplishment

- Presented the model outline in last year's (2023) ASCENT report. The focus of this year's efforts was on understanding how the modeling chain can be used to understand how existing SAF production pathways can be electrified to reduce their carbon intensity (see Task 5).

Publications

None.

Outreach Efforts

None.

Student Involvement

During the reporting period, TJ Park (MIT graduate student) worked on this task. The student calculated the embodied carbon intensity of wind electricity with battery storage using existing data in GREET, and developed the structure to analyze electrified variants of existing SAF pathways. This included data gathering from the literature for energy, emissions, and cost data of electrified alternatives to SAF production steps and subsequent adaptation for use in LCAs and TEAs.

Plans for Next Period

- Apply the method to additional pathways (e.g., HEFA soybean & tallow) and summarize the findings in a paper.

References

Argonne National Laboratory. (2022a). *GREET: The greenhouse gases, regulated emissions, and energy use in Transportation Model*. U.S. Department of Energy. https://www.energy.gov/eere/bioenergy/articles/greet-greenhouse-gases-regulated-emissions-and-energy-use-transportation

Argonne National Laboratory. (2022b*). Energy systems and infrastructure analysis – GREET aviation module*. https://greet.es.anl.gov/greet_aviation

Argonne National Laboratory (2022c). *ICAO-GREET model*. https://greet.anl.gov/greet_icao

Engineer Live. (2021, December 10). *The move to electric boilers*. Engineer Live. https://www.engineerlive.com/node/20952

Henrio, M., van der Ende, O., Motta, G., & Ray, R. K. (2023). *Mining electrification could double their electricity demand*. McKinsey & Company. https://www.mckinsey.com/industries/metals-and-mining/our-insights/electrifying-mines-could-double-their-electricity-demand

Honda. (2023). *Honda IGX800 engine*. https://www.hastingshonda.co.nz/power-equipment/honda-igx800/

Husker Power Products. (2023). *NGE 14.6L spec sheet*. Husker Power Products. https://www.huskerpowerproducts.com/assets/site/specsheets/irrigation/psi-14.6l-nglpg-specsheet.pdf

ICAO. (2022). *CORSIA eligible fuels – life cycle assessment methodology (CORSIA supporting document)*. International Civil Aviation Organization (ICAO), Montreal, Canada. https://www.icao.int/environmental-protection/CORSIA/Documents/CORSIA_Eligible_Fuels/CORSIA_Supporting_Document_CORSIA%20Eligible%20Fuels_LCA_Methodology_V5.pdf

Korberg, A. D., Brynolf, S., Grahn, M., & Skov, I. R. (2021). Techno-economic assessment of advanced fuels and propulsion systems in future fossil-free ships. *Renewable and Sustainable Energy Reviews*, *142*. https://doi.org/10.1016/j.rser.2021.110861

Lagnelöv, O., Dhillon, S., Larsson, G., Nilsson, D., Larsolle, A., & Hansson, P.-A. (2021). Cost analysis of autonomous battery electric field tractors in agriculture. *Biosystems Engineering*, *204*, 358–376. https://doi.org/10.1016/j.biosystemseng.2021.02.005

Popovich, N. D., Rajagopal, D., Tasar, E., & Phadke, A. (2021). Economic, environmental and grid-resilience benefits of converting diesel trains to battery-electric. *Nature Energy*, *6*(11), 1017–1025. https://doi.org/10.1038/s41560-021-00915-5

U.S. Department of Energy. (2023). *Determining electric motor load and efficiency*. https://www.energy.gov/eere/amo/articles/determining-electric-motor-load-and-efficiency

Tesla. (2023). *Tesla Semi*. https://www.tesla.com/semi

Task 5 - Analyze the Economic and Environmental Footprint of SAF Production Pathways

Massachusetts Institute of Technology

Objective

The objective of this task is to provide harmonized assessments of the minimum selling price and lifecycle GHG emissions of different SAF pathways. During the reporting period, the ASCENT Project 080(B) team analyzed the economic and environmental implications of different measures, including using renewable electricity and hydrogen, in selected CORSIA-eligible SAF pathways to improve carbon intensity scores. In addition, the costs of these strategies and the carbon abatement costs were calculated to provide a more holistic view of the impacts associated with SAF electrification.

Research Approach

Figure 2a shows the GHG emissions reduction potential of electrifying the ETJ supply chain. Differences in GREET 2011 and 2022, partially attributed to decreases in methane (CH_4) emission factors in newer NG boilers and efficiency improvements throughout the process, result in a new baseline of 82.7 g CO_2e/MJ. All reduction measures considered (see Figure 1), the GHG emissions of the electrified ETJ corn grain fuel is estimated at 16.8 g CO_2e/MJ (82% reduction), meeting the minimum SAF Grand Challenge target of 50% reduction relative to fossil Jet A fuel. The remaining emissions include farming (9.8 g CO_2e/MJ), the majority of which is attributed to nitrous oxide (N_2O) emissions from nitrogen fertilizer use in the soil with mitigation options currently in an experimental phase (Itakura et al., 2013), and induced land use change (ILUC) emissions (25.1 g CO_2e/MJ). No change is assumed in the value of the ILUC with electrification. There may be reduction opportunities with cover crops, double cropping, and sustainable land management practices which remain an area of research.

Figure 2b shows the cost changes associated with the electrification strategies. The two largest GHG reduction mechanisms, CCS in corn fermentation and electric heat for jet upgrading, incur the largest cost increases. In total, there is a 34% cost penalty ($0.55/L) for implementing electrification throughout the supply chain. However, the GHG reductions now qualify for the electrified fuel for SAF and H_2 credits. If 40B and 45V tax credits are assumed to be directly applied without amortization, the new minimum selling price (MSP) with credits is 11% higher than the baseline, with the credits partially mitigating the more expensive equipment and operating costs of electrification.

Figure 2c shows the carbon abatement costs of each electrification step applied independently, and a value for the electrified fuel with all steps applied. Since the CORSIA default carbon intensity value for the U.S. corn ETJ process is above that of fossil jet, no carbon is abated; thus, there is no associated abatement cost. Instead, the updated GREET value is used as the basis for calculating the baseline abatement costs. Every electrification method results in a reduction in abatement cost, with the final value an 85% decrease from the baseline, and with credits, a 90% reduction. This shows that the GHG emissions saved outweigh the cost increases from electrification.

Figure 2. (a) Greenhouse gas (GHG) emissions reduction potential jet fuel supply chain from ETJ corn grain via electrification. (b) MSP impacts from fuel electrification, in $2017USD/L. (c) Abatement cost of electrification strategies. HEFA: hydro-processed ester and fatty acid; Model Ver.: Differences in calculation of CORSIA U.S. baseline value using GREET 2022 vs. 2011; Elec. Farm: electrified farming, including equipment, fertilizer, input material transport; Elec. Oil Extr.: electrified oil extraction, including resistance heating; Elec. H2: electrolytic proton exchange membrane H2; Wind Elec.: wind electricity replacing U.S. grid electricity in fuel conversion; Elec. Heat: electric heating; Elec. Trans: battery electric trucks, rail, and ammonia fuel cell power. Red ocean tankers and barges; ILUC: induced land use change (remains constant).

Milestone

- Presented the initial modeling approach to the FAA and other stakeholders.

Major Accomplishment

- Presented initial model results which will provide the basis for further modification of the model and expansion to other pathway and feedstock combinations.

Publications

A paper summarizing the results is currently under preparation.

Outreach Efforts

- Presented results during the Spring and Fall 2024 ASCENT meetings.

Student Involvement

During the reporting period, TJ Park (MIT graduate student) worked on this task. The student performed the LCA and TEA of the baseline and electrified ETJ corn grain pathway for SAF production. The student calculated the change in abatement cost for each electrification strategy applied independently, as well as all strategies combined. The student included the impact of SAF and hydrogen credits on the minimum selling price and abatement cost of the fully electrified process.

Plans for Next Period

- Roll out the model for additional CORSIA-eligible pathways and summarize results in a paper.

References

Itakura, M., Uchida, Y., Akiyama, H., Hoshino, Y. T., Shimomura, Y., Morimoto, S., Tago, K., Wang, Y., Hayakawa, C., Uetake, Y., Sánchez, C., Eda, S., Hayatsu, M., & Minamisawa, K. (2013). Mitigation of nitrous oxide emissions from soils by Bradyrhizobium japonicum inoculation. *Nature Climate Change*, *3*(3), 208–212. https://doi.org/10.1038/nclimate1734

Task 6 - Analyze the Prospects of Direct Air Capture of Atmospheric CO_2 to Provide a Carbon Source for SAF Production

Massachusetts Institute of Technology

Objectives

The objective of this task is to evaluate the current and future costs of liquid and solid DAC through component-based learning curves. These projections were utilized to compare two pathways for decarbonization of aviation with DAC: (1) DAC with carbon capture and sequestration (DACCS) to offset emissions from continued use of fossil Jet A fuel, and (2) production of PtL fuels with DAC as a carbon source. The economic and environmental impact of these pathways were evaluated under various technology and cost assumptions in the near-term and long-term.

Research Approach

During the past year, the ASCENT Project 080(B) team determined the current cost of DAC through TEA. The future cost of DAC was determined by applying learning curves. The learning curves were estimated by applying learning rates (LR) to the capital, labor, and energy costs for DAC. The capital LR's for liquid DAC (5-10%) are lower than solid DAC (10-20%) because the equipment utilized in liquid DAC has already been developed in mature industries such as cooling towers and paper/pulp mills (Fasihi et al, 2019). Learning rates of 10-20% are assumed for labor and energy costs. As shown in Figure 3, the cost of DAC declines from $450-$600 to $200-$400 depending on the learning rate applied.

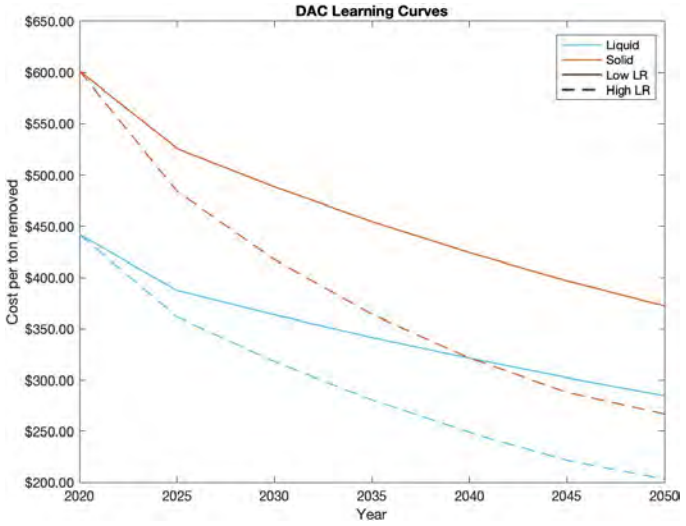

Figure 3. Learning curves for liquid and solid DAC with low and high LRs.

Our team compared two pathways for decarbonization of aviation with DAC: (1) DACCS to offset emissions from continued use of fossil Jet A fuel, and (2) production of PtL with DAC as a carbon source. To compare these pathways, a net-zero emissions target is established for both pathways via supplemental DACCS as needed. This includes accounting for the emissions from the DAC and storage process itself by including additional compensation DACCS. We determined PtL has life-cycle emissions of approximately 15.6 gCO2e/MJ without supplemental DACCS, driven largely by embodied emissions of the electricity.

The cost of these pathways is compared in the near-term and long-term considering both low and high LRs for DAC. In the near term, the cost of PtL is 2.5 times higher than Jet A fuel with DACCS (Figure 4a). Both pathways are not cost-competitive with biofuels in the short term, largely due to the high DAC cost (ICAO, 2022). However, in the long term, as the costs of DAC and fuel synthesis decrease, the price of both the PtL and Jet A fuel with DACCS may fall by 35-40% and 16-24% respectively. Consequently, Jet A fuel with DACCS could become cost-competitive with biofuels, while the PtL cost stabilizes at double the cost of Jet A fuel with DACCS.

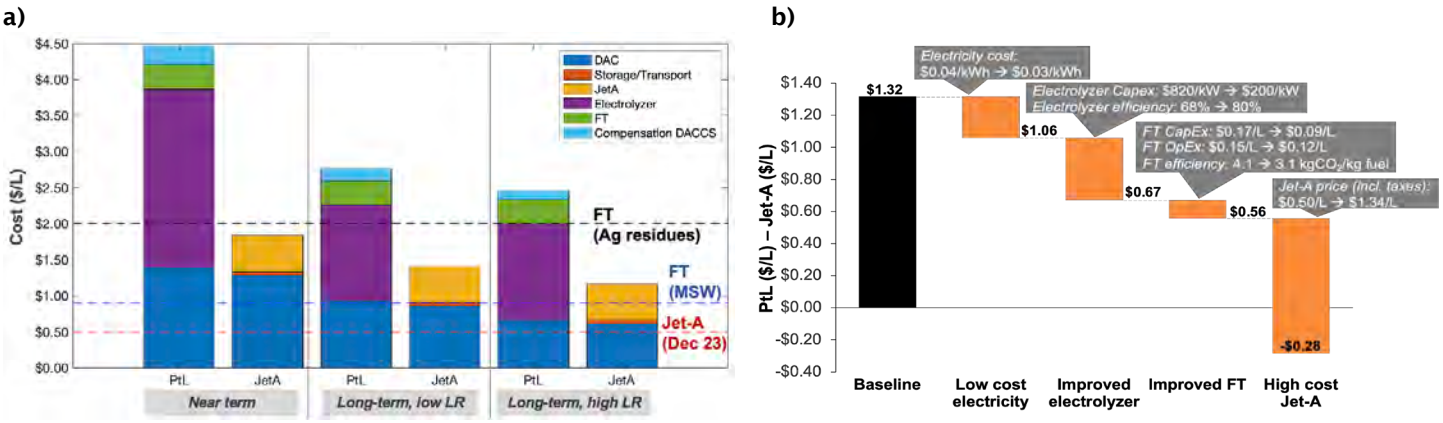

Figure 4. (a) Cost ($/L) of PtL vs. DACCS to offset emissions from Jet A fuel in the near-term and long-term. (b) Combination of factors to improve cost gap between PtL and DACCS to offset emissions from Jet A fuel.

Our team conducted a sensitivity analysis to evaluate whether the cost gap between PtL and Jet A fuel with DACCS could be closed with technology improvements and changes in energy prices. As depicted in Figure 4b, by combining low-cost electricity, advancements in electrolyzer and Fischer-Tropsch (FT) technologies, and high-cost Jet A fuel, the cost of PtL is $0.28 less than the Jet A fuel with the DACCS pathway.

Milestone

- Completed the results for DAC learning curves and analysis of DAC-based pathways for decarbonization of aviation are complete. A paper summarizing the results is under preparation.

Major Accomplishments

- Completed the results for projection of cost of liquid and solid DAC by applying learning curves.
- Completed the results for cost comparison of two DAC-based pathways for decarbonization of aviation: (1) DACCS to offset emissions from continued use of fossil Jet A fuel and (2) production of PtL with DAC as a carbon source.

Publications

Housen, T., (2024). *Climate impact analysis of direct air capture deployment* [Master's thesis, Massachusetts Institute of Technology]. MIT Libraries. https://hdl.handle.net/1721.1/155419

Outreach Efforts

- Presented our results during the Spring 2024 ASCENT meeting.

Student Involvement

During the reporting period, Tara Housen, an MIT graduate student, analyzed cost projections for liquid and solid direct air capture (DAC) technologies. She developed learning curves to compare two aviation decarbonization pathways and assessed their economic and environmental impacts under various assumptions.

Plans for Next Period

- Finalize a paper for publication.

References

Fasihi, M., Efimova, O., & Breyer, C. (2019). Techno-economic assessment of CO_2 direct air capture plants. *Journal of Cleaner Production, 224*, 957-980.

International Civil Aviation Organization. (2022). *Guidance on sustainable aviation fuel policies* (Version 3).

Project 082(A) Integrated Noise and CO_2 Standard Setting Analysis

Georgia Institute of Technology

Project Lead Investigators

Prof. Dimitri N. Mavris
Director, Aerospace Systems Design Laboratory
School of Aerospace Engineering
270 Ferst Dr, Mail Stop 0150
Georgia Institute of Technology
Atlanta, GA 30332-0150
404-894-1557
dimitri.mavris@ae.gatech.edu

Dr. Michelle Kirby
Chief, Civil Aviation Division
Aerospace Systems Design Laboratory
School of Aerospace Engineering
270 Ferst Dr, Mail Stop 0150
Georgia Institute of Technology
Atlanta, GA 30332-0150
404-385-2780
michelle.kirby@ae.gatech.edu

University Participants

Georgia Institute of Technology (Georgia Tech)

- P.I.s: Dr. Dimitri N. Mavris, Dr. Michelle Kirby
- FAA Award Number: 13-C-AJFE-GIT-117
- Period of Performance: September 21, 2022, to March 31, 2025
- Task:
  1. Dual stringency analysis support

Project Funding Level

The Federal Aviation Administration (FAA) provided $514,500 in funding, and Georgia Tech has agreed to a total of $514,500 in matching funds. This total includes salaries for the project director, research engineers, and graduate research assistants, as well as funds for computing, financial, and administrative support, including meeting arrangements. Georgia Tech has also agreed to provide tuition remission for the students, paid from state funds.

Investigation Team

Prof. Dimitri N. Mavris (P.I.), Task 1
Dr. Michelle Kirby (co-P.I.), Task 1
Dr. Jimmy Tai (senior research engineer), Task 1
Dr. Burak Bagdatli (research engineer), Task 1
Dr. Holger Pfaender (research engineer), Task 1
Dr. Jiacheng Xie (research engineer), Task 1
Mr. Brennan Stewart (research engineer), Task 1
Ms. Melek Ozcan (graduate researcher), Task 1
Mr. Zelin Hu (graduate researcher), Task 1

Mr. Andy Tan (graduate researcher), Task 1
Ms. Niharika Akula (graduate researcher), Task 1
Mr. Srikanth Tindivanam Varadharajan (graduate researcher), Task 1
Mr. Kumanan Srinivasan (graduate researcher), Task 1
Ms. Anna L Brongniart (graduate researcher), Task 1
Mr. Kevin Florian (graduate researcher), Task 1
Mr. Thibault Ly (graduate researcher), Task 1
Mr. Zakaria Zbakh (graduate researcher), Task 1
Mr. Raphael Rocher (graduate researcher), Task 1

Project Overview

This project has provided technical support to the FAA for the assessment of the 13th cycle of the Committee on Aviation Environmental Protection (CAEP/13) stringency analysis, including cost estimates of various stringency options (SO). Prior CAEP stringency analysis included a cost-benefit assessment of different scenarios on the basis of outdated information and relied on industry subject-matter input. This project has enhanced and updated the assumptions, on the basis of a quantitative assessment of technological benefits and the costs associated with achieving those benefits. The results will provide the FAA with a data-driven process for decision-making, including the interdependencies between carbon dioxide (CO_2) and noise, as well as the costs associated with their mitigation.

Task 1 – Dual Stringency Analysis Support

Georgia Institute of Technology

Objectives

The objective of this task is to support the FAA in conducting a cost-benefit stringency analysis for CAEP/13 while considering the interdependencies between CO_2 and noise. Although analyses of this type have been conducted previously, The ASCENT Project 082A seeks to update the assumptions and modeling capabilities to provide a data-driven decision-making process for the FAA. This research used the CAEP/10 approaches as starting points to assess the manufacturer non-recurring cost and the price premium of an aircraft after technology response to a SO. The Georgia Tech team is assisting the broader United State (U.S.) research team to accomplish the goals of the dual-stringency analysis.

Research Approach

In support of the broader U.S. research team, the Georgia Tech team has focused on the following main research thrusts:

- Help with the price after technology response (PATR) method.
- Provide input and guidance for the public Growth and Replacement Database (GRdB).
- Provide input to various papers and reports.
- Updating the technology responses possible for various SOs.
- Providing broad technical support for the CAEP working groups.

Methods and Implementation

Each research thrust is an independent effort and thus has different approaches and results, as described below.

Price After Technology Response (PATR) Model Development

The Georgia Tech team conducted a thorough review of the previous PATR methodologies developed during the CAEP/10 CO_2 stringency analysis, with particular emphasis on evaluating the underlying assumptions. In December 2023, the team convened a side meeting with the original developers of the PATR methodology during a joint session of the CAEP Modelling and Databases Group (MDG) and the Forecasting and Economic Analysis Support Group (FESG) hosted at Georgia Tech.

During this meeting, the participants collectively agreed to adopt a simplified approach, acknowledging that the previous methodology was overly resource-intensive for sensitivity analysis and lacked consensus among CAEP members. The Georgia Tech team actively supported this initiative and contributed to the development of an empirical approach for PATR, leveraging changes in an aircraft's CO_2 metric value improvement and its price to estimate the price premium for the new aircraft.

Alternative Growth and Replacement Database (GRdB) Development
Due to restrictions on data sharing, it became necessary to identify an alternative method for developing technology responses as part of the CAEP/13 analysis, leveraging publicly available data. In response, Working Groups 1 (WG1) and 3 (WG3) collaborated to form a dedicated group named PUBahg, tasked with advancing this effort. The Georgia Tech team took a part in supporting this initiative, offering both technical expertise and strategic guidance throughout the process.

Literature Review
The Georgia Tech team contributed input and feedback to several working papers over the course of the year, including the final Integrated Dual Stringency (IDS) report, which was the most extensive and demanding effort. The team conducted a thorough review of the nearly 300-page document and provided detailed feedback to support its development.

Technology Response
The Georgia Tech Aerospace Systems Design Laboratory has used an approach similar to that of the CAEP's Independent Expert Integrated Review and Long-Term Aspiration Goal studies in lieu of specific technology modeling. These two studies considered technologies as "bundles" of improvements in key disciplinary areas on the airframe and engine. For example, specific composite materials were not modeled, but structural weight improvements were included. A stringency analysis requires that technologies be at technology readiness level 8 each year, thus limiting the scope of applicability of the possible technology "bundles" according to the year of application of the stringency. The outcome of the subtask is a set of technology assumptions to be used in modeling for the interdependency trades in the sample problem and full analysis, to provide a Pareto front[1] of the maximum available technology response for a given aircraft class.

The methods for determining the impact of technology responses are represented in Figure 1. The system-level model calibration for the technology reference aircraft (TRA) vehicle is described in the Vehicle Model Calibration Section. The Vehicle Acoustic Calibration provides more detail on the calibration of the acoustic properties of the TRA vehicle from certification databases. The remaining sections describe how technology responses are applied to the vehicle model in a design space exploration and outline the optimization process for analyzing the design space, presenting preliminary results of generating Pareto fronts from the data.

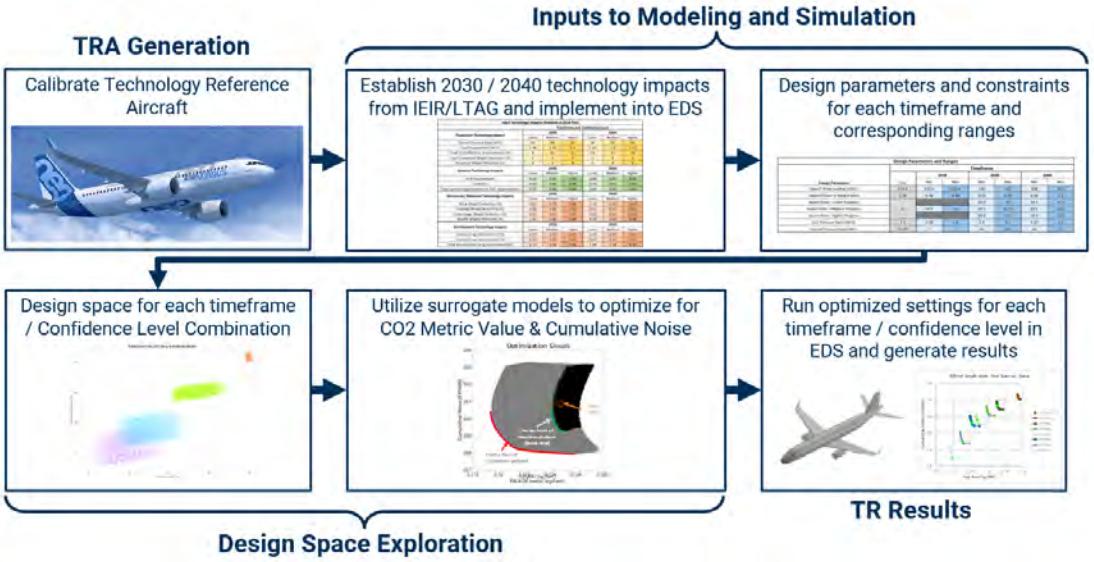

Figure 1. Process for determining a technology response (TR). IEIR: independent expert integrated review; LTAG: Long-Term Aspiration Goal; MV: metric value; TRA: technology reference aircraft; EDS: Environmental Design Space.

[1] A Pareto front is a set of solutions in a multi-objective optimization problem where no metric can be improved in one objective without worsening another, in this case CO2 Metric Value and Cumulative Noise. It represents the best possible trade-offs between different objectives.

Vehicle Model Calibration

The process for vehicle model calibration is nominally a two-stage process, starting with engine calibration followed by airframe calibration, matching with publicly available data for engine performance and geometry of the vehicle.

The notional engine model is calibrated using publicly available data from the engine Type Certificate Data Sheet (TCDS) and the International Civil Aviation Organization (ICAO) engine emissions databank. The TCDS provides information on the engine's weight and geometry, while the ICAO databank supplies key performance values including thrust, fuel flow, emissions indices, overall pressure ratio (OPR), and bypass ratio (BPR) under sea level static (SLS) uninstalled standard day conditions. These data points form the basis for calibrating the model to reflect publicly reported engine performance and physical attributes. Environmental Design Space (EDS) integrates various modeling tools to simulate and evaluate engine performance, such as compressor map generation in CMPGEN,[2] flow path and weight modeling through Weight Analysis of Turbine Engine (WATE++),[3] and engine cycle analysis via Numerical Propulsion System Simulation (NPSS). These tools work in concert to model the engine's performance at multiple design points, including takeoff, hot day sea level static, top-of-climb, and cruise conditions.

The notional aircraft model is calibrated using publicly available data from the aircraft's airport planning manual (APM). The geometric data, taken from three-dimensional-view published drawings, include information on the control surfaces of the airplane. Various measurements of the airframe are taken, for example, the height of the tail and the chord length of the leading-edge slats and many more. The payload-range diagram of the APM is used to determine a design mission for the notional aircraft model. These values are used in various calculations to be implemented in the Flight Optimization System (FLOPS) model. In EDS, FLOPS is executed immediately after the engine design loop has been completed and converged. The engine loop provides an engine deck, basic nacelle dimensions (length and diameter), and weight. Additionally, FLOPS requires aircraft geometry and mission details (i.e., design range, Mach numbers, altitudes, etc.). It also offers options for more detailed landing and takeoff (LTO) data, along with performance constraints, FLOPS begins with an initial guess for gross weight (GW) and vehicle geometry, then estimates the weight of internal components like the fuselage, wings, and tail, and results in the estimation of the operating empty weight (OEW). The available fuel capacity is calculated by subtracting OEW and payload weight from the gross weight. Using this fuel capacity, FLOPS simulates the mission and determines the maximum achievable range.

Included in this report is a sample of results from the calibrated notional narrow body and regional jet models, the Airbus® A320-271N weight variant WV055 with reference engine Pratt & Whitney® PW1127G-JM and Embraer® E190-E2 with reference engine Pratt & Whitney PW1922G. The Airbus A320neo represents the narrow body (NB) class of aircraft whereas Embraer E190-E2 represents the regional jets (RJ) class. Calibrated summary along with high level geometry data of Airbus A320neo and Embraer E190-E2 are shown in Table 1. The Airbus A320neo was calibrated to a design payload of 28,500 lb for a design range of 3,420 nmi, while Embraer E190-E2 was calibrated to a design payload of 21,660 lb and design range of 2,850 nmi.

Previous work by the Aerospace Systems Design Laboratory has defined component weights as percentages of the OEW. These percentages are based on a statistical approach for historical values of each component of the wide-body class aircraft. From these percentages, target component weights are defined and calibrated for the correct OEW (found in the airport planning manual) of the specified weight variant of the chosen aircraft, by using the class specific percentages for weight components, as listed in Table 2 and Table 3. The component weight calibration is performed by iteratively varying weight factors in FLOPS to reach the desired OEW. After this process is complete, the airframe model, together with correct engine cycle parameters, is implemented in the EDS to generate a baseline model. Using this process many other aircraft models have also been calibrated which are given in Table 4.

[2] CMPGEN is a modeling tool used to compute off-design performance of axial fans, booster, and compressors.
[3] WATE++ is an object-oriented computer code for gas turbine weight estimation.
® Airbus is a registered trademark of Airbus Operations GmbH, Hamburg, Germany.
® Pratt & Whitney is a registered trademark of RTX Corporation, Farmington, Connecticut.
® Embraer is a registered trademark of Embraer S.A., San Jose Dos Campos, Brazil.

Table 1. Calibration summary for Airbus A320neo and Embraer E190-E2. MTOW: maximum take-off weight.

Parameter	A320-271N	E190-E2
MTOW (lb)	174,165	124,341
OEW (lb)	100,962	69,941
Thrust (lb)	27,076	23,814
Aspect Ratio	9.5	10.5
Wingspan (ft)	117.5	110.7

Table 2. Calibrated mass and balance summary Airbus A320-271N.

Mass and balance summary	% OEW	Pounds
Wing	17.959%	18,132
Horizontal tail	1.936%	1,955
Vertical tail	1.047%	1,057
Vertical fin	0.000%	-
Canard	0.000%	-
Fuselage	18.168%	18,343
Landing gear	6.637%	6,701
Nacelle (air induction)	3.733%	3,769
Structure total	49.48%	49,956
Engines	16.273%	16,430
Thrust reversers	0.000%	-
Miscellaneous systems	0.000%	-
Fuel systems: tanks and plumbing	0.649%	655
Propulsion total	16.92%	17,085
Surface controls	2.397%	2,420
Auxiliary power	0.977%	986
Instruments	0.409%	413
Hydraulics	1.288%	1,300
Electrical	1.637%	1,653
Avionics	1.382%	1,395
Furnishings and equipment	18.665%	18,845
Air conditioning	1.343%	1,356
Anti-icing	0.155%	156
Systems and equipment total	28.25%	28,525
Weight empty	94.66%	95,566
Flight crew and baggage	0.445%	450
Cabin crew and baggage	0.594%	600
Unusable fuel	0.485%	490
Engine oil	0.124%	125
Passenger service	2.476%	2500
Cargo containers	1.220%	1232
Operating weight	100%	100,962
Passengers, 150		28,500
Passenger baggage		4,500
Cargo		0
Zero fuel weight		133,962
Mission fuel		41,085
Ramp (gross) weight		175,047

Table 3. Calibrated mass and balance summary Embraer E190 – E2.

Mass and balance summary	% OEW	Pounds
Wing	16.974%	11872
Horizontal tail	1.673%	1170
Vertical tail	1.035%	724
Vertical fin	0.000%	-
Canard	0.000%	-
Fuselage	18.956%	13258
Landing gear	7.300%	5106
Nacelle (air induction)	1.568%	1097
Structure total	47.507%	33,227
Engines	16.505%	11544
Thrust reversers	0.000%	-
Miscellaneous systems	0.000%	-
Fuel systems: tanks and plumbing	0.967%	676
Propulsion total	17.472%	12,220
Surface controls	1.814%	1269
Auxiliary power	0.914%	639
Instruments	0.000%	-
Hydraulics	1.220%	853
Electrical	2.062%	1442
Avionics	1.275%	892
Furnishings and equipment	19.432%	13591
Air conditioning	1.314%	919
Anti-icing	0.000%	-
Systems and equipment total	28.031%	19,605
Weight empty	93.010%	65,052
Flight crew and baggage	0.643%	450
Cabin crew and baggage	0.858%	600
Unusable fuel	0.655%	458
Engine oil	0.164%	115
Passenger service	4.670%	3266
Cargo containers	0.000%	-
Operating weight	100%	69,941
Passengers, 114		21,660
Passenger baggage		3,420
Cargo		0
Zero fuel weight		95,021
Mission fuel		29,760
Ramp (gross) weight		124,781

Table 4. Available notional aircraft models and their associated engine.

Aircraft	Engine
G650ER	RR BR725
E190-E2	PW1922G
A320-271N	PW1127G-JM
A330-941N	RR Trent 7000-72
Boeing 737-MAX-8	LEAP-1B28
Boeing 787-8	GEnx-1B70/P2
Boeing 787-10	GEnx 1B76-P2
Boeing 747-8	GEnx-2B67/P

Vehicle Acoustic Calibration

Several options for calibration, (or lack thereof), exist in EDS. Using default Aircraft Noise Prediction Program (ANOPP) predictions and declining to calibrate a model is a valid option when modeling an advanced configuration for which no calibration basis exists, or when modeling an airframe/engine which is similar to the basis for the acoustic regressions which form ANOPP. However, if a calibration basis exists in the form of test/certification data, and the aircraft feature airframe/engines designs which are outside of the regression basis of ANOPP or feature more advanced acoustic technologies not captured in ANOPP, then acoustic calibration should be performed. The two methods for calibrating vehicles in EDS are calibrating through the application of suppression factors developed by an airframe/engine reference calibration study across a range of similar vehicles and calibrating based on a comparison of the ANOPP-generated noise power distance (NPD) curves for Aerospace Systems Design Laboratory (ASDL) notional aircraft to NPDs measured from real aircraft, (the public “legacy” Aircraft Noise and Performance (ANP) Database has been the source for this test data). All of these options are implemented in EDS, and Figure 2 compares their usages, although the preferred noise calibration method, and the method used in A82A, is the NPD comparison to the ANP database. Noise produced by the vehicle is calibrated to known data taken from European Union Aviation Safety Agency (EASA) databases for aircraft noise (European Union Aviation Safety Agency, 2022; Eurocontrol Experimental Center, 2020). Currently, the ASDL only has access to the "Legacy" ANP database. These data were collected before Article 7(3) Regulation (EU) No 598/2014 came into effect by the European Organization for Safety of Air Navigation (EUROCONTROL) and FAA and was previously verified by the FAA/Volpe National Transportation Systems Center. Data collected by the Legacy ANP Database are publicly available on EASA's website; however, data collected under Article 7(3) Regulation (EU) No 598/2014 are restricted in their use by a limited rights agreement which ASDL has not consented to and which may exclude using that data for the purposes of acoustic calibration. Alternative means of collecting these data for more recent aircraft are being explored.

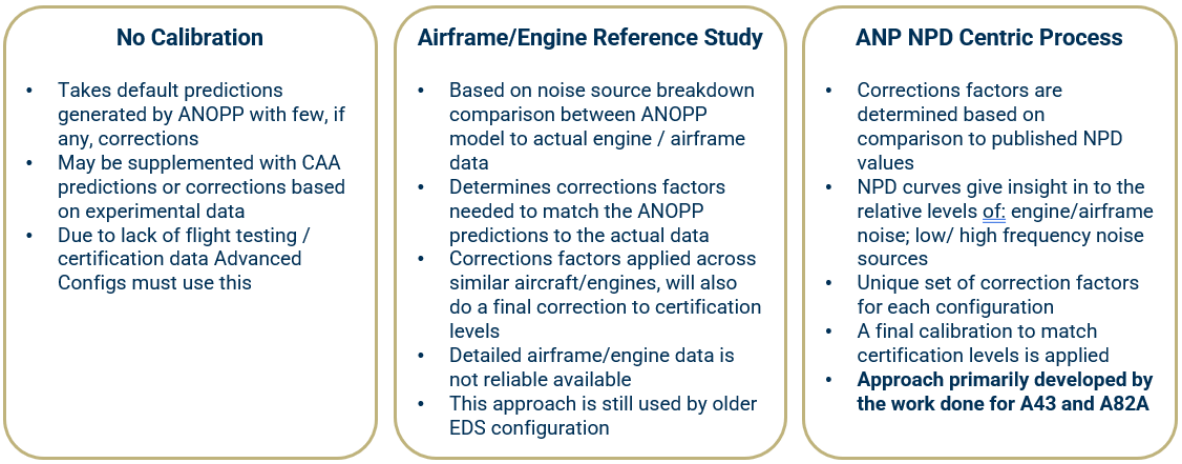

Figure 2. Comparison of acoustic calibration options used in EDS modeling.

The aircraft noise is predicted in the EDS off-design loop through an ANOPP model, which is parametrically constructed from engine geometry, trajectory predictions, airframe geometry, and engine cycle data predicted in the EDS model. This capability supports both mixed-flow turbofans and separate-flow turbofans architectures. The baseline noise predictions can be calibrated through ANOPP's General Suppression (GENSUP) module by adjusting each individual noise source in the ANOPP model at each power setting related to each of the three certification observers (i.e., approach, cutback/flyover, and sideline). Calibration variables are implemented in EDS via several variable parameters that represent the noise produced by the engine (i.e., combustor, turbine, fan, and jet sources) and the airframe including the tail, flaps, slats, and landing gear. Each noise source has a variable corresponding to noise perceived at each of the three observer positions as a result of the respective noise source (i.e., approach, cutback/flyover, and sideline). The aircraft noise source predictions are calibrated to the ANP NPD data using the method described in the following section and shown in Figure 3.

Figure 3. Overview of acoustic calibration method.

The noise modeling process begins with collecting certification data from the EASA, which include effective perceived noise in decibels (EPNdB) for cutback, approach, and sideline observer positions during takeoff and landing. These data are supplemented with NPD curves to provide more comprehensive information for various operational scenarios. NPD curves consider different acoustic measurements at various intervals and thrust settings. For recently certified aircraft not included in the NPD database, ICAO provides methods for using proxy vehicles and adjusting NPD curves based on certification noise data differences. The ICAO substitution method states which published NPD is most similar to the vehicle, and how many decibel (dB) of adjustment of the takeoff and approach NPD is required. However, caution must be used when applying ICAO substitution methods as the adjustment is only a shift in the curves and does not reflect how that shift is achieved (for example, it would not capture whether an upward shift in dB was needed due to more airframe or more engine noise). This method should only be used for very similar vehicles, such as estimating the 787-9 NPD by using the published 787-8 NPD.

To calibrate the acoustic model, noise suppression factors are adjusted to match the sound exposure levels (SELs) of the ANP NPD curves. NPD curves are valuable calibration parameters as they provide data across altitude and thrust levels. This information can be used to estimate the relative contributions of the engine and airframe noise, as well as the relative contributions of low- and high-frequency noise, which can provide insight into where the ANOPP model differs from the NPD data. The EDS model's predicted NPD curves are compared to the ANP database NPD curves and calibrated using vehicle calibration parameters in EDS to adjust ANOPP suppression factors. Due to the under-constrained nature of the calibration problem, a human-in-the-loop optimization approach is employed. An optimizer provides an initial guess for vehicle calibration parameters, which an engineer then refines based on empirical data and trends in aircraft noise source distribution. The result is a set of EDS variables representing noise from specific vehicle components at different observer points. The variables used to acoustically calibrate the aircraft are the following:

- **COR - AP/TO/MX**: Suppression factor on core (combustor) noise for approach/cutback/full-power thrust settings
- **DIS - AP/TO/MX**: Suppression factor on fan discharge noise for approach/cutback/full-power thrust settings
- **INL - AP/TO/MX**: Suppression factor on fan inlet noise for approach/cutback/full-power thrust settings
- **JET - AP/TO/MX**: Suppression factor on jet noise for approach/cutback/full-power thrust settings
- **LES - AP/TO/SL**: Suppression factor on leading edge slats noise for approach/cutback/full-power thrust settings
- **MGRAP**: Suppression factor on main landing gear noise for approach thrust settings
- **NGRAP**: Suppression factor on nose landing gear noise for approach thrust settings
- **TEF - AP/TO/SL**: Suppression factor on trailing flap noise for approach/cutback/full-power thrust settings
- **TEH - AP/TO/SL**: Suppression factor on wing trailing edge noise for approach/cutback/full-power thrust settings
- **TEH - AP/TO/SL**: Suppression factor on vertical tail trailing edge noise for approach/cutback/full-power thrust settings
- **TEV - AP/TO/SL**: Suppression factor on horizontal tail trailing edge noise for approach/cutback/full-power thrust settings
- **TUR - AP/TO/MX**: Suppression factor on turbine noise for approach/cutback/full-power thrust settings

Once calibrated via this method, the suppression factors are frozen for further trade studies.

Next, a LTO trade study is performed to match the vehicle certification noise found in the EASA Jet Certification database. Inaccuracies in takeoff and landing trajectories will affect the certification noise levels. The LTO study utilizes detailed FLOPS LTO results from the vehicle model, which are then used in the National Aeronautics and Space Administration ANOPP code to calculate the noise emission from the vehicle. Four parameters are varied in this trade study; the ranges over which these parameters were varied are listed in Table 5. The first two variables are scaling factors that scale the drag coefficients for the LTO polar. The EDS vehicle modeling process utilizes a low-fidelity method of predicting LTO performance, and it is recognized that those predictions could potentially have high errors. Since most of the approach trajectory parameters are fixed by regulation, landing drag is scaled until approach thrust levels match performance predictions for thrust from Aviation Environmental Design Tool (AEDT) landing predictions. A trade study examining the parameters is performed. The takeoff drag polar scaler is studied along with the other two variables related to the takeoff operation of the vehicle: the flight path angle during post-obstacle acceleration, the fixed climb speed, and the location at which cutback is performed (this can be done by either distance from brake release or altitude, but note that regulations specify a minimum altitude for cutback based on the number of engines).

Table 5. LTO study variables and design ranges. HSTOP: Transition Altitude to Next Trajectory Step

Variable	Takeoff drag scaling factor	Landing drag scaling factor	Flight path angle (degrees)	HSTOP (ft)
Design range	0.5–1.2	0.5–1.2	3.0–9.0	300–1,000

The design of experiments is run with roughly 600 cases that span the design space of this study. Of those cases, the one that best matches the published certification noise for the considered aircraft is selected. A 1 EPNdB error per observer is considered acceptable, while a 0.5 EPNdB error per observer would represent a great success for this process. Once this design point is verified, the selected design parameters are included in the EDS baseline model. One last iteration of calibration is undertaken, adjusting all parameters uniformly to eliminate the error between the predictions post-trajectory study and the published certification data. The overall noise calibration method is as follows:

- Determine target values for certification noise from the EASA database and for NPD data points using the ICAO-defined substitution method from the NPD database.
- Optimize suppression factors to match NPD data points freeze suppression factors.
- Perform an LTO study to find a combination of parameters that meet target certification noise points.
- Make a final uniform adjustment to match published certification noise values.

NO_x and CO_2 Mandatory Ventilation (MV) Prediction Enhancements

The current P3T3 method estimates the EINOx value based on detailed engine data, with the following formula (Norman et al., 2003) (Equation 1):

$$\mathrm{EINOx_{FLT}} = \mathrm{EINOx_{REF}} \left(\frac{P3_{\mathrm{FLT}}}{P3_{\mathrm{REF}}}\right)^{a} \left(\frac{FAR_{\mathrm{FLT}}}{FAR_{\mathrm{REF}}}\right)^{b} \exp\left(19(h_{\mathrm{REF}} - h_{\mathrm{FLT}})\right) \quad \text{(Eq. 1)}$$

where "REF" is sea level static reference condition, "FLT" is flight condition, and "a" and "b" are exponents based on combustor information. A correlation upon T3 is required for the reference EINOx value.

EDS enables those calculations, first by taking into account the effects on EINOx from technology infusion that are modeled directly through changes in detailed engine parameters and also, because EDS can provide predictions of P3, T3 and FAR engine parameters using its physics-based engine model.

In addition, EDS provides an alternative to the P3T3 method depicted in Figure 4. The EINOx metric is compared to ICAO engine emissions databank, over four points per engine rating. By relating the P3 and T3 to thrust, with data from the EDS engine model, the following correlation could be written (*Eq. 2*):

$$\mathrm{EINOx_{FLT}} = P_3^{0.4}\left(aT_3^6 + bT_3^5 + cT_3^4 + dT_3^3 + eT_3^2 + fT_3 + g\right) \quad \text{(Eq. 2)}$$

This method captures the effects of combustor architecture using a statistical approach.

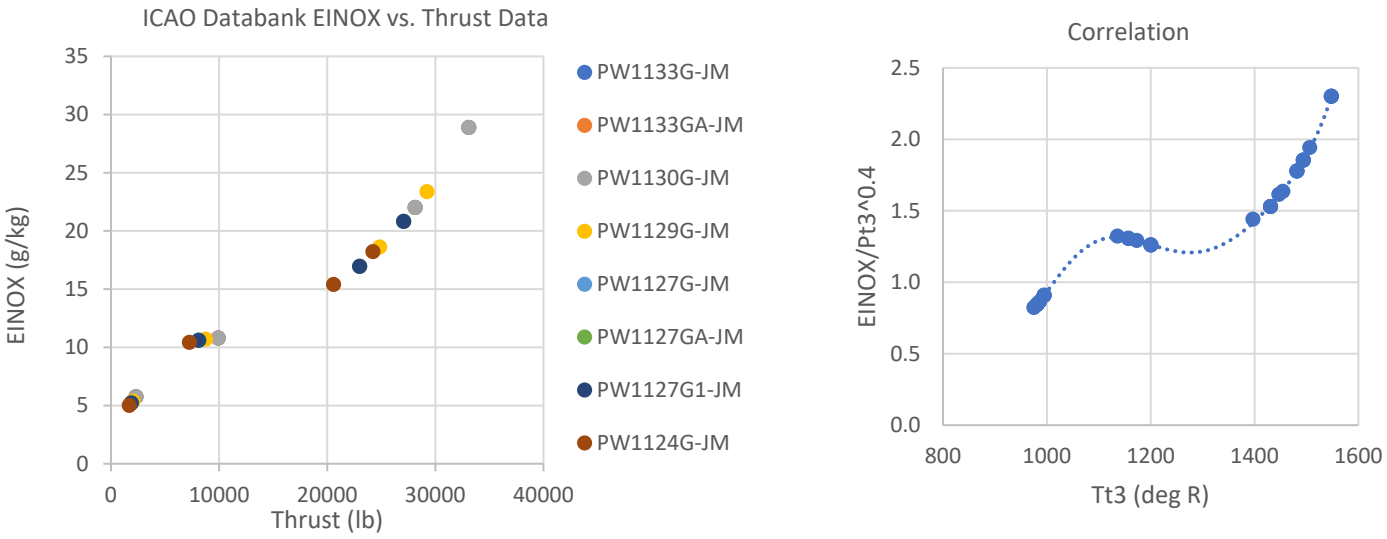

Figure 4. EINOX versus thrust data from different engines from the ICAO databank.

The CO_2 metric value (MV) is automatically calculated in EDS based on aircraft configuration/engine architecture and technology level, and is calculated as defined by (Federal Aviation Administration, 2023) (*Eq. 3*):

$$CO2\ MV = \frac{\left(\frac{1}{SAR}\right)_{avg}}{RGF^{0.24}} \quad \text{(Eq. 3)}$$

where “SAR” is the specific air range and “RGF” is the reference geometry factor based on the cabin floor area. For NB and wide body (WB) aircraft, the maximum takeoff weight is estimated at three different flying points, for supersonic and business jet aircraft only two points are required. In addition, for supersonic aircraft EDS can explore specific air ranges to assess how different maximum take-off mass (MTOM) definitions could affect the $C0_2$ metric value as illustrated in Figure 5.

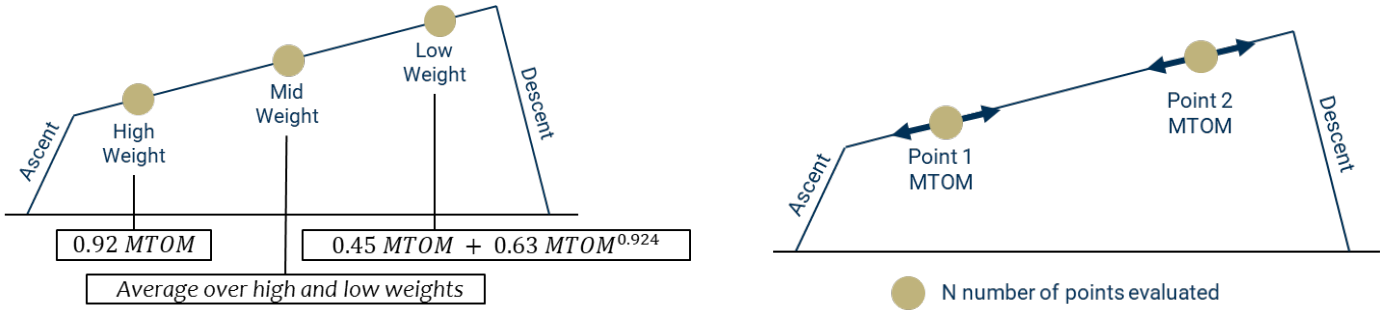

Figure 5. Representation of the MTOM points on a mission profile to calculate CO_2 MV, for subsonic aircraft (left) and the notional equivalent for supersonic jets (right)

Noise Prediction Enhancements

The aircraft noise certification process involves comprehensive measurements at multiple key points: approach, flyover, sideline, and cumulative noise positions. The measurement points for flyover and approach are strictly regulated at fixed positions, while Sideline measurements capture the maximum effective perceived noise level (EPNL) along the lateral reference line. The EPNL can be computed by adding a duration correction factor to the maximum tone-corrected perceived noise level (PNLT).

For trajectory modeling, several distinct takeoff procedures are implemented. The certification takeoff follows 14 CFR Part 36 specifications for EDS at maximum takeoff weight. NADP 1 and NADP 2 procedures, designed by the ICAO, focus on airport noise mitigation and accommodate various takeoff weights based on mission ranges. The broadband noise (BBN)/all takeoff, known as the "standard" procedure in FAA's Integrated Noise Model Software, and Variable Noise Reduction System (VNRS) takeoffs are also modeled, with VNRS specifically incorporating novel approaches like programmed lapse rate (PLR) for supersonic transports.

Currently, technology impact prediction employs two primary methodologies for acoustic modeling. The first approach applies an overall component-level acoustic benefit, providing general suppression per engine/airframe component. The second method offers detailed technology modeling, examining how specific technologies affect individual engine/airframe components and their acoustic signatures. These methods are visualized through spectral analysis, where the first approach shows uniform reduction across the emission spectrum, while the second method targets specific prominent tones for attenuation.

Parametric Engine Architectures

Currently EDS can model dual-spool direct drive turbofans that are paired with the NB and RJ classes, and triple-spool turbofan engine for the WB class. Each engine architecture runs through NPSS and WATE++ solvers to generate engine decks, powerhook, weights and geometry that are unique to them. This involves solving flow paths, pressure losses, thermodynamic efficiencies for turbo machinery components, power extraction used to drive the fan, compressors and bleed flow. Different engine architectures are enabled by passing engine specific parameters in the Design of Experiments (DoE) table. Since these variables are part of DOE and can be adjusted independently to make a calibrated aircraft engine, they can also be parametrically adjusted to infuse technology factors that are applicable to that engine type. This parametric approach also enables the generation of technology responses for any available airframe concept and propulsion architecture combination in ASDL EDS Vehicle Model Library. In recent efforts to expand EDS’s capability, new architectures are constantly developed including mixed-flow turbofan, geared turbofan, turbo prop and future concepts like hydrogen engine, electric hybrid engines.

Aircraft Library Expansion
EDS also allows for the modeling of next-generation aircraft. The technology response methodology provides an approach to modeling project aircraft announced by manufacturers, by leveraging existing notional models of the project aircraft's predecessor and applying technology impacts informed by data from public announcements to obtain information on project aircraft.

It is also possible to model novel configurations (e.g., box wings or over wing nacelles) paired with advanced propulsion concepts such as open rotors or electric powertrains using EDS, in addition to conventional concepts. This allows for the modeling of novel aircraft including ASDL designs such as the hydrogen electric NB Advanced Technology Hydrogen Electric Novel Aircraft (ATH2ENA).

Technology Sensitivity Analysis
This project employs a top-down approach that relies on the concept of technology "buckets." A technology bucket refers to the grouping of multiple technological advancements, whose combined effects are assessed collectively to understand their influence on broader systems. This method is informed by the ICAO independent expert integrated review (IEIR) and Long-Term Aspiration Goal (LTAG) technology impact tables, providing a framework to evaluate the aggregated impact of these buckets across different timeframes and confidence levels. By organizing technologies into these overarching categories, this approach enables a systematic assessment of their potential contributions to overall system improvements.

In addition to the top-down methodology, technology evaluations can also be conducted using a bottoms-up approach. This alternative approach focuses on the detailed assessment of individual technologies, examining their specific impacts and contributions. By breaking down technological advancements into their distinct components, the bottoms-up method provides valuable insights into how each innovation directly enhances system performance. This level of precision ensures a comprehensive understanding of the role each technology plays in driving progress.

Technology Reference Aircraft (TRA) Generation and Optimization
Since there are many different aircraft models from different manufactures and these aircraft were designed with different priorities in mind, there is a need to create a single aircraft that represents the entire class. This would become the TRA for the said class to which emerging technologies can be applied. For this purpose, a single variant of any in service aircraft is chosen, and once the calibration is done, it will be considered as the TRA or baseline. The next step is creating an optimized version of TRA that represents the whole class as many aircraft could have been introduced into service over a span of many years that have varying levels of technology. The generation of this optimized TRA (also called a TRA OPT) involves optimizing an existing in-service aircraft to align with specific environmental objectives, such as reducing fuel burn, CO_2 emissions and noise. This optimization ensures that advancements in aircraft design can be fairly evaluated against a relevant benchmark, ultimately guiding improvements in aviation's environmental performance.

This optimization focuses on improving fuel burn for the aircraft's respective fixed design mission by adjusting key design parameters, including aspect ratio, fan pressure ratio, and maximum turbine entry temperature (TET or T4). These changes are subject to critical constraints, such as the wingspan for gate constraint, fan diameter for ground clearance, and maximum compressor exit temperature. The resulting model will be used for assessment and technology infusion.

Design of Experiments Generation
With the baseline model calibrated to match publicly available data for the Airbus A320-271N and Embraer E190-E2, followed by optimization to get TRA OPT, the model can be adjusted to simulate technology infusion. One possible method for analyzing how current vehicles could meet future dual-stringency limits would be to predict which specific technologies might be applied by industry to their designs and then to model the impacts of those technologies on performance. However, this process would require proprietary information from the company designing and manufacturing the aircraft and engine. This approach is not feasible for the scope of this study.

Instead, the baseline is varied by applying *k*-factors that represent technology buckets, wherein a vehicle can make technology improvements in a certain aspect, such as the wing drag coefficient, without specifying what specific technology is used to achieve the improvement. In this fashion, the technology response is measured for various *k*-factors in mission parameters, and a wider design space is available.

Using these technology buckets provides a parametric approach for capturing stringency responses; however, this method results in a very large design space that can become computationally expensive to explore. An appropriate design of

experiments enables efficient exploration of the technology space with maximum knowledge gained. Specifically, the baseline case is taken along with edge cases at the extremes of the *k*-factor ranges. The design of experiments is then filled in with an appropriate number of random points to be run in EDS. The key metrics, which are measured outputs of the technology space exploration, are listed in Table 6.

Table 6. Key metrics for technology space exploration. CAEP: Committee on Aviation Environmental Protection; MTOW: maximum takeoff weight.

Key Metrics	
Wingspan	Cutback noise
Approach noise	Sideline noise
Cumulative noise	dPfooNOx
CO_2 metric value	MTOW
Maximum T3	Fan diameter
Noise margin relative to CAEP Ch. 14	Fuel burn per available ton kilometer

Results

To find the best design, in terms of our metrics of interest, all possible designs in the design space must be evaluated. This will be computationally expensive. Instead, surrogate models are created based on the cases run with the design of experiments. These models capture the complex relationship between the varied input parameters to the key metric outputs. Two of key metrics of interest are cumulative noise and CO_2 metric, the primary metrics for the dual stringency approach. This approach of creating surrogate models enables further study and additional insight for the future without the need for additional design runs. For this study, surrogate models based on neural network algorithms (consisting of either a single or dual hidden layer network of hyperbolic tangent neurons) are created to best fit the data from our design of experiment runs.

The surrogate generation process is followed by Pareto optimization for all the classes, performed for several timeframes of interest with increasing technology impacts over further timeframes. The 2029 Medium Confidence timeframe is discussed further. Pareto optimization is an algorithm that considers two or more metrics, defines a “best in class” for each metric, and then performs tradeoffs on the priority of each metric to draw a curved line between best-in-class points. The two metrics of interest to perform tradeoffs against are cumulative noise and the CO_2 metric value. The metric for nitrogen oxide emissions is the mass in grams (Dp) of NO_x pollutants emitted during the reference LTO cycle, divided by the rated output (Foo) of the engine (dPfooNOx). Although dPfooNOx is not included in the optimization, the metric is calculated to assess changes in NO_x emissions as a result of noise and CO_2 tradeoffs.

At a high level, the optimization method is as follows. Several million points are generated via random sampling within the ranges of the design space. Key points along the Pareto front with different importance weightings assigned to the dual-stringency metrics are found through a particle swarming optimization approach. The full Pareto front between these key points is generated by a genetic algorithm process. The Pareto fronts for the two class aircrafts NB and RJ are shown in Figure 6.

The results for NB class show a total variation of 2.8 EPNdB for cumulative noise and 5.5% for CO_2 metric along the Pareto front, which is well below the TRA OPT values and well above the acceptable error percentages. On the other hand, RJ class indicated a total variation of 1.0 EPNdB for cumulative noise and 1.5% for CO_2 metric along the Pareto front. It is surely a reduction from the TRA OPT values, but the variation is still not as wide as seen in NB class. This can be a combination of factors like the RJ class not having as aggressive technology improvements that NB class is expected to see in the short term or local buckets in design space preventing wider ranges. As Improvements to modeling and optimization are ongoing, it could help capture the sensitivity and improvement in the design space.

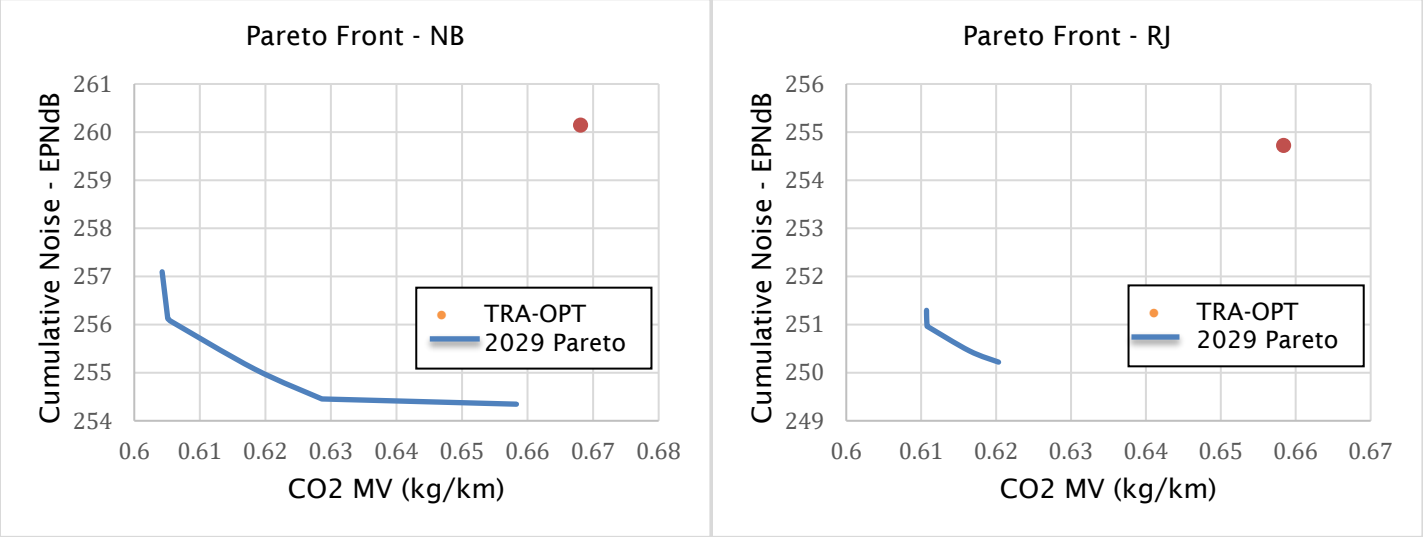

Figure 6. 2029 Pareto fronts for CO_2 metric value versus cumulative noise for NB (left) and RJ (right).

CAEP Working Group and Industry Collaboration
The research team participated in numerous CAEP working groups including the WG1 (noise), WG3 (emissions), and Modeling and Database Group (MDG) and Forecasting and Economics Support Group (FESG) working groups. Working with the broader U.S. research team, the Georgia Tech team developed a method to address the dual-stringency analysis sample problem, including assessments of current noise margins of the in-production fleet, development of technology response methods, contributions to the growth and replacement database, and development of an initial Non-Recurring Cost (NRC) function.

Milestones

- Developed an initial version of the NRC function for use in the sample problem.
- Developed notional technology responses across seat classes for use in the sample problem.
- Contributed to the CAEP technical working groups.

Major Accomplishments

NRC Function:

- Reviewed and reported previous CAEP work on NRC modeling.
- Developed an approach to include both CO_2 and noise MV improvements in the NRC function.

Technology response for the Sample Problem:

- Developed technology responses available across four vehicle classes.

CAEP Working group and industry collaboration:

- Contributed to the work plan of each of the CAEP working groups.

Publications

None.

Outreach Efforts

- Participated in bi-annual ASCENT meetings, various CAEP working group meetings and calls, and weekly U.S. research team meetings.

Awards

None.

Student Involvement

Melek Ozcan, Antoine Marin, Zelin Hu, David Mothershed, Gabriel Fronk, Andy Tan, Niharika Akula, Jayaprakash Kambhampaty, Kumanan Srinivasan, Anna L Brongniart, Kevin Florian, Thibault Ly, Raphael Rocher and Zakaria Zbakh (graduate research assistants, Georgia Tech) participated in the efforts in Task 1.

Plans for Next Period

- Continue to support the broad technical needs of the U.S. research team and CAEP working groups.

References

EASA. (2022). *EASA certification noise levels*. European Union Aviation Safety Agency (EASA).https://www.easa.europa.eu/en/domains/environment/easa-certification-noise-levels

Eurocontrol Experimental Center. (2020). *Aircraft Noise and Performance (ANP) Database: An international data resource for aircraft noise modellers*. https://www.aircraftnoisemodel.org

FAA. (2023). *Introduction to the ICAO airplane CO_2 certification database.* Federal Aviation Administration (FAA). https://www.faa.gov/media/70976

ICAO. (2018). *Recommended method for computing noise contours around airports* (2nd Ed.). International Civil Aviation Organization (ICAO), Doc 9911.

Norman, P.D., Lister, D.H., Lecht, M., Madden, P., Park, K., Penanhoat, O., Plaisance, C., & Renger, K. (2003). Development of the Technical Basis New Emissions Parameter Covering the Whole Aircraft Operation. NEPAIR, Final TR NEPAIR/WP4/WPR/01, Sept. 2003.

Project 082(B) Integrated Noise and CO_2 Standard Setting Analysis

Massachusetts Institute of Technology

Project Lead Investigator

Raymond L. Speth
Senior Research Scientist
Department of Aeronautics & Astronautics
Massachusetts Institute of Technology
77 Massachusetts Ave, Building 33-316
Cambridge, MA 02139
617-253-1516
speth@mit.edu

University Participants

Massachusetts Institute of Technology (MIT)

- P.I.: Dr. Raymond L. Speth
- FAA Award Number: 13-C-AJFE-MIT, Amendment Nos. 095, 102, 115, 119, and 133
- Period of Performance: June 14, 2022, to September 30, 2025 (with the exception of funding and cost-sharing information, this report covers the period from October 1, 2023, to September 30, 2024)
- Tasks:
  1. Data anonymization and comparison of original equipment manufacturer data with public data
  2. Development of an aircraft conceptual design tool for policy analysis

Project Funding Level

The ASCENT Project 082(B) has received $1,400,000 Federal Aviation Administration (FAA) funding and $1,400,000 matching funds. Sources of matching funds are approximately $185,200 from MIT, plus 3rd party in-kind contributions of $274,000 from Savion Aerospace Corp., and $532,000 from NuFuels, LLC, and $408,800 from Earth Force Technologies.

Investigation Team

Dr. Raymond L. Speth (P.I.), Tasks 1 & 2
Dr. Prakash Prashanth (co-investigator), Task 2
Dr. Jayant Sabnis (co-investigator), Task 2
Jonas J. Gonzalez (PhD student), Tasks 1 & 2
Aditeya Shukla (MS student), Task 2

Project Overview

To evaluate the economic reasonableness of proposed aircraft environmental standards, the International Civil Aviation Organization's (ICAO) Committee on Aviation Environmental Protection (CAEP) requires tools for assessing the impacts of technologies and design changes intended to control aircraft noise and emissions, and for evaluating the costs of implementing such changes to aircraft and engine designs. Existing methods used to support decision-making in previous CAEP noise stringencies do not represent modern aircraft and propulsion designs and technologies. The goal of this project is to develop new tools that address the shortcomings of the previous methods, in support of CAEP/13 stringency analyses.

Task 1 – Data Anonymization and Comparison of Original Equipment Manufacturer Data with Public Data

Massachusetts Institute of Technology

Objective

The requirement to protect sensitive original equipment manufacturer (OEM) data in the current CAEP/13 cycle necessitates a new approach to the management of data in the CAEP standard-setting process. Any data presented to the full CAEP working groups (WG) must be anonymized to satisfy these needs. In addition, comparing publicly available data against OEM-provided data helps inform CAEP regarding the quality of publicly available data.

Research Approach

While the studies for this task were concluded in July 2023 within the CAEP/13 Data Processing ad hoc group (DPahg), the current period of performance also included support of the DPahg's data hand-off presentations following the easing of data restrictions. Technical review was also provided for subsequent publications of the data within the CAEP.

Milestones

- Provided data anonymization and presentation support to CAEP WGs.

Publications

None.

Outreach Efforts

- Circulated and submitted the resulting anonymized plots and hand-off data within CAEP WGs and to the CAEP/13 meeting.

Awards

None.

Student Involvement

MIT Graduate student, Jonas J. Gonzalez, conducted the analyses and presented this work to CAEP WGs.

Plans for Next Period

This task has been completed.

Task 2 – Development of an Aircraft Conceptual Design Tool for Policy Analysis

Massachusetts Institute of Technology

Objective

The goal of this task is to enhance the capability of our Julia[1]-based aircraft conceptual design software, Transport Aircraft and the Environment System Optimization in Julia (TASOPT.jl), to incorporate new disciplines and components, including noise analysis and optimization. The objective is to use this tool to estimate the sensitivities of design changes to the engine, structures, and aerodynamics on metrics of environmental performance, such as carbon dioxide (CO_2) and nitrogen oxides, in addition to the impact on certification noise.

[1] Julia is a high-performance, open-source, general purpose programming language designed for scientific computing, machine learning, and data mining.

Research Approach

Recent development of TASOPT.jl has focused on three specific areas: (1) assessing and deploying methods for efficient and robust optimization, (2) integration of a noise assessment tool, pyNA, and (3) code refactoring and documentation for accessibility.

TASOPT.jl now has the ability to optimize aircraft designs using both gradient and non-gradient based methods. The codebase has a sensitivity module that uses finite differences to calculate gradients. Work has also been done to introduce memorization in gradient based optimization to mitigate increases in computational cost as the number of design variables and constraints increases. Steps have been taken to incorporate automatic differentiation for faster and more accurate gradients.

TASOPT.jl–pyNA integration is complete from a software perspective, having required initial maintenance of the pyNA repository. The technical assumptions of the noise analysis, however, are in progress of being adapted from their original application to supersonic aircraft to the subsonic regime relevant to this task. This adaptation includes updates to noise source models and trajectory assumptions, and also includes iterative review of initial results as more recent source models in the literature are likely needed to meet the requisite fidelity.

Early in the reporting period, code refactoring focused on abiding by contemporary conventions, such as script modularization, redundancy elimination, in-code commenting, and readability. The team also generated comprehensive documentation on the technical models and the implementation. These products were published on GitHub® where active development continues.

Milestones

- Implemented gradient-based/gradient-free optimization modules.
- Completed basic noise assessment integration.
- Published on GitHub the initial version of codebase, documentation, and development for TASOPT.jl.

Major Accomplishments

- Published TASOPT.jl (v3.0.0-beta). It is available at https://github.com/MIT-LAE/TASOPT.jl.

Publications

None.

Outreach Efforts

- Communicated progress in method development to the FAA project managers during regular teleconferences.
- Presented the development plan and intended analyses to the CAEP Public Data ad hoc group (PUBahg). Feedback and coordination of future analyses is anticipated.

Awards

None.

Student Involvement

MIT graduate students, Jonas J. Gonzalez and Aditeya Shukla, were engaged in code refactoring, documentation, and development.

Plans for Next Period

- Update pyNA modelling for subsonic aircraft.
- Determine best practices for robust and efficient design optimization.
- Generate “benchmark” models for aircraft of varied class and technology level.
- Submit TASOPT.jl to the *Journal of Open-Source Software*.

® GitHub is a registered trademark of GitHub, Inc., San Francisco, California.

Project 083 NO_x Cruise/Climb Metric System Development

Massachusetts Institute of Technology

Project Lead Investigator

Raymond L. Speth
Principal Research Scientist
Department of Aeronautics & Astronautics
Massachusetts Institute of Technology
77 Massachusetts Ave
Building 33-310
Cambridge, MA 02139
617-253-1516
speth@mit.edu

University Participants

Massachusetts Institute of Technology (MIT)

- P.I.: Dr. Raymond L. Speth
- FAA Award Number: 13-C-AJFE-MIT, Amendment Nos. 103, 115, 117, 133, and 137
- Period of Performance: September 19, 2022, to December 31, 2025 (reporting here with the exception of funding level and cost-sharing only for the period October 1, 2023, to September 30, 2024)
- Tasks:
  1. Evaluation of Weightings for a New NO_x Emissions Metric
  2. Evaluation of possible new stringencies for nitrogen oxide (NO_x) emission regulations

Project Funding Level

The ASCENT Project 083 received $900,000 Federal Aviation Administration (FAA) funding and $900,000 matching funds. Sources of matching funding are approximately $129,500 from MIT, plus 3rd party in-kind contributions of $250,000 from NuFuels LLC, and $520,500 from Earth Force Technologies.

Investigation Team

Dr. Raymond L. Speth (P.I.), All Tasks
Prof. Steven Barrett (co-P.I.), Task 1
Wyatt Giroux (graduate student), Task 1
Sarah Reider (graduate student), Task 2

Project Overview

The International Civil Aviation Organization (ICAO) is responsible for setting emissions standards for aircraft engines to limit the environmental impacts of these emissions. To limit the impacts of aviation emissions, the FAA's Office of Environment and Energy is working with the ICAO Committee on Aviation Environmental Protection (CAEP) to establish updated emissions standards for aircraft engines by using metrics relevant to the full-flight emissions of these species, rather than only those emissions occurring during a standard landing and takeoff (LTO) cycle. Emissions standards set by ICAO will influence the development of future engine technologies, thus resulting in a reduction of emissions from future aircraft engines, and consequently improved human health and reduced environmental impacts. To this end, the FAA needs to understand and quantify how current and future standards may impact aviation emissions in the United States and worldwide, and how changes in these emissions may affect the environment and human health.

The objective of this project is to provide support for FAA decision-making related to potential certification standards that control emissions during cruise and climb, in addition to the current standards for LTO. The project includes analyses

important for understanding the costs and benefits of both current standards and policies that may be proposed in the future. By providing a rational, scientific basis for decisions regarding the implementation of emissions standards, this project contributes to an efficient implementation process and provides industry with regulatory certainty. The analyses provided in this project will allow the FAA to identify policy proposals that serve the national interest and advocate for those policies within the ICAO.

Task 1 – Evaluation of Weightings for a New NO_x Emissions Metric

Massachusetts Institute of Technology

Objective

The objective of this task was to evaluate the effect of a weighting factor on the performance of a weighted emission indices (EI) for nitrogen oxides (NO_x) ground metric at representing cruise and climb NO_x emissions. The analysis was performed for two possible ground metrics.

Research Approach

A modeling framework was previously developed to assess the Pearson correlation of various forms of a cruise/climb NO_x metric (Guenard, 2024). This framework leveraged aircraft performance data from the PIANO-X database (Simos, 2008) and emissions certification data from the ICAO Engine Emission Databank (EEDB) (EASA, 2023), to calculate full flight emissions using the Aviation Emissions Inventory Code (AEIC) (Simone et al., 2013), and Boeing Fuel Flow Method 2 (BFFM2) (DuBois & Paynter, 2006).

Metrics consisting of a weighted sum of sea-level-static (SLS) NO_x EI were considered. These metrics had the specific form:

$$\mathrm{MV} = \sum_i \mathrm{EI}_i w_i \quad \text{where} \quad \sum_i w_i = 1 \qquad \text{(Eq. 1)}$$

Two choices of emissions index sets were considered in this analysis. The first is a combination of the SLS points measured at 85% and 30% rated thrust, acting as upper and lower bounds on the cruise operation range. These correspond to the climb-out and approach, respectively. The second set consisted of SLS EI values at 85% and 57.5% rated thrust, raising the lower bound to the midpoint of 85% and 30% to better approximate cruise. While the 57.5% rated thrust point is not currently reported, the non-volatile particulate matter certification is being updated to include this point. As such, the 57.5% point is most pertinent to consider from a policy standpoint.

To assess the performance of these metrics, we examine their Pearson correlation with respect to the mission average NO_x emission index, defined for a given engine as

$$\mathrm{EI}_{\mathrm{avg}} = \frac{M_{NO_x}}{I} \quad \left[\frac{\mathrm{kg}}{\mathrm{kN{\cdot}s}}\right] \qquad \text{(Eq. 2)}$$

where M_{NO_x} is the total mass of NO_x emitted by all aircraft/engine pairs using the given engine and I is the impulse, calculated as the integral of thrust over flight time, for all aircraft/engine pairs using the given engine. Such a metric is beneficial due to remaining at the engine level (no aircraft data required). To estimate the SLS emissions at 57.5% rated thrust, detailed curves of thrust versus EI(NO_x) were constructed using derated versions of engines from the EEDB. The NO_x emissions at 57.5% rated thrust could then be estimated by interpolating along the resulting curve. Notably, due to a lack of published analysis and understanding of non-reported emissions of engines using staged combustors, these were not included in the 85%/57.5% metric analysis.

Using this, the weighting of the 85% rated thrust point was swept from 0 to 1 with the Pearson correlation being calculated as a function of weighting for each choice of secondary point (30% or 57.5% rated thrust). The resulting curves of correlation coefficient are shown for the 85%/30% metric and the 85%/57.5% metric in Figure 1and Figure 2, respectively. Correlations are broken down by aircraft application (i.e., all types, single aisle, and twin aisle) and by certification year. The correlation achieved by using the existing LTO metric, D_p/F_{oo}, is also shown as dotted lines for each subcategory. For both metrics, all type/all engines performance outperforms the existing LTO metric by around 12.7%. In addition, each metric exhibits an increasing maximum correlation over time for each aircraft application, suggesting the metric performs better for newer engines. The primary difference between the metrics is the specific shape of the correlation versus weight curves. For the 85%/30% metric, the correlation plateaus above an 85% weight of 0.4. However, the correlation of the

metric with single aisle aircraft emissions decreases monotonically after that point. The twin aisle performance largely mirrors the all-types performance, plateauing at roughly the same point. As such, while performance of the 85%/30% metric is approximately invariant to weighting past an 85%-point weighting of 0.4, a lower value would retain the best correlation with single aisle aircraft.

For the 85%/57.5% metric, the curves vary far less. The all type and twin aisle performance is nearly constant for all weighting factors. The single aisle performance still decreases as 85%-point weight increases but does so over a slightly smaller range of correlation values compared to the 85%/30% metric. This indicates that the 85% and 57.5% rated thrust points are performing roughly equally at representing cruise/climb NO_x. Due to the single aisle performance varying the most in this case, a low weighting of the 85% point would be preferable for the 85%/57.5% metric. When possible, engines utilizing staged combustors should be included to examine potential effects on these trends.

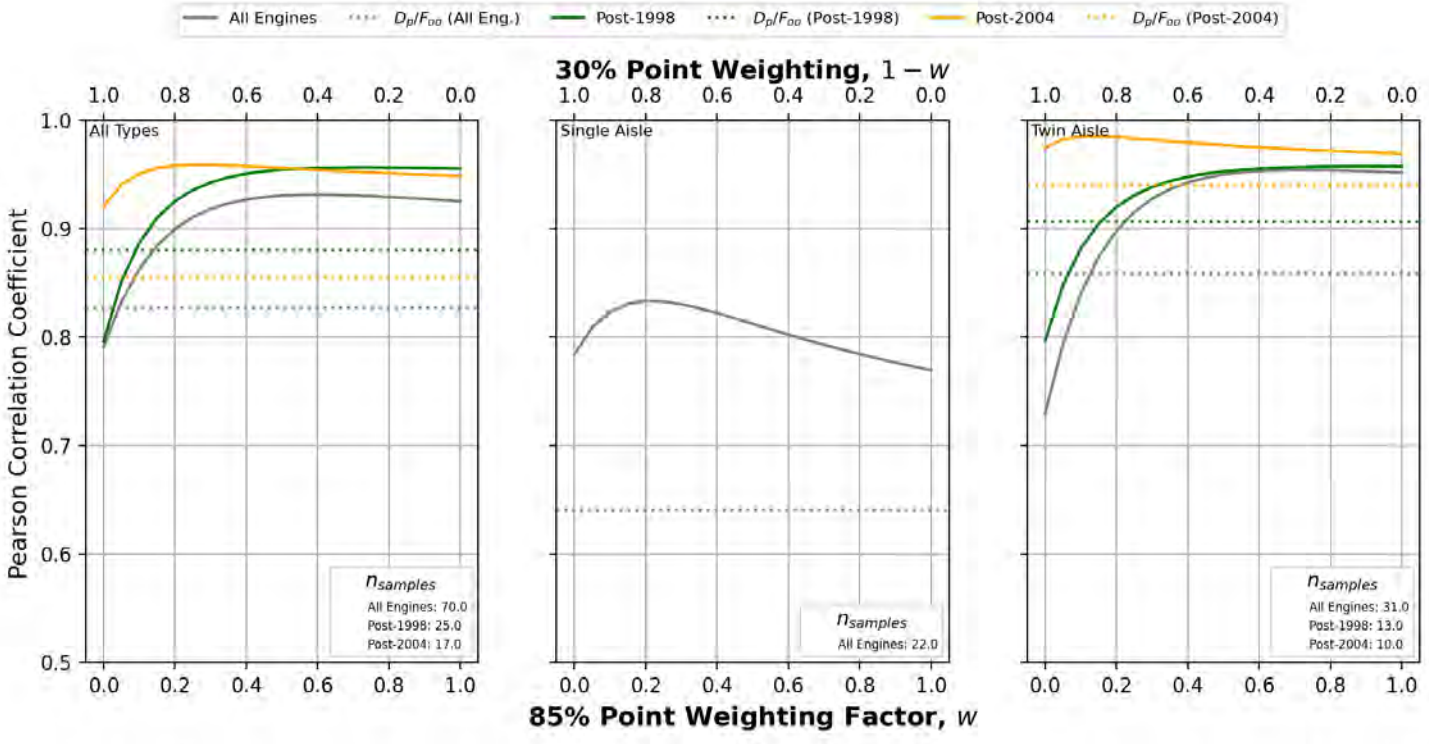

Figure 1. Correlation of 85%/30% metric by age and aircraft application (cases with at least 10 samples).

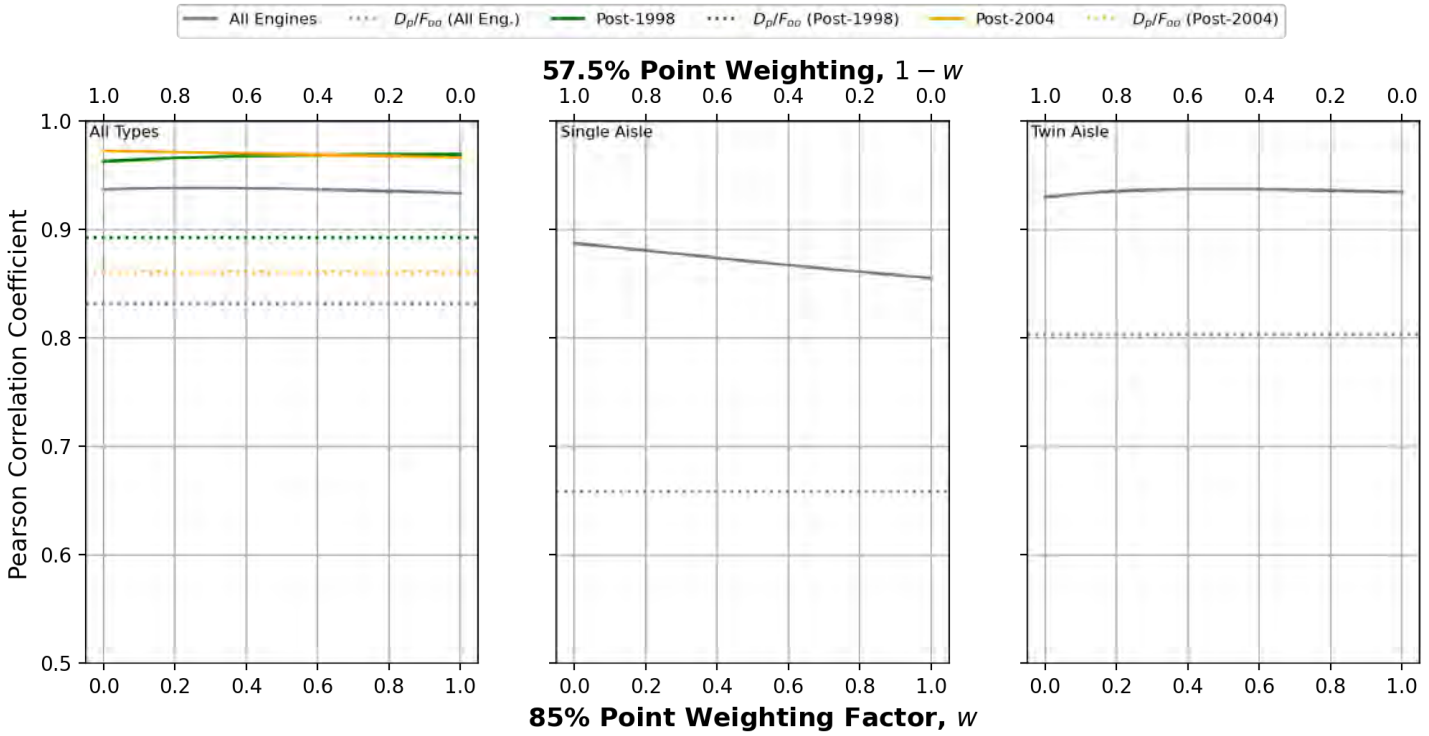

Figure 2. Correlation of 85%/57.5% metric by age and aircraft application (cases with at least 10 samples; staged combustors not included).

As a final step, the metric performance was compared between both metric choices. To do this fairly, the engines using staged combustion were removed from the 85%/30% dataset such that the metrics have equal weighting when the metric is determined only by the 85% rated thrust point. Looking at the results, near identical performance is observed between the metrics in the previously identified plateau regions, with the 85%/30% metric performance falling off at low 85% rated thrust point weighting. Most notably, the correlation for single aisle aircraft for the 85%/30% metric increases to approximately the same range seen in the 85%/57.5% metric, suggesting the removal of engines with staged combustors has a significant effect on the single aisle category (see Figure 3). This emphasizes the need for future work characterizing the non-reported performance of staged combustors.

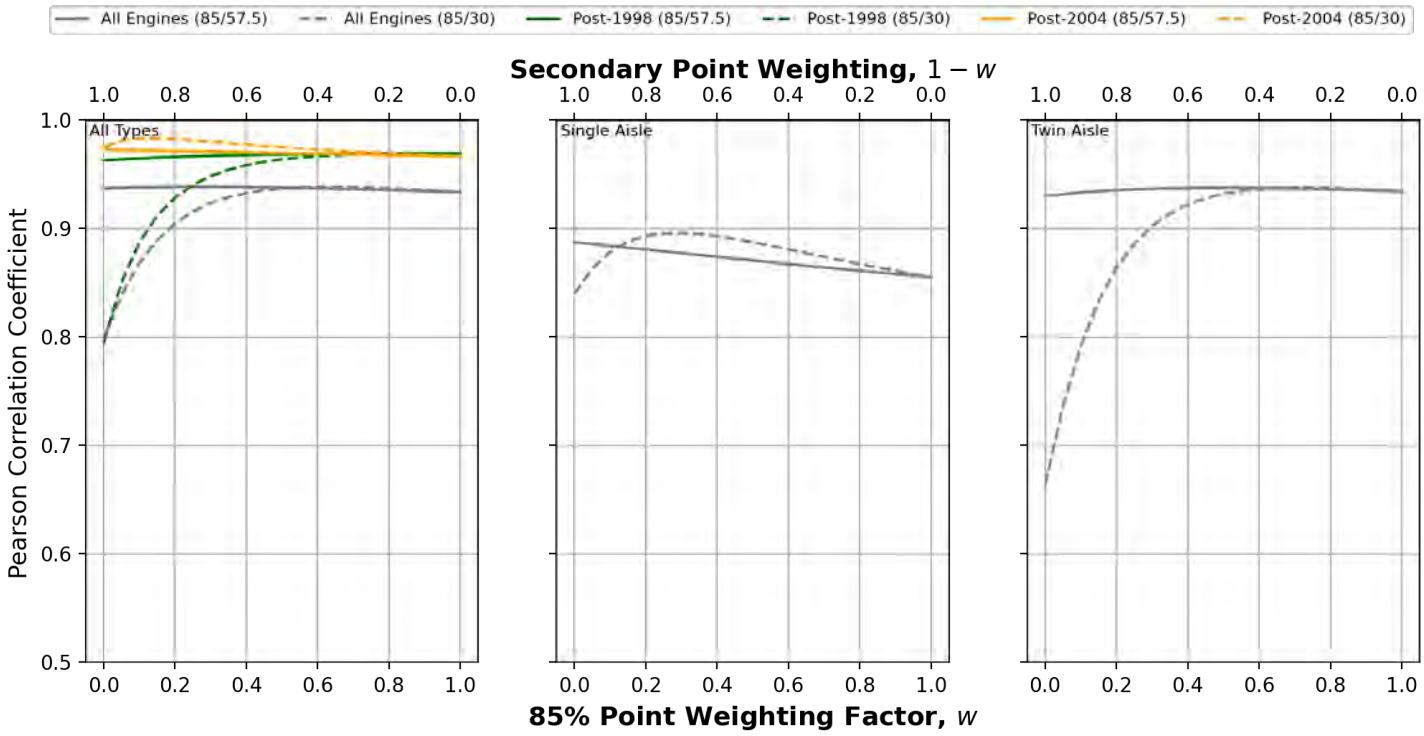

Figure 3. Correlation of 85%/57.5% and 85%/30% metric by age and aircraft application (cases with at least 10 samples; staged combustors not included)

Milestone

- Presented complete analysis was presented as a working paper at the 13th cycle of the ICAO Committee on Aviation Environmental Protection (CAEP/13)-Working Group 3 (WG3)/9-Emissions Characterization Task Group (ECTG) Meeting.

Major Accomplishments

The analysis demonstrated that metrics using different weights than the current LTO standard provide better representations of cruise NO_x emissions, and that including emissions data at intermediate thrust points could further improve this relationship.

Publications

None.

Outreach Efforts

- Presented at the CAEP/13-WG3/9-ECTG Meeting held September 30–October 4, 2024, in Montreal, Canada.

Awards

None.

Student Involvement

Graduate student Wyatt Giroux conducted the analyses and presented the work to the FAA and CAEP WG3.

Plans for Next Period

- Quantify the effect of engines utilizing staged combustion on metric correlation.
- Examine whether further increases to overall pressure ratio (OPR) should be expected to confer meaningful fuel burn benefits for the purpose of setting NO_x metric limits.

- Assess the performance of BFFM2 at representing cruise/climb emissions of modern and emergent engines.

References

DuBois, D., & Paynter, G. C. (2006). "Fuel Flow Method2" for estimating aircraft emissions (Section 1: *Journal of Aerospace*, Vol. 115, p. 1-14). In *SAE 1984 Transactions*. https://doi.org/10.4271/2006-01-1987

EASA. (2023). *ICAO aircraft engine emissions databank* (Issue 29). European Union Aviation Safety Agency (EASA). https://www.easa.europa.eu/en/domains/environment/icao-aircraft-engine-emissions-databank

Guenard, A. (2024). *Assessment of a new metric system to regulate NO_x aircraft emissions at cruise* [Master's thesis, Massachusetts Institute of Technology]. Massachusetts Institute of Technology. https://hdl.handle.net/1721.1/155378

Simone, N. W., Stettler, M. E. J., & Barrett, S. R. H. (2013). Rapid estimation of global civil aviation emissions with uncertainty quantification. *Transportation Research Part D: Transport and Environment*, *25*, 33–41. https://doi.org/10.1016/j.trd.2013.07.001

Simos, D. (2008) *PIANO-X user's guide*. Lissys, Ltd. https://lissys.uk/piano-x-guide.pdf

Task 2 – Evaluation of Possible New Stringencies for NO_x Emission Regulations

Massachusetts Institute of Technology

Objective

The objective of this task was to evaluate potential stringency setting options for emissions of NO_x at LTO and cruise that better represent the social cost tradeoffs between NO_x and carbon dioxide (CO_2) at high OPR.

Research Approach

The basis of this task involved developing a modelling framework for estimating cruise and LTO NO_x emissions. This was accomplished using the open-source aircraft optimization and design package, Transport Aircraft System OPTimization (TASOPT), which allowed us to determine the effect of varying OPR as a design parameter on NO_x emissions. TASOPT was run for a single engine flown on a 3000 nmi range mission at OPRs ranging between 10 and 60. This variation was ideal because it reflects the current LTO metric space, which is a function of OPR and NO_x emissions. Values for the emission index of NO_x at LTO and cruise were calculated using the P_3-T_3 curve in Equation 3, which was determined by fitting a combustor model in Cantera[1] to data for a CFM International CFM56 engine from the EEDB. In Equation 3, SH is the specific humidity and P_{t3} and T_{t3} are the pressures and temperatures at the compressor exit. Similarly, the impact of CO_2 is a function of thrust specific fuel consumption (TSFC), which is an output of TASOPT at all stages of the flown mission.

$$\mathrm{EI(NO}_x) = \exp\left(-19 \cdot (\mathrm{SH_{alt}} - \mathrm{SH_{SL}})\right) \cdot P_{t3}^{0.4} \cdot \left((4.85 \cdot 10^{-5})T_{t3}^4 - (6.51 \cdot 10^{-8})T_{t3}^3 + (7.19 \cdot 10^{-6})T_{t3}^2 + (2.07 \cdot 10^{-2})T_{t3} - 6.69\right) \quad \text{(Eq. 3)}$$

The equation representing the total environmental impact from NO_x emissions during LTO operations is

$$\text{Environmental Cost}_{\mathrm{LTO,NO}_x} = \frac{\mathrm{Dp}}{F_{oo}} \cdot \frac{1}{\text{LTO Test Time}} \cdot \text{Social Cost}_{\mathrm{NO}_x} \quad \text{(Eq. 4)}$$

where Dp/F_{oo} is the NO_x emissions during a standard LTO test cycle and the current estimate for the social cost of NO_x is \$48,000/tonne based on models estimating the health effects from ozone and fine particulate matter produced from aviation NO_x emissions (Grobler et al., 2019; Turner et al., 2016; Burnett et al., 2018; Quadros et al., 2020). A future cruise metric is likely to be EI(NO_x)-based. The social cost function for NO_x at cruise is

$$\text{Environmental Cost}_{\mathrm{cruise,NO}_x} = \mathrm{EI(NO}_x) \cdot \mathrm{TSFC} \cdot \text{Social Cost}_{\mathrm{NO}_x} \quad \text{(Eq. 5)}$$

[1] Cantera is an open-source suite of tools for problems involving chemical kinetics, thermodynamics, and transport processes.

This cruise impact includes thrust specific fuel consumption (TSFC) in its calculation to normalize the output by engine size and operating time. The impact of CO_2 is calculated in the same manner for LTO and cruise,

$$\text{Environmental Cost}_{CO_2} = \text{EI}(CO_2) \cdot \text{TSFC} \cdot \text{Social Cost}_{CO_2} \quad \text{(Eq. 6)}$$

where the social cost of CO_2 is taken to be \$168/tonne and the emission index is 3.15 kg CO_2/kg fuel (Howard & Sterner, 2017; Rennert et al., 2022).

The overall environmental cost was then determined by combining the NO_x and CO_2 costs at each OPR. Drawing lines of constant environmental cost on the LTO metric space showed that increasing OPR results in minimal fuel burn reduction. This causes a slope leveling effect in the constant cost contours, shown in Figure 4, meaning NO_x emissions are driving environmental costs at high OPRs. This contrasts with the current LTO limit, which is observed to increase the environmental cost with the increasing OPR in the same figure. Analysis of a potential cruise metric showed a corresponding effect as shown in Figure 5. This flat slope phenomenon remained even after accounting for uncertainties in the social costs for NO_x and CO_2. These results suggest that a different shape in the stringency line might more effectively constrain both LTO and cruise NO_x emissions.

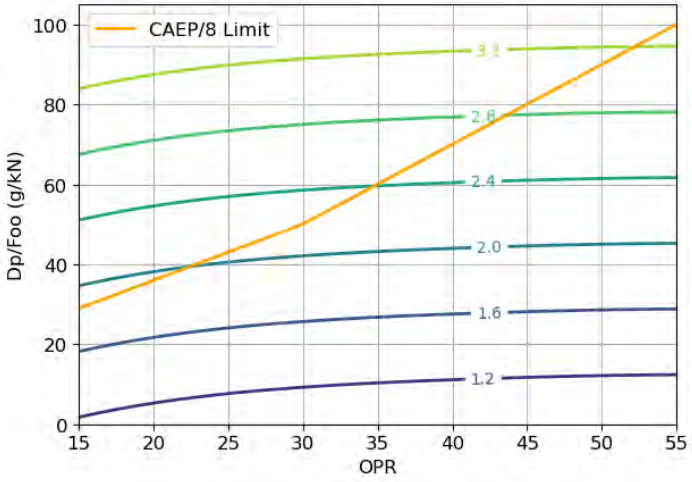

Figure 4. Contours of constant environmental cost in units of \$/MN-s combining NO_x and CO_2 emissions at varying OPRs for LTO operations. The CAEP/8 limit is shown in orange.

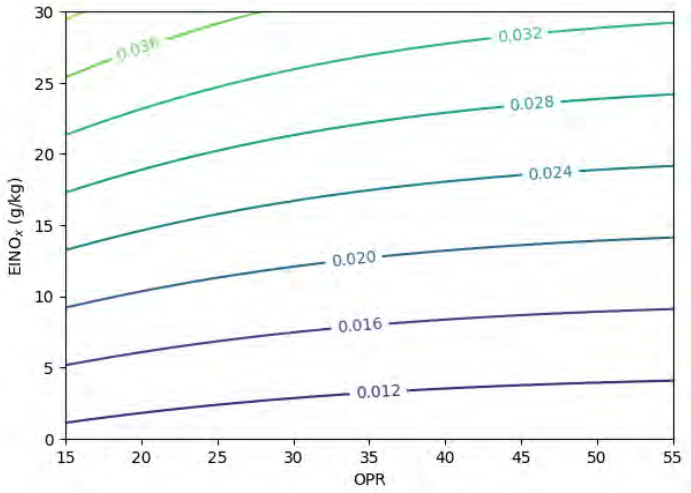

Figure 5. Contours of constant environmental cost in units $/kN-s combining NO_x and CO_2 emissions at varying OPRs for cruise.

Milestone

- Presented the complete analysis as a working paper at the CAEP13-WG3/9-ECTG meeting.

Major Accomplishments

This work demonstrated the ability to translate previously developed proposals for cost-effective NO_x stringencies into the new EI-based metric suggested for regulating cruise NO_x emissions.

Publications

None.

Outreach Efforts

- Presented at the CAEP/13-WG3/8-ECTG meeting (May 13–18, 2024).
- Presented at the CAEP/13-WG3/9-ECTG meeting (September 30–October 4, 2024).

Awards

None.

Student Involvement

Graduate student Sarah Reider conducted the analyses and presented the work to the FAA and CAEP WG3.

Plans for Next Period

- Conduct statistical analyses to determine the overall likelihood of reducing environmental damage given uncertainties in the social cost values and modeling approach under different stringency options for LTO and cruise.

References

Burnett, R., Chen, H., Szyszkowicz, M., Fann, N., et al. (2018). Global estimates of mortality associated with long-term exposure to outdoor fine particulate matter. *Proceedings of the National Academy of Sciences, 115*, 9592–9597. https://doi.org/10.1073/pnas.1803222115

Grobler, C., Wolfe, P., Dasadhikari, K., Dedoussi, I. C., Allroggen, F., Speth, R. L., Eastham, S. D., Agarwal, A., Staples, M. D., Sabnis, J., & Barrett, S. R. H. (2019). Marginal climate and air quality costs of aviation emissions. *Environmental Research Letters, 14*(11), 114031. https://doi.org/10.1088/1748-9326/ab4942

Howard, P. H. & Sterner, T., (2017). Few and not so far between: a meta-analysis of climate damage estimates. *Environmental and Resource Economics, 68*, 197–225. https://doi.org/10.1007/s10640-017-0166-z

Quadros, F. D. A., Snellen, M., & Dedoussi, I. C. (2020). Regional sensitivities of air quality and human health impacts to aviation emissions. *Environmental Research Letters, 15*(10), 105013. https://doi.org/10.1088/1748-9326/abb2c5

Rennert, K., Errickson, F., Prest, B. C., Rennels, L., et al. (2022). Comprehensive evidence implies a higher social cost of CO_2. *Nature, 610*, 687–692. https://doi.org/10.1038/s41586-022-05224-9

Turner, M. C., Jerrett, M., Pope, A. C., Krewski, D., et al. (2016). Long-term ozone exposure and mortality in a large prospective study. *American Journal of Respiratory and Critical Care Medicine, 193*(10), 1134–1142. https://doi.org/10.1164/rccm.201508-1633OC

Project 084 Noise Modeling of Advanced Air Mobility Flight Vehicles

Massachusetts Institute of Technology

Project Lead Investigators

R. John Hansman
T. Wilson Professor of Aeronautics & Astronautics
Department of Aeronautics & Astronautics
Massachusetts Institute of Technology
Room 33-303
77 Massachusetts Ave
Cambridge, MA 02139
617-253-2271
rjhans@mit.edu

Jacqueline Huynh
Assistant Professor of Mechanical and Aerospace Engineering
4212 Engineering Gateway
Irvine, CA 92697
949-824-3561
huynhlj@uci.edu

University Participants

Massachusetts Institute of Technology (MIT)

- P.I.: Prof. R. John Hansman
- FAA Award Number: 13-C-AJFE-MIT, Amendment Nos. 112, 115 and 131
- Period of Performance: January 1, 2023, to August 11, 2025
- Tasks:
  1. Identify target advanced air mobility (AAM) vehicle configurations for noise model development
  2. Identify noise modeling gaps for selected AAM configurations and operations
  3. Develop physics-based noise and flight profile model for representative AAM vehicles
  4. Incorporate noise results for representative AAM vehicles with the Aviation Environmental Design Tool
  5. Expand methods to additional vehicle sets
  6. Evaluate implications for noise mitigation and low-noise operations for AAM vehicles

University of California Irvine (UCI)

- P.I.: Prof. Jacqueline Huynh
- Award Number: MIT Subaward Purchase Order No. 883753
- Period of Performance: January 1, 2023, to August 11, 2025
- Tasks:
  1. Identify target AAM vehicle configurations for noise model development
  2. Identify noise modeling gaps for selected AAM configurations and operations
  3. Develop physics-based noise and flight profile model for representative AAM vehicles
  4. Incorporate noise results for representative AAM vehicles with the Aviation Environmental Design Tool
  5. Expand methods to additional vehicle sets
  6. Evaluate implications for noise mitigation and low-noise operations for AAM vehicles

Project Funding Level

The ASCENT Project 084 received $615,000 Federal Aviation Administration (FAA) funding and $615,000 matching funds. Sources of match are approximately $123,100 from MIT, and $44,900 from subrecipient UCI, and $447,000 from Electra.aero, Inc. (Electra™).

Investigation Team

Massachusetts Institute of Technology

Prof. R. John Hansman (P.I.), Tasks 1-6
Brandon Hadfield (graduate student), Tasks 1-6

University of California Irvine

Prof. Jacqueline Huynh (P.I.), Tasks 1-6
Victoria Pellerito (graduate student), Tasks 1-6
Nathan Yeung (graduate student), Tasks 1-6

Project Overview

This project develops first-principles noise models of urban air mobility (UAM) and AAM vehicle configurations to make community noise predictions of these aircraft flying at various operating states. Estimated noise levels from these models will be used to develop methods needed for a UAM/AAM-compatible the Aviation Environmental Design Tool (AEDT) to make preliminary noise estimates of these vehicles. Conventional aircraft configuration noise levels at both the source and procedural levels have been examined extensively in projects such as ASCENT Projects 011, 023, and 044. This project aims to expand upon this work for UAM/AAM. Various vehicle configurations are currently under consideration for feasibility for use in UAM and AAM operations, including short takeoff and landing (STOL) configurations, tilt-rotor vertical takeoff and landing (VTOL), and lift-plus-cruise (LPC) VTOL configurations, each of which has unique sources and operating modes. Thus, targets of opportunity are identified to estimate the noise levels and develop AEDT compatibility for these vehicles and operating modes. The work will be expanded to generalized AAM operations, and the models developed will be used to make preliminary noise footprint estimates for a variety of configurations. The goals of the project are thus to:

- Develop methods to model the noise levels at the source and due to different operations of UAM and AAM vehicle configurations.
- Develop methods needed for a UAM/AAM-compatible AEDT, to make preliminary noise estimates of AAM vehicles.

Task 1 – Identify Target AAM Vehicle Configurations for Noise Model Development

Massachusetts Institute of Technology
University of California Irvine

Objectives

The goals of this task are to determine target AAM vehicle configurations for development of the noise model. Various AAM configurations are under consideration in industry, such as STOL, as well as VTOL vehicles including tilt-rotor VTOLs. Various AAM vehicles across industry will be examined to determine which will be the most relevant for developing the noise modeling method. From this examination, one or more representative vehicles will be chosen as a focus in the initial noise modeling effort.

Research Approach

- Research candidate AAM configurations currently being proposed by the top industry contenders, such as Joby Aviation,® Wisk Aero (Wisk®), and Electra.
- Gather specifications and representative flight profile definitions for selected representative vehicle configurations needed for noise model development.

™ Electra is a trademark of Electra Aero, Inc., Falls Church, Virginia.
® Joby Aviation is a registered trademark of Joby Aero, Inc., Santa Cruz, California.
® Wisk is a registered trademark of Wisk Aero, LLC, Mountain View, California.

Milestones

- Selected three vehicle configurations for noise model development.
- Determined the geometry and performance specifications for vehicle configurations for noise model development from published resources and from discussions with industry.

Major Accomplishments

The research team identified three AAM vehicle configurations for the initial noise modeling development. In Figure 1, the vehicles examined include (a) a blown-flap STOL vehicle, (b) a lift-plus-cruise VTOL vehicle, and (c) a tilt-rotor VTOL vehicle.

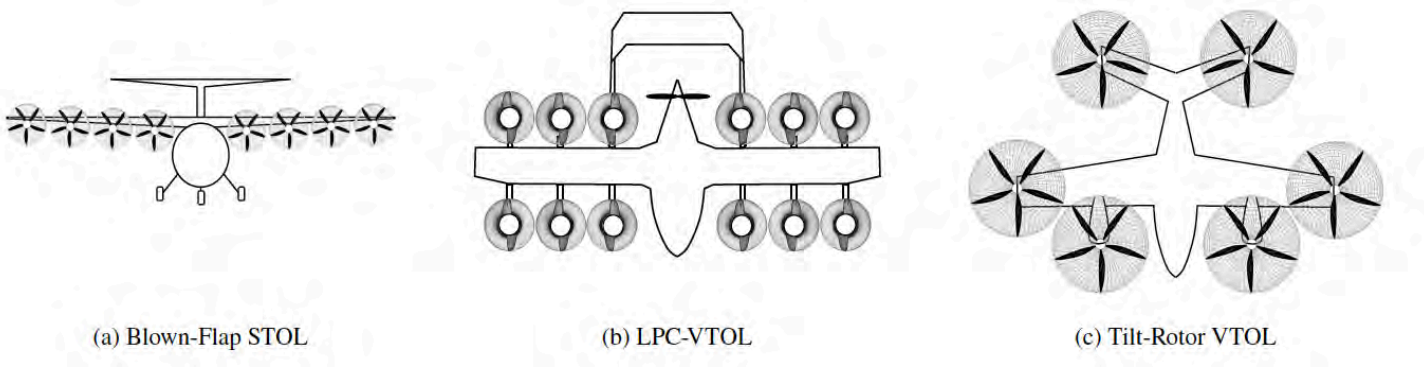

Figure 1. Selected AAM vehicle configurations for noise model development: (a) blown-flap STOL, (b) LPC-VTOL, (c) tilt-rotor VTOL.

For the purposes of modeling representative operations and noise models, an aircraft performance model that sizes and determines the off-design performance conditions of rotors for these vehicles was developed by using the XROTOR[1] blade element momentum model. Given design conditions such as the weight and required thrust of the representative vehicles, the ASCENT Project 084 team sized sample propellers for each of the vehicles to determine representative noise levels. For each of the vehicles selected, our team determined opportunities to obtain noise data for validation of the noise modeling done in Task 3. Electra provided data for the blown-flap STOL vehicle, Wisk provided data for the lift plus cruise vehicle, and published data from Joby Aviation was available for the tilt-rotor vehicle.

Depending on the type of vehicle, representative flight operations for each were conceptualized (Figure 2).

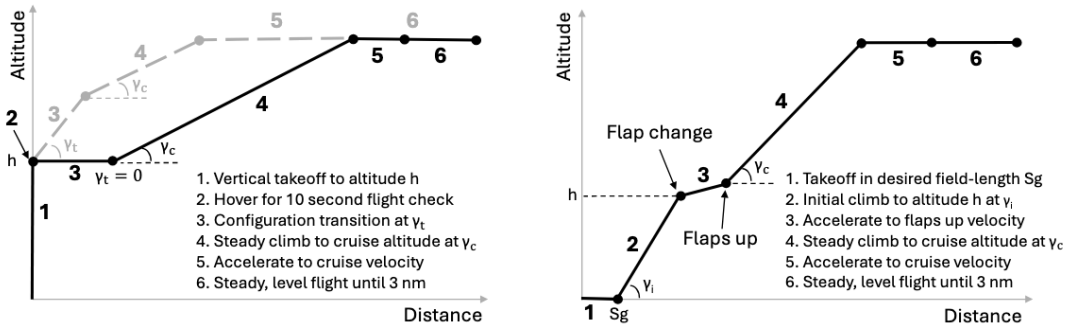

(a) eVTOL (b) eSTOL

Figure 2. Example control strategy for electric vertical take-off and landing (eVTOL) and electric short take-off and landing (eSTOL) AAM aircraft.

[1] XROTOR is an interactive program for the design and analysis of ducted and free-tip propellors and windmills

Publications
None.

Outreach Efforts
- Presented at biannual ASCENT Advisory Board meetings.
- Presented the project to engineers at Wisk.
- Collaborated with Electra to gather noise data for a full scale blown-flap STOL aircraft.
- Collaborated with Wisk to receive sample noise data for a full-scale lift plus cruise aircraft.
- Participated in weekly teleconferences and meetings with FAA Technical Monitor.

Awards
None.

Student Involvement
Graduate students have been involved in all aspects of this research, in terms of analysis, documentation, and presentation. These students conducted the research in selecting vehicles, and defining the representative vehicles used for Tasks 2 and 3 of the research goals.

Plans for Next Period
The primary objective for this task was met with the selection and development of specifications for representative vehicles to use for initial noise model development. However, as the project continues, opportunities to consider other vehicle configurations and flight procedures that will enrich the noise model development efforts will be considered, particularly via additional industry collaboration.

Task 2 – Identify Noise Modeling Gaps for Selected AAM Configurations and Operations
Massachusetts Institute of Technology
University of California Irvine

Objective
The objective of this task is to identify noise modeling gaps for selected AAM configurations and operations. According to the target AAM vehicle configuration to focus the noise model in effort on in Task 1, in Task 2, current gaps in noise modeling that must be addressed to formulate the noise modeling method for AAM vehicles will be identified. The noise modeling literature will be consulted, and the effort will leverage collaboration with the National Aeronautics and Space Administration (NASA) UAM and AAM work as appropriate. Noise sources most likely to dominate for different configurations and operations will also be identified. The task will focus primarily on the target vehicles identified Task 1, while considering additional gaps for other vehicle configurations on an ongoing basis.

Research Approach
- Examine the configurations and potential operating procedures of the AAM vehicles determined in Task 1 via performance modeling and consultation with industry.
- Research potential noise sources from the AAM vehicles and determine modeling approaches of the current state-of-the-art noise models.

Milestones
- Examined potential noise modeling operations for each of the three vehicle configurations from Task 1.
- Identified gaps in noise modeling, according to the three vehicle configurations from Task 1.

Major Accomplishments
The AAM vehicles examined in Task 1 feature unique sources of noise stemming from different numbers of rotors and their placements, which interact with one another and with the airframe. These features were examined during this task and the noise levels the ASCENT Project 084 team modeled in Task 3 were compared to the available noise data from

industry. The tilt-VTOL vehicle's noise directivity changes with the tilt of the rotor; the lift-plus-cruise vehicle has varied rotor sizes; and the blown-flap STOL vehicle features noise levels arising from the blown lift. The operating procedures for each of these vehicles also varies and must be considered in the noise modeling. For example, the tilt-VTOL vehicle and lift-plus-cruise vehicle can operate in both vertical and forward flight conditions and must feature transition modes. In addition, the blown-flap STOL vehicle has different flight path angles depending on the flap setting and amount of blowing, thus making the flight profile and produced noise levels a coupled system.

For each of the vehicles, noise was modeled in Task 3 and compared to the available data for each of these vehicles as described in the accomplishments in Task 1. The results indicate that modeling noise using a simple uniform inflow model results in reasonably close results compared to the validation data (within 1-3 dB) for steady state conditions for the tilt rotor and STOL vehicle, however results in very different results compared to the validation data for transition in the lift plus cruise vehicle. Thus, more sophisticated modeling of the aerodynamics and loading of the blades during the transition phase may be needed and will be examined in the next year of this project.

Publications
None.

Outreach Efforts
- Presented at the biannual ASCENT Advisory Board meetings.
- Collaborated with Electra.aero to understand blown-flap STOL aircraft flight profiles.
- Participated in weekly teleconferences and meetings with FAA Technical Monitor.

Awards
None.

Student Involvement
Graduate students have been involved in all aspects of this research, in terms of analysis, documentation, and presentation. These students conducted the research in determining noise modeling gaps for Task 3 of the research goals.

Plans for Next Period
As the project continues, our team will continue seeking industry collaboration opportunities to share concepts for AAM vehicle flight operations. As we examine additional vehicles of interest for the project, gaps in noise modeling and operation design will continue to be documented.

Task 3 – Develop Physics-Based Noise and Flight Profile Model for Representative AAM Vehicles

Massachusetts Institute of Technology
University of California Irvine

Objective
The objective of this task is to develop a physics-based noise and flight profile model for representative AAM vehicles. A first-principles modeling method for the flight profiles and noise of the target AAM vehicle configurations identified in Tasks 1 and 2 will be developed, with the ability to make community noise predictions for these aircraft flying at different operating states. Component-based noise models for the key sources identified in Tasks 1 and 2 will be developed primarily from the methods in the NASA Aircraft Noise Prediction Program (ANOPP2). As data become available, the noise source models will be validated. More complex sources, such as propulsion-airframe interaction noise, may be modeled with external computational fluid dynamics tools such as Comprehensive Hierarchical Aeromechanics Rotorcraft Model (CHARM), and the results will be incorporated into ANOPP2 as needed. In addition, a first-principles flight profile generator applicable to the target AAM vehicle configuration from Tasks 1 and 2 will be developed and incorporated into the noise model. Noise at a variety of velocities, flight path angles, and operating modes will be estimated to construct noise-operation mode-distance curves to adapt the data to AEDT. In this process, the operational drivers with the greatest impact on varying the vehicle noise levels will be identified, to determine which modes should be focused on when forming

the curves. The potential to expand the noise modeling to other vehicle configurations will be considered on an ongoing basis.

Research Approach

- Develop a method to model the noise of flight operations of representative AAM vehicles.
- Use methods to generate noise–operation mode–distance curves to adapt noise results on the AEDT to determine operational drivers with the greatest impact.

Milestones

- Developed an AAM noise modeling method utilizing a uniform inflow method for the propeller loading.
- Conducted several flight operations for the three vehicle types determined in Task 1 to determine how noise varies for different operations and to determine potentially relevant operations that will be needed to represent these vehicles in the AEDT.

Major Accomplishments

Compared to Year 1, a more robust method to determine the performance and noise characteristics of given AAM aircraft was developed (Figure 3). The blade element momentum theory propeller design program XROTOR is used to design AAM aircraft propellers that can operate in relevant flight conditions and minimize induced losses at the rotors by constraining a low Mach tip number, to decrease community noise levels with a feasible motor torque. Operating states, including propeller revolutions per minute, power, thrust, and aircraft drag characteristics, are predicted according to flight procedure conditions throughout feasible trajectories modeled according to the AAM aircraft flight dynamics. A flight trajectory generator was developed to assess the envelope of feasible trajectories for the AAM aircraft being studied. For modeling the noise, methods from ANOPP2, including the advanced blade element acoustic model (ABEAT), were used in the Source Noise Module to determine the noise levels over a hemisphere at significant transition segments of the flight procedure. The hemispheres were computed over a variety of operational states for each vehicle to develop an AAM vehicle source noise database. Given the hemispherical source noise around the vehicle during each flight segment, the noise is propagated from the aircraft source to the ground at the desired observer locations, such as a population grid surrounding an airport, given assumed atmospheric conditions within the Observer Noise Impact Module. The preliminary noise sources that are modeled are the rotor self-tonal and broadband noise sources, as well as airframe noise sources. For the case of blown-flap STOL, an estimate of blown-flap noise was made by using the flap edge model in ANOPP, with the mean propeller wake velocity as the input velocity. The propeller loading in this current method is determined by assuming uniform inflow into the propellers and that the propellers are not interacting with each other. As such, the presented framework enables the preliminary assessment of community noise levels for various AAM types and operations.

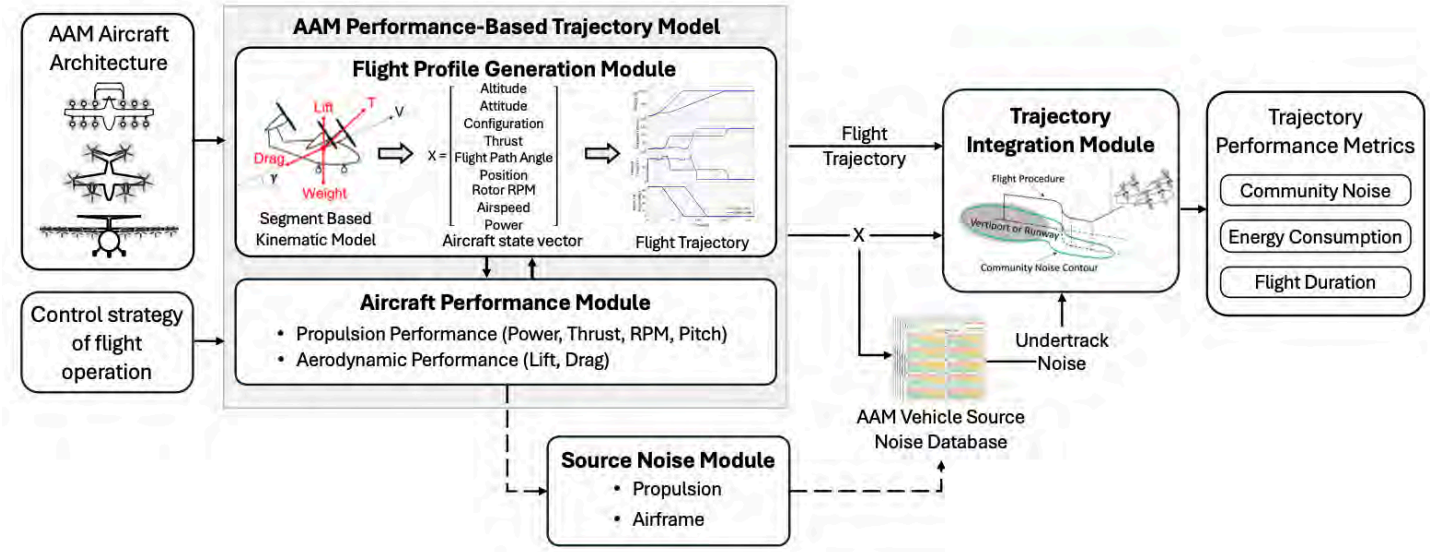

Figure 3. Performance and noise modeling framework for AAM.

Publications

Pellerito, V., Yeung, N., Huynh, j., & Hansman, R. J. (2024, July 29 – August 2). *Impact of flight trajectory design on performance and noise for AAM aircraft* [Conference presentation]. AIAA Aviation Forum and ASCEND 2024. https://doi.org/10.2514/6.2024-4076

Outreach Efforts

- Presented at the biannual ASCENT Advisory Board meetings.
- Presented at the AIAA Aviation Forum and ASCEND 2024
- Participated in weekly teleconferences and meetings with FAA Technical Monitor.

Awards

None.

Student Involvement

Graduate students have been involved in all aspects of this research, in terms of analysis, documentation, and presentation. These students conducted the research formulating the overall framework.

Plans for Next Period

Future iterations of the noise framework and vehicle noise analysis will feature additional interaction noise sources, such as rotor–wake interaction noise, fuselage–wake interaction noise, and blade vortex interaction noise which will be modeled using the CHARM model. In addition, future flight procedures could be assessed and tailored to minimize community noise exposure. Opportunities for noise validation via industry collaborations will also be conducted on an ongoing basis.

Task 4 – Incorporate Noise Results for Representative AAM Vehicles with the Aviation Environmental Design Tool

Massachusetts Institute of Technology and University of California, Irvine

Objective

The objective of this task is to incorporate noise results for representative AAM vehicles in the AEDT. Based on the results of Tasks 1, 2, and 3, an appropriate approach to model the representative vehicle in the AEDT will be determined. The existing AEDT structure will be evaluated, and operating modes necessary for the representative vehicle configuration will be identified. The noise estimates from Task 3 as a function of flight procedure characteristics will be incorporated into the AEDT. Preliminary modeling of AEDT-compatible vehicles and flight procedures will be performed as a test. In addition, the use of this technique to evaluate the noise impact of AAM of flight procedures will be examined.

Research Approach

- Evaluate the existing AEDT structure to determine operating modes necessary for the representative AAM vehicle configurations.
- Perform initial modeling of AEDT compatible vehicles and flight procedures.

Milestones

- Developed concepts for a process to determine the variety of operations that will be relevant to include in the AEDT for modeling AAM vehicles.

Major Accomplishments

The process to determine the variety of operations that will be relevant to include in the AEDT for modeling AAM vehicles involves simulating viable operations for different takeoff and landing segments. This process is based on the flight profile and noise modeling development and validation efforts from Task 3. Preliminary examples of this for different tilt rotor segments have been done.

Publications

None.

Outreach Efforts
- Presented to the Airborne Tactical Advantage Company (ATAC) on AAM modeling in the AEDT.
- Participated in weekly teleconferences and meetings with FAA Technical Monitor.

Awards
None.

Student Involvement
Graduate students have been involved in all aspects of this research, in terms of analysis, documentation, and presentation.

Plans for Next Period
The process to determine the variety of operations that will be relevant to include in the AEDT for modeling AAM vehicles will continue to be developed to simulate different performance states for each of the vehicles that our team will be assessing. The current AEDT structure will be examined to determine its suitability for assessing AAM noise operations in its current state and identify gaps in the modeling approaches. Our team will consult with technical experts at the Volpe National Transportation Systems Center regarding the existing AEDT structure.

Task 5 – Expand Methods to Additional Vehicle Sets
Massachusetts Institute of Technology
University of California Irvine

Objective
The objective of this task will be to expand the methods developed in Tasks 3 and 4 to more complex vehicles featuring additional noise components that have not yet addressed the initial target vehicle configuration. In collaboration with FAA Technical Monitors, the noise model will be updated to incorporate these noise levels and demonstrate their utilization in the AEDT, as was done in Task 4.

Research Approach
- Determine complex candidate vehicle sets via examination of current common vehicle configurations being proposed in industry.
- Update noise modeling methods by using advanced analysis approaches or noise data.

Milestones
To be determined for Year 3.

Major Accomplishments
To be determined for Year 3.

Publications
To be determined for Year 3.

Outreach Efforts
To be determined for Year 3.

Awards
None.

Student Involvement
To be determined for Year 3.

Plans for Next Period
Opportunities for gathering noise data that can be used for validation and the assessment of more complex noise sources beyond the initial modeling framework developed in Task 3 will be determined on an ongoing basis.

Task 6 – Evaluate Implications for Noise Mitigation and Low-Noise Operations for AAM Vehicles
Massachusetts Institute of Technology
University of California Irvine

Objective
The objective of this task will be to determine implications for noise mitigation and low-noise operations for AAM vehicles. The development of the AEDT for the study of AAM vehicle noise is likely to yield implications for noise mitigation and low-noise operations of AAM vehicles. These implications, along with the AAM-compatible AEDT tool, will allow future research teams to continue to use the AEDT to assess AAM vehicle noise. Implications for the development of low-noise procedures for AAM will also be evaluated. The results of the previous tasks have the potential to indicate the need for additional noise model development and validation. Validation of the noise models or flight procedures as data become available will be the goals of future research efforts.

Research Approach
- Assess the noise of candidate vehicles performing several advanced flight procedures.
- Determine low-noise operations and flight procedure design for different candidate vehicles that can be assessed in the AEDT.

Milestones
To be determined for Year 3.

Major Accomplishments
To be determined for Year 3.

Publications
To be determined for Year 3.

Outreach Efforts
To be determined for Year 3.

Awards
None.

Student Involvement
To be determined for Year 3.

Plans for Next Period
After examination of the noise of the representative vehicles operating in multiple operating conditions, the flight procedures and noise operations resulting in the lowest noise levels will be documented.

Project 085 Strategies for Improving En-Route Fuel Efficiency

Georgia Institute of Technology

Project Lead Investigator

Professor Dimitri N. Mavris
Director, Aerospace Systems Design Laboratory
School of Aerospace Engineering
Georgia Institute of Technology
Phone: (404) 894-1557
Fax: (404) 894-6596
Email: dimitri.mavris@ae.gatech.edu

University Participants

Georgia Institute of Technology (Georgia Tech)

- P.I.s: Dr. Dimitri N. Mavris, Dr. Michelle Kirby
- FAA Award Number: 13-C-AJFE-GIT-161
- Period of Performance: March 19, 2024, to September 30, 2025
- Tasks:
  1. Literature Review of Operational Improvement Strategies
  2. Development of a path optimization algorithm
  3. Use case example

Project Funding Level

Georgia Tech has received $400,000 in funding from the Federal Aviation Administration (FAA) for this project. In terms of cost-share details, Georgia Tech has agreed to a total of $400,000 in matching funds. This total includes salaries for the project director, research engineers, and graduate research assistants, as well as computing, financial, and administrative support, including meeting arrangements. Georgia Tech has also agreed to provide tuition remission for the students, paid for by state funds.

Investigation Team

Prof. Dimitri N. Mavris, (P.I.), Tasks 1-3
Dr. Michelle Kirby, (co-Investigator), Tasks 1-3
Dr. Ameya Behere, (research faculty), Tasks 1-3
Dr. Holger Pfaender (research faculty), Tasks 1-3
Dr. Cedric Justin (research faculty), Tasks 1-3
Mr. Jirat Bhanpato, (research faculty), Tasks 1-3
Jouwairia Ahabchane (graduate student), Tasks 1-3
Titien Berberian (graduate student), Tasks 1-3
Ghizlane Jari (graduate student), Tasks 1-3
Vishva Rana (graduate student), Tasks 1-3

Project Overview

In the face of anticipated increased aviation demand for the future, multiple avenues exist to achieve carbon neutral growth including aircraft and engine technologies, operational improvements (OI), and policy measures. This research project focuses on the strategies of near and long-term OIs and quantify their impact on reducing the carbon footprint of

aviation, with specific focus on en-route efficiency. The anticipated outcomes for the FAA are a series of recommended strategies for improving the en route fuel efficiency of aviation.

Task 1 - Literature Review of Operational Improvement Strategies

Georgia Institute of Technology

Objectives

The objectives of the literature review were to evaluate existing OIs in air traffic management and identify strategies to address inefficiencies such as weather disruptions, restricted airspace, and unpredictable wind conditions. By examining current efforts, the team gained a comprehensive understanding of available solutions and their limitations. This process led to a focused selection of two key strategies: (1) speed control, to absorb delays while maintaining fuel efficiency and (2) wind-optimal routing, to leverage real-time weather data for fuel-efficient long-range trajectories. These options were chosen for their potential to address opportunities for enhanced benefits in existing operations.

Research Approach

The literature review was conducted to identify key inefficiencies in airspace operations and explore potential solutions for improving efficiency and reducing delays. The process involved analyzing various sources of inefficiencies, evaluating OIs, and reviewing existing algorithms and strategies to address these challenges. The findings are summarized in the following sections.

Defining the Ideal Airspace and Sources of Inefficiency

The review began by defining the concept of an ideal airspace. Key en route inefficiencies were identified, including:

- **Weather Disruptions:** Adverse weather conditions that affect flight trajectories.
- **Restricted Airspace:** Airspace limitations that necessitate deviations from optimal routes.

Operational Improvements

To address these weather-related inefficiencies, the team narrowed its focus to two key OIs:

- **Wind-Optimal Routing:** Leveraging wind patterns to optimize flight paths.
- **Speed Control:** Managing aircraft speeds to reduce delays and improve flow.

The evaluation of algorithms capable of generating wind-optimal trajectories led to the selection of the kinematic A* algorithm as a starting point. This choice was based on the algorithm's ability to integrate weather data into trajectory optimization.

Investigating Lateral/Vertical Inefficiencies and Delay Absorption

In the second spiral of the review, the team explored inefficiencies in both lateral and vertical dimensions of air traffic management.

- **Airport Capacity and Weather:** Unplanned weather events and a lack of airport capacity can cause airspace congestion, leading to significant delays. Current delay absorption practices include holding stacks at terminal airports, vectoring, ground stops, route optimization, speed control, and metering. While ground stops prove to be the most fuel efficient, they cannot be utilized for flights already en route. As a result, holding and vectoring are commonly used strategies,
- **Holding and Vectoring:** Identified as major contributors to routing inefficiencies, these practices often result in significant fuel inefficiencies despite being used to absorb delay.

Speed control emerged as a promising method to absorb delays at more efficient altitudes during cruise and to avoid holding or vectoring in the terminal area at lower, less efficient altitudes. This approach became the focus of ongoing research.

Analysis of FAA's Current Efforts and Potential Gaps

The team conducted an in-depth review of the FAA's Time-Based Flow Management (TBFM) system, which aims to optimize air traffic sequencing. Key findings include:

- The identification of gaps in TBFM that could be addressed by speed control, particularly during convective weather events.

- The potential for speed control to complement existing strategies, enhancing their effectiveness and reducing delays.

Milestones
- Compiled a list of OIs possible in the near and far term.
- Scoped the improvements to a handful to model.

Major Accomplishments
The literature review enhanced team understanding of existing OIs and identified gaps/challenges that exist. In particular, existing systems often degrade during poor weather events or become less efficient when faced with uncertain headwinds or tailwinds, resulting in increased cost and fuel burn. As a result, speed control and wind-optimal routing are essential strategies to maintain optimal fuel burn levels while absorbing delay. These insights clarified the nature of the problem and enabled the team to define a practical use case for further development.

Publications
None.

Outreach Efforts
- Participated in ASCENT biannual meetings.

Awards
None.

Student Involvement
- Jouwairia Ahabchane (graduate student)
- Titien Berberian (graduate student)
- Ghizlane Jari (graduate student)
- Vishva Rana (graduate student)

Plans for Next Period
The team will conduct a deeper analysis of existing efforts to gain a clearer understanding of the gaps and limitations. Additionally, the focus will be on defining the appropriate scenario for this research, with particular emphasis on flights during unplanned weather events that hinder the effectiveness of TBFM.

Task 2 - Development of a Path Optimization Algorithm
Georgia Institute of Technology

Objectives
The objective of this task is to develop a path optimization algorithm integrating speed control, wind-optimal routing, and a surrogate model for accurate fuel burn estimation. Currently, the focus is on the holding pattern identification process as a key use case for slowing down aircraft (use of speed control), with future plans to include vectoring.

Research Approach
The surrogate model is designed to accurately estimate fuel burn by leveraging key parameters such as altitude, Mach number, air temperature, rate of climb, air density, and aircraft weight. This model plays a pivotal role in dynamic speed control as it gives insight into the most economically viable speed at which to operate, enabling the minimization of fuel burn. Additionally, with this model, a comprehensive comparison can be made between predicted fuel burn using optimized routes with speed-control and fuel burn using no speed-control but extended times in holding patterns or vectoring in terminal areas. This enables airlines to tactically adjust flight operations for maximum efficiency under varying environmental conditions.

The sections below highlight key steps that were taken towards building the fuel burn surrogate model as well as the holding pattern identification process and finally the development of the path algorithm.

Fuel Burn Surrogate Model

In the context of improving flight efficiency, the incorporation of a fuel burn surrogate model is essential to addressing challenges such as increased fuel consumption during cruise to minimize holding patterns. Therefore, to achieve the most efficient experience, the goal is to essentially 'slow-down' the aircraft such that it arrives at the end of the holding pattern event. This highlights the need for a fuel burn surrogate model to enable effective speed control and ensure minimal overall fuel burn under varying flight conditions.

Data Preparation

Flight operations quality assurance (FOQA) data focusing on the cruise phase of flight was prepared by segmenting flights based on aircraft types (e.g., A330-300) and engine types (e.g., General Electric, Pratt & Whitney) and filtering for cruise-specific conditions using rate of climb and Mach number thresholds (i.e., -200 ft/min to +200 ft/min for the rate of climb threshold, and 0.7 for the Mach threshold). Metrics of interest such as air density, temperature, pressure, Mach number, rate of climb, gross weight, mean sea level altitude and total fuel flow were normalized, and smoothing was applied to reduce noise. In the end, the extracted and filtered segments were combined in a single file that is used to train the surrogate model. The logic for the FOQA data processing steps is depicted in Figure 1.

Data smoothing is a critical part of the FOQA data processing. For example, smoothing was applied to the total fuel flow to reduce noise and enhance the model's ability to capture true trends in the data, as illustrated in Figure 2. This smoothing is applied for each identified cruise segment separately.

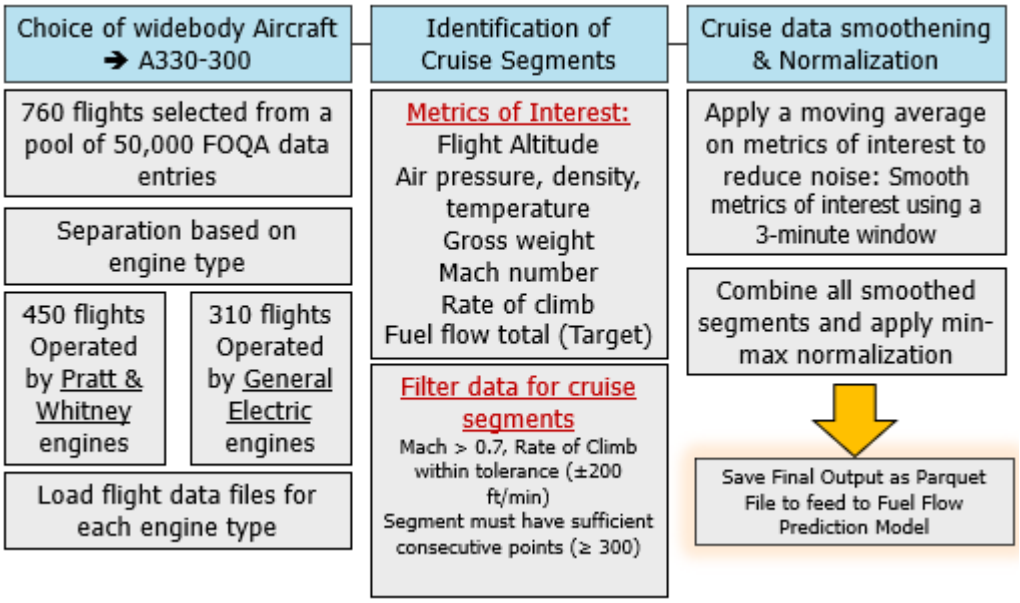

Figure 1. FOQA data processing logic.

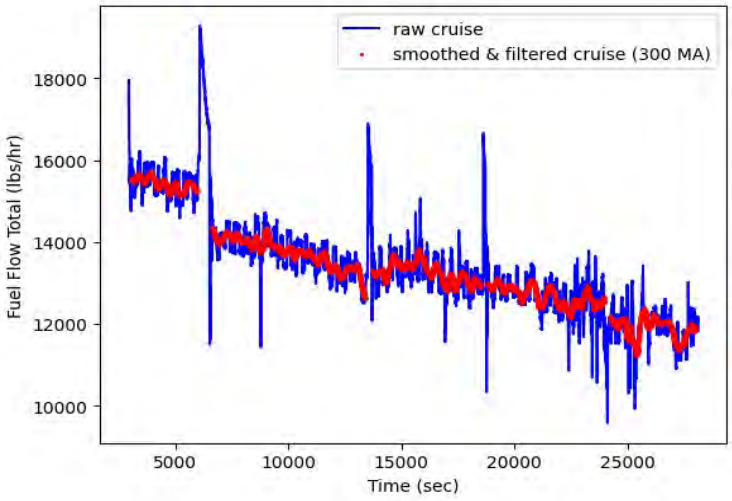

Figure 2. Total fuel flow noise reduction.

Model Development

The surrogate model development begins by splitting the data into training (70%) and validation (30%) sets and polynomial feature expansion (third degree terms) was applied to capture the nonlinear interactions between the different metrics of interest. The surrogate model uses XGBoost (XGBoost Developers, n.d.) for robust regression performance and handling of large complex datasets.

Model Evaluation

The goodness of the fit of the model was evaluated based on a few metrics, namely, the coefficient of determination (R^2) and root mean square error (RMSE), for which strong predictive performance is highlighted by a high R^2 and low RMSE. Additionally, scatter plots of the actual vs predicted fuel flow values were plotted, in which most of the points were falling along the diagonal indicating strong predictive performance.

The performance of the predictive surrogate model for the instantaneous fuel flow, specific to the A330-300 sub-fleet equipped with Pratt & Whitney engines, is highlighted in Figure 3. The dataset consists of 8 million points, split into 67% training and 33% validation subsets. The training data achieves a high R^2 value of 0.9992, with a RMSE of 31.37 lb/hr and a mean percentage error (MPE) between the actual vs predicted fuel flow values of 0.18%. Similarly, the validation data maintains robust performance with a R^2 value of 0.994, an RMSE of 83.475 lb/hr and a MPE between the actual vs predicted fuel flow values of 0.41%. The scatterplots illustrate the correlation between the actual and predicted fuel flow values for both training and validation datasets, with the points tightly clustered along the diagonal, indicating high model accuracy. These metrics affirm the reliability of the model in predicting fuel flow in this fleet and engine configuration during the cruise phase of flight.

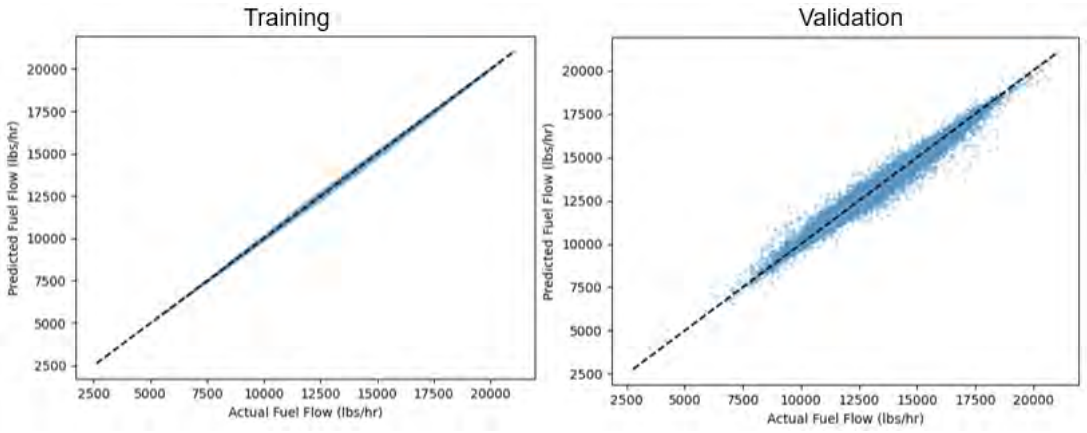

Figure 3. Model performance for predicting fuel flow in A330-300 aircraft with Pratt & Whitney engines: training and validation results.

Holding Patterns Identification

Flight delays can be caused by congestion, bad weather, or unexpected runway closures. These delays are sometimes handled by putting the aircraft into a holding pattern at lower altitudes near the arrival airport. However, this approach is highly inefficient because aircraft engines are not designed to operate optimally at these lower altitudes. The increased air density results in higher drag, forcing engines to burn more fuel than they normally would at cruising altitudes. This raises operational costs and leads to higher carbon dioxide (CO_2) emissions. Additionally, prolonged holding patterns can complicate air traffic management, leading to delays for other flights. Therefore, to address the inefficiencies caused by holding patterns, early identification of the likelihood of a holding pattern allows preventing them by reducing speed during cruise phase.

Data Preparation for FOQA Calendar Year (CY) 2023

Due to the large amount of data, a data preparation step is first applied to shortlist flights which could potentially have holding patterns. The initial filtering process of the FOQA data focused on extracting the time series from top of descent to touchdown. Next, the flights were further filtered within a 400 nautical mile radius from the landing airport. Flight paths with self-intersections as determined by analyzing latitude and longitude were identified as potential holding patterns. From this set, flights involving go-around maneuvers are excluded. An example result of this process at Hartsfield-Jackson Atlanta International Airport (KATL) is shown in Figure 4. For this analysis, 1,142 such flights were identified from the 50,000 FOQA CY2023 records.

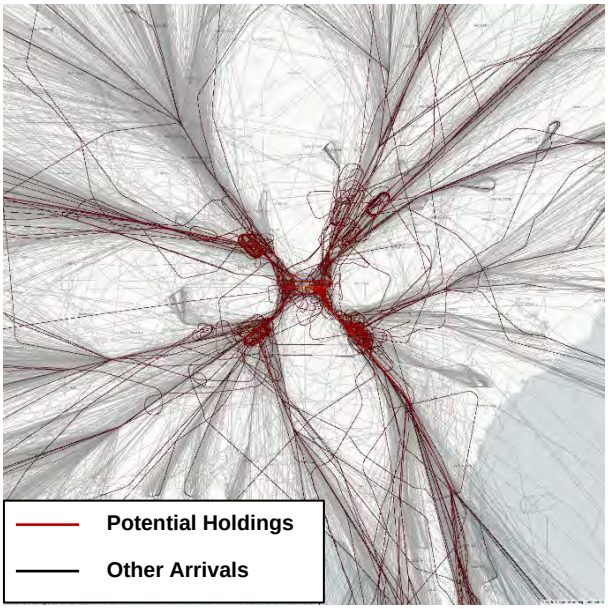

Figure 4. Example FOQA flights with potential holding pattern identification at KATL.

Holding Pattern Identification Process

The shortlisted flight from the previous step is further processed in more detail to verify presence of holding pattern. The process of identifying holding patterns involved a structured algorithm for analyzing flight paths. The process begins with data preparation, where flight data were filtered to include only the segment from top of descent to touchdown, while excluding flights with go-around maneuvers. The flights paths were then divided into short line segments based on latitude and longitude. An R-tree spatial index was applied to efficiently detect intersections between segments, identifying nonadjacent intersection segments as potential loops. These loops were refined by combining overlapping intersections and filtering them based on time gaps. Finally, the start and end points of holding patterns were determined by analyzing the indices of the interesting segments with additional refinements using time and geographic proximity. This approach reduced the FOQA dataset to 731 flights across 15 different aircraft types.

Extracting Threaded Track Flights Associated with FOQA Flights

The process of extracting threaded track flights associated with FOQA flights was implemented using a structured query approach. The approach involves identifying threaded track flights within a spatial and temporal radius, which can be adjusted around the detected FOQA holding pattern. The extracted threaded track flights are linked to their corresponding FOQA flight IDs, with additional adjustments applied to ensure accurate event associations. The grey lines in Figure 4 depict other threaded track flights meeting the spatial and temporal query but did not land at the same airport (i.e., departures, flyovers, or flights landing at other airports).

An example of the associated threaded track flights linked to a single FOQA with a holding pattern near LaGuardia Airport (KLGA) is highlighted in Figure 5. In Figure 5, the red line represents the path of the FOQA flight landing at KLGA, while the blue lines illustrate the threaded track flights that came within a 25 nautical mile radius during a two-hour window before and after the associated FOQA flight's holding pattern and are also landing at KLGA.

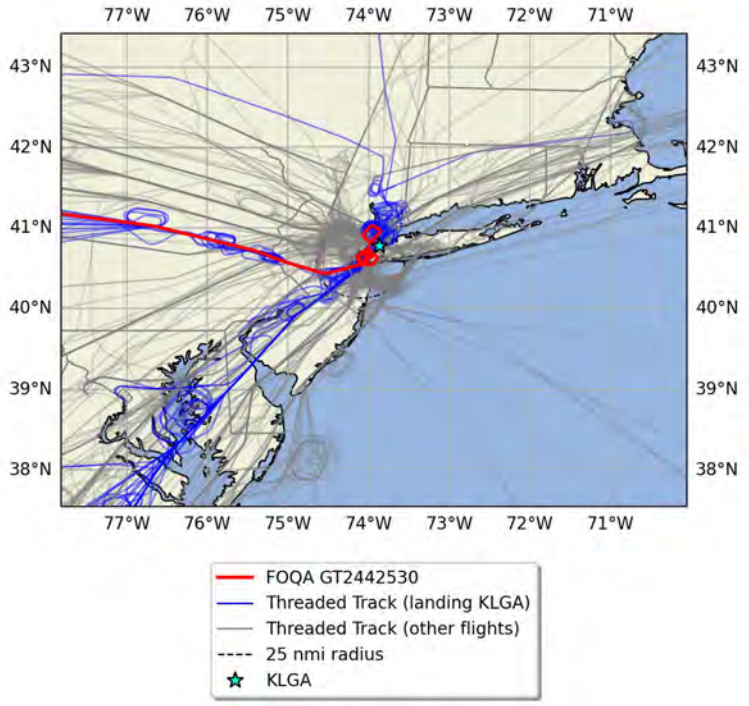

Figure 5. Threaded track flights associated with the GT2442530 FOQA flight.

Data Preparation for Threaded Track CY2023 and Holding Pattern Identification Process
From the 45,984 threaded track CY2023 flights associated with the FOQA CY2023 flights with holding patterns, 8,255 flights were initially identified as potentially having holding patterns based on self-intersecting flight paths; however, flights with go-arounds were not excluded at this stage. These flights were additionally filtered by aircraft type to exclude general aviation aircraft. After applying the holding pattern identification process, 3,014 flights across 40 different aircraft types were confirmed as flights with holding patterns. This number is expected to be further reduced once flights with go-around maneuvers are excluded.

The threaded track holding stack timeline for a specific FOQA flight is illustrated in Figure 6, showing the duration of holding patterns over time that occurred within a 2-hour window before and after the FOQA flight holding pattern. In Figure 6, the red dashed line represents the earliest start of a holding pattern detected from the threaded track data associated with the chosen FOQA flight, while the blue dashed line marks the latest end of the holding pattern. The green dashed line, indicating the selected FOQA holding pattern start, falls within this window, showing that many flights were impacted by holding patterns around the same time as the FOQA flight. This overlap shows that a holding pattern on one flight can indicate the presence of widespread holding patterns, affecting multiple flights and reducing the overall operational efficiency.

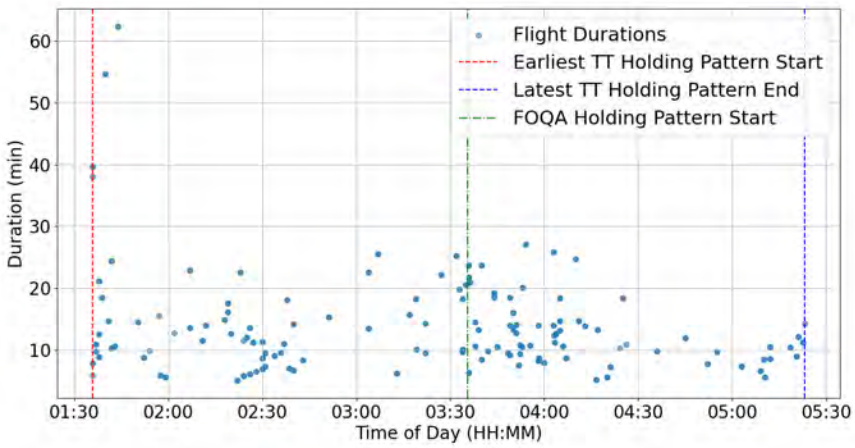

Figure 6. Threaded track holding stack timeline associated with FOQA flight GT2442530.

Results and Discussion

To evaluate the impact of holding patterns on fuel burn (from take-off to rollout) and flight duration, a specific aircraft sub-fleet is selected from FOQA data. This was followed by identifying an origin-destination (OD) pair that has a substantial number of flights. This filtering process was validated to confirm that the chosen aircraft type and OD pair included flights with holding patterns.

A comparison of the total fuel burn (from take-off to rollout) distribution for A321-200 flights with and without holding patterns operating the route between KATL and Ronal Reagan Washington National Airport (KDCA) is shown in Figure 7. In Figure 7, the blue distribution represents flights without holding patterns, with a mean fuel burn of 9,604.35 lb, while the red distribution represents flights with holding pattern, showing a higher mean fuel burn of 10,688.11 lb. In this case, flights with holding patterns consume approximately 11% more fuel compared to those without holding, which shows that on average holding patterns lead to higher total fuel consumption during flight.

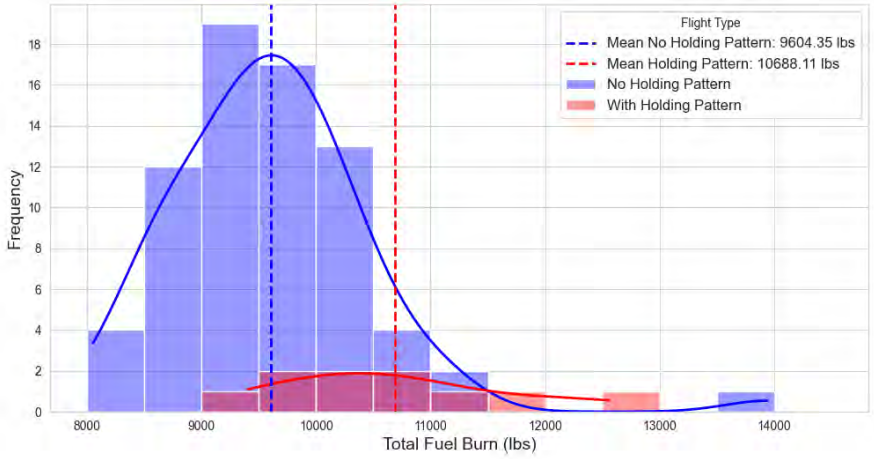

Figure 7. Fuel burn distribution of A321-200 flights with holding patterns vs flights without holding patterns on the KATL-KDCA route.

The flight duration distributions for A321-200 flights on the KATL-KDCA route, comparing flights with and without holding patterns is illustrated in Figure 8. In Figure 8, the blue distribution represents flights without holding patterns, with a mean flight duration of 1.36 hours, while the red distribution corresponds to flights without holding patterns, showing a higher

mean flight duration of 1.63 hours. In this case, flights with holding patterns last approximately 20% longer than those without holding patterns, which indicates that on average holding patterns lead to a longer flight duration.

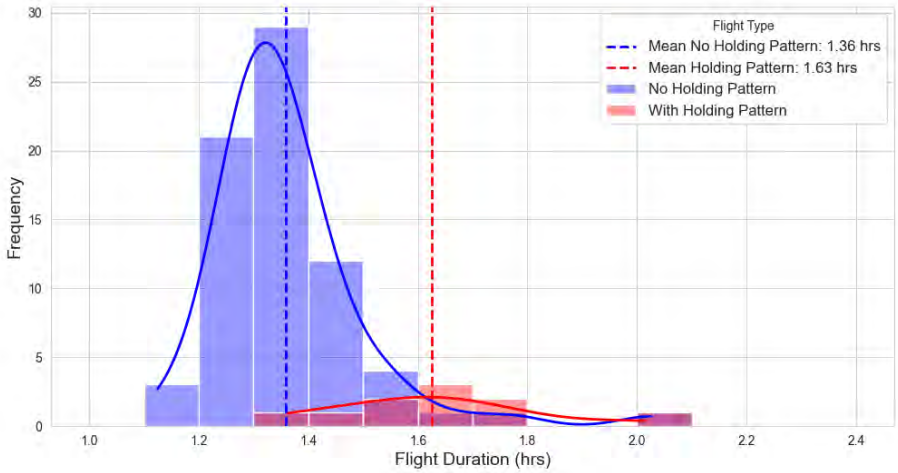

Figure 8. Flight duration distribution of A321-200 Flights with holding patterns vs flights without holding patterns on the KATL-KDCA route.

Path Optimization algorithm

In the context of improving fuel efficiency, the development of a path optimization algorithm is essential to understand the potential benefits of wind optimal routing and speed control. This path optimization algorithm integrates fuel burn calculations to quantify the benefits between the different strategies or routes that can be flown. The wind data used to perform wind optimal routing is coming from the "ERA5 hourly data on pressure levels from 1940 to present" dataset (Hersbach et al., 2023). This dataset is a reanalysis dataset with a horizontal resolution of 0.25° and a vertical resolution of 37 pressure levels, from 1000 hPa to 1 hPa. This dataset gives us access to the horizontal wind speed in m/s and to the vertical wind speed in Pa/s. Therefore, the vertical must be converted from Pa/s to m/s before being able to use the data in the kinematic equations that will be presented in this section.

Fuel Burn Calculation

Before being able to use the fuel burn surrogate models, the path optimization algorithm was built using the base of aircraft data (BADA[1]) Family 3 (BADA3) model fuel burn calculations for the "en route" section of a flight. The goal of those equations is to calculate the fuel flow and multiply it by segment duration. The different equations to calculate the nominal f_{nom} and cruise f_{CR} fuel flow are:

$$f_{nom} = \left(1 + \frac{V_T}{C_{f_2}}\right) C_{f_1} F \quad \text{(Eq. 1)}$$

$$f_{CR} = C_{f_{CR}} f_{nom} \quad \text{(Eq. 2)}$$

where F is the calculated thrust, V_T is the true airspeed, and the C_f are fuel coefficients specific to each aircraft:

- C_{f_1}: Aircraft-specific 1st thrust specific fuel consumption coefficient (kg/min/kN)
- C_{f_2}: Aircraft-specific 2nd thrust specific fuel consumption coefficient (kt)
- $C_{f_{CR}}$: Aircraft-specific cruise fuel flow correction coefficient (dimensionless)

[1] BADA is the international reference for aircraft performance modelling for the purposes of trajectory predictions and simulation (EUROCONTROL, 2025).

The thrust is calculated through the following equations:

$$D = \left[C_{D_0,CR} + C_{D_2,CR}\left(\frac{mg}{\frac{1}{2}\rho V_T^2 S cos(\varepsilon)}\right)^2\right]\frac{1}{2}\rho V_T^2 S \quad \text{(Eq. 3)}$$

$$F = m\left(\frac{g}{V_T}\frac{dh}{dt} + a\right) + D \quad \text{(Eq. 4)}$$

To calculate the thrust and the drag, the equations require:

- m: aircraft mass
- V_T: true airspeed
- ρ: air density
- ε: bank angle
- a: Acceleration
- $\frac{dh}{dt}$: ROC

The air density can be obtained through the standard atmospheric equation and the bank angle is approximated from the turn angle, the speed and the turn radius. The fuel burn calculation will be both used in the function that drives the algorithm (discussed in the next paragraph) and to assess the overall fuel burn of a flight.

Path Algorithm

The first step was to identify the most suitable algorithm for our problem. After a comparison of several algorithms (i.e., Dijkstra, Greedy Best First Search, etc.), the choice was made to use the Kinematic A* algorithm. This algorithm is an evolution of the A* algorithm that is already a combination of Dijkstra and Greedy Best First Search algorithms. Compared to the A* algorithm, the Kinematic A* algorithm considers the kinematics of the aircraft, allowing for a better compatibility with fuel burn calculations and wind data processing. Instead of using a regular node space like the other pathfinding algorithm, this algorithm uses a state space, each state is composed of the position of the aircraft and its turning angle. The position of the aircraft is calculated using the following equations that consider the effect of the wind:

$$X_i = X_s + \left(\frac{R_{min}}{u_i}\right)\cdot cos(\gamma_{max}\cdot w_i)\cdot\left[sin\left(\chi_s + \frac{V}{R_{min}}\cdot u_i\cdot \Delta t\right) - sin(\chi_s)\right] + W_x\cdot\Delta t \quad \text{(Eq. 5)}$$

$$Y_i = Y_s - \left(\frac{R_{min}}{u_i}\right)\cdot cos(\gamma_{max}\cdot w_i)\cdot\left[cos\left(\chi_s + \frac{V}{R_{min}}\cdot u_i\cdot \Delta t\right) - cos(\chi_s)\right] + W_y\cdot\Delta t \quad \text{(Eq. 6)}$$

$$Z_i = Z_s + V\cdot sin(\gamma_{max}\cdot w_i)\cdot\Delta t + W_z\cdot\Delta t \quad \text{(Eq. 7)}$$

$$\chi_i = \chi_s + \frac{V}{R_{min}}\cdot u_i\cdot\Delta t \quad \text{(Eq. 8)}$$

At each state, the algorithm explores a number of next states and calculates the cost for each of those states. It then chooses the state with the minimum cost as the next state. The cost function is composed of two different cost functions. The first cost function is the "cost-to-go" function. It is the cost between the current state and the next state. The second cost function is a "heuristic cost" function. It makes an optimistic estimation of the remaining cost between the next state and the goal. For our version of the algorithm, the cost functions are composed of fuel burn, time and distance metrics. The detailed "cost-to-go" and "heuristic cost" functions are shown in the following equations:

$$G(n) = \alpha\frac{D_n}{D_{GC}} + \beta\frac{T_n}{T_{GC}} + \gamma\frac{F_n}{F_{GC}} \quad \text{(Eq. 9)}$$

$$H(n) = \alpha\frac{Dr_n}{D_{GC}} + \beta\frac{Tr_n}{T_{GC}} + \gamma\frac{Fr_n}{F_{GC}} \quad \text{(Eq. 10)}$$

Since each metric has a different unit, they had to be normalized by values calculated through the Great Circle Trajectory. Each metric has an associated coefficient as they can have different orders of magnitudes. Finally, the algorithm minimizes this function at each step to give the optimal trajectory to reach the goal.

Milestones

- Developed a surrogate model for predicting total fuel flow at various air speed during the cruise phase of flight.
- Developed an initial path algorithm to account for wind and speed for a benchmark case in Task 3, which includes the creation of fuel burn surrogate models from the FOQA data.
- Identified holding patterns in both FOQA CY2023 and threaded track CY2023 flights.

Major Accomplishments

- Developed a surrogate model for prediction of fuel consumptions under varied flight conditions. The surrogate model enables precise predictions of fuel consumption under varying flight conditions, making it integral to optimizing speed control as OI strategy. By accurately estimating fuel flow at different speeds, it helps determine the optimal reduced speed that minimizes fuel burn while absorbing delays at congested terminal areas. This ensures a balance between efficient delay management and sustainable fuel use, supporting overall flight efficiency goals.
- Successfully implemented a wind optimal path algorithm allowing for speed control corrections. Fuel burn for each trajectory has been implemented but could be improved by replacing the BADA3 calculations by the fuel burn surrogate models.

Publications

None.

Outreach Efforts

- Participated in ASCENT biannual meetings.

Awards

None.

Student Involvement

- Jouwairia Ahabchane (graduate student)
- Titien Berberian (graduate student)
- Ghizlane Jari (graduate student)
- Vishva Rana (graduate student)

Plans for Next Period

- For the holding pattern detection, finalize the threaded track holding pattern logic by excluding flights with go-arounds and identify how far in advance a holding pattern can be detected to allow for speed reduction during the cruise.
- Create the fuel burn surrogate model tailored to the descent and climb phases to address holding patterns.
- Conduct an in-depth analysis of the FOQA data available to extract key pieces of information. The objective is to identify patterns and trends, pinpoint inefficiency hotspots, and compare fuel usage across flights operating on the same route (e.g., low fuel vs high fuel consumption flights).
- Use FOQA data to develop a method to identify flights utilizing speed control and quantifying its effect on fuel consumption.

References

EUROCONTROL. (2020). *Base of Aircraft Data (BADA) Family 3 Model.* Bruxelles, Belgium. https://www.eurocontrol.int/sites/default/files/2020-06/bada-standard-licence-information.pdf

Hersbach, H., Bell, B., Berrisford, P., Biavati, G., Horányi, A., Muñoz Sabater, J., Nicolas, J., Peubey, C., Radu, R., Rozum, I., Schepers, D., Simmons, A., Soci, C., Dee, D., & Thépaut, J-N. (2023). *ERA5 hourly data on pressure levels from 1940 to present*. Copernicus Climate Change Service (C3S) Climate Data Store (CDS). doi: 10.24381/cds.bd0915c6.

XGBoost Developers. (n.d.). *XGBoost documentation*. Retrieved November 21, 2024, from https://xgboost.readthedocs.io/en/stable/

Task 3 - Use Case Example

Georgia Institute of Technology

Objective

The objective of the use case is to assess the potential fuel savings of speed control by comparing a flight with a holding pattern and the same flight but slowed down to avoid the holding pattern. This task is therefore going to explain how each of the holding pattern identification, fuel burn surrogate models, and path algorithm are going to interact.

KATL was selected as the arrival airport for this use case; due to its status as the world's busiest airport, it is likely to experience holding patterns. FOQA CY2023 holding patterns around KATL are illustrated in Figure 9, reinforcing the selection of the airport due to the high likelihood of holding patterns.

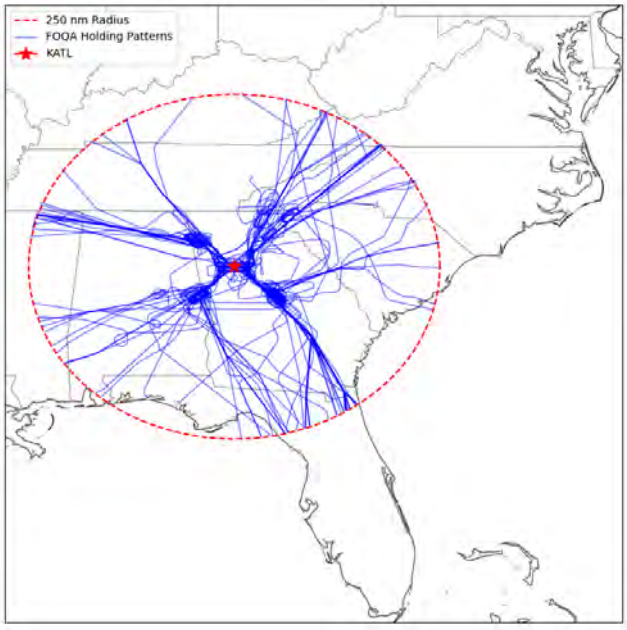

Figure 9. FOQA CY2023 holding patterns around KATL.

Research Approach

The research approach includes a thorough review of existing studies on air traffic congestion, fuel burn surrogate models, and flight path optimization. The methodology involved developing an algorithm to detect holding patterns, a fuel burn surrogate model and a wind optimization algorithm. Three different flights were analyzed for fuel consumption during cruise using the wind optimization algorithm for two different aircraft types, Airbus A330-300 and Airbus A350-900. A comparison is then made using a flight with holding pattern to highlight the impact of speed control on fuel efficiency.

Fuel Burn Comparison

To assess the path algorithm performance, the algorithm had to be tried on different flights and different aircraft. The first test case was an Airbus A350-900 flight from Los Angeles International Airport (KLAX) to KATL on February 2, 2023. The cruise phase began at a latitude of 33.486 and a longitude of -114.949, ending at a latitude of 34.799 and a longitude of -88.493. The aircraft consumed 27194.59 lb of fuel during the cruise segment. The second test case was an Airbus A350-900 flight Amsterdam Schiphol Airport (EHAM) to KATL on June 21, 2023. The cruise phase began at a

latitude of 53.339 and a longitude of-0.025, ending at a latitude of 35.337 and a longitude of -82.540. The aircraft consumed 27194.59 lb of fuel during the cruise segment. The third test case was an Airbus A330-300 flight from EHAM to KATL on February 10, 2023. The cruise phase began at a latitude of 51.46891 and a longitude of -0.042, ending at a latitude of 35.45472 and a longitude of -82.2553. The aircraft consumed 114,565.47 lb of fuel during the cruise segment. The results from the different test cases are summarized in Table 1.

Table 1. Fuel burn comparison for the three test cases.

Flight	Aircraft	Date	FOQA Fuel burn (lb)	Wind Algorithm Fuel Burn (lb)	Fuel Burn Percentage Difference
KLAX-KATL	A350-900	2/2/2023	27194.59	34547.06	+27.04%
EHAM-KATL	A350-900	6/21/2023	94537.02	86906.69	-8.07%
EHAM-KATL	A330-300	2/10/2023	114565.47	109280.36	-4.61%

The fuel burn output by the algorithm and therefore calculated with the BADA3 equations are off by a significant percentage for each of the different test cases. By changing the fuel burn calculation method and by using the fuel burn surrogate models, the algorithm should increase its precision in the fuel burn calculation.

Holding and Speed Control Comparison

Our use case aims at combining the different efforts that have been detailed in Task 2, which are the holding pattern identification and the fuel burn surrogate model. The first step would be to integrate the fuel burn surrogate into the path optimization algorithm. The fuel burn surrogate would replace the current BADA3 calculations to obtain better accuracy and prediction of the fuel burn. Indeed, the result of the previous section shows that there is a lot of improvement that can be made in the fuel burn calculations. Once the fuel burn surrogates are integrated to the algorithm, the goal is to use the results from the holding patterns identification to have a list of “holding pattern” flights and simulate them with the path algorithm. The simulation would use the holding pattern results that are the duration and the location to rerun the same trajectory and implement a speed control strategy that would help avoid the holding pattern. Finally, the fuel burn from that flight would be compared to the original flight and the fuel burn savings would be assessed.

Milestones

- Developed a methodology combining holding pattern identification, fuel burn surrogate model and flight path optimization. Continued algorithm development in preparation to integrate fuel burn surrogate models.
- Quantified the fuel burn through both wind algorithm calculations and surrogate models.

Major Accomplishments

- Selected KATL as the focus of this study due to its high likelihood of holding patterns. Conducted thorough review of existing studies on air traffic congestion, fuel burn surrogate models and flight path optimization.
- Conducted fuel burn comparisons using wind optimization algorithm for three test cases featuring A330-300 and A350-900 domestic and transatlantic flights.

Publications

None.

Outreach Efforts

- Participated in ASCENT biannual meetings.

Awards

None.

Student Involvement

- Jouwairia Ahabchane (graduate student)
- Titien Berberian (graduate student)
- Ghizlane Jari (graduate student)
- Vishva Rana (graduate student)

Plans for Next Period

The next steps involve integrating the fuel burn surrogate into the current algorithm to replace the BADA3 calculations, thereby enhancing the accuracy of fuel burn predictions. Once integrated, the algorithm will leverage holding pattern identification results to compile a list of flights with holding patterns, as discussed previously. The next step will involve comparing the fuel burn from the adjusted flight trajectories to the original flights to quantify the potential fuel savings. For the test flight with holding, metering fixes will be used to develop a queuing model for analyzing aircraft operations under different weather conditions. The model evaluates a baseline scenario comparing clear weather operations with those during bad weather. The objective is to determine the benefits of implementing speed control during adverse weather conditions, particularly in terms of reducing fuel burn and improving operational efficiency.

Project 086 Study on the Use of Broadband Sounds to Mitigate Sleep Disruption Due to Aircraft Noise

University of Pennsylvania

Project Lead Investigator

Mathias Basner, MD, PhD, MSc
Professor of Psychiatry
Department of Psychiatry
University of Pennsylvania
1019 Blockley Hall, 423 Guardian Dr.
Philadelphia, PA 19104-6021
215-573-5866
basner@pennmedicine.upenn.edu

University Participants

University of Pennsylvania

- P.I.: Prof. Mathias Basner
- FAA Award Number: 13-C-AJFE-UPENN, Amendment No. 015
- Period of Performance: October 1, 2023, to September 30, 2024
- Tasks:
  1. Complete measurement campaigns in the sleep laboratory
  2. Start data analysis

Project Funding Level

Project funding support from the Federal Aviation Administration (FAA) for the Year 2 award (January 1, 2024, to December 31, 2024) for this 2-year project totals $520,700. The cost-sharing requirement for this project is met by our international collaborators at the German Aerospace Center (DLR) and at St. George's University of London.

Investigation Team

University of Pennsylvania

Mathias Basner, MD, PhD, MSc (P.I.), All Tasks
Christopher Jones, PhD (co-investigator), All Tasks
Matthew Kayser, MD, PhD (co-investigator), Task 1
Haochang Shou, PhD (statistician), Task 2
Quy Cao, MS (statistician), Task 2
Michel Carlin (other professional), All Tasks
Adrian Ecker (other professional), All Tasks
Sierra Park-Chavar (other professional), All Tasks
Victoria Schneller (research assistant), All Tasks
Sinead Walsh (research assistant), All Tasks

Civil Aerospace Medical Institute (CAMI)

Hilary Uyhelji, PhD, PMP (co-investigator), All Tasks

Project Overview

Sound insulation of bedrooms is expensive and is typically provided only to residents living near an airport. The goal of this project is to investigate the effects of different types of aviation noise (AN) on sleep under controlled laboratory conditions, and to determine whether some of the sleep-disturbing effects can be mitigated by introduction of pink noise

(PN) into the bedroom or by wearing earplugs (EPs). The study will be performed in the Chronobiology Isolation Laboratory at the Hospital of the University of Pennsylvania. This newly constructed facility includes four acoustically isolated bedrooms and a high-fidelity sound system.

Objectives

- Investigate the following hypotheses on the whole night level:
  - AN disturbs sleep and reduces time spent in slow wave sleep + rapid eye movement sleep.
    AN vs. control
  - PN mitigates the negative effects of AN in a dose-dependent manner.
    AN + 50-dBA PN (PN50) vs. AN + 40-dBA PN (PN40) vs. AN
  - EPs mitigate the negative effects of AN.
    AN + EPs vs. AN
  - PN promotes sleep.
    PN50 vs. control
- Investigate the following hypotheses on the event-related level:
  - Various types of AN differ in their awakening potential.
  - The masking effects of PN differ by AN type.
  - PN masks meaningful sounds (e.g., fire alarm or baby crying).

Research Approach

Study design

The sleep of 24 participants will be monitored through polysomnography (PSG) over seven consecutive nights in groups of four participants. After an adaptation night, participants will be exposed to the following conditions:

1. Control night without noise and without EPs (control)
2. AN only
3. PN50
4. AN + EPs
5. AN + PN40
6. AN + PN50

Our team will investigate participants in six groups of four participants each. Each participant in a given group will be exposed to the same condition in each study night. Each group will receive the six exposure conditions in a randomized and balanced fashion, according to the randomization table below (see Table 1). Of note, in this randomization paradigm, each exposure appears in each position exactly once and is preceded by each other exposure exactly once (letters A–F will be randomly assigned to exposure conditions 1–6 listed above):

Table 1. Randomization of exposure conditions for the sleep research study using PSG.

Group	Night 1	Night 2	Night 3	Night 4	Night 5	Night 6	Night 7
1	Adaptation	A	B	C	D	E	F
2	Adaptation	B	D	A	F	C	E
3	Adaptation	C	A	E	B	F	D
4	Adaptation	D	F	B	E	A	C
5	Adaptation	E	C	F	A	D	B
6	Adaptation	F	E	D	C	B	A

Measurements during sleep

Participants' sleep will be measured polysomnographically with the Prodigy® system, which includes electroencephalography with frontal electrodes only, electrooculography, and electromyography. Data will be transmitted wirelessly to a bedside tablet. The tablet will also record sound pressure levels to help synchronize the polysomnographic and acoustic data. Participants will also wear a Bittium Faros™ device that measures the electrocardiogram (1 kHz) and body movements (25 Hz).

® Prodigy is a registered trademark of Younes Medical Technologies, Winnipeg, Manitoba, Canada.
™ Bittium Faros is a trademark of Bittium Oyj, Oulu, Finland.

Noise exposure

The AN night will consist of 93 noise events with maximum sound pressure levels (i.e., $L_{AS,\,max}$ of 45, 55, or 65 dB), including noise from jet engine aircraft, helicopters, drones, low sonic booms, rail, and road traffic. The jet engine, and road and rail noise events will be identical to events used in a prior study at the DLR and another study on broadband sounds on sleep performed by collaborator Dr. Michal Smith in Sweden, thus enabling direct comparison with those studies. Our team will choose several events within each noise level category and repeatedly play those events back. Each aircraft noise event is played back three times at three different maximum sound pressure levels (45, 55, and 65 dBA) for a total of nine times. Because of the limited sample size, playing every event back only once would not provide sufficient data for averaging. An alarm sound and the sound of a baby crying will also be included because a potential caveat of using EPs/PN is that meaningful sounds may be missed. The sequence and spacing of noise events will be identical within a study group but different across study groups. Noise scenarios will be preprogramed and will start 15 min after the lights are turned off (PN playback will start immediately after lights out). The lights are planned to be turned off at 11:00 p.m. and turned on at 7:00 a.m. for an 8-hour sleep opportunity.

Evening and morning procedures

Participants will arrive at the laboratory at approximately 7:00 p.m. and will be able to leave the laboratory at approximately 9:00 a.m. Because our noise exposures can affect sleep and impair recuperation to some degree, participants will be informed in the consent form that they should not operate heavy machinery during the study. A taxi will also be offered for participants who would otherwise use a car to travel to the Chronobiology Isolation Laboratory. Snacks will be provided in the evening and a light breakfast in the morning. Participants will be able to shower in the morning (after all tests) if they wish.

In the evening (before bed) and in the morning (after waking up), the following will be conducted:

1. Blood draw (for untargeted messenger RNA analyses expected to be performed by the FAA CAMI, morning only)
2. Completion of a survey asking participants about the previous day (evening survey) or the previous night (morning survey)
3. Cognition test battery (10 cognitive tests)
4. Driving simulator task
5. Hearing test (up to 16 kHz)
6. Blood pressure and heart rate variability measurements

The four participants of a group will be rotated through the six tasks. Each participant will perform the different tasks always in the same order.

Participant recruitment

Participants will be screened on two occasions. The first screening will include blood draws with drug screening, electrocardiography, and a hearing test. Participants will receive a pulse oximeter, which they will return at the second screening. At the second screening, participants will be familiarized with the cognitive tests and the driving simulator. They will also receive an actigraph that they will wear in the week before the start of their study run. They will be asked to adhere to a sleep schedule of 11:00 p.m. to 7:00 a.m. to the extent possible in the week before participation. We plan to conduct a seventh backup study run if participants drop out during the first six study runs.

Study inclusion criteria:

- Age between 21 and 50 years
- Absence of psychological/psychiatric conditions precluding participation
- Body mass index < 35 kg/m^2
- Self-reported regular sleep schedule; ability to maintain sleep schedule during the course of the study
- Self-reported sleep duration of 6–8.5 hours per night (verified by six workdays of ambulatory sleep monitoring with wrist actigraphy and daily logs)
- Ability to read and write in English
- Full vaccination against, or recovery from, COVID-19

Study exclusion criteria:

- Hearing loss > 25 dB in any frequency band up to 8 kHz
- History of neurological, psychiatric, or other medical conditions precluding participation

- Current mania or psychosis
- Current depression, according to the Beck Depression Inventory (Beck, 1996)
- Excessive alcohol or drug use in the past year, on the basis of history and urine toxicology screening
- Excessive alcohol intake (≥ 21 drinks per week) or binge alcohol consumption (more than five drinks per day)
- Excessive caffeine consumption (> 650 mg/day from all caffeinated drinks regularly absorbed during the day)
- Current use of cigarettes/tobacco, or nicotine replacement therapy (those nicotine-free for 30 days will be included)
- Body mass index ≥ 35 kg/m^2
- Acute, chronic, or debilitating medical conditions, major axis I psychiatric illness, according to history, physical examination, blood and urine chemistry, and complete blood count
- Self-reported history of recurrent seizures or epilepsy or a history of medical conditions that could increase the chance of seizure (e.g., stroke, aneurysm, brain surgery, or structural brain lesion)
- Cardiovascular, neurological, gastrointestinal, or musculoskeletal problems that preclude participation
- Major controlled or uncontrolled medical conditions, such as congestive heart failure, neuromuscular disease, renal failure, cancer, chronic obstructive pulmonary disease, respiratory failure or insufficiency, cardiac arrhythmia, or a need for oxygen therapy (as determined by self-report)
- Current night, swing, split, or rotating shift work
- Current use, or use of within the prior month, of a prescription or over-the-counter sleep medication or stimulant; use of psychoactive medication (based on self-report and review by a study clinician)
- Pregnancy or current breastfeeding
- Prior history or diagnosis of any sleep disorder including obstructive sleep apnea (Apnea-Hypopnea Index ≥15 events/hour) from ambulatory or in-laboratory PSG; restless legs syndrome or periodic limb movement disorder; insomnia; parasomnia; high risk of obstructive sleep apnea, according to the STOP-BANG Questionnaire ("yes" on at least four of eight questions); high risk of restless legs syndrome, according to the Cambridge-Hopkins Screening questionnaire; or high risk of insomnia, according to the Insomnia Severity Index (score of 22 or higher)
- Self-reported severe contact dermatitis, or allergy to silicone, nickel, or silver
- Planned travel across more than one time zone 1 month before and/or during the anticipated study period
- Intentional naps during the week
- Habitual use of broadband noise to facilitate sleep

Endpoints and power considerations
The primary outcome of the study is time spent in slow wave sleep plus rapid eye movement sleep during an 8-hour sleep opportunity (11:00 p.m. to 7:00 a.m.). Our team will investigate several other outcomes related to the entire night (e.g., sleep efficiency or wake after sleep onset); to outcomes before and after sleep (e.g., cognitive performance and driving); or to individual noise events (e.g., event-related analysis).

All power calculations were conducted in the Power Analysis & Sample Size (PASS) (Version 21; NCSS, 2021), by assuming a 5% type I error rate and using two-sided hypothesis tests. The data collected in the AIRORA study (Study on the effects of Air, Road, and Rail traffic noise on sleep) was used performed at DLR to inform power calculations. With a proposed sample size of 24 participants, our team expects to have at least 80% power to detect a medium effect size of 0.60 for the mitigation effect of PN on our primary outcome due to aviation noise.

Milestone

- Commenced data acquisition in the laboratory in November 2023 and finalized data acquisition in June 2024.

Major Accomplishments

- A total of 27 subjects were enrolled in the study, three of which withdrew early from the study. Partial data of two subjects withdrawing early can still be used for analysis. Thus, complete data of n=24 participants and partial data of n=2 participants will be used for data analysis (planned total was n=24).
- Preliminary analyses on morning blood pressure and heart rate variability; cognitive and driving simulator performance, hearing test data, and subjective assessments provided by participants were analyzed and presented at the ASCENT fall meeting.
- Data analysis on PSG data and blood samples (CAMI) is ongoing.

Publications
None.

Outreach Efforts
None.

Awards
None.

Student Involvement
Six temporary undergraduate or post-baccalaureate student workers are supporting participant screening and data acquisition in the sleep laboratory.

Plans for Next Period
- Data analysis
- Report generation

References
Beck, A.T., Steer, R.A., Ball, R., & Ranieri, W.F. (1996). Comparison of Beck Depression Inventories-IA and -II in psychiatric outpatients. *Journal of Personality Assessment,* 67(3):588-597.

NCSS. (2021). *Power Analysis & Sample Size* (Version 21) [Computer software]. https://www.ncss.com/download/pass/updates/pass-2021/

Project 088 A Method for Rapidly Assessing Jet Fuel Compatibility with Non-Metallic Materials

University of Dayton Research Institute

Project Lead Investigator

John Graham, PhD
Distinguished Research Engineer
Sealants and Elastomeric Materials Address, Nonstructural Materials Division
University of Dayton Research Institute
1700 S. Patterson Blvd. Dayton, OH 45459
937-229-2807
John.Graham@udri.udayton.edu

Project Co-Lead Investigator

Gina Roesch, PhD
Research Chemist
Sealants and Elastomeric Materials Address, Nonstructural Materials Division
University of Dayton Research Institute
1700 S. Patterson Blvd. Dayton, OH 45459
937-229-3488
Gina.Roesch@udri.udayton.edu

University Participants

University of Dayton Research Institute (UDRI)

- P.I.s: John Graham and Gina Roesch
- FAA Award Number: 13-C-AJFE-UD
- Period of Performance: February 2023 to September 2025
- Tasks:
  1. Material Selection and Acquisition
  2. Detailed Fuel Composition
  3. Volume Swell
  4. Analysis of Absorbed Fuels
  5. Statistical Analysis
  6. Multiple Regression Modelling
  7. Reporting

Project Funding Level

The Federal Aviation Administration (FAA) provided $350,000 for ASCENT Project 088. The funds from the FAA were matched by several cost-sharing partners including Global Bioenergies, The Boeing Company, General Electric (GE) Aviation, National Research Council (NRC) Canada, Lanzatech, Neste, Shell, and IHI Corporation.

Investigation Team

Dr. John Graham, PhD (P.I.), performs aspects of all parts of Project 088 from ideation, data acquisition, data analysis and reporting, as well as is the primary lead on statistical analysis and modeling of the data.

Barbara Miller (Sealants and Elastomer Group Leader) oversees all technical outputs and controls the financial aspects of ASCENT Project 088.

Dr. Gina Roesch, PhD (Co-P.I.), performs data acquisition and analysis as well as all project briefings.

Mary Galaska (technician) acquires analytical measurements including but not limited to volume swell and gas chromatography–mass spectrometry in support of ASCENT Project 088.
Wesley Waldron (technician) assists in the mechanical testing of the materials used in ASCENT Project 088.

Project Overview

The goal of ASCENT Project 088 is to create a prescreening method to assess whether a given synthetic aviation fuel (SAF) is a good candidate for the rigorous fuel certification process established in ASTM D4054 (ASTM International, 2022). As an evaluation method, ASTM D4054 is time-consuming (turnaround times of months to years), expensive, and requires large sample volumes. In the ASTM D4054 qualification process, material costs and sample sizes are substantial barriers to entry for original equipment manufacturers (OEMs) to submit candidate fuels, especially SAFs which often have vastly different compositions compared to traditional Jet A fuels. As a result, ASCENT Project 088 was proposed and designed to develop a low-cost, small-sample-volume method to assess fuel interactions with a list of the most common non-metallic materials. The advantage of the approach proposed in ASCENT Project 088 is that it is less expensive, has a faster turnaround time (weeks), and requires smaller sample volumes (<250 ml). To keep the requirements to a minimum, the ASCENT Project 08 team chose volume swell as the physical property of interest. In tandem with volume swell experiments, gas chromatography mass spectrometry (GC-MS) quantifies the interaction and exchange between fuels and materials. Using these two techniques as the foundation, statistical models will be generated to predict SAF compatibility with non-metallic materials. Additionally, the experimental data gathered in ASCENT Project 088 can be used as a method to down select which materials are of greatest importance to a particular OEM.

ASCENT Project 088 involves two crucial deliverables. The first is the creation of a reference dataset by using a population of Jet A fuels gathered from ten sites across the continental United States (CONUS). This sample of 12 Jet A fuels represents the population of Jet A fuels currently in service. Using the reference dataset of Jet A fuels, ASCENT Project 088 will study and characterize how the materials on the ASTM D4054 Non-metallic Short List (Table A3.2) interact with the current Jet A fuel population thus providing information on the interaction between non-metallic materials and fuels currently in service. The second deliverable for ASCENT Project 088 is a set of statistical models. The data points gathered for non-metallic materials and the survey of Jet A fuels will be used to build a statistical model by utilizing key class fractions as fitting parameters. Both single and multivariate models will be explored. At the end of ASCENT Project 088, the volume swell, absorbed fuel analysis, and material exchange results will be used as a method to predict and evaluate whether the candidate SAFs are likely or unlikely to be compatible with fuels currently used throughout the aviation industry today.

The tasks, deliverables, and current progress for ASCENT Project 088 are discussed in detail below with one amendment. This report was written prior to realizing that two materials had been overlooked on the ASTM D4054 Non-metallic Materials Short List. This report represents the progress of ASCENT Project 088 without the inclusion of the two materials, but they will be completed prior to the publication of the final report.

References

ASTM International. (2022). ASTM D4054-22L: Standard Practice for Evaluation of New Aviation Turbine Fuels and Fuel Additives. https://store.astm.org/d4054-22.html

Task 1 – Material Selection and Acquisition

University of Dayton Research Institute

Objective

The objective of this task is to select the list of non-metallic materials to evaluate in the survey of Jet A fuels, request quotations, and purchase all necessary materials for the project.

Research Approach

The 12 fuels were selected from a stock of 93 fuels obtained from 10 geographically dispersed locations across the CONUS. One fuel was selected from each of the 10 locations, and the fuels with the highest and lowest percentages of aromatic compounds were also selected, for a total of 12 sample Jet A fuels.

Milestones
A survey of Jet A fuels was acquired from the various locations across the CONUS so that the population could be considered a statistical representation of fuels being flown at the time of the study. This suite of Jet A fuels includes a variety of compositions (i.e., low aromatic compounds, high aromatic compounds, etc.). Additionally, all materials of interest have been acquired.

Major Accomplishments
Task 1 was completed during the previous reporting year.

Publications
None.

Outreach Efforts
None.

Awards
None.

Student Involvement
None.

Plans for Next Period
Task 1 is complete.

Task 2 – Detailed Fuel Composition
University of Dayton Research Institute

Objective
The objective of this task is to provide a detailed chemical analysis of current, in-service Jet A fuels. To achieve this objective, a survey of Jet A fuels was gathered from across the CONUS and characterized using two-dimensional gas chromatography (GCxGC) to determine the fuel composition against which future candidate SAFs can be compared.

Research Approach
The approach to evaluate the selection of the 12 Jet A fuels involved GCxGC, with emphasis placed on a selected set of class fractions known to affect the volume swell of non-metallic materials. Table 1 shows the class fractions of interest for ASCENT Project 088. Additionally, GCxGC analysis and simulated distillation curves were provided for each of the 12 fuels.

Table 1. Fuel Composition by GCxGC.

Class	Class Fraction
Aromatics	Alkyl benzenes
	Diaromatics (Naphthalenes, Biphenyls, etc.)
	Cycloaromatics (Indans, Tetralins,etc.)
Paraffins	iso-Paraffins
	n-Paraffins
	Monocycloparaffins
	Dicycloparaffins
	Tricycloparaffins

Milestone
Task 2 was completed during the past year.

Major Accomplishments
The completion of Task 2 confirmed that the fuels selected for ASCENT Project 088 was representative of the population of in-service Jet A fuels. Namely, the fuels were all qualified Jet A fuels and had sufficiently different aromatic contents. In the future, if the composition of the SAF is known, the results of Task 2 can be used as representative upper and lower bounds of acceptable composition with respect to current, in-service fuels. Comparing a new SAF's composition to the reference set of Jet A fuels will help inform fuel producers on how the composition of the SAF compares to what was being flown at the time of the study.

Publications
None.

Outreach Efforts
None.

Awards
None.

Student Involvement
None.

Plans for Next Period
Task 2 is complete. The GCxGC data will be used for the remainder of the project, to understand material compatibility with the reference fuels and, in the future, with candidate SAFs.

Task 3 – Volume Swell
University of Dayton Research Institute

Objective
Task 3 is the mission-critical task of ASCENT Project 088 as it provides the experimental data for the selected representative physical property, the volume swell of each material in the ASTM D4054 Non-metallic Short List in each of the 12 Jet A fuels selected in Task 2.

Research Approach
Experimental Approach
Volume swell was chosen as the keystone physical property for ASCENT Project 088 because it captures the overall exchange of components between the material and the fuel. In order to align with the goal of ASCENT Project 088 being a prescreening method, UDRI developed a technique called optical dilatometry that uses small sample and fuel volumes (mms in size and mL in volume). Task 3 hinges on using optical dilatometry to measure the volume swell of all the materials in the ASTM D4054 Non-metallic Short List in the candidate Jet A fuels selected in Task 2.

Figure 1 shows a schematic of an optical dilatometer on the left and an example system on the right. Up to four small samples are placed in an optical cell with 3–5 mL of test fluid at room temperature (approximately 75°F). The vial is placed on an optical stage that is lit form above with a light-emitting-diode (LED) strip. Below the optical cell is a digital camera. The camera photographs the materials every 10 s for the first 3 min and then every 10 min for the remainder of the experiment. The length of the swelling experiments is variable. For ASCENT Project 088, the duration of the soak was chosen to be 160 hours such that an equilibrium or near-equilibrium state was reached for each material.

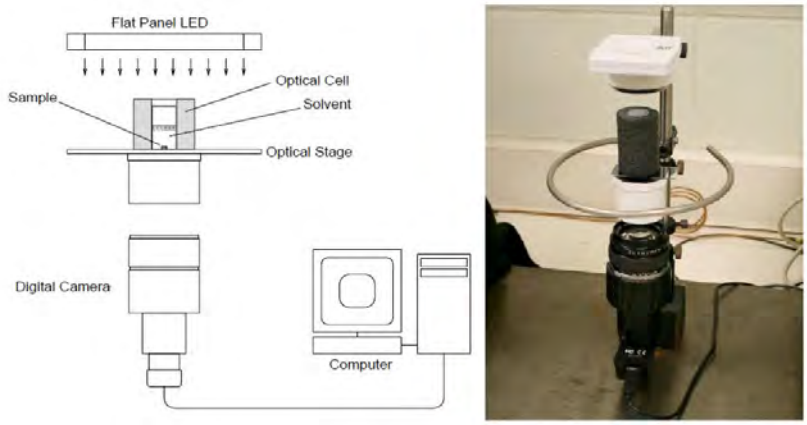

Figure 1. Schematic (left) and photograph (right) of an optical dilatometer.

Data Processing

When imaging is complete, the photographs are analyzed in ImageJ, a software program used to extract the cross-sectional area of each of the samples. Assuming isotropic swelling of the material, the two-dimensional (2D) area from the image can be extrapolated to a three-dimensional (3D) volume for each sample over the duration of the experiment. The final volume swell is recorded as an average of ±10 images surrounding the 160-hour mark. Figure 2 shows the volume swell of all O-rings in the ASTM D4054 Non-metallic Short List.

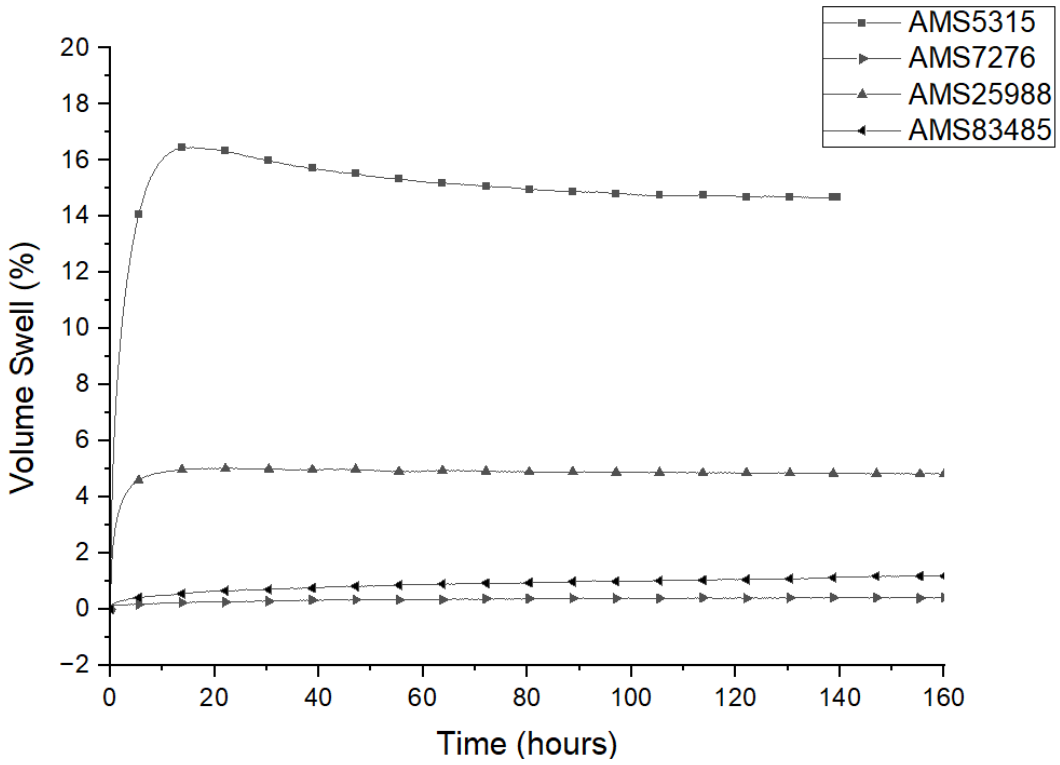

Figure 2. Volume swell of AMS5315, AMS7276, AMS25988, and AMS83485 O-rings over an aging period of 160 hours. Note that one material, AMS5315, was only run for 140 hours due to a change in the experimental parameters extending the soak time to 160 hours such that equilibrium or near-equilibrium exchange was reached.

Figure 3 shows a summary of the results of Task 3. More explicitly, Figure 3 shows the average volume swell of each material in the ASTM D4054 Non-metallic Short List across all 12 Jet A fuels. Two major conclusions arise from Figure 3. The first conclusion is that the soak duration of 160 hours was enough for all materials to reach equilibrium or near-equilibrium states. This is clearly seen by the flatlining of nearly all materials at 160 hours on the x-axis of Figure 3. The second conclusion is that only 6 of the 34 materials tested showed a significant (greater than 3% swell) response to fuel exposure. For clarity, they are named, along with their material type, in Figure 3. With these conclusions in mind, Figure 3 serves as one potential manner to use the experimental results of ASCENT Project 088 to down select the ASTM D4054 Non-metallic Materials Short List if a material's response to fuel exposure is a high priority.

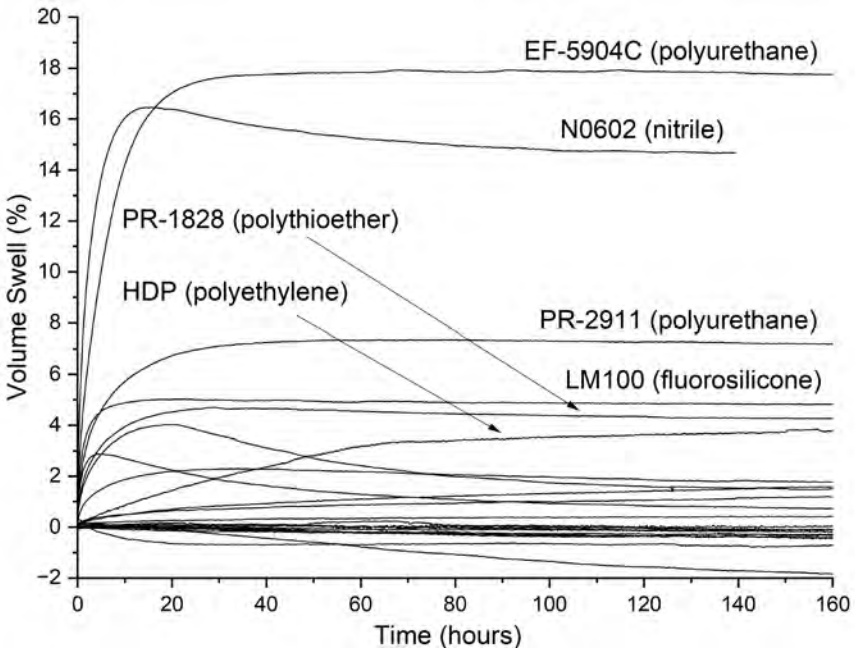

Figure 3. Task 3 Summary Graph showing the volume swell of all the materials in the ASTM D4054 Non-metallic Short List in all 12 Jet A fuels selected in Task 2.

Milestones

Task 3 was completed during 2024 and it provided the data necessary to generate statistical models in Tasks 5 and 6.

Major Accomplishments

None.

Publications

None.

Outreach Efforts

None.

Awards

None.

Student Involvement

During 2024, UDRI hired a technician and a research engineer who both learned the technique of optical dilatometry while acquiring Task 3 data for ASCENT Project 088. The technician, who is a full-time student at the University of Dayton, also learned how to analyze the volume swell data.

Plans for Next Period
Task 3 is complete.

Task 4 – Analysis of Absorbed Fuels
University of Dayton Research Institute

Objectives
Task 4 is included to complement the results of Task 3 and gain a fundamental understanding of how the materials and fuels interact with one another over the duration of exposure. Task 3 can be described as the "what," i.e., what happens to a material when it is exposed to fuel and Task 4 is the "why," i.e., why the material does or does not swell. To study what causes the swelling (or lack thereof), GC-MS will be used. GC-MS is a technique that identifies which, if any, of the selected class fractions are absorbed into the material from the fuel and/or what parts of the material are extracted into the fuel. The class fractions of interest are listed in Table 2 and were selected according to previous studies of material interactions with fuels and to align with several of the class fractions identified in the Jet A fuels in Task 2. Of note in Table 2, the class fraction labeled "naphthalenes" encompasses all alkyl naphthalene species. Alkyl naphthalenes usually consist of but are not limited to methyl or ethyl groups ($-CH_3$ or $-CH_2CH_3$) across different carbons in the aromatic structure.

Table 2. Class fractions investigated via GC-MS.

Class	Class Fraction
Aromatics	Alkyl benzenes
	Diaromatics (Naphthalenes, Biphenyls, etc.)
	Cycloaromatics (Indans, Tetralins, etc.)
Paraffins	iso-Paraffins
	n-Paraffins
	Monocycloparaffins
	Dicycloparaffins
	Tricycloparaffins

Research Approach
Experimental Approach
GC-MS is performed with an Agilent® 7890A gas chromatograph equipped with an Agilent 5975C VL Mass Selective Detector (MSD). The sample preparation for the material is as follows:

1. Remove aged samples from fuel, and pat dry three times with laboratory wipes to remove any fuel residing on the outside of the material (i.e., not absorbed by the material).
2. Place one piece of test material in a 1.5-ml GC vial with 1 ml methylene chloride (MeCl).
3. Repeat steps 1 and 2 with a second aged test material from the sample vial.
4. Place the samples sitting in solvent (MeCl) on the autosampler and run under UDRI's standard method/temperature ramp.
5. After GC-MS analysis is complete, decant the residual solvent and dry the test material and vial in an oven for 30 min using a predetermined heating cycle.
6. Remove and weigh the dried test material. Record the final weight of the sample for quantitative analysis.

Steps 1–4 should be repeated for the sample Jet A fuels (1 µL of fuel in 1 ml of MeCl) to quantitatively compare the material's ability to extract from the fuel (and vice versa).

Data Analysis

® Agilent is a registered trademark of Agilent Technologies, Inc., Santa Clara, California.

Data analysis for Task 4 consists of integrating the area under the curve of each peak present in the overall chromatogram (total ion chromatogram [TIC]) and the extracted ion chromatograms (EIC) for the representative class fractions. Integration is performed using Agilent ChemStation® Analysis software and Agilent MassHunter,® both via manual integration methods. The area under each curve for TICs and EICs are exported to another software program in which partition coefficients (K_{pf}) are calculated. The K_{pf}, the ratio of a class fraction in the polymer relative to its concentration in the neat fuel, is the metric used to summarize the interaction between the non-metallic material and the surveyed Jet A fuels. Figure 4 provides a visual representation of the two-way exchange that occurs between the material extracting from the fuel and the fuel extracting from the material. The bottom panel of Figure 4 shows the test fuel (sample Jet A), and the top panel shows the absorbed fuel in a sample O-ring (AMS5315). The ratio of the two spectra shows that the material only absorbed a fraction of the fuel components because it has a lower overall signal response.

As shown on the left side of Figure 4, K_{pf} values can fall into three regions. A $K_{pf} < 1$ indicates that the material is resistant to the class fraction of interest. A $K_{pf} > 1$ indicates that the material absorbs or extracts a substantial portion of the class fraction of interest. Finally, a K_{pf} of approximately 1 indicates relatively equal exchange in material and fuel. The K_{pf} values calculated for the materials can be used to predict the swelling behavior of fuels with similar class fractions in the future.

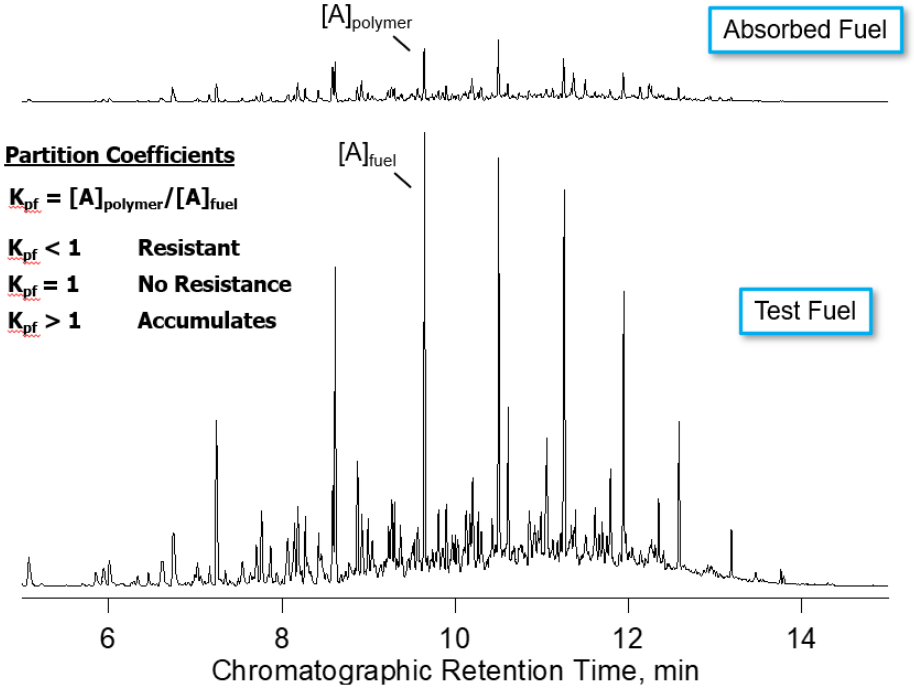

Figure 4. Absorbed fuel analysis, comparing a sample polymer (AMS5315) and a reference Jet A fuel.

Tables 3 and 4 contrast experimental K_{pf} values associated with O-rings and Films found in the ASTM D4054 Non-metallic Short List. These two examples show a stark contrast in experimental partition coefficients and, by extension, starkly different responses to fuel exposure. In Table 3, AMS5315 (Table 3, Column 1) has K_{pf} values that are all greater than 0.10 with some values even nearing 1.0. On the other hand, Kapton (Table 4, Column 3) showed so little of a response to fuel exposure that it could not be quantified via GC-MS, which is approximately a 10 ppm technique. This result is confirmed by the low volume swell experimentally determined in Task 3 (0.02% volume swell). A more quantitative example compares AMS5315 and polyethylene (Table 4, Column 2). Even the most readily absorbed class fraction (the naphthalenes), had experimental K_{pf} value of 0.21 indicating that approximately less than 1/5 of the class fraction was absorbed into the

® ChemStation is a registered trademark of Agilent Technologies, Inc., Santa Clara, California.
® MassHunter is a registered trademark of Agilent Technologies, Inc., Santa Clara, California.

material. The large K_{pf} values in AMS5315 (large values relative to high-density polyethylene (HDP) and many other non-metallic species in the ASTM D4054 Non-metallic Short List) indicate that AMS5315 responds to all class fractions in a significant amount relative to other materials. Comparing materials, both within a material class and externally between material classes, demonstrates the power of Task 4's quantitative approach to material-fuel interactions. The quantitative approach enhances the understanding of what class fractions play a role in volume swell, lifetime, hardness and other physical and mechanical properties of materials.

Table 3. Experimental K_{pf} values for all O-rings across sample Jet A fuels.

Class Fraction	AMS5315 N0602	AMS25988 LM100	AMS7276 V0747	AMS83485 VM125
Overall	0.17	0.04	0.01	0.02
n,i-Paraffins	0.12	0.04	0.01	0.01
Cycloparaffins	0.15	0.04	0.01	0.01
Alkyl Benzenes (C10 Bz)	0.37	0.09	0.03	0.07
Naphthalene	0.94	0.16	0.07	0.17
Naphthalenes (C11 & 12)	0.60	0.09	0.03	0.09

Table 4. Experimental K_{pf} values for all films across sample Jet A fuels. HDP: High-density polyethylene is below the detection limit (bdl).

Class Fraction	Nylon Dupont Zytel 101	Polyethylene HDP	Kapton UPILEX
Overall	bdl	0.10	bdl
n,i-Paraffins	bdl	0.09	bdl
Cycloparaffins	bdl	0.14	bdl
Alkyl Benzenes (C10 Bz)	bdl	0.20	bdl
Naphthalene	bdl	0.31	bdl
Naphthalenes (C11 & 12)	bdl	0.21	bdl

Milestones

Task 4 is a work in progress. Most K_{pf} analysis is complete, but some analysis remains including sealant materials.

Major Accomplishments

Over the past year, Dr. John Graham and Dr. Gina Roesch created separate templates to account for the characteristic sealant peaks. While ultimately Dr. Graham's will be used, this was a huge growth opportunity for Dr. Roesch to practice and compare approaches to complex data analysis problems.

Publications

None.

Outreach Efforts

None.

Awards

None.

Student Involvement
None.

Plans for Next Period
The plan for the next reporting period is to complete Task 4.

Task 5 – Statistical Analysis
University of Dayton Research Institute

Objective
The primary objective of this task is to explore if there is a correlation between the volume swell of a given material and the aromatic content of the fuel to which it was exposed. To achieve this objective, the volume swell data will be fit with a linear model against the aromatic content of the fuels, thus providing a line of fit in which experimental data points of candidate SAFs can be plotted and referenced against. This fit, along with the associated confidence and prediction intervals, will be the primary point of comparison used to evaluate the viability of future SAF candidates.

Research Approach
Task 5 models the relationship between aromatic compounds and volume swell as a linear relationship, which is easily generated by Statistical Analysis System (SAS) statistical modeling software. SAS is equipped with a suite of methods used to correlate new test subjects (in the case of ASCENT Project 088's future, materials aged in SAFs) to the reference dataset (materials aged in in-service Jet A fuels). The model produces three key variables: (1) the slope of the line, (2) the intercept, and (3) the coefficient of determination. These variables provide three critical outcomes: (1) the average response of the material to the aromatic content of the fuel, (2) the estimated volume swell for a Jet A fuel with 0% aromatic compounds in the fuel, and (3) the strength of correlation between the measured aromatic content of the fuel and volume swell. All these parameters contribute to the overall understanding of the aromatic content of the fuel's effect on a material. Figure 5 shows an example of the model on a sample material (AMS5315).

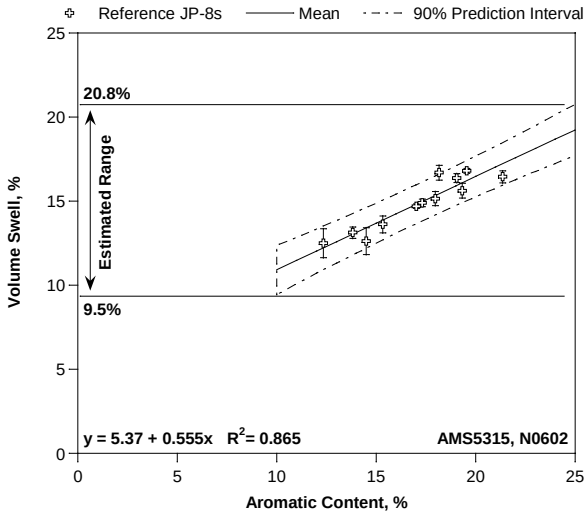

Figure 5. Sample model including the mean and 90% prediction interval of a set of reference JP-8 fuels in AMS5315, N0602.

Additionally, as shown in Figure 5, SAS generates a 90% prediction interval. The 90% prediction interval is distinct from a traditional confidence interval in that it is a quantification of individual fuels within a population and is not based on the mean value of only the 12 sample fuels. This aspect is key to Project 88 because it contextualizes the model to 90% of ***all*** in-service Jet A fuels being flown at the time of the study as opposed to the small sample of 12 Jet As that were tested. In

the future, the individual graphs in Task 5 will act as road maps for future SAF compatibility. For example, if a new SAF's experimental volume swell falls within the prediction interval produced in Task 5, it would be reasonable to suggest (not guarantee but suggest) that the SAF will be compatible with that material type. This type of analysis will provide OEMs with invaluable guidance regarding when a fuel is a good candidate to submit for ASTM D4054 testing.

Table 5 and Figure 6 present yet another approach to providing OEMs with information about a candidate fuel in the context of in-service, safe-to-fly Jet A fuels. Many material compatibility questions in the realm of synthetic fuels revolve around the concentration of aromatics in the fuel because they are known to contribute to the volume swell. To address this question, the linear model's coefficient of determination, the R^2 value, is the critical result to consider. Because the coefficient of determination defines the 'goodness' of the linear model, the materials that have high swelling character and high coefficients of determination would be of main interest for a fuel producer that is concerned about their low or no aromatic fuel being compatible with a non-metallic material that would normally only see Jet A fuels.

Table 5. Experimental coefficients of determination (R^2 values) for all O-rings in the ASTM D4054 Non-metallic Material Short List.

O-ring Material	Task 5 R^2 Values
AMS5315 (N0602)	0.865
AMS25988 (LM100)	0.028
AMS83485 (VM125)	0.184
AMS7276 (V0747)	0.112

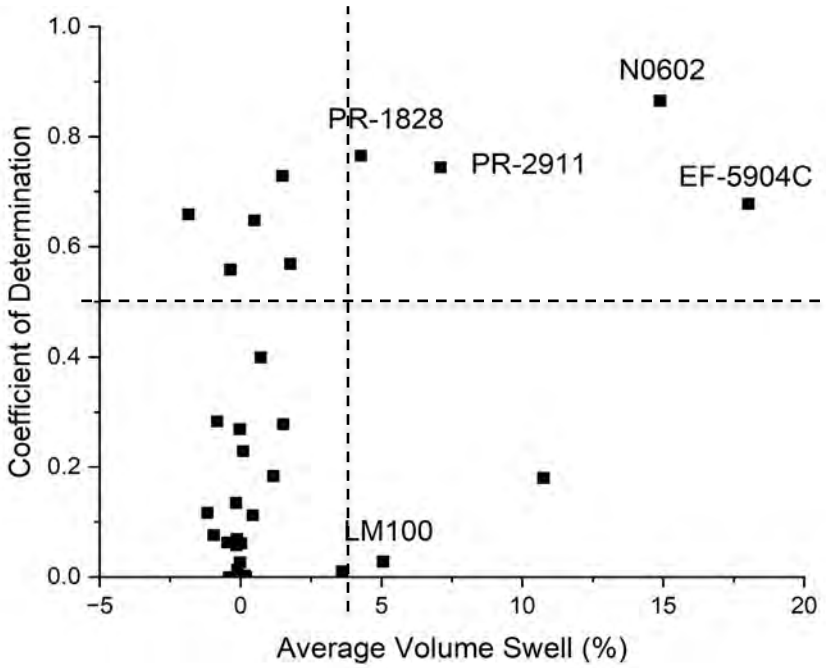

Figure 6. Average volume swell as a function of the coefficient of determination for the single variable model for all materials on the ASTM D4054 Non-metallic Short List.

As an example, Table 5 shows the coefficients of determination for all O-rings listed in the ASTM D4054 Non-metallic Short List. AMS5315 has an R^2 value of 0.865. This means that 86.5% of the observed volume swell of AMS5315 (14.9% average volume swell) is correlated to the aromatic content of the fuel. As a result of high swelling character and high correlation to the aromatic content, AMS5315 lands on the top right quadrant of the graph in Figure 6. Contrasting AMS5315,

AMS25988 has an R^2 value of 0.028. This means that only 2.8% of the observed volume swell of AMS25988 (5.1% average volume swell) is correlated to the aromatic content of the fuel. More succinctly, less than 5% of the volume swell of AMS25988 is described by the aromatic content. As a result, AMS25988 shows up in the lower left quartile of Figure 6. Using the information from the example, a potential suggestion for an OEM to decrease the testing matrix would be to test only AMS5315 in the candidate SAF. If the swelling profile falls within the range of standard Jet A fuels for AMS5315, the OEM could extrapolate that it is likely to fall within the range established for AMS25988 as well since the swell of AMS25988 is not as highly correlated with the aromatic content. This is just one example related to the aromatic content of the fuel. Similar comparisons can be made for other material classes and with respect to other class fractions.

Milestones
Task 5 was completed for 32 of the 34 materials of interest in ASCENT Project 088.

Major Accomplishments
The statistical models created in Task 5 will achieve one of the primary goals of implementing ASCENT Project 088 as a prescreening method. First, Task 5 summarizes the results of Task 3 (volume swell) as a function of the aromatic content of the fuels. Additionally, Task 5 provided reference data sets and associated models for comparing a material's response in the candidate SAF to its response in what fuels are currently being flown. Thus, OEMs and researchers now a have a point of reference.

Publications
None.

Outreach Efforts
None.

Awards
None.

Student Involvement
None.

Plans for Next Period
In the next calendar year, Task 5 will be completed for the remaining two materials and, ultimately, completed.

Task 6 – Multiple Regression Modeling
University of Dayton Research Institute

Objective
The objective of this task is to expand on the statistical models generated in Task 5. Task 6 will incorporate how and if additional class fractions contribute to the volume swell of materials. While there is no doubt about the relationship between the volume swell of a material and the aromatic content of a fuel, the results of Task 5 show that not all volume swell is a result of the aromatic content. Thus, there must be other chemical components that participate in material-fuel exchange. Consequently, the final step of ASCENT Project 088 will be to provide a broader statistical model that encompasses all class fractions identified in Task 2. This process will provide a more holistic picture of material and fuel interactions.

Research Approach
Task 6 will combine the results of Task 2 and Task 3 to create a more robust predictive model. The model will relate the measured fuel composition (Task 2) and the measured volume swell (Task 3) via a multiple regression linear model. The model will be fit to Equation 1:

$$\text{Volume Swell} = \sum_{i=1}^{n} ki[Ai] \qquad \text{(Eq. 1)}$$

where *ki* is the regression coefficient for a given component or class fraction, *i* is the class fraction, and *[Ai]* is the concentration of the component or class fraction *i*. The regression coefficient is calculated using Equation 2:

$$\text{Regression coefficient} = \frac{\text{Percentage volume swell of material in fuel}}{\text{Percentage concentration of class fraction in fuel}} \quad \text{(Eq. 2)}$$

for all class fractions, *n,* which will be used in the model. In ASCENT Project 088, the class fractions of interest are normal and iso-paraffins, cycloparaffins, alkyl benzenes, diaromatic compounds, and cycloaromatic compounds (Table 2, above). In addition to fitting the class fractions based on results from Tasks 2 and 3, the model will include a term to account for the average molecular weight because molecular weight of the fuel impacts the swell. This aspect will be an essential component enabling extension of the model to the candidate SAFs in the future that are also likely to have different molecular weight distributions.

Table 6. Full model volume swell coefficients for AMS5315 at 75°F in Jet A fuels.

Model Coefficients, %/%							
Aromatics			Paraffins		Average M.W.	Intercept	R^2
Alkyl-	Cyclo-	Di-	n, i-	Cyclo-	%/(g/mol)	%v/v	Value
-1.891	-2.045	-1.605	-2.530	-2.452	-0.159	279.951	0.950

Table 6 shows the coefficients generated for the Task 6 model for a sample material (AMS5315). While a good predictive tool, the model coefficients do not have physical meaning. In order to make the Task 6 model an interpretive tool for SAF producers and other OEMs, the model is under further investigation. Task 6 is a work in progress.

Milestones

During the previous year, Task 6 (as-written) was completed for 32 of the 34 materials on the list. Additionally, multiple versions of the code were written so that Task 6 could be used as both an interpretive and predictive tool for SAF samples as well as future SAF development.

Major Accomplishments

Task 6 expands ASCENT Project 088's prescreening toolkit for SAF and Jet A fuel compatibility with non-metallic materials beyond the singular contributions of the aromatics to volume swell. The model built in Task 6 will incorporate the effects of selected class fractions on volume swell both in terms of concentration and molecular structure. In the long term, the model in Task 6 will help OEMs understand the broader picture of a fuel's impact on non-metallic materials. On a fuel-design level, the model will provide OEMs with numbers indicating which class fractions play the greatest role in a material's swell, thus informing the design of future SAFs.

Publications

None.

Outreach Efforts

None.

Awards

None.

Student Involvement

None.

Plans for Next Period

In the next calendar year, Task 6 will be completed for the remaining two materials.

Task 7 – Reporting

University of Dayton Research Institute

Objective

The objective of this task is to document and report the results of ASCENT Project 088 in both quarterly and annual reports. Additionally, at the end of ASCENT Project 088, the results will be compiled into a final report and shared with the FAA.

Research Approach

None.

Milestones

None.

Major Accomplishments

Dr. Gina Roesch provided status updates for ASCENT Project 088 at the Spring SAF Meeting in Honolulu, Hawai'i, and the Fall ASCENT Meeting in Alexandria, VA.

Publications

None.

Outreach Efforts

None.

Awards

None.

Student Involvement

None.

Plans for Next Period

The remaining parts of Task 7 involve successful execution of the remainder of ASCENT Project 088 (Tasks 4-6) and generation of a final report. Additionally, participation in the biannual ASCENT meeting is a priority for all personnel involved in ASCENT Project 088.

Project 089 Characterization of Compositional Effects on the Dielectric Constant

University of Dayton Research Institute

Project Lead Investigator

Zachary West, PhD
Principal Research Engineer
Group Leader, Fuel Science
University of Dayton
300 College Park
Dayton, OH 45458
937-255-4062
zachary.west@udri.udayton.edu

University Participants

University of Dayton Research Institute (UDRI)

- P.I.: Zachary West, PhD
- FAA Award Number: 13-C-AJFE-UD, Amendment 056
- Period of Performance: January 1, 2024, to December 31, 2024
- Task:
  1. Measurement of dielectric constant and density

Project Funding Level

Amendment No. 47	$499,999.67
Amendment No. 54	$110,607.00
Total	**$610,606.67**

Investigation Team

Dr. Zachary West (P.I.)
Shane Kosir (Staff Scientist)
Dr. William H. Steinecker (Staff Scientist)
April Landsaw (Other Professional)
Taylor Nicely (Undergraduate Student)

Project Overview

Aircraft fuel tanks use capacitive gauges to determine fuel capacities during flight. Two crucial fuel properties, the dielectric constant and density, are used to calculate fuel capacity from the response determined from the concentric, cylindrical gauging sensors. In recent years, the airframe original equipment manufacturers (OEM) have closely monitored the behavior of the dielectric constant (also referred to as relative permittivity) of candidate synthetic aviation turbine fuels (SATF), sometimes referred to as sustainable aviation fuels (SAF), because even small changes in this property can result in large errors in fuel tank gauging. This project involves the measurement of the behavior of fuel dielectric constants over a range of temperatures and fuel blends, by using a new dielectric constant instrument. Conventional petroleum-based jet fuels, synthetic blend components (SBC) (some SBCs are produced to ASTM D7566 [ASTM International, 2022]) and blends of both, reflecting a range of hydrocarbon compositions, will be included. A primary goal of this effort is to determine the typical range of dielectric values for conventional fuels, which will be compared with the SATFs to determine any observed

differences and attempt to correlate any of these differences with specific hydrocarbon compositions. These measurements will help minimize errors in fuel tank gauging when aircraft are operated with SATFs.

Task 1 – Measurement of Dielectric Constant and Density

University of Dayton Research Institute

Objective

The primary objective of this effort is to determine the typical range of dielectric constant values for conventional fuels, which will be compared with the range for SATFs to determine any observed differences and attempt to correlate any of these differences to specific hydrocarbon compositions.

Research Approach

The approach of this program is to measure the behavior of fuel dielectric constants over a range of temperatures and fuel blends, by using a new dielectric constant instrument conforming to method IP 638. Both conventional petroleum-based jet fuels and SATF produced to ASTM D7566, reflecting a range of hydrocarbon compositions, will be included. If differences are observed, proposes to determine the causes of these differences by measuring dielectric properties of various species mixtures and/or pure compounds. For example, we can determine the roles of various species classes, e.g., *n*-alkanes, iso-alkanes, aromatic compounds, and cycloparaffins in influencing dielectric property behavior. This work can be performed by using commercial solvents (e.g., Aromatic 150) and/or jet fuels with unique compositions (e.g., Shell IH2 high-cycloparaffin fuel) that have already been characterized.

Historically, airframe OEMs have used a Clausius–Mossotti relationship,[1] wherein $(K - 1)/D$ is plotted vs. $(K - 1)$, where K is the dielectric constant, and D is density, to characterize the relationship between K and D. Figure 1 shows this relationship for measurements from an ARINC 611-1 (Aeronautical Radio, Inc., 1999) survey and high-cycloparaffin SBCs and their blends with petroleum fuels. The fits shown for the petroleum fuels are close to the OEM-assumed slope and intercept values of approximately 0.3658 and 1.00, respectively (Edwards, 2020). Airframe OEMs are concerned when the slope and intercept values differ from those assumed in their fuel quantity indicating systems (Moses, 2013; Parmenter, 2013).

[1] Clausius-Mossotti relationship is an equation that represents the relative permittivity (ε r) of a dielectric material and its molecular polarizability (α). The equation is used to predict the dielectric properties of a material based on its molecular structure.

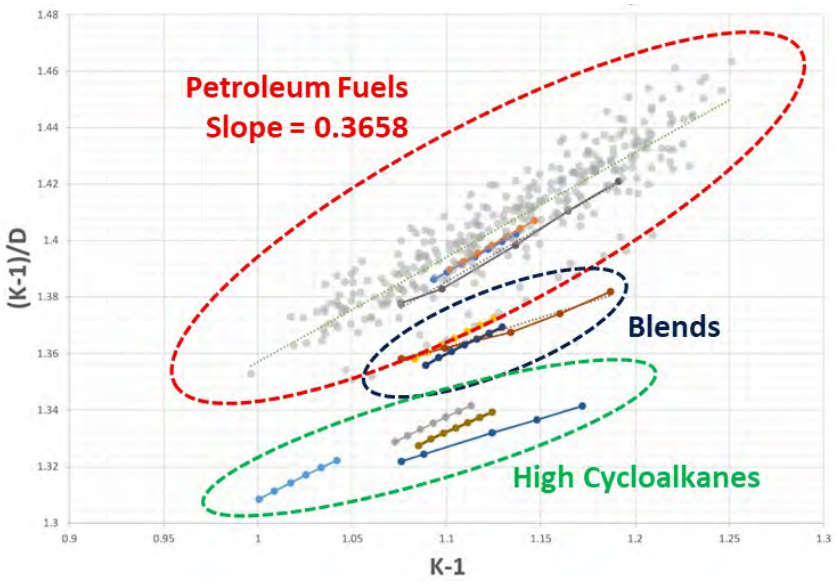

Figure 1. Clausius-Mossotti relationship plot for ARINC 611-1 fuels (Aeronautical Radio, Inc., 1999) and high-cycloparaffin SBCs and their blends with petroleum fuels (plot adapted from Griffin Valentich, Shell [personal communication]).

UDRI has purchased and commissioned the recently developed Stanhope-Seta® instrument JetDC, which meets the requirements of specification IP 638 "Determination of relative permittivity (dielectric constant) of aviation fuels, small scale automated temperature scanning method" The instrument allows for the rapid measurement of both the dielectric constant and density over a temperature range of 0-40°C. Examples of fuels and their blends that will be evaluated include on-specification Jet A fuels, approved ASTM D7566 blendstocks and their blends with Jet A fuels, and ASTM D7566 candidate blend components (i.e., Shell® IH²®, Global Bioenergies, Revo, IIP, etc.)

UDRI has worked with airframe OEMs, such as Airbus® and Boeing,® to determine how the measured results influence the ability to correctly determine aircraft fuel tank quantities. In addition, UDRI has participated in the Energy Institute Task Group SC-B-11 "Dielectric Constant Test Method Task Group," which organized an interlaboratory study (ILS) of the new instrument and method. UDRI participated in the ILS effort which contributed to the development of a precision statement for, and ultimately the full adoption of, IP 638.

Research Results and Discussion

The program began with a review of historical dielectric constant data for jet fuels. Our team was able to acquire the dielectric and density data from both the ARINC study (Aeronautical Radio, Inc., 1999) and a Coordinating Research Council (CRC) World Survey (Hadaller & Johnson, 2006); both datasets help to define the conventional jet fuel baseline. Figure 2 shows histograms of the Clausius-Mossotti slopes for the ARINC study, the CRC World Survey, and the two datasets combined. Interestingly, the data show that petroleum fuels exhibit a very broad range of slopes from 0.30 to 0.45, with an approximately normal distribution. Each of the three datasets shows an average slope in the range 0.35-0.36, in agreement with the 0.3658 slope assumed by at least one airframe OEM in their fuel quantity indicating system (Moses, 2013; Parmenter, 2013). These historical data were acquired with a variety of methods, probably following ASTM D924 (ASTM International, 2015).

® Seta is a registered trademark of Stanhope-Seta Limited, United Kingdom.
® Shell is a registered trademark of Shell Trademark Management BV, The Hague, The Netherlands.
® IH² is a registered trademark of Gas Technology Institute, Des Plaines, Illinois.
® Airbus is a registered trademark of Airbus Operations GmbH, Hamburg, Germany.
® Boeing is a registered trademark of The Boeing Company, Seattle, Washington.

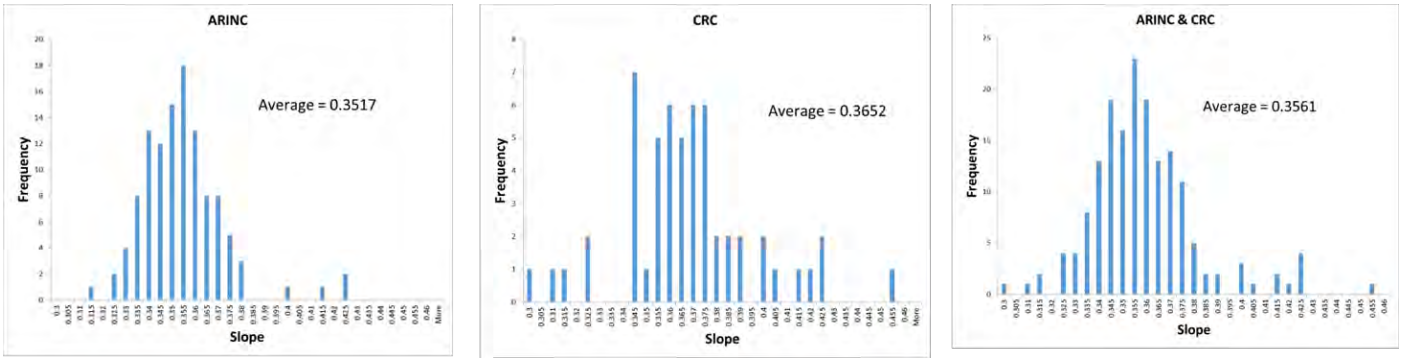

Figure 2. Histograms of the Clausius–Mossotti slopes for the ARINC data, the CRC data, and the combined set of fuels from both studies (Aeronautical Radio, Inc., 1999; Hadaller & Johnson, 2006).

This historic data for conventional fuels laid the groundwork for more recent investigations under ASCENT Project 089 (i.e., the investigation of bulk hydrocarbon compositional effects on dielectric constant). Our efforts have been documented in detail in the recent publication by Kosir et al. (2024); however, excerpts from that will be provided herein. The study by Kosir et al. (2024) involved blends of one Jet A fuel and four SBC materials as listed in Table 1 (additional reference fluids were also examined, e.g., Norpar 13, Isopar M, and Aromatic 150). As Table 1shows, the SBC materials consist of specific hydrocarbon classes (e.g., iso-alkanes or aromatics); none would be considered 'fully formulated' jet fuel as each is enriched with single hydrocarbon classes rather than a distribution of all classes like conventional fuels.

Table 1. Samples used in blending studies.

Fuel/SBC Type	Composition Description	H/C Ratio	Density at 20°C (kg/m³)	Dielectric Constant at 20°C
Jet A (POSF 10325)	Conventional/Fully formulated	1.9	800.4	2.116
ATJ-SPK	High *iso*-alkane	2.1	754.8	2.023
CPK	High cycloalkane	1.9	829.9	2.107
HEFA-SPK	High *n*/*iso*-alkane	2.2	759.1	2.030
SAK	High aromatic	1.4	870.1	2.365

ATJ = alcohol-to-jet fuel
CPK = cycloparaffinic kerosene
HEFA = hydrotreated esters and fatty acids
SAK = synthesized aromatic kerosene
SPK = straight paraffinic jet fuel

Volumetric blends of the materials listed in Table 1 were prepared and subjected to the simultaneous measurement of the dielectric constant and density (as a function of temperature) using the JetDC instrument. Figure 3 shows the resulting measurements at 20°C (markers) along with contours of historic ARINC and CRC data for comparison. Figure 3a shows binary blends of components at 0, 25, 50, 75, and 100 percentage volume (vol%); the dashed lines of same color connect markers for each binary pairing. The synthesized aromatic kerosene (SAK) material has the highest dielectric constant and density values, whereas the alcohol-to-jet fuel (ATJ) and hydrotreated esters and fatty acids (HEFA) materials have the lowest K and D values. The reference Jet A fuel is centrally located within the historic data, while the cycloparaffinic kerosene (CPK) material has a dielectric constant like the Jet A fuel but significantly higher density. The various binary blends demonstrate the linear blending behavior of the dielectric constant with respect to density. Figure 3b shows similar information for pure compounds and narrow distillates of specific hydrocarbon types (e.g., n-alkanes, iso-alkanes, and aromatics). These data confirm that iso- and n-alkanes drive both density and K to lower values, aromatics drive density and K to higher values, and cycloalkanes drive density to higher values with minimal change to K.

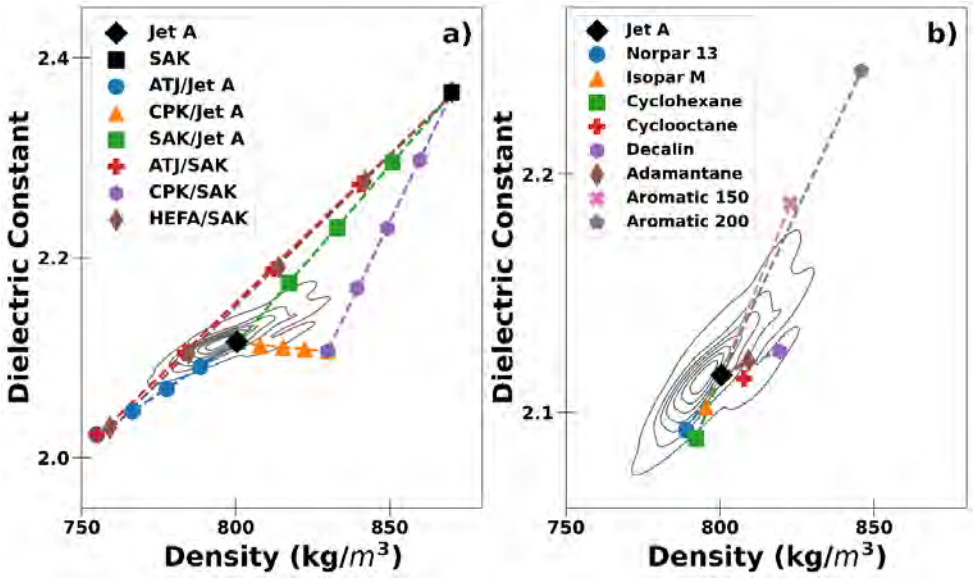

Figure 3. Dielectric constant versus density at 20°C for (a) SBC/Jet A fuel and SBC/SAK blends and (b) 25 vol% reference fluid/Jet A fuel blends, except for adamantane, which was blended at 5 vol% in Jet A fuel. The contour plot represents dielectric constant versus density interpolated to 20°C for ARINC and CRC data (Aeronautical Radio, Inc., 1999; Hadaller & Johnson, 2006).

The behavior of the iso-/normal- alkanes (e.g., HEFA and ATJ) and aromatic materials (e.g., SAK) shown in Figure 3 were within expectations; however, the cyclo-alkane material behavior (e.g., CPK) was unexpected. That is, the dielectric constant response for CPK was lower than anticipated based on the material's high density. Mixtures of CPK and Jet A were explored, and the results (at various blend percentages and temperatures) are shown in Figure 4. As Figure 4 shows, the higher the CPK percentage the more significant the gauging slope deviates from the typical industry value of about 0.36. However, blends with CPK were not the only materials that have gauging slopes that deviate from the typical industry value. Figure 5 shows gauging slopes as a function of blend percentage of binary blends of (a) SBC and Jet A fuel, (b) SBC and SAK, and (c) the distribution of conventional gauging slopes for ARINC and CRC data (Aeronautical Radio, Inc., 1999; Hadaller & Johnson, 2006). As Figure 5 shows, mixtures with extreme levels of aromatics (e.g., no aromatics or greater than 50% aromatics) demonstrated gauging slopes outside of the 95% confidence range for historic data. Aromatic level correlates proportional to gauging slope, while alkane (i.e., n-, iso-, and cyclo-alkanes) content appears to be inversely proportional to gauging slope. Regardless, there were several combinations of materials that fell within the expected/historic range of gauging slopes. This indicates that careful formulation of synthetic materials can meet existing experience, thus helping to de-risk the introduction of SAF materials in the future.

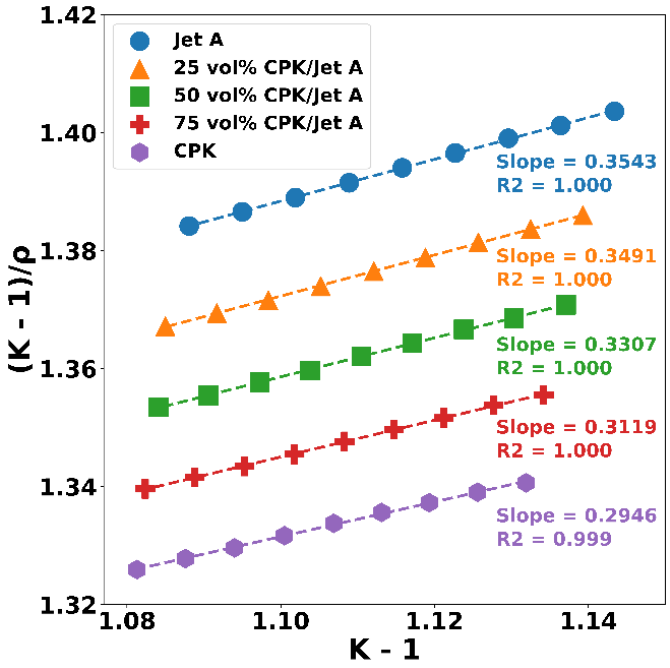

Figure 4. Clausius-Mossotti style gauging plot for blends of CPK with Jet A fuel. Each binary blend was measured from 0 to 40°C, with slopes and the coefficient of determination (R^2) values reported for the resulting linear regressions.

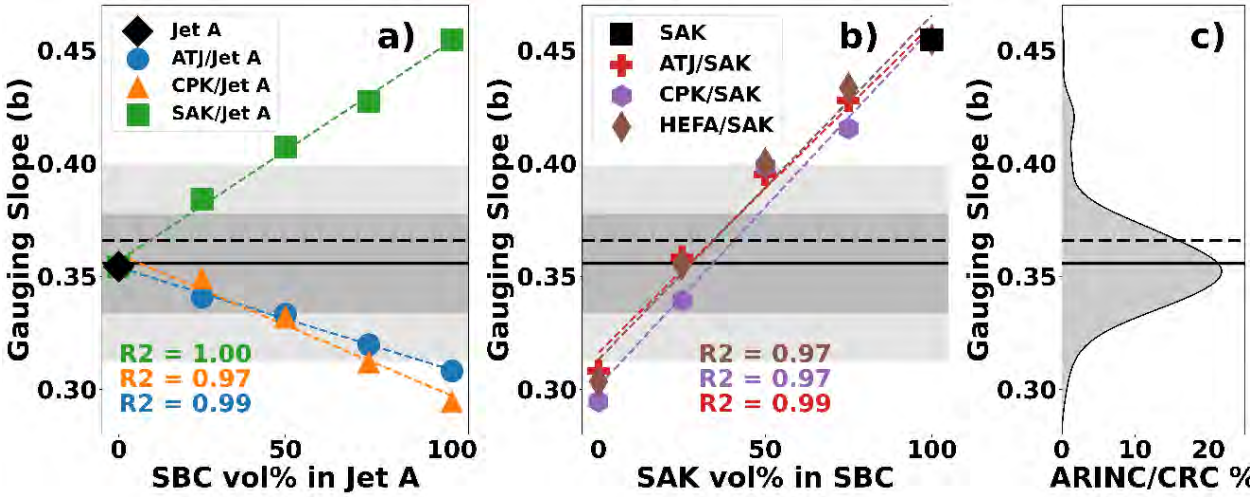

Figure 5. Gauging slope as a function of (a) SBC vol% for the SBC/Jet A fuel blends, (b) SAK vol% for the SAK/SBC blends, (c) histogram of gauging slopes for ARINC and CRC fuels. The horizontal shaded regions show the 68% (dark gray) and 95% (light gray) confidence intervals for the ARINC/CRC data (Aeronautical Radio, Inc., 1999; Hadaller & Johnson, 2006).

To more quantitatively predict mixture behavior, for future SAF adoption, efforts were made to develop predictive tools/models. Partial least squares (PLS) predictions were made using hydrocarbon type data for the blends measured and results are shown in Figure 6. The PLS model produced a root mean-square error (RMSE) of 0.0103 with three latent variables. The RMSE of 0.0103 is an order of magnitude lower than the average gauging slope of 0.3557. The inclusion of Tier 3 carbon number regions (i.e., hydrocarbon class and carbon number) produced a lower RMSE of 0.0059 (Kosir et al.,

2024), which indicates that the dielectric constant is somewhat sensitive to molecular weight in addition to hydrocarbon class. Nevertheless, the model coefficients for the dielectric constant using only Tier 2 data are shown in Figure 6b. The coefficients indicate that aromatics increase the slope, while alkanes decrease the slope in the order iso-alkanes ≈ n-alkanes > monocycloalkanes ≈ dicycloalkanes. The trends with hydrocarbon classes are as expected, except for diaromatics, which had a relatively low model coefficient. Diaromatics were only present in the training data for Jet A fuel, Aromatic 150, and Aromatic 200. The low concentration of diaromatics in the training data may have contributed to its unexpected low model coefficient in Figure 6b. The Tier 3 model coefficients mirrored the Tier 2 model coefficients. These models should allow future prediction of dielectric behavior of SAF and SAF blends; however, they may also require updating based on novel hydrocarbons that arise.

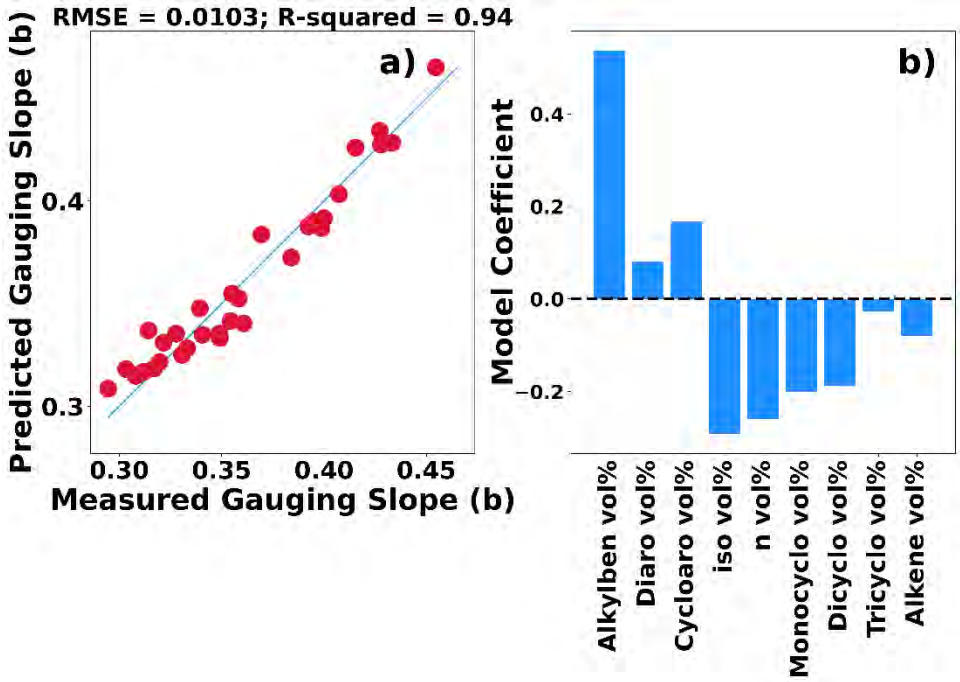

Figure 6. (a) Parity plot of PLS prediction vs. measured industry gauging slopes for SBC blends. (b) Model coefficients for Tier 2 hydrocarbon groups, which served as PLS training features.

Milestones

- Acquired and commissioned the Jet DC instrument,
- Participated in the ILS and measurements of dielectric and density on fuel/SBC blends.
- Presented our work at two major international conferences, and published journal publication of major findings.

Major Accomplishments

- Published peer reviewed journal publication in *Energy & Fuels*.
- Presented our work at two major international fuels conferences: 2024 CRC Aviation Committee Meeting and 18th International Conference on Stability, Handling, and Use of Liquid Fuels (September 2024).

Publications

Peer-Reviewed Journal Publication

Kosir, S., Landsaw, A., Steinecker, W. H., West, Z. J., Zabarnick, S. (2024). Synthetic blend component study: the effects of hydrocarbon composition on aviation fuel dielectric constant. *Energy & Fuels, 38*(17), 16451-16457, doi: 10.1021/acs.energyfuels.4c02342.

Presentations

Kosir, A., Landsaw, A., West, Z., Zabarnick, S. (2024, September 8-12). *Synthetic blend component study: the effects of hydrocarbon composition on aviation fuel dielectric constant* [Conference presentation]. 18th International Conference on Stability, Handling and Use of Liquid Fuels, Louisville, Kentucky.

Kosir, S., Landsaw, A., West, Z., Zabarnick, S. (2024, April 29 - May 2). *Composition effects on the dielectric constant for blends of aviation fuel synthetic blend components (SBCs)* [Conference presentation]. 2024 CRC Aviation Committee Meeting, Alexandria, Virginia.

Outreach Efforts

A presentation was made at the ASCENT Spring 2024 meeting, and a poster was presented at the Fall 2024 ASCENT meeting. Presentations were also made at the 2024 CRC Aviation Committee Meeting and the 18th International Conference on Stability, Handling and Use of Liquid Fuels; both meetings are well attended by aviation fuels industry experts (from OEMs and producers). The goal of these meetings is to receive feedback from industry experts on future steps to enable this work to most effectively contribute to the approval of new SAF candidates.

Awards

- Dr. Steven Zabarnick, ASTM D02 Award of Excellence, December 2023

Student Involvement

Undergraduate student, Taylor Nicely, was responsible for taking dielectric constant measurements.

Plans for Next Period

- Explore the impact(s) of trace species, such as water and fuel additives, on the dielectric constant.
- Work with OEMs to determine what, if any, additional information is necessary regarding dielectric constant and composition for further SAF adoption.

References

Aeronautical Radio, Inc., (1999). *Guidance for the design and installation of fuel quantity systems* (ARINC Report 611-1). https://img.antpedia.com/standard/files/pdfs_ora/20230613/ARINC/ARINC%20REPORT%20611-1-1999.pdf

ASTM International. (2022). *ASTM D7566-22a: standard specification for aviation turbine fuel containing synthesized hydrocarbons.*

ASTM International. (2015). *ASTM D924-15: standard test method for dissipation factor (or power factor) and relative permittivity (dielectric constant) of electrical insulating liquids.*

Edwards, J. T. (2020). *Jet fuel properties* (Report No. AFRL-RQ-WP-TR-2020-0017). Air Force Research Laboratory. https://apps.dtic.mil/sti/pdfs/AD1093317.pdf

Hadaller, O. J., & Johnson, J. M. (2006). *World fuel sampling program* (CRC Report No. 647), Coordinating Research Council, Inc.

Kosir, S., Landsaw, A., Steinecker, W. H., West, Z. J., & Zabarnick, S. (2024). Synthetic blend component study: the effects of hydrocarbon composition on aviation fuel dielectric constant. *Energy & Fuels, 38*(17), 16451—16457, doi: 10.1021/acs.energyfuels.4c02342.

Moses, C. (2013, April 29 - May 2). *Concern about density-dielectric correlation in synthesized kerosenes* [Conference presentation]. 2013 CRC Aviation Meeting, Savannah, Georgia.

Parmenter, D. (2013, April 29 - May 2). Assessing gauging performance of synthetic fuels [Conference presentation]. 2013 CRC Aviation Meeting, Savannah, Georgia.

Project 090 World Fuel Survey

University of Dayton Research Institute

Project Lead Investigator

Zachary West, PhD
Principal Research Engineer
Group Leader, Fuel Science
University of Dayton
300 College Park
Dayton, OH 45458
937-255-4062
zachary.west@udri.udayton.edu

University Participants

University of Dayton Research Institute (UDRI)

- P.I.: Zachary West, PhD
- FAA award number: 13-C-AJFE-UD
- Overall Period of Performance: January 1, 2023, to September 30, 2025
- Tasks:
  - Period of Performance: January 1, 2023, to December 31, 2023; Amendment No. 048
    1. Conduct a survey of commercial jet fuels and develop a modern technical dataset for relevant fuel samples
  - Period of Performance: September 22, 2023, to September 30, 2024; Amendment No. 049
    - No-Cost Extension
  - Period of Performance: March 19, 2024, to March 18, 2025; Amendment No. 051
  - Period of Performance: September 23, 2024, to September 30, 2025; Amendment No. 057
    - No-Cost Extension

Project Funding Level

Amendment	Funding
Amendment No. 048	$749,886.56
Amendment No. 051	$999,998.00
Total	**$1,749,885.00**

In-kind cost sharing has been obtained from the following organizations. Additional cost-sharing will be obtained from fuel refineries for the cost of fuel samples and testing services.

Organization	Amount	Year
Marathon Petroleum Corporation	$30,120	2023
ASG Analytik-Service AG	$9,357	2024
Total	**$39,477**	

Investigation Team

Dr. Zachary West (P.I.)
Carlie Anderson (staff scientist)
Dr. Amanda Arts (staff scientist)
Shane Kosir (staff scientist)
Susan Mueller (staff scientist)
Linda Shafer (staff scientist)
Dr. Willie Steinecker (staff scientist)
Taylor Nicely (undergraduate student)

CJ Nesbit (undergraduate student)
Maria Baker (other professional)
Lisa Brown (other professional)
April Landsaw (other professional)

Project Overview

Jet fuel is defined by a robust physicochemical and performance specification; however, the exact chemical composition is variable and depends on numerous market factors, such as petroleum crude sources, production/refinery techniques, and impacts from transportation/handling in the fungible fuel system. As the United States and other countries are accelerating the pace of fuel certification (via the ASTM D4054 standard practice [ASTM, 2022]) and production of synthetic aviation turbine fuels (SATF) to include sustainable aviation fuels (SAF), having a robust and representative set of data for comparison is critically important to the safe adoption of SATF/SAF fuels. Almost two decades have passed since the last major survey of commercial jet fuels (CRC Report No. 647, 2006 [Hadaller & Johnson, 2006]); therefore, this project aims to collect a contemporary set of representative jet fuel samples and conduct both specification and non-specification testing on the subject samples. The results of this survey will be used to inform how to accelerate SAF adoption in the market.

Task 1 – Conduct a Survey of Commercial World Jet Fuels

University of Dayton Research Institute

Objectives

The objectives of this task are to (1) secure relevant jet fuel samples directly from refineries around the world, (2) analyze the fuel samples to create a robust set of physicochemical and property technical data, and (3) make the test data available to the aviation fuels community, to enhance and expedite decisions regarding current and future SATF/SAF compositional requirements.

Research Approach

Our research approach has been two-fold where the first part involved collecting industry stakeholder interest/feedback and building partnerships with fuel refiners. The second portion of the project has involved the development and execution of the process shown in Figure 1. The execution of the process includes soliciting fuel samples from refiners, coordinating the shipping and handling of the samples to UDRI, subjecting fuel samples to testing at both UDRI and other vetted contracted laboratories, and reporting test data through partnerships with both the Coordinating Research Council (CRC) and Volpe National Transportation System Center (Volpe Center).

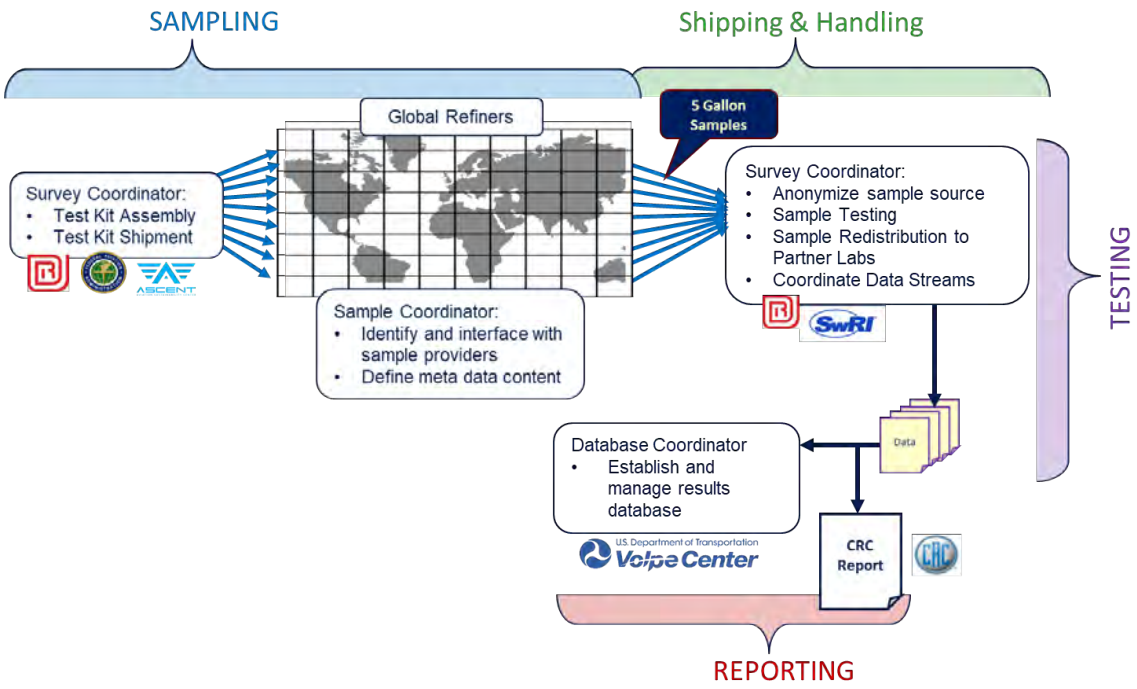

Figure 1. Schematic representation of the world jet fuel survey process.

Solicitation of samples

Targeted email solicitations requesting samples of 5 gal were sent to our fuel producer partners. After obtaining positive responses, UDRI sent sampling kits and instructions to fuel producers to submit samples along with certificates of analysis. The ASCENT Project 090 team have received a total of 45 jet fuel samples as of November 4, 2024, which represents over 121 million gal of product as self-reported by refiner batch volumes). The first 38 of these samples will be included in the first-year data reporting with the CRC and Volpe Center. Our team is actively soliciting additional samples to increase the total observed sample population and increase both the depth and breadth of the dataset.

Testing

In addition to the refiner's reported specification data (i.e., Refiner's Certificate of Quality [RCQ]), fuels are being subjected to 25 chemical, physical, and performance tests (Table 1). Testing is being performed at both UDRI and Southwest Research Institute (SwRI).

Table 1. Jet fuel survey fit-for-purpose test plan.

Property	Test method
Detailed Hydrocarbon Type	UDRI FCM-101/FED-STD-791, Method 7508
Olefins	ASTM D1319
Hydrogen content	ASTM D3701
Organic compounds	UDRI FCM-102
Inorganic compounds: N, total, and basic	ASTM D4629
Trace Metals	UDRI FCM-107
Distillation	ASTM D86
Simulated distillation	ASTM D2887
Thermal stability, breakpoint	ASTM D3241
Lubricity	ASTM D5001
Viscosity vs. temperature	ASTM D7042
Density vs. temperature	ASTM D4052
Specific heat vs. temperature	ASTM E2716
Surface tension vs. temperature	ASTM D1331
Isentropic bulk modulus vs. temperature and pressure	FED-STD-791, Method 7507
Thermal conductivity vs. temperature	ASTM D7896
Refractive index (nD20)	UDRI In-House
Water solubility vs. temperature	ASTM D6304
Air solubility (oxygen/nitrogen)	UDRI FCM-103
True vapor pressure vs. temperature	ASTM D6378
Dielectric constant vs. density	IP PM FC/21
Autoignition temperature	ASTM E659
Hot surface ignition temperature	ISO 20823
Derived cetane number	ASTM D6890
Thermal stability, QCM	ASTM D7739
Note: ASTM methods are available at https://www.astm.org/products-services/standards-and-publications.html.	

Reporting

UDRI will anonymize all test data before reporting, to protect fuel producers' commercial interests. The ASCENT Project 090 team is working with the Volpe Center to establish an online database to archive test data. Our team also intends to report the test data in a CRC report. Preliminary test data have been presented at the CRC Aviation Meeting, International Association for Stability, Handling and Use of Liquid Fuels, Inc. (IASH) conference, the Original Equipment Manufacturers (OEM) review panel meeting, and various ASCENT meetings. Already, some interesting comparisons can be made between the current ASCENT Project 090 world jet fuel survey and the prior CRC 2006 survey.

Detailed hydrocarbon type data (via FED-STD 791, Method 7508) are shown in combined violin plot format for subsets of both the 2024 and 2006 jet fuel surveys in Figures 2 to 9. In Figures 2 to 9, the violin plots include median (solid lines)

and interquartile ranges (dashed lines) for the respective datasets. The CRC 2006 data (shown on the left half of the violin plots in blue) include 51 petroleum derived Jet A, Jet A1, and JP-8 grade fuels. The 2024 ASCENT Project 090 survey data (shown on the right half of the violin plots in red) include 38 petroleum derived Jet A and Jet A1 fuel samples. Figure 2 shows Tier 2 hydrocarbon type for the seven most abundant classes of hydrocarbons in typical jet fuel. As Figure 2 shows, the median concentrations of n-alkanes, iso-alkanes, and alkylbenzenes is reduced from 2006 to present, while the median concentrations of both monocyclo- and dicyclo-alkanes increased from 2006 to present.

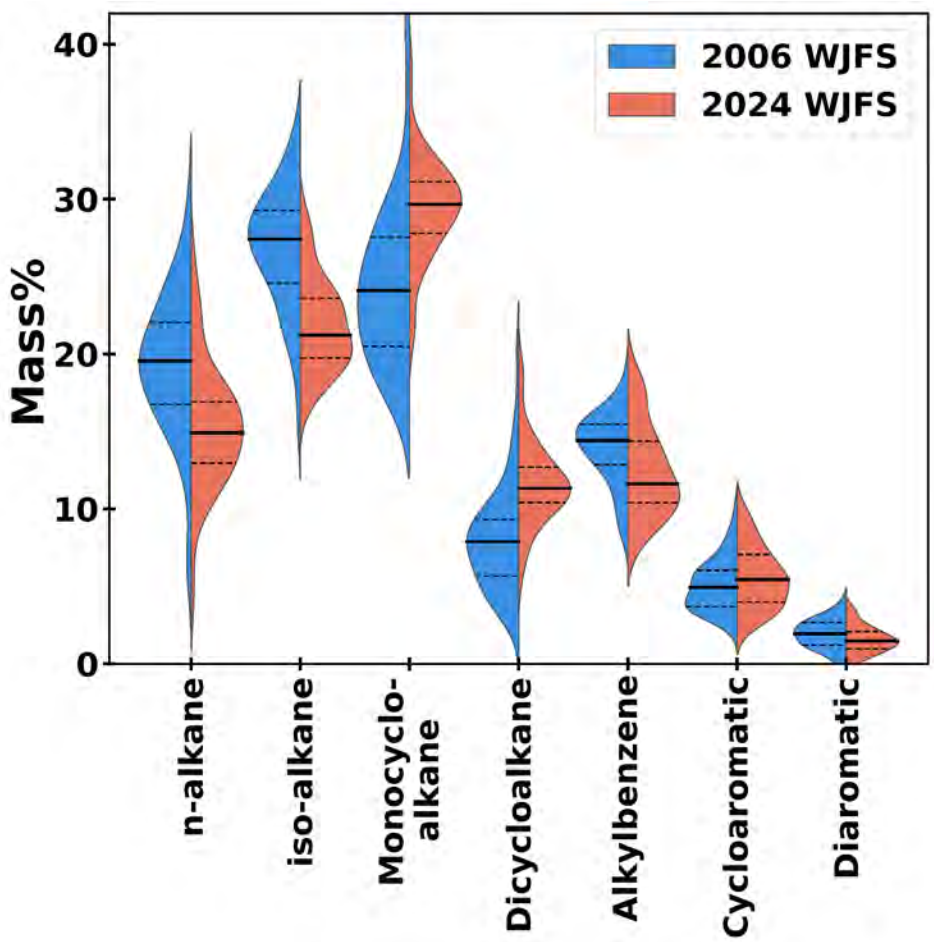

Figure 2. Comparison of Tier 2 hydrocarbon classes for 2006 and 2024 surveys.

Figures 3 through 9 show Tier 3 level hydrocarbon class with respect to carbon number data. Observations of these data, from 2006 to 2024, include reductions of the median concentrations of "light" (e.g., C7 to C12, n-alkanes and iso-alkanes), increased median concentrations of all monocyclo- and dicyclo-alkanes but especially the "heavier" (e.g., C13 to C17) range of compounds, and an increase in the median concentration values of C14 and C15 cycloaromatics.

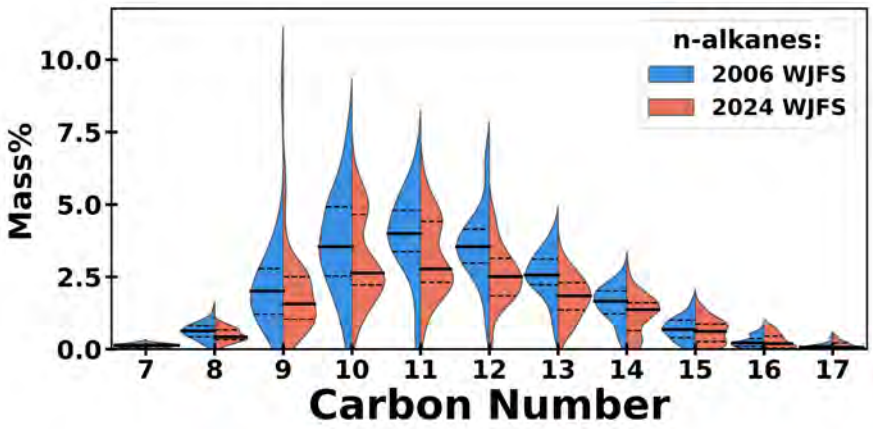

Figure 3. Comparison of Tier 3, n-alkanes for 2006 and 2024 fuel surveys.

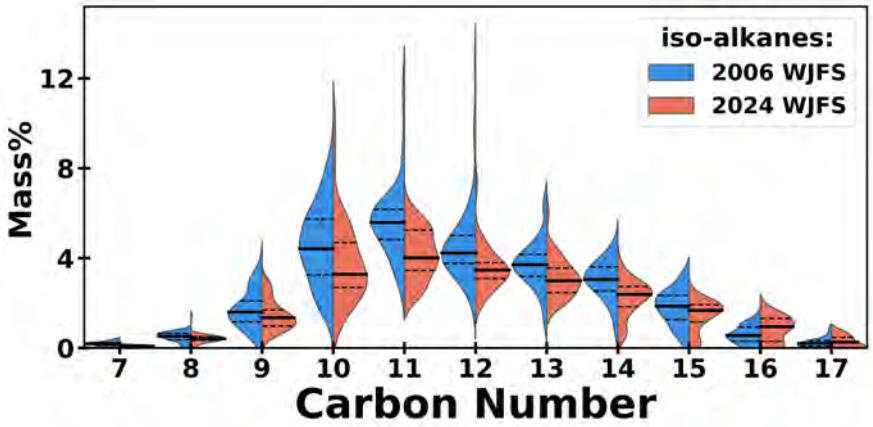

Figure 4. Comparison of Tier 3, iso-alkanes for 2006 and 2024 fuel surveys.

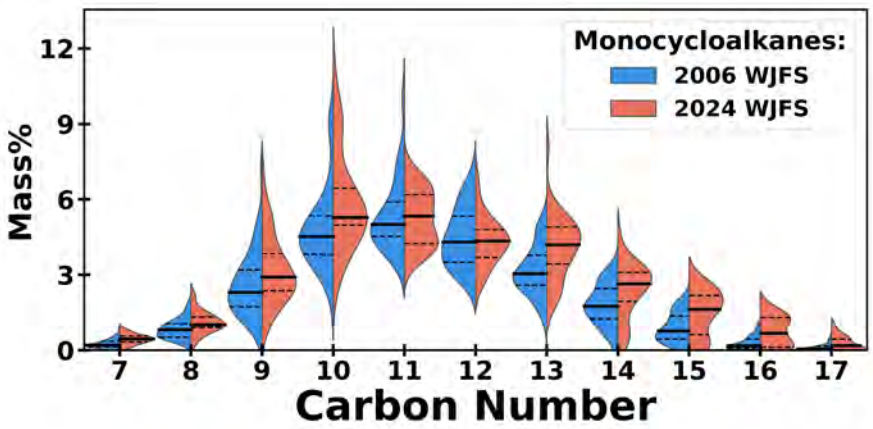

Figure 5. Comparison of Tier 3, monocycloalkanes for 2006 and 2024 fuel surveys.

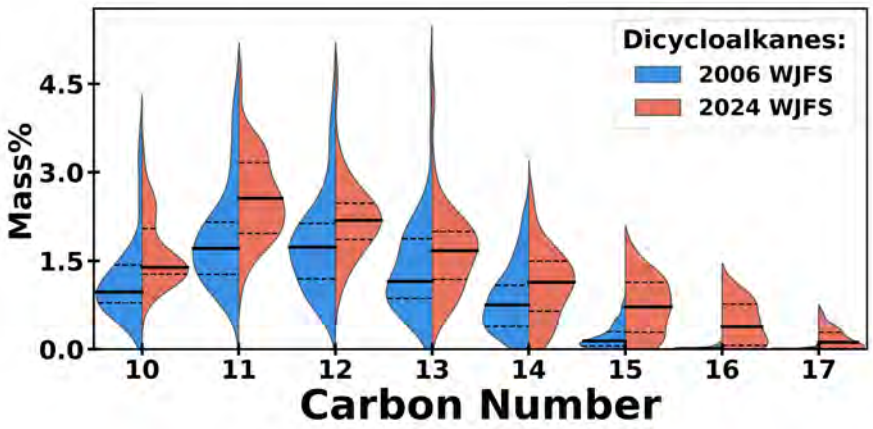

Figure 6. Comparison of Tier 3, dicycloalkanes for 2006 and 2024 fuel surveys.

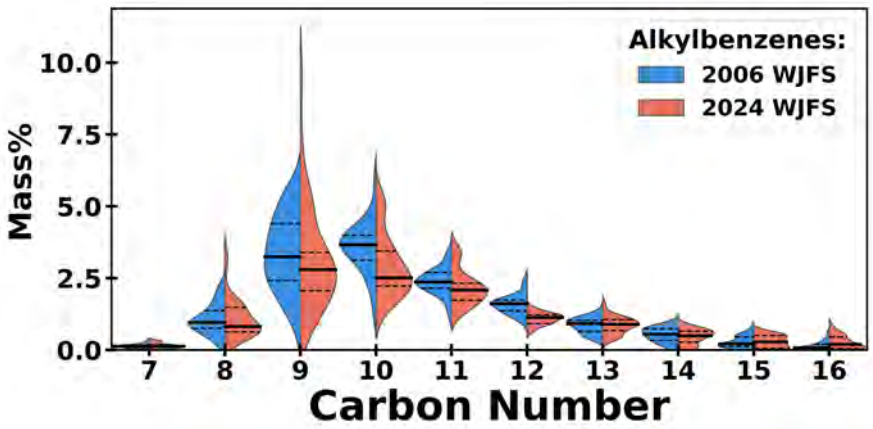

Figure 7. Comparison of Tier 3, alkylbenzenes for 2006 and 2024 fuel surveys.

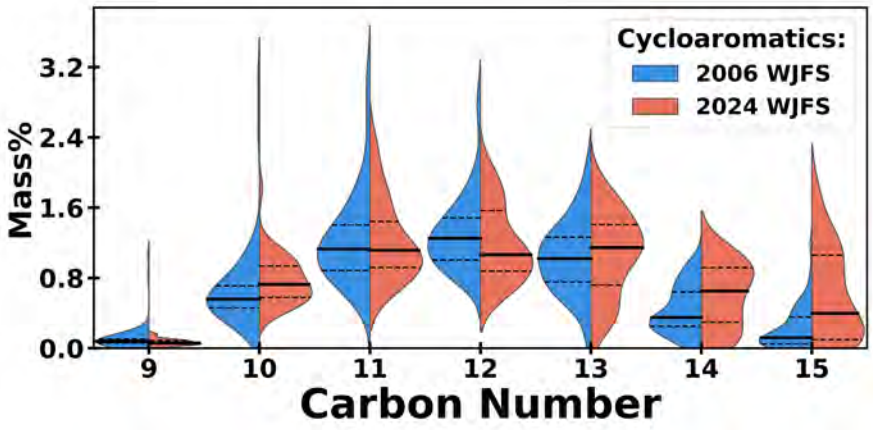

Figure 8. Comparison of Tier 3, cycloaromatics for 2006 and 2024 fuel surveys.

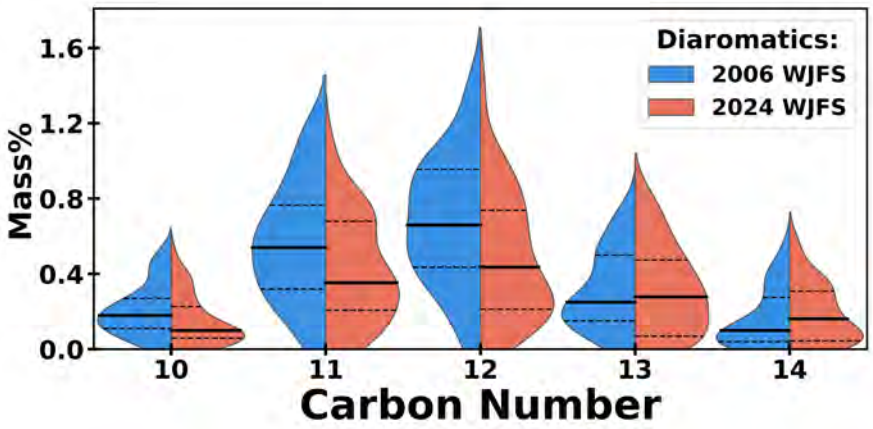

Figure 9. Comparison of Tier 3, diaromatics for 2006 and 2024 fuel surveys.

Changes in jet fuel composition will inevitably result in changes in the physicochemical and performance properties. For instance, Figure 10 shows the comparison of the ASTM D86 (ASTM, 2023) distillation data between 2006 and 2024 fuel surveys. Figure 10 shows that the median values for both the 90% volume recovery temperature (T90) and the final boiling point (FBP) are increased. The increase in distillation end point temperatures correlates with the elevated median concentrations of "heavier" hydrocarbons. In practice, the refiner defines the fractionation "cut points" (i.e., initial boiling point [IBP] and FBP) and the compound class sizes follow from those production variables.

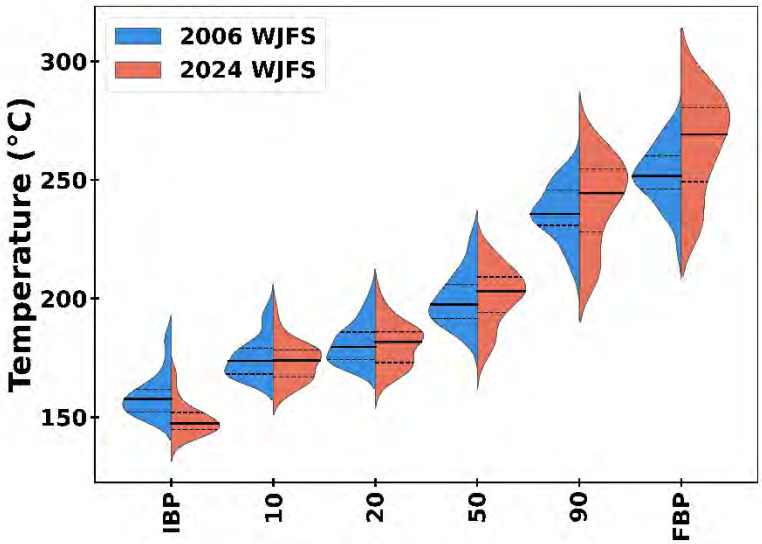

Figure 10. Comparison of ASTM D86 distillation data between 2006 and 2024 fuel surveys.

Milestones

The original project proposal indicated that sample testing would be completed by July 1, 2023, and a final report and analysis would be complete by September 30, 2023. However, this timeline failed to account for fuel producer schedules to provide samples and the time required for outside/sub-contracted testing services. The updated schedule for ASCENT Project 090 is dependent on the continued receipt of fuel samples for testing and the time associated with contracted laboratory testing. Our current best estimate for a major test data package is April 30, 2025, with a first-year data report completed by May 31, 2025.

Major Accomplishments

To date, 45 jet fuel samples have been received, which represent over 121 million gal of product (as self-reported by the refinery batch volumes). The ASCENT Project 090 has presented preliminary data at two major, international jet fuel conferences.

Publications

West, Z. (2024, April 29-May 2). *World jet fuel survey* [Conference presentation]. 2024 CRC Aviation Committee Meeting, Alexandria, Virginia.

Kosir, S., & West, Z. (2024, September 8-12). *World jet fuel survey (preliminary results)* [Poster presentation]. 18th International Conference on Stability, Handling and Use of Liquid Fuels (IASH 2024), Louisville, Kentucky.

Outreach Efforts

The ASCENT Project 090 activities were presented at the April 2024 Spring and October 2024 Fall ASCENT semi-annual meetings. Additionally, the project has been briefed during a regular original equipment manufacturer panel meeting, at the CRC Aviation Committee Meeting (April 29-May 2, 2024), the 18th International Conference on Stability, Handling and Use of Liquid Fuels (September 8-12, 2024), and has been discussed in numerous industry forums, such as ASTM.

Awards

None.

Student Involvement

Two undergraduate chemical engineering students that have been involved with the preparation of samples for solid phase extraction, two-dimensional gas chromatography with tandem flame ionization detection and mass spectrometry detection analysis for polar organic compounds (UDRI FCM-102) and investigating simulated distillation data analysis techniques.

Plans for Next Period

Over the next year, the ASCENT Project 090 team will continue to solicit samples from fuel producers, and we will collect test data in earnest (i.e., fit-for-purpose property data). First-year data will be reported (e.g., CRC report) and archived (e.g., Volpe Center database).

References

ASTM International. (2022). *Standard practice for evaluation of new aviation turbine fuels and fuel additives* (ASTM D4054-22).

ASTM International. (2023). *Standard test method for distillation of petroleum products and liquid fuels at atmospheric pressure* (ASTM D86-23ae1).

Hadaller, O. J., Johnson, J. M. (2006). *World Fuel Sampling Program* (CRC Report 647). Coordinating Research Council, Inc., Alpharetta, Georgia.

Testing Method of Lubricants, Liquid Fuels, and Related Products: 7508.0—Method for Detailed Hydrocarbon Analysis of Middle Distillate Fuels by Two-Dimensional Gas Chromatography, Fed.-Std.-791F (2024). https://assist.dla.mil

Project 091(A) Environmental Impacts of High-Altitude and Space Vehicle Emissions

Massachusetts Institute of Technology

Project Lead Investigators

Raymond L. Speth
Principal Research Scientist
Associate Director, Laboratory for Aviation and the Environment
Massachusetts Institute of Technology
77 Massachusetts Ave, Building 33-310, Cambridge, MA 02139
617-253-1516
speth@mit.edu

University Participants

Massachusetts Institute of Technology (MIT)

- P.I.: Raymond L. Speth
- FAA Award Number: 13-C-AJFE-MIT, Amendment Nos. 113, 115, 122, and 133
- Period of Performance: January 1, 2023, to September 30, 2025 (reporting here with the exception of funding level and cost sharing only for the period October 1, 2023, to September 30, 2024)
- Tasks:
  1. Creation of Emissions Inventories for Launch Vehicles
  2. Refining and Running GEOS-Chem High-Performance (GCHP) Simulations
  3. Quantifying Environmental Impacts of Emissions from Each Scenario

Aerospace Corporation

- Co-investigator: Martin Ross
- FAA Award: MIT Subaward Purchase Order No. 855789
- Period of Performance: January 1, 2023, to September 30, 2025 (reporting here with the exception of funding level and cost sharing only for the period October 1, 2023, to September 30, 2024)
- Task:
  1. Creation of Emissions Inventories for Launch Vehicles

Project Funding Level

ASCENT Project 051A was provided with $518,775 Federal Aviation Administration (FAA) funding and $258,775 matching funds. Sources of match are approximately $69,421 from MIT, plus 3rd party in-kind contributions of $225,327 from NuFuels LLC, and $224,027 from Earth Force Technologies.

Investigation Team

Massachusetts Institute of Technology

Dr. Raymond L. Speth (P.I.), All Tasks
Dr. Sebastian Eastham (co-investigator), All Tasks
Clara Ziran Ma (graduate research assistant), Tasks 2 and 3
Helena McDonald (graduate research assistant), All Tasks

Aerospace Corporation

Dr. Martin Ross (co-investigator), Task 1

Project Overview

The growth rate of the commercial space industry is projected to be at least 7% per year over the coming decades, thereby supporting rapid advancement in Earth observation, telecommunications, navigation technology, and space exploration. This development is supported by a rapidly growing launch industry: 180 launches were performed globally in 2022 alone (Witze, 2023).

Depending on the propellant used in each launch vehicle, the resulting emissions can have widely varying impacts on atmospheric chemistry. Species such as hydrogen chloride, aluminum, or nitrogen oxides (NO_x) can deplete ozone in the stratosphere, whereas others, such as methane (CH_4) and H_2O, can contribute to significant radiative forcing.

Given the projected rapid growth in launch numbers over the coming decades, quantitative data are needed to assess the magnitude of the impacts of emissions on atmospheric chemistry and thereby support robust decision making. The work performed under ASCENT Project 091A is designed to provide such data, and comprises four parts:

1. Development of future scenarios for the launch industry.
2. Creation of emissions inventories for launch vehicles for each scenario.
3. Refinement, running, and gathering results of GCHP simulations for each scenario.
4. Quantifying the environmental impacts of each scenario.

The ASCENT Project 091A team will first analyze the past growth rate of the launch industry and project the number of launches that will occur in 2050, their spaceport of origin, and the fuel used. Our team will then create and examine three future scenarios for the launch industry in 2050: one in which methane vehicles are dominant, one in which hydrogen (H_2) vehicles are dominant, and one in which kerosene (Rocket Propellant-1 [RP-1]) vehicles are dominant. Emissions inventory will then be created from the launch profiles of the vehicles, considering the rocket model, launch trajectory, and distribution by spaceport. The launch emissions' impact on atmospheric chemistry is simulated with GCHP. The output of the model is used to quantify the steady-state impact of the launch emissions on air quality, ozone, and radiative forcing.

References

Witze, A. (2023). 2022 was a record year for space launches. *Nature*. https://www.nature.com/articles/d41586-023-00048-7

Task 1 – Creation of Emissions Inventories for Launch Vehicles

Massachusetts Institute of Technology and Aerospace Corporation

Objective

Using the three future scenarios developed in the previous year of this project, emissions inventories needed to be developed for the three scenarios: (1) CH_4-fueled vehicles, (2) hydrogen (H_2)-fueled vehicles, and (3) RP-1-fueled vehicles.

Research Approach

A constant mass payload, target orbit, and flight trajectory were calculated for every launch vehicle. An emissions profile was created for the dominant vehicle in each scenario: CH_4-, H_2-, and RP-1-fueled vehicles. A script to rescale the emissions profile to fit the gridding structure of GEOS-Chem[1] was created and can be adjusted for other atmospheric chemistry models, such as Whole Atmosphere Community Climate Model (WACCM). This GEOS-Chem script was provided to ASCENT Project 091B. A script was created to generate input files for GEOS-Chem simulations: this script combines the emissions profiles from individual launches, the latitudes and longitudes of the spaceports, and the distribution of launches by spaceport. This script was provided to ASCENT Project 091B. Input files were generated for each of the three scenarios (CH_4-, H_2-, and RP-1-fueled vehicles) in preparation for GEOS-Chem simulations.

Milestone

- Created initial emissions inventories for the CH_4-, H_2-, and RP-1-fueled vehicles in the previous project year. In this project year, an error was discovered in the RP-1 inventory, so a corrected inventory for RP-1 was created.

[1] GEOS-Chem is a global three-dimensional model of atmospheric chemistry driven by meteorological input from the Goddard Earth Observing System (GEOS) of the National Aeronautics and Space Administration Global Modeling and Assimilation Office.

Major Accomplishments
Task 1 was determined to be complete in 2024.

Publications
None.

Outreach
Progress on all ASCENT Project 091A tasks was communicated in biweekly calls with the FAA, as well as collaborators at the University of Illinois Urbana-Champaign (from ASCENT Project 091B) and Aerospace Corporation. A summary of updates was presented at the Aviation Emissions Characterization (AEC) Roadmap meeting in May 2024, and the fall ASCENT meeting in Virginia in October 2024.

Awards
None.

Student Involvement
During the current reporting period, the MIT graduate students involved with Task 1 were Clara Ziran Ma and Helena McDonald.

Plans for Next Period
Task 1 is complete.

References
None.

Task 2 – Refining and Running GEOS-Chem High-Performance (GCHP) Simulations

Massachusetts Institute of Technology

Objective
To calculate the effects of the previously developed launch scenarios, the GCHP model needed to be modified to include the launch emissions from each scenario, and to allow for simulation of 2050 rather than the present day.

Research Approach
Previously as part of this project, GCHP was refined and updated to include input for launch emissions, in addition to existing inputs for background anthropogenic emissions, meteorology, and emitted chemical species. Several short GCHP test runs were completed to verify that the total mass and distribution of the species across the latitudes, longitudes, and altitudes are correct. The GCHP test run results and run configurations were compared with those of University of Illinois Urbana-Champaign's simulations using the WACCM to verify that the runs are comparable.

At the start of this period of performance, there were remaining necessary modifications to the GCHP code to include the boundary conditions and background emissions specified in the Intergovernmental Panel on Climate Change's (IPCC) Shared Socioeconomic Pathway (SSP) scenario SSP245. Once these were complete, the final four simulation runs would then be executed. Preliminary 1-year runs were completed.

During the current period of performance, these modifications were completed, and full chemistry was activated in the mesosphere (50-80 km altitude). Four simulations (baseline, RP-1, CH_4, and H_2) were conducted for 10 years at C24 resolution (approximately 400 km). The data from these simulations were used to analyze the three scenarios' impact on ozone and black carbon chemistry. Results from this analysis were presented as part of the ASCENT 2024 Fall Meeting.

Milestones
- Modified the GCHP source code to extend mesospheric chemistry for certain species above 50 km of altitude to the model top at 80 km altitude.

- Conducted four simulations of the baseline, RP-1, CH_4, and H_2 simulations for 10 years at C24 resolution, until the atmosphere reached a steady state.

Major Accomplishments
- Completed the baseline, RP-1, CH_4, and H_2 GCHP simulations with mesospheric chemistry added.

Publications
None.

Outreach
Progress on all ASCENT Project 091A tasks was communicated in biweekly calls with the FAA, as well as collaborators at the University of Illinois Urbana-Champaign (from ASCENT Project 091B) and Aerospace Corporation. A summary of updates was presented at the AEC Roadmap meeting in May 2024, and the fall ASCENT meeting in Virginia in October 2024.

Awards
None.

Student Involvement
During the current reporting period, the MIT graduate students involved with Task 2 were Clara Ziran Ma and Helena McDonald.

Plans for Next Period
- Make a second mesospheric chemistry modification to GCHP to adjust the ozone chemistry at high altitudes. Although chemistry has been added for altitudes from 50 km to 80 km in GCHP, there is an excess accumulation of ozone in the mesosphere.
- Execute the final four high-resolution simulations for the baseline scenario, CH_4 scenario, H_2 scenario, and RP-1 scenario. Each simulation will be set in the year 2050, with a duration of 10 years, and will be executed at a grid resolution of C90.
- Rerun the 10-year simulations at a higher horizontal resolution (a minimum of C48, or 200 km) for the purposes of publication.
- Run a series of radiative transfer simulations over the final simulation year to determine the radiative forcing (RF) for each launch scenario.
- Conduct an analysis of baseline conditions between GCHP and WACCM in conjunction with ASCENT Project 091B.

References
None.

Task 3 – Quantifying Environmental Impacts of Emissions from Each Scenario

Massachusetts Institute of Technology

Objective
After the modifications to GCHP described in Task 2, Task 3 is aimed at quantifying how atmospheric composition and metrics of environmental impact, including ozone depletion and air quality, are affected by the choice of future launch vehicle scenario.

Research Approach
Analysis of the results of the four completed simulations (baseline, RP-1, CH_4, and H_2) was conducted. The first species of interest is ozone. Graphs of the net change in ozone due to emissions from each launch vehicle type were created, including the change in ozone column, and the change in ozone mass concentration. Figure 1 displays zonal mean plots of the net change in mass concentration of ozone between the RP-1, CH_4, and H_2 simulations. In general, for all three launch vehicles, there is a slight increase in ozone in the stratosphere, centered at around 20 km altitude, and towards the poles.

The magnitude of this increase is highest with the RP-1 launch vehicles, with the highest concentration being about 20 μg/m^3. The ozone increase is second highest with CH_4 launch vehicles at about 6 μg/m^3.

The specific chemical mechanisms causing this increase in ozone could potentially be a decrease in photolysis rates (Matsumi & Kawasaki, 2003), due to the accumulation of stratospheric black carbon in the RP-1 and CH_4 scenarios, which would block a portion of incoming solar radiation.

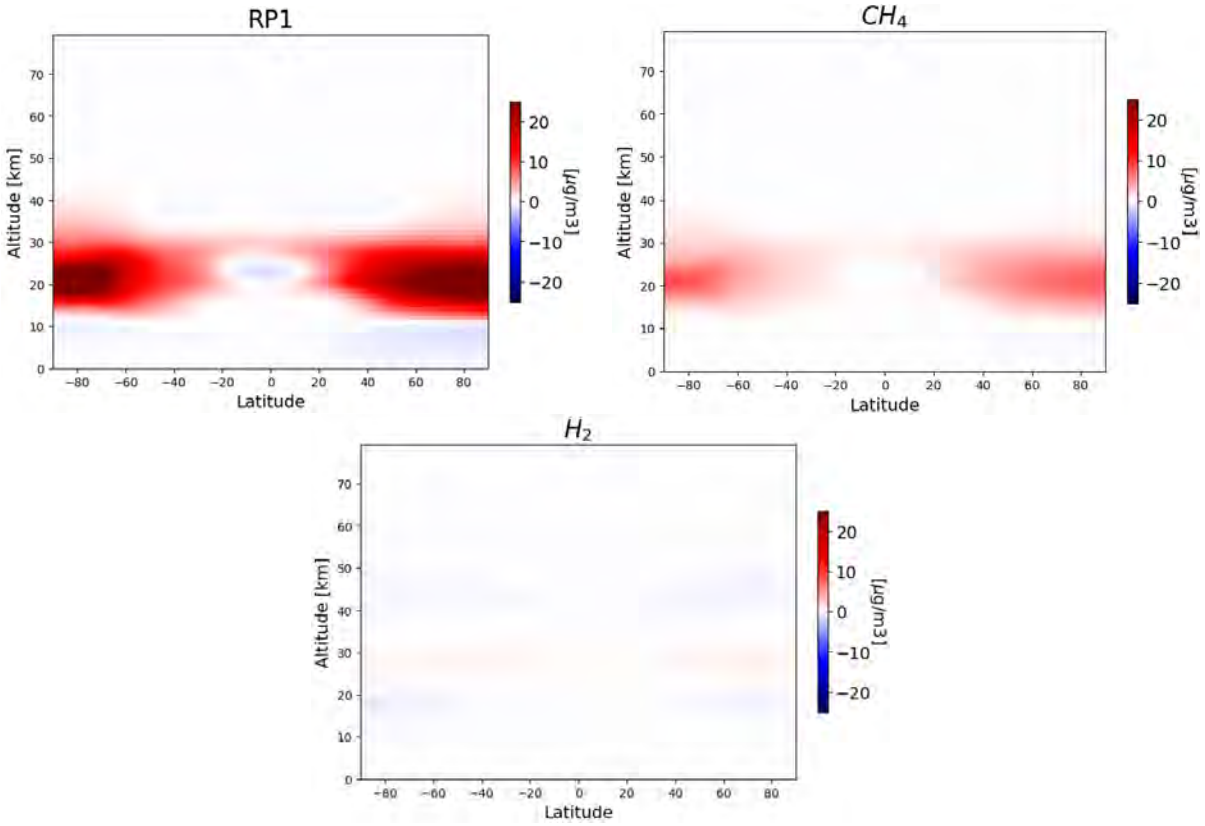

Figure 1. Net change in the mass concentration (μg/m^3) of ozone in the atmosphere as a result of RP-1, CH_4, and H_2 launch emissions respectively. The net ozone impact in the stratosphere, centered around 20 km altitude, and concentrated towards the poles, is positive in all three scenarios. The magnitude is highest in the RP-1 scenario, followed by the CH_4 and H_2 scenarios.

Milestone

- Conducted analysis of output from the four completed simulations, focusing on changes in ozone.

Major Accomplishments

- Quantified net impacts of launch emissions in each scenario on ozone column and ozone mass concentration.

Publications

None.

Outreach

Progress on all ASCENT Project 091A tasks was communicated in biweekly calls with the FAA, as well as collaborators at the University of Illinois Urbana-Champaign (from ASCENT Project 091B) and Aerospace Corporation. A summary of updates was presented at the AEC Roadmap meeting in May 2024, and the fall ASCENT meeting in Virginia in October 2024.

Awards
None.

Student Involvement
During the current reporting period, the MIT graduate students involved with Task 3 were Clara Ziran Ma and Helena McDonald.

Plans for Next Period

- Conduct further analysis will be conducted of the output from these four simulations. For example, Hovmöller plots will be created to assess seasonal changes in ozone concentration.
- Run further simulations, including radiative forcing calculations, using the output from the current simulations. Other simulations including sensitivity tests may be completed to better understand the chemical mechanisms causing the increase in ozone.
- After additional modifications are made to the GCHP code to correct the ozone chemistry in the mesosphere, conduct the four simulations (baseline, RP-1, CH_4, H_2) at a higher resolution of C90 (approximately 100 km).

References
Matsumi, Y., & Kawasaki, M. (2003). Photolysis of Atmospheric Ozone in the Ultraviolet Region. *Chemical Reviews, 103*(12), 4767-4782. https://doi.org/10.1021/cr0205255

Project 091(B) Environmental Impacts of High-altitude and Space Vehicle Emissions

University of Illinois at Urbana-Champaign

Project Lead Investigator

Dr. Donald Wuebbles
Department of Atmospheric Sciences
University of Illinois
105 S. Gregory Street
Urbana, IL 61801
217-244-1568
wuebbles@illinois.edu

University Participants

University of Illinois at Urbana-Champaign

- P.I.: Dr. Donald Wuebbles
- FAA Award Number: 13-C-AJFE-UI-048
- Period of Performance: January 1, 2023, to September 30, 2024 (partial year; project started January 1, 2023)
- Tasks:
  1. Examine the environmental impacts of technologies related to scenarios for extensive potential use of high-altitude vehicles, including rockets, and their associated emissions by mid-century
  2. Coordinate with Massachusetts Institute of Technology (MIT) and Aerospace Corporation in these studies

Project Funding Level

Project funding support from the Federal Aviation Administration (FAA) over this time period was approximately $175,000; an additional $175,000 of in-kind matching support was provided by the University of Illinois.

Investigation Team

Dr. Donald Wuebbles (P.I.), project oversight

Swarnali Sanyal and Rachana Pradhan (postdoctoral associates), conducting studies and performing analyses with the Community Earth System Model Whole Atmosphere Community Climate Model (WACCM), a three-dimensional atmospheric climate-chemistry model including the whole atmosphere.

Task 1 – Revisiting High-Speed Civil Transports and Their Potential Effects on Ozone and Climate

University of Illinois at Urbana-Champaign

Major Goals

This project uses state-of-the-art modeling capabilities for atmospheric climate and chemistry processes in association with expert analysis to develop an assessment of the potential impacts of rockets (i.e., high-altitude and space vehicle emissions) on the global environment, specifically the compositions of gases and particles in the global atmosphere (troposphere, stratosphere, mesosphere, and above) and the resultant potential impacts on the Earth's climate. These analyses are useful for policymakers to understand the potential effects of projected rocket emissions on the environment.

Objectives

This project uses state-of-the-art geophysical models of the Earth's climate and chemistry system that fully represent atmospheric processes from the ground to the top of the mesosphere (and above), to further improve understanding and evaluation of the environmental impacts of technologies related to scenarios for extensive potential use of high-altitude vehicles, including rockets, and their associated emissions by mid-century (approximately the year 2050). The aim, in coordination with the FAA, the Aerospace Corporation (which will develop the rocket emission scenarios), and Massachusetts Institute of Technology (MIT) (which will also use its global modeling capabilities) is to further assess the state of understanding of potential high-altitude and space vehicle emissions on the global environment, and to publish these analyses in major science journals.

Research Approach

The study uses the state-of-the-art WACCM model that is part of the range of models within the Community Earth System Model (CESM), developed through community-coordinated efforts by the National Center for Atmospheric Research (NCAR). The version of the WACCM model used here has 66 layers from the ground to above the mesosphere and provides a comprehensive treatment of tropospheric and stratospheric (and above) chemical processes. WACCM is one of the most advanced models worldwide for studying atmospheric processes and one of the few with a complete representation of stratospheric and mesospheric processes and higher; for example, it is one of very few models to represent the quasi-biennial oscillation that is important to stratospheric ozone. It has a comprehensive treatment of gas phase, particle based and heterogeneous chemistry. This model extends higher in the atmosphere than any other atmospheric model in existence except for another version of this model that goes even higher (to be considered for later studies but it is computationally very expensive). Therefore, the model used here is ideal for studying the environmental impacts from rockets.

Results and Discussion

Emissions from rockets and their effects on stratospheric ozone have been a subject of research since the 1970s (e.g., Prather et al., 1990; Harris & Wuebbles, 2014; Dallas et al., 2020). However, research in this area has comprised largely incomplete evaluations and has relied on poorly understood emission assumptions. A major need exists for assessment of the state of the science for understanding the environmental impacts according to the most up-to-date understanding of the potential future annual rocket emissions over the coming decades. Below, the existing research is summarized relating to such emissions.

More satellites have been launched into low Earth orbit during the past few years than during the previous 60 years, as a result of a combination of larger rockets and higher launch rates. Most of this growth has come from kerosene-fueled rockets, from which black carbon (BC) emissions have doubled in the past four years (Miraux, 2022). Emissions from solid fuel rockets have increased only slightly. Hydrazine-fueled rocket launches have decreased during this period, because of propellant toxicity concerns. Hydrogen-fueled launches have been constant but have represented only a small fraction of all launches. Methane-fueled rockets in advance testing are expected to play a major role in the future, although the rate at which methane would replace existing rocket fuel is uncertain.

Rocket propulsion systems typically combine the exhausts from several of the four primary propellant types (by fuel: kerosene, ammonium perchlorate, hydrazine, and hydrogen). Mixed rocket emissions into the stratosphere are mostly (>90% of approximately 8 Gg/yr) a combination of carbon dioxide (CO_2), carbon monoxide (CO), H_2O, and hydroxide (OH); the exact amounts vary, depending on propellant and altitude. None of these major emission components significantly affect stratospheric ozone, even at implausibly higher launch rates (Larson et al., 2017). Nitrogen oxide emissions (<1%) from some rocket types can affect ozone (Ross et al., 2004), although to a lesser degree than solid fuel chlorine emissions.

Direct ozone loss caused by chlorine emissions (0.2 Gg/yr) from solid fuel rockets is well understood. Models agree on the amount and distribution (Voigt et al., 2013). Alumina emissions from solid fueled rockets (0.4 Gg/yr) cause ozone loss through heterogeneous chlorine-involving Cl_y activation reactions; the importance of these reactions are less well bounded because of uncertainties in the alumina surface area density, the extent of sulfate coating, and reaction coefficients (Danilin et al., 2003). In situ plume data suggest that ozone loss from alumina might be larger than that from chlorine (Danilin et al., 2001).

Indirect ozone loss caused by the absorption and scattering of solar radiation by rocket BC and alumina particles in the stratosphere has not yet been investigated. General principles of stratospheric processes suggest that rocket BC and alumina increase heating rates and temperatures in the stratosphere, and cause ozone loss (Lee et al., 2021). Linear scaling of solid aerosol climate mitigation models and models of rocket BC emissions (Maloney, 2022) suggest that the

ozone loss from rocket BC and alumina stratospheric heating is comparable to that from chlorine emissions (Weisenstein et al., 2015).

Hydrogen-fueled projected space travel has been estimated to enhance stratospheric water by as much as 9%, thus leading to a potential 20% increase in polar stratospheric clouds in both hemispheres (Larson et al., 2017). An even larger effect of hydrogen-based space travel may arise from the expected increases in stratospheric nitrogen oxides, which, combined with hydrogen oxide (HO_x) cycle perturbations, leads to a 0.5% loss of the globally averaged ozone column, with column losses in the polar regions exceeding 2%.

New space technologies, such as large low Earth orbit constellations and active removal of space debris, dispose of derelict spacecraft into the middle atmosphere. The effects of stratospheric aerosols generated by destruction of space debris during reentry is a new area of research (Boley & Byers, 2021). Reentry vaporization and lower mesosphere particle production and sedimentation are a source of stratospheric particles likely to exceed present-day launches by 2030 (Boley & Byers, 2021). Very little is known regarding the composition, sizes, and steady-state distribution of reentry particles, or their possible impact on stratospheric ozone.

Three scenarios have been developed through our coordination with ASCENT Project 091A at MIT. These scenarios for 4,000 launches per year projected to occur annually by 2050 were evaluated with the WACCM model. These scenarios correspond to assuming the use of (1) fossil fuel, (2) methane fuel, and (3) hydrogen fuel. A series of meetings has been jointly held with MIT and Aerospace Corporation over the past project year towards not only developing the scenarios, but also to coordinate the modeling studies done with WACCM and with the MIT model. Our team is coordinating with MIT to evaluate the results from the model calculations and to complete a joint journal paper.

Milestones

- Prepared emissions for three scenarios developed by Aerospace Corporation for the modeling studies in coordination with MIT.
- Completed modeling studies for the scenarios and largely completed analyses for comparison with similar modeling studies made by MIT for the potential impacts on ozone and climate. That comparison is now underway, and the journal article is being written.

These studies will provide important context for further studies of rocket use projections, which our team will be examining next.

Publications

None. Journal article being completed.

Outreach Efforts

- Presented at ASCENT Meetings in October 2023, May 2024, and October 2024.
- Presented at the FAA Aviation Emissions Characterization (AEC) Roadmap meeting in November 2023 and October 2024.
- Participated in biweekly meetings with the project manager.
- Participated in monthly International Civil Aviation Organization (ICAO) Impacts and Science Group (ISG) meetings (Dr. Wuebbles).

Student Involvement

Two postdoctoral associates, Swarnali Sanyal and Rachana Pradhan, were responsible for the analyses and modeling studies within the project, and for leading the preparation of the journal article.

Plans for Next Period

- Complete and publish studies based on the rocket emissions scenarios, in coordination with MIT and Aerospace Corporation
- Complete development of additional scenarios to examine potential rocket launch issues and key questions to enhance understanding of the envelope (range) of potential impacts on ozone and climate from such vehicles. Complete modeling studies for these new scenarios.

References

Boley, A. C., & Byers, M. (2021). Satellite mega-constellations create risks in Low Earth Orbit, the atmosphere and on Earth. *Scientific Reports, 11*(1), 10642. https://doi.org/10.1038/s41598-021-89909-7

Dallas, J. A., Raval, S., Alvarez Gaitan, J. P., Saydam, S., & Dempster, A. G. (2020). The environmental impact of emissions from space launches: A comprehensive review. *Journal of Cleaner Production, 255*, 120209. https://www.sciencedirect.com/science/article/pii/S0959652620302560

Danilin, M. Y., Popp, P. J., Herman, R. L., Ko, M. K. W., Ross, M. N., Kolb, C. E., Fahey, D. W., Avallone, L. M., Toohey, D. W., Ridley, B. A., Schmid, O., Wilson, J. C., Baumgardner, D. G., Friedl, R. R., Thompson, T. L., & Reeves, J. M. (2003). Quantifying uptake of HNO_3 and H2O by alumina particles in Athena-2 rocket plume. *Journal of Geophysical Research: Atmospheres, 108*(D4). https://agupubs.onlinelibrary.wiley.com/doi/abs/10.1029/2002JD002601

Danilin, M. Y., Shia, R.-L., Ko, M. K. W., Weisenstein, D. K., Sze, N. D., Lamb, J. J., Smith, T. W., Lohn, P. D., & Prather, M. J. (2001). Global stratospheric effects of the alumina emissions by solid-fueled rocket motors. *Journal of Geophysical Research: Atmospheres, 106*(D12), 12727-12738. https://agupubs.onlinelibrary.wiley.com/doi/abs/10.1029/2001JD900022

Harris, N. R. P., & Wuebbles, D. J. (Eds.). (2014). *Chapter 5 in Scientific Assessment of Ozone Depletion: 2014, Scenarios and information for policymakers* (Vol. Global Ozone Research and Monitoring Project – Report No. 55). Geneva, Switzerland: World Meteorological Organization.

Larson, E. J. L., Portmann, R. W., Rosenlof, K. H., Fahey, D. W., Daniel, J. S., & Ross, M. N. (2017). Global atmospheric response to emissions from a proposed reusable space launch system. *Earth's Future, 5*(1), 37-48. https://agupubs.onlinelibrary.wiley.com/doi/abs/10.1002/2016EF000399

Lee, W. R., MacMartin, D. G., Visioni, D., & Kravitz, B. (2021). High-Latitude Stratospheric Aerosol Geoengineering Can Be More Effective if Injection Is Limited to Spring. *Geophysical Research Letters, 48*(9), e2021GL092696. https://agupubs.onlinelibrary.wiley.com/doi/abs/10.1029/2021GL092696

Maloney, C. (2022). The Climate and Ozone Impacts of Black Carbon Emissions from Global Rocket Launches. *J. Geophys. Res., submitted*.

Miraux, L. (2022). Environmental limits to the space sector's growth. *Science of The Total Environment, 806*, 150862. https://www.sciencedirect.com/science/article/pii/S0048969721059404

Prather, M. J., García, M. M., Douglass, A. R., Jackman, C. H., Ko, M. K. W., & Sze, N. D. (1990). The space shuttle's impact on the stratosphere. *Journal of Geophysical Research: Atmospheres, 95*(D11), 18583-18590. https://agupubs.onlinelibrary.wiley.com/doi/abs/10.1029/JD095iD11p18583

Ross, M. N., Danilin, M. Y., Weisenstein, D. K., & Ko, M. K. W. (2004). Ozone depletion caused by NO and H_2O emissions from hydrazine-fueled rockets. *Journal of Geophysical Research: Atmospheres, 109*(D21). https://agupubs.onlinelibrary.wiley.com/doi/abs/10.1029/2003JD004370

Weisenstein, D. K., Keith, D. W., & Dykema, J. A. (2015). Solar geoengineering using solid aerosol in the stratosphere. *Atmos. Chem. Phys., 15*(20), 11835-11859. https://acp.copernicus.org/articles/15/11835/2015/

Project 092 Advanced Two-stage Turbine Rig Development

The Pennsylvania State University

Project Lead Investigator

Reid A. Berdanier
Associate Professor
Department of Mechanical Engineering
The Pennsylvania State University
START Lab, 3127 Research Drive
State College, PA 16801
814- 863-3972
rberdanier@psu.edu

University Participants

The Pennsylvania State University (Penn State)

- P.I.: Dr. Reid A. Berdanier
- FAA Award Number: 13-C-AJFE-PSU-104
- Period of Performance: January 1, 2023, to March 14, 2025
- Tasks:
  1. Oversee new turbine rig design
  2. Design motor generator to dissipate the turbine power
  3. Order remaining air compressor components and complete manufacturing

Project Funding Level

For the two-year effort, the Federal Aviation Administration (FAA) provided $2,000,000 and matching funds of $2,125,000 were provided by Pratt & Whitney® and Penn State.

Investigation Team

Reid A. Berdanier (P.I.), Management, reporting, and oversight of all technical tasks Karen Thole, Affiliate Professor, Tasks 1–3
Tom Houck, Project Manager, Tasks 1–3
Assoc. Res. Prof. Michael Barringer, Research Advisor, Tasks 1–3
Justin Brumberg, Research Engineer, Tasks 1–3
Jeremiah Bunch, Engineering Technician, Tasks 1–3
Asst. Res. Prof. Matthew Meier, Research Engineer, Tasks 1-3

Project Overview

This project will significantly advance the efficiency levels of small-core gas turbines relevant to current engines, as well as future propulsion architectures such as hybrid electric propulsion systems for large single- and twin-aisle aircraft. The motivation for this research is aimed at reducing the carbon footprint of aviation through increasing turbine thermal efficiency, while maintaining or even improving component durability. This project will expand the infrastructure and research scope of the Steady Thermal Aero Research Turbine (START) Lab at Penn State, in which a two-stage, small-core, test turbine will be designed, manufactured, commissioned, and put to use in acquiring the necessary data to meet the proposed goal. The new infrastructure will be referred to as START⁺. The proposed expansion will result in a research

® Pratt & Whitney is a registered trademark of RTX Corporation, Farmington, Connecticut.

turbine facility like no other in the world and will situate turbine research in the United States at the leading edge in efficiency improvement and emissions reduction for future propulsion applications.

Task 1 – Oversee New Turbine Rig Design

The Pennsylvania State University

Objectives

The objectives of this task include (1) overseeing the design of the new START⁺ turbine rig and laboratory expansion, (2) integrating the entire facility by having the mechanical engineering firm work with the building design firm to layout piping, building penetrations, supports, and ensure proper access for lab personnel, (3) ensuring the new compressors and test turbine can be appropriately accommodated in the new laboratory building, and (4) beginning the preliminary design of the rig layout, and confirming with Pratt & Whitney the entire scope of the test turbine.

In the oversight of the design of the new START turbine rig and laboratory expansions, this objective includes pursuing the selection of a turbine engineering firm by interviewing multiple firms and creating a request for quotation, to enable selection of the firm that best meets the cost, schedule, and quality requirements of the program. The new building construction (which is funded by the Penn State and Pratt & Whitney cost share) is required to meet the research objectives of this project since the current START Lab does not have enough space for the new START⁺ two-stage turbine rig and compressors. The new START⁺ building expansion will add more than 10,000 ft^2 of space to the START Lab to house the new research equipment, rig, and turbine.

Research Approach

The START Lab, Penn State's lead architect, and the Office of Physical Plant (OPP) drafted a specific request for proposal (RFP) to hire a new engineering firm to create the START⁺ building design. After reviewing proposals from firms all over the United States, Gannett Fleming (GF) was selected. They were the lowest cost and had the best technical proposal. A kickoff meeting was held on February 5, 2024, and since the team has made significant progress. The team worked together to layout all rooms and equipment using cloud drafting software and reviewing them during weekly updates. During early 2024, the floor plan, building concept, and storm water preliminary designs were completed that are shown in Figures 1 through 3.

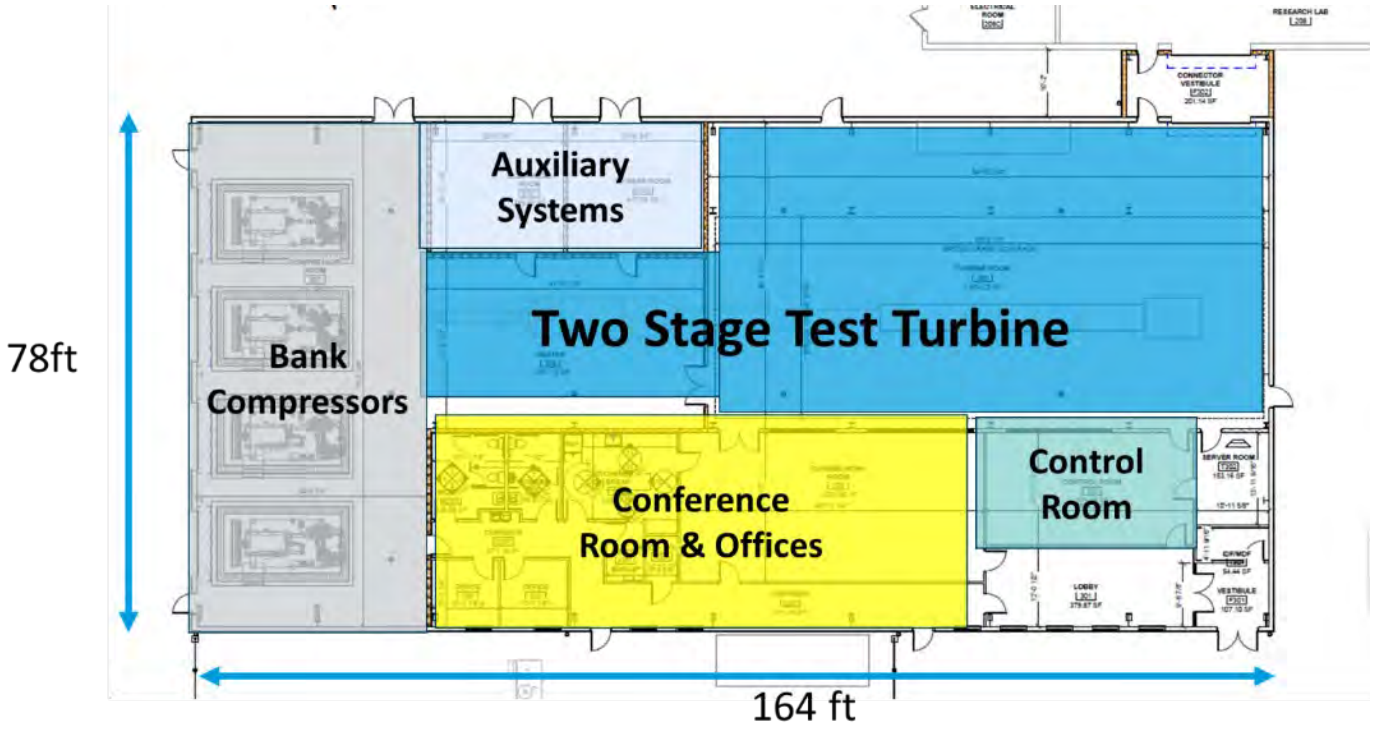

Figure 1. Floor plan of START⁺.

Figure 2. Conceptual START⁺ building.

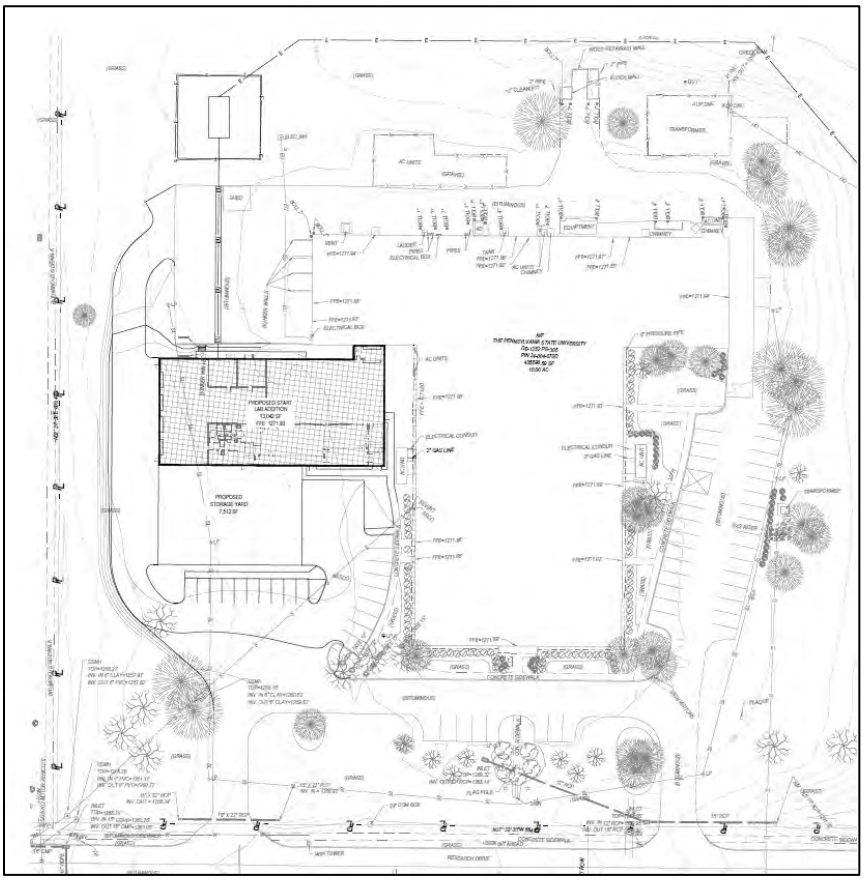

Figure 3. First submission of the START⁺ stormwater design.

The geotechnical engineering study of the START⁺ property site was generated during 2024 by GF related to the project critical path for the storm water design permit. The study was submitted to the local municipality government for their review and was approved. Water infiltration testing within selected basins on the property site was also completed. Because of the approval of the geotechnical study by the local government and the satisfactory infiltration testing results, the legal permit for the storm water management design was issued. Final land development permits by the local municipality are anticipated for issue during late 2024.

The START research group also worked during 2024 with GF to accomplish the 60%, 90%, and 100% completion milestones for the detailed design of the START⁺ laboratory addition. Significant progress was made on the detailed designs of the building addition, property stormwater management, and electrical systems including developing all details of the facility architecture, civil and structural designs, electrical and lighting plans, plumbing, fire safety, and telecommunications. Example excerpts from the detailed design completion package are shown in Figure 4. An updated solid model of the new START⁺ building addition is shown in Figure 5. After the detailed design 100% completion milestone was met, the project began coordinating the open-bidding process during the end of 2024 for construction companies to submit their proposals.

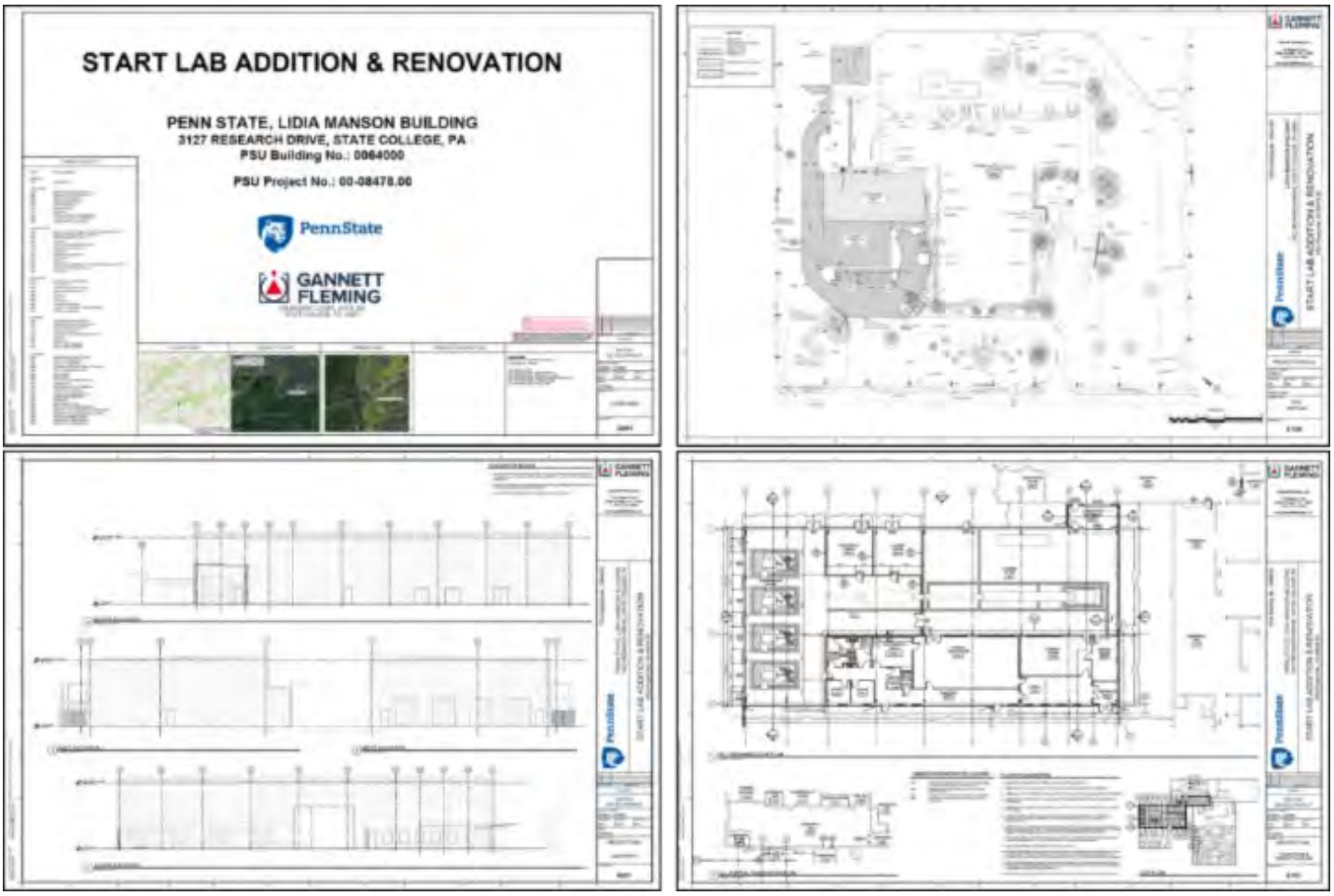

Figure 4. Detailed design of START+ (example excerpts).

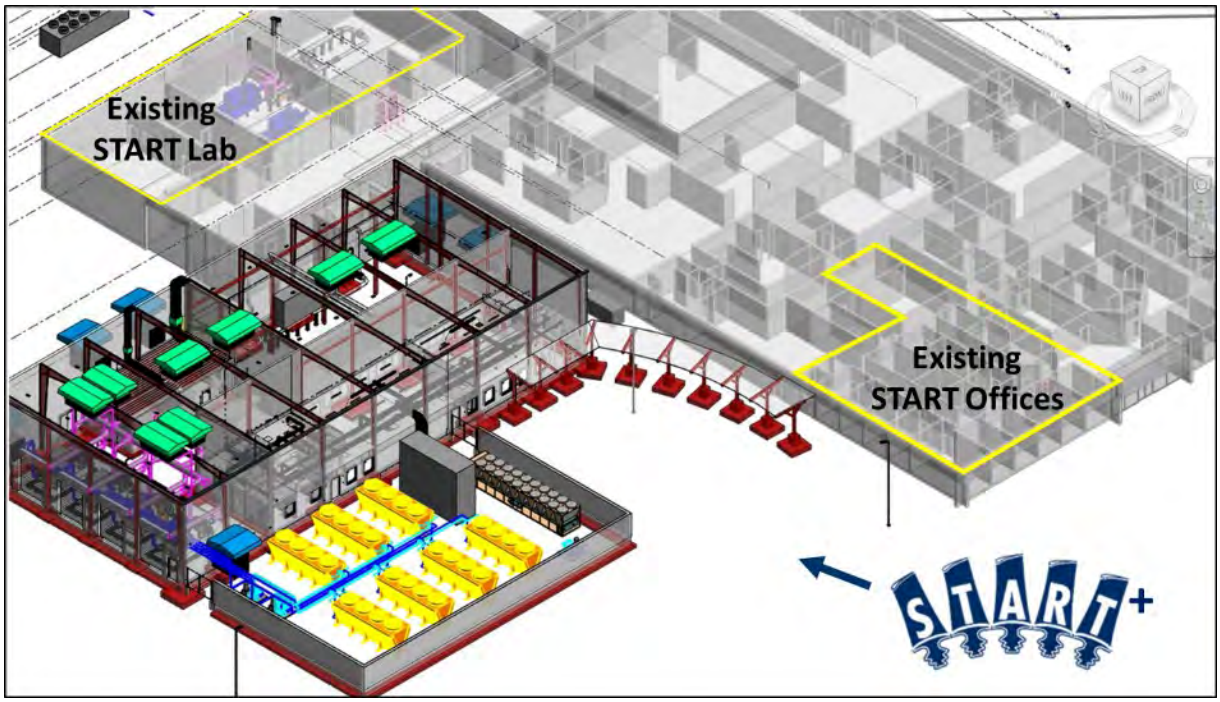

Figure 5. Updated solid model rendering of the new START⁺ building addition.

A schedule was developed in 2024 by the Penn State START team that enables the selection of an engineering design firm by the end of 2024 to begin design work on the START⁺ turbine integration plan. This plan includes the design firm working closely with both the START team and Pratt & Whitney to perform the detailed design of the hardware components that define the primary test section of the new two-stage turbine rig. The design scope for the START⁺ turbine test section is shown in Figure 6. A statement of work (SOW) and RFP were generated by the START team which were then submitted to multiple engineering design firms for review. The proposal bids from the design firms are due to Penn State at the end of November 2024 at which time they will be evaluated enabling the selection of the final design firm to take place.

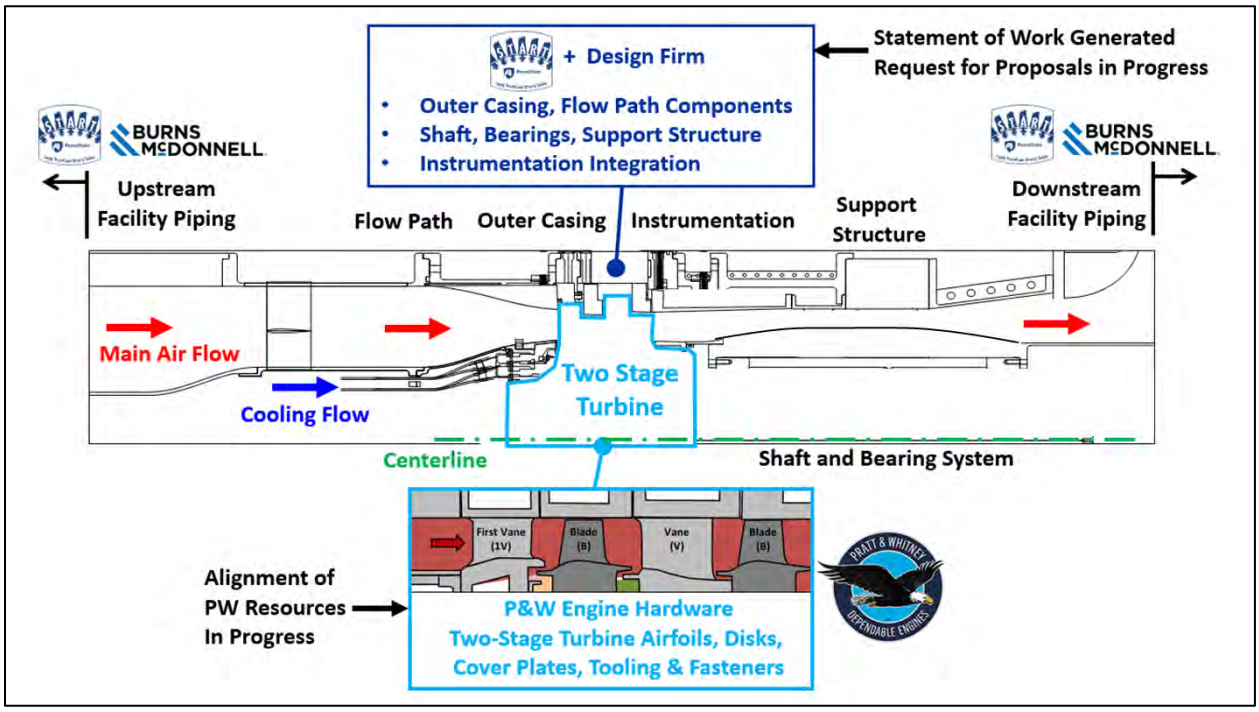

Figure 6. Design scope for the START⁺ two-stage turbine test section (cross-section diagram).

An interface control plan was also developed in 2024 related to the ownership of hardware design for the START⁺ two-stage turbine test section. All facility piping and equipment located upstream and downstream of the turbine test section will be the design responsibility of the Penn State START research group and design firm Burns and McDonnell (BMCD). The two-stage turbine hardware including the airfoils, disks, cover plates, and fasteners will be sourced by Pratt & Whitney directly from one of their current production aircraft engines. Pratt & Whitney in conjunction with the selected design firm will be responsible for designing any modifications to enable the engine hardware to be installed and operate within the START⁺ turbine test section. The hardware components within the turbine test section that define the outer casing walls, inner flow path walls, rotor shaft and bearing system, and bearing support structure will be the responsibility of the START research group and selected design firm. A summary of this interface control plan is shown in Figure 6.

The preliminary design of the rig process and equipment arrangements were also finalized during 2024 for the pipe network related to the large air compressors. The pipe network includes the air flow pipes and equipment necessary to deliver air flow from the compressors to the turbine test section, as shown in Figure 7. For each compressor, there are three main pipe branches including an inlet, exit, and unloading bypass. The inlet pipe branch directs air flow from outdoors to the compressor inlet using an intake filter housing located outdoors, a muffler silencer located indoors, and interconnecting pipes. The exit pipe branch directs airflow from the compressor exit to the turbine using a flow control valve and interconnecting pipes all located indoors. The unloading bypass branch is used temporarily each day during the startup and shutdown of the compressor and includes a flow control valve and muffler silencer both located indoors, and an exhaust pipe located outdoors. In addition to completing the preliminary design of the compressor pipe network, a RFP document was generated by the START research group and was submitted to BMCD that enabled the transition from preliminary design to the detailed design phase of their project work scope. Their proposal package was then received and is currently being reviewed by the START team to enable the detailed design work to begin as soon as possible.

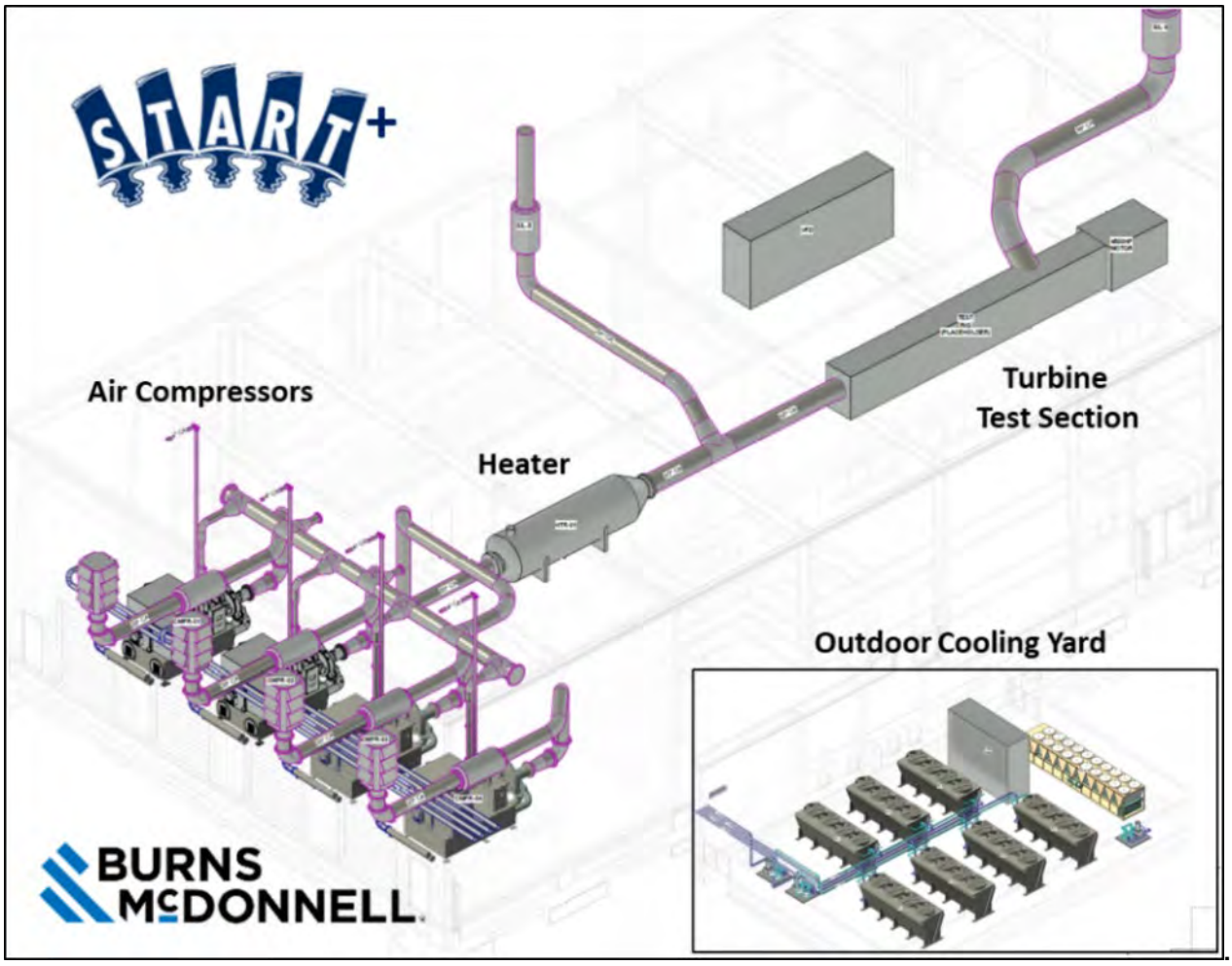

Figure 7. Preliminary design layout of the START⁺ rig piping and equipment integration.

The baseline sound study for outdoor noise on the property was also performed. This baseline study was performed by the START research group and the acoustics consulting firm SLR, which included sound level measurements at multiple locations on the property while the existing START laboratory had its equipment active in operational mode. The results of the baseline study indicated acceptable sound levels within the 54-62 dBA range as shown in Figure 8. The baseline results were combined with the sound level specifications of the new START⁺ equipment items in order to establish a total sound model and map for both the existing START rig and the START⁺ rig operating simultaneously. The new sound model and map were completed by SLR during 2024.

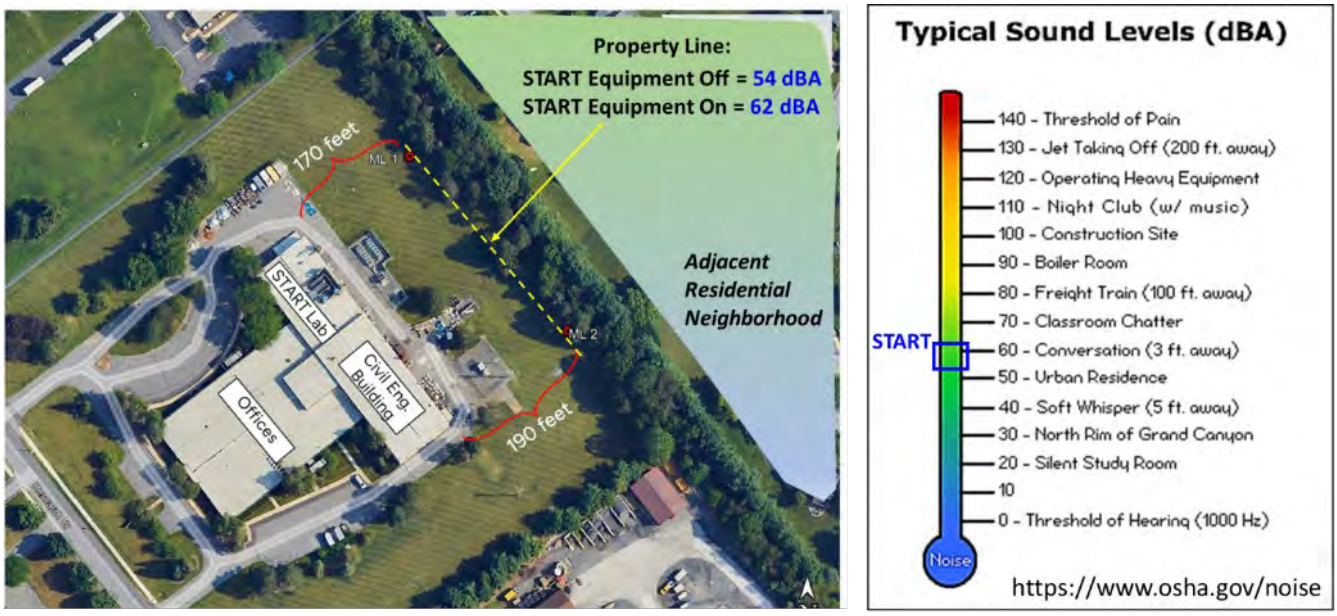

Figure 8. A baseline sound study was conducted for the existing START lab operation.

The START team worked with the exhaust vent silencer vendor to iterate on the preliminary design of the main exhaust silencer for air flow exiting the new START⁺ turbine. The focus was centered on the base structure and overall height of the vent silencer stack. The base structure will be designed for high temperature capability to avoid excessive thermal stress to the concrete foundation. The height of the silencer outlet from ground level was shortened to help reduce direct line of sight to the property line. The acoustics consultant firm SLR that was added to the team used their baseline sound survey results of the existing START lab operation and combined the results with the sound specifications and layout of the new equipment for the START⁺ addition. The combined acoustics information was used to create a new detailed sound model of the entire START and START⁺ operation, which was used to identify additional noise mitigation measures needed to meet the sound ordinance for the property. A few of these noise mitigation measures include (1) extending the sound curtains on the existing roof platform to completely obstruct direct line of sight of all equipment items, (2) wrapping the existing START facility vent silencers with additional noise reduction material, and (3) installing at ground-level sound curtains adjacent to specific pieces of heat rejection equipment.

Task 2 – Design Motor Generator to Dissipate the Turbine Power

The Pennsylvania State University

Objectives

The objectives of this task are to create a request for quotation for a motor generator system to dissipate the turbine power, review all bids, and select the company that best meets the cost, schedule, and quality requirements of the program. Collaborate with the selected vendor to develop manufacturing drawings so the turbine and motor generator system layout can be completed.

Research Approach

To help with the mechanical equipment design for START⁺, the team continued to collaborate in 2024 with BMCD. BMCD is a large engineering firm with past experience in designing turbine test facilities similar to START⁺. BMCD and START selected ACS to provide a motor generator solution. The ACS proposal met all technical requirements and was over $1 million less expensive than other vendor quotes. ACS will provide a 4,500-hp motor generator solution shown in Figure 9 that can absorb the targeted testing conditions from the START⁺ turbine. The solution also includes the auxiliary equipment required such as a gear box, oil system, variable frequency drive, and load bank to dissipate the power. The START Lab confirmed with the West Penn Power electric company that sending the turbine power back to the local

electricity grid is not an option for this project. West Penn Power requires continuous operation throughout the year. A purchase order was submitted to ACS in 2024 to perform the detailed engineering phase of the motor generator system. A preliminary layout plan of the motor generator equipment was also developed including the physical arrangement of the equipment components in the new turbine room as shown in Figure 10. An official project kickoff meeting was also held to review the preliminary design concept of the motor generator system components and overall project schedule.

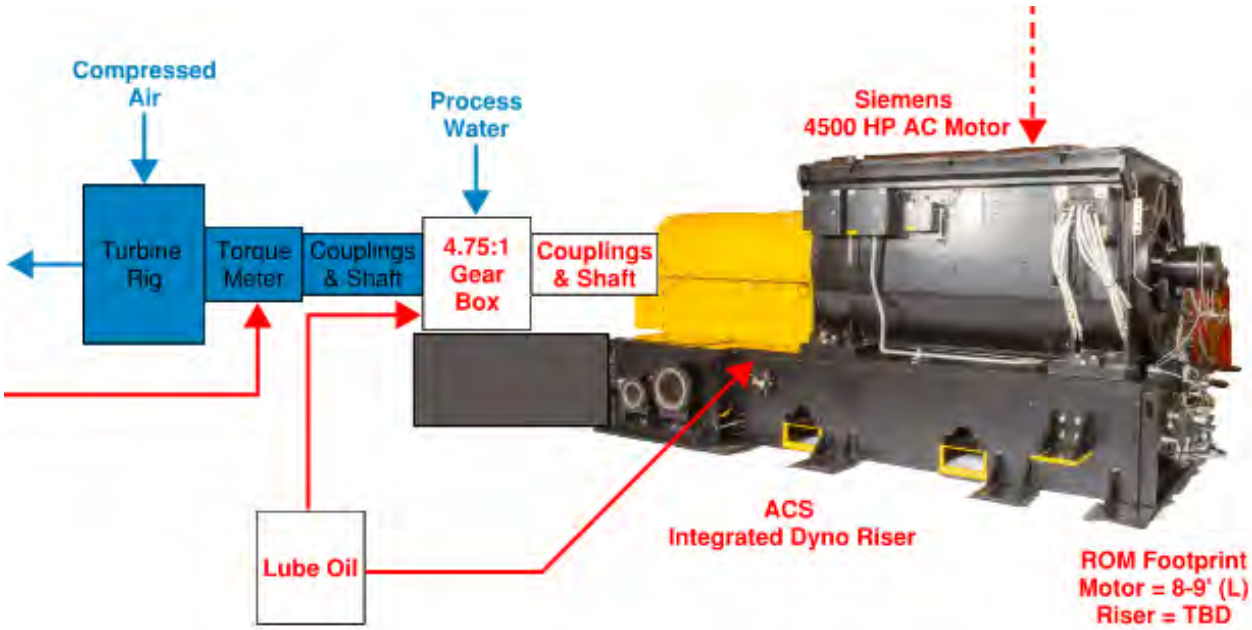

Figure 9. The ACS motor generator solution for START+ turbine power control.

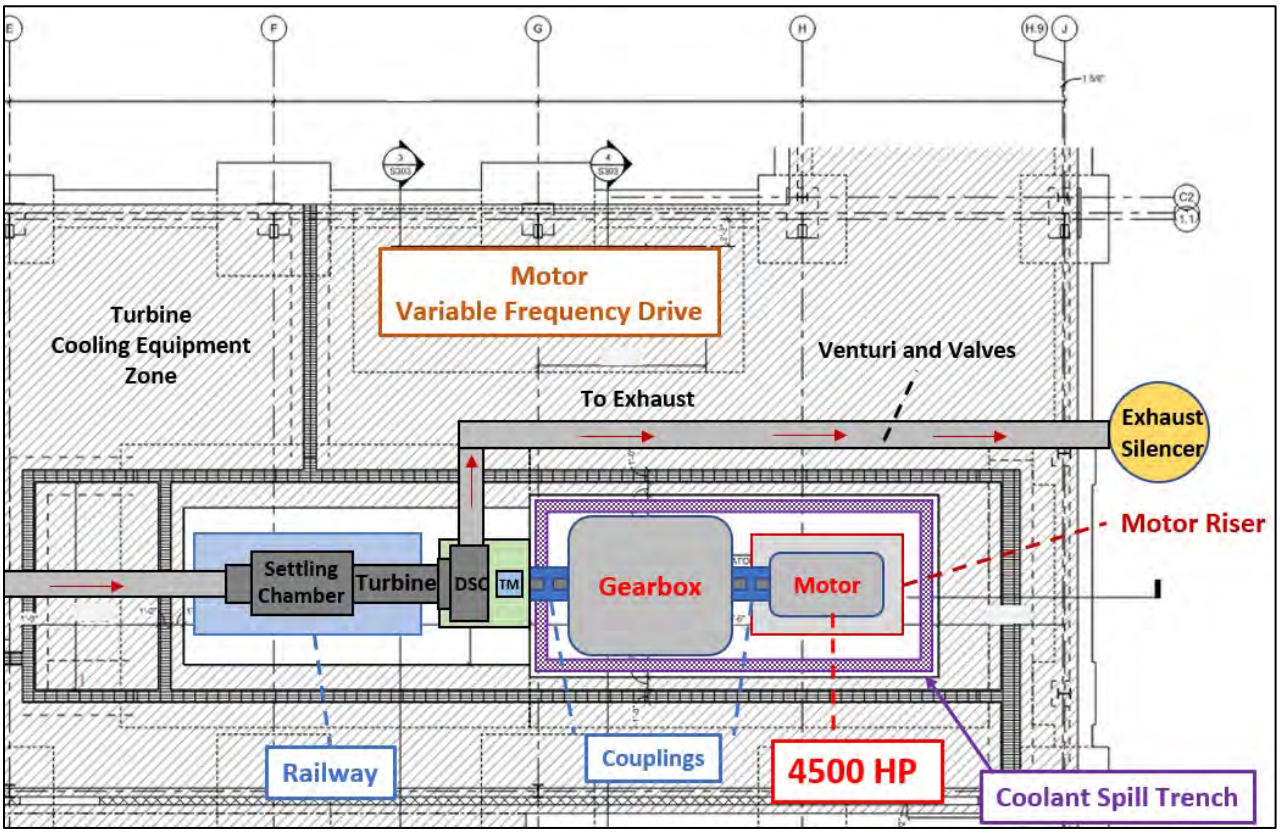

Figure 10. Preliminary layout of the motor generator equipment in the START⁺ turbine room.

Task 3 – Order Remaining Air Compressor Components and Complete Manufacturing.

The Pennsylvania State University

Objectives

The objectives of this task are to (1) review manufacturing quality documents related to the compressor starters, variable frequency drive (VFD) layout, cooler general arrangement drawings, and manufacturing reports, as well as to resolve non-conformances and approve final inspection reports, (2) attend factory performance testing and ensure the compressors meet all of the quoted performance metrics, review testing data such as hydrotests, flow, and pressure results, and (3) oversee the installation of equipment in START⁺ to ensure the compressors fit on their anchor bolts, are grouted in to place per the compressor vendor's requirements, and all lifting requirements are met.

Research Approach

The START research group continued to work in 2024 with the compressor manufacturer F.S. Elliott to complete the engineering design of the new air compressors and their subsystem equipment. Drawings of the compressors, motors, motor starters, and electronic control systems were obtained and reviewed. Drawings of the air intake systems, sound silencers, valves, and cooling systems were also obtained and reviewed. An updated sales quotation was obtained to allow a new purchase order to be submitted for manufacturing the compressors and subsystem equipment. A relatively small (5%) inflationary increase in cost was noted for the compressors in the updated 2024 sales quotation, compared to the original preliminary August 2023 quotation. However, this cost adjustment was able to be managed without any change overall project cost. A summary of the new START⁺ compressor designs is shown in Table 1 in relation to the existing START lab compressors. A drawing of the new F.S. Elliott air compressor that will be installed in START⁺ is shown in

Figure 11 in its three-stage centrifugal configuration, along with selection notes for the compressor motor and motor starter.

Table 1. Summary of the START⁺ compressor designs.

Compressor Specification	Existing START	START⁺
Compressor Stages	2	3
Total Horsepower	3000	9000
Flow Rate per Unit	12 lbm/s	10 - 11 lbm/s
Discharge Pressure	60-80 psia	125 psia, 165 psia
Discharge Temperature	225°F	225°F, 110°F
Number of Compressors	2	2 + 2 = 4
Number of Outdoor Fluid Coolers	2	7

Turbine Main Gas Path Flow
Turbine Cooling Air Flow + Supplemental Flow

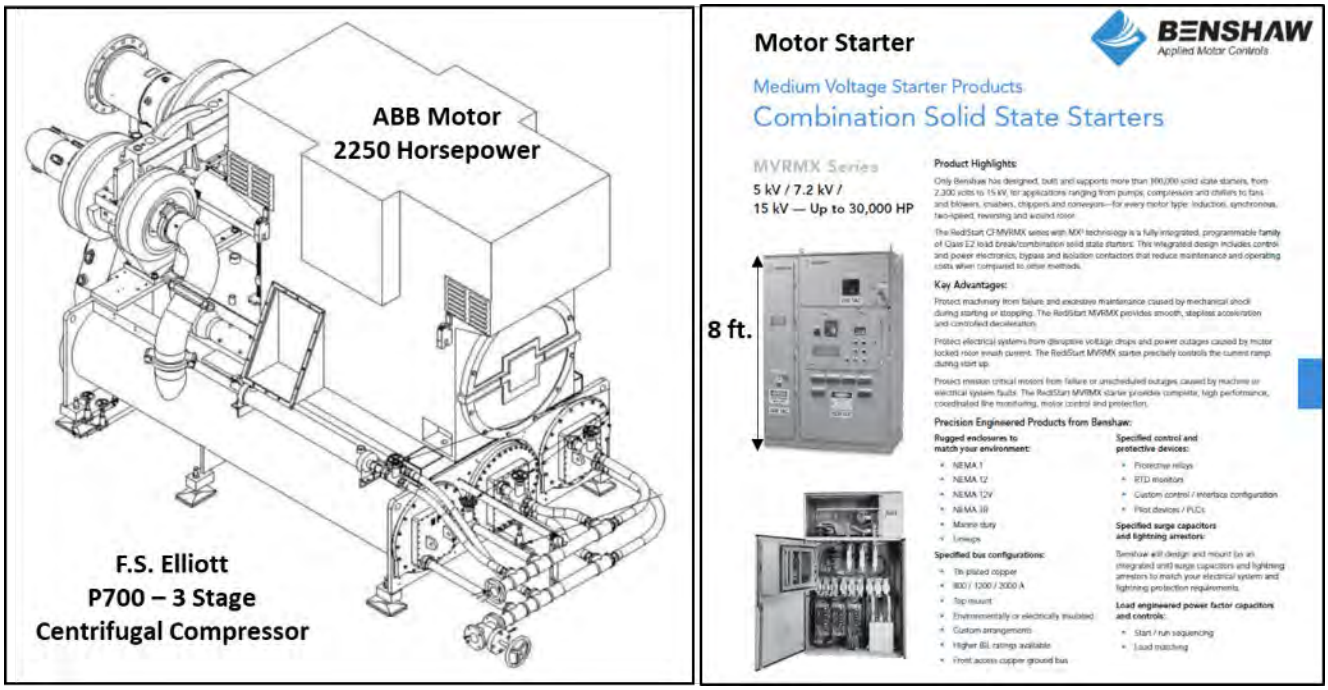

Figure 11. New START⁺ air compressor with motor and motor starter.

GF and West Penn Power completed the high voltage electrical design for supplying power to the four new air compressors. Preliminary sales quotations with lead times were obtained including 40-55 weeks for the main new 46 kV transformer that will be housed in a new substation yard shown in Figure 12. The transformer and switch gear equipment will be ordered during the initial phase of the building construction so that the overall schedule of the START⁺ project is not impacted.

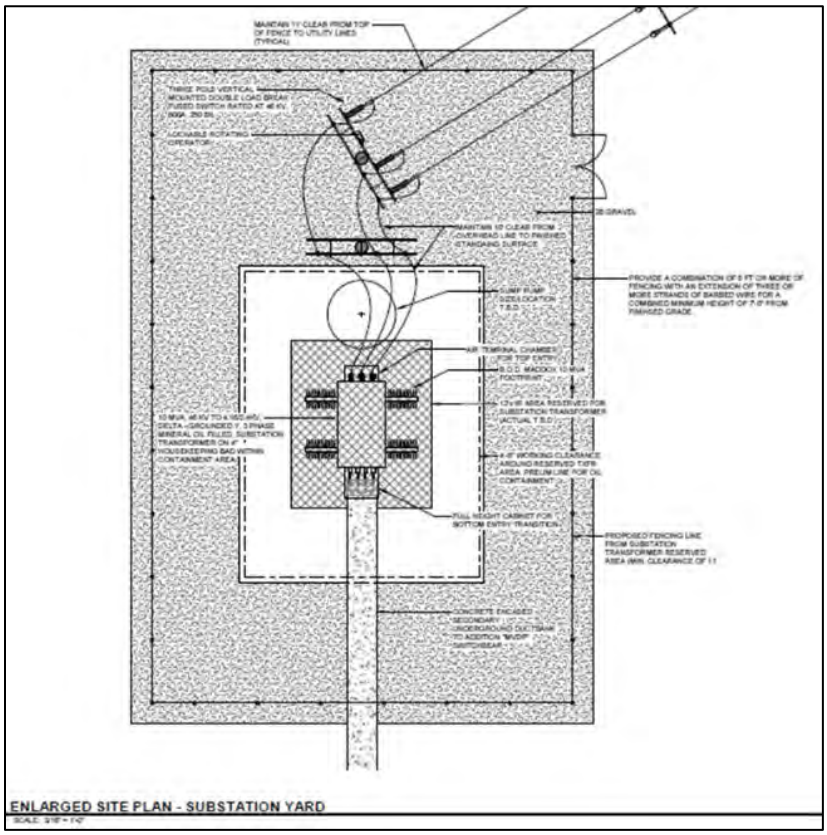

Figure 12. Design of the new electrical substation with main 46 kV transformer for the air compressors.

Milestones

Milestone	Completed or planned date
Design Development Kickoff with Gannett Flemming	February 1, 2024
60% Detailed Design Completed	March 18, 2024
90% Detailed Design Completed	July 9, 2024
Geological (Storm Water) Review Completed	July 18, 2024
100% Detailed Design Completed	August 30, 2024
Board of Trustees Approval	September 6, 2024
Compressors Ordered	October 31, 2024
Parking Study Completed	November 1, 2024
Groundbreaking Ceremony	November 8, 2024
Township Land Development Permit Submitted	November 11, 2024
Project Released for Bidding (Pending)	December 9, 2024

Major Accomplishments

Task 3.1- Review manufacturing quality documents related to the compressor starters, VFD layout, cooler general arrangement drawings, manufacturing reports, as well as, to resolve non-conformances and approve final inspection reports

GF was selected as the START+ building engineering design firm. They immediately began working on the program in February 2024 and kept the new building project on schedule.

An interface control plan was developed by the START research group related to the ownership of hardware design for the START+ two-stage turbine test section. The preliminary design of the rig process and equipment arrangements were also finalized for the pipe network related to the large air compressors. A RFP document was generated by the START group and was submitted to BMCD to transition from preliminary design to the detailed design phase of their project work scope. The START research group and GF completed the 60%, 90%, and 100% detailed design milestones for the new START+ building addition. The START group and SLR completed the baseline sound study for the existing START lab operation, and simultaneously acquired detailed sound level specifications for the new START+ equipment that were incorporated into the new sound model of the entire laboratory operation.

A schedule was developed by the Penn State START team that enables the selection of an engineering design firm by the end of 2024 to begin design work on the START+ turbine integration plan. A SOW and RFP were generated by the START team which were then submitted to multiple engineering design firms for review. The START team generated a SOW and RFP related to the detailed design phase of the rig piping and equipment integration. Both the SOW and RFP were submitted to BMCD for their review, and their proposal package was then received and is currently being reviewed. The START team and GF met the 100% completion milestone for the detailed design of the START+ laboratory building addition including the final design details of the building addition and electrical systems. The geotechnical engineering study of the START+ property site was completed related to the project critical path for the storm water design permit in which water infiltration testing within selected basins on the property site were completed.

Task 3.2 - Attend factory performance testing and ensure the compressors meet all of the quoted performance metrics, review testing data such as hydrotests, flow, and pressure results

START and BMCD selected ACS to provide the turbine power control solution. It will be a 4500-hp motor generator with associated equipment that will maintain the speed of the turbine and extract the energy from its shaft. A purchase order was submitted to ACS for the detailed engineering phase of the project to design the electrical motor dynamometer, gear box, oil system, variable frequency drive, and load bank to dissipate the power.

Task 3.3 - Oversee the installation of equipment in START+ to ensure the compressors fit on their anchor bolts, are grouted in to place per the compressor vendor's requirements, and all lifting requirements are met

An updated sales quotation was obtained for the new air compressor systems and their cooling systems to allow a new purchase order to be placed for their manufacturing. The purchase order for manufacturing was submitted in 2024.

All of the equipment details were reviewed necessary for submitting purchase orders for the engineering phase of (1) the ACS turbine motor generator system, (2) the heater chamber and process combustion system, and (3) the conceptual design of the new magnetic bearing system for the turbine rotor shaft. The purchase orders for the engineering phase of these equipment items will be submitted at the end of 2024.

Publications

Pennsylvania State University. (2024). Plan advances for addition, renovation to build START+ Lab at CATO Park. https://www.psu.edu/news/administration/story/plan-advances-addition-renovation-build-start-lab-cato-park

Outreach Efforts

Dr. Karen Thole presented in 2024 an update on the project to the American Institute of Aeronautics and Astronautics (AIAA) Science and Technology Forum and Exposition on January 9, 2024. The conference included multiple government agencies, academia, and industry representatives. On March 11, 2024, Dr. Anna Oldani, Arthur Orton, and Joshua Glottmann (all representing FAA ASCENT) visited START. Dr. Thole and the START team gave an update on the project to them along with the other START Ascent Grant. Finally, during the first quarter of 2024, the project was reviewed with multiple industry partners. The project was reviewed with Solar Turbines on January 18, 2024, during the semiannual

Center of Excellence Review. During the 2024 period, multiple Pratt & Whitney executives, including Geoff Hunt, Senior Vice President of Engineering were given updates on the project during visits to the lab.

During June 2024, the project was also presented to the several people that visited the START laboratory from the U.S. Department of Energy (DOE) National Energy Technology Laboratory including John Crane (Technology Manager). In August 2024, this project was presented to visitors from National Aeronautics and Space Administration (NASA) and Pratt & Whitney.

Dr. Reid Berdanier presented this work as part of program discussions at the Turbine Engine Technology Symposium in September 2024, in collaboration with the Propulsion Instrumentation Working Group. Dr. Berdanier also shared updates on this project at a DOE meeting in September 2024. Dr. Berdanier and Dr. Meier shared updates on the progress at a NASA meeting in October 2024.

In November 2024, an event was held at Penn State to celebrate the formal beginning of development efforts for a new construction project to house the equipment outlined in this project. The celebration was well-attended by guests from across Penn State, including the Board of Trustees, Deans, Vice Presidents, and University President. A collection of executive guests from Pratt & Whitney were also in attendance, including Senior Vice President Geoff Hunt and Senior Vice President of Engineering Michael Thacker. This event was also acknowledged through a local news report: https://www.wtaj.com/news/local-news/penn-state-announces-expansion-to-start-lab-to-expand-research/

Awards

None.

Student Involvement

Although no formal student support was included in this project for the reporting year, the students in the START Lab are provided regular updates on the status of this project through weekly team meetings.

Plans for Next Period

- Complete the detailed design of the two-stage test turbine.
- Begin procurement of the turbine components.
- Complete the designs of instrumentation including cameras and efficiency traverse.
- Attend weekly construction review meetings (Penn State START and OPP team) to ensure that the schedule and budget remain within the plan.
- Solve any issues as they arise between the new building contractor and Penn State OPP.
- Facilitate planning installation between the contractor and equipment vendors.
- Review quality documents to verify that all drawings and standards by the construction firm are maintained.
- Conduct walkthrough inspections with the design firm to ensure that drawing requirements and tolerances are within specifications.

During the next reporting period, the START team will also perform the following main steps to accomplish the goals and objectives of the project.

1. Oversee the beginning of construction on the new laboratory building addition.
2. Work with Pratt & Whitney and the selected design firm to begin the integration design of the two-stage turbine and primary test section.
3. Work with BMCD to begin the detailed design of the rig piping and equipment integration.
4. Oversee manufacturing and designing the major equipment items including the air compressors, cooling systems, motor generator, bearing system, and combustion heater.

Project 093(A) Collaborative Research Network for Global SAF Supply Chain Development

Massachusetts Institute of Technology

Project Lead Investigators

Dr. Florian Allroggen
Executive Director Aerospace Climate & Sustainability; Research Scientist
Laboratory for Aviation and the Environment
Massachusetts Institute of Technology
77 Massachusetts Ave, Building 33-328
Cambridge, MA 02139
617-715-4472
fallrogg@mit.edu

Dr. Raymond L. Speth
Principal Research Scientist
Department of Aeronautics & Astronautics
Massachusetts Institute of Technology
77 Massachusetts Ave, Building 33-316
Cambridge, MA 02139
617-253-1516
speth@mit.edu

University Participants

Massachusetts Institute of Technology (MIT)

- P.I.s: Dr. Raymond L. Speth; Dr. Florian Allroggen,
- FAA Award Number: 13-C-AJFE-MIT, Amendment Nos. 114, 115, 118, and 133
- Period of Performance: January 1, 2023, to September 30, 2025
- Tasks (for reporting period October 1, 2023, to September 30, 2024):
  1. Assess global biomass availability for sustainable aviation fuel (SAF) production
  2. SAF supply chain design for Africa, with specific focus on sub-Saharan Africa
  3. Facilitate a network for capability building for global SAF supply chain development
  4. Support knowledge sharing and coordination across ASCENT Project 093 universities

Hasselt University (UHasselt, through subaward from MIT)

- P.I.: Professor Robert Malina
- Period of Performance: January 1, 2023, to September 30, 2025
- Tasks (for reporting period October 1, 2023, to September 30, 2024):
  1. *(omitted, led by MIT)*
  2. SAF supply chain design for Africa, with specific focus on sub-Saharan Africa
  3. Facilitate a network for capability building for global SAF supply chain development
  4. Support knowledge sharing and coordination across ASCENT Project 093 universities

Project Funding Level

The ASCENT Project 093(A) received $1,150,000 Federal Aviation Administration (FAA) funding and $1,150,000 matching funds. Sources of matching funds are approximately $90,000 from MIT, plus 3rd party in-kind contributions of $1,060,000 from Earth Force Technologies.

Investigation Team

Dr. Raymond L. Speth, Principal Investigator (MIT), all tasks
Dr. Florian Allroggen, Principal Investigator (MIT), all tasks
Prof. Robert Malina, Principal Investigator (UHasselt), all UHasselt tasks
Dr. Niamh Keogh, Co-Investigator (MIT), Tasks 1 and 3
Dr. Alessandro Martulli. Postdoctoral Associate, Task 3
Dr. Sumit Maharjan, Postdoctoral Associate, Task 2
Francis Mwangi, Graduate Research Assistant (UHasselt). Task 2 and 3
Teshome Deressa, Graduate Research Assistant (UHasselt), Task 3
Andy Eskenazi, Graduate Research Assistant (MIT), Task 1

Project Overview

Large-scale production of SAF around the globe is needed to meet aviation's ambitious decarbonization goals. Production scale-up will require identification of waste feedstocks and land for energy crop cultivation, sustainable farming and land use practices, and investments in conversion capacity as well as fuel and feedstock logistics. Access to data, expertise, and capital remains a major roadblock towards successfully creating these supply chains around the globe. Under ASCENT Project 093, MIT aims to (1) assess global biomass availability, broken down by region, and the associated potential for SAF production with current and improved conversion technologies, (2) analyze opportunities and roadblocks for supply chain designs, specifically focusing on Africa, (3) share supply chain designs and feedstock availability assessments with other members of the ASCENT Project 093 team, and (4) facilitate a network of academics around the globe to support capacity building for SAF production.

Task 1 – Assess Global Biomass Availability for SAF Production

Massachusetts Institute of Technology

Objective

The objective of this task is to develop a detailed assessment of biomass availability for producing bio-based aviation fuels in different world regions. The biomass feedstock could originate from two sources: (1) expanding land use, as modeled from current and future land and sustainability practices, considering competing demands for land from agriculture and other uses, and (2) waste streams, such as agricultural residues, forestry residues, animal manure, and municipal solid waste. Work during Year 2 focused primarily on agricultural residues.

Research Approach

While there a number of prior studies that have aimed to quantify the energy potential of agricultural residues, these works generally (a) do not pursue a consistent methodology for categorizing the computed energy potentials (e.g., only consider the theoretical potential), (b) do not incorporate ecological criteria when assessing the availability of residues (e.g., do not take into consideration requirements to maintain soil health), and (c) do not appropriately model the uncertainty and variability in the quantification of residue production (e.g., assume a single residue-to-product ratio for a crop). To this end, MIT efforts over the past year have sought to create a standard approach for categorizing energy potentials from waste streams, with the option to be extended to other waste feedstocks, Furthermore, the uncertainty in residue production, recoverability, and availability was quantified via a statistical method.

Figure 1 provides an illustration of the various energy potential categories for crop residues. The first of these is the *Theoretical Potential*, which refers to the maximum amount of agricultural residues resulting from crop cultivation. The *Technical Potential* refers to the quantity of residues (energy equivalent) that could be collected after considering harvesting equipment limitations, while *Sustainable Potential* represents the residual biomass that could be collected ensuring that soil health is maintained (i.e., primarily by keeping the amount of carbon in the soil constant). The combination of the *Technical Potential* and *Sustainable Potential* is the *Technical Sustainable Potential*, which satisfies both ecological and environmental limitations. Finally, the *Available Potential* represents the amount of residue that is available for fuel conversion after accounting for other competing uses, such as cooking or animal feed.

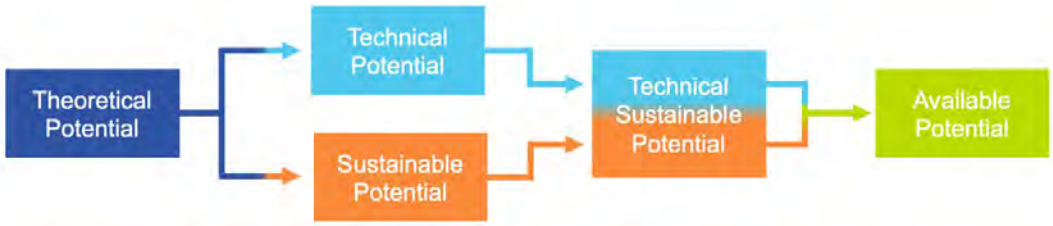

Figure 1. Five categories of energy potentials. Here, *technical potential* and *sustainable potential* are considered independently of each other, out of *theoretical potential*. As a result, the *technical sustainable potential* seeks to balance the trade-offs between the two categories.

These five categories of energy potential can be modelled via a set of crop-specific factors. These include (a) the residue-to-product ratio (RPR) (i.e., the amount of residue generated per unit of crop produced), (b) the technical recoverability ratio (TRR) (i.e., the percentage of residues that can be collected with typical harvesting machinery), c) the sustainable removal ratio (SRR) (i.e., the percentage of residues that can be collected less what must remain in the field to maintain soil health), d) the technical sustainable removal ratio (TSRR) (defined as the minimum between TRR and SRR), and e) the residue availability ratio (RAR) (i.e., the percentage of residues available after considering competing uses).

Our team conducted a literature review to derive RPR, TRR, and RAR values (the SRR and TSRR were computed using a custom geospatial methodology) for each crop. The results exhibit variation. For example, for corn, the RPR ratio (amount of stover per kilogram of grain) varies between 1.4 to 2.55, mostly due to (a) the differences in the methodologies to quantify the residue amounts and (b) the geospatial differences in crop residue production. To account for this variability, for each crop, all possible combinations between the RPR, TRR, SRR, TSRR, and RAR ratios were considered, creating a distribution of all possible energy potentials within each category. The results were aggregated for over 180 crops and are shown in Figure 2. Figure 2a summarizes the distribution of availability estimates. Figure 2b displays a Sankey diagram with the (mean) flow of residual energy across four of the potential categories. Overall, using crop production data for 2021, the analysis found that of the starting (theoretical) 122.2 EJ of energy in the crop residue biomass, only 33.8 EJ, or 27.7% of that energy would be fully available for biofuel conversion.

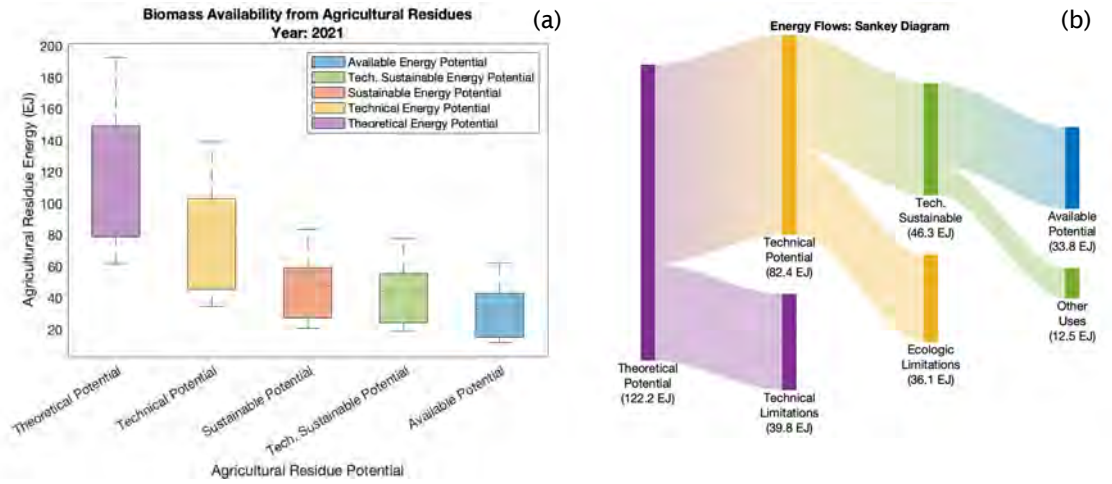

Figure 2. (a) Statistical evaluation of energy potentials, considering residual biomass from the production of +180 crops. The 25th and 75th percentiles and median are in the main box, as well as the mean with one standard deviation above and below, shown in the whiskers. (b) Sankey diagram for the flow of energy potential. Of the starting (theoretical) energy potential, 32.6% can't be recovered due to technical limitations, while an additional 29.5% (on top of what can't be recovered) must remain in the fields to maintain soil health conditions. In essence, the TSRR, on average, only allowed for a sustainable recovery of 37.9% of the theoretical amount of energy produced in agricultural residues.

Figure 3 provides an illustration to the 0.1-degree resolution of available crop residue energy potential. Five countries stand with significant potential: China (3.72 – 14.03 EJ/yr), Brazil (1.06 – 10.05 EJ/yr), India (2.08 – 9.39 EJ/yr), Indonesia (2.13 – 9.37 EJ/yr), and the United States (1.84 – 7.00 EJ/YR). Together, these five countries contribute to 57% of the global mean available crop residue energy potential.

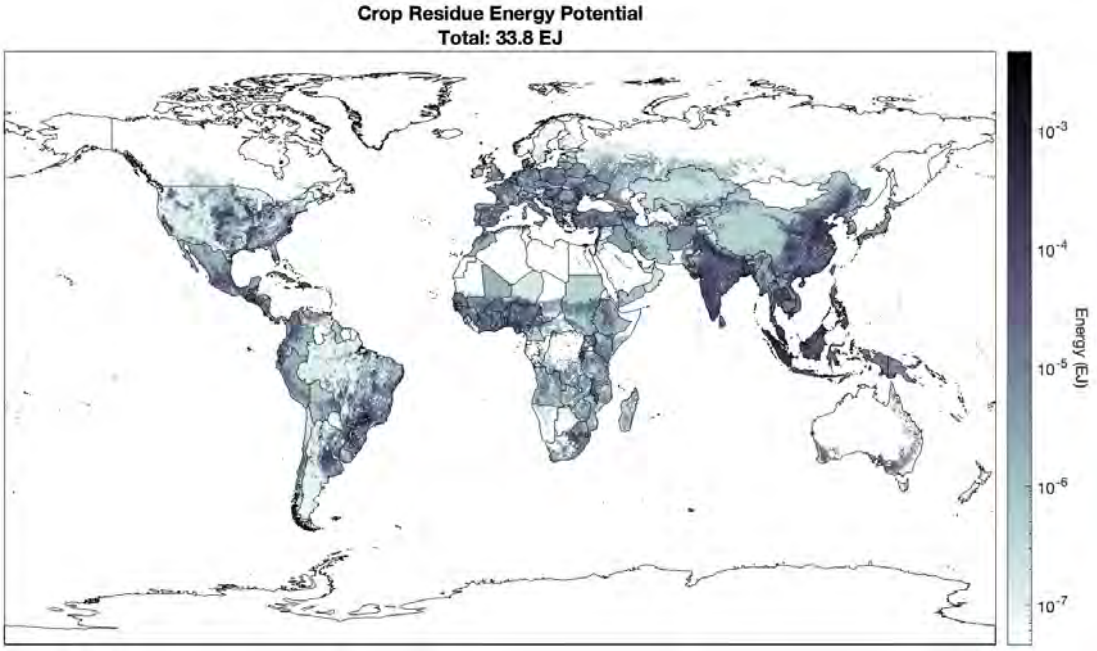

Figure 3. Global distribution of the available energy potential stemming from crop residue production to the 0.1-degree resolution.

Milestones

- Developed a standardized methodology for evaluating the energy potential from waste streams in a stochastic manner.
- Created a database containing production, recoverability, and availability factors for agricultural residues associated with +180 crops.

Major Accomplishments

- Completed the evaluation of the global energy potential for agricultural residues.

Publications

A paper summarizing the approach and results is under preparation.

Outreach Efforts

- Presented the approach to the ASCENT Spring 2024 Meeting.

Awards

None.

Student Involvement

Andy Eskenazi (MIT graduate student) was involved in this task.

Plans for Next Period

- Extend the framework to three other residual categories (i.e., municipal solid waste, animal manure, and forestry residues).
- Identify geographic clusters of high available energy potential where residues with similar characteristics could be processed.

Task 2 – SAF Supply Chain Design for Africa, with Specific Focus on Sub-Saharan Africa

Massachusetts Institute of Technology
University of Hasselt

Objectives

The objectives of this task are (1) to study the current hurdles for the development of a local SAF industry in Africa, (2) to develop science-driven advice to help overcome these hurdles, and (3) to help kick-start the SAF industry in Africa. For this purpose, our team has developed an understanding of the current economic, social, environmental, technological, logistical, and legal hurdles for SAF development in Africa. We then create quantitative assessments of supply chain designs that leverage the specific opportunity space on the African continent. This entails (techno-) economic assessments and environmental lifecycle assessments of selected supply chain designs, and the inclusion of regulatory and policy considerations.

During the current reporting period, this task focused on working with local partners in Kenya to advance supply chain development there.

Research Approach

A set of frameworks were developed and applied for the Kenyan context, which informed the “Second High-Level Meeting on SAF Development and Deployment” held in October 2024 in Nairobi, Kenya (see Task 3).

Finalization of Green Premium Study for Kenya

During the reporting period, an analysis on the green premium allocation of a SAF production facility was finalized and prepared for journal submission.

The green premium study explores the potential for deploying SAFs in developing countries, with Kenya as a case study, focusing on the allocation of the "green premium," (the cost differential between SAF and conventional jet fuel). This research aims to quantify the impact of the green premium on the cost of air travel, particularly for international flights. Despite its environmental benefits, SAF production is currently limited, with most facilities located in developed nations, where infrastructure, financing, and policy support are more robust. In developing countries, barriers to SAF production include high investment costs, limited policy frameworks, lack of technical expertise, and insufficient infrastructure.

Kenya presents a compelling case for SAF production due to its existing SAF ambitions, a well-connected international aviation network, and progress in renewable energy deployment. However, SAF costs in Kenya are estimated to range between 2.3 and 5 times those of conventional jet fuel, creating a substantial cost barrier. The study utilized data from Jomo Kenyatta International Airport (HKJK) and Moi International Airport (HKMO) for 2019 to model the green premium associated with SAF implementation. It applied the International Civil Aviation Organization (ICAO) Carbon Emissions Reporting Tool (CERT) to estimate fuel consumption per passenger and developed a cost model for SAFs, conventional jet fuel prices, and Carbon Offsetting and Reduction Scheme for International Aviation (CORSIA) carbon credits for greenhouse gas avoidance. Scenario analysis was used to evaluate the impacts of various SAF cost multipliers and blending ratios on air travel pricing.

The findings show that implementing a 10% SAF blend across all international flights from HKJK and HKMO would increase ticket prices by approximately 16%. If intra-African flights are excluded from bearing SAF-related costs, this cost shift results in a 29% price increase for intercontinental flights. The green premium varies significantly based on flight distance and geography; short-haul intra-African routes experience the lowest additional costs, ranging from $1 to $10 per passenger, while long-haul intercontinental flights, such as those to North America and East Asia, face costs between $41 and $90 per passenger (see Figure 4). While CORSIA carbon credits provide a marginal reduction in the green premium, their current value is insufficient to offset the high costs of SAF adoption meaningfully. SAF offtake agreements, in which airlines commit to purchasing SAF before production begins, can reduce investment risks, but financially constrained African carriers often lack the capacity to participate in such arrangements.

Origin	Destination	No. of Flights	Aircraft Type	Fuel burn per flight per Passenger carried (tons)	Cost of jet fuel per flight per pax carried (USD)	Cost of blended fuel per flight per passenger in USD	CORSIA GHG avoidance benefit per passenger per flight USD	Green premium cost allocation per passenger in USD	Green Premium Cost Range
HKJK	OOMS	277	B738	0.09	57.24	68.69	0.56	10.89	$11-$20
HKJK	FACT	28	B738	0.10	63.92	76.70	0.63	12.16	$11-$20
HKJK	FACT	226	B737	0.11	71.49	85.79	0.70	13.60	$11-$20
HKMO	EDDF	35	B763	0.20	129.76	155.72	1.27	24.68	$21-$30
HKMO	EDDF	51	B763	0.20	129.76	155.72	1.27	24.68	$21-$30
HKJK	EDDF	211	A333	0.21	137.41	164.89	1.34	26.14	$21-$30
HKJK	ZGGG	108	A332	0.30	197.65	237.18	1.93	37.60	$31-$40
HKJK	KJFK	221	B788	0.36	240.92	289.11	2.36	45.83	$41-$50

Figure 4. Green premium impact on ticket prices on select routes, if premium is allocated to all intercontinental flights from HKJK and HKMO airports.

The study underscores the necessity of policy interventions to reduce the green premium and foster SAF production in emerging economies. Governments need to establish robust SAF policies, supported by international financial mechanisms, to bridge the cost gap and promote sustainable aviation technologies and practices. Redirecting SAF costs primarily to intercontinental flights helps minimize disruptions to regional air travel while addressing emissions from fuel-intensive long-haul routes. In Kenya, integrating SAF initiatives with broader climate policies and securing development finance could significantly enhance the feasibility of SAF deployment, contributing to national climate goals and the decarbonization of international aviation. The insights and methodologies presented in this research are applicable to other developing countries seeking to address similar challenges and align with global climate objectives.

Milestone

- Presented the first set of techno-economic analyses and stakeholder mappings during the 2nd meeting of the National SAF Steering Committee on October 3-4, 2024, in Mombasa, Kenya.

Major Accomplishments

- Briefed the results on the analysis of green premium coverage for Kenya during the 2nd meeting of the National SAF Steering Committee on October 3-4, 2024, in Mombasa, Kenya.

Publications

None.

Outreach Efforts

- Presented the results of initial analyses during the 2nd meeting of the National SAF Steering Committee on October 3-4, 2024, in Mombasa, Kenya.
- Presented a summary of the efforts during the ASCENT Spring and Fall 2024 meetings.

Awards

None.

Student Involvement

Francis Mwangi (UHasselt graduate student) was involved in this task.

Plans for Next Period

- Further refine the analyses for Kenya.

Task 3 – Facilitate a Network for Capability Building for Global SAF Supply Chain Development

Massachusetts Institute of Technology
University of Hasselt

Objective

The objective of this task is to interface with partners to build the skills, expertise, and capacities needed for scaling up SAF development and deployment around the globe. During the current reporting period, the focus of this task was to deepen ties with external partners and establish an official group for advancing SAF development in Kenya.

Research Approach

To meet the goals of this task, the MIT/UHasselt team followed three approaches: (1) Capability building in Kenya, (2) developing a structure capability building with the ASCENT Project 093, and (3) country workshop of SAF development in sub-Saharan Africa. These approaches are further discussed below.

Capability Building in Kenya

A key objective during this reporting period was to establish a formal forum tasked with advancing a SAF production facility in Kenya. To achieve this, the team supported the Kenyan Civil Aviation Authority (KCAA) in the formation of a National Steering Committee for the acceleration of development and deployment of Sustainable Aviation Fuels in Kenya. Three MIT and UHasselt team members are members of the National Steering Committee.

The Steering Committee held two meetings, a meeting in June 2024 and a meeting in October 2024. While the first meeting was an initial kick-off, the 2-day meeting (October 3-4, 2024, in Mombasa, Kenya) focused on key supply chain challenges for SAF production in Kenya. It brought together key governmental and private stakeholders to work on issues such as feedstock sourcing and sustainability certification, plant financing, SAF policy, and fuel blending and certification. Having developed concrete workstreams, responsible parties for each were identified. The Committee also visited the idle petroleum refinery in Mombasa, Kenya, to initiate a dialogue on the potential for retrofitting parts of the refinery for SAF production.

A second objective was to foster a network to support stakeholders interested in building the capabilities and knowledge for analyzing, developing, and deploying SAF production capacity in Kenya. For this purpose, the team continued engaging with KCAA, the Deutsche Gesellschaft für Internationale Zusammenarbeit (giz), and the World Bank. A new collaborator, the European Union Aviation Safety Agency (EASA), brought forward resources for capacity building in Kenya. The MIT/ UHasselt team also held talks with other international stakeholders to help leverage additional resources for SAF supply chain development in Kenya.

Developing a Structured Capability Building with the ASCENT Project 093

Together with the University of Hawaii and Washington State University, the team has built a lecture series teaching the fundamentals of SAF production and deployment from multiple perspectives. The course was first introduced in November 2023 for a cohort from Latin America and the Caribbean. The MIT/Hasselt team developed and led several lectures in this lecture series.

Country-Workshop on SAF Development in Sub-Saharan Africa

During the reporting period, the team developed a program for a workshop to advance SAF development in sub-Saharan Africa. The workshop aims to address the underrepresentation of middle- and low-income countries in the global SAF industry. It will support SAF projects, enhance understanding of SAF's technical, financial, and policy dimensions, and establish a network of first-mover countries in Africa.

Designed for key stakeholders, including aviation, agriculture, energy, and treasury, as well as representatives from the aviation industry in selected African nations, the workshop underscores the importance of participants' influence within their domains. Only those who play a strategic role in their respective sectors can inform the development of policies and frameworks that support SAF implementation.

The planned program comprises expert-led thematic sessions and country-specific workshops. Expert sessions will cover topics such as SAF feasibility studies, feedstock sourcing, financing strategies, certification standards, sustainability requirements, and leveraging international support mechanisms. These sessions aim to provide both technical insights and strategic approaches to overcoming challenges associated with SAF deployment. The country workshops will focus on identifying existing challenges, formulating actionable solutions, and outlining next steps to advance SAF projects in each participating nation. Cross-country roundtables will facilitate the exchange of insights and best practices among participants.

The outcomes of the workshop are intended to strengthen the capacity of African countries to establish SAF production facilities, integrate SAF into national decarbonization strategies, and position themselves as active participants in the global SAF market.

Milestone

- Successfully delivered a lecture series in November 2023.

Major Accomplishments

- Co-organized (MIT/UHasselt team) the 2nd meeting of the National SAF Steering Committee on October 3-4, 2024, in Mombasa, Kenya.

Publications

None.

Outreach Efforts

- Co-organized (MIT/UHasselt team) the 2nd meeting of the National SAF Steering Committee on October 3-4, 2024, in Mombasa, Kenya.
- Presented a summary of the efforts during the ASCENT Fall 2024 meeting.

Awards

None.

Student Involvement

Francis Mwangi and Teshome Deressa (UHasselt graduate students) were involved in this task.

Plans for Next Period

- Deepen the ASCENT Project 093(A) team's engagement in Kenya. This will include supporting follow-up action from the 2nd National Steering Committee.
- Seek additional engagement in other sub-Saharan countries, which are deemed to provide substantial benefits.
- Review the course developed together with the ASCENT Project 093 universities.

Task 4 - Support Knowledge Sharing and Coordination Across all ASCENT Project 093 Universities

Massachusetts Institute of Technology
University of Hasselt

Objective

The objective of this task is to share best practices and coordinate efforts with other ASCENT Project 093 universities (Washington State University and University of Hawaii). The sharing of approaches minimizes duplication of ASCENT Project 093 universities' work on similar topics and can help develop transferable approaches for stakeholder engagement across various geographical regions.

Research Approach
The MIT/UHasselt team participated in regular ASCENT Project 093 coordination teleconferences, which served as a venue to discuss progress in the various geographies and to learn about the activities of other ASCENT Project 093 universities.

Milestone
- Shared their progress in Kenya and helped set up the joint lecture series on SAF.

Major Accomplishments
- Developed and delivered a joint course on the fundamentals of SAF to a first cohort in November 2023.

Publications
None.

Outreach Efforts
- Developed and delivered a joint course on the fundamentals of SAF to a first cohort in November 2023.

Awards
None.

Student Involvement
Francis Mwangi (UHasselt graduate student) was involved in this task.

Plans for Next Period
- Continue engagement in regular teleconferences and the development and delivery of the SAF lecture series.

Project 093(B) Collaborative Research Network for Global Sustainable Aviation Fuel Supply Chain Development

University of Hawai‘i

Project Lead Investigator

Scott Q. Turn
Researcher
Hawai‘i Natural Energy Institute
University of Hawai‘i
1680 East-West Rd., POST 109
Honolulu, HI 96822
808-956-2346
sturn@hawaii.edu

University Participants

University of Hawai‘i (UH)

- P.I.: Scott Q. Turn, Researcher
- FAA Award Number: 13-C-AJFE-UH, Amendment 020
- Period of Performance: January 1, 2023, to December 31, 2023
- Tasks:
  1. Establish a collaborative research network for sustainable aviation fuel supply chain development in southeast Asia
     - 1.1 Identify partner universities (and other entities) in the southeast Asian region
     - 1.2 Organize and conduct a sustainable aviation fuel supply chain workshop in southeast Asia
     - 1.2 Develop a plan for an education and exchange program with collaborating universities in southeast Asia and with ASCENT Project 093 universities

- FAA Award Number: 13-C-AJFE-UH, Amendment 024
- Period of Performance: March 19, 2024, to March 18, 2025
- Tasks:
  2. Collaborative research network for sustainable aviation fuel supply chain development in southeast Asia
     - 2.1 Develop sustainable aviation fuel research themes of common interest for Association of Southeast Asian Nations countries
     - 2.2 Hold sustainable aviation fuel supply chain workshop in Indonesia

Project Funding Level

Under Federal Aviation Administration (FAA) Award Number 13-C-AJFE-UH, Amendment 020, the ASCENT Project 093B Collaborative Research Network for Global sustainable aviation fuel (SAF) Supply Chain Development received $250,000 in funding from the FAA and cost-share funding of $250,000 from UH.

Under FAA Award Number 13-C-AJFE-UH, Amendment 024, the ASCENT Project 093B Collaborative Research Network for Global SAF Supply Chain Development received $250,000 in funding from the FAA and cost-share funding of $250,000 from UH.

Investigation Team

University of Hawai‘i

Dr. Scott Turn (P.I.; Hawai‘i Natural Energy Institute)
Dr. Quang-Vu Bach (assistant researcher; Hawai‘i Natural Energy Institute)

Dr. Elmar Villota (postdoctoral fellow, Hawai‘i Natural Energy Institute)

Other Lead Personnel

Washington State University
Prof. Manuel Garcia-Perez (co-P.I.)
Michael Wolcott (P.I.)

Volpe National Transportation Systems Center
Kristin Lewis (P.I. and principal technical advisor)

Massachusetts Institute of Technology
Florian Allroggen (P.I. and research Scientist)

Project Overview

UH will engage universities (and other entities) in southeast (SE) Asian countries and develop collaborative research programs focused on SAF supply chains. These activities will identify information shortfalls and generate fundamental data necessary for the design of engineered SAF production systems. Research activities will include supporting analyses related to the assessment of available feedstocks, supply chains, infrastructure needs, and stakeholder engagement. Planned activities under the program include support of research projects, workshops, and student and researcher exchanges.

The key objectives for this project are as follows:

- Establish a collaborative research network for SAF supply chain development in SE Asia.
- Provide technical support to other Project 093 ASCENT university and partner activities for which tropical feedstocks are relevant.

Task 1 – Establish a Collaborative Research Network for Sustainable Aviation Fuel Supply Chain Development in Southeast Asia

University of Hawai‘i

Objectives

This task includes three subtasks:

- Subtask 1.1 Identify partner universities (and other entities) in the SE Asian region
- Subtask 1.2 Organize and conduct a SAF supply chain workshop in SE Asia
- Subtask 1.3 Develop a plan for an education and exchange program with collaborating universities in SE Asia and with ASCENT Project 093 universities

Research Approach

UH has led the tropical regional supply chain effort under ASCENT Project 001 since 2015. Activities under this effort have focused on tropical energy crops and agriprocessing residues and urban residues as candidate feedstocks for SAF production. This experience forms the basis for the development of SE Asian SAF supply chains.

Background

Regional supply chain development is informed by crop-science-based evaluations of plants for feedstock production, analyses of crop production potential based on geographic information systems, development of advanced feedstock processing and conversion systems, assessments of the compatibility of biomass and bioderived products with existing infrastructure and logistical resources, and evaluations of biomass-based energy systems based on life cycle and economic approaches. The results of past efforts have provided a baseline of information to be accessed and built upon in developing scenarios of future SAF production along regional supply chains in Hawai‘i and the tropics. Pretreatment and conversion options for materials from potential SAF feedstock crops in the tropics are shown in Figure 1.

In August 2017, the Hawai‘i Natural Energy Institute at UH initiated efforts under a five-year grant from the Office of Naval Research for the Asia Pacific Regional Energy System Assessment. The objective of this 5-year grant was to develop comprehensive energy system assessments that include strategy, policy, regulation, technology options, demonstrations,

implementation plans, and training for energy system transitions in select locations throughout the Asia-Pacific region, based on the specific requirements or needs of the targeted jurisdictions and strategic alliances. The first three years of this program laid a firm foundation for continued success built upon the development of solid partnerships with national, regional, and local jurisdictions as well as private and public stakeholders, including utility companies, universities, and other research and international aid and development entities. Relationships developed in SE Asia (i.e., Thailand, Indonesia, and Vietnam) through the Asia Pacific Regional Energy System Assessment were leveraged to facilitate the ASCENT Project 093B global supply chain development effort. The Association of Southeast Asian Nations (ASEAN) includes the countries of Brunei Darussalam, Cambodia, Indonesia, Lao PDR, Malaysia, Myanmar, Philippines, Singapore, Thailand, and Vietnam. Universities (and other entities) from ASEAN countries, with the exception of Cambodia and Myanmar, were the initial target participant group in the collaborative research network for SAF supply chain development in SE Asia under this ASCENT project.

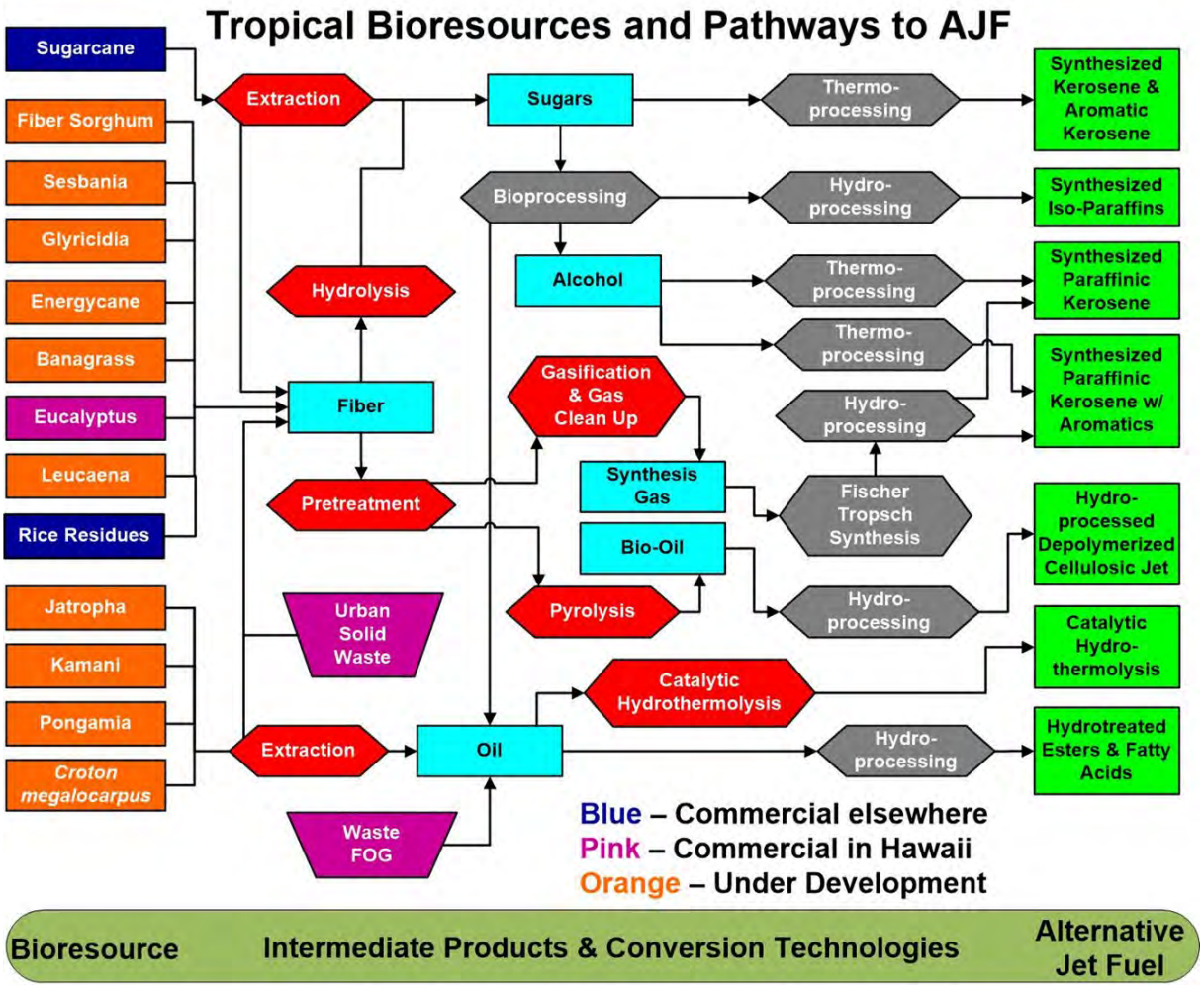

Figure 1. Tropical bioresources and pathways to alternative jet fuel/sustainable aviation fuel. FOG: fats, oils, and greases.

Subtasks 1.1 and 1.2

Activities conducted to accomplish Subtasks 1.1 and 1.2 were coordinated in planning the SAF supply chain workshop held in Bangkok in May 2023. The workshop was coordinated with the U.S. Trade and Development Agency (Commerce Department) as part of their effort to support the SAF business development of United States (U.S.) companies in the region. Thailand's National Energy Technology Center and Chiang Mai Rajabhat University were instrumental in the planning process, providing contacts at universities and government agencies throughout the ASEAN region. Staff from the

U.S. Embassy in Bangkok and FAA Asia Pacific Office at the U.S. Embassy in Singapore supported workshop planning by contacting and coordinating with government agencies across the region.

The archival literature was reviewed to identify universities and entities from ASEAN countries with either ongoing SAF-related development activities or prior work in biomass resource assessment or biomass supply chains. Based on the results, researchers from 13 universities across the region (i.e., Philippines, Indonesia, Thailand, Vietnam, Malaysia, and Brunei) were contacted to assess interest in workshop participation. Twelve researchers from seven universities attended the SAF workshop in Bangkok.

The workshop objectives were as follows:

- Connect stakeholders.
- Foster collaboration.
- Drive innovation in the adoption of SAF.

The FAA-supported section of the workshop was held on May 22–23, 2023, at the Conrad Hotel in Bangkok, Thailand. More than 100 attendees from eight countries participated in the workshop (see Figure 2). Participants self-identified their organization's place in the SAF value chain, as shown in Figure 3.

Figure 2. Country of origin of participants at the sustainable aviation fuel workshop.

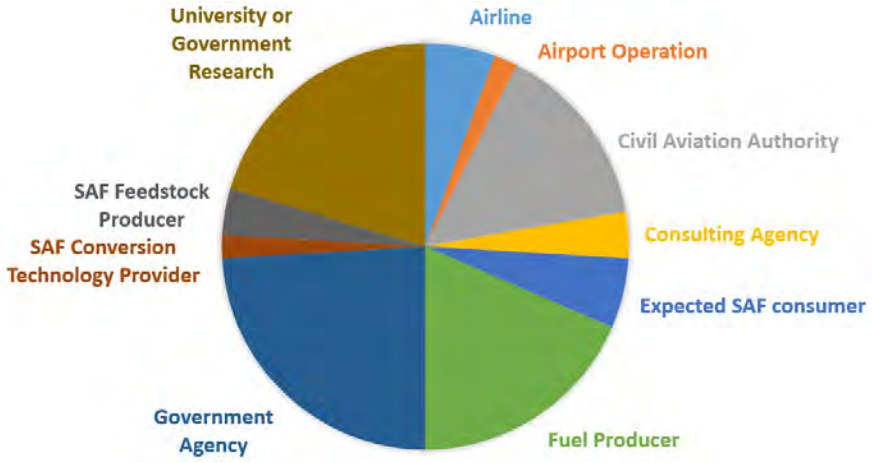

Figure 3. Organizations of sustainable aviation fuel (SAF) workshop attendees.

The two days of the workshop were organized as shown below:

Day 1, Morning
- Workshop overview and introduction
- Keynote address: International Civilian Aviation Organization
- Civil aviation authority perspectives
- Energy policy perspectives on SAF

Day 1, Afternoon
- Panel on SAF production: Upstream considerations/logistics
- Update on the Commercial Aviation Alternative Fuels Initiative
- Summary and close out of Day 1

Day 2, Morning
- Recap from Day 1
- Keynote address: SAF sustainability criteria
- Agricultural industry: Feedstocks for SAF production
- Airport fuel system operator perspectives

Day 2, Afternoon
- University research in support of SAF development
- Panel discussion: Way forward
- Summary and close out of Day 2

Participants who gave presentations were provided with five motivational prompts:
- Tell us about your organization (e.g., private/public, size, authority, etc.).
- What role will your organization play in the transition to SAF use in your country?
- How will your organization plan for the expanded use of SAF?
- What barriers will need to be overcome for SAF deployment in your country?
- What tools and resources are needed to overcome those barriers?

Workshop participants identified common themes that need to be addressed across the region, as summarized below:
- Sustainable funding models and strategies are needed for the aviation industry's transition to SAF.
- There is a lack of discussion on sustainability and economic viability of feedstocks.
- Investments in research and development are required to diversify feedstock options and promote sustainable alternatives that do not compete with food supplies.
- Infrastructure development is crucial for the production, storage, and distribution of SAF.

Workshop recommendations included the following:
- Explore and establish supporting policy (e.g., the use of incentives and carbon credits) to promote SAF production and adoption.
- Raise awareness and develop education initiatives to inform stakeholders, including the public, about the benefits and importance of SAF.

Participant feedback identified the sessions on civil aviation authorities' perspectives, energy policy perspectives on SAF, and the agricultural industry feedstocks for SAF production as the most useful.

Subtask 1.3
A meeting was held with the Dean of Education Programs and the Deputy Director of Research Programs at the East-West Center (www.eastwestcenter.org) adjacent to the UH campus. The purpose of the meeting was to inform the Dean and Deputy Director about ASCENT Project 093B goals and activities and to explore opportunities to integrate East-West Center educational and research networks and infrastructure with the ASCENT Project 093B goals of recruiting and educating SE Asian postdoctoral fellows and visiting scholars. UH faculty members that are actively engaged in research on ecosystem services and transportation networks have been recruited as mentors for the ASCENT Project 093B-supported postdoctoral fellows and visiting scholars.

Milestones

- Identified partner universities for the SAF research network.
- Selected a venue and support organizations for the SE Asia SAF workshop.
- Held the SAF supply chain workshop in SE Asia.

Major Accomplishments

The major accomplishment of the project was holding the highly successful SAF supply chain workshop in Bangkok, Thailand, on May 22–23, 2023. The workshop established ASCENT Project 093B as a leader in supporting the development of global SAF supply chains in the ASEAN region. Participants expressed great interest in FAA support for a similar workshop in 2024.

Publications

None.

Outreach Efforts

Organizing and conducting the SAF supply chain workshop in Bangkok, Thailand, provided outreach and education to the SAF supply chain stakeholder community. Presentations were made by Dr. Prem Lobo and Dr. Scott Turn during the workshop. Electronic communications were made with all the workshop participants, either directly or through in-country partners.

A presentation describing the workshop, its goals, and its outcomes was presented at the Third ASEAN International Conference on Energy and Environment held in Bali, Indonesia, on August 23–25, 2023.

Awards

None.

Student Involvement

None.

Plans for Next Period

- Submit a manuscript for publication in the journal *IOP Sustainability Science and Technology*. The prepared manuscript describes the 2023 workshop in Bangkok, Thailand, and details its outcomes.

Task 2 –Collaborative Research Network for SAF Supply Chain Development in SE Asia

University of Hawai'i

Objectives

This task includes two subtasks:

- Subtask 2.1 Develop SAF research themes of common interest for ASEAN countries
- Subtask 2.2 Hold SAF supply chain development workshop in Indonesia

Research Approach

Subtasks 2.1. and 2.2

A snapshot of jet fuel consumption and development plants for SAF in SE Asia is shown in Figure 4. Across the region, annual jet fuel consumption approaches 25 million metric tonnes. Planned and operating SAF annual production capacity is less than 3 million metric tonnes.

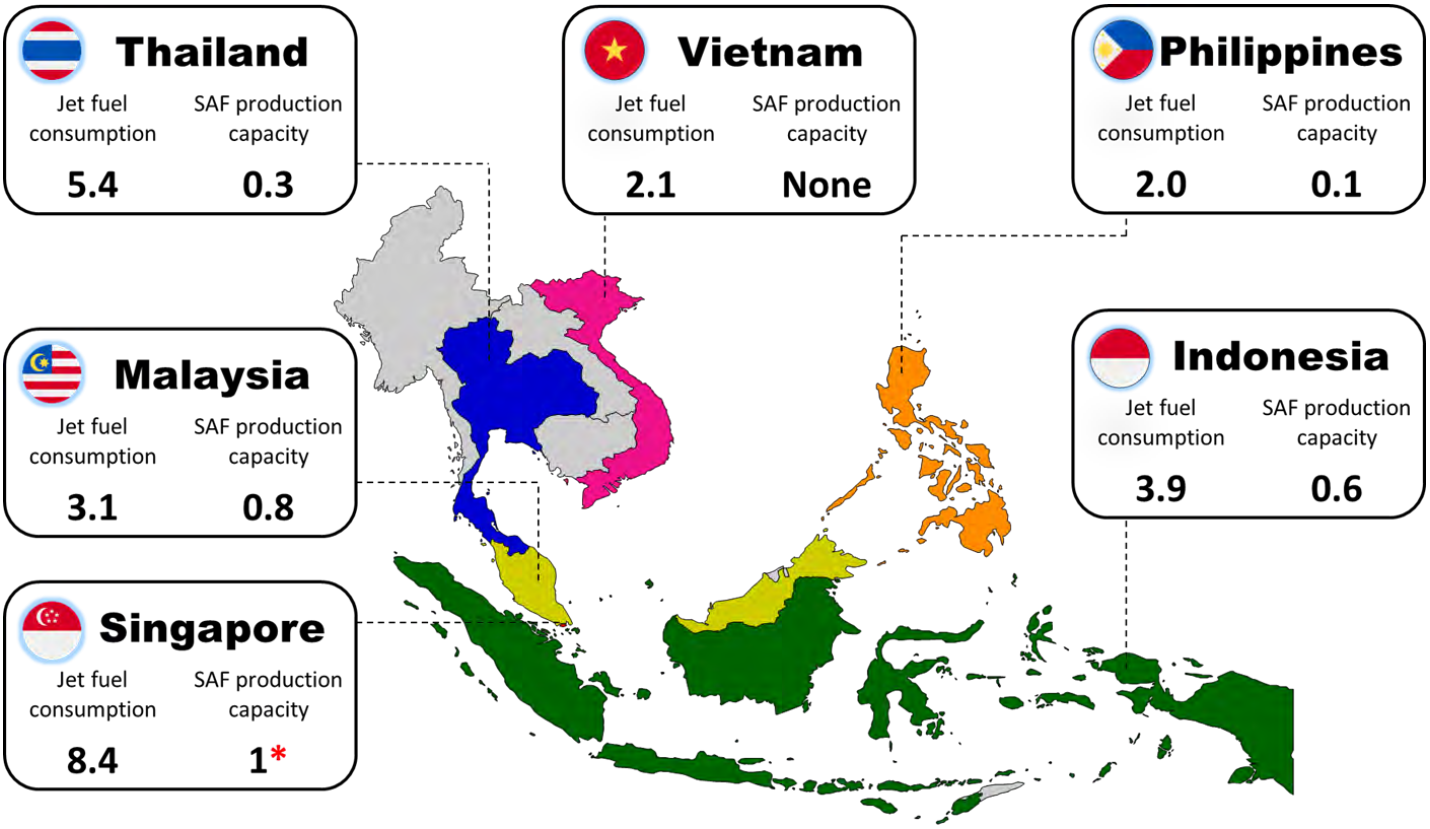

Figure 4. Summary of jet fuel consumption (U.S. Energy Information Administration, 2019) and planned SAF production capacity (Argus Media, 2024) in southeast Asia (* facility currently in operation). Units = million metric tonnes.

The SAF supply chain development workshop was organized and held on July 10-12, 2024, in Bali, Indonesia, to support and coordinate ongoing SAF development activities across the region. The workshop was co-organized by the FAA through ASCENT, the Indonesian Directorate General for Civilian Aviation, the Energy Technology Center of Thailand, and the UH.

The workshop registered 95 participants from Malaysia, Indonesia, Philippines, Thailand, Singapore, Vietnam, the U.S., and the European Union and included representatives from agricultural commodity groups, airlines, airport operations, civil aviation authorities, consulting groups, fuel producers, government energy and transportation agencies, SAF conversion technology providers, feedstock producers, university and research organizations, and aircraft manufacturers. Data on attendees and their organization are presented in Figure 5 and Figure 6, respectively.

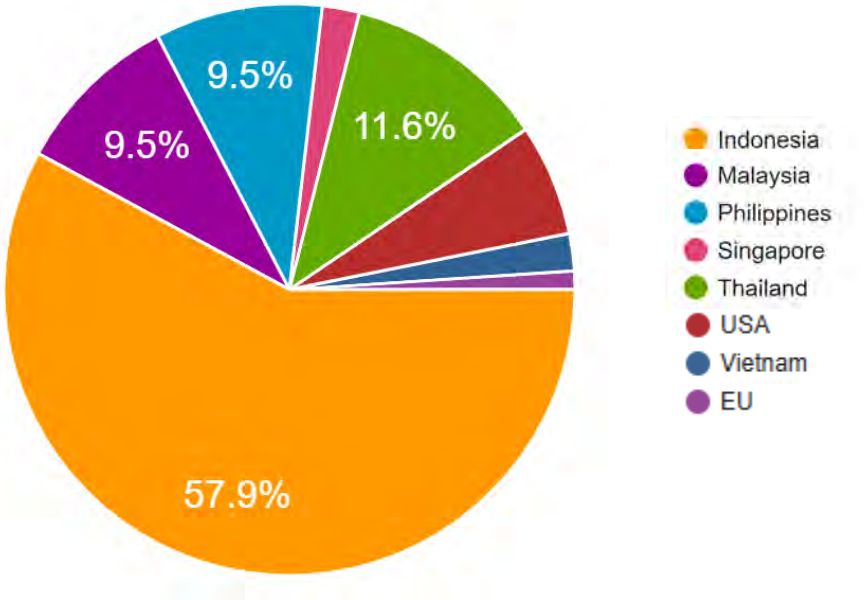

Figure 5. Country of origin of participants at the 2024 sustainable aviation fuel workshop in Bali.

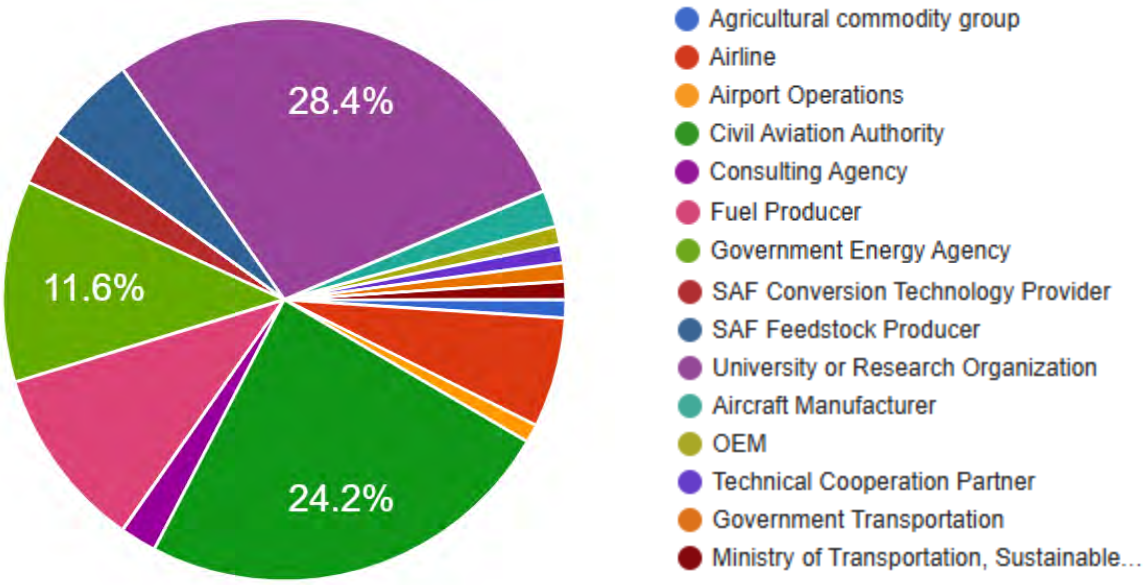

Figure 6. Organizations of sustainable aviation fuel (SAF) 2024 workshop attendees.

The workshop agenda included sessions on perspectives of civil aviation authorities, energy policy, SAF fuels/airports/airplanes, airline perspectives, feedstocks, feedstocks production and logistics, SAF conversion technologies, climate finance, SAF policy development, and university research. The first two days of the workshop were organized as shown below:

Day 1, Morning
- Workshop overview and introduction
- Civil aviation authority perspectives

Day 1, Afternoon
- Energy policy perspectives on SAF
- SAF Fuels: Airports and Airplanes
- Airline Perspectives on SAF
- Summary and close out of Day 1

Day 2, Morning
- Recap from Day 1
- Keynote address: Feedstocks for SAF: The Realm of Possibilities
- SAF Feedstocks: Production and Logistics
- SAF Conversion A-Z

Day 2, Afternoon
- Keynote: Climate Finance Options for SAF
- Development of SAF Policy
- University Research Activities
- Summary and close out of Day 2

Participants who gave presentations were provided with five motivational prompts:
- Tell us about your organization (e.g., private/public, size, authority, etc.).
- What role will your organization play in the transition to SAF use in your country?
- How will your organization plan for the expanded use of SAF?
- What barriers will need to be overcome for SAF deployment in your country?
- What tools and resources are needed to overcome those barriers?

An evaluation of workshop effectiveness was provided by 50 attendees who participated in an exit survey on the workshop content and organization. Participants found sessions on feedstock production and logistics, SAF policy development, energy policy, and SAF conversion technologies to be the most useful, demonstrating the value of an inter-agency approach to moving the SAF agenda forward.

The survey also queried participants on important research questions that needed to be addressed in order to advance SAF production in the region. Suggestions coalesced around common themes of (1) feedstock diversification and supply chains, (2) conversion technology advancement, and (3) environmental/sustainability certification. Cross cutting themes included funding, finance, and long term economic, social and environmental impacts of SAF implementation/utilization. This information was used as motivation in a four-hour session for university and research organization participants where they were encouraged to workshop on (1) specific research questions to include in a proposal, (2) funding sources, and (3) approaches to collaboration between their organizations for proposal development.

Central Luzon State University (CLSU) in the Philippines is undertaking a national biomass resource assessment in support of SAF development efforts. Dr. Elmar Villota, a postdoctoral fellow at UH, is coordinating with CLSU faculty and staff to serve as a resource person.

Milestones

- Identified partner universities for the SAF research network.
- Held the SAF supply chain workshop in SE Asia. This effort required identifying co-organizer groups for the SAF workshop in Bali, Indonesia; finalizing the workshop terms of reference, selecting and contracting a venue for the workshop and support organizations, and holding the SAF supply chain workshop in SE Asia.

Major Accomplishments

The major accomplishment of the project was holding the highly successful SAF supply chain workshop in Bali, Indonesia, on July 10-11, 2024. The workshop established ASCENT Project 093B as a leader in supporting the development of global

SAF supply chains in the ASEAN region. Participants expressed great interest in FAA support for a similar workshop in 2025.

Publications
None.

Outreach Efforts
Organizing and conducting the SAF supply chain workshop in Bali, Indonesia, provided outreach and education to the SAF supply chain stakeholder community. Electronic communications were made with all the workshop participants, either directly or through in-country partners.

On October 13, 2023, Dr. Manuel Garcia-Perez and Dr. Scott Turn presented information on SAF production and ASCENT global engagement to students from Taylor University in Malaysia at the request of the U.S. Grains Council.

Two lectures (February 15 and May 16, 2024) were presented as part of the ASCENT Project 093b Latin America training course organized by Washington State University.

Presentations on ASCENT Project 093b activities were delivered at the ASCENT review meetings in Honolulu, Hawai‘i (April 2024) and Alexandria, Virginia (October 2024).

Dr. Scott Turn participated in the Asia Pacific Air Transport Forum in Bali, Indonesia, and attended the release of Indonesia’s SAF road map at the Bali Airshow in September 2024.

Meetings were held with the Indonesian Directorate General for Civil Aviation (January, July, and September 2024) to discuss SAF development in the region and preparation and timelines for the release of Indonesia’s SAF road map.

Awards
None.

Student Involvement
None.

Plans for Next Period
- Draft and submit a manuscript that will be submitted for publication in the journal *IOP Sustainability Science and Technology.* A report was prepared describing the 2024 workshop in Bali, Indonesia, and detailing its outcomes. This report will be used to draft the manuscript.
- Continue efforts to develop regional projects for southeast Asian universities currently involved with SAF development work.

Project 093(C) Collaborative Research Network for Global Sustainable Aviation Fuel Supply Chain Development: Latin America Case

Washington State University

Project Lead Investigators

Manuel Garcia-Perez
Professor and Chair
Biological Systems Engineering Department
Washington State University
LJ Smith, Room 205, PO Box 646120
Pullman, WA 99164-6120
509-335-7758
mgarcia-perez@wsu.edu

Michael P. Wolcott
Regents Professor
Department of Civil & Environmental Engineering
Washington State University
PO Box 642910
Pullman, WA 99164-2910
509-335-6392
wolcott@wsu.edu

University Participants

Washington State University (WSU)

- P.I.s: Manuel Garcia-Perez and Michael P. Wolcott
- FAA Award Number: 13-C-AJFE-WaSU-037
- Period of Performance: October 30, 2023, to October 30, 2024
- Tasks:
  1. Create working groups in each Latin America and Caribbean (LAC) country involved in this project.
  2. Conduct the design and analysis of sustainable aviation fuel (SAF) supply chains in each of the LAC countries involved in this project.
  3. Create training modules/courses and graduate programs to train students.

Project Funding Level

The ASCENT Project 093C received $306,586 Federal Aviation Administration (FAA) funds and $306,586 in matching funds from WSU. Faculty time for Michael Wolcott, Manuel Garcia-Perez, Erik Jessup, Allyson Beall King, and Hanwu Lei contribute to the cost share. WSU funding is reported for this reporting period.

Investigation Team

Washington State University

Manuel Garcia-Perez (P.I.), Tasks 1, 2, and 3
Michael Wolcott (P.I.), Task 1
Hanwu Lei (co-P.I.), Task 3
Kristin Brandt (co-P.I.), Tasks 2 and 3

Lina Martinez (research staff), Tasks 1, 2, and 3
Dane Camenzind (research staff), Tasks 2 and 3
Allyson Beall King (research staff), Tasks 2 and 3
Eric Jessup (research staff), Tasks 2 and 3
Claudia Marcella Valderrama (graduate research assistant), Task 3
Robert Macias (graduate research assistant), Task 3
Volpe National Transportation Systems Center (Volpe)
Kristin Lewis (co-P.I.), Tasks 2 and 3

Project Overview

SAFs offer the potential to reduce the net environmental impact of aviation-related emissions while enhancing United States (U.S.) energy security and diversifying energy supplies. As a result, these technologies are receiving considerable attention from policymakers, industry, and academia. Most importantly, SAF has been included in the International Civil Aviation Organization (ICAO)'s Carbon Offsetting and Reduction Scheme for International Aviation (CORSIA), which aims to stabilize the carbon dioxide (CO_2) emissions of international aviation at year-2019 levels. Using SAF, aircraft operators can reduce their offsetting requirements using the reduced CORSIA values of CO_2 emissions from SAF using their well-to-wake lifecycle greenhouse gas (GHG) emissions (including credits for biogenic carbon emissions during combustion).

Significant progress has been made over the past decade in assessing SAF's economic and environmental properties. This includes studies that have fostered our general understanding of life cycle analysis (LCA) (Stratton et al., 2010). In addition, work has focused on the economic and environmental properties of specific pathways, including jet fuel produced from hydroprocessed esters and fatty acids (HEFA) (Stratton et al., 2011; Pearlson et al., 2013; Olcay et al., 2013; Seber et al., 2014), from Fischer-Tropsch (FT) pathways (Stratton et al., 2011; Suresh, 2016; Suresh et al., 2018), and from biomass-derived sugars using a variety of chemical and biological techniques (Bond et al., 2014; Staples et al., 2014; Winchester et al., 2015). Most recently, Monte Carlo approaches have been systematically introduced for quantifying uncertainty and stochasticity in LCA and techno-economic analysis (TEA) (Bann et al., 2017; Suresh, 2016; Yao et al., 2017; Suresh et al., 2018; Oriakhi, 2020).

A suite of decision-support tools for assessing SAF supply chains has been developed within ASCENT Project 001 and ASCENT 93C. These tools can be used to assess the economics of SAF production, the optimization of SAF supply chain logistics, and the configuration of supply chains to consider both the sale of the fuel commodity and the commensurate environmental benefits. This suite of tools has been widely applied within regions of the U.S. and has potential for use internationally. Of particular interest is gaining an understanding of feedstock availability and financial considerations for delineating both the minimum selling price and capital investment requirements for SAF production and regions outside the U.S. This project has the potential to benefit our understanding of the worldwide production of SAF to inform the ICAO.

ASCENT Project 001 has made progress in harmonizing TEAs across technology pathways and feedstock selections for both technical and financial assumptions. Five SAF production pathways have been completed and are publicly available TEAs: (1) HEFA, (2) alcohol to jet (ATJ), (3) FT, (4) pyrolysis, and (5) catalytic hydro thermolysis (CH) (Brandt et al., 2021a, 2021b, 2021c, 2022a, 2022b). These TEAs have been used extensively in work within ASCENT and for the ICAO Committee on Aviation Environmental Protection (CAEP) analysis. As part of the ICAO tasks, the TEAs were updated to allow for regional variables to be changed based on global location. These include local consumable prices such as feedstock and electricity, as well as equipment capital costs and labor. Location-specific financial assumptions, including tax rate, inflation rate, and terms of loans, are also customizable. With expertise from Latin American colleagues, these TEAs can be rapidly deployed for use in member countries.

The process of siting facilities consists of two steps: (1) generating an initial set of candidates, and (2) using mixed integer optimization to select facilities from the candidate locations. The candidate generation phase uses geospatial data to evaluate a location's compatibility with specific facility types. The optimization phase allows for the locations of facilities to be found that result in systemwide minimum costs for a specific set of variables, like fuel cost, tariffs, and feedstock availability. Batch processing allows for the rapid iteration of variables so that a supply chain's sensitivity can be evaluated in different scenarios. During the past decades, Latin America has grown its bioethanol and biodiesel production. Brazil, Argentina, and Colombia have the largest production of biofuel in the region (IEA, 2021). In addition, the LAC region is classified as a high-potential area for producing energy crops (Acharya & Perez-Pena, 2020; Trindale et al., 2019).

Currently, interest in the production and consumption of SAF has spiked in the region. Omega Green® is the first renewable diesel and SAF project under construction in Paraguay, with Brazilian investment, and it is expected to be in operation by 2025 (ECB Group, 2021). Legal framework and initiatives to produce or import SAF are being initiated in the Dominican Republic, Mexico, Costa Rica, and Colombia (Argus, 2021). LATAM,® a South American airline with main hubs in Chile, Peru, Brazil, and Colombia, plans to use 5% SAF for its operations by 2030, favoring producers throughout South America (LATAM, 2022). To date, no comprehensive assessment exists of the potential for SAF production in Latin America.

During Year 1, our team focused on three countries in Latin America and the Caribbean: (1) Colombia, (2) Dominican Republic, and (3) Ecuador. In the second year, we expanded our scope by adding Costa Rica. So far, our team has conducted literature reviews on biomass and SAF-related publications and existing infrastructure for Colombia, Dominican Republic, and Ecuador. The study of Colombia has been socialized with the Colombian stakeholders and is now published. We are now socializing our literature reviews with our stake holders from Ecuador and Dominican Republic. These literature reviews are being used as a supporting source of information to create the Road Maps in these countries.

The overall objectives of this project are to (1) create working groups in each of the LAC focus countries involved in this project that will work directly with the students on the development of SAF supply chains, (2) design and analyze SAF supply chains in Latin American and the Caribbean, and (3) create training modules, courses, and graduate programs to train students and stakeholders in Latin America and the Caribbean on the design and analysis of SAF production and supply chains.

References

Acharya, R. N., & Perez-Pena, R. (2020). Role of comparative advantage in biofuel policy adoption in Latin America. *Sustainability*, *12*(4), 1411.

Argus. (2021) *Jet fuel insights: The move to SAF in Latin America*. https://www.argusmedia.com/en/blog/2021/august/31/podcast-jet-fuel-insights-the-move-to-saf-in-latin-america

Bann, S. J., Malina, R., Staples, M. D., Suresh, P., Pearlson, M., Tyner, W. E., Hileman, J. I., & Barrett, S. (2017). The costs of production of alternative jet fuel: A harmonized stochastic assessment. *Bioresource technology*, *227*, 179-187.

Bond, J. Q., Upadhye, A. A., Olcay, H., Tompsett, G. A., Jae, J., Xing, R., Alonso, D. M., Wang, D., Zhang, T., Kumar, R., Foster, A., Sen, S. M., Maravelias, C. T., Malina, R., Barrett, S. R. H., Lobo, R., Wyman, C. E., Dumesicb, J. A., & Huber, G. W. (2014). Production of renewable jet fuel range alkanes and commodity chemicals from integrated catalytic processing of biomass. *Energy & Environmental Science*, *7*(4), 1500-1523. http://dx.doi.org/10.1039/c3ee43846e

Brandt, K., Geleynse, S., Martinez-Valencia, L., Zhang, X., Garcia-Perez, M., & Wolcott, M. P. (2021a). *Alcohol to jet techno-economic análisis* (v. 2.1). doi:10.7273/000001461

Brandt, K., Tanzil, A. H., Martinez-Valencia, L., Garcia-Perez, M., & Wolcott, M. P. (2021b). *Fischer Tropsch techno-economic analysis* (v. 2.1). doi:10.7273/000001459.

Brandt, K., Tanzil, A. H., Martinez-Valencia, L., Garcia-Perez, M., & Wolcott, M. P. (2021c). *Hydroprocessed esters and fatty acids techno-economic analysis* (v. 2.1). doi:10.7273/000001460

Brandt, K., Eswaran, S., Subramaniam, S., Zhang, X., & Wolcott, M. P. (2022a). *Catalytic hydrothermolysis techno-economic análisis* (v. 2.1). doi:10.7273/000002564

Brandt, K., Tanzil, A. H., Martinez-Valencia, L., Garcia-Perez, M., & Wolcott, M. P. (2022b). *Pyrolysis techno-economic analysis* (v. 2.1). doi: 10.7273/000002563

ECB Group. 2021. *Omega Green*. https://www.ecbgroup.com.br/en/group/bsbios-paraguay/omega-green

IEA. (2021). *Renewables 2021: Analysis and forecast to 2026*. https://iea.blob.core.windows.net/assets/5ae32253-7409-4f9a-a91d-1493ffb9777a/Renewables2021-Analysisandforecastto2026.pdf

LATAM. (2022, April 6). LATAM seeks to reach 5% sustainable fuel use by 2030, favoring producers throughout South America. Wings of Change. https://www.latamairlines.com/us/en/press-room/releases/latam-sustainable-aviation-fuel

Olcay, H, Seber, G, Malina, R. (2013). *Life cycle analysis for fully-synthetic jet fuel production*. MIT Support for Honeywell Continuous Lower Energy, Emissions and Noise (CLEEN) Technologies Development, Report to the FAA.

® Omega Green is a registered trademark of BSBios Indústria e Comércio de Biodiesel sul Brasil S/A, Passo Fundo, Brazil.
® LATAM is a registered trademark of LATAM Airlines Group S.A., Las Condes, Chile.

Oriakhi, U. M. (2020). *A stochastic life cycle and greenhouse gas abatement cost assessment of renewable drop-in fuels* (Doctoral dissertation, Massachusetts Institute of Technology). Massachusetts Institute of Technology.
Pearlson, M., Wollersheim, C., & Hileman, J. (2013). A techno-economic review of hydroprocessed renewable esters and fatty acids for jet fuel production. *Biofuels, Bioproducts and Biorefining*, *7*(1), 89-96.
Seber, G., Malina, R., Pearlson, M., Olcay, H., Hileman, J., & Barrett, S. (2014). Environmental and economic assessment of producing hydroprocessed jet and diesel fuel from waste oils and tallow, *Biomass and Bioenergy, 67*.
Staples, M. D., Malina, R., Olcay, H., Pearlson, M. N., Hileman, J. I., Boies, A., & Barrett, S. R. (2014). Lifecycle greenhouse gas footprint and minimum selling price of renewable diesel and jet fuel from fermentation and advanced fermentation production technologies. *Energy & Environmental Science*, *7*(5), 1545-1554.
Stratton, R., Wong, H. M., & Hileman, J. (2010). *Life cycle greenhouse gas emissions from alternative jet fuels* (No. PARTNER-COE-2010-001). Partnership for Air Transportation Noise and Emissions Reduction.
Stratton, R. W., Wong, H. M., & Hileman, J. I. (2011). Quantifying variability in life cycle greenhouse gas inventories of alternative middle distillate transportation fuels. *Environmental science & technology*, *45*(10), 4637-4644.
Suresh, P., Malina, R., Staples, M. D., Lizin, S., Olcay, H., Blazy, D., Pearlson, M. N., & Barrett, S. R. (2018). Life cycle greenhouse gas emissions and costs of production of diesel and jet fuel from municipal solid waste. *Environmental Science & Technology*, *52*(21), 12055-12065.
Suresh, P. (2016). *Environmental and economic assessment of alternative jet fuel derived from municipal solid waste* [Master's thesis, Massachusetts Institute of Technology]. Massachusetts Institute of Technology.
Trindade, S. C., Nogueira, L. A. H., & Souza, G. M. (2019). Relevance of LACAf biofuels for global sustainability. *Biofuels*, 1-11.
Winchester, N., Malina, R., Staples, M. D., & Barrett, S. R. (2015). The impact of advanced biofuels on aviation emissions and operations in the US. *Energy Economics*, *49*, 482-491.
Yao, G., Staples, M. D., Malina, R., & Tyner, W. E. (2017). Stochastic techno-economic analysis of alcohol-to-jet fuel production. *Biotechnology for Biofuels*, *10*, 1-13.

Task 1 - Create Working Groups in Each of the LAC Countries Involved in This Project

Washington State University

Objective

The objective of this task is to engage with stakeholders from Ecuador, Dominican Republic, Costa Rica, and Colombia.

Research Approach

Under Task 1, the team has been working with groups in each of the LAC countries involved in this project. For Colombia, Dominican Republic, and Ecuador, our team took advantages of activities in these countries. Last year, we expanded our work to cover Costa Rica. A new graduate student from Costa Rica (Raymond Angulo Gutierrez) will join our research program in January 2025. Our team is in contact with stakeholders in all these countries (leaders: Lina Martinez [Colombia]; Manuel Garcia-Perez [Ecuador, Dominican Republic and Costa Rica]).

Milestones

- Expanded our team to include three students (Micaela Peralta, Paulina Paredes, and Raul Perez) from Ecuador and the Dominican Republic in Spring 2024. Rayman Angulo, a student from Costa Rica joined our program in Spring 2025.
- Prepared and released a technical report (by Claudia Valderrama and Lina Martinez) for Colombia in March 2024. Tittle: Sustainable Aviation Fuel Production in Colombia: Opportunities and Challenges. DOI: https://doi.org/10.7273/000006281
- The report was released during a visit to the Latin American and Caribbean Air Transport Association (ALTA) meeting in Bogota, Colombia. This report supported the creation of a roadmap approved by the government in the fall of 2024. According to the resolution 00090 of 2025 Colombia aim to produce 100 million gallons of SAF by 2025 and 450 millions by 2050. https://www.presidencia.gov.co/prensa/Paginas/Colombia-definio-hoja-de-ruta-para-producir-combustible-sostenible-de-aviacion-SAF-250122.aspx
- Participated in the SAF round table and worked on the creation of working groups on oils to jet, ATJ, municipal solid waste to jet, and energy crops to jet.

- Travelled to Ecuador (Paulina Paredes) in Fall 2024.

Major Accomplishments

- Worked with active working groups in Colombia, the Dominican Republic, Ecuador and Costa Rica. The First Workshop was hosted by ASCENT Project 093 by WSU in Bogota, Colombia, (March 15, 2024) with 37 attendees from diverse industries, universities, and the government.
- Worked closely (Lina Martinez and Marcela Valderrama) in 2024 with the Colombian Civil Aviation Authority (Aerocivil) on the Colombian SAF roadmap. This roadmap was released to the group in the Dominican Republic. The group is formed by academic partners coordinated by the Ministry of Higher Education and existing SAF round table coordinated by Instituto Dominicano de Aviacion Civil (IDAC). Universities and industries mainly form the working group from Ecuador. We are working to attract more industries (especially Petro-Ecuador) and government agencies.
- Made first contracts and recruited a graduate student from Costa Rica to work on this project with their civil aviation authority.

Publications

None.

Outreach Efforts

- Hosted the First Workshop: ASCENT 093 – Colombia Stakeholder meeting (Bogota D.C., Colombia, March 15, 2024).
- Presented at the Aerocivil round table meeting about chain of custody methods (Virtual, June 28, 2024).
- Supported Colombia's SAF roadmap by providing resources on tracking methods, setting direction, and reviewing documents.
- Organized a workshop on SAFs by the University of San Francisco de Quito on July 2024 with the participation of our two graduate students (Paulina Echeverria and Micaela Del Rocio).
- Participated (Raul Perez) in the 8th and 9th SAF Dominican Republic Roundtable (April 24 & 29, 2024) facilitating stakeholder engagement on SAF opportunities.

Student Involvement

Claudia Marcela Valderrama has been supporting the Colombian working group. Raul Perez has been supporting the Dominican Republic working group. Paulina Echeverria and Micaela Peralta are in contact with stakeholders in Ecuador.

Plans for Next Period

- Participate in the ALTA conference in March 2025 at the Dominican Republic. During this conference, our team will release our literature review supporting the work of the Dominican Republic SAF round table.

Task 2 - Conduct the Design and Analysis of SAF Supply Chains in Each of the LAC Countries Involved in the Project

Washington State University

Objective

The objective of this task is to estimate cost reduction opportunities if emerging hydrogen production technologies are co-located with SAF production technologies and existing infrastructure.

Research Approach

Under Task 2, our team will conduct the design and analysis of SAF supply chains in each of the focus countries in LAC. It will start as soon as students from Latin America start receiving the training prepared under Task 1. In these studies, we will try to answer the following questions: (1) LCA value for the feedstock and sustainability criteria compliance, (2) what public policies the countries should develop to grow the production of SAF in Latin America, and (3) design of supply chain and sitting of facilities.

Milestone

- Recruited graduate students from each of the countries and provided graduate courses for graduate students and technical support to the SAF round tables.

Major Accomplishments

The *Sustainable Aviation Fuel Production in Colombia: Opportunities and Challenges* report was published in March 2024 (Valderrama M and Martinez L, 2024). This report covers technical expertise, infrastructure, access to funding, biofuel policies, economic incentives, sustainability issues, and suitable land and crops. The students (Raul Perez, Paulina Echeverria, and Micalea Peralta) are currently drafting reports for the Dominican Republic and Ecuador. The first draft of the Dominican Republic report will be sent to stakeholders in March 2025. The Ecuadorian first draft report was completed in December 2024 and is now under internal review. Our goal is to share with the relevant stakeholders in Ecuador.

All the students are developing system dynamics models to describe the effect of policies and other incentives on feedstock availability and the number of facilities developed in the region. The conversion technologies included in the studies are HEFA, ATJ, Pyrolysis, and Gasification/FT plants.

Volpe started to collaborate with our Colombian partners, introducing the road network and running an initial proof of concept for the biodiesel supply chain. Volpe started initially with an analysis of Fuel Transportation Optimization Tool (FTOT) of the biodiesel industry to validate the model. The biodiesel supply chain includes crude palm oil extraction, biodiesel production, and truck distribution to the main blending facilities listed by the Energy and Mines Ministry. Information regarding pipelines was provided to Volpe. This model is now expanded to study HEFA production scenarios from the Colombian palm oil industry.

Publications

Martinez-Valencia, L., & Valderrama-Rios, C. (2024). *Sustainable aviation fuel production in Colombia: Opportunities and challenges*. Washington State University. https://doi.org/10.7273/000006281

Outreach Efforts

- Worked with Volpe to implement a FTOT proof of concept, focusing first on a road-only network. This model maps Colombia's road system, mills, biorefineries, and blending sites for the palm oil biodiesel supply chain.

Awards

None.

Student Involvement

Claudia Marcela Valderrama has been working on this task. Paulina Echeverria Paredes, Micaela Peralta, and Raul Perez Mena started on January 1, 2024. Rayman Angulo will start in January 2025.

Plans for Next Period

- Continue working with Volpe to refine the base case scenario for the supply chain in Colombia using FTOT, focusing on optimizing the existing biodiesel supply chain, including biodiesel conversion and blending facilities.
- Start FTOT work with Ecuador and the Dominican Republic.
- Continue developing system dynamics models for the main SAF technologies which will be used in the analysis of the potential to grow the industry in the different regions.
- Prepare a final version of the Dominican Republic Report and a revised version of the Ecuadorian overview socialized with our stakeholders.

Task 3 - Creating Training Modules, a Course, and Graduate Programs for Training Students

Washington State University

Objective

The objective of this task is to create a year-long training program to introduce the stakeholders to the design of SAF supply chain, as well as a master's program.

Research Approach

Under Task 3, the team will create training modules, a course, and graduate programs for the preparation of personnel involved in the design of SAF production supply chains. The training will start with students from Latin America.
The materials to be created will be based on methodologies and tools developed as part of ASCENT Project 001 and that have been used in the design of supply chains in the U.S. Our training materials will include (1) methodologies for the creation of waste biomass feedstock databases, geographic information systems (GIS), and facility siting (leaders: Michael Wolcott, Dane Camenzind, and Kristin Lewis), (2) supply chain configurations to capitalize on sale of the fuel commodity and valorizing environmental services (leaders: Lina Martinez, Michael Wolcott, Allyson Beall King), (3) logistics optimization (leaders: Eric Jessup, Dane Camenzind), and (4) SAF production technologies (mass and energy Balances [Aspen], TEA, and LCA) (leaders: Kristin Brandt, Manuel Garcia-Perez, Hanwu Lei). These training materials will gradually evolve into courses that will be offered in a certificate and a master's program (Hanwu Lei).

Milestones

- Completed the SAF lecture series (21 lectures in total) in October 2024. World lead experts in SAF participated in the lecture series. In total, 31 students participated in more than 75% of the lectures.
- Submitted the first draft of a SAF master program to the WSU senate.

Major Accomplishments

Our team made progress in two areas: (1) the lecture series and (2) the professional master's program and associated courses. The lecture series was launched on November 2, 2023, with participation from stakeholders in academia, government, and industry across four prioritized countries in Latin America and the Caribbean (Colombia, Costa Rica, the Dominican Republic, and Ecuador). During the reporting period, we covered lectures on the fundamentals of transportation economics, biofuel logistics, supply chain optimization, and systems dynamics. The program concluded on October 17, 2024, after a total of 21 lectures. In total, 31 students participated in more than 75% of the lectures and received a certificate of completion.

On October 1, 2024, the Department of Biological Systems Engineering submitted the curriculum design for a master's program in SAF production to the WSU Senate. To complete this program, students must complete two common classes, seven courses, and a capstone project. The common courses are: Sustainable Aviation Fuels Technology, Feedstock Assessment, and SAF Law, Policies, and Regulations. Students can obtain three certificates that, when combined, result in a master's degree. The first certificate, in SAF production technologies, comprises three courses: Biomass Conversion Technologies, SAF Techno-Economic Analysis (TEA), and Financing and Investment in Renewable Electricity and Hydrogen. The second certificate, in SAF law, policies, and systems view, includes three courses: Life Cycle Assessment (LCA), Supply Chain Analysis and Optimization, and Systems Dynamics. The final certificate, in SAF fuel certification, consists of two courses (SAF Fuel analysis Certification and Standarization and SAF Combustion and Emissions). This will be the first professional master's program in the world and will start in January 2026.

Publications

None.

Outreach Efforts

- Completed a series of 21 lectures as part of our *Sustainable Aviation Fuels Supply Chains Design and Analysis* program. In total, 101 participants registered initially; 31 received a certificate as an attestation of at least 75% attendance.

Student Involvement

Claudia Marcela Valderrama, Paulina Echeverria Paredes, Micaela Peralta, and Raul Perez Mena participated in the 2023–2024 lecture series.

Plans for Next Period

- Hold additional workshops with international organizations to enhance stakeholder engagement in Colombia, the Dominican Republic, and Ecuador.
  Continue working with the WSU Senate to secure approval for our master's program and develop new courses, aiming for a start in January 2026.

Project 094 Probabilistic Unmanned Aircraft System (UAS) Trajectory and Noise Estimation Tool

Georgia Institute of Technology

Project Lead Investigator

Prof. Dimitri N. Mavris
Director, Aerospace Systems Design Laboratory
School of Aerospace Engineering
Georgia Institute of Technology
Phone: (404) 894-1557
Fax: (404) 894-6596
Email: dimitri.mavris@ae.gatech.edu

Dr. Holger Pfaender
Aerospace Systems Design Laboratory
School of Aerospace Engineering
Georgia Institute of Technology
Phone: (404) 385-2786
Fax: (404) 894-6596
Email: holger.pfaender@ae.gatech.edu

University Participants

Georgia Institute of Technology (Georgia Tech)

- P.I.s: Dr. Dimitri N. Mavris (P.I.), Dr. Holger Pfaender (Co-P.I.)
- FAA Award Number: 13-C-AJFE-GIT-143
- Period of Performance: January 1, 2024, to December 31, 2024
- Tasks:
  1. Investigate statistical sampling techniques
  2. Investigate surrogate noise modeling approaches
  3. Develop an integrated probabilistic noise computation methodology
  4. Extend existing prototype noise engine capabilities
  5. Coordinate with the Federal Aviation Administration (FAA) and Volpe National Transportation Systems Center (Volpe)
  6. Documentation

Project Funding Level

The ASCENT Project 094 is funded by the Federal Aviation Administration (FAA) at the following levels: Georgia Institute of Technology ($335,000).

The Georgia Institute of Technology has agreed to a total of $335,000 in matching funds. This total includes salaries for the project director, research engineers, and graduate research assistants and for computing, financial, and administrative support, including meeting arrangements. Georgia Tech has also agreed to provide tuition remission for students whose tuition is paid via state funds.

Investigation Team

Georgia Institute of Technology

Dimitri N. Mavris (P.I.)
Holger Pfaender (co-P.I.), Tasks 1-5
Raphaël Gautier (research faculty), Tasks 1-5
Jiacheng "Albert" Xie (research faculty), Tasks 1-5
Venkat Sai Chinta (graduate student), Task 5
Nada Himdi (graduate student), Task 3 and 4
Lloyd Teta (graduate student), Task 2 and 5
Xi Wang (graduate student), Task 1

Project Overview

Context and Motivation

The unmanned aircraft system (UAS) market is expected to grow rapidly in coming years, with projections estimating the civil UAS market at $121 billion in the next decade. Multiple operators are currently developing and testing various concepts of operations that fall within the umbrella of urban air mobility (UAM), with the two main use cases being drone delivery and electric-vertical takeoff and landing (e-VTOL) air taxis. Like traditional aircraft operations, these novel concepts are expected to have an impact on the environment in which they operate, particularly regarding noise. Just as noise assessments of traditional commercial and general aviation fixed wing and rotary aircraft operations are completed today, similar noise assessments for UAM operations will be necessary.

Problem Definition

UAM operations bring unique requirements. First, UAM operations are expected to be denser than current general or commercial aviation operations, possibly by orders of magnitude. Thus, a noise assessment method should be able to manage large vehicle densities. Second, UAM vehicles are expected to be smaller and therefore quieter (for example, small drones for deliveries or helicopter-sized vehicles for e-VTOL air taxis, benefiting from novel electric propulsion systems). As a result, the noise footprint of such vehicles is expected to be more localized. Therefore, noise exposure levels should be estimated with sufficient resolution. Third, instead of primarily following fixed trajectories dictated by approach and departure routes around airports, UAM vehicles are expected to operate point-to-point within populated areas. Departure and arrival locations are expected to vary from day to day; delivery drones may depart from warehouses and deliver goods to different customers every day, and e-VTOL air taxis may allow their customers to be picked up and dropped off all around an urban area. Thus, a noise assessment method should be flexible enough to accommodate changing flight paths, and the resulting noise assessment should account for the variability introduced by these changes.

Research Objective

The objective of this research is to develop a novel noise estimation method/tool that supports the computation of noise resulting from the stochastic operation of UASs and other upcoming vehicle concepts with irregular locations and operations in large numbers.

Research Approach

While the outcome of ASCENT Project 009 provided a solid base for the noise engine, it lacked several capabilities needed to realistically simulate UAS operations and account for the different sources of uncertainty that are the focus of ASCENT Project 094. Thus, in the first phase of this project, the effort primarily consisted of developing these capabilities, which include (1) modeling customer demand, (2) introducing more varied operational concepts beyond simple point-to-point flights, (3) generating realistic trajectories that account for obstacles found in urban areas, (4) updating the simulation logic to provide computational speed-ups and modeling flexibility, and (5) improving the visualizations of probabilistic quantities over a study area. These efforts led to an updated workflow for the integrated capability developed in this project, which is depicted in Figure 1. In addition to capability developments, two collaborations were initiated that aim at validating the approach proposed and implemented for this project.

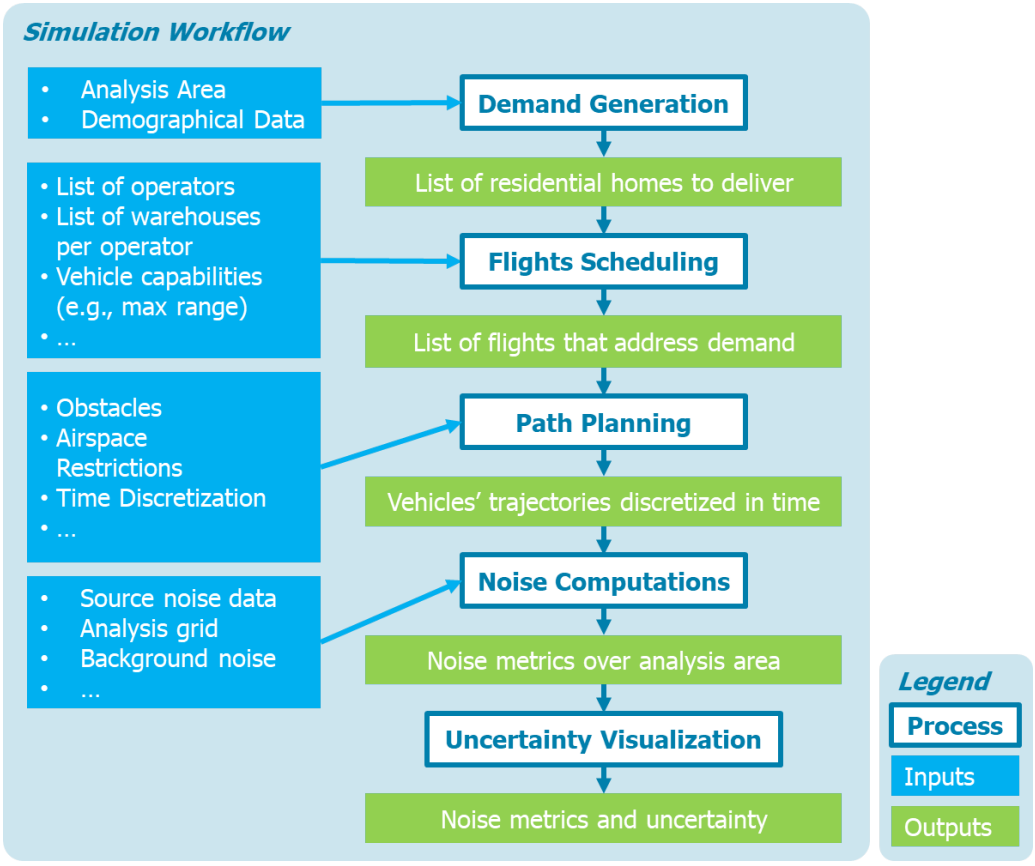

Figure 1. Workflow of the noise assessment logic in Phase 1.

Task 1 – Investigate Statistical Sampling Techniques

Georgia Institute of Technology

Objective

The objective of this task is to produce likelihood distributions for noise exposure maps at every receiver point, it is necessary to assign distributions to the variables that are the primary cause of the associated variability. In the case of UAS noise, these variables are thought to primarily be the day-to-day operations and trajectories. The first experiments performed in ASCENT Project 009 were conducted via Monte Carlo simulations; however, this brute force method is computationally expensive, requiring full reruns of the entire noise modeling with different inputs adjusted to the input variability. Other sampling methods are available that, if applied correctly, allow the computation of identical likelihood distributions but with a significantly reduced number of samples required. In this task, the ASCENT Project 094 team will investigate several sampling techniques and assess their applicability to the noise domain as well as their potential to reduce the computational time required to produce the desired probabilistic noise results.

The goal of the first task is to incorporate demand modeling as part of the analysis workflow such that the time and space distributions of flights match expected operations. In concrete terms, this means that instead of being sampled according to a uniform distribution within the analysis area under study, package delivery destinations are sampled according to the projected demand for online orders, which is estimated based on actual demographical information. To achieve this goal in an efficient manner, the proposed approach applies probabilistic and statistical computations and methods in an openly available demand model with openly available United States (U.S.) Census data.

Research Approach

Background

This task utilizes existing multinomial regression models from a published article (Jaller & Pahwa, 2020) to determine the online shopping demand in the study area. In that study, Jaller and Pahwa (2020) delved into the environmental impact of online shopping, focusing on how it influenced ground vehicle miles traveled and emissions. A key question addressed was whether and to what extent online shopping effectively reduces emissions compared with traditional in-store shopping. The findings revealed that the most significant factor in determining the environmental impact is the degree to which orders are consolidated.

The approach taken in this research involved a three-step modeling process. Firstly, the team utilized publicly available U.S. Census data to select representative individuals from two distinct areas: San Francisco, California, and Dallas, Texas. This method ensures that the study is both relevant and reproducible, as it relies on data that are easily accessible. Next, they developed their own demand model, drawing on data from the American Time Use Survey (Hofferth et al., 2017). The relevance of this model is underscored by the fact that the authors have made the resulting demand model available for public use.

Finally, the team conducted a straightforward environmental impact analysis. This analysis aimed to calculate the total number of miles traveled, differentiating between personal vehicle trips and delivery truck journeys. It also estimated the resulting emissions from these trips. However, this particular aspect of the study was deemed irrelevant to our current research interests. Overall, the study provides valuable insights into the environmental consequences of online shopping, particularly in terms of vehicle usage and emissions. Only regression coefficients from their model were used in this subtask, with the required input shown in Figure 2.

Factors and associated categories used to characterize individuals in the demand model

Gender	Male
	Female
Family Income	Poverty Level
	Low
	Lower Middle
	Median
	Middle Middle
	Upper Middle
	High

Age (as of 2016)	Silent [71,91]
	Baby Boomer [52,70]
	Generation X [37,51]
	Millennials [22,36]
	Gen Z [4,21]
Education level	No education
	Primary
	Secondary
	Graduate
Employment status	Employed
	Unemployed
	Not in labor force

Mobility-related difficulty	Has no difficulty in mobility
	Has difficulty in mobility
Region	Northeast
	Midwest
	South
	West
Metropolitan Statistical Area	Population > 1 million
Season	Winter
	Spring
	Summer
	Fall

Figure 2. Demand model inputs (Jaller & Pahwa, 2020).

Sampling Approach

The team developed a sampling method similar to that of Jaller and Pahwa (2020), as shown in Figure 3. In the demand model used for assessing the impact of online shopping, the Census data play a crucial role by providing the proportion of the population across various categories. These categories are used to create a synthetic population sample by sampling from these categorical distributions. However, it is important to note that this method does not account for dependencies between different factors, such as the relationship between age and family income level. Improvements to the model could be made by investigating ways to incorporate these dependencies.

The core of the demand model is a multinomial logit model, a type of classification model that predicts the probability of belonging to a certain class. In this context, the model considers four classes for a given individual on any given day, based on American Time Use Survey data: (1) no shopping ($k = 1$), (2) in-store shopping only ($k = 2$), (3) online shopping only ($k = 3$), and (4) both in-store and online shopping ($k = 4$).

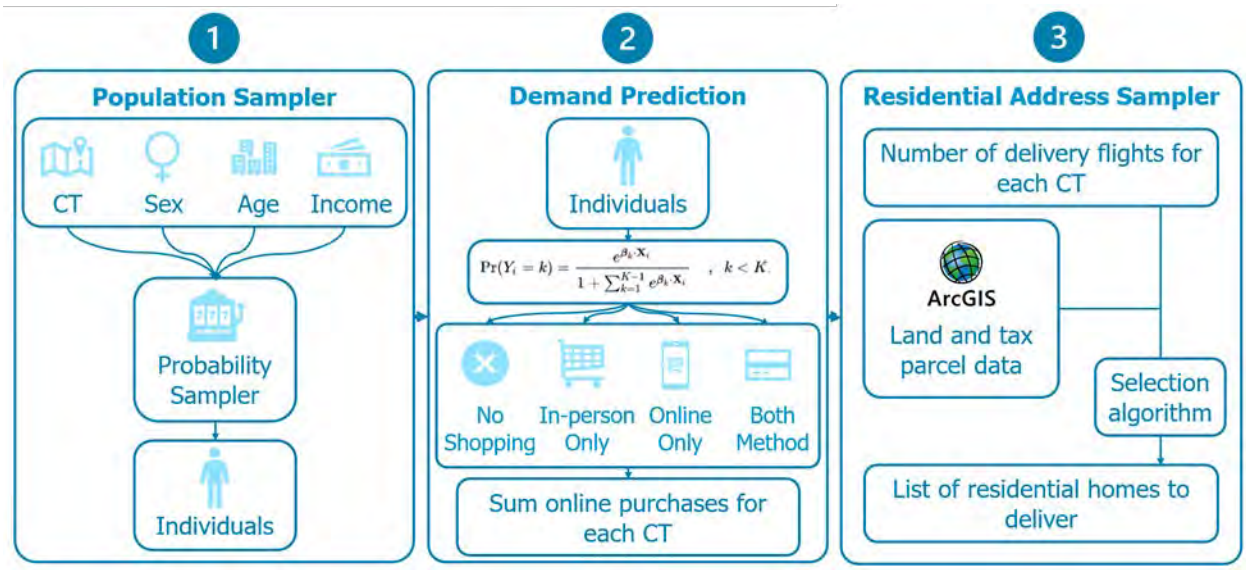

Figure 3. Sampling method workflow (Jaller & Pahwa, 2020). CT: Census tract.

The probability of an individual, characterized by their features $\boldsymbol{X}$, falling into one of these classes k is given by the following formula:

$$p(k|\boldsymbol{X}) = \frac{e^{\boldsymbol{\beta_k} X}}{1+\sum_{i=1}^{4} e^{\boldsymbol{\beta_i} X}} \quad \text{(Eq. 1)}$$

In this equation, the individual's features $\boldsymbol{X}$ are derived from the Census categories. The $\boldsymbol{\beta_k}$ coefficients ($1 \leq i \leq 4$) are the model coefficients provided by the authors of the study. For the purposes of this research, the primary interest lies in outcomes (3) online shopping only and (4) both in-store and online shopping. These outcomes are particularly relevant for understanding the shift in shopping behaviors toward online platforms and its subsequent impact on environmental factors such as vehicle miles traveled and emissions. A sampling method was first created following the process described in the published article, using Atlanta Regional Committee's census data (Atlanta Regional Committee, 2024).

Probabilistic Approach

To avoid the randomness of the sampling process for individuals in step 1, a probabilistic approach was developed as follows:

1. For every Census tract T_i, generate all possible combinations of household features, and for every combination of household features, evaluate the demand model to obtain the probability for that combination of household features, which allows us to evaluate the following formula:

$$p(household\ orders\ online|household\ in\ census\ tract\ T_i) = \Sigma_k^{N_{household\ info}} \left(p(household\ orders\ online|household\ info = H_k) \times p(household\ info = H_k|censu\ tract = T_i)\right) \quad \text{(Eq. 2)}$$

There is one such probability per Census tract.

2. For every Census tract, compute $p(household\ in\ census\ tract\ T_i)$ using the numbers of households in each Census tract.

3. At this point, for every Census tract, the actual probability sought can be computed:

$$p(household\ in\ census\ tract\ T_i|\ household\ orders\ online) = \frac{p(household\ orders\ online|household\ in\ census\ tract\ T_i)\ p(household\ in\ census\ tract\ T_i)}{\Sigma_{k=1}^{N_{tracts}} p(household\ orders\ online|household\ in\ census\ tract\ T_k) p(household\ in\ census\ tract\ T_k)} \quad \text{(Eq. 3)}$$

4. At this point, the information needed to sample from the multinomial distribution for which each category's probability is provided by $p(household\ in\ census\ tract\ T_i |\ household\ orders\ online)$. Sampling from the multinomial distribution gives us a number of deliveries per Census tract.

5. Within each Census tract for which there are deliveries, uniformly sample the corresponding number of homes among this tract's homes.

The strength of this approach lies in its reliance on publicly available nationwide statistics. By using data that are accessible and standardized across different regions, this methodology is not only relevant to the specific areas of study but also generalizable to other regions. This broader applicability is particularly valuable for elucidating and predicting the implications of online shopping and drone delivery in diverse contexts across the country.

Milestones

- Completed the sampling method in September 2023 and integrated with the flight scheduling task.
- Implement the probability approach (in process).

Major Accomplishments

From the implemented demand model, the online shopping demand for the State of Georgia was created using demographic data obtained from the census database (Atlanta Regional Committee, 2024), as presented in Figure 4. The demand was created with Census-tract resolution, corresponding to the smallest demographic data area, thus providing a more detailed and accurate representation of its population characteristics and therefore the online shipping demand.

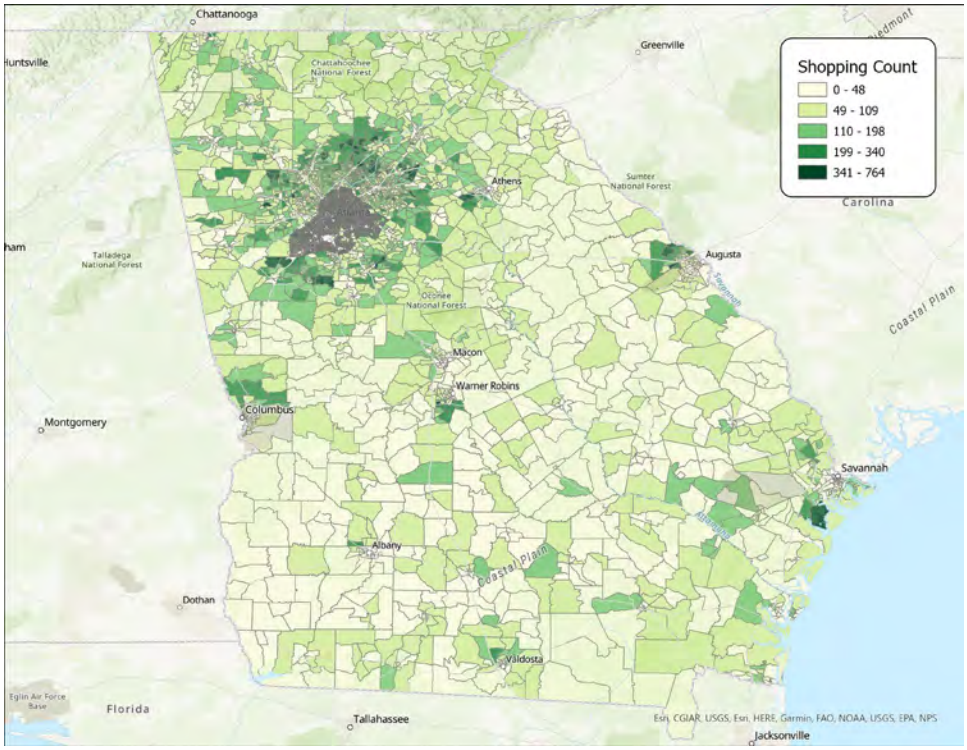

Figure 4. Online shopping demand for the state of Georgia.

Plans for Next Period

- Finalize the updated probabilistic approach for the demand model implementation.

Task 2 – Investigate Noise Surrogate Modeling Approaches

Georgia Institute of Technology

Objectives

In addition to the simplified sampling techniques, it is also possible to replace the full noise modeling with a reduced-order model. This surrogate model is a simplified mathematical representation of a high-fidelity noise study. To generate such a simplified model, a complete high-fidelity study will be created. This high-fidelity study can then be used to sample the input parameter space. Subsequently, the results can be applied to generate a much-simplified reduced-order model. This resulting surrogate model will serve as a stand-in for the full high-fidelity study with high statistical confidence. However, this surrogate model can also be used as a simplified transfer function to which the required input distributions, such as flight operations and trajectory variations, can be rapidly sampled in order to produce the desired output likelihood distributions with significantly reduced computational effort. This aspect is important for achieving rapid and efficient modeling of a potentially large number of vehicles and operations or a large area while still producing distributional results.

The first two efforts undertaken in the context of this task are (1) to reduce the geographical area over which the vehicle noise is propagated to the area in which the propagated sound level is noticeable instead of propagating over the complete analysis area (Subtask 2.a) and (2) to identify and compare a number of surrogate modeling approaches to replace the noise model (Subtask 2.b).

The potential for significantly decreasing the number of computations by reducing the geographical area over which noise is propagated, and therefore the number of receptors to which the noise must be propagated, was identified at the conclusion of ASCENT Project 009 and can be pursued in addition to surrogate modeling. To enable this, a systematic approach for computing a threshold distance around simulated vehicles must be developed that accounts for the fact that the noise level at one receptor location may originate from multiple vehicles.

Research Approach –

Subtask 2.a – Limit Range of Noise Computations

The granularity identified as appropriate in ASCENT Project 009 for obtaining sub-decibel accuracy leads to an analysis grid whose cells are separated by a distance on the order of 15 ft. To cover the geographical spread of a major U.S. city's urban area, this results in an analysis grid comprised of millions of points. In the simulation approach developed in ASCENT Project 009, the noise produced by every simulated vehicle at every time instant of the simulation was propagated to all cells in the analysis grid, resulting in a high computational burden and high computational times. This first effort aimed at assessing the feasibility and expected gains to be obtained by restricting the range around simulated vehicles over which noise would be propagated, on the basis that noise levels rapidly diminish with increasing distance from the noise source because of energy conservation and atmospheric absorption.

Figure 5 depicts the evolution of the sound pressure level as a function of distance from the noise source. The vehicle considered here is a small unmanned hexacopter manufactured by DJI® whose noise footprint was experimentally determined by Heutschi et. al. (2021). We observe that beyond approximately 1.1 km, the sound pressure level falls below typical background noise levels (30 dB). In this case, limiting the propagation distance to this threshold, instead of conducting propagation to all virtual receptors in the study area, would provide significant performance improvements.

® DJI is a registered trademark of Sz DJI Technology Co., Ltd., Shenzhen, China.

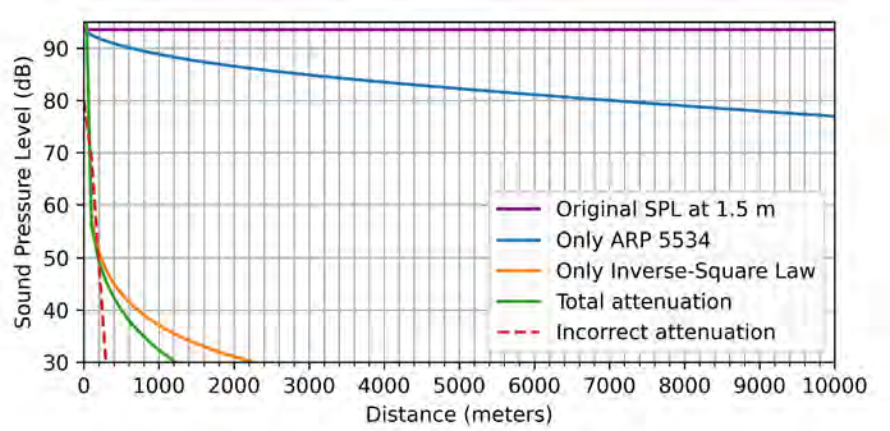

Figure 5. Evolution of sound pressure level (SPL) as a function of distance.

To generalize this approach to all vehicles considered in the simulation, it will be necessary to introduce a step in which this distance threshold is computed for each considered vehicle based on its specific source frequency distribution and amplitude. In addition, the possibility of interactions between multiple vehicles simultaneously located within the range of a given receptor will require additional logic to ensure that such situations do not lead to an underestimation of the resulting sound exposure level. Preliminary formulation work has shown that an analytical approach would allow the threshold distance to be updated based on the maximum number of vehicles concurrently operating within the simulation.

Subtask 2.b – Surrogate Modeling Study

1. *Objectives*

We aim to develop a surrogate model that replicates the output of a high-fidelity noise model with reduced computational complexity. The surrogate model should ensure a high degree of accuracy (high statistical confidence) while offering a considerable time improvement compared with the actual noise model.

2. *Approach*

The methodology involves three high-level steps, starting by identifying and fitting different types of surrogate models and then assessing these surrogate techniques based on computational time and accuracy. The final step is to select the most suitable approach. The following surrogate modeling techniques were considered in the modeling study.

Polynomial Response Surface Equations

The response surface equations (RSE) involve fitting a polynomial equation to the data points generated by the high-fidelity noise model. The general form of a second-order polynomial RSE is as follows:

$$\hat{f}(x) = \beta_0 + \sum_{i=1}^{n} \beta_i x_i + \sum_{i=1}^{n} \sum_{j=1}^{n} \beta_{ij} x_i x_j \quad \text{(Eq. 4)}$$

where $\hat{f}$ is the response variable, x_i and x_j are predictor/weight basis functions, and the β terms are coefficients determined by training/fitting the model. The linear regression found in the "scikit-learn" Python® library was used to fit the model (Scikit-Learn Developers, 2023a).

Radial Basis Functions

Radial basis functions (RBFs) are used for interpolation in multidimensional space. They depend on the radius between two training points. Typically, the 2-norm Euclidian radial distance is used to develop an RBF of the following form:

$$\hat{f}(x) = \beta_0 + \sum_{i=1}^{n} \lambda_i \phi(\|x - x_i\|) \quad \text{(Eq. 5)}$$

® Python is a registered trademark of Python Software Foundation, Beaverton, Oregon.

where λ_i are the weights, ϕ is the RBF, x is the input vector, and x_i are the centers of the RBF. The RBF was implemented by using SciPy's cdist, with a focus on multiquadric functional basis forms and a simple linear solver (Scikit-Learn Developers, 2023b).

Artificial Neural Networks

Artificial neural networks (ANN), inspired by biological neural networks, consist of layers of interconnected nodes. This model can learn nonlinear relationships and is thus capable of capturing complex patterns in data. A typical ANN has a structure with an input layer, one or more hidden layers, and an output layer. The neurons in these layers are interconnected with adjustable weights. The multi-layer perceptron regressor model from the "scikit-learn" Python package was employed (The Scipy Community, 2019).

3. Interpolation

Interpolation involves constructing new data points within the range of a discrete set of known data points. Linear interpolation is the simplest form, but higher-order polynomials can also be used for more complex datasets. The model was implemented through SciPy's interp1d (The Scipy Community, 2023).

4. Surrogate Modeling Process

Figure 6 depicts the surrogate modeling process.

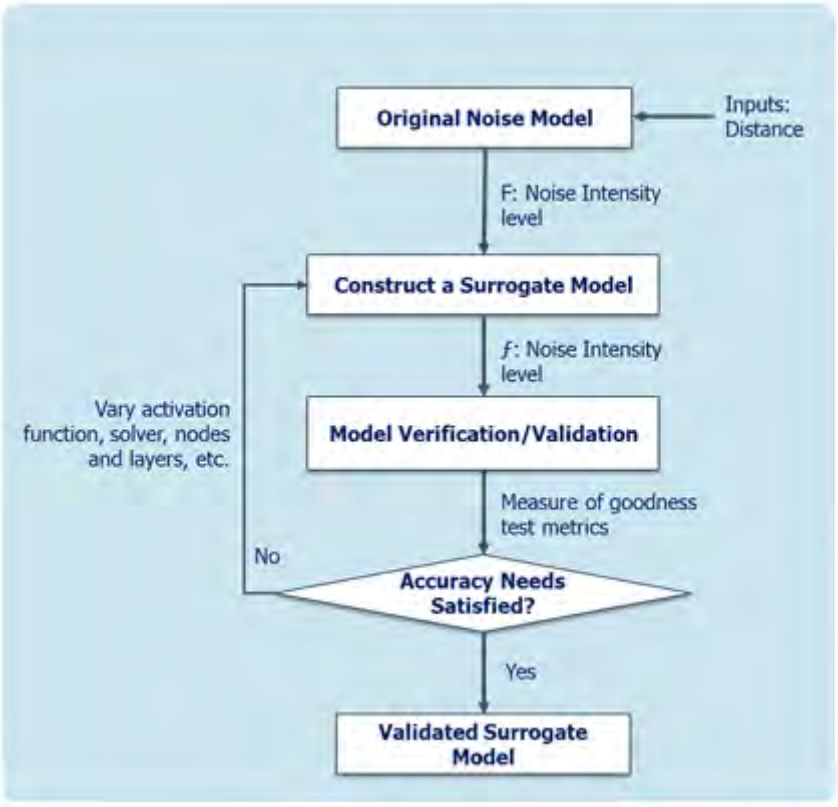

Figure 6. Surrogate modeling workflow.

Data Sampling

The high-fidelity study is used to sample the input parameter space. This step involves selecting a representative subset of the original model's input–output pairs.

Model Training and Validation

The surrogate models are trained on the sampled data. The training process involves adjusting the model parameters to minimize the difference between the model predictions and the actual data. Model validation is then performed on validation data, a set of model observations that were not used to train the surrogate model, thus ensuring the ability of the model to generalize.

5. *Surrogate Assessment*

The trained models were assessed based on two high-level metrics, surrogate accuracy and surrogate computational time. The accuracy of the model was verified based on validation metrics and validation plots.

Validation Metrics

- **Coefficient of determination (R^2):** This metric indicates the proportion of variance in the dependent variable predicted from the independent variables. A value closer to 1 suggests higher model accuracy. The lower the R^2 value, the greater the variance of the error compared with the response variance.
- **Mean absolute error:** This metric measures the average magnitude of the errors in a set of predictions, without considering their direction.

Validation Plots

- **Actual vs. predicted plots:** These plots compare actual values from the high-fidelity noise model with values predicted by the surrogate models. Ideally, the points should lie close to the 45° line, indicating high accuracy. Deviations from this straight diagonal line are due to inaccuracies introduced by surrogate modeling. Figure 7 presents examples of the actual vs. predicted plots used in the validation process.
- **Residuals vs. predicted plots:** These plots illustrate the difference (residuals) between actual and predicted values against the predicted values. The residuals should be randomly distributed and centered around zero.

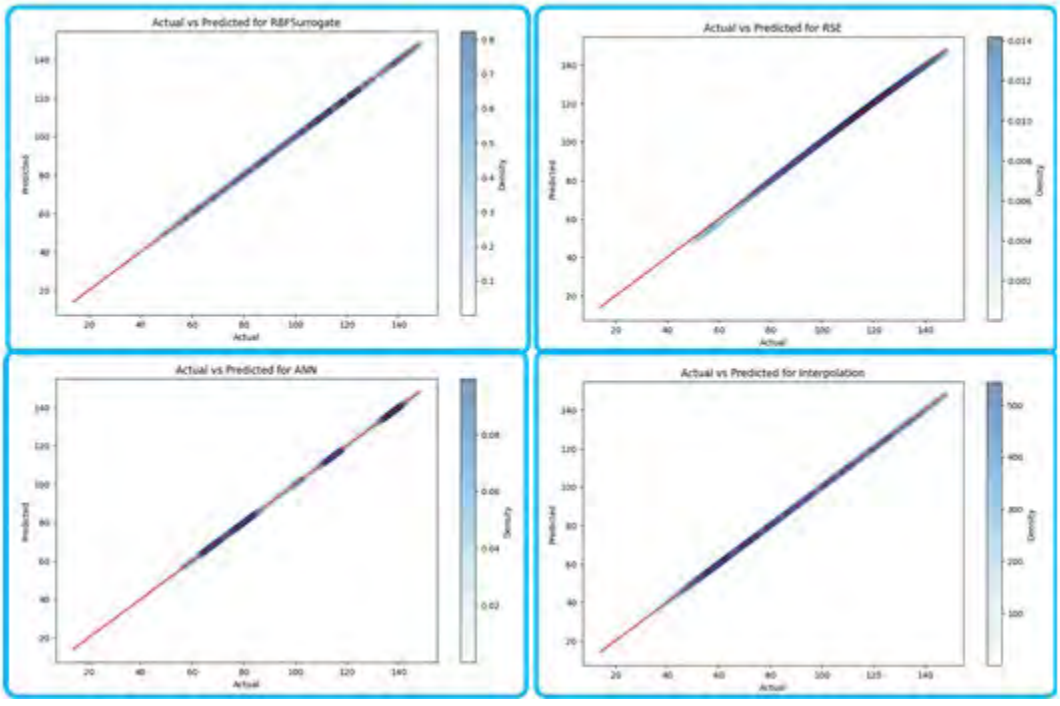

Figure 7. Actual vs. predicted plots for different surrogate modeling approaches. ANN: artificial neural network; RBF: radial basis function; RSE: response surface equation.

6. Computational Time Evaluation

The surrogate computational time represents the time needed to run a trained model for predictions. Note that the time needed to train a model is not considered in the study because we are assessing the computational time required to make predictions: Are we going faster than the original model?

7. Implementation

It is important to note that different sizes of prediction samples result in different prediction times; that is, a prediction with many sample points requires more prediction time. However, the computational time may not be linear with respect to the number of prediction samples; thus, we also study the evolution of prediction time vs. the number of prediction points. Prediction batches of different sizes, ranging from 100 to 100,000, were considered. The time is measured using the "timeit" Python module to evaluate the computation time for each prediction batch size. The surrogate is trained once using the same number of points, with the training dataset fixed at 30,000 points.

8. Results and Surrogate Model Selection

To ensure surrogate accuracy, validation metrics and plots for different surrogates were assessed. Figure 7 and Figure 8 display the validation plots of actual vs. predicted and residuals vs. predicted, respectively, for each considered surrogate modeling approach. The actual vs. predicted present a 45˚ diagonal line as desired. As stated, any deviations from a straight diagonal line are due to inaccuracies in surrogate modeling. The R^2 values are also assessed to check for the best fit for each surrogate model. The results in Table 1 show that that RBF and interpolation surrogate models have R^2 values of 1, indicating an almost perfect fit. The RSE and ANN models also demonstrate high R^2 values, suggesting a high level of accuracy, as the amplitude of the error is insignificant compared with the total amplitude of the response variations.

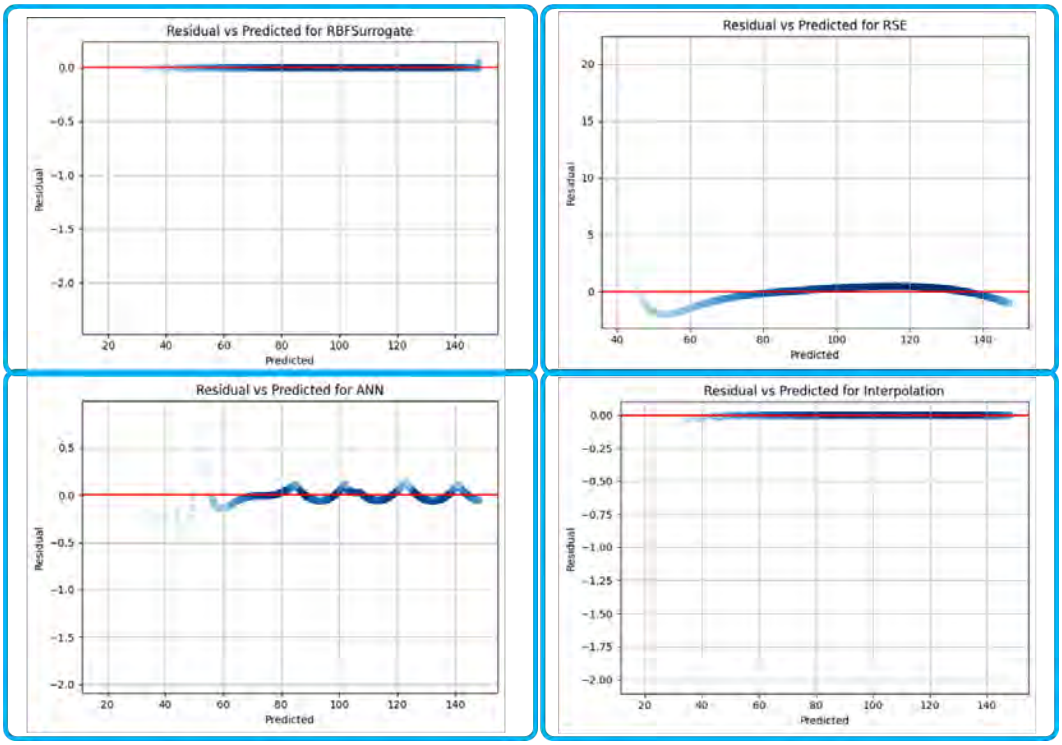

Figure 8. Residuals vs. predicted plots for different surrogate modeling approaches. ANN: artificial neural network; RBF: radial basis function; RSE: response surface equation.

Table 1. Quality of surrogate models.

Surrogate model	R^2
Radial basis function	1
Response surface equation	0.99695
Artificial neural network	0.99998
Interpolation	1

The residual plot results are consistent with the actual vs. predicted plots: the residuals for the RBF and interpolation models show less deviation, indicating that these models have a higher accuracy in emulating the high-fidelity noise model. The spread of residuals in the RSE and ANN models is wider, indicating a lower degree of accuracy.

1. *Impact of Prediction Points*

Figure 9 shows two plots depicting the computational time and relative computational time as a function of the number of prediction points for each surrogate model and the actual model. Figure 9 (left) shows the computational time (in seconds, on a logarithmic scale) required by each model as the number of prediction points increases. The surrogate models all start with relatively low computational times for small numbers of prediction points, with the time increasing sharply as the number of prediction points grows. As the number of prediction points increases, the ANN and RBF models show a steady increase in computational time, but they remain significantly faster than the actual model. The RSE and interpolation models demonstrate the best performance among the surrogates, with interpolation being the most efficient. Their computational times increase more slowly and remain several orders of magnitude lower than that of the actual model, even at 100,000 prediction points.

Figure 9 (right) presents the relative computational time, which is a ratio of the computational time of each surrogate model to that of the actual model (on a logarithmic scale). The relative computational time for the ANN and RBF models is above 1, indicating that these models are both less efficient than the actual model, whereas the RSE and interpolation models have relative computational times of less than 1, thus reinforcing their status as being more computationally efficient than the actual model. It is also noted that the efficiency gains of the surrogate models are more pronounced at higher numbers of prediction points.

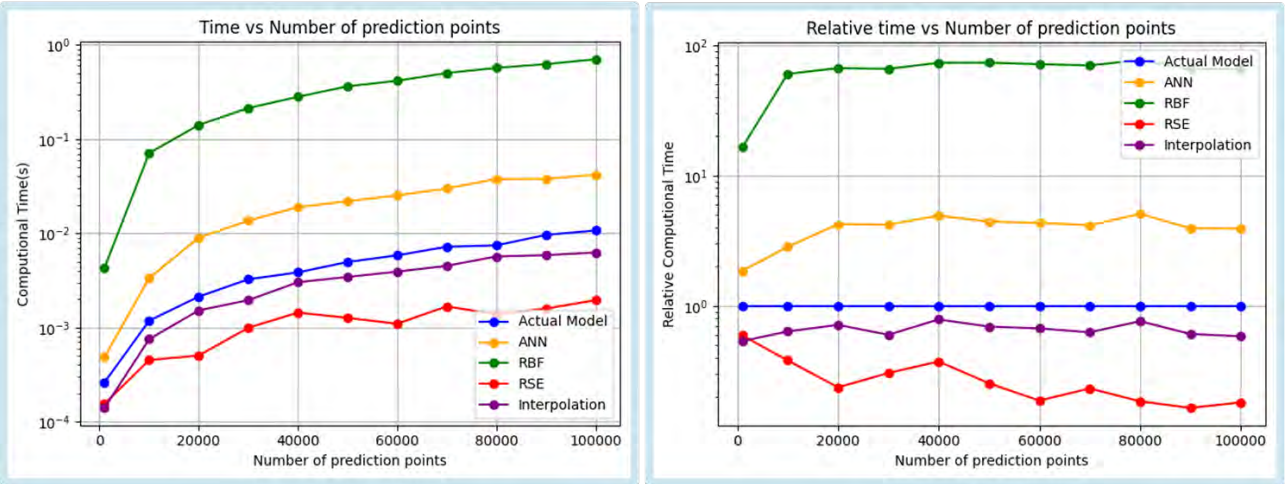

Figure 9. Left: Computational time vs. number of prediction points. Right: Computational times relative to the computational time of the actual model.

2. *Surrogate Accuracy vs. Computational Time*

Considering that the two attributes assessed for surrogate performance are surrogate accuracy and computational time, we provide a scatter plot for surrogate accuracy vs. computational time to determine whether any of the surrogate models

dominate the other surrogates in all attributes, as shown in Figure 10.

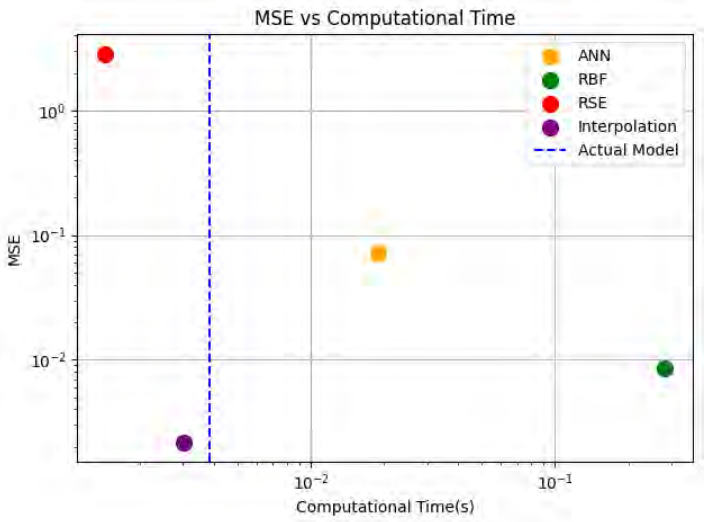

Figure 10. Mean squared error (MSE) vs. computational time.

3. Observations

Interpolation achieves the lowest mean squared error (MSE), indicating that it is the most accurate in making predictions among the surrogates evaluated. The ANN and RSE models have higher MSE values, suggesting that their predictions are less accurate compared with the interpolation and RBF models. The hierarchy of the testing error margin is $\epsilon_{RSE} > \epsilon_{ANN} > \epsilon_{RBF} > \epsilon_{Interpolation}$; thus, interpolation has the lowest error margin, followed by RBF, ANN, and finally RSE with the highest.

4. Actual Model Comparison

The blue dashed line in Figure 10 represents the computational time of the actual noise model. This serves as a benchmark for comparison. The computational times of both the interpolation and RSE models are to the left of this line, indicating that these models are faster than the actual model. Because we seek to accelerate the process, the interpolation and RSE models are the preferable options because of their lower computational times relative to the actual model.

5. Trade-off Analysis

There is an evident trade-off between accuracy and computational time among the surrogate models. Although the interpolation model is the most accurate, it has a higher computational time than the RSE model. In contrast, the RSE model offers a lower computational time at the cost of a higher MSE compared with the interpolation model.
The trade-offs highlighted by Figure 10 suggest that if the highest accuracy is required, interpolation is the best surrogate, given its lower MSE despite its slightly higher computational time compared with RSE. If the computational speed is more critical and some loss of accuracy can be tolerated, RSE might be the preferred choice.

Milestones

None.

Major Accomplishments

Identified and demonstrated multiple avenues for speeding up the noise assessment and making probabilistic assessments more practical. An initial study showed great potential for speeding up the noise assessment compared with the approach previously applied in ASCENT Project 009 by limiting the range of noise propagation. A comparison study of multiple surrogate approaches showed additional promise for speeding up this process.

Plans for Next Period

- Propagate the approach aimed at limiting the range over which noise is simulated.
- Implement and integrate the most promising surrogate modeling approaches into the noise assessment tool.

Task 3 – Develop an Integrated Probabilistic Noise Computation Methodology

Georgia Institute of Technology

Objectives

The objective of this task is to recommend a combined methodology that can quickly determine the statistical likelihood of where operations may occur, accompanied or integrated with a probabilistic determination of the resulting UAS noise exposure. ASCENT Project 009 provided a foundational noise engine but lacked several critical capabilities required to simulate UAS operations realistically and address the uncertainties emphasized in ASCENT Project 094. The first phase of this project concentrated on addressing these gaps by developing the ability to generate realistic two-dimensional (2D) path plans from staging locations to surrounding areas, compute flight probabilities to assess the likelihood of deliveries from specific staging locations and perform noise computations to produce time- and spatially dependent single-event noise metrics. Additionally, daily simulations were conducted to calculate probabilistic noise metrics over extended periods. These developments led to an updated workflow for the integrated capabilities, depicted in Figure 11.

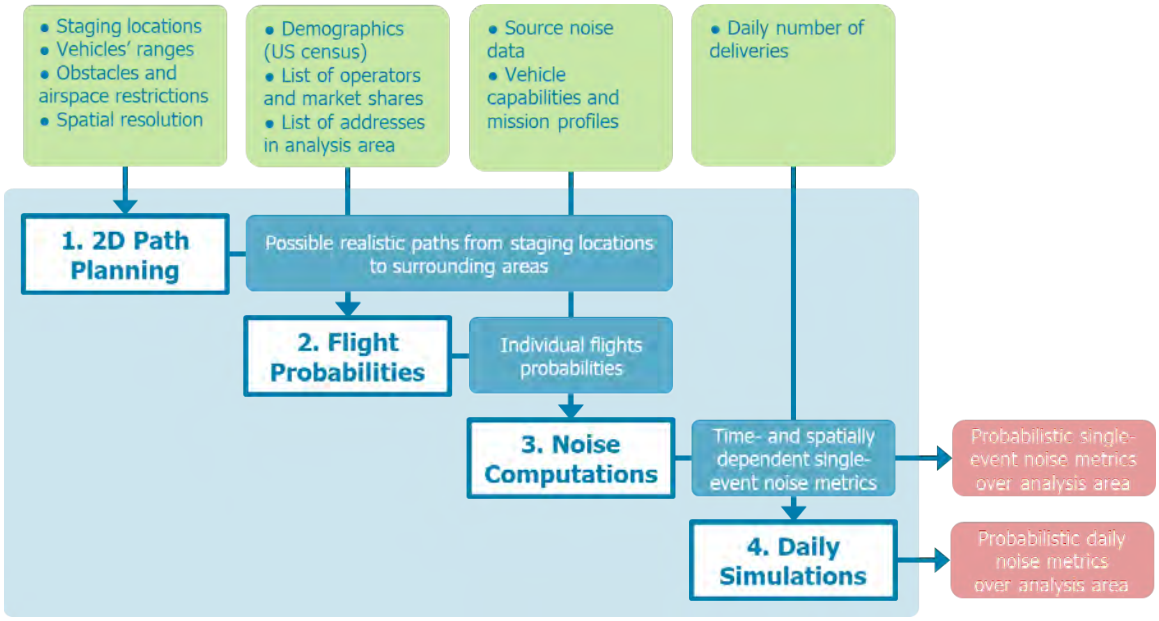

Figure 11. Updated workflow of drone delivery noise assessment.

This task will integrate the approach investigated in Tasks 1 and 2 and demonstrate the combined efficiency of the improved methodologies investigated to assess the wider noise implications of UAS operations as they expand and include larger operating areas, multiple operators, and multiple vehicles. More specifically, the dynamic nature of UAS operational drivers, including effects of market demand, service point locations (e.g., operating nests or delivery locations), airspace constraints, and possible operator/vehicle limitations, will require more flexible environmental analysis methods that can consider semi-randomization and statistically based quantification of unmanned aircraft activities.

The first effort of Task 3 was to develop the capability to model various operational concepts. Subtask 3.a aims to create a flight scheduling algorithm that produces a list of flights addressing the generated demand while accounting for the fact that multiple operational scenarios are possible, such as departures from multiple staging locations, multiple deliveries per flight, or the presence of multiple operators within the study area. Once the flights have been scheduled, their exact path can be planned, which is the focus of Subtask 4.a.

Research Approach –

Subtask 3.a – Modeling of Diverse Operational Concepts

1. *Introduction*

The input parameters for the system include (1) a comprehensive list of staging locations, typically warehouses, from where the UAS/drone will initiate the delivery journeys, and (2) a list of delivery locations, primarily residential homes, which will be the end points for these deliveries. Additionally, the system considers the maximum delivery radius for each drone, ensuring that deliveries are feasible given the drone's range. Lastly, the number of deliveries each drone can make per day is considered, which plays a vital role in scheduling and resource allocation.

The operational process of the drone delivery system involves two key steps. In the first step (i.e., the pairing step), each home within the service area is evaluated to determine whether it falls within the maximum delivery radius of any warehouse. If a warehouse is within range, the closest warehouse is assigned to that home. However, if no warehouse is within the maximum delivery radius, the home is not assigned a warehouse, and delivery to that location is deemed not possible. The second step involves the actual scheduling of deliveries. On each simulation day, delivery locations are randomly selected from the list of potential delivery locations. The corresponding warehouse for each delivery location is then identified using a lookup method, ensuring an efficient allocation of resources and timely deliveries.

2. *Newly Implemented Operational Concepts*

Per-Company List of Warehouses

The first improvement brought to the simulation is the ability to have multiple operators simultaneously operating in the study area, where each operator relies on its own staging locations. At this point, staging locations are assumed to be warehouses; thus, these two terms are used interchangeably in this discussion. This operational concept was implemented as follows, as presented in Figure 12:

- Each company has an attribute "list_of_warehouses" that consists of a list of warehouse identification numbers (ID).
- If warehouse W's ID is on the list, the company's delivery UAS can depart from that warehouse.
- When a company schedules a flight, its warehouses are located to determine from where the vehicle can take off.

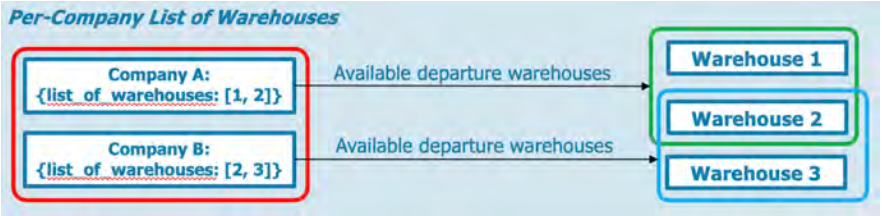

Figure 12. Notional illustration of the operational concept of "per-company list of warehouses."

Flights Between Warehouses

The second newly implemented operational concept allows us to model flights between warehouses. Such flights could be used to rapidly balance stocks between warehouses. This ability was implemented by extending the existing scheduling logic to include warehouses as possible destinations, as presented in Figure 13.

Figure 13. Notional illustration of the operational concept of "flights between warehouses."

Multi-Delivery Flights

The fourth and last additional operational concept is presented in Figure 14. This concept enables multiple deliveries within a single flight based on an optimization function that maximizes the number of houses associated with each drone and minimizes the number of drones used and the total distance flown by each drone. This feature would allow us to assign to each drone a list of houses that are relatively close for delivery.

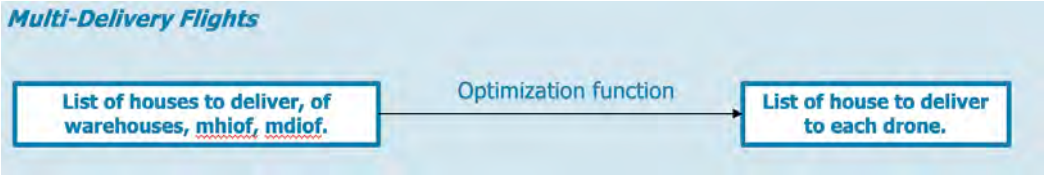

Figure 14. Notional illustration of the operational concept of "multi-delivery flights."

Examples of New Operational Scenarios

Figure 15 depicts the results obtained by applying the new operational concepts to two study areas: (1) the Memphis, Tennessee, study area (left), and (2) the Atlanta, Georgia, study area (right). All staging and delivery locations are notional at this point. We observe that the optimization algorithm efficiently places the mobile staging locations in order to maximize the number of reachable customers. On the right, it can be observed that the delivery radius of one of the warehouses (green) overlaps with the delivery radius of one of the staging locations (blue); this overlap occurs because the locations correspond to two different operators.

Figure 15. Example of a flight scheduling result over the Memphis, Tennessee, analysis area (left). Example of a flight scheduling result over the Atlanta, Georgia, analysis area (right).

3. Probabilistic Approach

To eliminate randomness in pairing warehouses and companies with delivery locations, a probabilistic framework was developed. Singular probabilities are computed at the household, company, and warehouse levels, considering factors

such as Census tract demographics, market share, and proximity. These probabilities are then combined to determine the likelihood of a specific warehouse delivering to a particular household. The detailed process is outlined below.

Household-Level Delivery Probability

The household-level delivery probability leverages the approach developed in Task 1, which evaluates the demand model for all possible combinations of household features within each Census tract. By applying this probabilistic framework, the likelihood of a household generating an order is determined based on Census tract demographics and feature probabilities.

Figure 16 illustrates the probability distribution of addresses for potential daily orders. Addresses are color-coded based on the likelihood of an order being placed within a day, with all addresses within a given Census tract sharing the same probability. Order probabilities range between 1% and 6%, but absolute values are not applied directly, as the total number of deliveries is determined by user input. This setup allows flexibility in adjusting delivery volumes while maintaining spatial probability patterns.

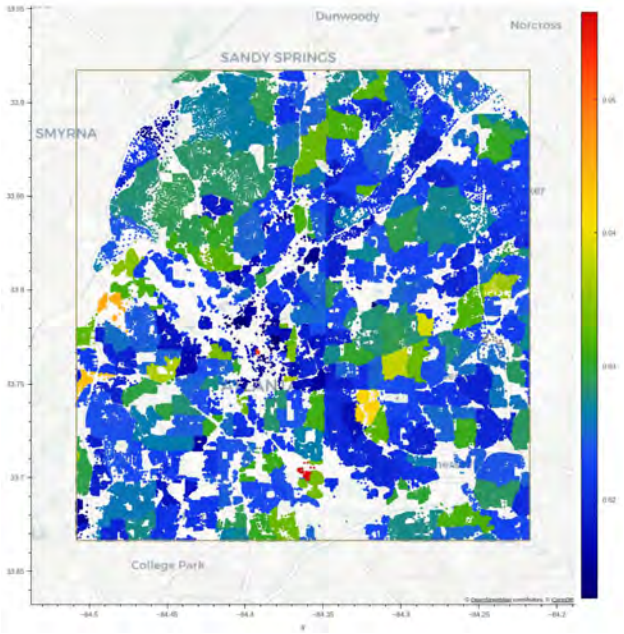

Figure 16. Probability distribution of daily UAS deliveries across addresses in Atlanta.

Company-Level Delivery Probability

This step was introduced to eliminate randomness in determining which operator performs the delivery, as the probability is heavily influenced by the market share of each operator. Operators with a larger market share have a higher likelihood of delivering to a household compared to others. To account for this, in the updated workflow, once the probability of a household receiving a delivery for being in a specific Census tract is determined, it will incorporate the market share of each company. Specifically, we multiply the household probability by the company's market share and then normalize it by dividing by the total market share of all companies delivering to that household:

$$p(household\ online\ order\ delivered\ by\ company\ C_j) = p(household\ in\ census\ tract\ T_i |\ household\ orders\ online) * \frac{Company\ C_j\ market}{Total\ market} \quad \text{(Eq. 6)}$$

Warehouse-Level Delivery Probability

This level was introduced to address the scenario where a company has multiple warehouses capable of delivering to the same household. Instead of randomly assigning a warehouse, we compute the distance between each warehouse and the delivery address, giving the highest probability of delivery to the closest warehouse. This probability is a user-defined parameter. Therefore, the probability of receiving a delivery from a specific warehouse is given by:

$$p(household\ delivered\ by\ warehouse\ W_k\ of\ C_j) = p(household\ online\ order\ delivered\ by\ company\ C_j) * p(warehouse\ w_k) \quad \text{(Eq. 7)}$$

This final probability is the one we ultimately consider for each household to receive a delivery, as it is more precise and takes all relevant factors into account.

Summary of Flight Probability Computation Process

Figure 17 summarizes the methodology for calculating the probability of occurrence for each flight based on demand distribution. The demand from each address is allocated across the various flights that can reach it, allowing orders at a single address to be fulfilled by different companies or staging locations. Market share is incorporated to determine each company's relative probability of servicing the demand, with preference given to the closest staging location for a given company. In this example, a specific flight pairs address 3,568 with Company A's staging location A2, demonstrating the assignment logic used to optimize fulfillment probability.

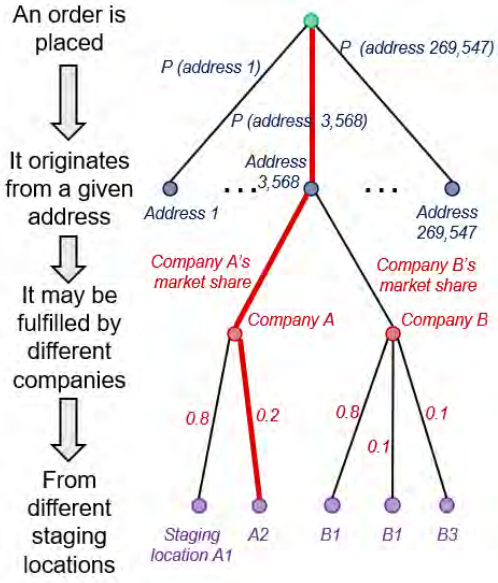

Figure 17. Logical breakdown of flight probability computation for UAS deliveries.

Figure 18 presents the results of applying the new approach to the households in the Atlanta, Georgia, area. Different colors in the figure indicate if a household's online order can be delivered by multiple companies and/or multiple warehouses. The probability of each household's online order being delivered by a specific warehouse of a specific company is calculated using the workflow illustrated in Figure 17.

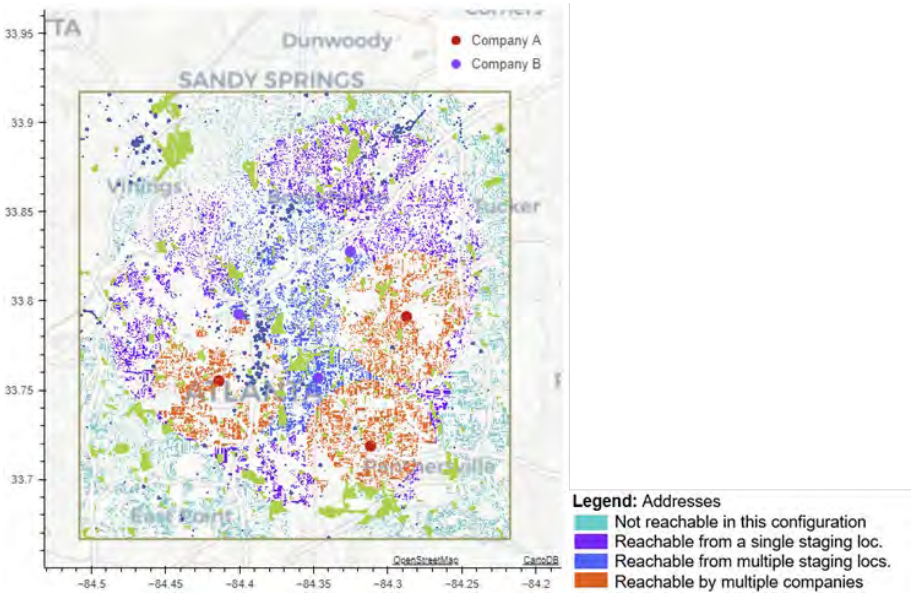

Figure 18. Spatial probability distribution of daily UAS delivery demand across addresses in Atlanta.

Subtask 3.b – Probabilistic Operational Noise Computation

1. Three-dimensional (3D) Path Planning

Before performing the noise computation, the 2D paths generated within the grid need to be transformed into 3D paths. To achieve this, optimal 2D paths that enable shortest distance while avoiding obstacles and restricted airspaces are selected and applied with vertical profiles. The details of the 2D generation are provided in Task 4. Two types of vertical profiles are considered, depending on the length of the path. The determination of the appropriate mission type involves evaluating both the horizontal distance of the path and the travel time, calculated using predefined inputs. The required inputs for the mission include cruise velocity, cruise altitude, climb/descent speed, and rate of climb/descent. Using these inputs, the horizontal distance traveled during each segment of the mission (i.e., climb, descent, cruise, etc.) is computed.

Two possible mission profiles are considered: (1) only vertical climb and vertical descent, and (2) vertical climb, cruise climb, vertical descent, and cruise descent. To determine the appropriate mission profile, the total horizontal distance of the path is compared against the requirements for the extended mission. Specifically, the horizontal distance covered during cruise climb and cruise descent is subtracted from the total path length. If the remaining distance is positive, then cruise climb, and descent will be applied in the mission profile. If not, the vehicle will only climb and descent vertically.

Once the vertical profile is determined, it is discretized into segments for further analysis. The discretized profile incorporates altitude variations and serves as the foundation for subsequent noise computations, enabling a detailed assessment of noise emissions along the selected path.

2. Noise Computations

Using the discretized 3D trajectories from the previous step, the actual noise computations are performed to analyze the impact of UAS operations on the surrounding environment. This process begins by propagating source noise from the vehicle's position at each time step along its trajectory to virtual receptors distributed across the analysis grid as shown in Figure 19. The propagation accounts for the spatial relationship between the vehicle and each receptor, ensuring precise modeling of noise exposure at different locations.

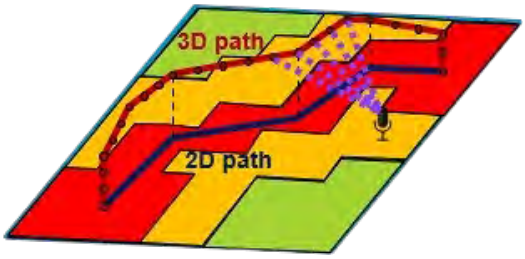

Figure 19. Noise computation along 3D trajectories.

For each flight, the propagated noise data are aggregated over time to calculate single-event noise metrics at each receptor. These metrics provide a detailed snapshot of noise exposure for a specific flight event. Additionally, probability distributions of these single-event noise metrics are generated at each receptor, incorporating the likelihood of different flight scenarios. This probabilistic approach ensures that variations in flight occurrences and trajectories are reflected in the noise analysis.

The outcomes of this step include pre-computed noise footprints for each flight and distributions of single-event noise metrics, such as sound exposure level (SEL), at the grid receptors' locations. These results are critical for understanding the spatial and temporal patterns of noise exposure and provide a foundation for further noise impact assessments.

3. *Daily Simulations*

Using the daily number of deliveries as input, the fourth and final step involves simulating the cumulative noise exposure over an entire day. This process begins by leveraging the pre-computed flight noise footprints, which contain detailed data such as grid cell locations, timestamps, and SPL in decibels. These footprints form the basis for constructing a realistic daily noise simulation.

A sample of flights is drawn to represent the expected number of daily deliveries, and these flights are scheduled across the simulated day. The schedule accounts for temporal distribution, ensuring that flights occur at realistic intervals. The simulation also considers potential interactions between flights, where overlapping noise events may occur due to simultaneous operations.

At each virtual receiver location, the sound levels from individual events are aggregated over time to capture the cumulative noise exposure throughout the day. This process is repeated multiple times using Monte Carlo simulations, where new samples of daily flights are drawn for each iteration. This approach enables the generation of probability distributions for daily noise metrics, such as the day-night average sound level (DNL), at every virtual receptor on the grid.

The outcome of this step is a detailed and probabilistic representation of daily noise exposure. The aggregated sound levels over time reveal the varying intensity of noise at each location, reflecting the effects of multiple single events within the day.

Subtask 3.c – Revised Computational Approach

The research conducted as part of ASCENT Project 009 identified a few shortcomings in the computational approach then adopted. In particular, that approach implicitly assumed that all vehicles independently contributed to the sound level received at receptors; however, it was demonstrated that when operations become sufficiently dense in a given geographical area, multiple vehicles may simultaneously emit noise to receptors at the same location, and the independence assumption may lead to a significant underestimation of the resulting sound level at the receptor. As a consequence, the computational approach was reformulated in order to account for instances in which multiple vehicles may simultaneously contribute to the sound level received at one given receptor location. The revised approach proceeds through time, timestep by timestep, instead of systematically vectorizing all computations.

The revised approach brings two additional benefits. First, because fewer operations are vectorized, a substantial reduction is expected for the memory requirements of the system on which the simulation is run. Second, stepping through time in the simulation is expected to allow for additional flexibility when identifying single events from the

viewpoint of individual receptors, allowing us to clearly identify when an event starts and ends based on a pre-defined rule, such as the common "10 dB down" rule.

Milestones

- Completed Subtask 3.a. The different flight scheduling algorithms are fully functional.
- Partially completed Subtasks 3.b and 3.c. The noise analysis modules will be integrated with the flight path generation modules of Subtask 3.a.

Major Accomplishments

- Implement the newly formulated revised simulation approach that provides more flexibility in defining events and computing various noise exposure metrics. Multiple operational concepts have been identified and implemented.

Plans for Next Period

- Finish the integration between the flight trajectory generation modules with the noise analysis module.
- Complete single-event simulations and perform daily simulations with uncertainties using the computed flight probabilities.

Task 4 – Extend Existing Prototype Noise Engine Capabilities

Georgia Institute of Technology

Objectives

The objectives of this task are to (1) implement a path planning algorithm to generate more realistic vehicle trajectories that avoid obstacles found in the study area, such as buildings and other landmarks, and 2) provide the review and selection of a visualization method that would enable the depiction of noise exposure metrics of interest along with the uncertainty associated with these metrics on a geographic information system (GIS)-like dashboard.

Development and testing in Ascent Project 009 demonstrated the potential for possible speed-ups to accelerate the computation of noise grids by using novel computational technologies such as cluster computation. As part of this effort, a prototype was developed that also includes user-interactive visualizations of UAS noise for specific study areas on map displays. This task will be updated to include the estimation of probabilistic distributions of UAS operations based on scalable numbers and locations for service points and stochastic operational frequencies and trajectories over large geographic areas. This task will also extend the prototype to include the capability to integrate the methods proposed in Tasks 1 and 2 and combined in Task 3 to visually present probabilistic distributions of UAS operations and UAS noise exposure over the analyzed geographic areas.

Research Approach

Subtask 4.a – Modeling of Realistic Vehicle Trajectories

1. *Analysis Grid Definition*

Each company operates its own set of warehouses, from which its delivery UAS can depart. These warehouses are considered fixed staging locations. When a company schedules a flight, the company's list of warehouses is checked to determine the vehicle's take-off location.

To define the delivery areas, the range around each warehouse based on the drone's maximum delivery range is calculated, considering half of that range in all directions. Additionally, we factor in the maximum distance at which the drone can be heard, which is controlled by a user-defined noise threshold. Finally, by combining the delivery areas from all warehouses, the total coverage area for the entire delivery network can be established.

2. *Environment Definition*

Before generating the paths, the operational environment was defined to account for obstacles that the UAS must avoid, with these obstacles being user-provided and discretized over the grid. Leveraging the FAA obstacles database, we included critical structures such as buildings and antenna towers, as well as parks, which serve as examples of restricted airspace. Additionally, delivery addresses were sourced from county databases to accurately represent customer locations within the analysis area.

In the context of ASCENT Project 009, vehicles were expected to fly straight from the origin to their destination according to a fixed-altitude profile. Although this approach offered a simple and convenient starting point for the initial proof-of-concept approach, it does not account for the possibly trajectories that vehicles will eventually need to follow in order to avoid the many obstacles existing in an urban environment where package delivery is expected to take place.

To account for this feature, we considered multiple path planning approaches from the literature. Because of its relative simplicity and maturity, the class of path planning over a discrete grid, including the well-known A* algorithm, was adopted. These algorithms operate over a discretized grid, which is already the case for the analysis grid used for the virtual receptors in the noise simulation. The grid cells obstructed by obstacles are identified and stored. The algorithm finds, if it exists, the shortest path between any starting cell to any destination cell in the grid, while avoiding all cells marked as obstacles.

In the context of ASCENT Project 094, the obstacles currently under consideration are buildings, which are obtained from the FAA obstacle list, and parks, which are obtained from openly available GIS databases. A custom approach was developed to effectively discretize these obstacles on the grid used for path planning. We note here that the developed approach is generalizable to all obstacles defined in the FAA obstacle database; therefore, new updates to the database can easily be imported in the simulation. Similarly, the logic developed for discretizing parks in the path planning grid relies on the definition of obstacles as a set of polygons, which is a generic method that can be generalized to other types of restricted geographical areas beyond parks.

The implementation effort started with a review of existing, off-the-shelf implementation of selected path planning algorithms. This initial review identified a lack of efficient Python implementations. Efficient implementation is crucial in the context of ASCENT Project 094 because path planning must be repeated at the beginning of every simulation run for every scheduled flight. Because probabilistic assessments require many simulation runs to generate distributional results, computational efficiency is a priority. Thus, we developed a custom implementation of the A* algorithm on a two-dimensional grid that does not require instantiation of the full grid, allowing the algorithm to run on a typical personal computer.

Because it only allows movements from one grid cell to its neighbors, the A* algorithm leads to unrealistic trajectories, such as “zig-zag”-shaped paths. A straightforward improvement to this is the Θ* (Theta) algorithm, which allows straight paths between any cells of the grid as long as the path is not obstructed by an obstacle. While conceptually simple, going from A* to Θ* requires the ability to check for obstructions between any two grid cells. This problem can be solved by ray-tracing algorithms. In this instance, computational efficiency is of utmost importance, as this process is repeated at every step of the path planning algorithm. Early testing indicated that a poor implementation could lead to a slowdown by orders of magnitude. As a result, a line-of-sight algorithm was efficiently implemented in Cython, a programming language and suite of tools that allows one to essentially write C code using a Python-like syntax. The resulting code can be compiled and easily called from the main Python program.

The resulting implementation allows one to generate a trajectory on the order of a tenth of a second. The actual duration depends on the granularity of the path planning grid and the distance between the departure and arrival locations; the further the distance between these locations, the greater the number of grid cells that must be explored to find the shortest path. An example of an outcome of path planning process is shown in Figure 20, where approximately 100 flights were generated over the Atlanta Midtown area. The green area in the center is Piedmont Park. Toward the west, multiple tall buildings are present that must be avoided by the vehicles. We observe that all red trajectories successfully reach their destination while avoiding obstacles.

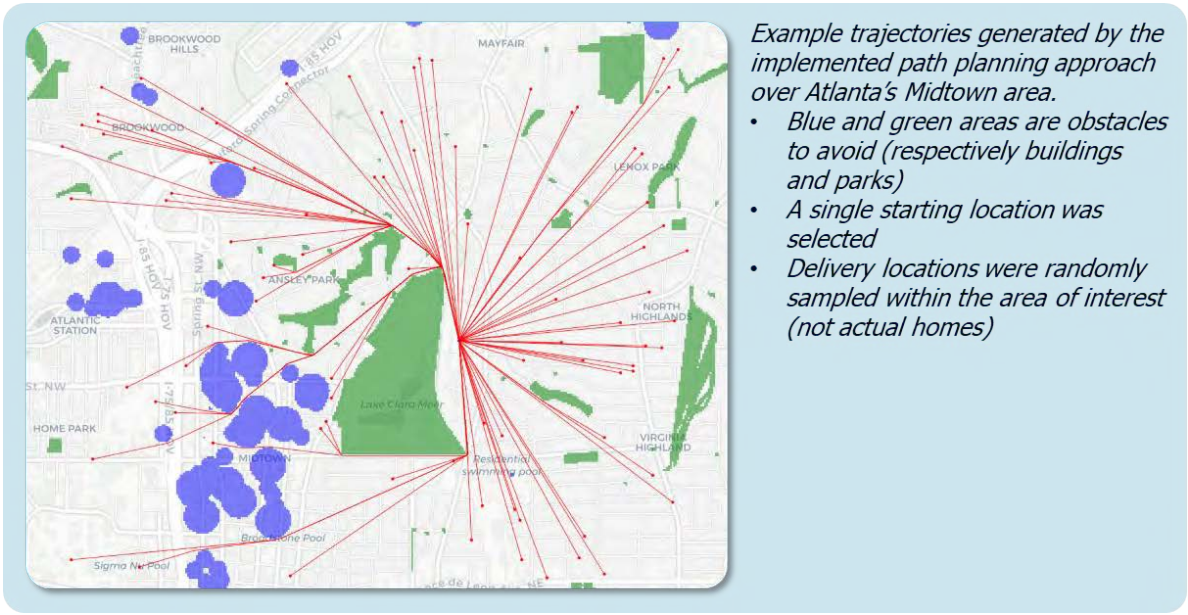

Figure 20. Example trajectories generated by the developed path planning logic. The study area under consideration is the Atlanta, Georgia, Midtown area.

Nevertheless, a critical issue with Θ* alone was that it required recalculating the path for every new flight, which is computationally expensive. This led us to adopt Dijkstra's algorithm[1] (further referred to as "Dijkstra'), which guarantees an optimal path for all grid cells from a given source without needing to recompute the entire path for every flight. Dijkstra allows us to precompute the shortest paths from a warehouse to all potential delivery locations, thus avoiding the need for repeated computations. This feature is particularly valuable when considering multiple delivery locations and obstacles across large urban environments.

The combination of Dijkstra and Θ* provided the optimal balance: Dijkstra ensures that the shortest path is computed once and reused, while Θ* smooths the paths by allowing direct, realistic trajectories as long as obstacles are avoided. This hybrid approach reduced computational overhead while ensuring realistic and efficient path planning in urban environments, where many obstacles like buildings and parks must be considered.

For example, Figure 21 showcases a study area of approximately 25 mi by 15 mi, divided into 50-ft cells (totaling over 5.6 million cells), Dijkstra efficiently planned paths for around 165,000 reachable grid cells marked in (in yellow) in about 5 min. The planned paths, marked in red, avoid obstacles (green) and extend the previously shown examples to longer and more complex paths.

[1] Dijkstra's algorithm is an algorithm for solving many single-source shortest path problems having non-negative edge weight in the graphs i.e., it is to find the shortest distance between two vertices on a graph. It was conceived by Dutch computer scientist Edsger W. Dijkstra in 1956.

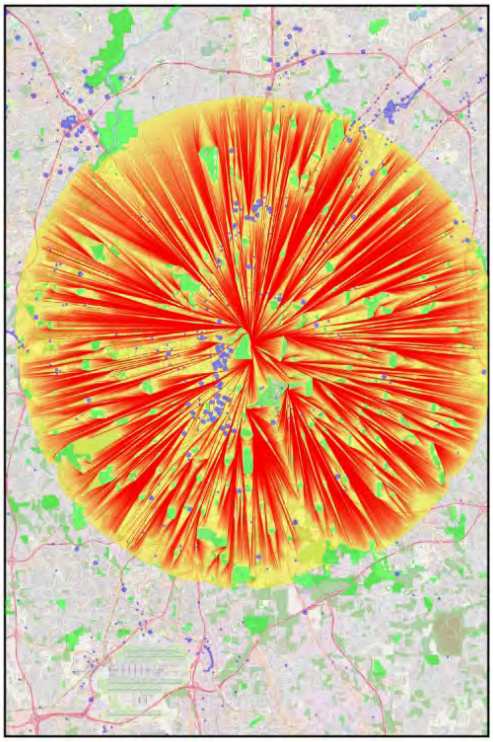

Figure 21. Reachable grid cells using Dijkstra/Theta*.

Upon identifying the reachable grid cells for each warehouse, the next step involves mapping the list of delivery addresses to these grid cells. Each address is checked against the reachable cells to determine if it falls within the delivery range of any warehouse. Addresses that do not correspond to any reachable grid cell are filtered out, ensuring that only addresses within the operational delivery zones are considered for planning. This step is crucial for optimizing the delivery process, as it removes unreachable locations, focusing the path planning on viable delivery targets within the grid.

On a larger scale, a notional example of path planning over the Atlanta, Georgia, area using Dijkstra, starting from six different staging locations is showcased in Figure 22. In this illustration, 1,000 paths are generated from each staging location to visualize potential routes toward customer addresses. The example includes a total of 285,789 addresses within the analysis area, resulting in 303,118 unique paths. This configuration highlights the variability in reachability, as some addresses are accessible from multiple staging locations while others remain unreachable due to environmental constraints and mapped obstacles.

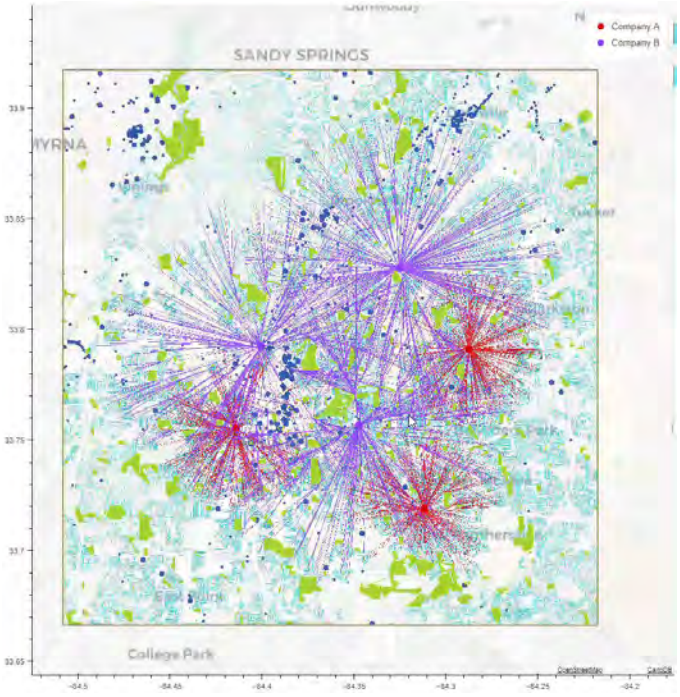

Figure 22. UAS path planning in Atlanta, Georgia, using Dijkstra/Theta.

Subtask 4.b – Visualization of Probabilistic Noise Exposure Metrics Over a Geographical Area
This task commenced with an intense literature review on different frameworks for visualizing uncertainty. Based on the review, we selected the Perlin noise model to visualize the uncertainty for our noise tool.

1. *Perlin Noise Model*

To visualize uncertain data fields, the Perlin noise model integrates color-scale visualization methods by controlling the model parameters. Based on the uncertainty of the data, the model effectively visualizes the uncertain scalar data fields in a combined manner, showing local data value and quality. The color-scale lookup is biased by a Perlin noise weighted by uncertainty data, allowing for a visualization of both the mean value and uncertainty information.

2. *Algorithmic Principle*

The objective of this study is to propose a universal method for visualizing both scalar data and associated uncertainty information, such as the error or standard deviation. The proposed method adheres to the following constraints:

- The approach should extend traditional one-dimensional color maps, ensuring that the resulting visualization remains readily comprehensible to individuals familiar with color maps.
- The representation of uncertainty data should not mask the fundamental data, nor should it introduce complexities, inaccuracies, or challenges in interpretation.

In a conventional 3D color-scale visualization, the data value $V(\vec{x})$ is mapped linearly to a color map coordinate and then to the corresponding red–green–blue color value, which is subsequently displayed in the 3D visualization. The proposed method introduces a modulation to this visualization by applying an uncertain value $U(\vec{x})$. The values generated by the Perlin noise model $n_{f_o,p}(\vec{x})$ are linearly scaled to ensure a null mean and to fall within the range of [-1,1]. Subsequently, the scaled noise is multiplied by the uncertainty value and added to the base value $V = (\vec{x})$.

The result is $V(\vec{x}) + n_{f_o,p}(\vec{x}) * U(\vec{x})$, which spans the range $[V(\vec{x}) + U(\vec{x}), V(\vec{x}) - U(\vec{x})]$. The range of the above resulting distribution will have a mean of $V(\vec{x})$ and serves as a color map coordinate in the visualization.

We implemented the Perlin noise model on a simple normal distribution with varying standard deviation to show the level of increasing uncertainty in the dataset. We employed the same algorithm as detailed above, with the results of the use case shown in Figure 23. The uncertainty of the data is shown to increase from left to right based on our Perlin noise texture without a masking of scalar data. A detailed level of pixel displacement can be achieved by tweaking the parameters of the Perlin noise model that will be employed for our noise computational model.

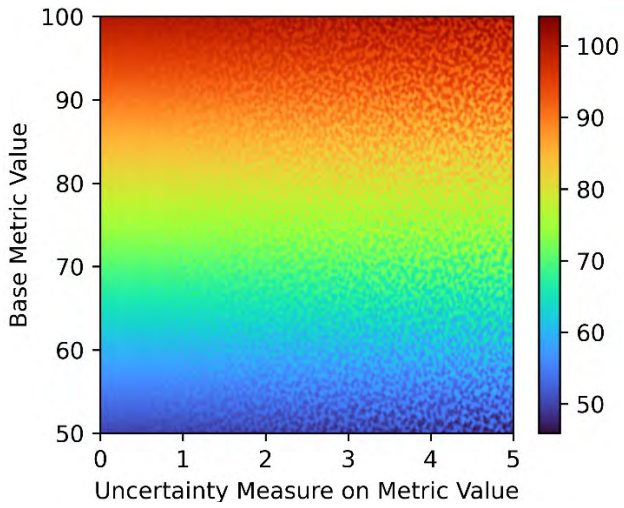

Figure 23. Test case result obtained by using the Perlin noise model.

Milestones

- Completed Subtask 4.a.
- Completed Subtask 4.b (stand-alone). This subtask will be integrated into the entire workflow.

Major Accomplishments

- Implemented and test a first version of the path planning algorithm.
- Selected the Perlin noise model as a method for visualizing noise assessment results.

Plans for Next Period

- Extend the path planning algorithm to the 3D case and integrate all steps of the noise assessment.

Task 5 – Coordinate with the FAA and Volpe

Georgia Institute of Technology

Objectives

The research team will utilize key noise computation methods for which experts reside at the FAA and Volpe. Likewise, to identify potential UAS noise source data and sample study data, it may also be necessary to coordinate with experts at the FAA and Volpe. This includes consultations regarding which noise metrics (e.g., A-weighted, equivalent continuous sound level [LA_{eq}], maximum noise level [LA_{max}], SEL, NA60[2], and potentially others) are the most appropriate for UAS noise and are amenable to probabilistic representations.

Two key collaborations were identified to enhance and validate the noise assessment tool under development. First, through collaboration with the FAA aeroacoustics team, flight test data for UAS vehicles of the relevant size class were obtained. These measurements should (1) enable the introduction of realistic source noise spheres in the simulation and (2) validate the noise propagation technique used in the noise engine. Second, through collaboration with the National Aeronautics and Space Administration (NASA) aeroacoustics team, input data were obtained for a UAM study conducted

[2] Number of flights above the 60 dB (A) per time period (NA = number above)

using the Aviation Environmental Design Tool (AEDT). For this case, replicating this study using the capabilities developed as part of ASCENT Project 094 would enable a higher-level validation.

Research Approach

Subtask 5.a – Leveraging of Causey Airport Measurements

1. *Objectives*

This subtask aims to validate the in-house noise analysis tool (ASCENT Project 094 approach) using Causey Airport UAS acoustics measurements. In 2021, an FAA-led team conducted a set of noise measurements at Causey Airport to characterize the noise produced by UASs during ground and airborne operations. In this experiment, the noise from three vehicles with different weights, speeds, and flight conditions was measured by two sets of microphone arrays: (1) for the flyover and (2) for the hover. Both ground-based and cable-suspended microphones were utilized in both layouts. The measurements were presented in terms of pressure time-history acoustic data stored in American Standard Code for Information Interchange (ASCII) files. This subtask uses the Causey Airport measurements to validate the in-house noise analysis used in this project, which was developed in ASCENT Project 009.

2. *Approach*

The validation involves two major steps. First, vehicle noise source data based on the Causey Airport measurements are generated by using the noise analysis tools developed by Volpe. Second, the in-house noise analysis code is used to re-generate the measured acoustics data based on the generated noise source data and the vehicle trajectories used in the Causey Airport measurements.

Noise Sphere Generation

Generating noise source data for UASs relies on two analysis tools from Volpe: (1) the Advanced Acoustics Model (AAM) and (2) the Acoustic Repropagation Technique (ART). The atmospheric conditions, microphone locations, and flight trajectories used in the Causey Airport measurements are first input to the AAM. Using time- and geometric-based analyses, the AAM calculates the propagation physics and geometric relationship between the noise source (i.e., UAS aircraft) and microphones; it then outputs a time-history file, including the mapped relationship on a sphere for each trajectory point. Along with the aircraft specifications and microphone measurement data, the generated time-history file is given as input to the ART to generate noise source data for the vehicle in terms of a noise sphere. This noise sphere is obtained by applying the propagation corrections determined by the AAM to the measured microphone spectral time histories.

Simulation of Noise Propagation

The generated noise sphere is then provided to the in-house noise analysis code. Using the same flight trajectory applied in the Causey Airport measurements, the noise levels at different points of interest are computed by the analysis code based on the noise sphere. In this validation, the points of interest are set to the microphone locations used in the Causey Airport measurements. If the computed noise levels match the measured acoustic data, the accuracy of the in-house noise analysis code will be validated. Running the in-house noise analysis tool for validation consists of five high-level steps. More details about each step are described in the following section.

3. *Replace point noise sources with noise spheres*

To ensure an apples-to-apples comparison between our results (ASCENT Project 094 tool) and results generated using the ART, we needed to provide the same inputs as such as the source noise, grid definition (receptor positions), and series of vehicle positions. Previously, the ASCENT Project 009 tool assumed that the noise source is isotropic, hence additional development was done to add the capability to take a noise source sphere as an input. In addition to computing the distance from a vehicle (source) position to each grid point (receptor), the extra steps added include computing the 3D angles between vehicle location/direction and grid receptor points. The computed angles are then used to interpolate the noise source data for noise propagation.

4. *File Parsing*

The inputs: grid definition, vehicle trajectory and noise source used for AAM propagation are provided as ART file formats that cannot be directly implemented in our Python-based noise analysis tool. The ART input(.INP) file contains Causey Airport trajectories, receptor points are in the comma-separated values (CSV) file and the noise source data are stored as a NetCDF (.NC) format. As such, file parsing algorithms were developed to seamlessly load the input(.INP) file, CSV file and NetCDF (.NC) file in the format expected by the tool. Figure 24 shows an example of extracting flight trajectory data, coordinates and time step from the input file to a data frame.

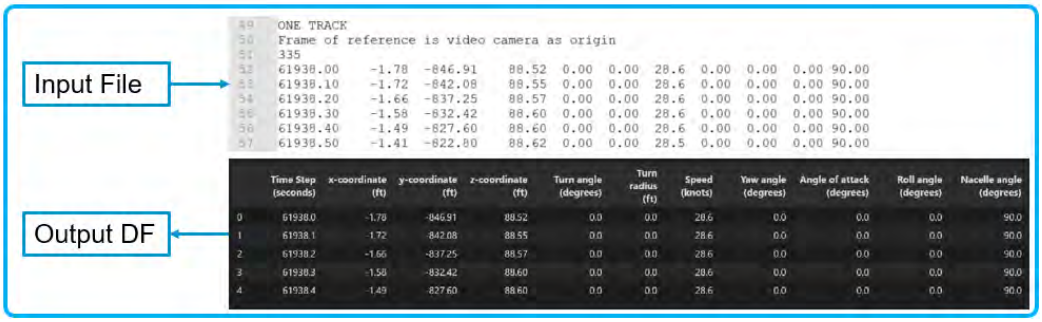

Figure 24. Parsing the .inp file to a Pandas DataFrame

5. Distance and Sphere Computation

The sound sphere angles were computed based on the description in the AAM technical manual (U.S. Department of Transportation Volpe Center, 2020). Figure 25 shows the description of the polar angle (theta) and azimuth (phi).

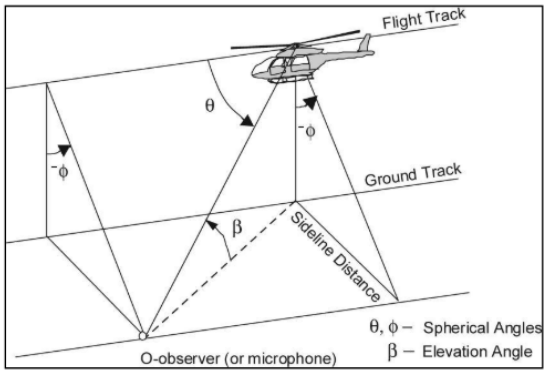

Figure 25. Sound sphere angles, adapted from U.S. Department of Transportation Volpe Center (2020).

For each point on the grid, the tool computes the:

- Distance from a vehicle (source) position to each grid point. This is computed as the length of the line segment between them$d(p,q) = \sqrt{\sum_{i=1}^{3}(q_i - p_i)^2}$ where p, q are two points (receptor and source) in the 3D space.
- The 3D angles; the elevation angle (angle with the z-axis) and the azimuth angle (angle in the x-y plane with respect to vehicle direction) from the source to each point in the grid. The vehicle direction at the point (x_i, y_i, z_i) is calculated as $\vec{v}_i = (dx, dy, dz) = (x_{i+1} - x_i, y_{i+1} - y_i, z_{i+1} - z_i)$. The vector is then normalized to give a unit direction of the vehicle at each point along the trajectory.

As an example, Figure 26 depicts a noise source as a red dot and the grid of virtual receivers as a scatter plot colored according to the distance from the source. The source coordinates and the angles between the source and one of the receivers are also shown for illustration.

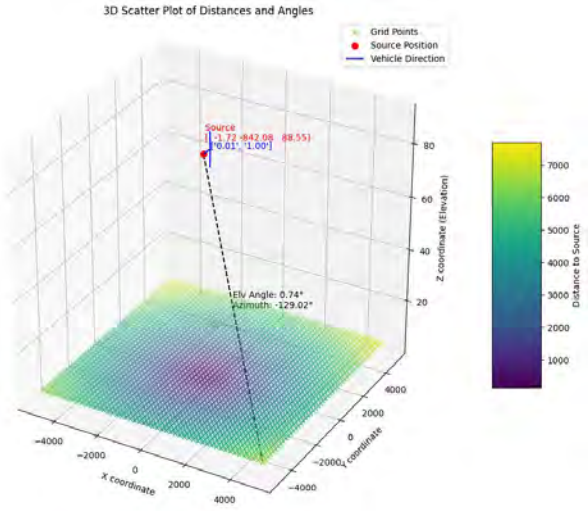

Figure 26. A 3D scatter plot illustrating distances and angles in a spatial context.

6. Validation Distance and Sphere Computation

As stated, ensuring the input fed into our tool is the same as for the AAM is important. Thus, after computing the distances and angles, the values were compared with the corresponding values in the time history file generated by the AAM. The scatter plot shown in Figure 27 was utilized to check the evolution of the results with time. This helped identify discrepancies in the azimuth computation which later updated.

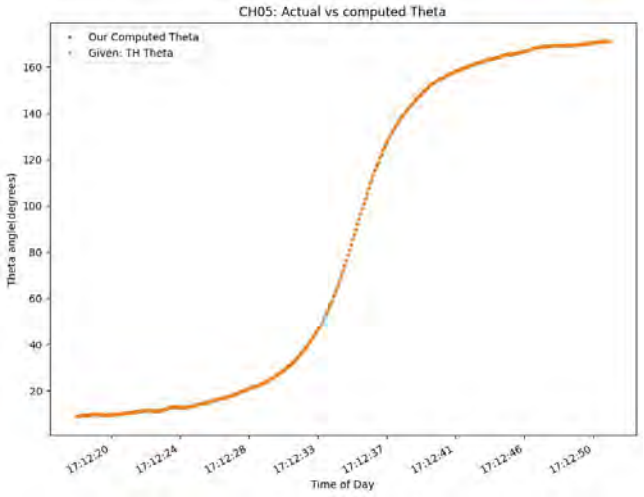

Figure 27. Actual vs. computed polar angle (theta).

7. Noise Sphere interpolation

The goal is to interpolate the noise source data (frequency and amplitudes) based on the input noise source angles. The loaded NetCDF noise source has 'PHI', 'THETA', 'FREQUENCY,' and 'AMPLITUDE' which are of shapes (37,), (37,), (31,), (37, 37, 31) respectively. AMPLITUDE data are in the shape of (37, 37, 31) suggests that for each (phi, theta) pair, there are 31 amplitude values, one for each frequency. The Scipy's RectBivariateSpline is used for interpolation due to its ability for vectorization to manage multiple (phi, theta) pairs of inputs.

8. Validating Interpolation

Figure 28 presents the contour plots of the noise levels with and without the interpolation. The left subplot displays the contours for the original amplitudes at the given 37×37 (phi, theta) pair values. A new finer grid of 100×100 (phi, theta) pair values were generated, and the amplitude corresponding to these pairs were interpolated and plotted in the right subplot. These two contour plots are almost the same, indicating that the interpolator is working correctly.

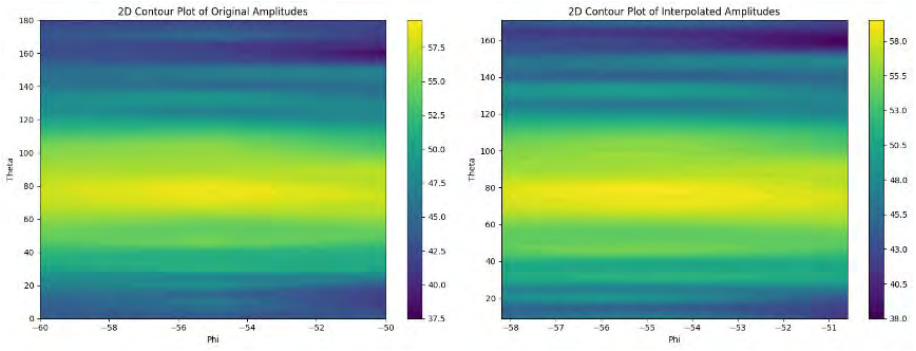

Figure 28. Comparison of 2D contour plots of original and interpolated amplitudes

9. Implementation and Results

Once all the inputs were validated to match the AAM inputs, they were fed into ASCENT Project 094 noise analysis tool for acoustic regeneration. The noise source sphere currently being used for noise propagation is the "FTREX094.nc" for Causey RUN #94. Data from the Causey RUN #94, such as the trajectory, were utilized for the initial validation efforts.

Loading Vehicle Trajectories

Figure 29 showcases the trajectory points for Causey RUN #94. Although the trajectory seems to be changing on the left plot, the vehicle change in the x and z are insignificant as compared to the y-axis. The trajectory contains 335 coordinates.

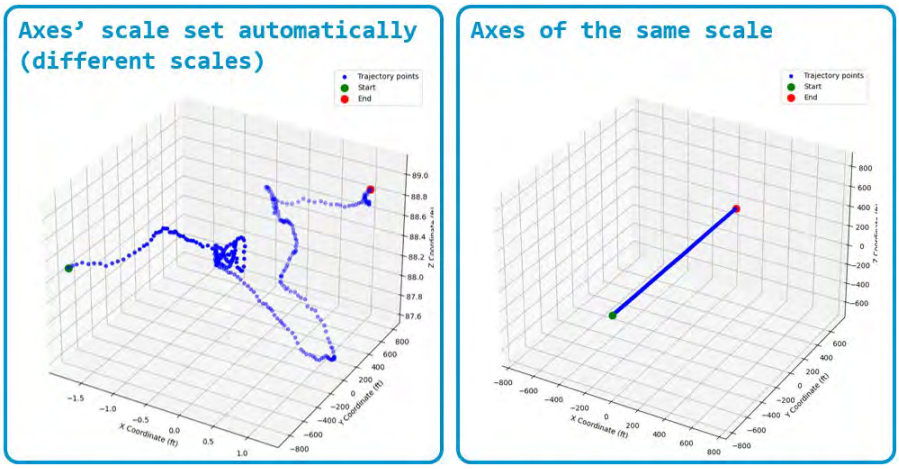

Figure 29. Trajectory points for Causey run #94.

Loading Receptor Locations

The file parsing algorithm is used to load the Causey Airport measurements receptor points. These consist of five receptor points at an altitude z>0 (crane microphones) and nine receptor points on the ground (z=0). In Figure 30, the picture on the left shows the Causey Airport measurement receptor points whereas the plot on the right is the 3D visualization of the loaded points in coordinate system.

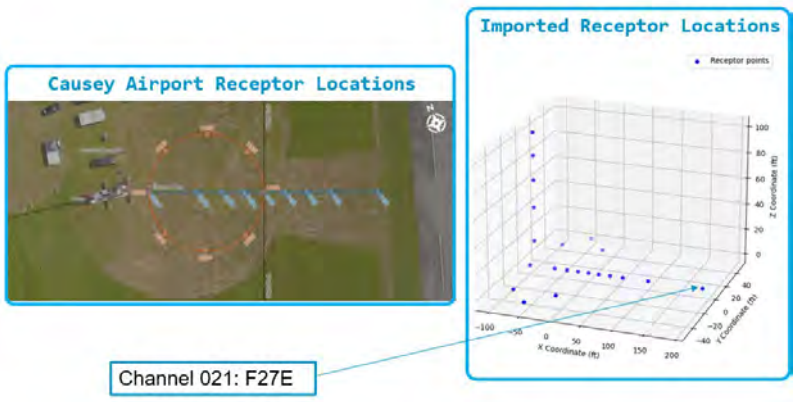

Figure 30. Location of the receivers used in the Causey Airport measurements.

A-Weighting Factors

The acoustic data/results generated by the AAM are A-weighted decibels (dBA). As such A-weighting factors were implemented in the noise analysis tool for both frequency SPL and total SPL. These were implemented based on the standard weighting function which is applied to the amplitude spectrum of unweighted sound level.

$$R_A(f) = \frac{12193^2 f^4}{(f^2+20.6^2)\sqrt{(f^2+107.7^2)(f^2+737.9^2)}(f^2+12194^2)} \quad \text{(Eq. 8)}$$

The weighting factor becomes:

$$A(f) = 20\log_{10}\big(R_A(f)\big) - 20R_A(1000) \quad \text{(Eq. 9)}$$

AAM Propagation

To compare the AAM and ASCENT Project 094 tool results at the receptor points of interest, "Detailed Time History at Points of Interest (poitime)" study was adapted. This requires the "COMPUTEPOI" input file, with the Points of Interest, and Vehicle Trajectory NetCDF Noise Sphere File clearly defined. Figure 31 shows the "COMPUTEPOI" input file required to run the "Detailed Time History at Points of Interest (poitime)."

Figure 31. Required data to run the detailed time history at the points of interest.

Comparison Between the ASCENT Project 094 Noise Analysis Tool and AAM Results

Our first approach started by comparing total SPL (dBA) for a single Causey run (94). Receiver #5 was randomly chosen for initial comparison. Initially, the raw measurements for the Causey Airport measurements were included to determine how the ASCENT Project 094 tool and AAM results compare to the actual data. Figure 32 displays the discrepancies between SPL propagated using the ASCENT Project 094 tool and AAM especially at the maximum SPL.

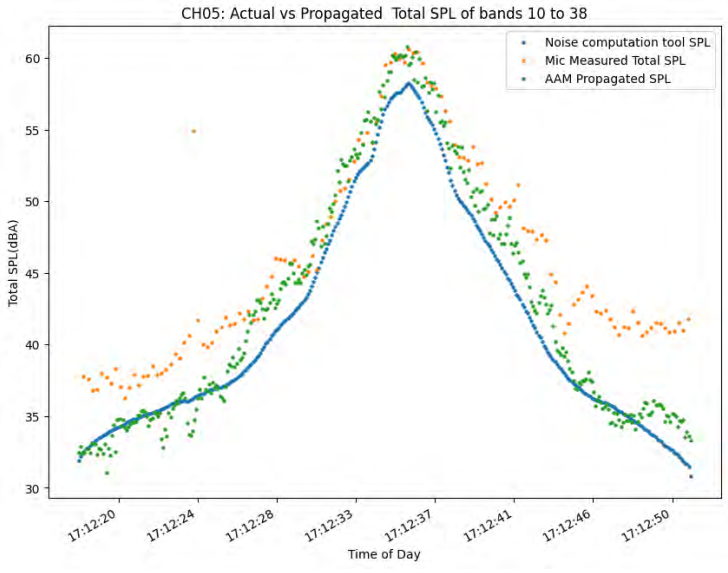

Figure 32. Discrepancies in propagated SPL between the A94 tool and AAM.

ASCENT Project 094 Tool Modifications to Match AAM Results

Studies were conducted to investigate the cause of the discrepancies between the ASCENT Project 094 tool and AAM. There appears to be a shift in time between the tool results, hence sound propagation delay was implemented. Also, as stated, the ASCENT Project 094 tools underestimates the maximum SPL in the middle, as such, reflected sound was added.

The receiver effectively receives sound from two sources at any given time: the "direct" noise and the "reflected noise" as depicted in Figure 33. Also accounted for is the difference in time.

- t_{direct} comes from trajectory information.
- $t_{received}$ comes from the sound propagation delay.
- $t_{reflected}$ computed such that reflected sound arrives to the receiver at $t_{received}$.

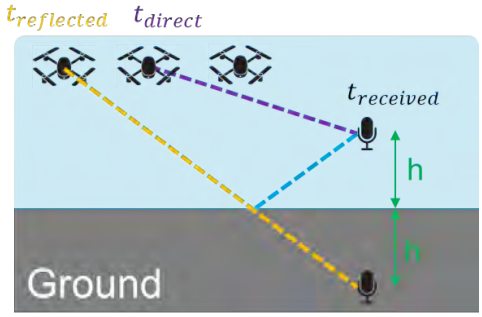

Figure 33. Representation of direct and reflected noise contributions to the receiver.

Notional View of the Reflected Sound Implementation

The SPL from the ASCENT Project 094 tool matches the AAM well in the region of highest SPL. It can be observed in Figure 34 that there is a good match in the 10dB down region which is used to compute integrated noise metrics. However, there is some overestimation of the sound level at higher distances between the vehicle and receiver. This is likely due to other phenomena not modeled in the tool. Note that the goal is not to perfectly match the AAM, but to have reasonable accuracy. Since this is for a single receptor, the next step will be to extend the validation to more Causey runs and receivers, to get a more global view of the tool's performance.

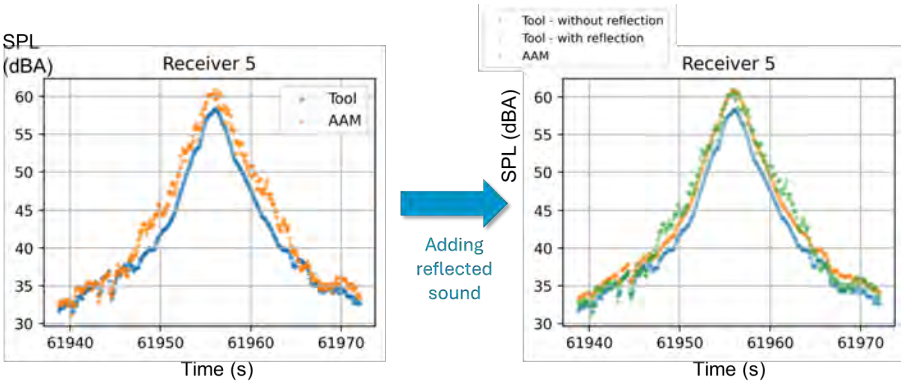

Figure 34. Impact of reflected sound on SPL prediction: A94 tool vs. AAM at receiver #5.

Global View of the Tool on All Receptor Points

Recalling that there are 14 receptor points, 5 receptors at an altitude and 9 receptors on the ground. Figure 35 shows the plots for 3 randomly chosen receptors on the crane (first row) and 3 ground receptors. The results for elevated (Crane) receptors better match the AAM results as compared to ground receptors (non-elevated receptors).

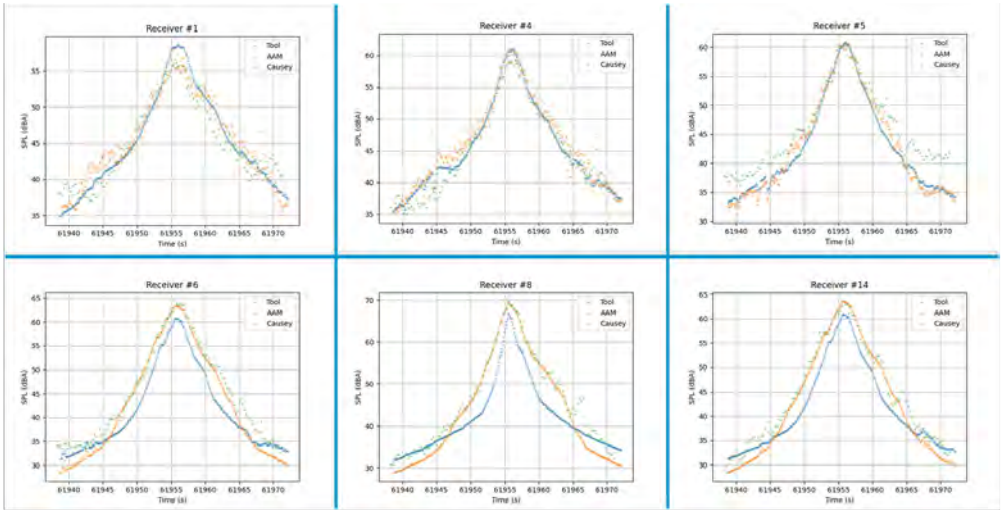

Figure 35. Results on all elevated receptors vs. ground receptors.

To investigate other phenomena not modelled, we suspected that it could be due to the terrain data implementation (e.g., hard impedance vs soft impedance). AAM terrain settings were varied from the original terrain data to ALL SOFT and ALL HARD impedances. The results were compared with the ASCENT Project 094 tool results to see which one matches better. Comparison for all the microphones are shown in Table 2. R^2 and root mean squared error (RMSE) were utilized to determine how the SPL results vary from each other.

Table 2. R^2 and RMSE of validation cases at different terrain settings.

Receiver		Actual		All Hard		All Soft	
		R^2	RMSE	R^2	RMSE	R^2	RMSE
1	Crane(z>0)	0.94792	1.362349	0.933965	1.451822	0.944285	1.444153
2		0.942718	1.436716	0.913427	1.64664	0.959348	1.215486
3		0.958022	1.296058	0.917934	1.64686	0.969325	1.077937
4		0.96588	1.24599	0.912512	1.79198	0.9741	1.035376
5		0.976521	1.301706	0.968509	1.371292	0.978963	1.15623
6	Ground(z=0)	0.911015	3.267892	0.844822	3.581061	0.972215	1.654723
7		0.867932	4.232326	0.815986	4.216348	0.941784	2.595165
8		0.83607	4.924783	0.784359	4.784754	0.910603	3.364589
9		0.772057	5.964834	0.705923	5.783041	0.850319	4.496555
10		0.72452	6.500523	0.619793	6.47318	0.801354	5.150109
11		0.760995	6.121138	0.689866	5.942117	0.839909	4.66193
12		0.81923	5.182726	0.761971	5.041571	0.899291	3.58118
13		0.865213	4.287818	0.8141	4.260886	0.93982	2.647602
14		0.91063	3.288102	0.854286	3.495203	0.969865	1.732736

Comparing results obtained when running the AAM and ASCENT Project 094 tool with (1) the actual terrain data file, (2) all hard, and (3) all soft terrain data, shows that the AAM results with all soft terrain data appear to match the ASCENT Project 094 tool results better than compared to the actual and all hard impedance terrain data. Results are worse for all hard impedances which may suggest that the ASCENT Project 094 tool is not implemented to consider hard impedance phenomenon. The same observations were observed on other Causey runs (91, #340 and #342) as depicted in Figure 36.

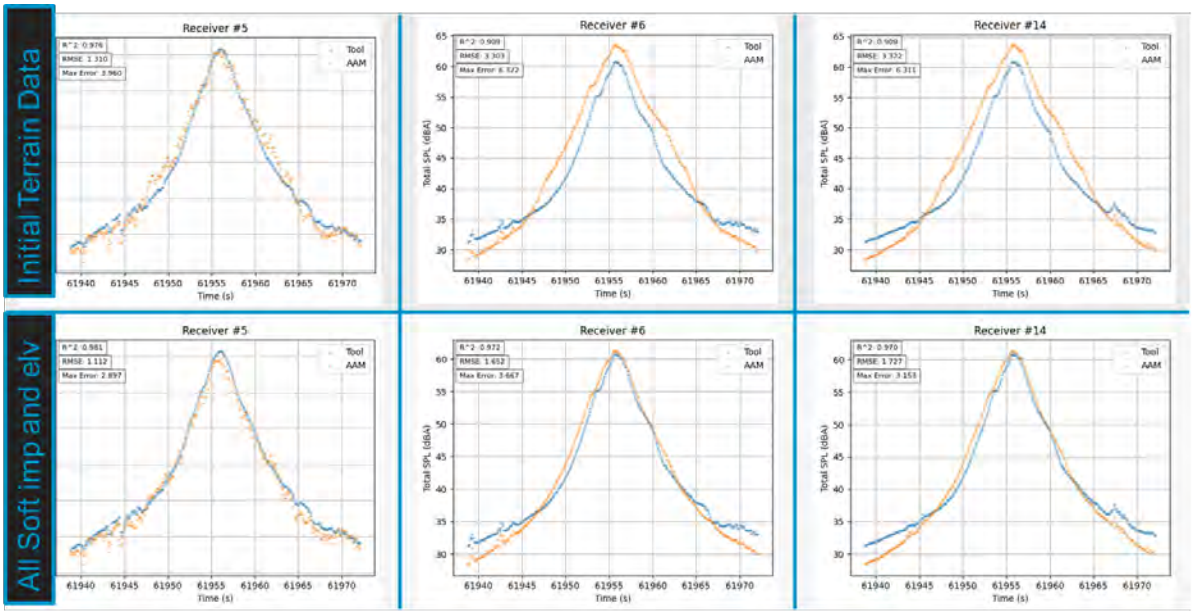

Figure 36. Graphical representation of the previous results.

Single-Event Metrics

R^2, $RMSE$ are not proper metrics for 10dB down comparison because the time/points events do not match. As such, the three single event metrics were implemented.

- L_{AE}: Sound exposure level (SEL)
  - L_{AE} is generally preferable because it accounts for the duration of the event as well as its intensity.
  - L_{AE} measurements are more susceptible to interference from background noise.
  - Sometime difficult to implement because L_{AE} usually exceeds L_{max} numerically, typically by around 10dB for the same event.
  - $L_{AE} = 10 \log_{10}\left(\frac{1}{t_0}\int_{t_1}^{t_2} 10^{\frac{L(t)}{10}} dt\right)$, t_1 and t_2 are the start and end times.
- L_{max}: Max A-weighted Sound level
- L_{EPN}: Effective Perceived Noise Level (EPNL)
  - metric for aircraft noise certification limits laid down by International Civil Aviation Organization.
  - $L_{EPN} = L_{max} + 10 \log_{10}\left(\frac{t_e}{t_0}\right)$, t_0 is a reference time, usually 1 s.

Figure 37 shows the heatmap for the difference between the ASCENT Project 094 tool and AAM results across receivers and metrics. Note that, on the one hand, negative values mean that the value obtained with the tool is smaller than the value obtained with the AAM. In other words, the ASCENT Project 094 tool underestimates the noise level compared to the AAM. On the other hand, positive values indicate that the ASCENT Project 094 tool overestimates the noise level compared to AAM. Metrics were also computed for 10dB down. As shown previously, results almost match for non-elevated (crane) receptors, where the difference between the ASCENT Project 094 tool and AAM results is the largest for on-ground receptors (numbered 8, 9, and 10).

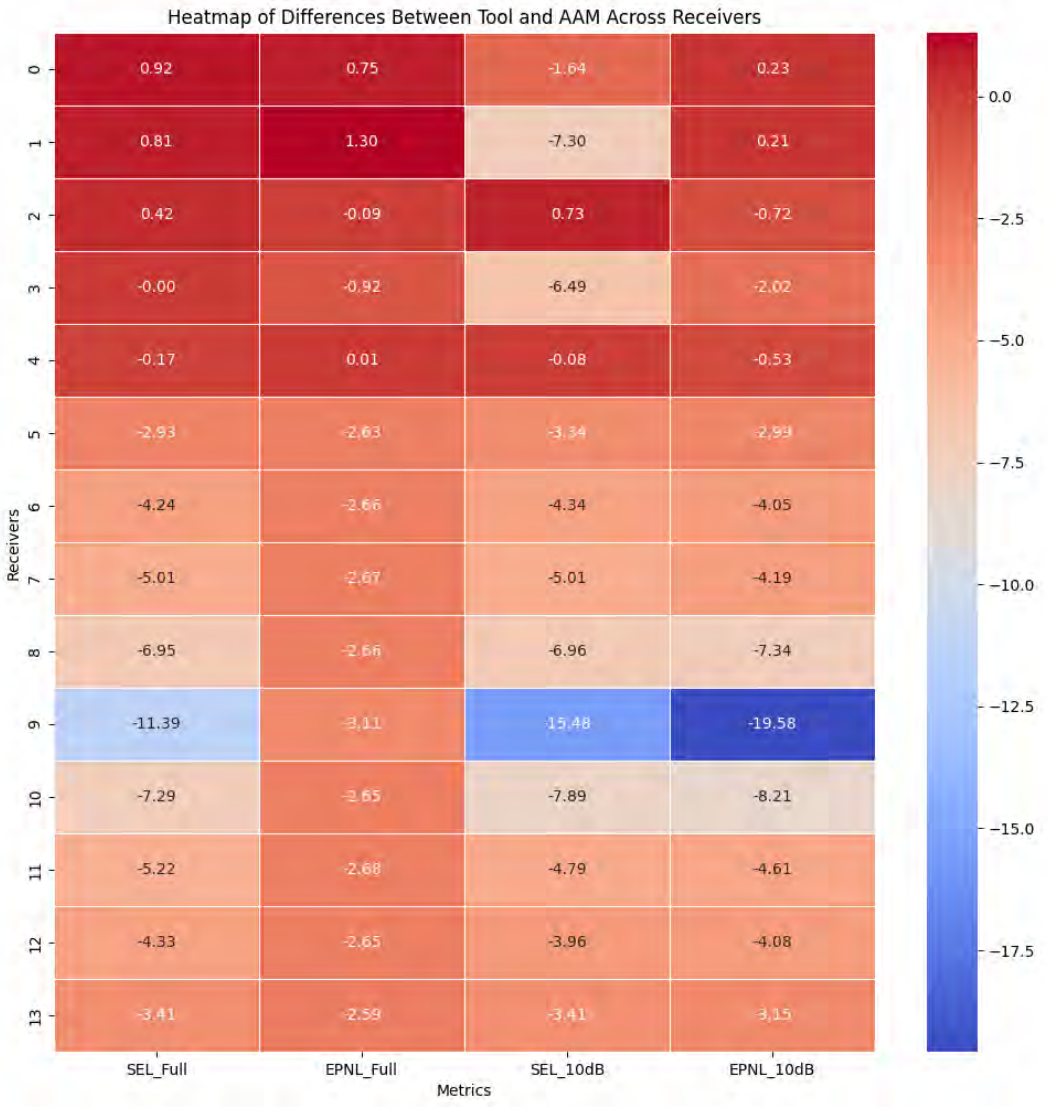

Figure 37. Heatmap for the difference between the A94 tool and AAM results across receivers.

Subtask 5.b – Validation of the Approach for Leveraging the NASA AEDT UAM Study

1. Objectives

The objective of this subtask is to validate the in-house noise analysis tool (ASCENT Project 094 approach) using a NASA UAM study conducted using AEDT (Rizzi and Rafaelof, 2023). Given the unique operational and acoustic characteristics of UAM vehicles, the study aims to overcome limitations in existing AEDT frameworks by generating noise-power-distance (NPD) data based on advanced simulation tools like NASA's Aircraft Noise Prediction Program (ANOPP2). The research focuses on segmenting point-to-point UAM operations into distinct departure, overflight, and approach phases, comparing noise exposure levels for fixed-wing, helicopter, and hybrid modeling approaches. The input data provided by the NASA UAM study group, along with the data generated by the AEDT, are utilized to replicate the study within the ASCENT Project 094 tool. This implementation serves as a critical component of the validation study, ensuring consistency and accuracy in noise modeling methodologies.

2. Approach

The validation process comprises two primary steps. The first step involves replicating the NASA UAM study within the FAA's AEDT, utilizing the input data provided by the NASA acoustics team. The output generated by the AEDT plays a crucial role in the second step of the validation process. In this step, the NASA UAM study is implemented within the ASCENT Project 094 tool, leveraging both the input data from NASA and the processed data from the AEDT. This phase requires extensive parsing and integration of multiple data files into the ASCENT Project 094 environment to ensure accurate and reliable implementation.

Replication of NASA UAM Study in the AEDT

The first phase of the validation study was conducted using the AEDT to ensure the accurate replication of results produced by the NASA acoustics group with the same input data. The input data, provided by the NASA acoustics team, consisted of CSV and structured query language (SQL) files, including information on receptor locations, vertiports, flight profiles (e.g., fixed-wing [FW] and helicopter), operations, and annualization settings for FW, helicopter, and hybrid models. These data files were imported into the AEDT using SQL scripts that facilitated the integration into specific modules, streamlining the replication process, Figure 38 compares the results from the NASA UAM study and replicated data. Additionally, terrain files for the corresponding UAM study location were loaded into the AEDT prior to running the simulations. All tasks specified in the input files were executed within the AEDT, and a comparative analysis was performed to verify the accuracy of the replication process and ensure consistency with the original UAM study results as shown in Figure 39.

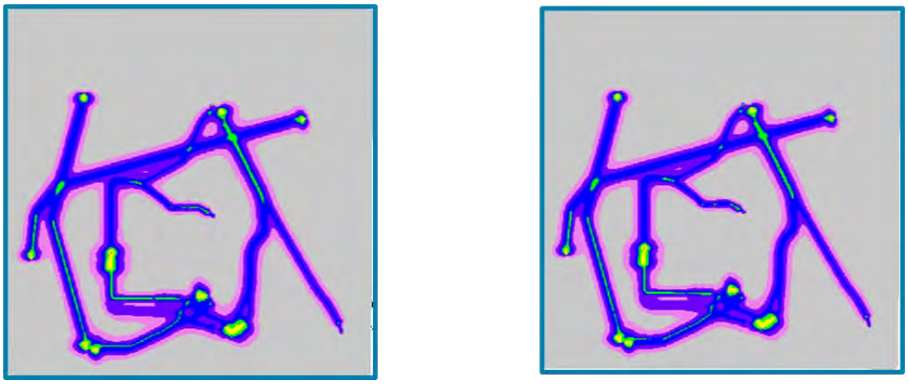

Figure 38. Results of NASA UAM study (left) and replicated UAM study (right).

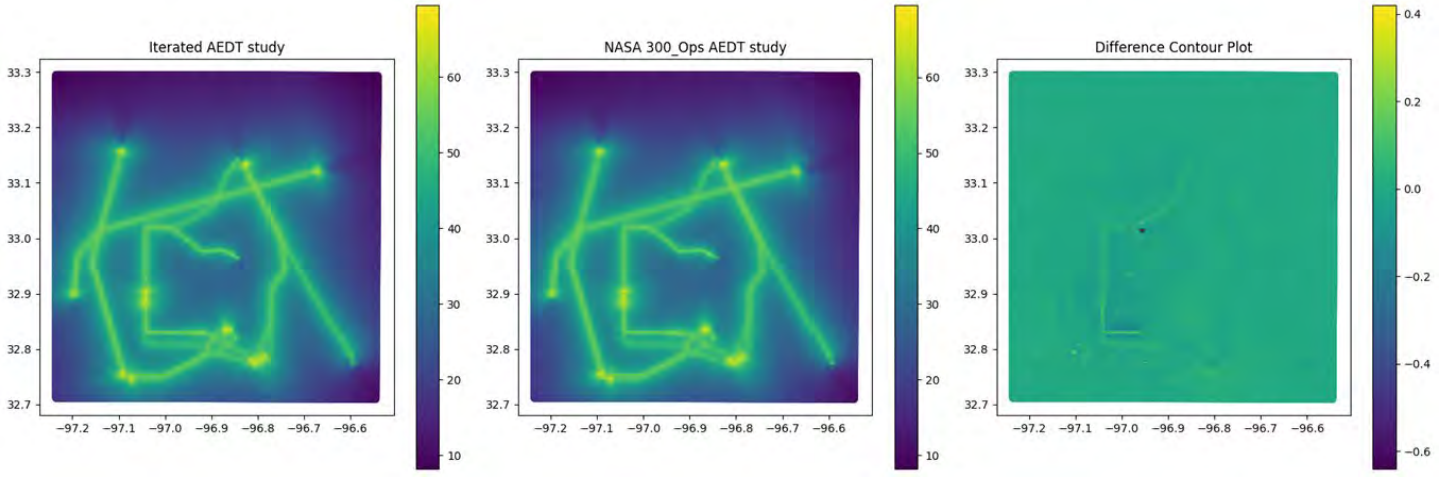

Figure 39. Results of the comparison study between NASA UAM study and replicated study.

Implementation of the AEDT Study in A94 Tool

The second phase of the validation study focuses on extracting trajectory data from the replicated UAM study in the AEDT, parsing the data files, and running noise simulations in the ASCENT-Project 094 tool. This phase adopts the noise sphere approach, as utilized in the Causey UAS validation study, in place of the traditional NPD approach. The noise spheres for FW and quadrotor configurations were provided by the NASA acoustics team and were specifically tailored for velocity and climb angle combinations corresponding to the vehicle profiles in the UAM study. Using the trajectory data generated in the AEDT, the noise levels at the receivers (virtual grid points from the AEDT) were calculated within the ASCENT Project 094 tool as part of the validation process. The implementation required substantial data extraction from the AEDT, parsing of the files for integration into the ASCENT Project 094 environment, computation of noise levels for various operations, and a comparative analysis between the AEDT results and outputs from the ASCENT Project 094 tool. The detailed process is depicted in Figure 40.

- **Loading Vehicle Locations/Source Points:** The vehicle coordinates along the trajectory were imported.
- **Loading Receiver Locations:** The coordinates of the points where noise levels were measured were defined.
- **Loading Noise Spheres:** Preconfigured noise spheres were loaded for specific velocity and climb angle combinations.
- **Noise Calculation for Each Vehicle Location and Receiver Point:**
  - **Velocity and Climb Angle Determination:** For each trajectory point, velocity and climb angle were computed.
  - **Noise Sphere Selection:** The nearest noise sphere corresponding to the computed velocity and climb angle was identified.
  - **Distance and Angle Computation:** The distances and angles (polar, θ, and azimuth, φ) between source and receiver were calculated.
  - **Source Noise Retrieval:** Noise values were interpolated from the noise sphere data based on θ and φ.
  - **Noise Propagation:** The source noise was propagated to the receptor locations.

Detailed explanations of each step and its sub-processes are provided in the Causey UAS validation study (Subtask 5.a). This comprehensive implementation ensures consistency and accuracy of the ASCENT Project 094 tool in replicating and validating the results of the UAM noise study.

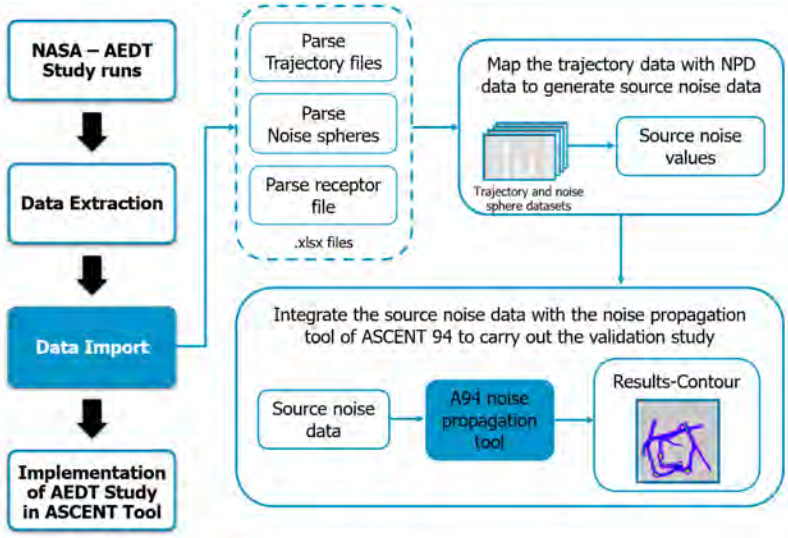

Figure 40. Detailed validation process using Causey Airport measurements. A94: ASCENT Project 094.

Implementation and Results

Following the formatting of input data from the NASA UAM study and the extraction of receptor locations and trajectory data for all operations from the AEDT, the parsed data files were imported into the ASCENT Project 094 tool to calculate noise levels at the receptor locations. To initiate the validation process, a single-event analysis was conducted as a test case, focusing on the trajectory from the KADD airport to the KDF5 airport with helicopter annualization. Subsequently, the

trajectory data for all annualization settings across all operations, including both single-event and multiple-operation scenarios, were extracted and parsed.

Loading Vehicle Trajectories

The trajectory of the quad vehicle from KADD airport to KDF5 is visualized in Figure 41, illustrating the three distinct phases of flight: (1) departure, (2) overflight, and (3) approach. Each waypoint in the trajectory represents the transition between segments, marking the start of one segment and the end of another. Initially, the trajectory data extracted from the AEDT is in global positioning system (GPS) coordinates and converted into the Web Mercator coordinate system for consistency. The trajectory comprises 188 segments, corresponding to 188 waypoints, with unique timestamps and a total flight time of 809 seconds for the vehicle to complete its journey. To standardize the data for implementation, the trajectory was converted into 1-s interval segments using linear interpolation. This approach facilitated a more efficient and consistent processing of the trajectory data during the analysis.

Loading Noise spheres

The noise spheres provided by the NASA team were integrated into the ASCENT Project 094 environment using the NetCDF package. These noise spheres were accessed based on the calculated velocity and climb angle of the vehicle at specific instances, as shown in Figure 41. To ensure accuracy and avoid potential errors, the nearest value approach was employed instead of interpolation, Figure 42 compares the trajectory obtained with original and interpolated data points. This method was chosen to eliminate the risk of extrapolation caused by outliers in the trajectory data and to prevent miscalculations during transitions in hybrid models.

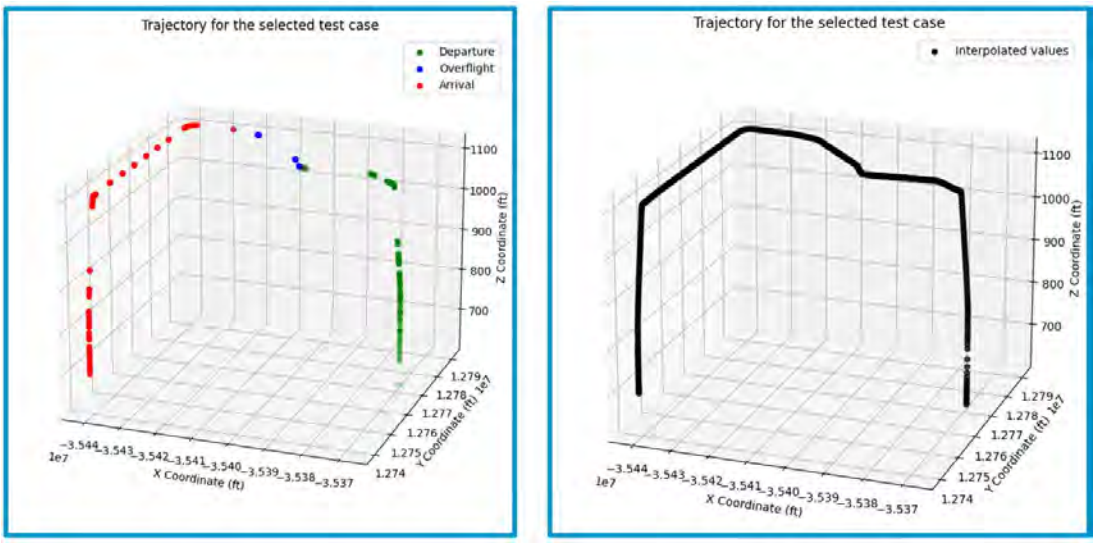

Figure 41. Comparison of the original trajectory (left) and trajectory interpolated at 1-second time intervals (right).

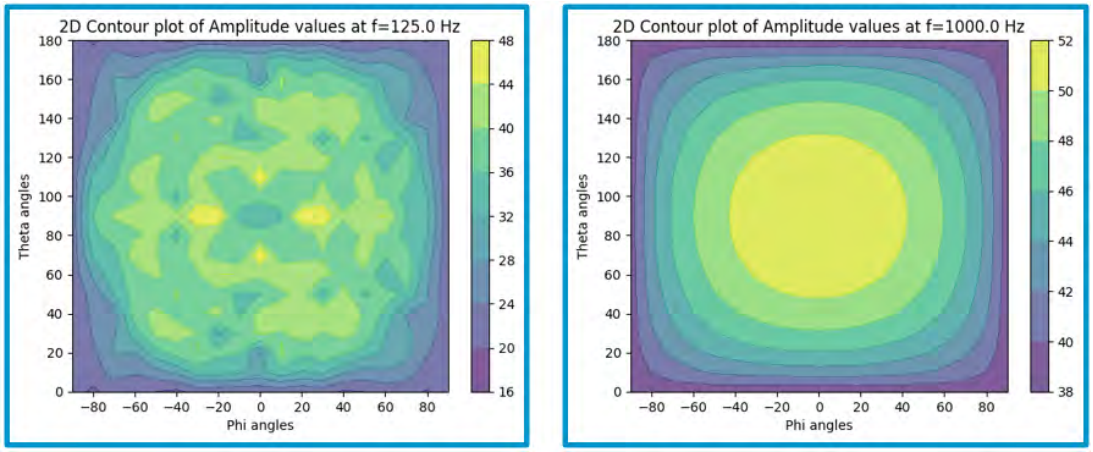

Figure 42. Noise sphere of quad vehicle (zero velocity and zero climb angle).

Loading Receptor Locations

In the AEDT, receptors are virtual grid points where the noise levels of the vehicle are calculated. The precise locations of these receptors are extracted from the AEDT in GPS coordinates. To ensure consistency in unit measurements, the GPS coordinates were converted into the Web Mercator coordinate system. A virtual grid comprising 501 × 501 points was established, with the elevation set to mean sea level (MSL), corresponding to 0 ft above ground. Figure 43 illustrate the virtual grid in relation to the trajectory of the vehicle.

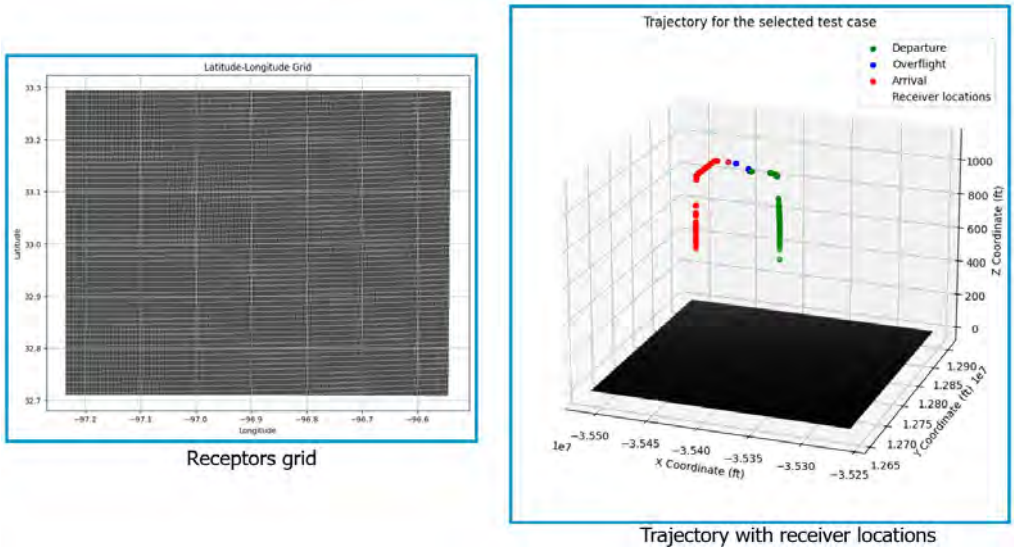

Figure 43. Receptors and flight trajectory

Milestones

- Set-up and configure the AAM and ART analysis tools. (Subtask 5.a)
- Received and translated Causey Airport UAS measurement data into a format that can be processed by the AAM and ART. (Subtask 5.a)
- Modified microphone measurement files in terms of the maximum number of bands to account for the limitation of ART. (Subtask 5.a)
- Decoded and executed the AAM and ART input files created for the Causey Airport UAS measurements. (Subtask 5.a)

- Replicated the NASA UAM study in the AEDT using the provided input data, and conducted a comparative analysis to evaluate the accuracy of the replicated study. (Subtask 5.b)
- Imported and parsed the trajectory data, receptor locations, and noise spheres into the ASCENT-Project 094 environment for the implementation of the AEDT study. (Subtask 5.b)
- Formatted the imported data to align with the requirements of the in-house tool, streamlining the implementation process and ensuring compatibility. (Subtask 5.b)

Major Accomplishments

- Implemented run cases 15 and 20 from the Causey Airport measurements were successfully implemented in the AAM and ART. (Subtask 5.a)
- Obtained Noise spheres for run cases 15 and 20 by using the terrain files provided in the AAM tutorial. (Subtask 5.a)
- Conducted an iterative AEDT study using the input data files provided by the NASA study group. (Subtask 5.b)
- Performed a comprehensive comparison study to validate the results to ensure accuracy. (Subtask 5.b)

Plans for Next Period

- Generate elevation and impedance files using the software BaseOps based on the experimental conditions applied in Causey Airport measurements. (Subtask 5.a)
- Select test cases from the Causey Airport measurements for validation purposes. (Subtask 5.a)
- Generate noise spheres for selected test cases using updated terrain files. (Subtask 5.a)
- For each test case, run the in-house noise analysis code using the generated noise sphere. (Subtask 5.a)
- Implement single-event analyses and multiple operations from the AEDT study in the ASCENT-Project 094 tool to further validate its functionality. (Subtask 5.b)
- Conduct a comprehensive comparison study between the results generated by the AEDT and ASCENT-Project 094 tool to assess the accuracy and reliability of the validation process. (Subtask 5.b)

References

Heutschi, K., Ott, B., Nussbaumer, T., & Wellig, P. (2021). Virtual microphone signals of flying drones (pp. 27–29). *Proceedings of the NATO STO MSG-SET-183 Specialists' Meeting on Drone Detectability: Modelling the Relevant Signature*, Wakefield, Massachusetts.

Jaller, M., & Pahwa, A. (2020). Evaluating the environmental impacts of online shopping: A behavioral and transportation approach. *Transportation Research. Part D, Transport and Environment, 80*, 102223-. https://doi.org/10.1016/j.trd.2020.102223

Hofferth, S., Flood, S.M., & Sobek, M. (2017). *American Time Use Survey Data Extract System: Version 2.6* [Machine-readable database]. In: College Park, M.U.o.M.a.M., MN: University of Minnesota. (Ed.).

Atlanta Regional Committee. (2024). *Census Data Manifest 2019-2023*. Georgia Association of Regional Commissions. Retrieved January, 2024, from https://opendata.atlantaregional.com/pages/census-data-arc

Volpe Center. (2020). *Advanced Acoustic Model (AAM) Technical Reference and User's Guide*. U.S. Department of Transportion.

Rizzi, S. A., & Rafaelof, M. (2023). On the modeling of UAM aircraft community noise in AEDT helicopter mode. In *AIAA AVIATION 2023 Forum* (p. 3363).

Scikit-Learn Developers. (2023a). *1.1. Linear models — user guide.* https://scikit-learn.org/stable/modules/linear_model.html

Scikit-Learn Developers. (2023b). 1.17. *Neural network models (supervised) — user guide.* https://scikit-learn.org/stable/modules/neural_networks_supervised.html

The Scipy Community. (2019). *Scipy.Spatial.Distance.Cdist — SciPy v1.3.2 reference guide.* https://docs.scipy.org/doc//scipy-1.3.2/reference/generated/scipy.spatial.distance.cdist.html

The Scipy Community. (2023). *Scipy.interpolate.intErp1d — SciPy v1.11.4 manual.* https://docs.scipy.org/doc/scipy/reference/generated/scipy.interpolate.interp1d.html

Project 095 Assessment of Fuel Cells for Powering Modern Business Jets

Georgia Institute of Technology

Project Lead Investigator

Principal Investigator
Professor Dimitri N. Mavris
Director, Aerospace Systems Design Laboratory
School of Aerospace Engineering
Georgia Institute of Technology
Phone: (404) 894-1557
Fax: (404) 894-6596
Email: dimitri.mavris@ae.gatech.edu

University Participants

Georgia Institute of Technology (Georgia Tech)

- P.I.: Dr. Dimitri N. Mavris
- FAA Award Number: 13-C-AJFE-GIT-158
- Period of Performance: March 19, 2024, to September 30, 2024
- Tasks:
  1. Developing a baseline vehicle model
  2. Creating an off-line Proton Exchange Membrane Fuel Cell (PEMFC) system model
  3. Integrating PEMFC model into the baseline aircraft model and conducting trade studies

Project Funding Level

This research was funded by the Federal Aviation Administration (FAA) Office of Environment and Energy through ASCENT, the FAA Center of Excellence for Alternative Jet Fuels and the Environment, Project 095 through FAA Award Number 13-C-AJFE-GIT-158 under the supervision of Joshua Glottmann. Any opinions, findings, conclusions or recommendations expressed in this material are those of the authors and do not necessarily reflect the views of the FAA.

The FAA provided $200,000 in funding to Georgia Tech. Georgia Tech has secured in-kind cost share from both Gulfstream® and Honeywell® in the amount of $100,000, respectively, totally $200,000.

Investigation Team

Georgia Institute of Technology

Dr. Dimitri N. Mavris, Principal Investigator
Dr. Jimmy Tai, Co-Principal Investigator
Mr. Berkay Terzi, Task 2 and 3
Mr. Jeremy Decroix, Task 1, 2 and 3
Mr. Leo Wattebled, Student Researcher, Task 2 and 3
Mr. Axel Jazzini, Student Researcher, Task 2 and 3

® Gulfstream G280 is a registered trademark of Gulfstream Aerospace Corporation, Savannah, Georgia.
® Honeywell HTF7250G and GTCP36-150 are registered trademarks of Honeywell International Inc., Charolotte, North Carolina.

Project Overview

The purpose of this research project is to identify opportunities for utilizing fuel cells on regional jet class aircraft to displace traditional power systems and reduce the total fossil fuel consumption of these vehicles. Fuel cell modeling and simulation will be performed for integration alongside an appropriate regional jet aircraft model.

Task 1 – Developing a Baseline Vehicle Model

Georgia Institute of Technology

Objective

The objective of this task is to model and calibrate a notional Gulfstream G280™ aircraft model powered by a notional Honeywell HTF7250G engine model and a notional Honeywell GTCP36-150 auxiliary power unit (APU). The modeling and simulation environment used for this task is the Environmental Design Space (EDS). The notional aircraft model is calibrated against publicly available data.

Research Approach

The notional Gulfstream G280 aircraft calibration process is performed using the Environmental Design Space (EDS) and the results are validated against public available data from Gulfstream and the European Union Aviation Safety Agency EASA (EASA; EASA, 2020). Figure 1 shows the EDS design loop segment for ASCENT Project 095.

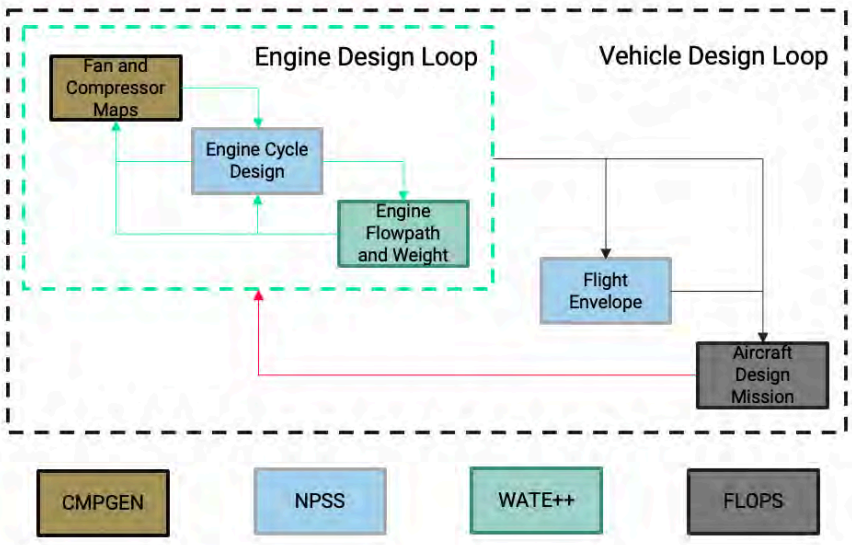

Figure 1. Environmental design space vehicle design loop segment.

EDS is an aircraft modeling and simulation environment developed by Georgia Tech and based on validated National Aeronautics and Space Administration (NASA) software tools, e.g., Flight Optimization System (FLOPS), Weight Estimation for Turbine Engines (WATE++[1]), and Numerical Propulsion System Simulation (NPSS). EDS was used to develop a physics-based model of a notional Gulfstream G280 aircraft (Figure 2), so that a parametric approach can be used to evaluate the effects of various design parameters. Built on the NPSS object-oriented framework, EDS supports automated data exchange between modules, allowing for comprehensive analysis of engine architectures and airframe configurations, including multi-design point cycle designs. The comprehensive suite of software tools which comprise EDS are integrated and designed to enable a thorough assessment of the environmental impacts associated with aviation.

[1] WATE++ is an object-oriented computer code for gas turbine weight estimation.

Figure 2. Gulfstream G280 business jet.

The G280 is a super mid-size business jet designed and manufactured jointly by U.S.-based Gulfstream Aerospace and Israel Aerospace Industries. The G280 is equipped with two HTF7250G engines with a rated takeoff thrust of 7,624 lbf each. The notional HTF7250G mixed flow turbofan engine model was sized using the multi design point (MDP) methodology and calibrated using International Civil Aviation Organization (ICAO) databank to match the thrust-specific fuel consumption (TSFC) at four different points (i.e., take-off, climb-out, approach, and idle). The results of the very close calibration are shown in Figure 3.

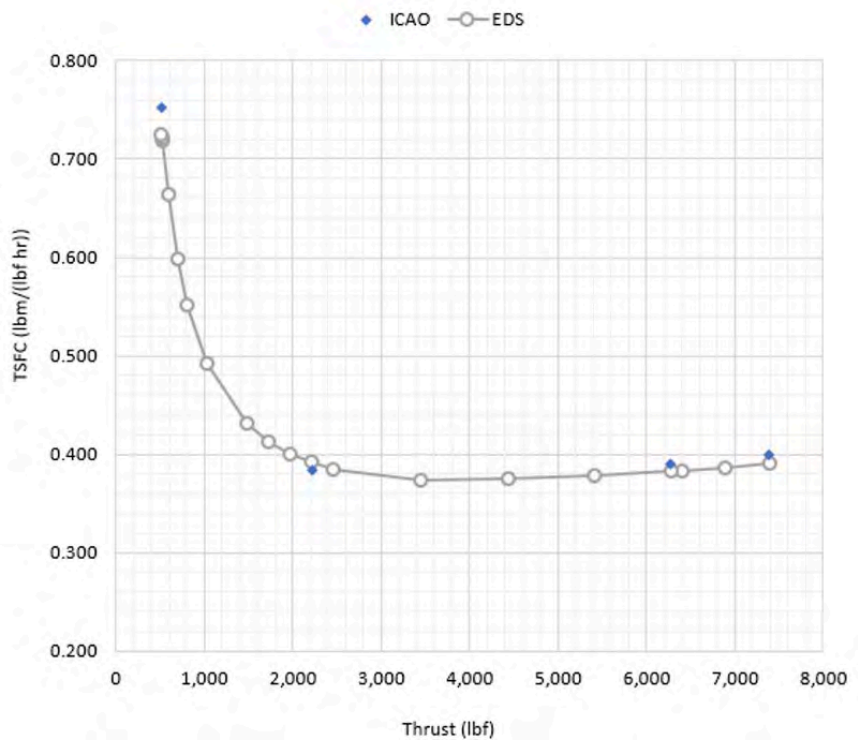

Figure 3. HTF7250G engine calibration using ICAO databank.

The APU being displaced onboard of the aircraft during this research effort is the GTCP36-150 (Figure 4). It has a single-stage centrifugal compressor and a single-stage radial turbine architecture. Its weight varies between 113 lb (51 kg) and 168 lb (76 kg) depending on the standard and high flow rates. With the integration of a k-factor of 2.2, the group weight value of 370 lb (168 kg) can be obtained. The rated horsepower can go up to 40kVA (59 F, SL) and the bleed airflow goes up to 70lb/min (59 F, SL). The rotor speed ranges from 58,737 to 62,000 rpm with a maximum operating altitude of 20,000 ft (Honeywell, 2024).

Key Performance Data	
Weight:	125 – 168lbs
Digital Control Weight:	6lbs
Basic Spec:	FAA TSO-C77a Category 1 (Essential)
Rated Horsepower:	Up to 40kVA, 59F, SL
Bleed Airflow:	Up to 70lb/min, 59F, SL
Rated EGT:	1230F
Rotor Speed:	58,737 – 62,000 rpm

Figure 4. GTCP36-150 APU characteristics.

The role of the APU is to provide electrical and pneumatic power to the aircraft during the ground operations while the engines are turned off. Its role can also be to start the main engines. After the main engines start, the APU system is turned off. In case of an engine failure, the APU will be turned on after an emergency descent under 20,000 ft. For on the ground operations, if the APU is running for 20 minutes, assuming a fuel consumption of 230 lb/hr (104 kg/hr) it will consume 77 lb (35 kg) of fuel before the taxi out segment.

Using the previous technical specification of the G280 found in Table 1and Table 2 and leveraging the engine deck of the notional HTF7250G mixed flow turbofan engine model, the notional G280 model was calibrated by performing a mission analysis with the FLOPS software. FLOPS takes the statistical weights fractions of each subsystem on the aircraft as input, the geometry of the aircraft from the computer-aided design (CAD) three-dimensional view rendering and the payload and range values.

Table 1. Notional G280 weight breakdown.

G280 Weight Breakdown	
Ramp Weight (RAMPWT)	39,750 lb (18,030 kg)
Taxi In Fuel Weight	150 lb (68 kg)
Maximum Takeoff Weight (MTOW)	39,600 lb (17,962 kg)
Design Landing Weight (DLDWT)	32,700 lb (14,832 kg)
Operating Empty Weight (OEW)	24,150 lb (10,954 kg)
Maximum Fuel	14,600 lb (6,623 kg)
Maximum Payload Full Fuel	1,000 lb (454 kg)
Passenger	4
Crew Member	2
Maximum Range	3,600 nmi

Table 2. G280 aircraft specifications.

G280 Aircraft Specifications	
Overall Wingspan	63 ft
Fuselage Length	66.8 ft
Fuselage Height	11.2 ft
Fuselage Width	7.9 ft
Passenger Compartment Length	25.8 ft
Maximum operating Mach number	0.85
Long Range Cruise Mach Number	0.8
Maximum Cruise Altitude	45,000 ft

The baseline calibration was performed using the maximum payload (1,000 lb [454 kg]) and the maximum mission fuel weight (14,600 lb [6,623 kg]) for the maximum range (3,600 nmi) with a reserve mission of 30 minutes at 10,000 ft. A cruise climb schedule was implemented. The results of the calibration show a very close percentage error for the aggregated weights as indicated in Table 3.

Table 3. Notional G280 model detailed weight breakdown.

Notional G280 Model		
Mass Breakdown	**Weight (lb [kg])**	**Error (%)**
Wing	3,802 (1,724)	
Horizontal Tail	716 (325)	
Vertical Tail	405 (184)	
Fuselage	5,750 (2,608)	
Landing Gear	1,100 (499)	
Nacelle (Air Induction)	250 (113)	
Structure Total	12,023 (5,454)	
Engines	3,682 (1,670)	
Fuel Systems - Tanks and Plumbing	290 (132)	
Powerplants Total	3,972 (1,802)	
Surface Controls	627 (284)	
Auxiliary Power	370 (168)	0
Hydraulics	613 (278)	
Electrical	341 (155)	
Avionics	350 (159)	
Furnishings and Equipment	4,023 (1,825)	
Air Conditioning	327 (148)	0
Systems and Equipment Total	6,652 (3,017)	
Empty Weight	22,646 (10,272)	
Crew and Baggage	450 (204)	
Unusable Fuel	337 (153)	
Engine Oil	54 (25)	
Passenger Service	666 (302)	
Operating Empty Weight	**24,153 (10,956)**	**0.01**
Passengers	760 (345)	
Passenger Baggage	240 (109)	
Zero Fuel Weight	25,153 (11,409)	
Mission Fuel	**14,602 (6,623)**	**0.01**
Max Design Taxi Weight	**39,755 (18,032)**	**0.01**
Taxi Out Fuel	**151 (68)**	**0.67**
Maximum Takeoff Weight	**39,604 (17,964)**	**0.01**
Design Landing Weight	**32,705 (14,834)**	**0.01**

Milestones

- Performed notional HTF7250G engine model calibration.
- Performed notional G280 aircraft model calibration.

Major Accomplishments

- Performed a notional baseline aircraft model of the G280 super mid-size business jet allowing the integration of the PEMFC system impact.

Publications

None.

Outreach Efforts

- Scheduled monthly meetings with Gulfstream, Honeywell, and FAA to guide this research effort.
- Attended ASCENT biannual meetings.

Awards

None.

Student Involvement

This task involves one graduate student, Jeremy Decroix, who is a PhD candidate at Georgia Tech.

Plans for Next Period

- Continue the study of the calibration mission schedule to ensure the integration of the PEMFC system is accurate.

Task 2 – Creating Off-line Proton Exchange Membrane Fuel Cell System Model

Georgia Institute of Technology

Objective

The objective of this task is to develop a comprehensive modeling and simulation environment for fuel cells, with potential application in the target aircraft. After evaluating traditional power system alternatives for APUs, solid oxide fuel cells (SOFCs) and PEMFC emerge as the most promising options (Daggett et al., 2003). Given PEMFCs' lower operating temperature, high efficiency, and their power output profiles that align with the typical power demands of business jets, PEMFCs are considered the preferable option for APU applications in business jets. Therefore, the modeling and simulation environment developed in this task will focus on PEMFC technology.

Research Approach

In contrast to conventional gas turbine APU systems, where the main component is a gas turbine, PEMFC systems consist of several key components, both from both fluidic and electrical perspectives. To address this complexity, system architectures are designed to create a comprehensive model. The system architecture, with a focus on the fluidic components, is illustrated in Figure 5. In this architecture, liquid hydrogen (LH_2) is preferred due to its superior gravimetric efficiency compared to gaseous hydrogen. LH_2 is pressurized using an electrically driven pump, while the thermal management system helps address the challenges associated with storing cryogenic fuel onboard. Another important aspect of this system architecture is the inclusion of compressors, which ensure compatibility for high-altitude operations.

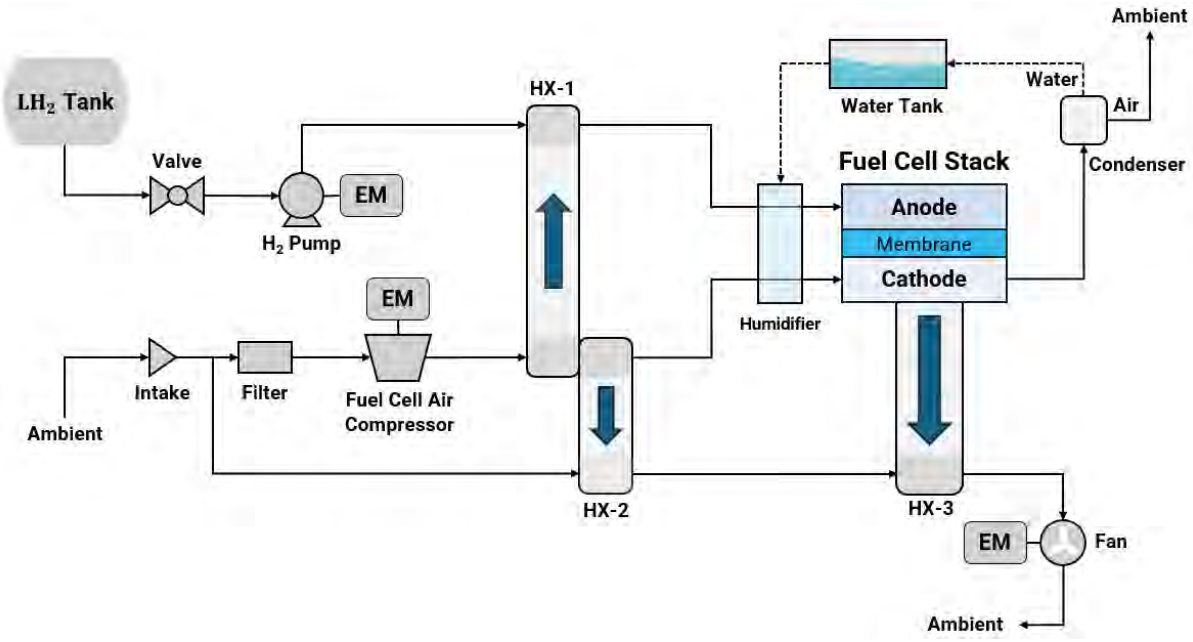

Figure 5. Fuel cell system architecture.

One of the main objectives of this task is to quantify the parasitic power demands, or in other words, the power requirements of the auxiliary components in the PEMFC system. To achieve this, the electrical system architecture shown in Figure 6 is proposed. As illustrated in Figure 6, the power sources for the auxiliary components include both the PEMFC stack and a parallel battery. The battery serves as an additional power source to assist the fuel cell stack during rapid transients in power demand, periods of high-power demand, or emergency situations. The outputs of the proposed system include DC) electrical power for use in aircraft subsystems and pressurized air for the aircraft's environmental control system (ECS).

The modeling of the proposed system is carried out in the NPSS environment, due to its advantages such as built-in components and solvers, as well as its ability to easily handle both on- and off-design conditions. The fuel cell modeling process is divided into five main steps.

Step 1: Determination of longest flight mission and selecting design point
To replace the current APU system without any gaps in performance and without altering the aircraft's range, it is necessary to consider the longest possible mission. Based on publicly available data and FAA reserve mission requirements, a notional flight mission is created, which includes altitude, Mach number, and power demand by the aircraft subsystems.

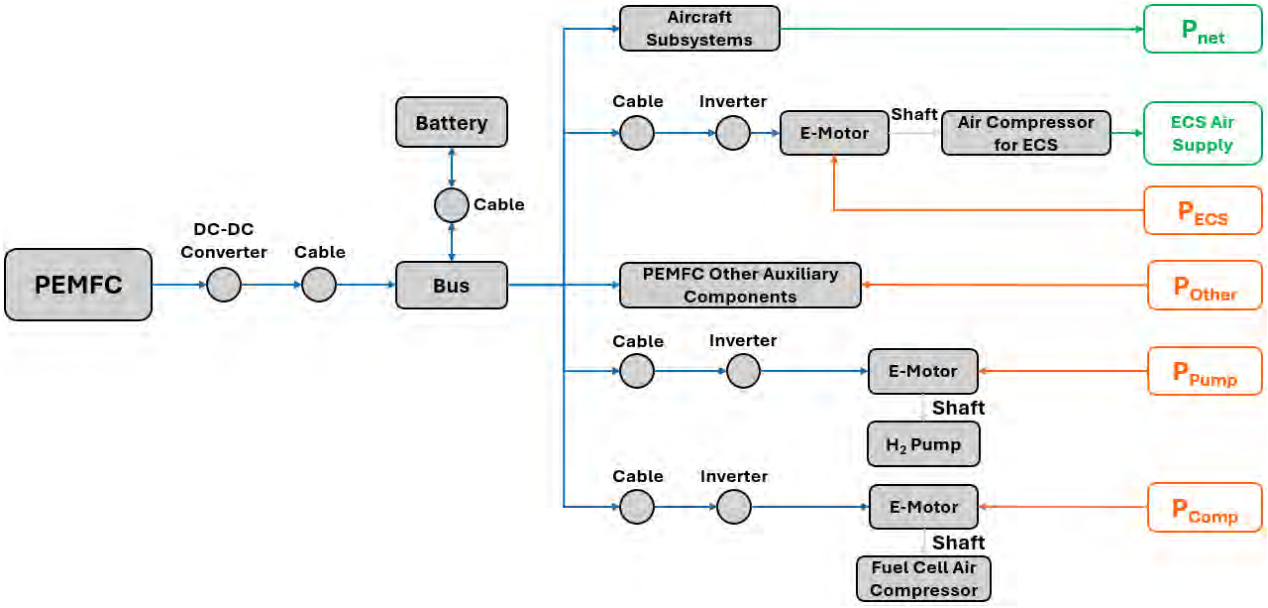

Figure 6. Fuel cell electrical system architecture.

The flight mission is critical in determining the design point of the new system and in properly sizing the LH_2 tank. For the design point of this project, the maximum possible altitude is selected, where the air density will be lowest for the given flight mission.

Step 2: PEMFC stack sizing

The modeling and simulation of the PEMFC stack are conducted using a simple semi-empirical model. This model considers three major losses to mimic the performance of a typical fuel cell (i.e., activation, ohmic, and concentration losses). These losses exhibit distinct characteristics, which are illustrated in Figure 7.

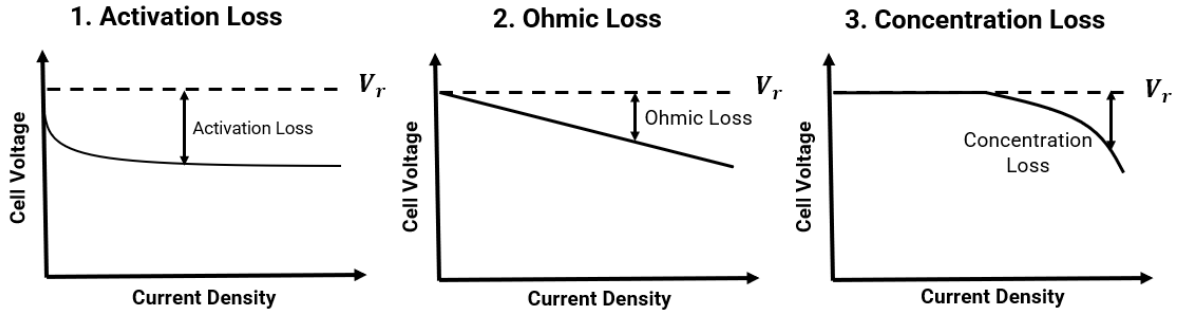

Figure 7. Typical losses in a fuel cell.

The equations used to model these losses are listed below (Equation 1). The coefficients in these equations are functions of the operating pressure and temperature of the stack. When combined, these losses produce a cell voltage curve, as shown in Figure 8.

$$\eta_{act} = [a_A + b_A \ln(i + i_{leak})] + [a_C + b_C \ln(i + i_{leak})] \quad \text{(Eq. 1)}$$
$$\eta_{ohm} = i\, ASR_{ohmic}$$
$$\eta_{conc} = C \ln \frac{i_L}{i_L - (i + i_{leak})}$$
$$v = V_r - \eta_{act} - \eta_{ohm} - \eta_{conc}$$

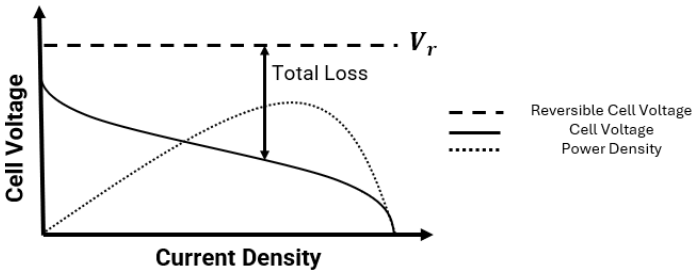

Figure 8. Current, voltage and power design plot of a typical fuel cell stack.

The power density of a fuel cell peaks at a point where the losses exceed those in the low power density zone. Therefore, when sizing a fuel cell, it is crucial to determine the operating range, as it directly impacts cell efficiency. For the selected design point in the flight mission, cell design efficiency and cell design voltage, the fuel cell stack is sized in terms of weight, volume, number of cells, and active area. The stack's current, voltage, and power performance curves are established and fixed before simulating the system under off-design conditions. For off-design conditions, the built-in solvers of NPSS determine an appropriate current and voltage combination while accounting for the power demand by the auxiliary components of the fuel cell system, as will be explained in the next step, to ensure the system meets the electrical power and bleed air demands of the aircraft.

Step 3: Balance of plant (BoP) sizing and modeling
As shown in Figure 5 and Figure 6, the fuel cell system consists of various fluidic and electrical auxiliary components. For modeling these components, both built-in NPSS components and newly developed components are used. The efficiencies and power-to-weight ratios of these components are set to match the corresponding aviation-grade industrial goal values (see Table 4) and are sized to accommodate the full operating range, ensuring that the system can provide the required power reliably. Additionally, any minor auxiliary power demands that required electrical power from the fuel cell stack are accounted for under the "Other Auxiliary Components" section given in the system architecture. The power required for these components is assumed to be 5% of the total power generated by the stack. For off-design performance, preloaded performance maps of the auxiliary components are used to determine their corresponding efficiency at a given set of operating conditions.

Table 4. Power-to-weight ratios of components.

Components	Power-to-Weight Ratio (kW/kg)
Fuel Cell Stack	2
DC-DC Converter	6
Inverter	5
AC Electric Motor	8
Other Auxiliary Components	1
Battery	100 (Wh/kg)

To estimate the weight of the different centrifugal turbomachinery components, regressions based on historical data are built. Relevant independent parameters are determined, and databases are created with existing commercial components. Fitting models are then implemented to obtain predicted values for the weight. This methodology is used for components such as compressors, pumps, and ECS.

Step 4: Liquid hydrogen (LH_2) tank sizing
PEMFCs require pure hydrogen, as they are sensitive to impurities. Hydrogen can be stored in either liquid or gaseous form, but due to its higher gravimetric efficiency, liquid hydrogen is typically preferred. However, storing cryogenic liquid hydrogen onboard presents some challenges. It must be stored in a tank designed to minimize heat transfer with the environment and heated using a heat exchanger to reach the appropriate temperature before being supplied to the fuel

cell stack. Although hydrogen offers excellent performance in terms of mass energy density, its volumetric performance is poor, making accurate estimation of both is crucial. Once the PEMFC components are sized, the power requirements for each component and the flow rates of air and hydrogen are calculated for each phase of the flight mission. The entire flight profile is simulated to determine the hydrogen flow rates during each mission phases. By integrating the hydrogen flow rate over the mission profile's block time, the total amount of liquid hydrogen required is calculated.

Given that hydrogen will be stored in liquid form, the storage system must account for thermal management and fuselage constraints. To minimize boil-off of hydrogen, maintain internal design pressure, and prevent air liquification, the tank's outer surface will be insulated. At the end of the sizing process, the total weight estimation will include all components and systems, as well as insulation and storage considerations. Different tank and insulation materials are considered and the best performing combination leading to the lowest hydrogen tank system will be selected.

To preserve the current cabin layout, the fuel cell system and its BoP will be located in the tail cone. Since this system will occupy more space than the traditional APU, elongating the cabin has been identified as the most viable option. This modification will be factored into the aircraft-level analysis.

Step 5: Thermal management system (TMS) sizing and modeling
The TMS is a critical component of the PEMFC architecture, designed to maintain optimal operating conditions for both the fuel cell and its associated subsystems. The presented TMS is composed of three distinct heat exchangers (see Figure 5), each tailored for specific thermal management needs.

The first heat exchanger (labeled HX-1 in Figure 5) is responsible for the transition of cryogenic liquid hydrogen to gaseous hydrogen, a necessary step to prepare the fuel for use in the PEMFC. Initial sizing utilized the log mean temperature difference (LMTD) method, which calculates the average temperature driving force across the exchanger to estimate heat transfer rates. To enhance accuracy, future iterations will incorporate an advanced version of the LMTD method tailored for phase-change conditions, addressing the complex thermal properties during hydrogen's liquid-to-gas transition. Compressed air serves as the heating medium, ensuring efficient energy transfer.

The second heat exchanger (labeled HX-2 in Figure 5) regulates the temperature of compressed air entering the system to meet the working temperature of the PEMFC stack. Sizing again employed the LMTD method, offering a straightforward yet effective approach for determining heat transfer capacities under steady-state conditions.

The third heat exchanger (labeled HX-3 in Figure 5) ensures effective cooling of the PEMFC using a liquid coolant system, which has been identified as the most efficient approach for this application. At its on-design point, corresponding to the PEMFC's maximum thermal load, this heat exchanger is required to dissipate peak heat generation to maintain stable operation. Sizing was conducted using the number of transfer units (NTU) method, which offers a robust framework for evaluating heat exchanger effectiveness based on heat capacity rates and temperature differentials without requiring detailed outlet temperature data. This method allows accurate modeling under high-heat rejection scenarios, critical for maintaining fuel cell performance.

To efficiently size the TMS, it is critical to determine the on-design point of each heat exchanger. For the HX-1 and HX-3, they both have been designed for the worst case. As said previously, the role of the second heat exchanger (HX-2) is to adjust the temperature of air to meet the working temperature of the PEMFC stack. The first study sized this heat exchange for flight operation where air must be cooled down. Yet, on ground operations especially, air must be heated up to meet the working temperature of the PEMFC. The sizing of the second heat exchanger is still in progress.

Milestones

- Step 1 has been completed. The flight mission used in EDS has been imported into the NPSS environment, and the average electrical power and bleed air requirements for the aircraft have been provided by the manufacturer.
- Step 2 has been completed. The fuel cell stack element has been established for use in the NPSS environment, with both on-design and off-design capabilities.
- Step 3 is in progress. The elements and their connections within the NPSS environment have been established. Work is ongoing to refine some weight estimation models which are used in this task.
- Step 4 has been completed. A cryogenic tank sizing function with the capability to handle several material types has been implemented into the model.

- Step 5 is in progress. Thermal management system requirements have been identified, and the corresponding models have been developed. Further development of the models is ongoing.

Major Accomplishments

- Synthesized the APU system requirements.
- Developed a comprehensive modeling and simulation environment for PEMFC in APU applications.

Publications

None.

Outreach Efforts

- Scheduled monthly meetings with Gulfstream, Honeywell, and FAA to guide this research effort.
- Attended ASCENT biannual meetings.

Awards

None.

Student Involvement

This task involves four Georgia Tech graduate students: Berkay Terzi (PhD candidate), Jeremy Decroix (PhD candidate), Leo Wattebled (Master of Science [M.S.] candidate), and Axel Jazzini (M.S. candidate).

Plans for Next Period

- Refine weight estimation models which are used in Task 2.
- Integrate the off-line PEMFC code into the EDS environment to enable seamless data transformation between them and centralize control from a single hub.

Task 3 – Integrating Vehicle and Proton Exchange Membrane Fuel Cell Models and Conducting Trade Studies

Georgia Institute of Technology

Objective

The objective of Task 3 is to integrate the off-line PEMFC code and EDS environment to make an assessment at aircraft level and conduct feasibility studies with the new proposed fuel cell system.

Research Approach

The proposed fuel cell system must satisfy three primary objectives: supplying electrical power to aircraft subsystems, providing pressurized air for the ECS, and independently starting the engine without external power sources. The existing conventional gas turbine APU in the baseline aircraft meets these needs by providing backup alternating current (AC) power up to an altitude of 20,000 ft, in-flight bleed air for air-conditioning up to 15,000 ft, and pneumatic air for engine startup. These functions in the baseline aircraft are accomplished by extracting shaft power from the engine and pressurized air from the engine compressor (Honeywell, 2024).

The new PEMFC APU system can be designed to replicate the capabilities of the current APU; however, it also offers opportunities for more innovative solutions. One such approach could involve sizing the fuel cell system to provide continuous electrical power and pressurized air for the ECS throughout the entire flight, thus reducing Jet-A fuel consumption and overall emissions. In Task 3, the weight balance considerations for this proposed system will be explored.

Step 1: PEMFC integration weight breakdown

Using the tool created in Task 2, a PEMFC system has been designed to provide electrical power and bleed air for both ground and flight operations, as specified in the system requirements defined in the use case. For the given flight mission and aircraft requirements, the stack has been sized such that, when the electrical power required by the auxiliary

components of the fuel cell is subtracted, the remaining power matches the net power demand of the aircraft. The I-V-P plot is shown in Figure 9, while the operating conditions and stack design details are presented in Table 5.

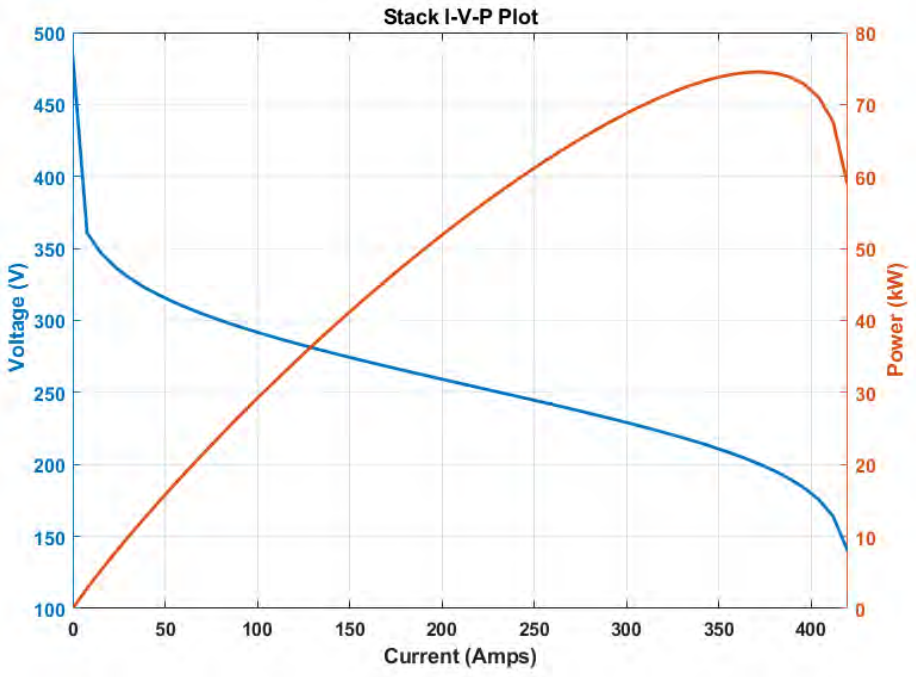

Figure 9. Current – voltage –power plot of the PEMFC stack.

Table 5. PEMFC stack parameters.

PEMFC Stack Parameters	Value
Internal Temperature Setpoint	176˚F
Internal Pressure Setpoint	14.7 psi
Max. Power	74.5 kVA
Stack Voltage at Max. Power	200 Volts
Stack Current at Max. Power	372.6 Amps

Hydrogen tank material and geometry are studied to achieve the lowest tank total weight. The hydrogen is at a temperature of 20K in the tank to be in liquid form. The tank internal design pressure is 20 psi. Three materials are investigated, and their properties are described in Table 6.

Table 6. Hydrogen tank material characteristics.

Tank Material	Stainless steel (SS304)	Aluminum (L5083)	Composite (Cycom5320-1)
Allowable Stress (psi)	31,200	33,000	190,000
Density (kg/m^3)	8,000	2,660	1,310
Thermal Conductivity [W/(m K)]	2.2	17.2	0.167

The selected material for the hydrogen tank is the composite CYCOM® 5320-1 attributed to its very low density and high allowable stress. The choice of insulation material for the tank is also explored. Three insulation materials are investigated with their properties listed in Table 7.

Table 7. Hydrogen tank insulation material characteristics.

Tank Insulation Material	Glass Microsphere Vacuum Jacket (GMVJ)	Multi-Layer Insulation Vacuum Jacket (MLIVJ)	Quest Light Vacuum Jacket (QVJ)
Density Insulation (kg/m^3)	65	80	0
Thickness Insulation (in)	2	1	1
Density Jacket (kg/m^3)	1.1	1.1	2
Thermal Conductivity [W/(m K)]	8.25E-04	2.2E-04	2.1E-04

The selected material for the hydrogen tank insulation material is the composite quest light vacuum jacket attributed to a very low thermal conductivity. The total tank weight found is 135.1 lb with a gravimetric index of 0.64. A breakdown of the designed hydrogen tank can be found in the following Table 8.

Table 8. Hydrogen tank insulation material characteristics.

Hydrogen Tank Design		
Weights	**lb (kg)**	**%**
LH_2 Consumed	79.9 (36.2)	59.1
LH_2 Boiloff	2.0 (0.9)	1.5
GH_2 Vented	0.03 (0.014)	0.02
LH_2 Final	4.6 (2.1)	3.4
Tank	15.6 (7.1)	11.5
Insulation	16.7 (7.6)	12.4
Fuel System	16.2 (7.3)	12.0
Total Weight	**135.1 (61.3)**	**100**

Table 9 depicts the weight of the PEMFC heat exchanger for different coolant types. The best coolant is the 25/75 propylene glycol mix, while the worst-case scenario occurs during ground operations on a hot day, defined using the SAE AS210 atmospheric model with an offset temperature of 58°F at sea level. Consequently, the considered weight for the PEMFC heat exchanger is 103 kg. For the first and second heat exchangers, preliminary results show a weight of 60 kg and 55kg, respectively. Therefore, the overall weight of the three heat exchangers is 140 kg.

Table 9. PEMFC heat exchanger weight for different coolant types.

Coolant Type	Heat exchanger weight (lb [kg])	Design Point
50/50 Propylene Glycol Mix	328 (149)	Ground Operations on Hot Day
	15 (75)	Ground Operations on Standard Day
25/75 Propylene Glycol Mix	227 (103)	Ground Operations on Hot Day
	128 (58)	Ground Operations on Standard Day

Regressions based on historical data are used to compute the weight of the turbomachinery components. The three systems considered are the PEMFC compressor, the ECS compressor and the hydrogen pump. The results obtained are

® CYCOM is a registered trademark of Cytec Technology Corp., Princeton, New Jersey.

summarized in Table 10. For the hydrogen pump, the model is still in development, therefore the weight used is an intermediate weight corresponding to a pump that can be purchased commercially and that has similar characteristics.

Table 10. Turbomachinery weight breakdown.

Turbomachinery	Number of Stages	Weight (lb [kg])
PEMFC Compressor	2	74.5 (33.8)
ECS Compressor	2	43.7 (19.8)
H_2 Pump	1	15.9 (7.2)

As shown in Table 11, the interim estimated weight of the PEMFC system is approximately 753.7 lb (341.9 kg). To account for any missing components such as membrane humidifier system or high voltage cables, the total weight is multiplied by a k-factor of 1.15. Therefore, for the next step, the PEMFC system weight which will be added to the aircraft, will be considered as 866.7 lb (393.1 kg).

Table 11. PEMFC system weight breakdown.

Components	Weight (lb [kg])	Weight Percentage (%)
Fuel Cell Stack	82.1 (37.3)	10.9
DC-DC Converter	27.4 (12.4)	3.6
Inverters	20.4 (9.2)	2.7
Electric Motors	11.5 (5.2)	1.5
Turbomachinery	134.0 (60.8)	17.8
Other Auxiliary Components	8.2 (3.7)	1.1
Thermal Management System	308.6 (140.0)	41.0
Battery	26.5(12.0)	3.5
LH_2 Fuel	86.4 (39.2)	11.5
LH_2 Empty Tank System	48.5 (22.0)	6.4
PEMFC Overall System	753.7 (341.9)	100

The aircraft model will also benefit from the removal of several systems' weights. Firstly, the APU system group weight of 370 lb (168 kg) will be removed. Then, the ECS system will be replaced by an electrical ECS system. Therefore, the air cycle machine (ACM) system weight will be reduced by 20% amounting to an ACM weight of 262 lb (119 kg) instead of 327 lb (148 kg). Moreover, the fuel consumption for the ground operations of the APU amounting to 77 lb (35 kg) is also to be removed. On top of these weight reductions, the load on the main engines will be reduced. In fact, no customer bleed extraction from the main engines will be performed nor any horsepower extraction since the PEMFC system will provide electrical power and the bleed air for the cabin.

Step 2: Aircraft level assessment of the new system

The notional baseline G280 aircraft model will be modified to assess the impact of integrating a PEMFC system to replace the APU. Firstly, the operating empty weight (OEW) will be increased by around 431 lb (866 lb - 370 lb - 65 lb) from 24,150 lb (10,954 kg) to around 24,581 lb (11,150 kg). The corresponding maximum ramp weight needs to be assessed by finding the mission fuel weight needed to complete a 3,600 nmi mission with the same aircraft. The modification of the baseline by replacing the APU and integrating a PEMFC system leads to the weight breakdown in Table 12 when performing a 3,600 nmi mission. While performing the fuel burn assessment the fuselage length is assumed to stay the same.

Table 12. The PEMFC system weight breakdown.

G280 with PEMFC Weight Breakdown	
Ramp Weight (RAMPWT), lb (kg)	39,984 (18,136)
Taxi In Fuel Weight, lb (kg)	150 (68)
Maximum Takeoff Weight (MTOW), lb (kg)	39,834 (18,069)
Design Landing Weight (DLDWT), lb (kg)	32,693 (14,829)
Operating Empty Weight (OEW), lb (kg)	24,577 (11,148)
Maximum Fuel, lb (kg)	14,407 (6,535)
Maximum Payload Full Fuel, lb (kg)	1,000 (454)
Passenger, number	4
Crew Member, number	2
Maximum Range, nmi	3,600

The weight distribution is maintained the same as the baseline except for the PEMFC weight addition, the APU weight removal and the ECS weight reduction of 20%. The weight breakdown of the aircraft with the PEMFC can be found in Table 13.

Table 13. The PEMFC system weight breakdown.

Notional G280 Model with PEMFC				
Mass Breakdown	**Weight (lb [kg])**		**Mass Breakdown**	**Weight (lb [kg])**
Wing	3,801 (1,724)		**Air Conditioning**	**262 (119)**
Horizontal Tail	716 (325)		Systems and Equipment Total	7,082 (3,212)
Vertical Tail	405 (184)		Empty Weight	23,071 (10,465)
Fuselage	5,750 (2,608)		Crew and Baggage	450 (204)
Landing Gear	1,100 (499)		Unusable Fuel	336 (152.4)
Nacelle (Air Induction)	248 (112.5)		Engine Oil	54 (24.5)
Structure Total	12,019 (5,452)		Passenger Service	666 (302)
Engines	3,680 (1,669)		**Operating Empty Weight**	**24,577 (11,148)**
Fuel Systems - Tanks and Plumbing	289 (131)		Passengers	760 (345)
Powerplants Total	3,969 (1,800)		Passenger Baggage	240 (109)
Surface Controls	627 (284)		Zero Fuel Weight	25,577 (11,602)
Auxiliary Power	**866 (393)**		**Mission Fuel**	**14,407 (6,535)**
Hydraulics	612 (278)		**Max Design Taxi Weight**	**39,984 (18,137)**
Electrical	341 (155)		**Taxi Out Fuel**	**150 (68)**
Avionics	350 (159)		**Maximum Takeoff Weight**	**39,834 (18,069)**
Furnishings and Equipment	4,023 (1,825)		**Design Landing Weight**	**32,693 (14,829)**

Finally, the comparison between the design mission of 3,600 nmi and two economic missions of 900 nmi and 500 nmi is performed. It can be observed in Table 14 that the aircraft fuel savings benefits vary from 2% to 3.16% block fuel reduction showcasing the potential for PEMFC systems to replace conventional APU systems.

Table 14. The PEMFC system weight breakdown.

Mission Fuel Burn Assessment			
Range (nmi)	3,600	900	500
Baseline Block Fuel (lb [kg])	13,207.1 (5,990)	3,478.8 (1,578)	2,216.8 (1,006)
PEMFC Aircraft Block Fuel (lb [kg])	12,944.1 (5,871)	3,388.9 (1,537)	2,146.8 (974)
Fuel Savings (lb [kg])	263 (119)	90 (41)	70 (32)
Percentage Reduction in Block Fuel (%)	**1.99**	**2.59**	**3.16**

Milestones

- Steps 1 and 2 are in progress. The two modeling and simulation environments were run separately to generate interim results, demonstrating their usefulness. Once the fuel cell model is finalized, efforts will be focused on integrating into these environments.

Major Accomplishments

- Examined the weight effects at the aircraft level using the interim results from the fuel cell sizing tool.

Publications

None.

Outreach Efforts

- Scheduled monthly meetings with Gulfstream, Honeywell, and FAA to guide this research effort.
- Attended ASCENT biannual meetings.

Awards

None.

Student Involvement

This task involves four Georgia Tech graduate students: Berkay Terzi, Jeremy Decroix, Leo Wattebled, and Axel Jazzini.

Plans for Next Period

- Integrate the off-line PEMFC code into the EDS environment to enable seamless data transformation between them and centralize control from a single hub.
- Conduct more comprehensive design studies by expanding the design space following the integration of the two environments.
- Evaluate the volumetric impact of the new system on the aircraft.

References

EASA. (2020). *Type-certificate data sheet for noise, No. EASA.IM.A.348 for Gulfstream G280*. European Union Aviation Safety Agency (EASA). https://www.easa.europa.eu/en/downloads/8117/en

Honeywell International, Inc. (2024). *Honeywell 36-150 ported shroud APU, advanced APU design for custom applications*. https://www.redimec.com.ar/contenido/productos/pdf/1425325504_1.pdf.

Daggett, D., Eelman, S., & Kristiansson, G. (2003). Fuel cell APU (p. 2660). In *AIAA International Air and Space Symposium and Exposition: The Next 100 Years*. AIAA Meeting Paper. https://doi.org/10.2514/EOF03

Project 096 Future Transportation System Opportunities and Constraints

Georgia Institute of Technology

Project Lead Investigator

Principal Investigator:
Professor Dimitri N. Mavris
Director, Aerospace Systems Design Laboratory
School of Aerospace Engineering
Georgia Institute of Technology
Phone: (404) 894-1557
Fax: (404) 894-6596
Email: dimitri.mavris@ae.gatech.edu

Co-P.I.:
Dr. Holger Pfaender
Aerospace Systems Design Laboratory
School of Aerospace Engineering
Georgia Institute of Technology
Phone: (404) 385-2786
Fax: (404) 894-6596
Email: holger.pfaender@ae.gatech.edu

University Participants

Georgia Institute of Technology (Georgia Tech)

- P.I.s: Dr. Dimitri N. Mavris, Dr. Holger Pfaender
- FAA Award Number: 13-C-AJFE-GIT-159
- Period of Performance: March 19, 2024, to September 30, 2024
- Tasks:
  1. Develop Background Scenarios
  2. Commercial Aviation
  3. Non-traditional Vehicle Scenarios
  4. Regional Passenger Demand Estimation
  5. Vehicle Technology Specific Scenarios
  6. Coordination with FAA
  7. Documentation

Project Funding Level

This research was funded by the U.S. Federal Aviation Administration (FAA) Office of Environment and Energy through ASCENT, the FAA Center of Excellence for Alternative Jet Fuels and the Environment, Project 096, through FAA Award Number 13-C-AJFE-GIT-159 under the supervision of Joshua Glottmann. Any opinions, findings, conclusions or recommendations expressed in this material are those of the authors and do not necessarily reflect the views of the FAA.

This project is funded at the following levels: Georgia Institute of Technology ($400,000). The Georgia Institute of Technology has agreed to a total of $400,000 in matching funds. This total includes salaries for the project director, research engineers, and graduate research assistants and for computing, financial, and administrative support, including meeting arrangements. The institute has also agreed to provide tuition remission for students whose tuition is paid via state funds.

Investigation Team

Georgia Institute of Technology

Dimitri N. Mavris (P.I.), Tasks 1-7
Holger Pfaender (co-P.I.), Tasks 1-7
Raphaël Gautier (research faculty), Tasks 1-7
Cedric Justin (research faculty), Tasks 1-7
Paul Boyer (graduate student), Tasks 1-7
Cristobal Garces (graduate student), Tasks 4, 6, 7
Anand Belsare (graduate student), Tasks 1, 2, 6, 7
Autumn Edwards (graduate student), Tasks 1-6
Anass Jari (graduate student), Task 4, 6, 7
Yilin Deng (graduate student), Tasks 1-6
Xi Wang (graduate student), Tasks 1-6

Project Overview

The primary objective of this research project is to support the FAA in modeling and assessing the potential future evolution of the next generation aircraft fleet while supporting the FAA Office of Environment and Energy goals and objectives. Research under this project will consist of three integrated focus areas: (1) developing a set of harmonized scenarios investigating what the air transportation system will look like in 2050, 2075, or 2100; (2) modeling advanced aircraft technologies and advanced vehicles expected to enter the fleet through 2100; and (3) performing vehicle and fleet level assessments based on input from the FAA and the results of (1) and (2).

Task 1 – Develop Background Scenarios

Georgia Institute of Technology

Objective(s)

The study will begin with a comprehensive literature review to provide an overview of the current state of the aviation industry and identify the challenges facing the sector. The research will also potentially include interviews with aviation experts, policymakers, and industry leaders to gain insights into the industry's current state and future direction. This review will be used to define macroeconomic and general technological advancements expected during this extended time horizon to 2100.

Research Approach

Literature Review

A review of the aviation sector's impacts to global carbon dioxide (CO_2) emissions is presented in the Sixth Assessment Report (AR6) of the Intergovernmental Panel on Climate Change (IPCC) prepared by Working Group (WG)-III. The review emphasizes that around 65% of the sector's emissions are from international flights, with total emissions in 2018 adding to about 1 gigaton (Gt) of CO_2. The research focuses on the alarming acceleration of emission rates, which increased by 2.5% annually over the previous 20 years to almost 4% annually between 2010 and 2018. The study examines the net warming effects of aviation's CO_2 and non- CO_2 emissions, such as water vapor, soot, sulfur dioxide, and nitrogen oxides.

Since net-zero emissions are a requisite for 1.5° scenarios, it calls for sweeping transformations in both technology and fuel types. It also asserts current technological advances, like blended wing body aircraft that could deliver about 10% fuel savings, will not be able to offset projected emissions growth due to their slow introduction into the market. The AR6 IPCC report also examines operational inefficiencies and potential improvements, including a finding that better air traffic control could reduce emissions by 13% globally by the year 2050. It points to major uncertainties about non- CO_2 impacts of liquid hydrogen powered aircraft and suggests a move toward high-speed rail as a practical substitute for regional travel, which could significantly lower the demand for short-haul flights (Guivarch et al., 2022).

The process for generation of scenarios is a major component of the IPCC AR6 reports, involving collaboration between the IPCC's working groups to combine socio-economic storylines with environmental impacts. This comprehensive approach to

scenario planning has been explained in the report, showing how socio-economic data is used with climate simulations to yield accurate and relevant policy scenarios (IPCC, 2023).

The report presents mid- to long-term projections through 2050 to illustrate how technology and infrastructure improvements could reduce aviation emissions, discusses hybrid modelling approaches used to project developments in the sector, and describes the top-down/bottom-up hybrid approach it uses which captures a wide range of drivers. It also rates potential mitigation pathways across three levels of concern based on a multidimensional feasibility framework that considers their transformative impact and feasibility, providing a systematic method for measuring the efficacy of different policymaking and technological approaches in addressing climate impacts from aviation (Lee et al., 2021).

To gain an understanding of how one of the models used by IPCC works, the Global Change Analysis Model (GCAM) was studied. GCAM integrates environmental, economic, and energy systems to forecast global future scenarios effectively. GCAM calculates transportation service demand using a sophisticated formula that includes variables such as per-capita gross domestic product (GDP), service price, population, and elasticity measures, which enables the prediction of future transportation needs under various socio-economic conditions.

More details in GCAM (discussing competition between different transportation subsectors, technology share, and time value of transport) also show how the model handles competition. The cost calculation method for alternative transportation technologies is also overly broad with respect to fuel price, vehicle fuel intensity factors, non-fuel costs and load factors (Joint Global Change Research Institute, 2024).

Another aviation model designed to quantify environmental and economic impacts of policies related to the emission reduction is the Aviation Emissions and Evaluation of Reduction Options Modelling System (AERO-MS). The AERO-MS is a framework built to provide a comprehensive quantitative system analysis of the present and future air transport system with special emphasis on assessing emissions from aircraft engines. The AERO-MS evaluates the downstream effect of policy change-related impact on supply-side costs, which in turn affects demand for air travel. The system evaluates global emissions under different emission mitigation scenarios, incorporating responses from all key stakeholders, including supply (airlines), demand (consumers), and policy sector (governments and manufacturers).

The AERO-MS has five linked modules: (1) the Unified Database, Airport Technology Model (ATEC), (2) Air Transportation Demand Module (ADEM), (3) Aviation Cost Module (ACOS), (4) Flights and Emissions Modules (FLEM), and (5) the Direct Economic Impacts Module (DECI). Together, these modules provide complementary perspectives on developments in the aviation system, with the DECI offering detailed assessments of volumes of air transport traffic, airline revenues and fleet and flight activity—all according to data from the other modules (European Commission, 2004).

The model organizes its analysis according to three scenarios: (1) the Base scenario, which demonstrates what would happen in a business as usual global air transportation system, (2) the datum scenario, consisting of projections for technical and economic progress that continue with no policy changes, and (3) the Forecast situation which inspects the impacts of various policy alternatives. The comparison of alternative mitigation policy measures against a common baseline enables the AERO-MS to provide high-resolution projections of future states, making the assessments applicable to real-world policy evaluation and subsequent efforts at mitigation with robust estimates.

In general, the AERO-MS is an important and necessary tool to better understand and predict the consequences of policy and technology changes on the aviation sector (European Union Aviation Safety Agency, 2009).

In addition to these models, trend projection is an important part of aviation forecasting. Trend projection is a process of making educated predictions of the future by using the known past as a basis. This approach necessitates in-depth knowledge of a large number of factors that affect the predicted outcomes. Trend projection should consider the consistency and variability of the main economic indicators, the technological advances, and the demographic changes.

To effectively project trends, the focus needs to dive into the inner structure and reasoning behind each variable. This requires examining how GDP, population, and technological advancement interacted with aviation demand in the past and how these can be projected to affect industry in the future under different conditions. For instance, when GDP is stable, air travel demand may be more predictably rising; whereas, when the economy is unstable, travel behavior can become more challenging to predict.

Apart from that, long-term forecasting should also take into consideration the probable occurrences of disturbances that can cause the trends to break. These disturbances might include, for instance, recent breakthroughs in aircraft technologies that would cut down the operation costs or new regulations that make flight operations difficult. In a like manner, there can be a massive geopolitical incident or a significant economic crisis that will highly affect the market conditions, which in turn would force changes in the trend projections. Besides, the forecast changes must be capable of bending if the baseline ideas turn out to be different than expected or if future circumstances exhibit unexpected behavioral changes. This versatility guarantees the survival of the methodology over time and its high predictive capability as to the strategic decisions of the aviation sector. The skill of recalibrating forecasts in the face of new developments or adaptations in the underlying assumptions is key for the accuracy and credibility of long-term aviation forecasts (Ashford et al., 2011).

Given the importance of trend projections, understanding the underlying assumptions in any forecast becomes important. The FAA forecast implements both optimistic and pessimistic scenarios to consider changes in national and global economic markets, which requires flexibility in bringing in the effects of various uncertainties that might impact the aviation sector, such as the economic recession or geopolitical conflicts (Federal Aviation Administration, 2020).

The FAA's forecasting methodology is based on economic data and assumptions from IHS Markit® Economics. The data are divided into data, such as the Consumer Price Index (CPI) and unemployment rates, to form baseline, optimistic, and pessimistic economic scenarios. The scenarios typically do not consider factors such as recessions, changes in consumer behavior, and the overall economic effect of international conflicts.

Among the specific data sources utilized in the FAA forecast are the historical data from the Bureau of Labor Statistics (BLS) and the Bureau of Economic Analysis (BEA) including forecasts from IHS Markit® These sources provide economic information that the FAA uses to make economic assumptions which, in turn, guides forecasts of future domestic aviation demands (Federal Aviation Administration, 2023).

Milestone(s)

- Examined the scenarios in the studies covered in Task 1 for how they include aviation and the emissions estimates.
- Identified how aviation is integrated into global change analysis models, including their links to the global economy and emissions impacts.

Major Accomplishments

The research team identified potential data sources for the development of very long-term trends. The IPCC scenarios are still a benchmark for climate analyses and therefore are useful in identifying the circumstances aviation will have to operate in. In addition, the scenarios for the 7th Assessment Cycle are currently under development. The research team therefore anticipates that this project will be able to assimilate data produced for this purpose.

Publications

None.

Outreach Efforts

- Presentations at biannual ASCENT Advisory meetings
- Biweekly teleconferences with the FAA Technical Monitor

Awards

None.

Student Involvement

Graduate students have been involved in the research of the background scenarios. This includes documentation and presentation of their findings. The students conducted research into how global change scenarios include or at least are connected to aviation-specific scenarios.

® IHS Markit is a registered trademark of S&P Global Limited, in the United States and other countries.

Plans for Next Period

The main objective of this task is to be able to connect aviation scenarios to high level global change scenarios. In this context, the modeling efforts are an attempt to cover a wide range of plausible outcomes of aviation sector scenarios. As the project continues, opportunities to enrich the development efforts will be considered.

References

Ashford, N. J., Mumayiz, S., & Wright, P. H. (2011). *Airport Engineering: Planning, Design, and Development of 21st Century Airports* (4th ed.). John Wiley & Sons, Hoboken, New Jersey.

European Commission. (2004, November 19). *Aviation Emissions and Evaluation of Reduction Options Modelling System (AERO-MS), Policy Model Inventory*. Joint Research Centre. https://web.jrc.ec.europa.eu/policy-model-inventory/explore/models/model-aero-ms

European Union Aviation Safety Agency. (2009). *SAVE - Study on Aviation and Economic Modelling - Final Report*. European Union Aviation Safety Agency, 2009/OP15. https://www.easa.europa.eu/en/document-library/research-reports/easa2009op15

Federal Aviation Administration. (2020). *FAA U.S. Passenger Airline Forecasts, Fiscal Years 2020-2040*. Version 1.1. https://www.faa.gov/sites/faa.gov/files/data_research/aviation/aerospace_forecasts/FY2020-40_Passenger_Airline_Forecast.pdf

Federal Aviation Administration. (2023). *FAA Aerospace Forecast Fiscal Years 2023–2043 - Appendix A: Alternative Forecast Scenarios*. https://www.faa.gov/sites/faa.gov/files/FY%202023-2043%20Full%20Forecast%20Document%20and%20Tables_0.pdf

Guivarch, C., Kriegler, E., Portugal-Pereira, J., Bosetti, V., Edmonds, J., Fischedick, M., Havlík, P., Jaramillo, P., Krey, V., Lecocq, F., Lucena, A., Meinshausen, M., Mirasgedis, S., O'Neill, B., Peters, G. P., Rogelj, J., Rose, S., Saheb, Y., Strbac, G., Hammer Strømman, A., van Vuuren, D. P., & Zhou, N., (2022). Annex III: Scenarios and modelling methods. In: *IPCC 2022: Climate Change 2022: Mitigation of Climate Change. Contribution of Working Group III to the Sixth Assessment Report of the Intergovernmental Panel on Climate Change.* Eds. Shukla, A.R., Skea, J., Slade, R., Al Khourdajie, A., van Diemen, R., McCollum, D., Pathak, M., & Some, S., pp. 1842-1908 Cambridge, United Kingom and New York, New York, United States: Cambridge University Press. doi: 10.1017/9781009157926.022

IPCC. (2023). *Climate Change 2023: Synthesis Report. Contribution of Working Groups I, II and III to the Sixth Assessment Report of the Intergovernmental Panel on Climate Change* [Core Writing Team, H. Lee and J. Romero (eds.)]. Intergovernmental Panel on Climate Change (IPCC), Geneva, Switzerland, 184 pp., doi: 10.59327/IPCC/AR6-9789291691647

Joint Global Change Research Institute. (2024). *GCAM v7.1 Documentation: Demand for Energy*. https://jgcri.github.io/gcam-doc/demand_energy.html

Lee, J.-Y., Marotzke, J., Bala, G., Cao, L., Corti, S., Dunne, J. P., Engelbrecht, F., Fischer, E., Fyfe, J. C., Jones, C., Maycock, A., Mutemi, J., Ndiaye, O., Panickal, S., & Zhou, T. (2021). Future Global Climate: Scenario-Based Projections and NearTerm Information. In: *Climate Change 2021: The Physical Science Basis. Contribution of Working Group I to the Sixth Assessment Report of the Intergovernmental Panel on Climate Change.* 'Eds.' Masson-Delmotte, V., Zhai, P., Pirani, A., Connors, S. L., Péan, C., Berger, S., Caud, N., Chen, Y., Goldfarb, L., Gomis, M. I., Huang, M., Leitzell, K., Lonnoy, E., Matthews, J. B. R., Maycock, T. K., Waterfield, T., Yelekçi, O., Yu, R., & Zhou, B. Cambridge University Press, Cambridge, United Kingdom and New York, New York, United States, pp. 553–672. doi:10.1017/9781009157896.006

Task 2 – Commercial Aviation

Georgia Institute of Technology

Objectives

This task includes the extension of existing commercial aviation forecasts with long-term trends to the year 2100. Additionally, this task will address potential vehicle and operational changes that could have larger scale effects on airline operating models. For example, reducing cruise Mach numbers to allow more efficient vehicles to operate could require significant airline schedule changes. A transition to smaller vehicle sizes and more direct service would also require significant route and schedule changes, which will also be among the potential changes to commercial aviation considered in this task.

Research Approach
The rapid technology estimation tools developed under prior PARTNER and ASCENT projects (A10, A11, etc.) are being examined for how they could allow categorizing into smaller, well organized and tested components that can be used to quickly explore commercial aviation and the emissions estimates for future years.

Milestone
Examine the scenarios in the studies covered in Task 1 for how these scenarios include aviation and the emissions estimates.

Major Accomplishments
The team made progress on establishing the reference datasets like the well published forecasts. In addition, initial mockups of this capability have progressed to the prototyping phase.

Publications
None.

Outreach Efforts
- Presentations at biannual ASCENT Advisory meetings
- Biweekly teleconferences with the FAA Technical Monitor

Awards
None.

Student Involvement
The students have undergone training to familiarize themselves with the existing tools and their heritage.

Plans for Next Period
The goal is to quickly move to a functional prototype so that its usefulness can be evaluated and expanded from there.

Task 3 – Non-traditional Vehicle Scenarios
Georgia Institute of Technology

Objective
Several new vehicles with capabilities that are completely different from conventional commercial airlines are expected to enter service and potentially become widely adopted. For this reason, traditional airline demand projections are not appropriate and are also not able to define future projections of these vehicles.

For example, intra-regional air travel in the United States is an economically challenging endeavor as the demand on any given route is minor compared to inter-regional travel which typically consists of flights to, from, and between large hub airports connecting these regions. Given the limited demand and shorter ranges, regional aircraft serving these intra-regional markets tend to be smaller, which leads to direct operating costs amortized over a smaller number of passenger seat-miles compared to larger aircraft. Regional aircraft usually have lower daily average utilization owing to the time spent on the ground in between flights. This increases the significance of fixed costs which are amortized over fewer passenger seat-miles. Short-range missions also result in more takeoffs and landings on average for each flight hour. Proportionally more time is thus spent during takeoff and climb, where power settings are high, and more takeoffs and landings are performed. This increases the wear and tear on the aircraft structure. All this tends to increase the maintenance costs and therefore the operating costs of regional air transportation.

The core of this research effort and its objective is to generate an optimized operational model to allow the construction of a potential future state of aviation where new types of mobility are enabled by highly efficient vehicles.

Research Approach
This task tries to connect the conventional commercial business models with new types of operation also supported by the results of Task 4.

Milestone(s)
Not started yet.

Major Accomplishments
Not started yet.

Publications
None.

Outreach Efforts
Not started yet.

Awards
None.

Student Involvement
Student researchers will be involved in all aspects of this task.

Plans for Next Period
The team will consult in collaboration with FAA Technical Monitors to determine the specific scope of this task.

Task 4 – Regional Passenger Demand Estimation
Georgia Institute of Technology

Objective
Regional aviation in the United States has seen a significant decline, with many routes left abandoned due to a multitude of challenges. This study aims to assess the feasibility of revitalizing regional aviation by forecasting passenger demand using more advanced modeling techniques under various macroeconomic and energy price scenarios.

Research Approach
To model regional aviation demand effectively, this task was divided into two interconnected parts:

1. Creating scenarios to evaluate the impact of different effects on current aircraft configurations and estimate change of aviation demand from the baseline scenario, including:
    a. Operating cost breakdown
    b. Categorization and evaluation of impacts on direct operating costs (DOC)
    c. Technology impacts
    d. Energy impacts
    e. Operations impacts
    f. Scenarios generation
2. Investigation and evaluation of demand models to:
    a. Explore forecasting methods, including statistical time-series methods such as Auto-Regressive Integrated Moving Average (ARIMA) and machine learning/deep-learning techniques (ML/DL).
    b. Seek models that can incorporate both internal and external factors.

Modeling Techniques
Air travel demand forecasting is an important task for understanding and planning the future of any aviation system. The choice of an appropriate forecasting model is heavily dependent on the type of factors and goals of the forecast itself. In the case of modeling the demand for regional aviation, historical data is sparse. Additionally, regional aviation is influenced by advancements in technology and the fluctuation of energy prices. Recent advancements in ML and DL have

motivated many researchers to explore the applicability of these techniques to aviation-related problems such as forecasting passenger demand (Zachariah et al., 2023). The ability of ML and DL to learn complex patterns and incorporate high-dimensional data offers the potential to create more accurate and robust forecasting models. Figure 1 shows a breakdown of common techniques to forecast passenger demand.

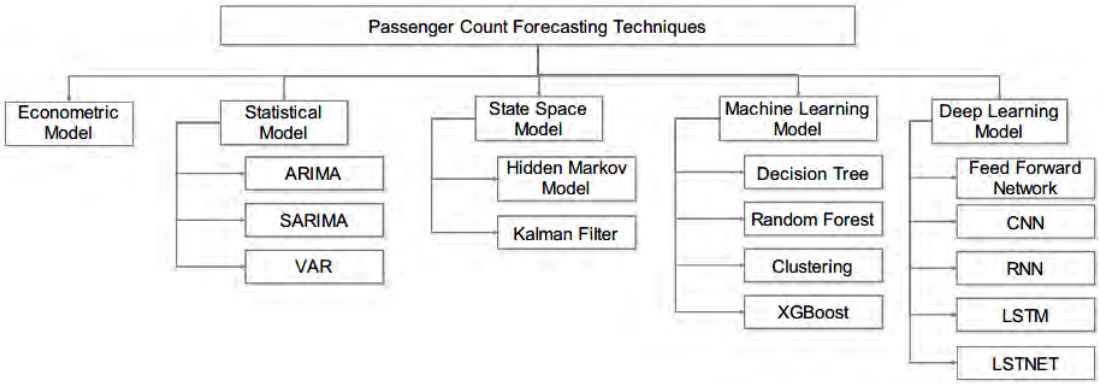

Figure 1. Aviation demand forecasting techniques.

Statistical forecasting techniques encompass traditional econometric models and time-series models. Econometric models are commonly used to study long-term economic trends in data, such as GDP growth. These models help with identifying which economic factors influence passenger demand within a region or country. Additionally, the models are built from economic theories and may use time-series data, cross-sectional data (data collected at a single point in time), and panel data (a combination of the two previously mentioned data types). Econometric models, for this reason, are both theory driven and data driven, which may result in misleading forecasts due to underlying assumptions in economic theory.

Time-series forecasting is used to predict future trends based on historical data that is observed over regular intervals, much in an analogous way to econometric models. However, these models can be specifically designed to analyze and forecast data points ordered sequentially over time. A pure time-series forecasting method for aviation has increased challenges associated with the increased uncertainty and irregularity of air passenger movement. Two popular and well-known statistical time-series models are the ARIMA and Seasonal Auto-Regressive Integrated Moving Average (SARIMA) models. ARIMA and SARIMA both rely on linear assumptions between data points and thus limit their ability to accurately forecast high dimensional and nonlinear behavior as commonly found forecasting passenger demand. These models are typically used in hybridized models since alone, they often have poor performance at long time horizons (Kanavos et al., 2021).

ML provides a powerful framework for addressing the challenges of forecasting regional passenger demand. Unlike traditional models, ML techniques excel at identifying nonlinear relationships and dependencies between variables, making them more suitable to handle the complexity of factors influencing demand. Additionally, with the decrease in computational cost and increase of memory capacity, ML methods have already been utilized to solve real-world problems (Kanavos et al., 2021). Additionally, ML techniques are more flexible and adaptable to varying scenarios such as shifts in energy price or macroeconomic conditions. Most ML techniques work primarily with cross-sectional data but may be used in hybrid models to boost performance in forecasting by better relating macroeconomic factors to demand.

DL is a subcategory of ML that is based on iterative learning from the method's own error. DL is nonlinear by its very nature and, thus, is capable of modeling highly complex and nonlinear time-series data. Additionally, DL models can receive both time-series and cross-sectional data to capture patterns between variables automatically (Do et al., 2020). However, DL is much more computation intensive than ML methods and requires more resources and time to model with an additional tendency to overfit data. Long Short-Term Memory (LSTM) models are a type of recurrent neural network (RNN) that solves many faults of RNN-based models: long-term dependency problem and vanishing gradient problem which occurs during backpropagation (Do et al., 2020). This allows the model to capture long-term effects on demand from factors such as population and GDP.

Hybrid models combine the strengths of multiple modeling approaches and balance each other's shortcomings. By integrating more traditional methods such as basic econometric or time-series methods (i.e., SARIMA) with more modern techniques like ML and DL, hybrid models can capture both simple and complex behaviors in the data. Hybrid models typically are a combination of statistical+ML, statistical+DL, and ML+DL. One side of the hybrid model can analyze the linear trends and seasonality while the ML or DL portion can account for the more complex relationships and interactions between diverse variables.

The performance of various forecasting techniques in predicting aviation demand varies significantly, as shown in Table 1. Hybrid models outperformed single method forecasting approaches. However, these models have primarily been evaluated for short- to medium-term forecasts. Although their effectiveness for long-term forecasting remains untested, their strong performance in shorter timeframes suggests they could be adapted successfully for long-term forecasting problems.

Table 1. Comparison of aviation demand models.

Model Description	Mean Absolute Percentage Errors (MAPE)
Random Forest (RF)	6.76%
Deep Neural Network	7.98%
Particle Swarm Optimization Support Vector Regression (PSO-SVR)	2.38%
SARIMA-SVR Passenger Traffic Volume	2.31%
Regression+SVM Model	5.07%
Long Short-Term Memory (LSTM)	4.00%

Modeling Validation
A backcasting approach on historical data will be used to validate the selected forecasting model. Backcasting involves applying the model to a historical dataset, where actual results are already available. Backcasting is a widely used method for validating forecasting models, providing a benchmark for how well the model can replicate real-world outcomes. By comparing the model's predictions against these known values, performance parameters such as mean absolute error (MAE), mean absolute percentage error (MAP), root mean square error (RMSE), and coefficient of determination (R^2) can be calculated. These performance parameters quantitatively assess a model's accuracy, consistency, and ability to generalize, allowing for a more objective evaluation of the chosen model.

Scenario Analysis

Given the gradual change in commercial aviation to hub and spoke operations as well as other factors, the regional aviation sector has seen a decrease in attractivity which is estimated to be reversed given an introduction of technologies that can revitalize the sector with newer and more efficient configurations. These configurations may enable lower emissions and noise within urban areas. However, the inclusion of modern technologies that prompt new configurations makes it hard to predict what future configurations would be flown in 2050, 2075, and 2100. Therefore, there is a need to find a modeling approach for new emerging configurations.

Operating Cost Breakdown
To forecast different scenarios for future aviation demand, it is imperative to assess the pricing strategies that airlines use to generate "airfare" or "ticket prices" since it is one of the most important socio-economic factors behind air travel demand (Clark, 2017). The pricing system used by airlines currently is summarized in Revenue Management Systems (RMS), which enables airlines to maximize revenue by using multiple pricing strategies such as dynamic pricing, route-based pricing, and more. These pricing strategies are often a mix of three main pricing principles as laid out by Lesgourgues and Malavolti (2023):

- Cost-based pricing
- Demand-based pricing
- Service-based pricing

Cost-based pricing refers to a system of pricing in which the airline sets its prices equal to the marginal cost of producing an incremental unit of output. This practice is one of the theoretically optimal conditions of "perfectly competitive" markets. Demand-based pricing is based on consumers' "willingness to pay," as defined by the price–demand curve in each origin-destination market. Finally, service-based pricing refers to differences in the quality of services (and, in turn, in the cost of providing these services) as a basis for pricing (Belobaba et al., 2009). For the scope of this task, the ASCENT Project 096 team will be using a cost-based model to derive the airfares to be set by the airlines in the future since other pricing principles require access to more data and more complex models that are not within the scope of this task. To use the cost-based pricing principle, our team will lay out a few assumptions such as a fixed marginal cost across all airlines which will in turn disregard pricing based on services and time of purchase of tickets.

The use of cost-based pricing principles causes us to investigate costs related to airline operations and more specifically direct operating cost, which is the cost related to the operations of the aircraft. The direct operating cost is usually expressed as a function of block hours to normalize the data collected from large and small fleets, long and short flights, and so on. In order to only consider the direct operating cost of airlines to predict future airfare, it is assumed that the indirect operating cost of airlines would not contribute to the airfare and thus is assumed to be constant. The direct operating cost can be further broken down into two categories: (1) fixed direct operating cost and (2) variable direct operating cost. Fixed direct operating cost refers to operating cost components that are expenses directly tied to operating the aircraft but do not vary significantly with flight hours or distance flown. Variable operating cost refers to expenses directly tied to operating the aircraft and which vary with flight activity. Therefore, in order to further investigate the impact of effects on the direct operating cost, the focus is on the variable direct operating cost and the assumption that effects do not impact the fixed direct operating cost.

The literature review revealed that there are two main approaches to direct operating cost estimation. Both approach methodologies use historical data to a certain extent. The first approach, mean based methodologies, use large datasets of reported direct operating cost broken down by component. The direct operating cost is categorized by aircraft category or by engine configuration and by using the mean of the cases selected from the datasets. The second approach uses historical data of the operating cost of certain aircraft, and performance and general data about the aircraft such as maximum takeoff weight to create a regression curve linking both variables, and is thereby able to predict the direct operating cost of an aircraft given its general information.

For the task, our team will use the mean-based methodology to determine the direct operation cost breakdown by component for the respective aircraft categories within regional aviation as well as what might become part of regional aviation in the future due to effects.

When discussing effects that can impact the direct operating cost, the different advancements in other scientific fields as well as aviation that can directly decrease the cost associated with fuel, crew, and maintenance as defined in Federal Aviation Administration (2024) are discussed.

Categorization and Evaluation of Impacts on DOC

The consideration of effects that can impact the future direct operating cost of aircraft is something that other research papers have tangentially explored (ICAO, 2022; Air Transport Action Group, 2021). ICAO (2022), for example, explores how different effects impact the CO_2 emissions of aircraft to meet future environmental aspirational goals. The report categorizes these effects into three main categories: (1) operations, (2) technologies, and (3) fuels. Operations effects are defined by opportunities for reducing costs and improving energy efficiency by improving the way existing aircraft operate. Technologies effects pertain to the development of evolutionary aircraft and engine technology such as incremental improvements of established architectures, development of novel aircraft concepts, and significant changes at the propulsion level. Fuels effects refer to the development of fuels and new energy carriers that can lead to decrease in fuel cost. Our team will use the same categorization to refer to the different impacts on the direct operating cost with a slight modification to the nomenclature referring to fuels, which will be rather referred to as energy, to better encapsulate a wider range of energy carriers that can be considered in the long future under the assumption that some future aircraft configurations may not rely on fuel to operate.

Technology Impacts

The technologies that have been considered have been carefully selected as potential implementations in future configurations of aircraft due to their impact on the performance of the aircraft as well as their readiness level. The technologies are divided into the following categories:

- Aerodynamics
  - Laminar flow control
- Powertrain efficiency
  - Geared turbofan engine
  - Electric powertrain
  - Open rotor engine
- Maintenance, repair, and operationsimprovement
  - Simplified vehicle operations
  - Predictive maintenance
- Noise improvement
  - Blown flap short takeoff and landing (STOL)
  - Lift-plus-cruise (LPC)-vertical takeoff and landing (VTOL)
  - Tilt-rotor VTOL

The infusion of technologies on future aircraft configurations would enable many improvements in terms of performance. Given that certain technologies that have widely developed over the last century have reached their limits in terms of improvements, there is a need for a paradigm shift to enable more growth in the aviation industry. The technology sectors that would benefit the most from a paradigm shift would be the sectors that have a wide application of similar products such as the powertrain sector for which turbofans have been the standard choice despite their low efficiency compared to other powertrain configurations. One of the rapidly emerging technological advancements that could drive progress in the aerospace sector is the development of electric vehicles, which enables the use of electric powertrains in aircraft, resulting in higher efficiency and lower emissions. This is one of many examples of how a paradigm shift can largely impact future aircraft configuration, and thus, impact aviation demand.

Milestones

- Investigated use cases of various forecasting models.
- Evaluated different operating cost prediction methodologies.
- Examined the technologies to evaluate their impact on operating cost for scenarios generation.

Major Accomplishments

None.

Publications

None.

Outreach Efforts

None.

Awards

None.

Student Involvement

Graduate students are actively participating in research and performing literature review.

Plans for Next Period

Model Exploration and Selection

As discussed previously, a modeling method or hybrid model will be selected after a thorough comparison of existing models. The selected model will be trained in historical data and be evaluated accordingly. This will be accomplished by the following:

- Creation of forecasting model using split historical data
- Training of selected model
- Evaluation of forecasting model's performance parameters

Scenario Generation
The mean-based methodology will be used to generate a direct operating cost breakdown for the respective aircraft categories that is to be assessed. A range of impacts from the different technologies on the aircraft performances will be created, which will then be used to generate the scenarios.

References

Air Transport Action Group. (2021). *Waypoint 2050* (2nd ed.). https://aviationbenefits.org/media/167417/w2050_v2021_27sept_full.pdf

Belobaba, P., Odoni, A., & Barnhart, C. (Eds.). (2009). *The global airline industry*. John Wiley & Sons.

Clark, P. (2017). *Buying the Big Jets: Fleet Planning for Airlines* (3rd ed.). Routledge. https://doi.org/10.4324/9781315570662

Do, Q. H., Lo, S. K., Chen, J. F., Le, C. L., & Anh, L. H. (2020). Forecasting air passenger demand: A comparison of LSTM and SARIMA. *Journal of Computer Science, 16*(7), 1063–1084. https://doi.org/10.3844/jcssp.2020.1063.1084

Federal Aviation Administration. (2024). *Economic values for FAA investment and regulatory decisions*, *Section 4: Aircraft Operating costs*. https://www.faa.gov/regulations_policies/policy_guidance/benefit_cost/econ-value-section-4-op-costs.pdf

ICAO. (2022). *Report on the feasibility of a long-term aspirational goal (LTAG) for international civil aviation CO_2 emission reductions*. Committee On Aviation Environmental Protection (CAEP), International Civil Aviation Organization (ICAO). https://www.icao.int/environmental-protection/LTAG/Documents/REPORT%20ON%20THE%20FEASIBILITY%20OF%20A%20LONG-TERM%20ASPIRATIONAL%20GOAL_en.pdf

Kanavos, A., Kounelis, F., Iliadis, L., & Makris, C. (2021). Deep learning models for forecasting aviation demand time series. *Neural Computing and Applications, 33*, 16329–16343. https://doi.org/10.1007/s00521-021-06232-y

Lesgourgues, A., & Malavolti, E. (2023). Social cost of airline delays: Assessment by the use of revenue management data. *Transportation Research Part A: Policy and Practice, 170*. https://doi.org/10.1016/j.tra.2023.103613

Zachariah, R. A., Sharma, S., & Kumar, V. (2023). Systematic review of passenger demand forecasting in aviation industry. *Multimedia Tools and Applications, 82*, 46483–46519. https://doi.org/10.1007/s11042-023-15552-1

Task 5 – Vehicle Technology Specific Scenarios

Georgia Institute of Technology

Objectives

This task aims to capture the implications of vehicle specific technology and their potentially required infrastructure changes. This is intended to cover the adoption of electric or fuel cell aircraft as well as the potential large-scale adoption of sustainable aviation fuel and hydrogen vehicles. Combined with the results of Tasks 1, 2, 3, and 4 this will define combined scenarios that bring the various aspects of demand, operational changes, and new vehicle specific changes together in new scenarios for aviation.

Research Approach

- The team needs to narrow down the potential options in coordination with the FAA and industry.
- The team will perform initial tests of how the vehicle technologies intersect with the overall modeling framework.

Milestone

The team will work with FAA on identifying the specific technologies and scenarios that will be covered under this task.

Major Accomplishments

These vehicle-specific analyses will be integrated with the conventional aviation and the long-term scenarios from Tasks 1, 2, and 3. The goal is to show how certain technologies could help or hinder the adoption of certain types of vehicles.

Publications

None.

Outreach Efforts
None.

Awards
None.

Student Involvement
The graduate students that are part of this project will conduct most of this research under faculty supervision and with feedback from project management and other stake holders.

Plans for Next Period
The vehicle down select under Task 3 will also try to consider which specific technologies can enable new types of vehicles to be commercially and environmentally successful.

Project 097 FAST-Tech System Level Assessment

Georgia Institute of Technology

Project Lead Investigator

Principal Investigator:
Professor Dimitri N. Mavris
Director, Aerospace Systems Design Laboratory
School of Aerospace Engineering
Georgia Institute of Technology
Phone: (404) 894-1557
Fax: (404) 894-6596
Email: dimitri.mavris@ae.gatech.edu

University Participants

Georgia Institute of Technology (Georgia Tech)

- P.I.(s): Dr. Dimitri N. Mavris
- FAA Award Number: 13-C-AJFE-GIT-155
- Period of Performance: March 19, 2024, to September 30, 2024
- Tasks:
  1. FAST-Tech Fleet Benefit Assessment Problem Formulation
  2. Initializing Modeling of FAST-Tech Aircraft Technologies and Advanced Configurations

Project Funding Level

The Federal Aviation Administration (FAA) provided $200,000 in funding to Georgia Institute of Technology.

The Georgia Institute of Technology has agreed to a total of $200,000 in matching funds. This total includes salaries for the project director and research engineers, as well as funding for computing, financial, and administrative support, including meeting arrangements. Georgia Tech has also agreed to provide tuition remission for students, paid from state funds.

Investigation Team

P.I.: Prof. Dimitri N. Mavris
Co-P.I.: Dr. Jimmy Tai
Program Manager: Brennan Stewart
Supporting Engineers: Srujal Patel and Dr. Zhimin Liu
Students: Joao De Azevedo, Kavya Krishnan, Alexandre Masset, Clementin Leron, Benjamin Bashtovoi, Byron Chang, Saisruthi Bandla, and Naomi Michael

Project Overview

The objective of this research project is to support the FAA by independently modeling and assessing the technologies that are being developed under the Fueling Aviation's Sustainable Transition (FAST) Program. This will involve direct coordination and data sharing with FAST-funded companies to accurately model the environmental benefits of these technologies at the vehicle and fleet levels.

Georgia Tech was previously selected to perform all system-level assessments for the Continuous Lower Energy, Emissions and Noise (CLEEN) program under Partnership for Air Transportation Noise and Emission Reduction (PARTNER) Project 36, ASCENT Project 010, and ASCENT Project 037. As a result, Georgia Tech is in a unique position from both the technical and programmatic standpoints to perform system level assessments for the FAST Program. From a technical perspective,

Georgia Tech has significantly enhanced the Environmental Design Space (EDS) over the past five years to incorporate advanced, adaptive, and operational technologies targeting fuel burn and emissions.

The goal of this work is to conduct fleet-level assessments for aircraft representative of future "in-service" systems. To accomplish this goal, Georgia Tech requires system-level EDS models using a combination of both FAST Technologies and other public domain technologies and defining assumptions for future fleet scenarios. To expedite this study, Georgia Tech will leverage previously created EDS models, public technologies sets, and future fleet scenarios from Georgia Tech's work on ASCENT Project 037, in combination with the technology models created for the FAST technologies funded under ASCENT Project 097. This approach will allow Georgia Tech to complete the FAST fleet assessment quicker and for less cost than if Georgia Tech were to redevelop these assumptions using ASCENT Project 097 funds.

Work conducted during this period of performance focused on establishing which assumptions ASCENT Project 097 would utilize from Georgia Tech's ASCENT Project 037 program and assessing Georgia Tech's capabilities of modeling FAST technologies and performing background research on the technology concept. Georgia Tech has selected a fleet assessment methodology and a base year case from Georgia Tech's ASCENT Project 037. Since FAST awards were not announced until close to the end of this performance period, Georgia Tech has not had the opportunity to initiate discussions with FAST contractors and instead focused on understanding the announced technologies and assessing Georgia Tech capabilities for modeling the announced technologies.

Next year's work will focus on finalizing the fleet assessment assumptions, initiating contact with FAST contractors, and developing detailed modeling plans for the technologies which will be studied in the next performance period.

Milestones

The major milestones and their planned due dates are listed below:

Task No.	Milestone	Planned Due Date
1	Select Initial System Level Assessment Methodology	June 30, 2023
2	Evaluate Modeling Capabilities for FAST Technologies	September 30, 2024

Major Accomplishments

- Selected initial system level assessment methodology.
- Performed background research of FAST technologies.
- Assessed current capabilities for modeling of FAST technologies.

Task 1 - FAST-Tech Fleet Benefit Assessment Problem Formulation

Georgia Institute of Technology

Objective

The objective of Task 1 is to align the assumptions used in this FAST fleet benefit assessment with the most relevant assumptions used across similar recent assessments performed by Georgia Tech.

Research Approach

Georgia Tech has provided fleet benefit assessments regarding fuel burn, nitrogen oxides (No_x) emissions, and noise in a number of previous research efforts. Learnings from these previous fleet benefit assessments will set the starting point for this assessment. The FAA is interested not only in the effects of individual FAST technologies, but also the impact of combining various FAST and other public domain technologies across vehicle size classes. The fleet benefit assessment will be updated to match the most relevant assumptions constraining the FAST program in conjunction with the FAA. Georgia Tech and the FAA have agreed that methodology used in ASCENT Project 037 will serve as a useful starting point for the methodology for the FAST fleet benefit assessment (Mavris et al., 2023). Figure 1 shows an overview of the methodology for the FAST-Tech fleet benefits assessment based on the fleet assessment methodology used in ASCENT Project 037. The public set of technologies used in ASCENT Project 037 will also serve as the basis for the non-FAST technologies which will be infused into the mid- and far-term generations of aircraft analyzed in the FAST fleet benefits assessment.

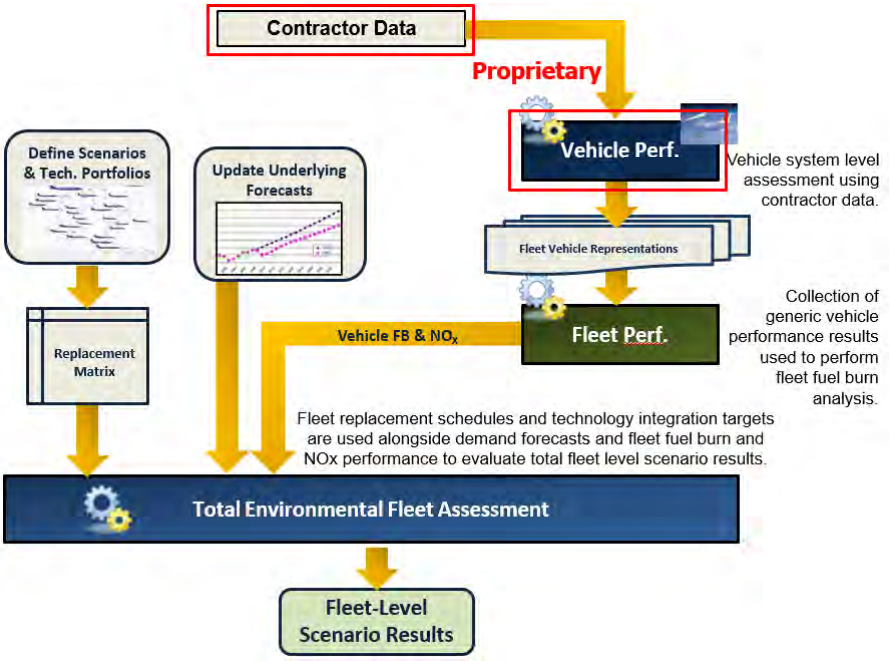

Figure 1. FAST fleet assessment initial methodology overview. FB: Fuel Burn, NO_x: nitrogen oxides.

Additionally, Georgia Tech has identified an appropriate set of baseline vehicles for the FAST fleet assessment and are shown below in Table 1. Notional vehicles models for these four vehicles were developed by ASCENT Project 037, and by leveraging for them for FAST fleet assessment, the process of modeling the baseline vehicles of the conventional Jet A Tube and Wing Architecture will not be required. This will allow additional effort to be focused on other areas of modeling.

Table 1. Initial FAST assessment baseline vehicle and vehicle classes.

Vehicle Class	FAST-Tech (2018 Baseline Year)
RJ (50 – 150pax)	E190-E2/PW1922G* + LEAP1B-28**
SA (151 - 235 pax)	B737-8/LEAP1B-28* + PW1127**
TA (236 - 400 pax)	B787-8/GEnX-1B70/P2* or B787-10/GEnX-1B76/P2*
F (400+ pax)	B747-8/GEnX-2B67*
* Entry into Service (EIS) Dates: E190-E2 (2018), B737-8 (2017). B787-8 (2011), B747-8 (2012) ** Notional System with alternative engine architecture	

Although FAST will be able to leverage much of the project formulation from ASCENT Project 037, the announced FAST awards will necessitate serval deviations from that methodology. FAST will need to consider alternative fuel sources, (i.e., electric and hydrogen fuel cell), and alternative vehicle architectures, (i.e., hybrid electric turboprop and blended wing bodies) due to the set of technologies funded by the FAA. Fuel burn alone may no longer be an appropriate metric when comparing vehicle architectures' performance on the fleet level. While electric and hydrogen concepts may reduce Jet A fuel consumption, there are still associated economic costs and net lifetime carbon dioxide (CO_2) emissions associated with both the generation and consumptions of those energy sources. The FAA is aware of Georgia Tech methodology towards comparing various vehicle fuel sources, but an agreement has not been reached on which, if any, additional fleet-level metrics should be used to compare fuel sources. This is due to the announcement of FAST awards occurring late in this period of performance. Discussions on the appropriate way to compare fleet level benefits will be ongoing towards in the next performance period. Additionally, the vehicle demand forecasts and fleet replacement assumptions will need to be updated to accommodate alternative vehicle architectures. The specifics of these assumptions will continue to be

discussed with the FAA in the next performance period and for the same reason discussions on metrics for comparing fuel sources will continue.

Task 2 - Initialize Modeling of FAST-Tech Aircraft Technologies and Advanced Configurations

Georgia Institute of Technology

Objectives

To estimate the impact of FAST relevant technologies at the vehicle-system level, each of these technologies must be modeled regarding their impacts to aircraft fuel burn and emissions using EDS.

Research Approach

To complete the FAST fleet benefit assessment outlined in Task 1, Georgia Tech must develop aircraft representative of future "in-service" systems, utilizing the technologies funded by FAST. Two necessary steps to accomplish the modeling of these future "in-service" systems are modeling all FAST technology in EDS and ensuring that new vehicle architectures are included in EDS modeling space. Once these tasks are completed, Georgia Tech will be able to develop the representative models of the future "in-service" systems and perform the fleet-level benefit assessment outlined in Task 1.

Table 2 shows the status of the modeling effort regarding each of the FAST relevant technologies. The announcement of the awards for the FAST contracts did not occur until August 2024, (Federal Aviation Administration, 2024), which was towards the end of this performance period. Additionally, Georgia Tech was not able to hold initial discussions with the contractors during the performance period due to the FAA contracting process not having been completed. Thus, Georgia Tech was limited to (1) performing background research on the technologies announced based on public sources and previous research effort into these technologies and (2) assessing current EDS capabilities to model these technologies.

Table 2. FAST technologies and their modeling status.

Contractor	Technology/Model Impact Area	Background Research Conducted and/or Modeling Capability Assessed	Initial Modeling Discussions Held with Contractor	Modeling Underway
AerSale, Inc.	Vertical Windshield Wipers	✓		
	Windshield Pillar Shock Bodies	✓		
Hamilton Sundstrand Corporation	Sustainable Aviation Fuel (SAF) Robustness	✓		
Green Taxi, Inc.	Green Taxi Electric Taxi (eTaxi) system for Embraer E-175 Aircraft	✓		
JetZero, Inc.	Blended Wing body Lightweight Composite Structures	✓		
Honeywell International Inc.	Sustainable Electrified Aircraft Power	✓		
APiJET, LLC	Optimizing Flight Routes using Real-Time Operating Constraints for Maximum			

Contractor	Technology/Model Impact Area	Background Research Conducted and/or Modeling Capability Assessed	Initial Modeling Discussions Held with Contractor	Modeling Underway
	Reduction of CO2 Emissions via Scalable Ground-Based Software			
Heart Aerospace Inc.	Total Hybrid Electric Management and Integration System	✓		
University of Michigan	Expanding Flight Operations-based Low Emissions Technologies: Fleet-wide and NAS-wide Arrival Flow Optimizer			
The Boeing Company	SAF Quality Indication	✓		
ZeroAvia Federal, Inc.	Project Hydrogen Aircraft Engine Zero Emission Leap	✓		
Otto Aviation Group, LLC	Wind-Tunnel Testing of a Transonic Aircraft with a Fully Integrated Slotted, Natural Laminar-Flow Wing	✓		
Wright Electric Inc.	Ultra-High Energy Battery			

FAST Technology Modeling Status Updates

- AerSale Inc. (AerSale)
  - Georgia Tech has evaluated that their technologies can likely be modeled in EDS through delta on-vehicle drag polar predictions, which is already a supported feature in EDS. However, final modeling plans cannot be developed until discussions with AerSale occur.
- Hamilton Sundstrand Corporation (Hamilton Sundstrand)
  - Georgia Tech has conducted background research on issues relating to the robustness of sustainable aviation fuel (SAF). Although literature found during this review assisted in furthering the Georgia Tech team understanding of SAF-related matters, the scope of Hamilton Sundstrand's technology is not clear from publicly available information; therefore, preliminary technology modeling plans will not be developed until discussions with the contractor can occur.
- Green Taxi, Inc (Green Taxi)
  - Georgia Tech has already developed electric taxi models featuring both fan-driven and wheel-based motor-driven propulsion, although the wheel-based motor design will need to be integrated into EDS. Georgia Tech will likely need to modify existing models to match the powertrain proposed by Green Taxi. Georgia Tech is confident that our previous work in this area will provide a strong foundation for this modeling effort.
- JetZero, Inc. (JetZero)
  - Georgia Tech has already conducted Blended Wing Body, (BWB), modeling efforts through our work with National Aeronautics and Space Administration (NASA) on the Sustainable Flight Demonstrator program and the Zero Emission Program. From public information, Georgia Tech cannot definitively state which lightweight composite structural technology JetZero has proposed; however, in general, Georgia Tech has experience with sizing non-cylindrical pressure vessels and structural sizing of composite technologies. Additionally, Georgia Tech has an existing workflow regarding integration of structural sizing estimate in the vehicle sizing analysis within EDS. Although these approaches may require modifications to capture the JetZero planned score,

Georgia Tech's background in BWB modeling and structural sizing positions the team to model JetZero's technology.

- Honeywell International, Inc. (Honeywell)
  - Georgia Tech's EDS tool has not historically developed auxiliary power unit (APU) numerical propulsion system simulator (NPSS) models as part of the aircraft sizing and synthesis process. Therefore, Georgia Tech has made it a focus to develop a baseline APU model in NPSS and will integrate it into the EDS design cycle to prepare for modeling work on Honeywell's proposed all-electric turbogenerator auxiliary power which Georgia Tech suspects will have a similar architecture as a baseline APU.
- ApiJET, LLC (ApiJET)
  - Due to the late announcement of awards, Georgia Tech will examine our capabilities to model ApiJET's technology in the next period of performance.
- Heart Aerospace, Inc. (Heart Aerospace)
  - Georgia Tech has developed a vehicle sketch pad (VSP) model of Heart Aerospace ES-30 aircraft concept, (Heart Aerospace, 2024), to support future modeling efforts and has been gathering public data about this concept. However, while hybrid aircraft concepts are currently supported in EDS, the combined gas turbine and electric motor turbo prop configuration proposed by Heart Aerospace is currently not an architecture established in EDS. The Georgia Tech team is working to include the combined gas turbine and electric motor turboprop configuration into EDS with the expectation that there will need to be some refinement to the electric powertrain once Georgia Tech can begin communications with Heart Aerospace.
- University of Michigan (Michigan)
  - Due to the late announcement of awards, Georgia Tech will examine our capabilities to model Michigan's technology in the next period of performance.
- The Boeing Company (Boeing)
  - Georgia Tech has conducted background research on issues relating to the SAF qualities during the flight mission and how fuel load is tracked over the course of the mission. Discussions with Boeing will be necessary to narrow down and define the scope of this technology and to develop a modeling plan.
- ZeroAvia Federal, Inc. (ZeroAvia)
  - Georgia Tech's work on ASCENT Project 095 has a heavy focus on modeling hydrogen fuel cell; it is expected that the FAST-Tech team will be able to heavily leverage these capabilities to model ZeroAvia technology. Once Georgia Tech can communicate with the contractor, more detailed modeling plans will be defined.
- Otto Aviation Group, LLC (Otto Aviation)
  - Georgia Tech has collected background information on previous research efforts regarding slotted, natural laminar-flow airfoils, and has developed an engineering sketch pad (ESP) model of Otto Aviation's public Celera 800 L aircraft concept, (Otto Aviation, 2023), to support future modeling efforts. Georgia Tech has evaluated that this technology can likely be modeled in EDS through a delta on vehicle drag polar predictions or through the implementation of a custom drag polar, which is already a supported feature in EDS. The FAA award to Otto Aviation announced that they would be performing wind tunnel testing; if possible, Georgia Tech would prefer to primarily utilize the wind tunnel test data generated by Otto Aviation to develop drag polar modifications. If the performance data required for that method cannot be provided by wind tunnel testing, Georgia Tech does have the ability to export the ESP model of Otto Aviation Concept and the ability to utilize high-fidelity and multi-fidelity Computation Fluid Dynamics (CFD) methods to generate drag polars. CFD simulations would be quite cost prohibitive and would only be considered if wind tunnel test data cannot provide all necessary information.
- Wright Electric Inc. (Wright)
  - Due to the late announcement of awards, Georgia Tech will examine our capabilities to model Wright's technology in the next period of performance.

Georgia Tech should complete preliminary assessment of its ability to model each of the FAST technologies by 1st Quarter (Q1) of 2025. Due to Georgia Tech's previous research and development efforts, Georgia Tech already has the capabilities to model most of these technologies and is focused on developing additional capabilities which are currently lacking. Task 2 will also be further advanced in Q1 2025, when Georgia Tech plans to complete initial discussions with each of the FAST award winners.

Publications

None.

Outreach Efforts

Georgia Tech presented our plans for the FAST Program as part of the CLEEN Consortium in Washington D.C. on May 7, 2024, to a mixed audience of industry and academia representatives.

Awards

None.

Student Involvement

Eight graduate students have been funded by the effort: Joao De Azevedo and Kavya Krishnan are PhD students, and the remaining six students, Alexandre Masset, Clementin Leron, Benjamin Bashtovoi, Byron Chang, Saisruthi Bandla, and Naomi Michael, are master's students.

Plans for Next Period

Durning the next performance period, Georgia Tech will:

- Refine the fleet assessment methodology to account for the modifications required to make the assessment appropriate for FAST's set of technology.
- Establish a relationship with the FAST contractors.
- Work with the FAST contractors to develop and refine a preliminary modeling plan for their technologies.

References

Federal Aviation Administration. (2024). Fueling Aviation's Sustainable Transition (FAST) Grants. *Federal Aviation Administration*. https://www.faa.gov/general/fueling-aviations-sustainable-transition-fast-grants

Heart Aerospace. (2024). Introducing the ES-30. *Heart Aerospace*. https://heartaerospace.com/es-30/

Mavris, D., Tai, J., & Brooks, J. (2023). *Project 037 CLEEN II System-level Assessment*. https://s3.wp.wsu.edu/uploads/sites/2479/2024/08/2023-ASCENT-Annual-Report.pdf

Otto Aviation (2023). Celera 800 L. *Otto Aviation*. https://www.ottoaviation.com/

Project 098 Low Emissions Lean Pre-Mixed Pre-Vaporized Combustion Technology for Subsonic Civil Transport

Georgia Institute of Technology

Project Lead Investigator

Adam Steinberg
Professor
School of Aerospace Engineering
Georgia Institute of Technology
Phone: (404) 897-1130
E-mail: adam.steinberg@gatech.edu

University Participants

Georgia Institute of Technology

- P.I.: Dr. Adam Steinberg
- FAA Award Number: 13-C-AJFE-GIT-150
- Period of Performance: March 19, 2024, to September 30, 2024
- Tasks:
  1. Experimental Measurement of Emissions, Lean Operation Limits, Spray, and Flame Structure
  2. CFD Simulations of LPP Combustor

Project Funding Level

Federal Aviation Administration (FAA): $1,000,000
Georgia Institute of Technology (Georgia Tech): $486,000
General Electric (GE) Aerospace Research: $514,000

Investigation Team

Dr. Adam Steinberg (Georgia Institute of Technology [GT], PD/PI)
Dr. Ellen Mazumdar (GT, Co-PI)
Dr. Joseph Oefelein (GT, Co-PI)
Dr. Jerry Seitzman (GT, Co-PI)
Mr. Arihant Jain (GT, PhD student)
Ms. Ijeoma Obi (GT, MS student)
Ms. Jananee Dhanasekaran (GT, MS student)
Dr. Krishna Venkatesan (GE Research [GER], Co-PI)
Dr. Victor Salazar (GER, Co-PI)
Ms. Sydney Borrello (GER)

Project Overview

Lean premixed prevaporized (LPP) combustion is a key enabling technology to further reduce nitrogen oxides (NO_x) and nonvolatile particulate matter (nvPM) emissions from aeronautical gas turbine engines, while achieving the necessary durability and robustness. However, achieving practical LPP combustion is challenging due to the need to rapidly vaporize and mix fuel, stabilize LPP flames across a wide operating envelope, and prevent unwanted combustion dynamics. Furthermore, the ability of current design methodologies to predict the operability and emissions of these combustors is unproven. Previous work during ASCENT Project 074 demonstrated positive results for an LPP combustor configuration at the conditions found in engines for supersonic transport aircraft and also encouraged further exploration at conditions relevant for the conventional subsonic fleet. This project will characterize the emissions and operability of the LPP

combustor at key operating points for such subsonic aircraft engines, including low power (i.e., idle and taxi), cruise, and approach. It will also develop measurement techniques needed to study high-power (i.e., takeoff and climb) conditions that are challenging for LPP combustors. High-quality experimental data at relevant conditions will be coupled with the development/validation of computational fluid dynamics (CFD) simulations and reduced order models. This forms a key first step in the development of both the LPP combustor technology and validated design tools for subsonic aircraft engine conditions.

Issues with contracting resulted in the GE Aerospace funding subaward not being executed until October 2024. As GE participation is essential for this project, the contracting issue delayed the project schedule by approximately six months. The project team is working to recover as much time as possible and has requested a no-cost extension for the current scope of work.

Task 1 – Experimental Measurement of Emissions, Lean Operation Limits, Spray, and Flame Structure

Georgia Institute of Technology and GE Aerospace.

Objectives

The objectives of this task under the current project scope are to:

- Redesign and optimize the ASCENT Project 074 LPP combustor geometry to have a pilot system that is more relevant for subsonic aircraft engines.
- Fabricate and commission this new combustor.
- Experimentally test the combustor at conditions representing idle, taxi, approach, and cruise to establish emissions levels and blow-off limits.
- Collect data using optical diagnostics with which to validate large eddy simulations (LES) and better understand the combustor.
- Develop and demonstrate novel measurement techniques that can be applied under high-power conditions (takeoff, climb) for studies in future years.

Research Approach

Experiments will be performed in the same basic test article as used for Experimental Campaign 2 in ASCENT Project 074 (see Figure 1), with some facility and premixer modifications to accommodate the different operating conditions for subsonic aircraft engines compared to supersonic aircraft. Due to the contracting delays, the experimental campaign currently is planned for the second and third quarters of 2025.

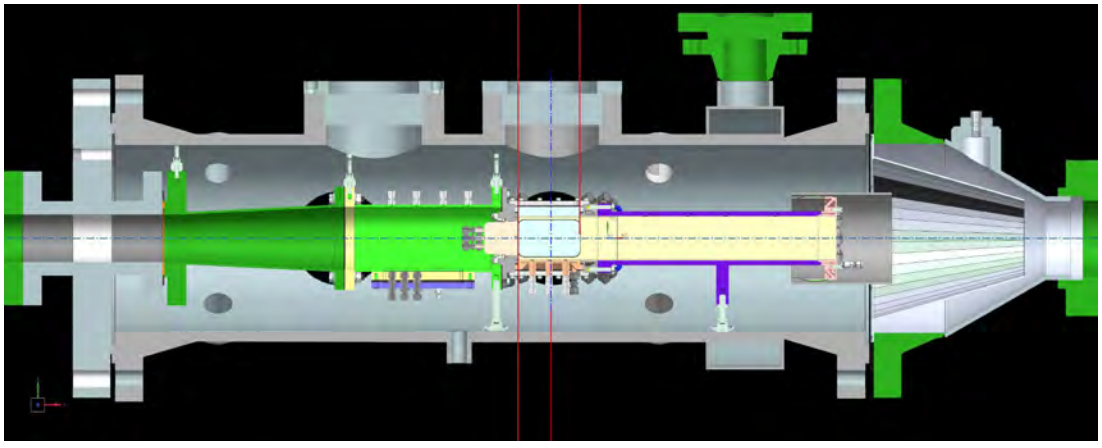

Figure 1. Conceptual schematic of experimental test article.

Activities to date have focused on three main areas:

1. Preliminary design of the new LPP combustor pilot and premixer by GE. The initial design concepts are complete, and GE Aerospace is currently running CFD simulations to aid in design and optimization.
2. Development of the overall experimental plan and schedule, including the test cells to be utilized and diagnostics to be deployed.
3. Continued training of the students on the diagnostic techniques.

The CFD simulations required to validate and optimize the combustor design are briefly described in Task 2. These are scheduled to be completed in January through February 2025. In parallel, the team is designing the accessory systems required for combustor operation in two GE test cells, designated "Cell 7" and "GEB." Component design is on track and scheduled for completion in December 2024. Fabrication of the combustor and components is scheduled for completion in April 2025, with final assembly and shakedown scheduled for May to June 2025.

Following commissioning of the experiment, two experimental campaigns will be performed back-to-back. The campaign in Cell 7 (June 2025) will map the operability and emissions of the combustor across the target range of conditions. Emissions data will include NO_x, unburnt hydrocarbons, carbon monoxide (CO), and carbon dioxide (CO_2), measured using an industry-standard protocol. In parallel, optical measurements of flame chemiluminescence and fuel spray Mie scattering will be made to characterize the heat release distribution, flame stability, and fuel spray pattern.

The campaign in GEB (July through August 2025) focuses on more detailed optical characterization of the combustor at a subset of operating conditions for LES validation, as well as the demonstration of the measurement techniques for high-power conditions. For the former objective, the team will deploy hydroxide (OH) planar laser induced fluorescence and particle image velocimetry to measure the flame surface topology and velocity field, respectively. These techniques have been successfully deployed in GEB during ASCENT Project 074 and provide critical LES validation data.

In addition, the team will develop and demonstrate two measurement techniques with the potential to be deployed at high-power conditions representative of takeoff and climb, which are challenging conditions for LPP combustors. Further, these conditions are difficult to study using advanced diagnostics because the combustors and pressure vessels generally cannot have large optical access, and optical techniques face challenges due to beam steering through refractive index gradients, signal trapping, spectral line broadening, etc.

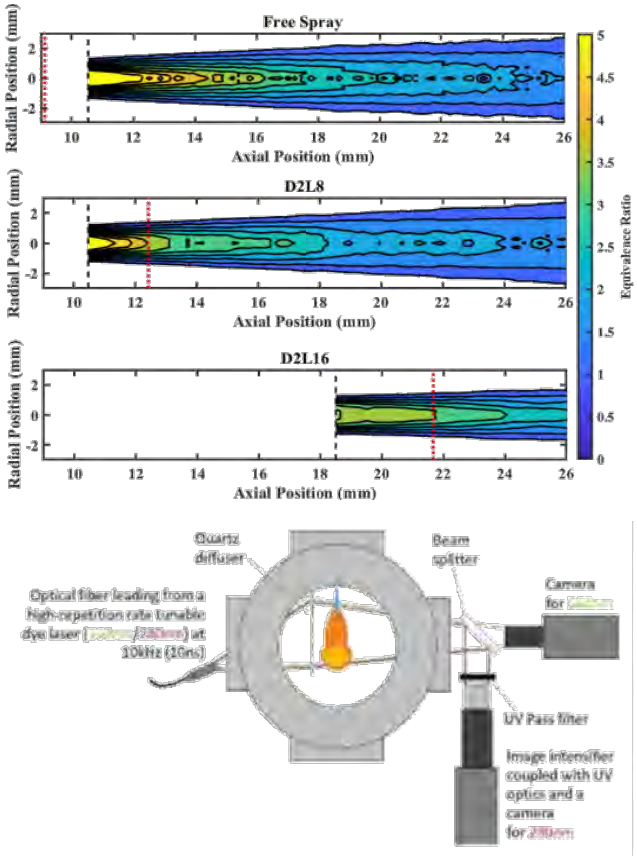

Figure 2. Example fuel/air equivalence ratio measurements using UV/visible laser absorption and scattering (top) and optical layout (bottom) (Godbold et al., 2024).

The two techniques to be demonstrated during the GEB campaign have the potential to be robustly deployed in such high-power conditions and provide significant new insights. The first technique to be demonstrated is based on simultaneous absorption and scattering of ultraviolet (UV) and visible laser light. This technique has previously been developed at Georgia Tech for measuring fuel vaporization and mixing at in diesel sprays, which occur at similar temperatures and pressures to those of interest here. In this technique, UV laser light is simultaneously absorbed by aromatic species in the fuel and scattered by fuel droplets. In contrast, the visible light is only scattered. Comparing the attenuation of the UV and visible lasers allows measurement of both vapor and liquid fuel through which the lasers traverse. An example of measured equivalence ratio fields in an evaporating diesel spray are shown in Figure 2. To date, this technique has been deployed in pressure vessels with windows, which simplifies the

optical arrangement. In ASCENT Project 098, the technique will need to be coupled into the test article by fiber optics. The optical system required for this coupling currently is being designed.

The second technique to be deployed will measure the spectrally-resolved light emissions from the flame as several discrete locations in the combustor. These emissions carry information on the heat release rate and fuel/air ratio at the measurement location (Sattelmayer et al., 2022). While such measurements are relatively routine in optical combustors with large fused-silica view ports, they have not been robustly performed in metal combustors without optical access. The team, therefore, is currently working on a method to directly braze sapphire optical fibers into effusion-cooled metal combustor liner panels. This method will allow many simultaneous optical emissions measurements to be collected. The fiber outputs are coupled into the slit of an imaging spectrograph, providing the desired spectral resolution for each fiber location.

Milestones

- Completed initiation of ASCENT Project 098.
- Completed and approved the ASCENT Project 098 year 1 detailed project plan and schedule with adaptations for contracting delays.

Major Accomplishments

None.

Publications

None.

Outreach Efforts

None.

Awards

None.

Student Involvement

- Arihant Jain (PhD Student)
- Ijeoma Obi (MS Student)
- Jananee Dhanasekaran (MS Student, Graduated)

Plans for Next Period

- Complete design, fabrication, and commissioning of ASCENT Project 098 combustor.
- Execute Cell 7 and GEB experimental campaigns.
- Analyze data.

References

Godbold, C., Gupta, I., Kurtz, E., Mueller, C. J., Genzale, C., & Steinberg, A. (2024). Experimental investigation of mixing phenomena for ducted fuel injection. *Proceedings of the Combustion Institute, 40*(1-4). https://doi.org/10.1016/j.proci.2024.105385

Sattelmayer, T., Fiala, T., & Lauer, M., (2022). Optical Diagnostics for Reacting and Non-Reacting Flows: Theories and Practice. In A. Steinberg & S. Roy (Eds.). *On Use of Chemiluminescence for Combustion Diagnostics* (pp. 931-1020). American Institute of Aeronautics and Astronautics. https://arc.aiaa.org/doi/abs/10.2514/5.9781624106330.0931.1020

Task 2 – CFD Simulations of Combustor Operation and Emissions

Georgia Institute of Technology and GE Aerospace.

Objective

The objective of this task under the current project scope is to perform CFD simulations of the LPP combustor to both aid in optimizing the combustor design and develop/validate best practices for simulating LPP combustors.

Research Approach

GE Aerospace will perform industry-scale "engineering" Reynolds averaged Navier-Stokes (RANS) and LES combustor test article. The solvers will be exercised to determine to what degree key processes can be represented both predictively and affordably. The central objective is to systematically establish a validated system of models for treatment of the device relevant processes emulated by the experimental rig. A major goal is to explore the ability of engineering-standard models to predict the trends observed as part of the experimental campaign and provide parametric analysis that provides additional insights with high levels of confidence.

Due to the contracting delays, this Task 2 was not initiated during the reporting period. Nonreacting CFD simulations of the pilot and mixer are scheduled for November 2024 to January 2025. Reacting CFD simulations are scheduled for January through February 2025. These simulations will primarily be used to optimize the combustor prior to fabrication. Ongoing LES will subsequently be validated against the experimental data from the Cell 7 and GEB campaigns.

Milestone

- Completed initiation of ASCENT Project 098.

Major Accomplishments

None.

Publications

None.

Outreach Efforts

None.

Awards

None.

Student Involvement

- Arihant Jain (PhD Student)

Plans for Next Period

- Complete nonreacting and reacting CFD for design optimization.
- Perform and validate LES of LPP combustor.

Project 101 Sustainable Aviation Fuel Repository

Washington State University

Project Lead Investigator

Joshua Heyne
Bioproducts, Sciences, and Engineering Laboratory Director, Associate Professor
School of Engineering and Applied Science
2710 Crimson Way, Richland, WA 99354
(937) 229-5319
joshua.heyne@wsu.edu

University Participants

Washington State University (WSU)

- P.I.: Dr. Joshua Heyne
- FAA Award Number: 13-C-AJFE-WaSU-043
- Period of Performance: March 15, 2024, to March 14, 2025
- Tasks:
  1. Investigating detailed needs and requirements of a SAF Repository
  2. Procuring SAF and conventional fuel samples for testing
  3. Testing procured samples for reference data to be leveraged by other partners
  4. Developing a data management protocol for sharing and distributing data
  5. Distributing fuel samples and data to partners per FAA prioritization

Project Funding Level

The ASCENT Project 101 received $2,000,000 from the Federal Aviation Administration (FAA) and cost sharing funding. In-kind cost share funding has been provided by Trinity College Dublin ($1,965,000) and Woodward ($35,000).

Investigation Team

Dr. Joshua Steven Heyne, P.I., Washington State University
Dr. Randall Boehm, Co-investigator, Washington State University
Dr. Tim Edwards (retired U.S. Air Force Research Laboratory), Consultant
Conor Faulhaber and Zhibin (Harrison) Yang, graduate students, Washington State University
Joshua Ledezma, Undergraduate Student, Washington State University

Project Overview

This project will serve to acquire, distribute, test, and document sustainable aviation fuels (SAF) and other reference conventional fuel samples. At present, accessing SAF samples is costly for the FAA and difficult for many research groups. Private, federal, and public research entities have issues collecting relevant SAF samples for testing. The lack of access inhibits progress in SAF research. Concurrently, procuring SAF materials is costlier for the FAA as samples are charged the full overhead rates, and individual acquisitions do not benefit from economies of scale. Fuel samples after acquisition will be tested for critical properties and then distributed to labs, per the preference of the FAA. A small portion of the acquired fuels will be retained for posterity and additional testing if anomalous observations are made.

Task 1 – Investigating Detailed Needs and Requirements of a SAF Repository

Washington State University

Objective

The objective of this task is to investigate detailed need and requirements of a SAF Repository. SAF is currently produced using novel feedstocks and conversion technologies. The combination of these novel feedstocks and conversion technologies results in unique compositions and properties in sustainable aviation fuel. As a result, the blend ratios for approved sustainable aviation fuel feedstocks vary between 10% and 50% as of November 21, 2024. The expectation is that several pathways will eventually be allowed at up to 100%. However, now, the limited blend ratios are the result of the unique properties and compositions of SAF relative to fossil fuel. For example, ASTM D7566 (ASTM International 2022b), the standard for synthetic aviation turbine fuel blend components, includes several annexes that have no aromatic content in the final product. The lack of aromatic content in the final product means that certain properties, such as seal swelling and dielectric constant, are outside of the experience range of 100% fossil fuels. This deviation is pronounced in the case of aromatics, but other more subtle deviations can also occur. For example, sustainable aviation fuels may be composed of only one or two molecules, as in the case of the iso-butanol to jet and Annex A3 in ASTM D7566. These compositions are very different from fossil jet fuel and, as a result, are not considered anything close to a conventional petroleum fuel.

Subtle and dramatic differences in composition can have substantial impacts on many safety and operability aspects. For example, changes in isomeric structure can impact a wide range of properties relevant to aviation. Properties like viscosity, for instance, can be increased substantially with changes in catalyst technologies, which is allowed under current ASTM D7566 (ASTM International 2022b) definitions. While there are no known issues with allowable blends or the current regulatory framework, it is critical to understand the scientific underpinnings of the impact of compositional variance on all aspects related to aviation fuel impacts on engines, infrastructure, aircraft, humans, and the environment. This task, investigating detailed needs and requirements of a sustainable aviation fuel repository, aims to identify the following characteristics required to assist in understanding the following compositional impacts:

- Types of fuels or synthetic blend components needed.
- Volumes of each needed fossil-synthetic blend component
- Number and type of fossil jet fuels for use as reference materials
- Number of entities that are needed to support this project
- Facilities needed to support activities SAF testing and research
- Forecasting future fuels and requirements several years in advance

Research Approach

Types of Fuels or Synthetic Blend Components Needed

There are three categories of fuels or synthetic blend components needed. The first category is reference conventional fuels. Conventional or petroleum-based fuels are needed to establish baseline experience ranges in various experimental architectures. Current aviation systems operate effectively, safely, and consistently on conventional fuels. However, all petroleum-based aviation fuels are not all the same. There are deviations across petroleum-based fuels in terms of their densities, viscosities, compositions, contaminants, etc. As a result, it is important to acquire several different petroleum-based fuels for testing in relevant architectures and configurations. Historically, three main petroleum-based fuels have been used for baselining. Under the National Jet Fuels Combustion Program (NJFCP), these fuels were defined as Category A fuels: A-1, A-2, and A-3. These three fuels were selected based on their combustor operability characteristics, namely their ability to resist or trigger lean blowout and ignite under altitude conditions. A-1 was selected to be the easiest to ignite and have the lowest flammability limit/lean blowout limit, making it a best-case fuel. A-2 was selected to be an "average" fuel, with properties similar to the average fossil fuel that aircraft in the United States were burning in 2014. The third fuel, A-3, was selected to be a "worst-case" fuel, with the poorest ignition characteristics and flammability limits relative to most conventional fuels used in the United States. Under this funded activity, the team has sought to acquire these Category A fuels from the U.S. Air Force Research Lab and gather additional fuels from other refineries in the United States. To the investigation team's knowledge, there are still some volumes of Category A fuels remaining; however, it is not yet known how many of these fuels are available for use under the FAA SAF repository project.

The second category of reference fuels sought under the SAF repository project are approved or candidate synthetic aviation turbine fuels. Now, there are eight annexes under ASTM D7566 (ASTM International 2022b). Additionally, there are

several producers globally producing materials with similar annexes, and at times with different technology providers/catalysts. For example, World Energy® in Paramount, California, and Montana Renewables in Great Falls, Montana, both produce synthetic blend components or SAF leveraging the ASTM D7566 Annex A2 pathway. Unfortunately, there are no commercially available synthetic blend components for some of the approved ASTM D7566 annexes. There are many SAF candidate pathways currently undergoing ASTM qualification or working towards entering the ASTM qualification process, ASTM D4054 (ASTM International, 2022b). The investigators have identified several institutions and products from these synthetic fuel routes.

The last broad category of synthetic blend components this program has sought to procure are solvents or other hydrocarbon materials that are not currently used as commercial fuels or being produced as an approved ASTM D7566 (ASTM International 2022b) pathway. Historically, programs have leveraged aromatic solvents such as aromatic (ARO) 100 and ARO 150. Furthermore, there are other solvents, such as NORPAR™ and ISOPAR,® which can be prepared to develop critical blends for testing various features or properties of aviation hardware.

Finally, under the NJFCP, combinations of all these categories were at times blended together to form mixtures that would stress-test various theories related to aircraft operability. These blends were collectively referred to as Category C fuels. Table 1 documents a range of fuels that have been selected based on the criteria above for inclusion in the repository.

Table 1. List of high interest materials for procurement under the repository project.

Category and motivation	Fuel description	Notes	POSF ID	Reason for Inclusion
SAF, emissions	HEFA (ASTM D7566 Annex A2) ($10/gal?)	Current producers: World Energy,® Montana Renewables, and Neste®	-	-
SAF	ATJ (ethanol) (ASTM D7566 Annex A5)	Lanzatech Global, Inc.	-	-
SAF	ATJ (isobutanol) (NJFCP C-1) (ASTM D7566 Annex A5) ($60/gal)	Gevo® or Global Bioenergies	Gevo: 11498 etc.	Historical, low cetane, narrow boiling
SAF	Power to liquids (Air Company)	In development toward ASTM D4054	-	-
Petroleum, operability	NJFCP A-2 "average" jet fuel, also used for blending ($3/gal)	-	10325, Jet A (also 4658)	Baseline for combustor operability testing
Petroleum, operability	NJFCP A-3 worst case jet fuel ($3/gal)	-	10289, JP-5	High viscosity, high flash
Petroleum, operability	NJFCP A-1 best case jet fuel	-	10264, JP-8	Low viscosity, low (but >38°C) flash
Petroleum, operability	New average Jet A fuel, also used for blending	-	-	-
Petroleum, operability	High flash JP-5 POSF 10370?	-	10376	70°C flash
SAF, emissions	Virent, Inc.,® SAK	Single-ring aromatics	12924, 13349, 13350	General Electric CLEEN II
SAF	CleanJoule LLC,® CycloSAF	1,4 dimethyloctane	-	-

® World Energy is a registered trademark of World Management Group, LLC, Boston, Massachusetts.
™ NORPAR is a trademark of Exxon Mobil Corporation, Spring, Texas.
® ISOPAR is a registered trademark of Exxon Mobil Corporation, Spring, Texas.

Category and motivation	Fuel description	Notes	POSF ID	Reason for Inclusion
SAF	Alder® Renewables pyrolysis pathways to Alder Renewable Crude (ARC) and Alder Pyrolytic Sugars (APS)	In development toward ASTM D4054	-	-
SAF	Visolis, Inc.	In development toward ASTM D4054		-
SAF historical	Amyris, Inc.,® fully synthetic	Contains farnesane, limonane, isopropyl methyl benzene	-	-
Operability	NJFCP C-8 (JRF-3)	-	12936	25% aromatic, maximum sulfur
SAF historical	Swedish Biofuels® ATJ SKA	ASTM D7566 Annex A8	12924, 7691	-
"SAF" historical	Sasol Ltd. IPK CTL	31 DCN, in production (coal)	7629	Baseline property data
"SAF" historical	Syntroleum Corp. S-8 or Rentech, Inc., GTL	GTL, a typical F-T product similar to HEFA	5018	Baseline property data
SAF historical	KiOR, Inc., HDCJ	Lignocellulosic pyrolysis, aromatic blend component (dormant)	-	-
SAF historical	Applied Research Associates CHJ	Aromatic-containing SAF, ASTM D7566 Annex A6	8455, 13676	-
SAF historical	IHI Corp. Bio-SPK	ASTM D7566 Annex A7	-	-
SAF historical	Shell International Ltd. CPK-0	High cyclo, on hold	-	-
SAF historical	Virent, Inc., HDO SK	High cyclo, on hold	8535	-
SAF historical	Honeywell International, Inc., UOP camelina HEFA	-	10301	-
SAF historical	Dynamic Fuels LLC, HEFA mixed fats	-	7635	-
SAF historical	Amyris, Inc., farnesane (DSH-76)	Trimethyl dodecane	12398	-
Operability	NJFCP C-2	-	12223, 11813	Asymmetric boiling range
Operability	NJFCP C-3	-	12341, 12363	Maximum viscosity
Operability	NJFCP C-4	-	12344, 12489	Low cetane, broad boiling
Operability	NJFCP C-5	-	12345, 12713, 12789, 12816	Flat/narrow boiling range
Operability	NJFCP C-7	-	12925, 12969, 12973	Maximum cycloparaffins
Operability	NJFCP C-9	-	12933, 12968	Maximum cetane

Category and motivation	Fuel description	Notes	POSF ID	Reason for Inclusion

ATJ = alcohol-to-jet
CHJ = catalytic hydrothermolysis jet
CLEEN = continuous lower energy, emissions and noise
CPK-0 = cycloparaffinic Kerosene
CTL = coal-to-liquids
DCN = derived cetane number
DSH = direct sugar to hydrocarbon
GTL = gas-to-liquids
HDCJ = hydroprocessed depolymerized cellulosic jet
HDO = hydrodeoxygenation
HEFA = hydroprocessed esters and fatty acids
IPK = iso-paraffinic kerosene
JRF = jet reference fluid
NJFCP = National Jet Fuels Combustion Program
UOP = Universal Oil Products
POSF = U.S. Air Force Research Laboratory fuel identification number prefix
SAF = sustainable aviation fuel
SAK = synthesized aromatic kerosene
SKA = synthetic kerosene with aromatics
SK = synthetic kerosene
SPK = synthetic paraffinic kerosene

ASTM International. (2022). *ASTM D7566-22: Standard specification for aviation turbine fuel containing synthesized hydrocarbons*. https://www.astm.org/d7566-22.html
ASTM International. (2022). *ASTM D4054-22: Standard practice for evaluation of new aviation turbine fuels and fuel additives*. https://www.astm.org/d7566-22.html
®World Energy is a registered trademark of World Management Group, LLC, Boston, Massachusetts.
®Neste is a registered trademark of Neste Oyj, Espoo, Finland.
®Gevo is a registered trademark of Gevo, Inc., Englewood, Colorado.
®Virent is a registered trademark of Virent, Inc., Madison, Wisconsin.
®CleanJoule is a registered trademark of CleanJoule, LLC, Salt Lake City, Utah.
®Alder is a registered trademark of Alder Energy, LLC, Washington, D.C.
®Amyris is a registered trademark of Amyris, Inc., Emeryville, California.
®General Electric is a registered trademark of General Electric Company, Schenectady, New York.
®Swedish Biofuels is a registered trademark of Swedish Biofuels AB, Stockholm, Sweden.
®Sasol is a registered trademark of Sasol Limited, Gauteng, South Africa.
®Syntroleum is a registered trademark of Emerging Fuels Technology, Inc., Tulsa, Oklahoma.
®Shell is a registered trademark of Shell Trademark Management B.V., The Hague, The Netherlands.
®Honeywell is a registered trademark of Honeywell International, Inc., Charlotte, New Jersey.
™Dynamic Fuels is a trademark of Dynamic Fuels, LLC, Springdale, Arkansas.

Facilities and Volumes of Each Needed Petroleum and Synthetic Blend Component

The volumes of each needed synthetic blend component were investigated based on the availability, needs, and storage availability. Two storage facilities have been identified to support the SAF repository project. One facility on campus at WSU is able to store 55-gal drum containers. The second facility, which is under development at Seattle Paine Field International Airport (hereinafter called Paine Field) in Snohomish County, Washington, can store tens of thousands of gallons of material. Finally, volumes needed for short-term distribution and use, have also been investigated and leveraged as will be reported later. Plans are underway to procure at least or up to 55 gal of each of the materials reported in Table 1. Ideally, the facility at WSU would be able to accommodate 55 gal or less of each of the materials reported in Table 1. Material volumes stored at Paine Field have emphasized large volumes with relatively limited number of samples. At present, the exact volumes and number of samples that can be stored there are still under investigation. Nominally it is anticipated to store roughly three samples at more than 6 to 10,000 gal each. In addition to these three samples, there has been designs develop that include five more containers which can store up to 5000 gal each. The volume stored at Paine Field would be able to support ASCENT projects and other global efforts in a manner that is substantial, or beyond current capabilities anywhere else.

Number and Type of Petroleum Jet Fuels for Use as Reference Materials

After consideration, there are no additional technical motivations for acquiring additional reference materials for petroleum jet fuel. There are, however, additional motivations to procure new reference materials composed of fossil carbon for this project. A key motivation for procuring new petroleum-based reference fuels is that the existing Category A fuels (i.e., Jet A-1, A-2, and A-3 fuels)—originally obtained over a decade ago—are nearly depleted. Replacing these diminishing stocks with updated standards is essential for ongoing and future research needs. Towards this end, several fuel suppliers have been contacted to source additional reference petroleum fuels. To date no additional fuels have been identified with certainty, this remains an ongoing subtask. Over the next year, it is anticipated that at least one new reference petroleum jet fuel will be identified.

Number of Entities that Could be Supported Under this Project
Domestic and international entities have been identified as potential users or entities that could be supported as a result of this project. Domestically, 16 ASCENT universities/principal investigators and 36 total entities or principal investigators have been identified as potential users of the repository project. Internationally, entities have queried for samples to be purchased and shipped to their locations. The major benefit of the repository project is that many experiments can study and explore the same fuel composition producing a key uncertainty in comparing results from numerous studies.

Currently, the facilities mentioned herein are sufficient to support the vast majority of programs domestically and internationally researching the compositional the property impacts of novel synthetic blend components on operability, emissions, various forms of compatibility, human health, and the environment. Unfortunately, current forecasts for large-scale flight and emissions campaigns, which require tens of thousands of gallons per campaign, are outside the scope of possibility for the two currently pursued facilities. This means that while many lower volume tests performed at ASCENT universities routinely can be supported sufficiently, years long investigations on the impacts of composition on emissions and the environment, will not be able to be supported by the size of facilities envisioned at present.

Milestone(s)

- Developed a short list of candidate materials for storage in the SAF repository.
- Worked with ASCENT stakeholders to identify compositional and volume interests for testing.

Major Accomplishments

- Developed a short list of candidate materials for storage in the SAF repository.
  - Candidate materials identified sought in the next federal fiscal year.
- Worked with ASCENT stakeholders to identify compositional and volume interests for testing.
  - Materials will be distributed more broadly once they are acquired in sufficient volumes quality.

Publications

None.

Outreach Efforts

In support of defining the repository's technical and capacity requirements, the ASCENT Project 101 team engaged multiple ASCENT principal investigators to learn about their specific demands for fuel volumes, compositional preferences, and testing frequencies. Our team also collaborated closely with original equipment manufacturer (OEM) partners—such as Gulfstream,® Airbus,® Pratt & Whitney,® World Energy, and CleanJoule®—to align the repository's capabilities with industry goals. These interactions, along with presentations at the Coordinating Research Council (CRC) aviation fuels meeting and the Commercial Aviation Alternative Fuels Initiative (CAAFI) webinar, helped refine our understanding of what a comprehensive SAF repository should encompass.

Awards

- Joshua Steven Heyne, American Chemical Society (ACS) Energy & Fuels, Rising Star

Student Involvement

None.

Plans for Next Period

Continue to add additional details and solicit feedback from stakholders.

References

ASTM International. (2022a). *ASTM D4054-22: Standard practice for evaluation of new aviation turbine fuels and fuel additives.* https://www.astm.org/d7566-22.html

® Gulfstream is a registered trademark of Gulfstream Aerospace Corporation, Savannah, Georgia
® Airbus is a registered trademark of Airbus Operations GmbH, Hamburg, Germany.
® Pratt & Whitney is a registered trademark of RTX Corporation, Farmington, Connecticut.
® CleanJoule is a registered trademark of CleanJoule, LLC, Salt Lake City, Utah.

ASTM International. (2022b). *ASTM D7566-22: Standard specification for aviation turbine fuel containing synthesized hydrocarbons*. https://www.astm.org/d7566-22.html

Task 2 – Procuring SAF and Conventional Fuel Samples for Testing

Washington State University

Objective

The objective of this task is to procure SAF and conventional fuel samples for testing under various ASCENT projects. Given the wide array of petroleum jet fuel producers, approved SAF producers, novel SAF producers, and manufacturers of relevant solvents for blend studies, it's essential to continually monitor the availability and changes in properties and compositions these producers offer. These variations can occur even over time at a given facility due to changes in production technology or feedstock.

To ensure quality and consistency, our team aims to:

- Gather certificates of analysis from various producers at different points in time to verify that the materials are consistent and are suitable for our research needs.
- Balance costs, availability, and desirability in terms of properties and compositions when procuring samples, ensuring we obtain high-quality materials within budget constraints.
- Identify cost-effective alternatives, such as contracting with petroleum fuel producers or solvent vendors who can provide products similar to expected SAF products.
- Monitor availability and property changes in producers' offerings on an annual or more frequent basis to support critical ASCENT projects.

Research Approach

Our approach involves collaborating with producers of sustainable fuels, conventional fuels, and solvent manufacturers to purchase and distribute the necessary materials. Our team will work closely with these suppliers to identify sources that meet the specific property and composition requirements for our research. This includes reviewing certificates of analysis and assessing the consistency of their products over time. By maintaining relationships with multiple producers, we ensure a reliable supply of samples for testing and blend studies.

Milestones

- Procured and distributed the first batch of large-volume samples for ASCENT Project 002, which included a Gulfstream emissions ground test.
- Collected sample materials involved in the emission ground test and sent them back to WSU for further testing and analysis.

Major Accomplishments

- Procured test volumes and distributed them to a research partner's test location for evaluation, ensuring that the necessary materials were available for timely testing.
- Established a procurement process that balances cost, availability, and quality, allowing for the acquisition of samples that meet research requirements without exceeding budget constraints.
- Supported for research initiatives enabling researchers to conduct fuel blend studies and other tests by providing appropriate samples sourced from various producers, thereby supporting the overall objectives of the ASCENT projects.

Publications

None.

Outreach Efforts

To streamline the procurement of various SAF and conventional fuel samples, our team proactively contacted ASCENT principal investigators to ascertain their project-specific requirements around fuel volumes, composition, and testing schedules. We also worked with the U.S. Navy, U.S. Air Force, and OEMs, such as Gulfstream, Airbus, Pratt & Whitney, World Energy, and CleanJoule, to ensure the correct types of fuel were sourced and supplied for research or operational needs.

Our team presented at the CRC aviation fuels meeting and the CAAFI webinar, further facilitating the sharing of procurement insights and best practices with a broader community.

Awards
None.

Student Involvement
None.

Plans for Next Period
- Support similar emissions campaign measurements.
- Procure additional materials for storage and distribution within the repository at WSU and Paine Field.

Task 3 – Testing Procured Samples for Reference Data to be Leveraged by Other Partners
Washington State University

Objectives
The objectives of this task are to (1) measure and disseminate standard reference data on materials associated with the repository project, (2) establish the extent of contamination from residual conventional fuels mixing with SAF in fuel storage tanks, and (3) provide reference test data to research partners to understand the variance in SAFs, specifically regarding sulfur content.

The success of the repository project critically depends on accurately measuring and disseminating standard reference data on materials associated with SAFs, reference petroleum fuels, hydrocarbon solvents, and blends of all these materials. SAFs can exhibit substantial variance in properties and compositions—from one ASTM D7566 (ASTM International, 2022) annex to another, and even within the same feedstock and process due to catalyst aging. Sulfur content plays a significant role in catalyzing contrail formation and persistent aviation-induced cloudiness, which contribute to the radiative forcing associated with aviation. Therefore, providing reliable data on sulfur content and other properties is essential for research partners and the broader scientific community.

Research Approach
During this initial, less-than-one-year period of performance, this task has focused on supporting three ASCENT research efforts: (1) providing fuel for an emissions campaign in coordination with Gulfstream and Missouri University of Science and Technology, (2) providing fuel for an emissions campaign in coordination with Pratt & Whitney and Missouri University of Science and Technology, and (3) a prescreening technology development effort led by Stanford University. The ASCENT Project 101 team received and tested dozens of samples associated with the Gulfstream emissions campaign. Our team focused on receiving and testing dozens of fuel samples associated with the Gulfstream emissions campaign. The primary emphasis was on testing the sulfur content of various SAF materials, particularly those compliant with ASTM D7566 (ASTM International, 2022) Annex A2, known as hydroprocessed esters and fatty acids (HEFA) (ASTM International, 2022). Recognizing that sulfur is a key component that catalyzes contrail formation and persistent aviation-induced cloudiness, we aimed to understand how even minimal sulfur levels could impact environmental outcomes.

HEFA fuel was procured from World Energy and sent to Gulfstream via World Fuel Services® in partnership with the Missouri University of Science and Technology. Samples were drawn at multiple locations throughout the fuel transport and distribution supply chain—from the refinery in Paramount, California, through various transfer points, to the final sampling from the airplane wing after testing. This comprehensive sampling provided a collective and traceable account of how sulfur was introduced or avoided in the HEFA material.

In addition to this emissions campaign, our team supported property measurement efforts associated with ASCENT Project 002, led by the Missouri University of Science and Technology. Pratt & Whitney procured jet fuel materials

® World Fuel Services is a registered trademark of World Kinect Corporation, Miami, Florida.

independently and conducted tests in coordination with ASCENT Project 002. They then sent us materials for reference property sampling, similar to the process undertaken with the Gulfstream project. While our team did not receive as many materials or samples from Pratt & Whitney as we did from Gulfstream, this collaboration allowed us to extend our research and contribute valuable data to the project.

Further tests were performed by distributing HEFA material to Stanford University for ASCENT Project 025 research. ASCENT Project 025 aims to develop low volume testing methodologies for prescreening and requires SAF materials for developing and validating their methods. Under all these programs, our team measured standard reference properties for the HEFA materials. These data are being prepared for public dissemination in accordance with FAA guidance.

Milestones

- Received and analyzed dozens of HEFA samples for sulfur content, establishing a thorough sampling process across the supply chain to trace sulfur introduction.
- Formed effective collaborations with key partners, including Gulfstream, the Missouri University of Science and Technology, and Stanford University.

Major Accomplishments

- Aided in the establishment of a high-resolution process for sampling sulfur at multiple locations throughout the fuel transport and distribution supply chain. This enabled comprehensive monitoring of sulfur content and efficient identification of potential contamination points.
- Procured and distributed HEFA samples with the necessary cleanliness to achieve sulfur concentration measurements below the limit of detection for the Missouri University of Science and Technology's experimental setup. This was crucial for providing ultra-pure samples that allowed for highly sensitive sulfur detection and analysis.
- Provided a comprehensive and traceable dataset demonstrating how sulfur contamination occurs in HEFA materials, enhancing the understanding of sulfur's role in the radiative forcing associated with aviation.
- Prepared data for public dissemination per FAA guidance, contributing to broader industry knowledge and efforts to mitigate environmental impacts.

Publications

None.

Outreach Efforts

To optimize our testing protocols and capture critical reference data, the ASCENT Project 101 team reached out to ASCENT principal investigators, confirming the volumes and compositional attributes they require for meaningful analysis. Our team also coordinated with OEMs—Gulfstream, Airbus, Pratt & Whitney, World Energy, and CleanJoule—to integrate feedback on how test results could support engine performance and emissions evaluations.

In parallel, our team engaged with Aerodyne® and other FAA program managers to clarify property measurement requirements that benefit broader SAF repository projects. For example, we discussed detection limits for total sulfur in HEFA blends—a key parameter for understanding contrail formation—and identified additional property measurements needed to address emerging research questions. By showcasing our testing objectives and methodologies at CRC aviation fuels meetings and CAAFI webinars, we fostered open discussion on these measurement needs, ensuring our approach remains aligned with the latest stakeholder and industry requirements.

Awards

- Joshua Steven Heyne - ACS Energy & Fuels, Rising Star

Student Involvement

Conor Faulhaber and Joshua Ledezma collaboratively measured sulfur concentrations from the Gulfstream emissions campaign. Harrison Yang measured other properties in support of the Stanford (ASCENT Project 025) and Pratt & Whitney emissions campaigns.

® Aerodyne is a registered trademark of Aerodyne Research, Inc., Billerica, Massachusetts.

Plans for Next Period

- Support similar research activities with other partners. Specifically, our team is looking to support a greater number of low-volume SAF requirements at partner institutions as well as at least two large-scale emissions campaigns.
- Aiming to develop new experimental methods to test sulfur concentrations lower than 1 part per million (ppm). Recently acquired equipment in the lab suggests the ability to test at lower volumes than current or typical ASTM sulfur concentration measurements are able to do.
- Measure sulfur concentrations down to single-digit parts per billion (ppb) levels after the awaited installation of additional equipment.

Reference

ASTM International. (2022). *ASTM D7566-22: Standard specification for aviation turbine fuel containing synthesized hydrocarbons*. https://www.astm.org/d7566-22.html

Task 4 – Developing a Data Management Protocol for Sharing and Distributing Data

Washington State University

Objectives

Building upon the experience gained from ASCENT Project 065A—which involved receiving and testing over 365 novel SAFs from approximately 38 institutions worldwide—the ASCENT Project 101 team aims to enhance our processes for the SAF repository project. The objectives for this task are to:

- Develop a Comprehensive Suite of Tests: Create and document a suite of tests specific to the SAF repository project, tailored to support airframers and engine companies in designing experiments for large-scale emissions tests.
- Collect and Database Property Data: Gather and systematically record property data and compositional information for all materials received under the repository project.
- Leverage Department of Transportation Resources: Collaborate with the developing resource within the U.S. Department of Transportation (DOT), as recommended by the FAA, to enhance our data collection and analysis capabilities.
- Support Critical Research Needs: Focus on properties like sulfur content, trace metals, thermal stability, and other critical measurements not commonly emphasized in previous projects.

Research Approach

The ASCENT Project 101 team is leveraging the robust, consistent, and streamlined processes established under ASCENT Project 065A for collecting and documenting relevant properties and compositions of aviation fuels. This existing system has been effectively utilized for materials processed under the repository project, including samples from Pratt & Whitney, Gulfstream, and those distributed to Stanford University.

Recognizing the different requirements of the SAF repository project, our team is developing a new suite of tests that may differ from those used in ASCENT Project 065A. Specifically, we are incorporating tests for properties such as sulfur content—which is of high importance for the repository project but not commonly measured under ASCENT Project 065A. Additional tests include, but are not limited to:

- Trace metals analysis
- Thermal stability (JFTOT®) tests
- Heat capacity measurements
- Dielectric constant measurements

® JFTOT is a registered trademark of Petroleum Analyzer Company, L.P., Housten, Texas. JFTOT is a globally recognized standard for jet fuel thermal oxidation testing.

These tests are critical for supporting airframers and engine companies as they design experiments for large-scale emissions tests. A comprehensive list of properties that has begun to be documented will be included for each material received.

Moving forward, our team plans to leverage the developing resource within the DOT, as suggested by the FAA, during the next period of performance. This collaboration will enhance our ability to collect, analyze, and disseminate critical fuel property data.

Milestones

- Collected and databased property data and compositional information for all materials received under the repository project.
- Began developing and documenting a full list of properties and tests specific to the SAF repository project.
- Applied the established processes from ASCENT Project 065A to streamline data collection and documentation efforts for the repository project.
- Initiated plans to collaborate with the DOT's developing resource, setting the stage for enhanced capabilities in the next performance period.

Major Accomplishments

- Established a robust and streamlined process for gathering and documenting aviation fuel properties, tailored to the needs of the SAF repository project.
- Developed a suite of tests focusing on critical properties such as sulfur content, trace metals, and thermal stability, which are essential for large-scale emissions testing.
- Provided vital property data to support airframers and engine companies in designing experiments, thereby facilitating advancements in emissions testing and environmental impact assessments.
- Positioned the project to leverage new tools and methodologies by preparing to collaborate with the DOT's developing resource, as recommended by the FAA.

Publications

None.

Outreach Efforts

In designing our data management framework, the ASCENT Project 101 team consulted multiple ASCENT principal investigators to gauge the types of data they collect (e.g., compositional or performance) and how frequently they need updates. This feedback, along with guidance from OEM partners, including Gulfstream, Airbus, Pratt & Whitney, World Energy, and CleanJoule, ensured the protocol would support both research and operational analytics. Our team presented at the CRC aviation fuels meeting and the CAAFI webinar allowing us to share draft data standards and solicit feedback for a more robust, user-oriented database system.

Awards

- Joshua Steven Heyne, ACS Energy & Fuels, Rising Star

Student Involvement

Conor Faulhaber, Harrison Yang, and Joshua Ledezma supported database upkeep and development.

Plans for Next Period

- Await FAA guidance to enable our team to put our research data onto databases.

Task 5 – Distributing Fuel Samples and Data to Partners per FAA Prioritization

Washington State University

Objectives

Distributing fuel samples is one of the most critical steps in the FAA SAF Repository project. The objectives of this task are to:

- Provide Appropriate Fuel Samples: Distribute relevant fuel samples—including neat SAFs, SAF candidates, reference fossil fuel materials, solvent materials, and blends—to partner institutions per the FAA's priority.
- Support Diverse Research Needs: Enable testing for operability, compatibility, emissions, human health impacts, and environmental impacts by ensuring that partner institutions receive fuel samples suited to their specific experimental hardware and testing motivations.
- Enhance Collaboration: Facilitate effective collaboration by matching partner institutions with the correct SAF repository materials, both within and outside of the ASCENT program.

Research Approach

Introduction

Distributing fuel samples is a critical component of the FAA SAF Repository project. The effectiveness of this task depends on matching partner institutions with fuel samples that meet their specific research needs. Partner institutions, both within and outside of the ASCENT program, receive reference materials from the repository. These materials may include neat SAFs, SAF candidates, reference fossil fuel materials, solvent materials, and blends of these hydrocarbon mixtures. These test materials enable experiments related to operability, compatibility, emissions, human health impacts, and environmental impacts.

Research Partner Material Requirements

The materials distributed need to align with partner experimental hardware and testing objectives. For example:

- Operability Testing: Institutions focusing on fuel operability in different hardware require fuel samples that reflect the operational conditions and stresses their equipment might encounter.
- Emissions and Environmental Impact Studies: Researchers examining emissions or performance metrics related to human health and the environment that need fuels with specific combustion characteristics or constituents.
- Flight Condition Testing: Facilities conducting tests under flight conditions require fuels that perform reliably and safely in those environments.

By understanding these specific needs, candidate materials are paired to the institution with the appropriate SAF repository material.

Material Selection and Preparation

Based on the needs assessment, our team selects and prepares the fuel samples for distribution. This process includes:

- Reviewing Repository Inventory: Evaluating available materials in the repository, including their properties, compositions, and suitability for the intended research.
- Custom Blending: Creating blends of fuels or adding specific additives when necessary to meet the precise needs of the partner institution.
- Quality Assurance: Verifying that all fuel samples meet the required quality standards and specifications before distribution.

Distribution Process

The distribution process is managed to comply with safety regulations and to maintain the integrity of the fuel samples. Materials are shipped with qualified hazardous material distribution entities such as FedEx,® UPS,® World Fuel Services, and Epic.® Steps of the distribution process include:

- Documentation: Preparing detailed documentation for each fuel sample, including certificates of analysis, safety data sheets, and handling instructions.

® FedEx is a registered trademark of Federal Express Corporation, Memphis, Tennessee.
® UPS is a registered trademark of United Parcel Service of America, Inc., Atlanta, Georgia.
® Epic is a registered trademark of World Kinect Corporation, Miami, Florida.

- Packaging: Using appropriate containers and packaging materials to protect the fuel samples during transit.
- Logistics Coordination: Arranging transportation while adhering to all relevant regulations concerning the shipment of hazardous materials.

Case Studies of Distribution
To date, materials have been distributed to two partner institutions:

- Missouri University of Science and Technology
  - Material Provided: HEFA fuel.
  - Purpose: Emissions testing to understand the environmental impacts of SAF usage.
  - Outcome: Enabled the institution to conduct emissions experiments with fuel samples suited to their testing apparatus and research goals.
- Stanford University
  - Material Provided: Fuel samples for developing low-volume prescreening test methodologies under ASCENT Project 025.
  - Purpose: To aid in the creation and validation of new testing methods that require minimal fuel volumes.
  - Outcome: Supported the advancement of testing techniques that can streamline future SAF research.

Data Sharing
In addition to physical fuel samples, our team provides data packages that include:

- Property Measurements: Information on fuel properties such as density, viscosity, sulfur content, and more.
- Compositional Analysis: Data on the chemical makeup of the fuels to assist partners in their analyses.

Conclusion
By assessing partner needs, selecting suitable materials, and managing the distribution process, our team has aimed to ensure that each research institution receives fuel samples appropriate for their specific projects. This approach supports the objectives of the SAF Repository project, facilitates research across multiple domains, and aligns with the FAA's priorities to advance the understanding and adoption of sustainable aviation fuels.

Milestones

- Distributed HEFA fuel samples to Missouri University of Science and Technology for emissions testing.
- Provided fuel samples to Stanford University for the development of low-volume prescreening test methodologies.
- Coordinated with producers by requesting additional materials to expand the repository's offerings and better meet partner needs.
- Established protocols for assessing partner needs and selecting suitable fuel samples for distribution.

Major Accomplishments

- Enabled critical research to occur at Missouri University of Science and Technology (ASCENT Project 002) and Stanford University (ASCENT Project 025).

Publications

None.

Outreach Efforts

To efficiently supply partners with the fuels and data they need, the ASCENT Project 101 team contacted a range of ASCENT principal investigators to ascertain their project timelines, fuel needs, and preferred reporting formats. We continued collaborating with OEMs such as Gulfstream, Airbus, Pratt & Whitney, World Energy, and CleanJoule to align sample distribution with ongoing testing programs. By participating in the CRC aviation fuels meeting and the CAAFI webinar, we demonstrated the distribution processes, addressed questions about sample integrity, and highlighted the broader benefits of a centralized, FAA-prioritized repository.

Awards

- Joshua Steven Heyne - ACS Energy & Fuels, Rising Star

Student Involvement

None.

Plans for Next Period

- Expand Sample Distribution to Additional Partners: Engage with more partner institutions, both within and outside of ASCENT per FAA guidance, to assess their specific fuel sample needs. We aim to provide appropriate materials from the repository to support their research projects.
- Process and Distribute New Materials: Upon receiving additional materials from various producers, we will incorporate these fuels into the repository. These new materials will be made available to partner institutions whose research requires specific fuel properties.

Project 102 Assessment on Contrail Formation via Combustion of SAF

University of Illinois at Urbana-Champaign

Project Lead Investigator

Tonghun Lee
Professor of Mechanical Science & Engineering
University of Illinois at Urbana-Champaign
1206 W. Green St., Urbana, IL 61801
517-290-8005
tonghun@illinois.edu

University Participants

University of Illinois at Urbana-Champaign (UIUC)

- P.I.: Professor Tonghun Lee
- FAA Award Number: 13-C-AJFE-UI-053
- Period of Performance: March 18, 2024, to September 30, 2024
- Task:
  1. Development of Environmental Test Chamber Platform

Project Funding Level

Federal Aviation Administration (FAA) funding level: $250,000
Cost sharing: 100% match provided by software license support from Converge, Inc.

Investigation Team

Prof. Tonghun Lee, (P.I.), All tasks
Sungho Hwang (graduate student), experimental efforts in designing and characterizing the combustor used in soot production.
Connor Malley (graduate student), experimental efforts in designing and characterizing the environmental chamber.
Anson Regi (graduate student), experimental efforts in laser and optical diagnostics.

Project Overview

Before discussing ASCENT Project 102, it is important to note that this study is in the initial stages of design and development and has only been actively worked on for roughly six months. As such, the results are limited. This study seeks to develop an environmental testing chamber to allow for the experimental creation and analysis of condensation trails (contrails) in a consistent and repeatable laboratory environment. The goals of this chamber will be to (1) understand the physics of contrail formation using advanced laser and optical diagnostics and potentially develop novel diagnostic methods for contrail characterization, (2) investigate contrail formation for fuels, including sustainable aviation fuels (SAF), and (3) integrate test data with both environmental modeling teams and flight-based tests. This study is done in collaboration with the Sandia National Laboratory (Livermore) where Dr. Lee is working as a part-time staff member.

Contrails are mainly composed of water (in the form of ice crystals) and contain a nucleus of soot particles. There is a major gap of knowledge in our understanding of the fundamental physics of contrail formation at the molecular level, but in certain supersaturate environments, contrails can form and then persist until they develop into high altitude cloud formations, which can impact the temperature of the Earth's atmosphere through radiative forcing. Due to this reflection of thermal radiation from the Earth's surface, it is believed that contrails contribute to greater than 50% of aviation's climate impact, the other portion being impacted by carbon dioxide (CO_2) and other greenhouse gases. This chamber will aim at

studying these various factors of contrails to better inform efforts to mitigate contrail formation through flight path adjustment, improve engine technologies, and characterize contrail development for SAFs to better predict the impact of fuel composition, potentially leading to developments in fuel composition standards with regards to contrails.

This project involves three main design considerations: (1) the environmental testing chamber, (2) the soot-generating combustor, and (3) the laser/optical diagnostic design. The environmental chamber is used to control the relevant conditions of contrail development in an optically accessible environment. The chamber consists of a co-flow section prior to the chamber where humidity and temperature are controlled for incoming air/soot mixtures. This is done using a chiller and heat exchanger, which cools both the chamber walls and the incoming air flow. Attached upstream of the chamber is a vacuum pump exhaust assembly that will control the pressure levels within the chamber and help regulate air speed throughout the system. The intended diagnostics systems consist of diffuse-back illumination imaging (DBI) for soot density, temperature and ice crystal formation, infrared (IR) spectroscopy and optics for soot composition and water-content, and laser induced illumination for soot diameters along with other non-in situ methods such as transition electron microscopy (TEM).

Task 1 – Development of Environmental Test Chamber Platform

University of Illinois at Urbana-Champaign

Objectives)

This task develops the test chamber, combustor, and laser/optical diagnostic systems. For the chamber, this involves defining the thermodynamic operating ranges for temperature, pressure, humidity, and air speed that are relevant to contrail formation. This then informs the design of the chamber itself, and the cooling, co-flow, and exhaust systems being utilized to control the relevant thermodynamic properties, which will then be assembled. For the combustor, this task involves defining the air-fuel mixing method, the injection method, flowrates, and soot particle sizes necessary to produce a usable sample that will properly represent the small soot particulates produced by a standard aviation turbine engine. This will help define the necessary design that will be assembled. Finally, the soot particulate properties relevant to the microphysics of contrail formation will be defined, which will inform the necessary laser/optical diagnostics required to gather useful data to help characterize contrail formation and help predict the effects of various SAF fuels as they relate to contrail formation.

Research Approach

The purpose of this study is to provide a controllable laboratory method for contrail formation and analysis to better inform environmental modeling of contrails and to corroborate and prevent the extensive need for expensive/difficult in situ methods directly involving aircraft (e.g., chase planes). This is conducted by developing a controllable environmental chamber in which sample soot and cold air flow through with diagnostic access through chamber viewports and soot sample collection methods. This task is completed by utilizing a cooling co-flow upstream of the chamber and a vacuum exhaust system downstream of the chamber. The primary concern of the chamber system is the control of pressure, temperature, humidity, and air speed. The soot particulates are provided through the burning of liquid aviation fuel in a characterized combustor. The combustor has the primary goal of controlling particulate sizes and maintaining a relatively uniform particulate size of roughly 10-30 nm in diameter. The relevant formation physics of the contrails are collected using laser/optical diagnostics utilizing both in situ (through the viewports) and non-in situ (collected soot particulates) methods. The properties that will be measured are soot density, soot diameter, soot composition, particle porosity, ice crystal growth, and temperature gradients within the flow as heat is transferred to create the ice crystals.

Environmental Test Chamber

The environmental test chamber is designed to mimic high atmospheric conditions in a controlled laboratory environment. It will do this through a co-flow and vacuum exhaust control system. Table 1 outlines the relevant operational ranges of the chamber. Pressure within the chamber will be able to range from 1 bar to near vacuum conditions with the standard experimental range being 0.2-0.5 bar. The temperature will have an ultimate range of 200-300K with the standard experimental range being 217K to 250K. The maximum water content within the chamber will be roughly 1000 ppm with the intent being able to create a supersaturated region with respect to water within the chamber. The maximum flow rate throughout the entire system will be 10 g/s with a maximum velocity of roughly 1.9 m/s. Normal experimental speeds will be significantly lower with the intent of producing the maximum residence time of 9 s with speeds as low as 0.1 m/s. The atmosphere within the system will be composed of air and nitrogen gas with soot included during operation.

Table 1. Operational conditions.

Parameter	Range
Pressure	0.01-1 bar
Temperature	200-300 K
Maximum Water Content	~1000 ppm
Maximum Flow Rate	10 g/s
Maximum Chamber Speed	1.9 m/s
Maximum Residence Time	~ 9 s
Chamber Atmosphere	Air/N_2

The chamber design is shown in Figure 1. The chamber will be double-walled stainless steel with coolant running between the walls to maintain the wall temperature to levels seen in the co-flow entering the chamber. The chamber will have four larger optical windows that are double-paned to allow their interior to be vacuum pumped to prevent condensation. Between the windows there are 12 general-purpose ports that can be utilized for sensors (i.e., thermocouples, pressure transducers, etc.) or specialty optical windows. The bottom of the chamber (not shown) has six to eight equidistant holes, which the co-flow will be pumped through, centered around a smaller hole where the sample exhaust from the combustor will be injected. The top of the chamber has an exhaust port that will connect to an Edwards® nES220 vacuum pump that will serve as the air speed and pressure control for the chamber.

Figure 1. Environmental chamber design.

Figure 2 and Figure 3 show the piping and instrumentation design (P&ID) and the computer-aided drawing (CAD) respectively for the co-flow system. This system modulates the humidity of the chamber through a moist air and nitrogen mixture and leads directly into the heat exchange system that will control the temperature of the incoming air mixture into the chamber. The top stream comes from the moist air source and is modulated by a pressure gauge and throttling valve. Air leaves the source and travels through an on/off valve into the throttling valve where it then passes two sensors in a cross, one sensor measures humidity and temperature while the other is a pressure transducer. This then travels through a flow meter and finally a check valve before entering the mixing tee. The lower section has a nearly identical design but

® Edwards is a registered trademark of Edwards Limited, Burgess Hill, United Kingdom.

controls pure nitrogen gas (set at a slightly lower pressure to encourage mixing). The lower line has just one tee instead of a cross to accommodate a pressure transducer. After both streams pass their respective check valves, they are mixed and travel downstream to another cross where humidity, temperature, and pressure measurements are once again taken before passing through a solid particulate filter. Once it passes through the filter, the co-flow is sent to the heat exchanger where it will be dropped to the relevant high-atmosphere pressure.

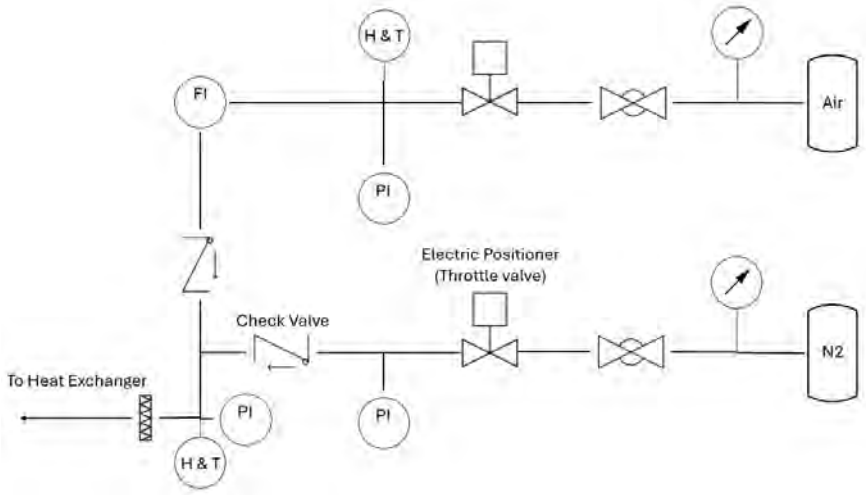

Figure 2. Co-flow piping and instrumentation diagram.

Figure 3. Co-flow computer-aided design model.

Figure 4 summarizes the control system in its entirety. The co-flow system outputs “hot” air into a heat exchanger which cools down the flow before it enters the testing chamber. The heat exchanger uses cold TMC HFE-347 coolant fluid from a

Thermonics® water-cooled chiller. The chiller has a temperature range of -80˚C to +25˚C with a cooling capacity of 1800W at -80˚C. It has an 8 GPM (50 psi at 60 Hz) pump and relies on 480V, three-phase power. A portion of this coolant is siphoned off prior to the external heat exchanger to be supplied into the interior of the double-walls to decrease the chamber wall temperature. The “hot” fluid from the heat exchanger and the chamber walls are then combined again before being pumped into the chiller to be cooled again by the in-house water system. After the chamber is the exhaust vacuum system. Detailed design has yet to be finalized but an Edwards® nES220 single-vane rotary vacuum pump (Figure 5) will be implemented with a back-pressure control system that will be used to modulate the pumping speed, which will be used to control both the pressure within the chamber and the air speed.

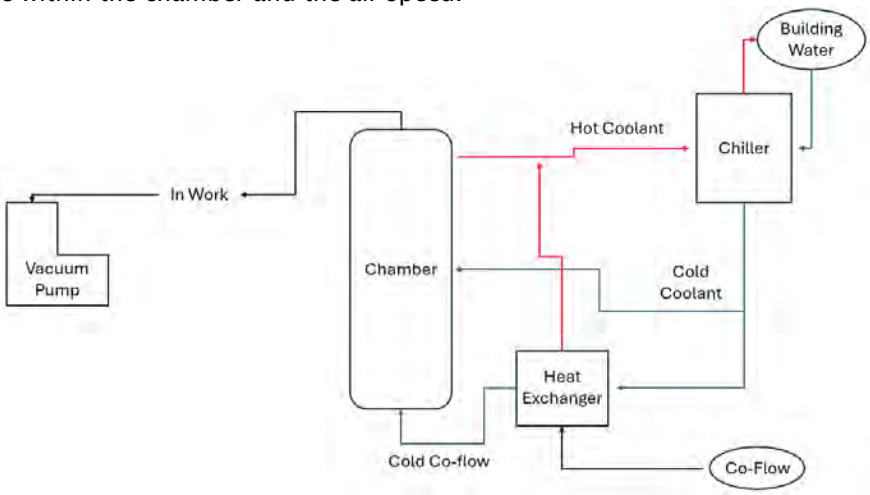

Figure 4. Control system overview.

® Thermonics is a registered trademark of Temptronic Corporation, Mansfield, Massachusetts.

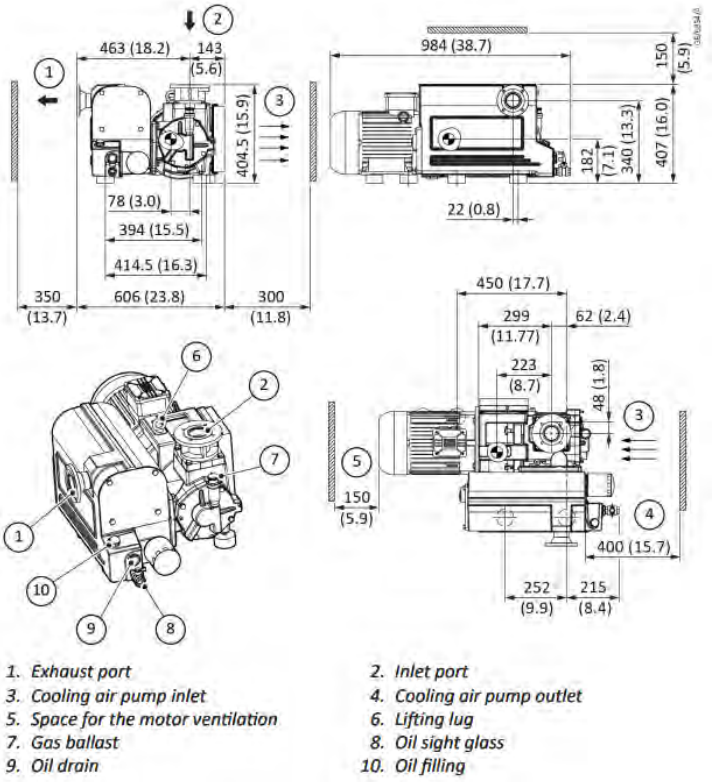

Figure 5. Edwards® nES220 vacuum pump schematic (from manual).

Combustor Design

The design of the combustor has just begun. The initial intent is to create a simple swirl burner that will take evaporated liquid fuel and ignite it with a pilot flame, which will be swirled to produce steady-sized soot particulates. Once this is developed, complexity will be added to reduce the particulate size as needed or to increase the consistency of the particulate diameters.

Laser/Optical Diagnostic System

The final portion of the environmental testing platform is the laser/optical diagnostic system. A preliminary design is shown in Figure 6, detailing a general (but incomplete) setup for initial testing. Like our partners at the Sandia National Laboratory, our initial focus will be applying DBI imaging to analyze soot density and temperature gradients, which has the possibility of assisting in the analysis of ice crystal formation. This system consists of a pulsing light-emitting diode (LED) laser that travels through a diffuser before interacting with the soot samples. DBI has the benefit of reduced scattering. Two cameras will be used to account for natural luminosity in the data collection. Laser Induced Incandescence (LII) has the potential to give information about primary particle sizes, but its application may be limited due to its nature of increasing temperatures in the soot, which could impact ice crystal formation. An infrared camera and other high-speed camera setups will be used to record water content within the system and to track the formation of ice crystals. Lastly, non-in situ methods such as IR spectroscopy will be utilized with sample streams of soot to analyze specific compositions of interest in the fuel exhaust, such as CO_2, nitrogen oxides (NO_x) and sulfur oxides (SO_x). Other non-in situ methods such as scanning mobility particle sizer (SMPS) and TEM will also be implemented with the support of UIUC's environmental engineering laboratories (through our graduate student, Anson Regi) to analyze both primary and mobility diameters of the soot samples. Soot for all non-in situ methods will be inputted into such devices either directly (after being cooled) or will be captured on filters to be brought to the analyzers.

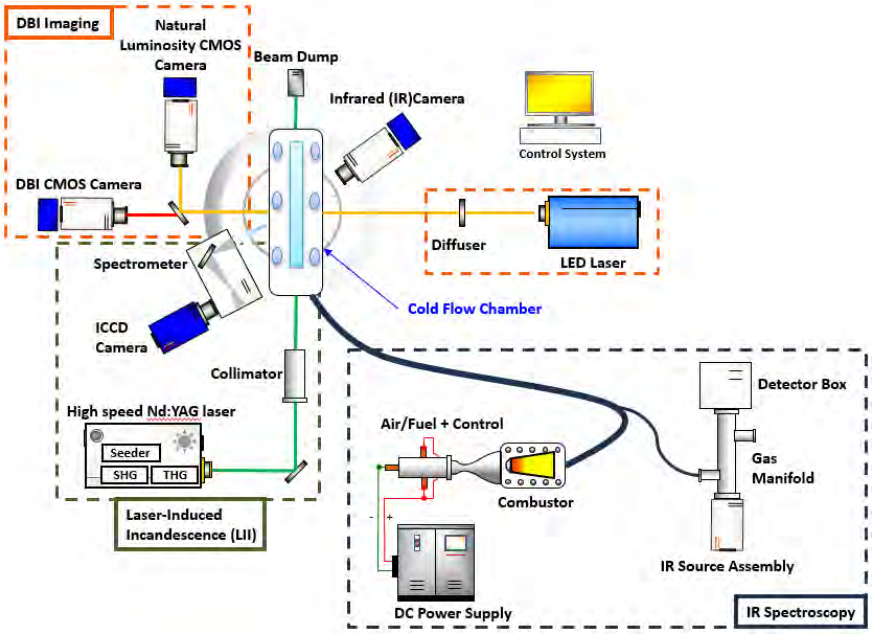

Figure 6. Laser/optical Diagnostic Setup

Milestones

- At three months, identified thermodynamic target ranges for operation of the chamber and facility.
- At six months, established the design of the chamber and co-flow system, shakedown of co-flow components, and began establishing the combustor design.

Major Accomplishments

The most important accomplishment to date is the establishment of a partnership with the Sandia National Laboratory (Livermore), of which Dr. Lee is now an employee. The Sandia National Laboratory has already developed their own contrail chamber, and with their advisement, we have been able to properly identify operation goals and methods to explore in the development of our own chamber.

Publications

None.

Outreach Efforts

All test data will be made accessible through https://altjetfuels.illinois.edu/.

Awards

None.

Student Involvement

This project was conducted by PhD student, Sungho Hwang, who is developing the combustor for the chamber; PhD student, Connor Malley, who is developing the chamber and environmental control systems; and master's student, Anson Regi, who is developing the laser/optical diagnostic systems.

Plans for Next Period

The next period will start with the design of the vacuum system design of the combustor, and assembly of the chamber, co-flow, and chiller systems. Once the systems are designed and fully assembled, characterization of both the chamber and the combustor will occur. For the chamber, this will consist of confirming operational environmental ranges for temperature, pressure, humidity, and air speed at various points along the optically accessible portion. For the combustor,

this will involve determining the effect of air-fuel ratio on particle diameter size and the nature of uniformity of produced soot particles. After both characterization tasks are complete, the ASCENT Project 102 team will develop a test plan and perform our first attempt at creating a contrail in a controlled experimental environment utilizing a generic fuel (e.g., Jet A fuel). This will involve using our laser/optical diagnostics to gather data on soot density, diameter, composition, and ice crystal growth.

Project 103 Pareto Efficient SAF Yield and Blending

Washington State University

Project Lead Investigator

Joshua Heyne
Bioproducts, Sciences, and Engineering Laboratory Director, Associate Professor
School of Engineering and Applied Science
2710 Crimson Way, Richland, WA 99354
(937) 229-5319
joshua.heyne@wsu.edu

University Participants

Washington State University

- P.I.: Dr. Joshua Heyne
- FAA Award Number: 13-C-AJFE-WaSU-044
- Period of Performance: March 15, 2024, to March 14, 2025
- Tasks:
  1. Distillation optimization tool and procedure improvement
  2. Vapor pressure measurement for sustainable aviation fuel

Project Funding Level

The Federal Aviation Administration (FAA) provided $350,000 in funding, cost sharing is provided by Air Company ($200,000) and Trinity College Dublin ($150,000).

Investigation Team

Washington State University

P.I. Joshua Heyne, Coordinating all team members (both ASCENT and non-ASCENT efforts) and communicating distillation results with SAF producers.
Randall Boehm, Research Engineer, Overseeing the project and providing guidance.
Zhibin (Harrison) Yang (Ph.D. candidate), Conducting distillation optimization and property measurements.
Joshua Ledezma (an undergraduate student), Conducting vapor pressure measurement.

Project Overview

The ASCENT Project 103 supports the conversion of pilot-scale bio-crude samples into plausible aviation fuel blend components, up to 100%, with the balance coming from a petroleum distillate. For non-selective sustainable aviation fuels production processes, the product stream could contain species ranging from as few as five to many (>26) carbon atoms per molecule (distillation range, 36 to >450°C), which is broader than the jet fuel range. In these cases, distillation can be used to separate the product stream into fractions, where the monetary value of each fraction varies based on contemporary policies, and the properties of that fraction. While this is essentially the same process as petroleum refining, the population distribution of different molecular species within a given distillation cut could be markedly different depending on the pathway, and those composition differences result in significant property differences.

Task 1 – Distillation Optimization Tool and Procedure Improvement

Washington State University

Objectives

The objectives of this task are intended to improve the current distillation optimization tool, Jet Fuel Blend Optimizer (JudO), and procedures associated with distillation processes to improve yield for a given sustainable aviation fuel (SAF) candidate while keeping the properties within the specification limits.

Research Approach

Introduction

SAF has taken center stage in the commercial aviation industry's attempt to achieve net-zero carbon emissions by 2050 (Air Transport Group, 2021; Collins & McLarty, 2020; Nicolay et al., 2021; Ng et al., 2021). Any novel SAF production pathway must be qualified through a process described in ASTM D4054 (ASTM International, 2022a), a process which requires between one hundred and hundreds of thousands of gallons of fuel, and years of rigorous testing to complete. The approved pathway will receive a new or edited annex in ASTM D7566 (ASTM International, 2020), describing the feedstock, process, and synthetic fuel specification limit. To date, there are eight annexes in ASTM D7566-23b, as they describe the different synthetic blending components (SBC) produced by different feedstock and conversion technologies, which have been qualified for up to 50 percent volume (%v) blends with conventional jet fuels (Jet A3 and A7 fuels are limited to 10 %v).

Given the current SAF production capability, it is well understood that a multitude of new production pathways will be developed and qualified in the next 25 years to achieve the 2050 goal. There has been much attention to the use of single/few components as blending components for both Jet A fuel and/or 100% paraffinic SAF to achieve 100% drop-in SAF (Baral et al., 2021). Based on the current experience and already known insight around these types of fuels (i.e., JP-10). It is unlikely a single/limited component fuel will be widely adopted for gas turbine applications as it is. However, blending such fuel with conventional fuels or other SAF may offer increased market opportunity for the producer and entail further investigation.

Acceptable alternatives to conventional jet fuel are composed of four hydrocarbon families in varying proportions including aromatics, cycloalkanes, iso-alkanes, and n-alkanes. The jet fuel property specifications leave little to no tolerance for olefins and heteroatom-containing species and exclude the possibility of an acceptable fuel being exclusively composed of species belonging to the same hydrocarbon family. This is significant because several biomass-to-hydrocarbon conversion technologies may not produce, for example, the required aromatic content (Huq et al., 2021). To resolve this issue, the hydrocarbon products from a variety of conversion technologies may be blended to yield an acceptable SAF. The presumption (and technical requirement) here is that any approved SAF could be mixed with any other approved SAF at any ratio, without risk of the resultant mixture falling out of specification. Although reasonable, testing is required to confirm this presumption. The current work presents such testing in the form of analyzing the simulated distillation curves of 41 different combinations of five different SAFs, prepared at their respective maximum blend ratios with an average Jet A fuel. The resultant dataset is then used to develop a predictive blending rule for determining the distillation profile of SAF blends, based on the known distillation profiles of the individual components and their respective ratios.

The effect of single components blending with fuel has yet to be explored. Upon blending a single component bioproduct into conventional jet fuel, the hydrocarbon population distribution grows increasingly atypical as its blend ratio increases. As a result, its distillation curve is expected to exhibit increasing atypical characteristics, and the impact of such anomalies on combustor operability is not known and therefore feared and consequentially regulated by the safety-conscious aviation industry (Colket et al., 2017).

The distillation curve of jet fuel correlates with a multitude of other jet fuel properties (Colket & Heyne, 2021). For example, the front end of the distillation curve determines its flash point, and the back end of the curve strongly impacts its fluidity characteristics (Yang et al., 2023). Five test methods for distillation curve measurement are referenced in the jet fuel specification ASTM D1655 (ASTM International, 2022b), where ASTM D86 is the referee method and other alternative methods are ASTM D2887/IP 406, ASTM D7344, ASTM D7345, and IP 123. ASTM D86 is essentially a one-plate atmospheric pressure distillation. The ASTM D2887 approach is to use data from a gas chromatography experiment to represent an infinite-plate distillation, and a numerical method is presented in Appendix X4 (ASTM International, 2024) to correlate that data with the results of an ASTM D86 distillation. ASTM D7344 and ASTM D7345 are the mini/micro versions

of ASTM D86. Due to the reduced volume involved, the resulting raw data must be corrected for relative bias as described in each method.

To the best of the authors' knowledge, studies on a single component's effect on the blended fuel distillation curve have not been documented to date. Here, we explored two single-component SAF candidates blending with either petroleum jet fuel or previously approved (ASTM D7566) SAF. A comparison is drawn between the experimental and simulated one-plate distillation curves.

Materials and methods

1. Materials

The materials used in this study are shown in Table 1. The materials consist of three reference conventional jet fuels from the National Jet Fuel Combustion Program (NJFCP) (Colket et al., 2017), four SAFs which meet ASTM D7566 requirements, and two single-component SAF candidates that are being considered for evaluation as described by ASTM D4054.

Table 1. Materials used in the current study and their respective class and supplier.

Description	Class	Reference Code
NJFCP A-1	Jet A (POSF 10264)	A-1
NJFCP A-2	Jet A (POSF 10325)	A-2
NJFCP A-3	Jet A (POSF 10289)	A-3
S8 Fischer Tropsh (FT)-synthetic paraffinic kerosene (SPK)	Annex 1 (FT). POSF 5018	5018
Hydroprocessed Renewable Jet (HRJ) Camelina	Annex 2 (HEFA). POSF 7720	7720
World Energy Hydrotreated Esters and Fatty Acids (HEFA)	Annex 2 (HEFA)	WE
Amyris Farnesane	Annex 3 (HFS-SIP) POSF 11832	11832
Gevo (limited components)	Annex 5 (Alcohol-to-Jet [ATJ]). POSF 13718	13718
Single component sustainable aviation fuel (SAF) candidate A	A cycloalkane species of C chain length 10	C10-Cy
Single component SAF candidate B	An aromatic species of C chain length 10	C10-Ar

2. Distillation (ASTM D86)

The Anton Paar® atmospheric distillation analyzer, Diana 700, was used to measure distillation curves via ASTM D86 (ASTM International, 2023). Diana 700 is an automated ASTM D86 analyzer with a temperature resolution of 0.1°C and a sample volume scan to the resolution of 0.01 ml. ASTM D86 is a basic test method of determining the boiling point distribution of petroleum fuel by performing a simple batch distillation. This method has been used since 1921, and historical data date back as long as the petroleum industry has existed. A brief version of the automated procedure follows: Initially, 100 ml of the sample and a boiling stone are introduced into the distillation flask. Subsequently, the apparatus administers heat to the distillation flask in a regulated manner. This heating process is meticulously controlled to ensure that the time interval from the first application of heat to the determination of the initial boiling point (IBP) adheres to predefined specifications. The IBP is identified by the occurrence of the first droplet in the receiving cylinder. Then, the heat is adjusted to achieve a uniform average rate of condensation. While the implementation of the automated ASTM D86 procedure may not necessarily enhance the accuracy of the distillation curve, it is anticipated to improve the consistency of results significantly. This improvement is crucial in mitigating potential errors introduced by inexperienced human operators during experimentation, such as variations in temperature probe depth, receiving rate, and recovered volume readings.

® Anton Paar is a registered trademark of Anton PAAR USA, Inc., Ashland, Virginia.

3. Simulated Distillation (ASTM D2887)

Simulated distillation was performed in accordance with ASTM D2887 (ASTM International, 2024) using an Agilent® 6890N gas chromatograph, configured with a flame ionization detector and a 10 m x 530 μm x 2.65 μm DB-1 capillary column. An injection volume of 0.1 mL was used, applying a split ratio of 2:1 and an inlet temperature of 350°C. Helium was used as the carrier gas at a rate of 14 mL/min. The oven temperature was ramped from 40 to 350°C at 20°C/min and then held for 8 min.

As specified by ASTM D2887, this method is applicable to petroleum products and fractions having an initial boiling point greater than 55°C and a final boiling point less than 538°C. A quantitative calibration solution and reference gas oil sample (RGO) (Sigma-Aldrich®) were analyzed in triplicate immediately prior to studied sample analyses, confirming that the RGO analysis results were within the acceptable specification range. Each sample was also analyzed in triplicate, with a blank analyzed immediately prior and after to confirm baseline consistency.

4. Distillation (ASTM D86) and Simulated Distillation (ASTM D2887) Data Correlation

The results obtained by ASTM D86 and ASTM D2887 are not comparable in the raw data format since ASTM D86 is one-plate atmospheric distillation and ASTM D2887 is a close to infinite-plate simulated distillation. However, the results obtained by ASTM D2887 can be used to obtain an ASTM D86 approximation via a correlation documented in ASTM D2887 appendix X4 (ASTM International, 2024). This correlation model is based on 46 conventional jet fuel and 39 diesel fuel samples with data from both experiments: ASTM D86 and ASTM D2887. It relates specific points on the respective distillation curves (i.e., IBP, T5, T10, etc.) to one another. Any deviation from these fuel samples, with respect to the shape of the distillation curve, could potentially cause a drive error in the simulated distillation. Such deviation of distillation curve shape is particularly notable with SAF and motivating for this study.

5. Blending Rules

Another goal of this work is to develop a blending rule to predict the blended fuel distillation curve using only the component fuels' distillation curves. Blending rules are critical for understanding how to optimize blend ratios while still meeting specification requirements.

ASTM D2887 distillation curves are interpreted from gas chromatographic data. As such, the response from common peaks in each chromatogram can be combined in proportion to their mass fraction, consistent with the mass response of the flame ionization detector. However, if some of these data are obscured by reporting only discrete values of the ASTM D2887 distillation curve (i.e., IBP, T10, T20, etc.), an alternate approach must be used. In this work, the ASCENT Project 103 team proposes the method which is outlined the next paragraph.

Each distillation curve is converted from a volume percentage to absolute volume consistent with the blend fraction. Each curve is then dissected into small segments. The segments from each of the curves are then spliced together in order of boiling point. The newly formed dataset is the predicted blended distillation curve. This method is fundamentally consistent with the physics and theory founding the ASTM D2887 method. This method is verified in the following sections.

For a one-plate distillation (such as ASTM D86), the blending rule is more elusive. Such distillations involve vapor equilibrium calculations of unknown accuracy and may involve non-ideal behavior. A similar approach as described in the paragraph above may be the best proxy for blended fuels ASTM D86 distillation curve as well, although this hypothesis is not directly tested in this work.

Results and Discussion

To represent potentially industrial scale mixing of two or more approved SAF products, 41 different mixtures were prepared from five different SAFs. Each of these mixtures and the five SAF components unmixed with other SAF were then blended with a reference jet fuel, called A-3, at the maximum allowable blending ratio as permitted by ASTM D7566. The composition of each of the blends prepared is described in Table 2. The 41 mixtures, five pure SAFs, five Jet A-3 blended SAFs, and three Jet A fuel samples (i.e., A-1, A-2, & A-3) were analyzed in triplicate via simulated distillation (ASTM D2887).

® Agilent is a registered trademark of Agilent Technologies, Inc., Santa Clara, California.

® Sigma-Alrich is a registered trademark of Sigma-Aldrich Co., LLC, St. Louis, Missouri.

Table 2. Composition of samples analyzed via simulated distillation (ASTM D2887): A-3 and SAF components.

Code	Composition (vol %)					
	A-3	5018	7720	13718	WE	11832
5018	-	100.0	-	-	-	-
7720	-	-	100.0	-	-	-
13718	-	-	-	100.0	-	-
WE	-	-	-	-	100.0	-
11832	-	-	-	-	-	100.0
B-5018	50.0	50.0	-	-	-	-
B-7720	50.0	-	50.0	-	-	-
B-13718	70.0	-	-	30.0	-	-
B-WE	50.0	-	-	-	50.0	-
B-11832	90.0	-	-	-	-	10.0
1	50.0	25.0	25.0	-	-	-
2	60.0	25.0	-	15.0	-	-
3	50.0	25.0	-	-	25.0	-
4	70.0	25.0	-	-	-	5.0
5	60.0	-	25.0	15.0	-	-
6	50.0	-	25.0	-	25.0	-
7	70.0	-	25.0	-		5.0
8	60.0	-	-	15.0	25.0	-
9	80.0	-	-	15.0	-	5.0
10	70.0	-	-	-	25.0	5.0
11	50.0	5.0	45.0	-	-	-
12	68.0	5.0	-	27.0	-	-
13	50.0	5.0	-	-	45.0	-
14	86.0	5.0	-	-	-	9.0
15	68.0	-	5.0	27.0	-	-
16	50.0	-	5.0	0.0	45.0	-
17	86.0	-	5.0	-	-	9.0
18	52.0	-	-	3.0	45.0	-
19	88.0	-	-	3.0	-	9.0
20	86.0	-	-	-	5.0	9.0
21	50.0	45.0	5.0	-	-	0.0
22	52.0	45.0	-	3.0	-	-
23	50.0	45.0	-	-	5.0	-
24	54.0	45.0	-	-	-	1.0
25	52.0	-	45.0	3.0	-	-
26	50.0	-	45.0	-	5.0	-

Code	Composition (vol %)					
	A-3	5018	7720	13718	WE	11832
27	54.0	-	45.0	-	-	1.0
28	68.0	-	-	27.0	5.0	-
29	72.0	-	-	27.0	-	1.0
30	54.0	-	-	-	45.0	1.0
31	56.7	16.7	16.7	10.0	-	-
32	50.0	16.7	16.7	-	16.7	-
33	63.3	16.7	16.7	-	-	3.3
34	56.7	16.7	-	10.0	16.7	-
35	70.0	16.7	-	10.0	-	3.3
36	63.3	16.7	-	-	16.7	3.3
37	56.7	-	16.7	10.0	16.7	-
38	70.0	-	16.7	10.0	-	3.3
39	63.3	-	16.7	-	16.7	3.3
40	70.0	-	-	10.0	16.7	3.3
41	62.0	10.0	10.0	6.0	10.0	2.0

The interpreted gas chromatography data were used to represent an infinite-plate distillation curve, and this curve was then converted in the manner described in ASTM D2887, Appendix A4 (ASTM International, 2024) so as to be comparable to data obtained during a distillation per ASTM D86. These calculated curves were then used to estimate some of the distillation properties specified for SAF in ASTM D7566. Specifically, for the blended SAFs, and blends thereof, the converted data can be used to verify that the temperature corresponding to 10% recovery has a maximum value of 205°C, and the final boiling temperature has a maximum value of 300°C. Analysis of this data confirms that all SAF blends prepared conform to this required specification.

The ASTM D2887 distillation curve of blended mixtures is predicted utilizing fundamental chromatographic concepts. The elution times of chromatographic peaks provide the data for ASTM D2887 analysis. The flame ionization detector (FID) in the gas chromatograph exhibits a linear response in relation to mass. Consequently, the blended mixture will demonstrate a proportional response to the mass of its individual fuels. With only ASTM D2887 results and without the raw data, the prediction is made by splicing each curve into infinitesimally small segments with widths proportional to their respective mass concentration for all the fuels in the blend. The segments are then combined and sorted by temperature. An example of this blending rule is shown in Figure 1 for reference.

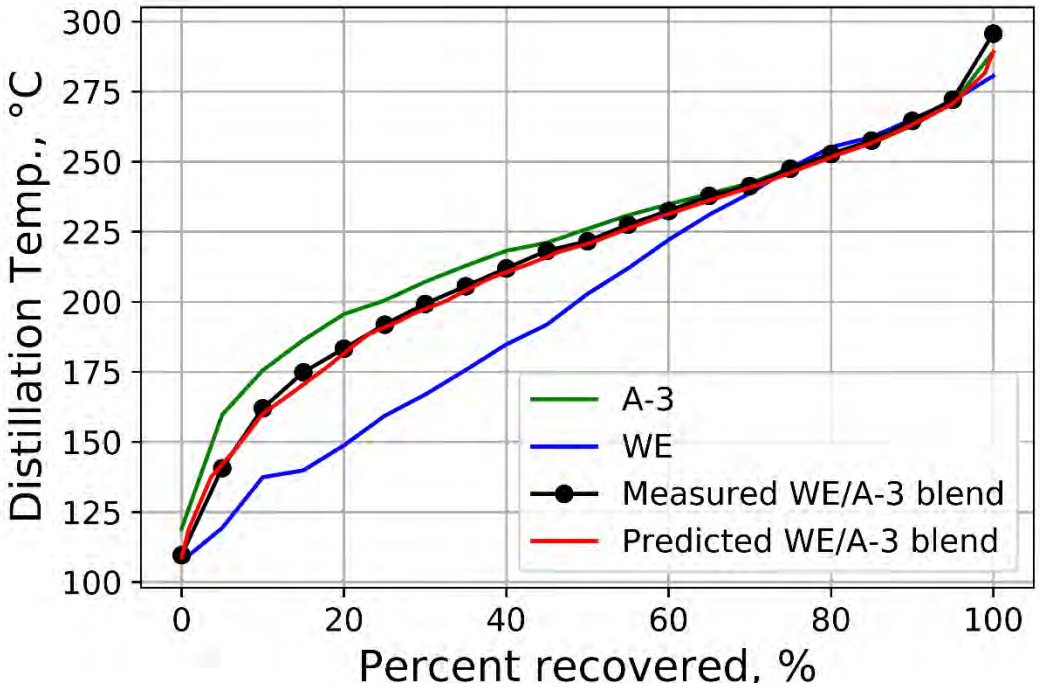

Figure 1. Example of D2887 blending rule. Where both measurement (black circles with line) and prediction (red line) of the blends are reported for comparison.

The method described above was tested with the five SAFs blended with Jet A-3 fuel at their maximum allowed blending ratio, and the range of 41 blends produced thereof which are described in Table 2. The results are summarized in Figure 2. The accuracy is exceptional across the whole dataset. The mean absolute error of the distillation temperature is 1.50°C. The largest error is seen at the initial and final boiling point. These are typically reported as the temperatures at 0.5% and 99.5% distilled, respectively. For the splicing, the distillation from 0 to 0.5% and 99.5 to 100% are assumed to be constant, a potential minor source of error. This is observable in Figure 2 where greater diversion from the unity line is present near the extremes.

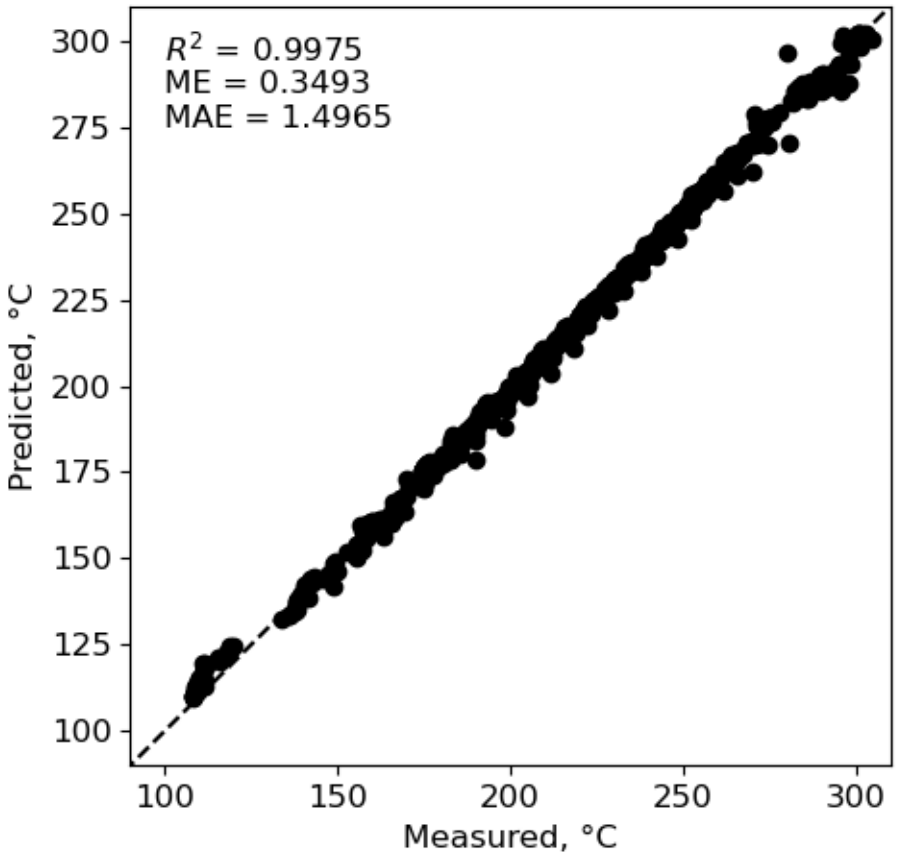

Figure 2. Unity plot for ASTM D2887 blending rule.

The impact of single component blending on SAF was also investigated. There has been community interest in blending aromatics and/or cycloalkanes with hydrotreated esters and fatty acids (HEFA) to meet a certain specification limit. The idea behind blending aromatic and cycloalkanes with HEFA is that both aromatics and cycloalkanes could bring HEFA (n- and iso-alkanes) density and seal swell back to the conventional jet fuel range. HEFA would, in return, make up for the low derived cetane number that is inherently associated with aromatics and cycloalkanes. Two single-component SAF candidates were blended with HEFA to evaluate the impact on the distillation curve. The single-component aromatic was blended at 8 and 25 vol%, which is motivated by the composition limits on aromatics in ASTM D7566. The single-component cycloalkane was blended at 10 and 50 vol%, and this is motivated by ASTM D4054 fast track and standard approval blend limits. The ASTM D86 and correlated ASTM D86 from ASTM D2887 results of neat HEFA and blended HEFA are shown in Table 3.

Table 3. Experimental data obtained for single-component SAF blends using ASTM D86 data (left) and ASTM D86 data correlated from ASTM D2887 data (right). The fuel consisting of 'Pure HEFA', 8% C10-Ar', '25% C10-Ar', '10% C10-Cy', and '50% C10-Cy' (Table 1).

	Distillation temperature (°C)				
Precent recovered (%)	Pure HEFA	8% C10-Ar	25% C10-Ar	10% C10-Cy	50% C10-Cy
0	141/139	142/140	146/147	143/143	153/152
5	150/152	151/153	156/156	151/153	162/170
10	156/153	157/158	160/165	157/158	167/180
20	163/164	163/170	166/176	165/170	172/188
30	172/175	171/176	171/178	173/176	176/189
50	194/203	189/195	183/184	191/195	183/184
70	222/228	216/223	203/209	215/223	192/187
80	234/240	231/236	223/226	229/236	201/203
90	244/249	243/247	242/242	242/247	225/229
95	249/254	248/254	248/251	248/254	242/247
100	255/263	254/263	257/261	255/263	254/259
T10 < 205 °C	TRUE	TRUE	TRUE	TRUE	TRUE
FBP < 300 °C	TRUE	TRUE	TRUE	TRUE	TRUE
T50-T10 (min 15°C)	38/50	32/37	23/19	34/37	16/4
T90-T10 (min 40°C)	88/96	86/89	82/77	85/89	58/49

Besides the 10% recovered temperature (T10) and finial boiling point (FBP), there are other property requirements on fuel's volatility. The T50-T10 and T90-T10 limits were established for jet fuel containing synthesized hydrocarbons. Those limits are based on current experience with the approved synthetic fuels and what is typical for refined jet fuel (Hadallar & Johnson, 2006; Edwards, 2020).

The effect on distillation curve of blending single component into HEFA is illustrated in Figure 3. Both ASTM D7566 specification limit (red line) and violation of specification limit (red shaded region) are shown as well. Blending 8 vol% aromatic or 10 vol% cycloalkane did not significantly change the distillation curve of the neat HEFA, and these blends present distillation curves that are well within the distillation slope limit. Even with the blend fraction increased to 25 vol% aromatic, distillation slope remains within the specification limit. Quite expectedly, the initial boiling point increases noticeably with increasing blend fraction of the less volatile component. Moreover, the distillation curve grows increasingly flatter in the T20 to T80 region as increasingly more of the single component is blended into HEFA. At 50 %v cycloalkane blended with HEFA, the mixture passes the T50-T10 limit by just 1°C.

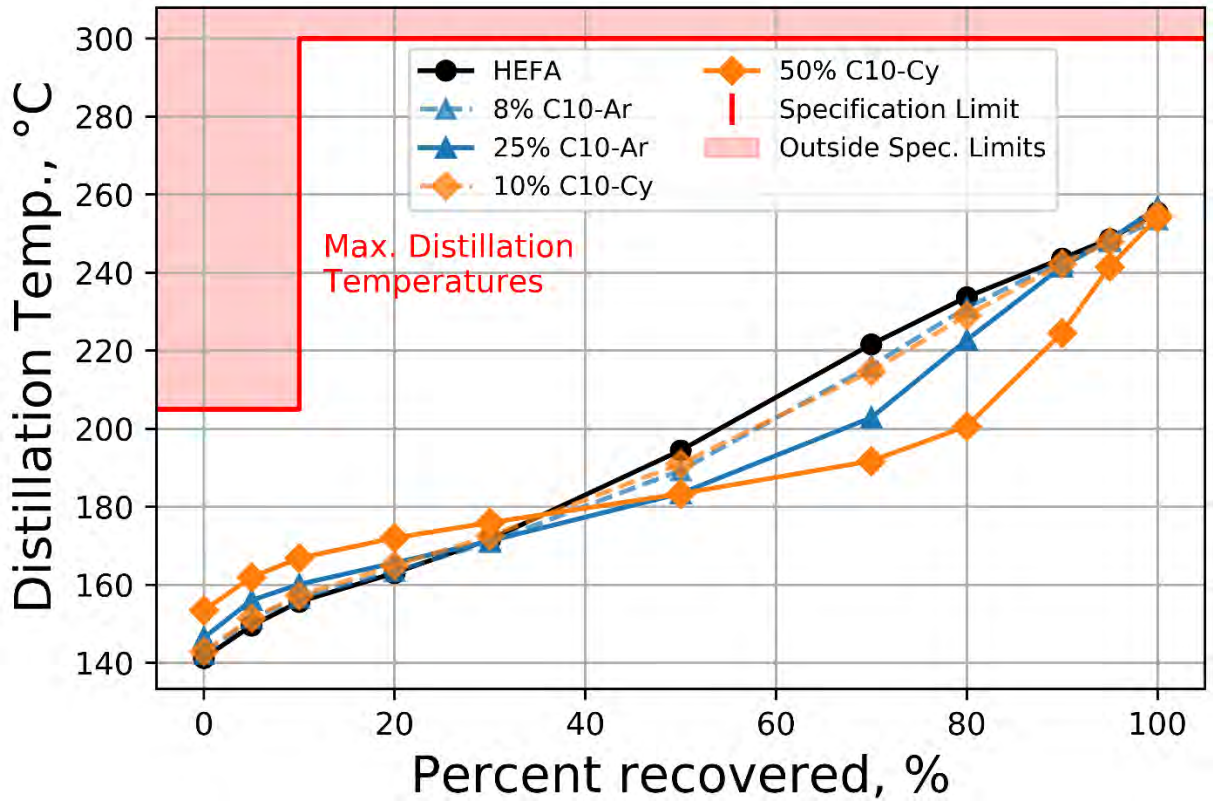

Figure 3. Distillation curve (ASTM D86) for single component blended with SAF mixtures.

Another concern raised by the SAF community is that the ASTM D86 correlation from ASTM D2887 data may not always adequately capture the shape of the distillation curve for SAF because of dramatic composition differences relative to the conventional fuels (46 jet fuels and 39 diesel fuels) upon which the correlation was derived. Most of the conventional jet fuels have a normal population distribution around carbon number 11. Figure 4 illustrates both ASTM D86 experimental data and simulated ASTM D86 from ASTM D2887 data corresponding to various SAF blends. The ASTM D86 results are represented by the black circles and lines, while the simulated ASTM D86 results are shown in yellow or blue colors. The specification limits derived from D7566 (red line and red-shaded region), and ASTM D4054 Fast track (red dashed line) are shown for reference.

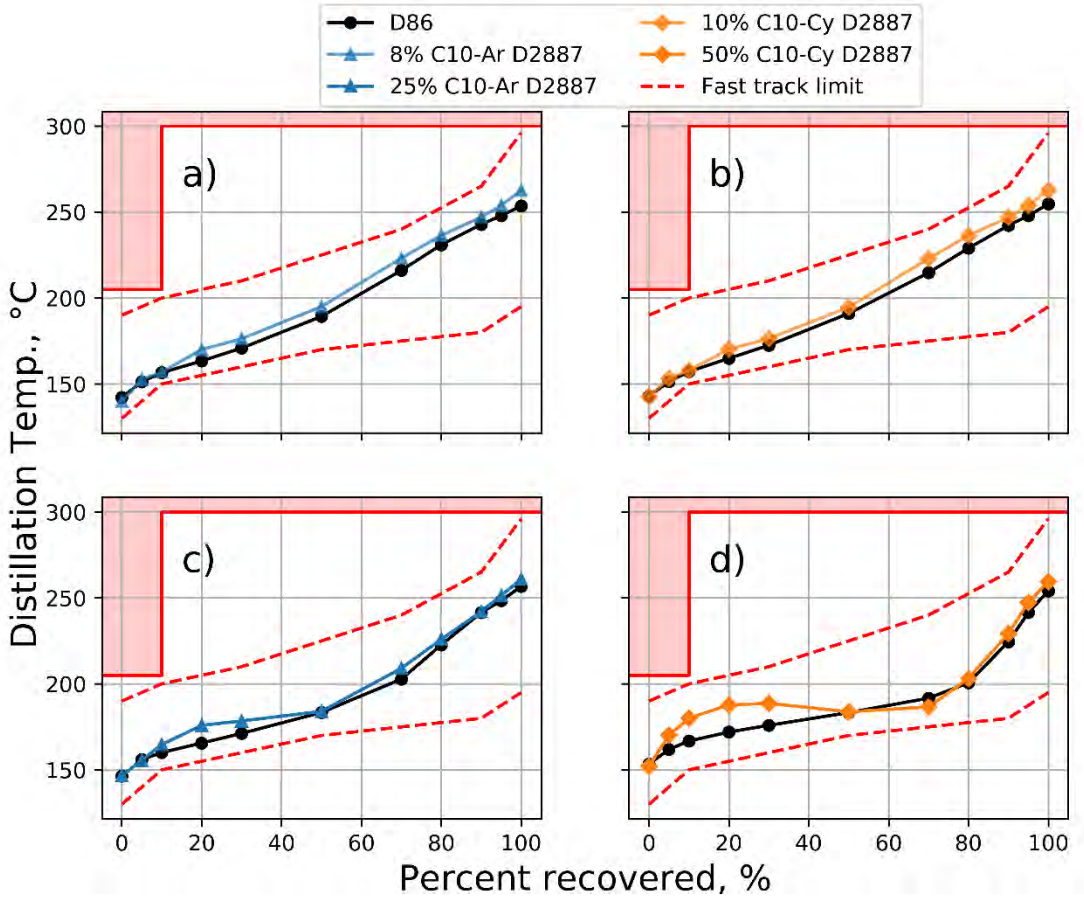

Figure 4. Distillation curve data (ASTM D86) for single-component blended SAF mixtures, and the data obtained through correlation from simulated distillation (ASTM D2887); (a) 8% C10-Ar, (b) 10% C10-Cy, c) 25% C10-Ar, & d) 50% C10-Cy.

At or below 10 vol% of single component blended with HEFA (Figure 4 (a) and (b), the discrepancy between ASTM D86 and simulated ASTM D86 is small, where the absolute average temperature deviation is 4.5°C and the absolute maximum temperature deviation is 9.0°C, which occurred at T70. As the single molecule concentration increased to 25 vol%, a visible discrepancy between ASTM D86 and simulated ASTM D86 emerged. The average absolute average temperature deviation is 3.6°C, and the absolute maximum temperature deviation is 10.3°C, which occurred at T20. When the concentration of a single molecule increases to 50 vol%, the ASTM D86 correlation predicts a non-physical distillation curve. The simulated ASTM D86 suggests that both T50 and T70 are smaller than T30, which is not possible in any real distillation. This discrepancy is even more clear in Table 3, where the actual ASTM D86 result passed the T50-T10 slope limit, while the simulated ASTM D86 predicted an off-spec result.

Conclusion

The effect of blending sustainable aviation fuel on the distillation curve is investigated here. The reported predictions by blending rule distillation curve exhibited remarkable consistency with ASTM D2887 data, with a minimal mean absolute error (MAE) of just under 1.5°C. Investigating the impact of blending high concentrations of single components in HEFA, two potential SAF candidates were blended with HEFA, and their ASTM D86 distillation curves were measured. Notably, even at blending levels as high as 50%v of a single-component SAF candidate, no violation of volatility limits was observed. However, a substantial discordance emerged between the simulated one-plate distillation curve (via ASTM D2887, Appendix X4 [ASTM International, 2024]) and the directly measured one-plate distillation curve (via ASTM D86) for SAFs, particularly accentuated at higher concentrations of a single component in the fuel.

Milestone

- Performed distillation optimization for eight SAF candidates from five different pathways.

Major Accomplishments

- Investigated and compared two existing distillation curve measurements ASTM D86 and ASTM D2887 for SAF candidates.

Publications

Yang, Z., Bell, D. C., Cronin, D. J., Boehm, R., Heyne, J., & Ramasamy, K. K. (2024). Volatility measurements of sustainable aviation fuels: a comparative study of D86 and D2887 methods. *ACS Sustainable Chemistry & Engineering, 12*(19), 7414-7420. https://doi.org/10.1021/acssuschemeng.4c00678

Yu, S., He H., Summers, S., Yang, Z., Si, B., Heyne, J., Zhang, Y., Yang, H. (In review). Upgrading of biocrude oil into sustainable aviation fuel using molybdenum carbide nanocatalysts, *Science Advances*.

Outreach Efforts

Presentation

Yang, Z., Bell, D. C., Cronin, D. J., Boehm, R., Heyne, J., & Ramasamy, K. K. (2024, August 15). *Volatility measurements of sustainable aviation fuels: a comparative study of D86 and D2887 methods* [Meeting presentation]. VTO SAF End-Use Review Meeting, Golden, Colorado.

Awards

- Joshua Heyne – 2024 Energy and Fuels Rising Starts

Student Involvement

Washington State University PhD student, Zhibin (Harrison) Yang, leads this effort. Joshua Ledezma, an undergraduate student at Washington State University, participated in this effort.

Plans for Next Period

- Continue improvement on the distillation optimization tool and procedure.
- Coordinate with novel fuel producers to optimize their distillation process.

References

Air Transport Action Group. 2021. *Waypoint 2050*. (2nd Ed.). https://aviationbenefits.org/media/167417/w2050_v2021_27sept_full.pdf

ASTM International. (2020). *ASTM D7566-20: standard specification for aviation turbine fuel containing synthesized hydrocarbons*. doi:10.1520/D7566-22A.

ASTM International. (2022a). *ASTM D4054-22: standard practice for evaluation of new aviation turbine fuels and fuel additives*. doi:10.1520/D4054-22.

ASTM International. (2022b). *ASTM D7566-22a: standard specification for aviation turbine fuel containing synthesized hydrocarbons*. doi:10.1520/D1655-10.2.

ASTM International. (2023). *ASTM D86-23ae2: standard test method for distillation of petroleum products and liquid fuels at atmospheric pressure*. doi:10.1520/mnl10832m.

ASTM International. (2024). *ASTM D2887-24: standard test method for boiling range distribution of petroleum fractions by gas chromatography*. doi:10.1520/mnl10902m.

Baral, N. R., Yang, M., Harvey, B. G., Simmons, B. A., Mukhopadhyay, A., Lee, T. S., & Scown, C. D. (2021). Production cost and carbon footprint of biomass-derived dimethylcyclooctane as a high-performance jet fuel blendstock. *ACS Sustainable Chemistry & Engineering*, 9(35), 11872–11882. https://doi.org/10.1021/acssuschemeng.1c03772

Collins, J. M., & McLarty, D. (2020). All-electric commercial aviation with solid oxide fuel cell-gas turbine-battery hybrids. *Applied Energy*, 265. https://doi.org/10.1016/j.apenergy.2020.114787

Colket, M., Heyne, J., Rumizen, M., Gupta, M., Edwards, T., Roquemore, W. M., Andac, G., Boehm, R., Lovett, J., Williamns, R., Condevaux, J., Turner, D., Rizk, N., Tishkoff, J., Li, C., Moder, J., Friend, D., & Sandaran, V. (2017). Overview of the national jet fuels combustion program. *AIAA J*, 55(4), 1087–1104. https://doi.org/10.2514/1.J055361

Colket, M., & Heyne, J. (2021). *Fuel effects on operability of aircraft gas turbine combustors*. American Institute of Aeronautics and Astronautics, Inc. https://doi.org/10.2514/4.106040

Edwards, J. T. (2020). *AFRL-RQ-WP-TR-2020-0017: Jet fuel properties*. Air Force Research Laboratory. https://apps.dtic.mil/sti/pdfs/AD1093317.pdf

Hadaller, O. J., & Johnson, J. M. (2006). *World fuel sampling program* (CRC Report No. 647). Coordinating Research Council, Inc., Alpharetta, Georgia.

Huq, N. A., Hafenstine, G. R., Huo, X., Nguyen, H., Tifft, S. M., Conklin, D. R., Stück, D., Stunkel, J., Yang, Z., Heyne, J. S., Wiatrowski, M. R., Zhang, Y., Tai, L, Zhu, J., McEnally, C. S., Christensen, E. D., Hays, C., Van Allsburg, K. M., Unocic, K. A., . . . Vardon, D. R. (2021). Toward net-zero sustainable aviation fuel with wet waste-derived volatile fatty acids. *Proceedings of the National Academy of Sciences*, 118(13) https://doi.org/10.1073/pnas.2023008118

Ng, K. S., Farooq, D., & Yang, A. (2021). Global biorenewable development strategies for sustainable aviation fuel production. *Renewable and Sustainable Energy Reviews*, 150. https://doi.org/10.1016/j.rser.2021.111502

Nicolay, S., Karpuk, S., Liu, Y., & Elham, A. (2021). Conceptual design and optimization of a general aviation aircraft with fuel cells and hydrogen. *International Journal of Hydrogen Energy*, 46(64), 32676-32694. https://doi.org/10.1016/j.ijhydene.2021.07.127

Yang, Z., Boehm, R. C., Bell, D. C., & Heyne, J. S. (2023). Maximizing sustainable aviation fuel usage through optimization of distillation cut points and blending. *Fuel*, 353. https://doi.org/10.1016/j.fuel.2023.129136

Task 2 – Vapor Pressure Measurement for Sustainable Aviation Fuel

Washington State University

Objectives

The objectives of this task are intended to improve the current understanding of vapor pressure of approved SAF pathways and develop and/or validate blending rules for vapor pressure.

Research Approach

There are several technical issues related to fuel vapor pressure. One key issue is the evaporation rate at temperatures below the boiling point. This rate is influenced by factors such as mass transfer rate, vapor pressure, and surface area. The evaporation rate directly affects droplet evaporation and the dry-out rate of purged staged circuits. Another concern is the pressure inside closed vessels, which can lead to "burping" and coking issues. These arise in systems such as the fuel metering unit and the fuel nozzle valve inlets during shutdown. Vapor pressure is also critical in simulated distillation modeling. During evaporation or vaporization, the composition of both liquid and gas-phase fuel evolves. This causes variations in chemical properties, such as derived cetane number (DCN) or threshold soot index (TSI), in the vapor phase. Furthermore, as the composition of lighter and heavier fractions changes, the vapor pressure and, consequently, the evaporation rate of the liquid phase will fluctuate throughout the process.

The vapor pressure measurement was conducted on PAC®-Herzog HVP 972 and according to ASTM D6378.
The repeatability and reproducibility of the machine was initially investigated and plotted in Figures 5 to 9. The initial measurements indicate that the machine is working as intended and measurements are within the ASTM D6378 reported repeatability reproducibility.

® PAC is a registered trademark of PAC L.P., Housten, Texas.

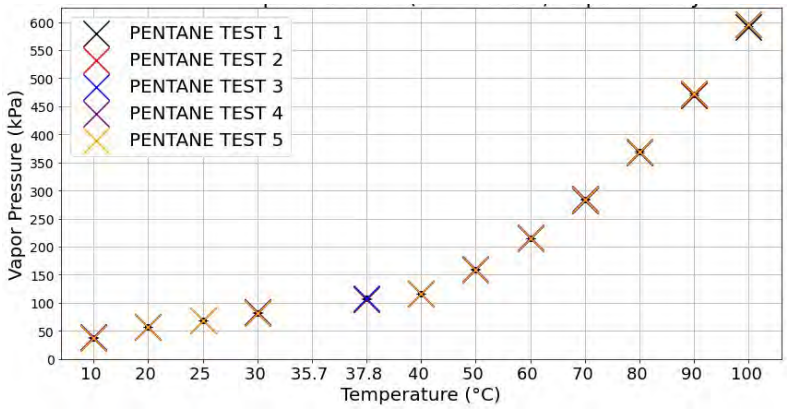

Figure 5. Pentane vapor pressure measurements.

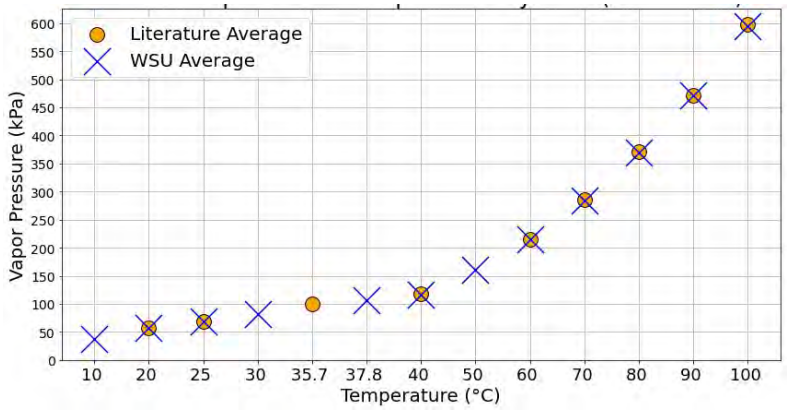

Figure 6. Pentane vapor pressure measurements against literature data.

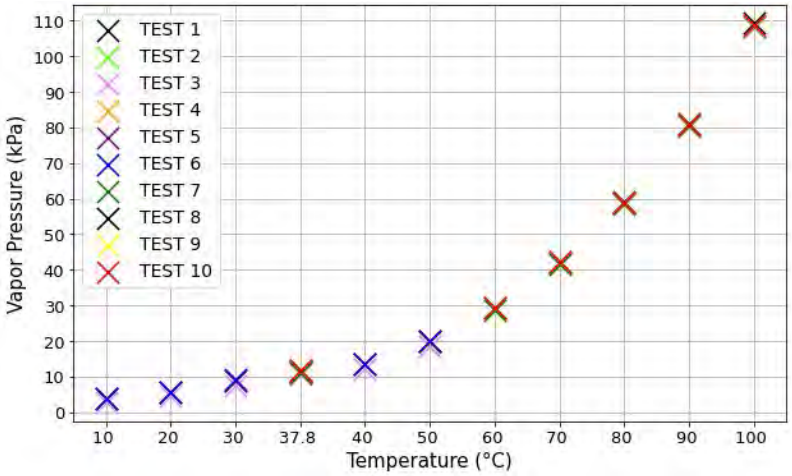

Figure 7. Heptane vapor pressure measurement.

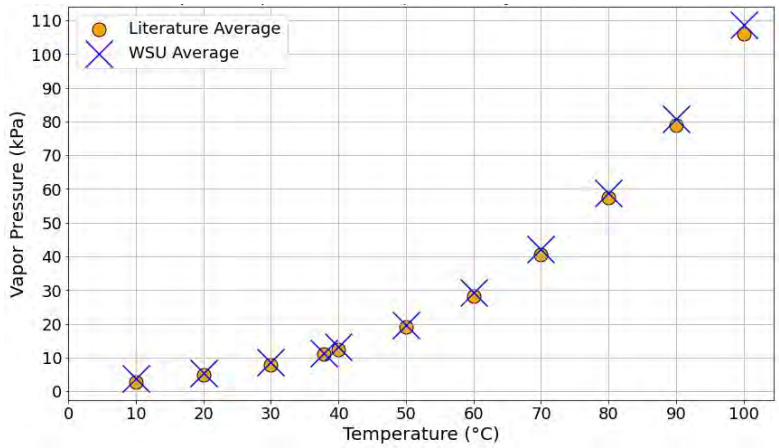

Figure 8. Heptane vapor pressure measurement against literature data.

After the validation of vapor pressure measurement, subsequent measurements were then conducted on SAF, SAF blend, and potential SAF candidate. Figure 9 illustrates these results where H164 is HEFA, C1 is Gevo alcohol-to-jet (ATJ), H233 is dimethycyclooctane (DMCO) or cycloSAF, and H140 is synthetic aromatic kerosene (SAK). As shown in Figure 9, significant variation exists in the vapor pressure profiles of approved SAFs and SAF candidates.

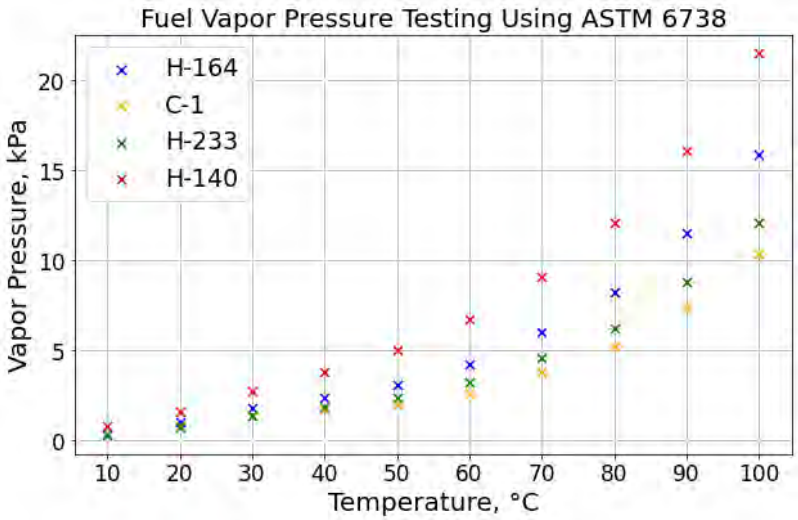

Figure 9. Vapor pressure measurement for SAFs and SAF candidates. H164 is HEFA, C1 is Gevo ATJ, H233 is DMCO, and H140 is SAK.

Another interest of this project is the vapor pressure blending rule development. Here the ASCENT Project 103 team mixed two neat molecules together at different ratios and measured the vapor pressures shown in Figure 10 and 11. With more measurements like this, a mixing rule could be established or validated for vapor pressure of jet fuel range hydrocarbons.

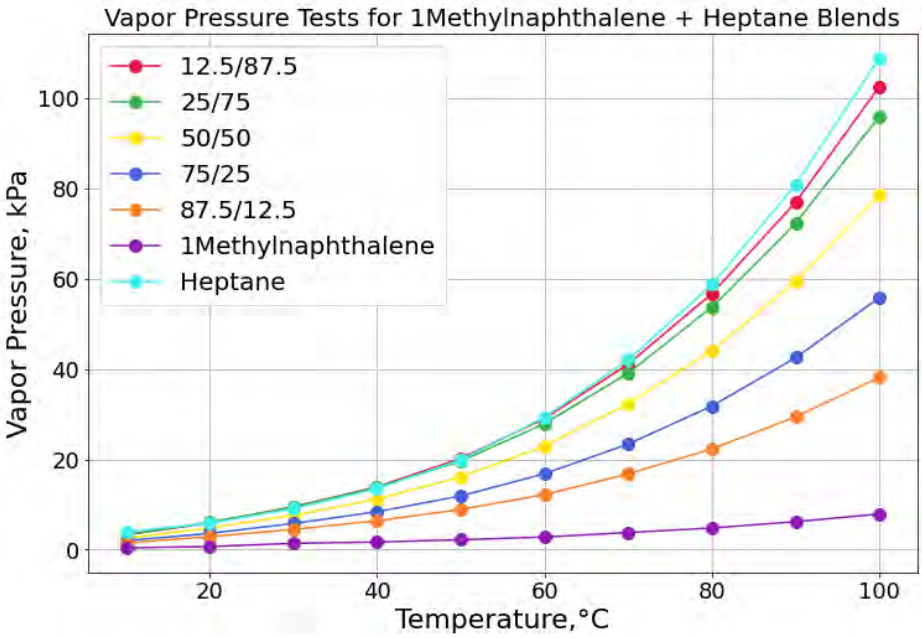

Figure 10. Vapor pressure measurements for 1-methylnaphthalene and heptane mixtures.

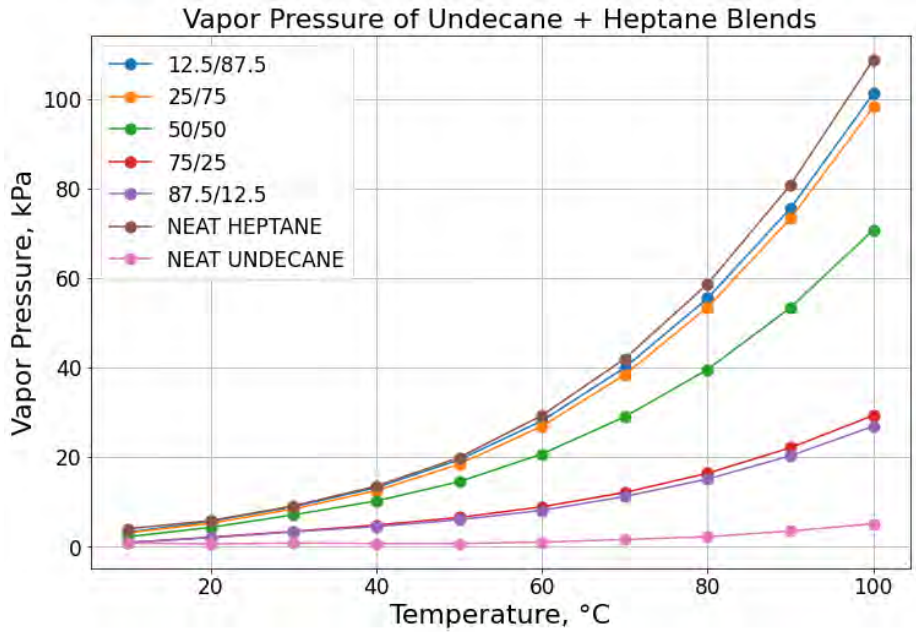

Figure 11. Vapor pressure measurements for heptane and undecane mixtures.

Milestone(s)

- Measured vapor pressure for two approved SAFs and two SAF candidates.

Major Accomplishments

- Validated the vapor pressure machine measurements for jet fuel range hydrocarbons.

Publications
None.

Outreach Efforts
None.

Awards
- Joshua Heyne – 2024 Energy and Fuels Rising Starts

Student Involvement
Washington State University PhD student, Zhibin (Harrison) Yang, leads this effort. Joshua Ledezma, an undergraduate student at Washington State University, participated in this effort.

Plans for Next Period
- Continue measurements for vapor pressure of neat molecules, blends, and SAFs.

Publications Index

Project 001

Fourteen graduate students and five undergraduate students involved.

Publications

- Benavidez, L., Baldos, U., Zhuang, Q., Chen, S., and Yuan, Y. (2024, June 5-7**).** *New induced land use change (ILUC) emissions assessment: Updates from IPCC guidelines and new estimates of soil carbon from the Harmonized World Soil Database (HWSD)* [Conference paper]. 27th Annual Conference on Global Economic Analysis. Colorado State University, Fort Collins, Colorado.
- Bolakhe, K., T.E. Yu, V. Sykes, A. Smith, and C.N. Boyer. "Assessing a Sustainable Aviation Fuel Supply Chain from Winter Canola and Its Carbon Intensity Considering Feedstock Yield Variations." Under review.
- Bolakhe, K. (2024). *Stochastic Optimization of Canola-Based Sustainable Aviation Fuel in the Southeastern US* [Master's Thesis, University of Tennessee]. https://trace.tennessee.edu/utk_gradthes/11777/
- Chen, S., Zhuang, Q., Yuan, Y. and Benavidez, L., (2024, June 5-7). *Global land cover changes under changing climate and socioeconomic conditions from 2001 to 2020* [Conference paper]. 27th Annual Conference on Global Economic Analysis. Colorado State University, Fort Collins, Colorado.
- Chen, S., Zhuang, Q., Taheripour, F., Yuan, Y., & Benavidez, L. (2025). Assessment of global land cover changes using satellite data: intermittent and long-term land cover changes from 2001 to 2020. *Environmental Research Letters*, *20*(3). http://dx.doi.org/10.1088/1748-9326/adb5a3
- Garcia, A., Sierra-Jimenez, V., Brandt, K., Martinez-Valencia, L. P., Wolcott, M., Male, J., & Garcia-Perez, M. (2024). Holistic methodology to guide the evolution of sustainable aviation fuel production technologies. *Energy & Fuels*, *38*(18), 17706-17716.
- Li. P., Yu, T. E., Trejo-Pech, C., Larson, J. A., English, B. C., & Lanning, D. (2024). Assessing the Impact of Preprocessing and Conversion Technologies on the Sustainable Aviation Fuel Supply from Forest Residues in the Southeast U.S. *Transportation Research Record, 2678*(9). https://doi.org/10.1177/03611981241230508
- Lynd, L., Kemanian, A., Smith, J., Richard, T. L., Arifi, A., Bozzetto, S., Fabbri, C., Field, J., Pries, C. H., Kubis, M. (2024). Soil application of high-lignin fermentation byproduct to increase the sustainability of liquid biofuel production from crop residues, *Environmental Research Letters, 19*(8). DOI 10.1088/1748-9326/ad601a
- Rubin, H.J., J.S. Fu, and T.E. Yu. "Mapping Historical Soil Carbon in the U.S. with Machine Learning." Under review.
- Taheripour, F., Mueller, S., Emery, I., Karami, O., Sajedinia, E., Zhuang, Q., & Wang, M. (2024). Biofuels induced land use change emissions: The role of implemented land use emission factors. *Sustainability (2071-1050)*, *16*(7).
- Trejo-Pech, C. O., Yu, T. E., Lanning, D. N., Dooley, J. H., Larson, J. A., & English, B. C. (2024). A Techno-economic Analysis Comparing a Hammermill and a Rotary Shear System to Process Woody Biomass for Biofuel Production. *Energies, 17*, 886. https://doi.org/10.3390/en17040886

Reports

- CAEP13/FTG06/WP05: SAF projection process, February 2024
- CAEP/13-FTG/06-WP/07: Summary of the progress of the CLCA subgroup, February 2024
- CAEP/13-FTG/06-WP/08: Summary of the progress of consideration for fuels with high electricity input in CORSIA
- CAEP/13-FTG/06-WP/11 – *Soil organic carbon double counting*, February 5-9, 2024, Geneva, Switzerland.
- CAEP/13-FTG/06-WP/12 – *Modelling Brazil corn ATJ pathway*, February 5-9, 2024, Geneva, Switzerland.
- CAEP/13-FTG/06-WP/13 – *Updating approved ILUC values according to 2019 IPCC guideline*, February 5-9, 2024, Geneva, Switzerland.
- CAEP/13-FTG/06-WP/14 – *Cut-off dates for Low LUC risk practices*, February 5-9, 2024, Geneva, Switzerland.
- CAEP/13-FTG/06-WP/15 – *Definition of marginal land*, February 5-9, 2024, Geneva, Switzerland.
- CAEP/13-FTG/06-WP/16 – *New GTAP-BIO data base and ILUC modelling*, February 5-9, 2024, Geneva, Switzerland.
- CAEP/13-FTG/07-WP/04: Summary of the progress of the CLCA subgroup, May 2024
- CAEP/13-FTG/07-WP/05: Summary of the progress of consideration for fuels with high electricity input in CORSIA
- CAEP/13-FTG/07-WP/08 – *ILUC values for significant multicropping cases*, May 13-17, 2024, Virtual.
- CAEP/13-FTG/07-WP/09 – *Key discussion points regarding the proposal for significant multicropping cases*, May 13-17, 2024, Virtual.

- CAEP/13-FTG/07-WP/10 – *Definition of marginal land for pathway specification*, May 13-17, 2024, Virtual.
- CAEP/13-FTG/07-WP/11 – *Proposed revisions in DLUC methodology*, May 13-17, 2024, Virtual.
- CAEP/13-FTG/07-WP/12 – *Removing SOC from ILUC, GLOBIOM ILUC values with 2019 IPCC guidelines, sharing AEZ-EF*, May 13-17, 2024, Virtual.
- CAEP13/FTG07/WP15: Update on the SAF database, May 2024
- CAEP13/FTG07/WP16: Proposal for non-standard coconut LCA (FTG Board), May 2024.
- CAEP/13-FTG/08-WP/09: Consideration of additional carbon sources for fuels with high electricity input in CORSIA
- CAEP/13-FTG/08-WP/10: Accounting of Electricity for fuels with high electricity input in CORSIA
- CAEP/13-FTG/08-WP/15 – *Proposed revisions in DLUC methodology*, September 20-27, 2024, Montreal, Canada.
- CAEP/13-FTG/08-WP/17 – *Future ILUC tasks and a proposal for ILUC modelling improvements*, September 20-27, 2024, Montreal, Canada.
- CAEP13/FTG08/WP20: Core-LCA-related items for the FTG Board, September 2024.

Presentations

- Benavidez, L., Baldos, U., Zhuang, Q., Chen, S., and Yuan, Y. (2024, June 5-7**).** *New induced land use change (ILUC) emissions assessment: Updates from IPCC guidelines and new estimates of soil carbon from the Harmonized World Soil Database (HWSD).* 27th Annual Conference on Global Economic Analysis. Colorado State University, Fort Collins, Colorado.
- Bolakhe, K., Yu, T. E., Sykes, V., & Smith, A. (2024, March 18-20). *Developing Sustainable Aviation Fuel System from Winter Oilseeds," Annual International Symposium* [Conference presentation]. Food-Energy-Water Bioeconomies for Net-Zero Transition, Knoxville, Tennessee.
- Bolakhe, K., Yu, T. E., Sykes, V., & Smith, A. (2024, May 22-24). *Sustainable Aviation Fuel Supply Chain from Winter Oilseeds and Its Carbon Intensity* [Conference presentation]. 2024 International Transport Forum Summit, Leipzig, Germany.
- Bolakhe, K., Yu, T. E., Sykes, V., Smith, A., & Boyer, C. N. (2024, July 28-30). *Evaluating a Stochastic Optimized Sustainable Aviation Fuel Supply Chain from Winter Canola and Its Carbon Intensity* [Poster presentation]. 2024 AAEA Annual Meeting, New Orleans, Louisiana.
- Brandt, K., & Malina, R. (2024, February 6). *Process for SAF announcement tracking and short-term projections.* CAEP: CAEP/13 (FTG) Meeting, Geneva, Switzerland.
- Brandt, K. (2024, July 3). *ICAO rules of thumb and related TEA tools developed by ASCENT* [Meeting presentation]. ICAO Assistance, Capacity-building and Training for SAF (ACT SAF), 13, virtual.
- Camenzind, D., Brandt, K., Martinez-Valencia, L., Wolcott. M. (2024, September 10*). Drivers of current biofuels development and opportunities for the future* [Conference presentation]. National Sustainability Society Inaugural Conference, Seattle, Washington.
- Chen, S., Zhuang, Q., Yuan, Y. and Benavidez, L., (2024, June 5-7). *Global land cover changes under changing climate and socioeconomic conditions from 2001 to 2020.* 27th Annual Conference on Global Economic Analysis. Colorado State University, Fort Collins, Colorado.
- Garcia-Perez, M., Garcia, A., & Wolcott, M. (2024, October 2-4). *Methodology to guide the evolution of sustainable aviation fuel production technologies* [Conference presentation]. Sustainable Aviation Futures, North America, Houston, Texas.
- Garcia, A., & Garcia-Perez, M. (2024, June 26). *Holistic methodology to guide the evolution of sustainable aviation fuel production technologies* [Conference presentation]. 32nd European Biomass Conference & Exhibition, Marseille, France.
- Helbing, M, & Korkut, E. (2024, February). *Exploring the Policy Landscape for Livestock Anaerobic Digesters* [Oral presentation]. C-CHANGE Grass2Gas Webinar Series hosted by Penn State Extension. (Renewable natural gas is seen as a potential part of the supply chain for SAF.)
- Kemanian A., et al. (2023, October 29-November 1). *Understanding how manure and digestate composition affect crop production and nitrogen losses in corn-based systems* [Poster presentation]. Agronomy Society of America meeting, St Louis, MI, United States.
- Li. P., T.E. Yu, C. Trejo-Pech, J.A. Larson, B.C. English, & D. Lanning. (2024). *Assessing the Impact of Preprocessing and Conversion Technologies on the Sustainable Aviation Fuel Supply from Forest Residues in the Southeast U.S.* 2024 TRB Annual Meeting presentation.
- Li. P., Yu, T. E., Labbe, C. N., Abdoulmoumine, N., Garcia-Perez, M. Hoyt, K., & English, B. C. (2025, January 5-9). *Optimizing Sustainable Aviation Fuel Supply Chains from Forest Residues Considering the Impact of Feedstock Ash Content Variability* [Conference presentation]. TRB Annual Meeting 2025, Washington, D.C.

- Turn, S., et. al. (2024). Thermochemical Equilibrium Prediction of Ash Behavior during Gasification of Construction and Demolition Waste. Poster presented at The International Conference on Thermochemical Conversion Science: Biomass & Municipal Solid Waste to RNG, Biofuels & Chemicals September 10–12, 2024, Westin Hotel, Itasca, IL.
- Yu, T. E., Li, P., Labbe, C. N., Abdoulmoumine, N., Garcia-Perez, M., & Hoyt, K. (2024, November 20-22). *Sustainable Aviation Fuel Supply Chains Optimization from Forest Residues Considering Feedstock Ash Content Variability* [Conference presentation]. 2024 AFCC Global Biobased Economy Conference and Exhibition, Washington, D.C.
- Yu, T.E. (2024, September 30 – October 3). *Biomass Feedstock Supply Chain Modeling and Decision Tools for Sustainable Aviation Fuels* [Conference presentation]. 2024 Frontiers in Biorefining 7th International Conference, St. Simons Island, Georgia.

Project 002

One graduate student and five undergraduate students involved.

Project 003

One graduate student involved.

Publications

- Peters, J.L., Grady, S.T., Laden, F., Nelson, E., Bozigar, M., Hart, J.E., Manson, J.E., Huang, T., Redline, S., Kaufman, J.D., Forman, J.P., Rexrode, K.M., & Levy, J.I. (2024) Long-term nighttime aircraft noise exposure and risk of hypertension in a prospective cohort of female nurses. *International Journal of Hygiene and Environmental Health*, *12(263): 114457*. doi: 10.1016/j.ijheh.2024.114457. PMID: 39270405.
- Bozigar, M., Laden, F., Hart, J.E., Redline, S., Huang, T., Whitsel, E.A., Nelson, E.J., Grady, S.T., Levy, J.I., & Peters, J.L. (2024). Aircraft noise exposure and body mass index among female participants in two Nurses' Health Study prospective cohorts living around 90 airports in the United States. *Environment International, 187: 108660*. doi: 10.1016/j.envint.2024.108660. PMID: 38677085.

Project 018

Two graduate students and four undergraduate students involved.

Presentations

- Mueller, S., Patil, P., Levy, J. I., Hudda, N., Durant, J. L., Gause, E., Loenen, B. V., & Lane, K. J. (2024, October 20-24). *Examining Impacts of Cross-Validation Approaches on Machine Learning Model Performance for Ultrafine Particle Exposure Assessment* [Oral presentation]. International Society for Exposure Science 2024 Annual Meeting, Montreal, Canada.
- Lane, K. J. & Durant, J. (2024, May 21-23). *Airport Air Quality Monitoring and Source Apportionment* [Oral presentation]. 2024 Aviation Emission Characterization Roadmap/Emissions Research Meeting, Washington DC.

Project 019

One graduate student involved.

Publications

- Venkatram, A., Pandey, G., & Arunachalam, S. (2024). Incorporating meander in area source modeling in AERMOD. *Journal of Air & Waste Management Association*, 1-10.

- Pandey, G., Venkatram, A., & Arunachalam, S. (2024). Accounting for plume rise of aircraft emissions and shoreline meteorology enhances AERMOD's description of concentrations measured around Los Angeles airport. *Journal of Air & Waste Management Association*, *74,* 726-742.
- Pandey, G. Venkatram, A., & Arunachalam, S. (2024). Modeling the air quality impact of aircraft emissions is area or volume the appropriate source characterization in AERMOD. *Air Quality, Atmosphere & Health, 17,* 1425-1434.

Project 022

No students involved.

Publications

- Singh, D. K., S. Sanyal, and D. J. Wuebbles, 2024: Understanding the role of contrails and contrail cirrus in climate change: A global perspective. *Atmospheric Chemistry and Physics*, 24, 9219-9262. https://doi.org/10.5194/acp-24-9219-2024.
- Eastham, S. D., Wuebbles, D. J., Sparrow, V. W., Rhodes, D., Grewe, V., Baughcum, S. L., Delhaye, D., & Penanhoat, O. (2024). *I.03 Update on Understanding of Potential Impacts of Supersonic Aircraft.* Special report for the International Civil Aviation Organization (ICAO), The United Nations, Montreal.
- Lee, D. S., Dickson, N., Altuntas, O., Arunachalam, S., Barrett, S., Baughcum, S., Bonne, N., Block, A., Boehm, A., Brons, R., Burkhardt, U., Carter, W., Catalano, F., Claro, G., Delhaye, D., Eastham, S., Gettelman, A., Goobie, S., Johansson, D., Kagaya, R., . . . Yin, F. (2024). *CAEP Impacts and Science Group (ISG) Contrail Science Workshop Report.* Special report for the International Civil Aviation Organization (ICAO), The United Nations, Montreal.
- Prashanth, P., Hauglustaine, D., Arunachalam, S., Eastham, S., Grewe, V., Miake-Lye, R., Skowron, A., Speth, R., Turgut, E. T., Van Velthoven, P., and Wuebbles, D. (2024). *I.01 Air Quality and Climate Impacts Interdependencies and Trade-Offs of Aviation Emissions.* Special report for the International Civil Aviation Organization (ICAO), The United Nations, Montreal.

Project 023

Two graduate students involved.

Publications

- Cezairli, M., Salgueiro, S., & Hansman, R. J. (2024). Analysis of the Implementation of Low-Noise PBN Flight Procedures at Boston Logan Airport. AIAA Aviation Forum, AIAA 2024-3856. https://doi.org/10.2514/6.2024-3856

Presentations

- Cezairli, M., Salgueiro, S., & Hansman, R. J. (2024). Analysis of the Implementation of Low-Noise PBN Flight Procedures at Boston Logan Airport. AIAA Aviation Forum, 29 July – 2 August, Las Vegas, NV, United States.

Project 025

Two graduate students involved.

Publications

- Boddapati, V., Ferris, A. M., & Hanson, R. K. (2024). Predicting the physical and chemical properties of sustainable aviation fuels using elastic-net-regularized linear models based on extended-wavelength FTIR spectra, *Fuel,* 356, 129557. https://doi.org/10.1016/j.fuel.2023.129557

Project 031

Two undergraduate students involved.

Publications

- Testing Method of Lubricants, Liquid Fuels, and Related Products: 7508.0—Method for Detailed Hydrocarbon Analysis of Middle Distillate Fuels by Two-Dimensional Gas Chromatography, Fed.-Std.-791F (2024). https://assist.dla.mil

Presentations

- Arts, A. M., Landsaw, A., West, Z. J. (2024, August 20). *Determination of Trace Metals in Aviation Turbine Fuel via ICP-MS* [Poster presentation]. American Chemical Society Fall 2024, Denver, Colorado.
- Arts, A. M., Landsaw, A., West, Z. J. (2024, September 8-12). *Determination of Trace Metals in Aviation Turbine Fuel via ICP-MS* [Poster presentation]. 18th International Conference on Stability, Handling and Use of Liquid Fuels, Louisville, Kentucky.
- West, Z., Zabarnick, S. (2024, March 19-20). *FAA ASCENT Center of Excellence D4054 Clearinghouse Update* [Conference presentation]. U.K. Ministry of Defense (MoD) Aviation Fuels Conference Meeting, Bristol, United Kingdom.
- West, Z. (2024, April 29-May 2). *D4054 Clearinghouse* [Meeting presentation]. 2024 CRC Aviation Committee Meeting, Alexandria, Virginia.

Project 033

One graduate student involved.

- Database made accessible through https://altjetfuels.illinois.edu/

Publications

- Wiersema, P., J. Oh, K. Kim, A. Godsell, & T. Lee. (2024). Analysis of constraining a chemical kinetic mechanism using hybrid response surface networks. *Proceedings of the Combustion Institute*, 40, 105522. https://doi.org/10.1016/j.proci.2024.105522
- Wiersema, P., K. Kim, E. Mayhew, J. Temme, C. Kweon, & T. Lee. (2024). Development of a gasoline and jet fuel blend kinetic mechanism using hybrid response surface networks. *Proceedings of the 2024 AIAA Science and Technology Forum and Exposition, 0176.*. https://doi.org/10.2514/6.2024-0176

Presentations

- Wiersema, P., K. Kim, E. Mayhew, J. Temme, C. Kweon, & T. Lee. (2024). Development of a gasoline and jet fuel blend kinetic mechanism using hybrid response surface networks. SciTech 2024, January 8-12, Orlando, FL.
- Wiersema, P., J. Oh, K. Kim, A. Godsell, & T. Lee. (2024). Analysis of constraining a chemical kinetic mechanism using hybrid response surface networks. 40th International Symposium on Combustion, Milan, Italy in July 2024

Project 37

Eighteen graduate students currently involved.

Project 038

One graduate student and one undergraduate student involved.

Publications

- Peddanarappagari, S. (2024). *Updates to Penn State Rotor Noise Prediction System* [Master's thesis]. The Pennsylvania State University.

Project 044

Four graduate and one undergraduate student involved.

Publications

- Salguiero, S., Huynh, J. & Hansman. R. J. (2025). Aircraft Takeoff and Landing Weight Estimation from Surveillance Data. *Journal of Air Transportation, 33*(1). https://doi.org/10.2514/1.D0370

Project 047

One graduate student involved.

Publications

- Voet, L. J. A., Prashanth, P., Speth, R. L., Sabnis, J. S., Tan, C. S., & Barrett, S. R. H. (2024). Automatic Continuous Thrust Control for Supersonic Transport Takeoff Noise Reduction. *Journal of Aircraft*, *61*(1), 291–306. https://doi.org/10.2514/1.C037394

Project 049

Two graduate students involved.

Publications

- Gan, Z. F. T., Tumelero Valente, V., Brentner, K. S., & Greenwood, E. (2024a). Broadband noise modulation of multirotor aircraft, *Journal of the Acoustical Society of America*, *157*, 924–939. https://doi.org/10.1121/10.0035646
- Gan, Z. F. T., Tumelero Valente, V., Brentner, K. S., & Greenwood, E. (2024b). Time-varying broadband noise of multirotor aircraft. *Proceedings of Meetings on Acoustics, 54*(1). https://doi.org/10.1121/2.0001946

Presentations

- Gan, Z. F. T., Tumelero Valente, V., Brentner, K. S., & Greenwood, E. (2024c, May 13-17). *Multirotor broadband noise modulation* [Conference Presentation]. 186th Meeting of the Acoustical Society of America/Acoustics Week in Canada, Ottawa, Ontario.

Project 051

One graduate student involved.

Project 052

One graduate student involved.

Project 053

One graduate student involved.

Publications

- Rindfleisch, T. C., Alonso, J. J., Jackson, D. C., Munguia, B. C., & Bowman, N. W. (2024). A Large-Scale Validation Study of AEDT Noise Modeling for Aircraft Arrivals, *Journal of the Acoustical Society of America,* 155 (3). https://doi.org/10.1121/10.0025276

Project 054

Ten graduate students involved.

Project 055

Four graduate students involved.

Publications

- Ha, S., & Lieuwen, T. (2024, January 8-12). Coherence between the globally integrated heat release rate and acoustic pressure in an enclosed duct [Conference paper]. AIAA SCITECH 2024 Forum, Orlando, Florida. https://doi.org/10.2514/6.2024-0795
- Ha, S., & Lieuwen, T. (2025). Direct combustion noise: Nearfield and non-compactness influences on pressure–heat release coherence. Combustion and Flame, 271, 113811. https://doi.org/10.1016/j.combustflame.2024.113811
- Patki, P. A., Emerson, B. L., & Lieuwen, T.C. (2025. Global stability and forced response analysis of swirling flows in aviation combustors. *Journal of Engineering for Gas Turbines and Power, 147*(1).

Presentations

- Ha, S., & Lieuwen, T. (2024, January 8-12). Coherence between the globally integrated heat release rate and acoustic pressure in an enclosed duct. AIAA SCITECH 2024 Forum, Orlando, Florida.

Project 056

Two graduate students involved.

Project 057

One graduate student involved.

Publications

- V. Sparrow & K. Riegel. (2024). Multipath interpretation of secondary sonic boom signatures. In 30th AIAA/CEAS Aeroacoustics Conference, Paper AIAA-3187. Manuscript available at DOI: 10.2514/6.2024-3187

Presentations

- V. Sparrow & K. Riegel. (2024). Multipath interpretation of secondary sonic boom signatures. Presented at 30th AIAA/CEAS Aeroacoustics Conference, Rome, Italy, June 4-7 2024.

Project 058

Three graduate students involved.

Publications

- Grobler, C. (2024). *Past, present, and future climate impacts of aviation* [Doctoral dissertation, Massachusetts Institute of Technology]. Massachusetts Institute of Technology. https://dspace.mit.edu/handle/1721.1/154000

Presentations

- Grobler, C., Agarwal, A., Fritz, T., Elmourad, J., Prashanth, P., Xu, X., Meijer, V., Florian, A., Eastham, S. D., & Barrett, S. R. (2023, December 11-15). *Assessing the evolution of contrail impacts from 1980 to 2019* [Conference presentation]. The American Geophysical Union (AGU) Fall Meeting 2023, San Francisco, California.
- Hagström, C., Waitz, I., Eastham, S., & Barret, S. (2024, April 14-19). *Uncertainty quantification of contrail climate impacts using non-intrusive polynomial chaos* [Poster presentation]. The 2024 General Assembly of the European Geosciences Union, Vienna, Austria.

Project 059

Five graduate students involved.

Publications

- Martin, O. G., Wu, G. J., & Lele, S. K. (2024, July 29-August 2). *Noise predictions of a dual-stream jet with forced internal mixing* [Conference paper]. AIAA Aviation Forum and ASCEND 2024, Las Vegas, Nevada.
- Mikkelsen, D. (2024). *Large-eddy simulation of jet noise using the energy cascade* {Master's thesis, Pennsylvania State University]. Pennsylvania State University.
- Shanbhag, T. K., Zhou, B., Ilario, C., & Alonso, J. J. (2024). An AD framework for jet noise minimization using geometrical acoustics. In *AIAA SCITECH 2024 Forum* (p. 2309). https://doi.org/10.2514/6.2024-2309
- Shanbhag, T. K., Zhou, B. Y., Ilario, C. R. S., & Alonso, J. J. (2024, June 4-7). *Adjoint-based jet noise minimization using geometrical aeroacoustics* [Conference paper]. 30th AIAA/CEAS Aeroacoustics Conference, Rome Italy.
- Shanbhang, T. K. (2024). *RANS-based methods for the prediction and reduction of jet noise* [Doctoral dissertation, Stanford University]. Stanford University.
- Woo, J., Murthy, S. R., & Bodony, D. J. (2024). Resolvent-based framework for jet noise reduction of a low-bypass ratio coannular nozzle, AIAA Paper 2024-2805, In AIAA SciTech 2024 Forum, Orlando, FL, 8-12 January.
- Wu, G. J. (2024). Towards quieter supersonic flight: a computational aeroacoustic study of high-speed jets, Chapter 4. PhD. Thesis. Stanford University.
- Wu, G. J., Martin, O. G., & Lele, S. K. (2024, June 4-7). *Computational aeroacoustic study of coannular nozzles with internal mixing geometries at high transonic Mach numbers* [Conference paper]. 30th AIAA/CEAS Aeroacoustics Conference, Rome, Italy.

Presentations

- Martin, O. G., Wu, G. J., & Lele, S. K. (2024, July 29-August 2). *Noise predictions of a dual-stream jet with forced internal mixing*. AIAA Aviation Forum and ASCEND 2024, Las Vegas, Nevada.
- Shanbhag, T. K., Zhou B. Y., Ilario, C. R. S., & Alonso, J. J. (2024). An AD framework for jet noise minimization using geometrical acoustics. Presented at the AIAA SciTech 2024 Forum, Orlando, FL.
- Shanbhag, T. K., Zhou, B. Y., Ilario, C. R. S., & Alonso, J. J. (2024, June 4-7). *Adjoint-based jet noise minimization using geometrical aeroacoustics*. 30th AIAA/CEAS Aeroacoustics Conference, Rome Italy.
- Woo, J., Murthy, S. R., & Bodony, D. J. (2024). Resolvent-based framework for jet noise reduction of a low-bypass ratio coannular nozzle, Presented at the AIAA SciTech 2024 Forum, Orlando, FL, 8-12 January.
- Wu, G. J., Martin, O. G., & Lele, S. K. (2024, June 4-7). *Computational aeroacoustic study of coannular nozzles with internal mixing geometries at high transonic Mach numbers*. 30th AIAA/CEAS Aeroacoustics Conference, Rome, Italy.

Project 060

Three graduate students involved.

Project 061

Six graduate students involved.

Publications

- Ravikanti, B., Ali, H., Balchanos, M., Harrison, E. D., & Mavris, D. N. (2024). *MBSE-Enabled System Verification of Unmanned Aerial System Noise Certification.* AIAA SciTech 2024 Forum, Orlando, FL, January 8-12, 2024.
- Balchanos, M., Ravikanti, B., Ali, H., Mali, H., D Harrison, E., & N Mavris, D. (2024). *A Regulatory Analysis and Process Improvement Decision Support Framework for Unmanned Aerial System (UAS) Noise Certification.* 2024 Quiet Drones Symposium, Manchester, U.K., September 2024.

Presentations

- Ravikanti, B., Ali, H., Balchanos, M., Harrison, E. D., & Mavris, D. N. (2024). *MBSE-Enabled System Verification of Unmanned Aerial System Noise Certification.* Presented at the AIAA SciTech 2024 Forum, Orlando, FL, January 8-12, 2024.
- Balchanos, M., Ravikanti, B., Ali, H., Mali, H., D Harrison, E., & N Mavris, D. (2024). *A Regulatory Analysis and Process Improvement Decision Support Framework for Unmanned Aerial System (UAS) Noise Certification.* Presented at the 2024 Quiet Drones Symposium, Manchester, U.K., September 2024.

Project 062

Four graduate students involved.

Publications

- Willitt, A., Bendarkar, M. V., Bhanpato, J., Kirby, M., Abelezele, S., & Mavris, D. N. (2024, Jan). Preliminary AEDT Noise Model Validation using Real-World Data. AIAA SCITECH 2024 Forum. Orlando, FL, January 2024.

Project 064

Five graduate students involved.

Publications

- Patel, D., Ergan, T., Cai, Y., Gladin, J., and Mavris, D., “Performance Assessment and Mission-Based Optimization for Next-Generation Single-Aisle Aircraft Conceptual Design,” accepted by *AIAA SciTech 2025 Forum*, American Institute of Aeronautics and Astronautics, 2025.
- Ergan, T., Parashar, A., Xie, J., Kirby, M., and Mavris, D., “Fleet-Level and Global Emissions Impact Analysis of Mission-Optimized Next-Generation Single-Aisle Aircraft,” accepted by *AIAA SciTech 2025 Forum*, American Institute of Aeronautics and Astronautics, 2025.

Presentations

- Patel, D., Ergan, T., Cai, Y., Gladin, J., and Mavris, D., “Performance Assessment and Mission-Based Optimization for Next-Generation Single-Aisle Aircraft Conceptual Design,” accepted by *AIAA SciTech 2025 Forum*, American Institute of Aeronautics and Astronautics, 2025.
- Ergan, T., Parashar, A., Xie, J., Kirby, M., and Mavris, D., “Fleet-Level and Global Emissions Impact Analysis of Mission-Optimized Next-Generation Single-Aisle Aircraft,” accepted by *AIAA SciTech 2025 Forum*, American Institute of Aeronautics and Astronautics, 2025.

Project 065

Four graduate and two undergraduate students involved.

Publications

- Boehm, R. C., Yang, Z., Bell, D. C., Faulhaber, C., Mayhew, E., Bauder, U., Eckel, G., & Heyne, J. S. (2024). Perspective on fuel property blending rules for design and qualification of aviation fuels: A review. *Energy and Fuels, 38*(18), 17128–17145. https://doi.org/10.1021/acs.energyfuels.4c02457
- Dasgupta, D., & Som, S. (2024, June). Fuel Property Impact on Lean Blow Out for Sustainable Aviation Fuels in Gas Turbine Combustors. In *Turbo Expo: Power for Land, Sea, and Air* (Vol. 87943, p. V03AT04A073). American Society of Mechanical Engineers.
- Faulhaber, C., Bell, D. C., Boehm, R., & Heyne, J. S. (2024). Dielectric constant predictions for jet-range hydrocarbons: Evaluating the Clausius–Mossotti relation and correcting for molecular dipole moments. *Energies, 17*(18), 4700. https://doi.org/10.3390/en17184700
- Hall, C., Bell, D. C., Feldhausen, Rauch, B., & Heyne, J. (2024). Quantifying isomeric effects: A key factor in aviation fuel assessment and design. *Fuel, 357 Part C*, 129912, https://doi.org/10.1016/j.fuel.2023.129912
- Kumar, A., Bell, D. C., Yang, Z., Heyne, J., Santos, D. M., Wang, H., Zuo, P., Wang, C., Mittal, A., Klein, D. P., Manto, M. J., Chen, X., & Yang, B. (2024). A simultaneous depolymerization and hydrodeoxygenation process to produce lignin-based jet fuel in continuous flow reactor. *Fuel Processing Technology, 263*. https://doi.org/10.1016/j.fuproc.2024.108129
- Yang, Z., Bell, D. C., Boehm, R. C., Marques, P. F., Boze, J. A., Kosilkin, I. V., & Heyne, J. S. (2024). Assessing the effect of composition on dielectric constant of sustainable aviation fuel. *Fuel, 380*. https://doi.org/10.1016/j.fuel.2024.133230
- Yang, Z., Bell, D. C., Cronin, D. J., Boehm, R. C., Heyne, J., Ramasamy, K. K. (2024). Volatility measurements of sustainable aviation fuels: A comparative study of D86 and D2887 methods. *ACS Sustainable Chemistry and Engineering, 12*(19), 7414–7420. https://doi.org/10.1021/acssuschemeng.4c00678

Presentations

- Dasgupta, D., & Som, S. (2024, June). Fuel Property Impact on Lean Blow Out for Sustainable Aviation Fuels in Gas Turbine Combustors. In *Turbo Expo: Power for Land, Sea, and Air* (Vol. 87943, p. V03AT04A073). American Society of Mechanical Engineers.
- Heyne, J. S. (2024, September). *SAF center at Paine Field* [Panel]. Aerospace Futures Alliance, 19th Annual Aerospace Summit, Tacoma, Washington.
- Heyne, J. S. (2024, September). *Towards decarbonizing aviation with sustainable aviation fuel: Some technical challenges and opportunities* [Seminar]. University of Georgia – Athens, School of Engineering and Chemistry Department, Athens, Georgia.
- Heyne, J. S. (2024, September 16). *Drop-in solutions to minimize aviation fuel sooting* [Panel]. International Civil Aviation Organization (ICAO), Symposium on non-CO_2 Aviation Emissions, Montréal, Canada.
- Heyne, J. S. (2024, July 26). *Towards biobased sustainable aviation fuel: Some technical challenges and opportunities in sustainable aviation fuels* [Keynote presentation]. NSF Innovative Nexus for Food, Energy and Water Systems, University of Illinois Urbana-Champaign, Urbana, Illinois.
- Heyne, J. S. (2024, May). *SAF property predictions from gas chromatography predictions* [Panel]. United Kingdom Department for Transport's Advanced Fuel Fund: Sustainable Aviation Fuel Innovation Programme, QEII Centre, London, United Kingdom.
- Heyne, J. S. (2024, March 4). *Fuel analysis, qualification, and standardization* [Seminar]. University of Washington, William E. Boeing Department of Aeronautics and Astronautics, Seattle, Washington.
- Fuller, C & Heyne, J. S. (2024, January). Some local SAF efforts and overviews [Keynote presentation]. CleanTech Alliance, Perkins Coie, Seattle, Washington.
- Heyne, J. S. (2024, January). *Navigating the shift: understanding fuel property variations in the move to 100% SAF* [Panel]. 2024 AIAA SciTech Forum, Sustainable aviation fuels: Moving towards 100% SAF, Orlando, Florida.
- Heyne, J. S. (2023, October). *Clear skies ahead: The evolution and expansion of sustainable aviation fuel* [Keynote presentation]. Discovery Series: A Technology Alliance Program, Perkins Coie, Seattle, Washington.
- Heyne, J. S. (2023, October). *WSU Tri-Cities bioenergy: research, programs, & priorities* [Keynote presentation]. Northwest Environmental Business Council, Northwest Bioenergy Summit, Three Rivers Convention Center, Kennewick, Washington.
- Heyne, J. S. (2023, October). *Sustainable aviation fuel: existing pathways, contemporary developments, and a potential future fuels* [Panel]. Northwest Environmental Business Council, Northwest Bioenergy Summit: Biofuels section, Kennewick, Washington.

Project 066

One graduate student involved.

Publications

- Boehm, R. C., Faulhaber, C., Behnke, L., & Heyne, J. S. (2024). The effect of theoretical SAF composition on calculated engine and aircraft efficiency. *Fuel, 371*(B). https://doi.org/10.1016/j.fuel.2024.132049

Project 067

Four graduate students involved.

Publications

- Hodge, A., Shahin, T., McLean, T., Gejji, R., Lucht, R., & Slabaugh, C. (2024, January 8-12). *Fuel temperature effects on combustion stability of a high-pressure liquid-fueled swirl flame.* AIAA SciTech 2024 Forum, Orlando, Florida. https://doi.org/10.2514/6.2024-1241
- Hodge, A. J., Shahin, T. T., Gejji, R. M., Philo, J. J., Lucht, R. P., & Slabaugh, C. D. (2025). Fuel temperature effects on combustion stability of a high-pressure liquid-fueled swirl flame. *Journal of Propulsion and Power, 41*(1), 53-63. https://doi.org/10.2514/1.B39592
- McDonald, C. T., Shahin, T. T., Philo, J. J., Gejji, R. M., Fish, D. D., Slabaugh, C. D., & Lucht, R. P. (2025). Emissions measurements in a liquid-fueled aviation gas turbine combustor with heated fuels. *ASME Journal of Engineering for Gas Turbines and Power, to be submitted.*
- McLean, T. N., Koenig, K. C., Murdock, B. K., Shahin, T. T., Hodge, A. J., Gejji, R. M., Slabaugh, C. D., & Lucht, R. P. (2025, January 6-10). *Laser-induced incandescence measurements in a high-pressure swirl-stabilized flame.* AIAA SciTech 2025 Forum, Orlando, Florida. https://doi.org/10.2514/6.2025-1580

Presentations

- Hodge, A., Shahin, T., McLean, T., Gejji, R., Lucht, R., & Slabaugh, C. (2024, January 8-12). *Fuel temperature effects on combustion stability of a high-pressure liquid-fueled swirl flame* [Conference presentation]. AIAA SciTech 2024 Forum, Orlando, Florida. https://doi.org/10.2514/6.2024-1241
- McLean, T. N., Koenig, K. C., Murdock, B. K., Shahin, T. T., Hodge, A. J., Gejji, R. M., Slabaugh, C. D., & Lucht, R. P. (2025, January 6-10). *Laser-induced incandescence measurements in a high-pressure swirl-stabilized flame* [Conference presentation]. AIAA SciTech 2025 Forum, Orlando, Florida. https://doi.org/10.2514/6.2025-1580

Project 068

Two graduate students involved.

Publications

- McFerran, K., Thole, K. A., & Lynch, S. P. (2025). Dirt ingestion impacts on cooling within a double-walled combustor liner. *ASME Journal of Turbomachinery, 147*(8), 081019. https://doi.org/10.1115/1.4067464
- Schaeffer, C. B., Barringer, M. D., Lynch, S. P., & Thole, K. A. (2025). Influence of dilution and effusion flows in generating variable inlet profiles for a high-pressure turbine. *ASME Journal of Turbomachinery*, 147(3), 031003. https://doi.org/10.1115/1.4066560
- Schaeffer, C. B., Barringer, M. D., Lynch, S. P., & Thole, K. A. (2025). *Comparison of predicted and measured combustor-relevant flow fields* (GT2025-15782). (in progress).

Presentations

- McFerran, K., Thole, K. A., & Lynch, S. P., (2024). Dirt Ingestion Impacts on Cooling within a Double-Walled Combustor Liner. Turbo Expo, London, June 24

- Schaeffer, C. B., Barringer, M. D., Lynch, S. P., & Thole, K. A. (2024). Influence of Dilution and Effusion Flows in Generating Variable Inlet Profiles for a High-Pressure Turbine. Turbo Expo, London, June 24

Project 069

One graduate student and two undergraduate students involved.

Presentations

- Whitefield, P and Offert, J. (2024, January). *Transitioning a research nvPM mass calibration procedure to operations* [Oral presentation]. SAE E31 Meeting, Albuquerque, New Mexico.

Project 070

Four graduate students involved.

Publications

- McGrath, R., Juergensmeyer, J., Bond, R., Bugay, E., Wehe, S., Wu, D., Steinberg, A., Sun, W., & Mazumdar, Y. C. (2024). Planar laser-induced incandescence for the study of soot production in a multi-sector RQL Jet A combustor. *Applications in Energy and Combustion Science, 18*, 100269. https://doi.org/10.1016/j.jaecs.2024.100269
- Vishwanath, R., Bibik, O., Olimid, D., Douglas, E., Wehe, S., Mazumdar, Y. C., Steinberg, A., & Sun, W. (2025, January 12-16). *Drop-size measurements using phase doppler particle anemometry in a confined high-pressure sector combustor*. AIAA 2025-1519, AIAA SciTech 2025 Forum, Orlando, Florida. https://doi.org/10.2514/6.2025-1519
- Juergensmeyer, J., Miller, J., Bond, R., Mcgrath, R., Wehe, S., Sun, W., Mazumdar, Y. C., & Steinberg, A. (2025, June 16-20). Measurement of particulate matter and its oxidation in a multi-sector rich-quench-lean combustor. ASME Turbomachinery Technical Conference & Exposition 2025, Memphis, Tennessee.

Presentations

- Vishwanath, R., Bibik, O., Olimid, D., Douglas, E., Wehe, S., Mazumdar, Y. C., Steinberg, A., & Sun, W. (2025, January 12-16). *Drop-size measurements using phase doppler particle anemometry in a confined high-pressure sector combustor* [Conference presentation]. AIAA SciTech 2025 Forum, Orlando, Florida.
- Juergensmeyer, J., Miller, J., Bond, R., Mcgrath, R., Wehe, S., Sun, W., Mazumdar, Y. C., & Steinberg, A. (2025, June 16-20). Measurement of particulate matter and its oxidation in a multi-sector rich-quench-lean combustor. ASME Turbomachinery Technical Conference & Exposition 2025, Memphis, Tennessee.

Project 071

Two graduate students involved.

Project 072

One graduate student involved.

Project 073

No students involved.

Project 074

Five graduate students and seven undergraduate students involved.

Publications

- Jain, A., Obi, I., Mazumdar, Y. C., Salazar, V., Kodali, M., Venkatesan, K., & Steinberg, A. M. (In preparation). Flame structure, spray, and blowout of a lean premixed prevaporized combustor with conventional and sustainable jet fuels. *AIAA Journal*.
- Jain, A., Obi, I., Mazumdar, Y. C., Salazar, V., Kodali, M., Venkatesan, K., & Steinberg, A. M. (2025, January 6-10). *Flame structure, spray, and blowout of a lean premixed prevaporized combustor with conventional and sustainable jet fuels* [Conference paper]. AIAA SCITECH 2025 Forum, Orlando, Florida.
- Passarelli, M. L., Wonfor, S. E., Zheng, A. X., Mazumdar, Y., Steinberg, A. M., Bower, H., Hong, J., & Venkatesan, K. (2024, June 24-28). *Blowoff characteristics of a bluff-body stabilized, multi-element, lean premixed pre-vaporized combustor for supersonic transport applications* [Conference paper]. ASME Turbo Expo 2024: Turbomachinery Technical Conference and Exposition, London, United Kingdom. https://doi.org/10.1115/GT2024-129322

Presentations

- Jain, A., Obi, I., Mazumdar, Y. C., Salazar, V., Kodali, M., Venkatesan, K., & Steinberg, A. M. (2025, January 6-10). *Flame structure, spray, and blowout of a lean premixed prevaporized combustor with conventional and sustainable jet fuels*. AIAA SCITECH 2025 Forum, Orlando, Florida.
- Passarelli, M. L., Wonfor, S. E., Zheng, A. X., Mazumdar, Y., Steinberg, A. M., Bower, H., Hong, J., & Venkatesan, K. (2024, June 24-28). *Blowoff characteristics of a bluff-body stabilized, multi-element, lean premixed pre-vaporized combustor for supersonic transport applications*. ASME Turbo Expo 2024: Turbomachinery Technical Conference and Exposition, London, United Kingdom.

Project 075

Two graduate students and one undergraduate student involved.

Publications

- Li, N., Zhange, Y., Winkler, J., Reinmann, C. A., Voytovych, D., Joly, M., Lore, K. G., Mendoza, J., & Grace, S. M. (2024). Development of fully low-order prediction of fan broadband interaction noise via integration of machine learning. *AIAA Journal, 62*(6). https://doi.org/10.2514/1.J063148
- Li, N., Winkler, J., Reinmann, C. A., Voytovych, D., Mendoza, J., & Grace, S. M. (2024). Effect of straight and swept FEGV placement on fan broadband interaction noise. In *30th AIAA/CEAS Aeroacoustics Conference (2024)* (p. 3161). https://doi.org/10.2514/6.2024-3161

Presentations

- Li, N., Winkler, J., Reinmann, C. A., Voytovych, D., Mendoza, J., & Grace, S. M. (2024). Effect of straight and swept FEGV placement on fan broadband interaction noise. *30th AIAA/CEAS Aeroacoustics Conference (2024)*, 4 - 7 June, Rome, Italy.

Project 077

Three graduate students involved.

Publications

- Chaudhary, R., Valente, V., Mukherjee, B., Jue, A., Brentner, K. S., & Greenwood, E. (2024, May 7-9). *Understanding takeoff and landing noise for small multirotor vehicles*. Vertical Flight Society's 80th Annual Forum & Technology Display, Montreal, Canada.

- Rachaprolu, J., & Greenwood, E. (2024). Helicopter noise source separation using an order tracking filter. *Journal of the American Helicopter Society, 69*, 012006. https://doi.org/10.4050/JAHS.69.012006
- Rachaprolu, J., Valente, V. T., ElSharkawy, E., & Greenwood, E. (2024, May 7-9). *Multirotor noise source separation and characterization from ground-based acoustic measurements.* Vertical Flight Society's 80th Annual Forum & Technology Display, Montreal, Canada.
- ElSharkawy, E., Valente, V.T., Rachaprolu, J.S., Greenwood, E. (2024, July 29-August 2). *Calibration of an air data system for small multirotor aircraft.* AIAA AVIATION Forum and ASCEND 2024, Las Vegas, Nevada. https://doi.org/10.2514/6.2024-4393
- ElSharkaway, E., Valente V.T., Rachaprolu, J., Greenwood, E. (2024, September 7-9). *Effect of wind on multirotor UAS noise measurements.* Quiet Drones 2024 Symposium, Manchester, United Kingdom.
- Valente, V., Johnson, E., & Greenwood, E. (2024, May 7-9). *An experimental evaluation of electronic propeller phase synchronization.* Vertical Flight Society 80th Annual Forum & Technology Display, Montreal, Canada. https://doi.org/10.4050/F-0080-2024-1194
- Valente, V., Johnson, E., & Greenwood, E. (In revision). An experimental evaluation of electronic propeller phase synchronization. *Journal of American Helicopter Society*.
- Valente, V. (2024). *Multiple rotor acoustic control* [Doctoral dissertation, The Pennsylvania State University]. The Pennsylvania State University.
- Valente, V., Khamvilai, T., Greenwood, E., Johnson, E. (2025, May 20-22). *Combining attitude and phase control for noise attenuation on multiple rotor vehicles* [Abstract submitted]. Vertical Flight Society Forum 81, Virgina Beach, Virginia.

Presentations

- Chaudhary, R., Valente, V., Mukherjee, B., Jue, A., Brentner, K. S., & Greenwood, E. (2024, May 7-9). *Understanding takeoff and landing noise for small multirotor vehicles* [Conference presentation]. Vertical Flight Society's 80th Annual Forum & Technology Display, Montreal, Canada.
- Rachaprolu, J., Valente, V. T., ElSharkawy, E., & Greenwood, E. (2024, May 7-9). *Multirotor noise source separation and characterization from ground-based acoustic measurements* [Conference presentation]. Vertical Flight Society's 80th Annual Forum & Technology Display, Montreal, Canada.
- ElSharkawy, E., Valente, V.T., Rachaprolu, J.S., Greenwood, E. (2024, July 29-August 2). *Calibration of an air data system for small multirotor aircraft* [Conference presentation]. AIAA AVIATION Forum and ASCEND 2024, Las Vegas, Nevada.
- ElSharkaway, E., Valente V.T., Rachaprolu, J., Greenwood, E. (2024, September 7-9). *Effect of wind on multirotor UAS noise measurements* [Conference presentation]. Quiet Drones 2024 Symposium, Manchester, United Kingdom.

Project 078

Four graduate students involved.

Publications

- Barbosa, M. P. (2024). *Relationship between synoptic scale meteorology, aircraft parameters, and observable contrails* [Master's thesis, Massachusetts Institute of Technology]. Massachusetts Institute of Technology. https://hdl.handle.net/1721.1/157807
- Kigotho, O. N. (2024). *Design of experiments for contrail avoidance* [Master's thesis, Massachusetts Institute of Technology]. Massachusetts Institute of Technology. https://hdl.handle.net/1721.1/155413
- Meijer, V. R. (2024). *Satellite-based analysis and forecast evaluation of aviation contrails* [Doctoral dissertation, Massachusetts Institute of Technology]. Massachusetts Institute of Technology). Massachusetts Institute of Technology. https://hdl.handle.net/1721.1/155350

Presentations

- Meijer, V., Eastham, S. D., Barrett S. R. H. (2023, December 11-15). *Contrail height estimation using geostationary satellite imagery* [Poster presentation]. AGU Fall 2023 Meeting, San Franscisco, California.
- Robion, L., Meijer, V., Speth, R., Eastham, S. D., Barrett S. R. H., (2023). *Enabling contrail avoidance through robust contrail detections* [Poster presentation]. AGU Fall 2023 Meeting, San Franscisco, California.

- Barbosa, M. P., Barrett, S. R. H., Eastham, S. D., Meijer, V., Robion, L. (2024, April 14-19). *Evaluation of robust flight attribution algorithm for contrail avoidance* [Poster presentation]. EGU24, Vienna, Austria.
- Robion, L., Meijer, V., Speth, R., Eastham, S. D., Barrett S. R. H., (2024, April 14-19). *Robust satellite-based tracking of contrail forming regions* [Conference presentation]. EGU24, Vienna, Austria.
- Robion, L., Prashanth, P., (2024, October 1-2). *Contrail modelling informed by flight campaign measurements* [Conference presentation]. 2024 LEAD Symposium, Niskayuna, New York.
- Euchenhofer, M. V., Ross, I., Eastham, S. D., Meijer, V., & Waitz, I. A. (2024, April 14-19). *A comparison of contrail detectability from LEO and GEO satellite images* [Poster presentation]. EGU24, Vienna, Austria.

Project 079

Three graduate students involved.

Publications

- Packer, A., Nelson, E., Mavrudieva, D., Liedtke, P., Winkler, J., Reimann, C., Homma, K., Goldberg, E., Mendoza, J., Simpson, T., & Manahan, M. (2024). A Design Optimization Framework Applied to Additively Manufactured Acoustic Liners. *Additive Manufacturing*. In Review.
- Goldberg, E. (2024). *Polymer prototyping of acoustic liner designs to support transition to metal additive fabrication*. [Master's thesis, The Pennsylvania State University]. The Pennsylvania State University, University Park, Pennsylvania.

Project 080

Six graduate students involved.

Publications

- Garcia, A., Sierra-Jimenez, V., Brandt, K., Martinez-Valencia, L. P., Wolcott, M., Male, J., & Garcia-Perez, M. (2024). Holistic methodology to guide the evolution of sustainable aviation fuel production technologies. *Energy & Fuels, 38*(18), 17706–17716. https://doi.org/10.1021/acs.energyfuels.4c02795
- Sierra, V., Wolcott, M., Zhang, X., Ha, S., Male, J., Garcia, A., Brand, K., Garcia-Perez, M., Drennan, C., & Holladay, J. (Under review). *Emerging and commercial hydrogen production technologies for SAF manufacturing: A comparative literature review*. Washington State University.

Presentations

- Garcia, A., & Garcia-Perez, M. (2024, June 24-27). *Holistic methodology to guide the evolution of sustainable aviation fuel production technologies* [Conference Presentation]. European Biomass Conference, Marseille, France.
- Garcia-Perez, M., Garcia, A., & Wolcott, M. (2024, October 2-4). *Holistic methodology to guide the evolution of sustainable aviation fuel production technologies* [Conference presentation]. Sustainable Aviation Futures, North America, Houston, Texas.
- Garcia-Perez, M., Garcia, A., & Wolcott, M. (2024, July 28-31). *Holistic methodology to guide the evolution of sustainable aviation fuel production technologies* [Conference presentation]. American Society of Agricultural and Biological Engineers (ASABE) 2024, Anaheim, California.
- Garcia-Perez, M., Garcia, A., & Wolcott, M. (2022, October 24-27). *Production of cheap sustainable aviation fuels (SAFs):Balancing economic and environmental imperatives* [Conference presentation]. Sustainable Energy for a Sustainable Future, San Pedro, San Jose.
- Sierra-Jimenez, V., Brandt, K., Wolcott, M., Male, J., Garcia-Perez, M. (2024, November 20-21). *Hydrogen Production Techno-economic and Carbon Intensity Insights for a Sustainable Energy Transition in the U.S.* [Poster presentation]. Re+CHARGE H_2 Conference (PNWH2 Hub), Seattle, Washington.

Project 082

Thirteen graduate students involved.

Project 083

Two graduate students involved.

Project 084

Three graduate students involved.

Publications

- Pellerito, V., Yeung, N., Huynh, j., & Hansman, R. J. (2024). *Impact of flight trajectory design on performance and noise for AAM aircraft*. AIAA Aviation Forum and ASCEND 2024. https://doi.org/10.2514/6.2024-4076

Presentations

- Pellerito, V., Yeung, N., Huynh, j., & Hansman, R. J. (2024, July 29 – August 2). *Impact of flight trajectory design on performance and noise for AAM aircraft* [Conference presentation]. AIAA Aviation Forum and ASCEND 2024.

Project 085

Four graduate students involved.

Project 086

Six undergraduate students involved.

Project 088

No students involved.

Project 089

One undergraduate student involved.

Publications

- Kosir, S., Landsaw, A., Steinecker, W. H., West, Z. J., Zabarnick, S. (2024). Synthetic blend component study: the effects of hydrocarbon composition on aviation fuel dielectric constant. *Energy & Fuels, 38*(17), 16451-16457, doi: 10.1021/acs.energyfuels.4c02342.

Presentations

- Kosir, A., Landsaw, A., West, Z., Zabarnick, S. (2024, September 8-12). *Synthetic blend component study: the effects of hydrocarbon composition on aviation fuel dielectric constant* [Conference presentation]. 18th International Conference on Stability, Handling and Use of Liquid Fuels, Louisville, Kentucky.

- Kosir, S., Landsaw, A., West, Z., Zabarnick, S. (2024, April 29 - May 2). *Composition effects on the dielectric constant for blends of aviation fuel synthetic blend components (SBCs)* [Conference presentation]. 2024 CRC Aviation Committee Meeting, Alexandria, Virginia.

Project 090

Two undergraduate students involved.

Presentations

- West, Z. (2024, April 29-May 2). *World jet fuel survey* [Conference presentation]. 2024 CRC Aviation Committee Meeting, Alexandria, Virginia.
- Kosir, S., & West, Z. (2024, September 8-12). *World jet fuel survey (preliminary results)* [Poster presentation]. 18th International Conference on Stability, Handling and Use of Liquid Fuels (IASH 2024), Louisville, Kentucky.

Project 091

Two graduate students involved.

Project 092

No graduate students involved.

Publications

- News article: https://www.psu.edu/news/administration/story/plan-advances-addition-renovation-build-start-lab-cato-park

Project 093

Five graduate students involved.

Publications

- Martinez-Valencia, L., & Valderrama-Rios, C. (2024). *Sustainable aviation fuel production in Colombia: Opportunities and challenges*. Washington State University. https://doi.org/10.7273/000006281

Project 094

Four graduate students involved.

Project 095

Four graduate students involved.

Project 096

Seven graduate students involved.

Project 097

Eight graduate students involved.

Project 098

Three graduate students involved.

Project 101

Two graduate and one undergraduate student involved.

Project 102

Three graduate students involved.

Project 103

One graduate student and one undergraduate student involved.

Publications

- Yang, Z., Bell, D. C., Cronin, D. J., Boehm, R., Heyne, J., & Ramasamy, K. K. (2024). Volatility measurements of sustainable aviation fuels: a comparative study of D86 and D2887 methods. *ACS Sustainable Chemistry & Engineering, 12*(19), 7414-7420. https://doi.org/10.1021/acssuschemeng.4c00678
- Yu, S., He H., Summers, S., Yang, Z., Si, B., Heyne, J., Zhang, Y., Yang, H. (In review). Upgrading of biocrude oil into sustainable aviation fuel using molybdenum carbide nanocatalysts, *Science Advances*.

Presentations

- Yang, Z., Bell, D. C., Cronin, D. J., Boehm, R., Heyne, J., & Ramasamy, K. K. (2024, August 15). *Volatility measurements of sustainable aviation fuels: a comparative study of D86 and D2887 methods* [Meeting presentation]. VTO SAF End-Use Review Meeting, Golden, Colorado.

Project Funding Allocations by Federal Fiscal Year

Breakout by Project*

Project		Funding Based on award date											
		2014	2015	2016	2017	2018	2019	2020	2021	2022	2023	2024	Total
001	Alternative Jet Fuel Supply Chain Analysis	$1,599,943	$1,425,000	$1,498,749	$1,855,461	$1,102,865	$1,034,039	$3,214,455	$1,412,313	$1,569,136	$936,344	$2,688,115	$18,336,420
002	Ambient Conditions Corrections for Non-Volatile PM Emissions Measurements	$2,800,000	$750,000	-$147,766	$725,500	-	$1,217,221	-	$521,246	-	$3,050,812	$2,513,003	$11,430,016
003	Cardiovascular Disease and Aircraft Noise Exposure	$200,000	$200,000	$200,000	$340,000	-	$1,729,286	-	-	-	$1,999,608	$162,001	$4,830,895
004	Estimate of Noise Level Reduction	$150,000	-	-	-	-$ 8,845	-	-	-	-	-	-	$141,155
005	Noise Emission and Propagation Modeling	$212,000	$200,000	-	-	-	-	-	-	-	-	-	$412,000
006	Rotorcraft Noise Abatement Operating Conditions Modeling	$250,326	-	-	-	-	-	-	-	-	-	-	$250,326
007	Civil, Supersonic Over Flight, Sonic Boom (Noise) Standards Development	$100,000	$200,000	-	-	-	-	-	-	-	-	-	$300,000
008	Noise Outreach	$ 30,000	$ 50,000	$ 75,000	$ 25,000	-	$ 30,000	-	-	-	-	-	$210,000
009	Geospatially Driven Noise Estimation Module	-	-	-	-	-	-	$250,000	$249,999	-	-	-	$499,999
010	Aircraft Technology Modeling and Assessment	$549,979	$550,000	$310,000	$669,567	$764,185	-	$2,747,116	$700,000	-	$200,000	-	$6,490,847

Project		Funding Based on award date											
		2014	2015	2016	2017	2018	2019	2020	2021	2022	2023	2024	Total
011	Rapid Fleet-wide Environmental Assessment Capability	$600,000	$270,000	$299,999	-	-	-	-	-	-	-	-	$1,169,999
012	Aircraft Design and Performance Assessment Tool Enhancement	$ 90,000	-	-	-	-	-	-	-	-	-	-	$90,000
013	Micro-Physical Modeling & Analysis of ACCESS 2 Aviation Exhaust Observations	$200,000	-	-	-	-	-	-	-	-	-	-	$200,000
014	Analysis to Support the Development of an Aircraft CO2 Standard	$520,000	-	-	-	-	-	-	-	-	-	-	$520,000
017	Pilot Study on Aircraft Noise and Sleep Disturbance	$154,000	$343,498	$266,001	$134,924	-	-	-	-	-	-	-	$898,423
018	Health Impacts Quantification for Aviation Air Quality Tools	$150,000	$150,000	$200,000	$270,000	-	-	$1,299,991	$599,371	$549,921	-	$649,915	$3,869,198
019	Development of Aviation Air Quality Tools for Airport-Specific Impact Assessment: Air Quality Modeling	$320,614	$369,996	-	$625,378	-	$300,000	$919,064	$650,000	-	$650,000	$300,000	$4,135,052
020	Development of NAS wide and Global Rapid Aviation Air Quality	$150,000	$200,000	$250,000	$250,000	-	-	-	-	-	-	-	$850,000
021	Improving Climate Policy Analysis Tools	$150,000	$150,000	$150,000	$150,000	-	-	-	-	-	-	-	$600,000
022	Evaluation of FAA Climate Tools	$150,000	$30,000	$ 75,000	$100,000	-	-	$200,000	$150,000	$199,999	-	$200,000	$1,104,999

Project		Funding Based on award date											
		2014	2015	2016	2017	2018	2019	2020	2021	2022	2023	2024	Total
023	Analytical Approach for Quantifying Noise from Advanced Operational Procedures	-	$286,711	$250,000	$250,000	-	$250,000	$500,000	-	-	$125,000	$125,000	$1,786,711
024	Emissions Data Analysis for CLEEN, ACCESS, and Other Recent Tests	$244,975	-	$ 75,000	-	-	-	-	-	-	-	-	$319,975
025	National Jet Fuels Combustion Program – Area #1: Chemical Kinetics Combustion Experiments	-	$615,000	$210,000	$200,000	$ 2,556	$110,000	$300,000	$200,000	$200,000	-	$300,000	$2,137,556
026	National Jet Fuels Combustion Program – Area #2: Chemical Kinetics Model Development and Evaluation	-	$200,000	-	-	-$ 2,556	-	-	-	-	-	-	$197,444
027	National Jet Fuels Combustion Program – Area #3: Advanced Combustion Tests	-	$1,010,000	$580,000	$265,000	-	$ 30,000	-	-	-	-	-	$1,885,000
028	National Jet Fuels Combustion Program – Area #4: Combustion Model Development and Evaluation	-	$470,000	$ 55,000	-	-	-	-	-	-	-	-	$525,000
029	National Jet Fuels Combustion Program – Area #5: Atomization Tests and Models	-	$640,000	$360,000	$150,000	-	$120,000	-	-	-	-	-	$1,270,000
030	National Jet Fuels Combustion Program – Area #6: Referee Swirl-Stabilized Combustor Evaluation/Support	-	$349,949	-	-	-	-	-	-	-	-	-	$349,949

Project		Funding Based on award date											
		2014	2015	2016	2017	2018	2019	2020	2021	2022	2023	2024	Total
031	Alternative Jet Fuels Test and Evaluation	-	$489,619	$744,891	$999,512	$183,019	-	$2,976,134	$499,784	$1,499,940	-	$2,101,722	$9,494,621
032	Worldwide LCA of GHG Emissions from Petroleum Jet Fuel	-	$150,000	-	-	-	-	-	-		-	-	$150,000
033	Alternative Fuels Test Database Library	-	$199,624	$119,794	$165,000	-	$163,584	$330,000	$150,000	$150,000	-	$150,000	$1,428,002
034	National Jet Fuels Combustion Program – Area #7: Overall Program Integration and Analysis	-	$234,999	$635,365	$192,997	$374,978	-	$582,983	-	-	-	-$101,888	$1,919,434
035	Airline Flight Data Examination to Improve flight Performance Modeling	-	$150,001	-	-	-	-	-	-	-	-	-	$150,001
036	Parametric Uncertainty Assessment for AEDT2b	-	$ 65,000	$175,000	$380,000	-	$300,000	-	-	-	-	-	$920,000
037	CLEEN II Technology Modeling and Assessment	-	$200,000	$150,000	$170,000	-	$170,000	$490,000	-	$250,000	-	$472,000	$1,902,000
038	Rotorcraft Noise Abatement Procedures Development	-	$150,000	$150,000	$150,000	$150,000	-	$300,000	$150,000	-	$170,000	$181,000	$1,401,000
039	Naphthalene Removal Assessment	-	-	$200,000	$290,000	-	$350,000	-	-	-	-	-	$840,000
040	Quantifying Uncertainties in Predicting Aircraft Noise in Real-world Situations	-	-	$218,426	$200,000	-	$255,000	-		-	-	-	$673,426

Project		Funding Based on award date											
		2014	2015	2016	2017	2018	2019	2020	2021	2022	2023	2024	Total
041	Identification of Noise Acceptance Onset for Noise Certification Standards of Supersonic Airplane	-	-	$160,000	$221,000	-	$390,000	-	-	-	-	-	$771,000
042	Acoustical Model of Mach Cut-off	-	-	$255,000	$150,000	$170,000	-	-$120	-	-	-	-	$574,880
043	Noise Power Distance Re-Evaluation	-	-	$150,000	$ 75,000	-	$220,000	$400,000	-	-	-	-	$845,000
044	Aircraft Noise Abatement Procedure Modeling and Validation	-	-	-	-	$350,000	-	$370,000	-	-	$125,000	$150,000	$995,000
045	Takeoff/Climb Analysis to Support AEDT APM Development	-	-	$250,000	$ 75,000	$ 8,845	$175,000	-	-	-	-	-	$508,845
046	Surface Analysis to Support AEDT APM Development	-	-	$ 75,000	$ 75,000	$ 75,000	-	$400,000	-	$75,000	-	-	$700,000
047	Clean Sheet Supersonic Engine Design and Performance	-	-	-	-	-	$250,000	$800,000	$200,000	-	$400,000	-	$1,650,000
048	Analysis to Support the Development of an Engine nvPM Emissions Standards	-	-	$150,000	$200,000	-	$200,000	$200,000	$200,000	-	-	-	$950,000
049	Urban Air Mobility Noise Reduction Modeling	-	-	-	-	-	-	$560,000	$280,000	-	$280,000	$305,000	$1,425,000
050	Over-Wing Engine Placement Evaluation	-	-	-	-	-	-	$590,000	-	-	$300,000	-	$890,000
051	Combustion Concepts for Next-Generation Aircraft Engines	-	-	-	-	-	-	$600,000	-	$300,000	-	$350,000	$1,250,000

Project		Funding Based on award date											
		2014	2015	2016	2017	2018	2019	2020	2021	2022	2023	2024	Total
052	Comparative Assessment of Electrification Strategies for Aviation	-	-	-	-	-	-	$600,000	-	$460,000	-	$600,00	$1,660,000
053	Validation of Low Exposure Noise Modeling by Open Source Data Management and Visualization Systems Integrated with AEDT	-	-	-	-	-	-	$569,903	-	$90,000	$250,000	-	$909,903
054	AEDT Evaluation and Development Support	-	-	-	-	-	-	$1,400,000	-	$900,000	-	$700,000	$3,000,000
055	Noise Generation and Propagation from Advanced Combustors	-	-	-	-	-	-	$2,999,984	-	$500,000	$1,000,000	$500,000	$4,999,984
056	Turbine Cooling through Additive Manufacturing	-	-	-	-	-	-	$800,000	-	$400,000	-	$300,000	$1,500,000
057	Support for Supersonic Aircraft En-route Noise Efforts in ICAO CAEP	-	-	-	-	-	-	$420,000	-	$110,000	$220,000	$400,000	$1,150,000
058	Improving Policy Analysis Tools to Evaluate Higher-Altitude Aircraft Operations	-	-	-	-	-	-	$500,000	$150,000	$500,000	-	$570,000	$1,720,000
059	Modeling and Measurements of Supersonic Civil Transport Jet Noise	-	-	-	-	-	-	$849,956	$849,999	-	$850,000	$499,999	$3,049,954
060	Analytical Methods for Expanding the AEDT Aircraft Fleet Database	-	-	-	-	-	-	$150,000	$150,001	$150,000	-	-	$450,001

Project		Funding Based on award date											
		2014	2015	2016	2017	2018	2019	2020	2021	2022	2023	2024	Total
061	Noise Certification Streamlining	-	-	-	-	-	-	$250,000	$250,000	$250,000	-	$250,000	$1,000,000
062	Noise Model Validation for AEDT	-	-	-	-	-	-	$350,000	$375,000	$375,000	-	$375,000	$1,475,000
063	Parametric Noise Modeling for Boundary Layer Ingesting Propulsors	-	-	-	-	-	-	$300,000	-	-	-	-	$300,000
064	Alternative Design Configurations to Meet Future Demand	-	-	-	-	-	-	$250,000	$1,199,999	$500,000	-	$600,000	$2,549,999
065	Fuel Testing Approaches for Rapid Jet Fuel Prescreening	-	-	-	-	-	-	$559,998	$150,000	$345,000	$300,000	$550,000	$1,904,998
066	Evaluation of High Thermal Stability Fuels	-	-	-	-	-	-	$284,997	$100,000	-	$200,000	$350,000	$934,997
067	Impact of Fuel Heating on Combustion and Emissions	-	-	-	-	-	-	$250,000	$250,000	$250,000	-	$200,000	$950,000
068	Combustor Wall Cooling with Dirt Mitigation	-	-	-	-	-	-	$150,000	$150,000	-	$800,000	$150,000	$1,250,000
069	Transitioning a Research nvPM Mass Calibration Procedure to Operations	-	-	-	-	-	-	$846,707	$100,853	$99,999	-	-	$1,047,559
070	Reduction of nvPM Emissions from Aero-engine Fuel Injectors	-	-	-	-	-	-	$500,000	$500,000	$500,000	-	$500,000	$2,000,000
071	Predictive Simulation of nvPM Emissions in Aircraft Combustors	-	-	-	-	-	-	$500,000	$500,000	-	$500,000	-	$1,500,000

Project		Funding Based on award date											
		2014	2015	2016	2017	2018	2019	2020	2021	2022	2023	2024	Total
072	Aircraft Noise Exposure and Market Outcomes in the United States	-	-	-	-	-	-	$380,000	-	$100,000	$300,000	$300,000	$1,080,000
073	Fuel Composition Impact on Combustor Durability	-	-	-	-	-	-	$299,148	$199,865	$200,000	-	$130,000	$829,013
074	Low Emissions Pre-Mixed Combustion Technology for Supersonic Civil Transport	-	-	-	-	-	-	$1,000,000	$999,995	-	$1,099,999	-	$3,099,994
075	Improved Engine Fan Broadband Noise Prediction Capabilities	-	-	-	-	-	-	$300,000	$300,000	-	$400,160	$201,044	$1,201,204
076	Improved Open Rotor Noise Prediction Capabilities	-	-	-	-	-	-	$300,000	$300,00	-	-	-	$600,000
077	Measurements to Support Noise Certification for UAS/UAM Vehicles and Identify Noise Reduction	-	-	-	-	-	-	$500,000	$500,000	-	$500,000	$500,000	$2,000,000
078	Contrail Avoidance Decision Support & Evaluation	-	-	-	-	-	-	-	$550,000	$550,000	-	$500,000	$1,600,000
079	Novel Noise Liner Development Enabled by Advanced Manufacturing	-	-	-	-	-	-	-	$299,867	-	$900,000	$1,200,000	$2,399,867
080	Hydrogen Production Alternatives for Sustainable Aviation Fuel (SAF) Production	-	-	-	-	-	-	-	$600,000	$758,026	-	$758,026	$2,116,052

Project		Funding Based on award date											
		2014	2015	2016	2017	2018	2019	2020	2021	2022	2023	2024	Total
081	Measurement and Prediction of nvPM size and number emissions from sustainable and convention al aviation fuels	-	-	-	-	-	-	-	-	$2,050,000	-$2,050,000	-	-
082	CAEP Stringency Analysis Modeling	-	-	-	-	-	-	-	-	$1,890,000	-	$1,662,938	$3,552,938
083	NOx Cruise/Climb Metric System Development	-	-	-	-	-	-	-	-	$250,000	-	$250,000	$500,000
084	Noise Modeling of Advanced Air Mobility Flight Vehicles	-	-	-	-	-	-	-	-	-	$315,000	$300,000	$615,000
085	Strategies for Improving En-Route Fuel Efficiency	-	-	-	-	-	-	-	-	-	-	$400,000	$400,000
086	Study on the Use of Broadband Sounds to Mitigate Sleep Disruption Due to Aircraft Noise	-	-	-	-	-	-	-	-	-	$1,077,621	-	$1,077,621
088	A Method for Rapidly Assessing Jet Fuel Compatibility with non-Metallic Materials	-	-	-	-	-	-	-	-	-	$350,000	$350,000	$700,000
089	Characterization of Compositional Effects on Dielectric Constant	-	-	-	-	-	-	-	-	-	$500,000	$110,607	$610,607
090	World Fuel Survey	-	-	-	-	-	-	-	-	-	$749,887	$999,998	$1,749,885
091	Environmental Impacts of High Altitude and Space Vehicle Emissions	-	-	-	-	-	-	-	-	-	$433,775	$435,000	$868,775

Project		Funding Based on award date											
		2014	2015	2016	2017	2018	2019	2020	2021	2022	2023	2024	Total
092	Advanced Two-Stage Turbine Rig Development	-	-	-	-	-	-	-	-	-	$1,100,000	$2,000,000	$3,100,000
093	Collaborative Research Network for Global SAF Supply Chain Development	-	-	-	-	-	-	-	-	-	$1,131,586	$1,175,000	$2,306,586
094	Probabilistic Unmanned Aircraft Systems (UAS) Trajectory and Noise Estimation Tool	-	-	-	-	-	-	-	-	-	$300,000	$335,000	$635,000
095	Assessment of Fuel Cells for Powering Modern Business Jets	-	-	-	-	-	-	-	-	-	-	$200,000	$200,000
096	Future Transportation System Opportunities and Constraints	-	-	-	-	-	-	-	-	-	-	$400,000	$400,000
097	FAST-Tech System Level Assessment	-	-	-	-	-	-	-	-	-	-	$200,000	$200,000
098	Low Emissions Lean Pre-Mixed Pre-Vaporized Combustion Technology for Subsonic Civil Transport	-	-	-	-	-	-	-	-	-	-	$999,979	$999,979
099	Conceptual Analysis of Cryogenic Hydrogen Distribution to Airports	-	-	-	-	-	-	-	-	-	-	$199,911	$199,911
100	U.S.-Canada Cross-Border SAF Supply Chain Analysis	-	-	-	-	-	-	-	-	-	-	$200,000	$200,000
101	Sustainable Aviation Fuel Repository	-	-	-	-	-	-	-	-	-	-	$2,000,000	$2,000,000

Project		Funding Based on award date											
		2014	2015	2016	2017	2018	2019	2020	2021	2022	2023	2024	Total
102	Assessment on Contrail Formation via Combustion of SAF	-	-	-	-	-	-	-	-	-	-	$250,000	$250,000
103	Pareto Efficient SAF Yield and Blending	-	-	-	-	-	-	-	-	-	-	$350,000	$350,000
		-	-	-	-	-	-	-	-	-	-	-	
		-	-	-	-	-	-	-	-	-	-		
	Total	**$105,000**	**$9,304,992**	**$10,598,440**	**$8,620,458**	**$9,754,341**	**$3,170,047**	**$7,685,041**	**$34,159,207**	**$14,438,292**	**$16,022,021**	**$19,464,791**	**$167,304,974**

Breakout by University*

	Funding Based on award year												
University	**2013**	**2014**	**2015**	**2016**	**2017**	**2018**	**2019**	**2020**	**2021**	**2022**	**2023**	**2024**	**Total**
Boston University	$5,000	$350,000	$350,000	$400,000	$610,000	-	$1,729,286	$1,599,962	$899,371	$549,921	$2,399,768	$1,012,960	$9,906,269
Georgia Institute of Technology	$5,000	$1,310,000	$1,975,001	$1,434,999	$1,468,500	$650,000	$895,000	$12,264,984	$5,434,994	$4,275,000	$3,749,999	$6,954,917	$40,418,394
Massachusetts Institute of Technology	$10,000	$1,153,927	$1,169,073	$1,855,000	$1,690,000	$1,000,000	$1,050,000	$5,250,000	$1,700,000	$3,885,000	$2,098,775	5,305,000	$26,166,775
Missouri University of Science and Technology	$5,000	$2,800,000	$750,000	-$147,766	$725,500	-	$1,217,221	$846,707	$622,099	$2,149,999	$1,000,812	$2,513,003	$12,482,575
Oregon State University	$5,000	-	$160,000	$80,000	$59,000	-	-	-	-	-	-	-	$304,000
Pennsylvania State University	$5,000	$862,301	$766,711	$958,426	$890,424	$320,000	$797,623	$2,945,000	$1,619,867	$750,000	$4,220,000	$5,476,000	$19,611,352
Purdue University	$5,000	$389,979	$1,030,000	$763,750	$747,067	$114,185	$605,000	$1,220,116	$600,000	600,000	$394,844	$599,865	$7,069,806
Stanford University	$5,000	$380,000	$1,155,000	$345,000	$200,000	-	$110,000	$1,069,903	$400,000	$290,000	$450,000	$499,999	$4,904,902
University of Dayton	$5,000	-	$906,196	$1,349,087	$1,192,509	$574,944	-	$4,553,260	$799,649	$1,894,940	$1,599,886	$3,590,439	$16,465,910
University of Hawaii	$10,000	-	$75,000	$100,000	$125,000	-	$200,000	$200,000	$100,00	-	$400,000	$400,000	$1,610,000
University of Illinois	$5,000	$349,943	$553,000	$375,000	$265,000	-	$130,000	$879,956	$649,999	$499,999	$375,000	$1,125,000	$5,207,897
University of North Carolina	$5,000	$320,614	$369,996	-	$625,378	-	$300,000	$919,064	$650,000	-	$650,000	$300,000	$4,140,052
University of Pennsylvania	$5,000	$154,000	$343,498	$266,001	$134,924	-	-	-	-	-	$1,077,621	-	$1,981,044
University of Tennessee	$5,000	$200,000	$100,000	$100,000	$225,000	-	$260,000	$500,000	$100,000	$200,000	$241,500	$200,000	$2,131,500

	Funding Based on award year												
University	**2013**	**2014**	**2015**	**2016**	**2017**	**2018**	**2019**	**2020**	**2021**	**2022**	**2023**	**2024**	**Total**
University of Washington	$5,000	$60,000	$29,997	$15,000	-	-	-	-$120.15	-	-	-	-	$109,877
Washington State University	$20,000	$974,228	$864,968	$725,961	$796,039	$510,918	$390,911	$1,910,374	$862,313	$927,162	$806,586	$6,005,161	$14,794,621

Breakout by State*

	Funding Based on award year												
State	**2013**	**2014**	**2015**	**2016**	**2017**	**2018**	**2019**	**2020**	**2021**	**2022**	**2023**	**2024**	**Total**
California	$5,000	$380,000	$1,155,000	$345,000	$200,000	-	$110,000	$1,069,903	$400,000	$290,000	$450,000	$499,999	$4,904,902
Georgia	$5,000	$1,310,000	$1,975,001	$1,434,999	$1,468,500	$650,000	$895,000	$12,264,984	$5,434,994	$4,275,000	$3,749,999	$6,954,917	$40,418,394
Hawaii	$10,000	-	$75,000	$100,000	$125,000	-	$200,000	$200,000	$100,000	-	$400,000	$400,000	$1,610,000
Illinois	$5,000	$349,943	$553,000	$375,000	$265,000	-	$130,000	$879,956	$649,999	$499,999	$375,000	$1,125,000	$5,207,897
Indiana	$5,000	$389,979	$1,030,000	$763,750	$747,067	$114,185	$605,000	$1,220,116	$600,000	600,000	$394,844	$599,865	$7,069,806
Massachusetts	$15,000	$1,503,927	$1,529,073	$2,255,000	$2,300,000	$1,000,000	$2,779,286	$6,849,963	$2,599,371	$4,434,921	$4,498,543	$6,317,960	$36,073,044
Missouri	$5,000	$2,800,000	$750,000	-$147,766	$725,500	-	$1,217,221	$846,707	$622,099	$2,149,999	$1,000,812	$2,513,003	$12,482,575
North Carolina	$5,000	$320,614	$369,996	-	$625,378	-	$300,000	$919,064	$650,000	-	$650,000	$300,000	$4,140,052
Ohio	$5,000	-	$906,196	$1,349,087	$1,192,509	$574,944	-	$4,553,260	$799,649	$1,894,940	$1,599,886	$3,590,439	$16,465,910
Oregon	$5,000	-	$160,000	$80,000	$59,000	-	-	-	-	-	-	-	$304,000
Pennsylvania	$10,000	$1,016,301	$1,110,209	$1,224,427	$1,025,348	$320,000	$797,623	$2,945,000	$1,619,867	$750,000	$5,297,621	$5,475,000	$21,592,396
Tennessee	$5,000	$200,000	$100,000	$100,000	$225,000	-	$260,000	$500,000	$100,000	$200,000	$241,500	$200,000	$2,131,500
Washington	$25,000	$1,034,228	$894,965	$740,961	$796,039	$510,918	$390,911	$1,910,254	$862,313	$927,162	$806,586	$6,005,161	$14,904,498

*Totals include administrative funds not associated with specific NFOs